VOLUMES 273–274
DECEMBER II 1999

ISSN 0921-4526

PHYSICA

B

CONDENSED MATTER

1999
July 26–30
BERKELEY

Proceedings of the 20th International Conference on Defects in Semiconductors

ICDS-20

held in Berkeley, CA, USA
26–30 July 1999

Guest Editors:

C. Van de Walle
W. Walukiewicz

NORTH-HOLLAND

http://www.elsevier.com/locate/physb

PHYSICA B

An interdisciplinary journal of research on condensed matter

Aims and scope
Physica B (*Condensed Matter*) contains papers and review articles in the realm of physics of condensed matter. Both experimental and theoretical contributions are invited, although theoretical papers should preferably be related to experimental results.

Abstracted/indexed in:
Current Contents: Physical, Chemical and Earth Sciences; Aluminium Industry Abstracts, EI Compendex Plus, Engineered Materials Abstracts, Engineering Index, INSPEC, Metals Abstracts, Physics Briefs

Subscription information
Physica B (ISSN 0921-4526) is published monthly. For 2000, volumes 275–290 are scheduled for publication. Subscription prices are available upon request from the Publisher. A combined subscription with *Physica A*, *Physica C*, *Physica D* and *Physica E* is available at a reduced rate.

Subscriptions are accepted on a prepaid basis only and are entered on a calendar year basis. Issues are sent by surface mail except to the following countries where air delivery via SAL is ensured: Argentina, Australia, Brazil, Canada, China, Hong Kong, India, Israel, Japan, Malaysia, Mexico, New Zealand, Pakistan, Singapore, South Africa, South Korea, Taiwan, Thailand, USA. For all other countries air mail rates are available upon request. Please address all enquiries regarding orders and subscriptions to:

Elsevier Science B.V.
Customer Support Department
P.O. Box 211, 1000 AE Amsterdam
The Netherlands
Telephone: +31-20-485 3757; Telefax: +31-20-485 3432

Claims for issues not received should be made within six months of our publication (mailing) date.

US Mailing Notice
Physica B (ISSN 0921-4526) is published monthly by Elsevier Science, Molenwerf 1, P.O. Box 211, 1000 AE Amsterdam, The Netherlands. The annual subscription price in the USA is US$ 4648 (valid in North, Central and South America only), including air speed delivery. Second class postage paid at Jamaica, NY 11431.
USA postmasters: Send address changes to Physica B, Publications Expediting Inc., 200 Meacham Avenue, Elmont, NY 11003.
Airfreight and mailing in the USA by Publications Expediting Inc., 200 Meacham Avenue, Elmont, NY 11003.

♾ The paper used in this publication meets the requirements of ANSI/NISO Z39.48-1992 (Permanence of Paper).

North-Holland, an imprint of Elsevier Science **Printed in The Netherlands**

PHYSICA B

VOLUMES 273–274, 1999

PHYSICA B
CONDENSED MATTER

NORTH-HOLLAND

Proceedings of the 20th International Conference on Defects in Semiconductors

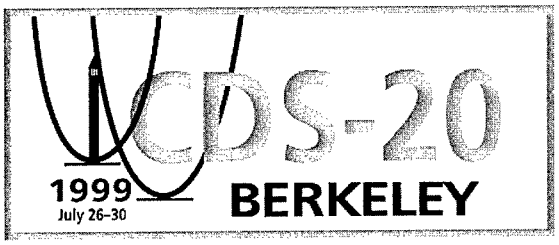

ICDS-20

held in Berkeley, CA, USA
26–30 July 1999

Guest Editors:

Chris Van de Walle
Xerox PARC
3333 Coyote Hill Road
Palo Alto, CA 94304
USA

Wladek Walukiewicz
E. O. Lawrence Berkeley National Laboratory
1 Cyclotron Road, MS 2-200
Berkeley, CA 94720
USA

ELSEVIER

Conference Photograph

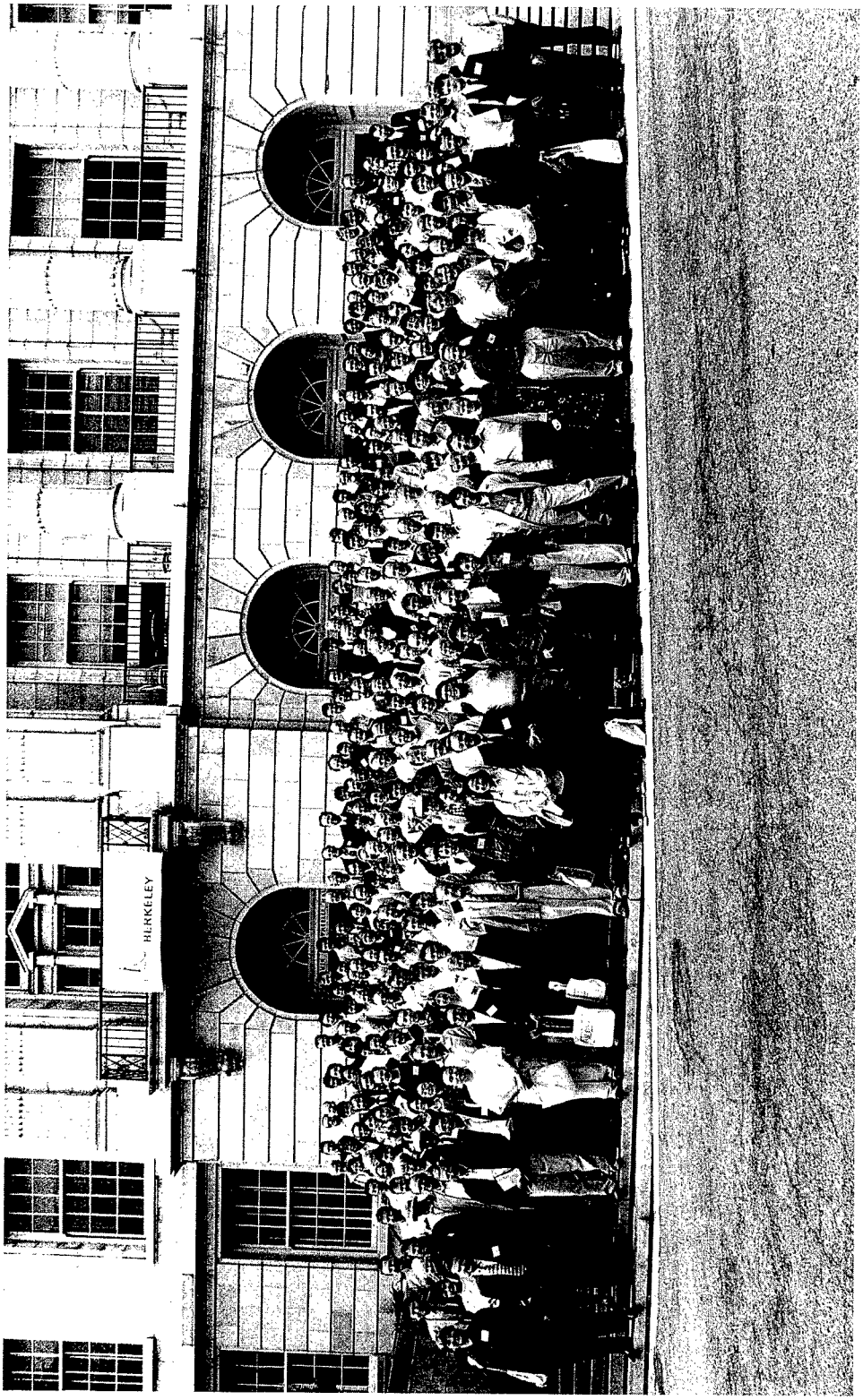

Foreword and Acknowledgments

These are the proceedings of the 20th International Conference on Defects in Semiconductors, ICDS-20, which was held in Berkeley, California, between July 26–30, 1999. It has been 40 years since the first conference in this series was organized in Gatlinburg, Tennessee, and we take this opportunity to identify and congratulate two of our friends and colleagues, Professors Anant K. Ramdas and George D. Watkins, for their seminal contributions to this field of research over the entire time span covered by the series.

The advent of new materials and materials systems, together with the ever increasing technological demands regarding the sub-micrometer control of the distribution and concentrations of numerous types of dopants and defects, have kept the field of physics of imperfections vibrant and full of surprises.

The 278 registered attendees from 25 countries presented and discussed a wide range of new experimental and theoretical results. Three plenary talks, all focusing on wide bandgap semiconductors, nineteen invited presentations, eighty-two contributed talks and 218 posters, for a total of 322 presentations, gave a comprehensive panorama of the continuously evolving field. The group III-nitrides and related materials, diamond and the effects of hydrogen represented a major portion of the conference content with the remaining contributions covering many exciting findings in elemental and compound semiconductors and their alloys.

Placing the three poster sessions midday between the morning and the afternoon oral sessions was considered by a large majority of the attendees to be a significant improvement over the traditional evening poster sessions. Another much appreciated change was the return to an archival journal, Physica B, for publishing the proceedings. Professor C.A.J. Ammerlaan last chose this journal for the proceedings of ICDS-12. We expect that publication of the proceedings in an archival journal with worldwide distribution will be an incentive for ICDS attendees to publish new work.

The costs incurred by a conference like ICDS-20 exceed the funds collected from attendees. We are very grateful for the generous contributions by government organizations and by private firms. Their support allowed us to bring many young researchers to Berkeley and to partially cover the costs for scientists from developing nations and countries of the former Soviet Union.

It gives us great pleasure to thank the members of the International Advisory and the Program committees for their active participation in planning the conference. Special thanks go to the local "student group" (made up of students, postdocs and young PhDs) for their expert help in a very wide range of activities, including manuscript processing, session support, conference photography, e-mail access and much personal advice and guidance. The session chairs are thanked for their dedicated efforts in keeping sessions on time and in encouraging interesting questions and discussion. Last but not least, we would like to thank all the attendees for making this another interesting and exciting conference in this long and established series of meetings.

N.M. Johnson, *Program Chair*
E.E. Haller, *Chair*

Conference Information

International Advisory Committee

F.D. Auret, South Africa
M.J. Caldas, Brazil
J. Chadi, USA
V.V. Emtsev, Russia
G. Davies, UK*
H.-J. Gossmann, USA
E.E. Haller (Chair), USA*
W. Jantsch, Austria*
L.C. Kimerling, USA
H. Kukimoto, Japan
J. Langer, Poland
B.A. Monemar, Sweden
M.H. Nazare, Portugal*
R.C. Newman, UK
J.M. Späth, Germany
M.J. Stavola, USA
K. Sumino, Japan*
K. Wada, Japan
G.D. Watkins, USA
J. Weber, Germany

Program Committee

B. Bech Nielsen, Denmark
M.S. Brandt, Germany
M.J. Caldas, Brazil
P. Clauws, Belgium
B. Clerjaud, France
J.M. Gibson, USA
E.R. Glaser, USA
E.E. Haller, USA
K.M. Itoh, Japan
W. Jantsch, Germany
N.M. Johnson (Chair), USA
M. Mizuta, Japan
P.M. Mooney, USA
A.R. Peaker, UK
T. Suski, Poland
C.G. Van de Walle, USA
W. Walukiewicz, USA
J. Weber, Germany
I.N. Yassievich, Russia

Local Organizing Committee

J.W. Ager III, Secretary
M.O. Field, Conference Coordinator
M.D. Giles, Member
E.E. Haller, Chair
D. Hom, Assistant Secretary
N.M. Johnson, Program Chair
C.G. Van de Walle, Proceedings
W. Walukiewicz, Proceedings
E.R. Weber, Fundraising
K.M. Yu, Member
P.Y. Yu, Treasurer

*International Steering Committee

Student Support Group

J. Bandaru, M. Benamara, B. Cardozo, D. Chamberlin, Y. Cho, M. Cich, J. Colton, S. Kellermann, J. Li, R. Lutz, S. Nicols, M. Norseng, L. Schloss, H. Silvestri, P. Specht, R. Wong, J. Wu, R. Zhao

Session Chairs

J.W. Ager III
C.A.J. Ammerlaan
F.D. Auret
B. Bech Nielsen
P. Blöchl
H.A. Bracht
M.J. Caldas
G. Davies
V.V. Emtsev
W. Frank
M.D. Giles
E.R. Glaser
E.E. Haller
W. Jantsch
N.M. Johnson
L.C. Kimerling
J. Langer
Z. Liliental-Weber
B.A. Monemar
P.M. Mooney
R.C. Newman
A.K. Ramdas
L.T. Romano
M.J. Stavola
T. Suski
C.G. Van de Walle
H.-H. Vuong
G.D. Watkins
E.R.Weber
J. Weber
K.M. Yu
P.Y. Yu

Sponsors

Air Force Office of Scientific Research
American Xtal Technology, Inc.
Applied Materials, Inc.
Bell Labs, Lucent Technologies
Hewlett-Packard Laboratories
IBM
Intel Corporation
Lawrence Berkeley National Laboratory
Office of Naval Research
Sula Technologies
Xerox Palo Alto Research Center

Contents

7. Silicon carbide

8. GaAs and AlGaAs

8.1. Point and extended defects

9. Other III–V compounds

10. II–VI compounds

11. Other semiconductors

14. Defects in devices

ELSEVIER

Physica B 273–274 (1999) 1–6

PHYSICA B

www.elsevier.com/locate/physb

To 40 years of defects in semiconductors: may the problem never be solved!☆

Michael Stavola*

Department of Physics, Lehigh University, 16 Memorial Drive East, Bethlehem, PA 18015, USA

Abstract

In the closing remarks presented at the end of ICDS-20, the ICDS meetings held in 1959 and 1980 were contrasted with ICDS-20 to provide perspective on progress in the field of defects in semiconductors.

Keywords: Closing remarks; Gatlinburg meeting; Oiso meeting

1. Introduction

The field of defects in semiconductors is now sufficiently broad that it would be difficult to provide a summary of the International Conference on Defects in Semiconductors in a closing talk. The last time this was done was in 1982 by L.C. Kimerling at ICDS-12 held in Amsterdam [1]. (Prior to 1982, many of the conferences began with a report on the status of the field and a summary of important unanswered questions. It is fun to look back at these status reports and to see how relevant some of these early surveys still are.) The plan for this talk is to take a naive look back at the ICDS series to gain perspective on how the field has evolved. Table 1 shows a list of the ICDS meetings. I will focus on just three of the conferences, ICDS-1 held in Gatlinburg, Tennessee in 1959, ICDS-11 held in Oiso, Japan in 1980, and the present ICDS-20 held in Berkeley. These three meetings provide snap-shots of the field, taken roughly 20 years apart.

The 1959 meeting is, of course, the first. The 1980 meeting is also fun to look at because it was here that Watkins suggested that "radiation effects" be dropped from the title of the conference, and the meeting began to be called the "International Conference on Defects in Semiconductors" as it is now [2]. Furthermore, none of the conference chairs prior to 1980 is still active in the field of defects with the sole exception of Watkins. Table 1 also shows that R.R. Hasiguti chaired the meeting *three* times, a service to the field of defects in semiconductors that has clearly been above and beyond the call of duty.[1]

2. The 1959 Gatlinburg Conference, ICDS-1

The conference on radiation effects in semiconductors, held on May 6–9, 1959 in Gatlinburg, Tennessee, is the first of the ICDS series. The meeting was chaired by J.W. Cleland of the Oak Ridge National Laboratory. The proceedings of the meeting were published in the Journal of Applied Physics, Vol. 30 [3]. A glance at the table of contents shows that at ICDS-1 there was a *total of only 31 papers*, not too many more than in the invited programs of recent meetings. And the proceedings are only ~ 200 pages in length, considerably shorter than, say, the ~ 1800 pages of the proceedings of ICDS-19 held in Aveiro [4]. There were many papers on radiation

☆The title of this talk is a paraphrase of a toast made by A. Seeger at ICDS-8 held in Freiberg in 1974, loosely remembered as: "To the defect problem: may it never be solved!"

* Fax: + 1-610-758-5730.

E-mail address: mjsa@lehigh.edu (M. Stavola)

[1] The author, who frequently misspeaks during presentations, may actually have said: "... service ... above and beyond the call of sanity."

0921-4526/99/$ - see front matter
PII: S0921-4526(99)00725-5

Table 1
The International Conference on Defects in Semiconductors series listed with the conference location, meeting date, and conference chairs

1.	Gatlinburg	1959	J.W. Cleland
2.	Kyoto	1962	R.R. Hasiguti and T. Fujiwara
3.	Royaumont	1964	P. Baruch
4.	Tokyo	1966	R.R. Hasiguti
5.	Santa Fe	1967	F. Vook and J.C. King
6.	Albany	1970	J.W. Corbett and G.D. Watkins
7.	Reading	1972	E.W.J. Mitchell
8.	Freiburg	1974	A. Seeger
9.	Dubrovnik	1976	N.B. Urli
10.	Nice	1978	J.H. Albany
11.	Oiso	1980	R.R. Hasiguti
12.	Amsterdam	1982	C.A.J. Ammerlaan
13.	Coronado	1984	L.C. Kimerling
14.	Paris	1986	M. Lannoo and J.C. Bourgoin
15.	Budapest	1988	G. Ferenczi
16.	Bethlehem	1991	M. Stavola and G.G. DeLeo
17.	Gmunden	1993	W. Jantsch
18.	Sendai	1995	K. Sumino
19.	Aveiro	1997	G. Davies and M.H. Nazaré
20.	Berkeley	1999	E.E. Haller
21.	Giessen	2001	B.K. Meyer and J.-M. Spaeth

damage in Ge, several on Si, and a few on compound semiconductors. At this time it was just being recognized that the vacancy in Si was mobile at room temperature. The technological driving force for studies of radiation effects was the interest in using semiconductor devices near nuclear reactors.

Two of the attendees of the Gatlinburg Conference were also present at ICDS-20 in Berkeley, George Watkins and Anant Ramdas. Also present at ICDS-1 was Walter Brown who is known to many of us and currently heads a department at Bell Laboratories. (Incidentally, Brown was in the same class at Harvard as Watkins, making it clear that one route to a long and productive career would be to become a member of that class.) Industrial participation at the meeting was particularly strong, as was the presence of researchers from Purdue University.

The following sentences, taken from the forward of the Gatlinburg conference proceedings [3], give a sense of the meeting's flavor:

> The use of semiconductors as convenient systems in which to study the nature of radiation effects originated in 1947 as a result of the discovery of the profound sensitivity of their electrical properties to energetic particle bombardment. The late Professor Karl Lark-Horovitz at Purdue University gave the first correct interpretation of these effects in terms of the generation of point defects by the interaction of nuclear particles with atoms of the crystal lattice.... Not only has the choice of materials been *broadened to include the elemental substances of the fourth column* of the periodic table and a number of compounds, but a variety of radiations has been used as well.... However, although the field has increased in complexity, *it has also attained a certain maturity.*

From these sentences one can see that the importance of radiation effects and the resulting native defects in semiconductors was recognized as early as 1947 by Lark-Horovitz and also that Lark-Horovitz had died before the first ICDS occurred. Then there is the statement that the choice of materials had been *broadened* to include group IV substances. While I am too young to remember a time when radiation and defect studies were not performed on group IV substances, it was pointed out to me by Watkins that in 1959 one usually thought of color centers in the alkali halides when one talked of radiation effects in solids. Finally, already in 1959, it was thought that this field had achieved a certain maturity. Of course, there have been many surprises since then!

3. The 1980 Oiso Conference, ICDS-11

We now jump forward by 20 years to ICDS-11. A glance at the conference photograph in the ICDS-11 proceedings volume [5] shows that many of the attendees of ICDS-20 were also present at ICDS-11 and have been loyal attendees of the conference series. Fig. 1 shows an enlargement of the center section of the conference photograph. The conference chair, R.R. Hasiguti, is in the

Fig. 1. Enlargement of the center section of the ICDS-11 conference photograph, Oiso, Japan.

front row, center. Two of the plenary speakers at ICDS-20 are present; George Watkins stands to the right of Hasiguti and Gordon Davies is one row back and to the left of Hasiguti. Near the upper left corner of Fig. 1 is Tom Kennedy, the chair of the next Gordon Research Conference on defects in semiconductors. The strong influence of the groups from Stuttgart can also be seen, with J. Weber, R. Sauer, H. Baumgart, and H. Queisser, standing nearly in a horizontal line drawn across the center of the photograph. (Weber and Sauer are also attendees of ICDS-20.)

Watkins presented the closing talk of the Oiso conference and summarized the status of the field, incorporating ideas that arose during the discussions of the International Advisory Committee at the meeting [2]. Quoting from Watkins's summary paper:

> ... there is presently a great resurgence and growth of interest and activity in the field of defects in semiconductors .... (The) proliferation of new experimental techniques has greatly increased the experimental facts at our disposal. At the same time, the strides made by large quantum mechanical computer techniques has made the theoretical treatment of a localized defect (the 'deep level' problem) begin to look tractable.
>
> In addition, there are new technological needs that are supplying the driving force and support for this study ... . So again there is developing a close symbiotic relationship between real technological needs and the associated fundamental science of defects.

Two years later, at the Amsterdam ICDS-12 meeting, Kimerling gave the closing summary and wrote the following sentences [1]:

> The (tighter) materials tolerances and complexity of fabrication of modern integrated circuits have added new demands for fundamental knowledge concerning defects in Si. The arrival of III-V compounds and related alloys as important materials for light emitter and detector applications has heightened the need to understand imperfection in multicomponent systems ... .

Watkins and Kimerling made two important points that still characterize much of the work done now, nearly 20 years later. New experimental and theoretical capabilities continually lead to advances in our understanding. And the demands of a rapidly advancing technology provide a rich source of interesting and important research problems.

While, from these quotations, it might seem that little has changed in defect studies since the early 1980s, the invited program of ICDS-11 (Table 2) gives a truer benchmark of the status of the field. Theoretical calculations by local density methods were beginning to make an important impact, but computational capabilities were insufficient to treat simple defect complexes [6]. The ability to calculate total energies was promised, but was not yet possible. There was, as there continues to be, interest in native defects with the negative U character of the Si vacancy being correctly described [7] nearly two decades after the vacancy was first seen by EPR [8]. Transition metals in the III-Vs and Si-processing problems also play a prominent role in the program. It is also fun to think about what is absent from the invited program. There were no invited talks on EL2 and antisite defects, DX, thermal donors, or metastability. These problems, that became the focus of much attention during the 1980s and early 1990s, were just emerging (or, for the thermal donor, re-emerging).

4. The 1999 Berkeley Conference, ICDS-20

A comparison of the invited program of the Oiso ICDS-11 meeting with the invited program of the 1999 Berkeley meeting shows that the field of defects in semiconductors has advanced dramatically since 1980. New materials systems have gained prominence. GeSi [9], the III–V nitrides [10], novel microstructures [11], and defects near interfaces [12,13] have been the focus of much recent attention and are well-represented in the ICDS-20 program. Lattice mismatch in epitaxial structures has led to the need to understand and control misfit strain [9,10]. As the dimensions of Si-integrated circuits have rapidly decreased, with oxide-layer thicknesses of tens of angstroms and circuit-design rules of tenths of microns, new defect-related problems like stress-induced leakage in MOSFETs [14] and transient enhanced diffusion [15] demand attention. The rapidly growing cost of integrated circuit fabrication drives the development of increasingly more accurate process models, which requires a sophisticated understanding of defects and their effects. Defect control has also led to novel processes such as smart-cut, which offers a new means to fabricate semiconductor-on-insulator structures [16].

A variety of new experimental methods has appeared since 1980 and contributes to our understanding of defects. There are the nuclear methods such as perturbed angular correlation, positron annihilation, and muon spin resonance. The direct imaging of defects and interfaces by high-resolution microscopies [17,18], while commonplace, continues to advance at a rapid pace. The recent achievement of control of the isotopic content of the *host crystal* [19] has led to advances in spectroscopy [20,21] and diffusion studies [22,23]. Heterostructures are used to probe defect properties, a strategy that is often coupled with the high-resolution imaging methods [17]. The ability to probe defects in device structures,

Table 2
Invited program from the 1980 ICDS-11 meeting held in Oiso, Japan. [From ref. [5]]

Theory of point defects and deep impurities in semiconductors *J. Bernholc, N.O. Lipari, S.T. Pantelides, and M. Scheffler*
Theory of the silicon vacancy: an Anderson negative-U system *G.A. Baraff, E.O. Kane and M. Schlüter*
Interstitials in germanium *J.C. Bourgoin, P.M. Mooney, and F. Poulin*
Electron spin resonance of defects in III–V semiconductors *J. Schneider and U. Kaufmann*
Optical resonance and magneto-optical measurements of defects in GaP and GaAs *B.C. Cavenett*
Electron paramagnetic resonance of native defects in diamond *C.A.J. Ammerlaan*
In situ x-ray topographic study of dislocations in silicon crystals growing from the melt *J. Chikawa and F. Sato*
Channeling studies of defect-impurity interactions in silicon *F.W. Saris*
Oxidation-and diffusion-induced defects in Si *M. Watanabe, Y. Matsushita, and K. Shibata*
Summary of the 1980 conference *G.D. Watkins*

which is a strength of the now classic capacitance spectroscopies, has been extended to highly structure-sensitive methods, with the electrical detection of magnetic resonance being a prominent example.

Considering theory, we look back at Watkins's 1980 summary where he wrote: "... it is refreshing to hear the theorist begin to talk back, begin to be a participating partner in the field". Things have certainly changed since then (and maybe Watkins should have been more careful about what he wished for). Now theorists have the ability to calculate electronic structure, total energies, and many experimentally observable properties such as vibrational frequencies, hyperfine parameters, levels positions, etc. The calculations include the effects of host relaxations in large supercells or clusters. Powerful molecular dynamics calculations have become possible [24,25]. At ICDS-20 Tsuneyuki et al. [26] reported path integral molecular dynamics calculations performed to study quantum effects for H and muonium that took one month at computational rates of 30 terraflops/h. Even to someone who does not understand these words, this sounds impressive.

So, looking over the ICDS-20 program, one sees that in addition to the progress made on classic problems, there are new research topics and new experimental and theoretical capabilities, many of which had not even been envisioned in 1980.

5. Conclusion

Even from a naive and superficial look over the 40 years of progress in the field of defects in semiconductors, one learns several lessons:

(i) Understanding takes time. Solutions to problems promised for the "next meeting" often take 20 years (or more). The vacancy in Si is a good example. The observation of the isolated vacancy was reported in 1962 at the Kyoto meeting (ICDS-2) [8]. Its electronic structure and negative U properties were explained nearly 20 years later at ICDS-11 [7]. The vacancy's partner, the native interstitial, remains a subject of active research in a variety of host materials [20,21,27].

(ii) The field continues to evolve. The people who are active in our field have continually changed. As was already mentioned, only two people who were at ICDS-1 were at the ICDS-20 meeting held 40 years later, and this is no surprise. Of greater concern might be the number of retirements of some of the best research workers in the field that have occurred during recent years. These include the retirements of Ron Newman (celebrated at this meeting) and several others such as Professors Ammerlaan, Grimmeiss, Queisser, Schneider, and Watkins. And additional retirements of key people, for example Professors Spaeth and Schröter, will occur soon.

Fortunately, many of these people remain active, and, at the same time, a number of talented young people emerge. This evolution of active researchers in the field requires us to encourage and promote the best of our students and young people if the field is to remain healthy.

One also often hears that our goals have changed, that understanding the fundamental microscopic properties of defects is no longer sufficient, and that applications dominate our interests. A look over 40 years of work in the field shows that many of the most interesting problems have always been close to applications. During the 1970s, for example, there was interest in ion-implantation processes and also the effect of particle bombardment on solar cells in the Van Allen belt [28]. In the 1980s and 1990s, the fascinating DX, EL2 and metastability phenomena being studied all had important technological implications. Thus, our field has always benefited from its close links to technology, as was stressed by Watkins and Kimerling in their closing summaries from the 1980s [1,2]. At the ICDS-5 meeting held in Santa Fe in 1967, Corbett said [28], "The scientists in this area have the obligation and *opportunity* to be aware of the technical problems."

(iii) Studies of esoteric, fundamental phenomena have unforeseen consequences. For example, research on radiation damage begun in the 1950s led to studies of vacancies, multi-vacancy clusters, and interstitial impurities in the 1960s and subsequently. This early work provides a foundation for understanding the presence of voids in as-grown Si crystals and the transient enhanced diffusion encountered following ion-implantation processes. As another example, studies of hydrogen in semiconductors were begun in the 1970s [29,30] and were followed by the recognition during the 1980s that dopants could be passivated by hydrogen, either intentionally or unintentionally [31]. Unintentional hydrogen passivation turned out to be the source of the difficulty of p-doping wide band-gap materials [32]. This problem, once solved, has led to the tremendous interest in the application of wide band-gap semiconductors. As a final example, fundamental studies of the interaction of hydrogen with native defects in Si were begun in the 1970s [30]. During recent years the combination of experiment and theory has unraveled the detailed properties of a number of hydrogen-vacancy and hydrogen-interstitial complexes without any regard for applications [33]. The understanding of these defects has made it possible to propose a mechanism for the "smart-cut" exfoliation process [16] that provides a novel means to fabricate semiconductor-on-insulator structures. These few examples demonstrate that we are lucky to be working in materials systems where it is difficult to separate fundamental issues from technological concerns. Thus, the work in our field often has real technological impact, even when it has not been intentional!

I will close with some comments on the vitality of the ICDS series. In a letter to the International Advisory Committee of ICDS, Eugene Haller, the chair of ICDS-20, wrote, "With a large and growing number of competing, specialized conferences, we will have to be very creative in keeping ICDSes attractive." Haller is certainly correct; the competition from MRS and ECS meetings, new III–V nitride Conferences and Gordon Conferences, etc., is tough, especially for a conference chair that is trying to estimate attendance and a budget for his or her meeting. But, this competition also convincingly shows that we are working in an *active and important* field! So, while the competition is troublesome and requires the attention of conference organizers, it is also healthy.

Further, this competition with a variety of overlapping conferences is not new. Quoting again from Watkins's 1980 summary at ICDS-11 [2]: "... it is clear that this conference series can have a bright future. Although many new mini-conferences and symposia are springing up everywhere, this is the only established international conference concerned with the fundamental science of defects in semiconductors." These remarks remain true today.

After 40 years of study of defects in semiconductors, one might ask if we have solved the problem yet. It is clear that the technological potential of semiconductor materials has not been exhausted [34]. Thus, there will continue to be new, more demanding applications of semiconductors that will continue to reveal new defect problems and new surprises. These new problems and the persistent old ones will continue to be fun for us and will give us good reason to meet and talk at future ICDS meetings. We hope these future conferences will be as highly successful as ICDS-20, with its marvelous program and organization (and weather). We thank Eugene Haller, Noble Johnson and other members of the local organizing committee for their outstanding effort.

Acknowledgements

I thank G.D. Watkins and W.B. Fowler for several helpful conversations that occurred while this talk was being prepared and G.D. Watkins for access to his nearly complete collection of ICDS proceedings volumes. I also thank K.L. Stavola for preparing Fig. 1 from Watkins's copy of the Oiso conference photograph. The preparation of this manuscript was supported by NSF Grant No. DMR-9801843 and ONR Grant No. N00014-94-1-0117.

References

[1] L.C. Kimerling, in: C.A.J. Ammerlaan (Ed.), Defects in Semiconductors, North-Holland, Amsterdam, 1983, p. 1.

[2] G.D. Watkins, in: R.R. Hasiguti (Ed.), Defects and Radiation Effects in Semiconductors, 1980, Inst. Phys. Conference Series 59, Institute of Physics, Bristol, 1981, p. 139.
[3] Proceedings of the Conference on Radiation Effects in Semiconductors, Gatlinburg, 1959, J. Appl. Phys. 30 (1959) 1117.
[4] G. Davies, M.H. Nazaré (Eds.), Defects in Semiconductors, ICDS-19, Trans. Tech., Switzerland, 1997.
[5] R.R. Hasiguti (Ed.), Defects and Radiation Effects in Semiconductors, 1980, Inst. Phys. Conference Series 59, Institute of Physics, Bristol, 1981.
[6] J. Bernholc, N.O. Lipari, S.T. Pantelides, M. Scheffler, in: R.R. Hasiguti (Ed.), Defects and Radiation Effects in Semiconductors, 1980, Inst. Phys. Conference Series 59, Institute of Physics, Bristol, 1981, p. 1.
[7] G.A. Baraff, E.O. Kane, M. Schlüter, in: R.R. Hasiguti (Ed.), Defects and Radiation Effects in Semiconductors, 1980, Inst. Phys. Conference Series 59, Institute of Physics, Bristol, 1981, p. 19.
[8] G.D. Watkins, J. Phys. Soc. Jpn 18 (suppl. II) (1962) 22.
[9] P. Batson, Physica B 273–274 (1999) 593, These Proceedings.
[10] J. Speck, Physica B 273–274 (1999) 24, These Proceedings.
[11] M. Lannoo, Physica B 273–274 (1999), These Proceedings.
[12] A. Stesmans, Physica B 273–274 (1999) 1015, These Proceedings.
[13] R. Baierle, M. Caldas, J. Dabrowski, H.-J. Müssig, V. Zavodinsky, Physica B 273–274 (1999) 260, These Proceedings.
[14] P. Blöchl, J.H. Stathis, Physica B 273–274 (1999) 1022, These Proceedings.
[15] H.-H. Vuong, Physica B 273–274 (1999), These Proceedings.
[16] M.K. Weldon, Y.J. Chabal, Y. Caudano, B. Stefanov, K. Raghavachari, Physica B 273–274 (1999), These Proceedings.
[17] R. Feenstra, Physica B 273–274 (1999) 796, These Proceedings.
[18] S. Pennycook, Physica B 273–274 (1999) 453, These Proceedings.
[19] E.E. Haller, J. Appl. Phys. 77 (1995) 2857.
[20] G. Davies, Physica B 273–274 (1999) 15, These Proceedings.
[21] D.C. Hunt, D.J. Twitchen, M.E. Newton, J.M. Baker, T.R. Anthony, W.F. Banholzer, Physica B 273–274 (1999), These Proceedings.
[22] H. Bracht, Physica B 273–274 (1999) 981, These Proceedings.
[23] A. Ural, P.B. Griffin, J.D. Plummer, Physica B 273–274 (1999) 512, These Proceedings.
[24] R. Car, P. Blöchl, E. Smargiassi, in: G. Davies, G.G. DeLeo, M. Stavola (Eds.), Defects in Semiconductors 16, Trans. Tech., Switzerland, 1992, p. 433.
[25] S.K. Estreicher, P.A. Fedders, in: G. Davies, M.H. Nazaré (Eds.), Defects in Semiconductors, ICDS-19, Trans. Tech., Switzerland, 1997, p. 171.
[26] S. Tsuneyuki, T. Miyake, T. Ogitsu, Physica B 273–274 (1999), These Proceedings.
[27] G.D. Watkins, Physica B 273–274 (1999) 7, 861, These Proceedings.
[28] J.W. Corbett, in: F.L. Vook (Ed.), Radiation Effects in Semiconductors, Plenum, New York, 1968, p. 3.
[29] E.E. Haller, Phys. Rev. Lett. 40 (1978) 584 and in: J.H. Albany (Ed.), Defects and Radiation Effects in Semiconductors, 1978, Inst. Phys. Conference Series 46, Institute of Physics, Bristol, 1979, p. 205.
[30] S.T. Picraux, F.L. Vook, H.J. Stein, in: J.H. Albany (Ed.), Defects and Radiation Effects in Semiconductors, 1978, Inst. Phys. Conference Series 46, Institute of Physics, Bristol, 1979, p. 31.
[31] S.J. Pearton, M. Stavola, J.W. Corbett, in: G. Ferenczi (Ed.), Defects in Semiconductors 15, Trans. Tech., Switzerland, 1989, p. 25.
[32] C.G. Van de Walle, J. Neugebauer, in: G. Davies, M.H. Nazaré (Eds.), Defects in Semiconductors, ICDS-19, Trans. Tech., Switzerland, 1997, p. 19.
[33] B. Bech Nielsen, L. Hoffmann, M. Budde, R. Jones, J. Goss, S. Öberg, in: M. Suezawa, H. Katayama-Yoshida (Eds.), Defects in Semiconductors 18, Trans. Tech., Switzerland, 1995, p. 933.
[34] A.M. Stoneham, in: G. Davies, M.H. Nazaré (Eds.), Defects in Semiconductors, ICDS-19, Trans. Tech., Switzerland, 1997, p. 27.

ELSEVIER

Physica B 273–274 (1999) 7–14

PHYSICA B

www.elsevier.com/locate/physb

Self-interstitials in semiconductors: what we are learning from interstitial Zn in ZnSe

G.D. Watkins*, K.H. Chow

Department of Physics, Lehigh University, 16 Memorial Drive East, Bethlehem, PA, 18015-3182, USA

Abstract

Interstitial Zn_i^+ has been observed in ZnSe by optical detection of EPR to be on-center in either T_d interstitial site – that surrounded by four Se atoms, $(Zn_i)_{Se}^+$, or by four Zn atoms, $(Zn_i)_{Zn}^+$. This can be understood by a simple universal model which predicts stability for an interstitial atom in this site if its free atom valence configuration contains no p-electrons, as is the case for the $Zn_i^0(4s^2)$, $Zn_i^+(4s^1)$, and $Zn_i^{+\,+}(4s^0)$. Otherwise it predicts a distortion off-center into a bonded configuration with one or more of its neighbors. Unanticipated in the model is the observation that Zn_i^+ can be made to hop back and forth between the two sites by optical excitation at 1.5 K, a motion fully equivalent to the one jump process for its long-range diffusion. It is proposed that the process involves capture into an excited p-electron state, similar to the EL2 or DX phenomenon in GaAs or AlGaAs, so that the resulting distortion can give it a 'kick' in the direction between the two sites. The model also appears to account for the properties reported for the first time at this meeting for the self-interstitial in diamond, the only other identified self-interstitial in a semiconductor.

Keywords: Self-interstitial; Interstitial zinc; ZnSe; Recombination-enhanced migration

1. Introduction

A great deal has been learned concerning the structure and the optical and electronic properties of lattice vacancies in the elemental and compound semiconductors from electron paramagnetic resonance (EPR) and optical studies over the years [1,2]. The self-interstitials, on the other hand, have for the most part eluded detection, and their properties have therefore remained a challenging mystery.

The first, and, at least until this meeting, the only unambiguous experimental identification of a self-interstitial in any semiconductor is that of interstitial zinc in ZnSe. In the present paper, we will therefore review what has been learned recently about some of its properties. Combining this information with various hints from theory and experiment for other semiconductors, a simple predictive model will be described which has begun to emerge for the properties of self-interstitials throughout the semiconductor series. In addition, this model leads to the suggestion of a possible mechanism for the surprising recombination-enhanced migration discovered for interstitial Zn in ZnSe at cryogenic temperatures.

In the above paragraph we said 'at least up to this meeting' because in the following talk Gordon Davies [3] will tell us that the self-interstitial in diamond has now also been observed, and the details of its EPR identification will be described in another paper by Hunt et al [4]. We will leave the details of this exciting new result to these authors, but we will return to it at the end briefly to see how well it fits in with the model.

2. Interstitial Zn in ZnSe

2.1. Background

In 1974, the first indirect detection of interstitial Zn in ZnSe was reported [5]. In this work, EPR studies after

* Corresponding author. Fax: + 1-610-758-4561.
E-mail address: gdw0@lehigh.edu (G.D. Watkins)

0921-4526/99/$ - see front matter
PII: S0921-4526(99)00397-X

1.5 MeV electron irradiation in situ at 20.4 K observed that the Zn vacancies (V_{Zn}^-) which were being produced linearly versus the irradiation fluence were perturbed by the presence of a nearby defect. The nearby defect was unambiguously identified as the displaced interstitial Zn_i^{++} atom from the observation that its orientation from the vacancy was correlated to the irradiating electron beam direction. In addition to the linear production of these close Frenkel pairs, it was observed that unperturbed (isolated) vacancies were also being produced approximately quadratically versus electron fluence. This was the first hint that either the interstitial or the vacancy can migrate at this temperature under the influence of the ionization accompanying the electron irradiation, and that the migrating direction is in the direction of separation of the pair.

In 1986, optically detected EPR (ODEPR) studies after in situ 2.5 MeV electron irradiation of ZnSe at 4.2 K revealed for the first time a large number of well-resolved zinc-vacancy–zinc-interstitial close Frenkel pairs of various separations frozen into the lattice [6]. These were observed via photo-luminescence (PL) in the 700–1100 nm region, which arises from radiative electron–hole recombination involving the zinc-interstitial donor and its partner vacancy acceptor

$$Zn_i^+ + V_{Zn}^- \rightarrow Zn_i^{++} + V_{Zn}^= + h\nu, \quad (1)$$

where Zn_i^+ and V_{Zn}^- are the paramagnetic centers seen in the ODEPR. Typical spectra are shown in Fig. 1, where the centers labeled *A–D* are $S = 1$ strongly exchange-coupled very close pairs, those labeled X_1–X_{20} are less strongly exchange-coupled pairs of increasing separation, and finally 'distant' pairs are observed, Fig. 1(c), where the exchange interaction is too weak to resolve, and broadened spectra of the isolated $s = \frac{1}{2}$ partners are seen.

In 1987, the EPR spectrum of the truly isolated Zn_i^+ was also observed directly in these samples via a competing spin-dependent recombination process,

$$Zn_i^+ + \mathscr{D}^0 \rightarrow Zn_i^0 + \mathscr{D}^+ \quad (2)$$

which produces negative Zn_i^+ ODEPR signals in unrelated distant shallow donor $\mathscr{D}_0$ to deep acceptor $\mathscr{A}^0$ radiative recombination at ~ 625 nm [7],

$$\mathscr{A}^0 + \mathscr{D}^0 \rightarrow \mathscr{A}^- + \mathscr{D}^+ + h\nu. \quad (3)$$

Resolved hyperfine interactions could be observed with the central ^{67}Zn atom ($I = \frac{5}{2}$, 4.1% abundant), and with ^{77}Se atoms ($I = \frac{1}{2}$, 7.6% abundant) at the nearest and third-nearest shells, unambiguously identifying the ODEPR signal as arising from Zn_i^+ on-center in the T_d site surrounded by four Se atoms, $(Zn_i)_{Se}^+$.

The various radiative and spin-dependent processes of Eqs. (1)–(3) are summarized in Fig. 2. A complete description of these and subsequent detailed ODEPR studies of

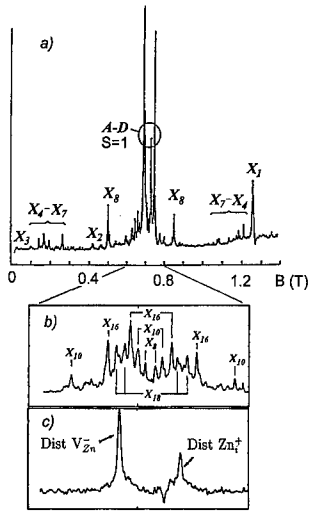

Fig. 1. (a) ODEPR spectra of the Frenkel pairs in ZnSe with (a) $\boldsymbol{B}\|\langle 1\,1\,1\rangle$, modulation frequency $f_m = 2$ kHz; (b) $\boldsymbol{B}\|\langle 1\,0\,0\rangle$, $f_m = 500$ Hz; and (c) $\boldsymbol{B}\|\langle 1\,0\,0\rangle$, $f_m = 20$ Hz. The strong *A–D* spectra are suppressed with $\boldsymbol{B}\|\langle 1\,0\,0\rangle$, revealing in (b) more of the intermediate pairs, and finally in (c) only the very distant pairs, as f_m is progressively decreased.

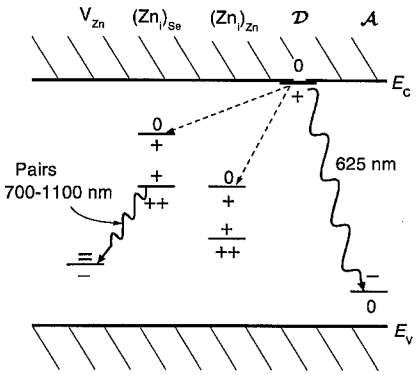

Fig. 2. Schematic of the energy level positions for the isolated zinc vacancy, V_{Zn} the isolated zinc interstitials, $(Zn_i)_{Se}$ and $(Zn_i)_{Zn}$, the shallow donor $\mathscr{D}$, and the deep acceptor $\mathscr{A}$ in ZnSe. The solid wavy lines indicate the observed radiative transitions, the dashed lines indicate the spin-dependent competitive processes (after Ref. [11]).

this fascinating system, and the information that has been learned, has recently been published [8,9].

More recently [10,11], we have returned to study this system again, this time motivated in part to try to understand the basic mechanisms operative in the degradation of ZnSe-based laser devices. It is generally agreed that the degradation arises from recombination-enhanced climb and glide of dislocations into the active region of the device which emanate from stacking faults at the lattice

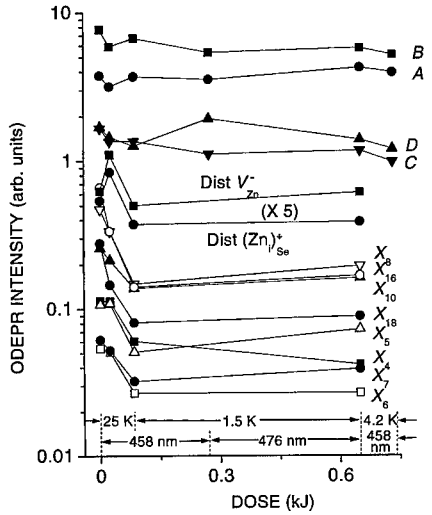

Fig. 3. ODEPR signal intensities of various Frenkel pairs in ZnSe after two 25 K anneals with 458 nm excitation, and subsequent 458 nm and 476.6 nm excitation at 1.5 and 4.2 K, as indicated (after Ref. [11]).

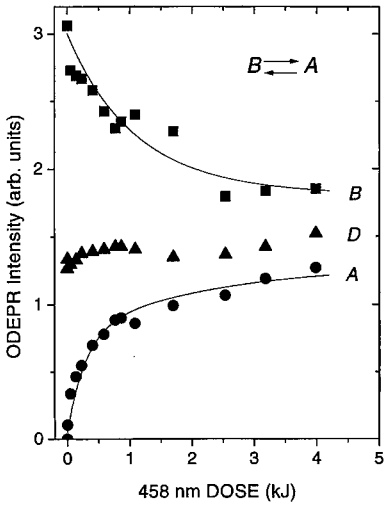

Fig. 4. Intensity of the ODEPR signals for three of the closer pairs in ZnSe vs. accumulated dose of 458 nm excitation at 1.5 K, after 150 K anneal in the dark (Ref. [10]).

mismatched interfaces [12,13]. For dislocations to climb, lattice atoms must be able to move into or out of the core, implying the motion of intrinsic defects. The many distinct close Frenkel pairs observable by ODEPR supply a unique opportunity to detect and unravel possible motion of the interstitial zinc or its zinc vacancy partner by monitoring their relative intensities during electronic excitation. In the next sections, we will describe some of the interesting results that have been found.

2.2. Conversion between Frenkel pairs

Under the normal low-power laser excitation (<3 mW at 458 nm) used for the ODEPR studies at 1.5 K, the intensity of each of the Frenkel pairs is quite stable, showing little evidence of change over several days of study. However, optical excitation at ~25 K produces significant changes, as illustrated in Fig. 3 for representative members of the pairs. Little change is seen for the *A–D* very close pairs, substantial decreases, but of differing magnitudes, are observed for the intermediate pairs, while the well-separated pairs first increase and then decrease. Shown in addition is that continuing with prolonged excitation at 1.5 K also produces further changes, albeit much more slowly. From this it is clear, consistent with the early EPR work, that one of the two constituents – the zinc vacancy or the zinc interstitial – must be being excited to migrate at these cryogenic temperatures, in this case optically, and that, as suggested in the early EPR studies, the net flow is one of separation.

Now, let us concentrate on conversion amongst the *A–D* very close pairs. We first anneal at 150 K in the dark which preferentially removes the *A* and *C* spectra, leaving *B* and *D* and all of the other spectra unchanged. The result of subsequent illumination with 458 nm light at 1.5 K is shown in Fig. 4. The reemergence of spectrum *A*, with a corresponding 1 : 1 decrease in *B*, reveals that *A* is being regenerated by conversion from *B*. The conversion is not complete revealing that the conversion goes in both directions, i.e., $B \rightleftharpoons A$. Here we are apparently monitoring directly the one jump process between the two configurations, which occurs under optical excitation even at 1.5 K.

2.3. Identification of $(Zn_i)_{Zn}$

In Fig. 5(a), we show the strong negative isolated $(Zn_i)_{Se}^{+}$ signal seen in the 625 nm luminescence, as described in Eqs. (2) and (3). Shown also at higher gain are two of the six weak satellites previously identified as arising from its central ^{67}Zn hyperfine interaction. In Fig. 5(b), the result of 458 nm excitation at 25 K followed by rapid cooldown is shown. The $(Zn_i)_{Se}^{+}$ signal has decreased substantially and a new signal at somewhat lower field has emerged. Shown also in the figure at increased gain are three of the six ^{67}Zn hyperfine satellites that identify this new signal as also arising from interstitial zinc, but in a new configuration. Angular dependence studies reveal the *g*-value for the resonance and the ^{67}Zn hyperfine interaction to be isotropic. Careful study of the partially resolved satellite structure visible on the signal in the figure reveals that it arises from ^{77}Se hyperfine interaction with the six equidistant next nearest neighbors surrounding the interstitial site with four Zn nearest

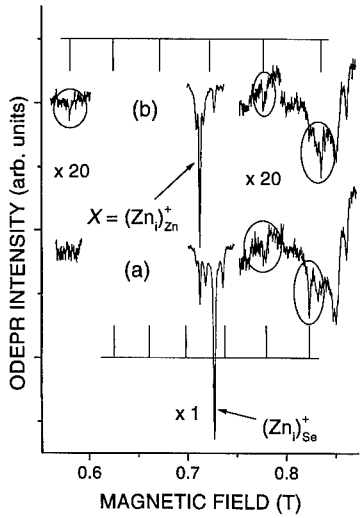

Fig. 5. The ODEPR spectra of the isolated zinc interstitials in ZnSe, with $\boldsymbol{B}\|\langle 1\,0\,0\rangle$. (a) After anneal at 25 K in the dark, the $(Zn_i)^+_{Se}$ is dominant. (b) After 458 nm excitation at 25 K, the $(Zn_i)^+_{Zn}$ signal dominates. In both (a) and (b), several observed satellites arising from hyperfine interaction with the central $^{67}Zn_i$ atom (4.1% abundant, $I = \frac{5}{2}$) are circled, and compared with the expected positions for all $2I + 1 = 6$ (Ref. [11]).

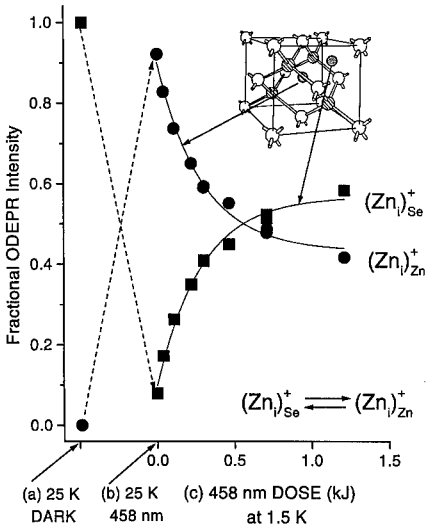

Fig. 6. The isolated $(Zn_i)^+$ ODEPR intensities in ZnSe after (a) 25 K anneal in the dark, (b) subsequent 458 nm excitation at 25 K with rapid cool down to 4.2 K, and (c) versus subsequent accumulated dose of 458 nm light at 1.5K (after Ref. [11]).

neighbors. This new signal is therefore unambiguously identified as arising from interstitial zinc, on-center in the T_d site surrounded by four Zn near neighbors, i.e., $(Zn_i)^+_{Zn}$.

The central ^{67}Zn hyperfine interaction is greater for $(Zn_i)^+_{Zn}$ than for $(Zn_i)^+_{Se}$ revealing that its electron is bound more strongly, and that its second donor level $(+/++)$ is therefore deeper in the gap. Analysis of the central and neighbor hyperfine interactions for each has allowed an approximate estimate for its second donor level position of $\sim E_C$-1.6 eV for $(Zn_i)_{Zn}$ and $\sim E_C$-1.0 eV for $(Zn_i)_{Se}$. These level positions and the corresponding observed central ^{67}Zn hyperfine interactions are in remarkable agreement with recent theoretical estimates [14–16], and the level positions have been incorporated into Fig. 2. In a companion paper at this conference [17], the details of the $(Zn_i)^+_{Zn}$ identification are described, as well as are those involved in the second donor level position estimates.

2.4. $(Zn_i)_{Se} \leftrightarrow (Zn_i)^+_{Zn}$ conversion

In Fig. 6, the result of sequential annealing and illumination steps on the intensity of the two Zn_i^+ signals is summarized. For this sample, annealing at 25 K in the dark completely removes the $(Zn_i)^+_{Zn}$ signal, with a corresponding increase in the $(Zn_i)^+_{Se}$ signal. Subsequent 458 nm illumination at 25 K with rapid cooldown regenerates it, with a corresponding decrease in the $(Zn_i)^+_{Se}$ signal. Upon subsequent 458 nm illumination at 1.5 K, slow, partial return conversion is observed, demonstrating that optically induced conversion is occurring in both directions, i.e. $(Zn_i)^+_{Se} \leftrightarrow (Zn_i)^+_{Zn}$, even at this low temperature. By repeating each of these injection and annealing processes, the interstitial can be controllably cycled back and forth many times between the two configurations.

These results unambiguously demonstrate that interstitial zinc is mobile under these excitation conditions, conversion between the two sites and back constituting a single diffusion jump, each site representing an intermediate position from which a return jump carries the atom to four possible choices for the other. This establishes unambiguously that the mobile species is interstitial zinc. A study of the temperature dependence of the process reveals no change in the rate between 1.5 and 4.2 K, but with an increase of $\sim 10^3$ already at 10 K. The process is therefore apparently athermal at the lowest temperatures, changing over to a more efficient phonon-assisted one by 10 K.

3. Model for interstitials in semiconductors

A simple model has previously been suggested for predicting the structure and properties expected of the various charge states of interstitials in semiconductors, which should be generally applicable to either impurities or self-interstitials [1,2]. It is summarized in Table 1,

Table 1
Interstitial atoms arranged according to their $s^m p^n$ free atom configuration

Host\config.	s^0p^0	s^1p^0	s^2p^0	s^2p^1	s^2p^2	s^2p^3	s^2p^4	s^2p^5
Si			$\mathbf{B_i^{+}}$*	$\mathbf{B_i^0}$	$\mathbf{B_i^{-}}$*			
Si				$\mathbf{C_i^{+}}$	$\mathbf{C_i^0}$	$\mathbf{C_i^{-}}$		
Si							$\mathbf{O_i^0}$	
Si		$\mathbf{Al_i^{++}}$	(Al_i^{+})	(Al_i^0)				
Si			Si_i^{++}*	Si_i^{+}*	Si_i^{0}*			
ZnSe	(Zn_i^{++})	$\mathbf{Zn_i^{+}}$	(Zn_i^0)	(Zn_i^{-})				
ZnTe						$\mathbf{Te_i^{+}}$	← or →	$\mathbf{Te_i^{-}}$
	On-center T_d			Jahn–Teller, off-center bonded				

The atom is predicted to be on-center in a T_d site if $n = 0$, but off-center and bonded to one or more of the host atoms if $1 \leqslant n \leqslant 5$. Confirming the model are those experimentally observed (bold), and those predicted by computational theory (*). Shown in parentheses are cases discussed in the text whose structures in the lattice are only predicted by the model.

where the free atom, with its valence orbital configuration given by $s^m p^n$ for its particular charge state, is considered to be placed on-center in a T_d interstitial site of the semiconductor. If $m = 0$, 1, or 2, and $n = 0$, the atom is in an S-state, with no orbital degeneracy. There is therefore no Jahn–Teller distortion and the atom should remain on-center. However, if $n = 1$–5, orbital degeneracy exists and the Jahn–Teller theorem predicts off-center distortion. Since we are dealing in this case with p-orbitals, which overlap strongly with the neighbors and have a tendency to form strong directed chemical bonds, we can expect strong distortions into bonded configurations with one or more of the host atoms.

This model was first proposed to help understand the properties of several experimentally observed impurity interstitials in silicon, and, in turn, therefore, to serve as a predictive tool for the properties of the silicon self-interstitial. As illustrated in the table, $B_i^0(2s^22p^1)$ [18], $C_i^+(2s^22p^1)$ [19], $C_i^0(2s^22p^2)$ [21], $C_i^-(2s^22p^3)$ [21] and $O_i^0(2s^22p^4)$ [22] have all been experimentally observed by EPR (or local mode vibrational studies in the case of C_i^0 and O_i^0) to be off-center in bonded configurations with nearby silicon host atoms, consistent with the model. $Al_i^{++}(3s^1)$, on the other hand, has been established by EPR to be on-center in the T_d site [23], again as expected. The model predicts, however, that $B_i^+(2s^2)$ goes to the on-center position, and conversely, that Al_i^0 goes off-center. Evidence of this predicted configurational change for both at the $+ \rightleftharpoons 0$ charge state change is found in the observation of substantial recombination-enhanced migration (REM) under electronic and/or optical excitation of both [24], the 'kick' given to the atoms upon charge state change presumably assisting the migration over the diffusion barrier. Confirmation also comes from recent state-of-the-art ab initio calculations in the case of interstitial boron, which have also predicted configurational changes from on-center to off-center bonded configurations at this particular charge state change [25]. Following the same arguments for the silicon self-interstitial, Table 1 predicts that $Si_i^{++}(3s^2)$ is on-center, but that $Si_i^+(3s^23p^1)$ and $Si_i^0(3s^23p^2)$ will go off-center into bonded configurations. Consistent with this prediction, theory predicts here also such changes [26–28], and experimentally strong REM is also observed [1,2]. As a result, it has been suggested [1,2] that a reasonable understanding of the self-interstitial in silicon may have actually emerged even though it has not been directly observed. (Recently, there have been several experimental studies that *indirectly* appear to reflect additional important properties of the silicon interstitial, which we will not attempt to describe here. To the interested reader we recommend particularly the extensive DLTS and EPR studies of Mukashev et al. [29], who present evidence that the interstitial may be stable up to room temperature in the absence of ionization, and the diffuse X-ray scattering experiments of Erhart and Zillgen [30], who conclude that the majority of close Frenkel pairs produced in a low-temperature electron irradiation may also actually be stable to above room temperature.)

It is interesting to point out that this very simple model says that the properties of an interstitial are determined primarily by the valence configuration of the atom itself, and relatively less dependent on the particular semiconductor into which it is placed. As a result it has also been used to predict the properties of interstitials in the compound semiconductors as well [1,2]. In this regard, additional possible confirmation of the model has come from ODEPR studies of what have been interpreted to be close Frenkel pairs produced on the Te sublattice of ZnTe [31]. There the symmetry of the ODEPR signals was interpreted to reflect a low-symmetry bonded configuration for the Te interstitial, as expected for the partial p-occupancy of its available charge states. (Similarly, but not shown in Table 1, ODEPR studies in as-grown GaP [32–34], GaAs [35,36], and AlGaAs [37] have detected

what have been suggested to be Ga_i^{++}-related centers. If correct, their mostly isotropic Ga hyperfine interactions confirm their non-bonded $4s^1$ character, as expected. On the other hand, in electron-irradiated GaN, two ODEPR centers tentatively identified with Ga_i-related defects have been observed which display substantial anisotropy in their hyperfine interactions suggestive of substantial 4p character [38]. To be consistent with the model, they could be related to Ga_i^0.) In any event, the results we have described for Zn_i^+ in ZnSe clearly supply a particularly critical test of the model, because it represents, at least up until now, the only direct and unambiguously observed self-interstitial. We note immediately that it does indeed fit the model accurately, being experimentally observed as on-center in either of the two T_d sites, as predicted for its $4s^1$ free atom configuration. The model predicts it to be on-center also for the other charge states involved in its spin-dependent processes as given in Eq. (1), $Zn_i^{++}(4s^0)$, and Eq. (2), $Zn_i^0(4s^2)$.

4. Mechanism for Zn_i enhanced migration

Here, we immediately run into what appears to be a possible problem with the model. We argued above that recombination-enhanced migration follows naturally from the configurational change associated with a change of charge state that involves change of occupancy of the p-orbitals. According to the model, Zn_i in its three charge states involves only s-electrons, and should stay on-center. There can be breathing vibrational modes excited upon charge change, but these supply no kick in a diffusion direction. In the notation of Stoneham [39], the 'accepting' and 'promoting' modes are orthogonal. Our model appears therefore to predict it to be safe and stable on-center, but in fact it clearly is not.

On closer examination, however, the model may actually also provide the answer. Two possibilities suggest themselves – (1) electron capture or optical excitation into an excited P state of the neutral interstitial, $Zn_i^0(4s^14p^1)$, or (2) electron capture into an additional, negative, charge state, $Zn_i^-(4s^24p^1)$. In either case, a single electron is now in a p-orbital, and a Jahn–Teller off-center distortion is predicted. It will be recognized that model (1) bears a close resemblance to the much-studied EL2 defect in GaAs [40,41], where, there, excitation into an excited state of the neutral defect leads to a metastable off-center distorted configuration. Model (2) bears a resemblance to the DX center in AlGaAs [42,43], in the sense that capture into an additional negative charged state is involved, made stable, or metastable, by the resulting distortion. In both of these cases also, the off-center instability has been satisfactorily explained as arising from the p-character of the excited state [44].

There is an additional confirming feature for this mechanism. Upon *thermal* annealing in the dark, the close Frenkel pairs have been found to disappear at the lowest temperatures, the more distant ones disappearing at progressively higher temperatures vs. their separation [8]. Their disappearance therefore clearly reflects vacancy-interstitial annihilation for the pairs, as expected from the Coulomb interaction between the negative vacancy and the more mobile positive interstitial. We have pointed out above, however, that the reverse is observed under REM conditions, the interstitial migrating away from its partner vacancy. This argues strongly that under these conditions the Coulomb attraction is absent. Since there is no evidence of a stable neutral state in the band gap for the vacancy, this argues that the interstitial must be in a neutral or possibly negative charge state when making the diffusive jump, again consistent with the model.

The barrier for thermally activated interstitial zinc migration has been estimated to be ~ 0.6–0.8 eV [8]. This comes from analysis of the annealing experiments in the dark, where, after the closer pairs have disappeared, the isolated Zn_i^+ ODEPR signal finally disappears after 15 min at ~ 220–260 K. The recombination event must therefore, in one way or another, supply this much energy to the interstitial atom.

5. Summary

Interstitial Zn_i^+ has been observed by ODEPR both as paired off with its partner vacancy in Frenkel pairs of various separations, and isolated, after 2.5 MeV electron irradiation in situ at 4.2 K. The isolated interstitial can be observed on-center in each of the two distinct T_d sites in the lattice – that surrounded by four Se atom nearest neighbors, $(Zn_i)_{Se}^+$, and that by four Zn nearest neighbors, $(Zn_i)_{Zn}^+$. The unpaired electron is more strongly bound for $(Zn_i)_{Zn}^+$, as evidenced by the central ^{67}Zn and neighboring ^{77}Se hyperfine interactions for each. Analysis of these interactions suggests the position of the second donor level to be at $\sim E_C - 1.6$ eV for $(Zn_i)_{Zn}^+$ and $\sim E_C - 1.0$ eV for $(Zn_i)_{Se}$ [17]. These values, as well as the hyperfine interactions themselves, are remarkably close to recent theoretical estimates [14–16]. Also, the experimental observation of both configurations for the interstitial is consistent with the conclusions of the theory that the two are very close in total energy.

Optical excitation in the temperature region 1.5–25 K causes the interstitial to hop between its two configurations, a motion fully equivalent to long-range diffusion. The remarkable fact is that in monitoring the process, we determine not only that it is diffusing, but the exact path it takes in the process, being 'caught in the act' of a half-jump from one T_d site to the other. To our knowledge, this observation is unique in solids. The process is temperature independent in the 1.5–4.2 K range, but

increases rapidly versus temperature by ~ 10 K. This motion is detected also by conversions between the Frenkel pairs of differing separations, the sense of the changes indicating diffusion of the interstitial away from its partner vacancy.

A previously proposed model for interstitials [1,2] envisions the atom as first placed on-center in a T_d site, its stability there depending upon the free-atom valence configuration $s^m p^n$ of its particular charge state. If $n = 0$, the atom is in a non-degenerate S-state and is stable on-center. If $1 \leqslant n \leqslant 5$, the state is degenerate due to its partial p-occupancy, and an off-center energy-lowering Jahn–Teller distortion is predicted. Since p-orbitals have a tendency to form strong directed chemical bonds, large distortions into bonding configurations with one or more of its neighbors are expected. The model predicts on-center configurations for $Zn_i^{++}(4s^0)$, $Zn_i^{+}(4s^1)$, and $Zn_i^{0}(4s^2)$, as confirmed here for Zn_i^{+}.

To explain the electronically stimulated migration of the zinc interstitial we have proposed that recombination occurs either via an excited $4s^1 4p^1$ neutral state, or via a negative $4s^2 4p^1$ state, the partial p-occupancy providing an off-center Jahn–Teller 'kick' to assist its migration. The lack of Coulomb attraction to its partner vacancy in these charge states would explain the tendency for the pair to separate. In view of the success of theory in treating the on-center T_d configurations for Zn_i in its $++$, $+$ and 0 states in ZnSe [14], and in handling the EL2 and DX problems [45–48], it would be highly desirable that the above EL2- or DX-like behavior be tested by similar calculations for Zn_i *in ZnSe*.

Finally, let us check the interstitial model against the very recent EPR results for the neutral self-interstitial in diamond. The neutral carbon free atom configuration is $2s^2 2p^2$ and an off-center bonded configuration is therefore predicted, fully consistent with the $\langle 1\,0\,0\rangle$-split configuration to be reported by these workers. In fact, the $\langle 1\,0\,0\rangle$-split configuration is identical to the structure observed for neutral $2s^2 2p^2$ interstitial carbon in silicon [20], and very similar to that predicted ($\langle 1\,1\,0\rangle$-split) for the neutral $2s^2 2p^2$ self-interstitial in silicon [27]. And, like the silicon self-interstitial, Hunt et al. report strong evidence for recombination-enhanced migration at cryogenic temperatures [4], indicative also of configurational changes versus charge state. Like these other systems, the ground state of the neutral system is non-paramagnetic, with electrons paired off, but for it there is a convenient excited $S = 1$ state nearby that can be thermally populated and observed by EPR. The energetically close availability of this state presumably reflects the increased exchange interaction between the more highly localized electrons in the wider band gap diamond.

We can conclude that the simple model we have described here for the behavior expected of interstitials in semiconductors continues to be remarkably reliable, with no exceptions encountered so far.

Acknowledgements

The research on the zinc interstitial has been supported by National Science Foundation Grant No. DMR-92-04114 and DMR-97-04386, and, in its initial stages, also by Office of Naval Research, Electronic Division, Grant No. N00014-94-0117.

References

[1] G.D. Watkins, in: W. Schröter (Ed.), Materials Science and Technology, Vol. 4, Electronic Structure and Properties of Semiconductors, VCH, Weinheim, 1991, pp. 105–141.
[2] G.D. Watkins, in: W. Schröter (Ed.), Handbook of Semiconductor Technology, Wiley, Weinheim, in press.
[3] G. Davies, paper MoM.2P, Physics B (1999), these proceedings.
[4] D.C. Hunt, D.J. Twitchen, M.E. Newton, J.M. Baker, T.R. Anthony, W.F. Banholzer, paper WeM4.3C, Physica B (1999), these proceedings.
[5] G.D. Watkins, Phys. Rev. Lett. 33 (1974) 223.
[6] F. Rong, G.D. Watkins, Phys. Rev. Lett. 56 (1986) 2310.
[7] F. Rong, G.D. Watkins, Phys. Rev. Lett. 58 (1987) 1486.
[8] F.C. Rong, W.A. Barry, J.F. Donegan, G.D. Watkins, Phys. Rev. B 54 (1996) 7779.
[9] W.A. Barry, G.D. Watkins, Phys. Rev. B 54 (1996) 7789.
[10] K.H. Chow, G.D. Watkins, Phys. Rev. Lett. 81 (1998) 2084.
[11] K.H. Chow, G.D. Watkins, Phys. Rev. B, 60 (1999) 8628.
[12] S. Guha, J.M. DePuydt, M.A. Hasse, J. Qiu, H. Cheng, Appl. Phys. Lett. 63 (1993) 3107.
[13] K. Nakano, S. Tomiya, M. Ukita, H. Yoshida, S. Itoh, E. Morita, M. Ikeda, A. Ishibashi, J. Electron. Mater. 25 (1996) 213.
[14] D.B. Laks, C.G. Van de Walle, G.F. Neumark, P.E. Blöchl, S.T. Pantelides, Phys. Rev. B 45 (1992) 10965.
[15] C.G. Van de Walle, P.E. Blöchl, Phys. Rev. B 47 (1993) 4244.
[16] M. Illgner, H. Overhof, Phys. Rev. B 54 (1996) 2505.
[17] K.H. Chow, G.D. Watkins, paper MoP.38, Physica B (1999), these proceedings.
[18] G.D. Watkins, Phys. Rev. B 12 (1975) 5824.
[19] G.D. Watkins, K.L. Brower, Phys. Rev. Lett. 36 (1976) 1329.
[20] J.F. Zheng, M. Stovola, G.D. Watkins, in: D.J. Lockwood (Ed.), 22nd International Conference on the Physics of Semiconductors, World Scientific, Singapore, 1995, pp. 2363–2366.
[21] L.W. Song, G.D. Watkins, Phys. Rev. B 42 (1990) 5759.
[22] H.J. Hrowstowski, R.H. Kaiser, Phys. Rev. 107 (1957) 966.
[23] G.D. Watkins, in: Radiation Damage in Semiconductors, Dunod, Paris, 1964, p. 97.
[24] G.D. Watkins, A.P. Chatterjee, R.D. Harris, J.R. Troxell, Semicond. and Insul. 5 (1983) 321.
[25] E. Tarnow, Europhys. Lett. 16 (1991) 449.
[26] R. Car, P.J. Kelly, A Oshiyama, S.T. Pantelides, in: L.C. Kimerling, J.M. Parsey Jr. (Eds.), 13th International Conference on Defects in Semiconductors, AIME, Warrendale, 1985, p. 269.

[27] Y. Bar-Yam, J.D. Joannopoulos, Phys. Rev. B 30 (1984) 2216.
[28] Y. Bar-Yam, J.D. Joannopoulos, in: L.C. Kimerling, J.M. Parsey Jr. (Eds.), 13th International Conference on Defects in Semiconductors, AIME, Warrendale, 1985, p. 261.
[29] B.N. Mukashev, Kh.A. Abdullin, Yu.V. Gorelkinskii, S.Zh. Tokmoldin, Mat. Sci. Eng. B 58 (1999) 171.
[30] P. Ehrhart, H. Zilgen, in: T.D. de la Rubia, S. Coffa, P.A. Stolk, C.S. Rafferty (Eds.), Defects and Diffusion in Silicon Processing, MRS Vol. 469, Pittsburgh, 1997, p. 175.
[31] B. Ittermann, F.K. Koschnick, W.A. Barry, M.J. Burnard, G.D. Watkins, Mat. Sci. Forum 143-7 (1994) 423.
[32] K.M. Lee, in: M. Stavola, S.J. Pearton, G. Davies (Eds.), Defects in Electronic Materials, MRS Vol. 104, Pittsburgh, 1988, p. 449.
[33] W.M. Chen, B. Monemar, Phys. Rev. B 40 (1989) 1365.
[34] M. Godlewski, B. Monemar, Phys. Rev. B 37 (1988) 2752.
[35] J.M. Trombetta, T.A. Kennedy, W. Tseng, D. Gammon, Phys. Rev. B 43 (1991) 2458.
[36] T. Wimbauer, M.S. Brandt, M.W. Bayerl, M. Stutzmann, D.M. Hofmann, Y. Mochizuki, M. Mizuta, Mat. Sci. Forum 258–263 (1997) 1309.
[37] T.A. Kennedy, R. Magno, M.G. Spencer, Phys. Rev. B 37 (1988) 6325.
[38] C. Bozdog, H. Przybylinska, G.D. Watkins, V. Härle, F. Scholz, M. Mayer, M. Kamp, R.J. Molnar, A.E. Wickenden, D.D. Koleske, R.L. Henry, Phys. Rev. B 59 (1999) 12479.
[39] A.M. Stoneham, Rep. Prog. Phys. 44 (1981) 1251.
[40] G.M. Martin, S. Markram-Ebeid, in: S.T. Pantelides (Ed.), Deep Centers in Semiconductors, 2nd edition, Gordon and Breach, Yverdon, 1992, pp. 457–545.
[41] G.A. Baraff, in: S.T. Pantelides (Ed.), Deep Centers in Semiconductors, 2nd edition, Gordon and Breach, Yverdon, 1992, pp. 547–589.
[42] D.V. Lang, in: S.T. Pantelides (Ed.), Deep Centers in Semiconductors, 2nd edition, Gordon and Breach, Yverdon, 1992, pp. 591–641.
[43] P.M. Mooney, in: S.T. Pantelides (Ed.), Deep Centers in Semiconductors, 2nd edition, Gordon and Breach, Yverdon, 1992, pp. 643–665.
[44] G.D. Watkins, Semicond. Sci. Technol. 6 (1991) B111.
[45] D.J. Chadi, K.J. Chang, Phys. Rev. Lett. 60 (1988) 2187.
[46] D.J. Chadi, K.J. Chang, Phys. Rev. B 39 (1989) 10063.
[47] J. Dabrowski, Matthias Scheffler, Phys. Rev. Lett. 60 (1988) 2183.
[48] J. Dabrowski, Matthias Scheffler, Phys. Rev. B 40 (1989) 10391.

ELSEVIER

Physica B 273–274 (1999) 15–23

PHYSICA B

www.elsevier.com/locate/physb

Current problems in diamond: towards a quantitative understanding

Gordon Davies*

Physics Department, King's College London, Strand, London WC2R 2LS, UK

Abstract

This paper discusses three major areas of current work on the properties of point defects in diamond: attempting to introduce a shallow donor centre, studying the rôle of transition metals, and achieving a quantitative understanding of radiation effects. Recent work on the first two topics is surveyed briefly. Published and new data on the problem of radiation damage are discussed in terms of: measuring the concentrations of the vacancy-related and self-interstitial centres; isotope effects on the vacancy and interstitial centres, including the identification of the self-interstitial 1.859 eV line as a vibrational feature; the rate of production of damage, including the influence of the nitrogen impurity; and the radiation-induced reactions. Some of the problems arising from the lack of current information are highlighted.

Keywords: Diamond; Radiation damage; Optical properties; Epr

1. Introduction

Today there are three major areas of work in progress on the properties of point defects in diamond: attempting to introduce a shallow donor centre, studying the rôle of transition metals, and achieving a quantitative understanding of radiation effects.

The problem of the shallow donor is primarily one of growth technology, and so the discussion here will be very short (Section 3). Studies of transition metals are at a better state of development: Ni is now known to form optical and paramagnetic centres, and both Ni and Co have complex interactions with another impurity, nitrogen. A considerable body of knowledge is building up, as outlined in Section 4, but there is not yet a complete picture of all the effects. The third topic, radiation damage, is at a more advanced state of study: the basic defects are rapidly being understood and our quantitative understanding is such that the gaps in our knowledge can be identified and addressed. For example, we now know the calibrations linking the concentrations of the damage centres to their optical absorption for the vacancy and vacancy-nitrogen centres (Section 5) and for self-interstitials (Section 6). One peculiarity is that the absorption per self-interstitial appears to be anomalously low. This paradox is solved by considering the effects of changing the isotopic content of the lattice from ^{12}C to ^{13}C: in Section 7 we will examine published and new data on the isotope dependence, derive the expected magnitude of the effect and show that the self-interstitial absorbs light through a different process from the typical defect in diamond. With the calibrations established, we can examine the rate of producing radiation damage (Section 8) and we will draw attention to the importance of the impurity nitrogen on the production of observable damage. Finally, in Section 9, we will look at the fate of the vacancy and self-interstitial during annealing, and their interactions with nitrogen. Given the importance of nitrogen in many of these processes we begin by gathering together the data which allow us to determine the concentrations of nitrogen in any sample.

* Corresponding author. Tel.: + 44-20-7848-2573; fax: + 44-20-7848-2420.

E-mail address: gordon.davies@kcl.ac.uk (G. Davies)

0921-4526/99/$ - see front matter
PII: S0921-4526(99)00398-1

2. Concentrations of nitrogen

The key to the recent increase in the understanding of radiation effects and transition metals in diamond has been the increased accuracy in the calibrations linking the concentration of nitrogen and the strength of the characteristic absorption produced in the one-phonon part of the infra-red absorption spectrum (at photon energies less than 1332 cm^{-1}). We will follow the convention that the absorption coefficient A_x at the wave number x (cm^{-1}) is measured in cm^{-1}, and the concentration, denoted [N], is in atomic parts per million (ppm); in diamond one ppm is $1.76 \times 10^{17}\,cm^{-3}$.

For the isolated substitutional N^0 atoms in the neutral charge state, the correlation has been made by comparing the strength of the 'P1' epr signal from N^0 with that of a $CuSO_4.5H_2O$ standard, and also by inert-gas fusion measurements (line 1 of Table 1) [1,2]. If a diamond which contains isolated N^0 atoms is subjected to radiation damage, the damage centres may be compensated by the N^0 producing N^+ centres, which have their own characteristic absorption spectrum. By using different optical excitations, the balance of N^0 and N^+ may be changed. From line 1 of Table 1, the change in $[N^0]$ is known, and so the absorption at 1332 cm^{-1} produced by $[N^+]$ can be found (line 2 of Table 2) [3]. An application of being able to measure $[N^+]$ is to estimate the amount of Ni in a sample, with the assumption that one N^0 atom can charge-compensate one Ni atom (Section 4). In contrast to N^+, there are currently no data for the absorption produced by N^-, given the great difficulty in producing a shallow donor in diamond (Section 3).

Annealing synthetic diamond at $\sim 1800^0$C under a stabilising pressure allows the N^0 atoms to aggregate into pairs of substitutional atoms (the 'A' centre) with the peak of their infra-red absorption at 1282 cm^{-1}. Chemical determinations, using the release of the nitrogen by combustion and using inert-gas fusion have given the correlation of line 3 of Table 1 [4,5]. A check on the consistency of the calibrations in lines 1 and 3 is that they are compatible with the changes in absorption during the conversion $2N^0 \rightarrow A$ [1]. Earlier calibrations were inconsistent in this regard as observed by Collins [6], and that inconsistency was a major motivation for the recent, apparently reliable, studies.

Table 1
Calibrations of the absorption produced by nitrogen

Line	Calibration	Reference
1	$[N^0] = (25.0 \pm 2)\mu_{N^0}(1130)$	[1,2]
2	$[N^+] = (5.5 \pm 1)\mu_{N^+}(1332)$	[3]
3	$[N_A] = (16.5 \pm 1)\mu_A(1282)$	[4,5]
4	$[N_B] = (79.4 \pm 8)\mu_B(1282)$	[7]

The concentration is in parts per million atomic, and the absorption coefficient $\mu(x)$ is in cm^{-1} measured at room temperature at the photon wave number x cm^{-1}. The overlapping absorption spectra are separated using the method described in Ref. [58].

Further heat treatment, at $\sim 2200^0$C, produces more aggregation of the nitrogen, converting the A centres into the 'B' form (4 N atoms around one vacancy). The calibration has been found from the loss of A-centre absorption assuming $2A \rightarrow B + I$, where I is the self-interstitial, line 4 of Table 1 [7]. This result is less certain, since the absorption of the B centres must be separated from those of the A pairs and the N^0 atoms.

Nitrogen does not act as a shallow donor in any of these structures: the least deep is the N^0 with a 1.7 eV ionisation energy.

3. The shallow donor problem

In diamond, substitutional boron forms a relatively shallow acceptor with a binding energy of 0.37 eV [8]. Considerable effort is being directed at the problem of doping diamond with a species which reproducibly produces a shallow donor. For example, in recent studies of P-doped CVD diamond, luminescence has been ascribed to excitons bound to a shallow donor and to donor (P)-acceptor (B) pairs [9], and photoconductivity has been reported from the ionisation of P donors [10], with donor binding energies of 560 meV [10] to 630 meV [9]. In addition to the challenge of creating a reproducible donor, it is desirable that the electron mobility μ_e is not reduced to unacceptable levels. Typical values in P-doped diamond are $\mu_e = 50\,cm^2\,V^{-1}\,s^{-1}$ [10], some 40 × smaller than in high-quality undoped diamond [8].

4. Transition metals in diamond

Transition metals, especially combinations of Ni, Co and Fe, are used as 'solvent-catalysts' in synthesising diamond under thermodynamically stable conditions, the high pressure, high temperature (HPHT) diamonds. The current interest in the metals arises because some of the metal becomes incorporated in the lattice, and Ni and Co are known to produce optical and epr centres. Ni, Co and Fe are also found in some inclusions inside natural diamonds, and some, relatively rare, optical and epr centres in natural diamond contain Ni [11].

The observed properties of the Ni-related centres are strongly affected by the nitrogen impurity in the diamonds. In as-grown HPHT diamond, either interstitial or substitutional Ni is observed, depending on the concentration of N^0, which controls the Fermi energy and hence the charge state of the active centres. In diamonds with low [N], < 10 ppm, two Ni *interstitial* epr centres are observed. The NIRIM1 epr centre has an isotropic

g-factor, and is assumed to be a tetrahedral Ni_i^+ atom [12]. NIRIM2, Ni_i^+ in a trigonal symmetry, is characterised by $g_\perp \sim 0$ [12]. Zeeman and stress perturbations [13] have established that the 1.4 eV optical band occurs at the same centre, and the g-factor has been rationalised recently by Mason et al. [14]. Samples with low [N] also show unexplored multiplet optical transitions at 1.2 and 3.1 eV [15].

In as-grown diamonds with higher [N], approximately > 50 ppm, charge compensation of the Ni by the N produces the W8 epr signal of *substitutional* Ni_s^- [16], and optical bands at 1.885 and 2.51 eV which correlate, within the uncertainties created by inhomogeneous distributions of Ni, with the strength of the Ni_s^- epr signal [17]. The relationship between the epr and optical signals is not yet clear. Applying 'detailed balance' arguments, which we will justify in Section 5, the data of Collins et al. [17] would link the strength of the 1.885 and 2.51 eV optical absorptions to the concentration of W8 epr centres if the oscillator strengths for the optical band were equivalent to radiative lifetimes of $\tau \sim 50\,\mu s$. Measured values are not available, but τ is comparable with values for some of the Ni-related centres (for example, 40 μs for the 2.968 eV band [18], 0.5 ms for the 'S2' 2.369 eV centre [19]), and Co-related centres in diamond (e.g. $63 \pm 1\,\mu s$ to $159 \pm 2\,\mu s$ for various bands [20]). The 1.885 eV transition occurs at a C_{2v} centre [21]; Zeeman measurements on the 1.885 and 2.51 eV transitions would clarify any link to the W8 centre.

Possibly both interstitial and substitutional forms coexist in the samples, but are separately observed depending on the Fermi level. Heat treatment from 1500°C to 1800°C results in considerable structural changes. The simplest Ni structure to emerge appears to be the NE4 epr centre, ascribed to a Ni atom at the centre of a divacancy [22]. This centre acts as the nucleus for the aggregation of N atoms, and many different condensates are formed as successive N atoms are trapped in sites adjacent to it [22,23]. The aggregation is enhanced by the increased mobility of the N atoms in Ni-doped diamond: at $\sim 1500^0$C, the reaction $N + N \rightarrow A$ increases with the concentration of N^+, in samples with the same total concentration of N [24]. Assuming that $[N^+]$ approximates to [Ni], as in Section 2, then the rate of aggregation of N is enhanced by the Ni, presumably by a vacancy- or self-interstitial process [25]; which process cannot be determined from the available data [24]. Corresponding changes occur in the optical spectra as the impurity-centres evolve, with the 1.883 and 2.51 eV bands being replaced by strong absorption at 1.693 eV (recently shown to occur at a monoclinic I centre [26]) and other multiple-line systems [27].

An analogous pattern is evolving for Co-doped diamond. Many optical bands are known [20], the effect of Co on the mobility of N has been noted [28] and resulting optical and epr centres are being identified [29,30].

It is clear from this short survey that a vast body of information is being gathered on the rôle of transition metals in diamond and their interactions with the N atoms. A full systematisation of the data will no doubt follow.

5. Concentrations of vacancy-related defects

To understand vacancy- or interstitial-mediated migration, as well as the rate of creation of defects and the kinetics of their annealing behaviour, we must be able to measure the concentrations of radiation-induced centres. In this section we report the recent substantial progress in this area, building directly from the calibrations of the nitrogen centres listed in Section 2.

In optical work, damage centres in diamond typically produce vibronic bands with well-resolved zero-phonon lines. The optical absorption is conventionally described using the integrated absorption A in the zero-phonon line, measured at liquid nitrogen temperature, with the absorption coefficient in cm^{-1}, the photon energy in meV, and the concentrations in cm^{-3}. For convenience, the known calibration constants are listed in Table 2.

First, we take the 'N3' optical centre (the 'P2' epr centre), a vacancy neighbouring three nitrogen atoms [31]. We [32] have compared the strength of the P2 epr signal with strength of the P1 epr signal of N^0 in a diamond for which $[N^0]$ is known from line 1 of Table 1. The resulting calibration for the integrated absorption A_{N3} in the 2.985 eV zero-phonon line is given in line 1 of Table 2 [32]. Confirmation is provided by charge-transfer effects, when excitation with 514.5 nm Ar^+ light produces an increase in N3 absorption along with an increase in N^0 [32]. Assuming the effect of the light is $N3^- + N^+ \rightarrow N3^0 + N^0$ then the change in N^+, using line 2 of Table 1, confirms the N3 value [32].

Table 2
Calibrations of the optical absorption in zero-phonon lines

Line	Calibration	Reference
1	$A_{N3} = (8.6 \pm 2) \times 10^{-17}[N3]$	[32]
2	$A_{ND1} = (3.9 \pm 1) \times 10^{-16}[V^-]$	[3]
3	$A_{ND1} = (4.8 \pm 0.2) \times 10^{-16}[V^-]$	[35]
4	$A_{GR1} = (1.2 \pm 0.3) \times 10^{-16}[V^0]$	(a)
5	$A_{NV} = 1.4 \pm 0.35 \times 10^{-16}[N - V]$	(a)
6	$A_{H3} = 1.0 \pm 0.35 \times 10^{-16}[H3]$	(a)
7	$A_{H4} = 1.0 \pm 0.35 \times 10^{-16}[H4]$	(a)
8	$A_{1.859} = 1.0 \pm 0.2 \times 10^{-17}[R2]$	[42]

A is the integrated absorption in the zero-phonon line of the transition, measured at 77 K, with the absorption coefficient in cm^{-1} and the photon energy in meV. The concentration is in cm^{-3}. (a) derived from lines 2 and 3 using the data of Ref. [36].

Next, we consider the V^- centre. Lawson et al. [3] have irradiated a specially grown diamond, which had a concentration of $[N^0]$ centres high enough to be measured using line 1 of Table 1, but low enough to be comparable to achievable radiation damage of isolated vacancies and self-interstitials. The high-Fermi energy created by the 1.7 eV ionisation energy of $[N^0]$ results in $V^0 + N^0 \rightarrow V^- + N^+$. V^- can be identified optically by the 'ND1' absorption line at 3.149 eV [33] and by the epr from its $^4A_2$ ground state [34]. *Assuming that the concentration of N^+ equals that of V^-*, Lawson et al. [3] have reported the calibration given in line 2 of Table 2. Direct measurement of the epr signal by Twitchen et al. [35] has recently refined this value (line 3 of Table 2). The agreement implies that the italicised assumption above is valid.

Extension to V^0 is indirect. Extensive annealing studies [36] suggest that when a nitrogen-rich diamond is irradiated and then annealed, the vacancies migrate to the nitrogen, regardless of its state of aggregation. Assuming that all the vacancies are trapped at nitrogen, Davies et al. [36] found that the data could be best fitted if the relative zero-phonon 'oscillator strengths' of V^0 and V^- are $f_{ND1}/f_{GR1} = 4.0 \pm 0.2$. Using this value the calibration for the GR1 zero-phonon line at 1.673 eV of V^0 follows immediately from the value for V^- (line 4 of Table 2). V^0 is a dominant product of primary radiation damage in diamond, but the centre is non-paramagnetic in its ground state, and so the determination of the rate of production of damage in pure diamond relies on this calibration factor.

Values for other nitrogen-vacancy aggregates are obtained using the relative zero-phonon 'oscillator strengths' of the aggregates of V and nitrogen [36]. These values, listed in Table 2, are determined directly from the loss of the vacancy absorption (in both V^0 and V^- forms) and the growth of the new zero-phonon lines produced by one V trapped at the nitrogen complexes. The specific lines are: the 1.945 eV zero-phonon line of one V at an isolated N atom, the 2.463 eV ('H3') line of one V at an A-centre (pair), and the 2.498 eV ('H4') line of one V at the B-centre (which itself is 4N plus V).

'Detailed balance' arguments to estimate the concentrations of centres from their radiative lifetimes τ_r were introduced in Section 4. We can now check the likely accuracy of this approach. The aim is to relate τ_r to the concentration $[C]$ of the optical centre and the total absorption integrated over the vibronic band:

$$[C] = \frac{9}{\pi^2}\frac{n^2}{(n^2+2)^2}\frac{E^2\tau_r g_f}{c^2\hbar^3 g_i}\int \mu(E)\,dE. \quad (1)$$

Here all quantities are measured in SI units, $n = 2.4$ is the refractive index of diamond, E is the mean energy of luminescence, and g_f and g_i are the degeneracies of the final and initial states of the luminescence band. The major problem is that the true radiative decay times are uncertain for many centres in diamond. For example, the measured lifetime of the N3 luminescence transition is $\tau = 41 \pm 1$ ns but after correction for non-radiative processes the true lifetime is estimated as ~ 150 ns [37]. For the N3 centre the mean energy of luminescence is 2.8 eV (4.5×10^{-19} J), and $g_f/g_i = \frac{1}{2}$. The integral in Eq. (1) is over the absorption band, including its phonon sideband, and for the N3 band is about 31 times the zero-phonon absorption. Evaluating we find $f_{N3} = 1.7 \times 10^{-16}$ meV cm^2. This value is a factor of two larger than the more reliable direct measures of f_{N3} in Table 2. The error may lie in estimating the effective electric field at the centre, but calculation for the other bands in Table 2 shows that there is no single expression for the effective electric field term which can be used for all the optical centres. Nevertheless, it would appear that Eq. (1) is likely to be valid to within an order of magnitude.

At this stage it is clear that by using Table 2 we can estimate the concentrations for many of the vacancy-related centres, supplemented where necessary by the use of detailed balance arguments.

6. The self-interstitial

Throughout our discussion of vacancy centres there was no mention of the rôle of self-interstitals, either in terms of their chemical reactions or their effect in determining the charge states of other centres. Very recent data have clarified the behaviour of the self-interstitial.

The 'R2' epr centre has been identified as being produced by the self-interstitial: a $\langle 0\,0\,1\rangle$ split-interstitial [38], the configuration that had been predicted theoretically [39,40]. The R2 epr centre has long been noted to correlate in strength with the 1.685 and 1.859 eV optical absorption lines [41]; very recently these correlations have been firmly established [42], allowing the calibration factor on line 8 of Table 2 to be derived. The absorption per centre is $10\times$ smaller than for the vacancy-related centres in Table 2. In fact, since the 1.859 eV line appears to have negligible phonon sidebands, all the absorption is concentrated in the sharp line rather than being spread out by vibronic coupling over a wide energy range. Allowing for this factor, the absorption per interstitial centre is over two orders of magnitude less than for each vacancy centre. This considerable difference is examined in Section 7.

The R2/[1.685, 1.859 eV] centre is destroyed by annealing at about 600 K, and the annealing rate has an activation energy of 1.6 ± 0.2 eV [38,43]. This is significantly lower than the 2.3 ± 0.3 eV for the vacancy [36]. Consequently, reactions involving the interstitial are completed before there is significant migration of the vacancy, justifying ignoring the interstitials in the vacancy reactions in Section 5 as long as the interstitial

traps are sufficiently stable that they do not release the interstitials.

7. Isotope effects

Recently, the control over the growth of HPHT diamonds has been exploited to investigate the effect of changing the lattice isotope on radiation damage centres. Natural carbon has an isotope content of 98.9% ^{12}C and 1.1% ^{13}C. ^{12}C has a nuclear spin $I = 0$, and so increasing the abundance of ^{13}C with $I = \frac{1}{2}$ allows paramagnetic centres to be more fully mapped out through the hyperfine splitting. We concentrate here on the optical data, and Table 3 lists new and existing data for features which are definitely or probably associated with vacancy and interstitial centres.

We will briefly review the mechanisms by which isotopic substitution changes the energies of zero-phonon lines (ZPLs). This discussion will allow us to establish the likely size of the effects, and so identify the very different behaviour of the self-interstitial.

Changing from ^{12}C to ^{13}C decreases the lattice volume. The change being $\Delta V/V = -4.5 \times 10^{-4}$ [44]. Compressing the lattice usually increases the zero-phonon energy. The detailed response varies between different ZPLs; for example, for the 1.945 eV line the change in energy is $\sim +0.9$ meV. A second effect is that the vibrational modes of the optical centre are likely to be different in the ground and excited electronic states, as a result of the change in the chemical bonding in the neighbourhood of the centre when the electronic transition occurs. The same physical origin results in a change in energy of the ZPL with increasing temperature T [45]. Usually the vibrational frequencies are lower in the excited electronic state, giving an increase in the energy of the ZPL with increasing vibrating mass. For example, for the 1.945 eV line we estimate the shift is by $\sim +1.0$ to 1.5 meV on moving from ^{12}C to ^{13}C. The two effects sum to a predicted shift of 1.9 to 2.4 meV, similar to observation (Table 3).

Local vibrational modes (LVMs) may have significantly different quanta in the ground and excited electronic states. For example, the '5RL' band has 3 LVMs with quanta $\hbar\omega_g$ 237, 193 and 175 meV in the ground electronic state, and $\hbar\omega_e$ of 202, 167 and (assumed) 151 meV in the excited state. Since, for non-degenerate orbital states, simple phonon sidebands are only seen in

Table 3
Isotope shifts for sharp optical lines in diamond on changing the ^{13}C content from 1.1 to 99%

Zero-phonon label	Energy in natural C (meV)	Shift (meV) relative to ^{12}C	Reference
Vacancy centres			
GR1 (V^0)	1673	2.9	[48]
GR2–8 (V^0)	2880–3005	+ 6.9 to 7.2	This work, [65]
ND1 (V^-)	3150	+ 4.0 ± 0.2	[65]
TH5 (V_2)	2543	+ 6.6 ± 0.5	This work
Nitrogen-vacancy centres			
H2	1257	+ 0.9 ± 0.1	[47]
H3	2463	+ 5.0 ± 0.2	[48]
N3	2985	+ 4.5 ± 0.2	[66]
"594 nm"	2086	+ 0.5 ± 0.3	This work
"575 nm" (N–V)	2156	+ 3.0	[48]
"640 nm" (N–V)	1945	+ 2.1	[48]
Interstitials			
H1b	612	0	[48]
1.40 eV Ni_i	1404	− 0.5	[48]
I	1685	+ 1.2 ± 0.2	This work
I	1859	− 5.2 ± 0.06	This work
3H	2463	+ 3.8 ± 0.06	This work
TR12	2638	+ 3.97 ± 0.06	This work
TR13	2672	+ 2.45 ± 0.06	This work
3.188 eV	3188	+ 3.3	[48]
5RL	4582	+ 8.0	[48]
Others			
M1	2400	+ 5.7 ± 0.2	This work
M2	2445	+ 4.2 ± 0.2	This work

Value quoted is from this work. Where other data exist they are referenced.

vibronic spectra for phonons which are totally symmetric in the point group of the centre, we would expect there to be other vibrational modes which are not being observed, but there are no supporting data yet from the observation of LVMs of the centre in the mid-infrared wavelengths. The contribution to the isotope shift of the ZPL is $[1-\sqrt{13/12}](\hbar\omega_e - \hbar\omega_g)$ and for the observed modes of the 5RL centre is $\sim +2$ meV.

An additional term, which is hard to estimate, comes from the anharmonicity of the vibrations of LVM and resonance modes. As a result of anharmonicity, the mean position of the vibrating system is not at the minimum point ($Q = 0$) of the potential. On increasing the vibrating mass, the system samples the space closer to $Q = 0$, and the change in equilibrium position is equivalent to a strain. Using anharmonicities which are typical of molecules and with $\hbar\omega = 40$ meV (as for vacancy centres), the effective strain is $\sim 4 \times 10^{-4}$. With a deformation potential of ~ 1 eV, this term produces a non-negligible shift of $\sim +0.4$ meV.

Finally, it is a working rule that for the vacancy-centres in diamond, significant dynamic Jahn–Teller coupling occurs in the electronic ground states (e.g. at V^0, the 575 and 594 nm centres) with weak or absent Jahn–Teller coupling at degenerate excited states (e.g. V^0, V^-, N3). For an e-mode (doubly degenerate), the zero-point energy is $\hbar\omega$ when there is no Jahn–Teller coupling, but is only $\frac{1}{2}\hbar\omega$ for large coupling [46]. For a transition between a JT-active ground state and a non-JT active excited state, the contribution to the zero-phonon energy is $+\frac{1}{2}\hbar\omega$, and the isotope shift from ^{12}C to ^{13}C would be $\frac{1}{2}\hbar\omega(\sqrt{12/13}-1)$. In contrast to the previous terms, this contribution is necessarily negative for the transition discussed here, and has a magnitude of 0.8 meV if $\hbar\omega = 40$ meV. It can therefore reduce the total shift, but is not expected to be dominant.

Our expectation is that the total shift will generally be about $+3$ meV, or larger with contributions from LVMs. These general arguments are supported by the results in Table 3. For some transitions the observed shift is zero or only slightly positive (H2, 594 nm, H1b) and in one case (1.40 eV) it is slightly negative, but these results are as expected from detailed analysis for these lines [47,48].

However, in one case, the 1.859 eV line, which correlates with the R2 self-interstitial (Section 6), the observed shift is large and negative, while the correlated 1.685 eV line has the expected size of shift (Table 3). This anomalous behaviour is rationalised by assuming that the 1.859 eV line is a phonon sideband of an electronic transition. Then we would expect the isotope shift to be $(\sqrt{12/13}-1)\ \hbar\omega$ relative to the ZPL of the transition, which is not known: the ZPL is not the 1.685 eV line for two reasons. First, the 1.685 eV line weakens with decreasing T, obeying a Boltzmann law with an activation energy of about 6 meV, while the 1.859 eV line grows in intensity as $T \to 0$, with an activation energy which has been measured here as close to 6 meV. Second, if the 1.859 eV line were a simple one-phonon replica of the 1.685 eV ZPL, the relative intensities $I(1859)/I(1685) \sim 10$ at 77 K [42] would give a Huang-Rhys factor S of that value, and hence a considerable two-phonon sideband ($S^2/2$ of the ZPL) would be expected. Such a two-phonon sideband is definitely not observed. These facts can be rationalised if the optical transition from the lowest energy state of the centre is forbidden, but its one-phonon sideband is induced by vibronic coupling to an allowed transition. Such a coupling does not induce a two-phonon sideband, in agreement with observation.

The importance of this discussion is that the oscillator strength of the 1.859 eV line may be significantly weaker than for a typical electronic transition, because its intensity depends on the details of the vibronic interaction. We see that there is no reason to doubt the very low f value of the 1.859 eV line (entry 8 in Table 2). This important parameter will be used in Section 8.

Before moving on we note that the GR2–8 lines all have the same (large) positive shift in Table 3. The similarity allows us to exclude the possibility that any of the GRn lines are phonon sidebands of other transitions, and it is consistent with their being effective-mass like excited states of an electron [49]. (The slight monotonic increase in the isotope shifts of transitions at the boron acceptor as the hole is progressively delocalised from the core [50], presumably reflecting the tightly bound nature of these 'Rydberg' states, is not be observed at the GRn lines.) The large magnitude of the shifts for GR2–8 emphasises that we know very little at present about V^+ which lies at the core of the effective-mass centre: the first possible identification of luminescence at the V^+ centre, with a ZPL at 1.95 eV, has very recently been reported, using heavily boron-doped diamond [51].

8. Rate of production of damage

The results reviewed in Sections 5–7 have shown how we can measure the concentrations of neutral and negative vacancies, and also of self-interstitials. The rate of producing damage can now be investigated quantitatively, in pure and in nitrogen-rich diamonds where the vacancies are likely to be predominantly in the neutral or negative charge states. We will not discuss p-type diamond, since no data have yet been obtained by monitoring the V^+ centres expected in that diamond.

Radiation studies of diamond have concentrated on using electrons of up to 2 MeV as the damaging agent, so that the damage occurs at predominantly isolated sites until very large doses are reached: in pure diamond, the observed rate of production of vacancies (GR1 absorption) is approximately linear in the dose for 1.9 MeV electrons up to $\sim 6 \times 10^{19}\,cm^{-2}$ [52]. However, the damage that is observed is that which is stable when the

measurement is made. It is necessary for the vacancy (V) and the self-interstitial (I) to separate from each other. If we assume that the I halves its kinetic energy each time it collides with lattice atoms, its energy will typically be reduced below its migration barrier of 1.6 eV (Section 6) after only about 4 collisions, and correlated recombination has to be considered. We may expect that the recombination will be influenced by nitrogen in the local environment, which may change the charge states of the V and I, and will also create local strains. Evidence for the influence of nitrogen on the rate of producing observable damage comes from annealing studies in diamonds with N-pairs (A-centres), in which the widths of the GR1 (V^0) and ND1 (V^-) zero-phonon lines sharpen during the first stages of annealing, as 40% of the vacancies are rapidly captured by the A-centres [36]. Estimates from the line widths suggest that these perturbed V's were within 0.7 nm of the nitrogen [36]. Apparently, within this small radius of the N aggregates, which contains 3% of the volume of the diamond, some 40% of the stable vacancies are produced. A significant change in bond-strength in this volume does not seem likely (e.g. by the small size of the perturbations of the V's), and so it is probable that the correlated recombination is being reduced near the A centres. Further evidence for this enhanced production rate is suggested in Section 9.

Recently, two direct measurements of the production rates of vacancies have been made, using the calibrations of Table 2. In pure diamond, the production of vacancies was $1.53 \pm 0.1\,cm^{-1}$ with 2 MeV electrons [42], and in diamond with 9 ± 1 ppm of isolated substitutional nitrogen the rate of creation of vacancies (V^0 and V^-) was only $0.50 \pm 0.05\ cm^{-1}$ for the slightly lower electron energy of 1.9 MeV [35]; it would appear that isolated N atoms reduce the creation rate in contrast to the apparent enhanced production near A centres.

The effect of temperature on the production of observable vacancies is not important at temperatures below 500 K [52,53]. In contrast, the rate of production of self-interstitials, as measured by the R2 epr and the 1.859 eV optical band is reported to decrease with increasing T [53]. In the limit of low T the production rate of I approaches that of V [53]; the implication is that with increasing bulk temperature of the sample the mobility of I increases during the irradiation. The fate of the mobile Is during the irradiation is not known: there is no increase in the (small) production of 'R1' (di-split-interstitials) and 'O3' (tri-split-interstitial) centres at higher T [53].

9. Capture of mobile V and I

In pure diamond, ~ 30% of the V^0's are annihilated when the I's become mobile (e.g. [36,38]) as a result of recombination of V^0 and I. The remainder of the I's escape, and simultaneously the '3H' (ZPL at 2.463 eV) and the '5RL' (ZPL 4.581 eV) centres appear: both have rhombic I symmetry [54,55], and are candidates for some form of self-interstitial complex. It should be possible to detect the LVMs of the centres by mid-infra-red absorption spectroscopy; possibly the $1531\,cm^{-1}$ LVM occurs at I, and the $1570\ cm^{-1}$ LVM at an early aggregate [56]. Paramagnetic resonance measurements have identified the R1 epr centre as a pair of split-interstitials [53] and the O3 centre as possibly three split-interstitials [57]. The picture for the early stages of aggregation of the self-interstitials is not yet clear, and this is a significant problem since the aggregates may be the nuclei of the 'platelets', essentially two-dimensional precipitates which are produced in natural diamond by the aggregation of A centres, $A + A \rightarrow B + I$ (Section 2) [58].

In diamond rich in A-centres, annealing at 300°C produces the H1a centre [59], observed by its LVM at $1450.3\ cm^{-1}$ but, surprisingly, not detected in epr [60]. Isotope data are consistent with the centre being one N atom in a bond-centred configuration, but displaced from the *C–C* axis [60]. One striking aspect of the production of the H1a centre is that for a given electron-irradiation dose and a given annealing, the H1a strength increases linearly with the local concentration of nitrogen A centres [60]. The effect could be caused by an increase in production of stable damage near the nitrogen (Section 8).

Mobile vacancies (V) are readily captured by all forms of nitrogen, limiting the diffusion lengths of the V's. Quantitatively, annealing studies [36] show that the capture time in diamonds with 100 ppm A-centres is, within the margin of uncertainty, as expected for a random walk by the V's, so that capture occurs after $\sim 10^4$ to 10^5 jumps. There is no evidence for a significant energy barrier before the final capture of V at the nitrogen, as predicted [61], although experiments to test this have not been carried out. The distance within which V is captured by a nitrogen centre (the 'capture radius') is not known for any of the aggregates, but relative radii can be established easily. In a sample with two forms of N, the probability of capture at one aggregate is proportional to the concentration of the aggregate and the capture radius. Knowing the relative oscillator strengths (Tables 1 and 2) we can now calculate the ratio of the capture radii of V at A and B aggregates (at the anneal temperature of 800°C) using old data [62]: $R(V,A)/R(V,B) = 1.7$. Counter-intuitively, the capture radius of the smaller A-aggregate is larger than that of the B-aggregate. For the single N atom, the capture radius is estimated at ~ 20 times larger than for V at the A-centre [25]. Further investigation of these radii is important given the importance of damage centres created by radiation [25] or by transition metals (Section 4) in enhancing the mobility of nitrogen.

In the absence of other traps two V's will aggregate to form a divacancy. The divacancy has long been reported to give the 'TH5' optical band [63], Table 3, and very recently has been identified with the R4/W6 epr centre [64]. Larger aggregates are not yet identified.

10. Summary

The ability to synthesise diamond with control over its isotope and, increasingly, impurity content are allowing quantitative arguments to be developed in the area of defect engineering in diamond. The immediate impact of these arguments is that they reveal how little we still know about many key issues. This paper has attempted to point out some of the targets which need to be addressed next.

Note added in proof

In Section 4 it was noted that the electron mobility with shallow n-type dopants is currently low. Sakaguchi et al. [67] have reported a shallow donor with an ionisation energy of 0.38 eV following doping with sulphur; the samples had the significantly better electron mobility at room temperature of 597 $cm^2 V^{-1} s^{-1}$.

Acknowledgements

I am grateful to Alison Mainwood, Alan Collins, Michael Baker, Jonathan Goss, VA Nadolinny, Armando Neves and John Steeds for discussions, to Daniel Twitchen for the loan of samples, and to Hannah Smith for experimental assistance.

References

[1] I. Kiflawi, A.E. Mayer, P.M. Spear, J.A. van Wyk, G.S. Woods, Philos. Mag. B 69 (1994) 1141.
[2] G.S. Woods, J.A. van Wyk, A.T. Collins, Philos. Mag. B 62 (1990) 589.
[3] S.C. Lawson, D. Fisher, D.C. Hunt, M.E. Newton, J. Phys.: Condens. Matter 10 (1998) 6171.
[4] S.R. Boyd, I. Kiflawi, G.S. Woods, Philos. Mag. B 69 (1994) 1149.
[5] G.S. Woods, G.C. Purser, A.S.S. Mtimkulu, A.T. Collins, J. Phys. Chem. Solids 51 (1990) 1191.
[6] A.T. Collins, J. Phys. C 13 (1980) 2641.
[7] S.R. Boyd, I. Kiflawi, G.S. Woods, Philos. Mag. B 72 (1995) 351.
[8] A.T. Collins, Israel J. Chem. 38 (1998) 121.
[9] H. Sternschulte, K. Thonke, R. Sauer, S. Koizumi, Phys. Rev. B 59 (1999) 12924.
[10] M. Nesládek, K. Meykens, K. Haenen, L.M. Stals, T. Teraji, S. Koizumi, Phys. Rev. B 59 (1999) 14852.
[11] C.J. Noble, Th. Pawlik, J.-M. Spaeth, J. Phys.: Condens. Matter 10 (1998) 11781.
[12] J. Isoya, H. Kanda, Y. Uchida, Phys. Rev. B 42 (1990) 9843.
[13] M.H. Nazaré, A.J. Neves, G. Davies, Phys. Rev. B 43 (1991) 14196.
[14] P.W. Mason, F.S. Ham, G.D. Watkins, Phys. Rev. B 60 (1999) 5417.
[15] S.C. Lawson, H. Kanda, M. Sekita, Philos. Mag. B 68 (1993) 39.
[16] J. Isoya, H. Kanda, J.R. Norris, J. Tang, M.K. Bowman, Phys. Rev. B 41 (1990) 3905.
[17] A.T. Collins, K. Kanda, J. Isoya, C.A.J. Ammerlaan, J.A. van Wyk, Diamond Related Mater. 7 (1998) 333.
[18] E. Pereira, L. Santos, L. Pereira, Mater. Sci. Forum 143–147 (1994) 57.
[19] E. Pereira, in: Tabulation of luminescence decay times in diamond, in: G. Davies (Ed.), The Properties and Growth of Diamond, Inst. of Electrical Engineers, London, 1994, pp. 228–232.
[20] S.C. Lawson, H. Kanda, K. Watanabe, I. Kiflawi, Y. Sato, A.T. Collins, J. Appl. Phys. 79 (1996) 4348.
[21] M.H. Nazaré, L.M. Rino, H. Kanda, Mater. Sci. Eng. A 209 (1996) 302.
[22] V.A. Nadolinny, A.P. Yelisseyev, O.P. Yuryeva, B.N. Fergelson, Appl. Magn. Reson. 12 (1997) 543.
[23] V.A. Nadolinny, A.P. Yelisseyev, private communication, 1999.
[24] I. Kiflawi, H. Kanda, A. Mainwood, Diamond Related Mater. 7 (1998) 327.
[25] A.T. Collins, J. Phys. C 13 (1980) 2641.
[26] M.H. Nazaré, A. Neves, private communication, 1999.
[27] S.C. Lawson, H. Kanda, J. Appl. Phys. 73 (1993) 3967.
[28] D. Fisher, S.C. Lawson, Diamond Related Mater. 7 (1998) 299.
[29] K. Johnston, A. Mainwood, A.T. Collins, G. Davies, D. Twitchen, J.M. Baker, M. Newton, Physica B (1999), these proceedings.
[30] D.J. Twitchen, J.M. Baker, M.E. Newton, K. Johnston, private communication, 1999.
[31] J.A. van Wyk, J.H.N. Loubser, J. Phys. C.: Solid State 5 (1993) 3019.
[32] G. Davies, D. Fisher, D.J. Twitchen (1996) unpublished.
[33] G. Davies, Nature 269 (1977) 498.
[34] J. Isoya, H. Kanda, Y. Uchida, S.C. Lawson, S. Yamasaki, H. Itoh, Y. Morita, Phys. Rev. B 45 (1992) 1436.
[35] D.J. Twitchen, D.C. Hunt, V. Smart, M.E. Newton, J.M. Baker, Diamond Related Mater. 8 (1999) 1572.
[36] G. Davies, S.C. Lawson, A.T. Collins, A. Mainwood, S.J. Sharp, Phys. Rev. B 46 (1992) 13157.
[37] M.F. Thomaz, G. Davies, Proc. Roy. Soc. A 362 (1978) 405.
[38] D.C. Hunt, D.J. Twitchen, M.E. Newton, J.M. Baker, T.R. Anthony, W.F. Banzoler, S.S. Vagarali, Phys. Rev. B (1999) in press.
[39] A. Mainwood, F.P. Larkins, A.M. Stoneham, Solid State Electron. 21 (1978) 1431.
[40] S.J. Breuer, P.R. Briddon, Phys. Rev. B 51 (1995) 6985.
[41] J. Walker, Rep. Prog. Phys. 42 (1979) 1605.
[42] D.J. Twitchen, D.C. Hunt, M.E. Newton, J.M. Baker, T.R. Anthony, W.F. Banzoler, Phys. Rev. B (1999) in press.
[43] L. Allers, A.T. Collins, J. Hiscock, Diamond Related Mater. 7 (1998) 228.

[44] H. Holloway, K.L. Hass, M.A. Timor, T.R. Anthony, W.F. Banholzer, Phys. Rev. B 45 (1992) 6353.
[45] A.E. Hughes, Proc. Phys. Soc. 88 (1966) 449.
[46] H.C. Longuet-Higgins, U. Öpik, M.H.L. Pryce, R.A. Sack, Proc. R. Soc. A 224 (1958) 1.
[47] S.C. Lawson, G. Davies, A.T. Collins, A. Mainwood, J. Phys.: Condens. Matter 4 (1992) 3439.
[48] A.T. Collins, G. Davies, H. Kanda, G.S. Woods, J. Phys. C 21 (1988) 1363.
[49] A. Mainwood, A.M. Stoneham, J. Phys.: Condens. Matter 9 (1997) 2453.
[50] H.J. Kim, R. Vogelgesang, A.K. Ramdas, S. Rodriguez, M. Grimsditch, T.R. Anthony, Phys. Rev. B 57 (1998) 15315.
[51] J.W. Steeds, private communication, 1999.
[52] E.A. Burgemeister, C.A.J. Ammerlaan, G. Davies, J. Phys. C 13 (1980) L691.
[53] D.J. Twitchen, M.E. Newton, J.M. Baker, O.D. Tucker, T.R. Anthony, W.F. Banholzer, Phys. Rev. B 54 (1996) 6988.
[54] J. Walker, Inst. Phys. Conf. Ser. 23 (1975) 317.
[55] A.T. Collins, P.M. Spear, J. Phys. C 19 (1986) 6845.
[56] A.T. Collins, in: R. Messier, J.T. Glass, J.E. Butler, R. Roy (Eds.), New Diamond Science and Technology, Material Research Society, Pittsburgh, PA, 1991, pp. 659–670.
[57] J.M. Baker, private communication, 1999.
[58] G.S. Woods, Proc. Roy. Soc. London A 407 (1986) 219.
[59] G.S. Woods, Philos. Mag. B 50 (1984) 673.
[60] I. Kiflawi, A. Mainwood, H. Kanda, D. Fisher, Phys. Rev. B 54 (1996) 16719.
[61] A. Mainwood, Phys. Rev. B 49 (1994) 7934.
[62] G. Davies, J. Phys. C 5 (1972) 2534.
[63] C.D. Clark, R.W. Ditchburn, H.B. Dyer, Proc. Roy. Soc. A 237 (1956) 75.
[64] D.J. Twitchen, M.E. Newton, J.M. Baker, T.R. Anthony, W.F. Banholzer, Phys. Rev. B 59 (1999) 12900.
[65] S.C. Lawson, Ph.D. Thesis, University of London, 1992.
[66] G. Davies, I. Kiflawi, G. Sittas, H. Kanda, J. Phys.: Condens. Mater. 9 (1997) 3871.
[67] I. Sakaguchi, M.N. Gamo, Y. Kikuchi, E. Yasu, H. Haneda, T. Suzuki, T. Ando, Phys. Rev. B 60 (1999) R2139.

ELSEVIER

Physica B 273–274 (1999) 24–32

PHYSICA B

www.elsevier.com/locate/physb

The role of threading dislocations in the physical properties of GaN and its alloys

J.S. Speck[a,*], S.J. Rosner[b]

[a]*Materials Department, University of California, Santa Barbara, CA 93106, USA*
[b]*Hewlett-Packard Laboratories, 3500 Deer Creek Rd., Palo Alto, CA 94303, USA*

Abstract

In this paper, we review progress on understanding the role of threading dislocations (TDs) in the physical properties of GaN and its alloys. A growing body of work provides compelling evidence that TDs in the group-III nitrides behave as non-radiative recombination centers, have energy levels in the otherwise forbidden energy gap, act as charged scattering centers in doped materials, and provide a leakage current pathway. In comparison with conventional III–V semiconductors, the relatively small minority carrier diffusion length L_d ($\sim$ 50 nm) in the III-nitrides, combined with favorable TD geometries, minimize dislocation-related degradation. The small value of L_d also allows for appreciable optical emission in materials with TD densities as high as 10^{10} cm^{-2}.

Keywords: Gallium nitride; Extended defects; Threading dislocations; Non-radiative recombination; Deep levels; Traps; Carrier scattering; Leakage

1. Introduction

The 1990s have been a time of remarkable progress in wide band-gap semiconductors, particularly in the group III-nitride system. The 'nitride revolution' was motivated by the early pioneering work of Pankove [1]. The two singular achievements which have enabled current nitride technology were the development of two-step growth by Akasaki and co-workers at Nagoya University which lead to high structural quality GaN films on sapphire substrates [2,3], and the subsequent developments of an efficient route to p-type doping by Nakamura and co-workers at the Nichia Chemical company [4]. These two results were followed by the development by Nakamura of InGaN quantum well structures and the demonstration of bright nitride-based blue LEDs [5]. The realization and early commercialization of Nichia LEDs catalyzed most of the recent work on nitride semiconductors.

Currently, there are still no widely available lattice-matched substrates for the growth of wurzitic GaN. As a result, most materials today still have high threading dislocation (TD) densities. Transmission electron microscopy (TEM) studies on early Nichia LEDs showed that the material had TD densities in excess of 10^{10} cm^{-2} passing through the active region, which is approximately four to six orders of magnitude higher than TD densities in conventional III–V optoelectronic devices [6]. The remarkably high TD densities in the III-nitrides lead to speculation that TDs were benign in the nitrides or perhaps even beneficial for the optoelectronic properties. However, there is a continually increasing body of work that shows TDs are indeed deleterious for the physical properties of the nitrides.

In this paper, we review the key work elucidating the role of extended defects in the physical properties of the nitrides. We begin by briefly reviewing current state-of-the-art microstructures for GaN on sapphire and SiC substrates, followed by a brief discussion of the role of TDs in the morphology of growing nitride surface, and then we review key papers which focus on the physical properties of TDs in the nitrides. We concentrate on III-nitride films grown by metal-organic chemical vapor

* Corresponding author. Tel.: + 1-805-893-8005; fax: + 1-805-893-8983.
E-mail address: speck@mrl.ucsb.edu (J.S. Speck)

0921-4526/99/$ - see front matter
PII: S0921-4526(99)00399-3

deposition (MOCVD) either on (0 0 0 1) sapphire or SiC substrates.

2. Background on extended defects in the nitrides

During the past ~5 yr there has been extensive work on understanding the extended defect structure in the nitrides. The commonly observed extended defects in (0 0 0 1) oriented GaN grown on sapphire substrates include (0 0 0 1) stacking faults and stacking disorder and related Shockley and Frank partial dislocations, inversion domains, and TDs [7]. In high-quality MOCVD-grown GaN films, the stacking disorder and partial dislocations usually only occur in the region in immediate adjacency to the substrate and are associated with the growth of a disordered low-temperature nucleation layer (NL) [8]. Inversion domains are normally associated with nitrogen polar domains that have grown either through to the free surface of an otherwise Ga-polar film (which is the usual polarity for high quality MOCVD films) or are overgrown by Ga-polar material. The TDs have typical total densities in the range 10^8–10^{10} cm^{-2}. There are two different predominantly observed TDs: pure edge, with Burgers vectors in the family $\frac{1}{3}\langle\bar{2}\,1\,1\,0\rangle$ and [0 0 0 1] line directions; and mixed character, with Burgers vectors in the family $\frac{1}{3}\langle\bar{2}\,1\,1\,3\rangle$ and line directions inclined ~10° from [0 0 0 1] towards the Burgers vector. Pure screw TDs (b = [0 0 0 1] and line direction [0 0 0 1]) represent a small fraction (~0.1–1%) of the total density of TDs [7].

In previous work, we have shown that for MOCVD growth of GaN on sapphire, the TDs form as a consequence of the coalescence of slightly misoriented GaN high-temperature islands (this work is reviewed in detail in Ref. [9]). Fig. 1 shows a representative cross-section TEM micrograph of a 5 μm thick MOCVD film grown on sapphire grown at UCSB. Note that TDs are the only extended defect that grow through to the free surface of the film. The microstructure of GaN grown on a more closely lattice matched substrate, namely SiC, shows very similar characteristics. However, it should be noted that the dislocation formation mechanisms are not fully understood for GaN growth on SiC. Thus, TDs are the most important extended defect to study in the context of understanding the physical properties of GaN thin films grown on Al_2O_3 substrates.

3. The role of threading dislocations in growth

Before reviewing the effects of TDs on the physical properties, we briefly review the important role of TDs in the growth of nitrides, namely the formation of 'V-defects' [10]. Many nitride-based device heterostructures require reduced growth temperature. For example, InGaN layers are typically grown at ~750–800°C in MOCVD, which is ~300°C lower than optimal MOCVD growth conditions for GaN — the lower temperature is necessary because of the high volatility of indium. Similarly, the growth temperature for AlGaN is generally limited by reactor or heater considerations. The low growth temperatures facilitate the formation of 'V-defects' which consist of six $\{1\,0\,\bar{1}\,1\}$ family planes and form an inverted hexagonal pyramid, as shown schematically in Fig. 2. The V-defects always form at TDs, with a higher propensity for formation at mixed character TDs, but they also form at pure edge TDs.

Wu et al. attributed the formation of V-defects to a kinetically limited growth process in which the surface depression associated with a TD (as predicted by Frank [11]) assists in the formation of $\{1\,0\,\bar{1}\,1\}$ facets [10]. Under kinetically limited growth conditions, the surface morphology will be dominated by the slowest growing planes, and thus in this scenario the $\{1\,0\,\bar{1}\,1\}$ planes have a slower growth rate in the [0 0 0 1] direction. Subsequent high-temperature growth of GaN will cause the

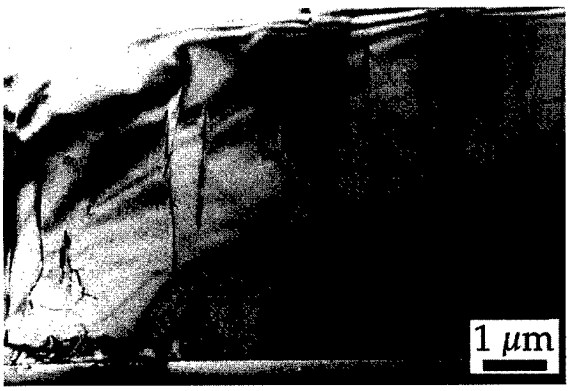

Fig. 1. Representative microstructure of a 5 μm thick MOCVD-grown GaN film on a sapphire substrate.

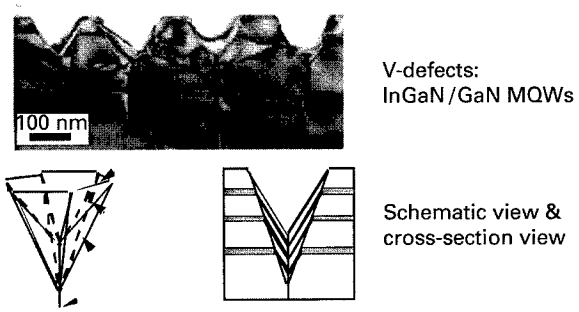

Fig. 2. Cross-section view of 'V-defects' in InGaN/GaN multiple quantum well structures (see Ref. [10] for further details) and schematic structure of the V-defect.

V-defects to be filled and there will be no surface morphological evidence for their presence. More recently, Northrup et al. have performed first-principle calculations of the energies of the (0 0 0 1) and the {1 0 1 1} planes for GaN and InGaN. Northrup has shown that V-defects at energically favorable for InGaN growth and their formation is driven by a balance of surface energy increase (due to the increased total surface area of the six $\{1\,0\,\bar{1}\,1\}$ planes of the V-defect relative to the area of the (0 0 0 1) plane) and strain energy reduction due to the open defect volume which would otherwise have a TD [12].

V-defects are deleterious for the growth of both optoelectronic and electronic device heterostructures. For InGaN/GaN quantum well structures, the V-defects cause the wells to be non-planar and may also lead to changes in the indium composition through a series of wells. As will be discussed later, V-defects are important sources of reverse leakage in diodes, and have been correlated to the very poor electro-static discharge (ESD) in these structures. For laser structures, the V-defects will be light scattering centers. Nitride-based high electron mobility transistor (HEMT) structures consist of AlGaN/GaN layers. It is quite common for V-defects to form during the growth of the AlGaN cap layer. In the case of HEMT structures, there is no further nitride growth after the AlGaN layer and thus the V-defects can concentrate electric fields both at ohmic source/drain contacts and more importantly at the Schottky gate contact.

4. Key work on the role of threading dislocations in the physical properties of the group III nitrides

Table 1 provides a summary of the key studies that have focused on the role of TDs in the physical properties

Table 1
List of key references on the physical properties of threading dislocations in GaN and its alloys

Topic	Reference
Modification of minority carrier concentrations	
Cathodoluminescence Studies:	
S.J. Rosner et al., Appl. Phys. Lett. 70 (1997) 420.	[13]
T. Sugahara et al., Jpn. J. Appl. Phys. (1998) L398.	[15]
S.J. Rosner et al., Appl. Phys. Lett. 74 (1999) 2035.	[16]
Photo-electro-chemical etching (PEC):	
C. Youtsey, L.T. Romano, I. Adesida, Appl. Phys. Lett. 73 (1998) 797.	[19]
C. Youtsey et al., Appl. Phys. Lett. 74 (1999) 3537.	[20]
Traps/deep levels	
Electronic structure calculations:	
'No states in the gap'	
J. Elsner et al., Phys. Rev. Lett. 79 (1997) 3672.	[22]
J. Elsner et al., Phys. Rev. B. 58 (1998) 12571.	[23]
'States in the gap'	
A.F. Wright, Ulrike Grossner, Appl. Phys. Lett. 73 (1998) 2751.	[25]
K. Leung, A.F. Wright, E.B. Stechel, Appl. Phys. Lett. 74 (1999) 2495.	[26]
Transport studies and transport modeling:	
Nils G. Weimann et al., J. Appl. Phys. 83 (1998) 3656.	[30]
H.M. Ng et al., Appl. Phys. Lett. 73 (1998) 821.	[31]
D.C. Look and J.R. Sizelove, Phys. Rev. Lett. 82 (1999) 1237.	[32]
Scanning capacitance microscopy:	
P.J. Hansen et al., Appl. Phys. Lett. 72 (1998) 2247.	[35]
Leakage Paths	
Ballistic electron emission microscopy (BEEM):	
E.G. Brazel et al., Appl. Phys. Lett. 74 (1999) 2367.	[36]
Reverse bias diodes on LEO versus normal GaN:	
P. Kozodoy et al., Appl. Phys. Lett. 73 (1998) 975.	[37]
G. Parish et al., Appl. Phys. Lett. 75 (1999) 247.	[38]
Shuji Nakamura, MRS Bulletin, May 1998, 37.	[39]
Degradation	
Long life laser diodes on LEO GaN:	
Shuji Nakamura, MRS Bulletin, May 1998, 37.	[39]

of the group III-nitrides. In this section, we summarize this work.

4.1. Non-radiative recombination centers

4.1.1. Cathodoluminescence (CL) studies

In 1997 Rosner et al. reported on a CL study on MOCVD grown n-type GaN on sapphire substrates [13]. This study involved correlated atomic force microscopy (AFM) and CL studies, in which the investigators used a combination of fiducial marks on their samples and a registered specimen stage to ensure imaging of exactly the same region by both techniques. It had been demonstrated in other studies that TDs affect the surface morphology of GaN, namely that mixed character TDs and sometimes edge TDs give rise to surface depressions (again, as predicted by Frank and recently discussed by Heying et al. [14]). Rosner et al. found that the 'pit' features in the AFM images were strongly correlated with dark regions in the CL images. Rosner et al. were able to generate maps of the pit locations, corresponding to the intersection of the TDs with the film-free surface, and then calculate CL images based on known solutions for the minority carrier concentration from a dislocation, which was assumed to be a line of non-radiative (NR) recombination centers. In this study the fits were done visually and it was found that the best agreement between the calculated and observed CL images was realized for a minority carrier diffusion length of 250 nm. An example of a calculated and observed image from this work is shown in Fig. 3. This study used bulk GaN samples and 10 keV primary electrons which broaden into a bulb-like volume with a radius of ~ 250 nm, which then provides an upper bound on the diffusion length.

The concepts developed by Rosner et al. were further advanced in a coupled plan-view TEM and CL study reported by Sugahara et al. on n-type MOCVD-grown GaN [15]. In this study, CL images were recorded on TEM foils prior to TEM investigation (apparently, there is sufficient radiation damage to the samples such that no CL was observable if the TEM studies were performed on the foils before CL studies). The authors found a one-to-one correspondence between the position of dark spots in the CL images and TDs in the plan-view TEM. The authors estimated a hole diffusion length of 50 nm based on the width of the dark regions in the CL maps. The lower minority diffusion length in these studies, in comparison with those reported by Rosner et al., is primarily due to the minimal probe broadening in a thin TEM foil.

In a more recent study, Rosner et al. used CL mapping to study the dislocation structure in GaN grown by lateral epitaxial overgrowth (LEO) [16]. Full details of the LEO process can be found elsewhere [17], but in summary, this technique involves first growing a GaN layer, then masking this layer with SiO_2 or a similar material while leaving openings into which the GaN can be grown, and subsequently regrowing material through the window opening and then laterally over the mask. When the orientation of window openings and growth conditions are optimized, it is possible to grow material with a TD density of $\sim 10^4$–$10^6\,cm^{-2}$ in the window region. Rosner et al. demonstrated the possibility of imaging individual TDs which propagate laterally into the overgrown region. This work included studies of InGaN single quantum wells which were grown on LEO stripes. It was found that there was a correspondence between dark regions, associated with vertically propagating TDs, in the GaN luminescence at 365 nm and the $In_{0.15}Ga_{0.85}N$ at 421 nm, as shown in Fig. 4, thus demonstrating that TDs also behave as NR centers in InGaN. The image widths for the dark regions was

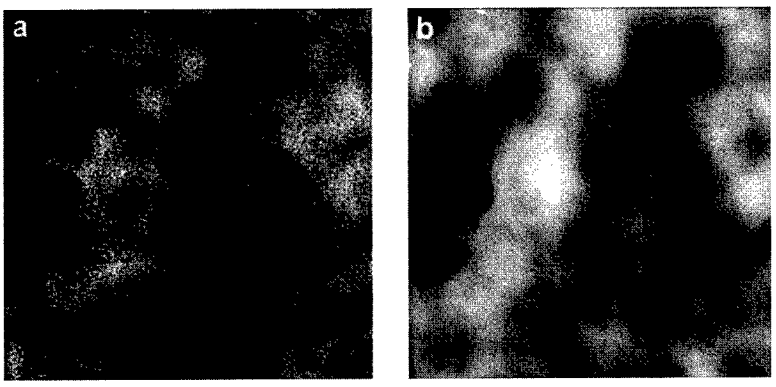

Fig. 3. Experimental and calculated CL images from n-type GaN: (a) 365 nm CL map showing dark regions (the image size corresponds to 2.5 μm × 2.5 μm); (b) Calculated CL map from the same region, based on TD positions from registered AFM studies. The map is calculated by convoluting the TD positions with a simple exponential model of NR recombination at the TDs (see Ref. [13] for further details).

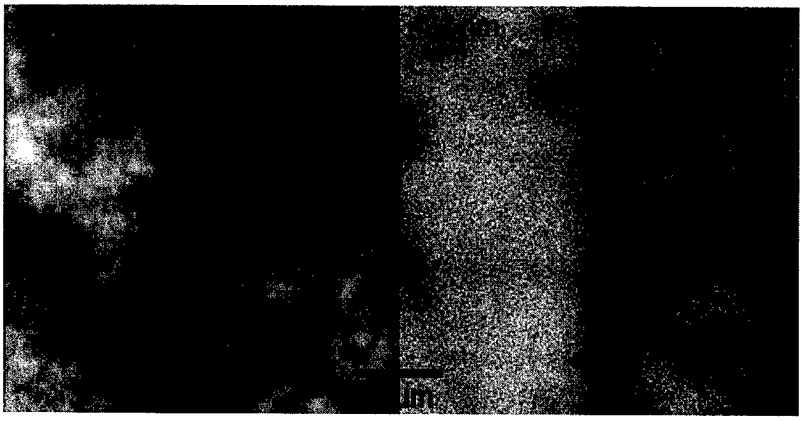

Fig. 4. CL images from a $In_{0.15}Ga_{0.85}N$ single quantum well structure grown on LEO GaN. The LEO wing is on the left-hand side of each image and the LEO window opening is on the right-hand side of the image. Left panel: GaN-related 365 nm map; right panel: $In_{0.15}Ga_{0.85}N$ 421 nm map. For further details, see Ref. [16].

comparable for the GaN and InGaN luminescence and an upper bound of 200 nm was determined for the minority carrier diffusion length for both GaN and InGaN. In the overgrown regions, where there were few, if any TDs propagating to the growth surface for this sample set, the InGaN luminescence was homogeneous, demonstrating that any heterogeneity in the InGaN was limited to a length smaller than 200 nm.

A simple model was used by one of the authors to understand the apparent contradiction of radiative devices (e.g., LEDs) with high internal quantum efficiency, coincident with high concentrations of NR recombination centers at dislocations. In this model, the dislocations are modeled as a line parallel to the film surface normal (taking advantage of the orientation habit of TDs in this material) with infinite recombination velocity. This effectively pins the excess minority carrier concentration to zero. Using a single parameter for diffusion length allows calculation of the minority carrier concentration gradient about a single dislocation. Using an array of such dislocations, the average excess minority carrier concentration can be calculated under conditions of constant carrier generation. This carrier population should be exactly proportional to light production in a diode active region. Fig. 5 shows the results of such a calculation for a range of minority carrier diffusion lengths L_d. For L_d near 50 nm, it is clear that high-efficiency devices can be obtained for dislocation densities below $10^{10}\,cm^{-2}$.

It is additionally important to note that in conventional III–V technology, devices can be fabricated with dislocations (dark line defects) present and still achieve reasonable quantum efficiencies. However, since diffusion lengths are typically greater than 1 μm and defects often have glide habits (in the case of strained layer cubic materials) that put the line parallel to the surface of the

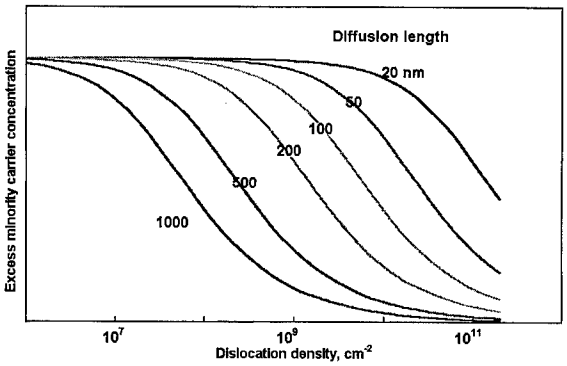

Fig. 5. Light removal due to threading dislocations for a range of minority carrier diffusion lengths. The luminescence intensity is proportional to the excess minority carrier concentration.

film, the tolerable density is several orders of magnitude lower than in the group III-nitride technology. More importantly, in the conventional III–V systems, these defects move and multiply under a combination of applied stress and current injection, and this process causes rapid degradation of the devices. This often requires extremely small numbers of defects to be present initially to guarantee reasonable lifetimes for the devices. In (0 0 0 1) oriented wurtzitic group III-nitride films, the TDs experience no shear stress because they lie on vertical planes, so dislocation multiplication and motion is not a contributor to device degradation. It appears that the differences between conventional III–V and III-nitride technologies do not require new physics as suggested by early reports, but rather can be accounted for by these two properties, the very short diffusion lengths and the relative immobility of the defect structures.

4.1.2. Photoelectrochemical (PEC) etching studies

Photoelectrochemical wet etching is a technique in which a semiconductor is illuminated with above gap radiation to generate minority carriers at the semiconductor surface [18]. The photogenerated minority carriers facilitate the etching by weakening near-surface bonds and allowing surface atoms to dissolve into the electrolyte. In two important papers, Youtsey et al. described PEC etching studies of n-type GaN films (prepared either by MOCVD or by hydride vapor phase epitaxy) [19,20]. They found under certain conditions, GaN 'whiskers' formed with a density on the order of 10^9 cm^{-2}. The whiskers had diameters between 10 and 50 nm and lengths up to 1 μm. Subsequent TEM studies on the whiskers showed that each whisker contained a TD. The authors speculated that the TDs could either behave as NR centers, thus inhibiting minority carriers (holes) from reaching the sample surface near TDs, or behave as charged lines which repel minority carriers.

4.2. Traps/deep levels

The work described above, which has provided a strong basis that TDs do behave as NR centers in GaN, implies that the TDs have deep acceptor levels for n-type material and presumably donor levels for p-type material (indeed CL images on p-type material also show dark regions associated with TDs [21]). We now address the studies which have provided further insight on whether there are indeed deep levels associated with the nitrides.

4.2.1. Electronic structure calculations

Currently, there are two different views that have resulted from electronic structure calculations of TDs and GaN. Elsner et al. presented the first electronic structure calculations for pure screw and for pure edge TDs in GaN [22]. These studies used both ab initio local-density functional (LDF) methods and density functional tight binding methods. For closed core pure screw TDs, the authors found deep states with energies 0.9 to 1.6 eV above the valence band maximum and states 0.2 eV below the conduction band minimum. The authors then addressed open core screw TDs, in which the inner most 1–2 unit cells of material were removed. This core structure was found to yield only shallow states which were related to the high local shear strains from the dislocation displacement field. Calculations of the energies of pure edge TDs showed no deep levels and the energetically favorable structure had a closed core. In a subsequent paper, Elsner et al. considered oxygen impurities, gallium vacancies, and clusters of these two species in the vicinity of edge TDs in GaN [23]. It was found that gallium vacancy–oxygen complexes are favorably trapped at the dislocation core and that these complexes do give rise to deep acceptor levels. The authors concluded that these acceptor levels may be responsible for yellow luminescence in the nitrides.

In a separate set of papers, Wright and co-workers calculated the formation energies and energy levels for pure edge TDs in AlN and GaN using density functional theory [24,25]. For both AlN and GaN, Wright et al. considered full core, open core, group III-vacancy core, and N-vacancy core structures. All calculations were performed for Fermi levels ranging from the valence band maximum to the conduction band minimum for both nitrogen-rich and gallium-rich growth conditions. For both AlN and GaN, the edge dislocation was found to have levels in the forbidden energy gap for all core structures that were studied. Subsequently, Leung et al. calculated the formation energies for the four different core structures as a function of donor (assuming Si dopants) and acceptor (assuming Mg dopants) concentrations for both gallium-rich and nitrogen-rich growth conditions [26]. The TDs had both acceptor and donor energy levels. In this work, Coulomb interactions were explicitly considered, namely, charge could transfer between dopants and TDs. The line charges per site were then calculated for TD densities of 10^8, 10^9, and 10^{10} cm^{-2} as a function of dopant concentration for both n- and p-type material for the two most favorable core structures. The transition from uncharged to fully charged TDs occurred at a dopant density corresponding to the bulk density of dislocation-related sites (assuming one site per unit cell), e.g., a TD density of 10^9 cm^{-2} corresponds to 2×10^{16} cm^{-3} TD-related defect sites — this is the approximate transition from uncharged to charged dislocations shown in Leung et al.'s work for 10^9 cm^{-2} TD density material. Leung et al. noted that for low n-type dopant densities, the number of defect sites will be much larger than the number of donors, and thus all carriers are transferred to dislocation-defect levels. In this case, the Fermi energy will be pinned near the defect level and there will be no free carriers — this is consistent with semi-insulating behavior in high-TD density GaN. At large donor densities, the TDs are fully charged, but there are excess free carriers which cause the Fermi level to rise toward the donor level.

4.2.2. Transport studies and transport modeling

The concept of carrier scattering by charged dislocation lines can be found in textbooks on semiconductor physics [27]. Weimann et al. used the formalism first developed by Bonch–Bruevich and Kogan [28] and later by Pödör [29] to obtain a transverse carrier mobility [30]. In this work, Weimann first calculated the trap occupation, apparently by assuming a dislocation trap level 2.2 eV below the conduction band minimum. Then the scattering amplitude was calculated for the charged line which was then used to determine the transverse mobility. The overall transverse mobility was calculated using Matthiesen's rule. In this model, the mobility first

increases with increasing free carrier concentration, which is attributed to screening of the dislocation charge, and then decreases due to ionized impurity scattering. Weimann et al., and Ng et al. in a related study [31], verified the predicted trends on a series of GaN samples grown by molecular beam epitaxy (MBE) with varying TD density and free carrier concentrations.

More recently, Look and Sizelove have rigorously developed the transverse mobility in material with charged TD lines [32]. Then, the theory was applied to the temperature-dependent mobility and carrier concentration data for two sets of samples with well characterized microstructures. Look and Sizelove were able to obtain excellent fits for both the temperature dependence of the carrier concentration and mobility for both samples with no arbitrary fitting parameters — the only adjustable fitting parameters were the donor concentration and energy and the TD density, all of which are known within reasonable bounds. The fitted TD density for the first sample ('sample A') was in the range $4–8 \times 10^8\ cm^{-2}$, depending on details for the screening, whereas the measured TD density was $4 \times 10^8\ cm^{-2}$. For the second sample, the fitted TD density was in the range $2–3.5 \times 10^{10}\ cm^{-2}$, whereas the experimentally observed TD density was $2 \times 10^{10}\ cm^{-2}$ (note that the TD densities were determined by plan-view TEM). The rigor of Look and Sizelove's work and the ability to accurately predict experimentally observed TD densities is remarkable. It is important to emphasize that Look and Sizelove modeled the TD as having one acceptor state per unit translation (*c*-axis translation) along the TD, in accordance with the model of Wright et al. Look and Sizelove noted that V_{Ga}–O_N complex could also give rise to the acceptor state. However, it seems unlikely that each TD line would be fully decorated with oxygen for the range of TD densities and growth techniques. Rather, it seems that Look and Sizelove's work supports the ideas of Wright et al. — namely, TDs, independent of impurities or kink sites, have deep levels in the forbidden gap.

4.2.3. Scanning capacitance microscopy (SCM)

SCM is a scanning probe microscope technique closely related to AFM. In this technique, a low-frequency (5–100 kHz) AC field with amplitude of ~1–5 V is applied between a metallized AFM tip and a semiconductor sample (which presumably has a native oxide) at a defined DC offset bias. At the same time, the capacitance is measured at high frequency (915 MHz) with a small superimposed voltage swing [33,34]. The SCM images then are typically displayed as changes in capacitance DC in response to the low-frequency AC voltage swing dV. Concurrent dC/dV maps and contact mode AFM images were recorded. The surface morphology of high-quality MOCVD-grown GaN films shows Ga-N bilayer steps. Terminations of pairs of steps correspond to the intersection of screw-component TDs with the surface. Hansen et al. carried out SCM and local C–V studies of unintentionally doped n-type GaN ($n \sim 5 \times 10^{16}\ cm^{-3}$) [35]. In these studies there was a strong correlation with the SCM (dC/dV) contrast and positions of TD intersections with the film surface. Local C–V curves recorded from regions near TDs in comparison to those away from TDs were consistent with a flatband shift due to negative charge accumulation at the TDs.

4.3. Leakage paths

Several studies are now appearing in the literature that demonstrate that TDs behave as current leakage pathways in GaN. The development of LEO for the nitrides has lead to clear demonstrations of the dramatic contrast in leakage currents between normal GaN with TD densities on the order of $10^9\ cm^{-2}$ and LEO material with TD densities in the range 10^4–$10^6\ cm^{-2}$.

4.3.1. Ballistic electron emission microscopy (BEEM)

Brazel et al. reported on BEEM studies of unintentionally doped n-type GaN films ($n \sim 5 \times 10^{16}\ cm^{-3}$) in which the Schottky barrier was formed by depositing 7 nm Au layer on the GaN [36]. Surprisingly, the Au layer had pit features with a density and distribution similar to the mixed character TD density, and thus it was inferred that the pits in the Au layer corresponded to the position of screw-component TDs in the underlying GaN layer. Simultaneously recorded collector current images and STM images showed high-collector current density regions associated with the pit features for both negative (electron) and positive (hole) tunneling bias. The threshold bias varied from 0.3 to 0.95 V for electron injection and from 0.3 to 1.3 eV for hole injection. The authors attributed the high current densities and reduced Schottky barrier heights to acceptor and donor-like traps in the vicinity of screw-component TDs.

4.3.2. Reverse bias diodes on LEO GaN

Kozodoy et al. used the high contrast in TD density in LEO structures to study the effect of TDs on reverse bias leakage currents in p–n junctions [37]. In this study, p–n junctions were formed on uncoalesced GaN LEO stripes, where the junctions were placed either over the wing region (TD density $< 10^6\ cm^{-2}$) or over the window region (TD density $\sim 10^9\ cm^{-2}$) on the same LEO stripe. Under reverse bias, the leakage current densities were at least three orders of magnitude higher for the window regions in comparison with the wing region, as shown in Fig. 6. In a similar study, Parish et al. fabricated AlGaN-based p–i–n UV solar detectors on LEO GaN [38]. The diodes on the wing regions typically had six to eight orders of magnitude lower reverse bias leakage current than for diodes grown on conventional ('dislocated') GaN. Additionally, the LEO-based diodes had sharper current cutoffs and much more sharply defined spectral

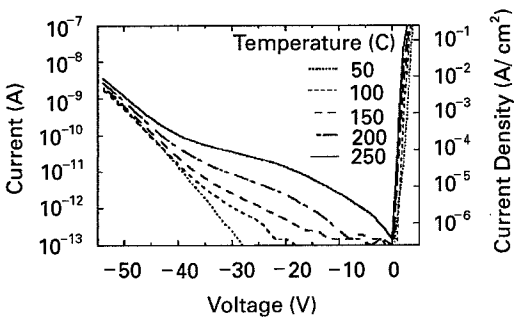

Fig. 6. *I–V* characteristics for pn junction diodes grown on LEO GaN (also referred to as the 'wing' region) and dislocated GaN (window region). For further details, see Ref. [37].

response curves in comparison with diodes produced on conventional GaN.

5. Summary

The body of work described above provides a picture in which the TDs in the group III-nitrides are electrically active and clearly deleterious for transport, emission, and detection properties. The CL, PEC etching, and transport studies are all consistent with dislocation-related deep acceptor levels for n-type GaN. In this case of optical-related properties, these levels appear to act as NR centers. For low doping densities, the TD-related deep levels can fully deplete the material of free carriers, rendering it semi-insulating. For high doping densities, the TD-related traps act as a charged line scattering centers. Dislocation-related deep levels may also play a role in leakage. It remains unclear whether the TD-related traps are an intrinsic feature of dislocations in the nitrides or if they are cause by impurity segregation. Continued progress in high purity growth techniques, such as MBE, may eventually resolve this issue.

The prospects appear to be excellent for achieving GaN single crystal 'pseudo-substrates' using techniques such as LEO, thick hydride vapor phase epitaxy, and laser-assisted substrate removal and combinations of these techniques. The economic advantages are minimal for developing single crystal GaN substrates for high volume commodity devices such as LEDs. However, for low volume, technology-enabling devices, such as laser diodes and possibly high performance transistors, the performance improvement on low TD density material appears to merit the use of single crystal substrates. Although Nakamura realized cw emission in GaN-based laser diodes in normal dislocated material, his realization of 10,000 h cw nitride-based laser operation was facilitated through the use of thick GaN on LEO substrates [39]. Fortuitously, the technological drive for single crystal GaN substrates will provide material with sufficiently low TD densities that many of the properties will unambiguously fall within the 'point-defect' limited regime. This exciting possibility should provide a wide variety of opportunities for the defect science community.

Acknowledgements

The authors thank all of the members of the nitride groups at UCSB and HP Laboratory. Financial support for the work at UCSB was provided by ONR (Colin Wood and John Zolper, contract monitors) and by Hewlett-Packard Laboratories.

References

[1] J.I. Pankove, E.A. Miller, J.E. Berkeyheiser, J. Lumin. 5 (1972) 84.
[2] Y. Koide, N. Itoh, K. Itoh, N. Sawaki, I. Akasaki, Jpn. J. Appl. Phys. 27 (1988) 1156.
[3] I. Akasaki, H. Amano, Y. Koide, K. Hiramatsu, N. Sawaki, J. Crystal Growth 98 (1989) 209.
[4] S. Nakamura, T. Mukai, M. Senoh, N. Iwasa, Japn. J. Appl. Phys. 31 (1992) L139.
[5] S. Nakamura, T. Mukai, M. Senoh, Appl. Phys. Lett. 64 (1994) 1687.
[6] S.D. Lester, F.A. Ponce, M.G. Craford, D.A. Steigerwald, Appl. Phys. Lett. 66 (1995) 1249.
[7] X.H. Wu, L.M. Brown, D. Kapolnek, S. Keller, B. Keller, S.P. DenBaars, J.S. Speck, J. Appl. Phys. 80 (1996) 3228.
[8] X.H. Wu, D. Kapolnek, E.J. Tarsa, B. Heying, S. Keller, B.P. Keller, U.K. Mishra, S.P. DenBaars, J.S. Speck, Appl. Phys. Lett. 68 (1996) 1371.
[9] X.H. Wu, P. Fini, E.J. Tarsa, B. Heying, S. Keller, U.K. Mishra, S.P. DenBaars, J.S. Speck, J. Crystal Growth 189–190 (1998) 232.
[10] X.H. Wu, C.R. Elsass, A. Abare, M. Mack, S. Keller, P.M. Petroff, J.S. Speck, S.J. Rosner, Appl. Phys. Lett. 72 (1998) 692.
[11] F.C. Frank, Acta. Crystallogr. 4 (1951) 497.
[12] J.E. Northrup, L.T. Romano, J. Neugebauer, Appl. Phys. Lett. 74 (1999) 2319.
[13] S.J. Rosner, E.C. Carr, M.J. Ludowise, G. Girolami, H.I. Erikson, Appl. Phys. Lett. 70 (1997) 420.
[14] B. Heying, E.J. Tarsa, C.R. Elsass, P. Fini, S.P. DenBaars, J.S. Speck, J. Appl. Phys. 85 (1999) 6470.
[15] T. Sugahara, H. Sato, M. Hao, Y. Naoi, S. Kurai, S. Tottori, K. Yamashita, K. Nishino, L.T. Romano, S. Sakai, Jpn. J. Appl. Phys. (Part 2) 37 (1998) L398.
[16] S.J. Rosner, G. Girolami, H. Marchand, P.T. Fini, J.P. Ibbetson, L. Zhao, S. Keller, U.K. Mishra, S.P. DenBaars, J.S. Speck, Appl. Phys. Lett. 74 (1999) 2035.
[17] H. Marchand, J.P. Ibbetson, P.T. Fini, S. Keller, S.P. DenBaars, J.S. Speck, U.K. Mishra, J. Crystal Growth 195 (1998) 328.
[18] M.S. Minsky, A.M. White, E.L. Hu, Appl. Phys. Lett. 68 (1996) 1531.

[19] C. Youtsey, L.T. Romano, I. Adesida, Appl. Phys. Lett. 73 (1998) 797.
[20] C. Youtsey, L.T. Romano, R.J. Molnar, I. Adesida, Appl. Phys. Lett. 74 (1999) 3537.
[21] S.J. Rosner, J.S. Speck, unpublished.
[22] J. Elsner, R. Jones, P.K. Sitch, V.D. Porezag, M. Elstner, T. Frauenheim, M.I. Heggie, S. Oberg, P.R. Briddon, Phys. Rev. Lett. 79 (1997) 3672.
[23] J. Elsner, R. Jones, M.I. Heggie, P.K. Sitch, M. Haugk, T. Frauenheim, S. Oberg, P.R. Briddon, Phys. Rev. B 58 (1998) 12571.
[24] A.F. Wright, J. Furthmuller, Appl. Phys. Lett. 72 (1998) 3467.
[25] A.F. Wright, U. Grossner, Appl. Phys. Lett. 73 (1998) 2751.
[26] K. Leung, A.F. Wright, E.B. Stechel, Appl. Phys. Lett. 74 (1999) 2495.
[27] K. Seeger, Semiconductor Physics, 4th Edition, Springer, New York, 1989.
[28] V.L. Bonch-Bruevich, S.M. Kogan, Sov. Phys.-Solid State 1 (1959) 1118.
[29] B. Pödör, Phys. Stat. Sol. 16 (1966) K167.
[30] N.S. Weimann, L.F. Eastman, D. Doppalapudi, H.M. Ng, T.D. Moustakas, J. Appl. Phys. 83 (1998) 3656.
[31] H.M. Ng, D. Doppalapudi, T.D. Moustakas, N.G. Weimann, L.F. Eastman, Appl. Phys. Lett. 73 (1998) 821.
[32] D.C. Look, J.R. Sizelove, Phys. Rev. Lett. 82 (1999) 1237.
[33] C.C. Williams, J. Slinkman, W.P. Hough, H.K. Wickramasinghe, Appl. Phys. Lett. 55 (1989) 1662.
[34] Y. Huang, C.C. Williams, J. Vac. Sci. Technol. B 13 (1994) 369.
[35] P.J. Hansen, Y.E. Strausser, A.N. Erickson, E.J. Tarsa, P. Kozodoy, E.G. Brazel, J.P. Ibbetson, U. Mishra, V. Narayanamurti, S.P. DenBaars, J.S. Speck, Appl. Phys. Lett. 72 (1998) 2247.
[36] E.G. Brazel, M.A. Chin, V. Narayanamurti, Appl. Phys. Lett. 74 (1999) 23672369.
[37] P. Kozodoy, J.P. Ibbetson, H. Marchand, P.T. Fini, S. Keller, J.S. Speck, S.P. DenBaars, U.K. Mishra, Appl. Phys. Lett. 73 (1998) 975.
[38] G. Parish, S. Keller, P. Kozodoy, J.P. Ibbetson, H. Marchand, P.T. Fini, S.B. Fleischer, S.P. DenBaars, U.K. Mishra, Appl. Phys. Lett. 75 (1999) 247.
[39] S. Nakamura, MRS Bull. 23 (1998) 37.

ELSEVIER

Physica B 273–274 (1999) 33–38

PHYSICA B

www.elsevier.com/locate/physb

Observation of Ga vacancies and negative ions in undoped and Mg-doped GaN bulk crystals

K. Saarinen[a,*], J. Nissilä[a], J. Oila[a], V. Ranki[a], M. Hakala[a], M.J. Puska[a], P. Hautojärvi[a], J. Likonen[b], T. Suski[c], I. Grzegory[c], B. Lucznik[c], S. Porowski[c]

[a]*Laboratory of Physics, Helsinki University of Technology, P.O. Box 1100, 02015 HUT, Finland*
[b]*Technical Research Centre of Finland, Chemical Technology, P.O. Box 1404, 02044 VTT, Finland*
[c]*UNIPRESS, High Pressure Research Center, Polish Academy of Sciences, 01-142 Warsaw, Poland*

Abstract

Gallium vacancies and negative ions are observed in GaN bulk crystals by applying positron lifetime spectroscopy. The concentration of Ga vacancies decreases with increasing Mg doping, as expected from the behavior of the V_{Ga} formation energy as a function of the Fermi level. The concentration of negative ions correlates with that of Mg impurities determined by secondary ion mass spectrometry. We thus attribute the negative ions to Mg_{Ga}^{-}. The negative charge of Mg suggests that Mg doping converts n-type GaN to semi-insulating mainly due to the electrical compensation of O_N^+ donors by Mg_{Ga}^{-} acceptors.

Keywords: GaN; Vacancies; Compensation; Positrons

1. Introduction

Bulk GaN crystals are ideal substrates for the epitaxy of GaN overlayers for optoelectronic components at the blue wavelength. Such material can be synthesized of liquid Ga in high N overpressure at elevated temperatures [1]. Nominally undoped GaN crystals show usually high n-type conductivity with the concentration of electrons exceeding 10^{19} cm^{-3}. This is most likely due to the residual oxygen atoms acting as shallow donors [2,3]. When GaN is doped with Mg the electron concentration decreases and for sufficiently high amount of Mg dopants the samples become semi-insulating. It is interesting to study how the movement of the Fermi level toward the midgap changes the formation of charged native defects such as the Ga vacancy. Another basic question concerns the mechanism of the electrical deactivation. One can consider either (i) the gettering role of Mg leading to the formation of MgO molecules [4] or (ii) electrical compensation of O_N^+ donors by Mg_{Ga}^{-} acceptors.

Positrons in solids get trapped at neutral and negative vacancy defects, which can be experimentally detected by measuring the positron lifetime [5]. At low temperatures positrons are also captured at the hydrogenic states around negative ions. The positron experiments thus yield detailed information on the concentration and structure of intrinsic and extrinsic acceptors. Our previous results have indicated that negative Ga vacancies are formed during the growth of undoped n-type GaN crystals and epitaxial layers [6,7]. There is also evidence that the creation of V_{Ga} is less likely in semi-insulating or p-type GaN overlayers on sapphire [7,8].

In this paper we review our recent works [6,9] and show that Ga vacancy acts as a native defect in GaN crystals. We pay special attention to the identification of V_{Ga} by correlating the results of positron experiments with those of theoretical calculations. Our data indicate that the formation of Ga vacancies is suppressed by Mg doping. We show further that most of Mg is in a negative charge state, suggesting that the loss of n-type conductivity is due to compensation of O_N^+ donors by Mg_{Ga}^{-} acceptors.

* Corresponding author. Tel.: + 358-9-451-3111; fax: + 358-9-451-3116.
E-mail address: ksa@fyslab.hut.fi (K. Saarinen)

0921-4526/99/$ - see front matter
PII: S0921-4526(99)00400-7

2. Experimental details and data analysis

The bulk GaN crystals were grown at the nitrogen pressure of 1.5 GPa and temperature of 1500°C [1]. We studied three samples, where the Mg doping level was intentionally varied during the crystal growth (Table 1). The Mg and O concentrations of the samples were determined experimentally by secondary ion-mass spectrometry (SIMS). The absolute concentrations were calibrated by implanting known amounts of O and Mg to undoped epitaxial GaN layers, where the residual Mg and O concentrations were well below 10^{18} cm^{-3}.

The positron lifetime experiments were performed using conventional instrumentation by sandwiching two identical sample pieces with a 30 μCi ^{22}Na positron source [5]. The lifetime spectrum is a sum of exponential decay components $-dn(t)/dt = \sum_i (I_i/\tau_i)\exp(-t/\tau_i)$, where $n(t)$ is the probability of positron to be alive at time t. The positron in the state i (e.g. delocalized state in the lattice or localized state at a vacancy) annihilates with the lifetime τ_i and the intensity I_i. The increase of the average lifetime $\tau_{av} = \sum I_i\tau_i$ above τ_B obtained in the defect-free lattice is a clear sign of vacancy defects in the sample.

The Doppler broadening of the 511 keV annihilation radiation was recorded using a Ge detector with an energy resolution of 1.4 keV. These measurements yield the one-dimensional momentum distribution of electrons as seen by the positron. In order to observe annihilations with core electrons, the experimental background was reduced by detecting simultaneously the two annihilation photons [10]. For this purpose, a NaI detector was placed collinearly with the Ge detector and a coincidence between the two detectors was electronically required.

In order to help the interpretation of the experimental results we calculated the positron lifetime and core electron momentum density theoretically [10,11]. The electron densities were constructed using the atomic superposition method. The positron states were solved in a supercell of 256 atomic sites in a periodic superlattice using the generalized gradient approximation for electron–positron correlation. The core electron momentum distribution seen by the positron was calculated using atomic wave functions for core electrons and the state-dependent enhancement scheme [11].

3. Impurity concentrations

The secondary ion-mass spectrometry indicates that the oxygen concentration is about 4×10^{19} cm^{-3} in undoped GaN (Table 1). The concentration of conduction electrons ($n = 5 \times 10^{19}$ cm^{-3} at 300 K) in this sample is thus almost the same as oxygen concentration. This is in good agreement with the previous evidence [2,3] that the n-type conductivity of GaN is due to unintentional oxygen doping. In the lightly Mg doped GaN the concentration of oxygen is 12×10^{19} cm^{-3}, which is slightly larger than the Mg concentration of 6×10^{19} cm^{-3}. The electrical experiments indicate that the sample has n-type conductivity, but the carrier concentration is less than in the undoped sample. The heavily Mg-doped sample has the O concentration of 9×10^{19} cm^{-3} and the Mg concentration of 1×10^{20} cm^{-3}. According to the electrical experiments the sample is semi-insulating. This is reasonable since the impurity concentrations determined by SIMS show that [Mg] ≈ [O].

4. Positron lifetime results

Examples of positron lifetime spectra are shown in Fig. 1 and the temperature dependencies of the average lifetime τ_{av} and the second lifetime component τ_2 are presented in Fig. 2. In the lifetime experiment of Fig. 1, positrons enter the sample and thermalize at the time $t = 0$. The vertical axis gives the number of annihilations at a time interval of 25 ps. In the heavily Mg-doped sample the positron lifetime spectrum has a single component of 165 ± 1 ps at 300 K. The lifetime is almost constant as a function of temperature (Fig. 2).

Both these observations indicate that the heavily Mg-doped GaN is free of vacancy defects trapping positrons. In perfect GaN lattice the positron state is very delocalized and the positron density has its maximum in the interstitial region (Fig. 3). The calculated lifetime in defect-free GaN lattice is 154 ps, which is in reasonable agreement with the experimental result $\tau_B = 165$ ps. The lifetime $\tau_B = 165$ ps is also very close to our earlier estimate (166 ps) based on the lifetime decomposition at low temperature [6]. In heavily Mg-doped GaN all positrons

Table 1
The concentrations of impurities and defects in the studied GaN bulk crystals. The magnesium and oxygen concentrations were determined by secondary ion mass spectrometry. The concentrations of Ga vacancies and negative ions are obtained from the positron annihilation data [9]

Sample	Oxygen concentration (cm^{-3})	Magnesium concentration (cm^{-3})	Ga vacancy concentration (cm^{-3})	Negative ion concentration (cm^{-3})
Undoped	4×10^{19}	1×10^{18}	2×10^{17}	3×10^{18}
Lightly Mg doped	12×10^{19}	6×10^{19}	7×10^{16}	6×10^{19}
Heavily Mg doped	9×10^{19}	10×10^{19}	$< 10^{16}$	

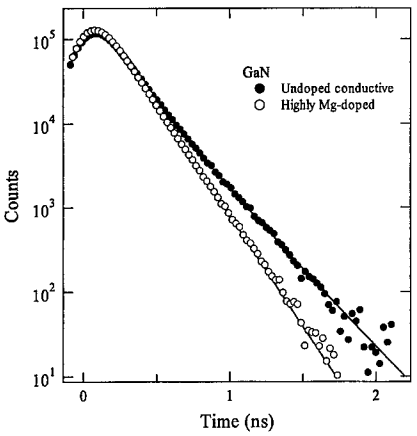

Fig. 1. Examples of positron lifetime spectra in undoped and highly Mg-doped GaN bulk crystals. The data are normalized to the typical experimental integral of 2×10^6 counts. The solid lines are fits to the sum of exponential decay components convoluted with the resolution function of the spectrometer. The data in the highly Mg-doped sample (recorded at 300 K) has only a single component of 165 ± 1 ps. The spectrum in the undoped crystal (recorded at 490 K) can be decomposed into two components of $\tau_1 = 150 \pm 10$ ps, $\tau_2 = 235 \pm 5$ ps, and $I_2 = 48 \pm 6\%$ [9].

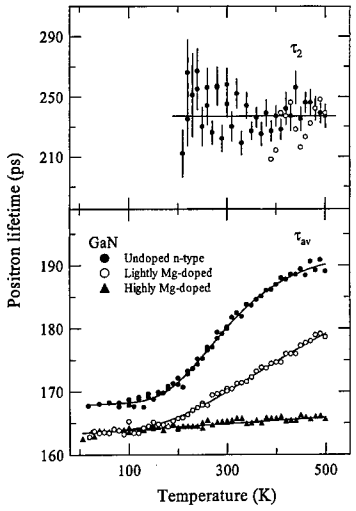

Fig. 2. The average positron lifetime and the second lifetime component τ_2 versus measurement temperature in GaN bulk crystals. The solid lines correspond to the analyses with the temperature-dependent positron trapping model, where concentrations of Ga vacancies and negative ions (Table 1) are determined as fitting parameters.

thus annihilate in the delocalized state in the GaN lattice with the bulk lifetime $\tau_B = 165$ ps. The slight increase of the bulk lifetime as a function of temperature (Fig. 2) can be attributed to the lattice expansion.

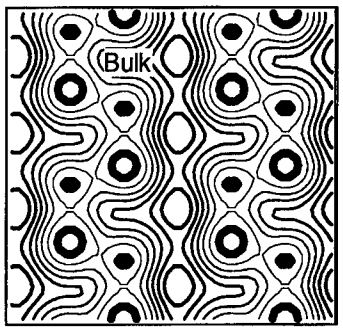

Fig. 3. The delocalized positron density in perfect GaN lattice according to theoretical calculations. The c-axis of the wurtzite structure is vertical in the figure. The positions of the Ga and N atoms are marked with open circles and diamonds, respectively. The contour spacing is $\frac{1}{6}$ of the maximum value.

The positron lifetime spectrum recorded in undoped GaN is clearly different from that in highly Mg-doped sample (Fig. 1). The annihilation probability at $t > 0.5$ ns is much larger in the undoped GaN, indicating that the average positron lifetime τ_{av} is longer than $\tau_B = 165$ ps. In fact, $\tau_{av} = 167$ ps at $T = 10$–150 K, and it increases up to $\tau_{av} = 190$ ps at 500 K (Fig. 2). In lightly Mg-doped GaN the positron lifetime is equal to $\tau_B = 165$ ps at low temperatures of 10–200 K (Fig. 2). At 200–500 K, however, τ_{av} is clearly larger than τ_B and reaches a value of 180 ps at 500 K. Since $\tau_{av} > \tau_B$ in both undoped and lightly Mg-doped samples, we can conclude that these GaN crystals contain vacancy defects.

The lifetime spectra recorded at 300–500 K in the undoped and lightly Mg-doped GaN can be decomposed into two exponential components (Figs. 1 and 2). The positrons trapped at vacancies annihilate with the longer lifetime $\tau_V = \tau_2 = 235 \pm 5$ ps. Within experimental accuracy this lifetime is the same in the n-type undoped crystal and in the lightly Mg-doped sample (Fig. 2), indicating that the same vacancy is present.

5. Doppler broadening results

The high-momentum part of the Doppler broadening spectrum was recorded in n-type GaN overlayers, which contain the same vacancy defect as the bulk crystals [6]. This experiment yields the superimposed electron momentum distribution $\rho(p) = (1 - \eta_V)\rho_B(p) + \eta_V \rho_V(p)$, where $\rho_B(p)$ and $\rho_V(p)$ are the momentum distributions in the lattice and at the vacancy, respectively. η_V is the fraction of positrons annihilating at the vacancy, which can be determined using the positron trapping model and the combination of positron lifetime and Doppler experiments [6]. Since the momentum distribution in the lattice $\rho_B(p)$ can be measured in the defect-free reference sample

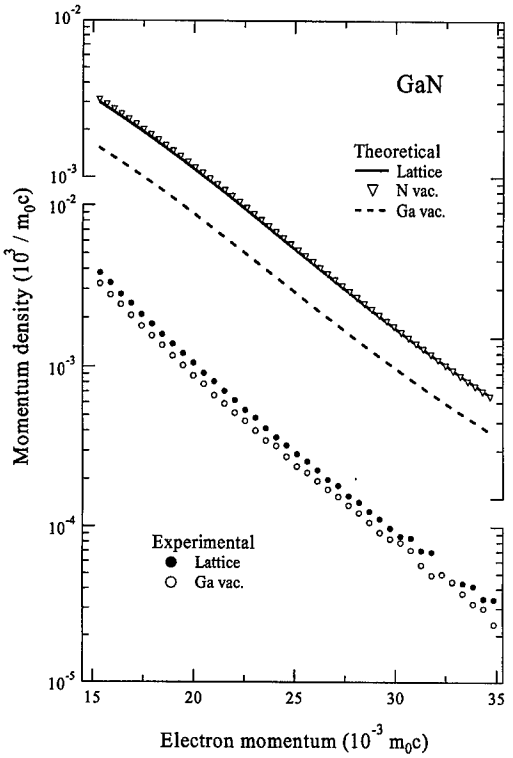

Fig. 4. The lower panel presents experimental core electron momentum densities at the perfect GaN lattice and at the Ga vacancy. The upper panel shows the result of the theoretical calculation at perfect GaN and at N and Ga vacancies. The momentum distibutions are normalized to unity.

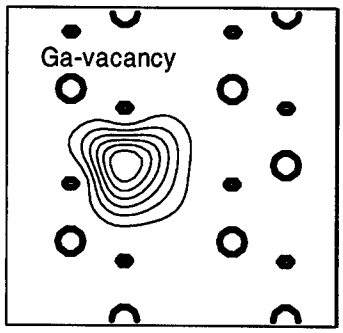

Fig. 5. The localized positron density in an ideal Ga vacancy in GaN according to theoretical calculations. The c-axis of the wurtzite structure is vertical in the figure. The positions of the Ga and N atoms are marked with open circles and diamonds, respectively. The contour spacing is $\frac{1}{6}$ of the maximum value.

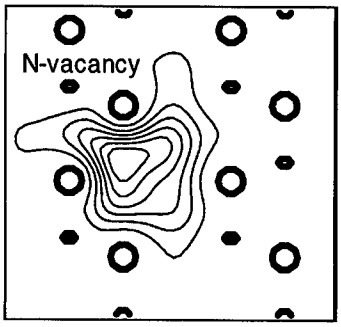

Fig. 6. The localized positron density in an ideal N vacancy in GaN according to theoretical calculations. The c-axis of the wurtzite structure is vertical in the figure. The positions of the Ga and N atoms are marked with open circles and diamonds, respectively. The contour spacing is $\frac{1}{6}$ of the maximum value.

such as heavily Mg-doped GaN crystal, the distributions $\rho_V(p)$ at vacancies can be decomposed from the measured spectrum $\rho(p)$.

Fig. 4 shows the core electron momentum distributions $\rho_B(p)$ and $\rho_V(p)$ in the perfect GaN lattice and at the vacancy defect, respectively. The intensity of the core electron momentum distribution is clearly smaller in the vacancy than in the GaN lattice. However, the momentum distributions at vacancies and in the bulk have clearly similar shapes over a wide momentum range.

6. Identification of the vacancy defect

Positron trapping and annihilation with the lifetime $\tau_V = 235$ ps is observed at native vacancies in n-type GaN crystals. This value is typical for a monovacancy in materials which have the same atomic density as GaN, such as Al. The calculated positron densities at Ga and N vacancies are shown in Figs. 5 and 6. Both vacancies are able to localize the positron. However, the localization is clearly stronger in the case of Ga vacancy, because the open volume of V_{Ga} is much larger than that of V_N. This fact is reflected in the calculated positron lifetimes, which are $\tau_V = 209$ and 160 ps for unrelaxed Ga and N vacancies, respectively. The experimental value of 235 ps can thus be associated with the Ga vacancy but not with the N vacancy.

The same identification can be deduced on the basis of the Doppler broadening experiments. The calculations show that the annihilations with Ga 3d electrons give the clearly dominant contribution to the measured core electron momentum distribution at GaN lattice as well as at Ga and N vacancies. The shape of the momentum distributions is thus similar in all these three systems. The calculated momentum distribution at the Ga vacancy clearly has a lower intensity than that in the GaN lattice (Fig. 4), because the contribution of Ga 3d is reduced due to the surrounding N atoms. At the N vacancy the neighboring Ga atoms yield a core annihilation component, which is as strong as in the bulk lattice

(Fig. 4). The experimental curve is compatible with the Ga vacancy, but not with the N vacancy.

The combination of positron lifetime and Doppler broadening experiments thus unambiguously shows that the native vacancies in GaN crystals belong to the Ga sublattice and have an open volume of a monovacancy. According to theoretical calculations [12,13], the Ga vacancy is negatively charged in n-type and semi-insulating GaN and thus acts as an efficient positron trap. On the other hand, the N vacancy is expected to be positive and repulsive to positrons [12,13]. The calculated difference $\tau_V - \tau_B$ becomes equal to the experimental value $\tau_V - \tau_B = 70$ ps when the neighboring N atoms are relaxed 5% outwards from the Ga vacancy. In fact, an outwards relaxation is expected for the Ga vacancy on the basis of theoretical calculations [12,13]. Unfortunately, the present positron experiments do not tell whether V_{Ga} is an isolated defect or part of a larger complex.

7. Positron trapping at negative ions

The decrease of the average lifetime at low temperatures (Fig. 2) indicates that the fraction $\eta_V = (\tau_{av} - \tau_B)/(\tau_V - \tau_B)$ of positrons annihilating at vacancies decreases. Since the positron trapping at negative Ga vacancies should be enhanced at low temperatures [14], the decrease of η_V is due to other defects which compete with Ga vacancies as positron traps. Negative ions are able to bind positrons at shallow (< 0.1 eV) hydrogenic states in their attractive Coulomb field [5]. Since they possess no open volume, the lifetime of positrons trapped at them is the same as in the defect-free lattice, $\tau_{ion} = \tau_B = 164 \pm 1$ ps. The average lifetime increases above 150 K when positrons start to escape from the ions and a larger fraction of them annihilates at vacancies.

The temperature dependence of the average lifetime can be modeled with kinetic trapping equations [5]. Positron trapping coefficients at negative Ga vacancies μ_V and negative ions μ_{ion} vary as $T^{-1/2}$, a function of temperature [5,14]. The positron detrapping rate from the ions can be expressed as $\delta(T) \propto \mu_{ion} T^{-3/2} \exp(-E_{ion}/k_B T)$, where E_{ion} is the positron binding energy at the Rydberg state of the ions. The fraction of annihilations η_V at Ga vacancies depends on the concentrations c_V and c_{ion} of Ga vacancies and negative ions, respectively, as well as on the detrapping rate $\delta(T)$. We take the conventional value $\mu_V = 2 \times 10^{15}\ s^{-1}$ for the positron trapping coefficient at 300 K [5]. The average lifetime $\tau_{av} = (1 - \eta_V)\tau_B + \eta_V \tau_V$ can be fitted to the experimental data of Fig. 2 with c_V, c_{ion}, μ_{ion} and E_{ion} as adjustable parameters. As indicated by the solid lines in Fig. 2, the fits reproduce well the experimental data with the positron binding energy of $E_{ion} = 60 \pm 10$ meV and trapping coefficient $\mu_{ion} = (7 \pm 4) \times 10^{16} (T/K)^{-0.5}$. These values are close to those obtained previously in GaAs [5].

8. Defect concentrations and electrical deactivation

The analysis explained above yields estimates for the concentrations of V_{Ga} and negative ions (Table 1). The Ga vacancy concentration is $c_V = 2 \times 10^{17}\ cm^{-3}$ in the undoped GaN and $c_V = 7 \times 10^{16}\ cm^{-3}$ in the lightly Mg-doped crystal. In the heavily Mg-doped GaN no Ga vacancies are observed indicating that their concentration is below the detection limit of $10^{16}\ cm^{-3}$. The concentration of V_{Ga} thus decreases with increasing Mg doping and the Ga vacancies disappear completely when the material gets semi-insulating, i.e. [O] $\approx$ [Mg]. The same observation has been done also in Mg-doped GaN layers on sapphire [8,15]. This behavior is in good agreement with the results of theoretical calculations, which predict a low energy formation for the Ga vacancy and V_{Ga}–O_N complex only in n-type material [12,13]. The creation of Ga vacancies in the growth of GaN crystals seems to follow thus the trends expected for acceptor defects in thermal equilibrium.

The concentration of negative ions is $3 \times 10^{18}\ cm^{-3}$ in undoped GaN and about $6 \times 10^{19}\ cm^{-3}$ in lightly Mg-doped crystal. The ion concentration cannot be determined in heavily Mg-doped sample because no competitive positron trapping at Ga vacancies is observed and the positron annihilations at the ions cannot be distinguished from those in the GaN lattice. Due to the uncertainties in the values of positron trapping coefficients μ_V and μ_{ion} the experimental errors of the absolute concentrations of negative ions are large, of the order of 50%. In the lightly Mg doped sample c_{ion} represents the lower limit concentration only, because at temperatures of $T < 200$ K the average lifetime saturates at the value τ_B corresponding to annihilations in the GaN lattice.

In spite of the experimental inaccuracies the data indicates clearly that the concentration of negative ions increases by at least an order of magnitude with the Mg doping. Furthermore, the estimated concentrations of negative ions are close to those of Mg impurities as determined by the SIMS measurements (Table 1). Hence, it is natural to attribute the negative ions to Mg_{Ga}^-. The positron results thus show that a substantial part of the Mg impurities is in the negative charge state in Mg-doped GaN bulk crystals. This suggests that the conversion of n-type GaN to semi-insulating with Mg doping is mainly due to an electrical compensation of oxygen donors with negatively charged Mg acceptors. The electrons originating from O donors are transferred to Mg acceptors charging them negatively. Since positron trapping at Mg_{Ga}^- requires long-range Coulomb attraction,

we can infer that Mg_{Ga}^{-} ions are not spatially correlated with positive O_N^+ donors. However, we cannot exclude the formation of MgO molecules [4], which may also contribute to some extent to the electrical deactivation of Mg-doped GaN crystals.

9. Conclusions

The positron experiments show the presence of Ga vacancies and negative ions in GaN crystals. The concentration of Ga vacancies decreases with increasing Mg doping, in good agreement with the trends expected for the V_{Ga} formation energy as a function of the Fermi level. The concentration of negative ions increases with Mg doping and correlates with the Mg concentration determined by SIMS. We thus associate the negative ions with Mg_{Ga}^{-}. The negative charge of Mg suggests that the loss of n-type conductivity in the Mg doping of GaN crystals is mainly due to compensation of O_N^+ donors by Mg_{Ga}^{-} acceptors.

Acknowledgements

The authors would like to acknowledge the financial support from the Academy of Finland (EPI-2 project) and the State Committee for Scientific Research (Poland) (Grant KBN 7T08A 007 13).

References

[1] S. Porowski et al., in: S.J. Pearton (Ed.), GaN and Related Materials, Vol. 2, Gordon and Breach, Amsterdam, 1997, p. 295.
[2] C. Wetzel et al., Phys. Rev. Lett. 78 (1997) 3923.
[3] T. Suski et al., in: J.I. Pankove, T.D. Moustakas (Eds.), Gallium Nitride (GaN) I, Vol. 50, Academic Press, San Diego, 1998, p. 279.
[4] J.I. Pankove et al., Appl. Phys. Lett. 74 (1999) 416.
[5] K. Saarinen et al., in: M. Stavola (Ed.), Identification of Defects in Semiconductors, Academic Press, New York, 1998, p. 209.
[6] K. Saarinen et al., Phys. Rev. Lett. 79 (1997) 3030.
[7] K. Saarinen et al., Appl. Phys. Lett. 73 (1998) 3253.
[8] L.V. Jorgensen et al., Mater Res. Soc. Symp. Proc. 449 (1997) 853.
[9] K. Saarinen et al., Appl. Phys. Lett. 75 (1999) 2441.
[10] M. Alatalo et al., Phys. Rev. B 51 (1995) 4176.
[11] M. Alatalo et al., Phys. Rev. B 54 (1996) 2397.
[12] J. Neugebauer et al., Appl. Phys. Lett. 69 (1996) 503.
[13] T. Mattila et al., Phys. Rev. B 55 (1997) 9571.
[14] M.J. Puska et al., Rev. Mod. Phys. 66 (1994) 841.
[15] J. Oila et al., 1999, unpublished.

ELSEVIER

Physica B 273–274 (1999) 39–42

PHYSICA B

www.elsevier.com/locate/physb

Mechanism of radiative recombination in acceptor-doped bulk GaN crystals

M. Godlewski[a,*], T. Suski[b], I. Grzegory[b], S. Porowski[b], J.P. Bergman[c], W.M. Chen[c], B. Monemar[c]

[a]*Institute of Physics, Polish Academy of Sciences, Al. Lotników 32/46, 02-668 Warsaw, Poland*
[b]*High Pressure Research Centre, Polish Academy of Sciences, 01-142 Warsaw, Sokołowska 29, Poland*
[c]*Department of Physics and Meas. Technology, Linköping University, S-581 83 Linköping, Sweden*

Abstract

Optical and electrical properties of acceptor-doped bulk GaN crystals are discussed. Though introducing Zn and Ca to bulk GaN does not significantly change electron concentration, it results in the appearance of a blue photoluminescence band accompanying the relatively strong yellow band usually present. Highly resistive GaN : Mg crystals are obtained when high amount of Mg is introduced to the Ga melt during high-pressure synthesis. Change of electrical properties of Mg-doped bulk crystals is accompanied by the appearance of a strong blue emission of GaN similar to that in Ca- and Zn-doped crystals. Optically detected magnetic resonance investigations indicate a multi-band character of this blue emission and suggest possible mechanism of compensation in acceptor-doped bulk GaN.

Keywords: GaN; Mg-doping; Photoluminescence; ODMR

1. Introduction

After successfully growing bulk GaN plates by means of high-pressure synthesis [1] these crystals of high structural quality were used as substrate materials in homoepitaxial MBE [2] and MOCVD [3] growth processes. This resulted in the best-quality GaN epilayers available at present, which show bright and sharp excitonic photoluminescence [2,3]. The intentionally undoped GaN crystals are however highly conductive, which may limit some possible applications. Recently, successful growth of resistive GaN bulk crystals was reported [4]. Resistive crystals were obtained by introducing Mg acceptors to the Ga melt. In this work we analyse the results of photoluminescence (PL), PL kinetics and optically detected magnetic resonance (ODMR) studies performed by us for a series of acceptor-doped/compensated bulk GaN crystals. Mechanisms of PL recombination and sample compensation are discussed.

2. Experimental

GaN bulk crystals were grown by high-pressure method employing crystallisation from liquid gallium solution at about 1500°C and at high nitrogen pressure ~15 kbar [1]. Hexagonal plates of the size approaching 1 cm were obtained by this method. The "undoped" crystals were highly n-type, with room temperature electron concentration above 10^{19} cm^{-3} [5]. Oxygen residual donor is the main source of electrons. Acceptor-doped crystals (introduced into melt with Zn, Ca or Mg) were either n-type or resistive (for heavily Mg-doped crystals).

PL and PL kinetics experiments were performed at 2 K. The 351 nm UV line of an Ar^+ laser was used for PL excitation. PL kinetics (for acceptor-compensated

* Corresponding author. Tel.: + 48-22-843-68-61; fax: + 48-22-843-09-26.
E-mail address: godlew@ifpan.edu.pl (M. Godlewski)

0921-4526/99/$ - see front matter
PII: S0921-4526(99)00401-9

crystals) was measured with a photon counting system. Pulsed excitation was provided by either a mode locked Ti : sapphire solid state laser with frequency doubling ($\lambda = 340$ nm, 2 ps pulses) or a frequency tripled YAG : Nd laser ($\lambda = 355$ nm, 2 ns pulses) with regulated repetition rate.

ODMR experiments were performed at 2 K using an X-band (9–10 GHz) system with on–off modulated microwave power (up to about 250 mW) under 351 nm UV line of an Ar^+ laser excitation. Microwave-induced PL changes were detected in phase with on–off modulated microwaves using a photomultiplier. The observed magnetic resonance signals were too weak to perform a detailed analysis of their spectral dependences. Instead, a set of five low-pass (LP) filters was used to select different spectral regions within a PL emission. These filters were passing PL of energy smaller than 3.1 (LP1), 2.5 (LP2), 2.17 (LP3), 1.92 (LP4) and 1.75 eV (LP5). This way we could establish an approximate spectral dependence of the observed ODMR signals.

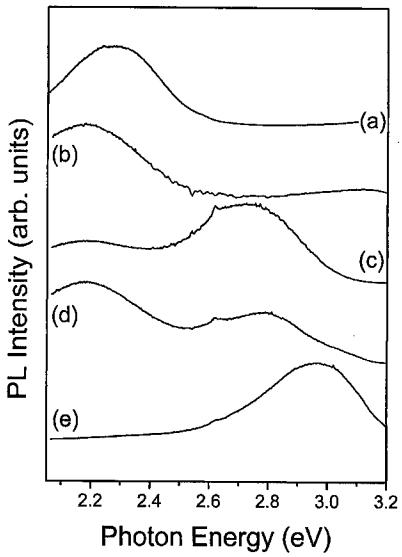

Fig. 1. 2 K PL spectra of bulk GaN samples undoped (a), Ca-doped (b), Zn-doped (c), lightly Mg-doped (d) and heavily Mg-doped (e).

3. Results and discussion

In Fig. 1 we show PL spectra observed for highly n-type sample (not intentionally doped) and for acceptor-doped crystals. The PL spectrum of the "undoped" sample is dominated by the yellow (YL) PL emission with maximum at 2.26 eV (2 eV for acceptor-doped samples). Weak blue-shifted "band-edge" PL was only observed, not shown in Fig. 1. YL still dominates for Ca and lightly Mg-doped samples, but becomes weak in Zn-doped crystal and is either very weak or is not observed in heavily Mg-doped sample. Instead a "new" PL band rises – blue PL (BL) with the maximum at about 3 eV (for Mg-doped sample), which dominates in heavily Mg-doped crystals. This PL is a close analogue of BL observed in Mg-doped GaN epilayers [6], suggesting a similar origin of BL emission in bulk crystals and in epilayers doped with Mg.

Large changes of electrical and optical properties of acceptor-doped crystals are accompanied by a significant change of PL kinetics. In "undoped" highly n-type sample an energy-independent decay of YL is observed with PL decay time in ns time range, which we explain by a degenerate n-type conductivity of uncompensated bulk crystals. A very different dependence is observed for YL and BL in acceptor-compensated crystals. In Fig. 2 we show the PL decay spectra taken at 2 K for heavily Mg-doped crystal. The observed PL kinetics is non-exponential. Fast decay is followed by a slow decay component, with a time constant up to 500 μs. PL decay is photon energy dependent. Longer decay times are observed at the low-energy tail of PL, which is a characteristic property of donor–acceptor pair (DAP) recombination transition [7].

The ODMR signals were detected via a change in the intensity (increase) of either the whole BL emission, or when using a set of low-pass filters for selecting different regions of the PL. In the second case no ODMR signals were observed only for the fifth low-pass filter (LP5). At least three slightly anisotropic and overlapping ODMR signals (D1, D2, A1) were observed, with g-factors (± 0.005): $g_{\|} = 1.995$ (D1), $g_{\|} = 1.982$ (D2), and $g_{\|} = 2.042$ (A1). The first two signals (D1 and D2) are relatively narrow (10 mT (D1), 19 mT (D2)), have g-factors close to 2 and are slightly anisotropic. They thus show properties of donor-related signals of GaN [8–10]. These signals were related to deeper donors. The shallow donor-related signal (slightly anisotropic signal with g-factors of $g_{\|} = 1.9514$, $g_{\perp} = 1.9486$ [11]), which was reported previously [8,9,11], was not resolved by us. The presence of shallow donors is however indicated by the observed fast components of the PL decay, and from the temperature dependence of the PL intensity, not discussed here. The third anisotropic signal (denoted as A1) with g-factor larger than 2 ($g_{\|} = 2.042 \pm 0.005$) shows properties of acceptor-related signal, which we tentatively relate to Mg acceptors. This signal is resolved for LP1 and LP2 filters but overlaps with D2 signal when PL is detected with LP3 and LP4 filters. Our ODMR data thus indicate that the same acceptor participates in all the PL transitions responsible for the BL.

The relative intensity of the D1 and D2 ODMR signals varies within the spectral region of the BL (see Fig. 3), but the A1 signal could be detected within the whole spectral region of this emission. These properties of the ODMR signals confirm a multi-band nature of the BL and prove

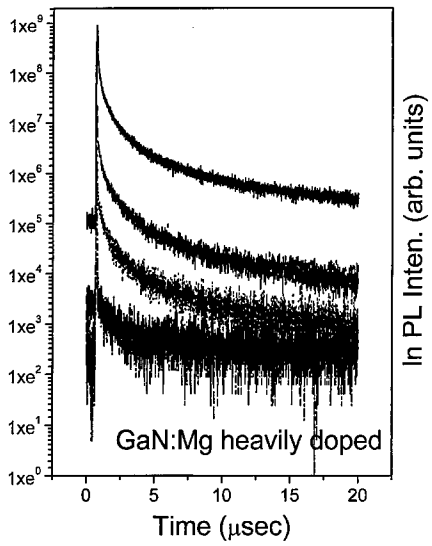

Fig. 2. 2 K PL decay spectra of bulk GaN crystal heavily doped with Mg measured at four different energies within broad blue band PL – at high-energy wing, at the maximum, at low-energy wing and at the position of the yellow PL, from top to the bottom.

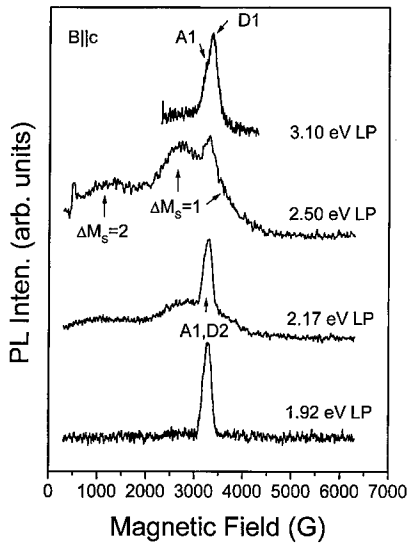

Fig. 3. The ODMR signals observed in heavily doped GaN : Mg with PL detected with LP1 to LP4 pass filters and magnetic field set along the c-axis of GaN.

the contribution of DAP transitions (donor- and acceptor-related signals are observed) to this PL.

In addition to the D1, D2 and A1 signals a new anisotropic ODMR signal is observed, which consists of a group of resonance lines around $g = 2$ and another group at about $g = 4$. This spectrum is the best resolved once using LP2 (optimum) and LP3 low-pass filters to select spectral region of the detection. Such ODMR spectra were previously observed for excitons bound at neutral complex centres and were explained by spin-triplet resonance [12]. We thus propose such an origin of the new spectrum. A detailed analysis of the angular dependence of the spectrum could not be performed, which is due to the large width of the resonance observed. We thus cannot directly conclude on the microscopic nature of the complex centre responsible for the resonance observed. The Mg–O origin of the resonance proposed below is thus tentative.

Oxygen is at present the best candidate for shallow donor species abundant in bulk GaN crystals [13]. A large change of resistivity following acceptor doping can be explained by a reduced oxygen incorporation to the crystals. This simple explanation is not, however, confirmed by the recent elastic recoil investigations of samples used in the present study [14], which shows a similar total concentration of oxygen in "undoped" and in acceptor-doped samples (between 5×10^{19} cm^{-3} and 1×10^{20} cm^{-3}). Recent calculations suggest another explanation of the observed rapid increase of the PL decay time and a triplet ODMR spectrum. Fairly low formation energy of Mg–O complexes is predicted from theoretical calculation [15]. The Mg–O complex consists of a single donor, which compensates a single acceptor; thus the Mg–O complex is a close associate of a donor–acceptor pair. It has thus the properties of the neutral complex centre observed in our ODMR experiments. We thus tentatively explain the appearance of the spin triplet ODMR spectrum by the probability of formation of close associates of Mg and O forming neutral complex centres. If so, introduction of Mg into the crystals not only charge compensates oxygen donors, but may also (for close associates) deactivate oxygen as a single donor.

4. Conclusions

The present ODMR studies indicate a multi-band DAP character of the blue PL, which is proved by the observation magnetic resonance signals of at least two donors (deep donors) and of one acceptor, which are coming from different spectral regions of a wide asymmetric BL. These centres, together with shallow donors and deep acceptors, provide initial states for radiative recombination responsible for the BL and partly the YL. The present PL and PL kinetics investigations also show that doping with acceptors steadily reduces the role of shallow donors in radiative recombination. Spin-triplet ODMR signal is attributed to magnetic resonance of exciton bound at neutral complex centre and Mg–O origin of this complex centre is proposed. Since oxygen is the main shallow donor in our bulk crystals, shallow donor concentration is reduced, i.e., doping with Mg

compensates shallow donors. A high efficiency of such compensation process can explain why concentration of shallow donors rapidly decreases in acceptor-doped samples, even though oxygen concentration remains unchanged. We further propose that similar compensation process occurs for Zn and Ca doped crystals.

Acknowledgements

This work was partly supported by National Committee for the Scientific Research under Grant KBN 2P 03B 018 13 (M. Godlewski) and 2P03B 101 14 (T. Suski)

References

[1] S. Porowski, I. Grzegory, in: S. Pearton (Ed.), GaN and Related Materials, Gordon and Breach Publishers, London, 1997, p. 295.
[2] M. Leszczynski, P. Prystawko, S. Porowski, in: J.H. Edgar, et al. (Eds.), Gallium Nitride and Related Semiconductors, Data Review Series No. 23, INSPEC, London, 1999, p. 391.
[3] P. Prystawko, M. Leszczynski, A. Sliwinski, H. Teisseyre, T. Suski, M. Bockowski, S. Porowski, J. Domagala, C. Kirchner, A. Pelzmann, M. Schauler, M. Kamp, J. Cryst. Growth 198/199 (1999) 1061.
[4] S. Porowski, Proceedings of The Second International Conference on Nitride Semiconductors, Tokushima, Japan 1997, p. 430.
[5] P. Perlin, T. Suski, M. Leszczynski, H. Teisseyre, in: S. Pearton (Ed.), GaN and Related Materials, Gordon and Breach Publishers, London, 1997, p. 315.
[6] U. Kaufmann, M. Kunzer, M. Maier, H. Obloh, A. Ramakrishnan, B. Santic, P. Schlotter, Appl. Phys. Lett. 72 (1998) 1326.
[7] D.G. Thomas, J.J. Hopfield, W.M. Augustyniak, Phys. Rev. 140 (1965) A202.
[8] E.R. Glaser, T.A. Kennedy, K. Doverspike, L.B. Rowland, D.K. Gaskill, J.A. Freitas, M.A. Khan, D.T. Olson, J.N. Kuznia, D.K. Wickenden, Phys. Rev. B 51 (1995) 13326.
[9] P.W. Mason, A. Dörnen, V. Haerle, F. Scholz, G.D. Watkins, in: F.A. Ponce, T.D. Moustakas, I. Akasaki, B.A. Monemar (Eds.), III–V Nitrides, MRS, Pittsburgh, Pennsylvania, 1997, MRS Symposium Proceedings, Vol. 449, p. 793.
[10] F.K. Koschnick, K. Michael, J.-M. Spaeth, B. Beaumont, P. Gibart, J. Off, A. Sohmer, and F. Scholz, Proceedings of The Second International Conference on Nitride Semiconductors, Tokushima, Japan 1997, p. 398.
[11] M. Palczewska, B. Suchanek, R. Dwilinski, K. Pakula, A. Wagner, M. Kaminska, MRS Internet J. Nitride Semicond. Res. 3 (1998) 45.
[12] W.M. Chen, B. Monemar, M. Godlewski, Defect Diffusion Forum 62/63 (1989) 133.
[13] C. Wetzel, T. Suski, J.W. Auger, E.R. Weber, E.E. Haller, S. Fischer, B.K. Meyer, R.J. Molnar, P. Perlin, Phys. Rev. Lett. 78 (1997) 3923.
[14] T. Suski, J. Jun, M. Leszczynski, H. Teisseyre, I. Grzegory, S. Porowski, G. Dollinger, K. Saarinen, T. Laine, J. Nissila, W. Burkhard, W. Kriegseis, B.K. Meyer, Mater. Sci. Eng. B 59 (1999) 1.
[15] C.G. Van De Walle, C. Stampfl, J. Neugebauer, Proceedings of The Second International Conference on Nitride Semiconductors, Tokushima, Japan 1997, p. 386.

ELSEVIER

Physica B 273–274 (1999) 43–45

PHYSICA B

www.elsevier.com/locate/physb

Mg acceptors in GaN: Dependence of the g-anisotropy on the doping concentration

Detlev M. Hofmann[a,*], Wolfgang Burkhardt[a], Frank Leiter[a], Walter von Förster[a], Helder Alves[a], Albrecht Hofstaetter[a], Bruno K. Meyer[a], Nikolai G. Romanov[b], Hiroshi Amano[c], Isamu Akasaki[c]

[a] *I. Physics Institute, Justus-Liebig-Universität Giessen, Heinrich-Buff-Ring 16, D 35392 Giessen, Germany*
[b] *A.F. Ioffe Physio-Technical Institute, RAS, 194021 St. Petersburg, Russia*
[c] *Department of Electrical and Electronic Engineering, 1-501 Shiogamaguchi, Tempaku-ku, Nagoya 468, Japan*

Abstract

Mg acceptors in GaN epitaxial layers grown by metal–organic vapour-phase epitaxy were investigated by optically detected magnetic resonance (ODMR) spectroscopy. The magnetic resonances were detected on the magnetic circular dichroism (MCD) of the acceptor bound exciton (Mg^0X) in the near bandgap region, and in the infrared spectral range on the MCD of the hole ionisation transition $Mg^0 + h\nu \rightarrow Mg^- + h_{VB}$. The observed g-values of the Mg^0 acceptors range for $g_{||}$ from 2.102 to 2.065 and for $g_\perp$ from 1.94 to 2.00, respectively. These variations depend on the Mg doping concentration.

Keywords: GaN; p-Doping; Mg-acceptor; Magnetic resonance

1. Introduction

Mg is the technological most relevant acceptor dopant for GaN. Compared to other acceptors such as Zn the Mg binding energy is rather small ($E_A = 260$ meV) and Mg can be doped in concentrations up to 10^{20} cm^{-3} [1]. This results in free hole concentrations at room temperature of the order of 10^{18} cm^{-3} being sufficient for many applications. However, compensation has been noticed already for low doping concentrations and photoluminescence shows in most cases that the shallow donor to shallow acceptor recombination at 3.2 eV is accompanied by a deeper band centred at about 2.8 eV. The 2.8 eV band is caused by a deep (compensating) donor to shallow Mg acceptor recombination [2].

To study the defects or impurities involved in detail magnetic resonance spectroscopy is an appropriate tool. Up to now the ODMR data reported on Mg-doped GaN give a non-coherent picture, g-values attributed to the Mg acceptor range from $g_{||} = 2.084$ to 2.02 and $g_\perp = 2.045$ to 1.990 (for a compilation of data, see Ref. [3]). One can speculate whether always the Mg acceptor acts as a isolated point defect or might be of more complex nature.

2. Experimental

Our experiments were performed on a series of Mg-doped GaN epitaxial layers grown by metal–organic vapour-phase epitaxy (MOVPE) on sapphire with AlN buffer layers. The thickness of the GaN layers were 0.9–1.4 μm. The Mg doping concentrations were determined by secondary-ion-mass spectroscopy (SIMS) and range from 9×10^{18} to 8×10^{19} cm^{-3}.

* Corresponding author: Fax: + 49-641-9933119.
E-mail address: detlev.m.hofmann@exp1.physik.uni-giessen.de (D.M. Hofmann)

0921-4526/99/$ - see front matter
PII: S0921-4526(99)00402-0

For the optical detection of the magnetic resonance spectroscopy we used a 24 GHz spectrometer described elsewhere [4]. As detection channel for the ODMR served the magnetic circular dichroism of the absorption (MCD) [5].

3. Results and discussion

In the Mg-doped GaN samples one can notice a shrinkage of the bandgap compared to the undoped reference material (see Fig. 1, dashed and dotted line). This additional absorption is likely to originate from impurity-to-band transitions, like $A^- + h\nu \rightarrow A^0 + e_{CB}$, or $D^+ + h\nu \rightarrow D^0 + h_{VB}$, or from the creation of excitons like $A^0 + h\nu \rightarrow A^0X$, or $D^0 + h\nu \rightarrow D^0X$. Among them the acceptor-bound exciton transition from the paramagnetic Mg^0 ground state to the neutral acceptor-bound exciton (Mg^0X) gives rise to a temperature and magnetic field dependent MCD (full line in Fig. 1).

It allows the optical detection of the magnetic resonance of the paramagnetic ground state of the Mg acceptors (Fig. 2). A single ODMR line is observed which corresponds to a decrease of the MCD of 30% for microwave powers of about 50 mW. The position of the ODMR signal varies with the sample orientation and reveals the axial symmetry of the centre. The experimental resonance position as a function of the angle θ between the magnetic field and the crystallographic c-axis of the sample is described by the relation

$$g(\theta) = (g_{\|}^2 \cos^2(\theta) + g_{\perp}^2 \cos^2(\theta))^{1/2}, \quad (1)$$

where $g_{\|}$ and $g_{\perp}$ correspond to the g-values parallel and perpendicular to the orientation of the c-axis in respect to the static magnetic field. The obtained pairs of g-values $(g_{\|}, g_{\perp})$ of all samples investigated are plotted as a function of the Mg-doping concentration in Fig. 3.

Extending the detection of the ODMR to longer wavelengths we find almost no response for energies down to 1.5 eV. However, below 1.5 eV we found paramagnetic MCD of increasing intensity which decreasing photon energy. The ODMR recorded on this MCD is identical to the ODMR detected on the Mg^0X. The open circles in Fig. 4 show the amplitude of the ODMR signals as a function of photon energy. It is well known that shallow acceptors give rise to photo-ionisation transitions of the type $A^0 \rightarrow A^- + h_{VB}$. The maximum of the corresponding absorption is located in the infrared

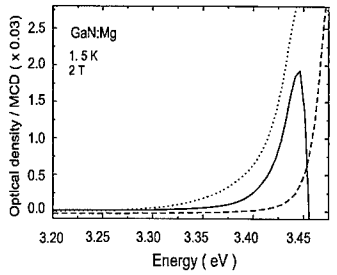

Fig. 1. Optical absorption in the near bandgap region of undoped GaN (dashed line) and Mg-doped GaN (dotted line). The full line shows the magnetic circular dichroism (MCD) observed in the Mg doped sample.

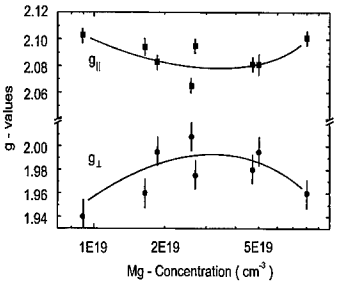

Fig. 3. Variation of the Mg^0-acceptor g-values in GaN as a function of the Mg doping concentration.

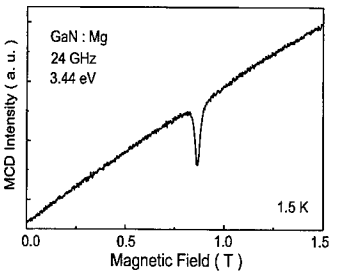

Fig. 2. Optically detected magnetic resonance spectrum observed on the magnetic circular dichroism (MCD) of the Mg^0-acceptor-bound-excitons in GaN.

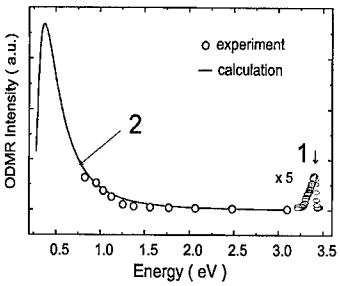

Fig. 4. Spectral dependence of the optically detected magnetic resonance of the Mg^0 acceptors in GaN. (1) Labels the acceptor bound exciton transition, and (2) the hole ionisation transition of the Mg^0-acceptors (for details see text).

and depends on the acceptor binding energy (E_A) but the spectrum can extend far to the visible spectral range. The spectral dependence of the photo-ionisation cross-section is given by [6]

$$\sigma(h\nu) = (h\nu - E_A)^{3/2}(h\nu)^{-5}. \quad (2)$$

The solid line in Fig. 4 shows the result of the calculation with $E_A = 260$ meV, the optical binding energy of the Mg acceptor.

The labels (1) and (2) indicate the two absorption transitions which enabled the observation of the ODMR of the Mg^0 acceptors: (1) the acceptor bound exciton (Mg^0X), and (2) the hole-ionisation transition $Mg^0 + h\nu \rightarrow Mg^- + h_{VB}$. These two transitions were observed in all the samples investigated and for which the Mg-acceptor g-values are plotted in Fig. 3. Although the Mg g-values show considerable scatter as a function on the doping concentration one can extract the following trend. The g-anisotropy decreases up to doping concentrations of about $2\text{–}3 \times 10^{19}$ cm^{-3}. For higher Mg concentrations it seems to increase again. An explanation can be given by the following considerations. The MOVPE GaN layers are compressive strained due to the difference in thermal expansion coefficients between GaN and the sapphire substrate. Mg substitutes Ga in the crystal lattice and it has a larger ionic radius. It can counteract to the thermal strain, and give an additional contribution to the g-anisotropy. This may be possible only to some extent, depending on the growth condition, buffer layer, annealing procedure for the acceptor activation, and layer thickness. For too high doping concentrations ($> 5 \times 10^{19}$ cm^{-3}) the lattice strain may shift back to a state similar to the conditions for low doping. Obviously, this model requires its justification by structure sensitive methods like X-ray reflection, these investigations are currently under the way, but preliminary results seem to support the model.

It should be noted that for the room temperature free hole densities in Mg-doped GaN a comparable trend on the doping concentration is observed as for the g-values [7]. The hole densities increase for doping concentrations up to 3×10^{19} cm^{-3} and start to decrease for higher concentrations. So far this behaviour is explained qualitatively by the formation of deep compensating donors only, but probably the formation of new Mg-related phases in GaN has also to be taken into account for the highly doped samples [8].

4. Summary

In summary, Mg acceptors in GaN epitaxial layers were investigated by ODMR spectroscopy using the magnetic circular dichroism (MCD). The MCD reveals the acceptor bound exciton (Mg^0X) in the near band gap region, and in the infrared spectral range the hole ionisation transition $Mg^0 + h\nu \rightarrow Mg^- + h_{VB}$. The observed g-values of the Mg^0 acceptors range for $g_{||}$ from 2.102 to 2.065 and for $g_\perp$ from 1.94 to 2.008, respectively.

References

[1] H. Amano, M. Kito, K. Hiramatsu, I. Akasaki, Jpn. J. Appl. Phys. 28 (1989) L2112.
[2] U. Kaufmann, M. Kunzer, H. Obloh, M. Maier, Ch. Manz, A. Ramakrishnan, B. Santic, Phys. Rev. B 59 (1999) 5561.
[3] B.K. Meyer, in: K.A Willardson, R.C. Beer (Eds.), Semiconductors and Semimetals, Vol. 57, Academic Press, London, 1999, p. 371.
[4] C. Schnorr, Dissertation, Gießen, 1996.
[5] E.F. Mollenauer, S. Pan, Phys. Rev. B 6 (1972) 772.
[6] J.S. Blakemore, S. Rahimi, in: K.A. Willardson, R.C. Beer (Eds.), Semiconductors and Semimetals, Vol. 20, Academic Press, London, 1984, p. 87.
[7] H. Obloh, K.-H. Bachem, D. Behr, U. Kaufmann, M. Kunzer, A. Ramakrishna, P. Schlotter, M. Seelmann-Eggebert, J. Wagner, in: B. Kramer (Ed.), Advances in Solid State Physics, Vol. 38, Vieweg, Braunschweig, 1999, p. 15.
[8] S. Liliental-Weber et al., Physica B 273–274 (1999) 124, These Proceedings.

ELSEVIER

Physica B 273–274 (1999) 46–49

PHYSICA B

www.elsevier.com/locate/physb

Electrical characterization of Mg-related energy levels and the compensation mechanism in GaN : Mg

D. Seghier, H.P. Gislason*

Science Institute, University of Iceland, Dunhagi 3, IS-107 Reykjavik, Iceland

Abstract

We investigated GaN : Mg samples grown by metalorganic chemical vapor deposition using various electrical measurement techniques. Annealing of as-grown samples for different duration of time gives gradual activation of acceptors. Conductance measurements of the annealed samples show the presence of a hole trap with concentration directly proportional to the electrically active acceptor concentration in the samples. This trap is the shallowest one in our samples with activation energy 130 from the valence band. We attribute it to an Mg acceptor. Electron traps observed in optical deep-level transient measurements have too weak concentrations to influence the free carrier concentration. We conclude that the hole conductivity observed in the annealed GaN samples is due to thermal dissociation of hydrogen from passivated Mg acceptors. Most of the Mg concentration in the samples however remains electrically inactive.

Keywords: GaN; Mg; Hydrogen; Passivation

High hole conductivity in GaN and other wide band gap III–V nitrides is the key for producing short-wavelength optical devices as well as high-power and high-frequency electronic devices. Mg is so far the only dopant in GaN which generates sufficient p-type conductivity in a reproducible manner. For reasons of inadvertent compensation in the as-grown GaN layers, treatments such as electron-beam irradiation or thermal annealing [1,2] are required in order to activate the p-type conductivity in layers grown by metalorganic chemical vapor deposition (MOCVD). Detailed characteristics of the electrical activity of Mg in GaN are not yet well understood. Several energy levels have been detected using various characterization techniques and have been attributed to Mg [3–7]. It can be argued that the literature does not provide a coherent picture of these acceptor levels. In this paper we report results from admittance spectroscopy, optical deep-level transient spectroscopy (ODLTS), dark current and thermally stimulated current (TSC) measurements on GaN : Mg. We show that the shallowest acceptor level which controls the conductivity in our samples is situated at 130 meV above the valence band and assign it to Mg. We suggest that the charge compensation of this acceptor level in MOCVD-grown GaN : Mg is caused by hydrogen passivation of the Mg acceptor.

The GaN : Mg epilayers were grown by the EMCORE corporation using MOCVD on *c*-plane sapphire substrates. The specified Mg concentration of the films is around $2–5 \times 10^{19}$ [8]. The measurements were conducted on Schottky devices made by evaporating Au on 2 μm thick layers of the as-grown or annealed GaN : Mg epilayers. Ohmic contacts were made by melting In on the front face of the GaN layer. Admittance measurements were performed in the dark using a Hewlett–Packard 4284A LCR meter at an AC-modulation signal level of 10 mV and frequencies ranging from 10 Hz to 1 MHz. Conductance and capacitance were monitored over a temperature range of 80–300 K using an MMR cryostat with a controllable heating rate. A standard set-up was used for measuring the ODLTS, which enables the

* Corresponding author. Fax: + 354-552-8911.
E-mail address: haflidi@raunvis.hi.is (H.P. Gislason)

0921-4526/99/$ - see front matter
PII: S0921-4526(99)00403-2

observation of electron traps in the upper part of the bandgap of p-type semiconductors. For measurements of the thermally stimulated current the samples were first illuminated at 80 K for about 10 min, then heated up to room temperature in the dark using different heating rates.

The aim of this study was to obtain a gradual electrical activation of the Mg acceptors through annealing as Table 1 shows. We performed capacitance–voltage (C–V) measurements at room temperature in order to determine the net acceptor concentration of the samples. Four pieces were cut from the same highly resistive as-grown wafer. For reasons of their high resistivity, it was not possible to measure the as-grown samples using Hall- or capacitance techniques. Three of the samples (denoted #1, #2 and #3 in Table 1) were annealed at 500°C under flowing N_2 for time duration 1, 3, and 6 min, respectively. This resulted in net acceptor concentrations in the range $N_a - N_d = 3\text{–}7 \times 10^{16}\ \text{cm}^{-3}$. We interpret this as a thermal activation of Mg-related acceptors. Sample #4 in Table 1 was annealed at 800°C under flowing N_2 for 20 min, which gave the highest net acceptor concentration $N_a - N_d = 1 \times 10^{17}\ \text{cm}^{-3}$. Under these optimal conditions of acceptor activation [8] about 1% of the Mg concentration is activated as acceptors. Most of the Mg in the samples remains electrically inactive under the annealing conditions of this work. The reasons for this are unclear. In the following we focus on the small fraction of the Mg concentration which causes the net acceptor concentration of the samples given in Table 1.

Fig. 1 shows the capacitance as a function of temperature measured at 10 kHz with a bias of 0 V. The capacitance shows a similar behaviour in all samples. After a smooth decrease between room temperature and approximately 150 K, it drops drastically to a level at which it remains at temperatures below 110 K. *C–V* measurements show that the samples are completely depleted at these low temperatures. Hence, we deduce that the abrupt decrease in capacitance is due to a freeze-out of free carriers. The results also underline that the shallowest acceptor level has similar ionization energies in all samples. The variation of conductance with temperature is shown in Fig. 2. The measurements were performed at 10 kHz under 0.5 V reverse bias. Two peaks, labelled H1 at lower temperature and H2 at higher temperature, are observed. Measurements at different frequencies show that the peaks are related to defects, since the corresponding plots of $\log(\omega/T^2)$ versus $1/T$ give straight lines, where ω is the angular frequency of the ac signal and T the temperature. The defects are hole traps since admittance spectroscopy only detects majority carrier traps. The hole activation energies deduced from the plots of $\log(\omega/T^2)$ versus $1/T$ are 130 and 170 meV for the H1 and H2 levels, respectively. A number of acceptor levels in GaN : Mg with activation energies close to that of the H1 and the H2 hole traps in this work have been reported in the literature. It is possible that the levels in the energy range between 124 and 136 meV [4–6], on the one hand, and 158 and 182 meV [4,5,7], on the other, are identical to the H1 and H2 levels, respectively, and related to Mg. The peak height of H1 is a linear function of $N_a - N_d$ in the four samples as shown in Fig. 3. Changes in the height of a conductance peak in admittance spectra can be interpreted as similar changes in the concentration of the corresponding trap [9]. Thus the straight line of Fig. 3 shows that the concentration of the H1 trap is

Table 1
Dependence of the net acceptor concentration on the annealing conditions

Sample	Annealing time and temperature	$N_a - N_d$ (cm^{-3})
1	1 min/500°C	3×10^{16}
2	3 min/500°C	4.5×10^{16}
3	6 min/500°C	7×10^{16}
4	20 min/800°C	1×10^{17}

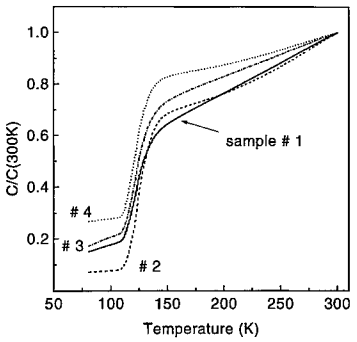

Fig. 1. Capacitance (C) as a function of temperature at AC frequency of 10 kHz. The value of the capacitance has been normalized to that at 300 K for each sample.

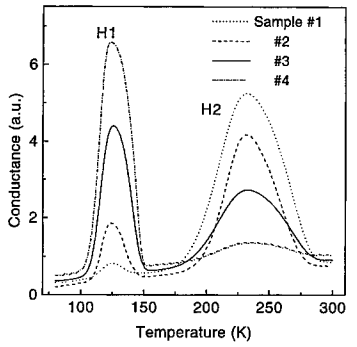

Fig. 2. Conductance as a function of temperature at AC frequency of 10 kHz.

directly proportional to the net concentration of active acceptors in the samples. For this reason we attribute it to a Mg acceptor. The temperature at which the H1 peak is observed coincides with the inflection point in the capacitance versus temperature curves measured at the same frequency, i.e. 10 kHz (see Fig. 2). Arrhenius plots of the dark current in the annealed samples give an activation energy of 136 meV, which agrees with that of the H1 trap. Therefore, we conclude that H1 originates from the shallowest acceptor level in the GaN layers. In contrast, the height of the H2 peak seems to decrease in a sublinear way with the net acceptor concentration. From the absence of a clear corresponding step in the capacitance versus temperature curves, we deduce that the concentration of the H2 trap is too weak to affect the carrier concentration in our samples.

In ODLTS spectra two positive peaks related to electron traps are observed in the annealed samples with activation energies 0.28 and 0.58 eV, respectively. The ODLTS spectra and the peak heights are quite similar in the samples. Electron traps with similar activation energy have been observed in n-type GaN [10,11]. The concentrations of the 0.28 and 0.58 eV electron traps as estimated from the spectra are 5×10^{13} and 2×10^{14} cm^{-3}, respectively. Hence, they have negligible effect on the carrier concentration in the samples. Given the different conductivity of the samples, we exclude the possibility that the charge compensation of the active acceptors is caused by the presence of electron traps.

Fig. 4 shows a thermally stimulated current spectrum typical of the highly resistive as-grown GaN : Mg samples. At least four peaks, denoted T1–T4, are observed. The peaks are only partially resolved and thus it is difficult to calculate their activation energies from the TSC spectra. In order to resolve the peaks we fitted the data for peaks T1 and T2 with Gaussian curves as shown in the figure. In this way we deduced the following activation energies: 180 ± 10, 250 ± 12, 540 ± 20, and 600 ± 20 meV for peaks T1–T4, respectively. Judging from its energy position, peak T1 may correspond to peak H2 in the conductance spectra of Fig. 2. Peak T2 possibly originates from the level observed by ODLTS at 0.28 eV below the conduction band. Peaks T3 and T4 are close in energy, and one of them may originate from the electron trap observed by ODLTS at 0.58eV below the conduction band. An important aspect of Fig. 4 is the absence of a peak corresponding to H1. In view of the low activation energy of the H1 trap we searched for the peak using various higher heating rates than in Fig. 4, without observing any trace of H1. The absence of this level in the as-grown samples suggests that the Mg acceptors are electrically inactive before heat treatment, which is consistent with the high resistivity of the as-grown samples. We conclude that they are most likely passivated by hydrogen, as already suggested by several authors [1,2].

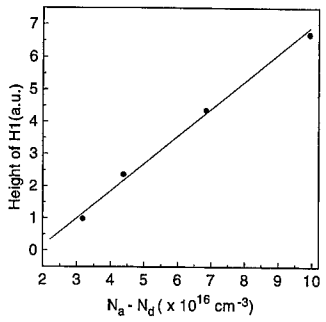

Fig. 3. Height of the H1 conductance peak as a function of net acceptor concentration.

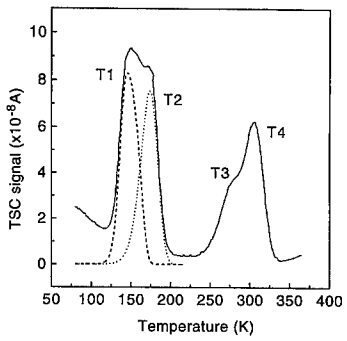

Fig. 4. TSC spectra measured in an as-grown sample. The dotted lines are Gaussian curves used for deconvolution of data.

In some reports the conductivity has been found to have an activation energy close to that of the H2 trap [4,5,7]. An acceptor level in the range 170–182 meV (depending on the active acceptor concentration) is the dominating level in the MOCVD-grown samples of Götz et al. [7] as determined from Hall effect measurements. However, the possible presence of a shallower level with much lower concentration would not be revealed in this kind of measurement. In our samples the H2 trap does not have a significant influence on the conductivity. Indeed, the capacitance versus temperature curves in Fig. 1 show that the concentration of H2 is much lower than that of the dominating H1 acceptor. Also, measurements of thermally stimulated current only reveal the H2 level in as-grown samples, where most of the H1 acceptors are absent. We do not know the reason why different acceptor levels dominate the p-type conductivity in the above cases, although different growth conditions may give a natural explanation for this experimental fact. Since the H2 level is only observed when the H1 level is weak in our samples, it is possible that it dominates the conductivity in samples with different Mg concentration from ours. In order to examine this hypothesis samples grown under other conditions with different Mg concentrations have to be investigated.

In summary, we investigated two hole traps H1 and H2 with activation energies 130 and 170 meV above the valence band, respectively, in GaN : Mg samples cut from the same as-grown highly resistive wafer annealed for different duration of time. The H2 trap has very low concentration. We attributed H1, the shallowest level in our samples, to an Mg acceptor which controls the conductivity in the samples. We demonstrated that it is absent from the as-grown samples, but activated by thermal annealing. The linear relation between the height of the H1 peak and the net acceptor concentration directly illustrates that the hole conductivity in the samples originates from the thermally activated H1 acceptor. To the best of our knowledge this is the first manifestation of such a relationship in GaN : Mg, which is usually attributed to hydrogen being extracted from the samples during the annealing [5]. We also observed two electron traps at 0.28 and 0.58 eV from the conductance band, with concentrations too low to influence conductivity of the samples. We conclude that the hole conductivity of GaN : Mg is due to thermal release of hydrogen from passivated Mg acceptors.

This work was supported by the Icelandic Research Council and the University Research Fund. We are grateful to EMCORE for providing the samples.

References

[1] S. Nakamura, T. Mukai, M. Senoh, N. Iwasa, Jpn. J. Appl. Phys. 31 (1992) L139.
[2] S. Nakamura, N. Iwasa, M. Senoh, T. Mukai, Jpn. J. Appl. Phys. 31 (1992) 1258.
[3] S. Fischer, C. Wetzel, E.E. Haller, B.K. Meyer, Appl. Phys. Lett. 67 (1995) 1298.
[4] T. Tanaka, A. Watanabe, H. Amano, Y. Kobayashi, I. Akasaki, S. Yamazaki, M. Koike, Appl. Phys. Lett. 65 (1994) 593.
[5] J.W. Huang, T.F. Kuech, Hongqiang Lu, Ishwara Bhat, Appl. Phys. Lett. 68 (1996) 2392.
[6] C. Johnson, J.Y. Lin, H.X. Jiang, Appl. Phys. Lett. 68 (1996) 1808.
[7] W. Götz, N.M. Johnson, J. Walker, D.P. Bour, R.A. Street, Appl. Phys. Lett. 68 (1996) 667.
[8] Emcore corporation. Private communication.
[9] D.L. Loose, J. Appl. Phys. 46 (1975) 2204.
[10] P. Hacke, H. Nakayama, T. Detchprohm, K. Hiramatsu, N. Sawaki, Appl. Phys. Lett. 68 (1996) 1362.
[11] W. Götz, N.M. Johnson, D.P. Bour, Appl. Phys. Lett. 68 (1996) 3470.

ELSEVIER

Physica B 273–274 (1999) 50–53

PHYSICA B

www.elsevier.com/locate/physb

Effect of Si doping on the strain and defect structure of GaN thin films

L.T. Romano[a,*], C.G. Van de Walle[a], B.S. Krusor[a], R. Lau[a], J. Ho[a], T. Schmidt[a], J.W. Ager III[b], W. Götz[c], R.S. Kern[c]

[a]*Xerox Palo Alto Research Center, 3333 Coyote Hill Road, Palo Alto, CA 94304, USA*
[b]*Materials Sciences Division, Lawrence Berkeley National Laboratory, CA 94720, USA*
[c]*Hewlett-Packard Company, Optoelectronics Division, San Jose, CA 95131, USA*

Abstract

The amount of strain was measured in GaN films using X-ray diffraction, Raman, and curvature techniques as a function of film thickness and the Si doping concentration. It was found that for a doping concentration of 2×10^{19}, the threshold thickness for crack formation was about 2.5 μm. Transmission electron microscopy observations showed that cracking proceeds without plastic deformation (i.e., no dislocation motion), and occurs catastrophically along the low-energy {1 $\bar{1}$ 0 0} cleavage plane of GaN.

Keywords: Residual stress; GaN films; Dislocations

1. Introduction

Residual strain in the III–V nitrides has been observed previously [1–5] and found to limit the alloying and doping concentrations necessary for optoelectronic devices [6,7]. Raman and X-ray diffraction studies performed on Si-doped GaN films have shown that the residual compressive strain decreased with increasing Si concentration [5]. Based on transmission electron microscopy (TEM) studies, Ruvimov et al. suggested that the strain relief for moderately doped Si samples ($\sim 3 \times 10^{18}$ cm^{-3}) was due to the formation of dislocations in the basal plane [3].

In this paper the relationship between the extended defect structure and strain is studied in order to understand the mechanism of crack formation in GaN films. Films doped with Si were measured as a function of both the doping concentration [Si] and film thickness t and compared with the microstructure. The films were grown by metal organic vapor deposition on (0 0 0 1) sapphire substrates up to 2.5 μm thick. Most of the samples were prepared by first depositing a low-temperature (LT) GaN buffer layer, followed by 100 nm of a high-temperature (HT) undoped layer, then introducing silane to begin the growth of the doped layer (A samples). Some of the 2 μm thick films were prepared by introducing the silane directly after growth of the LT buffer layer (B samples). Hall and secondary ion mass spectrometry (SIMS) were used to determine the carrier concentration and [Si]. In all the samples the agreement between the [Si] and carrier concentration indicated that all the Si was electrically active and therefore inferred to reside on the Ga site.

Strain was measured by using Raman, curvature, and X-ray diffraction (XRD) measurements. Raman study was measured by the shift in the E2 phonon with a lateral spatial resolution of 1 μm as discussed previously [4]. The a and c lattice constants were measured by XRD using the (1 0 $\bar{1}$ 5) and (0 0 0 2) reflections, respectively, and compared to values for bulk single crystal to determine the strain ($a_0 = 3.1876$ and $c_0 = 5.1846$ from porowski [8]. Strain from curvature measurements was calculated using the Stoney equation [9]. Atomic force microscopy (AFM), scanning (SEM) and transmission

*Corresponding author. Tel.: +1-650-812-4167; fax: +1-650-812-4140.
E-mail address: romano@parc.xerox.com (L.T. Romano)

0921-4526/99/$ - see front matter
PII: S0921-4526(99)00404-4

electron microscopy (TEM) were used to measure the roughness and structure of the material. TEM samples were prepared in the usual way by mechanically thinning and ion milling to electron transparency.

2. Results

Fig. 1 shows the residual strain measured by Raman, curvature, and XRD as a function of Si doping. The strain is found to increase with both the film thickness and [Si]. At low [Si], the films are in compression which is expected to occur on cooling due to the difference in thermal expansion coefficients between GaN and sapphire. However, as the Si concentration increases the films are found to be in tensile stress. For $t = 1.0\ \mu m$ the crossover from compressive to tensile strain is observed to occur at [Si] $\approx 10^{19}\ cm^{-3}$. The crossover for $t = 2.0\ \mu m$ occurs at [Si] $\approx 10^{18}\ cm^{-3}$. The highest tensile strain ($\varepsilon = 0.025$) was measured for $t = 2.5\ \mu m$ at [Si] $= 2 \times 10^{19}\ cm^{-3}$. The strains measured by the various techniques were in fairly good agreement for all the Si concentrations. Some exceptions were noted at the highest [Si] where cracking was also observed. The reason for this is related to the spatial resolution of the Raman probe and the difference in the strain near and away from the cracks as discussed below.

Cracking was present in films with a doping level of $2 \times 10^{19}\ cm^{-3}$ for $t \geqslant 2\ \mu m$. Subsurface cracking occurred for films with $t = 2\ \mu m$ whereas cracks extended to the surface for films with $t = 2.5\ \mu m$. The cracking occurred on the prismatic $\{1\ \underline{1}\ 0\ 0\}$ cleavage planes [10] of the GaN (i.e., parallel to the growth direction). The subsurface cracking suggests that the films cracked during growth at high temperature. Fig. 2a is a TEM micrograph of a subsurface crack in a 2.0 μm thick B film. The

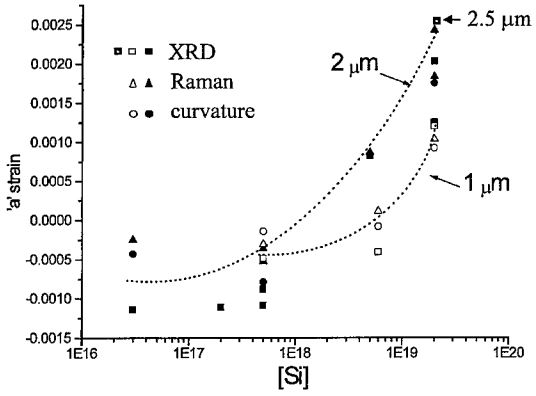

Fig. 1. The residual strain from Raman, curvature, and XRD measurements as a function of Si doping for $t = 1.0\ \mu m$ (unfilled symbols), 2.0 μm (filled symbols), and 2.5 μm (patterned symbol).

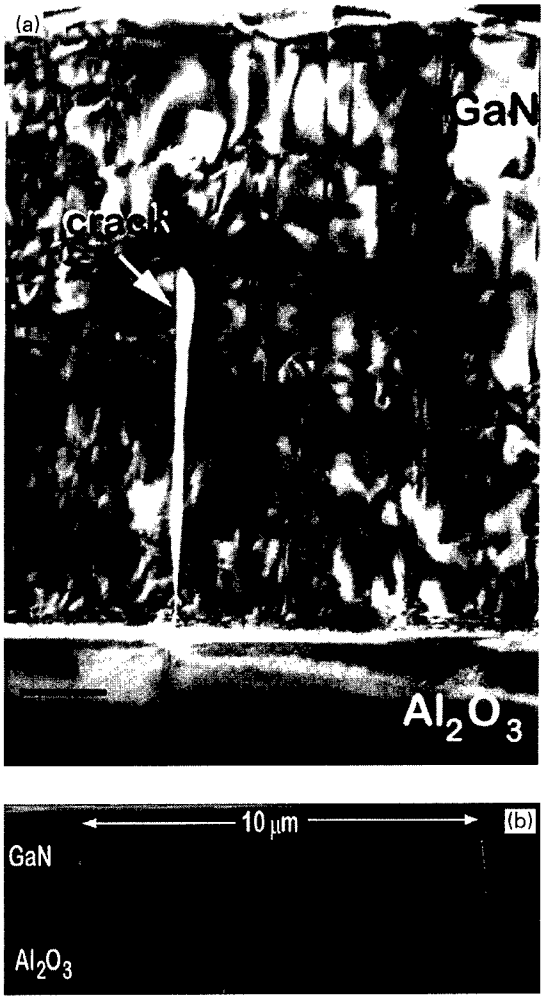

Fig. 2. (a) TEM micrograph of a subsurface crack in a 2.0 μm thick B film. (b) lower TEM magnification of the same film showing the separation between two subsurface cracks.

crack extends into the film/substrate interface and there are no additional dislocations observed near the crack. This suggests that plastic deformation does not take place to promote crack formation. The widest part of the crack is $\Delta L \sim 50$ nm and from Fig. 2b, the average crack spacing is shown to be $L \sim 10\ \mu m$. The amount of strain ε that has been relieved by the formation of the crack is $\varepsilon = \Delta L/L = 0.005$.

The surface of the overgrown cracks is found to be higher than the region of the away from the cracks. The AFM image in Fig. 3 shows lines of lighter contrast which correspond to the position of the cracks below the surface. A line scan taken across the lighter contrast regions indicates that the surface above the crack is ~ 15–20 nm higher compared to the surrounding region which has a root mean square (RMS) roughness of 3 nm.

The surface cracks on the 2.5 μm thick films occurred at larger separation distances than the subsurface cracks and were found to initiate at pits or irregularities on the surface. They were also found to be preferentially on the $\{1\bar{1}00\}$ planes. Raman measurements showed variations in the strain depending on the position of the probe relative to the crack. The measurements were taken linearly at 2 μm intervals on either side of the crack. Near the crack, the film was found to be in a small amount of compressive strain (0.05%) compared to a maximum tensile strain of 0.16% measured 100 μm from the crack. The compressive strain near the crack is due to the residual strain from cooling to room temperature. The strain becomes tensile at a position 20 μm from the crack which indicates that the strain relief induced by the crack occurs locally.

Small differences in strain were measured in films with [Si] at 2×10^{19} prepared with and without the undoped prelayer. The films with the undoped prelayer (samples A) had a lower tensile strain compared to the B films (no prelayer). This may be due to the difference in microstructure observed in the TEM (not shown). For samples B, a region containing basal plane dislocations extended approximately 1 μm above the LT buffer layer (i.e., half the total film thickness). The presence of these dislocations may have introduced larger strains in the material. For the A samples, no basal plane dislocations were generated at the doped interface. Instead threading dislocations that were generated in the undoped prelayer extended unperturbed into the doped portion of the film.

3. Discussion

The origin of the increase in tensile strain with Si doping is puzzling. We have shown elsewhere that the effect of incorporating Si in the GaN lattice (substituting on a Ga site) has no net effect on the lattice constant of the GaN lattice [11], if both the size effect and the deformation-potential effect are taken into account. The size effect would result in a net contraction of the lattice, since the Si–N bond length is smaller than the Ga–N bond length. However, for the doping concentrations used in this study, the change in lattice constant due to the size effect is an order of magnitude smaller than the strains we observe. In addition by taking into account that the Si is electrically active (the SIMS and Hall measurements indicated that the Si and electron concentrations were in good agreement up to 2×10^{19} cm^{-3}), the deformation-potential effect would lead to a net expansion of the lattice. The size effect and deformation-potential effects have similar magnitudes but are of opposite sign, resulting in no net change in strain with the addition of Si.

The observed changes in tensile strain when Si is incorporated can therefore not be attributed to a change in the lattice constant due to silicon. Silicon must therefore play a different role, presumably related to plastic deformation (or lack thereof). An understanding of this process would require better insight into the stress experienced by the film at the growth temperature, an issue that is only beginning to be explored. Recently, Hearne et al. reported in situ wafer curvature measurements that show

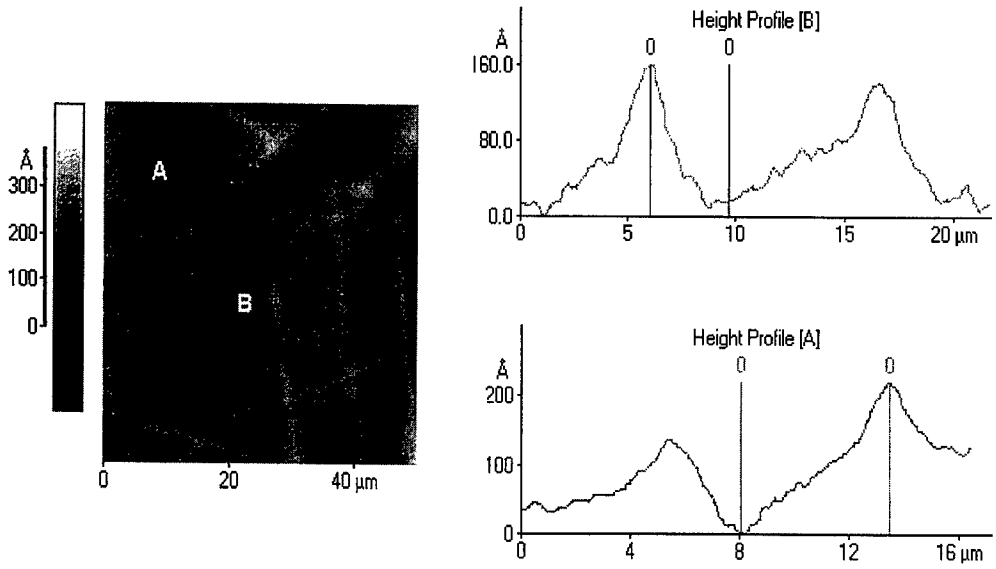

Fig. 3. (a) AFM micrograph of the surface of the same film in Fig. 2. (b) Line scans of the AFM image are taken through the regions of different contrast.

that tensile strains occur in GaN films at the growth temperature [9]. We suggest that this tensile strain may be related to the crystallite coalescence model developed recently by Nix and Clemens [12]. Their model shows that when the crystallite size decreases, the tensile stress increases. To address this issue we performed AFM measurements on 20 nm thick films grown over a 100 nm undoped layer. It was found that for $[Si] = 5 \times 10^{17}$ cm^{-3} the RMS roughness was 5.5 nm compared to 11.0 nm for $[Si] = 2 \times 10^{19}$ cm^{-3}. It is possible that gaps on the growing GaN surface, due to the roughness, coalesce in a similar way as the crystallites described in the model by Nix and Clemens. Therefore increasing the roughness of the surface would be analogous to decreasing the crystallite size and therefore lead to higher tensile strains. Limited surface diffusion of atoms on the growing surface would then attach to the strained crystal at their point of arrival, and the film would grow in a strained state.

4. Conclusions

Crack formation in GaN films doped with Si was studied by measuring the strain and comparing to the microstructure. The strain was found to increase with film thickness and Si concentration. Crack formation along the $\{1\,\bar{1}\,0\,0\}$ cleavage planes was found to be the major strain relief mechanism and occurred without creating additional dislocations. This suggests that plastic deformation is difficult in these materials at the temperatures used during growth. It was proposed that the increase in tensile stress with increasing [Si] may be related to the presence of tensile stress due to crystallite coalescence. The surface roughness increased with Si concentration, corresponding to an increased tensile stress by invoking a modified view of a coalescence model established recently by Nix and Clemens [12].

Acknowledgements

This work was supported partially by DARPA MDA972-96-3-0014.

References

[1] K. Hiramatsu, T. Detchprohm, I. Akaksaki, Jpn. J. Appl. Phys 32 (1993) 1528.
[2] C. Kesielowski, J. Kruger, S. Ruvimov, T. Suski, J.W. Ager III, E. Jones, Z. Liliental-Weber, M. Rubin, E.R. Weber, M.D. Bremser, R.F. Davis, Phys. Rev. B 54 (1996) 17745.
[3] S. Ruvimov, Z. Liliental-Weber, T. Suski, J.W. Ager III, J. Washburn, J. Krueger, C. Kesielowski, E.R. Weber, H. Amano, I. Akasaki, Appl. Phys. Lett. 69 (1996) 990.
[4] J.W. Ager III, T. Suski, S. Ruvimov, J. Krueger, G. Conti, E.R. Weber, M.D. Bremser, R.F. Davis, C.P. Kuo, Mater. Res. Soc. 449 (1997) 775.
[5] I. Lee, I. Choi, C. Lee, E. Shin, D. Kim, S.K. Noh, S. Son, K. Lim, H.J. Lee, J. Appl. Phys. 83 (1998) 5787.
[6] S. Nakamura, T. Mukai, M. Senoh, Jpn. J. Appl. Phys. Part 1 31 (1992) 2883.
[7] D.P. Bour, M. Kneissl, L.T. Romano, M.D. McCluskey, C.G. Van de Wall, B.S. Krusor, R.M. Donaldson, J. Walker, C.J. Dunrowiicz, N.M. Johnson, IEEE J. Sel. Top. Quantum Electron. 4 (1998) 498.
[8] S. Porowski, J. Crystal Growth 189/190 (1998) 153.
[9] S. Hearne, E. Chason, J. Han, J.A. Floro, J. Figiel, J. Hunter, H. Amano, I.S.T. Tsong, Appl. Phys. Lett., 1999.
[10] J.E. Northrup, J. Neugebauer, Phys. Rev. B 53 (1996) R10477.
[11] L.T. Romano, C.G. Van de Walle, J.A. Ager III, W. Gotz, S.A. Kern, in preparation.
[12] W.D. Nix, B.M. Clemens, J. Mater. Res. 14 (1999) 3467.

ELSEVIER

Physica B 273–274 (1999) 54–57

PHYSICA B

www.elsevier.com/locate/physb

Photo-enhanced dissociation of hydrogen-magnesium complexes in gallium nitride

Y. Kamiura[a,*], Y. Yamashita[a], S. Nakamura[b]

[a]*Faculty of Engineering, Okayama University, Tsushima-naka 3-1-1, Okayama, 700-8530 Japan*
[b]*Department of Research and Development, Nichia Chemical Industries, Ltd., 491 Oka, Kaminaka, Anan, 774-0044 Japan*

Abstract

We have studied the effect of UV light illumination during thermal annealing on the electrical properties of Mg-doped GaN films grown on (0 0 0 1) sapphire substrates by the two-flow MOCVD. We performed isochronal annealing up to 800°C for 1 h in a nitrogen atmosphere with and without UV light illumination, and measured annealing-induced changes in resistivity, hole density and mobility at 25°C using the van der Pauw method. Under no illumination, annealing around 550°C caused resistivity and mobility to decrease and simultaneously hole density to increase. This is consistent with the commonly accepted model that the hydrogen passivation of Mg is caused by the formation of electrically inactive Mg–H complexes and thermal annealing dissociates the complexes to activate Mg. The illumination of UV light with a peak wavelength around 350 nm greatly enhanced the dissociation of Mg–H complexes, reducing the temperature of resistivity reduction from 550°C to 450°C. These suggest that the dissociation of Mg–H complexes may be accelerated by the electronic excitation of the complexes and/or by the changes of their charge states. In view of application, such an effect may be useful to reduce the temperature of thermal annealing to make as-grown GaN films conductive.

Keywords: GaN; Magnesium; Hydrogen; Photo-enhanced dissociation

1. Introduction

Conductivity control of semiconductor materials is important to develop electronic and optical devices. A typical example is that the development of blue light-emitting diodes and lasers using wide-gap III–V nitride semiconductors was greatly indebted to the key technology to obtain p-type GaN material whose resistivity is low enough to form the p–n junction. As-grown Mg-doped GaN films fabricated by MOCVD normally showed high resistivity probably due to the formation of electrically inactive Mg–H complexes [1–4]. Low-energy electron irradiation [2] and thermal annealing [3] were discovered to cause the resistivity of as-grown material to decrease by several orders of magnitude. This was ascribed to the dissociation of Mg–H complexes, releasing hydrogen and electrically activating Mg [4–7]. Recently, some groups reported that minority-carrier injection greatly enhanced the Mg activation [8,9]. We have observed that the UV light illumination enhances the dissociation of Mg–H complexes [10]. These suggest that the dissociation of Mg–H complexes may be accelerated by the electronic excitation of the complexes and/or the changes of their charge states. Such phenomena have been commonly observed for the dissociation of hydrogen-related complexes in other semiconductors such as Si and GaAs [11–13]. In this paper, we describe the detailed results of the enhancement effects of UV light illumination on the dissociation of Mg–H complexes in GaN. We discuss possible mechanisms to cause the enhancement. We also report the effects of hydrogen plasma treatment

* Corresponding author. Fax: + 81-86-251-8237.
E-mail address: kamiura@elec.okayama-u.ac.jp (Y. Kamiura)

0921-4526/99/$ - see front matter
PII: S0921-4526(99)00405-6

and the subsequent thermal annealing with and without UV light illumination on the conductivity changes of GaN films, and propose the best conditions of thermal annealing and electronic excitation to obtain low-resistivity GaN films.

2. Experimental

The GaN films were grown on (0 0 0 1) sapphire substrates by the two-flow MOCVD. Trimethylgallium, ammonia and bis-cyclopentadienyl magnesium were used as Ga, N and Mg sources, respectively. A GaN buffer layer was first grown to a thickness of 25 nm at 510°C, and then a GaN film with a thickness of 3.5 μm was grown at 1035°C. The details of the growth techniques were described in the previous papers [3,4]. Samples of a square of $5 \times 5\ mm^2$ were cut, and prepared for resistivity and Hall measurements by applying indium contacts at the four corners of the samples. Resistivity and Hall measurements were performed at 25°C using the van der Pauw method. After the measurements, indium contacts were removed by immersing the samples into acid mixture ($HCl : HNO_3 = 3 : 1$). Subsequently, the samples were annealed in a nitrogen atmosphere with and without the illumination of UV light with a peak wavelength around 350 nm. In the case of UV light illumination, a UV lamp (Topcon FI-5L, 11VA) was used to illuminate the samples 8 cm apart during the annealing. Changes in resistivity, hole density and mobility due to the annealing were monitored.

3. Results and discussion

Fig. 1(a)–(c) show changes in resistivity, hole density and mobility, respectively, during the isochronal annealing for 1 h at each temperature. In the case of non-illumination of UV, resistivity and mobility decrease, and hole density increases simultaneously around 550°C. These results are consistent with the commonly accepted model of the mechanism of resistivity decrease [4–7]. In this model, neutral Mg–H complexes, which are formed by the hydrogen passivation of Mg, are assumed to exist in the as-grown state. Annealing dissociates these complexes to activate Mg. If the released hydrogen is desorbed out of the GaN layer or still remains in the layer in the neutral state, the annealing increases hole density and decreases mobility due to the increase of ionized-impurity density. On the other hand, our results contradict another possibility that hydrogen acts as a donor to compensate the Mg acceptor in the as-grown state. In this case, annealing should desorb the H donor out of the layer to cancel the electrical compensation. However, this should increase both hole density and mobility due to the decrease of ionized-impurity density.

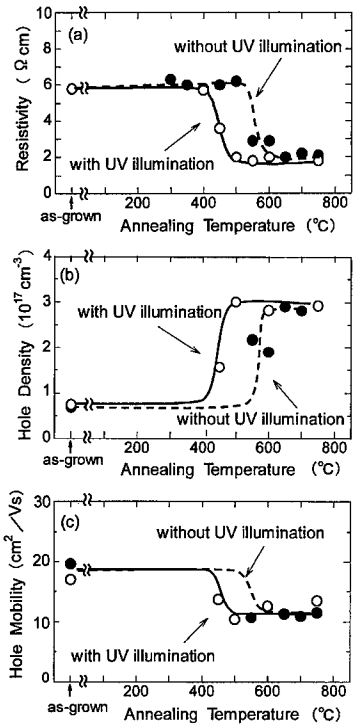

Fig. 1. Changes in resistivity (a), hole density (b) and hole mobility (c) during the isochronal annealing for 1 h at each temperature with and without the illumination of UV light with a peak wavelength around 350 nm.

Fig. 1(a)–(c) clearly show that the UV illumination reduces the temperature of changes in resistivity, hole density and mobility to 450°C. In the framework of the former model of the two described above, the enhancement effect of UV illumination on the resistivity decrease may be explained by the enhancement of the dissociation of Mg–H complexes. Many studies have observed that the dissociation of hydrogen-related complexes is enhanced by the excitation of their electronic states [11–13]. In most cases, the change of their charge states induces the instability of the complexes. We speculate that there are two possibilities for the cause of no electrical activity of Mg–H complexes. One possibility is that hydrogen removes the shallow acceptor level of Mg from the band gap, which makes Mg–H complexes to have no electronic level in the band gap. In this case, the UV illumination excites the electronic states of Mg–H complexes to change the charge distribution, and may reduce the binding energy between Mg and H to make the complexes unstable. The other possibility is that hydrogen perturbs the electronic state of Mg to change its shallow acceptor level to a deeper one. Thus, the Mg–H complexes have deep acceptor levels in the band gap and therefore are electrically inactive in p-type materials. In

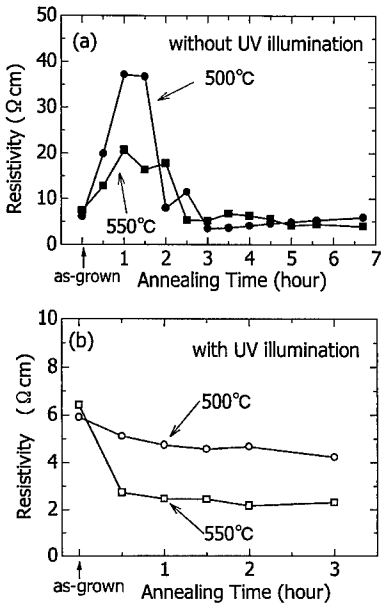

Fig. 2. Changes in resistivity during the isothermal annealing at 500°C and 550°C without (a) and with (b) the illumination of UV light.

this case, the excess electrons created by the UV illumination may be trapped by the deep acceptor levels of Mg–H complexes to change their charge states, making the complexes unstable. An alternative mechanism may be the so-called recombination-enhanced defect reaction, in which the electronic energy released by the electron–hole recombination at the deep acceptor levels of Mg–H complexes is converted into local vibrational energy to induce the atomic motion of hydrogen, causing the dissociation of the complexes.

Fig. 2(a) and (b) show resistivity changes due to isothermal annealing at 500°C and 550°C without and with UV illumination, respectively. In the case of non-illumination of UV, resistivity initially increases and then decreases to a value smaller than the as-grown resistivity. The amount of initial resistivity increase is larger at 500°C than that at 550°C. These features may be explained by the following reaction scheme.

$$(\text{X–H}) \rightarrow \text{X} + \text{H} \quad (1)$$

$$\text{Mg} + \text{H} \rightarrow (\text{Mg–H}) \quad (2)$$

$$(\text{Mg–H}) \rightarrow \text{Mg} + \text{H} \quad (3)$$

In the as-grown state, some of the hydrogen atoms passivate Mg to form the Mg–H complexes, and the rest are trapped somewhere in the form of X–H complexes, where X represents a defect or an impurity to trap hydrogen. Annealing around 500°C liberates hydrogen (reaction (1)), which passivates Mg further to form the Mg–H complexes (reaction (2)), making resistivity increase. Subsequently, the complexes begin to dissociate (reaction (3)), making resistivity decrease. Reaction (3) may be dominant at 550°C due to its higher activation energy than that of reaction (1), reducing a resistivity peak of the annealing curve from a high peak at 500°C. Such a model can reasonably explain rather large variations of resistivity around the resistivity peak (Fig. 2(a)). These variations may be due to the delicate balance between the formation and dissociation of the Mg–H complexes (reactions (2) and (3)) during the cooling period from the annealing temperature to room temperature. Under UV illumination, no resistivity increase but only resistivity decrease is seen in the initial period. This can be understood as the instability of the Mg–H complexes or the enhancement of reaction (3) under UV illumination, substantially suppressing their formation.

We have performed additional experiments on hydrogen-plasma irradiation and subsequent annealing to check our model. A sample was first annealed isochronally up to 750°C to reduce its resistivity to about 2 Ω cm. Subsequently, hydrogen plasma was irradiated to the sample at 600°C. This increased its resistivity to a high value of about 30 Ω cm, while plasma irradiation below 300°C did not induce any changes in resistivity. The subsequent isochronal annealing run completely reproduced the results of Fig. 1(a). We confirmed that the same resistivity changes as above were reversibly repeated by the cycle of plasma irradiation and subsequent annealing. These results indicate that the hydrogen passivation of Mg causes the high-resistivity in the as-grown state and the subsequent annealing induces the dissociation of the Mg–H complexes.

On the basis of the present results, we propose that the best conditions of thermal annealing and electronic excitation to obtain low-resistivity GaN films is the annealing at 550°C for 30 min under the illumination of intense UV light with a peak wavelength less than 350 nm. It is important to illuminate GaN films also during the cooling from the annealing temperature to room temperature.

4. Conclusions

We have studied the effect of UV-light illumination on annealing of as-grown Mg-doped GaN films by resistivity and Hall measurements. Annealing caused resistivity and mobility to decrease and simultaneously hole density to increase around 550°C. This is consistent with the commonly accepted model that the hydrogen passivation of Mg is caused by the formation of neutral Mg–H complexes and thermal annealing dissociates the complexes to activate Mg. The illumination of UV light with a peak wavelength around 350 nm enhanced the

dissociation of Mg–H complexes, reducing the temperature of resistivity reduction to 450°C from 550°C. This suggests that electronic excitation reduces the thermal stability of the neutral Mg–H complexes in GaN. Such an effect may be useful to reduce the temperature of thermal annealing to make the whole GaN films uniformly conductive.

Acknowledgements

We thank K. Seto and S. Senoh of Okayama University for their assistance in our experiments.

References

[1] H. Amano, M. Kito, K. Hiramatsu, I. Akasaki, Inst. Phys. Conf. Ser. No. 106 (1989) 725.
[2] H. Amano, M. Kito, K. Hiramatsu, I. Akasaki, Jpn. J. Appl. Phys. 28 (1989) L2112.
[3] S. Nakamura, T. Mukai, M. Senoh, N. Iwasa, Jpn. J. Appl. Phys. 31 (1992) L139.
[4] S. Nakamura, N. Iwasa, M. Senoh, T. Mukai, Jpn. J. Appl. Phys. 31 (1992) 1258.
[5] W. Götz, N.M. Johnson, J. Walker, D.P. Bour, H. Amano, I. Akasaki, Appl. Phys. Lett. 67 (1995) 2666.
[6] W. Götz, N.M. Johnson, J. Walker, D.P. Bour, R.A. Street, Appl. Phys. Lett. 68 (1996) 667.
[7] W. Götz, N.M. Johnson, D.P. Bour, M.D. McCluskey, E.E. Haller, Appl. Phys. Lett. 69 (1996) 3725.
[8] S.J. Pearton, J.W. Lee, C. Yuan, Appl. Phys. Lett. 68 (1996) 2690.
[9] M. Miyachi, T. Tanaka, Y. Kimura, H. Ota, Appl. Phys. Lett. 72 (1998) 1101.
[10] Y. Kamiura, Y. Yamashita, S. Nakamura, Jpn. J. Appl. Phys. 37 (1998) L970.
[11] N.M. Johnson, in: J.I. Pankove, N.M. Johnson (Eds.), Hydrogen in Semiconductors, Academic Press, New York, 1991, p. 113.
[12] S.J. Pearton, J.W. Corbett, M. Stavola, Hydrogen in Crystalline Semiconductors, Springer, Berlin, 1992, p. 91.
[13] Y. Kamiura, M. Hayashi, Y. Nishiyama, S. Ohyama, Y. Yamashita, Jpn. J. Appl. Phys. 36 (1997) 6579.

ELSEVIER

Physica B 273–274 (1999) 58–62

PHYSICA B

www.elsevier.com/locate/physb

Optically detected magnetic resonance of shallow donor – shallow acceptor and deep (2.8–3.2 eV) recombination from Mg-doped GaN

E.R. Glaser[a,*], T.A. Kennedy[a], J.A. Freitas Jr.[a], B.V. Shanabrook[a], A.E. Wickenden[a], D.D. Koleske[a], R.L. Henry[a], H. Obloh[b]

[a]*Naval Research Laboratory, Washington DC, 20375-5347, USA*
[b]*Fraunhofer-Institut für Angewandte Festkörperphysik, D-79108 Freiburg, Germany*

Abstract

Comprehensive photoluminescence (PL) and optically detected magnetic resonance (ODMR) experiments have been performed on a set of GaN epitaxial layers doped with Mg from 2.5×10^{18} to 5.0×10^{19} cm^{-3}. Strong shallow donor–shallow acceptor recombination at 3.27 eV is observed from the lowest-doped sample while broad emission bands at 2.8 and 3.2 eV were found from the more heavily doped films. ODMR at 24 GHz on these bands reveals evidence for effective-mass shallow donors and Mg-related acceptors with unique g-tensors, including the first observation of the resonance parameters ($g_{||} = 2.113(4)$ and $g_{\perp} = 1.970(5)$) associated with Mg shallow acceptors in GaN.

PACS: 71.55.Eg; 73.20.Hb; 78.55.Cr; 76.70.Hb

Keywords: Gallium nitride; Mg doping; Photoluminescence; Magnetic resonance

1. Introduction

A variety of recombination bands between 2.4 and 3.3 eV have been widely reported for GaN epitaxial layers doped with Mg impurities at concentrations between 10^{18} and 10^{20} cm^{-3}. Much activity is underway to provide information on the nature of the donors and acceptors that participate in these emission bands and to explore their roles in limiting the efficiency [1] of this p-type dopant. Earlier magnetic resonance studies have shown that Mg and Zn acceptors do not exhibit effective mass-like character in GaN [2]. More recently, it has been suggested that Mg concentration-induced deep donors are involved in the 2.8 eV photoluminescence (PL) band typically observed from highly-doped samples and, most significantly, act as self-compensating centers in films doped $\geqslant 10^{19}$ cm^{-3} [3–5].

In this work, comprehensive PL and optically detected magnetic resonance (ODMR) experiments have been performed on a set of GaN epitaxial layers doped with Mg impurities. Distinct PL bands are found for each sample. These include shallow donor–shallow acceptor (SD–SA) recombination at 3.27 eV from the lowest doped sample and broad emissions bands at ~ 2.8 and 3.2 eV from the more heavily doped films. The first observation of magnetic resonance associated with Mg shallow acceptors that participate in the 3.27 eV SD–SA PL is reported in this work. Overall, the ODMR on the different bands reveals evidence for shallow donors and Mg-related acceptors with unique g-tensors.

2. Experimental background

The PL and ODMR experiments were performed on three Mg-doped GaN epitaxial films (referred to as Nos.

*Corresponding author. Tel.: +1-202-404-4521; fax: +1-202-767-1165.

E-mail address: glaser@bloch.nrl.navy.mil (E.R. Glaser)

0921-4526/99/$ - see front matter
PII: S0921-4526(99)00406-8

1–3) grown by OMCVD on sapphire substrates. The total Mg concentration in the 1.5–2.0 μm-thick films is between 2.5×10^{18} and 5.0×10^{19} cm^{-3} as determined by secondary ion mass spectroscopy (SIMS). Only sample No. 3 exhibits clear p-type conductivity at room-temperature with a carrier concentration of 3×10^{16} cm^{-3} as found from Hall-effect measurements. The other two samples are highly resistive.

The PL at 1.6 K was generated by the 351 nm line of an Ar^+ laser at a power density of ~ 5 mW/cm^2. The emission was analyzed by a 0.25-m double-grating spectrometer and detected by a GaAs PMT. The ODMR at 24 GHz was carried out using the same spectrometer/detector combination in order to study the character of the magnetic resonance at several energy positions.

3. Results and discussion

3.1. Photoluminescence (PL)

The PL at 1.6 K from the three Mg-doped GaN layers is shown in Fig. 1. Distinct recombination bands are observed for each sample and are discussed in turn. We note that similar PL results as a function of the total Mg concentration have been previously reported [3,4,6–9].

Sample No. 1 ([Mg] $= 2.5 \times 10^{18}$ cm^{-3}) exhibits strong recombination at 3.27 eV and a series of LO-phonon replicas ($E_{LO} \sim 92$ meV) at lower energies. Following previous analyses [6], this PL is ascribed to recombination between shallow donors ($E_d \sim 30$ meV) of unknown origin and shallow Mg acceptors ($E_a \sim 200$ meV).

The dominant emission observed from sample No. 2 ([Mg] $= 1.4 \times 10^{19}$ cm^{-3}) is broad with peak energy at ~ 3.2 eV. Another characteristic of this band is its asymmetric line shape. The broad line width could arise from a strong electron (or hole)–lattice coupling interaction, typically associated with deep emission bands that involve a center with a very localized wave function. An alternate model to account for this line shape (with the donor and acceptor still of shallow character) involves the presence of large potential fluctuations that arise from a random distribution of positively- and negatively-charged impurities [10]. Potential fluctuations have been previously employed to model recombination of similar character from highly doped and compensated GaAs [11] and ZnSe [12] and more recently in GaN [3].

The strongest emission found from sample No. 3 ([Mg] $= 5.0 \times 10^{19}$ cm^{-3}) is also broad with peak energy at ~ 2.8 eV. This PL exhibits a nearly Gaussian lineshape, similar to that of the 2.2 eV "yellow" luminescence band commonly observed from undoped GaN epitaxial layers [13]. Several groups have proposed that the 2.8 eV band arises from recombination between Mg-related deep donors with $E_d \sim 0.3$ eV and shallow Mg acceptors [3–5].

3.2. Optically-detected magnetic resonance (ODMR)

The ODMR spectra obtained on the PL from the three Mg-doped GaN layers with $B \| c$ are shown in Fig. 2. ODMR spectral studies reveal that all of the emission contributes to the observed signals [14]. Two luminescence-increasing signals ascribed to shallow donors and Mg-related acceptors are found on each band. A summary of the resonance parameters is given in Table 1.

For the 3.27 eV SD-SA recombination, the first line is sharp (~ 5 mT) with $g_{\|} = 1.952(1)$ and $g_{\perp} = 1.94970(1)$. This feature is assigned to shallow, effective-mass (EM) donors based on previous work [13]. The second signal is broad (FWHM ~ 30 mT) with $g_{\|} = 2.113(4)$ and

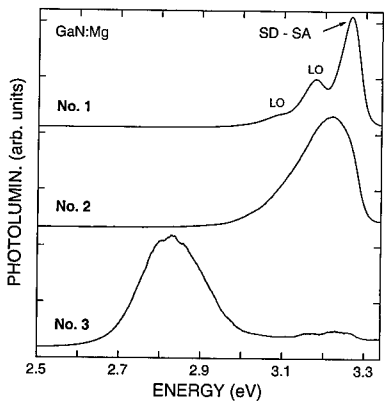

Fig. 1. PL spectra obtained at 1.6 K from three Mg-doped GaN layers under ~ 5 mW/cm^2 of 351 nm radiation (No. 1: [Mg] $= 2.5 \times 10^{18}$ cm^{-3}, No. 2: [Mg] $= 1.4 \times 10^{19}$ cm^{-3}, No. 3: [Mg] $= 5.0 \times 10^{19}$ cm^{-3}).

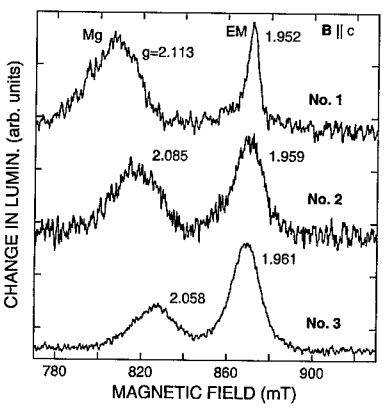

Fig. 2. ODMR spectra found on the dominant emission bands from three Mg-doped GaN films of varying concentration with $B \| c$ (EM ≡ effective-mass donor, Mg ≡ Mg-related acceptor).

Table 1
Summary of magnetic resonance parameters found on dominant emission bands from three Mg-doped GaN layers investigated in this work (NRL ≡ Naval Research Laboratory, FB ≡ IAF Freiburg)

Sample	[Mg][a] (cm^{-3})	PL band	ODMR	
			Donor	Accepter
No. 1 (NRL #980804)	2.5×10^{18}	3.27 eV SD–SA	$g_{\|\|} = 1.952(1)$, $g_\perp = 1.949(1)$ FWHM ~ 5 mT	$g_{\|\|} = 2.113(4)$, $g_\perp = 1.970(5)$ ($\Delta g = 0.143$) FWHM ~ 30 mT
No. 2 (FB #2947)	1.4×10^{19}	3.2 eV	$g_{\|\|} = 1.959(2)$, $g_\perp = 1.953(2)$ FWHM ~ 16 mT	$g_{\|\|} = 2.085(3)$, $g_\perp = 2.003(3)$ ($\Delta g = 0.082$) FWHM ~ 25 mT
No. 3 (NRL #980805)	5.0×10^{19}	2.8 eV	$g_{\|\|} = 1.961(2)$, $g_\perp = 1.957(2)$ FWHM ~ 17 mT	$g_{\|\|} = 2.058(3)$, $g_\perp = 2.018(3)$ ($\Delta g = 0.040$) FWHM ~ 26 mT

[a]Determined from SIMS.

$g_\perp = 1.970(5)$. This line is attributed to the shallow Mg acceptors based on the identical spectral dependencies of the ODMR and PL [14]. To the best of our knowledge, this represents the first observation of magnetic resonance associated with shallow acceptors in GaN. Overall, the resonance parameters of these shallow donors and Mg acceptors serve as an important benchmark for comparison with those obtained on the broad 2.8 and 3.2 eV PL emission bands discussed shortly.

The g-anisotropy (i.e., $\Delta g \equiv g_{\|} - g_\perp = 0.143$) for the shallow Mg acceptors is the largest found to date for any acceptor in GaN. However, this result differs significantly from the effective mass-like character that one may expect based on the high degree of g-anisotropy (i.e., $g_{\|} \sim 2$–4, $g_\perp \sim 0$) observed for several shallow acceptors in bulk 6H–SiC [15] and CdS [16], semiconductors with similar hexagonal symmetry, valence band parameters, and shallow acceptor binding energies. The g-tensor may reflect a symmetry-lowering local distortion of the Mg shallow acceptors as proposed recently by Malyshev et al. [17]. This can arise, for example, from local strain fields associated with the grain boundaries and/or that are generated from the size difference between the substitutional Mg atoms and the host Ga atoms they replace [18].

The ODMR on the 2.8 and 3.2 eV PL bands reveals similar donor-like resonances with $g_{\|} \sim 1.960(2)$ and $g_\perp \sim 1.955(2)$ and FWHM ~ 17 mT. Most notably, these features can still be ascribed to shallow states as found on the 3.27 eV SD-SA recombination. The small shift of the g-values towards 2 (i.e., shift of the resonance to lower magnetic fields) and the broadening can be accounted for by an increase in exchange interaction [19] due to the reduced average donor–acceptor pair separation in these more heavily doped samples. The influence of the exchange interaction on the donors is demonstrated from the ODMR obtained on the emission from sample No. 2 as a function of microwave modulation frequency (ν_{mod})

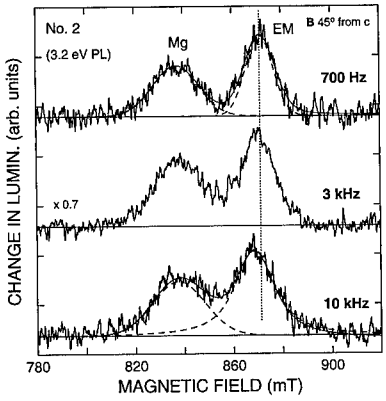

Fig. 3. ODMR spectra obtained on the 3.2 eV PL band from Mg-doped GaN sample No. 2 for several microwave modulation frequencies (ν_{mod}). The thin solid lines are fits to the spectra with $\nu_{mod} = 700$ Hz and 10 kHz as described in the text. The individual components are shown as the dashed curves. The dashed line indicates the position of the EM donor resonance at low ν_{mod}.

with B 45° from c (see Fig. 3). In particular, the donor resonance broadens and shifts to lower field (i.e., higher g-values) with a change in ν_{mod} from 700 Hz to 10 kHz. This behavior reflects an increase in the donor/acceptor exchange as closer pairs (with shorter recombination times) are emphasized with increasing modulation frequency. Fits made to the spectra using Gaussian and Lorentzian line shapes yield g-values of 1.955(2) and 1.961(2) and linewidths of 15 and 19 mT for ν_{mod} = 700 Hz and 10 kHz, respectively.[1]

[1] These fits reveal a similar broadening behavior for the Mg-related acceptor resonance but only $\sim \frac{1}{3}$ of the expected g-shift.

Distinct acceptor-like resonances with FWHM of ~ 26 mT are found on the 3.2 eV PL with $g_{||} = 2.085(3)$ and $g_{\perp} = 2.003(3)$ and on the 2.8 eV PL with $g_{||} = 2.058(3)$ and $g_{\perp} = 2.018(3)$. Several groups have reported such features on similar emission from Mg-doped GaN [13,20,21]. A comparison of these g-values with those observed on the 3.27 eV SD-SA band reveal a shift towards $g = 2$ and a monotonic decrease in the anisotropy from 0.143 to 0.040.[2] Combined with the shift of the PL energies and evidence for shallow donors from the ODMR, this behavior can be attributed to a deepening of the binding energy for the Mg-related centers. Alternatively, electric fields associated with large potential fluctuations that have been proposed to play a role in recombination from highly doped and compensated GaN films [3] can also produce a shift of the PL to lower energy and distortions at the Mg sites (resulting in further reductions of the g-anisotropy). In particular, this may account for the change in the acceptor ODMR found on the 3.2 eV PL band from sample No. 2. One expects a *continuous* shift of the PL bands to lower energy with increasing Mg concentration for such a mechanism. However, broad PL bands at discrete energies between 2.4 and 3.2 eV have been typically reported for GaN films doped $> 1 \times 10^{19}\,\mathrm{cm}^{-3}$ [3,4,9]. We suggest that Mg-related complexes, more likely to form in heavily doped GaN samples such as film No. 3, with levels in the lower half of the band gap may be responsible for these unique PL bands and the deep character of the acceptor ODMR. More work needs to be done to support this hypothesis. We note that in order to be consistent with the deep donor to shallow acceptor recombination model [3–5], the ODMR on the 2.8 eV PL would have to be described by an alternate mechanism such as a two-step process involving spin-dependent capture followed by radiative recombination.

4. Summary

PL and ODMR have been performed on three GaN epitaxial layers doped with Mg from 2.5×10^{18} to $5.0 \times 10^{19}\,\mathrm{cm}^{-3}$. Strong shallow donor–shallow acceptor recombination at 3.27 eV and several LO phonon replicas are found from the lowest-doped sample while broad emission bands at 2.8 and 3.2 eV are observed from the more heavily doped films. ODMR reveals evidence for effective-mass shallow donors whose resonance parameters in the higher-doped films are modified due to donor/acceptor exchange. In addition, Mg-related acceptors with unique g-tensors are found, including the first magnetic resonance of Mg shallow acceptors in GaN. More work is needed to better understand the nature of these acceptors.

[2] The donor/acceptor exchange interaction invoked to explain the shift of the donor g-values for samples No. 2 and 3 can only account for 10–20% of the shifts observed for the Mg-related acceptor g-values.

Acknowledgements

This work was supported by the Office of Naval Research. We thank R. Kotlyar (NRL), P.B. Klein (NRL), U. Kaufmann (IAF Freiburg), and M. Kunzer (IAF Freiburg) for ongoing discussions.

References

[1] D.P. Bour, H.F. Chung, W. Götz, L. Romano, B.S. Krusor, D. Hofstetter, S. Rudaz, C.P. Kuo, F.A. Ponce, N.M. Johnson, M.G. Craford, R.D. Bringans, Mater. Res. Soc. Symp. Proc. 449 (1997) 509.
[2] M. Kunzer, J. Baur, U. Kaufmann, J. Schneider, H. Amano, I. Akasaki, Solid-State Electron. 41 (1997) 189.
[3] M.A. Reschikov, G.C. Yi, B.W. Wessels, Phys. Rev. B 59 (1999) 13176.
[4] U. Kaufmann, M. Kunzer, H. Obloh, M. Maier, Ch. Manz, A. Ramakrishnan, B. Santic, Phys. Rev. B 59 (1999) 5561.
[5] S.G. Lee, K.J. Chang, Semicond. Sci. Technol. 14 (1999) 138.
[6] M. Ilegems, R. Dingle, J. Appl. Phys. 44 (1973) 4234.
[7] H. Amano, M. Kitoh, K. Hiramatsu, I Akasaki, J. Electrochem. Soc. 137 (1990) 1639.
[8] J.A. Freitas Jr., T.A. Kennedy, E.R. Glaser, W.E. Carlos, Solid-State Electron 41 (1997) 185.
[9] L. Eckey, U. von Gfug, J. Holst, A. Hoffmann, A. Kaschner, H. Siegle, C. Thomsen, B. Schineller, K. Heime, M. Heuken, O. Schöen, R. Beccard, J. Appl. Phys. 84 (1998) 5828.
[10] B.I. Shklovskii, A.L. Efros, Electronic Properties of Doped Semiconductors, Springer, Berlin, 1984.
[11] H.P. Gislason, B.H. Yang, M. Linnarsson, Phys. Rev. B 47 (1993) 9418.
[12] P. Bäume, J. Gutowski, D. Wiesmann, R. Heitz, A. Hoffmann, E. Kurtz, D. Hommel, G. Landwehr, Appl. Phys. Lett. 67 (1995) 1914.
[13] E.R. Glaser, T.A. Kennedy, K. Doverspike, L.B. Rowland, D.K. Gaskill, J.A. Freitas Jr., M. Asif Khan, D.T. Olson, J.N. Kuznia, Phys. Rev. B 51 (1995), and references therein.
[14] E.R. Glaser, T.A. Kennedy, J.A. Freitas, Jr., B.V. Shanabrook, A.E. Wickenden, D.D. Koleske, R.L. Henry, H. Obloh, to be published.
[15] Le Si Dang, K.M. Lee, G.D. Watkins, W.J. Choyke, Phys. Rev. Lett. 45 (1980) 390.
[16] J.L. Patel, J.E. Nicholls, J.J. Davies, J. Phys. C 14 (1981) 1339.
[17] A.V. Malyshev, I.A. Merkulov, A.V. Rodina, Physics of the Solid State 40 (1998) 917.
[18] T.N. Morgan, 10th International Conference on the Physics of Semiconductors, 1970, p. 266.

[19] T.A. Kennedy, E.R. Glaser, in: M. Stavola (Ed.), Identification of Defects in Semiconductors, Semiconductors and Semimetals, 51A, Academic Press, San Diego, 1998, pp. 93–136.
[20] U. Kaufmann, M. Kunzer, C. Merz, I. Akasaki, H. Amano, Mater. Res. Soc. Symp. Proc. 395 (1996) 633, and references therein.
[21] F.K. Koschnick, K. Michael, J.-M. Spaeth, B. Beaumont, P. Gibart, J. Off, A. Sohmer, F. Scholz, J. Crystal Growth 189–190 (1998) 561.

ELSEVIER

Physica B 273–274 (1999) 63–65

PHYSICA B

www.elsevier.com/locate/physb

The role of deep levels in the persistent photoconductivity in Mg-doped GaN grown by MOCVD

D. Seghier*, H.P. Gislason

Science Institute, University of Iceland, Dunhagi 3, IS-107 Reykjavik, Iceland

Abstract

Electrical properties of Mg doped GaN epilayers grown by metalorganic chemical vapor deposition were investigated using photocapacitance measurements. Annealing at different temperatures gave gradual activation of Mg-acceptors in samples taken from the same as-grown wafer. The samples exhibit a clear persistent photocapacitance at low temperatures. Measurements of the photocapacitance as a function of excitation energy show the presence of energy levels at 1.1 and 1.9 eV from the valence band. The concentration of both traps increases with the temperature and duration of the annealing. We show that the traps are metastable and conclude that they are related to the Mg doping. Our results support the hypothesis that the PPC observed in GaN : Mg originates from these metastable deep Mg-related centers.

Keywords: GaN : Mg; PPC; Deep defects; Photocapacitance

The success in obtaining hole conductivity in GaN through Mg doping has opened the door to III–V nitride-based optoelectronic devices [1,2]. However, crystallographic defects and impurities can be detrimental to the performance of the devices. Understanding and control of defects and p-type conduction in these materials remain one of the major obstacles to the device efforts. Recently, persistent photoconductivity (PPC) has been reported in n-type as well as p-type GaN [3–6]. Persistent photoconductivity is an increase of the conductivity in the material upon illumination, which persists for long time after the photoexcitation is terminated. PPC has been observed in other materials, the best known example being the GaAlAs system, where the effect is caused by the metastable DX centers [7,8]. However, the reasons for the PPC in GaN are not well understood. It has been suggested that it may involve a relaxation of Mg acceptors [4,9], or native defects in GaN [5]. In this paper we report results from photocapacitance measurements performed on Mg doped GaN : Mg. We show that there is a persistent photocapacitance at low temperatures. Measurements of the photocapacitance versus the photon energy show the presence of two energy levels at 1.1 and 1.9 eV from the valence band which we attribute to the Mg doping. We show that the PPC in our samples is associated with the metastability of the corresponding defects.

The GaN : Mg epilayers were grown by the EMCORE corporation using metalorganic chemical vapor deposition (MOCVD) on C-plane sapphire substrates. The Mg concentration of the films is around $2\text{–}5 \times 10^{19}$ cm^{-3}. We annealed two as-grown samples under flowing N_2. Sample 1 was annealed at 500°C for 1 min which resulted in a net acceptor concentration of $N_a - N_d = 3 \times 10^{16}$ cm^{-3}, while sample 2 was annealed at 800°C for 20 min which gave $N_a - N_d = 1 \times 10^{17}$ cm^{-3}. The measurements were conducted on Schottky devices made by evaporating Au on 2 μm thick layers of the annealed GaN : Mg epilayers. Ohmic contacts were made by melting In on the front face of the GaN layer. A 100 W Xe lamp was used as the photoexcitation light source. Samples were illuminated on the gold contact. In order to ensure the same initial conditions of each set of data obtained under different conditions, the system was always allowed to warm up to 350 K after each

* Corresponding author. Fax: + 354-552-8911.
E-mail address: seghier@raunvis.hi.is (D. Seghier)

0921-4526/99/$ - see front matter
PII: S0921-4526(99)00407-X

measurement, then cooled down in darkness. Different filters were used for selective spectral illumination of the samples with photon energies below the band gap of GaN. The same light flux was used for different excitation wavelengths.

Fig. 1 shows capacitance transients from a Schottky diode on sample 1. The diode was cooled down under zero bias and then measured at 80 K after illumination with different wavelengths. As can be seen from curve *a* in Fig. 1, there is an insignificant change in the photocapacitance for photon energies below about 0.9 eV. For photon energy around 1.5 eV, as shown in curve *b* in Fig. 1, the capacitance increases during illumination, and reaches a saturation value within the illumination time. When the light is turned off the capacitance decreases a little for a few seconds but thereafter it follows a very slow transient. The transient is slow enough that the capacitance virtually reaches a steady value which is higher than the dark value. If the sample is maintained at low temperature, the capacitance remains at this new value for a very long time. Similar results were obtained for sample 2. We conclude that there is a persistent photocapacitance in our samples. Curve *c* in Fig. 1 shows the behavior of the capacitance when the sample is illuminated with light of photon energy 2.5 eV. The capacitance increases more during illumination than in curve *b*. When the light is removed the capacitance again reaches a steady state at a higher value than in curve *b*. Thus, the 2.5 eV light induces additional persistent photocapacitance as compared with the 1.5 eV light. The same measurements were also performed at higher temperatures. We found that the decay rate of the capacitance transients increases with temperature.

Fig. 2 shows the dependence of the steady state photocapacitance ΔC_{ph} on photon energy measured at 80 K in samples 1 and 2. ΔC_{ph} is defined as the excess capacitance induced by the illumination. The samples were cooled down in the dark prior to illumination. After the thermal equilibrium was reached, a slow scan of the photon energy (about 1 h) was performed, with the diode kept at zero bias. There is a step in the capacitance at around 1.1 eV, and a second one more pronounced at around 1.9 eV. After termination of the illumination in Fig. 2, the capacitance variation with time is similar to the one described in curve *c* of Fig. 1, a weak relatively fast initial decrease followed by a much longer transient.

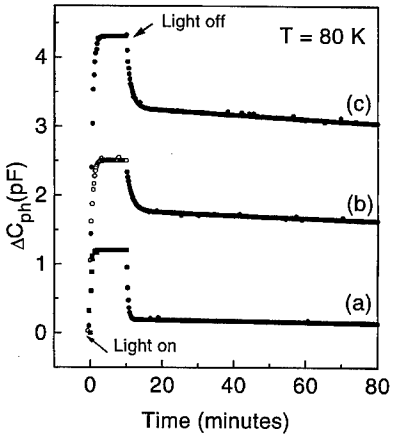

Fig. 1. Photocapacitance transients at 80 K. ΔC_{ph} is the excess capacitance induced by illumination at (a) 0.9 eV (b) 1.5 eV and (c) 2.5 eV.

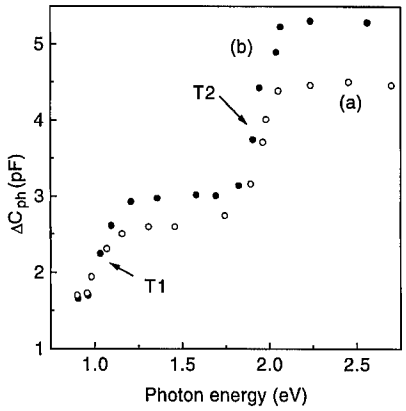

Fig. 2. The dependence of the photocapacitance on the photon energy of the illumination light for (a) sample 1 and (b) sample 2.

We interpret the increase of the capacitance upon illumination shown in Fig. 1 as the presence of deep energy levels in the band gap. In p-type samples the depletion region capacitance originates from the net electrical charge $N_a - N_d$ which is negative in the absence of free holes. Illumination affects the net charge by changing the population of optically active deep levels in the band gap. If the net negative charge density increases there is a corresponding increase of the capacitance. Each level introduces a step in the photocapacitance excitation spectrum near its optical threshold energy. Two such steps are evident in Fig. 2. Therefore, we attribute the steps in Fig. 2 to deep centers, T1 at $E_v + 1.1$ eV and T2 at $E_v + 1.9$ eV. This is in a general agreement with the literature [10] since several energy levels in this energy range have been observed in GaN. The height of each step of ΔC_{ph} in the spectrum of Fig. 2 is proportional to the concentration of the corresponding center. Since the capacitance increase due to T2 is larger than that of T1, the concentration of T2 is higher that that of T1. By comparing curves *a* and *b* in Fig. 2, measured in samples 1 and 2, respectively, it is clear that the concentrations of both traps are higher in sample 2.

As evident from Fig. 1, the photocapacitance induced by the ionization of the deep states does not return to its initial dark value when the light is turned off. Such

a remnant capacitance is typical of deep centers with a capture barrier such as the DX centers in III–V ternary materials [8]. Comparison of Fig. 2 and curve *a* in Fig. 1 suggests that the increase in photocapacitance upon illumination with light of photon energy 1.5 eV is mainly due to ionization of T1. Since the photocapacitance is persistent we conclude that T1 is a metastable state. After photoionization the free holes have to surmount an energy barrier in order to be captured by the metastable centers. At low temperatures the free carries do not have enough energy to overcome this barrier, which explains the persistent increase in the conductivity and the capacitance. The photocapacitance observed under illumination with light of photon energy 2.5 eV can be attributed to the ionization of both T1 and T2. Also, from the fact that this photocapacitance is persistent, as can be seen in curve *c* of Fig. 1, we deduce that T2 is similarly metastable. The centers are presumably acceptors which become negatively charged upon photoexcitation. Persistent photoconductivity has already been reported in MBE- and MOCVD-grown GaN [3–6]. However, its origin is still unclear. Chen et al. [5] assigned the PPC observed in n-type MOCVD grown samples to intrinsic defects in the material rather than extrinsic dopants. Qiu and Pankove [3], on the other hand, attributed the PPC in n-type GaN to the Ga vacancy, whereas in p-type GaN : Mg they detected metastable defects with levels 1.1, 1.4, and 2.04 eV above the valence band edge. It seems likely that the T1 and T2 centers are identical to these centers, although we do not see a separate step at 1.4 eV in Fig. 2. In photoemission spectroscopy several defects in MOCVD-grown GaN : Mg with levels close to the T1 and T2 centers have been observed [10]. Johnson et al. [4] also observed PPC in MOCVD-grown GaN : Mg and suggested that it may be due to isolated Mg acceptors or H–Mg complexes. In both our samples, we have the same concentration of Mg. The two samples were annealed under different conditions which resulted in different concentrations of activated acceptors. In a separate paper [11], we reported the effect of annealing on the acceptor activation and discussed the nature of the compensation in the as-grown GaN : Mg samples. We concluded that there were a higher concentration of electrically active Mg acceptors in sample 2 than in sample 1. Fig. 2 shows that centers T1 and T2 are present in higher concentrations in sample 2 than in sample 1. Hence, it seems that they are activated by the annealing in the same way as the Mg-acceptors. We therefore suggest that the centers T1 and T2 are related to Mg, presumably in a different lattice site than the shallow acceptor. It appears that our results support the hypothesis that the PPC in GaN : Mg is related to complex defects involving Mg, and consequently contradict the possibility of the PPC originating from a Mg–H complex. In this case, one should observe a decrease in the density of T1 and T2 with annealing, during which the Mg–H complexes are likely to dissociate.

In conclusion we annealed Mg doped MOCVD-grown GaN epilayers under different conditions obtaining a gradual increase of the acceptor concentration in the samples. A clear persistent photocapacitance was observed at low temperature. The dependence of the photocapacitance on light energy shows the presence of energy levels at 1.1 and 1.9 eV above the valence band. Their concentrations increase with temperature and the duration of the annealing which indicates that they originate from the Mg doping. We show that these centers are metastable and responsible for the PPC effect. Our results support the hypothesis that the PPC observed in GaN : Mg originates from metastable deep centers related to Mg.

This research was supported by the Icelandic Research Council and the University Research Fund. We are grateful to EMCORE for providing the samples used in this study.

References

[1] H. Amano, M. Kito, K. Hiramatsu, I. Akasaki, Jpn. J. Appl. Phys. 128 (1989) 2112.
[2] S. Nakamura, T. Mukai, M. Senoh, Jpn. J. Appl. Phys. 1 30 (1991) L1998.
[3] C.H. Qiu, J.I. Pankove, Appl. Phys. Lett. 70 (1997) 1083.
[4] C. Johnson, J.Y. Lin, H.X. Jiang, M. Asif Khan, C.J. Sun, Appl. Phys. Lett. 68 (1996) 1808.
[5] H.M. Chen, Y.F. Chen, M.C. Lee, M.S. Feng, J. Appl. Phys. 82 (1997) 899.
[6] G. Beadie, W.S. Rabinovich, A.E. Wickenden, D.D. Koleske, S.C. Binari, J.A. Freitas Jr., Appl. Phys. Lett. 71 (1997) 1092.
[7] D.V. Lang, R.A. Logan, Phys. Rev. Lett. 39 (1977) 635.
[8] D.J. Chadi, K.J. Chang, Phys. Rev. Lett. 57 (1988) 873.
[9] J.Z. Li, J.Y. Lin, H.X. Jiang, A. Salvador, A. Botchkarev, H. Morkoc, Appl. Phys. Lett. 69 (1996) 1474.
[10] W. Götz, N.M. Johnson, D.P. Bour, Appl. Phys. Lett. 68 (1996) 3470.
[11] D. Seghier, H.P. Gislason, Physica B 273–274 (1999) 46, These Proceedings.

ELSEVIER

Physica B 273–274 (1999) 66–69

PHYSICA B

www.elsevier.com/locate/physb

High-resolution PL spectra of donor- and acceptor-bound excitons in homoepitaxial GaN-layers

K. Kornitzer[a], M. Grehl[a], K. Thonke[a,*], R. Sauer[a], C. Kirchner[b], V. Schwegler[b], M. Kamp[b], M. Leszczynski[c], I. Grzegory[c], S. Porowski[c]

[a]*Abteilung Halbleiterphysik, Universität Ulm, D-89069 Ulm, Germany*
[b]*Abteilung Optoelektronik, Universität Ulm, D-89069 Ulm, Germany*
[c]*High Pressure Research Center, Polish Academy of Sciences, PL 02 668 Warsaw, Poland*

Abstract

Homoepitaxial GaN layers grown by MOVPE on a pre-treated GaN single crystal are almost strain-free, have very low defect densities and low impurity levels. These layers show strong, extraordinarily sharp photoluminescence spectra. Especially, the donor-(D^0, X) and acceptor-(A^0, X) bound excitons at $\approx$ 3.471 eV and 3.465 eV, respectively, exhibit line widths of $\approx$ 100 μeV, and ample fine structures can be resolved. For the (D^0, X), complicated spectra are observed in the spectral region of two-electron-transitions and in the excited bound exciton state. For both (D^0, X) and (A^0, X), the respective bound exciton states belonging to all three valence bands are found. By variation of the sample temperature and excitation density, we separate the spectral features contributed by different impurities and reassign several lines in the band gap region.

Keywords: GaN; Photoluminescence; Bound excitons; Excited states

1. Introduction

Nominally undoped state-of-the-art gallium nitride typically contains an uncontrolled amount of donors in the mid-10^{16} cm^{-3}-range, which is ascribed to extrinsic trace impurities like silicon or oxygen, or to intrinsic defects like gallium vacancies (see, e.g., Refs. [1] or [2]). These show up in low-temperature luminescence spectra as donor-bound excitons (D^0, X) $\approx$ 6 meV below the free exciton emission X_A, both linked to the topmost 'A' valence band (VB). Simultaneously, compensating acceptors of unidentified microscopic origin are present as well. The latter lead to the emission of acceptor-bound excitons (A^0, X) $\approx$ 12 meV below X_A [3] or, in the case of incorporation of magnesium, to an (A^0, X) with $\approx$ 19 meV localization energy. Typically, the partial compensation manifests itself also in the emission of broad donor–acceptor pair recombination bands (D^0, A^0) in the range between 2.5 and 3.3 eV. With the availability of purer epitaxial layers, especially those grown on bulk crystals, sharper shallow dopant-related bound-exciton PL features with ample fine structure were observed [4,5]. We report here on extremely sharp (D^0, X) and (A^0, X) PL spectra measured on such a pure layer, and try to identify the numerous new spectral features.

2. Experiment and results

For this study a bulk single crystal prepared by the high-pressure high-temperature method was pre-treated by chemically assisted ion-beam etching (CAIBE) and overgrown by metal–organic vapor-phase epitaxy (MOVPE) with a 1.5 μm thick layer with no intentional doping (for details see Ref. [6]). We performed high-resolution photoluminescence (PL) measurements on this layer of the sample over a wide temperature range

* Corresponding author. Tel.: + + 49-731-502-6131; fax: + + 49-731-502-6108.
E-mail address: klaus.thonke@physik.uni-ulm.de (K. Thonke)

0921-4526/99/$ - see front matter
PII: S0921-4526(99)00408-1

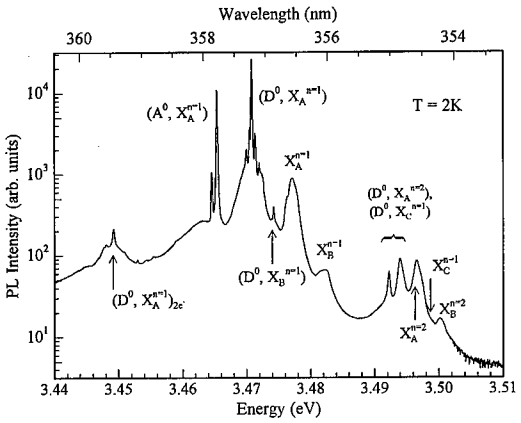

Fig. 1. Low-temperature, high-resolution PL spectrum of the band-edge region of a homoepitaxial, undoped GaN layer.

from 2 to 300 K. The sample was kept in a He gas- or fluid-cooled cryostat, and excited by a cw He–Cd laser (typically 10 mW on a sample spot of $\approx 1\,mm^2$). The emitted light was dispersed by a 2400 rules/mm grating mounted in a 1 m focal length monochromator, and detected either by a UV-optimized CCD camera using typically a resolution of $\approx 200\,\mu eV$, or with a photomultiplier in cases where a higher resolution of $\approx 30\,\mu eV$ was needed. A low-pressure Hg–Cd lamp served as wavelength calibration standard.

The PL spectra recorded at low temperature (see Fig. 1) are dominated by extremely sharp bound exciton emission lines at ≈ 3.465 eV (A^0, X) and at ≈ 3.471 eV (D^0, X) ('X' for brevity stands here for the ground state of an exciton with a hole from the A VB involved; full notation: '$X_A^{n=1}$'). Approximately 6 meV higher in energy, but one order of magnitude lower in its peak intensity, we detect the free exciton–polariton (EP) $X_A^{n=1}$ emission followed by the next valence band B related $X_B^{n=1}$ peak. Between 3.49 and 3.5 eV follows a complicated group of at least four lines. In order to distinguish between EP related features and those due to bound excitons, high-resolution reflectance spectra were taken on the same sample spots [7]. In reflectance, only free exciton–polariton resonances can show up, since only these have enough density of states to contribute to the total permittivity. We observe there no counterparts to the two lower peaks of this group at 3.492 and 3.494 eV. In temperature dependent PL measurements, both vanish already around 30 K in parallel to the dominant (D^0, $X_A^{n=1}$) ground state. The decrease of these two lower lines relative to the broader peak at 3.496_5 eV assigned to the $X_B^{n=1}$ EP corresponds to a thermal dissociation energy of ≈ 6 meV, similar to the energy spacing of these subgroups. Hence, we definitely can assign the lower two peaks to excited states of a donor bound exciton (D^0, $X_A^{n=1}$). Eventually, the lowest peak could also contain a contribution of the ground state of the donor-bound exciton (D^0, $X_C^{n=1}$) linked to the lowest C valence band.

Obviously, the thermalization of all bound and free exciton emission states is hampered at low temperatures, since otherwise all excited states should emit some ten decades less efficiently than actually observed. This is a common feature for EPs being blocked at 'bottleneck states' of the exciton–polariton dispersion as observed earlier for CdS [8]: Below ≈ 30 K the relaxation rates are extremely small and mainly governed by scattering processes at impurities. Since in the present sample the damping is very low as obvious from the shape of the reflectance peaks [7] and from the narrow line widths of the bound excitons in PL, these scattering mechanisms are expected to be rather inefficient.

A more detailed view onto the region of the dominant bound exciton emission is depicted in Fig. 2. The amplitude of the two dominant lines depends to a certain degree on the sample spot: In the center part the (D^0, X) line is by a factor of 2 higher, but towards the edges the (A^0, X) line approaches a comparable strength. This fact proves the independence of the underlying emission processes.

The narrowest emission signal is the line at 3.4655 eV marked as (A^0, X), which is essentially Lorentzian in shape with a slight asymmetry towards the high-energy side. If one tries to fit this line with symmetric Lorentzian lines, at least three sub-components are needed. The less intense adjacent line 0.76 meV lower in energy is by a factor of 16.3 smaller, but shows after expansion with this factor exactly the same shape within uncertainty. We assume internal couplings within the (A^0, X) complex, most presumably the hole–hole interaction, to be responsible for this substructure. The Lorentzian shape demonstrates that inhomogeneous strain broadening which would result in a Gaussian line shape plays only a minor role in this sample. From the full-width at half-maximum (FWHM) an effective (i.e. dominated mainly by Auger recombination) lifetime of 7 ps can be estimated. In time-resolved experiments typically 100–1000 ps are found [9] which are mainly governed by the slow feeding process from EP states. As typical for (A^0, X) emissions, we find for this line an A_1(LO) phonon replica 91.8 meV towards lower energies. Although the (D^0, X) is by a factor of 2 stronger, the respective A_1(LO) replica is only $\approx \frac{1}{10}$ of that of (A^0, X).

More complexities are contained in the (D^0, X) region, where on both sides of the main line two weaker components are resolved, respectively. For an exact decomposition even a sixth broader line at 3.472_3 eV is necessary. (This shoulder can be seen also in Fig. 1.) The central intense line is of Lorentzian type, symmetric and very narrow. The same holds for the two peaks at 3.4705_4 and 3.4720_0 eV (see Table 1), whereas the other two lines are somewhat broader. Again, the assignment remains largely unclear for the moment. We can rule out an isotope

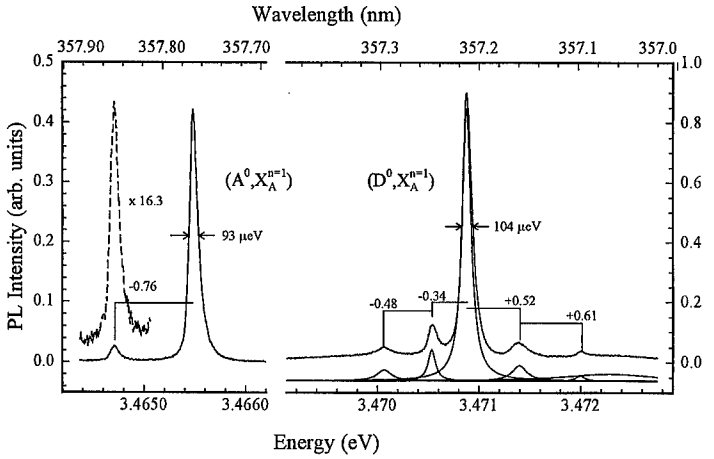

Fig. 2. PL spectra of the (A^0, X) (left) and (D^0, X) (right) region at 2 K. Spacings of lines are given in meV. The lower set of traces on the right side shows a decomposition into six lines of Lorentzian type (see Table 1). (Ordinate scale compressed by a relative factor of 2 for the right part.)

Table 1
Parameters for the (A^0, $X_A^{n=1}$) (upper two lines) and (D^0, $X_A^{n=1}$) (lower 6 lines) sub-components found by a line shape fit with Lorentzian lines as shown in Fig. 2. The main (A^0, $X_A^{n=1}$) line was fitted with one Lorentzian with two different full-widths at half-maximum (FWHM) for the right and left half

Energy (eV)	Relative line energy (meV)	Amplitude (arb. units)	FWHM (meV)
3.4647_2	− 0.76	0.026	0.037 + 0.059
3.4654_8	≡ 0	0.426	0.035 + 0.058
3.4700_7	− 0.81	0.035	0.170
3.4705_4	− 0.34	0.102	0.088
3.4708_8	≡ 0	0.906	0.106
3.4714_1	+ 0.52	0.050	0.175
3.4720_0	+ 1.12	0.016	0.106
3.472_3	+ 1.5	0.022	1.06

effect of a single silicon atom to account for the central plus the next two higher energy peaks, since the relative areas do not match the natural abundances of silicon isotopes. By variation of the excitation power over four decades, we find the two weak lines immediately adjacent to (D^0, X) to scale with (A^0, X), and at the same time the two subcomponents of (A^0, X) retain their relative strength. Based on energy arguments, we tentatively ascribe the line at 3.4705_4 to an acceptor bound exciton with one hole from the B VB: (A^0, $X_B^{n=1}$). Both the (D^0, X) and (A^0, X) region are superimposed on broader, weak bands which we believe to be emitted from the underlying, less pure substrate (see Fig. 1). The substrate could still be excited via diffusion of long-lived EPs generated close to the surface region.

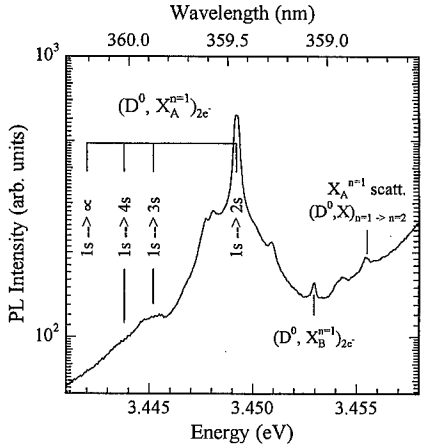

Fig. 3. PL spectrum of the two-electron-transition of the donor-bound exciton. The assignment of lines to different excited states of the donor electron after exciton annihilation are marked by lines.

For the (D^0, X) line, we find a 'two-electron'-replica, which is reduced in amplitude by a factor of ≈ 100, but is still sharp (Fig. 3). In this recombination process the donor electron in the final state is excited from the donor 1s ground state to the first excited 2s state. The (1s ↔ 2s) excitation energy is the spacing of this replica from (D^0, X): 21.6 meV. If central cell corrections are neglected, the binding energy E_D of the donor involved can be calculated within the frame of the effective mass theory as $\frac{4}{3} \times 21.6$ meV = 28.8 meV. This binding energy is commonly attributed to silicon impurities. From the fact, that the next two-electron with excitation into higher donor states (3s, 4s) are indeed found as weaker signatures

within an error of less than $\pm$ 0.5 meV, we expect central cell corrections to be small for this donor.

For donor-bound excitons with a hole from the B VB involved, a corresponding pair of lines exist: the $(D^0, X_B^{n=1})$ main transition at 3.474_3 eV and 21.3 meV lower in energy (at 3.452_9 eV) the $(D^0, X_B^{n=1})_{2e^-}$ two-electron replica, both scaled with the same factor relative to the $(D^0, X_A^{n=1})$ case.

There is an ongoing dispute in literature about the assignment of the 3.4655 eV line: Arguments were advanced, that this is not an (A^0, X), but instead an exciton bound to an ionized donor (D^+, X) instead [10]. Since we see this emission in nominally undoped (i.e. weakly n-type) GaN, and since the LO-phonon coupling is by at least a factor of 10 stronger than in the case of the (D^0, X), we consider this assignment as very unlikely. Recent Zeeman measurements confirm the (A^0, X) character [3].

Acknowledgements

We thank Wolfgang Limmer (Abt. Halbleiterphysik) for helpful discussions on phonon properties of GaN, and K.J. Ebeling (Abt. Optoelektronik) for continuous encouragement. The department of Optoelectronics acknowledges gratefully the financial support of the German ministry of science and education (BMBF).

References

[1] A.K. Viswanath, J.I. Lee, S. Yu, D. Kim, Y. Choi, Ch. Hong, J. Appl. Phys. 84 (1998) 3848.
[2] U. Kaufmann, M. Kunzer, H. Obloh, M. Maier, Ch. Manz, A. Ramakrishnan, B. Santic, Phys. Rev. B 59 (1999) 5561.
[3] R. Stepniewski, A. Wysmolek, M. Potemski, J. Lusakowski, K. Korona, K. Pakula, J.M. Baranowski, G.M. Martinez, P. Wyder, I. Grzegory, S. Porowski, Phys. Stat. Sol. B 210 (1998) 373.
[4] J.M. Baranowski, S. Porowski, in: M. Scheffler, R. Zimmermann (Eds.), Proceedings of the 23rd International Conference on Physics and Semiconductors, Berlin, 1996, World Scientific, Singapore, 1996, p. 497.
[5] M. Mayer, A. Pelzmann, M. Kamp, K.J. Ebeling, H. Teisseyre, G. Nowak, M. Leszczynski, I. Grzegory, S. Porowski, G. Karczewski, Jpn. J. Appl. Phys. Part 2 36 (1997) L1634.
[6] M. Schauler, F. Eberhard, C. Kirchner, V. Schwegler, A. Pelzmann, M. Kamp, K.J. Ebeling, F. Bertram, T. Riemann, J. Christen, P. Prystawko, M. Leszczynski, I. Grzegory, S. Porowski, Appl. Phys. Lett. 74 (1999) 1123.
[7] K. Kornitzer, T. Ebner, K. Thonke, R. Sauer, C. Kirchner, V. Schwegler, M. Kamp, M. Leszczynski, I. Grzegory, S. Porowski, Phys. Rev. B 60 (1999) 1471.
[8] P. Wiesner, U. Heim, Phys. Rev. B 11 (1975) 3071.
[9] B. Monemar, J.P. Berman, I.G. Ivanov, J.M. Baranowski, K. Pakula, I. Grzegory, S. Porowski, Solid State Commun. 104 (1997) 205.
[10] U. Kaufmann, C. Merz, B. Santic, R. Niebuhr, H. Obloh, K.H. Bachem, Mater. Sci. Eng. B 50 (1997) 109.

ELSEVIER

Physica B 273–274 (1999) 70–74

PHYSICA B

www.elsevier.com/locate/physb

Defect formation near GaN surfaces and interfaces

L.J. Brillson[a,*], T.M. Levin[a], G.H. Jessen[a], A.P. Young[a], C. Tu[b], Y. Naoi[b], F.A. Ponce[c], Y. Yang[d], G.J. Lapeyre[d], J.D. MacKenzie[e], C.R. Abernathy[e]

[a]*Department of Electrical Engineering, The Ohio State University, 2015 Neil Avenue, Columbus, OH 43210, USA*
[b]*Department of Electrical Engineering, University of California, San Diego, CA 92093, USA*
[c]*Department of Physics, Arizona State University, Columbus, OH 432210, USA*
[d]*Department of Physics, Montana State University, Bozeman, MT59717, USA*
[e]*Department Material Science and Engineering, Florida State University, Gainesville, FL 32611, USA*

Abstract

We have used low-energy electron-excited nanoscale-luminescence (LEEN) spectroscopy combined with ultrahigh vacuum (UHV) surface science techniques to probe deep level defect states at GaN free surfaces, metal-GaN contacts and GaN/InGaN quantum well interfaces. Employing energies as low as 100 eV and ranging up to 5 keV, we have been able to establish the local nature of these states and their spatial variation normal to the interface plane on an incremental 10–20 nm scale. Coupled with surface science techniques, these measurements show that a variety of discrete deep levels form deep within the GaN band gap due to (a) native defects, (b) metal-induced bonding, (c) reaction products, and (d), in the case of GaN/InGaN heterostructures, local interface phase changes. These results suggest that deep levels are a common feature at GaN interfaces and hence can play an integral role in charge transfer and the formation of local dipoles at GaN heterostructures.

Keywords: Gallium nitride; Surfaces and interfaces; New experimental techniques

1. Introduction

Deep electronic states are of central importance in determining the bulk emissive and transport properties of GaN. Theoretical calculations and experimental measurements show that the bulk defect and impurity states have energy levels ranging across the band gap [1–4]. While considerable attention has focused on the trapping and recombination properties of such bulk deep levels, relatively little is known about the electronic states at GaN surfaces and interfaces. The presence of localized states at such boundaries can affect Schottky barrier formation and heterojunction band offsets. The nanometer-scale film thicknesses now being used in numerous GaN heterostructures further amplifies the relative importance of such interface electronic features.

In this paper, we present evidence for a variety of discrete electronic states associated with GaN surfaces and interfaces. Such states are possible to identify and distinguish from bulk features with low-energy electron-excited nanoscale-luminescence (LEEN) spectroscopy. We have used the luminescence associated with optical transitions into or out of gap states in order to characterize electronic features near interfaces. This requires the ability to: (a) excite free electron–hole pairs, (b) produce such excitation near "buried" interfaces, and (c) vary this excitation in depth on a nanometer scale. These criteria are met by LEEN spectroscopy, which has already been applied to a wide variety of semiconductor–semiconductor and semiconductor–metal interfaces [5,6].

Considerable research has shown the strong dependence of bulk deep levels in GaN on the specifics of growth and subsequent processing [7,8]. Additional electronic

* Corresponding author. Fax: (614) 688-4688.
E-mail address: Brillson.1@osu.edu (L.J. Brillson)

0921-4526/99/$ - see front matter
PII: S0921-4526(99)00409-3

states may reside near surfaces and interfaces due to chemical and morphological changes in the crystal. All these extrinsic features can degrade the near band edge (NBE) optical emission as well as transport properties. In this paper, we present evidence for discrete gap states at GaN surfaces, metal-GaN interfaces, and III–V nitride heterojunctions. Furthermore, the use of surface science techniques permits the chemical origin of extrinsic, near-surface states to be investigated.

2. Experiment

The LEEN experiment consists of a low-energy (0.1–5 keV) electron beam impinging on a controlled surface in ultrahigh vacuum (UHV). The minority carriers generated recombine either across the band gap (near band edge (NBE) radiation), through deep levels in the band gap, or via (nonradiative) phonon generation. The depth of excitation can be varied as a function of incident electron beam energy from a few nm to a few hundred nm over this energy range [9]. The incident electron beam produces a cascade of secondary electrons and, subsequently free electron–hole pairs. One can calculate the maximum range of penetration R_B for the Everhart–Hoff relation [10] extending to low energies. The maximum electron–hole pair production of the electron cascade occurs for values approximately one-third of these values. Thus, for example, a 1 keV electron beam produces a cascade of secondaries and generates electron–hole pairs that extend 20 nm below the surface, peaking at $\sim$ 6–7 nm. Photon emission is collected via IR-UV transmitting optics to photodetectors. This experimental setup is described in previous publications [5,6].

3. Results and discussion

Fig. 1 shows LEEN spectra for GaN grown by molecular beam epitaxy (MBE) under different N deposition conditions. A biased electrode provided a means to deflect ionized N atoms from the plasma source away from the growth surface. Fig. 1 shows dramatically different spectral features for GaN grown with different deflection voltages applied to the electrode. The "yellow" luminescence (YL) that dominates the MBE GaN grown without removing N ions decreases with increasing deflection voltage. Likewise, a shallow defect transition at 3.37 eV decreases as well. A deflection voltage of 700 V can achieve almost two orders of magnitude decrease in these peaks. Furthermore, the electron mobility more than doubles from a value of 300–640 cm^2/V s from zero to the highest deflection voltage. These results indicate that the presence of N ions gives rise to yellow luminescence, which in turn corresponds to increased electron trapping

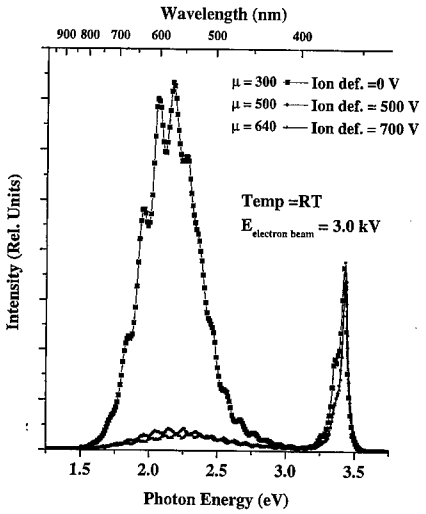

Fig. 1. LEEN spectra with 3.0 keV excitation energy of MBE-grown GaN versus ion deflection voltage. Increasing ion deflection voltage suppresses the midgap and 3.37 eV luminescence.

and reduced mobility. It should also be noted that this yellow luminescence is in fact comprised of at least three overlapping emission peaks centered at 1.75–1.8, 2.15, and 2.4 eV, rather than one broad peak distribution. Similar multiple peak structure in the YL energy range is evident in GaN grown by organometallic chemical vapor deposition (OMCVD) [4]. Finally, it should be noted that the emission spectra in Fig. 1 correspond to a total range of excitation R_B of 90 nm – well below the free surface. Depth-dependent spectra (not shown) reveal that the yellow luminescence is relatively constant versus depth for the GaN grown without deflection. On the contrary, the GaN grown with N ions deflected shows YL increases by over an order of magnitude for near-surface excitation ($\leqslant$ 1 keV corresponding to $R_B \leqslant 20$ nm). This increased emission suggests either defects formed preferentially near the free GaN surface or the influence of residual N ions associated with the termination of growth.

Fig. 2 illustrates a Ga-related defect at the surface of a GaN specimen grown by metallorganic MBE (MOMBE). The as-grown specimen shows YL with intensity completely dominating the NBE peak for all penetration depths. After annealing at $T > 1250$°C, dramatic new features appear, including a sharp (< 0.025 eV FWHM) peak at 1.81 eV and a broad (0.33 eV FWHM) peak centered at 1.66 eV. Similar emissions have been reported previously as "red luminescence" that appeared when excited via a broad C-excitation band [10]. Auger electron spectroscopy (AES) measurements of surface composition establish a $>10\%$ decrease in the Ga/N ratio and a residual C and O concentration of 6% C and $< 10\%$ O. Depth-dependent spectra reveal that the

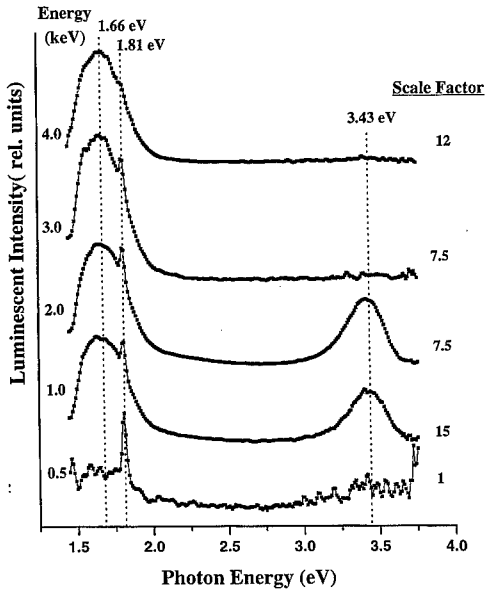

Fig. 2. LEEN spectra as a function of excitation energy and depth showing the near-surface features between 1.5 and 2.0 eV induced by 1250°C annealing.

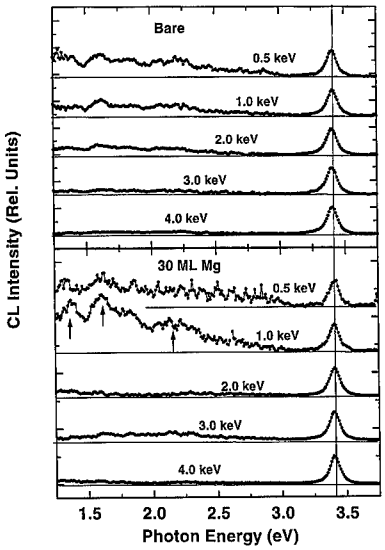

Fig. 3. LEEN spectra as a function of excitation energy and depth for a bare and a Mg-covered GaN single crystal showing the new emissions induced by the metal overlayer plus high-temperature anneal.

1.81 eV peak intensity decreases with deeper excitation. The sharpness of this feature, its near-surface location, and the decrease in relative Ga concentration together suggest emission either from a Ga-related nanostructure, e.g., Ga droplets, or a surface segregated impurity, e.g., Al or Cr. The broader feature corresponding to the Ga-deficient surface is at least 120 nm thick. The "bulk" nature of this emission suggests the formation of a defect complex associated with a Ga deficiency. Interestingly, this layer forms under high-temperature conditions usually associated with preferential N desorption. The YL emission does not appear to increase under these conditions. Subsequent UHV deposition of a 1 nm Ga overlayer on this heat-treated surface reduces (but does not eliminate) the 1.66 eV peak and, to a lesser extent, the YL shoulder within the top 6–20 nm, further confirming the Ga-deficient nature of the lower energy feature. The contrast in behavior between these red luminescence features versus the YL indicates that different defects can become dominant recombination sites with different surface treatments near the free GaN surface.

Defect formation also occurs at metal–GaN interfaces. Fig. 3 illustrates LEEN spectra taken at different depths below a bare, MBE-grown GaN surface versus that of a similar crystal coated with 30 monolayers (4.8 nm) of Mg [6]. This metal–GaN interface was formed by evaporation in UHV on a LEED-ordered, MBE-grown surface, then annealed at 1000°C [11]. Fig. 3 shows broad, nearly featureless emission extending from ~ 3 to below 1.4 eV and relatively uniform at all depths. In contrast the Mg-covered GaN shows a maximum in sub-gap emission at excitation depths of 3–6 nm. Despite the low signal intensities, this emission indicates peak features at 1.4, 1.6, and 2.15 eV. Soft X-ray photoemission spectroscopy (SXPS) measurement of the Fermi level movement for this same sample show that it stabilizes at 2.2 eV above the valence band (1.2 eV below the valence band) [12]. Interestingly, other metals on UHV-prepared n-type GaN surfaces are known to stabilize the Fermi level within a range of 2.0–2.6 eV [13]. This suggests that metal-induced states at the Mg-GaN interface play an active role in the Schottky barrier formation. However, the role of defects may not extend to all metal contacts with GaN. For example, Al–GaN interfaces annealed at 1000°C in UHV result in a reacted interface layer rather than new defect formation [6].

New localized states are also present at GaN heterojunctions. We obtained LEEN depth-dependent spectra from an InGaN quantum well "buried" 30 nm below the free GaN surface. These quantum well structures consisted of an $In_xGa_{1-x}N$ layer ($x = 0.14$ or 0.28) with an average thickness of 2 nm. This layer was confined between a 2 μm thick Si-doped ($n = 3 \times 10^{18}$ cm^{-3}) GaN layer grown at 1050°C over a (0 0 0 1) sapphire substrate and a 30 nm GaN capping layer not intentionally doped and grown at roughly 800°C, the same growth temperature as the $In_xGa_{1-x}N$ layer [14]. The bowing parameter calculations of In concentration due to McCluskey et al. [15] yield x values approximately one half of those extracted from a linear extrapolation between the GaN

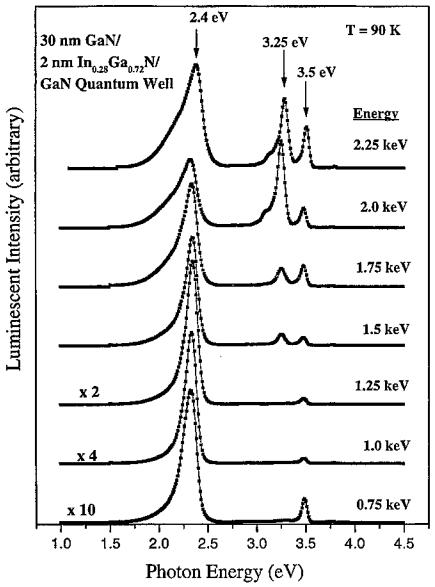

Fig. 4. LEEN spectra versus incident beam energy and depth for a relatively In-rich InGaN quantum well confined buried 30 nm below the GaN surface. At energies corresponding to depths just beyond the quantum well, new emission appears at 3.25 eV, corresponding to a localized electronic state at the deeper of the InGaN–GaN interfaces.

and InN band gaps (Vegard's Law) [14]. Fig. 4 illustrates for beam energies below 1 keV, showing quantum well emission at 2.4 eV that increases relative to the GaN NBE peak. This relative increase corresponds to an increasing penetration of the electron beam and an increase in minority carriers reaching the quantum well region. The quantum well versus NBE ratio reaches a maximum at 1 keV and corresponds to excitation of free electron–hole pairs peaking at depths of $\sim$ 6–7 nm and ranging down to $\sim$ 20 nm, followed by hole diffusion to the quantum well with a diffusion length $L_D < 25$–28 nm. The latter was extracted from a fit to the onset of quantum well emission in a $x = 0.14$ $In_xGa_{1-x}N$ layer that exhibited a similar ratio maximum at 750 eV [16].

In addition to the quantum well and NBE emissions, a new emission feature appears at 3.25 eV at excitation voltages above 1.25 eV. The intensity of this feature rises rapidly with increasing voltage, reaching a maximum relative to both the quantum well and NBE emissions at 2.0 keV. With further voltage increases, LEEN spectra show a decrease and disappearance of this 3.25 eV feature. The appearance of this feature at energies corresponding to the quantum well indicates that its location lies close to that of the quantum well. On the other hand, the 3.25 and 2.7 eV features have different depth dependences, indicating that the former is not a quantum well emission per se, but rather emission from a region localized near the quantum well. That it reaches a maximum relative intensity at voltages above the voltage at which the quantum well is maximum suggests that this localization is at or near the deeper quantum well interface. The line shape of the 3.25 eV peak is relatively unchanged with increasing energy. Researchers have found a nearly identical peak feature at 3.26 eV due to the NBE of cubic GaN [5]. Even the lower energy side bands in the LEEN spectra agree with the phonon replicas identified with the cubic phase emission. The formation of cubic GaN in a thin, interfacial region at the deeper quantum well interface is not unexpected, given the low temperature used to begin the InGaN growth and the relatively high In concentration, both of which could induce stacking faults, known to promote nucleation of cubic phase growth [17]. A new quantum well emission is a less likely explanation for this localized feature, given the difference in depth dependence of the quantum well versus 3.25 eV emission intensities. Phase segregation is also a less plausible explanation, given the lack of an even more In-rich peak emission at lower energies lower than 2.4 eV but above the InN band gap (e.g., 1.8 eV) [18]. Finally, transmission electron microscopy (TEM) images of the higher versus lower In concentration quantum well showed more complex lattice structure near the interface. Thus, the most likely origin for the "buried" interface feature is emission from a nanometer – scale layer of cubic GaN near the InGaN/GaN buffer layer interface due to the change in growth temperature and composition.

4. Discussion

The results presented above demonstrate that several types of localized electronic states can occur at GaN surfaces and interfaces. The deep level energies of these states appear at a wide range of energies across the GaN band gap. Incorporation of N ions in an MBE-grown film is shown to induce "yellow" luminescence features at multiple energies and with intensities that increase toward the free surface. The dependence of this intensity on the extent of ionized N incorporation suggests that point defects alone are not sufficient to account for YL emission. Other extrinsic parameters such as H incorporation may be required to account for the ion-dependent results. High-temperature annealing yields Ga-deficient surfaces and new features distinct from the YL emission. The correspondence of this luminescence with features associated with C doping suggests that changes in the near-surface C impurity bonding can alter the electrical activity of surface trap states. C redistribution in GaN is not expected even for higher temperatures (i.e., 1450°C) [19]. The lack of any increase in YL luminescence with a decrease in near-surface Ga suggests that more than Ga vacancies [1,2] are needed to account for this common defect feature. Mg–GaN Schottky barriers induce a set of

"buried" interface features localized at the intimate contact on a nanoscale with energies at and below that of "yellow" luminescence. The correspondence of the defect energies with the range of UHV Fermi level stabilization energies suggests that defects induced by GaN metallization play a significant role in Schottky barrier formation. Finally, we have observed localized states of an entirely different nature at heterojunction interfaces between GaN and InGaN. LEEN spectroscopy clearly highlights the localized nature of these states and provides strong evidence for cubic phase formation on a nanometer scale. The emission from such a cubic "interphase" is quite close to the band offset calculated for a "quantum-like region of zinc-blende material" surrounded by wurtzite GaN [20]. The change in electronic structure at all these "buried" GaN interfaces and free surfaces has until now not been available. Despite the highly localized nature of these states, it is possible to associate their energies with those of defects reported for bulk GaN. The results provided in this paper show that a complete understanding of surface recombination, charge transport across Schottky barriers, and heterojunction barrier confinement involving GaN surfaces and interfaces requires a determination of the extrinsic electronic states present at these junctions.

5. Conclusions

Low-energy electron-excited nanoscale-luminescence spectra demonstrate the ability to detect new electronic structure at GaN surfaces and interfaces. These results provide evidence for discrete native defect states across the band gap. Furthermore, both the free surface and heterointerface states display a strong dependence on growth techniques and specific chemical interactions. By feeding back to the growth process, this characterization provides a new approach to monitor and minimize localized deep levels at Schottky barriers and heterojunctions.

Acknowledgements

This work was supported in part by US Department of Energy grant DE-FG0297ER45666 (Craig Hartley) (LEEN experiments) and in part by NSF grant DMR-9711851 (LaVerne Hess) (depth calculations).

References

[1] J. Neugebauer, C.G. Van de Walle, Phys. Rev. B 50 (1994) 8067.
[2] P. Boguslawski, E.L. Briggs, J. Bernholc, Phys. Rev. B 51 (1995) 17255.
[3] J.I. Pankove, J.A. Hutchby, J. Appl. Phys. 47 (1976) 5387.
[4] W.J. Choyke, I. Linkov, Institute of Physics Conference Series No. 137, IOP Publishing Ltd, London, 1994, pp. 141–146 (Chapter 3).
[5] J. Schäfer, A.P. Young, L.J. Brillson, H. Niimi, G. Lucovky, Appl. Phys. Lett. 73 (1998) 791.
[6] A.P. Young, J. Schäfer, L.J. Brillson, Y. Yang, S.H. Xu, H. Curguel, G.J. Lapeyre, M.A.L. Johnson, J.F. Schetzina, J. Electron. Mater. 28 (1999) 308.
[7] T.D. Moustakas, in: Semiconductors and Semimetals, Vol. 57, Academic Press, New York, 1999, pp. 33–128.
[8] E.J. Tarsa, B. Heying, X.H. Wu, P. Fini, S.P. DenBaars, J.S. Speck, J. Appl. Phys. 82 (1997) 5472.
[9] L.J. Brillson, R.E. Viturro, Scanning Electron Microscopy 2 (1988) 789.
[10] T.E. Everhart, P.H. Hoff, J. Appl. Phys. 42 (1971) 5837.
[11] E.E. Reuter, R. Zhang, T.F. Kuech, S.G. Bishop, MRS Internet J. Nitride Semiconduct. Res. 4S1 (1999) G3.67.
[12] Y. Yang, S.H. Xu, G.J. Lapeyre, J.M. van Hove, J. Vac. Sci. Technol. B, in press.
[13] C.I. Wu, A. Kahn, J. Vac. Sci. Technol. B 16 (1998) 2218.
[14] F.A. Ponce, D. Cherns, W. Goetz, R.S. Kern, in: MRS Symposia Proceedings, Vol. 482, Materials Research Society, Pittsburgh, 1998, p. 453.
[15] M.D. McCluskey, C.G. Van de Walle, C.P. Master, L.T. Romano, N.M. Johnson, Appl. Phys. Lett. 72 (1998) 2725.
[16] T.M. Levin, G.H. Jessen, L.J. Brillson, F.A. Ponce, J. Vac. Sci. Technol., submitted for publication.
[17] A. Munkholm, C. Thompson, C.M. Foster, J.A. Eastman, O. Auciello, G.B. Stephenson, P. Fini, S.P. DenBaars, J.S. Speck, Appl. Phys. Lett. 72 (1998) 2972.
[18] A.F. Wright, J.S. Nelson, Appl. Phys. Lett. 66 (1995) 3051.
[19] X.A. Cao, R.G. Wilson, J.C. Zolper, S.J. Pearton, J. Han, R.J. Shul, D.J. Rieger, R.K. Singh, M. Fu, V. Scarvepalli, J.A. Sekhar, J.M. Zavada, J. Electron. Mater. 28 (1999) 261.
[20] C. Stampfl, C.G. Van deWalle, Phys. Rev. B 57 (1998) R15052.

ELSEVIER

Physica B 273–274 (1999) 75–79

PHYSICA B

www.elsevier.com/locate/physb

Selective excitation of the yellow luminescence of GaN

J.S. Colton[a,b,*], P.Y. Yu[a,b], K.L. Teo[c], P. Perlin[d], E.R. Weber[b,e], I. Grzegory[e], K. Uchida[f]

[a]*Department of Physics, University of California, Berkeley, CA 94720, USA*
[b]*Materials Sciences Division, Lawrence Berkeley National Laboratory, Berkeley, CA 94720, USA*
[c]*Department of Electrical Engineering, National University of Singapore, Singapore 119260, Singapore*
[d]*UNIPRESS, High Pressure Research Center, Polish Academy of Sciences, 01-142 Warsaw, Poland*
[e]*Department of Materials Science and Mineral Engineering, University of California, Berkeley CA 94720, USA*
[f]*Department of Communications and Systems, The University of Electro-Communications, 1-5-1 Choufugaoka, Choufu, Tokyo 182, Japan*

Abstract

The yellow luminescence of n-type GaN has been studied with selective excitation using a combination of Ar^+-ion and dye lasers. Narrower structures whose peak energies follow the excitation photon energy over the width of the yellow luminescence have been observed. Unlike the yellow luminescence excited by the above band gap excitations, these fine structures exhibit thermal activated quenching behavior. We propose that these fine structures are due to emission occurring at complexes of shallow donors and deep acceptors which can be resonantly excited by photons with energies below the band gap. The activation energy deduced from their intensity is that for delocalization of electrons out of the complexes. Our results therefore suggest that there is more than one recombination channel (usually assumed to be due to distant donor–acceptor pairs) to the yellow luminescence in GaN.

Keywords: Gallium nitride; Yellow luminescence; Selective excitation; Donor-acceptor pair complexes

In spite of the many technological advances in gallium nitride (GaN), one basic question concerning the origin of the ubiquitous yellow luminescence (YL) band remains unanswered. Many competing explanations for its origin have been proposed, including transitions from shallow-donor to deep-acceptor [1–6], shallow-donor to deep-donor [7,8], and deep-donor to shallow-acceptor [9], Even within these models, there are disagreements as to whether the YL originates from distant donor–acceptor pairs [10] (DAPs), or from localized DAP complexes [11].

One difficulty in studying the YL is its very large bandwidth (~0.5 eV). The technique of selective excitation (in which the incident laser is tuned to resonate with the emission) has become a well-established method to resolve fine structures within broad spectra as a result of inhomogeneous broadening. It has been applied successfully to materials, including ZnSe [12], CdSe [13], porous Si [14], Ge microcrystals [15], and most recently GaInN [16]. In this paper we use an Ar^+-ion laser as well as a continuously tunable dye laser to vary the exciting energy over the YL photon energies between 2.1 and 2.7 eV. We have observed several fine structures which we have attributed to emission from resonantly excited donor–acceptor complexes. This emission also differs from the "traditionally" excited YL (with incident photons having energy greater than the GaN band gap, $E_i > E_g$) in its temperature dependence, by exhibiting thermal quenching at temperatures above ~150 K. Our results suggest that there is more than one channel responsible for the YL. While the commonly observed YL using $E_i > E_g$ may involve distant donor–acceptor pair recombination, under resonant excitation the YL mainly originates from donor–acceptor complexes.

We have observed the same fine structures in selectively excited YL of three GaN samples. One is a 2.65 μm

* Corresponding author. 5721 San Diego St. 3, El Cerrito, CA 94530, USA. Tel.: + 1-510-642-8761; fax: + 1-510-643-8497.
E-mail address: colton@socrates.berkeley.edu (J.S. Colton)

0921-4526/99/$ - see front matter
PII: S0921-4526(99)00410-X

GaN film grown on sapphire by MOCVD, while two are bulk samples grown under high pressure. The film was heavily n-doped with Si ($n \approx 5 \times 10^{18}$ cm^{-3}). Although the bulk samples were not intentionally doped, they also had high carrier concentrations ($n \approx 5 \times 10^{19}$ cm^{-3}), most likely due to oxygen donors. Other details on their preparation and properties can be found elsewhere [17]. The photoluminescence (PL) spectra were excited by three lasers: a 50 mW HeCd laser at 325 nm (3.814 eV) for above band gap excitation, an Ar^+-ion laser with discrete laser lines between 2.4 and 2.7 eV, and a continuously tunable Coumarin 540 dye with output between 2.1 and 2.35 eV. The PL signal was analyzed with a SPEX double spectrometer and detected with a cooled GaAs photomultiplier tube and photon-counting system.

Fig. 1 compares the above-band gap-excited PL ($E_i > E_g$) with a resonantly excited YL in a bulk sample measured at 12 K. The smaller peak involving band gap recombination at 3.5 eV in the former spectra is not of interest to us. In that spectra, the broad band centered at 2.3 eV, with a line width of about 500 meV, is an example of the usual YL in GaN. When excited resonantly, however, at least three narrower peaks, each having line widths of $\sim$100 meV, become observable. For example, Fig. 1 shows excitation by the 2.541 eV Ar^+-ion line. By deconvoluting the resonantly excited YL spectra into a sum of Lorentzians (the solid and broken curves shown in the inset of Fig. 2 are, respectively, an experimental spectrum along with its fit), we can track their emission energies as a function of excitation photon energy E_i. We find that these peaks appear to "follow" the excitation laser energy, in that their emission energies E_{YL} are linearly dependent on E_i. This is shown in Fig. 2(a) and (b). We have labeled these narrower peaks observed under resonant excitation as A, B′, B, B″ and C and their energy shifts from the incident photon energy (i.e. $E_i - E_{YL}$) are equal, respectively, to 40, 170, 200, 240 and 370 meV (with uncertainties of $\pm$ 10 meV). The thin film

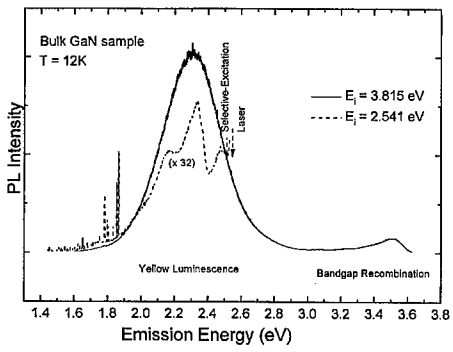

Fig. 1. Comparison of the 12 K yellow luminescence of a bulk GaN sample between above-gap excitation (solid curve) and selective excitation (broken curve).

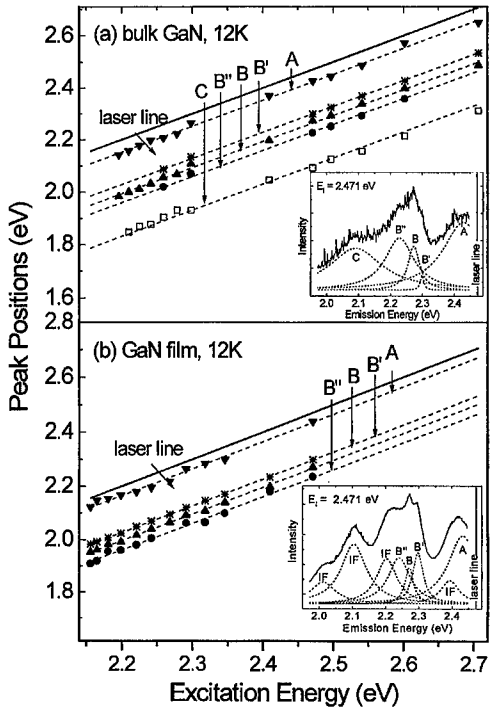

Fig. 2. Summary of the emission peak energies observed in the 12 K photoluminescence spectra of (a) bulk GaN sample and (b) GaN film, when excited by below the band gap photons of energies varying between 2.2 and 2.7 eV. Inset: examples of typical below band gap PL spectra in both bulk and thin film GaN, in this case excited at 2.471 eV. The broken curves represent a deconvolution of the experimental (solid curve) spectrum into a sum of Lorentzians. The peaks labeled "IF" in the inset of (b) are caused by interference fringes and are not plotted in the peak energy summary. The energies of peaks A, B, and C, are 40, 200, and 370 meV below the laser line, respectively.

sample shows additional peaks due to interference, labeled as IF in Fig. 2(b) inset, which are excluded from Fig. 2(b). The IF peaks can be easily distinguished from the YL peaks by noting that their energies do not change with E_i. The results from all three samples essentially agree within experimental uncertainties. The exceptions are that the finer structures B′ and B″ are not as clearly resolved in one bulk sample as in the other. Also, in the bulk samples peak A has a slightly larger $E_i - E_{YL}$ of 50 ± 10 meV. Otherwise the similarities in these results in GaN samples grown by two completely different methods is a strong indication that similar defects are involved in their resonantly excited emission. Moreover, the observations that these narrower peaks are only seen when excited in resonance with the YL, and that their intensity tends to decrease strongly as the excitation energy decreases below $\sim$2.35 eV, suggest that these peaks are related to the YL emission.

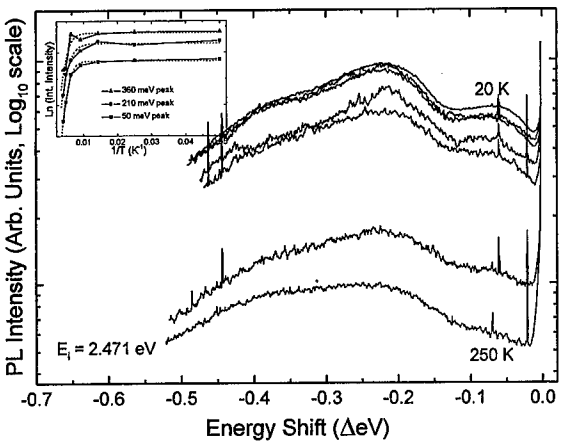

Fig. 3. Photoluminescence of selectively excited bulk GaN sample for various temperatures between 20 K (top spectrum) and 250 K (bottom spectrum). Inset: Arrhenius plot of the intensities of the peaks A, B, and C. By fitting the experimental points to Eq. (1) (broken curves), activation energies of 65, 57, and 73 meV ($\pm$ 10 meV) are obtained for peaks A, B, and C, respectively.

The selectively excited YL differs markedly from the $E_i > E_g$ excited YL in its temperature dependence. One distinctive feature of the $E_i > E_g$ YL noted in previous publications has been its lack of a dependence on temperature [10,18]. Fig. 3 shows the selectively excited YL spectra ($E_i = 2.471$ eV) of a bulk sample measured for several temperatures (T) plotted on the same intensity scale. A large thermal quenching effect is evident for T above $\sim$150 K. In addition to thermal quenching, all the peaks exhibit significant broadening so that fine structures are more difficult to discern at room temperature. The inset of Fig. 3 show an Arrhenius plot of the integrated intensities I of the three peaks A, B and C. The experimental points have been fit with the following formula:

$$I = \frac{I_0}{1 + Be^{-E_A/k_B T}} \tag{1}$$

with three adjustable parameters: I_0, E_A, and B. This equation has been derived by assuming a simple 2-level rate model:

$$\frac{dN_2}{dt} = G - \frac{N_2}{\tau_{rad}} - \frac{N_2}{\tau_{nonrad}}, \tag{2}$$

where N_2 is the population of the upper state (assumed to be proportional to the intensity I), G is the excitation rate, and τ_{rad} and τ_{nonrad} are the radiative and non-radiative times for relaxing back into the lower (ground) state, respectively. Eq. (1) is obtained as the steady-state solution (i.e. $dN_2/dT = 0$) if we assume that G and τ_{rad} are not dependent on temperature and τ_{nonrad} has an activated temperature dependence, given by

$$\frac{1}{\tau_{nonrad}} = Ae^{-E_A/k_B T}. \tag{3}$$

Here, E_A is the activation energy for an electron in level N_2 to recombine non-radiatively and A is the non-radiative recombination rate. Thus, $I_0 = G \times \tau_{rad}$ and $B = A \times \tau_{rad}$ (i.e., B = the ratio of non-radiative to radiative recombination efficiency). By fitting the experimental points in Fig. 3 with Eq. (1), we obtained for peaks A, B, and C the activation energies of 67, 57, and 73 meV (with uncertainties of $\pm$ 10 meV), respectively.

So far, several groups have presented evidence that the YL is due to recombination of shallow donors with deep acceptors, most likely isolated Ga vacancies. Based on this model we find it difficult to explain at least two aspects of our selectively excited YL: (1) given the high donor concentrations in our samples (above the Mott critical density), there should be large amount of free electrons present which could recombine with the photoexcited deep acceptors to produce YL as broad as in the $E_i > E_g$ case, and (2) the temperature dependence of the selectively excited YL should be no different than that of above-gap excitation. In the following sections we shall elaborate on these two points further.

The luminescence spectra of distant donor–acceptor pairs or DAPs (i.e., isolated donors and isolated acceptors not forming complexes) is known to be inhomogeneously broadened due to the dependence on emission energy on pair separation distance [19]. Selective excitation of ZnSe [12] and CdSe [13] has shown that narrow structures can be observed from DAP by removing the inhomogeneous broadening via resonant excitation of DAPs separated by a specific distance, determined by the excitation photon energy. However, in degenerate n-type samples, such as the GaN used in our study, the donors will form an impurity band and there will always be free electrons and neutral donors which can recombine with all photoexcited holes on the acceptors. As a result, if the YL is produced only by distant DAPs, the emission process would not necessarily involve the same donors as in the excitation process, and there would be no narrowing of the YL under selective excitation. In order to explain our results we therefore propose an alternate model in which radiative recombination of the resonantly excited YL takes place only at donor–acceptor complexes. It has already been suggested by both theoretical [3,20] and experimental [11,21] groups that the YL of GaN originates from complexes, or clusters, of shallow donor and deep acceptor pairs. However, within this model of donor–acceptor complexes, it is still necessary to assume that there is a large inhomogeneous broadening, since we are able to selectively excite the complexes over a large range of energies. At this point it is not clear as to its origin of this large

broadening. One can speculate that this may arise from variations in the distance or arrangement between the donor and acceptor within the complexes, or from variations in their surroundings. Further work is necessary to determine the microscopic structure of these complexes.

We find that the fine structures in the selectively excited YL actually still have rather large widths of ~ 0.1 eV. These large widths presumably result from homogeneous broadening. The origin of this broadening at low temperatures is most likely from the strong electron–phonon interaction which is often present in strongly localized defects. In fact, we attribute the peak A found in the resonantly excited YL to a phonon side-band of the donor–acceptor complex recombination. The origin of narrower peaks in the resonantly excited YL can in general be explained by (a) relaxation of photoexcited electrons and/or holes within the complex by emission of a phonon or (b) the complex being photo excited into a higher-energy electronic state, followed by relaxation into the ground state before emission. The former process most likely accounts for peak A since its energy shift of around 40 meV lies within the range of vibrational frequencies of GaN. On the other hand, the energy shifts of over 200 meV for peaks B and C are too high for one phonon modes. However, these energies are plausible for excited electronic states associated with a deep acceptor. We, therefore, tentatively attributed B and C to excited electronic states of the donor–acceptor complexes.

Nevertheless, our results must be reconciled with those of YL excited by $E_i > E_g$. Recently, the YL in GaN has been found to exhibit a "blue-shift" with excitation intensity [10]. These and other experiments have suggested that YL is due to recombination between spatially separated donors and acceptors. It is also necessary to develop a model which explains the different temperature dependence between the selectively excited and above-band gap excited YL. To account for all these experimental results, we propose that there may be multiple recombination channels which can contribute to the YL in GaN. In addition to recombination between the donor–acceptor complexes, there must also be recombination involving spatially separated or distant donors and acceptors pairs. In Table 1 we have listed a few other possible channels in addition to the two already mentioned. Whether a single channel is dominant will depend on many factors, such as: is the YL selectively excited (which tends to favor DAP complexes), or excited by above-band gap radiation (distant DAP pair recombination becomes possible), or excited strongly by high-power density light (not only distant DAP recombination will be possible but also free-to-bound and inter-complex recombination can occur). The possible recombination channels depends also on the sample doping and temperature. A highly doped sample will contain more isolated donors and hence tend to favor distant DAP recombination. On the other hand, extended defects may attract more DAP complexes leading to stronger recombination at complexes. In fact, one group has reported a correlation between the strength of YL and dislocation density leading to their conclusion that the YL involves DAP complexes.

Table 1
Various possible recombination channels contributing to the YL in GaN

Possible YL recombination channel	Name of channel
1. Donor (complex)–acceptor (same complex)	DAP complex
2. Donor (complex)–acceptor (different complex)	Inter-complex
3. Donor (isolated)–acceptor (isolated)	Distant DAP
4. Free electron–acceptor (complex or isolated)	Free-to-bound
5. Donor (isolated)–acceptor (complex)	"Hybrid complex"
6. Donor (complex)–acceptor (isolated)	"Hybrid complex"

The existence of more than one recombination channel responsible for the YL is a key to understand why its thermal properties depend on the excitation method. For example, when a highly n-doped GaN sample is strongly excited by photons above the band gap, the large concentration of free electrons generated tends to favor recombination via distant DAPs or even free-to-bound transitions. This recombination channel is not expected to be strongly dependent on temperature. On the other hand, during resonant excitation only a small number of DAP complexes will be selectively excited. Electrons can then be thermally excited out of these complexes. Once delocalized, these electrons will have higher probabilities of being annihilated non-radiatively. This process can lead to strong thermal quenching. Within our model, the measured activation energies of around 57–73 meV represent, therefore, the depth of traps localizing the electron in the DAP complexes. The holes are expected to be bound much more strongly to the deep acceptors.

In conclusion, we have been able to resolve fine structures in selectively excited YL of GaN samples. Unlike the YL excited by above band gap radiation, the selectively excited YL exhibits strong thermal quenching. Our results suggest that selectively excited YL involves recombination at donor–acceptor pair complexes, while the YL excited by above band gap radiation is dominated in most cases by recombination of distant donor and acceptor pairs.

The work at Berkeley was supported by the Director, Office of Energy Research, Office of Basic Energy Sciences, Materials Sciences Division, of the US Department of Energy under Contract No. DE-AC03-76SF00098.

References

[1] T. Ogino, M. Aoki, Jpn. J. Appl. Phys. 19 (1980) 2395.
[2] P. Perlin, T. Suski, H. Teisseyre, M. Leszczynski, I. Grzegory, J. Jun, S. Porowski, P. Boguslawski, J. Bernholc, J.C. Chervin, A. Polian, T.D. Moustakas, Phys. Rev. Lett. 75 (1995) 296.
[3] J. Neugebauer, C.G. Van de Walle, Appl. Phys. Lett. 69 (1996) 503.
[4] H.M. Chen, Y.F. Chen, M.C. Lee, M.S. Feng, Phys. Rev. B 56 (1997) 6942.
[5] K. Saarinen, T. Laine, S. Kuisma, J. Nissilä, P. Hautojärvi, L. Dobrzynski, J.M. Baranowski, K. Pakula, R. Stepniewski, M. Wojdak, A. Wysmolek, T. Suski, M. Leszczynski, I. Grzegory, S. Porowski, Phys. Rev. Lett. 79 (1997) 3030.
[6] W.G. Perry, M.B. Bremser, R.F. Davis, J. Appl. Phys. 83 (1998) 469.
[7] D.M. Hofmann, D. Kovalev, G. Steude, B.K. Meyer, A. Hoffmann, L. Eckey, R. Heitz, T. Detchprom, H. Amano, I. Akasaki, Phys. Rev. B 52 (1995) 16702.
[8] C.V. Reddy, K. Balakrishnan, H. Okumura, S. Yoshida, Appl. Phys. Lett. 73 (1998) 244.
[9] E.R. Glaser, T.A. Kennedy, K. Doverspike, L.B. Rowland, D.K. Gaskill, J.A. Freitas Jr., M. Asif Khan, D.T. Olson, J.N. Kuznia, D.K. Wickenden, Phys. Rev. B 51 (1995) 13326.
[10] U. Kaufmann, M. Kunzer, H. Obloh, M. Maier, Ch. Manz, A. Ramakrishnan, B. Santic, Phys. Rev. B 59 (1999) 5561.
[11] G. Li, S.J. Chua, S.J. Xu, W. Wang, P. Li, B. Beaumont, P. Gibart, Appl. Phys. Lett. 74 (1999) 2821.
[12] H. Tews, H. Venghaus, P.J. Dean, Phys. Rev. B 23 (1981) 4097.
[13] P.Y. Yu, C. Hermann, Phys. Rev. B 23 (1981) 4097.
[14] M. Rosenbauer, S. Finkbeiner, E. Bustarret, J. Weber, M. Stutzmann, Phys. Rev. B 51 (1995) 10539.
[15] A. Saito, T. Suemoto, Phys. Rev. B 56 (1997) R1688.
[16] N. Wieser, O. Ambacher, H.-P. Felsl, L. Görgens, M. Stutzmann, Astrphys. Lett. 74 (1999) 3981.
[17] S. Porowski, I. Grzegory, GaN and related materials, in: J. Pearton (Ed.), Optoelectronic Properties of Semiconductors and Superlattices, Vol. 2, Gordon and Breach, Amsterdam, 1997, p. 295.
[18] R. Zhang, T.F. Kuech, Appl. Phys. Lett. 72 (1998) 1611.
[19] P.Y. Yu, M. Cardona, Fundamentals of Semiconductors, Springer, Berlin, 1996, p. 344.
[20] T. Mattila, R.M. Nieminen, Phys. Rev. B 55 (1997) 9571.
[21] F.A. Ponce, D.P. Bour, W. Götz, P.J. Wright, Appl. Phys. Lett. 68 (1996) 57.

ELSEVIER

Physica B 273–274 (1999) 80–83

PHYSICA B

www.elsevier.com/locate/physb

Transient photoluminescence of defects in undoped GaN prepared by metal organic vapor phase epitaxy

R.Y. Korotkov, M.A. Reshchikov*,[1], B.W. Wessels

Department of Materials Sciences and Engineering and Materials Research Center, Northwestern University, Evanston, Illinois 60208, USA

Abstract

Transient behavior of the 2.3, 2.9 and 3.27 eV photoluminescence (PL) bands in undoped GaN is studied. A non-exponential decay of PL intensity is observed for all three bands after pulsed excitation at low temperature. Transition rates were measured for the three bands. Quantitative analysis of the PL decay indicates that all three bands are associated with donor acceptor pair (DAP) transitions involving a shallow donor and three acceptor states of different origins. The transition rate decreases with decreasing band energy or increasing thermal ionization energy of the acceptor.

Keywords: GaN; Photoluminescence; Donor-acceptor pairs; Defects

The nature and identity of point defects in GaN are still not well understood. This is especially the case for deep defects in undoped material. The yellow luminescence (YL), a broad band centered at around 2.2–2.3 eV has attracted considerable attention since it is universally present in the spectrum of undoped samples. Two principal recombination mechanisms for the YL band have been originally suggested: shallow donor–deep acceptor transition [1] and deep donor–shallow acceptor transition [2]. Later, various experiments, such as application of hydrostatic pressure [3], comparison studies of PL and photocapacitance [4] or surface photovoltage [5] confirmed that YL is related to transitions from a shallow donor or from the conduction band to a deep acceptor. The nature of the deep defect for this band is not established, however candidates such as the nitrogen antisite [3] gallium vacancy or its complexes with shallow donors [6,7] or carbon [1,8] have been suggested. Another defect-related PL band in undoped wurtzite GaN is observed with a zero-phonon line at about 3.27 eV followed by a set of LO phonon replicas. It is attributed to the inter-impurity transition involving a shallow donor and a shallow acceptor (SDA) [9]. Attribution of this band to the DAP transition is universally accepted. However, PL spectra corresponding to transitions from the shallow donor and from the conduction band to the same acceptor are very similar due to weak localization of electrons, and the predominance of one or the other mechanism depends on the sample (concentration of impurities) and experimental conditions (temperature, excitation intensity). In addition to these two bands, a blue luminescence (BL), a broad band with a maximum at about 2.9 eV is often observed in PL and cathodoluminescence (CL) spectra of undoped and Si-doped GaN [10–16]. CL images showed that defects responsible for the BL dominate in regions with weak near band edge luminescence [10–12]. Intensity of the BL, as well as YL band, varied in time under irradiation by electrons [13] or photons [14]. Transient behavior was explained by electromigration of ions [13] and by the metastability of the BL related defect [14]. BL in undoped GaN was related to V_{Ga} [14], to transition from O_N to multiply hydrogenated V_{Ga} [13] and to transition between deep donor V_NMg and shallow acceptor Mg [15]. The aim of this work is to elucidate the mechanism of the electron transition giving rise to the BL in undoped GaN and compare to that of the other PL bands. Our transient PL results give evidence that in

* Corresponding author. Fax: + 1-804-828-4269.

E-mail address: mreshchi@saturn.vcu.edu (M.A. Reshchikov)

[1] Permanent address: Ioffe Physical-Technical Inst., St.-Petersburg 194021, Russia

0921-4526/99/$ - see front matter
PII: S0921-4526(99)00411-1

pure undoped GaN at low temperature the defect PL bands are related to optical transitions involving a shallow donor and a series of acceptor states.

For the optical studies, wurtzite GaN layers about 2 μm thick that were grown by metal organic vapor-phase epitaxy on *c*-plane of sapphire were used. Concentration of free electrons and their mobility, obtained from the Hall measurements at room temperature (RT), varied in the ranges of 10^{17}–10^{18} cm^{-3} and 270–500 $cm^2V^{-1}s^{-1}$, respectively. PL was excited either with a continuous-wave He–Cd laser (photon energy 3.81 eV) or a pulsed nitrogen laser (4 ns pulses with repetition 20 Hz and photon energy 3.68 eV) and analyzed with a SPEX grating monochromator with Hamamatsu photomultiplier tube R928. Neutral density filters were used to attenuate the excitation density. The pump density was in the range 10^{-3}–1 W/cm^2 for continuous wave excitation and 10^2–10^4 W/cm^2 for pulsed excitation. The temperature of a sample was varied from 15 to 300 K using a closed-cycle cryostat.

In all the samples studied, the low-temperature steady-state PL spectrum near the band edge involved a rich exciton structure with the most intense peak at about 3.480 eV (3–8 meV wide), which has been attributed to an exciton bound to a shallow donor. Peak intensities of defect PL bands varied from sample to sample. For detailed study we measured samples simultaneously exhibiting three defect PL bands: YL, BL and SDA (Fig. 1). With increasing temperature, the integrated intensity of all defect bands increased up to 1.5 times in the range 15–100 K for a low excitation rate. We attribute this increase to the capture of holes released from the exciton dissociation by the acceptors responsible for the PL bands. The SDA PL band is quenched in the temperature range 120–180 K with a thermal activation energy of 0.17–0.19 eV. Quenching of the BL band begins at 200 K with a thermal activation energy of about 0.38 eV [16]. We attribute the quenching to the thermalization of holes from the acceptors to the valence band.

Transient PL measurements at 15 K showed that the luminescence decay is nonexponential for all defect

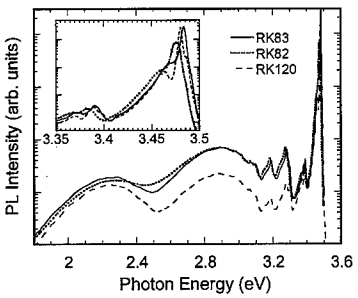

Fig. 1. PL spectrum for three GaN samples at 15 K. The inset shows the near band edge spectrum region.

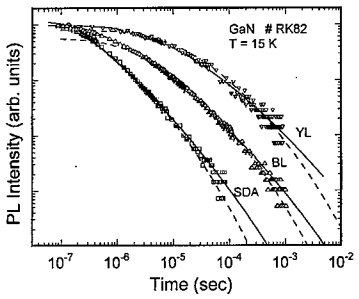

Fig. 2. Intensity decay of the YL (2.2 eV), BL (2.9 eV) and SDA (3.27 eV) bands at 15 K for the sample # RK82. The curves are calculated using Eq. (2) with parameters shown in the Table 1. Solid curves are the best fits with unknown W_{max} and N_D, dashed curves are the best fits with unknown W_{max} and $N_D = n(295\ K)$.

bands. The intensity decay curves for the three PL bands are shown in Fig. 2. The instantaneous lifetime of PL changes from several microseconds to milliseconds. Nonexponential decay is expected for DAP recombination and can be explained in terms of a recombination model whereby an electron on a donor recombines with a nonequilibrium hole bound to an acceptor. In this case, the radiative recombination rate W is not constant but depends exponentially on separation between donor and acceptor R [17]:

$$W(R) = W_{max}\exp\left(-\frac{2R}{a_D}\right), \tag{1}$$

where W_{max} is the transition probability in the limit $R \to 0$ and a_D is the Bohr radius for donor (the Bohr radius for acceptor, a_A, is much smaller). It is evident from Eq. (1) that the lifetime of the bound hole, $\tau = W^{-1}$, is much longer for distant pairs than for close ones. Thus, this results in an increase of instantaneous lifetime of the measured PL with the time delay. The transient PL depends on the detailed spatial distribution of pairs. Thomas et al. have previously treated the PL intensity decay in case of random distribution of DAP [18]. The intensity is given by

$$I(t) \propto N_D\exp\left[4\pi N_D\int_0^\infty (e^{-W(R)t}-1)R^2\,dR\right] \times \int_0^\infty W(R)e^{-W(R)t}R^2\,dR, \tag{2}$$

provided that $N_D \gg N_A$, where N_D and N_A are concentrations of bound electrons and holes on donors and acceptors, respectively. Eq. (2) assumes that most of donors are neutral, and that there are no charged donors between donor and acceptor in a pair. This is valid in the case of low compensation ratio or at high excitation rate.

The donor concentration was estimated from the Hall effect measurements in the temperature range 77–320 K. We have found that a shallow donor with activation energy of 10–27 meV is dominant in the samples studied. Estimates showed that its concentration is close to the room-temperature free electrons concentration, however the exact determination of the donor concentration is hampered by the unknown degree of compensation. We assumed that at low temperature the SDA, BL and YL bands are related to transitions from the same shallow donor to three different acceptors and that differences in the transient decay are due to different electron-capture cross-section of the acceptors. The possible effect of the electron–phonon coupling on transition rate has been neglected. The value of a_D for the shallow donor is calculated to be 24 Å for an electron effective mass of $0.22\,m_0$ and a static dielectric constant of 9.8 [19].

The results of the best fit of the transient PL by Eq. (2) are shown in Fig. 2 and in the Table 1 with N_D and W_{max} as fitting parameters. The fitting would be slightly different if the parameter N_D is taken equal to the RT concentration of free electrons (shown by dashed curves in Fig. 2 and in brackets in Table 1). Despite the uncertainty in N_D, the excellent fit of the PL decay to Eq. (2) for three bands with minimal number of fitting parameters supports the attribution of these bands to transitions from the same shallow donor to acceptors with different electron-capture cross-sections.

As seen in Table 1, the value of W_{max} increases with increasing PL band peak energy. The simplest explanation for this fact is that the Bohr radii of the acceptors (a_A) are different. Indeed, the maximum rate of the DAP transitions in the effective mass approximation upon neglecting many-body effects is given by [20]

$$W_{max} = 64A\left(\frac{a_A}{a_D}\right)^3, \tag{3}$$

where the parameter A depends on optical properties of the semiconductor and on the photon energy ω ($A \approx 4.5\times10^8\,\omega\,s^{-1}$ for GaN). The value of a_A is related to the ionization energy of an acceptor, E_A, and in the effective mass approximation is given as [21]

$$a_A = \frac{\hbar}{\sqrt{2m_h E_A}}, \tag{4}$$

where m_h is the effective mass of holes in the valence band ($m_h = 0.75m_0$ was taken after Ref. [22]). For thermal ionization energies of the acceptors, 0.86, 0.38 and 0.20 eV, taken for the YL, BL and SDA bands, respectively [1,16,9], the calculated Bohr radii are 2.4, 3.6 and 5.0 Å, respectively, according to Eq. (4). Taking $a_D = 24$ Å and $A = 4.5\times10^8\,\omega\,s^{-1}$ with $\omega = 2.3$, 2.9 and 3.27 eV for the YL, BL and SDA, from Eq. (3) one can estimate the values of W_{max} for these PL bands. The calculated values are listed in Table 1. A qualitative agreement between the transition rates predicted by Eq. (3) and the experimental values found from fitting Eq. (2) for W_{max} for three PL bands is evident. This agreement is consistent with the fact that the deeper the acceptor, the smaller the size of its wave function and the lower the transition rate. The observed difference between measured and calculated rates increases with depth of acceptor and presumably arises from utilization of the effective mass approximation for calculation of the Bohr radius for deep acceptors, as well as from neglecting the many-body effects. Indeed, if the acceptors responsible for the YL and BL involve a gallium vacancy and hence are multiply charged [6], the transition probability will be considerably reduced due to repulsive character of the negatively charged acceptors. Note that the values of W_{max}, found in this work, differ from the previously reported values for the YL ($2.5\times10^7\,s^{-1}$) [23] and SDA ($3\times10^7\,s^{-1}$) [9].

To support the findings that the shallow donor is involved in all DAP-type transitions in our samples, the PL spectra at different time delay were measured (Fig. 3). No difference is found between the steady state PL and transient PL spectra for a small time delay. With

Table 1
Parameters obtained from PL decay measurements by fitting with Eq. (2)

Sample #	W_{max} (MHz) for the 2.3 eV band	W_{max} (MHz) for the 2.9 eV band	W_{max} (MHz) for the 3.27 eV band	N_D (10^{17} cm^{-3})	n (10^{17} cm^{-3}) from the Hall data at RT
RK82	1.5 (0.6)[a]	15 (3)[a]	500 (60)[a]	2	5.5
RK83	1.5 (0.8)[a]	19 (6)[a]	750 (50)[a]	3	6.6
RK120	2.0 (1.2)[a]	18 (10)[a]	500 (100)[a]	0.4	1.8
RK170	1.4 (0.8)[a]	25 (6)[a]	550 (60)[a]	1	2.85
Average	1.6 (0.85)[a]	19 (6.2)[a]	575 (68)[a]		
Calculated from Eq. (3)	65	270	860		

[a]The fit with $N_D = n$ (295 K).

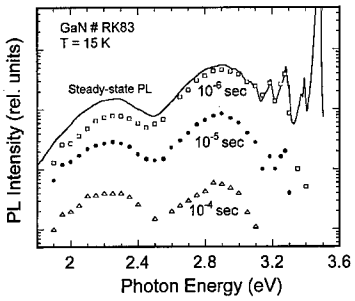

Fig. 3. Steady-state PL spectrum (solid curve) and transient PL spectrum (points) at time delays 10^{-6}, 10^{-5} and 10^{-4} s for the sample #RK83 at 15 K.

increasing time delay, relative intensities of the PL bands change, but no shift or change in the band shape is observed within the experimental accuracy < 30 meV. PL bands originating from the DAP-type transitions involving deep donors are expected to red-shift significantly with time delay [18,20]. This results from the faster recombination of the close pairs, which contribute to the high-energy side of the band due to stronger Coulomb interaction. The deeper the donor, the larger shift is possible but it still remains below the value of ionization energy of the donor [20]. The absence of a noticeable shift of the bands with the time delay indicates that only shallow donors are involved. Lack of variation in the band shape with time delay is consistent with our previous assumption that the electron–phonon coupling does not affect the transition rate.

In conclusion, we have studied the transient behavior of a series of PL bands with maxima at 2.3, 2.9, 3.27 eV in undoped GaN. A non-exponential transient decay is observed for all three bands. Good agreement between theoretical model for luminescence decay of Thomas et al. [18] for DAP-type transitions and experimental results indicates that these PL bands involve DAP-type transitions with the same shallow donor but different acceptor centers. The lower the peak photon energy of the PL band, the slower its intensity decay, which reflects an increase of the hole localization for deeper acceptors. Possible multiple charge states of deep acceptors, presumably enhance this tendency.

Acknowledgements

This work was supported by the National Science Foundation through the GOALI Program, under grant number ECS-9705134.

References

[1] T. Ogino, M. Aoki, Jap. J. Appl. Phys. 19 (1980) 2395.
[2] E.R. Glaser et al., Phys. Rev. B 51 (1995) 13 326.
[3] T. Suski et al., Appl. Phys. Lett. 67 (1995) 2188.
[4] E. Calleja et al., Phys. Rev. B 55 (1997) 4689.
[5] I. Shalish et al., Phys. Rev. B 59 (1999) 9748.
[6] J. Neugebauer, C.G. Van de Walle, Appl. Phys. Lett. 69 (1996) 503.
[7] T. Mattila, R.M. Nieminen, Phys. Rev. B 55 (1997) 9571.
[8] R. Zhang, T.F. Kuech, Appl. Phys. Lett. 72 (1998) 1611.
[9] R. Dingle, M. Ilegems, Sol. St. Comm. 9 (1971) 175.
[10] A. Cremades et al., Mat. Sci. and Eng. B 42 (1996) 230.
[11] M. Herrera Zaldivar et al., J. Appl. Phys. 83 (1998) 462.
[12] C. Trager-Cowan et al., Appl. Phys. Lett. 68 (1996) 355.
[13] M. Toth, K. Fleisher, M.R. Phillips, Phys. Rev. B 59 (1999) 1575.
[14] S.J. Xu, G. Li, S.J. Chula, X.C. Wang, W. Wang, Appl. Phys. Lett. 72 (1998) 2451.
[15] U. Kaufmann et al., Phys. Rev. B 59 (1999) 5561.
[16] M. A. Reshchikov, F. Shahedipour, R. Y. Korotkov, M. P. Ulmer, B. W. Wessels, unpublished.
[17] F.E. Williams, J. Phys. Chem. Solids 12 (1960) 265.
[18] D.G. Thomas, J.J. Hopfield, W.M. Augustyniak, Phys. Rev. 140 (1965) A202.
[19] W.J. Moore, J.A. Freitas Jr, R.J. Molnar, Phys. Rev. B 56 (1997) 12 073.
[20] A.P. Levanyuk, V.V. Osipov, Sov. Phys. Usp. 24 (1981) 187.
[21] A. G. Milnes Deep impurities in Semiconductors, A Wiley Interscience Publ., New-York, 1973, p. 6.
[22] D. Volm et al., Phys. Rev. B 53 (1996) 16 543.
[23] D.M. Hofmann et al., Phys. Rev. B 52 (1995) 16 702.

ELSEVIER

Physica B 273–274 (1999) 84–87

PHYSICA B

www.elsevier.com/locate/physb

Defect introduction in epitaxially grown n-GAN during electron beam deposition of Ru schottky contacts

F.D. Auret[a,*], S.A. Goodman[a], G. Myburg[a], F.K. Koschnick[b], J.-M. Spaeth[b], B. Beaumont[c], P. Gibart[c]

[a]*Department of Physics, University of Pretoria, Pretoria 0002, South Africa*
[b]*Fachbereich Physik, Universität GH Paderborn, Paderborn, Germany*
[c]*CRHEA-CNRS Valbonne, France*

Abstract

We have used deep-level transient spectroscopy (DLTS) to study the electrical properties of defects introduced in epitaxial n-GaN during electron beam (EB) deposition of Ru Schottky contacts. DLTS revealed that EB deposition introduces at least two defects, Ee1 and Ee2, with energy levels at $E_C - (0.19 \pm 0.01)$ eV and $E_C - (0.92 \pm 0.04)$ eV, respectively, in the band gap. The defect Ee1 has a similar signature as a radiation induced defect in GaN, speculated to be the V_N. The concentrations of Ee1 and Ee2 both decrease away from the interface into the GaN. The concentration of Ee2, the more prominent of the two defects, is estimated as about 10^{16} cm^{-3} at the GaN surface. The effect of the EB deposition induced defects on the current–voltage characteristics of the Schottky contacts thus formed is to introduce recombination and generation components to the reverse and forward currents, respectively.

Keywords: GaN; Electron beam metallization; DLTS; Defects

1. Introduction

Gallium nitride is a direct wide band-gap semiconductor which has unique applications in blue, green and ultraviolet light emitting diodes, detectors and blue lasers [1]. Because of its low thermal generation rates and high breakdown fields, an inherent property of wide bandgap semiconductors, it has also recently been shown that GaN is important in the field of high temperature and power electronics [2]. One of the critical processing steps during the fabrication of these devices is metallisation. The method chosen to deposit metal has to fulfil several requirements, including the ability to evaporate high melting point metals and that it should not introduce defects in the semiconductor. This latter requirement is particularly important for depletion layer based devices, such as metal–semiconductor field effect transistors and photodetectors. Defects that are introduced during metallisation processes of semiconductors have, amongst others, been shown to give rise to poor rectification quality of Schottky barrier diodes (SBDs), for example, a reduction in the free carrier concentration below the gate and high dark currents.

Sputter deposition is the metallisation method that yields the best metal adhesion to semiconductors and is also useful to deposit stoichiometric compounds [3]. However, it has been shown that it introduces defects at and below the surface of semiconductors, including GaN [4], which result in SBDs with poor rectification properties. Electron beam (EB) deposition, on the other hand, is widely used in the semiconductor industry, in particular where high melting point metals have to be evaporated. Also, for EB deposition it has been shown that, unless proper care is taken, stray particles originating in the region of the filament or molten metal can introduce

* Corresponding author. Tel.: + 27-12-420-2684; fax: + 27-12-362-5288.
E-mail address: fauret@scientia.up.ac.za (F.D. Auret)

0921-4526/99/$ - see front matter
PII: S0921-4526(99)00412-3

defects at and below the semiconductor surface which result in SBDs with degraded rectification properties [5–7]. Using deep-level transient spectroscopy (DLTS) [8], it was shown that, in the case of GaAs, this barrier height alteration was accompanied by the introduction of defects with discrete levels as well as continuous energy distributions in the band gap, at and below the semiconductor surface [9]. No studies pertaining to EB-induced defects in GaN have yet been reported.

In this paper we report the characteristics, determined by DLTS, of defects introduced in epitaxially grown GaN during EB deposition of Ru Schottky contacts thereon. Ru is the least expensive member of the platinum group metals, it is chemically inert and it has been successfully employed to fabricate high-quality Schottky and ohmic contacts to GaAs [10]. We show that EB deposition introduces at least two defects with energy levels at (0.19 ± 0.01) and (0.92 ± 0.04) eV below the conduction band.

2. Experimental procedure

For this study we used n-type GaN with a free carrier density of $(2\text{–}3) \times 10^{16}\ \text{cm}^{-3}$, grown by organo-metallic vapour-phase epitaxy (OMVPE) on sapphire substrates. Before contact fabrication, the samples were cleaned by first boiling them in aqua-regia and rinsing in de-ionised water, and then degreasing them by boiling in trichloroethylene followed by rinsing in boiling isopropanol and thereafter in de-ionised water. Finally, the samples were dipped in $HCl : H_2O$ (1 : 1) for 10 s. After this cleaning, Ti/Al/Ni/Au (150/2200/400/500 Å) ohmic contacts [11] were fabricated on the GaN and annealed at 500°C for 5 min in Ar. Prior to Schottky barrier diode (SBD) fabrication, the samples were again degreased and dipped in an $HCl : H_2O$ (1 : 1) solution. Following this, circular Ru Schottky contacts, 0.6 mm in diameter and 50 nm thick, were evaporated on the GaN by EB deposition through a metal contact mask, as close as possible to the ohmic contact to minimise series resistance. EB deposition was performed at a pressure of 2×10^{-6} mbar at a deposition rate of 0.01 nm s^{-1} *without shielding* the GaN, and at a rate of 0.05 nm s^{-1} *whilst shielding* the GaN from stray particles originating at the filament or molten metal. For control purposes, Au SBDs were resistively deposited next to the EB deposited SBDs.

Current–voltage (I–V) measurements were used to assess the quality of the Schottky contacts while the EB deposition induced defects were characterised by DLTS using a Stanford Research lock-in amplifier (model SR830) which facilitated measurements at a pulse frequency in the mHz range. The energy level, E_T, in the bandgap and apparent capture cross section, σ_a, of a defect (the combination of which is referred to as its DLTS "signature") were calculated from DLTS Arrhenius plots of T^2/e versus $1/T$, where e is the emission rate at a temperature T.

3. Results and discussion

I–V measurements (Fig. 1) revealed that for *unshielded* EB deposited SBDs (curves (b)), the current at a 1 V reverse bias is 2×10^{-9} A. These characteristics are poorer than those of the resistively deposited Au diodes (curves (a)), but much better than those of a sputter deposited contact (curves (d)) on the same sample. The forward log (I) versus V characteristics of the *unshielded* EB deposited diodes are linear only between 10^{-8} and 10^{-5} A. In this region the ideality factor and barrier height, calculated assuming thermionic emision, are 1.07 ± 0.02 and 1.00 ± 0.02 eV, respectively. From the shapes of curves (b) it is evident that in the low-current region recombination–generation (RG) currents dominate, whereas in the high-current region the series resistance limits the current. These I–V measurements confirm that, as for GaAs [5,6], EB deposition of Schottky contacts on n-GaN, *without shielding it from stray particles originating at the filament*, yields diodes with non-ideal rectification characteristics. Curve (c) in Fig. 1 was recorded from a diode that was *shielded from the filament* when metallizing at a deposition rate of 0.05 nm s^{-1}. It is clear that it has superior rectification properties. Its ideality factor and barrier height are 1.08 ± 0.01 and 1.08 ± 0.02 eV, respectively. No significant evidence of RG currents can be seen.

From a comparison of curves (b) and (c) in Fig. 1 it is clear that *shielding the GaN from the filament* and

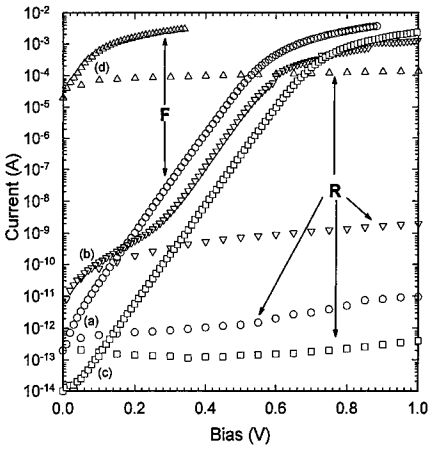

Fig. 1. I–V characteristics of resistively deposited Au contacts (curve (a)), EB deposited Ru contacts (curves (b) and (c)) and sputter deposited Au contacts SBDs (curve (d)) on n-GaN. "F" and "R" refer to the forward and reverse characteristics, respectively. Curves (b) and (c) are for contacts deposited at 0.01 nm s^{-1} *without shielding*, and at 0.05 nm s^{-1} *with shielding*.

depositing at higher rates, markedly improves the diode quality. This can be understood in that the GaN is exposed to energetic particles originating from, amongst others, a region close to the filament. These particles cause damage at and below the surface and this damage leads to the transport of charge by mechanisms in addition to thermionic emission, e.g. RG currents. When shielded from the filament and depositing at a high rate, the exposure of the surface to energetic particles originating at the filament is minimal and thus the defects that give rise to RG currents are few. On the other hand, when depositing *without shielding* the GaN from the filament and when *depositing at a low rate*, the total particle dose on the GaN is higher and therefore more defects are introduced which, in turn, cause poorer I–V characteristics.

Fig. 2 depicts the DLTS spectra of control (resistively deposited) and EB-deposited diodes. Curve (a) shows that the control sample contained two defects, labelled EO2 and EO5, with energy levels at 0.27 ± 0.01 and 0.61 ± 0.02 eV below the conduction band, respectively [14]. These have been correlated with as-grown defects reported by Hacke et al. in n-GaN grown by hydride vapour-phase epitaxy [12] and by Götz et al. in MOCVD-grown GaN [13]. Curves (b) and (c) in Fig. 2 show that after EB deposition, defects labelled Ee1 and Ee2 are detected. Note that in curves (b) and (c) the peak height of Ee2 has been reduced by a factor of ten with respect to that of Ee1. The energy and apparent capture cross section of Ee1, as determined from Fig. 3, are (0.19 ± 0.01) eV and $(1.2 \pm 0.2) \times 10^{-15}$ cm^2, respectively, while for Ee2 these parameters are (0.92 ± 0.04) eV and $(7.9 \pm 2) \times 10^{-14}$ cm^2, respectively. As can be seen from Fig. 3, the DLTS signature of Ee1 matches that of ER3 well. ER3 is introduced in n-GaN during high

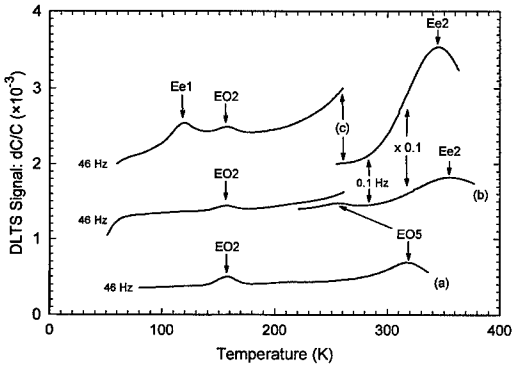

Fig. 2. Curve (a): DLTS spectrum of resistively deposited SBD on epitaxial n-GaN. Curves (b) and (c): DLTS spectra recorded from the EB deposited Schottky contact *without* and *with shielding*, respectively, using a filling pulse frequencies of 46 and 0.1 Hz, as indicated. All spectra were recorded using a filling pulse width of 0.2 ms and amplitude of 1.6 V, superimposed on a quiescent reverse bias of 1 V.

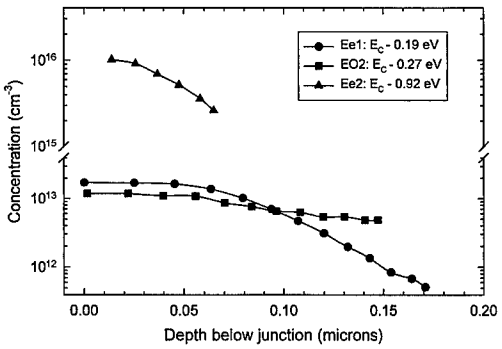

Fig. 3. DLTS Arrhenius plots of defects in as-grown and particle-processed epitaxial n-GaN. Open circles and triangles are for the defects present before and after EB deposition, respectively. Solid and broken lines without symbols are for defects characterised by other authors for irradiated [16] and unirradiated [13] epitaxial n-GaN, respectively.

energy (> MeV) proton [14] and He-ion irradiation [15]. ER3, in turn, is thought to be the same as a defect, labelled E, with a level at $E_C - 0.18$ eV, observed by Fang et al. [16] after MeV electron irradiation of MBE-grown GaN. These authors pointed out that, should the capture cross section of this defect be temperature activated, then its actual position in the band gap may be close to that of V_N ($E_C - 0.07$) [16], and on these grounds suggested that E (i.e. also the ER3) is the V_N. However, no firm identification has yet been made. The energy level of the major EB deposition-induced defect, Ee2, is similar to that of ER5, as yet unidentified, introduced during high-energy particle irradiation of GaN [17].

The depth distributions of Ee1 and Ee2 for *unshielded* deposited SBDs were calculated using the constant bias variable pulse DLTS technique. By applying a reverse bias of 1 V and increasing the pulse in steps of 0.1 V, a region up to 0.17 μm below the interface could be probed. Fig. 4 shows that within this region the concentration of the prominent defect, Ee2, decreases from about 1×10^{16} cm^{-3} just below the interface to 1×10^{15} cm^{-3} at 0.06 μm into the GaN. Clearly, it will significantly reduce the free carrier concentration directly below the Ru/GaN junction. Fig. 4 also shows that the concentration of Ee1 decreases from 2×10^{13} cm^{-3} just below the interface to 5×10^{11} cm^{-3} at 0.17 μm into the GaN. The concentration of Ee1 is too low to significantly affect the GaN free carrier concentration. For *shielded* diodes deposited at 0.05 nm s^{-1} the concentration of Ee2 is estimated (from (Fig. 2)) as about 4–5 times less than for *unshielded* diodes. The concentration of Ee1 (Fig. 2) is even more reduced than that of Ee2 with shielding and increased deposition rate.

When speculating on the origin of defects introduced during EB deposition, the different types of particles

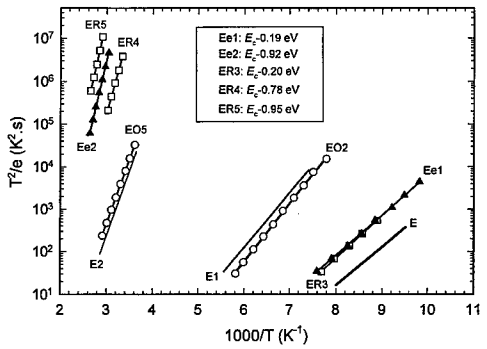

Fig. 4. DLTS depth profiles of defects in as-grown n-GaN before EB deposition (EO2), and after EB deposition *without shielding* (Ee1 and Ee2) of Ru SBDs.

present in the vacuum system during evaporation should be considered. Firstly, there are stray electrons which originate at the filament but which are not focussed on the metal because the filament is not a true point source of electrons. There may also be some other negatively charged particles (residual gas ions), originating in this region, which are not focussed on the metal because their mass is too high. Some of these particles impact on the sample where they cause damage and shielding the sample from the filament yields diodes with dramatically improved characteristics, similar to what has been reported for Ti and Pt EB-deposited Schottky contacts on n-GaAs [5,6]. Secondly, there are some ionised metal atoms, evaporated from the metal, which gain sufficient energy (by e.g. collisions with other particles) to produce damage when they reach the GaN surface.

4. Summary and conclusions

We have shown that EB metallisation of Ru Schottky contacts to n-GaN *at a low deposition rate, without shielding* the substrate from particles originating at the filament, results in SBDs with non-ideal rectification properties. On the other hand, *metallising at a higher deposition rate and shielding* the GaN from the filament results in SBDs with very good rectification properties. This I–V behaviour is explained by the fact that EB deposition introduces defects at and below the GaN surface. DLTS measurements revealed that EB metallisation introduces at least two electron traps, Ee1 and Ee2, located at $E_C - (0.19 \pm 0.01)$ and $E_C - (0.92 \pm 0.04)$ eV, respectively. Ee2 is by far the more significant defect and its concentration at the surface, in the case of *unshielded* SBDs deposited at 0.01 nm s^{-1}, is estimated to be about 10^{16} cm^{-3}. The concentrations of both these defects decrease when *shielding the sample* and when *increasing the deposition rate*. Ee1 has a similar DLTS signature as the E and ER3 defects, introduced in epitaxial GaN by high-energy (MeV) electron, proton and He-ion irradiation, speculated to be related to nitrogen vacancy, V_N.

Acknowledgements

We gratefully acknowledge financial assistance from the South African National Research Foundation (NRF).

References

[1] S. Nakamura, G. Fasol, The Blue Laser Diode, Springer, Berlin, 1997.
[2] K. Doverspike, A.E. Wickenden, S.C. Binarii, D.K. Gaskill, J.A. Freitas, Mat. Res. Soc. Symp. Proc. Vol. 395 (1996) p897.
[3] L.I. Maissel, in: L.I. Maissel, R. Glan (Eds.), Handbook of thin film technology, McGraw-Hill, New York, 1970, pp. 1–4.
[4] F.D. Auret, S.A. Goodman, F.K. Koschnick, J.-M. Spaeth, B. Beaumont, P. Gibart, Mater Sci. Eng. 1999, Submitted for publication.
[5] F.D. Auret, G. Myburg, H. Kunert, W.O. Barnard, J. Vac. Sci. Technol. B 10 (1992) 591.
[6] G. Myburg, F.D. Auret, J. Appl. Phys. 71 (1992) 6172.
[7] C. Christensen, J.F. Petersen, A.N. Larsen, Appl. Phys. Lett. 61 (1992) 1426.
[8] D.V. Lang, J. Appl. Phys. 45 (1974) 3023.
[9] F.D. Auret, G. Myburg, L.J. Bredell, W.O. Barnard, H.W. Kunert, Mater Sci. Forum 83-87 (1992) 1499.
[10] G. Myburg, W.O. Barnard, W.E. Meyer, C.W. Louw, N.G. van den Berg, M. Hayes, F.D. Auret, S.A. Goodman, Appl. Surf. Sci. 70/71 (1993) 511.
[11] S. Ruvimov, Z. Liliental-Weber, J. Washburn, K.J. Duxstad, E.E. Haller, Z.-F. Fan, S.N. Mohammed, W. Kim, A.E. Botchkarev, H. Morkoc, Appl. Phys. Lett. 69 (1996) 1556.
[12] P. Hacke, T. Detchprohm, K. Hiramatsu, N. Sawaki, K. Tadatomo, K. Miyake, J. Appl. Phys. 76 (1994) 304.
[13] W. Götz, N.M. Johnson, H. Amano, I. Akasaki, Appl. Phys. Lett. 65 (1994) 463.
[14] F.D. Auret, S.A. Goodman, F.K. Koschnick, J.-M. Spaeth, B. Beaumont, P. Gibart, Appl. Phys. Lett. 74 (1999) 407.
[15] F.D. Auret, S.A. Goodman, F.K. Koschnick, J.-M. Spaeth, B. Beaumont, P. Gibart, Appl. Phys. Lett. 74 (1999) 809.
[16] Z.-Q. Fang, D.C. Look, W. Kim, Z. Fan, A. Botchkarev, H. Morkoc, Appl. Phys. Lett. 72 (1998) 2277.
[17] F.D. Auret, S.A. Goodman, F.K. Koschnick, J.-M. Spaeth, B. Beaumont, P. Gibart, Appl. Phys. Lett. 73 (1998) 3745.

ELSEVIER

Physica B 273–274 (1999) 88–91

PHYSICA B

www.elsevier.com/locate/physb

Influence of generalized gradient approximations on theoretical hyperfine fields of paramagnetic defects

U. Gerstmann, H. Overhof*

AG Theoretical Physics, Physics Department, University of Paderborn, D33095 Paderborn, Germany

Abstract

We calculate isotropic hyperfine interactions for various paramagnetic defects in silicon and GaN. For *s*-like defect states the incorporation of GGA corrections in spherically symmetric geometry does not lead to significant changes, whereas for 3d transition metal defects the GGAs remove most of the deficits of the LSDA treatment only if an additional empirical correction is introduced. Possible reasons for the necessity of this correction are discussed.

Keywords: LSDA; GGA; Hyperfine interactions; Silicon; GaN

1. Introduction

The density functional theory (DFT) is widely used for self-consistent calculations of the electronic ground states of atoms, molecules, and solids. In this theory only the exchange-correlation energy must be approximated which is a functional of the spin density contribution. Up to now, all ab-initio calculations for the electronic structure of deep defects in semiconductors make use of the local spin density approximation (LSDA) which has proved to result in quite accurate total energies. In the LSDA the exchange-correlation energy functional is replaced by a local function of the local spin densities. This would be exact for homogeneous systems, but the requirement of a homogeneous spin density is not even approximately fulfilled for solid-state systems and is most strongly violated in the core regions near the nuclei. Thus, any improvement to the rather crude LSDA by gradient corrections should also influence hyperfine interaction data which are determined by the spin densities in this region.

Generalized gradient approximations (GGAs) are known to improve global results of the LSDA like total energies [1], but are often expected to fail in improving local quantities [2]. Recently, however, Battocletti et al. [3] presenting hyperfine field calculations for ferromagnetic metals using various parametrizations of GGAs obtained better agreement with the experimental data, but only in a statistical sense.

2. Computation of hyperfine interactions

We have self-consistently calculated the electronic structure of paramagnetic defects in silicon and GaN using the LMTO-ASA-Green's function method [4]. The ASA implies that only the spherically symmetric part of the densities is used to calculate a radial potential $V(r)$ for solving the Dirac equation in scalar relativistic approximation. In its present form, the method does not allow to include lattice relaxations. In principle, the LMTO-ASA method yields accurate information about the spatial distribution of the particle and magnetization densities, especially in the regions near the nuclei. Therefore, it is possible to calculate the hyperfine interaction (HFI) for the magnetic moments of the electrons with that of the nuclei.

In a relativistic treatment, the isotropic part of the HFI (the Fermi-contact term) is due to the magnetization density averaged over the Thomson sphere (a sphere of

* Corresponding author. Tel.: + 49-5251-602334; fax: + 49-5251-603435.

E-mail address: h.overhof@phys.upb.de (H. Overhof)

0921-4526/99/$ - see front matter
PII: S0921-4526(99)00413-5

Table 1
Calculated isotropic HFI (in MHz) broken up into core (a_{core}) and valence band state (a_{vb}) contributions for the LSDA parametrization of Perdew and Wang [9–11]. Corresponding experimental data are also given

	$Si:Al_{int}^{2+}$	$Si:Fe_{int}$	$GaN:Mn_{Ga}^{-}$	$Si:Cd_{Si}^{+}$
Exp.	1320[a]	20.9[b]	209.9[c]	64.7[d]
LSDA	1370	−13.3	−105.1	−15.3
a_{vb}	1360	11.0	72.8	5.6
a_{core}	10	−24.3	−177.9	−9.7

[a]Niklas et al. [13].
[b]Greulich-Weber et al. [14].
[c]Baranov et al. [15].
[d]Näser et al. [6].

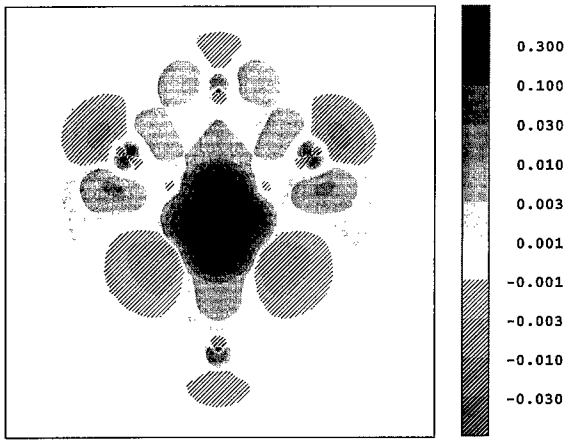

Fig. 1. Contour plot of the total magnetization density for isolated Fe_{int}^{-} in silicon in a (110) plane.

the Thomson radius $r_{Th} = ze^2/(mc^2)$, which is about 20 times the nuclear radius).

In Table 1, theoretical hyperfine values calculated in LSDA are given for various paramagnetic defects.

Al_{int}^{2+} in silicon represents a typical *s*-like defect state. As is shown in a recent review [5], for this class of defects the isotropic hyperfine interaction compares very well with the experimental value with differences in the range of a few percent.

Besides the vacancy, Cd_{Si}^{+} is one of the rare *p*-like defect states observed in EPR and ENDOR. For this unambigously identified defect the calculated isotropic HFI is 9.7 MHz only – about a factor of six smaller than the 64.7 MHz value observed experimentally by Näser et al. [6].

Fe_{int}^{0} in silicon (see Fig. 1) and Mn_{Ga}^{-} in GaN are typical 3d transition metal (TM) point defects which have been extensively investigated since the pioneering work of Ludwig and Woodbury [7]. As can be observed quite generally [8], the calculated LSDA-values are by about a factor of two smaller than the corresponding experimental values. This discrepancy is nearly proportional to the core hyperfine fields (see also Table 1). This suggests that the core polarization is not treated in a satisfactory way within the LSDA as already assumed by Blügel et al. [16] and by Ebert et al. [17].

3. Gradient corrections to the LSDA

Generalized gradient approximations (GGAs) can be interpreted as an attempt to resume the complete gradient expansion of the exchange-correlation energy functional (e.g. the exchange part) as well as possible by the form

$$E_x^{GGA}[n] = \int n \cdot \varepsilon_x^{LDA}(n) F(s)\, d^3r \quad \text{with } s = \frac{|\nabla n|}{2k_F n}, \tag{1}$$

which allows to derive an analytic expression for the exchange potential $V_x = \delta E_x/\delta n$, which is needed for self-consistent numerical calculations:

$$V_x^{GGA} = V_x^{LDA}\frac{3}{4}\left(\frac{4}{3}F - \frac{t}{s}\frac{dF}{ds} - \left(u - \frac{4}{3}s^2\right)\frac{d}{ds}\left(\frac{1}{s}\frac{dF}{ds}\right)\right), \tag{2}$$

where

$$t = \frac{1}{(2k_F)^2}\frac{\nabla^2 n}{n}, \tag{3}$$

and

$$u = \frac{1}{(2k_F)^3}\frac{\nabla n \cdot \nabla |\nabla n|}{n^2}. \tag{4}$$

For the correlation part similar expressions are valid [16]. It is the restriction to the reduced gradient s as a single nonlocal variable which makes the concept of GGAs so interesting for numerical calculations. At the same time $F(s)$ is the source of problems.

The semilocal form of $E_x^{GGA}[n]$ is still too restrictive to reproduce all features of an exact functional. E.g., it is not possible to optimize $F(s)$ in order to produce both correct exchange energies (PW91 [18], PBE96 [19]) and exchange potentials (EV93 [20]) simultaneously. Thus, $F(s)$ is not uniquely defined (see also Fig. 2) and it is not surprising that no unique picture for the validity of various GGAs has emerged. Therefore, we have to apply different parametrizations in order to obtain more information about the promises and limitations of GGAs when calculating the HFI for paramagnetic defects.

The results of our calculations in the *spherically symmetric* ASA geometry are compiled in Table 2. As already

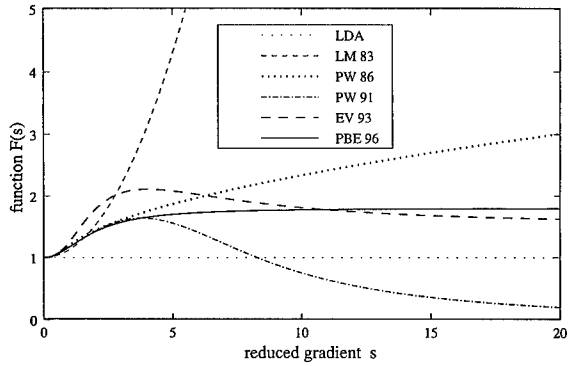

Fig. 2. Plot of the various parametrizations of GGA used for self-consistent calculations. Note the quite different behaviour for high values of s.

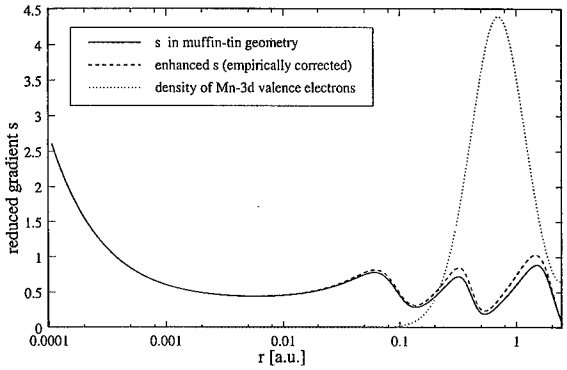

Fig. 3. Empirically enhancement of the reduced gradient s by about 20% in the range of the Mn-3d valence electrons for the Mn_{Ga}^{-} defect in GaN.

Table 2
Calculated isotropic HFI (in MHz) for various parametrizations of GGAs and LSDAs (LSDA[a]: Perdew, Wang [9–11]; LSDA[b]: Ceperley, Alder [12]). The corresponding experimental data are also given

	$Si:Al_{int}^{2+}$	$Si:Fe_{int}$	$GaN:Mn_{Ga}^{-}$	$Si:Cd_{Si}^{+}$
Exp.	1320	20.9	209.9	64.7
LSDA[a]	1370	−13.3	−105.1	−15.3
LSDA[b]	1365	−15.2	−98.9	−4.2
LM83	1394	−12.6	−97.1	—
PW86	1435	−12.1	−38.0	—
PW91	1379	−11.4	−83.3	−2.5
EV93	1285	−17.6	−110.7	—
PBE96	1359	−11.5	−85.6	−2.7

expected above, the results for different GGA parametrizations are by no means equivalent.

The parametrization of Engel and Vosko (EV93) improves the HFI predictions for the interstitials in Si and for Mn_{Ga}^{-} in GaN but the changes are small and comparable with differences between various LSDA parametrizations [9–12]. Unfortunately EV93 completely fails to predict the existence of the Cd_{Si}^{+} charge state in silicon, a state that has been unambigously observed in EPR measurements.

There are only minimal differences between the predictions using the PW91 and the PBE96 parametrization, since both parametrizations are analytical fits to the same numerical GGA [21]. Unfortunately, their use does not increase the modulus of the calculated HFI parameters with respect to results using the LSDA. In contrast, the discrepancy between theoretical and experimental values is even increased. The same is also observed for the exchange-only parametrizations LM83 [22] and PW86 [23].

Obviously, GGA corrections in the ASA treatment do not improve the LSDA predictions of hyperfine fields for paramagnetic defects, not even in a statistical sense as was observed by Battocletti et al. for ferromagnetic metals [3].

There are several possible sources for the still remaining discrepancies. First of all, for 3d TM defect states in semiconductors the core state and the valence band contributions to the HFI do not have the same sign. Thus, the simultaneous increase in modulus of both contributions of the HFI, which has also been observed in ferromagnetic metals, does not lead to significant changes in the total HFI.

Usually, the spin densities of paramagnetic defects in semiconductors are significantly more nonspherical (see Fig. 1) than those of ferromagnetic metals. Whereas the assumption of spherically symmetric densities is unproblematic in the LSDA, the only nonlocal variable $|\nabla n|$ and thereby s of all GGAs is *always* underestimated if the nonspherical parts of the densities are ignored

$$|\nabla n| = \sqrt{\left(\frac{\partial n}{\partial r}\right)^2 + \left(\frac{1}{r}\frac{\partial n}{\partial \vartheta}\right)^2 + \left(\frac{1}{r\sin\vartheta}\frac{\partial n}{\partial \varphi}\right)^2} > \left|\frac{dn}{dr}\right|. \tag{5}$$

In order to investigate whether a moderate increase (by about 20 %) of the reduced gradient s can improve the theoretical HFI, we simulate a full potential calculation by empirically enhancing the reduced gradient s for the valence electron densities (see Fig. 3), in order to get a more realistic exchange-correlation potential to be used in the self-consistent calculations. The corresponding results are compiled in Table 3.

Generally, this correction increases the modulus of the isotropic HFI parameters and eliminates the discrepancies between theory and experiment for 3d TM defects if the reduced gradient is increased by 20 % for the case of

Table 3
Calculated isotropic HFI (in MHz) for various parametrizations of GGAs with corrected reduced gradient s. Corresponding data for LSDA [9–11] and experimental values are also given

	$Si:Al_{int}^{2+}$	$Si:Fe_{int}$	$GaN:Mn_{Ga}^{-}$	$Si:Cd_{Si}^{+}$
Exp.	1320	20.9	209.9	64.7
LSDA	1370	−13.3	−105.1	−9.7
PW91	1337	−22.4	−171.2	−5.4
EV93	1265	−25.8	−181.5	—
PBE96	1316	−27.9	−228.5	−5.8

the parametrizations PW91 and PBE96, whereas in EV93 even a correction by five percent would suffice to this aim. Unfortunately, this enhancement of s does not remove the other main failure of the EV93 parametrization — the exclusion of an existing Cd_{Si}^{+} defect in silicon which is unambigously identified in EPR measurement. In contrast, EV93 leads to even lower lying single particle energy levels.

However, it seems promising that full potential GGA calculations give rise to significantly higher HFI parameters. In principle, this assumption is supported by results from Becke [24,25] who has performed full potential linear augmented plane wave (FPLAPW) calculations using a GGA parametrization equivalent to PBE96, but with empirical coefficients. The calculated magnetic moments in ferromagnetic metals are closer to experiment than those calculated in the muffin-tin approximation by Battocletti et al. [3]. These latter authors considered it unlikely that FP calculations have also a strong impact on HFI parameters, an assumption which must be questioned in the light of our present results for paramagnetic defects.

Cd_{Si}^{+} in silicon obviously presents a different case. For this defect, we assume at the moment that the neglect of lattice relaxations is the main reason for the striking discrepancy between experimental and calculated HFI by about a factor of six.

Of course, the influence of lattice relaxations cannot be ruled out for the 3d TM defects as well. We plan to calculate the relative importance of nonspherical corrections without empirical components and lattice relaxations of paramagnetic defects in semiconductors.

References

[1] J.P. Perdew, J.A. Chevary, S.H. Vosko, K.A. Jackson, M.R. Pederson, D.J. Singh, C. Fiolhais, Phys. Rev. B 46 (1992) 6671.
[2] E. Engel, S.H. Vosko, Phys. Rev. B 47 (1993) 13 164.
[3] M. Battocletti, H. Ebert, H. Akai, Phys. Rev. B 53 (1996) 9776.
[4] O. Gunnarsson, O. Jepsen, O.K. Andersen, Phys. Rev. B 27 (1983) 7144.
[5] H. Overhof, in: R.P. Agarwala (Ed.), Special defects in semiconducting materials, Solid State Phenomena, Trans-Tech Publications, Uerlikon, in press.
[6] A. Näser, W. Gehlhoff, H. Overhof, R.A. Yankov, Phys. Stat. Sol. B 210 (1998) 753.
[7] G.W. Ludwig, H.H. Woodbury, Sol. Stat. Phys. 13 (1962) 223.
[8] U. Gerstmann, M. Amkreutz, H. Overhof, Phys. Stat. Sol. B, in press.
[9] J.P. Perdew, Y. Wang, Phys. Rev. B 33 (1986) 8800.
[10] J.P. Perdew, Y. Wang, Phys. Rev. B 40 (1989) 3399.
[11] J.P. Perdew, Y. Wang, Phys. Rev. B 45 (1992) 13 244.
[12] D.M. Ceperley, B.J. Alder, Phys. Rev. Lett. 45 (1980) 566.
[13] J.R. Niklas, J.-M. Spaeth, G.D. Watkins, MRS Proc. San Francisco 46 (1985) 237.
[14] S. Greulich-Weber, J.R. Niklas, E.R. Weber, J.-M. Spaeth, Phys. Rev. B 30 (1984) 6292.
[15] P.G. Baranov, I.V. Ilyin, E.N. Mokhov, Mat. Sci. Forum 258–263 (1997) 1167.
[16] S. Blügel, H. Akai, R. Zeller, P.H. Dederichs, Phys. Rev. B 35 (1987) 3271.
[17] H. Ebert, P. Strange, B. L. Gyorffy, Z. Phys. B 73 (1988) 77.
[18] J.P. Perdew, in: P. Ziesche, H, Eschrig (Eds.), Electronic structure of Solids '91, Akademie Verlag, Berlin, 1991, p. 11.
[19] J.P. Perdew, K. Burke, M. Ernzerhof, Phys. Rev. Lett. 77 (1996) 3865.
[20] E. Engel, S.H. Vosko, Phys. Rev. B 47 (1993) 2800.
[21] J.P. Perdew, K. Burke, Y. Wang, Phys. Rev. B 54 (1996) 16 533.
[22] D.C. Langreth, M.J. Mehl, Phys. Rev. B 28 (1983) 1809.
[23] J.P. Perdew, Y. Wang, Phys. Rev. B 33 (1986) 8800.
[24] A.D. Becke, J. Chem. Phys. 84 (1986) 4524.
[25] A.D. Becke, Phys. Rev. A 38 (1988) 3098.

ELSEVIER

Physica B 273–274 (1999) 92–95

PHYSICA B

www.elsevier.com/locate/physb

Metastable-like behaviour of a sputter deposition-induced electron trap in n-GaN

F.D. Auret[a,*], W.E. Meyer[a], S.A. Goodman[a], F.K. Koschnick[b], J.-M. Spaeth[b], B. Beaumont[c], P. Gibart[c]

[a]*Department of Physics, University of Pretoria, Pretoria 0002, South Africa*
[b]*Fachbereich Physik, Universität GH Paderborn, Paderborn, Germany*
[c]*CRHEA-CNRS, Valbonne, France*

Abstract

We show that a deep level, the ES1, introduced in n-GaN by sputter-deposition of gold Schottky contacts exhibits metastable-like behaviour during temperature cycling between 55 and 250 K. The ES1 has an energy level 0.22 ± 0.02 eV below the conduction band. We provide some evidence that indicates that the defect responsible for the ES1 has a second energy level, the ES1*, and that the metastable behaviour of the ES1 may be due to negative-U ordering of these two energy levels. Furthermore, field effect measurements indicate that the ES1 level has a donor character, while the ES1* level is probably an acceptor.

Keywords: GaN; DLTS; Sputter deposition

1. Introduction

Gallium nitride, a direct, wide band-gap semiconductor, has a number of unique applications including blue, green and ultraviolet light emitting diodes, blue lasers, detectors and high temperature and power electronics devices [1,2]. An essential step in device manufacture is the deposition of a metal film that has to form ohmic or Schottky contacts to the semiconductor. This metal film is frequently deposited by means of sputter deposition. This technique has the advantage that it facilitates the stoichiometric deposition of compounds as well as the deposition of metals with a high melting point. In addition, sputter-deposited layers exhibit far better adhesion compared to layers deposited by other methods [3]. The main disadvantage of sputter deposition is that it involves energetic particles that may damage the crystal lattice and produce defects at and below the surface of the semiconductor [4]. In many cases these defects give rise to energy levels in the semiconductor band gap which are electrically active and may act as trapping or recombination levels. These defects can be observed by means of deep level transient spectroscopy (DLTS) [5].

Some defects in semiconductors exhibit charge state controlled metastable behaviour. That is, they can exist in different configurations, with the stable configuration depending on the charge state of the defect [6]. Such charge state controlled metastability allows for the reversible introduction and removal of defects in a semiconductor, and leads to a number of interesting phenomena, for instance the number and energy of the deep levels observed in a sample may depend on the bias conditions under which the sample was cooled. The metastability of defects is also of technologically importance, since the presence of a metastable defect in a device may lead to electrical properties that depend on the history of the sample, thus leading to unreliable device characteristics.

In this paper we discuss some of the metastable properties of defects introduced in n-GaN during sputter deposition of Au Schottky contacts.

* Corresponding author. Tel.: + 27-12-420-2684; fax: + 27-12-362-5288.

E-mail address: fauret@scientia.up.ac.za (F.D. Auret)

0921-4526/99/$ - see front matter
PII: S0921-4526(99)00414-7

2. Experimental procedure

We used epitaxial n-GaN grown by organo-metallic vapour-phase epitaxy (OMVPE), with a free carrier density of $2\text{–}3 \times 10^{16}\ \text{cm}^{-3}$ as determined by capacitance–voltage (CV) measurements. The samples were cleaned [7] by boiling them in aqua-regia. After rinsing the samples in de-ionized water, the samples were degreased in boiling trichloroethylene followed by rinsing in boiling isopropanol and in de-ionized water. Finally, the samples were dipped in a 50% HCl solution for 10 s. Ohmic contacts, consisting of 150 Å/2 200 Å/400 Å/500 Å layers of Ti/Al/Ni/Au [8], were deposited by means of electron beam evaporation and annealed at 500°C for 5 min in Ar. The samples were again degreased and dipped in a 50% HCl solution before deposition of the Schottky contacts. The Schottky contacts, 0.5 mm in diameter and 1 μm thick were sputter-deposited on the GaN through a metal contact mask [9]. For control purposes, Au SBDs were resistively deposited next to the sputter deposited SBDs.

The defects were characterized by means of a lock-in amplifier (LIA) based DLTS system, using a Boonton 7200 capacitance meter and a Stanford Research model SR830 LIA, which facilitates transient analysis at pulse frequencies as low as a few mHz. In order to measure single-shot events, an isothermal DLTS system was used. In this system, the capacitance transient from the Boonton 7200 was captured by an HP 3458 A multimeter and processed by a microcomputer. This isothermal DLTS system also allowed the measurement of DLTS transients lasting as long as a couple of hours. Therefore, it was possible to observe defects at temperatures much lower than those at which they are commonly observed by an LIA-based DLTS system.

The energy level in the band gap, E_T, and the apparent capture cross section σ_n of the defect (collectively known as the defect's 'signature'), were calculated from Arrhenius plots of T^2/e versus $1/T$, where e is the emission rate at temperature T.

In order to allow for measurements with short (down to 50 ns) filling pulses, a set of reed relays were used to connect the sample directly to the pulse generator and to disconnect the capacitance meter from the sample. To ensure that the sample was not inadvertently exposed to a filling pulse care was taken to ensure that the capacitance meter was only disconnected after the pulse generator was connected to the sample and no more contact-bounce was observed. Special precautions were taken to avoid any pulses being applied to the sample prior to the measurements. The absence of filling pulses was confirmed by monitoring the voltage across the samples with a fast (200 MHz) storage oscilloscope.

3. Results and discussion

The DLTS spectra of the resistively deposited control sample as well as the sputter-deposited diodes are shown in Fig. 1 curves (a) and (b), respectively. The energy levels and apparent capture cross sections of the sputter-induced defects are summarized in Table 1 [10].

Fig. 2 illustrates the metastable properties exhibited by the ES1 defect. Both curves (a) and (b) were recorded after cooling the sample under reverse bias. However, before curve (a) was recorded, the sample was exposed to a forward bias of 0.35 V. This forward bias pulse seems to reversibly remove the ES1 and ES2 defects. Both defects could be re-introduced by heating the sample under reverse bias to over 150 K. Further investigation using the isothermal DLTS system, showed that the height of the ES1 defect was decreased by an increase in the length of the filling pulse. This is contrary to the usual case, where an increase in the length of the filling pulse increases the height of the DLTS peak. It seems therefore that the capture of an electron in some way decreases the height of the ES1.

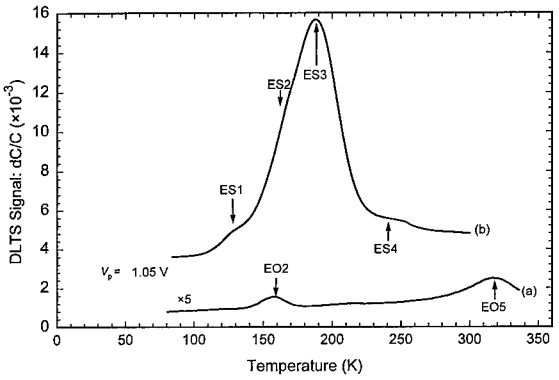

Fig. 1. DLTS spectrum of a resistively deposited control SBD (curve (a)) and a sputter deposited Schottky barrier (curve (b)) on epitaxial GaN ($V_p = 1.2$ V, $t_p = 0.2$ ms, $f = 46$ Hz).

Table 1
Electronic properties of sputter deposition induced defects in epitaxial n-GaN

Defect label	E_T (eV)	σ_a (cm^2)	T_{peak}[a] (K)
ES0	—	—	—
ES1	0.22 ± 0.02	$6.5 \pm 2.0 \times 10^{-16}$	< 120
ES2	0.30 ± 0.01	$4.4 \pm 1.0 \times 10^{-14}$	157
ES3	0.40 ± 0.01	$3.3 \pm 1.0 \times 10^{-13}$	192
ES4	0.45 ± 0.10	$8.1 \pm 2.0 \times 10^{-16}$	249

[a]Peak temperature at a lock-in amplifier frequency of 46 Hz, i.e. a decay time constant of 9.23 ms.

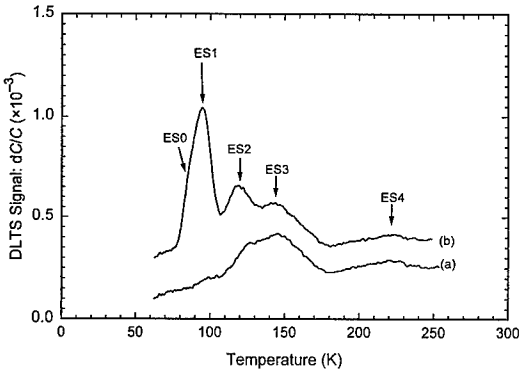

Fig. 2. DLTS spectra of a sputter deposited Schottky contact using $V_r = 1.0$ V, $V_p = 1.35$ V, $f = 0.22$ Hz. Curve (a) was recorded after cooling under reverse bias, while curve (b) was recorded after application of 0.35 V forward bias at 60 K.

One possible explanation for this behaviour is a phenomenon known as negative-U [11]. According to this explanation, the ES1 defect is one energy level of a defect that has two energy levels in the band gap (i.e. the defect can trap two electrons). If the defect has already captured one electron, the second electron the defect captures would be repelled by coulomb interactions with the first electron. This implies that the second electron should be less tightly bound than the first electron. This difference in binding energy is referred to as U, and is usually positive. However, in some defects, there may be some interaction with the lattice that causes the second electron to be more tightly bound than the first, i.e. U is negative. A classical case in which negative-U properties have been demonstrated is the boron interstitial in silicon [12].

In the case of the ES1 deep level, the short (50 ns) filling pulse is just long enough to fill the defect with one electron. After the defect has captured one electron, the capture cross section of the defect decreases dramatically, due to the change in the charge state of the defect. Therefore, the defect will not capture another electron as easily as it captured the first. After the filling pulse, the electron is easily emitted and gives rise to the ES1 peak observed in the DLTS spectrum.

If a long filling pulse is applied, the defect will capture a second electron. However, due to the negative-U ordering of these two energy levels, the second electron to be captured is more tightly bound than the first. Therefore this electron is emitted at a significantly lower rate than the first, and should give rise to another defect level with a lower emission rate, which we shall refer to as the ES1*. The first electron to be emitted is now rapidly followed by the emission of a second electron to be emitted (since the second electron is more weakly bound than the first). This implies that the ES1* should have twice the height of the ES1.

If a filling pulse with a length falling between the two extremes is applied, some of the defects will have captured a single electron, while others will have captured two electrons. Emission from these defects will give rise to both the ES1 and the ES1* DLTS peaks. It follows from the above argument that the heights of the peaks should be related by

$$2 \times [\mathrm{ES1}] + [\mathrm{ES1}^*] = \text{constant}. \quad (1)$$

In order to investigate the possibility of the ES1 belonging to a defect having negative-U properties, an attempt was made to look for evidence of a second energy level. Further investigations with the isothermal DLTS system showed that, as the peak due to the ES1 disappeared, a second peak with a much lower emission rate appeared. This second peak will be referred to as the ES1*. The isothermal DLTS spectrum obtained for the ES1 and ES1* after the application of different filling pulses is shown in Fig. 3. Here it can be clearly seen that the height of the ES1* (peak at 1000 s) increases as the height of the ES1 (peak at 0.6 s) decreases.

In order to confirm the relationship predicted by Eq. (1), the charge involved in each of the DLTS peaks was estimated by measuring the change in capacitance associated with each of the peaks. Fig. 4 shows this capacitance change for both peaks as a function of filling pulse length. Also shown is the value of $2 \times [\mathrm{ES1}] + [\mathrm{ES1}^*]$, which is approximately constant. The systematic deviation observed should still be investigated further, but it could be due to the field dependence of the emission rate or an inaccurate determining of the baseline position of partly overlapping peaks in Fig. 3.

In order to obtain some further insight into the properties of the ES1 and the ES1*, the field dependence of the emission rate from these defects was determined. This property is frequently used to estimate the shape of the potential well of a defect and to distinguish between

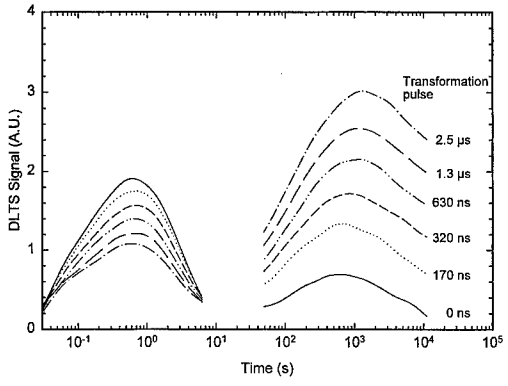

Fig. 3. Isothermal DLTS spectra obtained after the application of filling pulses with different lengths. Note that the height of the ES1 peak (at 0.6 s) decreases as that of the ES1′ (at 1000 s) increases. ($V_r = -1$ V, $V_p = 1.5$ V, $T = 100$ K).

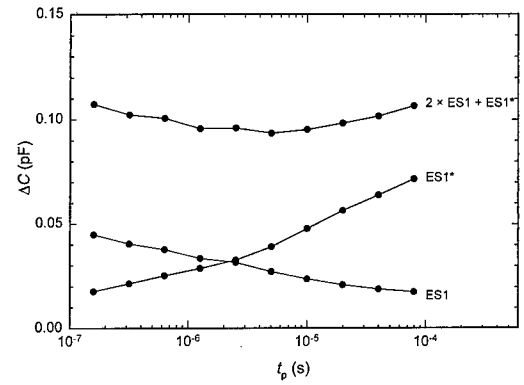

Fig. 4. Capacitance change associated with the ES1 and the ES1* after the application of different filling pules. The third curve corresponds to $2 \times [ES1] + [ES1^*]$.

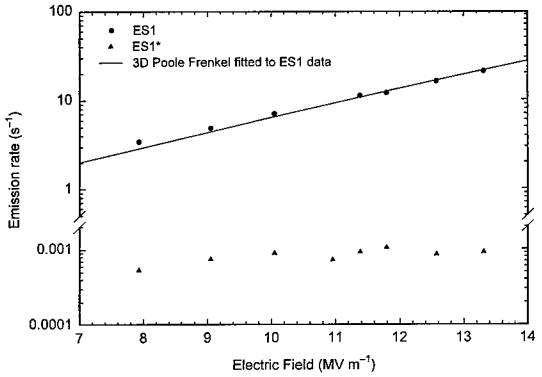

Fig. 5. Field dependence of the emission rate from the ES1 and ES1* defects as determined by means of isothermal DLTS at 100 K.

donor and acceptor levels [13]. The results of these measurements are shown in Fig. 5, which shows that the emission from the ES1 is strongly field dependent while the emission from the ES1* is much less dependent on the electric field.

If it is assumed that the field enhanced emission from the ES1 and ES1* is due to the Poole–Frenkel lowering of the barrier height, it follows that the potential well of the ES1 has to be much wider than that of the ES1*. A more quantitative approach can be followed by fitting the theoretical curve for the Poole–Frenkel field enhanced emission from a Coulombic well [13] to the field dependent emission data obtained for the ES1 (see Fig. 5). The excellent fit obtained indicates that the field enhanced emission from the ES1 is consistent with the Poole–Frenkel emission from a three-dimensional coulombic well, and therefore the ES1 is probably a donor. The weak dependence of the emission from the ES1* on the electric field, combined with the lower capture cross section, indicates that the ES1* is probably an acceptor.

4. Conclusions

We have reported some of the transformational properties of a sputter-induced metastable defect in n-GaN. The unusual transformational properties of the defect can be explained by assuming that the defect has two energy levels in the band gap, ES1 and ES1*, with negative-U ordering. The ES1 level is the same level that was previously reported in n-GaN with an energy level 0.22 ± 0.02 eV below the conduction band. We have used field effect measurements to show that this level is probably a donor. In contrast to the ES1, emission from the ES1* is much less sensitive to the electric field. It is therefore speculated that the ES1* is an acceptor. Although the evidence for the negative-U properties of this defect is not conclusive, it is hoped that further investigation could provide a definite answer.

Acknowledgements

We gratefully acknowledge financial assistance from the South African Foundation for Research Development. We also thank G. Myburg for ohmic contact metallization and C. Schutte and C. du Toit for sputter deposition.

References

[1] S. Nakamura, G. Fasol, The Blue Laser Diode, Springer, Berlin, 1997.
[2] K. Doverspike, A.E. Wickenden, S.C. Binarii, D.K. Gaskill, J.A. Freitas, Mater. Res. Soc. Symp. Proc. 395 (1996) 897.
[3] L.I. Maissel, in: L.I. Maissel, R. Glan (Eds.), Handbook of Thin Film Technology, McGraw-Hill, New York, 1970, pp. 1–4.
[4] F.H. Mullins, A. Brunnschweiler, Solid State Electron. 19 (1976) 47.
[5] D.V. Lang, J. Appl. Phys. 45 (1974) 3023.
[6] A. Chantre, Appl. Phys. A 48 (1989) 3.
[7] P. Hacke, T. Detchprohm, K. Hiramatsu, N. Sawaki, Appl. Phys. Lett. 63 (1993) 2676.
[8] S. Ruvimov, Z. Liliental-Weber, J. Washburn, K.J. Duxstad, E.E. Haller, Z.-F. Fan, S.N. Mohammed, W. Kim, A.E. Botchkarev, H. Morkoc, Appl. Phys. Lett. 69 (1996) 1556.
[9] F.D. Auret, S.A. Goodman, F.K. Koschnick, J.-M. Spaeth, B. Beaumont, P. Gibart, Appl. Phys. Lett. 74 (1999) 2173.
[10] F.D. Auret, S.A. Goodman, F.K. Koschnick, J.-M. Spaeth, B. Beaumont, P. Gibart, Mater. Sci. Eng. (1999), submitted for publication.
[11] G.D. Watkins, Negative-U properties for Defects in Solids, Festkörperprobleme XXIV, 1984, p. 163.
[12] J.R. Troxell, G.D. Watkins, Phys. Rev. B 22 (1980) 593.
[13] J.L. Hartke, J. Appl. Phys. 39 (1968) 4871.

ELSEVIER

Physica B 273–274 (1999) 96–100

PHYSICA B

www.elsevier.com/locate/physb

Annealing of ion-implanted GaN

A. Burchard[a], E.E. Haller[b], A. Stötzler[a], R. Weissenborn[a], M. Deicher[a,*], ISOLDE Collaboration[c]

[a]*Fakultät für Physik, Universität Konstanz, P.O. Box 5560, D-78457 Konstanz, Germany*
[b]*Department of Materials Science, University of California Berkeley, Berkeley CA 94270, USA*
[c]*CERN/PPE, CH-1211 Geneva 23, Switzerland*

Abstract

^{111m}Cd and ^{112}Cd ions have been implanted into GaN. With photoluminescence spectroscopy and perturbed $\gamma\gamma$ angular correlation spectroscopy (PAC) the reduction of implantation damage and the optical activation of the implants have been observed as a function of annealing temperature using different annealing methods. The use of N_2 or NH_3 atmosphere during annealing allows temperatures up to 1323 and 1373 K, respectively, but above 1200 K a strong loss of Cd from the GaN has been observed. Annealing GaN together with elementary Al forms a protective layer on the GaN surface allowing annealing temperatures up to 1570 K for 10 min.

PACS: 61.72V; 78.55.CR; 76.80.+Y

Keywords: GaN; Ion implantation; Annealing; Photoluminescence; PAC

1. Introduction

The advantage of doping semiconductors by ion implantation is the control of concentration, depth and lateral distribution of the dopants. However, ion implantation is always accompanied by structural damage to the crystal requiring thermal annealing to achieve electrical activation of the dopants. The reconstruction of the GaN lattice with a melting point of about 2800 K [1] requires annealing temperatures up to 1900 K and an external N_2 overpressure of several GPa to suppress the decomposition of the GaN due to the loss of N. It has been shown by RBS measurements [2] that a significant amount of damage remains in the material after annealing at 1370 K under N_2 atmosphere. On the other hand, implanted Zn acceptors have been efficiently optically activated by annealing at 1720 K under a N_2 overpressure of 1.6 GPa [3]. For the production of GaN-based devices it is necessary to have a practicable annealing technique which efficiently activates the implanted atoms. Several procedures for thermal processing of GaN have been investigated and were recently reviewed by Pearton et al. [4]. We report on the observation of implantation-induced defects and their annealing using the perturbed $\gamma\gamma$ angular correlation spectroscopy (PAC) [5]. This technique probes the immediate vicinity of a suitable radioactive dopant, ^{111m}Cd in this case. In a previous work, PAC has been used to study the annealing of the implantation-induced damage after implantation of the group-III element ^{111}In [6]. Here, we report on the annealing of Cd-implanted GaN under N_2, NH_3, and Al atmosphere. The achieved optical properties have been checked by photoluminescence spectroscopy (PL).

* Corresponding author. Tel.: +49-7531-883865; fax: +49-7531-883090.
E-mail address: manfred.deicher@uni-konstanz.de (M. Deicher)

2. Experimental details

The GaN samples used were epitaxial layers grown on AlN/c-sapphire by metal organic vapor-phase epitaxy

0921-4526/99/$ - see front matter
PII: S0921-4526(99)00415-9

(MOVPE) purchased from CREE Research or obtained from Hewlett-Packard Optoelectronics Division. For the PAC measurements the samples were doped by ion implantation (60 keV, 5×10^{11} ions/cm^2) at room temperature with ^{111m}Cd at the ISOLDE mass separator facility at CERN (Geneva). For the PL experiments, the samples have been implanted with stable ^{112}Cd (60 keV, 1×10^{11} – 1×10^{14} ions/cm^2). The implantation energy of 60 keV corresponds to a calculated depth distribution [7] of the implanted Cd ions centered at 190 Å below the surface with a width of 75 Å, i.e. the implanted dose range corresponds to mean Cd concentrations between 5×10^{16} cm^{-3} and 5×10^{19} cm^{-3}. To serve as reference, a part of each sample was not implanted. The samples were annealed for 10 min in sealed quartz ampoules either under N_2 or NH_3 atmosphere or in vacuum together with elementary Al up to 1623 K. The PAC technique [5] is sensitive to electric field gradients (EFG) present at the site of the probe atom, in our case ^{111m}Cd ($t_{1/2}$ = 48 min). An EFG causes a three-fold hyperfine splitting of an excited state of the ^{111}Cd nuclei. This splitting is observed by PAC and is characteristic for the defects in the immediate neighborhood of the probe atom. The EFG is described by the quadrupole coupling constant $\nu_Q = eQV_{zz}/h$(Q denotes the nuclear quadrupole moment, V_{zz} the largest component of the diagonalized EFG tensor) and the asymmetry parameter η. These quantities are unique for each defect and both, the symmetry of a formed probe-atom-defect complex and the fraction of probe atoms involved in this complex, can be determined from the characteristic modulation of the PAC spectrum $R(t)$. A damping of the observed modulation due to the superposition of different EFGs caused by the presence of different defect configurations is described by the width $\Delta\nu_Q$ assuming a Lorentzian distribution of these EFGs. All spectra have been recorded at room temperature with the c-axis of the GaN layer either oriented in the detector plane with an angle of 45° between two detectors or perpendicular to the detector plane. The photoluminescence (PL) experiments were carried out at 4.2 K using a He-flow-cryostat. The luminescence was excited by the 325 nm line of a HeCd laser. The luminescence was dispersed using a 0.75 m grating monochromator and detected with a photomultiplier.

3. Results and discussion

Fig. 1a shows a PAC spectrum $R(t)$ recorded directly after the implantation of ^{111m}Cd. The relaxation of the PAC signal within a few ns is caused by the superposition of many different EFGs. This is a clear sign for the presence of highly defective regions around all Cd atoms. These defect structures cause different EFGs and lead to the observed strong damping of the spectrum. These

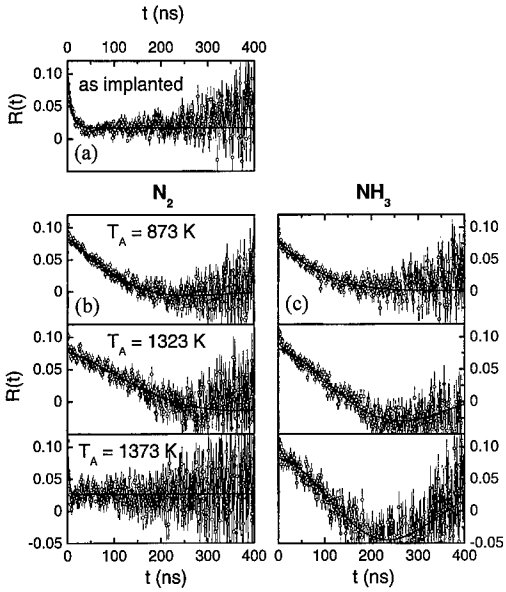

Fig. 1. PAC spectra recorded for GaN implanted with ^{111m}Cd ions (5×10^{11} cm^{-2}, 60 keV): (a) as implanted, after annealing under N_2 atmosphere (b) or NH_3 atmosphere (c) at 873, 1323, and 1373 K for 10 min.

defects act as non-radiative recombination centers and reduce strongly the total PL intensity observed from the implanted region of the sample. Increasing the implanted Cd dose to 10^{14} ions/cm^2 reduces the overall PL intensity to about 1% compared to an unimplanted sample. Immediately after the implantation no Cd-related luminescence is observable. Fig. 1b and c show PAC spectra recorded after different annealing steps under N_2 pressure (1 bar at 295 K) and NH_3 flow, respectively. Annealing at 873 K results in a partial recovery of the damage. Now, 60% of the ^{111m}Cd atoms are exposed to an EFG with ν_Q = 6.0(5) MHz which exhibits a large damping ($\Delta\nu_Q$ = 5 MHz). Increasing the annealing temperature to 1323 K continuously reduces this damping. For annealing under N_2 atmosphere, raising the annealing temperature to 1373 K drastically changes the spectrum: The unique EFG with ν_Q = 6.0 MHz is no longer observed and the spectrum looks similar to the one recorded directly after the implantation (Fig. 1a). This is an indication that the surface starts to decompose via the loss of N leading to a high concentration of defects in the GaN lattice reaching the depth where the implanted ions are located. This decomposition is shifted to higher annealing temperatures (above 1373 K) by the presence of NH_3 (Fig. 1c). The EFG characterized by ν_Q = 6.0 MHz is axially symmetric ($\eta = 0$) and its symmetry axis is oriented along the c-axis of the hexagonal structure of GaN. Both the symmetry and the small value of this EFG favors its association with the intrinsic EFG

detected by probe atoms located on Ga lattice sites with a defect-free nearest surrounding. This has been shown in an earlier work [6] observing the same EFG using the isotope ^{111}In which should occupy Ga lattice sites in GaN and is supported by emission channeling measurements [8] which show that at least 90% of the implanted ^{111}In atoms occupy substitutional lattice sites. In Fig. 2, the results for annealing under N_2 (filled symbols) and NH_3 (open symbols) are summarized. Annealing above 600 K leads to an increase of the fraction of ^{111m}Cd atoms with no defects in the immediate neighborhood (Fig. 2a). At 770 K, about 60% of the probe atoms observe the intrinsic lattice EFG but the rather broad distribution of about $\Delta\nu_Q = 5$ MHz (Fig. 2b) indicates that more distant defects are still present. As shown in Fig. 2b, the width of this distribution becomes more narrow with increasing annealing temperatures indicating a further removal of defects. After annealing between 873 and 1323 K, 60% of the ^{111m}Cd atoms reside on almost unperturbed lattice sites characterized by a minimum of the damping of $\Delta\nu_Q \approx 1$ MHz associated with $\nu_Q = 6$ MHz. This residual damping may be caused by the remaining implantation damage or dislocations present in the layer. Using NH_3 allows annealing temperatures up to 1373 K resulting in a further reduction of the damping $\Delta\nu_Q$. But even at these temperatures 40% of the implanted ions reside in highly perturbed surroundings. This is consistent with results obtained by RBS measurements and XTM images [2] of Si-implanted GaN which show the presence of implantation-induced defects and an electrical activation of about 50% of the dopants at these annealing temperatures. In Fig. 3, PL spectra of GaN implanted with ^{112}Cd (1×10^{12} cm^{-2}) recorded after annealing under NH_3 between 1000 and 1373 K are shown. For each annealing step the PL spectrum of an unimplanted part of the sample ("reference", dotted line) is shown. With increasing annealing temperature the concentration of non-radiative recombination centers decreases which is visible in the increase of the intensities of the transitions due to the donor-bound excitons (DX) and its phonon replicas (DX-LO, DX-2LO) which finally reach about 50% of the reference spectrum after annealing at 1373 K. At this temperature, the decomposition of the GaN surface already starts. This is expressed by a vanishing of the oscillations on the yellow luminescence (YL) located around 2.2 eV which are caused by Fabry–Perot interferences between the GaN/sapphire interface and the GaN surface. Increasing the annealing temperature to 1423 K destroys the GaN layer. The luminescence band centered at 2.7 eV and the transitions at 3.341, 3.328, and 3.272 eV were attributed to centers involving Cd (Fig. 3). The identification of these transitions is discussed in detail by Stötzler et al. [9]. Implanting radioactive isotopes makes it easy to follow up losses of the implanted species during annealing via detecting the radioactivity in the sample before and after

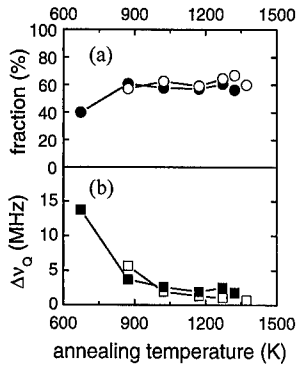

Fig. 2. Fraction of ^{111m}Cd on substitutional Ga lattice sites in GaN (a) and the damping of the observed EFG (b) as a function of the annealing temperature for annealing under N_2 (closed symbols) and NH_3 atmosphere (open symbols).

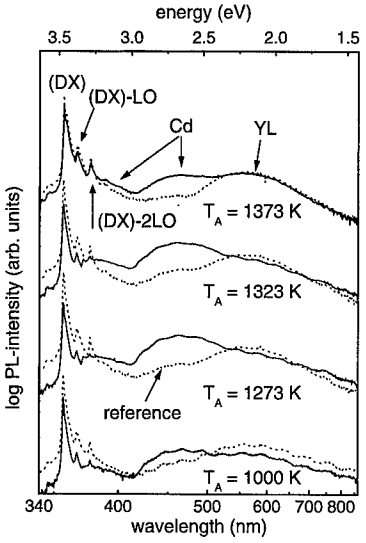

Fig. 3. PL spectra recorded for GaN implanted with ^{112}Cd (1×10^{12} cm^{-2}) after annealing under NH_3 between 1000 and 1373 K. The dotted curves show spectra recorded for a non-implanted part of the sample.

each annealing step. Fig. 4 shows the loss of implanted ^{111m}Cd atoms after annealing under N_2 and NH_3 atmosphere. After annealing for 10 min at 1323 K, about 75% of the Cd atoms have left the GaN sample. Increasing the annealing temperature to 1373 K results in a loss of more than 95% of the Cd atoms. This dramatic loss is less pronounced in the PL spectra shown in Fig. 3. It can be seen by comparing the intensities of the transitions related to donor-bound excitons (DX) and Cd, especially between 1323 and 1373 K. The observed PL intensities due to Cd transitions involve only Cd atoms which are optically active. This fraction of optically active Cd

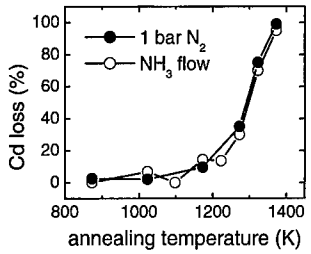

Fig. 4. Loss of Cd atoms out of GaN as a function of the annealing temperature and annealing under N_2 or NH_3 atmosphere.

atoms increases due to annealing whereas the total number of Cd atoms decreases due to out-diffusion. This is plausible because diffusion is enhanced by the presence of defects, especially vacancies. Therefore, optically inactive Cd atoms residing in highly defective regions leave the sample preferentially. Above 1300 K the observed decomposition of the surface may also contribute to the loss of ^{111m}Cd.

Another possibility to protect the GaN surface during high-temperature annealing is either the use of a protective layer like sputtered AlN [10,11] or the addition of nitrides like AlN or InN to supply an overpressure of N_2 during the annealing [4]. In the following, we present evidence for an alternative approach by adding elementary Al to the evacuated quartz ampoule containing the GaN sample. Fig. 5 shows PL spectra of GaN implanted with ^{112}Cd (3×10^{12} cm^{-2}, 60 keV) after using this procedure for annealing at 1473 and 1573 K for 10 min. The PL spectra show that the GaN layer is still intact and strong Cd bands are visible. Obviously, due to the vapor pressure of Al at these temperatures, a protective layer has formed on the GaN surface which effectively suppresses both the loss of N and of Cd. The existence of such a layer is visible in PL via a band normally not observed in GaN. Etching the sample with aqueous KOH at 360 K removes this layer. The samples appear optically smooth and the total PL intensity almost approaches the intensity of the non-implanted reference. Annealing above 1600 K destroys the GaN layer as can be seen by the drastic reduction of the observed PL intensity. The chemical nature of the layer formed on the GaN surface is not known up to now, it may consist of a thin AlN layer. XPS studies are on the way to clarify this question. This cheap and fast procedure may open the possibility to enhance the annealing of ion-implanted GaN.

4. Summary and conclusions

Using PAC and PL spectroscopy, the annealing of GaN implanted with Cd has been studied via both its structural and optical properties. Annealing under N_2 or NH_3 atmosphere leads to a partial structural and optical recovery but is accompanied by a strong loss of Cd at annealing temperatures above 1200 K. First promising results have been presented using elementary Al during annealing of GaN which forms a protective layer and allows annealing temperatures up to 1600 K. The chemical nature of this layer has to be determined in future experiments. Future work will also focus on the annealing behavior of GaN implanted with increasing doses and also the electrical properties will be determined using the same samples for all techniques.

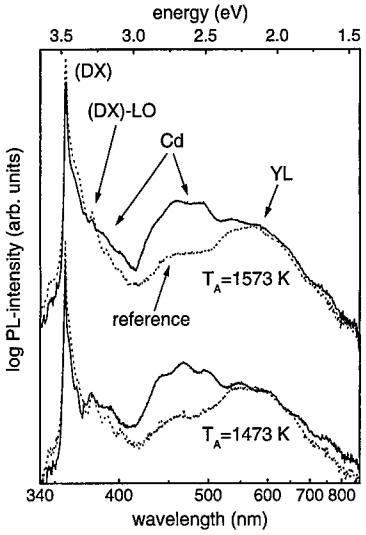

Fig. 5. Photoluminescence spectra recorded after annealing of Cd-implanted GaN (3×10^{12} cm^{-2}, 60 keV) at 1473 and 1573 K. The dotted curves show spectra recorded for a non-implanted part of the sample.

Acknowledgements

We acknowledge the Hewlett-Packard Optoelectronics Division for supplying us with GaN samples. We thank H. Hofsäss for performing some of the ^{112}Cd implantations. This work was financially supported by the Bundesminister für Bildung, Wissenschaft, Forschung und Technologie under Grant No. 03-DE5KO1-6.

References

[1] J.A. Van Vechten, Phys. Rev. B 7 (1973) 1479.
[2] J.C. Zolper, H.H. Tan, J.S. Williams, J. Zou, D.J.H. Cockayne, S.J. Pearton, M. Hagerott Crawford, R.F. Karlicek, Appl. Phys. Lett. 70 (1997) 2729.

[3] T. Suski, J. Jun, M. Leszczynski, H. Teisseyre, S. Strite, A. Rockett, A. Pelzmann, M. Kamp, K.J. Ebeling, J. Appl. Phys. 84 (1998) 1155.
[4] S.J. Pearton, J.C. Zolper, R.J. Shul, F. Ren, J. Appl. Phys. 86 (1999) 1.
[5] Th. Wichert, N. Achtziger, H. Metzner, R. Sielemann, in: G. Langouche (Ed.), Hyperfine Interactions of Defects in Semiconductors, Elsevier, Amsterdam, 1992, p. 77.
[6] A. Burchard, M. Deicher, D. Forkel-Wirth, E.E. Haller, R. Magerle, A. Prospero, A. Stötzler, Mater. Sci. Forum 258–263 (1997) 1099.
[7] J.B. Biersack, L.G. Haggmark, Nucl. Instr. and Meth. 174 (1980) 257.
[8] C. Ronning, M. Dalmer, M. Deicher, M. Restle, M.D. Bremser, R.F. Davis, H. Hofsäss, in: C.R. Abernathy, H. Armano, J.C. Zolper (Eds.), Gallium Nitride and Related Materials II, Material Research Society Symposium Proceedings, Vol. 468, Pittsburgh, 1997, p. 407.
[9] A. Stötzler, R. Weissenborn, M. Deicher, Physica B 273–274 (1999) 144, These Proceedings.
[10] J.C. Zolper, D.J. Rieger, A.G. Baca, S.J. Pearton, J.W. Lee, R.A. Stall, Appl. Phys. Lett. 69 (1996) 538.
[11] X.A. Cao, S.J. Pearton, R.K. Singh, C.R. Abernathy, J. Han, R.J. Shul, D.J. Rieger, J.C. Zolper, R.G. Wilson, M. Fu, J.A. Sekhar, H.J. Guo, S.J. Pennycook, MRS Int. J. Nitride Semicond. Res. 4S1 (1999) G6.33.

ELSEVIER

Physica B 273–274 (1999) 101–104

PHYSICA B

www.elsevier.com/locate/physb

Behavior of electrically active point defects in irradiated MOCVD n-GaN

V.V. Emtsev[a,*], V.Yu. Davydov[a], V.V. Kozlovskii[b], D.S. Poloskin[a], A.N. Smirnov[a], N.M. Shmidt[a], A.S. Usikov[a]

[a]*Ioffe Physicotechnical Institute, Russian Academy of Sciences, Politekhnicheskaya ulitsa 26, 194021 St. Petersburg, Russia*
[b]*Technical State University, 195251 St. Petersburg, Russia*

Abstract

Formation and annealing of radiation-induced defects in doped and nominally undoped n-GaN are investigated by means of electrical measurements and Raman spectroscopy. The production rate of defects turned out to be dependent on the dopant concentration. This suggests that at least one kind of native defects is involved in impurity–defect interactions at room temperature. Two prominent stages of defect annealing are revealed. The annealing processes at $T \geq 100$°C are associated with mobile native defects. A considerable fraction of radiation defects is still present in the materials after annealing to $T \geq 750$°C.

Keywords: Gallium nitride; Irradiation; Defect interaction

1. Introduction

It is well known that a great deal of information on defect behavior and properties in silicon and binary compounds, first of all in GaAs and GaP, has been gained from radiation experiments. In actual fact, irradiation of a semiconductor with fast electrons or gamma rays at energies of a few MeV provides a convenient tool for producing of native defects due to elastic displacement of host atoms. Annealing studies of irradiated semiconductors allow one to investigate important effects associated with mobile native defects and impurity–defect interactions.

The purpose of the present work is to study changes in the electrical and optical properties of wurtzite GaN layers with radiation-induced point defects.

2. Experimental

GaN layers of n-type were grown by the MOCVD technique using sapphire substrates. There were two groups of samples provided by two producers. The samples from the first group were two-layer structures of wurtzite GaN. The lower layer of a thickness of about 2 μm was doped with Si in concentrations of 1×10^{18}–3×10^{18} cm^{-3}. The growth process has been finished with deposition of another layer of undoped GaN. The undoped layer was about 0.1 μm thick. The samples from the second group were nominally undoped. Their thickness was about 4 μm. The electron concentration at room temperature varied from 7×10^{16} to 2×10^{17}cm^{-3}. The mobility of charge carriers was about 600 cm^2/(V s).

The samples were subjected to ^{60}Co gamma-irradiation at 8°C. In the case of ^{60}Co gamma rays the primary defects in GaN are introduced by means of the Compton electrons of a mean energy of about 700 keV, i.e. most of the produced defects are expected to be simple and point-like. The irradiated samples were then isochronically annealed up to $T = 750$°C in steps of $T = 100$°C and $t = 20$ min. Electrical data and Raman spectra were recorded for the samples under study prior to and after gamma-irradiation as well as at all annealing steps.

Hall effect and conductivity measurements were taken by the Van der Pauw technique over a temperature range of 78–300 K. The electrical measurements furnish

* Corresponding author. Tel.: + 7-812-247-9952; fax: + 7-812-247-1017.
E-mail address: emtsev@pop.ioffe.rssi.ru (V.V. Emtsev)

0921-4526/99/$ - see front matter
PII: S0921-4526(99)00416-0

information on the electron concentration and mobility vs. temperature, i.e. $n(T)$ and $\mu(T)$, respectively.

Raman scattering measurements were carried out at room temperature. The Ar^+ laser ($\lambda = 488$ nm) was used for excitation. The scattered radiation was analyzed with a help of a double grating monochromator connected to the computerized systems for scanning and data registration. Analysis of Raman data permits one to estimate the concentration and mobility of charge carriers in n-GaN; see for instance Ref. [1,2]. In this way we used the Raman spectroscopy as an independent source of information. This is especially useful in the case of a two-layer n-GaN structure, since the information can be gained separately for both layers.

3. Results and discussion

3.1. Irradiation of n-GaN

Let us first discuss the data obtained for the doped n-GaN. As can be seen from Fig. 1, the electron concentration over the entire temperature range studied increases in the course of gamma irradiation. This effect is also confirmed by Raman spectroscopy; see Fig. 2. In general, this observation is similar to that reported earlier for lightly doped n-GaN irradiated with fast electrons at 0.9 MeV [3]. Owing to the fact that the damage factors for fast electron and gamma irradiation are different the rates of change of the electron concentration in doped n-GaN differ substantially in both cases, about 1 and (0.01–0.04) cm^{-1}, respectively. However, there are reasons to believe that the rate of radiation-induced donors should be substantially higher than that given above. Actually, from Fig. 3 it is evident that the electron

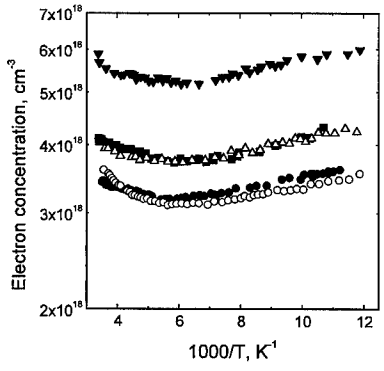

Fig. 1. Temperature dependence of the electron concentration in the doped n-GaN in the initial state (open circles), after gamma irradiation (black squares) and isochronal annealing at $T = 250$°C (black triangles), $T = 550$°C (black circles), and $T = 750$°C (open triangles). Irradiation dose $\Phi = 1.34 \times 10^{19}$cm^{-2}.

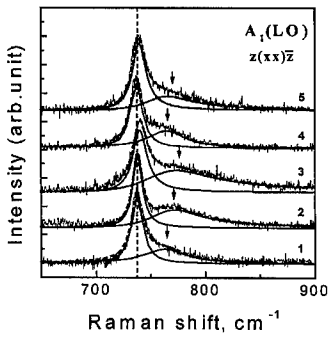

Fig. 2. Experimental Raman spectra and fitting curves for n-GaN : Si in the region of the coupled plasmon-LO phonon modes with higher eigenfrequencies. Spectra: *1*, initial; *2*, after gamma irradiation; *3*, annealing at $T = 250$°C; *4*, annealing at $T = 550$°C; *5*, annealing at $T = 750$°C. Irradiation dose $\Phi = 1.34 \times 10^{19}$cm^{-2}.

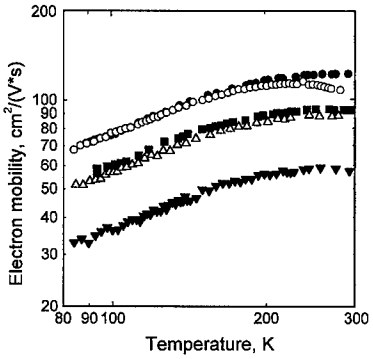

Fig. 3. Temperature dependence of the electron mobility in the doped n-GaN in the initial state (open circles), after gamma-irradiation (black squares) and isochronal annealing at $T = 250$°C (black triangles), $T = 550$°C (black circles), and $T = 750$°C (open triangles). Irradiation dose $\Phi = 1.34 \times 10^{19}$cm^{-2}. The corresponding $n(T)$ curves for this sample are shown in Fig. 1.

mobility in the n-GaN drops in the course of gamma irradiation. Strikingly, this decrease turned out to be much stronger as could be expected from the added concentration of charge carriers, presumably equal to the added concentration of scattering centers; cf. Ref. [4]. It is also true for electron-irradiated n-GaN [3]. Most likely, the effect stems from the appearance of very effective scattering centers, i.e. multiply charged acceptors in n-GaN. This, in turn, means that the added concentration of electrons in the irradiated n-GaN is only a small fraction of radiation-induced donors mostly compensated by the multiple acceptors. Taking into account that the Fermi level in the n-GaN at $T \leq 300$ K is in close proximity to the conduction band one can conclude that

the donors in question are very shallow or even in the conduction band; see also below.

Among the electrically active components of Frenkel pairs in n-GaN, close attention has to be given to the vacancies on both sublattices, V_N^+ (shallow donors) and V_{Ga}^{3-} (triple deep acceptors); see for instance Refs. [5–8]. Nothing is known about activation energies for migration of native point defects in this material. If the native defects are immobile at room temperature a simple interpretation of the experimental observation may be possible assuming that the production rate of V_{Ga}^{3-} is slightly less than one-third of the production rate of V_N^+. In this case the net effect in the n-GaN samples at the same irradiation dose should be the same, independent of the initial dopant concentration, provided that all the primary defects retain their charge states. However, the experimental data are not consistent with this model. The defect production rate drops significantly with decreasing dopant concentration; see also Ref. [3]. In an extreme case, for the undoped samples from the second group, the $n(T)$ curves display some features different from what is observed for the doped n-GaN after irradiation; cf. Figs. 1 and 4.

The effect appears to be associated with silicon impurity atoms or background impurities (oxygen, carbon, etc.) if their introduction in GaN is somehow correlated with the silicon doping. In other words, in such a case at least one of the components of Frenkel pairs should be mobile at room temperature. The mobile defects can be trapped by impurity atoms, thus forming impurity-related complexes. In view of poor identification of native defects in GaN any modeling of radiation-induced processes could be speculative at this stage. Additional information on the defect behaviour can be gained from annealing studies.

3.2. Annealing studies

Some experimental curves $n(T)$ and $\mu(T)$ for the doped n-GaN subjected to irradiation with subsequent annealing are shown in Figs. 1 and 3, respectively. Fig. 5 displays the annealing curves over the entire temperature range. As is seen from this figure, there is a good correlation between the electrical and optical data for the samples from the first group. Moreover, the annealing of defects in the undoped samples from the second group turned out to be similar in many respects, so we will discuss the question in general terms.

Surprisingly, the electron concentration still increases just at the beginning of annealing. This reverse annealing stage takes place up to $T \approx 300°C$; see Figs. 1 and 4. The effect is profound, so in the doped n-GaN the added concentration of charge carriers can be as large as 60% compared to the initial electron concentration; see Fig. 1. Further annealing revealed a broad stage ranging from $T \approx 300°C$ to 550°C. Over this temperature interval the concentration of charge carriers gradually reduced and it completely recovered at $T \approx 550°C$. The mobility of charge carriers also returned to the initial value; see Fig. 3. Interestingly, the EL3 ODMR spectrum, possibly associated with gallium-related defects, disappears in the temperature interval from $T \approx 300°C$ to 400°C [9] and, therefore, the contribution of these defects to the broad annealing stage at $T \geq 250°C$ may be taken into consideration, too.

Despite the seemingly complete recovery of $n(T)$ and $\mu(T)$, the annealing at $T \geq 550°C$ showed that a considerable fraction of radiation defects electrically neutral in the n-GaN survives. Actually, a new reverse annealing stage at $T \approx 650°C$ and its rapid disappearance at

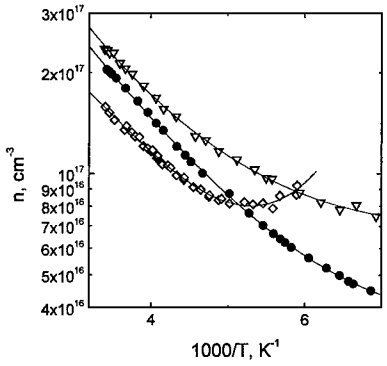

Fig. 4. Temperature dependence of the electron concentration in the undoped n-GaN in the initial state (open circles), after gamma-irradiation (crosses) and isochronal annealing at $T = 300°C$ (black triangles). Irradiation dose $\Phi = 1.18 \times 10^{19} cm^{-2}$.

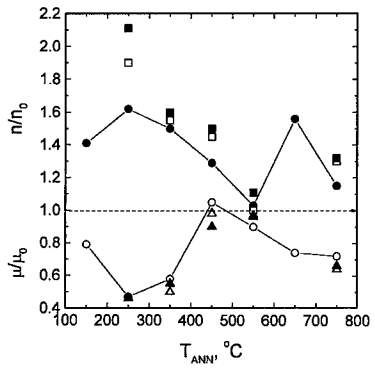

Fig. 5. Isochronal annealing of the irradiated n-GaN. Irradiation dose $\Phi = 1.34 \times 10^{19} cm^{-2}$. Electron concentration at room temperature: electrical measurements (black circles); optical measurements on the doped (black squares) and undoped (open squares) layers. Electron mobility at room temperature: electrical measurements (open circles); optical measurements on the doped (black triangles) and undoped (open triangles) layers.

$T \approx 750$°C are evident from Fig. 5. Two characteristic features of the defect annealing may be pertinent to note. First, the peak concentrations of charge carriers at both reverse annealing stages $T \approx 300$°C and 650°C were found to be nearly equal to one another. Second, after the annealing at $T \approx 750$°C the presence of radiation defects in the n-GaN is still observable, since both $n(T)$ and $\mu(T)$ are far from being recovered. The changes in the electron concentration upon annealing were found to be very similar for all the samples studied, whereas the mobility data differ somewhat in detail from the annealing processes in n-GaN layers with decreasing silicon concentration. Because of this, in drawing conclusions we lean mostly on the concentration data.

A considerable increase in the electron concentration is observed at two annealing stages starting from $T \geq 100$°C and 550°C, respectively. This provides strong support to the conclusion that the reverse annealing is related to the migration of native defects and their complexing with impurities rather than to annihilation of primary defects. The added concentration of shallow donors is estimated to be a few 10^{18} cm^{-3} for the n-GaN with higher silicon concentrations. In such a case, the production rate of primary defects involved in the donor formation is close to 0.1 cm^{-1}, in accordance with the conclusion given above for the irradiated n-GaN. Up to now there is no information on the threshold energy of elastic displacement of host atoms in GaN. Additional radiation experiments are needed to shed new light on the problems discussed.

4. Conclusions

The observed changes in the concentration and mobility of charge carriers in n-GaN as a result of gamma irradiation at room temperature can be explained in terms of the formation of multiply charged acceptors. The data presented furnish evidence that at least one of the components of Frenkel pairs is mobile at room temperature.

The annealing processes appear to be complex. Two prominent stages of reverse annealing of defects with shallow donor states are observed at $T \geq 100$°C. In the course of annealing, the mobile native defects can be trapped by impurities, first of all by silicon and oxygen. Based on the shallow donor concentration at the reverse annealing stages, the estimated production rate of primary defects in gamma-irradiated n-GaN is about 0.1 cm^{-1}, in contrast to the production rate of 0.03 cm^{-1} or less, simply determined from the added concentration of charge carriers in materials subjected to irradiation.

Acknowledgements

The authors are very grateful to Drs. J. Gaul and O. Semchinova for stimulating discussions and critical remarks.

References

[1] T. Kozawa et al., J. Appl. Phys. 75 (1993) 1098.
[2] H. Harima et al., J. Cryst. Growth 189–190 (1997) 672.
[3] V.V. Emtsev et al., Mater. Sci. Forum 258–263 (Trans Tech Publications, Switzerland, 1997) 1143–1148.
[4] D.L. Rode, D.K. Gaskill, Appl. Phys. Lett. 66 (1995) 1972.
[5] J. Neugebauer, C.G. Van de Walle, Phys. Rev. B 50 (1994) 8067.
[6] P. Boguslawski et al., Phys. Rev. B 51 (1995) 17255.
[7] J. Neugebauer, C.G. Van de Walle, Appl. Phys. Lett. 69 (1996) 503.
[8] T. Mattila, R.M. Nieminen, Phys. Rev. B 55 (1997) 9571.
[9] G.D. Watkins et al., Mater. Sci. Forum 258–263 (Trans Tech Publications, Switzerland, 1997) 1087–1092.

ELSEVIER

Physica B 273–274 (1999) 105–108

PHYSICA B

www.elsevier.com/locate/physb

Deep acceptors in undoped GaN

M.A. Reshchikov[a,*,1], F. Shahedipour[a], R.Y. Korotkov[a], M.P. Ulmer[b], B.W. Wessels[a]

[a]*Department of Materials Science and Engineering, Northwestern University, Evanston, IL 60208, USA*
[b]*Department of Physics and Astronomy, Northwestern University, Evanston, IL 60208, USA*

Abstract

Broad photoluminescence bands with maxima at 2.2, 2.5 and 2.9 eV in undoped GaN are studied. The bands are related to three deep acceptors, which are characterized by strong electron–phonon coupling. Vibrational properties of the defects are reported.

Keywords: GaN; Photoluminescence; Defects; Electron–phonon coupling

1. Introduction

Broad bands are often present in emission and absorption spectra of deep defects in semiconductors that are generally attributed to a strong electron–phonon interaction typical for deep localized centers [1–3]. Emission spectra of deep defects in ZnS [4], GaAs [5], GaP [6] and GaN [7] have been successfully described in terms of the one-dimensional configuration coordinate (CC) model, despite its simplicity. In undoped GaN, a broad photoluminescence (PL) band with a peak near 2.2 eV (yellow band) is universally observed [7–9]. Ogino and Aoki attributed this band to optical transitions from a shallow donor to a deep acceptor and explained its large width and temperature behavior using the CC model [7]. However, the broadening of the yellow luminescence has been also attributed to a broad distribution of closely spaced acceptor states [8,9]. Other broad bands have been observed in the luminescence spectrum of GaN whose properties have not been characterized. A broad band with a maximum near 2.9 eV (blue band) is often present in both PL and cathodoluminescence spectra of undoped GaN [10–15]. It is attributed to transitions from either the conduction band or a shallow donor to a deep acceptor, which is tentatively related to the Ga vacancy or its complex [13–15]. Some of our samples revealed a broad band with a maximum at about 2.5 eV (green band) [16]. In this work we show that the luminescence properties of the yellow, green and blue bands in undoped GaN are similar and can be best described by the CC model for defects with strong electron–phonon interaction.

2. Aspects of the configuration coordinate model [1–4]

The characteristic luminescence of the broad bands can be described by the CC model, which is shown in Fig. 1. Adiabatic potentials represent the total potential energy (electronic and nuclear) of the defect. The equilibrium positions of the ground and excited states are displaced from one another and the displacement R_0 is a measure of the electron–lattice coupling. In the simplest case the electronic state interacts with a single localized vibrational mode of frequency ω_0. For generality, the phonon frequencies in the ground and excited states are assumed to be different, ω_0^g and ω_0^e, respectively. At low temperatures ($kT \ll \hbar\omega_0^e$) optical transitions take place from the zero vibrational level and the maximum of

*Correspondence address: Department of El. Engineering/VCU, 601 W. Main str., Richmond, VA 23284-3072, USA. Fax: + 1-804-828-4269.

E-mail address: mreshchi@saturn.vcu.edu (M.A. Reshchikov)

[1] Permanent address: Ioffe Physical-Technical Institute, St.-Petersburg 194021, Russia.

0921-4526/99/$ - see front matter
PII: S0921-4526(99)00417-2

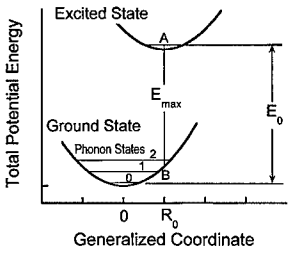

Fig. 1. Configuration coordinate diagram.

emission (E_{max}) corresponds to transition AB shown in Fig. 1. After emitting a photon, the system relaxes to the zero level of the ground state by emitting several phonons with an energy $\hbar\omega_0^g$ into the crystal.

The shape of the PL band depends on $\hbar\omega_0^e$ and the Huang-Rhys factor S, which may be different for absorption and emission, S_{ab} and S_{em}, yet there is a relation between these values:

$$\frac{S_{ab}}{S_{em}} = \frac{\hbar\omega_0^e}{\hbar\omega_0^g}. \tag{1}$$

In case of strong electron–phonon coupling ($S \gg 1$), S represents the mean number of the emitted phonons for each act of the photon absorption or emission. The larger S, the wider the band and the less resolved are transitions corresponding to different vibration levels. The full-width at half-maximum (FWHM, or W) of the PL band depends on temperature, T, and in the CC model is given by

$$W(T) = W(0)\sqrt{\coth\left(\frac{\hbar\omega_0^e}{2kT}\right)}$$

$$= \left(\sqrt{8\ln 2}\,\frac{S_{em}\hbar\omega_0^g}{\sqrt{S_{ab}}}\right) \times \sqrt{\coth\left(\frac{\hbar\omega_0^e}{2kT}\right)}. \tag{2}$$

At high temperatures the bandwidth is proportional to $T^{1/2}$ and at low temperatures it is temperature independent. Thus, it is possible to find $W(0)$ and $\hbar\omega_0^e$ from the temperature dependence of the FWHM of PL band. If position of the zero-phonon line (E_0) is known, one can estimate the quantity ($\hbar\omega_0^g S_{em}$) with the accuracy of $\frac{1}{2}(\hbar\omega_0^g - \hbar\omega_0^e)$

$$\hbar\omega_0^g S_{em} = (E_0 - E_{max}) + \tfrac{1}{2}\hbar\omega_0^g$$

$$\approx (E_0 - E_{max}) + \tfrac{1}{2}\hbar\omega_0^e \tag{3}$$

and then find parameters $\hbar\omega_0^g$, S_{em} and S_{ab} using Eqs. (1) and (2).

3. Experiment

For PL studies, GaN layers with thickness about 2 μm were grown by metal-organic vapor phase epitaxy onto c-plane sapphire. Concentration of free electrons and their mobility, obtained from the room-temperature Hall effect, are 10^{17}–10^{18} cm^{-3} and 100–500 cm^2 V^{-1} s^{-1}, respectively. PL was excited with 325 nm line of a cw He–Cd laser. The excitation density was varied from 2×10^{-5} to 10 W/cm^2 by means of neutral density filters. PL signal was dispersed by a 0.75 m Spex grating monochromator and detected by a Hamamatsu photomultiplier tube (PMT) and a photon-counting system. All PL spectra were corrected to account the spectral sensitivity of the PMT. The sample temperature was varied from 13 to 380 K in a closed cycle helium cryostat and up to 600 K using a heating stage.

4. Results and discussion

We have studied the PL spectra from more than 50 undoped GaN samples. The 2.2 and 2.9 eV bands are present in almost all samples, however their intensities vary. The 2.5 eV band has only been observed in two samples. The spectra of these three PL bands are shown in Fig. 2. The width of the bands was independent of excitation intensity and shape of the bands was the same in a large set of samples. These observations indicate that the PL bands in studied samples correspond to single point defects, rather than to a set of unresolved defects. The good quality of the samples is supported by intense near band-edge emission (FWHM in the range 3–10 meV) with rich fine structure.

With increasing temperature, integrated intensities of the PL bands are thermally quenched with activation energies (E_A) of about 0.38, 0.58 and 0.85 eV, respectively, for the 2.9, 2.5 and 2.2 eV bands (Fig. 3). We attribute this quenching to thermalization of holes from the acceptor level to the valence band. All three PL bands blue-shifted with increasing excitation intensity from 7 to 20 meV suggesting that at low temperature these bands involve

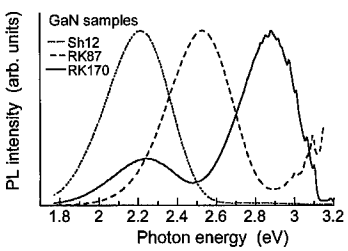

Fig. 2. PL spectrum of undoped GaN samples at $T = 15$ K.

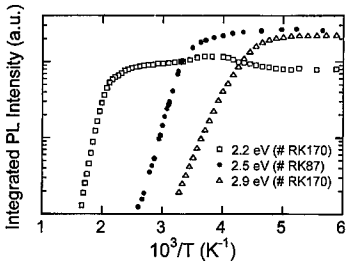

Fig. 3. Temperature dependence of the integrated PL intensity for three PL bands in undoped GaN.

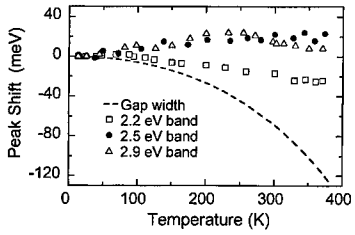

Fig. 4. Shift of the PL band maximum with temperature.

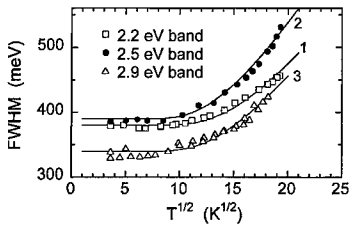

Fig. 5. Temperature dependence of FWHM for three PL bands. The solid curves are fit by Eq. (4) with the following parameters: $W(0) = 380$ (1); 390 (2); 340 (3) meV. $\hbar\omega_0^e = 52$ (1); 40 (2); 43 (3) meV.

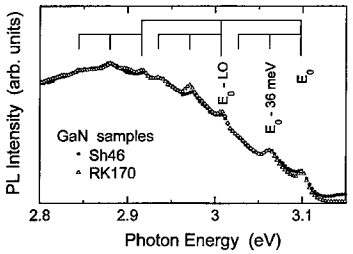

Fig. 6. Fine structure of the 2.9 eV PL band at $T = 15$ K.

transitions from a shallow donor to three different acceptors. Furthermore, the nonexponential decay of PL after pulsed excitation, observed for the yellow and blue bands [17], also implies donor–acceptor type transition. Note that the weakly bound electron on the shallow donor has almost no effect on position of atoms composing the defect and, hence, position and shape of adiabatic potentials should be the same for transitions from the conduction band and from the shallow donor to a deep acceptor. Distribution in the Coulomb interaction for pairs with different separation can also be ignored since it should be of the order of the donor ionization energy, which is much smaller than the observed broadening of the bands.

Temperature dependencies of the position and shape of the PL bands were studied over the range 15–380 K. Temperature-induced shift of the PL bands is different from the gap width variation (Fig. 4), which is typical for defects with strong electron-phonon coupling [4]. The positions of band maximum at low-temperature limit, $E_{max}(0)$, are 2.21, 2.51 and 2.88 eV, respectively, for the yellow, green and blue PL. Fig. 5 shows temperature dependencies of the FWHM of the 2.2, 2.5 and 2.9 eV PL bands. The experimental data for all studied PL bands are well described by Eq. (2) for parameters $W(0)$ and $\hbar\omega_0^e$ listed in captions of Fig. 5. Note that for the yellow band these parameters are slightly different from those found by Ogino and Aoki (430 and 40 meV) [7]. However, our results are consistent with the data of Kim et al. on YL, which attest also that the vibrational characteristics of the defect are invariant with hydrostatic pressure applied [18].

At low temperature, we have observed a fine structure on the high-energy side of the 2.9 eV band, associated with local and lattice phonons (Fig. 6). An analysis of the spectra from many samples has shown that the fine structure is formed by superposition of two series of sharp peaks [15]. First peak at 3.098 eV is attributed to the zero-phonon transition for the 2.9 eV band. Its replicas at the energy multiples of 36 ± 1 meV are attributed to transitions involving the local vibration mode of the acceptor. Repetition of this set over 91 meV is due to coupling with lattice phonons. Using the above-deduced parameters $W(0)$, E_0, $E_{max}(0)$ and $\hbar\omega_0^e$ for the 2.9 eV band we have calculated the parameters $\hbar\omega_0^g$, S_{ab} and S_{em} from Eqs. (1)–(3), which are 60 meV, 3.0 and 4.2 and respectively. The value of $\hbar\omega_0^g$ is consistent with the data measured from the fine structure of the PL band at low temperature. Indeed, contribution of the local (36 meV) and lattice (91 meV) phonons into the bandwidth is comparable and, hence, an effective phonon energy obtained from the band broadening may be expected to be something average. The calculated Huang-Rhys factor is consistent with the shape of the band. Thus, the magnitude $S_{em} = 4.2$ roughly correlates with the mean number of emitted phonons, which is 2.4 or 6 if solely lattice LO or defect local modes are considered. It is interesting to note that simplification $S_{ab} = S_{em}$, commonly accepted for calculation of quantity S from equation similar to Eq. (2) [3], leads to a large discrepancy, if the vibrational

Table 1
Parameters of broad PL bands in undoped GaN

PL band	$E_{max}(0)$ (eV)	E_A (eV)	E_0 (eV)	S_{ab}	S_{em}	$\hbar\omega_0^e$ (meV)	$\hbar\omega_0^g$ (meV)
Yellow	2.21	0.85	2.64[a]	8.0	8.4	52	55
Green	2.51	0.58	3.0 ± 0.05	9.5 ± 2	11 ± 2	40	46 ± 3
Blue	2.88	0.38	3.098	3.0	4.2	43	60

[a]After Ref. [7].

frequencies in the ground and excited states are actually different. So, assuming $S_{ab} = S_{em} = S$, one would obtain $S = 11.3$ from Eq. (2), which is inconsistent with the asymmetric shape of the 2.9 eV PL band. In contrast, the 2.2 and 2.5 eV bands have almost Gaussian shape, which implies stronger electron–phonon coupling (larger value of S). For the yellow band, taking $E_0 = 2.64$ eV from Ref. [7] and using the derived values of $W(0)$ and $\hbar\omega_0^e$ in this work, we obtain $S_{ab} = 8.0$, $S_{em} = 8.4$ and $\hbar\omega_0^g = 55$ meV. For the green band the value of E_0 was roughly estimated as 3.0 ± 0.05 eV from the analysis of the band shape. This results in $S_{ab} = 9.5 \pm 2$, $S_{em} = 11 \pm 2$ and $\hbar\omega_0^g = 46 \pm 3$ meV for this band. The obtained parameters of deep defects are given in Table 1.

Our results are consistent with association of broad PL bands in undoped GaN to a gallium vacancy and/or complexes involving it. Native acceptors, such as V_{Ga} or its complexes with Si, O and H are likely to be formed in the growth of n-type GaN [19]. Similar behavior of the "self-activated" luminescence in ZnS and GaAs, attributed to complexes including a cation vacancy [4,5], supports this.

5. Conclusions

We have studied broad PL bands with maxima at 2.2, 2.5 and 2.9 eV in undoped GaN epitaxial layers. We attribute these bands to optical transitions from a shallow donor (or conduction band) to three deep acceptors. Optical transitions are characterized by strong electron–phonon coupling responsible for the large width of the PL bands. Vibrational characteristics of the defects are found.

Acknowledgements

This work was supported by the NSF under grant ECS-9705134 and NASA under contract NAG5-8730.

References

[1] C.C. Klick, J.H. Schulman, Solid State Phys. 5 (1957) 97.
[2] K.K. Rebane, Impurity Spectra of Solids, Plenum Press, New York, 1970.
[3] A.M. Stoneham, Theory of Defects in Solids, Clarendon Press, Oxford, 1975.
[4] S. Shinoya, T. Koda, K. Era, H. Fujiwara, J. Phys. Soc. Japan 19 (1964) 1157.
[5] E.W. Williams, Phys. Rev. 168 (1968) 922.
[6] M. Tajima, M. Aoki, Jpn. J. Appl. Phys. 14 (1975) 1695.
[7] T. Ogino, M. Aoki, Jpn. J. Appl. Phys. 19 (1980) 2395.
[8] E. Calleja et al., Phys. Rev. B 55 (1997) 4689.
[9] I. Shalish et al., Phys. Rev. B 59 (1999) 9748.
[10] A. Cremades et al., Mater. Sci. Eng. B 42 (1996) 230.
[11] C. Trager-Cowan et al., Appl. Phys. Lett. 68 (1996) 355.
[12] J.C. Carrano et al., Appl. Phys. Lett. 70 (1997) 1992.
[13] M. Toth, K. Fleisher, M.R. Phillips, Phys. Rev. B 59 (1999) 1575.
[14] S.J. Xu, G. Li, S.J. Chua, X.C. Wang, W. Wang, Appl. Phys. Lett. 72 (1998) 2451.
[15] M.A. Reshchikov, F. Shahedipour, R.Y. Korotkov, M.P. Ulmer, B.W. Wessels, unpublished.
[16] N.N. Zinovev et al., Semicond. Sci. Technol. 10 (1995) 1117.
[17] M.A. Reshchikov, R.Y. Korotkov, B.W. Wessels, Physica B 273–274 (1999) 78, These Proceedings.
[18] S. Kim et al., Appl. Phys. Lett. 67 (1995) 380.
[19] J. Neugebauer, C.G. Van de Walle, Appl. Phys. Lett. 69 (1996) 503.

ELSEVIER

Physica B 273–274 (1999) 109–112

PHYSICA B

www.elsevier.com/locate/physb

Correlation of vibrational modes and DX-like centers in GaN:O

C. Wetzel[a,*], J.W. Ager III[b], M. Topf[c], B.K. Meyer[c], H. Amano[a], I. Akasaki[a]

[a]*High Tech Research Center, Department of Electrical and Electronic Engineering, Meijo University, 1-501 Shiogamaguchi, Tempaku-ku, Nagoya 468-8502, Japan*

[b]*Materials Sciences Division, Lawrence Berkeley National Laboratory, Berkeley, CA 94720, USA*

[c]*1. Physikalisches Institut, Justus-Liebig-Universität Giessen, 35392 Giessen, Germany*

Abstract

Vibrational modes in O-doped GaN have been observed at 544 cm^{-1} in Raman spectroscopy. Under perturbation of large hydrostatic pressure the mode appears as a set of three different lines $Q_{1...3}$ whose relative intensities change by pressure. A switching between the modes occurs near 10 and 20 GPa and is found to correlate with the electron capture process to the DX-like state of O. We employ a simple oscillator model to predict the vibrational frequencies of O_N. A localization energy of 23 cm^{-1} with respect to the optical phonon band is predicted. This is in reasonable agreement with the observed vibrational frequencies. Therefore, we assign the Q modes to the local vibration of O on N site in GaN. Modes $Q_{1...3}$ are tentatively assigned to three different charge states of the O defect center.

Keywords: Local vibration mode; Oxygen in GaN; DX-center

1. Introduction

Exciting opportunities for new optoelectronic devices with high-frequency, high-power, and high-temperature performance are arising with the development of wide band-gap group-III nitrides [1–3]. As in most semiconductor systems [4] the practical development of group-III nitrides (GaN in particular) is closely linked to the control of defects, dopants, and impurities. In the case of thin film epitaxy the lack of lattice-matched substrates required the development of suitable buffer layer techniques to achieve of high crystalline quality [1,3]. In addition, precursor purification and successful acceptor activation were essential steps in the development of the system [3]. Much attention has been paid to the problems of the structural defects and the acceptor activation; the donors have been less well studied. For example only recently has the role of O been clarified [5–8]. In contrast to Ge, Si, GaAs, and GaP, O in GaN turns out to be a highly effective donor and in the form of water is easily delivered (sometimes unintentionally) in large quantities during vapor phase growth with the ammonia precursor [9]. Furthermore, O is a difficult-to-avoid contaminant in high-vacuum systems. A role of O as a deep donor in irradiated GaN has also been reported [10].

Concerning electronic properties we recently identified a DX-like behavior of O, where its donor level converts into a deep gap state above a critical pressure of 20 GPa [5,11,12,8]. The free carrier concentration was measured via the phonon–plasmon coupling [11] of the GaN A_1 (LO) mode. The application of hydrostatic pressure to GaN is analogous with alloying in $Al_xGa_{1-x}N$, and we predicted that O should convert to a deep donor for $x > 0.40$. Recently these findings have been confirmed by both theory [6] and in transport experiments [7]. In the present work we focus on the vibrational properties of GaN:O under hydrostatic pressure perturbation.

* Corresponding author. Tel.: + 81-52-832-1151; fax: + 81-52-832-1244.

E-mail address: wetzel@meijo-u.ac.jp (C. Wetzel)

0921-4526/99/$ - see front matter
PII: S0921-4526(99)00418-4

2. Experimental

Epitaxial samples of GaN:O were grown by hydride vapor-phase epitaxy on *c*-plane sapphire at thicknesses of 20 μm [13]. O doping was achieved by water vapor. The concentration of typical donor-type dopants is $O: N_D = 2.0 \times 10^{19}$ cm^{-3}, $Si: N_D = 3.0 \times 10^{17}$ cm^{-3}. Free electron concentration are $N_{el} = 3.5 \times 10^{19}$ cm^{-3} at a mobility of 90 cm^2/Vs. Non-resonant Raman spectroscopy was performed using 100 mW of the 476.5 and 514.4 nm lines of an Ar ion laser. Scattering light was analyzed in either a single or a triple grating Raman spectrometer. Large pressure was applied by means of Mao–Bell-type diamond anvil cells using nitrogen as a pressure medium. All data were taken at room temperature.

3. Impurity modes in the linear chain model

The phonon dispersion in GaN has been calculated recently in first principles calculations [14,15]. For the purpose of impurity studies, however, a linear chain of springs and masses equivalent to its constituent nuclei has proven to be a suitable and descriptive model [16]. For example, such models have also been used to describe the effects of isotopical purification on the GaN phonon spectrum [17]. For our purpose, we consider the hexagonal basal plane of wurtzite GaN. In an approximation, we treat three bonds of the bonding tetrahedron as coplanar leading to a regular hexagonal mesh of coplanar lattice sites. A linear chain can be defined along any high symmetry axis with alternating masses of ^{69}Ga, $m_{Ga} = 69$ amu, and ^{14}N, $m_N = 14$ amu (solid line). To account for the alternating bonding angles we introduce two effective constants k_1 and k_2 ($k_1 > k_2$) of Hooke springs connecting adjacent nuclei. Imposing a superlattice on the Ga–N chain by such alternating spring constants induces an additional zone folding in reciprocal space. Consequently, Eigenvalues of modes in Γ are proportional to $m_{Ga}^{-1/2}$, $m_N^{-1/2}$, and $(1/m_{Ga} + 1/m_N)^{1/2}$, which can be identified as the E_2 (low), E_1, and E_2 (high) phonon modes.[1] The respective longitudinal vibration modes are depicted in Fig. 1(a). The two parameters of the system, k_1 and k_2, were adjusted to reproduce the two energies of E_2 (low) ($\bar{\nu} = 144$ cm^{-1}) and E_2 (high) ($\bar{\nu} = 570$ cm^{-1}). As a test a third value for E_1, $\bar{\nu} = 555$ cm^{-1}, was derived which closely coincides with the experimental E_1 (TO) mode and indicates the suitability of the model. The large ratio of m_{Ga}/m_N leads to a narrow optical phonon band and a large splitting of acoustical and optical phonons.

[1] TO–LO splitting is not considered for this purpose.

The role of O impurities on the N-site is studied in the same model by replacing one mass of 14 amu by the mass of 16 amu. This constitutes the case of isoelectronic doping, where the additional charge of O is neglected. The modified phonon modes and the mode associated with the O impurity are shown in Fig. 1(b). The O mode is limited to the two nearest neighbors on either side and strongly resembles the modal behavior of E_2 (high). In the larger vicinity of the impurity the amplitudes $\hat{e}$ and consequently the transition probability $\propto \hat{e}^2$ of E_2 (high) and E_1 phonons is strongly reduced. In turn the amplitude of the O atom is very strong and leads to a $(\hat{e}_O/\hat{e}_{E_2})^2 \approx 220$-fold increased transition probability with respect to the E_2 (high) mode in the unperturbed system. For a linear chain of 256 atoms the phonon dispersion including the one O_N impurity equivalent to a doping concentration of 0.4 at% was calculated leading to the density of states in Fig. 2 (the inset sketches the considered chain). The O mode appears as gap mode 23 cm^{-1} below the optical phonon band extending from

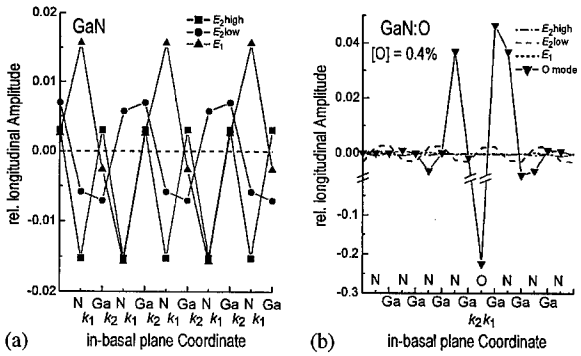

Fig. 1. Relative amplitudes of the atoms in a linear chain model for undoped GaN (a), and for GaN:O (b). In the doped case, the O-related mode draws much of the amplitudes from the phonon modes.

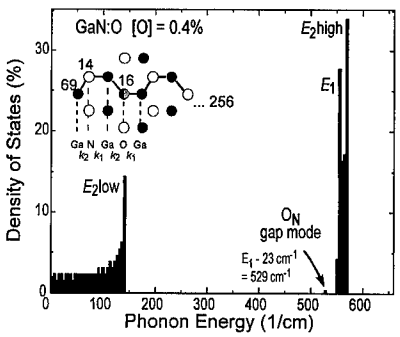

Fig. 2. Density of basal plane phonon modes in GaN in the linear chain model including one O_N impurity. An O-related gap mode appears with localization energy of 23 cm^{-1}.

E_1 to E_2 (high). Despite the small fraction of the O-related mode in the phonon density of states, becasue of its large oscillation amplitude it may be observable in experiment.

4. Raman spectra under hydrostatic pressure

A Raman spectrum of the GaN:O sample in $z(x, -)z$ forward scattering in the range of the optical phonons is shown in Fig. 3. According to the selection rules in wurtzite A_1 (LO), and E_2 (high and low) are allowed in this geometry and we identify E_2 (high) at 567 cm^{-1}. The peaks at 532 and 559 cm^{-1} are assigned to the A_1 (TO) and E_1 (TO), respectively. Their observation in this geometry is due to their coupling to the free electron plasmon due to the high electron concentration in the sample. An additional mode Q appears at 544 cm^{-1}; this mode is only seen in highly O-doped material in $z(x, -)z$ or $z(x, -)\bar{z}$ scattering. We cannot directly fit our phonon DOS in Fig. 2 to the data because modes of A_1 symmetry are not considered in the model. The experiment indicates a smooth background continuum between the A_1 (TO) mode and the considered E_1–E_2 band. The narrow line shape of the Q-mode, however, allows it to be distinguished clearly from the continuum.

Phonon quasi-modes in the range between E_1 (TO) and A_1 (TO) have been observed in GaN previously [18]. By observing scattering under a large variation of angle of incidence, the different branches of the phonon dispersion could be explored. Under these conditions a coexistence of the bare and the quasi modes could not be observed. Furthermore, due to its mixed nature, the quasi mode never appeared as the narrowest line. Therefore, we do not believe that the Q peak in our case is due to a quasi phonon mode has to be excluded in our case. Instead, we propose that the mode Q be associated with the O impurity substituting on the N-site in GaN. The small discrepancy in calculated localization (23 cm^{-1}) and the experimental observation (559–544 $cm^{-1} = 15$ cm^{-1}) is likely to be related to the insufficient treatment

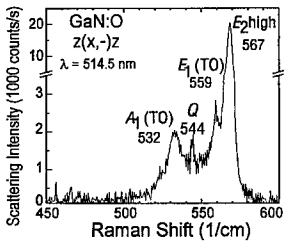

Fig. 3. Raman spectrum in the phonon range of GaN in forward scattering. The E_1 (TO) and E_2 (high) phonon modes form a narrow band. A mode Q appears with effective localization with respect to this band.

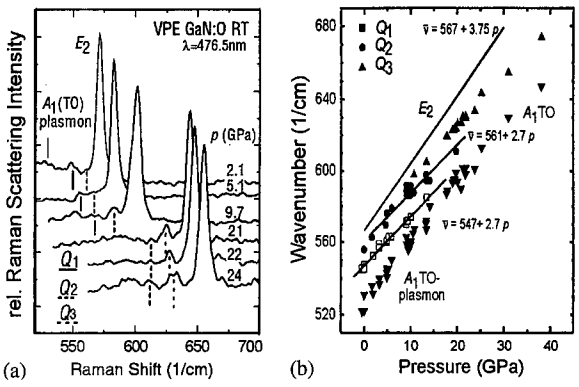

Fig. 4. (a) Raman spectra of GaN:O under variable hydrostatic pressure. Besides a pressure stiffening of phonon modes, Q_1, Q_2, and Q_3 appear with variable localization energy and intensities; (b) Phonon and Q-mode energies as a function of pressure. A significantly different behavior is observed for phonon mode E_2 and $Q_{1\ldots3}$.

of the charge state of the defect center in the present model [19].

Under application of large hydrostatic pressure, a more complex picture evolves. Spectra are shown in Fig. 4(a) and peak energies are graphed versus pressure in Fig. 4(b) (this data includes other O-doped samples reported elsewhere [19]. Mode Q appears as a set of three modes each of which shifts at a slightly smaller slope than E_2. As seen in Fig. 4(a) at a pressure of 10 GPa the second mode gains in intensity and at 21 GPa the third one prevails (labeled Q_1, Q_2, and Q_3, respectively).

5. Discussion

The mode switching between Q_1, Q_2, and Q_3 has strong parallels with the previously reported freeze-out [20] of the electron concentration in GaN:O under large hydrostatic pressure. This freeze-out was identified with the transformation of the O impurity states from a shallow donor to a DX-like center at pressures of 20 GPa [5]. This transition pressure closely coincides with the second mode switching step from Q_2 to Q_3 and could be due to the electron capture to the O impurity. A slight dependence of the impurity vibrational mode with the electronic charge state has previously been reported for Si in InP [21]. It is therefore also plausible that the step from Q_1 to Q_2 at 10 GPa is also caused by a charge trapping process of the O impurity. The results of a previously developed model [11] that calculates the pressure behavior of the $+/0$ electron capture level of the defect and GaN the band edges are shown in Fig. 5. For a free electron concentration of $N_{el} = 3.5 \times 10^{19}$ cm^{-3} the Fermi level meets the expected defect level near 10 GPa. This supports our claim that the Q_1–Q_2 mode switching

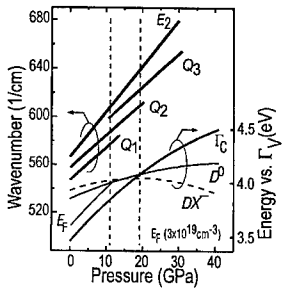

Fig. 5. Model of the theoretical pressure dependence of band gap, Fermi energy, and different charge states of the O DX-like donor states. The shown pressure slope of DX^- is an interpolation of the theoretical results in Ref. [6]. The different steps in the localization energy of Q closely corresponds to the crossings of the donor levels with the Fermi edge and the conduction band edge, respectively.

is caused by a charge trapping process at the O defect. Altogether, we observe three pressure ranges separated by two charge capture thresholds. This leads to the conclusion that three different charge states of the O defect should be involved.

Detailed theoretical models have been developed for the pressure behavior of O in GaN as well as the equivalent situation in AlGaN alloys [6]. According to these results the shallow donor state of O transforms into a DX-like center for pressures beyond 18 GPa. Accompanied by a large lattice relaxation of the O impurity two electrons can be trapped to a DX-center. In contrast to the present experimental observation of three different states in this process, theory has so far only identified the D^+ and the DX^- state. The fact that we count three different charge states strongly supports the models of a negatively charged DX^- state. Again, our results can be converted to AlGaN alloys where O vibration modes should indicate the charge state of the DX-state.

6. Conclusion

In vibrational spectra of GaN:O we observed a local mode at 544 cm^{-1} that show a strong correlation with the electron freeze-out dynamics to O induced DX-like centers in GaN under large hydrostatic pressure. In a model calculation, we find that O substituting on the N site should induce a strong gap mode in this energy range. Pressure-dependent variations indicate the presence of three different charge states of the defect. We conclude that the observed vibration mode at 544 cm^{-1} at ambient conditions originates in in-basal plane vibrations of substitutional O on N site in GaN.

Acknowledgements

The authors thank E.E. Haller and P.Y. Yu for the use of their pressure equipment. This work was supported by JSPS Research for the Future Program in the Area of Atomic Scale Surface and Interface Dynamics under the project of 'Dynamic Process and Control of the Buffer Layer at the Interface in a Highly Mismatched System'. Work at Berkeley Lab was supported by the Director, Office of Energy Research, Office of Basic Energy Sciences, Division of Materials Sciences, of the US Department of Energy under Contract No. DE-AC03-76SF00098.

References

[1] I. Akasaki, H. Amano, Jpn. J. Appl. Phys. 36 (1997) 5393.
[2] I. Akasaki, C. Wetzel, Proc. IEEE 85 (1997) 1750.
[3] I. Akasaki, Mater. Res. Soc. Symp. Proc. 482 (1998) 3.
[4] For a review see R.C. Newman, in: E.R. Weber (Ed.), Imperfections in III/V materials, Semiconductors and Semimetals, Vol. 38, Academic Press Inc, Boston, 1993, pp. 117–187.
[5] C. Wetzel et al., Phys. Rev. Lett. 78 (1997) 3923.
[6] C.G. Van de Walle, Phys. Rev. B 57 (1998) R2033.
[7] M.D. McCluskey et al., Phys. Rev. Lett. 80 (1998) 4008.
[8] For a review see C. Wetzel, I. Akasaki, in: J. Edgar, T.S. Strite, I. Akasaki, H. Amano, C. Wetzel (Eds.), Properties, Synthesis, Characterization, and Applications of Gallium Nitride and related Compounds, INSPEC, IEE, London, UK, 1999, pp. 284–293.
[9] W. Seifert et al., Cryst. Res. Technol. 18 (1983) 383.
[10] W.M. Chen et al., Phys. Rev. B 58 (1998) R13 351.
[11] C. Wetzel et al., Phys. Rev. B 53 (1996) 1322.
[12] T. Suski, P. Perlin, in: J.I. Pankove, T.D. Moustakas (Eds.), Gallium Nitride (GaN), Semiconductors and Semimetals, Vol. 50, Academic Press Inc, Boston, 1997, pp. 279–303.
[13] M. Topf et al., Proc. Mater. Res. Soc. 449 (1997) 307.
[14] K. Miwa, A. Fukumoto, Phys. Rev. B 48 (1993) 7897.
[15] K. Karch, J.-M. Wagner, F. Bechstedt, Phys. Rev. B 57 (1998) 7043.
[16] A.S. Barker, A.J. Sievers, Rev. Mod. Phys. 47 (1975) S1.
[17] J.M. Zhang et al., Phys. Rev. B 56 (1997) 14 399.
[18] L. Filippidis et al., Phys. Status Solidi B 198 (1996) 621.
[19] C. Wetzel, H. Amano, I. Akasaki, J.W. Ager III, T. Suski, M. Topf, B.K. Meyer, unpublished.
[20] P. Perlin et al., Phys. Rev. Lett. 75 (1995) 296.
[21] J.A. Wolk, W. Walukiewicz, M.L.W. Thewalt, E.E. Haller, Phys. Rev. Lett. 68 (1992) 3619.

ELSEVIER

Physica B 273–274 (1999) 113–115

PHYSICA B

www.elsevier.com/locate/physb

Effects of oxygen incorporation in p-type AlN crystals doped with carbon species

Tetsuya Yamamoto[a,*], Hiroshi Katayama-Yoshida[b]

[a]*Department of Electronic and Photonic Systems Engineering, Kochi University of Technology, 185 Miyanokuchi, Tosayamada-cho, Kami-gun, Kochi, 782-8502, Japan*

[b]*Department of Condensed Matter Physics, The Institute of Scientific and Industrial Research, Osaka University, 8-1 Mihogaoka, Ibaraki, Osaka 567-0047, Japan*

Abstract

We investigate the electronic structures of n-type O-doped and p-type C-doped AlN crystals with wurtzite structures based on ab initio electronic band-structure calculations. We find the strongly localized impurity states for p-type C-doped AlN compared with that for n-type O-doped AlN. For the materials design to fabricate high-conductive p-type C-doped AlN, we study the effects of oxygen incorporation on p-type C-doped AlN. We verify the delocalization of the impurity states for p-type AlN : (2C and O) with a decrease in the Madelung energy. © 1999 Elsevier Science B.V. All rights reserved.

Keywords: AlN; Oxygen; Carbon; p-type

1. Introduction

Wide-band gap semiconductors, GaN with a band gap of 3.4 eV and AlN with a band gap of 6.2 eV, are one of great interest for various applications in the blue and ultraviolet wavelength. For both AlN and GaN crystals, oxygen is a common impurity and the extent of O incorporation has substantial effects on the electric and optical properties.

In our previous work, we proposed a materials design, "codoping method", for the fabrication of low-resistivity p-type GaN using Be or Mg species as acceptors and oxygen as reactive donors based on ab initio electronic band-structure calculations [1–3]. Our prediction was verified by the experiments conducted by the German group [4]. The main effects of the oxygen codoping are as follows: (1) to increase the solubility of the acceptors with a decrease in the Madelung energy; (2) to lower the acceptor levels in the band gap due to the strong attractive interaction between the oxygen and the acceptors; (3) to increase the hole mobility due to the short-range dipole-like scattering mechanism. We note that AlN seems to present an extreme case with respect to oxygen incorporation compared to GaN, because of the possibility of several percent O incorporation [5]. On the other hand, several authors reported that C implantation in AlN produces no shallow acceptors [6]. In such a case, the impurity level in the band gap for carbon-doped AlN crystals is a key parameter to be controlled for the fabrication of high-conductive p-type AlN crystals.

The aim of this work is to investigate the effects of O incorporation on AlN : C crystals based on ab initio electronic-structure calculations. In addition, we propose materials design for the fabrication of high-conductive p-type AlN crystals.

2. Methodology

The results of our band structure calculations for AlN doped with O or C species are based on the local-density treatment of electronic exchange and correlation [7–9] and on the augmented-spherical-wave (ASW) [10] formalism. The Brillouin-zone integration was carried out

* Corresponding author. Fax: + 81-88-757-2120.
E-mail address: yamateko@ele.kochi-tech.ac.jp (T. Yamamoto)

PII: S0921-4526(99)00419-6

for 24-k points in an irreducible wedge. The Madelung energy, which reflects the long-range electrostatic interactions in the system, was assumed to be restricted to a sum over monopoles. For valence electrons, we employed the outermost s and p orbitals for all atoms under consideration.

We studied the crystal structure of doped AlN under periodic boundary conditions by generating supercells having 32 atoms that contain the object of interest as follows: (1) for AlN doped with O species (AlN : O_N), we replace one of the 16 sites of N atoms by an O atom site in model supercells; (2) for AlN doped with C species (AlN : C_{Al}), we replace one of the 16 sites of Al atoms by a C atom site; (3) for AlN doped with C species (AlN : C_N), we replace one of the 16 sites of N atoms by a C atom site; (4) for AlN : ($2C_N$ and O_N), we replace two of the 16 sites of the N atoms by C sites and one of the remaining N sites by the O site.

3. Results and discussion

We show the total density of states (DOS) of undoped AlN in Fig. 1(a) as the reference standard and the total DOS of AlN : O_N crystals in Fig. 1(b) and of AlN : C_N in Fig. 1(c). Energy is measured relative to the Fermi level (E_F). The arrows in Fig. 1(a)–(c) show N 2s band.

In Fig. 1(a), we find that while the mixing between N 2p and Al 3s orbitals shifts the center of gravity of the local DOS at the N sites towards lower-energy regions, charge transfers from Al 3p to N 2s and 2p give rise to the shift of Al 3p levels towards higher-energy regions above E_F. From the ionic characteristics of the chemical bonds in AlN, the Madelung energy is a key parameter to indicate a change in the stability of the ionic charge distributions caused by n or p-type doping. We verified

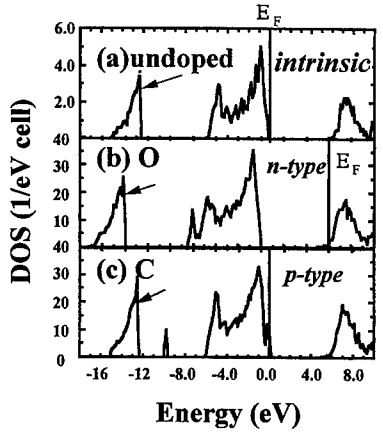

Fig. 1. Total DOS of (a) undoped, (b) O-doped and (c) C-doped AlN crystals.

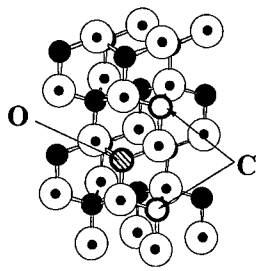

Fig. 2. Crystal structure of p-type AlN doped with $2C_N$ and O_N. The closed circle denotes N and the circle with dot denotes Al.

from ab initio total energy calculations that n-type doping using C species as donors, Al-substitution species, causes an almost 17.0 eV increase in the Madelung energy compared with p-type doping using C as acceptors, N-substitution species [11]. This indicates that C species will substitute for N, which is very reasonable considering the electronegativity and covalent radii estimated in the crystal with tetrahedral coordinates. Thus, we focus on carbon, N-substitution species, in this study.

Fig. 1(b) and (c) show that the conduction type of O- and C-doped AlN crystals is n- and p-type, respectively. For n-type AlN : O_N, we find that the strong attractive potential causes the shift of the weight of the impurity states, especially, s states at the O sites, towards lower-energy regions, resulting in a sharp DOS peak near at -12.0 eV below E_F. This gives rise to localized impurity states at O sites for n-type AlN : O_N crystals, in contrast to O_N in GaN [1–3,12,13].

A comparison of DOS near the top of the valence band between undoped AlN in Fig. 1(a) and p-type AlN : C_N in Fig. 1(c) shows the substantial localization of the impurity states for AlN : C_N due to the strong repulsive potential, resulting in a shift of the weight of C p states towards higher-energy regions. We find that the changes in the Madelung energy, compared with those for undoped AlN, for n-type AlN : O_N and for p-type AlN : C_N are a 2.09 decrease and a 6.64 eV increase, respectively. The above findings indicate that it is very difficult to fabricate p-type AlN using C species.

We investigate the effects of O incorporation on the electronic structures of p-type AlN : $2C_N$. We determined crystal structure of p-type AlN : ($2C_N$ and O_N) under the condition that the total energy is minimized. We show the crystal structure of p-type codoped AlN : ($2C_N$ and O_N) in Fig. 2. Total-energy calculations show that the formation of the complex including C–Al–O–Al–C is energetically favorable. In addition, O incorporation, or O-codoping, causes a 1.22 eV decrease in the Madelung energy compared with O-free p-type AlN : $2C_N$. We present the carbon-site decomposed DOS near E_F of p-type AlN : C_N in Fig. 3(a) and p-type AlN : ($2C_N$ and O_N) in Fig. 3(b). We note that the two crystals mentioned above

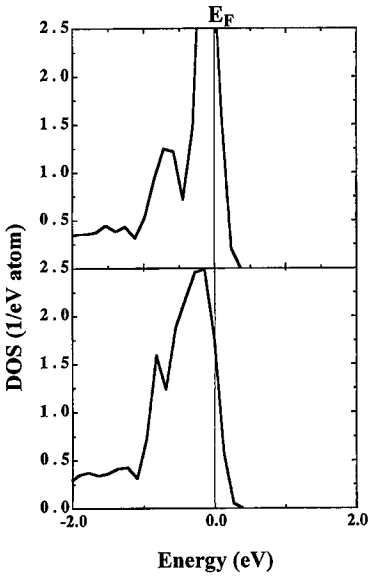

Fig. 3. Carbon-site decomposed DOS of p-type AlN (a) doped with C alone and (b) codoped with 2C and O.

have the same number of holes generated at the top of the valence band. Fig. 3(a) and (b) show that O-incorporation causes the delocalization of the impurity states near the top of the valence band, resulting in the lowered acceptor levels in the band gap compared with p-type AlN doped with C alone.

4. Conclusions

We have investigated the effects of O-incorporation on the electronic structure and the Madelung energy on p-type AlN : C_N crystals based on ab initio electronic-structure calculations. We find that O-codoping in p-type AlN : C_N causes the delocalization of impurity states of the acceptors with a decrease in the Madelung energy. We predict that codoping of C and O species is a very effective method for the fabrication of low-resistivity p-type AlN crystals. This awaits experimental verification.

Acknowledgements

The authors thank Dr. Jürgen Sticht for his technical support. In this work, we used ESOCS code of MSI.

References

[1] T. Yamamoto, H. Katayama-Yoshida, Jpn. J. Appl. Phys. 36 (1997) L180.
[2] T. Yamamoto, H. Katayama-Yoshida, J. Crystal Growth 189/190 (1998) 532.
[3] T. Yamamoto, H. Katayama-Yoshida, in: J.H. Edgar, S. Strite, I. Akasaki, H. Amano (Eds.), Properties, Processing and Applications of Gallium Nitride and Related Compounds, INSPEC, The Institution of Electrical Engineers (IEE), London, 1999, pp. 306–312.
[4] O. Brandt, H. Yang, H. Kostial, K.H. Ploog, Appl. Phys. Lett. 69 (1996) 2707.
[5] R.A. Youngman, J.H. Harris, J. Am. Ceram. Soc. 73 (1990) 3238.
[6] Y. Ueta, S. Sakai, Y. Kamiya, H. Sato, Mater. Res. Soc. (1994) 459.
[7] W. Kohn, L.J. Sham, Phys. Rev. 140 (1965) A1133.
[8] L. Hedin, B.I. Lundquist, J. Phys. C 4 (1971) 3107.
[9] U. von Barth, L. Hedin, J. Phys. C 5 (1972) 1629.
[10] A.R. Williams, J. Kübler, C.D. Gelatt, Phys. Rev. B 19 (1979) 6094.
[11] T. Yamamoto, H. Katayama-Yoshida, unpublished.
[12] T. Mattila, R.M. Nieminen, Phys. Rev. B 54 (1996) 16676.
[13] C.H. Park, D.J. Chadi, Phys. Rev. B 55 (1997) 12995.

ELSEVIER

Physica B 273–274 (1999) 116–119

PHYSICA B

www.elsevier.com/locate/physb

Negatively charged muonium states in gallium nitride

R.L. Lichti[a,*], M.R. Dawdy[a], T.L. Head[a], S.F.J. Cox[b,c], B. Hitti[d], C. Schwab[e]

[a]*Physics Department, Texas Tech University, Lubbock, TX 79409-1051, USA*
[b]*ISIS Facility, Rutherford Appleton Laboratory, Chilton OX11 0QX, UK*
[c]*University College, London WCE 6BT, UK*
[d]*TRIUMF, 4004 Wesbrook Mall, Vancouver, B.C., Canada V6T 2A3*
[e]*PHASE, Centre National de la Recherche Scientifique, 67037 Strasbourg, France*

Abstract

Muon nuclear-quadrupole level-crossing resonances (QLCR) and zero-field muon spin depolarization functions are identified for negatively charged muonium (Mu^-) centers in wurtzite-structured GaN.The QLCR spectra imply that Mu^- occupies interstitial locations next to Ga atoms, consistent with the two inequivalent Ga anti-bonding sites. Mu^- related depolarization shows an increase in average dipolar fields near 200 K and indicates motion above 500 K. Transitions suggested by relaxation features are briefly discussed.

Keywords: Muonium; Hydrogen; Gallium nitride; μSR

1. Introduction

Hydrogen is an important impurity in gallium nitride, as in other semiconductors, primarily because it interacts strongly with other defects forming complexes which modify the electrical activity [1]. The same interactions which make hydrogen important also make the study of *isolated* hydrogen impurities difficult. We have been investigating the very light, short-lived pseudo-isotope of hydrogen known as muonium, $Mu = [\mu^+, e^-]$. Muonium is formed when positive muons are implanted into the host material, and because the mean muon lifetime is only 2.2 μs, Mu nearly always occurs as an isolated defect center. The muon mass is only 1/9 th that of a proton, thus one expects large isotope and quantum effects to be important when inferring properties of hydrogen impurities from experimental results on muonium. Despite these complications, in the absence of experimental information directly on hydrogen, a great deal of qualitative information can be obtained from study of the Mu analogue. In situations where localization and quantum tunneling are important, significant differences between Mu and H must be kept in mind, particularly when translating parameters related to motion.

For diamond and zincblende materials in which previous studies of muonium in semiconductors have taken place, Mu occupies two different sites and occurs in three charge states. The bond-centered (BC) configuration is stable for positively charged centers. The other site is centered in the tetrahedral (T) interstitial region, and is stable for Mu^-. Theory places the potential energy minimum off-center at anti-bonding (AB) sites within this region. Mu^0 can occur in both sites and the stable location is material dependent. Extensive results [2,3] for Mu in the cubic structures transfer most directly to zincblende GaN, but also provide an excellent background for investigation of Mu in hexagonal GaN. The wurtzite structure has two inequivalent bonds, thus two different BC sites, two AB_{Ga} sites, and two AB_N locations. This structure does not have a T-site with a single type of nearest neighbor as is found in the zincblende structure, however there is a tightly confined cage region with four atoms of each type nearly equidistant from the center. Sites labelled AB^{II} lie within this cage and have Mu–Ga or Mu–N 'bonds' along the *c*-axis. Each atom also has three AB^{I} sites directed away from the cage at $\sim 70°$ to the *c*-axis. Locations within the cage should have higher

* Corresponding author. Tel.: 806-742-3697; fax: 806-742-1182.
E-mail address: xbrll@ttacs.ttu.edu (R.L. Lichti)

0921-4526/99/$ - see front matter
PII: S0921-4526(99)00420-2

energies than those outside due to spatial confinement. Three equivalent AB^I sites associated with different atoms are closely spaced within the *c*-axis channels providing an easy path for local motion, while the channels themselves are likely paths for diffusive motion. Theoretical studies of the structure of H/Mu defects in GaN [4–6] disagree on the most stable configurations for the neutral and positive charge states, yielding either BC or AB_N for Mu^+ and either BC or AB_{Ga} for Mu^0 with other possible locations [7] in the *c*-axis channels for an atomic-like neutral state. Most of these calculations agree that Mu^- should be stable at AB_{Ga} locations.

This contribution presents preliminary experimental results for the Mu^- center. Although less uncertainty surrounds the expected Mu^- location than for the other two charge states, Mu^- was studied initially because GaN samples of sufficient thickness for efficient muon implantation were available with the common n-type electrical characteristics. The results we present here are from two n-type GaN films grown by HVPE. One is nominally undoped and has a mid-$10^{16}cm^{-3}$ electron concentration. The second sample is doped with Si to produce an n-type concentration of $\sim 10^{18}\,cm^{-3}$. The spectral features associated with Mu^- states are essentially identical for the two samples; however, there are differences in other observed states and relative amplitudes, as well as in several relaxation features.

2. Experimental methods

We have used three of the standard muon spin research (μSR) techniques in this study. Muon production from pion decay and ordinary beam collection methods result in $\sim$100% spin-polarized muon beams. In a typical μSR measurement, information on the time evolution of the muon polarization following implantation is extracted from the measured asymmetry in positron emission rates resulting from parity violation in the muon decay. The 'surface' muon beams used in this work have a momentum of $\sim 29\,MeV/c$ (4.1 MeV energy) and the spin polarization is opposite to the momentum. The films on which these data were taken are approximately 150 μm thick and have areas of 2–3 cm^2, satisfying basic dimensional requirements for efficient implantation.

When a magnetic field is applied transverse to the initial polarization, the muon spin precesses at a frequency characteristic of the specific muonium state. For diamagnetic states including Mu^+ and Mu^- this is at the muon's Larmor frequency of 135.5 MHz/T. Applied fields of 6–10 mT were used to determine the total diamagnetic fractions. This signal includes any muons stopped in the sample holder; however, both samples show a weakly relaxing diamagnetic precession signal accounting for 40 – 60% of the muons at low and intermediate temperatures. The missing fractions imply that a significant number form Mu^0 centers which are not yet fully characterized. Two other techniques which probe the resonant and non-resonant cross relaxation between the muon and neighboring nuclei provide more easily distinguished signatures of different diamagnetic Mu states. Non-resonant dipolar interactions control the time evolution of the polarization in zero applied field. In a material such as GaN where the host nuclei all have dipole moments, each site has randomly oriented local fields of a characteristic strength. The resulting Kubo–Toyabe (K–T) depolarization function for a stationary diamagnetic Mu center is characterized by a width parameter Δ, which is related to the mean dipolar field strength and provides a site signature. When $Mu^{\pm}$ centers begin to hop among equivalent sites, the dynamic K–T derived from a strong collision model [8] is very sensitive to slow muon motion and the site-to-site hop rate becomes an additional parameter. Zero-field depolarization data for this study were obtained using the EMU spectrometer at the ISIS Facility of the Rutherford Appleton Laboratory in the UK. Finally, the resonant interactions involve quantum state mixing to avoid accidental degeneracy. In our specific situation, the quantum states are combined spin states for the muon and a neighboring nucleus. When the quadrupolar splitting of nuclear levels matches the muon Zeeman splitting, energy-conserving mutual spin-flips occur mixing the two muon spin states, thus reducing the polarization. This form of avoided level crossing is known as quadrupolar level-crossing resonance (QLCR). The muon Zeeman splitting is tuned by a weak magnetic field applied parallel to the polarization and stepped through the relevant range. The resulting spectrum is sensitive to the electric field gradient at the neighboring nucleus, which is dominated by effects from the muon and oriented along the muon–nucleus direction. QLCR data show the quadrupole characteristics of the nucleus thereby identifying the neighbor. QLCR spectra were obtained using the M20 beamline at TRIUMF in Vancouver, Canada.

3. Results and discussion

Both the zero-field depolarization data and QLCR spectra from the n-type GaN films show evidence of several different muonium centers, making detailed analysis somewhat tricky. However, a number of important conclusions can already be drawn from preliminary analysis. We have identified the QLCR spectra and zero-field depolarization associated with Mu^- states. The n-type nature and concentration of these films imply that Mu^- states are likely to occur. Secondly, the QLCR spectra appear identical in the two samples and relaxation parameters are nearly the same, implying an isolated Mu center. Finally, zero-field features assigned to Mu^- do not occur in a small compensated sample.

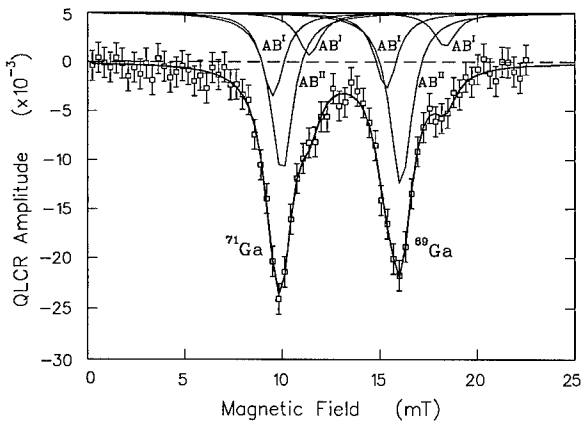

Fig. 1. The QLCR spectra for diamagnetic Mu states in (undoped) n-type GaN at 295 K is dominated by lines for Ga neighbors of Mu^-; site assignments are as noted.

We begin with a discussion of the QLCR spectra obtained with the magnetic field applied along the *c*-axis. A quadratic background and zero-field peak that is unrelated to QLCR were removed from the raw data to produce the results shown in Fig. 1. This spectrum, characteristic of the room temperature results, is clearly dominated by two strong, nearly identical features at 10 and 16 mT. The position ratio is extremely close to that expected for Ga nuclei where the ratio of quadrupole moments for the two $I = 3/2$ isotopes is $Q(69)/Q(71) = 1.589$. This alone might be sufficient to claim that these features represent a Ga neighbor; however, the amplitude ratio is also close to that expected from the product of natural abundance and dipole moment for the two Ga isotopes. The unresolved internal structure must be examined to obtain more detailed information. There is clearly a partially resolved smaller line on the high field side of each large resonance, and the central shape is not symmetric. Lorentzian lines were assumed in a preliminary six-line analysis. The displayed fit used a single width applied to all lines, while each amplitude, the position ratio, and the three higher-field positions were also free. The position ratio was 1.611 for this spectrum. Other constraints and the second sample yield similar results, differing mainly in exact positions and relative amplitudes for the satellites.

Comparison with simulated spectra [3] for various angles between the field and the Mu-nucleus direction provides insight into site assignments. A strong single line per isotope only comes from a bond direction parallel to the field (*c*-axis). The amplitude ratio and splitting for the satellites are consistent with the simulation for 70°, although neither is especially sensitive. Interestingly, the central line represents only about half as many muons as the satellites, and the field gradient for the satellites is slightly larger. These observations suggest that the subfeatures are from different sites. We therefore

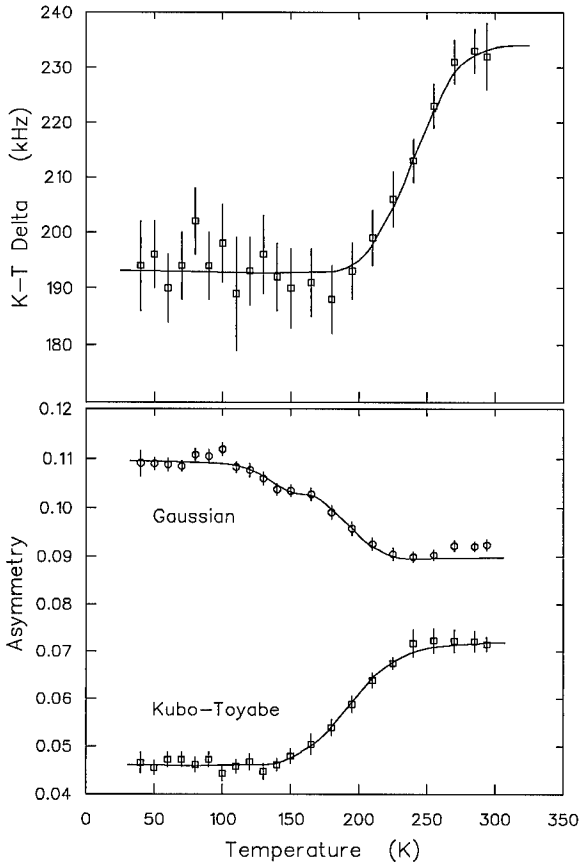

Fig. 2. The static Kubo–Toyabe linewidth Δ (a) and component amplitudes (b) from a two-signal fit to zero-field data on GaN:Si show a transition resulting in Mu^- at AB^{II}_{Ga} sites.

assign the central line to Mu^- at AB^{II}_{Ga} sites by the on-axis orientation, and assign the satellite lines to Mu^- at off-axis AB^{I}_{Ga} positions. The conclusion of separate sites is reinforced by spectra below 200 K where the central line is missing, but lines always occur at the satellite positions, implying that AB^{I}_{Ga} is occupied. Additional low-temperature lines do not have the Ga signature and may be Mu^+ near N atoms, but need to be confirmed in p-type material.

Fig. 2 summarizes preliminary zero-field results from a two-component fit, using a static Kubo–Toyabe and a weakly relaxing Gaussian. Both signals almost certainly result from more than one Mu state, and we are attempting to separate these contributions in a more complicated fit based on the preliminary conclusions. The static K–T linewidth Δ increases just below 200 K (Fig. 2a), correlating well with the onset of AB^{II}_{Ga} QLCR lines. Along with the absence of a similar K–T signal in a compensated sample, this allows the Kubo–Toyabe component to be assigned to Mu^- states. Δ is essentially the same for the two films at low temperatures where

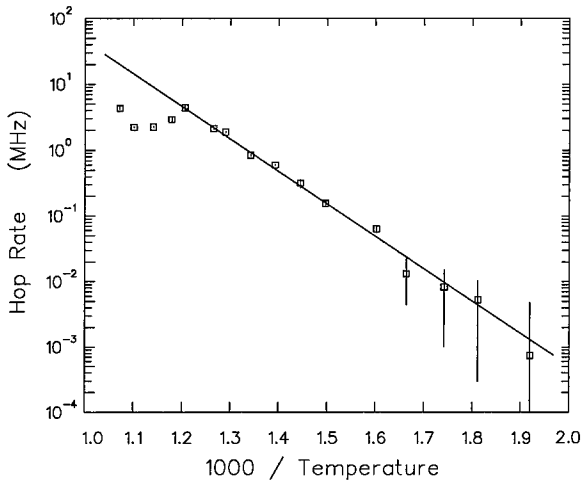

Fig. 3. Site-averaged hop rates for Mu^- from the dynamic Kubo–Toyabe component in zero-field data for undoped GaN yield an activation energy of 0.98 eV for 500–800 K.

only one site is occupied; therefore, we assign the average value of $\Delta = 192$ kHz to Mu^- at off-axis AB^I_{Ga} sites. The K–T signal above 200 K is a composite of the two sites, giving somewhat different Δ values for the two films. The temperature variation of the amplitudes are shown in Fig. 2b. A transition into the Mu^- K–T component is seen near the linewidth increase. The Gaussian amplitude decreases starting at a lower temperature and the data suggest two steps. Fits shown in Fig. 2b yield preliminary estimates for the transition energies of roughly 0.18 and 0.33 eV with large errors from the Gaussian decrease, and ~ 0.20 eV for the increase in K–T amplitude related to Mu^-. Assuming the step in Δ (Fig. 2a) properly reflects the transition into AB^{II}_{Ga} sites, one obtains about 0.30 eV. Correlation between the two-step Gaussian decrease and the two measurements of Mu^- growth, suggest that the lower-temperature step might increase the AB^I_{Ga} occupation while the higher-temperature transition may result in AB^{II}_{Ga} states.

Finally, Fig. 3 presents an important high-temperature zero-field result regarding motion of Mu^- states. When the Mu^- component is fit to the dynamic K–T function as a single signal, an activation energy ~ 1.0 eV is obtained for both samples. This value is likely to change when the data are fit to two separate K–T functions. Additional transitions between 600 and 800 K place nearly all muons into the mobile Mu^- state at the highest temperatures. Details are different for the two samples. The lower concentration film has an exponentially relaxing component in the zero-field data not present in the Si-doped sample. Correlation with the transverse-field missing fraction suggests that this signal is from Mu^0 states. The exponential rate constant diverges near 600 K, indicating a transition out of that state. Above 600 K about 10% of implanted muons show the relaxation signature of rapid cyclic charge-state transitions in that sample. These differences strongly suggest that Mu^- dominates in the higher concentration sample, while Mu^0 is more important at lower n-type concentrations, fully consistent with general expectations.

Overall, initial μSR results in n-type GaN are consistent with a model in which the stable Mu^- site is at the location we label as AB^I_{Ga}. This Mu^- state is mobile above about 500 K. Additional Mu^- states are formed at AB^{II}_{Ga} sites within the more confined region of the GaN wurtzite structure for $T > 150$ K, most likely via e^- capture by a Mu center already trapped in the cage. Muonium centers in high concentration n-type samples appear to undergo a series of transitions leading to the mobile Mu^- state at sufficiently high temperatures. Because of differences in the way H and Mu are introduced, we expect that only those aspects of this work which are related to Mu^- in its more stable AB^I_{Ga} site are applicable to hydrogen.

In conclusion, we have identified the QLCR spectra and zero-field muon spin depolarization components associated with Mu^- defect centers in wurtzite-structured GaN. Initial fits to these data provide preliminary characterization of the sites and dynamic properties of Mu^- and suggest a model that is generally consistent with theoretical expectations. The occupation of AB_{Ga} sites by Mu^- is verified by the QLCR spectra. A second round of fits to the zero-field data based on the emerging model will yield more realistic parameters characterizing Mu^- motion in GaN and the dynamics of transitions leading to the observed Mu^- states.

Acknowledgements

We wish to thank R.J. Molnar and R.P. Vaudo for providing the GaN samples. This work was supported by the U.S. National Science Foundation (DMR-9623823) and the Robert A. Welch Foundation (D-1321).

References

[1] S.J. Pearton et al., Mat. Res. Soc.Proc. 513 (1998) 229.
[2] T.L. Estle, R.L. Lichti, Hyperfine Int. 97–98 (1996) 171.
[3] R.L. Lichti, in: N. Nickel (Ed.), Hydrogen in Semiconductors, II, Academic Press, San Diego, 1999, p. 311.
[4] J. Neugebauer, C. Van de Walle, Phys. Rev. Lett. 75 (1995) 4452.
[5] S.K. Estreicher, Dj.M. Maric, Mat. Res. Soc. Proc. 423 (1996) 613.
[6] S.K. Estreicher, D.E. Boucher, in: S.J. Pearton (Ed.), GaN and Related Materials, Gordon and Breach, New York, 1997, p. 171.
[7] M.A. Roberson, S.K. Estreicher, Phys. Rev. B 44 (1991) 10578.
[8] R.S. Hayano et al., Phys. Rev. B 20 (1979) 850.

ELSEVIER

Physica B 273–274 (1999) 120–123

PHYSICA B

www.elsevier.com/locate/physb

ODMR of bound excitons in Mg-doped GaN

M.W. Bayerl[a,*], M.S. Brandt[a], T. Suski[b], I. Grzegory[b], S. Porowski[b], M. Stutzmann[a]

[a]*Walter Schottky Institut, Technische Universität München, D-85748 Garching, Germany*
[b]*High Pressure Research Center, Polish Academy of Sciences, Sokolowska 29, 01-142 Warsaw, Poland*

Abstract

GaN bulk crystals compensated with Mg exhibit a strong yellow photoluminescence (PL) band. However, optically detected magnetic resonance (ODMR) experiments show that the microscopic origin of this luminescence is completely different from the one observed in n-type GaN. The ODMR spectra of GaN:Mg bulk crystals are dominated by a fine-structure-split pair of lines. At magnetic field orientations between 45 and 60° from the *c*-axis, additional substructure on these peaks is resolved, characterized by a splitting of 14 mT, and tentatively assigned to a superhyperfine interaction. Additionally a half-field resonance split by 50 up to 70 mT is detected. The spectra are described by an electron–hole pair located at a close donor–acceptor pair. Axial donor and acceptor *g*-values of $g_{e||} = g_{e\perp} = 1.83$, $g_{h||} = 2.18$, and $g_{h\perp} = 2.22$ are found. The exchange interaction can be described by an axial fine-structure tensor with $D_{||} = 0.18\ \mathrm{cm}^{-1}$ and $D_{\perp} = 0.09\ \mathrm{cm}^{-1}$.

Keywords: Gallium nitride; Excitons; Optically detected magnetic resonance

1. Introduction

Most of the optically detected magnetic resonance (ODMR) experiments performed so far on the various photoluminescence (PL) bands of GaN show structureless inhomogeniously broadened lines [1,2] which do not allow the identification of the microscopic structure of the defects involved, with the notable exception of recent experiments on electron irradiated GaN [3,4]. In contrast, the ODMR of the yellow luminescence in Mg-compensated GaN bulk crystals exhibits finestructure due to optically excited donor–acceptor pairs. For a particular crystal orientation an additionally resolved hyperfine splitting is found. In this paper we summarize our experimental results and present a tentative model for the underlying complex.

2. Experimental background

The Mg-doped GaN bulk crystals (2×3 mm typical sample size) investigated by PL and ODMR were grown using a high-pressure high-temperature process [5]. Average Mg and O concentrations for these samples are of the order of $5 \times 10^{19}\ \mathrm{cm}^{-3}$ [6] leading to compensated material. PL at 5 K was excited by the 351 nm line of an Ar^+-ion laser at power densities of $\sim 1\ \mathrm{W/cm}^2$. The emission was analyzed with a 0.8-m double-grating spectrometer and detected with a GaAs photomultiplier. ODMR was measured at 34 GHz. Photoexcitation power densities near $1\ \mathrm{W/cm}^2$ and microwave modulation frequencies of 1 kHz gave the best signal-to-noise ratio.

3. Results and discussion

The photoluminescence of the GaN:Mg crystals is shown in Fig. 1. The samples exhibit a blue emission band, characteristic for Mg-doped material, as well as

* Corresponding author. Tel.: + 49-89-289-12755; fax: + 49-89-289-12737.
E-mail address: Martin.Bayerl@wsi.tum.de (M.W. Bayerl)

0921-4526/99/$ - see front matter
PII: S0921-4526(99)00421-4

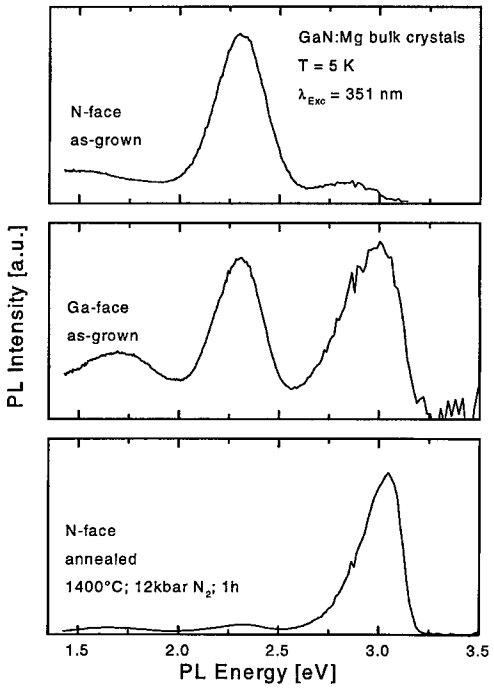

Fig. 1. PL spectra of Mg-doped GaN bulk crystals.

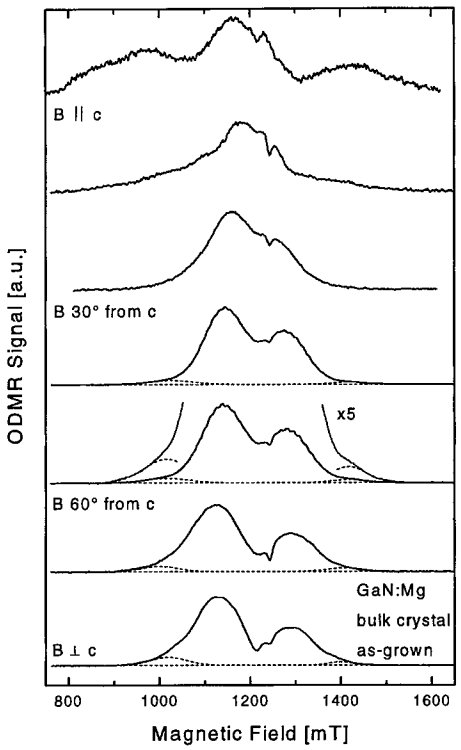

Fig. 2. Angular dependence of the 34 GHz ODMR spectra of the yellow PL from the as-grown crystals. For easier identification of the weak high- and low-field lines, the spectrum for B 60° from the c-axis has been magnified additionally.

yellow and red emission, the latter having been observed of Mg–Si codoped and Mg-doped GaN [7,8]. For the as-grown samples, the yellow emission from the Ga-face (smooth surface morphology) is considerably weaker than from the N-face (rough surface) [9]. Elastic recoil detection experiments show an inhomogeneous incorporation of oxygen into the crystals [6]. The oxygen concentration is a factor of two higher at the N-face, which suggests that oxygen is involved in the origin of the yellow luminescence. Upon annealing for 1 h at 1400°C and 12 kbar N_2 pressure, the intensity of the blue band increases dramatically while the yellow and red emission is reduced. Still, the Ga-face has a stronger blue and weaker yellow and red PL compared to the N-face.

ODMR experiments on the yellow luminescence of both surfaces from all samples show similar results. However, here we will only present spectra of the as-grown material since this gave the best signal-to-noise ratio. The angular dependence of the ODMR is shown in Fig. 2. For a crystal orientation $B \perp c$, the spectrum is dominated by a broad central feature consisting of two luminescence enhancing gaussian-shaped lines which are 80–100 mT wide and separated by 180 mT. In the high- and low-field wings, two additional resonances appear which are approximately 10–20 times weaker than the central lines. However, the intensity ratio of the two high-field lines is similar to that of the two low-field lines suggesting a common origin of the four constituents. Rotating the sample to $B \| c$, the two central resonances move together whereas the positions of the resonances in the wings seem to be fixed, at least up to angles of B 30° from c. Upon further rotation, strongly anisotropic features appear on both sides of the spectrum. As these lines have a slightly different phase with respect to the microwave power modulation than the previously discussed resonances, they probably have a different origin. Due to the experimental setup, these defect states could be located at the sample edge which is illuminated dominantly under this orientation. Note that the narrow dip at ~ 1.24 T in all the spectra arises from the well known effective-mass donor state with $g \approx 1.95$ [1] which is involved in a shunt process to this yellow luminescence band.

At angles between 60° and 45° from c additional substructure is resolved on the two central peaks (Fig. 3). Two sets consisting of more than 10 lines with an equal spacing of 13–14 mT are superimposed on the dominating central resonances. We tentatively assign these lines to a superhyperfine interaction with the nearest-neighbor shell of atoms. The hyperfine splitting due to ^{14}N atoms is expected to be comparatively small because of the small nuclear g_n-value of 0.4038. This is supported by the line width of 14–16 mT of the deep defect found in

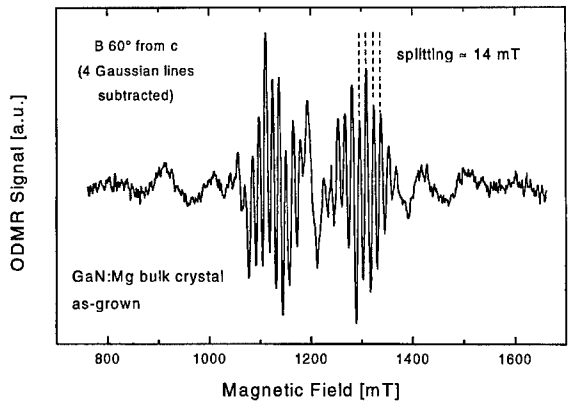

Fig. 3. Hyperfine structure on the central resonances after subtraction of a Gaussian line fit.

the ODMR of the yellow luminescence of n-GaN which is thought to arise from unresolved hyperfine splitting [1] most likely due to interaction with ^{14}N neighbors as the dominant defect in n-type GaN was calculated to be a V_{Ga}–O complex [10]. Therefore, a more likely explanation is hyperfine interaction with Ga neighbors ($g_n = 1.344$ and 1.708 for ^{69}Ga and ^{71}Ga resp.). To account for the observed number of lines at least three equivalent Ga atoms (nuclear spin $I = \frac{3}{2}$) have to be considered. Another interesting point is the integral intensity of the hyperfine lines which adds up to about 5% of the underlying resonances. This could indicate that the isotope causing the hyperfine splitting has a natural abundance of a few percent. Candidates are ^{29}Si ($I = \frac{1}{2}$; natural abundance 4.67%) and more likely ^{25}Mg ($I = \frac{5}{2}$; n.a. 10.00%). Further analysis is currently being performed.

In addition, at least two resonances are observed in the angular dependence of the half-field region around 0.6 T (shown in Fig. 4). These lines are quite symmetrically split around $g = 4.06$ by ~ 50 mT for $B \perp c$ and ~ 70 mT for $B \| c$. The angular dependence of the half-field splittings is opposite to that of the dominant full-field lines, but again the resonance at lower field is more intense than the corresponding resonance at higher field.

A summary of the peak positions derived from Fig. 1 is given in Fig. 5. The full squares represent the strong center resonances and their weaker companions in the tails of the spectra originating from the bulk states. The line positions of the defects thought to arise from the sample edge are represented by the open circles. The observation of half-field lines implies the presence of a finestructure-split triplet or higher-spin system. Thus, as a first model we describe the observed behavior of the main resonances (full squares) by a close donor–acceptor pair with an $S = \frac{1}{2}$ electron localized at the donor site and a $J = \frac{1}{2}$ hole localized at the acceptor site. Such a spin-

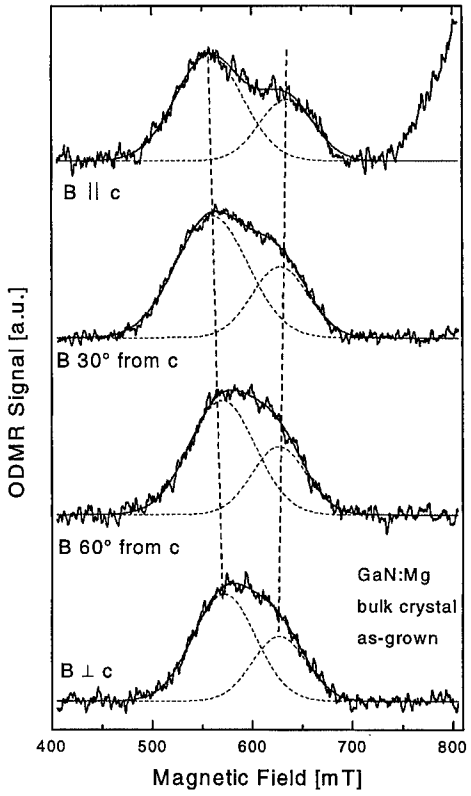

Fig. 4. Half-field ODMR spectra of the yellow PL from as-grown crystals. The spectra consist of at least two lines.

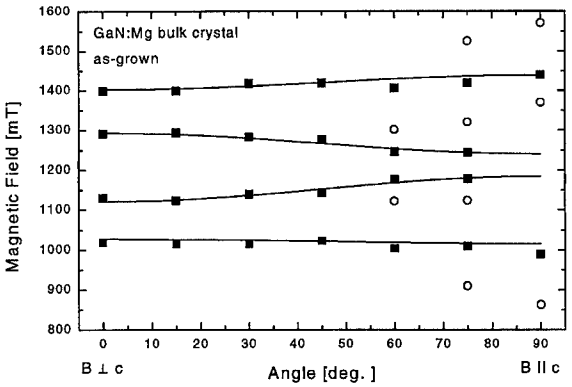

Fig. 5. Fit of the resonance positions of the donor–acceptor pairs (full squares). The open circles denote resonance positions assigned to defects located at the sample edge.

like hole is typical for deep acceptors [11]. The electron and hole are coupled via an axially symmetric finestructure tensor. The result of the fit is given by the lines in Fig. 5. This model is able to describe the resonance positions correctly. It also correctly predicts that the

Table 1
Comparison of the parameters used to describe the fit and recent magnetoluminescence results [12,13]

	Fit	Magnetoluminescence			
$g_{e\|\|}$	1.83	$g_{eD^0X\|\|}$	1.87		
$g_{e\perp}$	1.83	$g_{eD^0X\perp}$	1.87		
$g_{h\|\|}$	2.18	$g_{eA^0X\|\|}$	2.1	$g_{hA^0X\|\|}$	2.3
$g_{h\perp}$	2.22	$g_{eA^0X\perp}$	2.1	$g_{A^0X\perp}$	2.1
$D_{\|\|}$	0.18 cm^{-1}				
$D_\perp$	0.09 cm^{-1}				

lower field transitions are more intense than the high-field transitions, partially due to difference in the thermal occupation number. Finally, the center lines are expected to be stronger by a factor of ~ 6 compared to the outer resonances, while a ratio of 10–20 is observed experimentally. The parameters used for the fit are given in Table 1. The obtained g-values vary significantly from the effective-mass donor and magnesium acceptor g-values reported in previous ODMR experiments [1,2]. However, these experiments were performed on p-type material which has only a weak electron–hole coupling in contrast to the highly compensated samples studied here with a strongly coupled electron–hole system typical for donor or acceptor bound excitons. Similar g-factors indeed have been observed in recent magnetoluminescence experiments on bound excitons in GaN [12,13].

So far, the local symmetry of the complex giving rise to the hyperfine splitting was not taken into account. Assuming a substitutional donor–acceptor pair on the inequivalent nearest-neighbor Ga and N pair-sites leads to a broadening of the calculated lines rather than to the introduction of additional lines with a different angular dependence. This behavior could be the reason for the large line widths of 60–100 mT. The high concentrations of both Mg and O in the samples and their affinity to Ga and N sites, respectively, lead us to tentatively assign the origin of the ODMR to a Mg–O complex. However, the splitting of the half-field resonance and the hyperfine-split lines cannot be accounted for by this simple model and require further investigation.

4. Summary

ODMR on the yellow luminescence of highly Mg-compensated GaN bulk crystals exhibits new resonance features. The spectra are dominated by a fine-structure-split pair of lines accompanied by weaker lines on the high- and low-field tails of the spectra. This quartet of lines can be well described in terms of line positions, relative amplitudes and angular dependence using the model of a strongly fine-structure-coupled donor–acceptor pair. This pair is tentatively assigned to a Mg–O complex. At orientations of the crystal with B between 60° and 45° from the c-axis hyperfine splitting of a high-spin system with a separation of 14 mT is resolved. Additionally, a split half-field resonance is found for all orientations.

Acknowledgements

We thank B.K. Meyer and his group for help with the simulations. This work was supported by the Deutsche Forschungsgemeinschaft.

References

[1] E.R. Glaser, T.A. Kennedy, K. Doverspike, L.B. Rowland, D.K. Gaskill, J.A. Freitas Jr., M. Asif Khan, D.T. Olson, J.N. Kuznia, D.K. Wickenden, Phys. Rev. B 51 (1995) 13326.
[2] M. Kunzer, U. Kaufmann, K. Maier, J. Schneider, N. Herres, I. Akasaki, H. Amano, Mater. Sci. Forum 143–147 (1994) 87.
[3] C. Bozdog, H. Przybylinska, G.D. Watkins, V. Härle, M. Kamp, R.J. Molnar, A.E. Wickenden, D.D. Koleske, R.L. Henry, Phys. Rev. B 59 (1999) 12479.
[4] M. Linde, S.J. Uftring, G.D. Watkins, V. Härle, F. Scholz, Phys. Rev. B 55 (1997) R10177.
[5] S. Porowski, I. Grzegory, in: S.J. Pearton (Ed.), GaN and Related Materials, Vol. 2, Gordon and Breach, Amsterdam, 1997, p. 295.
[6] L. Görgens, private communication.
[7] M.W. Bayerl, M.S. Brandt, E.R. Glaser, A.E. Wickenden, D.D. Koleske, R.L. Henry, M. Stutzmann, Phys. Stat. Sol. B, accepted for publication.
[8] U. Kaufmann, M. Kunzer, H. Obloh, M. Maier, Ch. Manz, A. Ramakrishnan, B. Santic, Phys. Rev. B 59 (1999) 5561.
[9] M. Bockowski, I. Grzegory, S. Krukowski, M. Leszczynski, E. Litwin-Staszewska, B. Lucznik, G. Nowak, T. Suski, H. Teisseyre, J.L. Weyher, M. Wroblewski, S. Porowski, 1998, unpublished.
[10] J. Neugebauer, C.G. Van de Walle, Appl. Phys. Lett. 69 (1996) 503.
[11] For a review see W.M. Chen, B. Monemar, M. Godlewski, Defect and Diffusion Forum 62/63 (1989) 133.
[12] R. Stepniewski, A. Wysmolek, M. Potemski, J. Lusakowski, K. Korona, K. Pakula, J.M. Baranowski, G. Martinez, P. Wyder, I. Grzegory, S. Porowski, Phys. Stat. Sol. B 210 (1998) 373.
[13] A. Wysmolek, M. Potemski, R. Stepniewski, J. Lusakowski, K. Pakula, J.M. Baranowski, G. Martinez, P. Wyder, I. Grzegory, S. Porowski, Phys. Stat. Sol. B, to be published.

ELSEVIER

Physica B 273–274 (1999) 124–129

PHYSICA B

www.elsevier.com/locate/physb

Ordering in bulk GaN : Mg samples: defects caused by Mg doping

Z. Liliental-Weber[a,*], M. Benamara[a], W. Swider[a], J. Washburn[a], I. Grzegory[b], S. Porowski[b], R.D. Dupuis[c], C.J. Eiting[c]

[a]*Lawrence Berkeley National Laboratory, m/s 62/203, 1 Cyclotron Road, Berkeley, CA 94720, USA*
[b]*High Pressure Research Center "Unipress", Polish Academy of Sciences, Warsaw, Poland*
[c]*The University of Texas at Austin, Microelectronics Research Center, PRC/MER 1.606 D-R9900, Austin TX 78712-1100, USA*

Abstract

Transmission electron microscopy studies show evidence of spontaneous ordering in Mg-doped, bulk GaN crystals grown by a high-pressure and high-temperature process. The ordering consists of Mg-rich planar defects on basal planes separated by 10.4 nm and occurs only for growth in the N to Ga polar direction (0 0 0 $\bar{1}$ N polarity). These planar defects show characteristics of inversion domains and have a $\frac{1}{3}[1\ \bar{1}\ 0\ 0] + c/2$ shift vector. These monolayers are polytypoids. A model for these defects is suggested. No similar defects are formed on the opposite site of the crystal (Ga to N polar direction), where the growth rate is an order of magnitude faster compared to the growth with N-polarity, but pyramidal and rectangular defects, empty inside (pinholes) are observed. The same types of defects seen for the two growth polarities in the bulk crystals were also observed in MOCVD grown GaN samples with Mg delta doping.

Keywords: Mg doping; Ordering; Polytypoids; Polarity; Pinholes; Nanotubes

1. Introduction

In order to use GaN for electronic devices, p–n junctions need to be formed in this material. N-type GaN can easily be grown, but obtaining p-doping is more difficult. The most commonly used p-dopant is Mg. However, high hole concentrations can only be obtained after thermal annealing [1,2] which leads to the dissociation of Mg–H complexes. Material made using this process has been used to fabricate light emitting diodes (LEDs) [2] and lasers [3]. Despite this success, many aspects of Mg-doping in GaN are still not understood. We report here evidence that, under certain growth conditions, Mg causes the formation of several different types of defects depending on the growth polarity. For growth with N-polarity, planar defects, Mg-rich, form a superlattice-like array typical for polytypoids. Growth with Ga-polarity leads to the formation of pyramidal and rectangular defects; pinholes that are empty inside. These different types of defects, planar for growth with N-polarity, and three-dimensional for growth with Ga-polarity, were observed in bulk GaN : Mg as well as in heteroepitaxial samples grown on sapphire by metal-organic-chemical-vapor-deposition (MOCVD) with the delta doping method.

2. Experimental

Three different types of samples were studied: bulk samples, MOCVD samples with Mg delta doping and MOCVD samples doped with Mg throughout the layer (p–i–n structure). The bulk Mg-doped GaN crystals were grown by the high nitrogen pressure method [4] from

* Corresponding author. Tel.: + 1-510-486-6276; fax: + 1-510-486-4995.
E-mail address: z_liliental-weber@lbl.gov (Z. Liliental-Weber)

0921-4526/99/$ - see front matter
PII: S0921-4526(99)00422-6

a solution of liquid gallium containing 0.1–0.5 at% Mg [5]. They were grown at 1500–1600°C, with a N_2 pressure of 15 kbars for 100–150 h. P-type conductivity was not achieved but all crystals were highly resistive.

The Mg delta-doped structures were grown at 1030°C by MOCVD at 200 Torr in a hydrogen (H_2) ambient using trimethylgallium (TMGa) and ammonia (NH_3). Cp_2Mg was used as the Mg precursor. The superstructure of a 130-period GaN/Mg delta doped layer consisted of 104 Å-thick layers of GaN, each followed by a 15 s exposure of Cp_2Mg. During the Cp_2Mg exposure, the TMGa was vented, but the NH_3 and H_2 remained flowing into the chamber. Following the superlattice growth, the temperature was lowered to 850°C, the ambient was switched to nitrogen only, and a 10 min in situ anneal was performed to dissociate the Mg–H complexes and activate the Mg atoms [6].

The p–i–n structures were also grown by MOCVD at the same temperature (1030°C) but with continuous Cp_2Mg exposure and only slightly higher growth rate (5.5 Å/s) as compared to (5.3 Å/s) used for delta doping. The same annealing at 850°C for 10 min was performed.

All crystals have been studied using transmission electron microscopy (TEM). Dopant concentration and impurity levels were determined using secondary ion mass spectrometry (SIMS) and energy dispersive X-ray spectroscopy (EDX). Cross-section samples were prepared along the $[1\,\bar{1}\,0\,0]$ direction for convergent beam electron diffraction (CBED) in order to determine crystal polarity and along the $[1\,1\,\bar{2}\,0]$ direction for high-resolution cross-section studies (HREM).

3. Results

3.1. Bulk crystal growing with N-polarity

Fig. 1 shows cross-sectional TEM micrographs from the the bulk sample together with a ball model indicating crystal polarity determined by CBED. It can be seen that the upper and lower parts of the crystal are different in respect to the types of defect formed. This clearly shows that growth is very different for the two opposite crystal polarities. High-resolution images taken from the upper $(0\,0\,0\,\bar{1})$ side of the crystal (shown in Fig. 1) indicate the presence of planar defects (Fig. 2a). Every 10.4 nm (20 c-lattice parameters) a monolayer with an enhanced contrast was detected creating an equidistant layer structure which extended from the sample surface to a depth of a few micrometers, only about 10% of the sample thickness indicating a much smaller growth rate for the surface with N-polarity. This structure can be thought of as a monolayer thick quantum-well structure. The structure maintains its c-plane coherence along the whole length of the plate-shaped crystals (about 8 mm). Selective area

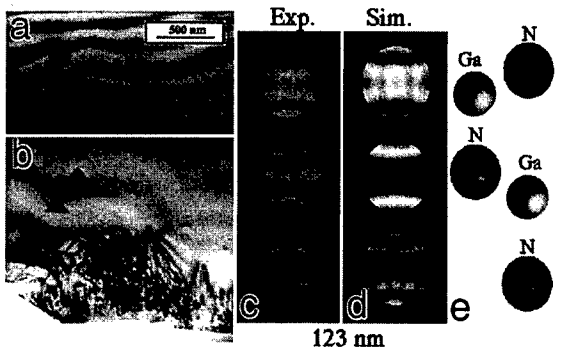

Fig. 1. Cross-section TEM micrograph showing GaN : Mg bulk sample: (a) shows an area near the surface with N-polarity and (b) near the opposite surface grown with Ga-polarity. Note the different types of defects formed for different growth polarity. The damage visible at the crystal edge for growth with Ga polarity was introduced by mechano-chemical etching and cannot be removed chemically; Experimental (c) and simulated (d) CBED patterns together with the atom arrangement (e) along the c-axis for polarity determination.

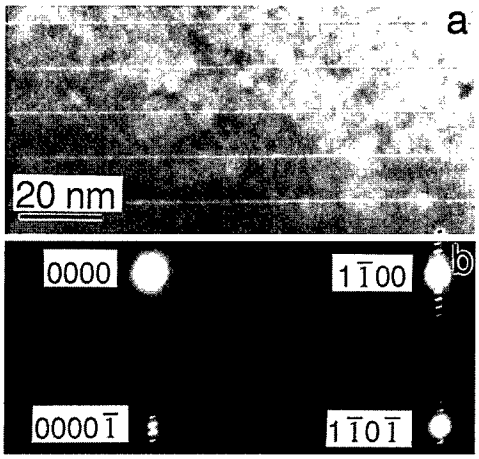

Fig. 2. (a) Higher magnification of the subsurface area grown with N polarity showing periodic arrangement of planar defects, (b) Diffraction pattern obtained from planar defects. Note satellite diffraction spots dividing (0 0 0 1) into 20 equal spacings.

diffraction pattern (SAD) show that the formation of these regularly spaced planar defects leads to additional diffraction spots dividing the (0 0 0 1) lattice distance into 20 equal parts which corresponds to a $0.52 \times 20 = 10.4$ nm distance between the monolayers in real space (Fig. 2b). Our earlier studies of these defects show that these monolayers have a $\frac{1}{3}[1\,\bar{1}\,0\,0] + c/2$ displacement vector [7,8] characteristic of a stacking fault. However, a splitting of the (0 0 0 1) and (0 0 0 3) reflections indicates that these defects contain inversion domain

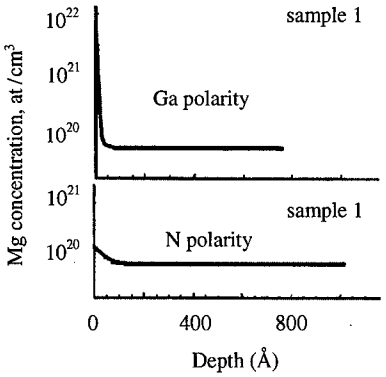

Fig. 3. SIMS measurements on the crystal surface with Ga and N polarity.

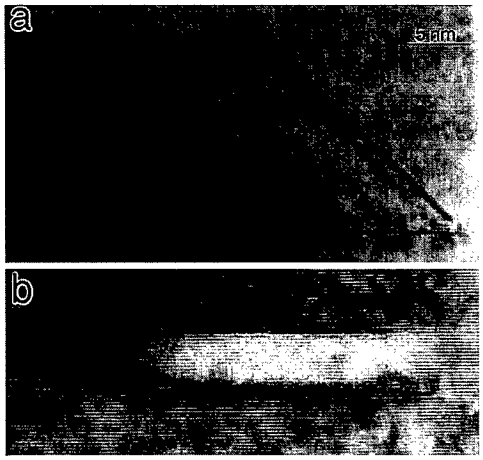

Fig. 4. Defects formed in the bulk crystal area grown with Ga polarity. (a) pyramidal defect and (b) rectangular defect. Note lighter contrast inside the defects indicating different sample thickness and contrast modulation due to Mg segregation at the base of the pyramidal defect.

boundaries (IDBs). This was also confirmed by a multi-beam dark field image obtained from the [1 1 $\bar{2}$ 0] zone axis. By placing either a (0 0 0 1) or a (0 0 0 $\bar{1}$) diffracted beam on the zone axis with a small objective aperture, reverse contrast on the defects was obtained. The contrast was symmetric on the defect edges, e.g. white–white or dark–dark and not asymmetric white–dark or dark–white as would be expected from stacking faults [9]. Both these observations, splitting of forbidden reflections and especially the reverse contrast for $\pm g$ of a polar reciprocal lattice vector indicate the presence of IDBs.

EDX analysis [8] with an electron beam size of the order of 1 nm which was placed either on the defect or in the area between these defects confirmed that these planar defects are Mg rich. SIMS studies show a constant Mg distribution at the level of 6×10^{19} cm^{-3} on both sides of the bulk sample (Fig. 3) with only a slight increase at the surface with N polarity to 2×10^{20} cm^{-3}. A high impurity level was also found in these samples. The oxygen concentration was 2.5×10^{19} cm^{-3}, [C] $\approx 1.5 \times 10^{17}$ cm^{-3} and [Si] $\approx 4 \times 10^{16}$ cm^{-3}.

The ordering close to the N polarity surface was not observed in all crystals studied. In some of them thick layers of regular hexagonal material were present, and some of them had no ordering at all. This suggests that the ordered structures form only for certain critical growth conditions.

3.2. Bulk crystals grown with Ga-polarity

The Ga-polarity side of the bulk crystals had a completely different defect structure as shown in Figs. (1b). The defects appear in [1 1 $\bar{2}$ 0] cross-section TEM micrographs as triangular features with a base on (0 0 0 1) c-planes and six {1 1 $\bar{2}$ 2} side facets. All these triangles were oriented in a direction with the base closest and parallel to the sample surface with Ga-polarity, e.g. from the triangle tip to the base a long bond direction along the c-axis is from Ga to N. No additional diffraction spots (or satellite spots) were observed on this side of the crystal. Some modulation of contrast is observed on the bases of these triangular figures (Fig. 4a). Especially for these areas some enhancement of Mg concentration is observed.

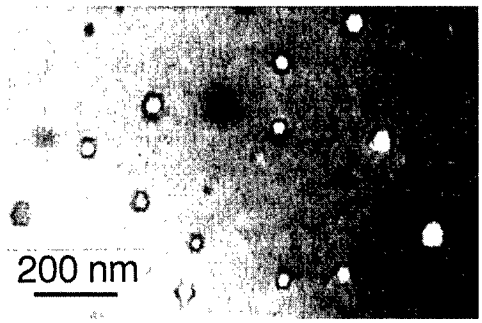

Fig. 5. Plan-view micrograph of the pyramidal defects.

Studies in plan-view configuration confirm that these defects are pyramids and that they are empty inside (Fig. 5). A change from dark to white contrast can be observed depending on whether the defect is located on a thickness fringe or between fringes. However, CBED studies applied for these defects (using a small beam size of 1.7 nm) show a change of symmetry from six-fold, obtained in the matrix, to very low symmetry (Fig. 6). This observation suggests that some reconstruction has occured on the internal surfaces of these pinholes probably caused by Mg segregation. The dimensions of the largest defects are in the range 100 nm (the measured length of their bases) and the smallest are about 3–5 nm.

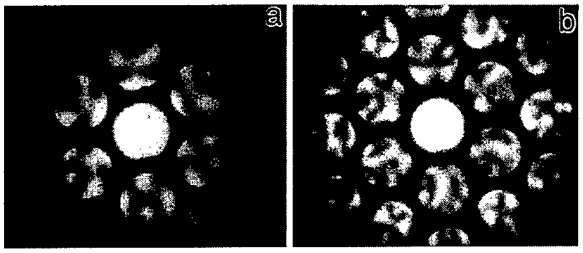

Fig. 6. Convergent beam electron diffraction taken in plan-view: (a) from the matrix, (b) on the defect. Note very low symmetry of the pattern obtained on the defect suggesting some surface reconstructions with different symmetry than the matrix.

The density of these defects is in the range of 2.5×10^9 cm^{-2}. A second type of hollow defect (empty inside) was observed in cross-section samples: a rectangular defect delineated by a cubic layer on top and bottom basal planes (Fig. 4b).The different types of defects observed on the crystal sides grown with N or with Ga-polarity are likely to be associated with different surface reconstructions and different positions within the unit cell where the Mg atoms are located.

These different types of defects formed for growth with different polarities have been observed initially in bulk crystals doped with Mg [7,8], where many crystals are grown during a single growth run, and the precise growth condition for each particular crystal is rather indeterminate. Therefore, experiments were also carried on heteroepitaxial samples grown by MOCVD, where growth conditions can be controlled for each crystal.

3.3. *Mg-delta-doped GaN samples grown by MOCVD*

TEM studies on cross-section Mg-delta-doped samples also show both types of defects formed for the two opposite polarities in bulk GaN : Mg, e.g. planar defects (polytypoids) which were characteristic for the growth with N-polarity and pyramidal and rectangular pinholes observed in the bulk GaN : Mg grown with Ga-polarity (Fig. 7a). This figure shows that growth of about 150 nm thickness above the buffer layer did not lead to any visible change in defect arrangement compared to undoped samples [10]. However, in the following layer, about 200 nm thick, planar defects, like those in bulk crystals grown with N-polarity were observed (Fig. 7b). In the layer following these planar defects, a high density ($\sim 10^{10}$ cm^{-2}) of triangular and rectangular defects like those observed in bulk crystals grown with Ga polarity was observed. SIMS analysis shows (Fig. 8) that much smaller Mg concentration was observed at the beginning of growth (7×10^{18} cm^{-3}), despite the fact that Mg delta doping was performed at each 104 Å through all of the sample. Mg concentration steadily increased to the level of 1×10^{19} cm^{-3} and then in the area with planar defects

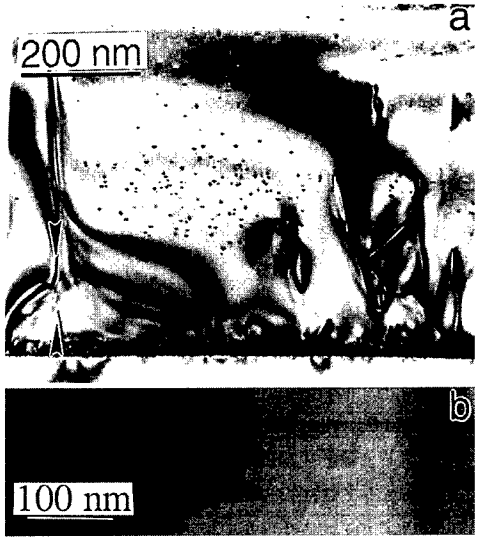

Fig. 7. (a) Micrograph showing cross-section sample grown by MOCVD with Mg delta doping. A part of the area marked by arrows is shown in (b) with planar defects similar to those observed in bulk samples grown with N-polarity. Note that above this area triangular and rectangular defects, similar to those in bulk samples for growth with Ga polarity, are formed.

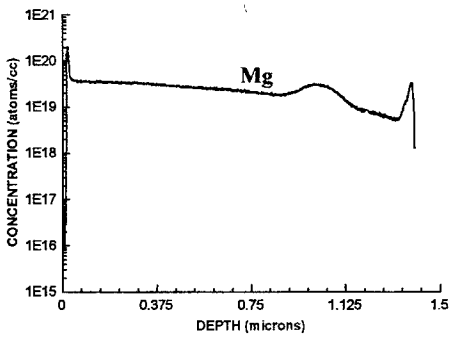

Fig. 8. SIMS measurements obtained from a MOCVD sample with Mg delta doping. A higher Mg concentration was measured in the area where planar defects were formed, similar to those observed in the bulk GaN samples grown with Ga polarity.

it reached 4×10^{19} cm^{-3}. At the layer thickness at which the hollow defects (rectangular and triangular) were formed, the Mg concentration dropped again to 2×10^{19} atoms/cm^3 and stayed almost constant with a slow increase to reach a concentration of 4×10^{19} cm^{-3} at the sample surface. No Mg fluctuation was observed, suggesting that detection of delta doping is beyond the resolution of the SIMS method. Impurity levels in this sample were very low showing carbon and oxygen concentrations on the level of $4–5 \times 10^{16}$ cm^{-3} (three

orders of magnitude lower than in the bulk samples), therefore, defects which were formed in these crystals must be caused by the Mg presence. The different defects formed in different parts of the layer suggest that during the MOCVD growth there are changes in growth polarity.

3.4. Continuous Mg-doped GaN samples grown by MOCVD

A minor change of growth conditions using the same MOCVD method, where Mg was supplied continuously and where a slightly higher growth rate was applied, did not lead to the formation of the previously described planar or three-dimensional defects. No changes of crystal polarity were observed, despite the fact that the average Mg concentration was at the same level as in the delta doped samples and the growth temperature was also the same. Therefore, it is not surprising that not all bulk samples showed ordering, since some deviations in composition, temperature or growth rate can be expected from crystal to crystal.

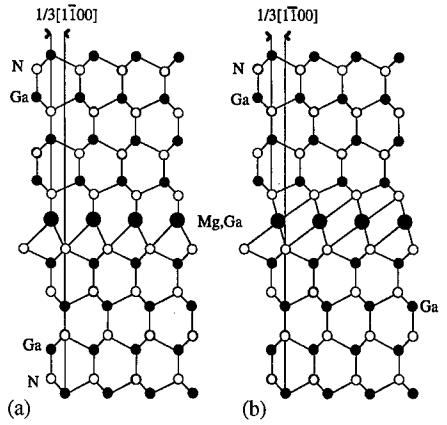

Fig. 9. Proposed models for the planar defects observed in bulk GaN : Mg samples formed for growth with N-polarity. The vertical lines indicate the shift of $\frac{1}{3}[1\ \bar{1}\ 0\ 0]$. (a) Mg four-fold coordinated and (b) Mg-six-fold coordinated. It is expected that some Ga atoms might remain also in this layer since Mg concentration in the sample is rather low. Some N atoms can also be substituted by oxygen or by N-vacancies to provide charge neutrality and stabilize this defect.

4. Discussion

Recent calculations by Bungaro et al. [11] show that the Mg arrangement on the GaN subsurface layer is dependent on crystal growth polarity and on the environment in which the crystal is growing (N-rich conditions versus Ga-rich conditions). For a Ga-polarity surface in a N-rich environment Mg would substitute Ga sites (Mg_{Ga}) and a Ga atom would be shifted to the surface. It is also expected that growth with Ga-polarity would be more favorable than growth with N-polarity. This is consistent with our studies which show much faster growth on the surface with Ga polarity. For a N-polar surface under N-rich conditions, the most stable configuration would be a complex consisting of a Ga_{H_3} together with Mg_{H_3} (H_3-center of the hexagonal atom arrangement).

Ordering observed in GaN : Mg for growth with N-polarity appears to be similar to the polytypoids formed in AlN rich in oxygen, or in Mg–Al–N–O–Si compounds [12–15]. Different types of polytypoids were observed depending on the M/X ratio (M-metal and X-nonmetal). The smaller the ratio, the longer the period of a polytype [12]. In all these samples, the oxygen concentration was at a level close to 1 at% or higher [12–15]. In our bulk samples, the oxygen concentration was high, but only in the range of $5 \times 10^{19}\ cm^{-3}$. However, in the samples with Mg delta doping, the oxygen concentration was only at the level of $5 \times 10^{16}\ cm^{-3}$, therefore, the polytypoids which are formed in our GaN : Mg samples are not oxygen related. It is anticipated that they must be caused by the Mg presence, which was confirmed by EDX studies [8]. Our experimental observations show that planar defects formed for growth with N-polarity, show the shift of $\frac{1}{3}[1\ \bar{1}\ 0\ 0] + c/2$ and contain an inversion.

Two possible models are proposed for the planar defect. Both models are shown in Fig. 9. The model shown in Fig. 9a would require Mg to be four-coordinated and the model shown in Fig. 9b would require Mg to be six coordinated, similar to what is observed in AlN : O [15]. Since the Mg concentration in these layers is rather low, it is expected that this is not a pure Mg layer but rather is mixed with Ga. For both models the $\frac{1}{3}[1\ \bar{1}\ 0\ 0] + c/2$ shift would be observed, however, six-coordinated Mg was not observed in these samples by X-ray studies [16]. Therefore, four-coordinated Mg is more likely. Since crystalline Mg has a lattice parameters ($a = 0.32$ nm and $c = 0.52$ nm) very similar to GaN ($a = 0.318$ nm and $c = 0.517$ nm), it explains why no change of the lattice parameter across the defect was detected in contrast to octahedrally coordinated oxygen in AlN : O [13–15]. It is also very likely that some N atoms surrounding a Mg-rich layer are substituted by oxygen atoms, in order to stabilize this defect and obtain the lowest possible formation energy. In order to verify this model the energy of such a defect needs to be calculated. Image simulations will be performed to compare the experimental and calculated image contrast of the defect.

5. Summary

In summary, this TEM study shows that ordered Mg-rich planar defects can be formed in Mg-doped GaN

crystals during growth in the N polar direction. These defects were formed in both bulk GaN samples as well in the MOCVD grown samples. Especially in the MOCVD grown samples a slightly higher Mg concentration was observed in the area with the planar defects. Regular spacing of these defects with a separation of only 10.4 nm was observed. This "microsuperlattice" leads to satellite diffraction spots dividing the (0 0 0 1) reciprocal lattice distance into 20 parts. A model for this defect was proposed.

A different type of defects is formed for growth with Ga polarity. The presence of Mg leads to formation of hollow defects in the form of pyramids and rectangular defects with surface reconstruction due to Mg segregation. This indicates that Mg segregating on particular planes can prevent further growth. These defects were observed in the majority of bulk GaN samples but also in Mg delta-doped samples grown by MOCVD. An extremely interesting observation in this study that deserves further investigation, is that in the MOCVD layers grown under similar conditions and with similar Mg concentration, but where Mg is introduced continuously rather than using the delta doping process, none of these defects were formed. Since growth of MOCVD layers can be better controlled than bulk growth this can lead to better understanding of the role of Mg in GaN structures. Optimum growth conditions can then be identified to obtain active dopant as needed for p-type conductivity and which avoid formation of defects.

Acknowledgements

This work was supported by the Director, Office of Basic Science, Materials Science Division, US Department of Energy, under the Contract No. DE-AC03-76SF00098. ZLW wants to thank Ch. Echer for EELS analysis. The use of the facility at the National Center for Electron Microscopy at E.O. Lawrence Berkeley National Laboratory is greatly appreciated. The work at UT-Austin was partially supported by the Office of Naval Research under N00014-95-1-1302 (monitored by Dr. J. C. Zolper) and the National Science Foundation under Grant CHE-89-20120.

References

[1] H. Amano, M. Kito, K. Hiramatsu, I. Akasaki, Inst. Phys. Conf. Ser. 106 (1989) 725.
[2] S. Nakamura, M. Senoh, T. Mukai, Jpn. J. Appl. Phys. 31 (1991) L1708.
[3] S. Nakamura, Paper Plenary 1, presented at the 24th International Symposium on Compound Semiconductors, San Diego CA, 8–11 September 1997.
[4] I. Grzegory, J. Jun, M. Bockowski, St. Krukowski, M. Wroblewski, B. Lucznik, S. Porowski, J. Phys. Chem. Solids 56 (1995) 639.
[5] S. Porowski, M. Bockowski, B. Lucznik, I. Grzegory, M. Wroblewski, H. Teisseyre, M. Leszczynski, E. Litwin-Staszewska, T. Suski, P. Trautman, K. Pakula, J.M. Baranowski, Acta Phys. Pol. A 92 (1997) 958.
[6] C.J. Eiting, P.A. Grudowski, J.S. Park, D.J.H. Lambert, B.S. Shelton, R.D. Dupuis, J. Electrochem. Soc. 144 (1997) L219.
[7] Z. Liliental-Weber, M. Benamara, J. Washburn, I. Grzegory, S. Porowski, Mater. Res. Soc. Proc. 572 (1999) 363.
[8] Z. Liliental-Weber, M. Benamara, J. Washburn, I. Grzegory, S. Porowski, Phys. Rev. Lett. 83 (1999) 2370.
[9] D.B. Williams, C.B. Carter, in: Transmission Electron Microscopy, Plenum Press, New York, 1996, pp. 386–390.
[10] Z. Liliental-Weber, M. Benamara, J. Washburn, I. Grzegory, S. Porowski, D.J.H. Lambert, C.J. Eiting, R.D. Dupuis, Appl. Phys. Lett. (1999) in press.
[11] C. Bungaro, K. Rapcewicz, J. Bernholc, Phys. Rev. B 59 (1999) 9771.
[12] K.H. Jack, J. Mater. Sci. 11 (1976) 1135.
[13] Y. Yan, M. Terauchi, M. Tanaka, Philos. Mag. A 77 (1998) 1027.
[14] R.A. Youngman, A.D. Westwood, M.R. McCartney, Mater. Res. Soc. Symp. Proc. 319 (1994) 45.
[15] A.D. Westwood, R.A. Yougman, M.R. McCartney, A.N. Cormack, J. Mater. Res. Soc. 10 (1995) 1270.
[16] K. Lawniczak-Jablonska, private communication.

ELSEVIER

Physica B 273–274 (1999) 130–133

PHYSICA B

www.elsevier.com/locate/physb

Structure of the $\{1\,1\,\underline{2}\,0\}$ inversion domain boundary in GaN

John E. Northrup*

Xerox Palo Alto Research Center, 3333 Coyote Hill Road, Palo Alto, CA 94304, USA

Abstract

A possible structure for inversion domain boundaries lying in the $\{1\,1\,\underline{2}\,0\}$ planes of wurtzite materials is presented. The formation energy of this defect is calculated for GaN using the local density approximation and first-principles pseudopotentials. The structure is generated by switching the chemical identity of Ga and N on one side of a $(1\,1\,\underline{2}\,0)$ plane followed by a translation $\boldsymbol{R} = \frac{1}{2}[0\,0\,0\,1]$. The resulting model, denoted IDB*-$\{1\,1\,\underline{2}\,0\}$, contains no Ga–Ga or N–N bonds. The translation vector $\boldsymbol{R}$ generating IDB*-$\{1\,1\,\underline{2}\,0\}$ is the same as that generating the IDB*-$\{1\,0\,\underline{1}\,0\}$ model determined previously for the $(1\,0\,\underline{1}\,0)$ inversion domain boundary in GaN. Therefore, inversion domains extending along the c-axis may be enclosed by a mixture of IDB*-$\{1\,0\,\underline{1}\,0\}$ and IDB*-$\{1\,1\,\underline{2}\,0\}$ boundaries without the need for additional dislocations. The predicted formation energy (29 meV/Å^2) of the IDB*-$\{1\,1\,\underline{2}\,0\}$ boundary is greater by 4 meV/Å^2 than that of the IDB*-$\{1\,0\,\underline{1}\,0\}$ boundary. This higher energy is attributed to a greater density of fourfold rings on the $(1\,1\,\underline{2}\,0)$ boundary.

PACS: 61.72.Nn

Keywords: GaN; IDB; Defect; Extended; Inversion; Domain; Boundary; Energy

1. Introduction

Growth of GaN on sapphire results in a complicated microstructure near the interface. Because of the chemical dissimilarity and the lattice mismatch (both laterally and vertically) between GaN and sapphire, the growth is three dimensional, and the initial stage of growth is the formation of a high density of islands. Adjacent islands will not necessarily be in registry with one another, and so the coalescence of the islands gives rise to stacking errors accommodated by the formation of dislocations and planar defects such as stacking faults and inversion domain boundaries. There is considerable interest in these defects and their effect on the optoelectronic properties of GaN-based devices (light-emitting diodes and lasers) that are grown on sapphire.

A large number of transmission electron microscopy studies have been performed to characterize dislocations and planar defects in GaN [1–17]. The most common types of threading dislocations are the pure edge dislocation, with a Burgers vector $\boldsymbol{b} = \frac{1}{3}[1\,1\,\underline{2}\,0]$, and the mixed dislocation, with $\boldsymbol{b} = \frac{1}{3}[1\,1\,\underline{2}\,3]$. A lattice image of an edge dislocation was recently reported by Xin et al. [4]. Based on this image, the core structure of this defect is thought to be comprised of a line of nearest neighbor pairs of threefold coordinated Ga and N atoms extending in the $[0\,0\,0\,1]$ direction, similar to the structure of the GaN$(1\,0\,\underline{1}\,0)$ surface [18]. Computations performed by Elsner et al. [19] suggest that such a dislocation would not be electrically active. However, such a dislocation could still be spatially correlated with non-radiative recombination events if impurities or native point defects would segregate to the core and induce states in the gap. Dislocations of mixed character ($\boldsymbol{b} = \frac{1}{3}[1\,1\,\underline{2}\,3]$), are also present in epitaxial GaN films, but little is known about the core structure of such defects. The question of whether a pure screw dislocation, with $\boldsymbol{b} = [0\,0\,0\,1]$, would have a filled or empty core has been investigated, [3,5,6]. Theoretical studies indicate that, in the absence of impurities, the equilibrium radius of an open core is less than ~ 3 Å. [19,20]. The energy cost of forming the internal GaN$(1\,0\,\underline{1}\,0)$ surfaces of the nanopipe outweighs the energy benefit of strain reduction when the nanopipe

* Corresponding author. Tel.: +1-650-812-4117; fax: +1-650-812-4140.

E-mail address: northrup@parc.xerox.com (J.E. Northrup)

0921-4526/99/$ - see front matter
PII: S0921-4526(99)00423-8

radius is greater than a few Angstroms. Thus, the presence in a few instances of open core screw dislocations (nanopipes) having radii on the order of 10 nm is probably due to the presence of impurity segregation to the internal surfaces or to growth kinetics.

There has also been progress in the identification of some of the planar defects as well as determinations of their atomic structure. For example, a stacking fault lying in the $\{1\,1\,\underline{2}\,0\}$ prism planes in GaN has been accounted for in terms of a structural model originally proposed by Drum for AlN [21]. This model is characterized by the fault displacement vector $\boldsymbol{R} = \frac{1}{2}[1\,0\,\underline{1}\,1]$. This vector agrees with the fault vector reported by Lee et al. [7] for a fault observed in GaN grown on sapphire and by Xin et al. [8] for a fault observed in GaN grown on GaP(1 1 1). Such faults also occur in GaN and AlN grown on SiC(0 0 0 1) and Al_2O_3 (0 0 0 1) [9,10]. The model of Drum has received strong support from a first-principles total energy calculation [22] which has shown it to be energetically favorable with respect to a competing, kinetically accessible, fault with $\boldsymbol{R} = \frac{1}{6}[2\,0\,\underline{2}\,3]$. The planar fault with $\boldsymbol{R} = \frac{1}{6}[2\,0\,\underline{2}\,3]$ is an example of a stacking mismatch boundary, and differs from the Drum structure by a rigid translation in the $[1\,0\,\underline{1}\,0]$ direction by 0.9 Å. The total energy calculation shows that the additional translation required to form the $\boldsymbol{R} = \frac{1}{2}[1\,0\,\underline{1}\,0]$ stacking fault is energetically favorable.

A second example of successful defect identification is the inversion domain boundary that is observed on the $\{1\,0\,\underline{1}\,0\}$ planes. The IDB*-$\{1\,0\,\underline{1}\,0\}$ model [23] is obtained by switching the chemical identity of atoms on one side of a $(1\,0\,\underline{1}\,0)$ plane followed by translation of the inverted region by $\boldsymbol{R} = \frac{1}{2}[0\,0\,0\,1]$. The translation eliminates the Ga–Ga and N–N bonds that would otherwise be present. This results in a very stable domain boundary having a formation energy cost of only 25 meV/Å^2. Simulations [11,12] of high-resolution electron microscopy images that employ the IDB*-$\{1\,0\,\underline{1}\,0\}$ model are consistent with the experimental images. A recent quantitative analysis of the structure employing convergent beam electron diffraction [13] also establishes the validity of this structure.

Almost all of the previous work on inversion domain boundaries in GaN has focussed on the part of the boundary that lies in the $(1\,0\,\underline{1}\,0)$ plane. However, there is some evidence that inversion domains extending in the [0 0 0 1] direction may exist with some part of their prismatic boundaries lying on the $\{1\,1\,\underline{2}\,0\}$ planes in ECR-MBE material [14]. Domains of irregular shape have also been observed in plan-view TEM images of high-quality MOCVD GaN [13,15].

In this paper total energy calculations for an IDB lying on the $\{1\,1\,\underline{2}\,0\}$ planes are reported. The proposed model is generated by a translation vector that is identical to that generating the boundary on the $\{1\,0\,\underline{1}\,0\}$ planes, and has an energy cost of formation that is just slightly greater than that of the $\{1\,0\,\underline{1}\,0\}$ boundary. These two features of the structure appear to be consistent with the existence of inversion domains enclosed by boundaries lying primarily, *but not invariably*, on the $\{1\,0\,\underline{1}\,0\}$ plane.

2. Calculations

We have performed total energy calculations for inversion domain boundaries using the plane-wave pseudopotential method and the local density approximation. The calculation method and pseudopotentials utilized here have been employed previously in calculations for GaN surfaces and extended defects [18,20,22,23]. The plane wave cutoff employed in the calculations is 60 Ry and the Ga 3d orbitals are included in the valence band. The domain boundary is modeled using a unit cell that contains 40 atoms. The cell is elongated in the $[1\,\underline{2}\,1\,0]$ direction: each cell contains two faults with five planes of atoms between the faults. The structure is periodic along the two orthogonal vectors $\boldsymbol{c} = [0\,0\,0\,1]$ and $3\boldsymbol{p} = [1\,0\,\underline{1}\,0]$ with repeat distances of $c = 5.18$ Å and $3p = 5.49$ Å. The formation energy for the fault is $E_{\text{form}} = 1/2(E - E_{\text{bulk}})$ where E is the total energy of a cell containing two equivalent faults and E_{bulk} is the energy of a bulk system with the same number of atoms. The domain wall energy is equal to E_{form}/A where $A = 28.44$ Å^2 is the area of the periodic unit cell of the boundary in the $(1\,\underline{2}\,1\,0)$ plane.

3. Results and discussion

The atomic positions are determined by energy minimization starting from an initial structure that corresponds to a switching of the chemical identity of the atoms on one side of the boundary plane followed by a rigid translation of these atoms by $\boldsymbol{R} = \frac{1}{2}[0\,0\,0\,1]$. The resulting structure contains no wrong bonds or dangling bonds. A ball-and-stick representation of the boundary structure is shown in Fig. 1. Careful examination of this figure reveals the presence of fourfold and eightfold rings of bonds across the boundary. A schematic model of the boundary is shown in Fig. 2. Note that the sets of atoms (1–2–3–4) and (5–6–7–8) each form a four-membered ring of bonds. However, the set (1–2–7–8) does not form such a ring because atom 1 is not bonded to atom 8. The smallest bond lengths are approximately 1.90 Å and the largest are 1.98 Å. The bonds between atoms 1–2, 3–4, 5–6, and 7–8 are almost identical to the bulk bond length in GaN, 1.94 Å. The largest deviations from the tetrahedral bond angle corresponds to the $\sim 90°$ bond angles in the fourfold rings. All other bond angles are within 10 degrees of the tetrahedral angle. Calculations of the Kohn–Sham eigenvalue spectrum for the IDB*-$\{1\,1\,\underline{2}\,0\}$

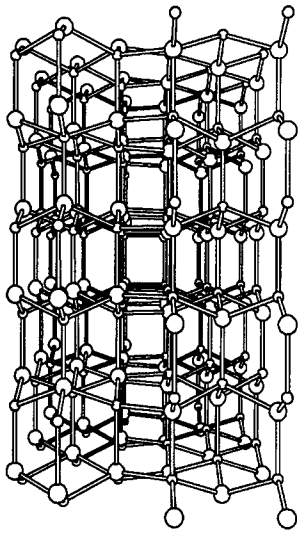

Fig. 1. This figure is a ball-and-stick representation of the IDB-$\{1\,1\,\bar{2}\,0\}$ model. The structure shown contains six $(1\,1\,\bar{2}\,0)$ planes of atoms. Three of these planes are to the left of the boundary and three planes are to the right. Examination of the structure reveals the existence of fourfold and eightfold rings of bonds that cross the boundary. Note that the polarity of the material on the left is inverted with respect to the polarity on the right. Large(small) circles represent Ga (N).

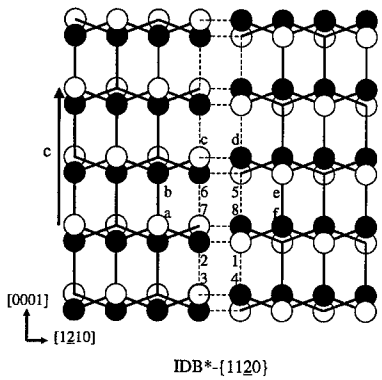

Fig. 2. Schematic representation of the inversion domain boundary on the $(1\,1\,\bar{2}\,0)$ plane. The sets (1–2–3–4) and (5–6–7–8) form fourfold rings. The set (1–2–a–b–c–d–e–f) forms an eightfold ring. The sets (1–2–7–8) and (5–6–c–d) do not form rings.

model do not indicate the presence of electronic states inside the band gap.

The calculated formation energy for the IDB*-$\{1\,1\,\bar{2}\,0\}$ model is equal to 0.83 eV/cell corresponding to a domain wall energy equal to 29 meV/Å^2. This energy is only slightly higher than that of the IDB*-$(1\,0\,\bar{1}\,0)$ boundary, 25 meV/Å^2 [23]. The low energy of these boundaries is attributed to the absence of wrong bonds and dangling bonds and the presence of a modest amount of strain. For perspective we point out that the energies of basal plane stacking faults [24,25] are typically only ~ 1 meV/Å^2 while the energies of the $(1\,0\,\bar{1}\,0)$ and $(1\,1\,\bar{2}\,0)$ surfaces are ~ 120 meV/Å^2 [18].

Given that the energy of the IDB*-$\{1\,1\,\bar{2}\,0\}$ boundary is only slightly greater than that of the $\{1\,0\,\bar{1}\,0\}$ boundary it seems plausible that closed domains could exist with boundaries on both sets of planes. The ratio of the domain wall energies for the IDB*-$(1\,0\,\bar{1}\,0)$ and the IDB*-$(1\,1\,\bar{2}\,0)$ is quite close to the ratio of the planar density of the fourfold rings of bonds in the two boundaries. The ratio of fourfold ring density is 1.15 while the ratio of the domain wall energies is 1.16. Thus the lower energy of the $(1\,0\,\bar{1}\,0)$ boundary is attributable to a reduced density of strained bonds rather than to a difference in the local bonding energetics. The situation is somewhat analogous to the difference between the energies of the $(1\,0\,\bar{1}\,0)$ and $(1\,1\,\bar{2}\,0)$ surfaces: The reduced density of Ga and N dangling bonds on the $(1\,0\,\bar{1}\,0)$ surface leads to a lower energy for this surface [18].

In a recent paper Elsner et al. presented theoretical work on domain boundaries in the $\{1\,1\,\bar{2}\,0\}$ plane [26]. They performed total energy calculations within a self-consistent tight binding approximation for several types of domain boundaries, but not the IDB*-$\{1\,1\,\bar{2}\,0\}$ model that we have presented here. Instead, they considered a model for an IDB on the $\{1\,1\,\bar{2}\,0\}$ plane characterized by a displacement vector of $\boldsymbol{R} = \frac{1}{2}[1\,0\,\bar{1}\,0]$. This model was initially suggested by Rouviere et al. [12]. Elsner et al. obtained a formation energy of 122 meV/Å^2 and attributed this very high formation energy to large deviations from tetrahedral coordination at the boundary. This energy is, of course, much greater than the value we have obtained for the IDB*-$\{1\,1\,\bar{2}\,0\}$ boundary. Because the IDB*-$\{1\,1\,\bar{2}\,0\}$ boundary would be kinetically accessible[1] to a system initially forming an $\boldsymbol{R} = \frac{1}{2}[1\,0\,\bar{1}\,0]$ boundary, it seems unlikely that a boundary with $\boldsymbol{R} = \frac{1}{2}[1\,0\,\bar{1}\,0]$ would be present over large areas.

In summary, we have presented a possible model for an inversion domain boundary on the $\{1\,1\,\bar{2}\,0\}$ planes of GaN. The model should also be applicable to other materials (e.g. 2H-SiC and AlN). The formation energy for this boundary was found to be slightly higher than that of the IDB*-$\{1\,0\,\bar{1}\,0\}$ model. The model can account for the existence of closed inversion domains observed in GaN having some segments of their boundary on $\{1\,1\,\bar{2}\,0\}$ planes.

[1] One should keep in mind that in addition to the domain wall energy global kinetic constraints play an important role in determining the atomic structure of a boundary. These kinetic hindrances make it possible for the crystal to exhibit more than one type of planar defect on a given plane.

References

[1] F.R. Chien, X.J. Ning, S. Stemmer, P. Pirouz, M.D. Bremser, R.F. Davis, Appl. Phys. Lett. 68 (1996) 2678.
[2] X.H. Wu, L.M. Brown, D. Kapolnek, S. Keller, S.P. DenBaars, J.S. Speck, J. Appl. Phys. 80 (1996) 3228.
[3] D. Cherns, W.T. Young, J.W. Steeds, F.A. Ponce, S. Nakamura, J. Crystal Growth 178 (1997) 201.
[4] Y. Xin, S.J. Pennycook, N.D. Browning, P.D. Nellist, S. Sivananthan, F. Omnes, B. Beaumont, J.P. Faurie, P. Gibart, Appl. Phys. Lett. 72 (1998) 2680.
[5] W. Qian, G. Rohrer, M. Skowronski, K. Doverspike, L. Rowland, D. Gaskill, Appl. Phys. Lett. 67 (1995) 2284.
[6] Z. Liliental-Weber, Y. Chen, S. Ruvimov, J. Washburn, Phys. Rev. Lett. 79 (1997) 2835.
[7] N.-E. Lee, R.C. Powell, Y.-W. Kim, J.E. Greene, J. Vac. Sci. Technol. A 13 (1995) 2293.
[8] Y. Xin, P.D. Brown, C.J. Humphreys, T.S. Cheng, C.T. Foxon, Appl. Phys. Lett. 70 (1997) 1308.
[9] P. Ruterana, B. Barbaray, A. Bere, P. Vermaut, A. Haire, E. Paumier, G. Nouet, A. Salvador, A. Botchkarev, H. Morkoc, Phys. Rev. B 59 (1999) 15917.
[10] P. Vermaut, P. Ruterana, G. Nouet, Philos. Mag. A 76 (1997) 1215.
[11] L.T. Romano, J.E. Northrup, M.A. Okeefe, Appl. Phys. Lett. 69 (1996) 2394.
[12] J.L. Rouviere, M. Arlery, B. Daudin, G. Feuillet, O. Briot, Mater. Sci. Eng. B 50 (1997) 61.
[13] D. Cherns, W.T. Young, M. Saunders, J.W. Steeds, F.A. Ponce, S. Nakamura, Philos. Mag. A 77 (1998) 273.
[14] L.T. Romano, J.E. Northrup, Mater. Res. Soc. Symp. Proc. 449 (1997) 423.
[15] F.A. Ponce, D. Cherns, W.T. Young, J.W. Steeds, S. Nakamura, Mater. Res. Soc. Symp. Proc. 449 (1997) 405.
[16] B.N. Sverdlov, G.A. Martin, H. Morkoc, D.J. Smith, Appl. Phys. Lett. 67 (1995) 2063.
[17] V. Ramachandran et al., Appl. Phys. Lett. 75 (1999) 808.
[18] J.E. Northrup, J. Neugebauer, Phys. Rev. B 53 (1996) 10477.
[19] J. Elsner et al, Phys. Rev. Lett. 79 (1997) 3672.
[20] J.E. Northrup, R. Di Felice, J. Neugebauer, Phys. Rev. B 56 (1997) 4325.
[21] C.M. Drum, Philos. Mag. 11 (1965) 313.
[22] J.E. Northrup, Appl. Phys. Lett. 72 (1998) 2316.
[23] J.E. Northrup, J. Neugebauer, L.T. Romano, Phys. Rev. Lett. 77 (1996) 103.
[24] A.F. Wright, J. Appl. Phys. 82 (1997) 5259.
[25] C. Stampfl, C.G. Van de Walle, Phys. Rev. B 57 (1998) R15052.
[26] J. Elsner, M. Kaukonen, M.I. Heggie, M. Haugk, Th. Frauenheim, R. Jones, Phys. Rev. B 58 (1998) 15347.

ELSEVIER

Physica B 273–274 (1999) 134–139

PHYSICA B

www.elsevier.com/locate/physb

Electronically induced dislocation glide motion in hexagonal GaN single crystals

Koji Maeda[a,*], Kunio Suzuki[b], Masaki Ichihara[c], Satoshi Nishiguchi[a], Kana Ono[a], Yutaka Mera[a], Shin Takeuchi[d]

[a]*Department of Applied Physics, Graduate School of Engineering, The University of Tokyo, 7-3-1 Hongo, Bunkyo-ku, Tokyo 113-8656, Japan*
[b]*Department of Materials Science, Nagasaki University, Nagasaki 852-8131, Japan*
[c]*Institute for Solid State Physics, The University of Tokyo, Roppongi, Tokyo 106-0032, Japan*
[d]*Department of Materials Science, Science University of Tokyo, Noda, Chiba 278-0022, Japan*

Abstract

Dislocations in crystalline powder of hexagonal GaN intentionally deformed by crushing were examined by transmission electron microscopy (TEM) in order to see if the recombination enhanced dislocation glide (REDG) effect is present in this solid. It was found that dislocations with a Burgers vector of *a*-type ($a/3\langle 1\,1\,\bar{2}\,0\rangle$) on the (0 0 0 1) basal plane and a $\{1\,\bar{1}\,0\,n\}$ pyramidal plane exhibit glide motion at room temperature under the influence of the electron beam used for TEM observations. From a quantitative comparison with the thermal mobility of basal dislocations empirically predicted for h-GaN, the authors concluded that the dislocation glides arose from the REDG effect induced by electronic excitation due to the TEM electron beam irradiation. Some implications of the results were discussed.

PACS: 61.70. – r; 61.70.Je; 61.80.Fe; 71.55.Fr

Keywords: Gallium nitride; Dislocation glide; Electronic excitation; Transmission electron microscopy

1. Introduction

Recent successful development of blue-light-emitting devices based on GaN or InGaN crystals is largely due to the innocuous nature of dislocations in this compound. Unlike the conventional photonic material such as GaAs and GaP, the presence of dislocations in an extremely high density does not much reduce the efficiency of light emission [1] and does not lead to rapid degradation in the dislocation multiplication mode [2]. These facts are surprising because the recombination enhanced dislocation glide (REDG) effect [3], which is a cause of the dislocation multiplication that is enhanced by minority carrier injection, has a tendency to become pronounced in widegap semiconductors.

One of the requisite conditions for the REDG effect to arise is the non-radiative recombination activity of the dislocations. Sugahara et al. [4] reported that individual dislocations in hexagonal (h-) GaN thin films grown on sapphire substrates are observed in dark contrasts in cathodoluminescence (CL) microscopy, which indicates that the dislocations act as non-radiative centers. However, these dislocations are those grown-in that were introduced during thin film growth at high temperatures and hence may be decorated with impurities and point defects, which could conceal the intrinsic nature of fresh dislocations. A more recent work done by Zaldivar et al. [5] showed that CL intensity is quenched in dislocated regions generated by micro-indentation at room temperature, which strongly suggests that the dislocations in the fresh state

* Corresponding author. Tel.: + 81-3-5841-6851; fax: + 81-3-5689-8268.
E-mail address: maeda@exp.t.u-tokyo.ac.jp (K. Maeda)

0921-4526/99/$ - see front matter
PII: S0921-4526(99)00424-X

as well act as non-radiative centers. Nevertheless, the lack of one-to-one correspondence between the dark contrasts and individual dislocations leaves the question above still open.

For the dislocation glide motion in GaN, Rocher and Jacob mentioned in their old paper [6] that dislocations in h-GaN grown on a sapphire substrate were observed to move during transmission electron microscopic (TEM) observations, though the details were not given in the short report. In order to clarify whether the REDG effect is really present or not, we have carried out TEM experiments using the electron beam as a source of electron-hole generation in the sample. We found that some of the dislocations introduced by intentional mechanical damage, hence believed to be fresh, really exhibit glide movement at room temperature. Experiments with interrupted electron beam irradiation revealed that the dislocation glides are induced reversibly by the electron beam. The effect was confirmed for dislocations on the basal slip plane and those on a pyramidal plane, but the magnitude of the effect depended on the dislocation type.

2. Experimental procedures

The samples used were single-crystalline powder of hexagonal (wurtzite) GaN (99.9%) purchased from Wako Chemicals Inc. The powder was crashed in an agate mortar at room temperature to introduce fresh dislocations and simultaneously to prepare thin specimens for TEM observations [7]. The specimens suspended upon a collodion mesh were examined at room temperature by either JEM-2010 (JEOL) or H-9000 (Hitachi) both operated at 200 kV with an electron beam density of the order of 10^3 A/m^2. Dislocation motion imaged by a TV camera was recorded by a video tape recorder. No intentional stress was applied to specimens during observations. When dislocations were isolated and remained in the crystal after they exhibited glides, the standard $\boldsymbol{g}\cdot\boldsymbol{b}$ analysis was performed to determine the Burgers vector.

3. Experimental results

The majority of the dislocations were stable during TEM observations, but some of them exhibited evident movement. Although most of those dislocations were densely tangled prohibiting comprehensive analysis, relatively detailed investigation was possible in the following two cases.

3.1. Basal dislocation

Fig. 1 shows a sequence of TV images that demonstrates shrinkage of a dislocation loop during TEM observation with a beam current density of 5×10^3 A/m^2. The dislocation motion was smooth and viscous which indicates that the dislocation glide is controlled by the Peierls mechanism. A notable fact is that the segment A running from top to bottom in Fig. 1(f) had a larger mobility than the segment A′ with the opposite sign that exhibited no movement. The similar difference in mobility was recognized between the segments B and B′ (Fig. 1(g)) with dislocation signs opposite to each other. Electron diffraction experiments indicated that the slip took place on the basal plane. In this specific sample, a direct analysis of the Burgers vector of that dislocation was not possible for the loop shrunk completely. However, among possible Burgers vectors, that are limited to the $a/3\langle 1\,1\,\bar{2}\,0\rangle$ type (a-type) on the basal plane in wurtzite structures, $\boldsymbol{b}=a/3[\,1\,1\,\bar{2}\,0]$ is most likely because in other cases, $\boldsymbol{b}=a/3[2\,\bar{1}\,\bar{1}\,0]$ and $\boldsymbol{b}=a/3[\bar{1}\,2\,\bar{1}\,0]$, the mobility difference between the segments A and A′ and the segments B and B′ cannot be explained since in both cases these segments would both be of screw character and therefore there would be no reason for the mobility to differ from each other as observed. The validity of the above assignment is supported by the fact that the Burgers vector of the dislocations around the annihilated loop, determined by the $\boldsymbol{g}\cdot\boldsymbol{b}$ analysis, are all identical to $\boldsymbol{b}=a/3[1\,1\,\bar{2}\,0]$. The mobility difference between the segments of opposite signs can be accounted for by the polarity-dependent behavior of α- and β-dislocations commonly observed in compound semiconductors [8], though the absolute polarity could not be determined in the present study.

Fig. 2 shows the displacement of the screw segment C and that of the 60° segment A in Fig. 1 and their velocity plotted as a function of elapsed time. Except for the final stage in which the movement was accelerated due to the mutual attraction of the segment B and B′, the velocity of the screw segment was kept at an almost constant level of $\sim 5\times10^{-9}$ m/s. The velocity of the 60° segment was of the similar order as the screw part.

The resolved shear stress τ acting locally on moving dislocation segments may be evaluated from the dislocation curvature ρ according to the relation [9]

$$\tau \approx G|b|/\rho \tag{1}$$

where G is the shear modulus. Fig. 3 shows the time variation of the curvature of the segment C. The stress level evaluated by (1) was almost constant around ~ 100 MPa, consistent with the constancy of the dislocation velocity.

3.2. Pyramidal dislocation

Fig. 4 presents a sequence of dislocation motion observed in a different sample that contained a dislocation line segment D penetrating the thin film. To see the

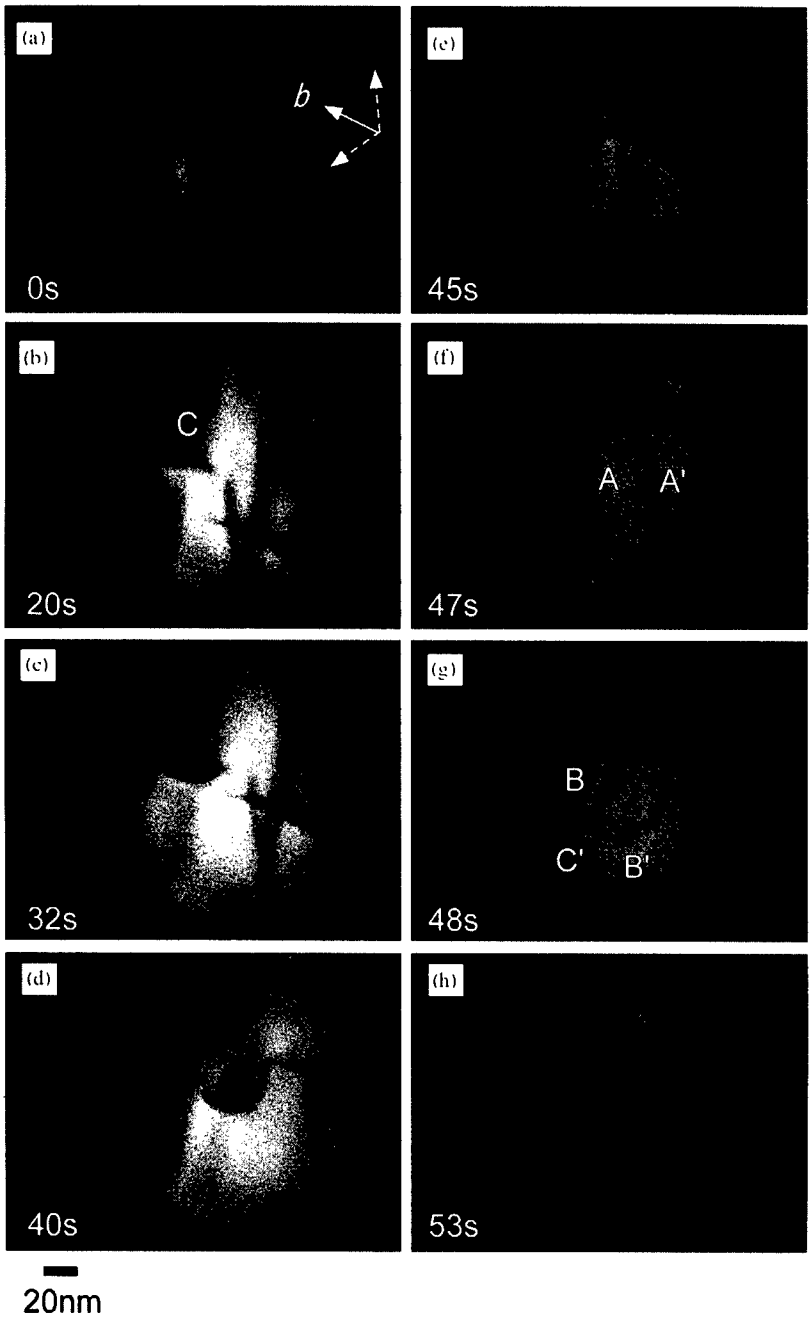

Fig. 1. A VTR image sequence showing shrinkage of a dislocation loop on the (0 0 0 1) basal plane in h-GaN. The solid arrow indicates the Burgers vector $\boldsymbol{b} = a/3[1\ 1\ \bar{2}\ 0]$ which is judged to be most likely from circumstantial evidences (see the text for the detail). Note the mobility difference between segments A and A′ and between B and B′. Note also that segment C advances in both concave ((a) and (b)) and convex ((d)–(f)) shapes.

irradiation effects of the TEM electron beam, a beam of 7×10^3 A/m^2 was switched off between images (f) and (g). As can be clearly seen in Fig. 5 plotting dislocation displacement with respect to time, the dislocation came to complete rest on interruption of electron beam irradiation and resumed its motion immediately after the irradiation was restarted.

The $\boldsymbol{g}\cdot\boldsymbol{b}$ analysis revealed that the Burgers vector of the dislocation is of a-type. The surface slip trace T left behind the dislocation passage is normal to the [0 0 0 1]

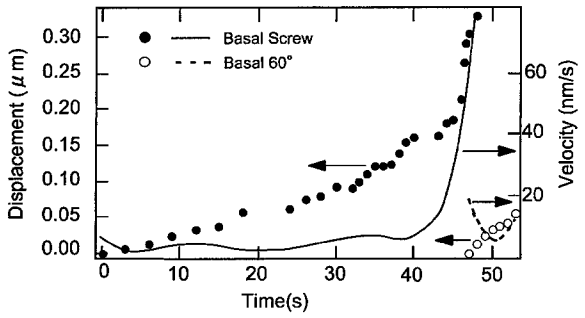

Fig. 2. The temporal variation of displacement and glide velocity of the screw segment C and the 60° segment A in Fig. 1.

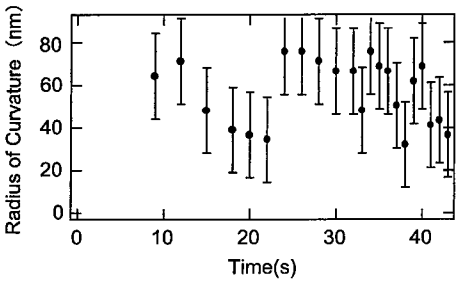

Fig. 3. The temporal variation of the curvature of the screw segment C. The time scale is the same as in Fig. 2.

c-axis, which indicates that the dislocation segment is not on the basal plane but on a pyramidal $\{1\,\bar{1}\,0\,n\}$ plane. The dislocation observed is therefore of a mixed character.

4. Discussion

The dislocation motion observed in the present study is evidently induced by irradiation of electron beam. A straightforward evidence in the pyramidal slip is provided by Fig. 5 in which dislocation mobility increases concomitant with electron beam irradiation. Although the evidence is not so direct as in the pyramidal slip, the basal dislocations became mobile only after we started TEM observations. To the authors' knowledge, there has been no report on direct measurements of thermal mobility of dislocations in h-GaN. The basal slip in wurtzite structures should not differ much from the slip on $\{1\,1\,1\}$ planes in zincblende and diamond structures. Also wurtzite GaN is not an exception in that the basal dislocations are dissociated into Shockley partials [7] as in other semiconductors. Empirically the dislocation velocity in covalent semiconductors depends on temperature T and stress τ in the form

$$V = A\tau^m \exp\left(-\frac{Q}{kT}\right), \tag{2}$$

where m is a numerical constant of 1–1.5 [10], and k the Boltzman constant. The pre-factor $A\tau^m$ is of the order of 10^4–10^6 m/s [10] at, e.g., $\tau \sim 100$ MPa. The literature accumulated for various semiconductors of zincblende and diamond structures shows that there is a good correlation as $Q \sim 0.3\,Gb_p^3$ [3] between the glide activation energy Q and a material parameter Gb_p^3 where b_p is the Burgers vector of the partial dislocations. The value of Q in GaN inferred from this correlation is ~ 4 eV while a different correlation with band gap energies yields a lower value of ~ 2 eV [11]. Whichever the case, if we try to explain the observed magnitude of dislocation velocity (of the order of 10^{-9} m/s at a shear stress of ~ 100 MPa) by electron-beam heating of the sample, we have to assume a temperature rise as high as 600–1400°C, which is totally unacceptable for the beam-current density (5×10^3 A/m^2) used in the present study. Similar reversible enhancement of dislocation velocity by TEM electron beam was never found in GaAs [12], ZnS [13], 6H-SiC [14] crystals. Thus, like these crystals, the most reasonable interpretation of the enhancement of dislocation mobility in GaN is the REDG effect.

The REDG effect could arise from enhancement in two different processes constituting the Peierls mechanism, kink-pair formation and kink migration. In the early stage of the movement of the screw segment C (Fig. 1 (a) and (b)) the dislocation is seen to proceed in a concave shape. Since the dislocation motion in such a concave motion is achieved by kink migration only, this fact indicates that the electronic enhancement takes place in the kink migration process. In the images that follow (Fig. 1(c)–(f)), the segment is seen to advance in a convex form. Since such a motion requires kink-pair formation, this behavior tells that the kink-pair formation is also enhanced by electron beam irradiation.

Another inference from the present results is that, if the electron-stimulated effect is brought about by the recombination enhanced defect reaction mechanism [15,16] (the phonon-kick model), the moving dislocations, that should be undecorated, act as non-radiative recombination centers. This is consistent with the report by Zaldivar et al. [5] on CL quenching in indented crystals. The dislocations that have been found to glide are basal dislocations and pyramidal dislocations both having the Burgers vector of a-type. The absence of the irradiation effects on the 60° segments A′ and B′ in Fig. 1 might indicate that these dislocations are electronically inactive. However, this interpretation is unlikely because, if the 30°-partials (either α- or β-type) common to 60° dislocations and screw dislocations were inactive so that they are unaffected by electron irradiation, the enhancement would not arise in the screw segments since the unstimulated component would retard glides of the perfect dislocations.

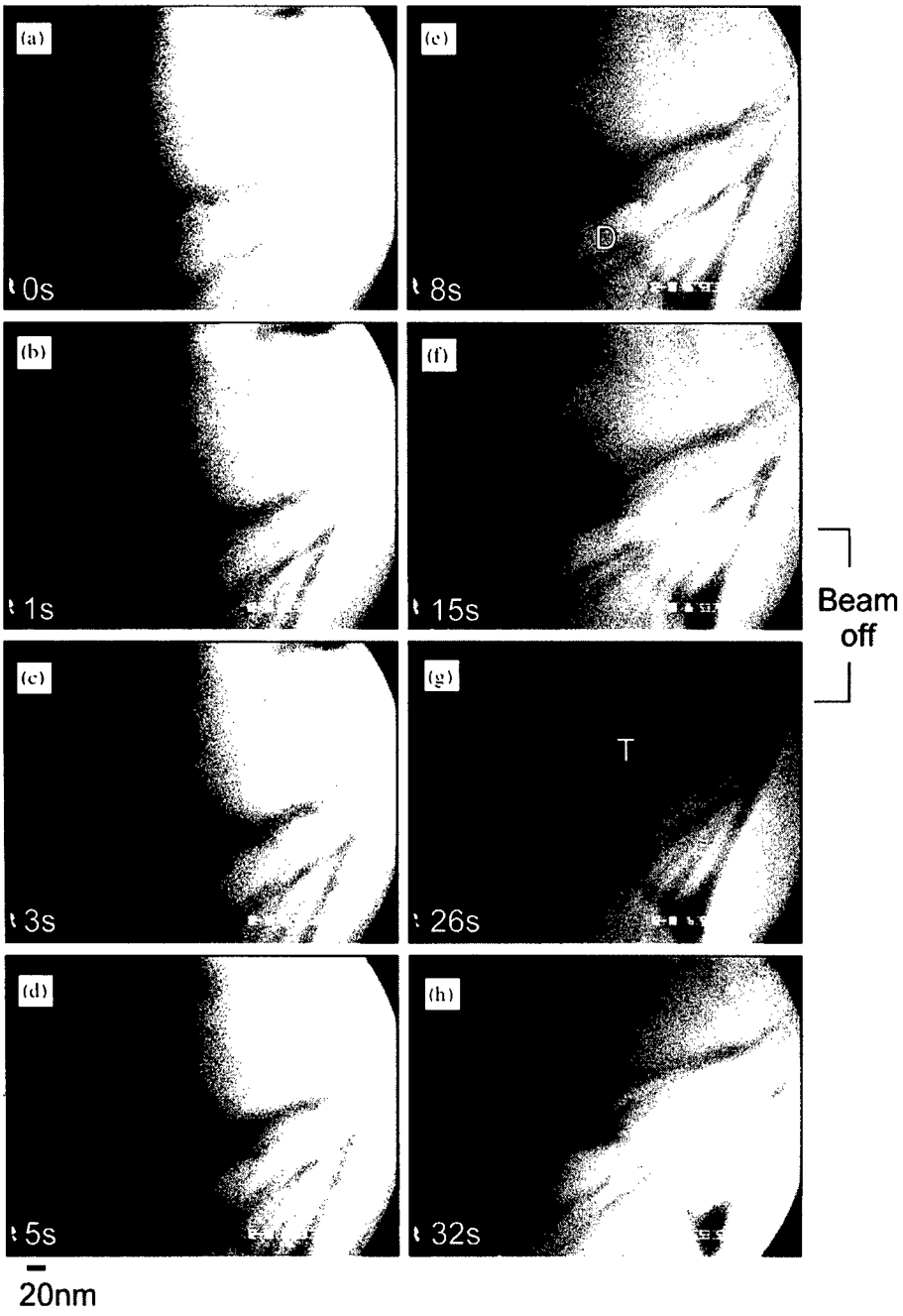

Fig. 4. A VTR image sequence showing glide of a dislocation segement D on a pyramidal $\{1\,\bar{1}\,0\,n\}$ plane in h-GaN. The electron beam was switched off between the frames (f) and (g).

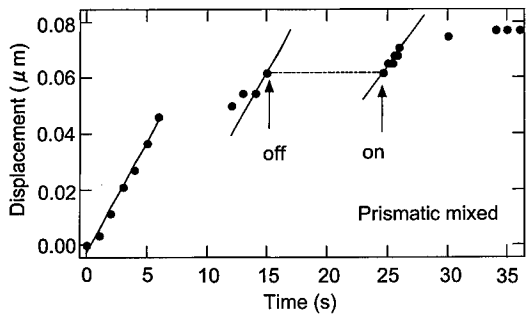

Fig. 5. The displacement versus time relation of the dislocation segment D in Fig. 4.

Acknowledgements

This work was supported by Grant-in-Aid for Scientific Research from MESC of Japan.

References

[1] S.D. Lester, F.A. Ponce, M.G. Craford, D.A. Steigerwald, Appl. Phys. Lett. 66 (1995) 1249.
[2] S. Nakamura, Science 281 (1998) 956.
[3] K. Maeda, S. Takeuchi, in: F.R.N. Nabarro, M.S. Duesbery (Eds.), Dislocations in Solids, Vol. 10, North-Holland, Amsterdam, 1996, pp. 443–504.
[4] T. Sugahara, H. Maosheng Hao, Y. Naoi, S. Kurai, S. Tottori, K. Yamashita, K. Nishino, L.T. Romano, Jpn. J. Appl. Phys. 37 (1998) L398.
[5] M.H. Zaldívar, P. Fernández, J. Piqueras, Semicond. Sci. Technol. 13 (1998) 900.
[6] A. Rocher, G. Jacob, J. Physique 39 (Suppl. 6) (1978) C2–121.
[7] K. Suzuki, S. Takeuchi, Philos. Mag. Lett. 79 (1999) 423.
[8] I. Yonenaga, J. Physique III 7 (1997) 1435.
[9] U. Messerschmidt, F. Appel, Kristal Technik 14 (1979) 1331.
[10] H. Alexander, in: F.R.N. Nabarro (Ed.), Dislocations in Solids, Vol. 7, North-Holland, Amsterdam, 1986, pp. 113–234.
[11] L. Sugiura, J. Appl. Phys. 81 (1997) 1633.
[12] K. Maeda, K. Suzuki, M. Ichihara, S. Takeuchi, J. Appl. Phys. 56 (1984) 554.
[13] G. Vanderschaeve, C. Levade, A. Faress, J.J. Couderc, D. Caillard, J. Physique III 1 (1991) C6–305.
[14] K. Maeda, K. Suzuki, M. Ichihara, Microsc. Microanal. Microstruct. 4 (1993) 211.
[15] J.D. Weeks, J.C. Tully, L.C. Kimerling, Phys. Rev. B 12 (1975) 3286.
[16] H. Sumi, Phys. Rev. B 29 (1984) 4616.

ELSEVIER

Physica B 273–274 (1999) 140–143

PHYSICA B

www.elsevier.com/locate/physb

Role of the defect microstructure on the electrical transport properties in undoped and Si-doped GaN grown by LP-MOVPE

J.-L. Farvacque[a,*], Z. Bougrioua[b], I. Moerman[b], G. Van Tendeloo[c], O. Lebedev[c]

[a]*LSPES, Université de Lille, Batiment C6, USTL, 59655 Villeneuve d'ascq, France*
[b]*INTEC, Gent University IMEC, Sint Pietersnieuwstraat 41, B-9000 Gent, Belgium*
[c]*EMAT, Department of Physics, University of Antwerp, B-2020 Antwerp, Belgium*

Abstract

Experimental results show that the room-temperature carrier mobility in bulk layers of undoped or Si-doped GaN grown by LP-MOVPE on sapphire substrate shows a sudden increase as soon as the carrier density exceeds a critical value of about 10^{18} cm^{-3}. We show that such a behavior can be theoretically reproduced by assuming that the columnar structure (i.e. the dislocation microstructure) is responsible for internal electronic barriers.

Keywords: GaN; Transport properties; Dislocations

1. Position of the problem

In the present state of the art, the GaN MOVPE growth on sapphire substrates leads to the appearance of columnar cells separated by walls mainly built from threading dislocations, some of them being also randomly distributed within the cells. In this paper we present a theoretical analysis of the role of this particular microstructure on the free carrier mobility. For the description of the dislocation effects, we consider their individual scattering potentials (core charge, strain fields) as well as their spatial distribution (dislocation walls).

We have measured the evolution of the Hall mobility and carrier density on several undoped and Si-doped GaN layers grown by low-pressure MOVPE on *C*-plane sapphire substrates using the two-steps procedure described in Ref. [1]. Silane was used as the dopant precursor. The carrier density measured at room temperature was found to increase linearly with the silane flow and to vary between 10^{17} and 10^{19} cm^{-3} [2]. As shown in Fig. 1, the corresponding Hall mobility versus the carrier density, at room temperature, exhibits a surprising behavior consisting of a low-mobility regime as long as the carrier density remains lower than typically 10^{18} cm^{-3} followed by a sudden increase within a factor which may reach 20 in some samples. To our best knowledge, such a behavior has not yet been reported. Mobility versus temperature has been respectively measured on samples belonging to either the low or the high mobility regime [3]. Most of the samples exhibit a two-channels conductivity. Fig. 2 shows the temperature dependence of the mobility contribution in the conduction band.

Parallely, the defect microstructure has been investigated for both kind of samples by TEM observations. As shown Figs. 3a and b, plane views perpendicular to the growth direction exhibit a columnar structure as usually reported. The dislocation distribution for both specimens is almost the same. They are generated at the interface and thread throughout the layer. We note, however, that the cell boundaries observed in undoped crystals are "well" shaped (well-marked contrasts) and that the various cells are more or less dislocation free. On the other hand, cell boundaries present in strongly doped materials look more "diffuse" and the

* Corresponding author. Tel.: + 33-3-20-43-48-67; fax: + 33-3-20-43-65-91.
E-mail address: jean-louis.farvacque@univ-lillel.fr (J.-L. Farvacque)

0921-4526/99/$ - see front matter
PII: S0921-4526(99)00431-7

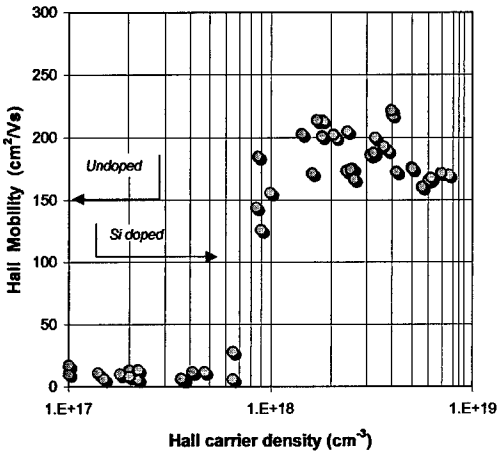

Fig. 1. Room-temperature carrier mobility versus the carrier density.

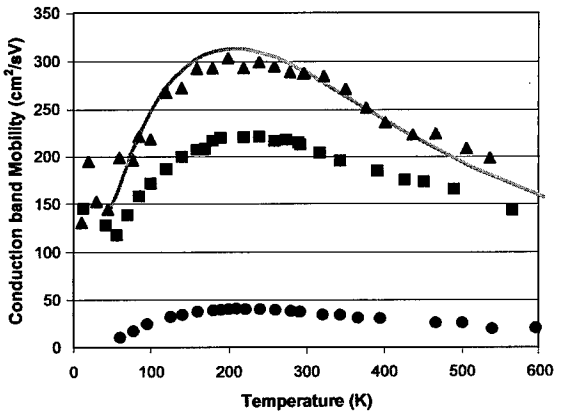

Fig. 2. Carrier mobility versus temperature: triangles: $n_{300\,K} = 3 \times 10^{18}\,cm^{-3}$, squares: $n_{300\,K} = 1.6 \times 10^{18}\,cm^{-3}$; circles $n_{300\,K} = 6 \times 10^{17}\,cm^{-3}$.

various cells also contain randomly distributed individual dislocations.

2. Theoretical analysis of transport

In view to understand the particular free carrier mobility behavior shown in Fig. 1, we have undertaken a theoretical description of the transport properties. We show, in the following, that a classical approach including the various classical scattering centers is unable to reproduce Fig. 1. Instead, we conclude that the present experimental results are likely described if we also introduce the presence of internal barriers leading to the modified mobility expression (4.1). Mainly, the present simulation of low-field transport properties is based on the use of the relaxation time approximation for solving Boltzmann's kinetic equation as long as scattering mechanisms are isotropic. It includes the standard scattering mechanisms like ionized impurities, acoustical and optical phonons, carrier–carrier scattering. However, anisotropic scattering centers (dislocations) which are of interest in the present study, cannot be properly taken into account in such approaches. Instead, we have used the concept of collision time tensor proposed in Ref. [4] for dealing with such anisotropic scattering centers. We now detail the various dislocation scattering mechanisms which have been introduced in our simulation.

Ab initio calculations unambiguously show that, in any studied semiconductor (see Ref. [5] for GaN), dislocation cores are strongly reconstructed and lead to band gaps which are generally free from deep states but which are systematically occupied by shallow states. These intrinsic shallow bound states are likely connected with the long-range strain field binding potentials. They have been numerically determined, solving the envelop function in the approximation of the effective mass [6]. In the particular case of GaN, these levels are found relatively deep and localized at 103 meV under the conduction band for threading dislocations whose lines are parallel to the *c*-axis. For other dislocation line orientations, the piezoelectric potential also has to be considered and leads to deeper ground states ranging between 150 and 250 meV. Moreover, extrinsic deep states associated with reconstruction defects or with the impurities of the Cottrell atmosphere may not be excluded. In any case, the dislocation traps are localized all along the dislocation line at very short distances from one another so that trapped carriers interact electrostatically. Their occupation rate is then selfconsistently regulated. Such effects have been included in the present calculation following the method described in Ref. [7] for the evaluation of the dislocation occupation rate.

There are mainly two ways by which dislocations act as scattering centers. As already noticed in the above section, the dislocation energy states, when filled, transform the defect into a charged line, the Coulomb potential of which acts as a scattering potential. Note that this scattering mechanism corresponds to the only one which is generally considered in the recent papers concerning GaN [8,9]. The dislocation strain field acts against the free carrier motion through the deformation potential and the piezoelectric coupling. These interactions have been included in the present calculation and numerical results show that they lead to scattering effects of the same order of magnitude than those associated with the dislocation core charge. However, in the particular case of wurtzite structures, owing to the shape of the piezoelectric tensor, this last contribution vanishes for a-edge and c-screw dislocations, i.e. for the threading dislocations [10].

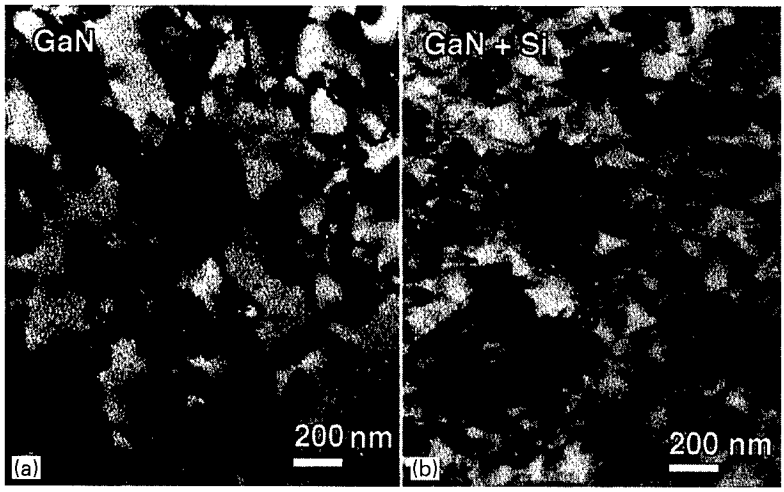

Fig. 3. TEM plane views showing the columnar structure in undoped (a) and strongly Si-doped GaN.

3. Discussion

Our simulation program, at room temperature, in low-doped, uncompensated and dislocation-free GaN ($N_D = 10^{15}\,cm^{-3}$) results in mobility values ranging between 1800 and 2200 $cm^{-2}\,s^{-1}\,V^{-1}$, in a good agreement with most of the previous published values [8]. Then, the various attempts to reproduce theoretically our experimental results shown in Figs. 1 and 2 allow us to draw the following comments:

- The full line shown in Fig. 2 demonstrates that good fits may always be done for the MOVPE samples chosen in the high-mobility regime. It is obtained by considering realistic parameter values for the sample represented by triangles: (i) a dislocation density of about $2 \times 10^{10}\,cm^{-2}$ (TEM) characterized by an energy level localized at 200 meV under the conduction band, (ii) a donor and acceptor density, respectively, equal to 8×10^{18} and $8 \times 10^{17}\,cm^{-3}$ (values consistent with those deduced from SIMS measurements [2]). Numerical values unambiguously indicate that dislocation scattering dominates the low-temperature range and that the effect of the deformation potential is quite equivalent to that of the core charge potential. Thus, at first sight, it is possible to get a correct theoretical description of the mobility of strongly Si-doped GaN, by just considering that it is regulated by a pure diffusion process, mainly governed by classical scattering centers (ionized impurities, phonons and dislocations).
- However, our simulation, based on a pure diffusion process, is unable to account for the low experimental values of the mobility found in the case of undoped materials, whatever the choice of the dislocation density and energy level and/or even the compensation ratio. Moreover, calculating the mobility versus the carrier density at room temperature does not allow to reproduce the behavior shown in Fig. 1.

Thus, assuming that the mobility is governed by a pure diffusion mechanism does not definitely allow to reproduce the experimental results observed in our MOVPE GaN materials. This suggests that some other mechanisms also control the mobility behavior. We note that the room-temperature effective density of states of the conduction band N_C is equal to $1.9 \times 10^{18}\,cm^{-3}$ (for an effective mass equal to $0.2m_0$). Thus, Fig. 1 covers two situations where the electronic gas starts being non-degenerated and progressively becomes fully degenerated. This implies that, at low dopant concentration, the carriers which participate in the conduction process are localized at the bottom of the conduction band. However, when the carrier density becomes larger than N_C, the carriers which participate in the conductivity are localized around the Fermi level E_F which quickly goes far above the bottom of the conduction band. Thus, if some internal barriers are present in the material, as already suggested in Ref. [11], they would not be able to strongly affect the carrier mobility as long as the barrier height is lower than the location of the Fermi level. On the contrary, such barriers would instantaneously decrease the conductivity in the low carrier density regime. It is straightforward to show that, in the presence of a barrier whose transmission power is $T(\varepsilon)$, the apparent current density is obviously given by

$$\mu_{app,j} = -\frac{e}{4\pi^3 n}\int T(\varepsilon_k)\left(\frac{\partial f_0}{\partial \varepsilon}\right)_k \tau_{D,j}(k) v_j^2(k)\,d^3k, \qquad (4.1)$$

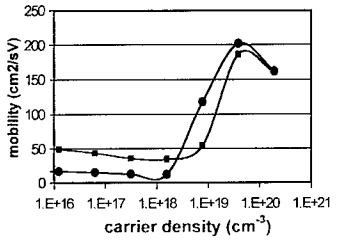

Fig. 4. Carrier mobility versus carrier density, simulated in the presence of a barrier: Squares: fixed barrier height $E_B = 0.15$ eV; circles: variable barrier height $E_B = 0.19$ eV for the low-mobility regime and $E_B = 0.13$ eV for the high-mobility regime.

where n is the carrier density and where the derivative of the f_0 Fermi–Dirac statistics has to be considered. $\tau_{D,j}$ is the component of the collision time tensor in the j-direction, $v_j(k)$ is the k state carrier velocity in direction j. Note that this last formula automatically accounts for both the thermal overcoming of the barrier and the tunneling possibility as soon as the barrier is sufficiently thin. Approximating the barrier by a squared potential, the theoretical mobility versus the free carrier density, deduced from Ref. (4.1) at room temperature, is shown in Fig. 4. The curve with "square" symbols is obtained considering a barrier with an identical height (0.15 eV above the bottom of the conduction band) for all the variously doped samples. The tunneling effect becomes noticeable when the barrier thickness falls below 10 nm and does not play a significant role in the present simulation. Mainly, our simulation displays the same features as those presented in Fig. 1. It clearly shows the existence of two mobility regimes versus the carrier density: (i) a low-mobility regime which slightly decreases with the carrier density, followed suddenly by a rapid increase after which the carrier mobility exactly behaves as if no internal barriers were present in the material (same temperature dependence, same order of magnitude). There is no reason to attribute the same barrier height for any value of the dopant density. This may be argued by the fact that the boundaries surrounding the various cells are not strictly identical as shown by electron microscopy. Furthermore, for larger dopant densities, screening effects are more efficient and may modify the barrier height. Consequently, considering a variable height barrier, leads to a better fit of the whole experimental behavior as shown by the curve with circle symbols. It is obtained attributing for the low-regime side, a barrier height of 0.19 eV while this barrier height is chosen to be 0.13 eV in the high-mobility side.

Thus, we conclude that the actual mobility behavior in columnar cell GaN materials is regulated by the presence of internal barriers probably associated by the particular dislocation microstructure arranged in the form of dislocation walls. The physical origin of such barriers may arise from the dislocation intrinsic properties themselves (strain fields, intrinsic states) as well as from exrinsic properties such as their impurity Cottrell atmosphere.

Acknowledgement

The authors are grateful to J. Harris for temperature measurements of the conductivity.

References

[1] W. van der Stricht, I. Moerman, P. Demeester, J.A. Crawley, E.J. Thrush, P.G. Middleton, C. Trager-Cowan, K. O'Donnell, Proceedings of MRS Fall Meeting, Boston, 1995, p. 231.
[2] Z. Bougrioua, I. Moerman, P. Demeester, E.J. Thrush, J.-L. Guyaux, J.C. Garcia, Proceedings of the eighth European Workshop on MOVPE, Prague, 1999, p. 61.
[3] Z. Bougrioua, J.-L. Farvacque, I. Moerman, P. Demeester, J.J. Harris, K. Lee, G. Van Tendeloo, O. Lebedev, E.J. Thrush, Proceedings ICNS3 Montpellier, 1999.
[4] J.-L. Farvacque, Semicond. Sci. Technol. 10 (1995) 914.
[5] J. Elsner, R. Jones, P.K. Sitch, V.D. Porezag, M. Eltsner, Th. Frauenheim, M.I. Heggie, S. Öberg, P.R. Briddon, Phys. Rev. Lett. 79 (1997) 3672.
[6] J.-L. Farvacque, Ph. François, Physica B 273–274 (1999) 995, These Proceedings.
[7] R. Masut, C.M. Penchina, J.-L. Farvacque, J. Appl. Phys. 53 (1982) 4964.
[8] N.G. Weimann, L. Eastman, D. Doppalapudi, H.M. Ng, T.D. Moustakas, J. Appl. Phys. 83 (1998) 3656.
[9] D.C. Look, J.R. Sizelove, Phys. Rev. Lett. 82 (1999) 1237.
[10] C. Shi, P.M. Asbeck, E.T. Yu, Appl. Phys. Lett. 74 (1999) 573.
[11] M. Fehrer, S. Einfeldt, U. Birkle, T. Gollnik, D. Hommel, J. Crystal. Growth 189/190 (1998) 763.

ELSEVIER

Physica B 273–274 (1999) 144–147

PHYSICA B

www.elsevier.com/locate/physb

Identification of Ag and Cd photoluminescence in ^{111}Ag-doped GaN

A. Stötzler[a,*], R. Weissenborn[a], M. Deicher[a], The ISOLDE Collaboration[b]

[a]*Fakultät für Physik, Universität Konstanz, P.O. Box 5560, D-78457 Konstanz, Germany*
[b]*CERN/PPE, CH-1211 Geneva 23, Switzerland*

Abstract

In order to unambiguously identify the chemical nature of Cd and Ag related optical transitions in GaN, epitaxial GaN layers were implanted with the radioactive isotope ^{111}Ag which decays into stable ^{111}Cd. This chemical transmutation was monitored by photoluminescence (PL) spectroscopy. Being an element specific property, the half-life of this decay was used to establish the chemical assignment of the optical transitions to a specific defect. We found that the Ag related transitions consist of a series of four single lines (1.610, 1.600, 1.594, and 1.573 eV), each accompanied by two phonon replicas separated by 63 meV. Cd produces two PL bands centered at 2.7 and 3.2 eV. Additional Cd-related single transitions at 3.341, 3.328, and 3.249 eV have been observed. Exponential fits to the PL intensities yield half-lives of $t_{1/2}^{Ag} = (7.61 \pm 0.27)$ d and $t_{1/2}^{Cd} = (7.60 \pm 0.27)$ d, respectively, in good agreement with the half-life of ^{111}Ag of 7.45 d.

Keywords: GaN; Ion implantation; Ag; Cd; Photoluminescence; Doping

1. Introduction

During the last years, there has been great interest in the study of the wide band gap semiconductor GaN, mainly due to its potential applications in optoelectronics in the UV and blue spectral region. As one of the most powerful tools for investigating defects in semiconductors, photoluminescence spectroscopy (PL) has been used to determine defect levels in GaN. But an unequivocal chemical identification of luminescence centers is often difficult due to the chemical blindness of PL and therefore the assignment of a luminescent transition to an element specific defect is often controversial. One element specific property that can be used to identify defect levels is the nuclear lifetime of a radioactive isotope undergoing a chemical transmutation. If the questioned level is due to a defect in which the parent or daughter isotope is involved the concentration of that defect will change with the characteristic time constant of the radioactive decay. This has been demonstrated for GaAs doped with radioactive ^{111}In decaying to ^{111}Cd, where ion implantation has been used for doping with the radioactive isotope and a quantitative link between PL intensity and defect concentration was obtained [1].

It has been established by PL that doping GaN with the group IIb element Cd leads to a blue luminescence band centered between 2.64 and 2.85 eV [2–5]. Ilegems et al. [2] associate the I_1-transition at 3.455 eV (also found by Lagerstedt et al. [3]) with an exciton bound to a Cd acceptor on a Ga site. They also report on additional Cd related lines (3.441 eV, 3.427 eV) lowered by 14 and 2×14 meV in energy relatively to the I_1-transition. In contrast to these results, only a blue Cd related luminescence band centered at 2.7 eV and in some cases an increased donor–acceptor-pair luminescence (DAP) at 3.26 eV [4,5] have been observed in GaN doped with Cd by ion-implantation. Having an atomic radius comparable to Cd, Ag should occupy a Ga lattice site (Ag_{Ga}) like Cd, and therefore act as double acceptor in GaN. Additionally, transition metals are known to produce deep

* Corresponding author. Tel.: + 49-7531-883866; fax: + 49-7531-883090.
E-mail address: arno.stoetzler@uni-konstanz.de (A. Stötzler)

0921-4526/99/$ - see front matter
PII: S0921-4526(99)00432-9

levels in the midgap, which often act as very efficient recombination centers [6]. A deep luminescence band centered at 1.52 eV has been attributed to Ag related defects by Pankove et al. [4]. But due to the high intrinsic defect concentration in GaN [7], and the remaining implantation damage even after annealing, this assignments are not conclusive. The aim of the experiment presented here is to uniquely identify the bands created by Cd and Ag in GaN.

2. Experimental details

The GaN samples used were 1.5 μm epitaxial layers grown on AlN/c-sapphire by metal–organic vapor-phase epitaxy (MOVPE) purchased from CREE Research. The nominally undoped layers were n-type with a free carrier concentration less than 5×10^{16} cm^{-3}. The samples were doped by ion implantation at room temperature with ^{111}Ag at the ISOLDE mass separator facility at CERN (Geneva). The implantation energy was 60 keV and a maximum dose of 3×10^{12} ions/cm^2 was used. To serve as reference, a part of the sample was not implanted. In order to reduce the implantation induced damage, the sample was annealed at 1270 K for 10 min in a sealed quartz ampoule with nitrogen gas at a pressure of about 1 bar at room temperature. The isotope ^{111}Ag transmutes into stable ^{111}Cd via a β-decay with a half-life of 7.45 d. Due to the radioactive decay the concentration of Ag decreases while the Cd concentration increases with time. Thus, the PL intensity of radiative transitions resulting from defects involving Ag or Cd atoms have to be correlated with the half-life of ^{111}Ag.

The PL experiments were carried out at 4.2 K using a He flow cryostat. The luminescence was excited by the 325 nm line of a HeCd laser with an excitation density of 160 Wcm^{-2}. The luminescence was dispersed using a 0.75 m grating monochromator and detected with a cooled GaAs-photomultiplier.

3. Results and discussion

Fig. 1 shows the PL spectra recorded after ion implantation and annealing. All spectra were recorded within 68 d after the implantation. For clarity only 7 of the 20 recorded spectra are shown. To minimize the intensity variations due to the experimental limitations in matching the same sample spot and focusing reproducibly onto the entrance slit of the monochromator it is necessary to normalize all spectra. In our case it is important to choose a transition for the normalization which PL intensity is independent from the Cd or Ag concentration. For this reason we normalize all spectra to the intensity of the yellow luminescence (YL) at 1.97 eV. In contrast to that a normalization to the I_2 line for

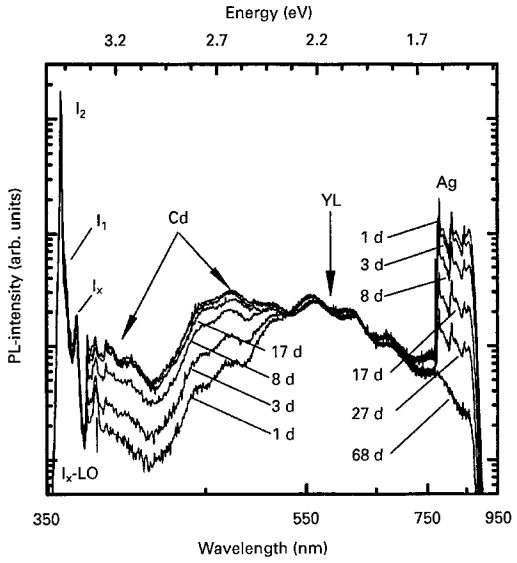

Fig. 1. Photoluminescence spectra of ^{111}Ag-doped GaN recorded at 4 K between 1 and 68 d after implantation and annealing. All spectra are normalized to the intensity of the yellow luminescence (YL) at 1.97 eV.

example, is not suitable since this transition overlap with to the I_1 transition which is believed to be Cd related [2,3].

The luminescence of the donor-bound exciton (I_2 at 3.471 eV) [8] and the transition labeled I_X at 3.395 eV and its LO phonon replica at 3.303 eV (I_X-LO) are observed in all spectra. The origin of the I_X line is not absolutely clear yet, but we do not observe any changes in the intensity of this transtion and we also observe this transitions in samples which are not implanted with Ag or Cd. In some samples the phonon replica I_2-LO of the donor-bound exciton has been observed at the lower energy tail of this transition. At 2.2 eV the commonly observed yellow luminescence (YL) can be seen. The oscillations on the YL are due to Fabry-Perot interferences between the GaN/sapphire interface and the GaN surface. The spectrum recorded one day after implantation shows a strong PL band centered at 1.5 eV not present in the unimplanted reference part of the sample. Only weak luminescence between 2.4 and 3.3 eV can be observed.

During the following 17 d, the PL intensity between 2.7 and 3.2 eV is increasing while the intensity of the 1.5 eV luminescence is decreasing continuously. After 70 d, no luminescence at 1.5 eV can be detected any more and no further increase of the two higher energetic PL bands can be observed. From this observations it is clear, that these bands decreasing and increasing in intensity with time have to be correlated with Ag or Cd, respectively.

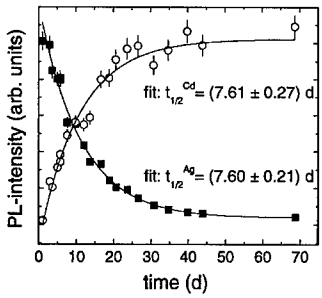

Fig. 2. Normalized PL intensity of the Cd band (circles) and the Ag band (squares) in GaN as a function of time. The solid lines correspond to exponential fits to the data using Eqs. (1) and (2).

The detailed spectral features of the PL bands described above will be discussed later (Figs. 3 and 4). In Fig. 2, the integral PL intensities of the Ag and Cd related PL bands are plotted as a function of time. The solid lines represent exponential fits to the data using the following fitting functions:

$$I^{Ag}(t) = I_0^{Ag} e^{-\ln 2t/t_{1/2}} \quad (1)$$

$$I^{Cd}(t) = I_0^{Cd}(1 - e^{-\ln 2t/t_{1/2}}). \quad (2)$$

These fits yield half-lives of $t_{1/2}^{Ag} = (7.60 \pm 0.21)$ d and $t_{1/2}^{Cd} = (7.61 \pm 0.27)$, respectively, both in very good agreement with the nuclear half-life of ^{111}Ag ($t_{1/2} = 7.45$ d) [9]. Since nothing else changes in the ^{111}Ag-doped sample but the decreasing Ag and the increasing Cd concentrations, the decreasing luminescence at 1.5 eV must be caused by recombination centers involving Ag. On the other hand, the two increasing PL bands centered at 2.7 and 3.2 eV have to involve Cd defects. Additionally, one must conclude that the involved defects contain only one Cd and Ag atom, respectively, since the intensities change exactly with the half-life of the radioactive decay. The involvement of more than one Ag or Cd atom in these defects would show up in slower time constants. The I_1 line shows no changes in intensity during the whole measure period, so we conclude that this transition is not due to an exciton bound to the Cd acceptor in contrast to earlier assignments [2,3]. We want to point out, that this conclusion is not compelling. It may be possible that we are not able to distinguish between the Ag bound exciton and the Cd bound exciton if the energy difference is below our spectral resolution.

Fig. 3 shows a blow-up of the Cd related luminescence recorded 68 d after the implantation. For comparison the spectrum taken 1 d after implantation is also shown. The blue luminescence band centered at 2.7 eV is clearly visible, which has also been observed by several authors in Cd doped GaN [2–5,10]. Our results support the radiation mechanism proposed by Bergman et al. which

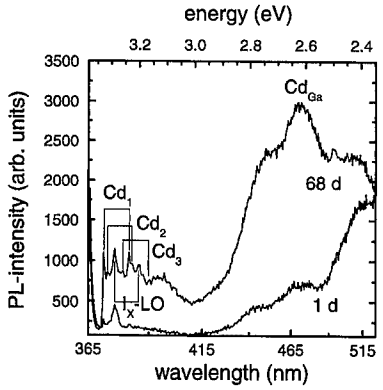

Fig. 3. Photoluminescence spectra of ^{111}Ag-doped GaN, recorded at 4 K one day after implantation and annealing and after 68 d, when nearly all Ag ions have transmuted into Cd.

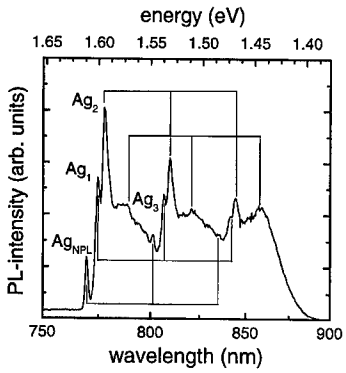

Fig. 4. Photoluminescence spectrum of ^{111}Ag-doped GaN measured at 4 K one day after implantation and annealing.

assumes the emission is due to the substitutional Cd_{Ga} single acceptor [10], since the recombination mechanism includes exactly one Cd atom. Additionally, the transition Cd_1 at (3.341 eV) and its LO phonon replica were found to be Cd related. We assume that the transitions Cd_2 (3.328 eV) and Cd_3 (3.272 eV) are also Cd related in spite of being poorly resolved in Fig. 3. We observe these transitions also in GaN implanted with stable Cd ions but the appearance and the intensity ratio between these three lines strongly depends on the sample quality. The line marked with I_X-LO corresponds to a phonon replica of the I_X transition discussed above and is also present in the PL spectrum of the unimplanted reference and thus not Cd related.

Fig. 4 shows a blow-up of the 1.5 eV emission, recorded one day after the implantation. Our results undoubtedly confirm the assignment by Pankove et al. that this luminescence band is Ag-related [4]. Fig. 4 shows clearly, that the Ag-related luminescence consists of a

series of four single transitions. Each line is accompanied by two additional lines separated by 63 and 126 meV, respectively. We assume that these transitions are caused by TO^L phonon replicas, although their energy has been determined to be 65.7 meV [11], but this value can be shifted by internal stress present in the GaN layer. Such shifts in energy have been observed by Kaschner et al. as a result of biaxial stress due to the incorporation of dopants [12]. As mentioned above, the blue emission results from a Cd atom at a Ga site. Since the recoil energy of the radioactive decay is much lower than the displacement energy of an atom from its lattice site (about 5 eV compared to 25 eV [13]) one can exclude a displacement of the Ag atom during its decay. As a consequence of that, also Ag is occupying a Ga site and therefore should act as a double acceptor.

4. Conclusions

In summary, using radioactive Ag isotopes we have proven that doping GaN with Ag produce a deep luminescence band centered at 1.52 eV, which is superimposed by four single transitions. Our results also confirm the assignments of the blue luminescence band centered at 2.7 eV to a Cd related defect. Furthermore transitions at 3.341, 3.328, and 3.272 eV were attributed to Cd. From the time dependence of the Ag and Cd related luminescence we conclude, that all recombination centers include exactly one Ag or Cd atom, respectively.

Acknowledgements

This work has been supported by the Bundesminister für Bildung, Wissenschaft, Forschung und Technologie under Grant No. 03-DE5KO1-6.

References

[1] R. Magerle, A. Burchard, M. Deicher, T. Kerle, W. Pfeiffer, E. Recknagel, Phys. Rev. Lett. 75 (1995) 1594.
[2] M. Ilegems, R. Dingle, R.A. Logan, J. Appl. Phys. 43 (1972) 3797.
[3] O. Lagerstedt, B. Monemar, J. Appl. Phys. 45 (1974) 2266.
[4] J.I. Pankove, J.A. Hutchby, J. Appl. Phys. 47 (1976) 5387.
[5] I.Sh. Khasanov, A.V. Kuznetsov, A.A. Gippius, S.A. Semiletov, Sov. Phys. Semicond. 17 (1983) 187.
[6] A.G. Milnes, Deep Impurities in Semiconductors, Wiley, New York, 1973.
[7] T. Mattila, R.M. Nieminen, Phys. Rev. B 55 (1997) 9571.
[8] A.K. Viswanath, J.I. Lee, S. Yu, D. Kim, Y. Choi, C. Hong, J. Appl. Phys. 84 (1998) 3848.
[9] V.S. Shirley, S.Y. Frank Chu (Eds.), Table of Isotopes, CD ROM Edition, Version 1.0, Wiley, New York, 1996.
[10] P. Bergman, G. Ying, B. Monemar, P.O. Holtz, J. Appl. Phys. 61 (1987) 4589.
[11] L. Bergman, D. Alexson, P.L. Murphy, R.J. Nemanich, M. Dutta, M. Stroscio, C. Balkas, H. Shin, R.F. Davis, Phys. Rev. B 59 (1999) 12977.
[12] A. Kaschner, H. Siegle, A. Hoffmann, C. Thomsen, U. Birkle, S. Einfeldt, D. Hommel, MRS Int. J. Nitride Semicond. Res. 4S1 (1999) G3.57.
[13] U.V. Desnica, N.B. Urli, B. Etlinger, Phys. Rev. B 15 (1977) 4119.

ELSEVIER

Physica B 273–274 (1999) 148–151

PHYSICA B

www.elsevier.com/locate/physb

Cathodoluminescence intensity and dislocation contrast evolutions under electron beam excitation in epitaxial GaN laterally overgrown on (0 0 0 1) sapphire

S. Dassonneville[a], A. Amokrane[a], B. Sieber[a,*], J.-L. Farvacque[a], B. Beaumont[b], V. Bousquet[b], P. Gibart[b], K. Leifer[c], J.-D. Ganiere[d]

[a]*Laboratoire de Structure et Propriétés de l'Etat Solide, UPRESA 8008, Bâtiment C6, Université des Sciences et Technologies de Lille, 59655, Villeneuve d'Ascq, Cedex, France*

[b]*CRHEA-CNRS, Parc Sophia Antipolis, 06560 Valbonne, France*

[c]*CIME, Ecole Polytechnique Fédérale de Lausanne, Switzerland*

[d]*IMO, Ecole Polytechnique Fédérale de Lausanne, Switzerland*

Abstract

We describe the first stage of the evolution of CL spectra, intensity and dislocation contrast under low keV electron beam for ELO-GaN with a low dislocation density. The UV and yellow intensities are decreased by beam irradiation. We have observed a broadening of the UV peak towards low energies followed by a red shift. This is explained in terms of an electron beam activation of non-radiative centers which relax partially the compressive strain. The dislocation contrast is lowered, but the dislocations become more non-radiative. We suggest that dislocations are preferential ways for the flux of non-radiative centers from the coalescence boundaries to the bulk.

PACS: 61.72.Ji; 61.72.Qq; 61.72.Ff; 77.84.Bv; 78.60.Hk

Keywords: GaN; Dislocations; Cathodoluminescence

1. Introduction

Despite the presence of a high dislocation density (10^8–10^{10} cm^{-2}), the band edge recombination in gallium nitride epilayers has a very large luminescence efficiency, compared to that exhibited by other III–V semiconducting compounds. So, in the past, dislocations in GaN have been thought not to be detrimental to the optical properties of this material. Only very recently, refutation of this statement came from cathodoluminescence (CL) imaging experiments which evidenced that dislocations quench the band edge UV luminescence [1–4]. Such experiments are more easily done on epitaxial laterally grown (ELO) GaN epilayers where the dislocation density is small enough ($\sim 10^7$–10^8 cm^{-2}) to allow spatially resolved CL imaging of dislocations [3–5]. On the other hand, an important pre-requisite to the development of gallium nitride as blue/UV lasers is the stability of its optical properties under photon and/or electron beam injection. But surprisingly, not many studies have been devoted to this subject [6–8]. In this paper we report on the evolution, under electron beam injection, of the CL intensity of bulk GaN as well as of dislocation contrasts. In situ irradiations of an ELO GaN specimen were made in a Cambridge scanning electron microscope (SEM) at 90 K; CL plan-view experiments, performed in the same experimental conditions that beam injection, were used to follow the luminescence variations.

2. Experimental

The main results presented here have been obtained after electron irradiation of the specimen at 10 kV, which

* Corresponding author. Fax: + 33-3-20-43-65-91.
E-mail address: brigitte.sieber@univ-lille1.fr (B. Sieber)

0921-4526/99/$ - see front matter
PII: S0921-4526(99)00434-2

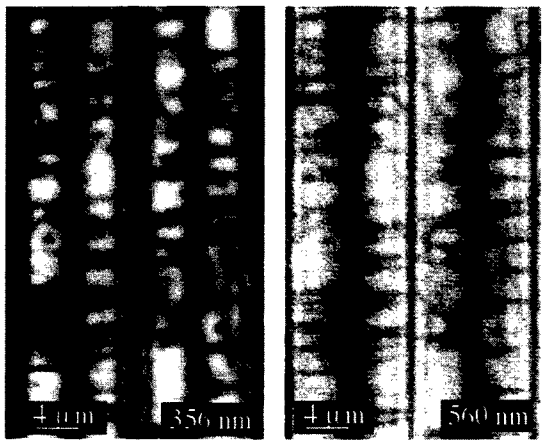

Fig. 1. Monochromatic UV and yellow plan-view CL images of two stripes of the ELO GaN specimen, recorded at 90 K before irradiation. The vertical dark line located in the middle of both images corresponds to the GaN seed. The horizontal dark lines are bent dislocations which end up on the coalescence boundaries.

gives the best spatial resolution of CL images. The time dependence of the CL signal varies with the experimental conditions: lower accelerating beam voltages and larger beam currents lead to a faster evolution. We have found that, at 10 kV, a beam current of 10 nA is adequate to follow the first stage of the luminescence evolution, as well as to change the recombination properties of the material in a reasonable time, i.e. here after scanning a 54 µm × 54 µm area in 90 min. The specimen temperature was 90 K. Very similar results have been obtained at 5 K. The CL signal was collected by an Oxford mirror and detected by a GaAs photomultiplier. Plan-view CL spectra and monochromatic images were recorded after irradiation nearly every 10 min. The ELO specimen of GaN has been grown on a (0 0 0 1) sapphire substrate by MOVPE with a two-step process in a home-made vertical reactor at atmospheric pressure using trimethyl species and NH_3. After the growth of a first GaN epilayer at 1080°C, on the sapphire substrate, a silicon nitride mask is deposited and stripe patterns are opened in this mask by photolithography to form a grating with a 10 µm period and 5 µm wide stripes typically. Stripes are aligned along $[1\,0\,\text{-}\,1\,0]_{GaN}$. Then, GaN seeds in the form of pyramids are grown at 1040°C. The growth temperature is then raised up to 1120°C to favor lateral growth from the seeds. A 2 µm thick GaN cap layer is deposited on the fully coalesced structure. This two step method reduces the dislocation density to few 10^7 cm^{-2} even above the seeds. The specimen is nominally undoped, and the electron concentrations in the range 5×10^{16}–10^{17} cm^{-3}. The extrinsic yellow band (YB) being absent in the cap layer, we have studied a piece of the specimen which was thinned from 9 to about 7 µm by ionic etching, in order to record the evolution of both the UV and yellow bands.

3. Results

3.1. CL mapping of two step ELO GaN

Lateral bending of dislocations from the GaN seed during the ELO process is well evidenced in Fig. 1. The dislocations are imaged, in both UV and yellow CL images, as dark lines perpendicular to the stripe direction. They end up on the coalescence boundary parallel to the stripe direction. A one-to-one correspondence between the dislocations is found in the UV and in the yellow images. Furthermore, no luminescence associated with dislocations was observed at larger wavelengths, until 1.1 µm. This evidences that they act as efficient non-radiative recombination centers. This observation definitely rules out the possibility that dislocations are at the origin of the yellow band. The spatial resolution of the CL images shows that they are surrounded by a cloud of non-radiative centers. Thus, dislocations are gettering centers for impurities and/or point defects. This is confirmed by the large value of the dislocation contrasts which, before electron beam irradiation, are in the range 20–50%.

3.2. Evolution of CL spectra and intensity under beam irradiation

The CL spectra of GaN are modified by electron beam irradiation, whatever is the specimen temperature. The intensity of the UV peak, which corresponds to the decay of the free exciton, decreases by about 50% in the first 20 mn, then broadens to lower energies, and red shifts by about 2 meV (Fig. 2). The full-width at half maximum increases from 25 meV initially to 33 meV after 90 min of irradiation. In parallel, the intensity of the yellow band

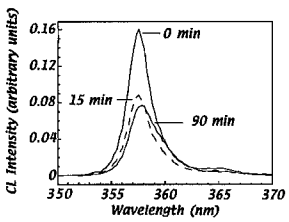

Fig. 2. Evolution of the UV part of the CL spectrum under electron beam irradiation, performed at 10 kV with a beam current of 10 nA. The specimen temperature is 90 K.

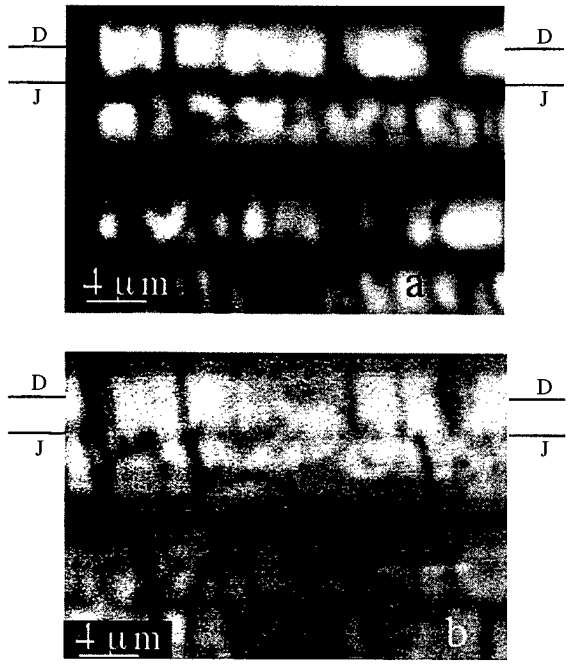

Fig. 3. Plan-view CL images of the same area recorded at 358 nm (a) before and (b) after 90 min irradiation.

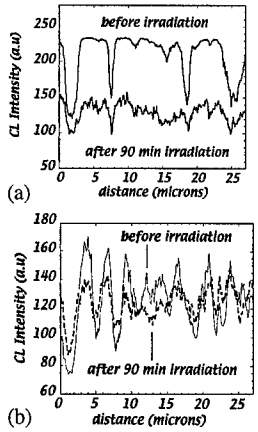

Fig. 4. Semi-quantitative CL line profiles. (a) Across dislocations (line D in Fig. 3), (b) along the coalescence boundary (line J in Fig. 3). The profiles have been recorded from the images taken with the same settings, and an offset line different from zero.

over the mask decreases by about a factor of 1.4, showing that there is no correlation between their effective evolution. No extra peak was detected after irradiation.

3.3. Evolution of dislocation contrast under beam irradiation

Figs. 3 and 4 display monochromatic ($\lambda = 358$ nm) CL images and semi-quantitative CL profiles recorded before and after 90 min of irradiation. They show that (i) the CL contrast of dislocations is lowered by electron irradiation, due to the larger decrease of the bulk. Very few or no dislocations are visible anymore after 90 min of irradiation. In fact, remaining dislocations exhibit a higher electrical activity after irradiation (Fig. 4) (ii) in the coalescence boundaries, the CL intensity of the darkest areas increases whereas it decreases for the brightest areas. The CL intensity along the boundary becomes homogeneous and tends towards that of the material located around it.

4. Discussion

Mainly, our experimental results show that the CL intensity of the whole spectrum (UV and YB) decreases under beam injection. It was suggested in Ref. [9] that such a decrease, and more especially in the UV and blue range spectrum side, could be due to a carbon contamination of the surface which acts as an absorption layer in the blue range. In the light of our results, this mechanism may be ruled out since a C deposited layer would equivalently affect any contrasts observed in same (UV or blue side) monochromatic image. Instead, we observe that the CL intensity decreases less quickly over dislocation areas than in bulk regions and, moreover, that it increases in the darkest regions of the coalescence boundaries. We then conclude that the whole effect is not a C induced artefact, but corresponds either to the introduction of non-radiative centers which compete with any initial radiative mechanisms, or to the destruction of radiative paths. Owing to the small accelerating voltage of the electron beam and the low incident electron flux [7,8], the direct creation of Frenkel pairs may be ruled out. As a consequence, we conclude that (i) some electron/hole pairs recombination mechanisms or again (ii) the beam induced electric field (due to secondary electron emission and beam charge deposition) activate the diffusion of points defects or impurities initially present in the structure. The activated displacement of initial point defects or impurities is particularly well supported in experiments where the degradation is obtained using a fixed position of the electron beam: a dark spot appears with time, surrounded by a brightest area.

The broadening of the intrinsic UV peak (Fig. 2) reflects that, within the area corresponding to the minority carrier generation volume, some spatial fluctuations of the band gap are induced by the incident electron beam. Parallely, the global red shift indicates that these fluctuations result into a strain relaxation. The material being initially in compression, it is likely that vacancy defects are necessarily involved in the process. Their activated

diffusion, which may also generate antisites, (i) may start breaking some initial complex defects in which they are involved (like V_{Ga}–Si, V_{Ga}–O or again V_{Ga}–H) restituting 'free vacancies' and (ii) may finally results into the formation of more elaborate defects, such as clusters or intrinsic dislocation loops, capable of strain relaxing the material. Both mechanisms result into the destruction of radiative paths (decomplexation) or in the appearance of non-radiative centers like dislocation loops which justifies the CL decrease.

As soon as the degradation is done in the scanning mode, it is observed that the whole areas between dislocations as well as the dislocations lose 'homogeneously' their UV and yellow luminescence. In this case, it is no more possible to evoke a redistribution of point defects initially distributed in the bulk. We therefore expect that some defects sources are also present in the structure. Obviously, such (vacancy) sources are naturally found in the coalescence boundaries which are probably made of vacuum areas, threading dislocations and impurities. Thus we expect that a flux of free vacancies is activated from the coalescence boundaries towards the material or, equivalently, a flux of matter is activated from the bulk towards these boundaries. This would explain why the luminescence recorded along the boundaries (Fig. 4a) decreases in the brightest areas while it increases in the darkest regions: the vacuum areas being progressively filled by matter and crystallographically reconstructed.

The UV and yellow luminescence at dislocations also decreases, but in a smaller relative ratio than that of the bulk. We speculate that, since dislocations may only end at the free surfaces of the coalescent boundaries (i.e. vacuum areas), they may act as preferential ways for the flux of matter (some pipe diffusion) and constitute the easiest ways for the vacancies flux towards bulk regions. However, their defect atmosphere is already quite saturated by points defects so that they are preferentially emitted towards the bulk and used for its strain relaxation. This would explain why their final contrasts become thinner.

The previous speculations which imply that a distribution of points defects more or less arranged in intrinsic dislocation loops or clusters is under investigation by transmission electron microscopy.

Acknowledgements

This work has been undertaken under the PICs 630. We greatly aknowledge C. VanMansart for his technical help in CL experiments.

References

[1] S.J. Rosner, E.C. Carr, M.J. Ludowise, G. Girolami, H.I. Erikson, Appl. Phys. Lett. 70 (1997) 420.
[2] T. Sugahara, H. Sato, M. Hao, Y. Naoi, S. Kurai, S. Tottaori, K. Yamashita, K. Nishino, L. Romano, S. Sakai, Jpn. J. Appl. Phys. 37 (1998) L398.
[3] S.J. Rosner, G. Girolami, H. Marchand, P.T. Fini, J.P. Ibbeston, L. Zhao, S. Keller, U.K. Mishra, S.P. DenBaars, J.S. Speck, Appl. Phys. Lett. 74 (1999) 2035.
[4] B. Beaumont, V. Bousquet, P. Vennéguès, M. Vaille, A. Bouillé, P. Gibart, S. Dassonneville, A. Amokrane, B. Sieber, Third International Conference On Nitride Semiconductors, Montpellier, 5–9 July, 1999.
[5] B. Beaumont, M. Vaille, G. Nataf, A. Bouillé, J.-C. Guillaume, P. Vénnègues, S. Haffouz, P. Gibart, MRS Int. J. Nitride Semicond. Res. 3 (1998) 20.
[6] M. Herrera Zaldivar, P. Fernandez, J. Piqueras, J. Solis, J. Appl. Phys. 85 (1999) 1120.
[7] F.D. Auret, S.A. Goodman, F.K. Koschnick, J.-M. Spaeth, B. Beaumont, P. Gibart, Appl. Phys. Lett. 74 (1999) 407.
[8] I.A. Buyanova, Mt Wagner, W.M. Chen, B. Monemar, J.L. Lindström, H. Amano, I. Akasaki, Appl. Phys. Lett. 73 (1998) 2968.
[9] M. Toth, K. Fleischer, M.R. Phillips, MRS Int. J. Nitride Semicond. Res. 4S1 (1999) G3.30.

ELSEVIER

Physica B 273–274 (1999) 152–163

PHYSICA B

www.elsevier.com/locate/physb

Spectroscopic studies of H-decorated interstitials and vacancies in thin-film silicon exfoliation

Y.J. Chabal*, M.K. Weldon, Y. Caudano, B.B. Stefanov, K. Raghavachari

Bell Laboratories, Lucent Technologies, 600 Mountain Avenue, Murray Hill, NJ 07974, USA

Abstract

In this paper, we review the pivotal role that defects (in particular vacancy structures) play in driving the H-induced exfoliation of Si. We highlight the central role that infrared spectroscopy has played in delineating the microscopic details of the exfoliation process. We show that when the results of such spectroscopic studies are combined with those obtained using a variety of other experimental probes as well as ab initio quantum chemical cluster calculations, an unambiguous mechanistic picture emerges. Specifically we find that H-terminated vacancy structures drive the formation of internal surfaces into cracks where H_2 is then evolved, resulting in the build-up of sufficient internal pressure to cause lift-off of the overlying Si. The role of coimplantation of He is also discussed.

1. Introduction

In 1995, the SmartCut™ process was described in the general literature [1,2]. The method provides an elegant way to exfoliate a thin crystalline Si layer onto an oxidized silicon wafer, by means of mono-energetic H-ion implantation of a wafer, a bonding step to a support (or handle) wafer, and then subsequent annealing (Fig. 1). While it was known that a medium dose of H + ions (5×10^{16}/cm^2) could lead to blistering, the central idea behind the SmartCut™ process is the realization that, with a support (e.g. another wafer), the blistering can be turned into a uniform exfoliation over the whole wafer surface with a thickness variation of only $\pm$ 50 Å. In so doing, the technique then becomes an ideal way to make silicon-on-insulator (SOI) wafers which are comprised of a thin crystalline film (500 Å — 1 μm thickness) on top of a silicon dioxide layer grown on the handle wafer [3]. It combines the advantages of the two more traditional ways of manufacturing SOI wafers, the separation by implantation of oxygen (SIMOX) and bonded-and-etch back silicon-on-insulator (BESOI), without the drawbacks: buried oxide thickness limitation (<2000 Å) for SIMOX and poor SOI thickness uniformity ($\pm$ 5000 Å) for BESOI [4].

As mentioned above, the SmartCut™ process depends critically on three steps: ion implantation, wafer joining, and annealing. The rapid development of this process to full production over the last five years can be largely attributed to an exquisite refinement of the implantation doses and conditions, the cleaning step prior to wafer joining and the rigorous annealing sequence. Its success is thus mostly due to excellent "engineering" rather than a thorough scientific understanding of the microscopic phenomena leading to exfoliation. The initial characterization, based on transmission electron microscopy (TEM) images of the implanted region [1,5], revealed the presence of cracks in Si samples implanted with 10^{17} H + /cm^2 and annealed to 400–500°C, but the underlying physics and chemistry that led to the development of such internal cracks was completely unexplored.

The purpose of this paper is to review the infrared spectroscopic studies of the thermal evolution of H-implanted Si wafers, along with complementary results from TEM, forward recoil scattering (FRS), atomic force microscopy (AFM) and mass spectrometry, that have been key in providing a mechanistic picture of the exfoliation process [6,7]. Along the way, it will be clear that a definitive assignment of the spectral features of H-defects in implanted/annealed silicon is critical. To this end, the importance of the many careful studies of

* Corresponding author. Tel.: + 1-908-582-4193; fax: + 1-908-582-3901.

E-mail address: yves@physics.lucent.com (Y.J. Chabal)

0921-4526/99/$ - see front matter
PII: S0921-4526(99)00435-4

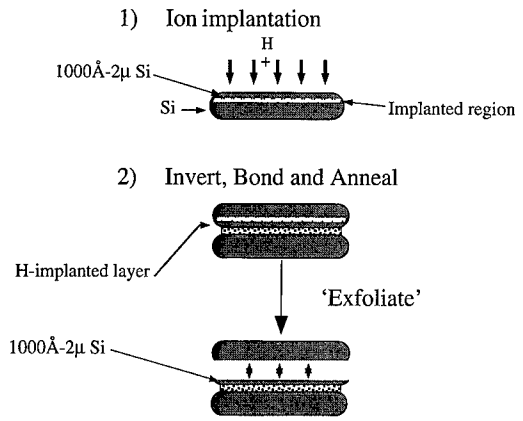

Fig. 1. Schematic illustration of the commercial SmartCut™ process, in which an oxidized Si wafer is pre-implanted with H^+, then joined to a second (handle) wafer and annealed, resulting in the direct formation of a high-quality SOI substrate.

H-decorated interstitials and vacancies that have emerged over the last decade cannot be overestimated. However, it is important to note that the H-implantation conditions leading to exfoliation are drastically different from those used in the exhaustive H-induced defect studies Bech Nielsen and coworkers [8,9]. In the latter, the implanted hydrogen is well isolated from other hydrogen by using a range of implantation energies (i.e. a range of different implantation depths). In contrast, to achieve exfoliation, it is critical that mono-energetic ions be used so as to achieve a local hydrogen density that is a couple of orders of magnitude higher than the hydrogen solubility in silicon. As a result, the interaction among implanted hydrogen atoms is significant, leading not only to defect agglomeration (key to exfoliation) and a tendency for H_2 to evolve into void spaces but also to a strong inhomogeneous broadening of Si–H vibrational lines. This inhomogeneous broadening precludes the use of low temperature spectroscopy to sharpen the spectral lines and makes the assignment particularly challenging. Consequently, it has become necessary to extend the vibrational characterization to include not only the Si–H stretching modes but also the accompanying bending modes in order to make definitive assignments. We will therefore highlight our recent efforts to measure and calculate the bending vibrations of VH_x vacancy defects in silicon.

2. Exfoliation by H implantation

The H-induced blistering of Si is, on first inspection (Fig. 2a), reminiscent of the well-known phenomenon of ion-implantation-induced blistering of metals under high implantation doses (10^{17}–10^{20} cm^{-2}). However, the

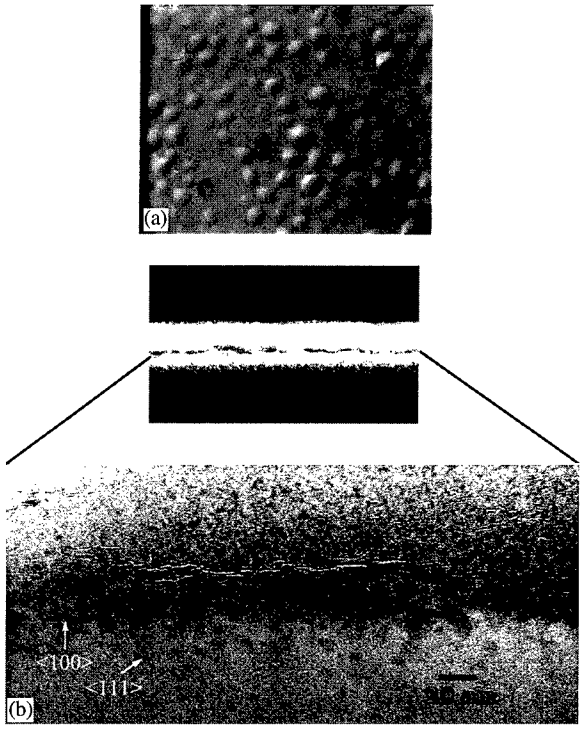

Fig. 2. (a) Optical micrograph of surface of exfoliated sample (Mag: ×80); (b) Low-resolution and high-resolution cross-sectional TEM images of Si(1 0 0) implanted with 1×10^{17} H/cm^2 after annealing to 475°C.

mechanism leading to the industrially viable process in silicon is in fact quite different; in metals, there is little chemical interaction between hydrogen and the lattice so that agglomeration of hydrogen depends solely on its diffusivity and solubility and can lead to high-pressure pockets (that lead to blistering) at low (ambient) temperature [10]. In silicon (and most semiconductors), hydrogen forms a strong chemical bond with lattice atoms. The energy of the defective lattice can therefore be dramatically altered with the development of H-stabilized internal structures. Thus, in addition to physical effects such as the generation of internal pressure, the chemistry of hydrogen with silicon plays an important role [6,7].

To underscore this point, it is informative to consider the number and type of cracks that develop under different implantation conditions. The defects originally created by H-implantation at room temperature evolve into internal surfaces (see Fig. 2b) that eventually join to form the macroscopic cracks leading to cooperative shearing of a Si layer. The spatial distribution of lattice damage closely follows the concentration profile of implanted hydrogen (i.e. spans the whole straggling region of several 1000 Å). Yet, upon exfoliation, the RMS roughness of the sheared layer is only 50–100 Å, clearly indicating that the development of macroscopic cracks only occurs in a very

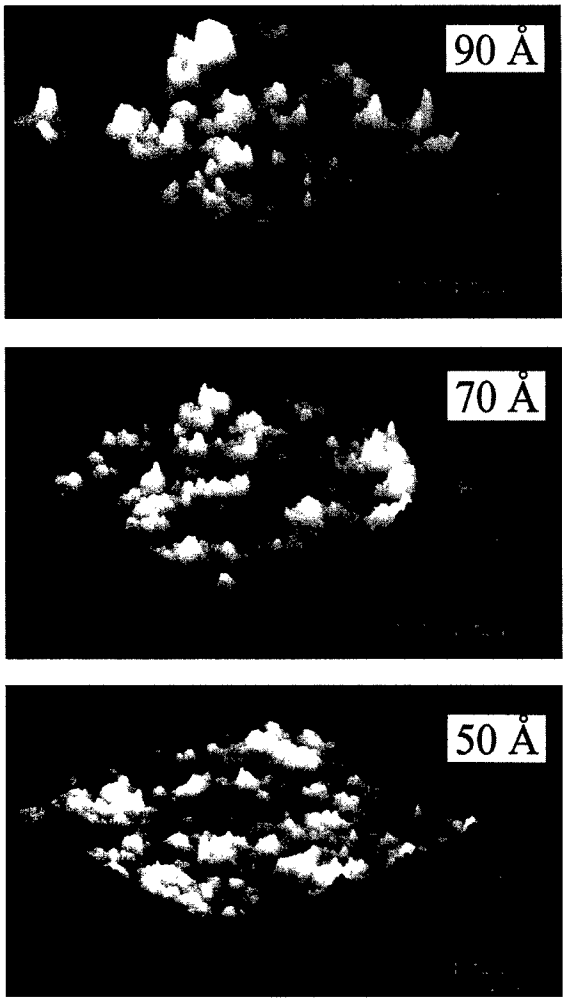

Fig. 3. Surface roughness measured by AFM over 15 μm × 15 μm regions of exfoliated samples implanted with 6×10^{16} H/cm^2 (top), 1×10^{17} H/cm^2 (middle) and 1.8×10^{17} H/cm^2 (bottom).

narrow region. Moreover, the RMS roughness decreases as the dose increases, as seen in Fig. 3, suggesting that the roughness arises from the intersection of H-terminated internal surfaces, such as the (1 1 1) and (1 0 0) planes identified by TEM [11] (Fig. 2b).

Annealing constitutes an important step in the SmartCut™ process for a number of reasons. Once the chemical activity of hydrogen is recognized, it is easy to understand that the degree of thermal activation will dictate the rate and extent to which the more energetically favorable internal surfaces form. In addition an increase in temperature will increase the rate of hydrogen diffusion, thereby enhancing the probability of agglomeration of H and H_2 in a reduced number of internal (vacancy-derived) traps. Consequently, the study of the thermal evolution of H-stabilized defects is central to any understanding of the exfoliation mechanism. The rest of this paper is therefore aimed at characterizing the H-induced defects and their thermal evolution into internal surfaces.

3. Thermal evolution of H-implantation-induced defects in silicon

The implantation of hydrogen into silicon has been extensively studied over the past four decades, using a wide variety of techniques such as TEM, IR, SIMS and electrical probes [12–17]. The vast majority of studies, however, were performed for doses well below 5×10^{16} H/cm^2, or for low local concentrations (i.e., non-interacting hydrogen). Above this dose the defect structures become "superimposed", hindering resolution of the discrete Si–H species that are formed. Yet, it is this higher dose range ($> 5 \times 10^{16}$ H/cm^2), that has been shown to be essential to cause blistering and exfoliation. [5,6,11]. Consequently, understanding the microscopic mechanism of this process presents a formidable challenge for which both the spectroscopic details and the macroscopic exfoliation process must be reconciled. A multifacetted experimental approach is clearly required; we have employed infrared absorption spectroscopy to probe the chemical nature of defects, as well as transmission electron microscopy (TEM) and atomic force microscopy (AFM) to uncover the physical structure, forward recoil scattering (FRS) to directly measure the total hydrogen content, and mass spectrometry (MS) to determine the composition of the gas evolved during annealing [6,7,11].

Previous infrared absorption spectroscopy studies by Stein et al. [13,14], Johnson et al. [15] and Bech Nielsen and coworkers [8] of hydrogen-related defects in semiconductors have played an important role in understanding the defect-based mechanism of exfoliation. In particular, the recent work of Bech Nielsen et al. [8] has made it possible to definitively identify a number of defect structures, by combining IR spectroscopy with selective isotopic substitution and uniaxial stressing. Some of these modes can be seen in the spectra of silicon implanted with higher local doses of hydrogen (Fig. 4). These spectra are typical of those reported in the literature for low (2×10^{16} H/cm^2 — does not exfoliate) and intermediate doses of hydrogen (6×10^{16} H/cm^2 — exfoliates), respectively [6,11]. In the as-implanted spectra, at least 12 discrete vibrational modes are observed in the Si–H stretching mode region, superimposed on a broad absorption band. The discrete features can be assigned to "point defects" (single Si vacancy or interstitial structures) formed at the periphery of the implanted region, whereas the broad band is due to an inhomogeneous distribution of "multivacancy" defects (by analogy to hydrogenated amorphous silicon) occurring near the

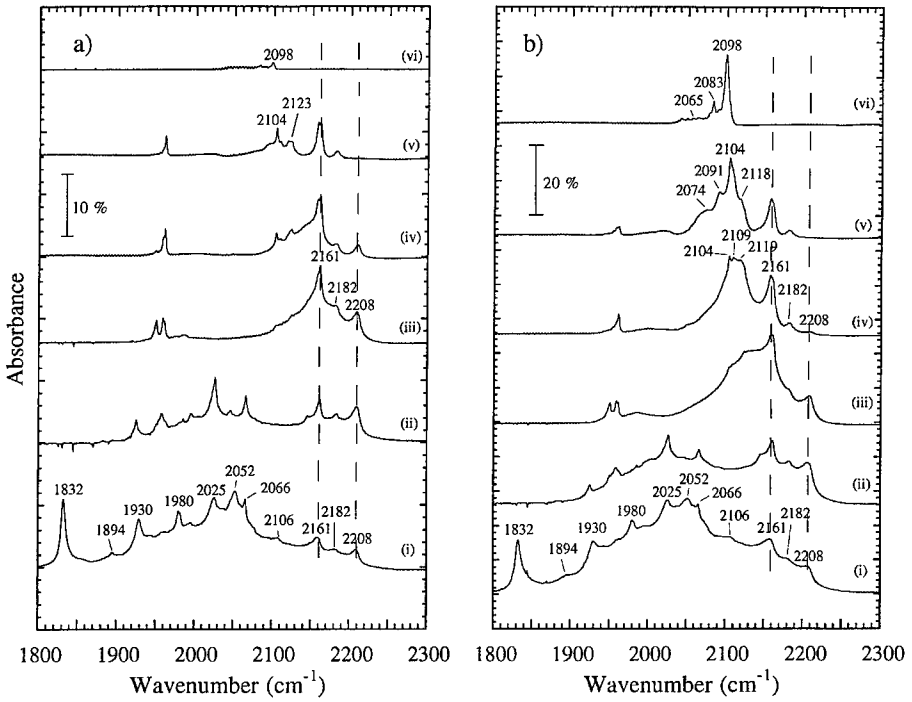

Fig. 4. Multiple internal reflection IR spectra of the Si–H stretching modes of hydrogen implanted 3300 Å into Si(1 0 0) at a dose of (a) 2×10^{16} H/cm^2 (low dose) and (b) 6×10^{16} H/cm^2 (intermediate dose) at (i) room temperature, and after annealing to (ii) 300°C, (iii) 425°C, (iv) 500°C, (v) 550°C, and (vi) 650°C. The annealing was performed sequentially in vacuum ($P\sim1\times10^{-8}$ Torr) for 30 min at each temperature (as for all other cases reviewed herein).

peak of the implantation profile [6]. This broad band component is found to scale with the hydrogen dose (as does exfoliation efficiency) whilst the point defect contribution remains essentially constant with change in [H], underscoring the central role of the multivacancies on the exfoliation process.

The nature of the point defects in the periphery is however still very relevant to a discussion of exfoliation because the higher H-concentration multivacancy region evolves into some of the same defect structures upon annealing. Drawing mostly from Bech Nielsen's work [8], the features at 2025, 2161/2182 and 2208 cm^{-1} are assigned to VH_1, VH_3 (or V_2H_6) and VH_4, respectively. The remainder of the sharp spectral lines observed in the as-implanted samples can be similarly assigned either to the H_2^* defect (1832, 2052 cm^{-1}), H-terminated divacancies $V_{2,3}H$ (2066 cm^{-1}), or hydrogenated interstitials, IH_2 (1980 cm^{-1}) [8,12].

The mechanism leading to the development of macroscopic cracks within the H-implanted silicon region can be inferred by considering the thermal evolution of the above mono- and multi-vacancy modes. Looking first at the IR data for both the low and high dose samples (Fig. 4a and b), we note that by 300°C, the most pronounced change (other than the loss of the relatively unstable H_2^* species) is the decrease in the concentration of hydrogenated multivacancies and the concomitant increase in the absorption of $VH_{3,4}$ species. Between 300°C and 425°C, complete attenuation of this multivacancy signature occurs with a corresponding increase of $VH_{3,4}$ species, and the monovacancy VH and interstitial IH_2 defects disappear in the periphery. The two samples differentiate themselves upon subsequent annealing; for the higher dose sample, there is a continuous attenuation of the $VH_{3,4}$ modes and a corresponding increase in absorption at 2100–2120 cm^{-1} (Fig. 4b) whereas minimal growth of these latter features is observed for the lower dose (2×10^{16} H/cm^2) sample (Fig. 4a). This frequency range is typical of that observed for extended H-terminated surfaces, with the 2104 and 2119 cm^{-1} features being suggestive of atomically rough, H-terminated internal (1 0 0) surfaces. Above 550°C, rearrangement of these internal surfaces occurs, leaving atomically smooth (1 0 0) and (1 1 1) surfaces, with characteristic frequencies of 2098 and 2083 cm^{-1}, respectively. Recent studies of the related bending modes have shown that the correct assignment of the 2104 cm^{-1} feature is in fact to a perturbed form of the same smooth monohydride reconstructed surface (see later). Important confirmation of these assignments is provided by TEM images of the annealed

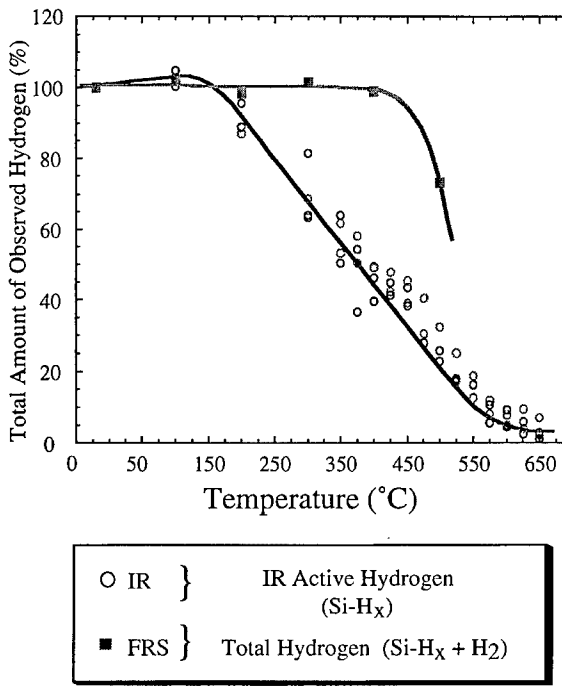

Fig. 5. Plot of the integrated hydrogen signal obtained using forward recoil scattering (FRS) and infrared (IR) absorption spectroscopy for H doses in the range 2×10^{16}–1×10^{17} H/cm^2.

samples which show that the growth of extended (1 1 1) and (1 0 0) type defects occurs exactly coincident with the development of these IR "internal surface" features.

Looking next at the FRS data together with a summary of the thermal dependence of the IR absorption (Fig. 5), we see that there is no loss of hydrogen up to 400°C, suggesting that the attenuation of the IR intensity (predominantly the broadband absorption) must be the result of conversion of bound Si–H into the IR inactive species, H_2. The increase in the $VH_{3,4}$ modes over the same temperature range indicates that transformation of both the mono- and multi-vacancy structure into such defects effectively competes with this molecular hydrogen production pathway, and it is these latter defects that couple (agglomerate) to produce the internal surfaces that are vital in order to trap the H_2 so-formed, as discussed below.

The observation that the growth of internal surface modes increases precisely at the temperatures at which surface blistering and flaking occur, and the absence of such blistering for the low H doses which do not develop high densities of internal surfaces, demonstrates the causal relationship between the two. Indeed, returning to the TEM images of the macro-crack that develops (Fig. 2), we know that the growth of H-passivated internal surfaces is a precursor to macroscopic cracking. Finally, mass spectrometry shows that H_2 is liberated when the surface flakes [6], confirming that H_2 accumulates in these internal surface (void) regions and acts as the source of internal pressure that drives exfoliation.

The spectroscopic observation that the internal surfaces persist even after flaking (> 550°C, Fig. 4) is also clear from TEM images (Fig. 2) that show a multi-tiered defect structure above and below the macroscopic crack. These unconnected (1 0 0) and (1 1 1) internal surfaces that give rise to the residual IR absorption only disappear after annealing to 700°C as the silicon heals. It is unlikely, however, that complete healing of the crystalline Si matrix occurs until substantially higher temperatures, by analogy to the 1000°C anneal required for the observed closure of the interface between two H-terminated Si bonded wafers [18].

To this point we have demonstrated the fact that hydrogen plays both a chemical (dictating defect structural evolution) and physical role (internal pressure) in the exfoliation process. The critical kinetic interplay of the two roles is highlighted by consideration of the low dose behavior: for H implantation at 2×10^{16} H/cm^2, FRS data indicate a similar fall-off in the H concentration with temperature as is observed for the higher dose samples (6×10^{16} H/cm^2), despite the absence of exfoliation. This is due to the insufficient density of internal surfaces (= traps for H_2) at these low doses, which permits loss of H by out-diffusion away from the implanted region as the temperature is raised, so that the internal pressurization does not occur to the necessary extent. Support for this model is provided by the observed accumulation of H_2 at the bonded interface when such low dose samples are pre-joined to a support wafer [6].

The theoretical limit for the minimum H dose required can be evaluated by quantification of mass spectrometry data [6]. Approximately, 30% of the total hydrogen dose is released upon exfoliation in the form of molecular hydrogen, which is $\sim$ an order of magnitude more than the amount of H decorating the surfaces of the macroscopic crack that develops (e.g. $2\times(1\,1\,1)$ surfaces = 1×10^{15} H/cm^2). Therefore, these data suggest that at most 2×10^{16} H/cm^2 is needed for exfoliation if all the hydrogen could be localized in one region.

In order to test this hypothesis we have investigated the effect of coimplanting a second insoluble species on the required H dose for exfoliation. Interestingly, we find that if He is coimplanted with H, exfoliation can indeed take place even with a dose as low as 1×10^{16} H/cm^2 [19,20]. As outlined above, this suggests that H and He act in complementary ways with H chemically stabilizing the internal surfaces and He providing the physical pressure necessary for exfoliation. However, a detailed investigation of the microscopic mechanism reveals an interplay between the two species wherein the presence of helium drives the reconversion of molecular H_2 into bound H that, in turn, enhances internal surface

formation, as described in the following. Both factors then serve to lower the hydrogen concentration necessary to achieve exfoliation.

The potential roles of He as a source of damage and/or internal pressure were investigated using infrared spectroscopy for samples implanted with H and He at the

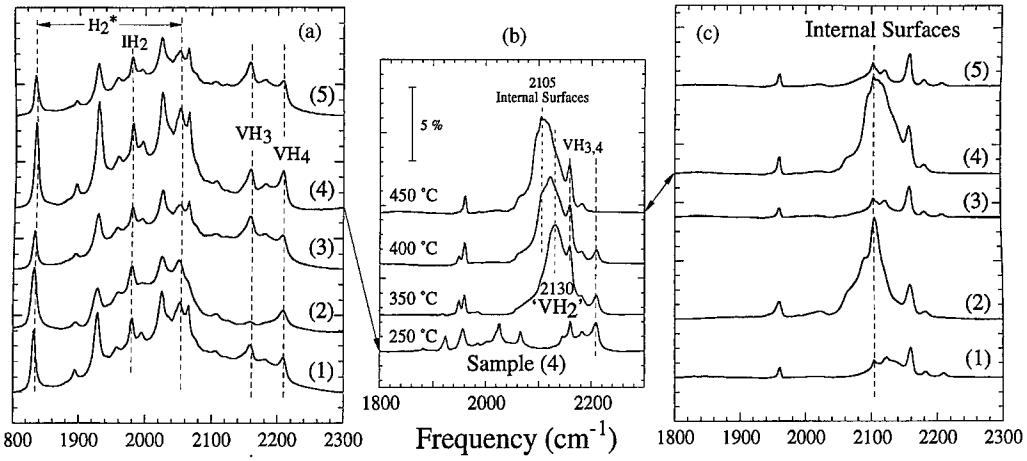

Fig. 6. Multiple internal reflection spectra of H/He coimplanted samples as a function of annealing temperature; (a) room temperature and (c) after a 450°C anneal. (b) detailed annealing data set for sample (4). Sample (1) 1×10^{16} H/cm^2 (depth = 0.3 μm); (2) 1×10^{16} H/cm^2 + 1×10^{16} He/cm^2 (same depth = 0.3 μm); (3) 1×10^{16} H/cm^2 + 1×10^{16} He/cm^2 (same depth = 0.3 μm) + He annealed out; (4) 1×10^{16} H/cm^2 (depth = 0.3 μm) + 1×10^{16} He/cm^2 (depth = 0.8 μm); (5) 1×10^{16} H/cm^2 (depth = 0.3 μm) + 1×10^{16} He/cm^2 (depth = 0.8 μm) + He annealed out.

Table 1
Comparison of theoretical and experimental frequencies for vacancy and surface structures

	Defect	Theory[a]		Experiment[b]	
		Stretching Modes	Bending Modes	Stretching Modes	Bending Modes
Vacancies	VH[c]	(2054)	(603)	2025	595
			(614)		606
	VH_2	2114	598	2125	~ 581
		2146	611	2144	611
			654		645
	VH_3	2166	596	2164	~ 581
		2197	634	2188	638
			662		669
	VH_4	2206	637	2219	633
Surfaces	Si(1 1 1) : H			2084	627
				2065[d]	
	Si(1 0 0)-(2 × 1)	2091	624	2088	619
		2098	640	2099	635
	Si(1 0 0) : H	2104	675	2110	656
		2115	895	2123	900
				2130	668
				2145	856

[a]The theoretical values for the VH defect are given in parentheses due to increased uncertainty resultant from convergence difficulties in the calculation.
[b]Experimental values for vacancies were taken from data in Fig. 9 or analogous data sets.
[c]Different scaling procedures were used for the surface and defect species (see text).
[d]Perturbed mode observed for two interacting surfaces.

same or different depths [21]. The role of damage was studied by similarly implanting He then diffusing it out (but maintaining the defect structure) prior to H implantation. The IR data (Fig. 6) clearly show that only the samples with He still present develop internal surfaces after the formation of a new intermediate. Initially, all the as-implanted silicon wafers (both with and without He coimplantation), are characterized by similar spectra with a broad band component and sharper features associated with H-decorated defects (Fig. 6a). However, upon a 450°C anneal (Fig. 6c), only the spectra in which He is still present (spectra 2 and 4) display a strong mode at 2105 cm^{-1}, characteristic of H-passivated internal surfaces. Interestingly, only these samples are observed to exfoliate. The fact that those samples in which the He was removed do not exfoliate indicates that damage is not responsible for the lower ion dose required for exfoliation of He/H coimplanted samples. Helium is therefore clearly taking an active role by providing the necessary internal pressure in the exfoliation process.

The presence of He also facilitates the formation of internal surfaces via a novel intermediate species, as illustrated in Fig. 6b where the spectral evolution of one of the exfoliating samples is shown (with He coimplanted deeper than H). Around 350°C, a strong mode appears at 2130 cm^{-1}, much stronger than the well-established bands at 2160 and 2208 cm^{-1} assigned to VH_3 and VH_4, respectively. This feature is unique to the coimplanted samples and is clearly the immediate precursor to the development of extended internal surfaces (2105 cm^{-1} mode). This mode has been assigned to "VH_2-like" defects, based on its frequency (Table 1). However, both its width and center frequency are not in exact agreement with the isolated VH_2 defect, suggesting that such VH_2-like species are significantly perturbed. This is consistent with the proposed mechanism which involves reconversion of H_2 to SiH as follows [21]:

$$He + V + H_2 \Rightarrow (He\text{-}VH_2)$$

with the He trapping within the hydrogenated divacancy that it helps form, thereby causing perturbation of the observed VH_2 frequencies.

An alternative scenario is that the VH_2 defects are strongly interacting or reside close to the advancing front

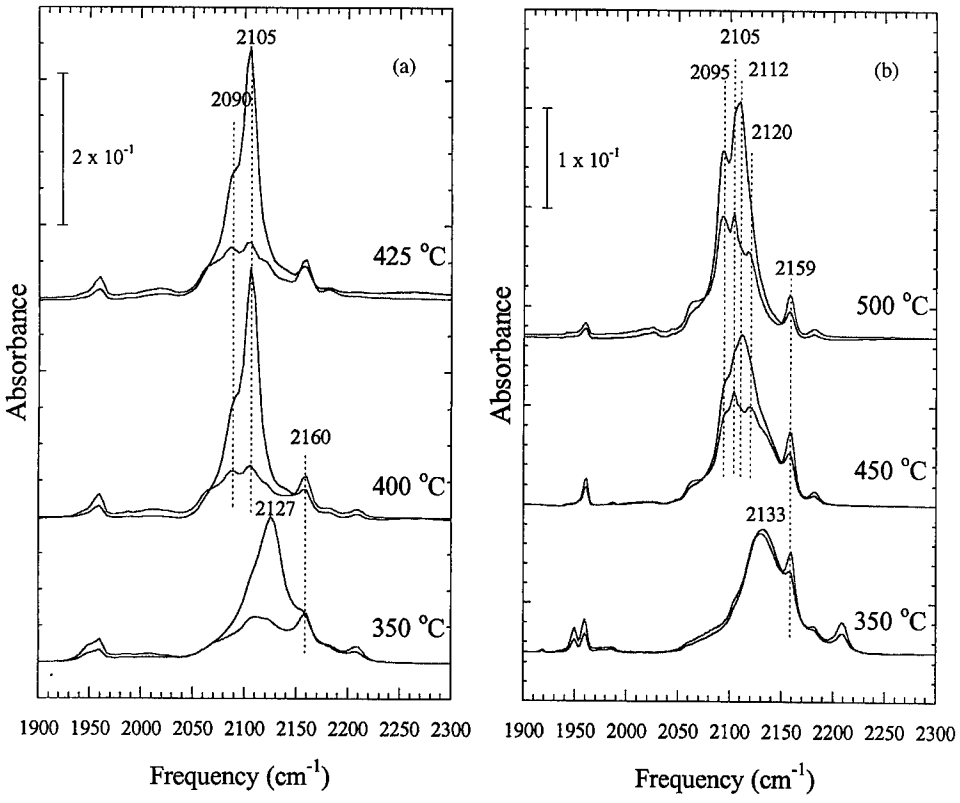

Fig. 7. Polarization dependent multiple internal reflection IR spectra of H/He coimplanted Si(1 0 0) as a function of annealing temperature. (a) 1×10^{16} H/cm^2 + 1×10^{16} He/cm^2 (same depth = 0.3 μm); (b) 1×10^{16} H/cm^2 (depth = 0.3 μm) + 1×10^{16} He/cm^2 (depth = 0.8 μm). In each case, the spectra with the most intense absorption bands were obtained using *p*-polarization (~ perpendicular to surface plane) and the lower intensity curves with *s*-polarization (parallel to surface plane).

of the expanding microcavities such that they cannot be thought of as true point defects. Some support for this conjecture is provided by the polarization dependence of the VH_2 signature (Fig. 7). The 2133 cm^{-1} feature observed for the [H shallow, He deep] sample shows no polarization dependence (Fig. 7b); in contrast when H and He are implanted at the same depth the analogous feature shifts to 2127 cm^{-1} and shows strong *p*-polarization (Fig. 7a). This observation is evidence for a more extended structure having formed ($\sim$10s of nm in size) so that an effective region of high dielectric contrast is formed in the Si substrate [22]. This argument is an extension of that demonstrated to be applicable for the interface formed between two bonded wafer surfaces [23] and also for internal surfaces in H-implanted Si [24]. The predicted polarization of such internal surfaces is clearly evident in the uppermost panels of Fig. 7, confirming that the He driven formation of VH_2 enhances subsequent internal surface formation.

To summarize the preceding, it is clear that in order to fully understand exfoliation, one must further delineate the formation and transformation of vacancy species into extended internal surfaces. In order to accomplish this a more complete spectroscopic characterization is required as is a correct theoretical description of the normal mode structure associated with each defect type. To this end we have extended our spectroscopic range to include the low-frequency Si–H bending modes, to provide important additional 'checkpoints' for the results of ab initio quantum chemical cluster calculations.

4. Silicon–hydrogen bending modes

The study of the bending modes is much harder than for the related Si–H stretching modes as their frequencies overlap the silicon phonon and multi-phonon bands, so that one cannot use the long optical pathlengths intrinsic to the multiple internal reflection geometry. A single-pass transmission geometry [25,26] must be used and, in addition, the temperature and thickness of the sample and reference must be identical. Even when these experimental criteria are satisfied, the spread of the Si–H bending frequencies is smaller ($\sim$250 cm^{-1}) than that for the stretching modes ($\sim$400 cm^{-1}), making it more difficult to distinguish various components.

The overall appearance of the bending mode region is illustrated in Fig. 8. For this survey spectrum, with bending modes on the left and stretching modes on the right, a high implantation energy (1 MeV) and a medium dose (6×10^{16} H/cm^2) were used to lower the inhomogeneous broadening. In the bending mode region, the modes of interest lie between 550 and 820 cm^{-1}, including a broad-band feature peaked at 650 cm^{-1}. The rest of the spectrum includes the interstitial IH_2 (746 cm^{-1} with the corresponding stretch mode at 1980 and 1990 cm^{-1}) and the H_2^* (814 cm^{-1} with the corresponding stretch modes at 1832 and 2052 cm^{-1}) [8]. The remainder of the bending modes have not been previously reported and therefore cannot be assigned without careful analysis of the thermal evolution in comparison with the (known) stretching modes, and also with theoretical frequencies. We will start our discussion by considering the modes associated with the well-characterized vacancy defects, then consider the Si–H bending modes associated with the internal surfaces and finally address the issue of the 2120–2135 cm^{-1} feature observed in H/He coimplanted samples.

The theoretical model we have employed is based on the well-documented B3LYP gradient-corrected density functional [27,28]. We start with a cluster containing

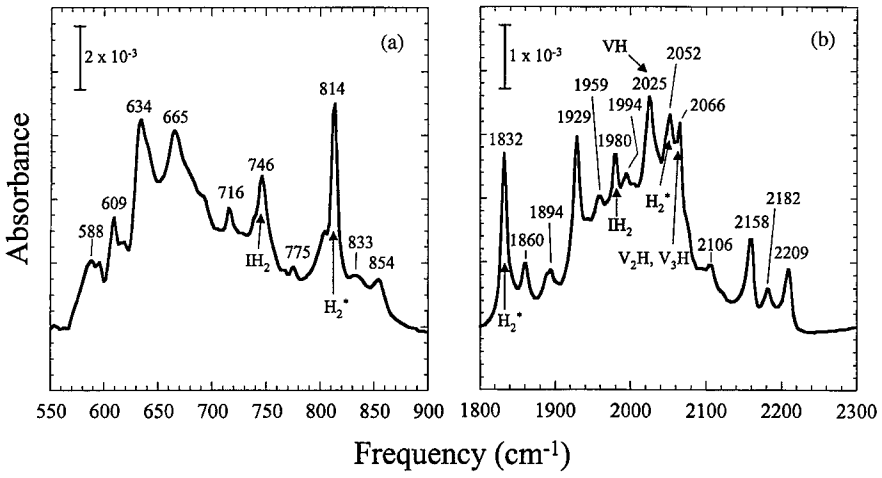

Fig. 8. Transmission IR spectra ((a) bending modes and (b) stretching modes) of H-implanted Si(1 0 0) at room temperature. The H dose is 6×10^{16} H/cm^2 and the implantation energy is 1 MeV (15 μm depth).

a tetrahedral core of 17 Si atoms (1 central Si + 4 first layer Si + 12 second layer Si) with an Si–Si distance of 2.35 Å as in the bulk. The 36 exterior broken bonds of the cluster are terminated with hydrogens (Si–H = 1.48 Å). The central Si atom is then removed to create a vacancy, and 1, 2, 3, or 4 hydrogens attached to the broken bonds in the central region to create the defects VH, VH_2, VH_3, and VH_4, respectively. In order to obtain optimized geometries, the exterior hydrogens terminating the cluster are frozen and the 16 remaining Si atoms along with the central hydrogens are allowed to relax. The polarized 6-31G** basis set (containing double-zeta valence orbitals + *d*-functions on Si + *p*-functions on H) was used for all the relaxing atoms while a 6-31G basis set was used for the exterior frozen hydrogens [29]. The complete matrix of harmonic force constants and the associated normal modes were then evaluated for each defect, and the results are summarized in Table 1 (top panel). In general, the frequencies are overestimated substantially, particularly for the defects containing multiple hydrogens in the vacancy region. This is partly because of neglect of anharmonicity but mostly due to the small size of the cluster which does not allow adequate relaxation from steric crowding. As a result, the stretching frequencies in particular tend to be increasingly overestimated as the number of hydrogens increases within the vacancy. For example, the stretching mode for the VH_4 defect which has been well characterized experimentally (2221 cm^{-1}) is overestimated by more than 200 cm^{-1}. The bending frequencies are also overestimated, but by smaller amounts. All these effects are taken into account by scaling the frequencies (stretches and bends are treated separately) using a linear regression method to the observed frequencies at low temperatures (i.e. to reduce anharmonicity effects). The scaled values of the frequencies are also listed in Table 1. Full details of our scaling procedure will be discussed in a future publication [24]. For comparison, the calculated stretching and bending frequencies of the monohydride and dihydride species on a Si(1 0 0)-2 × 1 surface are also listed in Table 1. The scaling procedure for the surface modes involves a uniform shift (102 cm^{-1} for stretches and 35 cm^{-1} for bends) and has been discussed in previous publications [30].

The thermal evolution of both the bending and stretching vibrations of Si(1 0 0) implanted with 6×10^{16} H/cm^2 at an energy of 1 MeV is summarized in Fig. 9. The data were collected with the sample held at low temperature (100 K) to minimize thermal broadening of the bands. In general, the evolution of the bending modes confirms the picture originally derived from the stretching mode behavior. The broad band peaked at 620 cm^{-1} in Fig. 8 is strongly attenuated upon annealing (Fig. 9), as was the 2000 cm^{-1} broad band in the stretching region. The frequency, breadth and thermal evolution of the bending modes is therefore consistent with a distribution of

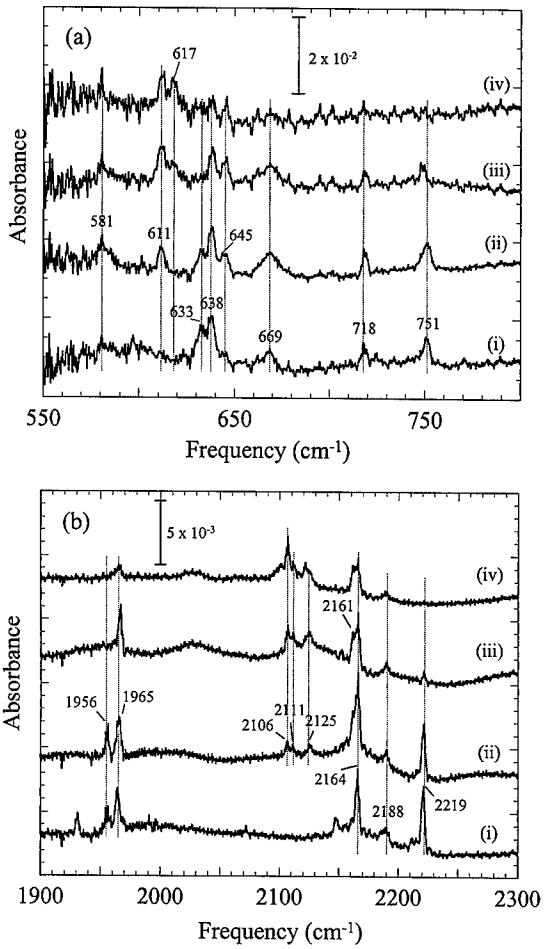

Fig. 9. Transmission IR spectra ((a) bending modes and (b) stretching modes) as a function of annealing temperature for Si(1 0 0) implanted with 6×10^{16} H/cm^2 at 1 MeV (15 μm depth); (i) 300°C anneal; (ii) 400°C; (iii) 500°C and (iv) 550°C. The data were taken at low temperature to reduce thermal broadening.

monohydride multivacancies, similar to those occurring in hydrogenated amorphous silicon and in accord with previous work [6,7,11]. Now, if we follow through the thermal evolution of each vacancy species in turn and compare experimentally correlated frequencies with theoretical calculation we find there is excellent agreement between the two. Starting with the VH_4 defect, which has previously been shown to be definitively characterized by a Si–H stretching frequency at low T of ~ 2220 cm^{-1} (cf. theory: 2206 cm^{-1}), we find a similar temperature dependence in the bending mode at 633 cm^{-1}, in very good agreement with the predicted frequency of 637 cm^{-1}. For VH_3 the stretching modes occur at 2164 and 2188 cm^{-1} and we find correlated bending modes at 638 and 669, with the possibility of a third band at ~ 581 cm^{-1}, which again compares favorably with the

calculated modes of 2166, 2197, 634 and 662 cm^{-1} with a weaker band at 596 cm^{-1}. Finally, the mode at 2125 cm^{-1} correlates with the 611 and 645 cm^{-1} features which are in good agreement with the calculated modes for VH_2 at 2114, 611 and 654 cm^{-1}, respectively.

The first conclusion from the preceding analysis is that the modes observed at 617 and 2106 cm^{-1} that predominate in the high-temperature limit cannot be attributed to a simple vacancy structure. Furthermore, the absence of related bending modes at 656 and ~ 900 cm^{-1} effectively precludes assignment to a (rough) Si(1 0 0) surface as had been previously proposed. A rough Si(1 0 0) surface contains dihydride SiH_2, characterized by modes at 2105–2115 cm^{-1} (stretch), 656 cm^{-1} (bend) and 910–920 cm^{-1} (scissor), and trihydride SiH_3, characterized by modes at 2120–2140 cm^{-1} (stretch) and 850 cm^{-1} (deformation), with unresolved bending modes in the 620 cm^{-1} range [31].

The most likely interpretation of the 617/2106 cm^{-1} pair is that they result from a monohydride-terminated reconstructed (2 × 1) Si(1 0 0) surface that is perturbed somewhat from the isolated surface frequency. This is illustrated in Fig. 10, where the transformation of these features is followed between 575 and 625°C. Starting with the high temperature data, the modes at 620, 634 and 2099 are in good agreement with known frequencies for (1 0 0) surfaces [31]; confirming our prior assignment of internal surfaces. Similarly, the 626, 2064 and 2083 cm^{-1} features are in excellent agreement with the known values for 2 mutually interacting monohydride terminated Si(1 1 1) surfaces (Table 1). Now, returning to the lower temperature 575°C data, the main (1 0 0) bending modes is observed as the stretching mode frequency shifts to 2104 cm^{-1}, strongly suggesting that the monohydride termination predominates at this temperature too. The possibility that the frequency perturbation from 2099 → 2104 cm^{-1} arises from direct interaction of the H's on the opposing surfaces can be refuted since such a dynamic coupling is known to *lower* the Si–H frequency [23]; the mode at 2064 cm^{-1} (reduced from 2083 cm^{-1}) for the two interacting (1 1 1) surfaces is quintessential in this regard. Interestingly, no shift in the bending mode frequency is observed to accompany this pronounced shift in (111) stretching frequency.

Thus, the constancy of bending mode frequency and upshift of stretching mode frequency suggests that the high Si–H stretching mode frequency (2104/5 cm^{-1}) is associated with a steric interaction with the overlying H_2 gas. Indeed, it has been shown that the steric effect of inert gases such as He, Ar, Kr adsorbed on Si(1 1 1) : H causes an 5–20 cm^{-1} increase in the Si–H stretching frequency [23], consistent with such an hypothesis. This steric interaction is then relieved as soon as the crack grows, as is the case at higher temperature and the frequency reverts to that of the unperturbed (1 0 0) surface. Clearly, such a conclusion represents a key additional piece of mechanistic information about the exfoliation process and could not have been arrived at by analysis of the stretching modes alone.

Before proceeding we note, in passing, that the remaining two bending modes at 718 and 751 cm^{-1} exhibit a similar temperature dependence to the 1956 and 1965 cm^{-1} stretching modes, and are therefore most likely due to hydrogenated interstitials (IH_x). These interstitials (which persist throughout the all-important 300–500°C temperature range) are distinct from IH_2 as it has possesses a characteristic stretching mode at 1980 cm^{-1}, although a more precise assignment is lacking at this time.

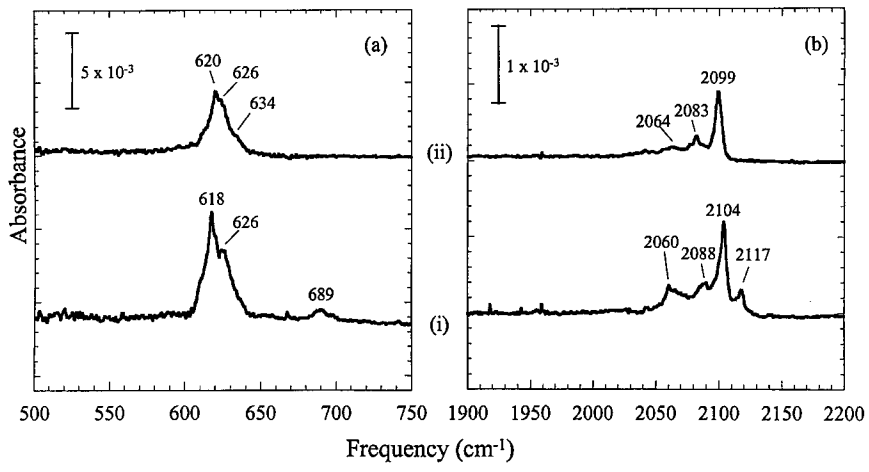

Fig. 10. Transmission IR spectra ((a) bending modes and (b) stretching modes) for Si(1 0 0) implanted with 6×10^{16} H/cm^2 at 75 keV (0.5 μm depth) after annealing to (i) 575°C and (ii) 625°C.

Finally, access to the lower-frequency bending modes is also important in the more complex study of He/H coimplantation. Specifically, the 2130 cm^{-1} mode could just as easily be assigned to the formation of trihydride on internal surfaces, as is the case for crystalline silicon hydrogenated by remote H plasma [32]. In the latter case, the observation of a mode at 850 cm^{-1} provided a positive identification of trihydride. The presence of this deformation mode is crucial because the SiH_3 stretch frequency is known to vary from 2120 to 2150 cm^{-1} with its immediate environment and cannot therefore be reliably used by itself. In the present case, the deformation mode is absent so that trihydride can be ruled out (data not shown). On the other hand, the spectra in the bending mode region are consistent with formation of a VH_2 species, although superposition of other modes makes it impossible to make an incontrovertible assignment. In fact, the possibility exists that the unique 2120–2133 cm^{-1} spectral frequency observed is indicative of a more exotic vacancy structure, such as the recently proposed ring hexavacancy (V_6H_{12}) [33]. Such a species is expected to exhibit a very similar IR activity to VH_2 (symmetry, mode frequencies, etc.) and is a natural precursor to extended surface formation, although clearly more detailed theoretical work is required to address this possibility.

5. Conclusions

In this paper, we have shown how IR spectroscopy can be used to uncover the important role that defects play in the exfoliation mechanism and have indicated future directions for characterizing the essential details of the process. For example, the ability to probe the lower-frequency bending and deformation modes of all H-stabilized defects within crystalline silicon will be necessary to arrive at a complete picture, particularly as more complex implantation conditions (e.g. with more than one species) are considered. In order to exploit the full potential of this new spectral region the development of a fingerprint map will be required. This can be achieved by combining first-principles calculations and extensive experiments, as was done for the stretching band region, with a good understanding of the effect of different perturbations on the mode frequencies. In this way, the ability to distinguish more complex defects such as the 'magic number' multivacancies should be possible in the near future.

Acknowledgements

Y. Candano is a research assistant of the Belgian National Fund for Scientific Research (FNRS).

References

[1] M. Bruel, Electron. Lett. 31 (1995) 1201.
[2] A.J. Auberton-Hervé, J.M. Lamure, T. Barge, M. Bruel, B. Aspar, J.L. Pelloie, Semicond. Int. 97 (1995) 97.
[3] C.E. Hunt, H. Baumgart, S.S. Iyer, T. Abe, U. Gösele (Eds.), Proceedings of the Third International Symposium on Semiconductor Wafer Bonding: Physics and Applications, The Electrochemical Society, Pennington, NJ, USA, 1995, PV95-7.
[4] P.L.F. Hemment, S. Christoloveanu, K. Izumi, T. Houston, S. Wilson (Eds.), Proceedings of the seventh International Symposium on Silicon on Insulator Materials, The Electrochemical Society, Pennington, NJ, USA, 1996, PV96-3.
[5] C. Maleville, B. Aspar, T. Poumeyrol, H. Moriceau, M. Bruel, in: P.L.F. Hemment, S. Christoloveanu, K. Izumi, T. Houston, S. Wilson (Eds.), Proceedings of the Seventh International Symposium on Silicon on Insulator Materials, The Electrochemical Society, Pennington, NJ, USA, 1995, PV96-3, p. 34.
[6] M.K. Weldon, V.E. Marsico, Y.J. Chabal, A. Agarwal, D.J. Eaglesham, J. Sapjeta, W.L. Brown, D.C. Jacobson, Y. Caudano, S.B. Christman, E.E. Chaban, J. Vac. Sci. Technol. B 15 (1997) 1065.
[7] M.K. Weldon, Y.J. Chabal, in: R. Hull (Ed.), The properties of Crystalline Silicon EMIS Datareviews Series, Vol. 20, 1999, p. 942.
[8] B. Bech Nielsen, L. Hoffmann, M. Budde, Mater. Sci. Eng. B 36 (1996) 259.
[9] M. Budde, B. Bech Nielsen, P. Leary, J. Goss, R. Jones, P.R. Briddon, S. Oberg, S.J. Breuer, Phys. Rev. B 57 (1998) 4397.
[10] B.M.U. Scherzer, in: R. Behrisch (Ed.), Sputtering by Particle Bombardment II, Topics in Applied Physics, 52, Springer, New York, USA, 1983 and references therein.
[11] M.K. Weldon, V.E. Marsico, Y.J. Chabal, A. Agarwal, D.J. Eaglesham, J. Sapjeta, W.L. Brown, D.C. Jacobson, Y. Caudano, S.B. Christman, E.E. Chaban, Proceedings of the Fourth International Symposium on Semiconductor Wafer Bonding: Science, Technology and Applications, The Electrochem. Society Proceedings, Vol. 97–36, Pennington, NJ, 1998, p. 229.
[12] S.J. Pearton, J.W. Corbett, M. Stavola, Hydrogen in Crystalline Semiconductors, Springer, Berlin, 1992 and references therein.
[13] H.J. Stein, S.M. Myers, D.M. Follstaedt, J. Appl. Phys. 73 (1992) 2755.
[14] S.M. Myers, D.M. Follstaedt, H.J. Stein, W.R. Wrampler, Phys. Rev. B 47 (1993) 13380.
[15] N.M. Johnson, F.A. Ponce, R.H. Street, R.J. Nemanich, Phys. Rev. B 35 (1987) 4166.
[16] J.N. Heyman, J.W. Ager III, E.E. Haller, N.M. Johnson, J. Walker, C.M. Doland, Phys. Rev. B 45 (1992) 13363.
[17] B. Bech Nielson, K. Bonde Nielson, J.R. Byberg, in: H. Heinrich, W. Jantsch (Eds.), Defects in Semiconductors 17, Mater. Sci. Forum, Vols. 143–147 (Trans. Tech. Aedermannsdorf, 1994) p. 909.
[18] D. Feijoo, Y.J. Chabal, S.B. Christman, Appl. Phys. Lett. 65 (1994) 2548.

[19] A. Agarwal, T.E. Haynes, V.C. Venezia, O.W. Holland, D.J. Eaglesham, Appl. Phys. Lett. 72 (1998) 1086.
[20] V.C. Venezia, T.E. Haynes, A. Agarwal, D.J. Eaglesham, O.W. Holland, M.K. Weldon, Y.J. Chabal, in: H. Huff, U. Gosele, H. Tsuya (Eds.), Semiconductor Silicon 1998, Proc. Electrochem. Soc., The Electrochemical Society, Pennington, NJ, 1998, p. 138.
[21] M.K. Weldon, M. Collot, Y.J. Chabal, V.C. Venezia, A. Agarwal, T.E. Haynes, D.J. Eaglesham, S.B. Christman, E.E. Chaban, Appl. Phys. Lett. 73 (1998) 3721.
[22] Y.J. Chabal, M.A. Hines, D. Feijoo, J. Vac. Sci. Technol. A 13 (1995) 1719.
[23] M.K. Weldon, V.E. Marsico, Y.J. Chabal, D.R. Hamann, S.B. Christman, E.E. Chaban, Surf. Sci. 368 (1996) 163.
[24] Y. Caudano, Y.J. Chabal, M.K. Weldon, B.B. Stefanov, K. Raghavachari, in preparation.
[25] K.T. Queeney, M. K. Weldon, J.P. Chang, Y.J. Chabal, A.B. Gurevich, J. Sapjeta, R.L. Opila, J. Appl. Phys. 87 (2000).
[26] Y. Caudano, M.K. Weldon, Y.J. Chabal, B.B. Stefanov, K. Raghavachari, D.C. Jacobson, S.B. Christman, E.E. Chaban, Proceedings of the fourth International Symposium on Semiconductor Wafer Bonding: Science, Technology and Applications, The Electrochem. Society Proceedings, Vol. 97–36, Pennington, NJ, 1998 p. 365.
[27] A.D. Becke, J. Chem. Phys. 98 (1993) 5648.
[28] C. Lee, W. Yang, R.G. Parr, Phys. Rev. B 37 (1988) 785.
[29] Gaussian 98, M.J. Frisch et al., Gaussian Inc., Pittsburgh, PA, 1998.
[30] A.B. Gurevich, B.B. Stefanov, M.K. Weldon, Y.J. Chabal, K. Raghavachari, Phys. Rev. B 58 (1998) R13434.
[31] M.K. Weldon, K.T. Queeney, Y.J. Chabal, B.B. Stefanov, K. Raghavachari, Chem. Phys. Lett. (1999), submitted for publication.
[32] W.B. Jackson, A. Franz, Y. Chabal, M.K. Weldon, H.-C. Jin, J.R. Abelson, in: N.H. Nickel, W.B. Jackson, R.C. Bowman, R.G. Leisure (Eds.), Hydrogen in Semiconductors and Metals, MRS Proceedings, 513, Warrendale, Penn, MRS, 1998, pp. 381–386.
[33] B. Mukashev, S. Tokmoldin, Kh. Abdullin, Yu. Gorelkinskii, Physica B 273–274 (1999). These Proceedings.

ELSEVIER

Physica B 273–274 (1999) 164–166

PHYSICA B

www.elsevier.com/locate/physb

The dipole moments of H_2, HD and D_2 molecules and their concentrations in silicon

R.C. Newman[a,*], R.E. Pritchard[a], J.H. Tucker[a], E.C. Lightowlers[b,1]

[a]*CEMD, The Blackett Laboratory, Imperial College of Science, Technology and Medicine, Prince Consort Road, London, SW7 2BZ, UK*
[b]*Physics Department, King's College London, Strand, London, WC2R 2LS, UK*

Abstract

The relative strengths of infrared active modes of H_2, HD and D_2, present as H_2–O_i centres (ν_1 and ν_2), or isolated molecules (ν_3) in Si pre-heat treated at 1300°C in a 50 : 50 mixture of H_2 and D_2 gases are reviewed. The effective charges $\eta(\nu_{1HH})$ and $\eta(\nu_{2HH})$ are equal to $\eta(\nu_{1DD})$ and $\eta(\nu_{2DD})$, respectively, but $\eta(\nu_{3HH}) = 0.08e$ is larger than $\eta(\nu_{3DD}) = 0.05e$. The relative strengths of the three HD modes are smaller than expected by a factor of ~ 3. Possible reasons for this discrepancy, including isotopic exchange, are discussed.

PACS: 81.05.Cy; 67.80.Mg; 63.20.Pw

Keywords: Silicon; Hydrogen Molecules; Dipole moments; Infra-red absorption

1. Introduction

Infrared (IR) active H_2, HD and D_2 molecules are detected in Czochralski (CZ) Si heated at 1300°C in mixtures of H_2 and D_2 gases, followed by a quench to 300 K [1]. Sets of modes, labelled ν_{1HH}(3788.9 cm^{-1}), ν_{1HD}(3304.3 cm^{-1}), ν_{1DD}(2775.4 cm^{-1}) and ν_{2HH}(3731 cm^{-1}), ν_{2HD}(3285.3 cm^{-1}), ν_{2DD}(2716.0 cm^{-1}) relating to H_2–O_i pairs have strengths correlated with the paired O_i absorption at 1075 cm^{-1}. Anneals at $50 \leqslant T \leqslant 150$°C lead to increases of the integrated absorption coefficients (IA) of a third set of modes ν_{3HH}(3618 cm^{-1}), ν_{3HD}(3264.8 cm^{-1}), ν_{3DD}(2642.5 cm^{-1}) of isolated molecules (ν_3), that had diffused away from O_i atoms: they are also present in float-zone (FZ) Si [2]. Measured effective charges η (dipole moment per unit displacement) are: $\eta(\nu_{1HH}) = 0.07e \sim \eta(\nu_{1DD}) = 0.06e : \eta(\nu_{2HH}) = 0.14e \sim \eta(\nu_{2DD}) = 0.17e : \eta(\nu_{3HH}) = 0.08e$ [2]: $\eta(1075) = 3.5e$, where e is the electron charge.

Permeation measurements imply that H atoms diffuse into Si at $T \sim 1200$°C [3], with H_2 formation during cooling. Concentration ratios of 1 : 2 : 1 are expected for $[H_2] : [HD] : [D_2]$ for Si heated in H_2(50%) and D_2(50%) gases. If the modes of a set have the same η, the expected IA ratios are 1 : 1.5 : 0.5, since IA is proportional to η^2/μ (μ is the reduced mass of the molecule). Measured ratios for both the ν_1 and ν_2 modes are 1 : 0.4 : 0.4. IA (ν_{HH}) : IA (ν_{DD}) is close to the prediction of 1 : 0.5 but IA (ν_{1HD}) and IA (ν_{2HD}) are too small by a factor greater than 3. For $\nu_{3HH} : \nu_{3HD} : \nu_{3DD}$, the IA ratios are 1 : 0.2 : 0.2 so that IA (ν_{3DD}) and IA (ν_{3HD}) are smaller than expected by factors of 2.5 and 7.5, respectively. We shall show that deuterium behaves in the same way as hydrogen but we find $\eta(\nu_{3DD}) < \eta(\nu_{3HH})$, explaining the discrepancy of 2.5. We then discuss the remaining discrepancies of ~ 3 and 7.5.

2. The pressure dependence of the solubilities of [H] and [D] in Si at 1300°C

Samples with $[B] = 10^{17}$ cm^{-3} were heated to 1300°C in mixtures of H_2 and Ar, with H_2 partial pressures $p = 0.17, 0.29, 0.40, 0.60$ or 1.0 bar, or in D_2 and Ar, with similar D_2 partial pressures (Fig. 1). Measured values

* Corresponding author. Tel.: + 44-201-594-6666; Fax: + 44-207-581-3817.

[1] Deceased.

E-mail address: r.newman@ic.ac.uk (R.C. Newman)

0921-4526/99/$ - see front matter
PII: S0921-4526(99)00436-6

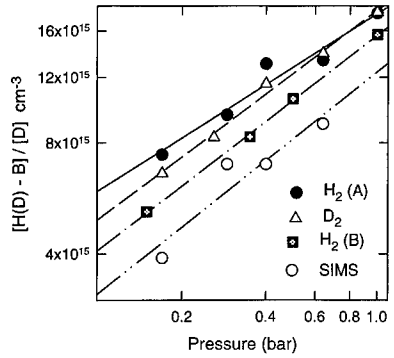

Fig. 1. Plots of log[H–B] versus the logarithm of the partial pressure (log p) of H_2 or D_2 gas in which Si samples were heated at 1300°C. H_2(A) and H_2(B) refer to the present and our previous [2] IR measurements, respectively. The average gradient of these lines is ~ 0.56.

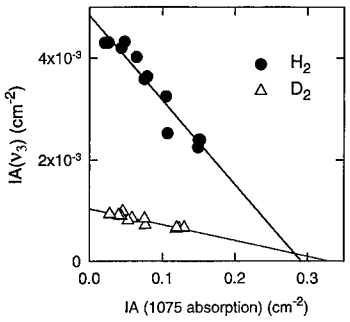

Fig. 2. The strengths (IA values) of the ν_{3DD} mode versus the strengths of the IR line at 1075 cm^{-1} from D_2–O_i pairs, showing a linear reversible anti-correlation, leading to $\eta(\nu_{3DD}) = 0.05e$. Corresponding data for [H_2–O_i], shown for comparison, yield $\eta(\nu_{3HH}) = 0.08e$.

of IA (1904 cm^{-1}), due to H–B pairs, increase to IA (1904_{MAX}) during anneals at 175°C [4]. The known IR calibration for the H–B mode [4] allows IA (1904_{MAX}) to be converted to $[H\text{–}B]_{MAX}$ that was equated to $[H]_{MAX}$ (Fig. 1). Measured values of IA (1390 cm^{-1}) due to D–B absorption at 1390 cm^{-1} leads to $[D\text{–}B]_{MAX}$, and hence $[D]_{MAX}$ for deuterated samples. $[H]_{MAX}$ and $[D]_{MAX}$ are consistent with SIMS measurements of [D] [5]. Plots of $\log[H(D) - B]_{MAX}$ and $\log[D]_{SIMS}$ versus $\log p$ (Fig. 1) yield lines with gradients of 0.48 ± 0.07 (H)(IR), 0.56 ± 0.03 (D)(IR), 0.57 (D)(SIMS) and 0.57 (H)(IR), in agreement with 0.56 (H) found in the early permeation measurements [3].

3. The effective charge of the ν_{3DD} vibrational mode

A CZ Si sample deuterated at 1300°C showed absorption from D_2–O_i pairs with IA ($1075 = 0.12\ cm^{-2}$) and the ν_{3DD} mode (D_2) with $IA(\nu_{3DD}) = 6.4 \times 10^{-4}\ cm^{-2}$. Thirty minutes isochronal anneals at $50 \leqslant T \leqslant 150$°C leads to a linear anti-correlation of the strengths of these modes (Fig. 2), and yields $\eta(\nu_{3DD}) = 0.05(\pm 0.001)e$, that is *smaller* than $\eta(\nu_{3HH}) = 0.08(\pm 0.001)e$ [2]. The concentrations, $[H_2]_{MAX}$ and $[D_2]_{MAX}$ of 2.6×10^{15} and $3.0 \times 10^{15}\ cm^{-3}$, derived from the values of η for samples heated in $[H_2] = [D_2]$ lead to $IA(\nu_{3HH}) : IA(\nu_{3DD}) = 1 : 0.2$. Thus, the apparent discrepancy of 2.5 identified in Section 1 is explained.

An Arrhenius plot Eq. (1) of the measurements is shown in Fig. 3. ΔE is the D_2–O_i

$$[D_2\text{–}O_i]_T/[\nu_{3DD}]_T = (g_1/g_2)\exp(+\Delta E/kT), \quad (1)$$

binding energy and g_1 and g_2 relate to the number of configurations accessible to bound and isolated D_2 molecules [2]. The gradient yields $\Delta E = 0.25 \pm 0.02$ eV and

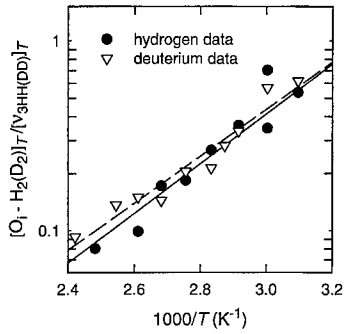

Fig. 3. An Arrhenius plot of $[D_2\text{–}O_i]_T/[\nu_{3DD}]_T$, yielding a binding energy of 0.25 eV for D_2 molecules paired to bond-centred O_i atoms in Si. The intercept on the y-axis leads to a density of accessible sites for isolated molecules close to $5 \times 10^{22}\ cm^{-3}$, corresponding to the density of interstitial lattice sites. Our previous data for [H_2–O_i] are included for comparison [2].

g_1/g_2 is found from the y-axis intercept. We took $g_1 = 6 \times 10^{18}\ cm^{-3}$ [2] and obtained $g_2 = 7(+8, -3) \times 10^{22}\ cm^{-3}$, the number density of interstitial lattice sites, $5 \times 10^{22}\ cm^{-3}$, multiplied by a small numerical factor. These values are close to $\Delta E = 0.26 \pm 0.02$ eV and $g_2 = 13(+10, -7) \times 10^{22}\ cm^{-3}$ for hydrogenated Si [2]. Thus, both H_2 and D_2 molecules can access all interstitial lattice sites.

4. Discussion

In summary, the behaviour of D_2 molecules is similar to that of H_2 molecules. We find, (a) $[H_2] = [D_2]$ for ν_1, ν_2 and ν_3 centres present in samples heated in a 50 : 50 mixture of H_2 and D_2 gases; (b) $IA(\nu_{1HD})$, $IA(\nu_{2HD})$ and $IA(\nu_{3HD})$ (compared with $IA(\nu_{3DD})$) are all smaller

than expected by a factor of ~ 3; (c) $\eta(\nu_{3DD})$ is smaller than $\eta(\nu_{3HH})$. We are unaware of such a difference, (c), for other isotopically related centres but, unusually, there is evidence that the dipole and molecular axes of ν_3 centres are not parallel [6,7], and so the molecular axes of H_2, HD and D_2 may all be different. Stress-alignment measurements of the ν_{3HH} mode [7] imply a static axis close to $\langle 0\,0\,1\rangle$ with the possibility of pairing of H_2 molecules with an impurity. H_2–O_i and D_2–O_i pairs may, however, have common axes due to the presence of the O_i atom.

The ν_{3HH} and ν_{3DD} modes are also detected by Raman scattering for samples pre-heated at 150°C in a mixed $H_2 : D_2$ plasma [8]. Pairing with an impurity would require its concentration to exceed $\sim 10^{18}\,cm^{-3}$. This is difficult to understand but a second H_2 molecule could be a candidate. We have considered but rejected the possibility that paired molecules are incorporated as $2H_2$–O_i centres (rather than H_2–O_i) [1] but we have found no evidence of pairing for ν_3 centres. Recent Raman measurements show that the ν_{3HD} mode is weaker than the H_2 and D_2 modes by a factor of ~ 10 [9]. Since the polarizability of HD molecules is likely to be similar to those of H_2 and D_2 molecules, it is implied that [HD] is much smaller than expected. We therefore calculated the kinetics of H_2, HD and D_2 formation from H and D atoms with various initial conditions. As an example, we assumed that the diffusion coefficient D_D of D-atoms is smaller than D_H ($= 2\times10^{-6}\,cm^2\,s^{-1}$ at 400°C) [3] by a factor of $\sqrt{2}$ and that samples initially contained [H] (0.55%) and [D] (0.45%) but the value of [HD] was still closely equal to ($[H_2] + [D_2]$). Thus, reducing D_D, and the value of [D], does not explain a low value of [HD].

We then supposed that [HD] might be reduced by isotopic exchange, i.e. $2HD \rightarrow H_2 + D_2$, since this reduces the total zero-point energy by $135\,cm^{-1}$. If $[H_2] = [D_2]$ and it is presumed that HD and DH are equivalent, the equilibrium relation becomes

$$[HD]/[H_2] = 2\exp(-\Delta E/2kT). \quad (2)$$

At 100°C ($kT = 260\,cm^{-1}$) the ratio $[HD]/[H_2] = 1.54$ is too close to 2 to explain the small IAs of the HD modes. However, HD may not be equivalent to DH (splitting of the ν_{3HD} modes is not detected) due to a preferred sense of alignment in an interstitial site. If the pre-exponential factor of 2 in Eq. (2) is then omitted, $[HD]/[H_2]$ is reduced to 0.77 and the concentration ratios of 1 : 0.77 : 1 lead to ratios of the IAs 1 : 0.58 : 0.5, close to those measured for the ν_1 and ν_2 modes. The ratios of the concentrations of the ν_3 modes would also be close to those predicted if $\eta(\nu_{3HD})$ were assumed to be equal to $\eta(\nu_{3DD}) = 0.05e$, rather than $\eta(\nu_{3HH})$. Consequently, we calculated the rate at which HD–HD collisions would occur at 100°C, leading to their loss by local rebonding and assuming that a large barrier did not exist for the latter process. Second order kinetics with $D(HD) = D(H_2) = 7.5\times10^{-15}\,cm^2\,s^{-1}$ (see Ref. [10]) leads to $d[HD]/dt = 6\times10^{10}\,s^{-1}$ at 373 K and equilibrium would be reached in ~ 10 h. The time increases to $\sim 10^3$ h at 300 K. This process of isotopic exchange could help explain the low values [HD] observed by IR absorption but it cannot explain the Raman results.

The IR discrepancies for the HD modes would also be removed if correlated H–H and D–D pairs diffuse into Si at 1300°C ($\sim 70\%$ of the hydrogen), as well as H- and D-atoms. A proposal for in-diffusion of molecules was made in Ref. [3] but it is difficult to reconcile this process with the pressure dependencies of H and D incorporation (Fig. 1). The situation is less clear for introduction of hydrogen from a plasma at a much lower temperature.

In summary, the effective charges of H_2 and D_2 molecules paired with O_i atoms are equal but η_{3DD} is smaller than η_{3HH} for isolated molecules. Small dipole moments of isolated and paired HD molecules or small reductions of [HD], by a factor of ~ 3, could explain the IR measurements. However, $[\nu_{3HD}]$ must be significantly reduced in relation to $[\nu_{3HH}]$ and $[\nu_{3DD}]$ to explain the Raman data. There are clearly on-going problems to be resolved.

Acknowledgements

We thank R. Jones for discussions, M. Stavola and J. Weber for communicating unpublished results and The EPSRC for contracts GR/K96977 (ICSTM) and GR/K30995 (KC), respectively. This paper is dedicated to the memory of Professor E.C. Lightowlers.

References

[1] R.E. Pritchard, M.J. Ashwin, J.H. Tucker, R.C. Newman, E.C. Lightowlers, M.J. Binns, S.A. McQuaid, R. Falster, Phys. Rev. B 56 (1997) 23118.
[2] R.E. Pritchard, M.J. Ashwin, J.H. Tucker, R.C. Newman, Phys. Rev. B 57 (1998) 15048.
[3] A. Van Wieringen, W. Warmoltz, Physica (Amsterdam) 22 (1956) 849.
[4] S.A. McQuaid, R.C. Newman, J.H. Tucker, E.C. Lightowlers, R.A.A. Kubiak, M. Goulding, Appl. Phys. Lett. 58 (1991) 2933.
[5] M.J. Binns, S.A. McQuaid, R.C. Newman, E.C. Lightowlers, Semicond. Sci. Technol. 8 (1993) 1908.
[6] B. Hourahine, R. Jones, S. Öberg, R.C. Newman, P.R. Briddon, E. Roduner, Phys. Rev. B 57 (1998) 12666.
[7] J.A. Zhou, E. Chen, M. Stavola, 273–274 (1999) 198, These Proceedings.
[8] A.W.R. Leitch, V. Alex, J. Weber, Phys. Rev. Lett. 81 (1998) 421.
[9] J. Weber, Private communication, 1999.
[10] V.P. Markevich, M. Suezawa, J. Appl. Phys. 83 (1998) 2988.

ELSEVIER

Physica B 273–274 (1999) 167–170

PHYSICA B

www.elsevier.com/locate/physb

Deep levels of vacancy-hydrogen centers in silicon studied by Laplace DLTS

K. Bonde Nielsen[a,*], L. Dobaczewski[b], K. Goscinski[b], R. Bendesen[a], Ole Andersen[a], B. Bech Nielsen[a]

[a]*Institute of Physics and Astronomy, University of Aarhus, DK-8000 Aarhus C, Denmark*
[b]*Institute of Physics, Polish Academy of Sciences, al. Lotników 32/46, 02-668 Warsaw, Poland*

Abstract

We identify the acceptor levels $(-/0)$ of the VH and V_2H defects in silicon from comparison of DLTS and EPR annealing data. The levels are very close to each other and close to the acceptor level of the PV defect (the E-center) as well. In order to separate them, we have applied the high-resolution technique of Laplace DLTS and compared the formation and annealing properties of defects generated by implantation of hydrogen or helium. We further applied Laplace DLTS in combination with uniaxial stress to study the acceptor level at $E_c - E_t = 0.31$ eV previously assigned to a vacancy-hydrogen–oxygen defect. We find, in accordance with recent EPR measurements, that the defect displays orthorhombic-I symmetry and rule out that it contains two hydrogen atoms. The defect can be understood as a single hydrogen atom bound inside the A-center, the well-known VO defect of silicon, and we denote it VOH accordingly. The observed orthorhombic-I symmetry arises because the hydrogen atom (at $T = 160$ K) swiftly jumps among two equivalent sites across the (1 1 0) plane that contains the Si–O–Si bond. Previous studies have shown that hydrogenation of oxygen-rich electron-irradiated samples leads to the formation of VOH with simultaneous depletion of the A-center. Our structural data are in accordance with this dynamic behavior.

Keywords: Silicon; Hydrogen; Laplace DLTS; Uniaxial stress

1. Introduction

Defects involving light and chemical active impurity atoms generally give rise to one-electron states within the semiconductor band gap. This is true not least for hydrogen for which several electrically active vacancy-related centers are expected to exist on the basis of electron paramagnetic resonance (EPR) and Fourier transform infrared (FTIR) data and theoretical results. The ability of hydrogen to be trapped at dangling bonds or even to break Si–Si bonds is well known. For instance, this occurs when a hydrogen atom binds to a vacancy complex in silicon since it is energetically favorable to form a Si–H bond at the expense of breaking an elongated bond in these complexes. The strong Si–H bond does not give rise to one-electron states within the bandgap, and hence does not determine the electrical properties of the defect. These are determined largely by the combination of the sp^3-like orbitals residing on the silicon neighbors to the vacant sites. A vacancy-hydrogen defect (V_nH) will typically contain a dangling bond with an unpaired electron or a lone pair in addition to the bond that has been saturated by hydrogen and may also contain elongated bonds forming bridges between Si–Si second neighbors. The electronic properties will be determined largely by the wavefunction of the dangling-bond electrons. This implies that V_nH defects may be expected to give rise to families of very similar deep levels in silicon. As

* Corresponding author. Fax: + 45-8612-0740.
E-mail address: kbn@ifa.au.dk (K. Bonde Nielsen)

0921-4526/99/$ - see front matter
PII: S0921-4526(99)00437-8

prominent examples of the effect of the bond reconstruction that occurs when hydrogen is incorporated in vacancy centers we investigate the modification of the acceptor levels of the monovacancy and divacancy. We find that the (0/−) levels of VH and V_2H are indeed very similar and similar to that of the E-center (VP). We explain this by noting that the lone pair attached to the phosphorus donor is electronically inert and plays a role equivalent to that of the Si–H unit. We further examine the analogous level introduced when the vacancy-oxygen center (the A-center) traps a single hydrogen atom.

2. Experimental method and details

So far none of the deep levels reported in the literature as vacancy-hydrogen related has been unambiguously assigned to a specific defect structure. This lack of definite assignments may be connected with the very similar electronic properties expected for these defects. Hence, their thermal emission properties may be difficult to discern by commonly used space-charge techniques like conventional deep-level transient spectroscopy (DLTS). In an attempt to separate the levels, we have taken advantage of the improved resolution offered by Laplace transform DLTS [1], which enabled us to separate the emission from similar centers and to follow their annealing behavior separately. This offers the possibility of correlating with the annealing of specific vacancy-hydrogen defects that have been structurally identified previously by EPR [2–4], and thereby identify the microstructure associated with the deep levels. Furthermore, from Laplace DLTS in combination with uniaxial stress the local symmetry of a center may be determined for direct comparison with FTIR and/or EPR data. We have applied mesa etched p^+n diodes with the p^+ layer grown epitaxially on 8 Ω cm FZ silicon substrate and Schottky diodes on 20 Ω cm CZ stress crystals. The diodes were implanted at or below room temperature with hydrogen or helium at equivalent (low) damage loads in order to distinguish between hydrogen-specific levels and intrinsic levels caused by the ion-beam damage. The implantation doses were chosen to generate the same number of primary vacancies at the end of range of the ions. The energies were chosen so that the range matched the middle of the depletion layer at 15 V reverse bias. The implantations were carried out at low temperature (60 K) and the samples were subsequently annealed at 400 K under reverse bias to remove the E-center [5]. We also compared with data for electron-irradiated diodes.

3. The VH and V_2H centers

The identification of two hydrogen-related centers by Laplace DLTS is illustrated in Fig. 1. Here we compare

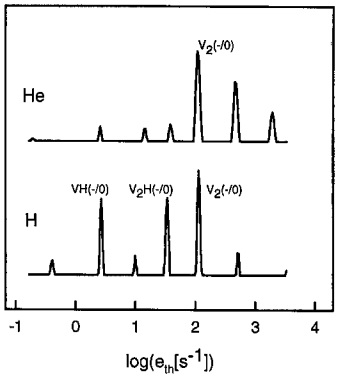

Fig. 1. Comparison of Laplace DLTS spectra measured at 225 K and displayed as function of the emission rate (e_{th}). Lower plot: Hydrogen-implanted sample ($\sim 10^{10}$ cm^{-2}), upper plot: Helium-implanted sample ($\sim 10^{9}$ cm^{-2}). The samples (FZ silicon) have been implanted at 60 K and reverse-bias annealed at 400 K. See Fig. 2 for the assignment of the emission-rate peaks to VH and V_2H.

spectra recorded with helium-implanted and hydrogen-implanted diodes. The Laplace transformed capacitance transients reveal three dominant peaks for the hydrogen-implanted sample and two for the helium-implanted sample. One of the peaks is common to both samples and can be assigned to the acceptor level of the divacancy $V_2(-/0)$ as identified previously [6]. The position of the $V_2(-/0)$ peak has been confirmed by measurements on electron-irradiated samples. Prior to the annealing of the E-center at 400 K, the Laplace spectra of the electron-irradiated samples contained two separated but very close lying peaks; the E-center and $V_2(-/0)$. After the annealing only the $V_2(-/0)$ signal remained. The origin of the second of the main signals in the helium-implanted sample is unknown. It may possibly come from a more complex vacancy center formed as a result of the denser collision cascades of the He implantation. After the 400 K anneal two hydrogen-related signals remain, which we tentatively ascribe to VH and V_2H as marked in the figure. We note that the V_2H and the (removed) E-center have practically equal emission rates and that VH is identical to the previously reported E5 center [7].

In order to confirm our tentative assignments we carried out a simultaneous annealing study of the hydrogen-related signals including also the oxygen-related VOH signal discussed below, and compared the results with recent EPR annealing data. This comparison is depicted in Fig. 2. As can be seen from the figure a clear correlation exists between our annealing data and the EPR results. In both cases the same sequence of annealing steps is observed, and also the individual absolute transition temperatures agree well considering the fact

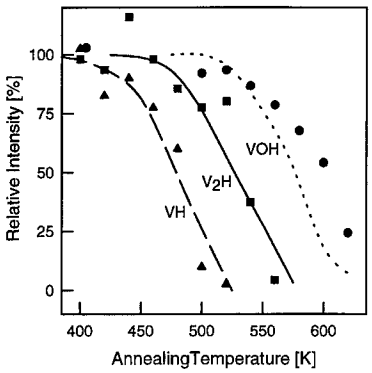

Fig. 2. Correlation of Laplace DLTS and EPR isochronal annealing data. The data points refer to emission peaks (see Fig. 1) and the smoothed curves to EPR data from Refs. [2–4]. The EPR data for VOH has been shifted slightly in temperature to comply with the 1 h annealing times applied in all other cases.

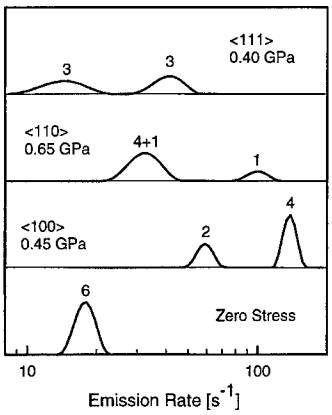

Fig. 3. Splitting of the Laplace DLTS emission-rate peak of VOH caused by uniaxial stress. Data for three different directions of stress (⟨1 0 0⟩, ⟨1 1 0⟩, and ⟨1 1 1⟩) obtained at 160 K with 20 Ω cm n-type CZ samples are shown. The numbers assigned to the individual peaks indicate the intensity ratios (normalized to the zero-stress intensity) expected for an orthorhombic center. The experimental relative intensities (summation over the number of equidistant data points in each peak) agree to within 10% with these numbers. For ⟨1 1 0⟩ stress the (4 + 1) component is unresolved.

that the implantation doses applied in the two kinds of measurements differ by more than three orders of magnitude. This may indicate that the annealing of the individual centers is governed by thermal dissociation rather than migration or trapping. We assert that the annealing data confirm the assignment of the DLTS peaks suggested in Fig. 1. For VH(0/−) and V_2H(0/−), we obtain the activation enthalpies 0.443 and ~0.43 eV, respectively. These values are practically indistinguishable from those obtained for V_2(0/−) and PV(0/−).

4. The VOH center

The annealing series depicted in Fig. 2 include data for an oxygen-related center denoted VOH. This center is abundant in oxygen-rich samples implanted with protons at low temperature when the samples are taken to room temperature under zero bias. The VOH center was originally studied in proton-implanted samples in Ref. [7] and ascribed to a vacancy-oxygen configuration partly saturated with hydrogen. The same center is formed when the A-center is passivated [8]. It forms, for instance, by wet chemical etching of electron-irradiated samples and this process has recently been studied in detail [9,10]. In the previous works, the center with an activation enthalpy of 0.31 eV has been denoted E3 [7], NH1 [9], or E4 [10]. The effect of uniaxial-stress on the emission rate of VOH measured at 160 K is shown in Fig. 3. The observed pattern and intensity ratio of the stress-split components are characteristic for a center with orthorhombic-I symmetry. The recently identified EPR signal of the A-center binding a single hydrogen atom displays the same symmetry [4] at this measurement temperature considering the different time scales of the measurements. On the basis of this and the correlation of the annealing behavior of the EPR and Laplace DLTS signals, we identify the VOH center with the A-center saturated by a single hydrogen atom. It has been suggested [10] that the VOH center contains two hydrogen atoms. This is at variance with our results. The low implantation dose ($< 10^{10}$ H/cm^2) makes it highly unlikely that hydrogen dimers should form below room temperature. In our experience, this requires at least ~4 orders of magnitude higher doses. More importantly, the EPR signal, which correlates with our data, unambiguously reveals that the center contains only one hydrogen atom [4].

5. Concluding remarks

From comparison with the available EPR data, we have ascribed specific vacancy-hydrogen defects to three deep acceptor states with similar properties. The electrical activity of all three centers can be understood in terms of characteristic and similar configurations of elongated-bond and dangling-bond orbitals as mentioned in the introduction. In particular for VH and V_2H the electronic structure should be extremely similar to that of the E-center, as confirmed by our results. The VOH level forms when a hydrogen atom breaks the elongated Si–Si bond in the VO-center, forms a Si–H bond, and leaves

a dangling-bond occupied by one or two electrons in the neutral or negative charge states, respectively. In the uniaxial-stress experiment, we observe orthorhombic-I symmetry because the hydrogen atom and the dangling bond swiftly interchange positions at the temperature at which the data is recorded. This interpretation is quantitatively consistent with the observation by EPR [4] of a monoclinic-I to orthorhombic-I transition at low temperature. Thus, the observed orthorhombic-I symmetry does not imply that two hydrogen atoms saturate the VO center. Actually, we expect this defect (VOH_2) to be electrically inactive since it does not possess any dangling bond.

Acknowledgements

This work has been supported by the Danish National Research Foundation through the Aarhus Center for Atomic Physics (ACAP) and the Committee for Scientific Research in Poland grant No. 8T11B00315. Pia Bomholt is gratefully acknowledged for preparation of samples.

References

[1] L. Dobaczewski, P. Kaczor, I.D. Hawkins, A.R. Peaker, J. Appl. Phys. 76 (1994) 194.
[2] B. Bech Nielsen, P. Johannesen, P. Stallinga, K. Bonde Nielsen, J.R. Byberg, Phys. Rev. Lett. 79 (1997) 1507.
[3] P. Stallinga, P. Johannesen, S. Herstrøm, K. Bonde Nielsen, B. Bech Nielsen, J.R. Byberg, Phys. Rev. B 58 (1998) 3842.
[4] P. Johannesen, B. Bech Nielsen, J. R. Byberg, contribution to ICDS20.
[5] L.C. Kimerling, H.M. DeAngelis, C.P. Carnes, Solid State Commun. 16 (1975) 171.
[6] A.O. Evwaraye, E. Sun, J. Appl. Phys. 47 (1976) 3776.
[7] B.G. Svensson, A. Hallen, B.U.R. Sundqvist, Mater. Sci. Eng. B 4 (1989) 285.
[8] S.J. Pearton, Phys. Stat Sol. A 72 (1982) K73.
[9] Y. Tokuda, H. Shimada, in: N.H. Nickel, W.B. Jackson, R.C. Bowman, R.G. Leisure (Eds.), Hydrogen in Semiconductors and Metals, Mater. Res. Soc., Warrendale, PA, Vol. 513, 1998, p. 363.
[10] O.V. Feklisova, N.A. Yarykin, Semicond. Sci. Technol. 12 (1997) 742.

ELSEVIER

Physica B 273–274 (1999) 171–175

PHYSICA B

www.elsevier.com/locate/physb

Hydrogen-induced extended complexes in silicon

Yu.V. Gorelkinskii*, Kh.A. Abdullin, B.N. Mukashev

Kazakhstan Academy of Sciences, Institute of Physics and Technology, 480082 Almaty, Kazakhstan

Abstract

New EPR spectrum, labeled Si-AA17, forms upon annealing at $\geqslant 200°C$ in irradiated high-purity hydrogen-containing silicon and is stable up to $\sim 450°C$. The AA17 defect has D_{3d} symmetry, electronic spin $S = 1$ and it is paramagnetic in a neutral charge state. An analysis of ^{29}Si hf interaction has shown that 62% of the resonant wave function belongs to two equivalent silicon atoms. The magnitude of zero-field splitting ($D = 16.8$ MHz) indicates that the distance between two equivalent Si sites (spins) creating the $S = 1$ state is ~ 12 Å along the $\langle 1\,1\,1\rangle$ axis. Piezospectroscopic measurements have also shown that vacancy-like defect should be sited between equivalent Si atoms. Tentative model of the defect is the $\{1\,1\,1\}$ planar hexavacancy centered between two $\langle 1\,1\,1\rangle$ dangling Si bonds separated by ~ 12 Å. Each of these dangling bonds is formed as a result of saturation of the nearest Si atom by one hydrogen. Si-AA1 EPR spectrum associated with the formation of self-interstitial aggregates is observed simultaneously with the Si-AA17.

Keywords: Hydrogen; Silicon; Defects formation; EPR

1. Introduction

The properties of hydrogen in crystalline silicon are extremely varied. For a long time hydrogen has been known to saturate dangling bonds at surface and grain boundaries, to passivate shallow impurities (such as boron, phosphorus, etc.), deep-level impurities and defects [1,2]. A number of hydrogen-related defects have been observed in silicon samples [3–5] after H-implantation or introduction of H atoms by other ways. It has been recently discovered that unique planar defects (described as "platelets") over diameters of many tens of nanometers are created in $\{1\,1\,1\}$ plane after hydrogenation of silicon and involve the coordinated formation of Si–H bond [6,7]. It has been suggested (from IR study) that two trigonal symmetry structures – di-hydrogen-saturated double vacancy layer and metastable di-hydrogen complex double layer (H_2^*), are most preferable models for the platelet structures [8]. Results of theoretical investigations of the H-platelets are generally in agreement with experimental data [9,10]. However, the formation mechanism of the H-platelets continues to be a puzzle and arouses applied and basic interest.

In this paper, we present hydrogen-induced defect extended along $\langle 1\,1\,1\rangle$ axis, which was detected by electron paramagnetic resonance (EPR) in irradiated silicon. The defect, labeled Si-AA17, has trigonal (D_{3d}) symmetry and spin $S = 1$. Characteristics of the AA17 EPR center allow to suggest that it can be considered as a precursor of platelets or microplatelets in silicon.

2. Experimental procedures

Samples used for our study were prepared from uncompensated high-purity, float-zone refined (FZ) silicon ingot with resistivity of $\sim 3000\,\Omega$ cm. Hydrogen was incorporated either by proton implantation or by thermal annealing of samples in the presence of water vapor. Implantation was carried out at the sample temperature of ~ 300 K with starting proton energy of 30 MeV and dose corresponding to a concentration of $\sim 1 \times 10^{17}$ H/cm^3. Alternatively, "as-grown" samples were sealed in a quartz ampoule containing $\sim 10^{-3}$ ml of H_2O, annealed at 1250°C for 30 min, and then cooled

* Corresponding author. Fax: + 7-3272-545-224.
E-mail address: yuvg@satsun.sci.kz (Yu.V. Gorelkinskii)

0921-4526/99/$ - see front matter
PII: S0921-4526(99)00438-X

rapidly to room temperature. Then the samples were irradiated at room temperature either by 50 MeV α-particles or by 30 MeV protons (with no implantation) with dose of $\sim 1 \times 10^{16}$ cm^{-2}.

After implantation (irradiation) the crystals were cut into small samples suitable for EPR measurements ($12 \times 1.4 \times 0.5$ mm^3) with long dimension along the $\langle 1\,1\,0 \rangle$ direction. The measurements were performed on 37 GHz (Q-band) EPR spectrometer with 100 kHz magnetic field modulation at sample temperature of 77 K mainly in dispersion.

3. Experimental results

After implantation (irradiation), several known EPR spectra (P3, P6, A5 [11]) are detected. A new Si-AA17 spectrum with low intensity is observed at sample temperature 77 K after brief illumination by white light. Heat treatment of sample at $\sim$200–300°C for 20 min increases significantly the AA17 intensity and produces three known spectra: Si-P1 (pentavacancy) [12], Si-A3 (tentatively is $\langle 1\,1\,1 \rangle$ planar tetravacancy) [13] and Si-AA1 (with C_{2v} symmetry) which was previously identified as hydrogen-induced double donor in a positive charge state and associated with self-interstitial aggregation [3,14]. So these four defects are dominant in the sample upon annealing at 350°C. Illumination of sample at 77 K leads to generation of AA17 spectrum, increases the intensity of AA1 and significantly decreases intensity of P1 and A3 (Fig. 1). It is important to note that AA17 and AA1 spectra are observed in both the H-implanted and irradiated H-containing samples. However, in irradiated hydrogen-free samples AA17 and AA1 spectra are absent while spectra characteristic of neutron or proton irradiation such as P3 (tetravacancy [15]) or following annealing P1 and A3 are predominant ones. The AA17 spectrum reaches the maximum intensity after annealing at $\sim$350°C and disappears completely in the temperature range from 425°C to 450°C (Fig. 2).

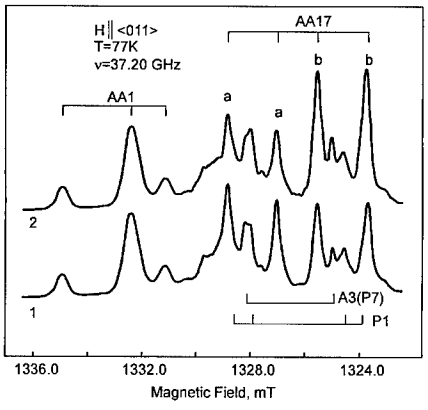

Fig. 1. EPR spectra of high-purity zone-refined silicon sample implanted with hydrogen (dose corresponding to $\sim 1 \times 10^{17}$ H/cm^3) upon annealing at 350°C for 20 min: (1) "as-annealed" (2) the sample was additionally annealed at 200°C for 1 h under stress of 150 MPa along $\langle 0\,1\,1 \rangle$ axis and then cooled to room temperature with stress on. Spectra were measured under band-gap illumination at 77 K in dispersion.

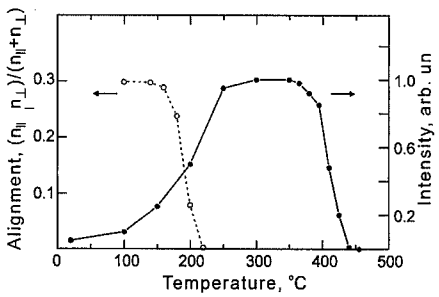

Fig. 2. Intensity of the Si-AA17 spectrum (filled circles) and recovery of the stress-induced alignment of the defect (open circles) versus temperature of a 15 min isochronal annealing of hydrogen-implanted FZ-Si sample.

The AA17 spectrum can be described as arising from an anisotropic defect of trigonal symmetry with the spin-Hamiltonian

$$H = \beta_B S \cdot g \cdot H + S \cdot D \cdot S + \sum_j I_j A_j S \qquad (1)$$

with $S = 1$. The first term presents the electronic Zeeman interaction, the second term is the fine structure, and the last one the magnetic hyperfine interaction with ^{29}Si nuclei. The spin-Hamiltonian parameters were found by fitting with the experimentally obtained spectrum and tabulated in Table 1. The positions of fine structure lines versus direction of magnetic field are shown in Fig. 3.

A low-intensity pair of satellites on the AA17 spectrum were interpreted as arising from a strong hyperfine (hf) interaction with a ^{29}Si isotope ($I_N = \frac{1}{2}$, naturally abundant of $\sim$4.7%). The intensity ratio of the hyperfine structure line to the corresponding central line is $\sim$5%. It indicates that two silicon equivalent sites participate in the hf interaction. Therefore, the symmetry of the AA17 defect is D_{3d}. An analysis of the hf interaction was performed in terms of a one-electron wave function for unpaired electron which is a linear combination of atomic orbitals centered on the atoms near the defect [12,16]. Using values of $|\psi^2(0)|_{3s} = 31.5 \times 10^{24}$ cm^{-3} and $\langle r^{-3} \rangle_{3p} = 16.1 \times 10^{24}$ cm^{-3} previously obtained for silicon [12], we have calculated that 62% of the spin wave function is located on the two equivalent silicon atoms, which has 91% 3p and 9% 3s character. The distribution of the wave function of the AA17 is thus characteristic of the dangling silicon bond in the vicinity of vacancy-like defect [16,17].

Table 1
Spin-Hamiltonian parameters of the Si-AA17 EPR center

Term	∥	⊥
g	2.0028 ± 0.0003	2.0106 ± 0.0003
D (MHz)	$\pm (33.6 \pm 0.5)$	$\mp (16.8 \pm 0.5)$
A (MHz)	$\pm (175 \pm 2)$	$\pm (89 \pm 2)$

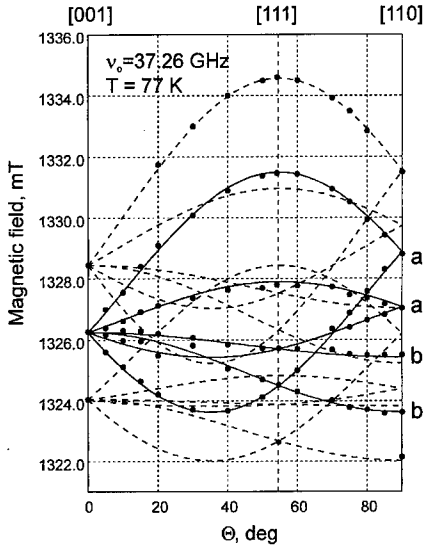

Fig. 3. Angular dependence of the Si-AA17 spectrum, with H in the $(0\,\bar{1}\,1)$ plane. Solid lines represent the fine structure and dashed lines the hyperfine structure from ^{29}Si nuclei. The circles are experimental points; curves are computer fit using constants from Table 1.

Distribution of the resonant wave function, electronic spin and D_{3d} symmetry of the defect indicate unambiguously that there are two equivalent Si sites with broken bonds oriented along the $\langle 1\,1\,1\rangle$ axis of symmetry of the AA17 defect. The distance between these two unpaired electrons (spins) can be determined from the magnitude of D-tensor (Table 1). Spin–orbit interaction cannot be a major origin of the fine structure of the AA17 spectrum because D_{ij} observed is too less and is not proportional to Δg_{ij} [18]. Therefore the D-tensor can be described as arising from interacting magnetic dipoles:

$$D_{ij} = \tfrac{1}{2} g_0^2 \mu_B^2 \langle S_1 \cdot S_2)/r^3 - 3(S_1 \cdot r)\cdot(S_2 \cdot r)/r^5\rangle. \quad (2)$$

Our estimation of distance between interacting dipoles is from 12 to 13 Å for the value $D = 16.8$ MHz of the AA17 center and it is in good agreement with previous investigations of the magnitude dependence of zero-field splitting versus distance between two dangling bonds of different vacancy-like defects in silicon [15,17]. In silicon lattice the distances between equivalent sites along $\langle 1\,1\,1\rangle$ axis are a, $3a$, $5a$, $7a$, etc., where a is the bond length (2.35 Å). The distance of ~ 12 Å is in good agreement only with the value of $5a$ (11.75 Å). The positions of dangling bonds resulting from experimental data are shown in Fig. 4.

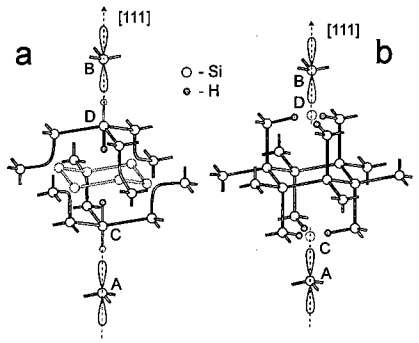

Fig. 4. Tentative models of Si-AA17 EPR center: hexavacancy with two equivalent hydrogen atoms (a) and two vacancies saturated with six hydrogen atoms (b).

Stress-induced preferential alignment of the AA17 center was also studied. The sample previously annealed at 350°C was subjected to uniaxial stress of 150 MPa along the $\langle 0\,1\,1\rangle$ axis at ~ 200°C for 1 h and then the sample was cooled to room temperature with stress on. The stress was then removed and the sample placed in the EPR cavity for observation at 77 K. A considerable alignment of the AA17 spectrum (Fig. 1) indicates that defect can be reoriented at this temperature range (Fig. 2). Recovery from the stress-induced alignment was studied by a series of isothermal anneals. The activation energy required for transition from one equivalent position to other was determined to be $E = (1.61 \pm 0.05)$ eV with a pre-exponential factor of $1/\tau = 1.8 \times 10^{14}\ s^{-1}$. The activation energy for the reorientation is large and exceeds those values of all known multiple-vacancy defects in irradiated silicon. The reason for this is the rearrangement of strong Si–H bonds at reorientation process of the AA17.

The energy of a defect in an applied strain field can be written as

$$E = \sum_{i,j} B_{ij}\varepsilon_{ij}, \quad (3)$$

where ε_{ij} are the strain tensor components and B_{ij} are the component of a "piezospectroscopic" tensor $\boldsymbol{B}$ [19]. For a center of trigonal symmetry, $\boldsymbol{B}$ has only two independent components. The procedure used to determine the $\boldsymbol{B}$ value has been described previously [20] in detail. In our case, we have measured the degree of equilibrium alignment $n_{\parallel}/n_{\perp} = 1.9$ under a stress of 150 MPa at

463 K and $B = +13.3$ eV/(unit strain) was obtained. The positive sign and magnitude of B-component means that the defect has a large tensile strain field along its trigonal axis. Energy of the defect is lowered if stress along $\langle 1\,1\,1\rangle$ axis and therefore defect prefers to align itself with $g_{||}$ parallel to the stress direction.

4. Discussion and model

The experimental results obtained by means of EPR (g-and D-tensors) have shown that AA17 spectrum arises from trigonal symmetry defect with spin $S = 1$. Magnitude of zero-field splitting (term D) of the AA17 indicates unambiguously that distance between two interacting spins (dangling bonds) creating triplet ($S = 1$) state is ~ 12 Å along the $\langle 1\,1\,1\rangle$ axis. Analysis of ^{29}Si hyperfine interaction has shown that two equivalent Si atoms are involved in the structure of the AA17 center. Resonant wave function is mainly ($\sim 62\%$) localized in these Si atoms (A and B on Fig. 4). Equivalence of these two silicon atoms means that the symmetry of the AA17 defect corresponds to D_{3d}. Strong localization ($\sim 62\%$) and hybridization (9% 3s and 91% 3p) of resonant wave function are typical for dangling bonds in the vicinity of vacancy-like defect [17,19]. Piezospectroscopic measurements have also revealed ($B = +13$ eV/unit strain) that there should be more void space between interacting dipoles (spins) (in comparison with normal lattice), i.e. vacancy-like defect should be situated between A and B atoms. On the other hand, only a circlet of the six vacancy at hexagonal site (centered between A and B atoms) allows to retain the D_{3d} symmetry of the defect. Therefore, the (1 1 1) planar hexavacancy situated between dangling bonds at A and B silicon atoms (Fig. 4a) is the most probable candidate for vacancy-like defect involving the structure of the AA17 center.

We note that among a variety of defects identified by means of EPR in irradiated silicon the hexavacancy has not been detected, so far. All stable above room temperature multivacancy-type defects such as di-vacancy (G6,G7 [21]) three vacancy (A4, [13]), tetravacancy (P3 and A3 [13,15]) and pentavacancy (P1 [12]) have been identified by EPR in electron, neutron or proton irradiated silicon. These defects have a symmetry of g-tensor lower than D_{3d} and, therefore, cannot be involved in the structure of AA17. However, recent [22,23] theoretical investigations have shown that $\{1\,1\,1\}$ planar hexavacancy is the most stable amongst the multiple-vacancy defects in silicon. Another important conclusion follows from theoretical study that the hexavacancy in silicon is an electrically (and hence in EPR) inactive defect [23]. These theoretical conclusions are in agreement with the properties of the AA17 defects.

In order to create spin-triplet ($S = 1$) state of the defect, the bonds between A–C and B–D atoms should be broken while dangling bonds at C and D atoms should be saturated (Fig. 4a). Hyperfine interaction with proton(s) was not detected in the AA17 spectrum. However the formation rate of the AA17 center reveals a strong dependence of hydrogen content in the sample. The AA17 spectrum dominates in hydrogen-implanted samples as well as in samples soaked in hydrogen with subsequent irradiation while in hydrogen-free samples irradiated by protons or α-particles the signal of AA17 is absent. Therefore, it is reasonable to propose that hydrogen is involved in the structure of the defect. Again, in view of high (D_{3d}) symmetry of AA17 it is logical to incorporate two equivalent hydrogen atoms located along [1 1 1] axis symmetrically to hexagonal site, i.e. at the anti-bonding or bonding positions at C and D atoms as shown in Fig. 4a. In both cases the bonds at A and B atoms should be broken to create $S = 1$ state.

As an alternative to V_6H_2 may be the defect of the two single vacancies (instead of C and D atoms on Fig. 4a) located on the same $\langle 1\,1\,1\rangle$ axis symmetrically to hexahedral site. Three broken bonds of each vacancy were saturated by hydrogen atoms (Fig. 4b). A pair of the dangling bonds of two vacancy creates the paramagnetic state with $S = 1$. This model also completely satisfies the AA17 parameters (D_{3d}-symmetry, distance of ~ 12 Å, etc.). However, six H atoms per defect is too much for samples with relatively low H concentration ($< 1 \times 10^{16}$ cm^{-3}). Moreover, more problems with reorientation of the defect appear.

It is important to note that conditions of formation and temperature range of stability of the AA17 EPR center and luminescence B_{41} (1.1509 eV) center [24,25] are very similar. The B_{41} center arises in irradiated H-containing silicon from defect with D_{3d} symmetry and two equivalent hydrogen atoms are incorporated in its structure [26,27]. Recently [28], on the basis of experimental data and theoretical ab inito cluster calculations the model of defect (V_6H_2) with D_{3d} symmetry has been proposed for B_{41} center luminescence. Distinction between models of AA17 EPR center (Fig. 4a) and the B_{41} luminescence center consists in location of hydrogen atoms. In the model of B_{41}, the dangling bonds of silicon atoms A and B (Fig. 4a) are saturated by hydrogen. For the AA17 center dangling bonds at A and B atoms should be free to create a state with $S = 1$. Significant similarity between properties of B_{41} and AA17 (conditions of formation, D_{3d} symmetry, region of stability, response on applied stress) strongly suggests that both spectra are derived from the same defect. Therefore, theoretical investigations of the configuration similar to the model of AA17 (Fig. 4a) as well as ENDOR measurements are required to establish exact model.

Model of AA17 (Fig. 4a) can be considered as a configuration arising on early stage of nucleation and growth of platelets or as a micro-platelet with characteristic properties such as a $\{1\,1\,1\}$ vacancies layer and two inversely

situated Si–H bonds. Behavior of the AA17 intensity upon annealing (Fig. 2) correlates well with that of platelets [10,29]. Assuming first-order kinetics with a characteristic frequency factor of 10^{13} c^{-1} for disappearance of the AA17 spectrum, we obtain from annealing data (Fig. 2) the activation energy of $\sim$ 2.1 eV for the process. This value is in good agreement with data obtained from Raman spectroscopy study ($\sim$ 2.3 eV) of a stability of the H_2 molecules possibly located in platelets [29].

Simultaneously with the AA17 the AA1 spectrum which derives from H-induced double donor in positive charge state is also dominated. Its structure associated with formation of self-interstitial aggregates ($\langle 0\,1\,1\rangle$ chain of $\langle 1\,0\,0\rangle$ oriented self interstitial complexes [14]). Therefore, AA1 defect also may be considered as a precursor of interstitial-type extended defects which recently [30] were observed by transmission electron microscopy in deuterium-implanted silicon.

References

[1] J.I. Pancove, N.M. Johnson (Eds.), Hydrogen in Semiconductors, Academic Press, San Diego, 1991.
[2] S.J. Pearton, J.W. Corbett, M. Stavola, Hydrogen in Crystalline Semiconductors, Springer, Berlin, 1992.
[3] Yu.V. Gorelkinskii, N.N. Nevinnyi, Physica B 170 (1991) 155.
[4] B.B. Nielsen, P. Johannesen, P. Stallinga, K.B. Nielsen, Phys. Rev. Lett. 79 (1997) 1507.
[5] S.J. Uftring, M. Stavola, P.M. Williams, G.D. Watkins, Phys. Rev. B 51 (1995) 9612.
[6] N.M. Johnson, F.A. Ponce, R.A. Street, R.J. Nemanich, Phys. Rev. B 35 (1987) 4166.
[7] S. Muto, S. Takeda, M. Hirata, Mater. Sci. Forum 143–147 (1994) 897.
[8] J.N. Heyman, J.W. Ager, E.E. Haller, N.M. Johnson, J. Walker, C.M. Doland, Phys. Rev. B 45 (1992) 13363.
[9] C.D. Van de Walle, P.J.H. Denteneer, Y. Bar-Yam, S.T. Pantelides, Phys. Rev. B 39 (1989) 10791.
[10] S.B. Zhang, W.B. Jackson, Phys. Rev. B 43 (1991) 12142.
[11] Y.H. Lee, P.R. Brosious, J.W. Corbett, Radiat. Effects 22 (1974) 169.
[12] Y.H. Lee, J.W. Corbett, Phys. Rev. B 8 (1973) 2810.
[13] Y.H. Lee, J.W. Corbett, Phys. Rev. B 9 (1974) 4351.
[14] Yu.V. Gorelkinskii, N.N. Nevinnyi, Kh.A. Abdullin, J. Appll. Phys. 84 (1998) 4847.
[15] K.L. Brower, Radiat. Effects 8 (1971) 213.
[16] G.D. Watkins, J.W. Corbett, Phys. Rev. 121 (1961) 1001.
[17] Y.H. Lee, J.W. Corbett, Phys. Rev. 13 (1976) 2653.
[18] M.H.L. Pryce, Proc. Phys. Soc. London A 63 (1950) 25.
[19] A.A. Kaplyanskii, Opt. Spektrosk. (USSR) 16 (1964) 329.
[20] G.D. Watkins, Phys. Rev. B 12 (1975) 5824.
[21] G.D. Watkins, J.W. Corbett, Phys. Rev. 138 (1965) A543.
[22] J.L. Hastings, S.K. Estreicher, P.A. Fedders, Phys. Rev. B 56 (1997) 10215.
[23] S.K. Estreicher, J.L. Hastings, P.A. Fedders, Appl. Phys. Lett. 70 (1997) 432.
[25] A.S. Kaminskii, E.V. Lavrov, V.A. Karasyuk, M.L.W. Thewalt, Phys. Rev. B 50 (1994) 7338.
[24] A.S. Kaminskii, E.V. Lavrov, V.A. Karasyuk, M.L.W. Thewalt, Solid State Commun. 97 (1995) 137.
[26] A.N. Safonov, E.C. Lightowlers, Mater. Sci. Eng. B 58 (1999) 39.
[27] A.N. Safonov, E.C. Lightowlers, G. Davies, Phys. Rev. B 56 (1997) R15517.
[28] B. Hourahine, R, Jones, A.N. Safonov, S. Öberg, P.R. Briddon, S.K.Estrricher. Workshop on Hydrogen in Semiconductors April 15–16 Exeter, UK, 1999, p. 11; Proceedings of E-MRS Spring Meeting, 1–4 June 1999, Strasbourg, France, to be published.
[29] A.W.R. Leitch, V.A. Alex, J. Weber, Mater. Sci. Forum 258–263 (1997) 241.
[30] S. Muto, S. Takeda, M. Hirata, Mater. Sci. Forum 196–201 (1995) 1171.

ELSEVIER

Physica B 273–274 (1999) 176–179

PHYSICA B

www.elsevier.com/locate/physb

Optically active hydrogen dimers in silicon

B. Hourahine[a,*], R. Jones[a], A.N. Safonov[b], S. Öberg[c], P.R. Briddon[d], S.K. Estreicher[e]

[a]*School of Physics, The University of Exeter, Stocker Road, Exeter EX4 4QL, UK*
[b]*Department of Physics, University of Durham, South Road, Durham, DH1 3LE, UK*
[c]*Department of Mathematics, University of Luleå, Luleå S-97187, Sweden*
[d]*Department of Physics, The University of Newcastle upon Tyne, Newcastle upon Tyne NE1 7RU, UK*
[e]*Department of Physics, Texas Tech University, Lubbock, Texas 79409-1051, USA*

Abstract

First-principles calculations are used to explore the structure and properties of several defects which are prominent luminescent centers in Si. The trigonal defects B_{41} and B_{71}^{1}, which are known to contain two hydrogen atoms in equivalent and inequivalent sites, respectively, are attributed to a hexavacancy containing two H atoms in different configurations. It is suggested that the *J* luminescence centers arises from a stable hexavacancy without hydrogen atoms. © 1999 Elsevier Science B.V. All rights reserved.

Keywords: Hydrogen; Silicon; Multivacancy; Photoluminescence

Hydrogen dimers were first suggested to exist in crystalline silicon in the form of molecules [1,2] sited at tetrahedral interstitial lattice positions. These molecules have subsequently been observed in hydrogen-soaked [3] and low-temperature plasma-treated silicon [4] (the substrate is held at $\leqslant 150°C$ during exposure). Higher-temperature plasma treatment instead forms hydrogen molecules inside platelet or void-like structures in the subsurface region of the silicon [4,5].

There are several other di-hydrogen and multi-hydrogen defects known to form complexes with native defects in implanted or irradiated silicon. A large number of vacancy-hydrogen complexes of the form V_mH_n $m = 1$, $n = 1 \cdots 4$; $m = 2$, $n = 1$ or 6, and $m = 3$ or 4 with $n = 1$ have been identified in proton-implanted silicon [6,7].

Similarly, electron paramagnetic investigations of multi-vacancy centers in Si have identified V_1, V_2 [8], V_3, V_4 and V_5 [9]. The last has been correlated with the *P*1 center and is a non-planar defect with C_{1h} symmetry. The larger vacancy centers are formed in irradiated material when subjected to a heat treatment. Thus V_5 is formed around 170°C and is stable until ~450°C.

Photoluminescence (PL) has revealed a large number of centers in silicon which has been treated by in-diffusion of hydrogen at high temperatures with a subsequent irradiation and heat treatment [10]. These centers were produced by irradiation with $6 \times 10^{17}\,cm^{-2}$ electrons, or $10^{17}\,cm^{-2}$ thermal neutrons, of silicon which has been soaked in hydrogen, followed by annealing at ~450°C.

Recent Zeeman and uniaxial studies demonstrate that the PL centers which are produced by irradiation bind an exciton consisting of a electron in a deep ($-/0$) level near E_c with a loosely bound hole [11,12]. These defects have labels of the form B_{yz}^{x}, which specifies the exciton binding energy associated with the strongest PL line as *xy.z* meV. So for example B_{71}^{1} has an exciton binding energy of 17.1 meV, and a strong PL line at 1.138 eV. In addition some of the transitions have specific names, such as the family of *J*-lines which are different exciton states of the B_{80}^{4} center giving a luminescence at around 1.108 eV [13,14].

Studies using H and D mixtures demonstrated that some of these centers contain two hydrogen atoms.

* Corresponding author. Tel.: + 44-1392-264-198; fax: + 44-1392-264-111.

E-mail address: bh@excc.ex.ac.uk (B. Hourahine)

0921-4526/99/$ - see front matter
PII: S0921-4526(99)00439-1

Zeeman splitting studies have shown that B^4_{80}, B_{41}, and B^1_{71} possess trigonal symmetry. In the absence of experiments performed in an electric field, the question of whether the defects have a center of inversion has not been resolved. B^4_{80} does not possess any hydrogen atoms; B^1_{71} contains two inequivalent hydrogen atoms, and B_{41} possesses two *equivalent* hydrogen atoms. The high symmetry of these centers strongly restricts possible structures of the defects, particularly in the case of B_{41}, which although is usually reported as possessing C_{3v} symmetry, actually requires the higher D_{3d}, D_3 or C_{3i} symmetries to give equivalent sites for the two hydrogen atoms.

There are few defect structures with such high symmetry in silicon, since the complex must possess a principle three-fold rotational axis along one of the $\langle 1\,1\,1\rangle$ directions. If the defect also possesses inversional symmetry as required by the D_{3d} and C_{3i} point-groups, or three coplanar two-fold rotation axes as required by D_3, then here are only two sites in the diamond lattice with such high symmetry at which the defect can sit. These are the bond-center and hexagonal lattice sites. The obvious structure, consisting of two anti-bonded hydrogen atoms attached to the pair of silicon atoms surrounding a bond-centered site must be discounted, since such a defects should be stable only at low temperatures.

The combined requirements of creation by irradiation and high thermal stability point towards a multivacancy-hydrogen complex. A plausible candidate is a complex between V_6 and hydrogen.

V_6 is expected to form in irradiated material which is heated. If the material contains hydrogen molecules these will readily react with V_6 to form dimer structures, which in turn suggests that the hydrogen free B^4_{80} defect should be V_6 itself. This is consistent with the strong preference this defect displays to align along [1 1 1] stress during formation [14], which is indicative of a vacancy center. Furthermore, this center appears to react with hydrogen to form B_{41} and B^1_{71} [15].

The defects considered were each constructed in a $Si_{154}H_{108}$ cluster centered on the hexagonal site. The wave function basis consisted of independent *s* and *p* Gaussian orbitals, with either four different exponents sited at each Si atom, or three at the H atoms of the dimers. A fixed linear combination of two Gaussian orbitals was sited on the H atoms which terminated the cluster. In addition, two Gaussian functions were placed across every Si–Si bond and the Si–H bonds of the defects. The charge density was fitted with five independent Gaussian functions with different widths on each Si atom, and four (three) on the central (terminating) H atoms. Two extra Gaussian functions were placed at each bond center. All atoms, including the terminating H ones, were allowed to relax by a conjugate gradient method. The second derivatives of the energy were found for the H atoms and the Si atoms they were bonded to. Further details of the spin-polarized LDF method can be found in Ref. [16].

We firstly simulate V_6 itself by removing the six atoms nearest to the hexagonal site. The resulting structure possesses D_{3d} symmetry and strongly reconstructs on relaxation to form six new bonds of length 2.60 Å between the twelve dangling bonds as shown in Fig. 1a. The resulting structure and electronic Kohn–Sham levels, display a well-defined band gap, which are consistent with previous calculations [17]. This defect possibly possesses states in the gap very near the conduction band, but it is difficult to decide whether such near-conduction levels are localized on the defect in cluster calculations. The character of the deepest of these shallow states is a_{1g}, and is anti-bonding to both the axial Si–Si bonds and the six reconstructed bonds. If the defect is identified with B^4_{80}, then this state corresponds to the $(-/0)$ Γ_1 level observed experimentally [11]. However, experimental measurement of the effect of an electrical field on this state would be required to confirm the proposed inversionally symmetric defect.

There are several potential models for B_{41} based on V_6, but all these require the hydrogen atoms to be sited at equivalent positions on the three-fold axis of the defect. One possible model would be a hydrogen molecule aligned along [1 1 1] and sited at the center of inversion of the defect. Alternately the H–H bond could be broken and the atoms placed at anti-bonding sites to the axial Si–Si bonds, as in Fig. 1b. A third possibility is that the hydrogen atoms are near the bond-centered sites within the axial Si–Si bonds. The second, anti-bonded structure is unstable and spontaneously relaxes back to the [1 1 1] aligned molecule structure. We calculate that the molecule itself is only metastable at the defect's center of inversion, and will dissociate with a barrier of 0.23 eV. It does this by breaking one of the reconstructed Si–Si bonds shown in Fig. 1a, to form two Si–H bonds, giving rise to a structure which is 1.76 eV lower in energy and of C_{1h} symmetry as shown in Fig. 1c. The third structure causes a further reconstruction of V_6, by breaking the two axial Si–Si bonds and forming Si–H bonds. The two dangling Si bonds thus formed pair together in the middle of the defect, leaving the structure with D_{3d} symmetry (shown in Fig. 1d). This reconstruction is energetically very favorable, being 0.80 eV lower in energy than the C_{1h} structure in Fig. 1c. The KS levels of this defect again show evidence for a very shallow $(-/0)$ level, of symmetry a_{1g} consisting of a combination of anti-bonding states around the defect. There are two high-frequency modes related to the hydrogen in this structure, of symmetries A_{1g} and A_{2u}, which we find to lie at 2033 and 2021 cm^{-1}, respectively. This structure posses properties consistent with B_{41}.

We now consider potential structures for B^1_{71}. Again this structure requires a C_3 axis, but due to the inequivalent hydrogen atoms the symmetry of the defect must be of lower order, i.e. C_{3v} or C_3. If it is assumed that dangling silicon bonds are energetically unfeasible, there

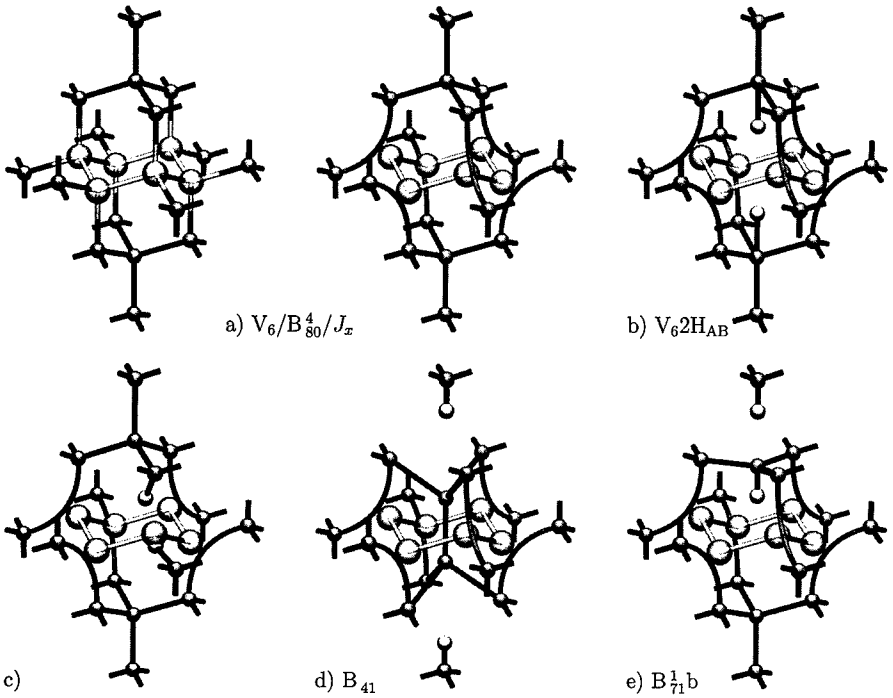

Fig. 1. Schematic diagrams of V_6 and related defects. (a) V_6 displaying the six vacancy sites, and the subsequent reconstruction caused by them. (b) V_6 plus two anti-bonding hydrogen atoms. (c) The structure formed by the dissociation of the H_2 molecule, which breaks one of the reconstructed bonds. (d) The proposed B_{41} structure is shown with the two equivalent hydrogen atom that force the further reconstruction of the two axial silicon atoms across the center of the defect. (e) The second proposed B^1_{71} structure with the two inequivalent hydrogen atoms arranged as in H^*_2.

is an obvious structure which can be derived from the bond-centered model for B_{41}. This defect consists of one hydrogen atom lying at a bond-centered site, and the other atom directly passivating the silicon atom which is displaced by the bond-centered H. There are two locations on either side of the silicon atom at which the hydrogen might be positioned. If the hydrogen were placed on the side nearest the other H atom, this would bring the two atoms into close proximity and thus raise the energy of the defect, this suggest that the hydrogen is sited on the opposite side of the silicon atom as shown in Fig. 1e. The relative energies of these defects are 0.13 eV in favor of the structure with the hydrogen atoms on opposite sides of the silicon. The more stable structure, which is reminiscent of H^*_2 [18], is 0.09 eV higher in energy than the C_{1h} defect formed by the dissociation a hydrogen molecule inside V_6. The KS levels again show evidence of a near conduction-band a_1 state localized on the defect in both cases. Both of these models possess two high-frequency A_1 vibrational modes, lying at 2149 and 2029 cm^{-1} for the structure with the two H atoms lying close together, or 2051 and 2010 cm^{-1} for the hydrogen on opposite sides of the silicon.

The dependence of the intensity of the PL due to B^4_{80} demonstrates that the exciton is thermally bound with an energy of 18 meV [19] and this can be taken to be the ionization energy of the hole. The exciton binding energy relative to a free electron and hole is the sum of 48.0 meV and the free exciton binding energy of 14.3 meV. From these results, we place the $(-/0)$ level of V_6 at $E_c - 44.3$ meV.

In conclusion, we have shown that complexes between V_6 and hydrogen have properties consistent with those of the photoluminescent B_{41} and B^1_{71} centers formed in irradiated silicon. We also suggest the J family of PL defects are due to the hydrogen-free hexavacancy.

S.Ö. thanks NFR and TFR for financial support. S.K.E. thanks the R.A. Welch Foundation (grant D-1126) and NREL (contract XAD-7-17652-01). We also thank the ENDEASD network and E.V. Lavrov for helpful discussions.

References

[1] A. Mainwood, A.M. Stoneham, Physica B & C 116 (1983) 101.
[2] J.W. Corbett, S.N. Sahu, T.S. Shi, L.C. Snyder, Phys. Lett. A 93 (1983) 303.

[3] R.E. Pritchard, M.J. Ashwin, J.H. Tucker, R.C. Newman, Phys. Rev. B 57 (1998) 15048.
[4] A.W.R. Leitch, V. Alex, J. Weber, Phys. Rev. Lett. 81 (1998) 421.
[5] B. Hourahine et al., Phys. Rev. B 57 (1998) 12666.
[6] B. Bech Nielsen, L. Hoffmann, M. Budde, Mater. Sci. Eng. B 36 (1996) 259.
[7] P. Stallinga et al., Phys. Rev. B 58 (1998) 3842.
[8] G.D. Watkins, in: S.T. Pantelides (Ed.), Deep Centers in Semiconductors, 2nd Edition, Gordon and Breach, Switzerland, 1992 (Chapter 3).
[9] Y.H. Lee, J.W. Corbett, Phys. Rev. B 9 (1974) 4351.
[10] A.S. Kaminskii, E.V. Lavrov, V.A. Karasyuk, M.L.W. Thewalt, Phys. Rev. B 50 (1994) 7338.
[11] A.N. Safonov, E.C. Lightowlers, G. Davies, Phys. Rev. B 56 (1997) 15517.
[12] A.N. Safonov, E.C. Lightowlers, Mater. Sci. Eng. B 58 (1999) 39.
[13] R. Sauer, J. Weber, Physica B & C 116 (1983) 195.
[14] A.S. Kaminskii, E.V. Lavrov, Solid State Commun. 106 (1998) 751.
[15] B. Hourahine et al., Phys. Rev. B, submitted for publication.
[16] R. Jones, P.R. Briddon, in: M. Stavola (Ed.), Identification of Defects in Semiconductors, Vol. 51A of Semiconductors and Semimetals, Academic Press, Boston, 1998 (Chapter 6).
[17] J.L. Hastings, S.K. Estreicher, P.A. Fedders, Phys. Rev. B 56 (1997) 10215.
[18] B. Bech Nielsen et al., Mater. Sci. Forum 845–852 (1994) 143.
[19] A.S. Kaminskii, B.M. Leiferov, A.N. Safonov, Sov. Phys. Solid State 29 (1987) 551.

ELSEVIER

Physica B 273–274 (1999) 180–183

PHYSICA B

www.elsevier.com/locate/physb

The *A* center binding a single hydrogen atom in crystalline silicon observed by EPR

P. Johannesen[a,*], J.R. Byberg[b], B. Bech Nielsen[a]

[a]*Institute of Physics and Astronomy, University of Aarhus, Ny Munkegade Bygn. 520, DK-8000 Århus C, Denmark*
[b]*Institute of Chemistry, University of Aarhus, DK-8000 Århus C, Denmark*

Abstract

Electron paramagnetic resonance measurements on proton- and deuteron-implanted silicon crystals reveal a new signal from a vacancy-type defect with spin $S = \frac{1}{2}$, which is observable only in oxygen-rich material. The signal is strongly temperature-dependent, displaying monoclinic-*I* symmetry below 180 K and orthorhombic-*I* symmetry above 240 K in the proton-implanted samples. Resolved proton-hyperfine splittings show that a single hydrogen atom is located ~ 2.5 Å from the silicon atom carrying the dangling bond. The observed properties, including the change of symmetry, allow an unambiguous identification of the signal with VOH^0, the neutral charge state of the monovacancy–oxygen complex (known as the *A* center) binding one hydrogen atom. The hydrogen atom is observed to jump readily between two equivalent sites in the (1 1 0) mirror plane of the defect.

Keywords: Silicon; Hydrogen; Oxygen; Vacancy

1. Introduction

The passivation of oxygen-related defects in silicon is of great technological as well as theoretical interest. From our previous studies of vacancy–hydrogen defects [1–3], it is known that hydrogen forms strong covalent bonds with silicon, even when this requires the breaking of elongated Si–Si bonds. The monovacancy–oxygen defect VO, also known as the *A* center [4], contains an elongated Si–Si bond in the plane perpendicular to that of the Si–O–Si unit, and may therefore be expected to bind one or two hydrogen atoms, thus creating the defects VOH and VOH_2. Pearton [5] observed that the deep level transient spectroscopy (DLTS) signal from VO decreased in intensity when the samples were exposed to either atomic or molecular hydrogen. However, the structure of the defects, into which VO is transformed when passivated by hydrogen, remains to be established experimentally.

It is expected that the hydrogen atom in VOH^0 (the neutral charge state) forms a strong covalent bond with one of the silicon atoms neighboring the vacancy that are not bonded to oxygen, whereas the remaining unsatisfied silicon orbital is left as a singly occupied dangling bond. Thus, the structure of VOH^0 should resemble closely that of VH^0 [2] with the Si–O–Si unit taking the place of the elongated Si–Si bond, as found also by ab initio calculations [6]. This expected structure is depicted in Fig. 1.

In this paper we report the identification of VOH^0 in proton-implanted silicon by electron paramagnetic resonance (EPR). The observed properties, including the electron–spin distribution, the proton hyperfine interaction, and a thermally activated change of the effective symmetry, all agree with the model of VOH^0.

2. Experimental

Samples grown by the Czochralski (CZ) and float zone (FZ) techniques were used. The CZ-samples were p-type with a boron concentration of $\sim 1 \times 10^{15}$ cm^{-3}, and the FZ-samples were n-type with a phosphorus concentration of $\sim 9 \times 10^{12}$ cm^{-3}. The oxygen concentration was

* Corresponding author. Tel.: +45-8942-2899; fax: +45-8612-0740.
E-mail address: pj@ifa.au.dk (P. Johannesen)

0921-4526/99/$ - see front matter
PII: S0921-4526(99)00440-8

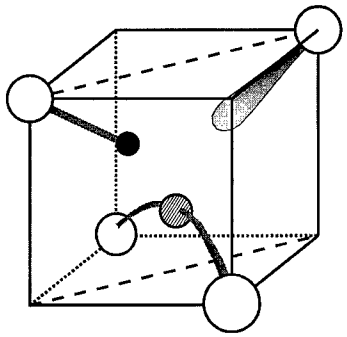

Fig. 1. Expected structure of the VOH^0 complex, showing the position of the hydrogen atom (black) and the dangling bond in the (1 1 0) mirror plane, and the oxygen atom (hatched) bonded to the remaining two silicon atoms neighboring the vacancy.

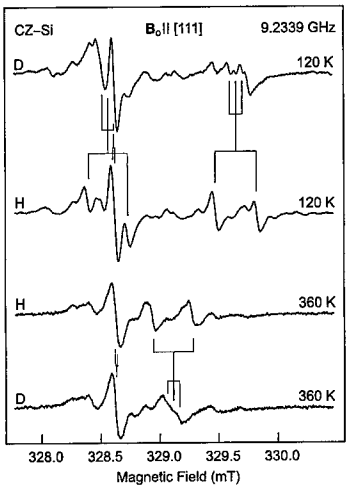

Fig. 2. EPR spectra from Czochralski-grown silicon implanted with protons (H) or deuterons (D), and recorded at low and high temperatures after heat treatment at 543 K. The stick diagrams depict the splittings from the hyperfine interactions with the two different hydrogen isotopes.

$\sim 6\times10^{17}$ and $\sim 5\times10^{15}\,cm^{-3}$ in the CZ- and FZ-samples, respectively, whereas the concentration of other impurities, mainly carbon, was below $5\times10^{15}\,cm^{-3}$ in all samples. Slabs measuring $0.6\times4\times15\,mm^3$ were cut with the large faces perpendicular to the (1 $\bar{1}$ 0) plane. After polishing, the large faces were implanted with protons (or deuterons) through 0.2-mm (0.1-mm) aluminium at 37 (40) successive energies in the range from 11.0 to 5.3 MeV (11.0–5.0 MeV). The dose implanted at each energy was calculated to ensure a uniform distribution of hydrogen throughout the sample, corresponding to a concentration of $\sim 3\times10^{17}\,cm^{-3}$. During the implantation, the sample temperature was kept below 120 K. Subsequently, the samples were warmed to room temperature and etched lightly in nitric and hydrofluoric acid to remove surface defects that might be paramagnetic.

A Bruker ESP300E spectrometer operating in absorption mode at X band ($\sim$ 9.2 GHz) was used to record the EPR spectra. During measurements, the sample temperature was controlled with a Varian E-257 variable temperature device by means of a thermostatted flow of nitrogen gas. The temperature could be set in the range 100–570 K and was monitored with one degree accuracy by means of a copper-constantan thermocouple. Further experimental details may be found in Ref. [3].

3. Results and discussion

The EPR spectra from proton- and deuteron-implanted CZ-samples contain the VH^0, $S1_a$, and $S1_b$ signals observed previously in FZ-material [2,3]. In addition, several intense lines are observed in the CZ-spectra, which are absent in the FZ-spectra, suggesting that they belong to an oxygen-related signal. Anticipating the identification made below, we denote this signal VOH^0. Heat treatment at 543 K greatly simplifies the spectra by removing the lines from the VH^0, $S1_a$, and $S1_b$ signals, while the lines from VOH^0 suffer only a small decrease in intensity. Therefore, the spectra presented here were recorded after annealing at 543 K. Below, proton- and deuteron-implanted CZ-samples will be denoted Si : H and Si : D, respectively.

A comparison of the spectra from Si : D and Si : H recorded with the magnetic field vector $\boldsymbol{B}_0$ along the [1 1 1] axis is shown in Fig. 2. At temperatures up to 120 K, the spectra look as shown in the upper part of the figure. The difference between the spectra from Si : D and Si : H directly shows that hydrogen is involved in the defect. Five strong lines are observed in the Si : H spectrum, four of which form two doublets originating from the hyperfine interaction with a single proton (nuclear spin $I_H = \frac{1}{2}$). No splitting of the remaining strong line is observed. This indicates a strong anisotropy of the proton–hyperfine interaction, which is confirmed by the angular variation of the line positions in the (1 $\bar{1}$ 0) plane (see Fig. 3, open circles). The solid curves represent the best fit to these data obtained with the spin Hamiltonian

$$H = \mu_B \boldsymbol{S}\cdot\boldsymbol{g}\cdot\boldsymbol{B}_0 + \boldsymbol{S}\cdot\boldsymbol{A}_H\cdot\boldsymbol{I}_H - \mu_N g_H \boldsymbol{I}_H\cdot\boldsymbol{B}_0, \quad (1)$$

with a monoclinic-I g tensor and a monoclinic-I tensor $\boldsymbol{A}_H$ describing the proton hyperfine interaction. μ_B and μ_N denote the Bohr and nuclear magneton, respectively, and g_H denotes the g factor of the proton. The principal values of $\boldsymbol{g}$ and $\boldsymbol{A}_H$ are listed in Table 1. The Si : D spectrum is also fully accounted for by Eq. (1), when $\boldsymbol{A}_H$ is scaled by the ratio (0.154) between g_H and g_D and the nuclear spin of the deuteron $I_D = 1$ is taken into account. However, the Si : D spectrum suffers from a heavy

Table 1
Spin-Hamiltonian parameters for VOH^0 at 120 K and for its motionally averaged state, both measured at 360 K ($g[m]$ and $A_H[m]$) and calculated from the low-temperature parameters ($g[c]$ and $A_H[c]$)

Term	X	Y	Z	Θ
g	2.0084	2.0086	2.0013	39.2°
A_H	−0.8	−0.3	15.2	1.0°
A_{Si}	−236	−236	−418	35.3°
$g[m]$	2.0057	2.0087	2.0043	0.0°
$g[c]$	2.0056	2.0086	2.0042	0.0°
$A_H[m]$	−0.6	−0.5	14.6	0.0°
$A_H[c]$	−0.8	−0.3	15.2	0.0°

The principal axis Y is along the $[1\,\bar{1}\,0]$ axis, and X and Z span the $(1\,\bar{1}\,0)$ plane, so that Z makes the angle Θ with the [1 1 0] axis. Principal values of A_H and A_{Si} are given in MHz. Limits of error: g, ± 0.0001; A_H, ± 0.3 MHz; A_{Si}, ± 1.0 MHz.

overlap with lines from weak unassigned signals. The stick diagram included in Fig. 2 represents the resonant field values of the allowed hyperfine signals. ($\Delta m_H = 0$) calculated from Eq. (1). A_H is axial with its unique axis close to a $\langle 1\,1\,0\rangle$ direction. The small isotropic component (4.7 MHz) indicates a near-vanishing electron–spin density at the proton. Consequently, the anisotropic component b may be ascribed to the dipole–dipole interaction between the spins of the proton and the electron, considered as classical dipoles with separation R. From the observed value of b we obtain $R = 2.5$ Å.

As the temperature is increased above 120 K, the spectra from Si : H change: Some VOH^0 lines first broaden and then disappear at ~ 180 K, while others persist. Above 240 K new lines emerge, which attain minimum line width at ~ 360 K. This temperature dependence is typical for a motional narrowing process [7]. The angular dependence of the signal at 360 K (see Fig. 3, solid circles) corresponds to orthorhombic-I symmetry. These spectral changes may be explained as the result of thermally activated jumps between the two equivalent configurations of the monoclinic-I defect that have the same (1 1 0) mirror plane. When this is in-plane motion becomes sufficiently rapid, the effective symmetry necessarily changes to orthorhombic-I. The dashed curves in Fig. 3 show the angular dependence of the motionally averaged signal, calculated (in the limit of infinite jump rate) from the low-temperature tensors g and A_H. The good agreement with the measured line positions corroborates the interpretation of the motional effect. The principal values of g and A_H of the motionally averaged signal, calculated from the low-temperature values, are included in Table 1 together with the corresponding values obtained from the best fit to the data at 360 K. As seen, the two sets of values are consistent within the limits of error.

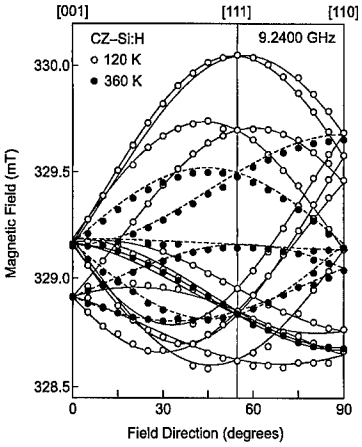

Fig. 3. Angular variation in the $(1\,\bar{1}\,0)$ plane of the positions of the EPR lines belonging to VOH^0. Open and filled circles represent the line positions measured in Si : H at low and high temperatures, respectively. Solid curves are calculated for a monoclinic-I defect with $S = \frac{1}{2}$ and the tensors g and A_H listed for VOH^0 in Table 1. Dashed curves represent an orthorhombic-I defect with $S = \frac{1}{2}$ and the tensors g and A_H calculated for the motionally averaged state of VOH^0 from the spin-Hamiltonian parameters obtained at 120 K.

Each of the main lines in the low-temperature spectra from Si : H and Si : D have a pair of satellites with an intensity of about 1 : 40 relative to the corresponding main line. Since the ^{29}Si nucleus has $I = \frac{1}{2}$ and is 4.67% abundant, we may ascribe these satellites to the hyperfine interaction with a ^{29}Si nucleus occupying a single silicon site. The principal values of the axial tensor A_{Si} describing the splittings of these satellites are given in Table 1. Similar ^{29}Si hyperfine satellites are observed at high temperatures. However, these have twice the relative intensity and about half the splittings of the low-temperature satellites, which shows that the averaged electron–spin density is now evenly divided among two equivalent silicon sites in the (1 1 0) mirror plane.

All properties derived from the low-temperature VOH^0 signal are consistent with the model of VOH^0 sketched in Fig. 1: (i) the signal is seen only in oxygen-rich material, indicating that oxygen is involved in the defect, (ii) it has monoclinic-I symmetry and displays hyperfine splittings from one proton, (iii) the tensors g and A_{Si} are both typical of paramagnetic vacancy-defects, in which the unpaired electron is confined mainly to a single dangling-bond orbital [8], and (iv) the distance $R =$ 2.5 Å, estimated from A_H, agrees with the distance between the hydrogen atom and the silicon atom carrying the dangling bond. Moreover, the observed change of the effective symmetry from monoclinic-I to orthorhombic-I at 180–240 K is in full agreement with the model. Thus, the fact that the dangling bond jumps between just two silicon atoms lying in the (1 1 0) mirror plane, indicates

the presence of the strongly bound Si–O–Si unit. The motion implies an interchange of the positions of the hydrogen atom and the dangling bond. The participation of the hydrogen atom in this process was directly confirmed by the observation of an isotope effect: in Si : D the change of the symmetry of the signal occurs at a significantly higher temperature than in Si : H.

We conclude that the EPR signal described here arises from VOH^0, the neutral charge state of an *A* center, in which a hydrogen atom satisfies one of the dangling bonds.

Acknowledgements

This work was supported by the Danish National Research Foundation through the Aarhus Center for Atomic Physics (ACAP).

References

[1] B. Bech Nielsen, L. Hoffmann, M. Budde, Mater. Sci. Eng. B 36 (1996) 259.
[2] B. Bech Nielsen, P. Johannesen, P. Stallinga, K. Bonde Nielsen, J.R. Byberg, Phys. Rev. Lett. 79 (1997) 1507.
[3] P. Stallinga, P. Johannesen, S. Herstrøm, K. Bonde Nielsen, B. Bech Nielsen, J.R. Byberg, Phys. Rev. B 58 (1998) 3842.
[4] See, e.g., G.D. Watkins, J.W. Corbett, Phys. Rev. 121 (1961) 1001.
[5] S.J. Pearton, Phys. Stat. Sol. A 72 (1982) K73.
[6] E. Artacho, F. Ynduráin, Solid State Commun. 72 (1989) 393.
[7] H.S. Gutowsky, A. Saika, J. Chem. Phys. 21 (1953) 1688.
[8] Y.H. Lee, J.W. Corbett, Phys. Rev. B 8 (1973) 2810.

ELSEVIER

Physica B 273–274 (1999) 184–187

PHYSICA B

www.elsevier.com/locate/physb

Effects of charge state on stress-induced alignment and relaxation of a hydrogen–carbon complex in silicon

K. Fukuda, Y. Kamiura*, Y. Yamashita

Faculty of Engineering, Okayama University, Tsushima-naka 3-1-1, Okayama 700-8530, Japan

Abstract

The local motion of hydrogen around carbon in n-type Si was studied by deep level transient spectroscopy (DLTS) under uniaxial compressive stress, combined with the technique of stress-induced alignment and subsequent relaxation. For the hydrogen–carbon (H–C) complex studied here, the hydrogen occupied the bond-centered site between silicon and carbon atoms. The H–C complex induced a donor level at 0.15 eV below the conduction band and was detected by DLTS as an electron trap. We have found that the compressive stress parallel to the C–H–Si bond raises the electronic energy of the bond. We have observed stress-induced alignment of the complex under ⟨1 1 1⟩ and ⟨1 1 0⟩ compressive stresses of 1 GPa at 250–300 K and subsequent relaxation of the alignment after removing the stress. This behavior can be understood as the motion of hydrogen under the stress from a high-energy to a low-energy bond with respect to the stress direction and the subsequent relaxation motion of hydrogen via bond-to-bond jumps in the absence of stress. By controlling the charge state of the complex with and without applying reverse bias to the Schottky junction, we have found that hydrogen moves more easily in the neutral charge state.

Keywords: Si; Carbon; Hydrogen motion; Stress-induced alignment; Stress DLTS

1. Introduction

The properties of hydrogen in semiconductors have been studied for many years. One of the most well-known properties of hydrogen is the passivation of electrically active defects. Though various static properties of hydrogen, such as electronic states and atomic configurations, have been studied extensively, its dynamic properties are not well known yet. It is difficult to experimentally observe the motion of isolated hydrogen because of its high mobility and high reactivity to other defects in semiconductors. Recently, it has widely been recognized that hydrogen is easily incorporated into the active region of silicon devices during various device processes even at room temperature. Therefore, the understanding of dynamic properties of hydrogen is important not only in basic researches but also from the viewpoint of applications.

We found that hydrogen, which was introduced into n-type silicon by chemical etching, formed a complex with a substitutional carbon atom. We have observed by DLTS technique that this hydrogen–carbon (H–C) complex acts as an electron trap with a donor level at 0.15 eV below the conduction band [1–5]. Recently, we have observed the stress-induced alignment of the H–C complex using the DLTS technique under uniaxial stress [6,7]. Since carbon is an isoelectronic impurity in Si, the study of the local motion of hydrogen around carbon is expected to provide important information about the motion of isolated hydrogen in silicon. In this paper, we report the results of the stress-induced alignment of the H–C complex and subsequent relaxation process after removing the stress, and discuss the local motion of hydrogen around carbon in silicon.

2. Experimental procedure

We used two n-type FZ silicon crystals, labeled FZ-P-10 and FZ-P-30, which had phosphorus densities of

*Corresponding author. Fax: + 81-86-251-8237.
E-mail address: kamiura@elec.okayama-u.ac.jp (Y. Kamiura)

0921-4526/99/$ - see front matter
PII: S0921-4526(99)00441-X

5.9×10^{14} and 1.7×10^{14} cm^{-3}, respectively. These crystals contained carbon at a density of approximately 1×10^{16} cm^{-3}. Many samples were cut from the crystals into square pillars with dimensions of $1 \times 1 \times 6$ mm^3, the longest of which was parallel to the ⟨1 1 1⟩ or ⟨1 1 0⟩ direction. Hydrogen (deuterium) was injected into samples by chemical etching (HNO_3 (DNO_3) : HF = 10 : 1) before the fabrication of Schottky contacts, which were formed by vacuum evaporation of gold. Capacitance DLTS measurements were performed with a reverse bias of 5 V and a filling pulse of 5 V under uniaxial compressive stresses up to 1 GPa applied to the ⟨1 1 1⟩ or ⟨1 1 0⟩ direction. Subsequently, samples were preannealed at 70°C for 90 min with a reverse bias of 5 V applied to the Schottky junction. This step increased the density of the H–C complex and made its depth profile flat. In our experiments, this preannealed state was taken as the initial state where the stress-induced alignment of the complex was performed under a compressive stress along the ⟨1 1 1⟩ or ⟨1 1 0⟩ direction.

3. Results and discussion

3.1. Lifting of orientational degeneracy

In Fig. 1(a), the dashed–dotted curve is a DLTS spectrum recorded without stress for a sample preannealed at 70°C. In this spectrum, a single DLTS peak due to the H–C complex appears at 93 K. The solid curve is a spectrum measured under a compressive stress of 1 GPa along the ⟨1 1 0⟩ direction. In this measurement, the stress was applied to the sample at 70 K, and was held during the DLTS run. The peak is split into two due to the lifting of orientational degeneracy of the complex, and is shifted toward lower temperature. Two dotted curves represent the fitting of two split peaks using the usual DLTS function, indicating that their intensity ratio was 1 : 1. In a preliminary paper, we reported that the DLTS peak of the complex was split into two under the ⟨1 1 1⟩ stress with an intensity ratio of 1 : 3, which was the ratio of the low-temperature to high-temperature peak [6,7]. We observed no splitting under ⟨1 0 0⟩ stress. From these results, we determined that the symmetry of the H–C complex is C_{3V}, and proposed a structural model, where a hydrogen atom occupied a bond-centered (BC) site between carbon and silicon atoms [Fig. 1(b)]. This model is consistent with the results of recent theoretical calculations [8–11]. Our results for the peak splitting under the ⟨1 1 1⟩ stress indicates that the applied stress induces the energy of one configuration of the complex, whose ⟨1 1 1⟩ symmetry axis along the C–H–Si bond is parallel to the ⟨1 1 1⟩ stress, to become higher than that of the other three configurations among four equivalent ⟨1 1 1⟩ orientations of the symmetry axis. This means that the compressive stress component parallel to the symmetry axis raises the energy of the C–H–Si bond, suggesting its anti-bonding nature. This result is also consistent with the theoretical calculations. In Fig. 1(b), the energy of the two bonds with an angle of 35° to the ⟨1 1 0⟩ stress direction is higher than that of the other two bonds perpendicular to the stress direction. In Fig. 1(a), the low-temperature peak arises from the former bonds and the high-temperature peak arises from the latter bonds.

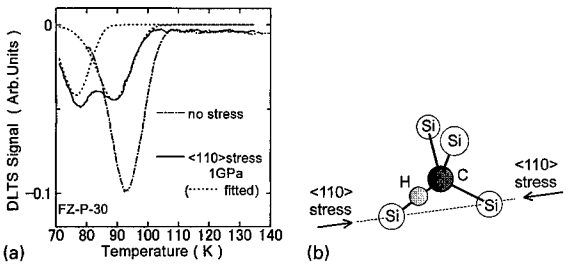

Fig. 1. (a) DLTS spectra after preannealing at 70°C for 90 min with a reverse bias, $V_R = 5$ V applied to the Schottky junction: the dashed–dotted curve is recorded without stress, the solid curve is measured under a stress of 1 GPa along the ⟨1 1 0⟩ direction and two dotted curves represent the fitting of two split peaks using the usual DLTS function. (b) Model of the atomic configuration of the hydrogen–carbon complex in Si.

3.2. Stress-induced alignment

The lifting of orientational degeneracy due to uniaxial stresses causes the hydrogen atom to jump from a high-energy to a low-energy bond to orient the symmetry axis of the complex toward the lowest-energy direction, provided that the temperature is high enough for hydrogen to move. This is called the stress-induced alignment of the H–C complex, and changes its DLTS peak from a split one to a single one. Such a change in the DLTS spectrum was actually observed in our experiments. The low-temperature peak decayed and simultaneously the high-temperature peak grew at 250 K under a ⟨1 1 1⟩ stress of 1 GPa. This clearly proves that a hydrogen atom jumps from one higher-energy bond parallel to the stress direction to the other three lower-energy bonds with an angle of 70° to the stress direction.

Fig. 2(a) shows the results of experiments on stress-induced alignment of the complex at 250 K under a ⟨1 1 0⟩ stress of 1 GPa without reverse bias, V_R, applied to the Schottky junction. It is seen in the figure that the low-temperature peak decays and simultaneously the high-temperature peak grows. This indicates that a hydrogen atom jumps from the two high-energy bonds with an angle of 35° to the stress direction to the other two low-energy bonds perpendicular to the stress direction. During this annealing, about 70% of H–C complexes

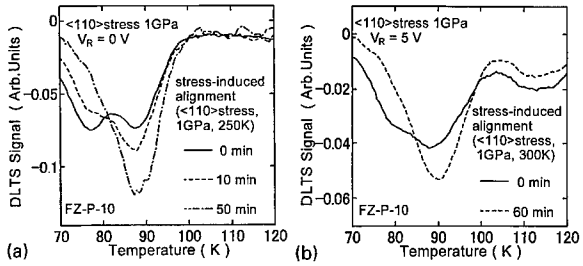

Fig. 2. Change of DLTS spectrum in the process of stress-induced alignment under a compressive stress of 1 GPa along the ⟨1 1 0⟩ direction, (a) at 250 K with $V_R = 0$ V, and (b) at 300 K with $V_R = 5$ V.

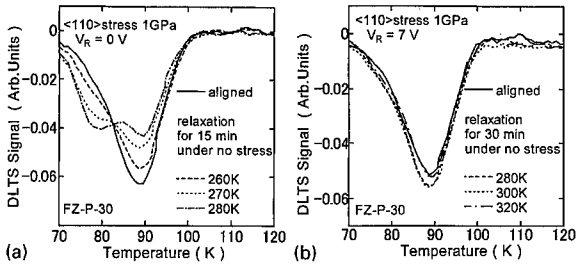

Fig. 3. Changes of DLTS spectra due to isochronal annealing to cause the relaxation from the alignment after removing the stress, (a) for 15 min at each temperature with $V_R = 0$ V, and (b) for 30 min at each temperature with $V_R = 7$ V.

were in the neutral charge state, and the rest were positively charged. To determine which of the charge states favors the stress-induced alignment, a reverse bias was applied to the Schottky junction during the stress-induced alignment to make the charge state of the complex completely positive. The results of our experiments indicated that stress-induced alignment did not occur at all during the annealing at 250 K for 60 min with a reverse bias of 5 V applied to the junction under a stress of 1 GPa along the ⟨1 1 0⟩ direction. Under such a reverse bias condition, the stress-induced alignment occurred at a higher temperature of 300 K, as shown in Fig. 2(b). Obviously, the alignment is suppressed by the application of reverse bias, indicating that stress-induced alignment occurs preferentially in the neutral charge state. This means that hydrogen moves more easily in the neutral charge state, at least under the compressive stress.

3.3. Relaxation of alignment

Fig. 3 shows the results of isochronal annealing in the relaxation process of stress-induced alignment after removing the stress. Again, the charge state of the H–C complex was controlled with and without the application of reverse bias to the Schottky junction. Fig. 3(a) shows the changes of the DLTS spectra due to isochronal annealing under no reverse bias, where about 70% of H–C complexes are in the neutral charge state and the rest are positively charged. The solid curve represents the spectrum just after the stress-induced alignment was completed at 250 K for 150 min. This spectrum shows nearly a single peak, the fitting of which indicates that about 70% of the H–C complexes originally oriented along the high-energy direction are aligned in the low-energy direction to yield the high-temperature DLTS peak. Isochronal annealing up to 280 K caused this peak to decay and the low-temperature peak to grow until the intensities of both peaks became the same. Since four BC sites around carbon are equivalent during this annealing without stress, the result of Fig. 3(a) can be explained as the loss of stress-induced alignment due to random jumps of hydrogen from bond to bond to recover the initial random orientations of the complex. These random jumps of hydrogen were greatly suppressed by the application of reverse bias of 7 V, as shown in Fig. 3(b). Under this bias condition, all of the H–C complexes were in the positive charge state. Therefore, we have reached the conclusion that under no stress hydrogen also moves more easily in the neutral charge state.

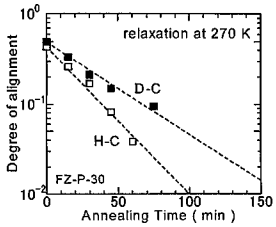

Fig. 4. Isothermal annealing at 270 K under no stress to cause the relaxation from the stress-induced alignment at 290 K for 10 min. The ordinate represents degree of alignment, $D = (N_1 - N_2)/(N_1 + N_2)$, where N_1 and N_2 are trap densities corresponding to high- and low-temperature DLTS peaks, respectively. Open squares represent the relaxation of the H–C complex and filled squares represent that of the D–C complex.

We have performed isothermal annealing experiments to check the effect of isotopic substitution of deuterium for hydrogen on the relaxation rate of stress-induced alignment of the H–C complex. Deuterium was introduced by chemical etching using deuterated nitric acid, and we observed that the DLTS peak due the deuterium–carbon (D–C) complex was the same as that of the H–C complex. Fig. 4 shows the results of isothermal annealing at 270 K under no stress after stress-induced alignment at 290 K for 10 min, which caused approximately 50% of the H–C complexes and the D–C complexes to become aligned. The ordinate represents the degree of alignment, D, defined by the equation, $D = (N_1 - N_2)/(N_1 + N_2)$, where N_1 and N_2 are trap densities corresponding to the high- and low-temper-

ature DLTS peaks, respectively. When all of the H–C complexes are aligned in the low-energy state responsible for the high-temperature peak, D is equal to unity, and when the relaxation of alignment is completely finished, D is equal to zero. Fig. 4 shows that the relaxation rate is lower by a factor of 0.6 for the D–C complex than that of the H–C complex. Since the relaxation rate is proportional to the jump rate of hydrogen (deuterium), the result of Fig. 4 proves that the relaxation of alignment of the H–C complex is certainly due to the motion of a hydrogen atom.

4. Conclusions

We have observed the stress-induced alignment and subsequent relaxation processes of the H–C complex in silicon by the DLTS technique under uniaxial compressive stresses along $\langle 1\,1\,1\rangle$ and $\langle 1\,1\,0\rangle$ directions. These two processes are due to hydrogen jumps from BC site to BC site around carbon with and without stress, respectively. By controlling the charge state of the complex with and without applying reverse bias to the Schottky junction, we have found that the motion of hydrogen is greatly influenced by the charge state of the complex and hydrogen moves more easily in the neutral charge state.

References

[1] M. Yoneta, Y. Kamiura, F. Hashimoto, J. Appl. Phys. 70 (1991) 1295.
[2] Y. Kamiura, M. Yoneta, F. Hashimoto, Appl. Phys. Lett. 59 (1991) 3165.
[3] Y. Kamiura, M. Yoneta, Y. Nishiyama, F. Hashimoto, J. Appl. Phys. 72 (1992) 3394.
[4] Y. Kamiura, M. Tsutsue, M. Hayashi, Y. Yamashita, F. Hashimoto, Mater. Sci. Forum 196–201 (1995) 903.
[5] Y. Kamiura, M. Hayashi, Y. Nishiyama, S. Ohyama, Y. Yamashita, Jpn. J. Appl. Phys. 36 (1997) 6579.
[6] Y. Kamiura, N. Ishiga, Y. Yamashita, Jpn. J. Appl. Phys. 36 (1997) L1419.
[7] Y. Kamiura, N. Ishiga, S. Ohyama, Y. Yamashita, Mater. Sci. Forum 258–263 (1997) 247.
[8] D.M. Maric, P.F. Meier, S.K. Estreicher, Phys. Rev. B 47 (1993) 3620.
[9] Y. Zhou, R. Luchsinger, P.F. Meier, H.U. Suter, D. Maric, S.K. Estreicher, Mater. Sci. Forum 196–201 (1995) 891.
[10] C. Kaneta, H. Katayama-Yoshida, Mater. Sci. Forum 196–201 (1995) 897.
[11] P. Leary, R. Jones, S. Öberg, Phys. Rev. B 57 (1998) 3887.

ELSEVIER

Physica B 273-274 (1999) 188-191

PHYSICA B

www.elsevier.com/locate/physb

A new type of hydrogen molecules in silicon

K. Murakami[a,*], K. Ishioka[b], M. Kitajima[b], S. Tateishi[a], K. Nakanoya[a], T. Mori[b], S. Hishita[c]

[a]*Institute of Applied Physics, University of Tsukuba, Tennoudai 1-1-1, Tsukuba 305-8573, Japan*
[b]*National Research Institute for Metals, Sengen, Tsukuba, Japan*
[c]*National Institute for Research in Inorganic Materials, Namiki, Tsukuba, Japan*

Abstract

The Raman line of a new hydrogen molecule at approximately 3820 cm^{-1} has been observed for the first time in silicon after Si^+ ion implantation with proper doses, followed by hydrogen atom treatment. The assignment was confirmed by isotope shifts to 2770 cm^{-1} for D_2 molecule and to 3353 cm^{-1} for HD molecule. Both the ion-dose dependence and hydrogenation-temperature dependence of the Raman intensity of the H_2 molecules correlate with those of the intensity of peaks of Si–H stretching observed at 1957 ± 1.8 cm^{-1} and at approximately 2185 and 2210 cm^{-1}. We propose a model where the hydrogen molecule corresponding to the 3820 cm^{-1} vibrational line is trapped in or adjacent to small H-terminated multivacancies.

Keywords: Hydrogen molecules; H-terminated multivacancies; Raman scattering

1. Introduction

Existence of hydrogen molecules H_2 in crystalline semiconductors had been predicted by many theoretical calculation, but had not been detected for a long time in crystalline semiconductors. Since the first observation of H_2 in crystalline silicon (Si) in 1996 [1], it has attracted much experimental and theoretical attention. So far two kinds of H_2 without impurities have been clarified in crystalline silicon; i.e., hydrogen molecules in platelets (4158 cm^{-1}) (let us denote it as type I; H_2(I)) and T_d interstitial sites (3601 cm^{-1}) (let us denote it as type II; H_2(II)) that have been observed by Raman scattering [1,2] and IR [3] measurements. On the other hand, infrared (IR) absorption measurements at low temperatures indicated that two IR lines (at 3788.9 and 3730.8 cm^{-1}) have been assigned as H_2 located at sites adjacent to interstitial oxygen atoms [3,4].

Several theoretical calculations [5–7] predict that H_2 in the valence electron's "sea" of crystalline silicon shows the downshift in the vibration frequency due to the charge redistribution in H_2 and/or between H_2 and the surrounding Si bonds. The difference in the vibrational frequencies of the two Raman lines, H_2(I) and H_2(II), is accounted for in terms of different interactions with the surroundings in different trapping environments; platelets and T_d sites are the two extremes in terms of the size. It is reasonable to expect a third vibrational frequency for H_2 that exists stably in a trap of a medium size or in the vicinity of Si–H bonds whose wave function is more localized than that of Si–Si bonds. Such medium-sized traps with H-terminated wall can be created by ion implantation into crystalline silicon [8,9] followed by hydrogenation.

In the present study we succeeded in observing H_2 trapped by multivacancies in silicon using Raman scattering spectroscopy. The vibrational frequency of the H_2 trapped by multivacancies was found to be between those of H_2(I) and H_2(II).

2. Ion implantation and experiments

There is a possibility that hydrogen molecules are effectively formed and incorporated in some types of

* Corresponding author. Tel.: + 81-298-53-5272; fax: + 81-298-53-7440.
E-mail address: murakami@ims.tsukuba.ac.jp (K. Murakami)

0921-4526/99/$ - see front matter
PII: S0921-4526(99)00442-1

multivacancies in silicon. Multivacancies were introduced into silicon in a controlled manner by means of Si^+ ion implantation. As reported [8,9], ion implantation is known to produce various kinds of multivacancies in Si; i.e., vacancies formed as primary product under ion implantation migrate quickly at room temperature and end up with multivacancies and impurity-vacancy complexes. Much less is known concerning the final state of interstitials; most probably they form interstitial-complexes.

FZ p-type Si (1 0 0) wafers were used as crystalline silicon samples. We implanted 200-keV Si^+ ions in the crystalline silicon at doses ranging from 1×10^{12} to 5×10^{15} Si/cm^2 at room temperature. The averaged project range is estimated to be 250 nm from the surface. The Raman spectrum of the silicon after implantation with a dose of 5×10^{15} Si^+/cm^2 showed the formation of continuous amorphous layer from the surface.

The implanted samples were treated with atomic hydrogen mainly at 250°C for 3 h in a remote downstream of hydrogen plasma. The samples were placed at a distance 60 cm apart from the plasma to suppress damage from the activated species in the plasma. Similar atom treatments were performed replacing hydrogen plasma with deuterium plasma or with plasma from hydrogen–deuterium 0.5 : 0.5 mixture gas to check the isotope shift. In order to investigate the temperature dependence of atomic hydrogen treatment, we performed hydrogenation of Si samples implanted with 2×10^{14} Si/cm^2 at various temperatures from 75°C to 450°C for 30 min. Details of the hydrogen atom treatment are described elsewhere [10,11]. In order to detect the third type of hydrogen molecules, we have measured Raman scattering for the Si samples at room temperature. Details of the Raman measurement are also described in the previous papers [10,11].

3. Results and discussion

Typical Raman spectra of hydrogen molecules are shown in Fig. 1 for silicon implanted with 2×10^{14} Si^+/cm^2 followed by the hydrogen atom treatment at 250°C. Two Raman lines were observed at 4158 and 3822 cm^{-1}. No Raman signals due to hydrogenation are observed at around 3600 cm^{-1} for any implanted samples studied in the present study. The 4158 cm^{-1} line is the Q_1 vibrational line of H_2(I) that was observed in unimplanted silicon after hydrogenation [1,2]. The 3822 cm^{-1} line was observed for the first time by the present authors [11,12], and was found to appear only for the silicon samples implanted with doses between 1×10^{13} and 5×10^{14} Si^+/cm^2. The peak of the Raman line is observed at approximately 3820 cm^{-1}, between 3813 and 3826 cm^{-1}, being dependent on the temperature of hydrogenation.

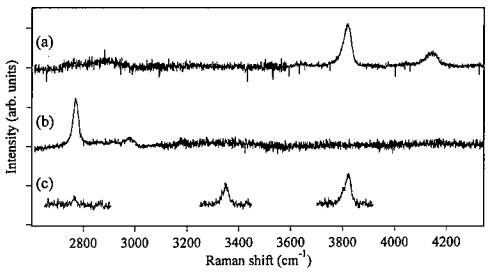

Fig. 1. Raman spectra of silicon after implantation with 200 keV Si^+ ions at a dose of 2×10^{14} Si^+/cm^2 followed by treatment with (a) H atoms, (b) D atoms, and (c) H + D atoms at 250°C for 3 h.

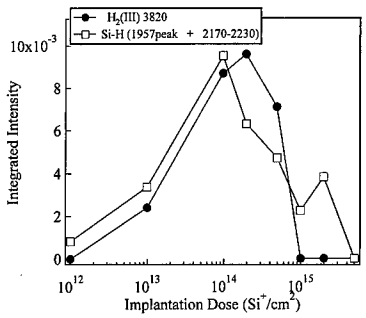

Fig. 2. The Raman intensities of the H_2 vibrational lines (H_2(I) and H_2(III)) and the three Si–H side peaks in silicon after implantation with different Si^+ doses followed by H atom treatment at 250°C for 3 h. The intensities are normalized by that of the optical phonon of silicon.

For investigation of the origin of the 3820 cm^{-1} peak we performed deuterium (D) atom treatment, as well as treatment using hydrogen-deuterium mixture (H + D atom treatment), at 250°C for 3 h. The Raman spectra of silicon after implantation with 2×10^{14} Si^+/cm^2 followed by different isotopic hydrogen atom treatment are compared in Fig. 1. The 3820 cm^{-1} line shows an isotope shift down to 2770 cm^{-1} for D atom treatment. After H + D atom treatment a peak was observed at 3353 cm^{-1} in addition to those at 3820 and 2770 cm^{-1}, which is apparently attributed to HD molecule. The isotope shifts confirm that the 3820 cm^{-1} line arises from H_2 in silicon (let us denote this hydrogen molecule as type III; H_2(III)), and not from any XH_2 complexes (e.g., H_2O).

In Fig. 2, the integrated Raman intensity of the vibrational line of H_2(III) is plotted as a function of the implantation dose. The intensity of H_2(I) not shown here decreased monotonically with increasing implantation dose, whereas that of H_2(III) has a maximum at 2×10^{14} Si^+/cm^2. The ion-dose dependence indicates that H_2(III) is not related to defects created during hydrogenation

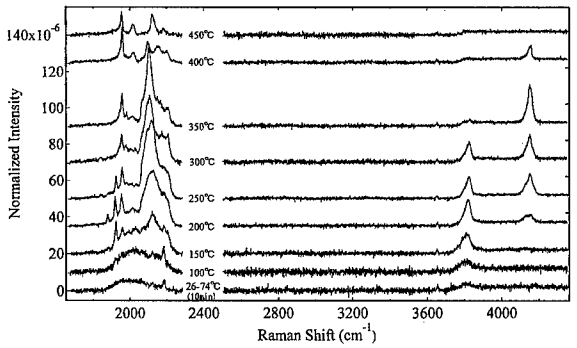

Fig. 3. Raman spectra of silicon after implantation with 200 keV Si^+ at a dose of 2×10^{14} Si^+/cm^2 followed by H atom treatment at various temperatures for 30 min.

(e.g. platelets), but to multivacancies and interstitial complexes created by ion implantation.

Here, let us consider the structures of H_2(III). It should be located in a trapping site whose size is greater than that of H_2(II) but smaller than that of H_2(I). Candidates for such traps are multivacancies created by Si^+ ion implantation. An electron paramagnetic resonance study was reported by Brower [8] on intrinsic and n-type silicon implanted with 160 keV O^+ ions, for example. It confirmed the formation of divacancy and 4-vacancy [8]. The 4-vacancy was observed for doses between 2×10^{12} and 2×10^{14} O^+/cm^2, with a maximum at around 2×10^{13} O^+/cm^2, while the negative divacancy is observed effectively at lower doses for n-type Si due to change of the Fermi level. The study suggests that the divacancy and multivacancies larger than the divacancy are effectively created in the ion dose range in which H_2(III) was observed.

Fig. 3 shows the Raman spectra of Si–H stretching at around 2000 cm^{-1} and of H_2(I)/(III) in silicon implanted with 2×10^{14} Si^+/cm^2, both after hydrogen atom treatment at various temperatures from 75°C to 450°C. The formation of H_2(III) can be observed between 75 and 350°C. The Si–H Raman band for silicon hydrogenated exhibits several side peaks around the broad Si–H spectrum due to platelet (approximately 2100 cm^{-1}) or due to amorphous phase (approximately 2000 cm^{-1}); i.e. there are at least three peaks at the low-frequency side (1882 ± 1.9, 1923 ± 2.2, and 1957 ± 1.8 cm^{-1}) and two relatively broad peaks at the high-frequency side (approximately 2185 and 2210 cm^{-1}). These side peaks are similar to those attributed to hydrogen-terminated dangling bonds observed by IR measurement in hydrogen-implanted Si [13]. Some of the side peaks have possibly originated from H-terminated multivacancies and/or complexes of Si interstitials and hydrogen [14]. H_2(III) is found not to be produced above a temperature of 400°C. In particular, the Raman spectrum for 300°C treatment in Fig. 3 indicates that the peaks of 1882 and 1923 cm^{-1} are not correlated with H_2(III), because they are not observed when the Raman line of H_2(III) is done. Consequently, the total integrated intensity of the 1957, 2185 and 2210-cm^{-1} side peaks is plotted in Fig. 2. The ion-dose dependence of the Si–H side peaks shows strong correlation with that of H_2(III), indicating that multivacancies and interstitial complexes play an important role in the formation of H_2(III), most plausibly as its trapping sites.

Calculations have shown that H_2 is stable in multivacancies with H-termination [14,15]. The vibrational frequency was calculated to be approximately 4000 cm^{-1} for H_2 in H-terminated 6- and 10-vacancies (V_6H_{12} and $V_{10}H_{16}$) [14,15], while it was approximately 3780 cm^{-1} for H_2 in the same vacancies without H-termination [15]. The vibrational frequency for H_2 trapped by H-terminated divacancy (V_2H_6) was approximately 3800 cm^{-1}, assuming H_2 to be trapped at T_d site adjacent to the Si–H bonds in the divacancy [14]. These calculations agree roughly with the experimentally observed frequency of H_2(III), 3820 cm^{-1}, and support its assignment as a hydrogen molecule trapped by small, H-terminated multivacancies in silicon. It is noted that the width of the H_2(III) line is about 30 cm^{-1}, being comparable to that of H_2(I) and much broader than that of H_2(II). The large width is interpreted by inhomogeneous broadening; i.e., H_2 molecules are trapped probably by small multivacancies with several different sizes (such as divacancy, 3 vacancy (3-V), and 4-V on (110) plane [8]). It is also possible that H_2 is located at several metastable sites in (or adjacent to) the same multivacancy.

4. Conclusions

We have presented the existence of the third type of H_2 molecule that is trapped without impurities by multivacancies in ion-implanted silicon. The isotope shifts confirmed the assignment of molecule. H_2(III) cannot be produced above a temperature of 400°C. Both the ion-dose dependence and hydrogenation-temperature dependence suggest that the Si–H at 1957, 2185 and 2210 cm^{-1} are correlated with H_2(III).

The findings of various types of hydrogen molecules such as H_2(I), (II) and (III) encourage us to investigate further useful possibilities of hydrogen molecules as a source for self-recovery or self-passivation of defects, through interactions between initially incorporated hydrogen molecules and defects induced during operation in Si devices.

Acknowledgements

The authors would like to thank A. Oshiyama, Y. Okamoto and M. Nimura for instructive discussion on

their theoretical calculations. They also thank S. Fujimura for his help in setting up the hydrogen atom treatment apparatus, and H. Haneda for his SIMS measurement of hydrogen in the samples. This work was partly supported by Grant-in-Aid (No. 11555001 and 10875066) for Scientific Researchers from the Ministry of Education, Science and Culture.

References

[1] K. Murakami, N. Fukata, S. Sasaki, K. Ishioka, M. Kitajima, S. Fujimura, J. Kikuchi, H. Haneda, Phys. Rev. Lett. 77 (1996) 3161.
[2] A.W.R. Leitch, V. Alex, J. Weber, Phys. Rev. Lett. 81 (1998) 421.
[3] R.E. Pritchard, M.J. Ashwin, R.C. Newman, J.H. Tucker, E.C. Lightowlers, M.J. Binns, R. Falster, S.A. McQuiaid, Phys. Rev. B 56 (1997) 13118.
[4] R.E. Pritchard, M.J. Ashwin, J.H. Tucker, R.C. Newman, Phys. Rev. B 57 (1998) 15048.
[5] Y. Okamoto, M. Saito, A. Oshiyama, Phys. Rev. B 56 (1997) R10016.
[6] C.G. Van. de Walle, Phys. Rev. Lett. 80 (1998) 2177.
[7] B. Hourahine, R. Jones, S. Oberg, R.C. Newman, P.R. Briddon, E. Roduner, Phys. Rev. B 57 (1998) R12666.
[8] K.L. Brower, W. Beezhold, J. Appl. Phys. 43 (1972) 3499.
[9] K. Murakami, K. Masuda, K. Gamo, S. Namba, Jpn. J. Appl. Phys. 12 (1973) 1307.
[10] N. Fukata, S. Sasaki, K. Murakami, K. Ishioka, K.G. Nakamura, M. Kitajima, S. Fujimura, J. Kikuchi, H. Haneda, Phys. Rev. B 56 (1997) 6642.
[11] K. Ishioka, M.Kitajima, S. Tateishi, K. Nakanoya, N. Fukata, T. Mori, K. Murakami, S. Hishita, Phys. Rev. B 60 (1999) 10852.
[12] M. Kitajima, K. Ishioka, K. Nakanoya, S. Tateishi, T. Mori, N. Fukata, K. Murakami, S. Hishita, Jpn. J. Appl. Phys. 38 (1999) L691.
[13] M.K. Weldon, V.E. Marsico, Y.J. Chabal, A. Agarwal, D.J. Eaglesham, J. Sapjeta, W.L. Brown, D.C. Jacobson, Y. Caudano, S.B. Christman, E.E. Chaban, J. Vac. Sci. Technol. B 15 (1997) 1065.
[14] T. Akiyama, Y. Okamoto, M. Saito, A. Oshiyama, Phys. Rev. Lett., submitted for publication.
[15] M. Nimura, private communication.

ELSEVIER

Physica B 273–274 (1999) 192–195

PHYSICA B

www.elsevier.com/locate/physb

Temperature dependence of the formation of hydrogen molecules in n- and p-type silicon

M. Kitajima[a,*], K. Ishioka[a], K. Murakami[b], K. Nakanoya[b], T. Mori[b]

[a]*National Research Institute for Metals, Sengen, Tsukuba, 305 Japan*
[b]*Institute of Material Science, University of Tsukuba, Tennoudai, Tsukuba, Japan*

Abstract

We report a Raman study on the hydrogenation–temperature dependence on the formation of hydrogen molecules in crystalline silicon. The 3601 cm^{-1} vibrational line for H_2, which has been attributed to hydrogen molecule in T_d site, is observed in p-type as well as in n-type crystalline silicon. This H_2 molecule exhibits significantly different temperature dependence in n- and p-type Si. It is suggested from the hydrogenation–temperature dependence that the charge states and the sites of atomic hydrogen affect the formation of this type of H_2. From the experiments using H + D atom treatments, there may be a significant isotope effect on the formation of the H_2 molecule.

Keywords: Hydrogen molecules; Raman scattering; Temperature effects; Doping effects

1. Introduction

Hydrogen is an important impurity and can be incorporated in Si in a number of different configurations. The hydrogen molecule has been long suggested to be one of most fundamental forms of hydrogen impurity in crystalline Si. Since the first observation of hydrogen molecules by means of Raman spectroscopy in 1996 [1], many authors have discussed this subject experimentally and theoretically [3–10]. Murakami et al. have revealed the existence of hydrogen molecules in crystalline silicon by observing a Raman vibrational line at 4158 cm^{-1} (let us denote this molecule as H_2(I)) [1,2]. The vibrational frequency is very close to that of gaseous hydrogen, and has been attributed to gaseous hydrogen molecules trapped in platelets [3].

Recently another vibrational Raman line of H_2 has been observed at 3601 cm^{-1} in FZ n-type silicon exposed to a hydrogen plasma at 150°C [4,5]. This correlates well with the low-temperature infrared (IR) spectroscopy local vibration modes of H_2 in crystalline Si after exposure to hydrogen gas between 1100 and 1300°C [6] (let us denote this molecule as H_2(II)). The downshift in the vibrational frequency with respect to gaseous H_2 implies a weakening of the H–H bond as a result of electron redistribution between H_2 and the surroundings. Several theoretical calculations predict that H_2 in the tetrahedral (T_d) site should show a significant downshift in the vibrational frequency compared with free H_2 [8–10]. H_2(II) has been attributed to hydrogen molecules at T_d sites of silicon on the basis of the theoretical predictions [4–6]. The H_2(II)-Raman line has been observed only for n-type Si hydrogenated at 150°C [4,5]. In this paper we present a detailed Raman study on both n- and p-type crystalline silicon hydrogenated at temperatures from 60°C to 400°C. The experimental observation of HD(II) molecules will be also described.

2. Experimental

FZ p-type Si (1 0 0) (resistivity > 50 Ω cm) and FZ n-type Si doped with phosphorus (3×10^{14} P/cm^2

* Corresponding author. Tel.: + 81-298-59-2836; fax: + 81-298-59-2801.
E-mail address: kitajima@nrim.go.jp (M. Kitajima)

0921-4526/99/$ - see front matter
PII: S0921-4526(99)00443-3

implantation) were used as crystalline silicon samples. The Si samples were treated with atomic hydrogen in a remote downstream hydrogen plasma at substrate temperatures between 60°C and 400°C for 30 min. They were first heated up to a desired temperature in vacuum and then treated with the atomic hydrogen. Similar atom treatments were performed replacing the H_2 plasma with a D_2 plasma or with $D_2 + H_2$ plasmas to check the isotope shifts. Details of the hydrogen atom treatment are described elsewhere [11]. All the Raman scattering measurements were performed at room temperature. A cw argon-ion laser with a wavelength of 514.5 nm and a power of 200 mW was used as the exciting source. Light scattered by the sample was collected in a 90° configuration, analyzed using a triple grating monochromator with a wavenumber resolution of 3 cm^{-1}, and detected with a CCD camera.

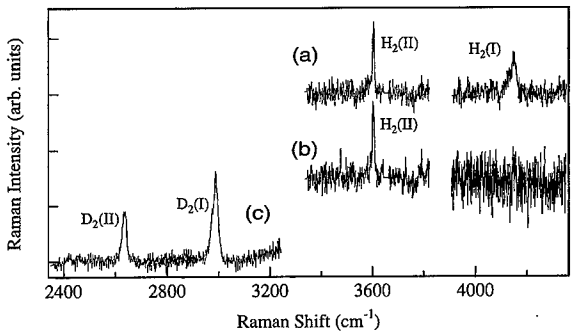

Fig. 1. Raman spectra of (a) n-type Si treated with H atoms at 250°C, (b) p-type Si treated with H atoms at 300°C, and (c) n-type Si treated with D atoms at 250°C.

3. Results and discussion

Typical examples of the Raman spectra of the silicon samples after hydrogen atom treatments are shown in Fig. 1. In both n- and p-type crystalline silicon after hydrogen atom treatment the vibrational Raman line of H_2(II) is observed at 3601 cm^{-1}, in addition to H_2(I) at 4158 cm^{-1}. The Raman line of H_2(II) has been reported only in n-type silicon so far [4,5], and here H_2(II) was found to be formed also in p-type silicon. The Raman line of H_2(II) was stable to irradiation of the incident laser, and did not disappear at all for Raman measurements for 5 h (It has been reported that this Raman line disappeared within several minutes during the Raman measurents when using an incident laser with a wavelength of 488 nm and a power between 50 and 300 mW, for further detail please see Ref. [12]).

In silicon crystal after deuterium atom treatment, the two vibrational lines show isotope shifts to 2990 cm^{-1} for D_2(I) and 2629 cm^{-1} for D_2(II). We have confirmed the HD(II) frequency, which has not been observed in the previous Raman study by Leitch et al. [4], using D_2-rich $H_2 : D_2$ gas mixtures. The HD(II) line was observed at 3177 cm^{-1} in crystalline silicon treated with H + D atoms using a $H_2 : D_2$ (10 : 90) plasma (Fig. 2b). However, neither the HD(II) line nor the D_2(II) but only H_2(II) was observed when using a $H_2 : D_2$(50 : 50) plasma for the hydrogenation (Fig. 2a). The results show that H_2(II) is formed preferential to HD(II) and D_2(II), and there may be an significant isotope effect on the formation of H_2(II).

The splitting due to the ortho- and para-H_2 states was not observed for H_2(II), in agreement with the previous study [4,5]. It is noted that the line of this H_2 became broadened as the mass of the molecular isotopes was increased: the half-width at half-maximum (HWHM) of H_2(II), HD(II) and D_2(II) were ca. 5, 9 and 11 cm^{-1},

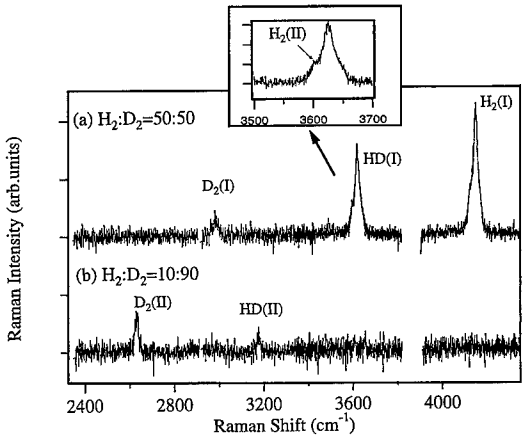

Fig. 2. Raman spectra of n-type Si treated with H + D atoms at 250°C using (a) a $H_2 : D_2$ (50 : 50) and (b) a $H_2 : D_2$ (10 : 90) plasmas.

respectively. This is contrary to the H_2(I) molecules: those of H_2(I), HD(I) and D_2(I) were ca. 34, 25 and 20 cm^{-1}, respectively. This result shows that the interactions of these molecular isotopes with the surroundings are different in such a small trap as T_d site. A plausible explanation for this difference in HWMH is motional broadening due to mass difference of the molecular isotopes. Note also that the widths of these H_2(II) lines are much broader than those seen by IR absorption for Si after exposure to hydrogen gas between 1100°C and 1300°C (ca. 0.1 cm^{-1}) [6]. The Raman line widths are over the wave number resolution in our monochromator, and are not instrumental. Actually the width of the H_2(II) line agrees well with that in the previous Raman study (ca. 6 cm^{-1}) [4,5]. IR measuremets of the Si samples treated with the hydrogen atoms are also required.

The formation of H_2(I) and H_2(II) strongly depends on the temperature during the hydrogen atom treatment.

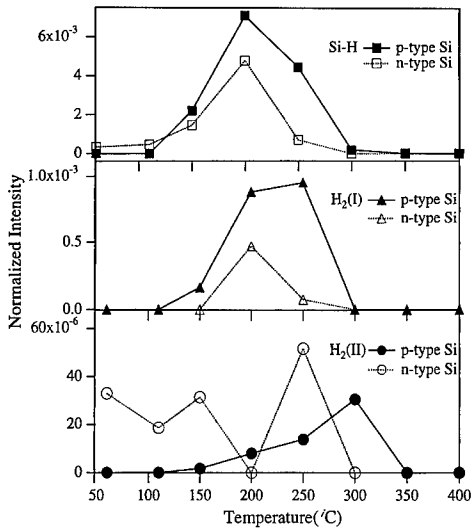

Fig. 3. Raman intensities of the vibrational lines of H_2 for n- and p-type Si as a function of the hydrogenation temperature. The intensity of the Si–H stretching line at around 2100 cm^{-1} showing the formation of platelet [2,3,13] is also shown. The intensities are normalized to that of the optical phonon line of Si. H_2(I) and H_2(II) are hydrogen molecules corresponding to the vibrational Raman lines of H_2 observed at 4158 and 3601 cm^{-1}, respectively.

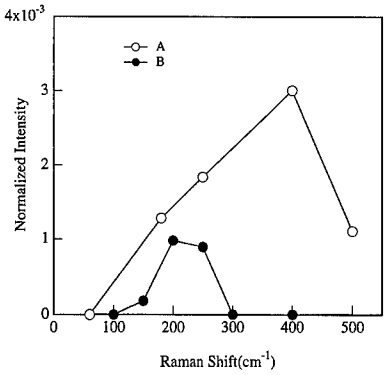

Fig. 4. Raman intensity of the vibrational line of H_2 observed at 4158 cm^{-1} (H_2(I)) for n-type Si as a function of the hydrogenation temperature, with different hydrogenation procedures. Two different procedures for hydrogenation were compared. The hydrogen plasma was ignited after the substrate temperature reached the desired level in procedure B, while it was before heating the substrate in procedure A.

Fig. 3 shows the hydrogenation–temperature dependence of the hydrogen molecules in n- and p-type crystalline silicon. H_2(I) and H_2(II) show different temperature dependence. The formation of H_2(II) has a maximum at higher temperature than that of H_2(I). The temperatures for the maximum formation of H_2(I), 200–250°C, corresponds roughly to the temperature of platelet formation [13]. The temperature dependence of the Si–H stretching band observed at 2100 cm^{-1} is similar to that of this H_2. It is found that H_2(II) exhibits significantly different temperature dependence in n- and p-type Si, while that of H_2(I) is similar in both types (although the intensities are different). In p-type the Raman line of H_2(II) occurs for hydrogenation between 150°C and 350°C and has a maximum in the intensity at 300°C. In n-type, in contrast, H_2(II) is formed from such a low temperature as 60°C up to 250°C. The different temperature dependence between n- and p-type suggests the importance of effects of Fermi-level on the formation of this H_2, that is, the formation of H_2(II) probably depends on the charge states and the sites of isolated hydrogen atoms [14].

It is also noted that H_2(II) has a tendency to decrease in the Raman intensity as H_2(I) increases. For example, the Raman intensity of H_2(II) is negligible when that of H_2(I) is very large, as seen for n-Si at 200°C in Fig. 3. The timing of the plasma ignition and the sample heating in the hydrogen atom treatment also strongly affected the formation of the H_2 molecules, as shown in Fig. 4. The temperature region where H_2(I) is formed was elevated when the hydrogen plasma was ignited before heating the substrate. The formation of H_2(I) has a maximum at 400°C where platelets are unstable, and no Raman line of H_2(II) was observed at any temperature. This result can be explained as follows: Exposure of the silicon to the plasma leads to the formation of platelets at lower temperatures while heating the sample. Once the platelets are formed, they become the preferential traps for further hydrogen introduced during hydrogen atom treatment to grow as hydrogen bubbles even at higher temperatures.

4. Conclusions

We have presented a Raman study on the hydrogenation–temperature dependence of the formation of hydrogen molecules in crystalline silicon. The 3601 cm^{-1} vibrational line for H_2(II), which has been attributed to the hydrogen molecule at the T_d site, was observed in p-type as well as in n-type crystalline silicon. It was found that the introduction of H_2(II) exhibits significantly different temperature dependence in n- and p-type Si. In p-type H_2(II) occurred for hydrogenation between 150°C and 350°C. In n-type, in contrast, H_2(II) was formed at as low a temperature as 60°C up to 250°C. It was suggested that the charge states and the sites of atomic hydrogen affects the formation of this type of H_2. From the experiments using H + D atom treatments, there may be an isotope effect on the formation of the H_2(II) molecules.

Acknowledgements

The authors would like to thank S. Fujimura and J. Kikuchi for their help in setting up the hydrogen atom treatment apparatus.

References

[1] K. Murakami, N. Fukata, S. Sasaki, K. Ishioka, M. Kitajima, S. Fujimura, J. Kikuchi, H. Haneda, Phys. Rev. Lett. 77 (1996) 3161.
[2] N. Fukata, S. Sasaki, K. Murakami, K. Ishioka, K.G. Nakamura, M. Kitajima, S. Fujimura, J. Kikuchi, H. Haneda, Phys. Rev. B 56 (1997) 6642.
[3] A.W.R. Leitch, V. Alex, J. Weber, Solid State Commun. 105 (1997) 215.
[4] A.W.R. Leitch, V. Alex, J. Weber, Phys. Rev. Lett. 81 (1998) 421.
[5] A.W.R. Leitch, J. Weber, V. Alex, Mater. Sci. Eng. B 58 (1999) 6.
[6] R.E. Pritchard, M.J. Ashwin, R.C. Newman, J.H. Tucker, E.C. Lightowlers, M.J. Binns, R. Falster, S.A. McQuiaid, Phys. Rev. B 56 (1997) 13118.
[7] R.E. Pritchard, M.J. Ashwin, J.H. Tucker, R.C. Newman, Phys. Rev. B 57 (1998) 15048.
[8] Y. Okamoto, M. Saito, A. Oshiyama, Phys. Rev. B 56 (1997) R10016.
[9] C.G. Van de Walle, Phys. Rev. Lett. 80 (1998) 2177.
[10] B. Hourahine, R. Jones, S. Öberg, R.C. Newman, P.R. Briddon, E. Roduner, Phys. Rev. B 57 (1998) R12666.
[11] N. Fukata, S. Fujimura, K. Murakami, Mater. Sci. Forum 196–201 (1995) 873.
[12] A.W. Leich, J. Weber, V. Alex, at European Materials Research Society Spring Meeting E-MRS'98, June 16–19, 1998, Strasbourg.
[13] N.M. Johnson, in: Hydrogen in Semiconductors, J.I Pankove (Ed.) (Academic Press, NY 1991) (Chapter 7).
[14] K. Murakami, Solid State Phys. (KOTAI BUTSURI) 33 (1998) 735 (in Japanese).

ELSEVIER

Physica B 273–274 (1999) 196–199

PHYSICA B

www.elsevier.com/locate/physb

Vibration of hydrogen molecules in semiconductors: anharmonicity and electron correlation

Mineo Saito[a,*], Yasuharu Okamoto[b], Atsushi Oshiyama[c], Toru Akiyama[c]

[a]*NEC Informatec Systems, Ltd., 34 Miyukigaoka, Tsukuba 305-8501, Japan*
[b]*Fundamental Research Laboratories, NEC Corporation, 34 Miyukigaoka, Tsukuba 305-8501, Japan*
[c]*Institute for Physics, Tsukuba University, Tennoudai 305-8573, Japan*

Abstract

Vibrational frequencies of hydrogen molecules trapped at a variety of crystal sites in semiconductors are studied based on the density functional theory and repeated cell model. Our calculation including the anharmonic effect well reproduces frequencies of molecules at the tetrahedral (T) sites in Si and GaAs and confirms the experimental identification. We also calculate the frequencies of molecules trapped at hydrogenated Si vacancies of a variety of sizes. The frequencies of the molecules at VH_4 and V_2H_6 are found to be inbetween those of the gas phase and of the T site. Meanwhile the frequencies of hydrogenated large (hexa- and deca-) vacancies are found to be close to that of the gas phase. It is suggested that the newly detected Raman line of 3822 (2770) cm^{-1} for $H_2(D_2)$ corresponds to the molecules trapped at V_2H_6.

Keywords: Hydrogen molecule; Density functional theory; Vibration; Anharmonicity

1. Introduction

Hydrogen impurity is important in semiconductor technology because of its unique properties of passivation. Atomic hydrogen and its complexes with a variety of impurity atoms have been extensively studied. As for dimerized hydrogen, two atoms located at the bond center and antibonding sites were observed in Si [1]. In addition to this H_2^*, recent experiments give clear evidence of molecular hydrogen and attract wide interests. First observation for Si shows that the Raman frequency ($\omega_I = 4158\ cm^{-1}$) is very close to that of the gas phase ($4161\ cm^{-1}$) [2]. In contrast, a Raman measurement for GaAs shows that the frequency ($3934\ cm^{-1}$) is substantially lowered [3]. Later further reduced frequency ($\omega_{II} = 3618\ cm^{-1}$) was observed by use of infrared (IR) light absorption spectroscopy for Si [4,5] and the same origin was detected by means of Raman spectroscopy [6]. Very recently, a new Raman frequency for Si^+ ion implanted Si ($\omega_{III} = 3822\ cm^{-1}$) lying in-between ω_I and ω_{II} was observed [7]. Theory is expected to identify the crystal sites where these observed molecules are located. Small cluster models based on the Hartree–Fock (HF) method and the hybrid-density functional theory (DFT) lead to the conclusion that the frequency of the molecule at the tetrahedral (T) site in Si is close to that of the gas phase, suggesting that ω_I corresponds to the T site [8,9]. Yet, the supercell model based on the generalized gradient approximation (GGA) as well as the local density approximation (LDA) [10,11] indicated that frequency is substantially lower than that of the gas phase. A cluster calculation based on the LDA also supported the substantial lowering [12].

In a previous study based on cluster models consisting of up to 84 sites [13], we found that the vibrational frequency of hydrogen molecules is very sensitive to the approximation used to include the electron many body effect. Further, the value was found to be affected by the anharmonic effect and the cluster size. In this paper, we adopt a method based on the GGA and the repeated cell

* Corresponding author. Tel.: + 81-298-50-1571; fax: + 81-298-56-6173.
E-mail address: mineo@nis.nec.co.jp (M. Saito)

0921-4526/99/$ - see front matter
PII: S0921-4526(99)00444-5

model and examine the validity of this method. The method is then applied to hydrogen molecules at the T sites of Si and GaAs. Further the molecules trapped at hydrogenated Si vacancies of a variety of sizes are investigated.

2. Method

To include the electron many body effects, the present study employs the GGA based on the type of Becke–Lee–Yan–Paar (BLYP) [14,15] unless otherwise stated since the method gives results comparable with those of accurate electron correlation calculations as will be discussed later. We use the repeated cell (supercell) containing up to 64 sites in order to simulate the impurities in a crystal. Special k points are used in Brillouin zone integration [16]. The pseudopotentials (bare Coulomb potentials) are used for the host (hydrogen) atoms and the 45 Ry cutoff energy for the plane wave basis set is employed: Soft pseudopotentials are constructed following Troullier and Martins [17] and the nonlinear core correction [18] is applied. In calculating vibrational frequencies, the anharmonic terms up to the fourth order are considered. We first fit the calculated total energies to the following expression:

$$E(x) = E(x_{eq}) + \frac{M\omega_H^2}{2}(x - x_{eq})^2 + \alpha(x - x_{eq})^3 + \beta(x - x_{eq})^4. \quad (1)$$

The vibrational frequency ω including the anharmonic effect is then given by the following equation:

$$\omega = \omega_H + \frac{3h}{(2\pi)^2 cM}\left[-\frac{5}{2}\left(\frac{\alpha}{M\omega_H^2}\right)^2 + \frac{\beta}{M\omega_H^2}\right], \quad (2)$$

where c, h, and M denote the speed of light, Planck constant, and reduced mass, respectively.

We here briefly discuss the validity of the present method. First, the GGA(BLYP) used in the present study is examined. Table 1 compares various types of calculations including the electron many body effects on H_2 molecules in the gas phase. The well-converged localized Gaussian basis set calculation indicates that the full configuration interaction (CI) method that includes the exact many body effect within the limitation of the given basis set well reproduces the experimental frequency. Compared with the LDA and HF methods employed in studies in the past, the GGA(BLYP) gives comparable results with the full-CI, though the hybrid DFT method [19] that is considered to be beyond the GGA gives a more accurate frequency. We next calculate the frequency of the molecule at the T site in the Si cluster ($Si_{10}H_{16}$) to examine the validity of the GGA for the interaction between the molecule and the host Si atoms (Table 2). Both the GGA and hybrid-DFT methods are found to give comparable results, suggesting the validity of the GGA: These methods lead to the conclusion that the frequency in the cluster is substantially lower (167–205 cm^{-1}) than that of the Møller–Plesset second-order perturbation theory (MP2) that corrects the HF method. As was stated above, we combine the GGA and the techniques of the repeated cell, pseudopotentials, and a plane wave basis set. The validity of the techniques is here argued. Tentative calculations lead to the conclusion that the present repeated cell model gives converged results within 80 cm^{-1}. The plane wave basis set is found to give accurate frequency of the hydrogen molecule in the gas phase: The calculated value is slightly (54 cm^{-1}) lower than that of the well-converged localized basis set (Table 2). Finally, the present calculational scheme using the pseudopotentials for the host atoms is found to give lattice constant of 5.52 Å (5.81 Å) for Si (GaAs)

Table 1
Frequencies of hydrogen molecules calculated by the use of a variety of methods to include electron many body effects. In the localized orbital calculations, we used the Gaussian orbitals for the H[311 G(2p)] and Si[6–31 G(2d)] atoms (Details of the description of the basis set was given previously [13]. ω(gas phase) is the frequency in cm^{-1} in the gas phase and $\Delta\omega$ is given by ω(cluster)–ω(gas), where ω(cluster) is the frequency of the molecules in the Si cluster

Basis set		ω(gas phase)	ω(cluster)	$\Delta\omega$
Experiment		4161	—	—
Localized orbital	Full-CI	4148	—	—
	Hybrid-DFT	4168	4001	− 167
	GGA(BLYP)	4064	3859	− 205
	MP2	4283	3992	− 291
	HF	4358	4568	+ 210
	LDA	3978	3436	− 542
Plane wave basis set	GGA (BLYP)	4011	—	—

Table 2
Calculated vibrational frequencies in cm^{-1} of hydrogen molecules in the gas phase and at some crystal sites in Si and GaAs. The experimental values are in parentheses

	$\omega(H_2)$	$\omega(D_2)$	$\omega(H_2)/\omega(D_2)$	
Gas phase	4011	2890	1.388	
	(4161)	(2994)	(1.390)	
T site in Si [1 0 0]	3478	2544	1.367	
T site in Si [1 1 0]	3520	2573	1.368	
	(3618)	(2643)	(1.369)	Ref. [5]
T_{Ga} site in GaAs	3817	2764	1.381	
	(3934)	(2843)	(1.384)	Ref. [3]
VH_4 in Si	3695	2702	1.368	
V_2H_6	3847	2790	1.379	
V_6H_{12}	4018	2900	1.386	
$V_{10}H_{16}$	3980	2879	1.382	

and the deviation from the experimental value is 1.6% (2.8%).

3. Results and discussion

We start the calculation with the frequency of H_2 in the gas phase (Table 2). The calculated frequency (4011 cm^{-1}) is consistent with the experimental one (4161 cm^{-1}) and is smaller by 155 cm^{-1} than the harmonic value, indicating that the anharmonic effect is important. Because of this effect, the calculated ratio ($r = 1.388$) in frequency between H_2 and D_2 deviates from that of the harmonic case (the square root of 2) and is consistent with the experimental value (1.390). Next we study the hydrogen molecule at the T site in Si based on the 32 site repeated cell calculation. The most stable orientation of the molecule is found to be [1 0 0]: The total energy for this orientation is lower by 11–12 meV than those of the [1 1 0] and [1 1 1] axes. The calculated frequency for the most stable orientation is 3478 cm^{-1} and is consistent with the observed value of ω_{II}, supporting that the mode II (ω_{II}) corresponds to molecules at the T site (Table 2). It was found that the frequency ratio (r) between H_2 and D_2 is 1.367 and is consistent with the observed value (1.369) [4,5]. This calculated value is slightly lower than that of the gas phase, indicating that the anharmonic effect is enhanced at the T site. It is finally noted that the most stable orientation [1 0 0] determined by the present study is IR inactive because of the high symmetry (D_{2d}) and thus seems to be inconsistent with the observation of the IR absorption [4,5]. This discrepancy between theory and experiment may be due to the error of the present calculation since the orientation dependence of the total energy is very small. We find that the orientation dependence of the frequency is small. For example, the frequency of H_2 and r are 3520 cm^{-1} and 1.368, respectively, in the case of [1 1 0]. Therefore, the above calculated frequency for [1 0 0] is reliable even when the stable orientation is different from [1 0 0].

We next calculate the hydrogen molecule at the T site of GaAs. There are two types of the T sites: One site (T_{Ga}) is surrounded by the nearest Ga atoms and the other (T_{As}) has the As nearest atoms. We found that the energy of the T_{Ga} site is lower by 0.16 eV than the T_{As} site and then conclude that the hydrogen molecule is trapped at the T_{Ga} site. Three molecular orientation [1 0 0], [1 1 0] and [1 1 1] have similar total energies within 3 meV less than the present calculational accuracy, indicating that the potential energy surface for the molecular rotation is very flat. This result seems to be consistent with the experimental result [6] that the splitting of the Raman line due to the molecular rotation is observed in GaAs. We then calculate the frequencies averaged over the orientation. The calculated frequency (3817 cm^{-1}) of H_2 and the value of r (1.381) are in-between those of the gas phase and of the T site in Si and agrees with the experimental values (3934 cm^{-1} and 1.384).

We finally study the interaction between the hydrogen molecule and vacancies in Si based on the 64 site repeated cell model [The calculated frequency of the molecule at the T site based on this model is 3559 cm^{-1}, which is more close to the experimental result (ω_{II}) than the value of the 32 site cell calculation (3478 cm^{-1})]. Mono- and di-vacancies are well studied but understanding of larger vacancies is insufficient. Theory predicted *magic numbers* of vacancies: It was concluded that the hexa-vacancy of a ring form and the deca-vacancy of a cage form are energetically stable [20–23]. We first consider hydrogenation of these four types of the vacancies (all the dangling bonds of the vacancies are terminated by hydrogen atoms):

$$V_n + n'H_2(T) \rightarrow V_nH_{2n'}, \quad (3)$$

where $H_2(T)$ indicates the hydrogen molecule at the T site. Our calculation shows that this reaction is exothermic[1] (the reaction energies are found to be 4.3–19.8 eV). Next the trapping of the hydrogen molecule by the hydrogenated vacancies is examined:

$$V_nH_{2n'} + H_2(T) \rightarrow H_2@V_nH_{2n'}. \quad (4)$$

It is found that this reaction is also exothermic: The gained energies are found to be 0.15–1.1 eV (see footnote 1). We then expect that hydrogen molecules trapped at hydrogenated vacancies are actually observed under

[1] The calculations on the energetics for vacancies [Eqs. (3) and (4)] are based on the GGA of the type of Perdew and Wang [24]. The pseudopotentials are used for both H and Si. Details of the calculational results will be presented elsewhere.

some experimental conditions and thus calculate vibrational frequencies of the molecules. The frequencies for H_2 and D_2 are found to be larger than those of the T site and increase as the vacancy size becomes large (Table 2). It is concluded that the frequencies of the hexa- and deca-vacancies are saturated and are close to those of the gas phase. These results indicate that observation of frequencies of molecules give important information on the size of hydrogenated vacancies. Recently, new Raman lines are observed in Si^+ ion implanted Si [7]. The observed frequencies are $3822\,cm^{-1}$ for H_2 and $2770\,cm^{-1}$ for D_2. The present calculation on frequencies (Table 2) suggests that these correspond to molecules trapped at hydrogenated di-vacancies: The calculated frequencies are 3847 and $2790\,cm^{-1}$ for H_2 and D_2, respectively, and the calculated frequency ratio (r) is 1.379, which is close to the experimental value (1.380).

4. Conclusion

We have performed first-principles calculations on a variety of types of hydrogen molecules in Si and GaAs. Our calculation has well reproduced experimental frequencies of the molecules trapped at T sites in Si and GaAs. It has been found that the frequency of molecules trapped at the hydrogenated vacancies is larger than that of the T site and increases as the size becomes large. It has been concluded that the frequencies are saturated in hexa- and deca-vacancies and are close to that of the gas phase. We have suggested that the newly found Raman line of ω_{III} corresponds to the molecules trapped at hydrogenated di-vacancies.

Acknowledgements

This work was supported in part by Japan Society for the Promotion of Science under Contract No. RFTF96P00203.

References

[1] J.D. Holbech et al., Phys. Rev. Lett. 71 (1993) 875.
[2] K. Murakami et al., Phys. Rev. Lett. 77 (1996) 3161.
[3] J. Vetterhöffer, J. Wagner, J. Weber, Phys. Rev. Lett. 77 (1996) 5409.
[4] R.E. Prichard et al., Phys. Rev. B 56 (1997) 13118.
[5] R.E. Prichard et al., Phys. Rev. B 57 (1998) R15048.
[6] A.W. Leitch, V. Alex, J. Weber, Phys. Rev. Lett. 81 (1998) 421.
[7] M. Kitajima et al., Jpn. J. Appl. Phys. 38 (1999) L691.
[8] K.G. Nakamura et al., Solid State Commun. 101 (1997) 735.
[9] K.G. Nakamura et al., J. Chem. Phys. 108 (1998) 3222.
[10] Y. Okamoto, M. Saito, A. Oshiyama, Phys. Rev. B 56 (1997) R10016.
[11] C.G. Van de Walle, Phys. Rev. Lett. 80 (1998) 2177.
[12] B. Hourahine et al., Phys. Rev. B 57 (1998) R12666.
[13] Y. Okamoto, M. Saito, A. Oshiyama, Phys. Rev. B 58 (1998) 7701.
[14] A.D. Becke, J. Chem. Phys. 88 (1988) 1053.
[15] C. Lee, W. Yang, R.G. Parr, Phys. Rev. B 37 (1988) 785.
[16] A. Baldereschi, Phys. Rev. B 7 (1973) 5212.
[17] N. Troullier, J.L. Martins, Phys. Rev. B 43 (1991) 1993.
[18] S.G. Louie, S. Froyen, M.L. Cohen, Phys. Rev. B 26 (1982) 1738.
[19] A.D. Becke, J. Chem. Phys. 98 (1993) 5648.
[20] D.J. Chadi, K.J. Chang, Phys. Rev. B 38 (1988) 1523.
[21] A. Oshiyama, M. Saito, O. Sugino, Appl. Surf. Sci. 85 (1995) 239.
[22] J.L. Hasting, S.K. Estrecher, P.A. Fedders, Phys. Rev. B 56 (1997) 10215.
[23] Akiyama, A. Oshiyama, O. Sugino, J. Phys. Soc. Jpn. 67 (1998) 4110.
[24] J.P. Perdew, in: P. Zeische, M. Eschring (Eds.), Electronic Structure of Solids 91, Akademie Verlag, Berlin, 1991.

ELSEVIER

Physica B 273–274 (1999) 200–203

PHYSICA B

www.elsevier.com/locate/physb

Microscopic properties of H_2 in Si from the dependence of the 3618.4 cm^{-1} line on temperature and stress

J. Anna Zhou, E Chen, Michael Stavola*

Department of Physics, Lehigh University, 16 Memorial Drive East, Bethlehem, PA 18015, USA

Abstract

The dependence of the 3618.4 cm^{-1} line assigned to interstitial H_2 in Si on temperature and stress has been studied to probe the structure and microscopic properties of this defect. The H_2 (and D_2) stretching lines broaden and shift to lower frequency with increasing temperature while the integrated intensity remains approximately constant. Uniaxial stress results are consistent with triclinic (C_1) symmetry and suggest a near $\langle 1\,0\,0\rangle$ orientation for the H_2 molecular axis. © 1999 Elsevier Science B.V. All rights reserved.

Keywords: Si; Hydrogen; Vibrational spectroscopy; Uniaxial stress

1. Introduction

While the importance of interstitial H_2 in semiconductors has been discussed for many years [1–4] (for a review of early theoretical work on H_2 see Ref. [5]), this defect was not observed spectroscopically so that its configuration and properties could be studied until recently [6–8]. The stretching vibration of an isolated interstitial H_2 molecule in a semiconductor was observed first in GaAs by Raman spectroscopy [6] with a frequency of 3934.1 cm^{-1} (77 K). The H_2 line is split by 8.2 cm^{-1}, leading to the conclusion that the H_2 molecule is freely rotating and that this doublet is due to the ortho and para nuclear spin states whose vibrational frequencies are split by ro-vibrational coupling. Subsequently, the stretching vibration of H_2 in Si was discovered at 3618.4 cm^{-1} (4.2 K) independently by Raman [7] and IR absorption [8] spectroscopies and strong evidence was presented that this line is indeed due to an isolated molecule [8]. In both GaAs and Si, lines due to D_2 and HD were also observed. In further support of these assignments, theoretical calculations [9–12] find vibrational frequencies for H_2 in GaAs or Si that are shifted to lower frequency from the gas-phase value by several hundred cm^{-1}, in agreement with experiment.

Several aspects of the results for H_2 in Si are surprising. In the gas phase, the stretching vibration of a homonuclear diatomic molecule does not give rise to an oscillating electric dipole moment and is IR inactive. The observation of a weak absorption line for interstitial H_2 in Si was, therefore, unexpected. Further, an important difference between H_2 in Si and in GaAs is that no ortho–para splitting was observed for H_2 in Si [8]. To explain the absence of an ortho–para splitting, it was suggested that there must be a barrier of at least 0.17 eV that prevents rotation of the molecule [11]. It has been found by theory that $\langle 1\,0\,0\rangle$, $\langle 1\,1\,1\rangle$ and $\langle 1\,1\,0\rangle$ orientations have similar energies [5,9–12], making it surprising that there is a substantial barrier to rotation and that the H_2 molecule in Si is static. Another important observation is that the vibrational line assigned to HD in Si is not split at 0.1 cm^{-1} resolution [13], suggesting that the two H atoms in the molecule remain equivalent. Based on the above results, a configuration with the H_2 molecule oriented along a $\langle 1\,1\,0\rangle$ direction and displaced from the T_d interstitial site along the perpendicular $\langle 1\,0\,0\rangle$ direction (C_{2v} point group) was proposed [11]. This configuration gives rise to a weak vibrational transition moment oriented perpendicular to the $\langle 1\,1\,0\rangle$ molecular axis while still leaving the H atoms equivalent.

* Corresponding author. Fax: + 1-610-758-5730.
E-mail address: mjsa@lehigh.edu (M. Stavola)

0921-4526/99/$ - see front matter
PII: S0921-4526(99)00445-7

In the work reported in this paper, the temperature and stress dependence of the 3618.4 cm^{-1} vibrational line have been studied to provide further information about the structure of the interstitial H_2 molecule in Si and its transition moment.

2. Experiment

For our experiments, H (or D) was introduced into lightly doped Si by annealing samples in sealed quartz ampoules containing H_2 (or D_2) gas ($\sim$0.7 atm at room temperature) for 30 min at 1250°C. IR spectra were measured with a Bomem DA3.16 Fourier transform spectrometer. For uniaxial stress measurements, oriented, bar-shaped samples with dimensions $3.5 \times 3.5 \times 10\ mm^3$ were prepared. Stress was applied with a push rod apparatus that was cooled to near liquid-He temperature in an Oxford CF1204 cryostat.

3. Results

IR absorption spectra for the interstitial D_2, HD, and H_2 molecules in Si are shown in Fig. 1 for a sample that contained both H and D. These frequencies are in excellent agreement with those observed previously by IR absorption [13] and Raman [7] spectroscopies. For samples ($\approx$15 mm thick) that contained either H or D, the temperature dependence of the frequencies, widths, and areas of the vibrational lines assigned to D_2 and H_2 were measured. The widths and areas of the lines could be measured with reasonable accuracy for the temperature range 4–200 K. The frequencies and linewidths are shown in Fig. 2 along with the previous results for the frequency of the H_2 line measured by Raman spectroscopy [14]. The integrated intensity of the H_2 line, which could be measured more accurately than

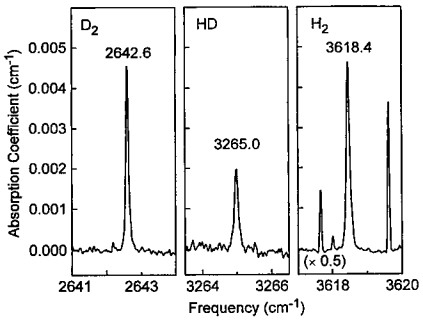

Fig. 1. IR absorption lines assigned to interstitial D_2, HD, and H_2 in Si. The sample temperature was near 4.2 K and the spectral resolution was 0.05 cm^{-1}. The sharp additional lines in the H_2 spectrum are due to H_2O vapor in the spectrometer.

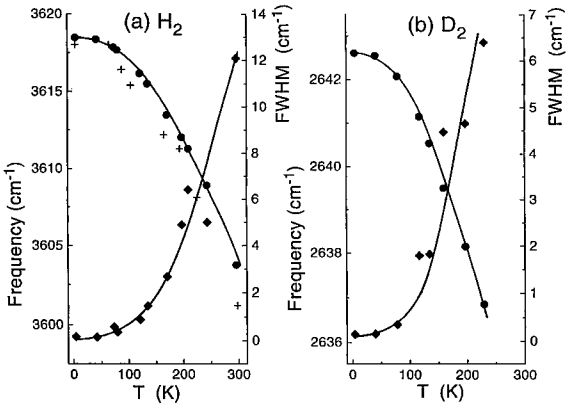

Fig. 2. The temperature dependences of the frequencies (●) and widths (◆) for the (a) H_2 and (b) D_2 IR absorption lines in Si. The H_2 frequencies (+) measured by Raman spectroscopy (Ref. [14]) are also shown.

that of the weaker D_2 line, was constant, within error ($\approx$10%), from 4 to 200 K.

The effect of uniaxial stresses on the 3618.4 cm^{-1} line is shown in Fig. 3. The frequencies of the stress-split components were measured for four different values of the stress from 0 to 0.2 GPa for each orientation and were found to depend linearly on the magnitude of the stress. The number of lines observed for each orientation is consistent with a nondegenerate vibrational mode of a triclinic center (C_1 point group). The shifts of the stress-split components, $\Delta\omega_i$, are given by

$$\Delta\omega_i = \sum_{ij} A_{ij}\sigma_{ji}, \tag{1}$$

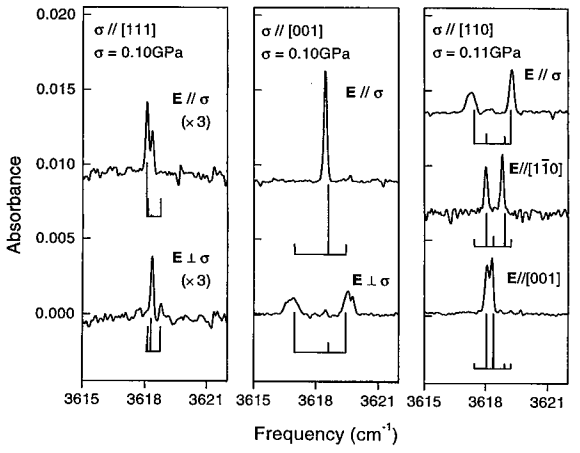

Fig. 3. Effect of stress, σ, on the 3618.4 cm^{-1} line assigned to interstitial H_2 in Si. The stress direction and magnitude and the polarization vector, $\boldsymbol{E}$, for the incident light are given.

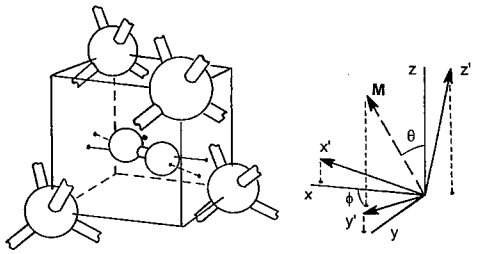

Fig. 4. A representative model for H_2 in Si is shown on the left. The molecular axis (dashed line) is rotated slightly from a $\langle 1\,0\,0\rangle$ direction (solid line) and the center of mass is displaced from the T_d interstitial position. The principal axes of the piezospectroscopic tensor and the direction of the IR transition moment, $\boldsymbol{M}$, are shown on the right. The direction cosines for the principal axes are as follows: $x' = (0.979, -0.090, 0.183)$, $y' = (0.061, 0.986, 0.156)$, $z' = (-0.194, -0.142, 0.971)$.

where A_{ij} are the components of a piezospectroscopic tensor, and σ_{ij}, defined here to be positive for compression, are the components of the stress tensor [15]. To model the polarization dependence of the spectra, the intensities of the stress-split components were written in terms of the angles, θ and ϕ, that characterize the direction of the vibrational transition moment, $\boldsymbol{M}$, in the cubic (x, y, z) defect coordinate system (Fig. 4). θ and ϕ were then varied to produce a fit to the observed intensity pattern for the [0 0 1] and [1 1 0] stress directions. ($\boldsymbol{M}$ was chosen to be nearest the z-axis in the defect coordinate system. This choice fixes A_3 as the parameter that describes the shift of the line observed for $\boldsymbol{E}//\sigma$ for [0 0 1] stress.) With the transition moment direction determined, it was then possible to assign the vibrational lines for the three stress directions and to fit the line positions with Eq. (1). The positions and intensities of the stress-split components, determined with the piezospectroscopic tensor given in Table 1 and with $\theta = 28°$ and $\phi = 45°$, are shown in Fig. 3 by vertical lines. While the fit to the IR-line positions shown in Fig. 3 is satisfactory, the direction of the transition moment is not precisely determined by our fit and there are a few weak components, especially for [1 1 1] stress, that are not well accounted for by our model.

The intensities of the stress-split components were found to be independent of the applied stress (up to 0.2 GPa), showing that the center does not reorient at low temperature. Experiments were also performed to investigate whether the H_2 molecule could be aligned by stresses applied at elevated temperatures. No such alignment-related intensity changes were observed. We note that the 3618.4 cm^{-1} line is weak so that a modest alignment would not have been detected.

Table 1
The piezospectroscopic tensor components, in units cm^{-1}/GPa, for the H_2 molecule in Si. Both the labels introduced by Kaplyanskii [15] and the conventional tensor notation are given for the components

$A_1(A_{xx})$	$A_2(A_{yy})$	$A_3(A_{zz})$	$A_4(A_{xy})$	$A_5(A_{yz})$	$A_6(A_{xz})$
9.6	−15.6	1.1	−1.8	−2.8	1.4

Our uniaxial stress data reveal a surprisingly low symmetry for H_2 in Si. The structural model we propose is based upon the form of the piezospectroscopic tensor whose largest components, A_1 and A_2, lie on the diagonal. The principal axes (x', y', z') of the piezospectroscopic tensor are shown in Fig. 4 and are rotated by less than 14° from the defect (x, y, z) axes. While the dominance of the effect of $\langle 1\,0\,0\rangle$ stresses suggests that the H_2 molecule is oriented approximately along a $\langle 1\,0\,0\rangle$ direction, the molecular axis must be rotated slightly away from a high symmetry $\langle 1\,0\,0\rangle$ direction to be consistent with C_1 symmetry. Furthermore, for C_1 symmetry, the molecule's center of mass is not required to be located at the T_d interstitial site. While our results suggest that the H_2 molecular axis is oriented near a $\langle 1\,0\,0\rangle$ direction, there is not a direct connection between the principal axes of the piezospectroscopic tensor and the direction of the molecular axis. Therefore, the small rotation angle of the molecular axis away from $\langle 1\,0\,0\rangle$ and the displacement of the molecule's center of mass from the T_d interstitial site are not determined by our results and Fig. 4 shows only a representative possibility.

For C_1 symmetry, the two H atoms in the molecule must be inequivalent, in apparent contradiction to the previous observation [13] that there are not two vibrational lines for the HD molecule. The spectrum shown in Fig. 1 for a sample that contained H and D reveals a single sharp line at 3265.0 cm^{-1} for HD, in agreement with the previously published result. One possibility suggested by this result is that the H and D atoms are nearly equivalent and a small splitting of the HD line remains unresolved. However, the evidence suggests an alternative possibility, that the H and D atoms are sufficiently inequivalent for only a particular arrangement of H and D to be observed. The alternative arrangement, with the H and D interchanged, would not be seen if it had sufficiently higher energy or if it had a much weaker IR transition moment. The inequivalence of H and D is supported further by the frequency position of the HD line that is found to be inconsistent with the model commonly used to characterize the anharmonic shift of the vibrational frequency. The observed frequency, ω, of a vibrational line is given by [16]

$$\omega = \omega_0 - B/m, \tag{2}$$

where $\omega_0 = (k/m)^{1/2}$ is the harmonic frequency, m is the reduced mass of the oscillator, and B is a parameter. The application of Eq. (2) to the H_2 (3618.4 cm^{-1}) and D_2

(2642.6 cm^{-1}) frequencies gives anharmonic shifts of 406 and 203 cm^{-1} for H_2 and D_2, respectively. From this analysis one then predicts an anharmonic shift of 305 cm^{-1} for HD and thus an HD frequency of 3180 cm^{-1}. This value determined from Eq. (2) differs from the experimental frequency (3265.0 cm^{-1}) by 85 cm^{-1}. A similar analysis for the frequencies of H_2 and D_2 in GaAs or in gas phase is consistent with the HD line positions in these cases to within a few cm^{-1}. This remarkable shift of the HD line in Si from its expected position would be consistent with two inequivalent arrangements of H and D and a large splitting of the HD line with only the higher frequency line being observed. (An additional HD line at lower frequency has not been found.)

4. Conclusion

Our new results on the symmetry and structure of the H_2 molecule in Si are unexpected. The C_1 symmetry found in our experiments is lower than has been suggested by theoretical calculations [5,9–12] and by an analysis of the vibrational spectrum [11]. The absence of a marked dependence of the magnitude of the IR transition moment on temperature or stress found in our experiments suggests that the existence of the nonzero transition moment is a simple consequence of this low symmetry. The absence of an ortho-para splitting of the H_2 vibrational line [8,11] and the lack of stress-induced alignment found here are consistent with a static center. All of these results for H_2 in Si are at variance with the theoretical expectation [9–12] that an isolated H_2 molecule will interact only weakly with its host cage (as seems to be the case for H_2 in GaAs [7]). A simple explanation, that the H_2 molecule is in the vicinity of another defect, conflicts with strong evidence that the H_2 molecule is isolated. For example, Raman experiments on H_2 in Si (Ref. [7]) were performed with samples treated in an H_2 plasma. The high concentration of H_2 molecules expected in these samples ($>10^{18}$ cm^{-3}) makes it unlikely that there is an additional impurity present in float zone Si at comparable concentration. An alternative possibility, that the H_2 molecule is part of a larger complex of hydrogen atoms or molecules, would have to be reconciled with the determination of the site degeneracy of H_2 in Si ($\approx 10^{23}$ cm^{-3}) which is consistent with an isolated interstitial site [8]. An explanation of the microscopic properties observed for H_2 in Si remains as a challenge.

Acknowledgements

We thank G.D. Watkins and W.B. Fowler for numerous helpful discussions. This work was supported by NSF Grant No. DMR-9801843 and NREL Subcontract No. XCE-8-18684-01.

References

[1] A. Mainwood, A.M. Stoneham, Physica B 116 (1983) 101.
[2] J.W. Corbett, S.N. Sahu, T.S. Shi, L.C. Snyder, Phys. Lett. 93A (1983) 303.
[3] R.N. Hall, IEEE Trans. NS-31 (1984) 220.
[4] S.J. Pearton, J.W. Corbett, M. Stavola, Hydrogen in Crystalline Semiconductors, Springer, Berlin, 1992.
[5] S.K. Estreicher, Mater. Sci. Eng. Rep. 14 (1995) 319.
[6] J. Vetterhöffer, J. Wagner, J. Weber, Phys. Rev. Lett. 77 (1996) 5409.
[7] A.W.R. Leitch, V. Alex, J. Weber, Phys. Rev. Lett. 81 (1998) 421.
[8] R.E. Pritchard, M.J. Ashwin, J.H. Tucker, R.C. Newman, Phys. Rev. B 57 (1998) 15048.
[9] Y. Okamoto, M. Saito, A. Oshiyama, Phys. Rev. B 56 (1997) 10016.
[10] C.G. Van de Walle, Phys. Rev. Lett. 80 (1998) 2177.
[11] B. Hourahine, R. Jones, S. Öberg, R.C. Newman, P.R. Briddon, E. Roduner, Phys. Rev. B 57 (1998) 12666.
[12] C.G. Van de Walle, J. Goss, in: J. Weber, A. Mesli (Eds.), Defects in Si: Hydrogen, Elsevier, Oxford, 1999, p. 17.
[13] R.E. Pritchard, M.J. Ashwin, J.H. Tucker, R.C. Newman, E.C. Lightowlers, M.J. Binns, S.A. McQuaid, R. Falster, Phys. Rev. B 56 (1997) 13118.
[14] A.W.R. Leitch, J. Weber, V. Alex, in: J. Weber, A. Mesli (Eds.), Defects in Si: Hydrogen, Elsevier, Oxford, 1999, p. 6.
[15] A.A. Kaplyanskii, Opt. Spectrosc. (USSR) 16 (1964) 329.
[16] R.C. Newman, Semicond. Sci. Technol. 5 (1990) 911.

ELSEVIER

Physica B 273–274 (1999) 204–207

PHYSICA B

www.elsevier.com/locate/physb

Hydrogen interactions with interstitial- and vacancy-type defects in silicon

S.Zh. Tokmoldin*, B.N. Mukashev, Kh.A. Abdullin, Yu.V. Gorelkinskii

Institute of Physics and Technology, Almaty, 480082 Kazakhstan

Abstract

IR and EPR studies of hydrogen interactions with defects in silicon implanted with protons and deuterons were carried out. An analysis of temperature dependence of Si–H local mode anharmonicity, using isotope substitution of H by D, revealed that anharmonicity is sensitive to the environment of a Si–H dipole. This enables to separate Si–H modes between H atoms in the vicinity of vacancy or Si interstitial conglomerates and to construct models for H-related complexes. It is shown that the 2107, 2122 cm^{-1} doublet may be assigned to V_6H_{12}, which can serve as nucleus of {1 1 1} platelets. Mechanisms of H interactions with ring hexavacancy and Si-B3 interstitial defect are considered and tentative models for a new Si-AA17 EPR center and for H-related shallow donor suggested.

Keywords: Silicon; Hydrogen; Vacancies; Interstitials

1. Introduction

IR studies of H-implanted Si : H revealed that chemical bonding of H in the vicinity of intrinsic defects leads to appearance of a number of Si–H local lines at 1800–2300 and 500–900 cm^{-1} [1,2]. Complexes responsible for strongest Si–H lines were investigated intensively using co-doping with H and D, uniaxial stress and impurity effect [3–7], however, these methods fail to discriminate between vacancy- and interstitial-type complexes and till now there are discrepancies in interpretation of experiments.

Earlier [8] we found a difference in temperature dependence of an anharmonicity between Si–H lines lying above and below 2000 cm^{-1} and have proposed that lines above 2000 cm^{-1} are related to vacancy-type complexes while lines below 2000 cm^{-1} are connected with interstitial-type complexes. The same trend was also shown in other works both theoretically [9–11] and experimentally [5,6,12–14].

An analysis carried out in this study reveals that the anharmonicity representing the coupling of a Si–H dipole to the defect host is sensitive to the character of hybridization and coordination of Si atom bonded to H. This enables to separate Si–H lines related to vacancy- and interstitial-type complexes. We also consider a mechanism of H interaction with Si-B3 interstitial center and discuss possible Si–H modes of a new H-related Si-AA17 EPR center [15] tentatively assigned to a complex of two H atoms with ring hexavacancy.

2. Experimental details

High-purity Si crystals ($N_B < 10^{14}\,cm^{-3}$, $N_{O,C} < 10^{15}\,cm^{-3}$) were implanted at near 300 K with 30 MeV protons and 25 MeV deuterons up to doses of 5×10^{17} ion/cm^2. Various thickness aluminum screens were used to reduce ion energy. A set of Si : H samples were heat-treated for 15 min 125–650°C with the step 25°C. Another set of samples were annealed at 400°C to 500°C for 15 min and then were kept for a long time at

* Corresponding author. Fax: + 7-327-2-545224.
E-mail address: serik@sci.kz (S.Zh. Tokmoldin)

0921-4526/99/$ - see front matter
PII: S0921-4526(99)00446-9

70–300°C, followed by quenching 300 K in water. IR spectra of Si : H and Si : D samples were measured with the spectral resolution of 0.5–2.5 cm^{-1} in the 400–2300 cm^{-1} range and at temperatures of 80 and 300 K.

3. Si–H bond anharmonicity

To characterize Si–H bond anharmonicity, in Ref. [8] we used a diatomic molecule approximation which enables to determine an anharmonic/harmonic frequency part Δ/ω via experimental Si–H and Si–D frequencies ν_H and ν_D. The anharmonicity may be also determined using a parameter χ included into the reduced mass as it was suggested in Ref. [16]. We measured ν_H and ν_D bond-stretching frequencies in as-implanted Si : H and Si : D spectra at 80 and 300 K and then calculated the values of $\omega, \Delta, \chi, \delta\omega = \omega(80\text{ K}) - \omega(300\text{ K}), \delta\Delta = \Delta(80\text{ K}) - \Delta(300\text{ K})$ and $\rho = \chi(80\text{ K})/\chi(300\text{ K})$.

Fig. 1 shows that $\delta\omega, \delta\Delta$ and ρ reveal correlated step function behavior along ν_H. Such a behavior of $\delta\omega, \delta\Delta$ and ρ representing temperature dependence of Si–H bond anharmonicity enables to separate lines lying above and below 2000 cm^{-1} into two groups (Fig. 1, *I*- and *V*-groups) and indicates that Si–H modes responsible for lines in a separate group have similar coupling to the defect host.

The values of Δ are varied from 70 to 95 cm^{-1} in good agreement with an estimation of $\Delta \approx -\text{const}/(\omega \times \tau) \approx -80\ cm^{-1}$ for a Si–H dipole located in a cavity with volume τ [17]. Taking into account this estimation one can expect that the decreasing of τ with temperature from 300 to 80 K will cause an increasing of $\delta\Delta$ and a deviation of ρ from 1. Indeed, it is observed for *V*-lines while $\delta\Delta$ and ρ for *I*-lines are only slightly deviated from 0 and 1. This indicates that Si–H bond coupling to surrounding atoms is larger in case of *V*-lines. The large value of coupling for *V*-lines implies the presence of neighbour H atoms because the coupling of a Si–H bond to Si host must be insensitive to temperature variation due to large mass difference for H and Si atoms.

Fig. 2 shows a coordination of Si–H bonds in the vicinity of vacancy- and interstitial-type complexes. In the case of a vacancy-type complex Si–H bond coordination is tetrahedral and a small distance between H atoms implies the noticeable coupling between Si–H bonds while in the case of an interstitial-type complex the coordination is non-tetrahedral and the distance between H atoms is larger. This enables to conclude that *V*- and *I*-lines are related to vacancy- and interstitial-type complexes, respectively.

According to Ref. [17] Si–H bond is a dipole with small negative charge on H atom. Therefore the lengths of Si–H bonds located in the vicinity of a vacant site must decrease in comparison with a single Si–H bond due to coulomb repulsion between H atoms. This implies an

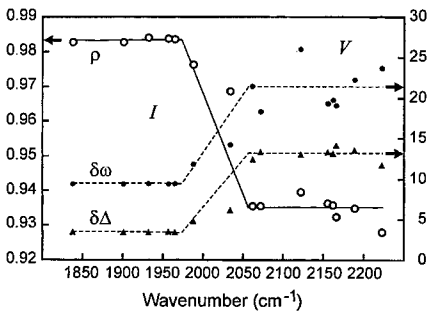

Fig. 1. Temperature dependence of Si–H bond anharmonicity in Si : H along ν_H.

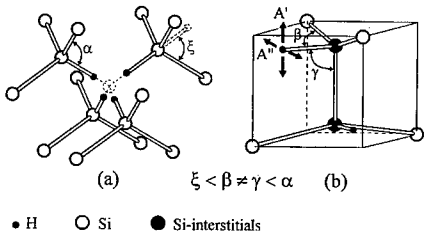

Fig. 2. Si–H bond coordination in the vicinity of vacancy-type and interstitial-type complexes.

increase of Si–H mode frequencies due to the increase of the s-orbital contribution into tetrahedral-coordinated Si–H bond formed by sp^3-hybridized Si-orbital. Indeed, it is seen in Fig. 1 that the parameter $\delta\omega$ representing harmonic part of Si–H mode frequency is increased greatly in case of *V*-lines. On the other hand, $\delta\omega$ for *I*-lines is deviated slightly and this may be explained by the fact that non-tetrahedral Si–H bond is formed by p-orbital of sp^2-hybridized Si-atom without noticeable s-orbital contribution (Fig. 2(b)).

Recent IR and EPR studies of Si : H [18] revealed that 2038 cm^{-1} line is related to VH complex. In this case single Si–H bond is coupled only to surrounding Si-host, therefore, the parameters $\delta\omega, \delta\Delta$ and ρ must be varied slightly in comparison with other *V*-lines. It is seen clearly in Fig. 1 and confirms our classification of *V*- and *I*-lines. Further confirmations come from detailed experimental and theoretical studies of 2223, 2191, 2166 cm^{-1} and 2145, 2122 cm^{-1} *V*-lines and 1990, 1987 cm^{-1} *I*-lines which were unambiguously identified with vacancy-type VH_4, V_2H_6, VH_2 and interstitial-type IH_2 complexes, respectively [5,6].

Fig. 2(a) illustrates also a coordination of Si–H antibond. As we argued in Ref. [19], Si–H antibond has ionic, non-covalent character, which is confirmed by the presence of 1599 cm^{-1} overtone mode of 818 cm^{-1} bond-bending mode. In this case the parameters $\delta\omega, \delta\Delta$ and ρ for related 1838 cm^{-1} bond-stretching line must be varied slightly that is seen in Fig. 1.

A confirmation of V- and I-lines classification comes also from the recent study of Si–H bond-bending modes in conjunction with Si–H bond-stretching modes [14]. We have found a correlation between the following sets of lines (wave numbers at 300 K): (1) 2211 and 634 cm^{-1}, (2) 2161, 2184 cm^{-1} and $\sim$610, 668 cm^{-1}, (3) 2104, 2120 cm^{-1} and $\sim$610, 694, 588 cm^{-1}, (4) 1950 cm^{-1} and 718, 750 cm^{-1}, and (5) 1960 cm^{-1} and 718, 750 cm^{-1}. One can also add to these sets the 1838 and 818 cm^{-1} lines and can then see that ordering of Si–H bond-bending lines is opposite to the ordering of V- and I-lines that may easily be explained by the difference of angles between Si–H and Si–Si bonds (Fig. 2). The ordering of Si–H bond-bending lines correlates with the relation between the angles $\xi < \beta \neq \gamma < \alpha$.

So Si–H bond anharmonicity is sensitive to coordination of bonds and to type (vacancy-type or interstitial-type) of complexes. The ordering of Si–H bond-stretching and bond-bending lines is characteristic of. Both anharmonicity and position of a Si–H line in the spectrum may be used to predict Si–H bond coordination and/or type of a related complex.

4. H-related shallow donor

H-related shallow donor (H-donor) is an important process-induced defect in Si. It appears in proton-implanted Si : H after subsequent annealing at 300–500°C [2]. It was shown that H-donor is a double donor with a ground spin-singlet state and correlates with C_{2v}-symmetry Si-AA1 EPR center with $S = \frac{1}{2}$ in positively charged state [20]. H-donor concentration can exceed 10^{16} cm^{-3} and may be reversibly changed by heat-treatment at 70–300°C with the following quenching to 300 K in water [21]. Si-AA1 also reveals quenching dependence, but opposite to that of H-donor.

It was found [22] that H-donor spatial distribution is close to that of Si-B3 EPR center assigned to a $\langle 1\,0\,0\rangle$ pair of Si atoms located at tetrahedral interstitial site [23]. It is reasonable to propose H-induced reconstruction of Si-B3 with the formation of H-donor responsible for C_{2v}-symmetry Si-AA1 EPR center. Recently we have found [24] that Si-AA1 spectrum derives from a C_{2v}-symmetry complex. An analysis of the effective piezospectroscopic tensor indicates that Si-AA1 produces strong compression strain field along both $\langle 0\,0\,1\rangle$ C_{2v}-axis and $\langle 1\,1\,0\rangle$ axis. This implies the presence of a chain of two or more $\langle 1\,0\,0\rangle$ Si-interstitialcies.

A tentative mechanism of H-induced Si-B3 reconstruction is shown in Fig. 3 where arrows indicate possible displacements of Si interstitials in the presence of H. The resulted complex (Fig. 3(b)) may be EPR active in neutral state. A low C_1-symmetry Si-AA3 EPR center with $S = \frac{1}{2}$ observed in Si : H in temperature range of H-donor activity [20] may be tentatively assigned to this complex because Si-AA3 intensity is reversibly changed by quenching at 100–300°C and the quenching dependence is similar to that of Si-AA1. The configurations shown in Fig. 3 (c and d) may be reversibly transformed into each other and may be responsible for H-donor and Si-AA1. They have to cause Si–H lines in I-line range. Indeed, analysis of annealing characteristics reveals that 1957 and 1967 cm^{-1} I-lines correlate with Si-AA1 and Si-B3. Fig. 4 shows that 1967 cm^{-1} line is raised with annealing of 1957 cm^{-1} line. Then 1957 and 1967 cm^{-1} lines may be assigned to configurations in Figs. 3(b) and (c and d), respectively. Recent IR study of H-donor [25] revealed that reversible changing of H-donor concentration does not cause appearing, displacement or splitting of any Si–H line.

The maximum of H-donor concentration derived from Hall measurements is close to that of 2107, 2122 cm^{-1} doublet V-lines. This is surprising because experimental data presented above indicate that H-donor is interstitial-type defect. Earlier [12] 2107, 2122 cm^{-1} doublet was assigned to vibrations of two Si–H bonds in the vicinity of a vacant site in V_2H_4 consisting of two VH_2 structural units. However the doublet may also be assigned to neutral V_6H_{12} also consisting of VH_2 units.

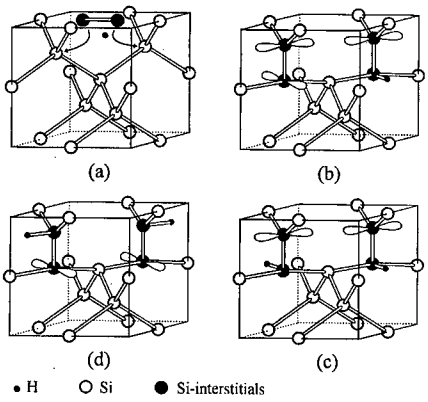

Fig. 3. Tentative mechanism of Si-B3 H-induced reconstruction.

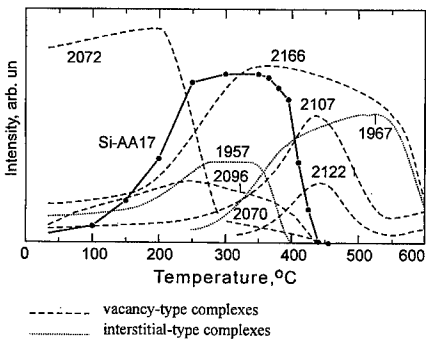

Fig. 4. Annealing characteristics for main Si–H lines and a new Si-AA17 EPR center.

Then correlation between H-donor and 2107, 2122 cm^{-1} doublet may be explained by hydrogen passivation and reactivation of acceptor-like complexes V_6H_x with $x < 12$. V_6H_{12} can serve as a nucleus of the {1 1 1} platelets [26]. Indeed, flaking-off of plates from Si samples implanted by protons at high doses after annealing at 500°C was observed in Ref. [2].

5. New SI-AA17 EPR center

Recently [15] a new H-related Si-AA17 EPR center with $S = 1$ and D_{3d}-symmetry was discovered. The Si-AA17 g-tensor and hyperfine structure reveal that 62% of spin-wave function is located on two equivalent Si atoms situated along ⟨111⟩ axis of defect. The wave function has 91% 3p and 9% 3s character that is characteristic of a dangling Si-bond in the vicinity of vacancy-type defect [27,28]. The magnitude of zero-field splitting (16.8 MHz) enables to estimate a distance of 12 Å between two unpaired electrons. Uniaxial stress applied along ⟨1 1 1⟩ axis leads to the lowering of Si-AA17 energy that implies the presence of a void space between two dangling bonds separated by distance of $5a$ (a – length of Si–Si bond).

A model for Si-AA17 is a complex of H atoms with ring hexavacancy, which was found to be the most stable defect among multivacancy complexes in Si [29]. Fig. 5 shows a tentative mechanism for the trapping of two H atoms in the vicinity of hexavacancy. Hexavacancy produces a tensile deformation of the A–B and A′–B′ bonds that enables H atoms to be trapped by B and B′ atoms. There are two possibilities: H atoms may be trapped on tetrahedral-coordinated Si–H bonds or on non-tetrahedral Si–H antibonds. The related Si–H lines are expected to appear in V- and I-lines ranges, respectively.

Recently [30] on the basis of experiments and theoretical calculations a similar V_6H_2 complex with D_{3d} symmetry has been suggested for B_{41} luminescence center [31,32]. B_{41} center arises from the defect with D_{3d} symmetry and two equivalent H atoms are incorporated in its structure. It is important that formation and temperature stability of B_{41} center correlate with those of Si-AA17.

Fig. 4 shows annealing behavior of Si-AA17 and some Si–H lines. It is seen that Si-AA17 is annealed at 450°C that correlates with annealing of 2070 and 2096 cm^{-1} Si–H lines situated in V-line range. There is no line in I-line range with behavior similar to that of Si-AA17. This means that two tetrahedral-coordinated Si–H bonds are preferable in Si-AA17 model.

Si-AA17 is annealed with increasing intensity of 2107, 2122 cm^{-1} doublet assigned to V_6H_{12}. This contributes a confirmation to Si-AA17 model suggested. Here it is necessary to note that {1 1 1} platelets produced in H_2 plasma-treated Si give rise to broad IR lines at 2065, 2075, 2095 and 2125 cm^{-1} [26].

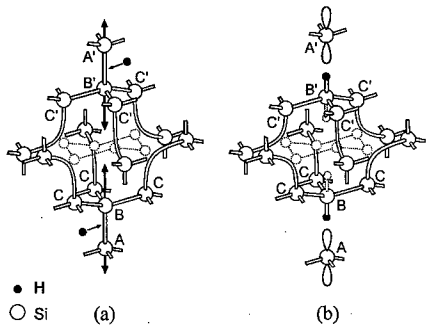

Fig. 5. Tentative mechanism of H-induced reconstruction of ring hexavacancy. Arrows show possible displacement of Si atoms.

References

[1] H.J. Stein, J. Electron. Mater. 4 (1975) 157.
[2] B.N. Mukashev et al., Phys. Stat. Sol. A 91 (1985) 509.
[3] G.R. Bai et al., Solid State Commun. 56 (1985) 277.
[4] B.B. Nielsen et al., Mater. Sci. Forum 143–147 (1994) 845.
[5] B.B. Nielsen et al., Mater. Sci. Eng. B 36 (1996) 259.
[6] M. Budde et al., Phys. Rev. B 57 (1998) 4397.
[7] M. Suezawa, J. Appl. Phys. 83 (1998) 1958.
[8] B.N. Mukashev et al., Mater. Sci. Forum 38–41 (1989) 1039.
[9] V.V. Frolov, B.N. Mukashev, Phys. Stat. Sol. B 148 (1988) K105.
[10] P. Deak et al., Mater. Sci. Eng. B 4 (1989) 57.
[11] P. Deak et al., Physica B 170 (1991) 253.
[12] B.N. Mukashev et al., in: K. Sumino (Ed.), Defect Control in Semiconductors, Elsevier Amsterdam, 1990, pp. 429–434.
[13] B.N. Mukashev et al., Physica B 170 (1991) 545.
[14] B.N. Mukashev, S.Zh. Tokmoldin, Mater. Sci. Forum 258–263 (1997) 223.
[15] Yu.V. Gorelkinskii et al., to be published.
[16] R.S. Leigh, R.C. Newman, Semicond. Sci. Technol. 3 (1988) 84.
[17] M. Cardona, Phys. Stat. Sol. B 118 (1983) 463.
[18] P. Johannesen et al., Mater. Sci. Forum 258–263 (1997) 515.
[19] S.Zh. Tokmoldin, B.N. Mukashev, J. Phys.: Condens. Matter 3 (1991) 9363.
[20] Yu.V. Gorelkinskii, N.N. Nevinnyi, Physica B 170 (1991) 155.
[21] Yu.V. Gorelkinskii, N.N. Nevinnyi, Nucl. Instr. and Meth. 209/210 (1983) 677.
[22] Yu.V. Gorelkinskii et al., Rad. Eff. 49 (1980) 161.
[23] K.L. Brower, Phys. Rev. B. 14 (1976) 872.
[24] Yu.V. Gorelkinskii et al., J. Appl. Phys. 84 (1998) 4847.
[25] S.Zh. Tokmoldin, B.N. Mukashev, Phys. Stat. Sol. B 210 (1998) 307.
[26] J.N. Heyman et al., Phys. Rev. B 45 (1992) 13363.
[27] G.D. Watkins, J. W Corbett, Phys. Rev. 121 (1961) 1001.
[28] Y.H. Lee, J.W. Corbett, Phys. Rev. 13 (1976) 2653.
[29] J.L. Hastings et al., Mater. Sci. Forum 258–263 (1997) 509.
[30] B. Hourahine et al., to be published.
[31] A.S. Kaminskii, Phys. Rev. B 50 (1994) 7338.
[32] A.N. Safonov et al., Phys. Rev. B 56 (1997) R15517.

ELSEVIER

Physica B 273–274 (1999) 208–211

PHYSICA B

www.elsevier.com/locate/physb

Vacancy–hydrogen complexes in group-IV semiconductors

M. Budde[a,b,*], B. Bech Nielsen[a], J.C. Keay[b], L.C. Feldman[b]

[a]*Institute of Physics and Astronomy, University of Aarhus, Aarhus, Denmark*
[b]*Department of Physics and Astronomy, Vanderbilt University, Box 1807, Nashville, TN 37235, USA*

Abstract

Hydrogen-related defects in proton-implanted crystalline Ge and 6H–SiC are studied with IR spectroscopy. Absorption lines at 1979.5, 1992.6, 2014.9, 2024.8 and 2061.5 cm^{-1} in Ge : H are identified as Ge–H stretch modes of three distinct vacancy–hydrogen complexes. The properties of H-related defects are very similar in Ge : H and Si : H. In contrast, no LVMs are observed in 6H–SiC : H, indicating that H behaves differently in this material.

Keywords: H; Ge; Vacancy; Local vibrational modes

1. Introduction

Hydrogen has, by far, the most diverse behavior of impurities in Si, reacting with lattice imperfections such as surfaces, interfaces, vacancies and self-interstitials, and impurities, including dopants, O, C, other H atoms and transition metals. In the last decade a variety of H-related defects have been identified in c-Si. Based on a strong interplay between experiment and theory, the microstructure of a series of these defects is now well understood. Considerable research is currently devoted to other group-IV semiconductors, such as $Si_{1-x}Ge_x$ alloys and SiC, motivated by the need for electronic devices beyond the reach of Si technology. To investigate the properties of H in these materials, we have performed IR absorption studies of proton-implanted Ge (Ge : H) and 6H–SiC (6H–SiC : H). In Ge : H, a series of Ge–H stretch modes is observed at and above room temperature (RT). Five of these modes are investigated in detail and ascribed to VH_2, VH_4, and V_2H_6, where V_mH_n consists of m vacancies and n H atoms. Apart from a downshift in frequency and decrease in thermal stability, the properties of these complexes are very similar to their counterparts in Si. In 6H–SiC : H, on the other hand, no H-related local modes are observed. The implications of this result are discussed.

2. Vacancy–hydrogen complexes in Si

The assignments of Ge–H modes to V_mH_n complexes are partly based on similar identifications carried out in Si : H using IR spectroscopy and EPR. The present section therefore gives a brief review of the identifications made in Si.

Vacancy complexes in Si can according to theory bind one H for each dangling bond. The structure of these complexes is essentially obtained by saturating the relevant number of dangling bonds with H. The interaction among the remaining dangling bonds inside the complex may distort the structure, leading to Si–H bonds that deviate from ⟨1 1 1⟩ directions. VH, VH_2, VH_3, VH_4 and V_2H_6 are predicted to have C_{1h} (monoclinic-I), C_{2v} (orthorhombic-I), C_{3v} (trigonal), T_d (cubic) and D_{3d} (trigonal) symmetry [1]. The calculated binding energy (per H) decreases and the Si–H stretch mode frequencies increase with the number of H bound to the vacancy due to repulsive inter-bond interactions. For the same reason, the total symmetric vibrational mode of each complex is predicted to have higher frequency than the asymmetric vibrational mode.

A series of single-hydrogenated complexes VH, V_2H and V_3H (or V_4H) were recently observed in Si : H by

* Correspondence address. Department of Physics and Astronomy, Vanderbilt University, Box 1807, Nashville, TN 37235, USA. Tel.: 615-322-2479; fax: 615-343-1708.

E-mail address: michael.budde@vanderbilt.edu (M. Budde)

0921-4526/99/$ - see front matter
PII: S0921-4526(99)00448-2

EPR [2,3]. Correlated IR measurements associated absorption lines at 2038.5, 2068.1 and 2073.2 cm^{-1} to these complexes [3]. In addition, a pair of absorption lines has been observed at 2121 and 2145 cm^{-1} in Si–H. The lines originate from an orthorhombic-I complex containing two equivalent Si–H bonds, and were assigned to VH_2 in Si [4]. Observation of the same complex by ODMR was reported by Chen et al. [5]. However, this assignment was recently questioned because the angular dependence of the ODMR signal is virtually identical that of the excited VO complex (A-center) [6]. The Si–H stretch mode with highest frequency in Si : H is observed at 2223 cm^{-1}. Isotope substitution [7] and uniaxial stress [8] measurements have shown that the mode is three-fold degenerate and originates from a cubic defect containing four equivalent Si–H bonds. These findings are all consistent with the 2223-cm^{-1} mode originating from VH_4. The last V_mH_n complexes in Si to be discussed in this context are VH_3 and V_2H_6, both of which have been associated with local modes at 2166- and 2191-cm^{-1} [4,9]. These modes originate from the same trigonal complex; the 2166-cm^{-1} mode being two-fold degenerate and the 2191-cm^{-1} mode non-degenerate [4]. The properties of the two modes are consistent with those expected theoretically for both VH_3 and V_2H_6, making identifications based on local mode spectroscopy virtually impossible. However, VH_3 was recently identified by EPR and shown to correlate with modes at 2155 and 2182 cm^{-1} [10]. This strongly suggests that the 2166- and 2191-cm^{-1} lines originate from V_2H_6. In summary, VH, VH_2, VH_3, VH_4, V_2H and V_2H_6 have been identified in Si.

3. Vacancy–hydrogen complexes in Ge

Hydrogen forms covalent bonds with Ge of similar strength as with Si [11]. Therefore, one would a priori expect that V_mH_n complexes also form in Ge : H. To test this hypothesis, we performed an IR study of Ge : H.

Ge samples were implanted with protons and/or deuterons at $\sim$ 70 different energies, yielding a uniform H and/or D concentration of 0.05 at% from 11 to 43 μm below the sample surface. After implantation at $\sim$ 30 K the samples were stored at RT.

Fig. 1 shows IR absorbance spectra of Ge : H annealed at RT and 513 K. The spectra were measured at 9 K using a closed-cycle cryostat and an FTIR spectrometer, as described elsewhere [12]. A series of absorption lines are observed in the range 1750–2100 cm^{-1}, close to the Ge–H stretch modes of molecular germane (GeH_4) at 2106 and 2114 cm^{-1} [11]. A similar series of lines is observed, shifted down in frequency by a factor of $\sim\sqrt{2}$, when deuterons are implanted instead of protons, showing unambiguously that the lines originate from excitation of Ge–H stretch modes [12]. Of particular interest to this work are the lines at 1979.5, 1992.6, and 2061.5 cm^{-1} observed after RT annealing and the 2014.9- and 2024.8-cm^{-1} lines present after annealing at 513 K for 15 min. Isochronal annealing studies show that the intensity ratio of the lines at 1979.5 and 1992.6 cm^{-1} is independent of annealing temperature, indicating that they originate from the same defect. The two lines have maximum intensity after annealing at RT and disappear after annealing at $\sim$ 400 K. Similarly, the annealing dependence shows that the lines at 2014.9 and 2024.8 cm^{-1} are correlated. They appear after annealing at $\sim$ 450 K and disappear at $\sim$ 620 K. Finally, it was found that the annealing behavior of the 2061.5-cm^{-1} line is different from that of any other line in the Ge–H spectra. This line is present after annealing at RT, but has maximum intensity at $\sim$ 500 K and disappears at 590 K.

Additional information on the microstructure of defects can be obtained by partial isotope substitution. For example, Fig. 2 shows that the 2061.5-cm^{-1} line splits

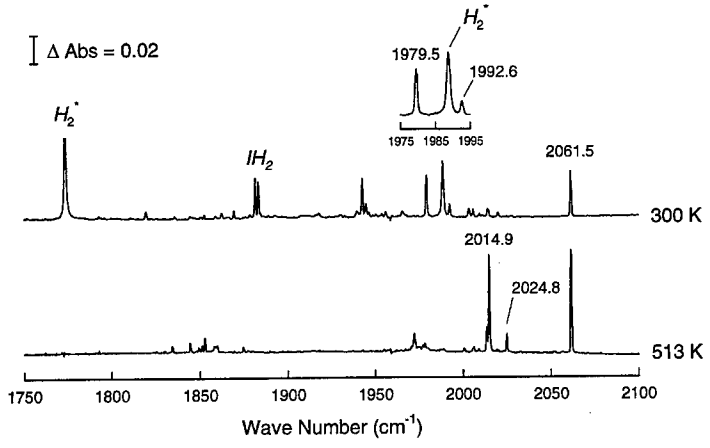

Fig. 1. Absorbance spectra of Ge : H stored at RT and annealed at 513 K.

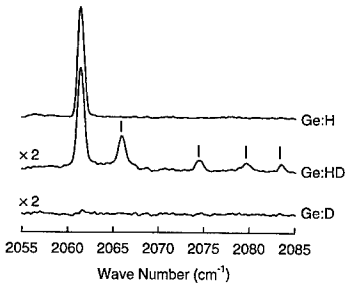

Fig. 2. Effect of isotope substitution on the 2061.5-cm^{-1} line in Ge : H.

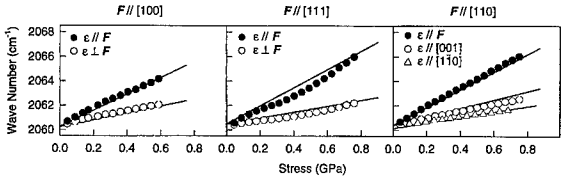

Fig. 3. Frequency shifts of the 2061.5-cm^{-1} line induced by uniaxial stress. The full (open) symbols are the line positions observed with the electric field of the IR light, ε, polarized parallel (perpendicular) to the applied stress $\boldsymbol{F}$. The solid lines represent the best fit of the theoretical shifts for a three-fold degenerate mode of a cubic defect to the experimental data.

into five, when deuterons and protons are coimplanted with spatially overlapping concentration profiles. All five lines have the same annealing behavior, and are ascribed to Ge–H stretch modes of the complexes obtained by isotopic mixing of the 2061.5-cm^{-1} complex. A corresponding set of lines is observed in the Ge–D stretch region (not shown). The isotopic splitting shows that the 2061.5-cm^{-1} complex contains at least four equivalent H atoms and has cubic symmetry. Similarly, partial isotope substitution shows that the complex giving rise to the 1979.5- and 1992.6-cm^{-1} lines contains two equivalent Ge–H bonds, whereas the lines at 2014.9 and 2024.8 cm^{-1} originate from a complex containing at least three Ge–H bonds.

The symmetry of point defects and their LVMs can be obtained by measuring the splitting and shifts of the absorption lines as a function of magnitude of uniaxial stresses applied along major crystallographic axes. Fig. 3 shows the uniaxial stress pattern of the 2061.5-cm^{-1} line. The line splits into two components when the uniaxial stress, $\boldsymbol{F}$, is applied along $\langle 1\,0\,0\rangle$ and $\langle 1\,1\,1\rangle$ directions, and into three components for $\boldsymbol{F}//\langle 1\,1\,0\rangle$. The components are fully polarized, i.e. only one component is observed when the IR light is polarized parallel and perpendicular to each of the three stress directions. Qualitatively, this stress pattern is consistent only with the 2061.5-cm^{-1} line originating from a three-fold degenerate T-mode of a cubic defect. A least-squares fit of the experimental frequency shifts to those expected theoretically for such a mode confirms this assignment, as evidenced by the good agreement between the experimental points and straight lines shown in Fig. 3. Similarly, uniaxial stress measurements show that the 1979.5-cm^{-1} line originates from a non-degenerate B_1-mode of an orthorhombic-I complex, and the 2014.9- and 2024.8-cm^{-1} lines from, respectively, a two-fold (E) and a non-degenerate (A) mode of a complex with trigonal symmetry.

Table 1 summarizes the properties of the five Ge–H modes, and compares them with the modes of the VH_2, VH_4 and V_2H_6 complexes in Si. There is clearly a one-to-one correlation between the modes in the two materials, establishing that they originate from the same defect. We therefore assign the lines at {1979.5, 1992.6}, 2061.5 and {2014.9, 2024.8} cm^{-1} to VH_2, VH_4, and V_2H_6 in Ge. Together with identifications of the H_2^* defect and the H-saturated self-interstitial (IH_2) in Si and Ge reported previously [12,13], the present work shows that H has very similar properties in the two materials. Table 1 shows that the stretch frequencies and annealing temperatures are ~8 and ~25% higher in Si than Ge. This is qualitatively consistent with the Si–H bond being ~10% stronger than the Ge–H bond [11].

4. Hydrogen in 6H–SiC

To further investigate the properties of H in group-IV semiconductors, IR absorption studies of 6H–SiC implanted with protons were carried out. Samples were implanted with protons at 13 different energies in the range 1425–2000 keV, resulting in a nearly uniform H concentration of 0.05 at% extending from 18–33 μm below the sample surface. The IR absorbance spectra of the samples were measured at 9 or 100 K with an FTIR spectrometer.

No absorption lines were observed in the Si–H or C–H stretch regions after implantation. This is very surprising considering that H may be expected to saturate implantation-induced dangling bonds in 6H–SiC, just as in Si and Ge. To test if thermal activation is required for H to react with the lattice defects, an isochronal annealing series was performed. One of the implanted samples was annealed at 673, 1073 and 1373 K for 15 min, and between the annealing steps, the IR absorption was measured at ~100 K. Annealing did not result in any detectable absorption lines. The failure to detect LVMs indicates that the properties of H in SiC are markedly different from Si and Ge. It can, however, not be ruled out that Si–H and C–H bonds actually are formed, but that the corresponding absorption lines are broadened beyond the limit of detection. In 6H–SiC there are two

Table 1
Properties of V_mH_n complexes in Si and Ge

Complex	Symmetry	Mode	Si		Ge	
			ω (cm^{-1})	T_{ann} (K)	ω (cm^{-1})	T_{ann} (K)
VH_2	Orthorhombic-I	B_1	2121	485	1979.5	400
		A_1	2145		1992.6[a]	
VH_4	Cubic	T	2223	775	2061.5	590
V_2H_6	Trigonal	E	2166	800	2014.9	620
		A	2191		2024.8	

[a]Symmetry not determined experimentally due to overlap with the 1989-cm^{-1} mode of the H_2^* defect (see inset in Fig. 1).

major sources of line broadening not present in Si and Ge. Ion implantation inevitably results in formation of lattice defects. In Si and Ge these defects recombine or agglomerate below RT, whereas much higher temperatures are required for intrinsic defects to become mobile in 6H–SiC. Even when they are mobile, a significant fraction of C-interstitials may recombine with Si-vacancies (and Si-interstitials with C-vacancies) leading to the formation of anti-site defects. This suggests that the concentration of intrinsic defects in 6H–SiC is considerably higher than in Si and Ge, which could lead to extensive inhomogeneous broadening of IR absorption lines. Another possible source of line broadening is the large number of inequivalent solution sites in the 6H–SiC lattice. For example, three distinct Si (and C) vacancies exist. For each of these vacancies, the dangling bond parallel to the hexagonal axis is distinguishable from the other three dangling bonds, which e.g. results in a total of 12 distinct VH complexes in 6H–SiC as compared to only one in Si and Ge. Depending on the stretch frequency difference of these VH complexes, the large number of inequivalent variants of each defect type can lead to either broadening or splitting of the absorption lines not present in Si and Ge.

5. Conclusion

Implantation of protons into Ge gives rise to Ge–H stretch modes at 1979.5, 1992.6, 2014.9, 2024.8 and 2061.5 cm^{-1}. Isochronal annealing, isotope substitution and uniaxial stress measurements revealed a clear one-to-one correlation between these modes and those of VH_2, VH_4 and V_2H_6 in Si : H. Evidently, the properties of H-related defects in Ge and Si are very similar. In contrast, no local vibrational modes are observed in 6H–SiC : H, indicating that H either behaves very differently in this material or that detection of Si–H and C–H stretch modes is impossible due to inhomogeneous broadening.

Acknowledgements

The work on Ge was funded by the Danish National Research Foundation through Aarhus Center for Atomic Physics (ACAP); the 6H–SiC studies were supported in part by ACAP, Oak Ridge National Laboratory (ORNL) contract DE-AC05-96OR22464 with Lockheed Martin Energy Res., and ARO grant #DAAG55-98-1-0449. Wayne Holland and the staff at ORNL are gratefully acknowledged for their hospitality during MB's stay at ORNL.

References

[1] See e.g. S.K. Estreicher, Mater. Sci. Eng. Rep. 14 (1995) 319.
[2] B. Bech Nielsen et al., Phys. Rev. Lett. 79 (1997) 1507.
[3] P. Stallinga et al., Phys. Rev. B 58 (1998) 3842.
[4] B. Bech Nielsen et al., Mater. Sci. Eng. B 36 (1996) 259.
[5] W.M. Chen et al., Phys. Rev. Lett. 64 (1990) 3042.
[6] P. Stallinga et al., Phys. Rev. Lett. 80 (1998) 422.
[7] T.S. Shi et al., Phys. Stat. Sol. B 131 (1985) 511.
[8] B. Bech Nielsen et al., Phys. Rev. B 39 (1989) 3330.
[9] B.N. Mukashev et al., in: K. Sumino (Ed.), Defect Control in Semiconductors, Amsterdam, North-Holland, 1990, p. 429.
[10] B. Bech Nielsen et al., to be published.
[11] CRC Handbook of Chemistry and Physics 73rd Edition, CRC Press, Boca Raton, FL, 1992.
[12] M. Budde et al., Phys. Rev. B 54 (1996) 5485.
[13] M. Budde et al., Phys. Rev. B 57 (1998) 4397.

ELSEVIER

Physica B 273–274 (1999) 212–215

PHYSICA B

www.elsevier.com/locate/physb

Nucleation mechanism of hydrogen-induced platelets in single crystal and polycrystalline silicon

N.H. Nickel[a,*], G.B. Anderson[b], N.M. Johnson[b], J. Walker[b]

[a]*Hahn-Meitner-Institut Berlin, Rudower Chaussee 5, 12489 Berlin, Germany*
[b]*Xerox Palo Alto Research Center, 3333 Coyote Hill Road, Palo Alto, CA 94304, USA*

Abstract

Hydrogen passivation of polycrystalline silicon (poly-Si) and single-crystal silicon (c-Si) at moderate temperatures causes the generation of platelets. These two-dimensional extended structural defects appear within 1500 Å of the surface and are predominantly oriented along {1 1 1} crystallographic planes. Platelet formation is observed only for Fermi energies of $E_C - E_F \leqslant 0.3$ eV. As the Fermi level moves closer to the conduction band the platelet concentration increases monotonically. It is demonstrated experimentally that platelet generation is driven by the Fermi energy. Based on our data we propose a model for platelet nucleation and growth that is consistent with experimental and theoretical studies of hydrogen in silicon. © 1999 Elsevier Science B.V. All rights reserved.

Keywords: Silicon; Hydrogen; Platelets; Fermi energy

It is well known that the introduction of hydrogen in single crystal (c-Si) and polycrystalline silicon (poly-Si) at temperatures below 300°C results in the formation of extended two-dimensional defects. These defects are known as platelets and are unrelated to plasma or radiation damage [1,2]. Platelets are predominantly oriented along {1 1 1} crystallographic planes and are a consequence of the coordination formation of Si–H bonds driven by strain [3].

In this paper we investigate the nucleation and growth mechanism of hydrogen stabilized platelets. Platelets are observed only in n-type silicon with a Fermi energy of $E_C - E_F \leqslant 0.3$ eV. The platelet concentration increases monotonically with increasing phosphorus concentration. Platelets are also observed in poly-Si. In samples with similar phosphorus concentrations the platelet densities at the surface of poly-Si and c-Si are comparable. Based on our data a model accounting for the nucleation and growth of platelets is proposed that is consistent with experimental and theoretical studies of hydrogen in silicon.

The experiments described in this paper were performed on undoped and phosphorus-doped fine grain polycrystalline silicon and n- and p-type single-crystal silicon. Poly-Si was prepared by laser crystallization of amorphous silicon. Hydrogen and deuterium exposures were performed in an optically isolated remote plasma system which eliminates surface damage resulting from direct immersion of the samples in the plasma. This has the additional advantage that defect passivation and generation is driven only by chemical reactions of hydrogen with the silicon lattice. Platelet formation was accomplished in a two-step hydrogenation process. Platelets were nucleated with a 20 min hydrogen exposure at 150°C. A second exposure to monatomic H at 275°C for 1 h caused the existing platelets to grow to a length of up to 150 nm[3]. Platelet concentrations were obtained from TEM micrographs. Deuterium concentration profiles were measured by secondary ion mass spectrometry (SIMS) using a Cs^+ ion beam. In the subsequent

* Corresponding author. Fax: + 49-30-67053-333.
E-mail address: nickel@hmi.de (N.H. Nickel)

0921-4526/99/$ - see front matter
PII: S0921-4526(99)00452-4

discussion the term hydrogenation will be used interchangeably with deuteration because no significant difference in platelet generation has been found for the two isotopes.

Typical deuterium depth profiles measured on undoped and phosphorus-doped poly-Si are shown in Fig. 1. The samples doped with a P concentration of 10^{17} cm^{-3} were exposed to monatomic D at 150°C for 5 and 30 min, respectively. In the first 300 Å of the depth profiles both samples reveal a striking peak in the D concentration. This is similar to D depth profiles reported for n-type c-Si [1]. For comparison a D depth profile (solid line) measured on undoped poly-Si is plotted in Fig. 1. The dashed line represents a least-squares fit to the convolution of an erfc and the SIMS depth resolution [4]. Fit and data are in good agreement for a depth greater than 0.1 μm. However, in the near-surface region data and fit deviate indicating an accumulation of D similar to that observed in P-doped specimens but more pronounced. In single-crystal silicon the deuterium accumulation in the near-surface region was attributed to the presence of D stabilized platelets [1]. The similarities of the deuterium depth profiles measured in poly-Si suggest that hydrogen passivation at low temperatures also causes the formation of platelets. On the other hand, it is conceivable that a high concentration of H traps [5] leads to the accumulation of H in the near surface region of poly-Si.

To clarify the origin of the high D concentration in the surface region of poly-Si TEM micrographs were taken on undoped and P-doped poly-Si. The bright-field images in Fig. 2 show a cross-sectional view of poly-Si prior to (a) and after a hydrogen plasma treatment (b). Plasma

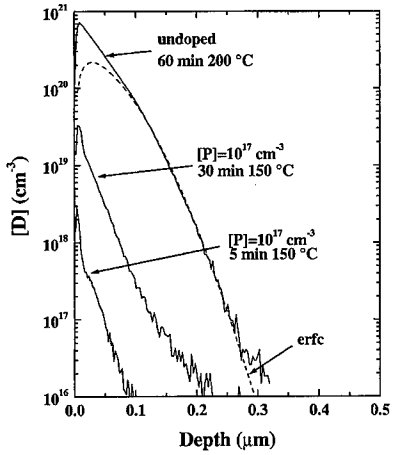

Fig. 1. D depth profiles in undoped and P-doped poly-Si. Plasma passivation parameters are indicated in the plot. The dashed line depicts a least-squares fit to the convolution of a complementary error function with the SIMS depth resolution [4].

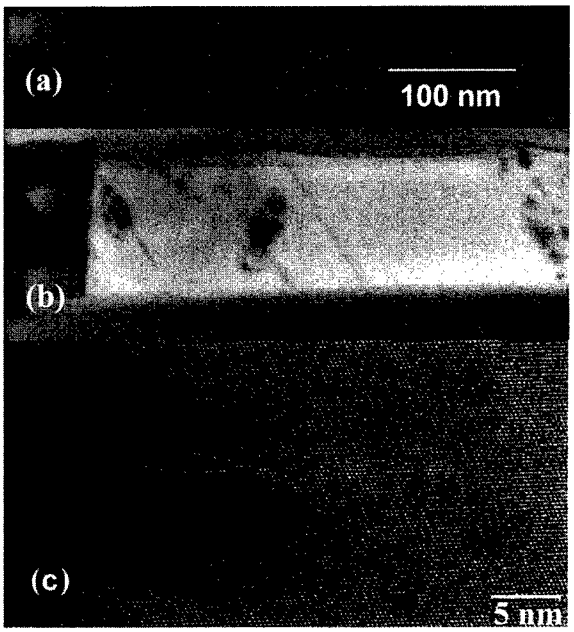

Fig. 2. Cross-sectional TEM micrographs viewed in a ⟨1 1 0⟩ projection. (a) bright-field image of poly-Si prior to the exposure to monatomic H; (b) after an exposure to monatomic H according to the two-step schedule; (c) high-resolution lattice image of a platelet viewed in a ⟨110⟩ projection.

hydrogenation of poly-Si resulted in the generation of H stabilized platelets. Since the micrographs show the poly-Si cross-section close to a ⟨1 1 0⟩ zone axis platelets in two of the 4 ⟨1 1 1⟩ planes appear as linear defects. Since the second ⟨1 1 1⟩ plane is rotated by 90° with respect to the first plane platelets in the second plane appear as two-dimensional discs. A high-resolution image of a single platelet is show in Fig. 2(c). A Burgers circuit analysis indicates no net displacement of the lattice eliminating dislocations as the origin of platelets in poly-Si. Similarly, no evidence was found that platelets consist of either interstitial or vacancy loops since contrast of typical stacking faults [6] was not observed.

In order to elucidate the microscopic mechanism governing platelet nucleation and growth a series of boron and phosphorus doped c-Si samples was hydrogenated according to the two-step passivation schedule. In Fig. 3 the platelet concentration is plotted as a function of the Fermi energy. Boron-doped samples (triangles) did not contain platelets while in phosphorus doped c-Si platelets were observed for Fermi level positions of $E_C - E_F \leqslant 0.3$ eV (diamonds). As the Fermi level moves closer to the conduction band the platelet concentration increases to 2.45×10^{17} cm^{-3}.

This result suggests that platelet generation is driven by the Fermi energy. However, it is also conceivable that platelet nucleation occurs at P sites. Hence, a series of

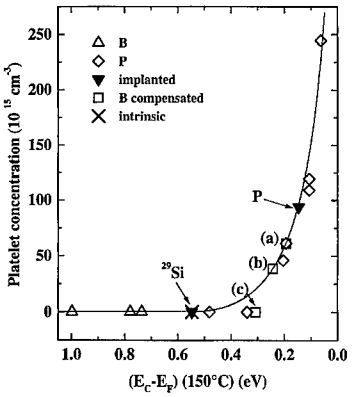

Fig. 3. Platelet concentration in c-Si vs. Fermi energy. Details are described in the text.

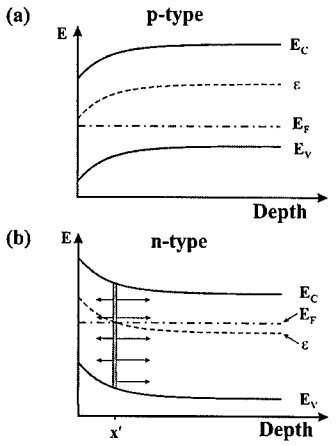

Fig. 4. Band diagram in the surface region of (a) p-type and (b) n-type silicon. ε is the mean value of the H donor and acceptor levels.

control experiments was performed to clarify the origin of the platelet nucleation mechanism. First, intrinsic c-Si ($E_C - E_F = 0.55$ eV) was implanted with P and ^{29}Si and subsequently annealed at 1200°C to remove the implantation damage and activate the dopants. Then, a control sample, the P-doped specimen, and the sample implanted with ^{29}Si were exposed simultaneously to monatomic H according to the two-step schedule. While the control sample (cross) and the specimen implanted with ^{29}Si (solid triangle at $E_C - E_F = 0.55$ eV) did not contain platelets the P-doped c-Si sample revealed a platelet concentration of approximately 9.4×10^{16} cm^{-3} (solid triangle at $E_C - E_F = 0.15$ eV). This result demonstrates that residual implantation damage does not give rise to platelet nucleation.

In the following experiment phosphorus-doped c-Si (labeled a) was electrically compensated by implanting boron to a depth of ≈ 1.0 μm with a concentration of 2×10^{17} and 2.6×10^{17} cm^{-3}, respectively (squares in Fig. 3). Again, the implanted atoms were activated in a 1200°C furnace anneal and subsequently the sample was exposed to monatomic H. Compensation resulted in a decrease of the platelet concentration in sample (b) to $\approx 3.8 \times 10^{16}$ cm^{-3} while platelet generation was suppressed in sample (c) (squares in Fig. 3). These experiments clearly demonstrate that H-induced generation of platelets is controlled by the Fermi energy.

Based on the observation that platelet generation is accompanied by an increase of the concentration of Si–H bonds [1] is has been suggested that the microscopic structure of platelets consists of aggregated H_2^* complexes [7]. This complex consists of one H in a Si–Si bond-center (BC) site forming a Si–H bond and the other H residing in the anti-bonding interstitial T_d site forming a Si–H bond with the remaining dangling bond [8]. The H_2^* complexes can be viewed as an intimate charged defect pair with a proton located in the BC site while the H^- prefers the T_d site since it has the lowest electron density. Therefore, the formation of H_2^* requires a positively and a negatively charged H atom. The concentrations of H^+ and H^- depend on the Fermi energy. In p- and n-type c-Si hydrogen prefers the positive and negative charge state, respectively. A change of the charge state occurs at a Fermi level position of $\varepsilon = E_C - E = 0.38$ eV. Neutral hydrogen is unstable which is characteristic for a negative-U impurity [9,10].

At the surface the Fermi energy is pinned approximately at midgap. It is conceivable, that the influence of a remote H plasma will not cause a significant deviation of the Fermi energy from its midgap position. Thus, in p-type and intrinsic c-Si the Fermi energy resides below ε (Fig. 4). Monatomic H introduced from the plasma donates electrons and becomes positively charged. Due to a lack of H^- platelets cannot nucleate. In the bulk of n-type c-Si the Fermi level resides between the conduction band and ε. Pinning of the Fermi energy at the surface causes band bending in the near-surface region and E_F crosses ε at a depth x' (Fig. 4). At x' the positive and negative charge states of H occur in similar concentrations permitting the nucleation of platelets.

Hydrogen introduced into silicon influences the Fermi energy. In the near surface region (Depth $< x'$) H becomes positively charged donating the electron. This causes the Fermi energy to move closer to the conduction band. Simultaneously, x' moves closer to the surface promoting the growth of platelets towards the surface. H at a depth greater than x' captures electrons and thus compensates the dopants. The Fermi energy moves closer to ε. As a consequence the depth of equal concentrations of H^+ and H^- moves deeper into the bulk promoting the growth of platelets in the bulk of c-Si.

Platelet nucleation and/or growth will terminate when the H concentration decreases below a threshold value of $10^{17}\,cm^{-3}$ or when the total H^- concentration is small compared to the doping concentration [11].

In summary, we have shown that nucleation and growth of H-induced platelets is controlled by the Fermi energy. Platelets are observed in n-type silicon with a Fermi energy of $E_C - E_F \leqslant 0.3$ eV. As the Fermi energy moves closer to the conduction band the platelet concentration increases monotonically. Platelet nucleation experiments performed on electrically compensated c-Si clearly established that the generation mechanism is driven by the Fermi energy. We propose a model for platelet nucleation and growth that is based on the idea that the microscopic structure of platelets consists of aggregated H_2^* complexes and that the formation of these H complexes requires charge neutrality.

References

[1] N.M. Johnson, F.A. Ponce, R.A. Street, R.J. Nemanich, Phys. Rev. B 35 (1987) 4166.
[2] N.H. Nickel, G.B. Anderson, J. Walker, Solid State Commun. 99 (1996) 427.
[3] N.M. Johnson, C. Herring, C. Doland, J. Walker, G.B. Anderson, F. Ponce, Mater. Sci. Forum 83–87 (1992) 33.
[4] P.V. Santos, W.B. Jackson, Phys. Rev. B 46 (1992) 4595.
[5] N.H. Nickel, W.B. Jackson, J. Walker, Phys. Rev. B 53 (1996) 7750.
[6] F.A. Ponce, T. Yamashita, R.H. Bube, R. Sinclair, in: J. Narayan, T.Y. Tan (Eds.), Defects in Semiconductors, Vol. 2, North-Holland, Amsterdam, 1981, Mat. Res. Soc. Symp. Proc., p. 503.
[7] W.B. Jackson, S.B. Zhang, Physica B 170 (1991) 197.
[8] K.J. Chang, D.J. Chadi, Phys. Rev. Lett. 62 (1989) 937.
[9] C.G. Van de Walle, P.J. Denteneer, Y. Bar-Yam, S.T. Pantelides, Phys. Rev. B 39 (1989) 10791.
[10] N.M. Johnson, C. Herring, C.G. Van de Walle, Phys. Rev. Lett. 73 (1994) 130.
[11] N. H. Nickel, G. B. Anderson, N. M. Johnson, J. Walker, 1999, submitted for publication.

ELSEVIER

Physica B 273–274 (1999) 216–219

PHYSICA B

www.elsevier.com/locate/physb

Hydrogen interactions with intrinsic defects in silicon

J.L. Hastings[a], M. Gharaibeh[a], Stefan K. Estreicher[a,*], P.A. Fedders[b]

[a]*Physics Department, Texas Tech University, Lubbock, TX 79409, USA*
[b]*Physics Department, Washington University, St. Louis, MO 63031, USA*

Abstract

The interactions between hydrogen and intrinsic defects in silicon are studied using ab initio molecular dynamics simulations in periodic supercells and Hartree–Fock in saturated clusters. The two issues discussed here are the complexes involving one neutral self-interstitial with one to four H's and the trapping of a single H at various vacancy aggregates. The binding energies, structures, and properties of these defects are calculated.

Keywords: Hydrogen; Vacancy; Self-interstitial; Silicon

1. Introduction

Hydrogen is a common impurity in silicon and other semiconductors. It diffuses rapidly and interacts with a wide range of impurities and native defects. These interactions often involve some degree of covalent bonding between H and Si atoms. The most common consequence is a change in the structure of the defect with which H interacts, a change in the energy spectrum associated with it, and a shift of levels within the gap, from the gap into a band (passivation), or from a band into the gap (activation) [1,2]. The thermal stability of most complexes containing H is of the order of a few hundred degrees Celsius. The most stable complexes are usually those involving H and intrinsic defects because of the presence of strong Si–H bonds. The simplest intrinsic defects [3] are the vacancy (V) and the self-interstitial (I), but aggregates of V's and I's are traps for H as well.

The isolated I has never been observed in Si, but several $\{I, H\}$ complexes have been detected by FTIR [4] and predicted by theory [4–6]. Possible structures have been calculated for such complexes [7–9].

It is now well-established [10] that a V has deep levels in the gap and can be fully passivated by four H atoms trapped in it, with all four Si–H bonds pointing toward the center of the vacancy. The $\{V, H_n\}$ complexes have now all been identified by FTIR [11,12]. The stretch mode at 2222 cm^{-1} with T_d symmetry has been assigned to both the $\{V, H_4\}$[1] complex [11,12] and to the interstitial silane (SiH_4) molecule [13–15]. Recent calculations [9] of vibrational modes found the stretch mode of interstitial SiH_4 to be close to 1800 cm^{-1}, far too low to be associated with the observed mode.

V–V interactions lead to the formation of vacancy aggregates V_n. One peculiar such aggregate, the ring-hexavacancy V_6, has been predicted [16] to be particularly stable and, in contrast to the other vacancy aggregates, have no localized (deep) levels in the gap. Thus, while four H's are needed to passivate the monovacancy, V_6 needs no H to be free of deep levels.

In the present work, we study two families of complexes: those of the form $\{I, H_n\}$ with $n = 1, \ldots, 4$, including the silane and silyl molecules, and those of the form $\{V_n, H\}$ with $n = 1, \ldots, 6$. We are interested in binding energies, equilibrium structures, and changes in the energy spectra of V_n caused by the trapping of a single H.

The stable and metastable configurations are obtained from ab initio tight-binding molecular-dynamics (MD) simulations [17,18] in periodic supercells containing 64

* Corresponding author. Tel.: + 1-806-742-3723; fax: + 1-806-742-1182.
E-mail address: bzske@ttu.edu (S.K. Estreicher)

[1] This line was reassigned to the $\{V, H_4\}$ complex in Ref. [15].

0921-4526/99/$ - see front matter
PII: S0921-4526(99)00456-1

and/or 216 Si atoms (not counting the defect). Four k-points in the Brillouin zone were included with the smaller cell but only $k = 0$ in the larger one. At first, a wide range of symmetrically inequivalent initial configurations were thermalized and quenched using the faster but less accurate Harris-functional version of the code. Then, the most stable configurations were used as inputs for slower but more accurate self-consistent calculations. Some of these calculations are still under way. All the MD calculations used a spin-averaged scheme.

Once the most stable structures were identified, approximate ab initio and ab initio Hartree–Fock (HF) calculations were performed to obtain molecular-orbital (MO) eigenvalues and chemistry of the various defects. All the configurations considered are closed-shell ones (spin 0). That is, in the HF calculations, the $\{V_n, H\}$ complexes are assumed to be in the $+1$ charge state, resulting from the trapping of H_{BC}^{+} by V_n^0.

2. Self-interstitial – hydrogen complexes

In agreement with other authors [19], we find that I^0 is stable in the split-$\langle 1\,1\,0\rangle$ configuration. There are numerous strained Si–Si bonds in the vicinity of the defect, and therefore numerous trapping sites for H. The binding energy ΔE_n of H to the $\{I, H_n\}$ complex, defined from $\{I, H_{n-1}\} + H_{BC} \rightarrow \{I, H_n\} + \Delta E_n$ is 1.45 eV for $n = 1$, 2.61 eV for $n = 2$, 0.42 eV for $n = 3$, and 1.35 eV for $n = 4$ (these are Harris functional energies). Thus, the most stable complex in the series is $\{I, H_2\}$, and the least stable one is $\{I, H_3\}$.

The lowest-energy structure of $\{I, H_1\}$ is a distortion of the split-$\langle 1\,1\,0\rangle$ configuration. I is shifted toward an adjacent T site and H is bound to it. Five Si host atoms are displaced from their perfect lattice sites.

The stable structure of $\{I, H_2\}$ (Fig. 1, left) is the same as that found by other authors. [4,7–9] It resembles a (distorted) split-$\langle 1\,0\,0\rangle$ interstitial with one H bound to each of the two Si atoms. The lowest-lying metastable configuration, 0.40 eV higher in energy, is a puckered bond-centered I with both H's bound to it [5].

The lowest-energy structure of $\{I, H_3\}$ (Fig. 1, right) is similar to $\{I, H_2\}$ with two H's bound to one Si atom and the third H to the second Si atom. A metastable configuration, only 0.1 eV higher in energy, has the three H atoms bound to three adjacent Si host atoms. The interstitial silyl molecule (SiH_3) with Si very near the T site, is 0.44 eV higher in energy. This is not only higher than two other configurations, but also than $\{I, H_2\}$ plus isolated H_{BC}.

The lowest-energy structure of $\{I, H_4\}$ consists of $\{I, H_2\}$ and two additional H atoms which are bound to a nearest neighbor (NN) and a second NN to I, respectively. The four H's are bound to four different Si atoms. The nearest metastable configuration, 0.2 eV higher in energy, is very similar to $\{I, H_3\}$ (Fig. 1, right) but with two H's bound to each of the two Si atoms. It is likely that the strain associated with this defect can trap additional H atoms, but is it not clear that the simple $\{I, H_n\}$ notation is still appropriate.

Interstitial silane, centered at the T site with the four H's pointing along the four $\langle 1\,1\,1\rangle$ axes, is 2.48 eV higher in energy. Since even $\{I, H_3\} + H_{BC}$ is more stable than interstitial silane, the molecule can be ruled out as a candidate as a model for the 2222 cm^{-1} line.

3. Hydrogen and vacancy aggregates

The binding energies of H to vacancy aggregates V_n, defined from $V_n + H_{BC} \rightarrow \{V_n, H\} + \Delta E_n$ and shown in Fig. 2, exhibit no correlation with the stability of V_n (Ref. [16]). ΔE_n increases up to $n = 5$ then remains constant at about 3.8 eV. In all the vacancy aggregates, H forms a strong Si–H bond with H pointing toward a perfect

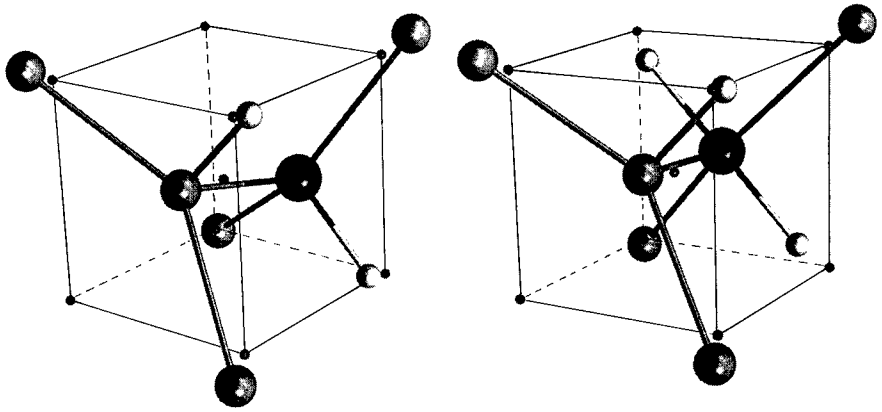

Fig. 1. Structures of the $\{I, H_2\}$ and $\{I, H_3\}$ complexes.

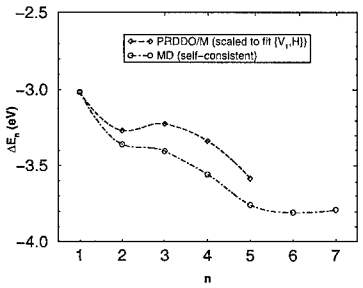

Fig. 2. Binding energy of H to V_n, defined as the difference between the total energies of $\{V_n, H\}$ and $\{V_{n-1}, H\} + H_{BC}$.

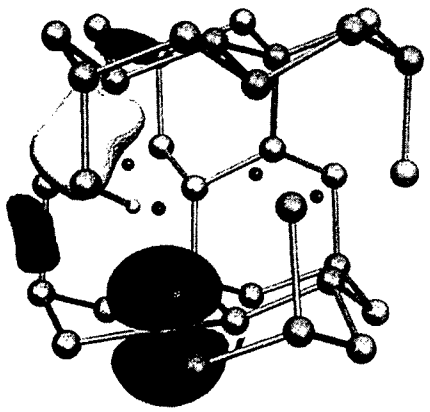

Fig. 3. Two MOs of the $\{V_4, H\}$ complex (see text). The small circles show the perfect lattice sites. Note that the Si–H bond points toward a perfect lattice site.

(vacant) lattice site. The defect reconstructs around that bond. The larger the defect, the more degrees of freedom, and the easier it is to realize a perfect reconstruction. The general features of the Si–H bond in $\{V_n, H\}$ are largely independent of n, and configurations such as H bridging a reconstructed Si–Si bond never occur.

A comparison of the energy spectra of V_n and $\{V_n, H\}$ shows that none of the V_n's which, by themselves, have deep levels in the gap ($n = 1, \ldots, 5$ and $n = 7$), are passivated by a single H. Some of the energy eigenvalues do shift, but they remain within the gap. On the other hand, V_6 by itself has no localized eigenvalue in the gap. Upon trapping one H, at least one deep level appears in the gap and H activates this defect.

Fig. 3 shows the structure of $\{V_4, H\}$ and several MO's. A 'dangling' p orbital is clearly visible on one of the Si atom. It is associated with one of the deep levels of this defect. Another MO, associated with a shallow level, extends over a reconstructed Si–Si bond with two small antibonding components on either side of it.

4. Discussion

The stable configurations for four $\{I, H_n\}$ complexes ($n = 1, \ldots, 4$) have been obtained. The most stable structures are those with an even number of H's, and of those $\{I, H_2\}$ is the most stable. More than four H's can bind to the region surrounding I because the strain associated with the defect provides a variety of distorted Si–Si bonds where H can trap. Interstitial silane is more than 2 eV higher in energy than at least two other configurations and that $\{I, H_3\}$ plus isolated H_{BC}. It is therefore not a possible defect.

H traps at V_n aggregates by forming a strong Si–H bond around which the rest of the defect reconstructs. The binding energy of H to V_n (relative to isolated H_{BC}) increases with n up to $n = 5$, then remains mostly constant. There is no correlation between the stability of V_n and the binding energy of H to it. None of the small V_n aggregates is passivated by trapping a single H, and V_6 is activated by it.

Acknowledgements

This work was supported in part by the grant D-1126 from the R.A. Welch Foundation and by the contract XAD-7-17652-01 from the National Renewable Energy Laboratory.

References

[1] S.J. Pearton, J.W. Corbett, M. Stavola, Hydrogen in Crystalline Semiconductors, Springer, Berlin, 1992.
[2] S.K. Estreicher, Mater. Sci. Eng. R 14 (1995) 319.
[3] G.D. Watkins, MRS Proc. 469 (1997) 139.
[4] M. Budde, B. Bech Nielsen, P. Leary, J. Goss, R. Jones, P.R. Briddon, S. Öberg, S.J. Breuer, Phys. Rev. B 57 (1998) 4397.
[5] S.K. Estreicher, J.L. Hastings, P.A. Fedders, Phys. Rev. B 57 (1998) R12663.
[6] S.K. Estreicher, J.L. Hastings, P.A. Fedders, Phys. Rev. Lett. 82 (1999) 815.
[7] P. Deák, L.C. Snyder, M. Heinrich, C.R. Ortiz, J.W. Corbett, Physica B 170 (1991) 253.
[8] C.G. Van de Walle, J. Neugebauer, Phys. Rev. B 52 (1995) R 14320.
[9] B. Hourahine, R. Jones, S. Öberg, P.R. Briddon, Phys. Rev. B 59 (1999) 15 729.
[10] Y.K. Park, S.K. Estreicher, C.W. Myles, P.A. Fedders, Phys. Rev. B 52 (1995) 1718.
[11] B. Bech Nielsen, L. Hoffmann, M. Budde, Mater. Sci. Engr. B 36 (1996) 259.
[12] P. Stallinga, P. Johannesen, S. Herstrom, K. Bonde Nielsen, B. Bech Nielsen, J.R. Byberg, Phys. Rev. B 58 (1998) 3842.
[13] T.S. Shi, L.M. Xie, G.R. Bai, M.W. Qi, Phys. Stat. Sol. b 131 (1985) 511.
[14] M. Suezawa, Jpn. J. Appl. Phys. 37 (1998) L259.

[15] M. Suezawa, Jpn. J. Appl. Phys. 38 (1999) L608.
[16] S.K. Estreicher, J.L. Hastings, P.A. Fedders, Appl. Phys. Lett. 70 (1997) 432.
[17] O.F. Sankey, D.J. Niklewski, Phys. Rev. B 40 (1989) 3979.
[18] O.F. Sankey, D.J. Niklewski, D.A. Drabold, J.D. Dow, Phys. Rev. 41 (1990) 12750.
[19] See the paper by M. Gharaibeh et al., Physica B 273–274 (1999) 532. These proceedings for details and references.

ELSEVIER

Physica B 273–274 (1999) 220–223

PHYSICA B

www.elsevier.com/locate/physb

Optical absorption study of Zn–H complexes in Si

Ryosuke Mori, Masashi Suezawa*

Institute for Materials Research, Tohoku University, Sendai 980-8577, Japan

Abstract

We studied electronic and vibrational properties of Zn–H complexes in Si based on optical absorption measurements. Specimens were prepared from floating-zone grown Si crystals of high purity and n-type. They were doped with Zn at 1200°C by the vapor pressure method. They were then doped with H and/or D by annealing in H_2 and/or D_2 gas followed by quenching. Optical absorption spectra were measured by an FT-IR spectrometer equipped with a continuous-flow-type liquid He cryostat. When specimens were doped with H at 1200°C, we observed optical absorption peaks due to electronic transition associated with the Zn–H pair. When specimens were doped with H at higher temperatures, intensities of above peaks decreased and two other peaks appeared at about 2214 and 2135 cm^{-1}, due to the vibration of the Zn–2H complex. The Zn–2H complex dissociated into Zn–H and H at around 450°C and the Zn–H pair dissociated at around 750°C due to isochronal annealing.

Keywords: Si; Zn; H; Optical absorption

1. Introduction

Hydrogen in semiconductors is chemically active and changes properties of other impurities and defects by forming pairs and complexes with them. Research on the properties of H in semiconductors has been extensively done since the pioneering study of Pankove et al. [1] on the hydrogen passivation of B in Si. Since the work of Pankove et al., many studies on group III acceptor-H pairs in Si have been done. Those pairs are electrically inactive but optically active since they have a vibrational frequency around 2000 cm^{-1}. In the case of group III acceptors in Si, they are monovalent acceptors and can form only one kind of pair with H.

On the other hand, group II acceptors are double acceptors. Hence, we expect two kinds of complexes with H, namely, a group II acceptor-H pair which is expected to be a monovalent acceptor, and a fully passivated group II acceptor-2H complex. There have been several studies on the properties of the former. Muro and Sieverse [2] studied the Be–H pair in Si by the measurement of its optical absorption spectrum. They found peaks associated with electronic transitions of a monovalent acceptor (Be–H pair). They also found an anomalous peak shift depending on the isotopes, H and D, and interpreted it as being due to the tunneling motion of H around Be. Later, Merk et al. [3] observed optical absorption peaks associated with a monovalent Zn–H pair. They also observed an anomalous peak shift depending on the isotopes, H and D. Suezawa and Mori [4] performed similar experiments and confirmed their results.

As shown above, studies based on the measurement of the optical absorption spectrum of group II acceptor-H complexes have been performed only for monovalent acceptors (group II acceptor-H pair). In this study, we investigated properties, namely, optical absorption spectra and thermal stability, of Zn–2H as well as of Zn–H based on the measurement of their optical absorption spectra. Thermal stability of pairs and complexes can yield invaluable information about their binding energies.

2. Experimental

Specimens were prepared from a floating-zone grown high-purity Si crystal (n-type, the phosphorus

* Corresponding author. Tel.: + 81-22-215-2040; fax: + 81-22-215-2041.

E-mail address: suezawa@imr.tohoku.ac.jp (M. Suezawa)

0921-4526/99/$ - see front matter
PII: S0921-4526(99)00457-3

concentration was $4.5 \times 10^{12}\,cm^{-3}$) and an n-type Si crystal (the phosphorus concentration was about $1 \times 10^{15}\,cm^{-3}$). After being cut from the above crystals, specimens were mechanically shaped with carborundum and chemically polished with a mixed acid ($HNO_3 : HF = 5 : 1$). Specimen size was about $6 \times 6 \times 12\,mm^3$. Then the specimens were doped with Zn by a vapor method: specimens were sealed in evacuated quartz capsules together with pieces of Zn foil. The weight of Zn was determined so as to obtain 1 atm Zn vapor at 1200°C. The quartz capsules were heated at 1200°C from 4 to 72 h, mainly 72 h, followed by quenching in water. After Zn doping, specimens were again sealed in quartz capsules together with H_2 and/or D_2 gas with a pressure of 1 atm at heat treatment temperature. After heating at an appropriate temperature, the quartz capsules were quenched in water. We measured their optical absorption spectra with an FT-IR spectrometer combined with a continuous-flow-type liquid helium cryostat. The resolution was $0.25\,cm^{-1}$ and the measured temperature was about 6 K.

3. Results and discussion

3.1. Optical absorption spectra

Fig. 1 displays the dependence of optical absorption spectra on the H-doping temperature. Peaks at 2099, 2130, 2171 and $2173\,cm^{-1}$ observed in the specimen doped at 1200°C are due to the electronic transitions associated with the Zn–H pair, a single acceptor. This was confirmed from a comparison of observed peak separations with those of the Zn acceptor. The separations of corresponding peaks agreed well. This means that they are well described by the effective-mass theory. After doping at 1250°C, two new peaks appeared at about 2214 and $2135\,cm^{-1}$. The relative intensities of these peaks with respect to those of the former four peaks became larger after 1300°C doping. This strongly suggests that these two peaks are due to the Zn–2H complex since the H concentration is larger at higher doping temperatures.

To confirm this interpretation for the $2214\,cm^{-1}$ peak, we performed two kinds of experiment, namely, use of an n-type specimen and co-doping with H and D. Fig. 2 displays spectra of originally n-type (the spectrum (a)) and high-purity (the spectrum (b)) specimens after H-doping at 1300°C. Absorption peaks due to the Zn–H pair disappeared in spectrum (a) in contrast with the existence of those peaks in spectrum (b). This is due to the compensation of the Zn–H pair acceptor due to P in the originally n-type specimen. On the other hand, the intensity of the $2214\,cm^{-1}$ peak is similar in both specimens. Hence, this clearly shows that the $2214\,cm^{-1}$ peak is not electrically active. Another interesting feature of Fig. 2 is,

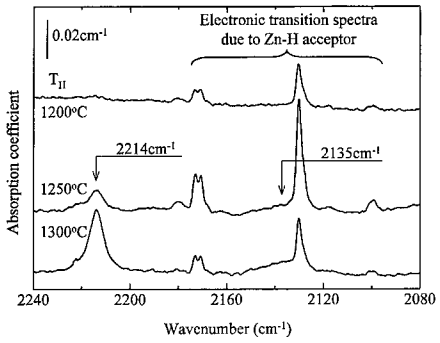

Fig. 1. Optical absorption spectra of specimens doped with H at various temperatures (T_H).

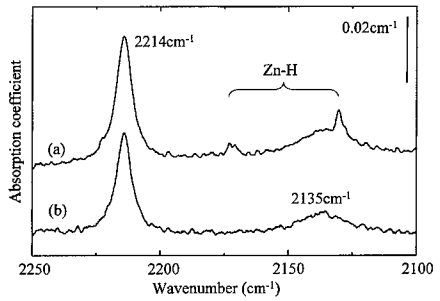

Fig. 2. Optical absorption spectrum of specimen of (a) high-purity and of (b) originally n-type. H doping was done at 1300°C.

as already described, that there is a broad peak at about $2135\,cm^{-1}$. We first hypothesized that this peak is due to the vibration of the Zn–H pair. This hypothesis, however, was incorrect according to the following experimental results. Firstly, this peak becomes noticeable when the optical absorption due to the Zn–H pair acceptor decreases. Secondly, the intensity of this peak also seems to be independent of the original conduction type. Finally, the annealing process was found to be similar to that of the Zn–2H complex as shown later. Hence, we did not detect the optical absorption due to the vibration of the Zn–H pair. Figs. 3 and 4 display spectra at around $2200\,cm^{-1}$ and $1600\,cm^{-1}$, respectively, of various specimens, all of which were doped with H and/or D at 1300°C. The $2214\,cm^{-1}$ in the H-doped specimen shifted to $2210\,cm^{-1}$ in the D-doped specimen. By co-doping of H and D, two peaks were observed at 2214 and $2210\,cm^{-1}$. Apparently, this result seems peculiar since two H atoms are thought to mainly bond with two Si atoms at the nearest-neighbor sites of the Zn atom and, consequently, there seems to be almost no direct interaction between two H atoms. However, it should be remembered that two H atoms migrate to the Zn atom because Zn is a double acceptor. Hence, in the discussion

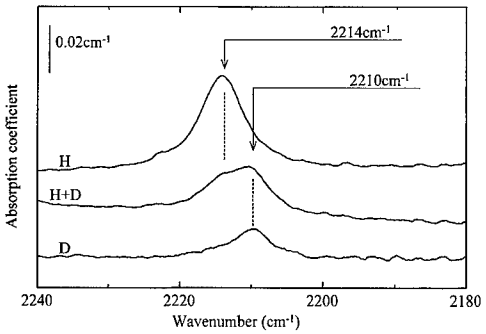

Fig. 3. Optical absorption spectra of H and/or D doped specimens around 2100 cm^{-1}.

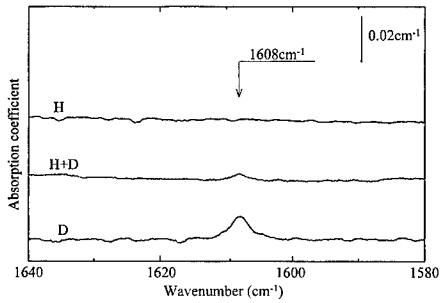

Fig. 4. Optical absorption spectra of H and/or D doped specimens around 1600 cm^{-1}.

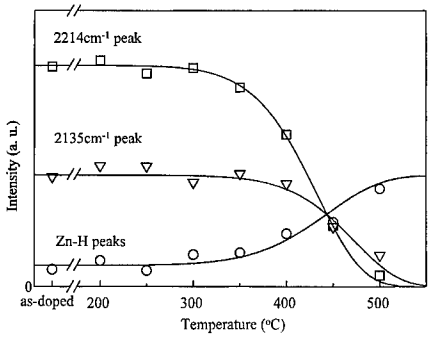

Fig. 5. Isochronal annealing behaviors of the Zn–2H complex (2214 and 2135 cm^{-1} peak) and the Zn–H pair. The annealing period was 30 min at each temperature.

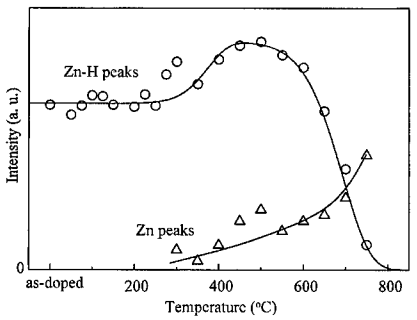

Fig. 6. Isochronal annealing behaviors of the Zn–H pair and Zn. Both intensities were determined from peak heights due to electronic transitions associated with them. The annealing period was 30 min at each temperature.

of vibrational properties, we regard a Zn–2H complex as a molecule. We applied the results of the H_2O model, a three-center model of molecular vibration, to explain the above observations and semi-quantitatively succeeded. According to this treatment, the 2214 and 2210 cm^{-1} peaks are due to the vibrations of H in the Zn–2H complex of H in the Zn–HD complex, respectively. A similar isotope shift was observed in the case of H_2^*, a metastable state of H_2, in Si [5]. At around 1600 cm^{-1}, a new peak appeared at 1608 cm^{-1} due to D-doping and H and D co-doping. This peak is probably due to the vibration of D in the Zn–2D complex since the frequency ratio (1.377) with 2214 cm^{-1} is slightly smaller than the square root of the mass ratio of H and D. This small ratio of isotope effect suggests that H mainly bonds to the Si atom. We expected another peak to exist near this peak due to D in the Zn–HD complex in the case of co-doping of H and D. However, we did not observe the splitting of the 1608 cm^{-1} peak upon co-doping. This may be due to a weak intensity.

3.2. *Thermal stabiltity of the Zn–H complex*

To determine the binding energy of the Zn–H complex and the Zn–H pair, we performed isochronal annealing experiments. Fig. 5 shows the results of isochronal annealing for 30 min at each temperature. The specimen was doped with H at 1300°C. The intensities of the 2214 (Zn–2H complex) and 2135 cm^{-1} peaks decrease above 350°C. Simultaneously, the intensity of 2130 cm^{-1} peak (Zn–H pair) increases. This clearly shows that one H atom dissociates from a Zn–2H complex, resulting in the Zn–H pair. Fig. 6 shows the result of the isochronal annealing experiment of the Zn–H pair. The specimen was doped with H at 1200°C. The slight increase around 300°C is probably due to dissociation of the Zn–2H complex and the decrease around 700°C is due to the dissociation of Zn–H pair. Assuming first-order reactions for the dissociations of the Zn–2H complex and the Zn–H pair, we obtained binding energies of about 2 and 3 eV, respectively. These are rough estimates but seem reasonable since the binding energy of Zn–2H complex is expected to be about $\frac{1}{2}$ that of Zn–H pair because the dissociation of the Zn–2H complex occurs by a reaction $Zn - 2H = Zn - H + H$ and because the Zn–H pair is

a monovalent acceptor. To obtain more accurate values, we need to perform an isothermal annealing experiment.

4. Conclusion

We studied optical absorption spectra due to a Zn–2H complex and a Zn–H pair. The vibrational frequency of the Zn–2H complex was 2214 cm^{-1}. On the other hand, we did not detect vibrational absorption due to the Zn–H pair. Instead, we observed electronic absorption due to the Zn–H pair, a monovalent acceptor, which is well described by the effective mass theory. The Zn–2H complex and Zn–H pair dissociate at above 450°C and 750°C, respectively.

Acknowledgements

The authors would like to thank the Laboratory for Developmental Research of Advanced Materials for allowing them to use an FT-IR spectrometer.

References

[1] J.I. Pankove et al., Phys. Rev. Lett. 51 (1983) 2224.
[2] K. Muro, A.J. Sievers, Phys. Rev. Lett. 57 (1986) 897.
[3] E. Merk et al., Mater. Res. Soc. Symp. Proc. 163 (1990) 15.
[4] M. Suezawa, R. Mori, Phys. Stat. Sol. B 210 (1998) 507.
[5] J.D. Holbech et al., Phys. Rev. Lett. 71 (1993) 875.

ELSEVIER

Physica B 273–274 (1999) 224–227

PHYSICA B

www.elsevier.com/locate/physb

Thermal properties of H-related complexes in electron-irradiated Si doped with H

Masashi Suezawa*

Institute for Materials Research, Tohoku University, Sendai 980-8577, Japan

Abstract

The annealing behaviors of H-point defect complexes in Si were investigated to determine their formation or dissociation processes. Specimens were doped with H by annealing in H_2 gas followed by quenching. They were then irradiated by 3 MV electrons at room temperature. Subsequently, they were annealed isochronally or isothermally. Optical absorption spectra of H-point defect complexes were measured at 7 K. Due to isochronal annealing, the 2122, 1838 and 817 cm^{-1} peaks disappeared below 200°C. On the other hand, 2223 and 2166 cm^{-1} peaks were formed at above 125°C and 175°C, respectively. From isothermal annealing experiments, the binding energies of H_2^* (1838 cm^{-1} peak) and I (I: a self-interstitial)·2H complex (1987 and 1990 cm^{-1} peaks) were determined to be about 1.5 and 2.0 eV, respectively. The generation of the 2223 cm^{-1} defect, V.4H (V: a vacancy), was due to the reaction between H_2 and the 2122 cm^{-1} defect, V·2H.

Keywords: H; Si; Point defect; Binding energy

1. Introduction

Hydrogen (H) is chemically active and forms pairs and complexes with impurities and defects in Si crystals. Its action was initially noticed by Pankove et al. [1] in their study on the hydrogen-passivation of B in Si. Although a number of results on the properties of H in semiconductors as well as in Si have been published, many properties of H, especially properties of complexes of H and other impurities and defects, remain to be further investigated.

We are particularly interested in the sort of point defects, namely, vacancies (V) or self-interstitials (I), included in H-point defect complexes since this is still controversial. One issue regarding the H-point defect complexes in Si is the sort of point defects, V or I, included in the complexes responsible for the 1987 and 1990 cm^{-1} peaks and the 2122 and 2223 cm^{-1} peaks. Some of the proposed models are reviewed below. Shi et al. [2] proposed that the 2223 cm^{-1} defect (we term the 2223 cm^{-1} defect which is responsible for the optical absorption at 2223 cm^{-1}) is an I·4H complex, based on the study of optical absorption spectrum of Si grown in H_2 gas and on a theoretical consideration. Bai et al. [3] proposed that the 1987 and 1990 cm^{-1} defects are the same, V·2H or V_2·2H, from the study of optical absorption spectra of electron-irradiated Si grown in H_2 gas. Xie et al. [4] proposed that the 1987 and 1990 cm^{-1} defects and the 2223 cm^{-1} defect are V·2H and V·4H, respectively. Bech Nielsen et al. [5] proposed that the 1987 and 1990, 2122, 2166, and 2223 cm^{-1} defects are I·2H, V·2H, V·3H, and V·4H, respectively, from the study of optical absorption spectra of proton-implanted Si. Their proposal was based on the ab initio calculation of the vibrational frequency of the H-point defect complex. On the other hand, Suezawa [6] focused on the impurity effect on the intensities of 1987 and 1990 cm^{-1} peaks and 2122 cm^{-1} peak. He measured the optical absorption spectra due to H-point defect complexes generated by electron irradiation of hydrogenated Si. According to him, the intensities of 1987 and 1990 cm^{-1} peaks in B- or C-doped Si were much weaker than those in high-purity Si. This result strongly supports the notion that the 1987 and 1990 cm^{-1} defect includes an I for the following

* Tel.: + 81-22-215-2040; fax: + 81-22-215-2041.
E-mail address: suezawa@imr.tohoku.ac.jp (M. Suezawa)

0921-4526/99/$ - see front matter
PII: S0921-4526(99)00458-5

reasons. An I is known to kick out B and C from substitutional site to interstitial site. Hence, the concentration of I is expected to be low in B and C-doped Si. Therefore, his results experimentally support Bech Nielsen et al.'s identifications quoted above.

As a further study, we performed experiments of isochronal and isothermal annealings to determine the thermal stability and the activation energy for the generation or annihilation of H-point defect complexes. In the case of H-point defect complexes, their generation or dissociation processes offer invaluable information about those complexes.

2. Experimental

Specimens were prepared from a high-purity (n-type, carrier concentration at RT was about 4×10^{12} cm^{-3}) floating-zone-grown Si crystal. After the specimens were cut from the crystal, they were shaped with carborundum and chemically etched with a mixed acid of HNO_3 : HF = 3 : 1. The specimen size was about $6 \times 6 \times 11$ mm^3. To dope the specimens with H, they were sealed in quartz capsules together with H_2 gas. They were heated at 1200°C for 2 h followed by quenching in water. Specimens were irradiated with 3 MV electrons at RT. During irradiation, the specimens were pressed onto a sample holder which was cooled with running water and blown air. The total dose of irradiation was 2×10^{16} cm^{-2}. To determine the thermal stability of H-point defect complexes, they were subsequently subjected to isochronal or isothermal annealing. In the former case, annealing was performed at 25°C intervals and an annealing duration of 30 min. Optical absorption spectra of those specimens at 7 K were measured with an FT-IR spectrometer and a continuous-flow-type liquid helium cryostat. The resolution was 0.25 cm^{-1}.

3. Results and discussion

3.1. Optical absorption peaks

Fig. 1 shows a part of the optical absorption spectrum after electron irradiation of hydrogenated Si. In an as-irradiated specimen, the observed peak positions are 2145.0, 2122.3 (abbreviated 2122 hereafter), 2072.4, 2062.2, 1989.9 (1990), 1987.0 (1987), 1952.9, 1952.4, 1870.0, 1838.5 (1838), 1599.6, 817.5 (817), 740.3, 736.4, 733.1, and 718.7 cm^{-1}, rounded off to the first decimal place. Many of those lines agree with those observed in a proton-implanted specimen [5]. As previously shown [7], the largest difference between the two specimens is that the 2222.9 (2223) and 2166. (2166) cm^{-1} peaks observed in proton-implanted specimen were not observed in our specimen in an as-irradiated state. Due to our

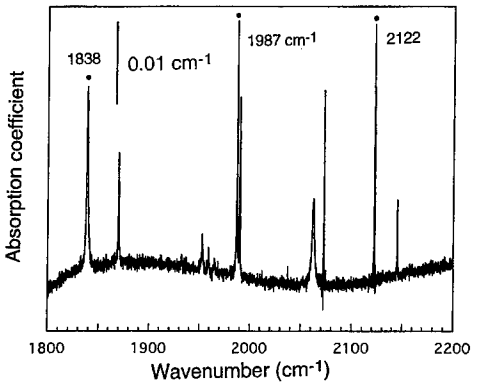

Fig. 1. The optical absorption spectrum of electron-irradiated Si doped with H around 2000 cm^{-1}.

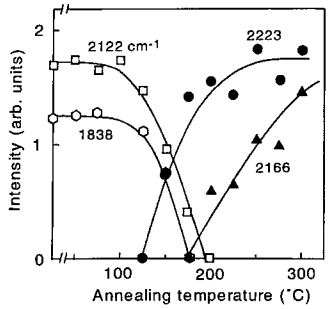

Fig. 2. Isochronal annealing curves of various defects in electron-irradiated Si doped with H. The ordinate corresponds to the peak intensity.

H-doping method, hydrogen existed in the form of H_2 in our specimen as first shown by Pritchard et al. [8]. We also detected it in our specimen. Hence, these results support Estreicher et al.'s prediction [9]: According to a theoretical study on the interaction between a V or an I and H_2, they concluded that V and I easily form complexes with H_2 such as a V·2H (or {V, H, H} according to their expression) and an I·2H (or {I, H, H}) complex, respectively.

3.2. Results of isochronal and isothermal annealing experiments

Fig. 2 shows the results of our isochronal annealing experiment. Both 2223 and 2166 cm^{-1} peaks were observed after annealing at high temperature. As shown below, the generation process of the 2223 cm^{-1} peak is well related to the annealing process of the 2122 cm^{-1} peak. The annealing behavior of the 817 cm^{-1} peak was similar to that of 1838 cm^{-1} peak. This result is consistent with Bech Nielsen et al.'s model [5] in which these peaks are due to vibration of the same defect, H_2^*, a metastable pair of H.

To determine the annealing kinetics and activation energy, we studied isothermal annealing behaviors of complexes responsible for various optical absorption peaks. All of the isothermal annealing processes were well described by first-order reaction kinetics, namely, dn/dt was proportional to n/τ where n was the defect density, t the annealing period and τ the time constant. Hence the dependence of n on the annealing period is given by

$$\text{annihilation: } n = n_0 \exp(-t/\tau), \tag{1a}$$

$$\text{generation: } n = n_0(1 - \exp(-t/\tau)), \tag{1b}$$

where n_0 is the initial concentration for the annihilation process and the saturation concentration for the generation process, $\tau = \tau_0 \exp(E/kT)$, and τ_0 and E are the pre-exponential factor of time constant and the activation energy, respectively. In the analysis of the experimental results by the above equations, we slightly modified them by introducing a small constant term to take experimental error and the short annealing period into account.

3.2.1. The 1838 cm^{-1} peak

We obtained the activation energy, 1.5 eV, from the isothermal annealing experiment. Two models have been proposed for the complex responsible for the 1838 cm^{-1} peak, VH [4] and H_2^* [5]. The effect of co-doping with H and D on the peak splitting supports the latter. This means that the activation energy corresponds to the binding energy of H_2^*. Van de Walle [10] calculated energies of various configurations of H in Si. According to him, the binding energy of H_2^* is about 1.2 eV, which is in good agreement with our result (1.5 eV). On the other hand, the theoretically estimated binding of H_2 is similar to that of H_2^*. It seems, however, much larger than that of H_2^* since H_2 disappeared after annealing at 350°C in our isochronal annealing experiment. If we assume a similar pre-exponential factor, the binding energy of H_2 is estimated to be about 2.2 eV. To confirm this, we need to perform isothermal annealing experiments about H_2.

3.2.2. The 2122 and 2223 cm^{-1} peaks

Fig. 3 shows the isothermal annealing behaviors of 2122 (triangles) and 2223 (circles) cm^{-1} peaks at 140°C. Both are well described by first-order reaction kinetics (solid lines). An interesting feature is that they have an almost mirror image relationship with respect to a horizontal line at about 1.1. By assuming the same oscillator strength for both lines, this means the conversion of the 2122 cm^{-1} defect to the 2223 cm^{-1} defect due to annealing. The activation energy is about 0.78 eV. This is in good agreement with the activation energy of H_2 diffusion determined by Markevich and Suezawa [11] from the generation process of the O–H_2 complex.

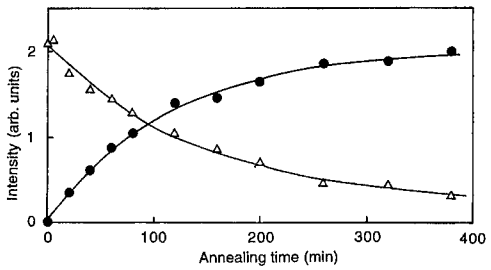

Fig. 3. Isothermal annealing curve of the 2122 (triangles) and 2223 (circles) cm^{-1} peaks at 140°C. The ordinate is the peak intensity. The solid lines are the fitting curves with Eqs. (1a) and (1b).

As mentioned, we detected H_2 in these specimens. Hence, we conclude that the 2122 cm^{-1} defect combines with diffusing H_2 and develops into the 2223 cm^{-1} defect. As shown above, the 2122 cm^{-1} defect is identified as being a V·2H complex. Hence the 2223 cm^{-1} defect is a V·4H complex.

3.2.3. The 2166 cm^{-1} peak

The activation energy is about 1.2 eV. A model [5] has been proposed for the 2166 cm^{-1} defect, VH_3. To generate VH_3 by the diffusion process, two mechanisms are possible, i.e., VH + H_2 or VH_2 + H. The vibrational frequency of VH is proposed to be 2068 cm^{-1}. However, this peak was not observed in our specimen. On the other hand, the activation energy of diffusion of atomic H in Si is too small (0.48 eV) to explain the above value. We therefore tentatively conclude that this energy (1.2 eV) is the binding energy of some defect by dissociation of which the 2166 cm^{-1} defect is generated.

3.2.4. The 1987 and 1990 cm^{-1} defects

The activation energy was determined to be about 2.0 eV. The annealing behaviors of 1987 and 1990 cm^{-1} peaks were the same. These defects were identified as I·2H in the above. Dissociation of I·2H probably occurs when one H atom leaves this complex. Hence, we must estimate the energy difference between two configurations, i.e., I·2H and I·H + H. According to Van de Walle [10], such difference is about 1.36 eV when I is a split-interstitial.

4. Conclusion

From the annealing study of electron-irradiated Si doped with H, we obtained the following conclusions. Due to isochronal annealing, the 2122, 1838 and 817 cm^{-1} peaks disappeared below 200°C. On the other hand, 2223 and 2166 cm^{-1} peaks were formed at above

125 and 175°C, respectively. From isothermal annealing experiments, the binding energy of H_2^* (1838 cm^{-1} peak) was determined to be about 1.5 eV, which is in good agreement with that (1.2 eV) estimated by theoretical calculation. The binding energy of I·2H (1987 and 1990 cm^{-1} peaks) was determined to be about 2.0 eV, which was slightly different from that (1.36 eV) of theoretical estimation. The generation of the 2223 cm^{-1} defect (V·4H) was due to migration of H_2 to the 2122 cm^{-1} defect (V·2H).

Acknowledgements

The author wishes to thank the Laboratory for Developmental Research of Advanced Materials for allowing him to use an FT-IR spectrometer. The author also thanks H. Sunaga of JAERI Takasaki Institute for his help in electron irradiation.

References

[1] J.I. Pankove et al., Phys. Rev. Lett. 51 (1983) 2224.
[2] T.S. Shi et al., Phys. Stat. Sol. B 131 (1985) 511.
[3] G.R. Bai et al., Solid State Commun. 56 (1985) 277.
[4] L.M. Xie et al., J. Phys. C 3 (1991) 8519.
[5] B. Bech Nielsen et al., Mater. Sci. Forum 196–201 (1995) 933.
[6] M. Suezawa, Jpn. J. Appl. Phys. 38 (1999) L608.
[7] M. Suezawa, Jpn. J. Appl. Phys. 37 (1998) L806.
[8] R.E. Pritchard et al., Phys. Rev. B 56 (1997) 13118.
[9] S.K. Estreicher et al., Phys. Rev. B 57 (1998) R12663.
[10] C.G. Van de Walle, Phys. Rev. B 49 (1994) 4579.
[11] V.P. Markevich, M. Suezawa, J. Appl. Phys. 83 (1998) 2988.

ELSEVIER

Physica B 273–274 (1999) 228–230

PHYSICA B

www.elsevier.com/locate/physb

Hydrogenation and passivation of electron-beam-induced defects in N-type Si

Y. Ohmura*, K. Takahashi, H. Saitoh, T. Kon, A. Enosawa

Department of Electronic Engineering, Iwaki Meisei University, 5-5-1 Iino Chuodai, Iwaki, Fukushima 970-8551, Japan

Abstract

Annealing and hydrogenation behaviors of electron-beam-induced defects in n-type Si have been investigated by deep-level transient spectroscopy. Hydrogenation has been performed by boiling samples in H_2O or D_2O at 120°C in an autoclave. The E1 level (A center: O–V complex), E2 level (double-negative charge state of the divacancy) and E3 level (single-negative charge state of the divacancy) are hardly annealed at as low a temperature as 120°C, while hydrogenation by boiling dramatically reduces the concentration of these levels. A new level emerges near 0.33 eV below the conduction band edge after boiling, which may be a radiation-induced defect-hydrogen or -deuteron complex. Reappearance of E1 level by annealing after hydrogenation suggests that disappearance of E1 level by hydrogenation is not due to the destruction of A center, but to a mere vanishing of the electronic level due to e.g. formation of the A center-hydrogen or -deuteron complex.

Keywords: Deep levels; Electron irradiation; Hydrogenation; n-Si

1. Introduction

In the past several decades, many investigations have been made on the electron or ion irradiation effects on Si. Pioneering works through electron paramagnetic resonance measurements by Watkins and Corbett [1–3] have shed light on the microscopic structures of these radiation defects. Evwaraye and Baliga [4] examined electron-beam-induced deep centers and their annealing behaviors by deep level transient spectroscopy (DLTS) [5] in connection with the minority carrier lifetime. It is well known that these defects are annealed out thermally at elevated temperatures or passivated by hydrogen. Hydrogen has been introduced into semiconductors by hydrogen plasma exposure of the semiconductors or low-energy hydrogen ion implantation. Recently, it has been reported that when B-doped p-type Si is boiled, the acceptor B is neutralized by hydrogen [6], and in pressurized water boiling, hydrogenation is enhanced significantly [7]. Water is ionized into H^+ and OH^-. It has been explained that the enhanced hydrogenation at elevated temperatures results from concentration increase of these H-related species in water. In this work, the hydrogenation and passivation of electron-beam-induced deep centers in n-type Si are investigated, the hydrogenation being achieved by boiling in light water (H_2O) or heavy water (D_2O).

2. Experimental

The samples used in this experiment were n-type (1 1 1) epitaxial Si wafers of 5 Ωcm resistivity. The thickness of the P-doped epilayer was about 14 μm. Wafers were irradiated at room temperature with 3×10^{14} electrons/cm^2 at 10 MeV. In the annealing experiment, Si chips from irradiated wafers were annealed in a gold-plated furnace in an Ar gas. In the hydrogenation experiment, the chips were boiled in deionized water at atmospheric pressure in the dark. Higher pressure boiling was performed in a medical autoclave which operates at 120°C and 2 atm using deionized light water or heavy water.

* Corresponding author. Fax: + 81-246-29-0577.
E-mail address: ohmura@iwakimu.ac.jp (Y. Ohmura)

0921-4526/99/$ - see front matter
PII: S0921-4526(99)00459-7

The autoclave is controlled not in the pressure but in the temperature. The boiling temperature of the heavy water is only slightly higher than that of the light water for the same pressure. In reality, the pressure shown by a Bourdon tube gauge was quite the same between the heavy water and the light water boiling. The heavy water used was of 99.9% purity. Most samples were boiled for 1 h. Au was evaporated both on the front surface (through the stencil mask) and the rear surface of the chip for Schottky and ohmic contact, respectively.

3. Results and discussions

Fig. 1 shows DLTS spectra for as-irradiated and thermally annealed samples. It is found that E1 (A center: oxygen-vacancy complex), E2 (the double-negative charge state of the divacancy) and E3 (the single-negative charge state of the divacancy) are hardly annealed at a low temperature of 120°C, while, at 200°C, E2 and E3 are obviously annealed. It is noted that E1 increases. At 300°C, however, all these levels are annealed out completely (not shown). It is also noted that the E4 level (Ec-0.36 eV) which Evwaraye and Baliga observed after annealing at 300°C and assigned to the dominant recombination center [4], has not emerged. Fig. 2 shows DLTS spectra for as-irradiated sample and those after boiling at 120°C in H_2O and D_2O. It is found that E1 and E2 levels as well as E3 have almost completely disappeared both for H_2O and D_2O boiling, which contrasts sharply with the thermal annealing behaviors in Fig. 1. In the samples boiled at 100°C, the E1 level is not annihilated completely, but remains at about one-fourth the height of that of the as-irradiated specimen (not shown). On the other hand, it is observed that in boiled samples, a new level En emerges. Also, the En level emerges both in H_2O and D_2O boiling at 100°C.

Table 1 shows energy levels obtained from the Arrhenius plot of DLTS data. The E1, E2 and E3 levels agree with previously reported ones. From the position

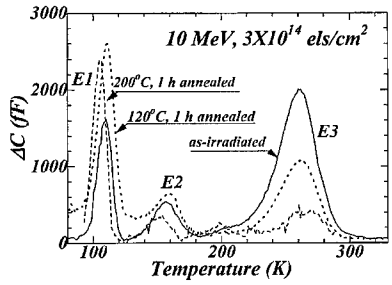

Fig. 1. DLTS spectra for as-irradiated and thermally annealed n-type epitaxial wafers which were irradiated with 3×10^{14} els/cm^2 at 10 MeV.

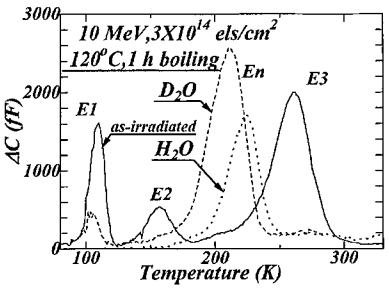

Fig. 2. DLTS spectra for as-irradiated and 120°C H_2O- and D_2O-boiled samples.

Table 1
Activation energies (eV) for defect levels E1, E2 and E3 in as-irradiated n-type Si and new levels En in irradiated and H_2O- and D_2O-boiled n-type Si

E1	E2	E3	En (H_2O)	En (D_2O)
0.17–0.21	0.22–0.25	0.41–0.45	0.31–0.34	0.32–0.35

of the energy level and the difference in appearance, it is clear that these new level En's are different from the E4 level. The origin of En must be an irradiation defect-hydrogen or -deuteron complex. It seems that the En level for D_2O boiling is slightly deeper than for H_2O boiling, although the data are scattered considerably.

Next, in order to investigate the stability of the new En levels, when annealed at elevated temperatures, boiled and hydrogenated samples were annealed also in an Ar gas for 1 h. Fig. 3 shows DLTS spectra for samples which were boiled in H_2O and subsequently annealed at various temperatures for 1 h. It is found that En level created by H_2O boiling is annealed out at 175°C. On the other hand, in Fig. 4, where DLTS spectra for samples which were boiled in D_2O and subsequently annealed are shown, En level remains up to 200°C for 1 h annealing. This difference of stability between En levels created by H_2O and D_2O boiling may be a strong evidence that the origin of En level is a radiation-induced defect-hydrogen or -deuteron complex. The deuteron-defect complex is thermally more stable than the hydrogen counterpart. This behavior is similar to that of the acceptor B in Si. Deuterated B is annealed at a higher temperature than hydrogenated B [8]. No such levels have been observed for Si wafers which were only boiled in H_2O or D_2O.

Finally, it must be noted that, in both Figs. 3 and 4, E1 levels reappear and seem to grow with the annealing temperature. In Fig. 2, the E1 levels must have been annealed out almost completely by boiling in H_2O or D_2O. In Fig. 5, the height of E1 levels are plotted against the annealing temperature for samples boiled in H_2O or D_2O as well as only thermally annealed samples. From

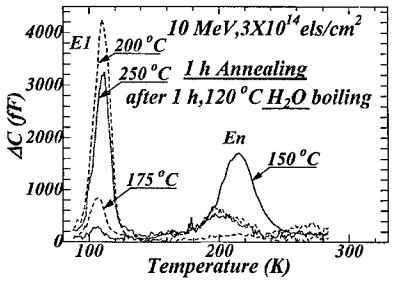

Fig. 3. DLTS spectra for 120°C, 1 h H_2O boiled and subsequently thermally annealed samples.

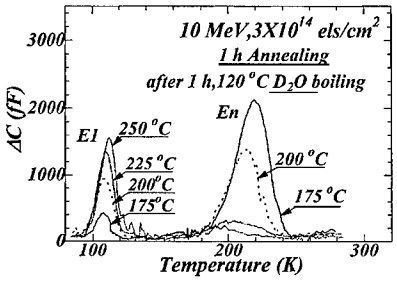

Fig. 4. DLTS spectra for 120°C, 1 h D_2O boiled and subsequently thermally annealed samples.

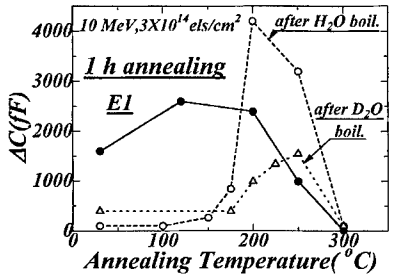

Fig. 5. Annealing behavior of E1 level (solid line) and reappearance and further annealing behaviors of E1 levels for H_2O- and D_2O-boiled samples.

this reappearance of E1 level by annealing, it is inferred that disappearance of E1 level by H_2O or D_2O boiling is not due to the destruction of A center but to a mere annihilation of the trap level, e.g. due to formation of the A center-hydrogen or -deuteron complex. Hence, when hydrogen or deuteron dissociates from the complex, the A center will recover. The A center that once recovered, however, will be annealed by higher temperature annealing. It seems, in Fig. 5, that recovering of H_2O-boiled samples takes place at a lower annealing temperature region than that of D_2O boiled samples, although the concentration of E1 level which recovered for H_2O boiling is much higher than that for D_2O boiling. Thus, it is found that deep centers such as E1 and En as well as acceptor B [8] passivated by deuteration require higher temperatures for annealing than those passivated by hydrogenation, which implies that deuteron forms stronger bonds with these centers, and which seems to be a general behavior for hydrogen and deuteron.

4. Summary

The effects of hydrogenation by boiling in pressurized light or heavy water on electron-induced defects in n-type Si have been investigated by DLTS measurements. The E1 (O–V complex), E2 (single-charge state of the divacancy) and E3 (double-charge state of the divacancy) levels disappear almost completely after boiling for 1 h at 120°C (2 atm), although they are hardly annealed thermally at 120°C. On subsequent thermal annealing after boiling, E2 and E3 levels do not appear any more for up to 300°C annealing, which suggests that divacancies are destroyed by hydrogenation or deuteration. On the other hand, E1 level reappears from about 150°C and grows with temperature. The decrease of E1 level by boiling may be not due to the destruction of the defect but to a mere annihilation of the trap level due to e.g. formation of the A center-hydrogen or -deuteron complex. The A center will recover, when hydrogen or deuteron dissociates from the complex. A new level emerges near 0.33 eV below the conduction band edge both for light- and heavy-water boiling. These new levels are subsequently annealed at different temperatures between H_2O- and D_2O-boiled samples; deuterated samples are annealed at about 50°C higher temperature. These results strongly suggest that the origins of these new levels are the radiation defect-hydrogen or -deuteron complexes.

Acknowledgements

The authors thank Dr. A. Yahata of Toshiba R&D Center for experimental aids and valuable discussions throughout this work.

References

[1] G.D. Watkins, J.W. Corbett, Phys. Rev. 134 (1964) A1359.
[2] G.D. Watkins, J.W. Corbett, Phys. Rev. 138 (1965) A543.
[3] J.W. Corbett, G.D. Watkins, Phys. Rev. 138 (1965) A555.
[4] A.O. Evwaraye, B.J. Baliga, J. Electrochem. Soc. 124 (1977) 913.
[5] D.V. Lang, J. Appl. Phys. 45 (1974) 3023.
[6] A.J. Tavendale, A.A. Williams, S.J. Pearton, Appl. Phys. Lett. 48 (1986) 590.
[7] Y. Ohmura, Y. Otomo, Y. Tago, N. Terakado, T. Satoh, Appl. Phys. Lett. 67 (1995) 64.
[8] Y. Ohmura. K. Abe, A. Enosawa, M. Ohshima, M. Yamaura, Abstract of the Eighth International Conference On Shallow-level Centers in Semiconductors, Montpellier, July, 1998, No. 154.

ELSEVIER

Physica B 273–274 (1999) 231–234

PHYSICA B

www.elsevier.com/locate/physb

Stability and vibrational modes of H_2 and H_2^* complexes in Si

Yong-Sung Kim, Young-Gu Jin, Ji-Wook Jeong, K.J. Chang*

Department of Physics, Korea Advanced Institute of Science and Technology, 373-1 Kusung-dong Yusung-ku, Taejon, 305-701, South Korea

Abstract

We investigate the stability and local vibrational properties of H_2 and H_2^* complexes in Si through first-principles pseudopotential calculations within the local-density-functional approximation (LDA) and the generalized gradient approximation (GGA). We find the energy difference between H_2 and H_2^* to be less than 0.05 eV per H atom, testing supercells containing up to 216 atoms. For the [1 0 0], [1 1 0], and [1 1 1] orientations of the H_2 molecule at or near a tetrahedral site, the vibrational frequencies by the GGA for the stretch mode lie in the range of 3556–3643 cm^{-1}, close to the experimental value of 3618 cm^{-1}, while they are underestimated by about 300 cm^{-1} in the LDA. A new local mode at 650–700 cm^{-1} is predicted for the H_2 molecule.

Keywords: Hydrogen; H_2; H_2^*; Vibrational mode

1. Introduction

The first proposal of a molecular form of interstitial hydrogen in Si was given by theory [1], and later experiments have proved the presence of the H_2 molecule [2–4]. The other stable form of H dimers was predicted to be the H_2^* complex [5], and also confirmed by infrared studies [6]. Most theoretical calculations showed that the H_2 molecule is more stable by about 0.2 eV per H atom than the H_2^* complex [5,7], with an exception that these complexes have very comparable energies [8]. For the H_2 molecule, experiments showed two different results for the stretch mode: a broad Raman line at 4158 cm^{-1} close to that of a free molecule in gas phase [2] and a substantial frequency shift to the infrared mode of 3618 cm^{-1} [3,4]. Although several theoretical studies predicted the vibrational frequencies of 3300–3700 cm^{-1} for the H_2 molecule [9–11], the infrared activity of molecule and the absence of a splitting of the stretch mode due to para- and ortho-forms of molecule still need to be understood.

In this work we perform real-space electronic structure calculations to investigate more precisely the stability of the H_2 and H_2^* complexes in Si, based on the pseudopotential method within the local-density-functional approximation (LDA). Increasing the supercell size up to a 216-atom cell, we find the H_2 molecule to be lower in energy by about 0.05 eV per H atom. We also investigate the vibrational modes of the H_2 and H_2^* complexes through plane-wave pseudopotential calculations and examine the effect of the generalized gradient approximation (GGA) on the vibrational frequencies. The details of the results will be published elsewhere [12].

2. Calculational method

The total energies are calculated using the first-principles pseudopotential method within the LDA and GGA. Norm-conserving pseudopotentials are generated by the scheme of Troullier and Martins [13], and transformed into a separable form of Kleinman and Bylander [14]. We use the Ceperley–Alder expression for the LDA exchange-correlation potential [15] and the PW91 form in the GGA calculations [16]. The wave functions are expanded in a plane-wave basis set with a kinetic energy cutoff of 64 Ry, which ensures the well convergence of

* Corresponding author. Tel.: + 82-42-869-2531; fax: + 82-42-869-2510.

E-mail address: kchang@hanbit.kaist.ac.kr (K.J. Chang)

0921-4526/99/$ - see front matter
PII: S0921-4526(99)00460-3

bond lengths and total energies. The Brillouin zone summation of the charge density is done with the use of a special $\boldsymbol{k}$-point set of uniform grids. The vibrational frequencies and normal modes of H_2 and H_2^* are determined using the dynamical matrix approach, where the force constants are calculated for atoms within the supercells containing 32 and 64 atoms. To determine the stability of the H_2 and H_2^* complexes, we test 64-, 128-, and 216-atom supercells. For the 216-atom supercell, we perform the calculations in real space using a 3-level multigrid method [17]. A higher-order finite-difference method is used to expand the kinetic energy operator up to the 12th order with a grid spacing of 0.35 a.u., which corresponds to the kinetic energy cutoff of at least 40 Ry in the plane-wave-basis calculations. Testing the 64-atom supercell, we find that the energy difference between the H_2 and H_2^* complexes varies by only 0.01 eV per H atom, compared with the plane-wave-basis calculations.

3. Results and discussion

The energy differences between the H_2^* and H_2 complexes are drawn for various supercell sizes and $\boldsymbol{k}$-point sets in Fig. 1. When only the Γ point is used for smaller supercells containing up to 128 atoms, the H_2^* complex is found to be more stable than the H_2 molecule, while the molecule becomes more stable by about 0.04 eV per H atom as the cell size increases to a 216-atom cell. For smaller 32- and 64-atom supercells, if a $\boldsymbol{k}$-point set generated from the $2\times2\times2$ Monkhorst–Pack mesh is used, the molecular form is more stable by about 0.05 eV per H atom. Thus, the stability of H_2^* and H_2 is very sensitive to the parameters used in calculations, with the energy difference less than 0.05 eV per atom, which is much smaller than the value of about 0.2 eV per atom in most previous calculations.

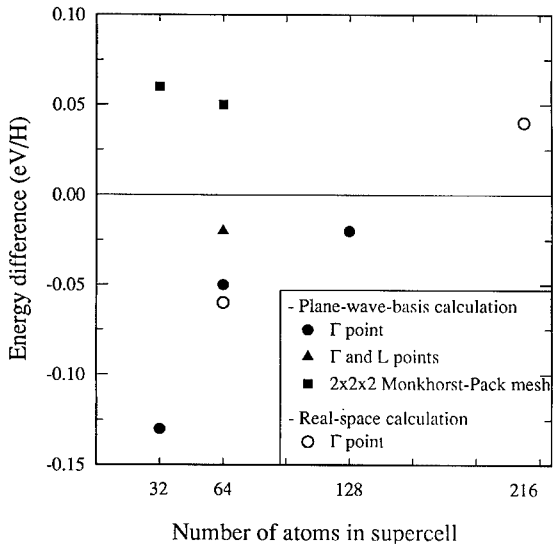

Fig. 1. The energy differences between H_2 and H_2^*, i.e., $E(H_2^*) - E(H_2)$, are drawn for various cell sizes and $\boldsymbol{k}$-point sets. Filled and open dots represent the results of plane-wave basis and real-space calculations, respectively.

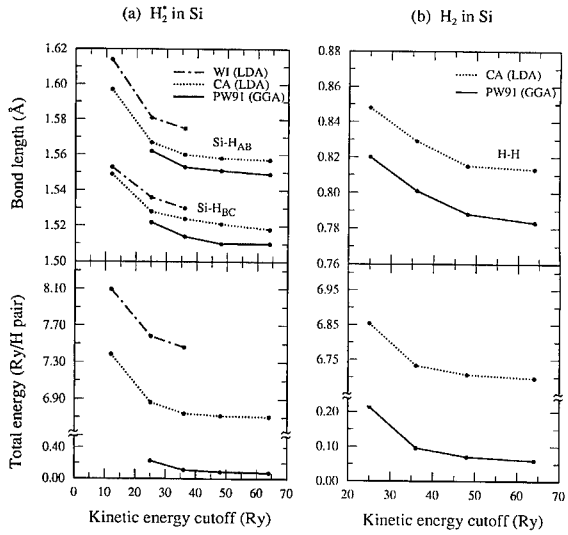

Fig. 2. The bond lengths and the total energies for (a) the H_2^* complex and (b) the H_2 molecule are plotted as a function of the kinetic energy cutoff. The LDA results using the Wigner (WI) and Ceperley–Alder (CA) expressions for the exchange-correlation potential are compared with the GGA results.

The vibrational frequency of a stretch mode strongly depends on the corresponding bond length, because a smaller bond length increases its vibrational frequency. Thus, it is important that the calculated bond lengths are fully converged. We find that the Si–H and H–H bond lengths of the H_2 and H_2^* complexes tend to decrease with increasing the kinetic energy cutoff, being well converged for the kinetic energy cutoff of 64 Ry, as shown in Fig. 2. In the LDA calculations, the Ceperley–Alder expression for the exchange-correlation potential gives shorter Si–H bond lengths in the H_2^* complex, compared with the Wigner interpolation formula. The Si–H and H–H bond lengths are further reduced in the GGA calculations, giving rise to higher vibrational frequencies for their stretch modes.

The H_2 molecule is found to be lowest in energy at a tetrahedral site with the [1 0 0] orientation. However, this molecular orientation is infrared inactive, in contrary to recent infrared measurements [3]. For the [1 1 0] and [1 1 1] orientations, the total energies increase by about 0.01 eV, and the position of the molecule is shifted slightly from the tetrahedral site, which is infrared active. If the

Table 1
The calculated relative energies (ΔE), bond lengths ($d_{H\text{-}H}$), and local vibrational frequencies (ω) for the H_2 molecules in the [1 0 0], [1 1 0], and [1 1 1] orientations by the LDA and GGA are listed and compared with other calculations and experiments

		LDA			GGA				
	Modes	[1 0 0]	[1 1 0]	[1 1 1]	[1 0 0]	[1 1 0]	[1 1 1]	Other calc.	Expt.
ΔE (eV/mol.)		0	0.008	0.012	0	0.008	0.011		
$d_{H\text{-}H}$ (Å)		0.813	0.810	0.808	0.783	0.780	0.779		
ω (cm^{-1})	Stretch	3260			3556	3603	3643	3363[a] 3396[d] 3708[e]	3618[b,c]
	Twist	605			651				
	Long. displ.					688	699		

[a]Ref. [9].
[b]Ref. [3].
[c]Ref. [4].
[d]Ref. [10].
[e]Ref. [11].

equilibrium position is shifted for the molecule in the [1 0 0] orientation, it may also give rise to the infrared activity, but, no shift is found. In GaAs, two stretch modes attributed to para- and ortho-H_2 molecules were observed by Raman spectroscopy [18], while only a single-stretch mode has been found so far for Si [3,4]. Since the ortho- and para-forms do not exist when the molecular rotation is frozen, Hourahine et al. suggested that the energy barrier of at least 0.17 eV to reorientation of the molecule is needed [11]. Our calculations show an extremely low energy barrier of about 0.01 eV, similar to other calculations for Si [9–11] and GaAs [19]. The infrared activity and the absence of para- and ortho-forms of the molecules in Si still need to be solved. One possible explanation is that unknown symmetry-breaking fields would exist, which shift the position of the molecule from the tetrahedral site and enhance the energy barrier to reorientation.

The vibrational frequencies for the H_2 molecules in the [1 0 0], [1 1 0], and [1 1 1] orientations are listed in Table 1. In the GGA calculations, we find the stretch modes in the range of 3556–3643 cm^{-1}, close to the experimental value of 3618 cm^{-1}. However, the LDA calculations underestimate the vibrations frequencies by about 300 cm^{-1}. Although the GGA frequencies for the stretch mode are in good agreement with experiments, these values would be lowered by considering the anharmonic effects [10,20]. For a H_2 molecule in gas phase, we estimate the lowering of the frequency by the anharmonic effect to be about 160 cm^{-1}, similar to the other calculated value of 190 cm^{-1} [10]. The lowering of the frequency may be remedied by including the accurate electron correlation effect beyond the LDA and GGA [20]. We find additional local modes that are infrared active. In a twist mode at 651 cm^{-1} for the [1 0 0] orientation, the center of mass of the molecule vibrates along either the [0 1 0] or [0 0 1] direction perpendicular to the [1 0 0] while the molecule rotates around the vibrational axis, while in longitudinal displacement modes at 688 and 699 cm^{-1} for the [1 1 0] and [1 1 1] orientations, respectively, the H atoms vibrate in-phase along the molecular direction. For the H_2^* complex, the GGA-calculated frequencies of the stretch mode are 1784 and 2071 cm^{-1} for the H atoms at the antibonding (AB) and bond-center (BC) sites, respectively, in good agreement with the measured values of 1838 and 2062 cm^{-1} [6]. The frequencies of the wagging mode are found to be 784 and 598 cm^{-1} for the Si–H_{AB} and Si–H_{BC} bonds, respectively. The experimental value for the wagging mode is only available for the Si–H_{AB} bond, which is 817 cm^{-1} [6].

4. Summary

In summary, we find that the H_2 molecule in Si is lower in energy by about 0.05 eV per H atom than the H_2^* complex. The stretch modes of the H_2 molecules lie in the frequency range of 3556–3643 cm^{-1}, close to the measured value of 3618 cm^{-1}. We predict an additional local mode at 650–700 cm^{-1} above the bulk phonon band for the H_2 molecule.

Acknowledgements

This work is supported by the MOST-FOTD and the CMS at KAIST.

References

[1] A. Mainwood, A.M. Stoneham, Physica B 116 (1983) 101.
[2] K. Murakami, N. Fukata, S. Sasaki, K. Ishioka, M. Kitajima, S. Fujimura, J. Kikuchi, H. Haneda, Phys. Rev. Lett. 77 (1996) 3161.
[3] R.E. Pritchard, M.J. Ashwin, J.H. Tucker, R.C. Newman, Phys. Rev. B 57 (1998) R15048.
[4] A.W.R. Leitch, V. Alex, J. Weber, Phys. Rev. Lett. 81 (1998) 421.
[5] K.J. Chang, D.J. Chadi, Phys. Rev. Lett. 62 (1989) 937.
[6] J.D. Holbech, B. Bech Nielsen, R. Jones, P. Sitch, S. Öberg, Phys. Rev. Lett. 71 (1993) 875.
[7] C.G. Van de Walle, Phys. Rev. B 49 (1994) 4579.
[8] D.J. Chadi, C.H. Park, Phys. Rev. B 52 (1995) 8877.
[9] Y. Okamoto, M. Saito, A. Oshiyama, Phys. Rev. B 56 (1997) R10016.
[10] C.G. Van de Walle, Phys. Rev. Lett. 80 (1998) 2177.
[11] B. Hourahine, R. Jones, S. Öberg, R.C. Newman, P.R. Briddon, E. Roduner, Phys. Rev. B 57 (1998) R12666.
[12] Y.-S. Kim, Y.-G. Jin, J.-W. Jeong, K.J. Chang, Semicond. Sci. Technol. (1999), unpublished.
[13] N. Troullier, J.L. Martins, Phys. Rev. B 43 (1991) 1993.
[14] L. Kleinman, D.M. Bylander, Phys. Rev. Lett. 48 (1982) 1425.
[15] D.M. Ceperley, B.J. Alder, Phys. Rev. Lett. 45 (1980) 566.
[16] J.P. Perdew, in: P. Zeische, M. Eschrig (Eds.), Electronic Structure of Solids '91, Akademie Verlag, Berlin, 1991.
[17] Y.-G. Jin, J.-W. Jeong, K.J. Chang, unpublished.
[18] J. Vetterhöffer, J. Wagner, J. Weber, Phys. Rev. Lett. 77 (1996) 5409.
[19] S.J. Breuer, R. Jones, P.R. Briddon, S. Öberg, Phys. Rev. B 53 (1996) 16289.
[20] Y. Okamoto, M. Saito, A. Oshiyama, Phys. Rev. B 58 (1998) 7701.

ELSEVIER

Physica B 273–274 (1999) 235–238

PHYSICA B

www.elsevier.com/locate/physb

Hydrogen interaction with defects in electron-irradiated silicon

O. Feklisova[a], N. Yarykin[a,*], Eu. Yakimov[a], J. Weber[b]

[a]*Institute of Microelectronics Technology RAS, 142432 Chernogolovka, Moscow region, Russia*
[b]*Max-Planck Institute FKF, D-70569 Stuttgart, Germany*

Abstract

Hydrogen-induced passivation and modification of radiation defect electrical activity in silicon are studied by deep-level transient spectroscopy. Hydrogen is incorporated into high-energy electron-irradiated crystals during chemical etching in acid solution at room temperature, followed by reverse-bias annealing of p-type samples at 380 K. It is observed that the concentrations of major radiation defects (divacancies, A- and K-centers) are reduced in the hydrogen-rich regions, while a number of novel hydrogen-related deep-level centers appear. The complexes with the energy level at $E_v + 0.28$ eV are formed due to hydrogenation of the *K*-centers.

Keywords: Silicon; Irradiation-induced defects; Hydrogen; Deep levels

1. Introduction

Hydrogen may be easily incorporated into crystalline silicon because of its presence in many chemicals used in semiconductor technology and, simultaneously, high enough diffusivity even at room temperature. In combination with the extremely high hydrogen chemical activity, this makes hydrogen one of the most important impurities in silicon. Investigations of last decades have established that hydrogen passivates the electrical activity of many defects in silicon [1,2]. However, while the mechanism of shallow acceptor and donor passivation is reasonably well understood, the hydrogen interaction with deep-level centers is still under study. Recently, the electrically active hydrogen-related centers have been observed in silicon with radiation defects and transition metal substitutional impurities [3–6]. These centers have been understood as intermediate complexes containing less hydrogen atoms than necessary for total defect passivation. In the present paper, we continue the work directed to ascertainment of the relationship between the non-hydrogenated radiation defects and the hydrogen-related complexes observed in Ref. [5].

* Corresponding author. Fax: + 7-95-962-8047.
E-mail address: nay@ipmt-hpm.ac.ru (N. Yarykin)

2. Results and discussion

2.1. Sample preparation

Radiation defects were introduced into n- and p-type silicon samples by bombardment with high-energy electrons. Hydrogen was incorporated into the irradiated samples during wet chemical etching in acid solution at room temperature. The energy spectrum of electrically active centers and their depth distributions were investigated by the deep-level transient spectroscopy (DLTS) on Schottky diodes prepared after chemical etching. In more detail, the sample preparation has been described in Ref. [5].

2.2. Overview

The effect of hydrogenation on the deep-level energy spectrum is shown in Fig. 1. In n-type silicon, the novel hydrogen-related centers appear in the near-surface region immediately after the chemical etching. Therefore, the DLTS curve taken from the layer located far enough from the treated surface is used as a reference. In p-type samples, only the radiation defect signatures can be found in the spectrum just after the etching, even when the reverse bias is totally removed from the diode during the DLTS filling pulse. We believe that the effective

0921-4526/99/$ - see front matter
PII: S0921-4526(99)00461-5

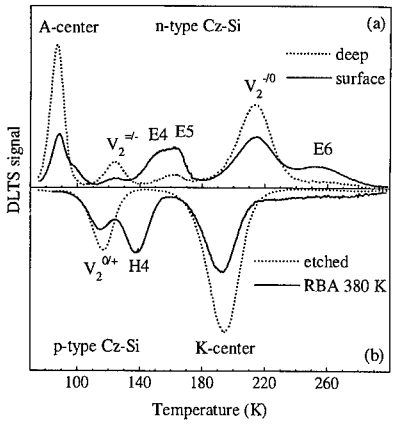

Fig. 1. DLTS curves taken from (a) n-type and (b) p-type irradiated silicon; the solid curves show the deep-level spectra in hydrogen-rich regions. The (reference) dotted curves are measured from the greater depth in the n-type crystal and before the reverse-bias annealing in the p-type sample.

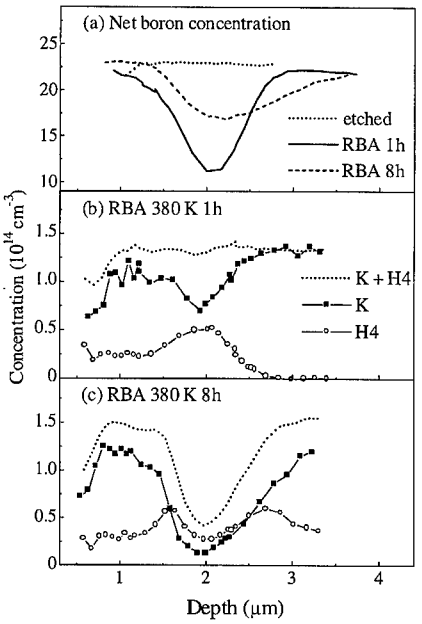

Fig. 2. Depth profiles (a) of the net acceptor concentration at different annealing stages and (b, c) deep-level centers in p-type Cz–Si taken after reverse-bias annealing at 380 K during (b) 1 h and (c) 8 h.

hydrogen–boron interaction [7] limits hydrogen penetration to a narrow, close to the surface layer. Therefore, the procedure of reverse-bias annealing (RBA) [7] at 380 K has been used to inject hydrogen deeper in the crystal. After the annealing, amplitudes of the radiation defect peaks are reduced and a novel peak appears. Note that the spectrum presented in Fig. 1(b) is much simpler as compared to that in Ref. [5]. Most probably, an unintentional sample contamination or heat treatment took place in the latter case. Summarizing Fig. 1, we can conclude that the spectrum of deep-level radiation point defects in the samples used in this work consists mainly of the divacancies, *A*-centers (vacancy-oxygen complex), and *K*-centers (carbon–oxygen pair). Incorporation of hydrogen at temperatures below 400 K results in the formation of the *E*4, *E*6, and *H*4 centers (the notations are chosen to be consistent with the previous paper [5]).

2.3. *H*4-center

The *H*4-center has been reported already as a hydrogen-related complex [8]; however, its nature has not been established. In this section, the results are presented, which allow us to state that the *H*4-center is a product of the *K*-center hydrogenation. The development of the depth profiles of the active boron concentration and the deep-level centers is presented in Fig. 2 for different annealing times. The boron passivation kinetics observed in our experiments agrees well with those reported in the literature [7]. This makes us confident that the processes of the defect transformations observed around the 2-μm depth are caused by hydrogen. Another important result presented in Fig. 2 is the constant sum of the *K*- and *H*4-center concentrations observed at earlier RBA stages, see curves for 1 h annealing. This constancy remains valid for a wide set of samples (both Cz and FZ) and irradiation doses, indicating that the *H*4-centers are formed at the expense of the *K*-centers. During further annealing, the constancy is broken, and the *H*4-center depth profile exhibits a local minimum in the region with the highest hydrogen concentration. This phenomenon is consistent with the model that another hydrogen atom is added to the *H*4-complex. Note that no defects with concentrations comparable to those of the *K*- and *H*4-centers, and with the energy level located between ~ 0.1 eV above the valence band and the midgap, appear due to this transformation.

2.4. *E*6-center

The *E*6-center has been already reported as a hydrogen-related defect [8]; however, the nature of the defect is still unknown. Our measurements characterize the *E*6-center by the energy level of 0.42 eV and the electron capture cross section of $\sim 1 \times 10^{-17}$ cm^{-2}. Taking into account the strong overlap of *E*6 with other peaks, the data are in a reasonably good agreement with the previously reported values. Investigations of a wide set of the *n*-type crystals grown with different techniques and irradiated with different electron fluences show that the *E*6-defect concentration is roughly proportional to the irradiation dose, but strongly varies from one crystal to

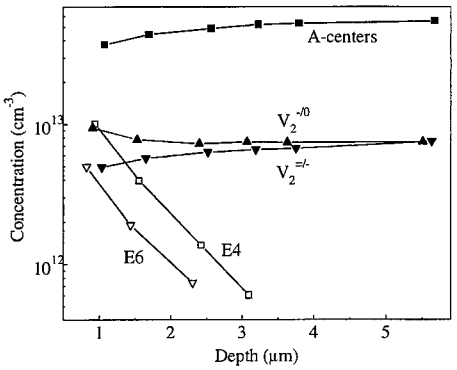

Fig. 3. Depth profiles of the deep-level centers detected in n-type electron-irradiated Cz–Si after chemical etching at room temperature.

another. In addition, *E*6 exceeds in some samples the divacancy concentration in the crystal bulk. All this indicates that the *E*6-center originates most probably from the impurity-related radiation defect like the *A*- or *K*-center. Along with other defects revealed in *n*-type crystals, the *E*6 depth profile is shown in Fig. 3. The characteristic length of its exponential decay from the chemically etched surface is practically the same as for the *E*4-center, indicating that these two defects contain the same number of hydrogen atoms. The *E*4-center was assigned to a complex of the *A*-center with two hydrogen atoms [5,8]. However, recent IR studies and theoretical calculations (see this volume) suggest that the electrically active product of the *A*-center hydrogenation should contain only one hydrogen atom. Extensive studies are underway to clarify this discrepancy. Different concentrations of the *E*4- and *E*6-centers and their different thermal stability ($\geqslant 350$°C and ~ 250°C, respectively) exclude the possibility that these are two levels of the same defect.

2.5. *A*-center passivation

It has been suggested [5] that hydrogenation of the *A*-centers produces the *E*4-complexes containing two hydrogen atoms. This conclusion was primarily based on the constant sum of the two defect concentrations observed after 150°C to 250°C annealing. The observation put forward the question about the existence of the *A*-center complex with one hydrogen atom (denoted further as A-H_1). It was assumed in the previous work [5] that A-H_1 avoids the detection since its energy level is almost coincident with the *A*-center level. This assumption is supported by the recent detection of another defect, which contributes to the *A*-center peak in hydrogenated samples (Peaker, this volume). On another hand, closer inspection of the defect depth profiles in the samples, which have not been annealed after chemical etching, shows that the deficiency of the *A*-center concentration near the surface is not totally compensated by the *E*4-centers. If this is due to missing A-H_1, the constancy of the *A*- and *E*4-center sum concentration after annealing indicates probably a relatively low thermal stability of the A-H_1 complex. Note that the problem with the A-H_1 complex totally disappears if the *E*4-center structure includes only one hydrogen atom.

2.6. Divacancy passivation

Incorporation of hydrogen leads to passivation of the divacancy levels both in n- and p-type silicon, see Figs. 2 and 3. At the moment, no deep-level centers are detected in a comparably high concentration which could be considered as partially hydrogenated divacancy. Note the apparent difference in the concentration of the first and second acceptor levels of divacancy, see Fig. 3. This difference is always observed near the chemically etched surface and is most probably determined by another defect, whose energy level is almost coincident with the divacancy acceptor level. Analysis of the depth profiles shows that only one hydrogen atom is needed for this unknown defect formation; however, the origin of the center contributed to the $V_2^{0/-}$ peak is still unknown.

3. Conclusion

Using the DLTS technique, we have found that the $E4(E_c - 0.32\,\text{eV})$, $E6(E_c - 0.42\,\text{eV})$, and $H4(E_v + 0.28\,\text{eV})$ are the most prominent deep-level centers that have resulted from hydrogen incorporation into the electron-irradiated silicon. It is shown that the *H*4-defects are formed at the expense of the *K*-centers. Both the *E*4 and *E*6-complexes are formed from the original radiation defects (A-center for the E4 complex) through the interaction with same number of hydrogen atoms.

Acknowledgements

We thank Dr. A. Mokrushin for help in the sample irradiation and W. Heinz and W. Krause for the technical assistance. Fruitful discussions with R. Jones, K. Bonde Nielsen, and A. Peaker are greatly appreciated. The work is supported by the Deutsche Forschungsgemeinschaft (Contract No. 436 RUS 113/166).

References

[1] S.J. Pearton et al., Appl. Phys. A 43 (1987) 153.
[2] S.J. Pearton et al., Hydrogen in Crystalline Semiconductors, Springer, Berlin, 1992.

[3] A.L. Parakhonskii et al., Semiconductors 30 (1996) 362.
[4] B. Bech Nielsen et al., Mater. Sci. Eng. B 36 (1996) 259.
[5] O.V. Feklisova, N. Yarykin, Semicond. Sci. Technol. 12 (1997) 742.
[6] N. Yarykin et al., Mater. Sci. Forum 259–263 (1997) 301.
[7] T. Zundel, J. Weber, Phys. Rev. B 39 (1989) 13549.
[8] K. Irmscher et al., J. Phys. C 17 (1984) 6317.

ELSEVIER

Physica B 273–274 (1999) 239–242

PHYSICA B

www.elsevier.com/locate/physb

Atomic and electronic structure of hydrogen-passivated double selenium donors in silicon

P.T. Huy[a,b,*], C.A.J. Ammerlaan[a], T. Gregorkiewicz[a]

[a]*Van der Waals-Zeeman Institute, University of Amsterdam, Valckenierstraat 65, NL-1018 XE Amsterdam, The Netherlands*
[b]*International Training Institute for Materials Science, ITIMS Building, Dai Hoc Bach Khoa Hanoi, 1 Dai Co Viet Road, Hanoi, Viet Nam*

Abstract

Selenium–hydrogen-related defects in silicon have been investigated by magnetic resonance. Two new electron paramagnetic resonance (EPR) spectra Si-NL60 and Si-NL61 of selenium–hydrogen complexes were observed. By application of the electron nuclear double resonance (ENDOR) and field scanned ENDOR (FSE) techniques the symmetry and spin-Hamiltonian parameters of the centers were determined. Based on the obtained information the atomic and electronic structures of the centers are discussed with two different models: one-chalcogen – one-hydrogen and one-chalcogen – two-hydrogen complexes. © 1999 Elsevier Science B.V. All rights reserved.

Keywords: Silicon; Hydrogen passivation; Chalcogen; Magnetic resonance

1. Introduction

Over the last ten years, the passivation by hydrogen of shallow single donors and acceptors in silicon has been extensively investigated, both by experimental and theoretical methods; as a result these passivated dopants have become well-understood defects. In some contrast, the understanding of the more complex and varied processes of passivation of deep electronic centers is still not on a satisfactory level. The structure and corresponding electrical activity of hydrogen complexes with deep centers have proven to be intriguing; results are controversial in several cases. The interactions of hydrogen with the chalcogen double donors are good examples of this situation. Experiments using deep level transient spectroscopy (DLTS) [1], infrared absorption [2] and magnetic resonance [3] showed that hydrogen could passivate the sulfur double donor in silicon. However, there still is dispute about the number of hydrogen atoms per sulfur atom participating in the passivation process, and about the question whether a S–H complex with a single hydrogen atom will behave as a, possibly shallow, single donor. In our experiments the hydrogen passivation of the double donor selenium was studied; new results were obtained.

In selenium-doped hydrogenated silicon two new electron paramagnetic resonance (EPR) spectra, labeled Si-NL60 and Si-NL61, were observed. The spectra, both revealing trigonal symmetry, have been investigated in detail by electron-nuclear double resonance (ENDOR) and field-scanned ENDOR (FSE). By the use of both natural and isotopically enriched selenium (isotope ^{77}Se, nuclear spin $I = \frac{1}{2}$, natural abundance 7.6%, enrichment 99.1%) the involvement of one selenium atom per center was conclusively established. From the hyperfine structure due to hydrogen or deuterium, using heavy water with 99.95% enrichment, the presence of hydrogen in the centers was concluded. The Si-NL60 spectrum displays the nuclear interaction due to one hydrogen atom. From the hyperfine and quadrupole interactions it is concluded that the corresponding center is very similar to the sulfur–hydrogen pairs (EPR spectra Si-NL54 and Si-NL55). The paramagnetic state most probably corresponds to the neutral charge state of a Si : Se, H single donor. The other spectrum, Si-NL61, reveals hyperfine interaction with two inequivalent hydrogen atoms. For this Si : Se,

* Corresponding author. Van der Waals-Zerman Institute, University of Amsterdam, Valckenierstraat 65, NL-1018 XE Amsterdam, The Netherlands. Tel.: + 31-20-525-5793; fax: + 31-20-525-5778.

E-mail address: pthuy@wins.uva.nl (P.T. Huy)

0921-4526/99/$ - see front matter
PII: S0921-4526(99)00462-7

H_2 center no corresponding sulfur — two-hydrogen complex was reported. Models for atomic and electronic structure will be discussed on the basis of the current findings.

2. Sample preparation and *K*-band spectrometer

The samples were prepared by thermal diffusion of natural selenium (7.6% of the magnetic isotope ^{77}Se) or of selenium enriched to 99.1% of the ^{77}Se into p-type float-zone silicon boron-doped with the room-temperature resistivity between 75 and 125 Ω cm. The samples shaped as rectangular bars with typical dimensions $2 \times 2 \times 15$ mm^3 were enclosed in quartz ampoules together with 0.5–1 mg of selenium powder mixed with an excess amount of silicon powder to create a SiSe atmosphere. They were heated to 1350°C for a period of 120–360 h. After the diffusion the rough surface layers of the samples were mechanically removed and the samples were etched in CP6 solution. Hydrogen or deuterium was introduced in a high-temperature treatment, at 1200–1350°C, in water vapor for 30–45 min, followed by a rapid quench to room temperature.

Magnetic resonance experiments were carried out using a superheterodyne spectrometer operating in the microwave *K*-band with the frequency near 23 GHz. For a more complete description of the equipment and the experimental techniques, see Ref. [4].

3. Resonance spectra of the defects

The two EPR spectra Si-NL60 and Si-NL61 of Se–H defects observed in the hydrogenated selenium-doped samples are given in Fig. 1 for magnetic field B parallel to a ⟨1 0 0⟩ crystal direction. The spectra of both centers are well characterized with pairs of satellites, symmetrically displaced with respect to the central component, which are due to the hyperfine interaction with isotope ^{77}Se, nuclear spin $I = \frac{1}{2}$. The total intensity of these hyperfine components fits precisely with the isotopic composition of natural selenium identifying the presence of one selenium atom in the structure of the defects. The central resonance is a superposition of two spectra, which can only be separated by the FSE technique. The superimposed EPR and the FSE spectra are given in Fig. 1. In order to confirm the conclusion on selenium participation, samples diffused with selenium enriched to 99.1% of ^{77}Se were prepared. The spectra of Si-NL60 and Si-NL61 are well reproduced in these samples with the central components almost absent and all intensity in the hyperfine components. The trigonal, ⟨1 1 1⟩-axial symmetry, of both central components (by FSE) and hyperfine components (by EPR) is observed for the Si-NL60 and Si-NL61 centers. The angular dependence patterns of the

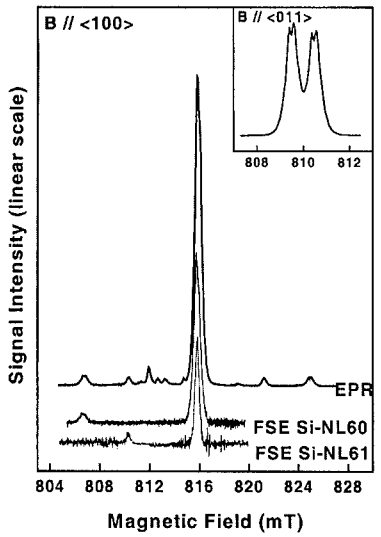

Fig. 1. EPR over full range and FSE spectra of Si-NL60 and Si-NL61 for $\boldsymbol{B}//\langle 1\,0\,0\rangle$, microwave frequency $f = 22.7536$ GHz, $T = 4.2$ K. The inset shows low-field hyperfine lines of Si-NL60 for $\boldsymbol{B}//\langle 0\,1\,1\rangle$ and $f = 22.8768$ GHz.

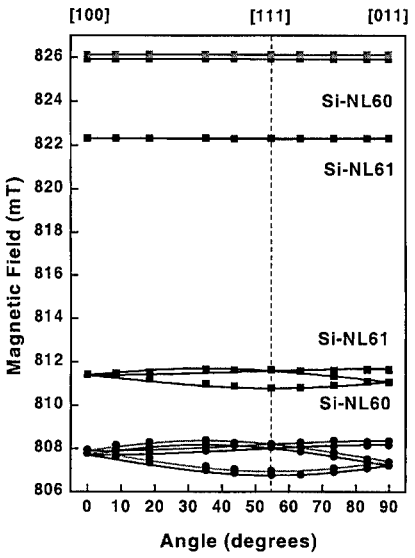

Fig. 2. EPR angular dependence of the ^{77}Se patterns, $T = 1.5$ K, $f = 22.8152$ GHz. The double loops observed for Si-NL60 are due to hydrogen hyperfine interaction.

resonance spectra when rotating the field from [1 0 0] to [0 1 1] in the (0 $\bar{1}$ 1) plane are given in Fig. 2.

Since the samples were intentionally doped with hydrogen at high temperature, the participation of hydrogen in the centers is anticipated. In EPR, the hyperfine interaction with hydrogen with nuclear spin $I = \frac{1}{2}$ is visible only for the Si-NL60 center. This splitting is about 0.24 mT creating the two loops in the angular

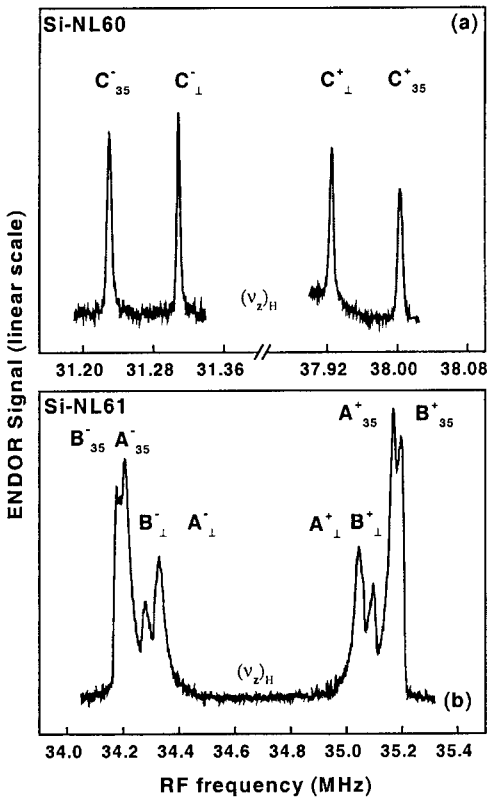

Fig. 3. ENDOR hydrogen spectra for $\boldsymbol{B}//\langle 0\,1\,1\rangle$ of (3a) Si-NL60, $B = 813.168$ mT, $f = 22.7067$ GHz, and (3b) Si-NL61, $B = 814.812$ mT, $f = 22.7553$ GHz. $T = 8.2$ K.

dependence pattern of the Si-NL60 center, see Fig. 2. Such a splitting is not observed in deuterated samples. A closer view on the hydrogen hyperfine splitting of Si-NL60 for $\boldsymbol{B}//\langle 0\,1\,1\rangle$ is given in the inset in Fig. 1.

To further verify the hydrogen involvement, ENDOR experiments have been performed. Typical hydrogen-ENDOR spectra are given in Fig. 3 for the magnetic field $\boldsymbol{B}//\langle 0\,1\,1\rangle$ mT. For the proton with $(g_n)_H = 5.58556$ the nuclear resonance frequency $(\nu_z)_H = (g_n)_H \mu_n B/h$ is near 34.7 MHz. The observed ENDOR spectra have two different groups of lines marked with A, B and C that correspond to ENDOR of three different hydrogen atoms. The first group (C lines) is, as seen in Fig. 3a, located about 3.3 MHz from the proton Zeeman frequency $(\nu_z)_H$. The second group (A and B lines), as given in Fig. 3b, is very close to $(\nu_z)_H$ with the hyperfine interaction being about 8 times smaller. Both groups of spectra are symmetric with respect to $(\nu_z)_H$ identifying the observed hyperfine interaction as being due to hydrogen. Detailed analysis of ENDOR and FSE spectra is given in Ref. [5]. The far group of spectra corresponds to a hyperfine interaction of about 6.7 MHz. In the EPR such a hyperfine interaction gives a splitting of 0.24 mT, which is indeed observed for the EPR spectrum Si-NL60. The other group of lines corresponds to two hydrogen atoms belonging to the Si-NL61 center; the hyperfine interaction constant of approximately 0.8 MHz leads to an EPR splitting of 0.03 mT which is too small to be observed in EPR. By measuring the hydrogen ENDOR and FSE angular patterns the trigonal symmetry of the centers is confirmed. The spin-Hamiltonian parameters are given in Table 1 of Ref. [5]

4. Atomic structure of the defects

From the experiment the participation of a single selenium and a single hydrogen atom in the microscopic structure of the Si-NL60, and a single selenium and two hydrogen atoms in the microscopic structure of Si-NL61 is established. As the isolated chalcogen (sulfur, selenium) is known to occupy a substitutional position in silicon (either in their single form or in S_2, Se_2 pairs), the substitutional position is also assumed to be true for the selenium–hydrogen complexes observed in this study. Since all observed tensors, which reflect interaction of the defect electron with nuclei involved, have trigonal symmetry, the $\langle 1\,1\,1\rangle$ direction must be assumed as the axis of the defect structure. Hyperfine interactions with the hydrogen or deuterium atoms, reflecting the local symmetry around these impurities, also have the perfect trigonal symmetry. It implies that the hydrogen/deuterium impurities are on the $\langle 1\,1\,1\rangle$ axis of the center. As the centers cannot have inversion symmetry, only one position is available in shells of the trigonal type. The defects as a whole therefore have an axial structure with the hydrogen impurities along a $\langle 1\,1\,1\rangle$-oriented line passing through the chalcogen atom. Such a linear model is shown in Fig. 4. Possible positions for hydrogen are a bond-centered site and anti-bonding sites with respect to chalcogen or silicon atoms. More detailed analysis of resonance data or advanced theoretical modeling are required to unambiguously conclude on the actual positions of the hydrogen atoms.

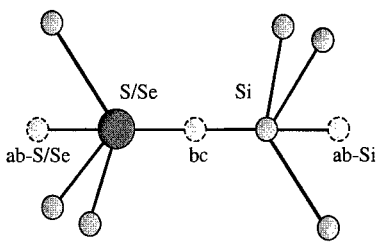

Fig. 4. Atomic model for chalcogen–hydrogen centers. Possible positions for the hydrogen atom are indicated by bc for a bond-centered site, ab-S/Se for anti-bonding site next to the chalcogen atom and ab-Si for the silicon anti-bonding site.

Table 1
Parameters related to the analysis of hyperfine interactions of the Si : Se, H spectra Si-NL60 and Si-NL61 and of the Si : S, H spectra Si-NL54 and Si-NL55

Parameter	Si-NL60	Si-NL61		Si-NL54	Si-NL55	Unit
Nucleus	^{77}Se	^{77}Se		^{33}S	^{33}S	
a	508.7	305.0		139.5	119.9	MHz
b	13.4	8.2		1.8	2.0	MHz
η^2	5.67	3.43		5.89	5.54	%
α^2	52	51		70	64	%
β^2	48	49		30	36	%
Nucleus	^{1}H	^{1}H	^{1}H	^{1}H	^{1}H	
a	6.663	0.897	0.830	4.718	5.600	MHz
b	0.060	0.081	0.095	0.782	0.100	MHz
η^2	0.47	0.063	0.058	0.33	0.39	%

5. Electronic structure of the defects

Based on LCAO analysis of observed values for the isotropic part a and anisotropic part b of the hyperfine interactions, the total localization η^2 of the electron, the s-character α^2 and p-character β^2 for selenium and hydrogen are calculated. As given in Table 1, the small localization of the paramagnetic electron ($\eta_{Se} \approx 5.7\%$ for Si-NL60, $\eta_{Se} \approx 3.4\%$ for Si-NL61, $\eta_H \approx 0.5\%$ for Si-NL60, $\eta_H \approx 0.06\%$ for Si-NL61) places the Si-NL60 and Si-NL61 in the group of the shallow single donors such as phosphorus, arsenic and antimony. For Si-NL60, the combination of single donor character and participation of a single hydrogen atom in the microscopic structure is very much similar to the Si-NL54 and Si-NL55 centers, which were identified with sulfur–hydrogen complexes [3]. Consequently, we identify this center as a form of a substitutional selenium double donor in the neutral charge state, passivated with a single hydrogen atom, i.e., (Se–H) pair. For the Si-NL61 center, evidence of the involvement of two hydrogen atoms has clearly been obtained leading to a conclusion that the center is observed most probably in an ionized state. With the trigonal arrangement of the impurities (hydrogen, selenium) this implies that no full passivation has taken place and the center is still electrically active regardless of complexing with two hydrogen atoms.

References

[1] G. Pensl, G. Roos, C. Holm, E. Sirtl, N.M. Johnson, Appl. Phys. Lett. 51 (1987) 451.
[2] R.E. Peale, K. Muro, A.J. Sievers, Mater. Sci. Forum 151 (1990) 65.
[3] I.S. Zevenbergen, T. Gregorkiewicz, C.A.J. Ammerlaan, Phys. Rev. B 51 (1995) 16746.
[4] M. Sprenger, Doctor Thesis, University of Amsterdam, 1986.
[5] P.T. Huy, C.A.J. Ammerlaan, T. Gregorkiewicz, D.T. Don, Phys. Rev. B, submitted for publication.

ELSEVIER

Physica B 273–274 (1999) 243–246

PHYSICA B

www.elsevier.com/locate/physb

Hydrogen reactions with electron irradiation damage in silicon

A.R. Peaker[a,b,*], J.H. Evans-Freeman[a], P.Y.Y. Kan[a], L. Rubaldo[b], I.D. Hawkins[a], K.D. Vernon-Parry[a], L. Dobaczewski[c]

[a]*Centre for Electronic Materials, UMIST, P.O. Box 88, Manchester, M60 1QD, UK*
[b]*CNRS/MPI, High Magnetic Field Lab, 25 ave des Martyrs, BP 166, Grenoble, France*
[c]*Institute of Physics, Polish Academy of Science, Al Lotnikow 32/46, Warsaw, Poland*

Abstract

We have irradiated n-type CZ silicon with 2 MeV electrons at room temperature, and atomic hydrogen has been introduced either before or after irradiation from the surface by wet etching. Quantitative comparisons of vacancy-related defects before and after the hydrogen reactions have been made using high-resolution (Laplace) DLTS. A deep level appears after hydrogenation at E_C — 0.311 eV, with two components detected by Laplace DLTS. This has previously been reported to be due to either VOH or VOH_2, and is accompanied by a decrease in the intensity of the A centre (VO). The Laplace DLTS shows that the A centre emission rate is modified by the hydrogen, and a slower emission rate from the A centre is observed in the presence of hydrogen. Depth profiling shows that this modification occurs in the expected spatial location of the introduced hydrogen.

Keywords: Silicon; Hydrogen; Vacancy; Laplace DLTS

1. Introduction

When silicon is irradiated with particles of sufficiently high energy (e.g. electrons, protons, ions and gamma rays), interstitials and vacancies are formed (Frenkel pairs) which then recombine. However, a fraction of the defects escape, leading to the formation of divacancies, oxygen–vacancy complexes (the A centre) and dopant–vacancy defects (the E centre in n-type material) [1]. A detailed understanding of the residual defects is essential for tracing the reaction kinetics in particle detectors and more generally in ion-implanted material.

It has recently become clear that significant concentrations of hydrogen can be introduced into silicon as a result of cleaning and etching processes, and that hydrogen has a role to play in many aspects of device and material technology. The presence of hydrogen is a key factor on MOS processing, in relation to hot electron degradation effects [2]. Hydrogen also forms complexes with transition metals hitherto used for modifying carrier lifetimes in power devices [3–5]. Hydrogen is well known for its ability to passivate shallow levels in the silicon band gap, and can also passivate some deep levels. It may form complexes which have different electronic properties to those of the original defect/species, but these differences could potentially be small, and beyond the reach of conventional Deep Level Transient Spectroscopy (DLTS) measurements. The technique of Laplace DLTS (LDLTS) [6] has high enough resolution that these small shifts in activation energy and emission rates can be detected, and the technique has recently been successfully applied to the study of Au–H complexes in silicon [5].

Passivation of irradiation defects by atomic hydrogen was reported many years ago [7,8], but the mechanism of the passivation is not clear. Vacancy–hydrogen defects are also known to exist, with, for example, the simple VH^0 defect expected to have a similar structure to that of VP^0, the E centre [9]. This paper reports a high-resolution DLTS study of electron irradiation induced defects in silicon, and the electrical effects of introducing

* Correspondence address. Centre for Electronic Materials, University of Manchester Institute of Science and Technology, P.O. Box 88, Manchester, M60 1QD, UK. Tel.: + 44-161-200-4704; fax: + 44-161-200-4770.

E-mail address: peaker@umist.ac.uk (A.R. Peaker)

0921-4526/99/$ - see front matter
PII: S0921-4526(99)00463-9

hydrogen into the samples, either before or after electron irradiation. We have applied Laplace DLTS to the study of the A centre in electron-irradiated silicon, before and after hydrogenation, and also to the study of a new centre at 0.311 eV which we ascribe to a vacancy–oxygen–hydrogen complex, VOH.

2. Experimental methods

Eight samples were irradiated with a dose of 10^{15} cm^{-2} electrons at 2 MeV. Half of the samples were irradiated through semi-transparent gold Schottky diodes, where the thickness of the gold was 20 nm. The other half had semi-transparent diodes evaporated after the electron irradiation. Chemical processing, to introduce hydrogen either by an HF dip or a CP4 etch ($HF : HNO_3 : CH_3COOH$, 3 : 5 : 3 for either 6 or 20 s), was carried out on some samples either before or after the electron irradiation. The introduction of hydrogen by etching avoids the formation of further defects, such as would occur in proton implantation or hydrogen plasma treatment. Table 1 lists the samples and the processing they have undergone.

Laplace DLTS is an isothermal technique, carried out in a high-stability cryostat. The temperature is maintained at a constant value, and several thousand capacitance transients are averaged. This should ensure that the signal-to-noise ratio is of the order of 1000, which is necessary to separate transients with closely spaced emission rates. The transient is then analysed by one of the three mathematical routines available, to produce a plot of peak intensity as a function of emission rate. If the transient is truly exponential, only one peak is visible in the LDLTS spectrum. The area under each sharp peak is proportional to the trap concentration.

3. Results and discussion

Fig. 1 shows the conventional DLTS spectra of an electron-irradiated CZ silicon sample. The defect present in highest concentration is the A centre (VO). The dotted line shows the DLTS spectrum on the same scale after hydrogen has been introduced by CP4 etching. It is very difficult to quantify the concentration of hydrogen introduced by this technique, but we can ascribe some relative measure by looking at the compensation of the shallow phosphorous donors. In the bulk of the material, the carrier concentration is 2×10^{15} cm^{-3}. At 0.9 μm this has been reduced to 0.4×10^{15} so that 6×10^{14} hydrogen atoms cm^{-3} are complexed with the phosphorous. After hydrogenation, the A centre peak is reduced to a quarter of its original concentration, and an additional peak at 180 K also appears. No other significant features are generated in the majority carrier DLTS spectrum. It

Table 1
Details of the electron irradiations and the hydrogen introduction method for the samples used in the study (all n-type (1 0 0) CZ silicon, resistivity 2–4 Ω cm). All samples were irradiated with 1×10^{15} cm^{-2} electrons at 2 MeV

Sample number	Hydrogen introduction method	Irradiated after H_2 introduction and diodes fabricated?
1	10% HF dip	Yes
2	CP4 6 s	Yes
3	None	Yes
4	None	Yes
5	CP4 20 s	No
6	CP4 20 s	No
7	None	No
8	None	No

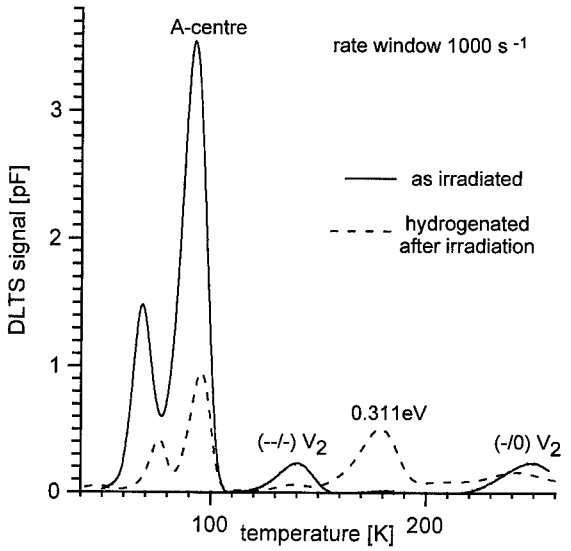

Fig. 1. DLTS plot of electron-irradiated Si before and after the introduction of hydrogen by chemical etching with CP4 solution.

seems unlikely that hydrogenation of the vacancy–oxygen centre would drive it into the lower half of the band gap and so it seems probable that the majority of the VO centre has been passivated and some complex of hydrogen and the VO centre is outside of the band gap. The state at around 180 K has been observed by many workers previously. Svensson et al. [10] observed it in proton-irradiated silicon and ascribed it to a vacancy–oxygen state complexed with hydrogen. More recently, Feklisova and Yarykin have produced the centre in the same way that we have, by wet etching, and ascribed it to VOH_2 [11], because the concentration as a function of depth exhibited a superlinear dependence

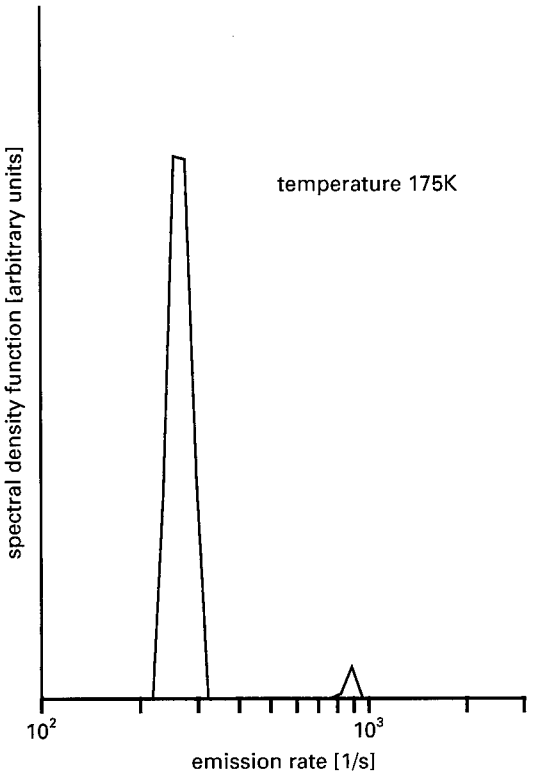

Fig. 2. LDLTS plot of 0.311 eV trap, showing two clear components exist in the capacitance transient, measured at 175 K.

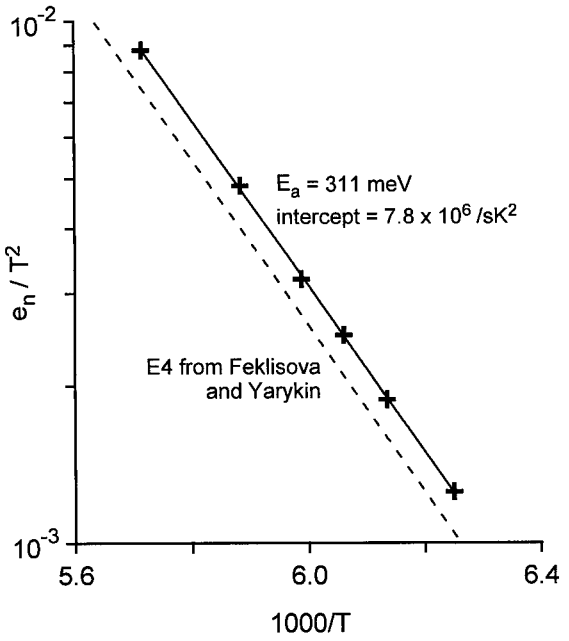

Fig. 3. The Arrhenius plot taken using Laplace DLTS of the peak in the 0.311 eV deep state with the lower emission rate.

on the hydrogen concentration. This assignment is somewhat controversial as Tokuda [12] ascribes the defect to VOH and, in addition, ab initio calculations indicate that VOH_2 should be inert, i.e., outside the band gap [13].

Fig. 2 shows the Laplace DLTS spectrum of this state taken at 175 K. The concentration in the presentation of Laplace spectra is proportional to the area under the curve, so the peak with the higher emission rate in Fig. 2 is of a larger concentration than is at first apparent because of the logarithmic scale. As a consequence, it appears that this centre contains more than one component. Fig. 3 shows the Arrhenius plot taken using Laplace DLTS of the peak with the lower emission rate. The Arrhenius line derived from the data of Feklisova and Yarykin [11] is drawn for comparison as a dotted line. Within the experimental error of the technique, these two are indistinguishable. From our experiments it is impossible to speculate on the nature of this complex. It is certainly associated with hydrogenation but we have also observed it, or at least a state with a very similar emission rate, in hydrogenated silicon that has not been irradiated [14]. In that work, the concentration of the state was increased if gold was present in the sample, but provided the hydrogen concentration was high enough, it could be seen in as-received CZ silicon.

If we now look in more detail at the peak associated with the vacancy–oxygen and the hydrogenated vacancy–oxygen defects using Laplace DLTS, some significant differences are evident. In Fig. 4, we show (on the left) the Laplace DLTS spectra of the irradiated sample 7 prior to the addition of hydrogen. A range of depths has been sampled, using voltages from 0.5 to 5 V, i.e., 0.9–2 μm. After hydrogenation of sample 7 (Fig. 4, centre), it is evident that two distinct peaks are present in the same region. One of these corresponds in emission rate exactly to that observed in sample 3 prior to hydrogenation while the other is a factor of two lower in emission rate. If we reduce the reverse bias to embrace only the region in which there is significant hydrogen concentration, i.e., 0.9–1.6 μm (as determined from the compensation of the phosphorus donors from the C–V plot), only the slower emission rate peak is present (Fig. 4, right). We interpret this as the complete conversion of the vacancy–oxygen centre into a vacancy–oxygen–hydrogen complex within the measured region. If we change the measurement conditions so that the reverse bias is changed over the entire accessible range, we see different ratios of the two peaks. These ratios change in a very systematic way and the emission rates are always exactly coincident. This suggests that neither the vacancy–oxygen centre nor the hydrogen complex are displaying a measurable Poole–Frenkel effect within our experimental conditions. Experiments on control samples without electron irradiation do not produce a defect with comparable

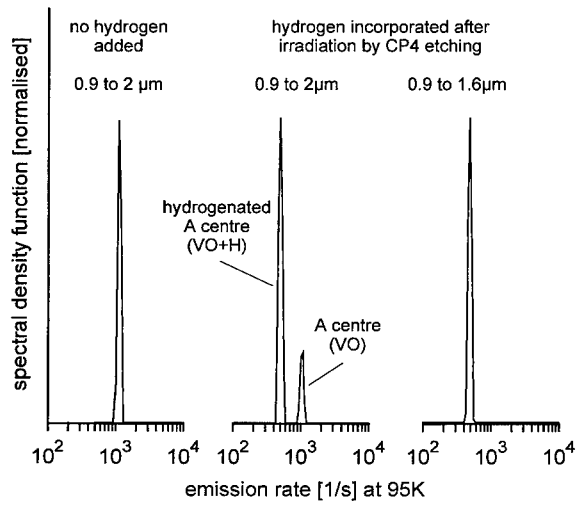

Fig. 4. The Laplace DLTS spectra of the irradiated sample 7 before (left-hand trace) and after the addition of hydrogen (right-hand trace), sampled from 0.5 to 5 V, i.e., 0.9–2 μm.

emission rates to the A centre, so supporting our assignment of this Laplace peak to the hydrogenated A centre.

4. Conclusions

Hydrogen passivates the A centre in electron-irradiated Si, and produces a trap at 0.311 eV, which has two emission rates detected by Laplace DLTS. The appearance of the 0.311 eV level is accompanied by a change in the properties of the A centre, resulting in a deep state with a lower emission rate detectable by high-resolution Laplace DLTS. Depth profiling studies show that this modification occurs in the spatial location predicted for the presence of the hydrogen from C–V measurements. The 0.311 eV centre is ascribed to the defect VOH, but the concentration of this defect does not fully account for the decrease in the number of A centres, modified or otherwise.

Acknowledgements

This work was funded by the United Kingdom Engineering and Physical Sciences Research Council. We gratefully acknowledge M. Brozel and M. Nicholls (UMIST) for the electron irradiations and discussion.

References

[1] G.D. Watkins, J.W. Corbett, Phys. Rev. 138 (1965) A543.
[2] J.W. Lyding, K. Hess, I.C. Kizlyalli, Appl. Phys. Lett. 68 (1996) 2526.
[3] J.-U. Sachse, E.O. Sveinbjornsson, W. Jost, J. Weber, Phys. Rev. B 55 (1997) 16176.
[4] J.A. Davidson, J.H. Evans, Semicond. Sci. Technol. 11 (1996) 1704.
[5] P. Deixler, J. Terry, I.D. Hawkins, J.H. Evans-Freeman, A.R. Peaker, L. Rubaldo, J.-C. Portal, L. Dobaczewski, K. Bonde Nielsen, A. Nylandsted Larsen, A. Mesli, Appl. Phys. Lett. 73 (1998) 3126.
[6] L. Dobaczewski, P. Kaczor, I.D. Hawkins, A.R. Peaker, J. Appl. Phys. 76 (1994) 194.
[7] J.L. Benton, C.J. Doherty, S.D. Ferris, D.L. Flamm, L.C. Kimerling, H.J. Leamy, Appl. Phys. Lett. 36 (1980) 670.
[8] S.J. Pearton, Phys. Stat Sol. A 72 (1982) K73.
[9] B.B. Nielsen, P. Johannesen, P. Stallinga, K.B. Nielsen, J.R. Byberg, Phys. Rev. Lett. 79 (1997) 1507.
[10] B.G. Svensson, A. Hallen, B.U.R. Sundqvist, Mater. Sci. Eng. B 4 (1989) 285.
[11] O.V. Feklisova, N.A. Yarykin, Semicond. Sci. Technol. 12 (1997) 742.
[12] Y. Tokuda, Jpn. J. Appl. Phys. 37 (1998) 1815.
[13] R. Jones, Private communication, presented at the Exeter Workshop on Hydrogen in Silicon, 1999.
[14] L. Rubaldo, P. Deixler, I.D. Hawkins, J. Terry, D.K. Maude, J.-C. Portal, J.H. Evans-Freeman, L. Dobaczewski, A.R. Peaker, Mater. Sci. Eng. B 58 (1999) 126.

ELSEVIER

Physica B 273–274 (1999) 247–250

PHYSICA B

www.elsevier.com/locate/physb

Optical absorption due to H-point defect complexes in quenched Si doped with C

Naoki Fukata*, Masashi Suezawa

Institute for Materials Research, Tohoku University, Sendai 980-8577, Japan

Abstract

We investigated the point defects, which exist at high temperatures in C-doped Si. Specimens were prepared from a floating-zone grown Si crystal doped with C (C concentration: 1.7×10^{17} cm^{-3}). They were sealed in quartz capsules together with hydrogen (H) gas, with pressure of 1 or 0.8 atm at high temperature, and were annealed at high temperature for 1 h followed by quenching in water. We measured their optical absorption spectra at about 7 K with an FT-IR spectrometer. Several peaks coincided with those observed in proton-implanted Si. We concluded that H-point defect complexes exist in those specimens. In C-doped Si, VH_4 (V: monovacancy) defects are formed by the reaction between VH_3 defect and H during quenching or annealing. The formation energy of V obtained in this study is smaller than the calculated one in intrinsic Si crystal by more than 1.5 eV.

Keywords: Si; Point defect; Hydrogen; Optical absorption

1. Introduction

It has not been clarified that the species of dominant point defect existed in Si at high temperatures is whether a vacancy (V) or a self-interstitial (I). Furthermore, their formation energies and their equilibrium concentrations also have not been determined experimentally since for ordinary quenching method to apply successfully for metals is almost impossible in the case of Si. Hence, it is important to make the properties of point defects existed at high temperature in Si clear. Suezawa performed a modified quenching method, namely, annealing specimens in a hydrogen atmosphere followed by quenching and measurement of optical absorption [1]. If point defects form complexes with H, they are stable at room temperature and can be investigated from their absorption peaks depending on the complexes. In Au-doped Si, an optical absorption peak at 2223 cm^{-1} and determined that the formation energy of point defect is about 2.1 eV from the quenching temperature dependence of the integrated intensity of the 2223 cm^{-1} peak. This peak has been observed in a proton-implanted crystal [2–5] and in a crystal grown in a hydrogen atmosphere [6–8]. The origin of the 2223 cm^{-1} defect, however, is still controversial. Two models have been proposed. One is the VH_4 (a vacancy saturated with four H atoms) model [3,7] and the other is the IH_4 (a self-interstitial saturated with four H atoms) model [1,9]. The former one was based on theoretical calculations of the vibrational frequency of H. The latter one was based on the effect of impurity on the peak. According to a very recent experiment of electron-irradiation of hydrogenated C- or B-doped Si by Suezawa [10], the 2223 cm^{-1} defect is VH_4 defect rather than IH_4 defect. Hence, it is considered that the formation energy of 2223 cm^{-1} defect determined in Au-doped Si is that of vacancy. The formation energy is smaller than the calculated one, about 4–5 eV [11,12], of point defects in intrinsic Si crystal.

In this study we investigated the optical absorption of H-point defect complexes in C-doped Si quenched from high temperature after annealing in a hydrogen atmosphere. We investigated the formation process of those

* Corresponding author. Tel.: + 81-22-215-2043; fax: + 81-22-215-2041.

E-mail address: fukata@imr.tohoku.ac.jp (N. Fukata)

0921-4526/99/$ - see front matter
PII: S0921-4526(99)00464-0

defects during quenching or annealing. We determined the formation energies of the point defects in C-doped Si from the quenching temperature dependence of the integrated intensity of the optical absorption peaks due to H-point defect complexes.

2. Experiment

We used n-type FZ-Si with a C concentration [C] of $1.7 \times 10^{17}\,cm^{-3}$. The specimens were sealed in quartz capsules together with H_2 gas with a pressure of about 1 or 0.8 atm at high temperature. They were heated at temperatures in the range of 1285–1375°C for 1 h followed by quenching. The quenching was performed by dropping the quartz capsules into water after the above-mentioned annealing. According to Takahashi et al. [13], temperature (T) during quenching is given by $T = (T_0 - T_f)\exp(-\alpha t) + T_f$ where α is the time constant, T_0 and T_f the quenching temperature and final (i.e., water) temperature, respectively, and t the quenching time. Optical absorption spectra were obtained by a Fourier transform infrared spectrometer at 7 K. The thickness of specimens was about 12.5 mm and the spectral resolution was $0.25\,cm^{-1}$. To investigate the annealing behaviors of H-point defect complexes, specimens were annealed in a furnace with an argon atmosphere at above 350°C.

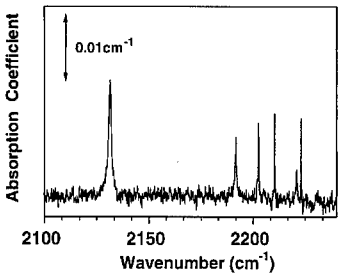

Fig. 1. Optical absorption spectra of C-doped FZ-Si sample annealed at 1360°C for 1 h in a hydrogen atmosphere with a pressure of about 1 atm followed by quenching in water.

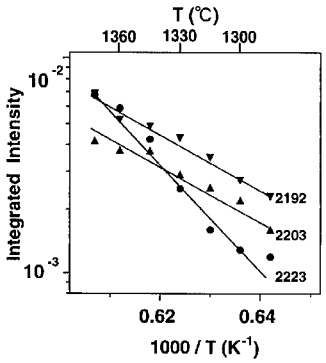

Fig. 2. The quenching temperature dependence of the integrated intensities of the 2192, 2203, and 2223 cm^{-1} peaks.

3. Results and discussion

Fig. 1 shows representative optical absorption peaks observed in the range from 2100 to 2250 cm^{-1} in C-doped FZ-Si annealed at 1360°C in a hydrogen atmosphere followed by quenching in water. These frequencies are, respectively, about 2131.5 (2132), 2191.8 (2192), 2202.7 (2203), 2210.4 (2210), 2220.8 (2221) and 2222.9 (2223) cm^{-1}. In addition to those peaks, four peaks were observed at about 792.0 (792), 1921.7 (1922), 1927.9 (1928), and 2752.4 (2752) cm^{-1}. To simplify the description of the peak, we use the value in the parentheses hereafter. These underlined peaks coincided well with those observed in proton-implanted Si [2–5] and in the Si crystal grown in H_2 gas [6–8]. As already reported, these peaks are due to H-point defects complexes or H-other impurities complexes [9].

We investigated the quenching temperature dependence of the observed optical absorption peaks. Fig. 2 shows the quenching temperature dependence of the integrated intensities of the 2192, 2203, and 2223 cm^{-1} peaks. The formation energies of the complexes responsible for the 2192 and 2203 cm^{-1} peaks are almost the same value, i.e., about 2.5 eV. This possibly suggests that these peaks originate from the same center with different stretching mode, namely, symmetric and asymmetric modes, respectively. The formation energy of the 2223 cm^{-1} defect is about 4.5 eV. The energy difference of the formation energy between 2192 and 2203 cm^{-1} defect and 2223 cm^{-1} defect is about 2 eV. This energy difference is in good agreement with the solution energy of H in Si, which is reported to be about 1.88 eV [14]. It is considered that the successive reactions ($VH_{n-1} + H \leftrightarrow VH_n (n = 1–4)$) between H and point defects occur during quenching. Considering the origin of the 2223 cm^{-1} peak and the above-mentioned energy difference of the formation energy between 2192 and 2203 cm^{-1} defect and 2223 cm^{-1} defect, we propose VH_3 defect as the origin of the 2192 and 2203 cm^{-1} defect.

To estimate the validity of the assignments, we performed isochronal annealings and investigated the annealing behaviors of these peaks. Fig. 3 shows the change of the 2192, 2203, and 2223 cm^{-1} peaks before and after an isochronal annealing. In this experiment, the specimen was annealed at 1360°C in H_2 gas with a pressure of about 0.8 atm for 1 h. The 2223 cm^{-1} peak was not observed before the isochronal annealing. After an isochronal annealing at above 350°C, the 2223 cm^{-1} peak appeared. The intensity increased accompanying with decreasing of those of the 2192 and 2203 cm^{-1} peaks.

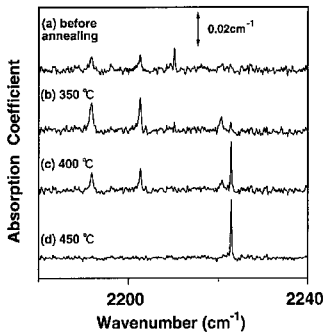

Fig. 3. H-related absorption spectra (a) before and after isochronal annealing at (b) 350°C, (c) 400°C, and (d) 450°C. Before an isochronal annealing C-doped FZ-Si sample was annealed at 1360°C for 1 h in a hydrogen atmosphere with a pressure of about 0.8 atm followed by quenching in water.

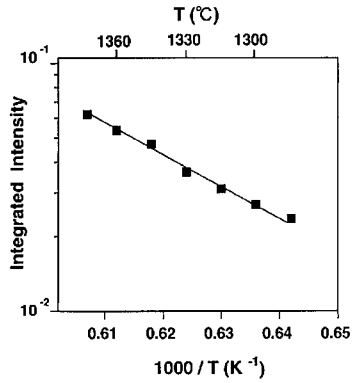

Fig. 4. The quenching temperature dependence of the sum of the integrated intensity of all peaks.

This result probably indicates that VH_3 defect capture one more H atom during isochronal annealings and become VH_4 defect, which is the most stable state of VH_n defect. Hence, we reconfirmed the 2192 and 2203 cm^{-1} peaks as the Si–H stretching mode of the VH_3 defect. In a study by Qi et al. [15], the 2191 cm^{-1} peak began to split at 250 K with a decrease in the measurement temperature and eventually split into two peaks (2192 and 2202 cm^{-1}) at 10 K. Based on this result, they proposed that the 2192 and 2202 cm^{-1} peaks may correspond to the symmetric and asymmetric stretching vibration of the same defect center. On the other hand, Nielsen et al. [3] assigned the 2166 and 2191 cm^{-1} peaks to the Si–H stretching mode of the VH_3 defect. In this experiment, the 2166 cm^{-1} peak, however, was not observed. Thus we consider that the 2166 cm^{-1} peak is not the Si–H stretching mode of the VH_3 defect.

We could not observe absorption peaks due to VH and VH_2 defects. We tentatively interpret that the reactions ($VH_{n-1} + H \leftrightarrow VH_n$) were so fast that only VH_3 and VH_4 defects were dominant after quenching. On the other hand, Suezawa observed optical absorption peak due to VH_2 defect at 2122 cm^{-1} in electron-irradiated Si doped with H at 1300°C [16]. In that experiment, he showed that the generation of the 2223 cm^{-1} defect by annealing is due to the reaction between 2122 cm^{-1} defect (VH_2 defect) and H_2. Hence, it is found that there are two different reactions for the formation of VH_4 defect. Namely, one is the reaction between VH_3 defect and H and the other is the reaction between VH_2 defect and H_2.

The above-mentioned formation energies of 2192, 2203, and 2223 cm^{-1} defects do not correspond to those of point defects which are constituent defects of the complexes, but rather to the values including the formation probability of H-point defect complexes during quenching. In the cases of defects such as vacancy-type defects (VH_n, $n = 1$–4), at least four kinds of species exist according to the number of H. Furthermore, in addition to the 2192, 2203, and 2223 cm^{-1} peaks, other peaks observed are also possibly vacancy related. The more detailed explanation will be described elsewhere [17]. In that case the contribution of all peaks must be considered. The quenching temperature dependence of the sum of the observed peak intensities is shown in Fig. 4. Taking into account of the contribution of all peaks, the formation energy of V is roughly estimated to be about 2.5 eV. The formation energy of V in intrinsic Si was calculated to be about 4–5 eV [11,12], as already described. Hence, the formation energy of V obtained in C-doped Si is smaller than the calculated one in intrinsic Si crystal and decreases more than 1.5 eV. For Au-doped Si, the formation energy of V was determined to be 2.1 eV from the quenching temperature dependence of the 2223 cm^{-1} peak [1] and the value also decreased in comparison with the calculated formation energy of V in intrinsic Si crystal. This formation energy is different from that in C-doped Si. The result suggests that the formation of V depends on the doped impurity.

In C-doped Si, C diffuses with the kick-out mechanism and introduces I into Si during high-temperature annealing. Furthermore, excess I are introduced into Si because of the effect of lattice strain due to small covalent radius of C. True enhancement of the formation of A-swirl defects, which are interstitial type dislocation loops, is observed when impurities such as C and B with smaller covalent radius than that of Si are doped during crystal growth [18]. From these results, concentrations of V([V]) and I([I]) are higher than those in intrinsic Si. This result throws a doubt on the rule that multiplication of [V] and [I] is constant [19].

4. Conclusion

We investigated the point defects, which exist at high temperatures in C-doped Si and determined their

formation energies from measurements of optical absorption due to H-point defect complexes. We assigned the 2192 and 2203 cm^{-1} peaks to the Si–H stretching mode of the VH_3 defect with different stretching mode, namely, symmetric and asymmetric modes, respectively. In C-doped Si, the reaction between VH_3 defect and H can be seen and VH_4 defect is formed through the reaction. The formation energy of V obtained in this study is smaller than the calculated formation energies of V in intrinsic Si crystal by more than 1.5 eV.

References

[1] M. Suezawa, Jpn. J. Appl. Phys. 37 (1998) L259.
[2] H.J. Stein, J. Electron. Mater. 4 (1975) 159.
[3] B. Bech Nielsen, L. Hoffman, M. Budde, Mater. Sci. Eng. B 36 (1996) 259.
[4] B. Bech Nielsen, L. Hoffman, M. Budde, R. Jones, J. Goss, S. Oberg, Mater. Sci. Forum 196–201 (1995) 933.
[5] B.N. Mukashev, M.F. Tambendarov, S.Zn. Tokmoldin, V.V. Frolov, Phys. Stat. Sol. A 91 (1985) 509.
[6] T.S. Shi, L.M. Xie, G.R. Bai, M.W. Qi, Phys. Stat. Solid. B 131 (1985) 511.
[7] L.M. Xie, M.W. Qi, J.M. Chen, J. Phys. C 3 (1991) 8519.
[8] B. Gu, Z. Xu, P. Ge, Sci. Sinica A 27 (1984) 213.
[9] N. Fukata, M. Suezawa, J. Appl. Phys. 86 (1999) 1848.
[10] M. Suezawa, Physica B 273–274 (1999) 222, These Proceedings.
[11] I. Kwon, R. Biswas, C.Z. Wang, K.M. Ho, C.M. Soukoulis, Phys. Rev. B 49 (1994) 7242.
[12] T. Akiyama, A. Oshiyama, O. Sugino, J. Phys. Soc. Jpn. 67 (1998) 4110.
[13] H. Takahashi, M. Suezawa, K. Sumino, J. Appl. Phys. 78 (1995) 3077.
[14] A. Van Wieringen, N. Warmoltz, Physica 22 (1956) 849.
[15] M.W. Qi, G.R. Bai, T.S. Shi, L.M. Xie, Mater. Lett. 3 (1985) 467.
[16] M. Suezawa, J. Appl. Phys., in press.
[17] N. Fukata, M. Suezawa, in preparation.
[18] T. Abe, H. Harada, J. Chikawa, Physica B 116 (1983) 139.
[19] T.Y. Tan, U. Goessele, Appl. Phys. A 37 (1985) 1.

ELSEVIER

Physica B 273–274 (1999) 251–255

PHYSICA B

www.elsevier.com/locate/physb

Breaking through the electrical saturation barrier: 2D- versus 3D-doping in n-type silicon

P.H. Citrin[a,*], D. Muller[a], H.-J. Gossmann[a], R. Vanfleet[b], P.A. Northrup[a]

[a]*Bell Laboratories, Lucent Technologies, Room 3L-403, 600 Mountain Avenue, Murray Hill, NJ 07974, USA*
[b]*Cornell University, Applied and Engineering Physics, Ithaca, NY 14850, USA*

Abstract

A novel application of scanning transmission electron microscopy, combined with data from X-ray absorption spectroscopy, establishes that high concentrations of n-type Sb dopants distributed within a two-dimensional (2D) layer in Si can contribute up to an order of magnitude higher free-carrier density than similar dopant concentrations distributed over a three-dimensional region. This difference is explained using a simple model in which formation of electrically deactivating centers is inhibited solely by geometric constraints. It should be possible to extend these ideas for obtaining even higher free-carrier densities in Si from 2D layers of Sb and other Group V donors. © 1999 Elsevier Science B.V. All rights reserved.

Keywords: Dopant activation; Point defects; Delta layers; Electron microscopy; X-ray absorption

The ubiquitous saturation and eventual loss of free-carrier densities, n_e, observed in Si at high donor-atom concentrations, $N_D \lesssim 2 \times 10^{21}$ cm^{-3}, has been generally believed to be due to the unavoidable formation of electrically inactive precipitates and/or deactivating dopant defects containing vacancies [1–7]. In the same vein, a new class of vacancy-free deactivating defects, called donor-pairs (DP), has recently been argued [8] to form in highly n-doped Si even in the absence of precipitates or vacancies, thus posing a fundamental barrier to achieving full dopant activity in highly doped Si. Such a barrier should be particularly severe for two-dimensional (2D) δ-layers of dopants, where even higher dopant densities can, in principle, be obtained [9]. Free-carrier concentrations of up to $\sim 3 \times 10^{14}$ cm^{-2} have been reported in 2D [10], but because the δ-layer thicknesses in those samples were not determined the effective volume concentration of dopants was not known. Conversely, samples from which reliably measured δ-layer widths were reported had no corresponding measurements of electrical activity [11,12]. The importance of DP defects in 2D-doped Si, and thus the inherent limitations on free-carrier densities, in general, has therefore not been possible to assess.

In this paper, we use a new application of scanning transmission electron microscopy (STEM) for directly measuring the widths of δ-layers from samples whose electrical properties have been well determined. This allows a consistent conversion of 2D to 3D dopant concentrations and free-carrier densities. Surprisingly, and contrary to expectations about forming DP defects, we find that electrical saturation in highly 2D-doped Si does not occur. Extended X-ray absorption fine structure (EXAFS) measurements confirm that in these samples neither precipitates nor vacancy-containing dopant defects are important. The results are explained using a simple model in which the formation of DP defects in 2D is geometrically frustrated at high dopant concentrations. The model thus predicts that in 2D-doped Si it should be possible to realize complete electrical activity even at the highest levels of n-type doping.

To illustrate the basic problem of characterizing dopant activity in 2D, we first show in the top of Fig. 1 an example of electrical saturation for the case of 3D Sb-doped Si. The samples were grown by low-temperature molecular beam epitaxy with the Sb atoms distributed

* Corresponding author. Tel.: + 1-908-582-5275; fax: + 1-908-582-3260.

E-mail address: phc@bell-labs.com (P.H. Citrin)

PII: S0921-4526(99)00465-2

over a 300-Å wide region [13]. Dopants are confined to a much narrower region in δ-doped samples grown under similar conditions [10]; their dopant and free-carrier concentrations are plotted at the bottom of Fig. 1 in areal rather than volume dimensions. The top and bottom plots span the same change in concentration of 10^3, but the electrical activity in the 3D and 2D samples, n_e/N_{Sb}, exhibits qualitatively very different behavior. One possible reason for this is that the dopant concentration in the sample labeled δ-VH is simply too low to display electrical saturation, but that explanation is purely speculative. Understanding the difference in electrical behavior clearly requires knowing the effective volume concentrations of dopants in the 2D samples, i.e., the widths of the δ-layers.

We use a combination of STEM and atomic-scale electron energy loss spectroscopy (EELS) [14–16] to determine the spatial distributions of the δ-layers. The Sb atoms are probed at internal interfaces by passing a focused 2–3-Å diameter 100-kV electron beam through a film that is thick enough to avoid significant surface state contributions to the transmitted signal, yet thin enough to avoid significant beam spread from multiple scattering. The interface is oriented parallel to the beam to allow atom columns within the interface to be measured separately from atoms in adjacent columns. Viewing the interface in projection means that any interfacial roughness, particularly on length scales thinner than the sample, leads to an apparent broadening of the interface. Accordingly, the δ-layer widths quoted here are upper-limit values.

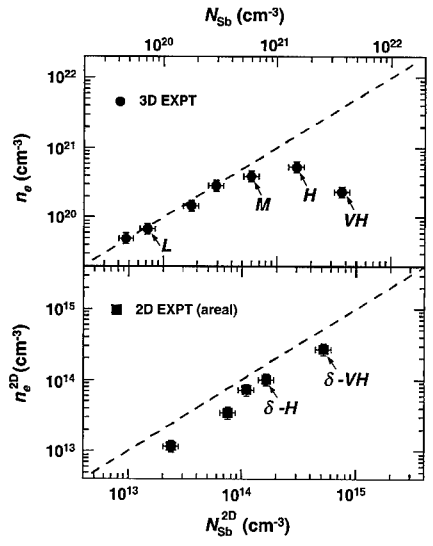

Fig. 1. Free-carrier concentrations, n_e, versus Sb-dopant concentrations, N_{Sb}, for Si(1 0 0) samples doped in ~ 300-Å-thick regions (i.e., 3D) and δ-layers (i.e., 2D). The sample labels are used for reference, and the dashed line indicates unity activation.

To map out the spatial distribution of the Sb $M_{4,5}$ EELS edge, which is sensitive only to chemical composition, the δ-layer is located using images from the stronger annular dark field (ADF) signal, which is sensitive to both chemical composition [17] and localized strain fields [18,19]. The ADF signal arises from electrons that have undergone Rutherford-like scattering to large angles, resulting in an intensity that is roughly proportional to the square of the atomic number in thin samples. Measurements were performed on the Cornell VG-HB501 STEM equipped with a cold field-emission gun and a McMullan-style parallel EELS spectrometer. Cross-sectioned samples were tripod polished to electron transparency, briefly ion milled, then dipped in HF to remove the damaged surface layer. EELS spectra were recorded simultaneously with the ADF signal under conditions optimized for atomic resolution imaging. A 100-Å-thick sample is expected to give an ADF resolution of 2.3 Å and an EELS spatial resolution at the Sb $M_{4,5}$ edge of 2.7 Å [20].

The top of Fig. 2 shows the ADF signal for the 2D-doped sample labeled δ-VH. Below is the corresponding intensity profile (composition + strain), which closely matches the superposed EELS intensity profile (composition) measured across one of the broadest regions of the δ-layer as shown in the figure. The full-width at half-maximum value of the δ-layer in this sample, averaged over several regions, is 16 ± 1 Å. Comparable values were determined for the other 2D-doped samples.

The measured δ-layer widths allow the 2D dopant and free-carrier areal densities in Fig. 1 to be converted to effective volume concentrations. This is done in Fig. 3, where the 3D-doped data are included for direct comparison. We see that the highest 2D- and 3D-doped samples, δ-VH and VH, respectively, are almost identical in dopant concentrations, contrary to the possible suggestion from Fig. 1 that they are dissimilar. On the other hand, the free-carrier concentration in the 2D-doped sample is very different, being almost an order of magnitude higher.

Further confirmation of this striking difference in electrical activity is found in our study of the local structure around Sb from a series of 2D and 3D samples using Sb L_3-edge EXAFS. Fluorescence-detection X-ray absorption measurements from samples cooled < 50 K (to minimize the effects of thermal disorder [21]) were obtained at the NSLS with the Bell Laboratories X15B beamline [22]. The Fourier transformed (FT) EXAFS data are shown in Fig. 4 for the two highest 2D-doped samples, δ-H and δ-VH, and the two highest 3D-doped samples, H and VH. Also included for reference is a low-concentration 3D-doped sample, labeled L, containing Sb in only substitutional sites [6,8]. In L, the FT peak at ~ 2 Å (uncorrected for phase shifts [21]) corresponds

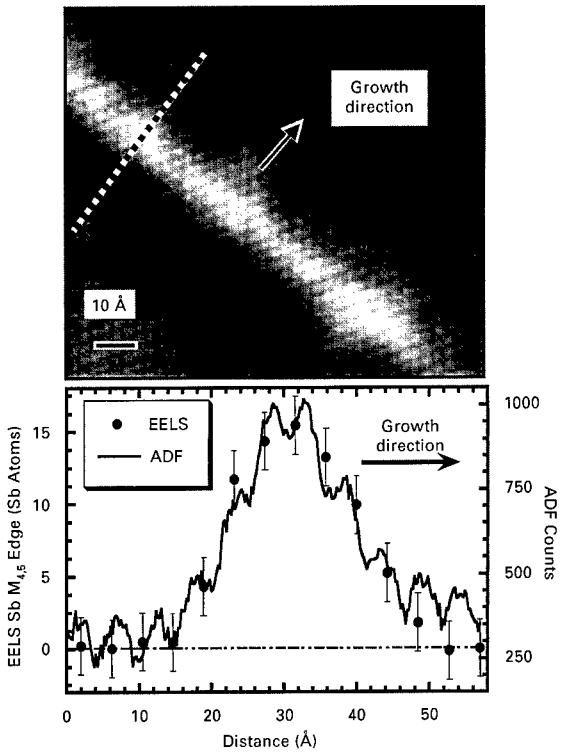

Fig. 2. Measuring the width of a δ-layer. Top: Annular dark field (ADF) image of the 2D Sb-doped layer in sample. The Sb atoms appear bright because they scatter more strongly than Si. Bottom: The electron energy loss spectroscopy (EELS) Sb $M_{4,5}$ edge is recorded across the δ-layer simultaneously with the ADF signal. The ~ 500-Å-thick sample, viewed in projection, contains $\lesssim$15 Sb atoms in the beam path.

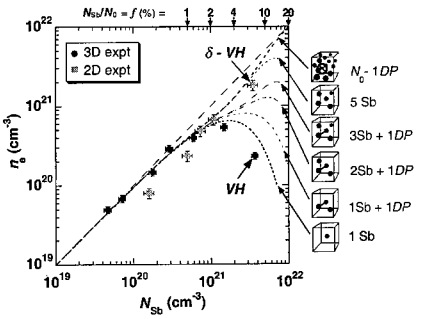

Fig. 3. Direct comparison of experimental free-carrier densities in 2D- versus 3D-doped Si. The differences in electrical behavior agree well with predictions of a simple model for creating dopant donor-pair (DP) centers in the cell volumes that are shown schematically in the legend (see text).

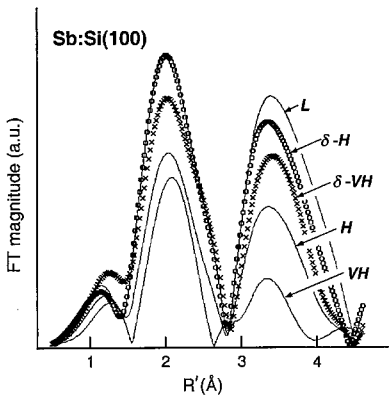

Fig. 4. Fourier transformed Sb L_3-edge EXAFS for different Sb concentrations in the 3D- and 2D-doped Si samples labeled in Fig. 1. The volume concentrations of Sb in δ-VH and VH are almost identical.

exclusively to first-neighbor Si atoms around Sb, while the peak at ~ 3.4 Å contains unresolved second- and third-neighbor Si atoms. Any surrounding Si atoms not at these distances, or any Sb neighbors within ~ 4 Å, will lead to destructively interfering EXAFS and a reduction of the FT-peak magnitudes. This is observed for both main peaks in the 3D-doped samples.[1] There is also evidence in VH of forming a Sb–Sb FT peak at ~ 2.9 Å [6], signaling the early stages of Sb clustering. By contrast, the 2D-doped samples show much less reduction in the FT peak intensities and no indication of Sb clustering.[2] These results therefore demonstrate that even in highly doped δ-layers, the Sb atoms still occupy predominantly substitutional Si sites, consistent with the high electrical activity displayed in Fig. 3.

Why do similarly high concentrations of n-type dopants in Si — differing only in their dimensionality — exhibit such different electrical behavior? Previous work [8] has shown that the dominant mechanism for deactivating free carriers in n-doped Si is the formation of DP defects, provided two conditions are satisfied. First, high annealing temperatures and excess vacancies are avoided in the sample preparation, i.e., formation of inactive precipitates and other deactivating centers is minimal. This is the case for the samples studied here. Second, the doping levels, and thus the number and energy of free carriers at the Fermi level, are high enough to create DP defects. This, too, is the case when $n_e \gtrsim 1\text{–}3 \times 10^{20}\,\text{cm}^{-3}$, corresponding to the energy range $E_F \approx 0.07\text{–}0.15\,\text{eV}$ needed to create the two

[1] The reduced FT peak intensities have been shown in Ref. [8] for sample H to be consistent with the formation of DP defects.

[2] EXAFS simulations for different sized Sb clusters, including dimers, were used to rule out the importance of Sb precipitation in the 3D-doped sample H and all of the 2D-doped samples.

lowest-energy DP defects. The formation of these two defects, denoted DP(2) and DP(4) because each contains a pair of substitutional donor atoms separated by second- or "fourth"-neighbor distances,[3] involves significant deformation of the surrounding Si lattice. It is therefore appropriate to look for a relationship between the concentration and dimensionality of donor atoms and the ability of the Si lattice to deform and create these defects.

Consider the consequences of randomly distributing N_d dopants in 3D among the N_0 substitutional sites in Si ($N_0 = 5\times10^{22}\,\mathrm{cm}^{-3}$). Any given dopant atom is surrounded by 28 sites, the occupation of which by a second dopant can lead to both dopants becoming electrically inactive, viz., there are four first-neighbor sites giving dimers and 24 other sites giving DP(2) and DP(4) defects. The total probability for all configurations in which other dopants occupy any of these 28 special sites can be expressed in terms of the fractional dopant population, $f = N_d/N_0$, by

$$1 = [f + (1-f)]^{28} = (1-f)^{28} + 28f(1-f)^{27} + (28\cdot 27/2!)f^2(1-f)^{26} + \ldots . \quad (1)$$

The first term in the expansion represents the probability that no other dopants will occupy any of the 28 special sites around a given dopant, the second that only one other dopant will occupy one of those sites, etc. The contribution to the total free-carrier concentration (absent any DP defects) is then obtained by multiplying each term by N_d. Previous work on 3D-doped Si considered only the effect of the first term on electrical activity because it dominates when f is small, i.e., $f \lesssim \frac{1}{29}$, or $\sim 3.5\%$ [8].[4] However, when f is no longer small, not only must the higher-order terms in Eq. (1) be considered, but so must the competing interactions between dopants, defects, and the Si lattice.

A simple way to see what happens as f increases is to picture N_d dilute dopants with each one lying at the center of its own 3D Si-lattice volume, or cell, containing the 28 special sites, giving a total of 29 relevant sites per cell per dopant (to simplify our discussion, we ignore dimers). As $f > \frac{1}{29}$, the probability increases for a second dopant to occupy this cell and form a DP defect, leading always to no free carriers from either dopant. Increasing f still further makes it likely that three dopants can occupy a cell, but now there are (at least) two possibilities to create one DP defect, leaving one dopant still active. The number of free carriers in this case is represented by multiplying the third term in Eq. (1) by $\frac{1}{3}$. Four dopants per cell leading to one DP defect is represented by multiplying the fourth term by $\frac{1}{2}$, etc. The electrical activities corresponding to configurations with up to 1, 3, 4, or 5 dopants per cell and at most 1 DP defect are plotted in Fig. 3, showing the increase in electrical activity with dopant density as each higher-order term in Eq. (1) is included.

The calculated activities in Fig. 3 reflect the statistics of occupying particular sites, not of actually forming defects. Increasing the density of dopants also means decreasing the density of ancillary Si atoms needed to create the DP defects through deformation of the surrounding lattice, a factor not included in Eq. (1). Consequently, there must be a threshold in f below which DP defect creation is favored and above which it is inhibited. When f is above threshold in 3D-doped Si, precipitates offer an alternative to DP defects because their formation requires comparatively less Si deformation; an example of this is seen in sample VH. However, above threshold in 2D-doped Si, forming DP defects or precipitates is inhibited still further because the choice between which dopants pair up and the ability of the lattice to deform are both constrained by the narrowness of the δ-layer, which we measure to be comparable to a single 3D-cell width. In effect, the 2D dopants are geometrically frustrated, analogous to antiferromagnetic Ising spins on a triangle [23].

The electrical activity from frustrated dopants has been represented in Fig. 3 by including two additional configurations. One is a cell with up to five dopants and no DP defect, i.e., the sum of the 1st, 3rd, 4th, and 5th terms in Eq. (1) and no corresponding multipliers of $\frac{1}{3}$, $\frac{1}{2}$ and $\frac{3}{5}$, and the other is the asymptotic limit of a cell with up to N_0 dopants and no DP defect, i.e., all terms but the second in Eq. (1). The predicted electrical activity for either configuration is seen to be in very good agreement with that measured for the highest 2D-doped sample studied here. Indeed, the trend towards obtaining even higher free-carrier densities from frustrated dopants is very encouraging.

In conclusion, we have demonstrated a simple and surprising result: constraining high concentrations of Sb dopants in 2D can strongly inhibit the formation of deactivating defects in Si, thereby surpassing the barrier to achieving full electrical activity. This finding should also apply to high doping levels of DP-defect-forming P and As dopants, with the understanding that the degree to which electrical deactivation will be inhibited depends on how narrow the δ-layer widths can be prepared.

The authors thank D.J. Chadi and A. Frenkel for helpful discussions. The X-ray absorption measurements were performed at the NSLS, Brookhaven National

[3] The "fourth"-neighbor dopant separation in DP(4) of $\sqrt{2}a_0$ is measured in the [1 1 0] plane, so is actually an eighth-neighbor Si distance.

[4] The fractional dopant population must still be large enough to form DP(2) and DP(4) defects, i.e $f \gtrsim (3\times10^{20})/(5\times10^{22}) \approx 0.006$.

Laboratory, which is supported by the DOE, Division of Materials Science and Division of Chemical Sciences. RRV was supported by Air Force grant F49620-95-1-0427. The Cornell STEM was acquired through the NSF (DMR-8314255) and is part of the Cornell CMR (DMR-9632275).

References

[1] R.O. Schwenker, E.S. Pan, R.F. Lever, J. Appl. Phys. 42 (1971) 3195.
[2] A. Nylandsted Larsen, F.T. Pedersen, G. Weyer, R. Galloni, R. Rizzoli, A. Armigliato, J. Appl. Phys. 59 (1986) 1908.
[3] K.C. Pandey, A. Erbil, G.S. Cargill, R.F. Boehme, D. Vanderbilt, Phys. Rev. Lett. 61 (1988) 1282.
[4] D. Mathiot, J.C. Pfister, J. Appl. Phys. 66 (1989) 970.
[5] P.M. Rousseau, P.B. Griffin, J.D. Plummer, Appl. Phys. Lett. 65 (1994) 578.
[6] C. Revenant-Brizard, J.R. Regnard, S. Solmi, A. Armigliato, S. Valmorri, C. Cellini, F. Romanato, J. Appl. Phys. 79 (1996) 9037.
[7] M. Ramamoorthy, S.T. Pantelides, Phys. Rev. Lett. 76 (1996) 4753.
[8] D.J. Chadi, P.H. Citrin, C.H. Park, D.L. Adler, M.A. Marcus, H.-J. Gossmann, Phys. Rev. Lett. 79 (1997) 4834.
[9] S.J. Bass, J. Crystal Growth 47 (1979) 613.
[10] H.-J. Gossmann, F.C. Unterwald, Phys. Rev. 47 (1993) 12618.
[11] W.F.J. Slijkerman, J.M. Gay, P.M. Zagwijn, J.F. van der Veen, J.E. Macdonald, A.A. Williams, D.J. Gravesteijn, G.F.A. van de Walle, J. Appl. Phys. 68 (1990) 5105.
[12] A.R. Powell, R.A.A. Kubiak, S.M. Newstead, C. Parry, N.L. Mattey, D.W. Smith, J.C. Brighten, C.J. Emeleus, T. Naylor, E. Basaran, T.D. Whall, M.G. Dowsett, R.D. Barlow, E.H.C. Parker, D.K. Bowen, J. Crystal Growth 111 (1991) 907.
[13] H.-J. Gossmann, F.C. Unterwald, H.S. Luftman, J. Appl. Phys. 73 (1993) 8237.
[14] P.E. Batson, Nature (London) 366 (1993) 728.
[15] N.D. Browning, M.M. Chisholm, S.J. Pennycook, Nature (London) 366 (1993) 143.
[16] D.A. Muller, Y. Tzou, R. Raj, J. Silcox, Nature (London) 366 (1993) 725.
[17] S.J. Pennycook, D.E. Jesson, Phys. Rev. Lett. 64 (1990) 938.
[18] D.D. Perovic, C.J. Roussouw, A. Howie, Ultramicroscopy 52 (1993) 353.
[19] S. Hillyard, J. Silcox, Ultramicroscopy 58 (1995) 6.
[20] D.A. Muller, J. Silcox, Ultramicroscopy 59 (1995) 195.
[21] P.A. Lee, P.H. Citrin, P. Eisenberger, B.M. Kincaid, Rev. Mod. Phys. 53 (1981) 769.
[22] A.A. MacDowell, T. Hashizume, P.H. Citrin, Rev. Sci. Instr. 60 (1989) 1901.
[23] A.P. Ramirez, Annu. Rev. Mater. Sci. 24 (1994) 453.

ELSEVIER

Physica B 273–274 (1999) 256–259

PHYSICA B

www.elsevier.com/locate/physb

Infrared absorption study of a new dicarbon center in silicon

E.V. Lavrov[a,b], B. Bech Nielsen[b,*], J. Byberg[c], J.L. Lindström[d]

[a]*Institute of Radioengineering and Electronics of RAS, Mokhovaya 11, 103907 Moscow, Russia*
[b]*Institute of Physics and Astronomy, University of Aarhus, Ny Munkegade, DK-8000 Aarhus, Denmark*
[c]*Institute of Chemistry, University of Aarhus, DK-8000 Aarhus, Denmark*
[d]*Linköping University, S-581 83, Linköping, Sweden*

Abstract

Infrared absorption measurements on n-type silicon doped with carbon and irradiated with electrons at room temperature have revealed new absorption lines at 527.4 and 748.7 cm^{-1}. The 748.7 cm^{-1} line is observed only when the sample is cooled down in the dark and the spectra are measured through a low-pass filter with cut-off frequency below 6000 cm^{-1}. Light of frequency above 6000 cm^{-1} removes this line and generates the 527.4-cm^{-1} line. Spectra recorded on silicon doped with ^{13}C show that the two lines represent local vibrational modes of a carbon defect. The annealing behavior of the 748.7-cm^{-1} line and of the EPR signal of two neighboring substitutional carbon atoms, $(C_s–C_s)^-$, are identical. The 527.4- and 748.7-cm^{-1} modes are identified as the modes of $C_s–C_s$ in neutral and negative charge states, respectively. The formation of $C_s–C_s$ is investigated, and it is shown that the center may arise when a vacancy is trapped by the metastable substitutional carbon-interstitial carbon center, $C_s–C_i$.

Keywords: Silicon; Carbon; Infrared absorption

1. Introduction

In crystalline silicon, carbon atoms are common and important impurities, which are present mainly as substitutional carbon, C_s [1]. Interstitial carbon, C_i, is produced by electron irradiation when mobile silicon interstitials become trapped by C_s [1–3]. At room temperature, C_i migrates through the lattice and becomes trapped at C_s, whereby a dicarbon center, $C_s–C_i$, is formed [4].

A recent EPR study of carbon-doped silicon, Si:C, showed that $C_s–C_i$ is not the only dicarbon center in silicon. After electron irradiation of n-type Si:C at room temperature a new paramagnetic center was observed and identified as a dicarbon center comprising two neighboring subsitutional carbon atoms, $C_s–C_s$ [5].

While an EPR experiment probes the electronic wave function, information about the identity of light impurity atoms can be obtained from the frequencies of their local vibrational modes (LVMs). Moreover, the LVMs serve to characterize the bonding of these atoms. In the present work the LVMs of $C_s–C_s$ are investigated by means of infrared absorption spectroscopy. Unlike EPR, this technique allows a study of both the negative and the neutral charge states of $C_s–C_s$. Moreover, the mechanism of formation of $C_s–C_s$ is addressed: From the electron dose dependence of the LVM intensities of C_s, C_i, $C_s–C_i$, and $C_s–C_s$ it is shown that $C_s–C_s$ may arise when vacancies become trapped by $C_s–C_i$.

2. Experimental

Samples with dimension $\sim 10 \times 7 \times 2\,mm^3$ were cut from three different float-zone (FZ) silicon crystals doped either with ^{12}C(Si:^{12}C) or predominantly with ^{13}C (Si:^{13}C). The samples were mechanically polished on the two opposite $10 \times 7\,mm^2$ faces to ensure maximum transmission of infrared light. One Si:^{12}C crystal was n-type and contained $4 \times 10^{17}\,cm^{-3}$ ^{12}C, $1 \times 10^{16}\,cm^{-3}$

* Corresponding author. Tel.: +45-8942-3716; fax: +45-8612-0740.

E-mail address: bbn@dfi.aau.dk (B. Bech Nielsen)

0921-4526/99/$ - see front matter
PII: S0921-4526(99)00469-X

oxygen, $5\times10^{16}\,cm^{-3}$ phosphorus, and $\sim1\times10^{18}\,cm^{-3}$ tin. A second Si:^{12}C crystal was nearly intrinsic (high-resistivity n-type) and contained $4.5\times10^{17}\,cm^{-3}$ ^{12}C and $1\times10^{16}\,cm^{-3}$ oxygen. The Si:^{13}C crystal was n-type and contained $8\times10^{17}\,cm^{-3}$ ^{13}C, $1\times10^{17}\,cm^{-3}$ ^{12}C, $1\times10^{17}\,cm^{-3}$ oxygen, and $4\times10^{14}\,cm^{-3}$ phosphorus.

The samples were irradiated with 2 MeV electrons supplied by a 5 MeV Escher Holland van de Graaff accelerator. The total irradiation dose varied from 5×10^{17} to $6\times10^{18}\,cm^{-2}$. The irradiation was carried out either at room temperature or below -20°C depending on the purpose of the experiment.

In order to study the annealing characteristics of the absorption lines, infrared absorbance spectra were recorded at 10 K after each step in a series of isochronal heat treatments at temperatures in the range from 300°C to 550°C. Each heat treatment had a duration of 40 min. and was carried out in a nitrogen atmosphere.

The infrared absorbance spectra were recorded with a Nicolet, System 800, Fourier-transform spectrometer equipped with a Ge-on-KBr beamsplitter, a glowbar as light source, and a mercury–cadmium–telluride detector. The spectra were recorded at 10 K with an apodized resolution of $2\,cm^{-1}$. Low-pass filters could be inserted between the glowbar and the sample. Spectra recorded with filters were obtained after cooling the sample in the dark from $\geqslant 200$ K to the temperature of measurement. A reference spectrum, recorded on pure silicon with a low carbon content, was subtracted from all spectra, unless otherwise stated. Moreover, the spectra shown in Figs. 1 and 3 were baseline corrected for presentation purposes, which could be done without introducing or removing any sharp absorption features.

In order to establish a correlation between the EPR signal of $(C_s–C_s)^-$ and the observed LVMs, EPR and infrared absorption measurements were performed on the same sample. The EPR spectra were recorded at room temperature with a Bruker ESP300E spectrometer operated in the absorption mode at ~ 9.5 GHz (X band).

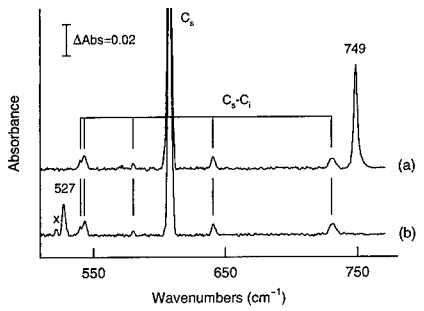

Fig. 1. Sections of absorbance spectra of electron-irradiated ($\sim 1\times10^{18}\,cm^{-2}$) Si:^{12}C recorded at 10 K: (a) through a low-pass filter with cut-off frequency at 3000 cm^{-1} and (b) without filter. The absorption line denoted by × is not related to the centers discussed in this work.

3. Results and discussion

3.1. Basic properties of absorption lines

Absorbance spectra of an n-type Si:^{12}C crystal irradiated with 2 MeV electrons at room temperature are shown in Fig. 1. The spectrum (a) was recorded with a low-pass filter with cut-off frequency at $3000\,cm^{-1}$, after cooling the sample to 10 K in the dark. Then the filter was removed, and the spectrum (b) was obtained. The intense absorption line at $607\,cm^{-1}$ associated with the LVM of $^{12}C_s$ dominates in the spectra. Much weaker absorption lines at 540.4, 543.3, 579.8, 640.6, and $730.4\,cm^{-1}$ are also seen. Recently, these were shown to represent the LVMs of C_s–C_i (see Ref. [6]). In addition, several other absorption lines appear in the spectra, among which those observed at 527.4 and $748.7\,cm^{-1}$ are discussed in this work. They lie in the region characteristic of LVMs of carbon defects in silicon. The 748.7-cm^{-1} line is observed only when the sample is cooled in the dark and the spectrum is recorded with a low-pass filter with cut-off frequency below $6000\,cm^{-1}$. Illumination with light of frequency above $6000\,cm^{-1}$ swiftly removes the 748.7-cm^{-1} line and generates the line at $527.4\,cm^{-1}$, as can be seen from comparison of spectra (a) and (b) in the figure. This process is reversible: After heating to 200 K and subsequent cooling in the dark, the line at $748.7\,cm^{-1}$ is restored, whereas the 527.4-cm^{-1} line disappears from the spectra. The 527.4- and 748.7-cm^{-1} lines display perfect anticorrelation, which implies that the same process controls the light-induced removal of the 748.7-cm^{-1} line and appearance of the 527.4-cm^{-1} line. At the same time, the annealing behaviors of these two lines are identical. These facts strongly indicate that the lines at $527.4\,cm^{-1}$ and $748.7\,cm^{-1}$ originate from two different charge states of the same defect. Moreover, since the 527.4-cm^{-1} line can be observed in both n-type and intrinsic material, whereas the 748.7-cm^{-1} line is observed only in n-type silicon we may expect the 527.4-cm^{-1} line to originate from a more positive charge state than the 748.7-cm^{-1} line.

Measurements on the Si:^{13}C sample showed that the 748.7-cm^{-1} line shifts down to $726.3\,cm^{-1}$. The frequency ratio between the two absorption lines is 1.031, which is very close to the value expected for a carbon atom bound to a silicon atom by a harmonic spring. Therefore, we ascribe the 748.7-cm^{-1} line to a LVM of a carbon defect presumably containing Si–C bonds.

No line corresponding to the 527.4-cm^{-1} line was observed in the Si:^{13}C sample. However, with the same frequency ratio as found above (1.031), this line should shift down to $\sim 512\,cm^{-1}$ and thus fall below the Raman

frequency 524 cm^{-1} in silicon [7]. Such modes normally couple strongly to the lattice phonons and cannot be detected. Hence, we may also ascribe the 527.4-cm^{-1} line to a LVM of carbon.

3.2. Assignment of absorption lines

So far, we have established that the center responsible for the 527.4 and 748.7-cm^{-1} lines is carbon related. Neither the number of carbon atoms involved nor their sites have been determined. The EPR signal arising from the negative charge state of C_s–C_s qualitatively displays the same sensitivity to light as discussed here for the 748.7-cm^{-1} line [5], which suggests that it may originate from $(C_s–C_s)^-$. To investigate this further, an n-type Si:^{12}C sample was first irradiated below $-20°C$ with 2 MeV electrons to a dose of 5×10^{17} cm^{-2}, in order to compensate the free carriers without creating much C_s–C_s (see Section 3.3). This compensation was required to ensure reliable intensities of the $(C_s–C_s)^-$ EPR signal at room temperature. Subsequently, the sample was electron irradiated at room temperature to a dose of 1.5×10^{17} cm^{-2} and the EPR as well as the infrared absorption spectra were recorded. Then the room temperature irradiation was repeated and the spectra remeasured until the total dose reached 9×10^{17} cm^{-2}. The results of this series of measurements are presented in Fig. 2, in which the intensity of the EPR signal from $(C_s–C_s)^-$ is plotted against the intensity of the 748.7-cm^{-1} line. As can be seen from the figure, the two data sets display a linear correlation, showing that the 748.7-cm^{-1} line originates from $(C_s–C_s)^-$. Thus, from the results described in the previous subsection we may conclude that the 748.7-cm^{-1} line represents a LVM of $(C_s–C_s)^-$. The 527.4-cm^{-1} line is observed both in n-type and intrinsic material, and no EPR signal correlates with it. Therefore, we identify this line as a LVM of $(C_s–C_s)^0$.

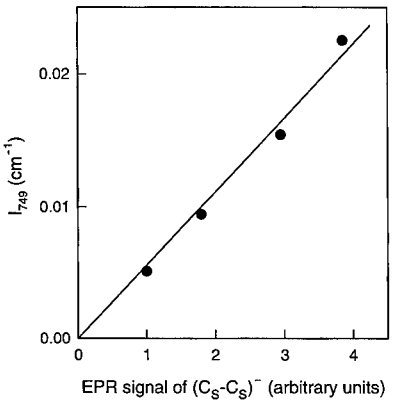

Fig. 2. The intensity (integrated absorbance) of the 748.7-cm^{-1} line shown against the intensity of the EPR signal associated with $(C_s–C_s)^-$. The solid line represents the least-square fit to the data.

3.3. Formation of C_s–C_s

Electron irradiation of virgin Si:C at low temperatures does not create any signals related to C_s–C_s. On the other hand, room-temperature irradiation is the most effective way to produce the center. Among the identified carbon-related centers, only C_i is mobile at room temperature, but as shown previously, C_i forms C_s–C_i rather than C_s–C_s (see Ref. [4]). We propose that C_s–C_i is a precursor for C_s–C_s and that the transformation of C_s–C_i into C_s–C_s may occur when C_s–C_i traps a vacancy produced by further electron irradiation. Accordingly, the proposed reaction scheme leading to formation of C_s–C_s is

$C_s + Si_i \rightarrow C_i$: Low temperatures,

$C_s + C_i \rightarrow C_s–C_i$: Room temperature,

$C_s–C_i + V \rightarrow C_s–C_s$: Above $\sim$K,

where Si_i denotes a silicon self-interstitial.

In Fig. 3, the experimental evidence for this reaction scheme is presented. As shown in part (a) of the figure, the dominant center produced by electron irradiation of virgin Si:C below room temperature is C_i, which has two infrared active LVMs at 922 and 932 cm^{-1}. When the sample is heated to room temperature the intensities of these LVMs decrease as a function of time, and after 210 min they can no longer be detected, see part (b) of the figure. The concurrent formation of C_s–C_i is demonstrated by the appearance of the LVMs of this complex at

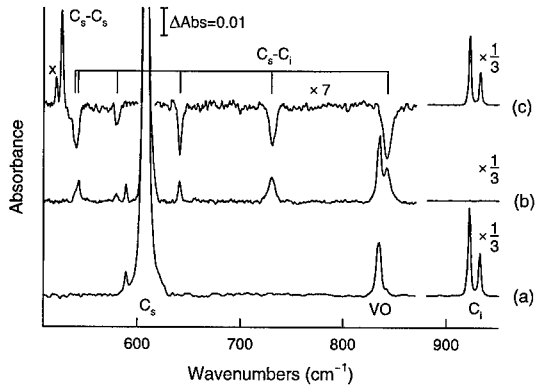

Fig. 3. Sections of absorbance spectra of Si:^{12}C recorded at 10 K: (a) just after electron irradiation below room temperature to a dose of 8×10^{17} cm^{-2}, (b) after subsequent room-temperature heat treatment for 210 min. The spectrum (c) is obtained by subtraction of spectrum (b) from a spectrum recorded after a second electron irradiation (6×10^{17} cm^{-2}) below room temperature. The absorption line denoted by × is not related to C_s–C_s.

540.4, 543.3, 579.8, 640.6, 730.4, and 842.4 cm^{-1} (see Ref. [6]). No C_s–C_s is formed at this stage. However, if the sample containing C_s–C_i is reirradiated with electrons below room temperature, but above ~ 200 K, the 527.4 cm^{-1} LVM of $(C_s–C_s)^0$ grows in and the LVMs of C_s–C_i decrease in intensity, as seen clearly from Fig. 3(c), in which the difference between the spectra recorded just after and before the second irradiation is shown.

The irradiation procedure described above was repeated several times on the same sample. For accumulated doses below $\sim 2 \times 10^{18}$ cm^{-2}, we find that the increase of the intensity of the $(C_s–C_s)^0$ line at 527.4-cm^{-1} is a linear function of the decrease of the intensities of the C_s–C_i lines, thus supporting the mechanism proposed above. When the accumulated dose exceeds 2×10^{18} cm^{-2}, the increase of the C_s–C_s lines falls below the linear relationship, and the intensity of the 527.4-cm^{-1} line saturates at $\sim 5 \times 10^{18}$ cm^{-2}. We take this to indicate that the accumulated radiation damage gives rise to additional processes that interfere with the simple reaction scheme proposed above.

4. Conclusions

Electron-irradiated n-type silicon doped with carbon has been studied by IR absorption spectroscopy. Absorption lines at 527.4 and 748.7 cm^{-1} have been identified as LVMs of $(C_s–C_s)^0$ and $(C_s–C_s)^-$, respectively. The formation mechanism of the center has been investigated and it is proposed that C_s–C_s is formed by the process $C_s–C_i + V \rightarrow C_s–C_s$.

Acknowledgements

We thank Pia Bomholt for preparing the samples for optical measurements. This work was supported by the Danish National Research Foundation through the Aarhus Center for Atomic Physics. E.V. Lavrov also acknowledges a grant from the Russian Foundation for Basic Research (grant No. 99-02-16652).

References

[1] G. Davies, R.C. Newman, in: T.S. Moss (Ed.), Handbook on Semiconductors, Vol. 3b, Elsevier Science, Amsterdam, 1994, p. 1557 and references therein.
[2] A.R. Bean, R.C. Newman, Solid State Commun. 8 (1970) 175.
[3] G.D. Watkins, K.L. Brower, Phys. Rev. Lett. 36 (1976) 1329.
[4] G.D. Watkins, in: M. Hulin (Ed.), Radiation Effects in Semiconductors, Dunod, Paris, 1965.
[5] J.R. Byberg, B. Bech Nielsen, M. Fancuilli, S.K. Estreicher, P.A. Fedders, Phys. Rev. B, submitted for publication.
[6] E.V. Lavrov, L. Hoffmann, B. Bech Nielsen, Phys. Rev. B, in press.
[7] J. Menendez, M. Cardona, Phys. Rev. B 29 (1984) 2051.

ELSEVIER

Physica B 273–274 (1999) 260–263

PHYSICA B

www.elsevier.com/locate/physb

A unified microscopic mechanism for donor deactivation in Si

R. Baierle[a], M.J. Caldas[b,*], J. Dąbrowski[c], H.-J. Müssig[c], V. Zavodinsky[d]

[a]*Departmento de Física, Universidade Federal de Santa Maria, 97105-900, Santa Maria, RS, Brazil*
[b]*Instituto de Física, Universidade de São Paulo, 05508-900 São Paulo, SP, Brazil*
[c]*Institute for Semiconductor Physics, Walter-Korsing-Str. 2, 15230 Frankfurt (Oder), Germany*
[d]*Institute for Automation and Control Processes, 5 Radio str., Vladivostok 690041, Russia*

Abstract

Dopant atoms segregate to SiO_2/Si(0 0 1) interfaces. This causes problems during manufacture of submicron microelectronic devices. On the basis of ab initio calculations, we identify the mechanisms by which P atoms are bonded and deactivated under the interface. We argue that P segregation occurs by (1) trapping at interfacial dangling bonds, (2) trapping at vacancies and vacancy–oxygen complexes bound under the interface, and (3) formation of pairs of threefold-coordinated P atoms. The first mechanism is important at low dopant concentrations and when no vacancies are available, the second one dominates at medium dopant concentrations after P implantation, the third one controls the segregation at dopant concentrations around 10^{19} cm^{-3} or higher.

Keywords: Si/SiO_2; Dopant deactivation; Dopant segregation

1. Introduction

Fabrication of silicon-integrated circuits involves implantation of a high concentration of donors. This is followed by processing at temperatures at which the dopants can migrate. CMOS technology relies on SiO_2 being placed next to doped regions of silicon. Segregation of dopants to SiO_2/Si interfaces causes a significant redistribution and deactivation of dopants, so that only a fraction of the dopant atoms remains electrically active [1]. As much as 50% of the implanted dopants can be lost during the pad oxide etch [2], and the interface can collect at least 3×10^{14}/cm^2 dopant atoms, that is, nearly a monolayer (1 ML $= 7 \times 10^{14}$/cm^2). Redistribution of the dopant atoms below gate oxides affects electrical parameters of MOS transistors. For example, the threshold voltage can be changed by 50% of its ideal value [3]. It is thus highly desirable to gain insight into the mechanisms for donor segregation and deactivation, since these effects will cause problems in the design and manufacture of ultra-sub-micron silicon devices.

In the literature, the segregation has been thus far treated at a phenomenological level. Details of dopant–interface interactions are unknown. It is unclear what causes the segregation, what are the atomic and electronic structures of the segregated donors, and what are their energies. A simple but physically correct description of the segregation mechanism would facilitate modeling of technological processes [1]. The purpose of this work is to provide fundamental insight into the physics of dopant segregation by ab initio studies of a typical donor, phosphorus.

The published segregation models [4–8] assume that the interface has a fixed number (~1 ML) of sites at which dopant atoms can be trapped, and do not differentiate between traps. However, this is inconsistent with the measured dependence of the dose loss on the implanted dose ("traps only", Fig. 1a). This inconsistency indicates that such models would fail when the dopant concentration changes strongly along the interface (as under oxide sidewalls in MOS transistors), even though these models work over a limited concentration range.

Here we formulate and discuss a general segregation model, based on results from ab initio calculations and

* Corresponding author. Tel.: 0055-11-818-6328; fax: 0055-11-818-6433.
E-mail address: mjcaldas@usp.br (M.J. Caldas)

0921-4526/99/$ - see front matter
PII: S0921-4526(99)00477-9

Auger electron spectroscopy measurements. We verify the model using published secondary ion mass spectroscopy (SIMS) data on P segregation [2,7,9]. Our results highlight the importance of mechanical strain near the interface, which promotes double-trapping (pairing) of dopants. We show that, as a consequence of pairing, the segregation mechanisms for high- and low-doping levels are qualitatively different.

We briefly describe in the next section the calculation methods and microscopic models for the interface and traps. In Section 3 we present and discuss the segregation model, and summarize our results.

2. Microscopic models

The calculations were done by ab initio supercell approaches.[1] Interface structures were calculated with the fhi96md code [10]. The reliability of results was verified by comparison with optimized geometries, electronic structures, and energy differences for test silicon–oxygen and silicon–oxygen–phosphorus structures computed with other ab initio codes (full-potential LMTO code [11,12] and LCAO-based ab initio pseudopotential code [13]) and with energy differences obtained by a semi-empirical method applied to clusters of roughly the same size as the supercells. The bulk defect calculations were done by the LCAO-based ab initio pseudopotential code SIESTA [13], using large cells.

We estimate that the numerical accuracy for energy differences between two atomic geometries associated with the same interface model is ~0.2 eV per unit cell (see footnote 1). The accuracy of binding energies is ~0.2 eV per phosphorus atom bonded in a complex. The numerical error is dominated by k-point sampling, small distance between defects in the neighboring supercells (in the interface models), and the LDA band-gap problem. The latter affects energy differences and binding energies when defects with deactivated donor atoms are compared to a substitutional donor. A band-gap correction was employed in such cases.

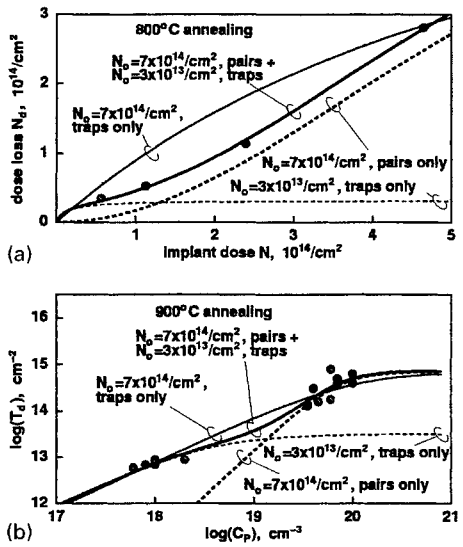

Fig. 1. Dopant pairing and dose loss: (Thin lines) trapping only, (Thick solid lines) pairing and trapping, (Broken lines) contributions from pairing (thick) and trapping (thin). (a) Dependence of P dose loss N_d on P implant dose N, SIMS data [2]. If traps only are assumed, the functional dependence is qualitatively wrong. Pairing and traps together give an excellent fit.(b) Dependence of P dose loss N_d on P concentration C_P close to the interface, SIMS data [9,7] The trap-dominated (low C_P) and pairing-dominated (high N_d) regimes are clearly visible.

The atomic geometries addressed in this work include (a) several models of the interface, (b) phosphorus atoms placed in various configurations at or near the interface, and (c) P atoms bonded in bulk-like defect complexes with and without oxygen. The details of these calculations will be given in a separate publication. Here, we focus on the hitherto unexpected effect of dopant pairing (that is, trapping of two P atoms at the same complex) below the interface.

The interfacial atomic structures were designed in such a way that as few atoms as possible represented the key features of the interface. These models were then systematically expanded towards increasingly realistic geometries. The fundamental geometry is built on the basis of a bulk Si(0 0 1) $1\times1\times8$ cell with two oxygen atoms inserted into Si–Si bonds in one of the (0 0 1) planes (Fig. 2a). The resulting SiOSi sandwich is stretched along the (0 0 1) axis to acommodate the compressive stress created by the insertion of oxygen. This makes a crude model of an amorphous SiO_2/Si(0 0 1) interface: each interfacial Si atom of the substrate has two O neighbors. There is no real SiO_2 in this system, but since phosphorus atoms are expelled from SiO_2 into silicon and since Si–O bonds are much stronger (stiffer) than Si–Si bonds, this numerically efficient model reasonably simulates an interface-like environment for exploratory

[1] Car-Parrinello type of pseudopotential calculations, with Local Density Approximation (LDA) after Ceperley and Alder [19] in the parameterization of Perdew and Zunger [20], and nonlocal pseudopotentials [21,22] in Kleinman-Bylander form [23]. Interface structures done by fhi96md code [10] in Si(0 0 1)-type supercells with lateral dimensions 2×2 to 4×4, typically six to eight Si layers and a single oxide layer with various boundary conditions described in the text. Convergence: 40 Ry cutoff for plane waves, tests between 16 Ry and 40 Ry; Brillouin zone sampled at the points equivalent to $(\frac{1}{4},\frac{1}{4})$ point of the fully symmetric 4×4 surface cell, test done at Γ and $(\frac{1}{4},\frac{1}{4})$ points from 4×4, 3×3, and 2×2 cells. Bulk defects with SIESTA [13] in FCC supercells based on a 128 Si bulk cell, double-zeta basis-set (tests with single-zeta).

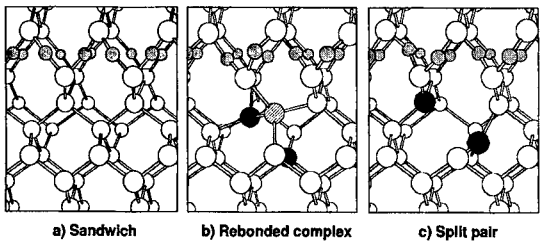

Fig. 2. Generic structures of phosphorus (black) trapped under SiO_2/Si(0 0 1). The phosphorus atoms of these P_2 complexes are deactivated (electrically neutral). (a) Idealized model of the SiO_2/Si(0 0 1) interface, (b) The dashed Si atom and its P neighbor form a pair of {1 1 3}-rebonded lattice atoms, (c) Threefold-coordinated P atoms of a distorted nearest-neighbor P_2 pair.

studies of the interaction between phosphorus, oxygen, and silicon atoms.

We found that at least two atomic configurations allow covering any SiO_2/Si(0 0 1) interface with nearly a full monolayer of P ($\sim 5 \times 10^{14}/cm^2$). (Fig. 2b and c). These structures involve no pre-existing defects, neither in Si nor in SiO_2/Si(0 0 1). Each of them is built on the basis of two threefold-coordinated, electrically neutral P atoms. One of these complexes (Fig. 2b) employs a local rearrangement of Si lattice bonds which we name "{1 1 3} rebonding" [14]. The geometry of {1 1 3}-rebonded atoms is analogous to the atomic configuration which is temporarily acquired near the barrier along the concerted-exchange path of Si self-diffusion [15]. The other structure is simply a distorted nearest-neighbor PP pair (Fig. 2c).

These complexes, in particular the PP pair, may be unstable in the bulk. But they are stabilized next to the interface, with the binding energy ~ 0.5 eV/mole in intrinsic material and ~ 1 eV/mole in n-type material. The stabilization takes place because the oxide helps to accommodate the stress caused by the deformation of the bonds around the defects and because the removal of a substrate bond makes the network more flexible, assisting in the relaxation of the interfacial stress.

In the bulk we found a stable complex between P and O in a P-decorated A-center (Fig. 3). The occurrence of the $V_{Si}P_{Si}$ complex (E-center) has been reported since a long time (donor trap) [16,17]. Pairing of P atoms has also been proposed at high doping levels. We found that in addition, in the presence of O atoms, the AP_2 complex is a strong candidate for double-trapping of donors. The complex is stable relative to various close associations of the component defects: the A-center (Fig. 3a) is stable relative to an interstitial oxygen O_i plus a vacancy V_{Si}, by ~ 2 eV; and AP_2 (Fig. 3c) is stable relative to $AP + P_{Si}$, and to $O_i + V_{Si}P_2$ (Fig. 3b), by ~ 0.5–1.3 eV. We thus find that two P donors and an O interstitial can lower their energy by ejecting a Si lattice atom to an interfacial step.

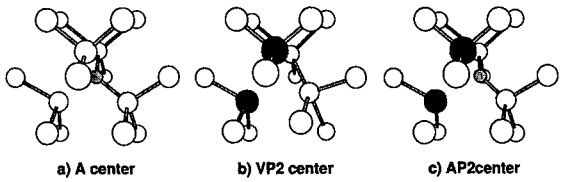

Fig. 3. Generic structures for phosphorus (black) trapped at vacancy defects in bulk Si. The phosphorus atoms of these P_2 complexes are deactivated (electrically neutral): (a) The oxygen(gray)-vacancy (V + O) neutral A-center, (b) The pair of P atoms trapped at a vacancy, (c) The pair of P atoms trapped at an A-center.

It is important to remark, however, that there are no PO bonds in the complex. The physical mechanism for P double-trapping and deactivation simple: through relaxation, each P atom assumes a three-fold coordination and re-traps an electron from the conduction band. This readily leads to a substantial energy gain, from electron-capture. There is also gain from exchanging the dimerized Si dangling bonds of the A-center (see Fig. 3) for the saturated inert lone-pairs of P (around ~ 0.7 eV). The pairing is in this case also favorable, relative to the simple PP complex, because there is no significant stress build-up compared to an already existing A-center. Summarizing our results up to this point, we found that not only P atoms may be trapped at vacancies and A-centers, they can also pair at such defects.

Turning now to Si processing, implantation creates interstitials and vacancies. Many of these recombine shortly after the implanted ion rests in the substrate, but some vacancies escape recombination and migrate to the interface. Implantation also kicks out some oxygen atoms from the screen oxide into the subsurface, where they will combine with vacancies and form A-centers. Annealing may then, instead of activating the P atoms, bring them close to the traps where they will be deactivated (as E or AP centers, single-trapping). However, if there is a high concentration of phosphorus, pairing may take place. Pairing can then happen as PP complexes, or as stable $V_{Si}P_2$, AP_2, or {1 1 3} rebonded complexes.

3. Thermodynamical model

We now perform an analysis of published SIMS data, using a thermodynamical model to estimate the dependence of the segregated dose N_d on the concentration C_P of active phosphorus under the interface. For this purpose, we assume that: (1) N_o deactivation sites exist under the interface. (2) Dopant atoms can be deactivated by pairing or trapping. (3) The corresponding reaction constants are thermally activated. (4) The active and

inactive dopants under the interface are in quasi-equilibrium (meaning here that activation rates = deactivation rates). This leads to

$$N_d = \frac{N_o C_P^2}{C_P^2 + B^2 \exp(-2E_s/kT)}. \quad (1)$$

When segregation is dominated by pairing and to the usual

$$N_d = \frac{N_o C_P}{C_P + B \exp(-E_s/kT)} \quad (2)$$

when trapping dominates. As explained below, analysis of the literature data in terms of this simple model (Fig. 1) verifies the plausibility of the segregation mechanism proposed in this work. The $N_d(C_P)$ dependence is recovered for the whole dopant concentration range under the gate and sidewall oxides in MOS transistors.

The segregation energy due to pairing is ~ 0.4 eV/mole from Fig. 1 (800°C and 900°C) and from the data in Ref. [18] (1000°C, not shown), while the segregation energy due to trapping is ~ 1.3 eV. These values are close to our ab initio estimates for pairing and trapping of phosphorus at broken bond sites, respectively. The density of "deactivating sites" of N_o for pairing corresponds to a monolayer, while N_o for trapping is $\sim 3 \times 10^{13}/\text{cm}^2$, which is about 10 times more than the typical number of electrically active interfacial defects. This indicates that defects such as nonstoichiometric sites (Si–Si bridges) may act as dopant traps, or, as discussed earlier, some phosphorus atoms may be trapped by silicon vacancies and A-centers. In order to account for $\sim 3 \times 10^{13}/\text{cm}^2$ trapping sites (5% of a monolayer, or 0.05 ML), one needs approximately 0.01–0.02 ML vacant sites (each A-center can trap two, and each vacancy can trap up to four P atoms). Assuming that these vacancies are localized between one to five atomic layers below the interface, the volume concentration of the segregated vacancies must be around $5\text{–}1 \times 10^{20}$ cm^{-3}. Calculations veryfying the stability of such a high vacancy concentration under SiO_2/Si(0 0 1) are in progress.

Our analysis indicates that any predictive simulation model which attempts to describe the segregation coefficient for P concentrations around 10^{18} cm^{-3} must account for the dopant pairing. The interface has much less than 1 ML of defect-related dopant traps, as expected of a high-quality boundary between two materials. The coexistence of pairing and trapping causes a two-regime dependence of the segregation coefficient on the implant dose (Fig. 1b). High- and low-coverage segregation are qualititatively different.

Concluding, we presented results of an ab initio study of dopant trapping and segregation to SiO_2/Si(0 0 1) interfaces. A simple and physically plausible model of the segregation of P atoms was formulated. We find that dopant segregation to the interface is aided by interfacial strain; so, segregation will also occur with any other dieletric that introduces strain. Moreover, losses at high implant doses are intrinsically nonlinear, because of pairing or double-trapping of dopants.

Acknowledgements

We are grateful to S. Dunham, A. Fischer, P. Masri, E. Artacho and A. Ourmazd for helpful discussions. This study was partially supported by the Deutsche Forschungsgemainschaft (DFG) project Nr. DA 308/5-1, by Conselho Nacional de Desenvolvimento Científico e Tecnológico (CNPq) and Fundaçao de Amparo à Pesquisa do Rio Grande do Sul (FAPERGS). The calculations were made possible by a grant of Cray T3E computer time by the von Neumann Institute for Computing (NIC) in Jülich, Germany; RB and MJC acknowledge use of the Laboratório de Computaç ao Científica Avançada, LCCA-USP.

References

[1] J. Dąbrowski, H.J. Müssig, M. Duane, S.T. Dunham, R. Goossens, H.-H. Vuong, Adv. Sol. State Phys. 38 (1999) 565.
[2] P.B. Griffin, S.W. Crowder, J.M. Knight, Appl. Phys. Lett. 67 (1995) 482.
[3] H.H. Vuong, C.S. Rafferty, S.A. Eshraghi, J.L. Lentz, P.M. Zeitzoff, M.R. Pinto, S.J. Hillenius, IEEE Trans. ED 43 (1996) 1144.
[4] M. Orlowski, Appl. Phys. Lett. 55 (1989) 1762.
[5] H. Sakamoto, S. Kumashiro, SISPAD (1997) 81.
[6] H.-H. Vuong, C.S. Rafferty, J.R. McMacken, J. Ning, S. Chaudhry, SISPAD (1997) 85.
[7] H.-H. Vuong, C.S. Rafferty, J. Ning, J.R. McMacken, J. McKinley, D.A. Stevie, SISPAD (1998) 380.
[8] R. Kasnavi, P.B. Griffin, J.D. Plummer, SISPAD (1998) 48.
[9] F. Lau, L. Mader, C. Mazure, Ch. Werner, M. Orlowski, Appl. Phys. A 49 (1989) 671.
[10] M. Bockstedte, A. Kley, J. Neugebauer, M. Scheffler, Comp. Phys. Commun. 107 (1997) 187.
[11] E. Bott, M. Methfessel, W. Krabs, P.C. Schmidt, J. Mat. Phys. 39 (1998).
[12] M. Methfessel, "NFP Manual", IHP Copyright, 1997.
[13] D. Sanchez-Portal, P. Ordejon, E. Artacho, J.M. Soler, Int. J. Quantum Chem. 65 (1997) 453.
[14] J. Dąbrowski, H.-J. Müssig, G. Wolff, S. Hinrich, Surf. Sci. 411 (1998) 54.
[15] K.C. Pandey, Phys. Rev. Lett. 57 (1986) 2287.
[16] G.D. Watkins, J.W. Corbett, Phys. Rev. 134 (1964) A1359.
[17] A. Fazzio, J.R. Leite, M.J. Caldas, Physica B 116 (1983) 90.
[18] Y. Sato, M. Watanabe, K. Imai, J. Electrochem. Soc. 140 (1993) 2679.
[19] D.M. Ceperley, B.J. Alder, Phys. Rev. Lett. 45 (1980) 567.
[20] J.P. Perdew, A. Zunger, Phys. Rev. B 23 (1981) 5048.
[21] D.R. Hamann, Phys. Rev. B 40 (1989) 2980.
[22] G.B. Bachelet, D.R. Hamann, M.A. Schlüter, Phys. Rev. B 26 (1982) 4199.
[23] L. Kleinman, D.M. Bylander, Phys. Rev. Lett. 48 (1982) 1425.

ELSEVIER

Physica B 273–274 (1999) 264–267

PHYSICA B

www.elsevier.com/locate/physb

EPR proof of the negatively charged acceptor state Zn^- in silicon

W. Gehlhoff[a,*], A. Näser[a], H. Bracht[b]

[a]*Institut für Festkörperphysik, Technische Universität Berlin, Sekr. PN5-2, Hardenbergstr. 36, D-10623 Berlin, Germany*
[b]*Institut für Metallforschung, Universität Münster, Wilhelm-Klemm-Straße 10, D-48149 Münster, Germany*

Abstract

The electronic properties of Zn in monocrystalline silicon were studied by means of electron paramagnetic resonance (EPR). In high-ohmic p- and n-type Si doped with Zn two new line sets were observed. One of them show the characteristic behavior of the $\frac{1}{2}\leftrightarrow -\frac{1}{2}$ and $\frac{3}{2}\leftrightarrow -\frac{3}{2}$ transitions of a Γ_8 state in tetrahedral symmetry and can be detected for all sample orientations. The line positions of this set can be well described with a spin Hamiltonian for $S=\frac{3}{2}$ including the linear and cubic Zeeman-interaction and the fitted parameters $|g|=1.1749\pm 0.0005$ and $|f|=0.0402\pm 0.0005$ ($g.f>0$). For magnetic field directions around $B\|\langle 1\,0\,0\rangle$, a second line set consisting of seven additional lines were detected which can be described by the spin transitions within a coupled (Γ_7–Γ_8)-ground state manifold. Based on the analysis of the experimental data this spectrum has been identified as arising from the negative charge state of the isolated substitutional Zn_s^- in silicon.

PACS: 61.72.Bb; 61.72.Ji; 71.55.Cn; 76.30.Lh

Keywords: Silicon; Paramagnetic defects; Spin resonance; Zinc

1. Introduction

In spite of a large number of investigations performed with different methods the electronic and geometric structure of isolated atoms of the group II impurity Zn ($[Ar]3d^{10}4s^2$) in Si still remains unclear. For isolated atoms of substitutional group II impurities in Si one expects singly and doubly charged acceptor levels to be positioned deep in the gap of silicon. Such deep acceptor levels assigned to $Zn^{-/0}$ (E_V+310 meV) and $Zn^{2-/-}$ (E_V+600 meV) were first established by Hall effect measurements [1,2]. In the following decades numerous investigations using photoconductivity and several variants of deep level transient spectroscopy (DLTS) confirmed this main result and exhibited some additional Zn-related centers. A summary of the results obtained, showing some scatter between the data, is given in Ref. [3]. Also, negative-U properties for Zn-related centers are discussed [4]. By infrared absorption spectroscopy only the transition $Zn^{-/0}$ at 320 meV could be identified [5,6]. In Si samples doped with Zn by high-temperature diffusion two trigonal spectra and several isotropic lines were observed by means of electric-dipole spin resonance (EDSR) [7]. However, direct experimental data for the microscopic structure of the singly and doubly charged acceptor states are not published up to now. Especially for the Zn_s^- charge state with one missing electron in the sp^3-orbitals of the Si bonding one might expect EPR or EDSR spectra analogous to those observed for the single acceptors B, Al, Ga and In in Si in the neutral charge state [8]. However, so far only various transition metal–Zn pairs have been identified by EPR in samples with corresponding co-doping [9].

In this paper the first EPR results on a Zn-related center with tetrahedral symmetry, which we assigned to isolated substitutional single ionized Zn_s^-, are presented.

* Corresponding author. Fax: + 49-30-314-22569.
E-mail address: gehlhoff@sol.physik.tu-berlin.de (W. Gehlhoff)

0921-4526/99/$ - see front matter
PII: S0921-4526(99)00481-0

2. Experimental

For the EPR experiments samples of about $12 \times 3 \times 3\,mm^3$ in size were cut from monocrystalline n- and p-type silicon. The material used was Czochralski grown as well as highly pure float-zone silicon with resistivities of 1.4 to 3000 Ω cm for p-type (B-doped) or 1.5 to 2100 Ω cm for n-type (P-doped) samples. For indiffusion of Zn the silicon samples together with a small amount of metallic Zn were encapsulated in an evacuated quartz ampoule and annealed between 1125°C and 1250°C for 24 h. Either Zn of the natural isotope composition as well as Zn enriched to above 92% with the isotope ^{67}Zn ($I = \frac{5}{2}$) was used. At the end of the diffusion process the silicon samples were rapidly quenched to room temperature by plunging the ampoule into water or ethylene glycol. Most of the samples were investigated before and after an additional annealing at 600–650°C for 30–60 min.

The EPR measurements were performed at the X-band in the temperature region 3.9–20 K using a Bruker ESP 300E spectrometer equipped with an Oxford ESR 900 helium gas-flow cryostat. In the most cases a special high sensitive TE_{011} resonator was used. The samples were always mounted with their long dimension perpendicular to the plane in which the external magnetic field B could be rotated. The samples could be illuminated with band-gap light from a halogen lamp through the sample holder or using a rectangular resonator by an opening in the resonator wall.

3. Results and discussion

In high-ohmic p- and n-type samples an EPR spectrum with trigonal symmetry very similar to the spectra described in Ref. [7] is dominant. The angular dependence of the EPR transitions is presented in Fig. 1 showing the typical behavior of the line positions, intensities and shapes for $\Delta M = 2$ spin transitions within a $S' = 1$ system with predominantly trigonal symmetry including random strains. In a first approach, the line positions can be described (within the error limit caused mainly by the misorientation of the samples and the error in the determination of the rotation angle) with $S' = 1, g'_{||} = 1.016, |D| \geqslant 10\,cm^{-1}$ and an effective orthorhombic distortion $E^* = 0.05\,cm^{-1}$. A more detailed discussion of the properties of this Zn-related center is given elsewhere [10].

After annealing of such samples at 600°C for 15–60 min we could observe several new lines, whose intensities increase in the most cases remarkably under illumination with band gap light. A typical example with dominating intensities of the new lines is given in Fig. 2. One of the EPR transitions shows the typical angular

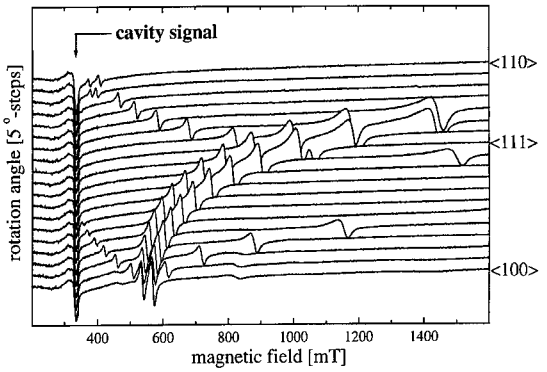

Fig. 1. Stack plot of the EPR transitions of a Zn-related center with dominantly trigonal symmetry at $T = 4$ K in the X-band ($\nu = 9.48$ GHz) using 2 mW microwave power. The magnetic field is rotated by 5° steps in a {1 1 0} crystal plane. The marked line splitting for one line set is caused by a small misorientation of the sample.

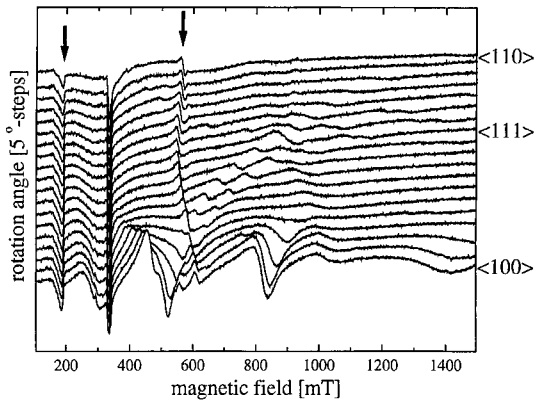

Fig. 2. Stack plot of the EPR transitions observed at 4.1 K for high-ohmic p-type Si after Zn diffusion and additional annealing at $T = 600$°C as well as in situ excitation of the sample with band-gap light. The magnetic field is rotated by 5° steps in a {1 1 0} crystal plane. Besides the weakened transitions of the trigonal center shown in Fig. 1 two new line sets are exhibited around $B||\langle 1\,0\,0\rangle$. The line sets indicated by arrows are observable for all sample orientations.

dependence of the $\frac{1}{2} \leftrightarrow -\frac{1}{2}$ transitions of a Γ_8 state in cubic (T_d, O_h, O) symmetry. This line set (right arrow in Fig. 2) can be well described using a spin-Hamiltonian with $S' = \frac{3}{2}$ including the linear and cubic Zeeman interactions

$$\mathcal{H} = g\beta \boldsymbol{B}\cdot\boldsymbol{S} + f\beta\{S_x^3 B_x + S_y^3 B_y + S_z^3 B_z - \tfrac{1}{5}(\boldsymbol{S}\cdot\boldsymbol{B})[3\boldsymbol{S}(\boldsymbol{S}+1) - 1]\}. \quad (1)$$

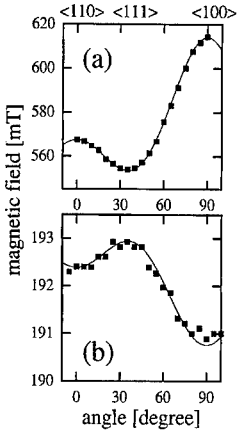

Fig. 3. a, b: Experimental line positions [■] of the two EPR transitions belonging to the line set which is observable for all sample orientations and are indicated by arrows in Fig. 2. The solid lines are calculated using the spin Hamiltonian (1) and the fitted parameter set given in Eq. (2). These transitions are assigned to the $\frac{1}{2} \leftrightarrow -\frac{1}{2}$ (a) and $\frac{3}{2} \leftrightarrow -\frac{3}{2}$ (b) transitions within a Γ_8 state arising from substitutional Zn_s^-.

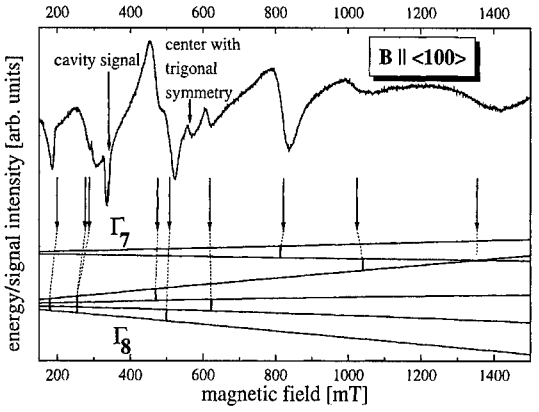

Fig. 4. EPR spectrum of substitutional Zn_s^- for the magnetic field $B \| \langle 1\,0\,0 \rangle$. Comparison of the experimental line positions with the calculated ones using a generalized spin Hamiltonian for a coupled (Γ_7–Γ_8)-manifold and the fitted parameter given in Eq. (3). Also the splitting of the energy levels of the (Γ_7–Γ_8)-manifold in the magnetic field B is shown.

In Fig. 3a the experimental angular dependence of the line positions of this transition is compared with the calculated one using the spin Hamiltonian (1) and the parameter set

$$|g| = 1.1749 \pm 0.0005, \quad |f| = 0.0402 \pm 0.0005$$

$$\text{with } gf > 0. \tag{2}$$

The excellent fitting indicates that these transitions can only arise in Si from a center with tetrahedral (T_d) symmetry. The characteristic cubic angular dependence could be also proved for the $\frac{3}{2} \leftrightarrow -\frac{3}{2}$ ($\Delta M = 3$) transitions (left arrow in Figs. 2 and 3b). But the line widths and the asymmetric line shapes caused by the random strains in the sample prevent a determination of the line positions with high accuracy. Another consequence of the large line width was that a hyperfine structure caused by ^{67}Zn ($I = \frac{5}{2}$) could not be resolved.

The saturation behavior of the $\frac{1}{2} \leftrightarrow -\frac{1}{2}$ transition reveals a very strong lattice coupling of the center, similar to the one observed for the Cd_s center [11] in Si. Therefore, it is reasonable to assign the spectrum with tetrahedral symmetry to isolated substitutional Zn in silicon. Such assignment is also corroborated by theoretical predictions. Total energy calculations for isolated Zn on the unrelaxed substitutional and tetrahedral interstitial sites in their different charge states suggest that the substitutional position should be the equilibrium site for Zn at the doping levels of our samples [12].

The fitted parameters given in Eq. (2) are similar to the ones obtained for the neutral charge state of the shallow single acceptors B^0, Al^0, Ga^0, In^0. This similarity suggests that the spectrum originates from the Zn_S^- state. This assumption is supported by the corresponding Fermi level in the band gap estimated from the preparation conditions and through the appearance of small lines from unintentionally doped impurities like Fe with well-known gap levels.

For magnetic field directions around $B \| \langle 1\,0\,0 \rangle$ a second set of lines consisting of seven lines could be detected (Fig. 2). Four lines can be attributed to the transitions $\pm\frac{1}{2} \leftrightarrow \pm\frac{3}{2}$ ($\Delta M = 1$) and $\pm\frac{1}{2} \leftrightarrow \pm\frac{3}{2}$ ($\Delta M = 2$) within the Γ_8 state. However, their shifted line positions in comparison with the calculated ones using the spin Hamiltonian (1) as well as the line position of three other lines demonstrate a strong admixture from a nearby twofold spin state. The spectrum can be analyzed within the manifold of the Γ_8 and Γ_7 states using a generalized spin Hamiltonian for the coupled ground state [10]. With the fitted parameter set

$$g_{81} = -1.09, \quad g_{82} = 1.28, \quad g_7 = -0.82,$$

$$g_{78} = 0.55, \quad E(\Gamma_7, \Gamma_8) = -1.4\,\text{cm}^{-1}, \tag{3}$$

the experimental line positions are well described (see Fig. 4). However the parameter set (3) is only a preliminary one, because there are five parameters for the description of such strongly coupled-manifold and an unambiguous assignment of all transitions and an accurate determination of all parameters require measurements at different magnetic field directions and microwave frequencies.

4. Conclusions

An EPR spectrum with cubic (tetrahedral) symmetry firstly observed could be identified as arising from the negatively charge state of isolated Zn on substitutional lattice site in Si. Parts of the spectrum can be well described by the spin transition within a Γ_8 state in cubic symmetry with similar parameters like the transitions for the neutral charge state of the single shallow acceptors B^0, Al^0, Ga^0, In^0 [8]. In contrast to these shallow acceptors for the deep Zn acceptor the influence of a nearby lying Γ_7-state must be considered and the whole EPR spectrum can be correctly described only within the resulting (Γ_7–Γ_8)-ground state manifold. The proof of a stable configuration of Zn^- gives evidence that the double acceptor Zn has no negative-U properties as claimed in Ref. [6].

Acknowledgements

The authors are indebted to W. Zulehner (Wacker Siltronic GmbH) for supporting us with high-ohmic Si starting material as well as H. Schroth and K. Laßmann (Univ. Stuttgart) for stimulating discussions.

References

[1] C.S. Fuller, F.J. Morin, Phys. Rev. 105 (1957) 379.
[2] R.O. Carlson, Phys. Rev. 108 (1957) 1390.
[3] S. Weiss, R. Beckmann, R. Kassing, Appl. Phys. A 50 (1990) 151.
[4] E. Merk, J. Heymann, E.E. Haller, Solid State Commun. 72 (1989) 851.
[5] A. Dörnen, R. Kienle, K. Thonke, P. Stolz, G. Pensl, D. Grünebaum, N.A. Stolwijk, Phys. Rev. 40 (1989) 12005.
[6] N.T. Bagraev, Solid State Commun. 95 (1995) 365.
[7] H. Schroth, K. Lassmann, H. Bracht, Proc. ICPS-23 (1996) 2725.
[8] A. Köpf, K. Lassmann, Phys. Rev. Lett. 56 (1990) 1122.
[9] H.E. Altink, T. Gregorkiewicz, C.A.J. Ammerlaan, Mater. Res. Soc. 262 (1992) 525.
[10] A. Näser, Doctoral Thesis, Technische Universität-Berlin, 1999.
[11] W. Gehlhoff, A. Näser, M. Lang, G. Pensl, Mater. Sci. Forum 258/263 (1997) 423.
[12] H. Bracht, H. Overhof, Phys. Stat. Sol. A 158 (1996) 47.

ELSEVIER

Physica B 273–274 (1999) 268–270

PHYSICA B

www.elsevier.com/locate/physb

Theoretical studies of interstitial boron defects in silicon

M. Hakala*, M.J. Puska, R.M. Nieminen

Laboratory of Physics, Helsinki University of Technology, P.O. Box 1100, FIN-02015 HUT, Finland

Abstract

We employ pseudopotential plane-wave calculations to study the interstitial B in Si in different ionic configurations and charge states. For all charge states the ground state is a B–Si pair in which the B atom is close to a substitutional site and the Si atom in a nearby tetrahedral position. The defect has negative-U property and exhibits a symmetry-lowering distortion. We also report several metastable configurations which are close in formation energy. The relation of the defects to B diffusion is discussed. © 1999 Elsevier Science B.V. All rights reserved.

Keywords: Silicon; Boron; Interstitials

1. Introduction

The understanding of dopant atom–native defect interactions is crucial for modeling diffusion in crystalline Si [1]. The formation of native point defects and the reactions of the dopant atoms with them determine the energetically favorable diffusion mechanisms. Excess native point defects, generated by surface oxidation or ion implantation, are the source of the often harmful enhanced dopant diffusion. For B in Si the diffusion has been shown to occur predominantly via interstitial B_i, which are generated by a kick-out reaction [2–4]. First, a Si self-interstitial interacts with a substitutional B so that the B atom ends up in the interstitial region. The B atom diffuses in the interstitial channel and finally recombines to a substitutional position. To understand the atomic structure of the defects and the possible charge state effects involved it is essential to perform first-principles calculations.

Experimental studies of electron-irradiated boron-doped Si at cryogenic temperatures have revealed an interstitial B defect [5–7]. The defect was found to show negative-U property. On the basis of experimental data several models have been proposed for the atomic structure of the defect [5,7]. Tarnow [8] employed first-principles total-energy calculations to investigate the microscopic structure of the defect, and found that it is a pair of a substitutional B and a Si self-interstitial. This defect has been considered to form an intermediate step in the kick-out process [4].

In the present study we go beyond the calculations by Tarnow [8] and study more systematically interstitial B in Si in different ionic configurations and charge states. We also report the metastable states of B_i. Results are presented for the formation and binding energies of the different configurations. Finally we discuss the implications of our results for B diffusion.

2. Methods

We use the plane-wave pseudopotential method [9] within the spin-polarized density-functional theory [10,11]. The electron exchange and correlation is taken into account in the local-spin-density approximation [11]. For Si we use a norm-conserving non-local pseudopotential [12,13] with the non-linear core-valence exchange-correlation scheme [14], whereas for B we have generated a non-norm-conserving Vanderbilt-type pseudopotential [15,16]. For the valence-electron wave

* Corresponding author. Tel.: + 358-9-451-3149; fax: + 358-9-451-3116.

E-mail address: mikko.hakala@hut.fi (M. Hakala)

PII: S0921-4526(99)00484-6

functions we use a plane-wave expansion with an 18 Ry kinetic-energy cutoff.

We employ 32-atom supercells with the $2\times2\times2$ Monkhorst–Pack [17] $\boldsymbol{k}$-point sampling throughout the calculations. For the interstitial configurations an extra atom is added to the supercell. For the total-energy differences we find the convergence within 0.1 eV with respect to increasing the supercell size to 64 atoms. In the structure minimization we move the ions according to the Hellmann–Feynman forces. No symmetry restrictions are imposed. Since the structure relaxes to the nearest (meta)stable minimum we use several initial positions to map all the minima. Further computational details will be reported in a later publication [18].

The formation energy of a given defect D can be defined as [19]

$$E_f^Q = E_D^Q + Q(E_v + \mu_e) - \sum_s n_s\mu_s, \quad (1)$$

where E_D^Q is the total energy of the supercell containing the defect, Q the charge state of the defect, E_v the top of the valence band, μ_e the electron chemical potential (i.e., the Fermi level) in the band gap relative to the top of the valence band, and n_s the number of atoms of type s. The chemical potential of a Si atom (μ_{Si}) is the total energy/atom in a perfect Si lattice. Since we compare only the formation energy differences it is not necessary to define the absolute value of the chemical potential of a B atom (μ_B). Thus, in practice, we scale the formation energy diagram so that the zero of energy corresponds to the formation energy of the substitutional B in the neutral charge state. To properly align the energy bands for different supercells a correction for E_v is also used [20,21].

3. Results and discussion

We have first studied the substitutional B in the absence of any other defects. We find that the negative charge state is stable for all the Fermi level positions in the band gap. In practice, the substitutional B binds a hole into a shallow effective-mass state producing in a subsequent ionization a delocalized hole in the valence band. The ionic relaxations around the B atom are inwards, about 12% of the Si bond length, in good agreement with the previous calculations for the neutral charge state [22–24]. The point symmetry of the negatively charged defect is T_d.

The formation energies of the most important interstitial B configurations (i.e., one extra B atom in the Si crystal) are shown in Fig. 1. Also shown is the formation energy of the isolated B_{Si}^-. The extra Si atom in the interstitial configurations is accounted for by using the chemical potential of a Si atom in a perfect lattice (i.e., subtracting μ_{Si} from the total energy of the defect). We discuss first the pair configuration B_{Si}–Si_i and then the other more prominently interstitial type structures B_i. It is noteworthy that the formation energies of the interstitial configurations are considerably higher than that for the isolated B_{Si}^- defect. The interstitial configurations cannot therefore cause acceptor compensation. The inactivation of B has to result e.g. from clustering of B atoms [25,26].

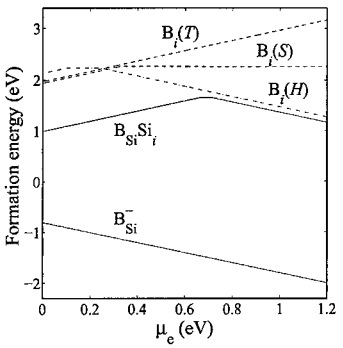

Fig. 1. Formation energies for the most important substitutional and interstitial B configurations as a function of the position of the Fermi level (μ_e). The zero of the formation energy corresponds to the substitutional B in the neutral charge state. The extra Si atom is taken into account by using the chemical potential of a Si atom in a perfect lattice. The experimental band gap is used as the upper limit of the Fermi level. T, S and H denote the tetrahedral, ⟨1 0 0⟩-split and hexagonal interstitial sites, respectively.

We study the pair configuration B_{Si}–Si_i in charge states 1+, 0, and 1−. Since the neutral charge state is stable for only a very small range of the Fermi level positions it can in practice be considered as metastable. The point symmetry of the neutral charge state is C_{1h}, which is consistent with experiments [5]. The 1+ charge state has the C_{3v} point symmetry and the 1− charge state the C_{1h} point symmetry. The geometry of the defect is qualitatively in accordance with the calculations by Tarnow [8]. The B atom stays close to its substitutional position and the Si atom close to a nearby tetrahedral position. The binding energy of the Si atom to the B_{Si}–Si_i defect is found to be 0.1–0.2 eV depending on the charge state. The weak binding is in accordance with the experimental observation that the Si interstitial is highly mobile also in B-doped Si (see, for example, Ref. [27]).

Troxell and Watkins have found enhanced migration of B_i under minority-carrier injection in n- and p-type material [7]. The enhanced migration was explained by a Bourgoin mechanism [28,29], in which the migrating defect alternates between two lattice configurations. The lattice configuration depends on the charge state, and cyclical trapping of electrons and holes leads to enhanced

diffusion. Our calculations support this kind of interpretation. The most important metastable configurations of B_i are the $\langle 1\,0\,0\rangle$-split (S), tetrahedral (T), and hexagonal (H) lattice sites (see Fig. 1). The bond-centered site is higher in formation energy for all the charge states. For the neutral and the negative charge state it lies more than 0.6 eV above the preceding sites. In p-type material the S and T sites are the energetically favorable interstitial positions for B_i, whereas in n-type material the H site is the favorable one. We also see from Fig. 1 that the change of the charge state leads to a change of the lowest-energy interstitial configuration B_i. However, the actual migration barriers between the sites should be analyzed to verify the proposed migration mechanism.

Under equilibrium concentrations of native point defects the activation energy of the defect-mediated B diffusion can be defined as a sum of the formation (E_f) and migration (E_m) energies for the diffusing species [22,23]. We calculate E_f as a sum of the formation energy of a Si self-interstitial ($\sim$3.3 eV) and the energy of exchanging a Si self-interstitial and a substitutional B ($\sim$0.7 eV). For E_m we use a value of 0.2 eV [30]. We obtain the activation energy of $\sim$4.2 eV when the Fermi level is at the midgap. This corresponds closely with the experimental range of 3.2–3.9 eV [1] and the earlier calculated value of 3.9 eV for the neutral charge state [22,23]. The relatively high activation energy is due to the formation of Si self-interstitials. However, the activation energy can be significantly smaller if excess Si interstitials are present in the crystal [27].

In conclusion, we have performed first-principles calculations for interstitial B in different ionic configurations and charge states. The lowest-energy structure exhibits the negative-U behavior and point symmetries in accord with experiment. The metastable interstitial configurations are the lowest-energy positions along the B migration pathway. We find that the metastable interstitial configurations depend on the charge state. The calculated activation energy of B diffusion agrees well with experiment.

Acknowledgements

This research has been supported by the Academy of Finland. We acknowledge the generous computing resources from the Center for Scientific Computing, Espoo, Finland.

References

[1] P.M. Fahey, P.B. Griffin, J.D. Plummer, Rev. Mod. Phys. 61 (1989) 289.
[2] N.E.B. Cowern, K.T.F. Janssen, G.F.A. van de Walle, D.J. Gravesteijn, Phys. Rev. Lett. 65 (1990) 2434.
[3] N.E.B. Cowern, G.F.A. van de Walle, D.J. Gravesteijn, C.J. Vriezema, Phys. Rev. Lett. 67 (1991) 212.
[4] N.E.B. Cowern, G.F.A. van de Walle, P.C. Zalm, D.J. Oostra, Phys. Rev. Lett. 69 (1992) 116.
[5] G.D. Watkins, Phys. Rev. B 12 (1975) 5824.
[6] G.D. Watkins, J.R. Troxell, Phys. Rev. Lett. 44 (1980) 593.
[7] J.R. Troxell, G.D. Watkins, Phys. Rev. B 22 (1980) 921.
[8] E. Tarnow, Europhys. Lett. 16 (1991) 449.
[9] M.C. Payne, M.P. Teter, D.C. Allan, T.A. Arias, J.D. Joannopoulos, Rev. Mod. Phys. 64 (1992) 1045.
[10] P. Hohenberg, W. Kohn, Phys. Rev. 136 (1964) B864.
[11] O. Gunnarsson, B.I. Lundqvist, Phys. Rev. B 13 (1976) 4274.
[12] G.B. Bachelet, D.R. Hamann, M. Schlüter, Phys. Rev. B 26 (1982) 4199.
[13] D.R. Hamann, Bull. Am. Phys. Soc. 33 (1988) 803.
[14] S.G. Louie, S. Froyen, M.L. Cohen, Phys. Rev. B 26 (1982) 1738.
[15] D. Vanderbilt, Phys. Rev. B 41 (1990) 7892.
[16] K. Laasonen, A. Pasquarello, R. Car, C. Lee, D. Vanderbilt, Phys. Rev. B 47 (1993) 10142.
[17] H.J. Monkhorst, J.D. Pack, Phys. Rev. B 13 (1976) 5188.
[18] M. Hakala, M.J. Puska, R.M. Nieminen, unpublished.
[19] J.E. Northrup, S.B. Zhang, Phys. Rev. B 47 (1993) 6791.
[20] A. Garcia, J.E. Northrup, Phys. Rev. Lett. 74 (1995) 1131.
[21] S. Pöykkö, M.J. Puska, R.M. Nieminen, Phys. Rev. B 53 (1996) 3813.
[22] C.S. Nichols, C.G. Van de Walle, S.T. Pantelides, Phys. Rev. Lett. 62 (1989) 1049.
[23] C.S. Nichols, C.G. Van de Walle, S.T. Pantelides, Phys. Rev. B 40 (1989) 5484.
[24] J. Zhu, T.D. Rubia, L.H. Yang, C. Mailhiot, G.H. Gilmer, Phys. Rev. B 54 (1996) 4741.
[25] P.A. Stolk, H.J. Gossman, D.J. Eaglesham, D.C. Jacobson, J.M. Poate, Appl. Phys. Lett. 66 (1995) 568.
[26] P.A. Stolk, H.J. Gossman, D.J. Eaglesham, J.M. Poate, Nucl. Instr. and Meth. 96 (1995) 187.
[27] G.D. Watkins, in: T. Diaz de la Rubia, S. Coffa, P.A. Stolk, C.S. Rafferty (Eds.), Defects and Diffusion in Silicon Processing, MRS Symposium Proceedings No. 469, Materials Research Society, Pittsburgh, 1997, pp. 139–150.
[28] J.C. Bourgoin, J.W. Corbett, Inst. Phys. Conf. Ser. 23 (1975) 149.
[29] J.C. Bourgoin, J.W. Corbett, Phys. Lett. 38A (1972) 135.
[30] J. Zhu, in: T. Diaz de la Rubia, S. Coffa, P.A. Stolk, C.S. Rafferty (Eds.), Defects and Diffusion in Silicon Processing MRS Symposium Proceedings No. 469, Materials Research Society, Pittsburgh, 1997, p. 158.

ELSEVIER

Physica B 273–274 (1999) 271–274

PHYSICA B

www.elsevier.com/locate/physb

Defects incorporating Ge atoms in irradiated Si : Ge

N.A. Sobolev[a,b,*], M.H. Nazaré[a]

[a]*Departamento de Física, Universidade de Aveiro, 3810-193 Aveiro, Portugal*
[b]*Institute of Solid State and Semiconductor Physics, ul. P. Brovki 17, 220072 Minsk, Byelorussia*

Abstract

Photoluminescence due to radiation defects in silicon doped with Ge at a concentration of 2×10^{20} cm^{-3} and subjected to neutron irradiation and subsequent annealing is analyzed and compared to that of silicon crystals containing less or no Ge. Several spectra are ascribed to centers incorporating Ge atoms. At concentrations of the order of 10^{20} cm^{-3} the Ge atoms are found to be the main sinks for the Frenkel pair components.

Keywords: Silicon; Germanium; Defects; Luminescence

1. Introduction

The influence of isovalent impurities, especially Ge, on the accumulation process of radiation defects (RDs) in silicon irradiated by gamma rays and elementary particles has been comprehensively studied (for a review, see, e.g., Refs. [1–3]). However, no defects incorporating Ge atoms have been identified which would be stable at room temperature and above it. The only positively identified defect incorporating Ge, namely, the Ge-vacancy pair, anneals well below room temperature [4]. Therefore, it has been believed that at $T \geqslant 300$ K Ge atoms act only as centers of indirect recombination of Frenkel pair components (vacancies and self-interstitials).

The near band edge photoluminescence (PL) of irradiated silicon doped with Ge concentrations $< \sim 10^{19}$ cm^{-3} brought new insights into the problem [5]. New lines labeled M80-83 were found in samples with $N(\mathrm{Ge}) = (1\text{–}2)\times10^{19}$ cm^{-3}. The appearance of the M80 and M82 lines could be well correlated with the presence of the Ge impurity. The impurity correlation of the centers M81 and 83 remained less certain.

In the present work, the investigated Ge concentration range is extended up to 2×10^{20} cm^{-3}. Supporting evidence for the incorporation of Ge atoms into the centers M80-83 is found. New centers (M86-88), presumably related to Ge, are encountered in the near band edge spectral range. The spectra of deeper centers will be treated in a forthcoming publication [6].

2. Experimental

Samples of monocrystalline, slightly P-doped silicon without Ge as well as of that doped with Ge at a concentration of 2×10^{20} cm^{-3} were investigated. The samples had a specific resistivity of $\geqslant 10^3\ \Omega\times$cm and contained carbon and oxygen in concentrations $(1\ldots7)\times10^{16}$ cm^{-3}. The Ge concentration was determined by neutron activation analysis and by X-ray microprobe analysis. The oxygen and carbon concentrations were measured by means of the IR absorption in the 1100 and 607 cm^{-1} bands. The neutron irradiation to a fluence of 6×10^{17} cm^{-2} was performed in a water reactor with a ratio of thermal to fast neutron fluxes of ca. 10 : 1 at a sample temperature of about 60°C. Irradiated samples were annealed in ambient air for 15 min over a temperature range $T_a = 50$–800°C in 25°C steps. The recombination radiation was excited by an Ar-ion laser, dispersed through a grating monochromator and detected by

* Correspondence address: Departamento de Física, Universidade de Aveiro, 3810-193 Aveiro, Portugal. Fax: + 351-34-424 965.

E-mail address: sobolev@fis.ua.pt (N.A. Sobolev)

0921-4526/99/$ - see front matter
PII: S0921-4526(99)00489-5

a cooled photomultiplier having an S-1-type cathode. All measurements were carried out at 4.2 K.

3. Results and discussion

In the PL spectra of all starting Si and Si : Ge crystals one observes lines caused by the radiative recombination of free excitons (Ex) as well as of excitons and multiexciton complexes bound to substitutional phosphorus and boron atoms (Fig. 1a). At high laser powers, the bands of electron–hole droplets (EHD) strongly appear. With increasing Ge concentration, the following phenomena are observed: (i) All lines are broadened due to a random band gap modulation and/or due to a random strain induced by fluctuations of the Ge concentration across the crystals. For $N(\mathrm{Ge}) = 2 \times 10^{20}\ \mathrm{cm}^{-3}$, the P_{NP} line (caused by the no-phonon recombination of the phosphorus-bound exciton) has a symmetric shape with an FWHM (full-width at half-maximum) of 0.7 meV. (ii) All lines are shifted toward lower energies. For $N(\mathrm{Ge}) = 2 \times 10^{20}\ \mathrm{cm}^{-3}$, the shift amounts to 1.7 meV, which exactly equals to the band gap shrinkage calculated using data of Ref. [7]. (iii) The no-phonon line (NPL) of the free exciton (Ex_{NP}) grows in intensity relative to its phonon replica due to perturbations of the translation symmetry of the lattice. (iv) The zero-phonon band of the EHDs emerges and grows due to the same reason. The magnitude of the effects listed in (i)–(iii) is in agreement with the previously published data [8].

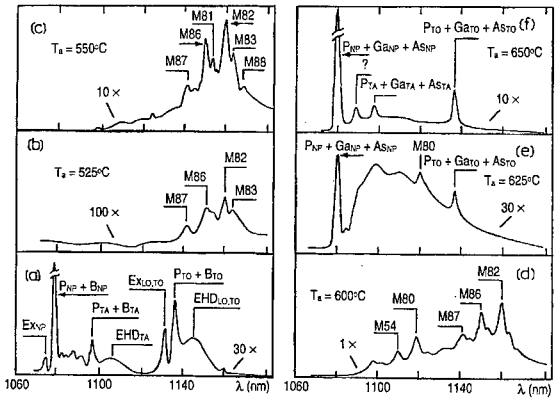

Fig. 1. Near band edge PL spectra of silicon containing 2×10^{20} Ge/cm^3 (a) as grown and after neutron irradiation and subsequent annealing at the following temperatures (°C): (b) 525, (c) 550, (d) 600, (e) 525 + 625, (f) 550 + 650. Ex means the free exciton. P, Ga, As, and B denote the lines of excitons bound to substitutional phosphorus, gallium, arsenic, and boron atoms, respectively. NP, TA, LO and TO designate no-phonon (NP) transitions and transitions with emission of TA, LO and TO phonons, respectively. It is worth noting that if a neutron-irradiated sample with $N(\mathrm{Ge}) = 2 \times 10^{20}\ \mathrm{cm}^{-3}$ was subjected to annealing at two subsequently increasing temperatures, a pronounced acceleration of annealing as compared to the heat treatment only at the higher one was observed. So, e.g., in the samples annealed at 525 + 625°C or at 550 + 650°C, phosphorus-bound excitons along with weak traces of some defect-related lines (e, f) and, at high excitation powers, also free excitons and EHDs are observed. In the samples annealed at 625°C or 650°C only, the spectra are very reminiscent of that characteristic of $T_a = 600$°C (see (d)).

Let us now consider the evolution of RD-related spectra. In contrast to the samples with $N(\mathrm{Ge}) < \sim 10^{19}\ \mathrm{cm}^{-3}$ (see Ref. [5]), those containing $N(\mathrm{Ge}) = 2 \times 10^{20}\ \mathrm{cm}^{-3}$ showed a behavior of the PL spectra being significantly different from that in 'pure' silicon. No near band edge PL is detected after neutron irradiation and annealing at $T_a \leqslant 500$°C. After annealing at 525°C $\leqslant T_a \leqslant$ 700°C, a group of lines emerges (Fig. 1b). An analysis has shown that this group includes the formerly observed centers M81–83 as well as new ones labeled M86-88 (for the line positions, see Table 1). Besides, the line M54 (nature unknown [5,9]), M80 and some weak unidentified features appear in the high-energy part of the spectrum of the sample annealed at $T_a = 600$°C. The lines M81–83, 86–88 are observed with the same relative intensities at all annealing temperatures, they always appear as a group. This fact may indicate a common origin of the lines. The observed correlation of the appearance of the centers M80–83 with the Ge content in the samples indicates the participation of Ge atoms in these centers. The lines M86–88 may also be ascribed to Ge-related centers, though with less certainty. The absence of almost all known PL features which are usually observed due to radiative recombination at impurity-related defects in silicon without Ge means that the Ge atoms, when they are present at a sufficient concentration, become the major sinks for defect components created by irradiation and/or released

Table 1
Parameters of PL lines in irradiated Si : Ge

Line	$h\nu$ (eV)	T_a (°C)	Line	$h\nu$ (eV)	T_a (°C)
M54	1.1196 (a)	500–650	M83	1.068 (a)	525–575
	1.1165 (b)	625–700		1.065 (b)	525–700
M80	1.1105 (a)	450–650	M86	1.077 (b)	525–700
	1.1075 (b)	625–700			
M81	1.075 (a)	525–575	M87	1.086 (b)	525–700
	1.073 (b)	525–700			
M82	1.071 (a)	525–575	M88	1.060 (b)	525–700
	1.068 (b)	525–700			

(a) Samples with $N(\mathrm{Ge}) = (1\text{–}2) \times 10^{19}\ \mathrm{cm}^{-3}$.

(b) Samples with $N(\mathrm{Ge}) = 2 \times 10^{20}\ \mathrm{cm}^{-3}$. Note that the lines M54, 80–83 are shifted in samples with $N(\mathrm{Ge}) = 2 \times 10^{20}\ \mathrm{cm}^{-3}$ by $-3 \ldots -3.5$ meV with respect to (a).

by the decay of other, less thermally stable damage centers. This refutes the formerly perceived view that the Ge atoms serve at $T \geqslant 300$ K only as centers of indirect recombination of vacancies and interstitials.

We propose the following explanation of the observed behavior. In Si crystals Ge atoms cause high internal strain. They form clusters with a high probability. The Frenkel pair components (vacancies and interstitials) created by irradiation migrate along strain field gradients and are captured by these clusters rather than by isolated oxygen, carbon or germanium atoms. The suppression of the creation of secondary defects in Si : Ge irradiated at 300 K is indeed well documented (see, e.g., Ref. [10]). The lack of a unique structure of such agglomerates prevents the observation of narrow spectral lines otherwise typical of point defects. In the case of neutron irradiation, disordered regions with a very high density of defects are formed. Upon annealing of these regions, intense fluxes of point defects emerge. Thus, there are sufficient components to be trapped by isolated impurity atoms. The absence of the known C-and O-related centers and the appearance of new, presumably Ge-related ones, means that, at elevated Ge concentrations and annealing temperatures, Ge atoms turn out to be major traps for defect components. In the framework of this model, a sufficient concentration of defects created by irradiation is necessary to saturate the trapping capacity of the Ge clusters. Otherwise complexes of Frenkel pair components with impurities, especially with dispersed Ge atoms, would not be created. Indeed, after irradiation of Si containing $N(\mathrm{Ge}) = 2 \times 10^{20}\ \mathrm{cm}^{-3}$ with 3–4 MeV electrons to a fluence of $3 \times 10^{17}\ \mathrm{cm}^{-2}$, the centers M81–83, 86–88 as well as other known defect-related PL centers in the near band edge spectral region could not be observed.

The sharp defect-related lines disappear almost completely for $T_a = 750$°C (only traces of M54, 80 could be registered at the highest sensitivity). For $T_a = 800$°C, only lines of free excitons and excitons bound to shallow impurities as well as EHD bands are observed. The bound exciton NPL consists of at least three partially resolved components (Fig. 2). The strongest is centered at 1.1483 eV, exactly as in the samples before irradiation, and has a FWHM of 0.7 meV. Another one, being somewhat weaker, is located at 1.1476 eV. There are as well one or more components with lower intensities centered at lower energies. The TO-phonon replica has nearly the same shape but a quantitative analysis was hampered by a poor signal-to-noise ratio due to a rapid drop of the sensitivity of the S-1 photocathode in this spectral region. Nevertheless, this observation rules out a possible defect-related nature of the satellite lines because the defect-related NPLs in the near band edge region have much weaker phonon replicas than P_{NP} has. It should be remembered that upon irradiation of Si and Ge with thermal neutrons, the (n,γ) nuclear reactions occur which transform ^{30}Si into ^{31}P, ^{70}Ge into ^{71}Ga, and ^{74}Ge into ^{75}As [11]. The Ge content in the samples under investigation is only 0.4 at% but the neutron capture cross section of ^{70}Ge is 214 times larger than that of ^{30}Si [12]. Thus, considering the natural abundance of the isotopes, we should expect the creation of comparable concentrations ($\sim 10^{14}\ \mathrm{cm}^{-3}$) of the P and Ga impurities. The concentration exceeds by more than one order of magnitude the P concentration in the as-grown crystals. The production of ^{75}As cannot be neglected either. The NPLs of the Ga and As bound excitons are shifted to lower energies with respect to P_{NP} by 1.0 and 0.6 meV, respectively (for a review, see, e.g., Ref. [13]). This agrees within the experimental accuracy with our experimental data. Therefore, the complex shape of the bound exciton NPL in the neutron irradiated and annealed Si : Ge samples is due to the presence of substitutional P, Ga, and As atoms introduced by means of nuclear transmutation reactions.

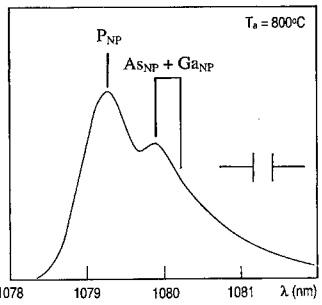

Fig. 2. PL spectrum in the bound exciton NPL region for Si doped with Ge to a concentration of $2 \times 10^{20}\ \mathrm{cm}^{-3}$ subjected to neutron irradiation and annealing at 800°C. As to the designations, see the caption of Fig. 1.

4. Conclusions

New supporting evidence of the Ge incorporation in the centers M80–83 was found. Several new centers (M86–88) with a similar behavior were observed. At concentrations of the order of $10^{20}\ \mathrm{cm}^{-3}$ the Ge atoms are found to be the main sinks for the Frenkel pair components in irradiated silicon. The presence of substitutional P, Ga and As atoms introduced by the nuclear transmutation reactions was verified in neutron irradiated and annealed Si : Ge samples.

Acknowledgements

This work was supported in part by the Fundaçâo para a Ciência e a Tecnologia of Portugal, Programa PRAXIS XXI/BCC/10003/96. The authors would like to thank A.A. Stuk for supplying the samples and to A.V. Voevodova for the help in performing luminescence

measurements. Fruitful discussions with M.C. Carmo are greatly appreciated.

References

[1] N.A. Sobolev, in: V.E. Borisenko et al. (Eds.), Physics, Chemistry and Application of Nanostructures, World Scientific, Singapore, 1997, p. 41, and references therein.
[2] A. Nylandsted Larsen, Mater. Sci. Forum 258–263 (1997) 83, and references therein.
[3] C.V. Budtz-Jorgensen, P. Kringhoj, A. Nylandsted Larsen, N.V. Abrosimov. Phys. Rev. B58 (1998) 1110, and references therein.
[4] G.D. Watkins, IEEE Trans. Nucl. Sci. NS-16 (1969) 13.
[5] A.V. Voevodova, F.P. Korshunov, N.A. Sobolev, A.A. Stuk, Fiz. Tekhn. Poluprov. 23 (1989) 1696 [Sov. Phys. – Semicond. 23 (1989) 1049]; and in: K. Sumino (Ed.), Defect Control in Semicond., Vol. 1, North-Holland, Amsterdam, 1990, p. 387.
[6] N.A. Sobolev, M.H. Nazaré, K. Thonke, R. Sauer, to be published.
[7] J. Weber, M.I. Alonso, Phys. Rev. B 40 (1989) 5683.
[8] A.B. Lopatin, Ya.E. Pokrovskii, Fiz. Tverd. Tela 28 (1986) 2373.
[9] F.P. Korshunov, N.A. Sobolev, V.A. Sheraukhov, Zh. Prikl. Spektroskopii 51 (1989) 248 [J. Appl. Spectroscopy 51 (1989) 797]; and in: K. Sumino (Ed.), Defect Control in Semicond., Vol. 1, North-Holland, Amsterdam, 1990, p. 559.
[10] V.G. Golubev, V.V. Emtsev, P.M. Klinger et al., Fiz. Tekhn. Poluprov. 26 (1992) 574.
[11] A.G. Zabrodskii, V.A. Yevseyev, R.F. Konopleva et al., Cryst. Lattice Defects Amorph. Mater. 13 (1987) 163.
[12] A.G. Zabrodskii, V.A. Evseev, R.F. Konopleva et al., Fiz. Tekhn. Poluprov. 20 (1986) 2042 [Sov. Phys. – Semicond. 20 (1986) 11278].
[13] R. Sauer, in: Landolt-Börnstein, Bd. 22b, Springer, Berlin, 1989, p. 338, and references therein.

ELSEVIER

Physica B 273–274 (1999) 275–278

PHYSICA B

www.elsevier.com/locate/physb

Local vibrational modes of a dicarbon–hydrogen center in crystalline silicon

L. Hoffmann[a,*], E.V. Lavrov[a,b], B. Bech Nielsen[a], J.L. Lindström[c]

[a]*Institute of Physics and Astronomy, Aarhus University, DK-8000 Aarhus C, Denmark*
[b]*Institute of Radioengineering and Electronics of RAS, Mokhovaya 11, 103907 Moscow, Russia*
[c]*Department of Physics, Linköping University, S-58183, Sweden*

Abstract

Carbon-doped silicon irradiated with electrons at room temperature and subsequently implanted with protons has been studied by infrared absorption spectroscopy. Isochronal annealing in the temperature range from 400°C to 800°C has revealed an absorption line at 2967 cm^{-1}. When protons are substituted by deuterons, the line shifts down in frequency to 2211 cm^{-1} and co-implantation of protons and deuterons gives rise to an additional line at 2218 cm^{-1}. Isotope shifts and similar annealing characteristics of the three lines show that the 2967 cm^{-1} line represents a local vibrational mode of a defect, which contains two equivalent hydrogen atoms. In samples co-doped with ^{12}C and ^{13}C, an additional mode is observed at 2963 cm^{-1}, which is about halfway between the modes involving only ^{12}C or ^{13}C. From the relative intensities of the isotope-shifted modes in silicon co-doped with ^{12}C and ^{13}C, it is concluded that the center contains two equivalent carbon atoms. The center is tentatively identified as two equivalent hydrogen atoms bound to two neighboring carbon atoms at substitutional sites.

Keywords: Carbon; Hydrogen; IR-spectroscopy

1. Introduction

Hydrogen and carbon are common impurities in crystalline silicon, which are involved in a variety of different point defects that have been studied for decades. Recently, also carbon–hydrogen complexes in silicon have been addressed experimentally [1–5] and theoretically [6]. The first experimental observation of a center, which includes both carbon and hydrogen was done by Endrös [1] in deep-level transient spectroscopy measurements. Since then, a number of carbon–hydrogen-related centers have been investigated by photoluminescence [2,5] and infrared absorption spectroscopy [3,4]. In spite of intense studies, the molecular structure of only one of them has been established. This center is known in photoluminescence as the *T*-line and it consists of an interstitial carbon pair, where one of the carbon atoms binds a hydrogen atom [2].

In the present work we report on a preliminary infrared absorption study of a new carbon–hydrogen center, which possesses an infrared active mode at 2967 cm^{-1}. The 2967 cm^{-1} line has recently been observed by Pajot et al. [3] and it has been ascribed to a nitrogen–hydrogen center. However, from carbon isotope substitution, we have proven that the center contains two equivalent carbon atoms and that the 2967 cm^{-1} mode originates from a direct carbon–hydrogen bond.

2. Experimental

The samples used in this work were cut from single-crystalline high-resistivity float-zone Si doped with ^{12}C (Si : ^{12}C) or predominantly with ^{13}C (Si : ^{13}C : ^{12}C). The Si : ^{12}C sample contained 5×10^{17} cm^{-3} ^{12}C atoms and less than 2×10^{16} cm^{-3} ^{16}O atoms. The Si : ^{13}C : ^{12}C

* Corresponding author. Tel.: + 45-89-42-28-99; fax: + 45-86-12-07-40.
E-mail address: hoff@ifa.au.dk (L. Hoffmann)

0921-4526/99/$ - see front matter
PII: S0921-4526(99)00503-7

sample contained 8×10^{17} cm^{-3} ^{13}C, 1×10^{17} cm^{-3} ^{12}C, and 1×10^{17} cm^{-3} ^{16}O atoms.

The samples were irradiated with 2 MeV electrons to a dose of 8×10^{17} cm^{-2} at room temperature (RT). Subsequently, the samples were implanted at RT with protons and/or deuterons at 30–50 different energies from both sides of the sample. The dose implanted at each energy was adjusted to yield an almost uniform depth distribution of implants. The local concentration of the hydrogen isotopes was 5×10^{17} cm^{-3}, and the depth profile ranged from 100 to 800 μm for protons and from 100 to 500 μm for deuterons from the surface of the sample. One sample was co-implanted with both isotopes in overlapping profiles. The total concentration of each isotope was 5×10^{17} cm^{-3}.

Infrared absorption measurements were carried out with a Nicolet, System 800, Fourier-transform spectrometer. The measurements were performed by use of a closed-cycle helium cryostat with CsI windows. In this configuration the spectrometer covers the spectral range from 450 to 7000 cm^{-1}. The resolution was 1 cm^{-1} and the sample temperature was 8 K during the measurements.

In order to study the thermal stability of the absorption lines, infrared absorption spectra were recorded at 8 K after each step in a series of isochronal annealings. Each annealing was performed in a furnace continuously supplied with nitrogen gas. The duration of each annealing was 30 min and during this time the temperature was stable within ± 2°C. The annealings were carried out at temperatures in the range from 400°C to 800°C, and in each step the temperature was increased by 25°C or 50°C.

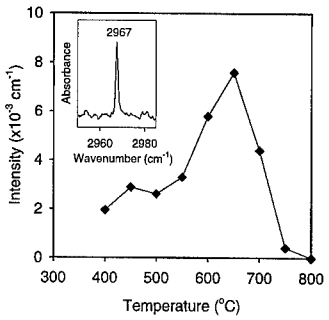

Fig. 1. Annealing dependence of the 2967 cm^{-1} line in the temperature range from 400°C to 800°C. The absorption line measured after annealing at 650°C is shown in the inset.

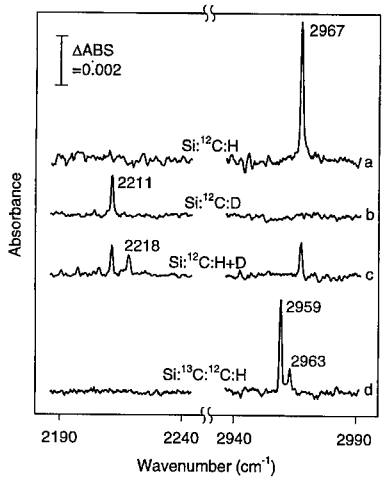

Fig. 2. Sections of absorption spectra measured after annealing at 650°C on: (a) Si: ^{12}C implanted with H^+, (b) Si: ^{12}C implanted with D^+, (c) Si: ^{12}C implanted with $H^+ + D^+$, and (d) Si: ^{13}C: ^{12}C implanted with H^+. Note that the implantation depth of samples implanted with pure hydrogen is twice the depth of other samples.

3. Results and discussion

After proton implantation of electron-irradiated Si: ^{12}C and subsequent annealing at 400°C an absorption line is observed at 2967 cm^{-1}. The frequency of the 2967 cm^{-1} line is in the typical range of C–H stretch modes, which are to be found from 2700 to 3100 cm^{-1} [7]. The 2967 cm^{-1} line displays high thermal stability reaching the maximum intensity after annealing at 650°C, as seen from Fig. 1, where the effects of isochronal annealing in the temperature range from 400°C to 800°C is shown.

Sections of the infrared absorption spectra measured after annealing at 650°C at carbon doped Si samples implanted with hydrogen isotopes are shown in Fig. 2. The absorption line at 2967 cm^{-1} is observed in the Si: ^{12}C sample implanted with protons (see Fig. 2(a)). The line shifts down in frequency to 2211 cm^{-1} when hydrogen is substituted with deuterium, as seen in part (b) of the figure. The frequency ratio of the two lines is 1.34, very close to the value expected for a hydrogen atom bound to a carbon atom by a harmonic spring: $\sqrt{m_r^D/m_r^H}$, where m_r^H and m_r^D are the reduced masses of ^{12}C–H and ^{12}C–D bonds, respectively. Therefore, we ascribe the 2967 cm^{-1} line to a local vibrational mode of hydrogen incorporated in a defect, which presumably involves carbon–hydrogen bonds. Only one additional line 2218 cm^{-1} is observed in the absorbance spectra of Si: ^{12}C co-implanted with protons and deuterons into overlapping profiles (see Fig. 2(c)), which indicates that the center contains two hydrogen atoms. The local modes at 2211, 2218, and 2967 cm^{-1} display similar annealing characteristics.

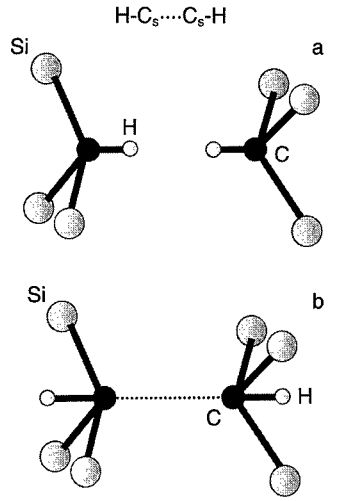

Fig. 3. Sketch of possible structures of the dicarbon–hydrogen defect. The two equivalent hydrogen atoms are located on the trigonal axis pointing either (a) towards or (b) outwards from the inversion center of the defect.

One more evidence for the incorporation of carbon in the center comes from carbon isotope substitution experiments. Fig. 2(d) shows the absorbance spectra of a Si : ^{13}C : ^{12}C sample implanted with protons. The relative concentration of ^{13}C and ^{12}C in the sample is 8 : 1. Two isotope-shifted lines at 2959 and 2963 cm^{-1} are clearly seen in the spectra, which shows that the center includes carbon atoms, presumably two carbon atoms. The relative content of the carbon isotopes in the sample together with the relative intensities of the 2959 and 2963 cm^{-1} lines, which is 4 : 1, shows that the two carbon atoms are equivalent. We note that we could not detect the 2967 cm^{-1} line in the Si : ^{13}C : ^{12}C sample, probably because its intensity falls below the noise level. From the relative content of ^{12}C to ^{13}C in the sample the intensity of the 2967 cm^{-1} line should only be $\frac{1}{64}$ of that of the 2959 cm^{-1} line.

Note that we could not detect any lines in the region characteristic of carbon defects in Si (500–1000 cm^{-1}) correlated to the 2967 cm^{-1} local mode of hydrogen.

Several possible models of a center consisting of two equivalent carbon and hydrogen atoms have been considered. We have found that the infrared absorption data are consistent only with a center comprising two carbon atoms occupying adjacent substitutional sites, with two equivalent hydrogen atoms located on the trigonal axis pointing towards or outwards from the inversion center of the defect, as illustrated in Fig. 3. We denote this defect H–C_s–C_s–H. The point group of H–C_s–C_s–H is D_{3d} and hence, the center possesses two hydrogen stretch modes denoted A_{1g} and A_{2u} in accordance with the irreducible representation describing its symmetry properties. Only the antisymmetric A_{2u} mode is infrared active, in agreement with the experimental findings. When both hydrogen and deuterium are incorporated in the center, its point group reduces to C_{3v}. A center with C_{3v} symmetry should, in principle, possess two infrared active modes. Therefore, the spectrum of the Si : ^{12}C sample implanted with protons and deuterons into overlapping profiles should contain four lines corresponding to two modes of H–C_s–C_s–H and D–C_s–C_s–D and two modes of H–C_s–C_s–D. We did only observe three correlated absorption modes in our spectra. However, the intensity of one of the modes, which involves both hydrogen isotopes, is expected to be weak as the two hydrogen isotopes counteract and, therefore the dipole moment is small. The other mode arises from a vibration, where the two hydrogen isotopes moves in the same direction, and this gives rise to a strong absorption line. This situation was observed in the case of H_2^*. This center consists of one hydrogen atom located at the bond-center site and one at the anti-bonding site [8].

The additional line in the Si : ^{12}C sample co-implanted with protons and deuterons is observed at 2218 cm^{-1}. This line is shifted upwards in frequency by only 7 cm^{-1} compared to the deuterium local vibrational mode at 2211 cm^{-1}. This suggests a weak coupling between the proton and the deuteron. Thus, the model in Fig. 3(b), where the two hydrogen isotopes point away from each other, is the most likely candidate. However, theoretical calculations are needed for a conclusive identification. Uniaxial stress measurements are also planned to establish the symmetry of the center.

4. Conclusion

Carbon-doped silicon irradiated with electrons at room temperature and subsequently implanted with protons has been studied by infrared absorption spectroscopy. Isochronal annealing in the temperature range from 400°C to 800°C has revealed an absorption line at 2967 cm^{-1}. It is shown that this line originates from a center, which consist of two equivalent hydrogen atoms bound to two neighboring substitutional carbon atoms.

Acknowledgements

This work has been supported by the Danish National Research Foundation through the Aarhus Center for Atomic Physics (ACAP). E.V. Lavrov also acknowledges a grant from the Russian Base Research Foundation (grant No 99-02-16652).

References

[1] A. Endrös, Phys. Rev. Lett. 63 (1989) 70.
[2] A.N. Safonov, E.C. Lightowlers, G. Davies, P. Leary, R. Jones, S. Öberg, Phys. Rev. Lett. 77 (1996) 4812.
[3] B. Pajot, B. Clerjaud, Z.-J. Xu, Phys. Rev. B 59 (1999) 7500.
[4] L. Hofmann, E.V. Lavrov, B. Bech Nielsen, Mater. Sci. Eng. B 58 (1999) 167.
[5] A.N. Safonov, E.C. Lightowlers, Mater. Sci. Eng. B 58 (1999) 39.
[6] P. Leary, R. Jones, S. Öberg, Phys. Rev. B 57 (1998) 3887.
[7] R.C. Weast (Ed.), CRC Handbook of Chemistry and Physics, 68th Edition, CRC Press, Inc., 1988, Boca Raton, p. F188.
[8] J.D. Holbech, B. Bech Nielsen, R. Jones, P. Sitch, S. Öberg, Phys. Rev. Lett. 71 (1993) 875.

ELSEVIER

Physica B 273–274 (1999) 279–282

PHYSICA B

www.elsevier.com/locate/physb

Identification of cadmium-related centers in silicon

A. Näser[a], W. Gehlhoff[a,*], H. Overhof[b]

[a]*Technische Universität Berlin, Institut für Festkörperphysik, Sekr. PN5-2, Hardenbergstr. 36, D-10623 Berlin, Germany*
[b]*Universität-GH Paderborn, Fachbereich Physik, AG Theoretische Physik, D-33098 Paderborn, Germany*

Abstract

The electronic and geometric structures of a new Cd-related center with trigonal symmetry is investigated by electron paramagnetic resonance (EPR). Isotope doping with the isotopes ^{111}Cd and ^{57}Fe confirmed, that the defect consists of one single Cd atom and one isolated Fe atom with a center axis in the ⟨1 1 1⟩-direction. The analysis of the spectra was performed within the $^4T_1$ ground state of interstitial Fe_i^+, which is distorted by a weak trigonal field caused by a substitutional Cd_S atom in the double negative charge state. For different Fe–Cd pairs the formation energies in dependence of the Fermi level were estimated by ab initio calculations.

PACS: 61.72.Bb; 61.72.Ji; 71.55.Cn; 76.30.Lh

Keywords: Silicon; Paramagnetic defects; Cadmium; Fe–Cd pairs

1. Introduction

The properties of different defects of the group IIb element Cd have been extensively studied with Hall effect techniques [1,2] and perturbed angular correlation (PAC) [3]. Recent deep level transient spectroscopy (DLTS) investigations of Si doped with Cd confirmed the expected two acceptor levels and a level tentatively ascribed to be due to a FeCd pair [4]. Interstitial Fe in Si tends to form complexes because of its low-migration energy [5]. Up to now for the group two elements only the isolated donor state Cd_S^+ [6] and several Zn related complexes [7] were identified by electron paramagnetic resonance (EPR). This method is an excellent tool to give direct structural information about isolated defects and complexes in a paramagnetic charge state.

2. Experimental

Monocrystalline Si samples of dimensions of about 12 mm × 3 mm × 3 mm were doped with natural Cd as well as with the isotopes ^{111}Cd (95%) or ^{113}Cd (96%) with a nuclear spin of $I = \frac{1}{2}$ by diffusion. The Cd diffusion of the crystals took place at 1250°C for 96 h in an evacuated quartz ampoule. The Fe doping was performed by encapsulating a small piece of Fe wire of natural isotope abundance or of the ^{57}Fe ($I = \frac{1}{2}$, 95%) isotope and a carefully etched Si : Cd sample in an evacuated quartz ampoule again. The samples were annealed at 1200°C for 10 min and subsequently quenched in H_2O. After the diffusion step the samples were etched again. The EPR measurements were performed at the X-band (microwave frequency $\nu \approx 9.4$ GHz) using a Bruker ESP300E spectrometer equipped with an Oxford ESR 900 helium gas-flow cryostat. The spectra were taken in the dark in absorption mode at a sample temperature of 4 K.

3. The Fe–Cd-pair in n-type Si

While in p-type Si the isolated Cd_S^+ defect could be identified [6], after Fe diffusion an additional EPR spectrum with ⟨1 1 1⟩-symmetry is observed in float zoned Si : Cd samples with a P background doping level of $[P] \approx 1 \times 10^{15}$ cm^{-3}. As expected, without Fe doping no Cd-related EPR transitions could be detected in this material. Fig. 1 shows the anisotropy of the line positions

* Corresponding author. Fax: 0049-30-314-22569.
E-mail address: gehlhoff@sol.physik.tu-berlin.de (W. Gehlhoff)

0921-4526/99/$ - see front matter
PII: S0921-4526(99)00504-9

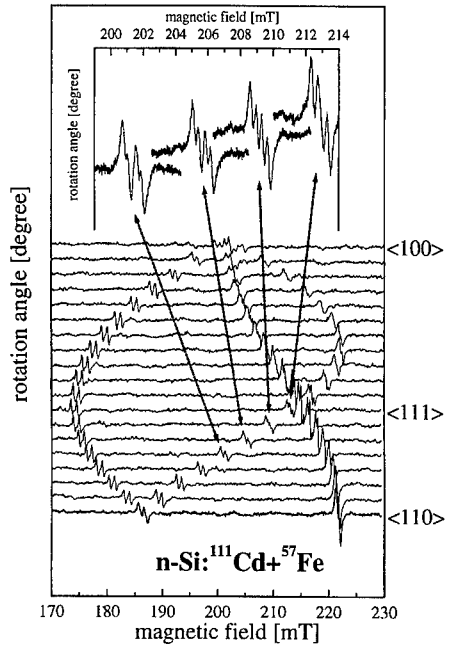

Fig. 1. Stack plot of the EPR spectra after doping n-Si with the isotopes ^{57}Fe and ^{111}Cd (both $I = \frac{1}{2}$). The magnetic field B is rotated by 5° steps in a {1 1 0} plane. The inset above shows the fourfold splitting of the EPR transitions induced by the hyperfine interactions of the two isotopes.

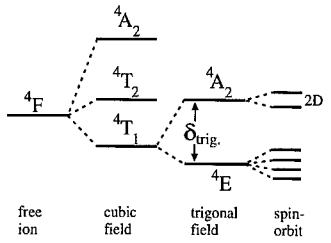

Fig. 2. Schematic term splitting of Fe_i^+ ($3d^7$, ^4F) in a crystal field lowered from cubic to trigonal symmetry including spin–orbit coupling.

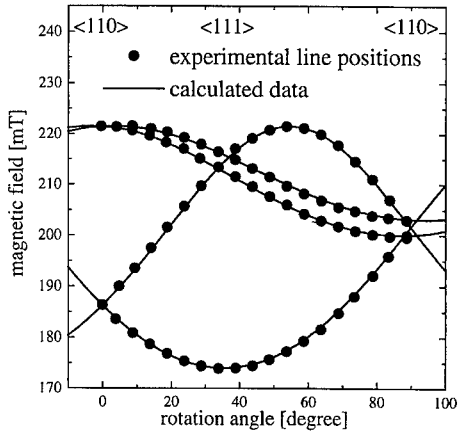

Fig. 3. Experimental X-band values of the electron-spin transitions for the Fe–Cd-complex (●) for rotation of the magnetic field in a {1 1 0} plane with a slight misorientation of about 1.5°. The solid lines are calculated from (1) using the parameters given in Table 1.

after doping of n-type Si with ^{111}Cd and ^{57}Fe. The fourfold splitting of the lines undoubtedly verifies that the center consists of one single Fe atom and one single Cd atom. The spectra can be interpreted as arising from the $^4T_1$ ground state of the interstitial Fe_i^+ in tetrahedral symmetry which is distorted by a very weak trigonal field (Fig. 2). The tetrahedral crystal field would split the ^4F ground state of the Fe_i^+ atom with its d^7 configuration into the threefold orbital degenerate $^4T_1$, $^4T_2$ and into the orbital singlet $^4A_2$ states, with the orbital triplet $^4T_1$ being the ground state. The trigonal distortion caused by the associated Cd splits the $^4T_1$ state into an orbital doublet ^4E and an orbital singlet $^4A_2$ of the group C_{3v}. In analogy to isolated Fe_i^+ and to pairs of iron with the shallow acceptors Al, Ga and In [8] we interpret the observed EPR spectra in terms of spin transitions within the lowest Kramers doublet of the ^4E ground state. Thus, the angular dependence of the Fe–Cd-pair can be described using an effective spin $S' = \frac{1}{2}$ and the spin Hamiltonian

$$\mathcal{H} = \beta g B S + \mathcal{H}_{HF} \tag{1}$$

with

$$\mathcal{H}_{HF} = \sum_{j=^{111}Cd,^{57}Fe} (A_j I_j S_j - \gamma B_j I_j). \tag{2}$$

The measured angular dependence of the electronic spin transitions is shown in Fig. 3 and compared with the calculated one using the g'-values given in Table 1, which summarizes the best fit parameters of the spin Hamiltonian and includes the hyperfine constants for the isotopes ^{57}Fe and ^{111}Cd. To confirm our assumption concerning the ^4E electronic ground state of the interstitial Fe_i^+ one can determine the sign and the size of the trigonal distortion in an approximation originally proposed by Abragam and Pryce [9,8]. Within this model the $^4T_1$ ground state of Fe_i^+ is treated by an fictitious orbital angular momentum $l' = 1$ and the real spin $S = \frac{3}{2}$. The admixtures of orbital contributions of excited states to the $(2l' + 1)(2S + 1)$ ground manifold were included by an effective Landé factor α. In completely cubic fields and without covalent effects α satisfies $-\frac{3}{2} \leqslant \alpha \leqslant -1$, where $\alpha = -\frac{3}{2}$ is in the weak field and $\alpha = -1$ is in the strong field case. Following the theory of Ref. [8], the influence of the orbital contributions on the Fe_i^+ ground state manifold can be calculated with the effective

Table 1
Spin Hamiltonian parameters of the Fe_i^+–Cd_s^{2-} pair

	Effective spin S′	$g_{\|\|}' \pm 0.0005$	$g_{\perp}' \pm 0.0005$		$A_{\|\|}'$ (10^{-4} cm^{-1})	$A_{\perp}'$ (10^{-4} cm^{-1})
Fe^+–Cd^{2-}	1/2	3.8972	3.0595	^{111}Cd	19.17	< 2.8
				^{57}Fe	< 3.3	6.5

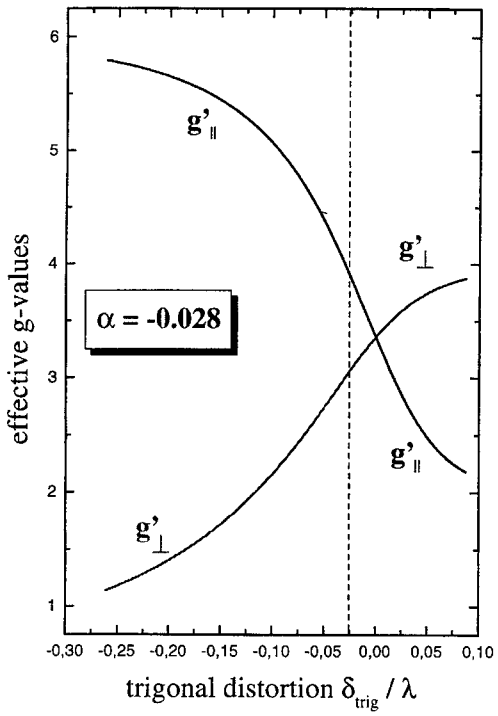

Fig. 4. Effective g' values for the Fe–Cd pair with trigonal symmetry calculated with the Hamiltonian (3) and the effective Landé factor $\alpha \approx -0.028$. The fitting point of the calculated g' values with the experimental ones is indicated by the dashed line.

Hamiltonian

$$\mathcal{H} = -\delta_{trig}[l_z'^2 - \tfrac{1}{3}l'(l'+1)] - \lambda(\alpha_x l_x' S_x + \alpha_y l_y' S_y + \alpha_z l_z' S_z). \quad (3)$$

We found the best fit to the experimental g' values of the Fe–Cd pair for $\alpha \approx -0.028$ (Fig. 4) which correponds to a value of $\delta_{trig}/\lambda \approx -0.025$. Therefore, the trigonal distortion results in a magnitude of $\delta_{trig} = 2.88$ cm^{-1} assuming the same value for the spin–orbit coupling constant $\lambda = -115$ cm^{-1} as for the free ion case. The positive sign of δ_{trig} indicates that in analogy to the complexes of interstitial Fe atoms with Al, Ga and In and in contrast to Fe–B pairs a ^{4}E ground state has to be assumed for the Fe–Cd pair.

4. Ab-initio calculations

We have performed ab initio calculations using the Green's function linear muffin-tin orbital method in the atomic-spheres approximation (LMTO-ASA) in order to theoretically investigate the electronic structure of the pairs. In our calculations we have investigated three different configurations of trigonal pairs: Cd is placed on the Si(0, 0, 0) position, the nearest neighbor ligand is Si($\bar{1}$, $\bar{1}$, $\bar{1}$). For pair 1 Fe is on the tetrahedral interstitial (1, 1, 1) site, for pair 2 Fe is placed on the interstitial (2, 2, 2) site, while for pair 3 it is on the ($\bar{2}$, $\bar{2}$, $\bar{2}$) site.

For pairs 1 and 2, the pair formation energies turned out to be very similar while for pair 3, the pair formation energy was about a factor of two smaller. The formation of this pair therefore appears to be rather unlikely. All pairs are most stable if E_F is close to the valence band with formation energies exceeding 1 eV for the more stable pairs 1 and 2. For n-type samples the pair formation energies tend to zero, while for intrinsic material the formation energies of pairs 1 and 2 are 0.6 eV.

The gap states and the valence band resonances of the pair originate from vacancy-like gap states of the Cd_{Si}^{2-} interacting with the *d*-like states of Fe_i^+ and, therefore, the individual gap states have a mixed character. Summing up over all occupied gap states and resonance states for the singly negative charge state of the pair we end up with a magnetic moment that is concentrated on the iron ASA sphere with $\mu_{Fe}^+ = 2.1\mu_B$ (for isolated Fe_i^+ the corresponding value is $2.37\mu_B$) whereas for the Cd partner we have $\mu_{Cd}^{2-} = 0.05\mu_B$ only. Thus the electronic structure of all negatively charged pairs closely resembles that of a Fe_i^+ isolated point defect which is slightly perturbed by the electrical field of the Cd_{Si}^{2-} partner.

For isolated Fe_i^+ the low-spin state does not exist — the $e_\uparrow$ state that should be unoccupied moves into the valence band — however in the repulsive field of the Cd_S^{2-} the single particle state is shifted upwards. We find for pair 1 a $^4A_2$ ground state (the ^{4}E state is higher in energy by 0.3 eV) while for pair 2 the ground state turns out to be a ^{4}E, 0.07 eV below the $^4A_2$ state. Clearly, the small energy differences do not allow to uniquely determine, which of the pairs and which ground state would be predicted by the local spin density approximation (LSDA). No attempt was made to calculate the hyperfine interactions. For the analogous case of iron-shallow acceptor pairs we have shown [10], that the experimental

values can fairly be reproduced by a theory that includes the spin–orbit interaction as a fitting parameter. Since the results sensitively depend on the choice of the fitting parameters, we shall not attempt to repeat the calculation for the $(Fe_i–Cd_S)^-$ pairs.

5. Conclusion

A Fe–Cd pair in monocrystalline Si was identified using samples doped with the isotopes $^{111}Cd/^{113}Cd$ and ^{57}Fe. For the observed Fe–Cd complex the values for the effective Landé factor α and the trigonal distortion δ_{trig} are by a factor of 10 smaller than for the Fe pairs with the shallow acceptors B, Al, Ga and In. The origin of the strong orbital quenching are speculative up to now. Ammerlaan et al. [11] favour in case of the Fe complexes with the shallow acceptors covalency effects as reason for the reduction of α. A dynamical Jahn–Teller effect as main reason for the orbital quenching as proposed by Ham [12] can be excluded because in case of dynamical Jahn–Teller effects one must assume the same value of quenching for different ground states and magnitudes of crystal field distortions.

Acknowledgements

The authors are indebted to Dr. W. Zulehner from Wacker Siltronic GmbH and Dr. H. Riemann from the Institute for Crystal Growth (Berlin) for supporting us with Si crystals. This work was partially supported by the BMFT under grant 03-GE4-TUB-5 which is greatfully acknowledged.

References

[1] S.S. Dzyundaidov, N.A. Urmanov, M.V. Gafurova, Phys. Stat. Sol. A 66 (1981) K79.
[2] M.A. Gulamova, I.Z. Karimova, P.I. Knigin, Sov. Phys. Semicond. 5 (1971) 687.
[3] Th. Wichert, N. Achtziger, H. Metzner, R. Sielemann, in: G. Langouche (Ed.), Hyperfine Interactions of Defects in Semiconductors, Elsevier, Amsterdam, 1992, p. 77.
[4] M. Lang, G. Pensl, M. Gebhard, N. Achtziger, M. Uhrmacher, Mater. Sci. Forum 83–87 (1992) 1097.
[5] E.R. Weber, Appl. Phys. A 30 (1983) 1.
[6] A. Näser, W. Gehlhoff, H. Overhof, R.A. Yankov, Phys. Stat. Sol. B 210 (1998) 753.
[7] H.E. Altink, T. Gregorkiewicz, C.A.J. Ammerlaan, Mat. Res. Soc. Symp. Proc. 262 (1992) 525.
[8] K. Irmscher, T. Kind, W. Gehlhoff, Phys. Rev. B 49 (1994) 7964.
[9] A. Abragam, M.H.L. Pryce, Proc. Roy. Soc. London Ser. A 206 (1951) 173.
[10] H. Weihrich, H. Overhof, Semicond. Sci. Technol. 13 (1998) 1374.
[11] C.A.J. Ammerlaan, J.J. van Knooten, Mater. Res. Soc. Proc. 45 (1985) 525.
[12] F.S. Ham, Phys. Rev. 138 (1965) A1727.

ELSEVIER

Physica B 273–274 (1999) 283–286

PHYSICA B

www.elsevier.com/locate/physb

Annealing kinetics of the di-carbon radiation-damage centre in edge-defined film-fed growth silicon

Seung-Chul Park*, Gordon Davies

Physics Department, King's College London, Strand, London WC2R 2LS, UK

Abstract

A systematic study of the isothermal annealing effect on the thermal destruction of the G centre was carried out at various annealing temperatures between 180°C and 240°C for e^--irradiated EFG Si samples with various radiation doses between 5×10^{16} and 8×10^{17} cm^{-2}. We show that the thermal decay of the concentration of the G centre (monitored by the 969 meV 'G' zero-phonon line absorption) can be explained by the combination of two independent processes through the break-up of the G centres and the capture of migrating defects. By analysing the rates of changes of $[G]$, $[C_i]$ (interstitial carbon atoms), and $[T]$ (migrating defects), the two exponential decay behaviour of the G centres during annealing was modelled successfully. With this decay model, it was shown that the time constant of the slow decay process has the temperature dependence with the two exponential factors of the break-up energy of the G centre (1.934 eV) and the migration energy of carbon atom (0.890 eV). For the fast decay process, the temperature dependence of the time constant was fitted with a single exponential curve and the migration energy of the defect was obtained as $E_m^d = 0.879$ eV.

Keywords: Di-carbon radiation-damage centre; EFG silicon; Thermal destruction

1. Introduction

The di-carbon centre, which is also known as the 'G' centre, is one of the most thoroughly investigated 'point defects' in silicon. There have been wealth of information on the G centre from the various studies [1]. The G centre is formed when one migrating interstitial carbon atom C_i is trapped at one substitutional carbon atom C_s [2]. The interstitial carbon atom may be produced by in-diffusion [3] or, as here, by radiation damage [4]. The destruction process of the G centre by thermal annealing is as yet uncertain. There have been several reports on the isothermal annealing of the G centre [5,6,1]. The destruction of the G centre has been considered as a simple break-up of the centre so that the decay of the concentration of the G centre was expressed with a simple exponential equation as

$$[G] = [G]_0 \exp(-t/\tau) \quad \text{with } \tau = \tau_0 \exp(E_b/kT), \qquad (1)$$

where τ_0 and E_b are the time constant factor and the activation energy for the break-up, respectively. However, since there occur multiple processes during annealing in reality, the equation for the time constant requires more parameters involving the carbon concentration and the radiation dose [1]. In addition, it has been observed that silicon crystal containing high carbon concentration ($> 2 \times 10^{17}$ cm^{-3}) show the two exponential decay behaviour rather than the single exponential decay [1,7].

Edge-defined film-fed growth (EFG) silicon is a ribbon crystal pulled from molten silicon through a graphite slot for solar cell production in economical way [8]. It was observed that EFG silicon contains high concentration of carbon over than 10^{18} cm^{-3} and that it has good optical characteristics comparable to single crystal silicon in spite of its poor crystallinity [9,7]. Thus EFG silicon can be useful as a sample material for understanding the decay process at higher carbon concentration. In this study, a systematic research of the isothermal annealing effect on the thermal destruction of the G centre was carried out at various annealing temperatures for EFG Si samples irradiated with various radiation doses.

* Corresponding author. Fax: + 44-20-7848-2420.
E-mail address: scp@maxwell.ph.kcl.ac.uk (S.-C. Park)

0921-4526/99/$ - see front matter
PII: S0921-4526(99)00505-0

2. Isothermal annealing statistics

As-grown EFG Si samples were cut typically to 1×1 cm^2 and loaded into an accelerator for e^--irradiation. The energy and current of the electron beam were set to 2 MeV and 25 μA, respectively. The radiation dose was controlled, by the radiation time, between 5×10^{16} and 8×10^{17} cm^{-2}. The temperature of the sample during the irradiation was typically 100°C [1]. To investigate the thermal destruction of the G centre, five samples with the same electron irradiation dose of 1×10^{17} cm^{-2} were annealed isothermally for several periods of annealing time up to 37 h at 180°C, 200°C, 210°C, 220°C, and 240°C. Another set of five samples irradiated with different electron doses, between 5×10^{16} and 8×10^{17} cm^{-2}, were annealed isothermally for various annealing time up to 37 h at 210°C. For temperatures up to 220°C, the annealing was carried out with samples immersed in a temperature stabilised silicon oil bath. For the annealing at 240°C, the sample was secured by Al-foil to the tip of a temperature probe and inserted into a horizontal ceramic tube furnace. The zero-phonon absorption line at 969 meV (G-line) from the G centre was measured, after each isothermal annealing period, using a dispersive spectrometer (SPEX 1 m) with the sample mounted in the full white light of a tungsten strip lamp. To avoid the noise in the signal caused by the bubbling of liquid helium at 4.2 K, all the absorption measurements were carried out with the sample immersed liquid helium, pumped below the λ point.

The decay of the G-line absorption intensity by the isothermal annealing is shown in Fig. 1(a) and (b). The absorption coefficients of the G line were normalised to the initial values before annealing. The decay patterns are not fit to the single exponential decay in Eq. (1) due to the slow decrease in the later stages of annealing. The solid curves in the figure are the least-squares fits obtained using the sum of two exponentials as

$$G = G_{0a} \exp(-t/\tau_a) + G_{0b} \exp(-t/\tau_b). \quad (2)$$

The decay may be slowed if the G centres are re-generated after the break-up. When the carbon concentration is high, a carbon escaping from the G centre can be captured at a different substitutional carbon atom to form another G centre. Thus, the sum of two exponentials would occur if there was inhomogeneity in the carbon distribution, since the decay time would be increased in regions of higher carbon concentration. However, it does not seem to be a plausible assumption that the carbon in EFG silicon is distributed as a mixture of micro-regions of two different concentrations: this assumption is a simple parametrisation of what is presumably a more complicated situation. From the double exponential decay, we can only say that at least two different processes are occurring independently for the destruction of

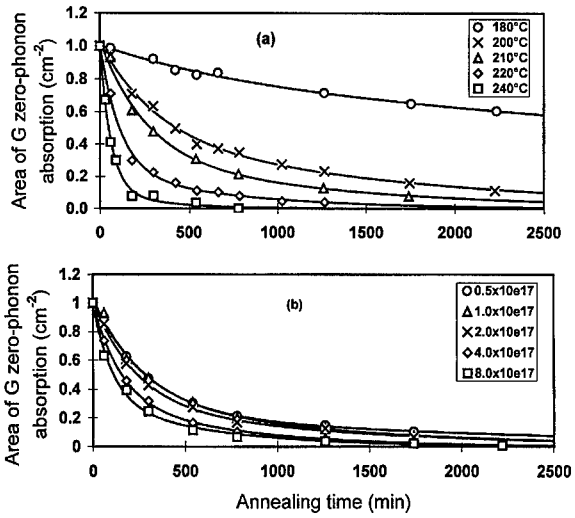

Fig. 1. The decay of G-line absorptions by the isothermal annealing (a) at different temperatures for samples irradiated with 1×10^{17} cm^{-2} 2 MeV electrons, (b) at 210°C for samples with different radiation doses. The solid curves are the least-square fits with the double exponential decay in Eq. (2).

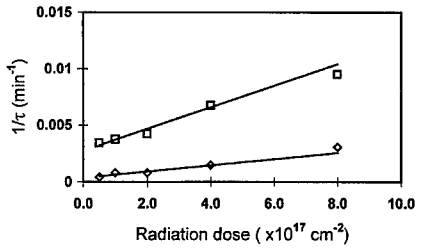

Fig. 2. Plot of the time constants obtained from the double exponential curve fits in Fig. 1(b). The fast decay (upper set of data) shows a greater dependence on the radiation dose than the slow decay.

the G centre in EFG silicon during annealing. The inverse of the time constants obtained from the double exponential curve fits in Fig. 1(b) are plotted for the different radiation doses in Fig. 2. The fast decay (upper set of data) shows a greater dependence on the radiation dose than the slow decay. This gives an important clue that the fast decay may be caused by defects created directly by the radiation damage but the slow decay may have a different cause.

3. Decay process model

To explain the thermal decay behaviour of the G centre, we consider several processes shown in Fig. 3. When the G centre breaks up, C_i escapes from the centre,

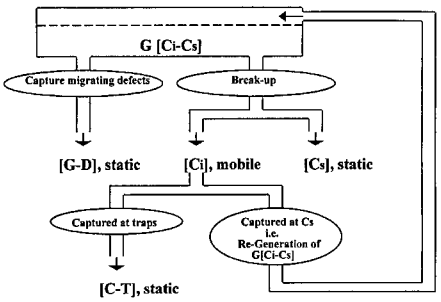

Fig. 3. Schematic diagram of the decay process model of the G centres.

leaving C_s, and moves around in the crystal. There may be two ways in which C_i ends its motion. One is to be trapped by another C_s resulting in a new G centre being created. Another is to be trapped by an unknown trap which forms a stable structure to hold C_i at the annealing temperature so that the destruction of the G centre is assured. On the other hand, some unknown radiation damages may contribute to the destruction of the G centre during annealing because the decay speed in the sample with higher radiation dose is faster than that of lower radiation dose. The unknown defects may migrate in the Si crystal with thermal energy during annealing and forms a complex by being trapped at the G centre, resulting in the destruction of the G centre.

The re-generation process may be considered as a feedback mechanism in the break-up process. Then the decay of the G centre can be expressed in two simultaneous equations as

$$\mathrm{d}[G]/\mathrm{d}t = -a[G] + c[C_i], \tag{3}$$

$$\mathrm{d}[C_i]/\mathrm{d}t = a[G] - b[C_i]. \tag{4}$$

Here a is the decay rate for the simple break-up of G centre and c is the re-generation rate by the capture of escaping C_i at another C_s, and b is the total loss rate of C_i atoms captured at C_s atoms or other traps. With the boundary conditions of $[G] = G_0$ and $[C_i] = 0$ at $t = 0$, the concentration of the G centre after annealing is obtained as

$$[G] = \frac{G_0}{2\omega}\left(\omega - \frac{a-b}{2} + \frac{ac}{b}\right)\exp -\left(\frac{a+b}{2} - \omega\right)t + \frac{G_0}{2\omega}\left(\omega + \frac{a-b}{2} - \frac{ac}{b}\right)\exp -\left(\frac{a+b}{2} + \omega\right)t, \tag{5}$$

where $\omega = \frac{1}{2}\sqrt{(a-b)^2 + 4ac}$.

If we choose the constants, a, b, and c, as positive values, ω is also positive. Then the first term in Eq. (5) has a smaller decay constant, i.e. a longer decay time, in its exponential function than that of the second term. Thus, the decay of the G centres in Eq. (5) can be interpreted as the sum of the slower decay (the first term) and the faster decay (the second term).

The fraction of the slow decay in Eq. (5) becomes larger with higher capture probability of C_i at C_s, e.g. when c approaches b, while the fraction of the fast decay becomes smaller. Since EFG Si samples used in this study contain a high concentration of carbon, we assume that the difference $(b - c)$ of the capture rate of C_i at C_s from the total capture rate at C_s and traps is sufficiently small compared to $(a + b)$. Then,

$$\omega = \frac{1}{2}\sqrt{(a+b)^2 - 4a(b-c)} \approx \frac{a+b}{2} - \frac{a(b-c)}{a+b} \tag{6}$$

and the fractions of the slow and fast decays are approximately unity and zero, respectively. The decay equation becomes one exponential form in this approximation. The decay time constant τ_s is obtained as

$$\tau_s = \frac{1}{s} = \frac{a+b}{a(b-c)} = \frac{1}{b-c} + \frac{b}{b-c}\frac{1}{a}. \tag{7}$$

The first term of τ_s corresponds to the time for a C_i atom to be captured at a trap and the second term is the time for the simple break-up of the G centre with a weight factor. Thus, the temperature dependence of the time constant is expressed as a function of the migration energy of C_i atom (E_m^c) and the break-up energy of the G centre (E_b).

$$\tau_s = A\exp(E_m^c/kT) + B\exp(E_b/kT), \tag{8}$$

where A and B are constants independent of temperature.

The destruction process by unknown migrating defects must be considered as an independent process to the break-up with re-generation process. To simplify the problem it is assumed that only one species of defect dominates the process. If there are migrating defects to the G centre, the number of the defects changes as

$$[T] = T_0\exp(-t/\tau_d), \tag{9}$$

where T_0 is the initial concentration of the defects and τ_d is a decay time constant. However, since the probability for the migrating defects to find the G centres varies with the concentration of the centre, the contribution by this process to the decay may be seen in the earlier stages of annealing. The temperature dependence of the time constant τ_d is expressed as a function of the migration energy of the defect as

$$\tau_d = D\exp(E_m^d/kT), \tag{10}$$

where D is a constant.

Consequently, with the decay process model, the decay of the G centres is considered as in two different circumstances. In the earlier stages of annealing it will be expressed as

$$[G] = G_0\exp(-t/\tau_s) - T_0[1 - \exp(-t/\tau_d)] \tag{11}$$

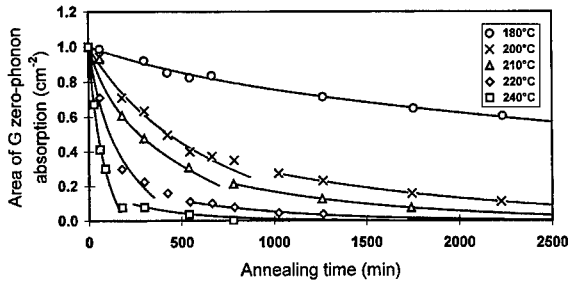

Fig. 4. The decay of G-line absorptions by the isothermal annealing as in Fig. 1(a). The solid curves calculated using Eq. (11) of the decay process model fit the data with good agreements.

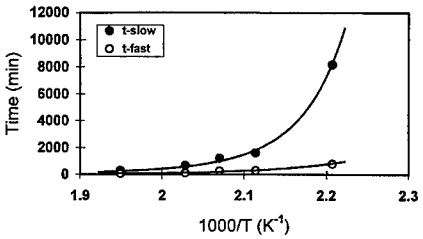

Fig. 5. The temperature dependence of time constants obtained from the curve fits in Fig. 4.

assuming all the possible processes occur simultaneously. In the later stages of annealing, the decay will be simplified to the the first term in Eq. (11). As seen in Fig. 4, the new fits from this model are in good agreements with the decay data. For the curve fits, 3–5 data points in the later stages at each annealing temperature were used and then, using the same time constants for the slow decays, the data values over 0.4 cm^{-2} in the earlier stages were fitted with the combination of two exponentials in Eq. (11).

The time constants obtained from the curve fits are plotted against the reciprocal temperature in Fig. 5. The time constant τ_s for the slow decay has the temperature dependence of the two factors from the break-up of the G centre and the migration of C_i atom. The curve fitted to the slower time constants is the two exponential combination in Eq. (8) with the barrier energy of the G centre $E_b = 1.934$ eV [1] and the migration energy of C_i atom $E_m^c = 0.890$ eV [10,11]. The curve fitted to the faster time constants is a single exponential curve and the migration energy E_m^d of the defect obtained from the fit is 0.879 eV. The energy values used and obtained from the fits are not very much significant due to the small number of data points and also due to the error range of the carbon contents about 20% in our samples. However, the good agreements of the decay data with the curve fits demonstrates that the suggested model for the decay of the G centre is a good approximation both qualitatively and quantitatively.

4. Summary

With the reliable experimental results, it was shown that EFG silicon is useful as a sample material for understanding the decay process at high carbon concentration. The two exponential decay behaviour of the G centres by isothermal annealing was explained successfully with a decay process model by the combination of the break-up and re-generation process and the destruction by migrating defects.

Acknowledgements

We thank W.D. Sawyer for providing EFG Si samples and useful discussions.

References

[1] G. Davies, T.K. Kwok, T. Reade, Phys. Rev. B 44 (1991) 12146.
[2] K.M. Lee, K.P. O'Donnell, J. Weber, B.C. Cavenett, G.D. Watkins, Phys. Rev. Lett. 48 (1982) 37.
[3] J. Weber, M. Singh, Appl. Phys. Lett. 49 (1986) 1617.
[4] G. Davies, E.C. Lightowlers, R.C. Newman, A.S. Oates, Semicond. Sci. Technol. 2 (1987) 524.
[5] E.H. Wong, B.G. Streetman, J. Appl. Phys. 42 (1971) 5882.
[6] G. Davies, T.K. Kwok, Semicond. Sci. Technol. 4 (1989) 327.
[7] S.-C. Park, G. Davies, W.D. Sawyer, V. Higgs, Mat. Sci. Forum 143–147 (1994) 1493.
[8] F.V. Wald, in: J. Grabmaier (Ed.), Crystals, Growth Properties and Applications, Vol. 5, Springer, Berlin, 1981, p. 147.
[9] G. Davies, S.-C. Park, V. Higgs, Appl. Phys. Lett. 63 (1993) 1783.
[10] G.D. Watkins, K.L. Brower, Phys. Rev. Lett. 36 (1976) 1329.
[11] S.P. Chappell, G. Davies, E.C. Lightowlers, R.C. Newman, Mat. Sci. Forum 10–12 (1987) 109.

ELSEVIER

Physica B 273–274 (1999) 287–290

PHYSICA B

www.elsevier.com/locate/physb

Electron irradiation of heavily doped silicon: group-III impurity ion pairs

V.V. Emtsev[a,*], P. Ehrhart[b], D.S. Poloskin[a], U. Dedek[b]

[a]*Division of Solid State Electronics, Ioffe Physicotechnical Institute, Russian Academy of Sciences, Politekhnicheskaya ulitsa 26, 194021 St. Petersburg, Russia*

[b]*Institut für Festkörperforschung, Forschungszentrum Jülich, D-52425 Jülich, Germany*

Abstract

Defect annealing processes in near-degenerate p-Si subjected to electron irradiation at cryogenic temperatures are investigated. A marked difference in the annealing behavior of defects in p-Si doped with boron and gallium is observed. It has been found that this effect is primarily due to the different charge states and stability of interstitial impurity ions. If mobile these ions form interstitial ion-substitutional ion pairs stable up to $T = 600$°C. The charge states and stability of impurity–vacancy complexes are also discussed.

Keywords: Silicon; Group III impurities; Electron irradiation; Impurity-related defects

1. Introduction

Boron in silicon is an impurity of great importance because of its wide use in the fabrication of silicon-based devices. A variety of technological steps in the treatment of Si, e.g. ion implantation, etching, oxidizing, heating, etc., gives rise to the production of intrinsic defects and their interactions with boron. This is why the properties of B-related defects generate deep interest for a long time.

It has been found that substitutional boron atoms B_S can trap mobile vacancies V and self-interstitials Si_I. The reaction products are boron–vacancy complexes [B_SV] [1] and interstitial boron atoms B_I [2,3]. Although the details of the production process are not clear at present [4] the interstitial boron atoms are easily produced in p-Si subjected to fast electron irradiation even at cryogenic temperatures. In contrast, boron–vacancy complexes are formed only at around $T = 200$ K when isolated vacancies in p-Si irradiated at low temperatures become mobile. Both the defects are not stable at room temperature giving rise to the appearance of other boron-related defects [5] which, in turn, can be annealed out at $T \leqslant 400$°C, with the exception of interstitial boron-substitutional boron pairs [B_IB_S]. The latter ones were found to be persistent at $T = 400$°C [6]. However, in lightly doped p-Si the boron pairing cannot be dominant because of very low formation rates [5] and the complete recovery of the hole concentration takes place at around $T = 350$°C [7].

The situation is different in degenerate p-Si irradiated at low temperatures [8,9]. Under such conditions, the presence of defects can be traced even at $T = 900$ K [4,9]. The defect interactions in heavily doped p-Si are far from being well understood. In this respect, the problem appears to be common for ion implantation of B in Si taking into account the complexity of defect reactions [10–12].

The aims of the present work is to examine the annealing behavior of defects in near-degenerate p-Si subjected to low-temperature electron irradiation and provide information on the defect interactions in Si : Ga. In contrast to B and Al, very little is known about Ga-related defects. The appearance of [Ga_IGa_S] pairs in irradiated p-Si after annealing to $T \approx 200$°C is the only observation by EPR [13] reported so far.

* Corresponding author: Tel.: + 7-812-247-9952; fax: + 7-812-247-1017.

E-mail address: emtsev@pop.ioffe.rssi.ru (V.V. Emtsev)

0921-4526/99/$ - see front matter
PII: S0921-4526(99)00506-2

2. Experimental

Czochralski grown Si doped with boron (Cz–Si : B) and gallium (Cz–Si : Ga) were used. The dopant concentrations in the initial materials were about 1×10^{18} cm^{-3}.

Electron irradiation experiments were performed at the low-temperature facility in Jülich, Germany [14]. The current density of 2.5 MeV electrons was 6.8 μA/ cm^{-2}. The samples were immersed in a stream of liquid helium. The irradiation dose was $D = 1.58 \times 10^{17}$ cm^{-2}.

The irradiation-induced defects were investigated by measurements of the electrical resistivity and of the Hall effect in the Van der Pauw geometry. Although there are many kinds of defects after irradiation and electrical measurements are not sensitive to all of them [4], they sensitively detect reactions of the dopant atoms. These reactions will be analyzed in the following on the basis of the published EPR-fingerprints on special defect complexes. Just after the electron irradiation at $T = 4.7$ K, conductivity was measured in situ on the irradiated samples up to $T = 100$ K. Since our preliminary experiments showed no recovery in the conductivity over a temperature range of $T = 40$–100 K the isochronal annealing procedure in steps of $\Delta T = 30$ K and $\Delta t = 10$ min was applied from $T = 100$ up to $T = 340$ K, with a reference point at $T = 40$ K. At higher temperatures the annealing studies were running in steps of $\Delta T = 100$ K and $\Delta t = 20$ min and Hall effect measurements were taken on all the samples studied.

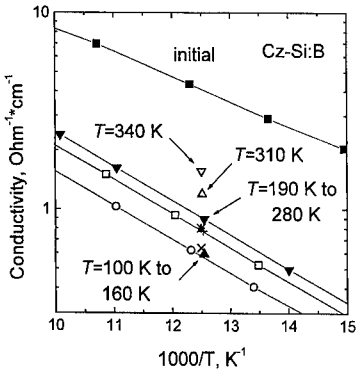

Fig. 1. Conductivity versus reciprocal temperature for the Cz–Si : B irradiated with fast electrons at $T = 4.7$ K and annealed up to $T = 340$ K. The concentration of charge carriers at room temperature is 8.1×10^{17} cm^{-3} before irradiation. Irradiation dose, $D = 1.58 \times 10^{17}$ cm^{-2}. The annealing temperature is indicated.

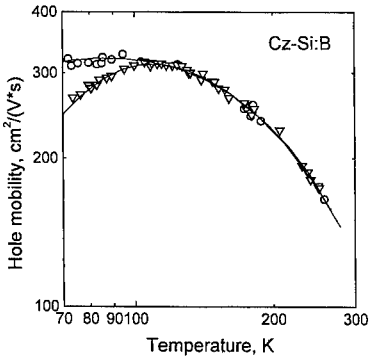

Fig. 2. Temperature dependence of the hole mobility in the Cz–Si : B before irradiation (circles) and after electron irradiation at $T = 4.7$ K with subsequent annealing up to $T = 340$ K (triangles). Irradiation dose, $D = 1.58 \times 10^{17}$ cm^{-2}.

3. Results and discussion

3.1. Defect annealing in irradiated Cz–Si : B below room temperature

As a result of the irradiation, the conductivity at the reference point dropped by an order-of-magnitude; see Fig. 1. As expected, the first signs of recovery occurred over an annealing temperature range of $T = 160$–220 K. This correlates well with the onset of migration of vacancies in p-Si and formation of boron–vacancy complexes [15]. Provided the [B_SV] complex is positively charged in p-Si [1] the hole concentration remains unchanged. However, the partial mobility of charge carriers by ionized defects should increase taking into account the charge states of V^{2+} and $[B_S V]^+$. Therefore, the conductivity is expected to increase as well, though the effect must be of minor importance. As a result, a relatively small recovery of the conductivity was observed. If the complexes [B_SV] were deep acceptors one could have observed a substantial increase in the conductivity after the annealing of V^{2+}.

The next annealing stage starts at $T = 280$ K and runs up to $T = 340$ K. As already mentioned above, both the boron-related defects B_I and [B_SV] are annealed out at room temperature. At the end of this stage, the hole concentration at room temperature was by 2.6×10^{17} cm^{-3} less than the initial one, though the mobility of charge carriers was practically restored; see Fig. 2. It means that most of the still existing defects are electrically neutral in p-Si.

3.2. Defect annealing in irradiated Cz–Si : Ga below room temperature

As can be seen from Fig. 3, there are no changes in the conductivity after annealing to $T = 340$ K. At this annealing step, the hole concentration at room temperature was by 2.8×10^{17} cm^{-3} less than the initial one. The mobility of charge carriers was found to be strongly suppressed at low temperatures; see Fig. 4. The concentrations of defects produced in the Cz–Si : Ga cannot

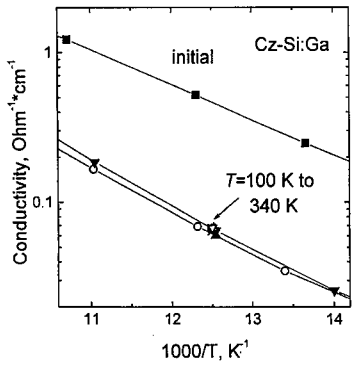

Fig. 3. Conductivity versus reciprocal temperature for the Cz–Si : Ga irradiated with fast electrons at $T = 4.7$ K and annealed up to $T = 340$ K. The concentration of charge carriers at room temperature is 8.8×10^{17} cm^{-3} before irradiation. Irradiation dose, $D = 1.58 \times 10^{17}$ cm^{-2}. The annealing temperature is indicated.

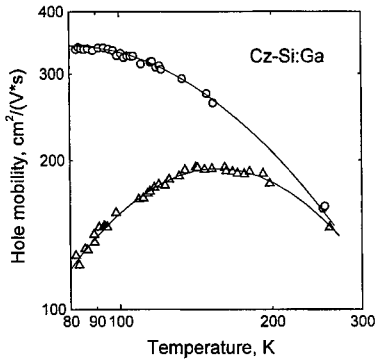

Fig. 4. Temperature dependence of the hole mobility in the Cz–Si : Ga before irradiation (circles) and after electron irradiation at $T = 4.7$ K with subsequent annealing up to $T = 340$ K (triangles). Irradiation dose, $D = 1.58 \times 10^{17}$ cm^{-2}.

differ greatly from those in the Cz–Si : B because of the same irradiation dose. Therefore, the low mobility of charge carriers is resulted from the effective scattering by multiply charged defects. Taking into account the EPR observation of $[Ga_i^{2+}Ga_s^-]$ pairs in electron-irradiated Cz–Si : Ga [13] the presence of isolated Ga_i^+ immobile at room temperature can explain the mobility suppression. The annealing processes at $T > 300$ K provides convincing evidence that this conclusion is true; see below.

The fate of vacancies in Cz–Si : Ga after annealing to $T = 220$ K should not be different from their fate in Cz–Si : B. We believe that the mobile vacancies V^{2+} are trapped by Ga_s^-, thus forming $[Ga_sV]$ complexes. These complexes must be positively charged, leaving the hole concentration unchanged. The lack of recovery of the conductivity up to $T = 340$ K can be accounted for

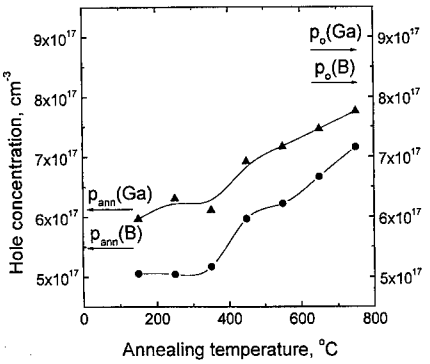

Fig. 5. Changes in the hole concentration as a result of isochronal annealing of the Cz–Si : B (circles) and Cz–Si : Ga (triangles) irradiated at $T = 4.7$ K. Irradiation dose, $D = 1.58 \times 10^{17}$ cm^{-2}. The hole concentration is measured at room temperature. Arrows show the hole concentrations $p_0(T = 280\text{ K})$ and $p_{ann}(T = 280\text{ K})$ before irradiation and after electron irradiation with subsequent annealing to room temperature, respectively.

a very low mobility of charge carriers at cryogenic temperatures; cf Figs. 2 and 4.

3.3. Defect annealing in irradiated Cz-Si : B above room temperature

As is apparent from Fig. 5, there is no recovery of the hole concentration up to $T = 300$°C. Starting from an annealing temperature of $T = 350$°C a gradual recovery process takes place and the recovery of the hole concentration after annealing to $T = 750$°C is 90% of the initial concentration of charge carriers. This is also true for the degenerate Cz–Si : B studied in Refs. [4,9].

The annealing behavior of the hole mobility shows a very interesting feature; see Fig. 6. Over a wide range of annealing, from $T \approx 100$°C to 600°C, the mobility of charge carriers at room temperature, being larger by 13% compared to the initial one, remains practically constant. This increase in the mobility is significant, since it means a decrease in the concentration of ionized scattering centers by about 1×10^{17} cm^{-3}. Among the defect interactions at room temperature, the formation of $[B_i^+B_s^-]$ pairs appears to be the only important process which provides a lucid explanation. Thus, one can conclude that these ion pairs formed as a result of the annealing of B_i^+ are stable up to $T \approx 600$°C.

3.4. Defect annealing in irradiated Cz–Si : Ga above room temperature

The defect annealing in the Cz–Si : Ga runs in a way very similar to that in the Cz–Si : B, apart from the

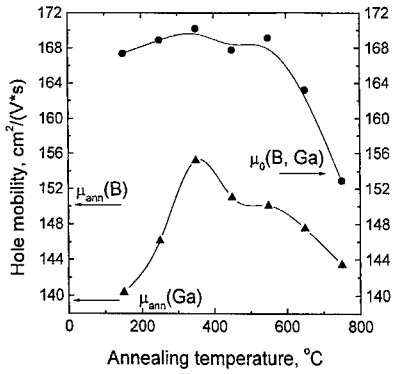

Fig. 6. Changes in the hole mobility as a result of isochronal annealing of the Cz–Si : B (circles) and Cz–Si : Ga (triangles) irradiated at $T = 4.7$ K. Irradiation dose, $D = 1.58 \times 10^{17}$ cm^{-2}. The hole mobility is measured at room temperature. Arrows show the hole mobilities $\mu_0(T = 280\ \text{K})$ and $\mu_{ann}(T = 280\ \text{K})$ before irradiation and after electron irradiation with subsequent annealing to room temperature, respectively.

formation of ion pairs. Really, the hole concentration remains unchanged after annealing to $T = 300$°C, whereas the mobility of charge carriers shows a considerable increase; see Figs. 5 and 6. The explanation based on the onset of migration of isolated Ga_i^{2+} at $T \approx 200$°C is straightforward, since the appearance of $[Ga_i^{2+}Ga_i^-]$ pairs in irradiated Cz–Si : Ga after annealing to $T \approx 200$°C was earlier observed by EPR [13]. The maximal increase in the hole mobility due to ion pairing did not exceed the initial mobility, in contrast to the case of Cz–Si : B; see Fig. 6. This is due to an extra charge in the $[Ga_i^{2+}Ga_i^-]$ pair versus the $[B_i^+B_s^-]$ pair.

A minor annealing stage taking place in both materials at $T \approx 400$°C (Fig. 4) is most likely associated with carbon-related complexes. The $[B_iC_s]$ complexes are known to be annealed out at this temperature [5].

As is seen from Fig. 5, the recovery processes at $T \geqslant 600$°C, resulted from the dissociation of ion pairs, run in a similar way in both Cz–Si : Ga and Cz–Si : B. However, the annealing behavior of the mobility of charge carriers at $T \geqslant 600$°C is more complicated and it appears to be dependent on both the chemical nature and concentration of dopants; cf present paper and Ref. [9].

4. Conclusions

The electrical data on the defect annealing in near-degenerate p-Si irradiated at low temperatures provide evidence that the boron- and gallium–vacancy complexes are deep donors. In contrast to the boron–vacancy complex which is unstable at room temperature, the gallium–vacancy complex appears to be stable at least up to $T = 400$ K.

The results obtained strongly suggest that interstitial ions Ga_i^{2+} are present in Cz–Si : Ga just after low-temperature electron irradiation, like B_i^+ in the case of Cz–Si : B. A marked difference between isolated B_i^+ and Ga_i^{2+} ions is their stability. The interstitial gallium ions start to migrate only at about $T = 200$°C, contrary to the interstitial boron ions mobile at room temperature. If mobile the interstitial ions can form ion pairs $[B_i^+B_s^-]$ and $[Ga_i^{2+}Ga_s^-]$. This ion pairing is a most prominent process in heavily doped p-Si. It has been shown that the ion pairs are stable up to $T = 600$°C. At elevated temperatures the pair dissociation takes place and the recovery of the hole concentration in p-Si is observed.

References

[1] G.D. Watkins, Phys. Rev. B 13 (1976) 2511.
[2] G.D. Watkins, Phys. Rev. B 12 (1975) 5824.
[3] J.R. Troxell, G.D. Watkins, Phys. Rev. B 22 (1980) 921.
[4] P. Ehrhart, H. Zillgen, Mater. Res. Soc. Symp. Proc. 469 (1997) 175.
[5] L.C. Kimerling et al., in: Materials Science Forum, Vols. 38-41, Trans Tech Publications, Switzerland, 1989, pp. 141–150.
[6] P.J. Drevinsky, in: Mat. Res. Soc. Symp. Proc., Vol. 104, Materials Research Society, 1988, pp. 167–172.
[7] V.S. Vavilov et al., in: Conference Series Number, 16, The Institute of Physics, London and Bristol, 1973, pp. 284–288.
[8] A.K. Tipping, R.C. Newman, Semicond. Sci. Technol. 2 (1987) 389.
[9] V.V. Emtsev et al., in: G. Davies, M.H. Nazaré (Eds.), Materials Science Forum, Vols. 258–263, Trans Tech Publications, Switzerland, 1997, pp. 575–580.
[10] T.E. Haynes et al., Appl. Phys. Lett. 69 (1996) 1376.
[11] S. Libertino et al., Appl. Phys. Lett. 70 (1997) 3002.
[12] L. Pelaz et al., Appl. Phys. Lett. 70 (1997) 2285.
[13] G.D. Watkins, in: Effets des Rayonnements sur les Semiconducteurs, Dunod Éditeur, Paris, 1964, pp. 97–113.
[14] J. Hemmerich et al., Z. Angew. Phys. 29 (1970) 1.
[15] G.D. Watkins, in: Conference Series Number, 23, The Institute of Physics, London and Bristol, 1975, pp. 1–22.

ELSEVIER

Physica B 273–274 (1999) 291–295

PHYSICA B

www.elsevier.com/locate/physb

Vibrational absorption from vacancy-oxygen-related complexes (VO, V_2O, VO_2) in irradiated silicon

J.L. Lindström[a,*], L.I. Murin[b], V.P. Markevich[b], T. Hallberg[c], B.G. Svensson[d]

[a]*Department of Physics, Solid State Physics, University of Lund, Box 118, S-22100 Lund, Sweden*
[b]*Institute of Solid State and Semiconductor Physics, 220072 Minsk, Belarus, Byelorussia*
[c]*National Defense Research Establishment, S-58111 Linkoping, Sweden*
[d]*Royal Institute of Technology, Solid State Electronics, S-16440, Kista-Stockholm, Sweden*

Abstract

Infrared absorption from oxygen-related defects in Si crystals irradiated with electrons (2.5 MeV) at room temperature (RT) and in the range 300–600°C has been investigated. Two new vibrational bands positioned at 10 K at about 1370 and 1430 cm^{-1} were observed in samples irradiated at RT. A good correlation is found between these lines and the bands at 836 and 885 cm^{-1} known to originate from asymmetrical stretching vibrations (B_1 mode) of an oxygen atom in the neutral and negative VO complex. An attribution of the 1370 and 1430 cm^{-1} bands to a combination of the B_1 mode with the symmetrical stretching A_1 mode (weakly IR active) for different charge states of VO is argued to be the most probable. A band at 833.4 cm^{-1} is found to increase in strength upon annihilation of divacancies at 250–300°C. The V_2O complex is suggested to give rise to this band. New experimental data confirming an attribution of the 895 cm^{-1} band to the VO_2 complex are presented as well.

PACS: 78.30.Am; 61.80.Fe; 63.20.Pw; 81.40.Wx

Keywords: Silicon; Electron irradiation; Oxygen; LVMs

1. Introduction

Oxygen is a very common and important impurity in silicon materials [1,2]. In as-grown crystals oxygen is mainly present in the form of an electrically inactive interstitial defect (O_i), where it binds with two neighboring Si atoms. Oxygen does not normally occupy a substitutional site. However, in irradiated crystals the mobile vacancy can be trapped at the O_i atom forming the vacancy-oxygen complex [3,4]. In this configuration oxygen bridges a pair of Si neighbors of the vacancy and is called an off-center substitutional oxygen, or A-center. Upon further irradiation the trapping of vacancies by the A-center can result in formation of a divacancy–oxygen V_2O complex [4]. Annihilation of both centers, VO and V_2O, occurs in the temperature range 300–400°C and is accompanied by the appearance of a number of new more complicated vacancy–oxygen complexes [5,6]. Among them the VO_2 complex, formed via the capture of a mobile A-center by an O_i atom, is the dominant one [6,7]. In this complex two oxygen atoms share a vacancy, each bonded between two Si neighbors.

Infrared (IR) absorption spectra of vacancy–oxygen-related complexes in Si have been intensively studied and a number of vibrational bands have been reported [3–10] (for a review, see Pajot [1, Chapter 6]). However, only the band at 836 cm^{-1} has been unambiguously identified as arising from the A-center [3,4]. The origin of all the others is still not fully understood and the experimental and theoretical studies of the appropriate local vibrational modes (LVMs) are currently active areas of research [11–13] (see Khirunenko et al. [Ref. 2, p. 403]).

* Corresponding author. Fax: + 46-46-2223637.
E-mail address: lennart.lindstrom@ftf.lth.se (J.L. Lindström)

0921-4526/99/$ - see front matter
PII: S0921-4526(99)00447-0

In the present paper we report on the observation of two new vibrational bands related to the A-center. An A-center satellite line at 833.4 cm^{-1} is argued to arise from the V_2O defect. A further support for the assignment of the well known 895 cm^{-1} band to the VO_2 complex is presented.

2. Experimental

In this study the IR absorption analysis was carried out using a Bruker 113v Fourier transform IR spectrometer. The measurements were performed at 10 K and at room temperature (RT), with a spectral resolution of 0.5–1.0 cm^{-1}. We used phosphorus and antimony doped Czochralski-grown (Cz) silicon with initial resistivity of 0.1–60 Ω cm. The concentration of oxygen in the crystals was $(9–17.5)\times10^{17}$ cm^{-3}. Carbon-lean ($N_C < 10^{16}$ cm^{-3}) and carbon-rich ($N_C = 3–5\times10^{17}$ cm^{-3}) samples as well as samples doped with the isotope ^{18}O were studied. The concentration of O_i and C_S was monitored by measuring the intensity of the absorption bands at 1107 [14] and 605 cm^{-1} [15], respectively. Irradiation with electrons (2.5 MeV) was performed at RT and in the range of 300–600°C. 30-min isochronal anneals were carried out up to 600°C in nitrogen ambient.

3. Results and discussion

3.1. V–O combination mode at 1370 cm^{-1}

The vacancy–oxygen complex is one of the dominant defects in Cz–Si after RT irradiation with MeV electrons. Its maximum concentration achievable at high doses of irradiation is usually limited by trapping of diffusing Si self-interstitial (I) by VO, i.e. due to the occurrence of the reaction $VO + I \Rightarrow O_i$. However, it is possible to suppress this reaction using the carbon-rich Cz–Si [15]. In such a material the main trap for I is substitutional carbon, and a much higher concentration of VO complexes can be attained. Accordingly, weak IR bands related to this defect can be detected in C-rich crystals.

Fig. 1 shows fragments of infrared absorption spectra in the regions 780–900 and 1300–1420 cm^{-1} for irradiated carbon-doped ^{16}O- and ^{18}O-enriched samples. In the former region the strong and well-known lines originating from the VO and C_i–O_i complexes are observed. In the latter region new lines positioned at 10 K at 1370.0 cm^{-1} for ^{16}O- and at 1332.5 cm^{-1} for ^{18}O-doped samples have been revealed. The lines are shifted to 1361.4 and 1323.9 cm^{-1} in the spectra measured at RT. The band at 1370.0 (1332.5) cm^{-1} was observed in all the irradiated Cz–Si samples including carbon-lean ones. The intensity of the line was found to be directly proportional to that of the 835.8 (799.9) cm^{-1} band, i.e. to the

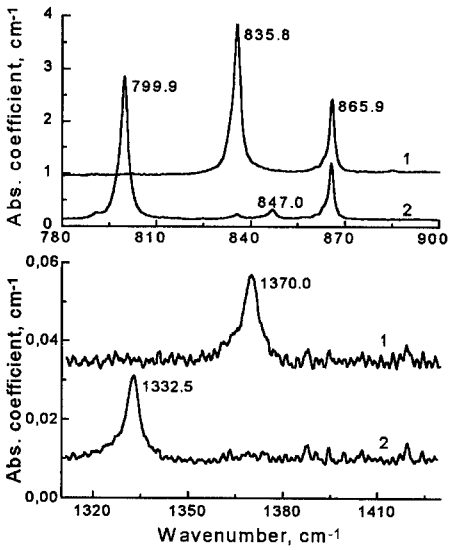

Fig. 1. Absorption spectra at 10 K for electron-irradiated (1×10^{18} cm^{-2}) Si crystals with (1) natural abundance of oxygen isotopes ($[^{16}O] = 9.5\times10^{17}$, $[^{12}C] = 3\times10^{17}$ cm^{-3}) and (2) ^{18}O enrichment ($[^{16}O] = 6.5\times10^{16}$, $[^{18}O] = 1.7\times10^{18}$, $[^{12}C] \approx 3\times10^{17}$ cm^{-3}.

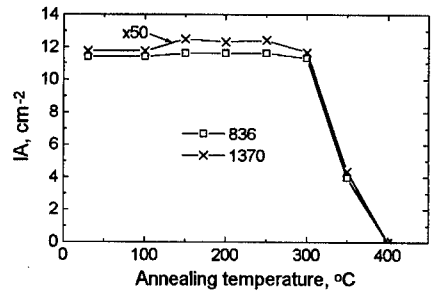

Fig. 2. Changes in integrated absorption due to lines at 836 and 1370 cm^{-1} with temperature of 30 min isochronal anneal.

A-center concentration. Besides, both lines (835.8 and 1370.0 cm^{-1}) exhibit the same thermal stability (Fig. 2). All these facts indicate that the line at 1370.0 cm^{-1} is most probably related to the A-center. To check this suggestion, we have studied the line behavior in samples with lower resistivity where an essential part of the A-center could be in the negative charge state giving rise to the IR band at 885 cm^{-1} [11].

Fig. 3 shows fragments of IR absorption spectra at 10 K for such samples. The strong lines positioned at 885.2 cm^{-1} for ^{16}O- and at 847.0 cm^{-1} for ^{18}O-doped samples originate from asymmetrical stretching vibrations (B_1 mode) of an oxygen atom in the negative VO. There are also two additional lines in the range of 1300–1420 cm^{-1}, positioned at 1430.1 and 1391.0 cm^{-1}

for ^{16}O- and ^{18}O-doped samples, respectively. The intensities of these lines were found to correlate with those of the 885.2 and 847.0 cm^{-1} bands.

These observations give an additional support for identification of the 1370 and 1430.1 cm^{-1} bands as arising from the neutral and negative A-center, respectively. The high-energy position of the lines with respect to the frequencies of fundamental modes (B_1) for VO implies that the lines could be related to a combination of fundamental vibrations. The oxygen isotopic shift of the 1370 cm^{-1} line is almost the same as that of the 836 cm^{-1} band. So, it appears likely that the 1370 cm^{-1} band is a combination band involving the B_1 mode and another mode positioned at about 534 cm^{-1}. However, no IR band related to the A-center has been clearly observed in the region of 525–550 cm^{-1}. It might be that the band is mainly Raman active. Besides, it should have a small oxygen isotopic shift (Table 1). All of these features of the second mode giving rise to the 1370 cm^{-1} band are rather close to those expected for the symmetrical stretching A_1 mode of the A-center. It appears that the 1370 cm^{-1} line related to off-center substitutional oxygen can be considered as an analogue of the 1748 cm^{-1} band originated from the bond-centered interstitial oxygen. The latter band was recently identified as a combination of symmetric and asymmetric stretching modes of a quasi-linear Si–O–Si unit [16].

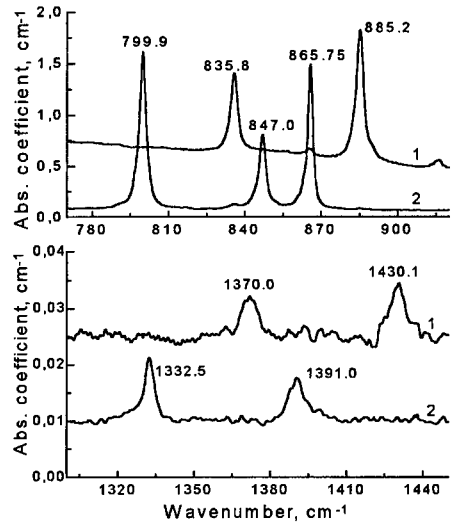

Fig. 3. Absorption spectra at 10 K for electron-irradiated (6×10^{17} cm^{-2}) highly doped Si crystals with (1) natural abundance of oxygen isotopes ($[^{16}O] = 9 \times 10^{17}$ cm^{-3}) and (2) ^{18}O enrichment ($[^{16}O] = 5 \times 10^{16}$, $[^{18}O] = 1.5 \times 10^{18}$ cm^{-3}).

3.2. V_2O vibrational mode

The V_2O complex was identified via a detailed EPR study of the A14 spectrum in heavily electron irradiated Si [5]. However, Corbett et al. [6] observed only the 836 cm^{-1} band with the same irradiation condition as the A14 spectrum. Since V_2O contains a Si–O–Si bonding structure like VO, it has been suggested [10] that an oxygen vibrational band of V_2O is very similar to that of VO and is not resolved from the more intensive 836 cm^{-1} band. Recent ab-initio calculations [12] have also predicted that the asymmetric stretching vibrations of VO and V_2O should be almost the same.

We have performed a careful analysis of a shape of the 836 cm^{-1} band using a fitting procedure with Lorentzian functions. It has been found that there is a clearly pronounced shoulder at about 833 cm^{-1} on the low-energy side of the band. The existence of such a shoulder; with a relative intensity of about 15%, is expected due to Si isotope effect, i.e. due to natural abundance of ^{29}Si (4.7%) and ^{30}Si (3.1%) isotopes (for a review, see Pajot [1, Chapter 6]). However, the relative intensity of the shoulder was found to be sample dependent, increasing up to 20–30% of the total absorption around the 836 cm^{-1} peak in the samples irradiated with a high fluence of electrons. This implies the existence of an additional satellite of the A-center at about 833 cm^{-1} and the latter one could be related to the V_2O defect.

An appearance of the A-center satellites, called S_1, S_2, S_3 and positioned at low temperature at about 829 (S_1), 833 (S_2), and 842 cm^{-1} (S_3) has been observed by

Table 1
Positions of vibrational IR modes (in cm^{-1}) related to the V–O complex in silicon

Mode	$(V–O)^0$				$(V–O)^-$			
	^{16}O		^{18}O		^{16}O		^{18}O	
	10 K	RT	10 K	RT	10 K	RT	10 K	RT
B_1	835.8	830.4	799.9	794.6	885.2	877.1	847.0	839. 0
$B_1 + A_1$	1370.0	1361.4	1332.5	1323.9	1430.1	—	1391.0	—
A_1	~ 534	~ 531	~ 533	~ 530	~ 545	—	544	—

different investigators upon heat-treatment at 210–400°C of Cz–Si irradiated with fast neutrons [8,13] (see Khirunenko et al. [Ref. 2, p. 403]) or electrons [9] (see Khirunenko et al. [Ref. 2, p. 403]). It has been suggested [8,13] that some of the satellites should be related to divacancy-oxygen complex formed via trapping of a mobile V_2 by an O_i atom. However, no correlation between the V_2 disappearance and formation of the satellites has been reported.

We have monitored the V_2 behavior during isochronal anneals by measuring the intensity of the well-known band at 2766 cm^{-1} [9]. It was found that the divacancies started to disappear at 250°C, and they annealed out completely at 300°C. This was followed by an essential increase in the strength of the band at 833.4 cm^{-1}, as it was inferred from the differential spectrum (Fig. 4). At the same time only a small decrease in the intensity of the 836 cm^{-1} band was detected. So, it appears likely that the growth of the 833 cm^{-1} band is associated with the disappearance of divacancies. Such a conclusion is also consistent with the results of Ref. [9], where an efficient formation of the S_2 satellite at $\geqslant$ 280°C has been observed in the samples irradiated with electrons and containing a high concentration of V_2. It should also be noted that the defect giving rise to the 833 cm^{-1} band is only slightly more stable than the A-center and anneals at 350–400°C.

All these observations allow one to suggest that the band at 833.4 cm^{-1} is related to the V_2O complex. However, further studies are needed to make a more definite conclusion.

3.3. The 895 cm^{-1} band

Disappearance of the A-center at 300–350°C is always followed by an appearance of the band at 895 cm^{-1}. It has been argued [6,7] that the vacancy–dioxygen complex formed via the capture of diffusing VO by an Oi atom is responsible for the band. However, there are still some doubts regarding such an identification (for a review, see Pajot [1, Chapter 6]). We present here some new experimental data supporting the original suggestions [6,7].

According to the results of ab-initio modeling [12], the LVM at 895 cm^{-1} represents independent motion of the two O atoms sharing a vacancy site, i.e. the both atoms contribute to the absorption. Hence, at the same concentration of the VO and VO_2 complexes the intensity of the 895 cm^{-1} band should be twice that of the A-center bands. However, in previous studies the intensity of the 895 cm^{-1} band has never been observed to exceed that of the 836 and 885.3 cm^{-1} bands implying that only a partial transformation of VO into VO_2 does occur, probably due to interaction of interstitial-type defects with VO etc. [6]. Recently we discovered [17] that upon annealing the samples irradiated with a small fluence of electrons the strength of the 895 cm^{-1} band could be actually twice that of the A-center bands. So, two oxygen atoms should be incorporated into the center responsible for the 895 cm^{-1} band. Besides, a complete transformation of the A-center into this complex can occur in some cases. Both obvservations are consistent with the VO_2 model for the 895 cm^{-1} band.

Additional support has come from the recent studies of defect production during electron irradiation at elevated temperatures [18]. A strong enhancement of the IR bands assigned to the oxygen dimer has been observed in carbon-lean Cz–Si irradiated at 300–400°C, and a correlation of that with the 895 cm^{-1} band generation has been found. These important findings can be easily explained assuming an occurrence of the reaction $VO_2 + I \Rightarrow O_{2i}$. Evidence for such interpretation is found from similar studies of carbon-rich Si. In this material only a small increase in the O_{2i} bands is detected, while the 895 cm^{-1} band is produced very efficiently (Fig. 5). It is well known [15] that the Watkins replacement mechanism $I + C_s \Rightarrow C_i$ is a dominating reaction in

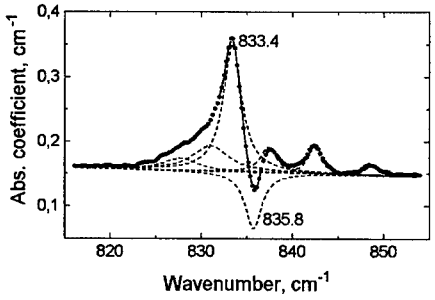

Fig. 4. Difference absorption spectrum at 10 K for sample 1 (see caption to Fig. 1) annealed at 300°C for 30 min. The spectrum recorded after irradiation was used as a reference. Dashed lines show a deconvolution of the spectrum onto the absorption peaks of Lorentzian shape.

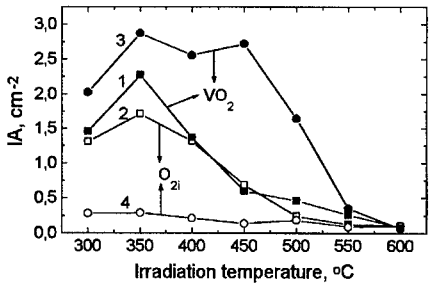

Fig. 5. Changes in integrated absorption at 10 K due to lines at (1,3) 895.3 and (2,4) 1012.4 cm^{-1} with temperature of irradiation (1×10^{18} e^-/cm^2) for (1,2) carbon-lean and (3,4) carbon-rich Cz–Si samples.

carbon-rich Si. An occurrence of this reaction suppresses the dimer formation, but stimulates the VO_2 growth. So, the results presented here seem to support strongly the identification of the 895 cm^{-1} band as arising from the VO_2 complex.

Acknowledgements

We thank TFR, KVA, SI, and FOA in Sweden for financial support. We also acknowledge financial support from the grant INTAS-Belarus 97-824. Useful discussions with R. Jones and S. Öberg are gratefully acknowledged.

References

[1] F. Shimura (Ed.), Oxygen in Silicon, Semiconductors and Semimetals, Vol. 42, Academic Press, London, 1994.
[2] R. Jones (Ed.), Proceedings of the NATO Advanced Workshop on the Early Stages of Oxygen Precipitation in Silicon, Exeter, UK, 1996, NATO ASI, Series 3, High Technology, Vol. 17, Kluwer, Dordrecht, 1996.
[3] G.D. Watkins, J.W. Corbett, Phys. Rev. 121 (1961) 1001.
[4] J.W. Corbett et al., Phys. Rev. 121 (1961) 1015.
[5] Y.H. Lee, J.W. Corbett, Phys. Rev. B 13 (1976) 2653.
[6] J.W. Corbett, G.D. Watkins, R.S. McDonald, Phys. Rev. 135 (1964) A1381.
[7] J.L. Lindström, B.G. Svensson, Mater. Res. Soc. Symp. Proc. 59 (1986) 45.
[8] A.K. Ramdas, M.G. Rao, Phys. Rev. 142 (1966) 451.
[9] A.R. Bean, R.C. Newman, R.C. Smith, J. Phys. Chem. Solids 31 (1970) 739.
[10] Y.H. Lee, J.C. Corelli, J.W. Corbett, Phys. Lett. 60A (1977) 55.
[11] B. Pajot et al., Mater. Sci. Forum 143–147 (1994) 969.
[12] C.P. Ewels, R. Jones, S. Öberg, Mater. Sci. Forum 196–201 (1995) 969.
[13] N.V. Sarlis, C.A. Londos, L.G. Fytros, J. Appl. Phys. 81 (1997) 1645.
[14] A. Baghdadi et al., J. Electrochem. Soc. 136 (1989) 2015.
[15] G. Davies, R.C. Newman, in: S. Mahajan (Ed.), Handbook on Semiconductors, Vol. 3, North-Holland, Amsterdam, 1994, p. 1557.
[16] E. Artacho et al., Phys. Rev. B 56 (1997) 3820.
[17] V.P. Markevich et al., Solid State Phenomena 69–70 (1999) 403.
[18] J.L. Lindström et al., Mater. Sci. Forum 258–263 (1997) 367.

ELSEVIER

Physica B 273–274 (1999) 296–299

PHYSICA B

www.elsevier.com/locate/physb

Assignment of EPR spectrum for bistable thermal donors in silicon

L.F. Makarenko[a,*], N.M. Lapchuk[b], Ya.I. Latushko[b]

[a]*Department of Applied Mathematics and Computer Science, Belarus State University, Minsk, 220050, F. Skaryna Avenue 4, Belarus*

[b]*Physics Department, Belarus State University, Minsk, 220050, F. Skaryna Avenue 4, Belarus*

Abstract

It has been shown that bistability of thermal double donors (TDD) in silicon can be observed by EPR technique. The spectrum of a bistable TDD species (TDD2) has been isolated using heat-treatment of Czochralsky-grown n-type silicon crystals with initial resistivity 4.5 Ω cm, at temperature 400°C and subsequent irradiation with electrons ($E = 3.5$ MeV). The principal values of the TDD2 g-tensor are determined as $g_1 = 1.9928, g_2 = 2.0009, g_3 = 1.9999$. An interpretation of some EPR data is given in the framework of the two-center model of the TDD structure.

Keywords: Silicon; Thermal donors; Bistability

1. Introduction

It is well known that in Czochralski-grown silicon crystals at temperatures lower than 500°C a series of divalent donor centers (which are called thermal double donors TDD) is formed. According to Ref. [1], these centers will be denoted hereafter as TDDn, where n is the center number. Minimal value of n is zero and maximal is $\geqslant 11$. The TDD1–11 are observed by IR spectroscopy [1]. Concentration of the TDD0 is rather small and it was attributed to the thermal donor family from the studies of persistent photoconductivity (PPC) decay [2].

In spite of a tremendous amount of experimental and theoretical studies on the problem of thermal donors their microscopic origin is poorly understood yet. And to decode their atomic structure new ideas and experimental data are required.

Significant information on atomic structure of TDD's can be obtained by studying variations in their properties while undergoing successive transformations TDD$n \rightarrow$ TDD$(n+1)$. A lot of such information was accumulated using IR absorption method [1]. Another sequence of data was obtained from magnetic resonance methods (see Ref. [3] and references therein). However, at present it is impossible to connect these two sets of data because there is no unambiguous relation of any EPR or ENDOR spectra to a certain TDD species. Therefore, to study the TDD's by magnetic resonance methods, Si crystals with an individual TDD should be prepared. Besides, it would be desirable to study first of all bistable TDDs as it was done for thermal donors in germanium [4].

2. Experimental details

Czochralski-grown silicon crystals with initial resistivity 4–20 Ω cm and oxygen content $(0.7–1.1)10^{18}$ cm^{-3} were investigated. Charge carrier concentration (n) was determined from Hall-effect measurements. The fraction of bistable TDDs was evaluated from PPC experiments. Infrared absorption spectra were obtained at 12 K with

* Corresponding author.
E-mail address: makarenko@fpm.bsu.unibel.by (L.F. Makarenko)

0921-4526/99/$ - see front matter
PII: S0921-4526(99)00449-4

"Specord-75IR" spectrometer. Conventional EPR investigations were performed with X-band spectrometer "PadioPAN SEX-2543" at 78 K.

3. Experimental results

3.1. Heat treatment conditions

To choose optimal annealing conditions two factors should be taken into account. First, concentration of the TDD2 should be high enough for EPR experiments and, second, this center should dominate. That is, its concentration should be at least twice larger than total concentration of all other TDDs. To prove simultaneous fulfillment of these two conditions we studied kinetics of TDD formation at different annealing temperatures. Concentration of individual TDD species was evaluated from intensities of absorption bands due to $1s–2p_{\pm}$ transitions of neutral TDDs. Experimental results for the TDD2 and TDD3 are shown in Fig. 1. For EPR studies, absorption coefficient of an individual TDD should be $\geqslant 10\,cm^{-1}$. As seen in the figure in order to realize the two necessary conditions, heat-treatment at temperatures $\leqslant 400°C$ must be used. In materials with oxygen content $[O] \geqslant 10^{18}\,cm^{-3}$ optimal annealing time is about 25–30 h.

3.2. Compensation conditions

Only singly ionized TDD are paramagnetic, and to study them using EPR it is necessary to use compensated materials where Fermi level is lower than the level $E(+/++) \approx E_C - 0.05$–$0.06\,eV$ of TDDs. Two compensation methods are possible. One is to use as-grown p-type crystals. The other is to create compensation centers by irradiation [5]. In Si : O crystals irradiated by γ-rays oxygen–vacancy complex (A-center) with acceptor level near E_C-0.18 eV is formed [6]. Under electron irradiation, divacancy with two acceptor levels $E(--/-) = E_C - 0.21$ and $E(-/0) = E_C - 0.40\,eV$ can be additionally created [6].

In order to compare these two compensation methods numerical simulations can be used. Let us suppose that in annealed crystals only the TDD2 center is available. As a rule its concentration is about $N_{TDD2} \approx 10^{15}\,cm^{-3}$. The Fermi level position (F) is determined from neutrality equation

$$N_P + N_{TDD2} f_{TDD2}(T,F) = n + N_B + N_A f_A(T,F),$$

where N_P and N_B are concentrations of shallow donor (phosphorus) and acceptor (boron), respectively; N_A is the concentration of deep acceptors (the A-center), $f_{TDD2}(T,F)$ and $f_A(T,F)$ are occupancy numbers of the TDD2 and A-center.

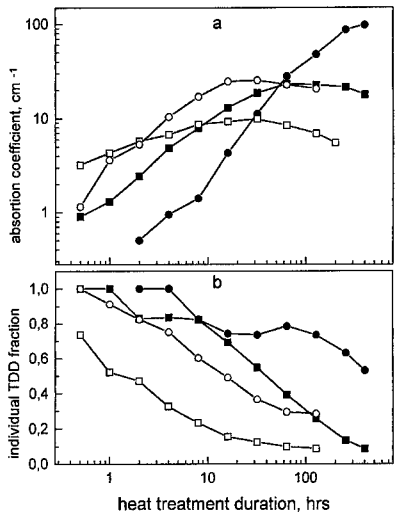

Fig. 1. Absorption coefficients (a) of $2p_{\pm}$ lines of neutral TDD2 (squares) and TDD3 (circles) and their fractions (b) versus annealing time at 400°C (solid squares and circles) and 475°C (open squares and circles). The fractions of TDD2 and TDD3 are equal to $[TDD2]/\sum[TDDn](n > 1)$ and $[TDD3]/\sum[TDDn](n > 2)$, respectively.

To maximize EPR signal in the first compensation method (when $N_P = N_A = 0$) it is necessary that $N_B = N_{TDD}$. In the second method ($N_B = 0$) the maximal $TDD2^+$ concentration will be achieved when $N_P + N_{TDD} = N_A$. Results of numerical simulations are shown in Fig. 2. Temperature dependencies of relaxation time for configurational transformation of the TDD2 were calculated according to Ref. [7].

As one can see from the figure the second compensation method is preferable. In the first compensation method in order to observe the 25% decrease of the NL8 signal one should store samples before measurements for some weeks at $T \sim 250$ K. In the second method a much shorter time is necessary to observe 4 times decrease of this signal.

As seen in Fig. 1, the TDD3 concentration can be much larger than that for the TDD2. If as-grown silicon crystals of p-type are used it is very easy to ensure conditions which correspond to the third case considered in Fig. 2. Then by storing annealed samples at about 250 K, we can achieve practically complete disappearance of the TDD2 signal. Hence, we can obtain samples with almost absolute domination of TDD3 and use these samples for EPR and ENDOR studies.

3.3. Experimental observation of bistable TDD spectrum

In accordance with the above IR absorption data we used samples annealed at 400°C during 26 h. Carrier concentration under illumination was $n = 2.6 \times$

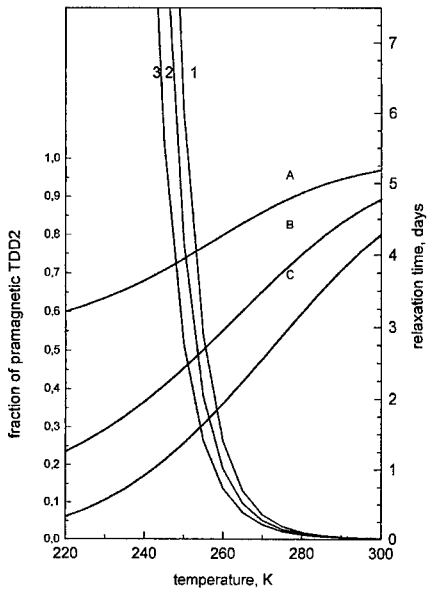

Fig. 2. Fraction of TDD2 in paramagnetic state ([TDD2$^+$]/[TDD2]) in equilibrium (A, B, C) and relaxation time to equilibrium state (1, 2, 3) versus storage temperature for samples with different concentration of centers (see equation in the text): 1, A — $N_P = 0$, $N_B = 10^{15}$ cm^{-3}, $N_A = 0$, $N_{TDD2} = 10^{15}$ cm^{-3}; 2, B — $N_P = 0$, $N_B = 0$, $N_A = 10^{15}$ cm^{-3}, $N_{TDD2} = 10^{15}$ cm^{-3}; 3, C — $N_P = 10^{15}$ cm^{-3}, $N_B = 0$, $N_A = 2 \times 10^{15}$ cm^{-3}, $N_{TDD2} = 10^{15}$ cm^{-3}.

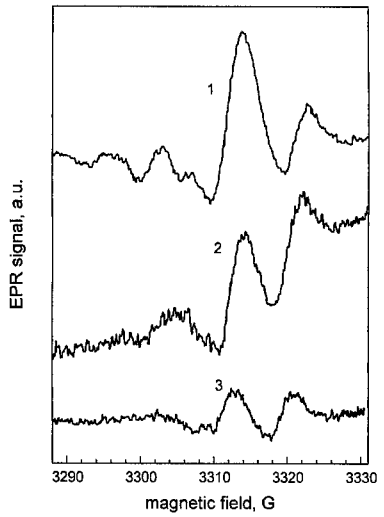

Fig. 3. EPR spectra of defects in Si crystals heat treated at 400°C during 26 h: 1 — after electron irradiation with the fluence 10^{16} cm^{-2}, 2 — after subsequent 30 min annealing at 250°C when cooling to measuring temperature from 300 K under illumination; 3 — the same as 2 but when cooling to measuring temperature after 4 days storage at 256 K in dark. The resonance frequency of our measuring cavity depends on the TDD2 concentration in paramagnetic state. That causes a shift of the third line as compared to the second one.

10^{15} cm^{-3}. Hence, the total TDD concentration was determined as $n = 0.7 \times 10^{15}$ cm^{-3} of which more than 80% was bistable. Then the samples were irradiated with 3.5 MeV electrons. The irradiation fluence was $\Phi = 10^{16}$ cm^{-2}. As a result of irradiation, carrier density diminished to the value $n = 1.9 \times 10^{15}$ cm^{-3}. In the as-irradiated sample, three centers were observed: A-center, divacancy (Si-G7) and thermal donor (Si-NL8) (Fig. 3, curve 1). To make experimental conditions more favorable from the point of view of relaxation time the samples were additionally annealed for 20 min at 275°C. After 275°C annealing, EPR signal related to divacancy essentially decreased and became indistinguishable because this annealing removed most part of divacancies and carrier density increases up to $n = 2.2 \times 10^{15}$ cm^{-3}.

From angular dependencies (Fig. 4) the principal values of TDD2 g-tensor were determined. According to the conventional notation, these values are $g_1 = 1.9928$, $g_2 = 2.0009$, $g_3 = 1.9999$.

The intensity of NL-8 signal depends on conditions of the sample cooling to the measuring temperature. If the sample was cooled down after a long period of storage at −17°C the signal intensity diminishes 4 times as compared to that after cooling from room temperature under illumination (Fig. 3, curves 2 and 3). The intensity changes observed are reversible. The higher signal is

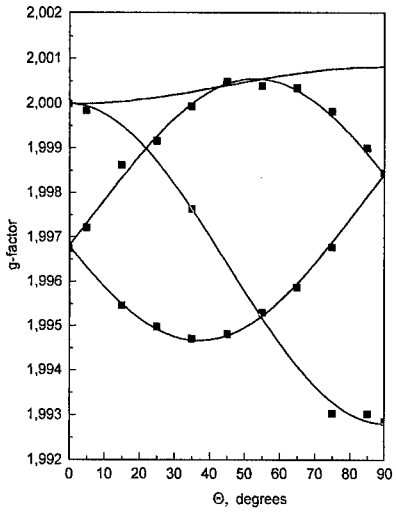

Fig. 4. Angular dependence of the TDD2 g-factor for magnetic field directions in the (0 1 1) plane.

restored after repeating the cooling regime under excitation. These data confirm the fact that the TDD2 was the dominating center in our samples.

It should be noted that although DC resistivity of irradiated crystal at 78 K was very high, there were essential microwave power losses in measuring cavity.

These losses seem to restrict the applicability of irradiation as a compensation method.

A possible explanation of the observed feature is that the losses are due to electron hopping between correlated TDD and A-centers. This problem however needs further investigation.

4. Discussion

Our data can be used as a reference point to the assignment of high-field EPR spectra $NL8_1$–$NL8_4$ observed in Ref. [8]. Since the g_1 value of TDD2 coincides with that of the $NL8_1$, therefore the $NL8_2$, $NL8_3$ and $NL8_4$ are TDD3, TDD4 and TDD5, respectively. This assignment is in accordance with the conclusion of Ref. [9] that the TDD3 has its g_1 value close to 1.9932.

Using this identification of the $NL8_i$ spectra we can compare the EPR data on the TDD structure obtained in Ref. [8] with the IR data of Ref. [1]. First of all the particular role of the TDD3 should be noted. As it is seen in Ref. [1] the transformation TDD3 → TDD4 leads to drastic changes in the optical characteristics of thermal donors and in Ref. [10] it is suggested that the optical characteristics of TDDs will recur with the periodicity of 4.

This periodicity is a natural consequence of the two-center model for the TDD structure. The model suggests that electrical activity of TDDs is due to two donor active atoms (DAA) and their optical properties can be explained using the theory of hydrogen molecular ion in an anisotropic medium. The donor active atoms are placed not in the core of the TDD complex but on its ends. New oxygen atoms joined to the complex build into the lattice between the DAAs. When four oxygen atoms are already inserted in the inner places of the complex, addition of the next atom leads to a drastic change in the distance between the DAAs. This change becomes apparent in the optical properties of the TDDs. From the point of view of this model the first three TDD of every four TDD can have some distortion from true C_{2v} symmetry and minimal distortion is awaited for TDD3, TDD7, etc. Therefore, the two-center model is consistent not only with the IR absorption data [1] but also with the EPR data of Ref. [8].

The sequential transformation of TDD structure is accompanied by the shift of only one of the principal values of the NL8 g-tensor — its component $g_1[1\,1\,0]$. In Ref. [11] it is shown that this variation cannot be related to the local lattice deformation around the TDD complex, rather it is due to a change of the TDD wave function. Because the $g_2[1\,1\,0]$ value practically does not shift, it would be awaited for more strong variation of the envelope function along the $g_1[1\,1\,0]$ axes. A similar behavior of wave function is revealed by hydrogen molecule when distance between atoms increases (see Ref. [12]). As a result of such a change, the region of maximal density of electron spreading ($|\psi| \geqslant |\psi|_{max}/2$) increases first of all along the axis of atom arrangement.

To test the applicability of this explanation, one should determine along what direction the TDD complex grows. To solve this problem let us use the results obtained in Ref. [13], where it is shown that $2p_{\pm l}$ and $2p_{\pm h}$ transitions have their dipole optical moments along the $g_1[1\,1\,0]$ and $g_2[\bar{1}\,1\,0]$ axes of NL8, respectively. According to Ref. [10] the $2p_{\pm 1}$ state corresponds to the $2p\sigma_z$ state of hydrogen molecular ion and the $2p\sigma_z$ wave function is extended along the TDD growth axis. So we obtained the expected correspondence which indicates the possibility of the suggested explanation of the TDD g-factor shift in Ref. [11].

5. Conclusions

From studies of TDD formation kinetics at 400°C and 475°C, conditions were determined which offer to observe EPR spectrum of individual TDD species. Using irradiation of Si crystals with 3.5 MeV electrons the spectra of the bistable TDD2 complex was registered. The obtained results make it possible to compare the EPR and IR spectroscopy data on individual TDD species.

References

[1] P. Wagner, J. Hage, Appl. Phys. A 49 (1989) 123.
[2] L.F. Makarenko, L.I. Murin, Sov. Phys. Semicond. 20 (1986) 1530.
[3] J.-M. Spaeth, in: R. Jones (Ed.), Early Stages of Oxygen Precipitation in Silicon, Kluwer Academic, Dordrecht, 1996, pp. 83–101.
[4] H.H.P.Th. Bekman et al., Phys. Rev. B 42 (1990) 9802.
[5] N. Meilwes et al., Mater. Sci. Forum 143–147 (1997) 141.
[6] F.P. Korshunov et al., Fiz. Techn. Poluprovodn. 26 (1992) 2006.
[7] L.F. Makarenko, Phys. Stat. Sol. A 106 (1988) K153.
[8] R. Dirksen et al., Mater. Sci. Forum 258–263 (1997) 373.
[9] J.M. Trombetta et al., J. Appl. Phys. 81 (1997) 1109.
[10] L.F. Makarenko, Solid State Commun. 98 (1996) 107.
[11] L.M. Roth, Phys. Rev. B 40 (1989) 5617.
[12] J.C. Slater, Electronic Structure of Molecules, McGraw-Hill, New York, 1963.
[13] P. Wagner et al., J. Appl. Phys. 61 (1987) 346.

ELSEVIER

Physica B 273–274 (1999) 300–304

PHYSICA B

www.elsevier.com/locate/physb

Local vibrational mode bands of V–O–H complexes in silicon

V.P. Markevich[a,*], L.I. Murin[a], M. Suezawa[b], J.L. Lindström[c], J. Coutinho[d], R. Jones[d], P.R. Briddon[e], S. Öberg[f]

[a]*Institute of Solid State and Semiconductor Physics, P. Brovki str. 17, 220072 Minsk, Belarus*
[b]*Institute for Materials Research, Tohoku University, Sendai 980-8577, Japan*
[c]*Department of Physics, University of Lund, S-221 00 Lund, Sweden*
[d]*Department of Physics, University of Exeter, Exeter EX4 4QL, UK*
[e]*Department of Physics, The University of Newcastle upon Tyne, Newcastle upon Tyne NE1 7RU, UK*
[f]*Department of Mathematics, University of Luleå, S-95187 Luleå, Sweden*

Abstract

H_2 molecules, which are introduced into moderately doped silicon crystals by high-temperature in-diffusion from H_2 gas ambient followed by fast cooling to room temperature, are found to interact effectively with the defects induced by irradiation of the crystals with fast electrons. In Czochralski-grown silicon crystals, the interaction of the mobile H_2 molecules with vacancy-oxygen defects (A centers) leads to the creation of V–O–H_2 complexes. This complex gives rise to infrared (IR) absorption lines at 943.5, 2126.4, and 2151.5 cm^{-1}. Ab initio calculations showed that the most stable configuration of V–O–H_2 consists of one oxygen and two hydrogen atoms sharing a vacancy site. It is suggested that the interaction of the V–O–H_2 complexes with interstitial oxygen atoms results in the formation of V–O_2–H_2 complexes, which are responsible for the IR absorption line at 891.5 cm^{-1}.

PACS: 78.30.Am; 61.80.Fe; 63.20.Pw; 81.40.Wx

Keywords: Silicon; Hydrogen; Oxygen; Vacancy; Absorption bands

1. Introduction

High-temperature heat-treatments of silicon crystals in H_2 gas ambient result in the incorporation of hydrogen atoms into the lattice up to the solubility limit at a treatment temperature [1]. It was found recently that after such treatments followed by fast cooling to room temperature, in moderately doped Si crystals practically all amount of hydrogen was in the form of hydrogen molecules (H_2) occupying tetrahedral interstitial (T_d) sites [2,3]. H_2 at the T_d sites are mobile in Si at $T \geqslant 50°C$, an activation energy for their migration was estimated as 0.78 eV [3]. In Czochralski-grown (Cz) Si crystals oxygen atoms were found to be effective traps for hydrogen molecules. The O_i–H_2 complex, however, is weakly coupled, the value of its binding energy was estimated as 0.28 eV [3].

Recent ab initio molecular dynamics calculations have shown that H_2 in Si interact effectively with silicon vacancies (V) and self-interstitials (I_{Si}) [4]. This interaction results in the breaking of a H–H bond and in the formation of two Si–H bonds, i.e., passivation of two dangling bonds of V or I_{Si} by hydrogen atoms occurs. Interaction of H_2 molecules with other radiation-induced defects having dangling bonds should be also expected in H-soaked Si crystals.

In Cz–Si crystals one of the dominant defects induced by irradiation is known to be a vacancy–oxygen complex (A center). Some evidences for the interaction of hydrogen atoms with the A centers were obtained by means of DLTS and infrared absorption measurements [5–7]. Absorption bands at 870 and 891 cm^{-1} were identified as related to the oxygen stretching vibrations for partially

*Corresponding author. Tel.: + 375-17-284-1290; fax: + 375-17-284-0888.
E-mail address: murin@ifttp.bas-net.by (V.P. Markevich)

0921-4526/99/$ - see front matter
PII: S0921-4526(99)00450-0

and fully passivated A center, i.e., the V–O–H and V–O–H_2 complexes, respectively [7]. It should be expected that these complexes beside the local vibrational modes (LVMs) related to the oxygen vibrations give rise to the LVM lines related to the hydrogen stretching vibrations. However, no clear information showing the existence of such bands was reported that makes the above mentioned identification of the lines at 870 and 891 cm^{-1} doubtful.

In the present work we report some new results related to the interaction of hydrogen with the vacancy-oxygen defects in Cz–Si crystals. The results were obtained using infrared absorption spectroscopy and ab initio modeling.

2. Experimental details

Samples for this study were prepared from an n-type phosphorus-doped Cz–Si crystal ($\rho \approx 1\ \Omega$ cm). The concentration of oxygen in the crystal was about $9.5 \times 10^{17}\ cm^{-3}$. Hydrogen (deuterium) was introduced into the samples by annealing at 1200°C for 1 h in a H_2 (D_2) gas ambient at a gas pressure of about 1.5 atm, and terminated by quenching. Irradiation with fast electrons (3 MeV in energy) was performed at about 50°C. Dose of irradiation was $1.6 \times 10^{16}\ cm^{-2}$. Isochronal annealing was carried out in an argon atmosphere in temperature steps of 25°C in the range of 100–600°C, for 30 min at each temperature. Isothermal annealing at 100°C was also studied.

Optical absorption spectra were measured by a Fourier transform infrared (FT-IR) spectrometer at 10 K. The spectral resolution was 0.5 or 1.0 cm^{-1}.

3. Experimental results and discussion

High-temperature heat-treatments of the samples in H_2 ambient were found to result in the appearance of a band at 1075.1 cm^{-1} with a shoulder at 1075.8 cm^{-1} in IR absorption spectra. Replacement of hydrogen by deuterium led to a shift of the lines to 1076 and 1076.6 cm^{-1}. These lines were earlier assigned to LVMs related to asymmetrical stretching vibrations of an interstitial oxygen atom perturbed by the presence of a H_2 (D_2) molecule at the nearest T_d site (O_i–H_2 complexes) [8].

The dominant centers produced by irradiation were found to be the same in both Si : O, H and as-grown materials: A center, C_i–O_i complex and divacancy. The intensities of the IR absorption bands due to these centers in hydrogenated samples were close to those in as-grown ones after irradiation.

A profound effect of the hydrogenation treatment was revealed in the annealing behavior of the radiation-induced defects. An enhanced disappearance of all the RDs occurred in hydrogenated samples. Isothermal annealing study of irradiated Si : O, H samples showed that the radiation-induced defects started to disappear at temperatures as low as 100°C. Simultaneously with the decrease in intensities of the lines due to RDs a substantial decrease in intensity of the line at 1075.1 cm^{-1} was observed after isothermal and isochronal anneals of hydrogenated samples. Further, it was found that the absorption spectra due to defects, which are formed upon annealing, differ significantly for the H-soaked and as-grown samples. Fig. 1 shows absorption spectra of the investigated samples at different stages of isochronal annealing. Consistent with the results of previous studies [9,10], the disappearance of the A centers in as-grown samples was accompanied by the formation of centers which give rise to a band at 895.3 cm^{-1} (VO_2), and, further, to ones at 910.0, 975.9, and 1005.3 cm^{-1} (VO_3). No band at 895.3 cm^{-1} was detected in hydrogenated samples. Other lines were found to be dominant in IR absorption spectra of these samples upon annealing. The most intense among them were the lines at 943.5 and 891.5 cm^{-1}. A number of lines in the range of 1900–2250 cm^{-1} were found to develop upon annealing of irradiated Si : O, H samples. The lines at 1956.0, 2126.4,

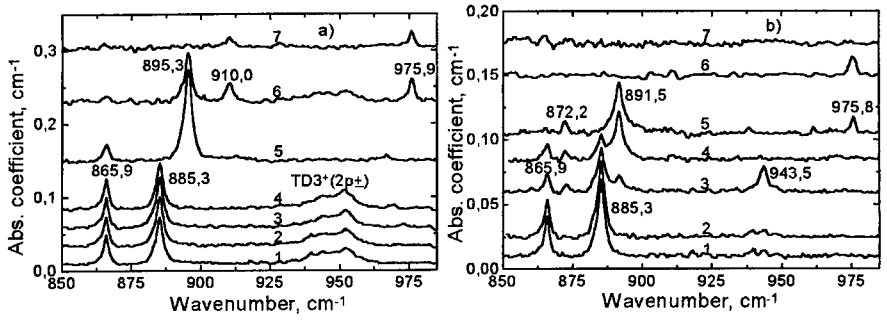

Fig. 1. Development of absorption spectra at 10 K for electron irradiated (a) as-grown and (b) hydrogenated Cz–Si samples with temperature of 30 min isochronal annealing: (1) as-irradiated, (2) 100°C, (3) 200°C, (4) 300°C, (5) 400°C, (6) 500°C, (7) 600°C.

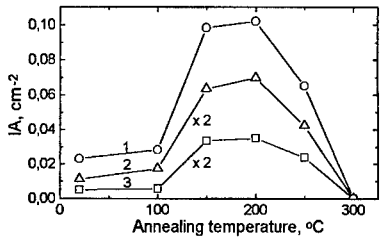

Fig. 2. Changes in integrated absorption due to the lines at (1) 943.5, (2) 2126.4, and (3) 2151.5 cm^{-1} with temperature of 30 min isochronal annealing for an irradiated Si : O, H sample.

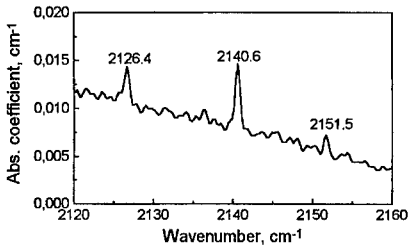

Fig. 3. Infrared absorption spectrum at 10 K for a Cz-Si sample which was co-doped with hydrogen and deuterium, irradiated with electrons and annealed at 100°C for 105 h.

and 2151.5 cm^{-1} were the strongest ones. This range is characteristic for the stretching vibrations of H atoms bonded to the host atoms in the Si lattice. No lines in this range were observed in as-grown samples.

Particular interests of the present work are the lines at 943.5, 891.5, 2126.4, and 2151.5 cm^{-1}. In the isothermal annealing study at 100°C a good correlation was found between a decrease in integrated absorption due to A center bands and an increase in that due to the line at 943.5 cm^{-1}. The lines at 2126.4 and 2151.5 cm^{-1} developed similar to the band at 943.5 cm^{-1}. Fig. 2 shows the development of these three lines upon isochronal annealing. It seems likely that all these bands are related to the same defect. The lines at 2126.4 and 2151.5 cm^{-1} are in the frequency range which is characteristic for stretching vibrations of H atoms in Si. As a rule, significant isotopic shifts of the lines in this range occur when hydrogen is substituted by deuterium. Indeed, in deuterated samples the lines at 943.2, 1549.1, and 1567.4 cm^{-1} were observed. They developed upon annealing similar to the lines at 943.5, 2126.4, and 2151.5 cm^{-1} in H-soaked samples. In the samples co-doped with hydrogen and deuterium in addition to these lines two new ones were observed at 1557.3 and 2140.6 cm^{-1}. Fig. 3 shows an infrared absorption spectrum of a sample which was co-doped with H and D and annealed for 105 h at 100°C after electron irradiation.

Disappearance of the lines at 943.5, 2126.4, and 2151.5 cm^{-1} in hydrogenated samples were found to occur simultaneously with the growth of a line at 891.5 cm^{-1}. A line at the same position was observed in deuterated samples. No correlation was found between the development of this band and any other bands in the range of 1900–2250 cm^{-1}.

O_i–H_2 complexes are not stable at temperatures exceeding 50°C in silicon, so heating the Si : O, H crystals results in the appearance of mobile H_2 molecules in the lattice. Under their motion the molecules can interact with RDs, forming the complexes. A correlation was found to occur between the disappearance of A centres and molecular hydrogen and development of the complex which gives rise to three IR absorption bands at

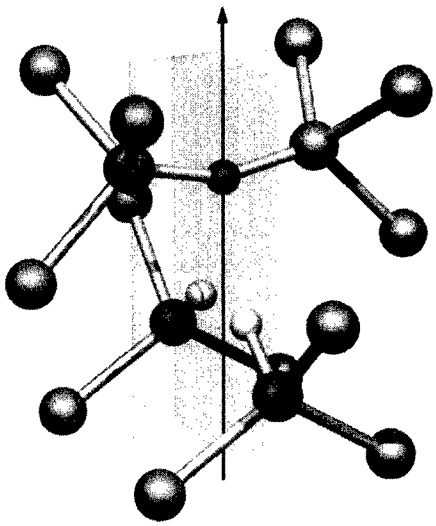

Fig. 4. Calculated ground-state structure for the V–O–H_2 center in silicon. The atom over the C_2-axis is oxygen and the white atoms represent hydrogen.

943.5, 2126.4 and 2151.5 cm^{-1}. It is likely that V–O–H_2 complexes formed by interaction of mobile H_2 with A centers are the defects responsible for these three lines. Positions (isotopic shifts) of the bands in Si : O, H and Si : O, D samples are consistent with those expected for V–O–H_2, in which an oxygen atom and two hydrogen atoms share a vacancy.

Disappearance of the V–O–H_2 complexes was found to occur simultaneously with the formation of a center, which gives rise to a band at 891.5 cm^{-1}. No isotopic shift due to substitution of hydrogen by deuterium as well as no correlation with any other lines was observed for this center upon its development. However, the center seems to be one of the dominant defects in proton implanted Cz-Si [9], as well as in electron irradiated Si : O, H crystals after heat-treatments at about 300°C. A V–O_2–H_2 complex can be suggested as a defect responsible for the 891.5 cm^{-1} line. The defect consists of two

Table 1
The ground-state structure of the V–O–H_2 center in silicon. All distances in Å

H–H	Si–H	Si–O	Si^H–^{H}Si	Si–O–Si
1.50	1.49	1.65	4.15	3.24

oxygen atoms sharing a vacancy with a hydrogen molecule in the vicinity. The H_2 only slightly perturbs the vibrations of oxygen atoms in VO_2 likely it does in the O_i–H_2 complex. For such a structure of the V–O_2–H_2 center there are not any Si–H bonds, that explains the absence of LVM lines in the range of 1900–2250 cm^{-1} for this hydrogen-related defect. The complex could be formed via the capture of mobile V–O–H_2 by interstitial oxygen atoms.

4. Theoretical calculations

We use an ab initio local density functional cluster method, AIMPRO [11], to determine the structure and vibrational modes of V–O–H_2. For this work 133 atom centered clusters were used with the composition $Si_{70}H_{62}O$. The O atom was placed at the center of the cluster within the vacancy and bridging two Si atoms.

The valence electronic wave functions were expanded in a set of s and p Gaussian orbitals placed at the atomic nuclei and at bond centers. The charge density was fitted to a sum of Gaussian functions placed at the same sites. Norm-conserving pseudo-potentials of Bachelet et al. [12] were used to eliminate the core electrons. Full details of the method have been described elsewhere [11].

Two configurations of V–O–H_2 defects were investigated. In the first, the two H atoms were placed inside the vacancy (see Fig. 4 and Table 1) in a manner similar with VH_2 [13]. In the second configuration, they lay outside, at anti-bonding sites, as in NiH_2 [14]. Both configurations have C_{2v} symmetry. We found that the second configuration was 1.25 eV higher in energy than the first one. For the stable configuration, the Si–O bond lengths were 1.65 Å compared with 1.75 Å in VO [15]. Clearly, the saturation of the Si dangling bonds has increased the strength of the Si–O bonds.

The LVMs for the defect along with their isotope shifts are given in Table 2. The two highest frequencies, at 2176 and 2173 cm^{-1}, are the symmetric and anti-symmetric Si–H stretch modes, respectively. The 1076 and 774 cm^{-1} frequencies are the anti-symmetric stretch and bend modes of the Si–O–Si complex, such that the oxygen

Table 2
Calculated LVMs for V–O–H_2 in Si. All frequencies and isotopic shifts (IS) are in cm^{-1}

	Exp. LVMs	IS	Calc. LVMs	IS	Mode
1	2151.5		2176		A_1
	2126.4		2173		B_1
V $^{16}OH_2$	943.5		1076		B_2
	N.D.		774		B_1
	N.D.		771		A_1
	1567.4	584.1	1559	617	A_1
	1549.1	577.3	1564	609	B_1
V $^{16}OD_2$	943.2	0.3	1076	0	B_2
	N.D.		765	9	B_1
	N.D		698	73	A_1
	2140.6	10.9	2174	2	A′
	1557.3	569.1	1562	611	A′
V ^{16}OHD	~943.5	~0	1076	0	A″
	N.D.		774	0	A′
	N.D		706	65	A′
			2176	0	A_1
			2173	0	B_1
V $^{18}OH_2$			1021	55	B_2
			753	21	B_1
			770	1	A_1

N.D. – Not detected.

atom vibrates in the two perpendicular (0 1 1) symmetry planes. Finally, the low frequency mode at 771 cm^{-1} corresponds to a symmetric Si–H wag-mode.

The isotopic shifts (Table 2) show that the oxygen- and hydrogen-related LVMs are completely decoupled: in either case, oxygen or hydrogen isotopic substitution, does not affect the LVMs in agreement with the experimental results in deuterated samples.

The two highest H-related LVMs are also almost independent. The highest LVM is an A_1 mode and lies 3 cm^{-1} above the anti-symmetric B_1 mode. This is in poor agreement with an experimental splitting of 25.1 cm^{-1} and suggests that the distance between the H atoms is too large. The observed splitting is similar to one found (22.5 cm^{-1}) for the VH_2 center [13].

All the shifts when one or both H atoms are replaced with D, largely agree with the experiment. The oxygen-related mode at 1076 cm^{-1} is much higher than that found for the VO at 787 cm^{-1} [15]. The increase mirrors what is seen experimentally, as the neutral VO center has a mode at 835 cm^{-1}.

Acknowledgements

We thank TFR, KVA and SI in Sweden for financial support. The support from the Belarussian Republican Fund of Fundamental Research and from the grant INTAS-Belarus 97-0824 is also acknowledged.

References

[1] M.J. Binns, R.C. Newman, S.A. McQuaid, E.C. Lightowlers, Mater. Sci. Forum 143–147 (1994) 861.
[2] R.E. Pritchard, M.J. Ashwin, J.H. Tucker, R.C. Newman, Phys. Rev. B 57 (1998) R15048.
[3] V.P. Markevich, M. Suezawa, J. Appl. Phys. 83 (1998) 2988.
[4] S.K. Estreicher, J.L. Hastings, P.A. Fedders, Phys. Rev. B 57 (1998) R12663.
[5] O.V. Feklisova, N.A. Yarykin, Semicond. Sci. Technol. 12 (1997) 742.
[6] S.J. Pearton, Phys. Stat. Sol. A 72 (1982) K73.
[7] B.N. Mukashev et al., Physica B 170 (1991) 545.
[8] R.E. Pritchard et al., Phys Rev. B 56 (1997) 13118.
[9] J.W. Corbett, G.D. Watkins, R.S. McDonald, Phys. Rev. 135 (1964) A1381.
[10] B.G. Svensson, J.L. Lindström, Phys. Rev. B 34 (1986) 8709.
[11] R. Jones, P.R. Briddon, in: M. Stavola (Ed.), Identification of Defects in Semiconductors, Semiconductors and Semimetals, Vol. 51A, Academic Press, Boston, 1998, p. 287.
[12] G.B. Bachelet, D.R. Hamann, M. Schluter, Phys. Rev. B 26 (1982) 4199.
[13] B. Bech Nielsen et al., Mater. Sci. Forum 196–201 (1995) 933.
[14] R. Jones, S. Öberg, J. Goss, P.R. Briddon, A. Resende, Phys. Rev. Lett. 75 (1995) 2734.
[15] C.P. Ewels, R. Jones, S. Öberg, Mater. Sci. Forum 196–201 (1995) 1297.

ELSEVIER

Physica B 273–274 (1999) 305–307

PHYSICA B

www.elsevier.com/locate/physb

Oxygen and peculiarities of its precipitation in $Si_{1-x}Ge_x$

L.I. Khirunenko[a,*], Yu.V. Pomozov, M.G. Sosnin[b,c], N.V. Abrosimov[a], M. Höhne[c], W. Shröder[c]

[a]*Institute of Physics of the National Academy of Sciences of Ukraine, Prospekt Nauki 46, 252650 Kiev-22, Ukraine*
[b]*Institute of Solid State Physics of Russian Academy of Sciences, 142432, Chernogolovka, Russia*
[c]*Institute of Crystal Growth, 12489 Berlin, Germany*

Abstract

The effect of germanium content ($N_{Ge} \leqslant 7.4 \times 10^{21}$ cm^{-3}) in solid solutions $Si_{1-x}Ge_x$ on the behavior of ν_3 vibrational mode of oxygen and kinetic formation of the low-temperature (450°C) thermal donors (TD) was investigated. It has been shown that the higher is Ge content in $Si_{1-x}Ge_x$, the lower are oxygen loss at heat treatment and TD formation rate. From the dependencies of the intensity of absorption band, corresponding to ν_3 vibrational mode of oxygen, TD concentration and oxygen loss at heat treatment on Ge content in $Si_{1-x}Ge_x$, an assumption is made that interstitial oxygen having Ge atoms in their second or third nearest-neighboring sites do not take part in low-temperature TD formation.

Keywords: Silicon; Germanium; Oxygen; Thermal donors

It has been known that germanium-doped silicon exhibits lower rates of low-temperature (450°C) thermal donors and radiation-induced defects formation [1–5]. The available data however were obtained for monocrystalline samples with germanium content $N_{Ge} \leqslant 5 \times 10^{20}$ cm^{-3}, that is when no significant change in the silicon energy structure occurred and germanium acted as isovalent impurity. The effect of Ge on the processes of defect formation can be considered here as the effect of internal elastic stress fields arising from the difference in Si and Ge covalent radii. The present work describes the data regarding oxygen properties and the features of low-temperature thermal donor formation in $Si_{1-x}Ge_x$ solid solutions with Ge content as high as 7.4×10^{21} cm^{-3}.

The samples of boron-doped $Si_{1-x}Ge_x$ grown by Czochralski method [6,7] in the Institute of Crystal Growth (Berlin, Germany) were investigated. The contents of oxygen and carbon determined using infrared (IR) absorption (1107 and 604 cm^{-1} lines) were $(7–9) \times 10^{17}$ and $(2–3) \times 10^{16}$ cm^{-3}, respectively. The germanium content was measured with X-ray analyzer SP-733 and varied from 3.5×10^{19} to 7.4×10^{21} cm^{-3}.

The crystals were investigated just after growth and after annealing in air atmosphere at 450°C. The maximum annealing time was 500 h. Every 10–15 h of annealing the IR oxygen absorption spectra were measured as well as oxygen content and charge carrier concentration were determined using Fourier-transform spectrometer IFS-113v and Hall effect technique.

Oxygen is known to be one of the most active elements taking part in the radiation-induced and thermal defect formation in silicon. Therefore, the acquisition of a new information about oxygen properties is of importance for an understanding of defect formation processes and a design of methods to control these processes. The role of oxygen in the defect formation processes in silicon is commonly judged from the behavior of IR absorption band corresponding to ν_3 vibrational mode (1107 cm^{-1} at 300 K). At 4 K the interstitial oxygen (Si_2O quasi-molecule) absorption spectrum in ν_3 vibrational mode region consists of 1136.4 cm^{-1} band with a fine structure at the right-hand side which is due to silicon isotopic content [8]. In germanium-doped silicon two additional absorption bands (1118.6 and 1130.2 cm^{-1}) were found

* Corresponding author. Fax: + 380-44-265-55-88.
E-mail address: lukh@iop.kiev.ua (L.I. Khirunenko)

0921-4526/99/$ - see front matter
PII: S0921-4526(99)00451-2

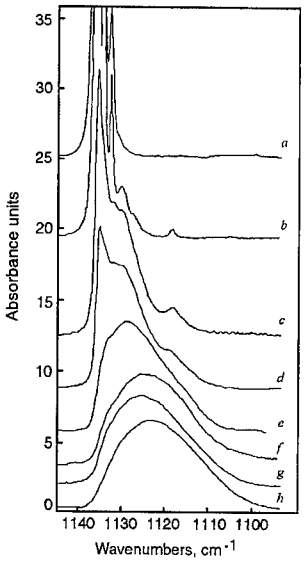

Fig. 1. Ge content dependence of an oxygen absorption spectrum in $Si_{1-x}Ge_x$. Resolution 0.5 cm^{-1}. $N_{Ge} \cdot 10^{21}$, cm^{-3}: (a) 0; (b) 0.11; (c) 1,25; (d) 1.8; (e) 3.2; (f) 4.4; (g) 5.8; (h) 7.4.

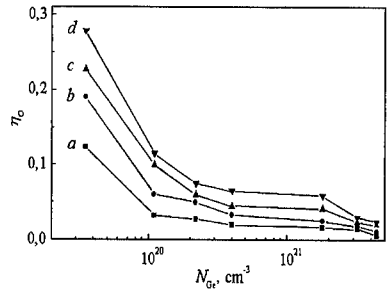

Fig. 2. Ge concentration dependence of relative oxygen loss η_o in $Si_{1-x}Ge_x$ at annealing. Time of annealing, hours: (a) 100; (b) 200; (c) 310; (d) 450.

at temperatures close to 4 K [9–12]. According to a model proposed in Ref. [9] these "new" bands are ascribed to the ν_3 vibrational mode of interstitial oxygen disturbed by germanium atom located in the second or third neighboring site, respectively.

The oxygen absorption spectra in ν_3 vibrational mode region for $Si_{1-x}Ge_x$ crystals with germanium content up to 7.4×10^{21} cm^{-3} measured at 4.2 K are shown in Fig. 1. It can be seen that the absorption spectrum is sufficiently transformed as germanium content increases. So with an increase of Ge content the 1136.4 cm^{-1} absorption band, which is intrinsic to the silicon, shifts toward the low-frequency side (the shift is about 0.75 cm^{-1} at $N_{Ge} \approx 2.2 \times 10^{20}$ cm^{-3}) and decreases in intensity. At the same time the intensity and half-width of absorption bands 1130.2 and 1118.6 cm^{-1} grow and the centroid of absorption spectrum shifts toward the low-frequency region. At $N_{Ge} \geqslant 5.5 \times 10^{21}$ cm^{-3} the 1136.4 cm^{-1} band virtually disappears and the spectrum becomes a wide structureless band shifted to the low-frequency region, i.e. the oxygen absorption spectrum completely changes as compared to that obtained from undoped silicon. Oxygen absorption spectrum transformation of this kind was not observed earlier whatever doping and/or treatment of Si was used. Thus in accordance with the model proposed in Ref. [9], the data obtained show that at Ge content $N_{Ge} \geqslant 5.5 \times 10^{21}$ cm^{-3} essentially all interstitials oxygen have Ge atoms in the nearest neighborhood.

The mutual arrangement of oxygen and germanium atoms in $Si_{1-x}Ge_x$ crystals at high Ge content and correspondingly changed potential reliefs in the vicinity of oxygen atoms and near thermal donors nuclei can have a sufficient effect on the formation of oxygen-containing thermal donor nuclei as well on the oxygen diffusion and precipitation during annealing.

The process of thermal donor formation in $Si_{1-x}Ge_x$ crystals was studied using measurement of the relative loss of optically active oxygen $\eta_o(t) = 1 - N_O(t)/N_O(O)$, where $N_O(O)$ is the initial oxygen concentration, $N_O(t)$ is the oxygen concentration after annealing for a time t. Fig. 2 shows the relative oxygen loss as a function of annealing time. From this figure it can be seen that regardless of the annealing time η_o decreases as Ge content increases and at $N_{Ge} \geqslant 5 \times 10^{21}$ cm^{-3} no oxygen loss is observed within the limits of experimental error at used annealing time values.

The dependence of thermal donor formation rate κ_{TD} on Ge content for the same samples annealed at 450°C is shown in Fig. 3. One can see a gradual decrease of thermal donor formation rate at $N_{Ge} > 3.5 \times 10^{19}$ cm^{-3}: the higher is Ge content, the lower is the thermal donor concentration. It should be noted that similar behavior of κ_{TD} was observed in the whole range of annealing time used in the present work. The comparison of the area under nondisturbed oxygen absorption band S_{1136}, obtained from spectrum decompositon, the thermal donor formation rate κ_{TD} and the loss of optically active oxygen η_o as functions of Ge content (Fig. 4) shows a correlation between these dependencies. Namely, oxygen transfer to the "new" state in $Si_{1-x}Ge_x$ as compared to Si results in the reduction of oxygen loss during annealing and in abrupt decrease of the thermal donor formation rate. From this fact it may be suggested that oxygen located close to Ge atoms does not take part in low-temperature thermal donor formation.

The obtained experimental results were also compared with the theoretical dependencies of relative oxygen loss versus Ge content, which we obtained earlier with only the internal elastic stress fields due to mismatch of Ge and Si covalent radii being taken into account [11].

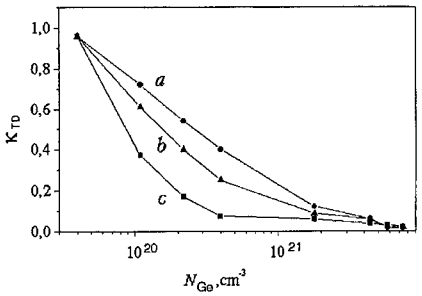

Fig. 3. Ge content dependence of an efficiency formation of thermal donors in $Si_{1-x}Ge_x$. Time of annealing, hours: (a) 100, (b) 300, (c) 450.

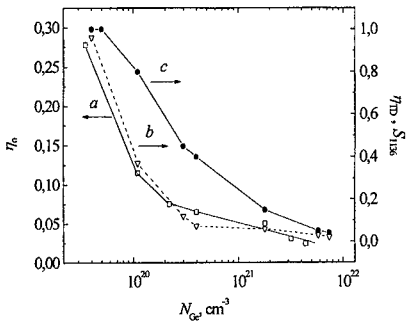

Fig. 4. The comparison of Ge content dependence of η_o (a), κ_{TD} (b) and S_{1136} (c) in $Si_{1-x}Ge_x$.

Fig. 5 shows the results for the relative oxygen loss. It can be seen that this model is applicable if Ge concentration does not exceed 1.1×10^{20} cm^{-3}. The similar situation is for the thermal donor concentration as a function of Ge content. It is apparent that the system of quasichemical equations used in Ref. [11] for the description of precipitation process does not work at high Ge concentrations. Here, the additional investigation of oxygen diffusion and thermal donor nucleation is needed as well as consideration of the change of energy structure and of the radius of oxygen capture by the thermal donor nucleus.

Thus, the study conducted shows that at Ge content in $Si_{1-x}Ge_x$ $N_{Ge} \geqslant 5.5 \times 10^{21}$ cm^{-3} virtually all interstitial oxygen have germanium atoms in the neighboring coordination spheres which results in abrupt decrease in low-temperature thermal donor formation rate.

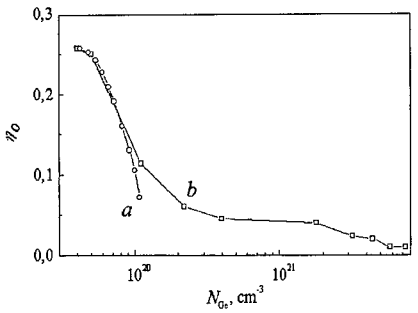

Fig. 5. Comparison between the experimental dependence of η_o on Ge content in $Si_{1-x}Ge_x$ (b) and its simulation according to Ref. [11] (a).

This work was supported by the Science and Technology Center in Ukraine (project No. 351).

References

[1] Yu.M. Babitskii, N.I. Gorbacheva, P.M. Grinshtein, M.G. Milvidskii, Fiz. Tekh. Poluprovodnikov 24 (1984) 1129.
[2] L.I. Khirunenko, V.I. Shakhovtsov, V.K. Shinkarenko, L.I. Shpinar, I.I. Yaskovetc, Fiz. Tekh. Poluprovodnikov 21 (1987) 562.
[3] T.V. Kritskaja, L.I. Khirunenko, V.I. Shakhovtsov, V.I. Yashnik, Fiz. Tekh. Poluprovodnikov 22 (1990) 1129.
[4] D.I. Brinkevich, V.P. Markevich, L.I. Murin, V.V. Petrov, Fiz. Tekh. Poluprovodnikov 26 (1992) 682.
[5] E. Hild, P. Gaworzewski, M. Franz, K. Pressel, Appl. Phys. Lett. 72 (1998) 1362.
[6] N.V. Abrosimov, S.N. Rossolenko, V. Alex, A. Gerhardt, W. Schröder, J. Crystal Growth 166 (1996) 657.
[7] N.V. Abrosimov, S.N. Rossolenko, W. Thieme, A. Gerhardt, W. Schröder, J. Crystal Growth 174 (1997) 182.
[8] D.R. Bosomworth, N. Hayes, A.R.L. Spray, G.D. Watkins, Proc. Roy. Soc. London 317 (1970) 133.
[9] H. Yamada-Kaneta, C. Kaneta, T. Ogawa, Phys. Rev. B 47 (1993) 9338.
[10] B. Pajot, Semiconduct. Semimet. 42 (1994) 191.
[11] L.I. Khirunenko, V.I. Shakhovtsov, V.V. Shumov, Mater. Sci. Forum 258–263 (1997) 1767.
[12] D. Wauters, P. Clauws, Mater. Sci. Forum 258–263 (1997) 103.

ELSEVIER

Physica B 273–274 (1999) 308–311

PHYSICA B

www.elsevier.com/locate/physb

Oxygen precipitation in nitrogen-doped Czochralski silicon

Deren Yang*, Xiangyang Ma, Ruixin Fan, Jinxin Zhang, Liben Li, Duanlin Que

State Key Lab of Silicon Material Science, Zhejiang University, Hangzhou 310027, People's Republic of China

Abstract

Oxygen precipitation in nitrogen-doped Czochralski (NCZ) silicon has been investigated by one-step and two-step annealing. It was found that nitrogen in NCZ silicon enhanced oxygen precipitation at lower temperatures ($< 750°C$), while it had no influence on oxygen precipitation at higher temperatures. We considered that nitrogen could enhance the nucleation of oxygen precipitation, rather than its growth. After two-step annealing, the samples were observed by means of a transmission Electronic Microscope (TEM). New morphology of oxygen precipitates was revealed. The size of the oxygen precipitates was about 300–500 Å. It is suggested that nitrogen interacted with oxygen to form nitrogen–oxygen complexes as heterogeneous nuclei which enhanced nucleation of oxygen precipitates.

Keywords: Oxygen precipitation; Nitrogen; Silicon

1. Introduction

Oxygen precipitation in Czochralski (CZ) silicon has been widely investigated for many years. It is believed that the number, density, size and morphology of oxygen precipitates are mainly dependent on the initial oxygen concentration, thermal history, annealing temperature and time. It was reported that carbon and metal impurities also play a role in oxygen precipitation. Since the last decade, nitrogen in silicon has attracted much attention because it can suppress microdefects and increase mechanical strength.

It has been reported that nitrogen in float-zone silicon could suppress the formation of swirl defects, and increased the mechanical strength by locking dislocations [1–3]. In CZ silicon, nitrogen atoms interacted with oxygen impurity to generate N–O complexes during crystal growth and subsequent heat treatment processes [4,5]. Recently, Yang et al. have pointed out that nitrogen in CZ silicon could suppress the formation of thermal donor [6] and new donor [7], and affect the electrical property of silicon while N–O complexes were formed [8]. Oxygen precipitates as intrinsic gettering sites have been intensively studied for more than 20 yr [9,10]. After investigating different intrinsic gettering processes, Shimura et al. [11] believed that oxygen precipitation was enhanced due to nitrogen in silicon lattice and so the denuded zone was narrow. However, a detailed study of nitrogen effect on oxygen precipitation has not yet been done.

In this paper, the behavior of oxygen precipitation in NCZ silicon isothermally and isochronically annealed in the temperature range 450–1150°C has been investigated. We considered that nitrogen could enhance the nucleation of oxygen precipitation, rather than its growth. New morphology of oxygen precipitation was found.

2. Experiment

The CZ silicon samples with and without nitrogen, which were respectively called CZ and NCZ–N samples, were used. The CZ and NCZ samples were cut from CZ single-crystal silicon grown in an argon atmosphere and in a nitrogen atmosphere, respectively. Both kinds of samples with resistivity in the range 1–10 Ω cm were

* Corresponding author. Tel.: + 86-571-795-1667; fax: + 86-571-795-1954.

E-mail address: mseyang@dial.zju.edu.cn (D. Yang)

0921-4526/99/$ - see front matter
PII: S0921-4526(99)00453-6

Table 1
The initial concentrations of oxygen and nitrogen in the samples

Sample	Oxygen ($\times 10^{17}$ cm^{-3})	Nitrogen ($\times 10^{15}$ cm^{-3})
CZ	8.8	—
NCZ	6.4	8.3
NCZ-T	7.1	13.8

about 2 mm in thickness and were polished on both sides. At first, the samples were preannealed at 1260°C for 1 h to dissolve as-grown oxygen precipitates and to remove the influence of the thermal history. Subsequently, the samples were annealed isothermally and isochronically up to 24 h at a differential of 100°C in the temperature range 450–1150°C. Heat treatments were carried out in a nitrogen protective gas. After annealing at each step, the samples were measured at room temperature by the Fourier transmission infrared spectroscopy (FTIR). The concentrations of oxygen and nitrogen were calculated. The FTIR measurement technique was the same as that reported in our previous work [6,7]. The concentrations of nitrogen and oxygen after the preannealing are given in Table 1. An as-grown NCZ sample, named NCZ-T (Table 1), was annealed at 700°C for 4 h following 1050°C for 16 h. And then the sample was observed by a JEOL 200CX high-resolution TEM.

3. Results and discussion

In general, oxygen atoms exist at interstitial positions in silicon lattice, and are related to the 1107 cm^{-1} absorption line in FTIR spectrum, which is the local vibration mode of oxygen. After heat treatments the decrement of interstitial oxygen concentration in silicon is usually considered to form oxygen precipitation. Fig. 1 shows the oxygen concentrations of the NCZ samples annealed up to 24 h as a function of temperature. It can be seen that the oxygen concentrations almost kept unchanged during annealing at temperatures less than 650°C, while the oxygen concentrations largely decreased due to the generation of oxygen precipitation during annealing at above 750°C. The maximum oxygen precipitation occurred at 1050°C.

The oxygen concentrations of the CZ silicon samples annealed as a function of temperature are shown in Fig. 2. The oxygen concentrations maintained the initial value while the samples were annealed at lower than 750°C. The oxygen concentrations decreased with annealing time due to the generation of oxygen precipitation during annealing at above 750°C. The maximum oxygen precipitation also occurred at 1050°C.

The oxygen concentration loss rate of the CZ and NCZ samples annealed for 24 h is given in Fig. 3. It can

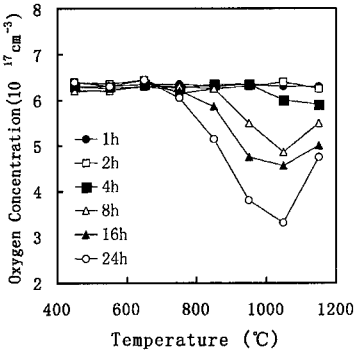

Fig. 1. The oxygen concentration of the NCZ samples annealed up to 24 h as a function of temperature.

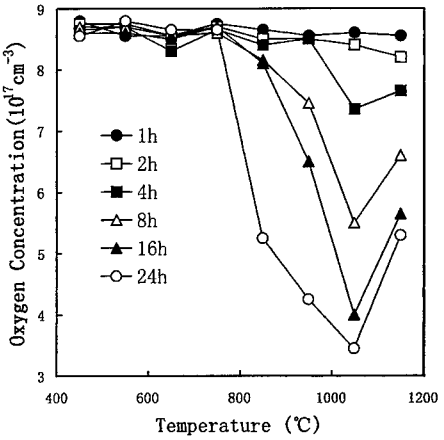

Fig. 2. The oxygen concentration of the CZ samples annealed up to 24 h as a function of temperature.

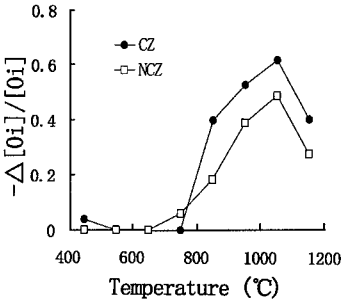

Fig. 3. Oxygen concentration loss rate of CZ-A and CZ-N samples annealed for 24 h.

be seen that the oxygen concentration of the CZ sample annealed at 450°C decreased slightly while that of the NCZ sample almost remained at the original value. During annealing at 750°C, the oxygen concentration loss rate, i.e., the oxygen precipitation rate, of the CZ sample

was lower than that of the NCZ sample even if the CZ silicon samples contained higher oxygen concentration (Table 1). On the contrary, the oxygen concentration loss rate of the CZ samples annealed at above 850°C was higher than that of the NCZ samples.

The experiments indicated that the oxygen concentration of the CZ sample annealed at 450°C for 24 h decreased slightly while that of the NCZ sample almost kept unchanged. It is well known that the thermal donors related to oxygen segregation are formed during annealing at about 450°C [12]. Due to the formation of the thermal donors some interstitial oxygen atoms in the CZ sample were consumed so that the oxygen concentration decreased slightly. It was proved that nitrogen could suppress the formation of thermal donors in silicon [6]. Therefore, the oxygen concentration of the NCZ sample roughly remained at the initial value during annealing at 450°C because of scarcely forming thermal donors.

When the NCZ samples were annealed below 650°C, several kinds of N–O complexes were formed [4–6]. Since the formation of the N–O complexes needs consumption of oxygen atoms, the oxygen concentration should decrease. However, the nitrogen concentration in the NCZ samples was two orders of magnitude lower than the oxygen concentration (Table 1). The consumption of the oxygen concentration due to the formation of the N–O complexes was much smaller than the initial oxygen concentration, and so the oxygen concentration of these samples remained unchanged during annealing.

During annealing at 750°C, the oxygen precipitate nucleation and the N–O complex formation simultaneously occurred in the NCZ silicon, while only the process of the oxygen precipitate nucleation occurred in the CZ silicon. After the formation of the N–O complexes in the initial period, the N–O complexes as heterogeneous nuclei of oxygen precipitates would easily attract oxygen atoms to enhance oxygen precipitation. Therefore, the oxygen precipitation in NCZ silicon was mainly based on the heterogeneous nuclei, rather than homogeneous nuclei. The density and size of the oxygen precipitates in NCZ silicon may be higher than that in CZ silicon. It is possible that the decrease of oxygen concentration in the NCZ silicon was more than that in the CZ silicon.

Furthermore, TEM results revealed that new morphology oxygen precipitates were generated in the two-step annealing NCZ silicon. Fig. 4 shows a TEM image of an oxygen precipitate in the NCZ-T sample annealed at 700°C for 4 h following that at 1050°C for 16 h. It is shown in the figure that the oxygen precipitate was square and was located on the (110) crystal plane. We observed the oxygen precipitate in different crystal directions. It was found that the oxygen precipitate was cubic and consisted of four {1 1 0} and two {1 0 0} crystal facets. The size of the oxygen precipitate was about 300–500 Å. It indicates that during annealing at 700°C, on the base of N–O complexes, the nucleus structure of

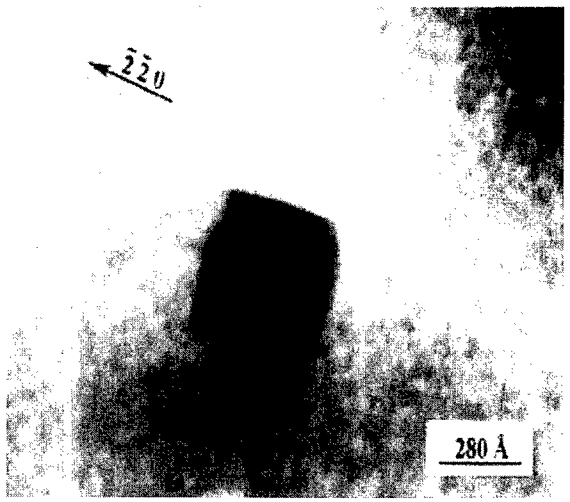

Fig. 4. TEM dark field image of an oxygen precipitate in the NCZ-T sample annealed at 700°C for 4 h following 1050°C for 16 h.

oxygen precipitates in the NCZ silicon was different from that in CZ silicon. After annealing at 1050°C, the oxygen precipitates grew and had a morphology different from that in common CZ silicon.

During annealing at high temperatures (> 850°C), the rates of the oxygen precipitation in the NCZ silicon were obviously lower than that in the CZ silicon containing higher oxygen concentration. It means that the oxygen precipitation predominantly depended upon the initial oxygen concentration, rather than the nitrogen concentration. According to dynamic principles, the higher temperatures favor the precipitate growth instead of the precipitate nucleation in single-crystal silicon. Precipitate nucleation is difficult at higher temperatures, but the nuclei, the radii of which are larger than the critical radius, one is easy to grow. In this case N–O complexes as heterogeneous nuclei are not important for the growth of oxygen precipitation. On the other hand, it has been reported that nitrogen atoms as a pair diffuse very quickly at higher temperatures [13,14]. During annealing at above 850°C, it is possible that nitrogen atoms directly diffuse into oxygen precipitates, rather than form N–O complexes. Thus, the oxygen precipitation at the higher temperatures mainly depends on the initial oxygen concentration. It is suggested that nitrogen atoms in NCZ silicon do not affect the growth of oxygen precipitates during higher temperature annealing (> 850°C), but enhance the nucleation.

4. Conclusion

The properties of oxygen precipitation in nitrogen-doped CZ silicon annealed at temperatures 450–1150°C

have been investigated in comparison with CZ silicon without nitrogen. Nitrogen was found to enhance the nucleation of oxygen precipitation at lower temperatures (< 750°C), but not to affect the growth at higher temperature (> 850°C). New morphology of oxygen precipitation, which was cubic and consisted of four {1 1 0} and two {1 0 0} facets of silicon, was found.

Acknowledgements

The authors would like to appreciate the financial supports of the Research Fund for the Doctoral Program of Higher Education (RFDP) and the Chinese Excellent Younger Teacher Fund.

References

[1] E. Wolf, W. Schroeter, H. Riemann, B. Lux, Mater. Sci. Eng. B 36 (1996) 209.
[2] K. Sumino, I. Yonenaga, M. Imai, T. Abe, J. Appl. Phys. 54 (1983) 5016.
[3] K. Sumino, in: H.R. Huff, R.J. Kriegler, Y. Takeishi, (Eds.), Semiconductor Silicon, ECS, 1981, p. 208.
[4] M. Suezawa, K. Sumino, H. Harada, T. Abe, Jpn. J. Appl. Phys. 27 (1988) 62.
[5] C.S. Chen, C.F. Li, H.J. Ye, S.C. Shen, D. Yang, J. Appl. Phys. 76 (1994) 3347.
[6] D. Yang, D. Que, K. Sumino, J. Appl. Phys. 77 (1995) 943.
[7] D. Yang, R. Fan, L. Li, D. Que, K. Sumino, Appl. Phys. Lett. 68 (1996) 487.
[8] D. Yang, R. Fan, L. Li, D. Que, K. Sumino, J. Appl. Phys. 80 (1996) 1493.
[9] A. Borghesi, B. Pivac, A. Sassella, A. Stella, J. Appl. Phy. 77 (1995) 4169.
[10] J. Vanhellemont, G. Kissinger, P. Clauws, A. Kaniava, M. Libezny, E. Gaubas, E. Simoen, H. Richter, C. Claeys, Solid State Phenom. 47-48 (1996) 229.
[11] F. Shimura, R.S. Hockett, Appl. Phys. Lett. 48 (1986) 224.
[12] S.A. McQuaid, M.J. Binns, C.A. Londos, J.H. Tucker, A.R. Brown, R.C. Newman, J. Appl. Phys. 77 (1995) 1427.
[13] T. Itoh, T. Abe, Appl. Phys. Lett. 53 (1988) 39.
[14] A. Hara, T. Fukuda, T. Miyabo, I. Hirai, Appl. Phys. Lett. 54 (1989) 626.

ELSEVIER

Physica B 273–274 (1999) 312–316

PHYSICA B

www.elsevier.com/locate/physb

An infrared investigation of the 887 cm^{-1} band in Cz–Si

L.G. Fytros[a], G.J. Georgiou[a], C.A. Londos[a,*], V.V. Emtsev[b]

[a]*Physics Department, Solid State Section, Athens University, Panepistimiopolis, Zografos, Athens 157 84, Greece*
[b]*Ioffe Physicotechnical Institute of the Russian Academy of Sciences, 26 Politekhnicheskaya st., St. Petersburg 194021, Russia*

Abstract

We report on infrared studies of the 887 cm^{-1} band arising in silicon, subjected to neutron irradiation with subsequent thermal anneals. Deconvolution of this band indicates the presence of two peaks: a strong one at 887 cm^{-1} and a weak one at 884 cm^{-1}. The 887 cm^{-1} peak is, generally, attributed to the VO_2 defect. We have tentatively correlated the 884 cm^{-1} peak to a [VO_2 + V] defect structure. Theoretical calculations of the vibrational frequencies of the two defects support the above hypothesis. The new picture for the 887 cm^{-1} band, could account for the exhibited uniaxial-stress behaviour.

Keywords: Silicon; Oxygen; Infrared; Neutron irradiation

1. Introduction

Upon irradiation of Czochralski-grown (Cz-grown) silicon, the VO pair is formed. Its presence in the IR spectra is verified by an LVM band at 830 cm^{-1} [1]. Upon annealing at temperatures of $\approx$ 300°C this band begins to disappear and another band arises with a frequency at $\approx$ 887 cm^{-1}. In general, this band is correlated with the VO_2 defect [2]. However, some aspects in the behaviour of the 887 cm^{-1} band cannot be explained if one correlates it only with the VO_2 defect. Thus, the VO_2 structure has a D_{2d} symmetry, although uniaxial stress studies [3] indicate a lower symmetry for the defect correlated with the 887 cm^{-1} band.

In this work we used IR spectroscopy to investigate the 887 cm^{-1} band in Si. Our results indicate the presence of two peaks in the band. We propose that the second peak originates from a [VO_2 + V] defect. Semiempirical calculations of the LVM frequency of this defect support such a correlation.

2. Experimental results and discussion

The material used was Cz-grown silicon crystals with an initial oxygen concentration of $[O_i]_0 \approx 10^{18}\,cm^{-3}$ and undetectable levels of the carbon impurity (i.e. $[C] < 10^{16}\,cm^{-3}$). The samples were irradiated by fast neutrons at a dose of $\approx 1 \times 10^{17}\,n\,cm^{-2}$, at room temperature. The IR spectra were obtained at room temperature.

Fig. 1 presents the region in the spectra around the 887 cm^{-1} frequency. Deconvolution of the band using Lorentzian profiles indicates the presence of two peaks. As is well established in the literature [2], VO_2 has an LVM frequency at 887 cm^{-1}, and therefore, one of the peaks is attributed to this defect. We have tentatively correlated the second peak at 884 cm^{-1} with a [VO_2 + V] structure, where a vacancy is trapped near a VO_2 defect. This is not unreasonable, since in the neutron-irradiated Si there are potential sources for vacancies. Thus, multivacancy clusters, like V_3,V_4,V_5, exist, and some of them, i.e. V_4, anneal out [4] at the

* Corresponding author. Tel.: + 301-727-4726; fax: + 301-725-7689.
E-mail address: hlontos@cc.uoa.gr (C.A. Londos)

0921-4526/99/$ - see front matter
PII: S0921-4526(99)00454-8

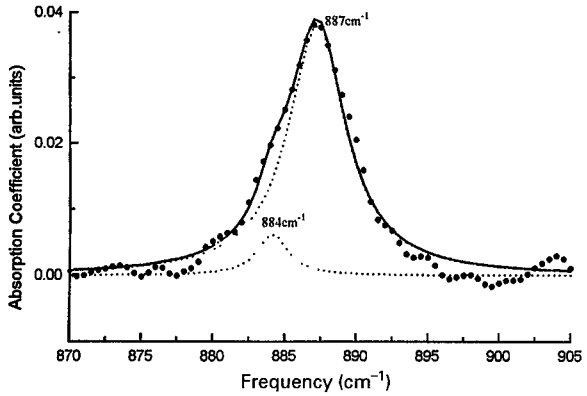

Fig. 1. Deconvolution of the 887 cm^{-1} region infrared band.

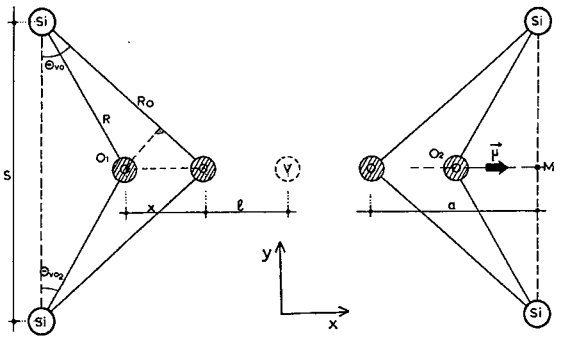

Fig. 2. The geometry of the VO_2 defect.

temperature range where this band arises, liberating the necessary vacancies. In principle, these vacancies could be trapped by VO_2 defects to form a [VO_2 + V] structure.

In what follows, we shall perform theoretical calculations, using semiempirical methods, of the LVM frequencies of the VO_2 and [VO_2 + V] defects. The results support the above assignments.

2.1. Calculation of the LVM frequency of the VO_2 defect

It is known [5] that VO is characterised by a ⟨1 0 0⟩ off-center configuration where the oxygen atom is displaced by 1.22 Å towards the two Si atoms to which it is bonded. The defect has a LVM frequency at about 830 cm^{-1}, which reflects the oscillation of the O(1) oxygen atom along the y-direction (Fig. 2).

We shall now try to calculate the frequency of the VO_2 defect, knowing the frequency of the VO defect. A reasonable approximation is to assume, according to the theory of the covalent bond Ref. [6], that the oxygen atom interacts with the two Si atoms to which it is bonded by a power-law potential which for the case of the O(1) oxygen atom (Fig. 2) has the form

$$U_{\text{tot}} = \varepsilon\left[\left(\frac{\sigma}{R + y\cos\theta}\right)^4 - \left(\frac{\sigma}{R + y\cos\theta}\right)^2 + \left(\frac{\sigma}{R - y\cos\theta}\right)^4 - \left(\frac{\sigma}{R - y\cos\theta}\right)^2\right], \quad (1)$$

where ε, σ are empirical parameters determined from independant measurements and R is the length of the Si–O bond. By making a Taylor expansion around the equilibrium position $y = 0$ we easily obtain

$$U_{\text{tot}} = \varepsilon\frac{\sigma^2}{R^4}\left[20\left(\frac{\sigma}{R}\right)^2 - 6\right]y^2\cos^2\theta + \mathrm{O}(y^4), \quad (2)$$

where $O(y^4)$ refers to higher-order terms. Thus, the force constant K_y in the y-direction would be

$$K_y = 2\varepsilon\frac{\sigma^2}{R^4}\left[20\left(\frac{\sigma}{R}\right)^2 - 6\right]\cos^2\theta, \quad (3)$$

We consider that the VO_2 defect forms from VO by the addition of a second oxygen atom, labelled O(2), at the same vacant site as that of O(1) atom. Upon introducing this oxygen atom, a new situation is established (Fig. 2). The effective charge "η" of the added atom O(2) has a value $\eta = 1.02|e|$ [7] leading to a dipole moment, $\boldsymbol{\mu} = -\eta(a - x)\hat{r}$, where $\hat{r}$ is the unit vector from the O(2) to the O(1) atom, which due to the two equivalent Si–O bonds lies on the x-axis, as depicted in Fig. 2. Assuming that this dipole moment lies in the middle of the O_2M segment its corresponding electric field will be given by the well-known expression: $\boldsymbol{E} = (1/4\pi\varepsilon_0)(3\hat{r}(\boldsymbol{\mu}\hat{r}) - \boldsymbol{\mu})/r^3$. Under the influence of this field the initial atom O(1) is pushed towards the Si atoms to which it is bonded. For the new equilibrium position the following relation holds: $E\eta = K_x x$, where K_x is the force constant in the x-axis direction and x is the displacement of the initial oxygen atom due to the addition of the second oxygen atom. Considering the geometry of VO_2 defect (Fig. 2), the last relation $E\eta = K_x x$ finally gives

$$K_x x = \frac{2\eta(a - x)}{4\pi\varepsilon_0(a + 2l + x)^3}\eta, \quad (4)$$

where l = 1.22 Å is the distance between the vacancy and the oxygen atom in the VO configuration. K_x has a value 92.16 Kgr/s^2 [8]. Taking into account [5], that R_0 = 1.66 Å and $\theta = 18°$ we easily find: $\alpha = R_0\sin\theta$ = 0.5129 Å, and substituting into Eq. (4) we obtain x = 0.08061 Å. Note that the oxygen atoms in both VO and VO_2 structures vibrate along the y-axis. Thus, from Eq. (3), the ratio of the force constants $K_{y,\text{VO}}$ and K_{y,VO_2} of the VO and VO_2 structures, is given by

the relation: $K_{y,\mathrm{VO}} : K_{y,\mathrm{VO}_2} = (8\varepsilon(\sigma^2/R_0^4)\cos^2\theta_{\mathrm{VO}}) : (2\varepsilon\sigma^2/R^4(20(\sigma/R)^2 - 6)\cos^2\theta_{\mathrm{VO}_2})$, where the relation for $K_{y,\mathrm{VO}}$ was obtained by setting $R = R_0 = \sqrt{2}\sigma$ in Eq. (3) where R_0 is the length of the Si–O bond at the equilibrium position. Since, in general, $K = m\omega^2$ and taking into account that $\cos\theta_{\mathrm{VO}} = (s/2)/R_0$ and $\cos\theta_{\mathrm{VO}_2} = (s/2)/R$ (Fig. 2) we finally obtain

$$\omega_{\mathrm{VO}_2} = \omega_{\mathrm{VO}}\left(\frac{R_0}{R}\right)^3 \frac{1}{2}\left[20\left(\frac{\sigma}{R}\right)^2 - 6\right]^{1/2}. \tag{5}$$

Assuming now that the displacement of the silicon atoms that are bonded to the oxygen impurity is negligible, we can write: $R = R_0 - x\sin\theta$ whereupon we get $R = 1.6351$ Å. Since $\sigma = R_0/\sqrt{2} = 1.1738$ Å, by substituting into Eq. (5) we finally have: $\omega_{\mathrm{VO}_2} = 901\,\mathrm{cm}^{-1}$, which is very close to the experimentally observed frequency of $887\,\mathrm{cm}^{-1}$, for the VO_2 defect.

2.2. Calculation of the LVM frequency of the $[VO_2 + V]$ defect

In this section we shall try to calculate the frequency of the $[VO_2 + V]$ defect, given the frequency of the VO_2 defect, by using the dipole–dipole interaction. We consider that due to the dipole moment $\boldsymbol{\mu}$ of the Si–O–Si chain, the neighbouring Si atoms are subjected to a corresponding electric field $\boldsymbol{E}$ which polarizes their bonds. The polarization $\boldsymbol{P}_{\mathrm{Si}}$ of each Si atom is given by the relation Ref. [9]: $\boldsymbol{P}_{\mathrm{Si}} = \alpha_{\mathrm{Si}}\varepsilon_0\boldsymbol{E}$, where α_{Si} is the polarisability of each silicon atom, due to the four bonds in which it participates. Due to the high-order symmetry of the silicon crystal, we assume that the polarizability is given by the Mossoti relation Ref. [9]: $\alpha_{\mathrm{Si}} = 3(\varepsilon - 1)/N(2 + \varepsilon)$, where $\varepsilon = 11.7$ [10] is the relative dielectric constant of silicon, and $N = 0.04969 \times 10^{-30}\,\mathrm{at/m}^3$ is the concentration of the silicon atoms per unit cell. Upon substituting these values we get: $\alpha_{\mathrm{Si}} = 4.68988 \times 10^{-29}\,\mathrm{m}^3$. Since there are two Si–O–Si chains in the VO_2 configuration, two permanent dipole moments $\boldsymbol{\mu}_1$ and $\boldsymbol{\mu}_2$ exist, where $\boldsymbol{\mu}_1$ is associated with the O(1) oxygen atom and $\boldsymbol{\mu}_2$ with the O(2) oxygen atom, as seen in Fig. 3. Due to these dipole moments, the Si atom, which will be removed from its lattice site, so that the remaining vacancy participates in the formation of the $[VO_2 + V]$ defect, is subjected to an electric field $\boldsymbol{E}_{\mathrm{tot}} = \boldsymbol{E}_1 + \boldsymbol{E}_2$, where $\boldsymbol{E}_1$ and $\boldsymbol{E}_2$ are related to $\boldsymbol{\mu}_1$ and $\boldsymbol{\mu}_2$ moments as follows:

$$\boldsymbol{E}_{\mathrm{tot}} = \boldsymbol{E}_1 + \boldsymbol{E}_2 = \frac{1}{4\pi\varepsilon_0}\left(\frac{3(\hat{r}_1\boldsymbol{\mu}_1)\hat{r}_1 - \boldsymbol{\mu}_1}{d_1^3} + \frac{3(\hat{r}_2\boldsymbol{\mu}_2)\hat{r}_2 - \boldsymbol{\mu}_2}{d_2^3}\right), \tag{6}$$

where $d_1 = 2.9842$ Å is the distance between the points where the dipole moment $\boldsymbol{\mu}_1$ is situated and the silicon atom Si(3) (Fig. 3), and $d_2 = 4.9939$ Å is the distance between the points where the dipole moment $\boldsymbol{\mu}_2$ is situated and the silicon atom Si(3). $\hat{r}_1 = (0.9098\hat{x} + 0.4151\hat{y})$ and $\hat{r}_2 = (0.5436\hat{x} + 0.8393\hat{y})$ are unit vectors on the d_1 and d_2 direction, respectively.

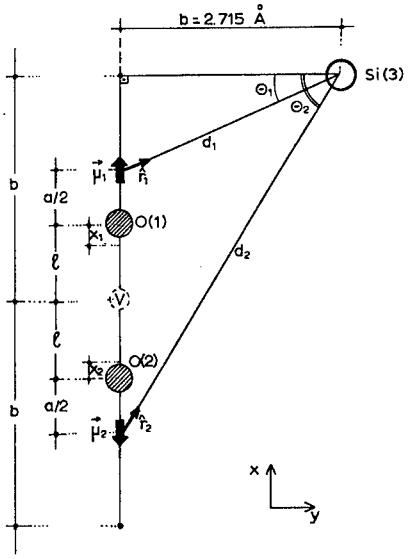

Fig. 3. The geometry of the $[VO_2 + V]$ defect in the plane where the dipole moments μ_1, μ_2 and Si(3) atom lie.

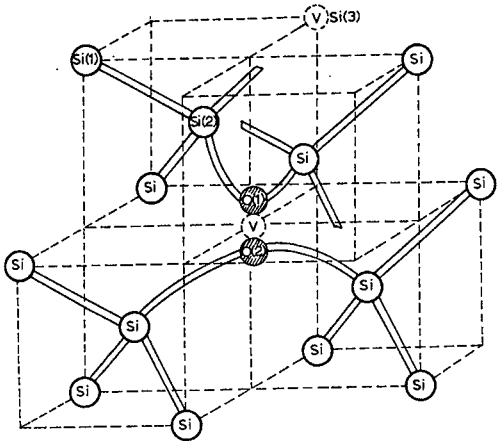

Fig. 4. The structure of the $[VO_2 + V]$ defect.

As stated above, in order to form a $[VO_2 + V]$ defect, a Si atom near a VO_2 defect must be removed. There are two possibilities for the formation of $[VO_2 + V]$: (i) to remove the Si(1) atom, (ii) to remove the Si(3) atom, Fig. 4. Only the second case is considered here. When the Si(3) atom is removed the displacement of the Si(2) atom is expected to be perpedicular to the Si–O(1)–Si plane and

therefore the bond length will remain almost the same. As a result, the vibration frequency of the O(1) atom will be affected slightly. The O(1) atom will move downwards and the Si–O(1) bond will expand. The vibrational frequency of the O(1) atom will be smaller than the corresponding frequency of this atom in the VO_2 structure. In contrast, the O(2) atom will move upwards and the Si–O(2) bond will contract. As a result, the vibration frequency of the O(2) atom will become larger than it is inside the VO_2 structure.

The interaction energy between the electric field and the neutral Si(3) atom is: $W = -\frac{1}{2}(\boldsymbol{P}_{Si}\boldsymbol{E}_{tot})$. However, when the Si(3) atom is removed, the four initial bonds in which it participates will be reduced to two. Therefore, assuming that the polarizability is slightly affected by the changes of the bond lengths, its value may be taken approximately equal to one-half of the initial value. Consequently, we obtain $W = -\frac{1}{2}(\alpha_{Si}/2)\varepsilon_0 \boldsymbol{E}_{tot}^2$.

Assuming that the displacements x_1 and x_2 of the two oxygen atoms, respectively, are quite small so that, $x_i \ll d_i$ $(i = 1, 2)$ and $x_1, x_2 \ll a$ (Fig. 3), we finally get that

$$W = -\frac{1}{2}\frac{1}{2}\frac{a_{Si}}{2}\frac{q^2}{(4\pi)^2\varepsilon_0}\left[\frac{(a+x_1)^2(1+3\sin^2\theta_1)}{d_1^6} + \frac{(a-x_2)^2(1+3\sin^2\theta_2)}{d_2^6}\right.$$
$$+ 2\frac{9(a+x_1)\sin\theta_1(a-x_2)(-\sin\theta_2)\hat{r}_1\hat{r}_2 - (a+x_1)(a-x_2)}{d_1^3 d_2^3}$$
$$\left. - 2\frac{3(a+x_1)\sin\theta_1(a-x_2)(-\sin\theta_1) + 3(a+x_1)\sin\theta_2(a-x_2)(-\sin\theta_2)}{d_1^3 d_2^3}\right], \quad (7)$$

where $\theta_1 = 24.5°$ and $\theta_2 = 57.1°$, as is shown in Fig. 3. Thus, the forces on the atoms O(1) and O(2) are given by the relations $F_1 = -\partial W/\partial x_1, F_2 = -\partial W/\partial x_2$, respectively, which for harmonic oscillators have the form,

$$F_1 = -\frac{\partial W}{\partial x_1} = -K_{x,VO_2}x_1,$$

$$F_2 = -\frac{\partial W}{\partial x_2} = -K_{x,VO_2}x_2, \quad (8)$$

where K_{x,VO_2} is the force constant along the x-axis direction of the VO_2 defect. Assuming that $K_{x,VO_2}/K_{x,VO} = K_{y,VO_2}/K_{y,VO} = (\omega_{VO_2}/\omega_{VO})^2$ and $K_{x,VO} = 92.16\,Kgr/s^2$ we get $K_{x,VO_2} = 105.25\,Kgr/s^2$. We have assumed that the angles θ_1 and θ_2 remain almost constant during the formation of $[VO_2 + V]$, considering that the displacements of the oxygen atoms are very small.

From Eq. (8) we get that the displacement of the O(1) atom is $x_1 = 0.00402$ Å and the corresponding one of the O(2) atom is $x_2 = 0.00023$ Å. Then, the vibrational frequencies of the two oxygen atoms of the $[VO_2 + V]$ structure are calculated from Eq. (5) by writing it down for $[VO_2 + V]$ and VO_2 defects, and their values are, respectively, found to be: $\omega_1 = 883.4\,cm^{-1}$ and $\omega_2 = 887.2\,cm^{-1}$. We therefore tentatively attribute the second peak in the spectra to ω_1 LVM of the $[VO_2 + V]$ structure. The peak with ω_2 frequency coincides with the $887\,cm^{-1}$ band of VO_2.

This new correlation of the $887\,cm^{-1}$ band with two defects, VO_2 and $[VO_2 + V]$ could explain its uniaxial-stress behaviour previously reported [3] in the literature. This behaviour is consistent with a defect structure having a symmetry lower than orthorhombic [3]. Actually, the VO_2 defect has D_{2d} symmetry, although the $[VO_2 + V]$ structure has apparently a symmetry lower than orthorhombic. The presense of two defects at this band could explain rather well this behaviour, since the measured piezospectroscopic tensor is related to both defects, and it is particulary affected by the piezospectroscopic tensor of the defect with the lower symmetry. This means that due to the presence of the $[VO_2 + V]$ defect the apparent symmetry of $887\,cm^{-1}$ is expected to become lower than D_{2d}, in agreement with the experimentally observed behaviour [3].

We should report here that the $887\,cm^{-1}$ band has been correlated also with the V_3O defect [11,12]. However, the results of the above analysis are more in line with a correlation with a $[VO_2 + V]$ defect.

3. Conclusions

We have performed a study of the $887\,cm^{-1}$ band in neutron irradiated silicon. Using computer deconvolution by employing Lorentzian functions, we found that this band consists of two peaks at 884 and $887\,cm^{-1}$. The $887\,cm^{-1}$ is generally attributed to the VO_2 defect. The $884\,cm^{-1}$ is tentatively atributed to a $[VO_2 + V]$ defect structure. These correlations are supported by theoretical calculations of their LVM frequncies. Our results could account for the behaviour of the band under uniaxial strees.

References

[1] J. Corbett, R. Watkins, G.D. Ghrenko, R. McDonald, Phys. Rev. 121 (1961) 1015.
[2] J. Corbett, G. Watkins, R. McDonald, Phys. Rev. 135 (1964) A1381.
[3] D. Bosomworth, W. Hayes, A. Spray, G. Watkins, Proc. Roy. Soc. Lond. A 317 (1970) 133.
[4] A. Li, H. Huang, D. Li, S. Zheng, H. Du, S. Zhu, T. Iwata, Jpn. J. Appl. Phys. 32 (1993) 1033.
[5] P. Deak, L.C. Snyder, J.W. Corbett, R.Z. Wu, A. Solyom, Mater. Sci. Forum 38–41 (1989) 281.
[6] W. Harrison, Electronic Structure and the Properties of Solids, Dover, New York, 1989.
[7] S. Pantelides, W. Harrison, Phys. Rev. B 13 (1976) 2667.
[8] G. DeLeo, C. Milsted, J. Kralik, Phys. Rev. B 31 (1985) 3588.
[9] J.D. Jacson, Classical Electrodynamics, Wiley, New York, 1975.
[10] C. Kittel, Introduction to Solid State Physics, Wiley, New York, 1976.
[11] Y. Lee, J. Corelli, J. Corbett, Phys. Lett. 60A (1977) 55.
[12] C.A. Londos, N.V. Sarlis, L.G. Fytros, J. Appl. Phys. 85 (1999) 8074.

ELSEVIER

Physica B 273–274 (1999) 317–321

PHYSICA B

www.elsevier.com/locate/physb

Oxygen in silicon doped with isovalent impurities

L.I. Khirunenko*, Yu.V. Pomozov, M.G. Sosnin, V.K. Shinkarenko

Institute of Physics of the National Academy of Sciences of Ukraine, Prospekt Nauki 46, 252650 Kiev-22, Ukraine

Abstract

Three additional infrared absorption lines of interstitial oxygen were found in silicon doped with isovalent impurities (Ge, Sn, or C). These lines are supposed to be associated with ν_3 vibration of Si_2O quasimolecules disturbed by isovalent impurity (IVI) atoms located in first, second and third coordination spheres. The shift of absorption band for IVI-disturbed quasimolecule is shown to be proportional to the deformation charge of IVI and independent of its sign. The results obtained confirm a presence of preferential arrangement of IVI atoms relative to interstitial oxygen in silicon lattice.

Keywords: Silicon; Oxygen; Isovalent impurity

1. Introduction

Czochralski-grown silicon remains the basic material for solid-state electronics. The oxygen content in this type of material can be as high as 10^{18} cm^{-3}. Being the most active impurity in defect–impurity interaction, oxygen forms a variety of defects [1–3] that can affect the electrical and optical properties of Si. In this connection the new information regarding microscopic origin and macroscopic behavior of oxygen-containing defects becomes rather important for control of defects as well as for the development of device parameter improvement techniques.

Considerable attention has been focussed recently on the silicon doped with isovalent impurities (IVI). This is due to the facts that IVI are electrically inactive and have almost no effect on the initial properties of silicon, but at the same time, being the sources of internal stress, they may have a pronounced effect on defect–impurity interaction and, hence on the Si parameters during material growth, heat treatment or irradiation [4–11]. So, a considerable decrease in formation rate of radiation- and thermally-induced defects was observed in tin- and germanium-doped silicon [5–9]. Carbon in silicon forms a series of radiation defects, including those in combination with oxygen, but suppresses the formation of thermal donors [10,11]. Hence, the investigation of oxygen properties in isovalently doped silicon is important from both applied and fundamental standpoints.

It has been known that infrared (IR) absorption spectrum of interstitial oxygen (which forms a quasimolecule Si_2O in silicon lattice) in the frequency region of ν_3 vibrational mode at 4.2 K consists of 1136.4 cm^{-1} band with a fine structure on the low-energy side due to isotopic silicon content (^{28}Si, ^{29}Si and ^{30}Si) [12]. In IR absorption spectra of interstitial oxygen in germanium-doped silicon [13,14] in addition to absorption bands intrinsic to silicon, two new vibrational modes near 1130 and 1118 cm^{-1} were found. In accordance with the model proposed in Ref. [13] by Yamada-Kaneta et al., these absorption bands are described to ν_3 vibration of interstitial oxygen which is disturbed by germanium atoms located, respectively, in the second and third coordination spheres.

In carbon-doped Si in addition to the vibrational band of substitutional carbon (607 cm^{-1}) there appear two other bands near 1103 (A) with two weak satellites, 1052 (B) cm^{-1}, and three weak satellite bands (X, Y, Z) located near 607 cm^{-1} band [10]. Replacement of ^{12}C by ^{13}C resulted in an isotopic shift of X, Y and Z bands, while A band did not shift. Nevertheless, an assumption was

* Corresponding author. Fax: + 380-44-265-55-88.
E-mail address: lukh@iop.kiev.ua (L.I. Khirunenko)

0921-4526/99/$ - see front matter
PII: S0921-4526(99)00455-X

made than A, B, X, Y and Z bands corresponded to the vibrational modes of interstitial oxygen with carbon atoms in the nearest second or third interstitial site [10].

There are no data available regarding the tin–oxygen interaction in tin-doped silicon.

Thus, the interaction between oxygen and isovalent substitutional impurities has not been adequately investigated. It is just this question which is the objective of the present work.

2. Experimental

Samples of Czochralski-grown silicon doped with germanium (Ge), tin (Sn) or carbon (C) were investigated. The oxygen and carbon content determined using infrared absorption (1107 and 604 cm^{-1} lines) were $(7–9)\times 10^{17}$ cm^{-3} and $(0.6–9)\times 10^{17}$ cm^{-3}, respectively. The germanium content was measured with an X-ray analyzer SP-733 and varied from 7×10^{18} to 1.1×10^{20} cm^{-3}. The concentration of tin measured by neutron-activation analysis was 2×10^{18}–2×10^{19} cm^{-3}. The IR absorption spectra in the region of ν_3 vibrational mode of interstitial oxygen in silicon doped with IVI were investigated. The measurements were carried out with the Fourier-transform spectrometer IFS-113v at 4.2 K with resolution 0.5–0.25 cm^{-1}.

3. Results and discussion

Fig. 1 shows IR absorption spectra measured at 4.2 K of interstitial oxygen in the region of ν_3 vibrational mode (1132–1050 cm^{-1}) for undoped silicon and for silicon doped with Sn, C, and Ge. The spectra are reduced to the same oxygen concentration and are shifted along the axis of ordinates for convenience. In the crystals of undoped Si only a week absorption maximum at ~ 1132.7 cm^{-1} is observed within the region under investigation (Fig. 1, curve d) which corresponds to ν_3 vibrational mode of $^{29}Si_2O$. Silicon doped with any of above-listed IVI exhibits additional low-frequency IR absorption (Fig. 1, curves a–c). The intensity of these additional absorption bands increases with increasing IVI content in Si. The results of decomposition of measured spectra are given in Fig. 2. It can be seen that, as opposed to the available data, three rather than two additional oxygen absorption lines appear in Ge-doped silicon — 1130.1, 1127.2 and 1118.4 cm^{-1}. A similar ternary structure is also observed in Sn-doped (1129.7, 1124.8, 1109.2 cm^{-1}) and C-doped (1129.1, 1104, 1052 cm^{-1}) Si. The 1104 cm^{-1} band in C-doped Si has also two satellite bands (1107.9 and 1099.5 cm^{-1}). With the assumption of the model proposed in Ref. [13], the observed absorption bands can be ascribed to the vibration of interstitial oxygen disturbed by IVI atoms located in the nearest 2nd, 3rd and 4th coordination spheres relative to an oxygen atom (or in the 1st, 2nd and 3rd spheres relative to Si_2O quasimolecule). As the perturbation is a maximum for Si_2O with IVI atom in the 1st coordination sphere and decreases with increasing distance between quasimolecule and the source of disturbance, we may suppose that 1118.4, 1109.2 and 1052 cm^{-1} absorption bands correspond to Si_2O disturbed by IVI atoms (Ge, Sn, C) located in the 1st coordination sphere; 1127.2, 1124.8 and 1104 cm^{-1} — in the 2nd one; 1130.1, 1129.7 and 1129.1 cm^{-1} — in the 3rd one. The possible origins of 1104 cm^{-1} band satellites may be the nonequivalency of carbon atom located in various site in the 2nd coordinate sphere relative to Si_2O or the presence of several C atoms in the 2nd sphere.

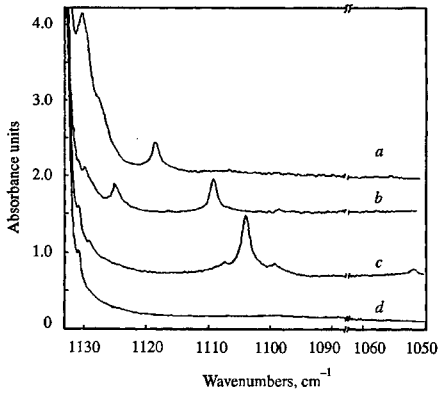

Fig. 1. Absorption spectra of interstitial oxygen on Si doped with Ge (a), Sn (b), C (c) and in Si (d). Resolution 0.25 cm^{-1}. $N_{Ge}\approx 2\times 10^{20}$ cm^{-3}; $N_{Sn}\approx 2\times 10^{19}$ cm^{-3}; $N_C\approx 8\times 10^{17}$ cm^{-3}.

Assuming a random distribution of IVI atoms in silicon lattice, the amount of quasimolecules with various sets of IVI atoms in the nearest coordination spheres may be estimated using probability theory. The probability P that i IVI atoms are in the jth coordination sphere containing m atoms is defined by the following expression:

$$P(i,j) = c_m^i x^i (1-x)^{m-i}, \tag{1}$$

where c_m^i is the number of i-combinations of m elements, x is the IVI content in Si ($0 \leqslant x \leqslant 1$).

Using Eq. (1) we have estimated the dependence of the probabilities that Ge atoms fall into the 1st, 2nd and 3rd coordination sphere relative to Si_2O quasimolecule, on the concentration of IVI in silicon. Fig. 3 shows the obtained values of the probabilities that (0–1) IVI atoms are located in the 1st, 2nd and 3rd coordination spheres, for IVI concentration $0 \leqslant N_{IVI} \leqslant 10^{20}$ cm^{-3}. It can be seen that the probability of IVI atom appearing in the nearest coordination spheres increases with increasing

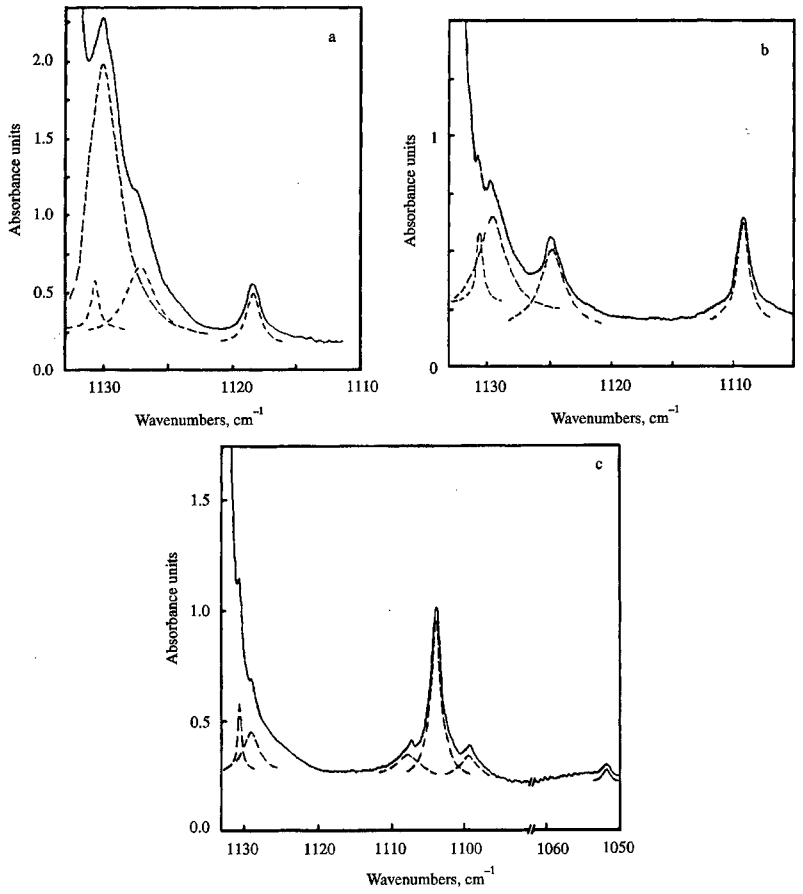

Fig. 2. Decomposition of the oxygen absorption spectrum for Ge-doped (a), Sn-doped (b) and C-doped (c) silicon.

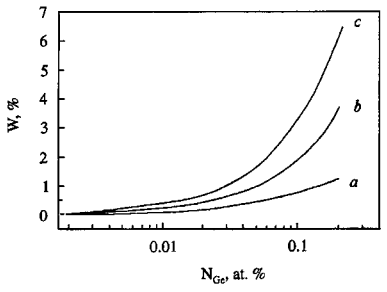

Fig. 3. Calculated dependencies of probability of IVI atoms situation in the 1st (a), in the 2nd (b) and in the 3rd (c) coordination sphere relatively of Si_2O quasimolecule on IVI content in Si.

IVI content and at given IVI content the probability of IVI atom appearing in the more distant spheres exceeds that for nearer spheres. The respective intensities of absorption components should then be proportional to the probabilities of IVI atom arrangement in the corresponding spheres.

However, the relationships between intensities of additional absorption bands which were experimentally observed and calculated from the probability values appear to vary for different IVI. Thus for IVI concentrations shown in Fig. 2, the most intensive absorption component in Si $\langle$Ge$\rangle$ corresponds to 1130.1 cm^{-1} (Ge atom in the 3rd coordination sphere), in Si $\langle$C$\rangle$ - 1104 cm^{-1} (C atom in the 2nd coordination sphere), while in Si$\langle$Sn$\rangle$ the 1129.7 cm^{-1} (Sn atom in the 3rd coordination sphere) component is only slightly greater than the other components. Note that the intensity ratio holds within the whole range of IVI concentration studied. For IVI concentrations corresponding to those shown in Fig. 3, the ratios of probabilities that IVI atom is located in 1st–3rd coordination spheres relatively Si_2O in silicon crystal are: 1.1 : 3.2 : 5.4 for Ge, 0.23 : 0.7 : 1.17 for Sn and 0.012 : 0.035 : 0.05 for C. Hence the experimental data indicate that there is a preferential arrangement of different IVI relative to Si_2O in silicon lattice: Ge atoms tend

to be located in the 3rd coordination sphere, C atoms — in the second one.

Note also the different shifts of absorption lines of interstitial oxygen disturbed by Ge, Sn or C atoms sited in the same coordination spheres. Thus for ν_3 vibrational mode of Si_2O quasimolecule disturbed by IVI atom in the first coordination sphere, the frequency shifts as compared with undoped Si are: $\sim 18\ cm^{-1}$ for Ge, $\sim 27\ cm^{-1}$ for Sn and $\sim 84\ cm^{-1}$ for C-doping, that is, a noticeable increase in shift is observed when passing from Ge to C impurity. A similar situation takes place for vibration of Si_2O quasimolecule having IVI atom in its 2nd coordination sphere, but the shift difference decreases (~ 9, ~ 11.6, ~ 32). The minimum shift difference is observed when IVI atom is in the 3rd coordination sphere (~ 6, ~ 6.7, ~ 7.3).

As indicated above, the effect of IVI on semiconductor properties is mainly associated with the deformation produced by IVI in the Si lattice. Deformation charge A (the change of crystal volume after introduction of a single point defect) of IVI in Ge, Sn, C series is known to increase more than the order of magnitude and is proportional to the difference between covalent radii of silicon ($r_{Si} = 1.17$ Å) and IVI ($r_{Ge} = 1.22$ Å; $r_{Sn} = 1.44$ Å; $r_C = 0.77$ Å) [15] (Fig. 4, curve d). Considering the dependencies of ν_3 absorption band locations on the difference between covalent radii of IVI and Si (Fig. 4, curves a–c), we can see that these relationships for quasimolecules disturbed by IVI atom in the 1st, 2nd and 3rd spheres are similar to that for the IVI deformation charge on covalent radius difference. That is, the shift of ν_3 vibrational mode is proportional to IVI-induced deformation charge. The value of deformation (shift) produced by the point source is known to follow the expression [16] $U = Ar/r^3$, where r is the distance from the point source of deformation. From here a small difference in the shift of absorption lines of oxygen with IVI atom in the 3rd coordination sphere becomes apparent. Fig. 4 shows a deviation from linear dependence as IVI atom passes into the 1st sphere. This can also be understood, because deformation changes of 2α angle between bonds in Si_2O, force constant (IVI is located very close to Si_2O) and mass correction M′ (which is due to the substitution of silicon atom by IVI atom [14]) are considerably large for IVI atom located in the 1st coordination sphere than those for IVI in 2nd and 3rd spheres.

Fig. 4 also illustrates the shift of absorption band for vacancy + oxygen center (VO^0) which is essentially Si_2O quasimolecule disturbed by neighbouring vacancy, which also is an isovalent "impurity" ($r_V \approx 0$) in silicon. As is seen from the figure, the point is in agreement with data obtained for IVI, but the deviation from linear dependence is more pronounced. In the case of VO-center the distance between oxygen atom and vacancy is very small which should result in more strong disturbance than produced by IVI. Accordingly, mass correction and force constant should also be changed to a greater extent. Thus the data obtained allow us to draw a conclusion that the value of interstitial oxygen absorption band shift resulted from IVI atom disturbance, is mainly due to the value of IVI-induced deformation in silicon.

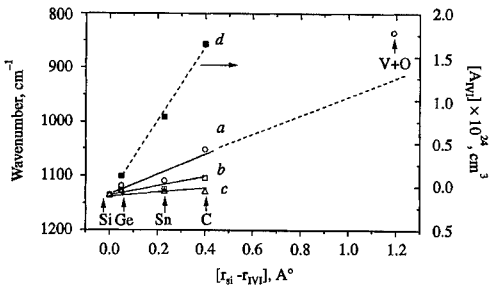

Fig. 4. Dependence of IVI deformation charge (d) and location of ν_3 mode for Si_2O perturbed by IVI atom situated in the1st (a), 2nd (b) or 3rd (c) sphere on the difference between r_{Si} and r_{IVI}.

Of some interest is the fact that regardless of the sign of IVI-induced deformation (r_C, $r_V < r_{Si}$; r_{Ge} $r_{Sn} > r_{Si}$), the absorption band of interstitial oxygen always shifts to the low-frequency side. According to reference data, the angle 2α between bonds in Si_2O quasimolecule in silicon is about 164°, while the distance between silicon atoms in quasimolecule (~ 3.16 Å) is considerably larger than the length of Si–Si bond (~ 2.35 Å) [14]. At the same time in organosilicon compounds, where Si_2O quasimolecule may be oriented rather freely and the angle between bonds remain close to tetrahedral [17], 2α angle is about 148°. Unlike these compounds, in Si lattice all six external bonds of Si_2O quasimolecule are rigidly fixed. A condition of minimum energy — minimum deviation from tetrahedral angles between Si atom bonds — is provided by some displacement of neighboring atoms and by the increase of angle in quasimolecule. Substitution of silicon atom in the vicinity of quasimolecule by IVI atom, regardless of the sign of deformation produced, results in local symmetry decrease. This probably permits some decrease of lattice deformation energy — the quasimolecule gains some degree of freedom, the decrease of the angle between bonds can occur and hence the distance between silicon atoms in quasimolecule also decreases. Thus a reduction of oxygen atom deformation potential may occur. This suggestion is supported by investigation of deformation charges in Czochralski-grown silicon — germanium as well as carbon doping were shown to result in compensation of oxygen-induced deformations [18,19]. The sign of IVI deformation potential is likely to determine the direction of oxygen atom displacement, rather than the value of displacement.

References

[1] J.L. Lindström, B.G. Svensson, Mater. Res. Soc. Symp. Proc. 59 (1986) 45.
[2] Y.H. Lee, J.W. Corbett, Phys. Rev. B 13 (1976) 2653.
[3] G. Davies, E.C. Lightowlers, R.C. Newman, A.S. Oates, Semicond. Sci. Technol. 2 (1987) 524.
[4] V.K. Bajenov, V.I. Fistul, Fiz. Tekh. Poluprovodnikov 18 (1984) 1345.
[5] Yu.M. Babitskii, N.I. Gorbacheva, P.M. Grinshtein, M.G. Milvidskii, Fiz. Tekh. Poluprovodnikov 24 (1984) 1129.
[6] L.I. Khirunenko, V.I. Shakhovtsov, V.K. Shinkarenko, L.I. Shpinar, I.I. Yaskovetc, Fiz. Tekh. Poluprovodnikov 21 (1987) 562.
[7] L.I. Khirunenko, V.I. Shakhovtsov, V.V. Shumov, Solid State Phenomena 57–58 (1997) 183.
[8] D.I. Brinkevich, V.P. Markevich, L.I. Murin, V.V. Petrov, Fiz. Tekh. Poluprovodnikov 26 (1992) 682.
[9] M.G. Sosnin, B.M. Turovskii, V.I. Shakhovtsov, V.L. Shindich, Soviet Phys. Semicond. 16 (1982) 577.
[10] A.R. Bean, R.C. Newman, J. Phys. Chem. Solids 33 (1972) 255.
[11] R.C. Newman, A.R. Bean, Radiat. effects 8 (1971) 189.
[12] D.R. Bosomworth, N. Hayes, A.R.L. Spray, G.D. Watkins, Proc. Roy. Soc. London 317 (1970) 133.
[13] H. Yamada-Kaneta, C. Kaneta, T. Ogawa, Phys. Rev. B 47 (1993) 9338.
[14] B. Pajot, Semicond. and Semimet. 42 (1994) 191.
[15] V. Kustov, M.G. Mil'vidskii, Yu.G. Semenov, B.M. Turovskii, V.I. Shakhovtsov, V.L. Shindich, Fiz. Tekh. Poluprovodnikov 20 (1986) 270.
[16] A.M. Stoneham, in: Theory of Defects in Solids 1, Mir, Moscow, 1978, p. 176.
[17] A.N. Lazarev, I.S. Ignat'ev, T.F. Tenisheva, in: Vibration of Simple Molecules with Si–O Bonds, Nauka, Leningrad, 1991, pp. 59–62.
[18] V.E. Kustov, T.V. Kritskaya, N.A. Tripachko, V.I. Shakhovtsov, Fiz. Tekh. Poluprovodnikov. 22 (1988) 313.
[19] V.E. Kustov, T.V. Kritskaya, N.A. Tripachko, L.I. Khirunenko, V.I. Shakhovtsov, V.I. Yashnik, Neorg. mater. 27 (1991) 1116.

ELSEVIER

Physica B 273–274 (1999) 322–325

PHYSICA B

www.elsevier.com/locate/physb

The temperature dependence of radiative and nonradiative processes at Er–O centers in Si

Thomas D. Chen*, Marlene Platero, Michal Opher-Lipson, Jörg Palm, Jurgen Michel, Lionel C. Kimerling

Massachusetts Institute of Technology, 77 Massachusetts Avenue, Cambridge, MA 02139, USA

Abstract

Er-doped silicon is a promising material for silicon microphotonics light sources. Luminescence from Er–O centers in silicon exhibits an intensity quenching as the temperature is raised from 4 to 300 K. We present the first unified description of the excitation and de-excitation processes over the entire temperature range. We model the phenomena in terms of exciton Auger, impurity Auger, and multiphonon transition processes. A set of rate equations that includes all of these processes is written to describe the energy transfer, and the normalized luminescence intensity versus temperature is computed and compared to experimental data. The proposed model fits the experimental photoluminescence data over the entire temperature range. Junction photocurrent spectroscopy measurements confirm the presence of a non-radiative multiphonon backtransfer mechanism. The photocurrent generated from the direct optical excitation of Er centers was found to increase with temperature in the form expected from the energy backtransfer model.

Keywords: Silicon microphotonics; Erbium doping; Energy backtransfer

1. Introduction

The sharp-line luminescence at $\lambda = 1.54\,\mu m$ from erbium-doped silicon arises from the $^4I_{13/2} \rightarrow {}^4I_{15/2}$ transition from the excited inner 4f shell of the Er^{3+} center [1]. Unlike luminescence in other semiconductors, rare-earth (RE) luminescence stems from spin-state transitions at the RE atomic site and does not involve radiative transitions from bandgap states or any other levels associated with the host lattice. Neglecting the possibility of direct optical or hot electron excitation, the excitation of an Er center in Si involves the generation of electron–hole (e–h) pairs, followed by a nonradiative energy transfer of the recombination energy to the Er inner 4f shell [2]. The e–h pairs can be generated either by above bandgap light or injection of minority carriers at a pn-junction. Room temperature electroluminescence (EL) of an erbium-doped silicon pn-junction has been demonstrated [3]. We have shown previously that the electroluminescence of Er in Si at 4 K and low excitation levels is up to 10^6 more efficient than direct optical pumping of Er centers in Er-doped fiber amplifiers [4]. The internal quantum efficiency decreases, however, strongly from about 5% as the power is increased and the temperature is raised. The photoluminescence (PL) intensity can decrease 3 orders of magnitude at low excitation powers when the sample temperature increases from 4 K to room temperature.

2. Background

Two distinct regimes with different activation energies have been identified on the PL versus temperature plot, suggesting two different processes of excitation and relaxation: 10–20 meV (below 100 K) and 160 mV (above 100 K) [4,5]. The temperature dependence of the PL

* Corresponding author. Tel.: + 1-617-253-6907; fax: + 1-617-253-6782.

E-mail address: tchen@mit.edu (T.D. Chen)

0921-4526/99/$ - see front matter
PII: S0921-4526(99)00466-4

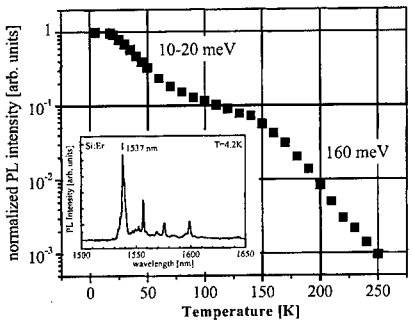

Fig. 1. Photoluminescence intensity at $\lambda = 1.537\ \mu m$ versus temperature for Er in silicon (excitation 60 mW). Two distinct de-excitation processes above and below 100 K can be identified. The inset displays the Si : Er PL spectrum.

intensity at $\lambda = 1.537\ \mu m$ is shown in Fig. 1. The understanding of these processes is critical for the optimization of the EL efficiency of Er-doped light-emitting diodes (LEDs). We have shown in Ref. [4] the importance of understanding the kinetic regimes of energy flow for recombination at RE centers in semiconductors. The energy transfer from an e–h pair to a radiated photon follows a multi-step pathway that is subject to non-radiative, alternative pathways. Due to the fairly long spontaneous emission lifetime of the 4f shell of about 1 ms, the energy is effectively stored in the excited erbium center. The long spontaneous emission lifetime of these centers makes them vulnerable to an energy back-transfer process. A nonradiative backtransfer process in direct competition with spontaneous emission will affect both emission intensity and luminescence decay time. A concomitant decrease in emission intensity and luminescence decay time has been observed in Si : Er, arguing strongly for the presence of a backtransfer mechanism [4,5].

We have demonstrated that the Impurity Auger effect with free carriers is responsible for the temperature quenching below 100 K [4]. Electroluminescence decay experiments under reverse bias show that despite the absence of free carriers, the decay time continues to decrease above 100 K with an activation energy of 150 meV. We concluded that there must be a second backtransfer process in addition to the Impurity Auger. In this article we will give direct evidence that this process involves energy transfer by phonons at an Er–O-related bandgap state. We will demonstrate the involvement of this donor level in a phonon-mediated energy backtransfer process by temperature-dependent junction photocurrent spectroscopy (JPCS) measurements. Moreover, this level will be featured in a rate equation model, which we will fit to experimental PL intensity versus temperature data.

3. Experimental procedure

Boron-doped, Czochralski (CZ) silicon wafers (0.5–2 Ω cm) were implanted with Er and O, resulting in peak concentration of $10^{18}\ cm^{-3}$. At an Er implantation energy of 320 keV the peak concentration depth was 0.1 μm. The oxygen was implanted to overlap the Er profile. Photoluminescence was performed at various temperatures on these samples by exciting with the 488 nm line of an Ar ion laser. A liquid nitrogen-cooled Ge detector, a grating spectrometer, and a lock-in amplifier were used for signal detection.

Mesa LED structures were fabricated on B-doped, CZ wafers by implanting As to form an n^+ emitter [3]. After performing a post-implantation damage anneal at 1000°C for 2 h, the wafers were then implanted with Er and O to a peak concentration of 5×10^{17} and $3 \times 10^{18}\ cm^{-3}$, respectively, at an implantation energy of 4.5 MeV (1.35 μm Er peak depth). The oxygen implant energy was chosen to match the Er profiles. The Er–O was optically activated by annealing at 900°C for 30 min in a nitrogen ambient. Aluminum backside and open front contacts were formed by evaporation. Mechanically chopped light from a tunable IR laser diode was focused into a spot onto the LED front surface. A reverse bias of 5 V was applied during the JPCS measurement. The current was measured by a current amplifier and a lock-in amplifier.

4. Results and discussion

The temperature dependence of the peak Er luminescence intensity at $\lambda = 1.537\ \mu m$ was shown in Fig. 1. Palm et al. [4], Priolo et al. [6], and Taguchi and Takahei [7] have written rate equations to describe the excitation and de-excitation of Er centers in silicon. Palm et al. included an Auger loss process in their description but did not include an explicit backtransfer mechanism by which energy is transferred from an excited 4f shell back to the silicon lattice. Priolo et al. also included an Auger loss but additionally modeled the back-transfer as a single exponential with an activation energy of 0.15 eV. Taguchi and Takahei utilized nonradiative multiphonon emission (MPE) rates to describe the backtransfer but did not include any Auger effects. The model submitted by Priolo et al. is able to describe the PL intensity from 4 K to room temperature, but it does not indicate a physical mechanism by which backtransfer occurs nor does it account for the excess energy that must be dissipated from an e–h pair.

We propose a model that includes Auger losses and the MPR mechanism utilized by Taguchi and Takahei. Fig. 2 shows an energy band diagram for the Si : Er system and illustrates the various excitation and de-excitation processes involved. The MPE rates W_e and W_a are given in

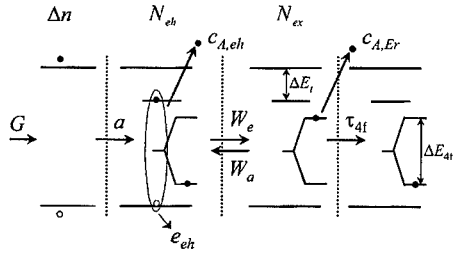

Fig. 2. Energy band diagram and energy transfer processes for Si : Er. An Er center is represented in the figure by an associated state in the bandgap at ΔE_T below the conduction band, along with the 4f shell with energy E_{4f}. The arrows that represent the excitation and de-excitation processes are discussed in the text.

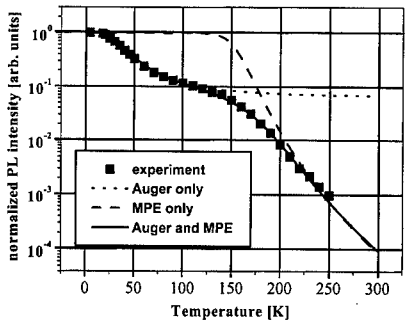

Fig. 3. Experimental and simulated normalized PL versus temperature. The solid line (—) combines Auger and MPE processes and gives good agreement between experiment and computation. Calculations for Auger only (···) and MPE only (- -) do not describe the temperature dependence over the entire range.

Ref. [7]. An e–h pair is first trapped at an Er center and then recombines to excite the 4f shell. The excess energy is dissipated by multiphonon emission. The reverse process, where an excited 4f shell generates an e–h pair, can occur by multiphonon absorption. The following rate equations, involving the excess carrier density Δn, the density of Er centers with a bound e–h pair N_{eh}, and the concentration of excited Er centers N_{ex}, reflect the excitation and de-excitation processes depicted in Fig. 2:

$$\frac{d(\Delta n)}{dt} = G - a(\Delta n)^2 \tag{1}$$

$$\frac{dN_{eh}}{dt} = a(\Delta n)^2 - c_{A,eh} n N_{eh} - W_e N_{eh} + W_a N_{ex} - e_{eh} N_{eh} \tag{2}$$

$$\frac{dN_{ex}}{dt} = W_e N_{eh} - W_a N_{ex} - N_{ex}\left(\frac{1}{\tau_{4f}} + c_{A,Er} n\right), \tag{3}$$

where G is the carrier generation rate, e_{eh} is the emission rate for a bound e–h pair at the Er center, n is the total electron concentration, and τ_{4f} is the spontaneous emission lifetime. Eq. (1) describes the generation of carriers and the formation of bound e–h pairs at Er centers [4]. The next equation accounts for the loss of bound e–h pairs by Auger or thermal emission processes. The MPE rates are included to reflect the excitation and de-excitation of the 4f shell. The last equation for the concentration of excited Er also reflects the MPE excitation and backtransfer pathways and includes the additional loss from impurity Auger quenching which is proportional to the density of free carriers.

The normalized PL intensity ($\propto N_{ex}/\tau_{4f}$) is computed and fitted to the experimental data by adjusting the emission cross section of the e–h pair. Values for a ($= 10^{-12}\,cm^{-3}\,s^{-1}$), $c_{A,eh}$ ($= 10^{-10}\,cm^{-3}\,s^{-1}$), and $c_{A,Er}$ ($= 10^{-10}\,cm^{-3}\,s^{-1}$) were taken from the results of power dependence simulations [4]. Fig. 3 displays the computed PL intensity versus temperature and demonstrates a good agreement between experiment and computation. The curve was fitted by adjusting the e–h cross section σ_{eh} to a value of $10^{-15}\,cm^2$. This cross section has been measured experimentally as the excitation cross section of e–h pairs [4,6]. The simulations for Auger only or MPE only are also shown for comparison. Clearly, the impurity Auger process dominates the quenching at low temperatures, and the MPE process accounts for the behavior at higher temperatures.

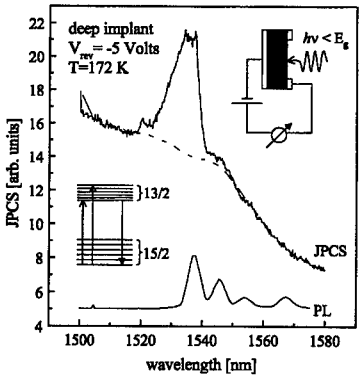

Fig. 4. JPCS spectrum at 172 K. A reverse-biased Si : Er diode is illuminated with IR light ($\lambda < E_g$). The JPCS signal peaks at $\lambda = 1.537$ μm, indicating that the measured current originates from photon absorption at Er centers.

The existence of a phonon-mediated process is directly measured by JPCS experiments. Fig. 4 shows a JPCS spectrum of a Si : Er diode at 172 K; a PL spectrum is provided for reference. The peak at $\lambda = 1.537$ μm demonstrates that the measured JPCS current is derived from direct optical absorption of photons at Er centers. A similar peak has been reported by Kik et al. [8]. The peak current is observed to increase with temperature. Fig. 5

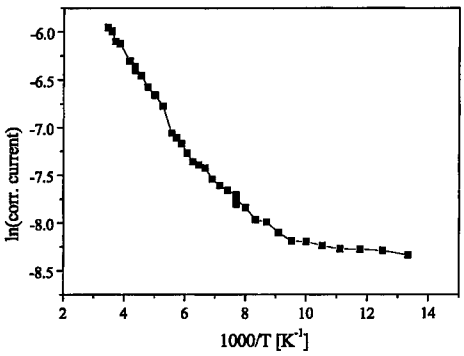

Fig. 5. The peak JPCS signal ($\lambda = 1.537$ μm) versus temperature. The JPCS signal increases with temperature as phonon-mediated transitions become more probable.

plots the JPCS peak current versus temperature. The slope of the curve in Fig. 5 indicates an activation energy of 0.04 eV. The generation of the JPCS current is possibly limited by multiphonon absorption, band bending effects in the Er-doped region of the material, exciton emission, or impurity Auger losses to bound electrons at shallow donor states [9]. These processes were not included in the present model for the PL. However, their importance is currently under investigation in light of the additional information provided by the JPCS data.

In summary, the excitation and de-excitation of Er centers in Si has been discussed. Auger and nonradiative multiphonon processes have been shown to cause the luminescence intensity quenching that occurs when the temperature is increased. The temperature dependence of the PL intensity was modeled by a set of rate equations. The computed and fitted results exhibited good agreement with the experimental data. The existence of a phonon-mediated backtransfer mechanism was directly observed by junction photocurrent spectroscopy. Direct optical excitation of Er centers result in the generation of e–h pairs. The backtransfer current was observed to increase with temperature in a manner consistent with phonon mediation. Without modifying the spontaneous emission lifetime, luminescence from Si : Er appears to be fundamentally limited by competitive, nonradiative processes, which are faster than the spontaneous emission rate.

Acknowledgements

Discussions with J.M. Langer are greatly appreciated. This work was supported by the AFSOR/DARPA/Rome Labs under contract F49620-95-1-0312.

References

[1] E. Ennen, J. Schneider, G. Pomrenke, A. Axmann, Appl. Phys. Lett. 43 (1983) 943.
[2] J. Michel, J.L. Benton, R.F. Ferrante, D.C. Jacobson, D.J. Eaglesham, E.A. Fitzgerald, Y.-H. Xie, J.M. Poate, L.C. Kimerling, J. Appl. Phys. 70 (1991) 2672.
[3] B. Zheng, J. Michel, F.Y.G. Ren, L.C. Kimerling, D.C. Jacobson, J.M. Poate, Appl. Phys. Lett. 64 (1994) 2842.
[4] J. Palm, F. Gan, J. Michel, L. Kimerling, Phys. Rev. B 54 (1996) 17603.
[5] S. Coffa, G. Franzò, F. Priolo, A. Polman, R. Serna, Phys. Rev. B 49 (1994) 16313.
[6] F. Priolo, G. Franzò, S. Coffa, A. Carnera, Phys. Rev. B 57 (1998) 4443.
[7] A. Taguchi, K. Takahei, J. Appl. Phys. 83 (1998) 2800.
[8] P. Kik, M.J.A. de Dood, K. Kikoin, A. Polman, Appl. Phys. Lett. 70 (1997) 1721.
[9] T. Gregorkiewicz, D. Thao, J. Langer, Phys. Stat. Sol. B 210 (1998) 737.

ELSEVIER

Physica B 273–274 (1999) 326–329

PHYSICA B

www.elsevier.com/locate/physb

Spectroscopic probing of defect-related energy storage in silicon doped with erbium

D.T.X. Thao[a,b,*], T. Gregorkiewicz[a], J.M. Langer[c]

[a]*Van der Waals-Zeeman Institute, University of Amsterdam, Valckenierstraat 65-67, NL-1018 XE Amsterdam, Netherlands*
[b]*International Training Institute for Materials Science, ITIMS building, Dai hoc Bach khoa, Hanoi, Viet Nam*
[c]*Institute of Physics, Polish Academy of Sciences, Al. Lotników 32/46, PL-02-668 Warszava, Poland*

Abstract

An enhancement of 1.5 μm Si:Er photoluminescence by a mid-infrared pulse from a free-electron laser is investigated in detail. It is concluded that the effect is a consequence of defect-related energy storage in Si:Er samples. Carriers generated by a band-to-band excitation are participating not only in the excitation of Er luminescence via the excitonic mechanism, but are also trapped at various defect states. The infrared pulse photoionizes them, thus promoting extra carriers into the excitation channel of the Er^{3+} ion and leading to an additional luminescence. By scanning the wavelength of the free-electron laser ionization spectra of shallow centers participating in the energy transfer are obtained. The results also elucidate a special role of oxygen in Si:Er luminescence.

Keywords: Silicon; Er doping; Photonics; Energy transfer; Free-electron laser

1. Introduction

Semiconductors doped with rare earths (RE) attracted much attention as new light-emitting materials. Narrow line emission characteristic for the 4f-shell transition and the temperature stability of the emission wavelength provide major motivation stimulating research in this area. Among various rare-earth doped semiconductor systems Si:Er is recognized as the most attractive [1]. This is due to the superior level of Si technology and the 1.5 μm emission wavelength of Er which matches exactly the optimal properties of light waveguides. Also, successful incorporation of the optically active Er centers into Si could open the possibility for direct light-electron integration [2]. Numerous studies are devoted to understanding the excitation and de-excitation mechanisms of this complex system. Full control of these processes is necessary for optimization of intensity and thermal stability of Er luminescence.

Recently, two-color spectroscopy with a pulsed free-electron laser (FEL) operating in the mid-infrared (MIR) range has been successfully applied to investigate the energy transfer process between 4f-electron shell of an Er^{3+} ion and silicon host. In these experiments changes of Er PL are followed as a function of FEL wavelength, power and timing with respect to the initial excitation in the visible region. Evidence has been obtained that luminescence of Er in Si can be generated also by energy transfer from shallow centers available in the material and not necessarily specifically related to erbium.

2. Experimental

In the experiments MIR pulses of approximately 5 μs duration and up to a few mJ energy have been used. For spectroscopic measurements the FEL wavelength

* Correspondence address: Van der Waals-Zeeman Institute, University of Amsterdam, Valckenierstraat 65-67, 1018 XE Amsterdam, The Netherlands. Tel.: + 31-20-525-5642; fax: + 31-20-525-5788.

E-mail address: thao@wins.uva.nl (D.T.X. Thao)

0921-4526/99/$ - see front matter
PII: S0921-4526(99)00467-6

λ_{FEL} was varied in the 7.5–17 μm range (70–170 meV). For initial band-to-band excitation the second harmonic of a pulsed Nd:YAG laser operating at $\lambda_{YAG} = 532$ nm or a cw solid-state laser with $\lambda_{DIODE} = 820$ nm were used. The signal was detected with a Ge-detector (North Coast, $\tau \approx 75$ μs) through a narrow band pass filter of 20 nm band width tuned to the Er-related emission at $\lambda_{Er} = 1.54$ μm. All the reported experimental data were obtained at a temperature of 5 K for samples placed in a helium gas flow cryostat (Oxford Instruments).

In the study two different kinds of samples have been used. One sample was prepared from oxygen-rich silicon material by Er and oxygen implantation (Cz-Si:Er), followed by a brief annealing in order to recrystallize the implantation damage. The PL spectrum of the sample contained predominantly emission from the so-called cubic Er center [3]. The second sample was prepared from oxygen-lean silicon material by Er implantation at an elevated temperature of 500°C (Fz-Si:Er). No coimplants have been used and no further heat treatment has been applied. The PL spectrum in this case was dominated by non-cubic components. The Er-related emissions of both samples used in the current study can be found in Ref. [4].

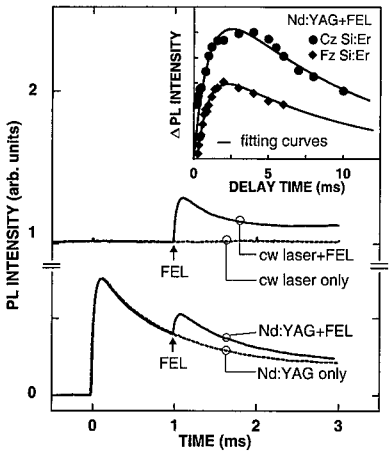

Fig. 1. Illustration of the MIR-induced Er PL; the delay time between the visible and the MIR pulses is $\Delta t = 1$ ms. The inset shows the dependence of the magnitude of the MIR-induced Er PL on the delay time Δt. The solid lines represent fits to the formula $\Delta I_{PL} = A[\exp(-t/\tau_d) - \exp(-t/\tau_r)]$. τ_r and τ_d correspond to the rise time and the decay time of the effect, respectively. The curves are plotted for $\tau_r \approx 1$ ms and $\tau_d \approx 10$ ms.

3. Results and discussion

MIR illumination of Si:Er samples optically excited in the visible region produces two effects. In the Fz-Si:Er sample quenching of the Er PL was observed for a small delay time between the visible and MIR pulses ($\Delta t \leqslant 250$ μs). This effect is interpreted as arising from the MIR-induced disruption of excitation path [5]. For a longer delay time the quenching is minimized and the enhancement of PL sets in. In the Cz-Si:Er sample only the enhancement effect is seen. The kinetics of the extra PL are independent of the band-to-band excitation type and the same as that of the standard Er PL excited in the visible region. Fig. 1 illustrates the time developments of Er PL intensity upon Nd:YAG and cw solid-state laser excitation and subsequent FEL irradiation (with a delay time of 1 ms in case of Nd:YAG). The magnitude of the additional PL intensity is bigger in oxygen-rich Cz-Si:Er than in oxygen-lean Fz-Si:Er material. The dependence of the magnitude of the effect on the delay time between the visible and the MIR pulses is presented in the inset of Fig. 1. It shows that the additional PL intensity increases gradually, attains a maximum at delay time of about 3 ms, and then decreases; practically no effect can be seen for $\Delta t \geqslant 30$ ms. Based on the experimental data we conclude that the Er-related emission can be generated with a light pulse in the mid-infrared range. The results show that the centers responsible for the MIR-induced Er PL have a long lifetime, of the order of 10 ms. Since the smallest energy necessary for generation of the $^4I_{13/2}$ excited state of Er^{3+} responsible for the observed luminescence at $\lambda \approx 1.5$ μm is approximately 800 meV, and therefore, much larger than the MIR quantum energy of 70–170 meV, the excitation effect could have been related to multiple-photon absorption only. The multiphoton absorption in an intense field of a free-electron laser is certainly plausible and has been reported in the studies of C60 [6]. In the current study, however, the visible excitation preceding the MIR pulse constitutes a necessary condition for the effect to occur. This is evident from the observation that the additional PL is not detected when the MIR pulse is applied prior to the Nd:YAG laser. We can therefore exclude the multiphoton absorption by Si crystal or directly by Er^{3+} ions as possible excitation mechanisms responsible for the additional PL signal. We propose that the energy provided by the excitation in the visible region is stored away for some time and is then transferred to Er ions upon application of the MIR pulse. This can indeed be expected if we assume that free carriers excited by the visible light undergo various recombinations. Some of them will result in Er excitation, giving rise to luminescence. In strongly defected material, however, many carrier-trapping centers will exist, the majority not being Er related and therefore not contributing to Er PL. These provide alternative channels of (mostly) nonradiative recombinations. Some of them will serve as efficient recombination centers, while others may have longer lifetimes. The intense MIR pulse applied after the excitation will ionize the longer-living traps. The condition for this to occur is a sufficiently small ionization

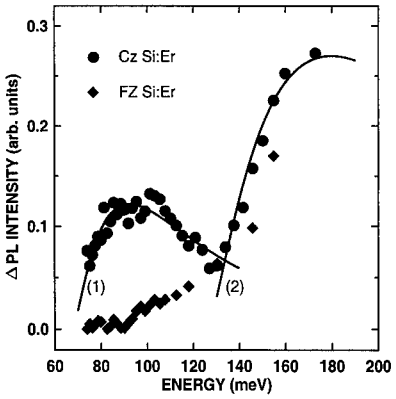

Fig. 2. The wavelength dependence of the magnitude of the MIR-induced Er PL. The solid lines represent fits to Eq. (1) with (1): $E_{D1} \approx 65$ meV; (2): $E_{D2} \approx 125$ meV. $\gamma_1 = \gamma_2 = 1$.

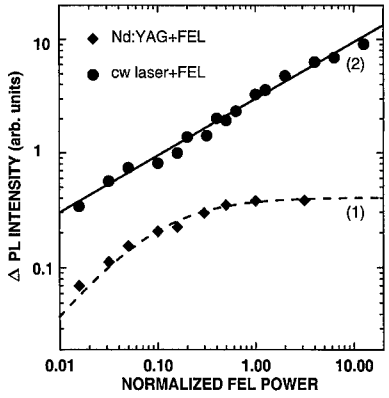

Fig. 3. The FEL power dependence of the MIR-induced Er PL signal for (1): primary pulsed excitation with a Nd:YAG laser; the broken line is a fit to Eq. (2); (2): primary excitation with a cw solid-state laser; the solid line is a fit to Eq. (3).

energy of the centers involved (shallow character), so that the process can be activated by the mid-infrared radiation. The chance exists that the free carriers generated in that way might be recaptured at Er-related centers capable of Er^{3+} core excitation. Consequently, additional PL will appear, with its magnitude governed by intensity of the free-electron laser, capture cross section, concentration and lifetime of the relevant traps.

The wavelength dependence of the MIR-induced Er PL, which was scaled for an identical number of photons per pulse at every wavelength, is shown in Fig. 2. The results for both samples show a clear difference at low energy ($h\nu < 125$ meV), followed by a rather similar behavior for the high-energy range. According to the above-proposed mechanism of the MIR-induced Er PL, results depicted in Fig. 2 represent ionization spectra of dominant traps contributing to the energy storage process. It has been shown [7] that the photoionization cross section σ of a trap can be described as

$$\sigma = \text{const.}\frac{E_D^{7/2}(h\nu - E_D)^{3/2}}{(h\nu)^{3+2\gamma}}, \tag{1}$$

where $h\nu$ and E_D correspond to the energy of the ionizing beam and the ionization energy of the trap, respectively. γ parameter ($0 \leqslant \gamma \leqslant 1$) depends on the particular form of the binding potential and is $\gamma = 0$ and 1 for the δ-like and Coulomb potentials, respectively. Eq. (1) gives a rather broad and featureless wavelength dependence, with an onset corresponding to $h\nu = E_D$, and a maximum at $h\nu = \frac{10}{7}E_D$ and $h\nu = 2E_D$ for de-localized and localized binding potentials, respectively. Comparing the wavelength dependencies obtained experimentally for Cz-Si:Er and Fz-Si:Er samples displayed in Fig. 2 we conclude that different traps are responsible for the MIR-induced excitation of Er in the two materials. The ionization spectrum in Cz–Si has a broad maximum at an energy around 90–100 meV and an extrapolated onset at 65 meV. Following our interpretation we conclude that the trap responsible for the MIR-induced Er PL is in that case characterized by an extended binding potential and an ionization energy $E_{D1} \approx 65$ meV. Both features agree well with typical shallow effective-mass-theory centers in silicon. We note that the observation of a shallow center participating in the energy transfer processes pertinent to Er core excitation in an oxygen-rich environment is the first spectroscopic evidence of the influence of oxygen on the optical activity of Er in silicon. For both samples the experimentally measured ionization cross sections show a very pronounced increase for the largest energies of the MIR beam. We assign this feature to a deeper trap characterized by a binding energy $E_{D2} \approx 125$ meV. This trap appears to be identical in both the investigated materials; it seems plausible that it is introduced by the Er ion itself.

The FEL power dependence of the additional PL intensity has been investigated and is illustrated in Fig. 3. For the pulsed Nd:YAG excitation the effect is initially linear and saturation sets in for higher power values. Experimental data could be fitted with a formula

$$\Delta I_{PL} = c_1 P/(1 + c_2 P), \tag{2}$$

where P is FEL power and c_1 and c_2 are fitting parameters. The integrated intensity of the additional PL signal is proportional to the number of Er^{3+} ions which attain the excited state following the MIR pulse. On the other hand, the operational power of FEL determines the actual number of photons contained in the MIR pulse. Therefore, the experimentally determined linear power dependence of the MIR-induced PL intensity shows proportionality between the number of MIR photons and

the number of additional recombinations leading to Er excitation. We conclude that a carrier (an electron or a hole) ionized from a trap by the photon absorption can recombine with a carrier of an opposite sign available in the material. In this case, the intensity of additional PL will increase linearly with MIR power until, at high densities of MIR photons, the saturation will appear, as populated traps become exhausted. This scenario is consistent with the experimental behavior obtained for both samples under conditions of the primary excitation by a pulsed Nd:YAG laser.

The situation was different for the case of cw solid-state laser excitation. As can be seen in Fig. 3, no saturation of the additional Er PL was observed over three decades of FEL power. The magnitude of the MIR-induced Er PL was found to be proportional to the square-root of the FEL power

$$\Delta I_{PL} = A\sqrt{P}. \quad (3)$$

Under condition of continuous excitation the system attains equilibrium and all shallow centers become completely filled, thus resulting in carrier storage. Assuming that the shallow traps are donors, the generation of extra carriers in the conduction band by the MIR pulse will resemble the generation of electron–hole pairs across a band-gap with the relations $\Delta n p_{imp} \sim P$ and $\Delta n = p_{imp}$, where Δn is the extra electron concentration in the conduction band and p_{imp} corresponds to the hole concentration at shallow states. This is different from that in the case of pulsed Nd:YAG excitation, where we had $\Delta n \ll p_{imp}$. The additional PL intensity under cw laser excitation will be proportional to the product Δnp, where p is the number of holes generated by the primary beam. This leads to $\Delta I_{PL} \sim \sqrt{P}$, in agreement with the experiments (see Fig. 3).

4. Conclusion

We have shown that the Er-related PL can be induced by a MIR pulse applied within several tens of milliseconds after the band-to-band excitation. We interpret this effect as being due to a release of energy generated with the band-to-band pulse and stored at shallow centers (predominantly of hydrogenic character). This effect is more prominent in oxygen-rich material, thus illustrating the special role of oxygen presence in Si:Er photoluminescence.

References

[1] L.C. Kimerling, K.D. Kolenbrander, J. Michel, J. Palm, In: H. Ehrenreich, F. Spaepen (Eds.), Solid State Physics, Vol. 50, Academic Press, New York, 1997, p. 333.
[2] E.A. Fitzgerald, L.C. Kimerling, MRS Bull. 23 (1998) 39.
[3] H. Przybylińska, W. Jantsch, Yu. Suprun-Belevitch, M. Stepikhova, L. Palmetshofer, G. Hendorfer, A. Kozanecki, R.J. Wilson, B.J. Sealy, Phys. Rev. B 54 (1996) 2532.
[4] T. Gregorkiewicz, D.T.X. Thao, J.M. Langer, Phys. Stat. Sol. B 210 (1998) 737.
[5] I. Tsimperidis, T. Gregorkiewicz, H.H.P.Th. Bekman, C.J.G.M. Langerak, Phys. Rev. Lett. 81 (1998) 4748.
[6] G. von Helden, I. Holleman, A.J.A. van Roij, G.M.H. Knippels, A.F.G. van der Meer, G. Meijer, Phys. Rev. Lett. 81 (1998) 1825.
[7] J.M. Langer, T. Langer, G.L. Pearson, B. Krukowska-Fulde, U. Piekara, Phys. Stat. Sol. B 66 (1974) 537.

ELSEVIER

Physica B 273–274 (1999) 330–333

PHYSICA B

www.elsevier.com/locate/physb

On the generation of optically active Er centers in Si light emitting diodes

W. Jantsch*, S. Lanzerstorfer, L. Palmetshofer, M. Stepikhova, G. Kocher, H. Preier

Institut für Halbleiterphysik, Johannes Kepler Universität, A-4040 Linz, Austria

Abstract

Room-temperature electroluminescence is obtained from erbium-doped Si diodes for heavily Er- and oxygen-doped material. Such diodes exhibit under reverse bias excitation a characteristic, about 10–20 nm wide emission spectrum which has a striking similarity to erbium-implanted silica (SiO_2 : Er) in contrast to the sharp line spectra of isolated Er centers seen at lower temperatures. The wide spectrum is thus attributed to the inhomogeneously broadened emission from Er in amorphous $SiO_{2-\delta}$ precipitates. We show that the isolated centers can be transformed into Er-containing precipitates for sufficient Er- and O-doses by proper choice of the annealing temperature after implantation.

Keywords: Rare earth centers; Electroluminescence from Si : Er

One of the present concepts to construct light emitting devices from silicon involves erbium as a dopant [1–3]. The Er^{3+} ion exhibits an internal radiative transition ($J = \frac{13}{2} \rightarrow \frac{15}{2}$) within the incompletely filled 4f shell at a wavelength of 1.54 μm. This transition is utilized already for optical amplification in silica fibers. In Si containing also oxygen, Er was shown to exhibit unexpectedly high quantum efficiencies at low temperatures both for interband excitation and for forward bias in an electroluminescence (EL) diode. At temperatures above about 150 K, however, the luminescence yield is strongly quenched and thus efficient room-temperature operation is not possible [4,5].

Nevertheless, room-temperature electroluminescence has been obtained by several groups from erbium- and oxygen-doped Si diodes operated under reverse bias with much weaker quenching [6–8]. In this paper, we investigate the origin of this type of electroluminescence. In particular, we show that it can be obtained in Er- and O-implanted samples after annealing at 1000°C. The resulting Er centers exhibit an inhomogeneously broadened spectrum that resembles strongly that of SiO_2 : Er, whereas after annealing at 900°C practically only the sharp lines of isolated centers with well-defined geometry and crystal field can be seen. The apparent "transition" temperature of 1000°C between the two types of spectra coincides with the threshold for the formation of SiO_2 precipitates in oxygen-doped Si [9]. We conclude thus that the SiO_2 : Er clusters are responsible for the reverse bias electroluminescence at 300 K and their formation conditions are specified. Embedding Er in SiO_2 provides also a plausible explanation for the inefficient quenching of this type of luminescence; because of the large energy gap, the backtransfer process has much higher activation energy.

The main tool for the identification of Er centers in Si is high-resolution photoluminescence (PL) spectroscopy [10,5]. In Fig. 1 we show spectra of Si implanted with Er with an energy of 300 keV at different doses at 300 K. A 10-times higher dose of O was coimplanted with energies to match the Er profile according to "TRIM"-code simulation. We use the 514 nm line of an Ar laser for the excitation and the spectra are recorded with a Bomem

* Corresponding author: Tel.: + 43-732-2468-9641; fax: + 43-732-2468-9696.

E-mail address: wolfgang.jantsch@jk.uni-linz.ac.at (W. Jantsch)

0921-4526/99/$ - see front matter
PII: S0921-4526(99)00468-8

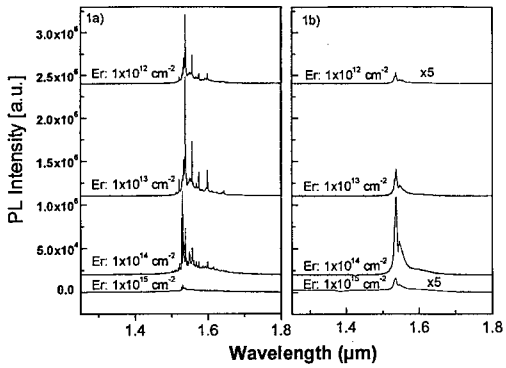

Fig. 1. Photoluminescence spectra at 77 K of Si implanted with Er and O after annealing for 30 min (a) at 900°C and (b) at 1000°C for various Er doses. The oxygen dose was 10 times higher than the Er dose.

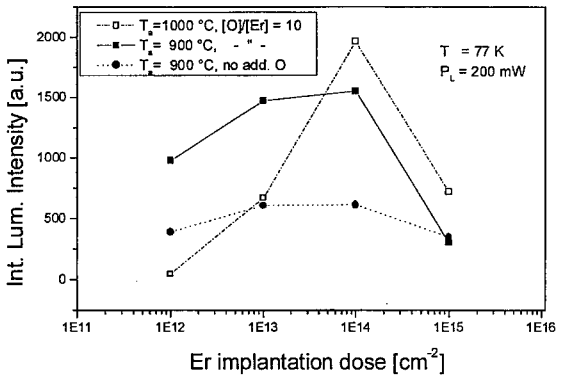

Fig. 2. Integrated PL intensity at 77 K of Si implanted with Er and O (squares) or Er only (dots). Samples were annealed after implantation at 900°C (full symbols) or at 1000°C (open symbols).

DA8 Fourier spectrometer set for $0.5\,cm^{-1}$ resolution. The spectra shown in Fig. 1a were obtained after annealing at 900°C for 30 min in forming gas atmosphere in a lamp-heated oven. The spectra show the sharp lines typical for isolated Er centers, namely the isolated Er interstitial and that of an Er–O complex with lower than cubic symmetry [5,10]. With increasing dose, the PL yield increases first, reaches a maximum for a dose of $1 \times 10^{13}\,cm^{-2}$ (corresponding to a volume concentration of $1.5 \times 10^{18}\,cm^{-3}$ according to TRIM code simulation) and decreases sharply for higher dose.

For comparison, in Fig. 1b PL spectra are given after annealing at 1000°C for 30 min. For these samples we obtain much wider spectra which are very similar to those obtained from Er-doped silica and also from oxidized porous Si [11]. There it was shown that not only the PL spectra are practically identical but also the PL excitation spectra. Attempts to detect the PLE here failed however, possibly because of strong coupling of the excited Er states to states of the surrounding Si host (to our knowledge, PLE due to the excited Er states was never observed for a single-crystal Si host).

Again the peak intensities increase with increasing dose but the maximum yield is obtained at higher dose ($1 \times 10^{14}\,cm^{-2}$ which corresponds to a volume concentration of $1.5 \times 10^{19}\,cm^{-3}$) than for the samples annealed at 900°C. The integral intensities for the two types of spectra are given in Fig. 2. For comparison, the integral PL intensity for a CZ-Si : Er sample without additional O implantation is also given. We observe a strong maximum in the integrated yield for the samples annealed at 1000°C at an Er dose of $1 \times 10^{14}\,cm^{-2}$. The corresponding curves for 900°C annealing show also a maximum, much flatter though. For this annealing temperature, however, the intensity comprises at least two different spectra due to the interstitial Er (dominant up to a dose of $1 \times 10^{14}\,cm^{-2}$) and that of Er–O complexes which become stronger for the higher doses. For high dose, the PL yield decreases for all types of Er centers, most likely because of the formation of other, non-radiative Er precipitates.

The annealing time is also of crucial importance as it was reported already in Ref. [12]. After annealing for a few seconds to minutes, only a wide, unidentified PL peak apparently close to 1.6 μm is seen. This peak is modified already by the sensitivity cut-off of the Ge detector. This luminescence may be connected with extended C-related radiation defects [13] (see also Fig. 3a). With increasing annealing duration, this type of luminescence decreases whereas the SiO_2 : Er luminescence increases. The latter finding is consistent with a migration of Er (and/or O) over some distances as necessary for the formation of clusters or precipitates.

In order to make use of the weaker quenching of the cluster luminescence we produced p–n junctions by implanting Er, O and P into Si : B. In Fig. 3 we compare EL spectra obtained for forward and for reverse bias obtained at 77 K, where both spectra show comparable intensity. The spectrum seen under forward bias shows also the cluster luminescence but in addition also some luminescence near the band edge and the broad peak at 1.6 μm. Under reverse bias, this peak is much weaker. The peak intensity at 1.54 μm is plotted in Fig. 4 for both polarities as a function of temperature. It is clearly seen that under reverse bias, quenching of the cluster luminescence is much less pronounced than under forward bias. For comparison, the intensity of the isolated centers is also shown for forward bias (or, completely equivalent, interband excitation). The excitation efficiency under reverse bias for this type of centers is much smaller than for forward bias and quenching is difficult to follow.

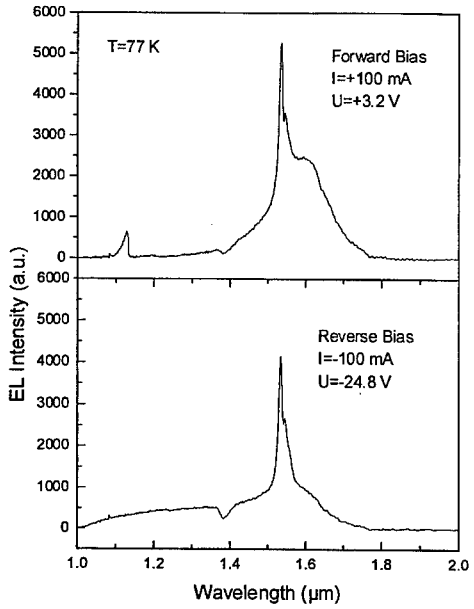

Fig. 3. Electroluminescence spectra of an Si : Er, O diode after annealing at 1000°C for forward and reverse bias.

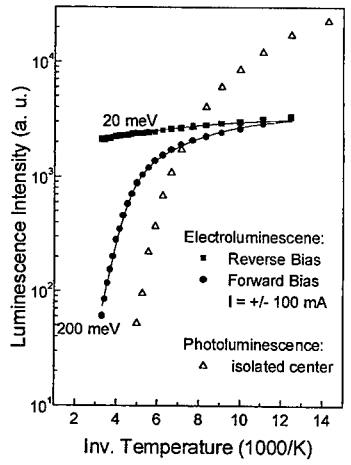

Fig. 4. Electroluminescence peak intensity as a function of inverse temperature for forward and reverse bias. For comparison typical results are given also for the PL peak intensity, in the case of interstitial Er.

The quenching behavior of the SiO_2 : Er clusters and the isolated centers under forward bias is clearly different. In the high-temperature regime, quenching has been attributed to a backtransfer process [4] in which the Er is de-excited non-radiatively by exciting an oxygen-related defect level. The latter is supposed to act as a co-activator, i.e., it participates in the energy transfer from the Si host to the Er 4f states. Apparently, this backtransfer process is less effective for the cluster luminescence. Within this model, the lower backtransfer efficiency is plausible since the backtransfer is a thermally activated process ruled by the difference in the Er activation energy and the activation energy of the coactivator level, and by the coupling between Er and the coactivator states (determined by the overlap of the relevant electronic states). For clusters, the energy gap is much bigger, so backtransfer may occur only to states outside the cluster whose coupling will depend on the cluster size and the distance of the Er within the cluster from its boundary. In any case we expect lower efficiency for the backtransfer for such clusters as seen here.

For reverse bias, quenching is least effective permitting thus room-temperature operation. Reverse bias excitation differs in two aspects: (i) the excitation is achieved by transfer of kinetic energy by hot carriers instead of energy transfer and (ii) the free carrier concentration in the p–n junction is drastically reduced. Free carriers are held responsible for PL quenching by an Auger process and it has been demonstrated that the luminescence decay time is shorter for forward bias than for reverse bias supporting the Auger model [14]. For forward biased diodes, the EL intensity and the decay time have slightly different temperature dependencies, demonstrating also a temperature dependence of the excitation efficiency [15]. Similar investigations for reverse bias are under way.

In summary, we have shown that room-temperature EL can be achieved from Er- and O-implanted Si after annealing at 1000°C under reverse bias. We attribute the spectra seen to SiO_2 : Er clusters formed at these temperatures. The superior quenching behavior of these clusters is attributed to the reduced coupling between the Er states and the Si host which prevents energy backtransfer, the mechanism held responsible for isolated Er centers.

Acknowledgements

Work supported in Austria by the Gesellschaft für Mikroelektronik, and the Fonds zur Förderung der Wissenschaftlichen Forschung, Vienna, Austria.

References

[1] H. Ennen, G. Pomrenke, A. Axmann, K. Eisele, W. Haydl, J. Schneider, Appl. Phys. Lett. 46 (1985) 381.
[2] S. Coffa, G. Franzo, F. Priolo, MRS Bull. 23 (1998) 25.
[3] J. Linnros, F. Priolo, L. Canham (Eds.), Light emission from silicon, progress towards Si-based optoelectronics, Proceedings of the Symposium B, E-MRS 1999, J. Lumin. 80 (1999) 1ff.
[4] F. Priolo, G. Franzo, S. Coffa, A. Carnera, Phys. Rev. B 57 (1998) 4443.

[5] H. Przybylinska, W. Jantsch, Yu. Suprun-Belevitch, M. Stepikhova, L. Palmetshofer, G. Hendorfer, A. Kozanecki, R.J. Wilson, B.J. Sealy, Phys Rev. B 54 (1996) 2532.
[6] J. Stimmer, A. Reittinger, J.F. Nützel, H. Holzbrecher, Ch. Buchal, G. Abstreiter, Appl. Phys. Lett. 68 (1996) 23.
[7] B. Zheng, J. Michel, F.Y.G. Ren, L.C. Kimerling, D.C. Jacobson, J.M. Poate, Appl. Phys. Lett. 64 (1994) 2842.
[8] G. Franzo, S. Coffa, A. Polman, A. Carnera, F. Priolo, Appl. Phys. Lett. 64 (1994) 17.
[9] A. Bourret, in: L.C. Kimerling, J.M. Parsey Jr. (Eds.), Proceedings of the 13th International Conference on Defects in Semiconductors, Metallurgical Society of AIME, New York, 1985, p. 130.
[10] H. Przybylinska, G. Hendorfer, M. Bruckner, L. Palmetshofer, W. Jantsch, Appl. Phys. Lett. 66 (1995) 490.
[11] M. Stepikhova, W. Jantsch, G. Kocher, L. Palmetshofer, M. Schoisswohl, H.J.v. Bardeleben, Appl. Phys. Lett. 71 (1997) 2975.
[12] J. Michel, F.Y.G. Ren, B. Zheng, D.C. Jacobson, J.M. Poate, L.C. Kimerling, Mater. Science Forum 143–147 (1994) 707.
[13] G. Davies, Phys. Rep. 176 (1989) 83.
[14] J. Michel, J. Palm, F. Gan, F.Y.G. Ren, B. Zheng, S.T. Dunham, L.C. Kimerling, Mater. Sci. Forum 585 (1995) 196.
[15] S. Lanzerstorfer, M. Stepikhova, J. Hartung, C. Skierbiszewski, W. Jantsch, Mater. Sci. Forum 1509 (1997) 258–263.

ELSEVIER

Physica B 273–274 (1999) 334–337

PHYSICA B

www.elsevier.com/locate/physb

Effective Auger excitation of erbium luminescence by hot electrons in silicon

M.S. Bresler[a,*], T. Gregorkiewicz[b], O.B. Gusev[a], P.E. Pak[a], I.N. Yassievich[a,c]

[a] *A.F. Ioffe Physico-Technical Institute, Politekhnicheskaya 26, 194021 St. Petersburg, Russia*
[b] *Van der Waals-Zeeman Institute, University of Amsterdam, NL-1018 XE Amsterdam, Netherlands*
[c] *Department of Theoretical Physics, Lund University, S-223 62 Lund, Sweden*

Abstract

In an electroluminescent structure based on erbium-doped crystalline silicon we have found and studied a new mechanism of excitation of erbium ions involving Auger recombination of electrons from the upper subband of the conduction band with holes from the valence band. The new excitation mechanism is weak at low temperatures, but it is resonantly enhanced at 160 K, when the energy distance of the edge of the upper subband of the conduction band from the valence band edge coincides with the energy of the second excited state of the erbium ion due to temperature shrinking of the silicon energy gap. © 1999 Elsevier Science B.V. All rights reserved.

Keywords: Erbium-doped crystalline silicon; Auger excitation; Electroluminescence

The interest to electroluminescent structures based on erbium-doped crystalline silicon is connected with their possible use as light-emitting diodes compatible with silica-glass optical fibers. The most promising results up to now were obtained with p–n junction electroluminescent structures operating at reverse bias in which the n-region was doped by erbium (it is well known that erbium–oxygen complexes introduce donor states in silicon) [1–7]. In these works [1–4,6,7] hot-electron luminescence besides erbium luminescence was observed and the excitation process was attributed to impact excitation of erbium ions produced by hot electrons.

In the present work we demonstrate that in a reversely biased p–n junction another efficient excitation mechanism can occur which is a resonance Auger process.

Electroluminescent structures with p^+–n^+ junctions provided by N.A. Sobolev (Ioffe Institute) were fabricated by co-implantation of erbium and oxygen in a crystalline silicon substrate doped by phosphorus (n^+-layer) and implantation of boron onto the substrate surface (p^+-layer) [7]. Our structures differed from those described in Refs. [1–6] in that they were fabricated from (1 1 1) rather than (1 0 0) substrates and erbium concentration in them was lower, not exceeding 2×10^{17} cm^{-3}. The I–V characteristics had a conventional rectifying shape. Erbium luminescence was measured at reverse bias on the structure as a function of temperature in the temperature range 77–300 K. Parallel with the measurements of the luminescence intensity the voltage on the structure at constant current through it or the current at constant voltage were registered during the temperature runs. The electroluminescence (EL) spectra at $T = 77$ and 300 K consisted of lines of erbium emission at 1.54 μm and a broad band of luminescence induced by hot electrons.

In Fig. 1a temperature dependences of the intensity of erbium EL are given and the voltage on p^+–n^+ junction of the electroluminescent structure for two values of current through the structure. In the temperature range 140–160 K, where the intensity of erbium EL at 1.54 μm sharply increases, a rise of the voltage on the p–n junction (in the constant current regime) simultaneously

* Corresponding author: Tel.: + 7-812-247-9140; fax: + 7-812-247-1017.
E-mail address: mikhail.bresler@pop.ioffe.rssi.ru (M.S. Bresler)

0921-4526/99/$ - see front matter
PII: S0921-4526(99)00470-6

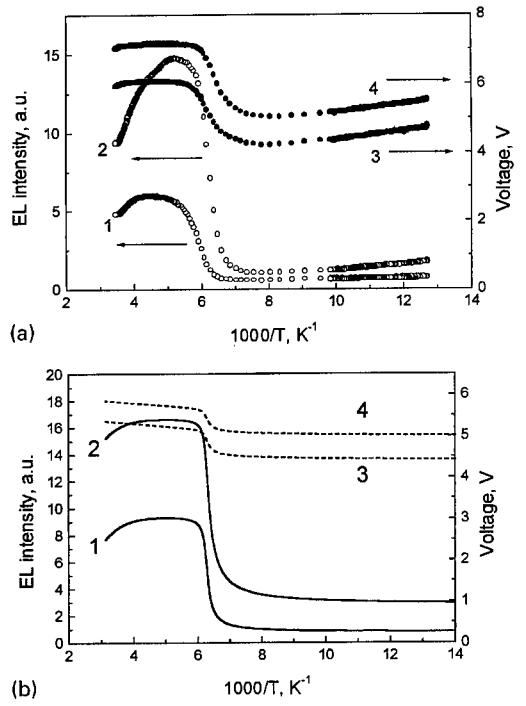

Fig. 1. Experimental (a) and calculated (b) temperature dependences of erbium EL intensity (1,2) and voltage drop on p–n junction (3,4) in the constant current regime for two values of current through the structure: (1,3) 60 mA; (2,4) 240 mA.

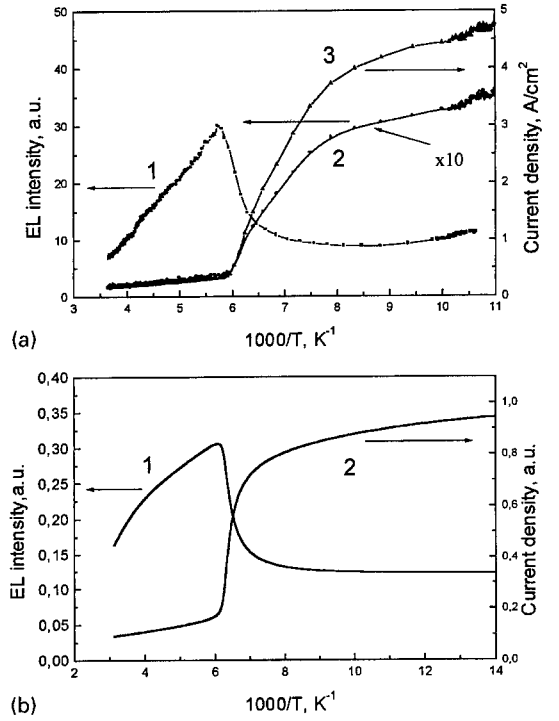

Fig. 2. Experimental (a) and calculated (b) temperature dependences of erbium EL intensity (1) and current through the structure (2) in the constant bias regime; (3) hot-electron EL intensity.

occurs. This fact points to annihilation of electron–hole pairs in the process of excitation of erbium EL, i.e. a strong recombination mechanism is switched on (the resistance of the p–n junction increases). To check this assumption we have measured temperature dependences of the intensities of erbium EL, hot electron EL ($\lambda = 1.35$ μm) and current through the sample at constant bias at p-n junction (Fig. 2a). In the temperature range around 160 K an abrupt jump of erbium EL is observed which is accompanied by a significant drop of the current through the p^+–n^+ junction and of the intensity of hot electron EL. This result draws unambiguously to the conclusion that the process of erbium excitation occurs via Auger recombination of nonequilibrium carriers rather than impact excitation.

Auger excitation of erbium ions involving the recombination of conduction electrons with free holes was considered by Yassievich and Kimerling [8]. (The energy band diagram demonstrating this process is shown in Fig. 3.) They have shown that in the case of recombination of electrons from the main Δ_1 subband of the conduction band with free holes the Auger process is highly inefficient, since the Bloch amplitudes of these bands are orthogonal. On the other hand, the probability of an Auger process with the participation of the electrons from the upper Δ_2' subband is fairly high. It is important

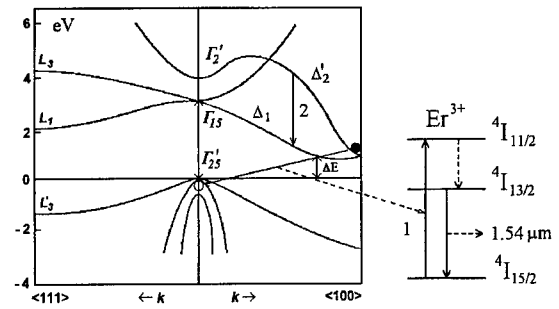

Fig. 3. Energy band diagram with schematic representation of the Auger process of erbium ion excitation (1) and optical transitions responsible for hot electron EL (2).

also that the recombination energy of the Δ_2' electrons with the holes is close to an energy of the transition of an erbium ion from the ground $^4I_{15/2}$ to the second excited state $^4I_{11/2}$(1.26 eV). We assume that the energy of Auger recombination of the Δ_2' electrons and the valence band holes at 77 K is slightly larger than that of the $^4I_{15/2}$–$^4I_{11/2}$ transition in the 4f shell of the Er^{3+} ion, and therefore such a transition can occur only with emission of phonons. The rise of the temperature to 160 K leads to a shrinking of the silicon energy gap by 10 meV approximately, and the Auger recombination with excitation of

Er^{3+} ion from the ground $^4I_{15/2}$ to the second excited state $^4I_{11/2}$ of 4f-shell becomes resonant. This results in a sharp increase of the rate of the Auger excitation process, the efficiency of which is very high (cf. Fig. 2a). Due to the symmetry properties of the Bloch amplitudes of the conduction and the valence bands [9] the electrons making tunnel transitions in the reversely biased p–n junction appear predominantly in the Δ_2' subband of the conduction band.

The broad band observed in the EL spectrum is caused by allowed optical transitions of electrons heated by electric field in the Δ_2' subband to the Δ_1 subband. The reduction of the intensity of hot electron EL simultaneously with the sharp rise of erbium EL in the same temperature range (cf. Fig. 2a) points directly to an Auger excitation of erbium ions with a participation of electrons from the Δ_2' subband of the conduction band.

The probability of the Auger process under discussion is proportional to a product of concentration of nonequilibrium electrons n by concentration of equilibrium holes in the depletion layer of the p–n junction, which is controlled by a temperature tail of the Boltzmann distribution: $p = p_0 \exp(-q\Phi/kT)$, where p_0 is the concentration of holes in the p^+ contact, Φ is a characteristic potential at the point of maximum electric field in the p–n junction (due to high concentration of holes in the p-region (5×10^{19} cm^{-3}) and comparatively low concentration of electrons in the n-layer (2×10^{17} cm^{-3}) this point is very close to the p-contact).

The experimental results can be described with the set of balance equations for the concentration of nonequilibrium electrons generated in the "active" zone (p–n junction) and the concentration of excited erbium ions

$$G = \gamma n p_0 \exp(-q\Phi/kT) N_t + nv/L, \tag{1}$$

$$\gamma n p_0 \exp(-q\Phi/kT)(N_{Er} - N^*_{Er}) = N^*_{Er}\left[\tau_r^{-1} + a p_0 \exp(-q\Phi/kT) + \tau_0^{-1} \exp\left(-\frac{E_{ac}}{kT}\right)\right], \tag{2}$$

where G is the generation rate of nonequilibrium carriers in the p–n junction due to tunnel transitions, γ is the coefficient of Auger-excitation of erbium ions, a is the coefficient of de-excitation of erbium ions due to their interaction with free holes, N^*, N_{Er}, and N_t are concentration of excited erbium ions, concentration of optically active erbium ions and total concentration of erbium ions, respectively, L is the thickness of the p–n junction, and τ_r is the radiative lifetime of an erbium ion in the excited state. We have included also the back-transfer de-excitation mechanism which contributes a term $\tau_0^{-1} \exp(-E_{ac}/kT)$ to the probability of de-excitation of erbium ion. (This back-transfer process corresponds to a generation of an electron on previously empty donor and a hole in the valence band; the donor states are depopulated in the high electric field of the p–n junction.) The characteristic energy of the back-transfer process is $E_{ac} = E_g - E_{ff'} - E_d$ where $E_g = 1.17$ eV is the silicon bandgap, $E_{ff'} = 0.8$ eV the excitation energy of an erbium ion and $E_d = 0.15$ eV the energy of the donor level connected with the erbium–oxygen complex.

The concentration of free electrons in the region of erbium ions excitation (in the p–n junction) is controlled by two factors: Auger recombination of free electrons with holes and drift of electrons from the "active" zone under the action of high electric field with a limiting velocity v.

In the regime of constant current through the structure j_0

$$I_{EL} = I_{EL}^{max} \frac{\gamma j_0}{va\,q}\left[\frac{\gamma j_0}{va\,q} + 1\right]^{-1} = I_{EL}^{max} \sigma\tau(j_0/q)[\sigma\tau(j_0/q) + 1]^{-1}, \tag{3}$$

where $I_{EL} = N^*/\tau_r$, $I_{EL}^{max} = N_{Er}/\tau_r$ and we have introduced the notations $\sigma = \gamma p_0 \exp(-q\Phi/kT)/v$ and $\tau^{-1} \approx (a p_0 \exp(-q\Phi/kT) + \tau_0^{-1} \exp(-E_{ac}/kT)) \gg \tau_r^{-1}$.

We assume that γ and a are independent of the temperature both below and above the resonance, but a does not depend on the temperature in the whole temperature range involved, while γ reveals a significant jump at the threshold (at $T = 160$ K). Then at low temperatures the intensity of erbium luminescence is proportional to the current whereas at high temperatures the system is close to saturation and the dependence on the current only demonstrates to what extent the saturation is incomplete.

At constant current through the p–n junction the electric field applied to the structure can be represented by the expression characteristic for thermally activated tunneling

$$E = E_c(\ln((j_0/(qGL))[\sigma N_t L + 1]))^{1/2}, \tag{4}$$

where E_c is a characteristic electric field.

A strong enhancement of σ at the resonance threshold leads to a marked rise of the voltage on the structure. Since σ enters the logarithm argument, the change in the voltage is much weaker than the variation of σ.

In the constant voltage regime according to the formula

$$j = j_0/(\sigma N_t L + 1), \tag{5}$$

the current starts to decrease compared to the j_0 value even below the resonance threshold due to an increase of hole concentration in the recombination region and

suffers an additional drop at the threshold. A further decrease of the current at higher temperatures is connected again with the rise of the hole concentration (γ is again constant above the threshold).

The intensity of electroluminescence in this regime is

$$I_{EL} \approx I_{EL}^{max}\sigma\tau(j_0/q)[\sigma\tau(j_0/q) + \sigma N_t L + 1]^{-1}. \quad (6)$$

We have calculated the intensity of erbium EL, voltage on the structure (in the constant current regime) and current through the structure (in the constant reverse bias regime) using formulas (3)–(6). The results of calculations are shown in Fig. 1b and Fig. 2b. It is clear that the calculated temperature dependences are in fair agreement with the experimental results.

In conclusion, we have demonstrated that a new mechanism of excitation of erbium ions, i.e. an Auger recombination process with participation of Δ_2' electrons and valence band holes, acts in reversely biased EL structures based on erbium-doped crystalline silicon.

This work was supported by the grants 98-02-18246 and 99-18079-a from the Russian Foundation of Basic Research, the grant 97-1036 of Russian Ministry of Science and NATO Linkage grant HTECH. LG 972032. I.N.Y. thanks Swedish Natural Science Research Council for financial support (grant O-AH/KG 03996-322).

References

[1] S. Lombardo, S.U. Campisano, J. Appl. Phys. 77 (1995) 6504.
[2] J. Stimmer et al., Appl. Phys. Lett. 68 (1996) 3290.
[3] S. Coffa, G. Franzo, F. Priolo, Appl. Phys. Lett. 69 (1996) 2077.
[4] G. Franzo, S. Coffa, F. Priolo, C. Spinella, J. Appl. Phys. 81 (1997) 2784.
[5] M. Matsuoka, Sh. Tohno, Appl. Phys. Lett. 71 (1997) 96.
[6] N.A. Sobolev, A.M. Emel'yanov, K.F. Shtel'makh, Appl. Phys. Lett. 71 (1997) 1930.
[7] A.M. Emel'yanov, N.A. Sobolev, A.N. Yakimenko, Appl. Phys. Lett. 72 (1998) 1223.
[8] I.N. Yassievich, L.C. Kimerling, Semicond. Sci. Technol. 8 (1993) 718.
[9] G.L. Bir, G.E. Pikus, Symmetry and strain-induced effects in semiconductors, Israel Program Sci. Translations, Jerusalem, 1974.

ELSEVIER

Physica B 273–274 (1999) 338–341

PHYSICA B

www.elsevier.com/locate/physb

The photoluminescence mechanism of erbium in silicon: intensity dependence on excitation power and temperature

D.T.X. Thao[a,b,*], C.A.J. Ammerlaan[a], T. Gregorkiewicz[a]

[a] *Van der Waals-Zeeman Institute, University of Amsterdam, Valckenierstraat 65-67, NL-1018 XE Amsterdam, Netherlands*
[b] *International Training Institute for Materials Science, ITIMS building, Dai hoc Bach khoa, Hanoi, Viet Nam*

Abstract

The photoluminescence intensity of erbium in silicon was measured as a function of laser excitation power and temperature. Results of these measurements are described on the basis of a physical model which includes the formation of free excitons, the binding of excitons to erbium ions, excitation of 4f-shell electrons of erbium ions and decay of excited erbium ions by light emission. An Auger energy transfer to free carriers by both erbium-bound excitons and excited erbium ions must be included in the model in order to obtain a quantitative agreement with experiment. From the temperature dependence two activation energies are derived, which are associated with the binding of excitons to erbium centers and with an energy transfer process from excited erbium ions back to erbium-bound excitons, respectively. The luminescence properties of the different types of Er-doped crystalline silicon are remarkably similar.

Keywords: Silicon; Erbium; Photonics; Photoluminescence

1. Introduction

The luminescence of erbium in silicon has triggered considerable research activity in recent years. From a fundamental point of view, the chain of processes through which the energy imparted to s and p electrons of the host crystal is transferred to the final step of light emission in the $^4I_{13/2}$ to $^4I_{15/2}$ transitions of 4f inner-shell electrons is a challenging topic. The particular emission wavelength of 1.54 μm, as a wide-band carrier for long-distance signal transport via glass fibers, stimulated application-oriented research. In particular, the efficiency of the light generation and its dependence on temperature are important topics.

In the present experiments, the photoluminescence (PL) from erbium in silicon was measured in crystalline float-zoned and Czochralski-grown samples and in a sample grown by a sublimation MBE method. The characteristic luminescence spectra, in the wavelength range between 1.5 and 1.6 μm, were observed. The different line structures of the spectra, which reflect the crystal-field effect, revealed the presence of optically active centers of different symmetry and/or atomic structure, in individual samples. The dependence of the photoluminescence intensity on Ar^+ laser excitation power and on the temperature was measured and analyzed on the basis of the excitonic luminescence model with the aim of achieving quantitative agreement.

2. Experimental

In the experiments three different kinds of samples were used. The first sample was prepared from

* Correspondence address: Van der Waals-Zeeman Institute, University of Amsterdam, Valckenierstraat 65-67, NL-1018 XE Amsterdam, Netherlands. Tel.: + 31-20-525-5642; fax: + 31-20-525-5788.

E-mail address: thao@wins.uva.nl (D.T.X. Thao)

0921-4526/99/$ - see front matter
PII: S0921-4526(99)00471-8

Czochralski-grown silicon by erbium and oxygen implantation (Cz-Si:Er,O), followed by annealing for 30 min at the temperature of 900°C. The peak Er concentration was $10^{17}\,cm^{-3}$. The second sample was prepared from float-zoned silicon implanted with Er (Fz-Si:Er) at an elevated temperature of 500°C to a peak concentration of $4\times10^{17}\,cm^{-3}$. No co-implants were done and no further heat treatment was applied. The third sample was a crystalline silicon layer of 2 μm thickness, which was grown by a sublimation MBE method at 500°C on top of a p-type silicon wafer, followed by annealing at 700°C for 30 min (MBE-Si:Er). The sample had an Er concentration of $10^{18}\,cm^{-3}$.

Luminescence was excited by the 514.5 nm line of an Ar^+-ion laser. The laser power could be varied in the range of 1 μW to 10 mW and was focused on a spot of about 1 mm diameter measured in front of the sample dewar. The temperature of samples was measured by a RhFe metallic resistor in a four-point-probe configuration to an accuracy of 0.1 K. Temperature measurements were performed in the range of 4–200 K. The PL signal was detected by a Ge-detector cooled by liquid nitrogen.

3. Model and discussion

3.1. Excitonic luminescence model

In the model the overall process of energy transfer in the Er-doped Si is considered. The process starts with the formation of electron–hole pairs by the incident light, at the rate G, followed by free-exciton creation with the rate $\gamma_x n^2$. Free excitons can be bound at erbium-related traps, which will occur proportional to their concentration n_{Er} and the available unoccupied fraction $[(n_{Er}-n_{xb})/n_{Er}]$, where n_{xb} denotes the concentration of excitons trapped at Er-related centers. Er-bound excitons can transfer their energies in an Auger process with a transfer time τ^* to the 4f electrons of a Er ion in the ground state, i.e., proportional to fraction $[(n_{Er}-n^*_{Er})/n_{Er}]$. Finally, the Er PL follows from decay of the excited Er ions with a temperature-stable radiative decay time τ_d: $I\propto n^*_{Er}/\tau_d$. Competing recombination paths included in the model are the alternative electron–hole recombinations with the rate γn^2, the direct recombination of free excitons or their recombination via alternative centers with the lifetime τ_x and the thermally induced dissociation of Er-bound excitons into free excitons. Apart from these, two Auger processes, which remove energy from the PL path, should be accounted for in the competition paths. They are related to Er-bound excitons and excited Er ions and dissipate energy to free electrons in the conduction band. Based on the above description the following balance equations can be written for free electrons (n), free excitons (n_x), Er-bound excitons (n_{xb}) and excited Er ions (n^*_{Er}), respectively:

$$G+fn_x=\gamma n^2+\gamma_x n^2, \tag{1}$$

$$\gamma_x n^2+cf_{xb}n_{xb}N_x=cn_xn_{Er}\frac{n_{Er}-n_{xb}}{n_{Er}}+fn_x+\frac{n_x}{\tau_x}, \tag{2}$$

$$cn_xn_{Er}\frac{n_{Er}-n_{xb}}{n_{Er}}+n^*_{Er}f_1\frac{1}{\tau^*}=n_{xb}\frac{n_{Er}-n^*_{Er}}{n_{Er}}\frac{1}{\tau^*}+cf_{xb}n_{xb}N_x+c_{Ax}nn_{xb} \tag{3}$$

and

$$n_{xb}\frac{n_{Er}-n^*_{Er}}{n_{Er}}\frac{1}{\tau^*}=\frac{n^*_{Er}}{\tau_d}+n^*_{Er}f_1\frac{1}{\tau^*}+c_{AEr}nn^*_{Er}, \tag{4}$$

where $f=\gamma_x(N_cN_v/N_x)e^{-E_x/kT}$, $f_{xb}=e^{-E_{xb}/kT}$ and $f_1=e^{-E_A/kT}$; E_x, E_{xb} and E_A are the binding energy of electron and hole in a free exciton, the exciton binding energy on the Er-related trap and the energy dissipated in the creation of an excited Er ion from the bound exciton situation, respectively. N_c, N_v and N_x are temperature-dependent densities of states in conduction, valence and exciton bands, respectively. Similar set of rate equations, but without Auger processes, has been developed earlier [1].

3.2. Excitation power dependence

The power dependence of the PL intensity was measured at low temperature. In this case, we can simplify the equations by putting $f=f_{xb}=f_1=0$. Solving Eqs. (1)–(4), an approximate solution for n^*_{Er}/n_{Er} is derived as

$$n^*_{Er}/n_{Er}=c_2G/(b_0+b_1G^{1/2}+b_2G+b_3G^{3/2}), \tag{5}$$

where b_0, b_1, b_2, b_3 and c_2 are temperature-independent factors. In the high-power limit this result yields $n^*_{Er}\sim 1/G^{1/2}$ or $n^*_{Er}\sim 1/n$ resulting in a decrease of PL intensity. This decrease of Er PL has not been observed in the present experiments, nor has it been reported in the literature. A numerical estimate [2] shows that such an effect corresponds to a high value of G, about $10^{26}\,cm^{-3}\,s^{-1}$, which is not reached in actual experiments. For this reason, under the usual experimental conditions linear increase at low power with $(c_2/b_0)G$ is observed, followed by saturation at the level c_2/b_2. Using the normalized units for power $P\equiv G/G_1$ with $G_1=b_0/b_2$ and for PL intensity $I\equiv(n^*_{Er}/n_{Er})/(c_2/b_2)$, Eq. (5), for the case of strong Auger processes, will read

$$I=\frac{P}{1+\beta\sqrt{P}+P} \tag{6}$$

with

$$\beta=\left(\frac{c_{AEr}\tau_d}{c_{Ax}\tau^*}\right)^{1/2}+\left(\frac{c_{Ax}\tau^*}{c_{AEr}\tau_d}\right)^{1/2}. \tag{7}$$

The PL has linear increase at low power with $I = P$ and saturates at high power at $I = 1$. Therefore, characteristic features of the luminescence process are only revealed at intermediate power, e.g. at $P = 1$, where $I = 1/(2 + \beta)$. In Fig. 1 theoretical curves for $\beta = 0$ and 2 are presented. The experimentally obtained power dependence of the PL intensity of sample Cz-Si:Er,O is plotted in the inset. The solid line is the best fit to the data with Eq. (6), yielding $\beta = 2.25$. Similar fits made for samples Fz-Si:Er and MBE-Si:Er gave $\beta = 2.63$ and 3.3, respectively. With Eq. (7) this result is converted to $(c_{AEr}\tau_d/c_{Ax}\tau^*)^{\pm 1} \approx 4$ for implantation samples and ≈ 9 for the MBE sample. This can be compared with the published data for $c_{AEr} = 10^{-12}\,\mathrm{cm^3\,s^{-1}}$, $\tau_d = 10^{-3}\,\mathrm{s}$, $c_{Ax} = 10^{-10}\,\mathrm{cm^3\,s^{-1}}$ and $\tau^* = 4 \times 10^{-6}\,\mathrm{s}$ [3]. One concludes that $c_{AEr}\tau_d/c_{Ax}\tau^*$ is very similar in the three kinds of investigated material. Although this can be due to an accidental combination of parameters, one is tempted to believe that all process parameters, i.e., c_{AEr}, τ_d, c_{Ax} and τ^*, have similar, material-independent values. In such a case the differences in structure of the luminescent centers in the three materials, as evidenced by their PL spectra, have very little influence on the efficiency of the Er PL process.

3.3. Temperature dependence

For an analysis of the Er PL temperature dependence, the set of Eqs. (1)–(4) is considered in its complete form. The solution of n^*_{Er}/n_{Er} is obtained also in the form of Eq. (5), but in this case the coefficients are temperature dependent as they include the state densities in conduction, valence and exciton bands and the functions f, f_{xb} and f_1. At low temperatures, Eq. (5) will give the solution $(n^*_{Er}/n_{Er})_{T=0}$. For the practical purpose of comparing model predictions with experimental results it is useful to express measured intensities normalized to the low-temperature value, i.e., $(n^*_{Er})_T/(n^*_{Er})_{T=0}$. After some approximations one can obtain a final solution

$$(n^*_{Er})_T/(n^*_{Er})_{T=0} = 1/[1 + AN_x\tau^* e^{-E_{xb}/kT} + BN_x\tau_d e^{-(E_{xb}+E_A)/kT}]. \quad (8)$$

Eq. (8) can be rewritten as

$$[(n^*_{Er})_{T=0}/(n^*_{Er})_T - 1]/T^{3/2} = N_x/T^{3/2}[A\tau^* e^{-E_{xb}/kT} + B\tau_d e^{-(E_{xb}+E_A)/kT}] \quad (9)$$

with $A \approx B$. Note that the binding energy of an electron–hole pair in a free exciton E_x does not appear in the solution. The ratio between the two pre-exponential factors is about equal to τ_d/τ^*. Fig. 2 represents experimental data for the sample Cz-Si:Er,O with the solid line as the best fit to Eq. (8). Two activation energies, which are necessary to fit the measured data, are represented in the inset by two straight lines. Results for the three samples measured at an intermediate power are given in Table 1. Fits are performed using a $T^{3/2}$ term in the pre-exponential factors. In the literature, however, analyses with temperature-independent pre-exponential factors prevail. The first activation energy is identified as the binding energy E_{xb} of an exciton at the Er-related trap. At temperatures above 100 K a second energy of about 110 meV becomes significant. At high temperatures the PL intensity has already decreased; this energy therefore cannot be determined with high accuracy. An error limit of at least 10 meV has to be accepted. Following our analysis, this energy corresponds to $E_{xb} + E_A$, leading to the experimental result $E_A \approx 100$ meV. By the physical model E_A is given as $E_A = E_g - E_x - E_{xb} - E_{PL} - E_d$. With estimates for silicon band gap energy $E_g =$

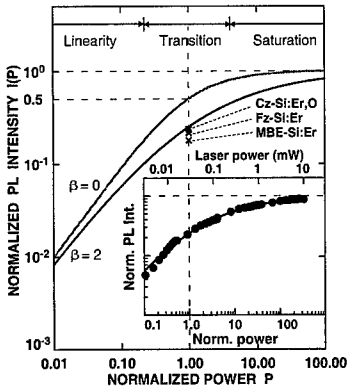

Fig. 1. Normalized luminescence intensity I as a function of normalized laser power P with $\beta = 0$ and 2. The experimental data points (×) at $P = 1$ are given for three samples. The inset shows the Er PL intensity versus excitation power with the solid line as the best fit to Eq. (6) for sample Cz-Si:Er,O.

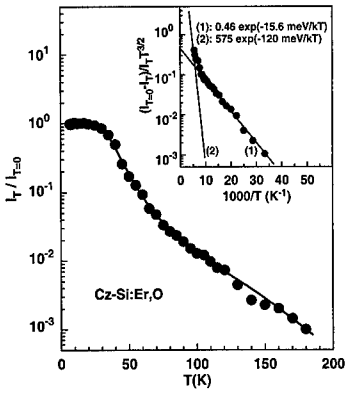

Fig. 2. PL intensity as a function of sample temperature normalized to the yield at low temperature. The solid line is the fit with Eq. (8). The inset plots $(I_{T=0} - I_T)/I_T T^{3/2}$ as a function of reciprocal temperature illustrating the analysis based on Eq. (9) for sample Cz-Si:Er,O.

Table 1
Activation energies and their corresponding pre-exponential factors following from the fits with Eq. (9) for the investigated samples. Notation $A_1 = A\tau^* N_x/T^{3/2}$ and $B_1 = B\tau_d N_x/T^{3/2}$ is used

Sample	A_1 ($K^{-3/2}$)	E_{xb} (meV)	B_1 ($K^{-3/2}$)	$E_{xb} + E_A$ (meV)
Cz-Si:Er,O	0.46	15.6	575	120
Fz-Si:Er	0.04	12.2	32	92
MBE-Si:Er	0.006	3.6	370	123

1170 meV, electron–hole binding energy $E_x = 15$ meV, exciton binding energy to Er center $E_{xb} = 15$ meV, PL energy $E_{PL} = 800$ meV, a donor ionization energy of $E_d = 240$ meV is required. This is close to the level position at 266 meV as reported in Ref. [4] for the same Fz-Si sample as used in this experiment. The order of magnitude between two pre-exponential factors estimated as $\tau_d/\tau^* \approx 10^3$ is in agreement with time constants found experimentally. The small E_{xb} in the MBE-Si:Er sample and the much larger τ_d/τ^* value may be related to a much larger Er concentration in this material.

4. Conclusion

The dependence of Er PL intensity on excitation power and temperature has been measured and analyzed by a physical model. A satisfactory agreement could be obtained by the consistent use of normalized units for both PL intensity and excitation power. The thermal dependence is governed by the binding energy of excitons to Er centers in the temperature range below 100 K. At higher temperatures, an activation energy about 100 meV becomes more prominent. This energy is associated with the energy back-transfer from an excited Er into an Er-bound exciton. The physical properties are similar for all Er-doped crystalline samples and are consistent with numerical data published in the literature.

Acknowledgements

Samples for the reported experiments were kindly provided by F.P. Widdershoven, Philips Research, Eindhoven, The Netherlands, by N.A. Sobolev, A.F. Ioffe Physico-Technical Institute, St. Peterburg, Russia and by B.A. Andreev and Z.F. Krasil'nik, Institute for Physics of Microstructures, Nizhny Novgorod, Russia.

References

[1] M.S. Bresler, O.B. Gusev, B.P. Zakharchenya, I.N. Yassievich, Phys. Solid State 38 (1996) 813 [translation from Fiz. Tverd. Tela 38 (1996) 1474].
[2] D.T.X. Thao, C.A.J. Ammerlaan, T. Gregorkiewicz, J. Appl. Phys., submitted for publication.
[3] J. Palm, F. Gan, B. Zheng, J. Michel, L.C. Kimerling, Phys. Rev. B 54 (1996) 17 603.
[4] F.P. Widdershoven, J.P.M. Naus, Mater. Sci. Eng. B 4 (1989) 71.

ELSEVIER

Physica B 273–274 (1999) 342–345

PHYSICA B

www.elsevier.com/locate/physb

Er–O clustering and its influence on the lattice sites of Er in Si

U. Wahl[a,*], J.G. Correia[b], J.P. Araújo[c], A. Vantomme[a], G. Langouche[a], the ISOLDE collaboration[b]

[a]*Instituut voor Kern-en Stralingsfysica, Universiteit van Leuven, Celestijnenlaan 200 D, B-3001 Leuven, Belgium*
[b]*CERN-EP, CH-1211 Geneva 23, Switzerland*
[c]*IFIMUP, University of Porto, P-4150 Porto, Portugal*

Abstract

We present emission channeling experiments on the lattice location of Er in CZ Si single crystals with a well-defined O concentration of $6.5–6.6 \times 10^{17}\,cm^{-3}$ and 60 keV-implanted Tm + Er doses ranging from 4.3×10^{12} to $3.6 \times 10^{13}\,cm^{-2}$. The experimental results are compared with the predictions of a simulator which models the formation of Er_nO_m clusters on the basis of simple diffusion and capture kinetics. We find that our experimental data compare favorably with a scenario where the formation of Er_nO_m defects with one or more O atoms is responsible for removing the Er atoms from their tetrahedral interstitial (T) sites. This suggests that Er does no longer occupy the T site even in simple (ErO) pairs.

Keywords: Lattice location; Er in Si; Implantation

1. Introduction

The presence of O is known to increase the luminescence from Er-related centers in Si. It can be regarded as proven that O forms complexes with Er which directly modify the structural, electrical and optical properties of Er [1–15]. However, there is also strong evidence that, possibly apart from ErO complex formation, additional mechanisms exist as to how O enhances the Er luminescence yield [6,7]. More knowledge on the composition and microscopic properties of ErO complexes can help to better understand the different mechanisms. Presently, engineering the optimum atomic neighborhood of Er in Si will be helpful in maximizing the luminescence output of Er-based light-emitting devices.

As a first step in order to allow a comparison of possible scenarios of Er_nO_m clustering with experimental data we have developed a simulator that allows to model the interaction of Er and O during high-temperature annealing on the basis of simple diffusion and capture kinetics [14]. Previously we have compared predictions of the simulator with experimental results on the lattice location of radioactive ^{167m}Er, which was determined by means of conversion electron emission channeling [14]. Experimentally, it was found that during annealing at 900°C the interaction of Er and O leads to a removal of Er from near-tetrahedral interstitial (T) lattice sites. In O-rich Czochralski (CZ) Si with a shallow Er profile close to the surface, the time scale for this process is limited by the out-diffusion of O from the bulk of the sample. The remaining fraction of Er on near-T sites therefore shows qualitatively a $1-C_{Ox}/(m_{av}\phi)(D_{Ox}t)^{1/2}$ behavior, where t is the time of annealing, C_{Ox} and D_{Ox} the concentration and diffusion coefficient of oxygen, ϕ the implanted Er dose, and m_{av} the average number of O atoms needed to remove one Er atom from its T site. However, since the oxygen concentration in our previous CZ Si samples was only known within an order of magnitude, an accurate estimate on the mean number m_{av} of O atoms was difficult. In this contribution we present the results of recent emission channeling experiments in CZ Si single crystals with a well-defined O concentration.

* Corresponding author. Tel.: + 32-16-327617; fax: + 32-16-327985.
E-mail address: ulrich.wahl@fys.kuleuven.ac.be (U. Wahl)

0921-4526/99/$ - see front matter
PII: S0921-4526(99)00472-X

2. Method

The preparation of 60 keV ^{167}Tm ($t_{1/2} = 9.45$ d) implanted samples at CERN's ISOLDE facility and the emission channeling lattice location experiments using conversion electrons from ^{167m}Er ($t_{1/2} = 2.28$ s) have been described in previous publications [8,13,16]. For our recent experiments we used *n*-Si : P CZ single crystals (⟨1 1 1⟩ orientation, 7.3–12 Ω cm) with an oxygen concentration of $6.5\text{–}6.6 \times 10^{17}$ cm^{-3}. The implanted doses of Er + Tm were 4.3×10^{12} cm^{-2} (sample A, resulting in a peak concentration of $[\text{Er} + \text{Tm}]_{max} = 2.0 \times 10^{18}$ cm^{-3}), 5.7×10^{12} cm^{-2} (B, 2.7×10^{18} cm^{-3}), 6.8×10^{12} cm^{-2} (C, 3.2×10^{18} cm^{-3}), 1.2×10^{13} cm^{-2} (D, 5.7×10^{18} cm^{-3}), 2.3×10^{13} cm^{-2} (E, 1.1×10^{19} cm^{-3}), and 3.6×10^{13} cm^{-2} (F, 1.7×10^{19} cm^{-3}). A filament that heats the back-side of the Ta sample holder allowed in situ thermal processing in the channeling goniometer at $< 10^{-6}$ mbar. The temperature was measured by two thermocouples attached to the sample holder, and the annealing time given is the time after reaching the setpoint temperature. Due to the temperature gradients between the thermocouples, the sample holder and the sample surface, the temperature uncertainty amounts to ± 15°C. Quantitative identification of Er atoms on near-T interstitial sites was achieved through fitting the experimental electron emission yields by theoretical channeling patterns calculated for these lattice sites [8,13,16].

The mathematical simulator which models the diffusion of Er and O and the formation of Er_n and Er_nO_m clusters has been described in Ref. [14]. The starting situation is a Gaussian depth profile of 60 keV implanted Er (mean depth 336 Å, FWHM 195 Å) and a constant O profile. Both Er and O are allowed to diffuse at 900°C, and, assuming that they interact with each other within certain capture radii which we derive from the mean volume of the defects, a set of coupled differential equations determines the concentrations $C_{Er(n)O(m)}$ of Er_nO_m complexes. These equations are solved by the method of finite differences. This means that the concentrations $C_{Er(n)O(m)}$ of all desired Er- and O-containing clusters are updated within finite time intervals Δt and depth intervals Δx. The diffusion coefficients of erbium ($D_{Er} \approx 10^{-15}$ cm^2 s^{-1} at 900°C) [2] and oxygen [$D_{Ox} = 0.13$ cm^2 s$^{-1} \times$ exp(− 2.53 eV/kT), corresponding to 1.8×10^{-12} cm^2 s^{-1} at 900°C] [17] are taken from the literature. All complexes are assumed to be thermally stable and immobile. However, formation of O_2 dimers and oxygen precipitation are neglected since the dimers are unstable at 900°C, and O precipitation occurs at this temperature only on time scales of the order of 100 h [17].

3. Results

Fig. 1 shows the normalized fraction of Er remaining on near-T sites as a function of isothermal annealing time

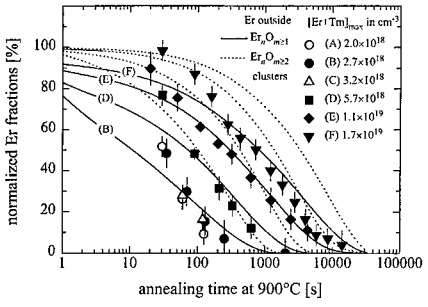

Fig. 1. The data points are the fractions of ^{167m}Er atoms which are left on near-T sites in CZ Si as a function of isothermal annealing time at 900°C, observed by emission channeling experiments in samples with an oxygen concentration of $6.5\text{–}6.6 \times 10^{17}$ cm^{-3}. Solid lines: fractions of Er remaining outside $Er_nO_{m\geq1}$ clusters calculated for four different Er + Tm peak concentrations according to the model described in the text; dashed lines: the same for all Er remaining outside $Er_nO_{m\geq2}$ clusters.

at 900°C for all 6 CZ Si samples investigated in the present study. The qualitative behavior with respect to the implanted Er dose is similar to the data we have published in Refs. [13,14], the removal of Er from near-T sites being fastest in low-dose implanted samples. The solid lines in Fig. 1 display the calculated fraction of free Er plus Er within Er_n clusters, i.e. all Er atoms remaining outside $Er_nO_{m\geq1}$ complexes, while the dotted lines show the calculated fraction of free Er plus Er within Er_n and $Er_{n\geq1}O_1$ clusters, i.e. all Er outside $Er_nO_{m\geq2}$ clusters. As can be seen, the assumption that all Er within $Er_nO_{m\geq1}$ clusters is removed from near-T sites agrees well with the experimental data for all implanted Er doses and annealing times, except for the initial 30 and 60 s anneal steps. While this may indicate that initially not all O is bound to Er, it is highly probable that during these relatively short annealing periods the implanted Si surface may not have fully reached 900°C. On the other hand, the scenario which considers only Er within $Er_nO_{m\geq2}$ clusters as being off the T sites (dotted lines) is clearly not in accordance with the experimental data.

The simulations confirm that the cluster distributions depend strongly on the processing conditions. In order to illustrate different scenarios, Fig. 2 displays calculated fractions of Er_nO_m clusters for three different sample treatments. For instance, annealing of the high-dose implanted sample F for 1800 s should favor mainly Er-rich clusters [Fig. 2(a)]. On the other hand, a short 120 s anneal of sample B should produce mainly O-rich clusters but still leave a relatively high amount (23%) of isolated Er [Fig. 2(c)]. An intermediate situation is suggested for typical processing conditions which are used to optimize the luminescence output of Er-implanted CZ Si, such as described in Ref. [12] (2 MeV implantation,

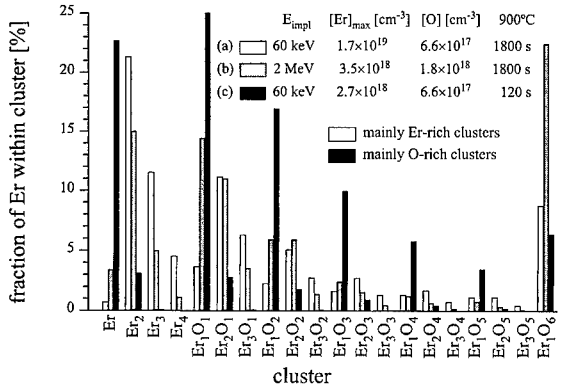

Fig. 2. Calculated distribution of Er_nO_m clusters for three different processing conditions using the model described in the text.

$[Er]_{max} = 3.5 \times 10^{18}$ cm^{-3}, $[O] = 1.8 \times 10^{18}$ cm^{-3}, 900°C for 1800 s). The simulator indicates 75% of Er bound in clusters with O, 19% in pure Er clusters and only 6% of free Er [Fig. 2(b)]. If we do not allow for Er_n cluster formation, as would be the case if these small clusters were unstable, 13% of Er would remain isolated.

Note that we have in all cases assumed that at maximum 6 O atoms can be bound to one Er atom. The high amount of Er within Er_1O_6 clusters reflects this boundary condition. From theoretical considerations it has been suggested that Er_1O_6 defects with Er on a hexagonal (H) site with respect to the Si lattice are particularly stable [11]. In order to check whether such defects are produced in substantial amounts, we have annealed sample B for a total of 2000 s at 900°C, which should result in the formation of Er_nO_m complexes with an O/Er ratio of 5.9. However, we only obtained flat electron emission patterns and thus did not find any indication for a preferred lattice site of Er.

4. Discussion

The results presented above have shown that the onset of O diffusion is of vital importance in producing complexes of Er and O. Concerning the Er lattice location following implantation and annealing, the emission channeling experiments with ^{167m}Er suggest three main structural stages, which are distinguished by the amount of remaining lattice damage and the possibilities for Er_nO_m complex formation. In the following we will discuss these three stages in comparison with the results of other techniques which have investigated Er-implanted Si samples.

4.1. The as-implanted state of Er

This situation is characterized by isolated Er atoms in defect-rich surroundings. For the lowest doses used in our studies (4–6 × 10^{12} cm^{-2} at 60 keV) we found already about 70% of Er close to tetrahedral interstitial sites (T) [13], with a mean displacement of 0.42 Å from the T site. As already remarked before [8,13,16], the displacement of 0.42 Å can also be interpreted as a mixture of several sites in the range 0– ≈ 0.6 Å from the T sites. Tetrahedral interstitial sites have also been predicted by theory to be the most stable sites for isolated Er in Si [11,18,19]. With increasing dose the observable near-T fraction decreases due to accumulation of damage. No difference is found between oxygen-rich CZ Si ([O] ≈ 10^{17}–10^{18} cm^{-3}) and oxygen-lean float zone (FZ) Si ([O] ≈ 10^{15}–10^{16} cm^{-3}). This is also indicated by extended X-ray absorption fine structure (EXAFS) experiments on Er and O co-implanted samples. Even following 30 min of annealing at 450°C, the surroundings of Er were still dominated by 6 ± 2 nearest-neighbor (NN) Si atoms [9]. Due to the remaining implantation damage, which forms efficient recombination centers for electrons and holes, luminescence from as-implanted samples is weak.

4.2. Recrystallization at 600–700°C

At these temperatures the implantation damage recovers to a large extent, resulting in more or less 80–100% of Er on near-T sites. The fact that we observe no difference between CZ and FZ Si [8,13] is in agreement with the low O and Er mobilities at 600°C and the small O/Er ratio of 0.02–1 in our CZ samples. Substantial formation of Er_nO_m complexes does not take place, and we suggest that in both CZ and FZ Si at low Er concentrations mainly isolated Er exists, however, in an environment where not all defects have been removed. It has been reported that the photoluminescence (PL) of FZ and CZ samples annealed at 600°C showed similar intensity [1,7] and even in the case of CZ Si annealed at 700°C was dominated by Er centers of cubic symmetry and a number of centers with lower than axial symmetry [7]. The cubic centers were attributed to isolated Er on T sites, while the low-symmetry Er centers were ascribed to complexes with implantation-induced defects [7]. Exceptions are samples co-implanted with high doses of Er and even higher doses of O (O/Er ≈ 10 or greater). In these samples Er_nO_m clusters can already form during solid-phase epitaxial regrowth, especially if the crystals have been amorphized during implantation [5]. This is due to the increased mobility of Er at the crystalline–amorphous interface. EXAFS analyses of FZ Si co-implanted with 10^{19} Er cm^{-3} and 10^{20} O cm^{-3} have observed 3 ± 2 NN Si and 4.4 ± 0.6 NN O atoms following recrystallization of the amorphized samples at 620°C for 3 h [9]. Electron paramagnetic resonance (EPR) of the same samples revealed several signals of trigonal and monoclinic symmetry, which were attributed to complexes including Er and O [15].

4.3. High-temperature annealing

At 900°C the diffusivity of Er is moderate while that of O is high. We believe that in CZ Si the high-temperature annealing results in a mixture of various Er_nO_m clusters with Er on different lattice sites. Since emission channeling cannot resolve such a mixture of sites, we simply observe random sites. Although we have some indication that in the case of FZ Si the disappearance of near-T Er is due to Er out-diffusion to the surface, occurring on a time scale of hours, the underlying processes are not yet fully understood. A key question, to be answered by future studies, is whether small Er_n clusters are actually formed, and which lattice sites Er might occupy in these complexes.

CZ Si samples implanted with Er resulting in O/Er ratios around 1 generally show an increase of the Er luminescence following annealing for not too long time periods (30 s–30 min) at 900°C. Usually the luminescence in such samples is still dominated by the cubic Er centers, while at the same time additional non-cubic, axial-symmetric Er centers increase in concentration [4,7,10,12,15]. The axial-symmetric Er centers are ascribed to ErO complexes [7]. In our opinion, the fact that the cubic PL signal increases in the presence of O, too, does not contradict our observation that Er is removed from T sites by reacting with one or more O atoms. It rather points out that there are additional mechanisms for O to enhance the Er luminescence, which are not due to the formation of optically active Er_nO_m centers. One such mechanism, which has already been suggested in the literature, is O passivation of Er-implantation-related recombination levels [6,7]. This additional role of O is also evidenced by the fact that the Si near-band-edge luminescence, which is not directly related to Er, was found to increase in the presence of oxygen [5,7].

A direct proof that Er acts as an efficient O getter comes from the EXAFS analyses of CZ Si which was implanted with 5×10^{17} Er cm^{-3} and annealed at 927°C for 30 min [3], and from EXAFS of amorphized FZ Si co-implanted with 10^{19} Er cm^{-3} and 10^{20} O cm^{-3} and annealed at 900°C for 30 s [9]. Under these conditions the Er neighborhood was characterized by 6 NN O atoms, and 5.1 ± 0.5 NN O atoms, respectively.

Following prolonged annealing at 900°C, e.g., for 60 h, especially with high O concentrations (O/Er $\approx$ 10), the Er PL spectra lose their sharp line features, giving way to a broad band luminescence at 1.54 μm, which was attributed to large ErO clusters [4].

5. Conclusions

In summary, we have shown that in CZ Si the fraction of Er which is removed from near-T sites shows a good correlation with the amount of O that can be delivered by the bulk of the wafers during the time of annealing. One O atom per Er_nO_m cluster is sufficient to remove Er from near-T sites. The structural properties which characterize the three different stages of Er-implanted Si samples (as-implanted, recrystallized, and high-temperature-annealed) have been discussed.

Acknowledgements

This work was partially funded by the FCT and ITN, Portugal, through project CERN/S/FIS/1048/98 (JGC).

References

[1] J. Michel, J.L. Benton, R.F. Ferrante, D.C. Jacobson, D.J. Eaglesham, E.A. Fitzgerald, Y.H. Xie, J.M. Poate, L.C. Kimerling, J. Appl. Phys. 70 (1991) 2672.
[2] F.Y.G. Ren, J. Michel, Q. Sun-Paduano, B. Zheng, H. Kitagawa, D.C. Jacobson, J.M. Poate, L.C. Kimerling, Mater. Res. Soc. Proc. 301 (1993) 87.
[3] D.L. Adler, D.C. Jacobson, D.J. Eaglesham, M.A. Marcus, J.L. Benton, J.M. Poate, P.H. Citrin, Appl. Phys. Lett. 61 (1993) 2181.
[4] J. Michel, F.Y.G. Ren, B. Zheng, D.C. Jacobson, J.M. Poate, L.C. Kimerling, Mater. Sci. Forum 143–147 (1994) 707.
[5] A. Polman, G.N. van den Hoven, J.S. Custer, J.H. Shin, R. Serna, P.F.A. Alkemade, J. Appl. Phys. 77 (1995) 1256.
[6] S. Libertino, S. Coffa, G. Franzò, F. Priolo, J. Appl. Phys. 78 (1995) 3867.
[7] H. Przybylinska, W. Jantsch, Y. Suprun-Belevitch, M. Stephikhova, L. Palmetshofer, G. Hendorfer, A. Kozanecki, R.J. Wilson, B.J. Sealy, Phys. Rev. B 54 (1996) 2532.
[8] U. Wahl, A. Vantomme, J. De Wachter, R. Moons, G. Langouche, J.G. Marques, J.G. Correia, the ISOLDE collaboration, Phys. Rev. Lett. 79 (1997) 2069.
[9] A. Terrasi, G. Franzo, S. Coffa, F. Priolo, F. D'Acapito, S. Mobilio, Appl. Phys. Lett. 70 (1997) 1712.
[10] K. Nakashima, O. Eryu, O. Iioka, T. Nakata, M. Watanabe, Nucl. Instr. and Meth. B 127 (1997) 475.
[11] J. Wan, Y. Ling, Q. Sun, X. Wang, Phys. Rev. B 58 (1998) 10415.
[12] S. Lanzerstorfer, L. Palmetshofer, W. Jantsch, J. Stimmer, Appl. Phys. Lett. 72 (1998) 809.
[13] U. Wahl, J.G. Correia, G. Langouche, A. Vantomme, the ISOLDE collaboration, Mater. Res. Soc. Proc. 486 (1998) 269.
[14] U. Wahl, A. Vantomme, G. Langouche, J.G. Correia, the ISOLDE collaboration, J. Lumin. 80 (1999) 303.
[15] J.D. Carey, R.C. Barkley, J.F. Donegan, F. Priolo, G. Franzò, S. Coffa, Phys. Rev. B. 59 (1999) 2773.
[16] U. Wahl, J.G. Correia, S. Cardoso, J.G. Marques, A. Vantomme, G. Langouche, the ISOLDE collaboration, Nucl. Instr. and Meth. B 136 (1998) 744.
[17] A. Borghesi, B. Pivac, A. Sassella, A. Stella, J. Appl. Phys. 77 (1995) 4169.
[18] M. Needels, M. Schlüter, M. Lannoo, Phys. Rev. B 47 (1993) 15533.
[19] F. Gan, L.V.C. Assali, L.C. Kimerling, Mater. Sci. Forum 196–201 (1995) 579.

ELSEVIER

Physica B 273–274 (1999) 346–349

PHYSICA B

www.elsevier.com/locate/physb

Impurity effects in silicon implanted with rare-earth ions

V.V. Emtsev[a,*], V.V. Emtsev Jr.[a], D.S. Poloskin[a], E.I. Shek[a], N.A. Sobolev[a], J. Michel[b], L.C. Kimerling[b]

[a]*Division of Solid State Electronics, Ioffe Physicotechnical Institute, Russian Academy of Sciences, 194021 Politekhnicheskaya ulitsa 26, St. Petersburg, Russia*

[b]*Materials Processing Center, MIT, MA 02139, USA*

Abstract

Formation of donor centers in Czochralski-grown silicon doped with Dy, Ho, Er, and Yb by means of ion implantation is studied. Three kinds of donors with ionization energies less than 0.2 eV make their appearance in implanted Cz-Si after annealing at $T = 700°C$ and 900°C. Shallow donor centers at $\approx E_C - 40$ meV are attributed to oxygen-related donors. Two kinds of deeper donors turned out to be associated with complex defects containing rare-earth ions.

Keywords: Silicon; Implantation; Rare-earth impurity; Oxygen-related donors

1. Introduction

The optical properties of rare-earth ions embedded in semiconductor materials are of scientific and practical interest, since their peculiarities stem from the intracenter f–f transitions. Among the covalent IV-group semiconductors, silicon with erbium ions is most extensively studied because of its possible applications in optoelectronics. Up to now the doping of Si with Er is very often performed by means of ion implantation with subsequent annealing at high temperatures for removal of the damage and activation of the implanted atoms. The interactions of Er impurity atoms with intrinsic defects and other impurities, first of all with oxygen in Czochralski-grown silicon (Cz-Si), result in the formation of various defect complexes in implanted materials. There are many papers concerning with deep centers in Si : Er and Cz-Si : Er studied thoroughly by DLTS; see for instance [1–3]. However, the information on donor centers with activation energies less than 0.2 eV was scanty until recently [4], though these donors govern the electron conductivity of Cz-Si : Er.

In the present work we concentrate on the behavior of rare-earth ions in Si, paying special attention to erbium impurity. The use of other rare-earth dopants helps us in identifying impurity centers by comparison. The results obtained throw new light on the formation processes of impurity-related donors.

2. Experimental

Wafers of carbon-lean Cz-Si with oxygen contents in the range from 2×10^{17} to 1×10^{18} cm^{-3} were used. All starting materials were of p-type, with the boron concentration in the range from 8×10^{13} to 2×10^{15} cm^{-3}.

The rare-earth doping was carried out by means of ion implantation at energies of 1.0–1.3 meV and doses up to 1×10^{13} cm^{-2}, i.e. beyond the onset of amorphization of the implanted layers. The implanted samples were annealed successively in two steps at $T = 700°C$ and 900°C for 30 min in a chlorine containing atmosphere. The radiation damage is mostly removed at $T = 700°C$ whereas the annealing at higher temperatures is used for the

* Corresponding author. Tel.: + 7-812-247-9952; fax: + 7-812-247-1017.

E-mail address: emtsev@pop.ioffe.rssi.ru (V.V. Emtsev)

0921-4526/99/$ - see front matter
PII: S0921-4526(99)00473-1

formation of the well-known Er-related centers with light emission at $\lambda \approx 1.54$ μm [5]. At implantation doses $\Phi \geqslant 5 \times 10^{11}$ cm^{-2}, the implanted layers of about 0.5 μm in thickness became n-type after the first annealing step. Under our experimental conditions the Er peak concentration at a largest dose of $\Phi(\mathrm{Er}) = 1 \times 10^{13}$ cm^{-2} was 3×10^{17} cm^{-3}.

Electrical measurements of the concentration of free electrons in the implanted layers vs. temperature, $n(T)$, were taken with the help of the Van der Pauw technique over the temperature range from $T \approx 20$ to 300 K. Analysis of the $n(T)$ curves was carried out on the basis of the corresponding electroneutrality equations.

3. Results and discussion

3.1. Formation processes in implanted Cz-Si after annealing to $T = 700$°C

By way of illustration, a typical curve of $n(T)$ for one of the samples studied is depicted in Fig. 1. A detailed analysis of such experimental curves based on the statistics of charge carriers allows one to determine the concentrations of centers with ionization energies less than 0.2 eV.

Three kinds of donor centers make their appearance in Cz-Si implanted with Dy, Ho, Er, and Yb.

First of all, shallow donor states with ionization energies from ≈ 30 to ≈ 40 meV are present in considerable concentrations; see Fig. 1. They resemble closely the oxygen-related shallow donors formed in Cz-Si [6] and Cz-Si irradiated with fast neutrons [7] during heat treatment over the temperature interval from $T = 600$°C to 700°C. In both cases [6,7] the shallow donors in Cz-Si are distributed over the ionization energy interval from ≈ 20 to ≈ 40 meV, the maximum of their distribution always being placed at around 40 meV. It has been found that a simple model of two donor levels at $E_1 \leqslant E_C - 30$ meV and $E_2 \approx E_C - 40$ meV used in the calculations of $n(T)$ curves can be a reasonable substitute for the real donor distribution. This is also true for Cz-Si implanted with rare-earth ions. For all the samples in this work, the calculated $n(T)$ curves fit the experimental ones at $T \leqslant 80$ K using a similar two-level model. This provides strong support to the conclusion that the nature of the shallow donors in Cz-Si after implantation is akin to the nature of oxygen-related shallow donors in Cz-Si, originating from oxygen aggregation at high temperatures [6,7]. However, there are some distinctions in their properties in the implanted layers, because in this case the formation of oxygen-related donors takes place in the presence of implantation-induced native defects in large concentrations. These defects can serve as nucleation sites for oxygen atoms. Actually, the total concentration of shallow donors turned out to be dose-dependent; see Fig. 2. The involvement of native defects in oxygen aggregation appears to contribute to higher thermal stability of the shallow donors as well as their higher production rate as compared to those formed under the "pure" heat treatment conditions; cf. Ref. [5] and present work.

The donor centers of the second kind are characterized by a single ionization energy of about 70 meV. Their concentration was found to be dose-dependent; see for instance Fig. 2. These donors are believed to be associated with rare-earth impurities, since their ionization energy turned out to be dependent on the impurity ions implanted, as can be seen from Fig. 3.

Along with the donors discussed above, additional deep donor centers have been found in implanted Cz-Si. As can be seen from Fig. 3, these donor centers are

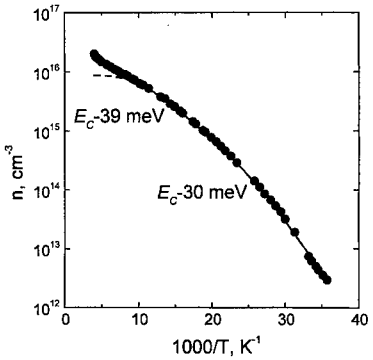

Fig. 1. Electron concentration vs. reciprocal temperature for Cz-Si implanted with Er and annealed at $T = 900$°C. $\Phi(\mathrm{Er}) = 1 \times 10^{12}$ cm^{-2}. Points, experimental; curves, calculated. The contribution of shallow donor centers at the saturation plateau is given by dashed line.

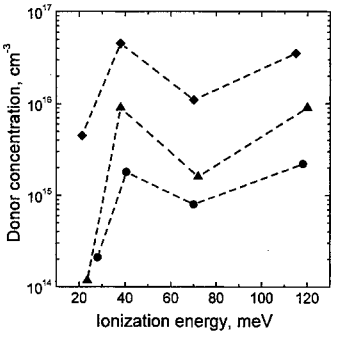

Fig. 2. Donor concentrations vs. ionization energies for Cz-Si implanted with Er and annealed at $T = 700$°C. $\Phi(\mathrm{Er}) = 5 \times 10^{11}$ cm^{-2} (circles); $\Phi(\mathrm{Er}) = 1 \times 10^{12}$cm^{-2} (triangles); $\Phi(\mathrm{Er}) = 1 \times 10^{13}$ cm^{-2} and $\Phi(\mathrm{O}) = 1 \times 10^{14}$ cm^{-2} (diamonds). Dashed lines are shown as a eye's guide only.

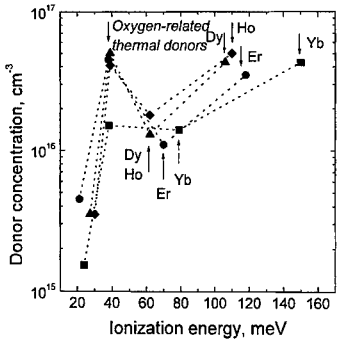

Fig. 3. Donor concentrations vs. ionization energies for the Cz-Si implanted with Dy (triangles), Ho (diamonds), Er (circles), and Yb (squares) and annealed to $T = 700°C$. Doses: Φ(Dy, Ho, Yb) $= 1 \times 10^{13}$ cm^{-2}; Φ(Er) $= 1 \times 10^{13}$ cm^{-2} and coimplantation with oxygen at Φ(O) $= 1 \times 10^{14}$ cm^{-2}.

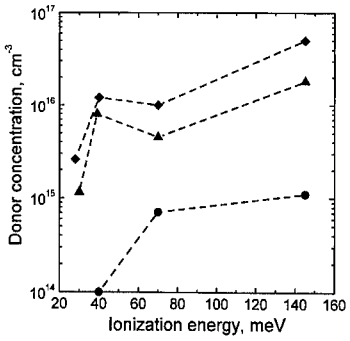

Fig. 4. Donor concentrations vs. ionization energies for Cz-Si implanted with Er and annealed at $T = 900°C$. Φ(Er) $= 5 \times 10^{11}$ cm^{-2} (circles); Φ(Er) $= 1 \times 10^{12}$ cm^{-2} (triangles); Φ(Er) $= 1 \times 10^{13}$ cm^{-2} and Φ(O) $= 1 \times 10^{14}$ cm^{-2} (diamonds). The sample implanted at Φ(Er) $= 1 \times 10^{13}$ cm^{-2} and Φ(O) $= 1 \times 10^{14}$ cm^{-2} was cut from another Cz-Si wafer with low oxygen concentrations (about 2×10^{17} cm^{-2}). Dashed lines are shown as a eye's guide only.

sensitive to the chemical nature of rare-earth impurities, too.

3.2. Formation processes in implanted Cz-Si after annealing to $T = 900°C$

At elevated temperatures of the postimplantation annealing the positions of two groups of donor states, the shallow ones and those with ionization energies of about 70 meV, remain practically unaltered. However, they appear to be partially annealed in some cases; cf. Figs. 2 and 4.

In Cz-Si doped with Dy and Ho after the second annealing step, our estimates showed little if any changes in the position of deep donor centers at $\approx E_C - 100$ meV, though their concentration decreased slightly; cf. Figs. 3 and 5. In contrast, we could not detect the presence of donor states at $\approx E_C - 120$ meV in Cz-Si : Er after annealing to $T = 900°C$. Instead, new donor states at $E_C - (145 \pm 5)$ meV are formed in this material (Fig. 5). As is seen from Figs. 2 and 4, the concentrations of these new donor states are comparable to those of donors at $\approx E_C - 120$ meV formed at $T = 700°C$, especially at heavy doses. Therefore, one can think of some transformations of the donor centers considered. Reliable analysis of the data concerning the deeper donors in Cz-Si : Yb presents difficulties which prevent arriving to a certain conclusion like in the case of Cz-Si : Er.

Let us briefly discuss the new information gained in this work paying attention to Cz-Si : Er annealed at $T = 900°C$.

The well-known quenching of an erbium-related photoluminescence band at $\lambda \approx 1.54$ μm at $T \geqslant 100$ K is said to be due to thermal ionization of donor centers at $\approx E_C - 150$ meV preventing from the formation of bound excitons at them; see for instance Ref. [10]. We

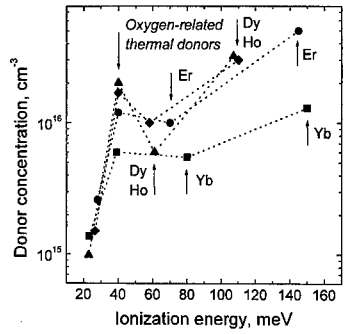

Fig. 5. Donor concentrations vs. ionization energies for the Cz-Si implanted with Dy (triangles), Ho (diamonds), Er (circles), and Yb (squares) and annealed to $T = 900°C$. Doses: Φ(Dy, Ho, Yb) $= 1 \times 10^{13}$ cm^{-2}; Φ(Er) $= 1 \times 10^{13}$ cm^{-2} and coimplantation with oxygen at Φ(O) $= 1 \times 10^{14}$ cm^{-2}. The Cz-Si : Er sample was cut from another Cz-Si wafer with low oxygen concentrations (about 2×10^{17} cm^{-3}).

believe that this quenching mechanism may not be very efficient, since at heavy doses of ion implantation most of these donors are neutral up to room temperature because of the presence of donor states at $E_C - 40$ meV and $E_C - 70$ meV in large concentrations.

In a recent paper [8] the nonradiative decay of the excited Er^{3+} ions in Cz-Si : P : Er at very low temperatures, at $T \leqslant 30$ K for the most part, is discussed in terms of the Auger impurity process with the energy transfer to free electrons; see also Ref. [9]. In the temperature range of interest, free electrons are thought to be released from shallow donor centers at $\approx E_C - 20$ meV [8]. However, these donor states were found to be present

only in a small fraction of the total concentration of shallow donors; see Fig. 4. Taking into account a more realistic donor distribution one can estimate that in the Cz-Si : P : Er studied in Ref. [8] the free electron concentration at $T \leqslant 30$ K may be much less than a critical one of about $7 \times 10^{14}\,\mathrm{cm}^{-3}$ and, hence, there is a need to examine this possible channel of Er deexcitation once again.

On the other hand, it is possible to suggest a unified model [11] which can provide a satisfactory description of the quenching of the characteristic Er luminescence on the basis of the dominant deexcitation mechanisms mentioned above. A careful analysis of optical and electrical data over the entire temperature range can help in clarifying the most important details of the underlying processes.

4. Conclusion

The present study on Czochralski-grown silicon implanted with different rare-earth impurities allows us to trace some general trend in the formation of donor centers with ionization energies less than 0.2 eV, responsible for the electrical properties of doped layers. Three kinds of donor centers are formed in Cz-Si after implantation with subsequent annealing to $T = 700$°C and 900°C. Shallow energy states at $E_C - 30 \ldots 40$ meV are attributed to oxygen-related donors. Other donor centers at $\approx E_C - (60 \ldots 80)$ meV and $\approx E_C - (100 \ldots 150)$ meV appear to be associated with rare-earth impurities. Some striking transformations of deeper donor centers in Cz-Si : Er takes place over an annealing temperature interval of $T = 700$°C to 900°C, leading to the appearance of donor centers at $\approx E_C - 150$ meV. These new centers are believed to be involved in the characteristic Er luminescence.

References

[1] J.L. Benton et al., J. Appl. Phys. 70 (1991) 2667.
[2] S. Libertino et al., J. Appl. Phys. 78 (1995) 3867.
[3] H. Przybylinska et al., Phys. Rev. B 54 (1996) 2532.
[4] V.V. Emtsev et al., J. Lumin. 80 (1999) 391.
[5] J. Michel et al., J. Appl. Phys. 70 (1991) 2672.
[6] V.V. Emtsev et al., in: H. Richter, M. Kittler, C. Claeys (Eds.), Sol. St. Phenomena, Vols. 47–48, Sci. Tech. Publications, Switzerland, 1996, pp. 259–266.
[7] V.V. Emtsev et al., Fiz. Tekh. Poluprovodn. 28 (1994) 1084 [Semiconductors (AIP) 28 (1994) 624].
[8] F. Priolo et al., Phys. Rev. B 57 (1998) 4443.
[9] J. Palm et al., Phys. Rev. B 54 (1996) 17603.
[10] F. Priolo et al., J. Appl. Phys. 78 (1995) 3874.
[11] T.D. Chen et al., Physica B 273–274 (1999) 320, These Proceedings.

ELSEVIER

Physica B 273–274 (1999) 350–353

PHYSICA B

www.elsevier.com/locate/physb

Structure of Er-related centers in Si

J.D. Carey[a,*], F. Priolo[b]

[a]School of Electronic Engineering, University of Surrey, Guildford GU2 5XH, Surrey, UK
[b]INFM and Dipartimento di Fisica, Università di Catania, Corso Italia 57, I95129 Catania, Italy

Abstract

Electron paramagnetic resonance (EPR) measurements have been performed on samples of Er implanted FZ Si which have been co-implanted with O ions. For an Er concentration of 10^{19}/cm^3 well-defined Er^{3+} centers with monoclinic and trigonal symmetry are observed in samples with 10^{20} O/cm^3 but are replaced by broad anisotropic resonances in samples with 3×10^{19} O/cm^3. The different centers are attributed to the formation of Er–O complexes with different configurations of O atoms. In the case of the trigonal Er–O center calculations reveal that this center cannot be associated with an Er atom residing at either the Si tetrahedral interstitial or substitutional site but is consistent with an Er atom located at the hexagonal interstitial site surrounded by six O atoms. The importance of the Er/O concentration ratio for the formation of the complexes is discussed.

PACS: 76.30.Kg; 78.55. – m; 61.72.Tt

Keywords: Erbium doped silicon; Electron paramagnetic resonance; Defects; Optoelectronics

1. Introduction

The incorporation of Er with light atoms such as O or F has been shown to be one of the most successful ways of obtaining room-temperature light emission at 1.54 μm from Si [1,2]. In the presence of a sufficient concentration of impurity atoms, the Er-related photoluminescence (PL) intensity on going from 77 K to room temperature was observed to only decrease by a factor of 30 compared to a reduction by over three orders of magnitude in the absence of sufficient impurity atoms [1]. This use of impurity codoping has led to the observation of room-temperature electroluminescence (EL) from Er-doped Si p–n diodes [2]. In addition, Er concentrations of $10^{19\text{-}20}$/cm^3 can now be obtained before the onset of precipitation [3]. These beneficial effects have been attributed to modifications of the local environment around the Er atom through the formation of Er-impurity complexes [1–3]. Consequently it is therefore of considerable interest to determine the structure of these complexes.

Some information has already been obtained from extended X-ray absorption fine structure (EXAFS) measurements of O-containing samples, which showed Er to be surrounded by a cage of 4–6 O atoms [4]. Recent ab initio cluster calculations have also suggested that there is a change to the environment around the Er atom which depends upon the number of O atoms present nearby [5]. These calculations also make predictions about the location and symmetry of the most stable configuration of Er atoms within the lattice which can be tested using electron paramagnetic resonance (EPR) spectroscopy and PL spectroscopy. In a recent paper we reported EPR measurements which have showed that in samples with concentrations of 10^{19} Er/cm^3 and 10^{20} O/cm^3 well-defined monoclinic and trigonal Er–O complexes are formed [6]. However, no well-defined centers were observed from a sample with only 3×10^{19} O/cm^3. Tentative models for the monoclinic centers were proposed but no attempt was made to describe the trigonal center nor any attempt to discuss how the Er–O complexes fit into the Si lattice. In this paper we discuss the lattice location and coordination of some of the

* Corresponding author. Tel.: + 44-1483-259841; fax: + 44-1483-534139.
E-mail address: d.carey@ee.surrey.ac.uk (J.D. Carey)

0921-4526/99/$ - see front matter
PII: S0921-4526(99)00474-3

centers and discuss the importance of the Er/O concentration ratio.

2. Experimental details

Samples of n-type FZ (1 0 0) Si wafers received multiple implants with Er ions (0.5–5 MeV) at 77 K to a total fluence of $10^{15}/cm^2$. This resulted in an approximately uniform concentration of 10^{19} Er/cm^3 to a depth of ~ 1.8 μm from the surface. Three samples were co-implanted with O ions (0.15–0.5 MeV) to give an approximately uniform impurity concentrations of $3 \times 10^{19}/cm^3$ (labelled sample O1) and 10^{20} O/cm^3 (O2 and O4). After implantation a continuous amorphous layer extends from the surface to a depth of 2 μm. All three samples were subsequently annealed at 450°C for 30 min, 620°C for 3 h and samples O1 and O2 were further annealed at 900°C for 30 s. Further details of the sample preparation conditions have been give elsewhere [6]. EPR measurements were performed in a modified Bruker EPR spectrometer employing 100 kHz field modulation and a TE_{102} rectangular cavity. The microwave frequency was approximately 9.23 GHz and the samples were cooled to approximately 10 K using an Oxford Instruments flow cryostat.

3. Results and discussion

The EPR spectrum from sample O4 for the magnetic field parallel to the [0 0 1] direction is shown in Fig. 1. A number of sharp lines can be observed and the lines labelled OEr-1′ and OEr-3 have each been shown to belong to monoclinic C_{1h} centers with effective spin $S = \frac{1}{2}$ and with principal g values given in Table 1 [6]. The intense line labelled OEr-2′ could be fitted [6] to a single spin $\frac{1}{2}$ exhibiting trigonal symmetry with principal g values $g_{||} = 0.69$ and $g_{\perp} = 3.24$. The weaker line

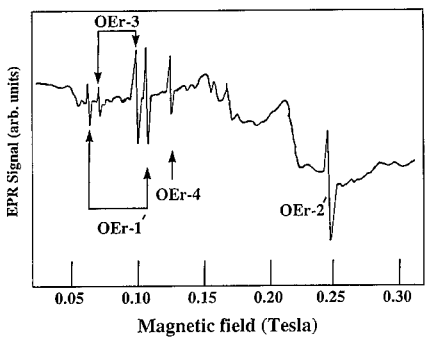

Fig. 1. Low-temperature EPR spectrum from sample O4 for the magnetic field parallel to the [0 0 1] direction.

Table 1
Principal g values for the different centers observed in sample O4

Center	g_1	g_2	g_3	Tilt angle[a] (deg)	g_{av}	Symmetry
OEr-1′	0.80	5.45	12.55	56.90	6.27	Monoclinic
OEr-3	1.09	5.05	12.78	48.30	6.31	Monoclinic
OEr-2′	0.69	3.24	3.24	54.74	2.39	Trigonal
OEr-4	2.00	6.23	6.23	54.74	4.82	Trigonal

[a]The tilt angle is the angle the 1-axis makes with the [0 0 1] direction as rotated about the [1 $\bar{1}$ 0] direction.

OEr-4 also exhibits trigonal symmetry and its principal g values are similarly reported in Table 1. Only centers OEr-1′ and OEr-2′ were clearly resolved in sample O2, where they have been labelled centers OEr-1 and OEr-2, respectively. Future discussion will concentrate on these two centers. The EPR spectrum from sample O1, (not shown), revealed only the presence of two broad anisotropic resonances [6]. The appearance of sharp lines in samples O2 and O4 is indicative of the formation of well-defined Er–O complexes. The transition from an Er/O concentration ratio of 1 : 3 to 1 : 10 implies that the environment around the Er has changed due to bonding with O atoms. It is known that the C-phase of Er_2O_3 occurs with two different coordinations each with Er^{3+} surrounded by six O atoms, though not in the form of an octahedron [7]. Previous EPR measurements of Er^{3+} in Y_2O_3, which has the same structure as Er_2O_3, reveal Er to be in sites with monoclinic C_2 and trigonal C_{3i} symmetry. In the case of the monoclinic site the principal g values are $g_z = 12.314$, $g_x = 1.645$ and $g_y = 4.892$ [7]. Not only are these principal g values similar to those observed for center OEr-1′ but also the average g value, g_{av}, as defined by

$$g_{av} = \tfrac{1}{3}(g_1 + g_2 + g_3) \quad (1)$$

is 6.28, almost identical to that obtained for center OEr-1′ (6.27). The average g value can be used as a quantitative measure of the local crystal field around a paramagnetic ion [8]. We thus suggest that center OEr-1′ consists of an Er^{3+} ion surrounded by six O atoms, however, in the absence of either hyperfine data or electron nuclear double resonance (ENDOR) measurements the exact arrangement of atoms remains unclear.

In the case of the OEr-2′ center since the g values of the trigonal C_{3i} center observed in $Y_2O_3 : Er^{3+}$, are $g_{||} = 12.17$ and $g_{\perp} = 3.32$ [7], are clearly different from the g values of center OEr-2′ we conclude that they are completely different centers. In order to determine the likely lattice location and coordination of center OEr-2′

it is necessary to calculate the g values for the different coordinations. When an Er atom is incorporated into Si, the 16-fold degenerate spin–orbit ground state is split into a number of Stark levels. The number and type of Stark levels can be obtained from group theory and can be shown, for T_d, symmetry, to be $\Gamma_6 + \Gamma_7 + 3\Gamma_8$ [9]. Which of these five levels lies lowest, and is thus the paramagnetic ground state, can be calculated from the crystal field Hamiltonian [10]

$$H = B_4(O_4^0 + 5O_4^4) + B_6(O_6^0 - 21O_6^4), \quad (2)$$

where O_n^m are the crystal field equivalent operators and the coefficients B_4 and B_6 determine the crystal field splitting [10]. Eq. (2) can be solved by the introduction of two parameters x and W defined such that

$$B_4F(4) = Wx \text{ and } B_6F(6) = W(1 - |x|), \quad (3)$$

where W is an energy scale factor and $F(4)$ and $F(6)$ are numerical constants [10]. The quantity x is the crystal field mixing term ($\sim B_4/B_6$) and runs from -1 to $+1$. With labelling appropriate to T_d symmetry, the Γ_7 representation lies lowest for $-1 < x < -0.46$, the Γ_6 representation for $-0.46 < x < 0.58$ and the Γ_8 representation for $x > 0.58$. Negative values of x correspond to a substitutional site, whereas positive values of x indicate an interstitial site. Using the crystal field eigenstates given elsewhere [10] the g values associated with transitions within the Γ_6 and Γ_7 states are 6.80 and 6.00, respectively, and are independent of x. In the case of the Γ_8 states, as these states occur more than once, the g values depend upon x [11]. For centers with less than cubic symmetry it is possible to use Eq. (1) to relate the observed principal g values to the g value associated with a center with cubic symmetry g_c [8]. This approach has been shown to be valid provided that the lower symmetry crystal field is small when compared to cubic crystal field. Since the average g value for center OEr-2′ is 2.39 and is far enough removed from the cubic g values for a Γ_6 state (6.8) or Γ_7 state (6.0) we can conclude that this center is not associated with an Er residing at a substitutional (T_s) site for which $x < 0$ or at a Γ_6 tetrahedral interstitial site (T_i) in the range $0 < x < 0.58$. For the remaining region of $0.58 < x < 1$, corresponding to a Γ_8 level lying lowest, the use of the average g value is not valid [11]. In this case it is necessary to calculate the g values for each value of x and use the associated cubic crystal field eigenstates, labelled P and Q in the notation of Ref. [11], to calculate the principal g values $g_{||}$ and $g_\perp$ via [11]

$$g_{||} = g_J(P - Q) \text{ and } g_\perp = g_J(P + Q), \quad (4)$$

where the Landé g value is taken to be $\frac{6}{5}$. Fig. 2 shows the calculated g values determined by this method using intervals for x of 0.01. It is clear from Fig. 2 that at no stage does $g_{||}$ approach the observed value of 0.69 and neither does $g_\perp$ approach 3.24 and we thus believe that

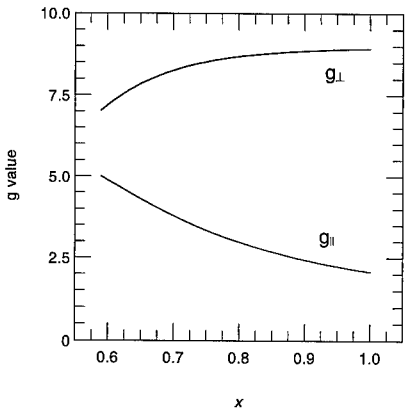

Fig. 2. The calculated principal g values $g_{||}$ and $g_\perp$ determined for an Er^{3+} center in trigonal symmetry.

center OEr-2′ does not originate from a trigonally split Γ_8 ground state. Consequently, OEr-2′ cannot be associated with either the T_s or T_i sites within the Si lattice. (It is also interesting to note that the g values of the other center which exhibits trigonal symmetry (center OEr-4) cannot be attributed to either the T_s or T_i sites either.) Since center OEr-2′ is observed in samples with an Er : O concentration ratio of 1 : 10, and not with 1 : 3.3, we believe that it is a well-defined Er–O complex with a large number of O atoms surrounding a central Er atom with trigonal point symmetry. Recent calculations by Wan et al. have predicted that in the presence of O, the Er atom tends to reside at the hexagonal interstitial (H_i site) surrounded by six O atoms [5]. Such an arrangement of atoms would have trigonal point symmetry and was found to be over 1 eV more stable than either of the T_s or T_i sites when Er is surrounded by four O atoms. In view of the fact that center OEr-2′ possesses trigonal symmetry, is only observed with a large number of O atoms surrounding it and cannot be associated with either the T_s or T_i sites, it is suggested that it may be the same as the trigonal center predicted by Wan et al. though other arrangements of atoms which would lead to trigonal symmetry are also possible.

Wan et al. have also calculated that in the absence of O, the most stable configuration consists of an Er atom residing at the T_i site surrounded by four Si atoms [5]. The observed PL spectrum from sample O1 could be fitted to an Er^{3+} center located at the T_i site with $x = 0.35$ [6]. This center has also been observed by Przybylinska et al. [12]. Such a value of x would indicate a Γ_6 ground state which should produce an isotropic EPR line with a g value of 6.8. No such line is observed though the broad anisotropic lines that are present may mask the signal from this center. The origin of these broad lines is unclear but Wahl et al. have recently

concluded that even 1–2 O atoms per Er atom are sufficient to remove an Er atom from the T_i site [13]. This will produce a large number of non-cubic centers which may be the reason for the broad EPR lines observed from sample O1. We believe that there is a minimum concentration ratio of O : Er required to form well required to form well-defined Er–O complexes consisting of one Er atom and six O atoms. When the O concentration is limited, corresponding to Er/O concentrations of 1 : 3 or less, no well-defined complexes will form. Only when the O concentration is large enough will the corresponding complexes form. An Er : O concentration ratio of 1 : 10 is sufficient for this to occur.

4. Conclusions

Electron paramagnetic resonance measurements made on samples of Er-doped Si co-implanted with O reveal the presence of monoclinic and trigonal centers. The monoclinic centers are attributed to an Er–O complex with six O atoms though the exact arrangement within the Si lattice is unclear. The dominant trigonal center is also attributed to an Er–O complex but cannot be associated with an Er atom at tetrahedral substitutional or interstitial sites. This center is consistent with the results of ab initio calculations that predict that Er resides at the hexagonal interstitial (H_i site) surrounded by six O atoms.

Acknowledgements

The authors would like to thank Dr. R. Barklie and Dr. J. Donegan from Trinity College, Dublin for help in the initial study of the monoclinic centers and also Dr. G. Franzò and Dr. S. Coffa from Catania.

References

[1] S. Coffa, G. Franzò, F. Priolo, A. Polman, R. Serna, Phys. Rev. B 49 (1994) 16313.
[2] G. Franzò, F. Priolo, S. Coffa, A. Polman, A. Carnera, Appl. Phys. Lett. 64 (1994) 2235.
[3] F. Priolo, S. Coffa, G. Franzò, C. Spinella, A. Carnera, V. Bellani, J. Appl. Phys. 74 (1993) 4936.
[4] A. Terrasi, G. Franzo, S. Coffa, F. Priolo, F. D'Acapito, S. Mobilio, Appl. Phys. Lett. 70 (1997) 1712.
[5] J. Wan, Y. Ling, Q. Sun, X. Wang, Phys. Rev. B 58 (1998) 10415.
[6] J.D. Carey, R.C. Barklie, J.F. Donegan, F. Priolo, G. Franzò, S. Coffa, Phys. Rev. B 59 (1999) 2773.
[7] G. Schafer, S. Scheller, Phys. Kondens. Mater. 5 (1966) 48.
[8] M.M. Abraham, R.A. Weeks, G.W. Clark, C.B. Finch, Phys. Rev. 148 (1966) 350.
[9] A. Abragam, B. Bleaney, Electron Paramagnetic Resonance of Transition Ions, Oxford University Press, Oxford, 1970, p. 858.
[10] K.R. Lea, M.J.M. Leask, W.P. Wolf, J. Phys. Chem. Solids 23 (1962) 1381.
[11] A. Abragam, B. Bleaney, Electron Paramagnetic Resonance of Transition Ions, Oxford University Press, Oxford 1970, p. 731.
[12] H. Przybylinska, W. Jantsch, Yu. Suprun-Belevitch, M. Stepikhova, L. Palmetshofer, G. Hendorfer, A. Kozanecki, R.J. Wilson, B.J. Sealy, Phys. Rev. B 54 (1996) 2532.
[13] U. Wahl, A. Vantomme, G. Langouche, J.G. Correia, J. Lumin. 80 (1998) 303.

ELSEVIER

Physica B 273–274 (1999) 354–357

PHYSICA B

www.elsevier.com/locate/physb

Mechanism of excitation of erbium electroluminescence in amorphous silicon

M.S. Bresler[a,*], W. Fuhs[b], T. Gregorkiewicz[c], O.B. Gusev[a], P.E. Pak[a], E.I. Terukov[a], K.D. Tsendin[a], I.N. Yassievich[a,d]

[a]*A.F. Ioffe Physico-Technical Institute, Politekhicheskaya 26, 194021 St.Petersburg, Russia*
[b]*Hahn-Meitner Institute, Abteilung Photovoltaik, D-12489 Berlin, Germany*
[c]*Van der Waals-Zeeman Institute, University of Amsterdam, NL-1018 XE Amsterdam, Netherlands*
[d]*Department of Theoretical Physics, Lund University, S-223 62 Lund, Sweden*

Abstract

We have studied electroluminescence (EL) in the amorphous silicon-based erbium-doped structures in the temperature range 77–300 K. The EL intensity at the wavelength of 1.54 μm corresponding to a radiative transition in the internal 4f-shell of the Er^{3+} ion is low at 77 K but sharply increases starting from 220 K and exhibits a maximum near the room temperature. Measurements of the resistance of the electroluminescent structure as a function of temperature performed in parallel with the measurements of the EL intensity demonstrated a correlation in behavior of these two quantities: a pronounced decrease of the resistance occurs at the same temperature where the EL intensity starts to rise. Our results can be explained by the excitation of erbium ions via an Auger process which involves the capture of conduction electrons by neutral dangling bonds (D^0) defects located close to erbium ions and thermally activated tunnel emission of electrons from deep donors to the conduction band that keeps the stationary current through the structure. A theoretical model proposed explains consistently all of our experimental data.

Keywords: Erbium-doped amorphous silicon; Auger excitation; Electroluminescence

Intense studies of erbium luminescence in semiconductor matrices in the last decade were motivated by the fact that the wavelength 1.54 μm of erbium luminescence corresponding to a transition from the first excited state $^4I_{13/2}$ to the ground state $^4I_{15/2}$ in the 4f-shell of an Er^{3+} ion coincides with the absorption minimum in silica-glass optical fibres.

Recently, in several works an efficient photoluminescence (PL) [1–3] and electroluminescence (EL) [4] from erbium in amorphous hydrogenated silicon (a-Si : H⟨Er⟩) was reported. The interest to this semiconductor matrix was drawn both by a simple and inexpensive method of doping it with erbium (magnetron sputtering of metallic erbium in the silane (SiH_4) atmosphere) and comparatively weak temperature quenching of erbium photoluminescence in amorphous silicon which makes this material promising for fabrication of light-emitting diodes operating at room temperature.

We have proposed that excitation of erbium ions in a-Si : H⟨Er⟩ occurs due to an Auger process in which an electron from the conduction band is captured by a neutral defect of the dangling bond-type D^0 with a formation of the D^- state. The energy released at this transition is transferred to an electron of the internal 4f-shell of the erbium ion exciting it from the ground $^4I_{15/2}$ to the first excited $^4I_{13/2}$ state (defect-related Auger excitation (DRAE) [5,6]. The efficiency of such a process is determined by a close coincidence of the energy of the $D^0 + e \rightarrow D^-$ transition and that of the $^4I_{15/2} \rightarrow {}^4I_{13/2}$ transition.

* Corresponding author. Tel.: + 7-812-247-9140; fax: + 7-812-247-1017.
E-mail address: mikhail.bresler@pop.ioffe.rssi.ru (M.S. Bresler)

0921-4526/99/$ - see front matter
PII: S0921-4526(99)00475-5

In the case of electroluminescence the capture of conduction electrons by D^0-centers leads to the disappearance of free charges transmitting the current, therefore a reverse process of ionization of deep centers should exist in high electric field. In the present work we demonstrate that excitation of erbium ions in electroluminescent structures is actually done by the DRAE mechanism and the role of reverse process supplying free electrons in the conduction band is played by multiphonon tunnel ionization of erbium-induced donors and D^--centers in electric field.

The structures studied were films of a-Si : H⟨Er⟩ with a thickness of ≈ 1 μm and a diameter of 1 mm deposited on a substrate from n-type crystalline silicon of 300 μm thickness. Aluminium electrical contacts were sputter deposited on the amorphous silicon film and the substrate. EL was measured in the regime of stabilized current pulses at 100 Hz with a duty cycle of 1 : 2. The light was collected by a system of lenses from the reverse side of the substrate and analyzed by double grating spectrometer supplied with a nitrogen-cooled germanium photodetector. At direct bias (" + " at the upper aluminum contact, " − " at the n-type crystalline silicon substrate) only EL of free excitations ($\lambda \approx 1.16$ μm) from the substrate was observed at room temperature. At reverse bias both erbium ($\lambda \approx 1.54$ μm) and defect ($\lambda \approx 1.34$ μm) luminescence were detected.

The temperature dependence of the erbium luminescence intensity for different currents through the structure is shown in Fig. 1a. Whereas the intensity of photo- and electroluminescence usually decreases at higher temperatures (i.e. suffers temperature quenching), in our case it is very low at liquid nitrogen temperatures but increases significantly while approaching the room temperature. For all the curves of Fig. 1a, maximum in the EL intensity is observed close to room temperature. The voltage drop on the structure measured as a function of the temperature in parallel with the EL measurements revealed a maximum at the temperature when EL intensity starts to increase, then decreased on the rise of temperature and had a slight minimum at the temperature of EL maximum (Fig. 1b).

The dependences of EL intensity and electric current through the structure on electric field measured at room temperature demonstrate close similarity: both quantities approach the exponential dependence on electric field squared at high values of electric field. The intensity of erbium EL depends linearly on the excitation current.

The electroluminescent structures studied are the structures of Al/a-Si : H⟨Er⟩/n^+-c-Si/Al type, i.e. they have a Schottky barrier at the aluminum contact and an a-Si/c-Si heterojunction at the contact with the substrate. However, as we shall see later, in the El regime when high electric field is applied to the structure, the role of contacts is of minor importance.

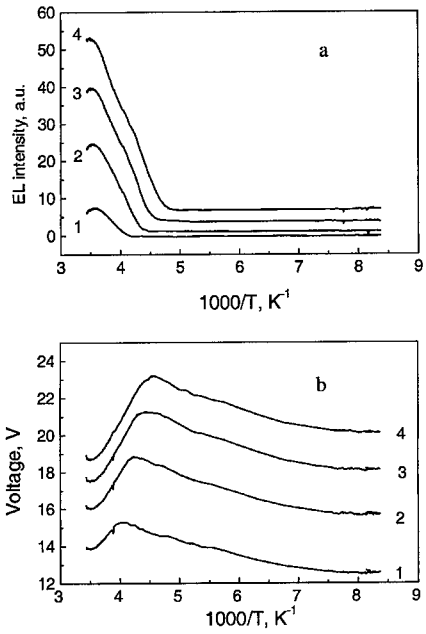

Fig. 1. (a) Temperature dependence of the intensity of erbium EL at 1.54 μm at reverse bias. (b) Temperature dependence of the voltage on the structure V. Currents through the structure: 5 mA (1), 10 mA (2), 15 mA (3), 20 mA (4).

Energy band diagrams of the electroluminescent structures studied are shown schematically in Fig. 2a and b for direct and reverse bias, respectively. In Fig. 2b the process of excitation of erbium ion is also shown. (It should be mentioned that due to a high resistance of the amorphous layer the potential drop concentrates on the bulk of it). When direct bias is applied to the structure, holes travel through the amorphous layer to the crystalline silicon substrate (cf. Fig. 2a) and luminescence of a free exciton from the n-type substrate is observed. At reverse bias erbium luminescence at the wavelength of 1.54 μm is only seen. No erbium luminescence in the structure with the n-type substrate is observed at direct bias demonstrating the absence of electron current in this case whereas no exciton luminescence from the substrate is seen at reverse bias. Thus, our experimental results indicate a monopolar conduction in the structure. The current is transferred by holes in the case of direct bias and by electrons at reverse bias. The erbium ions are excited only by electrons captured by D^0-defects.

The position of the Fermi level ζ determined from the temperature dependence of electrical conductivity indicates that in a large range of erbium concentrations (10^{18}–10^{20} cm^{-3}) it is nearly independent of the concentration of erbium ions $\zeta \approx 0.5$–0.45 eV below the edge of the conduction band), i.e. the Fermi level is pinned at a special position in the amorphous silicon bandgap,

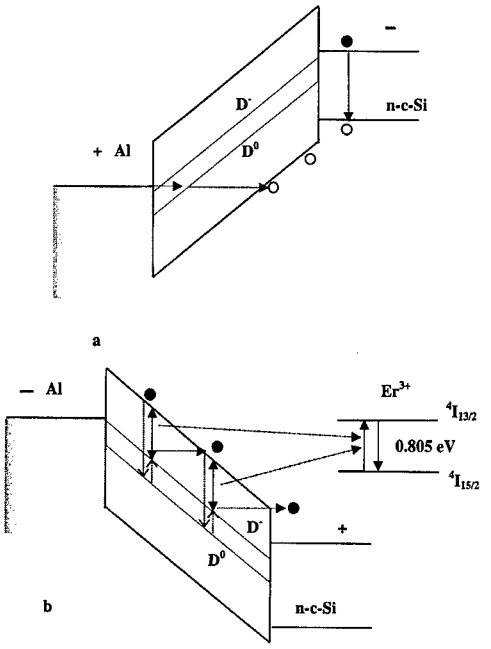

Fig. 2. Energy band diagrams of the EL structure: (a) at direct bias, (b) at reverse bias.

namely to the donor state induced by erbium–oxygen complex in amorphous silicon of the same nature as in crystalline silicon (cf. Ref. [7]).

From the defect absorption coefficient $\alpha \approx 10^3\ \mathrm{cm}^{-1}$ measured for our samples [5] the concentration of dangling bond defects (D-defects) $N_D \approx 10^{18}\ \mathrm{cm}^{-3}$ can be deduced. Since the concentration of erbium in our structures was by one order of magnitude higher, nearly all the D-centers captured additional electron from the donor levels and were in D^- state.

To construct a theoretical model which will permit the explanation of all our experimental results, we shall use two facts: (i) the erbium EL intensity I_L depends linearly on the current through the structure j in the whole range of currents studied and (ii) in sufficiently high electric fields applied to the structure both the EL intensity I_L and the current j approach asymptotically the exponential dependence on the electric field squared. We shall also introduce two assumptions the validity of which seems highly probable: (i) the mechanism of excitation of erbium ions in the case of electroluminescence is the same as that for photoluminescence [5], i.e. an Auger process of capture of free electrons from the conduction band by neutral dangling bonds (D^0-centers) while the energy released in this process is transferred by Coulomb interaction to a 4f-electron of a nearby Er^{3+} ion (DRAE-process); (ii) the electric field applied to the structure concentrates on the amorphous silicon layer whereas the voltage drop on the contact will be negligibly small. The validity of this assumption is based on a smallness of the characteristic field in the contact at no bias and the large resistance of the amorphous layer.

Now, we can write two principal equations of our model for the electric current and the EL intensity:

$$j = q\mu nE, \tag{1}$$

$$I_L = c_A n N_D^0 \frac{\tau}{\tau_r}, \tag{2}$$

where q is the electron charge, μ the mobility of electrons, n the concentration of conduction electrons, E the electric field applied to the structure, c_A the DRAE-process contribution to the capture coefficient of free electrons by D^0-centers, N_D^0 the concentration of D^0-centers, τ and τ_r are total and radiative lifetimes of erbium ion in the excited state, respectively.

To satisfy the conditions $I_L \propto j$, $I_L \propto j \propto \exp(E^2/E_c^2)$ we should admit that the only quantify which depends markedly on electric field is the concentration of conduction electrons n; the dependence of the concentration n on the electric field should be described by the formula

$$n = n_0 \exp(E^2/E_c^2), \tag{3}$$

where n_0 is the equilibrium concentration of conduction electrons, E_c is a characteristic electric field. The dependence given by Eq. (3) corresponds to thermally activated tunnelling of electrons from deep centers [8].

Since the dependence of both the current and the intensity of erbium luminescence on electric field is controlled mainly by exponent entering expression (3), these dependences as practically similar and the luminescence intensity is linear in electric current in agreement with the experiment. From the dependence $\ln(I_L) \sim E^2$ we have obtained the value of the characteristic field $E_c = 1.6 \times 10^5$ V/cm and calculated the tunnelling time $\tau_2 \sim 3 \times 10^{-14}$ s in an order-of-magnitude agreement with the results obtained for other defects and other semiconductors [8].

In the lowest approximation we should not consider the dependence on electric field of the electron mobility μ and concentration of D^0-centers N_D^0.

Therefore, the experimental results lead to the conclusion that the concentrations of negatively charged D-centers and neutral donors are nearly unaffected by the electric field and in the calculations we can use their equilibrium values.

It is the pinning of the Fermi level to the position of the donor state that makes possible the situation when electric field influences strongly the concentration of free electrons with nearly no effect on the concentrations of D^0 and D^--centers. However, these can be changed by the temperature: the rise of temperature will lead to a redistribution of electrons between D-levels and donors.

Using the expression for equilibrium concentration of D^0-centers, we arrive at the following formula for the

temperature dependence of EL intensity in the regime of constant current:

$$I_L = C_A N_D \exp\left(-\frac{\varepsilon_- - \zeta}{kT}\right)\frac{j}{q\mu E_j}\frac{\tau}{\tau_r}, \quad (4)$$

where E_j, the electric field applied to the structure at the current j, depends only weakly on the temperature, and ε_- is the position of the D^--level.

From the data presented in Fig. 1 it is seen that the $V(T)$ dependence, where $V = E/d$ is the voltage at the structure, has a maximum in the temperature region where the EL intensity rises with the temperature. This situation can be described within our model. In fact, we can express the electric field (voltage at the structure) via the current density.

$$E = E_c\sqrt{\log\frac{j}{q\mu n_0 E}}, \quad (5)$$

where in the logarithm argument we can approximately substitute E_c for E. For the temperature dependence of the field E which is determined both by the dependence $\log n_0 \sim \zeta/T$ and that of the characteristic field E_c we obtain

$$E \sim \frac{x^{1/2}}{(x + x_0)^{3/2}}, \quad (6)$$

where $x \equiv 1/T$, x_0 is a constant connected with the so-called tunnelling time of an electron (see Ref. [8]). The temperature dependence of the EL intensity I_L is given by

$$I_L \sim \frac{1}{E}\exp(-|\zeta - \varepsilon_-|x). \quad (7)$$

In Fig. 3 temperature dependences of $V = E/d$ and I_L calculated from formulae (6) and (7) are given. It is clear that the dependences obtained are in reasonable agreement with the experimental data.

At low temperatures the ionization of deep centers in strong field occurs due to tunneling without the participation of phonons and the EL intensity would be temperature-independent in agreement with our measurements.

In conclusion, we have studied electroluminescence (EL) of erbium-doped amorphous hydrogenated silicon in the temperature range 77–300 K. The intensity of erbium luminescence increased with the temperature rise and exhibited a maximum near room temperature.

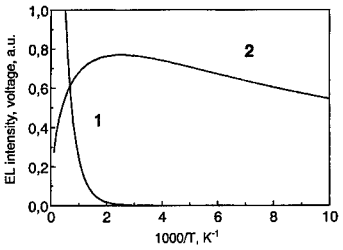

Fig. 3. Calculated temperature dependences of the intensity of erbium EL, I_L (curve 1) and the voltage on the structure, V (curve 2) in the constant current regime.

Excitation of erbium is determined by an Auger process involving capture of conduction electrons by D^0-centers with the energy transfer to 4f-electrons of the erbium ion due to Columb interaction. The stationary state is kept by multiphonon tunnel ionization of negatively charged dangling bonds (D^--centers) and donors induced by introduction of erbium ions into amorphous silicon. The theoretical model proposed describes quantitatively the whole collection of experimental data.

This work was partially supported by the Russian Foundation of Basic Research (grants 95-02-04163-a, 96-02-1693-a and 97-02-18079), INTAS grant 95-IN-RU-531, Copernicus program 977048-SIER and NATO Linkage grant HTECH.LG 972032.I.N.Y. thanks Swedish Natural Science Research Council for financial support (grant O-AH/KG 03996-322).

References

[1] M.S. Bresler et al., Appl. Phys. Lett. 67 (1995) 3599.
[2] J.H. Shin et al., Appl. Phys. Lett. 68 (1996) 997.
[3] A.R. Zanatta, Z.A. Nunes, Z.R. Tessler, Appl. Phys. Lett. 70 (1997) 511.
[4] O.B. Gusev et al., Appl. Phys. Lett. 70 (1997) 240.
[5] W. Fuhs et al., Phys. Rev. B 56 (1997) 9545.
[6] I.N. Yassievich, M.S. Bresler, O.B. Gusev, J. Phys.: Condens. Matter 9 (1997) 9415.
[7] V.F. Masterov et al., Appl. Phys. Lett. 72 (1998) 728.
[8] S.D. Ganichev, I.N. Yassievich, W. Prettl, Semicond. Sci. Technol. 11 (1996) 679.

ELSEVIER

Physica B 273–274 (1999) 358–362

PHYSICA B

www.elsevier.com/locate/physb

Transition metal defect behavior and Si density of states in the processing temperature regime

A.L. Smith[a,*], S.T. Dunham[b], L.C. Kimerling[a]

[a]*Massachusetts Institute of Technology, 77 Massachusetts Avenue, Cambridge, MA 02139, USA*
[b]*University of Washington, Box 352500, Seattle, WA 98195, USA*

Abstract

In order to make predictive models of transition metal gettering during semiconductor processing, a complete understanding of the process variables in high temperature ranges is essential. These variables are the internal gettering site density and capture radius, the intrinsic metal solubility, silicon doping level, the band gap, the effective density of states of the conduction and valence bands, and the transition metal defect level position in the gap. The least understood of these parameters is the temperature dependence of the transition metal defect level position. The work of Gilles et al. and McHugo et al. demonstrates that the doping enhancement of the solubility of Fe in p-type silicon vanishes at temperatures above 1000°C. They model this behavior by proposing movement at high temperature of the defect level for interstitial Fe from within the energy gap into the valence band. We explore the available models for Si effective density of states as a function of temperature and generate a third density of states model based on 0 K ab initio band structure calculations with the temperature-appropriate carrier occupations given by Fermi–Dirac statistics. We also consider uncertainty in E_G in the processing temperature regime. We show that uncertainties in the Si intrinsic properties database in the processing temperature regime can account for the available dopant-enhanced solubility data by assuming that E_T remain at a constant fraction of E_G. To quantitatively model gettering processes at high temperatures, more reliable estimates are needed for the densities of states of the conduction and valence bands, E_G and the behavior of defect levels as temperature rises.

Keywords: Si; Effective density of states; Fe; Defect level; Processing temperature

1. Introduction

The presence of transition metals in silicon device processing has deleterious effects on performance, yield and reliability. In silicon photovoltaics, we are concerned with the impact transition metals have on minority carrier lifetime and thereby efficiency. For integrated circuit applications, we are concerned with gate oxide integrity and device parameter homogeneity across a wafer. For this reason, a quantitative understanding of transition metal equilibria and kinetics at high temperature is needed in order to design gettering processes through accurate simulation. We explore the case of interstitial Fe (Fe_i), however, the method is quite general and can be extended to other deep-level impurities in a semiconducting host.

Researchers measuring Fe-dopant-induced solubility enhancement in p-type Si have found the enhancement to be less than they expected at temperatures $\sim$ 1000°C and have proposed an instability of the well-known Fe_i defect level (E_T) as these high temperatures are approached [1,2]. However, in order to infer the behavior of Fe in the processing temperature regime, we first need to complete our understanding of silicon at these temperatures.

In order to model dopant-enhanced solubility of defects in Si quantitatively, we need to understand the

* Corresponding author. Tel.: + 617-253-6907; fax 617-253-6782.

E-mail address: alsmith@mit.edu (A.L. Smith)

0921-4526/99/$ - see front matter
PII: S0921-4526(99)00476-7

temperature dependence of the various defect levels and Si parameters with precision. With regard to the defect Fe, E_T, the Fermi level (E_F), and the intrinsic carrier concentration (n_i) are the controlling parameters. The Si materials parameters, E_F and n_i, in turn depend on the effective density of states (DOS) of the conduction and valence bands (N_C and N_V, respectively) and the semiconductor band gap (E_G). In the work presented here, we demonstrate that uncertainties in the Si intrinsic properties database in the processing temperature regime can account for the available dopant-enhanced solubility data by assuming that E_T remain at a constant fraction of E_G.

2. Doping-enhanced solubility

Heavy p-doping increases the solubility of donor and interstitial transition metal impurities. This effect is driven by electron–hole equilibria and defect pairing to ionized acceptors which we model with defect reactions [3–7]. The intrinsic solubility of Fe in Si [8] represents the undoped reference level. The solubility in silicon is governed by the equilibrium between Fe from an external source with Fe_i donors in solid solution in the Si matrix. In p-type silicon, increased ionization of Fe_i and pairing of Fe_i^+ to ionized acceptors (A_s^-) contributes to solubility enhancement.

The quantitative calculation for the ratio of ionized to neutral charge states for Fe_i is given by Fermi–Dirac statistics for the defect level. The equilibrium constant for ionized $Fe_i^+ \cdot A_s^-$ pair formation is given by Kimerling et al.[9]. Increased p-type doping increases dopant-enhanced solubility by moving E_F with respect to the Fe_i ionization level. As more Fe_i is positively ionized, pairing becomes more likely.

3. Si in the processing temperature regime

Our interest in Si can be categorized into three temperature regimes: *measurement, device operation*, and *processing*. Most of our theoretical and experimental understanding of silicon is from very low temperatures, approximately 0 – 400 K, in the *measurement* temperature regime. This temperature regime overlaps reasonably with the temperature regime of *device operation*, predominantly between 200 and 500 K, providing accurate data for device simulation. For the case of the much higher temperatures of the *processing* temperature regime, approximately 700 – 1300 K, simulations currently rely heavily on extrapolations from the measurement temperature regime. In order to predict the interaction of defect levels with E_F, we need to understand the variation of N_C, N_V, and E_G at high temperature. It is necessary to extrapolate currently available values of these parameters well beyond the range of available measurements. In doing so, we gain an appreciation for how the uncertainty at processing temperatures will affect our calculations for dopant-enhanced solubility of Fe in Si.

The available models for N_C and N_V show disagreement even in the measurement temperature regime. The routinely used $T^{3/2}$ model found in classics such as Sze's *Physics of Semiconductor Devices* [10] is based on a parabolic band approximation. Si, however, is known to deviate from this approximation even at low temperatures. The valence band most strongly defies this categorization due to a lack of parabolicity in energy, anisotropy in the constant energy contours and the effect of spin–orbit coupling. At processing temperatures, the parabolic approximation is inadequate for both N_C and N_V. A more realistic empirical fit to data up to 500 K is provided by Green [11]. While the Green relation is a better fit to the experiment, it is only valid to 500 K and it is not valid when the Boltzmann approximation breaks down, such as in the case of degenerately doped material. This limitation is due to the fact that density of states effective mass is, in general, both temperature and energy dependent (see, for example Ref. [12]).

In order to generate a more physically reasonable method for E_F determination in the processing temperature regime, we determine the 0 K DOS from first principles using density functional theory within the local density approximation (LDA) with the Vienna ab inito simulation package (VASP) [13,14]. The LDA band structure-generated DOS has been shown to correlate with experiment better than the parabolic band model [15]. VASP numerically solves the LDA Kohn–Sham equations using ultra-soft pseudopotentials [16,17] and a plane wave basis set. A cut off energy of 300 eV was used. The exchange and correlation functional was that of Ceperley and Alder [18] as parameterized by Perdew and Zunger [19]. k-space sampling was performed with the method of Monkhorst and Pack [20] using an $18 \times 18 \times 18$ grid. k-space integrations were performed using the linear tetrahedron method including corrections according to Blöchl et al.[21]. We perform a rigid energy shift to correct for E_G which is well known to be underestimated by LDA. We then use Fermi–Dirac statistics (F-D) with numerical integration and $E_G(T)$ to determine $E_F(T)$ as dictated by the charge neutrality condition. Certain limitations of the calculation include neglecting spin–orbit coupling and greater inaccuracy in calculating excited states. On the other hand, this method can be used in the degenerately doped regime without resorting to the parabolic band approximation. In Fig. 1, we compare the calculated DOS with those given by a parabolic approximation to illustrate that they are very different even in the regions near the valence and conduction band edges. In fact, within $\sim kT$ of the band extrema, the DOS varies approximately linearly with E as opposed to the $E^{1/2}$ variation for the parabolic model.

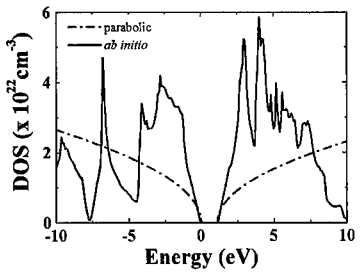

Fig. 1. Comparison of the density of states as a function of energy obtained ab initio to the density of states for a parabolic approximation to the valence and conduction bands.

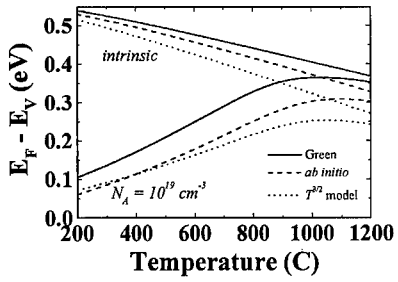

Fig. 2. Calculated values of E_F as a function of temperature for three different density of states approximations in the intrinsic (upper three curves) and heavily doped (bottom three curves) regimes. The dashed lines corresponds to E_F using the ab initio density of states the solid lines are determined with Green's N_C and N_V and the dotted lines were obtained with the $T^{3/2}$ using the data from Sze.

There are additional concerns with DOS modeling at processing temperatures. All three of these models rely on the assumption that the band structure is not significantly altered as temperature increases. In the processing temperature regime, we need to consider the influence of phonons on the band structure. Other factors that also need consideration are thermal expansion and the influence of the energy level occupations found at high temperature. The method we have developed for modeling DOS as a function of temperature is a physically reasonable starting place for determining E_F in the processing temperature regime, but it is by no means an ending point.

In Fig. 2, we compare E_F for both the case of intrinsic Si and for Si with an acceptor concentration (N_A) of 10^{19} cm^{-3} using the three DOS models discussed. The estimate using the ab initio calculated DOS falls between the curves calculated with N_C and N_V by the $T^{3/2}$ model and the extrapolation of Green's relations. It is important to note that E_F is quite sensitive to the DOS model used, varying by more than 0.1 eV at the highest temperatures shown.

Since E_F is not a measurable quantity, we look at estimates of dopant-enhanced solubility generated using the different DOS models. Fig. 3 displays calculations of Fe solubility for $N_A = 1.5 \times 10^{19}$ cm^{-3} with each DOS model assuming E_T remains at a constant fraction of the gap. The solid line shows the intrinsic Fe solubility. The curve predicting the greatest dopant-enhanced solubility was generated using again the $T^{3/2}$ model, however for this case, the Boltzmann approximation is used to determine E_F. The significant difference between this curve and that of the same DOS model with F-D integrals determining E_F demonstrates the importance of using the appropriate carrier statistics. Due to the extremely high doping level, F–D are needed.

Also in Fig. 3, we overlay the data of McHugo et al. The data is fit within error by the calculations using our DOS method and the $T^{3/2}$ model, with no instability of E_T required. The calculation using the Green extrapola-

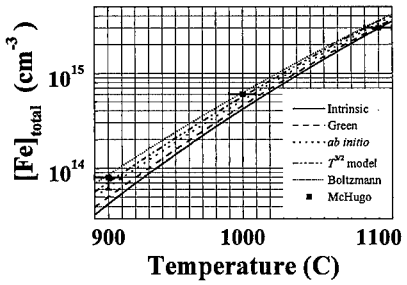

Fig. 3. Comparison of calculated dopant-enhanced solubility of Fe in Si as a function of temperature using different density of states approximations while assuming E_T remains at a constant fraction of E_G. The doping level is $N_A = 1.5 \times 10^{19}$ which corresponds to the doping level of the Si investigated by McHugo et al. (solid squares denote their data points). With the exception of the fine dotted line, all calculations were performed using Fermi–Dirac statistics to calculate E_F. A comparison between the fine dotted line (E_F obtained with the Boltzmann approximation for the $T^{3/2}$ model) and the dashed double-dot line illustrates the error generated using the Boltzmann approximation. The solid line represents the intrinsic Fe solubility.

tion underestimates for the data point at 1000°C. The $T^{3/2}$ model when used with the Boltzmann approximation overestimates the concentration at 1100°C.

The last parameter we require knowledge of in the processing temperature regime is E_G. Again, we have no reliable expression at these extreme temperatures. That most commonly used was derived by Varshni [22] with fitting parameters valid to 750 K extracted by Alex et al.[23]. We have used this relation in the calculations above, but note that extrapolations of empirically based polynomials beyond their regime of validity are notoriously unreliable.

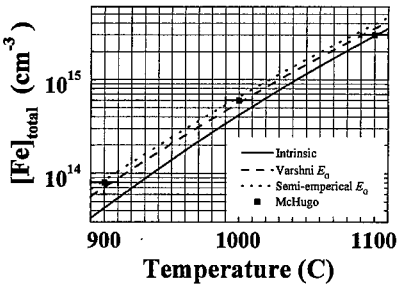

Fig. 4. Comparison of calculated dopant-enhanced solubility of Fe in Si for different temperature dependencies of E_G. E_T was held a constant fraction of the gap and we use the $T^{3/2}$ model for effective density of states. The dashed line was calculated using the Varshini relation for E_G with the parameters of Alex et al. while the dotted curve calculation relies on the extrapolation of a semi-empirical model for E_G.

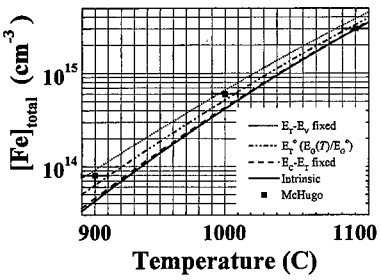

Fig. 5. Comparison of calculated dopant-enhanced solubility of Fe in Si for different temperature dependencies of the Fe defect level, E_T, in the gap. Dotted line was calculated assuming that E_T is a constant distance from the valence band edge. For the dot-dashed curve, E_T was held a constant fraction of the gap. The dashed curve was obtained by assuming that E_T is a constant distance from the conduction band edge. The solid line denotes intrinsic solubility.

A semi-empirical expression has been developed [24,25] and fit [26] over the 0 – 300 K temperature range. Extrapolations to higher temperatures are consistent with extrapolations of a linear fit valid up to 415 K[10]. The extrapolations of these relations from 415 to 750 K diverges significantly from the expression based on Varshni's model. Nevertheless, we calculate dopant enhanced solubility comparing the two sets of $E_G(T)$ to observe the impact that uncertainty in E_G has on our predictions. Fig. 4 shows these results where again we assume E_T remains at a constant fraction of the gap and we use the $T^{3/2}$ model for N_C and N_V. Note that for the data point at 1100°C, the semi-empirical E_G calculation is no longer within error.

4. Defect properties in the processing regime

In addition to the temperature dependence of fundamental properties of the host material, quantitative prediction of dopant-enhanced solubility for a defect requires the temperature dependence of (i) any defect level in the gap and (ii) relevant parameters for reactions of the defect with other species in the host matrix. For the case of Fe in p-type Si, these parameters are E_T and E_B.

For the dopant-enhanced solubility calculations contained in this paper, we focus on temperatures above 700°C where pairing has negligible impact on the solubility enhancement. Nevertheless, to generate a complete understanding of the dopant-enhanced solubility at all temperatures, the exact temperature dependence of E_B should be determined.

Motion of E_T within the gap will affect the ionization statistics and thereby the dopant enhanced solubility of Fe in p-type Si. The defect level of a species which is very foreign to its host matrix is expected to behave independently from the band edges.

In Fig. 5 we show calculations based on three cases of E_T behavior as temperature is increased and E_G narrows: (i) E_T stays at a constant fraction of E_G, (ii) E_T a fixed energy from the valence band edge, and (iii) E_T a fixed energy from the conduction band edge. Defect level position does affect the results, as expected, however, only the case with E_T a constant fraction of E_G is within error of the experimental data.

5. Conclusion

The commonly used $T^{3/2}$ model is not accurate even in the device operation regime and the available relations of Green do not extend past 500 K. We have constructed a DOS model using ab initio calculations and temperature-appropriate Fermi–Dirac statistics to generate a more physically motivated extrapolation of DOS into the processing temperature regime. Nevertheless, much remains to be explored about high temperature effects on the band structure. The available data of dopant-enhanced solubility of Fe in Si can be modeled within error assuming E_T remains at a constant fraction of E_G by either the $T^{3/2}$ model for N_C and N_V or the ab initio DOS. There is no evidence at this time for instability of E_T, however more accurate data for the Si DOS and E_G in the processing temperature regime will shed light on the temperature dependence of E_T.

Acknowledgements

The authors wish to thank K. Wada and M. Lipson for helpful discussions. This work was supported by NREL

under contract no. XD-2-11004-4 and by the Si-WEDS (Silicon Wafer Engineering and Defect Science) Consortium. One of the authors (ALS) is grateful for fellowship support from the DOE Fellowship for Integrated Manufacturing.

References

[1] Gilles, W. Schröter, W. Bergholtz, Phys. Rev. B 41 (1990) 5770.
[2] S.A. McHugo, R.J. McDonald, A.R. Smith, D.L. Hurley, E.R. Weber, Appl. Phys. Lett. 73 (1998) 1424.
[3] H. Reiss, C.S. Fuller, J. Metals 12 (1956) 276.
[4] H. M'saad, The role of surface and bulk perfection in the processing and performance of crystalline silicon, Ph.D. Thesis, Massachusetts Institute of Technology, 1994.
[5] J.L. Benton, P.A. Stolk, D.J. Eaglesham, D.C. Jacobson, J.-Y. Cheng, J.M. Poate, J. Appl. Phys. 80 (1996) 3275.
[6] L.L. Chalfoun Process optimization of alloyed aluminum backside contacts for silicon solar cells, Master's Thesis at MIT, June 1996.
[7] A.L. Smith, K. Wada, L.C. Kimerling, J. Electrochem. Soc. (1999), submitted.
[8] M. Hourai, K. Murakami, T. Shigematsu, N. Fujino, T. Shiraiwa, Jpn. J. Appl. Phys. 28 (1989) 2413.
[9] L.C. Kimerling, J.L. Benton, Physica B 116 (1983) 297.
[10] M.A. Greene, J. Appl. Phys. 67 (1990) 2944.
[11] S.M. Sze, The Physics of Semiconductor Devices, Wiley, USA, New York, 1981.
[12] F.L. Madarasz, J.E. Lang, P.M. Hemenger, J. Appl. Phys. 52 (1981) 4647.
[13] G. Kresse, J. Furthmuller, Phys. Rev. B 54 (1996) 11169.
[14] G. Kresse, J. Furthmuller, Comput. Mater. Sci. 6 (1996) 15.
[15] Landolt-Börnstein, in: O. Madelung (Ed.), Physics of Group IV Elements and III–V Compounds, Springer, Berlin, 1982.
[16] D. Vanderbilt, Phys. Rev. B 41 (1990) 7892.
[17] G. Kresse, J. Hafner, J. Phys: Condens. Matter 6 (1994) 8245.
[18] D.M. Ceperley, B.J. Adler, Phys. Rev. Lett. 45 (1980) 566.
[19] J.P. Perdew, A. Zunger, Phys. Rev. B 23 (1981) 5048.
[20] H.J. Monkhorst, J.D. Pack, Phys. Rev. B 13 (1976) 5188.
[21] P.E. Blöchl, O. Jepsen, O.K. Anderson, Phys. Rev. B 49 (1994) 16223.
[22] Y.P. Varshni, Physica 34 (1967) 149.
[23] V. Alex, S. Finkbeiner, J. Weber, J. Appl. Phys. 79 (1996) 6943.
[24] L. Viña, S. Logothetidis, M. Cardona, Phys. Rev. B 30 (1984) 1979.
[25] K.P. O'Donnell, X. Chen, Appl. Phys. Lett. 58 (1991) 2924.
[26] R. Pässler, Solid State Electron. 39 (1996) 1311.

ELSEVIER

Physica B 273–274 (1999) 363–366

PHYSICA B

www.elsevier.com/locate/physb

The electronic configuration of substitutional Fe in silicon

G. Weyer[a,*], A. Burchard[b], M. Fanciulli[a], V.N. Fedoseyev[c], H.P. Gunnlaugsson[a], V.I. Mishin[c], R. Sielemann[d], The ISOLDE Collaboration[b]

[a]*Institute of Physics and Astronomy, University of Aarhus, DK-8000, Aarhus C, Denmark*
[b]*EP Division, CERN, CH-1211 Geneva 23, Switzerland*
[c]*Institute of Spectroscopy, Russian Academy of Sciences, 142092 Troitsk, Russia*
[d]*Hahn-Meitner Institute, D-14109 Berlin, Germany*

Abstract

Ion implantations of radioactive $^{57}Mn^{+}$ into differently doped silicon single crystals held at 300–600 K have been utilized for ^{57}Fe Mössbauer studies of interstitial and substitutional Fe. Site and charge state assignments have been made on the basis of the determined hyperfine interaction parameters and Debye temperatures. Substantial fractions of substitutional ^{57}Mn probe atoms are proposed to occur due to annealing reactions. This site is maintained in the subsequent decay to ^{57}Fe by $\leqslant 50\%$ of the ^{57}Fe atoms, the remainder is displaced by recoil effects into interstitial sites.

Keywords: Mössbauer spectroscopy; Mn and Fe in silicon

1. Introduction

Among the 3d metal impurities in silicon iron can be said to be one of the best studied. However, this statement holds true almost exclusively for interstitial iron, Fe_i, only and complexes formed with it, whereas little is known about substitutional iron, Fe_s [1]. In intrinsic silicon the low total Fe solubility is attributed entirely to neutral Fe_i^0 and no signal from Fe_s has been detected [1]. This holds also for p- and p^+-type material, where, however, solubility enhancements by orders of magnitude are found for temperatures $< 1000°C$ [2,3]. This is due to both the occurrence of ionised Fe_i^+, related to the well-known $Fe_i^{0/+}$ donor level at $E_V + 0.38$ eV, and the formation of variously charged Fe_i-acceptor complexes at low temperature. The donor level was concluded to shift towards the valence band with increasing temperature and to merge with it at about 1000°C. In n^+-type material even larger solubility enhancements are attributed to the occurrence of substitutional Fe_s forming multiple acceptor centres and pairs with donors [2]. Simultaneously the Fe diffusivity decreases owing to the immobility of Fe_s and Fe_s-donor pairs. The behaviour of Co and Mn in heavily doped material was generally similar to that of Fe [2]. For Mn not only in n-type but also in intrinsic material substitutional Mn_s was concluded to be the dominant species. Utilizing radioactive ^{57}Co tracers, by ^{57}Fe Mössbauer spectroscopy (MS) assignments were made for both the spectra of Fe_s and Fe_s-donor pairs in n^+-type material and those of Fe_i-acceptor pairs in p-type material [2,4]. According to Ref. [1] all other experimental evidence for the existence of substitutional Fe was obtained in irradiated materials either by EPR [5] or by MS [6–8]. Theory predicts no band-gap states for Fe_s [9–11] and calculations of the $^{57}Fe_s$ isomer shift [7,12] are in reasonable agreement with each other and with the assignments made in Refs. [6–8], whereas these isomer shift values are significantly different from those given for $^{57}Fe_s$ in n^+-type silicon [2].

In this contribution we present further evidence for an unambiguous identification of the Mössbauer spectrum of Fe_s in differently doped materials and mention

* Corresponding author. Tel.: +45-894-22899; fax: +45-861-20740.
E-mail address: gw@ifa.au.dk (G. Weyer)

0921-4526/99/$ - see front matter
PII: S0921-4526(99)00478-0

briefly also new results for Fe_i. The experimental approach as described in Ref. [8] is different from previous procedures. Short-lived radioactive ^{57}Mn isotopes ($T_{1/2}$ = 1.5 min) are implanted and a substantial annealing of the radiation damage from the implantation process is achieved during the ^{57}Mn lifetime at 400–600 K prior to the decay and the measurement of the ^{57}Fe Mössbauer spectra at those temperatures. However, owing to an average decay recoil energy of $\langle E_R \rangle = 40$ eV imparted on the ^{57}Fe daughter atoms, a sizeable fraction is expelled mainly into interstitial sites. (Note that the recoil energy and the ^{57}Mn half-life were erroneous in Ref. [8].)

2. Experimental

Isotope separated beams of radioactive $^{57}Mn^+$ ions were implanted with an energy of 60 keV into silicon samples at the ISOLDE facility at CERN [13]. The samples were mounted in an implantation chamber [14] and held at temperatures of 300–600 K. About 10^{11} ions/cm^2 were implanted into each sample for each measurement at five different temperatures. P-type (3×10^{18} B/cm^3), n-type (5×10^{14} P/cm^3), and n^+-type ($3–4 \times 10^{20}$ P/cm^3) samples were employed. Mössbauer spectra were measured with a resonance detector [15] equipped with a stainless steel converter foil enriched in ^{57}Fe. The isomer shifts, δ, are given at 298 K relative to α-iron.

3. Results and discussion

As discussed previously [8], accurate determinations of the isomer shifts for the lines assigned to interstitial Fe on tetrahedral sites and substitutional Fe, revealing the anticipated Fermi-level dependence, have hitherto been hampered by the presence of a quadrupole-split line in spectra from ion implantation studies [6–8]. This line, attributed to a 'damage site' of unknown nature, showed substantial annealing between 77 and 297 K [6,8] and is here found to be annealed completely in p- and n-type material at 480 K, where only a 10% spectral fraction remained in n^+-type material. Spectra measured at 533 K are shown in Fig. 1, where the three lines found in the spectra are indicated; their parameters (from simultaneous fits for 480–573 K) are gathered in Table 1. The narrow lines are assigned to Fe_i(t) on tetrahedral sites and Fe_s, respectively, the broad lines, labelled Fe_u, have not been reported previously. The Debye temperatures, θ, obtained from the fit have large uncertainties, however, the more precise ratios of the corresponding Lamb-Mössbauer factors establishes their ordering. The Debye temperatures, deduced here for the first time, clearly reflect the substitutional and interstitial nature of Fe and

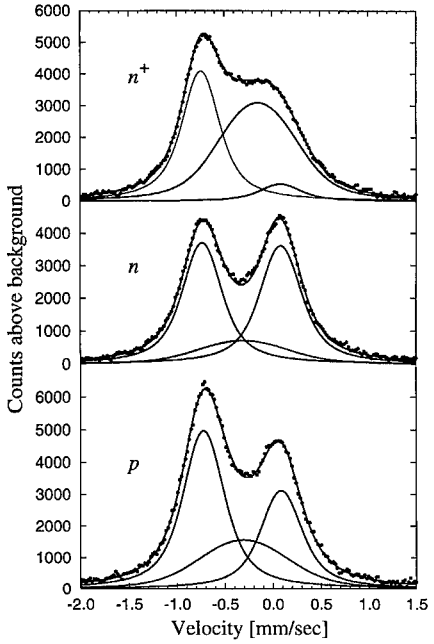

Fig. 1. ^{57}Fe Mössbauer spectra measured at 533 K for n^+-, n-, and p-type silicon single crystals. The analysis in terms of three different lines is indicated.

Table 1
Mössbauer parameters and site assignments for the individual components in the spectra

Line assignment	δ^a (mm/s)	$\sigma^{b,c}$ (mm/s)	Δ (mm/s)	θ_D (K)
$Fe_i(t, n^+)$	0.813(9)	0.09(1)	–	246(10)
$Fe_i(t, n)$	0.802(10)		–	
$Fe_i(t, p)$	0.790(9)		–	
Fe_s	−0.026(10)	0.11(2)	–	442(30)
$Fe_u(n, p)$	0.37(4)	0.24(4)	0.38(10)	232(80)
Fe_u (n^+)	0.21(3)	0.31(5)	0.41(10)	318(20)

[a] Relative to the center of the spectrum of α–Fe.
[b] The additional Gaussian broadening of the lines, all lines have the same Lorentzian width of 0.35(1) mm/s.
[c] The line broadening given for the interstitial iron is the line broadening at 480 K.

corroborate the site assignments made on the basis of the isomer shifts previously. For Fe_s a mass defect approximation yields a value of $\theta \approx 440$ K, which is in agreement with the experimental value. The pronouncedly lower value for Fe_i(t) suggests that the Debye temperatures enable a distinction between interstitial and substitutional sites. This then gives an indication as to the nature of the new broad lines. The Fe_u(n,p) lines have the same

Mössbauer parameters in n- and p-type material and the low Debye temperature implies an interstitial Fe location. The difference in the isomer shift to those for $Fe_i(t)$ and a small quadrupole splitting indicate a rather different location in a site of non-cubic symmetry. The line in n^+-type material, $Fe_u(n^+)$, is distinguished from this line by a different isomer shift and a larger Debye temperature in particular. This points to an unusually stable interstitial location or to a perturbed substitutional site.

In the analysis the line broadening due to the stainless steel absorber material was taken into account by a Gaussian broadening of the Lorentzian lines. At 480 K the Fe_i and Fe_s lines show no further broadening, however, at the highest temperatures the Fe_i lines broaden whereas the Fe_s line width stays constant. The line widths of the new broad lines are much larger and not well determined except for n^+-type material, where it is approximately constant. The broadening of the lines assigned to interstitial $Fe_i(t)$ sites is obviously related to the onset of diffusions, i.e. a few diffusional jumps occur within the lifetime of the excited nuclear state (140 ns), as observed previously [16]. This issue will be addressed in a forthcoming paper.

From the spectral intensities of the lines population fractions for the different Fe lattice sites have been calculated within a Debye model. The annealing of the quadrupole-split line of the 'damage site' leads predominantly to an increase of the Fe_s fraction, whereas the $Fe_i(t)$ fraction is approximately constant up to 480 K and the same ($\approx 60\%$) in all materials at that temperature. This gives evidence that the $Fe_i(t)$ fraction results from recoiling Fe atoms irrespective of the lattice location of the Mn parent atoms. The annealing behaviour observed concordantly in all experiments [6–8] with different implanted 3d probe atoms, i.e. Co, Fe, and Mn, suggests that substitutional sites are occupied by substantial fractions upon annealing. This can be attributed to the high concentration of vacancies in the radiation damage cascade created by the implanted ion. Given this lattice location, the Mn_s probe atoms can be considered immobile, whereas the diffusivity of Mn_i would result in diffusion lengths during its lifetime, which exceed the dimensions of the damage cascades and the implantation depth for the highest temperatures, if no trapping occurs. However, this fraction may interact with lattice defects and impurities. It is well known that in the temperature range investigated mobile Mn_i as well as Fe_i form pairs with B [17,1] in p-type material; the Mössbauer parameters of the Fe_i–B pairs are also known [4]. The absence of any indications for these lines in the present spectra is either due to a complete relocation of the recoiling Fe atoms from the pairs or a preferential substitutional location in the implantation and annealing processes. The recoil effects for atoms located initially on interstitial or substitutional sites are likely to be different. An interstitial relocation appears most probable in both cases, whereas the probability to remain on the initial site should be higher for substitutional than for interstitial location considering the difference in the Debye temperatures, i.e. in the bond strength. A replacement collision of a recoiling Fe atom with Si atoms should have a low probability due to the low recoil energy and the large mass difference. These considerations are in accordance with the dominant interstitial fractions observed. If those are recoil-produced, the atoms can be considered to be statistically distributed on interstitial sites making the probability of having a lattice defect or an impurity in the local atomic surrounding very small. Thus, the differences observed for the isomer shifts in n- and p-type material can be attributed to the Fermi-level dependence. The Fermi-levels are not accurately known due to an unknown potential influence of the residual radiation damage. However, for the heavily doped materials the Fermi levels can be safely assumed to be in the upper and lower halves of the band gap, respectively. As discussed previously [8] then the decay should lead to Fe_i^0 and Fe_i^+ states in n^+- and p-type material, respectively. The isomer shift values given in Table 1 at 298 K (corrected for the second-order Doppler shift) are more accurate than previous values [6–8], which mostly deviate from the present values however, by less than 2σ. A more detailed discussion of the results for $Fe_i^{0/+}$ is postponed until a further analysis of the more comprehensive set of data.

The origin of the substitutional fraction is to a large extent attributed to the substitutional location of the Mn parent atoms upon annealing of the 'damage site'. The recoil in the subsequent decay does not alter this location for a certain fraction of the Fe daughter atoms. The isomer shift for the substitutional line is the same in p- and n-type material within error bars. Considering the known $Mn_s^{0/+}$ band-gap state [18], Mn_s should be neutral in the n-type material and then the β^--decay leads to positively charged Fe_s^+. In the p-type material the decay of Mn_s^+ leads initially to Fe_s^{2+}. However, as this state is a resonance state in the valence band [9,18] it should be filled within times shorter than the lifetime of the Mössbauer state (140 ns) and thus again Fe_s^+ results. The narrow line width is consistent with T_d symmetry. The centre is therefore most likely not the same as a Fe_i^+-vacancy centre observed by EPR in e^--irradiated, moderately doped p- and n-type silicon, where the Fe atom is proposed to be slightly displaced from the substitutional site [5]. This should lead to a quadrupole-split or at least broadened Mössbauer line. This appears consistent with the characteristica of the $Fe_u(n^+)$ line, which, however, is unlikely also to be due to a Fe_s^+ charge state. If it is due to substitutional Fe, the MS data indicate a neutral charge state, i.e. the $Fe_s^{0/+}$ state would be in the upper half of the band gap. The isomer shift, $\delta = 0.41(1)$ mm/s, of a broad line ($\Gamma = 0.78$ mm/s) assigned previously to Fe_s in n^+-type material [2] is however, significantly different from

the present value. This line converts reversibly (600–900°C) into a quadrupole-split doublet with the parameters: $\delta = 0.07(2)$ mm/s, $\Gamma = 0.64$ mm/s and $\Delta = 0.79$ mm/s, assigned to Fe_s–P pairs. Both lines have the same but unknown Debye temperature. The former line could be contained in the $Fe_u(n^+)$ line found in the present investigation. Note that in our analysis this line was found to be analysed best with a quadrupole-split doublet, where the components, if interpreted as a single lines, would have isomer shifts of $+0.41$ and $+0.05$, respectively. The former value agrees with that of Ref. [2], the latter is close to that assigned here to Fe_s^+ and agrees with that of possibly neutral Fe_s^--P^+ pairs. Thus it appears conceivable that these lines could be due to the neutral Fe_s^0 and/or to (multiply) charged Fe_s^{-n} acceptor states in the upper half of the band gap. The relatively high Debye temperature determined here appears consistent with a substitutional Fe location. In this context, the large line width observed in both investigations could result from the simultaneous presence of different charge states having different isomer shifts. Theoretical values for the isomer shift of Fe_s^0 [6,7], are too uncertain to warrant a reliable identification of that charge state, however, they are not inconsistent with the supposition given above.

In summary: The generally similar behaviour of the 3d elements in question under ion implantation conditions in all material types and under diffusion conditions in n^+-type suggests that the occurance of substitutional impurities is correlated to the presence of high vacancy concentrations. In implanted material these are created athermally, whereas in n^+-type material evidence for their presence in high concentrations in thermal equilibrium has been found [19]. In n- and p-type material the Mössbauer parameters of substitutional Fe, assigned to Fe_s^+, are well determined and in reasonable agreement with theoretical expectations. The results for n^+-type material are less clear-cut. One or more broad lines are found within a range of isomer shifts, these are tentatively assigned to Fe_s^0 and differently charged Fe_s^{-n} states in the upper half of the band gap. The substitutional fractions are large in all ion implanted material types. Given the recoil production of the interstitial fraction, they amount to $\approx 100\%$. This finding for ion implanted material may be of relevance also with respect to the importance of a suppression of 3d metal impurity contaminations in device technologies.

Acknowledgements

This work has been supported by the Danish Natural Science Research Council within the CRAK center.

References

[1] A.A. Istratov, H. Hieslmair, E.R. Weber, Appl. Phys. A 69 (1999) 13.
[2] D. Gilles, W. Schröter, W. Bergholz, Phys. Rev. B 41 (1990) 5770.
[3] S.A. McHugo, R.J. McDonald, A.R. Smith, D.L. Hurley, E.R. Weber, Appl. Phys. Lett. 74 (1998) 1424.
[4] W. Bergholz, Physica 116B (1983) 312.
[5] S.H. Muller, G.M. Tuynman, E.G. Sieverts, C.A.J. Ammerlaan, Phys. Rev. B 25 (1982) 25.
[6] G. Langouche, Hyp. Int. 72 (1992) 217.
[7] J. Kübler, A.E. Kumm, H. Overhof, P. Schwalbach, M. Hartick, E. Kankeleit, B. Keck, L. Wende, R. Sielemann, Z. Phys. B 92 (1993) 155.
[8] G. Weyer, S. Degroote, M. Fanciulli, V.N. Fedoseyev, G. Langouche, V.I. Mishin, A.-M. Van Bavel, A. Vantomme, the ISOLDE Collaboration, Mat. Sci. Forum 258–263 (1997) 437.
[9] F. Beeler, O.K. Andersen, M. Scheffler, Phys. Rev. B 41 (1990) 1603.
[10] A. Zunger, U. Lindefelt, Phys. Rev. B 26 (1982) 5989.
[11] A. Zunger, U. Lindefelt, Phys. Rev. B 27 (1983) 1191.
[12] M. Lannoo, A. Svane, H. Overhof, H. Katayama-Yoshida, in: G. Langouche (Ed.), Hyperfine Interactions of Defects in Semiconductors, Elsevier, Amsterdam, 1992, p. 379.
[13] V.N. Fedoseyev, K. Bätzner, R. Catherall, A.H.M. Evensen, D. Forkel-Wirth, O.C. Jonsson, E. Kugler, J. Lettry, V.I. Mishin, H.L. Ravn, G. Weyer, the ISOLDE Collaboration, Nucl. Instr. Meth. B 126 (1997) 88.
[14] G. Weyer, Nucl. Instr. Meth. 186 (1981) 210.
[15] G. Weyer, in: I.J. Gruverman, C.W. Seidel, (Eds.), Mössbauer Effect Methodology Vol. 10, Plenum Press, New York, 1976, p. 301.
[16] P. Schwalbach, S. Laubach, M. Hartick, E. Kankeleit, B. Keck, M. Menningen, R. Sielemann, Phys. Rev. Lett. 64 (1990) 1274.
[17] H. Nakashima, K. Hashimoto, Mat. Sci. Forum 83–87 (1992) 227.
[18] R. Czaputa, H. Feichtinger, J. Oswald, H. Sitter, M. Haider, Phys. Rev. Lett. 55 (1985) 758.
[19] G. Weyer, M. Fanciulli, K. Freitag, A. Nylandsted Larsen, M. Lindroos, E. Müller, H.C. Vestergaard, the ISOLDE Collaboration, Mat. Sci. Forum 196–201 (1995) 1117.

ELSEVIER

Physica B 273–274 (1999) 367–370

PHYSICA B

www.elsevier.com/locate/physb

Lattice location of implanted Cu in Si

U. Wahl[a,*], J.G. Correia[b], A. Vantomme[a], G. Langouche[a], the ISOLDE collaboration[b]

[a]*Instituut voor Kern- en Stralingsfysica, University of Leuven, Celestijnenlaan 200 D, B-3001 Leuven, Belgium*
[b]*CERN-EP, CH-1211 Geneva 23, Switzerland*

Abstract

We have implanted the radioactive probe atom ^{67}Cu ($t_{1/2}$ = 61.9 h) into single-crystalline Si. Monitoring the β^- emission yield from the decay of ^{67}Cu to ^{67}Zn as a function of angle from different crystallographic directions allows to determine the lattice location of the Cu atoms by means of the emission channeling effect. We give direct evidence that the majority of implanted Cu occupies near-substitutional sites. As most-likely lattice location we suggest a displacement of 0.51(7) Å along ⟨1 1 1⟩ directions from substitutional sites to bond center positions. The annealing behavior shows that near-substitutional Cu is remarkably stable, and we estimate a dissociation energy of 2.2(3) eV.

Keywords: Cu in Si; Lattice location; Implantation; Gettering

1. Introduction

Cu represents a widespread contaminant in Si processing [1] and is responsible for several deep levels [2]. These deep levels act as recombination centers for electrons and holes, and hence are usually detrimental for the performance of electronic devices. Since Cu is also the fastest interstitial diffuser in Si (migration energy E_m = 0.18 eV) [3] with a very low intrinsic room-temperature solubility, it shows a strong tendency to precipitate or to react with various defects (cf. Ref. [1] and references therein). Among these are acceptors, and damage-related centers such as divacancies [4], dislocations, implantation defects, or voids [5]. The binding of Cu to these defects may be used beneficially in order to getter Cu within regions away from the active region of electronic devices.

The basic knowledge on the lattice sites of Cu in Si is very poor [1], despite its significance as a deep impurity and its technological role as potential contaminant in Si processing. Theory [6–8] as well as analogies to the other 3d and IB metals in Si [9,10] and to Cu in Ge [11,12] suggest that both tetrahedral interstitial and substitutional Cu may exist. Electron paramagnetic resonance (EPR) [13] and photoluminescence (PL) [14] have been able to detect a number of Cu-related signals with less than cubic symmetry which are supposed to be due to Cu–Cu pairs. *Direct* lattice location techniques such as ion beam channeling cannot be applied at low Cu concentrations, and at higher concentrations Cu forms precipitates.

In this contribution we report on first results of β^- emission channeling [15] lattice location experiments using the radioactive isotope ^{67}Cu ($t_{1/2}$ = 61.9 h) implanted into single-crystalline Si. The β^- particles emitted during the decay from ^{67}Cu to ^{67}Zn (maximum energy 577 keV) experience channeling effects along major crystal axes and planes. Monitoring the angular-dependent β^- emission yield by means of a position-sensitive electron detector as a function of angle from ⟨1 0 0⟩, ⟨1 1 0⟩ and ⟨1 1 1⟩ directions allows to directly determine the lattice location of ^{67}Cu.

2. Method

Clean beams of 60 keV radioactive Cu isotopes are available from newly developed laser ion sources at

*Corresponding author. Tel.: + +32-16-327617; fax: + +32-16-327985.
E-mail address: ulrich.wahl@fys.kuleuven.ac.be (U. Wahl)

0921-4526/99/$ - see front matter
PII: S0921-4526(99)00479-2

CERN's on-line isotope separator ISOLDE [16]. Implantations of ^{67}Cu into an n-Si : P float zone (FZ) grown single crystal (resistivity 700–1300 Ω cm, ⟨1 1 1⟩ orientation, implanted dose 3.8×10^{12} cm^{-2}) were done at room temperature, under 7° towards the surface normal of the sample and using a 1 mm beam spot. A position-sensitive Si detector was used in order to detect the emitted β^- particles. The same detection system was already applied in our previous experiments on the lattice location of rare earths in Si, and is described in more detail in Refs. [17,18]. Emission channeling patterns were extracted for the integral energy range from 97 to 600 keV. The value of 97 keV has been chosen as lower boundary in order to exclude the 84 and 92 keV conversion electrons emitted from the well-known 9.2 μs Mössbauer state in ^{67}Zn, which is populated from the ^{67}Cu decay.

In order to deduce the Cu lattice location from the β^- emission patterns we have carried out computer simulations of β^- emission yields, based on the dynamical theory of electron diffraction [15]. To approximate the continuous β^- energy spectrum of ^{67}Cu, simulations were done for electron energies from 100 to 550 keV in steps of 25 keV, and the results were averaged according to the theoretical spectral β^- distribution. We calculated characteristic two-dimensional patterns of electron emission probability within a range of ± 3° around the ⟨1 1 1⟩, ⟨1 0 0⟩ and ⟨1 1 0⟩ directions in steps of $\Delta x = \Delta y = 0.05°$. Due to limitations in computing time, however, we had to restrict ourselves to lattice sites with trigonal or tetragonal symmetry, and we considered substitutional (S), tetrahedral interstitial (T), hexagonal (H), bond center (BC), anti-bonding (AB), split ⟨1 0 0⟩ (SP) and the so-called Y and C sites (Fig. 1), as well as various ⟨1 1 1⟩ and ⟨1 0 0⟩ displacements between these sites. Quantitative information on the occupied sites was then obtained by comparing the fit of simulated patterns to the observed yields. The fit procedures used for this purpose have been discussed earlier [18].

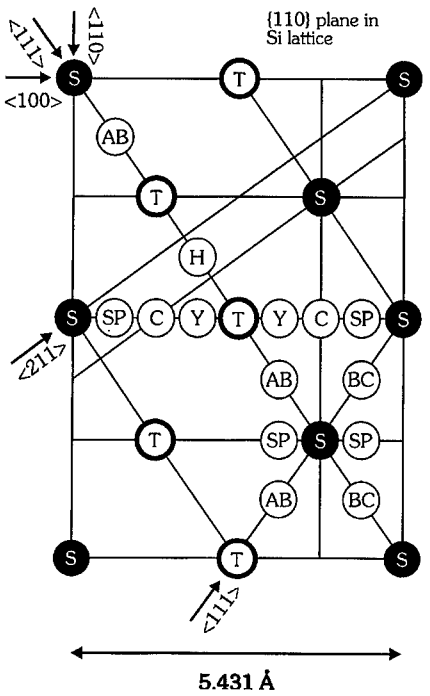

Fig. 1. High-symmetric lattice sites in Si. Cubic symmetry: S = substitutional, T = tetrahedral interstitial; trigonal symmetry: BC = bond center, AB = anti-bonding, H = hexagonal; tetragonal symmetry: SP = split ⟨1 0 0⟩, Y = the so-called Yb sites, and C = the so-called C-sites.

3. Results and discussion

Figs. 2(a)–(c) show the normalized β^- emission yields measured in the vicinity of the ⟨1 1 1⟩, ⟨1 0 0⟩ and ⟨1 1 0⟩ directions following room-temperature implantation of ^{67}Cu and annealing for 10 min at 100°C, 150°C and 200°C. An enhancement of β^- emission yield is visible along all of the axial directions, and also along the {1 1 1} and {1 1 0} planes. This proves that the majority of Cu is located close to substitutional sites, leading to channeling of emitted β^- particles along the closest-packed axial and planar directions. While {1 0 0} planar channeling in Si is usually not very pronounced (a few per cent above unity), in our case we even observe an electron emission yield below unity along the {1 0 0} planes. This gives evidence that the Cu atoms exhibit a significant displacement from ideal substitutional lattice sites.

More specific information on the occupied lattice sites is obtained by fitting the experimental yields with theoretical patterns. Figs. 3(a)–(c) show the calculated yields for 100% of emitter atoms on ideal S sites, assuming a root-mean-square (rms) thermal vibration amplitude of $u_1 = 0.079$ Å for the Cu atoms. For a fraction of 20% of emitter atoms on S sites and 80% on random sites these patterns reproduced most of the general features of the experimental yields shown in Figs. 2(a)–(c). Note that random sites are sites which cause an isotropic emission yield, for instance sites of very low crystal symmetry or in heavily damaged surroundings. However, the quality of fit considerably improved by introducing displacements from ideal S sites. The best fits, assuming a single Cu lattice site in addition to random sites, are shown in Figs. 2(d)–(f) and correspond to 70%, 62% and 76% of emitter atoms displaced from ideal S sites by 0.51(7) Å along ⟨1 1 1⟩ directions towards the bond center positions. The decrease in the chi square of fit, χ^2, compared to S sites was significant (20–40%). We also tried ⟨1 0 0⟩ displacements from S to SP (S → SP) and ⟨1 1 1⟩ displacements from S to AB (S → AB) sites. In the case of S → SP a local minimum of χ^2 was found for a distance of

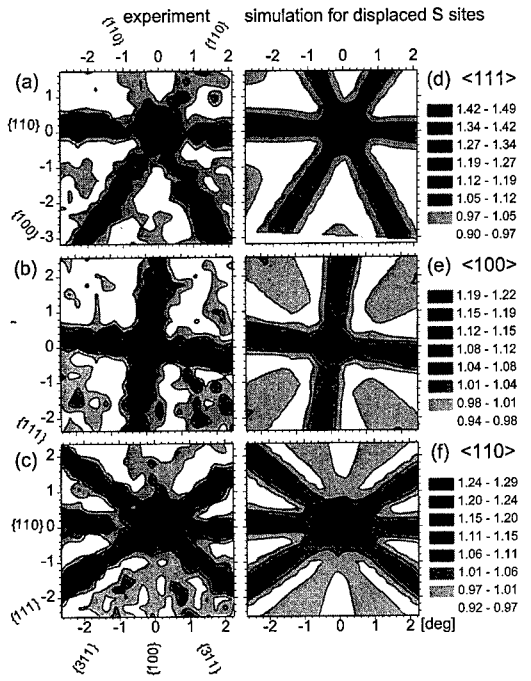

Fig. 2. (a), (b) and (c): β^- channeling patterns following room-temperature implantation of 3.8×10^{12} cm^{-2} of ^{67}Cu into *n*-Si : P FZ and annealing at 200°C. Shown are normalized emission yields from the integral β^- intensity in the vicinity of $\langle 1\,1\,1\rangle$, $\langle 1\,0\,0\rangle$ and $\langle 1\,1\,0\rangle$ directions. (d), (e) and (f) are best fits of simulated patterns to the experimental yields, corresponding to 70%, 62%, and 76% of emitter atoms on sites which are displaced by 0.51 Å from the S site towards the BC site.

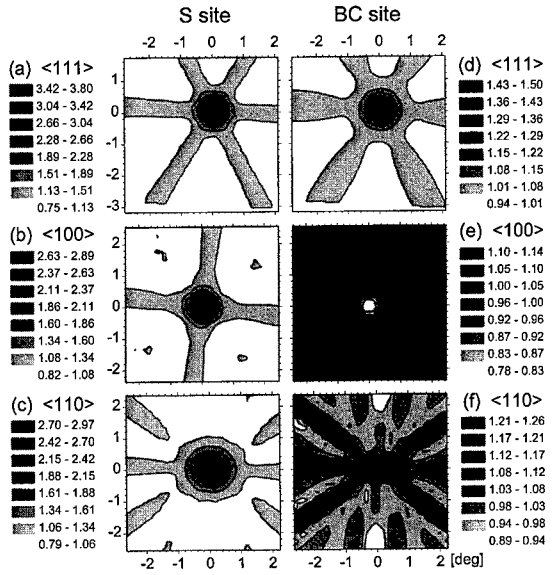

Fig. 3. (a), (b) and (c): Simulated angular-dependent β^- emission yields for 100% of ^{67}Cu atoms on ideal substitutional sites. (d), (e) and (f): Simulated yields for 100% on bond center positions. The angular resolution and orientation have been chosen corresponding to the experimental channeling patterns shown in Fig. 2(a), (b) and (c).

0.41 Å from the S site, but the absolute χ^2 values were up to 32% worse than for S → BC. Since the $\langle 1\,1\,1\rangle$ and $\langle 1\,0\,0\rangle$ channeling patterns for S → BC and S → AB sites are identical, only the $\langle 1\,1\,0\rangle$ pattern could be used in order to test for S → AB displacements. While a local minimum was found for a displacement around 0.51 Å from S to AB, the χ^2 values were 19% worse than for S → BC, and hence Cu on S → AB sites is less likely. We also considered Gaussian distributions of Cu atoms centered at the S sites. For an rms displacement of $u_1 = 0.40$ Å, these were also in agreement with the experimental data, so that an ensemble of Cu atoms with small but varying displacements from S sites cannot be ruled out.

On the other hand, major fractions of Cu on sites with displacements from the substitutional position larger than 0.6 Å were all clearly not in accordance with the experimental data. As an example we show the patterns due to the bond center positions [Figs. 3(d)–(f)], which are located at 1.17 Å from the S sites. Finally, we also investigated the possibility that, besides the near-substitutional Cu fraction, additional smaller fractions might be located on other high-symmetric sites. However, only the fits where we considered a combination of near-S sites and bond centered sites were compatible with the experimental data, indicating that a substantial part of the random fraction might be due to the occupancy of BC sites. Since the channeling patterns from BC sites are generally weak [Figs. 3(d)–(f)], an unambiguous identification of such a BC fraction will require measurements with improved statistics, though. In summary, we consider it most likely that the majority of Cu [69(6)%] is located at a position around 0.4–0.5 times the distance from S to BC sites, and the remainder on random sites. However, since we did not test these sites, we cannot exclude that the ~0.51 Å displacement occurs along other crystal directions such as $\langle 1\,1\,0\rangle$ or $\langle 2\,1\,1\rangle$, leading to a lower symmetry than trigonal or tetragonal.

In order to interpret the incorporation of Cu into near-substitutional sites, we have to consider the defect situation following ion implantation, which we have simulated using the MARLOWE code [19]. The mean implantation depth of 60 keV ^{67}Cu in Si is 494 Å with a straggling of 186 Å. The simulations indicate that around 800 vacancies are created for every implanted Cu atom, and that the mean distance to the nearest vacancy is less than 5 Å. Hence, Cu should have ample possibility to be trapped within vacancy-related defects.

Fig. 4 shows the isochronal (10 min) annealing behavior of the fraction of Cu on near-S sites for temperatures up to 600°C. Already in the as-implanted state we found

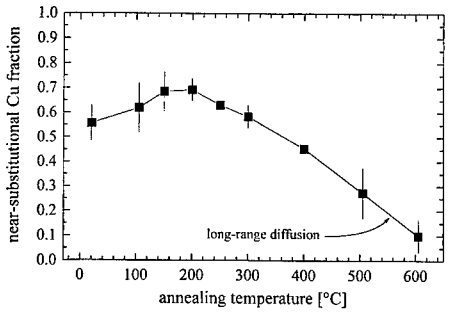

Fig. 4. Isochronal annealing sequence (10 min, measurements at 20°C) for the fraction of ^{67}Cu on near-substitutional sites.

56% of Cu atoms close to substitutional sites. Upon annealing to 200°C, the near-S fraction reached a maximum (cf. Fig. 2), and decreased continuously at higher temperatures along with an increase in the random fraction. Since the implantation damage, which is to some extent responsible for the random Cu fraction, decreases with increasing annealing temperature, the growth of the random Cu fraction must be associated with either a change in the local surroundings, or with Cu atoms changing to lattice sites of lower symmetry. A direct proof that Cu lattice site changes are involved, comes from the fact that following the anneal step at 600°C, the β^- count rate dropped by a factor of two. Since there was no detectable contamination outside the sample, we conclude that the radioactive Cu must have diffused throughout the bulk of the crystal. Assuming that the dissociation of Cu from near-substitutional sites follows an Arrhenius behavior with an attempt frequency of the order of the lattice vibrations ($\sim 10^{12}$ Hz), we estimate an activation energy of 2.2(3) eV for this process. This compares to the thermal stability of high-dose Cu implants into single-crystalline Si (>2.2 eV), Cu in Cu_3Si precipitates (2.2 eV) and Cu within voids (2.7 eV) [5], but is considerably higher than in amorphous Si, where an activation energy of 1.2 eV has been reported for Cu diffusion [20].

4. Conclusions

We have given direct evidence that the majority of implanted Cu occupies near-substitutional sites in Si. The displacement from S sites amounts to 0.51(7) Å and occurs most likely along the ⟨1 1 1⟩ directions towards the bond center positions. We suggest that this lattice position is due to Cu within a single or double vacancy. The annealing behavior shows that near-S Cu is remarkably stable, and that the room-temperature diffusion of Cu is suppressed once it occupies substitutional sites. This indicates that the formation of substitutional Cu is also involved in the initial stages of the radiation damage gettering mechanism.

Finally, the radioactive isotope ^{67}Cu has been found very suitable for lattice location studies of implanted Cu in semiconductors. Further experiments will be undertaken to study possible influences of doping type, crystal growth mode (FZ, CZ, epitaxial), or additional impurities on the lattice sites and stability of Cu in Si.

Acknowledgements

This work was partially funded by the TMR-LSF program of the European Union (UW) and the FCT and ITN, Portugal, through project CERN/S/FIS/1048/98 (JGC).

References

[1] A. Istratov, E.R. Weber, Appl. Phys. A 66 (1998) 123.
[2] S.D. Brotherton, J.R. Ayres, A. Gill, H.W. van Kesteren, F.J.A.M. Greidanus, J. Appl. Phys. 62 (1987) 1826.
[3] A. Istratov, C. Flink, H. Hieslmair, E.R. Weber, Phys. Rev. Lett. 81 (1998) 1243.
[4] M.O. Aboelfotoh, B.G. Svensson, Phys. Rev. B 52 (1995) 2522.
[5] S.M. Myers, D.M. Follstaedt, J. Appl. Phys. 79 (1996) 1337.
[6] A. Fazzio, M.J. Caldas, A. Zunger, Phys. Rev. B 32 (1985) 934.
[7] F. Beeler, O.K. Andersen, M. Scheffler, Phys. Rev. B 41 (1990) 1603.
[8] S.K. Estreicher, J.L. Hastings, Mater. Sci. Eng. B 58 (1999) 155.
[9] G.W. Ludwig, H.H. Woodbury, Solid State Phys. 13 (1962) 223.
[10] E.R. Weber, Appl. Phys. A 30 (1983) 1.
[11] F.C. Frank, D. Turnbull, Phys. Rev. 105 (1956) 617.
[12] R.N. Hall, J.H. Racette, J. Appl. Phys. 35 (1964) 379.
[13] P.N. Hai, T. Gregorkiewicz, C.A.J. Ammerlaan, D.T. Don, Phys. Rev. B 56 (1997) 4620.
[14] J. Weber, H. Bauch, R. Sauer, Phys. Rev. B 25 (1982) 7688.
[15] H. Hofsäss, G. Lindner, Phys. Rep. 210 (1991) 121.
[16] J. Lettry, R. Catherall, G.J. Focker, O.C. Jonsson, E. Kugler, H. Ravn, C. Tamburella, V. Fedoseyev, V.I. Mishin, G. Huber, V. Sebastian, M. Koizumi, U. Köster, and the ISOLDE collaboration, Rev. Sci. Instr. 69 (1998) 761.
[17] U. Wahl, A. Vantomme, J. De Wachter, R. Moons, G. Langouche, J.G. Marques, J.G. Correia, and the ISOLDE collaboration, Phys. Rev. Lett. 79 (1997) 2069.
[18] U. Wahl, J.G. Correia, S. Cardoso, J.G. Marques, A. Vantomme, G. Langouche, and the ISOLDE collaboration, Nucl. Instr. and Meth. B 136 (1998) 744.
[19] M.T. Robinson, Phys. Rev. B 40 (1989) 10 717.
[20] S. Coffa, J.M. Poate, D.C. Jacobson, W. Frank, W. Gustin, Phys. Rev. B 45 (1992) 8355.

ELSEVIER

Physica B 273–274 (1999) 371–374

PHYSICA B

www.elsevier.com/locate/physb

Metal impurity precipitates in silicon: chemical state and stability

Scott A. McHugo[a,b,*], A.C. Thompson[b], G. Lamble[a], C. Flink[c], E.R. Weber[c]

[a]*Advanced Light Source, Lawrence Berkeley National Laboratory, Berkeley, CA 94720, USA*
[b]*Center for X-ray Optics, Lawrence Berkeley National Laboratory, Berkeley, CA 94720, USA*
[c]*Materials Science Division, Lawrence Berkeley National Laboratory, Berkeley, CA 94720, USA*

Abstract

The chemical state and the stability of metal precipitates in silicon have been studied using synchrotron-based X-ray fluorescence and absorption. Specifically, we have studied the stability and chemical nature of iron and copper impurities in single and polycrystalline silicon. In polycrystalline silicon material, we observe the presence of iron oxide or silicate precipitates at dislocations. Furthermore, our results demonstrate dissolution of copper precipitates from oxygen precipitates and their growth-related defects. Based on these results, we suggest oxygen in silicon can complex and stabilize only some metal impurities, depending on the formation energies of the metal oxide compounds. © 1999 Elsevier Science B.V. All rights reserved.

Keywords: Silicon; Defects; Transition metals; X-ray analysis

1. Introduction

Transition metal impurities significantly affect the properties of silicon by acting as charge carrier recombination/generation centers or as electrical shorts. Even trace amounts of impurities, on the order of parts-per-trillion (ppt), within the active device region can create these deleterious conditions. The active device region of integrated circuits is generally within the first 10 μm from the surface. Therefore, removal or gettering of impurities into the bulk of the silicon is used to improve device performance via precipitation of impurities at oxygen precipitates and their growth-related defects [1]. The active device region of a solar cell is the entire thickness of the silicon wafer, therefore, gettering of impurities out to the frontside and/or backside layers is commonly attempted. For solar cells, an added complication is the presence of structural defects, such as oxygen precipitates and dislocations within the active device region. These defects act as precipitation sites for metal impurities, essentially competing for impurities with the front and backside gettering layers, such that localized regions of poor performance can form at the defects [2].

The dissolution rate or stability of metal precipitates with the application of a thermal treatment is an important factor for both integrated circuit (IC) devices and solar cells. For IC devices, stability is desired to retain metal impurities away from the active device region. Conversely, stability is not desired for solar cells where the impurities must be removed from the active device region.

Stability of precipitates is determined by the thermodynamic balance between metal precipitates and dissolved metal impurities in the silicon lattice. For nm-scale precipitates in silicon crystals, complete dissolution is possible since the silicon material generally is of sufficient volume to absorb all dissolved impurities afforded by the precipitates. The thermodynamic balance is primarily determined by the chemical state of the metal precipitate. The strain field of a structural defect and native point defect concentrations may slightly alter the

* Corresponding author. Lawrence Berkeley National Laboratory, MS 2-400, 1 Cyclotron Road, Berkeley, CA 94720, USA Tel.: + 1-510-486-4874; fax + 1-510-486-7696.
E-mail address: samchugo@lbl.gov (S.A. McHugo)

0921-4526/99/$ - see front matter
PII: S0921-4526(99)00480-9

balance but these effects are thought to be minor compared to a variation in the chemical state of the precipitate.

Past research has been only partially successful in determining the chemical state of metal precipitates at structural defects in silicon mainly because of the small sampling volume and poor sensitivity of standard characterization techniques. The chemical state of copper precipitates has only been identified when precipitated at unspecified structural defects, typically near the surface, where the copper was found to be in a low-temperature polymorph form of Cu_3Si [3,4]. The chemical state of nickel, cobalt and palladium precipitates has also been studied when precipitated near the surface [5]. Studies on iron have concentrated on iron reactions with a $Si–SiO_2$ surface, where both $FeSi_2$ and a modified form of Fe_2SiO_4 phases have been detected [6–8]. While these studies show which chemical phases could form in silicon, they do not directly show which phases form at structural defects such as oxygen precipitates, dislocations and stacking faults where the presence of oxygen, carbon and strain fields may modify the phase formation process. Identification of the chemical state at these defects is of critical importance to fully understand the stability of metal precipitates in IC devices and solar cells.

The work presented here is a study of the chemical state and stability of metal precipitates at dislocations in polycrystalline silicon and at oxygen precipitates and their growth-related defects in single-crystal silicon. We utilize the novel characterization techniques of synchrotron-based X-ray fluorescence and X-ray absorption microscopy to determine elemental distributions and the chemical state of nm-scale precipitates of iron and copper in silicon. Based on our results, we discuss the effect of oxygen–metal reactions in regards to precipitate stability.

2. Experiment

Boron-doped polycrystalline silicon (polysilicon) grown by a casting technique and single-crystal Czochralski (CZ) silicon was used in this work. Dissolved oxygen concentrations were $2–3 \times 10^{17}$ atoms/cm^3 for the polysilicon and 10^{18} atoms/cm^3 for the CZ silicon. The CZ silicon material was subsequently subjected to a series of heat treatments to produce an oxygen precipitate density of 10^{11} precipitates/cm^3. Descriptions of the precipitate-forming heat treatments are given in Ref. [9]. Prior to analysis, surfaces were cleaned with a VLSI grade piranha (H_2SO_4:H_2O_2) etch in a class 100 clean room. Cu was intentionally introduced in CZ material by dip-coating the samples in a solution of copper fluoride tri-hydrate, HF and H_2O followed by a 1170°C in-diffusion performed in a N_2 ambient. The anneal times used in these experiments were more than sufficient to establish the equilibrium concentration of 10^{18} Cu atoms/cm^3 throughout the thickness of the material [10]. The samples were air-cooled with a cooling rate of ≈ 25°C/s to allow for the Cu to precipitate. No dissolved Cu was detected with Transient Ion Drift (TID) measurements, which has a sensitivity of 10^{11} Cu atoms/cm^3. Dissolution anneals were performed at 460°C for 30 min in a quenching furnace with a quench rate of 1000°C/s, in order to freeze the dissolution process.

We performed X-ray fluorescence (XRF) and X-ray absorption spectroscopy (XAS) at the Advanced Light Source, Lawrence Berkeley National Laboratory in order to ascertain elemental distributions and chemical state, respectively, of metals in the silicon material. Both XRF and XAS analysis were performed with X-rays focussed to a spot size of 1–2 μm^2, with scan areas typically over hundreds of microns. Considering typical sampling depths for 3D transition metals with XRF and XAS are on the order of 10–80 μm, the sampling volumes are significant. Furthermore, the μ-XRF system is capable of detecting metal precipitates with radii > 20 nm, which is superior to other standard characterization techniques such as secondary ion mass spectroscopy, energy dispersive spectroscopy or auger electron spectroscopy. This combination of large sampling volume and high sensitivity allows for analysis that was previously unachievable.

The μ-XRF system detects fluorescent X-rays emanating from the material after excitation with a wide band pass, 12.4 keV energy X-ray beam. The energy of the fluorescent X-rays signifies the elements present. The μ-XAS system detects changes in the excitation of core-level electrons into empty valence band states with the use of a narrow band pass, variable energy X-ray beam. By monitoring the absorption of the impinging X-ray beam as the energy of the beams varied, we obtain a fingerprint for the chemical state of the element, which is compared to standard samples of known chemical state. Since the valence band electrons are sensitive to variations in chemical binding, this technique provides an excellent means for chemical state identification.

3. Results and discussion

Fe Kα and Kβ X-ray emission was detected in as-grown polysilicon with the μ-XRF system. The energy position and relative ratio of Fe Kα to Kβ clearly identified to fluorescent X-rays as those from Fe in the polysilicon. The Fe signal was compared to a standard sample of known Fe dose to obtain a peak concentration of 5×10^{16} Fe atoms/cm^2. If we assume the Fe is precipitated as one precipitate, located within the top 5 μm of the sample, the precipitate size can be calculated to be 288 nm. However, considering earlier work

[11], the Fe is more likely a fine dispersion of small precipitates.

The absorption spectra of the Fe precipitate(s) in the polysilicon sample is shown in Fig. 1, which is the summation of 19 spectral scans taken with the μ-XAS system. Multiple XAS scans are also shown in Fig. 1 for Fe, FeSi and $FeSi_2$ standards. Fe silicides would be expected to form in this material since silicide formation temperatures are in the same range as crystal growth temperatures. We observe little similarity between the absorption spectra, indicating the Fe in the polysilicon is not Fe, FeSi nor $FeSi_2$. This is unexpected considering the matrix is silicon.

The shift of the absorption edge for the Fe spectra suggests the Fe atoms have been elevated to a higher valence state. This is common for metal oxides and metal silicates but not for metallic iron or Fe silicides. Furthermore, the presence of the pre-edge structure indicates the local environment of the Fe atoms in this compound is highly asymmetric, which again is common for oxides and silicates but not for metallic Fe or Fe silicides. Further indications of Fe-oxygen complexes comes from other research, which has indicated that Fe may complex with oxygen precipitates in silicon [12].

With these possibilities in mind, we analyzed standard powders of α-Fe_2O_3 and Fe_2SiO_4 with the μ-XAS beamline for comparison to the Fe in the polysilicon. Results are shown in Fig. 2. We observe some similarity between the absorption spectra of the metal oxides and silicates with the Fe in polysilicon. In particular, the pre-edge structure is remarkably similar. Furthermore, the absorption edge of Fe in polysilicon falls between α-Fe_2O_3 and Fe_2SiO_4. Considering Fe in α-Fe_2O_3 is in a $+3$ charge state and Fe_2SiO_4 is in a $+2$ charge state, the Fe in polysilicon seems to be a mix of $+2$ and $+3$ charge states. From these comparisons, one may suggest the Fe in polysilicon is a mixed state of oxide and silicate. These results compare well with Kitano [7] who observed the formation of a mixed $+2, +3$ state of Fe_2SiO_4 with Fe reaction with a Si–SiO_2 interface.

With the iron in an oxide or silicate state, the ability to remove or getter the iron from the material is greatly hindered by to the high binding energy of iron to oxides and silicates relative to iron silicides. Table 1 lists the standard molar enthalpy of formation for iron silicides, oxides and silicates at 298 K, data from [13,14]. The data has not been corrected for compound formation within a silicon matrix, however, these numbers provide a relative indication of binding energy. From the data, the thermodynamic formation energies of iron oxides and silicate is significantly higher than iron silicides, thus, the binding energy of the iron atom to an oxide or silicate precipitate is higher than to a silicide precipitate. With a higher binding energy, the solubility of Fe in the presence of an oxide or silicate precipitate will be low, compared to the presence of a silicide precipitate. Since

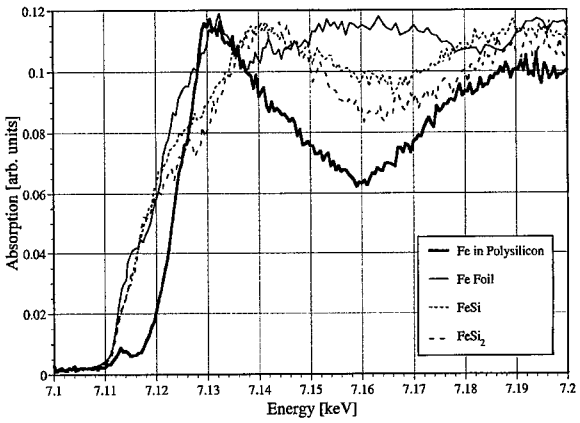

Fig. 1. X-ray absorption spectra from Fe in polysilicon, FeSi, $FeSi_2$ and metallic Fe.

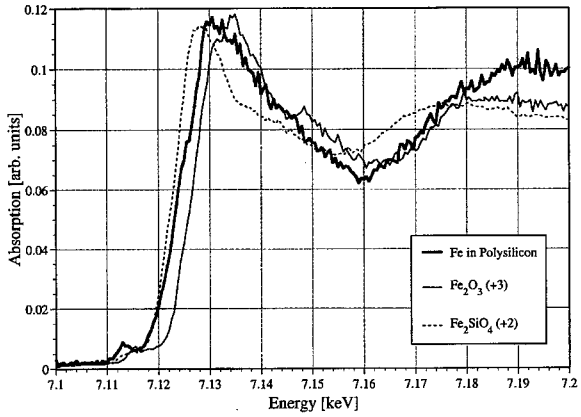

Fig. 2. X-ray absorption spectra from Fe in polysilicon, α-Fe_2O_3 ($+3$ charge state) and Fe_2SiO_4 ($+2$ charge state).

dissolution is a flux-limited process, this lower solubility decreases the dissolution rate, i.e. the gettering rate. This result has significant impact on solar cell improvements via gettering and for the robustness of gettering at oxygen precipitates in IC device silicon.

We have also studied the stability of Cu at oxygen precipitates and their growth-related defects after intentional contamination. Using the μ-XRF system, we have identified the positions of Cu precipitates with reference to an intentional scribe mark on the sample. The elemental map is shown in Fig. 3. Next, we annealed the sample at 460°C for 30 min to dissolve the Cu precipitates. Based on theoretical calculations of precipitate dissolution, [15], a Cu_3Si precipitate of radius smaller than 70 nm would fully dissolve for a 460°C, 30 min anneal. The sample was re-scanned in the same area with the μ-XRF system. We observe a decrease in the amount of Cu at each precipitate but the precipitates remain, suggesting

Table 1
Enthalpies of formation for Fe related compounds. Data from [13,14]

	ΔH_f° (kJ/mol)
FeSi	−39.3
$FeSi_2$	−30.6
1/2 Fe_2O_3	−412.1
1/3 Fe_3O_4	−372.8
1/2 Fe_2SiO_4	−740

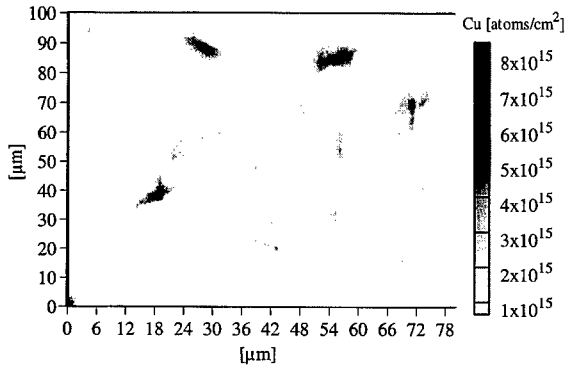

Fig. 3. Elemental map of precipitated Cu in single-crystal silicon taken with μ-XRF.

the 460°C anneal was not sufficient to fully dissolve the Cu precipitates. Considering we do not observe full dissolution in this study, the Cu precipitates are either larger than 70 nm or stabilized at the oxygen precipitate and/or growth-related defects. Stabilization may occur within the dislocation strain field or by chemical state change if the Cu reacts with the oxygen precipitates. We will perform further work to identify the chemical nature of the Cu and study dissolution at higher temperatures.

4. Conclusion

Based on our results we can conclude that Fe in polysilicon solar cells can be in the form of an oxide or a silicate. This is contrary to common thought, where a Fe silicide is expected to form. With the iron being in the form of an oxide or silicate, the rate of impurity removal is significantly reduced due to a higher binding energy of Fe atoms to oxides or silicates as compared to silicides. Furthermore, we have initial results indicating that Cu precipitates are stabilized to some extent in single crystal silicon with oxygen precipitates and their growth-related defects. This stabilization may be due to the formation of a chemical state different than Cu_3Si or to the strain fields associated with structural defects.

Acknowledgements

The authors would like to thank R. Gunion, R. Tackaberry, A. MacDowell, R. Celestre, Z. Hussain and H. Padmore for their help with the experiments. We would also like to thank S. Martinuzzi, I. Perichaud and R. Falster for samples. Funding for this work is by the National Renewable Energy Laboratory (NREL) under contract number XAF-8-17607-04 and by the Director, Office of Energy Research, Office of Basic Energy Sciences, Materials Sciences Division, of the U.S. Department of Energy, under Contract No. DE-AC03-76SF00098.

References

[1] W.K. Tice, T.Y. Tan, Mat. Res. Soc. Symp. Proc. 2 (1981) 367.
[2] S.A. McHugo, A.C. Thompson, I. Périchaud, S. Martinuzzi, Appl. Phys. Lett. 72 (1998) 3482.
[3] K.J. Solberg, Acta Crystallogr. A 34 (1978) 684.
[4] M. Seibt, Proceedings of the 6th International Symposium on Silicon Materials Science and Technology: Semiconductor 1990, Electrochem. Soc. 663 (1990)
[5] M. Seibt, K. Graff, J. Appl. Phys. 63 (1988) 4444.
[6] S. Sadamitsu, A. Sasaki, M. Hourai, S. Sumita, N. Fujino, Jpn. J. Appl. Phys. 30 (1991) 1591.
[7] T. Kitano, J. Electron Mater. 21 (1992) 1027.
[8] J. Wong-Leung, D.J. Eaglesham, J. Sapjeta, D.C. Jacobson, J.M. Poate, J.S. Williams, J. Appl. Phys. 83 (1998) 580.
[9] H. Hieslmair, A.A. Istratov, S.A. McHugo, C. Flink, T. Heiser, E.R. Weber, Appl. Phys. Lett. 72 (1998) 1460.
[10] E.R. Weber, Appl. Phys. A. 30 (1983) 1.
[11] S.A. McHugo, Appl. Phys. Lett. 71 (1997) 1984.
[12] B. Shen, J. Jablonski, T. Sekiguchi, K. Sumino, Jpn. J. Appl. Phys. 35 (1996) 4187.
[13] M.E. Schlesinger, Chem. Rev. 90 (1990) 607.
[14] D.R. Lide (Ed.), CRC Handbook of Chemistry and Physics, CRC, New York, NY, 1999.
[15] H.B. Aaron, G.R. Kotler, Metal. Trans. 2 (1971) 393.

ELSEVIER

Physica B 273–274 (1999) 375–378

PHYSICA B

www.elsevier.com/locate/physb

Evidence for deep recombination centers in high-purity silicon from photoluminescence measurements at elevated temperatures

Volker Alex[1], Jörg Weber*

Max-Planck-Institut für Festkörperforschung, Postfach 80 06 65, D-70506 Stuttgart, Germany

Abstract

Photoluminescence spectra of high-purity crystalline silicon samples are measured for temperatures up to 1000 K. The room-temperature lifetime of the near-edge-photoluminescence is in agreement with a coulomb-enhanced radiative decay of free excitons. However, the increase in lifetime with temperature asks for a Shockley–Read–Hall recombination process, which involves a deep-defect of unknown origin.

Keywords: Silicon; Recombination center; Photoluminescence

1. Introduction

Minority-carrier lifetimes in semiconductors are an important parameter in device performance. Defects and impurities strongly influence the lifetime of carriers and make the minority carrier lifetimes a sensitive probe for small defect concentrations. Usually, the measurements of the lifetimes are performed at room temperature but it was pointed out that differences in the lifetime of some samples show up only at elevated temperatures. [1] In this paper, we will present the lifetime of the near-band-gap photoluminescence (PL) from Si samples at elevated temperatures.

2. Photoluminescence line shape

The measured PL intensity is proportional to the emitted energy flux $j(E)$. For an indirect excitonic emission process $j(E)$ is given by [2]

$$j(\hbar\omega) \sim \frac{(\hbar\omega)^3}{\exp(\hbar\omega/kT)}\alpha(\hbar\omega). \tag{1}$$

Introducing the excitonic absorption coefficient from Ref. [3] yields

$$j(\hbar\omega) \sim \omega^2 \exp\left(\frac{-\hbar\omega}{kT}\right)\sum_b \sum_{\text{abs./em.}} a_{\text{abs./em.}} c_b \left(\sqrt{\hbar\omega - E_g - E_{exc} \pm k\Theta_b}\otimes G(\sigma_1) + rI(\hbar\omega - E_g - E_{exc} \pm k\Theta_b)\otimes G(\sigma_2)\right). \tag{2}$$

The first expression in the sum accounts for the absorption into bound states of the free exciton (FE), whereas the integral I takes care of the absorption into unbound excitonic states. The sum is over all phonon replicas b with energies $k\Theta_b$, which are weighted by c_b. The second summation is for the phonon absorption and emission processes. The Gaussian broadening G accounts for the different intrinsic as well as experimental broadening mechanisms. In Ref. [4] we have given the details of the photoluminescence line shape analysis. Only the LO and TO phonon replicas are included in the analysis, the TA phonon replica is too weak to be of any

* Corresponding author. Tel.: +49-711-689-1538; fax: +49-711-689-1602.

E-mail address: weber@kernix.mpi-stuttgart.mpg.de (J. Weber)

[1] Present address: McKinsey & Company, Inc., München, Germany.

0921-4526/99/$ - see front matter
PII: S0921-4526(99)00482-2

importance. We also neglect the small temperature dependence of the exciton binding energy E_{exc}, the near-infrared refractive index and the phonon energies in our analysis.

3. Experimental

Lifetime-measurements were carried out by modulating the laser beam (Ar^+-ion laser, 514.5 nm line) with an acousto-optical-modulator. The excitation powers were chosen to be sufficiently low (below 200 mW peak power) to justify the applicability of the low-injection-conditions of the decay-laws. The transients were detected by an InAs diode and stored in an transient recorder. The resolution of our time resolved measurements is ≈ 0.1 μs.

The sample was mounted in a clean quartz tube, which was inserted into the bore of a temperature controllable oven with high-thermal stability. Heating of the sample by the laser radiation was found to be negligible.

In total, we have investigated 9 different samples. In this report we will concentrate on two high-purity samples with the following specifications:

Si No. 1: p-type FZ Si, 3000 Ωcm, natural oxide,
Si No. 2: p-type FZ Si, 0.5 Ωcm, 104 nm thermal oxide,

Sample No. 2 showed the highest PL-intensity of all investigated samples. The minority carrier lifetime measured at room-temperature by laser/microwave lifetime measurement (μPCD) is 600 μs. All other high-purity samples show slightly smaller minority carrier lifetimes (100–400 μs).

4. Photoluminescence results

In Fig. 1 typical PL spectra at different sample temperatures are presented. At 35 K the spectrum exhibits the well known features of the near band-gap PL in Si. The exciton bound to the boron acceptor (BE) and the free exciton (FE) in different phonon replicas are clearly resolved. For details of the peak assignment see Ref. [5]. With increasing temperature a smooth change in the PL features occurs, there is an increasing broadening of the different lines, which results in only one broad PL band above around 100 K. A pronounced shift of the broad PL band with temperature is a direct indication for the reduction of the energy gap.

Fig. 2 gives three typical PL spectra at different sample temperatures along with the least-squares fits according to Eq. (2). The fitting procedure involved 5 free parameters: (1) the energy gap E_g, (2) the broadening $G(\sigma_1)$ of the absorption into the bound states of the FE, (3) the broadening $G(\sigma_2)$ of the absorption into the unbound

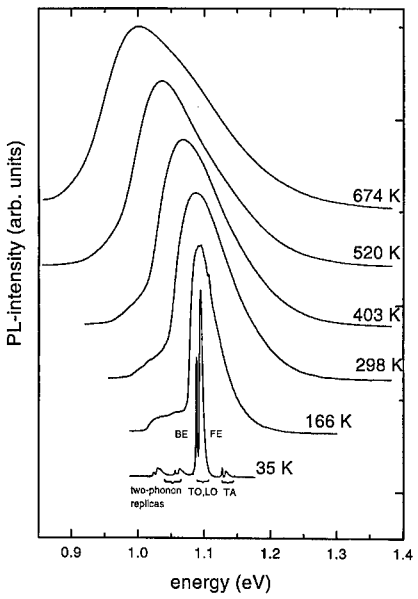

Fig. 1. Normalized photoluminescence spectra of the 0.5 Ωcm boron doped sample with surface passivation by a thermal oxide, recorded at different temperatures.

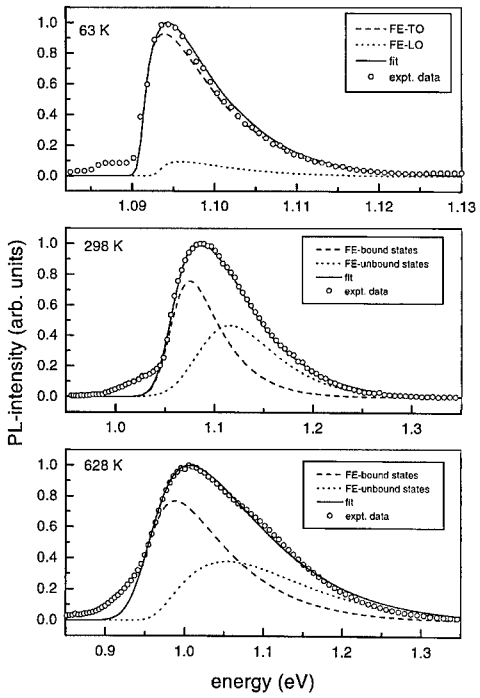

Fig. 2. Typical PL spectra at three different temperatures, (a) $T = 63$ K, (b) $T = 298$ K, (c) $T = 628$ K. The least-squares fits according to Eq. (2) are shown along with the different recombination processes contributing to the line shape.

states of the FE, (4) the ratio $a_{abs./em.}$ of the phonon absorption and emission processes, and (5) the ratio r of the relative strength of the unbound/bound FE processes (for details see Ref. [4]). The applicability of a pure excitonic recombination even at 600 K is justified by the calculations of Schlangenotto et al. The enhancement factor of recombination via excitonic states to the unmodified band–band transitions is ≈ 7 at 600 K. [6] Furthermore, the unmodified band–band transition has a similar spectral dependence as the unbound excitonic recombination and their influence can be incorporated in the parameter r.

The fitting parameter of main interest is the value of the fundamental indirect energy gap at high temperatures. Our results on the temperature dependence of E_g were already published in Ref. [4].

5. Life-time-measurements

The PL-decay of the two samples is shown in Figs. 3a and b. After a fast non-exponential decay, the PL-transients up to ≈ 700 K follow a simple exponential law. The lifetimes of the exponential part, show a remarkable increase with temperature. From room-temperature up to about 700 K the lifetimes of sample Nos. 1 and 2 rise by a factor of about three, the lifetime of sample No. 1 always being about half that of No. 2. At temperatures above 700 K lifetimes decrease very rapidly below the resolution of our set-up. The decrease corresponds to a drastic reduction of the PL-intensities in that temperature range. Auger-processes which should become important because of the $\approx 10^{17}$–10^{18} cm^{-3} free-carriers at these temperatures are a possible explanation of this behavior.

Radiative lifetimes in the millisecond range were calculated e.g. by Dumke [7] on the basis of indirect recombination. The calculations however neglected the coulomb-enhancement, i.e. the possibility of formation of excitons. The lifetime of free excitons is given by [6]

$$\tau_e(\mu s) = 210 \tanh \frac{\Theta_{TO}}{2T} \tag{3}$$

in agreement with an earlier estimation by Cuthbert [8]. At room-temperature Eq. (3) predicts a value of 120 μs, in the right order of magnitude compared to the measurements. The excitonic lifetime according to Eq. (3) is independent of doping, whereas the conventional radiative lifetime should vary with the inverse of dopant concentration and is therefore in contradiction to the comparitively small differences between the two investigated samples.

Although there is some evidence that the measured room-temperature-lifetime is in accordance with theoretical models of the coulomb-enhanced radiative process, the temperature-dependence of the lifetime according to Eq. (3) is contrary to the observed. Fig. 4 summarizes the measured lifetimes at different temperatures.

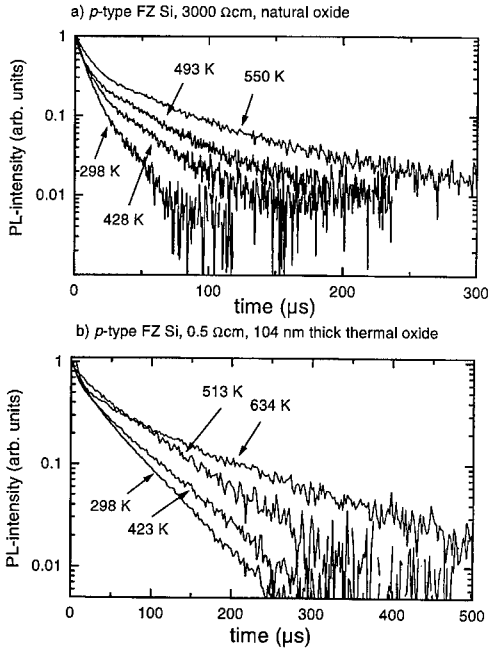

Fig. 3. Luminescence decay at different temperatures: (a) p-type FZ Si, 3000 Ωcm, with native oxide surface; (b) p-type FZ Si, 0.5 Ωcm, with thermal oxide.

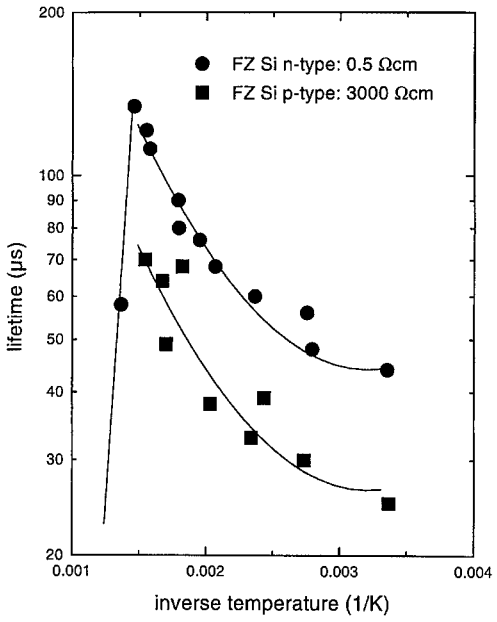

Fig. 4. Temperature-dependence of the lifetimes obtained from fitting the exponential parts in Fig. 3.

The influence of different recombination processes in high-purity Si was recently subject of several publications [9,10]. Above shallow dopant concentrations of $[C] \geqslant 10^{16}\ \mathrm{cm}^{-3}$ the lifetime is dominated in crystalline Si by intrinsic recombination processes, like the Coulomb enhanced Auger recombination, etc. below $[C] \approx 10^{16}\ \mathrm{cm}^{-3}$ recombination via defects and impurities determine the lifetime of carriers. The recombination process is described by Shockley, Read and Hall and the following temperature dependence of the lifetimes in the low injection limit is predicted [11,12]:

$$\tau_{\mathrm{SRH}} \approx \tau_{\mathrm{p0}}\left[1 + \exp\left(\frac{E_{\mathrm{T}} - E_{\mathrm{F}}}{kT}\right)\right] + \tau_{\mathrm{n0}}\left[\exp\left(\frac{2E_{\mathrm{i}} - E_{\mathrm{T}} - E_{\mathrm{F}}}{kT}\right)\right], \quad (4)$$

where E_{T} is the trap energy, E_{F} the Fermi energy and E_{i} the intrinsic Fermi energy. Eq. (4) gives the correct temperature dependence if we assume an acceptor level ($\tau_{\mathrm{p0}} \ll \tau_{\mathrm{n0}}$) in the middle of the band gap. A fit of the high-temperature regime gives a level position $E_{\mathrm{V}} = 450 - 650$ meV for the unknown defect. The difference in both samples is the τ_{n0} value ($\tau_{\mathrm{n0}} \propto 1/N_{\mathrm{T}}$). In sample No. 1 the concentration of the unknown defect N_{T} is a factor of $\approx$ two lower compared to No. 2.

Recombination via deep impurity levels as an explanation for the measured lifetimes in high-purity silicon was already discussed by Landsberg [13]. From numerous lifetime-measurements in silicon, which all gave values much lower than the predicted radiative lifetimes, which he assumed to be in the millisecond range, he concluded that there must be a residual "life-time-limitting" defect in silicon.

At present, the origin and the concentration of the deep level is not known, we find the same level energy in all studied p-type high-purity samples. One could speculate that the level is the acceptor level of substitutional Au, but further studies are necessary to establish this correlation.

6. Summary

The magnitude of room-temperature-PL lifetimes is in the correct order of excitonic recombination, but the temperature dependence can only be explained by an impurity-induced recombination process. The Shockley–Read–Hall recombination predicts the right temperature dependence, but to explain the absolute values of measured lifetimes, the introduction of a speculative deep defect is necessary. The level position of the unknown defect in high-purity Si is at $E_V + (0.55 \pm 0.1)$ eV, which makes the substitutional Au acceptor a possible candidate.

Acknowledgements

S. Finkbeiner was involved in the early stages of the experiments. W. Heinz and W. Krause gave excellent technical support.

References

[1] F. Shimura, T. Okui, T. Kusama, J. Appl. Phys. 67 (1990) 7168.
[2] H.B. Bebb, E.W. Williams, Semicond. Semimet. 8 (1972) 181.
[3] T.P. McLean, Prog. Semicond. 5 (1960) 53.
[4] V. Alex, S. Finkbeiner, J. Weber, J. Appl. Phys. 79 (1996) 6943.
[5] P.J. Dean, J.R. Haynes, W.F. Flood, Phys. Rev. 161 (1967) 711.
[6] H. Schlangenotto, H. Maeder, W. Gerlach, Phys. Stat. Sol. A 21 (1974) 357.
[7] W.P. Dumke, Phys. Rev. 1105 (1957) 139.
[8] J.D. Cuthbert, Phys. Rev. B 1 (1970) 1552.
[9] R. Häcker, A. Hangleiter, J. Appl. Phys. 75 (1994) 7570.
[10] J. Schmidt, A.G. Aberle, J. Appl. Phys. 81 (1997) 6186.
[11] W. Shockley, W.T. Read, Phys. Rev. 87 (1952) 835.
[12] R.N. Hall, Phys. Rev. 87 (1952) 387.
[13] P.T. Landsberg, Recombination in Semiconductors, Cambridge University Press, Cambridge, 1991.

ELSEVIER

Physica B 273–274 (1999) 379–382

PHYSICA B

www.elsevier.com/locate/physb

Lithium–gold-related complexes in p-type crystalline silicon

J.T. Gudmundsson*, H.G. Svavarsson, H.P. Gislason

Science Institute, University of Iceland, Dunhaga 3, IS-107 Reykjavík, Iceland

Abstract

Using Hall and conductivity measurements the formation of a Li–Au-related complex in p-type crystalline silicon is demonstrated. Substitutional gold is known to introduce two energy levels in the band gap of silicon, a deep acceptor level at $E_c - 0.56$ eV and a deep donor level at $E_v + 0.34$ eV. We observe two energy levels introduced by lithium diffusion of Au-doped silicon, a previously reported acceptor at $E_c - 0.41$ eV in n-type Si:Au and a new level at $E_v + 0.41$ eV in p-type Si:Au. In addition, control of the Li-doping level of p-type Si is found to shift the Fermi level position between the deep donor level to the deep acceptor level as expected, thus confirming their presence in the samples. We discuss the identity of these levels in comparison with theoretical predictions for the interaction between hydrogen and the energy levels of substitutional Au in silicon.

Keywords: Silicon; Gold–lithium complex; Electrical conductivity

1. Introduction

The well-known ampotheric gold center in Si [1,2] gives rise to an acceptor level at $E_c - 0.56$ eV and a donor level at $E_v + 0.34$ eV. It is well known that both hydrogen [3] and lithium [4] passivate gold acceptors in silicon. Lithium is the neighbour of hydrogen in the periodic table and is a fast interstitial diffuser in silicon with a high interstitial solubility. Due to the high solubility of lithium in silicon it is possible to obtain uniform lithium concentrations between 10^{14} and 10^{17} cm^{-3} throughout the bulk of the sample using diffusion below 300°C [4]. This is in contrast to hydrogen where the penetration depth is only a few micrometers after remote hydrogen plasma treatment [5]. The interaction of hydrogen with the gold center introduces at least six new energy levels observed in deep-level transient spectroscopy (DLTS) [5–8].

In an earlier study we reported that in n-type silicon, lithium interacts with the gold acceptor at $E_c - 0.56$ eV forming an electrically neutral center as well as an electron trap at $E_c - 0.41$ eV [4]. The lithium passivation of gold was previously studied in n-type material only [4] in which a uniform Au concentration of 2×10^{14} cm^{-3} had been produced by diffusion at 893°C. It was found that gold acceptors in silicon can be passivated by lithium as well as hydrogen [4]. There were two complexes of Au and Li observed, one of them being neutral, the other possessing a level at $E_c - 0.41$ eV in the bandgap, presumably an acceptor. Two gold–lithium centres have been identified in Si using EPR and double-ENDOR measurements, an orthorhombic Au–Li pair and a trigonal Au–Li_3 complex with a single donor level within the band gap above $E_c - 0.41$ eV [9].

Diffusion of gold into n-type silicon at temperatures below 750°C introduces the Au acceptor state at 0.56 eV below the conduction band which reduces the electron concentration. When the gold concentration exceeds the net concentration of residual donors the resistivity approaches that of intrinsic silicon [1]. Higher diffusion temperatures change the conductivity of the samples from n-type to p-type. The p-type conduction in highly gold-doped silicon is governed by the substitutional gold and its deep donor state at 0.34 eV above the valence band. In this investigation we focus the attention on Li-diffusion into p-type Au-doped Si. The purpose is to

*Corresponding author. Tel.: +354-525-4800; fax: +354-552-8911.

E-mail address: tumi@hi.is (J.T. Gudmundsson)

0921-4526/99/$ - see front matter
PII: S0921-4526(99)00483-4

monitor the dominating electrical levels using temperature-dependent resistivity and Hall coefficient measurements.

2. Samples preparation and experimental details

The silicon used in this work was n-type float zone phosphorus-doped (1 0 0)-oriented silicon with a nominal resistivity of 8.5–11 Ω cm. The wafers were coated with approximately 1500 Å thick gold layer on one side and gold was driven in at 1179°C for 4 h in nitrogen ambient. Details of the gold-doping procedure have been given elsewhere [10]. The concentration of gold diffused into the silicon starting material at 1179°C is estimated from the data of Collins et al. [1] to be roughly 6×10^{17} cm^{-3}. The lithium was predepositied at 300°C for 30 min, after which excess lithium was removed from the surface of the samples. Lithium was then driven in at 300°C for 10 h followed by a rapid quenching in liquid nitrogen.

Temperature-dependent Hall and conductivity measurements were made on samples of typical size 3×3 mm^2. Ohmic contacts were made to the four corners of the square samples using an alloy of aluminum and GaAl. The Hall coefficient was estimated from the slope of the Hall voltage versus the magnetic field in the range 0–0.75 T. In this range the product $\mu_H B$ is small compared to 1. Therefore, the Hall voltage will vary linearly with B. Electron and hole concentrations were calculated from the Hall coefficient R_H as $n = -1/eR_H$ and $p = 1/eR_H$, respectively. The sample resistivity ρ was measured applying the van der Pauw method [11]. The Hall mobility for electrons is then given by $\mu_H = 1/e\rho n$ with a similar equation for holes.

3. Experimental results

Fig. 1 shows the carrier concentration versus reciprocal temperature for Si:P samples diffused with gold and co-doped with lithium as described in Table 1. The carrier concentration increases again upon baking of the co-doped samples. When the Au concentration exceeds that of the shallow donors the samples turn p-type and the donor level at $E_v + 0.34$ eV is the only active level. Our samples became p-type after Au diffusion at 1179°C for 4 h. In agreement with expectations the slope of $\ln(pT^{-3/2})$ versus $1/T$ for a Si:P sample (S1), which was Au diffused at 1179°C for 4 h, shows p-type conductivity and a thermal activation energy of 0.36 eV.

Lithium co-doping of the samples increases their resistivity and thus decreases the carrier concentration. We find that Li diffusion at 300°C may or may not shift the Fermi level to the $E_c - 0.56$ eV acceptor level. Sample S2 which was Au-doped in a similar way as sample S1 but also Li diffused at 300°C for 10 h shows n-type conductivity with thermal activation energy of 0.56 eV as shown in Fig. 1. Some samples (such as sample S4) remained p-type with thermal activation energy of 0.36 eV after similar Li diffusion and further baking, however. This illustrates the fact that there is a delicate balance between the Au centres and the interstitial Li donors in our samples.

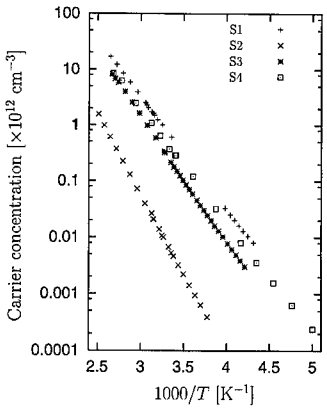

Fig. 1. The carrier concentration versus the reciprocal temperature for Si:P, + S1 Au diffused at 1179°C for 4 h, × S2 after Au diffusion Li diffused at 300°C for 20 min and baked at 300°C for 10 h,* S3 Au and Li diffused baked at 100°C for 10 h and 150°C for 30 min, ⊡ S4 Au and Li diffused baked at 100°C for 10 h and 205°C for 30 min.

In earlier work we reported that Li diffusion and a subsequent thermal annealing of weakly Au-doped Si:P samples produced a new electron trap at at $E_c - 0.41$ eV [4]. This level was observed in DLTS measurements and attributed to a complex of Au and Li. Au and Li diffused sample that is baked at 100°C for 10 h and 200°C for 30 min (sample S3) is expected to show the previously observed 0.41 eV Au–Li trap [4]. However, this is not the case for the more strongly Au-doped p-type samples in this study. A thermal activation energy of 0.41 eV is obtained. Hence, the corresponding level is located at $E_v + 0.41$ eV instead of $E_c - 0.41$ eV as found in samples which remain n-type after the initial Au diffusion. In view of the unexpected coincidence of the binding energies it must be pointed out that the p-type conductivity is firmly established in the case of Fig. 1 which places the 0.41 eV level in the lower half of the bandgap. The DLTS measurements of the n-type Au-Li co-doped samples, however, are only sensitive to traps in the upper half of the bandgap.

Fig. 2 shows the Hall mobility in the temperature range 170–390 K. The temperature dependence of the Hall mobility in this temperature range is expected to follow $\mu_H \propto T^{-\alpha}$ where α is a constant. The Hallmobility has a temperature dependence of $T^{-1.7}$ for samples where the 0.56 eV donor level governs the conductivity,

Table 1
Electrical parameters of Si:P, diffused by gold and lithium

Sample			n/p [m^{-3}]	ΔE [eV]	α	Type
S1	Au 1179°C 4 h		6.0×10^{12}	0.36	2.5	p
S2	Au 1179°C 4 h	Li 300°C 20 min baked 300°C 10 h	5.3×10^{10}	0.52	1.7	n
S3	Au 1179°C 4 h	Li 300°C 20 min baked 300°C 5 h baked 100°C 12h, 200°C 30 min	1.7×10^{12}	0.41	3.4	p
S4	Au 1179°C 4 h	Li 300°C 20 min baked 300°C 4 h baked 100°C 10 h, 205°C 30 min	1×10^{13}	0.35	2.3	p

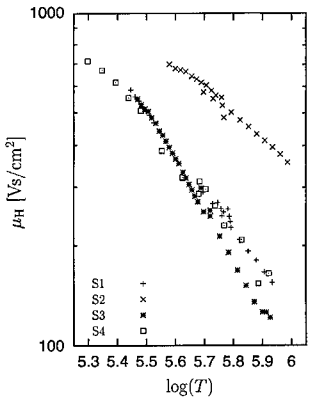

Fig. 2. The Hall mobility versus temperature for Si:P, +S1 Au diffused at 1179°C for 4 h, × S2 after Au diffusion Li diffused at 300°C for 20 min and baked at 300°C for 10 h, * S3 Au and Li diffused baked at 100°C for 10 h and 150°C for 30 min, ⊡ S4 Au and Li diffused baked at 100°C for 10 h and 205°C for 30 min.

such as sample S2. This is consistent with early measurements of the temperature dependence of the Hall mobility in n-type gold-doped silicon [1]. In samples where the 0.34 eV level controls the conductivity the temperature dependence of the Hall mobility is $T^{-2.5}$. This value is consistent with measurements by Weman et al. [12] and is slightly lower than what is generally expected for p-type silicon for temperatures $T > 100$ K, where optical deformation potential in addition to the acoustic deformation potential govern the scattering process [13]. When the new Au–Li level at $E_v + 0.41$ eV controls the conductivity the temperature dependence of the Hall mobility becomes $T^{-3.4}$ as seen for sample S3.

4. Discussion and conclusion

Deep-level passivation by hydrogen is commonly observed in semiconductors. In general, the passivation of deep levels is still incompletely understood. Neutral substitutional Au in silicon has the electronic configuration t_2^3. It is therefore expected to offer three possible configurations when forming complexes with hydrogen, Au–H_1, Au–H_2 and Au–H_3. The last configuration should be that of the passivated Au, since this defect has full t_2 manifolds if each hydrogen atom simply adds its electron to the t_2 subshell of Au. Recent calculations show that this simple model is not sufficient to explain the interaction between hydrogen and gold, since calculations predict that AuH_3 in fact has a shallow acceptor level [14].

Lithium ($1s^2 2s^1$) is a well known impurity in silicon, normally observed at the tetrahedral interstitial site acting as a shallow donor with a level at $E_c - 0.0338$ eV and as such its electronic structure is well understood [15,16]. Passivation of shallow and deep defects by lithium has been investigated in detail in GaAs and Si for reasons of comparison with hydrogen passivation. Experimental evidence suggests similarities between lithium and hydrogen as far as shallow acceptor passivation is concerned [17,18]. However, shallow donors in GaAs and Si are not passivated by lithium which suggests that a negative charge state of interstitial Li comparable to H^- does not exist in these materials. Deep donor levels are passivated by lithium, however. The passivation of the gold centre has been investigated for both hydrogen [3,19,20] and lithium [4]. The question whether one might expect differences between the interaction between hydrogen and gold, on the one hand, and lithium and gold on the other hand, has not been addressed theoretically yet.

In the present study the interaction between Au and Li has been investigated for the first time in p-type samples where the deep gold donor level at $E_v + 0.34$ eV governs the p-type conduction before Li diffusion. By controlling the Li concentration after the lithium-diffusion step we are able to maintain the p-type conductivity or convert the sample to n-type with the gold acceptor level at $E_c - 0.56$ eV governing the electron concentration in the conduction band. A schematic diagram of the energy levels of the ampotheric gold center in the band gap of silicon is shown in Fig. 3. Furthermore, the figure shows the levels introduced by hydrogenation and

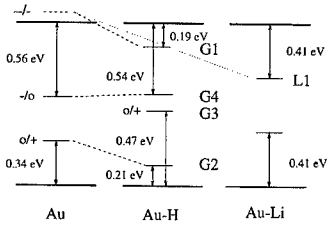

Fig. 3. Schematic diagram of the energy levels of the ampotheric gold center in the band gap of silicon on the left and energy levels introduced by co-doping with hydrogen and lithium.

lithium diffusion. The second acceptor level of gold has not been observed experimentally. A hitherto unknown level at $E_v + 0.41$ eV appears in Au–Li co-doped samples after baking at relatively low temperatures (100–200°C). In gold–hydrogen co-doped samples the closest resemblance to our observations is found in the Au–H_1 configuration where the –/– gold acceptor level is pulled down in the bandgap by the addition of one H atom to an acceptor level labeled G1 at $E_c - 0.19$ eV (observed in n-type samples) while a donor level G2 is found at $E_v + 0.21$ eV (observed in p-type samples) [4,19,20]. A deep level labeled G4 at $E_c - 0.54$ eV close to the gold level at $E_c - 0.56$ eV is also present in these samples [5,7]. Thus G1, G2 and G4 are believed to be different charge states of the same Au–H pair. Recent ab initio calculations suggest that G2 and G4 are due to the Au–H_1 configuration [14]. Furthermore, calculations suggest that the G3 level is due to the Au–H_2 configuration [14]. In our gold–lithium co-doped samples the three levels L1 at $E_c - 0.41$ eV (observed in n-type samples), the new level at $E_v + 0.41$ eV (observed in p-type samples), and the $E_c - 0.52$ eV level could well correspond to the levels G1, G2, and G4. The L1 level is then possibly due to a downward shift of the $Au^{-\ -/-}$ level and thus in the Au–Li_1 configuration. However, this assignment of the Au–Li levels is based on speculations alone in the absence of theoretical predictions. Thus, for instance, we cannot exclude the possibility that the $E_v + 0.41$ eV level corresponds to the G3 level and therefore the Au–Li_2 configuration.

In summary, at least five complexes of gold and lithium have been reported in silicon by different researchers: An electrically inactive complex and an electron trap at $E_c - 0.41$ eV were deduced from DLTS measurements in addition to the two centres observed by Alteheld et al. [9]. In this study a new center is observed in more strongly Au-doped silicon which is co-doped with lithium. Its binding energy is determined, placing its energy level at $E_v + 0.41$ eV.

Acknowledgements

The authors wish to thank Dr. Einar Örn Sveinbjörnsson for valuable discussion during the course of the experiment. This work was partially supported by the University of Iceland Research fund and the Icelandic Research Council.

References

[1] C.B. Collins, R.O. Carlson, C.J. Gallagher, Phys. Rev. 105 (1957) 1168.
[2] J.W. Petersen, J. Nielsen, Appl. Phys. Lett. 56 (1990) 1122.
[3] S.J. Pearton, A.J. Tavendale, Phys. Rev. B 26 (1982) 7105.
[4] E.Ö. Sveinbjörnsson, S. Kristjansson, H.P. Gislason, J. Appl. Phys. 77 (1995) 3146.
[5] E.Ö. Sveinbjörnsson, O. Engström, Phys. Rev. B 52 (1995) 4884.
[6] J.-U. Sachse, E.Ö. Sveinbjörnsson, N. Yarkin, J. Weber, Mater. Sci. Eng. B 58 (1999) 134.
[7] P. Deixler, J. Terry, I.D. Hawkins, J.H. Evans-Freeman, A.R. Peaker, L. Rubaldo, D.K. Maude, J.-C. Portal, L. Dobaczewski, K.B. Nielsen, A.N. Larsen, A. Mesli, Appl. Phys. Lett. 73 (1998) 3126.
[8] L. Rubaldo, P. Deixler, I. Hawkins, J. Terry, D. Maude, J.-C. Portal, J. Evans-Freeman, L. Dobaczewski, A. Peaker, Mater. Sci. Eng. B 58 (1999) 126.
[9] P. Alteheld, S. Greulich-Weber, J.-M. Spaeth, H. Overhof, M. Höhne, Mater. Sci. Forum 258–263 (1994) 1173.
[10] E.Ö. Sveinbjörnsson, O. Engström, U. Södervall, J. Appl. Phys. 73 (1993) 7311.
[11] L.J. van der Pauw, Philips Res. Rep. 13 (1958) 1.
[12] H. Weman, A. Henry, T. Begum, B. Monemar, O.O. Awadelkarim, J.L. Lindström, J. Appl. Phys. 65 (1989) 137.
[13] K. Seeger, Semiconductor Physics: An Introduction, Springer, Berlin, 1991.
[14] A. Resende, R. Jones, S. Öberg, P.R. Briddon, Phys. Rev. Lett. 82 (1999) 2111.
[15] R.L. Aggarwal, A.K. Ramdas, Phys. Rev. A 140 (1965) 1246.
[16] G.D. Watkins, F.S. Ham, Phys. Rev. B 10 (1970) 4071.
[17] G.G. DeLeo, W.B. Fowler, G.D. Watkins, Phys. Rev. B 29 (1984) 1819.
[18] B.H. Yang, H.P. Gislason, M. Linnarsson, Phys. Rev. B 48 (1993) 12345.
[19] E.Ö. Sveinbjörnsson, O. Engström, Appl. Phys. Lett. 61 (1992) 2323.
[20] E.Ö. Sveinbjörnsson, O. Engström, Mater. Sci. Forum 141–147 (1994) 821.

ELSEVIER

Physica B 273–274 (1999) 383–386

PHYSICA B

www.elsevier.com/locate/physb

Lattice defects in silicon rapidly solidified from the melt

H. Nishizawa, F. Hori, R. Oshima*

Research Institute for Advanced Science and Technology, Osaka Prefecture University, 1-2 Gakuen-Cho, Sakai, Osaka 599-8570, Japan

Abstract

The behaviors of melting and rapid solidification of Si have been studied by in situ ultra-high-voltage electron microscopy (UHVEM). Quenching experiments from a partly molten state have also been carried out. The lattice defects introduced are examined in detail by conventional transmission electron microscopy (C-TEM). Planar defects, dislocations, and defect clusters are found to form in the specimens. The results indicate that thermal point defects are associated with the formation of induced defects. Thermally formed stacking fault tetrahedra exhibit that clustering and the collapse of thermal vacancies actually occur in Si at high temperatures. Some dislocations are helical, and this shows that a strong interaction exists between induced dislocations and thermal point defects during cooling from high temperatures.

Keywords: Silicon; Defect cluster; Thermal vacancy; Stacking fault tetrahedron

1. Introduction

Diameters of Czochralski-grown Si crystals (CZ-Si) have been increased with the development of semiconductor device technology. At the beginning of the 21st century, crystals with diameters of 40 cm are expected to be produced commercially. This is all due to the remarkable refinement of device scales and higher integrated circuit densities. Accordingly, there are demands for the growth of higher quality Si crystals.

Among the various types of crystal defects, point defects are intrinsic ones thermodynamically, and are introduced into the bulk from the melt–solid interfaces during crystal growth. Point defects induced around the center of growing crystals become harder to diffuse out to a thermal equilibrium level with increasing crystal size during a period of crystal growth. Consequently, the supersaturated point defects become associated with various defect formations by the device processing; an example that is introduced is the formation of octahedral void defects [1,2].

Although a fast crystal growth rate is favorable from an economical stand point, thermal equilibrium conditions during crystal growth become highly disturbed in such a case. This results in poor-quality grown crystals. Therefore, knowledge on the behaviors of point defects in Si at high temperatures has become inereasingly important. Compared with work on point defects involving metals, however, few quenching experiments have been done for Si [3], possibly because the formation energy of a vacancy and that of an interstitial atom are large and comparable [4], making expectations low for the freezing of large amounts of point defects even by quenching from the melting temperature.

Our recent study has suggested the validity of quenching experiments for Si [5]. In this paper, we present results on the melting behaviors and the lattice defects introduced by the rapid solidification of Si studied by ultra-high-voltage electron microscopy (UHVEM) and the conventional transmission electron microscopy (C-TEM).

2. Experimental

2.1. Rapid cooling from a partly molten state in UHVEM

Disc specimens 2.4 mm in diameter cut from commercial float zone grown undoped Si (FZ-Si) and CZ-Si

* Corresponding author. Fax: + 81-722-51-6439.
E-mail address: oshima@riast.osakafu-u.ac.jp (R. Oshima)

0921-4526/99/$ - see front matter
PII: S0921-4526(99)00485-8

wafers were used in the experiments. A hollow 0.2 mm deep was made at the center of each specimen with an ultrasonic drill, and chemically thinned in a mixed solution of nitric acid and hydrofluoric acid. Each specimen mounted in a tantalum holder was heated on a specially designed heating stage able to accommodate temperatures of about 2300 K maximum. In situ observations were carried out in the Hitachi HU-2000 UHVEM of Osaka University operated at 2 MV. The images were continuously recorded on videotapes. Some specimens were cooled and solidified quickly by a sudden cut off of the electric power of the heating stage after a partly molten state, and they were recovered carefully at room temperature. They were further examined in detail by C-TEM using a JEOL-200CX electron microscope operated at 160 kV.

2.2. *Quenching of tiny FZ-Si crystals from a molten state*

Tiny crystals with a size of $5 \times 5 \times 1$ mm were cut from an FZ-Si single crystal using an ultrasonic cutting machine. Each specimen was melted quickly by infrared beam heating, and then solidified rapidly under an ambient condition. Although the cooling rate of the specimen itself was unable to be measured, it was estimated to be on the order of several thousand degrees per second or more near the melting temperature. The solidified spherical specimen about 2 mm in diameter was sliced to a disc 0.2 mm thick by a diamond wheel cutter, and mechanically dimpled slightly at the center. Then, chemical thinning was applied to make a small hole at the center, and observations were made by C-TEM.

3. Results and discussion

Fig. 1 is a sequence showing in situ observations of melting involving an FZ-Si specimen in UHVEM. In order to avoid the effect of additive electron irradiation, the electron dose rate was kept lower than $1 \times 10^{21} e/m^2$; this value is too low to induce a sufficient number of Frenkel pairs during observation. In this experiment, the heating rate was carefully controlled lest the whole specimen be melted and fall instantly from the sample holder. Ordinarily, melting started at the specimen edge and the profile of the edge gradually changed. As the melting proceeded, a marked mass flow took place on the specimen surface, and the surface morphology was drastically changed. Finally, an extremely thin constriction was formed at the root of each projected region as shown in Fig. 1(f).

When the heating rate was somewhat too large, the constriction was broken and the tip was lost. In most cases, however, the thinner the constriction was, the more strongly the attractive force acted at the thinnest part. When the diameter of the constriction became less than

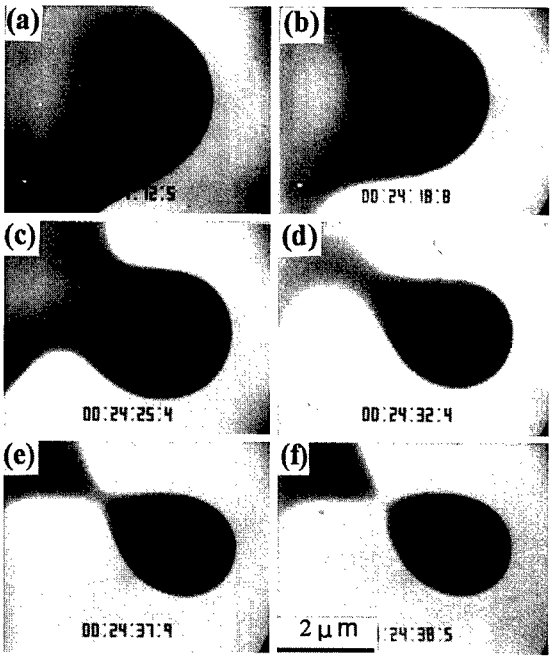

Fig. 1. Sequence for an in situ observation of melting of FZ-Si with UHVEM, taken from a videotape.

100 nm, and the temperature was under steady state, both sides of the constriction stuck together momentarily producing some thickness again by vigorous surface diffusion. This indicated that the surface tension of liquid Si is quite large.

It was also observed that thinner regions were formed near the roots of the projected regions due to an out diffusion of mass. Dislocation arrays were seen around the root of each projected part as shown in Fig. 2. Stereomicroscopy showed that the dislocation arrays lay on different sets of $\{1\,1\,1\}$ planes as indicated in the micrograph. It was found by dark field electron microscopy from various reflections that the Burgers vectors of both sets of dislocations were parallel to $\langle 0\,1\,1 \rangle$ and they were 60° dislocations.

Examples from different 400 type reflections are also shown in Fig. 2. These dislocations were considered to be responsible for the rapid flow of mass as well as the surface diffusion at high temperatures. Shape changes due to mass transportation at a high temperature by either shear or diffusion are illustrated in Fig. 3(a) and (b). Helical dislocations were frequently observed around the centers of the thinnest regions as shown in Fig. 4, indicating that absorption or emission of point defects of the dislocations actually took place during the cooling after the solidification. Tiny defects with bright dotted contrasts were also seen by the weak beam dark field electron micrograph. They were too small to determine, but were inferred to be small interstitial type dislocation loops from their contrasts.

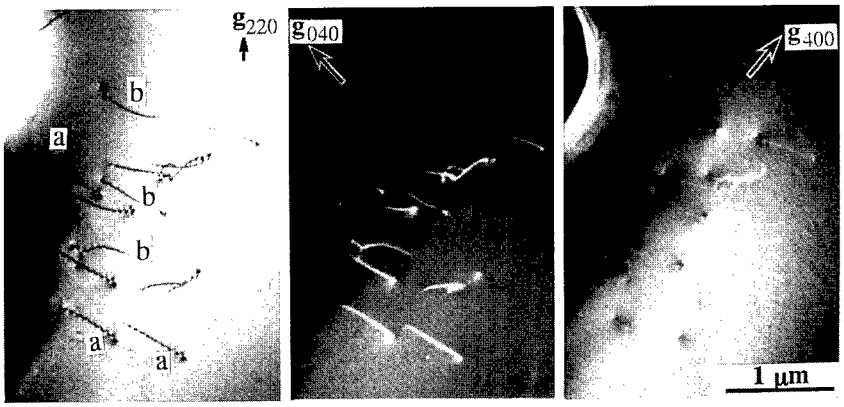

Fig. 2. Dislocation arrays formed near a root of a projected region of Si rapidly solidified in UHVEM, and the determination of their Burgers vectors; bright field image (left), and dark field images from $g = 040$ (center) and $g = 400$ (right). Most of the dislocation contrasts from $g = 400$ disappear. Dislocations indicated by a and b lie on the $\{1\,\bar{1}\,1\}$ and $\{\bar{1}\,1\,1\}$ planes, respectively.

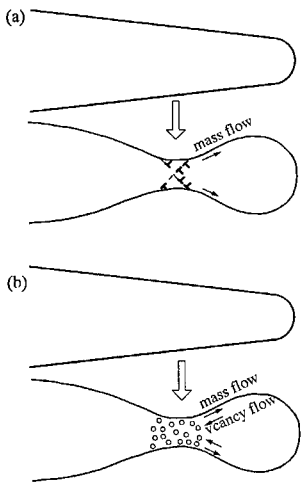

Fig. 3. Illustrations of shape changes of specimens due to mass flow by (a) shear and (b) diffusion.

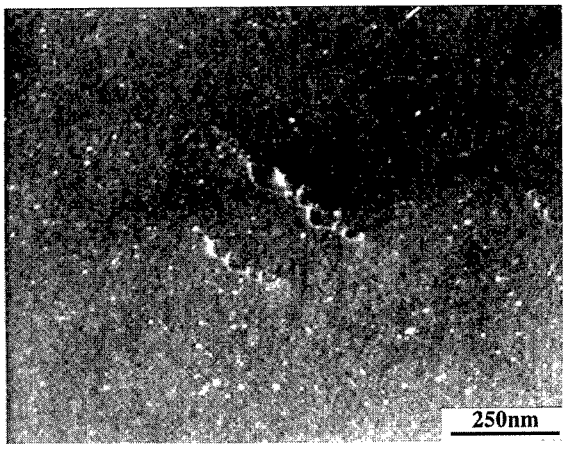

Fig. 4. Weak beam dark field micrograph from an 022 reflection showing helical dislocations and tiny defect clusters of FZ-Si rapidly solidified in UHVEM after a partly molten state.

Notable defects of another type were stacking faults. Fig. 5 shows various types of small stacking faults observed in FZ-Si specimens rapidly cooled from a molten state. These stacking faults were usually formed in regions whose thicknesses were abruptly changed by solidification after a partly molten state; this was confirmed by stereomicroscopy. However, since the widths of the stacking faults were too small, and they were confined in the specimens, their exact nature was difficult to determine by a conventional judgment technique using their fringe contrasts [6]. Some faults nonetheless did exhibit a triangular shape when viewed from the [1 1 1] direction as shown in Fig. 5(c). From dark field electron microscopy with systematic changes to the excited reflections, they were found to be stacking fault tetrahedra (SFT) surrounded by $\{1\,1\,1\}$ planes. The formation of stacking fault tetrahedra in Si has been reported only in ion-implanted [7] and neutron-irradiated specimens [8] so far, but not in thermally treated ones.

Since the nucleation of an SFT is considered to be induced by the clustering and the collapse of thermal vacancies on a $\{1\,1\,1\}$ plane [9], the present results clearly indicate that the interaction of thermal vacancies actually takes place at high temperatures. Concerning the formation mechanism of the present SFT, the nucleation and growth mechanism has already been discussed; see the previous letter of the present authors [5]. A similar SFT was also observed in a rapidly cooled CZ-Si specimen.

The present experiments exhibit that vacancy-type defect clusters are easily formed in Si rapidly cooled from a partly molten state by the local supersaturation of

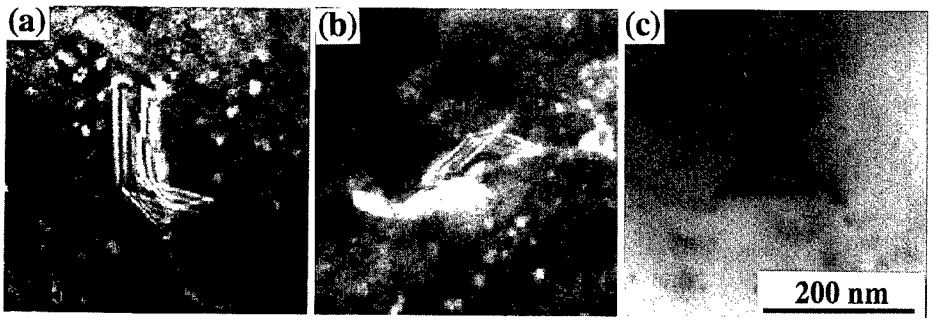

Fig. 5. A variety of small stacking faults formed in FZ-Si rapidly solidified in UHVEM after a partly molten state. (a) and (b) Weak beam dark field micrographs from 022 reflections, and (c) bright field micrograph viewed along the [1 1 1] direction.

Fig. 6. Electron micrograph showing planar defects and dislocations formed in FZ-Si quenched from a molten state. The defect with a fringe contrast at the left is a stacking fault, and the band at the right is a {1 1 1} twin.

vacancies. They also show that larger planar defects can be seen inside rapidly solidified specimens as shown in Fig. 6. This micrograph shows the formation of a {1 1 1} stacking fault, a {1 1 1} twin band, and some dislocations. In this case, stacking fault is determined to be of extrinsic type by the conventional fringe contrast method [6]. Therefore, the formation mechanism is different from that of the tiny planar faults mentioned above.

4. Conclusions

Although few quenching works have been performed on Si, the present study showed that quenching experiments are worth studying intrinsic point defects of Si. From TEM observations of various defects formed in Si by rapid cooling from a partly molten state, the results can be summarized as follows.

(1) Various types of lattice defects were found to form in the rapidly cooled specimens. They were stacking faults, twins, dislocations, and tiny defect clusters.

(2) The formation of stacking fault tetrahedra clearly exhibited the clustering and the collapse of thermal vacancies that took place on the {1 1 1} planes at high temperatures.

(3) The formation of helical dislocations indicated the interaction of dislocations induced by shear with thermal point defects in Si at high temperatures.

Acknowledgements

This work was partly supported by the Ministry of Education, Science, Sports and Culture of Japan (Grant-in-Aid for Scientific Research, C. No.10650015) and Japan Society for the Promotion of Science (JSPS) Research for the Future Program in the Area of Atomic Scale Surface and Interface Dynamics. We would like to acknowledge Professor H. Mori and his group members in the Ultra-high Voltage Electron Microscopy Center of Osaka University for their assistance in using the Hitachi HU-2000 electron microscope.

References

[1] M. Itsumi, M. Tomita, M. Yamawaki, J. Appl. Phys. 78 (1995) 1940.
[2] M. Kato, T. Yoshida, Y. Ikeda, Y. Kitagawara, Jpn. J. Appl. Phys. 35 (1996) 5597.
[3] P.V. Evans, S.R. Stiffler, Acta Metall. Mater. 39 (1991) 2727.
[4] A. Seeger, K.P. Chik, Phys. Stat. Solid. 29 (1968) 455.
[5] R. Oshima, F. Hori, M. Komatsu, H. Mori, Jpn. J. Appl. Phys. 37 (1998) L1430.
[6] G. Thomas, M.J. Goringe, Transmission Electron Microscopy of Materials, Wiley, New York, 1979, pp. 160–168.
[7] W. Coene, H. Bender, S. Amelinckx, Philos. Mag. A 52 (1985) 369.
[8] Y. Ohno, M. Hirata, S. Takeda, R. Fujimoto, R. Oshima, J. Electron Microsc. 45 (1996) 38.
[9] J.P. Hirth, J. Lothe, Theory of Dislocations, Wiley, New York, 1982 p. 332.

ELSEVIER

Physica B 273–274 (1999) 387–390

PHYSICA B

www.elsevier.com/locate/physb

Copper–hydrogen complexes in silicon

S. Knack[a,*], J. Weber[a], H. Lemke[b]

[a]*Max-Planck-Institut für Festkörperforschung, Heisengbergstrasse 1, Postfach 80 06 65, D-70506 Stuttgart, Germany*
[b]*TU Berlin, Institut für Werkstoffe der Elektrotechnik, Jebensstraße 1, D-10623, Germany*

Abstract

The deep levels of copper–hydrogen complexes in silicon were investigated by DLTS and MCTS. Copper-doped silicon was hydrogenated by wet chemical etching. Two deep levels at $E_c - 0.36$ eV and $E_v + 0.54$ eV were attributed to the Cu–H_1 complex. A third charge state of this defect might be overlapping with the Cu donor at $E_v + 0.21$ eV. The levels at $E_c - 0.25$ eV and $E_v + 0.27$ eV were assigned to the Cu–H_2 defect. The results are compared with former studies on the hydrogen complexing of Au and Ag.

PACS: 61.72.Ji; 78.66.Db

Keywords: Silicon; Copper; Hydrogen; DLTS

1. Introduction

Copper is an important and well-studied [1–5] metal impurity in silicon. It is the fastest diffuser in silicon [6,7] which makes it a feared contaminant in semiconductor technology.

Hydrogen is known to be able to form complexes with transition metals in silicon. The complexes can contain different numbers of hydrogen atoms, whereby in most, but not all, cases the complex containing the highest amount of hydrogen is electrically passive. The interaction between hydrogen and transition metals has been investigated for Au [8], Ag [9] and Pt [10] among others, but up to date not in the case of copper.

In this paper we report about first results from a DLTS study of the formation of copper–hydrogen complexes in silicon and compare our findings with results on complex formation of silver and gold with hydrogen.

2. Experimental

For our studies we used n- and p-type floating-zone silicon which was doped with copper during crystal growth and co-doped with phosphorous and boron, respectively. The shallow doping concentrations in the crystals were about $10^{14}\,cm^{-3}$ while the concentration of the substitutional copper was measured to be at $10^{13}\,cm^{-3}$.

Hydrogen was introduced into our samples by means of wet-chemical etching in an mixture of HF, HNO_3 and CH_3COOH (1 : 2 : 1) at room temperature.

Schottky contacts were formed by evaporating metal contacts of 1–2 mm diameter onto the sample surface without heating the sample. Gold was used as contact material for n-type samples and aluminium in the case of p-type material. An eutectic gallium–indium alloy was scratched onto the backside of the samples to give ohmic contacts.

Deep-level transient spectroscopy (DLTS) and minority carrier transient spectroscopy (MCTS) experiments were performed on the Schottky contacts. For the DLTS and MCTS experiments two different cryostats were used, which could be cooled down by liquid helium for DLTS and liquid N_2 for MCTS. The capacitance transients were analogue filtered, whereby different filters (first to third order) could be used for signal processing. The

* Corresponding author. Tel.: + 49-711-689-1543; fax: + 49-711-689-1602.

E-mail address: sknack@kernix.mpi-stuttgart.mpg.de (S. Knack)

0921-4526/99/$ - see front matter
PII: S0921-4526(99)00486-X

MCTS measurements were done by backside illumination of the samples. In order to get spatially resolved concentration profiles of the deep levels measured, DDLTS measurements at different voltages were performed. For the correct calculation of the concentrations the depth profiles of the free carriers as obtained by CV measurements were taken into account.

3. Results and discussion

The DLTS and MCTS spectra measured on our n- and p-type samples are shown in Fig. 1. The deep levels were labelled as shown in Fig. 1. (Electron traps are indicated by an E and hole traps by an H followed by the approximate peak temperature for an emission time of 50 ms.) There are three dominant peaks in the DLTS – spectrum of the n-type sample (E(100)–E(180)). The depth profiles of the concentration of these levels are shown in Fig. 2. As can be seen, the level E(100) is homogeneously distributed at greater depth and falls off towards the surface. This is consistent with the interpretation of E(100) as related to the substitutional Cu defect [3,4]. The missing concentration of isolated Cu_s near the surface is due to defect reactions. Contrary to E(100) the levels E(140) and E(180) are located near the surface and have an exponentially decreasing concentration at greater depth (Fig. 2). This is the expected behaviour for complexes containing hydrogen which has been introduced by wet chemical etching. The depth profiles clearly show that the two levels are related to different defects. Summing up the concentrations for E(100), E(140) and E(180) which accounts for all the defects containing copper, which can be measured in the upper half of the band gap, there is still a significant decrease in concentration in the near surface region. The copper might be either contained in a defect which leads to levels in the lower band gap only or is bound in an electrically passive complex.

The levels in the lower half of the band gap can be seen from the majority spectrum in p-type material as well as from the minority spectrum of the n-type sample. Due to the different filters used for analysing the transients the peak positions of the level vary slightly between the DLTS and MCTS measurements. Contrary to the DLTS measurements, the level H(260) can hardly be seen in the MCTS spectrum, which hints that the photocurrent and the hole capture coefficient of H(260) were too small to significantly fill the level. On the other hand, the levels H(200) and H(225) overlap in the DLTS-spectrum because of the lower-order filter. H(225) can only be seen as a shoulder to H(200). Fitting the two overlapping peaks shows that H(225) is smaller relative to H(200) in the majority spectrum compared to the minority spectrum. The reason for this might be that the formation of H(225) depends on the level of the Fermi energy and therefore differs between n- and p-type material or that H(200) is not completely filled in the MCTS experiment.

Fig. 3 shows the depth profiles of the deep levels measured in our p-type samples. Because of the strong overlap with H(200) no profile for H(225) could be obtained. The nature of this level is not known up to now. The profiles of levels H(100) and H(200) coincide deeper in the bulk material but show a significant differ-

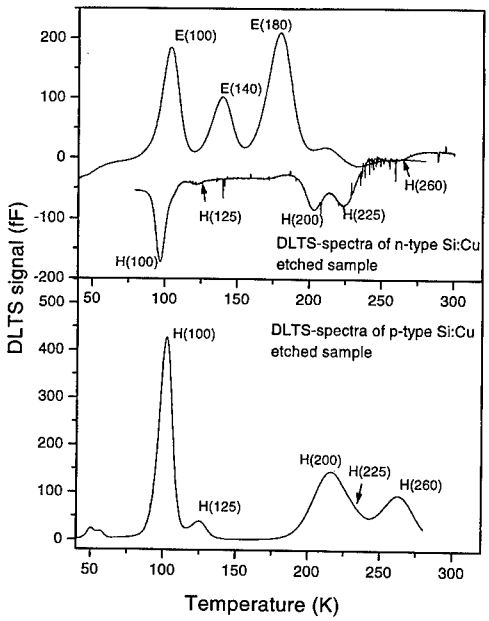

Fig. 1. DLTS and MCTS spectra of floating zone Si : Cu. Spectra were measured at an emission time of 50 ms. (a) Spectra of n-type material; (b) Spectrum of p-type material.

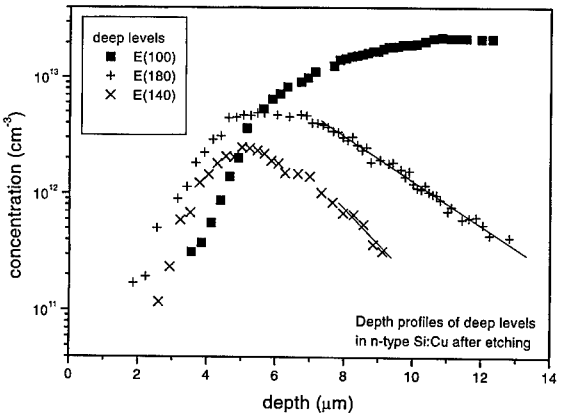

Fig. 2. Depth profiles of deep levels in n-type Si : Cu after etching of the samples.

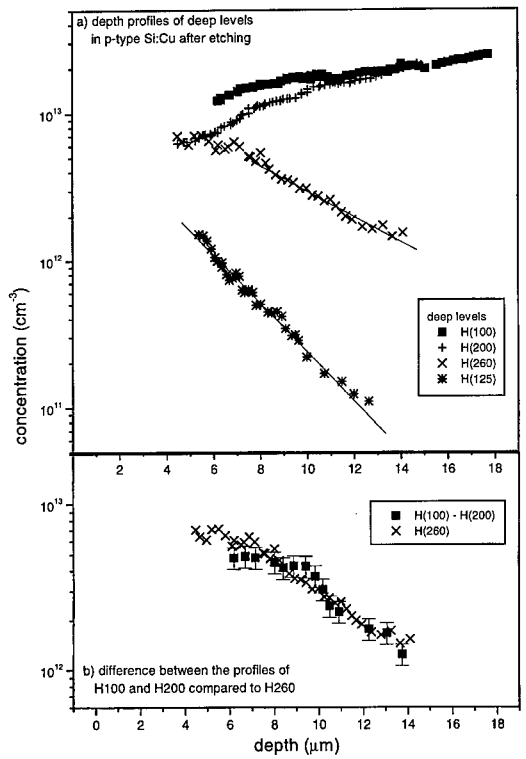

Fig. 3. (a) Depth profiles of deep levels in p-type Si : Cu after etching of the samples. (b) Difference of the profiles H(1 0 0) and H(2 0 0) compared to the profile of H(2 6 0).

ence in the near surface region. While both profiles decrease towards the surface, the reduction in concentration of H(200) is more pronounced. From the assignment of the two levels to the donor and acceptor state of substitutional copper [3,4] one would expect completely identical profiles. There have been previous reports [3] about this discrepancy in peak height between acceptor and donor level, which had been tentatively related to an insufficient evaluation of the space charge region at different temperatures. Our calculation of the profiles has taken into account this effect. We therefore can exclude space charge effects as a reason. The difference in concentration is real and can only be found near the surface.

For a more detailed analysis of the depth profiles, we used the model of Feklisova and Yarykin [11] describing the formation of complexes with hydrogen and an isolated centre under the conditions of wet chemical etching. The in-diffusing hydrogen is trapped by an isolated centre forming complexes containing one or more hydrogen atoms. An approximate solution in greater depth of the bulk shows that the concentrations of the different complexes decrease exponentially with depth, whereby the characteristic length is proportional to the inverse

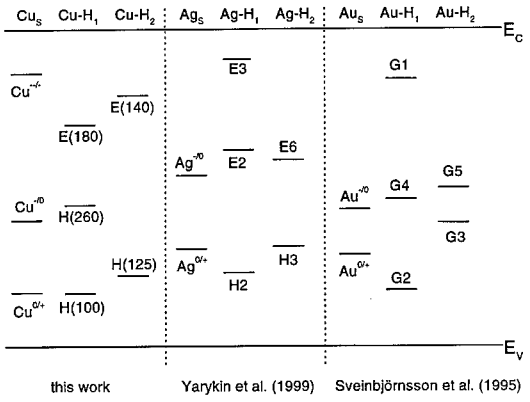

Fig. 4. Deep levels of the hydrogen complexes of the group IB elements, copper, silver [9] and gold [8].

number of hydrogen atoms. We fitted the exponential part of the concentration profiles obtaining a ratio of 1.8 ± 0.4 for the characteristic lengths of the levels E(140) ($L_{E(1\,4\,0)} = 2.8$ μm) and E(180) ($L_{E(1\,8\,0)} = 5.2$ μm) and of 1.8 ± 0.3 for H(125) ($L_{H(1\,2\,5)} = 6.7$ μm) and H(260) ($L_{H(2\,6\,0)} = 12$ μm). We conclude from the ratios that E(180) and H(260) are levels of a Cu–H_1 complex while E(140) and H(125) are different charge states of a Cu–H_2 defect. No level can account for the missing copper concentration in the near surface region. We propose that the Cu near to the surface is bound in an electrically passive complex containing three or more hydrogen atoms. This would be analogous to the cases of Au and Ag [8,9].

In Fig. 4, the difference in the concentrations of H(100) and H(200) is shown. For comparison the depth profile of H(260) is also given. If we allow a bigger error from the subtraction, the two profiles are comparable. This gives a possible explanation for the observed discrepancies in peak height for H(100) and H(200). H(100) is a superposition of the substitutional Cu double donor and a level of the Cu–H_1 defect. This suggestion is supported by the fact that by variation of the filling pulse length two capture coefficients differing by about one and a half order of magnitude could be extracted (see Table 1). At present the assignment is still very tentative and needs to be investigated further. It should be tried to resolve the presumed superposition of two levels either by high-resolution Laplace DLTS or by DDLTS in the time domain.

According to the vacancy model of Watkins [12] which has been very successful in describing the energy levels of substitutional transition metal defects, the energy level positions are derived from the energy levels of the vacancy and should be comparable for transition metals from the same group. This similarity also translates to the hydrogen complexes of the transition metals

Table 1
List of activation energies and carrier capture coefficients of the deep levels in copper-doped n- and p-type silicon

Level	ΔE (eV)	c_n ($cm^3\,s^{-1}$)	c_p ($cm^3\,s^{-1}$)	Assignment
E(100)	0.167(3)	3.2×10^{-10} (105 K)	6.5×10^{-6} (105 K)	$Cu^{--/-}$
E(140)	0.254(4)	4.6×10^{-11} (143 K)	7.0×10^{-6} (144 K)	$Cu\text{–}H_2$
E(180)	0.360(3)	7.5×10^{-11} (183 K)	1.3×10^{-5} (185 K)	$Cu\text{–}H_1$
H(100)	0.207(4)	—	2.4×10^{-5} (97 K)	$Cu^{0/+}$
			8.9×10^{-7} (97 K)	
H(125)	0.27 (1)	—	—	$Cu\text{–}H_2$
H(200)	0.478(5)	—	5.6×10^{-6} (204 K)	$Cu^{-/0}$
H(225)	0.506(7)	—	1.1×10^{-6} (233 K)	?
H(260)	0.54 (1)	—	—	$Cu\text{–}H_1$

as has e.g. been shown in the cases of Au and Ag [8,9]. One would therefore expect copper as the third element of this group to show an analogous picture. Fig. 4 shows an overview of the deep levels found for the hydrogen complexes of the group IB elements. While for Ag and Au the level schemes have a close qualitative resemblance, Cu as the first element of the group shows a different picture.

The properties of the discussed levels are summed up in Table 1. The activation energies are calculated using the standard T^2-correction. The capture coefficients for minority carriers were calculated assuming an average drift velocity $v_d = 2.5*10^6$ cm/s in the space charge region.

4. Conclusion

Substitutional copper in silicon forms defect complexes containing a different number of hydrogen atoms. We have found two different deep levels E(180) ($E_c - 0.36$ eV) and H(260) ($E_v + 0.54$ eV), which we assign to the $Cu\text{–}H_1$ complex. A possible third charge state of the defect at $E_v + 0.21$ eV overlaps with the copper donor. This explains the often reported difference in concentration for the donor and acceptor levels of copper. For the $Cu\text{–}H_2$ complex we have also found two deep levels at $E_c - 0.25$ eV and $E_v + 0.27$ eV. We have evidence for a passive copper complex which contains three or more hydrogen atoms.

Acknowledgements

We want to thank J. Bollmann for discussion about DDLTS and for help with the MCTS measurements. The technical assistance of W. Heinz and W. Krause is gratefully acknowledged.

References

[1] R.N. Hall, J.H. Racette, J. Appl. Phys. 35 (1964) 2.
[2] J. Weber, H. Bauch, R. Sauer, Phys. Rev. B 25 (1982) 7688.
[3] H. Lemke, Phys. Stat. Sol. A 95 (1986) 665.
[4] S.D. Brotherton et al., J. Appl. Phys. 62 (1987) 1826.
[5] E.R. Weber, Appl. Phys. A 30 (1983) 1.
[6] T. Zundel et al., Appl. Phys. Lett. 53 (1988) 1426.
[7] A. Mesli, T. Heiser, Phys. Rev. B. 45 (1992) 11 632.
[8] E.Ö. Sveinbjörnsson, O. Engström, Phys. Rev. B 52 (1995) 4884.
[9] N. Yarykin et al., Phys. Rev. B 59 (1999) 5551.
[10] J.-U. Sachse et al., Phys. Rev. B 55 (1997) 16 176.
[11] O.V. Feklisova, N.A. Yarykin, Semicond. Sci. Technol. 12 (1997) 742.
[12] G.D. Watkins, Physica B 117 & 118 (1983) 9.

ELSEVIER

Physica B 273–274 (1999) 391–394

PHYSICA B

www.elsevier.com/locate/physb

Dissociative diffusion of nickel in silicon, and sinks and sources of vacancy annihilation and generation in the crystal bulk

Hajme Kitagawa*, Shuji Tanaka

Department of Electronics, Fukuoka Institute of Technology, 3-30-1 Wajiro-Higashi, Higashi-ku, Fukuoka 811-0295, Japan

Abstract

In-diffusion and annealing processes of substitutional nickel atoms in dislocation-free silicon are studied at 960°C to distinguish between the site exchange mechanisms of the nickel atoms. The concentration of substitutional nickel atoms varies exponentially with time according to the theory of dissociative mechanism in both processes. Interstitial nickel atoms in dislocation-free silicon precipitate in the bulk as confirmed by an infrared microscopy. Nickel precipitates play an important role in the vacancy generation and annihilation. It is suggested that, in dislocation-free silicon, nickel diffuses under the dissociative mechanism, the dominant point defects mediating the site exchange of nickel atoms are vacancies, and that the crystal surfaces, and nickel precipitates or precipitate-induced lattice defects play a role as the sinks and sources of vacancy annihilation and generation. The rate-limiting step for the site exchange of substitutional nickel atoms is the diffusion of vacancies in the silicon crystal.

Keywords: Nickel; Dissociative diffusion; Vacancies; Nickel precipitation

1. Introduction

Nickel atoms in silicon occupy both interstitial and substitutional sites of silicon lattice [1]. A large fraction of nickel atoms occupies the interstitial sites, the rest, 10^{-4}–10^{-3} of total nickel atoms, remaining in the electrically active substitutional sites [2]. As a result of the fast interstitial diffusion, nickel is known as one of the fastest diffusers in silicon. It has been reported [1,3,4] that nickel atoms in dislocated silicon exchange their sites between the interstitial and substitutional sites via the dissociative mechanism, i.e., the dominant intrinsic point defects mediating the site exchange are vacancies. In dislocated silicon, both the crystal surfaces and dislocations play a role as sinks and sources (SS) of vacancy annihilation and generation. The site exchange process of nickel atoms is limited by the diffusion of vacancies. For dislocation-free silicon, however, experimental evidence allowing to distinguish between site exchange mechanisms and to examine the SS of the point defects involved in nickel diffusion is lacking. Thus, it is an open question which type of point defects, vacancies or self-interstitials, works, or which mechanism, the dissociative mechanism or the kick-out mechanism [5], operates in the site exchange of nickel atoms in dislocation-free silicon.

In present study, the in-diffusion of substitutional nickel atoms and the annealing of supersaturated substitutional nickel atoms in *dislocation-free silicon* are investigated experimentally. The purpose of the present study is to clarify which point defects dominate in the nickel diffusion in dislocation-free silicon. In the present paper, it will be shown that a small fraction of the nickel precipitates acts as SS of vacancy annihilation and generation, i.e., SS exist within the bulk even in dislocation-free silicon.

2. Experimental

N-type, phosphorus-doped, float-zoned, and dislocation-free silicon crystals were used in the experiment. Their phosphorus content ranged from 1.3×10^{13} to

* Corresponding author. Tel.: + 81-92-606-3131, ext.2405; fax: + 81-92-606-0726.

E-mail address: kitagawa@emat.fit.ac.jp (H. Kitagawa)

0921-4526/99/$ - see front matter
PII: S0921-4526(99)00487-1

1.5×10^{14} cm^{-3}. In-diffusion and annealing experiments were carried out at 960°C in a flowing nitrogen gas ambient after the nickel deposition by evaporation on both surfaces of the samples. For annealing experiment, samples were first saturated with nickel at 1020°C. In both processes, the samples were rapidly cooled at the rate of about 90 K/s to room temperature by pulling the samples out of the furnace. The concentration of substitutional nickel in the samples, C_s, was determined by measuring the change of the electrical resistivity by the four-point probe method at 20 ± 0.02°C under the assumption that nickel introduces an acceptor level at $E_c - 0.47$ eV in n-type silicon [6,7]. The concentration determined in this way is an average over the uniform region of the U-shaped distribution of nickel. We regarded the distribution as being uniform after the removal of a surface layer of the thickness of $0.2l$ from each surface of sample, where l is the thickness of the sample, to ensure the measurement of the increase (in-diffusion process) and the decrease (annealing process) of C_s while the heat-treatment time t elapses. Nickel precipitates were observed by an infrared microscopy (OLYMPUS BHSM-IR).

3. Results and discussion

The time dependence of C_s in the in-diffusion and annealing processes is shown in Fig. 1. The curves are calculated by Eqs. (1) and (2) predicted by the theory of the dissociative mechanism in which the time dependence of C_s is given by the exponential function of time t with time constant τ [3,4], i.e.,

$$C_s/C_s^0 = 1 - \exp(-t/\tau) \quad (1)$$

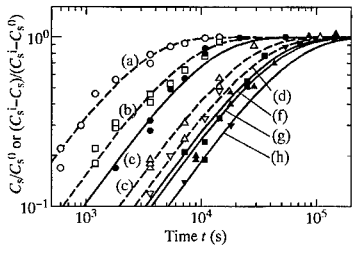

Fig. 1. In-diffusion and annealing processes of nickel in silicon. Diffusion temperature is $T_D = 960$°C in the in-diffusion processes. For the annealing processes, the sample was first saturated with nickel at $T_D = 1020$°C ($C_s^i \cong 8.5 \times 10^{13}$ cm^{-3}), then annealed at $T_A = 960$°C ($C_s^0 \cong 2.2 \times 10^{13}$ cm^{-3}). Curves are calculated from Eqs. (1) or (2) with τ listed below. (a): $l = 0.05$ cm, $\tau = 2.45 \times 10^3$ s (in-diffusion), (b) $l = 0.10$ cm, $\tau = 5.92 \times 10^3$ s (in-diffusion), (c): $l = 0.20$ cm, $\tau = 1.84 \times 10^4$ s (in-diffusion), (d): $l = 0.30$ cm, $\tau = 2.50 \times 10^4$ s (in-diffusion), (e): $l = 0.05$ cm, $\tau = 9.02 \times 10^3$ s (annealing), (f): $l = 0.10$ cm, $\tau = 3.11 \times 10^4$ s (annealing), (g): $l = 0.20$ cm, $\tau = 3.50 \times 10^4$ s (annealing) and (h): $l = 0.30$ cm, $\tau = 4.89 \times 10^4$ s (annealing).

for the in-diffusion process and

$$(C_s^i - C_s)/C_s^i - C_s^0) = 1 - \exp(-t/\tau) \quad (2)$$

for the annealing process, where the superscripts 0 and i denote the thermal equilibrium value of C_s and the value of C_s at $t = 0$, respectively.

Not only the in-diffusion and annealing processes shown in Fig. 1, but also the results obtained from a series of experiments performed so far at the temperature range from 940°C to 1020°C show that both processes obey Eqs. (1) or (2). Thus, we take the view that nickel atoms in dislocation-free silicon exchange their site between substitutional and interstitial sites via the dissociative mechanism and the dominant point defects working in the site exchange are vacancies as confirmed in dislocated silicon [1,3,4].

It was reported [8] that in in-diffusion process of substitutional impurity atoms, the relationship between the in-diffused concentration and time depends strongly on the thickness of the removed surface layers in the dissociative mechanism in dislocation-free silicon, provided the sinks of vacancy annihilation are only the crystal surfaces. In contrast to this theoretical prediction, the relationship between C_s and t in the present study was always in accordance with Eqs. (1) or (2), independent of the thickness of the removed surface sections. This suggests that some SS of vacancies exist in the bulk, even in the dislocation-free silicon.

The anticipation that the SS exists in the bulk is also in accordance with the dependence of τ of the in-diffusion and annealing processes on the sample thickness, l. The time constant τ obtained experimentally in the present study varied strongly from sample to sample. This is understood if the SS exist in the bulk and the density and size of the SS vary from sample to sample, depending on the diffusion and cooling conditions. If the SS of vacancies are only the crystal surfaces, as generally assumed for dislocation-free silicon, τ should only depend on l.

Nickel precipitates in the bulk, which are potential candidates for vacancy SS in the bulk, were investigated in the present study. Nickel precipitates, which were identified by comparison between infrared microscope images of nickel-doped and undoped silicon crystals, were distributed inhomogeneously within the bulk. We focused on the distribution, density and size of the precipitates. However, the morphology and composition of the precipitates could not be determined in the present study. Fig. 2 shows the two-dimensional display of the distribution of the nickel precipitates in the in-diffusion (a) and annealing (b) processes. In the in-diffusion process, the precipitate density in the center of the crystal was significantly lower than that in the vicinity of the surface. After annealing the density was reduced, indicating that interstitial nickel atoms diffuse out to the surface

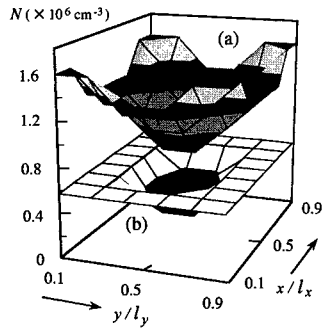

Fig. 2. Two-dimensional distribution of nickel precipitates in dislocation-free silicon of two samples: (a) doped with nickel at 1080°C for 120 min and (b) annealed at 940°C for 120 min after being doped with nickel at 1080°C for 120 min. Distribution in the plane of $z/l_z = 0.1$ is shown, where l_z is the thickness of samples and z is the distance from the surface.

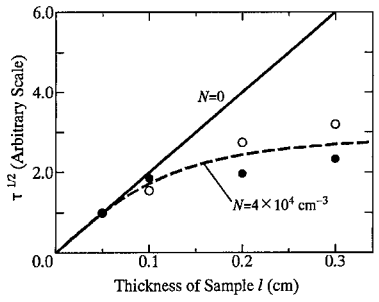

Fig. 3. Time constant of in-diffusion (○) and annealing (●) processes of nickel in dislocation-free silicon as a function of the thickness of the sample. Solid line and broken curve show the values of Eq. (3) calculated under the assumed values of $N = 0$ and $N = 4 \times 10^4\ \mathrm{cm}^{-3}$, respectively.

during annealing or cooling. The diameters of the precipitates ranged from 10 (or smaller) to 20 μm.

We assume that the precipitates of nickel in the bulk are formed not only during quenching, but also during the heat treatment in the in-diffusion and annealing process, and that the nickel precipitates or precipitate-induced lattice defects can act as SS of vacancies. In the dissociative mechanism, the reciprocal of the time constant, $1/\tau$, of in-diffusion and annealing processes is given by [9]

$$1/\tau = [(\pi/l)^2 + 4\pi r_0 N] \times C_v^0 D_v/(C_s^0 + C_v^0), \quad (3)$$

under the assumption that the precipitates are spherical (radius r_0 and number per unit volume N) and distribute randomly in the bulk. D_v and C_v^0 are the diffusion coefficient and the concentration of vacancies, respectively. The term $(\pi/l)^2$ on the right-hand side of Eq. (3) describes the contribution of the crystal surface to τ as the SS of vacancies, while $4\pi r_0 N$ describes the contribution of the spherical precipitates. Eq. (3) shows that $\tau^{1/2}$ is simply proportional to l when $N = 0$. For the display of this characteristic, the experimental data of $\tau^{1/2}$ as a function of l are plotted in Fig. 3 together with the semi-quantitative values of Eq. (3) in which $\tau^{1/2}$ at $l = 0.05$ cm is normalized to unity. It is worth mentioning that the contribution of internal sinks and sources increases with the increase of the sample thickness. Thus, Fig. 3 shows that a small fraction of nickel precipitates within the bulk or precipitate-induced lattice defects can work as SS of vacancies in silicon, and that the site exchange of nickel atoms is limited by the vacancy diffusion from the crystal surface and the vacancy SS in the bulk. To our knowledge, the present result is the first experimental indication of the effect of SS of vacancies in the bulk on site exchange of metal impurity atoms in dislocation-free silicon.

Since diffusion coefficient, D_i, of interstitial nickel atoms is high ($D_i \approx 10^{-4}$–$10^{-5}\ \mathrm{cm}^2/\mathrm{s}$ at 800–1200°C [1]) and the solubility decays exponentially with temperature, interstitial nickel atoms can diffuse out to the surface and form precipitates at the surface [10] which have been attributed to $NiSi_2$-type silicide. Seibt and Schröter [11] also reported that interstitial nickel atoms precipitate within the crystal bulk after rapid cooling from high temperatures. It was shown [11] that coherent platelets on Si {1 1 1} planes are formed, which consist of two {1 1 1} layers of $NiSi_2$ and are bounded by dislocations. Unfortunately, the composition and morphology of the nickel precipitates cannot be determined by infrared-microscope observations alone. From a series of in-diffusion and annealing experiments, $C_v^0 D_v$ or the vacancy contribution to the silicon self-diffusion coefficient, D_v^{SD}, has been found to range from 3.1×10^{-18} at 940°C to $1.0 \times 10^{-16}\ \mathrm{cm}^2/\mathrm{s}$ at 1020°C, which is in fairly good agreement with the result reported by Tan and Gösele [12]. However, since these temperatures are in the range in which the temperature dependence of D_v^{SD} almost coincides with that of D_I^{SD}, the self-diffusion coefficient via interstitial mechanism, it cannot be decided by means of the present experiments or nickel diffusion which mechanism predominates in self-diffusion of silicon.

In summary, in-diffusion and annealing processes of substitutional nickel atoms in dislocation-free silicon were studied at 960°C. It was suggested that nickel atoms in dislocation-free silicon exchange their sites via the dissociative mechanism and that the dominant point defects mediating the site exchange are vacancies. The crystal surfaces, and nickel precipitates or precipitate-induced lattice defects were found to play a role as SS of vacancy annihilation and generation. The site exchange of substitutional nickel atoms is limited by the diffusion of vacancies from the crystal surface and the vacancy SS in the bulk.

References

[1] M. Yoshida, K. Saito, Jpn. J. Appl. Phys. 6 (1967) 573.
[2] M. Yoshida, K. Furusho, Jpn. J. Appl. Phys. 3 (1964) 521.
[3] H. Kitagawa, K. Hashimoto, M. Yoshida, Jpn. J. Appl. Phys. 21 (1982) 276.
[4] H. Kitagawa, K. Hashimoto, M. Yoshida, Physica 116B (1983) 323.
[5] U. Gösele, W. Frank, A. Seeger, Appl. Phys. 23 (1980) 361.
[6] H. Kitagawa, H. Nakashima, Jpn. J. Appl. Phys. 28 (1989) 305.
[7] H. Kitagawa, S. Tanaka, H. Nakashima, M. Yoshida, J. Electron. Mater. 20 (1991) 441.
[8] M. Takahashi, M. Morooka, M. Yoshida, Jpn. J. Appl. Phys. 31 (1992) 1134.
[9] A.C. Damask, G.J. Dienes, Point Defects in Metals, Gordon and Breach, New York, 1963, p. 81.
[10] S. Sadamitsu, M. Sano, M. Hourai, S. Sumita, N. Fujino, T. Shiraiwa, Jpn. J. Appl. Phys. 28 (1989) L.333.
[11] M. Seibt, W. Schröter, Philos. Mag. 59 (1989) 337.
[12] T.Y. Tan, U. Gösele, Appl. Phys. A 37 (1985) 1.

ELSEVIER

Physica B 273–274 (1999) 395–397

PHYSICA B

www.elsevier.com/locate/physb

Drift of interstitial iron in a space charge region of p-type Si Schottky diode

S. Koveshnikov[a,*], B. Choi[a,b], N. Yarykin[c], G. Rozgonyi[d]

[a]*SEH-America, Inc., 4111 NE 112th Ave, Vancouver, WA 98682-6776, USA*
[b]*Arizona State University, Tempe, AZ, USA*
[c]*Institute of Microelectronics Technology RAS, Chernogolovka, Russia*
[d]*North Carolina State University, Raleigh, NC, USA*

Abstract

A novel straightforward method to determine the diffusion parameters of positively charged iron in p-type silicon has been developed. The method is based on application of high-frequency bias pulses to a Schottky diode, providing the total iron ionization and drift in the space charge region. Temperature-dependent measurements in the range from 25°C to 180°C revealed the migration energy of positively charged iron of 0.84 eV, thereby supporting the data obtained from the iron–boron pairing.

Keywords: Iron in silicon; Diffusion; Drift

1. Introduction

Iron in silicon is known to diffuse as an interstitial impurity. The effective diffusion coefficient of iron diffusing in both its neutral, Fe^0, and ionized, Fe^+, charged states is given by $D_{\mathrm{eff}}(\mathrm{Fe_i}) = f \times D(\mathrm{Fe_i}^+) + (1-f) \times D(\mathrm{Fe_i}^0)$, where f is the fraction of ionized iron, and can be described in the wide temperature range as $D(\mathrm{Fe_i}) = 1.3 \times 10^{-3} \times \exp(-0.68\ \mathrm{eV}/kT)\ \mathrm{cm}^2/\mathrm{s}$ [1,2]. However, due to the uncertainty in f at elevated temperatures, the specific migration barriers for Fe_i^+ and Fe_i^0 cannot be directly obtained from the temperature dependence of $D_{\mathrm{eff}}(\mathrm{Fe_i})$. Numerous FeB re-association experiments revealed the activation energy to be 0.8–0.9 eV [1,2], which was attributed to the diffusion barrier for Fe_i^+ [3]. In principle, the difference between the FeB re-association data and the overall fit for $D_{\mathrm{eff}}(\mathrm{Fe_i})$ can be explained under assumption that the Fe_i^+ migration energy is lower than the barrier for the last jump of Fe_i^+ to boron [2]. On the other hand, this barrier was experimentally measured in Ref. [3] to be 0.65 eV. Thus far, it is not clear whether or not the re-association kinetics represent the migration barrier for Fe_i^+. Therefore, an alternative method excluding the short-range Fe_i–B_s interaction is required for determination of the Fe_i^+ migration barrier.

In this work we have developed a novel method to measure the $D(Fe_i^+)$ via drift of positively charged iron in a space charge region (SCR) of a Schottky diode on p-type Si. The key experimental idea consists of the application of high-frequency reverse bias pulses, which provides favorable conditions for total ionization and drift of iron in the SCR. During the half period when the bias is *off*, the Fe_i traps are filled with holes, and become positively charged; while during the half period when the bias is *on*, iron is driven by the electric field towards the edge of the SCR. To keep iron within the SCR in a positively charged state at the annealing temperature, the pulse frequency, F_p, should be high enough to satisfy $e_h \ll F_p$, where e_h is the hole emission rate.

2. Experimental

We used double-side polished FZ Si wafers doped with boron to $2.0 \times 10^{14}\ \mathrm{cm}^{-3}$. Iron was introduced by

* Corresponding author. Fax: + 1-360-883-7240.
E-mail address: sergei_koveshnikov@seha.com (S. Koveshnikov)

0921-4526/99/$ - see front matter
PII: S0921-4526(99)00488-3

thermal annealing at 900°C for 2 h following "back-side" ion implantation with a dose of 1×10^{11} Fe/cm^2. The Fe_i and FeB traps were measured by DLTS on Al Schottky diodes formed on opposite wafer surface. The total Fe concentration was uniformly distributed up to, at least, 10 μm and equal to 2×10^{12} cm^{-3}. The samples from second set were doped with boron and iron to 8×10^{14} and 6×10^{13} cm^{-3}, respectively. The pulsed bias anneal experiments were carried out in the temperature range from 27°C to 180°C following thermal annealing at 180°C to dissociate the FeB pairs. The temperature dependence of Fe_i^+ mobility was determined via measurements of changes in the Fe_i concentration profiles using the depth-dependent DLTS technique. The concentration profiles of shallow acceptors were measured by the C–V method on each diode before and after annealing. The diode leakage current at room temperature did not exceed 100 nA at a reverse bias of 20 V.

3. Results and discussion

3.1. Drift of Fe_i^+ under pulsed bias annealing

Fig. 1 presents a direct evidence of the feasibility of pulsed bias annealing (PBA) method for studying Fe_i^+ drift across the SCR in p-type silicon. The diode was annealed at 50°C for 8 h, while the applied bias was switched between 8 and 2 V at the high frequency of 1 MHz. During annealing, the near surface layer $\Delta W_1 = W(2\text{ V}) - W(0\text{ V})$, was permanently depleted of charge carriers creating a zone of predominantly neutral iron. In spite of the strong electric field, the Fe concentration profile in Fig. 1 is uniformly flat within ΔW_1, indicating that the Fe_i^+ fraction was indeed negligibly small. Pulse biasing over the deeper layer defined by $\Delta W_2 = W(8\text{ V}) - W(2\text{ V})$ strongly enhances the fraction of positively charged Fe in the space charge region. The resulting drift of Fe_i^+ produces a dip in the Fe concentration profile. Note that pulsed bias annealing at a low pulse frequency (1 Hz) did not lead to a notable Fe redistribution. If the applied bias of 1 MHz was switched between 8 and 0 V, i.e. Fe_i^+ was present in the entire SCR, the dip initially formed close to the surface and then extended deeper with annealing time, as shown in Fig. 2. Note that the loss of the Fe concentration in the near surface region is compensated by an increase of Fe concentration deeper than ~ 5 μm. In Fe-doped samples with a boron concentration of 8×10^{14} cm^{-3} an Fe redistribution also occurred under pulsed bias annealing; however, the time needed for Fe_i^+ to drift the same distance was shorter by about a factor of two due to the higher electric field over the shallower SCR. Thus, based on the observed Fe profile dependence on annealing time, temperature, and electric field strength, we conclude that the observed iron redistribution is governed totally by drift and can be used for determination of its mobility.

3.2. Determination of Fe_i^+ mobility

A set of samples were subjected to 1 MHz pulsed bias annealing in the temperature range from 27°C to 180°C. The changes observed in the Fe concentration profiles were similar to those presented in Fig. 2. By solving the diffusion-drift equations and fitting the Fe concentration depth profiles obtained under pulsed bias annealing, the temperature dependence of $D(Fe_i^+)$ was determined, (see Fig. 3). The migration energy for positively charged iron is equal to 0.84 eV, which agrees well with previously published values derived from the FeB pair re-association kinetics [3]. We also measured FeB re-association

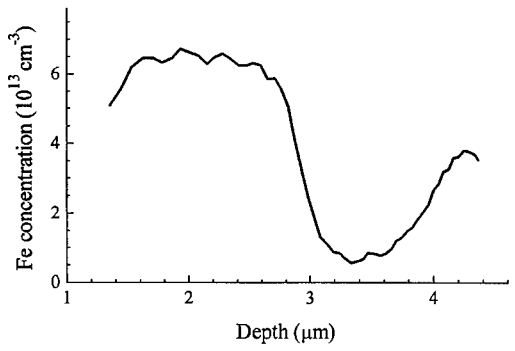

Fig. 1. The Fe_i concentration profile measured by DLTS on samples doped with boron and iron to 8×10^{14} and 6×10^{13} cm^{-3}, respectively, after 1 MHz pulsed bias annealing at 50°C for 8 hours. The reverse bias was switched between 8 and 2 V corresponding to the SCR width of 4.1 and 2.8 μm, respectively.

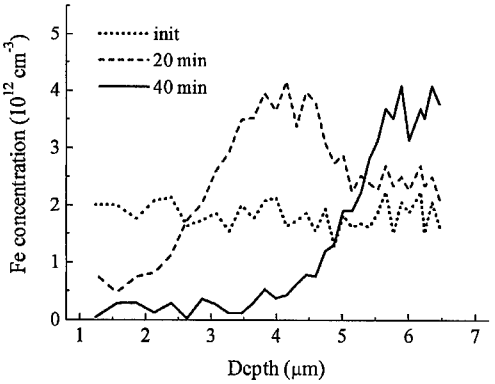

Fig. 2. Development of the Fe_i concentration profiles as measured by DLTS before and after pulsed bias annealing at 120°C for 20 and 40 min. The reverse bias was switched between 8 and 0 V at a frequency of 1 MHz. The boron and initial iron concentrations were 2×10^{14} and 2×10^{12} cm^{-3}, respectively.

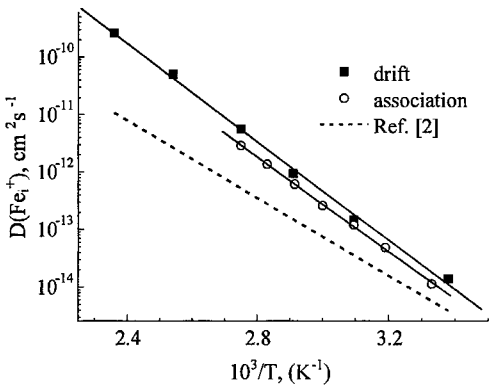

Fig. 3. Temperature dependence of $D(Fe_i^+)$ as determined from the Fe_i^+ drift experiments, and FeB pairing kinetics. The overall fit for $D_{eff}(Fe_i^+)$ from Ref. [2] is also presented.

kinetics on the same Si wafer to directly compare the migration energies determined by the two methods. The measurements were performed in the temperature range of 27°C to 90°C following thermal dissociation at 180°C for 3 min. The diffusion coefficient was calculate using the expression given in Ref. [3]. The temperature dependence of $D(Fe_i^+)$, also shown in Fig. 3, yielded a migration energy of 0.85 eV. It is important to note that: (i) the good agreement of the $D_{Fei+}(1/T)$ slopes implies that the activation energy obtained in the FeB re-association experiments indeed represents the diffusion barrier; and (ii) the close values for diffusion coefficients determined over wide temperature range confirm the validity of a pure Coulombic Fe–B interaction.

3.3. Determination of Fe_i^+ fraction under constant bias annealing

As it was shown above, annealing of the Schottky diodes under a constant bias at 50°C did not lead to redistribution of iron. By increasing the temperature to $\geqslant 90$°C the shape of the Fe concentration profiles changed in a similar fashion to that in Fig. 2, indicating the presence of a notable fraction of positively charged iron. To determine the fraction of Fe_i^+ from the dependence of the observed changes in iron concentration profiles on constant bias annealing time, one needs first to obtain reliable data for 100%-ionized iron. To evaluate the occupancy of the iron level with holes under 1 MHz pulsed bias, we used the values $E_{Fe} = E_v + 0.38$ eV, and σ_n, σ_p from Ref. [4]. The results of calculation predict full ionization of iron up to ~ 100°C, and a reduction of the Fe_i^+ fraction to 50% at 150°C. However, since the data in Fig. 3 does not reveal a notable deviation from a straight line, the occupancy of the Fe trap with holes must be 100%. As a check we calculated that an increase of the Fe ionization energy by only 0.02 eV provides total Fe ionization over the whole temperature range. Therefore, we used the data in Fig. 3 to calculate the Fe_i^+ fraction under constant bias annealing.

By comparing the results of the pulsed vs. constant bias annealing experiments performed at 90°C, we found the Fe_i^+ fraction under constant bias annealing to be $\sim 3\%$, while calculations using $E_{Fe} = E_v + 0.38$ eV, and σ_n, σ_p from Ref. [4] yielded a value of $\sim 0.5\%$. This discrepancy, by factor of 6, does reflect the uncertainty of the parameters of the Fe level extrapolated to elevated temperatures. Again, raising the Fe level position by only 0.02 eV accounts for this discrepancy.

4. Conclusion

Summarizing the experimental data on Fe_i^+ drift, we have demonstrated the feasibility of a novel method for determination of the diffusion parameters of Fe_i^+. The migration energy of 0.84 eV determined from the drift under pulsed bias annealing is higher than that derived from the overall fit of high- and low-temperature diffusion data. However, this value is in remarkable agreement with the iron migration energy measured by FeB pairing. This implies negligible impact of the barrier for the last jump of iron to boron. On the other hand, the direct determination of the diffusion coefficient supports the model of a pure Coulombic Fe–B interaction. Further investigation of the Fe drift as a function of annealing temperature, pulse frequency, and t_p/T ratio can help determine the fundamental properties of Fe at elevated temperatures.

Acknowledgements

The authors are grateful to A. Istratov for stimulating discussion of this work.

References

[1] E.R. Weber, Appl. Phys. A 30 (1983) 1.
[2] A.A. Istratov et al., Appl. Phys. A 69 (1999) 13.
[3] L.C. Kimerling, J. Benton, Physica B 116 (1983) 297.
[4] T. Heiser, A. Mesli, Phys. Rev. Lett. 68 (1992) 978.

ELSEVIER

Physica B 273–274 (1999) 398–403

PHYSICA B

www.elsevier.com/locate/physb

Impact of vacancies and self-interstitials on the formation of substitutional transition metal defects in float-zone silicon crystals

H. Lemke[a,*], W. Zulehner[b]

[a]*Institut für Mikroelektronik und Festkörperelektronik, Technische Universität Berlin, Jebensstrasse 1, 10623 Berlin, Germany*
[b]*Wacker Siltronic AG, Johannes-Hess-Straße 24, D-84489 Burghausen, Germany*

Abstract

It is shown that investigations on substitutional TM-defects grown-in by the FZ-technique can be used as a suitable detection method for vacancies and self-interstitials in silicon. For the interpretation of the experimental results, approximate analytical solutions are presented for the temperature field in the growing crystal, for the transport equations describing the diffusion and recombination of intrinsic point defects and for the capture process connected with the formation of substitutional TM-defects. The analysis is demonstrated on dislocation-free FZ-crystals doped with Pt and Rh, respectively. The capture of the interstitial TM-defects by the vacancies takes place in different temperature ranges depending on the metal type. First results about the capture coefficients for Si- and TM-interstitials are derived.

Keywords: Silicon; FZ-crystals; Intrinsic point defects; Substitutional TM-defects

1. Introduction

Four years ago, it was reported about the axial distributions of transition metal (TM) defects in float zone (FZ) silicon crystals [1]. It was shown that the defects for the doping metals with the valence $N > 8$, which were observed by deep-level transient spectroscopy (DLTS), are caused by substitutional TM-defects M_S. For the important metals Au, Pt, Ir and Rh (group II) nearly uniform axial distributions $N_S(z)$ were found. The almost complete incorporation of the doping concentration on lattice sites could be interpreted by the existence of a sufficiently high concentration of vacancies. But all crystals investigated at that time were grown in vacuum (type A) [1]. A different doping behavior was observed meantime in FZ-crystals grown in an argon ambient (type B) [2,3]. High concentrations N_S, comparable to those in A-crystals, could be detected only in the initial parts and in the quickly cooled end parts of the crystals. This behavior gave a first hint that the distributions of both vacancies and self-interstitials are important for the interpretation of the results found in B-crystals [3].

In this work, it will be shown that the axial distributions of substitutional TM-defects in dislocation-free crystals are mainly determined by the growth parameter $P = V/G$, where V denotes the growth velocity and G the temperature gradient at the melt/solid interface. Taking into consideration recombination and diffusion of intrinsic point defects, Voronkov [4] has shown already in 1982 that for $P > P_{crit}$ a vacancy-dominated (V) and for $P < P_{crit}$ an interstitial-dominated (I) region exists in grown Si-crystals. On the basis of these results the author presented for the first time a correct interpretation for the formation of microdefects (D-defects, A-swirls) in FZ-crystals. Recently Dornberger and v.Ammon [5] published extensive experimental results for large-diameter CZ-crystals, which are consistent with the critical growth parameter $P_{crit} = 2.23 \times 10^{-5}$ cm^2/(K s). In the present work the dependence of the growth parameter on

* Corresponding author. Fax: + 30-314-26804.
E-mail address: nell@imf.ee.tu-berlin.de (H. Lemke)

0921-4526/99/$ - see front matter
PII: S0921-4526(99)00490-1

the axial position will be derived from a simple analytical solution of the heat conduction equation. As representatives of the metals of group II, a detailed interpretation of the axial distribution $N_S(z)$ is presented for the dopants Pt and Rh in B-crystals. For the determination of the theoretical distributions $N_S(z)$, approximate solutions of the transport equations for vacancies and self-interstitials are used, which have been derived recently in Ref. [6]. Based on the results in Ref. [6] a theoretical critical growth parameter can be estimated in first approximation according to $P_{crit} = 2.26 \times 10^{-5}$ cm^2/(K s), which is in agreement with the experimental value cited above. For all numerical calculations presented in this work the same parameters of intrinsic point defect as published by Sinno et al. [7] will be used.

2. Experimental details

The crystals were prepared by the FZ-technique in an argon ambient close to atmospheric pressure with the following growth parameters: growth direction = ⟨1 1 1⟩, pull rate = 3.4 mm/min, seed rotation = 6 rpm, feed rod rotation = 10 rpm, crystal diameter $2r_0 = 2$ cm, crystal length $L = 10$–15 cm. For the TM-doping a metal amount of 3 mg for Pt and 8 mg for Rh was dissolved in the molten zone. The doping process was finished by quickly separating the crystal from the feed rod and switching off the inductor power. This process resulted in an average cooling rate of about 10 K/s in the last crystal part, whereas a broad middle region can be characterized by about 1 K/s. The electrically active defects were investigated with DLTS on samples near the radial position $r = r_0/2$ using Schottky contacts with a diameter 4–5 mm.

3. Theoretical and experimental results

3.1. Growth parameter

The formation of substitutional TM-defects depends strongly on the distributions of vacancies and self-interstitials in the grown crystal. The estimation of these distributions involves the temperature gradient G at the melt/solid interface and by this the growth parameter $P = V/G$ for each axial position z_{cryst} of the cylindrical FZ-crystal. We have solved the heat conduction equation taking into account adequate boundary conditions. During the growth of FZ-crystals the heat loss at higher temperatures is mainly determined by the heat radiation via the cylindrical surface. For small-diameter crystals the heat conduction is governed approximately by the one-dimensional differential equation [8]

$$\frac{d}{dz}\left[\frac{k(T)}{k_0}\frac{dT}{dz}\right] - b\frac{dT}{dz} = aT^4, \tag{1a}$$

$$a = \frac{2\varepsilon\sigma}{r_0 k_0}, \quad b = \frac{c_p \rho V}{k_0}, \tag{1b}$$

where z is the distance to the melt/solid interface, $T(z)$ the temperature, $k(T)$ the thermal conductivity, $\sigma = 5.7 \times 10^{-12}$ W/(cm^2 K^4) the Stefan–Boltzmann constant, $\varepsilon = 0.57$ the emissivity, $c_p = 0.922$ J/(g K) the specific heat, $\rho = 2.33$ g/cm^3 the density, V the growth velocity, and r_0 the crystal radius.

If the thermal conductivity is approximated by the function $k(T) = k_0/T$ [9], the differential equation (1a) can be solved in closed form for the growth rate $V = 0 (b = 0)$

$$T(z) = T_w \Big/ \sqrt{\cos[\sqrt{2a}wT_w^2(1 - z/w)]}, \tag{2}$$

where the heat conduction across the boundary between the cylindrical part and the seed cone ($z = w$) of the FZ-crystal has been neglected. Using the condition $T(0) = T_m$, where T_m denotes the melting temperature, the temperature T_w at the boundary can be determined. For $w/r_0 \geqslant 5$ the solution is approximately given by

$$T_w \approx \sqrt{\pi/2}T_m[1 + \sqrt{2a}wT_m^2]^{-1/2}. \tag{3}$$

For normal growth rates the second term in Eq. (1a) is sufficiently small and the complete solution can be estimated by a perturbation analysis. Inserting $T(z)$ according to (2) into the right-hand side of Eq. (1a) yields after integration the first approximation for the temperature gradient

$$G = \sqrt{\frac{a}{2}}T_m\sqrt{T_m^4 - T_w^4} - bT_m(T_m - T_w). \tag{4}$$

Using the approximation $k_0 = 360$ W/cm [10] the growth parameter $P = V/G$ was estimated for the growth rate $V = 3.4$ mm/min and $r_0 = 1$ cm. Fig. 1 shows the parameter in dependence on the axial position $z_{cryst} = w$ for both cases $b = 0$ and $b \neq 0$. The gradient is evidently lowered by the zone movement up to about 10%. In the first crystal part the gradient decreases strongly, which leads to the condition $P > P_{crit}$ in this range. But the main parts of our FZ-crystals are characterized by the reversed condition $P < P_{crit}$. The range of the stationary crystal growth starts evidently near the position $z_{cryst} = 9$ cm with $G = 390$ K/cm and $P = 1.45 \times 10^{-5}$ cm^2/(K s).

3.2. Intrinsic point defect distributions

For the interpretation of the substitutional TM-defect distributions it is assumed that the doping leads at first to the formation of interstitial TM-defects, which can be trapped by the vacancies during the cooling period in the temperature range $T \leqslant T_c$. In the range $T > T_c$, the distributions of vacancies and self-interstitials are

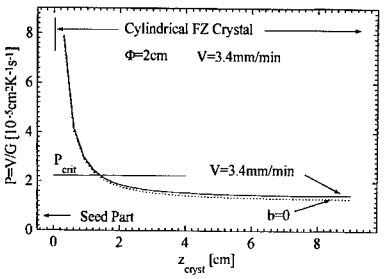

Fig. 1. Dependence of the growth parameter P on the axial position.

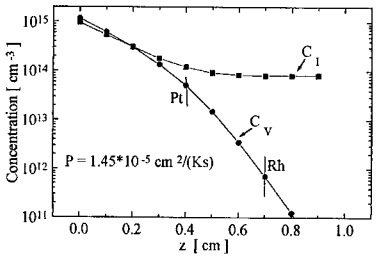

Fig. 2. Dependence of the vacancy and self-interstitial concentration on the distance to melt/solid interface for stationary growth conditions.

determined by diffusion and recombination processes. The basic differential equations could be recently solved by simple analytical approximations [6]. All experimental results presented in this work show that the recombination between vacancies and self-interstitials is sufficiently high, which can be described by the relation [6]

$$Q(T) = C_V C_I = C_V^{eq} C_I^{eq},$$

$$Q(T) = C_{Vm} C_{Im} \exp\left[-\frac{H}{kT_m}\left(\frac{T_m}{T} - 1\right)\right], \tag{5}$$

where C_V, C_I are respectively concentrations of vacancies and self-interstitials (thermal equilibrium values are labelled by the suffix eq), $H = 7.37$ eV is the activation energy characterizing the total temperature dependence of Q near the melting point [7], k the Boltzmann constant, $C_{Vm} = 11.7 \times 10^{14}$ cm^{-3}, $C_{Im} = 9.6 \times 10^{14}$ cm^{-3} [7].

In the case of high recombination the intrinsic point defect distributions depend only on the growth parameter P [6] according to

$$C_V(T) = C + \sqrt{C^2 + qQ(T)}, \tag{6a}$$

$$C = (C_{Vm} - C_{Im} q)/2, \tag{6b}$$

$$q = \left(P + \frac{HD_{Im}}{2kT_m^2}\right)\left(P + \frac{HD_{Vm}}{2kT_m^2}\right)^{-1} \tag{6c}$$

with $D_{Vm} = 4.3 \times 10^{-5}$ cm^2/s: diffusivity of vacancies at $T = T_m$, $D_{Im} = 3.8 \times 10^{-4}$ cm^2/s: diffusivity of self-interstitials at $T = T_m$ [7].

Knowing the characteristic temperature T_c, the relations (5) up to (6c) can be used as starting point to estimate the substitutional TM-defect distributions. The parameter T_c depends mainly on the binding energy of the metal atom on the lattice site which is not yet known at present. Hence, it is very important that T_c can be directly determined with our experimental results as will be shown below. The steep increase of the substitutional defect concentration at the crystal end is generally located in the range of the stationary crystal growth. The distributions of vacancies and self-interstitials for these growth conditions are shown in Fig. 2. For distances $z > 2$ mm to the melt/solid interface the concentration of the self-interstitials C_I is evidently the dominating species. Whereas C_I tends to a constant value given according to Eqs. (5) and (6a) by $2(-C)/q$, the vacancy concentration C_V decreases very quickly with increasing distance to the interface. The capture of the interstitial TM-defects by the vacancies starts near the positions $z = 4$ and 7 mm for Pt and Rh, respectively. These positions correspond to the temperatures $T_c = 1530$ K for Pt and 1410 K for Rh. Taking into account the growth parameter $P(z)$ as demonstrated in Fig. 1, the concentrations $C_V(T_c)$ and $C_I(T_c)$ can be estimated for each axial position. Fig. 3 shows these distributions for the dopants Pt and Rh. A sufficient high concentration C_V can be recognized only in the range $z_{cryst} < 1.5$ cm. In the main part of the crystal, on the other hand, the vacancy concentration is low and the formation of substitutional TM-defects is additionally hindered by a high concentration of self-interstitials.

Similar distributions can also be estimated for the rapidly cooled crystal end. Provided that Eq. (5) is fulfilled in the range $T \geqslant T_c$ even for the cooling rate $\beta = 10$ K/s, the concentrations $C_V(T_c)$, $C_I(T_c)$ can be derived from the distributions shown in Fig. 2. Neglecting a further diffusion during the fast cooling period the relation (5) yields

$$(C_V^0 - \Delta)(C_I^0 - \Delta) = Q(T_c), \tag{7}$$

where C_V^0, C_I^0 denote the initial concentrations according to Fig. 2. After solving the quadratic equation for $\Delta(z)$, both concentrations are known. The intrinsic point defect concentrations in this range are shown for Pt and Rh in Fig. 4.

3.3. Capture process

In the temperature range $T \leqslant T_c$ two capture processes have to be considered. The reaction of self-interstitials with vacancies leads to the formation of new

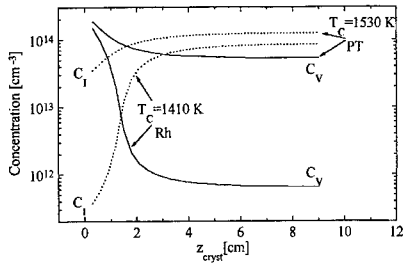

Fig. 3. Concentrations of vacancies and self-interstitials at two temperatures T_c in dependence on the axial position.

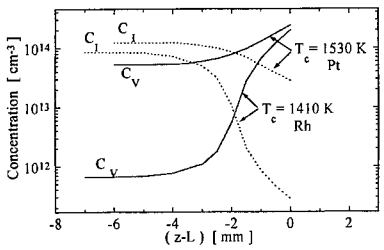

Fig. 4. Concentrations of vacancies and self-interstitials at two temperatures T_c in dependence on the distance to the crystal end.

ordinary lattice points with a concentration ΔN_L, whereas the capture of interstitial TM-defects generates substitutional TM-defects with a concentration N_S. Introducing the capture coefficients $R_c(T)$ for the first and $r_c(T)$ for the second process the coupled nonlinear differential equations can be written in the form

$$\beta \frac{d\Delta N_L}{dT} = -R_c(T)X(T)[N_I - \Delta N_L], \tag{8a}$$

$$\beta \frac{dN_S}{dT} = -r_c(T)X(T)[N_D - N_S], \tag{8b}$$

$$X(T) = N_V - N_S - \Delta N_L, \tag{8c}$$

where $N_V = C_V(T_c)$, $N_I = C_I(T_c)$, $N_D = [TM]_{tot}$, $\beta = VG$: cooling rate.

An approximate solution can be derived, if the temperature dependence of R_c/r_c can be neglected and if either $\Delta N_L \approx (p-1)N_S$ or $\Delta N_L \ll N_S$, where

$$p = 1 + (R_c N_I)/(r_c N_D). \tag{9}$$

The solution for $T \to 0$ can be written in the form

$$N_S = \sqrt{\frac{N_V N_D}{p}} \frac{\sinh[R/2]}{\sinh[R/2 + \ln\sqrt{pN_D/N_V}]}, \tag{10a}$$

$$\beta R = [pN_D - N_V]\int_0^{T_c} r_c(T)\,dT. \tag{10b}$$

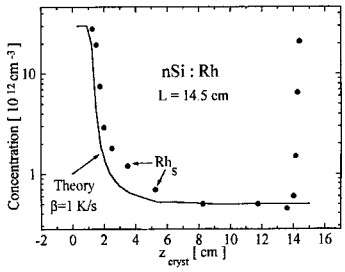

Fig. 5. Comparison between the experimental and theoretical distribution of Rh_S-defects for the range of normal crystal growth, $N_D = 3 \times 10^{13}$ cm^{-3}.

From Eq. (10a) it follows immediately that $N_S \approx N_V/p$ for $R \gg 1$ and $N_S \approx N_D$ for $-R \gg 1$. In our crystals the first case can be recognized in the I-dominated regions, whereas the second case is fulfilled whenever N_V is high. Using the capture coefficient $r_c(T) = r_0 \exp[-E_c/(kT)]$ the integration in Eq. (10b) yields approximately

$$\beta R = [pN_D - N_V]r_c(T_c)kT_c^2/E_c. \tag{11}$$

3.4. Comparison between theory and experiment

Since the capture coefficients are presently not known, a first rough determination was performed using our experimental results. Figs. 5 and 6 show the axial distributions of substitutional Rh- and Pt-defects measured in dislocation-free FZ-crystals. For Rh a steep decrease of the concentration is observed in the first crystal part. For $z_{cryst} > 3$ cm the concentration is small and tends to a constant value near 5×10^{11} cm^{-3} in the range of the stationary crystal growth. The steep increase at the crystal end is caused by the fast cooling process. A qualitatively similar behavior can be observed for Pt (see Fig. 6). But the concentration in the middle region is much higher compared to that of Rh. A first important information about the capture coefficients can be derived from the concentration of substitutional defects in (or near) the range of the stationary crystal growth. Using the results in Fig. 3 and Eqs. (9) and (10a) leads to the numerical relations $r_c/R_c \approx 9$ for Rh and ≈ 10 for Pt, provided that $R \gg 1$ is fulfilled. A second important information can be derived from the results measured at the quickly cooled crystal end. If the relation (7) holds up to the temperature T_c, a condition for the recombination strength of intrinsic point defects must be fulfilled, which can be written in the form $R_c(T_m)/(\beta E_c) \geqslant A(T_c)$ [6]. According to the approximate analysis published in Ref. [6] the parameter A can be easily estimated with Bessel functions, which leads to the condition $R_c(T_m) \geqslant 2.2 \times 10^{-14}$ cm^3/s for $T_c = 1410$ K, $\beta = 10$ K/s and $E_c = 1.25$ eV. Since the activation energy for the recombination E_c cannot be directly determined with

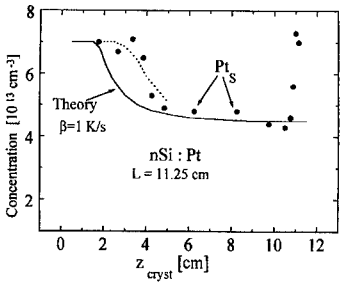

Fig. 6. Comparison between the experimental and theoretical distribution of Pt_S-defects for the range of normal crystal growth, $N_D = 7 \times 10^{13}\ cm^{-3}$.

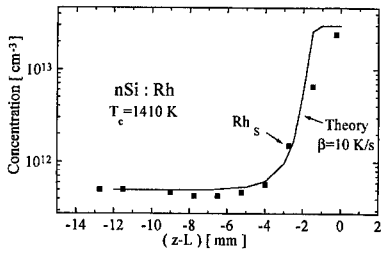

Fig. 7. Comparison between the experimental and theoretical distribution of Rh_S-defects for the quickly cooled end part of the crystal.

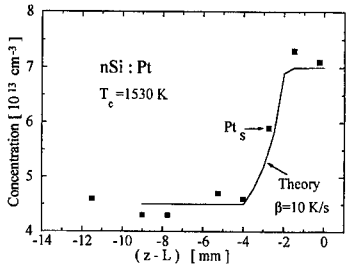

Fig. 8. Comparison between the experimental and theoretical distribution of Pt_S-defects for the quickly cooled end part of the crystal.

our experimental results, we have chosen a value, which is nearly equal to the migration energy of self-interstitials $E \approx 1$ eV [7]. Taking into account these results the capture coefficients of the interstitial TM-defects can be estimated according to $r_c \geqslant 3.5 \times 10^{-14}\ cm^3/s$ (Rh, $T_c = 1410$ K) and $r_c \geqslant 9.2 \times 10^{-14}\ cm^3/s$ (Pt, $T_c = 1530$ K). Inserting these relations into Eq. (11) leads to $\beta R/(pN_D - N_V) \geqslant 4.9 \times 10^{-12}\ cm^3\ K/s$ for Rh and $\geqslant 14.9 \times 10^{-12}\ cm^3\ K/s$ for Pt. For the estimations of the theoretical distributions $N_S(z)$, we have used the lower limit of these data and the cooling rate $\beta = 1$ K/s in the range of normal crystal growth and $\beta = 10$ K/s for the quickly cooled crystal end. The doping concentration N_D was estimated with the segregation coefficients [1] to about $3 \times 10^{13}\ cm^{-3}$ for Rh and $7 \times 10^{13}\ cm^{-3}$ for Pt. The theoretical results calculated with Eq. (10a) are demonstrated in Figs. 5 and 6 by the drawn curves. The steep decrease of the substitutional Rh-defects in the first crystal part (see Fig. 5) is evidently consistent with the theory, but systematic deviations can also be recognized. A similar comparison for the dopant Pt is shown in Fig. 6. The higher concentration of substitutional Pt-defects in the range $z_{cryst} > 2$ cm is obviously caused by the higher concentration of vacancies at the temperature T_c as demonstrated in Fig. 3. In the range of the stationary crystal growth $R = 437$ for Pt and 189 for Rh holds, consistent with the above postulated condition $R \gg 1$.

For a better fitting of the experimental results the growth parameter has to be changed up to about 15% around the position $z_{cryst} = 2.5$ cm as indicated by the dotted curve in Fig. 6. Such changes can be expected, for example, if a weak after-heating due to the inductor field near the melt/solid interface is taken into consideration. But also in the frame of the present theory a systematic deviation to the experimental results seems possible. Since the intrinsic point defect concentrations shown in Fig. 3 were calculated with approximations, which are valid only in the stationary case, a delay effect can be expected for quickly changing growth conditions (Fig. 1). In this case, all curves in Fig. 3 have to be shifted somewhat to the right consistent with the deviations shown in Figs. 5 and 6.

The distributions of substitutional TM-defects in the quickly cooled crystal ends are demonstrated in more detail in Figs. 7 and 8. For the representation of the experimental results the distances to the crystal end were measured on the cylindrical surface. Taking into account the concave shape of the melt/solid interface these data were lowered by an average distance of 1 mm. The experimental distribution for Rh in Fig. 7 shows that the increase of the concentration starts near to the distance $L - z_{cryst} = 7$ mm, which was used above for the determination of the important parameter T_c. Taking into account the intrinsic point defect distributions (see Fig. 4) the theoretical distribution of substitutional Rh-defects was estimated with Eq. (10a). The theoretical distribution is evidently in fair agreement with the experimental results. It can be concluded, therefore, that Eq. (7) used for the estimations is correct. Similar distributions are demonstrated for the dopant Pt in Fig. 8. The agreement between the theoretical and experimental results is again good.

4. Conclusion

A study was presented about the axial distribution $N_S(z)$ of substitutional Pt- and Rh-defects in small-diameter FZ-crystals. For dislocation-free crystals grown with a velocity $V = 3.4$ mm/min high concentrations N_S are

only observed in the initial parts and in the quickly cooled end parts of the crystals. With analytical approximations for the temperature field and for the distributions of vacancies and self-interstitials it could be proven that the concentration of substitutional TM-defects depends on the growth parameter $P = V/G$ at each axial position. In the interstitial-dominated regions, characterized by $P < P_{crit}$, markedly decreased concentrations N_S are observed. These concentrations depend strongly on the parameter T_c, which characterizes the temperature range $T \leqslant T_c$, where the interstitial TM-defects can be effectively trapped by the vacancies. Using the experimental results in the quickly cooled end parts, the important data $T_c = 1530$ K for Pt and $T_c = 1410$ K for Rh were determined. From the experimental results in the interstitial-dominated region and at the crystal end it was concluded that the capture coefficients of the interstitial TM-defects must be set according to $r_c \geqslant 3.5 \times 10^{-14}$ cm^3/s (Rh, $T_c = 1410$ K) and $r_c \geqslant 9.2 \times 10^{-14}$ cm^3/s (Pt, $T_c = 1530$ K). Using an approximate solution for the capture process theoretical distributions $N_S(z)$ could be derived for the range of the normal crystal growth and for the quickly cooled crystal end. A fair agreement between theory and experiment is found for both dopants. These results show that investigations on FZ-crystals doped with substitutional TM-defects can be used as a suitable tool to determine the concentration of vacancies and self-interstitials.

Acknowledgements

The work was performed at the-Institut für Mikroelektronik und Festkörperelektronik der Technischen Universität (TU-Berlin) in cooperation with Wacker Siltronic AG (Burghausen) and the -Institut für Kristallzüchtung (IKZ-Berlin). The authors would like to thank Mrs. H. Baumüller (IKZ-Berlin), A. Eckert and B. Tierock (TU-Berlin) for extensive technical assistance in sample preparation. The support by Dr. W. Schröder and Dr. H. Riemann (IKZ-Berlin) during the crystal growth experiments is gratefully acknowledged.

References

[1] H. Lemke, Mater. Sci. Forum 196–201 (1995) 683.
[2] H. Lemke, in: C.L. Claeys, P. Rai-Choudhury, P. Stallhofer, J.E. Maurits (Eds.), High Purity Silicon IV, The Electrochemical Society, Pennington, NJ, 1996, p. 272.
[3] H. Lemke, W. Zulehner, B. Hallmann, in: H.R. Huff, U. Gösele, H. Tsuya (Eds.), Semiconductor Silicon, The Electrochemical Society, Pennington, NJ, 1998, p. 572.
[4] V.V. Voronkov, J. Crystal Growth 59 (1982) 625.
[5] E. Dornberger, W. von Ammon, J. Electrochem. Soc. 143 (1996) 1648.
[6] H Lemke, W. Südkamp, Phys. Stat. Sol. (a) 176 (2) (1999) in press.
[7] T. Sinno, R.A. Brown, W. von Ammon, E. Dornberger, J. Electrochem. Soc. 145 (1998) 302.
[8] H.S. Carslaw, J.C. Jaeger, Conduction of Heat in Solids, Clarendon Press, Oxford, 1959.
[9] J.M. Ziman, Electrons and Phonons, University Press, Oxford, 1967.
[10] C.J. Glassbrenner, G.A. Slack, Phys. Rev. 134A (1964) 1058.

ELSEVIER

Physica B 273–274 (1999) 404–407

PHYSICA B

www.elsevier.com/locate/physb

Dependence of electrically detected magnetic resonance signal shape from iron-contaminated silicon wafers on the thermal treatment of the samples

T. Mchedlidze[a,*], K. Matsumoto[a], T.-C. Lin[a], M. Suezawa[b]

[a]*Komatsu Electronic Metals Co., Ltd., 2612 Shinomiya, Hiratsuka 2540014, Japan*
[b]*Institute for Materials Research, Tohoku University, Sendai 9808577, Japan*

Abstract

The shape of the electrically detected magnetic resonance (EDMR) signal from iron–contaminated Czochralski-grown silicon (CZ–Si) samples strongly depends on the thermal treatments applied to the samples before and after the contamination procedure, although the average g-value of the spectra apparently does not vary. A signal from an iron-contaminated float-zone grown silicon (FZ–Si) sample was detected employing an EDMR signal detection unit with enhanced sensitivity. For similar contamination levels, the signal from the FZ–Si sample has amplitude about $\frac{1}{45}$ that of the CZ–Si signal and has specific shape. Further study of the EDMR signals from iron-contaminated Si samples will be useful for the investigation of gettering and recombination processes in Si wafers. Besides that, dependence of the EDMR spectrum shape on the thermal processes employed can help to pinpoint the process responsible for wafer contamination during semiconductor device fabrication.

Keywords: EDMR; Iron in silicon; Contamination

1. Introduction

The electrical detection of magnetic resonance (EDMR) remains a largely unclaimed measurement technique in the silicon industry in spite of its extremely high sensitivity to several types of defects (see Refs. [1,2] and references therein). The absence of an established model for spin-dependent recombination (SDR) processes, which are responsible for the EDMR signal, is probably to be blamed for this situation. The SDR is only a part of the overall recombination processes in common silicon systems. Thus, the intensity of the EDMR signal of a sample will depend on the concentrations of SDR-active and other carrier recombination centers and cross sections of relevant recombination processes in a complex manner. Moreover, some known recombination centers that give rise to the ESR signal do not reveal EDMR activity. On the contrary, centers not participating in recombination processes are occasionally detected by the EDMR in the presence of SDR-active centers. Due to these factors, the EDMR is only a qualitative defect detection method at the present time. On the other hand, the EDMR can provide an important information for structure modeling of the detected defects in the same way, as does the ESR.

In the previous work [2], we detected SDR signals from iron-contaminated CZ–Si samples. These signals (KEM-1 and KEM-2 spectra) were different from the ESR signals in Si reported previously. The absence of signals in the non-contaminated reference samples and the dependence of the signal intensity on concentrations of oxygen and iron in the samples led us to hypothesize that the signals were related to some iron–oxygen complexes. Furthermore, the analysis of signal anisotropy as well as size/concentration calculations for oxide precipitates in the samples investigated enabled us to propose oxide precipitates decorated with iron atoms as a source

* Corresponding author. Fax: + 81-643-248915.
E-mail address: teimuraz@steppenstones.com (T. Mchedlidze)

0921-4526/99/$ - see front matter
PII: S0921-4526(99)00491-3

of the detected signal. The KEM-1 and KEM-2 signals differed only by the shape of the EDMR signal. We hypothesized that both signals originated from similar defects and that shape variation was stipulated by a difference in post-contamination thermal treatment of the samples. If the last hypothesis is correct, the EDMR method may be capable of pinpointing the process sequence responsible for the contamination during semiconductor device fabrication. To investigate this possibility, we decided to conduct EDMR measurements for the iron-contaminated samples subjected to different thermal processes before and after contamination.

2. Experimental

We used boron-doped ($\rho_{SUB} = 10\,\Omega$ cm) CZ–Si mirror-polished wafers, with a (1 0 0) surface planes as a starting material (interstitial oxygen concentration in the wafers was $O_i = 1.3 \times 10^{18}\,cm^{-3}$, as measured by Fourier transform infrared absorption method using the ASTM F 121-76 standard). FZ–Si wafers with similar resistivity were also investigated ($O_i \approx 1 \times 10^{16}\,cm^{-3}$). The starting sample wafers were subjected to various combinations of thermal processes prior to and after the iron-contamination procedure.

Below, the letters and numbers in the labels of samples correspond to the starting material (first letter 'C' for CZ–Si and 'F' for FZ-Si) and preparation procedures which were employed. The second position in the label identifies the procedure, used to create gettering sites in the wafers prior to contamination: 'I' – internal sites (IG process, two-step annealing at 650°C, 5 h + 900°C, 4 h) or 'E' – external sites (EG process, 0.8 μm thick poly-Si film deposition on the back surface of the wafer at 650°C for 3 h). The letter 'P' in the third position of a label indicates that an epitaxial layer about 4 μm thick was deposited on wafer surface ($T \approx 1000$–1200°C, $t <$ 10 min, $\rho_{EPI} \approx \rho_{SUB}$). The next number corresponds to the level of iron contamination: '1' – low, '2' – middle, '3' – heavy (sign '#' will stand for either contamination level). The contamination of wafers was done in SC-1 solution, containing iron atoms at concentrations of 1, 10, and 100 ppb. After dipping in the contaminated SC-1 solution, wafers were spin-dried. The last letter in the sample label specifies the post-contamination procedure employed. Thus, the letter 'T' corresponds to annealing of wafers at 1000°C for 1 h and cooling to 800°C in the furnace. The letter 'C' designates the CMOS process (1000°C, 5 h + 1175°C, 9 h + 800°C, 2 h + 1000°C, 4 h). The letter 'G' indicates gettering annealing (1000°C, 1 h + 600°C, 2 h) and the letter 'L' means low-temperature annealing (600°C, 17 h). '0' in the label instead of a letter means that the sample was not subjected to that particular treatment step.

We used deep-level transient spectroscopy (DLTS) and surface photovoltage (SPV) analysis to estimate iron concentration in the contaminated samples. The resultant iron concentration in the subsurface layer (about 1–3 μm from the wafer surface) was estimated from the intensity of the iron–boron pair peak in the DLTS spectra. The iron concentration in the bulk of the samples was calculated from results of SPV measurements according to the established procedure [3]. The iron concentration detected in the wafer subsurface region was generally lower than that in the bulk due to gettering processes.

Sample preparation for the EDMR measurements, installation and measurement procedures are described elsewhere [2]. In the present work we restricted our investigation to comparison of the EDMR signals obtained from different samples. Thorough investigation of EDMR spectra anisotropy and deduction of relevant microscopic models for the defects are tasks for the future. Spectra were measured for similar orientations of the samples (the static magnetic field vector was perpendicular to the wafer surface (1 0 0) direction, with precision better than 1°). The temperature during all measurements was (12 ± 0.3) K (we used an Oxford-type He-flow cryostat). The microwave frequency was 9.07 GHz and microwave power was 200 mW. The EDMR signals (differential of the sample resistance by the magnetic field) were detected using an EG&G model 5110 lock-in amplifier. For this purpose, magnetic field was modulated with 0.2 G amplitude on 100 KHz frequency. The samples were illuminated with a highly stable white light source to create charge carriers at low temperatures.

3. Results and discussion

In the all samples, except the non-contaminated starting wafers, we were able to detect EDMR signals of various shapes and intensities. The intensity of EDMR signals is usually expressed as $\Delta R/R$, where ΔR stands for sample resistivity change during the magnetic resonance and R – for sample resistivity out of resonance [4,5]. For our case, the shape of the spectra for different samples was significantly different. To compare signal intensity for different samples we integrated the EDMR spectra.

For the samples subjected to similar thermal procedures, the integrated intensity of the EDMR signal correlated well with the iron concentration measured by the SPV method. In Fig. 1a and b the EDMR spectra obtained from several samples are presented. As seen from the Fig. 1a, the intensity of the signal grows with the iron contamination level.

In Fig. 2, a correlation between the integrated EDMR signal and iron concentration for the different samples is presented. In the case of the samples subjected to similar thermal processes having different contamination levels

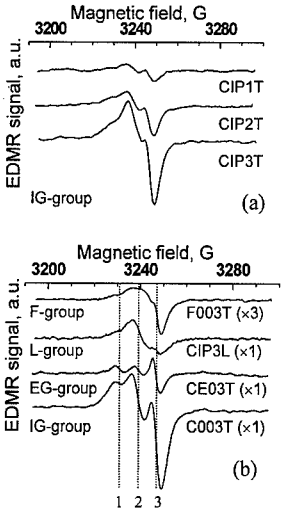

Fig. 1. The EDMR spectra obtained from iron-contaminated Si samples subjected to various treatments. (a) Samples with different levels of contamination subjected to similar treatments. (b) Samples with the same level of contamination subjected to different treatments. Sample labels with corresponding magnification factor for amplitude and corresponding groups are indicated beneath the curves. Three dotted lines are presented for eye-guide. Experimental conditions: $T_{MEAS} = 12$ K, $P_{MW} = 200$ mW, $f_{RES} = 9.06892$ GHz, $f_{MOD} = 100$ KHz, $H_{MOD} = 0.2$ G, $\boldsymbol{B}\|(0\ 1\ 1)$, measurements under illumination.

the correlation between these values is good. In the case of the samples subjected to different thermal processes, even for similar contamination levels the correlation seems to be significantly worse. Probably, the difference can be attributed to the influence of recombination centers not relevant to the iron. In the figure the re-measured result for the sample used in the previous work [2] is also presented (CZ-Si sample, $O_i = 1.5 \times 10^{18}$ cm^{-3}, contaminated in the SC-1 solution containing 13 ppm of iron).

Although contamination and annealing procedures for the F003T and C003T samples were similar as well as SPV measurement results for these samples, a large difference in the integrated intensity of the EDMR signals (about 45 times, see Fig. 2) was observed. We attribute this result to the lower concentration of oxygen in the FZ-Si sample.

The results presented in Fig. 2 once again prove the supposition [2,6] that the EDMR measurement method is unable to give quantitative results on defect concentrations at present. However, on the other hand, all the EDMR signals observed in iron-contaminated samples are under the detection limit of the ESR measurement method (about 10^{12} spin G^{-1} cm^{-3} for our case), indicating much higher detection possibilities of the EDMR for these defects.

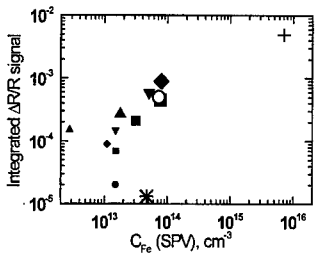

Fig. 2. Correlation between iron concentration in the samples (SPV measurement results) and integrated EDMR signals from different samples. The size of the symbols is related to the level of contamination. Squares correspond to CIP#T samples, up-triangles to CIP#C, diamonds to CEP#T, down-triangles to C00#T, circles to CE0#T, star to F003T sample, and cross to re-measured KEM-1 spectra.

Table 1
Groups of samples with similarly shaped EDMR spectra. The symbol '#' indicates that samples with either contamination level revealed similar signal shape

Group	Similar shape	Close shape
L	CIP#L	
	CEP#L	
	C0P#L	
	C00#L	
IG	C0P#T	CIP#G
	C0P#C	CEP#G
	C00#T	CE0#G
	C00#C	C0P#G
	CIP#T	C00#G
	CIP#C	
EG	CEP#T	
	CEP#C	
	CE0#T	
	CE0#C	
F	F003T	

The shapes of EDMR spectra, obtained from the samples subjected to similar heat treatments were very similar for all investigated contamination levels (see spectra in Fig. 1a for an example). On the contrary, the samples subjected to different heat treatment procedures prior to and/or after the contamination even with an equal iron contamination level revealed dissimilar shapes of the EDMR signal. Although exactly similar spectral shapes were not found for any two samples subjected to different thermal treatments, the spectra can be roughly divided into several groups. The representative spectra of each group are shown in Fig. 1b and the groups are defined in Table 1. We must stress here, that the classification given

in Table 1, is far from being explicit, because spectra from only one orientation of the samples were considered. An examination of spectral anisotropy may reveal more differences and/or similarities.

Let us first highlight the similarities among spectra presented in Fig. 1b. In the figure positions of dotted lines correspond to the g-factor values of ≈ 2.006 (dotted line 1), ≈ 2.001 (dotted line 2) and ≈ 1.996 (dotted line 3). The positions of respective peaks in the spectra do not vary much (compare positions of the three main respective peaks toward the dotted lines in Fig. 1b for different groups); also all the spectra can be fitted with similar number of gauss-shaped absorption line derivatives. The EDMR measurements at different temperatures for the newly obtained EDMR signals revealed temperature behavior similar to that reported previously for the KEM-1 and KEM-2 spectra [2]. All these facts, together with results reported previously, lead us to hypothesize that all the obtained spectra are due to similar defects, namely, iron–oxygen complexes. Anisotropy measurements and other investigations should be conducted to prove this supposition finally.

Additional investigations should be performed to discuss possible reasons for the behavior of individual lines in the spectra. Below we will present only some general consideration. Let us suppose that the classification given in Table 1 is correct. In such a case we can conclude that the low-temperature processes, near to 600°C, mainly determine the shape of the EDMR spectra. The best example supporting this supposition is probably the similarity of the spectra obtained from the L-group samples. For these samples, their 'thermal history' was almost eliminated during the prolonged annealing at 600°C. Also, EDMR signals from several samples subjected to the EG process revealed similar shapes regardless of the other procedures applied during their preparation. Similarly, for the large IG group, the main process, which determined the shape of the EDMR spectra, was probably the oxide precipitate creation during the IG process. Surprisingly, C00#T and C00#G samples also revealed similarly shaped spectra. We can assume that the stable embryo of oxide precipitates already existed in the starting Si material due to high oxygen concentration.

According to previously published results [6–8], the gettering process of iron occurs in a relatively low-temperature range (<700°C). Thus, it can be assumed that different structures of iron–oxygen complexes created during low-temperature processes are responsible for the observed differences in the shape of the EDMR signal.

4. Summary

For the CZ–Si and FZ–Si samples contaminated with iron and subjected to various thermal treatments prior to and after the contamination, EDMR signals were observed. The EDMR signal intensity roughly correlated with the iron concentration in the samples estimated from the SPV measurements.

The shape of the EDMR signal was different for samples subjected to various thermal processes prior to and/or after the contamination procedure. The processes conducted at relatively low temperatures (400–650°C) had an especially strong effect on the shape of the EDMR signal. We suppose that such behavior can be explained by the fact that gettering of the iron atoms occurs in that temperature range.

Further investigations of EDMR signal anisotropy will probably yield important information on gettering processes and the structure of the defects relevant to the detected signals. Besides that, the data herein presented indicates the possibility that EDMR signal shape can pinpoint the process responsible for wafer contamination. Such information would be of extreme importance in the fabrication of semiconductor devices.

References

[1] B. Stich, S. Greulich-Weber, J.-M. Spaeth, J. Appl. Phys. 77 (1995) 1546.
[2] T. Mchedlidze, K. Matsumoto, J. Appl. Phys. 83 (1998) 4042.
[3] J. Lagowski, P. Edelman, Electrochem Soc. Proc. 96-13 (1996) 523.
[4] D. Lepine, Phys. Rev. B 6 (1972) 1436.
[5] I. Solomon, Solid State Commun. 20 (1976) 215.
[6] T.Y. Tan, E.E. Gardner, W.K. Tice, Appl. Phys. Lett. 30 (1977) 175.
[7] R.B. Fair, C.W. Pearce, J. Washburn (Eds.), Impurity Diffusion and Gettering in Silicon, Materials Research Society Proceedings, Vol. 36, Materials Research Society, Pittsburgh, PA, 1985.
[8] H.R. Huff, W. Bergholz, K. Sumino (Eds.), Semiconductor Silicon 1994, The Electrochemical Society, Pennington, NJ, 1994.

ELSEVIER

Physica B 273–274 (1999) 408–411

PHYSICA B

www.elsevier.com/locate/physb

Out-diffusion profiles of supersaturated substitutional gold in silicon

Masami Morooka*

Fukuoka Institute of Technology, Wajirohigashi, Higashi-ku, Fukuoka 811-0295, Japan

Abstract

Out-diffusion profiles of supersaturated high-temperature substitutional gold and low-temperature substitutional gold in silicon have been measured by two heat-treatment methods. The profiles of high-temperature substitutional gold show those for a kick-out mechanism, and supersaturated high-temperature substitutional gold is annealed near the specimen surface. On the other hand, the profiles of low-temperature substitutional gold show a flat distribution even after the annealing, and supersaturated low-temperature substitutional gold agglomerates in the silicon resulting in electrically inactive during the heat-treatment.

Keywords: Si : Au; Impurity diffusion; Substitutional and interstitial impurities

1. Introduction

Gold atoms in silicon occupy interstitial and substitutional sites, and the substitutional gold exists in three states: low-temperature substitutional gold in a condition of supersaturation below 850°C, high-temperature substitutional gold in a condition of supersaturation above 850°C or undersaturation, and agglomerations of substitutional gold [1]. High-temperature substitutional gold diffuses slowly, and their effective atomic-flow is dominated by an interchange mechanism of silicon atom with interstitial gold atom [2]. On the other hand, low-temperature substitutional gold diffuses rapidly by a ring mechanism [3] and the atomic-flow is limited by the diffusion [4].

During the heat-treatment for gold-indiffusion, most of gold atoms exist as high-temperature substitutional gold, because total concentration of gold atoms is nearly equal to the concentration of electrically active gold atoms [5] and the concentration of substitutional gold is less than thermal equilibrium value. Limiting process for the gold indiffusion depends on silicon crystals such as intrinsic defects and specimen thickness [6]. On the other hand, during the heat-treatment for the annealing of supersaturated gold atoms, namely, during the re-heat-treatment below the temperature for the indiffusion, supersaturated substitutional gold exists as high-temperature substitutional gold or low-temperature one depending on temperature history of the specimen after gold-indiffusion [1].

In this paper, out-diffusion profiles of supersaturated high-temperature substitutional gold in silicon and supersaturated low-temperature one have been investigated by two types of heat-treatment, after gold-indiffusion at 1150°C, and out-diffusion mechanisms of the supersaturated substitutional gold have been discussed.

2. Two types of heat-treatment for annealing of supersaturated substitutional gold

High-temperature substitutional gold in the heat-treatment for gold-indiffusion at 1150°C changes into the condition of supersaturation by cooling to 1000°C as shown in Fig. 1(a) called as "*continuous annealing*". In this case, during the heat-treatment at 1000°C, substitutional gold is still in the configuration of high-temperature substitutional gold in spite of the supersaturation

* Corresponding author. Tel.: + 81-92-606-3131 ext. 2426; Fax: + 81-92-606-0751.

E-mail address: morooka@ee.fit.ac.jp (M. Morooka)

0921-4526/99/$ - see front matter
PII: S0921-4526(99)00492-5

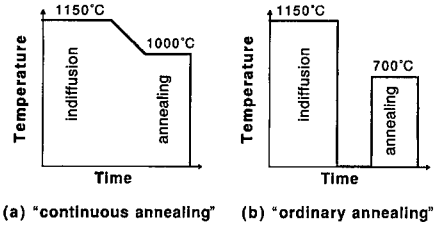

Fig. 1. Two types of heat-treatment for annealing of supersaturated substitutional gold. (a): annealing of high-temperature substitutional gold, "continuous annealing", and (b): annealing of low-temperature one, "ordinary annealing".

due to the annealing temperature above 850°C, and the supersaturated concentration of high-temperature one decreases to a thermal equilibrium value with the increase of annealing time.

High-temperature substitutional gold in the gold-indiffusion at 1150°C changes into low-temperature substitutional gold by rapid cooling to room temperature after the indiffusion, and the supersaturated concentration of low-temperature one decreases to a thermal equilibrium value by the subsequent heat-treatment at 700°C as shown in Fig. 1(b) called "*ordinary annealing*".

3. Measurement of out-diffusion profile of substitutional gold in silicon

Most of low-temperature substitutional gold remaining upto the end of heat-treatment is frozen in the specimen at room temperature by the rapid cooling after the heat-treatment for the annealing as shown in Fig. 1(b). Even in the case of heat-treatment for the annealing of high-temperature substitutional gold as shown in Fig. 1(a), most of high-temperature substitutional gold remaining till the end of heat-treatment is frozen in the specimen as low-temperature substitutional gold by the rapid cooling [7]. Therefore, we have measured the concentration of low-temperature substitutional gold, which is electrically active with dominant deep level of $E_c - 0.54$ eV, after the cooling, and the obtained concentration of the deep level is regarded as the final concentration of high-temperature or low-temperature substitutional gold during the heat-treatment for the annealing.

The concentration profile of the deep level was obtained by a capacitance measurement in lines with Au-Si Schottky diodes on an angle-lapped surface of the specimen, as shown in Fig. 2 [8]. Here, the diameter of gold dot is 0.15 mm and the lapped-angle is 11.3°. We used n-type silicon crystals containing phosphorus concentration of $8 \times 10^{16}\,\mathrm{cm}^{-3}$, and the capacitance of the Schottky diode was about 14 pF.

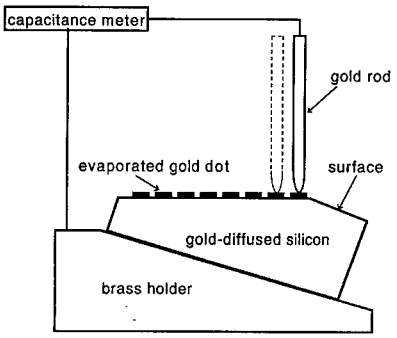

Fig. 2. Measurement of out-diffusion profile of substitutional gold in silicon by a capacitance method on an angle-lapped surface.

Total concentration of gold atoms on several points of the angle-lapped surface was also measured by SIMS method to compare with the concentration of substitutional gold.

4. Out-diffusion profiles of supersaturated high-temperature substitutional gold in silicon

Gold atoms were indiffused into several silicon specimens of 2.1 mm thickness from Au–Si surface layer at 1150°C for 90 h. After a rapid cooling to room temperature, one of the specimens was used for the measurement of indiffusion profile of high-temperature substitutional gold, whose profile was regarded as the initial concentration profile for the subsequent annealing of supersaturated one. The obtained profile is shown in Fig. 3 as the initial profile, but the specimen surface in the data retreats behind that in the indiffusion, which is the surface in the annealing as mentioned below.

The other specimens were heat-treated again at 1150°C for 30 min after removing 0.1 mm thickness of specimen surface layer by a mechanical and subsequent chemical method. Most of substitutional gold, which has changed into low-temperature substitutional gold from high-temperature one by the rapid cooling after the gold-indiffusion, becomes again high-temperature substitutional gold by this heat-treatment. The concentration of high-temperature substitutional gold exists in a condition of supersaturation by cooling to 1000°C as shown in Fig. 1(a) and the specimens were heat-treated subsequently at the temperature for a long time for the annealing of supersaturated high-temperature substitutional gold. The concentration profiles after the annealing were measured by the capacitance method, as shown in Fig. 3. The heat-treatment time at 1000°C is indicated for each sign in the figure. The profiles show a typical out-diffusion to surface of supersaturated impurities in solid.

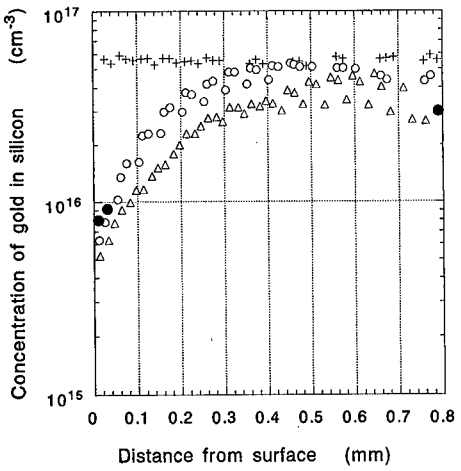

Fig. 3. Out-diffusion profiles of high-temperature substitutional gold in silicon after the annealing of supersaturated one at 1000°C. Specimen thickness is about 1.8 mm. (+) initial profile before the annealing, (○) profile after the annealing for 240 h, (●) total concentration of gold atoms measured by SIMS on the sample signed by (○), and (△) profile after the annealing for 480 h.

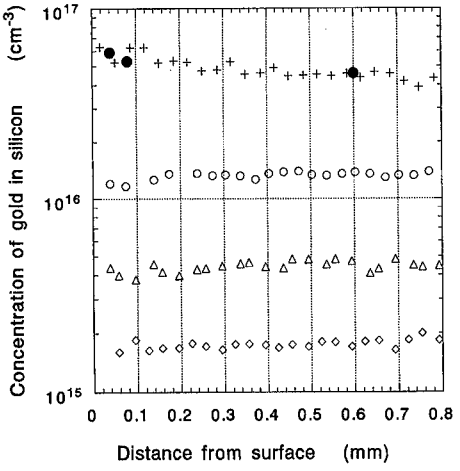

Fig. 4. Concentration profiles of low-temperature substitutional gold in silicon after the annealing of supersaturated one at 700°C. (+) initial profile before the annealing, (○) profile after the annealing for 0.1 h, (△) profile after the annealing for 0.2 h, and (◇) profile after the annealing for 0.4 h [4], (●) total concentration of gold atoms measured by SIMS on the sample signed by (○).

Total concentration of gold atoms measured by SIMS method on several points on the angle-lapped surface of the same sample signed by ○ are shown by ●, for comparison with the concentration of high-temperature substitutional gold in the annealing.

5. Concentration profiles in the annealing of supersaturated low-temperature substitutional gold in silicon

After the heat-treatment at 1150°C for 90 h for the gold indiffusion, the specimens were cooled rapidly to room temperature, and most of substitutional gold changes into low-temperature substitutional gold by this cooling. Then, the specimens were heat-treated again at 700°C as shown in Fig. 1(b), and the concentration profile of substitutional gold, which is an annealing profile of supersaturated low-temperature substitutional gold, was measured by the capacitance method, as shown in Fig. 4 [4]. Specimen thickness in the heat-treatment was about 2.5 mm, and the difference between initial profiles in Figs. 3 and 4 was made by the difference of specimen thickness. In the case of annealing of low-temperature substitutional gold, the concentration profile shows a flat type profile, and the concentration decreases uniformly in the whole of the specimen without relation to the distance from specimen surface. The concentration of low-temperature substitutional gold decreases with the increase of annealing time due to its supersaturation.

On the other hand, total concentration of gold atoms measured by SIMS method does not decrease in spite of the decrease of low-temperature substitutional gold, and the total concentration is intact as the initial concentration of low-temperature substitutional gold as shown in Fig. 4.

6. Discussion

The concentration of high-temperature substitutional gold in the heat-treatment for the annealing of supersaturated one is nearly equal to total concentration of gold atoms as shown in Fig. 3. Therefore, most of gold atoms are located at the center of substitutional site [1] during the heat treatment for the annealing as shown in Fig. 1(a), and the supersaturated high-temperature substitutional gold is annealed near the specimen surface. The profiles are very similar to those for a kick-out mechanism limited by the diffusion of interstitial silicon atoms from a specimen surface. In this case, the concentration at the specimen surface should be a thermal equilibrium value and the concentration increases with increasing the distance from the surface. However, the surface concentration in the annealing is slightly smaller than that in the indiffusion at the same temperature as shown in Fig. 5. The difference of the surface concentration between them seems to be caused by the difference of chemical situation of the surface, that is, the silicon surface is bounded by argon ambiance in the annealing but the surface is bounded by Au–Si fusion in the indiffusion.

The concentration of low-temperature substitutional gold decreases uniformly in the specimen by the

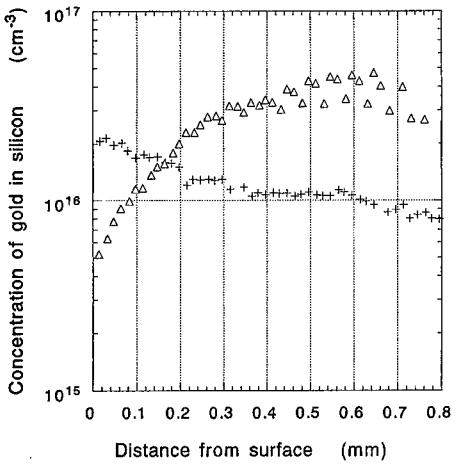

Fig. 5. Difference of the concentration of high-temperature substitutional gold near the surface between the concentration in the indiffusion and that in the annealing. (△) profile after the annealing at 1000°C for 480 h show in Fig. 3, and (+) indiffusion at 1000°C for 480 h. Specimen thickness is same in both cases.

heat-treatment for the annealing of supersaturated one, and the decrease is very fast in spite of low temperature in contrast to the annealing of high-temperature substitutional gold. The evidence that the total concentration is nearly equal to the initial concentration of low-temperature substitutional gold, supports the annealing mechanism of supersaturated low-temperature substitutional gold, that is, supersaturated one agglomerates by a ring diffusion with homogeneous nucleation resulting in electrically inactive gold atom [4].

7. Conclusions

Out-diffusion profiles during the heat-treatment of supersaturated high-temperature substitutional gold and low-temperature one in silicon have been investigated. The results are summarized as follows.

(1) Those of high-temperature substitutional gold show a profile of kick-out mechanism limited by the diffusion of interstitial silicon atoms from the specimen surface. In this case, gold atoms are annealed out near specimen surfaces.
(2) Those of low-temperature substitutional gold show a flat distribution due to agglomeration of homogeneous nucleation. In this case, gold atoms exist in the specimen as electrically inactive agglomeration.

Acknowledgements

This work was supported in part by Grant-in-Aid for Scientific Research from the Ministry of Education, Science, Sorts and Culture of Japan.

References

[1] M. Morooka et al., Jpn. J. Appl. Phys. 24 (1985) 133.
[2] U. Gösele, W. Frank, A. Seeger, Appl. Phys. 23 (1980) 361.
[3] M. Morooka, H. Tomokage, M. Yoshida, Jpn. J. Appl. Phys. 25 (1986) 1161.
[4] M. Morooka, Mater. Sci. Forum 258–263 (1997) 1789.
[5] M. Morooka et al., Jpn. J. Appl. Phys. 23 (1984) 124.
[6] M. Morooka, Jpn. J. Appl. Phys. 35 (1996) 2537.
[7] M. Morooka, H. Tomokage, M. Yoshida, in: K. Sumino (Ed.), Defect Control in Semiconductors, Elsevier, Amsterdam, 1990, pp. 291–296.
[8] M. Morooka, Res. Bull. Fukuoka Inst. Technol. 31 (1998) 43.

ELSEVIER

Physica B 273–274 (1999) 412–415

PHYSICA B

www.elsevier.com/locate/physb

What do we know about iron in silicon after 45 yr of research

A.A. Istratov[a,*], H. Hieslmair[a], E.R. Weber[b]

[a]*University of California at Berkeley, LBNL, MS 62-203, 1 Cyclotron Road, Berkeley, CA 94720, USA*
[b]*University of California at Berkeley, 577 Evans Hall, Berkeley, CA 94720-1760, USA*

Abstract

Iron is the most investigated metallic impurity in crystalline silicon. It is thought that the fundamental physical properties of Fe in Si, such as diffusivity, solubility, and reaction constants of pairing with boron, are firmly established. However, our analysis shows that there remains a good deal of contradiction in the literature data, and that the uncertainty of the reaction constants is too large for quantitative predictive simulations of iron defect reactions, such as gettering simulations. Possible reasons for discrepancies in the literature data are discussed, and improved measurement procedures are suggested. Finally, the current state of understanding of the reactions of iron to form iron oxides and silicates, which may be responsible for lifetime-killing intragranular defects in solar cells, is discussed.

Keywords: Iron; Silicon; Iron–boron pairs; Iron oxide; Iron silicate; Oxygen

Iron is one of most ubiquitous and detrimental metal impurities in silicon technology, and has been intensively studied over the past 45 yr. Recently, we have undertaken an extensive critical analysis of the current state of understanding of properties of iron in silicon. This analysis revealed that some of the fundamental properties of iron, such as its diffusivity or interaction with shallow acceptors, which were thought to be fully understood, are actually uncertain or inaccurate. Additionally, a number of other important defect reactions of iron, such as interaction of iron with oxygen, are hardly studied at all. A complete report on our study, which includes more than a thousand references, will be published elsewhere [1,2]. In this article, we present some of our conclusions, discussed at this conference, which we believe will have a strong effect on further studies of iron in silicon.

Currently high-end technology requires maintaining the surface iron contamination at the level of 10^{11} cm^{-2} and below. Since ultrapure technology is extremely expensive, it has become increasingly important to understand and model the behavior of iron and its gettering during thermal processing of silicon wafers. We have recently developed a gettering simulator, capable of modeling of relaxation and segregation gettering (see, e.g., Ref. [3]). Besides the parameters of the silicon wafer itself, such as its doping level and thickness of the epilayer or denuded zone, input parameters for the simulator include several fundamental physical parameters specific for iron in silicon. It is well known that segregation of iron in p^+ substrates is driven by pairing of iron with boron. The kinetics of pairing is determined by diffusivity of iron in p- and p^+-Si. The equilibrium segregation coefficient is determined by the fraction of iron that is ionized and can be efficiently trapped, and by the pairing constants of Fe_i^+ and B^-. The fraction of the ionized interstitial iron is determined by the position of its energy level with respect to the Fermi level. The available experimental data [4–6] indicate that the energy level of iron is strongly temperature dependent at high temperatures, as shown in Fig. 1. McHugo et al. [5,6] and Gilles et al. [4] concluded that the position of the iron level at $T = 800$°C coincides with that measured by DLTS and Hall effect ($E_V + 0.38$ eV), whereas at $T > 900$°C the iron level dives towards the valence band and nearly merges with it at $T > 1100$°C. McHugo et al. [5,6] pointed out that the iron level shifts so closely to the valence band at 1100°C that the Boltzmann approximation was no longer valid, and he could not accurately calculate the

* Corresponding author. Fax: + 1-510-486-4995.
E-mail address: istratov@socrates.berkeley.edu (A.A. Istratov)

0921-4526/99/$ - see front matter
PII: S0921-4526(99)00493-7

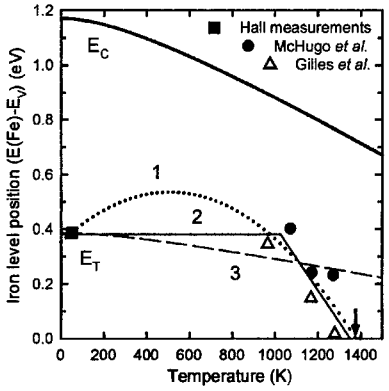

Fig. 1. Temperature dependence of the position of the donor level of iron in the band gap with respect to the valence band edge.

position of the iron level at 1100°C (arrow in Fig. 1). The absence of experimental data between the temperatures where the DLTS and Hall effect data were obtained, and 1000 K, which was the lowest temperature of the solubility studies, makes the interpolation of the iron level position over the whole temperature range difficult, although such interpolation is unavoidable in simulations of segregation gettering. One can imagine three substantially different simple approximations for the intermediate temperature range, as indicated in Fig. 1: a parabolic fit to the experimental data (curve 1), a step-like function (curve 2) and a smooth curve given by $(E_{Fe}(T) - E_V)/E_g(T) = \text{const}$ (curve 3), where $E_g(T)$ is the temperature-dependent band-gap width. The parabolic dependence is the only curve of the three, which is smooth and fits well the experimental data. Although it would be premature and speculative to conclude that the temperature dependence of the iron level position in the band gap is described by this parabolic function, we want to attract attention of the scientific community to this possibility. Experimental studies at $T < 1000$ K are required to determine which of the three models provides a better description for the temperature dependence of iron in silicon. Note that the difference between the curves 1, 2, and 3 results in orders of magnitude of difference in segregation coefficient of Fe_i^+ in p^+-Si substrates in the intermediate temperature range.

Another factor, that affects both the effective diffusivity of ionized iron and its segregation coefficient in p^+ substrates, is the kinetics of formation and dissociation of FeB pairs. These kinetics are characterized by the equilibrium binding energy E_b, diffusion barrier of interstitial iron E_m, and potential barrier for dissociation of FeB pairs E_{diss}. The equilibrium binding energy E_b can be obtained from the analysis of the temperature dependence of the equilibrium fraction of Fe_i, paired with boron, as it follows from the law of mass-action:

$$\frac{N(\text{FeB})}{N(\text{Fe}_i^+)N(\text{B}_s^-)} = \frac{Z}{N_i}\exp\left(\frac{E_b}{k_B T}\right) \quad (1)$$

where N_i is the density of interstitial sites in the silicon lattice (5×10^{22} cm^{-3}), $Z = 4$ is the number of possible orientations of an FeB pair with tetrahedral symmetry around an acceptor atom, and N(FeB), $N(Fe_i^+)$, and $N(B_S^-)$ are the concentrations of FeB pairs, ionized interstitial iron, and negative boron acceptors, respectively. The binding energies obtained by using Eq. (1) vary from 0.45 [7], 0.53 [8], and 0.58 [9] to 0.6 [10,11] and 0.65 eV [12,13]. While the scatter by 0.1–0.2 eV is not very important from the point of view of fundamental physics of semiconductors, it is unacceptable for the task of quantitative prediction of gettering. A scatter in the binding energies reported by different groups can be partly ascribed to the interaction of iron with other impurities, unintentionally introduced in silicon samples, and by the narrow temperature range of the measurements.

A similar, if not greater, uncertainty was found in the reported association and dissociation energies of FeB pairs. The association kinetics of FeB pairs can be described using the theory of diffusion-limited precipitation/trapping, developed by Ham [14]. It can be shown [15] that the association rate of FeB pairs is given by the following expression:

$$\tau_{ass} = \frac{\varepsilon\varepsilon_0 k_B T}{q^2 N_A D(\text{Fe}_i)} \approx \frac{566.7T}{D(\text{Fe}_i)N_A} \quad (2)$$

where N_A is the concentration of shallow acceptors (in our case, boron) in cm^{-3}, T is the temperature in Kelvin, and $D(Fe_i)$ is the iron diffusivity in cm^2/s. This equation was extensively used for determining the diffusion barrier of ionized iron at low temperatures, and yielded strongly scattered values for the diffusion barrier from 0.58 to 0.81 eV (see Ref. [1] for more detail), which is certainly not accurate enough for the purpose of predictive modeling.

The dissociation kinetics of FeB are determined by the potential barrier E_{diss} for a jump of the Fe_i ion away from the first closest neighbor position to the boron atom. The dissociation time constant is given by

$$\tau_{diss}^{-1} = \nu\exp\left(-\frac{E_{diss}}{k_B T}\right), \quad (3)$$

where ν is the attempt frequency. To the best of our knowledge, only two values of E_{diss} were reported in the literature by the same group: $E_{diss} = 1.17$ eV ($\nu = 1.8 \times 10^{10}$ s^{-1}) [16], and 1.2 eV ($\nu = 5 \times 10^{10}$ s^{-1}) [17]. The accuracy of these values is unknown, since no independent data are available.

It is important to note that the association or dissociation energies of the pairs were calculated from the temperature dependence of the reaction rate. In most studies

it was assumed that the reaction is either purely dissociation or purely association. This assumption is generally incorrect and may lead to substantial errors since in fact, the rate of the observed reactions is determined by both, the association rate $r_{ass} = \tau_{ass}^{-1}$, and the dissociation rate $r_{diss} = \tau_{diss}^{-1}$. This point can be illustrated by the analysis of a simple differential equation, describing the reaction kinetics. If we neglect the precipitation of iron, assume that most of the interstitial iron is ionized ($N(Fe_i) = N(Fe_i^+)$), and that the concentration of iron is much less than the concentration of boron, then the iron–boron pairing reaction is given by the following differential equation:

$$\frac{dN(FeB)}{dt} = r_{ass} \times (N(Fe_i) - N(FeB)) - r_{diss} \times N(FeB). \quad (4)$$

The solution of this equation is given by

$$N(FeB) = \frac{r_{ass}}{r_{ass} + r_{diss}} \times N(Fe_i) - \left\{ \frac{r_{ass}}{r_{ass} + r_{diss}} \times N(Fe_i) - N_0(FeB) \right\} \times \exp(-(r_{ass} + r_{diss})t) \quad (5)$$

where $N_0(FeB)$ is the initial concentration of FeB pairs at the beginning of the measurement ($t = 0$). It is important to keep in mind that the reaction rate is always given by the sum of association and dissociation rates, $r = r_{ass} + r_{diss}$. The common assumption $r = r_{ass}$ or $r = r_{diss}$ may lead to significant errors, and the apparent activation energy of the reaction as reported in the literature may actually come out to be between the true dissociation and association barriers. This may be a possible explanation for the disagreement of pairing constants reported by different groups. Thus, a careful re-examination of the pairing reactions using state-of-the-art silicon material and modern cleanroom facilities, and taking into account both association and dissociation reactions, is required to obtain the FeB pairing constants with a better accuracy.

Another important defect reaction of iron, which is poorly understood, is its interaction with oxygen, dissolved in the silicon lattice. These reactions may take place either at the Si/SiO_2 interface during wafer oxidation, or in the bulk of the wafer during nucleation and growth of oxygen precipitates. The possibility of a chemical reaction of iron with oxygen and silicon, resulting in the formation of iron oxides or iron silicates, is frequently neglected in favor of the formation and growth of iron-silicide precipitates, and was not explored until highly sensitive synchrotron-radiation-based X-ray techniques which can distinguish different types of bonding were developed and applied to silicon materials. Kitano [18] diffused iron into boron-doped CZ silicon wafers through a 20 nm SiO_2 film at 750°C and 900°C, removed oxide by HF chemical etching, and studied the state of iron at the silicon surface (former Si/SiO_2 interface) by using angular-dependent TXRF and total reflection fluorescence X-ray absorption fine structure technique, using synchrotron radiation as a source of X-rays. X-ray analysis revealed that significant amount of iron concentrated at the SiO_2/Si interface formed chemical bonds of the type Fe–O, Fe–Si and Fe–Fe. The valence of iron was a mixture of Fe^{3+} and Fe^{2+}, mostly Fe^{3+}. From these observations Kitano [18] inferred that the layer formed by iron at the SiO_2/Si interface is iron silicate, in which a portion of Fe^{3+} ions is reduced to Fe^{2+}, similar to the natural iron silicate $Fe^{3+}Fe^{2+}_{0.5}$ $[SiO_4]$, known as laihunite [18]. Recent studies of McHugo [19], who studied iron precipitates, located by XRF microprobe in the bulk of mc-Si, revealed that a similar reaction may take place in the bulk of a wafer. He analyzed near-edge X-ray absorption fine-structure spectroscopy (NEXAFS) spectra of detected iron agglomerates and compared them with those from the samples of iron oxides and silicides. Although unambiguous identification of the phase of iron was not achieved, it was concluded that agglomerated iron was certainly not in the form of silicide, but rather iron silicate, primarily with the valence Fe^{3+}. This is in agreement with the findings of Ref. [18]. The possibility of formation of iron silicates or oxides was also discussed in studies, which investigated TEM images of iron precipitates in silicon dioxide or at the Si/SiO_2 boundary [20–24]. The available thermodynamical data on enthalpy of formation of iron oxides and silicates in the silicon lattice are scarce, but they indicate that these compounds should be much more stable during anneals than iron silicide. Thus, iron-oxide and iron-silicate precipitates will not be dissolved during standard gettering anneals. If the following studies will show that these precipitates are electrically active, the physics of formation of iron oxides and silicates may provide an important key to the understanding of the nature of gettering-resistant intragranular recombination centers in solar cells [25,26].

In conclusion, we have analyzed the available data on the position of the electrical level of iron in the silicon band gap and its pairing with shallow acceptors, demonstrated that the accuracy of these data is not sufficient for quantitative modeling of iron in silicon, and suggested an explanation for disagreement between different groups. Furthermore, we have emphasized the importance of understanding of poorly studied defect reactions of iron and oxygen.

References

[1] A.A. Istratov, H. Hieslmair, E.R. Weber, Appl. Phys. A 69 (1999) 13.

[2] A. A. Istratov, Appl. Phys. A 70 (2000), in press.
[3] H. Hieslmair, A.A. Istratov, S.A. McHugo, C. Flink, E.R. Weber, J. Electrochem. Soc. 145 (1998) 4259.
[4] D. Gilles, W. Schroter, W. Bergholz, Phys. Rev. B 41 (1990) 5770.
[5] S.A. McHugo, R.J. McDonald, A.R. Smith, D.L. Hurley, E.R. Weber, Appl. Phys. Lett. 73 (1998) 1424.
[6] S.A. McHugo, R.J. McDonald, A.R. Smith, D.L. Hurley, A.A. Istratov, H. Hieslmair, R. Weber, in: S. Ashok, J. Chevallier, K. Sumino, B.L. Sopori, W. Gotz (Eds.), Defect and Impurity Engineered Semiconductors and Devices II, Materials Research Society, Warrendale, PA, 1998, p. 361.
[7] L.C. Kimerling, in: J. Narayan, T.Y. Tan (Eds.), Defects in Semiconductors, Amsterdam, North-Holland, 1981, p. 85.
[8] K. Wunstel, P. Wagner, Appl. Phys. A 27 (1982) 207.
[9] W. Wijaranakula, J. Electrochem. Soc. 140 (1993) 275.
[10] H. Lemke, Phys. Stat. Sol. A 76 (1983) 223.
[11] J.H. Reiss, R.R. King, K.W. Mitchell, Appl. Phys. Lett. 68 (1996) 3302.
[12] H. Lemke, Phys. Stat. Sol. A 64 (1981) 215.
[13] L.C. Kimerling, J.L. Benton, Physica B & C 116 (1983) 297.
[14] F.S. Ham, J. Phys. Chem. Solids 6 (1958) 335.
[15] H. Hieslmair, A.A. Istratov, T. Heiser, E.R. Weber, J. Appl. Phys. 84 (1998) 713.
[16] H. Feichtinger, Acta Phys. Aust. 51 (1979) 161.
[17] H. Feichtinger, Inst. Phys. Conf. Ser. 46 (1979) 528.
[18] T. Kitano, J. Electron. Mater 21 (1992) 1027.
[19] S.A. McHugo, (1999), to be published.
[20] S. Sadamitsu, A. Sasaki, M. Hourai, S. Sumita, N. Fujino, Jpn. J. Appl. Phys. 30 (1991) 1591.
[21] H. Shimizu, J. Electrochem. Soc. 144 (1997) 4335.
[22] T. Abe, T. Itoh, Y. Hayamizu, K. Sunagawa, S. Yokota, H. Yamagishi, in: K. Sumino (Ed.), Defect Control in Semiconductors, Elsevier, Amsterdam, 1990, p. 297.
[23] S. Saito, K. Hamada, D.J. Eaglesham, Y. Shiramizu, J.L. Benton, H. Kitajima, S.D.C. Jacobson, J.M. Poate, in: G.S. Higashi, M. Hirose, S. Raghavan, S. Verhaverbeke (Eds.), Science and Technology of Semiconductor Surface Preparation, Materials Research Society, Pittsburgh, PA, 1997, p. 81.
[24] N. Fujino, K. Hiramoto, M. Sano, K. Murakami, H. Horiye, Y. Oka, S. Sumita, in: H.R. Huff, K.G. Barraclough, J.I. Chikawa (Eds.), Semiconductor Silicon 1990, The Electrochemical Society, Pennington, NJ, 1990, p. 709.
[25] E.R. Weber, A.A. Istratov, S.A. McHugo, H. Hieslmair, C. Flink, in: D.C. Gupta, F.R. Bacher, W.M. Hughes (Eds.), Recombination Lifetime Measurements in Silicon, ASTM, West Conshohocken, PA, 1998, p. 18.
[26] M. Werner, E.R. Weber, S. McHugo, K.L. Chapman, Solid State Phenom. 51–2 (1996) 81.

ELSEVIER

Physica B 273–274 (1999) 416–419

PHYSICA B

www.elsevier.com/locate/physb

Iron-related defect model in n-type silicon based on the electrical and diffusion properties

Hajime Kitagawa*, Shuji Tanaka

Department of Electronics, Fukuoka Institute of Technology, 3-30-1 Wajiro-Higashi, Higadhi-ku, Fukuoka 811-0295, Japan

Abstract

We review the electrical and diffusion properties of iron-related electrically active defects (IRDs) in floating zoned (FZ) and Czochralski (CZ)-grown n-type silicon. A small fraction of iron atoms dissolved into n-type silicon forms electrically active IRDs. From in-diffusion and annealing properties, IRDs can be related to interstitial iron atoms independent of phosphorus, oxygen and hydrogen atoms. We propose a model that IRDs observed in the present study are due to intermediate states in consecutive reactions of iron-related complex formation process. IRDs observed in CZ and FZ n-type silicon are identical. © 1999 Elsevier Science B.V. All rights reserved.

Keywords: Iron, n-type silicon; Electrical activity; Iron complexes

1. Introduction

In spite of the principal importance of iron impurity in semiconductor device technology, the diffusion and electrical properties of iron in n-type silicon are much less established than those in p-type silicon. While it has been generally accepted that iron atoms in n-type silicon do not electrically ionize [1,2], a few researchers [3–5] have reported the observation of iron-related levels in n-type silicon. We have shown [6] from deep-level transient spectroscopy (DLTS) and Hall effect that iron in n-type silicon is electrically ionized and introduces a donor level at $E_c - 0.41$ eV (hereafter referred to as the level C in FZ silicon and level E_3 in CZ silicon) and, at least, one acceptor level at $E_c - 0.21$ eV (hereafter referred to as the level B in FZ silicon and level E_2 in CZ silicon). Since the first report by our group in 1992 [6], some fundamental aspects of the diffusion and electrical properties of iron-related defects (IRDs) have been clarified by electrical measurements. It has been found, from a series of studies [6–12], that IRDs observed in the present study are due to intermediate states in consecutive reactions of iron-related complex formation process. IRDs observed in CZ and FZ n-type silicon have been found to be identical.

The purpose of the present report is to review the results of our studies on the diffusion and electrical properties of IRDs in floating zoned (FZ) and Czochralski (CZ)-grown n-type silicon. Based on the in-diffusion and annealing processes of IRDs, we will propose a possible model on the composition of the electrically active IRDs.

2. Experimental

The silicon crystals used for the experiment were phosphorus-doped dislocation-free, FZ and CZ n-type silicon. Their phosphorus content ranged from 4×10^{13} to $4 \times 10^{14}\,cm^{-3}$ in both FZ and CZ silicon. CZ silicon contained oxygen of $18 \times 10^{17}\,cm^{-3}$ (ASTEM F121-79) and carbon of $5.0 \times 10^{16}\,cm^{-3}$. The oxygen content in CZ silicon was about two orders of magnitude higher than that in FZ silicon. Iron was diffused in flowing nitrogen gas ambient after iron was deposited on the surfaces of the silicon slices by vacuum evaporation. The diffusion heat treatment was terminated by pulling

* Corresponding author: Tel.: + 81-92-606-3131, ext. 2405; fax: + 81-92-606-0726.

E-mail address: kitagawa@emat.fit.ac.jp (H. Kitagawa)

0921-4526/99/$ - see front matter
PII: S0921-4526(99)00494-9

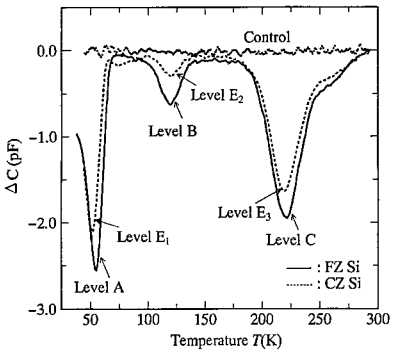

Fig. 1. DLTS spectra of iron-doped n-type CZ and FZ silicon. Iron diffusion was performed at 1160°C for 30 min. The reverse bias was 5 V, filling pulse bias 0 V, rate window 0.5/5.0 ms and injection pulse width 500 μs.

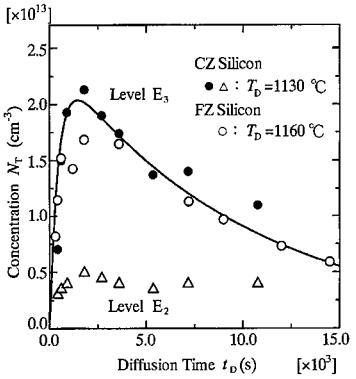

Fig. 2. In-diffusion process of IRDs as a function of diffusion time, t_D. Solid curves show the calculated values based on the consecutive reaction model (see text).

the slices out of the quartz furnace tube to the cool region. DLTS measurement was performed on a Schottky barrier diode formed by gold evaporation. The samples were always stored in a liquid-nitrogen bath except during measurements because it was needed that special attention was paid to keep the sample always below room temperature since interstitial iron atoms are mobile even at room temperature. The concentration of the iron-related defect centers was evaluated from DLTS peak height and the steady-state capacitance.

3. Results and discussion

3.1. Electrical properties of iron-related defects

Electrically active iron-related defect centers were observed by DLTS and Hall effect in the sample prepared under the rapid cooling condition. Their levels, donor and acceptor characters and concentration have been evaluated by combined analyses of Hall coefficient and DLTS [6,10,12]. The DLTS spectra of iron-doped n-type CZ and FZ silicon are shown in Fig. 1. Among electron trap centers observed, those labeled as E_3 and C are donors and the others are acceptors. Hereafter we confine ourselves to the analyses for the levels C, E_3, B and E_2. The electron thermal emission rates of levels B and C observed in FZ silicon have been found [10] to be equivalent to those of levels E2 and E3 observed in CZ silicon, respectively.

3.2. In-diffusion characteristics of iron-related defects

The introduced concentrations of IRDs in the in-diffusion process at 1160°C are shown in Fig. 2 as a function of the diffusion time, t_D. The characteristics common to the in-diffusion processes are as follows: (1) the concentration higher than the order of 10^{13} cm^{-3} cannot be introduced at elevated diffusion temperature, hence the thermal equilibrium concentrations of IRDs are not defined, (2) in a longer diffusion time, DLTS signal becomes broadened and eventually disappears, and (3) the introduction processes of levels E_2 and E_3 in CZ silicon are qualitatively the same, respectively, as those of levels B and C for FZ silicon, except for longer time region at which the IRDs seem to dissociate into many other defects. Therefore, the abnormal behavior of introduced concentration of IRDs could not be attributed to single interstitial iron atom, Fe_i. For such abnormal in-diffusion characteristics of IRDs, a model has been proposed [7–12], on the basis of a consecutive progress of iron precipitation reaction or complexes of Fe_i with other defects which cannot be identified yet.

3.3. Isothermal annealing of iron-related defects

Under an isothermal annealing, concentrations of electrically active IRDs decay exponentially with the annealing time, t_A. Fig. 3 shows the concentrations of levels E_3 and C as a function of t_A, the isothermal annealing process at temperatures from room temperature to 150°C, where the sample was subjected to the isothermal experiment immediately after iron was diffused at 1160°C for 30 min. The decay constants, τ, of the levels E_3 and C are expressed by $\tau = 1.2 \times 10^{-4} \exp(0.65\ \mathrm{eV}/kT_A)$, where k is the Boltzmann's constant and T_A is the annealing temperature. The activation energy of τ, 0.65 eV, is close to the binding energy, 0.65 ± 0.05 eV [13], for the pairing of positively charged interstitial iron and negatively charged substitutional boron in p-type silicon, suggesting that electrostatic force is included in the iron-related defect formation.

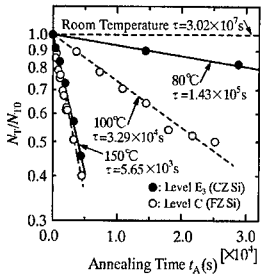

Fig. 3. Isothermal annealing of level E_3 (CZ silicon) and level C (FZ silicon) at temperatures from room temperature to 150°C. The concentration of defects, N_T, is normalized by the concentration, N_{T0}, at $t_A = 0$.

3.4. Proposed defect model

The present results indicate that only a small fraction of iron atoms forms electrically ionizable complexes, identical IRDs being formed in both CZ and FZ n-type silicon. Their complexes behave as acceptors and a donor. Thus negatively charged and positively charged iron-related states coexist in n-type silicon. Although substitutional iron atoms can be a candidate of the ionizable species, the presence of substitutional iron atoms in silicon has not yet been confirmed.

The in-diffusion and annealing processes of IRDs suggest that the electrically active IRDs are complexes of Fe_i with other defects [7–12]. Especially, the abnormal behavior of introduced iron-related levels B, C, E_2 and E_3 could not be attributed to single Fe_i atoms. The model of the consecutive defect reaction model [5,9–12] has been proposed. Consider the reaction process that the formation of electrically active complex, β, which is composed of the combination of Fe_i and other defects, α, present in the crystal, followed by the defect reaction for the formation of another complex, γ, which is electrically inactive. Then the concentration of β, N_β, as a function of time t is given by $N_\beta = k_1 N_{\alpha 0}/(k_1 - k_2)[\exp(-k_1 t) - \exp(-k_2 t)]$, where k_1 and k_2 are the rate constants of the consecutive reactions $Fe_i + \alpha \rightarrow \beta$ and $\beta \rightarrow \gamma$, respectively, and $N_{\alpha 0}$ is the concentration of defect α at $t = 0$. The values of N_β fitted to the experimental in-diffusion data are shown in Fig. 2 by solid curves for levels B and C. The calculated numerical values are given in Fig. 2. The agreement between the calculated and experimental values are good. If this model is valid, the introduction of levels B and C implies that the observed defects are due to intermediate states of iron-related complexes formed by consecutive defects reaction including Fe_i.

Simple exponential decay of the concentration in the isothermal annealing as shown in Fig. 3 is equivalent to that of a first-order chemical reaction. Therefore, the relationship, $dN_T/dt_A = -KN_T$, or $N_T = N_{T0}\exp(-Kt_A)$, should hold in the isothermal annealing process, where K is the rate constant independent of the concentration of annealing species, N_T, and proportional to the diffusion coefficient, D, of the annealing species associated with, for example, level C. Assuming random distribution of spherical complex of the radius, r_0, with the number per unit volume, N_0, we have $D = (4\pi r_0 N_0 \tau)^{-1}$ [14], where τ is the decay constant in isothermal annealing. Assuming $r_0 = 2.35 \times 10^{-8}$ cm, $N_0 = 9.0 \times 10^{12}\,\mathrm{cm}^{-3}$ and $\tau = 3.0 \times 10^7$ s at room temperature and $\tau = 5.1 \times 10^3$ s at 150°C, we obtain $D = 1.3 \times 10^{-14}\,\mathrm{cm}^2/\mathrm{s}$ at room temperature and $D = 1.5 \times 10^{-12}\,\mathrm{cm}^2/\mathrm{s}$ at 150°C These values of D are in good agreement with diffusion coefficient of Fe_i reported in Refs. [15,16] and give an evidence that Fe_i takes part in the iron-related complex formation.

3.5. Discussion

DLTS observations have shown [8] that the donor state (level C) is dissolved into two or more different electron-trap states after the storage of the sample at room temperature for longer than 200 d. Eventually all traps become unobservable electrically upon annealing at room temperature for a period longer than one year. Since the observation of IRDs using electrical measurements exhibits strong dependence on thermal history, it is considered inappropriate to use routinely iron-related levels as an indication of iron contamination in n-type silicon.

An identical nature of IRDs observed between CZ and FZ silicon suggests that IRDs cannot be attributed to oxygen atoms. Furthermore, we could not find any effect of phosphorus atoms, nitrogen or hydrogen on the characteristics of IRDs.

The IRDs can be re-generated by a successive iron diffusion [9,10]. This fact indicates that the IRDs are generated during iron diffusion at high temperature. However, the introduced concentration of IRDs strongly depends on the cooling rate [10]. As stated in Section 3.4, we interpret the electrical activity of the observed IRDs on the basis of the composition of the electrically active species related to Fe_i. Another mechanism that may be electrically observable is space-charge region around the complex as discussed in Ref. [17]. However, DLTS and Hall effect might not be so powerful as to give a conclusive picture of the mechanisms involved.

4. Conclusion

Electrical properties of iron-related defects in n-type CZ and FZ silicon were studied using DLTS and Hall effect. We proposed a model that electrically active iron-related complexes are due to intermediate states in consecutive reactions of iron-related complex formation

process. The iron-related defects observed in CZ silicon are identical to those observed in FZ silicon.

References

[1] C. Schmidt, Appl. Phys. 17 (1978) 137.
[2] G.A. Adegboyega, A. Poggi, A. Susi, Phys. Status Sol. A 118 (1990) 491.
[3] L.C. Kimerling, J.L. Benton, J.J. Rubin, Inst. Phys. Conf. Ser. 59 (1981) 217.
[4] K. Nakashima, M. Chijiwa, Jpn. J. Appl. Phys. 25 (1986) 234.
[5] K. Kakishita, K. Kawakami, S. Suzuki, E. Ohta, M. Sakata, J. Appl. Phys. 65 (1989) 3923.
[6] H. Kitagawa, L.C. Kimerling, S. Tanaka, J. Electron. Mater. 21 (1992) 863.
[7] H. Kitagawa, S. Tanaka, B. Ni, Jpn. J. Appl. Phys. 32 (1993) L1645.
[8] S. Tanaka, H. Kitagawa, Jpn. J. Appl. Phys. 34 (1995) L721.
[9] H. Kitagawa, S. Tanaka, Mater. Res. Soc. Symp. Proc. 378 (1995) 983.
[10] S. Tanaka, H. Kitagawa, Jpn. J. Appl. Phys. 37 (1998) L4.
[11] H. Kitagawa, S. Tanaka, Mater. Res. Soc. Symp. Proc. 510 (1998) 47.
[12] S. Tanaka, H. Kitagawa, Jpn. J. Appl. Phys. 37 (1998) 4656.
[13] L.C. Kimerling, J.L. Benton, Physica B 116 (1983) 297.
[14] A.C. Damask, G.J. Dienes, Point Defects in Metals, Gordon and Breach, New York, 1963, p. 81.
[15] E.R. Weber, Appl. Phys. A 30 (1983) 1.
[16] H. Nakashima, T. Isobe, Y. Yamamoto, K. Hashimoto, Jpn. J. Appl. Phys. 27 (1988) 1542.
[17] A.A. Istratov, E.R. Weber, Appl. Phys. A 66 (1998) 123.

ELSEVIER

Physica B 273–274 (1999) 420–423

PHYSICA B

www.elsevier.com/locate/physb

The 777 meV photoluminescence band in Si : Pt

J.P. Leitão[a], M.C. Carmo[a], M.O. Henry[b,*], E. McGlynn[b], J. Bolmann[c], S. Lindner[b]

[a]*Departamento de Física, Universidade de Aveiro, 3810 193 Aveiro, Portugal*
[b]*School of Physical Sciences, Dublin City University, Collins Avenue, Dublin 9, Ireland*
[c]*Max-Planck Institut FKF, D-70506 Stuttgart, Germany*

Abstract

In this paper we present a photoluminescence study of a platinum centre with zero-phonon lines at ≈ 777.5 and ≈ 778.8 meV. Uniaxial stress data show that these transitions occur at an axial defect with C_{2v} symmetry aligned along a (1 0 0) axis and exhibiting strong stress-induced reorientations even at low temperature. The centres are shown to align parallel to the stress axis. The observed stress shift rates are very similar to the shift rates of the conduction band edges, suggesting that these transitions occur at a centre containing a loosely bound electron. Experiments on samples produced by the decay of radioactive Au to Pt show that, in p-type material, the defect anneals out in the region of 100 K, while it remains stable in n-type material.

Keywords: Silicon; Platinum; Stress

1. Introduction

The study of Pt-doped silicon has a long history, and is interwoven with the case of Si : Au [1–5]. For Si : Pt, the negatively charged centre Pt^- has been studied in great detail, and several key properties of this centre have emerged from EPR measurements, in particular the alignment under stress of defects into one preferred orientation [6,7]. By the signs of the piezospectroscopic tensor it was concluded that the sense of this alignment was opposite to that occurring in the single negative vacancy, i.e. under stress the Pt^- defects realigned parallel to the stress axis. No corroborative evidence for this description of the Si : Pt^- centre has been reported. For the case of Si : Au^0, on the other hand, which is isoelectronic to Si : Pt^-, good data are available from optical measurements, but the EPR is famously absent, although strong arguments to explain its absence have been advanced [8]. (One report of the Si : Au^0 EPR has been published [9] but the identification has been questioned [3]). Here we provide some details of a photoluminescence (PL) centre, previously confirmed as involving one Pt atom [10], which shows some strong parallels to the Si : Au^0 centre, but which proves to be difficult to definitively assign to Si : Pt^-.

2. Experimental details

The samples were prepared from n- and p-type silicon ingots with resistivities in the order of 12 Ω cm. Platinum was introduced by ion implantation at 170 KeV and a flux of 10^{13} ions/cm^2. Following implantation the samples were annealed at 900°C in a tubular furnace in inert atmosphere for 1 h followed by a rapid thermal quench. Details of the experimental procedures, including the preparation of samples containing radioactive isotopes, are described elsewhere [10].

3. Results

A typical spectrum is shown in Fig. 1 for 4.2 and 17 K. The spectrum is dominated by two zero-phonon lines (ZPL) labelled A and B at 777.55 and 778.85 meV with instrument-limited half-widths of 0.2 meV at 12 K. The

* Corresponding author. Tel.: + 353-1-704-5390; fax: + 353-1-704-5384.
E-mail address: martin.henry@dcu.ie (M.O. Henry)

0921-4526/99/$ - see front matter
PII: S0921-4526(99)00495-0

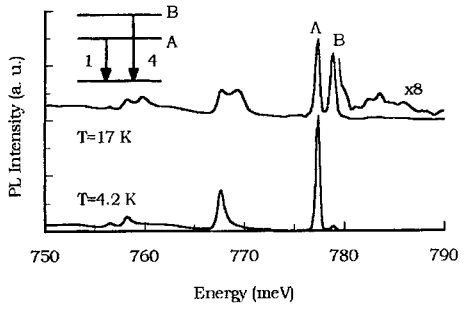

Fig. 1. Photoluminescence spectra recorded at 4.2 and 17 K for Si : Pt. The inset shows that the two lines share a common ground state and that the upper line oscillator strength is four times that of the lower. Some structure in the region of 785 meV in the 17 K spectrum is due to anti-Stokes sidebands.

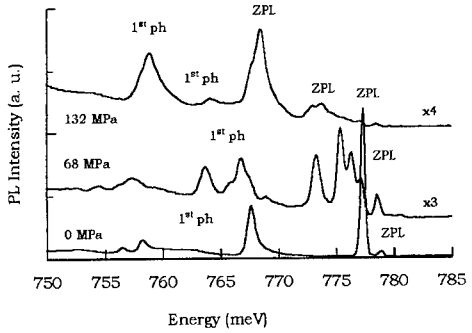

Fig. 2. Uniaxial stress data for the two zero-phonon lines. The solid lines are fits obtained for transitions at a C_{2v} centre.

temperature dependence of the zero-phonon lines (ZPL) reveals that the splitting occurs in the excited state as shown in the inset of Fig. 1. The transition probability from the higher-energy excited level is four times the transition probability from the lower level. The spectral sideband shows a maximum at ≈ 30 meV from the ZPL and is dominated by strong local vibrational modes. This shape can be reproduced with two local modes for each ZPL: a weak phonon of 7.5 meV and a strong mode of 9.6 meV. Several replica and combinations of these modes can be identified in the phonon side band (up to four). The temperature dependence of the integrated intensity of the ZPL can be measured giving an ionisation energy E of ≈ 13 meV.

The phonon sideband can be reproduced using the theory of linear electron–phonon coupling and a Huang–Rhys factor $S \approx 1.2$. From the energy of the ZPL we can measure a spectroscopic localisation energy of 378.6 meV (measured from the free exciton energy of 1155.7 meV). Taking out a value of 13 meV as the ionisation energy we are left with ≈ 366 meV. The electron-phonon coupling contributes with a relaxation energy that accounts for $E_R \cong 36$ meV and so we get a residual binding energy ≈ 330 meV, in agreement with the measured substitutional platinum donor level reported in the literature to be in the region of 320–330 meV [11].

3.1. Uniaxial stress

Uniaxial stresses up to 250 MPa were applied along the three major crystallographic axis of Si : Pt samples at 4.2 K. The effect of these perturbations can be seen in Fig. 2. These effects are unusual in one aspect: under $\langle 1\,0\,0\rangle$ stress the zero-phonon lines start by splitting in three components but at even moderate stresses the higher-energy components begin to lose intensity, and the spectrum becomes identical to the spectra of stress free samples (except for a shift in energy). The intensity ratio of the two zero-phonon lines at high stress is different from that measured in stress free samples due to the fact that the two stress components shift at different rates under $\langle 1\,0\,0\rangle$ and are thus further apart in energy. Under $\langle 1\,1\,1\rangle$ stress the lines are not split by the external field although some line broadening is observed. Under $\langle 1\,1\,0\rangle$ three components are observed. Considering only the splitting patterns at low stresses the data can be fitted considering that the electronic transitions are between non-degenerate states at a centre of C_{2v} symmetry with a C_2 axis along the $\langle 1\,0\,0\rangle$ axis of the silicon crystal. The stress perturbation can be written as

$$H = A_1 s_{xx} + A_2 s_{yy} + A_3 s_{zz},$$

where s_{ij} denotes the stress tensor components defined relative to the local defect axis and A_1, A_2 and A_3 are stress parameters that in principle can be different for each line. With this perturbation the secular matrix of the system can be solved considering the set of parameters shown in Table 1.

The fit shown in Fig. 3 was obtained using these parameter values and setting the interaction between the two neighbouring excited states to zero. In this notation the line in $\langle 1\,0\,0\rangle$ that goes to lower energy corresponds to centres oriented parallel to the applied stress. Fig. 4 shows the log plot of the intensities of the three components seen in $\langle 1\,0\,0\rangle$ as a function of applied stress for the stress range in which they can be clearly observed. It is clear that they project out, in the limit of zero stress, to the intensity ratios $I_1 : I_2 : I_3 = 1 : 1 : 2$ in accordance with the theoretical prediction by Kaplianskii for a C_{2v} centre [12]. As the stress components all come from the differently oriented centres relative to the stress axis we have to interpret this stress-induced dichroism as due to reorientations between the differently oriented centres. We note that this reorientation process occurs at very low temperature and stress.

Table 1
Stress parameters according to Kaplyanskii notations

Line (meV)	A (meV/Gpa)	B (meV/Gpa)	C (meV/Gpa)
778.85	−15.0	33.0	−45.0
777.75	−17.0	17.4	−56.8

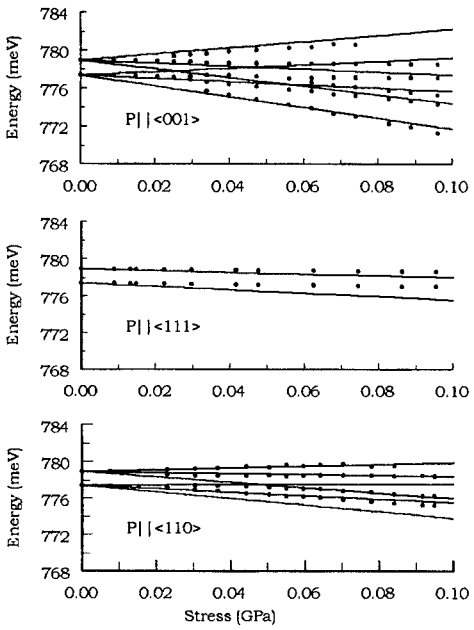

Fig. 3. PL spectra recorded for several stress values showing the loss of signal from the upper components as the stress increases.

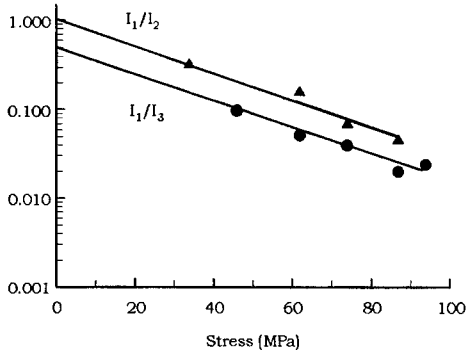

Fig. 4. The intensity ratios of the 777.5 meV line components as a function of stress.

3.2. Zeeman effect

Magnetic fields were applied along the ⟨1 0 0⟩ and ⟨1 1 0⟩ axes. No measurable broadening of the higher-energy ZPL is detected. The splitting pattern of the low-energy component is more complex and the number of observable components varies according to the orientation of the field to the crystal axis. This confirms the axial nature of the defect. The data shown in Fig. 5 for B‖⟨1 1 0⟩ was fitted modelling the defect as an exciton in a negative axial field along the ⟨1 0 0⟩ axis and using the parameters of Table 2, according to the model developed in Refs. [13,14].

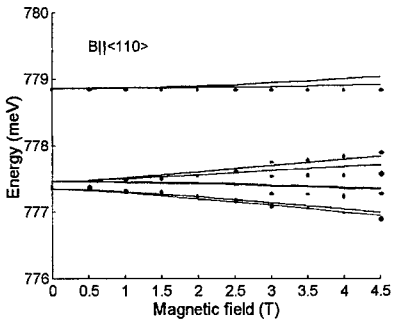

Fig. 5. Zeeman data for the magnetic field along the ⟨1 1 0⟩ direction. The solid lines are fits to the data in terms of the states expected for an exciton under a local compressive stress.

Table 2
Fitting parameters for the splitting under magnetic field considering the tetrahedral base. The Bohr magneton is $\mu = 0.05788$ meV T^{-1}

$E_1 = 1.56$	$A = -0.17\mu$
$E_2 = 2.95$	$C = -0.97\mu$
$P = -1.60$	$D = 2.69\mu$
$Q = 1.84$	$F = 1.48\mu$
$R = -1.47$	$G = -1.63\mu$
$S = -1.44$	

3.3. Thermal stability

One important result to emerge from studies with implanted radioactive Au atoms which decay to Pt was the loss, for p-type samples only, of the 777 meV centres produced at low temperatures when the sample temperature was allowed to rise to ≈ 100 K and cooled again to repeat the PL measurement. For n-type samples, the PL centre is stable for long periods at room temperature. The activation energy and attempt frequency for the annealing out of the centre in p-type material have not been established, but the critical temperature lies between 80 and 120 K.

4. Discussion

The observed stress shift parameters are very similar to the perturbations of the conduction band minima. Under

⟨1 1 1⟩ stress the lines shift (without splitting) to lower energy at a rate of -10 meV/GPa compared to the conduction band shift rate of -15 meV/GPa. Under ⟨1 0 0⟩ stress the separation between the high- and the low-energy components increases by ≈ 80 meV/GPa, with the lowest-energy component shifting at twice the rate of the high-energy component, both results being the same as for the conduction band edges. Thus, we can conclude that the centre contains a loosely bound electron. The thermal data gives an ionisation energy of ≈ 13 meV, close to the ionisation energy of the free exciton and in the order of magnitude of other excitonic centres [12]. The full set of uniaxial stress and Zeeman data can be accounted for satisfactorily in terms of an axial isoelectronic centre with a negative local strain (Tables 1 and 2), after the model of Davies [14]. While the theoretical fits favour this generic assignment, they do not establish the identity of the Pt centre.

We now consider whether the main results can be accounted for in terms of the Si : Pt^- centre. The C_{2v} symmetry, the reorientation under stress at 4.2 K, including the lowest-energy orientation, closely parallel the properties of the EPR centre [15]. This correspondence, together with the donor nature and the energy position, constitutes a strong argument for attributing the 777 meV PL to transitions from shallow excited states to the deep donor level of Si : Pt^-, analogous to the 793 meV PL and absorption line in Si : Au^0 [5]. The Zeeman data pose a problem, however. Taking the known g-values for the Pt^- centre ($g_\perp = 1.4$ and $g_{//} = 2.1$) and assuming an isotropic g-value of 2 for the excited state, in the manner used by Watkins et al. [5] for the Si : Au^0 case, produces the correct number of components and reasonably close agreement with the shift rates observed in the available Zeeman data (⟨1 0 0⟩ and ⟨1 1 0⟩ directions only) for the lower-energy line. However, the upper luminescence line, which involves transitions into the same ground state, does not show any splitting, and this cannot be reconciled with the donor model which otherwise seems to meet many of the essential features. The loss of the defect (when produced from the decay of radioactive Au) in p-type material at ≈ 100 K we interpret as due to a thermally activated relaxation from the configuration of the mother Au defect into a new configuration which results in the defect acquiring a different charge state thereby losing its luminescence property.

5. Conclusions

The 777 meV centre in Si : Pt has been shown to be due to transitions at a C_{2v} centre from shallow donor-like excited states to a deep ground state lying in the region of Ev + 330 meV. The centre shows many of the characteristics of the Pt^- donor, but the available Zeeman data appear to rule out this identification. The centre belongs to the family of axial isoelectronic centres possessing a negative local strain in the silicon lattice.

References

[1] H.H. Woodbury, G.W. Ludwig, Phys. Rev. 126 (1962) 466.
[2] G.W. Ludwig, H.H. Woodbury, Solid State Phys. 13 (1962) 223.
[3] M. Kleverman et al., Solid State Commun. 93 (1995) 383.
[4] D. Thébault et al., Phys. Stat. Sol. B 125 (1984) 357.
[5] G.D. Watkins et al., Phys. Rev. Lett. 67 (1991) 1149.
[6] J.C. Henning, E.C. Egelmeers, Phys. Rev. B 27 (1983) 4002.
[7] F.G. Anderson et al., Phys. Rev. B 45 (1992) 3279.
[8] F.G. Anderson, J. Phys.:Condens. Matter 3 (1991) 4421.
[9] N.T. Son et al., Phys. Rev. Lett. 69 (1992) 3185.
[10] M.O. Henry et al., in: M. Scheffler, R. Zimmermann, (Eds.), Proceedings of the 23rd International Conference on Physics Semiconductors, World Scientific, 1996, Singapore, 2713.
[11] S. Mayo, J.R. Lowney, J. Appl. Phys. 61 (1987) 2626.
[12] A.A. Kaplyanskii, Optics Spectrosc. 16 (1964) 329.
[13] N. Killoran et al., J. Phys. C 15 (1982) 6067.
[14] G. Davies, J. Phys. C 17 (1984) 6331.
[15] R.F. Milligan et al., Phys. Rev. B 29 (1984) 2819.

ELSEVIER

Physica B 273–274 (1999) 424–428

PHYSICA B

www.elsevier.com/locate/physb

Copper-related defects in silicon

Stefan K. Estreicher*

Physics Department, Texas Tech University, MS 1051, Lubbock, TX 79409-1051, USA

Abstract

Copper-related defects in Si are studied at the ab initio Hartree–Fock level in clusters containing up to 100 Si atoms. The defects studied are interstitial and substitutional copper, as well as one through five Cu's trapped at an internal void modeled by the ring-hexavacancy. Configurations, electronic structures, and binding energies are calculated. The origin of the electrical activity of copper precipitates and trends are discussed.

Keywords: Copper; Gettering; Silicon; Theory

1. Introduction

Copper is a common impurity in silicon [1–4]. Interstitial copper is believed to exist almost exclusively as the Cu_i^+ ion. It is the fastest-diffusing impurity in Si known to date [5] with $D = (3.0 \pm 0.3) \times 10^{-4} \exp -(0.18 \pm 0.01)$ eV/k_BT cm^2/s. The activation energy is close to the 0.24 eV predicted by ab initio Hartree–Fock (HF) calculations [6] for the diffusion of Cu_i^+ along the interstitial tetrahedral–hexagonal–tetrahedral (T–H–T) path. It has been assumed that the reason for this low value is that Cu^+ has an ionic radius of only 0.75 Å and the closed-shell $[Ar]3d^{10}4sp^0$ configuration. It should therefore behave like a small ball which does not interact covalently with the host crystal.

Yet, copper has a strong tendency to precipitate at dislocations [1,4,7], grain boundaries [8], nanocavities [9–11] radiation-damaged regions [12,13], stacking faults [14], etc. It forms star-shaped etch pits, and platelets in {1 1 1} planes [4]. Such precipitates reduce carrier lifetimes [15,16]. A range of gap levels observed by deep-level transient spectroscopy (DLTS) have been assigned to copper precipitates [3,4]. Thus, even though isolated copper is thought to exhibit little electrical activity and be mostly inert, its interactions with defects result in the appearance of deep levels in the gap.

In this work [17], interstitial and substitutional copper, as well as the trapping of copper at a model internal void, the ring-hexavacancy (V_6) [18,19] are studied at the ab initio Hartree–Fock level. Similar calculations have successfully predicted the activation energy for diffusion [6] of Cu_i^+ and the structure [20] of the passivated {Cu,B} pair.

Except for these two HF studies, the theoretical work published so far has dealt with the prediction of trends for *isolated* transition metal (TM) impurities at *undistorted* sites. DeLeo et al. [21,22] used the scattered-wave Xα method to calculate the gap-level positions of interstitial TMs. Hemstreet et al. [23,24] applied the same technique to substitutional TMs.

Zunger and Lindefelt [25–28] started with a perfect-crystal Green's function and added the TM as a perturbative potential. Beeler et al. [29,30] performed spin-unrestricted linear muffin-tin orbital Green's function calculations for all the 3d TMs at interstitial and substitutional sites. Finally, Lindefelt [31] estimated the magnitude of the relaxations around substitutional copper using an empirical valence-force potential, and found a symmetric outward relaxation of the NNs by 0.24 Å.

The aim of the present paper is quite different. The positions of gap levels obtained at the ab initio HF level are well-known to be only qualitative, and no attempt is made here at predicting the position of DLTS levels. Further, only copper is discussed. However, these are ab initio total-energy quantum chemical calculations.

The geometries were gradient optimized with no symmetry assumptions using the 'approximate ab initio' HF

* Tel.: + 1-806-742-3723; fax: + 1-806-742-1182.
E-mail address: bzske@ttu.edu (S.K. Estreicher)

0921-4526/99/$ - see front matter
PII: S0921-4526(99)00496-2

method of PRDDO [32,33]. The optimized geometries were used as inputs for single-point ab initio HF calculations [34] with split-valence polarized basis sets. Pseudopotentials [35,36] were used to remove the core electrons from the calculations. The host crystal was represented by saturated clusters [37] up to 100 Si atoms.

2. Interstitial and substitutional copper

The lowest-energy configuration of Cu_i^+ in Si is almost exactly at the T site, off by less than 0.1 Å toward one of its four Si nearest neighbors (NNs). The energy spectrum shows no state in the gap, but for a very shallow level near the conduction band.

It *costs* 1.67 eV to insert the free Cu^+ ion into the T site in Si. This value matches the measured heat of solution from the silicide, 1.7 eV [1,10]. The electronic configuration of Cu_i^+ is *not* the free ion's $3d^{10}4sp^0$. Instead, interstitial copper promotes several electrons from the 3d into the 4sp shell. Thus, Cu_i^+ *does not* resemble a tiny sphere, as shown in Fig. 1. The promotion of some electrons from the 3d to the 4sp shells allows Cu_i^+ to interact covalently with impurities and defects, and to hybridize in a variety of ways.

When Cu_i^+ and a (neutral) vacancy (V) get close to each other, copper becomes substitutional Cu_s^+. The energy spectrum shows that several energy levels are present in the gap. Their number and position are basis-set dependent, but their presence is not. The Koopman-theorem ionization potential for this defect is negative, implying that adding one (or more) electron(s) occurs at a gain in energy. Cu_s is four-fold coordinated and binds to its four NNs. None of the Cu–Si bonds are true 2-electron covalent bonds. The bond orders are small. The four NNs to copper relax outward by less than 0.1 Å.

The energy gained in the reaction $Cu_i^+ + V \rightarrow Cu_s^+$ is 2.71 eV, which does not include the formation energy of the vacancy. This is not a large energy gain for a reaction involving an interstitial impurity and a vacancy and corresponds to about 0.6 eV for each of the four Cu–Si bonds. For comparison, ones gains more than 3 eV by inserting a single H atom into a vacancy [38] or a cluster of vacancies [39]. When H is placed in the vicinity of substitutional copper, it traps inside the vacancy and forces Cu into a 3-fold coordination. A second H appears to expel copper from the substitutional site. Since the standard preparation of Schottky diodes results in some H penetrating into the sub-surface layer [40], this could explain why it is difficult to detect substitutional copper by DLTS.

3. Copper precipitation at internal voids

The model internal void considered here is V_6, a defect predicted [18,19] to be extremely stable and electrically inactive. It consists of a hexagonal ring missing from the crystal. V_6 is an ellipsoidal void of diameter 7.8 Å and thickness 4.4 Å. It has trigonal symmetry, with 12 Si NNs around the $\langle 1\,1\,1\rangle$ axis and two Si NNs on the trigonal axis which also participate in the reconstruction. These 14 host atoms must be included in all the geometry optimizations, in addition to any impurities inside V_6.

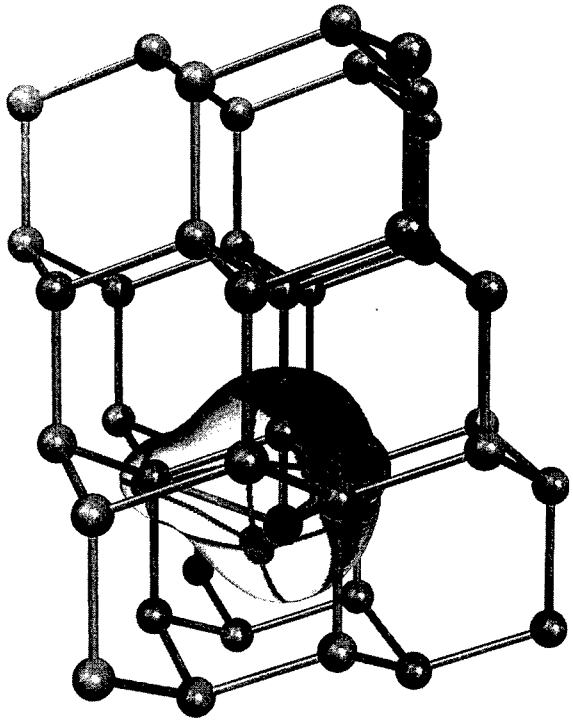

Fig. 1. Cross-section of the electrostatic potential around Cu_i^+ (at the center, in black).

In order to avoid the build-up of positive charge as Cu^+ precipitates in the void, I assumed that $\{Cu_{n-1},V_6\}^+$ traps an electron before the next copper binds to the defect. Such a process was proposed [41] as the reason why copper precipitates faster in n- than in p-type Si. However, since copper precipitates are also observed in p-type material, electrons must trap at the defect to maintain a small or zero net charge. Further, since restricted and unrestricted HF energies are not comparable, only total energy differences involving closed-shell (spin 0) configurations are included. The precipitation of Cu_i^+ at V_6 was handled as follows.

(1) Cu^+ is placed inside V_6, the geometry optimized, and the binding energy ΔE_1 is defined as $Cu_i^+ + V_6 \rightarrow \{Cu_1,V_6\}^+ + \Delta E_1 = 3.36$ eV. It is then assumed that $\{Cu_1,V_6\}^+$ captures an electron, then traps Cu_i^+. This defect traps a second electron and the geometry of $\{Cu_2,V_6\}^0$ is optimized. This defect, a closed shell, is the trap for the next Cu_i^+.

(2) Cu^+ is placed inside $\{Cu_2,V_6\}^0$, the geometry optimized, and the binding energy ΔE_3 is defined as $Cu_i^+ + \{Cu_2,V_6\}^0 \rightarrow \{Cu_3,V_6\}^+ + \Delta E_3 = 4.94$ eV. It is then assumed that $\{Cu_3,V_6\}^+$ captures an electron, then traps Cu_i^+. This defect traps a second electron and the geometry of $\{Cu_4,V_6\}^0$ is optimized. This defect, a closed shell, is the trap for the next Cu_i^+.

(3) Cu^+ is placed inside $\{Cu_4,V_6\}^0$, the geometry optimized, and the binding energy ΔE_5 is defined as $Cu_i^+ + \{Cu_4,V_6\}^0 \rightarrow \{Cu_5,V_6\}^+ + \Delta E_5 = 2.01$ eV. Note that this value coincides with the measured [10] dissociation energy of copper from Cu-saturated internal voids, 2.2 ± 0.2 eV.

This complex could continue to grow, for example involving sites for Cu outside V_6. This possibility is not considered here. The configurations of the $\{Cu_n,V_6\}$ complexes [17] with $n = 0,\ldots,5$ are as follows.

In $\{Cu_1,V_6\}$, copper binds to four Si atoms on the inner surface of the void. The four Cu–Si distances range from 2.38 to 2.68 Å, and the degrees of bonding [42] from 0.6 to 0.4. For a perfect 2-electron covalent bond, this number is 1.0.

In $\{Cu_2,V_6\}$, the two copper atoms are as far from each other as possible (4.55 Å), at opposite inner surfaces of V_6. The Cu–Si bond lengths vary from 2.38 to 2.62 Å, and the degrees of bonding from 0.7 to 0.5.

In $\{Cu_3,V_6\}$, the three copper atoms form an almost perfect isosceles triangle in the plane of V_6. The Cu–Cu distances are 2.75, 2.77, and 4.08 Å, respectively. One Cu is bound to the two other Cu's, but the overlap is very small (degree of bonding $\leqslant 0.2$ and overlap population ~ 0.1). This Cu is mostly bound to only two Si atoms, at 2.28 and 2.33 Å, with degrees of bonding of 0.7 and 0.8. The other two coppers form four Cu–Si bonds, with bond lengths varying from 2.38 to 2.71 Å and degrees of bonding from 0.6 to 0.4.

The copper atoms in $\{Cu_4,V_6\}$ form a perfect rectangle of width 2.36 Å and length 3.67 Å in the plane of V_6. There are two weak Cu–Cu bonds (degree of bonding 0.4), that is each of the four Cu's is bound to one Cu and four Si atoms. These bonds are similar to those described above.

Finally $\{Cu_5,V_6\}$, is a slightly distorted version of $\{Cu_4,V_6\}$, with the fifth Cu forming the tip of a pyramid with a rectangular base, the tip being on the trigonal axis of V_6. The fifth Cu is eight-fold coordinated (!) but the degrees of bonding vary only from 0.2 to 0.4. The other coppers are as in $\{Cu_4,V_6\}$.

The following trends are apparent.

(1) Cu impurities trap on the inner surface of the void and remain as far apart as possible from each other.

(2) Cu–Si bonding is preferred over Cu–Cu bonding. As long as there is enough space, each Cu binds to different Si atoms. As the void fills up, some Cu–Cu overlap becomes unavoidable, and a few Si atoms bind to two Cu atoms.

(3) Cu prefers to form four weak Cu–Si covalent bonds. The degrees of bonding are in the 0.4–0.8 range.

(4) The sum of the degrees of bonding associated with each Cu lies in the narrow range 2.3–2.6 for all the copper complexes studied here. Thus, the total number of electrons participating in the covalent bonding of Cu is very near five. These electrons are distributed among four Cu–Si bonds (plus any Cu–Cu bonds).

(5) The binding energies of Cu to an internal void vary with the number of copper impurities in the void. For a saturated void, it is 2 eV.

(6) The maximum strength of each of the Cu–Si bonds is 0.9 eV. This estimate is obtained by dividing the binding energy of Cu to $\{Cu_n,V_6\}$ (relative to $\{Cu_{n-1},V_6\} + Cu_i^+$) by the number of Cu–Si bonds involved. Since each copper forms four inequivalent Cu–Si bonds with degrees of bonding ranging from 0.4 to 0.8, some of the bonds are necessarily weaker than 0.9 eV. This has the following two consequences.

(6a) Some of the energy eigenvalues associated with the bonding/antibonding orbitals of the weak Cu–Si (and Cu–Cu) bonds are in the gap. Fig. 2 shows the wavefunction associated with the highest-occupied orbital in the gap. It is clearly localized on the Cu–Si bonds. This implies that the electrical activity of copper precipitates in internal voids is caused by the energy levels associated with the many weak Cu–Si and Cu–Cu bonds.

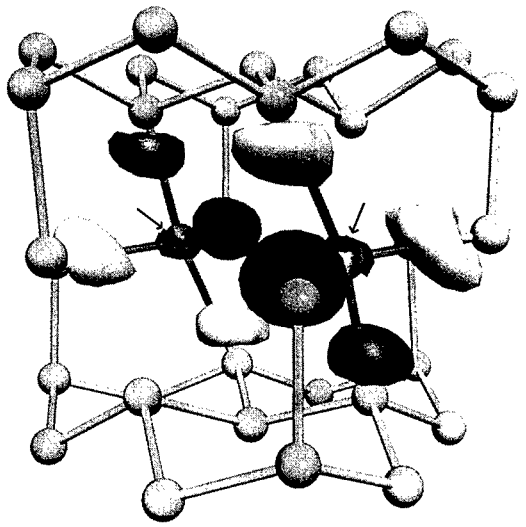

Fig. 2. Wave function associated with the highest-occupied molecular orbital of the $\{Cu_2,V_6\}$ complex. The two Cu atoms are marked by arrows.

(6b) The binding energy of a single hydrogen to a vacancy [38] or vacancy aggregate [39] is of the order of 3 eV and results from the formation of a single strong Si–H bond. Thus, if hydrogen is present, it should easily displace Cu from internal voids, since replacing even the strongest Cu–Si bond by a Si–H bond results in a gain of the order of 2 eV. Such an effect has indeed been reported [10].

4. Conclusions

The Cu_i^+ ion is at (or very near) the T site. It is not in the chemically inert $3d^{10}4sp^0$ configuration. Instead, several electrons are promoted from the 3d into the 4sp shell. This allows copper to form weak but covalent bonds to a wide range of impurities and defects. Even the isolated interstitial ion shows some covalent overlap with its four Si NNs.

The activation energy for diffusion [6] of Cu_i^+ along the T–H–T path is 0.24 eV, very close to the experimental [5] value, 0.18 ± 0.01 eV. It costs 1.67 eV to insert the free copper ion into the T site in Si. This value coincides with the experimentally determined heat of solution from the silicide (1.7 eV) [1,10].

Substitutional copper, Cu_s^+, is four-fold coordinated. Its binding energy (relative to Cu_i^+) is 2.7 eV. It is an electron trap.

Copper precipitates at internal voids such as V_6. The common features of the complexes studied here are as follows. (1) The Cu's stick to the inner surface of the void and remain as far away from each other as possible. (2) Cu–Si bonding is preferred over Cu–Cu bonding. (3) Each Cu normally binds to four Si atoms. (4) A total of about five electrons participate in the bonding of each Cu (this includes the electrons associated with the Cu and Si atoms). (5) The binding energies of $\{Cu_n,V_6\}^+$ relative to $\{Cu_{n-1},V_6\}^0 + Cu_i^+$ vary with n. For $n = 1$, it is 3.36 eV. For $n = 3$, it is 4.94 eV. For $n = 5$, it drops to 2.01 eV, which matches the experimental [10] binding energy of Cu at internal voids, 2.2 ± 0.2 eV, relative to the solution in Si. (6) The Cu–Si bond strengths are less than 0.9 eV, and at least some of the bonding and antibonding energy levels associated with the Cu–Si (and Cu–Cu) lie in the gap. They are responsible for the electrical activity of Cu precipitates. H should easily displace Cu from such precipitates, as observed [10].

Acknowledgements

This work was supported in part by the grant D-1126 from the R.A. Welch Foundation and by the contract XAD-7-17652-01 from the National Renewable Energy Laboratory.

References

[1] E.R. Weber, Appl. Phys. A 30 (1983) 1.
[2] A. Mesli, T. Heiser, Defect Diff. Forum 131–132 (1996) 89.
[3] T. Heiser, A.A. Istratov, C. Flink, E.R. Weber, Mater. Sci. Eng. B 58 (1999) 149.
[4] A.A. Istratov, E.R. Weber, Appl. Phys. A 66 (1998) 123.
[5] A.A. Istratov, C. Flink, H. Hieslmair, E.R. Weber, T. Heiser, Phys. Phys. Lett. 81 (1998) 1243.
[6] D.E. Woon, D.S. Marynick, S.K. Estreicher, Phys. Rev. B 45 (1992) 13 383.
[7] J. Weber, Solid State Phenom. 37–38 (1994) 13.
[8] J.-L. Maurice, C. Colliex, Appl. Phys. Lett. 53 (1989) 241.
[9] J. Wong-Leung, C.E. Ascheron, M. Petravic, R.G. Elliman, J.S. Williams, Appl. Phys. Lett. 66 (1995) 1231.
[10] S.M. Myers, D.M. Follstaedt, J. Appl. Phys. 79 (1996) 1337.
[11] M. Zhang, C. Lin, X. Duo, Z. Lin, Z. Zhou, J. Appl. Phys. 85 (1999) 94.
[12] S. McHugo, E.R. Weber, S.M. Myers, G.A. Petersen, Appl. Phys. Lett. 69 (1996) 3060.
[13] S. Koveshnikov, O. Kononchuk, Appl. Phys. Lett. 73 (1998) 2340.
[14] M. Kaniewska, J. Kaniewski, A.R. Peaker, Mater. Sci. Forum 83–87 (1992) 1457.
[15] A. Rohatgi, J.R. Davis, R.H. Hopkins, P. Rai-Choudhury, P.G. McMullin, J.R. McCormick, Solid State Electron 23 (1980) 415.
[16] A.A. Istratov, C. Flink, H. Hieslmair, T. Heiser, E.R. Weber, Appl. Phys. Lett. 71 (1997) 2121.
[17] S.K. Estreicher, Phys. Rev. B 60 (1999) 5375.
[18] S.K. Estreicher, J.L. Hastings, P.A. Fedders, Appl. Phys. Lett. 70 (1997) 432.
[19] J.L. Hastings, S.K. Estreicher, P.A. Fedders, Phys. Rev. B 56 (1997) 10 215.
[20] S.K. Estreicher, Phys. Rev. B 41 (1990) 5447.
[21] G.G. DeLeo, G.D. Watkins, W.B. Fowler, Phys. Rev. B 23 (1981) 1851.
[22] G.G. DeLeo, G.D. Watkins, W.B. Fowler, Phys. Rev. B 25 (1982) 4962 and 4972.
[23] L.A. Hemstreet, Phys. Rev. B 15 (1977) 834.
[24] L.A. Hemstreet, J.O. Dimmock, Phys. Rev. B 20 (1979) 1527.
[25] A. Zunger, U. Lindefelt, Phys. Rev. B 26 (1982) 5989.
[26] A. Zunger, U. Lindefelt, Phys. Rev. B 27 (1983) 1191.
[27] A. Zunger, Phys. Rev. B 28 (1983) 3628.
[28] A. Zunger, Sol. St. Phys. 39 (1986) 275.
[29] F. Beeler, O.K. Anderson, M. Scheffler, Phys. Rev. Lett. 55 (1985) 1498.
[30] F. Beeler, O.K. Anderson, M. Scheffler, Phys. Rev. B 41 (1990) 1630.
[31] U. Lindefelt, Phys. Rev. B 28 (1983) 4510.
[32] A. Derecskei-Kovacs, D.S. Marynick, Int. J. Quant. Chem. 58 (1996) 193.
[33] A. Derecskei-Kovacs, D.S. Marynick, Int. J. Quant. Chem. 61 (1997) 67.
[34] M.W. Schmidt, K.K. Baldridge, J.A. Boatz, S.T. Elbert, M.S. Gordon, J.H. Jensen, S. Koseki, K.A. Nguyen, S. Su,

T.L. Windus, M. Dupuis, J.A. Montgomery Jr., J. Comp. Chem. 14 (1993) 1349.
[35] P.J. Hay, W.R. Wadt, J. Chem. Phys. 82 (1985) 270.
[36] W.J. Stevens, H. Bash, M. Krauss, J. Chem. Phys. 81 (1984) 6026.
[37] S.K. Estreicher, Mater. Sci. Eng. R 14 (1995) 319.
[38] Y.K. Park, S.K. Estreicher, C.W. Myles, P.A. Fedders, Phys. Rev. B 52 (1995) 1718.
[39] S.K. Estreicher, J.L. Hastings, P.A. Fedders, Mater. Sci. Eng. B 58 (1999) 31.
[40] W. Jost, J. Weber, H. Lemke, Semicond. Sci. Technol. 11 (1996) 525.
[41] A.A. Istratov, O.F. Vyvenko, C. Flink, T. Heiser, H. Hieslmair, E.R. Weber, MRS Proc. 510 (1998) 313.
[42] D.R. Armstrong, P.G. Perkins, J.J.P. Stewart, J. Chem. Soc. Dalton Trans. (1973) 838.

ELSEVIER

Physica B 273–274 (1999) 429–432

PHYSICA B

www.elsevier.com/locate/physb

Depth profiles of palladium–hydrogen complexes in silicon

J. Weber*, S. Knack, J.-U. Sachse[1]

Max-Planck-Institut für Festkörperforschung, Postfach 80 06 65, 70506 Stuttgart, Germany

Abstract

Wet-chemical etching of palladium doped silicon introduces at least seven new levels in the band gap. The depth profiles of the levels associate them with three different palladium–hydrogen complexes. An analysis of the profiles allows us to correlate the levels to complexes with one, two or three hydrogen atoms. Evidence for a complete electrical passivation of substitutional Pd is presented by a complex which contains at least four hydrogen atoms.

Keywords: Silicon; Transition metal; Hydrogen; DLTS

1. Introduction

The effect of hydrogen on the electrical properties of transition metals in silicon, especially the formation of electrically active complexes, is currently an active area of research [1–6]. DLTS measurements combined with depth-profile and annealing studies showed, e.g. that platinum forms several hydrogen-related complexes after hydrogenation by wet-chemical etching [7,8]. The complexes differ in the number of hydrogen atoms, most of them are electrically active, but one complex PtH_4 was proposed to be electrically neutral. In an early study on Pd-related defects no electrically active complexes were detected, only a complete passivation of the Pd-donor and acceptor level by hydrogen plasma treatment was reported [9]. In Ref. [10] we have presented new DLTS data on electrically active PdH complexes. Fig. 1 gives an example for the variety of new levels in Pd doped Si, which was wet-chemically etched and afterwards annealed at 400 K for 30 min. The new levels are characterized by the temperature of the DLTS maximum. Experimental details can be found in Ref. [10]. Table 1 summarizes all PdH levels giving their energy positions and assignments. In the present paper the number of H atoms involved in the PdH complexes is identified from the concentration depth profiles.

2. The formation of hydrogen complexes

Depth profiles of hydrogen complexes that result from wet-chemical etching were described recently by Feklisova and Yarykin in a simple model [11]. The complex formation is understood as a subsequent addition of hydrogen atoms to the defects. A numerical integration of the set of differential equations which describe the formation process is possible for the different experimental conditions, e.g. after wet chemical etching, after annealing, etc. In the limit of larger depth an exponential behavior of all profiles is found. A detailed investigation of the numerical fitting of the total depth profiles is presently performed.

An analytical solution of the differential equations can be derived in the limit of large depth, provided that all complexes are thermally stable, i.e. a hydrogen atom once captured remains attached to the complex and the concentration of the different hydrogen defects A_i decreases with the number i of hydrogen atoms ($[A_i] \gg [A_{i+1}]$). The approximations lead to a simple exponential decay of the complex concentration:

$$[A_i] \sim \exp\left(\frac{x}{L_i}\right) \tag{1}$$

* Corresponding author. Tel. +49-711-689-1538; fax: +49-711-689-1602.

[1] Present address: Infineon Technologies Dresden, 01099 Dresden, Germany.

E-mail address: weber@kernix.mpi-stuttgart.mpg.de (J. Weber)

0921-4526/99/$ - see front matter
PII: S0921-4526(99)00497-4

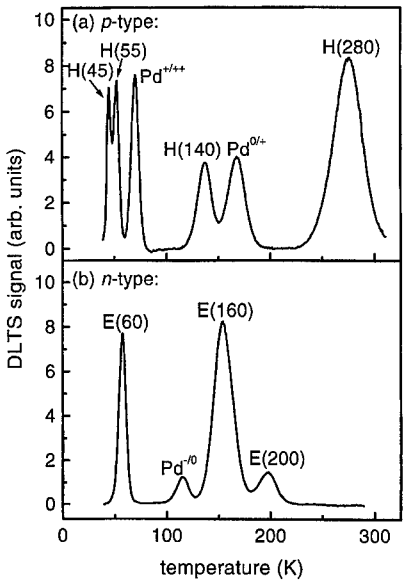

Fig. 1. DLTS spectra of Pd-doped Si after wet-chemical etching and subsequent annealing at 400 K for 30 min ($e_n = 42\ s^{-1}$, $V_r = -2$ V, $t_f = 3$ ms). (a) p-type sample, (b) n-type sample.

Table 1
Energy levels E_A determined from Arrhenius plots of emission rates and assignment of the deep levels based on the analysis of the depth profiles

Level	E_A (eV)	Assignment
E(60)	$E_C - 0.18$	PdH_2
Pd-acceptor	$E_C - 0.23$	Pd_s
E(160)	$E_C - 0.29$	PdH_3
E(200)	$E_C - 0.43$	PdH_1
H(280)	$E_V + 0.55$	PdH_2
Pd-donor	$E_V + 0.31$	Pd_s
H(140)	$E_V + 0.55$	PdH_3
Pd double donor	$E_V + 0.14$	Pd_s
H(55)	$E_V + 0.08$	PdH_3
H(45)	$E_V + 0.07$	PdH_3

with a characteristic length L_i which is derived to be inversely proportional to the number i of hydrogen atoms

$$L_i \approx 1/i\,. \tag{2}$$

The simple relation offers a correct description in the case of PtH complexes in Si, even for samples, which were annealed at moderate temperatures [8].

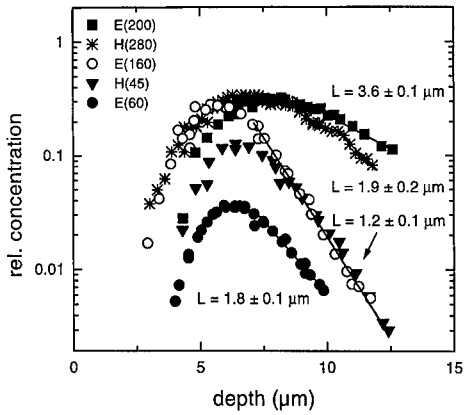

Fig. 2. Depth profiles of all PdH defects in p- and n-type Si after wet-chemical etching and annealing at 470 K for 1 h.

3. Analysis of the PdH depth profiles in n- and p-type samples

The formation of hydrogen complexes after wet-chemical etching or additional low-temperature annealing is quite different for n- or p-type material. A direct comparison of profiles in different samples is only possible if we omit the influence of shallow-dopant hydrogen pairs and different Pd concentrations. In the present analysis only those samples were considered which were measured after an anneal above 450 K. Under these conditions all boron– and phosphorus–hydrogen pairs are dissociated. The influence of different Pd concentrations is corrected by scaling the profile of the Pd-acceptor in n-type Si to the Pd-donor level in p-type Si. The profiles of the PdH defects are then scaled with the same factor. The result of such a comparison of n- and p-type samples is given in Fig. 2. For clarity only the profiles for the levels E(200), H(280), E(160), H(55) and E(60) are given. The profiles of H(45) and H(140) are identical to H(55). The error bar in concentration and depth is estimated to be 10% of the values given in the figure. The profiles of all PdH levels follow an exponential decrease for larger depth and can be grouped into four sets according to their slopes. The slope of level E(160) coincides with level H(55) only for large penetration depth. Level E(200) has the largest penetration into the sample. We therefore assume that E(200) belongs to the PdH_1 complex. The defect profiles show the expected integer ratios for the characteristic length. The ratio $L_{E(200)}/L_{E(60)} = 2$ relates E(60) to a PdH_2 complex, $L_{E(200)}/L_{E(160)} = 3$ associates E(160), H(45), H(55) and H(140) with PdH_3 complexes. However, there is a problem with the assignment of E(160), H(55), H(45) and H(140) to PdH_3 complexes. One would expect that all profiles coincide in the whole depth regime. But level E(160) has a higher maximum concentration compared to the other levels.

Level H(280) has the same slope as E(60). If we assign H(280) also to a PdH_2 complex we have to explain the large concentration differences in n- and p-type samples.

We can resolve the difficulties by reevaluating the approximations made in modeling the formation process of the hydrogen defects. A major simplification is the use of charge-state independent capture radii r_i. In the n-type samples obviously a much faster trapping of hydrogen to the PdH_2 complex seems to occur, compared to p-type samples. This leads to a strongly reduced PdH_2 and an increased PdH_3 concentration in n-type samples. The behavior is different to the results on Pt-doped samples and can be related to the level positions of the PdH_2 complex. In n-type samples at the temperature of annealing most of the PdH_2 complexes are in the negative state and an efficient trapping of positively charged hydrogen occurs. In p-type samples the PdH_2 complex is neutral and trapping by the positively charged hydrogen is less efficient. The H(280) level of the PtH_2 is closer to midgap, which leads in n- and p-type samples to the same interaction of the negatively charged PtH_2 complex with positively charged hydrogen.

The behavior of the PdH_2 depth profile in p-type samples needs further discussion. The total concentration of the PdH_2 complex is identical to that of the PdH_1 complex at the maximum. Apparently for the PdH complexes the capture radii are not decreasing with complex size, as was found for Pt doped samples. To explain the behavior of the PdH_2 depth profile in p-type samples we have to assume a much faster capture of H to PdH_1 than H to Pd. Only for small hydrogen concentrations, which occur at larger depth, the PdH_2 profile will follow the expected slope.

If we sum up the concentration of all electrically active Pd-defects we find in the range from 4 to 6 μm a concentration which is identical to the Pd concentration before wet-chemical etching. Below 4 μm the concentration of Pd-related centers decreases strongly towards the surface. Because all electrically active defects are included in this profile the decrease has to be due to the formation of an electrically passive PdH defect, which is only formed in the region with the highest hydrogen concentration. We therefore assume that the passive complex contains at least three, probably four hydrogen atoms.

4. Level scheme for the PdH-levels

Fig. 3 gives schematically the derived level positions for the different PdH_i complexes. A clear trend for the acceptor level is seen, which systematically is lowered with the addition of another hydrogen to the defect. This behavior can be expected from the simple vacancy model of the substitutional TMs. The t_2-level of the vacancy shifts towards the valence band for increasing nuclear charge [12]. Apparently, the addition of protons has the same effect as increasing the nuclear charge.

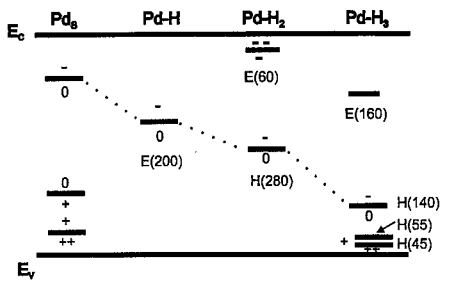

Fig. 3. Energy levels of the substitutional Pd and the PdH_i complexes.

5. Comparison with theoretical calculations

Recent calculations by Jones et al. [13] give for the PdH_1 complex an acceptor level at $E_C - 0.30$ eV in close agreement with E(200) at $E_C - 0.43$ eV. The acceptor level shifts weakly in the PdH_2 complex to $E_C - 0.36$ eV, which corresponds to H(280) at $E_V + 0.55$ eV. The acceptor level of PdH_3 was calculated at $E_C - 1.15$ eV compared to $E_C - 0.93$ eV for the H(140) level. Further agreement can be found for the double acceptor state of the PdH_3-complex: The calculated value of $E_C - 0.29$ eV could correspond to $E_C - 0.29$ eV of the E(160) level. From our experiments no assignment to a double donor state could be made.

There are, however, also some discrepancies between the theoretical results and our assignment of the levels. Jones et al. calculate a donor level for the PdH_1 complex at $E_V + 0.62$ eV. This level does not appear in our experiments. The proposed coincidence of this level with the level of the Pd donor ($Pd^{0/+}$) can be excluded from the identical profiles for the Pd-donor and double donor ($Pd^{0/+}$, $Pd^{++/+}$). The calculations give for the PdH_4 complex an acceptor and a donor level. No support is given from the calculation that a substitutional PdH defect is electrically passive. This strongly contradicts the measurements where an electrically inactive complex accounts for the missing concentration of all electrically active Pd-defects in the sample.

6. Conclusions

We have studied the interaction of hydrogen with substitutional Pd in Si. A careful investigation of the electrical properties of wet-chemically etched samples revealed seven new hydrogen-induced levels. From the analysis of the defect profiles we were able to correlate the new levels to Pd complexes which contain up to three hydrogen atoms. A neutral PdH complex is found to contain four hydrogen atoms. The behavior of the PdH complexes is very similar to PtH complexes, however, some refinements in the simple model of hydrogen defect

formation have to be included for the Pd-complexes. The trend of the energy levels with the number of hydrogen atoms in the complexes reflects the simple vacancy like structure of the complexes.

Acknowledgements

We thank M. Stavola and R. Jones for many helpful discussions and comments. We acknowledge the technical assistance and continuous help of W. Heinz and W. Krause.

References

[1] E.Ö. Sveinbjörnsson, O. Engström, Phys. Rev. B 52 (1995) 4884.
[2] T. Sadoh, H. Nakashima, T. Tsurushima, J. Appl. Phys. 72 (1992) 520.
[3] T. Sadoh, M. Watanabe, H. Nakashima, T. Tsurushima, J. Appl. Phys. 75 (1994) 3978.
[4] J.-U. Sachse, E.Ö. Sveinbjörnsson, W. Jost, J. Weber, H. Lemke, Appl. Phys. Lett. 70 (1997) 1584.
[5] J.-U. Sachse, E.Ö. Sveinbjörnsson, N. Yarykin, J. Weber, Mater. Sci. Eng. B 58 (1999) 134.
[6] N. Yarykin, J.-U. Sachse, H. Lemke, J. Weber, Phys. Rev. B 59 (1999) 5551.
[7] J.-U. Sachse, E.Ö. Sveinbjörnsson, W. Jost, J. Weber, H. Lemke, Phys. Rev. B 55 (1997) 16 176.
[8] J.-U. Sachse, J. Weber, E.Ö. Sveinbjörnsson, Phys. Rev. B 60 (1999) 1474.
[9] S.J. Pearton, E.E. Haller, J. Appl. Phys. 54 (1983) 3613.
[10] J.-U. Sachse, J. Weber, H. Lemke, Mater. Sci. Forum 258–263 (1997) 307.
[11] O.V. Feklisova, N.A. Yarykin, Semicond. Sci. Technol. 12 (1997) 742.
[12] G.D. Watkins, Physica 117B and 118B (1983) 9.
[13] R. Jones, A. Resende, S. Öberg, P.R. Briddon, Mater. Sci. Eng. B 58 (1999) 113.

ELSEVIER

Physica B 273–274 (1999) 433–436

PHYSICA B

www.elsevier.com/locate/physb

Deep level anomalies in silicon doped with radioactive Au atoms

J. Bollmann[a,*], S. Lindner[b], M.O. Henry[b], E. McGlynn[b], S. Knack[a], ISOLDE collaboration[c]

[a]*Max-Planck-Institut FKF, 800665, D-70506 Stuttgart, Germany*
[b]*Dublin City University, Dublin 9, Ireland*
[c]*CERN, CH-1211 Geneva, Switzerland*

Abstract

DLTS investigations on n- and p-type silicon samples implanted with various radioactive Hg isotopes which decay fully or partly through the series Au/Pt/(Ir) are reported. The deep Au-donor level at $E_v + 0.374(3)$ eV is observed in all cases. In p-type silicon its energy differs significantly ($E_v + 0.438(3)$ eV). Both Au and Pt are found to produce two acceptor levels in n-type material. An additional donor-like level at $E_v + 0.499(4)$ eV is shown to be due to Au. In all detected levels, one atom of Au or Pt is involved and the concentration decreases towards crystal surface. A key result is that, despite the presence of the Au donor in the samples, for all decay series involving Au to Pt conversion we have never observed the appearance of the Pt-donor.

PACS: 61.72.Ji; 61.72.Tt; 78.55.Ap; 81.05.Cy; 85.40.Ry

Keywords: Silicon; Defects; DLTS; 5d transition metals

1. Introduction

After some decades of intensive investigation of 5d noble metal impurity centres in silicon the details of electronic and optical properties of isolated Au and Pt atoms appear finally established [1,2]. However, the interpretation of combined electrical, optical and structural sensitive measurements give sometimes controversial results. The values quoted for energy positions, capture cross sections, IR absorption bands, PL features, etc., available in literature have various discrepancies indicating that Au and Pt do not produce a well-defined set of simple defects in silicon. Because 5d elements tend to be incorporated ionised and favour interstitial lattice position, they show a strong tendency to form complexes with trace metal impurities as well as with fast-diffusing contaminants like H, Li, Fe, Cu, etc. Frequently, the study of Au impurities involves the comparison with Pt defects because $Au^{(o)}$ and $Pt^{(-)}$ have the same electron configuration and show similar trends in the formation of defect complexes.

A unique method to examine these similarities is the use of radioactive isotopes of Au transforming to Pt within a suitable half-life [3]. Ion implantation in materials with high purification, perfection, and controlled trace contamination can ensure an adequate purity standard for such experiments.

2. Experimental

The samples used have been dislocation free floating zone refined phosphorus-doped n-type (1×10^{14} cm^{-3}) and boron-doped p-type (4.5×10^{14} cm^{-3}) silicon. Doping with radioactive atoms was carried out using the facilities of the isotope on-line separator ISOLDE at CERN. Bombardment of lead targets with GeV protons leads via spallation reactions to a broad spectrum of

* Corresponding author. Fax: + 49-0711-689-1602.
E-mail address: bollmann@kernix.mpi-stuttgart.mpg.de (J. Bollmann)

0921-4526/99/$ - see front matter
PII: S0921-4526(99)00498-6

proton enriched nuclei with somewhat lighter mass decaying into the stability region of nuclei. Of all the produced isotopes Hg can be most easily vaporised and ionised. A key feature of the ISOLDE facility is the high mass resolution (approximately 2000) achievable, which enables a single isotopic mass to be selected for implantation. Depending on the Hg isotope yield, implantation times from minutes up to 1 h give fluxes of $\sim 10^{12}\,cm^{-2}$ which are suitable limits for radiation safety considerations. In our experiments we find no evidence that for ^{193}Hg and ^{191}Hg implantation a significant fraction of stable Pt and Au or Ir is within the beam. X-ray spectroscopy measurements after implantation as well as after annealing give the amount, purity and loss of implanted unstable elements. The annealing and in-diffusion were carried out in quartz ampoules under He atmosphere (0.5 atm) at 950°C for 10 min and completed by dropping the ampoules into water or by slow cooling down with initial rates of about 1 K/s. Schottky contacts for electrical measurements were prepared by standard technology. For reference measurements we used contacts on a not implanted area of all our samples.

All measurements were carried out with a special DLTS set-up based on a fast capacitance meter with a signal frequency of 5 MHz and a modified lock-in filtering of transients in higher order. The resolvable emission rates are within the range 10^{-1}–$10^{5}\,s^{-1}$ and filling pulses as short as 10 ns can be applied. The detection of minority carrier traps was realised by pulsed backside illumination causing a diffusion of minorities up to sample front side, filling there the traps inside the space charge region.

To create deep level centres of 5d elements in silicon evaporation is commonly used followed by a long-term in-diffusion at temperatures approaching the melting point. The achieved bulk concentrations are limited by solubility and precipitation and the electrical activation depends on the application of controlled quenching procedures. Bulk densities of up to $10^{16}\,cm^{-3}$ for Au and $10^{17}\,cm^{-3}$ for Pt, resulting from the so-called "kick-out" diffusion mechanism (assumed to bring the atoms to rest on a substitutional lattice site), have been reported [4]. As little as one thousandth of a monolayer of surface contamination may create defect densities as high as $10^{14}\,cm^{-3}$ if distributed homogeneously throughout a sample with typical thickness. To ensure adequate conditions in our experiments far from solubility limits, we used mass separated ion beams for crystal doping. The disadvantage of generated radiation damage is overcome by annealing and diffusion at moderate temperatures and by studying regions far beyond the implanted layer.

The amplitude of the DLTS signal reflects directly the actual trap density and one can readily and accurately identify the kind and number of atoms involved in a defect from the known values of half-life [5,6].

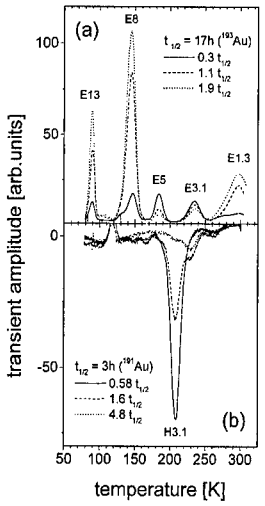

Fig. 1. Typical DLT-spectra of n-type silicon doped with radioactive ^{193}Au ($e_{n,p} = 500\,s^{-1}$) showing the evolution of deep level densities at different times after annealing. (a) majority carrier spectrum; (b) minority carrier spectrum generated by optical backside excitation.

The radioactive Hg isotopes used in this study decay according to the following series:

$$^{191}Hg \xrightarrow{50\ m} {}^{191}Au \xrightarrow{3.18\ h} {}^{191}Pt \xrightarrow{2.8\ d} {}^{191}Ir(\text{stable})$$

$$^{193}Hg \xrightarrow{11.8\ h} {}^{193}Hg \xrightarrow{17.65\ h} {}^{193}Pt(50\ y)$$

3. Results

For all samples, annealing treatments were carried out at a time when the Au content reached its maximum. In case of ^{191}Hg implants that means 3.5 h after beam stop, 55% of the implanted mercury has decayed to Au, 24% has already become Pt, but less than 0.2% is Ir. In the case of ^{193}Hg ions after 20 h the samples contain 40% Au and again 27% Pt. Since in practice virtually all mercury is lost from the samples during annealing, the time scale to fit time-dependent defect densities should begin with the annealing time.

3.1. n-type material

The starting material had a phosphorus concentration of $1 \times 10^{14}\,cm^{-3}$. Fig. 1(a) shows DLT spectra for ^{193}Hg recorded immediately after annealing and contact preparation (0.3 half-life after implantation) and after 1.1 and 1.9 half-life intervals. Two peaks labelled E5/E3.1 decrease at a rate in agreement with the ^{193}Au half-life, while concurrently three features labelled E13/E8/E1.3, clearly due to Pt, increase. We did not observe a mid-gap

Au acceptor level in the measurements. In all n-type samples studied, the Au donor appears as the dominant minority carrier trap decreasing in time as the Au population decreases, as shown in Fig. 1(b). Surprisingly, there is no evidence of the corresponding Pt donor level expected to be produced in the samples following the decay of Au. The in-depth profiles of the Au-related level E5 and the Pt-related level E8, obtained using double DLTS and shown in Fig. 2, are nearly identical in shape as expected if the Pt levels arise from the transmuting Au atoms. All profiles from deep levels of Au or related daughter Pt isotopes show a significant decrease of defect density towards crystal surface. A possible explanation would be, that Pt and Au atoms solved at high temperatures diffuses out at near-surface regions during slow cooling down.

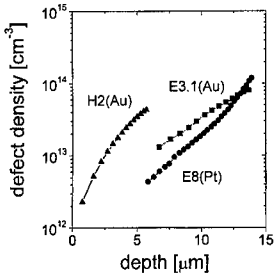

Fig. 2. In-depth distribution of Au- and Pt-correlated deep level centres in silicon detected by double correlation technique (DDLTS). Given defect densities are corrected to their maximum (Au) and to their final (Pt) concentration according to the decay series.

The densities given in Fig. 2 are corrected to their starting value (Au after annealing) or to the final concentrations (Pt after transmutation). It is obvious, that the observed Pt defects are of the same order of magnitude compared to the acceptor-like Au defects E5 and E3.1.

3.2. *p-type material*

The p-type starting material was boron-doped to a concentration of 4.5×10^{14} cm^{-3}. In Fig. 3 we show DLT spectra recorded for a sample implanted with ^{191}Hg for which the decay sequence is Au/Pt/Ir. The hole trap H3 decays away in accordance with the ^{191}Au half-life. The level marked H2 decays initially at this rate

Table 1
Summary of detected defect parameters of Au and Pt correlated deep level centres in silicon doped with radioactive Au isotopes. $e_{n,p} = S_n \exp(-\Delta E)$, $^{(*)}v_p^{dr}$ – drift velocity assumed to be 2.5×10^6 cm/s

Au-correlated deep centres in silicon					Detected in samples implanted with		
n-type silicon	E_T (eV)	S_n (10^{12} s^{-1})	C_n (10^{-8} cm^3 s^{-1})	C_p (10^{-8} cm^3 s^{-1})	^{191}Hg	^{193}Hg	Stable Au
E.31	$E_c - 0.490(10)$	20(6)	0.33(233 K)	—	X	X	X
	$E_c - 0.503(5)$	60(10)					
E5	$E_c - 0.385(1)$	18(1)	7(157 K)	—	X	X	X
H3.1	$E_v + 0.374(2)$	0.6(1)	—	$\approx 20^{(*)}$ (174 K)	X	X	X
p-type silicon							
H3.2	$E_v + 0.438(2)$	0.001	—	6(121 K)	X	X	X
H2	$E_v + 0.499(4)$	2.2(5)	—	0.08(262 K)	X	X	X
Pt-correlated deep centres in silicon					Detected in samples implanted with		
n-type silicon	E_T (eV)	S_n (10^{12} s^{-1})	C_n (10^{-8} cm^3 s^{-1})	C_p (10^{-8} cm^3 s^{-1})	^{191}Hg	^{193}Hg	Stable Pt
E1.3	$E_c - 0.58(1)$	4(2)	—	—	X	X	X
E3	$E_c - 0.516$	70(20)	3.3(182 K)	—	X	X	X
	$E_c - 0.432$	0.8(1)					
E8	$E_c - 0.281(1)$	10(1)	—	—	X		X
	$E_c - 0.248(2)$	1.6(1)	5(131 K)	—		X	
	$E_c - 0.243(8)$	0.8(1)				X	
	$E_c - 0.258(8)$	2.6(2)					
E13	$E_c - 0.165(1)$					X	
	$E_c - 0.151(1)$	30(3)	—	—	X		X
	$E_c - 0.153(2)$	3.6(1)	—	—	X		X

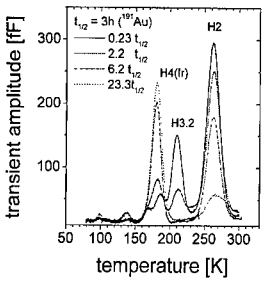

Fig. 3. Typical DLT-spectra of p-type silicon doped with radioactive ^{191}Au ($e_{n,p} = 500\,s^{-1}$) at different stages of radioactive transmutation.

also, but then more slowly, at an effective half-life value comparable to the Pt decay. The level H4 is attributed to Ir, the final product of the decay sequence. Profile measurements on level H2, shown in Fig. 2, reveal again that the defect densities increase with distance below the surface.

The parameters obtained for all observed traps are tabulated in Table 1 for the experiments described here and also for control experiments using stable Au and Pt implantations.

4. Discussion

The data for n-type material produce clear evidence for the deep Au donor attributed to substitutional Au atoms as a minority carrier trap. We have never observed any evidence of the growth of the corresponding Pt donor level in any of the samples implanted with radioactive Au. For our measurement system, this places an upper limit of $3 \times 10^{-10}\,cm^3s^{-1}$ on the hole capture coefficient of the Pt donor, a factor of 100 lower than the Au counterpart. This compares to factors of between 4 and 20 in the literature for the two cases [4]. We are forced to conclude either that the position of the Pt donor believed to be at $E_v + 0.348$ eV is incorrect or that the $E_v + 0.398$ eV level observed for Au is not due to the single substitutional Au centre.

In addition to the $E_v + 0.499(4)$ eV trap, we can also assign the levels at $E_c - 0.385(1)$ eV and $E_c - 0.503(5)$ eV to defects involving one Au atom. Similarly, only one Pt atom is involved in the $E_c - 0.248(5)$ eV and $E_c - 0.153(2)$ eV Pt-related levels. The absence of any Pt-related DLTS features immediately after annealing, despite the presence of Pt in the samples at roughly 50% of the Au concentrations, shows that the diffusion processes are markedly different in the two cases. Corroborative evidence for this has been obtained in experiments with stable isotopes.

5. Summary

DLTS measurements on silicon implanted with radioactive ions have enabled us to identify five defects due to Au, four due to Pt, and one additional hole trap due to Ir [5]. In all cases, only one Au/Pt/Ir atom is involved in the defects. The defects observed are likely to be due to the combination of trace impurities with the implanted species. We have observed the DLTS peak normally attributed to the substitutional Au donor, but the Pt counterpart, which is expected to grow in the samples to the same concentration, has never been observed in any measurement to date. This re-opens the question of the interpretation of DLTS spectra for Si : Au and Si : Pt.

References

[1] G.D. Watkins, P.M. Williams, Phys. Rev. B 52 (1995) 16575.
[2] G.D. Watkins, M. Kleverman, A. Thilderkvist, H.G. Grimmeiss, Phys. Rev. Lett. 67 (1991) 1149.
[3] J.W. Peterson, J. Nielson, Nucl. Instr. and Meth. B 63 (1992) 186.
[4] W. Schröter, M. Seibt, R Hull (Eds.), Properties of Crystalline Silicon, EMIS Datareviews Series No. 20, Short Run Press Ltd., Exeter, U.K.
[5] J. Bollmann, S. Lindner, E. Alves, J. Soares, C.A.J. Ammerlaan, M. Deicher, M. H. Knopf, R. Magerle, A. Stötzler, M. O. Henry, E. McGlynn, A. Burchard, D. Forkel-Wirth, M. Fanciulli, G. Weyer, ICPS-24, Jerusalem, 1998.
[6] M.O. Henry, E. Alves, J. Bollmann, A. Burchard, M. Deicher, M. Fanciulli, D. Forkel-Wirth, M.H. Knopf, S. Lindner, R. Magerle, E. McGlynn, K.G. McGuigan, J. Soares, A. Stötzler, G. Weyer, Phys. Stat. Sol. B 210 (1998) 853.

ELSEVIER

Physica B 273–274 (1999) 437–440

PHYSICA B

www.elsevier.com/locate/physb

Formation of copper precipitates in silicon

Christoph Flink*, Henning Feick, Scott A. McHugo[1], Amna Mohammed[1], Winfried Seifert, Henry Hieslmair, Thomas Heiser[2], Andrei A. Istratov, Eicke R. Weber

Department of Materials Science, University of California at Berkeley and Lawrence Berkeley National Laboratory, MS 62-203, Cyclotron Road, Berkeley, CA 94720, USA

Abstract

The formation of copper precipitates in silicon was studied after high-temperature intentional contamination of p- and n-type FZ and Cz-grown silicon and quench to room temperature. With the Transient Ion Drift (TID) technique on p-type silicon a critical Fermi level position at $E_C - 0.2$ eV was found. Only if the Fermi level position, which is determined by the concentrations of the acceptors and the copper donors, surpasses this critical value precipitation takes place. If the Fermi level is below this level the supersaturated interstitial copper diffuses out. An electrostatic precipitation model is introduced that correlates the observed precipitation behavior with the electrical activity of the copper precipitates as detected with Deep Level Transient Spectroscopy (DLTS) on n-type and with Minority Carrier Transient Spectroscopy (MCTS) on p-type silicon.

Keywords: Silicon; Copper; Precipitation formation

The reaction path of interstitial copper in silicon and the formation of copper precipitates in silicon are poorly understood. The use of copper interconnects in silicon integrated circuit technology, and the drastically increased danger of unintentionally contamination of the silicon substrates with copper has triggered new efforts to study the physical behavior of copper in silicon.

Interstitial copper is a single donor with a level close to or even in the conduction band [1]. Among all transition metals, copper has the highest solubility in the silicon lattice at elevated temperature [1,2]. While at room temperature the equilibrium concentration of interstitial copper drops to a negligible level, it remains highly mobile [3]. Most of the supersaturated interstitial copper follows one of two distinct reaction paths discussed in literature: out-diffusion to the surface and precipitation in the bulk. Transmission Electron Microscopy (TEM) studies demonstrate that after introduction of 10^{17}–10^{18} cm^{-3} of copper, most of the copper precipitates in the bulk upon cooling [4–6]. In n-type silicon it was found that after a fast quench the precipitates form plate-like defects throughout the bulk of presumably Cu_3Si. These defects introduce band-like states in the upper half of the band gap, as has been studied with Deep Level Transient Spectroscopy (DLTS) [6,7]. In contrast to silicon contaminated with very high copper concentrations, Total X-Ray Fluorescence (TXRF) studies on p-type silicon with copper contamination levels around 10^{13}–10^{15} cm^{-3} demonstrated complete out-diffusion of copper to the surface after both slow cool [8] and quench [9]. In this study we present the conditions under which the interstitial copper in p-type silicon diffuses out or precipitates. We propose an electrostatic model for the formation of copper precipitates in p- and n-type silicon based on the charge state of the copper precipitates.

We have investigated p-type dislocation free FZ and Cz-grown silicon with various doping concentrations after

* Corresponding author.

[1] At the Advanced Light Source (ALS) at the Lawrence Berkeley National Laboratory (LBNL), MS 2-400, 1 Cyclotron Rd., Berkeley, CA 94720, USA.

[2] Now at the Laboratore de Physique et Application des Semiconducteurs, CNRS, Universite Louis Pasteur, BP 20, F-67037, Strasbourg Cedex 02, France.

E-mail address: cflink@lbl.gov (C. Flink)

0921-4526/99/$ - see front matter
PII: S0921-4526(99)00499-8

intentional copper contamination of 10^{13}–10^{18} cm^{-3}. The in-diffusion process has been terminated by quenching the samples in ethylene glycol, silicon oil or 10% NaOH, resulting in cooling rates between 200 and 2000 K s^{-1}. Details of the sample preparation can be found elsewhere [10,11]. Interstitial copper concentrations in p-type silicon have been measured with the Transient Ion Drift (TID) technique. The electrical activity of the copper precipitates has been characterized with Deep Level Transient Spectroscopy (DLTS) in n-type silicon and with Minority Carrier Transient Spectroscopy (MCTS) in p-type silicon.

TID is a technique that measures interstitial copper concentrations in p-type silicon in the space charge region of a reverse biased Schottky diode. Despite the high diffusivity of interstitial copper even at room temperature [3], it has been shown that quenching rates above 100 K s^{-1} are sufficiently fast to keep the copper in the interstitial state after quench [11]. In our recent publication we have shown that TID monitors the interstitial copper concentrations diffusing out [12]. In the case of copper precipitation, the precipitation process takes place during or immediately after the quench, while the first TID measurement points can be taken 30 min after quench. Computer simulations of the out-diffusion kinetics, which include a boron and copper dependent effective diffusion coefficient of the interstitial copper, are in very good agreement with the TID results [12].

To demonstrate the conditions for out-diffusion and precipitation of the interstitial copper, in Fig. 1 we show the interstitial copper concentration as measured with TID 30 min after quench versus the Fermi level position at room temperature. Both, the concentration of shallow acceptors and the concentration of the mobile interstitial copper, which serves as a donor, determine the Fermi level position. Motivated by the fact that the interstitial copper concentrations measured with TID 30 min after quench could be found close to the solubility concentration at the in-diffusion temperature and did not depend on the quenching rate, the Fermi level position was calculated with the initial copper concentration at the in-diffusion temperature given in Ref. [2]. In Fig. 1 the results of three boron concentrations of 4×10^{14}, 4×10^{15} and 2×10^{16} cm^{-3} are presented. The TID results did not differ for FZ and Cz-grown silicon. For this reason we do

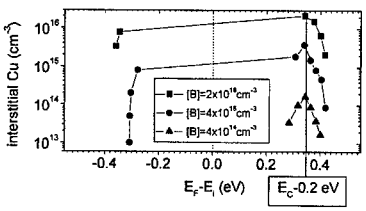

Fig. 1. Interstitial copper concentration as measured with TID 30 min after quench at room temperature vs. the Fermi level position immediately after quench.

not distinguish these parameters here. A lower and a higher copper contamination region can be recognized. These regions are divided by a critical Fermi level position at $E_C - 0.2$ eV. In the lower copper contamination region, out-diffusion is the dominant reaction path of the interstitial copper and the interstitial copper concentrations measured with TID follow the solubility concentration of the copper at the in-diffusion temperature, i.e., they increase with an increasing Fermi level position. Because the measurement volume of the TID technique is within the first microns of the near surface region, the interstitial copper concentrations measured with TID depend on the slope of the out-diffusion profile, i.e., on the effective diffusion coefficient. Consequently, for the lower-doped sample, the interstitial copper concentrations can be orders of magnitude higher in the bulk than measured within the surface near region. If the interstitial copper concentration exceeds the acceptor concentration, the Fermi level position rises above the intrinsic level and the conductivity type changes from p- to n-type. This is, however, not sufficient to change the precipitation behavior of copper. Only when the Fermi level position surpasses the critical value of $E_C - 0.2$ eV the copper precipitates, and the interstitial copper concentrations decrease drastically with increasing copper contamination.

Such precipitation behavior of copper in p-type silicon is confirmed by synchrotron based X-Ray Fluorescence (XRF) measurements. With XRF on silicon with 2×10^{16} boron atoms per cm^3, we have detected bulk concentrations of precipitated copper that equal the solubility concentration of copper at the in-diffusion temperature only if the copper contamination was high enough to drive the Fermi level position above $E_C - 0.2$ eV. If the Fermi level is below this critical value no precipitated copper was detected, indicating that the copper has diffused out.

Due to the fact that TID can only be applied to p-type silicon and that no DLTS level of the interstitial copper has been found, no direct measurment method is available to detect low concentrations of interstitial copper in n-type silicon. Resistance measurements that take advantage of the donor nature of the interstitial copper can only measure interstitial copper concentrations above or in the range of the doping concentration of the uncontaminated wafer. Utilizing resistance measurements we have not found any clear evidence of the presence of low concentration of interstitial copper in n-type silicon after in-diffusion and quench. Shabani et al. [8] have reported that in contrast to p-type silicon, in n-type silicon with a doping concentration in the range of 10^{15} cm^{-3} after copper in-diffusion of about 10^{15} cm^{-3} and slow cool with TXRF, they could not detect any interstitial copper diffusing to the surface. Only when they increased the temperature of the sample to 200°C they saw the copper coming to the surface. This suggests that in n-type silicon

the copper precipitates even if the Fermi level position is below the critical level of $E_C - 0.2$ eV, as found for p-type silicon. In n-type silicon this level corresponds to a total donor concentration of 1×10^{16} cm^{-3}.

Concentrations of precipitated copper above 10^{16} cm^{-3} can be detected with synchrotron based XRF. For such high copper contamination in n-type silicon after quench it is found that the amount of precipitated copper follows the solubility concentration of copper at the in-diffusion temperature. Despite the differences in the precipitation behavior of copper in p- and n-type silicon, we have found that the morphology of the copper precipitates is identical. As has been reported in literature previously for n-type silicon [6,7], in p-type silicon with cooling rates larger than 100 Ks^{-1} the precipitates form plate-like defects throughout the bulk of presumably Cu_3Si, mainly on the {111} habit planes. Their size, density, and their morphology depend on the quenching rate.

To further investigate the formation of the copper precipitates we measured the electronic properties of the copper precipitates with DLTS on n-type and with MCTS on p-type silicon. In both cases we detect the electronic levels in the upper half of the band gap. Fig. 2 shows DLTS spectra, taken with a rate window of 250 ms, of Cz-grown silicon doped with phosphorus of 2×10^{15} cm^{-3} and with initial copper concentrations between 5×10^{14} and 1×10^{16} cm^{-3}, after quench in ethylene glycol. The spectra reveal the development of the band-like states of the copper precipitates with increasing copper contamination. The defect band between 50 and 225 K is well known in literature and is associated with the electronic properties of the copper precipitates between about $E_C - 0.15$ eV and $E_C - 0.35$ eV [6,7]. However, for a copper contamination of 1×10^{16} cm^{-3} we see that the defect band is split into two peaks separated at about $E_C - 0.2$ eV. Fig. 3 shows MCTS spectra, taken with a rate window of 250 msec, of FZ silicon doped with boron of 4×0^{14} cm^{-3} and with initial copper concentrations between 5×10^{15} and 2×10^{16} cm^{-3}, after quench in ethylene glycol. The critical Fermi level position of $E_C - 0.2$ eV for such a low doped sample equals a copper contamination of 1×10^{16} cm^{-3}. The spectrum with a copper contamination above this critical concentration for the formation of copper precipitates shows a strong similarity with the electrical activity found with DLTS for n-type silicon in Fig. 2. The peaks between 50 and 100 K and between 100 and 225 K are observed. Decreasing the initial copper concentration below the critical contamination level shows a much less developed spectrum, and the low temperature peak can not be observed. Because most of the copper has diffused out under this condition, see Fig. 1, we account the electrical activity of this sample to the copper precipitate embryos. With a copper contamination around the critical concentration, i.e., with a copper contamination of 1×10^{16} cm^{-3}, the MCTS spectrum reveals that the high-temperature peak has not developed yet its full width and structure, while the low-temperature peak is disclosed. Obviously, the precipitates undergo a transition from the embryo-state to the fully developed copper precipitates, which are observed with TEM for high copper contamination. From Fig. 2, at this stage of our research, the conditions for the transition of the copper precipitates from the embryo-state to their full development in n-type silicon cannot be decided unambiguously. We note that the shape of the spectra of the copper precipitates in n- and p-type show similar peaks, while the temperature range of those in n-type silicon are slightly shifted to higher temperatures as compared to p-type silicon.

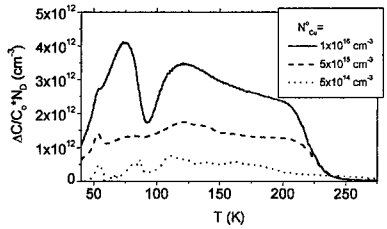

Fig. 2. DLTS spectra of n-type silicon with 2×10^{15} cm^{-3} doping for varying initial copper contamination.

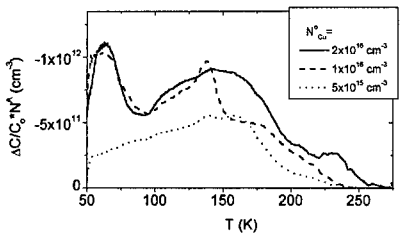

Fig. 3. MCTS spectra of p-type silicon with 4×10^{14} cm^{-3} doping for varying initial copper contamination.

Due to the fast internal electronic transitions of band-like states, the defect bands of the copper precipitates can be described by a quasi-Fermi distribution [6,7]. Correlation of DLTS spectra of the high-temperature defect band in n-type silicon with computer simulations suggests that the copper precipitates are amphoteric in nature. The simulations of the DLTS spectra could be fitted successfully if the band-like states in n-type silicon were defined between $E_C - 0.15$ eV and $E_C - 0.35$ eV with a neutrality occupation level at about $E_C - 0.2$ eV. Remarkably, this neutrality occupation level corresponds to the critical Fermi level position at about $E_C - 0.2$ eV, as found for copper precipitates in p-type silicon in Fig. 1. This enables us to put forward the model that the precipitation of copper is determined by the electrostatic interaction between the positively charged copper ions and

the copper precipitates. The precipitates are positively charged if the Fermi level is below their neutrality level and Coulomb repulsion will retard precipitation. If the Fermi level rises above the critical level of $E_C - 0.2$ eV, the precipitates become neutral or negatively charged and precipitation can occur uninhibitedly. As the copper precipitates, the interstitial copper concentration decreases and eventually the Fermi level drops below its critical value, resulting in positively charged precipitates, and the precipitation process slows down drastically.

This model explains consistently the obtained data of the formation of copper precipitates in p-type silicon. With MCTS the electronic properties of the embryos, as well as of the fully developed copper precipitates could be found. As a consequence, we would expect that copper precipitates completely and independently of the contamination level in n-type silicon with a doping concentration of at least 1×10^{16} cm^{-3}. This copper contamination level corresponds to a Fermi level position at room temperature of $E_C - 0.2$ eV, and must be understood as an upper limit of a critical Fermi level position. The reason why copper precipitates in n-type silicon with a doping concentration in the range of 10^{15} cm^{-3} [8] could be due to the slight shift to higher temperatures of the defect bands of the precipitates in n-type silicon. Such a shift could correspond to a lower critical Fermi level position in n-type silicon, and thus to a lower doping concentration needed to exceed this critical level.

Acknowledgements

The authors are very grateful to G. Nimtz of the University of Cologne, Germany, for his support. The use of experimental facilities at the Lawrence Berkeley National Laboratory, which is funded through the DOE, is acknowledged. This work was supported by Si-WEDS consortium, which is supported by the NSF, and by NREL, which is funded through the DOE, under Contract No. XAF-8-17607-04.

References

[1] R.H. Hall, J.H. Racette, J. Appl. Phys. 35 (1964) 379.
[2] E.R. Weber, Appl. Phys. A 30 (1983) 1.
[3] A.A. Istratov, C. Flink, H. Hieslmair, E.R. Weber, T. Heiser, Phys. Rev. Lett. 81 (1998) 1243.
[4] K. Graff, Metal Impurities in Silicon-Device Fabrication, Springer, Berlin, 1995.
[5] M. Seibt, M. Griess, A.A. Istratov, H. Hedemann, A. Sattler, W. Schroeter, Phys. Stat. Sol. A 166 (1998) 171.
[6] M. Seibt, H. Hedemann, A.A. Istratov, F. Riedel, A. Sattler, W. Schroeter, Phys. Stat. Sol. A 171 (1999) 301.
[7] A.A. Istratov, H. Hedemann, M. Seibt, O.F. Vyvenko, W. Schroeter, T. Heiser, C. Flink, H. Hieslmair, E.R. Weber, J. Electrochem. Soc. 145 (1998) 3889.
[8] M.B. Shabani, T. Yoshimi, H. Abe, J. Electrochem. Soc. 143 (1996) 2025.
[9] C. McCarthy, M. Miyazaki, H. Horie, S. Okamoto, H Tsuya, in: H.R. Huff, H. Tsuya, U. Goesele (Eds.), Semiconductor Silicon-1998, The Electrochem. Soc., Pennington, NJ, 1998, p. 629.
[10] T. Heiser, E.R. Weber, Phys. Rev. B 58 (1998) 3893.
[11] T. Heiser, S. McHugo, H. Hieslmair, E.R. Weber, Appl. Phys. Lett. 70 (1997) 3576.
[12] C. Flink, to be published.

ELSEVIER

Physica B 273–274 (1999) 441–444

PHYSICA B

www.elsevier.com/locate/physb

Experiments and computer simulations of iron profiles in p/p^+ silicon: segregation and the position of the iron donor level

H. Hieslmair*, A.A. Istratov, C. Flink, S.A. McHugo, E.R. Weber

Lawrence Berkeley National Laboratories and the Materials Science Department, University of California at Berkeley, MS 7-222, 1 Cyclotron Road, Berkeley, CA 94720, USA

Abstract

The position of the iron donor trap level in the silicon band gap at processing temperatures determines numerous important properties of iron such as its solubility and effective diffusivity. Thus this position influences the time and efficiency of the widely used p/p^+ segregation gettering, i.e. the removal of iron from an epitaxial p-type silicon layer (the device region) by a heavily p^+-doped silicon substrate. In this work, the iron concentration profiles within a 70 μm p-type epitaxial layer on a p^+-type substrate were quantitatively measured using deep level transient spectroscopy in order to determine the position of the iron donor level. The samples are first intentionally contaminated with iron at 920°C and then annealed at 472°C for various times. The measured iron profiles are fitted with computer simulations in order to determine the iron trap level and the segregation coefficient at 472°C. The results indicate that the iron trap level is at Ev + 0.32 eV at 472°C. The results of this study and of previous studies indicate that the iron donor level decreases in proportion to the band-gap narrowing.

Keywords: Iron; Donor level; Heavily doped silicon; Segregation

Utilization of a moderately p-doped epitaxial layer on a heavily p-doped substrate helps to prevent the "latch-up" problem in CMOS devices [1]. There is an additional benefit of gettering iron out of the epitaxial layer and into the substrate. The equilibrium solubility concentration of iron has been shown to increase with the doping level in p-type silicon [2–4]. The enhanced solubility of iron in a heavily doped substrate [2] with respect to a moderately doped epitaxial layer is the fundamental driving force for this segregation gettering [5–8]. While the segregation effect is most significant in the 300–650° temperature range, the exact position of the iron donor level in the silicon band gap has a large influence on the magnitude of the segregation and the effective diffusivity of iron during semiconductor processing.

The general approach in this work is to experimentally measure iron concentration profiles in a 70 μm p-type epitaxial layer on a p^+ substrate, and then fit these profiles using computer simulations in order to determine the position of the iron trap level at 472°C. The samples were prepared by growing a 100 nm oxide on p/p^+ (1.8×10^{15} B/cm^{-3}/4.5×10^{18} B/cm^{-3}) silicon samples to avoid out-diffusion of the iron to the frontside. The oxide was removed from the backside of the samples (p^+) using a plasma etch and iron was scratched on the bare backside. The samples were then annealed at a high temperature (≈ 920°C) where the segregation between the p and p^+ material is minimal, followed by a quench in silicon oil. These samples were then annealed at a lower temperature of 472°C, where segregation is significant, for various times. The iron concentration was measured using deep level transient spectroscopy (DLTS). The magnitude of the iron–boron peak was measured after the samples were given time for the iron to pair with boron. After each DLTS measurement, the samples were chemically etched and new diodes were evaporated. The results of these experiments are shown by the symbols in Fig. 1. The lines are from computer simulations. In order to fit the experimental results using computer simulations, the following expressions for the iron solubility and effective diffusivity were used.

* Corresponding author.
E-mail address: hhiesl@argon.berkeley.edu (H. Hieslmair)

0921-4526/99/$ - see front matter
PII: S0921-4526(99)00500-1

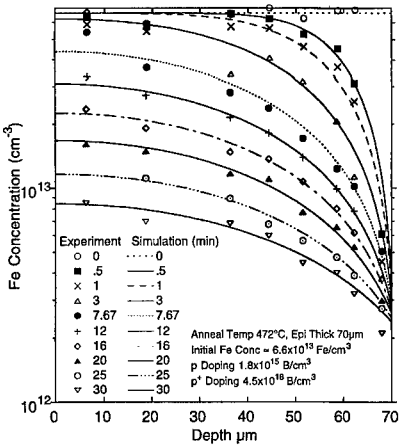

Fig. 1. The experimental data (symbols) and the computer simulations (lines) are shown and make a satisfactory fit.

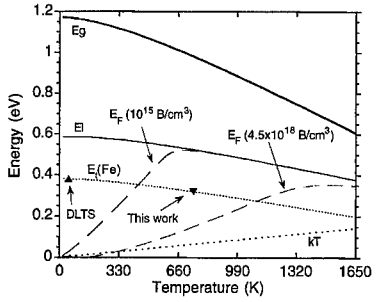

Fig. 2. Schematic of the energy levels in silicon with respect to the valance band. The iron trap level, E_t(Fe), is shown as proportional to the band-gap shrinkage. Additionally, the Fermi levels of a p (10^{15} B/cm^3) and a p$^+$ (4.5×10^{18} B/cm^3) are also shown.

The segregation coefficient for iron in a p/p$^+$ structure is simply defined as the ratio of the total equilibrium iron concentration in the p region to the p$^+$ region. The total iron concentration consists of three separate species, neutral interstitial iron, Fe^0, interstitial ionized iron, Fe^+, and iron paired with an acceptor such as boron, FeB. Fe^0 is the species which is in actual equilibrium with the boundary phase $FeSi_2$. The amount of each iron species present depends on the equilibrium reactions,

$$[Fe_i^0]_{FeSi_2} \leftrightarrow [Fe_i^0]_{Si} \leftrightarrow [Fe_i^+]_{Si} \leftrightarrow [Fe^+B^-]_{Si},$$

$$i = \text{interstitial.} \tag{1}$$

In a recent review, Istratov et al. [9] showed the best expression for the equilibrium iron concentration in *intrinsic* silicon to be

$$C_{Fe}^{eq} = C_0 e^{-E_f/kT}, \quad C_0 = 8.4\times10^{25}, \quad E_f = 2.86\,\text{eV} \tag{2}$$

additionally,

$$\frac{[Fe^+]}{[Fe^0]} = \frac{1}{2} e^{(E_i - E_F)/kT} \tag{3}$$

and [10,11]

$$\frac{[FeB]}{[Fe^+]} = [B^-]\frac{4}{5\times10^{22}} e^{0.65/kT}. \tag{4}$$

In the case of intrinsic silicon, Eq. (2) the boron concentration is low, i.e. [FeB] ≈ 0, and the total iron is interstitial in either the positive or neutral state depending on the temperature and where the iron trap level actually is (Eq. (3)). For doped material, the concentration of the neutral interstitial iron is the same as that of the intrinsic silicon since the first step of Eq. (1), $[Fe_i^0]_{FeSi_2} \leftrightarrow [Fe_i^0]_{Si}$, does not depend upon doping. However Fe_i^+ and FeB concentrations increase in p-doped materials. In the computer simulations in this work, the following procedure was used to calculate solubilities in doped materials, (a) an iron trap level was chosen (for Eq. (3)), (b) the neutral iron concentration in intrinsic silicon was calculated (from Eqs. (2) and (3)), (c) the positively charged iron concentration for the p-doped materials was calculated from the intrinsic neutral iron concentration (from b and Eq. (3)), (d) the paired iron concentration is determined from the positively charge iron concentration (using c and Eq. (4)). The computer simulation was run and the iron trap level was adjusted until a good match between the simulations and the experimental results was obtained.

From the above discussion, one can see that the total iron segregation behavior depends on the Fermi level and iron trap level which are both temperature dependent. At high temperatures, the narrowing of the silicon band gap must also be taken into account and is given by Thurmond [12] as

$$E_g = E_g^0 - \frac{AT^2}{B+T}, \quad A = 4.73\times10^{-4}, \quad B = 635,$$

$$E_g^0 = 1.17\,\text{eV}. \tag{5}$$

Standard equations for the intrinsic level, Fermi level, and density of states were used to determine the Fermi levels in p and p + materials as a function of temperature and are shown in Fig. 2. The iron trap level shown, proportionally follows the narrowing of the band gap.

In order to accurately simulate the iron concentration profiles, the effective diffusivity of iron in p + materials must be calculated from $D_{total}^{eff} = (N_{Fe^+})D_{Fe^+}^{eff} + (N_{Fe^0})D_{Fe^0}$. The effective diffusivity of positively charged iron, for [Fe]$\ll$[B], depends upon the concentration of boron as [13]

$$D_{Fe^+}^{eff} \approx \frac{D_{Fe^+}^{int}}{1+\Omega[B]}, \tag{6}$$

where

$$\Omega = \frac{\tau_c^{-1}}{[B] \times \tau_{diss}^{-1}} = \frac{4\pi D_{Fe^+}^{int} R_c}{\tau_{diss}^{-1}}. \quad (7)$$

There have been various reports of values for D_{Fe^0} and $D_{Fe^+}^{int}$. Istratov et al. [9] showed that a single line could be fit through the literature data for both low- ($D_{Fe^+}^{int}$) and high-temperature studies (D_{Fe^0}). Thus, in these simulations, we used 0.67 eV for E_m of both D_{Fe^0} and $D_{Fe^+}^{int}$. In Eq. (7), one can see that the dissociation time constant of FeB pairs needs to be known. We have determined the dissociation time constant of the iron–boron pairs and details are published elsewhere (see Ref. [14]). The dissociation rate of iron–boron was measured using SPV by monitoring the decrease of the minority carrier diffusion length as iron dissociated from boron. The resulting expression for the dissociation of FeB is $\tau_{diss} = 9.35 \times 10^{-16} e^{1.40/kT}$.

The experimental results and computer simulations are shown in Fig. 1. The computer simulation fits are satisfactory and indicate an Fe 0/+ trap level at 0.32 ± 0.02 eV at 472°C. The 0.32 level coincides with the proportional curve (E_{trap}) in Fig. 2. Thus, from this result, it appears that the iron donor level moves toward the valance band in proportion with the band-gap shrinkage. The proportional temperature dependence closely predicts the high-temperature solubility data obtained by McHugo et al. [4]. The total iron solubility data obtained by McHugo are shown in Fig. 3 (squares) with the iron solubility predicted by this model (circles). However, the dependence of the iron solubility on the position of the iron trap level at such high temperatures is very weak, and thus it is difficult to determine the trap level from such solubility measurements. For example, a change of 0.2 eV in the iron trap level results in a solubility change of less than 25% at 1100°C, and approximately 60% at 800°C assuming a doping concentration of 1.5×10^{18} B/cm^3.

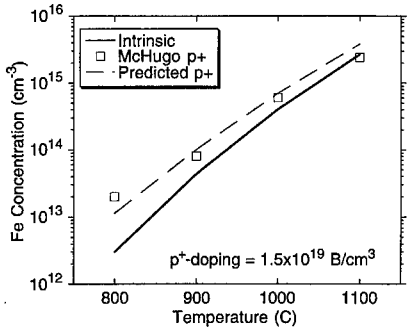

Fig. 3. The high-temperature solubility data from McHugo et al. [4] and the predicted iron solubility based on the proportional temperature dependence of the iron trap level. The predicted values match the experimentally obtained values well.

The total iron concentration in silicon is given as $Fe_{tot} = Fe_i^0 + Fe_i^+ + Fe^+B^-$. The intrinsic neutral iron concentration, assuming the iron trap level is proportional to the band gap, is slightly less than the total intrinsic iron solubility and is given as $[Fe^0] = 7.58 \times 10^{25} \exp(-2.85/kT)$. The total iron concentration in boron-doped materials can then be calculated as

$$[Fe_{tot}] \cong (7.58 \times 10^{25} e^{(-2.85/kT)}) \left[(1 + \tfrac{1}{2} e^{(E_i - E_f)/kT}) \times \left(1 + [B^-] \frac{4}{5 \times 10^{22}} e^{0.65/kT}\right)\right]. \quad (8)$$

There are numerous possible sources of error in this work, either from the experimental error or from the values used in the computer simulations. For example, the intrinsic diffusivity of iron is assumed to be the same for neutral and positively charged iron. Clearly, the two values are not expected to be the same, yet the empirical fit of the literature data described by Istratov et al. [9] may well describe the diffusivity of iron in both states, or it may be the case that the diffusing species is always the Fe_i^+ species. The dissociation energy of FeB pairs may also be revised in the future as different techniques and approaches are used to measure this value, and as the definition of "dissociated" versus "associated" FeB itself, becomes clarified. Additionally, band-gap narrowing due to heavy doping was not taken into account. On the experimental side, the repeated etchings resulted in a non-smooth surface which increases the uncertainty in depth. This uncertainty becomes more pronounced near the p/p^+ junction and is not the same for each sample. Thus additional experiments are underway at different temperatures to try to obtain better profiles and conclusively determine the iron trap level from 400°C to 650°C. It is not expected, however, that these new experiments will result in a large deviation from the 0.32 eV level determined by this work. With this temperature dependence of the iron trap level, the effective diffusivity and segregation behavior of iron can be simulated. Such simulations are useful in optimizing semiconductor processes to maximize gettering of iron.

The use of the experimental facilities at the Lawrence Berkeley National Laboratories is acknowledged. This work was supported by the Silicon Wafer Engineering and Defect Science (SiWEDS) consortium and by the National Renewable Energy Laboratory (NREL) under Contract No. XAF-8-17607-04.

References

[1] R.R. Troutman, IEEE Electron Dev. Lett. EDL-4 (1983) 438.
[2] D. Gilles, W. Schröter, W. Bergholz, Phys. Rev. B 41 (1990) 5770.

[3] S.A. McHugo, R.J. McDonald, A.R. Smith, D.L. Hurley, A.A. Istratov, H. Hieslmair, E.R. Weber, Defect and Impurity Engineered Semiconductors and Devices II, Vol. 510, 1998, in print
[4] S.A. McHugo, R.J. McDonald, A.R. Smith, D.L. Hurley, E.R. Weber, Appl. Phys. Lett. 73 (1998) 1424.
[5] J.L. Benton, P.A. Stolk, D.J. Eaglesham, D.C. Jacobsen, J.-Y. Cheng, J.M. Poate, N.T. Ha, T.E. Haynes, S.M. Myers, J. Appl. Phys. 80 (1996) 3275.
[6] P.A. Stolk, J.L. Benton, D.J. Eaglesham, D.C. Jacobson, J.-Y. Cheng, J.M. Poate, S.M. Myers, T.E. Haynes, Appl. Phys. Lett. 68 (1996) 51.
[7] M. Sano, S. Sumita, T. Shigematsu, N. Fujino, in: H.R. Huff, W. Bergholz, K. Sumino (Eds.), Semiconductor Silicon 1994, The Electrochemical Society, Pennington, NJ, 1994, p. 784.
[8] Y. Hayamizu, S. Tobe, H. Takeno, Y. Kitagawara, in: H. Huff, U. Gösele, H. Tsuya (Eds.), Semiconductor Silicon — 1998, The Electrochemical Society, Pennington, NJ, 1998, p. 1080.
[9] A. Istratov, H. Hieslmair, E.R. Weber, Appl. Phys. A 69 (1999) 13.
[10] H. Lemke, Phys. Stat. Sol. A 76 (1983) 223.
[11] L.C. Kimerling, J.L. Benton, Physica 116B (1983) 297.
[12] C.D. Thurmond, J. Electrochem. Soc. 122 (1975) 1133.
[13] H. Reiss, C.S. Fuller, F.J. Morin, Bell Systems Tech. J. 35 (1956) 535.
[14] H. Hieslmair, A. Istratov, H. Kohno, C. Flink, E.R. Weber, to be published.

ELSEVIER

Physica B 273–274 (1999) 445–448

PHYSICA B

www.elsevier.com/locate/physb

ESR study of Fe–H complexes in Si

Toru Takahashi*, Masashi Suezawa

Institute for Materials Research, Tohoku University, Sendai 980-8577, Japan

Abstract

We studied the influence of hydrogen (H) on the properties of Fe in Si crystals based on ESR measurement. Specimens were prepared from an n-type Si crystal (phosphorus concentration; 1.5×10^{16} cm^{-3}). After chemical polishing, they were doped with ^{57}Fe by a vapor method and with H by annealing in H_2 gas followed by quenching. ESR spectra were measured at 10 K by an X-band spectrometer. Two and three ESR lines were observed in specimens doped with ^{57}Fe and co-doped with ^{57}Fe and H, respectively. We interpreted the latter to be due to a ^{57}Fe–H complex. Due to isochronal annealing, the ^{57}Fe–H complex disappeared at around 220°C. From the results of the isothermal annealing experiment, the binding energy of ^{57}Fe–H complex was determined to be about 1.3 eV. The temperature dependence of the total concentration of Fe, namely, the sum of the concentrations of isolated Fe and the Fe–H complex, was 1.9 eV, which is smaller than that without H by about 1 eV.

Keywords: Si; Fe; H; ESR

1. Introduction

Hydrogen (H) is one of the impurities which easily enters Si crystals. It is chemically active and forms pairs and complexes with other impurities and defects, resulting in the modification of their electrical properties. Research related to H in semiconductors has been actively performed since Pankove et al.'s pioneering study [1] on the hydrogen passivation of B in Si.

We are interested in the interaction between H and transition metal (TM) impurities in Si. We herein briefly review studies on TM–H complexes in Si. Properties of TM and TM–H complexes have been investigated based on the measurements of DLTS, ESR, optical absorption and so on [2,3]. Among TM-related complexes, TM which occupies substitutional sites, for example, Pt and Au, has been investigated most extensively. From the measurement of DLTS spectra, TM-H complexes are known to have different energy levels from those of isolated TM [4,5]. From the measurement of ESR spectra, they are known to have different symmetries from those of isolated TM. How about Fe which occupies an interstitial site? Fe easily enters Si during various processes and is a harmful impurity for Si devices. It is important to know the properties of the Fe–H complex since it may be possible to passivate Fe by H. Its energy level is known to shift by forming a complex with H [6]. Their detailed properties, however, have not been investigated.

We studied some properties of the Fe–H complex from the measurement of its ESR spectra. The ESR method is a non-contact method which enables systematic study of the same specimen, a necessity when investigating the thermal stability of complexes.

2. Experimental

The Si crystal used in this experiment was grown by the floating-zone growth method. The phosphorus concentration was 1.5×10^{16} cm^{-3}. We did not use p-type Si since the concentration of H reacting with Fe probably becomes small because of B–H pair formation. After cutting out parallelpiped-shaped specimens, $3 \times 3 \times 12$ mm^3, the longest side of which was parallel to the [0 1 1] direction, from the above crystal, we shaped and polished them mechanically and chemically with

* Corresponding author. Tel.: + 81-22-215-2043; fax: + 81-22-215-2041.

E-mail address: toru@imr.tohoku.ac.jp (T. Takahashi)

0921-4526/99/$ - see front matter
PII: S0921-4526(99)00501-3

carborundum and a mixed solution of HNO_3 : HF = 5 : 1, respectively. We doped the specimens with ^{57}Fe by a vapor method, namely, we sealed specimens in evacuated quartz capsules together with pieces of ^{57}Fe (purity: 95.73 at%) foil. We then annealed them at high temperatures, between 950°C and 1250°C, for appropriate durations estimated from the diffusion constant of Fe, followed by quenching in iced water. We used ^{57}Fe to avoid confusion due to possible ^{56}Fe-contamination during high-temperature annealing. Next, we doped H by annealing specimens at the Fe-doping temperature in H_2 gas (1.5 atm) followed by quenching. After quenching, we kept specimens in liquid nitrogen till measurement since Fe and H are known to diffuse at room temperature but not at 77 K. We measured the ESR spectra by an X-band spectrometer at 10 K to determine the concentrations of Fe and the Fe–H complex separately. The modulation magnetic field was 0.08 mT.

3. Results and discussion

3.1. The ESR spectrum of Fe–H complex

Fig. 1 shows the ESR spectra of a ^{57}Fe-doped specimen (spectrum (a)) and a ^{57}Fe and H co-doped specimen (spectrum (b)). They were doped at 1250°C followed by quenching. The microwave frequency was about 9.068 GHz. As shown in Fig. 1, two ESR peaks were observed when the specimen was doped with only ^{57}Fe. This is due to the hyperfine interaction between the electron spin and the nuclear spin, $\frac{1}{2}$, of ^{57}Fe. On the other hand, three peaks were observed after ^{57}Fe and H co-doping. Two of these peaks, outer peaks, coincide with those of isolated ^{57}Fe as shown in Fig. 1(a). There are four possible explanations for this spectrum. The first and second possibilities are that the two outer peaks are due to isolated ^{57}Fe and the central peak is of different origin, namely, ^{56}Fe and an Fe–H complex, respectively. The third is that all three peaks are due to an Fe–H complex. The fourth possiblity is that the two outer peaks overlap the spectra due to ^{57}Fe, and the ^{57}Fe–H complex and that

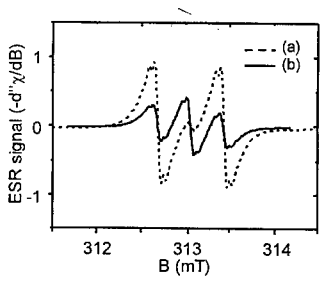

Fig. 1. ESR spectra around 313 mT of ^{57}Fe-doped (dashed line) and ^{57}Fe and H co-doped (solid line) specimens. The applied magnetic field was parallel to ⟨1 1 0⟩.

the central peak is due to ^{57}Fe–H complex. The first possibility seems not to be the case since the central peak was observed only when the specimen was co-doped with H. This result indicates that the contamination due to Fe (mainly ^{56}Fe, since its natural abundance is 91.7%) was very small in our experiment. To investigate the second, third and fourth possibilities, we doped Fe and H at various temperatures. The relative intensity of the central and outer peaks depended on the doping temperature. This strongly supports the fourth possibility that the observed signal is the overlap of spectra due to the isolated ^{57}Fe and ^{57}Fe–H complex, taking into account the result of isochronal annealing which is presented in Section 3.2.

One peculiar point of the ^{57}Fe–H complex is its symmetry. Usually the symmetry of a TM–H complex is different from that of an isolated TM, for example, Pt–H_2 [2]. On the other hand, in the case of the Fe–H complex, its ESR signal was isotropic indicating T_d symmetry. This suggests that Fe in the Fe–H complex also occupies an interstitial site having T_d symmetry as an isolated Fe. One possibility for T_d symmetry is the high jumping rate of H at equivalent positions around the Fe atom. If this is the case, the jumping rate of H should be much greater than 10^{10} s^{-1}, which is the microwave frequency. Assuming a thermally activated H jump, $\nu \exp(-E/kT)$, and the magnitude of pre-exponential factor (ν) of H jump to be 10^{13} s^{-1}, the activation energy (E) is estimated to be smaller than 1.1 meV, which seems too small to be realized. Hence, we do not have a clear explanation for the isotropic signal of Fe–H complex. Another peculiar point is the number of ESR peaks. The H atom has $\frac{1}{2}$ of nuclear spin. We thus expect many ESR lines when ^{57}Fe and H form a complex. If an Fe–H pair is formed, for example, the number of ESR lines is expected to be 4, contrary to the experimental result of 3. If the interaction between the electron spin and nuclear spin of H is very weak, the splitting should be small. There may be line broadening instead of splitting. However, we did not detect any change of line width (around 0.08 mT) due to the Fe–H complex. We do not have any plausible explanations for line number 3 of the Fe–H complex.

There are two ways to determine the number of H atoms included in TM–H complexes. One is to observe the number of ESR lines. The other is to observe splitting of optical absorption peaks due to co-doping with H and deuterium. We did not succeed in the former as shown above. We also tried to observe optical absorption due to H included in the Fe–H complex and failed. Hence, we could not determine the number of H included in the Fe–H complex.

3.2. Thermal properties of Fe–H complex

To determine the thermal stability of the Fe–H complex, we first performed an isochronal annealing

experiment. The annealing period was 10 min at each temperature. Fig. 2 shows the results of this experiment after H and Fe co-doping at 1250°C. As described in Section 3.1, our tentative interpretation was that the observed signal was the overlap of those of isolated Fe and the Fe–H complex. According to this interpretation, the central peak correponds to Fe–H complex and the outer two peaks are due to both isolated Fe and the Fe–H complex. To determine the separate behaviors of isolated Fe and the Fe–H complex with isochronal annealing, we plotted the intensities of the central and outer lines. As shown in Fig. 2, they show similar behavior. This is probably due to predominance of the Fe–H complex compared with isolated Fe after quenching from 1250°C. The increase around 100°C is probably due to the formation of the Fe–H complex from unreacted Fe and H since Fe and H_2 are known to diffuse around this temperature. This increase is very small which indicates a small concentration of isolated Fe after H doping. Hence, most part of outer peaks are due to the Fe–H complex. They disappeared at about 225°C.

To determine the activation energy, we performed isothermal annealing experiments as shown in Fig. 3. Lines are fitting curves with first-order reaction kinetics. From these, we determined the time constants. Fig. 4 shows the relation between the time constant and annealing temperature. Solid circles correspond to specimens doped with Fe only and open circles represent specimens co-

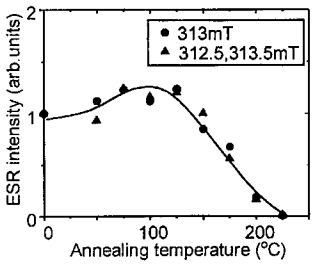

Fig. 2. Annealing behaviors of the central peak (circles) and outer peaks (triangles) of specimen co-doped with ^{57}Fe and H due to isochronal annealing for 10 min at each temperature. The specimen was co-doped with ^{57}Fe and H at 1250°C.

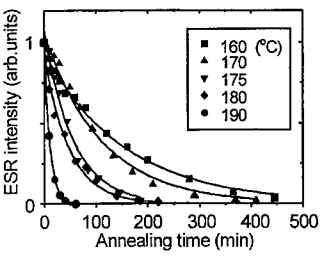

Fig. 3. Behaviors due to isothermal annealings at various temperatures. Specimens were co-doped with ^{57}Fe and H at 1250°C.

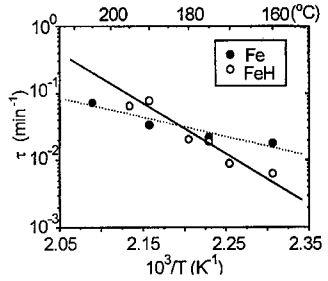

Fig. 4. Arrhenius plot of time constants of ^{57}Fe doped (solid circles) and ^{57}Fe and H co-doped (open circles) specimens determined from isothermal annealing experiments.

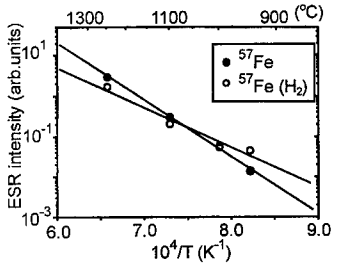

Fig. 5. Dependence of the sum of intensities of specimens doped with ^{57}Fe and co-doped with ^{57}Fe and H.

doped with Fe and H. The activation energies of the former and the latter were about 0.6 and 1.3 eV, respectively. The former value agrees well with that of a previous study [7]. The latter value is very large. Taking the large value of the pre-exponential factor, $7 \times 10^{11}\ s^{-1}$, into consideration, our interpretation is that the annealing process represented by the open circles in Fig. 3 corresponds to the dissociation of the Fe–H complex.

Fig. 5 shows the quenching temperature dependence of the concentration of Fe. In this figure, the ordinate is the sum of the intensities of three ESR lines, namely the total concentrations of isolated Fe and the Fe–H complex. Solid and open circles correspond to Fe-doped and Fe and H co-doped specimens, respectively. From the slopes of the solid lines, the solution energies of Fe are estimated to be about 2.8 and 1.9 eV from solid and white circles, respectively. The former agrees well with that determined from neutron activation analysis method [8]. On the other hand, the latter agrees well with that (1.8 eV) of H. It is difficult to determine the pre-exponential factor c_0 from the measurement of only ESR, when the solubility (c) is given by $c = c_0 \exp(-E/kT)$. We assumed that the solid circles agreed well with those determined by the neutron activation analysis, $c = 1.8 \times 10^{26} \exp(-2.94\ \text{eV}/kT)$. Then we obtained the pre-exponential factor of 2.1×10^{22} atoms/cm^3. This value is smaller by a factor of about 10^4 than that without H doping, and it is larger than that of the solubility of H [9] by a factor of about 2. This discrepancy may be due to the scatter of

data since this value is determined by extrapolation. We therefore tentatively propose that the formation of the Fe–H complex is dominated by H. To confirm this experimentally, the same study should be conducted under a lower concentration of H.

At above 1000°C, the number of Fe atoms, i.e., isolated Fe and Fe–H complex, becomes smaller after H doping. Extra Fe atoms probably form precipitates. On the other hand, the number of Fe atoms becomes greater than that of isolated interstitial Fe after H doping. Several possible sources of Fe, such as Fe precipitate, Fe on the surface, and so on, were experimentally excluded. Thus we propose substitutional Fe as the Fe source, the existence of which has been detected by Moesbauer spectroscopy [10].

4. Conclusion

Fe atoms form an Fe–H complex in Si when Fe and H are co-doped. The binding energy of this Fe–H complex is about 1.3 eV. By co-doping of Si with Fe and H, the solute concentration of Fe in the forms of isolated Fe and a complex of Fe and H has a temperature dependence, 1.9 eV, which is much different from that (2.8 eV) of doping with Fe only. This temperature dependence agrees well with that of H solubility (1.8 eV).

References

[1] J.I. Pankove et al., Phys. Rev. Lett. 51 (1983) 2224.
[2] P.M. Williams et al., Mater. Sci. Forum 143–147 (1994) 891.
[3] M.J. Evans et al., Mater. Res. Soc. Sympo. Proc. 442 (1997) 275.
[4] E.O. Sveinbjornsson et al., Phys. Rev. B 49 (1994) 7801.
[5] J. Weber, Mater. Res. Soc. Symp. Proc. 513 (1998) 345.
[6] T. Sadoh et al., J. Appl. Phys. 82 (1997) 3828.
[7] H. Takahashi et al., Phys. Rev. B 46 (1992) 1882.
[8] E.R. Weber, Appl. Phys. A 30 (1983) 1.
[9] R.C. Newman et al., Solid State Phenom. 32/33 (1993) 155.
[10] P. Schwalbach et al., Phys. Rev. Lett. 64 (1990) 1274.

ELSEVIER

Physica B 273–274 (1999) 449–452

PHYSICA B

www.elsevier.com/locate/physb

Pt and Li complexes in silicon. 99-07-22 16.52

Mats Kleverman*, Xinhui Zhang, Janos Olajos

Solid State Physics, University of Lund, Box 118, S-221 00 LUND, Sweden

Abstract

Two different Pt- and Li-related centers in silicon have been studied by excitation spectroscopy combined with uniaxial stress and isotope doping experiments. The dominating spectrum consists of a series of sharp lines between about 5000 and 8000 cm^{-1} and is due to excitation from a deep initial state to various shallow donor states. The energy positions of the electronic lines in Li^6-doped samples shift by about 1 cm^{-1} to lower energies compared to those in Li^7 samples. Phonon replicas of the no-phonon lines are detected with $\hbar\omega(Li^7) = 528.6\ cm^{-1}$ and $\hbar\omega(Li^6) = 547.8\ cm^{-1}$. Other replicas of the no-phonon lines are also observed involving an energy of about $\Delta = 2229\ cm^{-1}$ as well as combinations of Δ and $\hbar\omega$. The uniaxial stress data indicate that the center has either tetrahedral or orthorhombic I symmetry. The second center gives rise to sharp lines at 1965.64, 1974.12, and 2001.00 cm^{-1} at $T < 30$ K. The 2001 cm^{-1} line has a full width at half maximum of 1.4 and 0.12 cm^{-1} at room temperature and $T = 10$ K, respectively. Uniaxial stress experiments show that all three lines originate from excitations of a trigonal center. The isotope shift is small and for Li^6 samples the 2001 cm^{-1} line shifts only by 0.06 cm^{-1} to higher energy compared to Li^7 samples.

Keywords: Silicon; Platinum; Lithium

1. Introduction

Lithium is a fast diffuser in silicon and has a high tendency to form complex centers with other impurities present in the crystal. Recently, several investigations on Li-related complexes involving gold [1–4] and platinum [3–5] have been carried out using a variety of experimental methods as well as ab initio calculations [6]. In this work, results from detailed optical investigations of two different PtLi complexes in silicon are reported.

Pt resides on substitutional site whereas Li preferably occupies an interstitial position. The excitation spectrum of platinum has been investigated in detail previously and it is dominated by the acceptor spectrum at about 7400 cm^{-1} [7] and the T-line spectrum consisting of three lines at about 8000 cm^{-1} [8]. None of these spectra are observed in our samples co-doped with Pt and Li; instead, two other series of sharp lines are observed. The first at about 2000 cm^{-1} and the second in the range between approximately 5000 and 8000 cm^{-1}. The disappearance of the Pt lines could in principle be caused by a change of the Pt centers charge states since isolated Li acts as a shallow donor center. However, the results from the Li isotope experiments to be presented here unambiguously show that Li indeed forms complexes with Pt.

2. Experimental details

The sample preparation procedure and the experimental setup are in described detail in Ref. [5]. In this work, however, all samples were diffused under Li-rich conditions as described in Ref. [5].

3. The Si : Pt–Li donor lines

In Fig. 1, a typical excitation spectrum for a Si : Pt–Li^6 sample is presented. It is virtually identical to the Si : Pt–Li^7 spectrum previously presented in Ref. [5] but

* Corresponding author: Fax: 46-46-222-3637.
E-mail address: mats.kleverman@ftf.lth.se (M. Kleverman)

0921-4526/99/$ - see front matter
PII: S0921-4526(99)00502-5

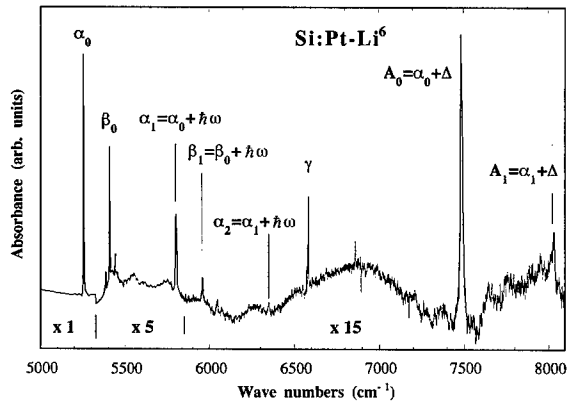

Fig. 1. A typical absorption spectrum of a Pt and Li^6 diffused silicon sample showing the PtLi donor lines.

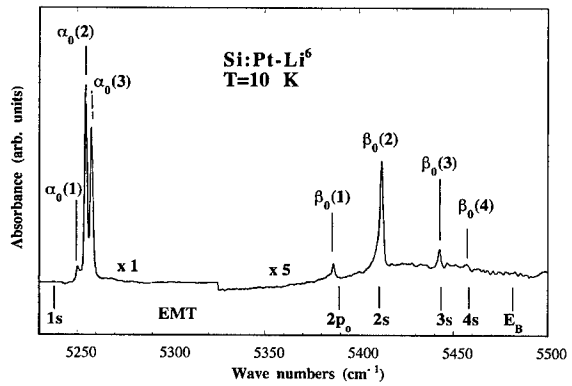

Fig. 2. The no-phonon lines energy positions compared to those predicted by EMT.

with important isotope-dependent differences that will be discussed below. The main groups of lines are labeled α_n, β_n where n indicates the number of local phonons involved in the transitions.

Uniaxial stress data [5] have shown that the final states of the transitions involve shallow donor states. Furthermore, it was suggested that the three α_0 lines are due to transitions to states in the 1s manifold and that $\beta_0(2)$, $\beta_0(3)$, and $\beta_0(4)$ lines correspond to excitation to the 2s, 3s, and 4s manifolds, respectively. The energy differences between the lines are close, but somewhat smaller, to those predicted by effective mass theory, EMT [9]. The $\beta_0(1)$ line must then be identified to be due to excitation to the $2p_0$ state. The zero-phonon lines in Fig. 2 are presented in more detail and their energy positions are compared to those of EMT. It is interesting to note that the final s-states have binding energies that are smaller than the EMT energies whereas the $2p_0$ state experiences a net attractive central-cell shift. This may be understood by noting that the one-particle shallow donor states must be orthogonal to the remaining core state. This implies that the shallow donor states may be pushed up in energy compared to their EMT values. However, in the case where the core state is s-like this orthogonalization only affects the excited s states. The s-states are thus believed to shift due to two contributions [5]; an attractive contribution due to, e.g., a reduced screening close to the impurity site and a stronger repulsive effective potential due orthogonalization effects. The $2p_0$ state is expected to shift to smaller binding energy since it is in a zeroth-order approximation already orthogonal to an s-like core state and is only affected by the electron attractive part of the potential. The PtLi and Ag [10] excitation spectra are similar since they are both dominated by transition to s states and that only one p-line, $2p_0$, is observed.

All no-phonon lines shift by about 1 cm^{-1} to lower energies in Li^6-doped samples compared to the energy positions in Li^7-doped material. In Fig. 3 this isotope shift is presented in more detail for the three α_o lines. This unambiguously shows that Li indeed is one of the constituents of the complex. Diffusion experiments using both Li^6 and Li^7 could, in principle, give information on the number of Li ions in the complex. Unfortunately, several attempts to incorporate both isotopes simultaneously have failed.

Additional lines in the Li^7 spectrum were interpreted as phonon replicas of the no-phonon lines [5]. In Fig. 1, the α_1 and β_1 lines are one-phonon replicas whereas the α_2 line is due to excitation to the $n = 2$ phonon state. This interpretation is strongly supported by the isotope doping experiments presented in Fig. 4. In this way the phonon energy for the two different Li isotopes could accurately be determined and they were found to be $\hbar\omega(Li^7) = 528.6\ cm^{-1}$ and $\hbar\omega(Li^6) = 547.8\ cm^{-1}$. The phonon energies are in the range previously found for several other Li-related complexes in silicon [11]. Direct observation of Li^7 local vibration mode, LVM,

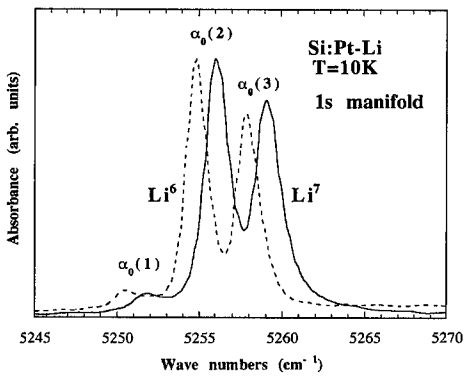

Fig. 3. The isotope shift of the α_0-lines in the 1s manifold of shallow donor states.

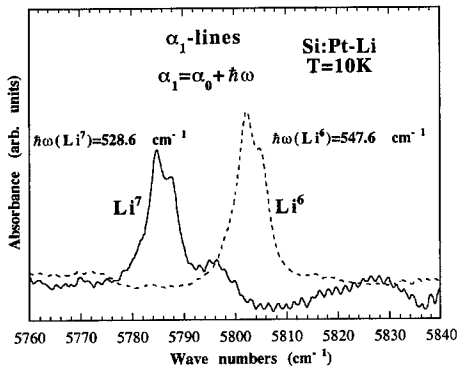

Fig. 4. The one-phonon replica of the α_0-lines.

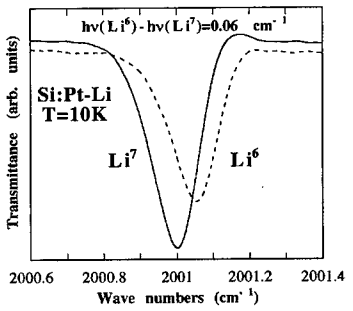

Fig. 5. The isotope shift of the 2001 cm^{-1} PtLi line.

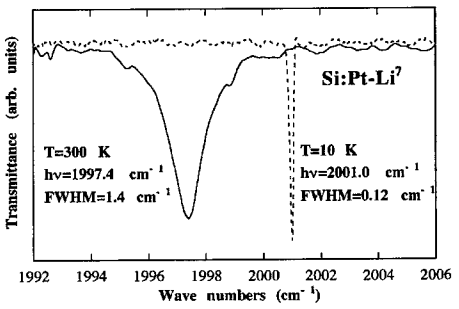

Fig. 6. The 2001 cm^{-1} line measured at two different temperatures.

was reported in Ref. [5] but attempts to observe the corresponding Li^6 mode have hitherto been unsuccessful.

At higher energies other lines labeled A_0 and A_1 are detected (Fig. 1). A closer inspection and a comparison with the α_0 and α_1 series shows that A_0 and A_1 are their corresponding replicas, respectively, displaced about $\Delta = 2229$ cm^{-1} to higher energies. This energy is, within experimental error, identical for the two Li isotopes. The A_1 line is thus correspondingly a double α_0 replica involving both $\hbar\omega$ and Δ. This interpretation is supported by the fact that in the case of Li^6 samples the A_1 line is found at about 8032 cm^{-1} which exceeds the Li^7 energy by about 20 cm^{-1} which is equal to the energy difference of the corresponding local phonons. If the Δ replicas are due to a local phonon mode, the high-energy modes indicates that H-stretching modes may be involved. It should be pointed out that the Li source is immersed in mineral oil and traces of mineral oil in the ampoule during the diffusion could be a source of hydrogen. We have compared the spectral results presented here with those obtained from samples diffused in H atmosphere. No differences have been detected which indicate that the Δ energy does not correspond to a hydrogen LVM. These findings support our previous assignment that the Δ replicas are due to shake up effects in the final core-state, i.e., that two different final core-states, separated in energy by Δ, are reached in the transitions.

4. The 2001 cm^{-1} line center.

Sharp lines at 1965.64, 1974.12, and 2001.00 cm^{-1} are detected in all our Pt-Li^7 samples where the energies refer to sample temperatures $T < 30K$. The 2001 cm^{-1} line has high intensity whereas the other two have considerably lower intensity. All three lines are only observed when co-doping with Pt and Li which indicates that they are related to both Pt and Li. We will here focus on the properties of the 2001 cm^{-1} line since all experimental data indicate that all three lines belong to the same center. In Fig. 5 the 2001 cm^{-1} line is presented for a Li^6- and a Li^7-doped samples measured at $T = 10$ K. The apodized resolution was 0.04 cm^{-1}. Only a very small isotope shift of about 0.06 cm^{-1} was detected, which, nevertheless, shows that Li indeed is involved in the center. The 2001 cm^{-1} line is easily observed also at higher temperatures and Fig. 6 shows the line measured at room temperature (RT) and 10 K. Interestingly, the full-width at half-maximum (FWHM) is as small as 1.4 cm^{-1} at RT which is in the range found for many electronic lines in silicon at cryogenic temperatures. When decreasing the sample temperature the line position shifts to higher energies and the FWHM value decreases and, finally, it reaches its low temperature value of 0.12 cm^{-1} for temperatures below about 30 K.

To the best of our knowledge very few electronic lines in silicon, if any at all, are observed at room temperature and then with such a low FWHM value. This suggests that the lines are due to local vibrational modes. This tentative identification suffers, however, from the difficulty to understand what is vibrating that gives rise to a vibrational energy of about 2000 cm^{-1}. The small isotope shift revealed in Fig. 5 shows that the vibration does not involve Li. As discussed above, a natural candidate is of course hydrogen but also in this case the results of

co-doping with H do not support this suggestion. Whether the 2001 cm^{-1} lines have electronic or vibrational origin is still unclear.

The 2001 cm^{-1} lines were also investigated by uniaxial stress spectroscopy [12]. The lines do not split for stress parallel to $\langle 1\,0\,0\rangle$ but splits into two components for stress in the $\langle 1\,1\,0\rangle$ and $\langle 1\,1\,1\rangle$ directions. This splitting pattern is typical for transitions at a trigonal center [13]. The relative intensity of the split components as well as the polarization rules show that the transitions take place between orbital singlet states.

Platinum- and lithium-related complexes in silicon have been studied previously by other techniques. Two different centers were observed by electron paramagnetic resonance (EPR) and electron nuclear double resonance (ENDOR)), one with orthorhombic I (C_{2v}) and one with trigonal symmetry (C_{3v}) [3,4].

In silicon, isolated Li normally occupies an interstitial position and forms a shallow donor center. In the case of the C_{2v} PtLi center, calculations [6] have suggested that the center consists of substitutional Pt^- and a Li^+ ion on next nearest interstitial position. The candidate suggested for the trigonal PtLi paramagnetic center was Pt^{3-} surrounded by three Li^+ ions on nearest-neighbor interstitial positions. Yet another PtLi complex was found to be stable. It consists of Pt^{4-} surrounded by four Li^+ ions and has tetrahedral symmetry. However, this center is not paramagnetic when neutral and is expected to be formed in higher concentration in Li-rich material.

Ab initio calculations thus result in three stable Pt–Li complexes whereas our experimental results are interpreted to be due to excitation of two centers. However, it is tempting to assign the Pt–Li donor center to be either the tetrahedral Pt^{4-} Li_4^+ complex or the C_{2v} Pt^- Li^+ pair center. Unfortunately, our evaluation of the data has hitherto not resulted in a definite identification of the symmetry of the donor center. It is our hope the high-resolution stress data at lower stresses than those used in Ref. [5] will give the information needed. We, finally, assign the trigonal 2001 cm^{-1} center to be trigonal Pt^{3-} Li_3^+ center.

Acknowledgements

The authors acknowledge financial support from the Swedish Natural Science Research Foundation (NFR).

References

[1] P. Tidlund, M. Kleverman, Phys. Rev. B 58 (1998) 4517.
[2] E.Ö. Sveinbjörnsson, S. Kristjansson, H.P. Gislason, J. Appl. Phys. 77 (1995) 3146.
[3] S. Greulich-Weber, P. Alteheld, J. Reinke, H. Weihrich, H. Overhof, J.- M Spaeth, Semicond. Sci. Technol. 10 (1995) 977.
[4] P. Alteheld, S. Greulich-Weber, J.- M Spaeth, H. Overhof, H. Weihrich, M. Höhne, Phys. Rev. B 52 (1995) 4998.
[5] P. Tidlund, M. Kleverman, P. Hazdra, Phys. Rev. B 59 (1999) 4858.
[6] H. Weihrich, H. Overhof, P. Alteheld, S. Greulich-Weber, J.- M Spaeth, Phys. Rev. B 52 (1995) 5007.
[7] M. Kleverman, J. Olajos, H.G. Grimmeiss, Phys. Rev. B 37 (1988) 2613.
[8] J. Olajos, M. Kleverman, H.G. Grimmeiss, Phys. Rev. B 40 (1989) 2613.
[9] E. Janzén, R. Stedman, G. Grossmann, H.G. Grimmeiss, Phys. Rev. B 29 (1984) 1907.
[10] J. Olajos, M. Kleverman, H.G. Grimmeiss, Phys. Rev. B 38 (1989) 10633.
[11] W.G. Spitzer, in: O. Madelung (Ed.), Festkörperprobleme XI, Fr. Vieweg and Sohn, Braunschweig, 1971, p. 1.
[12] Mats Kleverman, Xinhui Zhang, Janos Olajos, unpublished.
[13] A.A. Kaplyanskii, Optika Spectrosk. 16 (1964) 602.

ELSEVIER

Physica B 273–274 (1999) 453–457

PHYSICA B

www.elsevier.com/locate/physb

A combined experimental and theoretical approach to grain boundary structure and segregation

S.J. Pennycook[a,b,*], M.F. Chisholm[a], Y. Yan[c], G. Duscher[a,b], S.T. Pantelides[a,b]

[a]*Solid State Division, Oak Ridge National Laboratory, PO Box 2008, Oak Ridge, TN 37831-6030, USA*
[b]*Department of Physics and Astronomy, Vanderbilt University, Nashville TN 37235, USA*
[c]*National Renewable Energy Laboratory, Golden, CO 80401, USA*

Abstract

Recently, the scanning transmission electron microscope has become capable of forming electron probes of atomic dimensions. Through the technique of Z-contrast imaging, it is now possible to form atomic resolution images with high compositional sensitivity from which atomic column positions can be directly determined. An incoherent image of this nature also allows atomic resolution chemical analysis to be performed, by locating the probe over particular columns or planes seen in the image while electron energy loss spectra are collected. Such data represent either an ideal starting point for first-principles theoretical calculations or a test of theoretical predictions. We present several examples where theory and experiment together give a very complete and often surprising atomic scale view of complex materials. © 1999 Elsevier Science B.V. All rights reserved.

Keywords: Grain boundaries; Atomic structure; Impurities; Segregation; Transformation; Electron microscopy; Total energy calculations

1. Direct imaging with electrons

The images we see with our eyes generally appear to be a direct representation of the world around us. This is because they are formed *incoherently*; objects are illuminated by light over a large range of directions and the intensity scattered depends primarily on the nature of the object and not on the direction of illumination. If objects are illuminated by coherent laser light they show a speckle pattern, which is due to interference effects. These are directly related to the object, but not in a manner that can be directly interpreted. Except for special applications, optical instruments such as a projector or a microscope invariably use incoherent illumination to maintain this capability for direct interpretation.

It is over one hundred years since Lord Rayleigh first explained the difference between coherent and incoherent imaging in the context of the light microscope. He clearly pointed out the advantages of incoherent imaging: absence of interference artifacts, and in addition a factor of two improved resolution [1]. Ideally, a self-luminous object is required for perfect incoherent imaging, so that each point will emit light independently. But Lord Rayleigh showed how the condenser lens can be used to give a close approximation to incoherent imaging. If the condenser lens subtends a sufficiently large range of angles, then we approach the incoherent imaging conditions of normal vision. Specifically, for an illumination semiangle θ, the transverse coherence length in the sample, ℓ_T, is $0.61\lambda/\theta$, which can be made comparable to the resolution limit.

In the conventional transmission electron microscope (CTEM), historically, a small condenser aperture has been used to give an approximation to perfect coherent imaging. This is necessary for low-resolution diffraction contrast imaging of defects such as dislocations, but this

* Correspondence address. Solid State Division, Oak Ridge National Laboratory, P.O. Box 2008, Oak Ridge, TN 37831-6030, USA. Tel.: + 1-423-574-5504; fax: + 1-423-574-4143.
E-mail address: pky@ornl.gov (S.J. Pennycook)

0921-4526/99/$ - see front matter
PII: S0921-4526(99)00521-9

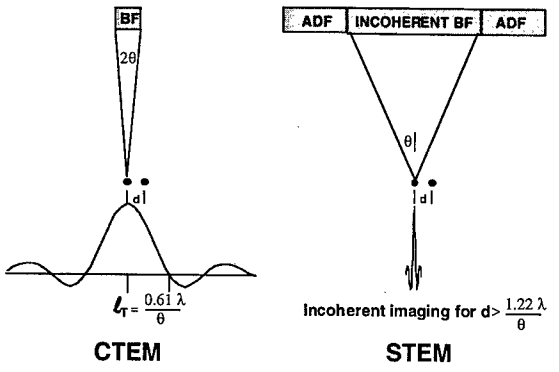

Fig. 1. Schematic comparing the transverse coherence lengths for coherent and incoherent imaging. In bright field (BF) conventional TEM the coherence length is large compared to interatomic spacings, whereas in the STEM, a large-angle BF or annular dark field (ADF) detector effectively breaks the coherence between neighboring atoms.

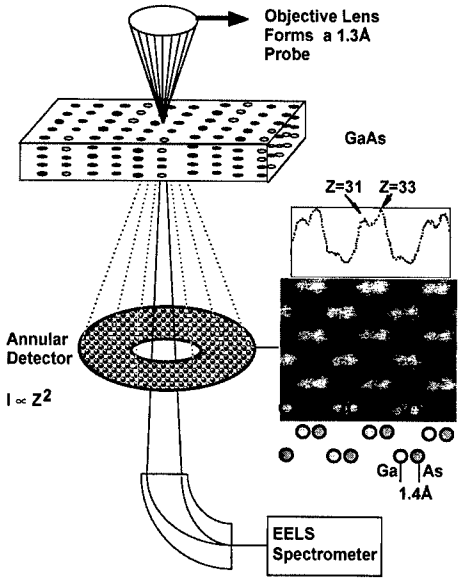

Fig. 2. Schematic showing a fine probe formed by the objective lens of an STEM. A Z-contrast image is formed by mapping high-angle scattered electrons as the probe is scanned across the sample, while atomic resolution electron energy loss spectroscopy is possible with the probe stationary on specific columns selected from the image. The Z-contrast image of GaAs shows As columns with higher intensity than Ga.

leads to a transverse coherence length much greater than typical interatomic spacings as shown in Fig. 1. As electron microscope resolution gradually improved it became possible to resolve atomic-scale features, but the coherent imaging conditions were maintained. In a coherent image (referred to as a phase contrast image) atomic columns can be bright or dark depending on specimen thickness and objective lens focus (which alter the relative phases of the scattered beams). It is clear that simply increasing the illumination aperture will reduce the transverse coherence length. Eventually, it will reduce below the typical interatomic spacings of materials, and the coherence between columns will be broken. We would then achieve incoherent imaging, and we would expect atomic images to become directly interpretable. This has indeed proved to be the case. In practice, however, it is more efficient and results in higher image contrast to reverse the direction of the electrons, and to use the complementary high-angle annular *detector* shown in Fig. 1. Then the image is formed by scanning the illumination across the sample, a scanning transmission electron microscope (STEM).

The principle of Z-contrast imaging in the STEM is shown schematically in Fig. 2. A small electron probe is scanned across a thin specimen, and the Z-contrast image results from mapping the intensity of electrons reaching the annular detector [2–7]. The detector performs the function of Lord Rayleigh's condenser lens. But it not only breaks the coherence in the *transverse* plane [8], it enforces high scattering angles, so that Rutherford scattering dominates and atoms contribute to the image with a brightness determined by their mean square atomic number Z. For this reason the image is referred to as a Z-contrast image. In a crystal, Rutherford scattering becomes phonon scattering, and effectively breaks the coherence through the *thickness* of the sample [9]. The thickness dependence of the image becomes relatively intuitive, and atomic images from thicker materials can be interpreted equally well on the basis of Z-contrast.

In the image of GaAs shown in Fig. 2, bright features correspond directly to columns of As, and the less bright features to columns of Ga. Unlike the coherent imaging of conventional high-resolution electron microscopy (HREM), the positions of atomic columns can be determined directly and uniquely from the image to a high accuracy, without the need for extensive image simulations of model structures. Incoherent imaging effectively bypasses the phase problem of HREM, a particular advantage for complex materials. The VG Microscopes HB603U STEM at ORNL has a 300 kV accelerating voltage, and a directly interpretable resolution of 1.26 Å, although recently information transfer at 0.78 Å has been demonstrated in Si⟨1 1 0⟩ [10]. This also demonstrates the factor of two improved resolution available with incoherent imaging; the comparable phase contrast image resolution on this microscope is 1.93 Å. There are now many examples where the high resolution and the direct interpretability of Z-contrast imaging have proved very successful. Examples include the direct determination of dislocation core structures in GaN [11] and at CdTe/GaAs interfaces [12], and in imaging structure and

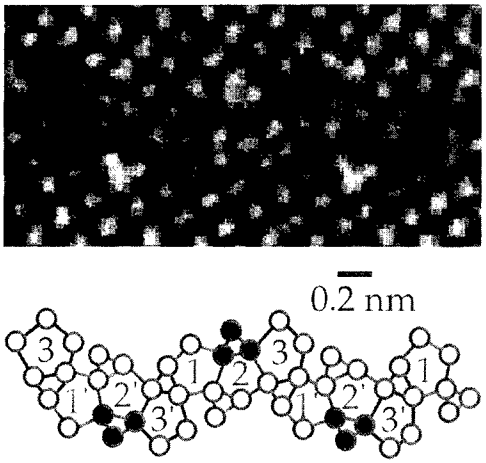

Fig. 3. Z-contrast image of a 23° ⟨0 0 1⟩ tilt grain boundary in Si showing its unexpectedly complex structure. The five-fold rings (with black centers in the image) are dislocation cores arranged in a repeating sequence along the boundary. Columns shown black in the schematic are those seen brighter in the image due to segregated As.

impurity sites at grain boundaries, as shown in the examples below.

The ability to retrieve atomic structures directly from experiment is a great advantage for first principles simulations, as it avoids the need to calculate large numbers of trial structures. This is especially true for complex materials where there are a great many possibilities. A further advantage of the STEM is that it allows electron energy loss spectroscopy (EELS) to be performed simultaneously with the Z-contrast image, allowing compositional analysis and local band structure to be determined at atomic resolution [13,14].

2. Arsenic segregation sites at a silicon grain boundary

Z-contrast imaging enables low concentrations of high-Z impurities to be directly observed. A recent example of this capability is shown in Fig. 3, a Z-contrast image from a 23° grain boundary in Si, after doping with As [15].

The atomic structure of the boundary is directly determined from the positions of the bright features in the image, and is different from all structures proposed previously. It comprises a continuous sequence of dislocation cores, a perfect edge dislocation (1) and two perfect mixed dislocations (2,3) arranged as a dipole, followed by the same sequence (1′,2′,3′) mirrored across the boundary plane. In the ⟨0 0 1⟩ projection, these dislocations appear as a connected array of pentagonal and triangular arrangements of atomic columns. The presence of the dipoles is surprising, as being of equal and opposite Burgers vector they could equally well be replaced by perfect crystal. However, precisely the same atomic arrangement is seen in the undoped boundary given the same annealing treatment.

Looking closely at the relative intensities of the columns in the doped sample, it is seen that one of the dislocation cores contains columns that are 20% brighter on average than other similar columns. This must be due to the presence of the As dopant. Taking into account the scattering cross section, the increased intensity corresponds to an average of only 5% As concentration, approximately two As atoms in each atomic column.

In a previous theoretical study of the shorter-period 36° grain boundary, it was found that isolated As atoms have only a small segregation energy of ~ 0.1 eV, too small to account for the concentrations observed experimentally [16]. However, as arsenic prefers to be three-fold coordinated, calculations were performed for arsenic dimers. It was found that the two As atoms repel and become three-fold coordinated without having to create an Si dangling bond. Thus binding of the dimer occurs through repulsion. After the image of Fig. 3 was obtained, calculations were repeated for the 23° boundary, and preference was found for those sites seen bright in the image. The segregation energy was again increased, becoming consistent with the As solubility limit in the bulk at the annealing temperature of 700°C. This combined use of experimental and theoretical techniques produced a remarkably detailed and consistent atomic-scale picture of impurity segregation at this grain boundary.

Very recently, an extensive ab initio study has confirmed the observed grain boundary structure, with its redundant dislocations, to be energetically preferred in the undoped grain boundary [17]. Further theoretical work could build on these results to determine grain boundary diffusion coefficients, as well as to extend studies to other boundaries and polycrystalline materials.

3. Impurity-induced grain boundary transformation in MgO

In Fig. 4, STEM imaging of an MgO grain boundary [18] reveals a structure that is inconsistent with the widely accepted structure of the boundary proposed by Harris et al. [19], based on theoretical modeling using classical potentials. The observed structure is similar to that proposed much earlier by Kingery [20]. The large empty core of the Harris structure is obviously very different from the more dense core of the Kingery model. On careful examination of the intensity in the experimental image, it can be seen that certain specific atomic columns at the grain boundary are again significantly brighter than neighboring columns, as arrowed in the figure. This suggests that impurities, with $Z > 12$, may be segregated at these sites. EELS measurements indeed

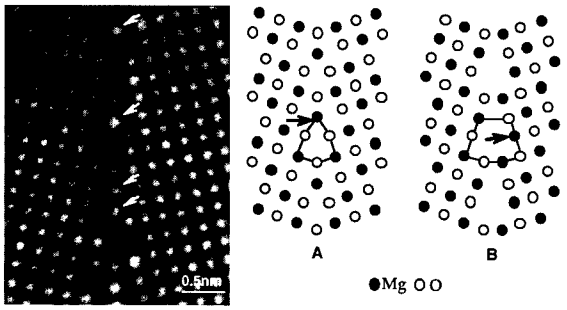

Fig. 4. Z-contrast image from a 24° ⟨0 0 1⟩ tilt grain boundary in MgO showing occasional bright atomic columns at the grain boundary (arrowed), compared to two structures for the 36° ⟨0 0 1⟩ tilt grain boundary proposed by (a) Kingery [20] and (b) Harris et al. [19]. Sites of Ca segregation are arrowed.

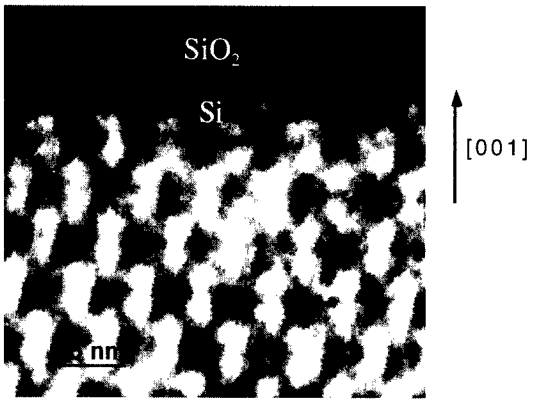

Fig. 5. Z-contrast image of a sharp Si/SiO_2 interface showing the last monolayer of Si in atomic positions close to those of the bulk.

established that significant concentrations of Ca were present in the grain boundary, approximately 0.3 monolayers, consistent with the bright intensity in the image.

To reconcile these observations with the apparently conflicting prior experimental and theoretical work, first-principles theoretical calculations were performed. These calculations in fact reproduced the results of the classical potential calculations for the clean grain boundary, indicating the open structure to be 0.5 eV lower in energy per periodic repeat unit. Theory further determined that Ca has a large segregation energy in both boundary structures, but *significantly higher* in the dense structure, sufficient to make the dense structure the lower energy boundary. These calculations therefore established that the dense structure is in fact *stabilized* by the Ca segregation, an example of a segregation-induced structural transformation [18]. Examination of the electronic charge distribution revealed just a small perturbation to the oxygen ions next to the Ca atom, indicating that the transformation is structural and not electronic in origin, i.e. it is driven by the size difference between Ca and Mg ions.

4. Structure and composition of the Si–SiO_2 interface

In the case of an amorphous material, no channeling of the probe can occur, and a Z-contrast image reflects only changes in projected atomic density. This is in marked contrast to conventional HREM images where amorphous materials always show a speckle pattern due to random interferences, and interfaces show Fresnel fringes and other coherent interference phenomena that can obscure the structure. In the Z-contrast image of Fig. 5, the last monolayer of the crystalline Si is clearly visible, and the Si columns are in almost exactly the expected positions for bulk Si [21]. Here again theory can be very useful in establishing the relative energies of various possible interface structures. Recent calculations have established that atomically abrupt interfaces are in fact energetically preferred over structures involving suboxides [22]. This is due to the softness of the Si–O–Si bond which allows strain relaxation to occur. Experimentally, however, suboxides are always found, presumably due to the non-equilibrium nature of the oxidation process and indicating the potential for improved characteristics. EELS provides a sensitive means to detect suboxides at the Si/SiO_2 interface, with high sensitivity and spatial resolution [23]. An example of an extended zone of suboxide is seen in Fig. 6, where Si-L edge spectra are plotted for a series of beam positions moving from the crystal into the oxide. The edge onset is 99 eV in the crystal, moving to 104 eV for stoichiometric SiO_2, but for approximately 2 nm both features are seen indicative of suboxide. The width of the suboxide zone is an order of magnitude greater than the beam size; this is confirmed also by profiles of the O-K edge [21], where there can be no contribution from the crystalline Si.

5. Conclusions

It is now possible to determine, without prior knowledge, the structure, impurity content and local electronic states, at grain boundaries, dislocations and interfaces by the combination of Z-contrast imaging and electron energy loss spectroscopy in the STEM. Atomic-scale total energy calculations are a natural complement and extension to these STEM techniques, giving critical insight into the underlying physics through the ability to study segregation energies, electronic states, and atomic-scale dynamics.

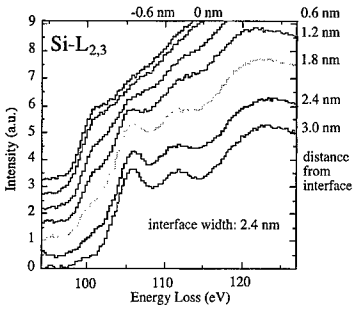

Fig. 6. Si-$L_{2,3}$ EELS profiles across a Si/SiO_2 interface showing evolution of the SiO_2 band gap. The full gap is not established until 2.4 nm into the oxide.

Acknowledgements

This research was supported by Lockheed Martin Energy Research Corp. under DOE Contract No. DE-AC05-96OR22464, ONR Grant No. N00014-95-1-0906, AFOSR Grant No. F-49620-99-1-0289 and by appointment to the ORNL Postdoctoral Research Associates Program administered jointly by ORNL and ORISE.

References

[1] L. Rayleigh, Philos. Mag. 42 (5) (1896) 167.
[2] S.J. Pennycook, in: S. Amelinckx, G. Van Tendeloo, D. Van Dyck, J. Van Landuyt (Eds.), Handbook of Microscopy, VCH Publishers, Weinheim, Germany, 1997, pp. 595–620.
[3] S.J. Pennycook, D.E. Jesson, Phys. Rev. Lett. 64 (1990) 938.
[4] S.J. Pennycook, D.E. Jesson, Ultramicroscopy 37 (1991) 14.
[5] S.J. Pennycook, D.E. Jesson, Acta. Metall. Mater. 40 (1992) S149.
[6] R.F. Loane, P. Xu, J. Silcox, Ultramicroscopy 40 (1992) 121.
[7] P.D. Nellist, S.J. Pennycook, Ultramicroscopy 78 (1999) 111.
[8] D.E. Jesson, S.J. Pennycook, Proc. Roy. Soc. A 441 (1993) 261.
[9] D.E. Jesson, S.J. Pennycook, Proc. Roy. Soc. A 449 (1995) 273.
[10] P.D. Nellist, S.J. Pennycook, Phys. Rev. Lett. 81 (1998) 4156.
[11] Y. Xin, S.J. Pennycook, N.D. Browning, P.D. Nellist, S. Sivananthan, F. Omnès, B. Beaumont, J.-P. Faurie, P. Gibart, Appl. Phys. Lett. 72 (1998) 2680.
[12] A.J. McGibbon, S.J. Pennycook, J.E. Angelo, Science 269 (1995) 519.
[13] N.D. Browning, M.F. Chisholm, S.J. Pennycook, Nature 366 (1993) 143.
[14] G. Duscher, N.D. Browning, S.J. Pennycook, Phys. Stat. Sol. A 166 (1998) 327.
[15] M.F. Chisholm, A. Maiti, S.J. Pennycook, S.T. Pantelides, Phys. Rev. Lett. 81 (1998) 132.
[16] A. Maiti, M.F. Chisholm, S.J. Pennycook, S.T. Pantelides, Phys. Rev. Lett. 77 (1996) 1306.
[17] J.R. Morris, Z.-Y. Lu, D.M. Ring, J.B. Xiang, K.M. Ho, C.Z. Wang, C.L. Fu, Phys. Rev. B 77 (1998) 11241.
[18] Y. Yan, M.F. Chisholm, G. Duscher, A. Maiti, S.J. Pennycook, S.T. Pantelides, Phys. Rev. Lett. 81 (1998) 3675.
[19] D.M. Harris, G.W. Watson, S.C. Parker, Philos. Mag. A 74 (1996) 407.
[20] W.D. Kingery, J. Am. Cer. Soc. 57 (1974) 1.
[21] G. Duscher, S.J. Pennycook, N.D. Browning, R. Rupangudi, C. Takoudis, H.-J. Gao, R. Singh, in: D.G. Seiler, A.C. Diebold, W.M. Bullis, T.J. Shaffner, R. McDonald, E.J. Walters (Eds.), Characterization and Metrology for ULSI Technology: 1998 International Conference, The American Institute of Physics, Woodbury, New York, 1998, pp. 191–195.
[22] R. Buczko, S. J. Pennycook, S. T. Pantelides, submitted for publication.
[23] D.A. Muller, T. Sorsch, S. Moccio, F.H. Baumann, K. Evans-Lutterodt, G. Timp, Nature 399 (1999) 758.

ELSEVIER

Physica B 273–274 (1999) 458–462

PHYSICA B

www.elsevier.com/locate/physb

Native defects and their interactions in silicon

Luciano Colombo*

INFM and Department of Materials Science, University of Milano-Bicocca, via Cozzi 53, I-20125 Milano, Italy

Abstract

We discuss the application of various quantum-mechanically based computational models to the investigation of microstructural evolution in crystalline silicon mediated by intrinsic defects. Focus is on the formation of like-defect clusters. © 1999 Elsevier Science B.V. All rights reserved.

Keywords: Silicon; Self-interstitial defect; Vacancy defect; Like-defect cluster; Tight-Binding molecular dynamics; Lattice kinetic Monte Carlo

1. Introduction

The dynamics of intrinsic defects causes the microstructural evolution of bulk silicon in many diverse real-world conditions, including Czochralski crystal growth, ion-beam processing, and rapid thermal annealing. Its accurate understanding represents in fact a great challenge for the materials theorist who aims at bringing the simple modeling of known (or predicted) defect properties up to the controlled tailoring of silicon bulk processing. This challenge basically consists in reaching the detailed atomic-scale characterization of the following scenario: defect-mediated self-diffusion brings to the clustering of like-defects that, in turn, eventually drives to formation of more extended defect structures (like dislocation loops, nanovoids, and {311} planar defects).

We are still quite far from reaching such a thorough theoretical picture on silicon microstructural evolution. Nevertheless, quite a few specific defect-related phenomena have been recently indentified, characterized and even predicted by combining different theoretical quantum mechanical models. More specifically, semi-empirical tight-binding molecular dynamics (see the special topic issue [1]) (TBMD) has been widely used to find the most stable defect structures, to compute their energetics, and to investigate defect–defect interactions and coalescence mechanisms. On the other hand, more refined ab initio electronic structure calculations [2,3] — at the Hartree–Fock (HF) level — have been perfomed to investigate the intimate nature of chemical bonding at (or nearby) defect complexes, thus provindig robust arguments for the a posteriori interpretation of the various features emerging from TBMD simulations. Furthermore, TBMD results represented a valuable set of data to be used for developing defect–defect interaction models which, finally, have been adopted in Monte Carlo (MC) simulations on the mesoscopic length and time scales [4].

The quantum-mechanical level of description, although quite heavy to be carried on systematically, is indeed mandatory. Nearly any problem related to intrinsic defect dynamics requires an accurate description of the sizeable bonding and re-bonding mechanisms occurring during microstructural evolution. This concept is clearly illustrated by evolution dynamics of the topological bond defect (BD) [2]. The BD complex is formed by the incomplete annihilation of a self-interstitial/vacancy pair: its structure is displayed in Fig. 1 (upper panel) and compared to the normal crystalline bond environment (Fig. 1, bottom panel). Although no excess or defect atoms are present, the local atomic arrangment is nevertheless quite different in the two cases. The BD structure is quite stable, being the energy recombination barrier as large as $\sim$ 1.3 eV [2]. TBMD simulations have provided

*Tel.: + 39-02-6448-5218; fax: + 39-02-6448-5403.
E-mail address: luciano.colombo@mater.unimib.it (L. Colombo)

PII: S0921-4526(99)00522-0

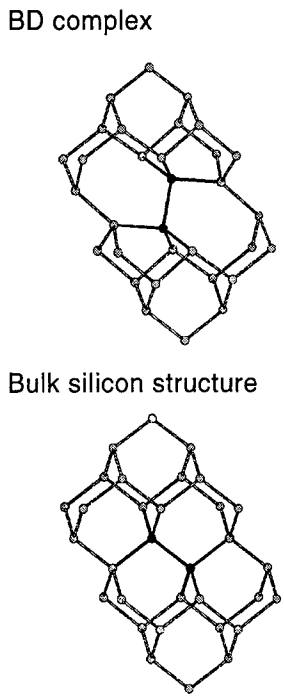

Fig. 1. Stick-and-ball representation of the equilibrium geometry of the BD complex.

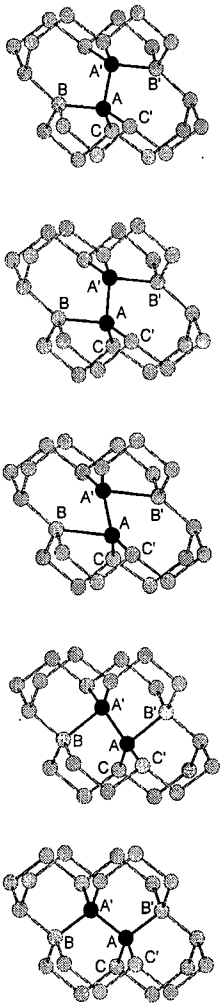

Fig. 2. Representation of the BD complex along the reaction path for its annihilation. Top: BD complex; bottom: non-defective crystal.

the reaction path for BD recombination: it is reported in Fig. 2. The work needed to recombine the defect must be spent in breaking the $A'B'$ and AB bonds and to form the new $A'B$ and AB' ones. Under this respect, namely taking into account the crucial importance played by purely quantum-mechanical features like the illustrated BD dynamics, empirical model-potential simulations have been proved to have serious limitations in the quantitative modeling of experimental data, as well as in the qualitative prediction of new features.

In this paper we briefly review our recent work on the formation of vacancy (V) and self-interstitial (SI) clusters, where all the computational tools mentioned above have been systematically used and hierarchically combined to provide a consistent picture covering both the atomic and meso-scale.

2. Self-interstitial clusters

TBMD simulations — performed by means of the TB representation by Kwon et al. [5] and O(N) formulation of TBMD by Goedecker et al. [6] — were aimed at annealing defect structures at finite temperature and at characterizing the energetics of the resulting complexes. Present simulation cells contained as many as 512 atoms (in addition to the atoms forming the SI cluster) [3]. In Table 1 we report the formation energy E_f and binding energy $E_b = 1/n[nE_f(1) - E_f(n)]$ for SI clusters containing up to 11 self-interstitial atoms, while Fig. 3 shows the atomic structure of the smaller ones. The stick-and-ball picture was drawn on the basis of the topological analysis of the valence charge density provided by HF calculations [3]. According to this quantum-chemical analysis we term as Si defective atoms (DAs) only those atoms that are filled in black in the figure, while bulk-like atoms are represented in gray.

In I1 (the well known $\langle 110 \rangle$ dumbbell) the DAs are 4-fold coordinated as is the Si atom in the bulk, while by increasing the cluster size the coordination raises from 5- in I2 to 6-fold in I3. Up to and including I3, all DAs in

Table 1
Formation E_f and binding E_b energy for SI-clusters

Cluster size I_n	E_f (eV)	E_b (eV)
I1	3.87	—
I2	4.91	1.41
I3	6.69	1.63
I4	9.41	1.51
I5	11.08	1.65
I6	14.37	1.47
I7	15.95	1.58
I8	19.14	1.47
I9	20.13	1.62
I10	24.05	1.45
I11	24.97	1.60

a given SI cluster exhibit the same connectivity. The structural evolution emerging from Fig. 3 is towards the formation of a tetrahedral cage symmetrically embedded into the crystalline environment, the "nucleation catalyst" being a dumbbell defect. We remark that in fact the assumed growth mechanism is "by last interstitialcy added". This noticeable symmetry is broken in I5 following the transition from three-dimensional to rod-like defect structures discussed below. Indeed the average coordination in I5 is 5.75, a value somewhat smaller than that found in I3, which has the highest average connectivity in the investigated SI cluster series.

As for the energetics of larger complexes, while formation energy increases linearly with cluster size, the binding energy data indicate that the average energy content per self-interstitial is about 1.55 eV, in rather good agreement with the 1.8 eV experimental data provided by Chason et al. [7]. Moreover, larger complexes behave differently as far as cluster shape is concerned. We observed that during the TBMD finite-temperature annealing process SI cluster self-organize so to form rod-like defects with an intriguing structure. The I5 SI defect is in fact the smallest rod-like structure of this kind. A careful analysis on atomic coordination and bonding provides a rationale for the evolution of SI cluster shape towards rod-like structures. The atomic coordination increases linearly with cluster size up to 6 for I3. Above this value Si atoms cannot form new bonds (the maximum average coordination is 6.5, as observed in liquid silicon [10]) and therefore a new growth pattern for larger complexes must be followed. Our conclusion is that I5 cluster plays a special role, being a sort of basic building block for the formation of more extended complexes. The reliability of the present structural model for small I-clusters is confirmed by the experimental evidence of rod-like structures reported by Benton et al. [8] and Libertino et al. [9].

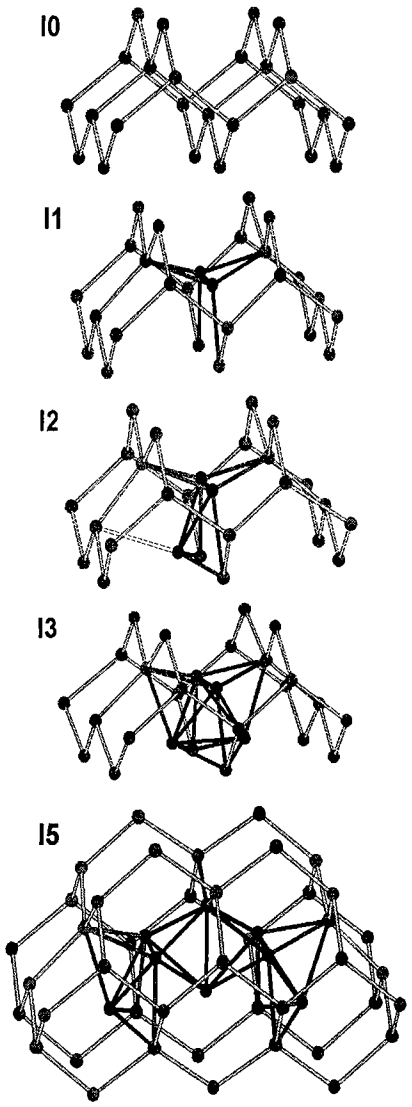

Fig. 3. Equilibrium structure of I1, I2, I3, I5 SI clusters after TBMD annealing, including bulk-like structure I0. Black: Si defect atoms (DAs); gray: bulk-like atoms.

3. Vacancy clusters

By means of O(N)-TBMD it has been possible to investigate the aggregation of vacancy defects using very large simulation cells, containing as many as 1000 atoms each. The large bulk-Si sample guarantees that the lattice strain field — which is particularly long-ranged for vacancies [11] — created by the cluster is well contained in the simulation cell.

In principle, the creation of a vacancy cluster is equivalent to: (i) breaking bonds; (ii) forming internal surfaces; (iii) incorporating a new structure (i.e. the cluster itself)

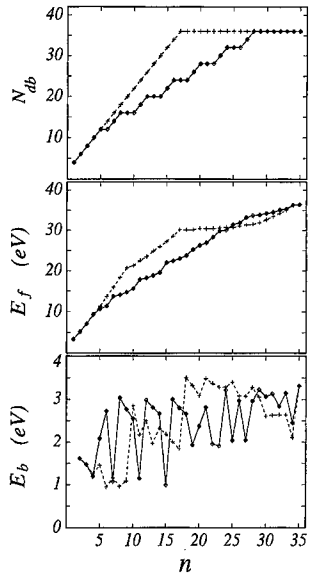

Fig. 4. Number of dangling bonds N_{db} (top), formation energy E_f (middle) and binding energy E_b (bottom) of vacancy clusters in silicon as function of the cluster size n. Full line with ◇ symbols: HRC clusters; dashed line with + symbols: SPC clusters.

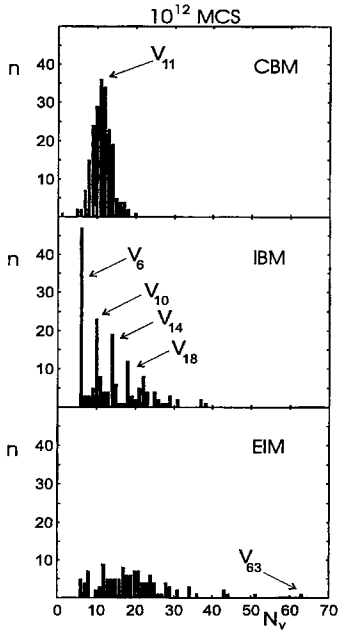

Fig. 5. Vacancy cluster size distribution after $\sim 10^{12}$ MCS using (a) a continuous binding model (CBM); (b) an Ising-type model (IBM); (c) an extended Ising model (EIM).

into an host lattice. Therefore, vacancy coalescence is affected by the variation of the angular coordination, by the relaxation of the internal surface, and by the interplay between the symmetry of the diamond lattice and cluster topology. As for point (iii) we identified at least two different growth patterns [12]. We can simply take out Si atoms from the successive shells of neighbours of a given atom or Si atoms can be removed from the 6-fold rings present in the diamond lattice. It resulted that the former pattern (named spheroidal clusters — SPC) is much more energy expensive than the second one (named hexagonal ring cluster — HRC), since a much higher number of dangling bond is created at cluster surface [12]. These results are summarized in Fig. 4 where the number of dangling bonds before surface reconstruction (top panel), formation energy (middle panel), and binding energy (bottom panel) are represented as function of cluster size (n represents the number of vacancies).

The main feature showed in Fig. 4 is that the binding energy is not a monotonically increasing function of the cluster size n, as often assumed in continuum binding models. Vacancy aggregates corresponding to $n = 6,8,10,12$, and 16 vacancies display much larger binding energies than clusters with slightly different size. In order to find the most stable clusters (having larger binding energies) we need, as discussed above, to select those aggregates obtained by extracting Si atoms from completed 6-fold rings: they correspond to cluster size $n = 6,10$, and 18. Furthermore, the relaxation of the new internal surface can energetically promote a given cluster which does not strictly fullfill the previous topological condition. This is, for instance, the case of cluster size $n = 8,12$, and 16. In any case the aggregation of a new vacancy to a stable cluster always gives rise to a less stable structure.

The detailed modeling of V-clusters binding energetics opens a new perspective, namely the investigation of the riping mechanism of nanovoids occurring at the meso-scale. To this aim we have recently developed a lattice kinetic Monte Carlo code [4], where different V–V interaction models have been implemented. In particular, we used a (over)simplified continuum binding model (CBM) according to Ref. [13], an Ising-like binding model (IBM) with 1nn interactions only, and another Ising-like binding model (EIM) where V–V interactions have been extended up to the second next neighbors. We then performed a *gedanken* computer experiment where we measured the V-cluster size distribution — after thermal annealing — of a given initial configuration, as produced by the three different interaction models. The basic idea was to check whether different energetics models could provide different pictures for microstructural evolution. Since the V-cluster distribution is, in principle, an observable quantity, this simulation could be related to experiments.

The results of the simulations for a system of $\rho = 10^{19}$ vacancy/cm^3 at $T = 900$°C are summarized in Fig. 5. Significant differences in the distributions can be

observed. In the case of CBM the distribution shows peaks at the cluster size dominant at the time considered. The distribution for the IBM case is, in turn, dominated by hexagonal ring aggregates ($n = 6,10,14,\ldots$). This feature, which causes a bottleneck of the growth process, appears during the time evolution soon after the dissolution of smaller clusters. Finally, the kinetics appears strongly modified in the EIM case. The distribution shows an increased spreading and reveals the presence of very large clusters (containing as many as 63 vacancies). It is worth remarking that the origin of these observed features is the mobility of small V-aggregates which allows the coalescence and self-organization and it boosts considerably the ripening process.

The results presented in Fig. 5 have several implications on our current understanding of the ripening of voids in Si. Indeed, the use of EIM, introduced to recover vacancy static energetics calculated by TBMD (see Fig. 4), affects the mechanism through which void ripening takes place. Void evolution does not occur only through a standard Ostwald ripening mechanism, as predicted by MC simulations using a CBM model, but a rather through a mixed mechanism of Ostwald ripening and coalescence. Furthermore, the presence of particularly stable V-clusters, which produces severe bottleneck for void evolution using IBM, is completely overwhelmed by the motion of small clusters induced by second neighbors interaction.

4. Conclusions

We presented a thorough theoretical picture on intrinsic point defect interaction and clustering in silicon which is both consistent with experimental data, and predictive under many circumstances. The theoretical framework consists in a combination of quantum-mechanical methods, ranging from semi-empirical tight-binding molecular dynamics to ab initio electronic structure calculations, performed at the Hartree–Fock level. In addition, our molecular dynamics data represent a useful information to set up Monte Carlo models aimed at modeling bulk silicon microstructural evolution over a longer time scale and a larger length scale than the atomic one.

The results obtained so far allow for the definition of a challenging roadmap for future works consisting in the study of: (i) the structural transition from self-interstitial clusters to extended defects (like dislocation loops or planar {311} defects); (ii) the interaction among vacancy and self-intertitial defects; (iii) the dissolution/aggregation kinetics of large complexes; (iv) the like-defect cluster mobility; and, finally, (v) the defect-mediated dopant atoms diffusion.

Acknowledgements

I acknowledge longstanding collaborations with A. Bongiorno, F. Cargnoni, S. Coffa, T. Diaz de la Rubia, C. Gatti, A. La Magna, and M. Rosati. I also acknowledge computational support by INFM under Parallel Computing Initiative and by CASPUR (Rome). Finally, financial support by CNR under project "Progetto 5% Microelettronica" is acknowledged.

References

[1] Tight-Binding Molecular Dynamics Simulations in Materials Science, L. Colombo (Ed.), Comput. Mater. Sci. 12 (1998) 157.
[2] F. Cargnoni, C. Gatti, L. Colombo, Phys. Rev. B 57 (1998) 170.
[3] A. Bongiorno, L. Colombo, F. Cargnoni, C. Gatti, M. Rosati, 1999, submitted for publication.
[4] A. La Magna, S. Coffa, L. Colombo, Phys. Rev. Lett. 82 (1999) 1720.
[5] I. Kwon et al., Phys. Rev. B 49 (1994) 7242.
[6] S. Goedecker, L. Colombo, Phys. Rev. Lett. 73 (1994) 122.
[7] E. Chason et al., J. Appl. Phys. 81 (1997) 6513.
[8] J.L. Benton et al., J. Appl. Phys. 82 (1997) 120.
[9] S. Libertino et al., Appl. Phys. Lett. 71 (1997) 389.
[10] I. Stich et al., Phys. Rev. B 44 (1991) 4262.
[11] C.Z. Wang, C.T. Chan, K.M. Ho, Phys. Rev. Lett. 66 (1991) 189.
[12] A. Bongiorno, L. Colombo, T. Diaz de la Rubia, Europhys. Lett. 43 (1998) 695.
[13] M. Jaraiz, G.H. Gilmer, J.H. Poate, T. Diaz de la Rubia, Appl. Phys. Lett. 68 (1996) 409.

ELSEVIER

Physica B 273–274 (1999) 463–467

PHYSICA B

www.elsevier.com/locate/physb

The structure of vacancy–impurity complexes in highly n-type Si

K. Saarinen*, J. Nissilä, H. Kauppinen, M. Hakala, M.J. Puska, P. Hautojärvi, C. Corbel

Laboratory of Physics, Helsinki University of Technology, P.O. Box 1100, 02015 HUT, Finland

Abstract

We show that the detailed atomic structure of vacancy–impurity complexes in Si can be experimentally determined by combining positron lifetime and electron momentum distribution measurements. The vacancies complexed with a single impurity, V–P and V–As, are identified in electron irradiated Si. The formation of native vacancy defects is observed in highly As-doped Si at the doping level of 10^{20} cm^{-3}. The defects are identified as monovacancies surrounded by three As atoms. The formation of V–As_3 complex is consistent with the theoretical descriptions of As diffusion and electrical deactivation in highly As doped Si.

Keywords: Si; Diffusion; Compensation; Positrons

1. Introduction

In the As and Sb doping of Si the concentration of free electrons saturates at the level of $\leqslant 5 \times 10^{20}$ cm^{-3} when the impurity concentration is increased [1]. This behavior is indicative of the formation of inactive impurity clusters or compensating defects that trap free electrons. There is presently no consensus on the detailed nature of these defects. Experimental evidence has been obtained on impurity precipitation as well as on the formation of vacancy-impurity complexes (see Refs. [2–4] and citations therein). Theoretical results propose that the vacancy-impurity complexes are formed very abundantly and they may also play distinct roles in the diffusion and clustering of impurities [3]. However, recent calculations and X-ray absorption measurements suggest that the deactivating defects are not associated with vacancies [4]. There is thus a need for new experimental information on the atomic structure of defects in heavily n-type Si.

Positron annihilation spectroscopy is a method for the direct identification of vacancy defects [5]. Thermalized positrons in solids get trapped at neutral and negative vacancies because of the missing positive charge of the ion cores. At vacancies positron lifetime increases and positron–electron momentum distribution narrows due to the reduced electron density. Positron experiments have been applied to study defects in heavily As or Sb doped Si in this work and earlier [6–9].

2. Experimental details

We studied Czochralski grown (Cz) Si(1 1 1) bulk crystals doped with [As] = 10^{19} and 10^{20} cm^{-3} and [P] = 10^{20} cm^{-3}. Experiments were done both in as-grown samples as well as after 2 MeV electron irradiation at 300 K. The positron experiments were performed in the conventional way by sandwiching two identical sample pieces with a 30 μCi ^{22}Na positron source [5]. A fast–fast coincidence system with a time resolution of 230 ps was used in the positron lifetime experiments. The positron-electron momentum distribution was measured as a Doppler broadening of the 511 keV annihilation radiation, using a Ge detector with an energy resolution

* Corresponding author. Tel.: + 358-9-451-3111; fax: + 358-9-451-3116.

E-mail address: ksa@fyslab.hut.fi (K. Saarinen)

0921-4526/99/$ - see front matter
PII: S0921-4526(99)00523-2

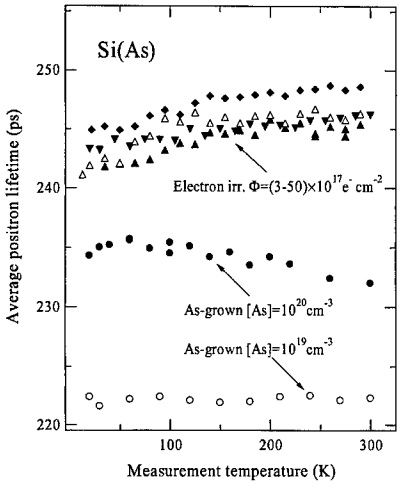

Fig. 1. The average positron lifetime versus temperature in as-grown and electron irradiated Si(As). The irradiation fluences are 3×10^{17} cm^{-2} (△) for the Si([As] = 10^{19} cm^{-3}) sample and 3×10^{17} cm^{-2} (▲), 1×10^{18} cm^{-2} (▼), and 5×10^{18} cm^{-2} (◆) for the Si([As] = 10^{20} cm^{-3}) sample [6].

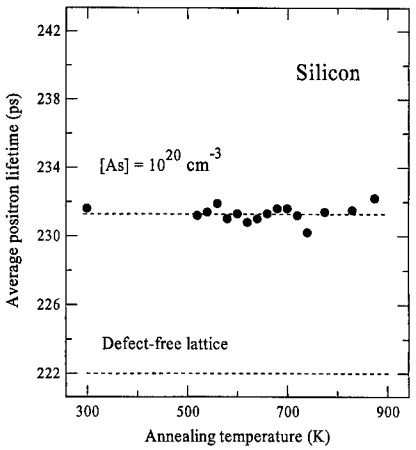

Fig. 2. The average positron lifetime as a function of annealing temperature in as-grown Si([As] = 10^{20} cm^{-3}). The measurements were performed at 300 K and the annealing times were 30 min.

of 1.4 keV. In order to observe positron annihilations with core electrons, the experimental background was reduced by detecting simultaneously the two annihilation photons [10]. For this purpose, a NaI detector was placed collinearly with the Ge detector and a coincidence between the two detectors was electronically required.

3. Positron lifetime results

The positron lifetime spectra in the as-grown Si([As] = 10^{19} cm^{-3}) and Si([P] = 10^{20} cm^{-3}) samples have a single component of 222 ps at 300 K. The lifetime is the same as often reported for defect-free Si (τ_B = 220 ps) [11], and depends very little on temperature (Fig. 1). This behavior is typical when all positrons annihilate at a delocalized state in the lattice, and it can be attributed to the thermal expansion [5]. The Si([As] = 10^{19} cm^{-3}) and Si([P] = 10^{20} cm^{-3}) samples are thus free of vacancies trapping positrons.

The positron average lifetime is clearly higher in the as-grown Si([As] = 10^{20} cm^{-3}) sample, τ_{av} = 232 ps at 300 K. The lifetime spectrum has two components, the longer of which is $\tau_2 = 250 \pm 3$ ps. Both τ_{av} and τ_2 are almost constant as a function of temperature. The two-componential lifetime spectrum and the increase of τ_{av} above the bulk lifetime τ_B are clear signs that native vacancies exist in the Si([As] = 10^{20} cm^{-3}) sample. The second lifetime component $\tau_2 = 250 \pm 3$ ps is characteristic for the positron annihilations at the vacancy [5]. These vacancies are stable at least up to 900 K since no change is observed in the average positron lifetime up to this annealing temperature (Fig. 2).

In all electron irradiated samples the average positron lifetime is longer than in as-grown samples indicating that irradiation-induced vacancies are observed. In the Si(P : 10^{20}) sample irradiated to the fluence $\Phi = 5 \times 10^{17}$ cm^{-2} the lifetime spectrum can be decomposed and the vacancy component $\tau_2 = 250 \pm 3$ ps is obtained. Both irradiated Si([As] = 10^{20} cm^{-3}) samples have only a single positron lifetime of about 247 ± 2 ps, almost independently of the irradiation fluence (Fig. 1). This behavior can be explained by a total positron trapping at irradiation-induced vacancy defects. When the vacancy concentration exceeds 10^{18} cm^{-3} [5,11], all positrons annihilate at the irradiation-induced vacancy defects with the lifetime 247 ± 2 ps and no annihilations take place at the delocalized bulk state or at the native vacancies detected only before irradiation.

The same positron lifetime at the vacancy, $\tau_V = 248 \pm 3$ ps, is thus observed for three different types of samples: (i) as-grown Si([As] = 10^{20} cm^{-3}), (ii) electron-irradiated Si([As] = 10^{20} cm^{-3}), and (iii) electron-irradiated Si([P] = 10^{20} cm^{-3}). The positron lifetime at the vacancy characterizes the open volume of the defect. According to experiments [11,12] and theoretical calculations [13], the lifetime of 248 ± 3 is typical for the single vacancy in Si, whereas for a divacancy much larger values of about 300 ps are observed [13–15]. In all three systems listed above, the open volume of the dominant vacancy defect is the same, and equal to that of a monovacancy.

4. Doppler broadening results

In order to identify the monovacancies in greater detail, we have performed Doppler broadening experiments using the two-detector coincidence technique [10]. These

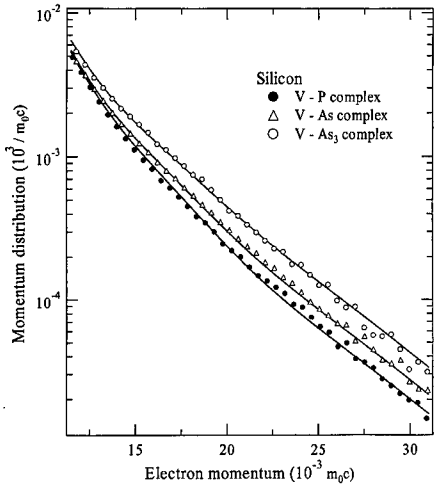

Fig. 3. The high momentum part of the positron–electron momentum distribution at the various vacancy–impurity pairs, identified in electron irradiated Si([P] = 10^{20} cm^{-3}) (•) and in as-grown (○) and irradiated (△) Si([As] = 10^{20} cm^{-3}). The results of theoretical calculations are shown by the solid lines [6].

measurements yield the one-dimensional momentum distribution of electrons as seen by the positron. In the samples containing vacancy defects we obtain the superimposed distribution $\rho(p) = (1-\eta)\rho_B(p) + \eta\rho_V(p)$, where $\rho_B(p)$ and $\rho_V(p)$ are the momentum distributions in the lattice and at the vacancy, respectively. The lifetime results (Fig. 1) can be used to determine the fraction of positrons annihilating at vacancies $\eta = (\tau_{av} - \tau_B)/(\tau_V - \tau_B)$. Since the momentum distribution in the lattice $\rho_B(p)$ can be measured in the reference sample, the distributions $\rho_V(p)$ at vacancies can be decomposed from the measured spectrum ρ(p).

The momentum distributions $\rho_V(p)$ at vacancies are very different in the higher momenta ($p > 12 \times 10^{-3}$ m_0c), where the annihilation with core electrons is the most important contribution (Fig. 3). This result indicates that the vacancy is surrounded by different atoms in each of the three cases. Because both in Si ($Z = 14$) and P ($Z = 15$) the 2p electrons constitute the outermost core electron shell, the core electron momentum distributions of these elements are very similar. The crucial difference in the core electron structures of Si, P, and As is the presence of 3d electrons in As. The overlap of positrons with the As 3d electrons is much stronger than with the more localized Si or P 2p electrons. The increased intensity of the core electron momentum distribution is thus a clear sign of As atoms surrounding the vacancy.

5. Identification of the vacancy defects

The 2 MeV electron irradiation creates vacancies and interstitials as primary defects, both of which are mobile at 300 K [16]. In heavily n-type Si the donor atom may capture the vacancy and form a vacancy–impurity pair [16]. The monovacancy detected in heavily P-doped Si is thus the V–P pair. Similarly, it is natural to associate the electron irradiation-induced vacancy in Si([As] = 10^{20} cm^{-3}) with a V–As pair surrounded by a single As atom. The influence of As next to the vacancy is clearly visible as the enhanced intensity in the high momentum region (Fig. 3). Since even stronger signal from As is seen in the as-grown Si([As] = 10^{20} cm^{-3}), we can conclude that this monovacancy is surrounded by at least two As atoms.

To analyze quantitatively the chemical environment of the monovacancies we define the conventional W parameter as an integral of the momentum distribution at $20 \times 10^{-3} < p/m_0c < 25 \times 10^{-3}$ (Table 1). Because of the similar core electron structures of Si and P the value $W_V/W_B = 0.71$ measured for the V–P pair is expected to be close to that of an isolated vacancy (for a theoretical verification, see below). The W_V/W_B increases by 0.28 between the V–P pair (isolated vacancy) and the V–As pair found in electron irradiated Si([As] = 10^{20} cm^{-3}). For the vacancy in as-grown Si([As] = 10^{20} cm^{-3}) the ratio $W_V/W_B = 1.49$. The change of W_V/W_B from the irradiation-induced V–As pair to the native V–As_n

Table 1
Experimental (exp.) and theoretical (theor.) positron annihilation characteristics at vacancy–arsenic complexes in Si. The leftmost column indicates the number of As atoms neighboring the vacancy. τ_V, W_V and W_B are the positron lifetime and the high electron-momentum parameters in the bulk (subscript B) and at the vacancy (subscript V), respectively [6]

Number of As atoms	τ_V (ps) (exp.)	τ_V (ps) (theor.)	W_V/W_B (exp.)	W_V/W_B (theor.)
0	248(3)	257	0.71(3)	0.74
1	248(3)	254	0.99(3)	0.98
2		253		1.23
3	248(3)	252	1.49(3)	1.49
4		250		1.76

complex is thus about twice the difference between the V–P (isolated vacancy) and V–As defects. A linear extrapolation of the W_V/W_B ratio on the number of neighboring As atoms thus indicates that the native complex is $V–As_3$, i. e. the vacancy is surrounded by three As atoms.

In order to put the above ideas on a firmer basis we calculated the momentum distributions of annihilating electron–positron pairs theoretically [13,17]. The valence electron densities were calculated self-consistently employing the plane-wave pseudopotential method. Atomic wave functions were used for core electrons. A supercell of 64 atomic sites in a periodic superlattice was used to describe defects which were assumed to be neutral and ideal, i.e., the atoms were at the ideal lattice sites. The positron states and annihilation characteristics were calculated within the local density approximation for electron–positron correlation.

The theoretical results reproduce well the experimental observation that the positron lifetime is rather insensitive to the substitutional impurities surrounding the vacancy (Table 1). The calculations verify further that nearly the same W parameter is obtained for an isolated vacancy and a V–P pair. The theoretical and experimental momentum distributions are in a good agreement at high momenta (Fig. 3). The theoretical W_V/W_B ratio increases by about 0.26 for each As atom added. This is the same difference as deduced above from the experimental results for V–P and V–As pairs and used further to identify the $V–As_3$ native defect. The calculated W_V/W_B ratio for $V–As_3$ complex is in very good agreement with the experimental result, whereas those of $V–As_2$ and $V–As_4$ are much too small or large, respectively. The experimental and theoretical results for V–As and $V–As_3$ are in good agreement even in the valence electron momentum range [6]. The theoretical calculations thus strongly support the experimental defect identifications that (i) vacancies complexed with a single donor impurities are detected in electron irradiated P and As-doped Si, and (ii) the native defect in Si([As] = 10^{20} cm^{-3}) is a vacancy surrounded by three As atoms.

6. Diffusion and deactivation of arsenic

The existence of $V–As_3$ complexes in heavily As-doped Cz Si is consistent with the defect formation and diffusion mechanisms described theoretically by Ramamoorthy and Pantelides [3]. At high temperature, the diffusion of As starts by the formation of V–As pairs, which can migrate, if two As atoms are fifth neighbors or closer to each other, thus enabling the formation of $V–As_2$ complexes [18]. The calculations predict that this complex can diffuse fast through the sample even at moderate temperatures [3]. At the high growth temperature of Cz Si, the $V–As_2$ complexes thus migrate until they stop at the substitutional As forming the $V–As_3$ complex. In perfect agreement with this theoretical scheme, the $V–As_3$ complex is observed in the experiments in the Si([As] = 10^{20} cm^{-3}) sample. This defect complex is stable over the 700–800 K annealing stage (Fig. 2), which is seen in ion-implanted or low-temperature grown Si and is most likely related to the migration of V–As and $V–As_2$ (see e.g. Refs. [1,3]). No $V–As_3$ are found at the lower doping level of [As] = 10^{19} cm^{-3}, most likely because the average distance between the donor atoms is too large to form the migrating $V–As_2$ in the process described above.

The concentration of free electrons in heavily doped Si saturates at $\leqslant 5 \times 10^{20}$ cm^{-3} due to the formation of compensating defects [1]. The deactivation has been theoretically explained by the creation of vacancy–impurity complexes V_m–As_n, but there is no agreement on the value of m and n [2,3,19]. The present results show that $V–As_3$ is the dominant vacancy defect in Cz grown Si([As] = 10^{20} cm^{-3}), i.e. $m = 1$ and $n = 3$. The concentration of $V–As_3$ in our samples is $\sim 10^{17}$ cm^{-3}, which is a typical value for compensating centers at the doping level of 1×10^{20} cm^{-3} [1,4,9,19]. Recently, the deactivation of dopants has been attributed to the formation of defects containing pairs of dopant atoms without vacancies [4]. The present experiments do not give information on these defects, because the open volume in them is too small to trap positrons.

7. Conclusions

The present results show that positron lifetime and core electron momentum distribution experiments can yield detailed information on the open volume and atomic surrounding of vacancy–impurity complexes in Si. In electron irradiated material, we identify vacancies complexed with single P and As impurities. In as-grown Si we observe the formation of vacancy defects when the As doping level increases up to 10^{20} cm^{-3}. The native defect is identified as a monovacancy surrounded by three As atoms. The formation of $V–As_3$ complex is consistent with the theoretical predictions on the As diffusion and electrical deactivation in highly doped Si.

References

[1] A. Lietoila et al., Appl. Phys. Lett. 36 (1980) 765.
[2] K.C. Pandey et al., Phys. Rev. Lett. 61 (1988) 1282.
[3] M. Ramamoorthy et al., Phys. Rev. Lett. 76 (1996) 4753.
[4] D.J. Chadi et al., Phys. Rev. Lett. 79 (1997) 4834.
[5] K. Saarinen et al., in: M. Stavola (Ed.), Identification of Defects in Semiconductors, Academic Press, New York, 1998, p. 209.
[6] K. Saarinen et al., Phys. Rev. Lett. 82 (1999) 1883.

[7] D.W. Lawther et al., Appl. Phys. Lett. 67 (1995) 3575.
[8] U. Myler et al., Appl. Phys. Lett. 69 (1996) 3333.
[9] S. Szpala, Phys. Rev. B 54 (1996) 4722.
[10] M. Alatalo et al., Phys. Rev. B 51 (1995) 4176.
[11] J. Mäkinen et al., Phys. Rev. B 39 (1989) 10162.
[12] J. Mäkinen et al., J. Phys.: Condens. Matter 4 (1992) 5137.
[13] M. Hakala et al., Phys. Rev. B 57 (1998) 7621.
[14] V. Avalos et al., Phys. Rev. B 54 (1996) 1724.
[15] H. Kauppinen et al., Phys. Rev. B 55 (1997) 9598.
[16] G.D. Watkins, in: S. Pantelides (Ed.), Deep Centers in Semiconductors, Gordon and Breach, New York, 1986, p. 147.
[17] M. Alatalo et al., Phys. Rev. B 54 (1996) 2397.
[18] D. Mathiot et al., Appl. Phys. Lett. 42 (1983) 1043.
[19] M.A. Berding et al., Appl. Phys. Lett. 72 (1998) 1492.

ELSEVIER

Physica B 273–274 (1999) 468–472

PHYSICA B

www.elsevier.com/locate/physb

Defect states at silicon surfaces

A.J. Reddy[a,*], J.V. Chan[a], T.A. Burr[a], R. Mo[b], C.P. Wade[b], C.E.D. Chidsey[b], J. Michel[a], L.C. Kimerling[a]

[a]*Department of Materials Science and Engineering, Massachusetts Institute of Technology, Cambridge, MA 02139, USA*
[b]*Department of Chemistry, Stanford University, Stanford CA 94305, USA*

Abstract

We demonstrate that surface defects can be characterized in terms of the same parameters that are used for studying bulk defects. We have a model for defect formation on the surface that allows us to estimate formation energies. By combining our contactless surface recombination velocity (SRV) measurement with other surface analysis techniques, we are able to determine the electrical activity of many surface species. We demonstrate observation of surface dangling bonds created by O_2 dissolved in dilute hydrofluoric acid (HF). Immersion in a methanol/I_2 solution is shown to produce electronically passive Si–OR bonds. Minority carrier capture cross sections for metal defects are calculated based on independent measurement of metal surface coverage. Through the understanding of surface defects, we apply our lifetime measurement to monitor metal contamination from dilute HF solutions. A model relating metal deposition rate to HF dilution is developed. We demonstrate sensitivity of 20 parts per trillion (ppt) Cu in a 500 : 1 HF solution.

Keywords: Surface defect; Passivation; Dangling bond; Lifetime

1. Introduction

Understanding of surface defects is important for many processes in semiconductor manufacturing. For wafer cleans to produce surfaces that meet the guidelines specified in the SIA National Technology Roadmap for Semiconductors [1], the fundamentals of surface contamination need to be understood. The thinner oxides required for future CMOS generations require defect-free Si/SiO_2 interfaces. The growing demand for epitaxial wafers requires understanding how surface defects affect the quality of epi-layers. Fermi-level pinning due to the presence of surface states can cause problems in the formation of ohmic or Schottky contacts. Understanding of surface defects is required in all these cases to achieve required performance of advance semiconductor devices.

Our goal is to characterize surface defects in terms of the same parameters employed in the study of bulk defects. A surface defect is defined as any surface or interface deviation from the Si–Si sp^3 bond configuration of the bulk. Fig. 1 shows schematics of representative surface defects that we have studied: a silicon dangling bond, hydrogen and fluorine terminations, our novel –OR termination, and a metal adsorbate. In this work, we demonstrate observation of dangling bonds created at the surface by reaction with O_2 dissolved in solution. We provide data that shows that the Si–OR termination does not introduce surface states. For metal adsorbates, we calculate capture cross sections for both Au and Cu and present a model for the role of HF dilution in metal deposition rate. Based on this understanding, we demonstrate a method to monitor metal contamination in HF at part per trillion (ppt) sensitivity.

2. Defect formation

One can understand the driving force for defect formation by directly comparing electron energy levels in the silicon with energy levels of the terminating species in

* Corresponding author. Fax: + 1-617-253-6782.
E-mail address: ajreddy@mit.edu (A.J. Reddy)

0921-4526/99/$ - see front matter
PII: S0921-4526(99)00527-X

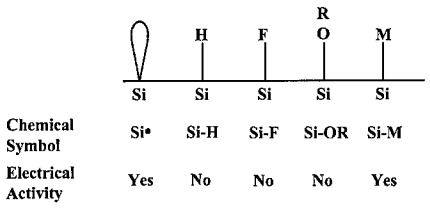

Fig. 1. Possible silicon surface defects: Surface dangling bond, H-terminated Si, F-terminated Si, OR-terminated Si, and metal defect. The electrical activity of each defect is determined by minority carrier recombination lifetime measurements.

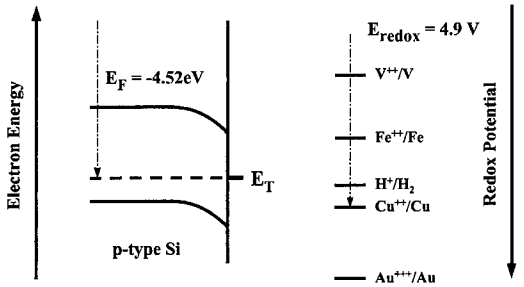

Fig. 2. Thermodynamic model for surface defect formation. Comparison of electron energies of the silicon wafer and electron energies of the terminating group determines the driving force for defect formation.

solution. Fig. 2 shows band energies for p-type Si compared to redox potentials for metal contaminants. The bands bend near the surface due to the charging of surface states. For a high density of surface states, the Fermi level will be pinned at the trap level of the surface defect, as shown in the diagram. Energy levels for the contaminant species are represented by their redox potentials.

Alignment of these two energy scales at the vacuum level shows the driving force for electron transfer [2]. For redox potentials which lie below E_F, electron transfer from the silicon to the metal ion is thermodynamically favorable. These ions will form bonds with the silicon surface. Redox potentials which lie above E_F have a positive formation energy and surface defects are not expected to form spontaneously.

3. Electrical activity

We probe the electrical activity of surface defects through the contactless measurement of minority carrier recombination lifetime. The recombination activity of the surface is characterized by the surface recombination velocity

$$S = N_s \sigma v_{th},$$

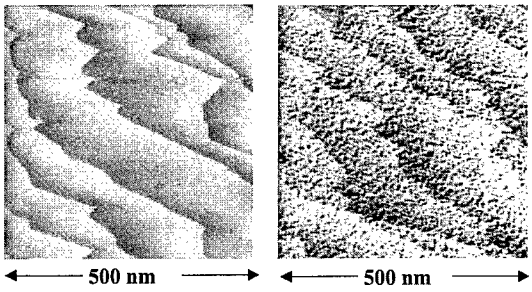

Fig. 3. Scanning tunneling microscopy images for Si (111) surfaces exposed for 3 min to different 50 : 1 HF solutions. The HF for image (a) was sparged with Ar, while that for (b) was saturated with O_2. The roughness of image (b) shows that O_2 is responsible for initiating etch pits.

where N_s is the density of surface defects, σ is the minority capture cross-section, and v_{th} is the carrier thermal velocity. By using wafers with high bulk lifetime, one can extend detection sensitivity to surface defects below 10^9 cm^{-2} [3].

3.1. Dangling bonds on Si–H

The mechanism for surface roughening was studied using scanning tunneling microscopy (STM) [4]. Fig. 3 shows images obtained of Si (111) wafers immersed for 3 min in 50 : 1 HF solutions. The solution used for the wafer in image (a) was bubbled with Argon to remove all O_2, while the solution for (b) was saturated with O_2. The wafer in the Ar-sparged solution shows atomically flat terraces, extending for hundreds of atoms, with clearly defined step edges. In image (b), meanwhile, there are numerous etch pits and no clearly-defined step edges. By repeating these experiments with the addition of H_2O_2, the superoxide anion radical (O_2^-•) has been identified as the active species. The reaction by which etch pits are initiated is

$$O_2^-\bullet + Si - H \rightarrow Si\bullet + HO_2^-,$$

where Si• is a dangling bond. The etch pits grow as the dangling bonds are attacked by the F^- in solution.

We observe these dangling bonds directly by their role in surface recombination activity. Fig. 4 shows our data for p-Si (100) wafers exposed to 100 : 1 HF solutions. We calculate the density of dangling bonds from the lifetime by assuming a typical value for the electron capture cross section of 10^{-16} cm^2. The correlation shown between defect density of the wafer surface and dissolved O_2 concentration confirms the theory for dangling bond formation shown above.

3.2. Termination with Si–OR

The termination of the silicon surface is modified by immersing a H-passivated surface in a solution of iodine

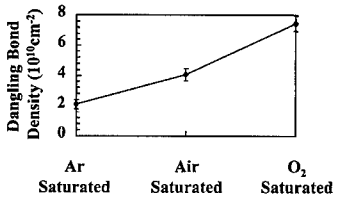

Fig. 4. Dangling bond density, calculated from lifetime measurements, for Si (100) wafers exposed to different 100 : 1 HF solutions. The increase for the O_2-saturated solution confirms the role of O_2 in removing hydrogen from Si–H bonds.

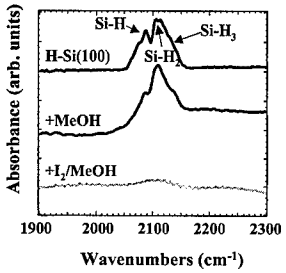

Fig. 5. Attenuated total reflection fourier transform infrared spectroscopy (ATR-FTIR) data showing the Si–H stretching region. The disappearance of all peaks for the I_2/MeOH line indicates that iodine is required to catalyze the replacement of Si–H bonds with Si–OCH_3.

and methanol (CH_3OH). Fig. 5 shows ATR-FTIR data in the region of the Si–H stretch. The top spectrum is for a wafer that has been passivated in dilute HF and clearly shows mono- and di-hydride peaks with a small tri-hydride shoulder. Immersion in pure methanol does little to modify the spectrum, while the I_2/methanol solution removes nearly all the hydrogen. X-ray photoelectron spectroscopy (XPS) was used to provide positive identification of the surface species. Fig. 6 shows XPS data of a wafer that has been exposed to a solution of I_2 in methanol and corresponds to surface coverage by C, O and I in a ratio of 10 : 10 : 1. This ratio implies a reaction mechanism in which iodine serves as a catalyst for the attachment of methoxy groups:

$$CH_3OH + Si - H \xrightarrow{I_2} Si - OCH_3 + 2H\bullet.$$

Lifetime measurements of this surface provide us with a direct measure of the electrical activity of the Si–OR bond. Fig. 7 shows lifetime data comparing this novel methoxy-passivated surface to the passivation achieved by dilute (100 : 1) HF and concentrated HF. The density of trap states is again calculated by assuming $\sigma = 10^{-16}$ cm^2. The estimated trap density of 6×10^9 cm^{-2} represents 6 parts per million of the surface terminations and shows clearly that Si–OR, the majority species on the surface, is not electrically active.

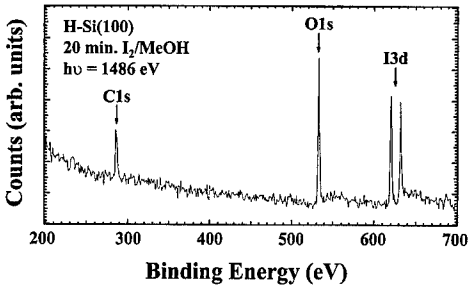

Fig. 6. X-ray photoelectron spectrum (XPS) of a Si (100) wafer immersed in a MeOH/I_2 solution. The 10 : 10 : 1 C : O : I ratio suggests that iodine is a catalyst for methoxy attachment.

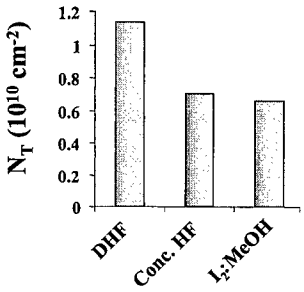

Fig. 7. Surface trap state density, calculated from lifetime measurements, for Si (100) wafers immersed in HF and I_2/methanol solutions. The trap density for the I_2/MeOH surface indicates that the Si–OR termination is not electrically active.

3.3. Metal adsorbates

In our model for defect formation, we discussed how metal ions in solution deposit on the wafer surface. The entire reaction scheme also involves silicon corrosion and hydrogen gas evolution, and can be represented by

$$6F^- + M^{++} + 2Si - H \rightarrow Si - M + H_2 + SiF_6^{--}.$$

Table 1 summarizes our sensitivity to metal defects. Independent measurement of the surface coverage by total-reflection X-ray fluorescence (TXRF) combined with our lifetime data allows us to calculate the capture cross-section of a single metal adsorbate site. We estimate the resolution for metal adsorbate detection as a 2% change in the lifetime.

4. Application to contamination monitoring

Based on the understanding of surface defects outlined above, we have developed a method for in-situ monitoring of metal contamination in dilute HF [5]. In our system, dilute HF is pumped from a 20 l tank through

Table 1
Summary of recombination activity of Au and Cu adsorbates (on n-type Si). The surface coverage, measured independently by Total-reflection X-Ray Fluorescence (TXRF), allows us to calculate capture cross sections. The detection limit is calculated based on measuring a 2% change in lifetime.

	Surface coverage (cm^{-2})	τ_{meas} (ms)	Cross-section (σ_n) (cm^2)	Resolution (cm^{-2})
Au	3.4×10^{11}	1.05	1×10^{-17}	6.3×10^9
Cu	6.5×10^9	5.96	9.6×10^{-17}	6×10^8

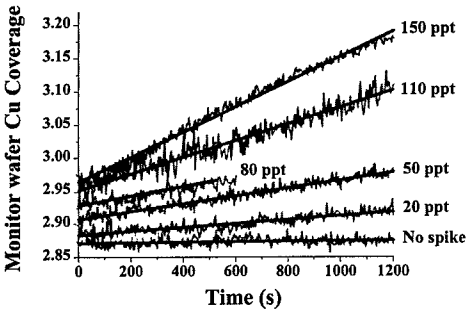

Fig. 8. Surface metal coverage versus time for the monitor wafer used in detection of metal contamination. The slope of each line is a measure of the metal deposition rate.

a Teflon flow cell that houses a $1'' \times 1''$ piece of silicon. Reducible metals present in the HF will deposit on the surface of the wafer, as described above. By continuously measuring the lifetime of this monitor wafer, we can directly observe the rate of metal deposition, and hence, extrapolate the concentration of metals in the solution.

A set of data we obtained using a 500 : 1 HF solution is shown in Fig. 8. The metal surface coverage is calculated from the inverse of the lifetime and is plotted in arbitrary units. The line labeled 'No spike' shows that the lifetime remains constant when there are no contaminants in the bath. With the addition of just 20 parts per trillion (ppt) of Cu, we see that the lifetime changes noticeably over the range of 20 min. With the addition of more Cu, we see that the lifetime degrades more rapidly, indicating that the deposition rate is strongly dependent on the Cu concentration.

By measuring the slope of each of these lines and using the cross sections calculated above, we can determine the rate of metal deposition corresponding to each Cu concentration. This data is shown in Fig. 9, along with similar data taken for a 100 : 1 HF bath. For both sets of data, we see that there is a linear relationship between deposition rate and metal concentration. In the 500 : 1 solution, though, deposition occurs nearly 15 times as fast. We can explain this sharp dependence by considering that Cu deposition and evolution of H_2 gas compete for available electrons. The hydrogen evolution current drops off when $[H^+]$ is reduced, and Cu reduction can therefore proceed more rapidly. A more complete explanation is presented elsewhere [6] based on analysis of all the electron transfer reactions occurring between the silicon wafer and the solution.

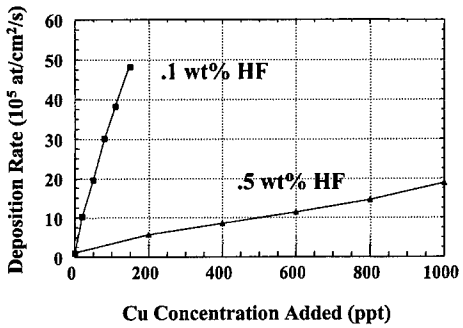

Fig. 9. Deposition rate versus Cu concentration for 500 : 1 HF and 100 : 1 HF. The line for the 500 : 1 bath is 15 times as steep at the line for the 100 : 1 solution.

5. Conclusion

By combining conventional tools for surface analysis with electrical measurements of surface recombination, we are able to determine the electrical activity of a number of surface defects. In dilute HF we have observed surface recombination at dangling bonds introduced by dissolved O_2. Our studies of I_2/methanol passivation show that the Si–OR termination is not electrically active. We calculate capture cross-sections for atomic Au and Cu adsorbates. Based on this fundamental knowledge of surface defects, we have developed a monitor for in-situ detection of metal contamination in HF. The rate of degradation of the lifetime provides quantitative assessment of contamination in the bath. Deposition is shown to be much more rapid in dilute solutions and allows for detection of 20 ppt Cu in a 500 : 1 HF bath.

Acknowledgements

The authors at MIT would like to thank Patrick Taylor at Mitsubishi Silicon America for providing silicon wafers. Laurie Johnston and Tom Blanchard at Kanto Chemical Corporation were helpful in providing ultrapure chemicals. This research was funded by the NSF-SRC Center for Environmentally Benign Semiconductor Manufacturing.

References

[1] National Technology Roadmap for Semiconductors, Semiconductor Industry Association, San Jose CA, 1997.
[2] S.R. Morrison, Electrochemistry of Semiconductors and Oxidized Metal Electrodes, Plenum, New York, 1980.
[3] G.J. Norga, Ph.D. Thesis, Massachusetts Institute of Technology, Cambridge, MA, 1996.
[4] C.P. Wade, C.E.D. Chidsey, Appl. Phys. Lett. 71 (1997) p. 1679.
[5] A.J. Reddy, G.J. Norga, Park, A.L. Smith, J. Michel, L.C. Kimerling, Mater. Res. Soc. Symp. Proc. 447 (1997) 1.
[6] A.J. Reddy, S. McDonald, J. Michel, L.C. Kimerling, in press.

ELSEVIER

Physica B 273–274 (1999) 473–475

PHYSICA B

www.elsevier.com/locate/physb

Effects of extended defects on the properties of intrinsic and extrinsic point defects in silicon

J.F. Justo[a,*], A. Antonelli[b], T.M. Schmidt[c], A. Fazzio[a]

[a]*Instituto de Física da USP, CP 66318, CEP 05315-970, São Paulo-SP, Brazil*
[b]*Instituto de Física Gleb Wataghin, UNICAMP, CEP 13083-970, Campinas-SP, Brazil*
[c]*Universidade Federal de Uberlândia, CP 593, CEP 38400-902, Uberlândia-MG, Brazil*

Abstract

We investigated the interaction of intrinsic and extrinsic point defects with stacking faults in silicon. The calculations were carried out using ab initio total energy methods. The results show that the formation energies of intrinsic defects and impurities (P, As, and Al) are lower at the stacking fault as compared to the respective defects in crystalline environment. Therefore, stacking faults should have a large concentration of defects, and they should play an important role on the mechanisms of dislocation motion. © 1999 Elsevier Science B.V. All rights reserved.

Keywords: Extended defects; Point defects; Stacking faults

The interaction of point defects with extended defects (grain boundaries, dislocations, and stacking faults) in semiconductors has been the subject of interest over the last decade [1]. Impurities have been observed to segregate at extended defects. This effect, called gettering, shows how extended defects may play an important role in controlling the detrimental effects of impurities in the active region of the semiconducting devices. At the same time, extended defects may themselves be detrimental to the performance of such devices. Therefore, understanding the properties of extended defects and their interactions with point defects is crucial to develop better semiconducting devices.

Studies on extended defects and their interactions with point defects have focused on the properties of grain boundaries and dislocations. Although stacking faults (SF) play a central role in the mobility of dissociated dislocations, they have not received attention until very recently [2,3]. In zincblende semiconductors, dislocations belonging to the {1 1 1} glide planes dissociate into partial dislocations having an SF between the partials [4]. This dissociation is energetically favorable and facilitates the dislocations to glide conservatively. Dislocations glide by the thermally activated mechanisms of kink formation and migration [4,5]. However, point defects interact with the dislocation and the SF which may affect the dislocation mobility. Several theoretical studies have explored the interaction of defects with the dislocation cores [6,7]. What is not clear so far is how or whether the interaction of point defects with the SF may also affect the dislocation mobility. Here we investigated the interactions of intrinsic (vacancies and interstitials) and extrinsic (dopants) point defects with an SF in silicon. We compared the electronic and structural properties of point defects at an SF with the respective defects in the crystalline environment. We showed that the formation energies of intrinsic and extrinsic defects at the SF are lower, by up to 0.6 eV, than in the crystalline environment. Therefore, there should be segregation of impurities to the SF, which could affect the mobility of the dislocations.

We computed the properties of the defects using the density functional theory and local density approximation framework. The Kohn–Sham equations were solved using the Car-Parrinello scheme [8,9] with norm-conserving pseudopotentials [10,11]. The basis-set was expanded in plane-waves, with kinetic energy up to 12 Ry

* Corresponding author. Tel.: + 55-11-818-7018; fax: + 55-11-818-6831.
E-mail address: jjusto@if.usp.br (J.F. Justo)

0921-4526/99/$ - see front matter
PII: S0921-4526(99)00528-1

(see Ref. [3]). The sampling in the Brillouin zone was performed using the Γ-point. An orthorhombic supercell of 160 atoms was used as reference. It consisted of five double planes stacked along the [1 1 1] direction, simulating an infinite SF in the [1 1 1] plane. This supercell has the dimensions: 13.7 Å × 15.6 Å × 15.3 Å. It may not be large enough to prevent interaction between the defects and their images, specially in the case of impurities. However, we stress that we used the same cell to compute all the defects, which allowed to compare total energies among the defects in different sites of the cell. The optimization of the atomic structure was performed by allowing atoms to move until the Hellmann–Feynman forces were smaller than 10^{-3} Ha/au.

Fig. 1 shows a side view of the simulation cell, with the SF perpendicular to the [1 1 1] direction. The calculations were performed considering each defect in two distinct sites in the cell: the crystalline-like (CL) site and the SF site. Atoms at the CL layer in Fig. 1 are at a distance of 7.8 Å from the SF or of its image. The surrounding environment of an atom in the CL site is that of an atom in a perfect crystal up to the fourth nearest neighbor.

We considered the case of intrinsic point defects, in their neutral charge state, interacting with an SF. We computed the vacancy at the SF or in the crystalline environment by removing atoms in SF or CL sites respectively from the 160-atom supercell shown in Fig. 1. The formation energy of a vacancy in the crystalline-like site is 3.06 eV, which is in agreement with other theoretical calculations (3.27 eV) [12]. However, a vacancy at the SF has formation energy lower by 0.23 eV. In both cases, there is an inward relaxation of the four nearest neighbors of the vacancy. Apart from an inward relaxation, a Jahn-Teller distortion takes place, breaking up the tetrahedral symmetry, lowering it to a C_{2v} symmetry. The C_{2v} symmetry, instead of the usual a D_{2d}, is likely caused by the lowering of the symmetry of the system due to the presence of the stacking fault.

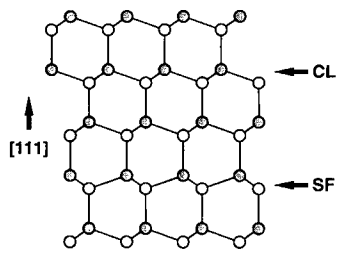

Fig. 1. Side view of the orthorhombic supercell consisting of 160 atoms used as a reference cell. The figure shows the [$\bar{1}$ 1 0] plane of a diamond cubic lattice in Si having an SF in the [1 1 1] glide plane. SF and CL sites represent the stacking fault and the crystalline-like environments.

The [1 1 0]-split dumbbell in Si is regarded to be the interstitial with the lowest formation energy [13]. The geometry of this defect consists of an empty lattice site with two atoms aligned along the [1 1 0] direction forming a dumbbell. The presence of the SF affects the [1 1 0]-split interstitial more strongly than the vacancy. As a result, the change in the formation energy between the CL and SF sites is larger: 3.10 and 2.49 eV at the CL and SF sites, respectively. This large difference in the formation energy is a result of the local structure close to the fault. Although the planar {1 1 1} packing is identical in the crystal and at the SF, the local structure around the defect at the SF site allows a larger relaxation than in the CL site. As a result, the distance between the two dumbbell atoms in the SF site is 2.52 Å which should be compared to the distance in the CL site of 2.48 Å. For the hexagonal interstitial, the difference in energy between the CL and SF sites is smaller: 3.43 and 3.28 eV at the CL and SF layers. This is because the hexagonal structure is very similar at the fault and in the crystal, and the six-atom ring of first neighbors is equivalent in both cases.

We now consider the interaction of substitutional impurities (P, As, and Al) with an SF. We used the same procedure as in the case of intrinsic defects. The difference in the calculated total energy for the impurity in the CL and in the SF sites gives the segregation energy of such defects at the SF [14]. For P, As, and Al the calculated segregation energies were 0.09, 0.07 and 0.09 eV, respectively. These results should be compared with the segregation energies of As in a dislocation core, at 0.33 eV [6]. Considering the case of As in a grain boundary, recent theoretical studies have reported a segregation energy of 0.11 eV [14]. Therefore, segregation of dopants is possible at all those extended defects.

In the case of intrinsic point defects, outstanding differences in the atomic relaxations were observed between the defects in the SF or CL sites. That was not the case for impurities, the atomic relaxation was equivalent in both SF and CL sites. For the substitutional impurities (P, As, and Al) there was no distortion which destroyed the tetrahedral symmetry. The first neighboring atoms only relaxed outward to accommodate the impurity atom. Therefore, the calculated segregation energy is not resulting from relaxation, instead it results from electronic effects. The P and As atoms in a crystalline substitutional site are donors, giving partially occupied shallow levels near to the bottom of the conduction band. In contrast, an Al atom is an acceptor, giving a partially occupied shallow level near to the top of the valence band. The interaction of those impurities with the SF changed the positions of these shallow levels with respect to the crystalline bands. For the impurities at the SF sites, the levels moved deeper into the gap, reducing the delocalization of the electronic wave functions.

In summary, we investigated the interaction of an SF with point defects in silicon. We found that formation

energies are lower at the SF than in the crystalline environment for all the cases studied here. Therefore, in thermodynamic equilibrium, concentrations of intrinsic and extrinsic defects should be larger at the SF than in the crystalline environment.

The interaction of impurities with dislocations has been measured to affect strongly the dislocation mobility [1]. This interaction can manifest itself as non-local or local effects. The non-local effect, called Pattel effect, results from the displacement of the Fermi level due to the doping of donors and acceptors. There is an increase (decrease) in the dislocation mobility by the presence of donors (acceptors). In that model, the increase in dislocation mobility is a result of a negatively charged dislocation core, which facilitates kink formation and migration. In our study, we observed that when the donor atoms were placed in the CL site, the SF became negatively charged. Therefore, not only dislocation core becomes negatively charged as a result of donor doping but also the SF. It would be of interest to investigate to what extent this non-local effect would affect the dislocation motion. The local effect would be the result of segregation of impurities in the dislocation core, pinning the dislocation. Measurements have shown that the binding energies of impurities in the dislocation core are as large as 0.5 eV [1]. Our results show that impurities may also segregate to the SF, and provide additional dislocation pinning.

Acknowledgements

The authors acknowledge partial support from Brazilian agencies FAPESP and CNPq. The calculations were performed at the facilities of the LCCA-USP and CENAPAD-SP.

References

[1] H. Alexander, in: F.R.N. Nabarro (Ed.), Dislocations in Solids, Vol. 7, Elsevier, Amsterdam, 1986, p. 115.
[2] M.Y. Chou, M.L. Cohen, S.G. Louie, Phys. Rev. B 32 (1985) 7979.
[3] A. Antonelli, J.F. Justo, A. Fazzio, Phys. Rev. B 60 (1999) 4711.
[4] J.P. Hirth, J. Lothe, Theory of Dislocations, Wiley, New York, 1982.
[5] V.V. Bulatov, J.F. Justo, W. Cai, S. Yip, Phys. Rev. Lett. 79 (1997) 5042.
[6] A. Maiti, T. Kaplan, M. Mostoller, M.F. Chisholm, S.J. Pennycook, S.T. Pantelides, Appl. Phys. Lett. 70 (1997) 336.
[7] N. Lehto, S. Öberg, Phys. Rev. B 56 (1997) 12 706.
[8] R. Car, M. Parrinello, Phys. Rev. Lett. 55 (1985) 2471.
[9] M. Bockstedte, A. Kley, J. Neugebauer, M. Scheffler, Comp. Phys. Commun. 107 (1997) 187.
[10] G.B. Bachelet, D.R. Hamann, M. Schluter, Phys. Rev. B 26 (1982) 4199.
[11] L. Kleinmann, D.M. Bylander, Phys. Rev. Lett. 48 (1982) 1425.
[12] M.J. Puska, S. Pöykkö, M. Pesola, R.M. Nieminen, Phys. Rev. B 58 (1998) 1318.
[13] P.E. Blochl, E. Smargiassi, R. Car, D.B. Laks, W. Andreoni, S.T. Pantelides, Phys. Rev. Lett. 70 (1993) 2435.
[14] A. Maiti, M.F. Crisholm, S.J. Pennycook, S.T. Pantelides, Phys. Rev. Lett. 77 (1996) 1306.

ELSEVIER

Physica B 273–274 (1999) 476–479

PHYSICA B

www.elsevier.com/locate/physb

Electron irradiation effects in Si observed at 4.2–25 K by means of in situ transmission electron microscopy

S. Takeda[a,*], J. Yamasaki[a], Y. Kimura[b]

[a]*Department of Physics, Graduate School of Science, Osaka University, 1-16 Machikane-yama, Toyonaka, Osaka 560-0043, Japan*
[b]*Department of Structural Biology, Biomolecular Engineering Research Institute, 6-2-3 Furuedai, Suita, Osaka 565, Japan*

Abstract

We have observed electron-irradiation effects in Si at low temperature, utilizing in situ transmission electron microscopy. Amorphization is induced in crystalline silicon (*c*-Si) by high-energy electron (MeV) irradiation at low temperatures. The mechanism of amorphization in Si is discussed in terms of self-interstitial clustering. In addition, we have also observed the electron (0.3 MeV) irradiation effects at 4.2 K in *c*-Si by means of high-resolution transmission electron microscopy. We have found that numerous defects of a few nanometer in diameter are introduced. The characteristics of the defects differs from those of the known interstitial clusters such as the {1 1 3} defects. The accumulation of the defects never leads to amorphization.

Keywords: Silicon; Electron irradiation; Amorphous; Electron microscopy

1. Introduction

Dynamic motions of covalent-bonded silicon atoms under electron irradiation have not entirely been revealed at low temperature. Defects introduced by electron irradiation at low temperature were extensively studied by electron paramagnetic resonance (EPR) and electronic measurements. In addition to the analysis of the atomic and electronic structures of the defects, it was also shown that self-interstitials were moveable under electron irradiation even at 4.2 K [1]. On the other hand, attempts have been made to pursue the nucleation and growth of defects in real space at low temperature utilizing transmission electron microscopy (TEM) [2,3]. Nevertheless, a lack of the stability of cryo-TEM has prevented us from observing the phenomena at high magnification.

It is usually thought that TEM cannot contribute significantly to the study of point defects in Si. In fact, individual point defects have not yet been clearly revealed by TEM. However, TEM studies of electron irradiation effects have brought the reliable atomic data about the clusters of self-interstitials [4,5], which has led us to, for instance, a novel picture of self-interstitials in Si [6,7]. Furthermore, TEM observation has occasionally led us into finding novel phenomena involving point defects under electron irradiation [8,9]. With the background, we have re-examined the electron-irradiation effects at low temperature by advanced cryo-TEM. In this presentation, we report our recent finding that crystalline silicon (*c*-Si) is rendered to amorphous silicon (*a*-Si) by electron irradiation at near 20 K [10]. We also show in situ high-resolution TEM observation of electron irradiation effects at 4.2 K.

2. Experimental procedures

Thin Si specimens were made of a P-doped Czochralski (CZ) Si {1 1 0} wafer. The specimens were set on a cooling specimen container for electron irradiation and observation in transmission electron microscopes (TEM). The electron energies for irradiation, E were 0.3, 1.0, 1.5 and 2.0 MeV. The direction of an incident electron beam

* Corresponding author. Tel.: + 81-6-6850-5752; fax: + 81-6-6850-5764.
E-mail address: takeda@phys.wani.osaka-u.ac.jp (S. Takeda)

0921-4526/99/$ - see front matter
PII: S0921-4526(99)00529-3

was set parallel to the ⟨1 1 0⟩ zone axis. The irradiation temperature, T ranged from 4.2 K to 297 K. For irradiation, an electron beam was focused on a specimen of about 1 μm in diameter in this study. The fluxes in 0.3, 1, 1.5 and 2 MeV irradiations were estimated to be 3.5×10^{19}, $1.8\text{–}2.6 \times 10^{20}$, 2.5×10^{20} and $0.84\text{–}8.1 \times 10^{20}$ $cm^{-2}\,s^{-1}$, respectively. The irradiation effects were observed by means of in situ TEM and recorded in photographic films with a smaller flux, roughly estimated to be 10^{17} $cm^{-2}s^{-1}$. After electron irradiation, the samples were transferred to a 200 keV TEMs, and post-irradiation examined at room temperature.

3. Results and discussion

3.1. *In situ lower voltage (0.3 MeV) TEM observation*

Electron (0.3 MeV) irradiation at 4.2 K induces a number of defects of a few nm in diameter (Fig. 1). They appear to be black in bright field TEM images (Fig. 2). The nucleation of similar defects was observed in *c*-Si thin foil coated by aluminum by lower magnification high-voltage (0.65 MV) TEM [2]. The energy of incident electrons (0.3 MeV) is sufficient to create Frenkel pairs, and insufficient to create cascade damages, since the threshold electron energy for displacement damage is about 0.15 MeV. Therefore, we conclude that the defects are secondary defects which are due to the agglomeration of point defects at 4.2 K. A preliminary analysis of the defects shows that they do not exhibit the habit planes, in contrast to the well known planar clusters of self-interstitials such as the {1 1 3} defects. Some of the defects exhibit void-like contrast. Increasing the doses, we observed the accumulation of the defects with the crystallinity retained.

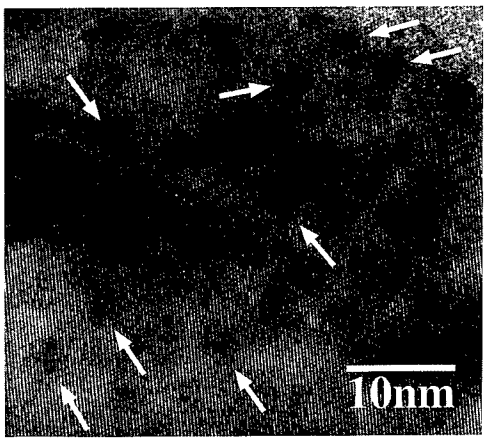

Fig. 2. Defects introduced by electron (0.3 MeV) irradiation at 4.2 K. The arrows indicate the defects.

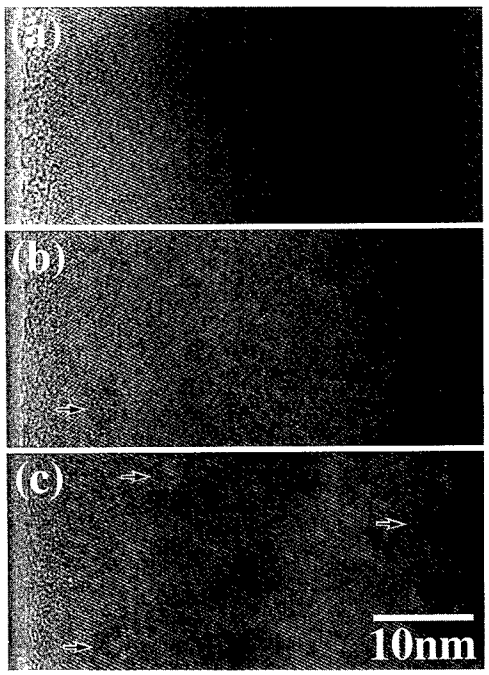

Fig. 1. In situ high-resolution TEM observation of a Si crystal under electron (0.3 MeV) irradiation at 4.2 K. The arrows indicate the defects introduced by electron irradiation.

3.2. *In situ higher voltage (2 MV) TEM observation*

Electron (2 MeV) irradiation at 25 K induces similar defects as those introduced by the irradiation of 0.3 MeV electrons. With the increase of the dose, the halo rings appeared in electron diffraction patterns and their intensities increased. Accordingly, the white TEM contrast came out in bright-field TEM images, indicating that the non-crystalline materials, i.e. *a*-Si is formed (Fig. 3(a)). The defects of a few nm in diameter are observed at the periphery of the irradiation spot where the dose is lower.

As seen in Fig. 3(b), electron (2 MeV) irradiation at room temperature introduces numerous {1 1 3} defects with the crystallinity retained.

Our experimental finding of the amorphization was surprising. It was long thought that *c*-Si cannot be rendered into *a*-Si by electron irradiation [3]. Therefore, we found a new route for amorphization in Si in addition to the previously reported routes by ion-implantation, indentation, laser melting and surface scratch etc. The new route has the potential application of fabricating artificial structures of the two Si structures with different dielectric and electronic transport properties, since a MeV electron beam can be focused on an area smaller than 0.2 μm in diameter, can be scanned and can penetrate about 0.5 μm into *c*-Si.

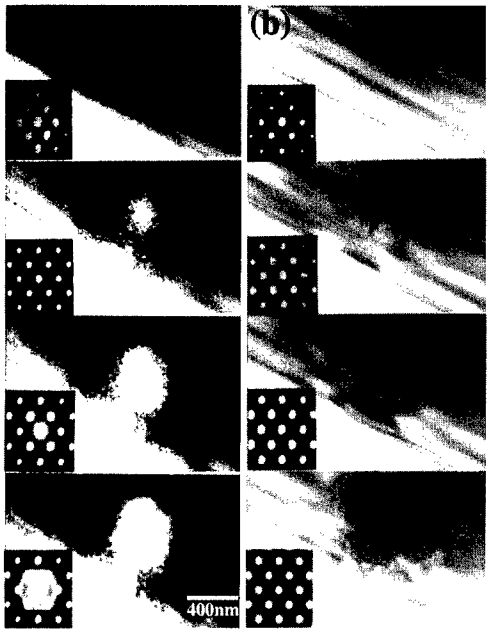

Fig. 3. In situ high voltage TEM observation of a Si crystal under electron (2 MeV) irradiation (a) at 25 and (b) at 293 K.

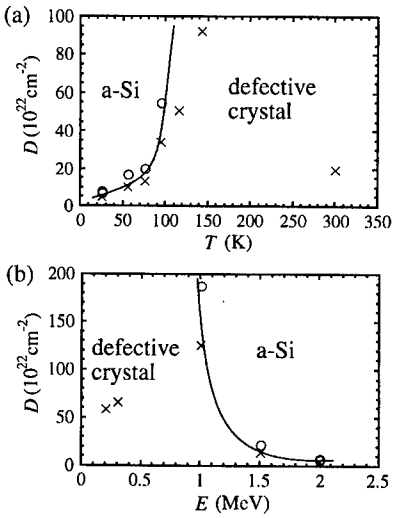

Fig. 4. Silicon structures under electron irradiation as a function of dose D and electron energy, E in (a) and that of D and irradiation temperature, T in (b). Circles and crosses represent amorphous and defective crystal, respectively. All the data in (a) were obtained by 2 MeV electron irradiation. Data in (b) were obtained at 25 K, except that the data of 0.3 MeV were taken at 4.2 K.

The halo intensity profiles in Fig. 3(a) were converted to the radial distribution functions (RDF) using an ordinary method. The peaks in the RDF are located at 0.235, 0.382, 0.588 and 0.755 nm. All of them correspond to those obtained in evaporated pure a-Si [3]. This means that, in terms of pair-wise atomic correlation, the structure of the a-Si induced by electron irradiation is similar to those of a-Si created by other existing techniques.

3.3. Diagram of the steady states under electron irradiation

The steady states under electron irradiation at low temperature are summarized in Fig. 4. The dose needed for amorphization increases steeply with the decrease of electron energy (Fig. 4(a)). The dose over 115 displacement / atom (dpa) is needed for amorphization by 1 MeV electron irradiation. The threshold electron energy for amorphization probably exists slightly below 1 MeV at 25 K. Clearly, the accumulation of point defects is insufficient to account for the amorphization under electron irradiation. It is known that the production rate of divacancies at 1.5 MeV is approximately 3–3.5 times larger than that at 1.0 MeV. In fact, the maximum recoil energy of a Si atom is of the order of 10^2 eV under MeV electron irradiation. Therefore, we suggest that the complex collision events, which create extremely small cascades such as divacancies and clusters of self-interstitials, are needed for the amorphization.

3.4. Mechanism of amorphization

It was suggested that self-interstitials and their clusters are embryos of a-Si [3,11], since they may include odd-membered atom rings as a-Si does. The simple clusters of vacancies are unlikely to contain odd-membered rings in their structures. However, the moveable self-interstitials may interrupt the amorphization and recover the crystallinity. A possible picture of the amorphization is the accumulation of small clusters of self-interstitials which possess a certain life time during electron irradiation. The cluster of four self-interstitials, i.e. I4 [5–7] may be an embryo of a-Si, since I4 consists of 5-, 6- and 7-membered rings, has the six-orientation variants as seen in Fig. 5 and is stable once it is formed. We suggest that the clustering of four self-interstitials takes place heterogeneously via the complex collision events and the accumulation of the clusters with dose induces amorphization. It is generally described that transformation from crystal to amorphous occurs whenever the average squared displacement of atoms from their equilibrium positions reaches a critical value. Accumulation of the I4 clusters increases the *static* average squared displacement monotonously with dose, naturally leading to amorphization.

4. Conclusion

In conclusion, we have observed electron irradiation effects in thin Si crystals at low temperature by means of

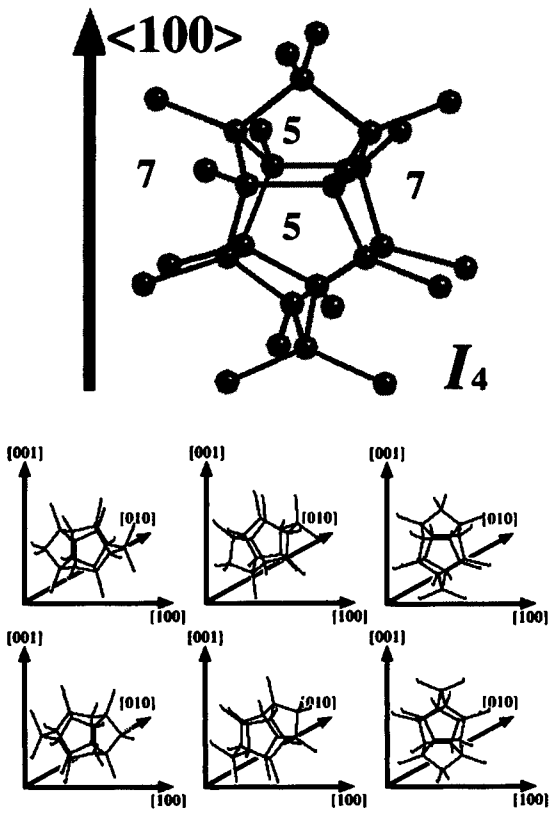

Fig. 5. The structure of I4 and its six orientation variants. In contrast to the {1 1 3} defect structure, the I4 structure has no periodicity in any direction. The structural characteristic of I4 is compatible with the structure of *a*-Si.

in situ TEM. We found that a new route exists for amorphization in Si. We observed the nucleation and growth of the secondary defects by high-resolution TEM at 4.2 K. We discussed the mechanism of amorphization in Si in terms of the clustering of self-interstitials.

Acknowledgements

This work was partially supported by the Ministry of Education, Science, Sports and Culture, Grant-in-Aid for Scientific Research (A)(2) No. 10305006, 1998.

References

[1] G. D. Watkins, Institute Conference Series No. 23, 1975, p. 1.
[2] H. Föll, Proceedings of the Lattice Defects in Semiconductors, Institute Physics Conference Series No. 23, 1974, p. 233.
[3] D.N. Seidman, R.S. Averback, P.R. Okamoto, A.C. Baily, Phys. Rev. Lett. 58 (1987) 900.
[4] S. Takeda, S. Muto, M. Hirata, Proceedings of the 16th International Conference Defects in Semiconductors (Lehigh) 1991: Materials Science Forum 83–87, 1992, p. 309.
[5] S. Takeda, Proceedings of the 10th International Conference Microscopy of Semiconducting Materials, Oxford, 1997: Institute Physics Conference Series No., 157, 1997, pp. 25–34.
[6] N. Arai, S. Takeda, M. Kohyama, Phys. Rev. Lett. 78 (1997) 4265.
[7] S. Takeda, N. Arai, J. Yamasaki, Proceedings of the 19th International Conference on Defects in Semiconductors (Aveiro) 1997: Materials Science Forum 258–263, 1997, p. 535.
[8] S. Takeda, K. Koto, S. Iijima, T. Ichihashi, Phys. Rev. Lett. 79 (1997) 2994.
[9] S. Takeda, K. Koto, Y. Kuno, S. Iijima and T. Ichihashi, Proceedings of the 19th International Conference on Defects in Semiconductors (Aveiro) 1997: Materials Science Forum 258–263, 1997, p. 553.
[10] S. Takeda, J. Yamasaki, Phys. Rev. Lett. 83 (1999) 320.
[11] V.J.B. Torres, P.M. Masri, A.M. Stoneham, J. Phys. C: Solid State Phys. 20 (1987) L143.

ELSEVIER

Physica B 273–274 (1999) 480–484

PHYSICA B

www.elsevier.com/locate/physb

Positron annihilation study of dopant effects on proton-irradiation defect in silicon

F. Hori[a,*], T. Chijiiwa[a], R. Oshima[a], T. Hisamatsu[b]

[a]*Research Institute for Advanced Science and Technology, Osaka Prefecture University 1-2, Gakuen-cho, Sakai, Osaka 599-8570, Japan*
[b]*National Space Development Agency of Japan, Tsukuba, Ibaragi 305-8505, Japan*

Abstract

Positron annihilation lifetime and doppler broadening measurements have been performed to examine the effects of B, Al and Ga dopants of Czochralski-grown Si (CZ-Si) on defects induced by 10 MeV proton irradiations at room temperature with a total dose from 3×10^{12} p/cm^2 to 5×10^{14} p/cm^2. Isochronal annealing experiments were also carried out after the irradiations. In spite of the high-energy proton irradiation, a short lifetime component τ_1 of about 100 ps was observed in all of the specimens, which is considered to be responsible for dopant–oxygen–vacancy complexes. The long lifetime component becomes remarkable in specimens with irradiation more than 10^{14} p/cm^2. In isochronal annealing experiments, annealing stages at 527 and 552 K were observed for the irradiated B doped CZ-Si with resistivities of 10 and 2 Ωcm, respectively. This corresponds to the formation of larger vacancy clusters. We found that the formation of the vacancy–oxygen complex depends on the species of dopant atoms of silicon, especially at irradiation below 10^{14} p/cm^2.

Keywords: Positron annihilation; Silicon; Proton irradiation; Dopant atoms

1. Introduction

The nature of radiation-induced vacancy-type defects in silicon has been well established by positron annihilation techniques [1–5]. High-energy particle irradiation with high fluence on the order of above 10^{14} p/cm^2 [1,2] and 10^{17} e/cm^2 [3,4] has mainly been used in previous experiments. Since positron annihilation experiments can detect defects with a concentration greater than the order of ppm, it is natural that few data for experiments with fluences under 10^{14} p/cm^2 have been analyzed. On the other hand, recent studies have shown that serious problems concerning interactions between small amounts of dopants, oxygen, and point defects arise during crystal growth process such as the formation of octahedral voids. The concentrations of these defects should be considerably low. The atomic concentrations of interstitial oxygen in the bulk silicon were of $9.5 \times 10^{17} \sim 1.6 \times 10^{18}$ cm^{-3} for CZ-Si and were of the order of 10^{15} cm^{-3} for float zone grown Si (FZ-Si). Dopant atom concentrations were about 4 orders of magnitude lower than those of oxygen in CZ-Si. These interactions have not been clarified yet. In this paper, positron annihilation experiments after low dose proton irradiation into silicon were performed to examine the interactions among oxygen, dopants and vacancy type defects.

2. Experiment

CZ-Si wafers with B, Ga and Al dopants were prepared as shown in Table 1. Samples (8 mm × 8 mm, 0.23 mm thick) for positron annihilation measurements were cut from the wafers. The 10 MeV-proton irradiations with total doses from 3×10^{12} to 5×10^{14} p/cm^2 were performed at room temperature with an AVF cyclotron at Takasaki Radiation Chemistry Research Establishment

*Corresponding author: Phone: +81-722-54-9812; fax: +81-722-54-9935.
E-mail address: horif@riast.osakafu-u.ac.jp (F. Hori)

0921-4526/99/$ - see front matter
PII: S0921-4526(99)00530-X

Table 1
Summary of CZ-Si samples and the total dose of proton irradiations with energy of 10 MwV

Dopant	Resistivety (Ω cm)	Fluence (10^{13} p/cm^2)
B	10	0.3, 1, 6, 10, 20, 50
B	2	0.3, 1, 6, 10, 20, 50
Al	10	0.3, 1, 6, 10, 20, 50
Ga	10	0.3, 1, 6, 10, 20, 50
None	862	0.3, 1, 10

of the Japan Atomic Energy Research Institute (JAERI). The total doses of proton employed in this study were lower than the previous ones used in most positron annihilation studies on proton-irradiated Si with doses above 10^{14} p/cm^2. The penetration depths of 10 MeV-protons were calculated to be at a maximum of 700 μm. Therefore, protons were thought to penetrate and only create cascade-type defects homogeneously in all specimens. Positron annihilation γ-ray energy spectrum doppler broadening measurements and positron lifetime measurements were simultaneously performed at room temperature. The isochronal annealing was carried out in a vacuum with a heating rate of 0.8 min/K. The positron source was ^{22}NaCl of 570 kBq that was sealed by 3 μm thickness Kapton foils and sandwiched between two identical Si samples. The full-width at half-maximum (FWHM) of a resolution curve for all positron lifetime spectra with total counts of 1.1×10^6 was about 220 ps. To evaluate the contribution from source components, we measured the positron lifetime spectrum of FZ-Si before irradiation. All of the positron lifetime spectra were analyzed with "RESOLUTION" and "POSITRONFIT" programs by Risø [6]. In the analyses, the lifetime spectra could be fitted by applying a two state trapping model with sufficient precision. Observations of doppler broadening distributions using an energy dispersive Ge detector were performed. The resolutional γ energy (FWHM) at 122 keV γ-line of ^{57}Co was about 581 eV. The spectrum with a total count of 3.5×10^7 was measured for each measurement.

3. Results and discussion

3.1. As-irradiated specimen

Fig. 1 shows the fluence dependence of positron annihilation lifetimes on 10 MeV proton irradiated non-doped CZ-Si. The long lifetime component of positron τ_2 and its relative intensity I_2 are almost unchanged with increases in the dose of proton up to 5×10^{14} p/cm^2. This is because low fluence irradiation induces an extremely

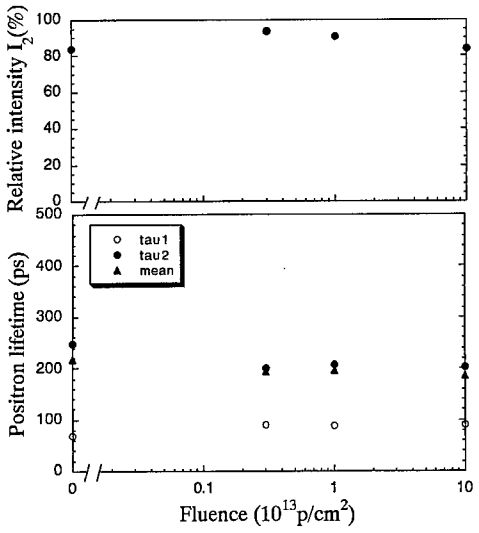

Fig. 1. Positron annihilation lifetime versus fluence of 10 MeV proton irradiation for non-doped CZ-Si. Filled and open circles denote the long- and short-lifetime components, respectively.

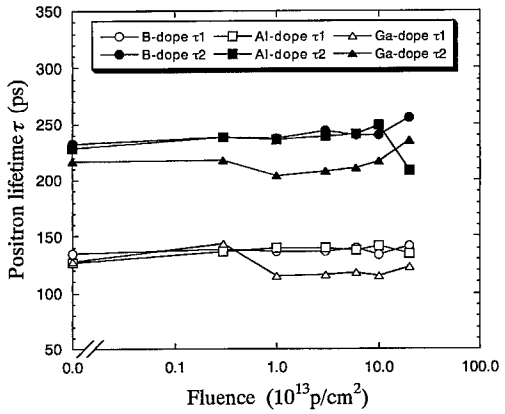

Fig. 2. Positron annihilation lifetimes τ_1 and τ_2 versus fluence of 10 MeV proton irradiation for B, Al and Ga doped CZ-Si. Filled and open marks denote the long- and short-lifetime components, respectively.

low concentration of defects, and it is hard to decompose vacancy type defects from the positron lifetime spectra. Fig. 2 shows the result of positron lifetime measurements for B, Al and Ga doped CZ-Si after proton irradiations. In Figs. 1 and 2, a short lifetime component $\tau 1$ of nearly 100 ps appeared in each case. This short lifetime component did not appear in FZ-Si before irradiation. In another positron experiment for Si with proton irradiation more than 10^{14} p/cm^2, only long lifetime components related to vacancy clusters were detected and no indication of short lifetime components could be found [1,2].

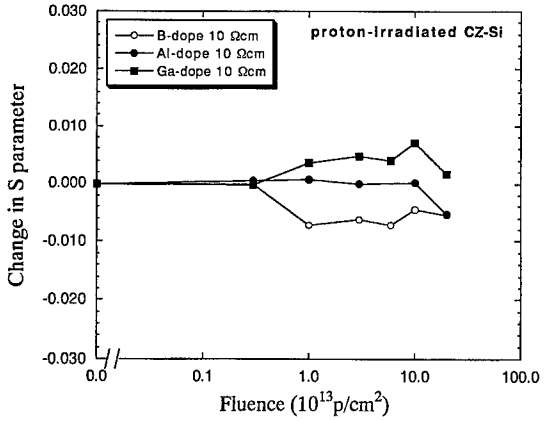

Fig. 3. Change in S parameters versus fluence of 10 MeV proton irradiation for B (open circle), Al (filled circle) and Ga (closed square) doped CZ-Si.

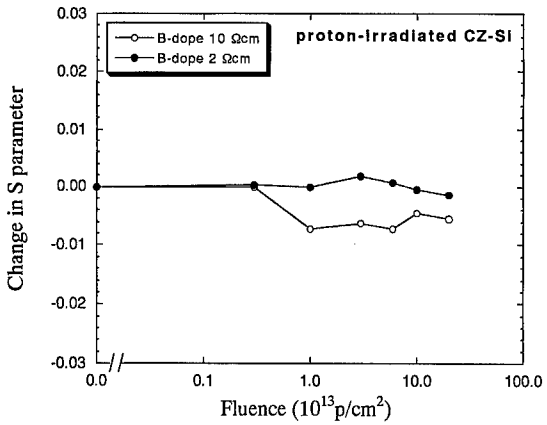

Fig. 4. Change in S parameters as a function of total dose of 10 MeV proton for B-doped CZ-Si with the resistivety of 10 and 2 Ω cm.

According to the two-state trapping model, the deduced lifetime of the Si matrix from the lifetime component of defect τ_d and its intensity I_d are calculated by the equation

$$\tau_{bulk}^{cal} = (1 - I_d)/(1/\tau_f - I_d/\tau_d), \quad (1)$$

where τ_f is the positron lifetime of bulk Si to be referred, and $\tau_f = 216$ ps, which is obtained for un-irradiated FZ-Si, is used in the present case. In this equation, we assume that the short lifetime component τ_1 is the defect component, and τ_{bulk}^{cal} agrees with the analyzed bulk component τ_2. Short lifetime components of positron annihilation experiments for Si have been reported by Dannefear et al. [7,8]. They suggest that this type of defect is associated with oxygen clusters. Our result is in good agreement with their results. Moreover, τ_1 components in B, Al and Ga doped Si are slightly higher than those in non-doped Si. Therefore, oxygen–impurity complexes most likely formed in the CZ-Si during proton irradiation with a total dose less than 5×10^{14} p/cm^2, could be detected in the experiments.

Fig. 3 shows the change in doppler broadening S parameters versus the fluence of proton irradiation. All of these S values are normalized by the value of each specimen before irradiation. The S parameter changes with the proton fluence do not have the same tendencies among B, Al and Ga doped Si. The S values slightly decreases with increase of the dose of proton irradiation only in B doped Si. This is because the electron densities around complexes depend on the species of the dopant atoms, and their charge states of the complexes are reflected in the S value. Fig. 4 shows the changes in S parameters for specimens of B doped CZ-Si with the resistivities of 2 and 10 Ω cm as a function of irradiation fluence. The S value of the 2 Ω cm sample slightly decreases with increasing fluence. This is also because the electron densities around the defects formed by irradiation depend on the amount of dopant. The value of doppler broadening S parameter for neutral charged VO (A center) has been reported larger than that for the bulk silicon, while that for VO_2 is smaller than that for the bulk [9]. The potential energy of a positron associated with coulomb correlation and its annihilation rate are mainly related to the surrounding electron density. In a condensed oxygen cluster, the atomic density and the electron density will be higher than in the bulk Si, and hence the positron lifetime will become shorter and the S parameter will be smaller than in the bulk Si. Therefore, it is believed that complexes consisting of oxygen, dopant atoms and radiation-induced defects are formed during proton irradiation, and such complexes exhibit different lifetimes and S parameters depending on the species of dopant atoms in positron annihilation experiments.

3.2. Annealing experiment after irradiation

Figs. 5 and 6 shows the positron lifetimes and their relative intensities for B-doped CZ-Si with electrical resistivities of 2 and 10 Ω cm after 1×10^{13} p/cm^2 proton irradiation as a function of annealing temperature. After prolonged annealing, long lifetime components corresponding to vacancy clusters appeared in both cases. A marked annealing stage varied from 527 to 552 K with increased B content. It is well known that di-vacancy migration takes place in Si around these temperature ranges. Accordingly, it is believed that this stage corresponds to the formation of larger vacancy clusters due to the clustering of free vacancies produced by the dissociation of the preexisting oxygen–vacancy-B complexes. The

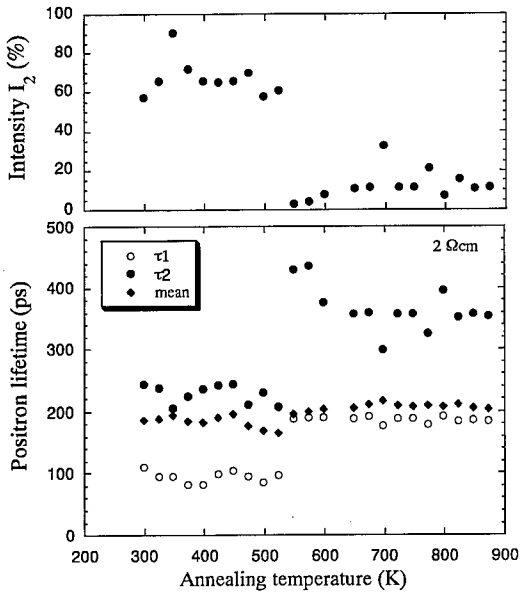

Fig. 5. Positron annihilation lifetimes τ_1, τ_2 and its relative intensity I_2 after 10 MeV proton irradiation with the fluence of 1×10^{13} p/cm^2 as a function of annealing temperature for B-doped CZ-Si with the resistivety of 2 Ω cm.

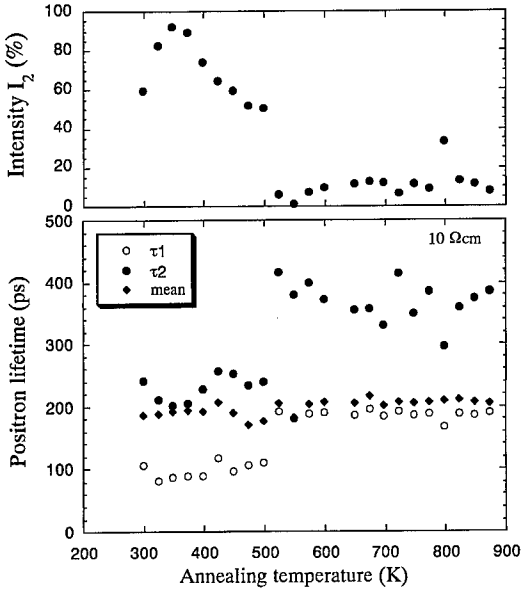

Fig. 6. Positron annihilation lifetimes τ_1, τ_2 and its relative intensity I_2 after 10 MeV proton irradiation with the fluence of 1×10^{13} p/cm^2 as a function of annealing temperature for B-doped CZ-Si with the resistivety of 10 Ω cm.

difference in the temperature stage by 25 K is considered to result from the amount of dopant. Therefore, it can be concluded that more dopant B atoms result in greater suppression of the dissociation and the formation of vacancy clusters. This result is in good agreement with the positron annihilation results of dopant effect of Si with no irradiation [10]. The present results show that radiation-induced excessive vacancies play an important role in the agglomeration of supersaturated oxygen atoms via vacancy mechanism, and also play a role in the formation of their complexes with oxygen and dopant atoms during the process of agglomeration.

4. Conclusions

The effect of dopant atoms on the defect complex formation in Si after low-dose proton irradiation has been investigated. In CZ-Si containing a small amount of point defects induced by low-dose proton irradiations up to 10^{14} p/cm^2, both oxygen and dopant-related complexes were formed. These complexes account for the positron annihilation lifetimes of about 100 ps, exhibiting that the defects have higher electron densities than those in Si with no defects and impurities.

Annealing stages that correspond to the dissociation of vacancies from the oxygen–vacancy–impurity complexes and the formation of larger clusters depend on the concentration of dopant atoms. The number of dopant atoms in the complexes increases with dopant atom concentrations.

These complexes were detected only in CZ-Si irradiated with proton at low doses less than 10^{15} p/cm^2, and vacancy-type defects were detected in the specimens with irradiation more than 10^{15} p/cm^2 by positron techniques.

Acknowledgements

The authors would like to express their cordial thanks to the staff of JAERI Takasaki facility for the proton irradiation.

References

[1] A. Uedono, Y.K. Cho, S. Tanigawa, A. Ikari, Jpn. J. Appl. Phys. 33 (1994) 1.
[2] S. Dannefaer, P. Mascher, D. Kerr, J. Appl. Phys. 73 (1993) 3740.
[3] P. Mascher, S. Dannefaer, D. Kerr, Phys. Rev. B 40 (1989) 11764.
[4] V. Avalos, S. Dannefaer, Phys. Rev. B 54 (1996) 1724.
[5] G. Dlubek, C. Ascheron, R. Krause, H. Erhard, D. Klimm, Phys. Stat. Solid A 106 (1988) 81.

[6] P. Kirkegaard, M. Eldrup, O.E. Mogensen, N.J. Pedersen, Comput. Phys. Commun. 23 (1981) 307.
[7] S. Dannefaer, Phys. Stat. Solid A 102 (1987) 481.
[8] S. Dannefaer, D. Kerr, J. Appl. Phys. 60 (1986) 1313.
[9] A. Uedono, Y. Ujihira, A. Ikari, O. Yoda, Material Science Forum. 105–110 (1992) 1301.
[10] W. Puff, P. Mascher, D. Kerr, S. Dannefaer, Materials Science Forum. 38–41 (1989) 225.

ELSEVIER

Physica B 273–274 (1999) 485–488

PHYSICA B

www.elsevier.com/locate/physb

In-situ studies of point-defect complexes in silicon implanted with heavy MeV ions

N. Yarykin[a,b,*], C.R. Cho[a], R. Zuhr[c], G. Rozgonyi[a]

[a]*Department of Materials Science and Engineering, North Carolina State University, Raleigh, NC 27965, USA*
[b]*Institute of Microelectronics Technology RAS, 142432 Chernogolovka, Moscow region, Russia*
[c]*Solid State Division, Oak Ridge National Laboratory, Oak Ridge, TN 37831, USA*

Abstract

In-situ deep-level transient spectroscopy measurements have been performed on silicon implanted with MeV ions at 85 K. It is observed that the implantation of heavier ions results in the formation of novel deep-level centers; their formation/annealing kinetics and depth distributions are studied. Divacancy formation in silicon implanted with Si^+ and Ge^+ MeV ions is found to occur at higher temperatures than expected from the isolated vacancy mobility, and to exhibit a strong dependence on the electrical bias applied during annealing. The phenomena are discussed under the assumption that vacancies and interstitials are trapped in clusters/disorder regions immediately after low-temperature implantation of heavier ions, and are released during subsequent annealing.

Keywords: Silicon; Ion implantation; Defects; Deep levels

1. Introduction

Ion implantation, the most intensively used technique to form the well-defined impurity spatial profile in silicon wafers, is always accompanied by creation of a significant number of structural defects. This damage may strongly impact the redistribution of implanted impurity during subsequent annealing, the very harmful phenomenon known as transient enhanced diffusion [1 and references therein]. To enable us to predict the final impurity distribution, a knowledge about the behavior of the implantation-induced defects, their aggregation and annealing is needed. However, the properties of intrinsic point defects and their complexes have mainly been learned from electron-irradiated silicon [2], where isolated Frenkel pairs are only created; although formation of higher-order aggregates is generally expected in dense collision cascades of implanted ions [2]. The investigations of electron-irradiated samples have demonstrated that both vacancies and self-interstitials are extremely mobile in silicon at room temperature; therefore, in situ measurements of the defects created at low temperatures are required. As for ion-implanted silicon, until recently, such measurements have only been reported for the lightest ions, H^+ and He^+ [3–5]. Except Ref. [3], these investigations have not found any essential divergence from the results obtained on electron-irradiated samples. However, the first in situ studies for heavier ions, Si^+ and Ge^+ [6,7], have revealed several novel electrically active defects and unexpected kinetics of the well-known complex formation. In this work, further results of the in situ deep-level transient spectroscopy (DLTS) measurements on silicon self-implanted with MeV ions are presented.

2. Experimental

Schottky diodes fabricated on the as-received silicon wafers were implanted with MeV ions at 85 K. Immediately after the implantation, the diodes were connected to computerized setup for the DLTS and CV measurements. Data were collected during heating/cooling cycles, the highest cycle temperature being continuously

* Corresponding author. Fax: + 7-095-962-8047.
E-mail address: nay@ipmt_hpm.ac.ru (N. Yarykin)

0921-4526/99/$ - see front matter
PII: S0921-4526(99)00531-1

increased. Details about the experimental procedure can be found elsewhere [6–8].

The DLTS technique relies on thermally stimulated emission of carriers from deep level traps. Generally, this is a disadvantage of the technique for in-situ study of the defect evolution. Indeed, to record the DLTS signal from a particular deep-level center with the activation energy for carrier emission E_t, it is necessary to raise the sample temperature to $\sim E_t/25\,k$, where k is the Boltzmann constant. If the defect annealing/transformation temperature is lower, it can never be detected by DLTS. Fortunately, this is not the case for many defects of interest, as it will be seen below. On the other hand, the extremely low DLTS detection limit allows one to study deep-level centers induced by implantation with as low as 10^8–$10^9\,cm^{-2}$ dose. Overlapping of the collision cascades is not significant under these conditions, and effectively, defects produced by single incident ion can be studied.

3. Results and discussion

3.1. Defect formation kinetics

A typical development of the deep-level spectrum in p-type Cz–Si self-implanted with MeV ions at low temperature is shown in Fig. 1. The first DLTS scan has been started in few minutes after the implantation at 85 K. It is seen that except small features at $\sim$ 100 and 150 K, no DLTS signal occurs until the sample temperature exceeds 180 K. The scan has been interrupted at 200 K, the sample has been kept at this temperature for 1 min again and cooled down to 85 K. The second DLTS scan, denoted as '200 K' to indicate annealing at this temperature, shows only a very small peak at 120 K, which could be correlated with the divacancy donor level. At the same time, significant signal occurs at $\sim$ 180 K. Also, the H1 peak maximum [6] is reached during this scan. Increase in the annealing temperature by 20 K only, leads to the DLTS signal growth in the whole temperature range from 100 to 200 K, and a shoulder corresponding to the K2 center [6] can be clearly seen. Well-resolved divacancy peak appears in the DLTS spectrum only after annealing above 230 K and reaches saturation due to annealing at 270–300 K. The H1 centers gradually decay during in situ measurements and totally disappear due to room-temperature storage for several days, allowing to resolve the presence of the H2 centers. Storage at room temperature removes also the DLTS signals at $\sim$ 100 K (of still unknown nature) and $\sim$ 150 K (could be related with interstitial carbon), while the peak at $\sim$ 180 K increases. The latter increase is caused by the well-known C_iO_i pair formation [6,9].

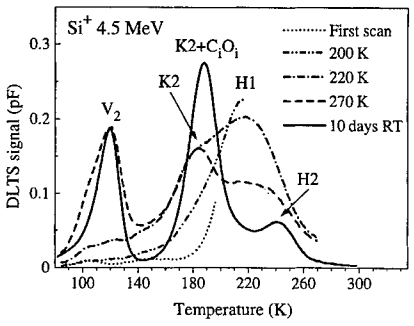

Fig. 1. Deep-level spectrum development due to low-temperature annealing of p-type Cz-Si ($[B] = 7 \times 10^{14}\,cm^{-3}$) implanted with $1 \times 10^8\,cm^{-2}$ of 4.5 MeV Si^+ ions at 85 K.

3.2. Depth profiles

Further information about the nature of the K2 and H1 centers can be obtained from the analysis of their spatial distributions. Note that the depth profiles presented in Fig. 2(a) have been measured after annealing at 270 K for 5 min. It is clear from the data in Fig. 1 that the H1 peak is still reasonably high after such annealing, the V_2 and K2 concentrations have already reached their saturated values, while there is yet no contribution from the C_iO_i pairs. It is seen that the K2 and H1 centers exhibit similar profiles with the maxima near the ion projective range (R_p). The profiles can be reasonably well fitted by the curve obtained for the implantation-induced

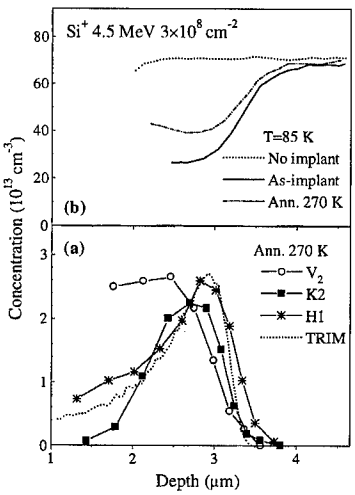

Fig. 2. Depth profiles of (a) deep-level centers and (b) space-charge density in Schottky diode on p-type Cz-Si implanted with $3 \times 10^8\,cm^{-2}$ of 4.5 MeV Si^+ ions at 85 K and annealed at 270 K during DLTS measurements. For comparison, the vacancy distribution calculated by the TRIM program is shown in the plot (a). All CV profiles presented on the plot (b) were measured at 85 K.

damage from the Monte-Carlo TRIM simulations. Divacancy distribution is much wider and shifted to the surface.

For comparison, the depth profiles of the active boron concentration calculated from CV measurements are shown in Fig. 2(b). Greater part of the compensation caused by the implantation has remained after 270 K annealing; only ~ 30–50% of the dip around 2.5–3 μm depth can be explained by hole trapping to the deep-level centers. This phenomenon was related to deactivation of acceptor impurity due to moving out of the substitutional position [10].

3.3. Vacancy source in MeV-implanted silicon

It has been found from the in situ EPR studies on electron-irradiated samples [2] that isolated vacancies are mobile in silicon above 200 K independent of their charge state. Therefore, divacancy formation at much higher temperatures leads us to the conclusion that most of the vacancies created in the collision cascades are trapped in some clusters or disordered regions. This conclusion is supported by the fact that no signature of isolated vacancies at $E_v + 0.13$ eV [2] has been detected in our samples immediately after implantation at 85 K. The existence of structural defects, which emit vacancies during annealing of MeV-implanted silicon, has also been postulated for n-type crystals [7,11,12].

Analysis of the data in Fig. 2 shows that V_2 profile does not resemble the TRIM simulation, but follows restoration of the compensated boron. It is more obvious from the following experiment. Two Schottky diodes prepared on p-type Cz–Si were implanted in identical conditions at 85 K. After CV measurements at implantation temperature, the diodes were annealed at 280 K for 1 min; the reverse bias (but no DLTS pulses) was applied to one diode during annealing, while the other diode was kept at zero bias. The CV profiles and DLTS curves taken from these diodes after annealing are presented in Figs. 3 and 4, respectively. It is seen that the implantation-induced damage is more stable in the crystal neutral volume as compared to the space-charge region, see Fig. 3. Simultaneously, the DLTS spectra show a radical difference in the defect concentrations. Zero bias almost totally suppresses divacancy and interstitial carbon formation during annealing. We believe that this is primarily a result of the smaller number of vacancies and interstitials released from the highly damaged regions. If the annealing temperature is increased up to 300–320 K, practically equal divacancy concentrations are found in biased and unbiased diodes. Note that different annealing conditions show no effect on the H1 defect concentration, indicating most probably that these centers are formed immediately during implantation.

It is clear from a comparison with Fig. 4 that the data in Fig. 1, as well as in earlier publications [6,8], demonstrate defect transformations in intrinsic silicon rather than in p-type crystals. This example shows that one should be more careful in interpreting data obtained under annealing in the 'DLTS condition' as presented in Fig. 1. This is also valid for the results on n-type crystals [7,11], where in contrast to p-type samples, divacancies are detected as soon as the sample temperature reaches the corresponding peak at ~ 120 K. Generally, it can be assumed that the DLTS measurement itself, as repeated changing of the defect charge state, impacts the defect transformation.

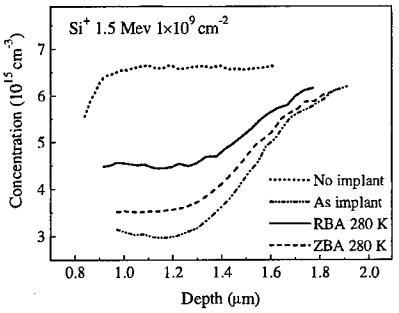

Fig. 3. Space-charge density in 4.5 MeV Si^+-implanted Schottky diodes annealed at 280 K for 1 min under reverse (RBA) or zero (ZBA) bias. The curves measured before and immediately after implantation are the same for both diodes inside 3% error.

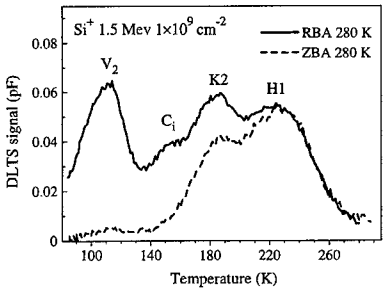

Fig. 4. DLTS curves for the same diodes as in Fig. 3.

3.4. Novel defect nature

In-situ DLTS measurements both on p- and n-type crystals implanted with different MeV ions revealed two defects, K2 and H1, which were not known from studies on electron-irradiated samples. Moreover, the defects are created in significant concentrations only due to implantation of sufficiently heavy ions [6,8]. This is consistent with the model that they include several Frenkel pair components. Concentrations both of the K2 (after annealing) and of the H1 defects are very similar in Cz, FZ, and epi-crystals, indicating that such impurities as

carbon and oxygen are not included in the centers. However, both these centers have been observed only in p-type samples; therefore, boron cannot be excluded from the possible constituents of the K2 and H1 defects.

The H1 center is the only defect, which exhibits decay below room temperature in ion-implanted silicon. We have not observed an unambiguous correlation of this decay with any other center formation. However, this extended over ~ 100 K annealing resembles the A-center formation in n-type MeV-implanted silicon [7,11]. If we suppose that the H1 center decay results in vacancy release, then it is not clear why the V_2 formation in p-type crystals reveals no correlation with the H1 behavior.

The K2 nature is also unknown. Only the coincidence of the K2 formation with the freeze-out temperature for neutral vacancies gives some advantage to the vacancy-related model. Note in this connection that the conclusion about the equal number of vacancies and interstitials included in the electrically active complexes in ion-implanted silicon has been made in Ref. [13] implying the interstitial nature of the K2 centers. On the other hand, the statement about the equal number of vacancies and interstitials, being reasonable in electron-irradiated samples, might be not valid in MeV-implanted silicon, since we admitted the formation of multi-defect clusters, part of which could be stable even above room temperature [12].

4. Conclusion

In-situ DLTS studies have been performed on silicon implanted with MeV ions at 85 K. It is observed that in addition to the point-defect complexes well known from the experiments on electron irradiation, novel electrically active deep-level centers are formed due to implantation of Si^+ and Ge^+ ions. The H1 defect is most probably formed immediately during implantation and is unstable at room temperature. The K2 center appears during annealing at 200–230 K; after room-temperature storage, its DLTS signature is hidden in the peak usually ascribed to the C_iO_i pairs. Divacancy formation temperature is strongly dependent on whether the reverse bias has been applied to the implanted Schottky diode during annealing. In either case, this temperature is much higher than expected from the isolated vacancy mobility. The entirety of the results lead us to the conclusion that complicated defect clusters/disorder regions are formed in the heavy-ion collision cascades. Most of the vacancies and interstitials generated by energetic ion remain trapped in these clusters after low-temperature implantation, and can be released during subsequent annealing. It is the cluster thermal stability that determines the defect formation kinetics in heavy-ion-implanted silicon.

Acknowledgements

This study was supported in part by NSF grant DMR-96 28695. The work at ORNL was sponsored by US DOE under contract DE-AC05-96OR22464.

References

[1] P.A. Stolk et al., J. Appl. Phys. 81 (1997) 6031.
[2] G.D. Watkins, Electrochem. Soc. Proc. 99-1 (1999) 38.
[3] L.C. Kimerling et al., Inst. Phys. Conf. Ser. 46 (1979) 273.
[4] K. Irmscher et al., J. Phys. C 17 (1984) 6317.
[5] K.A. Abdullin et al., Semiconductors 28 (1994) 1012.
[6] C.R. Cho et al., Appl. Phys. Lett. 74 (1999) 1263.
[7] N. Yarykin et al., Appl. Phys. Lett. 75 (1999) 241.
[8] C.R. Cho et al., Mater. Res. Soc. Symp. Proc. 532 (1998) 253.
[9] P.J. Drevinsky et al, in: K. Sumino (Ed.), Defect control in Semiconductors, North-Holland, Elsevier, 1990 p. 341.
[10] E. Rimini et al., Mater. Sci. Forum 153–155 (1998) 137.
[11] C.R. Cho et al., Electrochem. Soc. Proc. 99-1 (1999) 172.
[12] P. Pellegrino et al., Nucl. Instr. and Meth. B 148 (1999) 306.
[13] S. Libertino et al., Appl. Phys. Lett. 71 (1997) 389.

ELSEVIER

Physica B 273–274 (1999) 489–492

PHYSICA B

www.elsevier.com/locate/physb

Impurity-assisted annealing of point defect complexes in ion- implanted silicon

Paolo Pellegrino*, Andrej Yu. Kuznetsov, Bengt G. Svensson

Department of Electronics/Solid State Electronics, Royal Institute of Technology, P.O. Box E229, S-164 40 Kista, Sweden

Abstract

Annealing of vacancy-related defect complexes in CZ and FZ n-type silicon crystals has been studied by means of deep level transient spectroscopy. Characteristic vacancy-related defects such as VO and V_2 were introduced by electron irradiation or implantation with C^+, Si^+, Ge^+, and I^+ ions using very low doses. It was found that the overall thermal stability of both V_2 and VO is almost independent on the mass of the primary projectile. However, after initial annealing stages ($T \leqslant 200°C$) a significant increase of the normalized V_2 and VO signals was detected for heavy ions (Ge^+, I^+). Moreover, depth profiling of the CZ samples implanted with Si^+ ions reveals a substantial narrowing of the V_2 and VO distributions after initial annealing stages. Both phenomena may be interpreted in terms of a preferential formation and subsequent dissociation of high-order vacancy clusters at the depth corresponding to the peak of the implantation damage.

PACS: 61.82.F; 61.80.Jh; 61.72.Cc; 61.72.Ji

Keywords: Point defects; Silicon; Annealing; Ion implantation; DLTS; Lattice disorder

1. Introduction

Our present knowledge about the mechanisms responsible for the thermal stability of defects created by ion implantation is still limited in spite of its great technological importance. Most of the fundamental studies have been dedicated to the investigation of defects induced by MeV electron irradiation (see Ref. [1,2]), but still our understanding of the annealing mechanisms of such defects is not complete.

In contrast with MeV electron irradiation, ion implantation gives rise to a highly localized defect distribution, with a characteristic shape of a peak-like damage region and a long tail towards the surface. The local disorder created at the end of the ion range is a strong function of the projectile mass. This high concentration of point- and cluster-like defects in the peak region can result in a strain enhancement and local changes in the Fermi level, and eventually it causes amorphization of the material [3]. The mechanism which is responsible for the production of the vacancy- and interstitial-like defects during ion bombardment has been extensively explored [3,4]. In this work we focus our experimental investigation on the thermal stability of the electrically active defects, which are introduced by ion implantation in n-type silicon.

2. Experimental

The n-type ($8–9 \times 10^{14}$ P/cm^3) silicon samples used in this study were cut from (1 0 0) Czochralski (CZ) and float-zone (FZ) wafers. Shallow p^+n diodes were fabricated using the FZ material according to a procedure described elsewhere [5].

Low-dose (from 5×10^7 to 1×10^9 cm^{-2}) implantations into the p^+n-diodes and the CZ samples using C^+, Si^+, Ge^+ and I^+ ions were carried out in the Uppsala EN tandem accelerator, where a scanning facility is reserved

* Corresponding author. Tel.: + 46-8-752-1423; fax: + 46-8-752-7782.

E-mail address: paolo@ele.kth.se (P. Pellegrino)

0921-4526/99/$ - see front matter
PII: S0921-4526(99)00532-3

for homogeneous low-dose implantations [6]. The implantation energies were chosen to create a defect distribution suitable for monitoring by deep level transient spectroscopy (DLTS), while the ion doses were tuned to avoid a "macroscopic" doping compensation effect. Careful attention was given to accurate dosimetry, and the error in nominal doses never exceeded 10%. As a reference, part of the samples were instead electron irradiated (2 MeV) to a dose of 1×10^{15} cm^{-2}. Subsequently, Schottky barrier junctions were manifactured on CZ samples using Au contacts.

Isochronal and isothermal anneals were performed in the temperature range between 100°C and 300°C in nitrogen atmosphere. DLTS measurements were carried out using an in-house setup described in Ref. [7]. The macroscopical lateral uniformity of the defect concentration was checked in all samples before annealing.

3. Results and discussion

Fig. 1 shows DLTS temperature scans after isochronal (30 min) annealing of CZ silicon implanted with 5.6 MeV silicon ions. Characteristic signatures of the vacancy-related defects created by ion bombardment dominate the spectra. The vacancy–oxygen complex (VO) at E_C-0.17 eV and the double and single negative charge states of the divacancy (V_2) at E_C-0.23 and E_C-0.42 eV, respectively, were identified (E_C denotes the conduction band edge). Two annealing stages can be distinguished in Fig. 1. For anneals below 200°C the intensity of E_C-0.42 eV peak decreases, mainly due to the dissociation of the overlapping phosphorous–vacancy (PV) center [8], while the "original" V_2 and VO signals appear to be stable or to increase slightly, respectively. Anneals at temperatures $T \geqslant 200$°C result in a progressive reduction in the concentration of both V_2 and VO. The concentration of V_2 centers is below the detection limit after annealing at 300°C, while VO still persists at temperatures well above 300°C. One can also observe a gradual increase in the level at E_C-0.32 eV, originating from a defect which was

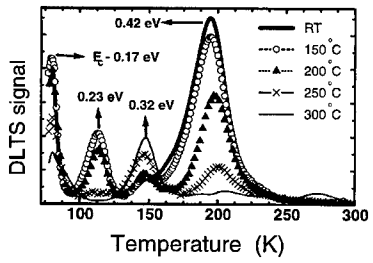

Fig. 1. DLTS spectra of CZ n-Si diodes after isochronal (30 min) anneals at different temperatures. The diodes were implanted with 5.6 MeV silicon ions to a dose of 2×10^8 cm^{-2}. The rate window is (640 ms)$^{-1}$.

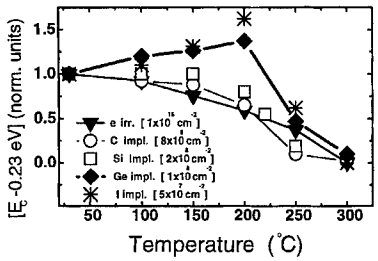

Fig. 2. Amplitude of the E_C-0.23 eV level (V_2 center) in CZ samples after electron irradiation or ion implantation and subsequent isochronal 30 min anneals. For each ion, energy and dose, the values have been normalized to the initial V_2 concentrations in unannealed samples. Error bars are not shown, being smaller than the symbol sizes.

already present in a small concentration directly after ion implantation. The exact identification of this defect is still uncertain, but there is strong evidence that it is a defect involving hydrogen [9].

The role of the implanted specie on the annealing behavior of V_2 in CZ silicon is illustrated in Fig. 2, where the DLTS intensities after isochronal annealing for 30 min are normalized to the value measured before the heat treatment. It is seen that the overall thermal stability of V_2 is almost independent on the mass of the impinging particle. However, after anneals at and below 200°C a significant increase of the normalized intensity is detected for heavy ion (Ge^+ and I^+) implants. A similar trend is also observed for the VO center.

It is known that the elastic energy deposition per incoming ion around the projected range becomes larger with an increase of the projectile mass. This enhances the formation of high-order vacancy clusters (V_n, with $n > 2$). Some of these centers have a poor thermal stability, e.g. V_4 [10], and they can dissociate during subsequent anneals and release vacancies and/or divacancies. The concomitant increase of VO and V_2 signals supports this hypothesis. Only the dissociation of PV centers cannot account for this effect since in samples implanted with heavy ions the production of PV pairs is anticipated to be strongly suppressed relative to higher-order vacancy complexes [11].

Since the probability to create V_n : s is anticipated to be strongly depth dependent, defect concentration versus depth profiling of the observed levels has been performed. The evolution of the VO and V_2 depth profiles in CZ silicon after Si^+ implantation and isothermal annealing at 220°C is shown in Fig. 3. The profiles are normalized with respect to the peak concentration value in order to facilitate a comparison of the profile shape.

In accordance with previously reported measurements [10,12], the annealing of the V_2 centers is found to be faster than the one of VO, due to the higher dissociation rate of divacancy complexes in comparison to the

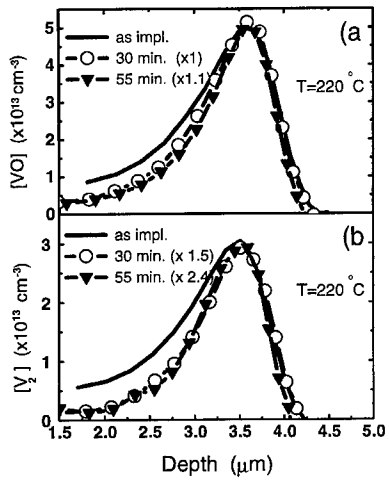

Fig. 3. Concentration versus depth profiles of E_C-0.17 eV (VO center) and E_C-0.23 eV (V_2 center) levels in a CZ n-Si Schottky diode. The sample was implanted with 5.6 MeV silicon ions to a dose of 2×10^8 cm^{-2} and, then, isothermally annealed at 220°C.

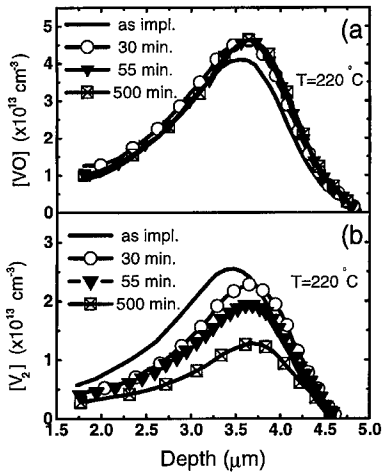

Fig. 4. Concentration versus depth profiles of E_C-0.17 eV (VO center) and E_C-0.23 eV (V_2 center) levels in a FZ p^+/n-Si diode. The sample was implanted with 5.6 MeV silicon ions to a dose of 2×10^8 cm^{-2} and, then, isothermally annealed at 220°C.

"simple" vacancy–oxygen defect. Nevertheless, both sets of curves present a common very interesting feature: under the current annealing conditions no broadening of the VO or V_2 depth profiles is detected. On the contrary, during the initial annealing stage (30 min) the defect distributions become narrower around the projected range (see Fig. 3(a), where the decrease of the DLTS signal is only detected in the "tail" region). Further, relative to the 30-min anneal the 55-min anneal results in a depth independent decrease of the VO and V_2 intensities. This characteristic behavior has also been observed in other CZ samples implanted with different types of ions and subsequently annealed at various temperatures for different durations.

This observation is interesting because the dissociation of either VO or V_2 might immediately result in a gradient of monovacancy concentration through the depth of the damaged region in Fig. 3. Monovacancies should succesively redistribute in accordance with the concentration gradient, and the probability of clustering reactions in the "tails" might thus increase. However, we do not observe any signs of additional VO and V_2 clustering in the tail regions in Fig. 3. This discussion readily brings us to an hypothesis of an efficient trapping of migrating mono- and/or divacancies by impurities or implantation-induced defects in CZ silicon.

In order to investigate the role of background impurities on the vacancy diffusion, isothermal anneals were repeated in FZ silicon, where the concentration of impurities (in particular O_i and C_s) is expected to be significantly lower. The results are illustrated in Fig. 4.

Also in this material the VO and V_2 concentration in the peak damage region increases relatively to the tail after a 30-min annealing. However, one can observe also an apparent shift. In our opinion, it was not possible to detect a similar shift in CZ samples because of the following two facts. Due to lower concentration of impurities and, consequently, higher effective diffusivity for vacancies created by the implantation, the profiles in Fig. 4 are much broader than in CZ samples. Moreover, both VO and V_2 were found to be much less stable in the CZ material compared to the results for the FZ samples, see also Ref. [13].

However, even for a 500-min anneal, when a significant dissociation of V_2 centers was detected, no indication of a substantial broadening of the depth profile was observed, Fig. 4(b). Few alternatives may be considered in order to interpret the absence of broadening in the depth profiles in both CZ and FZ materials. First, the content of potential traps for mono- and/or divacancies may be high enough to suppress long-range vacancy diffusion even in the FZ samples. At the same time, vacancy diffusivity may be high enough to allow vacancies to reach macroscopic sinks, e.g., surfaces.

In addition, and because of the application of very low doses, only isolated defect-rich zones have been introduced into the sample in the present experiment (the average distance between adjacent ion trajectories is around 1.4 μm). Thus, we cannot exclude a preferential lateral diffusion of the released vacancies on a microscopic scale. Such diffusion would stem from a strong concentration gradient in the plane perpendicular to the direction of the implantation, but not detectable in our measurements.

As we can see in Figs. 3 and 4, the narrowing around the projected range during early stages of annealing can be due to a fast dissociation of V_n complexes, which are mainly localized near the implantation damage peak. This leads to a formation of more "simple" vacancy-type defects, like VO and V_2, at the depth of the ion range, while at the same time such defects can already start to dissociate in the sample in a quite uniform manner. As shown in Fig. 2 this phenomenon should be more pronounced after implantation with heavy ions.

4. Conclusions and summary

Annealing of vacancy-related defect complexes in CZ and FZ n-type silicon crystals has been studied by means of deep level transient spectroscopy. Characteristic vacancy-related defects such as VO and V_2 were introduced by electron irradiation or implantion with C^+, Si^+, Ge^+, and I^+ ions using very low doses.

It was found that the overall thermal stability of both V_2 and VO is almost independent on the mass of the primary projectile. However, after initial annealing stages ($T \leqslant 200°C$) a significant increase of the normalized V_2 and VO signals was detected for heavy ions (Ge^+, I^+). Moreover, depth profiling of the CZ samples implanted with Si^+ ions reveals a substantial narrowing of the V_2 and VO distributions after initial annealing stages. Both phenomena may be interpreted in terms of a preferential formation and subsequent dissociation of high-order vacancy clusters at the depth corresponding to the peak of the implantation damage.

Acknowledgements

Financial support from the Swedish Research Council for Engineering Science is kindly acknowledged.

References

[1] B.G. Svensson, J.L. Lindström, Phys. Rev. B 34 (1986) 8709.
[2] A. Polity, F. Börner, S. Huth, S. Eichler, R. Krause-Rehberg, Phys. Rev. B 58 (1998) 10363.
[3] N. Keskitalo, A. Hallén, J. Lalita, B.G. Svensson, Mater. Res. Soc. Proc. 469 (1997) 233.
[4] B.G. Svensson, B. Mohadjeri, A. Hallén, J.H. Svensson, J.W. Corbett, Phys. Rev. B 43 (1991) 2292.
[5] N. Keskitalo, A. Hallén, F. Masszi, J. Olsson, Solid State Electron. 39 (1996) 1087.
[6] A. Hallén, P.A. Ingemarsson, P. Håkansson, B.U.R. Sundqvist, G. Possnert, Nucl. Instr. and Meth. B 36 (1989) 345.
[7] B.G. Svensson, K.H. Rydén, B.M.S. Lewerentz, J. Appl. Phys. 66 (1989) 1699.
[8] L.C. Kimmerling in: N.B. Urli, J.W. Corbett (Eds.), Radiation Effect in Semiconductor 1976, Institute of Physics, Bristol, 1977 p. 221.
[9] J. Lalita, B.G. Svensson, C. Jagadish, A. Hallén, Nucl. Instr. and Meth. B 127 (1997) 69.
[10] J.W. Corbett, J.C. Bourgoin in: J.H. Crawford, L.M. Slifkin (Eds.), Point Defects in Solids Vol. 2, Plenum Press, New York, 1975, p. 27.
[11] B.G. Svensson, C. Jagadish, A. Hallén, J. Lalita, Phys. Rev. B 55 (1997) 10498.
[12] O.O. Awadelkarim, B. Monemar, Phys. Rev. B 38 (1988) 10116.
[13] S. Dannefaer, P. Masher, D. Kerr, J. Appl. Phys. 73 (1992) 3740.

ELSEVIER

Physica B 273–274 (1999) 493–496

PHYSICA B

www.elsevier.com/locate/physb

Concentration of point defects in growing CZ silicon crystal under the internal stresses: effects of impurity doping and thermal stress

K. Tanahashi[a,*], M. Kikuchi[a], T. Higashino[a], N. Inoue[a], Y. Mizokawa[b]

[a]*RIAST, Osaka Prefecture University, 1-2, Gakuencho, Sakai, Osaka 599-8570, Japan*
[b]*CIAS, Osaka Prefecture University, 1-1, Gakuencho, Sakai, Osaka 599-8531, Japan*

Abstract

Behavior of point defects under the internal stress in a growing Czochralski (CZ) silicon is theoretically examined. The changes of point defect concentration by the impurity doping and by the thermal stress are quantitatively estimated. Contributions of them to the formation of secondary defects are discussed. © 1999 Elsevier Science B.V. All rights reserved.

PACS: 61.72 J; 67.80 6b

Keywords: Silicon; Point defect; Concentration; Impurity doping; Thermal stress

1. Introduction

It is well known that various secondary defects are formed in silicon crystal during crystal growth, i.e. voids and interstitial-type dislocation loops. Secondary defects are aggregates of point defects, vacancies (V) and interstitials (I). Since such defects degrade very large-scale integrated circuit performance, it is necessary to eliminate them. It has been reported that the type of secondary defects in FZ-Si changes either to interstitial type or to vacancy type by various impurity doping [1], and that the location of oxidation induced stacking fault ring (OSF-ring) moves inward [2] and the number of void defects decreases [3] by high concentration B doping in CZ-Si. However, behavior of point defects in a highly doped Si, especially the change of concentration, has not been known yet. We consider that these are the results of internal stress effect on point defect concentration due to doping of impurities which have different size from matrix Si [4]. Theoretical analyses and quantitative evaluation are performed here. There is another source of internal stress in a growing Si: growing crystal has thermal stress caused by temperature gradient. We have made the preliminary study on the thermal stress effect [5]. In this paper the effect of thermal stress is quantitatively investigated and compared with the impurity doping effect.

2. Impurity doping effect

2.1. Analysis

Analysis on the effect of stress by doping of impurities has been given by Rytova et al. [6]. Considering the potential for formation of vacancies around an impurity as shown in Fig. 1, they obtained the phenomenological formula for the vacancy concentration. The formula, however, was complicated and ambiguous in physical meaning, mainly due to the statistical treatment based on the assumption of non-uniform impurity distribution. We have improved it as follows [4]. We assumed, for simplicity, the uniform impurity distribution.

* Corresponding author. Tel.: + 81-722-51-5634; fax: + 81-722-54-9935.
E-mail address: tanahasi@riast.osakafu-u.ac.jp (K. Tanahashi)

PII: S0921-4526(99)00534-7

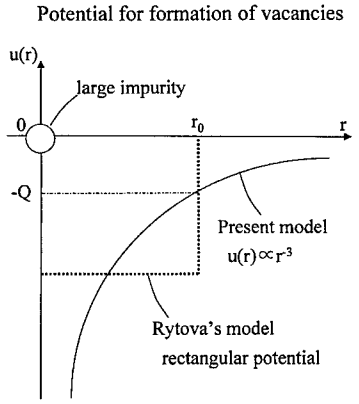

Fig. 1. Potential for the formation of vacancy formation around a large impurity.

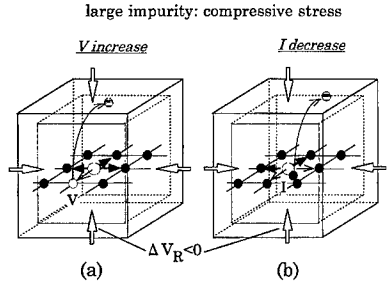

Fig. 2. Relaxation of internal stress around large impurity by increase of vacancy (a) and decrease of interstitial (b).

Compressive stress occurs around large size impurity as shown by black arrows in Fig. 2(a). It is relaxed by vacancy as shown by white arrows. Therefore, vacancy formation is energetically favorable and enhanced. On the contrary, interstitials around small size impurity are increased due to the tensile stress. Internal stress by the impurity decreases as the distance from the impurity increases. It was assumed that the potential $u(r)$ for formation of point defects, is inversely proportinal to the cubic of the distance r from impurity as shown in Fig. 1, $u(r) = -Qr_0^3/r^3$, where Q is the potential at a fixed position with distance r_0 from the impurity. We considered the potential overlap between the adjacent impurities to involve the impurity concentration dependence. The increased concentration of point defects was given by the following equation by averaging local concentration:

$$N_{I,V}^{+} = N_{I0,V0}\exp(16Qr_0^3n/kT),$$

(V for large impurity, I for small impurity), (1)

where N_0 is the equilibrium concentration of point defects in undoped Si and n is the impurity concentration. This formula is simple and has clear physical meaning. Moreover, it reproduces the reported exponential dependence on the impurity concentration [6] well. To formulate the impurity size dependence, we assumed that the potential energy change Q is given by the strain energy which is proportional to the volume difference between Si and the dopant atom. Then we obtain the formula $Q = K|V - V_{Si}|$ where V and V_{Si} are the atomic volumes of impurity and Si and K is constant. We determined K by fitting Eq. (1) to the vacancy reported related donor concentration in Sn doped Si film [6]. The values of parameters are described in Ref. [4] in detail.

In this report, we further examine the relaxation of internal stress by the decrease of unfavorable point defects as follows. Compressive stress around large impurity can be relaxed by decrease of interstitials as shown in Fig. 2(b). On the other hand, tensile stress around small impurity can be relaxed by decrease of vacancies. Therefore, $-u(r)$ is regarded as the potential for the decrease of point defects. By the same treatment as above, the concentration of decreased point defects is given as follows

$$N_{I,V}^{-} = N_{I0,V0}\exp(-16Qr_0^3n/kT),$$

(I for large impurity, V for small impurity). (2)

Further, we obtain simpler formula, because Q and r_0 are the constants [4] as follows:

$$N_{I,V}^{\pm} = N_{I0,V0}\exp(\pm Cn/T), \quad (3)$$

where C is given in Table 1. This is convenient for concentration estimation.

2.2. Change of point defect concentration

Now, we calculate the change of point defect concentration. Fig. 3 shows the calculated change of point defect concentration corresponding to the defect type change in doped FZ-Si: for smaller impurities than Si, A-defects increase with doped B for $5\times10^{16}/cm^3$ and with C for $5\times10^{16}/cm^3$ (corresponding to filled circles), for larger impurities than Si, D-defects increase when doped with Sb for $3\times10^{17}/cm^3$ and with Sn for $3\times10^{18}/cm^3$ (corresponding to open circles). The calculated change of point defect concentration by these impurities are above 0.1%.

Table 1
The value of C in Eq. (3) for various impurities

Atomic species	C
C	8.455×10^{-17}
B	6.747×10^{-17}
P	1.964×10^{-17}
Ge	1.537×10^{-17}
Sb	6.747×10^{-17}
Sn	8.455×10^{-17}

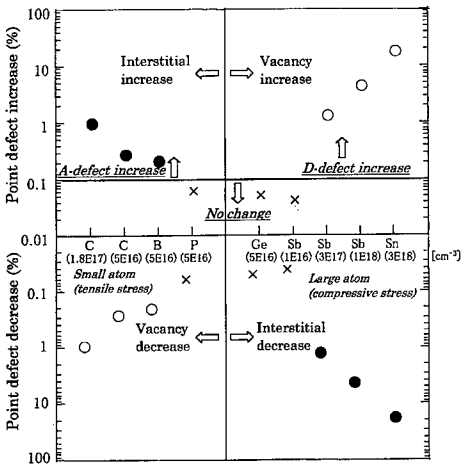

Fig. 3. Change of point defect concentration by impurity doping corresponding to the secondary defect type change.

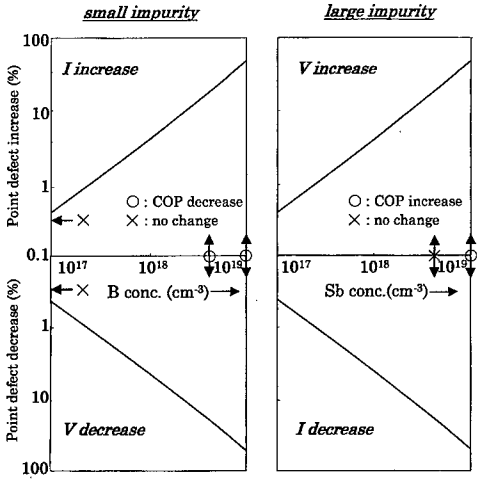

Fig. 4. Change of point defect concentration depending on the impurity concentration.

Increase and decrease of point defect concentration are nearly equal. This suggests that it is necessary to consider not only increase but also decrease of point defects by the impurity doping effects because the decrease of opposite type of point defects also enhances the secondary defect formation. For similar size impurities of Si, P and Ge, which do not affect secondary defects formation (corresponding to crosses), the change is below 0.1%. These results show that the change for only 0.1% determines the secondary defect type, independent on the atomic species. This means that the point defect formation and secondary defect formation only depend on the volume change. This strongly suggests that it is mainly internal stress effect [7].

Fig. 4 shows the impurity concentration dependence of the change of point defects in CZ-Si. The calculated threshold increase of interstitial concentration corresponding to the shrinkage of OSF-ring and the decrease of COP density by B doping in CZ-Si is estimated to be above a few percent. This agrees with the assumed increase of 2%, which is expected value to be necessary for secondary defect change [8]. Thus, the reported doping effect in CZ-Si is also well explained by the internal stress effect on point defect concentration. Suhren et al. assumed the concentration to be the order of $10^{18}/cm^3$ [3], which might be overestimated. Recently, it is reported that Sb doping increases the number of COP [9]. The calculated increase of vacancies of $10^{18}/cm^3$ Sb doping is several per cent. Thus, the internal stress model well predict the experiment. Compared with FZ-Si, the change of point defect concentration in CZ-Si, which effects the formation of secondary defects, is larger by an order of magnitude. In CZ-Si, doping effect on the point defect concentration may be affected by the interstitial oxygen.

3. Thermal stress effect

As shown above, since we know the magnitude of change of point defect concentration affecting secondary defects by analyses on the doping effect, we can quantitatively examine the thermal stress in growing crystal by comparison to the doping effect. We have made the non-equilibrium thermodynamic analysis under the internal stress as follows [5]. Gibbs free energy for formation of point defects under the stress is given as

$$\Delta G = nE_F - n\sigma\Delta V_F - T\Delta S \tag{4}$$

where E_F is the increase of internal energy due to the formation of a point defect, ΔV_F is the volume change of the crystal under stress and ΔS is the entropy change. $\sigma\Delta V_F$ is the work by the internal stress. As there is no external stress at the interface, the internal volume relaxation ΔV_R is taken into account. The concentration of point defects is given by $d(\Delta G)/dn = 0$.

$$C = C^{eq}\exp(\sigma\Delta V_R/kT). \tag{5}$$

In case of vacancy formation, neighboring atoms around vacancy are relaxed inward ($\Delta V_R < 0$). This means the increase of vacancies under the compressive stress like the effect of doping of large impurity discussed in Section 2.

Here, we calculate the point defect concentration change. Usually, the growing crystal has the compressive stress in the center and tensile stress in the periphery. Thus, C_V increases and C_I decreases under a compressive stress in the center ($\sigma < 0$). This matches with the observed distribution of vacancy type defects in the center and interstitial type defects in the periphery. Growth front immediately above the solid–liquid interface has

the maximum stress along both axial and radial directions. We calculate the thermal stress using the reported temperature distribution in 150 mm-diameter crystal [10], and considering the temperature dependence of elastic modulus [11] as shown in Fig. 5. It is − 0.44 MPa (compressive) in the center and + 1.97 MPa (tensile) in the periphery. These are a little smaller than the yield stress at melting temperature, 2.2 MPa [10]. The resultant change of point defect concentration is up to 0.01% under a usual growth condition as shown in Fig. 5. Compared with doping effect in CZ-Si, thermal stress does not seem to have major contribution at present. However, since it is supposed that the thermal stress increases with crystal diameter, it will be an important factor for the future.

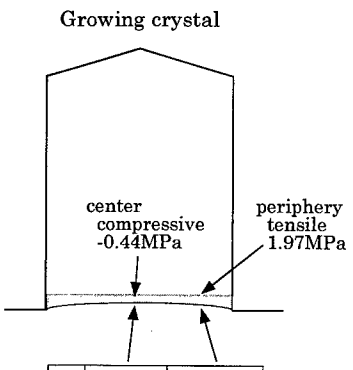

	center	periphery
V	+0.009%	-0.016%
I	-0.004%	+0.044%

Fig. 5. Calculated value of thermal stress in a growing Si and change of point defect concentration.

4. Summary

We quantitatively examine the internal stress effect on the change of point defect concentration. The changes of concentration for 0.1% in FZ- and a few % in CZ-Si due to impurity doping determine the secondary defects formation. Compared with the impurity doping effect, the change of 0.01% by thermal stress is small now, but will be important factor for the large diameter crystal.

Acknowledgements

We are grateful to K. Wada, W. Walukiewicz, K. Nakamura and M. Suezawa for stimulating discussions and Y. Yokono for help in preparation of the manuscript. This work was partially supported by JSPS Research for the Future Program.

References

[1] T. Abe, Silicon, Baifukan, Tokyo, 1994, p. 263 (in Japanese).
[2] E. Dornberger et al., J. Crystal Growth 180 (1997) 343.
[3] M. Suhren et al., J. Electrochem. Soc. 144 (1997) 4041.
[4] M. Kikuchi et al., Defects in Silicon III, The Electrochemical Society, 1999, p. 491.
[5] K. Tanahashi, N. Inoue, J. Mater. Sci. 10 (1999) 1.
[6] N.S. Rytova, Sov. Phys. Semicond. 20 (1986) 869.
[7] F. Ishikawa et al., The Japan Society of Applied Physics and Related Societies, Autumn, 1997, Extended Abstracts, Vol. 1, p. 423 (in Japanese).
[8] W. Walukiewicz, Appl. Phys. Lett. 54 (1989) 2009.
[9] T. Ono et al., Defects in Silicon III, The Electrochemical Society, 1999, p. 300.
[10] T. Abe, Defects in Silicon III, The Electrochemical Society, 1999, p. 414.
[11] W. Wijaranakula, J. Electrochem. Soc. 140 (1993) 3306.

ELSEVIER

Physica B 273–274 (1999) 497–500

PHYSICA B

www.elsevier.com/locate/physb

Annealing of the photoluminescence W-center in proton-irradiated silicon

Henning Feick*, Eicke R. Weber

Department of Materials Science and Mineral Engineering, University of California at Berkeley, 1 Cyclotron Road, Berkeley, California 94720, USA

Abstract

We study radiation defects generated by 55 MeV protons in float-zone silicon using photoluminescence (PL) and deep-level transient spectroscopy (DLTS). The investigated material is weakly phosphorus-doped and contains varying amounts of interstitial oxygen ($< 2\times10^{14} \ldots 1.7\times10^{17}$ cm^{-3}). Special attention is paid to the as of yet unidentified luminescence W-center. Its isochronal annealing behavior (40–160°C) is discussed in conjunction with the evolution of the cluster damage-related features in the DLTS spectrum. We find the annealing rate of the W-center to be independent of the oxygen content and thus exclude oxygen as a constituent of the center. There is no evident correlation between the main peaks in the DLTS spectrum and the W-center. However, a weak signal at E_C-0.075 eV is found to be a good candidate for a DLTS signal of the center. Further studies are needed to relate the formation of the W-center to the interstitials and/or vacancies released from damage clusters during annealing, which might help in identifying the constituents of the complex defect.

Keywords: W-center; Luminescence; DLTS; Radiation damage

1. Introduction

Ion-implantation or irradiation of silicon with high-energetic particles produces the luminescence W- or I1-band with zero-phonon line at 1018 meV (for a review, see for example Ref. [1]). A comprehensive study on the uniaxial stress and magnetic field perturbation of the luminescence band carried out by Davies et al. has revealed the trigonal symmetry of the center [2]. From a detailed analysis of the vibronic properties of the defect they further conclude that it incorporates silicon self-interstitials: (i) the defect is harder to compress than the bulk lattice and (ii) it displays a local mode involving predominantly the motion of a silicon atom. This finding has recently renewed the interest in the center, as a more detailed understanding of the defect might shed light on the formation of rod-like defects, which play a crucial role in the transient-enhanced diffusion phenomenon [3]. Another observation of relevance made on the W-center refers to the broad correlation between its concentration and the radiation-induced negative charge in the depletion region of silicon detectors, deteriorating their performance within harsh radiation environments like high-energy physics experiments [4].

Even though most studies carried out so far claim the W-center to be an intrinsic defect, the saturation of the production reported in Ref. [2] might be due to the exhaustion of an impurity in the material. It is therefore very interesting to study whether the formation of the center can be influenced by incorporation of impurities, e.g. oxygen [5].

As the structure of the center is expected to be simple, and as slightly modified luminescence bands are introduced by bombardment with inert-gas ions, the center has also become an interesting subject for theoretical calculations. In fact, two different models for the center

* Corresponding author. Tel.: + 1-510-486-5569; fax: + 1-510-486-4995.

E-mail address: hfeick@lbl.gov (H. Feick)

0921-4526/99/$ - see front matter
PII: S0921-4526(99)00536-0

causing the luminescence band have recently been put forward: the divacancy by Estreicher et al. [6] and one possible model of the tri-interstitial by Coomer et al. [7]. Due to the fact that there is no direct experimental evidence for the involvement of either vacancies or interstitials in the defect, the debate about its microscopic structure continues.

As the W-band is typically observed after heavy-particle damage one would expect the defect to be located in a terminal cluster of a damage cascade initiated by a high-energetic primary knock-on atom. Here it is interesting to note that the luminescence band emerges only after annealing at elevated temperature, being maximized at about 250°C. Transformations in the cluster region involve reactions between intrinsic point defects, and interstitials and/or vacancies are likely to be released during this process. For the weakly doped materials studied here, the vacancies will be trapped at interstitial oxygen, forming A-centers VO_i. The interstitials will kick out substitutional carbon (Watkins-replacement), which in turn complexes with oxygen and carbon to form C_iO_i and C_iC_s defects, respectively. The concentration of these secondary defects can be very accurately measured using deep-level transient spectroscopy (DLTS). Our approach to unravel the formation of the W-center is therefore to study the evolution of DLTS spectra within an isochronal annealing experiment and to look for a direct correlation with the photo luminescence (PL) spectra. The investigated materials thereby contain different amounts of carbon and oxygen.

2. Experimental procudure

Table 1 lists the main properties of the materials used in this work. The samples were obtained through, and characterized by, the ROSE/CERN-RD48 Collaboration [8]. They include specimen from an FZ ingot that has been enriched with oxygen during growth using a jet-doping technique. For the DLTS measurements, diodes with diffused p–n junctions (6.25 mm^2) were used, allowing for minority carrier injection under forward bias. Sample irradiations with 55 MeV protons were carried out at the 88-Inch Cyclotron of the Lawrence Berkeley National Laboratory. At 55 MeV the proton range in silicon is of the order of centimeters, ensuring homogeneously distributed damage defects. For the DLTS samples the proton fluence was chosen between 5×10^{10} and 5×10^{11} p/cm^2 whereas all PL samples were stacked and exposed to 5×10^{13} protons/cm^2. The irradiations were performed at room temperature. The time to achieve 5×10^{13} protons/cm^2 was about 1 h. Isochronal annealing ($\Delta t = 15$ min, $\Delta T = 20$°C) was done in air. Between the annealing procedures the samples were stored in a freezer. For the PL studies the samples were mounted in a closed-cycle helium cryostat and maintained at 20 K. An Argon-ion laser (514.5 nm) was used for luminescence excitation. The optical power was controlled to be 20 mW in front of the cryostat window. The luminescence light was dispersed with a dual grating spectrometer (0.23 m focal length, blazed at 1.5 μm) and then directed onto a liquid-nitrogen-cooled germanium diode. Conventional lock-in detection with the chopper (50 Hz) placed in the exciting laser beam was employed. DLTS measurements were carried out in a liquid-helium cryostat in the temperature range from 30 K, at which the carriers typically started to freeze out, to 280 K. Majority and minority carrier filling pulses allowed to investigate levels within the whole silicon band gap. Transients observed with a 1 MHz capacitance meter were digitized on a 250 ms rate window, averaged 20 times, and analyzed with a rectangular lock-in correlation function on the full transient and the first $\frac{1}{2}, \frac{1}{4}, \ldots$ fraction, resulting in about five useable DLTS signals. A long filling pulse (100 ms) was used to ensure complete filling of the traps in the high-resistivity material.

Table 1
Properties of the studied materials obtained through the ROSE CERN/RD48 Collaboration [8]. Carbon and oxygen concentrations were characterized by the collaboration using SIMS and/or infrared absorption

Designation	Resistivity	Carbon	Oxygen
standard FZ	110 Ω cm	2×10^{16} cm^{-3}	$<5\times10^{16}$ cm^{-3}
oxygenated FZ	800 Ω cm	$<2\times10^{16}$ cm^{-3}	1.7×10^{17} cm^{-3}
oxygen-lean FZ	4 kΩ cm	$<3\times10^{16}$ cm^{-3}	$<2\times10^{14}$ cm^{-3}

3. Results and discussion

In Figs. 1 and 2 we present selected PL, respectively, DLTS spectra obtained on the standard FZ material in

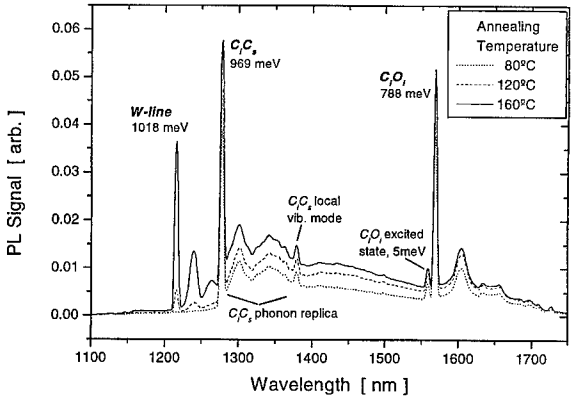

Fig. 1. Selected PL spectra obtained on the standard FZ material within the isochronal annealing experiment. The data are not corrected for the spectral sensitivity of the set-up.

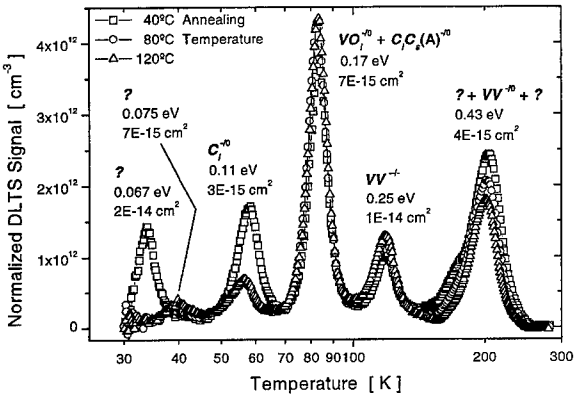

Fig. 2. Selected DLTS spectra obtained on the standard FZ material within the isochronal annealing experiment. The given energies (referring to the conduction band) and cross sections were determined from Arrhenius plots.

the course of the isochronal annealing experiment. The PL spectra display the well-known bands for the W-center as well as the C_iC_s and C_iO_i defects. Each band is bounded by a sharp zero-phonon line at short wavelength followed by phonon and local-mode replica towards longer wavelengths. We observe a significant population of the 5 meV excited state of the C_iO_i defect resulting from the comparatively high measuring temperature of 20 K. At about 1125 nm we can detect a small signal from the optical phonon assisted free exciton recombination, which stays constant during the isochronal annealing. We assume therefore that the main recombination path for the excitons is not altered during our experiment and that the height of the zero-phonon transitions gives a good relative value for the defect concentration.

In the majority carrier pulse DLTS spectra we see the deep acceptor levels of interstitial carbon C_i, vacancy–oxygen VO_i, carbon–carbon C_iC_s, and the two charge states of the divacancy VV. C_i anneals-out rapidly and forms C_iC_s and/or C_iO_i. The latter defect introduces a deep donor level at $E_V + 0.36$ eV, which we can easily observe in our minority carrier injection spectra (not shown) as the hole-capture coefficient is much larger than the electron-capture coefficient [9]. The samples were always cooled down under zero bias to ensure that the carbon-pair freezes in the bistable state (A) giving rise to a DLTS peak very close to the $VO_i^{-/0}$ transition [10]. The apparent remnant of the C_i anneal at about 60 K in the spectrum did not give a reasonable Arrhenius plot. We assume it to be related to the (B) configuration of the C_iC_s defect, which would introduce a DLTS signal at about that temperature. In the context of this study the peculiarities of heavy-particle damage are of special interest. This refers mainly to the broadened DLTS signal of the $VV^{-/0}$ transition, which is now well known to display two characteristic annealing stages at 170°C and 70°C. They can be attributed to two additional defect levels at E_C-0.4 and E_C-0.45 eV, respectively [11,12]. It will be noted that the right-hand shoulder of the divacancy transition can not be due to the E-center, VP_s, since the unknown signal displays a second ionization state in the left-hand shoulder of $VV^{-/0}$, as is demonstrated by the identical annealing behavior (cf. Fig. 2). Also, the formation of E-centers is unlikely in the weakly doped material studied, since most vacancies will be trapped by interstitial oxygen. Finally, we observe a quickly annealing electron trap at E_C-0.067 eV and a level at E_C-0.075 eV, which was documented previously, see e.g. Ref. [13] where the peak was labeled E(34 K).

Fig. 3 summarizes the evolution of defect concentrations as derived from the PL and DLTS spectra. During the initial stages of the annealing of the W-line, which we

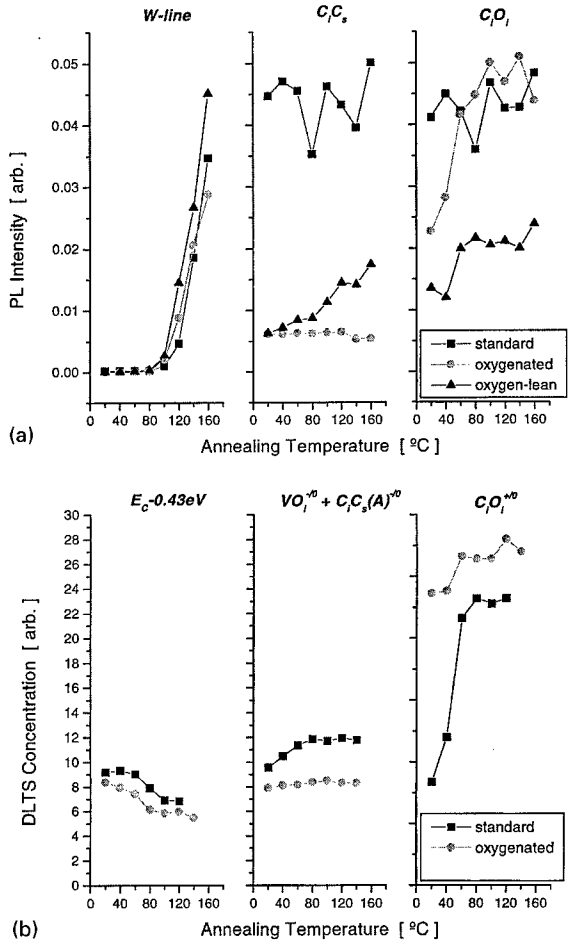

Fig. 3. Isochronal annealing of trap concentrations, (a) taken from the height of the zero-phonon lines in the PL spectra, (b) taken from the DLTS spectra.

have covered at the current state of our experiment, the W-line annealing rate does not depend on the specific material investigated. Like Nakamura et al. [5] we therefore exclude oxygen as a possible constituent of the center, as the oxygen content in our samples varied by more than three orders of magnitude (cf. Table 1).

None of the major peaks in the DLTS spectrum correlates with the annealing behavior of the W-line. This is in particular true for the cluster-related DLTS signal in the right-hand shoulder of the $VV^{-/0}$ transition. However, the weak signal at E_C-0.075 eV shows qualitatively a similar formation behavior as the W-line. Here it will be noted that a possibly existing DLTS level of the W-center would be expected to be quite shallow. Given the luminescence is due to a radiative recombination at the defect, which can be described in the framework of a pseudo donor/acceptor model, one would expect a DLTS level at about the band-gap energy minus the energy of the photon emitted during the recombination. Examples for such a relation are given for the C_iO_i defect and the copper–copper pair [14]. The E_C-0.075 eV level would therefore be a good candidate for a DLTS level of the W-center.

During the initial stages of the annealing of the W-line, no correlated increase in the VO_i and C_iO_i concentrations is observed. Further studies, especially at higher annealing temperature where the W-line signal is maximized, are needed to decide unambiguously whether the formation of the W-line is due to a mere reconfiguration in the damage cluster core or if interstitials and/or vacancies are released from the cluster region.

Acknowledgements

This work was supported by the Director, Office of Energy Research, Office of Basic Energy Sciences, Materials Sciences Division, of the US Department of Energy under Contract No. DE-AC03-76SF00098. H.F. acknowledges the Alexander von Humboldt foundation for a Feodor Lynen fellowship.

References

[1] G. Davies, Phys. Rep. 176 (1989) 83.
[2] G. Davies, E.C. Lightowlers, Z.E. Ciechanowska, J. Phys. C 20 (1987) 191.
[3] D.J. Eaglesham, P.A. Stolk, H.J. Gossmann, T.E. Haynes, J.M. Poate, Nucl. Instr. and Meth. B 106 (1995) 191.
[4] B.C. MacEvoy, S.J. Watts, Diffusion and Defect Data, Part B, 57–58 (1997) 221.
[5] M. Nakamura, S. Nagai, Y. Aoki, H. Naramoto, Appl. Phys. Lett. 72 (1998) 1347.
[6] S.K. Estreicher, J. Weber, A. Derecskei-Kovacs, D.S. Marynick, Phys. Rev. B 55 (1997) 5037.
[7] B.J. Coomer, J.P. Goss, A. Resende, R. Jones, S. Öberg, P.R. Briddon, in: C. Claeys (Ed.), Proceedings of the first ENDEASD Workshop, Santorini, Greece, April 21–22, 1999.
[8] The ROSE/CERN-RD48 Collaboration works on the improvement of the radiation tolerance of silicon particle detectors used in high-energy physics experiments. For further details see the second RD48 Status Report, CERN/LHCC 98-39, October 1998, or http://www.brunel.ac.uk/research/rose/.
[9] A. Hallen, N. Keskitalo, F. Masszi, V. Nagl, J. Appl. Phys. 79 (1996) 3906.
[10] L.W. Song, X.D. Zhan, B.W. Benson, G.D. Watkins, Phys. Rev. B 42 (1990) 5765.
[11] E. Fretwurst, C. Dehn, H. Feick, P. Heydarpoor, G. Lindström, M. Moll, C. Schütze, T. Schultz, Nucl. Instr. Meth. A 377 (1996) 258.
[12] S.J. Watts, J. Matheson, I.H. Hopkins-Bond, A. Holmes-Siedle, A. Mohammadzadeh, R. Pace, IEEE Trans. Nucl. Sci. NS-43 (1996) 2587.
[13] H. Feick, M. Moll, Diffusion and Defect Data, Part B 57–58 (1997) 233.
[14] J. Weber, H. Bauch, R. Sauer, Phys. Rev. B 25 (1982) 7688.

ELSEVIER

Physica B 273–274 (1999) 501–504

PHYSICA B

www.elsevier.com/locate/physb

Magic number vacancy aggregates in Si and GaAs – structure and positron lifetime studies

T.E.M. Staab[a,*], M. Haugk[b], A. Sieck[b], Th. Frauenheim[b], H.S. Leipner[c]

[a]*Helsinki University of Technology, Laboratory of Physics, P.O. Box 1100, FIN-02015 HUT, Finland*
[b]*University GH Paderborn, Department of Physics, Theoretical Physics, D - 33098 Paderborn, Germany*
[c]*Martin-Luther-University Halle-Wittenberg, Department of Physics, Friedemann-Bach Platz 6, D-06108 Halle, Germany*

Abstract

We investigate structural properties of large vacancy agglomerates in Si and GaAs using a self-consistent-charge density-functional based tight-binding method. We also calculated the defect-related positron lifetimes. Strong evidence is found for the existence of vacancy aggregates with unusual magic numbers in GaAs. In contrast to Si – the first stable agglomerate consists 12 vacancies instead of 6. This findings fit into experimental observations on deformed and irradiated samples.

Keywords: Positron annihilation spectroscopy; Magic number vacancy clusters; Deformation; Irradiation

1. Introduction

Neutron or electron irradiation as well as plastic deformation [1–3] are well known to produce vacancies and vacancy agglomerates in semiconductors. Vacancy agglomerates may also be present in as-grown silicon [4]. When excess vacancies are mobile but cannot find sinks (like surfaces or dislocations) to anneal, they are likely to agglomerate – e.g. into stable three-dimensional vacancy clusters.

Positron annihilation spectroscopy (PAS) is a suitable tool to detect small vacancy clusters. Since positron lifetime spectroscopy (POLIS) measures the electron density at the trapping site of the positron, this method is sensitive to the size of open-volume defects [5]. Hence, it is possible to distinguish between monovacancies, vacancy chains, and three-dimensional agglomerates. Vacancy agglomerates are generically detected by POLIS in deformed or irradiation-damaged materials (see e.g. Refs. [1,6,7] and for an overview [8]). Positron lifetimes as in monovacancies (Si: 270 ps (GaAs: 260 ps) – bulk lifetime: 218 ps (230 ps)) or divacancy-type defects have been attributed to vacancy-type defects bound to the dislocation core [1,3]. Long positron lifetime components of about 500 ps are an indication of large vacancy agglomerates created during deformation [3,8].

Only in covalently bound materials there exist some indications that stable vacancy clusters of certain sizes should be present, since a low number of dangling bonds is considered to be favorable. This led Chadi and Chang [9] to the conclusion that there should be the so-called *magic numbers* ($N = 6$, 10, and 14) of vacancies in diamond-like homonuclear structures like silicon. This may be expanded in a straightforward manner to $N = 4i + 2$; $i = 1,2,3,\ldots$ [10]. It may now be interesting to investigate this for compound semiconductors like GaAs, where the existence of dangling bonds of the different atomic species makes reconstruction and relaxation of the surrounding atoms much more important. Therefore, we examine the formation energy for three-dimensional agglomerates as well as for vacancy chains in Si and GaAs, and we calculated the corresponding positron lifetimes to be able to compare our data to experimental results. To avoid defect–defect interactions we use very large supercells of 512 atoms [10,11]. Since this cannot be achieved by fully SCF methods, one has to apply a more approximate scheme.

* Corresponding author. Tel.: + 385-9-451-3107; fax: + 385-9-451-3116.
E-mail address: tst@fyslab.hut.fi (T.E.M. Staab)

0921-4526/99/$ - see front matter
PII: S0921-4526(99)00537-2

2. Methodology

A self-consistent charge density-functional based tight-binding (SCC-DFTB) method, which also takes charge transfer into account, has been used for total energy calculations and structure relaxation [12,13].

The method gives very good results for surface reconstructions of GaAs [12] compared to self-consistent field local density approximation (SCF-LDA) calculations. Test calculations [10,11] indicate that SCC-DFTB allows the determination of defect formation energies with an accuracy comparable to SCF-LDA calculations. But the computing time and memory usage of SCC-DFTB is up to two orders of magnitude smaller allowing the modeling of large supercells, which are needed to avoid defect–defect interaction of large vacancy aggregates (details may be found in Ref. [10]). We used only charge-neutral supercells (for GaAs: vacancy clusters consisting of an equal number of missing arsenic and gallium atoms). Due to the electron counting rule, this should lead in GaAs to configurations which are charge-neutral over a wide range of the position of the Fermi level, and the defect formation energies are then independent of the relative chemical potential and have an absolute value. This allows a direct comparison of the defect formation energies of the vacancy aggregates.

The formation energies Ω_n for neutral defects in Si and GaAs (with an equal number of Ga and As vacancies) have been obtained using [14]:

$$\begin{aligned} \Omega_n^{\mathrm{Si}} &= E_{\mathrm{tot}}^{\mathrm{Si}} - \mu_{\mathrm{Si}}^{\mathrm{bulk}}(n_{\mathrm{Si}}), \\ \Omega_n^{\mathrm{GaAs}} &= E_{\mathrm{tot}}^{\mathrm{GaAs}} - \mu_{\mathrm{GaAs}}^{\mathrm{bulk}}(n_{\mathrm{Ga}} + n_{\mathrm{As}}), \end{aligned} \tag{1}$$

where n_{Si} (n_{Ga} and n_{As}) denotes the number of Si (Ga and As) atoms in the supercell and $\mu_{\mathrm{Si}}^{\mathrm{bulk}}$ ($\mu_{\mathrm{GaAs}}^{\mathrm{bulk}}$) is the chemical potential of Si (the Ga and As pair in bulk GaAs), which we obtained in a SCC-DFTB total energy calculation for the Si (GaAs) single crystal.

The positron lifetimes for the perfect lattice and for different vacancy cluster configurations are calculated using the superimposed-atom model by Puska and Nieminen [15]. The lattice relaxations under the influence of the trapped positron can be neglected for large open volume defects (cf. e.g. Refs. [16,17]). We took the unrelaxed atomic positions as well as those determined by the SCC-DFTB method. The theoretical data will be scaled to the experimental bulk lifetime [18].

3. Results

Our calculations show that the formation energy for chains of vacancies is much higher than that for vacancy clusters. Hence, if the vacancies are able to move along this vacancy chain, they will re-arrange from the initial chain configuration and aggregate as 3D clusters, which have a much lower formation energy. Clustering can happen even below the temperature of vacancy diffusion [10].

We then examined different three-dimensional vacancy aggregates in order to determine the stability of clusters with different numbers of missing atoms. Since a huge number of possible candidates for clusters consisting of up to 15 vacancies exists, but obviously only closed structures will have a minimal energy, we used a straightforward way to construct these vacancy aggregates and checked only a small number of different configurations for some vacancy complexes (details may be found in Refs. [10,11,19]). First, we tried to form hexagonal ring-like structures for Si and GaAs (3 V_{Ga} and 3 V_{As}). The sequence in which the atoms were removed in larger vacancy clusters can be seen for GaAs in Fig. 4. Other configurations which do not follow this straightforward way of construction were checked and found to be significantly higher in energy. They are consequently not considered here.

To compare the energies of the different clusters we calculated for Si (GaAs) the energy gained by adding an isolated monovacancy (divacancy) to the most stable aggregate consisting of $n-1$ ($n-2$) vacancies. In our calculations this is

$$\Delta E_n = \Omega_n - (\Omega_{n-1} + \Omega_1) \text{ (Si-}case\text{)}$$

$$\Delta E_n = \Omega_n - (\Omega_{n-2} + \Omega_2) \text{ (GaAs-}case\text{)},$$

which sets the energy zero at ΔE_1 (ΔE_2). Note that ΔE_n is the negative dissociation energy of V_n into $V_{n-1} + V_1$ ($V_{n-2} + V_2$) for Si (GaAs) (Fig. 1).

This energy is plotted in Figs. 2 and 3 for the most stable aggregates of vacancies. The *smallest* stable structure, with respect to dissociation, is found to be V_{12} in GaAs, whereas in Si it is V_6. The next larger stable agglomerates in Si are the cage-like structures V_{10} and V_{14}.

We assumed in our calculations that the vacancy aggregates grow by the addition of monovacancies (divacancies). Of course these aggregates can dissociate into other fragments. However, SCC-DFTB predicts the lowest dissociation energies for $V_n \rightarrow V_{n-1} + V_1$ ($V_n \rightarrow V_{n-2} + V_2$).

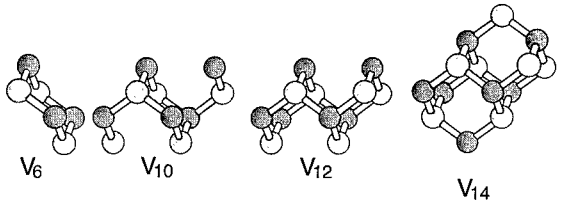

Fig. 1. Structures of some V_n in GaAs are shown (missing As atoms dark grey, missing Ga Atoms light gray). For Si V_6 and V_{14} are the same as show here while V_{10} has the 4 most upper right vacancies from V_{14} removed.

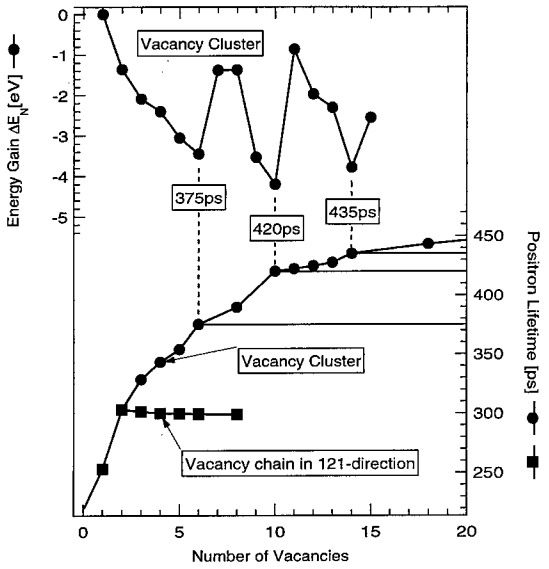

Fig. 2. Energy gained by adding a monovacancy to an aggregate of $(N-1)$ vacancies in Silicon (upper part) and the corresponding positron lifetime (lower part) for unrelxed structures. Theoretical positron lifetimes for V_6, V_{10}, and V_{14} are indicated.

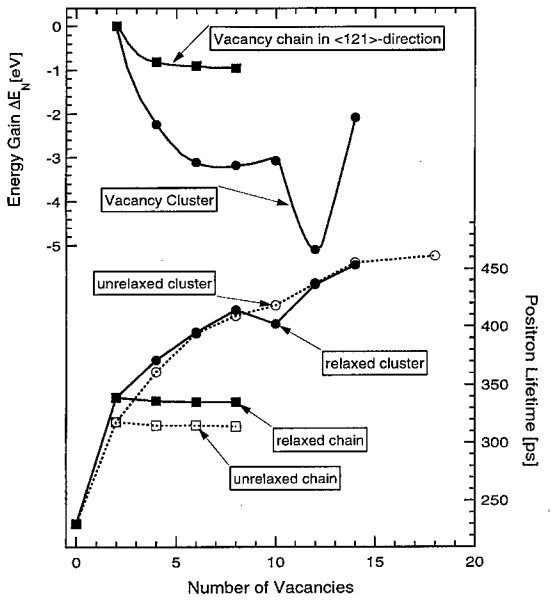

Fig. 3. Energy gained by adding a divacancy to an aggregate of $(N-2)$ vacancies in GaAs (upper part) and the corresponding positron lifetime (lower part).

A general feature of all GaAs-relaxed structures is that threefold coordinated Ga atoms undergo a sp^2 hybridization by emptying all dangling bonds, whereas all threefold coordinated As atoms show p^3 bonding configuration with filled dangling bonds. This is typical for GaAs and can be illustrated by the electron counting rule. Following this rule a Ga atom contributes $\frac{3}{4}$ electrons per bond, whereas As contributes $\frac{5}{4}$ electrons. Since the energy states created by Ga dangling bonds are higher than the energy states by As dangling bonds, the electrons are transferred from gallium to arsenic atoms. As a result the atoms will change the hybridization state to further minimize the total energy.

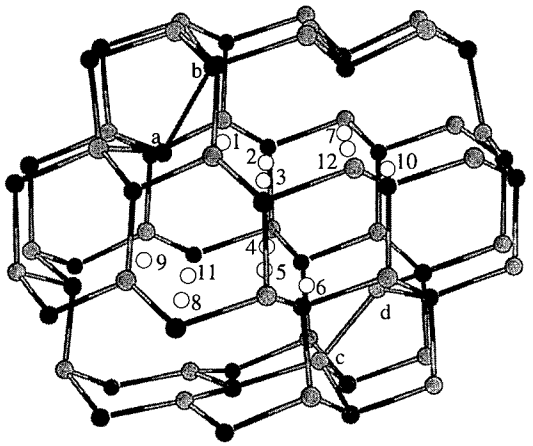

Fig. 4. Structure in GaAs consisting of 12 vacancies. Dark grey balls denote As and light grey balls Ga atoms. The white spheres are the vacancies. The numbers give the order in which the atoms have been removed, starting from V_2 to V_{12}. Atoms a and d are removed to get V_{14}.

It can be seen from Fig. 3 that V_{12} is by far the most stable configuration in GaAs, which can be understood by looking at the relaxed structure of V_{12} in Fig. 4. The dominant feature of this structure is the formation of an As–As and a Ga–Ga dimer (a–b resp. c–d in Fig. 4). This reduces the number of dangling bonds and, therefore, lowers the total energy. Additionally, it can be seen that the threefold coordinated As atom (a in Fig. 4) is in a p^3 configuration state, whereas the Ga Atom (d in Fig. 4) prefers a planar structure with sp^2-character. Furthermore, V_{12} has a band gap which is larger than that for the other structures except the divacancy. This additional fact supports the stability of this structure. In contrast to Si, where one hexagonal ring is the first stable structure, the vacancies in GaAs are arranged here in two hexagonal rings placed one upon the other (see Fig. 4).

The dimer formation of inner surface atoms (a–b resp. c–d in Fig. 4) is responsible for the lower energy for certain configurations of vacancy agglomerations in compound semiconductors. Since in GaAs – in contrast to Si – the energy of a structure can already be lowered by transferring electrons from Ga dangling bonds to As dangling bonds, a remarkable reduction of energy can only be achieved when dangling bonds are saturated by dimer formation. This explains why in Si the hexagonal

ring with a minimal number of dangling bonds is the first stable cluster, whereas in GaAs it is the double hexagonal (V_{12}) structure, which shows an energetically favorable dimer configuration.

We calculated the positron lifetimes for the unrelaxed and the relaxed structures in GaAs (for Si only the unrelaxed one are considered). The calculated positron lifetime related to trapping into a zig-zag chain is roughly that of a divacancy. For clusters consisting of more than four vacancies no significant change in positron lifetime before and after relaxation can be observed. An exception is V_{10} in GaAs, where the unfavorable configuration of some Ga atoms leads to an increase in the electron density within the open volume.

Recent result on positron annihilation in neutron irradiated silicon [7,20] and on high dose electron-irradiated Silicon [6] give a quite consistent picture on stable agglomeration formed during annealing by mobile primary defects: Considering neutron irradiation larger vacancy agglomerate were formed around 870 K and gave defect-related positron lifetimes of 420 ± 20 ps [20] and 430 ± 30 ps [7]. Concerning high-dose electron irradiation vacancy agglomeration was found in the same temperature range (around 870 K) and defect-related positron lifetimes of 415 ± 20 ps [6] were obtained. This experimental finding would correspond within the errors very well to the most stable agglomerate found by us: the V_{10} vacancy cluster in Si.

4. Conclusions

In conclusion, the calculations prove that vacancy chains are energetically unfavorable. We can assume that these vacancy chains, generated during deformation by jog-dragging, collapse instantaneously by atomic rearrangement to 3D vacancy clusters. While we are able to obtain the same magic numbers for Si as predicted by qualitative arguments, we find a new type of *magic number* vacancy clusters in GaAs. We believe that these result can be generalized also to other III–V semiconductors with zincblende structure. For the smallest stable structure we find – in contrast to Si (V_6, V_{10}, V_{14}) – for GaAs a V_{12} vacancy cluster consisting of two staggered hexagonal rings. The reason is – unlike the Si case – not only a minimization of the number of dangling bonds, but a lowering of the energy by re-hybridization caused by charge transfer from Ga to As. This one stable vacancy cluster configuration up to a size of 12 vacancies for GaAs may be a good candidate for the large vacancy agglomerates observed with POLIS in deformed GaAs. For Si, comparison to experiments indicate a cluster size of V_{10} after high dose electron or neutron irradiation followed by partial annealing.

Acknowledgements

This work was supported by the Deutsche Forschungsgemeinschaft (DFG) and by the European Union (Marie-Curie research grant).

References

[1] R. Krause-Rehberg et al., Phys. Rev. B 47 (1993) 132 66.
[2] R. Krause-Rehberg et al., Phys. Rev. B 49 (1994) 2385.
[3] H. Leipner et al., Phys. Stat. Sol. A 171 (1999) 377.
[4] T. Tan, P. Plekhanov, U. Gösele, Appl. Phys. Lett. 70 (1997) 1715.
[5] M. Puska, R. Nieminen, Rev. Mod. Phys. 66 (1994) 841.
[6] Motoko-Kwete et al., in Positron Annihilation Proceedings of the ICPA-8 Gent, World Scientific, Singapore, 1989, pp. 687–689.
[7] Z. Shenyun et al., Mater. Sci. Forum 175–178 (1995) 609.
[8] R. Krause-Rehberg, H. Leipner, Defects in Semiconductors, 1st Edition, Springer, Berlin, 1999.
[9] D. Chadi, K. Chang, Phys. Rev. B 38 (1988) 1523.
[10] T. Staab, M. Haugk, T. Frauenheim, H. Leipner, Phys. Rev. Lett., accepted October 1999.
[11] T. Staab et al., Phys. Rev. B, submitted for publication.
[12] M. Haugk, J. Elsner, T. Frauenheim, J. Phys.: Condens. Matter 9 (1997) 7305.
[13] M. Haugk et al., J. Comp. Mater. Sci. 13 (1998) 239.
[14] S. Zhang, J. Northrup, Phys. Rev. Lett. 67 (1991) 2339.
[15] M. Puska, R. Nieminen, J. Phys. F: Metal Phys. 13 (1983) 333.
[16] M. Saito, A. Oshiyama, Phys. Rev. B 53 (1996) 7810.
[17] M. Hakala, M. Puska, R. Niemienen, Phys. Rev. B 57 (1998) 7621.
[18] F. Plazaola, A. Seitsonen, M. Puska, J. Phys: Condens. Matter 6 (1994) 8809.
[19] J. Hastings, S. Estreicher, P. Fedders, Phys. Rev. B 56 (1997) 10215.
[20] M. Huang et al., Mater. Sci. Forum 105–110 (1992) 1071.

ELSEVIER

Physica B 273–274 (1999) 505–508

PHYSICA B

www.elsevier.com/locate/physb

Interstitial aggregates and a new model for the I_1/W optical centre in silicon

B.J. Coomer[a,*], J.P. Goss[a], R. Jones[a], S. Öberg[b], P.R. Briddon[c]

[a]*School of Physics, The University of Exeter, Exeter EX4 4QL, UK*
[b]*Department of Mathematics, University of Luleå, Luleå S-97187, Sweden*
[c]*Department of Physics, The University of Newcastle upon Tyne, Newcastle upon Tyne NE1 7RU, UK*

Abstract

First principles local-density-functional (LDF) theory is employed to investigate the properties of di-interstitial (I_2), tri-interstitial (I_3) and tetra-interstitial (I_4) structures in silicon. We show that a tri-interstitial defect can account for many of the fundamental properties of the I_1/W-optical centre which is observed in irradiated, annealed silicon.

Keywords: Silicon; W-line; Interstitial; Aggregation

It is well known that following the annealing of electron or ion irradiation of silicon or germanium, extended structures are generated that are observable with transmission electron microscopy (TEM). These 'rod-like' defects lie along [1 1 0] on a {3 1 1} habit-plane. The proposed model [1] is that of a [1 1 0] chain of self-interstitials which is inserted down a [1 1 0] channel. The TEM results are well matched by this model if a bonding rearrangement on both sides of the chain is included. This 'bond-switching' process has been shown to significantly lower the energy of the extended structure [2].

In contrast to the wealth of information on the extended defects, there is little published data concerning the first stages of the aggregation process of self-interstitials. One assignment has been made of a di-interstitial structure to the electron paramagnetic resonance (EPR) spectrum, P6 [3]. However, this model is not universally accepted.

The I_1/W-optical centre is observed in silicon which has been exposed to lattice damaging treatments with subsequent annealing at around 500 K. It is seen in both n- and p-type silicon following self-ion irradiation [4]. The centre is characterised by a sharp peak at 1018.2 eV and an associated phonon sideband, containing local vibrational modes (LVMs). Uniaxial stress measurements reveal the defect symmetry to be trigonal. Although this intriguing centre has received much attention by both experimentalists and theorists, a definitive model is still lacking.

It is generally accepted that the W-centre arises from the agglomeration of an intrinsic species. Much work in the past has concentrated on the defect being vacancy related [5–7] but more recent experiments [4,8,9] have supported the interstitial nature of the W-centre. We review this information now:

1. The LVM detected in luminescence, with energy 70.0 meV is consistent with a strengthened Si–Si bond. Calculations [10] have shown that the optimisation of vacancy defects leads to the lengthening of Si–Si bonds and such defects could not give rise to local modes lying above the Raman frequency [8].
2. The stress response of the W-optical line is two orders of magnitude smaller than that of the 1039 meV line in silicon which is believed to be a vacancy aggregate [8]. Also, the shift of the W-luminescence line with stress is very much smaller than that of V_6 (the B^4_{80} luminescence centre) [11,12]. Analysis of the W-vibronic

* Corresponding author. Tel.: + 44-1392-264198; fax: + 44-1392-264111.
E-mail address: coomer@excc.ex.ac.uk (B.J. Coomer)

0921-4526/99/$ - see front matter
PII: S0921-4526(99)00538-4

sideband suggests that the W-defect is less compressible than bulk Si [8]. Such a low stress response would be expected for an interstitial defect where bonds are compressed.

3. The release of interstitials from irradiation damage regions during annealing has been tentatively correlated with the growth of the W-centre [13].
4. Although the existence of the W-centre is not dependent on the presence of any impurity, the effect of carbon and oxygen impurities on the defect concentration has also been used to argue that the defect is interstitial related [9].

Following annealing at around 500 K of He, Ne, Ar or Kr ion-bombarded silicon, a new family of trigonal centres are observed. Although the new zero-phonon lines and associated LVM sideband structures are qualitatively the same as the W-centre, the system is red-shifted by between 1–10 meV, depending upon the identity of the noble-gas atom. The one-phonon replicas of the noble-gas-related defects are also shifted slightly relative to the W-centre one-phonon replica. Davies et al. [8] claims that this effect is consistent with a strain interaction between the noble-gas atom and the W-centre, i.e., the noble-gas atom lies close to the W-centre and, although no *chemical* bonding takes place, the presence of the noble-gas atom perturbs the electronic and geometric structure of the W-centre.

Comprehensive studies of Ar ion-beam etched silicon [14] have indicated that an unexpected and enhanced diffusion process takes place before the W-like defect forms. The observed depth profile of the noble-gas-related centres suggests that the argon atoms are penetrating deeper into the sample than expected – up to 1 μm. The diffusion co-efficient was estimated to be $D = 5 \times 10^{-14}$ cm^2 s^{-1}. Using $D = va^2 e^{E_b/kT}$ where v is the attempt frequency ($\sim 10^{13}$ Hz) and a is the diffusion length (~ 3.0 Å), this leads to a barrier height of $E_b = 0.65$ eV. Implantation [15] and permeation [16] studies show that helium diffuses with an activation energy between 0.8 and 1.3 eV. Since the argon atom has almost twice the covalent radius of He, one would expect the diffusion barrier of Ar to be significantly greater than 0.65 eV.

Although it is thought that the thermal migration barrier for the self-interstitial is greater than 1 eV, the interstitial has been observed to undergo an enhanced diffusion at cryogenic temperatures [17]. Recent studies of irradiated silicon [18] have obtained a value of 0.065 ± 0.015 eV for the migration energy of the silicon self-interstitial under ionising conditions. Therefore, the anomalous diffusion of Ar could be explained by an interstitial mechanism if:

(a) A binding energy exists between the isolated self-interstitial and the noble-gas atom.
(b) The presence of the self-interstitial significantly reduces the energy required for the noble-gas atom to move through the lattice.

It has also been suggested [7] that the enhanced diffusion of the noble-gas atom could be due to repulsion from a wave of vacancies released during implantation. However, a microscopic model for this process has not been put forward.

We present the results of state-of-the-art calculations investigating the structures and electronic properties of interstitial defects. The properties of the lowest energy tri-interstitial are compared with the W-optical centre.

A local density-functional (LDF) code (AIMPRO [19]) is used. Large, hydrogen-terminated clusters are used with composition $Si_{181+n}H_{116}$ ($n = 2,3,4$) to investigate the interstitial defects. Several models for I_2 and I_3 are compared in energy. For I_4, the structure proposed by Aria et al. [20] is optimised. The total energy of the structure is compared with a [1 1 0] interstitial-chain element. The positions of all the Si atoms were optimised using a conjugate gradient method. Electrical levels were calculated using a transition-state method described elsewhere [21].

Several structures were considered for I_2. Two similar structures [22,23] were found lowest in energy and both consist of three Si atoms sharing a single substitutional site. The lowest energy form of this type of I_2 defect was found to possess C_{1h} symmetry (see Fig. 1). In this case the two interstitial atoms lie along [1 1 0] [23]. Two other structures were found to lie around 0.4 eV higher in energy. The first is formed by placing two parallel [1 0 0] split-interstitials at next-nearest-neighbour sites. The second is formed by placing the additional atoms in opposing bond-centred sites either side of a hexagonal ring. Both structures include two atoms which are three-fold co-ordinated, all other atoms being fully coordinated. The model assigned by Lee [3] to the P6 EPR centre was calculated to lie ~ 3.0 eV higher in energy with the symmetry constrained to D_{2d}. Removal of symmetry

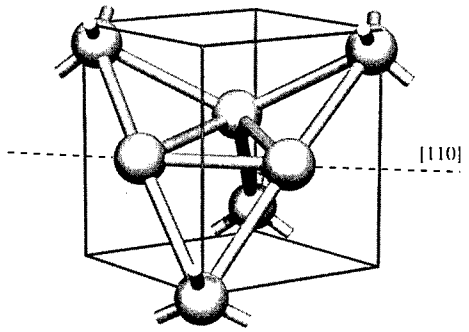

Fig. 1. Optimised structure of the lowest energy form of I_2 investigated. Three Si atoms share a single substiutional site. The two interstitial atoms lie along [1 1 0] as indicated.

constraints results in a new structure and an energy lowering of 1.1 eV. However, the resultant defect has little in common with the ground state structure proposed by Lee.

The lowest energy tri-interstitial investigated possesses C_{3v} symmetry. The structure is formed by placing each additional Si atom at the centre of three parallel bonds which surround a tetrahedral interstitial site (see Fig. 2). Structural optimisation of this structure involves the formation of a three-atom ring resulting in full four-fold coordination of all atoms. The optimisation was repeated from an asymmetric starting configuration resulting in the same relaxed structure. It is interesting to note that this structure is a three atom section of a [1 1 0] interstitial-chain which is a basic element of the {3 1 1} planar defects observed following high-temperature annealing of irradiated silicon [1].

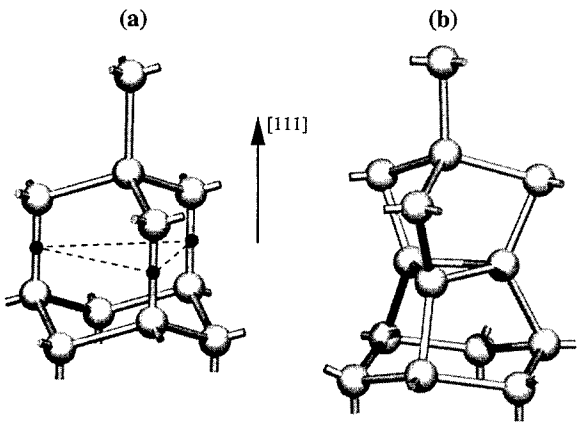

Fig. 2. (a) A section taken from the ideal diamond structure. To form the tri-interstitial, additional atoms are placed at the bond-centred sites indicated by the black circles. The bond reconstruction that results from the structural optimisation is indicated by the dashed lines (b) The fully optimised structure. A possible site for a noble-gas atom is along $[\bar{1}\,\bar{1}\,\bar{1}]$ in the cage adjacent the three-atom ring.

The electrical levels of the tri-interstitial were calculated. The defect does not appear to possess an $(-/0)$ acceptor level but a possible $(0/+)$ donor level was calculated to lie close to the valence band edge ($\sim E_v + 0.1$ eV).

The I_3 defect possesses a number of LVMs. A symmetric vibrational mode lies at 74 meV, consistent with experiment (70.0 meV). This mode is localised upon unique atoms lying on the principal [1 1 1] axis of the defect. The mode shifts by 12 cm^{-1} when one atom is replaced by ^{30}Si, which is in reasonable agreement with the experimentally observed shift of 16 cm^{-1} [8].

A slightly enlarged interstitial cage lies along the principal [1 1 1] axis of the tri-interstitial, providing a possible site for noble-gas atoms. The effect of placing an argon atom at this site is to perturb the electronic structure of the tri-interstitial and enlarge the cage surrounding the argon atom. The bond which gives rise to the 74 meV symmetric mode is only slightly perturbed by the presence of the argon. To show that the trigonal symmetry structure was a local minimum, the argon was displaced from its optimised trigonal axis site by ~ 1.0 Å. In the subsequent optimisation the Ar relaxed back to the high symmetry site.

Two I_4 models were optimised. The model suggested by Aria et al. [20] was found to be significantly lower in energy than a 4-atom [1 1 0] interstitial chain element. The optimised structure (Fig. 3) compares well with that

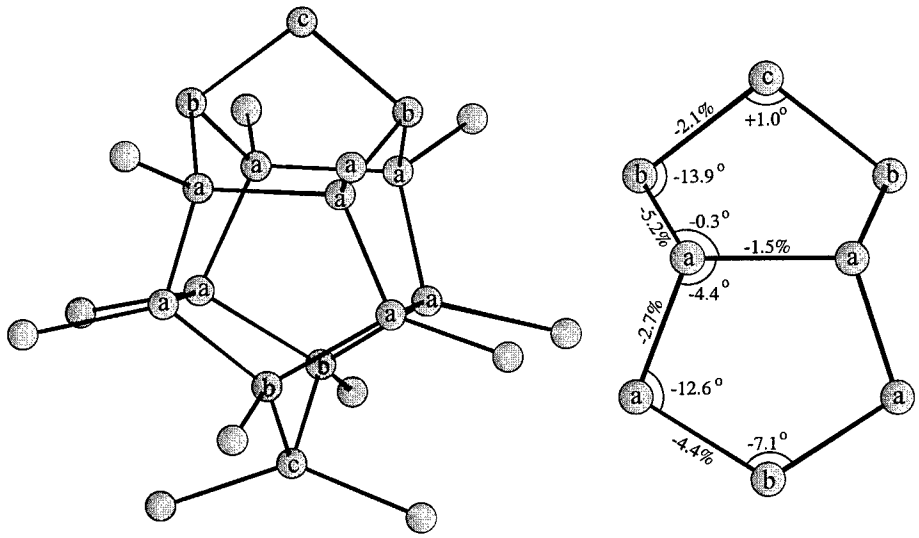

Fig. 3. Optimised structure of I_4. Distortions from the ideal bond lengths and angles are shown.

calculated by Aria et al. All atoms are four-fold coordinated with bond lengths and bond angles distorted from their ideal values by no more than $\sim 10\%$. Preliminary calculations suggest that the $(-/0)$ and $(0/+)$ levels lie within ~ 0.1 eV of E_c and E_v respectively.

In conclusion, we propose a new model for the tri-interstitial in silicon. Its calculated properties agree well with experimental information on the W-optical centre. The structure is closely related to the $\{3\,1\,1\}$ defect structure proposed by Takeda et al. [1]. We propose a suitable site for a noble-gas atom nearby the tri-interstitial. This structure gives rise to the correct symmetry and the inert-gas atom is expected to perturb the W-centre as observed.

Energy comparisons between di-interstitial defects reveal four low-energy structures within 0.5 eV of each other. Optimisation of the [1 0 0] oriented I_4 structure results in a geometry close to that reported in the previous theoretical calculations of Aria et al.

Acknowledgements

S.Ö. thanks NFR and TFR for financial support. We also thank the ENDEASD network.

References

[1] S. Takeda, Jpn. J. Appl. Phys. 30 (1991) L639.
[2] J. Kim, J.W. Wilkins, F.S. Khan, A. Canning, Phys. Rev. B 55 (1997) 16 186.
[3] Y.H. Lee, Appl. Phys. Lett. 73 (1998) 1119.
[4] P.J. Shultz, T.D. Thompson, R.G. Elliman, Appl. Phys. Lett. 60 (1992) 59.
[5] C.G. Kirkpatrick, J.R. Noonan, B.G. Streetman, Radiat. Effects 30 (1976) 97.
[6] N.S. Minaev, A.V. Mudryi, V.D. Tkachev, Phys. Status. Solidi B 108 (1981) K89.
[7] S.K. Estreicher, J. Weber, A. Dereckei-Kovacs, D.S. Marynick, Phys. Rev. B 55 (1997) 5037.
[8] G. Davies, E.C. Lightowlers, Zofia E. Cienchanowska, J. Phys. C: Solid State Phys. 20 (1987) 191–205.
[9] M. Nakamura, S. Nagai, Y. Aoki, H. Naramoto, Appl. Phys. Lett. 72 (1998) 1347.
[10] B.J. Coomer, A. Resende, J.P. Goss, R. Jones, S. Öberg, P.R. Briddon, Physica B 273–274 (1999) 518, These Proceedings.
[11] A.S. Kaminskii, E.V. Lavrov, Solid State Commun. 106 (1998) 751.
[12] B. Hourahine, R. Jones, A.N. Safonov, S. Öberg, P.R. Briddon, S.K. Estreicher, Physica B 273–274 (1999) 174, These Proceedings.
[13] H. Feick, E.R. Weber, Physica B 273–274 (1999) 495, These Proceedings.
[14] J. Weber, Physica B 170 (1991) 201.
[15] P. Jung, Nuc. Inst. Meth. in Phys. Res. B 94 (1994) 362.
[16] A. Van Wieringen, N. Warmholtz, Physica XXII (1956) 849–865.
[17] G.D. Watkins, in: Radiation Damage in Semiconductors, Dunod, Paris, 1964, p. 97.
[18] A. Hallén, N. Keskitalo, L. Josyula, B.G. Svensson, J. App. Phys. 86 (1999) 214.
[19] R. Jones, P.R. Briddon, in: M. Stavola (Ed.), Identification of defects in semiconductors, Vol 51A of Semiconductors and semimetals, Academic press, Boston, 1998 (Chapter 6).
[20] N. Aria, S. Takeda, M. Kohyama, Phys. Rev. Lett. 78 (1997) 4265.
[21] A. Resende, R. Jones, S. Öberg, P.R. Briddon, Phys. Rev. Lett. 82 (1999) 2111.
[22] A. Bongiorno, L. Colombo, F. Cargnoni, C. Gatti, M. Rosati, ICPS-21 Conference Proceedings, Jerusalem, 1998.
[23] S.K. Estreicher, Hydrogen '99 workshop, Exeter University, 1999.

ELSEVIER

Physica B 273–274 (1999) 509–511

PHYSICA B

www.elsevier.com/locate/physb

Thermal equilibrium concentrations and diffusivities of intrinsic point defects in silicon

Takahisa Okino[a,*], Toshitada Shimozaki[b]

[a]*College of Liberal Arts and Sciences, Nippon Bunri University, Ichigi, Oita 870-0327, Japan*
[b]*Center for Instrumental Analysis of Kyushu Institute of Technology, Kitakyushu 804-8550, Japan*

Abstract

Recently, inherent defects in silicon crystal cause a serious problem resulting from the trend toward small scale and highly integrated circuits used in semiconductor devices. There is no doubt that intrinsic point defects in silicon are closely related to the formation mechanisms of these defects. Understanding the behavior of the point defects is thus extremely important. The equations for dopant diffusions and oxidation stacking faults in silicon, considering the intrinsic point defect concentrations as unknowns, are solved by mathematically self-consistent method and also the mechanisms of silicon self- and dopant-diffusions are determined. The thermal equilibrium concentrations and diffusivities of self-interstitials and vacancies in silicon, $^*C_I$, $^*C_V$, D_I and D_V are obtained as functions of the absolute temperature T. Consequently, the relations of $^*C_I < (^*C_I{}^*C_V)^{1/2} < {}^*C_V$ and $\partial_T \ln(D_V) < \partial_T \ln(D_I)$ are derived for an arbitrary temperature.

Keywords: Thermal equilibrium concentration; Diffusivity; Point defect

1. Introduction

The process related to thermal oxidation of the bulk surface or a dopant diffusion in silicon is an indispensable one for silicon semiconductor device fabrication. The thermal oxidation of the silicon surface generates extrinsic stacking faults and enhances or retards a dopant diffusion in silicon. This fact indicates that self-interstitials generated at the Si/SiO_2 interface diffuse into the bulk inside. And self-interstitials are still in the supersaturated state although they are captured by vacancies in the bulk, while vacancies are in the undersaturated state. Furthermore, it is assumed that the local equilibrium relation given by

$$C_I C_V = {}^*C_I {}^*C_V \tag{1}$$

is valid [1,2], where $^*C_I$ and $^*C_V$ are the thermal equilibrium values of self-interstitial and vacancy concentrations C_I and C_V.

To clarify the mechanisms of the grown-in defect formation and the diffusion of a dopant deliberately introduced into the bulk is useful in the semiconductor device fabrication. There is no doubt that the intrinsic point defects are closely related to their mechanisms. Therefore, understanding of self-interstitial and vacancy concentrations $^*C_I$ and $^*C_V$ as well as their diffusivities D_I and D_V is extremely important. At present, however, these values are not conclusively determined, although various results have been reported. Since there is no way to directly investigate them through experimentation, the best method is to determine them from investigating the phenomena of the dopant diffusions and the oxidation stacking faults.

Antoniadis [3] used an equation of C_I and C_V for analysis of oxidation-enhanced/-retarded diffusion (OED/ORD). Tan et al. [4] proposed an equation of C_I and C_V for oxidation stacking faults (OSF). These

* Corresponding author. Fax: + 81-97-593-2071.
E-mail address: okino@la.nbu.ac.jp (T. Okino)

0921-4526/99/$ - see front matter
PII: S0921-4526(99)00540-2

OED/ORD and OSF equations considering C_I and C_V as unknowns have been solved by many researchers. However, the conclusive solutions have not been reported because they are not mathematically self-consistent [5,6]. Therefore, we first contrive an analytical method to obtain mathematically self-consistent solutions of these equations, using the experimental results of the OED/ORD [1,2] and the OSF [7]. As a result, the analytical solutions are obtained and also the mechanisms of P, Sb, B and silicon self-diffusions are determined. Furthermore, $^*C_I$ and $^*C_V$ as well as D_I and D_V are determined as functions of the absolute temperature T.

The reproducible diffusivity values of the self-diffusion were experimentally obtained by Mayer et al. [8]. The self-diffusion coefficient resulting from the obtained $^*C_I$, $^*C_V$, D_I and D_V agreed well with Mayer et al.'s result. As seen from Figs. 1 and 2 in ref. [9], there are no reliable results to each of their values. As there are necessary conditions to be satisfied between them, the relations of $^*C_I < (^*C_I{}^*C_V)^{1/2} < {}^*C_V$ and $\partial_T \ln(D_V) < \partial_T \ln(D_I)$ are obtained for an arbitrary temperature.

2. Basic equations and analytical method

The self-diffusion diffusivity based on the interstitialcy and vacancy mechanisms is generally expressed as

$$D_{sd} = f_I D_I {}^*C_I/C_0 + f_V D_V {}^*C_V/C_0, \tag{2}$$

where f_I (= 0.7273) [10,11], f_V (= 0.5) [10,11] and C_0 ($= 5 \times 10^{22}$ cm^{-3}) are the correlation factors of the interstitialcy and vacancy mechanisms for the self-diffusion and the atom numbers in a unit volume of the perfect crystal. Using $F(t)$ derived from analyzing the experimental results of the OED or the ORD for n species dopants in silicon, the functional equation of I($= C_I/{}^*C_I$) and V($= C_V/{}^*C_V$) are written as [12]

$$F(t) = d_F I + (n - d_F)V, \tag{3}$$

where d_F is the summation of the fractional component values of the interstitialcy mechanism for diffusions of n species dopants. Using the notation of $G(t) = (A\alpha_{\text{eff}} D_{sd} C_0)^{-1} \mathrm{d}r/\mathrm{d}t$ and d_S($= f_I D_I {}^*C_I/D_{sd}C_0$), the OSF equation is expressed as [4]

$$G(t) = d_S(I - 1 - \gamma/kT)/f_I - (1 - d_S)(V - 1 + \gamma/kT)/f_V, \tag{4}$$

where r, k, A($= 6.38 \times 10^{-6}$ cm^2), α_{eff} ($\fallingdotseq 4$), γ($= 2.4 \times 10^{-2}$ eV) are, respectively, the radius of the dislocation loop surrounding the stacking fault, the Boltzmann constant, the area per atom in the stacking fault, the geometrical constant and the stacking fault energy per atom with respect to the shrinkage.

Assuming the local equilibrium relation of (1) and using the notation of

$$\begin{bmatrix} A(t) \\ B(t) \\ C(t) \\ D(t) \end{bmatrix} = \begin{bmatrix} fvG(t) - 1 + \gamma/kT & -fvF(t) \\ fvG(t) + 1 + \gamma/kT & fiF(t) + 2nfv \\ fiG(t) - 1 + \gamma/kT & fvF(t) + 2nfi \\ fiG(t) + 1 + \gamma/kT & -fiF(t) \end{bmatrix} \begin{bmatrix} \mathrm{d}F(t)/\mathrm{d}t \\ \mathrm{d}G(t)/\mathrm{d}t \end{bmatrix},$$

(3) and (4) yield [6]

$$A(t)I^3 + B(t)I^2 - C(t)I - D(t) = 0. \tag{5}$$

In the present case, using the notation of $\Omega = [B(t)^2 + 3A(t)C(t)]^{1/2}/3|A(t)|$ and $\phi = \cos^{-1}(q\Omega^{-3/2})$, the analytical solution of (5) is

$$I = 2\Omega \cos(\phi/3), \tag{6}$$

where $q = [A(t)^2 D(t) - A(t)B(t)C(t)/3 - B(t)^3/27]/2A(t)^3$. Note that V is obtained by substituting I into (1).

The fractional component of the interstitialcy mechanism for k-th dopant among n species dopants d_k and that of the self-diffusion d_S are obtained as

$$d_k = (F_k(t) - V)/(I - V), \tag{7a}$$

$$d_S = (G(t) + H_V)/(H_I + H_V), \tag{7b}$$

where $F_k(t)$ is determined from the experimental results of kth dopant diffusion and $H_I = (I - 1 - \gamma/kT)/f_I$ and $H_V = (V - 1 + \gamma/kT)/f_V$. The fractional component is defined as $d_k = D_{Ik}/(D_{Ik} + D_{Vk})$, where D_{Ik} and D_{Vk} are dopant diffusion coefficients related to the interstitialcy and the vacancy mechanisms. Table 1 in Ref. [13] shows that d_k increases with the temperature increase. This indicates that the useful relation of

$$\partial_T \ln(D_V) < \partial_T \ln(D_I) \tag{8}$$

holds for an arbitrary temperature.

3. Diffusivities and thermal equilibrium concentrations of point defects

$F(t) = 5.3t^{-0.0924} + 0.24t^{0.0738} + 2.58t^{-0.0428}$ and $G(t) = 2.9t^{-0.08}$ determined from the experimental results of P, Sb and B diffusions and the oxidation stacking faults at 1100°C [1,2,7] yield the numerical solution I of Eq. (6). Substituting this solution into Eq. (1) gives the solution V. Correlating these solutions I and V with the approximate equations [5] $I = 1 + {}^*I \exp[-\alpha_I D_I(\pi/w)^2 t]$ and $V = 1 - {}^*V \exp[-\alpha_V D_V(\pi/w)^2 t]$, the empirical equations [13] $D_I {}^*C_I = 4.57 \times 10^{25} \exp[-4.84\ \text{eV}/kT]$ and $D_V {}^*C_V = 3.0 \times 10^{22} \exp[-4.03\ \text{eV}/kT]$ and the well-known defining equation ${}^*C_X = C_0 \exp[-E_{FX}/kT]$, $^*C_I$ and $^*C_V$ as well as

D_I and D_V are obtained as

$$*C_I = C_0 \exp[-1.44\,\mathrm{eV}/kT], \quad (9a)$$

$$*C_V = C_0 \exp[-1.13\,\mathrm{eV}/kT] \quad (9b)$$

and

$$D_I = 914 \exp[-3.4\,\mathrm{eV}/kT], \quad (10a)$$

$$D_V = 0.6 \exp[-2.9\,\mathrm{eV}/kT] \quad (10b)$$

for an arbitrary T. Here, $*I$ and $*V$ are the integral constants, α_I and α_V the fitting parameters, w the bulk thickness and E_{FY} ($Y = I$ or V) the self-interstitial or vacancy formation energy.

Note that the obtained D_I and D_V satisfy Eq. (8) and the relation of

$$*C_I < (*C_I *C_V)^{1/2} < *C_V \quad (11)$$

is valid between $*C_I$ and $*C_V$ obtained for an arbitrary T.

Although the various values of $*C_I$, $*C_V$, D_I and D_V have been reported [9], Eqs. (8) and (11) should be adopted as the necessary conditions of their validity.

4. Conclusions and discussion

We first contrived the method to obtain mathematically self-consistent solutions of the OED/ORD and OSF equations. These functional equations were analytically solved. Using the experimental results of P, Sb and B diffusions and the oxidation stacking faults, the numerical solutions were determined. At the same time, it was found that the diffusions of self-, P and B depend on the interstitialcy mechanism by about 50%, 35% and 30%, respectively, while Sb diffusion is mainly governed only by the vacancy mechanism. That the fractional component of the interstitialcy mechanism for a dopant diffusion increases with the temperature increase led to the relation $\partial_T \ln(D_V) < \partial_T \ln(D_I)$. Furthermore, $*C_I$, $*C_V$, D_I and D_V were derived as functions of an arbitrary temperature.

Figs. 1 and 2 in Ref. [9] show various results of $*C_I$, $*C_V$, D_I and D_V. Thus, we cannot conclusively determine them because there is no clear way to investigate the behavior of the point defects through experimentation. Hence, we cannot estimate the validity of the present results through comparison with previous ones. On the other hand, Mayer et al. [8] obtained the reproducible result of the self-diffusion coefficient via the silicon tracer diffusion experiment. The substitution of Eqs. (9a), (9b), (10a) and (10b) into Eq. (2) showed a good agreement with Mayer et al.'s result. This gives evidence of the validity of Eqs. (9a), (9b), (10a) and (10b) although it is indirect.

Although a number of researchers have investigated the behavior of the intrinsic point defects in silicon, even the thermal equilibrium concentrations as well as their diffusivities have not been conclusively determined. Based on the fact that the swirl A defects are formed by the interstitial-type dislocations or clusters, many researchers insist that $*C_V < *C_I$ is valid at a high temperature. In contrast to this however, we concluded the relation $*C_I < (*C_I *C_V)^{1/2} < *C_V$ in this study. It was found that the formation mechanisms of the grown-in defects in CZ silicon as well as the swirl defects in FZ silicon are systematically explained using this relation [5,14]. Therefore, we propose $\partial_T \ln(D_V) < \partial_T \ln(D_I)$ and $*C_I < (*C_I *C_V)^{1/2} < *C_V$ as necessary conditions to be satisfied in this field.

References

[1] S. Mizuo et al., Jpn. J. Appl. Phys. 20 (1981) 739.
[2] S. Mizuo et al., Jpn. J. Appl. Phys. 21 (1982) 281.
[3] D.A. Antoniadis, Electrochem. Soc. Proceedings International Symposium on Semiconductor Silicon, Pennington, 1981, p. 947.
[4] T.Y. Tan et al., Appl. Phys. Lett. 40 (1982) 616.
[5] T. Okino et al., Jpn. J. Appl. Phys. 33 (1994) 3362.
[6] T. Okino, Jpn. J. Appl. Phys. 30 (1991) L857.
[7] S.P. Murarka, J. Appl. Phys. 48 (1977) 5020.
[8] H.J. Mayer et al., Inst. Phys. Conference Series. Vol. 31, 1977, p. 186.
[9] W. Zulehner, in: G. Harbeke, M.J. Schulz (Eds.), Materials Science Vol. 13, Semiconductor Silicon, Springer, Berlin, 1988, pp. 127–152.
[10] K. Compaan et al., Trans. Farady Soc. 52 (1956) 786.
[11] K. Compaan et al., Trans. Farady Soc. 54 (1958) 1498.
[12] T. Okino, Defect Diffusion Forum 148–149 48 (1997) 48.
[13] T.Y. Tan et al., J. Appl. Phys. A37 (1985) 1.
[14] T. Okino et al., to be published.

ELSEVIER

Physica B 273–274 (1999) 512–515

PHYSICA B

www.elsevier.com/locate/physb

Nonequilibrium experiments on self-diffusion in silicon at low temperatures using isotopically enriched structures

Ant Ural*, P.B. Griffin, J.D. Plummer

Department of Electrical Engineering, Stanford University, Stanford, CA 94305, USA

Abstract

Self-diffusion in silicon has been studied using epitaxially grown isotopically enriched structures under nonequilibrium concentrations of native point defects created by thermal oxidation and nitridation. Comparing identical anneals for phosphorus, antimony, and self-diffusion in Si, we obtain experimental evidence for a dual vacancy–interstitial mechanism of self-diffusion with the possibility of a small substitutional exchange component. We determine that in the temperature range 800–1100°C, the interstitial-mediated fraction of self-diffusion is confined between 0.50 and 0.62. The corresponding activation enthalpies are 4.68 and 4.86 eV for the interstitial and vacancy mechanisms, respectively. Furthermore, both mechanisms exhibit large activation entropies. This constitutes direct experimental evidence of the remarkable similarity between the energetics of these native point defects in silicon.

Keywords: Self-diffusion; Silicon; Self-interstitial; Vacancy

1. Introduction

Self-diffusion is the most fundamental diffusion process in silicon. Experimental study of atomic-scale mechanisms of Si self-diffusion reveals information about the thermodynamic properties of the native point defects in this material. In this respect, it provides direct quantitative comparison to ab initio and atomistic theoretical calculations. Moreover, it supplies key parameters for predictive modeling of dopant diffusion in Si device technology.

On the atomic-scale, diffusion in Si can be mediated by either native point defects, namely self-interstitials (I) and vacancies (V), or by a direct substitutional exchange mechanism (E) which occurs in their absence [1–6]. It is the competition between these three microscopic mechanisms that we study in this work.

2. Experiment

Experimentally, this study relies on two key components. The first is the use of isotopically enriched Si structures. The growth of these structures by chemical vapor deposition (CVD) has been possible only very recently [7–10]. Using these structures has advantages over metal-diffusion and radioactive tracer experiments, since direct measurement of the diffusion of Si atoms over a wide temperature and time range becomes possible. The isotope structures used in this experiment had a surface layer of approximately 170 nm containing the three stable isotopes of Si in their natural abundances, and a buried layer heavily depleted in ^{29}Si and ^{30}Si. For example, ^{30}Si, the isotope used to monitor self-diffusion, was reduced from a natural abundance of 3.10% at the surface to 0.002% at the buried layer.

The second key component of this study is using nonequilibrium experiments, where native point defect concentrations are perturbed from their equilibrium values by well-studied surface reactions, to determine the fractional contributions of the three microscopic mechanisms to Si self-diffusion. Two such surface reactions are

* Corresponding author. Tel.: + 1-650-725-6078; fax: + 1-650-723-4659.

E-mail address: antural@leland.stanford.edu (A. Ural)

0921-4526/99/$ - see front matter
PII: S0921-4526(99)00541-4

oxidation and nitridation. It has been well established that thermal oxidation of the surface injects I into the bulk, whereas nitridation results in V injection. Anneals in an inert ambient, on the other hand, give the equilibrium diffusion coefficient. Inert anneal data alone, however, cannot reveal which microscopic diffusion mechanisms are actually involved.

In order to obtain quantitative information about these microscopic mechanisms of self-diffusion, a comparison to dopants under identical oxidation and nitridation anneals is necessary. A well-suited set of dopants is P, which diffuses mainly by an I-mechanism, and Sb, which is a vacancy diffuser. Therefore, in addition to the isotope structure, P and Sb structures were also fabricated for this experiment, using ion implantation followed by a drive-in inert anneal, and epitaxial growth of intrinsic Si to from a surface layer.

After growth, these three structures were annealed in a furnace in an oxidizing (100% O_2) ambient at 800–1100°C for times between 1 and 100 h, and in a nitridizing (100% NH_3) ambient at 1000 and 1100°C for 1–5 h. In addition, all structures were annealed in an inert ambient (100% Ar) at temperatures ranging from 900°C to 1100°C for times between 1 and 72 h.

The diffusion profiles resulting from all anneals for ^{30}Si, P, and Sb were obtained by secondary ion mass spectrometry (SIMS). The details of the SIMS analysis has been given elesewhere [9,10].

3. Results and discussion

The P, Sb, and self-diffusion coefficients in Si under both inert and oxidizing ambients were extracted by taking the as-grown profile, and using TSUPREM-4, a simulation program, to numerically diffuse it by solving the appropriate form of Fick's second law until a least-squares fit was achieved to the SIMS profile after annealing. Fig. 1 shows the SIMS profiles and the simulation fits of the 900°C anneals for ^{30}Si, P, and Sb under inert and oxidizing ambients. Nitridation experiments were only performed at 1000°C and 1100°C. SIMS plots at these higher temperatures, including nitridation, have already been given elsewhere [9,11,12]. The extracted equilibrium (inert anneal) coefficients show a good fit to Arrhenius behavior with a single activation enthalpy in all cases. For P and Sb, we find that

$$D_P^{eq} = 1.37 \exp(-3.55/kT) \quad (1a)$$

and

$$D_{Sb}^{eq} = 49 \exp(-4.19/kT)\ \mathrm{cm}^2/\mathrm{s}, \quad (1b)$$

respectively. These values agree well with previously published data [13]. In addition, the equilibrium self-diffusion coefficients exhibit an excellent fit to the expression

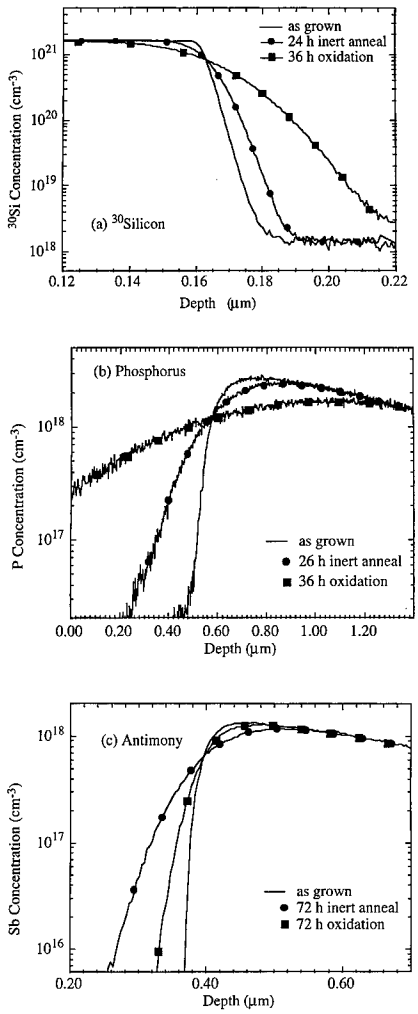

Fig. 1. Diffusion profiles of 900°C anneals under inert and oxidizing ambients for (a) ^{30}Si (b) P (c) Sb. The duration of each anneal is indicated on the figures. The solid lines are the actual SIMS profiles measured, whereas the symbols show the simulation best fits used for extracting diffusivity enhancements or retardations. The as-grown profile for each case is also given for reference.

obtained in Refs. [7,8] using similar isotope layers,

$$D_{Self}^{eq} = 560 \exp(-4.76/kT)\ \mathrm{cm}^2/\mathrm{s}, \quad (1c)$$

and lie well within the error bars reported in that work. In Eqs. (1), k is the Boltzmann's constant and T denotes absolute temperature.

It is evident from Fig. 1 that self- and P diffusion are enhanced during oxidation at 900°C, whereas Sb diffusion is retarded. The same behavior is observed for oxidation in the whole temperature range 800–1100°C. During nitridation at 1000 and 1100°C, however, Sb and self-diffusion are enhanced, whereas P diffusion is

Table 1
Measured diffusivity ratios for ^{30}Si, P, and Sb under oxidation. The oxidation times are 1, 5, 36, and 100 h, respectively, at 1100, 1000, 900, and 800°C. Values of f_{SiI} are also given

Temperature (°C)	Diffusivity ratios under oxidation			
	^{30}Si	P	Sb	f_{SiI}
1100	1.53	2.69	0.349	0.502
1000	2.46	4.09	0.260	0.575
900	5.16	8.39	0.198	0.605
800	14.57	23.60	< 0.194	0.614

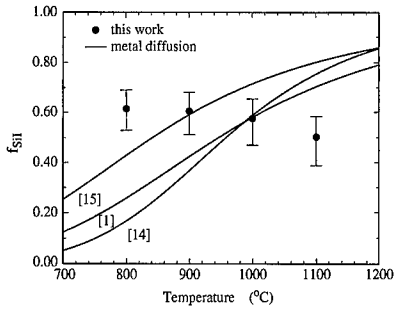

Fig. 2. The I-mediated fraction of self-diffusion as a function of temperature in the range 800–1100°C. The symbols show the data points including the error bars. Solid lines are the predictions of metal diffusion experiments where the corresponding reference number is cited in square brackets.

retarded [9]. These results qualitatively show that P diffuses mainly by an I-mechanism, whereas Sb diffusion is V mediated. The fact that Si self-diffusion is enhanced by both V and I injection gives a clear hint that it has non-negligible vacancy and interstitial components. Indeed, if either one of the point defect mechanisms were solely dominant, a retardation in diffusivity would have been observed when the opposite type of defect is injected. On the other hand, if the exchange mechanism were dominant, perturbing the point defect concentrations as above would not have any effect on the self-diffusion coefficient.

The ratio of the diffusivity under oxidation to that under inert annealing for each species is listed in Table 1 at temperatures of 800–1100°C. These diffusivity ratios under oxidation are related to the fractional contributions of atomic-scale diffusion mechanisms by [2,11],

$$\frac{D_A^{ox}}{D_A^{eq}} = f_{AI}\frac{C_I^{ox}}{C_I^{eq}} + f_{AV}\frac{C_V^{ox}}{C_V^{eq}} + f_{AE}, \tag{2}$$

where A represents the diffusing species (A = P, Sb, or in the case of self-diffusion, Si), and f_{AI}, f_{AV}, and f_{AE} are the I, V, and E fractions, respectively, of A diffusion under equilibrium conditions. The ratios involving the I and V concentrations on the right-hand side are the perturbation levels of these defects under nonequilibrium conditions. The superscripts eq and ox denote equilibrium and oxidation, respectively. Diffusivity ratios and point defect perturbation levels measured at the end of the experiment are time averaged values. Furthermore, all results reported in this work represent an average over possible charge-states of the native point defects present under intrinsic conditions.

Assuming $f_{PI} = 1$, $f_{SbI} = 0$, and $f_{SiE} = 0$, we have solved Eq. (2) for f_{SiI}, and listed the values obtained in the temperature range 800–1100°C in the last column of Table 1. These values are plotted in Fig. 2 including the error bars. These error bars are due partly to relaxing the above assumptions on f_{PI}, f_{SbI}, and f_{SiE}, and partly to taking into account experimental uncertainty. The high-temperature experiments have shown that at 1000°C and 1100°C, $f_{PI} \geqslant 0.96$ and $f_{SiE} \leqslant 0.14$, and in conjunction with the low-temperature data, at 800–1100°C, $f_{SbI} \leqslant 0.03$ [9,11]. Solving the system of three equations (one equation each for P, Sb, and self-diffusion) having the form Eq. (2) with these upper and lower bounds, and taking into account our estimate of the experimental error, ± 5%, in the measured diffusivity ratios listed in Table 1, we arrive at the error bars shown in Fig. 2.

In the same figure (Fig. 2), we have also plotted, represented by solid lines, f_{SiI} extracted from experimental studies of substitutional–interstitial metal diffusers (e.g., Au, Zn, and Pt) in Si [1,14–16]. Results from other similar experiments (see the references in Refs. [1,14–16]), a combination of Zn and self-diffusion data [7,8], and tight-binding calculations [17] exhibit similar trends. In striking contrast to these results, f_{SiI} obtained directly using isotopically enriched structures manifests a much weaker dependence on temperature. Furthermore, we observe an increase in f_{SiI} with decreasing temperature, which is exactly the opposite of the trend extracted from metal diffusion experiments. Our findings show that within the temperature range 800–1100°C, f_{SiI} is confined between 0.5 and 0.62.

The temperature dependence of the X component of self-diffusion D_{Self}^X, is given by

$$D_{Self}^X(T) = f_{SiX}D_{Self}^{eq} = d_{0X}\exp(-H_X/kT), \tag{3a}$$

with the temperature independent pre-factor

$$d_{0X} = l_X g_X a_0^2 v_X \exp(S_X/k), \tag{3b}$$

where X = I, V, or E, l_X is the correlation factor (we do not use the traditional notation of f_X for the correlation factor in order to distinguish it from f_{SiX}), g_X is the geometry factor, a_0 is the lattice constant, and v_X is the attempt frequency. Furthermore, for the point defect

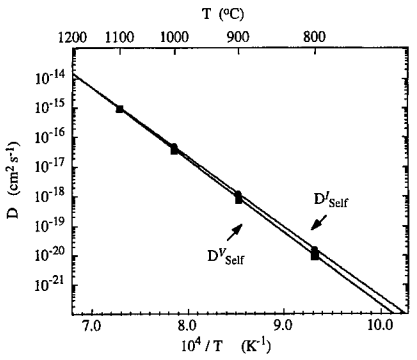

Fig. 3. Arrhenius plots of the I and V components of the Si self-diffusion coefficient. The symbols are the actual data points, and the solid lines show the best-fits as given in the text.

mechanisms, the activation enthalpy H_X equals the sum of the formation and migration enthalpies of the defect X, and similarly the activation entropy S_X equals the sum of the respective entropies. Eqs. (3) show clearly that an Arrhenius fit of the product of f_{SiX} and D^{eq}_{Self} yields H_X and S_X. As a result, we find that the I and V components of Si self-diffusion exhibit excellent fit to $D^I_{Self} = 149 \exp(-4.68/kT)$ and $D^V_{Self} = 636 \exp(-4.86/kT)$ cm^2/s, respectively, as plotted in Fig. 3. Using the same values for the constants in Eqs. (3) as in Ref. [7,8], and taking into account the error bars in our measured results, we get $H_I = 4.68^{+0.12}_{-0.15}$ eV and $H_V = 4.86^{+0.19}_{-0.15}$ eV, and $S_I = 10.2^{+1.2}_{-1.5}k$ and $S_V = 12.8^{+1.8}_{-1.5}k$. These results, on the other hand, strongly suggest the converse, with the difference between H_I and H_V is on the order of only a few tenths of an eV. The value of H_I obtained in this work agrees, within error bars, with that extracted recently from the energetics of self-interstitial clusters in Si [18]. Focusing on the results for S_I and S_V, we see that both entropies are large and comparable in magnitude. Our results agree with the theoretical findings of Ref. [19] that even simple native point defects can have large entropies of formation, and that they are similar in magnitude.

In conclusion, we have studied Si self-diffusion under nonequilibrium conditions using isotopically enriched structures in the temperature range 800–1100°C. We find that, on the atomic-scale, self-diffusion is mediated by a dual vacancy–interstitial mechanism with the possibility of a small exchange component. These results constitute direct experimental evidence of the strong competition between the I- and V-mechanisms of self-diffusion and of the remarkable similarity between the energetics of these native point defects in silicon.

Acknowledgements

We would like to thank S. Burden of Isonics Corporation for providing the enriched ^{28}Si. This work was funded by the Semiconductor Research Corporation.

References

[1] W. Frank, U. Gösele, H. Mehrer, A. Seeger, in: G.E. Murch, A.S. Nowick (Eds.), Diffusion in Crystalline Solids, Academic press, New York, 1984, p. 63.
[2] P.M. Fahey, P.B. Griffin, J.D. Plummer, Rev. Mod. Phys. 61 (1989) 289.
[3] C.S. Nichols, C.G. Van de Walle, S.T. Pantelides, Phys. Rev. Lett. 62 (1989) 1049.
[4] C.S. Nichols, C.G. Van de Walle, S.T. Pantelides, Phys. Rev. B 40 (1989) 5484.
[5] K.C. Pandey, Phys. Rev. Lett. 57 (1986) 2287.
[6] A. Antonelli, S. Ismail-Beigi, E. Kaxiras, K.C. Pandey, Phys. Rev. B 53 (1996) 1310.
[7] H. Bracht, E.E. Haller, R. Clark-Phelps, Phys. Rev. Lett. 81 (1998) 393.
[8] H. Bracht, E.E. Haller, K. Eberl, M. Cardona, R. Clark-Phelps, in: Y. Mishin, G. Vogl, N. Cowern, R. Catlow, D. Farkas (Eds.), Diffusion Mechanisms in Crystalline Materials, Mater. Res. Soc. Proc. 527, Warrendale, PA, 1998, p. 335.
[9] A. Ural, P.B. Griffin, J.D. Plummer, Appl. Phys. Lett. 73 (1998) 1706.
[10] A. Ural, P.B. Griffin, J.D. Plummer, Phys. Rev. Lett. 83 (1999) 3454.
[11] A. Ural, P.B. Griffin, J.D. Plummer, J. Appl. Phys. 85 (1999) 6440.
[12] A. Ural, P.B. Griffin, J.D. Plummer, in: H.-J.L. Gossmann, T.E. Haynes, M.E. Law, A.N. Larsen, S. Odanaka (Eds.), Si Front-End Processing—Physics and Technology of Dopant-Defect Interactions, Mater. Res. Soc. Symp. Proc. 568, Warrendale, PA, 1999, p.97.
[13] R.B. Fair, in: F.F.Y. Wang (Ed.), Impurity Doping Processes in Silicon, North-Holland, Amsterdam, 1981, p. 315.
[14] H. Bracht, N.A. Stolwijk, H. Mehrer, Phys. Rev. B 52 (1995) 16542.
[15] H. Bracht, Proceedings of the Electrochemical Society Meeting, Vol. 99-1, 1999, p. 357.
[16] A. Giese, H. Bracht, N.A. Stolwijk, J.T. Walton, J. Appl. Phys. 83 (1998) 8062.
[17] M. Tang, L. Colombo, J. Zhu, T. Diaz de la Rubia, Phys. Rev. B 55 (1997) 14279.
[18] N.E.B. Cowern, G. Mannino, P.A. Stolk, F. Roozeboom, H.G.A. Huizing, J.G.M. van Berkum, F. Cristiano, A. Claverie, M. Jaraiz, Phys. Rev. Lett. 82 (1999) 4460.
[19] P.E. Blöchl, E. Smargiassi, R. Car, D.B. Laks, W. Andreoni, S.T. Pantelides, Phys. Rev. Lett. 70 (1993) 2435.

ELSEVIER

Physica B 273–274 (1999) 516–519

PHYSICA B

www.elsevier.com/locate/physb

Magic numbers of multivacancy in silicon and its hydrogen decoration

Toru Akiyama*, Atsushi Oshiyama

Institute of Physics, University of Tsukuba, Tennodai, Tsukuba 305-8571, Japan

Abstract

We report microscopic calculations performed for a variety of multivacancies V_n in Si and their hydrogen decoration. We find that there are stable sizes and structures (magic numbers), and that with any value of chemical potential of hydrogen atom the stable multivacancy is either free from or completely decorated with hydrogen atoms. Moreover, we find that the H-decorated multivacancy is capable of trapping an H_2 molecule even after its hydrogen decoration. © 1999 Elsevier Science B.V. All rights reserved.

Keywords: Multivacancy; Silicon; Density functional theory; Hydrogen

The vacancy in crystalline silicon is a paradigm of defects in materials. In mono- and divacancy, for instance, dangling bonds induce electron states in the energy gap (deep levels) and these deep levels split upon symmetry-lowering lattice relaxation. This picture is well known from earlier experiments [1–4] and recent total energy calculations [5–7]. Vacancy aggregates (multivacancy) in Si, that are regarded as negative clusters, however, have been less intensively pursued. In spite of their undoubted existence, little is known about microscopic identification of the multivacancy. Electron spin resonance (ESR) measurements suggest existence of the tri-, tetra-, pentavacancies [8,9]. A simple dangling-bond counting model [10], preliminary density-functional calculation with the local density approximation (LDA) [11], and the LDA-based tight-binding molecular dynamics and the Hartree–Fock calculation [12] predict that there are stable sizes and structures (magic numbers) for multivacancy. For the microscopic identification of the multivacancy, detailed and systematic calculations on the stable size, the lattice relaxation around multivacancy, and the electronic structure near the band gap are imperative.

Another aspect of the multivacancy is its capability of containing impurities such as hydrogen: The negative cluster may serve as a trap of impurity atoms or molecules in Si. For instance, recent Raman scattering and infrared absorption experiments have detected several peaks which are attributed to the stretching mode of H_2 molecules in Si [13–17]: The observed several peaks are attributed to H_2 at the tetrahedral interstitial (T_d) site (3618 and 3601 cm^{-1} [13–15]), in the platelet defects or voids (4158 cm^{-1} [16]), or possibly trapped in the multivacancy (3822 cm^{-1} [17]). We here discuss stable forms and structures of hydrogen-decorated multivacancy in Si.

Most of calculations are performed based on density functional theory. We use norm-conserving pseudopotentials [18], the LDA [19] or the GGA-PW91 [20] for the exchange-correlation energy, and the conjugate-gradient minimization technique both for ionic and electronic degrees of freedom [21,22]. The vacancy in an otherwise perfect crystal is simulated by a supercell. We find that the 64-site supercell is sufficient to obtain the formation energy of the small vacancy V_n ($n \leqslant 7$) but that for the large vacancy ($n \geqslant 8$) the 216-site supercell is necessary to take into account medium-range lattice relaxation and then obtain sufficiently accurate formation energies. We use the Γ-point sampling in the Brillouin zone integration, and the 14-Ry cutoff energy for the 64-site supercell and the 8-Ry for the 216-site supercell.

* Corresponding author. Tel.: + 81-298-53-4203; fax: + 81-298-53-4492.

E-mail address: akiyama@cm.ph.tsukuba.ac.jp (T. Akiyama)

0921-4526/99/$ - see front matter
PII: S0921-4526(99)00542-6

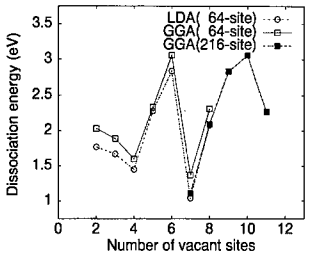

Fig. 1. Dissociation energy $D(n)$ as a function of the size of the multivacancy V_n ($2 \leqslant n \leqslant 11$) obtained by the LDA with the 64-site supercell or by the GGA with either the 64- or the 216-site super cell. Lines are guides for eyes.

Larger multivacancies V_n ($n \leqslant 36$) are treated by a transferable tight-binding (TTB) model [23]. In the TTB calculations we use the 512-sites supercell. In order to obtain the optimized geometry, we use the conjugate-gradient technique [24] instead of the molecular dynamics scheme. Preliminary results using the TTB model have been published previously [25].

In order to discuss stability of the multivacancy V_n, we consider the dissociation reaction, $V_n \rightarrow V_{n-1} + V_1 - D(n)$. The dissociation energy $D(n) \equiv E_f(n-1) + E_1(1) - E_f(n)$ is a measure of the stability of V_n: The value of $D(n)$ defined above are large positive for the stable multivacancies. We find that $D(n)$ obtained by the TTB calculations has large positive for V_6,V_{10},V_{14},V_{17},V_{22},V_{26}, and V_{35}: The magic numbers of V_n are 6, 10, 14, 17, 22, 26 and 35. Fig. 1 shows calculated $D(n)$ as a function of the size of the multivacancy obtained by density functional calculations. It is clear that the dissociation energy $D(n)$ becomes positively large for the closed hexagonal V_6 and the adamantine shaped V_{10}, indicating that 6 and 10 are the magic numbers. The magic numbers for the small multivacancy are identical to those obtained by the TTB calculations.

Lattice relaxation around the hexavacancy V_6 and its electronic structure near the energy gap are unusual. Fig. 2(a) shows the valence electron density around V_6. It is prominent that each 2 nearest-neighbor atoms belonging to one vacant site are distorted to form a pair. The length of the bond due to the paring is 2.86 Å (20% longer than the bulk bond length). Interestingly, this pairing distortion keeps the threefold symmetry of the unrelaxed V_6. Due to the paring, 12 dangling bond states become 6 bonding and 6 antibonding states. Analysis of the calculated wave functions leads to a conclusion that the bonding states are resonant in the valence bands and that at least 4 antibonding states appear in the gap with 0.3–0.1 eV below the conduction band bottom. Fig. 2(b) shows a wave function of shallow level, which is located at 0.3 eV below the conduction band bottom. This wave function has the character of antibonding state between

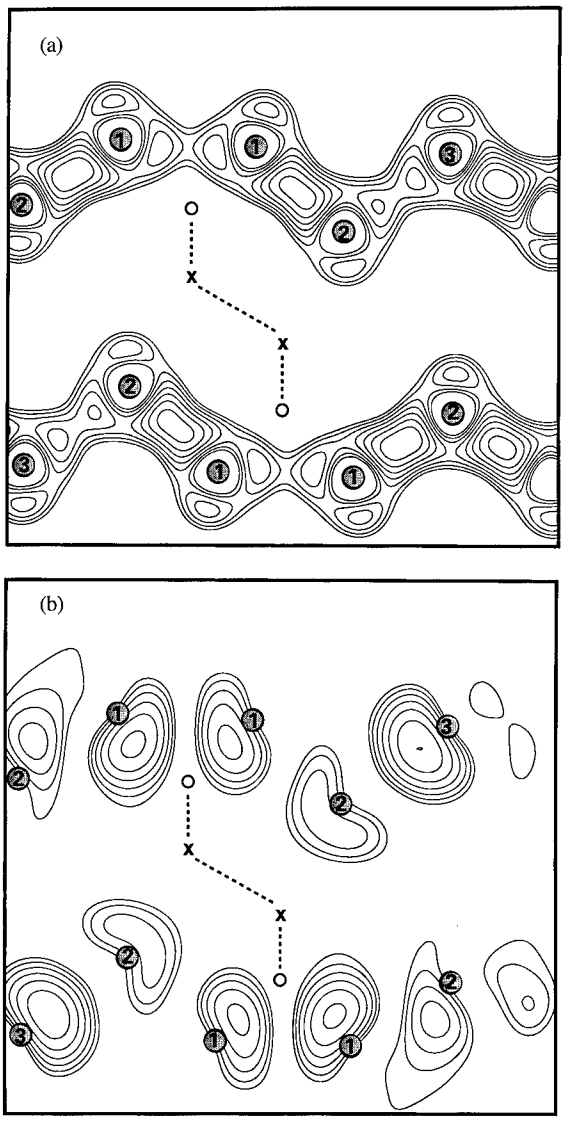

Fig. 2. Contour plots of the valence electron density (a) and the wave function of a shallow level located at 0.3 eV below the conduction band bottom (b) on the (1 1 0) plane around V_6 obtained by the GGA with the 216-site supercell. The mth neighbor Si atoms around the vacant sites are shown by shaded circles with the number m, while the vacant sites are shown by open circles. The vacant sites not on the plane are also shown by crosses for clarity. The maximum value of the contour lines are $0.55/\text{Å}^{-3}$ (a) and $1.5 \times 10^{-2}/\text{Å}^{-3}$ (b), and the subsequent lines differ by a factor of 1.1 (a) and 1.25 (b).

the first neighbor Si atoms. For neutral V_6 these rather shallow levels are empty.

Electronic structure of the stable decavacancy V_{10} is rather different from that of V_6. Fig. 3(a) shows the valence electron density around V_{10}. In the optimized geometry, 12 of the 16 nearest neighbors are rebonded

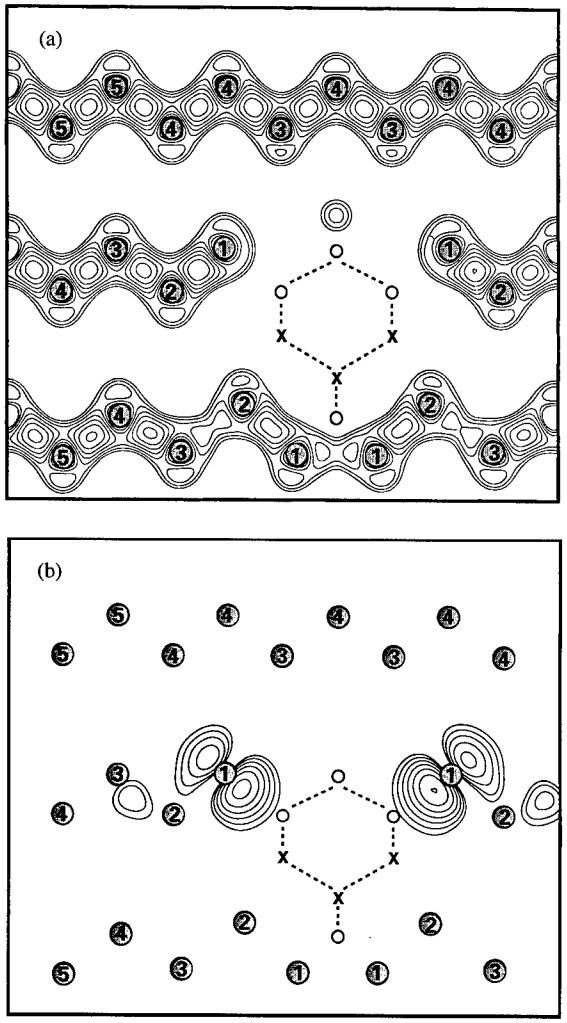

Fig. 3. Contour plots of the valence electron density (a) and the wave function of a deep level located at 0.7 eV below the conduction band bottom (b) on the (1 1 0) plane around V_{10}. Notation is the same as in Fig. 2. The maximum value of the contour lines are $0.60/Å^{-3}$ (a) and $1.1 \times 10^{-2}/Å^{-3}$ (b), and the subsequent lines differ by a factor of 1.1 (a) and 1.5 (b).

(the bond length is 2.80 Å) and this pairing distortion induces relatively shallow levels near the conduction band bottom. Yet even after relaxation there remains 4 nearest-neighbor Si atoms. This causes dangling bonds which induce deep levels in the gap. However, the T_d symmetry of the unrelaxed V_{10} is almost kept in the relaxed V_{10}.[1] Therefore there appear a deep level at 0.8 eV and almost triply degenerate levels at 0.7 eV below the conduction band bottom. The latter level is occupied by 2 electrons in neutral V_{10}. Fig. 3(b) shows a wave function of deep level, which is located at 0.7 eV below the conduction band bottom. This wave function clearly shows the character of dangling bond state.

Next, we consider the stable form and structure of hydrogen-decorated multivacancy, in particular, accommodation of an H_2 molecule in the pristine multivacancy and also in the H-decorated multivacancy. When an H_2 molecule is located in the pristine multivacancy, one of the possible reactions is

$$H_2@V_n \rightarrow V_nH_2, \tag{1}$$

where $H_2@V_n$ means a trapped H_2 in V_n, and V_nH_2 does the corresponding geometry with two of the dangling bonds in V_n being terminated. We have calculated total energies of these geometries for $n = 2,6,10$, and obtained following results: $H_2@V_6$ and $H_2@V_{10}$ is higher in energy than V_6H_2 and $V_{10}H_2$ by 0.94 (1.07) eV and 1.00 (0.99) eV in the LDA(GGA), respectively. In V_2 the H_2 molecule is unable to exist: it spontaneously dissociates and become V_2H_2. It is thus likely that the vacancy is fully decorated with H atoms. We also consider the reaction for all dangling bonds in V_n being terminated by hydrogen atoms,

$$mH_2 + V_n \rightarrow V_nH_{2m}, \tag{2}$$

where H_2 indicates an H_2 at the stable T_d interstitial site along $\langle 1\,0\,0 \rangle$ direction. Table 1 shows energy gains $E_{mH_2}(n)$ for this reaction. It is confirmed that multivacancy favor being fully decorated with hydrogen atoms.

In order to discuss accommodation of an H_2 in the H-decorated multivacancy, we consider the reaction,

$$H_2 + V_nH_{2m} \rightarrow H_2@V_nH_{2m}, \tag{3}$$

where $H_2@V_nH_{2m}$ means an H_2 trapped in the completely H-decorated multivacancy V_nH_{2m}. We have calculated total energies of (i) the fully decorated vacancy, and (ii) an H_2 molecule in the fully decorated vacancy. The calculated energy gains $E_{H_2}(n)$ for this reaction are also listed in Table 1. Since this reaction is exothermic, it is concluded that H_2 favors being trapped in the multivacancy rather than being at the T_d site.[2]

We have also calculated vibrational frequencies of stretching modes in various location. Anharmonic effects are fully considered by the 4th-order polynomial expansion (Electron correlation is also important to obtain reliable frequencies. For further deteail please see

[1] Jahn–Teller-type relaxation is not recognized in the present calculation. It is likely that separation of these 4 dangling bonds (the distance is 6.53 Å) leads to reduction of the electronic energy gain by the symmetry-lowering relaxation.

[2] Calculated energy gains in the reaction (3) are larger than 0.15 eV which assures thermal stability of the trapping. Yet at high temperature the H_2 could be released from the vacancy.

Table 1
Calculated energy gains (eV) of the vacancy fully decorated with hydrogen $E_{mH_2}(n)$, and an H_2 trapped in the resulting H-decorated vacancy $E_{H_2}(n)$ (see text)

Vacancies	$E_{mH_2}(n)$	$E_{H_2}(n)$
V_1H_4	4.26	0.15
V_2H_6	6.41	0.29
V_3H_8	8.56	0.53
V_4H_{10}	11.0	0.70
V_5H_{12}	12.6	0.77
V_6H_{12}	13.3	0.91
$V_{10}H_{16}$	19.8	1.12

Table 2
Calculated bond lengths and vibrational frequencies of Si–H in the hydrogen-decorated V_n and of H–H of the H_2 molecule at various locations obtained by the GGA

	Bond length (Å)	Frequency (cm^{-1})
Si–H		
Si(111): H	1.53	1984
V_1H_4	1.49	2294
V_2H_6	1.51	2037
V_6H_{12}	1.52	1763
	1.52	1841
$V_{10}H_{16}$	1.52	1838
	1.53	2046
H–H		
Vacuum	0.739	4077
T_d interstitial	0.767	3475
V_1H_4	0.761	3583
V_2H_6	0.746	3834
V_6H_{12}	0.738	4008
$V_{10}H_{16}$	0.739	4042

Note: For comparison, the calculated bond length and the vibrational frequency of Si–H on the Si(111): H surface are shown. In V_6H_{12} and $V_{10}H_{16}$, there are two types of the Si–H bonds due to the symmetry of V_n.

Ref. [26]). Table 2 shows the calculated bond length and the frequency of the Si–H for the H-decorated vacancies, along with the calculated bond length and stretching frequencies of an H_2 in H-decorated multivacancies. From the calculated frequencies of H_2 it is confirmed that the previous peak at 3618 and 3601 cm^{-1} [13–15] is due to H_2 at T_d site [27–29]. In V_1 and V_2 we find the systematic increase on frequencies with increasing size of the H-decorated vacancies. However, the frequency of an H_2 in V_6H_{12} already saturates to that in vacuum. Moreover, it is reasonable to conclude that the newly observed peak at 3822 cm^{-1} [17] is due to the H_2 trapped in V_2H_6.

In conclusion, we have performed microscopic calculations for the pristine and the H-decorated multivacancy in Si and also for the H_2 molecule trapped there. The results provide a firm theoretical framework to clarify microscopic structures of the multivacancy and its capability of incorporating the H_2 molecule. Comparison of the calculated H–H frequencies with the Raman experiments leads to a new interpretation of the observed peaks.

This work was supported in part by JSPS under Contract No. RFTF96P00203.

References

[1] See, for instance, G.D. Watkins, in: S.T. Pantelides (Eds.), Deep Centers in Semiconductors, Gordon and Breach, New York, 1986, p. 147.
[2] G.D. Watkins, J.W. Corbett, Phys. Rev. 138 (1965) A543.
[3] J.W. Corbett, G.D. Watkins, Phys. Rev. 138 (1965) A555.
[4] C.A.J. Ammerlaan, G.D. Watkins, Phys. Rev. B 5 (1972) 3988.
[5] O. Sugino, A. Oshiyama, Phys. Rev. Lett. 68 (1992) 1858 and references therein.
[6] O. Sugino, A. Oshiyama, Phys. Rev. B 42 (1990) 11869.
[7] M. Saito, A. Oshiyama, Phys. Rev. Lett. 73 (1994) 866 and references therein.
[8] Y-H. Lee, J.W. Corbett, Phys. Rev. B 8 (1973) 2810.
[9] Y-H. Lee, J.W. Corbett, Phys. Rev. B 9 (1974) 4351.
[10] D.J. Chadi, K.J. Chang, Phys. Rev. B 38 (1988) 1523.
[11] A. Oshiyama, M. Saito, O. Sugino, Appl. Surf. Sci. 85 (1995) 239.
[12] J.L. Hastings, S.K. Estreicher, P.A. Fedders, Phys. Rev. B 56 (1997) 10 215.
[13] R.E. Prichard et al., Phys. Rev. B 56 (1997) 13 118.
[14] R.E. Prichard et al., Phys. Rev. B 57 (1998) R15 048.
[15] A.W.R. Leitch, V. Alex, J. Weber, Phys. Rev. Lett. 81 (1998) 421.
[16] K. Murakami et al., Phys. Rev. Lett. 77 (1996) 3161.
[17] K. Murakami et al., private communication.
[18] N. Troullier, J.L. Martins, Phys. Rev. B 43 (1991) 1993.
[19] D.M. Ceperley, B.J. Alder, Phys. Rev. Lett. 45 (1980) 566.
[20] J.P. Perdew, in: P. Zeische, M. Eschrig (Eds.), Electronic Structure of Solids '91, Akademie Verlag, Berlin, 1991.
[21] M. Saito, O. Sugino, A. Oshiyama, Phys. Rev. B 46 (1992) 2606.
[22] A. Oshiyama, Phys. Rev. Lett. 74 (1995) 130.
[23] I. Kwon, R. Biswas, C.Z. Wang, K.M. Ho, C.M. Soukoulis, Phys. Rev. B 49 (1994) 7242.
[24] M.C. Payne et al., Rev. Mod. Phys. 64 (1992) 1045.
[25] T. Akiyama, A. Oshiyama, O. Sugino, J. Phys. Soc. Jpn. 67 (1998) 4110.
[26] Y. Okamoto, M. Saito, A. Oshiyama, Phys. Rev. B 58 (1998) 7701, and further results will be published elsewhere.
[27] Y. Okamoto, M. Saito, A. Oshiyama, Phys. Rev. B 56 (1997) R10016.
[28] C.G. van de Walle, Phys. Rev. Lett. 80 (1998) 2177.
[29] B. Hourahine et al., Phys. Rev. B 57 (1998) R12 666.

ELSEVIER

Physica B 273–274 (1999) 520–523

PHYSICA B

www.elsevier.com/locate/physb

The divacancy in silicon and diamond

B.J. Coomer[a,*], A. Resende[a], J.P. Goss[a], R. Jones[a], S. Öberg[b], P.R. Briddon[c]

[a]*School of Physics, The University of Exeter, Stocker Road, Exeter EX4 4QL, UK*
[b]*Department of Mathematics, University of Luleå, Luleå S-97187, Sweden*
[c]*Department of Physics, The University of Newcastle upon Tyne, Newcastle upon Tyne NE1 7RU, UK*

Abstract

First-principles studies of the divacancy (V_2) in both silicon and diamond are reported. We demonstrate that the contrasting experimental spin-density localisation of both systems can be explained through the one-electron pictures arising from opposing distortions.

Keywords: Silicon; Diamond; Divacancy; Jahn–Teller

The removal of two neighbouring atoms from the diamond structure results in a defect with D_{3d} symmetry (see Fig. 1). A linear combination of atomic orbitals (LCAO) approach shows that the six dangling bonds of the divacancy give rise to four electronic levels in D_{3d} – two doublets, e_u and e_g (see Fig. 2) and two singlets, a_{1g} and a_{1u} which are lower in energy. In the neutral charge state the singlets are filled and two electrons occupy the lower doublet, e_u. The one-electron configuration $a_{1g}^2 a_{1u}^2 e_u^2 e_g^0$ gives rise to three multiplets: $^3A_{2g}$, $^1A_{1g}$ and ^1E_g. The $S = 1$ state, $^3A_{2g}$, is orbitally non-degenerate and hence no Jahn–Teller distortion is expected. If the divacancy has spin 0, however, then a Jahn–Teller distortion is expected to lower the ground state symmetry and split the one-electron levels, e_u and e_g.

The silicon divacancy is observed by electron paramagnetic resonance (EPR) in two charge states [1]. The $S = \frac{1}{2}$ spectra labelled G6 and G7 arise from V_2^+ and V_2^- respectively. The neutral charge state of the silicon divacancy is not observed by EPR, presumably because it possesses zero spin. Both G6 and G7 were found to possess C_{2h} symmetry below 40 K. Above this temperature the signals undergo motional broadening and narrowing effects resulting from thermally activated reorientations of the defect between three equivalent Jahn–Teller distortions. Above 110 K, the effective symmetry arising from the rapid reorientation was observed to be trigonal. The spin-density is found to be localised largely ($\sim 60\%$) on the two atoms in the defect mirror plane.

Watkins et al. [1] explain the low symmetry structure and spin-density results in terms of a strong 'pairing' distortion. Two pairs of dangling bonds may be reconstructed to produce a defect with C_{2h} symmetry. The LCAO method shows that the e_u and e_g doublets split under the pairing distortion as shown in Fig. 2(d). Two of the resultant singlet levels, b_u and a_g are localised on the mirror plane atoms, whereas the b_g and a_u wave functions are nodal on the mirror plane. Therefore, since the positive charge state has electronic configuration $b_u^1 a_u^0$, the unpaired electron occupies an orbital which has amplitude on the mirror plane, consistent with experiment.

For V_2^-, a small pairing distortion would give rise to the electronic filling $b_u^2 a_u^1$. In this case the unpaired electron occupies an orbital which is nodal in the mirror plane. In order to explain the observed spin-density localisation, Watkins suggested that the Jahn–Teller distortion is strong enough to cause cross-over of the a_g and a_u levels thus giving $b_u^2 a_g^1$.

* Corresponding author. Tel.: + 44-1392-264198; fax: + 44-1392-264111.
E-mail address: coomer@excc.ex.ac.uk (B.J. Coomer)

0921-4526/99/$ - see front matter
PII: S0921-4526(99)00543-8

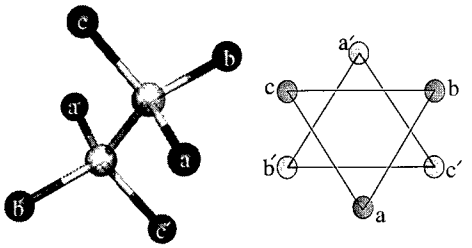

Fig. 1. (a) Schematic of the ideal divacancy in silicon or diamond. The atoms are labelled following the notation used by Watkins and Corbett [1]. (b) We summarise the structure of the divacancy with a view down the principal [1 1 1] axis.

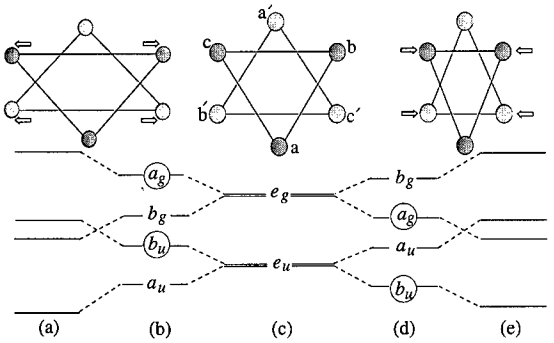

Fig. 2. The effect of symmetry lowering distortions to C_{2h} on the one-electron levels of the ideal, D_{3d} divacancy. For clarity, circles indicate the orbitals with finite amplitude on the defect mirror plane. (a) and (b): A large (a) and small (b) resonant bonding, 'outward' distortion. The four equivalent atoms move out in pairs so that $l_{ac} = l_{ab} < l_{bc}$ and $l_{a'c'} = l_{a'b'} < l_{b'c'}$. (c) The D_{3d} structure. (d) and (e): A small (d) and large (e) pairing distortion. A bond is formed between the two atom pairs b, c, and b', c' such that the distances $l_{ac} = l_{ab} > l_{bc}$ and $l_{a'c'} = l_{a'b'} > l_{b'c'}$.

An alternative explanation for the spin-density localisation results of V_2^- has arisen from LDF supercell studies of Saito et al. [2]. A distortion which is inverse to the pairing distortion (see Fig. 2(b)) gives rise to a different one-electron ordering. Here, an outward displacement of four equivalent atoms leads to five-fold coordination with three strong covalent back-bonds and a pair of "resonant bonds" across the divacancy. A modest distortion of this type results in the electronic filling $a_u^2 b_u^1$. The unpaired electron then occupies an orbital with amplitude on the mirror plane consistent with experiment. Watkins points out [3], however, that only the pairing distortion appears consistent with stress alignment measurements. The application of compressive stress along $[0\,1\,\bar{1}]$ lifts the degeneracy of the three Jahn–Teller distortion directions. One of the distortion directions is observed to be enhanced at the expense of the other two. Although the pairing model appears consistent with this observation, it is unclear why such an effect should arise from the resonant-bonding structure.

Further large-scale LDF super-cell calculations [4] have also found that the resonant-bonding structure to be stable. However, the study finds a new low symmetry structure is lowest in energy.

The R4/W6 EPR centre observed in irradiated diamond is attributed to the neutral charge state of the divacancy. The centre possesses effective spin 1 and so has a non-degenerate ground state, $^3A_{2g}$. It is then intriguing that the ground state of the defect also has C_{2h} symmetry, even though no simple Jahn–Teller effect can be responsible.

Hyperfine measurements [5] have shown that, in contrast to the divacancy in silicon, the diamond divacancy has very little spin-density ($< 2\%$) localised on the mirror plane atoms. This observation may be explained through the one-electron picture only by the electronic configuration $a_u^1 b_g^1$ or $b_g^1 a_u^1$.

LDF theory (AMP [6]) has been employed in this study using large, hydrogen terminated silicon (diamond) clusters of composition $Si_{146}H_{98}$ ($C_{96}H_{78}$). The wave function basis consisted of independent s and p Gaussian orbitals with four different exponents, sited at each Si (C) site. A fixed linear combination of two Gaussian orbitals was sited on the terminating H atoms. In addition, a Gaussian s and p orbital was placed at each Si–Si (C–C) bond centre. The charge density was fitted with four independent Gaussian functions with different widths on each atom and three on the terminating H atoms. One extra Gaussian function was placed at each bond centre. All atoms were optimised using a conjugate gradient method. The total energy of each stable cluster was calculated and the character of each Kohn–Sham level introduced into the gap was determined.

V_2^+, V_2^0 and V_2^- in silicon were optimised with symmetry constrained to D_{3d}. An inward breathing motion of atoms resulted in a lengthening of Si–Si bonds around the divacancy so that the optimised distances, $l_{ab} = l_{ac} = l_{bc}$ (see Fig. 2(c) for atom labelling) were reduced from the ideal value of 3.83 Å. Structures are reported in Table 1.

The distorted structures were investigated using two different initial structures corresponding to distortions of the pairing and resonant bonding types. During relaxation, symmetry was constrained to C_{2h}. In silicon, no outward (resonant bonding) distortion was found to be stable in any charge state. Stable pairing structures, however, were located for all charge states investigated.

In both the single negative and single positive charge states the pairing distortion is found to be sufficient to cross the a_g and a_u levels as shown in Fig. 2(e). The energy of the optical transition between the a_g and

Table 1
Distances (Å) between atoms surrounding the divacancy for the relaxed D_{3d} and C_{2h} structures in silicon and diamond. Distances are given with reference to Fig. 1

Charge state	Silicon				Diamond			
	D_{3d}	C_{2h}			D_{3d}	C_{2h}		
	$l_{ab} = l_{ac} = l_{bc}$	l_{ab}	l_{ac}	l_{bc}	$l_{ab} = l_{ac} = l_{bc}$	l_{ab}	l_{ac}	l_{bc}
V_2^+	3.77	3.92	3.92	2.94	—	—	—	—
V_2^0	3.71	3.78	3.78	2.92	2.75	2.87	2.87	2.68
V_2^-	3.66	3.71	3.71	2.76	—	—	—	—

a_u levels for V_2^- was calculated using a transition state method [7] to be 0.4 eV in excellent agreement with the experimental value, 0.34 eV [8].

In diamond, the $S = 1$, D_{3d} defect was found to have four Kohn–Sham levels in the band gap with two doublets, e_g and e_u lying above two singlet levels b_u and a_g. All six atoms surrounding the divacancy relaxed outwards from their ideal positions by about 0.17 Å during optimisation.

The pairing distortion was found to be unstable in diamond, spontaneously relaxing to a D_{3d} structure. An outward distortion was located with energy 0.1 eV higher than that of the D_{3d} structure. In this distortion the b singlet levels cross giving b_u higher in energy than b_g (Fig. 2(a)). This results in the unpaired electrons occupying orbitals with nodes on the mirror plane. The angles made by the back-bonded atoms to each of the four atoms out of the mirror plane were determined to be 115.4°, 115.9°, 118.5° giving an average angle of 116.6° in reasonable agreement with experiment ($\sim 115°$). The distances between the atoms of the defect were found to be $l_{ac} = l_{bc} = 2.87$ Å and $l_{bc} = 2.68$ Å as compared with $l_{ac} = l_{ab} = l_{bc} = 2.75$ Å for the relaxed D_{3d} defect.

Although care must be taken, particularly in the case of diamond, where many electron effects are greater, the observed distortion of the spin $S = 1$ divacancy in diamond may be understood by consideration of the one-electron picture. In D_{3d} (Fig. 2(c)) the e_u doublet is occupied by two electrons with parallel spins. When a modest distortion to lower symmetry occurs (Fig. 2(b) or (d)) the combined one-electron energy of the two electrons is expected, to first order, to remain constant, but the distortion is disallowed because of the energy cost from increased strain around the defect. However, our calculations demonstrate that a larger distortion causes cross-over of the one-electron levels. This means, for example, that an outward distortion to C_{2h} symmetry can cause the b_g level to fall below the b_u level (Fig. 2(a)). Hence, it is apparent that the sum of the one-electron energies of the unpaired electrons is now reduced in the distortion. If this reduction exceeds the strain energy, then the distortion will be stable. Although this pseudo-Jahn–Teller effect holds equally for the pairing case, this distortion involves a larger movement of atoms from their ideal positions. We find that the associated strain energy is prohibitively large. However, an outward distortion may be expected, a priori, to be favourable in diamond due to the capability for sp^2 hybridization of carbon.

To conclude, we have successfully modelled the distortions required to explain the experimental observations for the divacancy in silicon and diamond. Calculations support the rebonding-by-pairs model for the divacancy in silicon for *both* positive and negative charge states. The spin-density in both cases is localised predominantly on the two silicon atoms in the mirror plane of the defect, in agreement with EPR studies. The calculated optical transition of V_2^- in silicon, which is a good measure of the magnitude of the distortion is in excellent agreement with experiment. The resonant-bonding distortions previously reported are found to be unstable and may arise because the volume of the unit cells were kept constant or from limitations in unit cell or basis size. In diamond, however, an outward distortion can account for the observed spin-density measurements.

References

[1] G.D. Watkins, J.W. Corbett, Phys. Rev. 138 (1965) A543.
[2] M. Saito, A. Oshiyama, Phys. Rev. Lett. 74 (1994) 866.
[3] G.D. Watkins, Phys. Rev. Lett. 74 (1995) 4353.
[4] M. Pesola, J. vonBoehm, S. Poykko, R.M. Nieminen, Phys. Rev. B 58 (1998) 362.

[5] D. Twitchen, M.E. Newton, J.M. Baker, T.R. Anthony, W.F. Banholzer, Phys. Rev. B 59 (1999) 12900.
[6] R. Jones, P.R. Briddon, Chapter 6 in: M. Stavola (Ed.), Identification of Defects in Semiconductors, Vol. 51A of Semiconductors and Semimetals, Academic Press, Boston, 1998.
[7] A. Resende, R. Jones, S. Öberg, P.R. Briddon, Phys. Rev. Lett. 82 (1999) 82.
[8] J.H. Svensson, B.G. Svensson, B. Monemar, Phys. Rev. B 38 (1988) 4192.

ELSEVIER

Physica B 273–274 (1999) 524–527

PHYSICA B

www.elsevier.com/locate/physb

Tin-vacancy complexes in e-irradiated n-type silicon

Marco Fanciulli[a,*], Jørgen R. Byberg[b]

[a]*Laboratorio MDM - INFM, Via C. Olivetti 2, I-20041 Agrate Brianza (MI), Italy*
[b]*Institute of Chemistry, University of Aarhus, DK-8000 Aarhus C, Denmark*

Abstract

Electron irradiated n-type float-zone silicon containing tin has been investigated by EPR. In addition to the well known Si-G29 signal due to the SnV^0 complex we have observed a group of similar EPR signals with strongly anisotropic, near-trigonal g tensors, which we label DK4. The corresponding defects have $S = \frac{1}{2}$ and contain one tin atom. Exposure to light at low temperatures reduces the G29 signal and increased the DK4 signals, whereas subsequent annealing at 200 K restored the initial signal strengths. A linear relationship between the light-induced decay of G29 and the growth of DK4 was established, indicating that DK4 arises from SnV^0 by a change of the charge state. From the observation of DK4 in the n-type material after cooling in the dark we assign DK4 to SnV^-. The acceptor level $E_{-/0}$ (SnV) implied by this assignment has not been determined, but the observations indicate a position below the single-acceptor level of the divacancy ($E_c - 0.42$ eV).

PACS: 76.30.Mi; 61.72.Ji; 71.55.Cn; 61.82.Fk

Keywords: EPR; Si; Sn; Vacancy

1. Introduction

Tin, introduced as an isoelectronic impurity in silicon, has several intriguing properties such as its diffusivity [1] and the unique structure of the only tin-related defect in silicon described so far: the neutral charge state of the Sn–V complex [2,3]. In contrast to the group V-vacancy complexes (E-centers) where the impurity (P, Sb or As) is substitutional [4,5], or even to the Ge-vacancy complex where the group IV element occupies also a regular lattice site [6], the tin atom in SnV^0 sits in a "bond-center" position between two empty lattice sites, the defect thus constituting a divacancy with a tin atom at the center [2,3]. In addition, SnV^0 is the only center derived from the monovacancy that has a triplet ($^3A_{2g}$) ground state.

Sn has come to be considered one of the most efficient vacancy traps in silicon since the early infrared absorption measurements performed by Brelot on e-irradiated CZ-grown silicon samples [7,8]. A reduction of the formation of A-centers (V–O complex) by a factor of 13 was observed in tin-containing samples (relative to control samples). Annealing at about 200°C produced an increase of the A-center and divacancy concentrations, a result interpreted as the release of the vacancies trapped by tin and a subsequent formation of these complexes. Similar results were obtained by Svensson et al. [9]. Brelot pointed out the possibility of using tin and carbon as traps for vacancies and interstitials, respectively, to investigate the radiation induced degradation of devices and eventually develop a radiation hardening based on a self-annealing mechanism [7]. This idea has recently been revived as part of the quest for long-life solid state detectors and other silicon-based devices suitable for high-energy particle physics enterprises such as the CERN large hadron collider (LHC) presently under construction, and space applications. Simulations based on a numerical model for the build-up of electrically active defects during neutron- and γ-irradiations point to the divacancy (V_2) as the principal villain, and suggest that detectors would be extremely radiation hard if the

* Corresponding author. Tel.: + 39-039-6036253; fax: + 39-039-6881175.

E-mail address: mfanciulli@mdmlab.mi.infm.it (M. Fanciulli)

0921-4526/99/$ - see front matter
PII: S0921-4526(99)00544-X

formation of V_2 could be suppressed [10]. Divacancies arise both athermally, as an immediate result of the collision of the projectile with atoms of the target, and in thermally activated processes involving diffusion of monovacancies. Evidently, the latter process may be intercepted by impurities acting as traps for vacancies, and tin would seem a good choice. Indeed, Watkins [2] and Watkins and Troxell [11] observed by EPR and DLTS a quantitative conversion at ≈ 200 K of the isolated monovacancies into SnV, indicating that the thermal formation of V_2 was effectively blocked by the presence of tin. However, this clear-cut result was obtained under the simplifying conditions of low-dose electron irradiation carried out at low temperature, where no interplay of thermal- and radiation-induced processes can occur.

Irradiation of tin-doped silicon to higher doses at room temperature lead to the formation of other types of tin-related defects. Thus, we have recently detected three new EPR signals DK1, DK2, and DK3, from electron-irradiated float-zone silicon containing tin, which we could assign to SnV_2^- and to two configurations of $Sn_2V_2^-$, respectively [12]. These tin–divacancy complexes arise mainly from the thermal decay of SnV, however. It therefore appears that the feasibility of defect-engineering schemes based on tin depends primarily on the stability and, in particular, on the electrical properties of SnV. The DLTS measurements performed by Watkins and Troxell [11] showed that SnV has two levels in the band gap at $E_v + 0.07$ and $E_v + 0.32$ eV, associated with double- and single-donor states, respectively. Moreover, Nielsen et al. observed a DLTS signal at $E_c - 0.57$ eV in electron-irradiated float-zone n-type silicon implanted with tin which they tentatively attributed to a deep acceptor level of the Sn–V complex [13]. In the present EPR study of electron-irradiated silicon doped with tin we identify a new EPR signal arising from the negative charge state of SnV, thus corroborating the proposed existence of an acceptor level in the band gap.

2. Experimental details

The investigated samples were float-zone silicon containing 1×10^{18} cm^{-3} Sn enriched to $\approx 85\%$ ^{119}Sn and 5×10^{16} cm^{-3} P. From the intensity of the infrared absorption line at 607 cm^{-1} ascribed to substitutional carbon, the carbon concentration was estimated to be 3×10^{17} cm^{-3}. Discs of thickness 2 mm cut parallel to (0 0 1) were irradiated at room temperature with 2 MeV electrons to a dose of 1×10^{18} e cm^{-2}. From these discs EPR samples measuring approximately $8 \times 4 \times 2$ mm^3 were cut with faces parallel to (1 1 0) and (0 1 0) and subsequently etched with HNO_3 and HF to remove paramagnetic surface defects.

EPR spectra were recorded with a Bruker ESP300E spectrometer operated at X-band (9.3 GHz) in the absorption mode. The static magnetic field was modulated at 100 kHz. The microwave frequency ν_0 and the magnetic field $\boldsymbol{B}_0$ were monitored continuously with an electronic counter and an NMR gaussmeter.

Sample temperatures in the range 5–300 K were obtained with an APC Heli-Tran liquid-helium flow cryostat. Annealings in the temperature range 300–570 K were carried out in situ in a N_2 flow.

The samples were mounted on the $(1\,\bar{1}\,0)$ face, i.e. with $[1\,\bar{1}\,0]$ along the axis of the cryostat-cavity assembly. The magnet could be rotated about this axis, thus causing $\boldsymbol{B}_0$ to scan the $(1\,\bar{1}\,0)$ plane. The spin Hamiltonian parameters reported here were derived from an angular scan in this plane, recorded at 5° intervals.

3. Results and discussion

As expected the Si-G29 signal (SnV^0) dominates the EPR spectrum of the as-irradiated n-type samples. Owing to the large D-tensor of SnV^0, the G-29 signal is, for most orientations of $\boldsymbol{B}_0$, located outside the spectral region characteristic of defects with $S = \frac{1}{2}$ and g-values near 2. Here a group of closely related weak signals, collectively denoted DK4, may be observed after cooling the samples to temperatures below 15 K in the dark. Illumination with visible or near-infrared light at any temperature below 170 K reduces the intensity of Si–G29 by $\approx 40\%$ and increases that of DK4 by a factor of about six. Simultaneously, the Si–G7 (V_2^-) signal emerges along with the DK1 signal assigned to SnV_2^- [12]. These light-induced changes are all reversible: heating the sample to 200 K and recooling in the dark restores completely the initial EPR spectrum.

At 5 K, microwave power levels in the mW range lead to complete saturation of the G7 and DK1 signals, but maximizes the height of the DK4 signals, which are shown in Fig. 1 for $\boldsymbol{B}_0 \| \langle 100 \rangle$. The three groups of lines indicate a hyperfine interaction with one tin nucleus: The outer groups arise from hyperfine interaction with ^{119}Sn nuclei ($I = \frac{1}{2}$), whereas the central group represents those defects containing an even isotope of tin ($I = 0$). However, the fact that the right-hand group contains four lines shows the presence of more than one signal. The angular variation of the line positions confirms that DK4 consists of several signals, corresponding to a set of defects having $S = \frac{1}{2}$ and similar, strongly anisotropic g tensors as well as similar ^{119}Sn hyperfine interactions. The apparent intensities of the individual hyperfine transitions depend strongly on the sample temperature and on the orientation of $\boldsymbol{B}_0$ with respect to the principal axes of the spin Hamiltonian. Thus, the signals virtually disappear in an angular region around the unique axes of the strongly axial g tensors. These complications, together with an extensive overlap of the very similar signals, precluded a complete analysis. However, the g

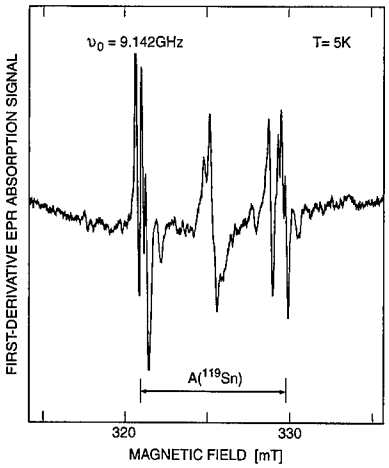

Fig. 1. The group of EPR signals DK4 (SnV^-) recorded at 5 K with $\boldsymbol{B}_0 \parallel [0\,0\,1]$ and 2 mW microwave power. Under these conditions the signals from divacancies are completely suppressed by saturation. The overall spectral pattern correspond to an electron spin ($S = \frac{1}{2}$) interacting with one tin nucleus, while the number of lines within the three groups indicates the presence of several slightly inequivalent configurations of the defect.

tensor and the ^{119}Sn hyperfine tensor could be determined with fair accuracy for two DK4 signals, one of which has monoclinic-I symmetry, whereas the other is triclinic. These parameters are given in Table 1. Moreover, from the observation of six clearly resolved lines in the right-hand group of ^{119}Sn hyperfine transitions for $\boldsymbol{B}_0 \parallel [1\,1\,1]$, the presence of a third DK4 signal of unknown symmetry could be inferred, because one monoclinic and one triclinic signal can account for at most five lines in this region of the spectrum. Satellite hyperfine lines arising from ^{29}Si nuclei were detected in the DK4 signals, but the data did not allow a derivation of the corresponding hyperfine tensors. The *relative* intensities of lines belonging to the individual DK4 signals depend neither on the temperature at which the illumination is carried out nor on subsequent annealings.

The DK4 signals were only observed in samples displaying also the G29 signal. Thus both signals disappeared by annealing at 428 K. This observation suggested a connection between the light-induced decay of G29 and the simultaneous growth of DK4. The use of a very weak light source (a pen-light filtered through 0.5 mm of germanium) allowed us to monitor these processes. As shown in Fig. 2, a linear relationship between the signal heights measured after seven successive illuminations was obtained, indicating that the rate of formation of DK4 is proportional to the rate of decay of G29. The same anticorrelation of DK4 and G29 was observed during the reverse, thermal process: the pairs of corresponding signal heights measured at low temperature between isochronal annealings from 170 to 190 K (also shown in Fig. 2) retrace backwards the linear relationship characterizing the light-induced process.

The anticorrelation of the DK4 and G29 signals observed both when DK4 increases during illumination and

Table 1
Spin Hamiltonian parameters of tin-vacancy complexes discussed in the present work. For comparison, those for SnV^0 are also reported. The principal values of the hyperfine interaction tensors, given in MHz, refer to ^{119}Sn

Term		DK4a (SnV^-) (5 K)	DK4b (SnV^-) (5 K)	Si-G29[a](SnV^0) (20 K)
	S	1/2	1/2	1
	g_X	1.9982(5)	1.998(1)	2.0025
$\boldsymbol{g}$	g_Y	1.9927(5)	1.998(1)	2.0025
	g_Z	2.0335(5)	2.034(1)	2.0107
	ϕ,θ,ψ[b]	0, − 50,0	−, − 59,−	0, − 54.74,0
	$\lvert A_X\rvert$	228(5)	260(10)	393
A^{Sn}	$\lvert A_Y\rvert$	219(5)	180(10)	393
	$\lvert A_Z\rvert$	268(5)	240(10)	374
	ϕ,θ,ψ[b]	0, − 13,0	−, − 10,−	0, − 54.74,0

[a]Data from Ref. [2].

[b]Eulerian angles ϕ,θ,ψ (in degrees), defined in Ref. [14], specify the principal axes (XYZ) for one of the 24 orientations of the defect with respect to a reference coordinate system with axes $[1\bar{1}0]$, $[1\,1\,0]$, and $[0\,0\,1]$. With this choice of reference system θ is the rotation angle from $[0\,0\,1]$ to Z. For terms with $(1\,1\,0)$ mirror symmetry X coincides with $[1\bar{1}0]$, and $\phi = \psi = 0$. Eq. (4.47) of Ref. [14] gives the coordinates of X, Y, and Z in the reference coordinate system as functions of the Eulerian angles (ϕ,θ,ψ).

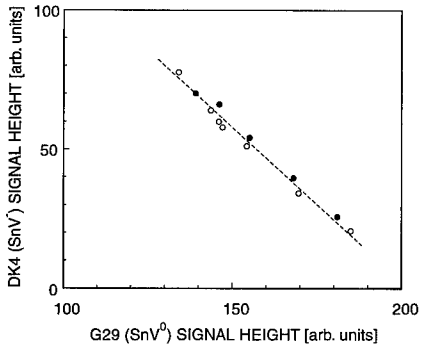

Fig. 2. Heights of the DK4 signal versus the height of the G29 (SnV^0) signal measured between successive illuminations through a germanium filter at 5 K (open circles: the light-induced process runs from upper left to lower right), and measured between 10 min annealings at temperatures increasing from 170 to 190 K in 5° steps (solid circles; the thermal process runs from lower right to upper left). The linear plot indicates a reversible transformation of SnV^0 into the defects giving rise to the DK4 signals.

when DK4 decays thermally at ≈ 180 K indicates that DK4 represents either the positive or the negative charge state of SnV, formed from SnV^0 by photoionization or by electron capture, respectively. Recalling that the DLTS measurements placed the single-donor level $E_{0/+}$ of SnV at $E_v + 0.32$ eV [11] and that DK4 can be observed after cooling to 5 K in the dark, so that an equilibrium population of defect levels may be assumed, we then find that association of DK4 with SnV^+ would imply a radiation-induced lowering of the Fermi level at 5 K to near $E_v + 0.32$ eV. This virtually eliminates SnV^+ as a candidate, and we therefore assign the group of DK4 signals to SnV^- in a set of slightly different configurations. This assignment implies that SnV has an acceptor level $E_{-/0}$ in the band gap.

SnV is isoelectronic with the well-known group V – vacancy pairs (E-centers), but its structure appears to deviate significantly from those of the E-centers, in which the electron spin resides predominantly in a single dangling bond on a silicon atom adjacent to the vacancy, and the impurity atom has a near-substitutional position [4,5]. Thus, the strongly axial g tensor of SnV^- has $\Delta g_{||} \approx 0.03$, $\Delta g_{\perp} \approx -0.006$ (see Table 1), while the E-centers have $\Delta g_{||} \approx 0$, $\Delta g_{\perp} \approx 0.01$. If the three principal components of the ^{119}Sn hyperfine tensor of SnV^- all have the same sign, as observed for SnV^0 and SnV_2^- [12], the spin density on the tin atom is of the order of 0.02e. Hence, a substantial contribution to the g shifts from the spin–orbit coupling of that atom is unlikely. In any case, the "deviating" g tensor of SnV^- indicates that the electron spin cannot be confined to a single dangling bond. However, we may explain the observed properties of SnV^- in terms of the description of SnV^0 given by Watkins [2]. In SnV^0 (point group D_{3d}) the uppermost occupied orbitals, a degenerate pair belonging to the representation E_g, are half-filled, which results in a $^3A_{2g}$ ground state of the defect. Adding an extra electron to the e_g orbitals generates the orbitally degenerate ground state ^2E_g. Hence the defect is expected to distort spontaneously so as to lift the degeneracy of the E_g level. If only a moderately large splitting occurs, a low-lying excited state will exist, which may give rise to the dominant g-shift. Alternatively expressed, the undistorted ^2E_g state has a non-zero orbital angular moment along [1 1 1]. A small distortion quenches this moment to some extent, but the residual angular moment generates a large positive g-shift approximately along [1 1 1] as well as a small negative g-shift perpendicular to [1 1 1]. The observation that the unique axis of the g tensor of SnV^- deviates by only a few degrees from [1 1 1] suggests that the distortion of the D_{3d} shape of SnV^0 upon electron capture is indeed small, thus supporting the notion of a moderate splitting of the E_g level. The occurrence of several inequivalent distortions may be interpreted as reflecting an energetic advantage of a four-coordination of the tin atom: if two of the six initially equivalent silicon neighbours are somehow made inequivalent to the other four, 15 configurations arise which constitute three sets belonging to the three point groups $C_{2h}(3)$, $C_{1h}(6)$, and $C_1(6)$, respectively. Because three DK4 signals are detected and those two that have been analyzed display symmetries consistent with these point groups, it is tempting to associate the structure responsible for the three DK4 signals with three such sets of "four-coordinated" configurations of SnV^-. That a highly symmetric system may distort in several inequivalent ways is quite common. The unusual feature here is that three different distortions apparently yield almost the same stabilization so that none of the configurations alone represents a ground state of the system into which the other configurations can be converted thermally. The energy barriers between the configurations are probably very low since the DK4 signals broaden beyond detection already at ≈ 15 K.

The assignment of the DK4 signals to SnV^- implies that SnV has an acceptor level ($E_{-/0}$) in the band gap. The position of this level has not been determined, but the fact that DK4 are observed after cooling in the dark whereas G7 (V_2^-) is not, indicates that $E_{-/0}(SnV)$ lies below the single-acceptor level of the divacancy, $E_{-/0}(V_2) = E_c - 0.42$ eV. Hence this level might correspond to the DLTS peak found at $E_c - 0.57$ eV in tin-implanted silicon after electron-irradiation, in which case the accumulation of SnV in silicon-based devices exposed to radiation could be even more harmful than the accumulation of divacancies. Irrespective of the exact position of $E_{-/0}(SnV)$, the present results indicate, however, that the prospects of making devices radiation-resistant by including tin to trap vacancies are unpromising.

References

[1] P. Kringhoj, A. Nylandsted Larsen, Phys. Rev. B 56 (1997) 6396.
[2] G.D. Watkins, Phys. Rev. B 12 (1975) 4383.
[3] G.D. Watkins, Solid State Commun. 17 (1975) 1205.
[4] G.D. Watkins, J.W. Corbett, Phys. Rev. 134 (1964) A1359.
[5] E.L. Elkin, G.D. Watkins, Phys. Rev. 174 (1968) 881.
[6] G.D. Watkins, IEEE Trans. Nucl. Sci. NS-16 (1969) 13.
[7] A. Brelot, IEEE Trans. Nucl. Sci. NS-19 (1972) 220.
[8] A. Brelot, in: J.E. Whitehouse (Ed.), Radiation Damage and Defects in Semiconductors, Conference Series No.16, Institute of Physics, London and Bristol, 1973, p. 191.
[9] B.G. Svensson, J. Svensson, J.L. Lindström, D. Davies, J.W. Corbett, Appl. Phys. Lett. 51 (1987) 2257.
[10] B. MacEvoy, K. Gill, G. Hall, Mater. Sci. Forum 258–263 (1997) 671.
[11] G.D. Watkins, J.R. Troxell, Phys. Rev. Lett. 44 (1980) 593.
[12] M. Fanciulli, J.R. Byberg, Phys. Rev. B, to be published.
[13] J. Nielsen, K. Bonde Nielsen, A. Nylandsted Larsen, Mater. Sci. Forum 38–41 (1989) 439.
[14] H. Goldstein, Classical Mechanics, Addison-Wesley, Reading, MA, 1950, p. 109.

ELSEVIER

Physica B 273–274 (1999) 528–531

PHYSICA B

www.elsevier.com/locate/physb

Effect of high-temperature electron irradiation on the formation of radiative defects in silicon

I.A. Buyanova[a,*], T. Hallberg[b], L.I. Murin[c], V.P. Markevich[c], B. Monemar[a], J.L. Lindström[d]

[a]*Department of Physics and Measurement Technology, Linköping University, S-581 83 Linköping, Sweden*
[b]*Swedish Defence Research Establishment, Box 1165, S-581 11 Linköping, Sweden*
[c]*Institute of Solid State and Semiconductor Physics, Minsk 220072, Byelorussia*
[d]*Solid State Physics, University of Lund, Box118, S-221 00 Lund, Sweden*

Abstract

Defect formation processes in silicon caused by electron irradiation performed at elevated temperatures are studied in detail using photoluminescence (PL) spectroscopy. The use of high temperature during electron irradiation has been found to affect considerably the defect formation process. In particular, several new unknown excitonic PL lines were discovered in carbon-rich Si wafers subjected to electron irradiation at temperatures higher than 450°C. The dominant new luminescent center gives rise to a bound exciton PL emission at 0.961 eV. The center is shown to be efficiently created by electron irradiation at temperatures from 450°C up to 600°C. The electronic structure of the 0.961 eV PL center can be described as a pseudodonor case, where the hole is strongly bound at a level 187 meV above the valence band, while the electron is a effective-mass-like particle weakly bound by ≈ 21 meV in the BE state.

Keywords: Silicon; Electron irradiation; Photoluminescence; Defect

1. Introduction

Irradiation of silicon by high-energy electrons produces lattice defects (vacancies and interstitials) which can participate in different reactions with defects/impurities present in the sample. The sequence of the reactions depends on the temperature of the irradiation and impurity content. Previously reported studies have nearly all referred to irradiation at room temperature (RT) or lower. A subsequent annealing at elevated temperatures causes two major effects on the defect system [1] due to thermal activation of defect reactions involving radiation-induced defects, i.e. (i) thermal annealing of the created defects and/or (ii) creation of new defects. The sequence of radiation-initiated reactions between impurities, present in the samples, and the created defects should depend on the temperature of irradiation, thus providing a method of controlling the material properties. However, the effect of electron irradiation performed at elevated temperatures (i.e. hot irradiation) has been studied to a much less extent [2].

In this study we have employed photoluminescence (PL) spectroscopy to investigate radiative defect formation in silicon caused by the electron-irradiation at elevated temperatures. Several new excitonic PL emissions have been found in carbon-rich Si. The electronic structure of the dominant new luminescent center, responsible for a bound exciton (BE) PL emission at 0.961 eV, has been analyzed based on temperature-dependent and magneto-optical studies.

* Corresponding author. Tel.: + 46-13-281795; fax: + 46-13-142337.
E-mail address: irb@ifm.liu.se (I.A. Buyanova)

0921-4526/99/$ - see front matter
PII: S0921-4526(99)00564-5

2. Experimental

In this study Cz-grown Si wafers with high (3×10^{17} cm^{-3}) and low (5×10^{15} cm^{-3}) concentration of carbon were used. The concentration of oxygen in all samples was about 1×10^{18} cm^{-3}. The concentration of carbon and oxygen was monitored by measuring the optical absorption bands at 605 and 1107 cm^{-1} related to the C atoms at substitutional site (C_s) and oxygen atoms at interstitial site (O_i), respectively [3,4]. The samples mounted on a temperature-regulated holder were irradiated in air at temperatures in the range 20–600°C to a dose 1×10^{18} cm^2, using 2.5 MeV electrons.

The PL measurements were performed in a SM 4000 magnetooptical system (Oxford Instruments) equipped with a 5 T split-coil superconducting magnet, allowing variable temperature measurements in the range from 1.4 up to 300 K. The PL was excited by the 514.5 nm line of an Ar^+ laser and was detected using a 0.8 m Spex-double-grating monochromator equipped with a nitrogen-cooled North-Coast Ge-detector.

3. Experimental results and discussion

PL spectra of carbon-rich and carbon-lean silicon subjected to hot electron irradiation are shown in Fig. 1a and b, respectively. In addition to known BE emissions at 0.767 eV (P-line) and 0.925 eV (H-line) the PL spectra of carbon-rich Si contain more than 10 unknown excitonic lines. The dominant new luminescent center gives rise to a BE PL emission at 0.961 eV — see Fig. 1a. The comparison with reference samples where the electron irradiation was performed at room temperature with subsequent annealing at elevated temperatures suggests that the 0.961 eV PL defect can be created only under hot electron irradiation conditions. In the following we will concentrate on the analysis of the electronic structure of this new PL center. The detailed analysis of the other observed effect of hot irradiation, i.e. an enhancement in the formation of known point and extended defects, involving the carbon and/or oxygen impurities will be given elsewhere.

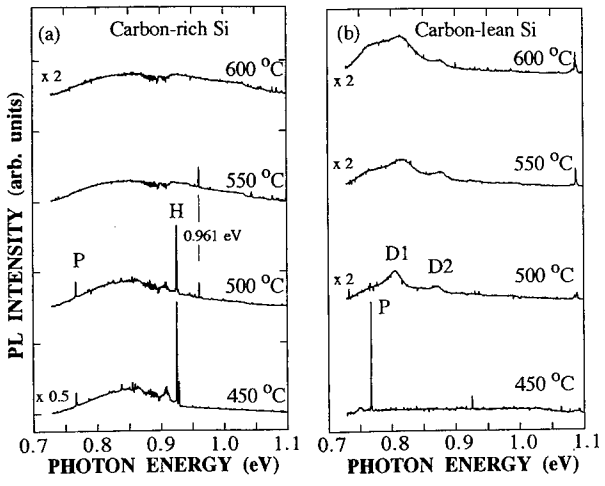

Fig. 1. Low-temperature PL spectra of electron-irradiated carbon-rich silicon (a) and carbon-lean silicon (b), respectively, as a function of irradiation temperature.

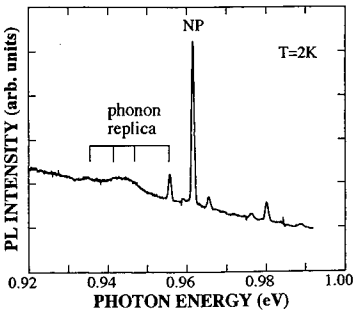

Fig. 2. High-resolution spectrum of the 0.961 eV PL emission. The NP denotes the no-phonon PL transition.

A high-resolution spectrum of the 0.961 eV emission is shown in Fig. 2. The spectrum contains the dominant narrow (~0.25 meV) no-phonon (NP) line at 0.961 eV followed at lower energies by much weaker satellite lines located at around 5.7, 14, 20 and 26.5 meV from the NP emission. Since the appearance of these satellite lines always occurs simultaneously with the main 0.961 eV peak, we tentatively ascribe them to phonon-assisted transitions related to the same PL defect.

The electronic structure of the 0.961 eV defect has been studied by applying a number of external perturbations, including the measuring temperature and a magnetic field. An increase in temperature above 30 K leads to a rapid thermal quenching of the 0.961 eV emission with an activation energy of ~ 21 meV, as estimated from the Arrhenius plot of the integrated PL intensity. This locates the shallow excited state E^* of the defect at around 21 meV from the band edge. Based on the energy of the NP PL transition, the position of the defect-related deep ground state E° can be deduced as ~187 meV from the band edge ($E^\circ \approx E_G - E_{NP} - E^*$). The increase in temperature does not lead to an energy shift in the NP line position, and no additional PL lines are observed.

Zeeman measurements have revealed that the radiative transitions occur between spin-singlet excited and ground states, since no splitting or shift of the NP line has been observed in a magnetic field up to 5 T. The magnetooptical data provide evidence that the 0.961 eV PL defect is a neutral isoelectronic defect of low symmetry with a tightly bound spinlike hole in the BE state. This is because in all other possible cases (i.e. acceptor BE,

donor BE, as well as exciton bound to an electron-attractive isoelectronic center or to a hole-attractive isoelectronic center but retaining orbital angular momentum) a splitting of the NP line in an applied magnetic field is expected [5]. The excited state of such a defect is expected to consist of a spin triplet and a spin singlet, with the triplet state being the lowest [6]. However, for the majority of carbon-related defects in Si, the optical transition from the spin-triplet excited state to the spin-singlet ground state is spin forbidden and cannot be observed via PL spectroscopy [1]. The electronic structure of the 0.961 eV PL center can therefore be described as a pseudodonor case, where the hole is strongly bound at a level 187 meV above the valence band, while the electron is a effective-mass-like particle weakly bound by ≈ 21 meV in the BE state.

Let us briefly discuss the possible model of the 0.961 eV defect. This defect is formed within a relatively narrow range of the temperatures of electron irradiation, i.e. from 450°C up to 600°C, as shown in Fig. 3. According to IR absorption measurements the formation of the 0.961 eV PL defect occurs at the temperatures when oxygen atoms become mobile. This is evident from the thermal annealing at $T > 400$°C of the IR absorption bands related to the oxygen dimer and the VO_2 complex, as have been discussed in Ref. [7]. In addition, the creation of the 0.961 eV PL correlates with the appearance of several new IR absorption bands (compare Figs. 3 and 4) also related to the oxygen impurity [8], based on the observed isotopic shift of the IR bands in the samples enriched with ^{18}O. Thus, the participation of oxygen in the formation of the 0.961 eV PL defect is rather probable. On the other hand, the observation of the corresponding PL emission only in carbon-rich Si suggest that C atoms could either be directly involved in the defect structure or may stimulate its formation. This is supported by the observed strong decrease in the concentration of isolated substitutional carbon atoms after the hot irradiation (Fig. 5) also indicating the formation of some complex defect involving carbon.

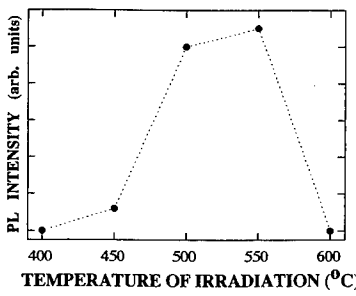

Fig. 3. Dependence of the intensity of the 0.961 eV PL emission on the temperature of electron irradiation. The points represent experimental data. The line is a guide for the eye.

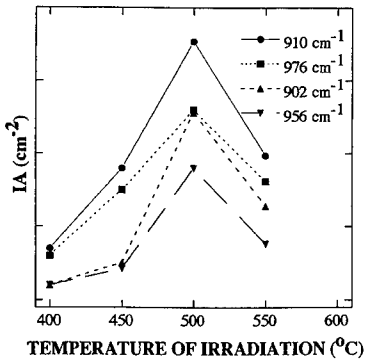

Fig. 4. Dependence of the integrated intensity of the oxygen-related infrared absorption bands on the temperature of electron irradiation. The points represent experimental data. The lines are a guide for the eye.

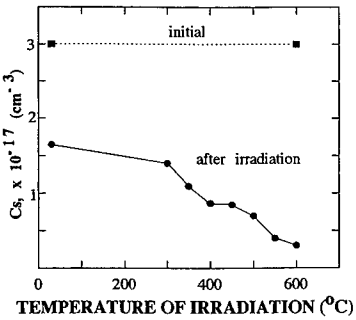

Fig. 5. Dependence of the integrated intensity of infrared absorption related to the subtitutional carbon (C_s) on the temperature of electron irradiation. The points represent experimental data. The lines are a guide for the eye.

4. Summary

We have employed PL spectroscopy to investigate radiative defects created in Si during electron irradiation at elevated temperatures. Several new excitonic PL emissions have been found in carbon-rich silicon subjected to electron irradiation performed at temperatures higher than 450°C. The dominant new PL center gives rise to a BE PL emission at 0.961 eV. Based on temperature-dependent and magnetooptical studies, the electronic structure of the 0.961 eV defect has been shown to be characteristic of a pseudodonor BE at an isoelectronic center, where the hole of the BE is strongly bound at a level 187 meV above the valence band, while the electron is a weakly bound effective-mass-like particle.

Acknowledgements

Financial support was received from Teknikvetenskapliga Forskningsrådet (TFR) and from the National

Defense Research Establishment. We also acknowledge financial support from the Swedish Institute and from The Swedish Royal Academy of Sciences, making it possible for L.I. Murin and V.P. Markevich to visit Linköping University.

References

[1] G. Davies, Phys. Rep. 176 (1989) 83.
[2] L.N. Safronov, L.S. Smirnov, E.G. Tishkovskii, Sov. Phys. Semicond. 14 (1980) 67.
[3] A. Baghdadi, W.M. Bullis, M.C. Croarkin, Y.-Z. Li, R.I. Scace, R.W. Series, P. Stallhofer, M. Watanabe, J. Electrochem. Soc. 136 (1989) 2015.
[4] ASTM Book of Standards, Test Method for Substitutional Carbon Atom of Silicon by Infrared Absorption, F123-86, American Society for Testing and Materials, Philadelphia, 1986, p. 252.
[5] B. Monemar, CRC Crit. Rev., Solid State Mater. Sci. 15 (1988) 111.
[6] B. Monemar, U. Lindefelt, W.M. Chen, Physica B 146 (1987) 256.
[7] J.L. Lindström, T. Hallberg, D. Åberg, B.G. Svensson, L.I. Murin, V.P. Markevich, Mater. Sci. Forum 258–263 (1997) 367.
[8] J.L. Lindström, T. Hallberg, L.I. Murin, V.P. Markevich, unpublished.

ELSEVIER

Physica B 273–274 (1999) 532–534

PHYSICA B

www.elsevier.com/locate/physb

Molecular-dynamics studies of self-interstitial aggregates in Si

M. Gharaibeh[a], S.K. Estreicher[a,*], P.A. Fedders[b]

[a]*Physics Department, Texas Tech University, Lubbock, TX 79409, USA*
[b]*Physics Department, Washington University, St. Louis, MO 63031, USA*

Abstract

The interactions between neutral self-interstitials in silicon are studied using ab initio tight-binding molecular-dynamics simulations in periodic supercells containing 64 up to 216 Si atoms. A number of configurations with three or more self-interstitials are found, and the lowest-energy ones are discussed. The binding energies of I_n relative to $I_{n-1} + I$ show that the first 'magic number' (particularly stable aggregate) is I_3. The potential energy surfaces for aggregates of three or more I's have several local minima, leading to a range of metastable configurations.

Keywords: Self-interstitial; Silicon; Molecular-dynamics

1. Introduction

The fundamental intrinsic defects in c-Si are the vacancy (V) and the self-interstitial (I). Self-interstitials are not observed directly because their activation energy for diffusion in the presence of minority carriers is so low that they trap at shallow donors or H, form I_n precipitates, kick-out substitutional impurities such as B or C, or recombine with vacancies before they can be observed [1].

Many models have been proposed for the isolated I, including the tetrahedral interstitial (T) or hexagonal interstitial (H) sites, [2] the bond-centered (BC) site, [2,3] and a split-$\langle 100 \rangle$ structure [4]. The high-symmetry configurations are Jahn–Teller unstable in most charge states and symmetry-lowering distortions occur when lattice relaxations are allowed to take place. Recent calculations favor the split-$\langle 110 \rangle$ configuration [5–11].

Calculations of the structures of small I_n precipitates have also been performed. Rasband et al. [11] used empirical methods and proposed several structures for the di-interstitial I_2. Arai et al. [12] also used empirical methods to obtain the structure of the I_4 aggregate. Lee proposed a di-interstitial model based on an EPR spectrum [13]. Finally, Coomer et al. [14] performed ab initio density-functional calculations in H-saturated clusters for various structures of I_n aggregates, with $n \leqslant 4$.

In this work, we calculate systematically the structures and binding energies of neutral I_n aggregates with $n = 1, \ldots, 6$. The potential energy surfaces are explored using ab initio tight-binding molecular-dynamics (MD) simulations [15,16] in periodic supercells containing 64, 128, and 216 Si atoms, not including the self-interstitials. The smaller cell uses four k-points and the larger ones only the Γ point. A wide range of plausible initial configurations for each I_n aggregate are tested. In order to identify any metastable configuration, simulated quenching is used to force convergence toward the nearest local minimum of the potential energy. Thermal anneals around 500 K for several hundred time steps followed by quenching are also performed to identify the more stable local minima. The time step for all the calculations is 2 fs.

Most of the calculations have been done using the Harris energy functional and minimal basis sets on all the Si atoms. Cell size effects are monitored by repeating the calculations in the 64- and 216-atom cells. The more stable structures are further studied with the self-consistent version of the code and large basis sets. Many of the

* Corresponding author. Tel.: + 1-806-742-3723; fax: + 1-806-742-1182.

E-mail address: stefan.estreicher@ttu.edu (S.K. Estreicher)

0921-4526/99/$ - see front matter
PII: S0921-4526(99)00566-9

latter calculations are still under way and the results presented below are preliminary.

Note that the configurations of the I_n aggregates in Si all involve substantial lattice relaxations and distortions, and one or more host atoms often end up quite far from ideal crystalline sites. As a result, the same aggregate can often be described differently depending on which atoms are taken to be the I's and which the host atoms. We generally define the I's as those atoms located the furthest away from perfect crystalline sites.

2. Results and discussion

In agreement with other authors [5–11], we find that the stable configuration for I^0 is the split-$\langle 1\,1\,0\rangle$, but the center of the split is shifted by about 0.7 Å in the $\langle 0\,0\,1\rangle$ direction. The split-$\langle 1\,0\,0\rangle$ and BC configurations are shallow minima of the potential energy, and 4000 time-steps anneals at 1000 K forces those configurations toward the split-$\langle 1\,1\,0\rangle$ one.

Three initial configurations of I_2 have been considered: two $\langle 1\,1\,0\rangle$ splits (perpendicular and parallel to each other), and a 'zig-zag' structure. The first two initial configurations lead to the same final configuration for I_2. It has the two I's bound to each other and aligned along a $\langle 1\,1\,0\rangle$ direction. This can also be viewed as two I's bridging the same BC site. The I–I internuclear distance is 2.23 Å. The 'zig-zag' initial guess leads to a metastable configuration, more than 1 eV higher in energy.

We considered almost a dozen initial structures for I_3. Systematic quenches and/or high-T anneals followed by quenches have led to five local minima of the potential energy. Several structures of I_3 are likely to coexist. Our lowest-energy one consists of three I's forming an equilateral triangle in a $\langle 1\,1\,1\rangle$ plane, the center of the triangle lying at a BC site (I_3^a, Fig. 1, top). A competing structure, also with trigonal symmetry, [14] consists of an equilateral triangle but with the three I's bridging three adjacent BC site (I_3^b, Fig. 1, bottom). Both structures have large binding energies and are quite stable. The energy difference between them varies with the level of theory, the size of the basis set as well as the size of the cell. At this point, we cannot say with certainty which of the two structures is the most stable one and believe that both coexist. Further, we cannot exclude the possibility that I_3 may be a mobile complex, moving for example from I_3^a to I_3^b.

Half-a-dozen possible initial configurations leading to different structures for I_4 aggregates were considered. Our lowest-energy structure looks similar to that proposed by Aria et al. [12]. It consists of a square in a $\langle 1\,0\,0\rangle$ plane. The metastable structures are about 0.5 eV higher in energy.

Our lowest-energy structure of I_5 consists of I_4 plus an adjacent split-$\langle 1\,1\,0\rangle$ interstitial. As for I_6, numerous configurations can be constructed starting with $I_5 + I$, $I_4 + I_2$, etc. The lowest-energy ones are obtained from combinations of nearby I_3^a and/or I_3^b complexes. These structures are all calculated in the $216 + I_6$-atoms cell.

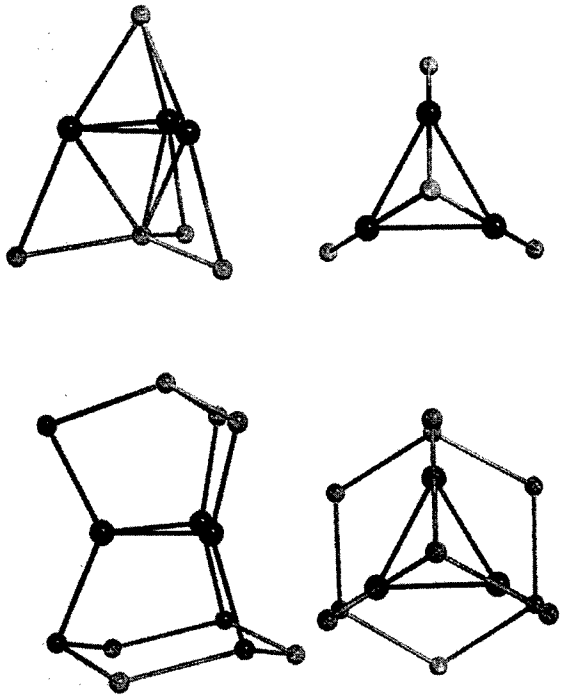

Fig. 1. Views in and along the $\langle 1\,1\,1\rangle$ axis of I_3^a (top) and I_3^b (bottom). Both are equilateral triangles. The three I's are either around a single BC site (top) or bridge adjacent BC sites (bottom).

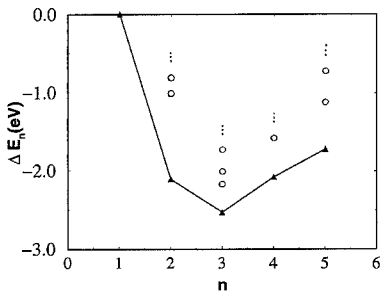

Fig. 2. Binding energies of I_n aggregates vs. n, calculated in the 64 atom cell. The open circles show the energies of some metastable configurations.

Calculations involving I_n aggregates with n larger than 3 involve a surprisingly large number of local minima of the potential energy surfaces. Further, cell size effect begin to play a role with I_3 already. This shows that the 'small' cells (32 and 64 atoms) often used today to study increasingly larger complexes should be used with care.

The (Harris functional) binding energies ΔE_n, defined as the energy gained by forming I_n from I_{n-1} and an isolated I, are shown in Fig. 2. In agreement with Coomer et al. [14], we predict that the trigonal I_3 complex is particularly stable, but caution the reader that much work remains to be done on that issue.

Acknowledgements

This work was supported in part by the grant D-1126 from the R.A. Welch Foundation and by the contract XAD-7-17652-01 from the National Renewable Energy Laboratory.

References

[1] G.D. Watkins, MRS Proc. 469 (1997) 139.
[2] J.W. Corbett, J.P. Karins, T.Y. Tan, Nucl. Instr. and Meth. 182/183 (1981) 457.
[3] R. Car, P.J. Kelly, A. Oshiyama, S.T. Pantelides, Phys. Rev. Lett. 52 (1984) 1814.
[4] C. Weigel, J.W. Corbett, Z. Phys. B 23 (1976) 233 and references therein.
[5] Y. Bar-Yam, J.D. Joannopoulos, Phys. Rev. Lett. 52 (1984) 1129.
[6] R. Car, P.J. Kelly, A. Oshiyama, S.T. Pantelides, Phys. Rev. Lett. 54 (1985) 360.
[7] D.J. Chadi, Phys. Rev. B 46 (1992) 9400.
[8] P.E. Blöchl, E. Smargiassi, R. Car, D.B. Laks, W. Andreoni, S.T. Pantelides, Phys. Rev. Lett. 70 (1993) 2435.
[9] C.G. Van de Walle, J. Neugebauer, Phys. Rev. B 52 (1995) R14320.
[10] A. Mainwood, Mater. Sci. Forum 196–201 (1995) 1589.
[11] P.B. Rasband, P. Clancy, M.O. Thompson, J. Appl. Phys. 79 (1996) 8998.
[12] N. Aria, S. Takeda, M. Kohyama, Phys. Rev. Lett. 78 (1997) 4265.
[13] Y.H. Lee, Appl. Phys. Lett. 73 (1998) 1119.
[14] B.J. Coomer, A. Resende, J.P. Goss, R. Jones, S. Öberg, P.R. Briddon, Physica B 273–274 (1999) 518, These proceedings.
[15] O.F. Sankey, D.J. Niklewski, Phys. Rev. B 40 (1989) 3979.
[16] O.F. Sankey, D.J. Niklewski, D.A. Drabold, J.D. Dow, Phys. Rev. B 41 (1990) 12 750.

ELSEVIER

Physica B 273–274 (1999) 535–539

PHYSICA B

www.elsevier.com/locate/physb

On the fluence dependence of radiation-induced carrier removal in moderately doped Si

H. Amekura*, K. Kono, N. Kishimoto

National Research Institute for Metals, 1-2-1 Sengen, Tsukuba, Ibaraki 305-0047, Japan

Abstract

Two different empirical rules have been proposed for the fluence dependence of the radiation-induced carrier removal, i.e., the exponential rule and the linear rule. In order to distinguish which rule is more adequate, in-situ measurements of carrier concentration in moderately doped n-type Si have been carried out under 17 MeV proton irradiation. The results at $T = 200$ and 300 K are well fitted by the linear relation, while the result at 450 K is relatively well fitted by the exponential one. The experimental results are reproduced by a numerical calculation based on the Oerlein model which includes 15 reactions of 14 defect species. The change from the linear to the exponential rule is mainly ascribed to increased thermal excitation of carriers from defect levels.

Keywords: Carrier removal; Radiation damage; Si; Proton irradiation; High fluence

1. Introduction

Although the carrier removal, i.e., decrease in carrier concentration due to radiation-induced defects, has been well known for several decades, it has again become a critical issue in recent high-fluence applications, e.g., anomalous degradation of Si solar cells for space satellites [1,2], particle detectors at the CERN Large Hadron Collider [3] and optical detectors for plasma diagnostics of nuclear fusion reactors [4]. For understanding the device degradation, fluence dependence of the carrier removal is extremely important.

Up to the present, two different *empirical* rules have been proposed for the fluence dependence of the carrier removal [5]; the exponential rule

$$n(\phi) = n_0 \exp(-R\phi/n_0) \quad (1)$$

and the linear rule

$$n(\phi) = n_0 - R\phi, \quad (2)$$

where n_0, R and ϕ denote the initial carrier concentration, the carrier removal rate and the fluence, respectively. Since both rules are almost identical in the low-fluence region ($\phi \ll n_0/R$) where most of the past devices were used, the difference between two rules was not significant. However, the difference is critical in the high-fluence applications described above. In this paper, we discuss which empirical rule is more adequate for the fluence dependence of the carrier concentration in n-type Si under 17 eV proton irradiation.

2. Experimental conditions and results

Experimental procedures are similar to those described in Ref. [6]. Samples were fabricated from a commercially available n-type CZ Si wafer. The dopant (P) concentration is $3.1 \times 10^{15}\,\mathrm{cm}^{-3}$. A 17 MeV proton beam for the NRIM cyclotron was used for irradiation. The proton flux was about $40\,\mathrm{nA/cm}^2$. A sample was mounted on a temperature-stabilized holder in the irradiation chamber. In order to precisely determine the fluence dependence, the irradiation and the measurements were repeated on the same sample in the chamber.

* Corresponding author. Fax: + 81-298-59-5010.
E-mail address: ame@nrim.go.jp (H. Amekura)

0921-4526/99/$ - see front matter
PII: S0921-4526(99)00567-0

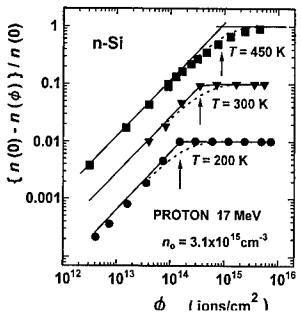

Fig. 1. The fluence dependence of carrier concentration in n-Si under 17 MeV proton irradiation. The experimental results are indicated by symbols. The solid and broken lines indicate the linear and the exponential rules, respectively. The ordinate $\{n(0) - n(\phi)\}/n(0)$ indicates the removed carrier fraction. The arrows indicate the critical fluence defined in Ref. [6].

The projectile range of 17 MeV protons is 1.7 mm in Si [6], which is much larger than the sample thickness. The large range guarantees that the irradiated samples are free from hydrogen implantation and that they have a homogenous damage distribution along the depth. These are advantageous for experimental simplicity. The carrier concentration was determined from the conductivity [6].

The fluence dependences of carrier concentration $n(\phi)$ at three different temperatures, 200, 300 and 450 K, are shown in Fig. 1. The ordinate designates a removed carrier fraction, $\{n(0) - n(\phi)\}/n(0)$, where $n(0)$ is the carrier concentration before irradiation. If the linear rule holds, the data fall on a straight line in the plot. While the linear rule is observed at 200 and 300 K, the exponential rule is observed at 450 K. The critical fluence ϕ_c where the removed carrier fraction is expected to be unity from extrapolation of lower fluence [6] is indicated by arrows in Fig. 1. As the temperature increases ϕ_c shifts higher.

3. Numerical calculation

In principle, the carrier concentration can be determined from the charge neutrality condition, if the concentration and the energy levels of *all* the defects are known. This method is, however, almost impossible to be applied for radiation damage of semiconductors in general. Since a huge amount of knowledge is accumulated for the radiation-induced defects in Si, we tried to reproduce the experimental results using a numerical model based on the accumulated knowledge.

Based on the Oerlein model [7], defect evolution was calculated using the rate equations [8] partially shown in Table 1, which express defect reactions described in

Table 1
Only a part of rate equations used in the calculation are shown here. All the equations are shown in Ref. [8].

$$\frac{d[V]}{dt} = G_V F - R'(V,I)(D_V + D_I)[V][I] - 4R'(V,V)D_V[V]^2 - R'(V,P)D_V[V][P] + R'(V_2,I)D_I[V_2][I] - R'(C_I,V)(D_{CI} + D_V)[C_I][V] - R'(V,V_2)D_V[V][V_2] - R'(V,VO)D_V[V][VO] \quad (B.1)$$

$$\frac{d[I]}{dt} = G_I F - R'(V,I)(D_V + D_I)[V][I] - R'(VO,I)D_I[VO][I] - R'(C_S,I)D_I[C_S][I] - R'(V_2,I)D_I[V_2][I] - R'(VP,I)D_I[VP][I] - R'(C_IC_S,I)D_I[C_IC_S][I] - R'(V_3,I)D_I[V_3][I] - R'(V_2O,I)D_I[V_2O][I] \quad (B.2)$$

$$\frac{d[V_2]}{dt} = G_{V_2} F + 2R'(V,V)D_V[V]^2 - R'(V_2,I)D_I[V_2][I] - R'(V_2,V)D_V[V_2][V] + R'(V_3,I)D_I[V_3][I] \quad (B.3)$$

$$\frac{d[VO]}{dt} = R'(V,O)D_V[V][O] - R'(VO,I)D_I[VO][I] - R'(VO,C_I)D_{CI}[VO][C_I] - R'(VO,V)D_V[VO][V] + R'(V_2O,I)D_I[V_2O][I] \quad (B.4)$$

...
...
...

$$\frac{d[V_2O]}{dt} = R'(V,VO)D_V[V][VO] - R'(V_2O,I)D_I[V_2O][I] \quad (B.14)$$

Table 2
Defect reactions considered in the calculation

$V + I = \phi$	(A.1)		
(1) V-*related*			
$V + V = V_2$	(A.2)	$V + O = VO$	(A.3)
$V + P = VP$	(A.4)	$V + V_2 = V_3$	(A.5)
$V + C_I = C_S$	(A.6)	$V + VO = V_2O$	(A.7)
(2) I-*related*			
$I + V_2 = V$	(A.8)	$I + VO = O$	(A.9)
$I + VP = P$	(A.10)	$I + V_3 = V_2$	(A.11)
$I + C_S = C_I$	(A.12)		
(3) C_I-*related*			
$C_I + C_S = C_IC_S$	(A.13)	$I + C_IC_S = CCI$	(A.14)
$C_I + VO = CO$	(A.15)		

Table 3
Parameters used in the calculation

$R'(X, Y) = 4\pi R(X, Y)$
$R(X, Y) = 0.5$ nm for all sets of X and Y [7]
$D_j(T) = D_{j,o} \exp(-\Delta H/kT)$, ($j$ = V, I, C_I).
$D_{V,O} = 2.19 \times 10^{-3}$ cm^2/s, $\Delta H = 0.34$ eV for V [7,8]
$D_{I,O} = 3.16 \times 10^{-4}$ cm^2/s, $\Delta H \sim 0$ eV for I [7]
$D_{CI,O} = 3.76 \times 10^{0}$ cm^2/s, $\Delta H = 0.78$ eV for C_I [7]
$G_I = G_V + 2G_{V2}$ (defects ion^{-1}cm^{-1}).
where R: effective defect reaction radius
D: diffusion constant
ΔH: migration enthalpy
F: proton flux (ions/cm^{2}s)
G_j: defect creation rate for j = V, I, V_2
Initial values [P] $= 3.1 \times 10^{15}$ cm^{-3},
[C_S] $= 5.0 \times 10^{17}$ cm^{-3},
[O] $= 1.0 \times 10^{18}$ cm^{-3}

Table 2. The defect reactions are assumed to occur via diffusion of mobile defects. The reaction rate between any two defect species is assumed to be $4\pi(D_X + D_Y)R(X, Y)$, where D_X and D_Y are the diffusion coefficients of the defect species and $R(X, Y)$ is an effective reaction radius. Only three species, single vacancy (V), self-interstitial (I) and interstitial carbon (C_I) are assumed to be mobile, and to have diffusion constants of activation type as described in Table 3. In the Oerlein model, all reaction radii $R(X, Y)$ between any pairs of defects are assumed to be 0.5 nm, for simplicity.

Once the concentration of each defect species is determined from the rate equations, the free electron concentration n is derived from the charge neutrality condition:

$$n = \sum_i (N_{D,i} - n_{D,i}) - \sum_j (N_{A,j} - p_{A,j}) + p, \tag{3}$$

where p, $N_{A,j}$, $N_{D,i}$ $p_{A,j}$ and $n_{D,i}$ denote the free hole density, the jth acceptor defect density, ith donor defect density, hole density at the jth acceptor level and electron density at the ith donor level. The densities are given by

$$n = N_C \exp\left(\frac{\mu - E_G^*}{kT}\right), \tag{4}$$

$$p = N_V \exp\left(-\frac{\mu + E_G^*}{kT}\right), \tag{5}$$

$$n_{D,i} = \frac{N_{D,i}}{1 + (1/g_i)\exp((-E_{D,i} + E_G^* - \mu)/kT)} \tag{6}$$

$$p_{A,j} = \frac{N_{A,j}}{1 + g_j \exp((E_G^* - E_A + \mu)/kT)} \tag{7}$$

where $E_G^* = E_G/2$, and $E_{D,i}$ and $E_{A,j}$ denote the ith donor energies and the jth acceptor energies shown in Table 4, respectively.

During the irradiation, V, I and V_2 were assumed to be created directly at constant rates G_V, G_I and G_{V2}, keeping the relation $G_I = G_V + 2G_{V2}$. Even under the electron irradiation, the direct creation of V_2 was assumed in some past works [7], although other authors denied the possibility [9]. Under the proton irradiation, the direct creation of V_2 is more plausible. According to estimation with the SRIM-98 simulation [10], about 30% of vacancies are created within very close distance to each other, due to the cascade collisions under 17 MeV proton irradiation. The simulation cannot tell that all the adjacent two vacancies form V_2, but that the upper limit is 30%, i.e., $G_{V2}/G_V < 0.3$. The fluence dependence was calculated varying the ratio G_{V2}/G_V, by keeping a constant $G_I = G_V + 2G_{V2} = 9.6$ defects/ion·cm. As shown in Fig. 2, the fluence dependence does not greatly change, irrespective of the value of G_{V2}/G_V. From the insensitivity on G_{V2}/G_V, we can compare the calculation with the experimental results further, although we do not have exact information about the G_{V2}.

Using the value G_V as a fitting parameter, the experimental results have been reproduced by the calculation as shown in Fig. 3. Good agreement was attained with G_V = 6–8 cm^{-1}. From SRIM-98 code calculation [10], the *primary* defect creation rate $G_I^{(1)} = 143$ cm^{-1} was derived. In the Oerlein model, spatial correlation between I and V is neglected, although the spatially correlated I–V distribution enhances the I–V recombination in the early stage. The value G_V in the Oerlein model should be regarded as a creation rate of vacancies which survive

Table 4
Defect energy levels [3] considered in the calculation

V_2	$E_C - 0.23$ eV	($\mu > E_C - 0.23$ eV)	Acceptor
	$E_C - 0.42$ eV	($\mu < E_C - 0.23$ eV)	Acceptor
VO	$E_C - 0.17$ eV	Acceptor	
VP	$E_C - 0.23$ eV	Acceptor	
P	$E_C - 0.045$ eV	Donor	
C_I	$E_C - 0.12$ eV	Acceptor	
C_SC_I	$E_V + 0.36$ eV	Donor	
V_2O	$E_C - 0.50$ eV	Acceptor	
CO	$E_V + 0.34$ eV	Donor	

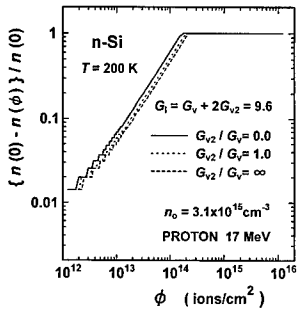

Fig. 2. The fluence dependence of carrier removal are calculated at $G_{V2}/G_V = 0$, 1 and ∞, respectively. The creation rate of interstitials $G_I = G_V + 2G_{V2}$ is fixed to be 9.6 cm^{-1}.

the early recombination. It should be noted that the primary defect creation rate $G_I^{(1)} = 248\ cm^{-1}$ was derived from TRIM-85, which was about twice larger than the value from SRIM-98. This difference is probably due to the improvement of potential energies.

Although the experimental result at 450 K shows the exponential rule, the result is also reproduced by the Oerlein model. The change from the linear rule to the exponential one is mainly ascribed to increased thermal excitation of carriers from some defect levels. Indicated by arrows in Fig. 3, the critical fluence increases as increased T. This is also reproduced well by the calculation. It is found from the calculation that there are two mechanisms for the critical fluence shift, i.e., the increased thermal excitation of carriers from defect levels, and temperature-dependent defect reactions. While the shift from 200 to 300 K is mainly due to the latter, the shift from 300 to 450 K is due to both the mechanisms.

Using the Oerlein model, the fluence dependence of the carrier removal was extrapolated to the wider temperature and wider dopant-concentration range than the experiments. Although the deviation from the linear rule

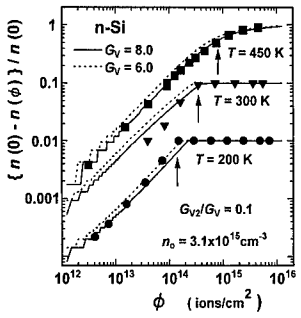

Fig. 3. Comparison between the experimental and the numerical results at 200, 300 and 450 K. The solid and broken lines indicate the numerical results with $G_V = 8.0$ and 6.0 cm^{-1}, respectively. The arrows indicate the critical fluence defined in Ref. [6].

is observed at higher than 300 K, the deviation is also observed at lower than 100 K where the dopants are not fully activated. Even at 200 K, the deviation is observed in highly doped samples ($n_0 > 10^{18}\ cm^{-3}$) at higher fluence. In the higher fluence region where 10^{18} carriers/cm^3 are trapped by the radiation-induced defects, the native impurities O and C whose concentration is about $10^{18}\ cm^{-3}$ cannot any more be regarded as infinite sources for the VO and C_I-related defects formation, respectively. Then, the carrier removal rate may change in the higher fluence, i.e., the fluence dependence may deviate from the linear rule.

4. Conclusion

The fluence dependence of carrier removal in n-type CZ-Si has been studied using the in-situ measurements under 17 MeV proton irradiation. The linear dependence is observed at 200 and 300 K, although the exponential one is observed at 450 K. The experimental results are well reproduced by numerical calculation based on the Oerlein model. The change from the linear- to the exponential rule is mainly ascribed to the thermal excitation of carriers from defect levels. It is also found from the calculation that the fluence dependence in general cannot be expressed by either the linear- or the exponential rule, but by the intermediate. The linear rule is confirmed between about 100 and 300 K, with dopant concentrations less than $10^{18}\ cm^{-3}$.

References

[1] M. Yamaguchi, S.J. Taylor, S. Matsuda, O. Kawasaki, Appl. Phys. Lett. 68 (1996) 3141.
[2] H. Amekura, N. Kishimoto, K. Kono, IEEE Trans. Nucl. Sci. NS-45 (1998) 1508.

[3] B.C. MacEvoy, G. Hall, K. Gill, Nucl. Instr. and Meth. A 374 (1996) 12.
[4] N. Kishimoto, H. Amekura, T. Saito, J. Nucl. Mater. 233–237 (1996) 1244.
[5] R.L. Pease, E.W. Enlow, G.L. Dinger, P. Marshall, IEEE Trans. Nucl. Sci. 34 (1987) 1140.
[6] H. Amekura, N. Kishimoto, T. Saito, J. Appl. Phys. 77 (1995) 4984.
[7] G.S. Oerlein, K. Krafesik, J.L. Lindstroem, A.E. Jaworwski, J.W. Corbett, J. Appl. Phys. 54 (1983) 179.
[8] K. Kono, H. Amekura, N. Kishimoto, Proc. Mater. Res. Soc. Symp. 540 (1999) 115.
[9] B.G. Svensson, M. Willander, J. Appl. Phys. 62 (1987) 2758.
[10] J. Ziegler, J.P. Biersack, U. Littmark, The Stopping and Range of Ions in Solids, Pergamon Press, New York, 1985 (Chapter 8) http://www.research.ibm.com/ionbeams/.

ELSEVIER

Physica B 273–274 (1999) 540–543

PHYSICA B

www.elsevier.com/locate/physb

Investigation of defect formation and electronic transport in microcrystalline silicon deposited by hot-wire CVD

M. Stöger[a], A. Breymesser[b], V. Schlosser[b,*], M. Ramadori[b], V. Plunger[b], D. Peiró[c], C. Voz[c], J. Bertomeu[c], M. Nelhiebel[a], P. Schattschneider[a], J. Andreu[c]

[a]*Institut für Angewandte und Technische Physik, Technical University Wien, A-1040 Wien, Austria*
[b]*Institut für Materialphysik, Universität Wien, Strudhofgasse A-1090, Wien, Austria*
[c]*Departament de Física Aplicada i Electrònica, Universitat de Barcelona, E-08028 Barcelona, Spain*

Abstract

We have investigated doped and undoped layers of microcrystalline silicon prepared by hot-wire chemical vapour deposition optically, electrically and by means of transmission electron microscopy. Besides needle-like crystals grown perpendicular to the substrate's surface, all of the layers contained a noncrystalline phase with a volume fraction between 4% and 25%. A high oxygen content of several per cent in the porous phase was detected by electron energy loss spectrometry. Deep-level transient spectroscopy of the crystals suggests that the concentration of electrically active defects is less than 1% of the undoped background concentration of typically $10^{17}\,cm^{-3}$. Frequency-dependent measurements of the conductance and capacitance perpendicular to the substrate surface showed that a hopping process takes place within the noncrystalline phase parallel to the conduction in the crystals. The parasitic contribution to the electrical circuit arising from the porous phase is believed to be an important loss mechanism in the output of a pin-structured photovoltaic solar cell deposited by hot-wire CVD.

Keywords: Microcrystalline silicon; Transmission electron microscopy; Deep-level transient spectroscopy; Nanopotentiometry

1. Introduction

In the last years the deposition of polycrystalline silicon on glass substrates has attracted great interest for the preparation of thin film transistors and thin film solar cells. For photovoltaic applications polycrystalline films are believed to combine the advantage of a low-temperature deposition technique similar to the preparation of amorphous silicon with the high long-term stability known from crystalline silicon solar cells. Recently, conversion efficiencies of 8.5% have been demonstrated for thin amorphous-microcrystalline silicon solar cells on glass substrates [1]. The limited thermal stability of the glass substrate which corresponds to about 550°C in the case of borosilicate glass requires deposition techniques at low temperatures. Several methods have been reported which allow the deposition of crystalline silicon layers at temperatures as low as 190°C [2]. At these temperatures which are several hundred degrees below the typical growth temperature used for epitaxial silicon deposition the morphology and the electronic quality of the deposited layers are extremely sensitive to the selected deposition parameters. In the present work microcrystalline silicon — μc-Si — deposited by Hot-Wire chemical vapour deposition (HWCVD), which is sometimes referred to as catalytic CVD, was investigated. Crystalline layer growth has been observed at substrate temperatures even below 190°C.

2. Experimental

Undoped μc-Si : H layers were deposited on Corning 7059 glass and on conducting zinc oxide (ZnO) coated glass in one of the chambers of an UHV multichamber

* Corresponding author. Tel.: +43-1-586-3409-27; fax: +43-1-586-34-0813.
E-mail address: viktor.schlosser@univie.ac.at (V. Schlosser)

0921-4526/99/$ - see front matter
PII: S0921-4526(99)00568-2

setup [3]. The ZnO layer served as a transparent, electrical contact. The deposition system consists of the gas inlet, the substrate holder and a basket shaped tungsten filament of 0.5 mm diameter. The distance between the filament and the substrates varies from 4 to 6 cm. The filament is heated by the Joule effect and catalytic cracking reactions at its surface decompose the silane-hydrogen mixture during the deposition process. The base pressure is lower than 10^{-8} mbar. The process parameters which were varied are (i) the silane to hydrogen ratio, (ii) the process pressure, (iii) the gas flow, (iv) the substrate temperature and (v) the filament temperature. For the formation of a pin-structure diborane was added to the gas flow in the case of p-Si deposition and phosphine was added in the case of n-Si deposition. For transmission electron microscopy (TEM) and electron energy loss spectrometry (EELS) thin specimen have been prepared by glueing together two pieces of a sample surface to surface thus preventing the thin film from splintering away during abrasion. Thinning was done mechanically and by the use of an ion polishing system. Two types of rectifying structures were prepared: (i) undoped μc-Si on transparent ZnO and (ii) a pin-device grown on ZnO. In the first case the thickness of the μc-Si film was about 1 μm. Onto the layer's surface small metallic circles of chromium were evaporated. The pin-diode consists of an about 100 nm thick highly boron doped layer grown onto the ZnO, followed by 800 nm of slightly boron doped μc-Si. The boron was added in order to compensate the donors present in undoped μc-Si. The highly phosphorous-doped top layer was about 50 nm thick. Chromium/gold was used as ohmic contact material. Mesa diodes were prepared by wet etching the silicon layers down to ZnO contact.

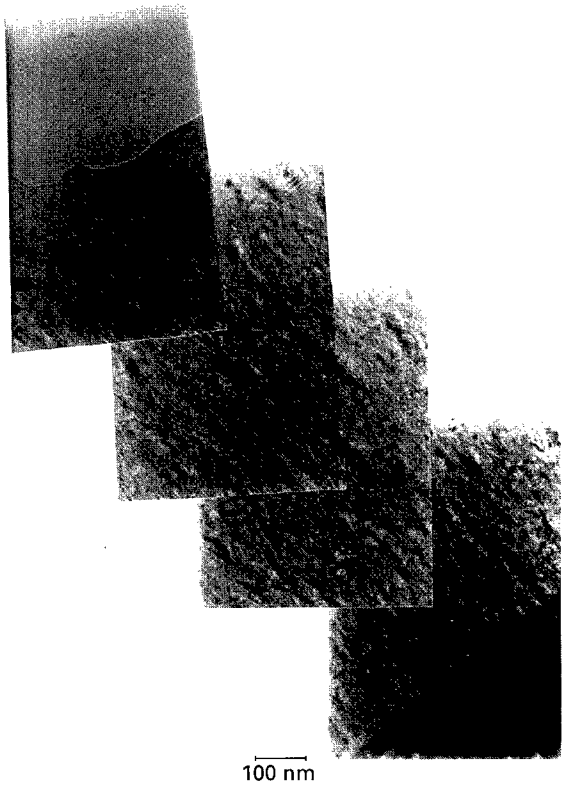

Fig. 1. TEM image of the cross-section of a microcrystalline silicon layer deposited on glass at $T = 225$°C by hot-wire CVD. The substrate is shown in the lower right corner.

3. Results and discussion

The TEM image in Fig. 1 shows a typical structure of an about 1.2 μm thick undoped microcrystalline layer deposited at 225°C onto glass. A needle-like structure surrounded by a noncrystalline phase can be seen. The diameter of a single crystal is about 30 nm whereas the length sometimes exceeds 300 nm. In order to get information about potential contamination from the substrate during deposition the barium content in the silicon layer was measured by EELS. Barium was chosen since Corning 7059 glass contains 25% bariumoxide. The oxygen content was determined with different electron beam configurations in order to distinguish between the concentration within or at the surface of a single grain and the concentration between the grains in the noncrystalline phase [4]. In order to demonstrate the porosity of the film the carbon concentration arising from the glue was determined. The results of the EELS analyses are shown in Fig. 2. In the porous phase the measured oxygen concentration is 2.15 higher than inside or on the nanocrystals. Due to the preparation of the ultrathin and porous specimen which were exposed to air prior to the transfer into the electron microscope it must be expected that native oxide formation occurs which significantly contributes to the measured oxygen content but was not introduced during the deposition of the μc-Si layer. All of the examined μc-Si layers had a porous phase. The volume fraction varied depending on the process conditions between less than 4% and more than 25%. Optical measurements on nearly all of the samples were dominated by the crystalline properties of the deposited films. Absorption measurements suggest an optical gap close to the one of crystalline silicon (1.12 eV) with a high density of subband gap states [5]. Raman spectroscopy usually showed a dominant line close to 519 cm^{-1} which is typical for crystalline silicon and the two reflectance maxima in the photon energy range between 3 and 6 eV well known from single-crystal surfaces were found in our samples. When exposed to air the lateral conductivity of undoped μc-Si films grown on glass usually exhibits an unstable behaviour which was found to be mainly due

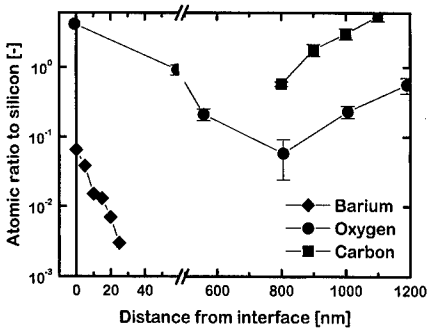

Fig. 2. Distribution of oxygen, barium and carbon in the μc-Si film shown in Fig. 1 as detected by EELS. The distance is taken from the glass/silicon interface.

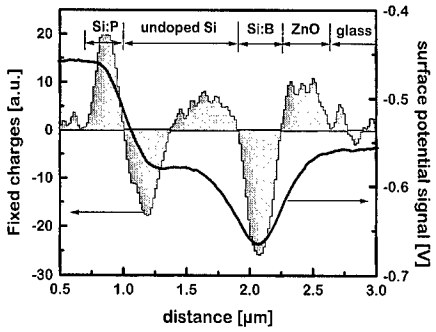

Fig. 3. Surface potential variation across a pin-structure of μc-Si deposited on conducting ZnO measured by SFM and calculated charge distribution.

to the adsorption and desorption of gases. Some of the films were heat treated in Ar, N_2 and O_2 and subsequently heated up under high-vacuum conditions. A quadrupol mass spectrometer was used to detect the partial pressure of the gases of interest released from the sample as a function of the temperature. Up to 100°C the outgasing of nonreactive N_2 and Ar as well as the outgasing of O_2 obeyed the thermal activation law with activation energies, E_{act}, between 0.1 and 0.3 eV. No significant difference between the use of oxygen and nonreactive gases was found. Above 100°C E_{act} for oxygen changes to values greater than 2 eV indicating that oxidation takes place whereas E_{act} of N_2 and Ar remains unchanged up to 200°C. The simple structure of undoped μc-Si deposited on ZnO exhibited a Schottky-type behaviour where the space charge region was located at the ZnO/μc-Si interface and the undoped layer was slightly n-type. These structures have been used to carry out deep-level transient spectroscopy (DLTS). Capacitance–voltage and conductance–voltage measurements as a function of the frequency showed that the measured capacitance was given by two capacitors in parallel. One capacitor was determined by the space charge region assumed to be located within the nanocrystals and the other capacitor was independent of the bias voltage. However, it obeyed a power law in the frequency dependence which is typical for hopping conduction in highly disordered materials as one will expect for the noncrystalline phase. Despite the results from optical absorption measurements suggesting defect-induced subbands rather than distinguishable deep levels three easily resolvable donors with activation energies, ΔE, at 0.027, 0.185 and 0.336 eV were found. The capture cross-sections, σ_n assuming electronic properties of crystalline silicon were 4×10^{-22}, 4.4×10^{-19} and 2.5×10^{-18} cm^2 respectively. The concentration for all the three levels was less than 1% of the background concentration. One acceptor was resolved: $\Delta E = 0.104$ eV, $\sigma_p = 6 \times 10^{-21}$ cm^2. In the pin-device three more shallow donors with $\Delta E < 0.140$ eV were found. The shallow donor levels probably can be attributed to oxygen. The donor level at 0.336 eV may be caused by tungsten introduced by the filament. However, no evidence for iron coming from the chamber walls and zinc diffusion from the substrate was observed. Using conducting tips during the operation of a scanning force microscope (SFM) in the noncontact mode the potential distribution was recorded simultaneously during the topographic measurement on a cross section of the pin-structure. The averaged result of the surface potential and the calculated charge distribution is shown in Fig. 3. Since the measurements were carried out in air the magnitude of the measured values of the surface potential will diverge considerably from those obtained under ideal conditions in high vacuum [6]. It can be seen that the diode rather behaves like two junctions in series (at the n^-/i-interface and at the i/p^+-transition) than a pin-structure with no charges in the i-layer. The p^+–Si/n–ZnO transition acts as a reverse biased diode in the equivalent circuitry of the structure thus leading to a rather poor photovoltaic output under illumination.

4. Conclusions

The investigated microcrystalline silicon layers are composed of a crystalline and a porous, noncrystalline phase. During the layer deposition the porous phase has the capability to efficiently getter contaminants like oxygen and potentially other impurities and dopants. Impurity levels observed in the undoped crystalline needles are in the order of 1% of the background concentration and can mainly be attributed to oxygen. The electrical properties perpendicular to the substrate's surface, parallel to the main direction of the crystalline needles can be described by the semiconducting properties of the crystals in parallel with a hopping conduction coming from the

noncrystalline channels between the crystals. Although the presence of the porous phase during deposition is potentially advantageous its parasitic contribution to the output of photovoltaic devices prepared from HWCVD silicon must be further investigated.

Acknowledgements

The authors thank Prof. H. Kuzmany for the use of the scanning force microscope. This work was supported in part by the Joule-Thermie program of the European Commission, contract number JOR3-CT97-0126.

References

[1] J. Meier, H. Keppner, S. Dubail, Y. Ziegler, L. Feitknecht, P. Torres, Ch. Hof, U. Kroll, D. Fischer, J. Cuperus, J.A. Anna Selvan, A. Shah, in: J. Schmid, H.A. Ossenbrink, P. Helm, H. Ehmann, E.D. Dunlop (Eds.), Proceedings of the Second World Conference on Photovoltaic Solar Energy Conversion, Vienna, 1998, p. 375.

[2] P. Müller, W.M. Holber, W. Henion, E. Nebauer, V. Schlosser, B. Selle, I. Sieber, W. Fuhs, in: J. H. Werner, H.P. Strunk, H.W. Schock (Eds.), Proceedings of the International Conference on Polycrystalline Semiconductors, Schwäbisch-Gmünd, 1998.

[3] D. Peiró, J. Bertomeu, C. Voz, G. Robin, J. Andreu, in: J. Schmid, H.A. Ossenbrink, P. Helm, H. Ehmann, E.D. Dunlop (Eds.), Proceedings of the Second World Conference on Photovoltaic Solar Energy Conversion, Vienna, 1998, p. 766.

[4] M. Stöger, Diplomarbeit am Institut für Angewandte und Technische Physik, TU Wien, 1999, pp. 55–58.

[5] A. Breymesser, V. Plunger, M. Ramadori, V. Schlosser, M. Nelhiebel, P. Schattschneider, D. Peiró, C. Voz, J. Bertomeu, J. Andreu, in: J. Schmid, H.A. Ossenbrink, P. Helm, H. Ehmann, E.D. Dunlop (Eds.), Proceedings of the Second World Conference on Photovoltaic Solar Energy Conversion, Vienna, 1998, p. 1615.

[6] A. Breymesser, V. Schlosser, D. Peiró, C. Voz, J. Bertomeu, J. Andreu, J. Summhammer, Sol. Energy Mater. Sol. Cells, in preparation.

ELSEVIER

Physica B 273–274 (1999) 544–548

PHYSICA B

www.elsevier.com/locate/physb

Electronic transport properties of polycrystalline silicon films deposited on ceramic substrates

S. Bourdais[a,*], G. Beaucarne[b], J. Poortmans[b], A. Slaoui[a]

[a]*Laboratoire PHASE, CNRS, 23 rue du Loess, F-67037 Strasbourg, France*
[b]*IMEC vzw, Kapeldreef 75, B-3001 Leuven, Belgium*

Abstract

In this paper we first present our results on growth of silicon onto silicon oxide and ceramic (alumina, mullite) substrates in three chemical vapor deposition (CVD) reactors using chlorosilanes as precursor gases. The effect of operational parameters (substrate temperature and gas concentration) on growth rate and grain size were analyzed using scanning electron microscopy (SEM) technique. We show that deposition rates up to 5 μm/min can be reached. Furthermore, preferential (up to 80%) (220) oriented structure with grain size ranging from 0.5 to 10 μm can be generated for a 10 μm thick Si film. In the second part we report on electronic properties of the deposited poly-Si films through the layer resistivity, open-circuit voltage of photovoltaic devices, minority carrier diffusion length and spectral response data. We show that the grain size and the post-hydrogenation treatment affect mostly the open-circuit voltage and weakly the spectral response.

Keywords: Polycrystalline silicon; Electronic properties; Solar cells

1. Introduction

Recently, direct deposition of 5–20 μm polycrystalline silicon (poly-Si) films onto foreign substrates has been of great interest to manufacture thin film-silicon solar cells (TF-Si) [1]. Chemical vapor deposition (CVD) processing at temperatures above 1000°C allows rapid growth (> 1 μm/min) and large grain sizes formation but needs appropriate substrates that can withstand elevated temperatures and with a thermal expansion coefficient close to that of silicon [2]. In Si layers deposited by CVD on foreign substrates, the majority and minority carrier transport properties of the resulting poly-Si layer are dominated by the grain size and grain boundaries (GB's) activity which limit the photovoltaic performance [3].

In this paper, we first report on the growth of pc-Si films on thermal silicon oxide, alumina (Al_2O_3) and mullite ($3Al_2O_3$–$2SiO_2$) substrates using lamps heated CVD reactors. This leads to the formation of Si material with different grain size and structure. We looked at the electronic transport properties of the deposited layers in conjunction with the grains size and subsequent hydrogenation step for defect passivation.

2. Experimental

Three different CVD systems were used for Si deposition. The first one, a cold walls RTCVD reactor (Jipelec) described in Ref. [4] uses 12 tungsten halogen lamps as a heating source. The second one, the Epsilon reactor, combines radiation from lamps and conduction via a graphite susceptor to heat the substrate. The third CVD reactor is a batch-type where the samples are heated by IR radiation. The first two reactors work at atmospheric pressure (APCVD) whereas the third one is a low-pressure (LPCVD) reactor. The p-type Si films were deposited at high-temperatures (900–1250°C) in the different reactors by employing chlorosilanes ($SiHCl_3$ (TCS) or SiH_2Cl_2 (DCS)) as precursors diluted in hydrogen at various concentrations and adding BCl_3 or B_2H_6 for doping.

* Corresponding author. Tel.: 33-388-10-63-27/35.
E-mail address: Bourdais@phase.c-strasbourg.fr (S. Bourdais)

0921-4526/99/$ - see front matter
PII: S0921-4526(99)00569-4

The substrates used for silicon film deposition are thermally oxidized silicon (200 nm SiO_2), alumina and mullite. Investigation of the deposition kinetics revealed that the mass-transfer limited regime dominates at temperatures above 1000°C and leads to deposition rates in the range 1–5 μm/min, 0.1–4 μm/min and 0.1–0.5 μm/min in the Jipelec, Epsilon and LPCVD reactors, respectively.

3. CVD deposition

Fig. 1 shows SEM cross-section of views of polysilicon layers deposited on SiO_2 at 1050°C and 1200°C in the Jipelec reactor. At lower temperature, the film exhibits a columnar structure with small grains at the interface becoming larger as growth proceeds. At high temperature, deposition leads to much larger grains but with defects such as twins, and small grains still present. X-ray diffraction measurements revealed a very strong (2 2 0) preferential orientation on fine as well as on large-grained layers over a large range of experimental conditions [5].

Fig. 2 reports the average grain size (GS) dependence on the growth temperature for about 10 μm thick Si layers deposited on SiO_2 or Al_2O_3 in both atmospheric pressure CVD reactors. In the Epsilon reactor, increasing the deposition temperature up to 1190°C did not result in any improvement in the average GS and a maximum value around 1.5 μm is reached. Only a deposition in two steps led to grains up to 4 μm in size. In contrast, a strong dependence of the average GS on the deposition temperature in the Jipelec reactor is observed for all substrates used and values exceeding 10 μm are possible. All silicon layers deposited in the different reactors and on various foreign substrates result in polycrystalline films with a distribution in grain size. In particular, the smallest grains can have a detrimental effect both on majority and minority carrier transport.

The observed differences in average GS between the two systems at equal deposition temperatures are striking. A first possible explanation might be the extreme temperature gradients existing in the RTCVD-system between substrates and chamber wall, effectively suppressing any tendency towards homogeneous reactions [6]. However, in the Epsilon, no indication at all has been found for homogeneous reaction and the small grain sizes were observed even in extremely selective deposition conditions which, practically, rules out any homogeneous reaction pathway. A second possibility might be the different irradiation spectrum in the two systems which can influence surface mobility and adatom concentration, thereby influencing the nucleation rate

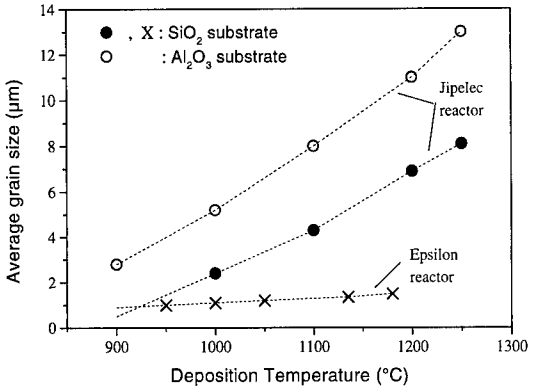

Fig. 2. Average grain size versus temperature for poly-Si films deposited on SiO_2 or Al_2O_3 substrates and in two different APCVD reactors.

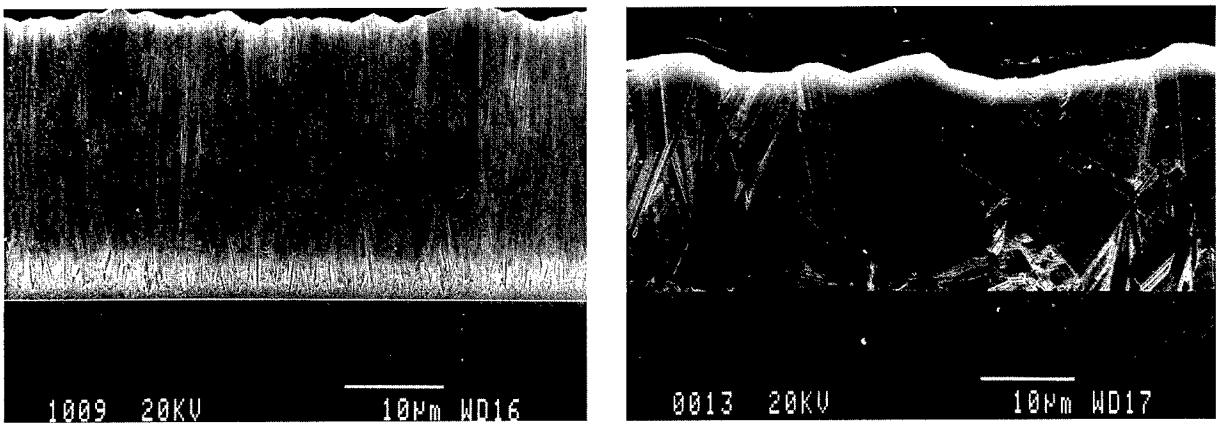

Fig. 1. SEM cross-sectional views of poly-Si layers deposited onto SiO_2 substrate at (a) 1100 and (b) 1250°C in the Jipelec reactor. Layer (a) presents small grains but a smoother surface whereas layer (b) exhibits large grains but a rough surface.

and GS. It is also possible that competitive grain growth is enhanced by the high-energy photons. However, further investigations are needed before this explanation can be confirmed.

The difference in grain-size evolution between Si deposits on alumina and SiO_2 in the RTCVD reactor, can be associated with the higher Si nucleation rate observed on ceramics. Furthermore, for increasing deposition temperatures, we observed higher nuclei size (and lower nuclei density) on alumina than on silicon oxide, which can be attributed unequivocally to an Ostwald ripening process [7].

4. Electronic transport properties

Fig. 3 plots the resistivity against measured carrier density for some RTCVD p-doped polysilicon layers obtained at high temperature and by varying the boron concentration. The resistivity of our pc-Si is found above that of single crystalline Si (sc-Si) and is consistent with results of Graef et al. [8] for comparable grain sizes. For low carrier densities, the measured Hall mobility of our poly-Si films are about 5 times below that of sc-Si but exhibit a slight increase, from 50 to 100 $cm^2/V\,s$ up to a doping level of $10^{17}\ cm^{-3}$. Beyond this level, the measured mobility is close to that of sc-Si, decreasing with increasing doping level. This evolution of the resistivity and mobility with doping level can be understood in the light of the conventional theory of pc-Si, where trapping of majority carriers by interface states N_T (in cm^{-2}) present at grain boundaries (GB's) is considered [9]. At a critical doping level N_A, namely when $N_A = N_T/L$ with L the average grain size, all mobile carriers are trapped at GB's thus giving a minimum in mobility (and sharp increase in resistivity). In our case, with a typical N_T value of $10^{12}\ cm^{-2}$ and an average grain size of 10 μm, the critical doping level is about $10^{15}\ cm^{-3}$ which is lower than the doping levels of all our samples. We indeed do not observe any minimum in mobility. For higher doping levels, grains are only partially depleted, the potential barrier decreases (increase in mobility) and the mobile carrier density gets close to N_A.

One approach to reduce the potential barrier in the as-grown poly-Si films can be seen in bulk passivation of these GB's interface states by monoatomic hydrogen. Fig. 4 plots the resistivity versus inverse temperature for pc-Si layers deposited on alumina in the RTCVD or LPCVD reactors (The average grain sizes are 4 and 0.5 μm, respectively). For as-grown layers, the deduced (conductivity) activation energies E_σ are around 214 meV for large grains and 169 meV for the small ones. The corresponding density of positively charged interface states N_T at the grain boundaries was estimated to be around $7 \times 10^{11}\ cm^{-2}$ and $1.3 \times 10^{12}\ cm^{-2}$, respectively. A hydrogenation treatment at 400°C for 1 h in a remote-plasma reactor results in a significant resistivity reduction. The observed increase with temperature is characteristic of mobility increase in the silicon grains, due to scattering by optical phonons (see the reference curve for single-crystal silicon). Therefore an almost complete passivation of grain boundaries in this RT-CVD layer has been achieved. On the small grained (LPCVD) layer, however, only a small reduction in $E_\sigma = 148$ meV is obtained after hydrogenation. In this case, the measured resistivity is governed by that at grain boundaries, with no conductivity contribution of intra-grains, that are still partly depleted. A possible explanation for the different passivation efficiencies can be found in the total amount (averaged over the volume) of GB interface states present in the different materials. This amount which is proportional to the product of N_T (cm^{-2}) by the total

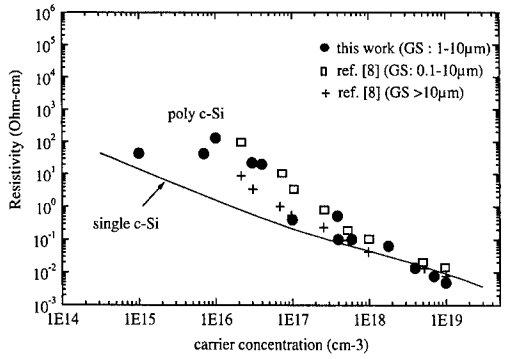

Fig. 3. Resistivity as a function of acceptor concentration for polycrystalline silicon on different substrates grown in the RTCVD reactor. Data from Ref. [8] are also plotted for comparison.

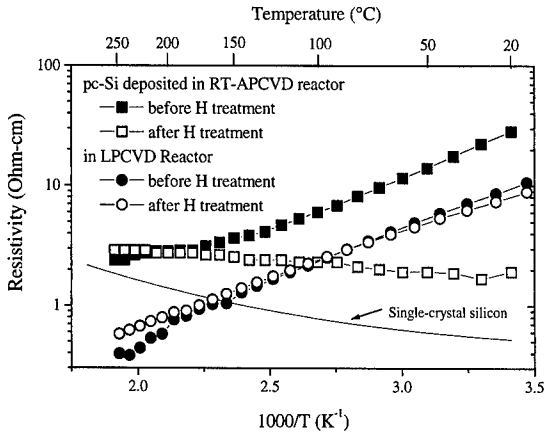

Fig. 4. Resistivity, before and after plasma hydrogenation (400°C, 1 h), of p-type polycrystalline silicon deposited on alumina substrate in the RTCVD and LPCVD reactors.

GB's surface (proportional to the grain size, for a given thickness) is indeed higher by a factor of at least 4 in the LPCVD material.

Despite a minor improvement in majority carrier transport, hydrogenation (performed after emitter formation), has a strong effect on the photovoltaic parameters of cells made on the fine-grained p-type Si layers. The results are reported in Table 1 where the largest improvement is observed on the open-circuit voltage V_{oc}. Since V_{oc} is mainly dominated by the second diode current J_{0r}, the higher V_{oc} value after hydrogenation results in a reduction of the total recombination in the device, especially at grain boundaries (Low N_t). On the other hand, the V_{oc} is also known to be limited by the grain size and distribution [10]. Indeed, in the fine-grained material, there are locally much smaller grains than average with particularly active grain boundaries; this high activity leads to complete depletion of these small grains. Even if all grains are not depleted, those which are depleted contribute more significantly to the recombination current and therefore limit V_{oc}. Increasing the grain size and narrowing their size distribution will result in much less depleted grains and therefore to lower recombination currents for equivalent doping level. This expectation is confirmed in Table 2 which reports a higher V_{oc} for solar cells made on hydrogenated polysilicon material with an average grain size of 4 μm compared to that of about 2 μm. The given V_{oc} values are averaged over 10 measured samples. However, no significant improvement is seen in the electron diffusion length in the pc-Si material (as derived from spectral response measurements), while the lifetime is expected to increase linearly with the grain size [11]. Possible explanations are that the lifetime is mainly controlled by non-passivated intra-grain defects and/or that the region over which minority carrier collection takes place is determined by the junction depth along the grain boundaries. Additional experiments are underway to clarify this point.

Table 1
Photovoltaic parameters before and after a remote plasma hydrogenation

Cell param.	I_{sc} (mA/cm^2)	V_{oc} (mV)	FF (%)	η (%)
No H	9.88	242.2	52.8	1.26
H, 1 h 400°C	10.57	286.6	56.7	1.71

The active layer is a 20 μm p-type silicon layer deposited on alumina in the LPCVD reactor. The average grain size in the layer is about 1 μm.

Table 2
Open-circuit voltage (deduced from I–V illumination) and effective electron diffusion length (deduced from spectral response) for n + pp + cells made on 30 μm thick poly-Si layers grown in Epsilon reactor with two different average grain size

Average grain size (μm)	Open-circuit voltage V_{oc}	Eff. electron diff. Length (μm)
1.7	Mean. 296 (7) Best. 303.6	3.7
4	Mean. 330 (10) Best. 347.1	3.8

5. Summary

In this work, polycrystalline silicon layers with crystallite size from 0.5 to 15 μm were grown on foreign substrates using three lamps based chemical vapor deposition (CVD) reactors. Deposition rates up to 5 μm/min and (2 2 0) oriented columnar structure are obtained. The grain size is found mostly influenced by deposition temperature, especially in the rapid-thermal CVD reactor.

We have shown that the majority-carrier transport in these films is controlled by the electrical energy barrier at the grain boundaries. Depending on the grain size, a post-hydrogenation step at 400°C for 1 h can dramatically improve this conductivity as well as the open-circuit voltage (V_{oc}) of photovoltaic devices. Increasing the grain size from 2 to 4 μm improves the V_{oc} value but has no significant effect on the collection efficiency in the device.

Acknowledgements

S. Bourdais acknowledges the support of EDF (Electricité de France) and G. Beaucarne that of IWT (Flemish Institute for Promotion of Scientific-Technology Research in Industry). This work was partially funded by the European Community under contract N°JOR3-CT98-0234 (COMPOSIT).

References

[1] A. Slaoui, J. Poortmans, T. Vermeulen, R. Monna, O. Evrard, K. Said, J. Nijs, J. Mater. Res. 13 (1998) 2763.
[2] J.E. Cotter, A.M. Barnett, D.H. Ford, R.B. Hall, A.E. Ingram, Prog. Photovoltaics: Res. Appl. 3 (1995) 351.
[3] A.K. Gosh, C. Fishman, T. Feng, J. Appl. Phys. 51 (1980) 446.
[4] R. Monna, A. Slaoui, A. Lachiq, J.C. Muller, Mater. Sci. Eng. B 39 (1996) 48.
[5] A. Slaoui, R. Monna, D. Angermeir, S. Bourdais, J.C. Muller, in: 26th IEEE Photovoltaic Conference 1997, pp. 627–630.
[6] D. Angermeier, R. Monna, A. Slaoui, J.C. Muller, J. Crystal Growth 191 (1998) 386.
[7] D. Angermeier, R. Monna, S. Bourdais, A. Slaoui, J.C. Muller, in: A. Slaoui, R.K. Singh, T. Theiler, J.C. Muller

(Eds.), Rapid Thermal Processing, Elsevier, Amsterdam, 1998, p. 293.
[8] M.W.M. Graef, J. Bloem, L.J. Giling, J.R. Monkowski, J.W.C. Maes, in: Second E.C. Photovoltaic Solar Energy Conference, 1979, pp. 65–72.
[9] J.Y.W. Seto, J. Appl. Phys. 46 (1975) 5247.
[10] M. Imaizumi, T. Itoh, M. Yamagushi, K. Kaneko, J. Appl. Phys. 81 (1997) 7635.
[11] H.W. Card, E.S. Yang, IEEE Trans. ED-24 (1977) 397.

ELSEVIER

Physica B 273–274 (1999) 549–552

PHYSICA B

www.elsevier.com/locate/physb

Defect diagnostics using scanning photoluminescence in multicrystalline silicon

I. Tarasov[a], S. Ostapenko[a,*], V. Feifer[a], S. McHugo[b], S.V. Koveshnikov[c], J. Weber[d], C. Haessler[e], E.-U. Reisner[e]

[a]*Center for Microelectronics Research, University of South Florida, 4202 E Fowler Avenue, Tampa, FL 33620, USA*
[b]*Advanced Light Source Center, Lawrence Berkeley Lab, Berkeley, CA 94720, USA*
[c]*SEH America, Vancouver, WA 98682, USA*
[d]*Max-Planck-Institut fur Festkorperforschung, D-70569 Stuttgart, Germany*
[e]*BAYER AG, D-47829 Krefeld, Germany*

Abstract

Scanning room-temperature photoluminescence (PL) spectroscopy was applied to multicrystalline silicon (mc-Si) wafers to assess electronic properties of the high-quality solar grade material. The intensity of band-to-band emission with the maximum at 1.09 eV measured across entire mc-Si wafer positively correlates with minority carrier lifetime measured concurrently using laser-microwave reflection technique. We have found in mc-Si wafers an intense "defect" PL band with the maximum at about 0.8 eV and half-width of ~ 75 meV at room temperature. It is strongly localized in "bad" areas possessing a reduced by a factor of two orders band-to-band PL intensity and a noticeable degraded lifetime. High-resolution PL mapping of the 0.8 eV band revealed a link to areas with high dislocation density. PL spectra down to 4.2 K were measured in regions with high and low "defect" band intensity demonstrating a correlation of the 0.8 eV band with distribution of the D3/D4 dislocation lines. The origin of the 0.8 eV band is discussed in a connection with dislocation network.

Keywords: Silicon; Photoluminescence; Dislocation; Defects

1. Introduction

A strong growth in the photovoltaic market is mainly based on crystalline silicon wafer technology. Specifically, multicrystalline silicon (mc-Si) is able to meet both the requirement of a cost-effective large-scale production technique and high solar cell efficiencies. One of the main limiting factors of mc-Si solar cell efficiencies, however, are so-called "bad regions" with enhanced recombination activity. A further substantial improvement of the efficiencies attainable with mc-Si solar cells can therefore be achieved by reducing and potentially eliminating "bad regions". In this paper, we report application of scanning, room-temperature photoluminescence (PL) spectroscopy in solar grade mc-Si.

2. Experimental

Multicrystalline silicon wafers were grown using block-casting technique for Baysix® mc-Si. Samples for scanning PL study were bare wafers of 5×5 cm^2 size.

The PL spectrum was analyzed using a SPEX-500M grating spectrometer coupled to a liquid-nitrogen-cooled Ge detector. The 800 nm AlGaAs laser diode (10 nm bandwidth) operating in a pulse mode with peak power up to 300 mW was used as the excitation source. The absorption coefficient of the AlGaAs laser in silicon is 12 μm^{-1}, which allowed us to reduce the influence

* Corresponding author. Tel.: 001-813-974-2031; fax: 001-813-974-3610.
E-mail address: ostapenk@eng.usf.edu (S. Ostapenko)

0921-4526/99/$ - see front matter
PII: S0921-4526(99)00570-0

of surface recombination on bulk PL intensity. PL mapping was performed by placing mc-Si wafers on X–Z moving stage with a spatial resolution controlled by the diameter of the laser spot, which ranged from 0.25 to 3 mm. The PL spectra were corrected to the spectral response of the optical system. The mapping of effective minority carrier lifetime was performed using a laser-microwave reflection technique with the spatial resolution identical to the PL mapping. Notice that both methods realize a high injection limit for the minority carriers in p-type Si. Concurrently, we have used the automatic system for measuring the dislocation density at a whole mc-Si wafer. The system capable of etch-pit-density (EPD) mappings over large areas up to 10 cm × 10 cm wafers. Basically, the EPD system consists of a microscope with computer-controlled automatic focusing, an x–y table, and an image analysis software program.

3. Results

Photoluminescence (PL) spectrum at room temperature in mc-Si wafer is generally composed of two broad bands shown in Fig. 1a: (i) a band-to-band emission with $h\nu_{max} = 1.09$ eV, and (ii) a "defect" band with the maximum changing across the wafer between 0.76 and 0.80 eV. Hereafter we give the assignment of "defect" band to the peak near 0.8 eV.

A room-temperature PL mapping was performed for both luminescence bands. First, we measured the band-to-band PL intensity (I_{bb}) in a scanning mode and compared this to a mapping of the effective minority carrier lifetime (τ_{eff}). In Fig. 2a and b, we presented a distribution of both values measured independently over the same mc-Si wafer with equal steps. We see that the low lifetime regions of the wafer (dark contrast) correspond to a noticeably reduced I_{bb} intensity (also dark), while the high-quality regions in lifetime and PL (white contrast), also are correlated. To illustrate this observation, one of the "bad regions" is framed. These data are supported and quantified in Fig. 3 as a point-by-point plot of I_{bb} versus τ_{eff} for 1680-points map collected from a 5 cm × 5 cm mc-Si wafer. Notice a wide range of values in Fig. 3 spanning as much as one order of PL intensity and lifetime across the wafer. This is a consequence of a strong inhomogeneity of the starting mc-Si, which justify the necessity of using scanning diagnostic techniques.

Based on data in Figs. 2a and b and 3 , it may be concluded that the band-to-band PL intensity positively correlates to a distribution of the minority carrier lifetime in mc-Si. In a simple approximation one can assume that non-radiative centers are a dominant recombination channel in mc-Si at room temperature. The following

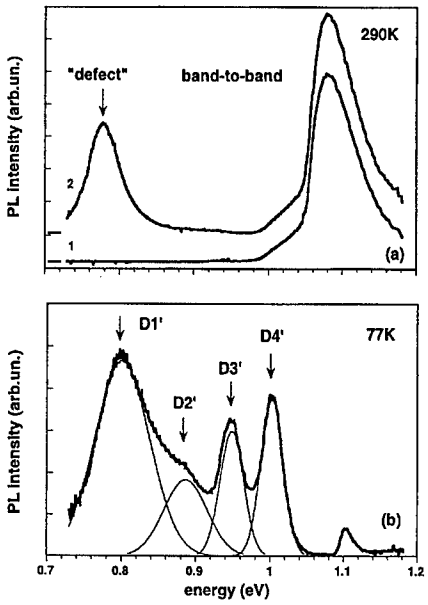

Fig. 1. (a) – room-temperature PL spectrum in high-lifetime (1) and low-lifetime (2) regions of mc-Si. (b) – PL spectrum at 77 K and a deconvolution on four sub-bands.

relation is valid in this case:

$$I_{bb} \sim \tau_r^{-1}/(\tau_r^{-1} + \tau_{nr}^{-1}) = \tau_{nr} = \tau_{eff}, \quad (1)$$

where τ_r^{-1} and τ_{nr}^{-1} are the rates of radiative and non-radiative recombination, assuming that $\tau_{nr} \ll \tau_r$. The Relation (1) is illustrated in Fig. 3. More detailed analyses accounting surface recombination, minority carrier diffusion, and penetration depth of the excitation light on I_{bb} and lifetime was consistent with data in Fig. 3.

We further observed that regions of mc-Si wafers possessing low lifetime values exhibit at room temperature an additional "defect" PL band (I_{def}). Typical spectrum is presented in Fig. 1a (curve 2). It was found previously that this band is observed in bare and processed polycrystalline EFG Si wafers and persists also in final solar cells [1]. Using PL mapping technique it was obvious that the 0.8 eV band is strongly localized in "bad regions" showing a reverse contrast to lifetime and band-to-band PL intensity (Fig. 2c). This is clearly observed in the framed area corresponding to one of the "bad regions" of the wafer. Concurrently with lifetime and PL mapping we performed at the same mc-Si wafer measurements of the dislocation density using EPD technique. The data presented in Fig. 2d document a positive correlation in distribution of the dislocation density with the "defect" PL band. Specifically, the 0.8 eV PL band is observed in areas with high dislocation density of $(1\text{–}8)E + 6\ \text{cm}^{-2}$. We may conclude at this point that the "defect" PL band is originating in areas with enhanced recombination activity and increased dislocation density.

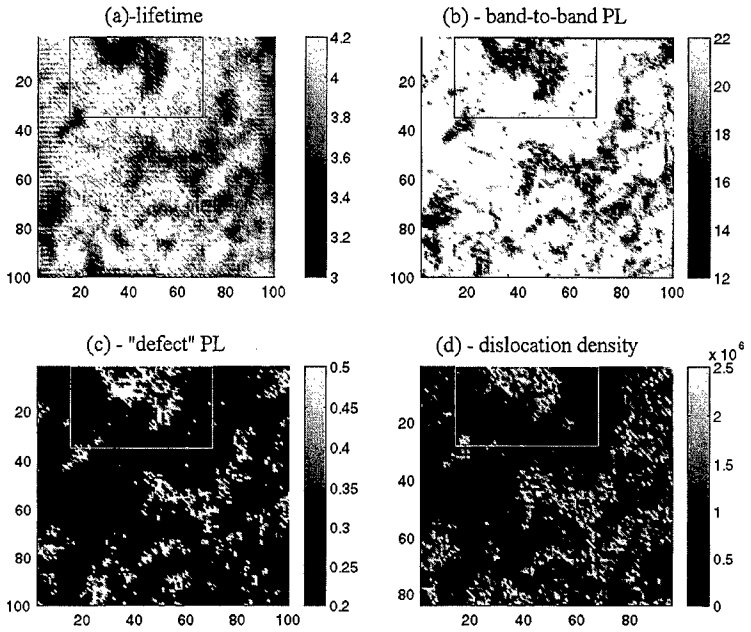

Fig. 2. (a) minority carrier lifetime (μs), (b) band-to-band PL, (c) "defect" PL, and (d) dislocation density (cm^{-2}). All mappings were performed at the same mc-Si wafer.

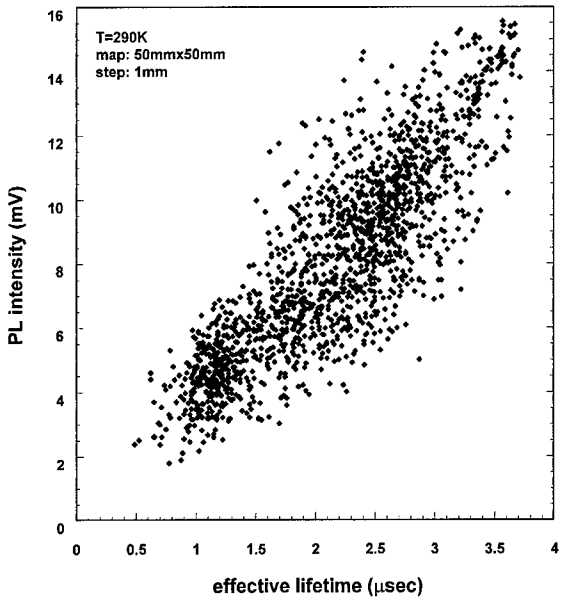

Fig. 3. Band-to-band PL intensity positively correlates to minority carrier lifetime.

To assess a possible origin of the "defect" luminescence, we measured PL spectra at low temperatures down to 4.2 K and compared the areas with different recombination activity. The PL spectrum at 77 K of a "bad region" in mc-Si wafer is depicted in Fig. 1b (thick line). The band-to-band luminescence is shifted to 1.1 eV due to temperature increasing of silicon band gap. Additionally, rich spectral features are now observed at energies below 1.05 eV. Two well-resolved bands have maxima at 0.95 and 1.00 eV correspondingly. At lower energies, the PL spectrum shows the maximum at 0.80 eV with barely resolved extra band as a shoulder. By increasing temperature up to 290 K we proved that the maximum at 0.8 eV is shifted toward lower energies and traceable to the previously described "defect" PL band. The PL spectroscopy was extended down to 4.2 K. At this temperature band-to-band emission is substituted with sharp excitonic lines dominated by the TO-phonon replica of the boron bound exciton at 1.093 eV. Aside from the total increase in PL intensity between 77 and 4.2 K, essentially no qualitative changes were observed in the PL spectrum below 1.05 eV. For this reason we limited our analyses with 77 K PL spectroscopy. We performed a numeric deconvolution of the 77 K PL spectrum in the range of 0.72–1.05 eV, and found that it can be satisfactorily decomposed by *four* individual Gaussian bands depicted by thin lines in Fig. 1b. It is remarkable that a set of *four* PL lines, known as D1–D4, with very close energies (see Table 1) was previously observed and studied in detail in plastically deformed Cz-Si and attributed to the dislocation network [2,3]. It is worth noting that the range of dislocation density measured by EPD technique in "bad regions" of mc-Si,

Table 1
Energies of dislocation PL-lines in Cz-Si [2,3] and D′-bands in mc-Si

	D1	D2	D3	D4
Cz-Si	0.812	0.875	0.934	1.000
	D1′	D2′	D3′	D4′
mc-Si	0.80	0.89	0.95	1.00

(1–8)E + 6 cm^{-2}, is close to that in plastically deformed Si exhibiting dislocation D-lines. Due to this similarity, we assigned the individual bands in mc-Si as D1′–D4′ in the same sequence as dislocation D1–D4 lines.

To challenge the dislocation origin of the D′-lines we measured the PL spectrum at 77 K under identical excitation in Cz-Si wafer with dislocations introduced by a laser annealing technique [4]. After laser annealing of Si wafer, four dislocation lines D1–D4 were clearly observed with maximum positions close to D′ bands (see the Table 1). It is important to note that a half-width of the D3′/D4′ lines in mc-Si (~ 30 meV) is close to the half-width of the D3/D4 in laser annealed Cz-Si. On the contrary, the D1′ and D2′ lines in mc-Si have an enlarged half-width by a factor of 2.5 compared to D1 and D2 lines in Cz-Si. Summarizing, a principal difference between D′-lines in mc-Si versus dislocation D-lines in Cz-Si is a substantial broadening (60–70 meV at 77 K) of the D1′/D2′ lines, which accompanied by a different T-quenching of the D1′-line tracing to the intense room-temperature "defect" luminescence. Therefore, low-temperature PL spectroscopy additionally confirmed a linkage of the "defect" luminescence in mc-Si to dislocations.

4. Discussion

It is recognized that recombination-active dislocations in solar-grade mc-Si are a limiting factor to high efficiency solar cells. In this regard, presented experimental data of the room-temperature PL mapping are consistent with the dislocation origin of "bad regions" in mc-Si wafers. Further, we can suggest that the "defect" 0.8 eV PL band in these regions originates from D1/D2 dislocation lines previously studied in plastically deformed Cz-Si. A unique feature of these PL lines in mc-Si is that they are observed as a broad PL band retaining at room temperature contrary to the fact of a fast D1/D2 quenching in Cz-Si [3]. This difference can be addressed to (i) a strain field, which modifies recombination parameters of relevant centers, or/and (ii) interaction of dislocations with contamination. Specifically, it was observed that oxygen precipitates in Cz-Si influence a spectral position, half-width and intensity of the D1 line presumably due to a relaxation of the dislocation strain field [5]. This is consistent with the room-temperature PL study of the 0.77 eV band attributed to oxygen precipitates in thermally treated Cz-Si [6]. Another possibility of D-line modification in mc-Si is an interaction of dislocations with heavy metal precipitates. A direct correlation has been recently observed between regions of high minority carrier recombination and Fe, Cr, and Ni precipitates [7]. Together these data imply that conventional hydrogenation employed to passivate recombination centers during solar cell processing may not be sufficient to eliminate a detrimental effect on carrier lifetime of oxygen or heavy metal precipitates at grain boundaries and dislocations.

In conclusion, scanning room-temperature PL was applied to solar-grade mc-Si providing a deeper insight and advanced diagnostics of the "bad regions" in solar cells. Band-to-band PL intensity is distributed similar to minority carrier lifetime and offers a reliable feedback to the bulk carrier recombination. A new advance to the scanning PL method is a mapping of the "defect" band. In wafer regions with low lifetime we observed a strong deep luminescence with the maximum at about 0.8 eV attributed to dislocation D1/D2 lines in silicon. We can postulate that improved passivation of the modified dislocations may be a passage way to high-efficiency mc-Si solar cells.

Acknowledgements

This work was supported by NREL grant XD-2-11004-5 and NSF cooperative research program INT-9725215.

References

[1] Y. Koshka, S. Ostapenko, I. Tarasov, S. McHugo, J.P. Kalejs, Appl. Phys. Lett. 74 (1999) 1555.
[2] N.A. Drozdov, A.A. Patrin, V.D. Tkachev, JETP Lett. 23 (1976) 598.
[3] R. Sauer, J. Weber, J. Stolz, E.R. Weber, K.-H. Kusters, H. Alexander, Appl. Phys. A 36 (1985) 1.
[4] W. Staiger, G. Pfeiffer, K. Weronek, A. Hopner, J. Weber, Mater. Sci. Forum 83–87 (1994) 1571.
[5] M. Bugajski, M. Goorsky, J. Lagowski, Electron. Technol. 24 (1991) 85.
[6] M. Tajima, M. Tokita, M. Warashina, Mater. Sci. Forum 196–201 (1995) 1749.
[7] S.A. McHugo, A.C. Thompson, I. Perichaud, S. Martinuzzi, Appl. Phys. Lett. 72 (1998) 3482.

ELSEVIER

Physica B 273–274 (1999) 553–556

PHYSICA B

www.elsevier.com/locate/physb

Effects of nitrogen on dislocations in silicon during heat treatment

Dongsheng Li, Deren Yang*, Duanlin Que

State Key Laboratory of Silicon Material Science, Zhejiang University, Hangzhou 310027, People's Republic of China

Abstract

By indentation at room temperature followed by annealing at high temperatures, the pinning effect of nitrogen on dislocations in nitrogen-doped Czochralski silicon (NCZ Silicon) has been studied. Experimental results showed that dislocations in NCZ Silicon moved slower and shorter than those in common Czochralski silicon (CZ Silicon) during the annealing. The results also indicated that the activation energy of the dislocations in NCZ Silicon was higher than that in CZ Silicon. The stress relaxing mechanism is discussed.

Keywords: Dislocation; Nitrogen; Silicon

1. Introduction

With the narrowing of the design rules of ULSI devices and the increasing of wafer diameter, maintaining the mechanical strength of silicon wafers becomes one of the most important factors in device fabrication processes. Various techniques such as compression [1], tensile testing [2–6], bending [7,8], and high-temperature indentation testing [9–13] have been used to investigate the mechanical strength of silicon wafers. Experimental results showed that the impurities in silicon wafers, such as oxygen and boron, reinforce the strength of the wafers [9–12]. It has been believed that the impurities can pin dislocations so as to increase the silicon wafer strength. The interaction of oxygen and dislocations has been discussed in the past few years [3–6].

Nitrogen is also an important impurity in silicon because it has many interesting behaviors, such as suppressing microdefects. Sumino et al. [2] found by means of tensile tests at high temperatures that the yield strength of nitrogen-doped float zone (FZ) silicon was much higher than that of common FZ silicon. They concluded that interstitial nitrogen atoms brought about the hardening of silicon crystal through locking dislocations. Jastrzebski et al. [15] pointed out the effect of nitrogen on the mechanical properties of FZ silicon wafers used for CCD devices. They indicated that not only the nitrogen concentration but also the state of the nitrogen were the critical factors that controlled silicon properties. However, there are few reports on the effect of nitrogen on dislocations in Czochralski silicon.

In this paper, we have investigated the pinning effect of nitrogen on dislocations in NCZ silicon by indention tests at room temperature and then annealing at high temperatures.

2. Experiment

Samples were 76 mm in diameter, n-type (phosphorus-doped, 10–12 Ω cm), ⟨1 1 1⟩ orientation NCZ silicon wafers grown in a nitrogen protective gas, or common CZ silicon wafers grown in an argon gas. The initial concentrations of the impurities in the samples (see Table 1) were detected by a Fourier transmission infrared spectrometer (FTIR). The thickness of the polished wafers was approximately 410 μm. Then the wafers were divided into 12 × 24 mm pieces and indented at 5 points with a load of 500 g for 15 s using a Vicker hardness tester at room temperature. These indented samples were annealed at 850°C, 900°C, 950°C, 1000°C, 1100°C and

* Corresponding author. Tel.: + 86-571-7951667; fax: + 86-571-7951954.

E-mail address: mseyang@dial.zju.edu.cn (D. Yang)

0921-4526/99/$ - see front matter
PII: S0921-4526(99)00571-2

Table 1
The concentration of impurities in silicon

Samples	O_i (cm^{-3})	C_s (cm^{-3})	N_p (cm^{-3})
NCZ silicon	1.4×10^{18}	$<1\times10^{15}$	2.0×10^{14}
CZ silicon	1.4×10^{18}	$<1\times10^{15}$	—

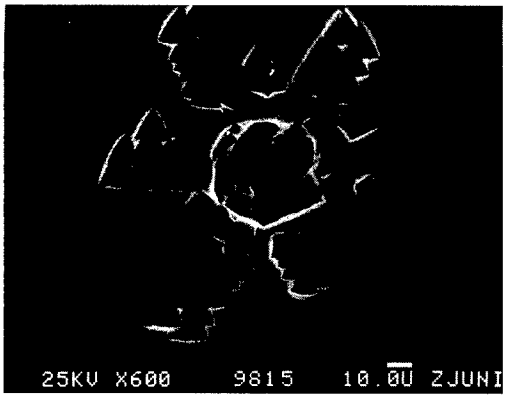

Fig. 1. Rosette patterns of dislocation in silicon.

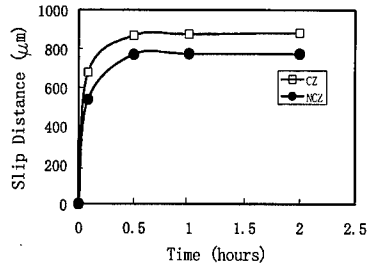

Fig. 2. The moving distance of dislocations in silicon annealed at 1200°C.

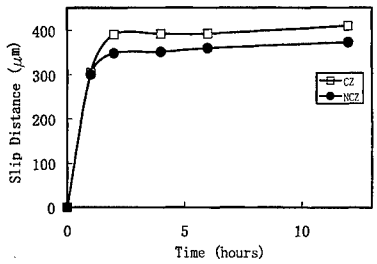

Fig. 3. The moving distance of dislocation in silicon annealed at 950°C.

1200°C up to 12 h in an argon ambient and cooled quickly in air. After the heat treatments, punched-out dislocations from the indentation points were revealed with Sirtl etching and were observed with an optical microscope and a scanning electron microscope. Fig. 1 shows the rosettes pattern observed with a scanning electron microscope. The moving length of punched-out dislocations was calculated by averaging the length over all orientations.

3. Results and discussion

Figs. 2 and 3 show the slip distance of dislocations in NCZ silicon and in common CZ silicon annealed at 950°C and 1200°C, respectively. With increasing annealing time, the slip distance of dislocations in NCZ silicon increased in the initial stage and then remained unchanged after annealing at 950°C for 2 h or at 1200°C for 0.5 h. The maximum slip distance of dislocations was about 371 and 774 μm in NCZ silicon when samples were annealed at 950°C and 1200°C, respectively. A similar in tendency slip distance of dislocations was observed in CZ silicon. But the maximum value was 409 μm for 950°C annealing and 882 μm for 1200°C annealing. All these indicated that dislocations in NCZ silicon moved slower than that in common CZ silicon under the same annealing conditions.

The experiments pointed out that the nitrogen atoms did lock dislocations efficiently in NCZ silicon during the annealing processes at high temperatures. This may be due to the following reasons: (1) Because of effect of nitrogen impurities in enhancing the formation of oxygen precipitate nuclei [14], there may be a high density of small N–O complexes which could be responsible for reducing the velocity of dislocations. But it remains to be explored which one of the states of nitrogen pins the dislocations most efficiently. (2) The nitrogen segregated along the dislocations and developed into clusters or complexes. The segregated atoms, clusters or complexes could have a high interaction energy with the dislocation [2]. Therefore, dislocations in NCZ silicon moved more slowly than in CZ silicon. It was seen that the moving distance of dislocations in NCZ silicon was shorter than that in common CZ silicon. (3) The activation energy for dislocation motion in NCZ silicon was higher than that in common CZ silicon. Fig. 4 shows the relation of the slip velocity of dislocations with temperatures. This indicates that the slip velocity of dislocations in NCZ silicon was smaller than that in common CZ silicon. The velocity of dislocations can be expressed as follows

$$V = A\exp(-E/kT), \tag{1}$$

where A is a constant. Thus the activation energy for dislocation slip was obtained from Eq. (1), and was found

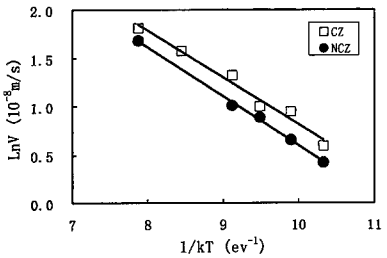

Fig. 4. The relation of the activation energy for dislocation slip and the slip velocity of dislocation in silicon after 2-h annealing.

to be 0.51 eV in NCZ silicon, and 0.48 eV in common CZ silicon, respectively. This indicates that the dislocations in CZ silicon were easier to move than in NCZ silicon. Sumino [15] has indicated that the velocity of dislocations is a function of stress (τ) and temperature (T) and can be expressed as

$$V = V_0 \tau \exp(-E/kT), \tag{2}$$

where V, V_0, τ, E, K, and T are the velocity of dislocations, constant, stress, the activation energy for dislocation slip, the Boltzman constant and temperature, respectively. But in our experiments it appeared that the average stress during annealing at different temperatures was almost the same.

With annealing time the rosette pattern size increased rapidly in the initial stage and then remained almost unchanged (see Figs. 2 and 3). The rosettes pattern size in 1200°C treated samples was much larger than that in 950°C treated samples. But in the samples annealed at 950°C the rosettes pattern size increased with annealing time until 2 h, while it did not change after annealing for 30 min in the samples annealed at 1200°C. This may be explained by the fact that the stress abd energy produced during indentation were relaxed by slip of dislocations. It was considered that if the stress and the energy were smaller than the critical value that equated with the total amount of the Peierls barrier and interactive force and energy between dislocations, the dislocations would not be able to move. With increasing annealing time the stress decreased rapidly in the initial stage by relaxing, and then was lower than the critical value. So the rosettes pattern size increased rapidly in the initial stage and the remained almost unchanged. And because the deformation in both kinds of silicon was the same, the plastic energy produced during indentation was also the same. However, due to the barrier at high temperature becoming lower, dislocations were easier to move. Thus the slip velocity of dislocations at high temperature was faster than that at lower temperature. At higher temperature the energy was released much more quickly than at lower temperature. Therefore, dislocations stopped moving early at high temperatures. It was suggested that the stress produced during indentation was released by dislocation moving and the residual stress could be expressed as the following equation:

$$\tau = ct^{-m(T)}, \tag{3}$$

where c is a constant concerned with the initial stress produced in the indentation, t is the annealing time and T the temperature, respectively. m increased with annealing temperature.

Since nitrogen atoms could efficiently lock dislocations, there still exists the question of why the dislocations stopped moving at the same time in both kinds of silicon under the same conditions. The reason may be ascribed to the stress relaxing mechanism. Because dislocations were driven by stress that was produced during indentation process, their movement was dependent on the stress field and the magnitude of residual stress. However, the stress field in both kinds of silicon was the same. And as mentioned above in Eq. (3), the relaxation of the residual stress was related to the annealing time and temperature. Thus at the same annealing temperature, the dislocations stopped moving at the same time in both kinds of silicon.

4. Conclusion

By indentation at room temperature and annealing at high temperatures the pinning effect of nitrogen on dislocations and the relaxing mechanism of the stress produced during indentation process were discussed. It is concluded that (1) The nitrogen atoms in silicon did pin the dislocations efficiently. (2) The stress was relaxed exponentially and the exponent increased with the temperature. It also indicated that the activation energy of dislocations in NCZ silicon was higher than that in CZ silicon.

Acknowledgements

The authors would like to appreciate the financial support of the Research fund for the Doctoral Program of High Education (RFDP) and the Chinese Excellent Younger Teacher Fund.

References

[1] K. Yasutake, M. Umeno, H. Kawabe, Appl. Phys. Lett. 37 (1980) 789.
[2] I. Yonenaga, K. Sumino, J. Appl. Phys. 56 (1984) 2346.
[3] K. Sumino, H. Harada, Philos. Mag. A 44 (1981) 1319.
[4] T. Fukuda, A. Ohsawa, J. Appl. Phys. 73 (1993) 112.
[5] T. Fukuda, M. Akatsuda, J. Appl. Phys. 74 (1993) 2420.

[6] K. Sumino, I. Yonenaga, M. Imai, J. Appl. Phys. 54 (1983) 5016.
[7] T. Fukuda, Jpn. J. Appl. Phys. 35 (1996) 3799.
[8] T. Fukuda, Jpn. J. Appl. Phys. 34 (1995) 3209.
[9] S.M. Hu, J. Appl. Phys. 46 (1975) 1470.
[10] S.M. Hu, Appl. Phys. Lett. 31 (1977) 53.
[11] M. Akatsuka, K. Sueoka, H. Katahama etc., Jpn. J. Appl. Phys. 36 (1997) L1422.
[12] M.J. Hill, D.J. Rowcliffe, J. Mater. Sci. 9 (1974) 1569.
[13] T. Fukuda, A. Ohsawa, Appl. Phys. Lett. 60 (1992) 1184.
[14] L. Jastrzebski, G.W. Cullen, R. Soydon etc., J. Electchem. Soc. 134 (1987) 466.
[15] K. Sumino, in: H.R. Huff, et al., (Eds.), Semiconductor Silicon 1981: Part II, Electrochem Soc, Pennington, NJ, 1981, pp. 208–219.

ELSEVIER

Physica B 273–274 (1999) 557–560

PHYSICA B

www.elsevier.com/locate/physb

Infrared vibrational mode absorption from thermal donors in germanium

P. Clauws*, P. Vanmeerbeek

Department of Solid State Sciences, Universiteit Gent, Krijgslaan 281-S1, B-9000 Gent, Belgium

Abstract

The infrared vibrational absorption attributed to thermal donors (TDs) in Ge has been investigated. Oxygen-doped Ge was annealed at 350°C and the spectrum was recorded after different annealing times. Absorption bands develop mainly around 600 and 780 cm^{-1}, in close correspondence with the increasing TD concentration and the loss of interstitial oxygen (O_i). At low temperature the bands are resolved into a number of components which appear sequentially and are assigned to the double donor configuration of TD2–TD9. The assignments are confirmed by the bistable properties of TD2–TD4 revealed in the vibrational spectrum. The low-energy configuration gives rise to three new bands in the same range. The absorption is interpreted as due to vibrational modes of oxygen incorporated in the TDs. The number of oxygen atoms involved is discussed taking account of the evolution of the O_i and TD concentrations and of the integrated absorption.

Keywords: Germanium; Thermal donors; Vibrational modes; Bistability

1. Introduction

Thermal annealing of oxygen-doped Ge in the 300–500°C temperature range results in the formation of oxygen-related thermal donors (TDs) at the expense of interstitial oxygen (O_i) [1,2]. As is the case for Si, the TDs in Ge are double donors with an effective mass-like level spectrum and a hierarchy of ground states [3–5]. The sequential formation of the TDn has led to the assumption that also in Ge the TDs are formed by agglomeration of oxygen species. The earliest members TD1–TD3 were found to display bistability between the shallow double donor configuration and a low-energy configuration, the latter remaining spectroscopically unobserved [6–8]. Kaiser [2] was the first to report a small infrared (IR) absorption band at 785 cm^{-1}, developing along with the TD formation; it was attributed to vibration of GeO_4. Similar observations were reported by Whan [9]. More recently, Clauws [5] reported two features in the IR spectrum of oxygen-doped Ge, the first one corresponding with the band found by Kaiser, the second one occurring at about 600 cm^{-1}. The similar behaviour of the two bands suggested that both belong to vibrational modes of the TDs. It is interesting to note that in Si also the TDs give rise to two groups of IR vibrational bands [10]; in Si the bands assigned to TD1 and TD2 display bistability [11].

In this paper we summarise the results of a more systematic investigation of the vibrational absorption attributed to the TDs in Ge. The line narrowing at low temperature makes it possible to resolve the TD-related bands into components belonging to different TDn and to follow their evolution upon thermal treatment. The assignment of the components is substantiated by comparing with far-IR electronic transition spectra and by the observation of bistable behaviour in the vibrational spectra.

2. Experimental

In this study oxygen doped Ge with $[O_i] = 3.0 \times 10^{17}$ cm^{-3} and with shallow dopant concentration below

* Corresponding author. Tel.: + 32-9-264-43-65; fax: + 32-9-264-49-96.

E-mail address: paul.clauws@rug.ac.be (P. Clauws)

0921-4526/99/$ - see front matter
PII: S0921-4526(99)00572-4

10^{13} cm^{-3} was used. Similar material is always n-type in the as-grown state ($n \approx 10^{16}$ cm^{-3}) as a result of uncontrolled TD formation during cooling of the crystal. Before annealing the samples are therefore submitted to a 5 min dispersion at 900°C followed by a quench to room temperature (RT). The samples were annealed in flowing Ar at 350°C; at this temperature a high degree of O_i to TD conversion may be achieved within a reasonable time [1]. The IR spectra were recorded with a Bruker IFS66v FT-IR instrument. The O_i concentration was determined from the amplitude of the 855 cm^{-1} band at RT using the conversion factor of Kaiser [2,12]:

$$[O_i] = \alpha_{max} \times (5 \times 10^{16})\ \text{cm}^{-2} \quad (1)$$

with α_{max} the amplitude in cm^{-1}. The TD vibrational spectra were recorded at RT, 80 and 6 K using a nominal resolution of 1 cm^{-1}. The electron concentration n was monitored by resistivity and Hall-effect measurements at RT.

3. Experimental results

The evolution of the RT spectrum during a 350°C annealing sequence is summarised in Fig. 1. As the anneal proceeds, two bands develop around 780 and 600 cm^{-1}, which gradually shift to higher average wave number. The bands (designated as "780" and "600") correspond with the earlier reported features [5]. A third and weaker band not earlier observed is seen to appear at about 740 cm^{-1} ("740"). The development of the absorption is accompanied with a similar increase of the electron concentration and a continuous decrease of $[O_i]$ (e.g. after 31 h at 350°C, $[O_i]$ has dropped to about one-fourth of the initial value). The correspondence in the evolution of the TD concentration (N_{TD} may be taken equal to $n/2$ regarding the double-donor nature) with that of the integrated absorption of the bands, supports the interpretation that the absorption is due to the TDs. The wave number range of the absorption and the oxygen loss agree with the assumption of local vibrational mode (LVM) absorption of oxygen species incorporated in the TD centres. Supposed the oxygen agglomeration influences the spectral position, the shift in average wave number of the bands would reflect the increasing average n-number of TDn members present, the components belonging to different TDn being probably too broad with respect to their separation in order to be resolved at RT.

In the spectra taken at low temperature, structure is revealed in the "780" and "600" bands (Fig. 2). The observations confirm that the bands are indeed composed of different lines becoming narrower with decreasing temperature. Lines on the low wave number side appear first in the annealing sequence while lines at higher wave numbers are gradually added as the anneal proceeds. It was possible to certify the occurrence of eight different components in the "600" band, the positions (6 K) of which are given in Table 1. Long annealing results in an almost structureless band with maximum at 619 cm^{-1} at 6 K (to be compared with 612 cm^{-1} at RT). Only 3–4 components can undoubtedly be resolved in the "780" band (Table 1); long annealing eventually yields one band with maximum at 788 cm^{-1} at 6 K

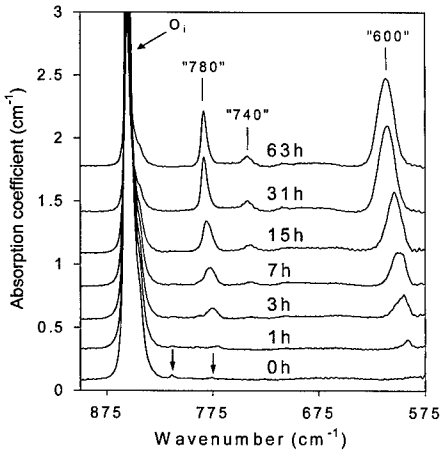

Fig. 1. Infrared absorption spectrum at room temperature of oxygen doped Ge annealed at 350°C. $[O_i]$ before anneal $= 3.0 \times 10^{17}$ cm^{-3}. The annealing time in hours is indicated with the graphs. The spectra are vertically shifted, lattice and free carrier absorption have been subtracted. The indicated features are explained in the text.

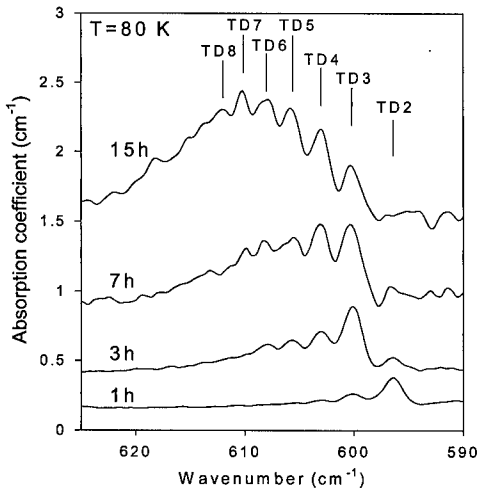

Fig. 2. Sequential appearance of TDn components in the "600" band measured at 80 K (cooling with illumination), after different annealing times at 350°C.

Table 1
Wavenumber position (cm^{-1}) at 6 K and assignment of resolved vibrational absorption bands belonging to TDs in Ge. DD: shallow double donor configuration. N: low-energy neutral configuration

	TD2	TD3	TD4	TD5	TD6	TD7	TD8	TD9
DD	597.0	600.6	603.5	606.1	608.5	610.6	612.5	(614.3)
	774.5	777.6	780.7	(782.7)				
N	583.5	587.4	590.4					
	712.9	706	706					
	791.9	790.5	790.5					

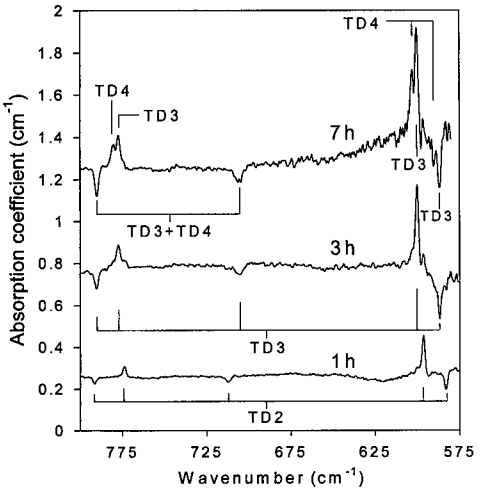

Fig. 3. Difference spectra ($T = 80$ K) showing bistability of TD2–TD4, after different annealing times. The positive features correspond with modes of the shallow double-donor configuration, the negative features are due to modes of the low-energy configuration.

(783 cm^{-1} at RT). No structure could be resolved in the weak "740" band; at 6 K the position after long annealing is 746 cm^{-1} (742 at RT).

The spectra in Fig. 2 were recorded after the sample was cooled under intense above band gap illumination, a procedure assumed to result in the conversion of virtually all TD centres into the shallow double donor configuration. A second series of spectra was taken after cooling in the dark. Important differences are observed in the amplitude of components at the low wave number side of the "780" and "600" bands, which as will be shown below is an effect of full or partial bistability of TD2–TD4. This may best be illustrated using difference spectra (the spectrum with illumination during cooling minus the spectrum with cooling in the dark) as in Fig. 3, corresponding with the first three anneals in the sequence. The effect of bistability is that "780" and "600" modes (positive lines) are replaced by new modes at 583–590, 712–706 and 790–792 cm^{-1} (negative lines). Obviously, three different TDn members are involved in the spectra shown.

4. Discussion

It seems obvious that we are dealing with vibrational absorption from the TDs in Ge. The integrated absorption of the "780" and "600" bands is almost independent of temperature between RT and 6 K (if cooled under illumination). We also observe a normal shift of the bands and their components towards higher wave number with decreasing temperature (4–7 cm^{-1}). The sequential appearance of the components in the "780" and "600" band suggests that each component belongs to a different TDn member. This is substantiated by the bistability of different components as seen in Fig. 3 and was confirmed by far-IR reference measurements. In the as-quenched sample $N_{TD} = 1.6 \times 10^{14}$ cm^{-3} and the far-IR electronic transition spectrum shows that this is mainly due to the presence of TD1, probably formed during the quench. No corresponding absorption fitting into the "780" and "600" sequence is, however, observed, probably because the TD1 concentration is too low. After 1 h of annealing N_{TD} has increased to 2.4×10^{15} cm^{-3} and the far-IR spectrum reveals that TD2 is predominant and displays 100% bistability, while the TD1 concentration remains very low. Comparison with Fig. 2 learns that in this sample the first component in the vibrational sequence is predominant and Fig. 3 confirms that this component displays full bistability, allowing to identify the corresponding modes with TD2. The other modes in the sequence are then labelled accordingly (Table 1). One difference with our earlier investigations is that TDs in Ge are now found to display bistable behaviour up to TD4 at least. This is an illustration of the advantage of vibrational spectroscopy to study Ge samples with high TD concentration, when electronic excitation spectroscopy suffers from line broadening. We conclude that the shallow double-donor configuration of TDs in Ge gives rise to three infrared active modes ("780", "600" and

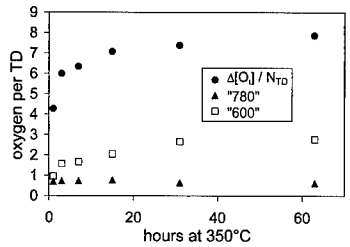

Fig. 4. Number of oxygen atoms in the TDs as a function of annealing, calculated from the disappeared O_i and the "780" and "600" bands.

probably also "740"). The low-energy configuration gives rise to three modes at wave numbers different from the former but in a comparable range. It may be remarked that this represents the first direct observation of the latter TD configuration in Ge. The lowest wave number mode of the deep configuration displays a sequence with distinctly different lines, while for the high wave number mode only a gradual shift to lower position appears.

In the assumption that all O_i which disappears during annealing goes into the TD centres, the number of oxygens per TD may be calculated from $\Delta[O_i]/N_{TD}$ with $\Delta[O_i]$ the O_i concentration lost. The result is displayed in Fig. 4 and obviously corresponds with an average over the TDn present in each particular situation. Decomposition of the "600" band for the shortest anneals (lower spectra in Fig. 3) indicates that the results seem to agree best with TD2 containing four oxygens. The average of eight after long anneals is in agreement with Ref. [1] (where the final donor, however, was identified as GeO_4 assuming single donors). Using the same conversion factor as for the integrated absorption of the O_i band (derived from formula (1)), the integrated absorption of the "780" and "600" bands may be used to estimate the number of oxygen oscillators per TD involved in the corresponding mode. The results are also shown in Fig. 4. The almost constant value yielded by the "780" band seems to indicate that only one oxygen is involved in the mode, while the "600" band follows the trend of the total oxygen per TD. An interpretation as the "780" band representing the TD core and the "600" band the clustered oxygen is tempting but seems premature. The results above depend on the accuracy of the conversion factor in formula (1); e.g. the other factor published in Ref. [13] would multiply the data in Fig. 2 by 2.5, yielding, however, rather high values for the early TD.

A final remark concerns the identification of TD1 which according to Chadi [14] may contain only two oxygen atoms; the vibrational spectrum attributed to the oxygen dimer in Si [15] may be interesting in this context. Application of a scaling factor of 1107/855 to relate O-vibrations in Si and Ge predicts the position of the "780" band very well from the $\approx 1000\ cm^{-1}$ position in Si. If we do the same for the dimer modes at 1060 and $1012\ cm^{-1}$ in Si, we obtain values of 819 and $782\ cm^{-1}$ for Ge. The latter values agree with peaks found by Whan [9] in irradiated oxygen doped Ge (819 and $780\ cm^{-1}$), which we also find in our samples after a dispersion quench. These are the weak features at 813.7 and $776.5\ cm^{-1}$ (RT values) indicated by arrows in Fig. 1. At least the correspondence of the $813.7\ cm^{-1}$ peak with the $819\ cm^{-1}$ peak of Ref. [5] is well established and assignment of this peak to TD1 would be in agreement with the integrated absorption at a concentration $\approx 10^{14}\ cm^{-3}$. This will be further investigated.

References

[1] C.S. Fuller, W. Kaiser, C.D. Thurmond, J. Phys. Chem. Solids 17 (1961) 301.
[2] W. Kaiser, J. Phys. Chem. Solids 23 (1962) 255.
[3] P. Clauws, J. Vennik, Phys. Rev. B 30 (1984) 4837.
[4] P. Clauws, J. Vennik, Mater. Sci. Forum 10–12 (1986) 941.
[5] P. Clauws, Mater. Sci. Eng. B 36 (1996) 213.
[6] V.V. Litvinov, G.V. Palchik, V.I. Urenev, Phys. Stat. Sol. A 108 (1988) 311.
[7] P. Clauws, J. Vennik, Mater. Sci. Forum 65 (1990) 339.
[8] P. Clauws, F. Callens, F. Maes, J. Vennik, E. Boesman, Phys. Rev. B 44 (1991) 3665.
[9] R.E. Whan, Phys. Rev. 140 (1965) A690.
[10] T. Hallberg, J.L. Lindström, J. Appl. Phys. 79 (1996) 7570.
[11] T. Hallberg, J.L. Lindström, Appl. Phys. Lett. 68 (1996) 3458.
[12] W. Kaiser, C.D. Thurmond, J. Appl. Phys. 32 (1961) 115.
[13] E.J. Millett, L.S. Wood, G. Bew, Brit. J. Appl. Phys. 16 (1965) 1593.
[14] J. Chadi, Phys. Rev. Lett. 77 (1996) 861.
[15] S. Öberg, C.P. Ewels, R. Jones, T. Hallberg, J.L. Lindström, L.I. Murin, P.R. Briddon, Phys. Rev. Lett. 81 (1998) 2930.

ELSEVIER

Physica B 273–274 (1999) 561–564

PHYSICA B

www.elsevier.com/locate/physb

Low-temperature spreading-resistance profiling for the characterization of impurity distributions in germanium

S. Voss*, H. Bracht, N.A. Stolwijk

Institut für Metallforschung, University of Münster, Wilhelm-Klemm-Strasse 10, D-48149 Münster, Germany

Abstract

We have designed and constructed a novel device to perform low-temperature spreading-resistance profiling (LTSRP) of electrically active impurities or defects in semiconductors. Unlike commercial SRP systems which are exclusively operated at room temperature, the present device allows for measurements in a temperature range typically from 150 to 300 K. The practical potential of the LTSRP concept is demonstrated — to the authors' knowledge for the first time — by the analysis of Ge samples diffused with Cu or Au. As a major feature, LTSRP combines the accurate resolution of an impurity profile with a determination of the dominating energy level associated with the impurity.

Keywords: Spreading resistance; Copper; Gold; Germanium

1. Introduction

Spreading-resistance profiling (SRP) [1,2] at room temperature is a powerful tool for measuring depth distributions of electrically active impurities in silicon [3,4]. A high spatial resolution of the resistivity is obtained by means of two-point probes at a mutual separation of typically 100 μm stepping across a specially prepared (bevel) plane of the sample. However, for Ge (or GeSi alloys with high Ge content) the method suffers from a limited dynamic range due to a relatively low intrinsic resistivity, i.e. a relatively high intrinsic carrier concentration, at room temperature. This drawback can be overcome by performing SRP measurements at lower temperatures (typically between 150 and 200 K).

The underlying physical concept makes allowance for the fact that the intrinsic carrier concentration n_i, the concentration of ionized impurities C_{ion}, and the mobility of the charge carriers change with temperature, but to dissimilar extents. More specifically, the mobility increases with decreasing temperature whereas n_i and C_{ion} decrease. The effect of temperature on the ratio C_{ion}/n_i depends on the position of the impurity energy level within the semiconductor band gap. Consequently, in Ge and GeSi alloys the detection limit of electrically active impurities is lowered and the resolution of the corresponding resistivity-depth profiles may be significantly improved. Furthermore, information about the energy levels of the impurity can be deduced from the temperature dependence of the measured resistivity.

In this work we will present the first results of low-temperature spreading-resistance profiles obtained with a self-designed device. The potential applications of LTSRP will be demonstrated on Ge samples diffused with Cu or Au. These impurities are suitable for our investigations since their diffusion behaviour [5,6] and their electrical properties in Ge [7,8] are well known. Cu and Au are incorporated predominantly on substitutional sites and introduce three acceptor states. In addition, Au also generates a deep donor state. For either impurity the dominating energy level is the first acceptor state (0/ −) above the valence band edge (E_V), i.e. E_V +

* Corresponding author. Tel.: + 49-251-83-39011; fax: + 49-251-83-38346.

E-mail address: vosst@nwz.uni-muenster.de (S. Voss)

0921-4526/99/$ - see front matter
PII: S0921-4526(99)00573-6

0.04 eV for Cu [7] and $E_V + 0.15$ eV for Au [8]. This offers the possibility to look for different influences on the measurements for impurities that change their charge state significantly (Au) or not (Cu) when the specimen is cooled.

2. Experimental

2.1. Device construction

To perform SRP-measurements below room temperature a self-designed SRP device was constructed. Core of the device is a vacuum chamber enclosing the two-point probes and the sample holder placed on a platform. This platform can be translated in all three space directions and rotated in the x–y plane (parallel to the measuring plane of the sample) by stepper motors. Cooling is mediated by thermal conduction to nitrogen at cryogenic temperature. A pipeline connected with a liquid-nitrogen reservoir enters the vacuum chamber and splits into three smaller pipes supplying either measuring probe and the sample holder. Temperature is measured with semiconductor sensors at each cold part and controlled by mutually adjusting the nitrogen flux and the resistance-wire counterheating. Thin plates of mica electrically isolate the probes and the sample holder from the cooling facilities. Positioning of probes and sample holder as well as data acquisition and storage are controlled by a computer.

2.2. Data analysis

The measured spreading-resistance values R_S are converted into electrical resistivities ρ with the aid of a calibration curve. A calibration is necessary since both the unknown contact resistances between the probe tips and the sample surface and the irregularly shaped contact areas of typically 5 μm in diameter do not allow for a direct calculation of ρ from R_S. Calibration measurements were done on homogeneously doped samples with known electrical resistivities ρ. Since the impurities investigated introduce acceptor states within the Ge band gap we produced p-type calibration samples by indiffusion of Cu into undoped material. Temperatures and times of diffusion anneals were chosen so that homogeneous distributions of Cu of different concentrations were achieved. Fig. 1 shows calibration data for room temperature (293 ± 1 K) and 180 K. The relation between R_S and ρ is well described by the equation

$$R_S = A\left(\frac{\rho}{\Omega\ \mathrm{cm}}\right)^B, \tag{1}$$

and represented by the fitted straight lines in Fig. 1. Here we obtain $A = 594.5\ \Omega$, $B = 0.8166$ for room temperature and $A = 860.1\ \Omega$, $B = 1.0216$ for 180 K, which may be considered as typical values for Ge. It should be emphasized, however, that the calibration parameters A and B are specifically determined in every profiling cycle for any individual measuring temperature.

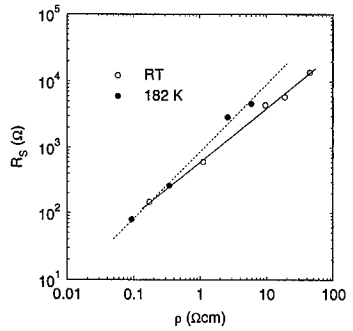

Fig. 1. Spreading-resistance R_S of the calibration samples versus resistivity ρ for different temperatures. The solid and dashed line represent best fits of Eq. (1).

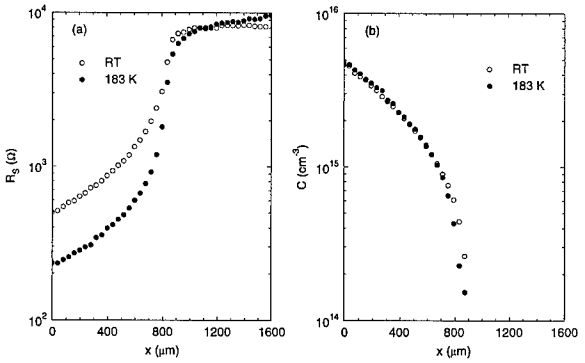

Fig. 2. Spreading-resistance profiles (a) at room temperature and 183 K of a Cu-diffused (706°C, 23 min) sample. The coincidence of the concentration profiles (b) demonstrates the consistency of our analysis.

The calculation of concentrations from resistivities is based on a numerical solution of the charge neutrality equation which contains the concentrations of the various charge states of the impurity depending on the position of the Fermi level E_F. To take into account the influence of phonon and impurity scattering of charge carriers we have parameterized the hole mobility data of Golikova et al. [9]. This enables us to interpolate for ionized impurity concentrations between 4.3×10^{13} and 2.2×10^{18} cm^{-3} and for temperatures between 77 and 300 K. In summary, for each R_S value an implicit equation in E_F is solved numerically by iterating the mobilities in dependence on the ionized impurity concentration until convergence is achieved.

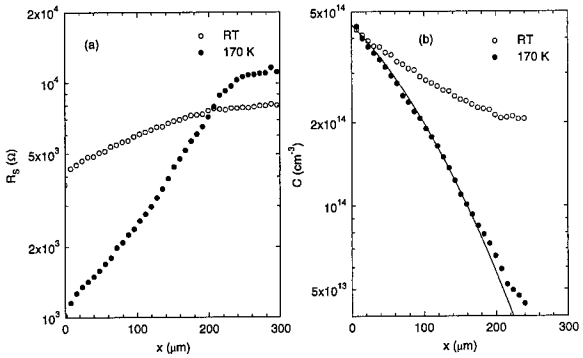

Fig. 3. Spreading-resistance profiles (a) at room temperature and 170 K of a Cu-diffused (577°C, 8 h) Ge sample. The improved resolution at 170 K allows for fitting of a complementary error function (solid line) to the concentration profile (b).

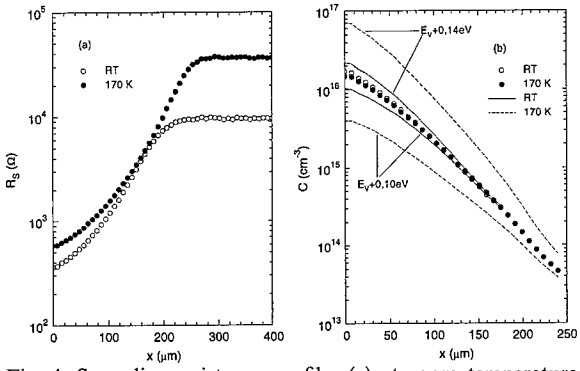

Fig. 4. Spreading-resistance profiles (a) at room temperature and 170 K for a Au-diffused (725°C, 24 h) Ge sample. The corresponding concentration data coincide for an ionization enthalpy of 0.12 eV for the $Au^{0/-}$ acceptor level. Solid and dashed curves illustrate the inconsistent results for other ionization enthalpies of $Au^{0/-}$.

2.3. *Proof of consistency*

To check the consistency of our method of analysis we performed measurements on the well-characterized Ge:Cu system [5,6]. Fig. 2 shows the two R_S profiles that were obtained from LTSRP at room temperature and 183 K on a Cu-diffused ($T = 706$°C, $t = 23$ min) Ge-sample. It is seen that the R_S profiles show pronounced differences. Nevertheless, the conversion of R_S to Cu concentration based on the dominant Cu level of $E_V + 0.04$ eV [7] lets the concentration profiles coincide, thus fulfilling the necessary condition that profiling at different temperatures must reveal the same unique Cu distribution present in the sample.

3. Results

3.1. *Copper in germanium*

Fig. 3 demonstrates the advantage of the new concept for samples diffused at relatively low temperatures, that is, for samples with impurity concentrations not much different from the intrinsic carrier concentration at room temperature. In this case we measured a Ge sample which was Cu-diffused at 577°C for 8 h. The R_S profile recorded at room temperature is barely resolved whereas the measurement at 170 K reveals a distinct profile which can be fitted by a complementary error function. The gain in dynamic range at the lower measuring temperature can be explained by the decrease of the intrinsic carrier concentration in conjunction with the increase of the hole mobility.

3.2. *Gold in germanium*

A further advantage of the LTSRP concept is the possibility to extract information about the dominating energy level of the impurity. This is demonstrated on a Au-diffused ($T = 725$°C, 24 h) Ge sample. The conversion of the R_S profiles recorded at room temperature and 170 K (Fig. 4) requires an energy level for the first Au acceptor state of $E_V + 0.12$ eV in order that the concentration profiles coincide. Combining all results from different Au-diffused samples yields as best estimation $E_V + (0.13 \pm 0.02)$ eV. This value is in accordance with the Hall-effect result of $E_V + 0.15$ eV given by Dunlap et al. [8]. This example reveals that LTSRP is able to combine the measurement of an impurity profile with the determination of the dominating energy level of the impurity.

4. Conclusions

In comparison with conventional SRP which is performed with commercially available spreading-resistance instruments at room temperature, the application of the LTSRP concept offers the following advantages: (i) Appreciably lower detection limit for electrically active impurities. (ii) Improved resolution of concentration–depth profiles. (iii) Determination of the major energy level characterizing an impurity or defect in the semiconductor host. In conclusion, LTSRP combines in a unique manner the electrical characterization of an impurity or defect with the resolution of its spatial distribution.

Acknowledgements

We thank L. Suwelack, R. Farke, K. Suwelack and F. Biermann from our institute for the construction of the LTSRP device, and H. Mehrer for critical reading of the

manuscript. We also gratefully acknowledge financial support by the 'Deutsche Forschungsgemeinschaft'.

References

[1] R.G. Mazur, D.H. Dickey, J. Electrochem. Soc. 113 (1966) 255.
[2] M. Pawlik, J. Vac. Sci. Technol. B 10 (1992) 388.
[3] N.A. Stolwijk, J. Hölzl, W. Frank, E.R. Weber, H. Mehrer, Appl. Phys. A 39 (1986) 37.
[4] H. Bracht, N.A. Stolwijk, H. Mehrer, Phys. Rev. B 52 (1995) 16542.
[5] N.A. Stolwijk, W. Frank, J. Hölzl, S.J. Pearton, E.E. Haller, J. Appl. Phys. 57 (1985) 5211.
[6] H. Bracht, N.A. Stolwijk, H. Mehrer, Phys. Rev. B 43 (1991) 14465.
[7] H.H. Woodbury, W.W. Tyler, Phys. Rev. 105 (1957) 84.
[8] W.C. Dunlap Jr., Phys. Rev. 97 (1955) 614.
[9] O.A. Golikova, B.Ya. Moizhes, L.S. Stil'bans, Sov. Phys. Sol. State 3 (10) (1962) 2259.

ELSEVIER

Physica B 273–274 (1999) 565–569

PHYSICA B

www.elsevier.com/locate/physb

Frenkel pairs, vacancies, and self-interstitials in Ge: identification and properties from PAC- and Moessbauer spectroscopy

R. Sielemann*, H. Haesslein, L. Wende, Ch. Zistl

Hahn-Meitner-Institut Berlin GmbH, Glienicker Strasse 100, 14109 Berlin, Germany

Abstract

Perturbed angular correlation spectroscopy (PAC) and the Moessbauer effect were utilized to study intrinsic point defects in Ge. In continuation of earlier work the production of Frenkel pairs in p-type Ge is studied microscopically by PAC utilizing the PAC probe as the primary knock-on atom receiving 29 eV recoil energy (Neutrino-recoil technique). Correlated recombination of the produced Frenkel pairs is observed between 205 and 238 K. This temperature agrees with the formerly determined migration temperature for long-range interstitial migration (220(5) K) and strongly corroborates the identification of the vacancy and self-interstitial in that former work. In a second type of experiment the Moessbauer probe ^{119}Sb, being a donor in Ge, is utilized to study the trapping of negative vacancies in n-type material induced by electron irradiation. The result is compared to the previously observed trapping of neutral vacancies in p-Ge at ^{111}In PAC probes.

Keywords: PAC; Moessbauer spectroscopy; Vacancies and self-interstitials in germanium

1. Introduction

The elementary point defects in Ge have attracted intensive research for a long time and numerous results have been obtained, mostly by electrical methods [1] and capacitance techniques [2,3]. However, no microscopic identification of either the vacancy or the self-interstitial has yet been accomplished. This is mainly due to the fact that methods suited to give microscopic information such as electron paramagnetic resonance (EPR) have, for various reasons, only limited successs when applied to Ge. Thus, a definite assignment of the collected data to the basic defects and their properties is still missing and interpretation of the results has remained largely speculative. An example is the migration enthalpy. There is a long-standing controversy over the question, at what temperature free defect migration occurs, speculative interpretations of various experimental results range from 50 to more than 200 K for vacancy diffusion, the situation for self-interstitials is even worse. The lack of a microscopic identification also implies that neither the geometrical structure nor electrical properties like charge states and ionization levels are definitely known. On the other hand, knowledge of these fundamental properties would not only be interesting for Ge itself but would be of considerable interest in relation to Si where a lot more data exist, in particular for the vacancy [4].

In a recent publication [5] we presented a different approach to identify and study the intrinsic defects in Ge. Perturbed angular correlation spectroscopy (PAC) was used which is based on the fact that defects in the immediate vicinity of a radioactive probe atom (^{111}In) can be studied via the induced hyperfine interaction. Defects were produced either by electron irradiation or by using the PAC probe itself as the primary knock-on

* Corresponding author. Tel.: + 49-30-8062-2725; fax: + 49-3080-622-293.

E-mail address: sielemann@hmi.de (R. Sielemann)

0921-4526/99/$ - see front matter
PII: S0921-4526(99)00574-8

atom effected by emission of a neutrino in the preceeding nuclear transmutation. From the combination of both types of techniques, identification of the vacancy and self-interstitial was proposed and numerous defect properties extracted. It turned out that long-range migration of the (neutral) vacancy occurs at 200 K and, most surprisingly, long-range migration of the self-interstitial takes place in the same temperature region, at 220 K. Both these annealing stages were found to be very sharp indicating that in each case a single activation process was involved. An acceptor level around $E_V + 0.20$ eV for the vacancy and a donor level very close to the conduction band for the self-interstitial was deduced from an analysis of the defect trapping process. Properties of the isolated defects' geometrical structure, however, cannot be inferred since the PAC derives its structural information always from a molecule-type defect, i.e., from the probe atom paired with a nearby defect.

Of course all properties assigned to a certain defect rest on a correct identification of this defect under study. The identification given in Ref. [5] is mainly based on the information obtained from the neutrino-recoil process [6]. In this experiment 29 eV is imparted to the probe atom ^{111}In by emission of a high-energy neutrino in the preceding decay from ^{111}Sn to ^{111}In thereby leading to the production of exactly one Frenkel pair (one vacancy and one interstital) in close vicinity of the probe atom. Strictly speaking, in order to identify the occuring PAC signal unambiguously the microscopic details of the Frenkel-pair production process must be known or, vice versa, with a definite knowledge of the PAC defect signals the production process can be studied. The interpretation in Ref. [5] uses plausible arguments as to how the production process occurs and combines it with the results of the trapping process following electron irradiation.

In order to further strengthen this assignment we have performed new experiments using PAC in connection with the neutrino-recoil technique. Emphasis was laid on the study of the annealing process of the produced Frenkel pair since in our former experiments only a rough scan of the annealing process had been obtained [7]. More precise data combined with the kinetic parameters obtained from the long-range defect migration [5] should help to elucidate the microscopic details of the Frenkel-pair production process and to distinguish between vacancy and self-interstitial. In the second part of this contribution we present experiments utilizing Moessbauer spectroscopy. The motivation for these experiments is the fact that the well suited standard PAC probe ^{111}In is an acceptor in Ge implying that all the defect information is obtained from the "acceptor standpoint". This fact is favourably used in the analysis of the trapping process [5], nevertheless, it is obvious that a donor probe atom would in addition be able to make those defects visible which preferably interact with donors and not with acceptors. Moessbauer spectroscopy (MS) has a suitable probe atom, ^{119}Sb, which is a common donor in Ge decaying to ^{119}Sn on which the Moessbauer effect is measured. We utilize this probe as a trapping agent for defects induced by electron irradiation and compare the results with former experiments obtained with PAC on the ^{111}In probe [5].

2. Neutrino-recoil experiments with PAC

2.1. Experimental

^{111}Sn nuclei ($T_{1/2} = 35$ min) were produced and implanted into Ge by a recoil implantation technique [7], see Fig. 1. By this procedure μm-deep implantation is achieved with a resulting probe concentration of 10^{13}–10^{14} cm^{-3}. We have used p-Ge (Ga) samples with Ga doping concentration of 6×10^{17} cm^{-3}. The sample dimensions were 10×20 mm with a thickness of 600 μm. Following implantation the samples were annealed for 3 min at 630°C and then transferred into a cryostat filled with liquid nitrogen. Due to the short halflife of ^{111}Sn we have added eight individual samples prepared in this way in order to get sufficient statistics in the PAC measurements. More details of the technique can be found in Ref. [7]. During the decay from ^{111}Sn to ^{111}In the probes suffer a monoenergetic recoil of 29 eV which leads to Frenkel-pair production. This can be studied in the following PAC experiments utilizing the standard PAC decay from ^{111}In to ^{111}Cd with the probe being the PKA. We mention that recoil energies resulting from the final decay ^{111}In to ^{111}Cd are smaller than 1 eV and do not contribute to defect production. Therefore the ^{111}In/Cd

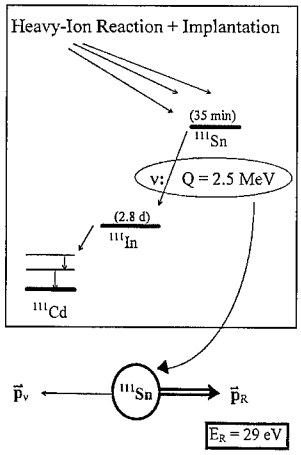

Fig. 1. Partial decay scheme illustrating the neutrino recoil effect. The neutrino emitted in the EC decay of ^{111}Sn carries an energy of 2.5 MeV leading to 29 eV monoenergetic recoil on the PAC probe ^{111}In/^{111}Cd.

decay, being the "standard" PAC probe activity, just plays the role of an analyzer of the defect situation caused by the precursor decay ^{111}Sn/In. To probe the thermal stability of the produced defects an isochronal annealing program is performed. For this purpose the samples are brought to the desired temperature, kept there for 10 min and are then transferred back to 77 K. After each annealing step a PAC spectrum is measured.

3. Results and discussion

As known from previous experiments [7] the PAC spectra contain a defect component characterized by a quadrupole interaction frequency $\nu_{Q1} = 54$ MHz. This component has axial symmetry (asymmetry parameter $\eta = 0$) and the main axis of the electric field gradient oriented in $\langle 111 \rangle$ directions. Fig. 2 shows a spectrum measured at 77 K, the spectral fraction of the defect component amounts to 11%. Fig. 3 shows the results of our annealing measurements in comparison with the formerly obtained data. The defect fraction stays constant within the experimental accuracy up to 205(3) K and is no longer present in the spectrum measured at 238(4) K (and above). The disappearance in exactly this small temperature interval now has far reaching implications. As discussed in Ref. [5], the 54 MHz defect is interpreted as a vacancy neighbouring the PAC probe in $\langle 111 \rangle$ directions. In the trapping experiment following electron irradiation this defect forms at 200 K and is thermally stable up to 400 K which is the break-up temperature of the defect pair with the vacancy escaping. The complete disappearance in the present experiment now reflects the different microscopic situation resulting from the neutrino recoil experiment. In this case the 54 MHz component represents the probe atom associated with

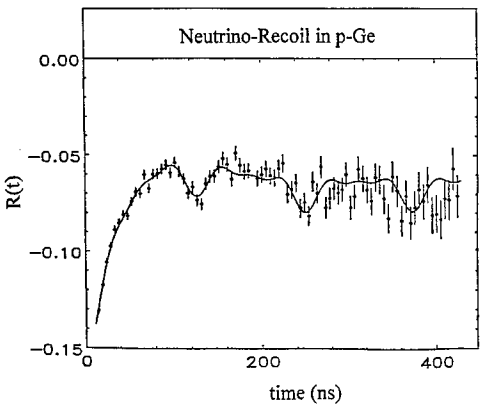

Fig. 2. PAC spectrum of ^{111}In/^{111}Cd in p-Ge following the decay of the precursor ^{111}Sn. Measurement at 77 K.

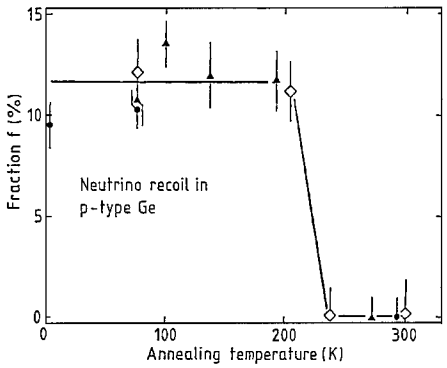

Fig. 3. Fraction of probe atoms decorated with the 54 MHz defect induced by neutrino recoil as function of the annealing temperature. Open symbols: this paper. Filled symbols: formerly obtained data.

one partner of the Frenkel pair with the other partner close by but sufficiently faraway that it is not seen by the PAC probe. The disappearance then can only be interpreted as the recombination of the defect bound to the probe atom with its near-by, but invisible, Frenkel partner; this process can be called a defect–antidefect reaction. Now, looking at the respective temperature (between 205 and 238 K) we note that it exactly overlaps the migration temperature (225 K) observed for the trapping process following electron irradiation leading to the defect frequency $\nu_{Q2} = 420$ MHz (tentatively interpreted as self-interstitial trapping in Ref. [5]). This clear agreement inevitably leads to the conclusion that the defects leading to 54 and 420 MHz quadrupole interaction, respectively, are antidefects and therefore must be the monovacancy and self-interstitial. The "invisible" defect causing defect annihilation is the one giving rise to the 420 MHz defect when trapped after electron irradiation. But there is more information in it. The annealing is complete, meaning that each defect bound to the PAC probe is annihilated by its antidefect. This implies that there is still an attractive correlation between the Frenkel partners, otherwise part of the invisible defect fraction would escape from the bound fraction after becoming mobile and would leave part of the bound fraction unannihilated. Thus we can speak of a correlated recombination. On the other hand, the temperature for this process and for free migration is identical within the measured interval of about 20 K. These two findings identify the process as correlated but almost free defect recombination which in metal physics usually is termed stage I_D. Of course one expects for the correlated recombination a small shift to lower temperatures to account for the smaller number of diffusion steps necessary for defect annihilation compared to the large number of steps necessary in the free migration process to reach

trapping at the PAC probe. This small expected shift is possible within the interval of our measurements.

The conclusions reached here assigning defect and antidefect then only leaves the question: which defect is which? This question is extensively discussed in Ref. [5] employing a model that the observed defect trapping following electron irradiation is determined by the defect's charge. Trapping can be explained with an acceptor behaviour for the defect leading to 54 MHz whereas the other defect (leading to 420 MHz) displays donor character. Taking the present paper's evidence and those results on the electrical properties we find a strong confirmation of our previous conclusion that the vacancy constitutes the 54 MHz defect and the self-interstitial the 420 MHz.

It is interesting to mention very recent experimental results obtained with other experimental methods. From positron annihilation experiments in undoped Ge a sharp annealing stage at 200 K is interpreted as free vacancy migration [8] in complete agreement with our result [5]. In another work, utilizing X-ray diffraction Ehrhart et al. [9] present strong evidence for the fact that Frenkel pairs produced by electron irradiation at 8 K are stable up to 150 K and annealing below that temperature is due to close Frenkel-pair recombination only. Long-range migration for both vacancies and self-interstitials, according to that paper, occurs only for $T > 150$ K again agreeing with our findings considering the fact that irradiation doses are extremely high in that work [9] which shifts annealing stages to lower temperatures.

4. Trapping experiments with (donor-) Moessbauer spectroscopy

4.1. Background

Employing the PAC probe ^{111}In for defect studies in Ge (or Si) it is obvious that the physical information is obtained from the viewpoint of an *acceptor* atom which, depending on the circumstances, may preselect or influence the attainable information. This is, on the one hand, a very desirable situation as has been demonstrated in the analysis of the trapping experiments in Ref. [5] which showed that interaction of the probe is only possible with positive or, under certain conditions, neutral defects. On the other hand, the interaction with negatively charged defects is impossible or at least strongly retarded. A donor probe, however, would open the field for studies of negative defects. To search for negative vacancies in Ge we have employed Moessbauer spectroscopy utilizing the probe atom ^{119}Sb which is, as non-radioactive Sb, a common donor in Ge and Si. ^{119}Sb decays to the Moessbauer-active ^{119}Sn state and is one of the best-suited Moessbauer probes for semiconductor studies, for details see Ref. [10].

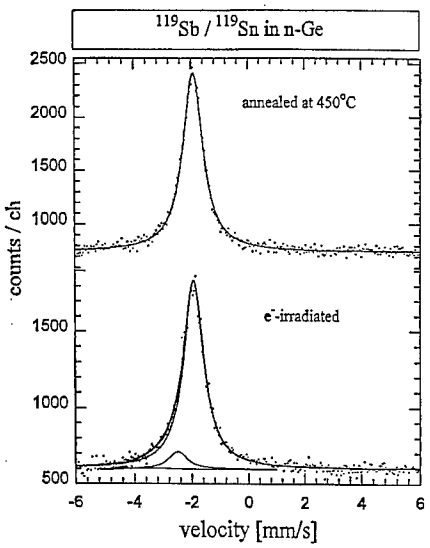

Fig. 4. Moessbauer spectra of ^{119}Sb/^{119}Sn in n-Ge. Top: measurement after probe implantation and annealing. Bottom: after additional electron irradiation. Measurement temperature is 4.2 K (versus a $CaSnO_3$ detector at room temperature).

4.2. Results and discussion

We have implanted n-type Ge predoped with Sb (1×10^{15} cm^{-3}) with ^{119}Sb Moessbauer atoms by using the recoil implantation technique mentioned above (for details see Ref. [11]). This results in 4 μm deep implantation and a probe concentration of about 10^{14} cm^{-3}. Following implantation the sample was annealed at 450°C for 10 min, a procedure already known to anneal all implantation-induced defects resulting from ^{111}In implantations [5]. Subsequently, a Moessbauer spectrum was measured at 4 K. Fig. 4 (top) shows the result. The spectrum can be well fitted with one single line having the smallest attainable linewidth under our experimental conditions, the parameters are 1.92(2) mm/s for the isomer shift and a Lorentzian line width of 0.84 mm/s (FWHM). Subsequently, the sample was irradiated with electrons of 1.2 MeV to a fluence of 5×10^{16} cm^{-2}. During irradiation the temperature was kept below 90 K. The sample then was transferred to the Moessbauer cryostat with an intermediate warm-up to room temperature. Fig. 4 (bottom) shows the result. The fit (outer line) shows a satellite component which is clearly seen when the defect-free line (top) is inserted as reference into the spectrum (inner line). The satellite spectrum has a isomer shift of 0.52 mm/s relative to the substitutional component (shifted to negative velocities corresponding to higher electron density), the spectral intensity amounts to 11%. The main component is due to the probe atom on a regular substitutional site, see also Ref. [12]. Since the spectral intensity of the defect line is rather small and the

isomer shift difference to the main component is also small there remains some uncertainty concerning the correct fitting of the spectrum. In a recent Moessbauer experiment large electric field gradients associated with simple defects have been observed in GaSb [13], so it cannot completely be excluded that a quadrupole splitting might be involved in the defect line with the visible part of the line as the left part of a doublet and an invisible (right) part inside the left wing of the main (substitutional) line. In the latter case one would still have an isomer shift with higher electron density compared to the main component which is expected for a vacancy associated with the substitutional probe atom. The dangling bond for such a configuration leads to a somewhat higher s-electron density than is usually contained in the unperturbed sp^3-configuration, see also the discussion in Ref. [12]. Detailed further studies employing higher electron irradiation fluences to produce more defects and a fine-step annealing program will be performed in the future. It is, however, already clear from the present experiments that defects induced by electron irradiation are trapped at the (donor-) ^{119}Sb probes which we tentatively assign to negatively charged vacancies (donor–acceptor pairs) not observable with ^{111}In. It is understood that self-interstitials (being positive up to very high n-doping levels [5]) cannot be trapped at the donor probes.

5. Conclusion

Experiments presented in this paper using the neutrino recoil technique in connection with PAC spectroscopy strongly support our previous conclusion that vacancies and self-interstitials in Ge undergo free migration around 200 K [5] implying that Frenkel pairs which are not too close are stable up to that temperature. Newly performed experiments utilizing other techniques [8,9] are in favour of that interpretation. In addition to using the ^{111}In acceptor probe we have presented experiments using the donor probe ^{119}Sb (employing Moessbauer spectroscopy) which enables the study of negative defects. Recently published results employing the DLTS technique on radioactive atoms in Ge [14] complement the achieved results so that a large body of kinetic, structural and electrical data on the intrinsic defects have become available.

Acknowledgements

We thank V.V. Emtsev for many enlightening discussions on the intricacies of defects in Ge.

References

[1] V.V. Emtsev, T.V. Mashovets, V.V. Mikhnovich, N.A. Vitovskii, Radiat. Eff. Defects Solids 111–112 (1989) 99.
[2] J.C. Bourgoin, P.M. Mooney, F. Poulin, Inst. Phys. Conf. Ser. 59 (1981) 33.
[3] A. Fourches, G. Walter, J.C. Bourgoin, J. Appl. Phys. 69 (1991) 2033.
[4] G.D. Watkins, Mater. Sci. Forum 143–147 (1994) 9.
[5] H. Haesslein, R. Sielemann, Ch. Zistl, Phys. Rev. Lett. 80 (1998) 2626.
[6] R. Sielemann, H. Haesslein, M. Bruessler, H. Metzner, Mater. Sci. Forum 83–87 (1992) 1109.
[7] Th. Wichert, N. Achtziger, H. Metzner, R. Sielemann, in: G. Langouche (Ed.), Hyperfine Interactions of Defects in Semiconductors, Elsevier, Amsterdam, 1992, p. 79.
[8] A. Polity, private communication, 1998.
[9] P. Ehrhart, H. Zillgen, J. Appl. Phys. 85 (1999) 3503.
[10] D.L. Williamson, L. Niesen, G. Weyer, R. Sielemann, G. Langouche, in: Hyperfine Interactions of Defects in Semiconductors, Elsevier, Amsterdam, 1992, p. 1.
[11] R. Sielemann, L. Wende, G. Weyer, Phys. Rev. Lett. 75 (1995) 1542.
[12] G. Weyer, S. Damgaard, J.W. Petersen, Phys. Lett. 76A (1980) 321.
[13] L. Wende, R. Sielemann, G. Weyer, International Conference Hyper. Int., Durban, South Africa, 1998.
[14] Ch. Zistl, R. Sielemann, H. Haesslein, S. Gall, D. Braeunig, J. Bollmann, Mater. Sci. Forum 258–263 (1997) 53.

ELSEVIER

Physica B 273–274 (1999) 570–574

PHYSICA B

www.elsevier.com/locate/physb

Local vibrational mode spectroscopy of thermal donors in germanium

V.P. Markevich[a], L.I. Murin[a], V.V. Litvinov[b,*], A.A. Kletchko[b], J.L. Lindström[c]

[a]*Institute of Solid State and Semiconductor Physics, 220072 Minsk, Belarus*
[b]*Belarusian State University, F. Scornia av. 4, 220050 Minsk, Belarus*
[c]*Department of Physics, University of Lund, S-221 00 Lund, Sweden*

Abstract

We report the observation of infrared (IR) vibrational bands related to individual thermal double donors (TDs) in Ge crystals enriched with either ^{16}O or ^{18}O isotopes of oxygen. The TDs were generated by heating the oxygen-doped Ge at 300°C and 350°C. IR absorption spectra were measured at room temperature (RT) and 10 K (LT). In the RT spectra two broad bands at about 600 and 780 cm^{-1} are found to develop upon the TD generation. In the LT spectra a splitting of the bands into series of rather sharp bands (up to 9 resolved lines) related to a double-donor (DD) configuration of individual TDs (TD1–TD9) is observed. A manifestation of bistability of the first four TD species (TD1–TD4) is observed in absorption spectra measured at 10 K after different cooling conditions. The pairs of lines due to bistable TDs in the DD configuration are detected after cooling under the band-gap illumination. They are found to transform to the sets of three lines after cooling in the dark. These triplets are assigned to the local vibrational modes (LVMs) of a neutral (X) configuration of bistable TDs. Oxygen isotopic shifts of LVMs due to TDs are determined and compared with those for vibrational modes of interstitial oxygen in Ge.

Keywords: Germanium; Thermal donors; Bistability; Local vibrational modes

1. Introduction

The oxygen-related thermal donors (TDs) in silicon and germanium are probably among the most studied defects in these semiconductors for the last four decades [1–4], because of high technological importance of the oxygen impurity in silicon [3,4]. Thermal donors are generated upon heating the oxygen-rich Si and Ge crystals in the temperature range of 300–500°C. In both semiconductors these centers have been identified as families of sequentially formed helium-like double donors (up to 16 species in Si [5]) with slightly different ground-state energies. The most recent progress in identification of the microscopic structure and formation mechanism of TDs has come from the discovery of the local vibrational modes (LVMs) related to the TDs in Si [6–8]. These give rise to two groups of the infrared (IR) vibrational bands in the regions of 716–748 and 975–1015 cm^{-1}. Three pairs of bands positioned at 716/975, 724/988, and 728/999 cm^{-1} are found to be related to the individual TDs (TD1, TD2, and TD3, respectively), while the pair at 734/1006 cm^{-1} is suggested to originate from the higher-order TDs (TDN, $N \geqslant 4$).

It is well established that the first TD species in Si and Ge are bistable [9–14], i.e., for these species beside the double-donor (DD) configuration there is a lower energy neutral configuration, usually labeled X. It has been found [8,14] that the transformation of TD1 and TD2 into the X configuration in Si is followed by the disappearance of the bands at 975 and 988 cm^{-1} and appearance of new ones with a common frequency of about 1020 cm^{-1}.

Infrared vibrational absorption from the TDs was observed in Ge crystals as well [15]. Two broad IR bands detected at room temperature at about 600 and

* Corresponding author. Fax: + 375-172-20-74-65.
E-mail address: litvvv@phys.bsu.unibel.by (V.V. Litvinov)

0921-4526/99/$ - see front matter
PII: S0921-4526(99)00575-X

786 cm^{-1} were suggested to originate from the TDs in Ge [15–17].

In the present paper a confirmation of this suggestion is given and positions of the IR vibrational bands related to the individual TD species are presented. A manifestation of bistability of the first four TDs is observed and for the bistable TD species different LVM lines are revealed to arise from the X configuration. Oxygen isotopic shifts of vibrational bands of TDs are reported.

2. Experimental details

Samples for this study were prepared from n-type Sb-doped Ge crystals ($\rho \approx 4{,}3$–$10\ \Omega$ cm), which were enriched with either ^{16}O or ^{18}O isotopes of oxygen up to concentration $(1.7\text{–}3) \times 10^{17}$ cm^{-3}. The concentration of ^{16}O and ^{18}O was determined from the intensity of the absorption bands at 856 and 812 cm^{-1}, a calibration coefficient of 1.25×10^{17} cm^{-2} [18] was used. Thermal donors were generated by heating the samples at 300°C and 350°C in nitrogen gas. The IR absorption measurements were carried out at 10 and 295 K using a Bruker 113v Fourier transform IR spectrometer. The spectral resolution was 0.5 or 1.0 cm^{-1}.

3. Experimental results and discussion

In the room temperature absorption spectra of as-grown Ge : ^{16}O (Ge : ^{18}O) crystals, two bands positioned at 856 (812) and 1264 (1209) cm^{-1} are observed. In the spectra measured at 10 K the bands are shifted by 6 cm^{-1} to higher frequencies. These bands are known to be related to interstitial bond-centered oxygen atoms (O_i) in Ge [2,16]. The band at 856 (812) cm^{-1} is attributed to the antisymmetric motion (ν_3 or A_{2u}) of the Ge–O–Ge unit and the band at 1264 (1209) cm^{-1} to the combination of the ν_3 mode with a symmetric motion (ν_2) of the same unit [19].

Heat-treatment (HT) of the Ge : ^{16}O (Ge : ^{18}O) samples results in appearance of two broad bands at about 600 (574) and 780 (738) cm^{-1} in the RT spectra. The development of the bands correlates well with the TD growth as deduced from the resistivity and Hall measurements. Both bands grow up in intensity and their peak positions are shifted to the high-energy side with the heat-treatment time. This implies that the individual TD species have slightly different LVMs, and their peak positions are shifted to higher frequencies for higher-order TDs.

The measurements performed at 10 K have confirmed this suggestion. It was found that lowering the measurement temperature results in splitting the broad bands into two series of rather sharp lines (see Fig. 1). The strength and number of the resolved lines depends strongly on the duration of HT and cooling conditions: under the band-gap illumination or in the dark.

Let us first consider the spectra obtained after cooling with the illumination (spectra I in Fig. 1). Two series of lines are observed in the regions of 595–615 and 770–790 cm^{-1}. The lines in the former region are narrower and up to nine species can be detected, while only a few bands can be resolved in the latter one (see Table 1). The lines in both series are formed in a sequential way, i.e. similar to that found for the first TD species in Ge by electrical [11] and optical (far-infrared) [13] measurements. Evidently, these series should correspond to the bands at 600 and 780 cm^{-1} observed in the RT spectra.

After cooling in the dark some of the lines disappear or their intensity decreases noticeably. Instead, a number of new lines appear in the ranges of 582–590, 705–715 and 790–793 cm^{-1} (spectra II in Fig. 1). It is natural to suggest that these lines are related to the X configuration of bistable thermal donors (BTDs). In Ge three first TD species (TD1–TD3) are well known to exhibit bistability [11–13,20]. The results of electrical measurements of Ref. [11] showed that the bistability of TD4 occurred as well.

The rates of the DD $\rightarrow$ X transformation are different for TD1–TD4 species, and strongly depend upon the free-electron concentration [11,12]. This allows one to distinguish the individual BTDs by studying the crystals with different TD concentrations. According to Ref. [11], the dominant centers after HT at 300°C and 350°C for 15 h were TD1 and TD2, with the density of the species of about $(2\text{–}4) \times 10^{14}$ and $(7\text{–}8) \times 10^{14}$ cm^{-3}, respectively. In our samples, which were similar to those studied in Ref. [11] and were treated for 15 h at 300°C and 350°C, the pairs of lines at 593.0/769 and 597.0/774.2 cm^{-1} were the dominant ones in LT spectra after cooling with the band-gap illumination. These bands were replaced by the lines at 581.0/715 and 583.8/712.9/791.8 cm^{-1} in the spectra measured after cooling in the dark (see Fig. 1a–d). On the basis of combined analysis of the data of electrical and optical measurements an identification of the appropriate lines with the LVMs of TD1 and TD2 in the DD and X configurations has been done (see Table 1).

After HT at 350°C for 50 and 90 h, a further increase in the TD concentration occurred and TD3 and TD4 became bistable (Fig. 1e–h). It should be noted that the transformation of the TD4 species was detected only by the decrease in intensity of a band at 603.5 cm^{-1} (DD state of TD4) and appearance of a line at 590.2 cm^{-1} (X state of TD4). Other vibrational modes of the TD4 in X configuration have not been detected because of two reasons: firstly, only the small part of these centers could be transformed into the X state under the used cooling conditions and secondly, rather strong absorption due to free charge carriers occurred.

An identification of LVM lines of the first numbers of TD family in Ge : ^{18}O crystals has been done in the similar way. Positions of all the observed lines are

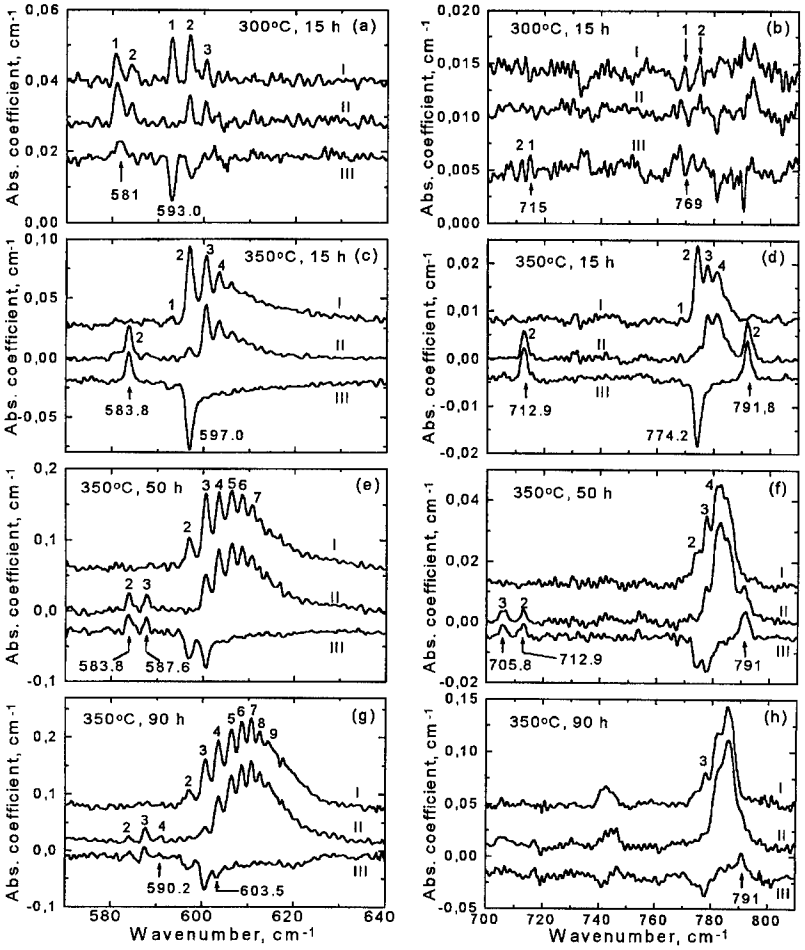

Fig. 1. Absorption spectra at 10 K for Ge : ^{16}O crystals annealed at (a, b) 300°C for 15 h and at 350°C for (c, d) 15 h, (e, f) 50 h and (g, h) 90 h. Spectra I and II were measured after cooling the samples with the band-gap illumination and in the dark, respectively. Spectra III are the difference of the spectra II and I.

Table 1
Positions of the vibrational IR modes (in cm^{-1}) of individual TDs in germanium at 10 K

TD species	State	Mode 1 (ν1)		Mode 2 (ν2)		Mode 3 (ν3)	
		Ge : ^{16}O	Ge : ^{18}O	Ge : ^{16}O	Ge : ^{18}O	Ge : ^{16}O	Ge : ^{18}O
TD1	DD	593.0	569	769	?	—	—
	X	581.0	555.8	?	?	715	?
TD2	DD	597.0	573.0	774.2	735.2	—	—
	X	583.8	559.4	791.8	750	712.9	672.5
TD3	DD	600.6	575.6	777.8	739	—	—
	X	587.6	562.5	791–792	750	705.8	?
TD4	DD	603.5	578.4	781.2	?	—	—
	X	590.2	?	?	?	?	?
TD5	DD	606.3	580.5	?	?	—	—
TD6	DD	608.6	?	?	?	—	—
TD7	DD	610.7	?	?	?	—	—
TD8	DD	612.8	?	?	?	—	—
TD9	DD	614.5	?	?	?	—	—

Table 2
Squares of the frequency ratios of different LVMs for individual TDs in Ge crystals doped with either ^{16}O or ^{18}O oxygen isotopes

TD state	$[\nu1(^{16}O)/\nu1(^{18}O)]^2$	$[\nu2(^{16}O)/\nu2(^{18}O)]^2$	$[\nu3(^{16}O)/\nu3(^{18}O)]^2$
DD	1.09	1.11	—
X	1.09	1.11	1.12

presented in Table 1. One can see some tendencies in the line positions. The $\nu1$ mode of TDs for both the DD and X configurations shifts to higher frequences by 2–4 cm^{-1} with increase in TD number (N). It is worth mentioning that the spacing between the neighboring $\nu1$ lines decreases with increase of N. The similar behavior is characteristic for the $\nu2$ mode of TDs in the DD configuration. The positions of $\nu2$-related LVM lines of BTDs in the X configuration are very close (in the range of 1 cm^{-1}). This mode might be considered as an analog of the band at 1020 cm^{-1} in Si, which was observed after the transformation of bistable TD1 and TD2 centers into the X configuration. The $\nu3$ mode of the bistable TDs shifts in opposite direction compared with the $\nu1$ and $\nu2$ modes with increase in TD number.

Some results of an analysis of oxygen isotopic shifts for the LVMs of individual TD species are presented in Table 2. It should be noted that the square of the frequency ratio of the $\nu2$ mode for Ge : ^{16}O and Ge : ^{18}O crystals is close to that for antisymmetric stretch mode ($\nu3$) of interstitial oxygen atoms in Ge (862/818 = 1.11). So, the $\nu2$ mode might be assigned to the antisymmeric stretching vibrations of divalent bond-centered oxygen atoms incorporated into TDs. The isotopic ratios for $\nu1$ and $\nu3$ modes of TDs differ from that for $\nu3$ mode of O_i in germanium. These modes are, probably, associated with other states of oxygen atoms in Ge lattice.

There is a consensus now [21–23], that the electrical activity of TDs in Si and Ge is associated mainly with the presence of trivalent oxygen atoms (O_y). The driving force for appearance of oxygen trivalency could arise from the stress produced by divalent oxygen atoms being attached to the TD core (located in the vicinity). It is obvious that the vibrational absorption from the O_y and O_i atoms should be different. The Ge–O (Si–O) bonds for the O_y atoms are softer than those for the O_i atoms [23], and accordingly the O_y stretching vibrations should have lower frequencies. It has been found in the calculations of Deak et al. [21,23], that the O_y atom in Ge should give rise to LVM at about 640 cm^{-1}. This is rather close to the positions of the TD lines observed in the region of 590–620 cm^{-1} (mode $\nu1$). Hence, we have suggested that the $\nu1$ mode bands (and the lines in the region of 716–744 cm^{-1} for Si) are related to the trivalent oxygen atoms in the TD core.

It is more difficult to interpret the lines in the region of 705–715 cm^{-1} ($\nu3$ mode). These lines are characteristic features for the X configuration only. Perhaps, they arise from the oxygen atoms in some metastable state being intermediate between O_i and O_y ones.

In conclusion, we have presented a further confirmation of the previous assignment of the bands at 600 and 780 cm^{-1} as arising from the TDs. The individual TD species are resolved in the low-temperature IR absorption spectra, and the LVM characterization of the lower energy X configuration of BTDs is performed. From the oxygen isotopic shift of vibrational bands of TDs a strong evidence for the incorporation of oxygen atoms into the structure of TDs is obtained.

Acknowledgements

We thank TFR, KVA and SI in Sweden for financial support. We also acknowledge financial support from the grant INTAS-Belarus 97-0824.

References

[1] C.S. Fuller et al., Phys. Rev. 96 (1954) 833.
[2] J. Bloem, C. Haas, P.J. Penning, J. Phys. Chem. Solids 12 (1959) 22.
[3] F. Shimura (Ed.), Oxygen in Silicon, in: Semiconductors and Semimetals, Vol. 42, Academic Press, New York, 1994.
[4] R. Jones (Ed.), Proceedings of the NATO Advanced Workshop on the Early Stages of Oxygen Precipitation in Silicon, Vol. 17 of NATO ASI Series, 3. High Technology, Kluwer Academic Publishers, Dordrecht, 1996.
[5] W. Götz, G. Pensl, W. Zulehner, Phys. Rev. B 46 (1992) 4312.
[6] J.L. Lindström, T. Hallberg, Phys. Rev. Lett. 72 (1994) 2729.
[7] T. Hallberg, J.L. Lindström, J. Appl. Phys. 79 (1996) 7550.
[8] J.L. Lindström, T. Hallberg, in: R. Jones (Ed.), Proceedings of the NATO Advanced Workshop on the Early Stages of Oxygen Precipitation in Silicon, Vol. 17 of NATO ASI Series, 3. High Technology, Kluwer Academic Publishers, Dordrecht, 1996 pp. 41–60.
[9] V.D. Tkachev et al., Sov. Phys. Semicond. 18 (1984) 324.
[10] Ya.I. Latushko et al., Phys. Stat. Sol. A 93 (1988) K181.
[11] V.V. Litvinov, G.V. Palchik, V.I. Urenev, Sov. Phys. Semicond. 19 (1985) 841.
[12] V. V Litvinov, G.V. Palchik, V.I. Urenev, Phys. Stat. Sol. A 108 (1988) 311.
[13] P. Clauws et al., Phys. Rev. B 44 (1991) 3665.

[14] T. Hallberg, J.L. Lindström, Appl. Phys. Lett. 68 (1996) 3458.
[15] W. Kaiser, J. Phys. Chem. Sol. 23 (1962) 255.
[16] P. Clauws, Mater. Sci. Eng. B 36 (1996) 213.
[17] N. Fukuoka et al., Jpn J. Appl. Phys. 30 (1991) 784.
[18] E.I. Millett, L.S. Wood, G. Bew, Brit. J. Appl. Phys. 16 (1965) 159.
[19] B. Pajot et al., Mater. Sci. Forum 258–263 (1997) 41.
[20] H.H.P.Th. Bekman, Phys. Rev. B 42 (1990) 9802.
[21] P. Deak, L.C. Snyder, J.W. Corbett, Phys. Rev. B 45 (1992) 11612.
[22] D.J. Chadi, Phys. Rev. Lett. 77 (1996) 861.
[23] P. Deak, in: R. Jones (Ed.), Proceedings of the NATO Advanced Workshop on the Early Stages of Oxygen Precipitation in Silicon, Vol. 17 of NATO ASI Series, 3. High Technology, Kluwer Academic Publishers, Dordrecht, 1996. pp. 163–177.

ELSEVIER

Physica B 273–274 (1999) 575–578

PHYSICA B

www.elsevier.com/locate/physb

Electronic and structural properties of vacancy and self-interstitial defects in germanium

A. Janotti[a], R. Baierle[b], Antônio J.R. da Silva[a], R. Mota[b], A. Fazzio[a,*]

[a]*Instituto de Física, Universidade de São Paulo, CP 66318, 05315-970 São Paulo, SP, Brazil*
[b]*Departamento de Física, Universidade Federal de Santa Maria, 97105-900, Santa Maria, RS, Brazil*

Abstract

The electronic and structural properties of an isolated vacancy and self-interstitial defects in germanium are studied through 'parameter free' calculations. We analyze the lattice relaxations and Jahn–Teller distortions for several charge states. Our results for ionization levels of the Ge-vacancy are in fair agreement with experimental results. In contrast to the silicon vacancy we obtain that the germanium vacancy does not present an Anderson negative-U. For the self-interstitial defect we obtain, similarly to silicon, that the lowest-energy configuration is the split dumbbell configuration.

Keywords: Ge vacancy; Ge self-interstitial; Ab initio calculations

1. Introduction

The vacancy and self-interstitial are among the simplest defects one can imagine. In silicon they have been thoroughly studied in the past [1–6]. The V_{Si} presents many interesting physical properties, such as: (i) several charge states in the gap; (ii) different local lattice relaxations for different charge states; (iii) the charge states (0), (+), and (++) form an Anderson negative-U system [7], with the (+) state being a missing (metastable) state. The silicon self-interstitial has also been well characterized, with the $\langle 1\,1\,0\rangle$ dumbbell configuration being the lowest-energy configuration [6], followed by the configuration with the Si interstitial at a hexagonal site.

As opposed to silicon, neither the vacancy nor the interstitial are well characterized in germanium. However, recent experiments [8–10] were able to provide some new microscopic information about these defects. Zistl et al. [8] used a combination of two different techniques, deep level transient spectroscopy (DLTS) and perturbed angular correlation spectroscopy (PAC) to obtain information about deep level defects in germanium. With the DLTS they were able to detect a level at 0.33 eV above the top of the valence band, and through the PAC measurements they related this level with a monovacancy. In another set of experiments [9,10], only the PAC technique was used. In these experiments, point defects produced by electron irradiation are trapped at ^{111}In probes, and their properties are studied as a function of the Fermi level. The authors concluded that the vacancy (0/−) level is 0.20 ± 0.04 eV above the top of the valence band. In the PAC experiments they also detected another type of defect, which they assigned, with a 'high degree of certainty', to a germanium self-interstitial. For the Ge_i, the dependence of the results on the Fermi level led the authors to conclude (tentatively) that the (+/0) level is located somewhere between 0.02 and 0.06 eV below the top of the conduction band.

The present paper, motivated by these experimental results, presents a detailed theoretical study of the germanium vacancy and self-interstitial. For the vacancy [11] we report results for the charge states (++), (+), (0), (−), and (− −), and for the self-interstitial we present results for the dumbbell configuration in the (+) and (0) charge states.

* Corresponding author. Tel.: + 55-11-818-7039; fax: + 55-11-818-6831.
E-mail address: fazzio@if.usp.br (A. Fazzio)

0921-4526/99/$ - see front matter
PII: S0921-4526(99)00576-1

2. Method

Our calculations are based on the density functional theory with the local density approximation (LDA) for the exchange-correlation potential [12]. We have performed total energy ab initio calculations using a supercell with 128 atoms to describe the germanium defects. The electrons–ions interactions were described using norm-conserving pseudopotentials of Bachelet et al. [13], in the Kleinman–Bylander [14] form. A plane wave basis set was used with an energy cutoff of 12 Ry, and the Brillouin zone was sampled using one $\boldsymbol{k}$-point (Γ-point). When performing geometry optimizations all the atoms were allowed to move until all components of the forces were smaller than 0.0005 hartree/bohr. No symmetry constraints were imposed in any of the geometry optimizations. To check the influence of the size of the supercell in the relaxed geometries, we embedded our 128 supercell (for the relaxed geometries of the vacancy) in a 216 supercell, and repeated the calculation without further atomic relaxation. We found that all the components of the forces were smaller than 0.003 hartree/a.u. This indicates that the atomic displacements are well represented in the 128 sites supercell. In order to have the system always charge neutral, when a calculation was performed with the system in charge state q, a uniform charge density of $\rho = -q/\Omega_{\text{cell}}$ was added to the unit cell of volume Ω_{cell}.

For the vacancy in charge state q, the formation energy was calculated as

$$E_q^{\text{v}}(\mu_e) = E_q^{N-1} + q(\mu_e + E_v) - \frac{N-1}{N}E^N, \quad (1)$$

whereas for the self-interstitial in charge state q it was calculated as

$$E_q^{\text{i}}(\mu_e) = E_q^{N+1} + q(\mu_e + E_v) - \frac{N+1}{N}E^N. \quad (2)$$

E^{N-1} is the total energy of the supercell with a vacancy in charge state q ($N-1$ atoms), E^{N+1} is the total energy of the supercell with a self-interstitial in charge state q ($N+1$ atoms), E^N is the total energy of the perfect lattice supercell (N atoms), and μ_e is the position of the Fermi level relative to the top of the valence band E_v. The top of the valence band has been corrected in the defect supercells by the average potential around the furthermost interstitial from the defect site [15–17].

3. Results

3.1. Vacancy

For the $(++)$ charge state we obtain an inward relaxation around the vacancy site, with a relative volume change of approximately 27% when compared to the perfect crystal. The point-group symmetry around the vacancy site is T_d, as expected. This result is the same as in silicon [18]. For the charge state $(+)$ there is a Jahn–Teller distortion to the D_{2d}-point symmetry. There is also an inward relaxation, with a contraction of 30% when compared to the unrelaxed structure. The same point-group symmetry (D_{2d}) is also obtained for the (0) charge state, and the lattice distortion is very similar to the $(+)$ state, with a contraction of 31% when compared to the unrelaxed structure. With the addition of another electron, i.e., the $(-)$ charge state, there is another Jahn–Teller distortion to a C_{2v} point-group symmetry. The relative volume contraction is now 40%. Finally, for the $(--)$ charge state the point-group symmetry is also C_{2v}, and the relative volume contraction is 41%, very similar to the $(-)$ charge state. Therefore, for all charge states, the point-group symmetries around the vacancy site are the same as in the case of the silicon vacancy.

Table 1
Vacancy and self-interstitial formation energies. The values were obtained from Eqs. (1) and (2) with $\mu_e = 0$ eV. The results for V_{Si} were obtained from Ref. [10] (we report their numbers for a cell with 216 sites). All results are in eV

	$(++)$	$(+)$	(0)	$(-)$	$(--)$
V_{Ge}	1.717	1.718	1.927	2.300	2.694
V_{Si}	3.01	3.20	3.27	3.88	4.29
Ge_i		2.05	2.20		

From Eq. (1) we can calculate the formation energies for all charge states. They are reported in Table 1 for $\mu_e = 0$ eV, where we also present the results for the V_{Si} [18]. As can be seen, the formation energies for the germanium vacancy are significantly smaller than the formation energies for the silicon vacancy, for all charge states. An important consequence is that the vacancy is much more important for the self-diffusion in germanium than in silicon [19,20]. The experimental results for the formation energy of a singly charged negative vacancy, which range from 1.7 to about 2 eV [21], are in good agreement with our value of 2.3 eV. From Eq. (1) we obtained the ionization levels, i.e., the values of the Fermi level μ_e where the formation energies of two charge states become equal. These values are reported in Table 2. The most important points are: (i) the $(++/+)$ level is almost resonant in the valence band. We cannot tell if it will be resonant or not at our level of calculation; (ii) as

[1] We calculated the value of U using the following expression: $U = E^{\text{v}}_{(++)}(\mu_e = 0) + E^{\text{v}}_{(0)}(\mu_e = 0) - 2E^{\text{v}}_{(+)}(\mu_e = 0)$. See Eq. (1) for definition of quantities.

Table 2
Ionization levels for the germanium vacancies. All the values are in eV

(+ +/+)	(+/0)	(0/−)	(−/− −)
0.001	0.209	0.373	0.399

opposed to the silicon vacancy, the (+ +), (+), (0) states do not form an Anderson negative-U system, and we obtain[1] a value of $U = 0.21$ eV. This value should be compared with the result for the V_{Si}, $U = -0.12$ eV, obtained using Puska et al.'s results; (iii) the (0), (−), (− −) states do not form an Anderson negative-U system; (iv) the (−) state has a small region of stability, of about 0.03 eV.

If the DLTS level at 0.33 eV above the top of the valence band [8] also corresponds to the (0/−) transition, we can conclude that it is somewhere between 0.20 and 0.33 eV above the top of the valence band. Our results give for this level a value of 0.37 eV, which is similar to the value obtained from the DLTS measurements. However, if we consider the large spin–orbit splitoff of the valence band in Ge, together with the fact that we do not include any spin–orbit effects in our calculations, we can conclude that one should be careful when comparing the absolute positions of our calculated levels with the experimental results.

An important question remains: why in germanium the charge states (+ +), (+), and (0) do not form an Anderson negative-U system, whereas in silicon they do. In order to answer this question, let us consider the total energies E^{++}, E^{+}, and E^{0} for the charge states (+ +), (+), and (0), respectively, as a function of the normal modes [22,23][2] Q_{A_1} and Q_E. If we expand them up to second order around the coordinates of the undistorted lattice, we obtain [4,5,7,24]:

$$E^{++}(Q_{A_1}, Q_E) = E_0 - \lambda_{A_1}^{++} Q_{A_1} + \tfrac{1}{2} k_{A_1}^{++} Q_{A_1}^2, \tag{3}$$

$$E^{+}(Q_{A_1}, Q_E) = E_0 + E_v^{+} - \lambda_{A_1}^{+} Q_{A_1} + \tfrac{1}{2} k_{A_1}^{+} Q_{A_1}^2 - \lambda_E^{+} Q_E + \tfrac{1}{2} k_E^{+} Q_E^2, \tag{4}$$

$$E^{0}(Q_{A_1}, Q_E) = E_0 + E_v^{0} - \lambda_{A_1}^{0} Q_{A_1} + \tfrac{1}{2} k_{A_1}^{0} Q_{A_1}^2 - \lambda_E^{0} Q_E + \tfrac{1}{2} k_E^{0} Q_E^2, \tag{5}$$

where E_v^q are the vertical (i.e., without any lattice relaxation or distortion) shifts in the total energies. For each normal mode of symmetry Γ_i, the $\lambda_{\Gamma_i}^q$'s are the electron–lattice coupling coefficients, and the $k_{\Gamma_i}^q$'s are the force constants. Minimization of the total energies for each charge state q, with respect to each normal mode coordinate, gives the equilibrium coordinates as

$$Q_{\Gamma_i}^{q,\mathrm{eq.}} = \frac{\lambda_{\Gamma_i}^q}{k_{\Gamma_i}^q}, \tag{6}$$

and the energy gain, for each normal mode and for each charge state, upon lattice relaxation or distortion is

$$\Delta E_{\Gamma_i}^q = -\frac{(\lambda_{\Gamma_i}^q)^2}{2k_{\Gamma_i}^q}. \tag{7}$$

The values of the $\lambda_{\Gamma_i}^q$'s and of the $k_{\Gamma_i}^q$'s were calculated by Öğüt et al. for silicon [24]. From the above equations, we can write[1] $U = U_v + U_{A_1} + U_E$, where $U_v = E_v^0 - 2E_v^+$ is the contribution coming from the vertical shifts, $U_{A_1} = \Delta E_{A_1}^{(++)} + \Delta E_{A_1}^{(0)} - 2\Delta E_{A_1}^{(+)}$ is the contribution coming from the energy gains associated with the A_1 mode, and $U_E = \Delta E_E^{(++)} + \Delta E_E^{(0)} - 2\Delta E_E^{(+)}$ is the contribution from the energy gains due to the E mode, or the energy gains due to the Jahn–Teller distortions. Using the results from Refs. [18,24], we estimate for the silicon vacancy $U_v = 0.4$, $U_{A_1} = -0.3$, and $U_E = -0.2$ eV. To obtain the numbers for germanium, we consider the following relation:

$$\Delta E_{\Gamma_i}^q(\mathrm{Ge}) = \left(\frac{Q_{\Gamma_i}^{q,\mathrm{eq.}}(\mathrm{Ge})}{Q_{\Gamma_i}^{q,\mathrm{eq.}}(\mathrm{Si})}\right)^2 \left(\frac{k_{\Gamma_i}^q(\mathrm{Ge})}{k_{\Gamma_i}^q(\mathrm{Si})}\right) \Delta E_{\Gamma_i}^q(\mathrm{Si}). \tag{8}$$

The values of the $Q_{\Gamma_i}^{q,\mathrm{eq.}}(\mathrm{Ge})$ were obtained by projecting, for each lowest-energy structure, our calculated atomic displacements from the undistorted structure into the normal coordinates [22,23] Q_{Γ_i}. The values for silicon were obtained in a similar way using the results from Puska et al. [18]. From the ratio between the atomic masses and the ratio between the phonon modes of silicon and germanium we can estimate $(k_{\Gamma_i}^q(\mathrm{Ge})/k_{\Gamma_i}^q(\mathrm{Si}))$. In this way we obtain for germanium $U_{A_1} = -0.2$ eV and $U_E = -0.01$ eV. By performing a calculation without letting the atoms relax, we calculated for germanium $U_v = 0.4$ eV. This gives for the $V_{\mathrm{Ge}a}$ $U = 0.19$ eV. This value is very similar to the value of $U = 0.2$ eV that we have obtained using our results for the formation energies. What we can conclude from these numbers is that the contribution U_{A_1} due to the breathing mode is similar in both silicon and germanium, but the contribution U_E due to the Jahn–Teller distortion is much smaller in germanium than in silicon. The main reason is a weaker electron–lattice coupling λ_E^q in germanium than in silicon. We obtain that λ_E^q is about six times smaller in Ge than in Si, which leads to values of $Q_E^{q,\mathrm{eq.}}(\mathrm{Ge})$ which are about three times smaller than $Q_E^{q,\mathrm{eq.}}(\mathrm{Si})$.

3.2. Self-interstitial

Similar to silicon, we obtain that the dumbbell configuration has lower energy than both the hexagonal and

[2] There are two E normal modes, but in order to have a D_{2d} distortion they cannot be independent of one another. Therefore, we can consider only one normal mode coordinate Q_E instead of two.

the tetrahedral configurations. We therefore concentrate on the analysis of the dumbbell structure. Using Eq. (2) we calculated the formation energies for the (+) and (0) charge states, for $\mu_e = 0$ eV, and we report the values in Table 1. For the dumbbell configuration in silicon the formation energy [6] for the (0) charge state is 3.2 eV. Once again we obtain that the defect formation energy in germanium is significantly smaller than in silicon.

From the results of Table 2 we calculate the (+ /0) levels. We obtain that the (+ /0) is an electronically inert level located at 0.15 eV above the top of the valence band. In accordance with Haesslein et al. [10], a donor state located at 0.04 eV below the bottom of the conduction band was tentatively identified with the self-interstitial (+ /0) level. This assignment was given because the authors supposed that the In^- probe ions were decorated by the (+) self-interstitial. However, there is no impediment for a coupling between the In^- and the neutral self-interstitial. Therefore, we tentatively assign the decrease in the PAC signal in the p(Ga)-type material (for $p > 10^{16}$ cm^{-3}) with the (+ /0) level, instead of the influence of the competing Ga^- trapping centers, as suggested by the authors. If we use the experimental data from Haesslein et al. [10] and an analysis similar to the one presented by the authors, we would give for this level a value around 0.1 eV, which is close to our result of 0.15 eV. The decrease in the PAC signal in the n(Sb)-type material (for $n > 2.8 \times 10^{17}$ cm^{-3}), which was assigned to the charge change (+) to (0) by the authors, may correspond to another transition, the (0) to (−), for example. Calculations to test this hypothesis are under way.

4. Conclusions

We have presented a detailed study of the germanium vacancy, and comparison of our results for the ionization levels are in fair agreement with recent experimental results [8–10]. We have shown that the germanium vacancy does not present a negative-U, and suggests as a possible explanation the small electron–lattice coupling for the mode responsible for the Jahn–Teller distortion, the E-mode.

We have also studied the germanium self-interstitial. The dumbbell configuration is the lowest-energy configuration, similarly to the silicon self-interstitial. In contrast to the assignment given by Haesslein et al. [10], we place the (+ /0) self-interstitial level at 0.15 eV above the top of the valence band, and not at 0.04 eV below the bottom of the conduction band, as suggested by the experimentalists.

Acknowledgements

This work was supported by the Brazilian agencies CNPq, FAPESP and FAPERGS.

References

[1] G.D. Watkins, in: B. Henderson, A.E. Hughes (Eds.), Defects and Their Structure in Non-metallic Solids, Plenum Press, New York, 1976, p. 203.
[2] G.D. Watkins, J.R. Troxell, Phys. Rev. Lett. 44 (1980) 593.
[3] G.D. Watkins, in: S.T. Pantelides (Ed.), Deep Centers in Semiconductors, Gordon and Breach, New York, 1986, p. 147.
[4] G.A. Baraff, E.O. Kane, M. Schlüter, Phys. Rev. Lett. 43 (1979) 956.
[5] G.A. Baraff, E.O. Kane, M. Schlüter, Phys. Rev. B 21 (1980) 5662.
[6] J. Zhu, T.D. dela Rubia, L.H. Yang, C. Mailhiot, G.H. Gilmer, Phys. Rev. B 54 (1996) 4741, and references therein.
[7] P.W. Anderson, Phys. Rev. Lett. 34 (1975) 953.
[8] C. Zistl, R. Sielemann, H. Hässlein, S. Gall, D. Bräunig, J. Bollmann, Mater. Sci. Forum 258–263 (1997) 53.
[9] H. Hässlein, R. Sielemann, C. Zistl, Mater. Sci. Forum 258–263 (1997) 59.
[10] H. Hässlein, R. Sielemann, C. Zistl, Phys. Rev. Lett. 80 (1998) 2626.
[11] A. Fazzio, A. Janotti, A.J.R. da Silva, R. Mota, Phys. Rev. Lett., submitted for publication.
[12] M. Bockstedte, A. Kley, J. Neugebauer, M. Scheffler, Comput. Phys. Commun. 107 (1997) 187.
[13] G.B. Bachelet, D.R. Hamann, M. Schlüter, Phys. Rev. B 26 (1982) 4199.
[14] L. Kleinman, D.M. Bylander, Phys. Rev. Lett. 48 (1982) 1425.
[15] A. Garcia, J.E. Northrup, Phys. Rev. Lett. 74 (1995) 1131.
[16] S. Pöykkö, M.J. Puska, R.M. Nieminen, Phys. Rev. B 53 (1996) 3813.
[17] T. Mattila, A. Zunger, Phys. Rev. B 58 (1998) 1367.
[18] M.J. Puska, S. Pöykkö, M. Pesola, R.M. Nieminen, Phys. Rev. B 58 (1998) 1318.
[19] W. Frank, N.A. Stolwijk, Mater. Sci. Forum 15–18 (1987) 369.
[20] H.D. Fuchs, W. Walukiewicz, E.E. Haller, W. Dondl, R. Schorer, G. Abstreiter, A.I. Rudnev, A.V. Tikhomirov, V.I. Ozhogin, Phys. Rev. B 51 (1995) 16817.
[21] C.J. Hwang, L.A.K. Watt, Phys. Rev. 171 (1968) 958 and references therein.
[22] M. Lannoo, A.M. Stoneham, J. Phys. Chem. Solids 29 (1968) 1987.
[23] F.P. Larkins, A.M. Stoneham, J. Phys. C 4 (1971) 143.
[24] S. Öğüt, H. Kim, J.R. Chelikowsky, Phys. Rev. B 56 (1997) R11353.

ELSEVIER

Physica B 273–274 (1999) 579–583

PHYSICA B

www.elsevier.com/locate/physb

Investigation of ion-bombardment effects on the formation of voids during deposition of a-Ge : H

Z.L. Peng[a], D. Comedi[b], F. Dondeo[b], I. Chambouleyron[b], P.J. Simpson[c], P. Mascher[a,*]

[a]*Ctr. for Electrophotonic Mat. & Dev., Department of Engineering Physics, McMaster University, Hamilton, Ont., Canada L8S 4L7*
[b]*Instituto de Física GlebWataghin, Universidade Estadual de Campinas - UNICAMP 13081-970 Campinas SP, Brazil*
[c]*Department of Physics and Astronomy, The University of Western Ontario, London, Ont., Canada*

Abstract

In this work, positron annihilation (PA) and infra-red (IR) spectroscopies are combined to obtain information on the H bonding and the void size distribution as a function of deposition parameters (substrate temperature and ion-bombardment) during reactive ion-beam sputtering deposition (IBSD) for the growth of a-Ge : H films. For a-Ge : H films obtained at substrate temperatures between 180°C and 260°C without ion bombardment of the growth surface, PA studies reveal low-value valence (S) parameters and high core (W) parameters as compared with films grown under less-favorable conditions. These data indicate a relatively low concentration of large voids, the annihilation process being controlled mainly by trapping at vacancies. IR and PA measurements on IBSD samples subjected to in-situ ion-bombardment during growth indicate ion irradiation of the growth surface as a major factor responsible for large void formation. It can thus be concluded that rather compact a-Ge : H films can be obtained by IBSD at substrate temperatures between 180°C and 260°C, by minimizing the ion bombardment of the growth surface.

Keywords: Positron annihilation; a-Ge : H; Ion-bombardment effects

1. Introduction

Hydrogenated amorphous germanium (a-Ge : H) is a natural candidate for amorphous semiconductor-based device applications requiring a small pseudo-gap. However, films of a-Ge : H have been reported to have poor electronic properties mainly due to the existence of a large number of dangling bonds, vacancies and voids which influence optoelectronic properties. Positron annihilation experiments have been shown to be a useful tool for the investigation of vacancy-type defects in materials [1]. The crux of this technique is that positrons are effectively trapped at neutral and negative vacancies due to the potential well formed by the missing positive charge of the ion cores. In this work we utilize beam-based Doppler broadening, and infra-red spectroscopies to obtain information on the microstructure of the samples and the concentration of vacancies and voids as a function of two deposition parameters, i.e., substrate temperature and ion-bombardment.

2. Experimental

The depositions were performed in a dual ion beam deposition chamber equipped with two Kaufman ion sources and a high-purity Ge target. The target atoms were sputtered by a 1000 eV Ar^+ beam and deposited onto c-Si or glass substrates placed at a distance of 15 cm from the target. Two sample series (samples #1–7 in Table 1) were grown: (1) the substrate was irradiated by

* Corresponding author. Tel.: + 1-905-5259140#24963; fax: + 1-905-5278409.
E-mail address: mascher@mcmail.cis.mcmaster.ca (P. Mascher)

0921-4526/99/$ - see front matter
PII: S0921-4526(99)00578-5

Table 1
Summary of the deposition conditions of a-Ge : H on c-Si substrate and positron-related parameters

Sample	Temp. (°C)	Deposit rate (Å/s)	I/A	Thickness (nm)	H%	L_+ (nm)	Defect concentration (cm^{-3})
#1	220	1.23	1.2	950	4.4	21.1	4.0×10^{18} (void)
#2	220	1.38	0.6	880	5.8	22.2	3.6×10^{18} (void)
#3	220	1.38	1.0	990	8.4	12.2	1.2×10^{19} (void)
#4	220	1.31	0	940	4.1	23.6	3.2×10^{19} (vacancy)
#5	260	1.28	0	930	0.5	46.0	8.0×10^{18} (vacancy)
#6	180	1.30	0	940	4.3	27.3	2.4×10^{19} (vacancy)
#7	25(RT)	1.51	0	1080	8.1	21.1	—
#10	220	0.74	0	530	0.0	22.6	3.7×10^{19} (vacancy)
#470	180	1.00	—	900	11.0	22.9	3.4×10^{18} (void)
c-Ge	—	—	—	—	—	200.0	—

a 100 eV $H_2^+ + Ar^+$ "assisting" beam, where the ion/atom arrival rate ratios (I/A) were varied from 0 to 1.2; (2) the samples were prepared by performing Ar^+ sputtering of the Ge target in a H_2 atmosphere ($P_{H_2} \sim 1 \times 10^{-3}$ mbar) with $I/A = 0$ and by varying the substrate temperature from 25°C to 260°C. Additional samples #10 (non-hydrogenated and not ion bombarded) and #470 (grown by RF-sputtering) were also investigated for comparison.

Doppler broadening spectra were measured as a function of positron energy, corresponding to implantation depth. The spectra were characterized by the usual line shape parameters S and W, defined as the number of counts in the central and wing regions of the 511 keV annihilation peak divided by the total number of counts. The S parameter is associated with annihilations with low momentum (valence) electrons, while the W parameters corresponds to annihilations with high momentum (core) electrons.

3. Results and discussion

The experimental results for the S parameter from depth profiling of a-Ge : H on c-Si substrates are plotted as a function of positron beam energy, E (Fig. 1). The sample depth can be calculated from the incident energy according to $z[\text{nm}] = (40/\rho)(E[\text{keV}])^{1.6}$, where ρ is the mass density. The solid lines through the data points are the results of a POSTRAP5 [2] analysis based on the positron diffusion model. The S–E curves for those samples can be divided into three regions. In the energy range up to 6 keV the S value increases due to the surface effect, then S attains a constant value above 6 keV which can be identified as the characteristic value of the a-Ge : H film. At larger positron energies, $E > 14$ keV, the S parameter starts to decrease and approaches the value of the c-Si substrate, $S = 0.507$. It can be seen that both the non-bombarded and bombarded samples are different in two ways from c-Ge: (1) the S value is considerably higher, and (2) the increase in S from the surface value is much steeper in a-Ge : H than in c-Ge. These differences indicate the presence of vacancy-type defects in a-Ge : H, where the defect type and concentration are related to the growth conditions. These defects are expected to act as traps for positrons, thus reducing the diffusion length (Table 1) and increasing the S parameter. Furthermore, it can be seen in Fig. 1 that the S value decreases with increasing substrate temperature, and larger S values are observed for the ion bombarded a-Ge : H as compared with films grown without ion bombardment. An increase of vacancy concentration, or the formation of larger microvoids due to the ion bombardment may explain the observed increase in S-parameter values. It should also be noted from these data that the films are uniform throughout their thickness.

Typical infrared spectra of high-quality a-Ge : H films show two main bands, namely the Ge–H wagging vibration mode at 570 cm^{-1} and two corresponding Ge–H stretching modes, which may have two components: one is due to bonded H atoms vibrating within a Ge vacancy (the so-called bulk mode at 1874 cm^{-1}) and the other is due to H atoms bonded to Ge atoms at the internal surface of voids considerably larger than a single vacancy (surface mode, at frequencies between 1970 and 2000 cm^{-1}). Two interesting effects are observed [3]: (1) for $I/A = 0$, the surface mode is below the detection limit. Decreasing the substrate temperature from 260°C towards room temperature leads to an asymmetrical broadening of the stretching mode peak and a slight shift to larger frequencies. The asymmetrical broadening is evidence for small but not negligible contributions from the surface-like modes, especially for the film deposited at room temperature; (2) for $I/A \neq 0$ and RF-sputtering

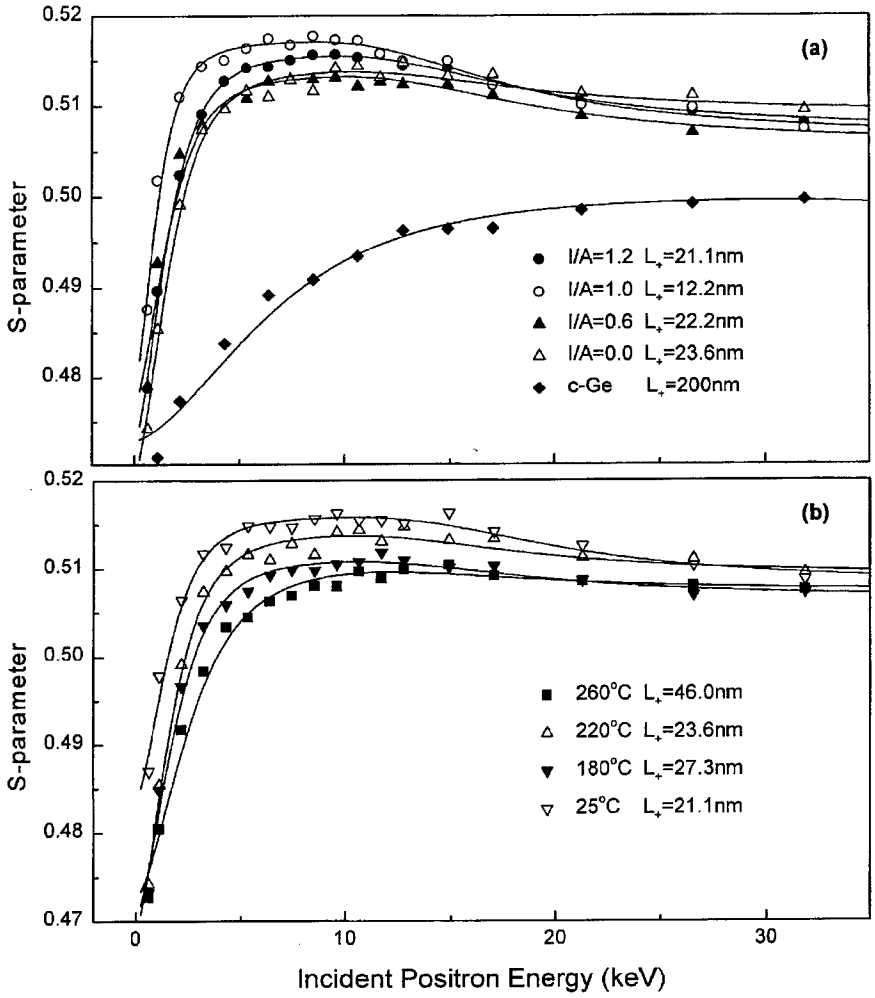

Fig. 1. S parameter versus incident positron energy for a-Ge : H on c-Si substrate deposited by ion-beam sputtering at (a) various ion-to-atom arrival rate ratios I/A; (b) different substrate temperatures T_s.

deposition, both the bulk and surface stretching modes are apparent and the surface-like mode frequency as well as the relative intensity increase with increasing ion current. The IR results show that ion-bombardment plays a crucial role in the formation of voids in a-Ge : H.

Previous experiments [4] performed on films deposited by magnetron and RF sputtering have shown, however, that ion bombardment during film growth can lead to a more compact network structure, which is in contradiction with our results. It should be noted that the amount of ion bombardment occurring in our deposition seems to be significantly larger than prevailing values during the deposition of compact a-Ge : H films by other groups. For increasing ion (especially Ar^+) currents striking the growth surface, an increasing number of coordination dangling bonds are expected to be created by knock-on processes. According to TRIM calculations, an average number of atoms equivalent to about $\frac{1}{4}$ of each deposited monolayer will be displaced by the Ar^+. At such a high defect production rate, it is conceivable that defects will easily agglomerate, leading to the formation of large voids. In addition, since the beam contains about 50% hydrogen, dangling bonds may be readily passivated thus favoring the formation of H-decorated voids as observed in the IR spectra. The observed effect of the substrate temperature on the S parameter and on the infrared stretching modes can also be expected. At higher substrate temperatures, atoms acquire more surface mobility, which tends to eliminate microstructure and results in a more relaxed amorphous network. As a consequence, the material will have a lower density of defects and thus smaller S-parameter values.

The number of different vacancy defects trapping positrons can be investigated through the relationship between the S- and W-parameters [5]. If there is only one dominant type of defect present, the W parameter depends linearly on the S parameter when the fraction of positron annihilations at defects varies due to variation in defect concentration. Fig. 2 shows the valence annihilation parameter, S, as a function of the core annihilation parameter, W, for a-Ge : H films on both c-Si and glass substrates. The S and W values of all samples were averaged for positron energies from 6 to 14 keV (except 6–10 keV for sample #10). It is obvious that the non-bombarded and bombarded samples can only be fitted well with different straight lines. This is a strong indication for the presence of different vacancy-type defects in the non-bombarded and bombarded samples. We also observe in Fig. 2 that the defect type in a-Ge is different from that in a-Ge : H. The decrease of the S values in a-Ge : H can be explained by the association of H with these defects. The hydrogen can bind to the dangling bonds of Ge, resulting in reduced positron trapping and thus giving a low S value. Based on the IR results, vacancies in the nonbombarded a-Ge : H samples may be responsible for the positron trapping, while vacancy clusters or microvoids are the dominant positron traps in the bombarded and RF-sputter deposited samples due to their much larger positron trapping rate. For the RF sputter deposition, significant uncontrolled ion bombardment is expected to occur as a result of the film being directly exposed to the plasma. Thus, we can conclude that the ion bombardment of the growing surface is the major factor for the formation of microvoids in the resulting film. Interestingly, we observed that the experimental (S, W) points for the films deposited at room temperature deviate from the straight line of nonbombarded samples and tend closer to that of the bombarded samples. IR spectra have shown that there are not negligible contributions from the surface for the films deposited at room temperature. Then, a possible explanation is that in addition to vacancies, larger voids are present in these samples due to the low growth temperature.

The defect concentration, C in a-Ge : H can be estimated from the positron diffusion lengths, L_+. The diffusion length, L_+ is related to the diffusivity, D and the effective positron trapping rate, λ_{eff}, as $L_+ = \sqrt{D/\lambda_{\text{eff}}}$. λ_{eff} is related to specific trapping rate μ and C according to $\lambda_{\text{eff}} = \lambda_b + \mu C$, where λ_b is the annihilation rate in trap-free a-Ge : H (assumed to be equal to that in c-Ge, $4.39 \times 10^9\ s^{-1}$ [1]). The positron diffusivity in c-Ge at room temperature is about $1.8\ cm^2/s$ [6]. Positron trapping rates in a-Ge : H are unknown, but some values have been reported for a-Si : H [7]. Experimental specific trapping rates for microvoids in a-Si : H, $\mu = 4 \times 10^{15}\ s^{-1}$, are 10 times higher than in vacancies. Using these coefficiencies and assumptions, and the above values for positron diffusivity and trapping, the concentration of microvoids/vacancies in bombarded/nonbombarded samples can be estimated, as shown in Table 1. We note that the microvoid concentration and hydrogen content in the bombarded a-Ge : H increase with increasing I/A up to $I/A = 1.0$ and then decrease for a larger ion current. The variation of hydrogen content with I/A is

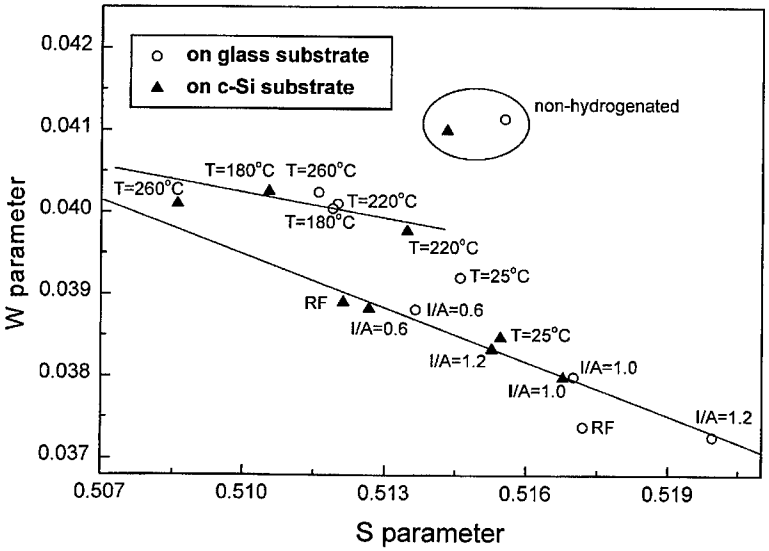

Fig. 2. The core annihilation parameter, W versus the valence annihilation parameter, S for differently grown a-Ge : H on c-Si and glass substrates.

due to the competition between H_2 incorporation by implantation and ion-induced removal of H by either sputtering, chemical etching, or direct heating of the near surface region. The comparison between the microvoid concentration and the hydrogen content gives evidence that hydrogen passivation is another major factor responsible for the formation of microvoids.

4. Conclusion

By means of beam-based Doppler broadening and infra-red spectroscopies, information on the microstructure and the concentration of vacancies and voids has been obtained as a function of two major deposition parameters, substrate temperature and ion-bombardment. It was found that hydrogen plus argon ion bombardment of the growing surface is responsible for the formation of microvoids in the resulting films. For a-Ge : H films obtained without ion bombardment of the growth surface, the positron annihilation process is being controlled mainly by trapping at vacancies, and increasing the substrate temperature can lead to a more ordered network structure. In addition, the difference of the S values in the a-Ge : H and a-Ge films reveals that the interaction of hydrogen with defect centers can be studied utilizing the property of positron trapping at defect sites that are also sensitive to hydrogen trapping.

Acknowledgements

This work was supported by the Natural Sciences and Engineering Research Council of Canada.

References

[1] R. Krause-Rehberg, H.S. Leipner, Positron Annihilation in Semiconductors, Springer, Berlin, 1999.
[2] G.C. Aers, in: P.J. Schultz, G.R. Massoumi, P.J. Simpson (Eds.), Positron Beams for Solids and Surface, Proceedings of the Fourth International Workshop, AIP Conference Proceeding, AIP, New York, 1991, p. 218.
[3] F. Origo, P. Hammer, D. Comedi, I. Chambouleyron, Mater. Res. Soc. Symp. Proc. 507 (1998) 477.
[4] T. Drüsedau, B. Schröder, J. Appl. Phys. 75 (1994) 2864.
[5] L. Liszkay, C. Corbel, L. Baroux, P. Hautojärvi, M. Bayhan, A.W. Brinkman, S. Tatarenko, Appl. Phys. Lett. 64 (1994) 1380.
[6] E. Soininen, J. Mäkinen, D. Beyer, P. Hautojärvi, Phys. Rev. B 46 (1992) 13104.
[7] H.E. Schaefer, R. Würschum, Appl. Phys. A 40 (1986) 145.

ELSEVIER

Physica B 273–274 (1999) 584–588

PHYSICA B

www.elsevier.com/locate/physb

Deep defects in n-type high-purity germanium: quantification of optical variants of deep level transient spectroscopy

A. Blondeel*, P. Clauws

Department of Solid State Sciences, University of Ghent, Krijgslaan 281/S1, 9000 Gent, Belgium

Abstract

The characterization of high-purity (HP) Ge for the fabrication of γ-ray detectors poses very specific demands due to the high degree of purity of the material (shallow concentration of the order 10^9–10^{10} cm^{-3}). Deep level transient spectroscopy (DLTS) may still be applied to this kind of material since the sensitivity is relative to the shallow doping concentration. In contrast with p-type HP Ge which was characterized extensively in the 1980s, very little is known about deep defects in n-type HP Ge. Two optical variants of DLTS have been applied to n-type HP Ge and quantified for the first time. Several deep minority carrier traps are detected and identified as mainly Cu-related traps with concentrations in the 10^6–10^8 cm^{-3} range. These Cu-related traps, which are well known as the majority carrier traps appearing in typical p-type HP Ge, are thus present as minority carrier traps in typical n-type HP Ge. The conclusion that deep-level defects in n- and p-type HP Ge are very similar could be expected from the similarity in growing conditions for the two types of materials. In the first DLTS variant, known as optical DLTS or ODLTS the deep levels are filled by optical injection (with light of above bandgap energy) at the back ohmic contact of a reverse biased diode. The spectrum is generated by the capacitance transients following the optical excitation. In the second variant, known as photo induced (Current) transient spectroscopy or PI(C)TS the deep levels are also filled optically with intrinsic light, but here a neutral structure is used with two ohmic contacts in sandwich configuration. The spectrum is generated by current transients instead of capacitance transients. This method is especially suited for high-resistivity or semi-insulating materials which cannot be measured with capacitance-based DLTS. PICTS was applied to n-type Ge with a shallow concentration as low as 10^9 cm^{-3}.

Keywords: DLTS; Deep level transient spectroscopy; Deep defects; High-purity germanium

1. Introduction

Since its early days, classical mode deep level transient spectroscopy (DLTS) [1], with voltage pulses and capacitance transients, has been used as a quantitative tool for the investigation of deep traps in semiconductor materials. The sensitivity of DLTS is relative to the shallow doping concentration, implying that this technique is especially suited for the detection of deep defects in high-purity (HP) Ge. The latter material with a residual shallow concentration of the order 10^{10} cm^{-3} is mainly used for the fabrication of γ-ray detectors. Already in the 1980s DLTS was applied to p-type HP Ge [2–6] and a series of deep majority carrier traps were detected. These traps with typical concentration in the 10^7–10^9 cm^{-3} range correspond mainly to defects involving Cu impurities. Since these traps represent majority carrier traps in p-type, quantitative DLTS analysis is straightforward. Nowadays more and more n-type HP Ge (10^{10} cm^{-3}) is used for detector fabrication mainly because this material is more resistant to radiation damage than p-type [7,8]. Besides this, there is also an evolution towards material with an even smaller residual shallow concentration: down to 10^9 cm^{-3} called ultrapure (UP) Ge. Classical DLTS of n-type HP Ge usually

* Corresponding author. Tel.: + 32-9-264-4364; fax: + 32-9-264-4996.

E-mail address: anja.blondeel@rug.ac.be (A. Blondeel)

0921-4526/99/$ - see front matter
PII: S0921-4526(99)00579-7

results in the detection of only a broad feature from majority carrier traps which was shown to be correlated with the presence of dislocations [9–11]. The Cu-related deep levels, known from p-type HP Ge, which are presumed to be present in n-type HP Ge too, are minority carrier traps in the latter material and their detection thus requires the injection of minority carriers. The present article deals with the detection and quantitative analysis of the Cu-related deep levels in n-type HP and UP Ge using two optical variants of DLTS.

2. n-type high-purity Ge

The most common way to inject minority carriers in DLTS of an n-type semiconductor is forward biasing of a p^+n junction. In contrast to p-type Ge where a n^+p junction is easily obtained by a low-temperature Li diffusion, a p^+n junction on n-type requires a high-temperature process (acceptor diffusion or implantation followed by post anneal). To avoid contamination of this delicate material with rapidly diffusing elements the temperature has to be kept below 300°C [9]. Therefore preparation of a p^+n junction is difficult and Schottky barriers are preferred combined with optical injection of minority carriers. The largest difficulty when quantifying optical DLTS (ODLTS) is the fact that both electrons and holes are present in the depletion area, giving rise to a combined majority-minority spectrum and to uncertainties in the filling of the deep traps. To avoid this complication, a specific sample configuration together with strongly absorbed light is used resulting in a flow of only minority carriers into the depletion region [11–13].

The main features of the sample are given in Fig. 1a. The sample has a Au Schottky contact on one side and a Li-diffused (250°C during 15 min in Ar atmosphere) ohmic contact on the other side. On the Li-diffused side a thin layer of InHg is rubbed on. Both Schottky and ohmic contact are then covered with a piece of In foil, leaving a circular hole in the middle of the In foil on the ohmic contact side to allow illumination. The diode is reversely biased and illuminated through the back (ohmic) contact with light of above band-gap energy resulting in the generation of electron–hole pairs. The reverse bias is kept constant during the whole experiment. The wavelength of the light is chosen so that all the light is absorbed in the neutral material and penetration of the light into the depletion area is negligible. The photogenerated carriers will diffuse away from the back ohmic contact following their concentration gradient. Due to the sign of the electric field, the current flowing through the space charge region will be mainly a minority carrier (hole) current. The holes are then available for capture in deep levels. A 905 nm laser diode was used as a light source in our experiment. Since in Ge the penetration depth at this wavelength is about 175 nm and the thickness of the neutral part of the sample is approximately 1 mm, no direct photoexcitation of the traps will occur [11,13].

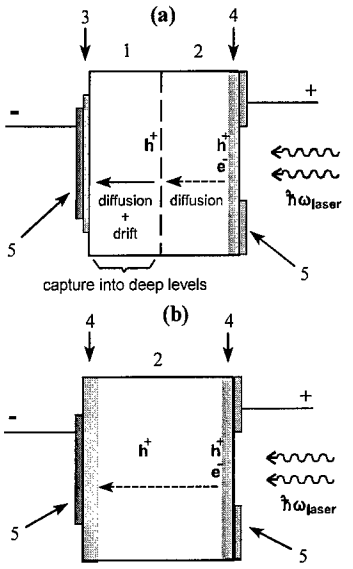

Fig. 1. Schematic representation of the sample in (a) ODLTS of n-type HP Ge, (b) PICTS of n-type UP Ge (1) depletion area; (2) neutral material; (3) Schottky-contact (Au); (4) n^+ ohmic contact (Li diffused); (5) In foil. Typical sample dimensions: area: 9×9 mm^2; thickness: 1–2 mm.

A typical ODLTS spectrum of n-type HP Ge is shown in Fig. 2a. Six peaks superimposed on a broad background are clearly resolved. Form the signature (E_T, K_T) of the levels they could be identified as the same levels that are commonly present in p-type HP Ge (assignment and signature of the peaks in Table 1). They correspond to residual impurities present in the crystal and are mainly Cu related [11,13]. A typical p-type spectrum is shown in Fig. 2b for comparison. In the situation as described above a simple concentration formula could be deduced [11,13]. This concentration formula was verified experimentally by comparing the results of DLTS and ODLTS measurements. For this purpose samples were cut from a crystal showing a p to n transition between head and tail end (caused by the difference in segregation behavior of the shallow donor phosphorus and the shallow acceptor aluminium). Three samples were cut from the p-type side and measured with classical voltage pulse DLTS, two from the n-type side and measured with ODLTS. The concentration of five different deep levels was calculated. No large changes in deep trap concentration (and certainly no abrupt changes) through the crystal and especially between two adjacent samples are expected. The results of these measurements are summarized in Fig. 3. From this figure it is clear that the changes in deep

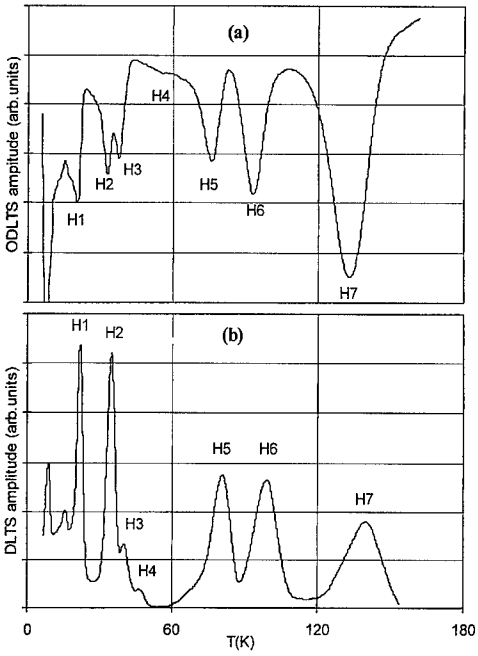

Fig. 2. (a) ODLTS spectrum of n-type HP Ge ($N_D - N_A \approx 10^{10}$ cm^{-3}): bias: -0.5 V; light pulses: 20 ms ($\tau_{window} = 47$ ms), (b) DLTS spectrum of p-type HP Ge ($N_D - N_A \approx 10^{10}$ cm^{-3}), bias: -4 V; electrical pulses: 1 ms; height: 2V ($\tau_{window} = 6$ ms). For peak labels refer to Table 1.

Table 1
Assignment and signature of hole traps commonly present in HP Ge [3]

Peak label	Assignment	Energy level	K_T (10^7 K^{-2} s^{-1})
H1	$Cu_s^{0/-}$	$E_V + 37$ meV	6.0
H2	Cu,H	$E_V + 62$ meV	8.6
H3	V_2H	$E_V + 71$ meV	6.2
H4	"O"	$E_V + 78$–87 meV	1.0–8.3
H5	Cu,Li,H	$E_V + 160$ meV	21.8
H6	Cu,H	$E_V + 185$ meV	4.5
H7	$Cu_s^{-/2-}$	$E_V + 322$ meV	146

trap concentration are smooth as expected, showing that the deduced concentration formula for ODLTS is valid.

3. n-type ultra-pure germanium

It can be shown experimentally as well as theoretically that conventional DLTS based on thermally stimulated capacitance transients is no longer reliable for material

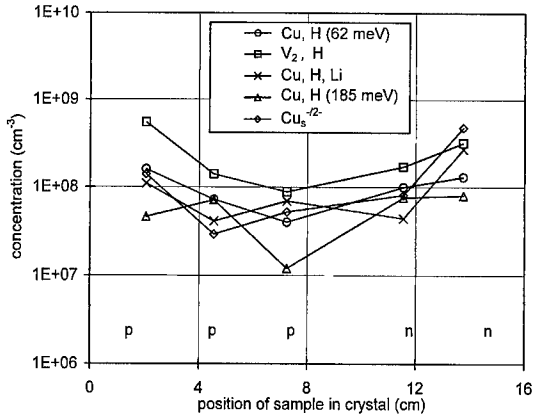

Fig. 3. Concentration of deep hole traps as a function of position in a HP germanium crystal showing a p to n transition. The samples cut from the p-type side were measured with voltage pulse DLTS. The samples cut from the n-type side were measured with ODLTS.

with a very low net shallow concentration (such as UP Ge): the samples dimensions become very stringent, the samples barely react or not at all react on the excitation pulses and calculation of the concentration becomes extremely complicated and inaccurate [11,14]. A DLTS variant which has shown to be useful for high-resistivity epitaxial layers or semi-insulating substrates is photo-induced (current) transient spectroscopy (PICTS or PITS) [11,14–18]. In this technique, thermally stimulated current transients are observed after optical excitation instead of capacitance transients. The technique was applied to UP Ge and has been quantified.

Fig. 1b is a schematic representation of an n-type sample in PICTS. The sample has two ohmic, Li-diffused contacts (250°C during 15 min in Ar atmosphere) applied on two opposite faces of the sample (sandwich configuration). On both sides a thin layer of InHg eutectic is rubbed on which is covered with a piece of In foil (with a circular hole in the middle of one side to allow illumination). A bias is applied to the sample and kept constant during the whole experiment. The sample is illuminated through one of the contacts with intrinsic light. The optical excitation source is the same as the one used for ODLTS. The sandwich configuration together with the strongly absorbed supra band-gap light results in a very superficial injection of electron–hole pairs in the sample. In this situation, the magnitude of the current will depend on the polarity of the applied bias allowing to make a distinction between electron and hole traps. When for instance the back Ohmic contact is negative (which is the situation used in our experiments), holes will be predominantly injected throughout the sample. These holes (minority carriers) are available for capture into deep levels

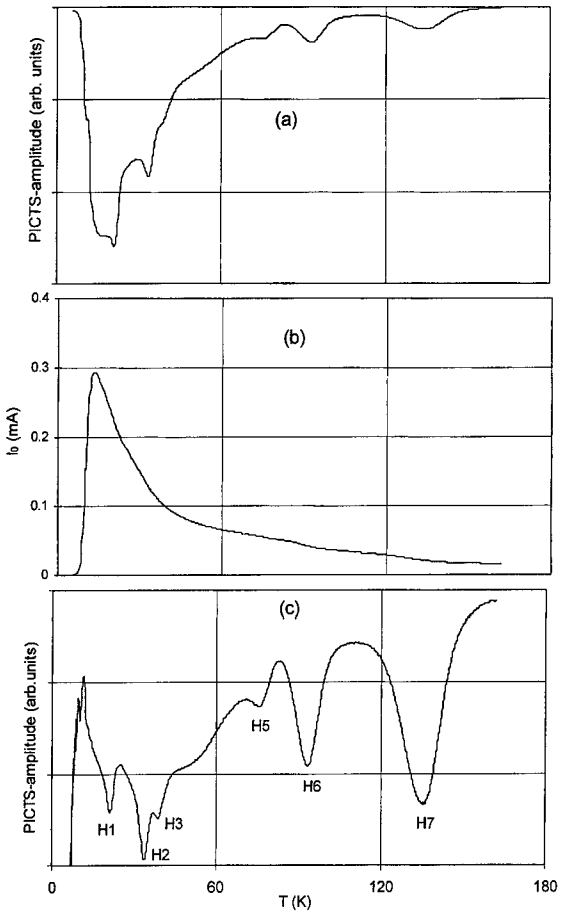

Fig. 4. (a) Original PICTS spectrum; bias: -0.5 V; light pulses: 20 ms ($\tau_{window} = 47$ ms), (b) Dark current at quiescent bias (c) PICTS spectrum corrected for the temperature dependence of the mobility. For peak labels refer to Table 1.

and after the light is switched off, the defect states which have been filled during the optical pulse will return to their initial state by hole emission, resulting in a current transient.

A typical PICTS spectrum is shown in Fig. 4a [11,14]. The PICTS peaks are always superimposed on a large background and hence is not very pronounced. This background increases with decreasing temperature. In Fig. 4b the dark current at quiescent bias corresponding with the PICTS spectrum of Fig. 4a is shown. The dark current increases when the temperature decreases which can be explained by the mobility dependence of the current (the mobility increases strongly with decreasing temperature). Since PICTS is basically a current measurement, the latter temperature dependence is also reflected in the PICTS spectra. This dependence can be eliminated by dividing the spectrum by its corresponding dark current. The corrected spectrum is given in Fig. 4c. As expected, the major part of the broad background is eliminated, leaving a spectrum with peaks that become well resolved. It was shown that the levels found in UP Ge with PICTS are the same as the ones found with ODLTS in HP n-type Ge and with DLTS in HP p-type Ge : mainly Cu-related deep levels.

In the configuration as described above it is possible to deduce a concentration formula [11,14]. This formula too was verified experimentally showing that PICTS can be used in a quantitative way for the evaluation of deep traps in material with a very low net shallow concentration.

Acknowledgements

This work was supported by the Flemish institute for stimulation of scientific-technological research in industry (IWT). The authors wish to thank M. Cauwe, D. Vyncke, B. Depuydt and C. Goessens from Union-Minière, BU Electro-Optic Materials (Olen) for supplying the high-quality germanium used in this work as well as for the use of their advanced DLTS instrument.

References

[1] D.V. Lang, J. Appl. Phys. 45 (1974) 3014–3023.
[2] E.E. Haller, P.P. Li, G.S. Hubbard, W.L. Hansen, IEEE Trans. Nucl. Sci. NS-26 (1979) 265.
[3] E. Simoen, P. Clauws, M. Lamon, J. Vennik, Semicond. Sci. Technol. 1 (1986) 53.
[4] E. Simoen, P. Clauws, J. Broeckx, J. Vennik, M. Van Sande, L. De Laet, IEEE Trans. Nucl. Sci. NS-29 (1982) 789.
[5] E. Simoen, P. Clauws, G. Huylebroeck, J. Vennik, L. Van Goethem, M. Van Sande, L. De Laet, H. Guislain, Nucl. Instr. and Meth. A 251 (1986) 519.
[6] E. Simoen, P. Clauws, J. Vennik, J. Phys. D: Appl. Phys. 18 (1985) 2041.
[7] R.H. Pehl, N.W. Madden, J.H. Elliott, T.W. Raudorf, R.C. Trammell, L.S. Darken, IEEE Trans. Nucl. Sci. NS-16 (1979) 321.
[8] T.W. Raudorf, R.H. Pehl, Nucl. Instr. and Meth. A 255 (1987) 538.
[9] M. Van Sande, L. Van Goethem, L. De Laet, H. Guislain, Appl. Phys. A 40 (1986) 257.
[10] E. Simoen, P. Clauws, J. Vennik, Solid State Commun. 54 (1985) 1025.
[11] A. Blondeel, Ph. D. Thesis, Universiteit Gent, Gent 1998.
[12] S.D. Brotherton, J. Appl. Phys. 55 (1984) 3636.
[13] A. Blondeel, P. Cauws, D. Vyncke, J. Appl. Phys. 81 (10) (1997) 6767.
[14] A. Blondeel, P. Clauws, J. Appl. Phys. 86 (1999) 940.

[15] C.H. Hurtes, M. Boulou, A. Mitonneau, D. Bois, Appl. Phys. Lett. 32 (12) (1978) 821.
[16] G.M. Martin, D. Bois, in: P.A. Barnes, G.A. Rozgonyi (Eds.), Semiconductor Characterization Techniques, PV 78-3, The electrochemical society, Princeton, NJ, 1978, pp. 32–42.
[17] O. Yoshie, M. Kamihara, Jpn. J. Appl. Phys. 22 (4) (1983) 621.
[18] J.C. Balland, J.P. Zielinger, C. Noguet, M. Tapiero, J. Phys. D: Appl. Phys. 19 (1986) 57.

ELSEVIER

Physica B 273–274 (1999) 589–592

PHYSICA B

www.elsevier.com/locate/physb

Initial stages of Ge growth on Si(1 0 0): ad-atoms, ad-dimers, and ad-trimers

G.M. Dalpian, A. Janotti, A. Fazzio, Antônio J.R. da Silva*

Instituto de Física, Universidade de São Paulo, CP 66318, 05315-970 São Paulo, SP, Brazil

Abstract

We study, using ab initio calculations, small structures that are present at the early stages of growth of Ge on the Si(1 0 0) surface. Ad-atoms, ad-dimers, and ad-trimers are investigated. We consider different configurations of the adsorbed structures, and present results for their relaxed geometries and relative energies.

Keywords: Ge on Si(1 0 0); Semiconductor growth; Ab initio calculations

1. Introduction

The microscopic understanding of the initial stages of growth of semiconductor materials has attracted a great deal of attention in the past few years [1]. The motivation behind all this activity has both an applied as well as a basic research connotation. The drive towards smaller devices and nanostructures has motivated the understanding of growth at the atomistic level. Because the Si(1 0 0) is the surface of choice for device growth, both the surface itself [2–5] as well as the growth of Si on it [6–15] has been studied in great detail. Careful experiments performed at ultra-high vacuum conditions, with coverages of a few percent of a monolayer, using scanning tunneling microscope (STM) were able to identify many adsorbed structures that participate at the initial stages of growth, and some of the dynamical processes that lead from these small structures to the epitaxial growth of a full layer [8–11,14,15]. From the theoretical point of view, many studies were also performed on these small structures [7,12,13]. The geometries and relative energies for the different adsorption sites and configurations have been studied, and these studies have been very helpful in the understanding of the Si growth on Si(1 0 0).

The growth of germanium on Si(1 0 0) has also been intensively studied, mainly motivated by the formation of Ge islands on silicon surfaces [16,17]. However, a relatively smaller number of studies [18–21] have focused on the initial stages of Ge growth when compared to the growth of Si on Si(1 0 0). From a theoretical point of view, only the adsorbed monomer has been studied in great detail at the ab initio level [19]. The objective of the present paper is to contribute to the characterization of these small Ge structures. We study monomers, dimers and trimers, their atomic relaxations and relative energies of each configuration.

2. Method

Our calculations are based in the density-functional theory (DFT), and we use the local density approximation (LDA) for the exchange-correlation potential [22]. We have performed total energy calculations for the different configurations, and the surface was simulated using the supercell approach. The supercell used in the present work was formed by a 4×4 surface unit cell, six atomic layers, five vacuum layers, and hydrogen passivation of the dangling bonds in one of the exposed surfaces.

* Corresponding author. Tel.: 55-11-818-7039; fax: 55-11-818-6831.

E-mail address: ajrsilva@if.usp.br (A.J.R. da Silva)

0921-4526/99/$ - see front matter
PII: S0921-4526(99)00580-3

All geometry optimizations were performed without any symmetry constraints, and all the atoms in the topmost five silicon layers were allowed to relax, including all the Ge adsorbed atoms. The atoms in the bottom layer were held at their bulk positions. We considered that the structures were relaxed when all components of the forces were smaller than 0.001 hartree/bohr. The ion–electron interactions were described using norm-conserving pseudopotentials of Bachelet et al. [23], in the Kleinman–Bylander form [24]. We used a plane wave basis set to expand the Kohn–Sham orbitals with a cutoff energy of 12 Ry. The Brillouin zone was sampled with one special $\boldsymbol{k}$-point at Γ. We have performed some tests with the dimer structures, and increasing the sampling from one special $\boldsymbol{k}$-point to four special $\boldsymbol{k}$-points changes the relative energies by less than 0.1 eV, but the ordering of the configurations with respect to their energies was not altered.

3. Results

We have chosen to study three small adsorbed structures, the ad-atoms, or monomers, the ad-dimers, and ad-trimers. For each structure we have selected few adsorption sites and configurations, and then we have allowed the system to relax, as described above. We report below the relaxed geometries for each configuration, and also their relative energies.

3.1. Ad-atoms

The monomers have been studied before by Milman et al. and they have obtained that the most stable position for the ad-atom is on the troughs between the substrate ad-dimers, almost directly above a second-layer substrate atom, the so-called M site. Almost degenerate in energy is a site on top of the substrate dimer rows, located in between two Si dimers, named H site. The energy difference between these two configurations obtained by Milman et al. was $\Delta E_{HM} = 0.06$ eV.

Similarly to Milman et al.'s result, we also obtain that the M site is more stable than the H site. However, we obtain a much larger energy difference: $\Delta E_{HM} = 0.30$ eV. Our relaxed geometries, reported in Fig. 1, are also different than the ones obtained by Milman et al. For site M, we found that the dimers bonded to the Ge ad-atom are still buckled as in the clean surface, only the buckling angle has changed. In the next Si dimer row, the two nearest dimers to the Ge ad-atom are buckled in such a way that the down atoms are closest to the Ge, as can be seen in Fig. 1. For the H site, the two dimers bonded to the ad-atom also did not have their buckling direction changed, the only change being again the amplitude of their buckling angle. All the other substrate dimers in the cell were almost unaffected (buckling directions and buckling angles). The inter-atomic distances between the Ge ad-atom and its nearest-neighbors are reported in Table 1 for both structures.

3.2. Ad-dimers

We consider four possible configurations for the ad-dimers: (i) ad-dimer on top of the substrate dimer rows, with the ad-dimer bond parallel to the substrate dimer bonds ($TOP_{\parallel}$); (ii) ad-dimer on top of the substrate dimer rows, with the ad-dimer bond perpendicular to the substrate dimer bonds ($TOP_{\perp}$); (iii) ad-dimer on the trough between the substrate dimer rows, with the ad-dimer bond parallel to the substrate dimer bonds ($TRO_{\parallel}$); (iv) ad-dimer on the trough between the substrate dimer rows, with the ad-dimer bond perpendicular to the substrate dimer bonds ($TRO_{\perp}$).

Our relaxed geometries are presented in Fig. 2, and their relative energies are shown in Table 2 (these numbers correspond to a calculation where the energies were

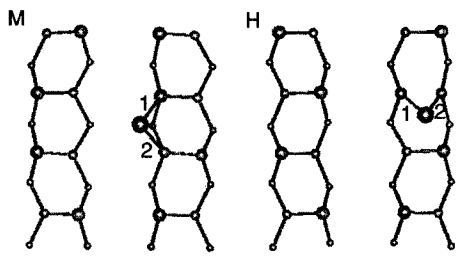

Fig. 1. Relaxed geometries for the two ad-atom configurations studied. The inter-atomic distances marked with numbers are presented in Table 1.

Table 1
Values of the inter-atomic distances for the bonds marked in Figs. (1)–(3). All the values are in Å

	1	2	3	4	5	6	7
ad-atoms							
M	2.44	2.43					
H	2.45	2.38					
ad-dimers							
$TOP_{\parallel}$	2.47	2.46	2.50	2.50	2.46		
$TOP_{\perp}$	2.46	2.38	2.36	2.40	2.44		
$TRO_{\parallel}$	2.69	2.48	2.47	2.48	2.48		
$TRO_{\perp}$	2.39	2.48	2.48	2.48	2.48		
ad-trimers							
a	2.63	2.47	2.47	2.46	2.46	2.43	2.43
b	2.51	2.43	2.48	2.46	2.51	2.49	2.46
c	2.69	2.50	2.46	2.45	2.48	2.43	2.44

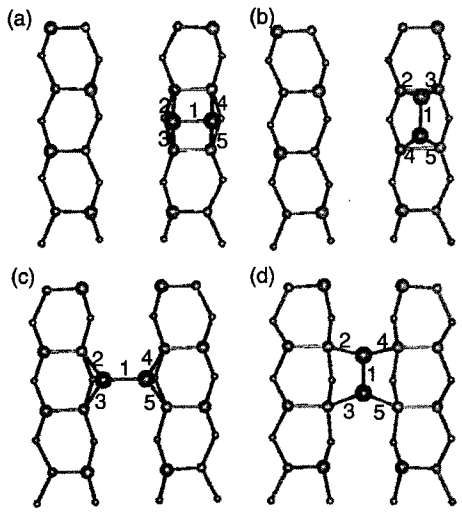

Fig. 2. Relaxed geometries for the four ad-dimer configurations studied: (a) $TOP_{\parallel}$; (b) $TOP_{\perp}$; (c) $TRO_{\parallel}$; (d) $TRO_{\perp}$ (see text for definition of labels). The inter-atomic distances marked with numbers are presented in Table 1.

Table 2
Relative energies for the four Ge ad-dimers (see text for definition of labels). All results are in eV

$TOP_{\parallel}$	$TOP_{\perp}$	$TRO_{\parallel}$	$TRO_{\perp}$
0.0	0.08	0.30	1.00

obtained using four special k-points for the geometries optimized using only one k-point). For Si ad-dimers on Si(1 0 0), experimental evidence [14] suggests that the $TOP_{\perp}$ is the most stable configuration, with the $TOP_{\parallel}$ only 0.06 eV higher in energy. For the Ge ad-dimers, on the other hand, we obtain that the most stable configuration is the $TOP_{\parallel}$ instead of the $TOP_{\perp}$. However, similarly to Si on Si(1 0 0), we obtain that the on-top structures are more stable than the on-trough ones. The main reason is that the on-top Ge ad-dimers cause a relatively small disturbance on the substrate Si dimers when compared to the on-trough structures. The Si–Si dimer bond lengths of the four Si dimers which are bonded to the Ge ad-dimers, on both on-trough configurations, are much longer than the corresponding bonds on the clean Si(1 0 0) surface, whereas the Si–Si bond lengths of the other four Si dimers in our (4×4) unit cell are shorter than the corresponding bonds on the clean Si(1 0 0) surface. This does not happen in the on-top configurations, where all the Si–Si bond lengths are much closer to their values on the clean Si(1 0 0) surface. This is similar to what was found by Brocks and Kelly [12] for Si ad-dimers on Si(1 0 0). We do not find any buckling for the Ge ad-dimers, in any one of the four configurations that we have studied. In Table 1 we report the Ge ad-dimers bond lengths and all the inter-atomic distances between the Ge atoms and their Si nearest neighbors.

3.3. Ad-trimers

Wingerden et al. [14] studied the early stages of Si growth on Si(1 0 0) using STM measurements. They have observed only one stable type of three-atom cluster on the surface, composed of a $TRO_{\parallel}$ ad-dimer plus an in-line ad-atom at the M site of an adjacent trough. They have also observed two pathways to form such a cluster. In one of them there is the simple binding of a diffusing ad-atom to an existing $TRO_{\parallel}$ ad-dimer, and in the other there is a more complex mechanism involving a $TOP_{\parallel}$ ad-dimer (which will have its dimer bond broken) plus a diffusing ad-atom.

Based on these observations, we have decided to study three configurations for the ad-trimers, whose relaxed geometries are presented in Fig. 3. We obtain that the most stable structure is composed by a $TRO_{\parallel}$ ad-dimer plus an in-line ad-atom at the M site, in agreement with Wingerden et al.'s [14] STM measurements. The relative energies for the three structures are presented in Table 3. All the relevant inter-atomic distances are presented in Table 1.

It is interesting to note that even though the $TOP_{\parallel}$ ad-dimer and the ad-atom at site M are the most stable structures among the dimers and monomers, respectively, the trimer formed by these two structures, our structure (b) in Fig. 3, is not the most stable configuration.

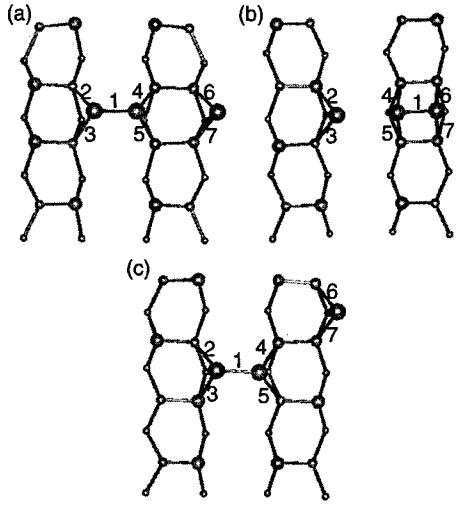

Fig. 3. Relaxed geometries for the three ad-trimer configurations studied. The inter-atomic distances marked with numbers are presented in Table 1.

Table 3
Relative energies for the three Ge ad-trimers (the labels refer to Fig. 3). All results are in eV

a	*b*	*c*
0.0	0.28	0.40

This indicates that the $TRO_{\parallel}$ ad-dimer plays a significant role in the growth of larger structures [20].

4. Conclusions

We have studied small adsorbed Ge structures on Si(1 0 0). In particular, we have focused on ad-atoms, ad-dimers, and ad-trimers. For the ad-atoms, we have obtained that the most stable site is the M site, similarly to Si on Si(1 0 0). For the ad-dimers, we have shown that the structure adsorbed on top of the substrate dimer rows are more stable than the structures adsorbed on the troughs between the substrate dimer rows. This is also similar to Si on Si(1 0 0). However, we obtain that the $TOP_{\parallel}$ is more stable than the $TOP_{\perp}$ structure, which is opposed to what is found for Si on Si(1 0 0). Finally, for the ad-trimers, we have obtained that the structure composed by a $TRO_{\parallel}$ ad-dimer plus an in-line ad-atom at the M site is the most stable structure. This is consistent with the STM measurements of Wingerden et al. [14] for Si on Si(1 0 0).

Acknowledgements

This research was supported by CNPq and FAPESP.

References

[1] Z. Zhang, M.G. Lagally, Science 276 (1997) 377.
[2] J. Dąbrowski, M. Scheffler, Appl. Surf. Sci. 56–58 (1992) 15.
[3] J. Fritsch, P. Pavone, Surf. Sci. 344 (1995) 159.
[4] A. Ramstad, G. Brocks, P.J. Kelly, Phys. Rev. B 51 (1995) 14 504.
[5] J.A. Kubby, J.J. Boland, Surf. Sci. Rep. 26 (1996) 61, and references therein.
[6] D. Srivastava, B.J. Garrison, J. Vac. Sci. Technol. A 8 (1990) 3506.
[7] G. Brocks, P.J. Kelly, R. Car, Phys. Rev. Lett. 66 (1991) 1729.
[8] Z. Zhang, F. Wu, H.J.W. Zandvliet, B. Poelsema, H. Metiu, M.G. Lagally, Phys. Rev. Lett. 74 (1995) 3644.
[9] P.J. Bedrossian, Phys. Rev. Lett. 74 (1995) 3648.
[10] R.A. Wolkow, Phys. Rev. Lett. 74 (1995) 4448.
[11] B.S. Swartzentruber, Phys. Rev. Lett. 76 (1996) 459.
[12] G. Brocks, P.J. Kelly, Phys. Rev. Lett. 76 (1996) 2362.
[13] T. Yamasaki, T. Uda, K. Terakura, Phys. Rev. Lett. 76 (1996) 2949.
[14] J. van Wingerden, A. van Dam, M.J. Haye, P.M.L.O. Scholte, F. Tuinstra, Phys. Rev. B 55 (1997) 4723.
[15] B. Borovsky, M. Krueger, E. Ganz, Phys. Rev. Lett. 78 (1997) 4229.
[16] M.G. Lagally, Phys. Today 46 (1993) 24.
[17] M. Kästner, B. Voigtländer, Phys. Rev. Lett. 82 (1999) 2745, and references therein.
[18] F. Iwawaki, M. Tomitori, O. Nishikawa, Surf. Sci. 266 (1992) 285.
[19] V. Milman, D.E. Jesson, S.J. Pennycook, M.C. Payne, M.H. Lee, I. Stich, Phys. Rev. B 50 (1994) 2663.
[20] X.R. Qin, M.G. Lagally, Science 278 (1997) 1444.
[21] X.R. Qin, F. Liu, B.S. Swartzentruber, M.G. Lagally, Phys. Rev. Lett. 81 (1998) 2288.
[22] M. Bockstedte, A. Kley, J. Neugebauer, M. Scheffler, Comp. Phys. Commun. 107 (1997) 187.
[23] G.B. Bachelet, D.R. Hamann, M. Schlüter, Phys. Rev. B 26 (1982) 4199.
[24] L. Kleinman, D.M. Bylander, Phys. Rev. Lett. 48 (1982) 1425.

ELSEVIER

Physica B 273–274 (1999) 593–597

PHYSICA B

www.elsevier.com/locate/physb

Atomic resolution EELS analysis of a misfit dislocation at a GeSi/Si interface

P.E. Batson*

IBM Thomas J. Watson Research Center, Yorktown Heights, NY 10598, USA

Abstract

A dissociated 60° misfit dislocation at the substrate interface of a Si/$Ge_xSi_{(1-x)}$ heterojunction has been examined using EELS and ADF imaging. New spectra are obtained at the intrinsic stacking fault, at the dislocation cores and in the strained regions on either side of the stacking fault. A splitting of the L_1 conduction band due to symmetry breaking at the stacking fault is observed. Near edge conduction band states are verified at the partial dislocation cores, but not at the stacking fault.

Keywords: Dislocations; Electronic structure; EELS; GeSi

1. Introduction

When the thickness of a thin film exceeds the Matthews–Blakeslee limit for pseudomorphic growth, misfit dislocations are introduced at the underlying heterojunction [1]. In the case for Si growth on the (0 0 1) surface of $Ge_xSi_{(1-x)}$, the misfit takes the form of a 60° dislocation dissociated into 30° (P30) and 90° (P90) partial dislocations separated by an intrinsic stacking fault (ISF). These structures also occur in heavily deformed silicon, and are believed to support electrically active states within 0.1 eV of the conduction band (CB) minimum [2]. TEM and luminescence studies have confirmed optical activity near the defect, but the atomic structure that gives rise to the activity is not yet known [3–5]. Optical activity has also been detected associated with misfit structures [4]. Theoretical work for the stacking fault [6], and for straight partial dislocations [7–9] have found that defect structures often reconstruct to clear the gap of electronic states. On the other hand, there has been some theoretical evidence for the existence of shallow valence band states [10].

2. Experimental details and description of the dislocation

I report here experiments using spatially resolved electron energy loss spectroscopy (EELS) to probe small regions of dissociated misfit dislocations in a strained Si quantum well imbedded in $Ge_{0.35}Si_{0.65}$. Atomic column positions in the [1 1 0] projection, and the spatial location for the spectral results are obtained using annular dark field (ADF) imaging [11,12] in the VG microscopes scanning transmission electron microscope (STEM), modified to operate at 120 kV to obtain a 0.2 nm diameter electron probe. In prior work with GeSi alloys, it has been shown that very detailed conduction band (CB) information is obtainable using high resolution, spatially resolved EELS measurements of the Si $2p_{3/2}$ core absorption edge [13,14]. The EELS spectrometer was a Wien Filter design with an energy resolution of ~200 meV and an absolute calibration of ± 20 meV [15]. Numerical deconvolution of the 0.3 eV wide field emission yielded a spectral resolution of 0.20–0.25 eV limited by statistical considerations [16].

The misfit dislocation was of the 60° type located at the substrate interface of a 15 nm Si quantum well structure [17] Fig. 1 shows an annular dark field (ADF) image of the [1 − 1 0] projection of the structure at high magnification. The Si well is at the bottom left, below the dashed line. The dislocation is extended about 3 nm in the [1 1 − 2] direction away from the Si interface. Since the

* Tel.: 914-945-2782; fax: 914-945-2141.
E-mail address: batson@watson.ibm.com (P.E. Batson)

0921-4526/99/$ - see front matter
PII: S0921-4526(99)00078-2

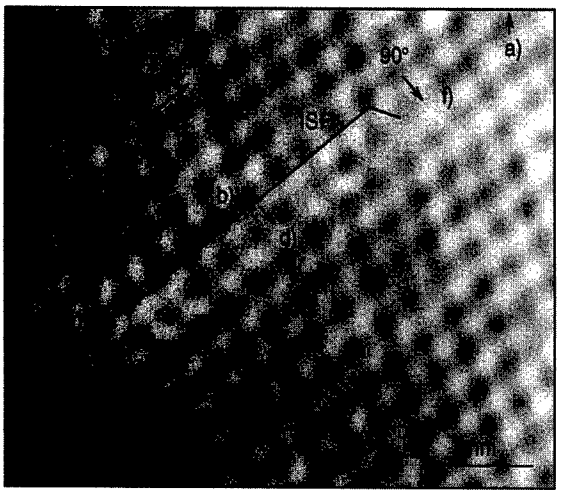

Fig. 1. ADF image of a second misfit dislocation structure. Detailed EELS results were obtained from the locations marked a–f.

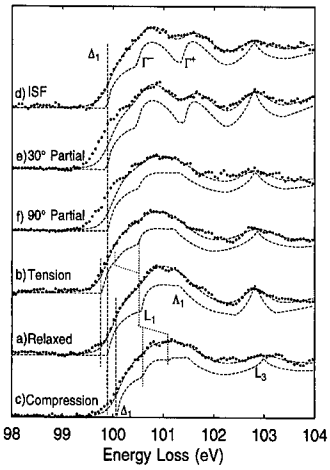

Fig. 2. Spatially resolved EELS results for the Si $2p_{3/2} \rightarrow$ CB absorption edge for various locations within the structure summarized in Fig. 1. There appear to be unoccupied electron states below the CB within the dislocation cores, but not within the ISF.

inter-column distance in the [0 0 1] direction in this projection is about 0.135 nm, this distance is not resolved using the 0.2 nm probe size. Instead, for each pair of columns, we see one spot, elongated in either the [0 0 1] direction in the bulk or in the [− 2 − 2 1] direction in the ISF. The measured distance between the two partial dislocations is 3.3 nm, or 10 "dumbbell" units. This distance was found in other simple misfit structures elsewhere in this sample. The P30 core is well defined, but the P90 core appears indistinct, probably due to kinks occurring along its length [18,19]. However, it can be located by considering continuity of (1 1 − 1) type atomic planes as they cross the ISF. This figure defines several unique locations for EELS analysis: (a) the bulk, relaxed GeSi alloy several tens of nm away from the defect, (b) the regions of tension and (c) compression within two (1 1 1) plane spacings on either side of the ISF, (d) the ISF itself, (e) the P30 dislocation core and (f) the P90 core.

3. Experimental results

Si 2p core absorption spectra are processed to remove a slowly varying background, to sharpen the energy resolution by deconvolution of the incident beam energy distribution, and to remove the $2p_{1/2} \rightarrow$ CB intensity. The shape of the remaining intensity is due to transitions to the s- and d-projected CB local density of states (LDOS). A model spectrum is made from a trial LDOS, using an inelastic scattering theory including core excitonic interactions, lifetime broadening and instrumental resolution. The model LDOS consists of parabolic effective mass contributions for the s-like band edges at Δ_1, L_1, and a saddle point at the d-like point L_3. These contributions are terminated linearly at the p-like points $\Gamma_{1,5}$ and $\Gamma_{2'}$ in the center of the Brillouin zone. The model positions for the important band edges Δ_1 and L_1 are then adjusted to fit the experimental data. Finally, there is a small contribution to the L_1 intensity due to a Ge-like saddle point in the Λ_1 band.

In Fig. 2 there are spectral results for each of the regions described above. Each spectrum includes the processed data, a trial LDOS and the fitted spectrum. The spectra are aligned on an absolute energy scale relative to the $2p_{3/2}$ core level. This level has been shown to be a constant for the relaxed alloy series [14], but it does shift with the addition of crystal strain [20].

3.1. Bulk relaxed and strained alloy areas

The bulk alloy results in Fig. 2 match the prior results closely for the alloy composition $Ge_{35}Si_{65}$ [13]. The four usual CB features, Δ_1, L_1, L_3, and Λ_1, are required to fully explain the measured data. In the regions of tension and compression, the most notable change is to shift the spectra lower or higher in energy. A secondary difference is an apparent broadening of the L_1 contribution in the compressed region. In order to understand these results, we need to consider both volume and uniaxial strain in [1 1 1] type directions.

The experimental data show a Δ_1 shift of − 0.085 eV for the region in tension and + 0.10 eV in compression. These shifts are opposite to those expected for the CB and so we expect a large core level shift. Within a couple (1 1 1) lattice planes on either side of the ISF, inspection of the image shows that this 10 unit ISF has 10 atomic planes on one side and 11 planes on the other, occupying roughly 10.5 bulk lattice units, giving a lattice strain of

$\pm$ 5% on either side. The deformation potential for the Si $2p_{3/2}$ core level is about $-$ 6 eV [20] giving a core level shift of $-$ 0.3 eV at 5% tension and + 0.3 eV in compression. Therefore these measurements place the Δ_1 CB at + 0.22 eV at (b) in tension, and $-$ 0.20 eV at (c) in compression, relative to the bulk alloy. The band offset in the Si well in this case is about $-$ 0.28 eV so this is a significant perturbation of a desired device quantity. The deformation potential for Δ_1 is + 4 eV, [20] and therefore provides a satisfying consistency to the interpretation.

The uniaxial strain is somewhat more difficult to deal with in that it results in splitting of the eight-fold degenerate L_1 bands into two-fold/six-fold combinations. Again, inspection of the image suggests that the uniaxial strain is about $\pm$ 5% within a (1 1 1) plane, but oriented in a [1 1 2] type of direction. The appropriate deformation potential for this process appears to be Ξ_u^L and is 15–16 eV [20]. The shifts are expressed relative to the strain $\varepsilon_{xy} = 1/3(\varepsilon_\perp - \varepsilon_{||}) \approx 0.1\varepsilon_{111}$ for this case, leading to a shift of two-fold part of the band by about 0.15 eV and the six-fold part by 0.05 eV in the opposite direction. An experimental determination of these quantities is made difficult by the disparity in degeneracy, making the two-fold contribution difficult to identify. In Fig. 2 the total splitting for the best fit to the data is indicated by the dotted lines attached to the L_1 point in the bulk results. In tension, the two-fold edge falls over the edge of the Δ_1 contribution, giving a spectrum that appears to have only one, less intense, L_1 peak. In compression, the two-fold piece shifts upwards in energy, where the underlying Δ_1 contribution is flat, leading to an apparent broadening of the L_1 peak. This modeling arrives at a total splitting of 0.26 eV, compared with 0.20 eV expected from the deformation potential.

3.2. Intrinsic stacking fault

Spectral results from position (d), the ISF, show a splitting of the L_1 peak, with no other apparent shifts or changes. In particular, there appears to be no shift or change in shape of the onset at Δ_1. The splitting can be understood using the calculations for Si of Mattheiss and Patel [21]. They predicted that the L_1 branch is affected in two ways. First, it is projected into the center of the 2-D hexagonal ISF Brillouin zone (BZ) by two-dimensional nature of the fault. Then it is split into two components by mixing of Si sp^3 orbitals from third-neighbor atoms on either side of the glide-cut plane. In the parent crystal, third-neighbor atoms occupy positions on either end of a structure commonly referred to as a "chair". In the ISF structure, as a consequence of the 180° rotation of the structure about the [1 1 1] direction, the third-neighbors form a "boat" structure, moving from their normal 0.45 nm distance apart to nearly the second neighbor distance of 0.38 nm. This structure can also be visualized as a two atom "dumbbell" with three neighbors at each end. In the bulk, the six end atoms transform into each other by a two-fold screw axis oriented along the "dumbbell". In the ISF, this screw axis is replaced by a mirror plane.

I model the band splitting that results from this by introducing a gap in the L_1 band, labeling the upper and lower branches, Γ^+ and Γ^-, following the notion that the band is projected into the 2-D zone center and split into symmetric and anti-symmetric parts by the third-neighbor interaction. This splitting is calculated to be about 1.5 eV for Si, while the lower band is calculated to shift about 0.25 eV down from the L_1 minimum in the bulk. These predictions strongly resemble the observed behavior. That work also predicts that the X_1 CB in the bulk lattice, for which Δ_1 is the band minimum, becomes the Γ–M band in the hexagonal ISF BZ and is not affected by the change in local symmetry at the ISF. Again this is reflected in the data of Fig. 2, which shows no change at the ISF Δ_1 onset relative to the bulk alloy.

This experimental result argues against the presence of in-gap empty states near the CB at the ISF. It obviously does not address the possibility of states near the valence band edge, although it indirectly supports that possibility because they are predicted within the Mathiess and Patel work, which appears consistent with these results in areas where it can be checked.

3.3. Dislocation cores

P30 spectral results in Fig. 2 show L_1 splitting that is very similar to that at the ISF. Referring to the model structure in Fig. 3a, we see, in the parent lattice, the

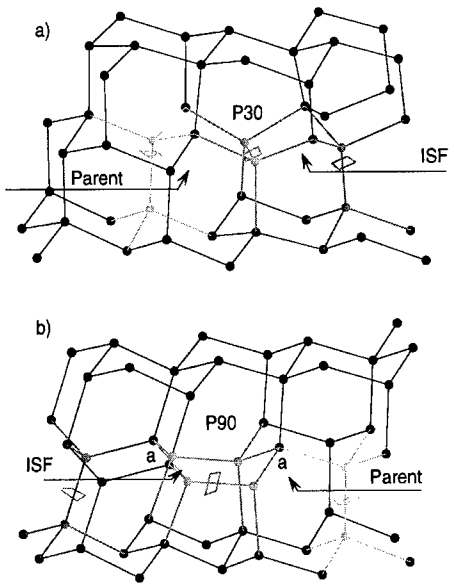

Fig. 3. P30 (a) and P90 (b) model structures. Note that the P30 resembles the ISF structure.

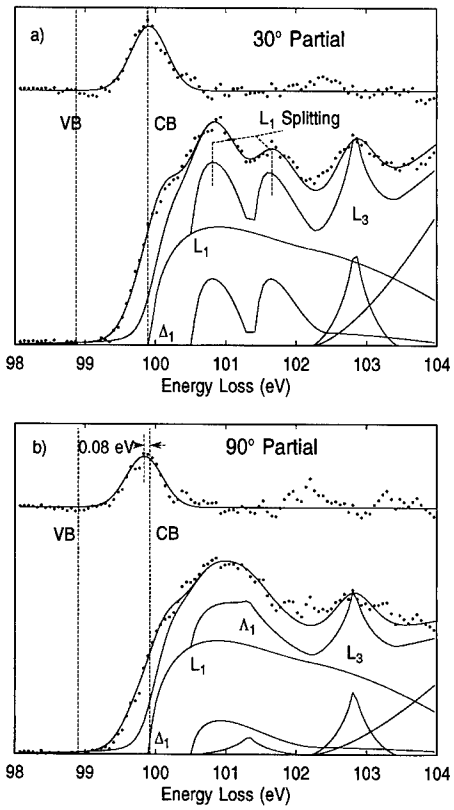

Fig. 4. EELS analysis for the P30 (a) and P90 (b) partial dislocation cores. The solid line reproduces the fit to the ISF data on the left and the bulk data on the right. There is extra intensity coincident with the CB onset in both cases.

two-fold screw operation for the bulk. In the ISF, this is replaced by a structure supporting a quasi-mirror plane. The P30 core structure is very similar to that in the ISF, although it has to be admitted that the mirror symmetry is not exact in the P30 case, either. Interestingly, the orientation of the core structure is in a [1 1 0] type direction rather than in a [1 1 1] direction as it is in the ISF. It appears that the reconstructed P30 core is consistent with the finding of splitting in the L_1 band at the dislocation core. This result is supported by a statistical analysis of the structure of the relaxed core to be reported elsewhere.

Examination of the P30 near edge structure at Δ_1, summarized in Fig. 4a, shows near edge gap states at the dislocation core. For everywhere except near Δ_1, the ISF model fit is a very good match to the data. When this fit is subtracted from the P30 data, a peak remains centered at the Δ_1 onset. It's width is close to the instrumental resolution of 0.2 eV. In addition, excess intensity remains near the L_3 peak. It is known that this peak is symmetry compatible with Δ_1 so that it shifts in a similar manner under the influence of strain [13]. Therefore, it is reasonable that any distortion in the crystal that splits off states into the gap from Δ_1 should also shift states downwards from L_3.

The P90 core EELS results present an interesting problem because they do not show the L_1 splitting. Fig. 3b shows the single period (SP90) reconstructed P90 structure. This consists of 5–7-fold rings joined across the core. In this model structure third-neighbor pairs (for instance, labeled a) mimic the ISF configuration, so it would seem that this structure might not be consistent with the spectral results.

A new model for the P90, recently suggested by Bennetto et al. [9] introduces a double period (DP90) reconstruction at the core through the addition of kinks in the plane of the ISF. Viewed in the [1 1 1] direction, these have the effect of creating 5–7-fold rings along the dislocation core. The model is interesting in the present context because the introduction of kinks reduces the number of ISF-like third-neighbor interactions. In fact, introducing many kinks within an extended core structure can completely eliminate ISF third-neighbor interactions near the P90 core. This would be more likely, therefore, to produce a spectrum that resembles the bulk result.

Fig. 4b shows the EELS analysis for the P90 core. In this case the fitted model for the bulk result has been subtracted from the data to reveal that a peak exists about 80 meV below the onset of Δ_1. Also in this case, a second peak exists near L_3, as it must if the near edge peak is actually due to the splitting of states from the CB edge.

These two results, together with the results from the ISF and strained regions above, suggest that optical activity involving empty states near the CB is likely to be confined to the dislocation cores. Electrical activity may also be associated with the regions of strain on either side of the ISF, since 200 meV peaks and valleys in the CB offset are certainly present there.

4. Conclusions

This report describes the EELS and atomic structure of the dissociated 60° misfit dislocation. Splitting of the L_1 CB peak is almost certainly due to local symmetry breaking by the presence of ISF-like atomic structure. Near edge gap states are found at the partial dislocation cores, leading one to surmise that optical activity exists at these locations. No information about near valence band (VB) edge states can be obtained from these results, so the possibility of optical activity near the ISF due to excitations from a shallow VB state remains. Future work on these structures will be undertaken using improved EELS and imaging capabilities that are currently under development.

Acknowledgements

Model structures for this work were relaxed by Y. Tu at IBM. I also acknowledge discussion with P.M. Mooney, F.K. LeGoues, and K. Ismail during this work. R.W. Nunes kindly provided atomic coordinates for the DP structure.

References

[1] J.W. Matthews, A.E. Blakeslee, J. Crystal Growth 27 (1974) 118.
[2] L.C. Kimerling, H.J. Leamy, J.R. Patel, Appl. Phys. Lett. 30 (1977) 217.
[3] H. Alexander, J. Phys. Coll. Paris 40 (1979) 1.
[4] Kai Shum, P.M. Mooney, J.O. Chu, Phys. Rev. Lett. 71 (1997) 1074.
[5] H. Alexander, J.C.H. Spence, D. Shindo, H. Gottschalk, N. Long, Philos. Mag. A 53 (1986) 627.
[6] M.Y. Chou, M.L. Cohen, S.G. Louie, Phys. Rev. B 32 (1985) 7979.
[7] J.R. Chelikowsky, Phys. Rev. Lett. 49 (1982) 1569.
[8] J.R. Chelikowsky, J.C.H. Spence, Phys. Rev. B 30 (1984) 694.
[9] J. Bennetto, R.W. Nunes, David Vanderbilt, Phys. Rev. Lett. 79 (1997) 245.
[10] F. Liu, M. Mosteller, V. Millman, M.F. Chisholm, T. Kaplan, Phys. Rev. B 51 (1995) 17192.
[11] S.J. Pennycook, L.A. Boatner, Nature 336 (1988) 565.
[12] R.F. Loane, E.J. Kirkland, J. Silcox, Acta. Crystallogr. A 44 (1988) 912.
[13] P.E. Batson, J.F. Morar, Appl. Phys. Lett. 59 (1991) 3285.
[14] J.F. Morar, P.E. Batson, J. Tersoff, Phys. Rev. B 47 (1993) 4107.
[15] P.E. Batson, Rev. Sci. Instr. 57 (1986) 43.
[16] P.E. Batson, D.W. Johnson, J.C.H. Spence, Ultramicroscopy 41 (1992) 137.
[17] K. Ismail, F.K. LeGoues, K.L. Saenger, M. Arafa, J.O. Chu, P.M. Mooney, B.S. Meyerson, Phys. Rev. Lett. 73 (1994) 3447.
[18] A. Olsen, J.C.H. Spence, Philos. Mag. A 43 (1981) 945.
[19] Y.M. Huang, J.C.H. Spence, O.F. Sankey, Phys. Rev. Lett. 74 (1995) 3392.
[20] C.G. Van de Walle, Phys. Rev. B 39 (1989) 1871.
[21] L.F. Matheis, J.R. Patel, Phys. Rev. B 23 (1981) 5384.

ELSEVIER

Physica B 273–274 (1999) 598–602

PHYSICA B

www.elsevier.com/locate/physb

Diffusion of gold in relaxed Si–Ge epi-layers

Roland Fischer[a], Werner F.J. Frank[a,*], Klara Lyutovich[b]

[a]*Max-Planck-Institut für Metallforschung, Heisenbergstraße 1, D-70569 Stuttgart, Germany*
[b]*Universität Stuttgart, Institut für Halbleitertechnik, Stuttgart, Germany*

Abstract

The diffusion of implanted ^{195}Au in relaxed, low-dislocation-density $Si_{1-y}Ge_y$ epi-layers has been measured as a function of temperature (700–950°C) and composition ($0 \leqslant y \leqslant 0.24$) by means of a radiotracer technique, where serial sectioning was done by precision grinding. In all cases, the diffusion takes place by the kick-out mechanism, which is self-interstitial-controlled at low Ge contents, low temperatures, or close to the epi-layer surface, but gold-interstitial-controlled otherwise. An interpretation is presented in which a novel mechanism of alloy-retarded substitutional–interstitial diffusion plays a major rôle.

Keywords: Si–Ge epi-layers; Diffusion of gold; Radiotracer technique; Kick-out mechanism

1. Introduction

Nowadays it is generally accepted that germanium and silicon differ considerably with respect to intrinsic-point-defect-mediated diffusion [1]. In Ge, the native point defects dominating under thermal-equilibrium conditions at all solid-state temperatures accessible in diffusion experiments are vacancies, and therefore Ge self-diffusion is vacancy-controlled. The same holds for the diffusion of substitutional solutes in Ge, particularly for dopants of the groups III and V of the periodic table. In Si, by contrast, self-interstitials and vacancies coexist in thermal equilibrium. Whereas in the most thoroughly investigated temperature regime above about 1000°C Si self-diffusion is self-interstitial-controlled, it is vacancy-controlled at lower temperatures. Under these circumstances it is not surprising that the diffusion behaviour of groups-III and V dopants in Si is quite sophisticated due to the different electrostatic and elastic interactions of these atoms with self-interstitials and vacancies. On the other hand, the group-IV element Ge has been found to diffuse in Si almost like Si, and therefore the radiotracer ^{71}Ge may be used as a Si substitute permitting the simulation of Si self-diffusion by ^{71}Ge diffusion in Si. McVay and DuCharme [2] have made use of this possibility by measuring the ^{71}Ge (self-) diffusion in $Si_{1-y}Ge_y$ alloys over the entire composition range $0 \leqslant y \leqslant 1$. In fact, they observed a changeover in the diffusion mechanism at $y = 0.35$ in accordance with the expected transition from the interstitialcy mechanism in Si to the vacancy mechanism in Ge.

Whereas the indirect (i.e. intrinsic-defect-mediated) diffusion of self-atoms or substitutional solutes — sometimes referred to as "slow diffusers" — reflects the properties of the dominating thermal-equilibrium defect species, this is obviously not the case for the "fast" direct interstitial diffusion of transition metals not involving native defects as diffusion vehicles (e.g., Fe in Si). However, there are "intermediate diffusers" — Au [1], Pt [1], or Zn [3] in Si and Cu [4] or Au [5–7] in Ge — which during diffusion repeatedly change from interstitial to substitutional sites, and vice versa, with the aid of intrinsic point defects. The fact that Au is an intermediate diffuser in both Si and Ge has prompted us to study the diffusion of Au in $Si_{1-y}Ge_y$ alloys as a function of composition in order to search for the changeover from Si-type self-interstitial-controlled to Ge-type vacancy-controlled interstitial–substitutional Au diffusion. This paper reports on our first results concerning the composition range $0 \leqslant y \leqslant 0.24$.

* Corresponding author. Tel.: + 49-711-689-1940; fax: + 49-711-689-1932.
E-mail address: wfrank@physix.mpi-stuttgart.mpg.de (W.F.J. Frank)

0921-4526/99/$ - see front matter
PII: S0921-4526(99)00582-7

2. Interstitial–substitutional diffusion mechanisms

Intermediate diffusivity in Si or Ge arises from the hybrid nature of the corresponding element, say, Au, i.e. its capability to occupy both interstitial (Au_i) and substitutional (Au_s) sites. While the interstitial diffusivity (D_i) of a hybrid is high compared to its substitutional diffusivity ($D_s \approx 0$), the opposite is true for the corresponding solubilities ($C_i^{eq} \ll C_s^{eq}$), so that C_s^{eq} is practically identical with the measured total solubility.

Depending on whether self-interstitials (I) or vacancies (V) dominate in thermal equilibrium, the site exchange required in interstitial–substitutional hybrid diffusion occurs either by the kick-out mechanism [8] (Si case),

$$Au_i \leftrightarrows Au_s + I, \tag{1}$$

or the dissociative mechanism [9] (Ge case),

$$Au_i + V \leftrightarrows Au_s. \tag{2}$$

In specimens containing internal sinks and sources for intrinsic point defects (e.g., dislocated specimens), in which the equilibrium concentrations C_l^{eq} of self-interstitials ($l = I$) or vacancies ($l = V$) may rapidly be established, the effective diffusivity $D_{s,eff}$ of the substitutional hybrid component is Au_i-controlled and given by

$$D_{s,eff} = D_i^* \equiv D_i(C_i^{eq}/C_s^{eq}), \tag{3}$$

irrespective of which of the two interstitial–substitutional diffusion mechanisms is operative.

In the absence of internal sinks and sources for point defects, the expressions for $D_{s,eff}$ are different for the two interstitial–substitutional diffusion mechanisms: (i) In the case of kick-out diffusion, $D_{s,eff}$ is controlled by the flux $D_I C_I^{eq}$ of the self-interstitials produced via the reaction (1) to the specimen surface and given by

$$D_{s,eff} = D_I^*[C_s^{eq}/C_s(x,t)]^2 \tag{4a}$$

with

$$D_I^* \equiv D_I C_I^{eq}/C_s^{eq} \tag{4b}$$

(D_I = diffusion coefficient of self-interstitials). It is noteworthy that, via the local, instantaneous Au_s concentration $C_s(x,t)$, the preceding expression for $D_{s,eff}$ is space-coordinate (x)- and time (t)-dependent. For this reason, self-interstitial-controlled kick-out diffusion produces diffusion profiles of extraordinary shapes. (ii) In the case of dissociative diffusion, $D_{s,eff}$ is controlled by the flux $D_V C_V^{eq}$ of vacancies from the surface to the interior of the specimens, where they are consumed by reaction (2). In this case

$$D_{s,eff} = D_V^* \equiv D_V C_V^{eq}/C_s^{eq} \tag{5}$$

(D_V = diffusion coefficient of vacancies).

Now, the attention is to be focused on two interesting features of interstitial–substitutional diffusion, which will play a rôle in the interpretation of our data (Section 4): (a) In the Au_i-controlled case, a distinction between the kick-out mechanism and the dissociative mechanism is not possible, since for both mechanisms $D_{s,eff}$ is the same [Eq. (3)]. (b) In in-diffusion experiments, in which $C_s^{eq}/C_s > 1$, self-interstitial-controlled kick-out diffusion tends to predominate over vacancy-controlled dissociative diffusion. This follows from Eqs. (4) and (5), according to which $D_{s,eff}$ for kick-out diffusion exceeds that for dissociative diffusion by a factor of $(C_s^{eq}/C_s)^2$ for $D_I C_I^{eq} = D_V C_V^{eq}$. The opposite is true for out-diffusion experiments ($C_s^{eq}/C_s < 1$).

In this section, the discussion of the interstitial–substitutional diffusion mechanisms has been restricted to limiting cases in order to bring out the physical base. However, the data evaluation (Section 4) has been done numerically by means of the computer program ZOMBIE [10] which is based on the theories of kick-out and dissociative diffusion in their general versions.

3. Experimental

The specimens used in the present investigations were 5×5 mm^2 square platelets sawn out from about 10 μm thick, relaxed, monocrystalline $Si_{1-y}Ge_y$ layers ($0 \leqslant y \leqslant 0.24$), which had been grown epitaxially from the vapour phase ($H_2, SiCl_4, GeCl_4$) on dislocation-free, 440 μm thick silicon substrates at 1100°C at the Institute of Electronics of the Academy of Sciences of Uzbekistan in Tashkent.

The thicknesses of the Si–Ge epi-layers were determined from raster electron micrographs of the cross-sections of cleft specimens or by means of spreading-resistance measurements across these cross-sections. The Ge contents of the layers were measured by means of energy dispersive X-ray spectroscopy. The dislocation densities in the layers were estimated by counting the etch pit densities on optical micrographs of Secco-etched layer surfaces. For instance, in $Si_{0.947}Ge_{0.053}$ the dislocation density was found to be 2.4×10^{10} m^{-2}. As revealed by transmission electron microscopy, the interfaces between the Si substrates and the Si–Ge epi-layers contain ladder-type networks of misfit dislocations, whose densities exceed the dislocation densities inside the epi-layers by several orders of magnitude.

The diffusion studies were performed by means of a modified radiotracer technique, in which radioactive ^{195}Hg and ^{195m}Hg ions were implanted with an energy of 60 keV into the Si–Ge epi-layers to depths of about 20 nm at the on-line isotope separator (ISOLDE) of the European Nuclear Research Centre (CERN) in Geneva, Switzerland. The decay of these implants via electron capture with half-lives of 10 and 41 h, respectively,

produces ^{195}Au atoms, which, due to their suitable half-life of 186 d, may serve as Au radiotracers in the subsequent diffusion experiments.

Isothermal diffusion anneals were performed in the temperature regime 700–950°C. Their durations t lay in the regime $10\ \mathrm{s} \leqslant t \leqslant 18$ d. The short-time anneals ($\leqslant 240$ s) were done in a computer-controlled rapid-annealing facility, in which for heating the light of two xenon arc lamps was focused on the specimens by means of mirrors and light-conducting glass rods [11].

After the diffusion annealing of a specimen, the Au distribution in the Si–Ge epi-layer and, in many cases, also in the adjacent part of the Si substrate was measured along the "depth coordinate" x perpendicular to the epi-layer surface $x = 0$. To this end, the specimen was serially sectioned by precision grinding, where the minimum thickness of the removed layers was about 0.5 μm. By layerwise counting the ^{195}Au atoms in the taken-off material, which was achieved in a liquid-scintillation counter by detecting the electrons emitted after the radioactive decay of ^{195}Au, it was possible to "construct" the Au concentration profile $C(x)$ in a diffusion-annealed specimen (C = total ^{195}Au concentration).

4. Results and interpretation

In order to test our measuring technique and, in particular, to find out whether the diffusion in thin epi-layers may be compared to bulk diffusion, the ^{195}Au diffusion in (Ge-free) Si epi-layers was investigated. The diffusion profiles show the typical features of I-controlled kick-out diffusion into thick, dislocation-free Si specimens [12]. The D_i^* values extracted from those profiles (Fig. 1, ∗) follow reasonably well the Arrhenius law

$$D_i^* = 9.1 \times 10^{-3} \exp(-2.94\ \mathrm{eV}/kT)\ \mathrm{m^2 s^{-1}} \qquad (6)$$

(k = Boltzmann's constant, T = diffusion temperature) for Au diffusion in dislocation-free bulk Si [12] (Fig. 1, solid line). As expected for Si epi-layers perfectly grown on Si substrates, there is no interface effect on the shapes of the profiles.

In Si–Ge epi-layers with $0 < y \leqslant 0.09$, ^{195}Au diffusion occurs via the I-controlled kick-out mechanism, too. An example is the U profile for $y = 0.013$, $T = 800$°C, and $t = 240$ s (Fig. 2, ▲), to which a solid curve was fitted by means of the computer program ZOMBIE (Section 2). From such fits, for $0 < y \leqslant 0.09$ the D_i^* values were found which are represented in Fig. 1 filled symbols. In accordance with what one expects in the case of low Ge contents for the low-dislocation-density epi-layers used in our investigations and in agreement with previous findings on bulk Si–Ge specimens of the same kind [13], these values are quite close to those for dislocation-free Si, though, in spite of their scatter, on the average a devi-

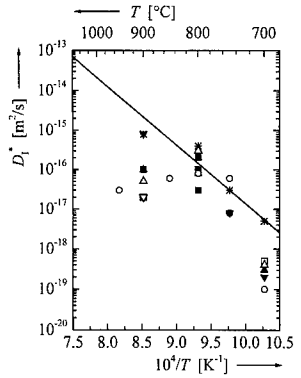

Fig. 1. Temperature dependence of the effective diffusion coefficient D_i^* [Eq. (4b)] of ^{195}Au in $Si_{1-y}Ge_y$ epi-layers (∗ $y = 0$, full symbols $0 < y \leqslant 0.09$ [■ $y = 0.013$, ▲ $y = 0.039$, ● $y = 0.053$, ▼ $y = 0.09$], empty symbols $0.09 < y \leqslant 0.24$ [□ $y = 0.102$, ▽ $y = 0.132$, △ $y = 0.196$, ○ $y = 0.239$]) and dislocation-free bulk Si (solid line) [12].

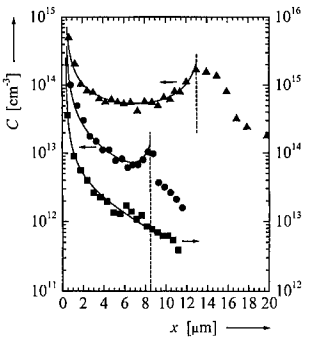

Fig. 2. ^{195}Au diffusion profiles $C(x)$ in $Si_{1-y}Ge_y$ epi-layers for 240 s anneals at 800°C (▲ $y = 0.013$, ● $y = 0.239$) and a 60 s anneal at 950°C (■ $y = 0.239$). The data points on the right-hand sides of the dashed vertical lines refer to the Si substrates.

ation to lower values is recognizable. In contrast to Si epi-layers, $Si_{1-y}Ge_y$ layers with $y \leqslant 0.09$ show a distinct increase of $C(x)$ in the vicinity of the interface (e.g., Fig. 2, ▲), particularly at low temperatures. In some cases, at the interface C even exceeds C_s^{eq} for Si. This increase in part arises from a local acceleration of the $Au_i \rightarrow Au_s$ transformation [Eq. (1)] due to the absorption of self-interstitials at the misfit-dislocation network in the interface (Section 3); however, conventional segregation of Au at the interface also contributes to this phenomenon.

In the regime $0 < y \leqslant 0.09$, at a given temperature D_i^* decreases to a value $D_i^*(0.09 < y \leqslant 0.24)$ which is considerably smaller than that in Si and y-independent for $0.09 < y \leqslant 0.24$. At 900°C, for instance, $D_i^*(0.09 < y \leqslant 0.24)$ is by more than two orders of magnitude smaller than $D_i^*(y = 0)$ (Fig. 3). As a consequence, in Si–Ge

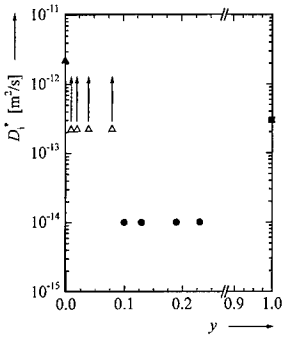

Fig. 3. Dependence of the effective diffusion coefficient D_i^* [Eq. (3)] of ^{195}Au at 900°C on the Ge content y for $Si_{1-y}Ge_y$ epi-layers in the regime $0.09 < y \leqslant 0.24$ (●). The empty triangles are lower limits of D_i^*(900°C) for $0 < y \leqslant 0.09$. Also included are the D_i^*(900°C) values for dislocated bulk Si [14] (▲) and dislocation-free bulk Ge [6] (●).

epi-layers with $0.09 < y \leqslant 0.24$, under certain circumstances to be specified at once, the ^{195}Au diffusion profiles show a transition from "I-controlled" to "Au_i-controlled". Whereas close to the epi-layer surface even after short annealing times the Au_i concentration has reached its saturation value C_i^{eq} and thus, at any rate, the in-diffusion of ^{195}Au is I-controlled, in greater depth it may be Au_i-controlled. For instance, this is the case for $y = 0.239$, $T = 800$°C, and $t = 240$ s (Fig. 2, ●). One realizes that in this case the in-diffusion rate is considerably lower than for $y = 0.013$ and otherwise identical conditions (Fig. 2, ▲) where the diffusion is I-controlled over the entire epi-layer thickness. It should be noted, however, that the moderate increase of the Au concentration close to the interface in the profile for $y = 0.239$, $T = 800$°C, and $t = 240$ s (Fig. 2, ●) cannot be due to a locally enhanced absorption of I, but must be a segregation effect, since that part of the profile is Au_i-controlled. At 700°C, the lowest diffusion temperature in our investigations, ^{195}Au diffusion takes place via the I-controlled kick-out mechanism over the entire thickness of the epi-layers even for $0.09 < y \leqslant 0.24$. This is only partly due to the extremely long duration (3d) of the anneals performed at this temperature. Rather for $0.9 < y \leqslant 0.24$, where D_i^* (Fig. 4, ●) obeys the Arrhenius equation

$$D_i^* = 4 \times 10^{-9} \exp(-1.3 \text{ eV}/kT) \text{ m}^2\text{s}^{-1} \quad (7)$$

(solid line in Fig. 4), I-controlled kick-out diffusion is also favoured by low temperatures, since, decreasing the temperature, $D_i^*(C_s^{eq}/C_s)^2$ (Fig. 1) finally drops below D_i^*. By contrast, at high temperatures $D_i^*(C_s^{eq}/C_s)^2$ exceeds D_i^*, and thus ^{195}Au diffusion becomes Au_i-controlled except near the surface. In these cases the interface leaves the profile shape unaffected, as shown in Fig. 2 (■) for $y = 0.239$, $T = 950$°C, and $t = 60$ s. The D_i^* values extracted from the I-controlled profiles or profile parts in the composition regime $0.09 < y \leqslant 0.24$ (Fig. 1, empty symbols) scatter considerably, but lie preferentially below the solid Arrhenius line for pure Si like those for $0 < y \leqslant 0.09$ (Fig. 1, filled symbols). In the entire composition regime investigated ($0 < y \leqslant 0.24$), a systematic dependence of D_i^* on y cannot be revealed.

An interpretation of the results reported above may be based on the dependences of D_i^* on composition (Fig. 3) and temperature (Fig. 4). In addition to the D_i^*(900°C) data in the regime $0.09 < y \leqslant 0.24$, the D_i^*(900°C) values for Si and Ge from the literature have been included in Fig. 3. Whereas the Si value refers to highly dislocated materials, in which Au undergoes Au_i-controlled kick-out diffusion [14], the Ge value has been measured on both dislocated and virtually dislocation-free crystals, in which the Au_i-controlled dissociative mechanism is operative [6,7]. For $0 < y \leqslant 0.09$ the kick-out profiles are I-controlled (see above), so that in this regime only lower limits of D_i^* can be determined. At first sight, one may speculate that alloying of Ge to Si, or vice versa, introduces sites at which the Au_i atoms may temporarily be trapped and that this leads to a reduction of D_i which, according to Eq. (3), is reflected by the small D_i^* values in the Si–Ge alloys with $0.09 < y \leqslant 0.24$ documented in Fig. 3. However, a closer inspection of the theory of trap-retarded diffusion shows that this kind of D_i reduction would involve an increase of the pre-exponential factor of D_i which is overcompensated by a simultaneous increase of the activation enthalpy entering D_i [15]. This is in contradiction to the finding that for Si–Ge both the pre-exponential factor and the activation enthalpy of D_i^* are smaller than for Si or Ge (Fig. 4). Hence, the small D_i^* values in Si–Ge must arise from a reduction of the ratio C_i^{eq}/C_s^{eq} in comparison to Si or Ge, for instance, by a decrease of C_i^{eq} as a result of the lattice distortions induced by Ge additions. At least in part, the reduction of C_i^{eq}/C_s^{eq} may also be achieved by an increase of C_s^{eq}. In fact, according to Eq. (4b) the preferential location of the D_i^* values for Si–Ge below the Si line (Fig. 1) is in accordance with an enhancement of C_s^{eq} in Si–Ge in comparison to Si. Such an enhancement is very likely, since the Au solubility is much greater in Ge [6] than in Si [12]. Presumably, this is related to the increase of the lattice parameter from Si to Ge [16].

The decrease of D_i^* as a result of a reduction of C_i^{eq}/C_s^{eq}, which has been postulated above, is an interesting phenomenon that leads to a retardation of the diffusivity of hybrid diffusers, which can exist in both a "sessile" and "mobile" configuration. This kind of diffusion retardation is a collective property of the matrix, in which the mobile fraction of the diffusers is lowered by alloying. It differs conceptually from conventional trapping [15] in which the reduction of the diffusivity results from a temporary immobilization of the diffusers at localized traps.

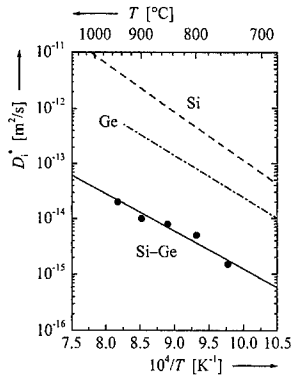

Fig. 4. Temperature dependence of the effective diffusion coefficient D_i^* [Eq. (3)] of ^{195}Au in a $Si_{0.761}Ge_{0.239}$ epi-layer (●). The straight lines represent Arrhenius laws for D_i^* in the $Si_{0.761}Ge_{0.293}$ epi-layer (solid line [Eq. (7)]), in dislocated bulk Si [14] (dashed line), and in dislocation-free bulk Ge [6] (dashed–dotted line).

5. Final remarks

The experimental data on the diffusion of Au in Si–Ge alloys presented in this paper have been discussed in terms of the kick-out mechanism, which — depending on the Ge content, the diffusion temperature, the annealing duration, and/or the location in the specimens — is either I- or Au_i-controlled. Whereas the assignment of diffusion profiles to the I-controlled kick-out mechanism is possible without any unambiguity, from diffusion data alone a discrimination between Au_i-controlled kick-out diffusion and Au_i-controlled dissociative diffusion is, in principle, not possible (Section 1). However, there is no physical reason why in the Au_i-controlled case the $Au_i \rightarrow Au_s$ transformation should be dominated by reaction (2), whereas in the I-controlled case the rate of reaction (1) obviously exceeds that of reaction (2). This view is confirmed by the fact that at 700°C, the lowest temperature in the present investigations, all diffusion profiles are I-controlled over the entire epi-layer thickness, though the likelihood that vacancies predominate over self-interstitials is expected to increase with decreasing temperature (Section 1). Hence, we conclude that in $Si_{1-y}Ge_y$ of the composition range $0 \leqslant y \leqslant 0.24$ the in-diffusion of Au occurs via I- or Au_i-controlled kick-out diffusion. This does not necessarily mean that in all our experiments $D_I C_I^{eq}$ has exceeded $D_V C_V^{eq}$. In in-diffusion experiments, a predominance of the kick-out mechanism over the dissociative mechanism may also occur due to its "$(C_s^{eq}/C_s)^2$ advantage" (Section 1). The physical cause of this is the need for vacancies for the $Au_i \rightarrow Au_s$ transformation in the dissociative mechanism [Eq. (2)] which has no analogue in the kick-out mechanism [Eq. (1)].

Acknowledgements

We are grateful to W. Jüngling and his collaborators for putting the computer program ZOMBIE at our disposal and to the ISOLDE Collaboration for the assistance in the implantation experiments.

References

[1] W. Frank, Def. Diff. Forum 75 (1991) 121.
[2] G.L. McVay, A.R. DuCharme, Phys. Rev. B 9 (1974) 627.
[3] N.A. Stolwijk et al., Def. Diff. Forum 59 (1988) 79.
[4] N.A. Stolwijk et al., J. Appl. Phys. 57 (1985) 5211.
[5] A. Almazouzi et al., J. Appl. Phys. 70 (1991) 1345.
[6] H. Bracht et al., Phys. Rev. B 43 (1991) 14 465.
[7] A. Strohm, Diplomarbeit, Universität Stuttgart, 1999.
[8] U. Gösele et al., Appl. Phys. A 23 (1980) 361.
[9] F.C. Frank, D. Turnbull, Phys. Rev. 104 (1956) 617.
[10] W. Jüngling et al., IEEE Trans. Electron. Dev. ED-32 (1985) 156.
[11] C. Rank, Vakuum Praxis 2 (1990) 286.
[12] N.A. Stolwijk et al., Physica 116 B (1983) 335.
[13] A. Giese et al., Verhandl. DPG 5 (1997) 722.
[14] B. Kühn, Dr. rer. nat. Thesis, Universität Stuttgart, 1991.
[15] M. Koiwa, Acta Metall. 22 (1974) 1259.
[16] J.P. Dismukes et al., J. Phys. Chem. 68 (1964) 3021.

ELSEVIER

Physica B 273–274 (1999) 603–607

PHYSICA B

www.elsevier.com/locate/physb

Deep state defects in strained and relaxed epitaxial $Si_{1-x}Ge_x$ on Si introduced by 3d transition metal and 5d noble metal impurities

K. Nauka*, T.I. Kamins

Hewlett-Packard Laboratories, 3500 Deer Creek Road, Palo Alto, CA 94304, USA

Abstract

This study describes deep state defects introduced in the epitaxial $Si_{1-x}Ge_x$ on Si substrates by 3d transition metal (Fe, Ti, Cr, Ni) and 5d noble metal (Au, Pt) impurities. The deep state activation energy is related to the Ge concentration and strain in the $Si_{1-x}Ge_x$. The strain dependence is described in terms of the deep state uniaxial and hydrostatic deformation potentials. The difference between the deep state activation energies in Si and $Si_{1-x}Ge_x$ does not agree with the independently determined Si–$Si_{1-x}Ge_x$ band offsets. This demonstrates that the concept of 3d state as an independent, internal reference level, well established for III–V and II–VI compounds, fails in the case of group IV semiconductors.

Keywords: Epitaxial $Si_{1-x}Ge_x$/Si; Deep state defects; Transition metal impurities; Noble metal impurities; Band offsets

1. Introduction

The successful application of $Si_{1-x}Ge_x$ to fabricate silicon-based heterojunction bipolar and MOSFET devices has created significant interest in the properties of $Si_{1-x}Ge_x$ epitaxial layers grown on Si substrates. The epitaxial $Si_{1-x}Ge_x$ on Si ($Si_{1-x}Ge_x$/Si) can be grown by chemical vapor deposition which is compatible with Si device processing, thus devices containing $Si_{1-x}Ge_x$ within their active region could become part of the mainstream Si integrated circuit (IC) technology [1]. The inherent difference of lattice constants between the epitaxial $Si_{1-x}Ge_x$ and Si substrate can be accommodated by tetragonal distortion of the cubic lattice cell of $Si_{1-x}Ge_x$ so its in-plane lattice constant matches the lattice constant of Si or by the formation of inferfacial misfit dislocations. Since device applications require the number of defects to be kept at a minimum, the $Si_{1-x}Ge_x$ epitaxial layers are grown commensurate with the substrate with no or very few misfit dislocations. Ge concentration, thickness of the epilayer, and its thermal history determine the amount of strain in the $Si_{1-x}Ge_x$.

Transition and noble metal impurities can have deleterious effects on Si IC devices. They can be present in various charge states and introduce an extensive network of deep level defects, acting as recombination–generation sites [2]. In addition, due to their large diffusivities and affinity to interact with the host atoms and other defects, they can form complexes and precipitates, degrading the device quality. Since these metallic contaminants can be introduced by device processing, it is important to understand their properties in $Si_{1-x}Ge_x$ epitaxial layers. The goal of this work is to evaluate the properties of deep states introduced in $Si_{1-x}Ge_x$ by selected 3d transition metals (Fe, Cr, Ni, Ti) and 5d noble metals (Au, Pt) as a function of the Ge concentration and the layer's strain, and their behavior within the $Si_{1-x}Ge_x$/Si heterojunction.

2. Experimental procedure

$Si_{1-x}Ge_x$ epitaxial layers were deposited by chemical vapor deposition (CVD) in a state-of-the art, commercial

*Corresponding author. Tel.: 650-857-5595; fax: 650-813-3279.

E-mail address: chris_nauka@hpl.hp.com (K. Nauka)

0921-4526/99/$ - see front matter
PII: S0921-4526(99)00584-0

single-wafer CVD epitaxial reactor on Si (1 0 0), 150 mm diameter substrates. Deposition temperatures were between 625°C and 700°C. Layers were grown either p-doped (B) or n-doped (As) on p- or n-type Si substrates, respectively. The layer thicknesses were between 150 and 500 nm, and Ge content varied from $x = 0$ to 0.28. The Ge concentration was constant within the $Si_{1-x}Ge_x$ epilayer. Different degrees of relaxation of the epilayers with the same Ge content were achieved by either growing films with different thicknesses or by post-deposition annealing at elevated temperatures. Reference p- and n-type Si epitaxial layers were grown under similar conditions.

Ge concentration and $Si_{1-x}Ge_x$ epilayer thicknesses were obtained by Rutherford Backscattering (RBS) analysis using 2 MeV H^{++} ions. Strain and degree of relaxation were determined by X-ray diffraction. Diffraction data were collected with a four-circle diffractometer equipped with a Ge crystal monochromator and Cu K-α_1 radiation off the (0 0 4) and (2 2 4) planes. Diffraction results were used to calculate lattice parameters of the measured epilayer, and then to calculate the lattice values for fully strained and fully relaxed films [3]. Because of the thickness difference (substrate thickness = 625 μm, epilayer thickness < 1 μm) virtually all the strain was present in the $Si_{1-x}Ge_x$ epilayer. Due to biaxial strain symmetry the strain tensor has only two components: $\varepsilon_{||}$ (parallel to the interface) and $\varepsilon_{\perp}$ (normal to the interface). $\varepsilon_{||} = (a_{meas} - a_{eq})/a_{eq}$, where a_{meas} is the in-plane lattice parameter of a given epilayer and a_{eq} is the corresponding equilibrium (completely relaxed) value. Analogous to bulk solids, biaxial strain can be expressed as the sum of the uniaxial (ε_{ax}) and the hydrostatic (ε_{vol}) stresses. For tetrahedral semiconductors $\varepsilon_{||} \cong -\varepsilon_{\perp}$, and ε_{ax} and ε_{vol} can be described as: $\varepsilon_{ax} \cong \varepsilon_{\perp} - \varepsilon_{||} = -2\varepsilon_{||}$ and $\varepsilon_{vol} \cong \varepsilon_{||}$ [4]. The degree of relaxation of an epilayer can be simply expressed as $100\% * [1 - (a_{meas} - a_{eq})/(a_{Si} - a_{eq})]$.

Deep level transient spectroscopy (DLTS) was employed to investigate deep level defects introduced by metallic impurities in $Si_{1-x}Ge_x$ epitaxial layers. DLTS measurements were conducted using Schottky diodes on the $Si_{1-x}Ge_x$. In order to avoid the potential ambiguities caused by interfacial band offsets or interfacial defects, the $Si_{1-x}Ge_x$ epilayer dopant concentration, its thickness, and DLTS bias/pulse voltages were selected to limit the probed region to the upper part of the epilayer. All as-grown $Si_{1-x}Ge_x$ epitaxial layers were free of deep level defects within the probed bulk region (detection limit $\approx 10^{10}$ cm^{-3}). Metallic impurities (Fe, Cr, Ni, Ti, Au, Pt) were diffused into the $Si_{1-x}Ge_x$ layer by rapid thermal annealing (RTA) with a metallic source in surface contact with the layer. Both surfaces were etched before the diffusion in order to remove surface oxide, which could impede the diffusion. Only one metallic impurity was introduced into each measured film in order to avoid overlapping of DLTS signals and any potential interactions between the impurities. RTA temperature and duration were selected to distribute metallic impurities almost uniformly within the upper part of the $Si_{1-x}Ge_x$ layers (no deep level gradients were observed with DLTS) and had concentrations from the range 10^{10} cm^{-3}–10^{12} cm^{-3}. In addition, RTA provided conditions close to quenching some of the metallic impurity-related point defects. Calculation of the deep state location within the $Si_{1-x}Ge_x$ band gap included correction due to the capture cross section.

3. Results and discussion

Table 1 presents the DLTS results obtained for an epitaxial Si ($x = 0$). Presented results are in agreement with previous reports on the metal-related deep states in Si [2]. The exact nature of deep state defects is known only in few cases; for example: $H1_{Fe} = Fe_{interstitial}$, $H1_{Cr}$ = Cr–B pair, $H1_{Au}$ is probably due to $Au_{substitutional}$ while $E1_{Au}$ might be caused by a Au complex. Introduction of Ge causes changes in the band structure; $Si_{1-x}Ge_x$ has a smaller band gap than Si. However, the conduction band minimum remains at the Δ point of the Brillouin zone within the range of Ge concentrations used in this experiment [5]. Biaxial strain causes further narrowing of the band gap and splits the valence band at the Γ point into the heavy- and light-hole bands. Behavior of the $Si_{1-x}Ge_x$ band structure as a function of x and strain has been previously studied using epitaxial samples grown under the same conditions as in the present experiment [6].

The presence of Ge causes the of DLTS peaks to shift as shown in Fig. 1. The corresponding deep state activation energy changes when the Ge concentration and the degree of epilayer's relaxation are changed. Two extreme cases of this evolution, namely 100% relaxed and 100% strained $Si_{1-x}Ge_x$, are shown in Figs. 2 and 3 for the Au-Fe- and Cr-related deep states. Similar behavior of the activation energy was observed for all the measured deep

Table 1
Activation energies of deep states introduced in epitaxial Si (measurement error ≈ 0.02 eV). Capture cross section correction has been included

Impurity	Hole trap (eV)	Electron trap (eV)
Fe	$H1_{Fe} = 0.410$	—
Cr	$H1_{Cr} = 0.270$	—
Ti	$H1_{Ti} = 0.265$	$E1_{Ti} = 0.300$
Ni	—	$E1_{Ni} = 0.425$
Au	$H1_{Au} = 0.345$	$E1_{Au} = 0.540$
Pt	$H1_{Pt} = 0.325$	$E1_{Pt} = 0.230$

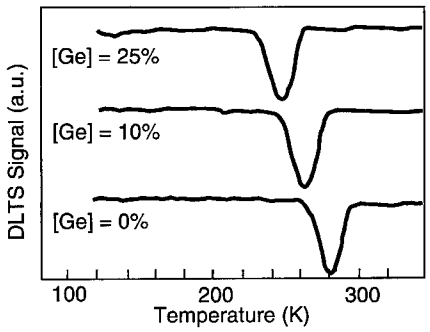

Fig. 1. $H1_{Au}$ DLTS peak in $Si_{1-x}Ge_x$ as a function of the Ge concentration. All samples were almost completely relaxed.

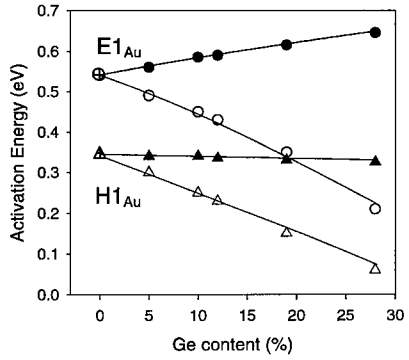

Fig. 2. Evolution of the Au-related deep states as a function of Ge concentration.Two extreme cases are shown:, 100% relaxed (open symbols) and 100% strained (closed symbols).

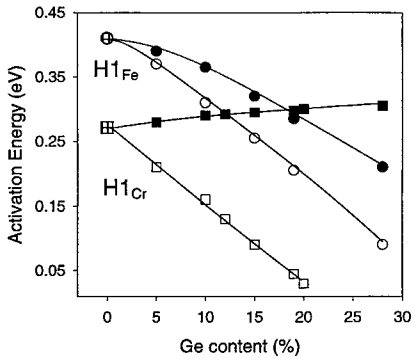

Fig. 3. Evolution of the Fe- and Cr-related deep states as a function of Ge concentration. Two extreme cases are shown: 100% relaxed (open symbols), 100% strained (closed symbols).

states (Table 2). None of the deep states appears to track either the conduction band minimum or the valence band maximum, in agreement with the fact that deep states are formed by wave functions originating from the

Table 2
Activation energies (eV) of the Ti- Ni- and Pt-related deep states (100% strained case/100% relaxed case)

Ge (%):	5	10	15	20
Ti: $H1_{Ti}$	0.26/0.22	0.252/0.18	0.245/0.12	0.235/0.09
$E1_{Ti}$	0.325/0.23	0.36/0.15	0.38/0.07	0.41/—
Ni: $E1_{Ni}$	0.45/0.365	0.48/0.28	0.50/0.19	0.515/0.12
Pt: $H1_{Pt}$	0.32/0.255	0.31/0.18	0.30/0.10	0.3/—
$E1_{Pt}$	0.22/0.21	0.20/0.19	0.19/0.175	0.18/0.16

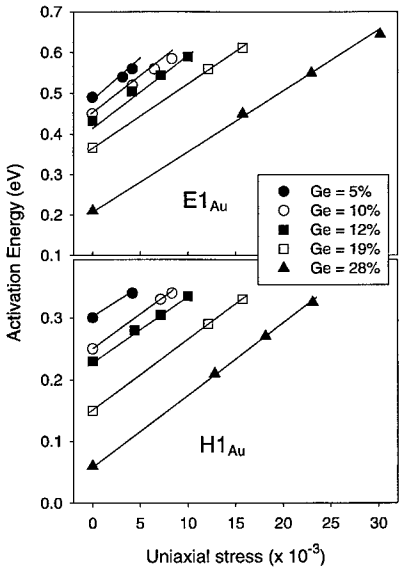

Fig. 4. Activation energy of the Au-related deeps states as a function of the uniaxial stress.

entire Brillouin zone [7]. The deep state activation energy depends on both the Ge concentration and the amount of strain present in a $Si_{1-x}Ge_x$ epilayer. In order to separate these two factors DLTS measurements were conducted for a series of samples containing the same amount of Ge but with different amounts of relaxation. Then, the activation energies (E_{act}) for all the measured deep states were plotted as a function of the corresponding uniaxial stresses (ε_{ax}), as shown in Figs. 4 and 5 for Au, Fe, and Cr impurities.

The slope of $\Delta E_{act}/\Delta\varepsilon_{ax} = \xi_{ax}$, analogously to the solid state deformation potentials, can be called the uniaxial deformation potential of a deep state. Due to the biaxial stress symmetry the hydrostatic deformation potential of a deep state ξ_{vol} is equal $-2\xi_{ax}$. Fig. 6 shows the relationship between the Ge concentration and ξ_{ax} for deep states introduced by Au, Fe, and Cr. ξ_{ax} depend only weakly on the Ge concentrations; their average values for

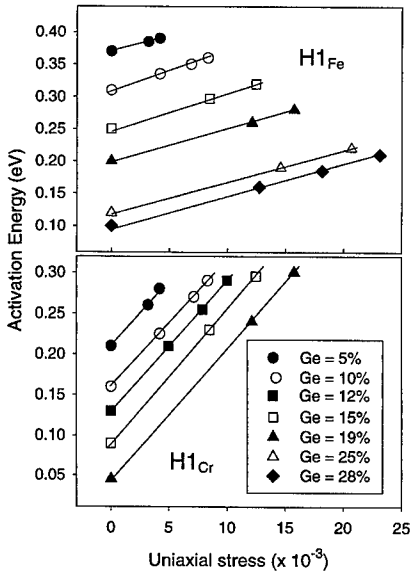

Fig. 5. Activation energy of the Fe- and Cr-related deep state as a function of the uniaxial stress.

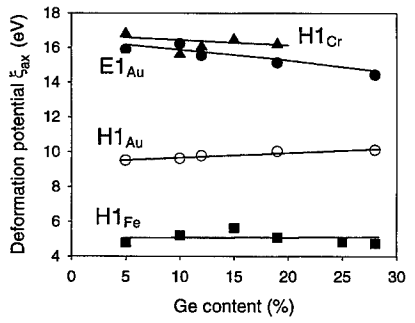

Fig. 6. Uniaxial deformation potential of the Fe- Cr- and Au-related deep states as a function of Ge concentration.

the remaining metallic impurities are equal: $\xi_{ax}(H1_{Ti}) = 8.3$ eV, $\xi_{ax}(E1_{Ti}) = 18.1$ eV, $\xi_{ax}(E1_{Ni}) = 23.8$ eV, $\xi_{ax}(H1_{Pt}) = 16.8$ eV, $\xi_{ax}(E1_{Pt}) = 1.5$ eV. ξ_{ax} values appear to fall into two groups: $\xi_{ax} < 10$ eV and $\xi_{ax} > 16$ eV. Although, the internal structure of the metallic impurity defects in Si and $Si_{1-x}Ge_x$ is poorly understood, the simple point defects with a high symmetry may be less sensitive to the stress changes and their values of ξ_{ax} may be smaller than in the case of complexes with lower symmetry. Supporting this idea is the observation that ξ_{ax} values of known simple point defects, like $Fe_{interstitial}$ ($H1_{Fe}$) $Au_{substitutional}$ ($H1_{Au}$) are low, while the complex defects (Cr–B pair ($H1_{Cr}$), Au complex ($E1_{Au}$)) have large ξ_{ax} values. Therefore, $H1_{Ti}$ and $E1_{Pt}$ are likely due to single point defects, while $E1_{Ti}$, $E1_{Ni}$, and $H1_{Pt}$ could be due to defect complexes with lower symmetry. Since, within the tested range of Ge concentrations ($x < 0.3$), ξ_{ax} is approximately constant for a given impurity, it can be used to calculate the location of a deep state within the gap when the degree of $Si_{1-x}Ge_x$ relaxation is known. Conversely, knowledge of the trap activation energy can be used to determine the amount of $Si_{1-x}Ge_x$ relaxation.

It has been demonstrated that 3d transition metal impurities introduce deep states that can be used as a reference for calculating band offsets in isovalent heterojunctions [8]. According to this approach, deep states introduced by the 3d metallic impurities align at the junction of two isovalent compounds and the band discontinuities result simply from the differences of the respective activation energies. This approach requires that the heterojunction is of a high quality, meaning that the bulk properties of both semiconductors rather than the interfacial defects determine the band alignment. This concept has been employed for a large number of III–V and II–VI compounds and provided the correct band alignment with accuracy and simplicity unmatched by any other method. Epitaxial $Si_{1-x}Ge_x$/Si offers a unique opportunity for testing this approach for a group IV semiconductor system. $Si_{1-x}Ge_x$/Si junction quality and cleanliness is at least as good as in the case of previously tested III–V and II–VI semiconductors, and its band alignment has been well established by independent calculations and measurements [5,6]. However, the measured difference between the deep state activation energies in Si and in $Si_{1-x}Ge_x$ did not agree with the known Si–$Si_{1-x}Ge_x$ band offsets for any of the 3d transition metal and the 5d noble metal impurities tested. Fig. 7 presents examples of this comparison for two extreme cases of 100% relaxed and 100% strained $Si_{1-x}Ge_x$, and the Fe- and Cr-related deep states. In the case of strained $Si_{1-x}Ge_x$ this lack of agreement is true whether the deep state location is calculated from the top of the highest valence band or from the weighted, intermediate position between the heavy- and light-hole bands. Occasionally, in isolated, intermediate cases of partial relaxation for some of the traps and some Ge concentrations, band offset appears to match the activation energy difference. However, this agreement is accidental, and it disappears when any one of the listed parameters is changed.

Thus, the concept of an internal, 3d deep state-related reference level for band alignment appears not to work in the case of the Si–$Si_{1-x}Ge_x$ system. Although the reason for its failure remains unclear, some potential explanations can be proposed: (A) Group IV semiconductors differ from the III–V and II–VI systems because their ionicity is zero. It has been shown that deep state activation energy depends on the crystal ionicity [9]. Perhaps the lack of such a link (zero ionicity, deep states exist in the gap) invalidates the use of the deep state as an internal reference for band alignment. (B) Stress in $Si_{1-x}Ge_x$ is an additional factor that needs to be taken

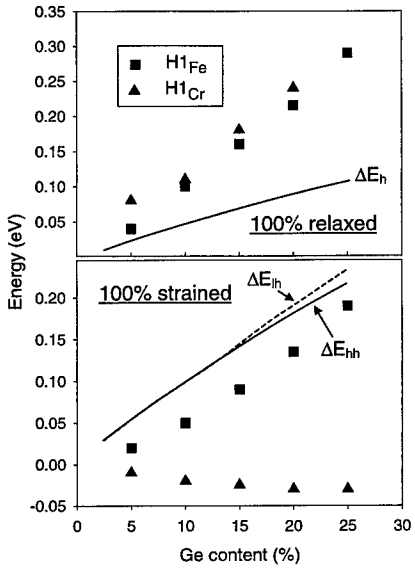

Fig. 7. Comparison between the valence band discontinuity at the $Si_{1-x}Ge_x$/Si heterojunction and the corresponding difference of the Fe- and Cr-related deep states in the case of 100% relaxed and 100% strained $Si_{1-x}Ge_x$.

into account. None of the previous reports on the use of the 3d metal deep state as a reference for band alignment in III–V or II–VI semiconductors included a strained semiconductor, as in the case of $Si_{1-x}Ge_x$. The uniaxial stress may perturb the atom-like 3d shell structure of the transition metal impurity, preventing it from being an independent reference level for band alignment. (C) Of course, the previous argument is incorrect in the case of completely relaxed $Si_{1-x}Ge_x$. However, the interface between the Si and partially or completely relaxed $Si_{1-x}Ge_x$ contains dislocations that might carry some electrical charges. Definition of band alignment as rearrangement of bands providing local charge neutrality is the basis of the concept of an internal reference level introduced by 3d impurities [8]. Lack of the means to account for the dislocation charges could invalidate the model when dislocations are present. Obviously, further study is needed to resolve why 3d deep states cannot be used as reference for aligning bands at the $Si/Si_{1-x}Ge_x$ interface.

In conclusion, deep states introduced by the selected 3d transition metals and 5d noble metals in $Si_{1-x}Ge_x$ ($x < 0.28$) have been described. Their activation energies depend on the Ge concentration and strain present in the $Si_{1-x}Ge_x$ epitaxial layer. The strain effect has been described by introducing the uniaxial and hydrostatic deep state deformation potentials. Their knowledge can be used to predict the strain in a $Si_{1-x}Ge_x$ epitaxial layer when the Ge content is known or, conversely, Ge concentration can be determined from the known activation energy and degree of epilayer relaxation. Unlike the previous studies of III–V and II–V compounds, deep states introduced by 3d transition metals cannot be used as a reference level for aligning bands at the $Si–Si_{1-x}Ge_x$ interface. It is proposed that this failure of the well established concept for band offset calculations could be linked to negligible crystal ionicity, stress, and electrical charges associated with misfit dislocations.

References

[1] T.I. Kamins, K. Nauka, J. Kruger, J.L. Hoyt, C.A. King, D.B. Noble, IEEE Trans. EDL10 (1988) 503.
[2] E.R. Weber, Appl. Phys. A 30 (1983) 1.
[3] K. Nauka, in: The Proceedings of the 22nd International Conference on the Physics of Semicond. (ICPS-22), World Sci. Publ., Singapore, 1995.
[4] E.R. O'Reilly, Semicond. Sci. Technol. 4 (1989) 121.
[5] R. People, Phys. Rev. B 32 (1985) 1405.
[6] K. Nauka, T.I. Kamins, J.E. Turner, C.A. King, J.L. Hoyt, J.F. Gibbons, Appl. Phys. Lett. 60 (1992) 195.
[7] K.A. Kikoin, V.N. Fleurov, Transition Metal Impurities in Semiconductors, World Sci. Publ., Singapore, 1994.
[8] J.M. Langer, C. Delerue, M. Lannoo, H. Heinrich, Phys. Rev. B 38 (1988) 7723.
[9] Z. Liro, C. Delerue, M. Lannoo, Phys. Rev. B 36 (1987) 9362.

ELSEVIER

Physica B 273–274 (1999) 608–611

PHYSICA B

www.elsevier.com/locate/physb

Images of local tilted regions in strain-relaxed SiGe layers

P.M. Mooney[a,*], J.L. Jordan-Sweet[a], I.C. Noyan[a], S.K. Kaldor[a], P.-C. Wang[b]

[a]*IBM Research Division, T.J. Watson Research Center, P.O. Box 218, Yorktown Heights, NY 10598, USA*
[b]*IBM Microelectronics Division, Hopewell Junction, NY 12533, USA*

Abstract

Strain-relaxed $Si_{1-x}Ge_x$ films have been investigated using X-ray microdiffraction with a diffracted beam footprint of 0.3 μm × 2 μm. Intensity variations in the diffracted beam at different positions on the sample are due to the presence of local tilted regions which are larger in area than the diffracted X-ray beam. These regions are shown to have the same lattice parameter but different orientation with respect to the Si substrate. These regions arise from dislocation pileups, which consist of a larger number of dislocations when larger mismatch strain is relieved.

Keywords: SiGe; Local tilted regions; Mosaic structure; X-ray microdiffraction

Heterostructures of $Si_{1-x}Ge_x$/Si(0 0 1) are currently used to fabricate heterojunction bipolar transistors (HBTs) for applications in wireless telecommunications. Other potential applications include high-speed field-effect transistors (FETs) having strained Si or $Si_{1-x}Ge_x$ carrier channels grown pseudomorphically on a strain-relaxed $Si_{1-x}Ge_x$ buffer layer [1–3]. When the lattice mismatch strain is less than 2%, epitaxial $Si_{1-x}Ge_x$ films grown on Si(0 0 1) relax by the introduction of 60° misfit dislocations. These nucleate by different mechanisms, depending on the lattice mismatch strain and growth temperature [2,4]. Cross-sectional transmission electron micrographs (XTEMs) show strikingly different arrangements of the misfit dislocations, depending on the nucleation mechanism [4–6]. A $Si_{0.7}Ge_{0.3}$ uniform-composition layer grown at about 550°C relaxes initially by surface roughening followed by nucleation of misfit dislocations in regions of high strain [4,7]. XTEM shows that the misfit dislocations are located at the $Si_{1-x}Ge_x$/Si interface and that high densities ($\sim 10^{10}$ cm^{-2}) of threading arms extend from the interface to the film surface [4–6]. Alternatively, if an intermediate layer in which the Ge mole fraction x is graded up from 0 to 0.3 is grown prior to the uniform-composition $Si_{0.7}Ge_{0.3}$ layer, dislocation nucleation occurs at low mismatch strain [2,8] by a multiplication mechanism [5,6]. In this case XTEM shows pileups of misfit dislocations extending several microns deep into the Si [5,6]. Graded buffer layers have low threading dislocation densities (typically 10^5–10^7 cm^{-2}, depending on the grading rate [2]), and are therefore suitable for a variety of device applications.

X-ray rocking curves taken with a standard double-axis laboratory diffractometer (beam size about 1 mm × 8 mm) are broadened when dislocations are present [9]. Triple-axis X-ray measurements [10] show that the peak broadening is primarily due to the bending of the lattice planes by the dislocations, which is usually referred to as mosaic broadening, and not to variations of the lattice parameters [8]. Despite the orders-of-magnitude difference in the density of the threading dislocations in the two types of samples, the peak broadening is comparable in both uniform-composition samples and samples with graded intermediate layers when the density of misfit dislocations is the same [9]. Thus the mosaic broadening results primarily from the misfit dislocations [9,11].

X-ray microdiffration measurements of strain-relaxed $Si_{1-x}Ge_x$ layers show a clear difference in the microstructure of samples that relaxed by these two different

* Corresponding author. Fax: + 914-945-4581.
E-mail address: mooneyp@us.ibm.com (P.M. Mooney)

0921-4526/99/$ - see front matter
PII: S0921-4526(99)00585-2

mechanisms [12]. Local tilted regions larger in size than the diffracted microbeam are observed when dislocation multiplication occurs. In contrast, the local tilted regions in samples that first relax by roughening are much smaller than the microbeam. Thus the size of the local tilted regions depends on the arrangement of the misfit dislocations, which differs greatly in samples that relax by these two dislocation nucleation mechanisms.

The $Si_{1-x}Ge_x$ samples investigated here were grown at 550°C by ultra-high vacuum chemical vapor deposition [13] on Si(0 0 1) substrates. XTEM images of all these samples show dislocation pileups penetrating several microns deep into the Si substrate, characteristic of dislocation multiplication. We show data from two samples: a 97% relaxed $Si_{0.83}Ge_{0.17}$ layer and a 49% relaxed $Si_{0.84}Ge_{0.16}$ layer. The alloy composition and the degree of strain relaxation were determined from diffraction data taken with a large area X-ray beam.

The microdiffraction experiments were performed at beamline X20A at the National Synchrotron Light Source at Brookhaven National Laboratory using a microdiffractometer described elsewhere [14–17]. The monochromatic X-ray beam at wavelengths close to Cu $K_{\alpha 1}$ is focused using a 60 μm-diameter capillary tapered down to 3 μm. The focused beam has a divergence of 0.3° and therefore only a small fraction of the incident beam, specifically the center of the fan where the intensity is a maximum, is at the proper angle for Bragg diffraction from our single crystal samples [17]. Thus, when a bare Si wafer is placed at about 1 mm from the tip of the capillary, the width of the 0 0 4 diffracted beam at the sample in the diffraction direction is only 0.3 μm for this capillary. The vertical receiving slits were set to accept the entire width of the diffracted beam from the bare Si wafer. In the horizontal (non-diffracting) direction the receiving slits were set to accept the center 2 μm of the diffracted beam.

Fig. 1 shows a microtopograph, a map of the diffracted beam intensity, from the 97% relaxed $Si_{0.83}Ge_{0.17}$ layer. To collect these data both the sample (θ and χ axes) and the detector (2θ axis) were positioned to obtain the maximum diffracted beam intensity from the 0 0 4 reflection of the layer. The sample was then translated under the incident beam in the two orthogonal directions parallel to the wafer surface (x is parallel and y is perpendicular to the diffraction plane) in steps of 2 and 5 μm, respectively. Note that the diffracted beam intensity varies from its maximum value to nearly zero at different positions on the sample, forming a "cross-hatched" pattern along the two 1 1 0 directions. This pattern is not surprising, since the 60° misfit dislocations lie along the two 1 1 0 directions of the crystal.

Fig. 2 shows the variation in diffracted intensity at different x positions (y held fixed) for a bare Si wafer and for the $Si_{0.83}Ge_{0.17}$ sample. As expected for a perfect crystal, the diffracted beam intensity is the same at all

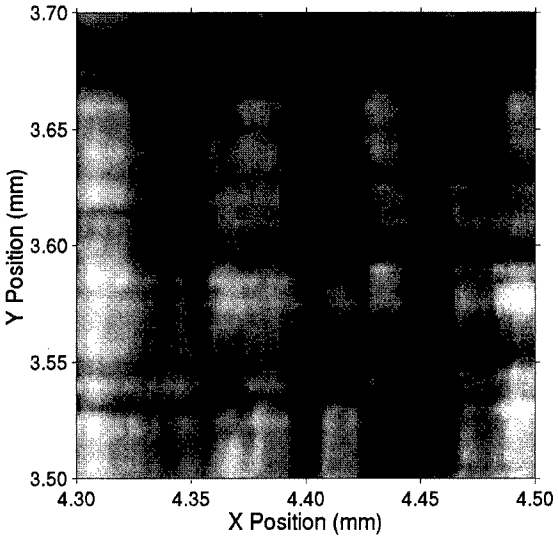

Fig. 1. Microtopograph showing the variation of the 0 0 4 diffracted beam intensity at different x, y positions on a 97% relaxed $Si_{0.83}Ge_{0.17}$ layer.

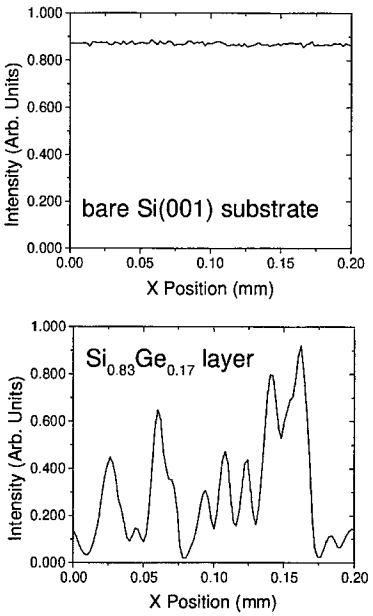

Fig. 2. Line scans showing the diffracted intensity at different x positions (y held constant).

points on the bare Si substrate. In contrast, the diffracted beam intensity from the relaxed SiGe layer is as low as about 5% of the maximum value at many x positions and is a significant fraction of the maximum value at only a few x positions, consistent with the data of Fig. 1.

To investigate the origin of the large intensity variation in the step-graded samples, rocking curves (θ scans) and

detector scans (2θ scans) were taken at various x positions to determine the sample orientation and Bragg angle that give the maximum diffracted beam intensity. Fig. 3(a) shows θ scans for the 97% relaxed $Si_{0.83}Ge_{0.17}$ layer. As the sample is translated under the beam, the maximum intensity shifts to different values of θ. Thus, the intensity variation observed in Figs. 1 and 2 results from a variation in the orientation of the crystal lattice planes at different positions on the sample. The angle of the lattice planes with respect to the incident X-ray beam varies by 0.21°. The FWHM of the most intense peaks is relatively narrow, ranging from 0.05° to 0.09°. Fig. 3(b) shows detector scans taken at the same x positions. Note that the variation in 2θ is very small (<0.02°), indicating that the Bragg angle ($2\theta/2$) and therefore the lattice parameter of all the local tilted regions varies by < 0.01°. These results are consistent with triple-axis data taken using a large area X-ray beam which indicate a large variation in the orientation (tilt) of the layer but only a very small variation in the lattice parameter. With X-ray microdiffraction, however, we are able to image the individual tilted regions since they are larger than the size of our diffracted beam.

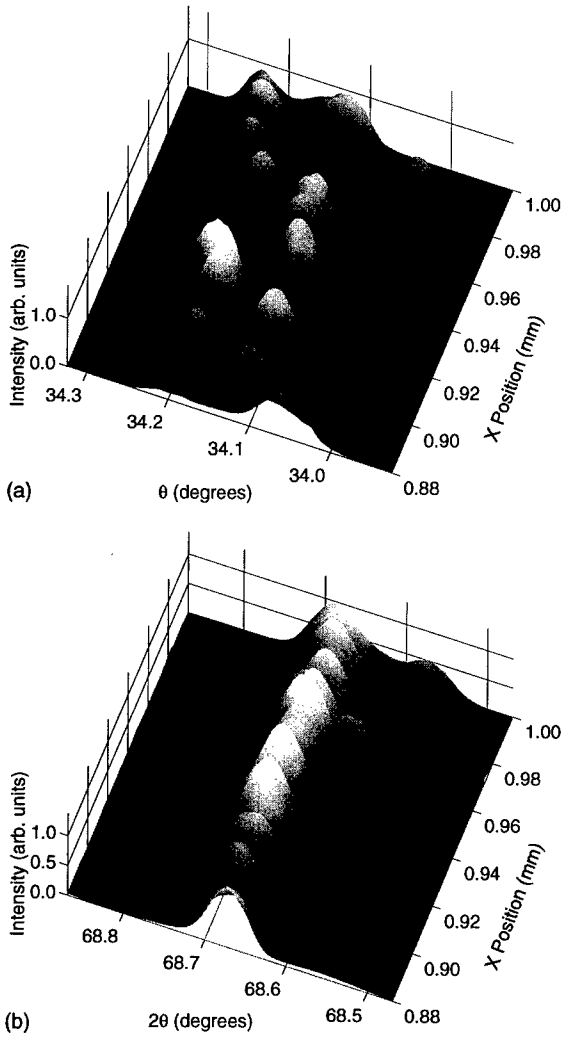

Fig. 3. (a) θ scans of the 0 0 4 reflection from the 97% relaxed $Si_{0.83}Ge_{0.17}$ sample taken at different x positions (y held constant) and (b) 2θ scans of the 0 0 4 reflection from the same sample.

Fig. 4 shows θ scans for a $Si_{0.84}Ge_{0.16}$ layer which is only 49% relaxed and thus has a misfit dislocation density which is about half that of the other sample. The total variation of θ is comparable for both samples, but neighboring tilted regions have a smaller change in θ in this sample than in the more relaxed sample, suggesting that the dislocation pileups that separate the local tilted regions consist of fewer dislocations when the total misfit dislocation density is lower. Quantitative analysis of data from a large number of samples us underway and will be published elsewhere.

Using X-ray microdiffraction, we have imaged the individual local tilted regions (mosaic structure) in SiGe layers that relaxed by dislocation multiplication. We have shown that these regions have the same lattice parameter but are tilted at various angles with respect to the Si substrate. The different distribution of the tilt angles in two samples having misfit dislocation densities which differ by a factor of 2 suggests that the dislocation pileups separating the local tilted regions have fewer dislocations in less relaxed samples. A comparison of the lateral size of the tilted regions in different samples indicates that the density of the dislocation pileups is comparable [12], consistent with the conclusion that the pileups in less relaxed samples consist of fewer dislocations.

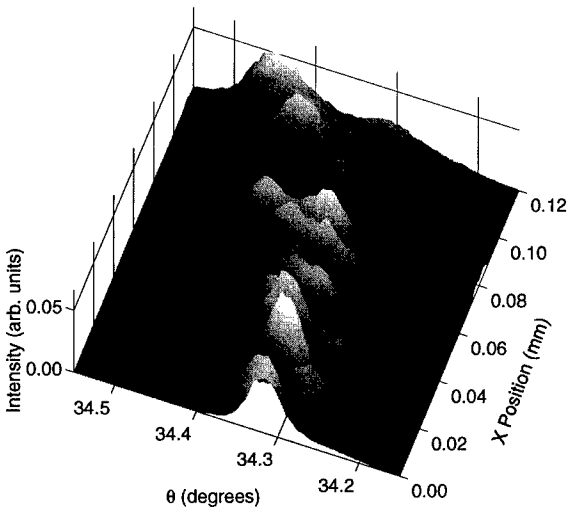

Fig. 4. θ scans of the 0 0 4 reflection from the 49% relaxed $Si_{0.84}Ge_{0.16}$ layer.

We gratefully acknowledge J.O. Chu, who prepared the samples, and E. Liniger, who made the tapered capillaries. The work was partially supported by DOE contract DE-AC02-76CH00016.

References

[1] B.S. Meyerson, Proc. IEEE 80 (1992) 1592 and references therein.
[2] P.M. Mooney, Mater. Sci. Eng. Rep. R17 (1996) 105 and references therein.
[3] M. Arafa, K. Ismail, J.O. Chu, B.S. Meyerson, I. Adesida, IEEE Elect. Dev. Lett. 17 (1996) 586.
[4] J. Tersoff, F.K. LeGoues, Phys. Rev. Lett. 72 (1994) 3570.
[5] F.K. LeGoues, B.S. Meyerson, J.F. Morar, Phys. Rev. Lett. 66 (1991) 2903.
[6] F.K. LeGoues, B.S. Meyerson, J.F. Morar, P.D. Kirchner, J. Appl. Phys. 71 (1992) 4230.
[7] D.E. Jesson, S.J. Pennycook, J.-M. Baribeau, D.C. Houghton, Phys. Rev. Lett. 71 (1993) 1744.
[8] P.M. Mooney, J.L. Jordan-Sweet, J.O. Chu, F.K. LeGoues, Appl. Phys. Lett. 66 (1995) 3642.
[9] P.M. Mooney, F.K. LeGoues, J.O. Chu, S.F. Nelson, Appl. Phys. Lett. 62 (1993) 3464.
[10] P.F. Fewster, Semicond. Sci. Technol. 8 (1993) 1915.
[11] V. Holy, J.H. Li, G. Bauer, F. Scheffler, H.-J. Herzog, J. Appl. Phys. 78 (1995) 5013.
[12] P.M. Mooney, J.L. Jordan-Sweet, I.C. Noyan, S.K. Kaldor, P.-C. Wang, Appl. Phys. Lett. 74 (1999) 726.
[13] B.S. Meyerson, Appl. Phys. Lett. 48 (1986) 797.
[14] I.C. Noyan, J.L. Jordan-Sweet, E.G. Liniger, S.K. Kaldor, Appl. Phys. Lett. 72 (1998) 3338.
[15] I.C. Noyan, S.K. Kaldor, P.-C. Wang, J.L. Jordan-Sweet, Rev. Sci. Instrum. 79 (1999) 1300.
[16] I.C. Noyan, P.-C. Wang, S.K. Kaldor, J.L. Jordan-Sweet, Appl. Phys. Lett. 74 (1999) 16.
[17] I.C. Noyan, P.-C. Wang, S.K. Kaldor, J.L. Jordan-Sweet, E.G. Liniger, submitted to Rev. Sci. Instrum.

ELSEVIER

Physica B 273–274 (1999) 612–615

PHYSICA B

www.elsevier.com/locate/physb

Growth and dislocation behavior in GeSi bulk alloys

Ichiro Yonenaga*

Institute for Materials Research, Tohoku University, Katahira 2-1-1, Aoba-ku, Sendai 980-8577, Japan

Abstract

Bulk crystals of $Ge_{1-x}Si_x$ alloys in the whole composition range $0 < x < 1$ were grown by the Czochralski technique. Full single crystals were obtained for the alloy composition $0 < x < 0.15$ and $0.9 < x < 1$. The dislocation velocity decreases with increasing Si content in the range $0 < x < 0.08$, while the dislocation velocity first increases and then decreases with increasing Ge content in the range $0.94 < x < 1$. The dislocation velocities were determined as functions of stress and temperature. The stress–strain behavior of the alloys becomes temperature-insensitive at high temperatures. The yield strength of the alloys depends on the composition, proportional to $x(1-x)$ over the whole composition range. Built-in stress fields related to local fluctuation of the alloy composition and the dynamic development of a solute atmosphere around dislocations, seem to suppress the activities of dislocation and bring about alloy strengthening.

Keywords: GeSi; Growth; Dislocations; Alloy hardening

1. Introduction

GeSi alloys are important microelectronic and optoelectronic materials in view of the possibilities of band gap engineering they offer. Usually these alloys are grown as thin films on Si substrates by various epitaxial techniques. The introduction of misfit dislocations is inevitable in such hetero structures due to the interfacial mismatch when the film thickness exceeds a critical value. To clarify the dislocation properties and utilize the potential of GeSi alloys, it is necessary to grow bulk crystals of low dislocation densities. From such a viewpoint, the present author grew crystals of Ge-rich GeSi alloys by the Czochralski method and studied the dislocation velocities and mechanical properties of the grown alloys. An athermal stress relating to the alloying has been deduced [1–5].

This paper reports on the Czochralski growth of $Ge_{1-x}Si_x$ alloys in the whole composition range $0 < x < 1$ and the unique properties of dislocations brought about by alloying.

2. Bulk crystal growth

Bulk crystals of $Ge_{1-x}Si_x$ alloys in the whole composition range $0 < x < 1$ were grown by the Czochralski technique at very low pulling rates ranging from 1 to 8 mm/h in a flowing Ar gas atmosphere [1,5,6].

Full single crystals 10–25 mm in diameter and 20–70 mm in length were successfully grown for GeSi alloys of the composition ranges $0 < x < 0.15$ and $0.9 < x < 1$. For alloys of intermediate compositions, single crystalline parts were obtained near the seeds of ingots, which relates to the polycrystallization due to the occurrence of the constitutional supercooling.

The critical growth velocity v_c for the polycrystallization caused by the constitutional supercooling was estimated as a function of the composition x by $v_c = D\nabla\Theta k/\nabla T_l x(k-1), (k > 1)$ using the distribution coefficient k and diffusion coefficient $D = (30 - 24x)\ 10^{-5}\ \mathrm{cm^2/s}$ [7]. $\nabla\Theta$ is the temperature gradient in the melt and ∇T_l is the slope of the liquidus. Fig. 1 shows the critical growth rates estimated for the temperature gradient of 50 K/cm as a function of the composition. The experimental results including those reported previously [5,6] are superimposed in the figure. The transition from a single crystal to a polycrystallinity seems to occur at pulling rate lower than the estimated critical growth

*Tel.: +81-22-215-2042; fax: +81-22-215-2041.
E-mail address: yonenaga@imr.tohoku.ac.jp (I. Yonenaga)

0921-4526/99/$ - see front matter
PII: S0921-4526(99)00586-4

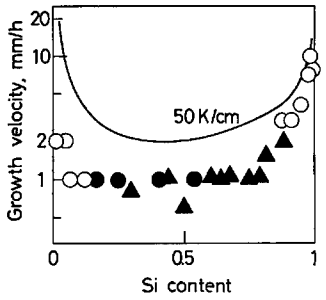

Fig. 1. Growth velocities of GeSi crystals as a function of the composition. Solid line shows the estimated critical growth rates for a temperature gradient of 50 K/cm. Open circles show the growth of full single, while solid circles and triangles the occurrence of polycrystallization in the position of the late stage of the growth and near the seed, respectively.

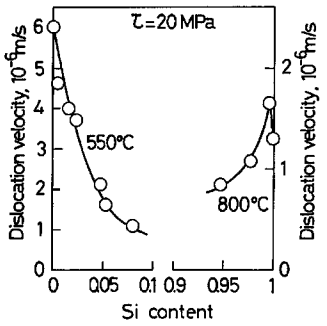

Fig. 2. Velocities of 60° dislocations in the Ge-rich and Si-rich GeSi alloy at 550°C and 800°C, respectively, under a shear stress 20 MPa as dependent on the Si content.

velocity, especially in the cases of low and intermediate Si content, though the temperature gradient $\nabla\Theta$ was measured to be ~ 50 K/cm by a thermocouple [5]. Possibly the temperature gradient was reduced with the low temperature available for growth of the GeSi alloys.

For any grown crystal the composition changes spatially in such a way that the Si content gradually decreases along the pulling direction, implying that Si in the melt is preferentially consumed and taken into the crystal during the growth. The composition variation of the grown crystals along the growth direction suggests that the growth of GeSi alloys is described in terms of the complete mixing model of the melt together with the gravity effect in the melt related to the large difference in the densities of Ge and Si [5].

Dislocations were generated mainly at the seed/alloy interface. The density of grown-in dislocations in the alloys was in the range 10^3–10^5 cm^{-2}. The generation process may be controlled by the magnitude of the misfit strain between the alloy and seed, the temperature, the temperature gradient and the mobility of generated dislocations in the alloy [5].

A large infra-red absorption peak is observed at the position centred at 1106 cm^{-1} in grown crystals of Si-rich alloys [6]. The absorption coefficient determined by the peak height is 3–4 cm^{-1} in the highest case, which corresponds to the oxygen concentration 12×10^{17} cm^{-3} if the conversion factor 3.06×10^{17} cm^{-2} is used. The peak height decreases with decreasing Si content in the alloys.

3. Direct measurement of dislocation velocities

In the Ge-rich GeSi alloys of composition range $0 < x < 0.08$, the dislocation velocity decreases monotonically with an increase in Si content, reaching about one-seventh of that in pure Ge at $x = 0.08$ as shown in Fig. 2. Contrarily, in the composition range $0.94 < x < 1$ the dislocation velocity first increases and then decreases with an increase in Ge content. The dislocation velocity for the Ge content $(1 - x) = 0.004$ is higher than that in pure Si.

The logarithms of the velocities of 60° dislocations in the Ge-rich GeSi alloys of the composition range $0 < x < 0.08$ show a linear relation against the logarithms of shear stress with approximately the same slope in the stress range 3–24 MPa in the temperature range 450–700°C. The dislocation velocity versus the stress relation at 750°C and 800°C in the Si-rich GeSi alloy with $x = 0.996$ also shows a linear relation against shear stress with approximately the same slope as in Si. Contrarily, in the GeSi alloys of $x = 0.979$ and 0.946 the velocity of dislocations is zero under stress lower than the threshold stress and then increases rapidly with increasing stress beyond the threshold stress. The threshold stress for dislocation generation from a scratch increases with decreasing the Si content.

The velocities of dislocations in the above GeSi alloys can be described in a similar way to those in various semiconductors as functions of the stress τ and temperature T by the following empirical equation:

$$v = v_0(\tau/\tau_0)^m \exp(-Q/k_B T), \quad \tau_0 = 1 \text{ MPa}, \tag{1}$$

where k_B is the Boltzmann constant. The experimentally determined magnitudes of v_0, m and Q in GeSi alloys and pure Ge and Si are given in Table 1.

4. Mechanical properties in compressive deformation

The stress–strain curves of the Si-rich GeSi alloys of the composition range $0.94 < x < 1$ are similar to those of pure Si at temperatures 800–1000°C, being characterised by a stress drop followed by an increase in the stress with strain. Such a stress drop is commonly found in various semiconductors at relatively low temperatures. The upper and lower yield stresses and flow stress

Table 1
Magnitudes of v_0, m and Q for 60° dislocations in $Ge_{1-x}Si_x$ and pure Ge and Si

Crystal	v_0 (m/s)	m	Q (eV)
Ge	2.9×10^2	1.7	1.62 ± 0.05
$Ge_{1-x}Si_x$ ($x = 0.016$)	4.6×10^2	1.7	1.68
($x = 0.047$)	2.8×10^2	1.7	1.68
($x = 0.080$)	2.3×10^2	1.6	1.70
($x = 0.946$)	9.4×10^1	2.1	2.30
($x = 0.978$)	2.1×10^2	1.9	2.30
($x = 0.996$)	1.4×10^4	1.0	2.40
Si	1.0×10^4	1.0	2.40

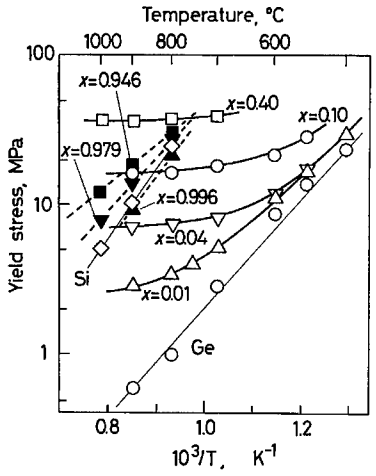

Fig. 3. Yield stresses of the GeSi alloys plotted against the reciprocal temperature for deformation under a strain rate of $1.8 \times 10^{-4}\,s^{-1}$.

increase with decreasing Si content. On the other hand, the stress–strain curves of the Ge-rich GeSi alloys with $x = 0.01, 0.10, 0.25$ and 0.40 show no stress drop at temperatures higher than 600°C, quite different from those of the Si-rich GeSi alloys.

The lower yield stresses of the GeSi alloys for various Si content and those for Si and Ge, for comparison, are plotted against the reciprocal temperature in Fig. 3. The logarithms of the yield stresses in Si and Ge are linear with respect to the reciprocal temperature in the whole temperature range investigated. The same holds in a limited temperature range of 500–700°C for the alloy of $x = 0.01$ and in a range of 550–600°C for the alloy of $x = 0.04$. In such temperature ranges the yield stresses of the alloys are slightly higher than that of Ge. The temperature dependencies of the yield stresses of the alloys become much weaker in a higher temperature range. Such a temperature range expands toward the low-temperature side with increasing magnitude of x. Thus, the yield stresses of the GeSi alloys are nearly

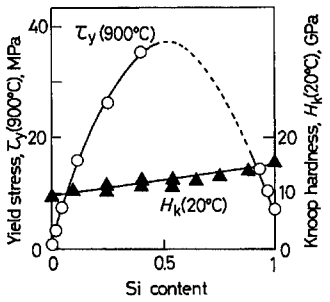

Fig. 4. Yield stresses τ_y of the GeSi alloy plotted against the Si content x for deformation at 900°C under a strain rate of $1.8 \times 10^{-4}\,s^{-1}$ together with Knoop hardness H_k at room temperature.

constant with respect to the temperature and are much higher than that of Ge in the high-temperature range. The magnitudes of the lower yield stress of the alloy $x = 0.996$ are slightly lower than those of Si and the temperature dependence of the lower yield stress is similar to that of Si as seen in Fig. 3. Then, with a decrease in the Si content to $x = 0.946$, the yield stress increases and the temperature dependence of the yield stress becomes weaker in the alloys $x = 0.979$ and 0.946.

Fig. 4 shows the composition dependence of the yield stress of the GeSi alloys. The yield stress increases with an increase in Si content in the composition range $x = 0$–0.4 and a decrease in Si content down to $x = 0.94$. The yield stresses of the alloys with $x > 0.10$ are much higher than those of pure Si. Over the whole composition range of the GeSi alloys, the yield stress seems to show the maximum around $x = 0.5$ and to be dependent on the composition as proportional to $x(1 - x)$. The room-temperature hardness of the GeSi alloys obtained with a Knoop indentor with a 25 g load for 10 s is shown by solid triangles in Fig. 4. The hardness at room temperature increases linearly with the Si content x from 0 to 1.

5. Alloying effects

The results in Fig. 3 mean that the yield stress of the alloys with any composition consists of two components: one decreases rapidly with increasing temperature in a similar manner as in Ge or Si and the other is almost independent of the temperature and depends on the Si content x. The former is the effective stress and the latter the athermal stress. The variation in the yield stress with temperature in the GeSi alloys can be understood that the flow stress of the alloy has an athermal stress that is absent in elemental and compound semiconductors. Such athermal stress related to alloying becomes maximum around the Si content $x = 0.5$ and leads the observed threshold stress for dislocation generation.

A few origins of athermal stress related to alloying are conceivable as discussed in the previous papers [2–4]. Long-range stress may be introduced with a relation to the local fluctuation of the alloy composition in a crystal. Since the bond lengths of Si and Ge differ by about 4%, local fluctuations of the alloy composition in a crystal, causing small regions of Si or Ge enriched, can induce a long-range stress field that cannot be surmounted by dislocations via a thermally activated process. The observed composition dependence of the yield stress in the GeSi alloys is in good agreement with that of the yield stress in ionic solid solutions reported by Kataoka and Yamada [8]. Immobilization of dislocations due to the dynamic development of a solute atmosphere around them during deformation leads to an extra stress necessary to release the dislocations from solute atmosphere. Although the release of a dislocation from its solute atmosphere is controlled by a thermal activation process, a solute atmosphere around a dislocation develops more pronouncedly at higher temperature. Thus, the contributions of these effects to the flow stress compensate each other and may become temperature-insensitive, apparently looking like an athermal stress.

References

[1] I. Yonenaga, A. Matsui, S. Tozawa, K. Sumino, T. Fukuda, J. Crystal Growth 154 (1995) 275.
[2] I. Yonenaga, K. Sumino, Appl. Phys. Lett. 69 (1996) 1264.
[3] I. Yonenaga, K. Sumino, J. Appl. Phys. 80 (1996) 3244.
[4] I. Yonenaga, K. Sumino, Mater. Sci. Forum 258/263 (1998) 159.
[5] A. Matsui, I. Yonenaga, K. Sumino, J. Crystal Growth 183 (1998) 109.
[6] I. Yonenaga, M. Nonaka, J. Crystal Growth 191 (1998) 393.
[7] W.A. Tiller, K.A. Jackson, J.W. Rutter, B. Chalmers, Acta Metall. 1 (1953) 428.
[8] T. Kataoka, T. Yamada, Jpn. J. Appl. Phys. 18 (1977) 55.

ELSEVIER

Physica B 273–274 (1999) 616–619

PHYSICA B

www.elsevier.com/locate/physb

Modelling of local modes in Si_xGe_{1-x} and $C_xSi_yGe_{1-x-y}$ alloys to explore the local clustering of the species

Simon Scarle, Alison Mainwood*

Physics Department, King's College London, Strand, London, WC2R 2LS, UK

Abstract

The frequencies of the local vibrational modes due to defects within group IV alloys are affected by the local environment of the defects; therefore by investigating known modes we get an insight into alloy fluctuations near the defects. The local modes are modelled around defects in a range of local alloy arrangements to investigate the effects of clustering alloy species. An interatomic potential has been fitted to phonon frequencies for the pure materials at symmetry points in k-space, to local vibrational modes of lighter elements in otherwise pure local environments and to atomic positions predicted by local density calculations for certain alloy structures. Using this potential, the frequencies of local modes of substitutional carbon are found in Si_xGe_{1-x} with various values of x. From a stochastic analysis of the local environs to the carbon, the modes are weighted to produce the expected local vibrational spectrum of a Si_xGe_{1-x} alloy. The experimental local mode line shapes in the alloys deviate sufficiently from those predicted to show that the carbon substitutes preferentially in regions of high silicon content.

Keywords: SiGe; CSiGe; Local vibrational modes; Defects

1. Introduction

Carbon is added in small amounts to SiGe alloys as a way of altering the average lattice constant, and thus reduce the strain in layered structures built on silicon [1]. It is also possible to grow ternary group IV alloy $Si_xGe_yC_{1-x-y}$, although since the solubility of carbon in bulk silicon or germanium is very low, only highly dilute carbon alloys are in equilibrium. The solubility of carbon can be orders of magnitude higher [2] near the surface.

Since the bonding of the group IV elements has the same sp^3 electronic structure, but the three elements have very different band gaps, once the problems of solubility and clustering of the alloy species have been overcome, band gap engineered, strain-free quantum wells and superlattices could be produced.

In this paper, we show how the local segregation of species in a SiGe or SiGeC alloy can be monitored by an examination of the local vibrational modes (LVMs) of defects in the alloy. A comparison of the observed LVM spectrum with the prediction produced by a stochastic arrangement of the species will allow one to investigate the local segregation of the alloy species.

2. Calculating the local mode spectrum

An LVM is present at a defect when the local bonds are stronger or when the defect atoms are lighter than in the perfect lattice. Therefore, substitutional carbon in otherwise pure silicon or germanium has a clear single LVM. For ^{12}C this LVM has a frequency of 605 cm^{-1} in silicon [3], and 531 cm^{-1} in germanium [4], whilst for ^{13}C it is at 590 cm^{-1} in silicon [4], and 512 cm^{-1} in germanium [4]. In the alloys the carbon has multiple LVMs, the frequencies of which depend on the environment about the carbon.

This can be seen as a two-level effect. The first level is from the direct nearest neighbours of the carbon. We are assuming here, that due to the low solubility, no carbon has another carbon as a nearest neighbour. This leaves

*Corresponding author. Tel.: +44-(0)-171-848-2044; fax: +44-(0)-171-848-2420.

E-mail address: alison.mainwood@kcl.ac.uk (A. Mainwood)

0921-4526/99/$ - see front matter
PII: S0921-4526(99)00587-6

Table 1
The local modes produced by each local environment [4]. In local environ, Si_nGe_m : C means a substitutional C with nearest neighbours of n Si's and m Ge's

Local environ	Number of modes	Symmetry in T_d point group
Si_4 : C	1	T_2
Si_3Ge : C	2	A_1 E
Si_2Ge_2 : C	3	A_1 B_2 B_1
$SiGe_3$: C	2	A_1 E
Ge_4 : C	1	T_2

five possible structures for the defect, as shown in Table 1. If all the next neighbours of the carbon are of the same type denoted by Si_4 : C or Ge_4 : C, the carbon is in a near tetrahedral environment and the mode is approximately triply degenerate with T_2 symmetry — approximately because the further neighbours to the carbon may break this symmetry and split the T_2 state slightly. For mixtures of species neighbouring the carbon, the symmetry is lower and there will be two or three LVMs. The second level of this effect depends on the overall ratio of SiGe, this affects the above splitting only very slightly, but the masses of the further neighbours shifts the frequencies of the LVMs between the germanium and silicon extremes.

These effects were demonstrated by Hoffman et al. [4], who observed the carbon LVM in Si_xGe_{1-x} alloys with x varying from 0.5 to 1, and also used an ab initio model to find the LVM frequencies. They were able to show the splitting due to the different species as nearest neighbours, but could not demonstrate the effect of the more distant neighbours because of the long computer time required to find the frequencies for each of a large number of alloy arrangements.

3. The model

A valence force potential with a large parameter set has been used.

i. Parameters for interactions between atoms of the same species have been fitted to phonon frequencies for the pure materials at symmetry points in k-space.
ii. The main interaction between an atom and a neighbour of a different species has been derived from LVMs of lighter atoms in otherwise pure local environments [3–5].
iii. The positions of the atoms in the alloys depend on the interatomic potential, so the positions calculated by local density approximation ab initio calculations, using a super-cell of 64 atoms of given SiGe and SiC structures, were used to optimise the remaining interaction parameters [6].

To calculate the LVM expected of carbon in a particular Si_xGe_{1-x} alloy, a super-cell of 64 atoms was used with the arrangement of species selected randomly in the correct ratio. This was repeated for each of the possible arrangements of nearest neighbours to the carbon and for 10 different random arrangements of further neighbours, leading to 50 runs for each value of x, giving 150 LVM frequencies, some of them degenerate. We assumed an intrinsic line width of 8 cm^{-1} taken from the experimental value for the LVM in germanium [4] and a Gaussian line shape. Thus we constructed a spectrum corresponding to each ratio.

If the species were arranged randomly, the probability of the neighbours to the carbon being Si_nGe_{4-n} in an alloy of Si_xGe_{1-x} would be

$$\frac{4!}{n!(4-n)!}x^n(1-x)^{4-n}. \quad (1)$$

We can, therefore, construct the expected spectra for the carbon LVM in Si_xGe_{1-x} for various values of x.

4. Results and discussion

The expected LVM spectra for four silicon-rich alloys ($Si_xGe_{1-x}, x = 0.95, 0.85, 0.75, 0.65$) are shown in Fig. 1. The modes due to the arrangement of species among the nearest neighbours can be distinguished clearly.

A comparison with the LVM spectra reported by Hoffman et al. [4] shows a rather different distribution of modes. Note that their SiGe samples were *implanted* with carbon, so we can assume that the site the carbon arrives at is determined by the implantation, carbon migration and substitutional processes, not by the growth of the SiGeC alloy.

Hoffman's spectra shows that the peak corresponding to four silicon neighbours around the carbon is the strongest feature for $0.5 < x < 1$, whereas we would expect from our spectra that other modes would dominate as x decreases below 0.75. This suggests that either:

1. There are regions of the alloy where the silicon and germanium are slightly segregated, or
2. Carbon substitutes preferentially into sites surrounded with silicon.

The second of these suggestions is supported by Kelires [7] and Berdin et al. [8], who have shown that Ge–C bonds are less strong than Si–C or Si–Ge bonds. In addition, Yang et al. [5] show that the Ge–Ge vibrational mode in the ternary SiGeC alloy is not affected by the concentration of carbon, whilst the Ge–Si mode is.

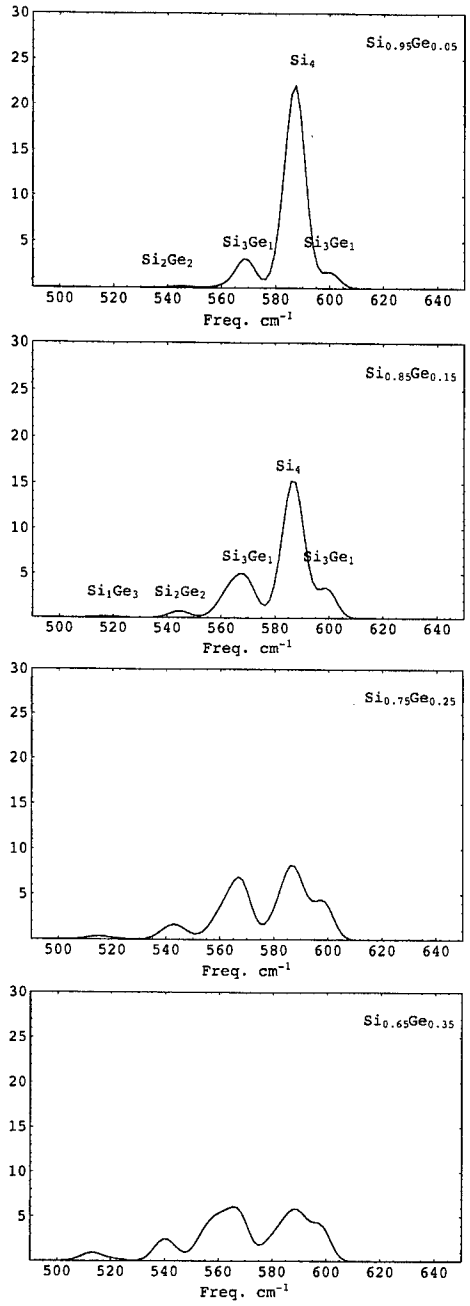

Fig. 1. Calculated LVM spectra for ^{13}C in Si_xGe_{1-x} alloys, assuming stochastic arrangements of species, with the modes identified by the number of neighbours to the carbon. The values of x are the same as those used by Hoffman et al. [4].

In the first case, we would expect the experimental spectra to show a wider spread of x values than the stochastic predictions — that is regions with x significantly *both* greater and smaller than average. In the second case, only regions with x greater than the average would be observed by monitoring the LVM spectrum of carbon.

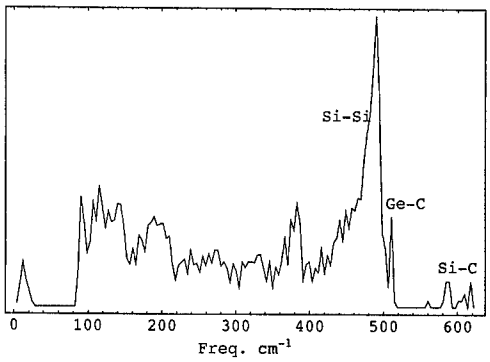

Fig. 2. Density of phonon states in arbitary units for a stochastic arrangement of $C_{0.01}Si_{0.80}Ge_{0.19}$ with the main modes identified.

We have analysed Hoffman's spectra qualitatively in the light of our calculated spectra, near the carbon atom, their spectra show a concentration of germanium which is consistently 5–10% lower than the x values implies. There is no evidence for a matching increase in x elsewhere in the crystal, so these results support the preferential substitution of carbon into regions of high silicon content. It was not possible to determine whether these silicon-rich regions were more abundant than the stochastic analysis would predict.

5. The ternary alloy

A similar investigation of the ternary alloy can be made by looking at the density of phonon states and identifying the modes associated with particular combinations of species. Fig. 2 shows an example of the density of phonon states that we predict for a stochastic ternary alloy ($C_{0.01}Si_{0.80}Ge_{0.19}$). The Si–C LVMs can clearly be seen, whilst the Ge–C modes are starting to be lost into the Si–Si peak.

An alternative approach is to look at the LVM spectra associated with an impurity. Boron is common in silicon and its alloys. It is a shallow acceptor, which means that the excess hole has a very large orbit, and the local *elastic* behaviour of the boron will be very similar to that of a carbon atom with the mass of boron. Therefore, apart from adjusting the parameters for B–C and B–Si to give the LVM frequencies observed [9,10] and scaling the B–Ge parameter by the same factor as B–Si, the parameters in the potential for boron and boron–carbon are the same as those for carbon.

With these assumptions, the LVM spectra for boron and carbon in stochastic arrangements of $C_{0.02}Si_{0.05}$

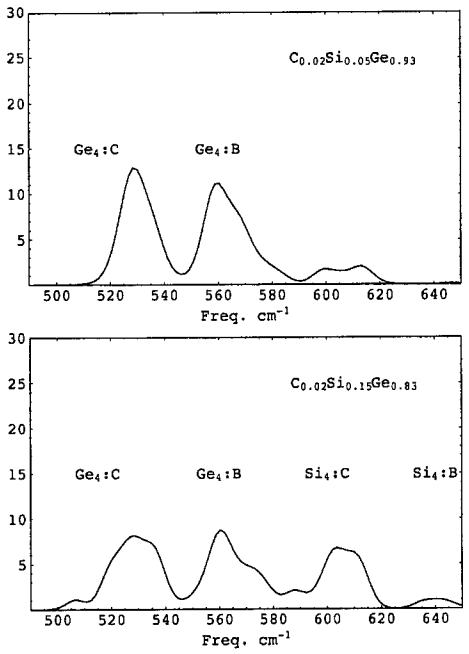

Fig. 3. Predicted LVM spectra for ^{10}B in $C_xSi_yGe_{1-x-y}$ assuming a stochastic arrangement of species.

$Ge_{0.93}$ and $C_{0.02}Si_{0.15}Ge_{0.83}$ are shown in Fig. 3. The inclusion of boron has clearly made the Ge_4:C peak wider than in the pure alloy, and most of the intermediate modes are now hidden under the Ge_4:B peak. The Si_4:C peak appears stronger due to the intermediate Si_nGe_m:B modes having similar frequencies. Although not shown on these graphs for reasons of clarity, modes for C–B nearest neighbours were found at around 1000 and 720 cm^{-1}. Again, all of these features shift with overall alloy ratios. Comparisons of these spectra with those observed experimentally will allow the segregation of the alloy to be quantified.

6. Conclusions

We have demonstrated a method by which the local segregation of the species in group IV alloys can be investigated by means of the LVM spectra of carbon or impurities in the alloy.

Acknowledgements

We thank J.E. Lowther for the results quoted as Ref. [6]. SS thanks the Engineering and Physical Sciences Research Council of the U.K. for a studentship.

References

[1] R.A. Soref, Proc. IEEE 81 (1993) 1687.
[2] J. Tersoff, Phys. Rev. Lett. 74 (1995) 5080.
[3] R.C. Newman, J.B. Willis, J. Phys. Chem. Solids 26 (1965) 373.
[4] L. Hoffman, J.C. Bath, J. Lundsgaard Hansen, A. Nylandsted Larsen, B. Bech Nielsen, P. Leary, R. Jones, S. Öberg, Mater. Sci. Forum 258–263 (1998) 97.
[5] B.-K. Yang, M. Krishnamurthy, W.H. Weber, J. Appl. Phys. 84 (1998) 2011.
[6] J.E. Lowther, private communication.
[7] P.C. Kelires, Phys. Rev. Lett. 75 (1995) 1114.
[8] M.A. Berding, A. Sher, M. van Schilfgaarde, Phys. Rev. B 56 (1997) 3885.
[9] S.J. Breuer, P.R. Briddon, Phys. Rev. B 49 (1994) 10332.
[10] C.P. Herrero, M. Stutzman, Phys. Rev. B 38 (1998) 12688.

ELSEVIER

Physica B 273–274 (1999) 620–623

PHYSICA B

www.elsevier.com/locate/physb

Site preference next to germanium atom of gold and platinum impurities in SiGe alloy

L. Dobaczewski[a,*], K. Bonde Nielsen[b], K. Gościński[a], A.R. Peaker[c], A. Nylandsted Larsen[b]

[a]*Institute of Physics, Polish Academy of Sciences, al. Lotników 32/46, 02-668 Warsaw, Poland*
[b]*Institute of Physics and Astronomy, University of Aarhus, DK-8000 Aarhus C, Denmark*
[c]*Center for Electronic Materials, University of Manchester Institute of Science and Technology, P.O. Box 88, Manchester M60 1QD, UK*

Abstract

The technique of Laplace transform deep level transient spectroscopy has been used to study the acceptor levels of platinum and gold diffused into dilute (0–5% Ge) SiGe alloys. The high-resolution spectra obtained display a fine structure that we interpret as the effect of alloy splitting in terms of the relative number of silicon and germanium atoms in the immediate proximity of the transition metal. We show that Ge atoms in the first and in the second shell of atoms surrounding the impurity perturb the electronic properties of the well-known Au and Pt acceptor defects. For both defects the spectral distributions indicate an overpopulation of Ge-perturbed sites as compared to randomly occupied sites. This can be quantitatively interpreted in terms of an enthalpy difference of ~ 60 meV between configurations with zero or one Ge in the first or second shell surrounding the impurity.

Keywords: SiGe; Laplace DLTS; Alloy splitting; Gold; Platinum

1. Introduction

Electronic levels of localized point defects in semiconductor materials are sensitive to the details of the atomic configuration in their close vicinity. For semiconductor alloys the spatial fluctuations in local alloy composition may then cause variations in the thermal emission rates of carriers from the defect. As a result, the thermal emission spectra obtained by deep level transient spectroscopy (DLTS) may reveal in the alloys a fine structure that can be interpreted in terms of "alloy splitting" of the bound-state total energy [1–3]. For this interpretation the effective radius of the bound carrier is the crucial parameter. The concept of a bound-carrier radius is less useful when both initial and final states are alloy sensitive, which happens when the ionization is accompanied with a notable lattice relaxation. However, as long as the alloy is macroscopically homogenous it may be assumed, that the observation of fine structure (or line broadening) in the ionization spectra of defects is a manifestation of spatial fluctuations in the alloy composition on the microscopic scale rather than variations in bulk band gap parameters.

One can expect that only one shell of atoms influences the level splitting in the case of a ternary alloy [4,5], whereas for binary alloys, such as SiGe, two shells may contribute. Taking this into account we show that the application of the high-resolution Laplace DLTS [6] enables a uniquely detailed mapping of environmental effects on deep centers within dilute SiGe. We show that emission spectra obtained for the platinum and gold acceptor states display a fine structure that can be interpreted as the effect of alloy splitting in terms of the relative number of silicon and germanium atoms in the immediate proximity of the transition metal. Both defects have been studied previously in great detail for pure Si [7,8] and some conventional DLTS results are available

* Corresponding author. Fax: + 48-22-843-09-26.
E-mail address: dobacz@ifpan.edu.pl (L. Dobaczewski)

0921-4526/99/$ - see front matter
PII: S0921-4526(99)00588-8

for SiGe alloys [9,10]. We further show by analyzing the relative concentrations of different local alloy configurations that both transition metals display a preference to end up next to Ge when they are diffused into the alloy.

2. Samples

The measurements were carried out using samples grown by molecular-beam epitaxy (MBE) on (1 0 0) Si substrates. The Ge content was varied between 0 and 5 at% in the 4 μm thick top layers of $Si_{1-x}Ge_x$. This was grown on top of compositionally graded buffer layers; details of the growth procedure can be found elsewhere [11]. The uniform top layers were n-type, doped with 5×10^{15} Sb cm^{-3}. Both p^+n-mesa diodes, formed by mesa etching a 200 nm thick MBE grown p^+-type $Si_{1-x}Ge_x$ top layer, and Schottky diodes, produced by e-gun evaporation of Au through a mask, were used. The dopant metals (either Pt or Au) were diffused into the layers at 800°C for 24 h. In the case of the mesa diodes this was done through the p^+ layer and in the case of the Schottky diodes prior to diode formation.

3. Results

The Laplace DLTS spectra of the gold acceptor in pure silicon show no structure. For the 0.5% SiGe alloy two lines are seen and for the samples with the germanium content between 1% and 5% always three lines forming a characteristic pattern are observed. Two Laplace DLTS spectra of the gold and platinum acceptors in an SiGe alloy with 1% Ge are shown in Fig. 1. The measurements have been carried out at different temperatures. However, for direct comparison of the spectra the commonly used frequency scale has been converted to a defect-energy scale using the formula: $\Delta E = kT*\ln(e_n/e_{n0})$, where e_{n0} is an arbitrary reference frequency, T is the measurement temperature, and k is the Boltzman constant. A substitutional atom has four nearest neighbors so from the binomial distribution governing the mixing of atoms in a random binary alloy the probability of finding a given number of germanium atoms, i.e. 0, 1, etc. out of 4 neighbors, in the first-nearest shell of an Si substitution site can be calculated. We assign these local configurations by 0, 1 and 2 Ge in the case of Au. The assignment of the individual peaks is based on the trend in the intensities and comparison with data obtained for pure silicon. It should be noticed, however; that the relative amplitudes of peaks corresponding to the 1 and 2 Ge configurations are somewhat larger than expected for a perfectly random alloy.

The depicted Pt spectrum has more features than the Au spectrum and does not display the same clear series of lines. However, when the center of gravity of three left-hand-side lines seen for the platinum spectrum is aligned with the 0 Ge line of the Au spectrum the remaining right-hand-side line for platinum aligns with the 1 Ge line for gold. In order to understand the differences one should remember that the energy resolution of the Laplace DLTS technique is inversely proportional to the temperature at which the spectrum is taken. This means that the platinum spectrum has been obtained with a factor of 2.5 higher resolution than the gold spectrum. As a result, an additional splitting of the gold 0 Ge line is revealed. We interpret this as a manifestation of the influence of the second-nearest shell of atoms on the electronic level of the platinum acceptor.

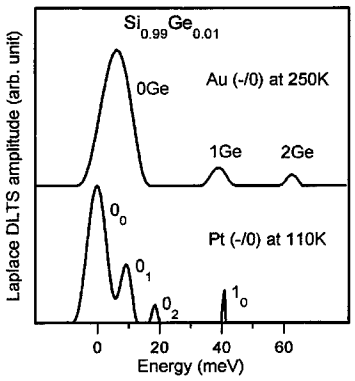

Fig. 1. Laplace DLTS spectra of gold and platinum acceptors in the 1% SiGe alloy. The usual frequency scale has been converted to a relative defect-energy scale using a formula given in the text. Note that a lower energy means a slower emission rate, and consequently a larger energy distance from the conduction band. The 0 Ge line for Au has been aligned with a center of gravity of the 0_0, 0_1, 0_2 lines for Pt.

In order to analyze this observation quantitatively we must consider both the first and the second nearest neighbors of the substitution-site Pt impurity. Analogous to binomial analysis for the gold case, when two shells of atoms are considered we may assign spectral features to two groups of peaks, those having zero and those having one germanium in the first nearest shell. Each feature on the platinum-related spectrum is assigned by a figure and a subscript denoting the number of germanium atoms in the first and second nearest shell, respectively. A consequence of the enhanced resolution of the Laplace DLTS measurements in the case of platinum is a limitation in the total width of the spectrum. As a result, weak peaks completing the series for the 1 Ge line, i.e. the 1_1 and 1_2 lines, practically cannot be observed for platinum.

In principle, one could expect that the peak assigned to the 0 Ge configuration for the gold center should be broadened by the unresolved splitting of the 0_0, 0_1, and 0_2 configurations which has been resolved in the Pt case. Furthermore, the 0 Ge line should be asymmetric.

However, due to limitations of the numerical method used for the Laplace transform inversion this asymmetry will not be seen in the spectra unless the line separation is larger than the characteristic resolution of the method (approximately, a factor of two in the emission rate difference) [12]. We conclude that there is no fundamental difference between the results for the gold and platinum as far as the alloy splitting is concerned. The differences seen in the displayed spectra may simply be a result of more advantageous experimental conditions in the platinum case.

The peak positions on the energy scale are indicative of how the electronic properties of the acceptor state are modified by alloying. Assuming that the defects in different configurations have equal capture cross-section we may conclude that the enthalpy for electron emission differ by $\Delta H_{\mathrm{th}}^{0/1} \approx 34$ meV for the gold 0 and 1 Ge configurations. This energy difference can also be found by evaluating the absolute values of the activation enthalpies relating to each particular configuration from the Arrhenius plots, i.e. from the $\ln(e_{\mathrm{th}}/T^2)$ versus $1/T$ dependence. A similar result can be obtained for platinum. For the enthalpy difference between the 0_0 and 1_0 configurations we derive the result $\Delta H_{\mathrm{th}} \approx 39$ meV, i.e. comparable to the value obtained for gold. When the germanium atom is present in the second nearest shell then the splitting is smaller. The energy difference for electron emission between the 0_0 and 0_1 configurations is ~ 12 meV.

4. Discussion

The sequences of peaks observed for both metals in different alloy compositions allowed us to identify unambiguously different configurations of the alloy in the closest vicinity to the defect. The peak amplitudes are measures of the relative concentrations of these configurations and can be compared to the theoretical concentrations expected for a truly random alloy. Table 1 presents such a comparison for two alloy compositions. The experimental values were taken from the peak amplitudes observed for many spectra measured at different experimental conditions. For the case of the gold acceptor the intensities of 1 and 0 Ge configuration are compared. For the case of platinum the results for the configurations having no germanium in the first- and differing in the number of germanium in the second-nearest shell are showed. In both cases a clear overpopulation of the germanium-rich configurations is observed. This suggests that during diffusion at 800°C the gold and platinum atoms prefer to occupy sites in the lattice next to germanium. For the case of gold we conclude that on average the relative concentration of the 1 Ge configuration is approximately twice as big as would be expected for a random siting. This site preference can be translated into a crude estimate of the difference in the enthalpy of formation for the 0 and 1 Ge configurations. The result is $\Delta H_{\mathrm{conf}}^{0/1} = kT(@800°C) * \ln(2) \cong 60$ meV (disregarding entropy terms other than configuration entropy). A similar enthalpy difference can be obtained for the 0_0 and 0_1 configurations for the case of platinum.

Table 1
Relative concentrations of different local environment configurations for two SiGe alloy compositions. Theoretical values inferred from an analysis of a perfectly random alloy are compared to ratios of peak amplitudes assigned on the Laplace DLTS spectra for both metal impurities

Composition (%)	Au: amp(1 Ge)/amp(0 Ge)		Pt: amp(0_1)/amp(0_0)	
	Theory	Experiment	Theory	Experiment
0.5	0.020	0.06 ± 0.03	0.062	0.10 ± 0.05
1	0.043	0.08 ± 0.03	0.12	0.21 ± 0.05

The site preference of the transition metal (i.e. the favoring of a germanium neighborhood) may be related to details of the microscopic mechanism of the diffusion of these metals in silicon. Both transition metals diffuse by the kick-out process. The diffusion proceeds as the metal impurity switches between an interstitial position and a substitutional position. The switching is accompanied by the movement of a host atom from the substitutional to the interstitial site. The driving force for the accumulation of substitutional Au or Pt is the removal of the self-interstitial atoms by sinks. Due to the fact that the germanium atom has a larger ionic radius than the silicon atoms, one may expect that it is easier for the metal to kick-out the silicon atoms rather than the germanium atoms from their substitutional positions. A smaller interstitial atom would mean that less energy is needed for a local lattice distortion to accommodate an extra atom. Thus, it would cost less energy to create the self-interstitial defect (silicon atom in the silicon host) than the pseudo-self-interstitial defect (germanium atom in the silicon host). This preference of an interstitial site by Si will be partially counteracted by the weakening of Ge-substitution-site bonds as compared to Si-substitution site bonds. Moreover, the self-interstitial creation from a site next to Ge may benefit from an easier relaxation (because of the longer and softer Si–Ge bonds) when the metal squeezes its neighbors. As a result of these competing energy terms, the metal atoms prefer during diffusion to reside as Si-substitutional atoms close to Ge.

5. Summary

The high-resolution Laplace DLTS spectra for gold- or platinum-diffused SiGe samples show an alloy

splitting that may be associated with the spatial alloy fluctuations of the total energy of the non-ionized Au and Pt acceptor states. For the case of platinum we can distinguish between the effect of the level splitting caused by alloying in the first and in the second shell of surrounding atoms. We have found that the electronic energy level is affected by the alloying in the first nearest neighborhood by a factor 2–3 more than by the alloying in the second nearest shell. A clear preference for gold and platinum to enter substitutional Si sites adjacent to Ge has been revealed. This may be interpreted in terms of an enthalpy lowering as a simple result of the fact that both metals are able to replace the host silicon atom more easily in the substitutional position than the germanium atom. As a result, for both cases we observed that the germanium atom effectively lowers the local minimum energy for these metals to occupy the substitutional site by approximately 60 meV.

Acknowledgements

This work has been supported in part by the Committee for Scientific Research grant No. 8T11B00315 in Poland, the Danish National Research Foundation through the Aarhus Center for Atomic Physics (ACAP), the Danish Natural Scientific Research Council, the UK Royal Academy of Engineering and the European Community grant No. CIPA-CT94-0172.

References

[1] P. Omling, L. Samuelson, H.G. Grimmeiss, J. Appl. Phys. 54 (1983) 5117.
[2] E. Calleja, F. Garcia, A. Gomez, E. Munoz, P.M. Mooney, T.N. Morgan, S.L. Wright, Appl. Phys. Lett. 56 (1990) 934.
[3] L. Dobaczewski, J.M. Langer, Mater. Sci. Forum 10–12 (1986) 399.
[4] L. Dobaczewski, P. Kaczor, M. Missous, A.R. Peaker, Z.R. Zytkiewicz, Phys. Rev. Lett. 68 (1992) 2508.
[5] L. Dobaczewski, P. Kaczor, M. Missous, A.R. Peaker, Z.R. Zytkiewicz, J. Appl. Phys. 78 (1995) 2468.
[6] L. Dobaczewski, P. Kaczor, I.D. Hawkins, A.R. Peaker, J. Appl. Phys. 76 (1994) 194.
[7] G.D. Watkins, M. Kleverman, A. Thilderkvist, H.G. Grimmeiss, Phys. Rev. Lett. 67 (1991) 1149.
[8] F.G. Anderson, R.F. Milligan, G.D. Watkins, Phys. Rev. B 45 (1992) 3279.
[9] F. Nikolajsen, P. Kringhøj, A. Nylandsted Larsen, Appl. Phys. Lett. 69 (1996) 1743.
[10] A. Mesli, A. Nylandsted Larsen, Materials Research Society Symposium Proceedings, Vol. 510 1998, p. 89.
[11] A. Nylandsted Larsen, Mater. Sci. Forum 258–263 (1997) 83.
[12] A.A. Istratov, O.F. Vyvenko, Rev. Sci. Instr. 70 (1999) 1233.

ELSEVIER

Physica B 273–274 (1999) 624–627

PHYSICA B

www.elsevier.com/locate/physb

Jahn–Teller splitting and Zeeman effect of acceptors in diamond

Hyunjung Kim[a,*], S. Rodriguez[a], M. Grimsditch[b], T.R. Anthony[c], A.K. Ramdas[a]

[a]*Department of Physics, Purdue University, West Lafayette, IN 47907, USA*
[b]*Argonne National Laboratory, Argonne, IL 60439, USA*
[c]*GE Corp. Research and Development, Schenectady, NY 12309, USA*

Abstract

Employing the high resolution of a 5 + 4 tandem Fabry–Pérot interferometer, we discovered that Δ', the Raman active electronic transition between the spin–orbit split $1s(p_{3/2}):\Gamma_8$ and $1s(p_{1/2}):\Gamma_7$ acceptor ground states, is a doublet for a boron impurity in diamond with a clearly resolved spacing of $0.81 \pm 0.15\,cm^{-1}$. The direct observation of a Stokes/anti-Stokes pair with $0.80 \pm 0.04\,cm^{-1}$ shift provides a striking confirmation that the lower $1s(p_{3/2}):\Gamma_8$ ground state has experienced a splitting due to a static Jahn–Teller distortion. The Zeeman effect of Δ' has been investigated with a magnetic field along several crystallographic directions. Theory of the Zeeman effect, formulated in terms of the symmetry of the substitutional acceptor and the Luttinger parameters of the valence band, allows quantitative predictions of the relative intensities of the Zeeman components in full agreement with experiments. The observation of transitions *within* the Γ_8 Zeeman multiplet, i.e., the Raman-electron-paramagnetic-resonances, is yet another novel feature to emerge from the present study. The investigation has also yielded g-factors characterizing the Zeeman multiplets.

Keywords: Jahn–Teller splitting; Zeeman effect; Acceptors; Diamond

1. Introduction

Bound states of electrons (holes) bound to Coulomb centers represented by substitutional group V (group III) impurities in group IV semiconductors, with small binding energies and extended wave functions (and hence labeled 'shallow' centers), are successfully described in the effective mass theory (EMT) [1,2]. The screened Coulomb potential; the effective mass parameters and the symmetry of the band extremum with which the electronic states are associated; and the site symmetry of the impurity — these are the basic ingredients of EMT. To the extent the wave functions of the bound states probe the immediate vicinity of the impurity, as those of the 1s-like ground state of these solid state analogs of the H-atom, relevant corrections to EMT are introduced. In the context of such considerations, the case of substitutional boron acceptors in diamond (in the so-called type IIb, blue diamonds) is particularly fascinating in view of distinctive underlying features: the largest departure from the spherical approximation [3–5] exhibited by any of the tetrahedrally coordinated semiconductors and the small spin–orbit splitting of the valence band.[1]

* Corresponding author. Present address: B4202, XFD/401, Advanced Photon Source, Argonne National Laboratory, 9700 S. Cass Ave. Argonne, IL 60439, USA. Tel.: + 1-630-252-9141; fax: + 1-630-252-3222.

E-mail address: hjk@physics.purdue.edu, hjk@aps.anl.gov (H. Kim)

[1] These authors have introduced valence band parameters $\mu = 2(3\gamma_3 + 2\gamma_2)/5\gamma_1$ and $\delta = (\gamma_3 - \gamma_2)/\gamma_1$ where γ_1, γ_2, and γ_3 are the Luttinger parameters; μ measures the strength of spherically symmetric contributions to the light and heavy hole kinetic energy while δ gives the deviation of the hole energies from sphericity. Among the tetrahedrally coordinated elemental group IV and the III–V and II–VI semiconductors (μ/δ) has the smallest value for diamond. We have used the γ_1, γ_2, γ_3 values of Reggiani et al. (see Ref. [5]).

0921-4526/99/$ - see front matter
PII: S0921-4526(99)00589-X

Spectroscopic investigations of the electronic states of holes bound to boron acceptors are particularly tractable thanks to its successful incorporation in sufficient concentrations in man-made diamonds [6–8], besides its occurrence in extremely rare natural specimens [9,10].

We recently reported the electronic Raman line associated with the transition between the spin–orbit split 1s ground states, i.e., the $1s(p_{3/2}):\Gamma_8 \rightarrow 1s(p_{1/2}):\Gamma_7$ (labeled Δ') in boron-doped diamonds with natural isotopic composition as well as in a ^{13}C specimen [7,8]. In this paper we present the results of a high-resolution investigation of the Δ' line of boron-doped diamond employing a tandem Fabry–Pérot interferometer. Further, we have fully characterized Δ' with its Zeeman splitting and the polarizations of the Zeeman components which have yielded insights into the mass anisotropy of the valence band maximum and the g-factors for the participating levels.

2. The Δ' line without perturbation

The energy levels of a hole bound to a boron acceptor in diamond are shown schematically in the inset to Fig. 1. The effective mass ground state shows a spin–orbit splitting into $1s(p_{3/2}):\Gamma_8$ and $1s(p_{1/2}):\Gamma_7$ states, separated by Δ' corresponding to Δ, the spin–orbit splitting of the valence band maximum. Also shown are the Lyman transitions originating from the $1s(p_{3/2})$ and $1s(p_{1/2})$ ground states. The transition *between* the two 1s ground states is strongly Raman allowed but infrared forbidden due to the approximate even parity of both levels.

In order to study the Δ' transition with precision as well as with the ability to observe small shifts, we resorted to a 5 + 4 tandem, piezo-electrically scanned Fabry–Pérot interferometer. We discovered that it is actually a doublet with a separation of 0.81 ± 0.15 cm^{-1} as shown in Fig. 1. Note that the lower electronic ground state, $1s(p_{3/2}):\Gamma_8$ is four-fold degenerate; as such, it is a prime candidate for a Jahn–Teller splitting into two Kramers doublets. We ensured that the doublet structure did not originate in the procedure adopted for mounting the diamond specimen. We observed it in four blue diamonds with natural isotopic composition; within experimental accuracy, the splittings are same in all the samples and in different crystallographic directions. Random strains introduced during crystal growth are not expected to be homogeneous and the same from specimen to specimen; thus they cannot produce identical splittings but will cause only broadening and hence can be ruled out as the origin of the splitting.

We have explored both static and dynamic Jahn–Teller effect as the microscopic underlying mechanisms for the above splitting [11] and concluded that the static Jahn–Teller approach provides a physically meaningful interpretation. A group theoretical analysis, taken together with the experimental results including polarization effects, shows that the $1s(p_{3/2}:\Gamma_8)$ level experiences a distortion along a cubic axis and splits it into $\psi_{\pm 3/2}$ and $\psi_{\pm 1/2}$ levels. It is specially significant that near ω_L, the unshifted exciting laser frequency, two new features identified with a star appear; they occur with a frequency shift of 0.80 ± 0.04 cm^{-1} from ω_L equal to the Jahn–Teller splitting of Δ'. We interpret them as the Stokes and the anti-Stokes Raman line corresponding to the transition within the Jahn–Teller split $1s(p_{3/2})$ levels, i.e., it corresponds to the $\psi_{\pm 3/2} \rightarrow \psi_{\pm 1/2}$ transition. This is one of the smallest Raman shifts reported in the literature other than those of Brillouin components.

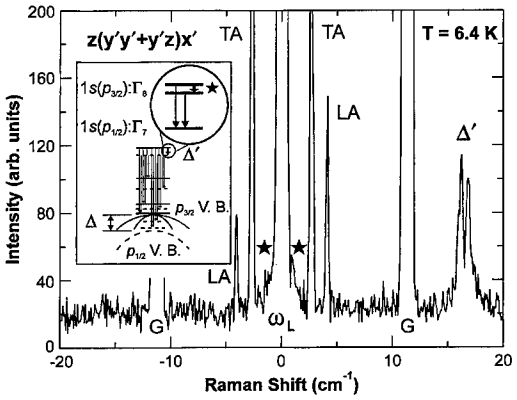

Fig. 1. The Δ' line as a Jahn–Teller doublet, the transition between the Jahn–Teller split $1s(p_{3/2})$ levels, labeled with a star (★), and the intrinsic transverse acoustic (TA) and longitudinal acoustic (LA) Brillouin components in the scattered light from a natural type IIb diamond spectrally analyzed with a high-resolution tandem Fabry–Pérot interferometer. The spectrum is recorded in the right angle scattering geometry $z(y'y' + y'z)x'$; here $x'\|[110]$, $y'\|[\bar{1}10]$ and $z\|[001]$ and the incident light along z is polarized along y' whereas the scattered light along x' is not analyzed. The wavelength of the exciting laser radiation (λ_L) is 5145 Å (Ar^+). ω_L is the unshifted laser frequency and ***G*** identifies its 'ghosts' due to leakage in the tandem operation. The inset shows energy levels of a hole bound to a substitutional boron acceptor in diamond. The Jahn–Teller split $1s(p_{3/2})$ levels and the transition between them, identified with a star (★), and the two transitions resulting in the Δ' line as a doublet are shown in the enlarged view presented within the circle. V. B. ≡ Valence Band.

3. The Zeeman effect of Δ'

The Zeeman effect of the Δ' Raman line, in an external magnetic field ***B*** of 4 T along $z\|[001]$ and the sample temperature of 5.3 K, is displayed in Fig. 2. The Raman spectrum, recorded with the tandem Fabry–Pérot interferometer in the right angle scattering geometry $y(zx + zy)z$ where x, y, and z are the cubic axes, shows four fully resolved Zeeman components of Δ' labeled

1′, 2′, 3′, and 4′. With incident light along y and polarized along z and the scattered light unanalyzed, the experiment allows the zx and zy components of the Raman tensors of the Zeeman transitions to appear [12].

The inset to Fig. 2 shows schematically the four sublevels of $1s(p_{3/2}):\Gamma_8$ and two of $1s(p_{1/2}):\Gamma_7$ for $\boldsymbol{B} \neq 0$. (The figure is appropriate for magnetic fields in which the Jahn–Teller splitting can be neglected in comparison to the Zeeman splitting.) The ordering of the Zeeman sublevels of the two 1s states is based on the polarization features of the Zeeman components and the negative sign for the g-factor of free hole, i.e., from an appeal to the experimental observations. The selection rules for the Zeeman transitions are: $\delta = m - M = 0, \pm 2$ for the transitions 1, 2, 3, and 4 while $\delta = \pm 1$ apply to 1′, 2′, 3′, and 4′, the Zeeman components observed under the experimental conditions of Fig. 2. Here $m = \pm \frac{1}{2}$ denote the magnetic quantum numbers of the $1s(p_{1/2})$ level while $M = \pm \frac{3}{2}$ and $\pm \frac{1}{2}$ those of the $1s(p_{3/2})$ [12].

In Fig. 2, in addition to the Zeeman components of Δ', and the intrinsic transverse acoustic (TA) and longitudinal acoustic (LA) Brillouin components, two Stokes/anti-Stokes pairs labeled $E1'$ and $E2'$ with significantly smaller shifts can be observed. They correspond to the electron-paramagnetic-resonances (Raman-EPR transitions) within the Zeeman multiplet of $1s(p_{3/2})$ satisfying $\Delta M = \pm 1$. In the linear approximation for the Zeeman effect, the sublevels of $1s(p_{3/2})$ are spaced equally leading to identical energies for the $E1'$ and $E2'$ lines. The experimental observation thus unambiguously shows the contribution of Zeeman energies quadratic in $\boldsymbol{B}$ making the spacings unequal [12]. The $\psi_{\pm 1/2} \rightarrow \psi_{\mp 1/2}$ as well as the $\psi_{\pm 3/2} \rightarrow \psi_{\mp 3/2}$ EPR transitions are forbidden by time-reversal symmetry in Raman effect.

The Zeeman effect of Δ' for $\boldsymbol{B}\|[110]$, employing a charge-coupled-device (CCD)-based triple grating spectrometer, is displayed in Fig. 3. It is recorded with incident radiation along $z\|[001]$, polarized along $y'\|[\bar{1}10]$ or $x'\|[110]$, and scattered along x', analyzed along z or y'. The polarization configurations accessible in this right angle scattering geometry allows the $x'z$, $x'y'$, $y'y'$, and $y'z$ components of the Raman polarizability tensors to be observed. It can be shown [12] that level scheme in the inset to Fig. 2 applies equally to this case for a given $\boldsymbol{B}$; hence, 1′, 2′, 3′, and 4′ can appear in $z(x'z)x'$, $\delta = \pm 1$, Fig. 3(a), whereas 1, 2, 3, and 4 can be seen in $z(y'y')x'$ conforming to $\delta = 0, \pm 2$, Fig. 3(b). Thus, one can deduce the distinct but small separation between the primed and the unprimed components, $(1, 1'), (2, 2'), (3, 3')$, and $(4, 4')$, i.e., the splitting of the $1s(p_{1/2}):\Gamma_7$ level. The significantly larger splittings of the $1s(p_{3/2}):\Gamma_8$ level are obtained from similar comparisons of spacings between 1 and 2′ and 1′ and 2 yielding the $(-1/2, -3/2)$ separation while the $(1/2, -1/2)$ and $(3/2, 1/2)$ intervals are given by the spacings of $(2, 3')$, $(2', 3)$ and $(3, 4')$, $(3', 4)$, respectively [12]. The $(x'y')$ polarization permits the observation of

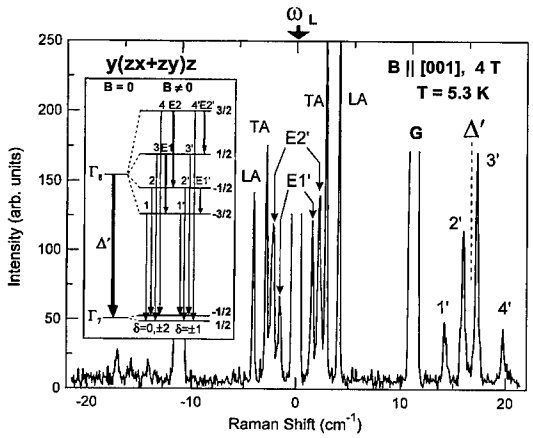

Fig. 2. The Zeeman splitting of the Δ' electronic Raman transition of a boron acceptor in a man-made type IIb diamond recorded with the tandem Fabry–Pérot interferometer. The experiment was carried out with: a 4 T magnetic field ($\boldsymbol{B}$) along [001]; temperature, $T = 5.3$ K; and $\lambda_L = 5145$ Å line of Ar^+ laser. The spectra are recorded in the right-angle scattering geometry, $y(zx + zy)z$; x, y, and z are along [100], [010], and [001], respectively; ω_L, $\boldsymbol{G}$, TA, and LA are defined in Fig. 1. The Zeeman components are labeled according to the inset.

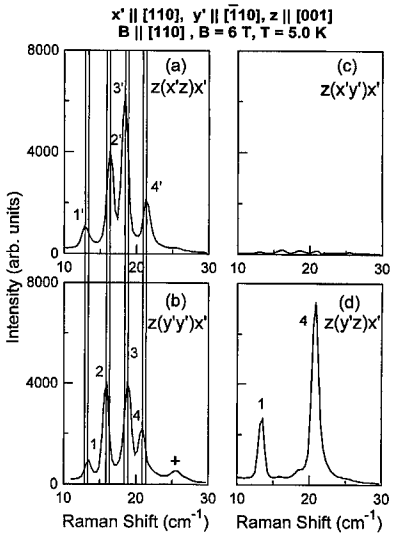

Fig. 3. The polarization features of the Zeeman components of Δ' of a natural type IIb diamond for $\boldsymbol{B}\|[110]$, recorded in a right-angle scattering geometry in which incident light is along z, polarized along y' or x', and scattered parallel to x', analyzed along z or y'. Here $x'\|[110]$ and $y'\|[\bar{1}10]$. The spectral analysis was performed with a CCD-based triple grating spectrometer; $\lambda_L = 6471$ Å (Kr^+) laser. The Zeeman components are labeled 1, 1′; 2, 2′; 3, 3′; and 4, 4′ following the energy level scheme shown in the inset of Fig. 2. The feature labeled with a ' + ' mark is of unknown origin.

1′, 2′, 3′, and 4′ but their conspicuous absence in Fig. 3(c) is due to their intensities being proportional to γ_2^2, where the γ_2 Luttinger parameter is an order of magnitude smaller than γ_3 [8], the Luttinger parameter which essentially controls the Raman intensities in Fig. 3(a), (b), and (d).

4. g-Factors

On the basis of the magnetic field dependence of the Zeeman components of Δ' and of the Raman-EPR lines, $g_{3/2}$ and $g_{1/2}$, the g-factors characteristic of $1s(p_{3/2})$ and $1s(p_{1/2})$ can be obtained. It can be shown that the $J = \frac{3}{2}$ and $\frac{1}{2}$ 'angular momentum' states split into $g_{3/2}\mu_B$ BM and $g_{1/2}\mu_B$ Bm, respectively. Here μ_B is the Bohr magneton, $g_{3/2} = \frac{1}{3}(2g_1 + g_2)$ and $g_{1/2} = \frac{1}{3}(4g_1 - g_2)$, g_1 and g_2 are the g-factors for the orbital and spin-angular momenta, respectively [12]. The magnetic field dependence of the energies of the Zeeman components of Δ' yield $g_{3/2} = -0.94 \pm 0.02$ and $g_{1/2} = 0.16 \pm 0.05$; in turn they lead to $g_1 = -0.39 \pm 0.04$ and $g_2 = -2.04 \pm 0.10$.

5. Concluding remarks

While Si and Ge, the other two elemental group IV semiconductors, have been intensively investigated in the context of shallow donors and acceptors, the corresponding studies in diamond could not be pursued with equal effort. The main bottleneck has been the limited and sporadic successes in the incorporation of dopants; until recently the technological challenges remained daunting. The case of boron acceptors in diamond shows how insightful spectroscopic techniques can be exploited when appropriately doped specimen become available. The studies on boron acceptors in diamond shows in a particularly striking manner the power of Raman techniques when applied to Lyman spectroscopy; they provide information complementary to that obtained from infrared. Finally, the high resolution and the freedom from parasitic radiation of a tandem Fabry–Pérot interferometer; the optical quality of diamond which makes it exceptionally suited for spectroscopy; and the electronic band structure with unusual features are some of the unique aspects of diamond in the context of impurity states of semiconductors.

Acknowledgements

The authors acknowledge support from the National Science Foundation Grant No. DMR 98-00858 at Purdue University and from the US Department of Energy, BES Material Sciences (Grant No. W-31-109-ENG-38) at Argonne National Laboratory.

References

[1] W. Kohn, in: F. Seitz, D. Turnbull (Eds.), Solid State Physics, Vol. 5, Academic Press, New York, 1957, p. 257.
[2] A.K. Ramdas, S. Rodriguez, Rep. Prog. Phys. 44 (1981) 1297.
[3] A. Balderschi, N.O. Lipari, Phys. Rev. B 8 (1973) 2697.
[4] A. Balderschi, N.O. Lipari, Phys. Rev. B 9 (1974) 1525.
[5] L. Reggiani, D. Waechter, S. Zukotynski, Phys. Rev. B 28 (1983) 3550.
[6] H. Kim, A.K. Ramdas, S. Rodriguez, T.R. Anthony, Solid State Commun. 102 (1997) 861.
[7] H. Kim, R. Vogelgesang, A.K. Ramdas, S. Rodriguez, M. Grimsditch, T.R. Anthony, Phys. Rev. Lett. 79 (1997) 1706.
[8] H. Kim, R. Vogelgesang, A.K. Ramdas, S. Rodriguez, M. Grimsditch, T.R. Anthony, Phys. Rev. B 57 (1998) 15315.
[9] J.F.H. Custers, Physica 18 (1952) 489.
[10] J.F.H. Custers, Physica 20 (1954) 183.
[11] H. Kim, A.K. Ramdas, S. Rodriguez, M. Grimsditch, T.R. Anthony, Phys. Rev. Lett. 83 (1999).
[12] H. Kim, A.K. Ramdas, S. Rodriguez, M. Grimsditch, T.R. Anthony, Phys. Rev. Lett. 83 (1999) 3254.

ELSEVIER

Physica B 273–274 (1999) 628–631

PHYSICA B

www.elsevier.com/locate/physb

Electron paramagnetic resonance (EPR) and optical absorption studies of defects created in diamond by electron irradiation damage at 100 and 350 K

D.J. Twitchen[a,*], D.C. Hunt[a], M.E. Newton[a], J.M. Baker[a], T.R. Anthony[b], W.F. Banholzer[b]

[a]*Department of Physics, Clarendon Laboratory, Oxford University, Parks Road, Oxford OX1 3PU, UK*
[b]*General Electric Company, Corporate Research and Development, Schenectady, NY, USA*

Abstract

We present a study, using electron paramagnetic resonance (EPR) and optical absorption spectroscopies, of high purity synthetic type IIa diamonds, which have been irradiated with 2 MeV electrons in a specially developed dewar; allowing irradiation at a measured sample temperature down to 100 K, at doses of $2\times10^{17}\rightarrow4\times10^{18}e^{-}$ cm^{-2}. The production rate of vacancies (1.53(10) cm^{-1}) was the same for irradiation at 100 as at 350 K; as was the production rate of the EPR centre R1, known to be two nearest-neighbour $\langle0\,0\,1\rangle$-split interstitials (0.014(4) cm^{-1}). However, the production rate of the $\langle0\,0\,1\rangle$-split self-interstitial (R2 EPR centre) is 1.1(1) cm^{-1} at 100 K and only 0.10(5) cm^{-1} at 350 K. That R1 is created at 100 K indicates that the self-interstitial is mobile under these conditions of irradiation. Production rates have also been measured for the R3 and R14 EPR centres and a new centre, labelled O3. © 1999 Elsevier Science B.V. All rights reserved.

Keywords: Radiation damage; Creation rates; Vacancies; Interstitials

1. Introduction

Over recent years there has been a resurgence of interest in radiation-induced defects in diamond (see for example Refs. [1–3]). The reasons include for instance, the possibility of using diamond in particle detectors [4,5] and exploitation of ion implantation techniques [6]. In view of this, the understanding of irradiation damage defects is vital for full exploitation of the properties of this material.

In this paper we present a systematic study of optical and EPR defects created in type IIa diamond after being irradiated with mono-energetic 2 MeV electrons. We compare the effects of irradiating diamond: (i) at 100 K and then annealed to 300 K before measurement; (ii) at 350 K before measurement at 300 K; and (iii) at 100 K and then transference to the EPR spectrometer without allowing the sample to warm up, followed by stepped annealing and measurement to 300 K.

2. Previous work

In 1993 Palmer [7] produced a review of the rate of production of radiation damage in diamond by electrons. His review covers the most investigated effects of irradiation-induced defects in single-crystal diamond, using techniques such as EPR, optical absorption and luminescence spectroscopies, and electrical conductivity [7]. The experimental results presented differ for different samples and it was clear to him at the time of writing the paper that further experimental investigations were required to understand the low-temperature (< 300 K) annealing properties of irradiation-induced defects in diamond, especially to try to establish the temperature at which interstitials are mobile. The early experiments reported were carried out in uncharacterized samples, which meant that a consistent picture of irradiation damage had not emerged. In this paper we present results on the

* Corresponding author. Fax: + 44-(0)-1865-272400.
E-mail address: D.Twitchen1@physics.ox.ac.uk (D.J. Twitchen)

0921-4526/99/$ - see front matter
PII: S0921-4526(99)00590-6

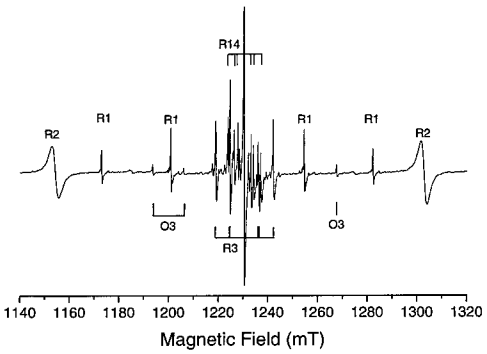

Fig. 1. First derivative 35 GHz EPR spectrum taken at 300 K with the Zeeman field oriented along a ⟨0 0 1⟩-crystallographic axis. The diamond had received a dose of 7×10^{17} 2 MeV e^- cm^{-2} while being held at 100 K.

production rate of the neutral vacancy V^0, and the EPR defects labelled R1 [3], R2 [8], R3 [9], R14 [9], and a new previously unreported defect, which we label O3, in high-quality IIa diamond (see Fig. 1). The R2 EPR centre, which has recently been shown to be the ⟨0 0 1⟩-split self-interstitial [8], and the vacancy are always the dominant defects created in IIa diamond on room-temperature irradiation with 2 MeV electrons. R1 is the next most dominant EPR centre after R2, and has no optical absorption associated with it. Since Palmer's review, R1, has been shown to be a pair of parallel ⟨0 0 1⟩-split interstitials at nearest-neighbour positions [3]. The R3 and R14 defects are as yet uncharacterized. A future publication will present a model for O3 in terms of three next-nearest-neighbour interstitials.

3. Experimental details

Six high pressure and temperature grown synthetic diamonds with parallel polished {0 0 1} faces and dimensions $\sim 2\times2\times0.5\,mm^3$ were supplied by the General Electric (GE) Company. Infrared and UV/visible absorption measurements prior to irradiation showed the samples to be type IIa. EPR measurements at 4 K determined that the concentration of neutral single substitutional nitrogen (P1) was less than 0.02 parts per million (ppm) carbon atoms, and infrared absorption measurements showed that the neutral boron concentration was less than 0.1 ppm.

The EPR measurements were made at room temperature using two spectrometers: a Bruker ER200D spectrometer equipped with an X-band (nominally 9.5 GHz) bridge (ER 041 XG) and Bruker TE_{104} cavity; and a Clarendon designed and built *Q*-band (nominally 35 GHz) spectrometer described previously [3]. EPR concentration measurements were made by comparing doubly integrated first derivative absorption spectra with those of a well-calibrated reference sample. The concentration of V^0 was determined by integrating over the optical absorption zero phonon line (ZPL) of GR1 (1.673 eV) and using the number determined by Twitchen et al. [10], which relates the integrated intensity of GR1 to the concentration of V^0.

The diamonds were irradiated at Reading University, UK using a van De Graaf accelerator, with 2 MeV electrons to doses which ranged between 2×10^{17} and 4×10^{18} e^- cm^{-2}. For irradiating the diamonds in contact with a heat sink at 77 K, modification to the end of the electron beam tube was needed. A dewar, shown in Fig. 2, was developed in the Clarendon Laboratory which bolted onto an adapted endplate of the beam tube. The dewar has vacuum walls and contains a large copper heat sink. Liquid nitrogen was gravity fed through the base of the dewar via a transfer arm connected to a large bucket-dewar ($\sim$ 30 l) of liquid nitrogen. The return pipe for the nitrogen was above the equilibrium position of the sample in the dewar during running conditions. The sample was mounted on the end of a copper screw insert.

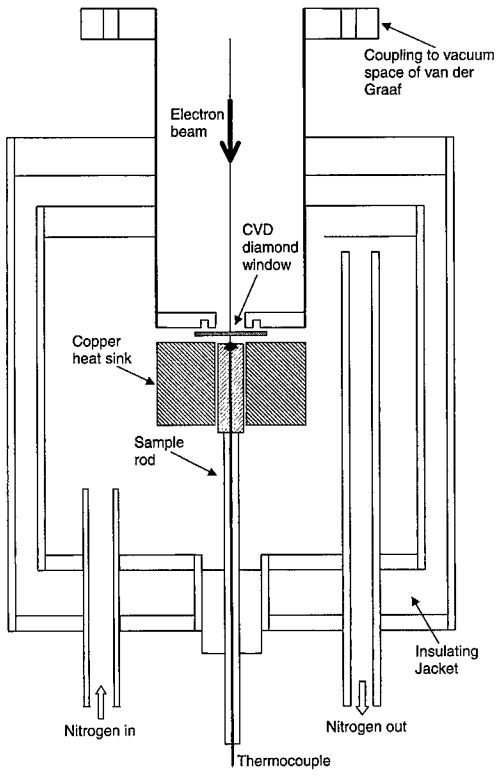

Fig. 2. Dewar developed for irradiating samples in thermal contact with a copper heat sink held at 77 K. The sample is mounted on the end of a copper rod, which is screwed into a large copper heat sink clamped against a thin CVD diamond window. Liquid nitrogen is gravity fed into the dewar. The dewar was designed to fit onto the existing technology at the Reading University van Der Graaf accelerator. The sample can be removed at 77 K and transferred to a pre-cooled EPR cavity.

This screwed into the centre of the large copper heat sink within the dewar, which is clamped against a thin CVD diamond window, which was held next to the exit window of the beam tube. A thermocouple, mounted in the indium just below the diamond sample, allowed the temperature to be measured continuously throughout the irradiation. The measured temperature varied as a function of beam flux: running at $9.4\times10^{13}\,e^-\,s^{-1}\,cm^{-2}$ the thermocouple measured 110 K, and at $5.0\times10^{13}\,e^-\,s^{-1}\,cm^{-2}$ measured 95 K. A compromise was decided on $7.5\times10^{13}\,e^-\,s^{-1}\,cm^{-2}$ and a sample temperature of $\sim$ 100 K. This represented a reasonable time to obtain the necessary irradiation doses without significantly warming the sample. Using this system we performed irradiation doses ranging between 2×10^{17} and $3\times10^{18}\,e^-\,cm^{-2}$. From now on we will refer to irradiation of the sample in contact with the heat sink at 77 K as the "100 K irradiation". Irradiation was also performed at a measured temperature of 350 K, which we refer to as "the 350 K irradiation".

One sample was irradiated at 100 K to a dose of $\sim 7\times10^{17}\,e^-\,cm^{-2}$, and transferred to the *X*-band cavity for measurement at 90 K, without the temperature of the sample rising above 110 K. The sample was then annealed in stages at temperatures of 150, 200, 250 and 293 K. At each temperature the sample was held for 2 h before cooling to 90 K to allow EPR measurements to be taken and compared at the same temperature.

4. Results

The stones used in this study, showed no EPR defects before irradiation. On irradiation with 2 MeV electrons at 350 and 100 K, V^0 and R2 were always formed, together with several other EPR centres (R1, R3 and R14). EPR and optical measurements showed that V^0 was always the dominant charge state of the vacancy produced. Fig. 3(a) shows the production of V^0 as a function of irradiation dose. The points represented by circles correspond to the 350 K irradiation and squares the 100 K irradiation. The straight line is a constrained fit to all the experimental points made to pass through the origin. The measured production rate at both temperatures was 1.53(10) $V^0\,cm^{-1}$ for 2 MeV electrons.

A typical EPR spectrum with the Zeeman field oriented along a ⟨001⟩-crystallographic axis taken at

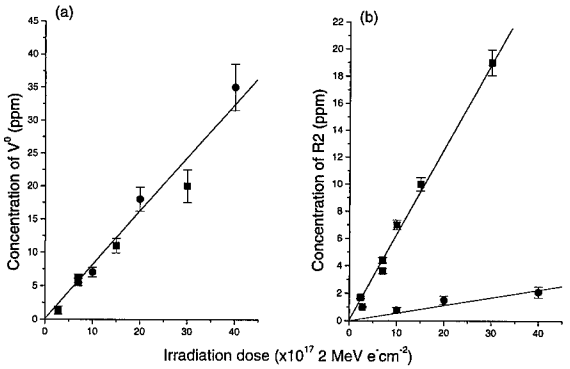

Fig. 3. Concentration of neutral vacancies, produced in type IIa diamond after irradiation with 2 MeV electrons. Circles and squares represent vacancies created after irradiating at 350 and 100 K, respectively. The production rate of vacancies at the two temperatures is the same (1.53(10) cm^{-1}). (b) Production rate of the EPR defect R2, after irradiation with 2 MeV electrons at 100 (squares) and 350 K (circles).

Q-band is shown in Fig. 1. The sample had been irradiated to a dose of $7\times10^{17}\,e^-\,cm^{-2}$ at 100 K. Fig. 3(b) shows the production of R2 in samples irradiated at 100 K (squares) (1.1(1) cm^{-1}) and 350 K (circles) (0.01(5) cm^{-1}). The measured EPR concentrations at 300 K have been corrected allowing for the fact R2 arises from an excited state [8]. The production rate of R1, shown in Fig. 4(a) is 0.014(1) cm^{-1}, which is the same at 100 and 350 K (see Table 1). Fig. 4(b) and (c) show the production rates of the R3 and R14 defects, respectively, at both 100 and 350 K. Fig. 4(d) shows the production rate of O3, which is only created in the 100 K irradiation. The production rates for R3, R14 and O3 will not be discussed further but it is worth making the point here that their production rates in such high-quality diamond means they can only be intrinsic-related defects. The production rates for all the defects are given in Table 1.

The results of irradiating a sample to a dose of $7\times10^{17}\,e^-\,cm^{-2}$ at 100 K and transferring to the spectrometer cold (see Section 2 for details) showed, on annealing in steps to 300 K, that there was no measurable change in the EPR intensity from R1 and R2. Thus, the difference between irradiating at 100 and at 350 K, does not result from some annealing stage which occurred between these two temperatures but must result from

Table 1
The production rates (cm^{-1}) in type IIa diamond for 2 MeV electrons for the sample irradiated at 100 K compared with the sample at 350 K. The V^0 concentration was determined from the integrated intensity of the GR1 ZPL. The R1, R2, R3, R14 and O3 concentrations were determined by EPR measurements.

Temperature of irradiation (K)	V^0 (cm^{-1})	R2 (cm^{-1})	R1 (cm^{-1})	O3 (cm^{-1})	R3 (cm^{-1})	R14 (cm^{-1})
100	1.53(10)	1.10(10)	0.014(1)	0.006(1)	0.018(1)	0.019(1)
350	1.53(10)	0.10(1)	0.014(1)	0.000(1)	0.009(1)	0.007(1)

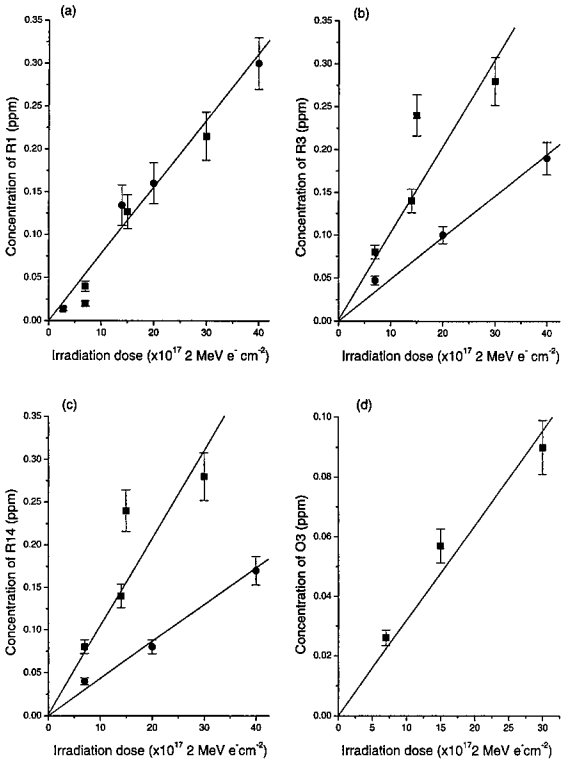

Fig. 4. Production rates of (a) the R1; (b) the R3; (c) the R14 and (d) the O3 EPR defects. The data points shown by circles and squares are taken from samples irradiated at 350 and 100 K, respectively. See Table 1 for a summary of the production rates determined by least-squares fitting constrained to pass through the origin – shown by solid lines in Figs. (a)–(d).

a genuine difference in irradiating at 100 compared with 350 K.

5. Discussion

We have found that for high purity type IIa diamonds the production rate of the vacancy is the same at 100 and 350 K. Contrary to early results, which found that no R1 was created after irradiating at 100 K [9], we found the production rate at 100 and 350 K to be the same. However, the early measurements used samples of uncertain purity and less sensitive spectrometers; it was only the enhanced sensitivity of *Q*-band, and the ability to get precise orientations, that allowed us to identify R1 at low irradiation doses. This identification of R1 indicates that at 100 K, at least under the conditions of irradiation the interstitial atom must be mobile.

The production rate for the ⟨0 0 1⟩-split interstitial (R2) at 100 K is so high, about 0.2 defects per incident 2 MeV electron, and not much smaller than the production rate for V^0, which indicates that at 100 compared with 350 K very few ⟨0 0 1⟩-interstitials are lost in aggregation processes. The explanation as to why the ⟨0 0 1⟩-split interstitial (R2) production is so different is not clear at this stage and warrants further investigation.

6. Conclusion

We have designed a dewar which can be attached to the Reading University van De Graaf accelerator, which enables electron irradiation at a measured temperature down to 100 K. This work represents the first study of the formation of intrinsic defects in high-quality synthetic IIa diamonds. The relative formation rates of the vacancy, ⟨0 0 1⟩-split interstitial (R2), di-⟨0 0 1⟩-split interstitial (R1), R3, R13 and O3 intrinsic defects for irradiation at 100 compared with 350 K are given in Table 1. The most dominant EPR defect formed on electron irradiation at 100 K is the ⟨0 0 1⟩-split interstitial (R2). It is created in similar concentration to vacancies at 100 K, but on irradiating at 350 K the creation rate is down by a factor of ten or more. The number of vacancies and R1 defects are the same independent of the irradiation temperature. The structure of R1 means that at 100 K, at least under the conditions of irradiation the interstitial atom must be mobile – this is an un-ambiguous and important result. Although R3 and R14 are unidentified, their production in these samples shows that they are intrinsic defects.

Acknowledgements

This work was supported by EPSRC grant GR/L65772. DJT thanks Merton College, Oxford for the Harmsworth Senior Scholarship and Linacre College, Oxford for a Junior Research Fellowship. DCH thanks EPSRC for financial support. We would like to thank Ian Thomas for invaluable help and advice with the Reading van Der Graaf accelerator.

References

[1] L. Allers, A.T. Collins, J. Hiscock, Diamond Relat. Mater. 7 (1998) 228.
[2] A. Mainwood, A.M. Stoneham, J. Phys. C 9 (1997) 2453.
[3] D.J. Twitchen, M.E. Newton, J.M. Baker, O.D. Tucker, T.R. Anthony, W.F. Banholzer, Phys. Rev. B 54 (1996) 6988.
[4] L. Allers, A.S. Howard, J.F. Hassard, A. Mainwood, Diamond Relat. Mater. 6 (1997) 353.
[5] A. Mainwood et al., J. Phys. D 28 (1995) 1279.
[6] J.W. Prins, Diamond Relat. Mater. 7 (1998) 1065.
[7] D.W. Palmer, in: G. Davies (ed.), Properties and Growth of Diamond, INSPEC, London, 1994, p. 143.
[8] D.C. Hunt, D.J. Twitchen, M.E. Newton, J.M. Baker, T.R. Anthony, W.F. Banholzer, Phys. Rev. B (1999) in press.
[9] M.A. Lea-Wilson, J.N. Lomer, J.A. van Wyk, Philos Mag. B 70 (1995) 101.
[10] D.J. Twitchen, D.C. Hunt, V. Smart, M.E. Newton, J.M. Baker, Diamond Relat. Mater. 8 (1999) 1572.

ELSEVIER

Physica B 273–274 (1999) 632–635

PHYSICA B

www.elsevier.com/locate/physb

Ab initio calculations of hyperfine interactions for vacancy and Ni point defects in diamond

U. Gerstmann, M. Amkreutz, H. Overhof*

AG Theoretical Physics, Physics Department, University of Paderborn, D33095 Paderborn, Germany

Abstract

We calculate total energies and hyperfine interactions for the V_C^- ground state and the V_C^{*0} excited state of the vacancy in diamond. The comparison with experimental data shows that the local spin density approximation gives reliable spin densities not only for ground states, but also for excited states. We extend our calculations to Ni_C and Ni_i defects and to trigonal (Ni–B_C) pairs.

Keywords: LSDA; Hyperfine interactions; Diamond

1. Introduction

The local spin density approximation (LSDA) has been most successful in determining the ground state properties of deep defects in semiconductors. It can be applied as well to those excited states, for which the symmetry differs from that of the ground state. The $^5A_2$ orbital singlet state of the excited neutral vacancy V_C^{*0} in diamond is an example for such an excited state, for which also experimental EPR data with resolved ligand hyperfine interactions (HFI) are available [1]. This offers the opportunity to check theoretical LSDA spin densities for an excited defect state against experimental ligand HFI data.

We have performed LSDA calculations using a Green's function approach. Since for the HFI we need magnetization densities which are accurate near the ligand nuclei, we have used the linear muffin-tin orbitals method in the atomic-spheres approximation (LMTO-ASA) [2].

In its present form the method does not allow to include lattice relaxations. However, several calculations show that the relaxation for the vacancy in diamond is of the breathing type and small: Li and Lowther [3] report a 10% inward relaxation, Breuer and Briddon [4] obtain a 13% outward relaxation, whereas according to Zywietz et al. [5] the outward relaxation is only 7.3%.

In diamond, nickel is still the only 3d transition metal (TM) defect, for which EPR data have been observed [6,7]. We report HFI calculations for Ni_C^-, Ni_C^+ and Ni_i^+ isolated point defects and also for trigonal (Ni–B_C) pairs in order to identify the NIRIM-1 point defect.

2. The vacancy

In its negative charge state the ground state of V_C^- is a $^4A_2$ orbital singlet state [8]. For the neutral vacancy the LSDA predicts a $^3T_1$ ground state of the $a_{1\uparrow}^1 a_{1\downarrow}^1 t_{2\uparrow}^2$ configuration, while from configuration interaction calculations [9–11] the ground state is known to be a ^1E singlet state. While the ground state of V_C^0 cannot be correctly given by the LSDA, the excited state V_C^{*0} with its $a_{1\uparrow}^1 t_{2\uparrow}^3$ configuration of $^5A_2$ symmetry is not affected by configuration interactions, since there are no further $a_1^{n_1} t_2^{n_2}$ configurations that could be admixed.

In a calculation for the $^5A_2$ excited state of V_C^{*0} the upper $a_{1\downarrow}$ orbital must be left unoccupied. This $a_{1\downarrow}$ orbital is a valence band resonance rather than a localized gap state [12], for which the occupancy could have been freely chosen. We see from Fig. 1, which displays the

* Corresponding author. Tel.: + 49-5251-602-334; fax: + 49-5251-603-435.

E-mail address: h.overhof@phys.upb.de (H. Overhof)

0921-4526/99/$ - see front matter
PII: S0921-4526(99)00591-8

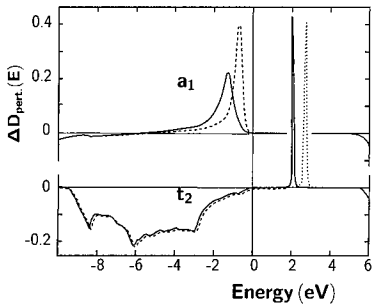

Fig. 1. Induced density of states $\Delta D_{\text{pert.}}(E)$ for the negatively charged vacancy V_C^- broken up into a_1 states (upper panel) and t_2 states (lower panel). Full lines mark spin-up states, broken and dotted lines denote occupied and unoccupied spin-down states, respectively.

density of states (dos) change induced by the vacancy, that the vacancy-induced $a_{1\uparrow}$ and $a_{1\downarrow}$ resonance states are reasonably well-defined [12]. We leave the upper $a_{1\downarrow}$ resonance unoccupied when calculating total energies and spin densities for V_C^{*0}.

The $^5A_2$ state of V_C^{*0} is observed under illumination only: absorption at the ND1 band with a 3.149 eV zero phonon line (ZPL) excites the $^4A_2$ ground state of V_C^- into a $^4T_1$ excited state of V_C^{*-}. For this excited state with one of the $a_{1\uparrow}^1 t_{2\uparrow}^3 t_{2\downarrow}^1$ configurations we find an excitation energy of 3.77 eV, in fair agreement with the experimental value for ND1. The excited $^4T_1$ state is ionized into the neutral orbital singlet $^5A_2$ state of V_C^{*0} with the $a_{1\uparrow}^1 t_{2\uparrow}^3$ high-spin configuration. For this V_C^{*0} state there are no spin-conserving transitions into lower-lying states of V_C^0, hence the excited $^5A_2$ state is long lived [1].

A comparison of the magnetization densities for V_C^{*0} and V_C^- in Fig. 2 shows characteristic differences: For V_C^{*0} the magnetization density is less confined to the nearest-neighbor ligands but extends slightly more towards the more distant ligands. Furthermore, the characteristic minimum at the vacancy center is no longer pronounced.

This difference of the magnetization densities for the two states is reflected by the calculated ligand HFI parameters (see Table 1), which compare well with experimental data. The agreement is excellent in particular for the dipolar terms and also for the isotropic HFI with the nuclei of the first shell of ligands. The isotropic HFI with the ^{13}C (2,2,0) ligands appears not to have the correct sign, but the modulus is very small corresponding to 10^{-4} of a C 2s electron only.

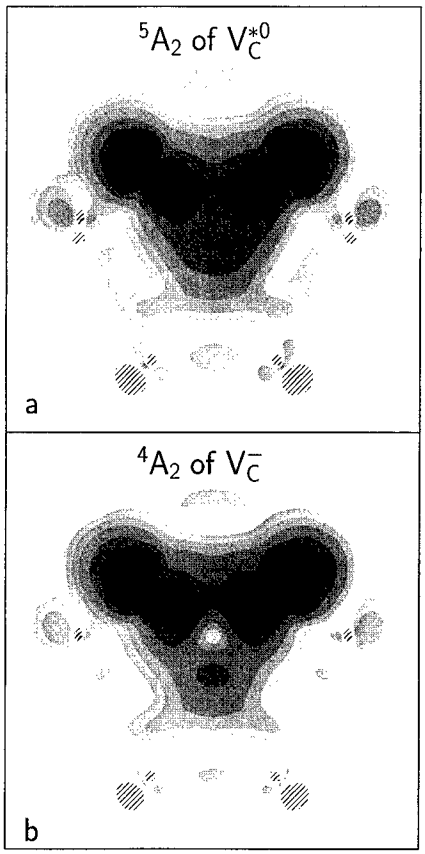

Fig. 2. Contour plot in the (1,1,0) plane of the total magnetization densities the $^5A_2$ excited state of V_C^{*0} (a) and for the $^4A_2$ ground state of V_C^- (b), respectively.

Table 1
Calculated ligand hyperfine interaction constants (in MHz) for the unrelaxed $^5A_2$ excited state of V_C^{*0} compared with experimental data from vanWyk et al. (1995) [1] and for the $^4A_2$ state of V_C^- compared with experimental data from Isoya et al. (1992) [8]

Ligand		$^5A_2$ V_C^{*0}		$^4A_2$ V_C^-	
		Theor.	Exp.	Theor.	Exp.
(1,1,1)	*a*	88.	53.73	126.0	101.7
	b	16.4	18.70	18.1	20.0
(2,2,0)	*a*	−4.7	6.36	−3.2	10.7
	b	1.2	1.2	1.2	1.37
	b'	0.2	—	0.3	0.085

3. Nickel defects in diamond

In contradiction to the famous LW model [13] the late 3d Tm defects in Si exhibit low-spin ground states both for the interstitial and for the substitutional sites [14,15]. According to our calculations the same is also true for all charge states of the tetrahedral Ni point defects in diamond.

3.1. Ni_C^- in diamond

For the substitutional site our results confirm the vacancy model [16–19], which must be modified because the V_C^- vacancy in diamond has a $^4A_2$ ground state with tetrahedral symmetry. The modified vacancy model predicts an $^4A_2$ ground state for Ni_C^- as well.

The Ni 3d states are lower in energy than the t_2 single particle gap states of V_C^-. Therefore, the occupied $t_{2\uparrow}$ gap states are predominantly dangling-bond like. As can be seen from Fig. 3, the gap state of the Ni_C^- defect resembles the gap state of the vacancy (see Fig. 2) augmented with a rather small (21%) admixture of Ni 3d states. This small admixture leads to a small (0.4 eV) exchange splitting for Ni_C^-, which is much smaller than the 3.4 eV crystal-field splitting. For Ni_C we find stable charge states from 2+ to singly negative, with the acceptor energy $E^{0/-} = E_v + 3.85$ eV, in general agreement with the 3.0 eV value deduced from photo-EPR [20].

Our results are similar to the results of a cluster calculation by Goss et al. [21]. In this calculation it was shown that the lattice relaxation preserves the T_d symmetry of both the Ni_i^+ and the Ni_C^- point defects. In contrast, the cluster calculations by Jinlong et al. [22] for Ni_i^+ predict a 0.1 Å trigonal distortion.

The magnetization density arises from the t_2 gap states with little contribution from the resonant $e_\uparrow$ and $e_\downarrow$ states. Comparing the calculated isotropic HFI with the 3d TM nucleus for Ni_C^- with experimental data of Isoya et al. [6] in Table 2, we find a discrepancy which amounts to nearly a factor of two. Similar discrepancies are found for 3d TM defects in Si and in 3C-SiC [23,24]. The calculated ligand HFI values are in fair agreement with the experimental data, demonstrating that the magnetization density distribution is well represented by the LSDA. The magnetization density at the C(1,1,1) ligands of the Ni_C^- defect is much smaller than the same density for the V_C^- vacancy in diamond. In agreement with the experimental ligand HFI data our results demonstrate that the vacancy model must not be taken literally.

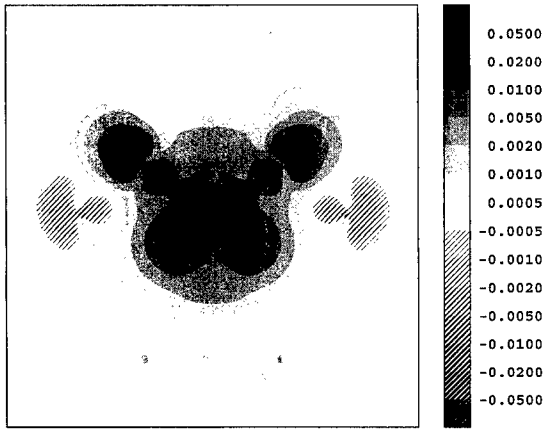

Fig. 3. Contour plot of the total magnetization density for isolated Ni_C^- in a (1 1 0) plane.

Table 2
Calculated hyperfine interactions (in MHz) for the unrelaxed $^4A_2$ state of Ni_C^- compared with experimental EPR data from Isoya et al. [6]. Theoretical hyperfine data for the $^2T_2$ state of Ni_C^+ and for the ^2E state of Ni_i^+ are also given

	^{61}Ni	(1,1,1) ligand		(2,2,0) ligand		
	a	a	b	a	b	b′
Ni_C^-						
Theor.	13.5	31.9	7.67	−4.12	0.38	0.14
Exp.	17.1	18.85	9.32	8.63	1.04	0.05
Ni_C^+						
Theor.	12.7	35.3	10.5	0.82	0.45	0.41
Ni_i^+						
Theor.	25.2	0.51	−0.90	5.99	3.4	0.43

3.2. The NIRIM-1 point defect

For the positive charge state of Ni_C^+ the LW model predicts an $S = \frac{5}{2}$ high-spin ground state. According to our calculation for Ni_C^+ no $S = \frac{5}{2}$ state can be constructed, the ground state being a low-spin $^2T_2$ state that should be subject to a Jahn–Teller distortion. Thus, in principle Ni_C^+ is a candidate for the NIRIM-1 point defect observed by Isoya et al. [7], for which no ligand HFI was resolved. Our results in Table 2 show, however, that for Ni_C^+ the HFI with the nn ^{13}C(1,1,1) ligand is too large to be hidden under the experimental EPR linewidth.

We therefore tentatively identify NIRIM-1 with the positive charge state Ni_i^+ of the interstitial Ni, which also has an $S = \frac{1}{2}$ ground state according to our calculations. The HFI calculated for the interaction with the nn ^{13}C(1,1,1) ligand is by at least one order of magnitude smaller than the corresponding value for Ni_C^+ (see Table 2). For Ni_i^+ the HFI interactions are small enough to be hidden under the broader NIRIM-1 line.

Upon heavy boron doping the NIRIM-1 spectrum disappears [7]. This disappearence is not explained by a Ni_i^{2+} charge state: Ni_i^{2+} does not exist according to our calculations. If it did, it would be in a $^3A_1$ state and not diamagnetic.

In order to explain the disappearence of the NIRIM-1 EPR spectrum in heavily B-doped diamond we have investigated pairing with B_C acceptors [24].

The trigonal $(Ni_i^- B_C)^+$ pair is tightly bound with a pair formation energy of 1.3 eV in p-type diamond.

However, for this doping state the pair is in the positive $^3A_2$ charge state as might be expected for a Ni_i^{2+} point defect interacting with a negatively charged B_C^- center.

The trigonal $(Ni_C–B_C)^+$ pairs are diamagnetic and have the same 1.3 eV pair formation energy. The formation of this pair in p-type diamond could easily explain why a Ni_C^+ EPR signal disappears. It does not explain, however, that the Ni_i^+ signal disappears upon heavy B doping.

A possible explanation can be given comparing the total energies of isolated Ni_C with those of isolated Ni_i point defects: For n-type material the substitutional Ni defect Ni_C^- has the lowest total energy. For intrinsic and for lightly p-doped diamond the interstitial Ni_i^+ is the most stable defect state, whereas for highly p-type material the diamagnetic Ni_C^{2+} defect on the carbon site is again the most stable defect.

A mystery remains: we have also studied other TM defects like Co, Fe, and Mn on tetrahedral interstitial and substitutional sites. We find that most charge states of these defects are paramagnetic, yet no EPR has been reported to date.

References

[1] J.A. vanWyk, O.D. Tucker, M.E. Newton, J.M. Baker, G.S. Woods, P. Spear, Phys. Rev. B 52 (1995) 12 657.
[2] O. Gunnarsson, O. Jepsen, O.K. Andersen, Phys. Rev. B 27 (1983) 7144.
[3] L.H. Li, J.E. Lowther, Phys. Rev. B 53 (1996) 11 277.
[4] S.J. Breuer, P.R. Briddon, Phys. Rev. B 51 (1995) 6984.
[5] A. Zywietz, J. Furthmüller, F. Bechstedt, Phys. Stat. Sol. B 210 (1998) 13.
[6] J. Isoya, H. Kanda, J.R. Norris, J. Tang, M.K. Bowman, Phys. Rev. B 41 (1990) 3905.
[7] J. Isoya, H. Kanda, Y. Uchida, Phys. Rev. B 42 (1990) 9843.
[8] J. Isoya, H. Kanda, Y. Uchida, S.C. Lawson, S. Yamasaki, H. Itoh, Y. Morita, Phys. Rev. B 45 (1992) 1436.
[9] C.A. Coulson, M.J. Kearsley, Proc. R. Soc. Lond. A 241 (1957) 433.
[10] G.T. Surratt, W.A. Goddard III, Solid State Commun. 22 (1977) 413.
[11] M. Lannoo, J. Bourgoin, Point Defects in Semiconductors I, Theoretical Aspects, Vol. 22, Springer Ser. Solid. State Sci., Springer, Heidelberg, 1981.
[12] G.B. Bachelet, G.A. Baraff, M. Schlüter, Phys. Rev. B 24 (1981) 4736.
[13] G.W. Ludwig, H.H. Woodbury, Solid State Phys. 13 (1962) 223.
[14] F. Beeler, O.K. Andersen, M. Scheffler, Phys. Rev. Lett. 55 (1985) 1498.
[15] F. Beeler, O.K. Andersen, M. Scheffler, Phys. Rev. B 41 (1990) 1603.
[16] G.W. Watkins, Physica (Amsterdam) 117B and 118B (1983) 9.
[17] A. Zunger, Phys. Rev. B 28 (1983) 3628.
[18] A. Zunger, Solid State Phys. 39 (1986) 276.
[19] A. Zunger, Phys. Rev. B 11 (1975) 849.
[20] D.M. Hofmann, M. Ludwig, P. Christmann, D. Volm, B.K. Meyer, L. Pereira, L. Santos, E. Pereira, Phys. Rev. B 50 (1994) 17 618.
[21] J. Goss, A. Resende, R. Jones, S. Öberg, P.R. Briddon, Mater. Sci. Forum 196–201 (1995) 67.
[22] Y. Jinlong, Z. Manhong, W. Kelin, Phys. Rev. B 49 (1994) 15 525.
[23] H. Overhof, Mater. Sci. Forum 258–263 (1997) 677.
[24] U. Gerstmann, M. Amkreutz, H. Overhof, Phys. Stat. Sol. B, in press.

ELSEVIER

Physica B 273–274 (1999) 636–639

PHYSICA B

www.elsevier.com/locate/physb

An orthorhombic nickel–nitrogen complex in high-pressure synthetic diamond

A.J. Neves[a,*], M.H. Nazaré[a], J.C. Lopes[a], H. Kanda[b]

[a]*Departamento de Física, Universidade de Aveiro, 3800 Aveiro, Portugal*
[b]*National Institute for Research in Inorganic Materials, Tsukuba, Japan*

Abstract

We report uniaxial stress measurements on the 1.693 eV zero-phonon line, observed on nickel- and nitrogen-containing synthetic diamonds after annealing at 1600°C. We show that the line is an electric dipole transition which occurs at a defect of rhombic I symmetry. The shape of the vibronic sideband and the temperature dependence of the zero-phonon intensity may be understood assuming linear coupling to totally symmetric vibrational modes. Quadratic coupling to a single quasi-localised non-symmetric mode is invoked to explain a temperature-induced transition 7 meV below the zero-phonon line energy.

Keywords: Synthetic diamond; Uniaxial stress; Vibronic properties

The 1.693 eV band is observed only in absorption (Fig. 1a) after annealing at 1600°C nickel- and nitrogen-containing synthetic diamonds [1]. Further, annealing at 1800°C destroys the band. The maximised integrated absorption of the band correlates with the pre-anneal integrated absorption of the 1.885 eV zero-phonon line (ZPL) [1].

In this study, we used two synthetic diamonds grown with Ni and annealed at 1600°C during 4 h under a stabilised ~ 6 GPa hydrostatic pressure, at NIRIM.

The behaviour of the 1.693 eV ZPL under uniaxial stress is shown in Figs. 2 and 3. The energy of the stress-split components varies linearly with the applied stress while their intensities are stress independent, which shows that there are no stress-induced interactions with any other electronic states. The number, intensity and polarisation of the stress-split components are consistent with the ZPL being an electric dipole transition between states that transform as A_1 and B_1 at a rhombic I centre [2]. In diamond a rhombic I centre has a C_{2v} point group, with C_2 along the $\langle 1\,0\,0\rangle$ axes. We define a set of local coordinates X, Y, Z for each of the six inequivalent orientations, one of them being $\boldsymbol{X} = [1\,1\,0]$, $\boldsymbol{Y} = [-1\,1\,0]$, $\boldsymbol{Z} = [0\,0\,1]$. For these low strains the stress perturbation H is linear in the stress tensor components S_{IJ} at each centre. For non-degenerate states – and since there are no stress-induced interactions of the states involved in the transition with any other electronic states – only the electronic operators which transform as the totally symmetric representation perturb the electronic states involved. The perturbation is then

$$H = aS_{XX} + bS_{YY} + cS_{ZZ}, \tag{1}$$

where a, b and c are electronic operators which transform as A_1 in the C_{2v} point group. The perturbation to the energy of the ZPL is expressed using the Kaplyanskii parameters [2], related to the electronic operators by

$$K_1 = \langle e|c|e\rangle - \langle g|c|g\rangle, \qquad K_2 = (\langle e|a + b|e\rangle - \langle g|a + b|g\rangle)/2,$$

$$K_3 = (\langle e|a - b|e\rangle - \langle g|a - b|g\rangle)/2, \tag{2}$$

where $|g\rangle$ and $|e\rangle$ are the ground and excited state of the transition. The relative intensities of the stress-split lines

* Corresponding author. Fax: + 351-34-424-965.
E-mail address: armando@fis.ua.pt (A.J. Neves)

0921-4526/99/$ - see front matter
PII: S0921-4526(99)00592-X

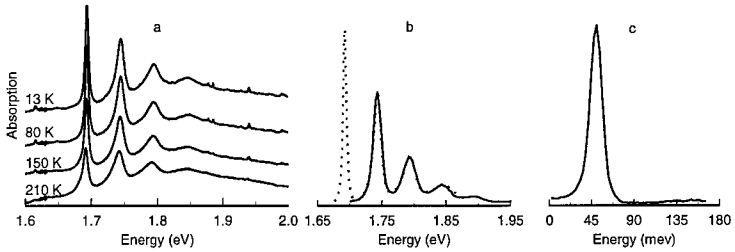

Fig. 1. (a) Absorption spectra measured at different temperatures. (b) Comparison of the measured and calculated absorption spectra for $T = 8$ K. (c) The one-phonon spectrum for $T = 0$ K.

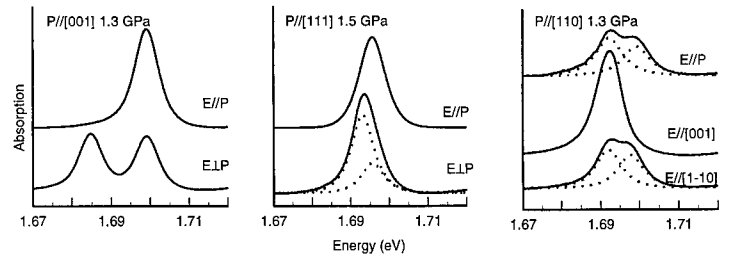

Fig. 2. Uniaxial-stress spectra: the stress axis $\boldsymbol{P}$ and the directions of the electric vector $\boldsymbol{E}$ are as shown. Dashed lines shows the calculated decomposition of the lines not clearly resolved.

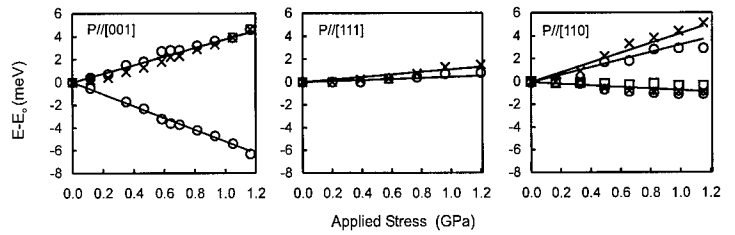

Fig. 3. Measured energies of the stress-split lines for each stress direction: × stands for $\boldsymbol{E}//\boldsymbol{P}$ and o for $\boldsymbol{E}\perp\boldsymbol{P}$ (□ for $\boldsymbol{E}//[0\,0\,1]$ when $\boldsymbol{P}//[1\,1\,0]$). The lines are the calculated energies using the expressions of Table 1 and the parameters given in text.

can be calculated taking into account that at a rhombic I centre an electric dipole transition can occur between $A_1(A_2)$ and $B_1(B_2)$ states if the electric dipole is parallel to the X axis. Table 1 summarises for each stress direction the shift rates and the expected relative intensities for π and σ polarisation of the stress-split components. A least-squares fit to the observed shift rates gives the values of the three parameters

$$K_1 = -5.2\ \text{meV/GPa}, \qquad K_2 = 3.8\ \text{meV/GPa}$$
$$\text{and } K_3 = 0.49\ \text{meV/Gpa}. \tag{3}$$

The lines in Fig. 3 are the calculated shifts, which are in very close agreement with the experimental values. A good agreement is also obtained for the measured and expected relative intensities as shown in Table 1.

Table 1
Uniaxial stress perturbation of the 1.693 eV ZPL. For stresses along [1 1 0] the relative intensities for electric vector $\boldsymbol{E}$ perpendicular to $\boldsymbol{P}$ are in the format $\boldsymbol{E}//[001]$: $\boldsymbol{E}//[1\text{-}10]$

Stress axis	Theoretical shift rate	Relative intensities			
		Theory		Measured	
		$\boldsymbol{E}//\boldsymbol{P}$	$\boldsymbol{E}\perp\boldsymbol{P}$	$\boldsymbol{E}//\boldsymbol{P}$	$\boldsymbol{E}\perp\boldsymbol{P}$
001	K_1	0	1	0	1.0
	K_2	2	1	1.9	1.0
111	$(K_1 + 2K_2 - 2K_3)/3$	2	0.5	2	0.6
	$(K_1 + 2K_2 + 2K_3)/3$	0	1.5	0	1.4
110	$K_2 + K_3$	1	0:0	0.9	0:0
	$K_2 - K_3$	0	0:1	0	0:0.9
	$(K_1 + K_2)/2$	1	2:1	1.1	2:1.1

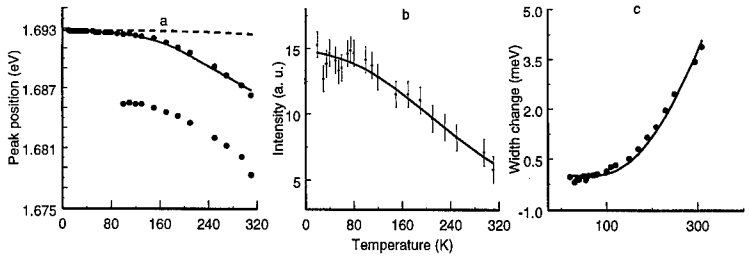

Fig. 4. Temperature dependence of the 1.693 eV ZPL. (a) Peak energy of the two components used to reconstruct the ZPL; dashed line shows the effect of lattice expansion; solid line the calculated total shift scaled to the α line. (b) Comparison of the measured and calculated intensity using Eq. (5) and the one-phonon spectrum I_1 of Fig. 1c. (c) Dots are the measured width change; The curve is calculated from Eq. (7).

Fig. 1a shows the absorption band recorded in the temperature range 13–210 K. The temperature dependence of the intensity, position and width of the ZPL are depicted in Fig. 4. At low temperatures (13 K) the ZPL full-width is about 5 meV, a value somewhat larger than the typical value in diamond. This is probably due to the samples large nitrogen content. The vibronic sideband shows dominant coupling to a 51 meV phonon. At high temperature the ZPL becomes asymmetrical, with a pronounced shoulder on the low-energy side.

To reproduce the line shape of the ZPL at the different temperatures we have to admit the existence of another transition 7 meV below the energy of the ZPL (Fig. 5). The intensity of this line (β) increases with temperature at the expense of the ZPL (α line). An Arrenhius plot gives an activation energy of 35 meV, five times larger than the spectroscopic splitting. This excludes the hypothesis that the lines arise from a split ground state. We believe that all these temperature effects can be explained with linear and quadratic coupling. Let us assume that the dominant interaction between electrons and phonons is linear in the vibrational coordinates. Since the optical transition is between two non-degenerate electronic states, the linear coupling must be to totally symmetric vibrational modes. In the limit of low temperatures the vibronic band can be regarded as the sum of individual components involving the emission of an integer number of phonons. If ν_0 is the ZPL frequency, the absorption coefficient $\mu(\nu)$ is the product of the total transition probability times frequency: $K(\nu) = \nu I_T(\nu - \nu_0)$, $I_T(x) = \sum_p I_p(x)$. If $I_1(\omega)$ is the transition probability for emitting one phonon with energy $\hbar\omega$, then the transition probability of emitting p phonons $I_p(\omega)$ is

$$I_p(x) = a_p \int_0^{\omega_M} d\omega\, I_1(\omega) I_{p-1}(x - \omega). \tag{4}$$

Each phonon sideband is normalised: $\int dx\, I_p(x) = e^{-S} S^p/p!$.

The Huang–Rhys factor, S, measures the linear coupling strength and can be obtained experimentally from the ratio between the whole band intensity and the ZPL intensity: $S = \ln[\int dx\, I_T(x)/I_0]$.

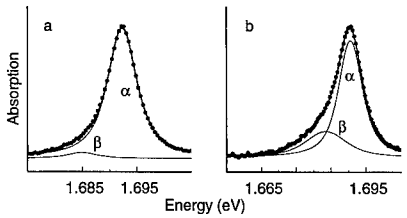

Fig. 5. Line shape of the 1.693 eV ZPL at (a) 100 and (b) 210 K. Thin lines show the calculated decomposition in two components.

Linear coupling can also be used to predict the changes in the intensity of ZPL with temperature. As temperature increases higher lying vibrational states become populated and the no-phonon transition intensity decreases as

$$I_0(T) = \exp[-\int d\omega\, I_1(\omega)(2n(\omega) + 1)] \tag{5}$$

with $n(\omega) = [\exp(\hbar\omega/K_B T) - 1]^{-1}$. Fig. 1b shows the comparison between the low-temperature experimental and theoretical spectra, using $S = 1.3$ and the one-phonon sideband of Fig. 1c. The curve in Fig. 4b, which shows the ZPL intensity change with temperature, was calculated using $I_1(\omega)$ and the Eq. (5). The agreement is very good and confirms the model.

Linear coupling cannot explain the temperature-induced transition nor the shift and broadening of the ZPL. The effect of quadrating coupling to a single mode is to make unequal the vibrational frequencies of the excited and ground states. The no-phonon transitions can occur between vibrational states with the same quantum number n, with energy $E_{n-n} \approx E + n\hbar(\omega_e - \omega_g)$. For $T > 0$ we can have a series of no-phonon lines, each separated by the difference in the vibrational quanta between

the ground and excited states. Then, assuming that the quadratic coupling changes the vibrational energies from 35 meV in the ground state to $35 - 7 = 28$ meV in the excited state, we can explain the temperature-induced transition (β line) 7 meV below the ZPL. As T increases, the $n = 1$ phonon state becomes populated and the transition is therefore observed. Since there can be quadratic coupling to modes belonging to a C_{2v} irreducible representation other than the totally symmetric one, the mode we are concerned with may not be active in producing side-bands.

However, if we had quadratic coupling to only one mode, then the shift with temperature of the no-phonon lines would due to lattice expansion only (given by the dotted curve in Fig. 4a). The observed shift is probably due to small quadratic electron–phonon coupling to the continuum of modes. The simplest assumption to make is that quadratic coupling to modes of frequency ω is proportional to the square of the linear coupling to those modes [3]. In this approximation the ZPL changes in energy by

$$\Delta E(T) = c_1 \int_0^{\omega_m} d\omega\, \omega^2 I_1(\omega)[n(\omega) + 1/2], \quad (6)$$

and the full-width at half-height W increases as

$$W(T) = c_2 \int_0^{\omega_M} d\omega [\omega^2 I_1(\omega)]^2 n(\omega)[n(\omega) + 1]. \quad (7)$$

The curves in Figs. 4a and c are calculated using Eqs. (6) and (7) and they agree very well with the experimental data.

Our study shows that the 1.693 eV line is an electric dipole transition which occurs at a defect of rhombic I symmetry. The shape of the vibronic sideband and the temperature dependence of the zero-phonon intensity may be understood assuming linear coupling to totally syimmetric vibrational modes. Quadratic coupling to a single quasi-localised non-symmetric mode explains a temperature-induced transition 7 meV below the zero-phonon line energy.

Acknowledgements

This work was supported in part by FCT under contract PRAXIS/PCEX/FIS/0012/96.

References

[1] S.C. Lawson, H. Kanda, J. Appl. Phys. 73 (1993) 6.
[2] A.A. Kaplyanskii, Opt. Spectrosc. 16 (1964) 329.
[3] A.A. Maradudin, Solid State Phys. 18 (1964) 273.

ELSEVIER

Physica B 273-641 (1999) 640-643

PHYSICA B

www.elsevier.com/locate/physb

Spin-orbit splitting of acceptor states in Si and C

J. Serrano[1], A. Wysmolek[2], T. Ruf*, M. Cardona

Max-Planck-Institut für Festkörperforschung, Heisenbergstr. 1, D-70569 Stuttgart, Germany

Abstract

We report calculations of the Γ_8-Γ_7 spin-orbit splittings of substitutional acceptor levels in silicon and diamond and corresponding Raman measurements for Si:X (X = B, Al, Ga, In). The calculations were performed using a Green's function method based on a full-zone 30×30 $\boldsymbol{k} \cdot \boldsymbol{p}$ Hamiltonian together with a Slater-Koster ansatz for the acceptor potential. The results are in reasonable agreement with experimental data. © 1999 Elsevier Science B.V. All rights reserved.

Keywords: Spin-orbit splitting; Acceptor; Slater-Koster

1. Introduction

In the last 30 years a lot of effort has been devoted to the study of impurity levels in semiconductors, partly because of their interest for doping applications. The knowledge of acceptor levels allows one to evaluate the effects of different dopant atoms on the carrier concentration. This is of crucial importance in the development of devices, such as transistors or diodes, which are widely employed in electronic systems. Despite the intensive study of these acceptor levels, especially by means of optical spectroscopies, there are some details of the observed spectra which are not completely understood. In the case of Si, a splitting, Δ_0^a, has been observed for B, In, Be^-, Zn^- substitutional impurities. This splitting varies from 23.7 to 0.3 meV depending on acceptor [1-4].[3] Its tentative assignment to spin-orbit interaction requires an enormous reduction of the corresponding spin-orbit splitting of the Γ_{25}^{+v} valence band states, $\Delta_0 \simeq 44$ meV [5]. In the case of diamond, the reported splitting is 6 meV [6],[4] while for the boron acceptor this splitting is reduced to 2 meV [7-11].

Baldereschi and Lipari showed in Ref. [12] that for silicon doped with boron, $\Delta_0^a \simeq \Delta_0/2$ if the acceptor binding energy, E_b^a, is close to Δ_0. For this purpose they used an effective mass approximation (EMA) involving a Kohn-Luttinger 6×6 Hamiltonian. Although they found a good agreement with the spin-orbit splitting of the ground state of the boron acceptor, their formalism cannot be applied for larger values of E_b^a, for which a large range of $\boldsymbol{k}$-space must be taken into account in describing the acceptor wave functions, leading to non-parabolicity effects, which cause the EMA to break down.

In this work we report calculations for the spin-orbit-induced splitting of substitutional acceptors in silicon and diamond. A Green's function method is used to estimate the splitting of Γ_8 and Γ_7 ground state levels for different impurities, using as input parameter only the experimentally determined value of E_b^a for the acceptor

* Corresponding author. Tel.: + 49-711-689-1735; fax: + 49-711-689-1712.

E-mail address: ruf@cardix.mpi-stuttgart.mpg.de (T. Ruf)

[1] On leave from University of Valladolid, Spain.

[2] On leave from Institute of Experimental Physics, Warsaw University, Poland.

[3] The splitting of 4.2 meV in the luminescence peaks of Si:In was attributed by Sauer et al. to vibronic structure. However, it is likely to correspond to the Δ_0^a discussed by us.

[4] No justification for the assignment to Δ_0 of structure seen in ir-induced cyclotron resonance is given in this work.

PII: S0921-4526(99)00593-1

under consideration. In order to calculate the Green function, the full-zone $\boldsymbol{k}\cdot\boldsymbol{p}$ Hamiltonian is used with a Slater–Koster ansatz for the impurity potential (this ansatz is equivalent to assuming that the hole interacts with the acceptor only if both are in the same primitive cell). The results are compared with previous experiments and with Raman data for Si:X, X being B, Al, Ga and In. Good agreement with the observed reduction of Δ_0^a with increasing E_b^a, as well as qualitative agreement with the absolute values of Δ_0^a, is obtained.

2. Theory: silicon

The electronic levels of acceptors in diamond- and zinc-blende-type semiconductors are usually described using a 4×4 Kohn–Luttinger effective mass Hamiltonian [13] which neglects the Γ_7^+ spin–orbit-split band. Baldereschi and Lipari [12] calculated for Si:B a spin–orbit splitting of $\Delta_0^a \simeq 23.8$ meV using a 6×6 Kohn–Luttinger–Hamiltonian, in which the Γ_7^+ spin–orbit-split bands were treated by perturbation theory. This treatment implies the assumption of parabolic bands which does not hold if E_b^a is larger than Δ_0. This scheme, therefore, does not allow one to explain the smaller splittings observed in Si for In (4.2 meV [3,4]), Be^- (0.6 meV [2]) and Zn^- ($\simeq 0.3$ meV [3]) acceptors. It is thus necessary to take into account the full details of the band structure in the calculation. In this work we used a Slater–Koster potential to represent the acceptor–hole interaction, i.e. we consider this interaction constant if both particles are in the same primitive cell and zero otherwise. This allows us to obtain the binding energy of an acceptor level Γ, $E_b^a(\Gamma)$, by using the equation

$$\frac{1}{V_0} \simeq G_r^\Gamma(E_b(\Gamma)), \tag{1}$$

where V_0 represents approximately the average of the potential over the primitive cell, and G_r^Γ is the real part of the Γ-projected Green function. G_r^Γ is obtained from the imaginary part of the Green function, G_i^Γ, by using a Hilbert transform. G_i^Γ is related to the Γ-projected density of states through

$$G_i^\Gamma(E) = -\pi N^\Gamma(E). \tag{2}$$

$N^\Gamma(E)$ is calculated from the 30×30 full-zone $\boldsymbol{k}\cdot\boldsymbol{p}$ Hamiltonian [14] using the tetrahedron method [15] with a grid of $\simeq 3\times10^5$ tetrahedra which was shown to yield adequately converged final results. The total valence density of states is plotted in Fig. 1 together with that calculated by means of ab initio pseudopotentials within the LDA-approximation, using the parametrization in Ref. [16] for the exchange-correlation potential. The agreement is shown to be remarkably good. The parameters used for the $\boldsymbol{k}\cdot\boldsymbol{p}$ Hamiltonian were adjusted from those

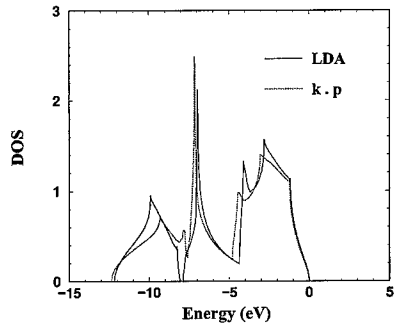

Fig. 1. Total density of valence states calculated for silicon with the 30×30 $\boldsymbol{k}\cdot\boldsymbol{p}$ Hamiltonian, and the LDA-pseudopotential technique, using a Troullier–Martins pseudopotential [23] and a plane-wave expansion with a cutoff energy of 40 Rydbergs and a grid of $20\times20\times20$ in reciprocal space.

Table 1
Parameters of the full-zone $\boldsymbol{k}\cdot\boldsymbol{p}$ Hamiltonian used for the calculation of the Green function of silicon, taken from Ref. [14] unless otherwise specified

	(eV)		(a.u.)
$E_{\Gamma_7^+}$	−12.36[a]	P	0.600
$E_{\Gamma_8^+}$	0.00	Q	0.525
$E_{\Gamma_8^-}$	3.40	R	0.415
$E_{\Gamma_7^-}$	4.185[a]	P′	−0.045
$E_{\Gamma_8^-}$	9.66	P″	0.050
$E_{\Gamma_7^-}$	7.075	P‴	0.660
$E_{\Gamma_7^+}$	13.47	Q′	−0.4035
$E_{\Gamma_8^+}$	12.79	R′	0.605
Δ_0	0.044	T	0.103
Δ_0'	0.040	T′	0.540

[a]Modified from those in Ref. [14], so as to reproduce the experimental data given in Ref. [22].

in Ref. [14] to reproduce the LMTO band structure corrected for the "gap problem" [17]; they are shown in Table 1.The density of states is projected via Γ_8^+ and Γ_7^+ admixture coefficients interpolated for each tetrahedron. Finally, we made the plausible assumption of equal values of V_0 for Γ_8^+ and Γ_7^+. The Γ_8–Γ_7 acceptor splitting Δ_0^a is then found by solving Eq. (1) for $E_b^a(\Gamma_7)$ after having determined V_0 using also Eq. (1) and the experimental value of $E_b^a(\Gamma_8)$. This procedure is illustrated by the horizontal line in the inset of Fig. 2. The values of Δ_0^a obtained for silicon by this procedure versus E_b^a are displayed in Fig. 3.

3. Experimental results: silicon

Together with the calculations presented above we performed Raman measurements in Si:X samples, X

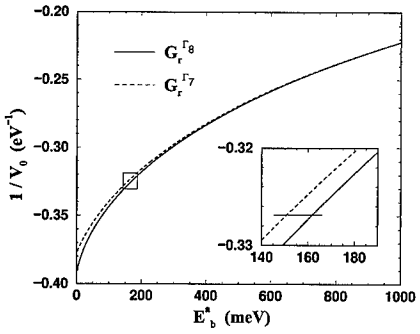

Fig. 2. Real part of the Green funtion of the valence band of silicon (labeled $1/V_0$ in the spirit of Eq. (1)) versus E^a_b. The inset represents a blowup of the rectangle drawn around the binding energy of the In acceptor. It allows one to see $G_r(\Gamma_8)$ and $G_r(\Gamma_7)$ separately and to determine Δ^a_0 as illustrated by the horizontal line (see also Fig. 3).

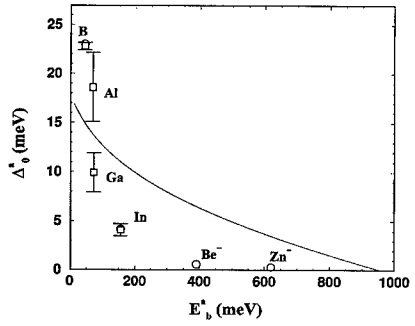

Fig. 3. Spin–orbit splitting Δ^a_0 of a substitutional acceptor in silicon versus binding energy, E^a_b. The circles represent EDSR data from Ref. [3], while the squares correspond to Raman measurements (see Fig. 4).

being B, Al, Ga and In. Most samples were cut from bulk material but we also used epitaxial layers. The carrier concentrations were in the 10^{16}–10^{18} cm^{-3} range. The 7993 Å krypton laser line was used for excitation in backscattering configuration with low power densities. A cold finger cryostat was used to hold the samples at 11 K. A Dilor XY multichannel spectrometer and a charge-coupled device detector were used to record the spectra. The spectral resolution was 1.5 cm^{-1}.

In Fig. 4 we show typical Raman spectra in the range of 4–30 meV, displaying structure that can be attributed to Δ^a_0, the Γ_8–Γ_7 spin–orbit splitting of the corresponding acceptor ground state levels. The peak positions were determined by subtracting a linear background, and taking the centroid of the resulting curves. The observed values of 22.8 (B) and 4.1 meV (In) are in good agreement with those previously reported, namely 22.7 [18] and 4.2 meV [3], from Raman and EDSR experiments, respectively. However, a strong broad structure was obtained for Si:Al. This increases the error for the determination of the splitting, although the energy at the maximum is in reasonable agreement with what would be expected from the calculations, as can be seen in Fig. 3. In the case of Si:Ga, two peaks occur in the range of interest, we thus cannot unambiguously assign one of them to Δ^a_0; on the basis of the general systematics (see Fig. 3) we assign the lower one (10 meV) to Δ^a_0. More work should be done to clarify the origin of these features which appeared in all samples investigated (epi-layers and bulk). Tentatively, however, we assign the additional peaks observed for Ga to disorder activated TA phonons (DATA). The shoulder in the Si:In spectrum at 8 meV is likely to be due to vibronic structure (dynamic Jahn–Teller effect) [19]. Our experimental data are compared with the calculation in Fig. 3 where we also show some results of electric-dipole spin resonance (EDSR) measurements [2,3]. The open circles represent the EDSR data, while the open squares stand for the Raman results. The theoretical curve describes the trend of the experimental data, namely a reduction of Δ^a_0 with increasing E^a_b, although considerable differences exist between the magnitudes of experimental and calculated splittings. These differences are less conspicuous if we look at the data in terms of the quenching of the Γ^+_8–Γ^+_7 band splitting which amounts to 44 meV for the experimental value in the case of the Zn^- acceptor and 41 meV for the calculated one.

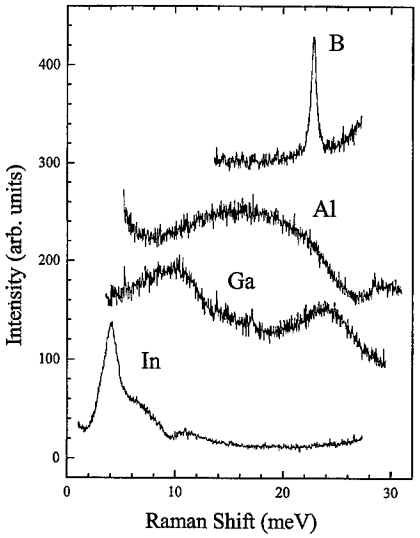

Fig. 4. Raman spectra of Si:X samples [X being B, Al, Ga and In]. The peaks can be assigned to the Γ_8–Γ_7 spin–orbit splitting of the corresponding substitutional acceptor. In the case of Ga doped samples two structures can be observed. The nature of these peaks is not understood.

4. Diamond

Similar calculations have been performed for acceptor states in diamond [20]. While lending support to the value of $\Delta_0 = 13$ meV calculated ab initio with the relativistic LMTO method [21] they lead to a calculated value of $\Delta_0^a = 3.9$ meV, in reasonable agreement with the 2 meV observed experimentally for substitutional boron, the only clearly identified acceptor. Because of the value Δ_0^{exc} reported for the splitting of the edge (indirect) excitons in diamond, we also performed a calculation of this splitting with a method similar to that used for acceptor levels, modified so as to take into account the indirect nature of the edge exciton. We obtained the value $\Delta_0^{exc} = 8.6$ meV and rather good agreement with the experimental one ($\simeq 7$ meV).

5. Conclusions

We have presented a calculation for the Γ_8–Γ_7 spin–orbit splitting of substitutional acceptor levels in silicon and diamond, using a Green's function formalism with a full-zone $\boldsymbol{k}\cdot\boldsymbol{p}$ Hamiltonian, and a Slater–Koster ansatz to describe the acceptor–hole interaction. We have also reported Raman measurements for the spin–orbit splitting of acceptor states in Si:X samples (X = B, Al, Ga, In) which reproduce the previously known splittings in the case of B and In. Two structures are observed in the case of Si:Ga which are not completely understood yet. For In, structure of possible Jahn–Teller origin has been also observed. Our calculation shows a reasonable agreement with the experimental quenching from the free band Γ_8^+–Γ_7^+ splitting of that of the acceptors in the case of silicon, although this simple model does not yield a quantitative description. In the case of diamond the observed quenching of 11 meV for boron, i.e. from 13 to 2 meV, can be also understood with our theory, which yields a quenching of 9 meV. A similar procedure has been applied for the free indirect exciton [20].

Acknowledgements

We would like to thank K. Lassmann, H. Schroth and M. Konuma for the silicon samples and stimulating discussions, and H. Schroth for communicating to us his unpublished results. Thanks are also due to D. Olguin, to A. Romero for computational help, and J. Weber for a critical reading of the manuscript. J.S. acknowledges support from Max-Planck-Gesellschaft and Ministerio de Educación y Ciencia (Spain) through the Plan Nacional de Formación del Personal Investigador. A.W. gratefully acknowledges financial support from the Alexander-von-Humboldt-Stiftung.

References

[1] G.B. Wright, A. Mooradian, Phys. Rev. Lett. 18 (1967) 608.
[2] H. Schroth et al., Phys. Stat. Sol. B 210 (1998) 747.
[3] H. Schroth, Doctoral Dissertation, University of Stuttgart, 1999, unpublished.
[4] R. Sauer, W. Schmid, J. Weber, Solid State Commun. 27 (1979) 705.
[5] S. Zwerdling, K.J. Button, B. Lax, L.M. Roth, Phys. Rev. Lett. 4 (1960) 173.
[6] C.J. Rauch, in: A.C. Stickland (Ed.), Proceedings of the International Conference on the Physics of Semiconductors, Exeter, 1962 (The Institute of Physics and the Physical Society, London, 1962), p. 276.
[7] E.C. Lightowlers, A.T. Collins, J. Phys. D 9 (1976) 951.
[8] P.A. Crowther, P.J. Dean, W.F. Sherman, Phys. Rev. 154 (1967) 772.
[9] D.M.S. Bagguley, G. Vella-Coleiro, Proceedings of the International Conference on the Physics of Semiconductors, Kyoto, 1966 (J. Phys. Soc. Japan 21 (Suppl.) (1966) 244).
[10] H. Sternschulte, T.R. Anthony et al., Mat. Sci. Forum 258–263 (1997) 757.
[11] H. Kim et al., Phys. Rev. B 57 (1998) 15315.
[12] N.O. Lipari, A. Baldereschi, Solid State Commun. 25 (1978) 665.
[13] W. Kohn, in: F. Seitz, D. Turnbull (Eds.), Solid State Physics, Vol. 5, Academic, New York, 1957, p. 257.
[14] M. Cardona, F.H. Pollak, Phys. Rev. B 142 (1966) 530.
[15] G. Lehmann, M. Taut, Phys. Stat. Sol. B 54 (1972) 469.
[16] D.M. Ceperly, B.J. Alder, Phys. Rev. Lett. 45 (1980) 566.
[17] U. Schmid, N.E. Christensen, M. Cardona, Phys. Rev. B 41 (1990) 5919.
[18] J.M. Cherlow, R.L. Aggarwal, B. Lax, Phys. Rev. B 7 (1973) 4547.
[19] J. Maier, E. Sigmund, Phys. Rev. B 34 (1986) 5562.
[20] J. Serrano, M. Cardona, T. Ruf, to be published.
[21] M. Willatzen, M. Cardona, N.E. Christensen, Phys. Rev. B 50 (1994) 18054.
[22] O. Madelung, M. Schulz, H. Weiss (Eds.), Landolt-Börnstein, New Series III, Vol. 22a, Springer, Berlin, Heidelberg, 1987, p. 14.
[23] N. Troullier, J.L. Martins, Phys. Rev. B 43 (1991) 1993.

ELSEVIER

Physica B 273–274 (1999) 644–646

PHYSICA B

www.elsevier.com/locate/physb

The production and annealing stages of the self-interstitial (R2) defect in diamond

D.J. Twitchen[a,*], D.C. Hunt[a], C. Wade[a], M.E. Newton[a], J.M. Baker[a], T.R. Anthony[b], W.F. Banholzer[b]

[a]*Department of Physics, Clarendon Laboratory, University of Oxford, Parks Road, Oxford OX1 3PU, UK*
[b]*General Electric Company, Corporate Research and Development, Schenectady, New York, USA*

Abstract

We report on the production rate of the neutral ⟨0 0 1⟩-split self-interstitial (measured via the electron paramagnetic resonance (EPR) concentration of the R2 defect) in type IIa diamond irradiated at a controlled and measured sample temperature in the interval 110–350 K with 2 MeV electrons and a beam flux of 7.5×10^{13} electrons $cm^{-2} s^{-1}$. On annealing at $\sim$ 700 K, we find that the neutral ⟨0 0 1⟩-split self-interstitial (R2) defect is mobile and anneals out with an associated energy of 1.6(2) eV and some loss of neutral vacancies. A significantly reduced production rate of R2 in the temperature interval 110–350 K is suggestive of a radiation enhanced annealing process.

PACS: 61.72.Ji; 61.80.Fe; 76.30.-V; 76.30.Mi

Keywords: Self-interstitial; Annealing; Irradiation damage

The paramagnetic R2 center, observed in all diamonds after irradiation, has recently been identified as the neutral ⟨0 0 1⟩-split self-interstitial (I_{001}) (see Fig. 1). This assignment is based on a range of results from EPR ^{13}C hyperfine coupling measurements, EPR line width measurements, stress alignment studies, annealing studies and optical absorption measurements that are reported elsewhere [1]. After more than 40 years of investigation of radiation damage defects in diamond this represents a significant breakthrough. Indeed, it is the first observation of an isolated self-interstitial in any group IV material. In this paper, we present the results of the production of this defect in extrinsic defect-free diamond produced by the HTHP method (type IIa, before irradiation extrinsic defect concentration < 0.2 ppm) as a function of sample temperature between 100 and 350 K during the irradiation, and annealing out of this defect at a temperature of $\sim$700 K.

The production rate of I_{001} (1.1 cm^{-1}) for irradiation with 2 MeV electrons at 100 K is nearly equal to the vacancy production rate (1.5 cm^{-1}) [1]. In these experiments the electron flux during irradiation was 7.5×10^{13} electrons $cm^{-2} s^{-1}$. For irradiation with 2 MeV electrons at 350 K (electron flux 20×10^{13} electrons $cm^{-2} s^{-1}$) the production rate of I_{001} is dramatically reduced from the low temperature value, whereas the vacancy production rate is the same as at 100 K [1].

Fig. 2 shows the isochronal annealing data of R2, in a sample which contained after electron irradiation an initial concentration of 0.45(5) ppm R2. The time of each anneal was 1 h. Assuming simple first-order kinetics and an Arrhenius annealing process for the loss in R2, the solid line in Fig. 2 shows a fit to:

$$I_n = I_{n-1} \exp(-t/\tau_0 \exp(-E/k_B T_n)),$$

where I_n is the intensity after the nth anneal at temperature T_n and E is an associated activation energy. The fit corresponds to $\tau_0 = 1 \times 10^{-8}$ s and $E = 1.6(2)$ eV. When the R2 center anneals out at $\sim$700 K, the measured concentration of neutral vacancies (integrated optical

* Corresponding author. Fax: + 44-1865-272400.
E-mail address: d.twitchen1@physics.ox.ac.uk (D.J. Twitchen)

0921-4526/99/$ - see front matter
PII: S0921-4526(99)00594-3

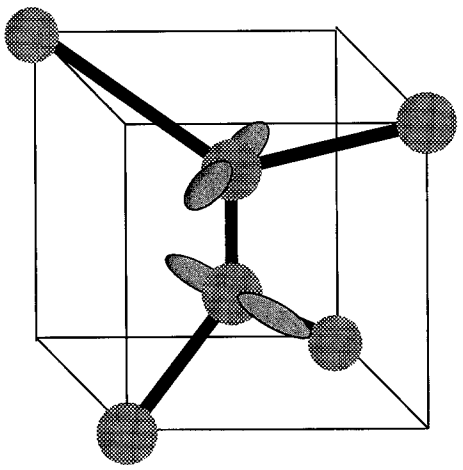

Fig. 1. The structure of the R2 EPR defect previously shown to be the neutral ⟨0 0 1⟩-split self-interstitial (I_{001}).

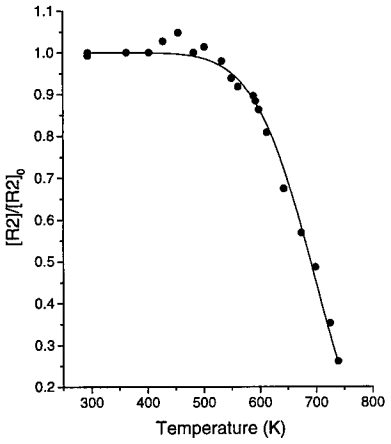

Fig. 2. The isochronal annealing of the I_{001} (measured R2 concentration). The solid line shows the best theoretical fit to first-order kinetics and an Arrhenius annealing process, with $\tau_0 = 1 \times 10^{-8}$ s and $E = 1.6(2)$ eV. The time of each anneal was 1 h. The initial concentration was 0.45(5) ppm R2.

absorption of the GR1 zero-phonon line at 1.673 eV [2]) decreases. In one sample irradiated with 2 MeV electrons at 100 K to a dose of 7×10^{17} e$^-$ cm^{-2}, the concentration of V^0 falls by 30(3)% from 1.4 to 1.0 ppm, while that of R2 falls from 1.00 ppm to zero. In a different study, the fall in concentration of V^0 is only 14(2)% from 1.4 to 1.2 ppm, while the smaller concentration of R2 falls from 0.45 ppm to zero. Allers et al. [3] have shown that the loss in vacancies on annealing at 700 K, a temperature when the vacancy in diamond is known not to be mobile [4], corresponds to a first-order process with an activation energy of 1.68(15) eV. To explain these results the I_{001} must be mobile in this temperature region but not at lower temperatures. However, the neutral di-⟨0 0 1⟩-split self-interstitial (R1) [5] is produced by electron irradiation damage at 100 K [6]. This latter result indicates that interstitials (not necessarily I_{001} in its neutral charge state) must be mobile during irradiation, since the di-⟨0 0 1⟩-split self-interstitial cannot plausibly be produced as a direct product of irradiation damage.

These results have led us to make a more careful and systematic study of the production rates of the vacancy and I_{001} centers. We report the results of an investigation of the production rate of I_{001} in synthetic type IIa diamond as a function of temperature. The electron energy (2 MeV) and flux (7.5×10^{13} electrons cm^{-2} s^{-1}) were held constant for all experiments. The temperature at the sample was controlled by a small heater coil placed near the sample mounted on a large copper heat sink kept at 77 K. Following irradiation, the samples were annealed to room temperature, where all EPR measurements were made. To check that no annealing was occurring when the samples were allowed to warm to room temperature, a sample was irradiated at 110 K and transferred to the EPR spectrometer without warming. No changes in the concentration of I_{001} were detected on annealing to temperatures between 120 and 350 K.

Fig. 3 shows the concentration of I_{001} produced for an irradiation dose of 7×10^{17} electrons cm^{-2} as a function of irradiation temperature. The production rate of I_{001} changes dramatically between 130 and 200 K. In the absence of electron irradiation we know that the I_{001} is not mobile in this temperature range. It is possible that we are observing radiation-enhanced diffusion of the I_{001} defect at temperatures above 150 K. Radiation-enhanced diffusion has not previously been reported for any other defects in diamond. Further studies are in progress to investigate the mechanism responsible for the

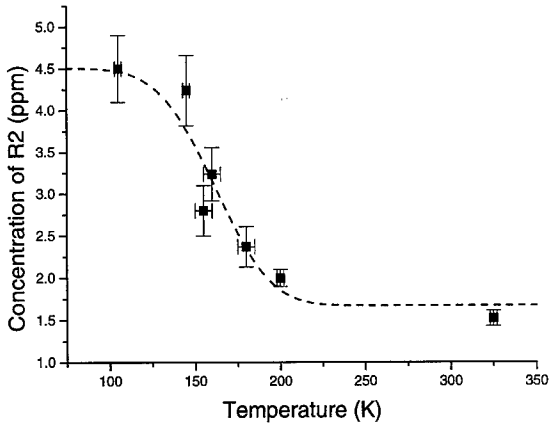

Fig. 3. The production of I_{001} (R2) as a function of temperature, in a suite of virgin IIa diamonds irradiated to a dose of 7×10^{17} e$^-$ cm^{-2} (2 MeV). All measurements were made at 300 K. The dashed line provides a guide to the eye.

change in the production rate of I_{001}. These studies include an investigation of the vacancy production rate in the same temperature region.

To conclude, the I_{001} defect center in diamond anneals out by migration at ~ 700 K with an associated energy of 1.6(2) eV, and at the same time there is a loss in the concentration of vacancies. It is not clear at this stage if the 1.6(2) eV corresponds to simply a migration energy for I_{001} or contains some factor associated with recombination/binding. Production of R2 as a function of temperature in the interval 110–350 K suggests a radiation-enhanced mechanism for the loss of I_{001}. A complete understanding of this process is of importance in understanding the formation mechanisms of intrinsic defects in diamond.

Acknowledgements

This work was supported by EPSRC grant GR/L65772. D.J.T. thanks Merton College, Oxford for the Harmsworth Senior Scholarship and Linacre College, Oxford for a Junior Research Fellowship. M.E.N. thanks EPSRC for an Advanced Fellowship. We would like to thank Profs. V. Nadolinny and A. Yelisseyev for their ideas and time to discuss some of this work, and Ian Thomas for his help with the use of the van Der Graaf machine at Reading University, U.K.

References

[1] D.C. Hunt, D.J. Twitchen, M.E. Newton, J.M. Baker, T.R. Anthony, W.F. Banholzer, Phys. Rev. B 8 (1999) 1572.
[2] D.J. Twitchen, D.C. Hunt, V. Smart, M.E. Newton, J.M. Baker, Diamond Related Mater. 9 (1999) in press.
[3] L. Allers, A.T. Collins, J. Hiscock, Diamond Related Mater 7 (1998) 228.
[4] G. Davies, S.C. Lawson, A.T. Collins, A. Mainwood, S.J. Sharp, Phys. Rev. B 46 (1992) 13157.
[5] D.J. Twitchen, M.E. Newton, J.M. Baker, O.D. Tucker, T.R. Anthony, W.F. Banholzer, Phys. Rev. B 54 (1996) 6988.
[6] D.J. Twitchen, D.C. Hunt, M.E. Newton, J.M. Baker, T.R. Anthony, W.F. Banholzer, Physica B (1999) submitted for publication.

ELSEVIER

Physica B 273–274 (1999) 647–650

PHYSICA B

www.elsevier.com/locate/physb

Transition metals in diamond: experimental and theoretical identification of Co–N complexes

Karl Johnston[a], Alison Mainwood[a,*], Alan T. Collins[a], Gordon Davies[a], Daniel Twitchen[b], J.M. Baker[b], Mark Newton[b]

[a]*Physics Department, King's College London, Strand, London WC2R 2LS, UK*
[b]*Clarendon Laboratory, University of Oxford, Parks Road, Oxford OX1 3PU, UK*

Abstract

Diamonds grown using a cobalt/iron catalyst and annealed at 1800°C were studied using two experimental techniques. A zero-phonon line, observed in photoluminescence at 2.367 eV, showed the splitting under uniaxial stress characteristic of an optical transition at a defect of trigonal symmetry. The same samples were measured by electron paramagnetic resonance (EPR) spectroscopy where they showed the defect labelled O4. This centre contains cobalt and possibly nitrogen, but has monoclinic symmetry. Ab initio modelling using the local density approach (LDA) with the code AIMPRO suggests that the optical transition is at a defect consisting of neighbouring substitutional cobalt and nitrogen atoms. A plausible model for the EPR data is a cobalt atom at the centre of a divacancy with a neighbouring nitrogen atom. We conclude that the defects giving rise to the 2.367 eV photoluminescence and EPR O4 centres are both simple cobalt–nitrogen pairs.

Keywords: Diamond; Cobalt; Uniaxial stress spectroscopy; Electron paramagnetic resonance spectroscopy; Ab-initio density functional theory

1. Introduction

Transition metals are crucial to the synthesis of large single crystal diamonds. By acting as a solvent-catalyst with graphite during the high-pressure high-temperature (HPHT) growth process, they enable samples with dimensions of several millimetres to be grown. The elements cobalt, iron, manganese and nickel are thought to be the most powerful catalysts for graphite to diamond conversion [1]. However, not all these metals have been identified in diamond as point defects. Nickel is now well known as an impurity in both synthetic and natural diamonds [2,3]. It can exist in a variety of forms. The interstitial atom has been investigated by EPR [4], optical spectroscopy [5] and magnetic circular dichroism in optical absorption [6]. High-temperature annealing allows migration of the nitrogen impurity [7] in these samples. The resulting complexes of nitrogen with nickel [8] have been investigated extensively using EPR [9].

Recently, a paper by Lawson et al. [10] identified optically active cobalt in diamond for the first time. Zero-phonon lines (ZPL) were reported in photoluminescence spectra at energies 1.989, 2.135, 2.207, 2.227, 2.367 and 2.590 eV. Most of these ZPLs are only observed after high-temperature annealing of samples containing nitrogen when, by analogy with nickel, cobalt–nitrogen complexes may be formed. In this paper, we give the first detailed study of some of the defects generated by this treatment.

2. Methods

The diamonds were grown using a Fe/Co catalyst in the absence of nitrogen getters and annealed at 1800°C

* Corresponding author. Tel.: + 44-(0)-171-848-2044; fax: + 44-(0)-171 848 2420.
E-mail address: alison.mainwood@kcl.ac.uk (A. Mainwood)

0921-4526/99/$ - see front matter
PII: S0921-4526(99)00595-5

for 20 h, enabling nitrogen to migrate [7] and the defect centres to form. The concentration of nitrogen was about 330 ppm of which less than 10% was left as isolated substitutional atoms after annealing. The crystals were then cut into cubes enabling uniaxial stress to be applied along the ⟨0 0 1⟩, ⟨1 1 0⟩ and ⟨1 1 1⟩ directions.

Luminescence was generated by the 351–364 nm lines of the Ar^+ laser and was collected using a $\frac{3}{4}$ m Spex monochromator. An oil-driven hydraulic ram delivered uniaxial stresses of up to 2.2 GPa and all the measurements reported here were carried out with the diamonds at 77 K.

For EPR measurements, a Bruker X-Band spectrometer was used operating at 9.5 GHz. The O4 EPR defect was only observable when the sample temperatures were below 30 K and our results were collected at ~ 5 K.

The modelling was carried out using an ab initio local density approximation (LDA) approach (AIMPRO) that has previously been successful in the treatment of both intrinsic and extrinsic defects in diamond [11,12].

A detailed account of the experimental and theoretical procedures is given in Ref. [13].

3. Results and discussion

3.1. Uniaxial stress on the 2.367 eV ZPL

Fig. 1 shows the splitting of the 2.367 eV line under stress along the high symmetry directions. According to the theory of Hughes and Runciman [14], the 2.367 eV centre is a trigonal defect with an optical transition between a singlet A state and a doublet E state. We show elsewhere [13] that the A state is the ground state.

The stress Hamiltonian is as that derived by Hughes and Runciman [14]. The basic trigonal centre is oriented along [1 1 1], defined as the Z-axis, and the X- and Y-axis are [1 1 $\bar{2}$] and [1 $\bar{1}$ 0], respectively. The Hamiltonian can then be written as

$$\Delta V = \hat{A}(\sigma_{xx} + \sigma_{yy} + \sigma_{zz} + \hat{A}'(\sigma_{yz} + \sigma_{zx} + \sigma_{xy}) + \hat{E}_X(2\sigma_{zz} - \sigma_{xx} - \sigma_{yy}) + \sqrt{3}E_Y(\sigma_{xx} - \sigma_{yy}) + \hat{E}'_X(2\sigma_{xy} - \sigma_{yz} - \sigma_{zx}) + \sqrt{3}\hat{E}'_Y(\sigma_{yz} - \sigma_{zx}), \quad (1)$$

where the σ_{ij} are the stress tensor components defined with respect to the *crystal* axis x, y, z, and the coefficients are coupling constant explained in Ref. [14]. The behaviour of the A to E transition under stress can be described by four parameters which can be derived from the experimental data. The calculated values for these are listed in Table 1 in the notation of Ref. [15], and are shown fitted to the experimental data in Fig. 1.

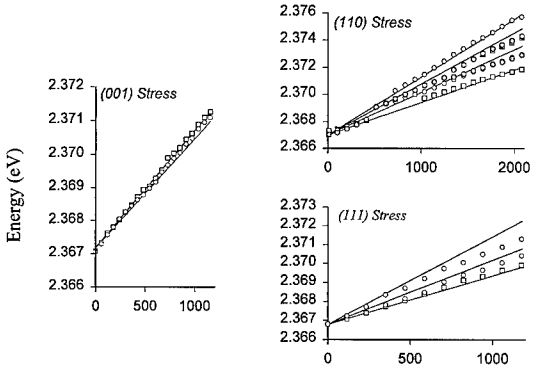

Fig. 1. The splitting of the 2.367 eV line under stress. The points are the experimental data while the lines are the calculated fits using the parameters listed in Table 1.

3.2. EPR results

In the same samples, the only Co-related EPR signal was O4 [16], which has spin $\frac{1}{2}$ and displays monoclinic I symmetry (see Fig. 2). It is only observed at low microwave powers (< 10 μW) and low temperatures (< 30 K). The characteristic eight line spectrum in Fig. 2 indicates a hyperfine interaction with a nucleus of spin $\frac{7}{2}$, consistent with cobalt [16]. The spin Hamiltonian describing the system can be written:

$$H = \mu_B S \cdot \underline{g} \cdot B + S \cdot \underline{A} I - \mu_N g_N I \cdot B \quad (2)$$

here the $\underline{g}$ and $\underline{A}$ matrices are given in Table 2 and $S = \frac{1}{2}$, $I = \frac{7}{2}$. The broad lines (about eight times as broad as for other centres in the same sample) indicate the possibility of a hyperfine interaction with nitrogen in the complex. If the cobalt atom is situated in the centre of a divacancy, similar to the nickel defects, then nitrogen at a nearest-neighbouring site will lower the symmetry to C_{1h}, the monoclinic symmetry that we observe.

3.3. Theoretical modelling

Nickel in diamond can be present at the centre of a divacancy (a "semi-divacancy" structure) – the NE4 EPR centre [9], the Co analogy of which is illustrated in Fig. 3a. Although this has trigonal symmetry, it is unlikely that this defect produces the 2.367 eV ZPL because we would expect such a structure to be grown-in rather

Table 1
The stress parameters for the 2.367 eV line. (meV GPa^{-1}). The uncertainty in the figures is approximately 0.06 meV GPa^{-1}.

A_1	3.40
A_2	0.62
B	0.06
C	0.31

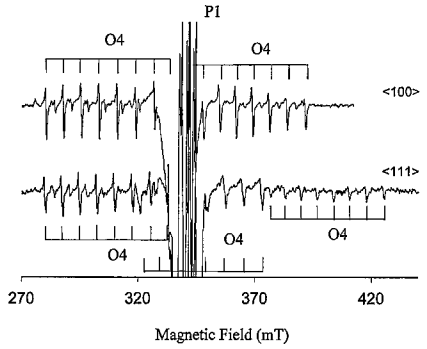

Fig. 2. The EPR spectrum of the O4 centre, with the magnetic field along ⟨1 0 0⟩ and ⟨1 1 1⟩ directions. Although each group of eight lines should have equal intensity, saturation has affected the spectra. The P1 signal is that of the residual isolated nitrogen [17].

Table 2
The g and $\underline{A}$ matrices of the O4 centre determined at X-band (9.59 GHz)

	θ	φ
g-matrix		
$\|g_x\| = 1.8438(5)$	90	315
$\|g_y\| = 1.7045(5)$	61(2)	45
$\|g_z\| = 2.3463(5)$	29(2)	225
A-matrix		
$\|A_x\| = 180(2)$	90	315
$\|A_y\| = 163(2)$	65(2)	45
$\|A_z\| = 248(2)$	26(2)	225

The angles θ, φ (in degrees) refer to spherical co-ordinates expressed in the crystal cubic axis scheme

than being dependent on annealing at 1800°C. Nevertheless, we have calculated the electronic states of the centre (shown in Fig. 4a), and find that the ground state transforms as E (in contrast to the observed A state of the 2.367 eV ZPL). Furthermore, the lowest transition energy is 3.4 eV, considerably higher than the observed 2.367 eV.

We therefore turn to the first-order stage of aggregation of cobalt and nitrogen. There are two basic possibilities: The N atom could be trapped as a nearest-neighbour to a substitutional cobalt atom to produce a trigonal centre (Fig. 3b) or at any one of the nearest-neighbour sites to the cobalt in a divacancy to give a monoclinic I centre (Fig. 3c). The LDA calculations show that both these configurations are energetically stable.

The d-shell of a cobalt substitutional atom is split into t_2 and e states by the crystal field of the diamond, and the t_2 state is further split into a_1 and e states in the trigonal

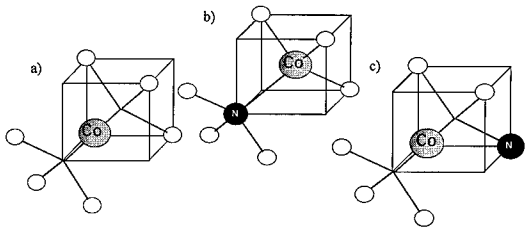

Fig. 3. Possible structures for cobalt and cobalt–nitrogen defects: (a) Cobalt in a divacancy, (b) Co-N trigonal defect, (c) Co–N monoclinic defect (the model for the O4 EPR centre). The unlabelled atoms are carbon.

field of the Co–N complex of Fig. 3b. The expected one-electron structure is either $e^4a_1^1e^1$ or $e^4a_1^2e^0$ depending on the detailed electron–electron interactions. The former configuration has a ^3E ground state, in contrast to the experimental requirement for an A ground state, as shown in Fig. 4b(i). (In fact, there is no evidence for a trigonal $S = 1$ EPR-active centre in these samples.) The $e^4a_1^2e^0$ configuration gives a $^1A_1$ ground state (see Fig. 4bii). The lowest energy transition is $^1A_1$ to ^1E, in agreement with experiment, and has an energy of about 1.7 eV, acceptably close to the 2.367 eV of the ZPL.

For the monoclinic I centre shown in Fig. 3c to be EPR-active with $S = \frac{1}{2}$, it must have an odd number of electrons. Given the presence of nitrogen in the sample, we chose the negative charge state. In that case the energy levels calculated are shown in Fig. 4c. Several transitions are possible near 2 eV, which provide an impetus to attempting to correlate another optical transition with this EPR centre.

More details of the results and their interpretation are given in Ref. [13].

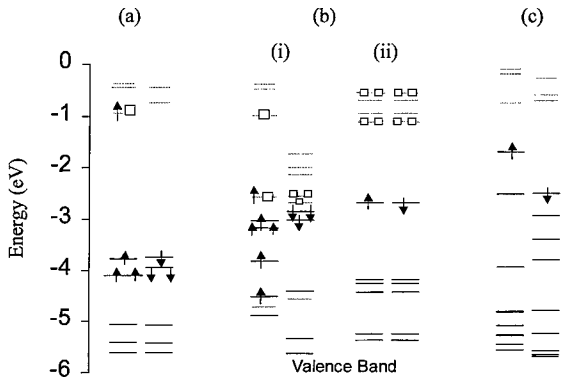

Fig. 4. The Kohn–Sham eigenvalues for the structures suggested in Fig. 3: (a) the cobalt atom in a divacancy; (b) the substitutional cobalt–nitrogen complex with (i) spin 1 and, (ii) spin 0; (c) The model of the monoclinic O4 defect. For each structure there are spin up and spin down eigenvalues. For significant levels, occupied states are represented by the appropriate arrow, indicating spin; empty states are shown by boxes.

4. Conclusions

A combination of experimental and theoretical methods has allowed us to suggest the structure of two cobalt–nitrogen defects in diamond. The centre at which the 2.367 eV PL line arises is consistent with a Co–N substitutional pair; a cobalt atom at the centre of a divacancy with a nitrogen neighbour is a plausible model for the O4 EPR defect. These are the two simplest cobalt–nitrogen aggregates; if cobalt behaves like nickel, we would expect other more complex cobalt–nitrogen defects to form after further annealing.

Acknowledgements

We thank the Diamond Research Laboratories in Johannesburg for the samples used, and DTC Research Centre for their preparation. K.J. thanks De Beers Industrial Diamond Division for a studentship. The work at Oxford was supported by EPSRC grant GR/L65772. D.T. thanks Linacre College, Oxford for a Junior Research Fellowship.

References

[1] C.-M. Sung, M.-F. Tai, Int. J. Refractory Metals Hard Mater. 15 (1997) 237.
[2] A.T. Collins, P.M. Spear, J. Physica D. 15 (1982) L183.
[3] C.J. Noble, Th. Pawlik, J.-M. Spaeth, J. Phys: Condens. Matter 10 (1998) 11781.
[4] J. Isoya, H. Kanda, Y. Uchida, 1990 Phys, Rev. B 42 (1990) 9843.
[5] M.H. Nazaré, A.J. Neves, G. Davies, Phys Rev B 43 (1991) 14196.
[6] P.W. Mason, F.S. Ham, G.D. Watkins, Phys. Rev. B 60 (1999) 5417.
[7] T. Evans, in: J.E. Field (Ed.), The Properties of Natural and Synthetic Diamond, Academic Press, New York, 1992, p. 259.
[8] V.A. Nadolinny, A.P. Yelisseyev, Diamond Related Mater. 3 (1993) 17.
[9] V.A. Nadolinny, A.P. Yelisseyev, O.P. Yureva, B.N. Feygelson, Appl. Magn. Reson. 12 (1997) 543.
[10] S.C. Lawson, H. Kanda, K. Watanabe, I. Kiflawi, Y. Sato, A.T. Collins, J. Appl. Phys 79 (1996) 4348.
[11] J.G. Goss, A. Resende, R. Jones, S. Öberg, P.R. Briddon, Mater. Sci. Forum 196-201 (1995) 67.
[12] R. Jones, P.R. Briddon, in: M. Stavola (Ed.), Semiconductors, Semiconductors and Semimetals, Academic Press, New York, 1998.
[13] K. Johnston, A. Mainwood, G. Davies, A.T. Collins, D.J. Twitchen, J.M. Baker, M.E. Newton, Phys. Rev. B, submitted to for publication.
[14] A.E. Hughes, W.A. Runciman, Proc. Phys. Soc. 90 (1967) 827.
[15] G. Davies, M.F. Hamer, Proc. Royal Soc London A 348 (1975) 285.
[16] D.J. Twitchen, J.M. Baker, M.E. Newton, K. Johnston, Phys. Rev. B (2000) to be published.
[17] W.V. Smith, P.P. Sorokin, I.L. Gelles, G.J. Lasher, Phys. Rev. 115 (1959) 1546.

ELSEVIER

Physica B 273–274 (1999) 651–654

PHYSICA B

www.elsevier.com/locate/physb

New paramagnetic defects in synthetic diamonds grown using nickel catalyst

A.J. Neves[a,*], R. Pereira[a], N.A. Sobolev[a], M.H. Nazaré[a], W. Gehlhoff[b], A. Näser[b], H. Kanda[c]

[a]*Departamento de Física, Universidade de Aveiro, 3810 Aveiro, Portugal*
[b]*Institut für Festkörperphysik, Technische Universität Berlin, 10623 Berlin, Germany*
[c]*National Institute for Research in Inorganic Materials (NIRIM), Namiki 1-1, Tsukuba, Japan*

Abstract

We report four new EPR spectra found in high-pressure synthetic diamonds with high nitrogen content, grown using nickel, and annealed at 1600°C. Analyzing the complex spectra around $g \approx 2$ two trigonal and two orthorhombic defects, all with $S = \frac{1}{2}$, were identified from the angular dependence and the different saturation behavior of the transitions. Besides optical and EPR investigations reveal several centers which have been previously ascribed to defects containing nickel and nitrogen. However, nitrogen is not involved in the new centers, since no evidence of an ^{14}N hyperfine structure could be found. Possible relations of the new defects with Ni are discussed.

PACS: 61.72Ji; 71.55.Cn; 76.30.Fc

Keywords: Synthetic diamond; EPR; Nickel

1. Introduction

In the high-pressure synthesis of diamond transition metals like Ni, Fe or Co and their alloys are used as solvent catalysts. If no special measures are taken, like the addition of a nitrogen getter (Ti and/or Zr) to the solvent catalyst, dispersed substitutional N (*C*-center) is the major impurity in these diamonds. When the solvent catalyst is Ni its incorporation into the diamond lattice in the form of dispersed atoms gives rise to several electron paramagnetic resonance (EPR) as well as to optical absorption spectra whose relative intensities are dependent on the nitrogen concentration in the sample. Synthetic diamonds with higher nitrogen content (> 50 ppm) exhibit typically optical centers with zero-phonon lines (ZPL) at 1.885 and 2.51 eV [1] and an EPR signal at $g = 2.0319$, which is attributed to substitutional Ni_s^- ($3d^7$) in tetrahedral environment with a spin ground state $S = \frac{3}{2}$ [2].

The annealing of this type of synthetic diamonds at temperatures in excess of 1600°C results in a growth of a complex absorption structure in the visible region at the expense of the optical transitions at 1.885 and 2.51 eV [3]. As well a diversity of EPR centers results from such heat treatments. Some centers, which were tentatively assigned to Ni-related defects (NE1–NE3 and NE5), have anisotropic g values with magnitudes between 2.00 and 2.14 and show characteristic superhyperfine (shf) splittings indicating interactions with two or three nitrogen atoms [4]. The proposed model assumes an Ni^+ in a di-vacancy position surrounded by two or three nitrogen atoms in different site positions [4]. Within the temperature range of these heat treatments nitrogen becomes mobile and aggregates to form pairs of neighboring substitutional nitrogen atoms (A-centers) [5]. The arising new optical and EPR features after different stages of annealing are then taken as evidence that complex defects involving nickel and nitrogen are also

* Corresponding author. Fax: + 351-34-424965.
E-mail address: armando@fis.ua.pt (A.J. Neves)

0921-4526/99/$ - see front matter
PII: S0921-4526(99)00596-7

formed. Monitoring simultaneously changes in the EPR and optical spectra an assignment between optical absorption and specific EPR spectra was attempted [4]. Very recently such correlation was achieved more directly using optical detection of electron paramagnetic resonance (ODEPR) via the magnetic circular dichroism of the optical absorption (MCDA) at least for two spectra of a synthetic diamond crystal, which was grown using Ni-catalyst and annealed at 1700–1800°C [6]. The observed single sharp line at 1.40 eV and a doublet structure at 1.72 eV in the MCDA spectra could be assigned to the NIRIM-2 [7] and NE4 [4] centers, respectively.

It should be pointed out that only for the center with $g = 2.0319$ the involvement of Ni was directly confirmed observing the resolved hyperfine splitting from ^{61}Ni isotope ($I = \frac{3}{2}$, natural abundance 1.2%) in isotopically enriched powder samples [8]. In all other cases the assignment of the EPR spectra to Ni-related centers was achieved only indirectly based on the fact that the corresponding signals only appeared in samples grown with Ni or Ni alloys as catalyst. The same holds true for the optical investigations, with the exception of the 1.40 eV center observed in synthetic diamonds with low N concentration, where an isotope related fine-structure has conclusively shown that nickel is part of the center [9].

The present study describes four new EPR spectra found in synthetic diamonds grown using only Ni catalyst and annealed during 4 h at 1600°C. All spectra can be described with an electron spin state $S = \frac{1}{2}$, anisotropic g-values with magnitudes greater than g_e and no indications of hyperfine or superhyperfine structure related to isotope ^{14}N ($I = 1$, natural abundance 99.63%). The possible nature of these centers is discussed.

2. Experimental details

The synthetic diamonds used for our study were grown at NIRIM by the temperature gradient method at temperatures in the range 1400–1450°C using only Ni as solvent-catalyst without nitrogen getters. Two samples were then annealed at 1600°C for 4 h under a stabilizing hydrostatic pressure of 6 GPa. The samples were polished into parallelepipeds with edges of ~ 1 mm linear length, with faces oriented along the $\langle 1\,1\,0\rangle$ and $\langle 1\,0\,0\rangle$ crystallographic directions.

EPR spectra were obtained using a Bruker ESP 300E spectrometer with X- and Q-band microwave bridges and equipped with an Oxford Instruments helium gas-flow cryostat. The measurements were performed either at room temperature or at temperatures in the range 50–100 K using a cylindrical $TE_{0\,1\,1}$ microwave resonator.

Infrared (IR) absorption were measured on a Bruker IFS66V FTIR spectrometer. The optical absorption and luminescence in the visible region in the temperature range of 15–20 K were recorded using a dispersive spectrometer fitted with a cooled photomultiplier. For the absorption experiments the diamonds were irradiated with light from a 100 W tungsten lamp, and for the photoluminescence studies with light from He–Ne and He–Cd lasers.

3. Results and discussion

For the characterization of the investigated diamond samples the optical absorption spectra were measured. Characteristic absorption spectra obtained for one annealed sample in the IR and the visible spectral region are shown in Fig. 1a and b, respectively. Isolated substitutional nitrogen, in the neutral and positively charged states, as well as nitrogen aggregates induces characteristic IR absorption in the one-phonon region. The IR spectrum observed at room temperature (Fig. 1a) is an admixture of these individual spectra, and was reconstructed using numerical minimization techniques. From the best fit, and using the relationships between nitrogen concentration and the infrared absorption coefficients given in Ref. [10–12] we can conclude that most of the nitrogen present in the sample is in the A-form, with an estimated concentration of 190 at ppm. The concentration of C and N^+ centers is about 70 and 38 at ppm, respectively. The corresponding optical absorption spectrum in the visible region (Fig. 1b) recorded at 15 K is dominated by a vibronic system with zero-phonon line (ZPL) at 1.693 eV, and a complex multiline array that extents from 2 to 2.8 eV, similar to the previously reported by Lawson and Kanda [3]. Photoluminescence spectra show several vibronic systems namely the broad bands associated with S2 and S3 defects.

In consequence of the small spin–orbit coupling for impurities in diamond many centers have EPR transitions near to g_e [13]. This makes their differentiation

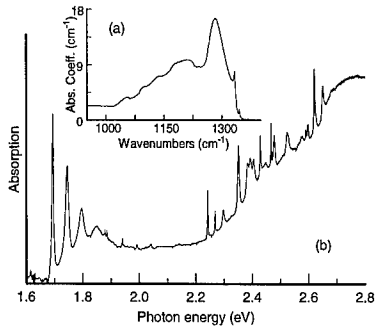

Fig. 1. Optical absorption spectra of an annealed diamond sample. (a) IR spectrum measured at room temperature. (b) Optical spectrum in the visible spectral region measured at $T = 15$ K showing the vibronic system with ZPL at 1.693 eV and a complex multiline array that extents from 2.2 to 2.8 eV.

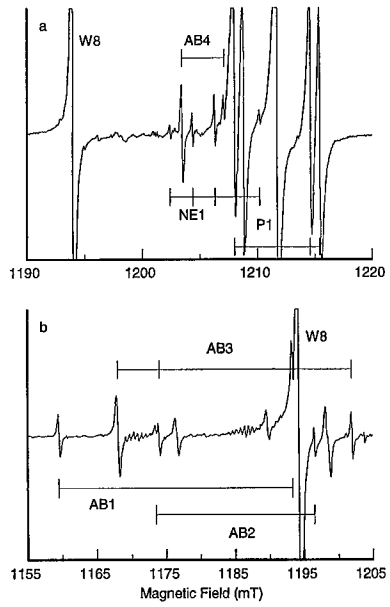

Fig. 2. EPR spectrum of an annealed synthetic diamond sample recorded at 70 K with the magnetic field parallel to ⟨1 1 0⟩ and a microwave power level of (a) 0.2 μW and (b) 0.8 mW in the Q-band. (100 kHz modulation frequency, and 0.1 mT modulation amplitude).

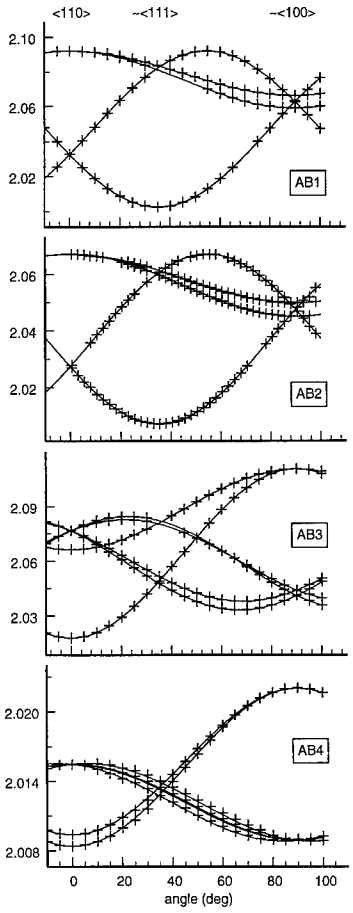

Fig. 3. Angular dependencies of the EPR lines for the centers AB1–AB4 for rotation of the magnetic field in a {1 1 0}-plane. The points represent the experimental line positions and the solid lines are computer fits using the numerical values for the g-values given in Table 1 for the corresponding main axes systems.

difficult especially using low microwave frequencies, because the transitions of the different centers overlap in many cases very strongly. Carefully controlled experiments at different microwave frequencies (X- and Q-band) and appropriate choice of microwave power (MWP) and sample temperature enabled us to find four new EPR spectra.

Fig. 2 shows an EPR spectrum of the annealed sample obtained at 70 K with low MWP (0.2 μW). The main features of this spectrum are the typical P1 center with a three-line hyperfine structure due to substitutional nitrogen ^{14}N [14], and the $g = 2.0319$ isotropic line associated with substitutional Ni^- [2]. By simulation of the EPR spectra using the spin Hamilton parameters given in the literature another spectrum with a five-line hyperfine structure was identified as the NE1 defect [4]. Some other lines correspond to a new center with orthorhombic (only weakly distorted tetragonal) symmetry labeled AB4. In addition several small unidentified lines with low intensity were observed. At a higher MWP (0.8 mW) the lines related to the P1, NE1 and AB4 centers are almost completely saturated, and the spectrum is dominated by a group of lines that we have assigned to three new centers labeled AB1, AB2 and AB3 in Fig. 2. The peak-to-peak line width of the spectral lines is about 0.1–0.2 mT. Below 50 K even at the lowest MWP available saturation effects impaired the observation of well-resolved spectra. In the used temperature range of the experiments no apparent motional effects and shifts of the EPR line positions could be detected.

The EPR angular dependencies of the new centers AB1–AB4 measured at ~ 34 GHz in a plane very close to a {1 1 0}-plane are presented in Fig. 3. (Analyzing the simultaneously measured angular dependence of the P1 hyperfine structure a small misorientation of 2° of the ⟨1 1 0⟩-rotation axis was determined.) The line positions can be well described with the spin Hamiltonian

$$H = \beta S \cdot g \cdot B$$

with $S = \frac{1}{2}$ and using the g-values and corresponding symmetries for the different centers given in Table 1.

As mentioned above the defect with trigonal symmetry responsible for the MCDA doublet at 1.72 eV detected

Table 1
g-values and center symmetries for the new EPR centers AB1–AB4. For comparison the data for the NE4 center and ODMR center (NE4*) taken from Refs. [4] and [6] are given

Center	Spin	Symmetry	g-values	Axis
AB1	$S=\frac{1}{2}$	Trigonal	$g_{\|\|}=2.0024$ $g_{\perp}=2.0920$	$\langle 1\,1\,1\rangle$
AB2	$S=\frac{1}{2}$	Trigonal	$g_{\|\|}=2.0072$ $g_{\perp}=2.0672$	$\langle 1\,1\,1\rangle$
AB3	$S=\frac{1}{2}$	Orthorhombic-I	$g_1=2.1105$ $g_2=2.0663$ $g_3=2.0181$	$\langle 1\,0\,0\rangle$ $\langle 0\,1\,1\rangle$ $\langle 1\,0\,-1\rangle$
AB4	$S=\frac{1}{2}$	Orthorhombic-I	$g_1=2.0220$ $g_2=2.0094$ $g_3=2.0084$	$\langle 1\,0\,0\rangle$ $\langle 0\,1\,1\rangle$ $\langle 1\,0\,-1\rangle$
NE4	$S=\frac{1}{2}$	Trigonal	$g_{\|\|}=2.023$ $g_{\perp}=2.098$	$\langle 1\,1\,1\rangle$
NE4*	$S=\frac{1}{2}$	Trigonal	$g_{\|\|}=2.004$ $g_{\perp}=2.093$	$\langle 1\,1\,1\rangle$

with ODEPR-techniques [6] was assigned to the NE4 center described in [4]. However, comparing the g-values of the trigonal centers AB1 and NE4 with the values determined from the angular dependence of the ODEPR measurements (see Table 1) it is obvious that the AB1 data fit the ODEPR angular dependence much better. Therefore, we believe that the MCDA doublet is more likely related to the AB1 defect as to the NE4 center.

The nature of the four EPR centers AB1–AB4 is unknown up to now, because there are no indications of hyperfine interactions related to these centers. Therefore, a direct chemical identification by this fingerprint was not possible. However, there are some hints concerning their nature. As a consequence of the high annealing temperature it can be excluded that these centers are caused by intrinsic defects only, because this kind of defects typically anneal out at a temperature lower than 1000°C [15].

Since these spectra only appear in diamond grown with Ni it is reasonable to assume that they are Ni related. Above all substitutional Ni_s^- and a complex of Ni and N (NE1) could be detected in our samples. Besides, like all Ni-related centers described up to now the g-values of the centers AB1–AB4 are greater than g_e. This is consistent with a more than half-filled d-shell. Because no hyperfine structure could be observed, nitrogen seems to be not directly involved in these centers. However, the observed different magnitudes and symmetries of the crystal-field distortions suggests associations with other impurities with low abundance of isotopes with non-zero nuclear spin like oxygen or intrinsic defects.

During crystal growth nickel being larger than carbon could act as a center for generation of vacancies and carbon interstitials, which in turn interact with nickel atoms and/or other imperfections to form the observed defects. From studies on the kinetics of the aggregation of nitrogen it is known that the rate of aggregation is increased by the nickel concentration [16,17]. This dependence was explained by the release of vacancies, which in turn assist in the migration of nitrogen, or through the release of carbon interstitials that in turn release high mobile nitrogen interstitials [16,17]. Another sources of mobile defect components are defect complexes, which dissociate at certain annealing temperatures. Since these processes occur in the vicinity of nickel we could admit that the new centers which results from substitutional nickel captures a vacancy, or that the dissociation processes leave a complex of Ni that becomes paramagnetic.

Acknowledgements

This work was supported in part by FCT under contracts PRAXIS/PCEX/FIS/0012/96, PRAXIS XXI/BD/18405/98 and PRAXIS XXI/BCC/10003/96.

References

[1] A.T. Collins, H. Kanda, R.C. Burns, Philos. Mag. B 61 (1990) 797.
[2] J. Isoya et al., Phys. Rev. B 41 (1990) 3905.
[3] S.C. Lawson, H. Kanda, J. Appl. Phys. 73 (1993) 3967.
[4] V.A. Nadolinny et al., J. Appl. Mag. Res. 12 (1997) 543.
[5] R.M. Chrenko, R.E. Tuft, H.M. Strong, Nature (London) 270 (1977) 141.
[6] Th. Pawlik, C. Noble, J.-M. Spaeth, J. Phys.: Condens. Matter 10 (1998) 9833.
[7] J. Isoya, H. Kanda, Y. Uchida, Phys. Rev B 42 (1990) 9843.
[8] M.I. Samoilovich, G.N. Bezrukov, V.P. Butuzov, JETP Lett. 14 (1971) 379.
[9] M.H. Nazaré, A.J. Neves, G. Davies, Phys. Rev. B 43 (1991) 14196.
[10] I. Kiflawi et al., Philos. Mag. B 69 (1994) 1141.
[11] S.R. Boyd, I. Kiflawi, G.S. Woods, Philos. Mag. B 69 (1994) 1149.
[12] S. Lawson et al., J. Phys.: Condens. Matter 10 (1998) 6171.
[13] J.M. Baker, M.E. Newton, Appl. Magn. Reson. 7 (1994) 209.
[14] W.V. Smith, P. P Sorokin, I.L. Gelles, G.J. Lasher, Phys. Rev. 115 (1959) 1546.
[15] C.A.J. Ammerlaan, in: O. Madelung, M. Schultz (Eds.), Landolt-Bornstein Numerical Data and Functional Relationships in Science and Technology; New Series III, Vol. 22b, Springer, Berlin, 1990, pp. 177–206.
[16] D. Fisher, S.C. Lawson, Diamond Rel. Mater. 7 (1998) 299.
[17] I. Kiflawi, H. Kanda, A. Mainwood, Diamond Rel. Mater. 7 (1998) 327.

ELSEVIER

Physica B 273–274 (1999) 655–658

PHYSICA B

www.elsevier.com/locate/physb

Electron-paramagnetic-resonance studies of defects in electron-irradiated p-type 4H and 6H SiC

N.T. Son[a,*], P.N. Hai[a], P.T. Huy[b], T. Gregorkiewicz[b], C.A.J. Ammerlaan[b], J.L. Lindström[a,1], W.M. Chen[a], B. Monemar[a], E. Janzén[a]

[a]*Department of Physics and Measurement Technology, Linköping University, S-581 83 Linköping, Sweden*
[b]*Van der Waals-Zeeman Institute, University of Amsterdam, Valckenierstraat 65-67, NL-1018 XE Amsterdam, Netherlands*

Abstract

Defects in p-type 4H and 6H SiC irradiated by 2.5 MeV electrons were studied by electron paramagnetic resonance (EPR). Two anisotropic EPR spectra, labeled I and II, were observed in both 4H and 6H SiC. These spectra demonstrating triclinic symmetry of the center can be described by an effective electron spin $S = \frac{1}{2}$. The angle α between the direction of the principal g_z of the g-tensors and the c-axis is determined as 63° and 50° for spectra I and II, respectively. In the 6H polytype, a third also similar EPR spectrum was detected. Based on their similarity in the electronic structure (electron spin, symmetry, g values), annealing behavior and temperature dependence, these spectra are suggested to be related to the same defect occupying different inequivalent lattice sites in 4H and 6H SiC. A pair between a silicon vacancy and an interstitial is a possible model for the defect.

Keywords: Silicon carbide; Defects; Electron paramagnetic resonance

1. Introduction

In a compound semiconductor such as SiC, vacancies, interstitials and also anti-site defects are created under high-energy-particle irradiation. The interaction between these primary defects leads to the formation of many possible complex centers. Although the vacancies in SiC seem to become mobile only at temperatures far above room temperature [1,2], different vacancy-associated complexes can already be formed without undergoing an anneal at higher temperatures [1]. An isolated defect such as a single vacancy will give rise to only one electron paramagnetic resonance (EPR) spectrum in the cubic lattice of the 3C SiC. In the 4H and 6H SiC, there are two and three inequivalent lattice sites, respectively, and hence a substitutional defect can give rise to two or three different spectra depending on its position. The one-to-one correspondence between the number of the spectra and the inequivalent lattice sites may also apply for vacancy-related complexes if the electron spins mainly locate in one of the constituents. A defect occupying different inequivalent lattice sites may give rise to different EPR spectra. This makes the defect study, which is already very complicated as experienced in electron-irradiated cubic semiconductors, more difficult in hexagonal SiC polytypes.

In the past, most of the EPR studies of intrinsic defects were reported for 3C and 6H SiC [1–5] and much less for the 4H polytype [6,7]. Recently, Cha and coworkers [8] have studied p-type 6H SiC irradiated with electrons and observed several low-symmetry EPR spectra (PC1, PC2 and PD), but no suggestion on defect identification has been made. In this work, we used EPR to study defects in p-type 4H and 6H SiC irradiated with 2.5 MeV electrons at room temperature. In 6H SiC, we also observed three anisotropic EPR spectra with an electron spin $S = \frac{1}{2}$,

* Corresponding author. Fax: + 46-13-142337.
E-mail address: son@ifm.liu.se (N.T. Son)
[1] Present address: Department of Solid State Physics, Lund University, Box 118, S-221 00 Lund, Sweden.

0921-4526/99/$ - see front matter
PII: S0921-4526(99)00597-9

which are very similar to those observed by Cha et al. [8]. Comparing the results in 6H and 4H SiC, it is suggested that all these EPR spectra are related to the same defect occupying different inequivalent lattice sites.

2. Experiment

Samples used in this work were p-type 4H and 6H SiC substrates from Cree Research Inc. The concentration of the Al acceptor is about $2.5 \times 10^{18}\,cm^{-3}$ in 4H SiC and $4.4 \times 10^{17}\,cm^{-3}$ in 6H SiC samples. These commercial substrates are off-axis wafers in which the plane's normal is not parallel to the c-axis but inclines an angle ($\sim 3.5°$ for 6H and $\sim 8°$ for 4H polytypes) towards the [1 1 $\bar{2}$ 0] direction. The samples were irradiated by 2.5 MeV electrons with doses in the range 10^{16}–$10^{17}\,cm^{-2}$ at room temperature. EPR measurements were performed on a K-band (~ 23 GHz), superheterodyne spectrometer, tuning to observe the dispersion of the susceptibility. During the experiments, the sample temperature can be regulated from 2.5 K to room temperature. For angular dependence studies of the EPR spectra the magnetic field was rotated in the (1 1 $\bar{2}$ 0) plane. Since the samples were cut from off-axis wafers, typical misalignments by an angle of about 3° and 8° for 6H and 4H SiC, respectively, were often present in the experiments. Due to this type of misalignment, the magnetic field was actually rotated in a plane, which inclined an angle φ with the (1 1 $\bar{2}$ 0) plane as illustrated in Fig. 1.

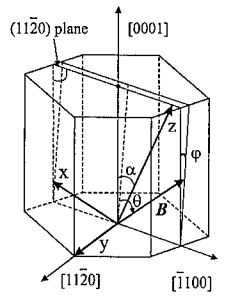

Fig. 1. Principal axes of the g-tensor and a typical sample misalignment occurring in the experiments. For off-axis samples, the magnetic field $\boldsymbol{B}$ was indeed rotating in a plane inclined an angle φ with the (1 1 $\bar{2}$ 0) plane.

3. Results and discussion

Several low-temperature EPR spectra were detected in p-type 4H and 6H SiC irradiated with electrons with a dose of $1 \times 10^{17}\,cm^{-2}$. Figs. 2(a) and 2(b) show the spectra in 4H and 6H SiC, respectively, recorded for the magnetic field $\boldsymbol{B}$ parallel to the c-axis. These spectra were not detected in as-grown materials. As can be seen in Fig. 2(a), three groups of lines with different intensities and line widths appear at around 825, 831 and 833 mT. The low-field lines in the region 823.5–826 mT as indicated by solid and dashed arrows in the figure belong to two different spectra, labeled I and II, respectively. The group of lines at around 831 mT belongs to unidentified defects. These lines severely overlap with each other at most directions of the magnetic field. The lines in the region 832–834 mT, labeled EI1 and EI2, belong to defects related to carbon and silicon vacancies [9], respectively. In the 6H polytype, similar groups of lines were also detected in the same region of the magnetic field [Fig. 2(b)] as in the case of 4H SiC. The low-field lines are also labeled I and II due to the similarity in the g-values and other aspects, which will be shown later. In addition to these, another more anisotropic spectrum was detected.

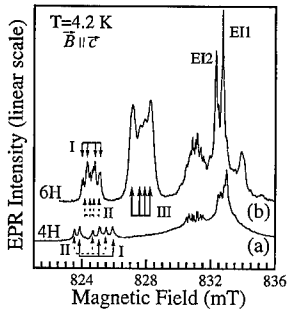

Fig. 2. EPR spectra observed in p-type (a) 4H and (b) 6H SiC irradiated with 2.5 MeV electrons with a dose of $1 \times 10^{17}\,cm^{-2}$ for $\theta = 0$. The lines belong to spectra I, II and III are indicated by solid, dashed and thick solid arrows, respectively. Due to misalignment (Fig. 1), at this direction of $\boldsymbol{B}$ each spectrum should be observed as a group of three lines. In (b) the angle θ is not exactly zero so each spectrum appears as a group of four broader lines. The microwave frequencies are (a) $\nu = 23.335636$ and (b) $\nu = 23.332216$ GHz.

These lines, labeled III, are indicated by thick arrows in Fig. 2(b). The intensity of spectra I–III increases with increasing the dose of irradiation. However, when the dose reaches about $5 \times 10^{17}\,cm^{-2}$, these spectra disappear and another anisotropic spectrum, with an electron spin $S = 1$ is detected in both 4H and 6H SiC [10]. These EPR signals disappear at measurement temperatures above 25 K.

At some angles of the magnetic field, where the resonance lines are relatively strong and well separated, weak hyperfine structure lines can be seen. Fig. 3 shows, as an example, the hyperfine structure of the spectrum III in 6H SiC for the magnetic field $\boldsymbol{B}$ perpendicular to the c-axis. There are three satellites on each side of the main line (one of these is overlapping with other EPR lines of spectrum I). The total intensity of these satellites is about

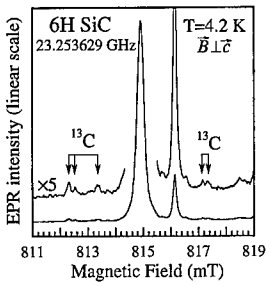

Fig. 3. Part of the EPR spectrum III in 6H SiC for $\boldsymbol{B} \| [\bar{1}\,1\,0\,0]$. The hyperfine structure due to the interaction with four ^{13}C atoms in the nearest-neighbor shell is indicated by arrows.

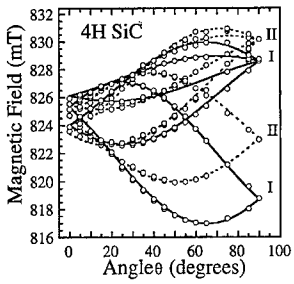

Fig. 4. Angular dependencies of spectra I and II in 4H SiC. The open circles represent the experimental data. The solid and dashed curves represent the simulated angular dependencies for spectra I and II, respectively, using the obtained parameters taking into account a misalignment angle $\varphi = 9°$. The microwave frequency is $\nu = 23.335788$ GHz. The zero degree corresponds to the direction closest to the c-axis in the rotation plane, see Fig. 1. The angle of 90°, on the other hand, corresponds exactly to $\boldsymbol{B} \| [\bar{1}\,1\,0\,0]$.

4.6% compared to that of the main line. This hyperfine structure is due to the interaction between the electron spin and the nuclear spins of the four ^{13}C atoms ($I = \frac{1}{2}$ and 1.1% natural abundance) in the nearest-neighbor shell. The hyperfine structure due to the interaction with ^{29}Si atoms ($I = \frac{1}{2}$ and 4.7% natural abundance) in the next-nearest-neighbor shell is not resolvable. This makes the line width of spectra I–III (typically ~ 0.3 mT) broader comparing to that of the carbon–vacancy-related EI1 center (~ 0.11 mT). Thus, the observation of the ^{13}C hyperfine structure indicates that the electron spin localizes at the silicon site in the lattice.

The experimental angular dependencies for spectra I and II in 4H SiC are shown in Fig. 4 by the open circles. As shown by the solid curves, each spectrum consists of three closed loops, which do not coincide at $\theta = 0$. This splitting is due to a sample misalignment off the c-axis as illustrated in Fig. 1. The fits to the experimental data were performed taking into account the sample misalignment and using the spin Hamiltonian

$$H = \mu_B \boldsymbol{B} \cdot \boldsymbol{g} \cdot \boldsymbol{S}, \tag{1}$$

where the effective electron spin $S = \frac{1}{2}$ and μ_B is the Bohr magneton. The g-tensor is diagonalized in the principal coordinate system with g_z and g_x lying in the $(1\,1\,\bar{2}\,0)$ plane and g_y along the $[1\,1\,\bar{2}\,0]$ direction as depicted in Fig. 1. α is the angle between the principal z-axis and the c-axis of the crystal. The principal g-values and angles α deduced from the best fits for spectra I and II in 4H SiC are given in Table 1. A misorientation angle in this case was $\varphi = 9°$. The simulated angular dependencies of spectra I and II using the obtained parameters and Eq. (1) are plotted in Fig. 4 as solid and dotted curves, respectively. The angular dependencies of the spectra in the 6H polytype are very similar to those in the 4H SiC. Least-squares fits to the experimental data using the spin Hamiltonian (1) with an effective electron spin $S = \frac{1}{2}$ were performed. The obtained g-values and corresponding angles α for spectra I–III are also given in Table 1.

Table 1
The principal g-values of spectra I–III in 4H and 6H SiC. α is the angle between the principal z and the c-axis. The error in the g-values is about ± 0.0003

Spectrum	Polytype	g_x	g_y	g_z	α (deg)
I	4H	2.0162	2.0035	2.0412	63 ± 0.5
	6H	2.0161	2.0061	2.0407	63 ± 0.5
II	4H	2.0144	2.0029	2.0337	50 ± 0.5
	6H	2.0139	2.0048	2.0323	50 ± 0.5
III	6H	2.0075	2.0021	2.0452	65.7 ± 0.5

The symmetry of spectra I–III is low (C_1). This suggests that the associated defects are not isolated impurities. Substitutional impurities in hexagonal SiC polytypes often have trigonal symmetry (C_{3v}) or, in the cases of off-center defects such as the shallow boron [11], both trigonal and monoclinic (C_{1h}) symmetries corresponding to the defect occupying the hexagonal and cubic sites, respectively. The symmetry axes in those cases usually coincide with the directions of the Si–C bonds, i.e. are either parallel to the c-axis or make an angle of about 71° with it. The same may apply for the cases of substitutional impurity–vacancy pairs. In our case, the spectra were only observed after irradiation and their intensities increase with increasing the dose of irradiation. This also indicates that they are related to intrinsic defects. The low symmetry in this case also rules out the possibility of an anti-site defect, which should have the same symmetry as the substitutional impurities. Together with the hyperfine structure described above, it can be concluded that the silicon vacancy is involved in the defects.

Experimental data [2,6] and a recent calculation [12] showed that the silicon vacancy in the hexagonal polytypes is undistorted or has axial (C_{3v}) symmetry depending on its charge states. According to this calculation [12], the geometrical changes around a silicon vacancy in the case of the positive charge state ($S = \frac{1}{2}$) will lead to the axial symmetry for the silicon vacancy at both cubic and hexagonal sites. Since its ground state lies close to the maximum of the valence band [12], the center would be observable in p-type material over a wide temperature range. These do not agree with our observation. Spectra I–III have a lower symmetry (C_1) and can be detected in a very narrow temperature range. Therefore, these spectra are attributed to complex centers involving a silicon vacancy.

Under high-energy electron bombardment, vacancies and interstitials are created. In SiC, vacancies are stable at room temperature [1,2]. A part of the interstitials may be recaptured by nearby vacancies–leading to either the restoration of the lattice from damages or the creation of antisites. In addition to these dominant isolated defects, other types of complex centers such as divacancies or vacancy–interstitial pairs may be possible. Coupling between the vacancies often leads to the formation of vacancy pairs with the electron spin $S = 1$ and specific directions of the defect axis as detected in 6H SiC [4]. Their formation may be enhanced under annealing at elevated temperatures when the vacancies become mobile. In the samples irradiated at ~ 400°C, these spectra were not detected, but instead a carbon vacancy pair was observed. The electron spin, the symmetry and the formation conditions of the studied centers are clearly different from that of the divacancies. In both polytypes, spectra I–III were found to be partially quenched after keeping the samples at room temperature for a few weeks. These signals gradually decrease with increasing the annealing temperature and disappear at around 700°C, which is close to the anneal-out temperature of the silicon vacancy [1]. A complex center involving a vacancy and an interstitial (or an impurity at interstitial positions) is a possible model for these centers. In this case, the electron spin may be localized mainly at the silicon vacancy but not at the interstitial. The defect is then site sensitive as a substitutional center and may give rise to different spectra corresponding to different inequivalent lattice sites.

In 4H and 6H SiC samples irradiated with different doses, spectra I–III always appear together with similar intensity ratios and line shapes. A similarity in temperature dependence and annealing behavior is also observed for these spectra. As can be seen from Table 1, the principal g-values of these spectra in both polytypes are very similar. Therefore, it is suggested that these spectra belong to the same defect. Spectra I and II may correspond to the defect occupying the quasi-cubic and hexagonal sites, respectively. Spectrum III then corresponds to the defect at the other cubic site of the 6H SiC lattice.

In summary, we have observed two and three EPR spectra in electron-irradiated, p-type 4H and 6H SiC, respectively. All the spectra have the same symmetry (C_1) and an effective electron spin $S = \frac{1}{2}$. A paired center between a silicon vacancy and an interstitial (or an impurity at an interstitial position) is a possible model of the defects. Based on the similarity in the electronic structure, annealing behavior, temperature dependence and formation conditions, these spectra are suggested to belong to the same defect, which occupies different inequivalent lattice sites in 4H and 6H SiC.

Acknowledgements

Support for this work was provided by the Swedish Research Council for Engineering Sciences (TFR), the Swedish Natural Science Research Council (NFR), the SSF program SiCEP and ABB Corporate Research.

References

[1] H. Itoh, A. Kawasuso, T. Ohshima, M. Yoshikawa, I. Nashiyama, S. Tanigawa, S. Misawa, H. Okumura, S. Yoshida, Phys. Stat. Sol. A 162, (1997) 173, and reference therein.
[2] J. Schneider, K. Maier, Physica B 185 (1993) 199.
[3] L.A. de S. Balona, J.H.N. Loubser, J. Phys. C 3 (1970) 2344.
[4] V.S. Vainer, V.A. Ilin, Sov. Phys. Solid State 23 (1981) 2126.
[5] E. Sörman, N.T. Son, W.M. Chen, O. Lindström, J.L. Kordina, E. Janzén, in: The Physics of Semiconductors, World Scientific, Singapore, 1996, p. 2649.
[6] T. Wimbauer, D. Volm, B.K. Meyer, A. Hofstaetter, A. Scharmann, in: The Physics of Semiconductors, World Scientific, Singapore, 1996, p. 2645.
[7] E. Sörman, N.T. Son, W.M. Chen, C. Hallin, J.L. Lindström, E. Janzén, Mater. Sci. Forum 258 (1997) 685.
[8] D. Cha, H. Itoh, N. Morishita, A. Kawasuso, T. Ohshima, Y. Watanabe, J. Ko, K. Lee, I. Nashiyama, Mater. Sci. Forum 264 (1998) 615.
[9] N.T. Son, W.M. Chen, J.L. Lindström, B. Monemar, E. Janzén, Mater. Sci. Eng. B. 61–62 (1999) 202.
[10] N.T. Son, W.M. Chen, J.L. Lindström, B. Monemar, E. Janzén, Phys. Scripta T 79 (1999) 46.
[11] T. Matsumoto, O.G. Poluektov, J. Schmidt, E.N. Mokhov, P.G. Baranov, Phys. Rev. B 55 (1997) 2219.
[12] A. Zywietz, J. Furthmüller, F. Bechstedt, Phys. Rev. B 59 (1999) 15166.

ELSEVIER

Physica B 273–274 (1999) 659–662

PHYSICA B

www.elsevier.com/locate/physb

Effective mass donors in silicon carbide — a study with electron nuclear double resonance

S. Greulich-Weber*, M. März, J.-M. Spaeth

Department of Physics, University of Paderborn, Warburger Strasse 100, 33095 Paderborn, Germany

Abstract

With electron nuclear double resonance the superhyperfine interactions of numerous ^{29}Si and ^{13}C lattice neighbours of ^{14}N donors in 3C and 4H–SiC have been measured. It was attempted to explain them using the effective mass theory (EMT). The interactions of N donors on cubic sites in 3C–SiC can be well explained with EMT assuming N to be on C sites, but not on Si sites. N in 3C–SiC represents probably the only true EMT donor, since for shallow donors in Si EMT is not sufficient as shown previously. The interactions of N on the hexagonal sites in 4H–SiC are still reasonably well explained, while the EMT approach fails to explain N on the quasi-cubic sites. Comparison between 3C–SiC and 4H–SiC shows that the "central cell corrections" due to the chemical nature of N introduced into EMT previously for silicon is very small. The major contribution comes from inter-valley interactions.

Keywords: Effective mass theory; ENDOR; Nitrogen donor; Silicon carbide

1. Introduction

It seems common place to regard shallow donors in semiconductors as sufficiently well understood by the effective mass theory (EMT) according to which the donor electron moves in a hydrogenic orbit, which is extended due to screening effects of the electronic atomic cores of the crystal lattice. The donor ionisation level and the effective Bohr radius are determined by the effective masses and the dielectric constant. However, already when trying to explain the ionisation levels and hyperfine (hf) interactions of P, As and Sb in Silicon, it was necessary to introduce the so-called "central cell correction" [1], which took the "chemical" nature of the donors into account in order to explain the ground state ionisation level and the hf interactions. Subsequent investigations with electron nuclear double resonance (ENDOR), in which also the superhyperfine (shf) interactions with a large number of ^{29}Si lattice neighbours could be resolved [2,3] showed that the EMT approach including central cell corrections failed and a pseudo-potential method gave better agreement with experiment [3]. Thus, strictly speaking, so far no real effective mass shallow donor has been observed.

Silicon carbide is an indirect semiconductor with the conduction band minima not at $k = 0$ as the silicon, but it provides in addition, a unique opportunity to study the same shallow donor on various inequivalent lattice sites because of its polytypism. Thus, one can investigate whether the central cell correction due to the chemical nature, as assumed in silicon, is similar here – it would be identical for all sites – or whether the so-called "inter-valley interaction" is more important. Recently, the different hf interactions for ^{14}N on inequivalent lattice sites in various polytypes of SiC have been discussed in the framework of EMT. Empirically, a linear correlation between the valley-orbit splittings observed experimentally by IR spectroscopy and the isotropic ^{14}N hf interactions has been detected [4]. In order to obtain more information on the electronic structure of the ^{14}N donors, an ENDOR investigation of ^{14}N donors in 3C–SiC and 4H–SiC was performed. In the cubic 3C–SiC

* Corresponding author. Tel.: + 49-5251-60-2740; fax: + 49-5251-60-3247.

E-mail address: greulich-weber@physik.uni.paderborn.de (S. Greulich-Weber)

0921-4526/99/$ - see front matter
PII: S0921-4526(99)00598-0

Table 1
g Values, hf and quadrupole interaction constants, ionisation levels E_D and valley-orbit splittings Δ"VO" for N donors in 3C–SiC and 4H–SiC

	Site	E_D/meV	Δ"VO"/meV	$g_\parallel$	$g_\perp$	a/h (MHz)	b/h (MHz)	q/h (MHz)
3C	k	54.2	8.34	2.0050[a]	2.0050	3.494	0.000	0.000
4H	h	91.8	7.6	2.0055[b]	2.0010	2.757	0.081	0.020
	k	52.1	45.5	2.0043[b]	2.0013	51.019	0.006	0.010

[a]After Ref. [13].
[b]After Ref. [14].

there is only one cubic site for N, while in 4H–SiC there is one quasi-cubic (k) and one hexagonal site (h). The ionisation level of N in 3C–SiC at E_{CB}-54.2 meV [5] is approximately as shallow as that of N on the h site in 4H–SiC (E_{CB}-52.1 meV), while N on the k site in 4H–SiC is much deeper (E_{CB}-91.8 meV) [6]. The hf interactions are similar for N in 3C–SiC as for N on the h site in 4H–SiC, while that of N on the k site is about a factor of 16 larger, which already shows that a simple EMT picture cannot apply [4].

We show from our ENDOR investigation that the N donor in 3C–SiC can be explained very well with an effective mass theory. It is probably the only donor known so far which has this property. In 4H–SiC this approach already breaks down.

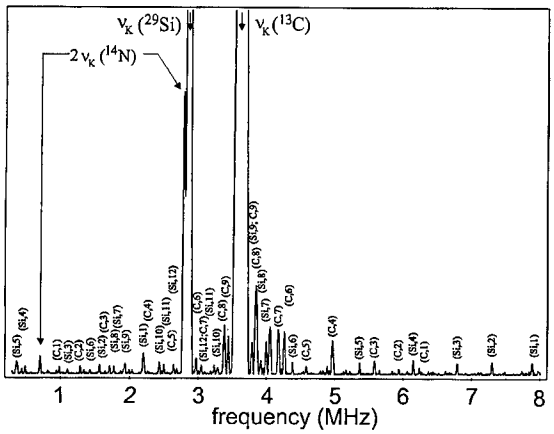

Fig. 1. ENDOR lines of ^{14}N donor in 3C–SiC measured at 4.2 K for $B\|[c]$.

2. Experimental results

EPR and ENDOR measurements were performed at 9.5 GHz and 4.2 K with a computer-controlled custom-built spectrometer. The samples of 3C–SiC and 4H–SiC were Lely-grown and doped with nitrogen during growth. The concentration was estimated to be $N_D \times 10^{18}$ cm^{-3} [7]. In Table 1 the EPR results are collected. The ^{14}N hf interaction is given in terms of the isotropic constant a/h and the anisotropic hf constant b/h (for axial symmetry), which are related to the hf interaction tensor A by

$$A_{zz} = a + 2b, \quad A_{xx} = A_{yy} = a - b. \tag{1}$$

Similarly, the quadrupole interaction constant q/h is related to the quadrupole tensor Q for axial symmetry by

$$Q_{zz} = 2q, \quad Q_{xx} = Q_{yy} = -q. \tag{2}$$

ENDOR spectra were recorded for $B\|[1\,1\,1]$ in 3C–SiC and for $B\|$ to the c-axis in 4H–SiC.

Fig. 1 shows an example of ENDOR spectra of N in 3C–SiC. There are numerous lines up to 8 MHz which belong either to ^{29}Si ($I = \frac{1}{2}$, 4.7% abundance) or to ^{13}C ($I = \frac{1}{2}$, 1.11% abundance) lattice neighbours and to the central ^{14}N nucleus ($I = 1$, 100% abundance). The ENDOR frequencies for each nucleus i are given in perturbation theory of first order by [8]

$$\nu_{ENDOR} = \frac{1}{h}|m_s A_i - \nu_{K,i}|, \tag{3}$$

where A_i is the shf (hf) interaction constant, $m_s = \pm\frac{1}{2}$ the electron spin quantum number and $\nu_{K,i}$ the Larmor frequency of the free nucleus i. The assignment of the lattice nuclei was made using Eq. (3). If $A_{i/2} > \nu_{K,i}$, because of $m_s = \pm\frac{1}{2}$, two lines separated by $2\nu_{K,i}$ are observed (see ^{14}N lines in Fig. 1). If $A_i/2 < \nu_{K,i}$, two lines symmetrical about $\nu_{K,i}$ are measured. The strongest lines are the so-called "distant" ENDOR lines of ^{29}Si and ^{13}C. In Fig. 1 for each line the assignment to a given specific nucleus or shell is indicated (for shell assignments see below). The ENDOR spectra for all lines in 3C–SiC and most of the lattice neighbour lines in 4H–SiC show no angular dependence. The largest interaction measured for ^{29}Si in 4H–SiC was 9.39 MHz. In 4H–SiC, because of bad signal-to-noise ratio in spite of long integration and accumulation times, it is possible that further lines exist between 10–40 MHz which could not be measured. The

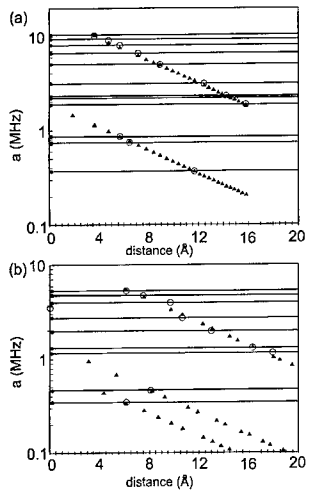

Fig. 2. (a) Experimental (full circles) and calculated (full triangles) ^{13}C shf interactions of ^{14}N donors in 3C–SiC as a function of shell distances. λ was fitted to be 236. Open circles represent those ^{13}C shells to which a measured shf interaction could be assigned; (b) Experimental (full circles) and calculated (full triangles) ^{29}Si shf interactions as a function of shell distances. λ was fitted to be 2100. Open circles and squares represent those ^{29}Si shells which could be assigned to measured shf interactions. The squares represent ENDOR lines which could not unambiguously be identified as ^{29}Si lines because of bad signal-to-noise ratio.

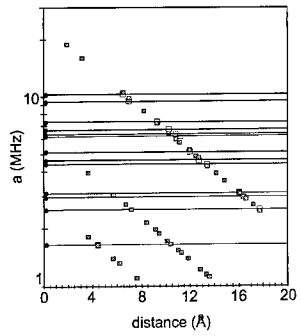

Fig. 3. Experimental (full cirlces) and calculated (full squares) ^{29}Si shf interactions as a function of shell distances. λ was fitted to be 1337. Open squares represent ^{29}Si shells which could be assigned to measured shf interactions. For distances < 5 Å, see text.

experimental shf data for 3C–SiC are presented in Figs. 2a and b, some for 4H–SiC in Fig. 3. The exact values can be found in Ref. [7]. Unlike in silicon [2,3], no anisotropic shf interactions could be detected in 3C–SiC, which would have enabled one to assign certain interactions to certain lattice shells from the ENDOR angular dependence by symmetry arguments. In 4H–SiC only some large interactions show some anisotropy, but not more than 0.1 MHz, which is not sufficient to assign shells.

3. Discussion

According to EMT the wave function of a shallow donor in an indirect semiconductor is the superposition of an expansion of Bloch functions on the conduction band (CB) minima at $\boldsymbol{k}_0$ [1,7]. The ground state 1 s is described by a hydrogenic wave function with an effective Bohr radius

$$a_{\mathrm{B,eff}} = \frac{\varepsilon m_0}{m^*} 0.529\,(\text{Å}) \tag{4}$$

and an ionisation level at

$$E_{\mathrm{EMT}} = E_{\mathrm{CB}} - \frac{m^*}{\varepsilon^2} 13.6\,(\mathrm{eV}). \tag{5}$$

In 3C–SiC and 4H–SiC there are 3 CB minima. The inter-valley interaction splits the ground state into three states, one with A_1 and two with E symmetry [1]. For the calculations we used $\varepsilon = 9.72$ for 3C–SiC and $\varepsilon = 9.84$ for 4H–SiC, which is the geometrical average of $\varepsilon_{\parallel}$ and $\varepsilon_{\perp}$. The effective mass values $m^*/m = 0.3$ for 3C–SiC and 0.19 for 4H–SiC were used according to Refs. [9] and [10]. Including a correction after Faulkner [11] taking the anisotropy of the effective masses into account, the ground state energy E_{EMT} for 3C–SiC was obtained to be 47.2 meV in rather good agreement with experiment (54.2 meV), while $E_{\mathrm{EMT}} = 27.6$ meV for 4H–SiC, which deviates considerably from the values $E(A_1, \mathrm{h}) = 52.1$ meV and $E(A_1, \mathrm{k}) = 91.8$ meV, demonstrating the importance of the inter-valley interaction for the A_1 ground state. The excited states are better explained in Ref. [7]. For the hf interaction calculation following Kohn [1], the effective Bohr radius of the hydrogenic function was "adjusted" to the experimentally observed E_{EMT} energies by

$$a_{\mathrm{B,eff}}^{\mathrm{Corr}} = a_{\mathrm{B,eff}} \left(\frac{E_{\mathrm{EMT}}}{E_{\mathrm{exp}}} \right)^{1/2}. \tag{6}$$

The following effective Bohr radii were obtained: 14.2 Å for 3C–SiC and 19.9 Å for the h site in 4H–SiC and 15.0 Å for the k site in 4H–SiC. For the calculation of the isotropic hf/shf constants one has [8]

$$a(r_1) = \frac{2}{3} \mu_0 g_e \mu_B g_n \mu_n |\Psi(r_1)|^2. \tag{7}$$

With Eq. (6) one obtains

$$a(r_1) = \frac{2}{3} \mu_0 g_e \mu_B g_n \mu_n \cdot \lambda |S(r_1)|^2 \frac{1}{\pi a_{\mathrm{B,eff}}^3} \mathrm{e}\left(\frac{-2r_1}{a_{\mathrm{B,eff}}} \right) \tag{8}$$

The factor λ has been introduced replacing the unknown amplitude of the Bloch functions. It was determined from the experimental values (see below). The Kohn–Luttinger interference factor $S(r)$ [1] was calculated taking the crystal symmetry into account following Patrick [12].

$S(r)$ causes the variation of the hf interactions in space and is responsible for the some-times large differences from shell to shell. It depends decisively on the position of the conduction (CB) minimum in k space (see Refs. [1,7]). Fig. 2a and b show the comparison with experiment for 3C–SiC where only λ had to be adjusted to the experimental values. Since we could not assign certain a-values to certain shells from experiment, the experimental values (solid circles) are represented on the left-hand side of the diagram and the values are compared to the calculated ones (solid triangles) by horizontal lines. λ was adjusted such that the difference between experimental and calculated values was minimal for those shells which could be assigned (open circles). In particular for the smaller values of a/h, the difference between the values of subsequent shells is so small that no decision was possible as to which shell the experimental value could be assigned. In these cases the horizontal lines are drawn to the right-hand side. We find good agreement between experimental and calculated values in 3C–SiC for the larger ^{29}Si and ^{13}C interactions as well as for the central ^{14}N nucleus (3.7 MHz calculated, 3.5 MHz measured). In the calculation it was assumed that N is on a C site. When placing N on a Si site, the agreement is much worse. In particular, the theoretical value of a/h for ^{14}N is three times the experimental value. Thus, the calculation supports the assumptions made previously that normally N replaces C. There are also more ^{29}Si interactions resolved than ^{13}C ones, which is expected for N on a C site from the Kohn–Luttinger factor [7].

The agreement between calculated and measured shf interactions in 4H–SiC for the hexagonal site is not as good as the one in 3C–SiC, but not bad either [7]. The calculated value of a/h for ^{14}N is 3.2 MHz and thus slightly bigger than the experimental one (2.8 MHz). The reason for this can be that there is some admixture from the next excited E state, which has a node on the N site and causes also a small anisotropy of the N hf interaction (Table 1) (see also Ref. [4] for further details). In comparison with the quasi-cubic site (k), the valley-orbit splitting is small enough (Table 1) to allow this admixture, which is practically zero in the case of the k-site. For the quasi-cubic site, the large number of ^{29}Si shf interactions measured (Fig. 3) can only be explained with the assumption that we have failed to measure the ENDOR lines of the nearer ^{29}Si shells (probably due to the very weak or very bad signal-to-noise ratio). In EPR at 10 K an anisotropic ^{29}Si shf doublet is resolved with $a/h = 40 \pm 1$ MHz. An estimate from the inhomogeneously broadened line width reveals that interactions up to 25 MHz may be hidden in the line width. Thus, the corrected Bohr radius according to Eq. (6) seems to describe well the asymptotic behaviour of the wave function, but not the more central part at distances smaller than 5 Å. In accordance with this the calculated value for a/h of ^{14}N is only 3.5 MHz compared to the experimental value one of 51 MHz, a typical result for the failing EMT approach also found in silicon. Here, apparently a central cell correction including mainly the valley-orbit splitting is needed. The part due to the "chemical nature" seems to be very small, since otherwise the good agreement in 3C–SiC would have not been possible. There, the deviation of the EMT value for the ground state energy is only 7 meV, very small in comparison to the gap energy of 2.9 eV. Thus, the central cell correction due to chemical shift for N must be very small. Therefore in SiC it must be concluded that the major contribution for any central cell corrections must come from the inter-valley interactions. It seems that only one "true" EMT donor has so far been identified and that is N on the C site in 3C–SiC.

References

[1] W. Kohn, in: Solid State Physics Vol. 5, S. 257ff., Academic Press, New York, 1957.
[2] E.B. Hale, R.L. Mieher, Phys. Rev. 184 (3) (1969) 739–759.
[3] J.L. Ivey, R.L. Mieher, Phys. Rev. B 11 (2) (1974) 822–848.
[4] S. Greulich-Weber, Phys. Stat. Sol. A 162 (1997) 95–151.
[5] W. Kohn, J.M. Luttinger, Phys. Rev. 98 (4) (1955) 915.
[6] W.J. Choyke, D.R. Hamilton, L. Patrick, Phys. Rev. 133 (4A) (1964) 1163.
[7] M. März, Doctoral Thesis, University of Paderborn, 1999.
[8] J.-M. Spaeth, R.H. Bartram, J.R. Niklas, Structural Analysis of Point Defects in Solids, Solid State Series 43, Springer, Berlin, 1992.
[9] C. Persson, U. Lindefelt, J. Appl. Phys. 82 (11) (1997) 5496.
[10] P. Käckell, B. Wenzien, F. Bechstedt, Phys. Rev. B 50 (15) (1994) 10761.
[11] R.A. Faulkner, Phys. Rev. 184 (3) (1969) 713.
[12] L. Patrick, Phys. Rev. B 5 (6) (1972) 2198.
[13] W.E. Carlos, in: G.L. Harris (Ed.), Properties of Silicon Carbide, Vol. 13, INSPEC IEE, 1995.
[14] E.N. Kalabukhova, S.N. Lukin, B.D. Shanina, E.N. Mokhov, Sov. Phys. Solid State 32 (3) (1990) 465.

ELSEVIER

Physica B 273–274 (1999) 663–666

PHYSICA B

www.elsevier.com/locate/physb

Zeeman spectroscopy of the neutral silicon vacancy in 6H and 4H SiC

Mt. Wagner[a,*], B. Magnusson[a], E. Sörman[b], C. Hallin[b], J.L. Lindström[c], W.M. Chen[a], E. Janzén[a]

[a]*Department of Physics and Measurement Technology, Linköping University, S-581 83 Linköping, Sweden*
[b]*ABB Corporate Research, S-721 78 Västerås, Sweden*
[c]*Swedish Defense Research Establishment, Box 1165, S-581 11 Linköping, Sweden*

Abstract

High-resolution photoluminescence (PL) and PL excitation (PLE) spectroscopy has been employed to reveal the electronic structure of the neutral silicon vacancy in 6H and 4H SiC. The defect gives rise to characteristic PL emissions with three no-phonon lines in 6H SiC and two in 4H SiC at around 1.4 eV. All of the no-phonon lines are shown to arise from transitions between singlet ($S = 0$) excited states and singlet ground states. Nevertheless, optically detected magnetic resonance (ODMR) signals typical for a spin triplet ($S = 1$) configuration can be obtained when monitoring the emission under resonant excitation. This observation can be explained by non-radiative recombination via a lower lying excited triplet state. In strained samples all no-phonon PL lines are split into a series of lines. For the highest energy lines the main splitting can be attributed to lifting of the orbital degeneracy of the excited states, the additional broadening or splitting is probably due to a strain distribution in the samples.

Keywords: Silicon carbide; Intrinsic defects; Magneto-optical spectroscopy

1. Introduction

Vacancies are among the primary defects introduced during bombardment of semiconductors with high-energy particles. They can also be incorporated under non-optimized growth conditions and during device processing such as ion implantation. Their presence has been shown both theoretically and experimentally to introduce defect levels in the forbidden energy bandgap in SiC. They therefore influence significantly the electrical and optical properties of the material and thus the performance of various devices. Though the importance of the vacancies has long been recognized, our understanding of their properties is still poor.

The aim of this work is to gain a better understanding of the electronic structure of the neutral silicon vacancy in 6H and 4H SiC, by employing magneto-optical spectroscopy. The samples used were CVD-grown free-standing epi-layers ($\sim 70\,\mu m$ thick) with low n-type doping (mid $10^{14}\,cm^{-3}$). Vacancies were created in the high-purity samples by irradiation with 2.5 MeV electrons at room temperature with a dose of $10^{17}\,cm^{-2}$. The luminescence was excited with a tunable Ti : Sapphire laser, and the spectra were recorded either through a SPEX 0.85 m double grating monochromator with a liquid-nitrogen cooled Ge-detector (model North Coast) attached at the exit slit or with a BOMEM FTIR spectrometer using a Ge-detector or a Si-avalanche photodiode. In PLE experiments the detection wavelength was fixed to typically 1.2 eV (i.e. at the maximum intensity of the phonon-assisted sideband) and the excitation wave-length of the Ti : Sapphire laser was varied. For the Zeeman experiments an Oxford split-coil superconducting magnet with optical access from all sides producing fields up to 5 T was used.

* Corresponding author. Fax: + 46-13-142337.
E-mail address: matwa@ifm.liu.se (Mt. Wagner)

0921-4526/99/$ - see front matter
PII: S0921-4526(99)00599-2

2. Results and discussion

We have revealed earlier that the neutral silicon vacancy gives rise to characteristic photoluminescence (PL) emissions with three no-phonon lines in 6H SiC and two in 4H SiC [1,2] around 1.4 eV. PL spectra of both polytypes are shown in Fig. 1 for easy reference. The number of PL lines corresponds to the number of inequivalent sites of point defects in each polytype. The identification of the defect was obtained through the resolved hyperfine interactions with the ligand atoms in optically detected magnetic resonance (ODMR) of the PL emissions. In these experiments a spin-triplet was observed under resonant excitation of the no-phonon line [1,2].

High-resolution spectroscopy reveals that in strained samples all of the no-phonon lines exhibit a fine structure. The highest energy line V1 in both polytypes consists of two main lines V1 and V1′, each of which has a shoulder on the high-energy side. This shoulder is also observed for V2 and V3 in 6H SiC (Fig. 2) and V2 in 4H SiC.

Zeeman experiments were performed in order to determine whether the triplet observed in ODMR is directly involved in the emission or indirectly as a non-radiative recombination channel. Fig. 2 shows PL spectra of the 6H polytype at 12 K without magnetic field and at 5 T. Even though the line width of typically 0.4 meV or better is smaller than the expected splitting of ~ 0.6 meV between two Zeeman split magnetic sublevels, no splitting or broadening of any of the lines at any angle between $B\|c$-axis and $B\perp c$-axis is observed.

Similarly PLE spectra have been recorded with and without magnetic field. In Fig. 3, the results of such experiments for 6H SiC are displayed. Again there is no splitting of any of the lines. Identical results have been obtained in 4H SiC in Zeeman PL and PLE measurements. From these experiments it can be concluded that both the excited states and the ground state involved in the radiative recombination are spin-singlet states for all inequivalent sites in both polytypes.

In order to understand the nature of the fine structure of the no-phonon lines the temperature dependence and the polarization of the various lines has been studied. In Fig. 4 PL spectra of 6H SiC are shown at 2 and 50 K. Clearly V1 and V1′ are thermalized, proving that V1′ is

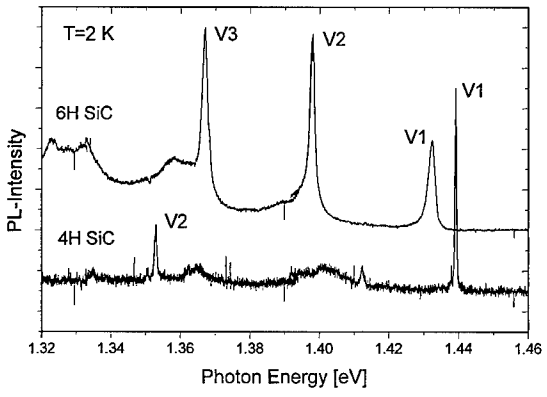

Fig. 1. Photoluminescence (PL) spectra of the neutral silicon vacancy in 6H SiC (upper curve) and 4H SiC (lower curve) at 2 K. The spectrum consists of three no-phonon lines in 6H SiC and two no-phonon lines in 4H SiC followed by a phonon structured side band. The number of lines corresponds to the number of inequivalent lattice sites in both polytypes.

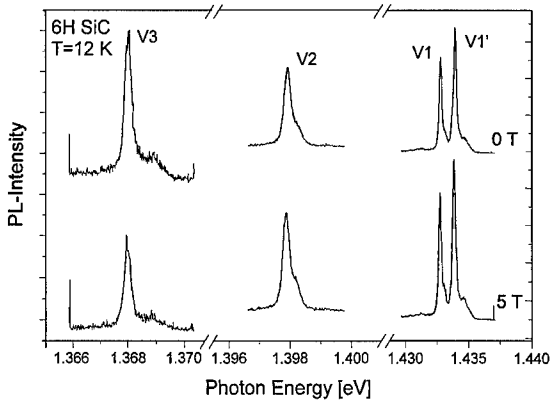

Fig. 2. High-resolution PL spectra at 12 K of the three no-phonon lines in 6H SiC without magnetic field (upper curve) and in a magnetic field of 5 T applied approximately 10° off the c-axis (lower curve). None of the lines split in the field, proving that both the excited states and the ground state are spin-singlets. All main lines are accompanied by shoulders on the high-energy side.

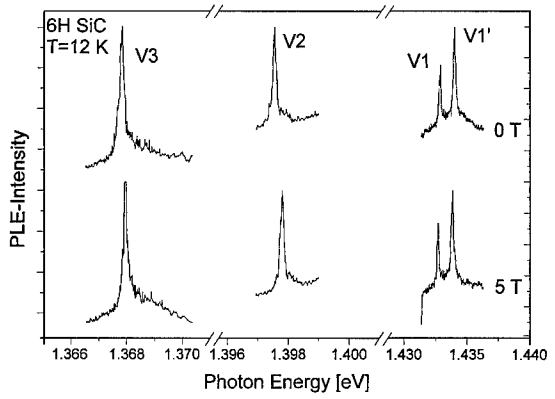

Fig. 3. PLE spectra of 6H SiC at 12 K detected in the phonon band at 1.21 eV with and without magnetic field. The absence of any splitting shows that the states involved in the transition are spin-singlets.

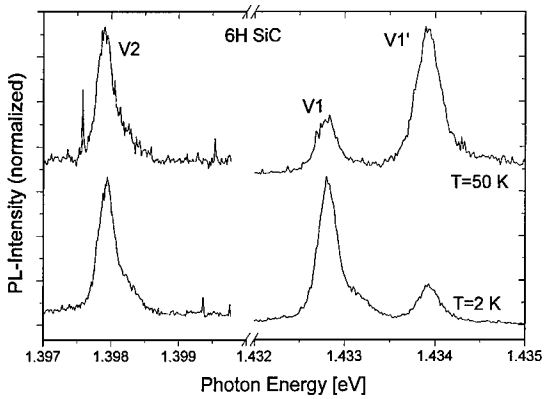

Fig. 4. Temperature dependence of V1 and V2 in 6H SiC. Carriers are redistributed between the two excited states giving rise to V1 and V1′ at elevated temperatures. The shoulder at the high-energy side of the no-phonon lines does not thermalize with the main line. As an example V2 is shown at two temperatures.

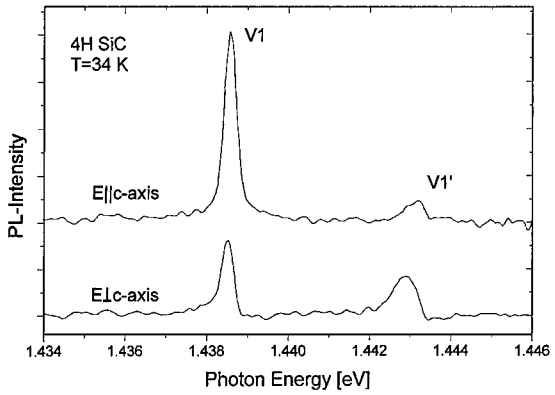

Fig. 5. Polarization spectra of V1 and V1′ in 4H SiC at 34 K. V1 is mainly polarized along the *c*-axis, whereas V1′ is stronger perpendicular to the *c*-axis. This behavior can be explained by a lifting of the orbital degeneracy of the level by strain.

due to a higher lying excited state of the same defect center than the one giving rise to V1. No such thermalization occurs in PLE experiments, confirming that the transitions V1 and V1′ are between two closely lying excited singlets to the singlet ground state.

V1 and V1′ exhibit different polarization (Fig. 5). V1 is mainly polarized parallel to the *c*-axis, whereas V1′ is stronger perpendicular to the *c*-axis. This can result from a different electronic character of the orbital states related to the two excited states. A possible explanation for the strain induced splitting between V1 and V1′ is then a lifting of their orbital degeneracy by the strain.

All main lines exhibit an additional shoulder on the high-energy side. An example of this is shown for line V2 in 6H SiC in Fig. 4 at two different temperatures. The strength of the shoulder relative to the main line depends on the angle of detection and/or excitation. In any case its intensity does not increase relative to the main line at elevated temperature. Even in PLE experiments there is no redistribution of intensity between the main line and the shoulder for any of the no-phonon lines.

Since the additional shoulders on the no-phonon lines do not thermalize with the main lines neither in the PL nor in the PLE experiments, they cannot be due to the levels lying close to the excited state or the ground state of the same defect. In the thin free-standing epilayers used in this study we certainly have a strong distribution of strain due to the glue used for mounting the samples on the sample holder. It has been shown before that the exact energetic position of the no-phonon lines varies strongly with strain [3], so we can expect a distribution of various line positions in our samples. Nevertheless, we would rather expect a broadening of the lines in this case and not well-defined shoulders. An alternative explanation could be that the strain is rather uniform, but it is sufficient to lift an existing orientational degeneracy of the defect. In this case however the symmetry of the defect has to be lower than C_{3v} for a simple, undistorted Si monovacancy. Further studies are necessary to clarify this point.

3. Electronic structure and recombination model

The Zeeman experiments clearly showed that both the excited states and the ground state of the defect involved in the radiative transitions are spin-singlet levels. A successful model of the electronic structure of the defect has to explain why an ODMR signal of a spin-triplet level can be detected via this recombination even under selective excitation of the no-phonon line. In Fig. 6, a possible model is sketched similar to the one proposed for a defect in silicon [4]. The ground state of the defect is a singlet and there are excited singlet states. Radiative recombination occurs between these singlet levels. There exists also a spin-triplet excited state at lower energy than the excited singlets. The radiative recombination via this triplet is spin-forbidden, resulting in a long recombination time of the level. Whenever a carrier instead of recombining directly from the singlet excited state to the ground state relaxes to the triplet level, it is trapped there for a long time and the defect cannot participate any more in the emission. Microwave-induced transitions between the magnetic sublevels of the triplet can change the effective recombination time of the triplet, and this will influence the luminescence intensity of the singlet-to-singlet transition.

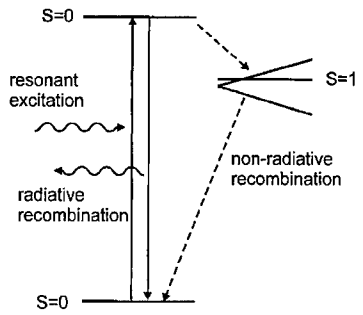

Fig. 6. Model explaining the observation of a spin-triplet ODMR signal via a singlet to singlet radiative recombination. The triplet is a lower lying excited state. The radiative recombination via this level is spin-forbidden, thus representing a bottleneck for the recombination. Microwave-induced transitions between the magnetic sublevels of the triplet state change the recombination rate via the triplet. This affects the luminescence intensity of the singlet to singlet transition indirectly.

The observation of a singlet ground state of the neutral silicon vacancy in SiC is in contrast to theoretical calculations predicting a triplet ground state [5], and calls for a close examination of the theoretical models and also the interpretation of the earlier experiments.

References

[1] E. Sörman et al., in: M. Scheffler, R. Zimmermann (Eds.), Proceedings of the 23rd International Conference on the Physics of Semiconductor, World Scientific, Singapore, 1996, p. 2649.
[2] E. Sörman et al., Mater. Sci. Forum 258 (1997) 685.
[3] A. Niilisk et al., Solid State Commun. 94 (1995) 71.
[4] K.M. Lee et al., Phys. Rev. Lett. 48 (1982) 37.
[5] A. Zywietz et al., Phys. Rev. B 59 (1999) 15166.

ELSEVIER

Physica B 273–274 (1999) 667–671

PHYSICA B

www.elsevier.com/locate/physb

Electron paramagnetic resonance of the scandium acceptor in 4H and 6H silicon carbide

J.-M. Spaeth[c], S. Greulich-Weber[a,*], M. März[a], E.N. Mokhov[a], E.N. Kalabukhova[b]

[a]*Department of Physics, University of Paderborn, 33095 Paderborn, Germany*
[b]*Ioffe Physico-Technical Institute, St. Petersburg, Russia*
[c]*Institute of Semiconductors, Kiev, Ukraine*

Abstract

In Sc-doped 6H–SiC epitaxial layers we observed several different electron paramagnetic resonance (EPR) spectra with a ^{45}Sc hyperfine interaction pattern. The spectra are explained as being due to the isolated $Sc^0(S = \frac{1}{2})$ acceptor on carbon sites but with different microscopic configurations. The spectra show a pronounced temperature dependence. At low temperatures the hole of the Sc^0 acceptor is located in a Sc^0–Si bond either along the *c*-axis forming an axial centre or along one of the three other C–Si bonds giving rise to a monoclinic centre. At higher temperature the hole changes place rapidly between the three Sc–Si bonds resulting in an axial centre. All three Sc^0 hole configurations have different ionisation levels. The ionization level of the low-temperature monoclinic–high-temperature axial centre is significantly influenced by an entropy term. In 4H–SiC spectra were only observed from a single Sc^0 centre with monoclinic symmetry.

Keywords: Silicon carbide; Scandium; EPR

1. Introduction

It is known that transition metal ions, such as in silicon, play an important role in silicon carbide too. In SiC only a few of such impurities were investigated, very few were identified by means of structure sensitive methods. Recently, the microscopic and electronic structure of the Sc impurity in SiC turned out be a controversial issue [1–3]. Sc is expected to act as an acceptor in SiC [4]. 6H–SiC doped with Sc was first investigated with photoluminescence showing a luminescence band with an onset at about 2.55 eV and a maximum at about 2.2 eV [4]. With electron paramagnetic resonance (EPR) detected via the photoluminescence (PL-EPR) several EPR lines were observed, but no hyperfine (hf) structure was resolved [1,3], leaving the origin of the observed lines open. With conventional EPR up to four different EPR spectra were reported for 6H–SiC, measured at different temperatures and all having the typical ^{45}Sc hf splitting of octets [2,3]. It was argued that these spectra have to be explained assuming two Sc defects [3]. In one EPR spectrum a resolved ^{29}Si superhyperfine (shf) interaction was found, from which it was concluded, that Sc replaces C [2] in contrast to other speculations that Sc occupies a Si site [3]. In order to further clarify the structure of the Sc acceptors, we present a new EPR investigation of the Sc acceptor at various temperatures, mainly in 6H–SiC, but also a few measurements in 4H–SiC.

2. Experimental

6H- and 4H–SiC epitaxial layers were grown on 6H- and 4H–SiC single crystal substrates, respectively, by a sublimation sandwich method [1,2] and doped with Sc during the growth. The measured sample contained the

* Corresponding author. Tel.: + 49-5251-60-2740.
E-mail address: greulich-weber@physik.uni-paderborn.de (S. Greulich-Weber)

0921-4526/99/$ - see front matter
PII: S0921-4526(99)00600-6

epitaxial layer with a Sc concentration of the order of $(1–3) \times 10^{17}$ cm^{-3} and an unknown degree of compensation with N. The n-type substrate contains N donors, which were seen in the EPR spectra.

3. Experimental results

In 6H–SiC an X-band EPR spectrum with axial symmetry about the c-axis was measured, which was published previously by the authors [2, Figs. 1 and 2]. It was reinvestigated in this study because of the controversial discussions about the microscopic structure of the Sc acceptor [2,3]. The spectrum could be observed between 4.2 and 70 K with signal intensities depending on temperature and illumination. In K-band three sets of eightfold split spectra were resolved (Fig. 1 in ref. [2]), while in X-band only one octet was resolved at slightly lower temperature under the same conditions otherwise (see Fig. 2 in Ref. [2] and Fig. 3). The eightfold split EPR lines were explained with an effective spin of $S = \frac{1}{2}$ and an anisotropic hf interaction of a 100% abundant nucleus with $I = \frac{7}{2}$ such as ^{45}Sc. The three octets observed in K-band were assigned to the three inequivalent defect sites in 6H–SiC (two quasi-cubic sites (k_1 and k_2) and one with hexagonal symmetry (h)). The hf parameters and g tensors are given in Table 1 (spectrum B, sites I–III). The three octets of sites I–III show only slightly different g tensors and very similar hf parameters indicating that Sc is in a very similar configuration on all three sites. An assignment to the specific sites k_1, k_2 and h could not be made. The axial Sc centre is not seen at low temperatures ($T < 15$ K) in the dark, but appears upon illumination with the above band gap light.

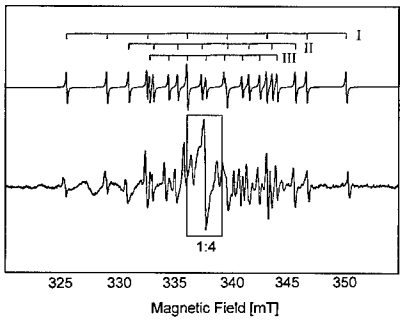

Fig. 1. Upper curve: EPR spectrum of defect A for $B \| c$-axis calculated with the parameters given in Table 1. Lower curve: EPR spectrum of Sc-doped 6H–SiC (X-band, $T = 4.5$ K) measured in the dark for $B \| c$. The central part of the spectrum shows the triplets of the N donors and is reduced by a factor of four for the sake of clarity.

Two small satellite lines measured symmetrically about the ^{45}Sc hf EPR lines (Figs. 1 and 2 in ref. [2] and Fig. 3) were previously analysed by März et al. [2]. It was concluded that these satellite lines are due to four equivalent nearest-neighbour Si nuclei (equivalent within the line width) and that therefore Sc is on a C site, in contrast to recent speculations that Sc resides on a Si site [3]. The analysis of März et al. [2] was checked again on the basis of new measurements confirming the previous results.

Below 15 K the axial spectrum B disappears in the dark and can only be measured under above band gap illumination. Yet another EPR spectrum is measured (Fig. 1, lower curve), which shows six octets corresponding to six defect orientations with different splittings. The eightfold splitting of each spectrum is again associated with Sc. Fig. 1 shows three octets which are seen for $B_0 \| c$. The symmetry observed is monoclinic, which made it necessary to measure the angular dependence in two planes ((1 1 $\bar{2}$ 0) and (0 0 0 1)) in order to determine

Table 1
Principal values of g tensors and hf tensors of Sc defects measured in 6H- and 4H–SiC at different temperatures

Polytype	Spectrum		Temperature (K)	Symmetry	g_{xx}	g_{yy} ($g_\|$)	g_{zz}	A_{xx}/h (MHz)	A_{yy}/h (MHz)	$A_{zz}/h(A_\|/h)$ (MHz)
	A		< 15	Monoclinic	1.999	1.996	2.002	0	17	106
					(0.001)	(0.001)	(0.001)	(15)	(15)	(1)
		I			1.9976		2.0029	22.8		116.6
					(0.0003)		(0.0003)	(0.4)		(0.2)
6H	B	II	4.2–70	Axial	1.9975		2.0026	22.3		116.5
					(0.0003)		(0.0003)	(0.4)		(0.2)
		III			1.9969		2.0020	22.7		116.4
					(0.0003)		(0.0003)	(0.4)		(0.2)
	C		> 25	Axial	2.000		1.998	56		26
					(0.001)		(0.001)	(1)		(1)
4H	D		< 15	Monoclinic	1.995	1.993	1.9976	13	0	104
					(0.001)	(0.001)	(0.001)	(15)	(15)	(1)

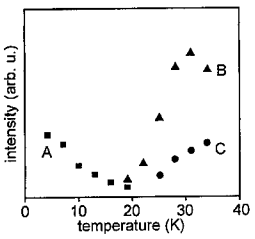

Fig. 2. Relative EPR line intensities of one Sc hf line of spectra A (full squares), B (full triangles) and C (full circles) at different temperatures. All spectra were measured with the same microwave power without illumination of the sample.

the spin Hamiltonian parameters. Fig. 1 (upper curve) shows the calculated spectrum for $S = \frac{1}{2}$ and for the parameters given in Table 1 for spectrum "A". The principal axis of the hf tensor with the largest interaction (z-axis) is oriented along the bond axis between Sc on the C site and a nearest Si neighbour in the plane perpendicular to the c-axis. The three inequivalent sites (h, k_1, k_2) were not resolved in X-band.

Upon increasing the temperature the line intensities of the monoclinic spectra A decrease until above about 15 K they vanish (see Fig. 2, squares). Until above 25 K a new octet spectrum appears having axial symmetry about the c-axis, which is also attributed to Sc. The intensity of the spectrum increases with temperature (see Fig. 2, circles). The g and hf tensors are collected in Table 1 (spectrum C). The ^{45}Sc hf splitting of the axial spectrum C is largest when the magnetic field is perpendicular to the c-axis. In contrast to this in spectrum B it is largest for the magnetic field parallel to the c-axis. At low temperature the EPR line intensity of spectrum B (measured under illumination) depends on the microwave power due to saturation effects. The line intensity increases with temperature above about 20 K (Fig. 2, triangles). Above 40 K the intensity does not change under illumination with above-band-gap light any more.

In 4H–SiC doped with Sc we observed an EPR spectrum only at low temperatures ($T < 15$ K) of which the g and hf tensors are given in Table 1. The symmetry is monoclinic and up to six octets were observed for an arbitrary orientation in the dark similar to what was observed in 6H–SiC at low temperature.

4. Discussion

We observed three different types of EPR spectra in Sc-doped 6H–SiC, all showing a pronounced temperature dependence. They all exhibit the Sc hf interaction pattern, however with different hf splittings, indicating Sc to be present in different configurations.

The EPR spectrum type A observed at low temperatures (< 15 K) have almost the same value of A_{zz} as that observed in the axial spectrum B (Table 1). Furthermore, A_{yy} of spectrum type A is much smaller than A_{zz} as is $A_\perp$ of spectrum type B compared to $A_{zz}(A_\parallel)$. Unfortunately, A_{xx} and A_{yy} of spectrum type A could not be determined precisely enough to check whether their average is close to $A_\perp$ of spectrum type B. Similarly, we observed for the g values that both the monoclinic spectrum A and the axial spectrum B show very similar values of g_{zz} (although of different orientations). Furthermore, $g_\perp$ of the spectrum type B is the average of g_{xx} and g_{yy} of the spectrum type A.

If one calculates an average of the g and hf tensors of the spectrum type A such that the orientations of the principal axes for the average tensors are parallel and perpendicular to the crystal c-axis, one finds approximately the hf tensors of the observed axial spectrum type C: About 55 MHz for $A_\perp$ and about 12 MHz for $A_\parallel$, in fair agreement with the experimental values.

From these observations, the following Sc defect model is proposed: Sc^0 ($4s^2\ 3d^1$) resides in a carbon vacancy (V_C). All three types of Sc EPR spectra (A–C) are due to the isolated Sc^0 acceptor only. The EPR spectra observed originate from different configurations of the Sc hole which is located in a bond to one of the four nearest silicon neighbours.

At low temperature the hole is in one of the C–Sibonds as shown in Fig. 3(a). There are six orientations for this configuration in the crystal: two groups of three in a C_{3v} arrangement, twisted with respect to each other by 60°. In this configuration one, measures the monoclinic spectrum type A. Upon raising the temperature the hole starts to hop between the bonds of the three next-neighbour Si in the plane perpendicular to the c-axis (Fig. 3(b)). Due to this thermally induced motion, the

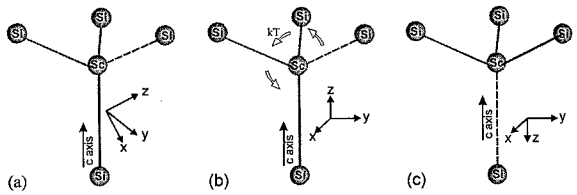

Fig. 3. Models of the Sc_C impurity in 6H–SiC explaining all EPR spectra observed (A–C). (a) At low temperatures ($T < 15$ K) the hole is oriented along one of the nearest neighbour Si bonds which are in a plane perpendicular to the c-axis (spectrum A) or along the c-axis, spectrum B. At higher temperatures the hole starts jumping about the three nearest neighbour Si bonds and the axial spectrum C is observed. (c) The axial orientation of the hole ($\|c$-axis) shows no change in spectral position of EPR lines as a function of temperature (spectrum B). The orientations of the g and hf tensors are also shown.

low-temperature g and hf tensors with monoclinic symmetry are averaged such that an EPR spectrum with axial symmetry about the c-axis (type C) is observed with $A_{\parallel} < A_{\perp}$ and with $g_{\parallel} < g_{\perp}$. In the case of the axial spectrum type B with $A_{\parallel} > A_{\perp}$ (Fig. 3(c)) and $g_{\parallel}$ parallel to the c-axis the bond direction is along the c-axis. There is no hopping process for center B, since the spectral positions of the EPR lines of spectra B do not change in the whole temperature range investigated.

The different hole configurations leading to spectra of types A, B or C lead to three different defect levels in the gap which is probably caused by different lattice relaxations and lattice vibrations. Their position relative to the Fermi level determines whether the EPR spectrum is observable in the dark or not. From the measured EPR line intensities as a function of temperature and illumination we propose that at low temperature (4.2 K) the ionization level of defect A is above that of defect B (see Fig. 4). At 4.2 K the Fermi level is near (slightly above) the ionization level of center A, which is then (at least partly) in the paramagnetic A^0 state, while center B remains in the diamagnetic A^- state. Above band gap illumination level B can catch holes to convert to the A^0 state and becomes visible in the EPR as observed.

Upon raising the temperature above 4.2 K the Fermi level drops and moves towards the ionization level of B (see Fig. 4) increasing more and more the hole occupancy there (A^0 occupancy). Therefore, the line intensity of center B increases with increasing temperature (Fig. 2, triangles) until a maximum is reached at about 40 K. Had the Fermi level been such that all centres B had been in the paramagnetic state at 4.2 K then the signal intensity would have been decreasing with increasing temperature due to the Boltzmann factor ($\propto 1/T$). The decrease of the signal intensity of the center A with increasing temperature is probably not due to the Boltzmann factor, but due to the thermal hopping of the hole resulting in the axial center C and disappearance of the ionization level A. It is proposed that the centre C has a level below that of B, certainly below the assigned position of the monoclinic centre A. It is probably near that of B. The reason is that because of the thermally activated hole hopping associated with soft local lattice modes the ionization level is determined by a larger entropy term compared to the low-temperature monoclinic configuration A. The importance of an entropy term has been demonstrated for two bistable defect configurations, where the bistability was thermally driven [6,7]. If we consider the Gibbs free energy

$$G = H - TS(T) \tag{1}$$

(H = configuration enthalpy, T = temperature and $S(T)$ = entropy of defect) the defect level is shifted downwards on raising the temperature. The entropy is thought to be associated with rather soft local lattice mode which also enables the thermal hopping of the hole. According to Eq. (1) the negative entropy term increases in magnitude rapidly with increasing temperature. For soft modes the entropy increases significantly with increasing temperature [6]. Whether also the level of B has an appreciable entropy term, we do not know. We think that relative to B the center C has the larger entropy term. Upon increasing the temperature above approximately 20 K the Fermi level is lowered and moves nearer to the C level resulting in an increase of its line intensities, which at 40 K has not yet reached a maximum.

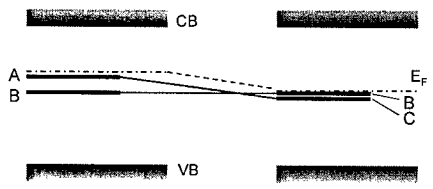

Fig. 4. Proposed ionisation level scheme for defects A–C. The low-temperature case is shown qualitatively on the left with centre A observed by EPR in the dark. With increasing temperature the Fermi level moves downwards towards level B. In the high-temperature case on the right, the level of defect C is below that of defect B. Therefore the intensity of lines of defect C is lower than that of defect B. Had it full hole occupancy the lines of defect C should have three times the intensity of those of defect B.

In contrast to our measurements Baranov et al. [3] claimed that they found in total four types of Sc EPR spectra instead of the three that we have observed. A closer inspection of Ref. [3] shows that their EPR spectra were not analysed satisfactorily. In fact, Baranov et al. measured the same low-temperature EPR spectrum as we did (spectrum type A in our notation). The interaction parameters given in Ref. [3] seem doubtful, since the largest hf splitting should occur at $B \| c + 70°$ (along the Si–C bond direction) and not for $B \perp c$ as stated in Ref. [3]. Furthermore, the two spectra labelled $Sc_{\alpha 1}(LT)$ and $Sc_{\alpha}(LT)$ in Ref. [3] are not due to two different centres as assumed there but are due to two different orientations of the low-temperature Sc configuration (labelled type A by us).

The spectra shown in Ref. [3] are the same as those measured here (spectra types B and C (Table 1)). We could explain the lines of Fig. 4 in Ref. [3] with the data presented in Table 1. However, the g and hf values given in Ref. [3] differ significantly from ours (Table 1) by about 15%. In both investigations the EPR of the shallow N donor was observed simultaneously, which could be used as an independent field marker for the determination of the g and hf values [5]. Probably the field calibration used in Ref. [3] was erroneous.

5. Conclusion

Various EPR spectra of Sc-doped SiC, measured at different temperatures, were explained as being due to isolated Sc^0-acceptors substituting for carbon. While at low temperatures EPR spectra of Sc^0 are observed to have hole orientations along the *c*-axis showing an axial center and in the three remaining Sc–Si bonds resulting in monoclinic centers, at higher temperatures the latter ones are averaged due to a thermally activated hopping of the hole between the three equivalent Sc–Si bonds giving rise to an axial center. The thermally driven dynamical properties of this axial center cause the defect level to be temperature dependent because of the importance of an entropy term. The axial EPR spectrum from the configuration having the hole along the Sc–Si bond parallel to the *c*-axis shows no change of the hf interactions or *g* tensor in the whole temperature range investigated.

Acknowledgements

This work was supported by the "Deutsche Forschungsgemeinschaft". The authors would like to thank H. Overhof for helpful discussions.

References

[1] P.G. Baranov, N.G. Romanov, V.A. Vetrov, V.G. Oding, Proceedings of the 20th International Conference Physics and Semiconductors Vol. 3, World Scientific, Singapore, 1990, pp. 1855–1858.
[2] M. März, J. Reinke, S. Greulich-Weber, J.-M. Spaeth, H. Overhof, E.N. Mokhov, A.D. Roenkov, E.N. Kalabukhova, Sol. Stat. Commun. 98 (5) (1996) 439.
[3] P.G. Baranov, I.V. Il'in, E.N. Mokhov, A.D. Roenkov, V.A. Khramtsov, Phys. Solid State 39 (1) (1997) 44.
[4] V.S. Ballandovich, Sov. Phys. Semicond. 25 (1991) 174.
[5] E.N. Kalabukhova, N.N. Kabdin, S.N. Lukin, Sov. Phys. Solid State 29 (8) (1987) 1461.
[6] H. Söthe, J.-M. Spaeth, F. Luty, Rad. Effects Defects Solids 119–121 (1991) 269–274.
[7] B. Hamilton, A.R. Peaker, S.S. Pantelides, Phys. Rev. Lett. 61 (1988) 1627.

ELSEVIER

Physica B 273–274 (1999) 672–676

PHYSICA B

www.elsevier.com/locate/physb

Low-dose ion implanted epitaxial 4H–SiC investigated by deep level transient spectroscopy

D. Åberg*, A. Hallén, B.G. Svensson

Department of Electronics/Solid State Electronics, Royal Institute of Technology, Kista-Stockholm, S-164 40, Sweden

Abstract

4H–SiC n-type epi-material of nitrogen doped to $1 \times 10^{15}\,cm^{-3}$ was implanted with low doses of B and He ions. The doses were extremely low, 1×10^{7}–$8 \times 10^{7}\,cm^{-2}$, to avoid dopant compensation. Deep level transient spectroscopy and capacitance–voltage measurements were then performed on the samples without needing an intermediate anneal to restore doping activation. Two levels were found in the energy band gap, $E_c - 0.70 \pm 0.02$ and $E_c - 1.6 \pm 0.07$ eV. The $E_c - 0.70$ level was found to grown linearly with dose but implantation at 500°C reduced the $E_c - 0.70$ level concentration.

Keywords: 4H–SiC; Deep acceptors; Implantation-related defects

1. Introduction

Silicon carbide has during recent years been in focus for industrial exploitation as a semiconductor material for high-power and high-frequency electronic devices. SiC appears in several polytypes of which 4H–SiC today is of highest interest, mostly due to its high and comparatively isotropic electron mobility. Intentional doping of SiC is preferably made by ion implantation technique, since dopant diffusion is very very limited up to the sublimation temperature of the material. However, ion implantation doping of SiC is a challenge for several reasons, e.g. it has been shown that SiC is dopant compensated five times more than Si for the same implantation dose at room temperature (RT) [1]. This results in a high degree of dopant compensation, which is furthermore much more difficult to anneal out, even after annealing at 1700°C.

In order to improve the implantation technology for SiC it is necessary to obtain insight in the defect formation processes. The purpose of this study is to gain a better understanding of the defect kinetics during implantation and to identify important implantation induced defects. Capacitance–voltage (CV) and deep-level transient spectroscopy (DLTS) have been used for characterization. By using low doses of ions it has been possible to avoid dopant compensation which otherwise disturbs the analysis.

2. Experiment

Low doped ($\sim 10^{15}\,cm^{-3}$), thick high-purity n-type 4H–SiC epi-layers were grown on Cree substrate wafers. Further details of the material are given in Ref. [2]. The samples (8 × 8 mm) were cut from the same wafer, with doping variation of 5% between samples, and then implanted at the Uppsala tandem accelerator facilities [3]. Both ^{4}He and ^{11}B ions were used, with energies of 1.7 and 5 MeV, respectively. According to TRIM [4] simulations these energies produce an implantation peak at a depth around 4 μm. The implantations were made at RT, and hence no electrical activation of B is expected. Implantation doses ranged from 1×10^{7} to $8 \times 10^{7}\,cm^{-2}$ for B while a dose of 2×10^{9} was used for all the He implanted samples. These extremely small doses are needed to avoid dopant compensation in this SiC material according to the previous study [1]. The He-implanted sample was subsequently annealed at 700°C and

* Corresponding author. Tel.: + 46-8-7521400; fax: + 46-8-7527782.

E-mail address: denny@ele.kth.se (D. Åberg)

0921-4526/99/$ - see front matter
PII: S0921-4526(99)00601-8

1000°C in vacuum. Furthermore, some samples were B implanted with dose $3 \times 10^7\,cm^{-2}$ both at RT and at elevated temperatures 400°C and 500°C. The samples were cleaned in Aqua Regia, followed by acetone and ethanol rinse and a dip in 10% hydrofluoric acid. Schottky contacts were made using Au or Ni, grown in a thermal evaporator or an e-beam evaporator, under base pressures of 2×10^{-5} and 1×10^{-8} mbar, respectively.

CV and DLTS measurements were then performed using both a Semilab cryostat ($T \lesssim 300\,K$) and an adapted cryostat ($\lesssim 800\,K$) from Schaefer. The high-temperature cryostat consists of a vacuum system with a 50 W heating element and, electrically isolated from the heater, the sample and a PT103 sensor are mounted in symmetric positions to ensure a high accuracy of the temperature reading. The temperature is varied using a Neocera PID-controller, with typical ramping rates between 0.1 and 10 K min. The DLTS spectrometer consists of a 1 MHz HP4280A C(t)-meter for time-resolved capacitance measurements, with the filling pulse produced by a HP8110A dual pulse generator. These instruments are computer controlled, so that each transient is recorded and stored. In this way one may apply different weight functions for maximum flexibility when extracting DLTS-signals during subsequent analysis. Transient times from μs to several seconds can be monitored.

Concentration versus depth profiles were determined by keeping the temperature constant within $\pm 0.5\,K$ at the temperature for the maximum of the selected DLTS peak and gradually increasing the filling pulse as described in Ref. [5].

3. Results and discussion

The compensation effects of the implantation, even at relatively low doses, are demonstrated in Fig. 1 where *CV* depth profile measurements from a helium implanted sample are shown after implantation and subsequent anneals. The occurrence of a deep acceptor, responding to the step voltage frequency (here 4 Hz) is known to produce an overshoot in apparent doping at depth larger than 4 μm. This is due to that the deep acceptors affect the capacitance signal within the depletion region separated from the depletion region edge, where the dopant ions affect the capacitance [6]. As the voltage bias is changed, this separation distance can in fact change dramatically, if the trap concentration is highly nonuniform. This will affect the *CV*-analysis, and give rise to an apparent increase in doping, trailing the actual compensation and with a strong concentration gradient, such as after He-implantation, this effect can be very large. The dose of $2 \times 10^9\,cm^{-2}$ corresponds to $\sim 2 \times 10^{13}\,cm^{-3}$ He atoms at the implantation peak. The dopant compensation is seen to widely exceed this concentration. However, annealing at 700°C for 30 min clearly reduces the compensation. An anneal at 1000°C for 30 min further reduces the compensation, although the majority of compensating defects have been annealed out between RT and 700°C.

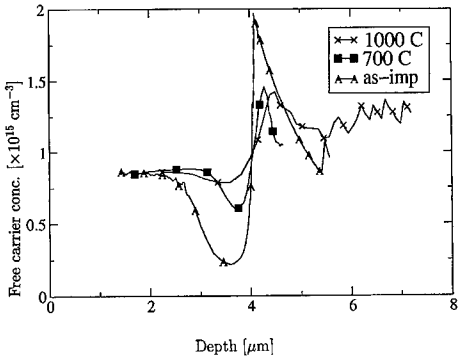

Fig. 1. *CV* plots of samples implanted with a He dose of $2 \times 10^9\,cm^{-2}$ measured after implantation and after anneals at 700°C and 1000°C for 30 min.

TRIM calculations for a corresponding He implantation show a peak in the vacancy distribution with a maximum value of $1 \times 10^{15}\,cm^{-3}$ at 4 μm. In Fig. 1, it can be seen that the dopant compensation appears at a similar depth. Although it is very difficult to obtain quantitative data from compensated *CV*-plots this indicates that a major part of the created defects are involved in the compensation. As a comparison, in Si less than 5% of the created vacancies survive the immediate annihilation and form compensating defects.

In Fig. 2, the DLTS spectra using a rate window $\tau = 0.3125\,s^{-1}$ from a sample implanted with B at a dose of $3 \times 10^7\,cm^{-2}$ is shown. At this low dose no dopant compensation is seen in *CV*-measurements, which otherwise could have affected the DLTS peak amplitudes. At 271 K a peak appears, with an energy position of $E_c - 0.70 \pm 0.02\,eV$, where E_c denotes the conduction band. This center, often referred to as the *Z*-center, is an intrinsic acceptor-like defect frequently found in as-grown as well as irradiated material [7]. This center is known to be stable up to temperatures of 2000°C [8], and it has been discussed in terms of a divacancy [9]. The nature of the $E_c - 0.70$ defect is, however, far from fully revealed. For instance, recently it was found in electron-beam irradiation experiments [10,11] that there exists two levels, within the *Z* spectra, called Z_1 and Z_2. These showed negative U-behavior where each center normally was in acceptor state after ionization (preferred energy position), but could be found in donor states by use of illumination during DLTS ($\lambda = 470$ nm).

The next broad peak at $\sim 580\,K$ comes from a deep electron trap. Assuming temperature-independent capture cross section yields an activation energy of $1.6 \pm 0.07\,eV$ below E_c and capture cross section of $9 \times 10^{-12}\,cm^2$ extrapolated from Arrhenius plot. The DLTS

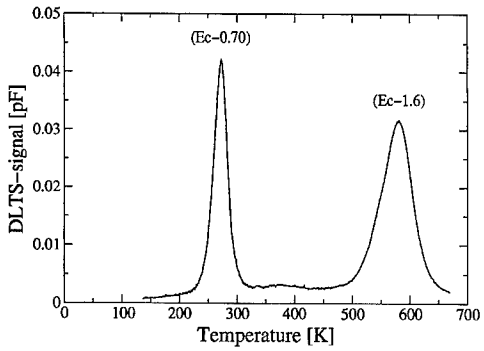

Fig. 2. DLTS temperature spectra of a sample implanted with a B dose of $3 \times 10^7\,cm^{-2}$. The measurement rate window was $\tau = 0.3125\ s^{-1}$.

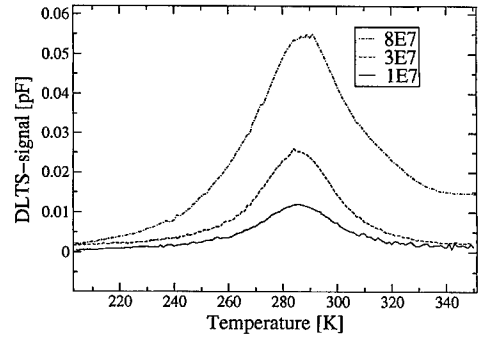

Fig. 3. DLTS temperature spectra of B implanted samples of 1×10^7, 3×10^7 and $8 \times 10^7\,cm^{-2}$ (with $\tau = 1.25\ s^{-1}$).

signal is broad, and may consist of several levels. Previously, a deep level has been seen at $E_c - 1.65\,eV$ after e-beam irradiation of 4H–SiC [12]. Only these two levels were found in the spectra when going from 80 to 700 K. The concentration of the two are apparently of the same order of magnitude.

In Fig. 3, the DLTS spectra of the $E_c - 0.70$ peak of B implanted samples using doses of 1×10^7, 3×10^7 and $8 \times 10^7\,cm^{-2}$ are shown. The peak amplitude is proportional to the concentration of defects and in Fig. 3 the dose dependence is seen to be roughly linear in this range although the accuracy of the dose measurements is poor at these low doses (relative error less than $\pm$ 15%). The peak broadens strongly with increasing dose, but it is known that two traps exist which closely relate to each other in this range [12,13] and the broadening is possibly caused by an overlap of these traps.

Concentration versus depth profile of the $E_c - 0.70$ peak is shown in Fig. 4, together with a profile of the free carriers. This sample was implanted with B of $8 \times 10^7\,cm^{-2}$ dose. Included is also a calculated B profile, using a Pearson distribution function with the moments taken from Ref. [14]. This dose is found to be the threshold of observable compensation for $1 \times 10^{15}\,cm^{-3}$ n-type material after implantation. The defect concentration is shown to have a maximum at the peak position of the implanted ions. The compensation effects which are on the order of $10^{14}\,cm^{-3}$ for this implantation dose, cannot be caused solely by the $E_c - 0.70$ defects, since they amount only to a concentration of $10^{13}\,cm^{-3}$. Likewise, the deep electron traps, seen in Fig. 2, occur with concentrations of the same order of magnitude as the $E_c - 0.70$ defects, suggesting that the compensation is caused mainly by defects in the lower half of the band gap. As the samples used in this study was of n-type with Schottky contacts, the lower half of the band gap could not be explored. It is possible that an acceptor level in the lower half of the band gap accounts for most of the compensation (≈ 5–$10 \times 10^{13}\,cm^{-3}$) and the highly gradient $E_c - 0.70$ concentration produce the overshoot in apparent doping.

In Fig. 5, is seen the effect of implantation temperature on the formation of the $E_c - 0.70$ level. These samples were implanted with B dose of $3 \times 10^7\,cm^{-3}$, which is

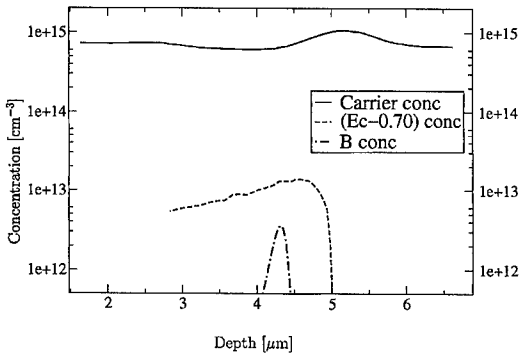

Fig. 4. Profile of carrier concentration and $E_c - 0.70$ concentration for sample implanted with 5 MeV B at $8 \times 10^7\,cm^{-2}$. Included is the calculated B concentration for the implantation.

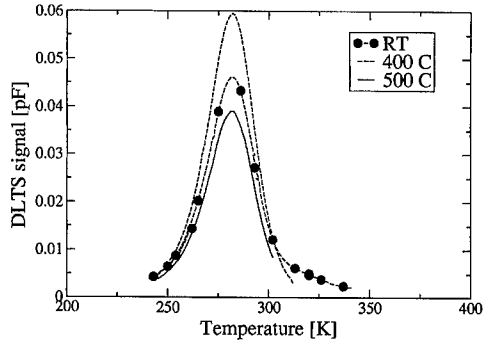

Fig. 5. DLTS spectra of $E_c - 0.70$ spectra for samples implanted with boron dose of $3 \times 10^7\,cm^{-2}$ at RT, 400°C and 500°C.

Table 1
Electron traps close to $E_c - 0.70$ eV found in different sample treatments

Activation energy ΔE (eV)	σ (cm^2)	Treatment		Ref.
$E_c - 0.62 \pm 0.02$	1×10^{-15}	H($2 \times 10^{10} - 1 \times 10^{11}$ cm^{-2})	Stable	[8]
$E_c - 0.62$	4×10^{-14}	e(1×10^{15} cm^{-2})	Annihilated at 100°C	[7,13]
$E_c - 0.68$	5×10^{-15}	e(1×10^{15} cm^{-2})	Annihilated at 200°C	[7,13]
$E_c - 0.70$	5×10^{-14}	e(1×10^{15} cm^{-2}) + 200°C	Stable	[7,13]
$E_c - 0.67 \pm 0.03$		B(2×10^{8} cm^{-2})	Stable	[1]
$E_c - 0.68$	1.3×10^{-14}	e(1×10^{14} cm^{-2})	Annihilated at 700°C	[12]

sufficiently low not to give rise to compensation. Implantations were made at RT, 400°C and 500°C. Is has previously been shown [1] that implantation at 700°C substantially reduces compensation compared to RT implant. The concentration of $E_c - 0.70$ defects is first seen to increase as the implantation temperature is raised from RT to 400°C. At higher temperatures it decreases in agreement with Hemmingsson [12] who reports a complete annealing of the $E_c - 0.70$ defect after post-irradiation anneal at 700°C.

There are several reports on electron traps situated close to $E_c - 0.70$ eV and these are summarized in Table 1. There is, however, a large inconsistency in the behavior of these levels. Dalibor et al. performed hydrogen implantations (hydrogen was confirmed not to be related to the generated defects) of doses 2×10^{10} and 1×10^{11} cm^{-2} followed by a 1700°C anneal for 10 min [8]. The implantations generates vacancy concentration of $\sim 10^{16}$ cm^{-3} according to TRIM. They reported a level at $E_c - 0.62$ eV, named the Z_1 level, existing in the as-grown material. The Z_1-level grew with implantation and was doubled in concentration with a 5 folded dose increase. An increased anneal temperature to 2015°C gave a tenfold increase in Z_1 concentration. In contrast to this report of the Z_1 level as a temperature stable defect are the results from e-beam irradiation experiments by Hemmingsson et al. [12]. After an electron dose of 10^{14} cm^{-3}, which is a considerably milder treatment than the ion implantations by Dalibor, a level named EH2 was found at $E_c - 0.68$ eV. This level was annealed out completely after 10 min at 750°C. Doyle et al. found in similar e-beam experiments [7,13] a level present in as-grown material at $E_c - 0.70$ eV. Directly after irradiation, this level was annihilated, and two levels at $E_c - 0.62$ and $E_c - 0.68$ eV had formed. Heat treatments at 100–140°C showed first a decrease of the $E_c - 0.68$ level and a comparable simultaneous increase of the $E_c - 0.62$ level. At 200–250° both levels were annihilated and instead the $E_c - 0.70$ level had formed. Hallén et al. showed from B implantations of 2×10^{8} cm^{-3} the rise and broadening of a level existing in the as-grown material at $E_c - 0.67 \pm 0.03$ eV [1]. This level was not annealed out after 1000°C. In the present study, after a lower B dose a level at $E_c - 0.70$ eV in agreement with Hallén, however, this level is not totally stable during implantation, but show a decrease at 500°C implantation temperature. These discrepancies needs to be examined further. The difference in temperature stability of the different levels seen by various authors can be indication on the existance of different centers with similar electrical characteristics.

4. Summary

We have performed ion implantations of 4H–SiC using 1.7 MeV He and 5 MeV B with low doses to avoid compensation. For B the dose need to be below 8×10^{7} cm^{-2}. Two DLTS peaks were found in the temperature range 80–700 K. These were positioned at $E_c - 0.70$ eV and at $E_c - 1.6$ eV. The concentration of the levels were found to be lower than the measured compensation, and hence a deeper lying compensating level exists roughly of 5 times higher concentration. The $E_c - 0.70$ level was found to grow linearly with B dose in the range 1×10^{7}–8×10^{7} (up to the threshold of detectable compensation). The $E_c - 0.70$ level was further found to grow with implantation temperature, up to 500°C, where a decrease was noted.

Acknowledgements

The Swedish Foundation for Strategic Research is kindly acknowledged for supporting this work within the SiCEP program and ABB Corporate Research (Script project) for providing the epitaxial material.

References

[1] A. Hallén, D. Åberg, P. Pellegrino, A. Henry, B.G. Svensson, Mater. Sci. Eng. B 61–62 (1999) 378.
[2] O. Kordina, C. Hallin, A. Henry, J.P. Bergman, I. Ivanov, A. Ellison, N.T. Son, E. Janzén, Phys. Stat. Sol. B 202 (1997) 321.
[3] A. Hallén, P.A. Ingemarsson, P. Håkansson, B.U.R. Sundqvist, G. Possnert, Nucl. Instr. and Meth. B 36 (1989) 345.

[4] J.P. Biersack, L.G. Haggmark, Nucl. Instr. and Meth. 174 (1980) 257.
[5] B.G. Svensson, M. Willander, J. Appl. Phys. 62 (1987) 2758.
[6] L.C. Kimerling, J. Appl. Phys. 45 (1974) 1839.
[7] J.P. Doyle, M.O. Aboelfotoh, M.K. Linnarsson, B.G. Svensson, A. Schöner, N. Nordell, C. Harris, J.L. Lindström, E. Janzén, C. Hemmingsson, Mater. Res. Soc. Symp. Proc. 423 (1996) 519.
[8] T. Dalibor, C. Peppermüller, G. Pensl, R.P. Devaty, W.J. Choyke, A. Ito, T. Kimoto, M. Matsunami, Proceedings from ICSCRM-95, September 1995, Kyoto, Japan.
[9] T. Dalibor, C. Peppermüller, G. Pensl, S. Sridhara, R.P. Devaty, W.J. Choyke, A. Itoh, T. Kimoto, H. Matsunami, Inst. Phys. Conf. Ser. No. 142 (1996) 517.
[10] C. Hemmingsson, N.T. Son, A. Ellison, J. Zhang, E. Janzén, Phys. Rev. B 58 (1998) R10 119.
[11] C. Hemmingsson, N.T. Son, A. Ellison, J. Zhang, E. Janzén, Phys. Rev. B 59 (1999) 7768.
[12] C. Hemmingsson, N.T. Son, O. Kordina, J.P. Bergman, E. Janzén, J.L. Lindström, S. Savage, N. Nordell, J. Appl. Phys. 81 (1997) 6155.
[13] J.P. Doyle, M.K. Linnarsson, P. Pellegrino, N. Keskitalo, B.G. Svensson, A. Schöner, N. Nordell, J.L. Lindström, J. Appl. Phys. 84 (1998) 1354.
[14] M.V. Rao, J.A. Gardner, P.H. Chi, O.W. Holland, G. Kelner, J. Kretchmer, M. Ghezzo, J. Appl. Phys. 81 (1997) 6635.

ELSEVIER

Physica B 273–274 (1999) 677–680

PHYSICA B

www.elsevier.com/locate/physb

Zeeman spectroscopy of the D_1 bound exciton in 3C–, and 4H–SiC

T. Egilsson*, I.G. Ivanov, A. Henry[1], E. Janzén

Department of Physics and Measurement Technology, Linköping University, S-581 83 Linköping, Sweden

Abstract

We have studied the D_1 bound exciton (BE) in 3C–SiC (cubic) and 4H–SiC (hexagonal) by means of Zeeman spectroscopy. We show that the D_1-BE can be described by an electron–hole pair consisting of an ($L_e = 0$, $S_e = \frac{1}{2}$) electron and a ($L_h = 1$, $S_h = \frac{1}{2}$) hole, influenced by a number of interactions. In order to model the behaviour of the D_1-BE in magnetic field, an appropriate Hamiltonian equation is solved by using perturbation theory. The spin–orbit parameter and orbital g-value are small, indicating that the hole is tightly bound.

Keywords: Excitons; SiC; Photoluminescence

1. Introduction

The D_1-BE photoluminescence (PL) usually dominates the spectrum of implanted and irradiated SiC after annealing. The D_1-defect persists to very high annealing temperatures (> 2000°C), and is thus difficult to get rid of. The structure of the defect is not known, although alternatives such as a di-vacancy, or a vacancy-interstitial complex have been proposed [1,2]. The D_1-BE lifetime [3] is much longer than the lifetime of common donor and acceptor BE's in SiC [4,5], indicating that the exciton is bound at an isoelectronic defect. The PL and PL excitation (PLE) spectra in Fig. 1 show the main no-phonon lines associated with the D_1-BE in 3C–, and 4H–SiC. At 2 K only the lowest-energy states of the D_1-BE are populated, and thus only the lowest-energy no-phonon lines are observed in the PL spectra. The PLE spectra are obtained by monitoring the low-temperature PL while scanning the excitation energy, and they therefore reveal all the states. However, since the L and L_1 lines happen to have very low oscillator strengths they are scarcely visible in the PLE spectra. In this paper we report and explain the Zeeman splitting of the no-phonon lines shown in Fig. 1.

2. Results and discussion

The behaviour of the D_1-BE in 3C–, and 4H–SiC in magnetic field was investigated using both PL and PLE measurements. D_1-defects were created in the samples by irradiation with 2 MeV electrons at a dose of 10^{17} cm^{-2}, and a subsequent annealing at 1500°C for 1 h. The maximum magnetic field used in the experiments was 5 T. Figs. 2 and 3a show the Zeeman splitting as a function of magnetic field for the D_1-BE in 3C–, and 4H–SiC, respectively. The M_1 and H_1 lines in 4H–SiC were not seen to split and are not included in Fig. 3. Furthermore, due to the weakness of the N_1 PLE peak and its close proximity to the strong M_1 peak, we were not able to establish its splitting. We did not observe any angular dependence of the Zeeman splitting in 3C–SiC, and thus conclude that it is isotropic. A strong angular dependence was on the other hand observed in the case of 4H–SiC, as is shown in Fig. 3. The population of the different magnetic field split states depends on temperature. By measuring at different

* Corresponding author. Materials Science, IFM, Linköping University, S-581 83 Linköping, Sweden. Fax: + 46-13-14-23-37.

[1] Also at ABB Corporate Research, S-721 78 Västerås, Sweden.

E-mail address: tryeg@ifm.liu.se (T. Egilsson)

0921-4526/99/$ - see front matter
PII: S0921-4526(99)00602-X

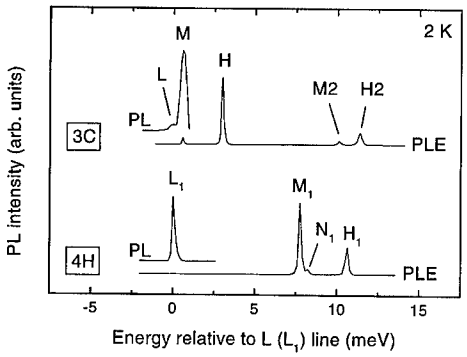

Fig. 1. PL and PLE spectra recorded at 2 K, showing the main no-phonon lines associated with the D_1-BE in 3C–, and 4H–SiC. The PLE spectra are obtained by monitoring in the phonon-assisted part of the low-temperature PL while scanning the excitation energy.

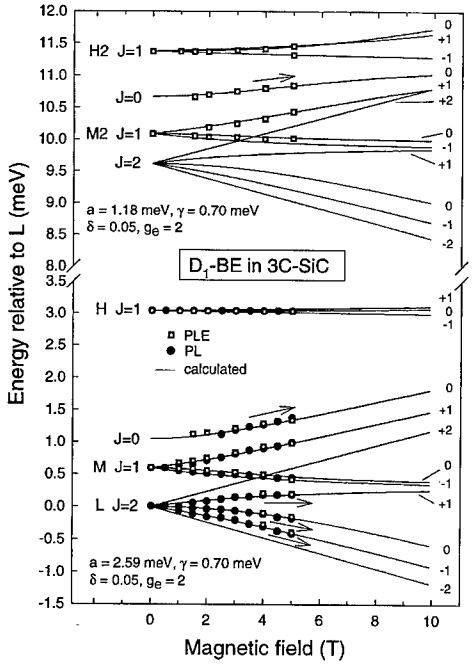

Fig. 2. Zeeman splitting as a function of magnetic field in the case of the D_1-BE in 3C–SiC. Arrows indicate the direction of increased oscillator strength. The solid curves in the figure are calculated. The parameters of the calculation are shown in the figure. The numbers in the rightmost part of the figure are the values of the M quantum number.

temperatures (1.5–5 K) we observed thermalization effects in the PL spectra (the relative intensities of the different lines changed). No such effects were observed in the PLE spectra however, their form was not affected by the temperature. This shows that the splitting only occurs in the initial state of the PL transitions (final state of the

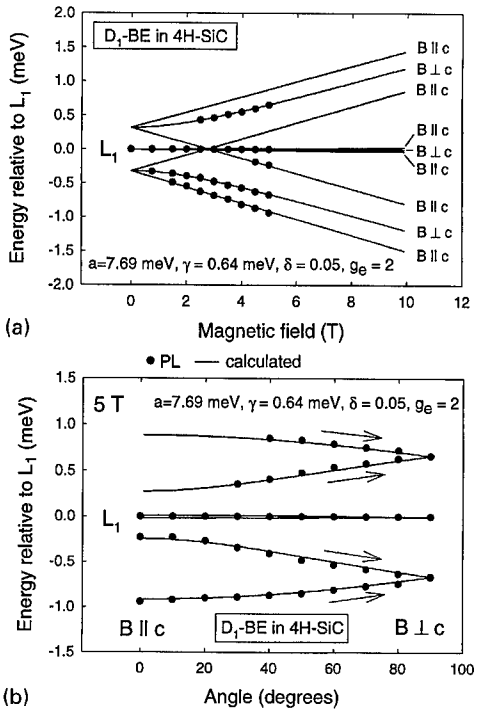

Fig. 3. Zeeman splitting of the L_1 PL line in 4H–SiC; (a) as a function of the size of the magnetic field in the case when the field direction is either parallel or perpendicular to the c-axis, and (b) as a function of the angle between the field and the c-axis at 5 T. Arrows indicate the direction of increased oscillator strength. The solid curves in the figure are calculated. The parameters of the calculation are shown in the figure.

PLE transitions). This is consistent with the D_1-defect being isoelectronic, since no splitting is in that case expected after the exciton has recombined (or before it is created). The Zeeman splitting of the D_1-BE in both 3C–, and 4H–SiC, can be explained by considering the BE to consist of an ($L_e = 0$, $S_e = \frac{1}{2}$) electron and a ($L_h = 1$, $S_h = \frac{1}{2}$) hole affected by a number of interactions. Here, L_e, L_h, S_e and S_h are the quantum numbers associated with the orbital angular momentum operators $\boldsymbol{L}_e$ and $\boldsymbol{L}_h$, and the spin operators $\boldsymbol{S}_e$ and $\boldsymbol{S}_h$. The energy splitting caused by the different interactions, is shown schematically in Fig. 4 for both 3C– and 4H–SiC. In the figure, L, S, and J are the quantum numbers of the total orbital angular momentum $\boldsymbol{L} = \boldsymbol{L}_e + \boldsymbol{L}_h$, total spin $\boldsymbol{S} = \boldsymbol{S}_e + \boldsymbol{S}_h$, and total angular momentum $\boldsymbol{J} = \boldsymbol{L} + \boldsymbol{S}$, and M_L, M_S and M_J are the quantum numbers of the z-components of $\boldsymbol{L}, \boldsymbol{S}$ and $\boldsymbol{J}$. The splitting is as follows: $[\Delta_{CF} >]\Delta_{VO} > \Delta_{EX} > \Delta_{SO}$, where CF stands for crystal field, VO for valley–orbit, EX for exchange and SO for spin–orbit. The crystal field splitting, Δ_{CF}, is due to the uniaxial crystal field present in the hexagonal 4H–SiC polytype. This field is not present in the cubic 3C–SiC

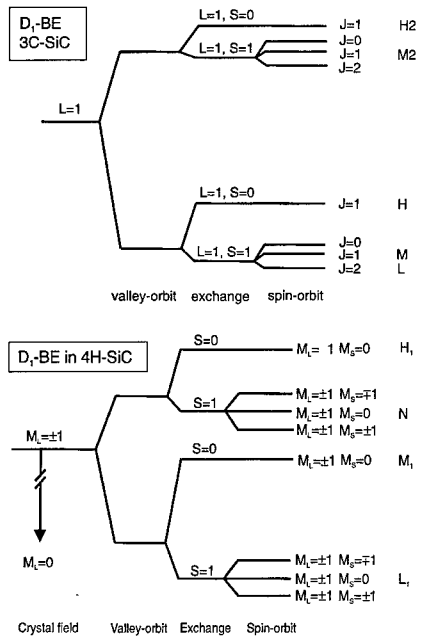

Fig. 4. Schematic figures showing the electronic structure of the D_1-BE ground state in 3C-, and 4H-SiC according to the model developed in this paper. Assignments to associated optical transitions observed in PL and PLE spectra are shown in the rightmost part of the diagrams.

polytype and therefore does not contribute in that case, hence the brackets. Our assignments to associated optical transitions observed in 3C- and 4H-SiC are given in the rightmost parts of the diagrams.

In order to model the behaviour of the D_1-BE in magnetic field ($\boldsymbol{B}$), we have used the following perturbation Hamiltonian:

$$H^1 = H_{EX} + H_{SO} + H_Z, \tag{1}$$

where H_{EX}, H_{SO}, and H_Z are the exchange, spin–orbit and Zeeman Hamiltonians, respectively. These three interactions are thereby treated on an equal footing. The three terms may be written as follows:

$$H_{EX} = -a\boldsymbol{S}_e \cdot \boldsymbol{S}_h, \quad H_{SO} = -\gamma \boldsymbol{L}_h \cdot \boldsymbol{S}_h,$$

$$H_z = \beta \boldsymbol{B} \cdot (\delta \boldsymbol{L}_h + g_e \boldsymbol{S}_h + g_e \boldsymbol{S}_e). \tag{2}$$

Here, a and γ are scalars describing the sizes of the exchange and spin–orbit interactions, β is the Bohr magneton, and g_e and δ are the spin and orbital g-values, respectively (for free electrons and holes $g_e = 2$ and $\delta = 1$). The effects of valley–orbit splitting and the polytype-dependent crystal field are taken into account in the unperturbed Hamiltonian H^0. In terms of orbital and spin quantum numbers the original BE state, before taking into account any of the above interactions, is described by $L_h = 1$, $S_h = \frac{1}{2}$, $L_e = 0$ and $S_e = \frac{1}{2}$. For the sake of convenience, we choose as a basis for this state the 12 wave functions $|L = 1, S = \{0,1\}, M_L, M_s\rangle$. In the case of the 4H-polytype, the crystal field splitting, Δ_{CF}, dominates. It is taken into account by defining the quantization axis as the crystal axis (c-axis), and removing functions with $M_L = 0$, since they are split off by the crystal field (see Fig. 4). The degeneracy of the electron state due to the multi-valley nature of conduction band minimum does not depend on the orbital or spin quantum numbers. Therefore, the valley–orbit interaction will not alter them. The classification of the states in terms of orbital and spin quantum numbers therefore remains the same in each of the valley–orbit split states, as it is without valley–orbit splitting (see Fig. 4). After establishing the matrix elements of H^1 within the set of basis functions the energy eigenvalues were calculated by numerically solving the corresponding secular equation. Fits to experimental results are shown in Figs. 2 and 3 (solid curves). The sizes of the parameters used for the fitting are also shown in the figures.

In magnetic field the M_J states associated with the different J numbers repel each other (see Fig. 2). This causes the rather complicated non-linear splitting pattern observed in the figure. In particular, it causes the $M_J = -1$ and 0 components of the $S = 1, J = 1$ state to be so closely spaced that they are observed as a single peak in the measurements. The two groups of lines in Fig. 2 corresponding to the two valley–orbit split electron states (see Fig. 4) were calculated separately. Since the properties of the hole are the same in both cases (same δ, and γ), the only difference between the two groups is the size of the exchange interaction (a). The spin–orbit parameter (γ), and the orbital g-value (δ) are approximately ten times smaller than the corresponding values for free holes. This shows that the hole is strongly localised, and can thus be considered to be the primary particle of the D_1-BE, whereas the electron is the weakly bound secondary particle.

For the D_1-BE in 4H–SiC, δ is the same as in the case of 3C–SiC, but the size of γ is slightly less. The lack of splitting in the case of the M_1 − and H_1 − lines (not shown in the figure) agrees with the model, since the splitting of the $S = 0, M_L = \pm 1, M_S = 0$ states is due only to the small residual orbital g-value (δ), and is therefore too small to be observed. The anisotropy and non-linearity of the Zeeman splitting in 4H–SiC may be understood qualitatively as follows. Since the exchange interaction is stronger than both the spin–orbit and Zeeman interaction, the two spins are tied together and cannot be de-coupled by these latter interactions. Furthermore, the orbital momentum is pinned to the c-axis by the crystal field. The spin–orbit interaction will thus try to align the total spin up with the c-axis. The Zeeman interaction will on the other hand try to align the spin up with direction of the magnetic field. It is this competition that explains the results. Consider for example the case

when the direction of the magnetic field is perpendicular to the c-axis ($B \perp c$). In order for the spin to be aligned up with the magnetic field, it needs to be decoupled from the orbital momentum. When the magnetic field is small it cannot do this and the states are therefore unaffected by the field. On the contrary, for large magnetic fields, the spin is decoupled from the orbital momentum and consequently the spin–orbit splitting disappears. The magnetic splitting becomes that of a simple $S = 1$ triplet.

Let us consider now the electric dipole selection rules governing the optical transition probabilities from the D_1-BE states shown in Fig. 4. The final state of the optical transitions, is the state of the bare isoelectronic defect. In this state the quantum numbers: L, S, J and M_J are zero. The selection rules for transitions between states with well defined L, S, J and M_J quantum numbers are

$$\Delta S = 0, \quad \Delta L = \pm 1, \quad \Delta J = 0, \pm 1, \quad \Delta M_J = 0, \pm 1 \quad (3)$$

with the exception that ($J = 0$) to ($J = 0$) is not allowed, and ($M_J = 0$) to ($M_J = 0$) is not allowed if $\Delta J = 0$. According to the spin selection rule, optical transitions from all the states associated with $S = 1$ in Fig. 4 are forbidden, whereas transitions from all states associated with $S = 0$ are allowed. This selection rule does not quite hold for the D_1-BE, however, since states with different S quantum numbers, are to some extent mixed by the interactions. We consider first the D_1-BE in 3C–SiC. H_{SO} mixes states with the same J and M_J numbers. The $S = 1$, $J = 1$ states are therefore mixed with the $S = 0$, $J = 1$ states and thereby optical transitions associated with the $S = 1$, $J = 1$ states acquire a non-zero transition probability. This explains the observation of the M-, and M2-lines in PLE spectra (see Fig. 1). The M-line is also observed in PL spectra. The smaller the energy separation between $S = 0$ and 1 states the larger the mixing. This also conforms with the experiments, since the oscillator ratio M2/H2 is larger than M/H. Similar arguments can be used to explain the observation of the L_1-, and N_1-lines in 4H–SiC. The mixing induced by spin–orbit interaction on the other hand does not explain the observation of the $J = 2$ related L-line in PL-spectra of 3C–SiC. Its appearance must be due to an effect not taken into account by the model. The oscillator strength of the L-line is very weak, however (approximately one hundred times lower than for the M-line), and is observed in PL measurements only at the lowest temperatures when the thermal population of higher-energy states of the D_1-BE is small.

A magnetic field will mix the different spin–orbit split states. In the case of the D_1-BE in 3C–SiC, the magnetic field mixes the states of adjacent J numbers which have the same M_J number. J will therefore not remain a good quantum number in the presence of a magnetic field, but M will. In this way, some of the transition probability associated with the $S = 0$, $J = 1$ state will be transferred to the $S = 1$, $J = 0$ and 2 states. This explains the observation of the latter states in PLE spectra in magnetic field (see Fig. 2). The outermost $M_J = \pm 2$ components of the $J = 2$ state are not enhanced in magnetic field, since they cannot be mixed with any other states. They are thus not observed in the PLE spectrum. They are not observed in PL spectra either, although the "forbidden" $J = 2$ related L-line can be observed at zero magnetic field, that is without any mixing of different J states (see Fig. 1). This indicates, that the oscillator strength of optical transitions from the $J = 2$, $M_J = \pm 2$ states is weaker than for transitions from the $J = 2$, $M_J = 0, \pm 1$ states, even at zero magnetic field, in agreement with the M_J selection rule (see Eq. (3)). The mixing of the different M_J components of the $S = 0$, $J = 1$ and $S = 1$, $J = 1$ states induced by the spin–orbit coupling also changes in magnetic field. This is due to the different energy separation between the various M_J components associated with the $S = 0$ and 1 states in magnetic field.

Acknowledgements

Financial support for this work was provided by the Swedish Council for Engineering Sciences (TFR), the SSF program SICEP, and ABB Corporate Research.

References

[1] W. J. Choyke, in: Proceedings of the International Conference on Radiation Effects in Semiconductors, IOP Conf. Proc., Institute of Physics and Physical Society, London, 1977, p.58.
[2] Yu.A. Vodakov, G.A. Lomakina, E.N. Mokhov, M.G. Ramm, V.I. Sokolov, Sov. Phys. Semicond. 20 (1986) 1347.
[3] T. Egilsson, J.P. Bergman, I.G. Ivanov, A. Henry, E. Janzén, Phys. Rev. B 59 (1999) 1956.
[4] J.P. Bergman, C.I. Harris, O. Kordina, A. Henry, E. Janzén, Phys. Rev. B 50 (1994) 8305.
[5] J.P. Bergman, O. Kordina, E. Janzén, Phys. Stat. Sol. A 162 (1997) 65.

ELSEVIER

Physica B 273–274 (1999) 681–684

PHYSICA B

www.elsevier.com/locate/physb

Effect of grown-in biaxial strain on deep level defects in $Si_{1-y}C_y/Si$ epitaxial heterostructures

D.V. Singh[a,*], T.O. Mitchell[a], J.L. Hoyt[a], J.F. Gibbons[a], N.M. Johnson[b], W.K. Götz[b,1]

[a]*Solid State Electronics Laboratory, CIS-X, Room 128X, Stanford University, Stanford, CA 94305, USA*
[b]*Xerox Palo Alto Research Center, Palo Alto, CA 94303, USA*

Abstract

We report the first study of traps in strained $Si_{1-y}C_y$ random alloys grown on Si ⟨1 0 0⟩ substrates using chemical vapor deposition. Deep level transient spectroscopy (DLTS) measurements of n-type Schottky diodes fabricated on $Si/Si_{1-y}C_y/Si$ heterostructures ($y < 0.02$) were used to study the impact of carbon and grown-in strain on the formation of deep levels. The observed deep level activation energies were found to vary with carbon fraction, and ranged between 0.175 and 0.225 eV, measured with respect to the conduction band. The systematic variation in the measured activation energies with carbon fraction suggests the splitting of a single deep level due to strain in the $Si_{1-y}C_y$ alloy layer. The DLTS peaks exhibit anomalous broadening which increases with increasing carbon fraction and can be explained using an alloy broadening model.

Keywords: $Si_{1-y}C_y$; DLTS; deep level; Alloy broadening; Stress; Splitting

The prospect of increased flexibility in band gap engineering and alleviation of critical thickness constraints has fueled interest in the study of substitutional carbon in Column IV heterostructures [1–4] such as $Si_{1-y}C_y/Si$ and $Si_{1-x-y}Ge_xC_y/Si$. Thin $Si_{1-y}C_y$ ([C] ⩽ 2 at%) films grown pseudomorphically on Si are under biaxial tensile strain in directions parallel to the growth plane. The uniaxial component of the strain perpendicular to the growth plane splits the six-fold degeneracy of the conduction band edge, E_c. The strain induced splitting of E_c in conjunction with the intrinsic alloying effect of carbon gives rise to a conduction band offset of ~65 meV/at% C at the $Si/Si_{1-y}C_y$ heterojunction [5,6]. The presence of a conduction band offset and no significant valence band offset is complementary to the band alignment in the $Si/Si_{1-x}Ge_x$ system, and has important device implications. In addition, C concentrations on the order of ~0.1 at% have been shown to eliminate transient enhanced diffusion of boron in Si [7]. However, in order to fully exploit the beneficial effects of carbon for device applications, it is essential to study its impact on the formation of deep levels. The study of deep levels is also an important tool in understanding how carbon interacts with the lattice.

In this paper we study the impact of carbon on the formation of deep levels in $Si_{1-y}C_y$ random alloys with varying carbon fractions using deep level transient spectroscopy (DLTS). The $Si/Si_{1-y}C_y/Si$ heterostructures were grown epitaxially on 4″ Czochralski n-Si ⟨1 0 0⟩ substrates in a rapid thermal chemical vapor deposition (RTCVD) reactor equipped with a load lock. The primary source gases were silane (SiH_4) for silicon and methylsilane (SiH_3CH_3) for carbon. Details of the growth and materials analysis have been discussed elsewhere [8–11]. A schematic representation of the sample structure is shown in Fig. 1. All samples have a thick

* Corresponding author. Fax: + 1-650-723-4659.
E-mail address: dinkar@cvd.stanford.edu (D.V. Singh)
[1] Presently at Hewlett Packard Company, San Jose, CA 95131, USA.

0921-4526/99/$ - see front matter
PII: S0921-4526(99)00603-1

n-type Si layer grown at 1000°C using dichlorosilane (DCS). A 2000 Å thick n-type silicon layer was then grown at 600°C, followed by the strained alloy layer grown at 550°C which was capped by a thick Si layer (~3300 Å) grown at 700°C. All samples were in situ doped n-type with phosphine to doping levels of $3–5 \times 10^{16}$ cm^{-3} in the vicinity of the heterojunction. The Si cap was made sufficiently thick to ensure that the alloy layer remains outside the depletion region at zero bias. Schottky diodes were formed by evaporating Au dots, 0.5–1 mm in diameter. Backside contacts were formed by aluminum deposition.

The substitutional carbon fraction was determined by high-resolution X-ray diffraction (XRD) using a Philips Materials Research Diffractometer. Excellent agreement is obtained between measured and simulated rocking curves, indicating material of high crystalline quality. The various assumptions made in the extraction of the carbon concentration have been described in earlier studies [9]. Good agreement is found between the carbon fractions obtained using secondary ion mass spectrometry (SIMS) and X-ray analysis for the samples used in this study, indicating that the carbon is mostly substitutional.

DLTS measurements were performed on $Si_{1-y}C_y$ samples with approximately 0.14, 0.5 and 0.95 at% carbon. A Si Schottky diode with identical growth and post-epitaxial processing conditions (except for the presence of carbon) served as a control device in order to isolate the effect of carbon on deep level formation. No DLTS signal was observed in the control device, for the same measurement conditions used for the test devices.

DLTS signals are sometimes associated with heterojunction band offsets. However, previous measurements of the band offsets using metal–oxide–semiconductor (MOS) capacitors [6] and admittance spectroscopy [12] indicate relatively small conduction band offsets (<70 meV) for all the samples studied here. In the temperature range scanned (80–300 K) the emission rates over the conduction band offset are sufficiently high to preclude any band offset related capacitance transients in the DLTS measurements.

Fig. 2(a), which shows the DLTS spectrum for $Si_{1-y}C_y$ ($y \sim 0.95$ at%) exhibits two distinct peaks, each of which is significantly broadened. The solid line represents the best fit to the data using the alloy broadening model proposed by Omling et al. [13]. This model accounts for the random positions of the Si and C atoms using a Gaussian distribution of the trap activation energy, $g(E_a)$, having a width, S, and centered about an average activation energy, E_{ao}. This model explains the anomalous broadening of the observed DLTS peaks, which cannot be accounted for by conventional analysis. The free parameters used to fit the DLTS spectra are E_{ao}, S, the temperature independent capture cross section σ_n and the height of the capacitance transient ΔC. For

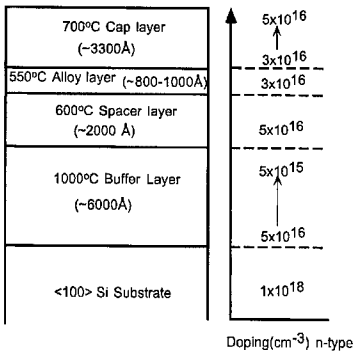

Fig. 1. Schematic representation of the structure of a typical sample used in this work for deep level transient spectroscopy.

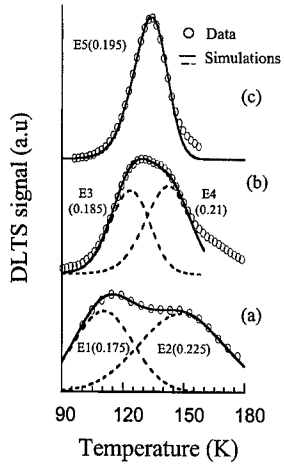

Fig. 2. DLTS signals for samples with layers of (a) $Si_{0.9905}C_{0.0095}$, (b) $Si_{0.995}C_{0.005}$, and (c) $Si_{0.9986}C_{0.0014}$. The solid line represents the best fit to the data (circles) using the alloy broadening model proposed by Omling et al. [13] and is the sum of the signals from the two trap levels (dashed lines).

a given sample, a single set of parameters (E_{ao}, S, σ_n) gives an excellent fit to the DLTS spectra over the entire range of rate windows studied. The two peaks in the spectra shown in Fig. 2(a) correspond to trap levels centered below E_c at E1(0.175) and E2(0.225), with alloy broadening widths, S, of 23 and 31 meV, respectively.

The $Si_{1-y}C_y$ sample with 0.5 at% C exhibits a broadened peak with a distinct shoulder as shown in Fig. 2(b). Due to alloy broadening, the two DLTS peaks are not fully resolved. Fitting the spectrum to two alloy broadened peaks yields levels at E3(0.185) and E4(0.21). Both peaks are alloy broadened with $S \sim 12$ and 14 meV, respectively. The decrease in alloy broadening width compared to the sample with [C] ~ 0.95 at% is consistent with the lower carbon fraction. Fig. 2(c) shows the DLTS spectra for $Si_{1-y}C_y$ with [C] ~ 0.14 at%. This

sample has a single peak at E5(0.195) and exhibits the least amount of alloy broadening ($S < 5$ meV). The alloy broadening effect of carbon in Si is illustrated in Fig. 3, which compares the measured DLTS data to simulations both with and without alloy broadening, for the sample with 0.95 at% C.

SIMS analysis of the samples indicates that methylsilane, which is the source gas for carbon, introduces oxygen (10^{17}–10^{18} cm^{-3}) in the $Si_{1-y}C_y$ layers. Several deep levels associated with carbon and oxygen in silicon have been reported in the literature. The trap levels E1(0.175) and E3(0.185) might be related to a C_s–C_i complex [14,15] or to the A center (oxygen–vacancy pair) [16], both of which have reported activation energies of E(0.17). A complex involving interstitial carbon, C_i, and phosphorus, P_s, [14] observed in electron irradiated silicon has metastable states with activation energies at E(0.27), E(0.23), E(0.21) and E(0.3). Since our samples contain both carbon and phosphorus (n-type dopant), it is possible that the levels at E2(0.225), E4(0.21) and E5(0.195) are related to a P_s–C_i complex.

Attributing the observed deep levels to different complexes cannot however provide a satisfactory explanation for the systematic variation in the measured activation energies with increasing carbon fraction. It seems likely that increasing strain with higher carbon fraction plays an important role in interpreting the DLTS results. Previous studies [17,18] have shown that deep levels under uniaxial stress can give rise to multiple DLTS peaks reflecting the symmetry of the defect. As mentioned earlier the incorporation of substitutional carbon in Si results in biaxial tensile strain parallel to the plane of growth. This is equivalent to a uniaxial component of strain perpendicular to the growth plane in addition to a hydrostatic component. Hence, it is possible that strain induced splitting of a single level at E5(0.195) may be responsible for the emergence of two distinct levels with increasing carbon fraction. From the DLTS spectra in Fig. 2, the splitting of a single peak into two signals is apparent. Fig. 4 illustrates the measured deep level activation energies as a function of carbon concentration and strain. The difference between the two activation energies (i.e. the measured splitting of the level) increases at the rate of approximately 61 meV/at% C. By assuming the mismatch, m, defined by $m = (a_{alloy} - a_{Si})/a_{Si}$ is -0.395%/at% C, the elastic modulus $s_{11} = 7.68 \times 10^{-13}$ dyn/cm^2 and using Poissons ratio $v = 0.278$, the observed splitting of 61 meV/at% C is equivalent to 67 meV/GPa in uniaxially strained Si, along $\langle 1\,0\,0\rangle$. Strain-induced splittings of similar magnitude have been observed previously for defect levels in Si, e.g. the splitting of the A-center under $\langle 1\,0\,0\rangle$ uniaxial stress is $\sim$74 meV/GPa [18].

Uniaxial strain along the $\langle 1\,0\,0\rangle$ direction also splits the six-fold degeneracy of the conduction band minima with the four in-plane valleys increasing and the two out of plane valleys decreasing in energy. This conduction band splitting is on the order of 65 meV/at% C, which is close to the measured value of 61 meV/at% C for the splitting of the deep level. The possibility of multiple activation energies due to emission by the same deep level to the split conduction bands must be considered. However, in the temperature range spanning the measured DLTS spectra, the calculated emission rates, $\tau_e(\tau_e \propto \exp\{(E_c - E_t)/kT\})$ to the upper and lower conduction bands differ by more than an order of magnitude. Thus, the observed signal will arise primarily from emission to the lower conduction band. This large difference in calculated emission rates between the upper and lower conduction bands ensures that the multiple activation energies observed are not due to the splitting of the conduction band, and are most likely associated with the energy splitting of a deep level.

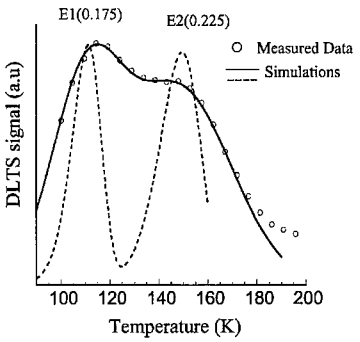

Fig. 3. Measured DLTS signal (circles) for $Si_{0.9905}C_{0.0095}$ and simulations with (solid line) and without (dashed line) alloy broadening. The alloy broadening parameters used to fit the two signals are S1 = 23 and S2 = 31 meV. Apart from the alloy broadening, identical trap parameters are used in the two simulations.

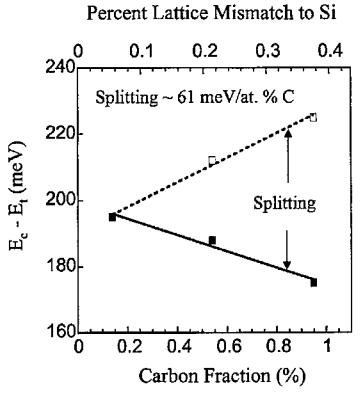

Fig. 4. Measured trap levels in $Si_{1-y}C_y$ as a function of carbon fraction and strain.

In summary, we have studied traps in strained, epitaxial $Si/Si_{1-y}C_y$ heterostructures using DLTS. The measured deep level activation energies exhibit a systematic variation with carbon fraction. This trend is consistent with a strain-induced energy splitting of a single level at $E_c - 0.195$ eV, where the strain originates during pseudomorphic growth of the epitaxial $Si_{1-y}C_y$ on Si. Alloy broadening of the deep level signals is significant in these samples, even for C concentrations on the order of 1 at%.

Acknowledgements

We are grateful to Gernot Pomrenke of the Defense Advanced Research Projects Agency and the Army Research Office for support of this work.

References

[1] S. Bodnar, J.L. Regolini, J. Vac. Sci. Technol. A 13 (1995) 2336.
[2] J. Mi, P. Warren, P. Letourneau, M. Judelewicz, M. Gailhanou, M. Dutoit, C. Dubois, J.C. Dupuy, Appl. Phys. Lett. 67 (1995) 259.
[3] Z. Atzmon, A.E. Bair, E.J. Jaquez, J.W. Mayer, D. Chandrasekhar, D.J. Smith, R. Hervig, M.J. Robinson, Appl. Phys. Lett. 65 (1994) 2559.
[4] C.W. Liu, A. St. Amour, J.C. Sturm, Y.R.J. Lacroix, M.L.W. Thewalt, C.W. Magee, D. EagleSham, J. Appl. Phys. 80 (1996) 3043.
[5] K. Rim, T.O. Mitchell, D.V. Singh, J.L. Hoyt, J.F. Gibbons, Appl. Phys. Lett. 72 (1998) 2286.
[6] D.V. Singh, K. Rim, T.O. Mitchell, J.L. Hoyt, J.F. Gibbons, J. Appl. Phys. 85 (1999) 978.
[7] H. Rucker, B. Heinemann, W. Ropke, R. Kurps, D. Kruger, G. Lippert, H.J. Osten, Appl. Phys. Lett. 73 (1998) 1682.
[8] T.O. Mitchell, J.L. Hoyt, J.F. Gibbons, Appl. Phys. Lett. 71 (1997) 1688.
[9] J.L. Hoyt, T.O. Mitchell, K. Rim, D.V. Singh, J.F. Gibbons, Thin Solid Films 321 (1998) 41.
[10] J.L. Hoyt, T.O. Mitchell, K. Rim, D.V. Singh, J.F. Gibbons, in: M.A. Allendorf, C. Bernard (Eds.), Chemical vapor deposition Proceedings of the XIV International Conference and EUROCVD-11, Electrochemical Society, Pennington, NJ, 1997, pp. 1254–1265.
[11] J.L. Hoyt, T.O. Mitchell, K. Rim, D. Singh, J.F. Gibbons, in: E.A. Fitzgerald, D. Houghton, P.M. Mooney (Eds), Material Research Society Symposium Proceedings, Spring Meeting, 1998, Epitaxy and applications of Si-based heterostructures, Material Research Society, Pittsburgh, PA, 1998, pp. 263–274
[12] D.V. Singh, K. Rim, T.O. Mitchell, J.L. Hoyt, J.F. Gibbons, J. Appl. Phys. 85 (1999) 985.
[13] P. Omling, L. Samuelson, H.G. Grimmeiss, J. Appl. Phys. 54 (1983) 5117.
[14] M.T. Asom, J.L. Bentom, R. Sauer, L.C. Kimmerling, Appl. Phys. Lett. 51 (1987) 256.
[15] L.W. Song, B.W. Benson, G.D. Watkins, Appl. Phys. Lett. 51 (1987) 1155.
[16] G.D. Watkins, J.W. Corbett, Phys. Rev. 121 (1961) 1001.
[17] J.M. Meese, J.W. Farmer, C.D. Lamp, Phys. Rev. Lett. 51 (1983) 1286.
[18] X.C. Yao, J.X. Mou, G.G. Qin, Phys. Rev. B 35 (1987) 5734.

ELSEVIER

Physica B 273–274 (1999) 685–688

PHYSICA B

www.elsevier.com/locate/physb

Self-diffusion on the arsenic sublattice in GaAs investigated by the broadening of buried nitrogen doping layers

N.A. Stolwijk[a,*], G. Bösker[a], J.V. Thordson[b], U. Södervall[b], T.G. Andersson[b], Ch. Jäger[c], W. Jäger[c]

[a]*Institut für Metallforschung, Universität Münster, Wilhelm-Klemm-Strasse 10, D-48149 Münster, Germany*
[b]*Division of Microelectronics and Nanoscience, Department of Physics and Engineering Physics, Chalmers University of Technology and Göteborg University, S-41296 Göteborg, Sweden*
[c]*Mikrostrukturanalytik, Technische Fakultät, Universität Kiel, D-24143 Kiel, Germany*

Abstract

We have studied the diffusion-induced broadening of a nitrogen doping region embedded in a GaAs layer that was grown by molecular beam epitaxy on a GaAs substrate. The markedly non-Gaussian shape of the N distribution measured by secondary ion mass spectroscopy after isothermal annealing at temperatures between 724°C and 922°C can be excellently described within the framework of a kick-out mechanism, i.e., $N_s + I_{As} \rightleftharpoons N_i$, which involves As interstitials I_{As}, N_s atoms substitutionally incorporated on the As sublattice, and interstitially dissolved N_i atoms. This yields not only nitrogen-related diffusivities based on the mobility of N_i but also As-sublattice-related self-diffusivities D^I_{As} associated with I_{As} movement. The latter data are represented by $D^I_{As} = 0.25 \exp(-3.88\ \mathrm{eV}/k_B T)\ \mathrm{cm}^2\ \mathrm{s}^{-1}$ and agree with directly measured As tracer diffusion coefficients. The present results provide evidence that self-interstitials are more important for atomic transport processes on the As sublattice than vacancies.

Keywords: Diffusion; GaAs; Interstitials; Nitrogen

1. Introduction

Over the past decades self-diffusion experiments in GaAs, which were carried out with the aid of radioactive tracers, have proven to be quite difficult. This is due to the smallness of the self-diffusion coefficients in conjunction with the high vapor pressure of As which tends to induce surface degradation and non-equilibrium of native point defects. For the Ga component, such complications could be eliminated in recent investigations of the interdiffusion in ^{69}GaAs/^{71}GaAs (stable-)isotope heterostructures [1]. For As, however, a similar approach is not possible since there exists only one stable As isotope (i.e. ^{75}As). Fortunately, in favorable cases pertinent information on self-diffusion can be obtained through impurity diffusion involving interstitial-substitutional exchange. Well-known examples are the vacancy-controlled diffusion of Cu in Ge [2] via the dissociative mechanism and the self-interstitial-controlled diffusion of Au [3] or Zn [4] in Si via the kick-out mechanism. Here we will show that the broadening of a buried N doping layer in GaAs upon annealing can be interpreted as As-interstitial-controlled diffusion of N via an As-sublattice-related kick-out mechanism. This enables us to deduce from the experimentally observed N profiles the interstitial component of the As self-diffusivity in a wide range of low temperatures and to compare the results with directly measured As tracer-diffusion coefficients reported earlier [5–7].

* Corresponding author. Tel.: + 49-251-83-39013; fax: + 49-251-83-38346.
E-mail address: stolwij@nwz.uni-muenster.de (N.A. Stolwijk)

0921-4526/99/$ - see front matter
PII: S0921-4526(99)00610-9

2. Experiment

Fig. 1 shows the as-grown structure used in our experiments. Semi-insulating GaAs served as substrate on which a ca. 1000 nm thick GaAs layer was grown at 580°C by solid-source molecular beam epitaxy (MBE). After 500 nm of buffer-layer growth, the process was interrupted to introduce the N_2 flow and to ramp up the RF power of the plasma source to 600 W for N_2 excitation, however, without igniting the plasma. In this way a nominally 30 nm thick GaAs:N doping layer with a comparatively low N concentration of about 10^{19} cm^{-3} was grown. Another growth interruption was made after completion of the GaAs:N layer in order to let the N_2 pressure drop to 5×10^{-7} Torr before growing the cap layer of 500 nm thickness.

Diffusion annealing of 5×5 mm^2 samples cut from a single as-grown wafer was performed between 724°C and 922°C in closed quartz ampoules. These also contained crushed undoped GaAs and pure As to reduce surface degradation and to establish a partial As_4 vapor pressure $P_{As_4} = 0.15 \pm 0.05$ atm. Nitrogen distributions before and after annealing were measured by secondary ion mass spectroscopy (SIMS) using Cs^+ as primary ions. GaN^- with mass 83 was selected as a secondary ion with sufficient yield. In order to distinguish $^{69}Ga^{14}N$ from $^{71}Ga^{12}C$ we also monitored mass 81 of $^{69}Ga^{12}C$. This procedure unambiguously revealed that the peak at 500 nm depth only contains nitrogen [8]. Conversion of the $^{69}Ga^{14}N$ signal into N concentration relied on a GaAs:N implantation standard for calibration.

Transmission electron microscopy (TEM) was used to check the presence or absence of microstructural defects after annealing. Examinations of cross-sectional samples were performed using a Philips CM30 microscope at 300 kV.

3. Results and analysis

Fig. 2 shows the N distribution of a sample annealed at 841°C for 5 h in comparison with the distribution recorded on the as-grown wafer. To evaluate the profile broadening process, sets of coupled diffusion–reaction equations were solved (cf. [4,9]) using the as-grown distribution as starting profile. The solid and dash-dotted line in Fig. 2 are the results of such simulations as will be elucidated in the following.

The broadened N profile of Fig. 2 has an anomalous shape as becomes obvious from the comparison with the Gaussian-like dash-dotted line. This implies that diffusion mechanisms predicting a concentration-independent diffusion coefficient such as the interstitial mechanism, the vacancy mechanism, and the dissociative mechanism (see below) cannot explain the experimental observations. Instead, a good fit (solid line in Fig. 2) is

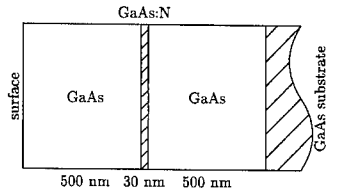

Fig. 1. Schematic of the GaAs:N buried layer structure grown by MBE on a semi-insulating GaAs substrate.

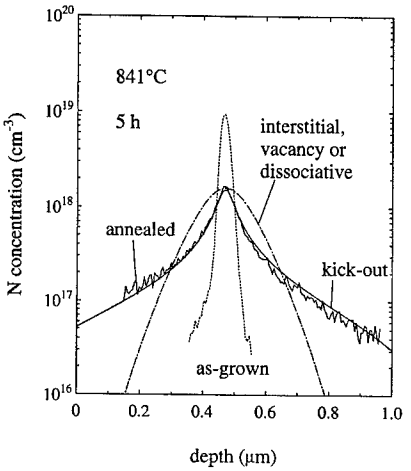

Fig. 2. N distribution after annealing compared with the as-grown starting profile. Computer-simulated curves demonstrate the validity of the kick-out mechanism as well as the failure of alternative mechanisms inducing Gaussian-like broadening.

obtained by the kick-out mechanism

$$N_s + I_{As} \rightleftharpoons N_i. \quad (1)$$

Here N_s denotes the immobile substitutional configuration of the group V element nitrogen, i.e. incorporated on the As sublattice, which may react with an As interstitial I_{As} to get into the mobile interstitial configuration N_i. Electric charges are neglected because N_s (with concentration C_s) does not introduce any doping effect while the concentrations C_i of N_i and C_I of I_{As} do not exceed the intrinsic carrier density at the diffusion temperature, i.e., $C_i, C_I \lesssim n_i(T) \approx 10^{17}$ cm^2 s^{-1}. The latter condition relates to the finding that meaningful results are only obtained when C_i, $C_I \ll C_s$ holds in the relevant parts of the profile with $C_s \leqslant 10^{19}$ cm^2 s^{-1} (cf. Fig. 2).

The special shape of the N profile is only reproduced by the kick-out model if, in addition, the following conditions are met: (i) The forward and reverse reaction rates associated with interstitial–substitutional exchange are much faster than any other step in the diffusion process. (ii) The diffusion region must be virtually free of sinks and

sources for N and I_{As}. This is evidenced by the TEM investigation of the annealed sample depicted in Fig. 2 showing no microstructural defects – either as-grown or diffusion-induced – in the cross-sectional region examined. From this we deduce a – probably overestimated – upper limit of the dislocation density of 2×10^6 cm^{-2}. These dislocations, however, can be neglected since their mutual separation ($\gtrsim 10$ μm) is much larger than the width of the diffusion zone, i.e., the epilayer thickness. (iii) Transport of I_{As} must be slower than transport of N_i, which is expressed by the relationship $C_I D_I < C_i D_i$. Here D_I and D_i are the diffusivities of I_{As} and N_i, respectively.

Under these circumstances a distinct I_{As} undersaturation develops as shown by simulation results displayed in Fig. 3. This undersaturation relates to the I_{As} equilibrium concentration C_I^{eq} which is supposed to be established at the onset of annealing throughout the epilayer and maintained during annealing both at the surface and the interface to the substrate. The C_I^{eq} value itself is not unambiguously resolved, however, and therefore has been arbitrarily chosen within the allowable range. Fig. 3 further reveals that N_i migrates comparatively fast towards the boundaries. In the simulation allowance is made for an (adjustable) outflux of N_i through either boundary, for which independent evidence is provided by the N accumulations at the boundaries observed in similar experiments. More details about the simulation can be found in Ref. [8].

Fitting of the broadened profiles within the above scenario yields information on both N diffusion and I_{As}-mediated self-diffusion [8]. In this paper we will focus on self-diffusion data which is contained in the parameter

$$D^I_{As} = C_I^{eq} D_I / C_0, \tag{2}$$

with $C_0 = 2.215 \times 10^{22}$ cm^{-3} denoting the density of As sublattice sites. The results are displayed in Fig. 4 (solid squares) and fitted by the Arrhenius expression (solid line)

$$D^I_{As} = 0.25 \exp(-3.88 \text{ eV}/k_B T) \text{ cm}^2 \text{ s}^{-1}. \tag{3}$$

Here the activation energy of 3.88 eV arises with a standard deviation of 0.10 eV while the corresponding uncertainty in the pre-exponential factor amounts to a factor of 2.8 in either direction.

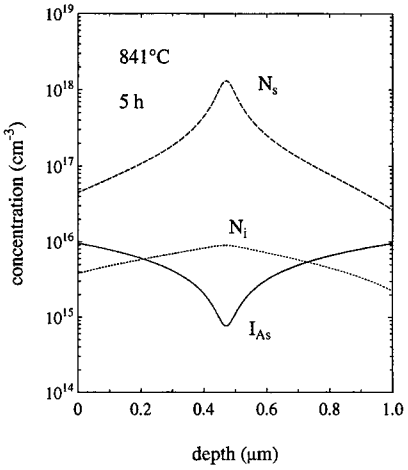

Fig. 3. Distributions of the species involved in the kick-out diffusion model which originate from the numerical simulation of the broadened N profile shown in Fig. 2. Concentration levels of I_{As} and N_i are arbitrary within allowable ranges.

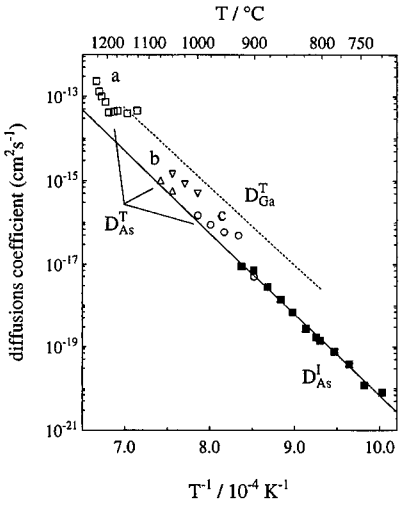

Fig. 4. Self-difusion coefficients in intrinsic GaAs under As-rich conditions: I_{As}-related D^I_{As} data deduced from N profile broadening (closed symbols and solid line; this work), As tracer data D^T_{As} (open symbols; a: [5], b: [6], c: [7]), and Ga tracer data D^T_{Ga} (dotted line; [1]). The data of Ref. [6] refer to two different As_4 ambient pressures (cf. [8]).

4. Discussion

Fig. 4 compares the present data with As tracer diffusion coefficients D^T_{As} from various authors [5–7]. All data are representative of intrinsic GaAs under As-rich ambient. Differences of up to one order of magnitude in P_{As_4} among the various studies may be ignored here since their influence on the diffusivity data is expected to be at most a factor of 2, i.e., from mass action law considerations [8].

D^T_{As} comprises, in addition to the interstitial component D^I_{As}, the vacancy component of As diffusion in GaAs, $D^V_{As} = C_V^{eq} D_V / C_0$, i.e.,

$$D^T_{As} = f_I D^I_{As} + f_V D^V_{As} \tag{4}$$

with the V_{As} equilibrium concentration C_V^{eq}, the V_{As} diffusivity D_V and the diffusion correlation factors f_I, $f_V \approx 1$ [10]. It is seen in Fig. 4 that D_{As}^I agrees with the lower D_{As}^T data. Moreover, there are indications that the higher D_{As}^T values may have been affected by surface evaporation effects [7]. This suggests that for intrinsic GaAs under As-rich conditions the contribution of I_{As} to As diffusion is substantial or even dominant.

It is noteworthy that in one of our experiments, i.e. at 859°C, elemental As was omitted in the diffusion ambient. However, no significant influence on N profile broadening was found. This can be understood from the notion that the annealing time used here (2.1 h) was too short to let the (buried) GaAs:N diffusion zone equilibrate with the ambient. This indicates that our D_{As}^I data are representative of the epilayer composition which thus rather seems to correspond to As-rich GaAs. This point, however, needs further clarification.

Fig. 4 also shows the Ga tracer diffusion coefficients in GaAs of Bracht et al. [1], $D_{Ga}^T = 0.64 \exp(-3.71\,\text{eV}/k_B T)\,\text{cm}^2\,\text{s}^{-1}$, which we regard as the most reliable data of this kind. Interestingly, activation energy and pre-exponential factor are comparable to those of D_{As}^I. Connected with this, D_{Ga}^T exceeds D_{As}^I (or D_{As}^T) by only one order of magnitude. In general, such findings may point to a common diffusion mechanism. One could think of joint diffusion of Ga and As via vacancy pairs ($V_{Ga}V_{As}$) or triple defects ($V_{As}As_{Ga}V_{As}$) following earlier suggestions for GaSb [11]. In the present case, however, these mechanisms seem hard to rationalize since Ga diffusion in GaAs is found to be dominated by V_{Ga} [12] but As diffusion rather by I_{As} (this work). Moreover, the vacancy-pair or triple-defect mechanism only sustains D_{Ga}^+/D_{As}^+ ratios between 2.6 and 1/2.6 [11]. Therefore we believe that the virtually equal magnitude of the Ga and As activation energies is rather fortuitous.

5. Conclusions

N profile broadening in MBE-grown intrinsic GaAs is governed by As interstitials which participate in N_i–N_s exchange through the kick-out mechanism. Comparing the I_{As} transport properties so-obtained with As tracer diffusion coefficients indicates that under As-rich conditions also As diffusion in GaAs proceeds to a major extent via As interstitials. These results support the view that self-interstitials may dominate over vacancies as diffusion vehicle on the As sublattice.

Acknowledgements

We thank H. Mehrer for reading the manuscript. Research funding by BMBF (Germany) and by TFR and NUTEK (Sweden) as well as travel grants from DAAD (Germany) and the Swedish Institute are gratefully acknowledged.

References

[1] H. Bracht, E.E. Haller, K. Eberl, M. Cardona, Appl. Phys. Lett. 74 (1999) 49.
[2] N.A. Stolwijk, W. Frank, J. Hölzl, S.J. Pearton, E.E. Haller, J. Appl. Phys. 57 (1985) 5211.
[3] N.A. Stolwijk, B. Schuster, J. Hölzl, Appl. Phys. A 33 (1984) 133.
[4] H. Bracht, N.A. Stolwijk, H. Mehrer, Phys. Rev. B 52 (1995) 16 542.
[5] B. Goldstein, Phys. Rev. 121 (1960) 1305.
[6] H.D. Palfrey, M. Brown, A.F.W. Willoughby, J. Electron. Mater. 12 (1983) 863.
[7] G. Bösker, N.A. Stolwijk, H. Mehrer, A. Burchard, U. Södervall, Mater. Res. Soc. Symp. Proc. 527 (1998) 347.
[8] G. Bösker, N.A. Stolwijk, J.V. Thordson, U. Södervall, T.G. Andersson, Phys. Rev. Lett. 81 (1998) 3443.
[9] G. Bösker, N.A. Stolwijk, H. Mehrer, U. Södervall, W. Jäger, J. Appl. Phys. 86 (1999) 791.
[10] J. Philibert, Atom Movements – Diffusion and Mass Transport in Solids, Les Editions de Physique, Les Ulis, 1991.
[11] D. Weiler, H. Mehrer, N.A. Stolwijk, Philos. Mag. A 50 (1984) 559.
[12] T.Y. Tan, U. Gösele, S. Yu, Crit. Rev. Solid State Mater. Sci. 17 (1991) 47.

ELSEVIER

Physica B 273–274 (1999) 689–692

PHYSICA B

www.elsevier.com/locate/physb

Hydrogen passivation of $Al_xGa_{1-x}As$/GaAs studied by surface photovoltage spectroscopy

H.Ö. Olafsson, J.T. Gudmundsson*, H.G. Svavarsson, H.P. Gislason

Science Institute, University of Iceland, Dunhaga 3, IS-107 Reykjavík, Iceland

Abstract

We study the effect of hydrogen passivation on $Al_xGa_{1-x}As$ grown by liquid-phase epitaxy (LPE) on semi-insulating GaAs. Using surface photovoltage (SPV) spectroscopy and Hall measurements we investigate the effect of hydrogenation on $Al_xGa_{1-x}As$ epilayers with electron concentrations in the range 10^{16}–$10^{17}\,cm^{-3}$. We measure the minority carrier diffusion length in the as-grown $Al_xGa_{1-x}As$ epilayers to be in the range 0.1–0.8 μm and to increase significantly upon hydrogenation. Hydrogen passivation of interface states at the heterojunction is demonstrated for epilayers with low carrier concentration. We apply the result from the SPV measurements to speculate on the band bending at the heterojunction.

Keywords: AlGaAs; Hydrogenation; Surface photovoltage; Passivation

1. Introduction

It is well known that atomic hydrogen passivates the electrical activity of both shallow acceptor and donor dopants in virtually all semiconductors. This has been the subject of extensive study and the passivation of shallow dopants and formation of hydrogen complexes with shallow levels are in most cases well understood [1,2]. It is well established that hydrogen diffusion into GaAs results in the neutralization of shallow donors and DX centers [3]. Furthermore, hydrogen also passivates deep levels and deep level passivation is found to be more stable than shallow level passivation. Currently, microscopic understanding of the passivation of deep levels is incomplete.

Surface photovoltage (SPV) spectroscopy is a powerful contact-less technique to study the diffusion length of minority carriers, variation of surface potentials, distribution of surface states and band bending at surfaces and interfaces [4,5]. Furthermore, applications in control of microcontamination and wafer mapping are of increasing interest [6]. In this work we demonstrate the use of SPV spectroscopy to examine the $Al_xGa_{1-x}As$/GaAs heterostructure. We investigate the effect of hydrogenation on the minority diffusion length of the $Al_xGa_{1-x}As$ epilayer. Furthermore, we demonstrate the use of SPV to study the influence of hydrogenation in passivating interface states and speculate on band bending at the interface.

2. Sample preparation and experimental details

The $Al_xGa_{1-x}As$ epilayer was grown by liquid-phase epitaxy (LPE) on semi-insulating (SI) GaAs. The four samples examined are denoted S1, S1* and S2, S2*. S1 and S1* are both from the same growth batch and samples S2 and S2* are from another growth batch. Samples S1 and S2 were measured as-grown while samples S1* and S2* were exposed to H_2/Ar plasma in a planar inductive discharge. The details of the inductive discharge used and the plasma properties during hydrogenation are given elsewhere [7,8]. The gas pressure was kept at 20 m Torr with fractional argon pressure of 0.3 and the power applied to the plasma was 400 W for 45 min. No external heating was applied to the sample. The plasma electron density was roughly $6\times10^{16}\,cm^{-3}$ [7]

* Corresponding author. Tel.: +354-525-4800; fax: +354-552-8911.

E-mail address: tumi@hi.is (J.T. Gudmundsson)

0921-4526/99/$ - see front matter
PII: S0921-4526(99)00611-0

and the mean ion bombarding energy was about 18 eV [8].

The majority carrier concentration of the $Al_xGa_{1-x}As$ epilayers was determined by Hall measurements. Using square samples in the van der Pauw configuration [9], ohmic contacts were welded on the four corners with tin coated gold wire. The Hall coefficient R_H was estimated from the slope of the Hall voltage versus the magnetic field B in the range 0–0.75 T.

The SPV measurements were made at room temperature. Following the ASTM standard [5] a lock-in amplifier measures the SPV signal in the chopped light geometry. The light source is a halogen lamp filtered through a 0.5 m monochromator. At each measured wavelength the light flux Φ is monitored by using a calibrated PIN Si photodiode. Power to the lamp is regulated by a computer so that light flux to the sample is constant within $\pm$ 1% for all wavelengths of interest. The SPV signal is capacitively coupled through a conducting transparent window which consists of an indium tin oxide coating deposited on glass. Light intensity was kept low so that the SPV signal is proportional to the light intensity. The modulation frequency was $f = 1097$ Hz. A detailed description of the experimental apparatus and method is given elsewhere [10].

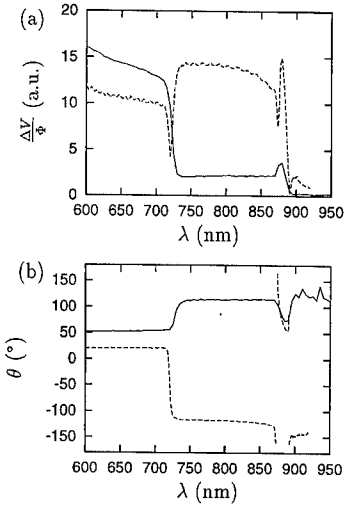

Fig. 1. (a) Normalized SPV amplitude $\Delta V/\Phi$ and (b) SPV phase as a function of wavelength λ for samples S1 (solid line) and S1* (dashed line). Measurements were made at room temperature using the constant flux method. The modulation frequency was $f = 1097$ Hz.

3. Results and discussion

The as-grown $Al_xGa_{1-x}As$ epilayer of sample S1 was found to be n-type with $n \approx 2 \times 10^{16}\,cm^{-3}$. After hydrogenation the $Al_xGa_{1-x}As$ epilayer of sample S1* was n-type with $n \approx 3 \times 10^{15}\,cm^{-3}$. The electron density concentration of the as-grown sample S2 was $n \approx 3 \times 10^{17}\,cm^{-3}$ and remained unchanged upon exposure to hydrogen plasma, referred to as sample S2*. In calculating these carrier concentrations we used the thickness of the $Al_xGa_{1-x}As$ epilayer deduced from photoacoustic spectroscopy (PAS) measurements, $d \approx 25$ μm [10]. The results of the Hall measurements are summarized in Table 1.

Fig. 1(a) shows the amplitude and Fig. 1(b) the phase of the SPV signal for samples S1 and S1*. The light intensity was the same for both samples. In Fig. 1(a) and (b) we see that an abrupt jump in the SPV amplitude and phase is present for both samples at $\lambda = 720$ nm. This corresponds to a photon energy of $E = 1.72$ eV which coincides with the band gap of $Al_{0.24}Ga_{0.76}As$ [11]. This value of the band gap was confirmed by PAS measurements [10]. Thus, for wavelengths $\lambda \in [600, 720\,nm]$ all the light absorption occurs in the $Al_{0.24}Ga_{0.76}As$ epilayer but for $\lambda \in [720, 870\,nm]$ light is absorbed within the SI-GaAs substrate. Let us consider the origin of the SPV signal in these two wavelength regions. For $\lambda \in [600, 720\,nm]$ electron–hole pairs are formed close to the surface. Here the oscillating SPV signal is due to alternations in the band bending near the surface. In the wavelength region $\lambda \in [720, 870\,nm]$ electron–hole pairs

Table 1
Properties of samples S1, S1*, S2 and S2* at room temperature. Here x is the alloy parameter for $Al_xGa_{1-x}As$. The carrier concentration, n_H, and the mobility, μ_H, were found using Hall measurements. The minority carrier diffusion length L_p was found using SPV measurements

Sample	x	n_H ($\times 10^{15}\,cm^{-3}$)	μ_H ($\times 100\,cm^2/(Vs)$)	L_p (μm)
S1	0.24 ± 0.01	20 ± 2	20 ± 2	0.8 ± 0.1
S1*	0.24 ± 0.01	3 ± 0.3	20 ± 2	1.7 ± 0.1
S2	0.21 ± 0.01	300 ± 30	19 ± 2	0.1 ± 0.02
S2*	0.21 ± 0.01	300 ± 30	22 ± 2	0.5 ± 0.1

are formed within the substrate, adjacent to the heterojunction. In this region, carriers diffusing into the heterojunction region will alter the band bending at the junction to produce the SPV signal.

It is well known that SPV spectra reveal the minority carrier diffusion length in extrinsic semiconductors provided that the absorption coefficient is known for the appropriate wavelengths [4,5,10]. Using the absorption coefficient for GaAs [12], but shifted appropriately towards higher energies to allow for the displacement of the band edge in $Al_xGa_{1-x}As$, we found the minority carrier diffusion length to be $L_p^{S1} = 0.8$ μm for the as-grown sample S1 and $L_p^{S1*} = 1.5$ μm for the hydrogenated sample S1*.

Consider the abrupt change in the SPV phase at $\lambda \approx 720$ nm in Fig. 1(b). The phase jump for sample S1 is $+50°$ while the phase jump for sample S1* is $-140°$. For the wavelength regions $\lambda \in [600, 710\,\text{nm}]$ and $\lambda \in [730, 870\,\text{nm}]$ both samples exhibit constant phase. In the wavelength region $\lambda \in [600, 710\,\text{nm}]$ the phase is $+50°$ in the as-grown sample but $+30°$ after hydrogenation. In the wavelength region $\lambda \in [730, 870\,\text{nm}]$ the phase is $+100°$ and $-180°$ for as-grown and hydrogenated sample, respectively. These observations are in accordance with the view that in these two wavelength regions, the SPV signal has different origins, the $Al_xGa_{1-x}As$ epilayer and the $Al_xGa_{1-x}As$/GaAs interface, respectively.

For $\lambda \in [870, 890\,\text{nm}]$ there is a common feature in the SPV spectra for samples S1 and S1*, both in phase and amplitude. Although more pronounced in sample S1*, both samples show a peak in SPV amplitude and a dip in phase. For these wavelengths, light penetrates the sample, reaching the backside which also has an LPE grown layer. Thus, for these wavelengths the backside contributes to the SPV spectra. For $\lambda > 890$ nm the SPV signal for sample S1 is almost zero. This is to be expected because the absorption coefficient is very low for photon energies below the band gap of GaAs. However, for sample S1* we see a hump in the SPV amplitude spectra for $\lambda > 890$ nm. This suggests that introducing hydrogen results in below band gap absorption.

Fig. 2(a) shows the amplitude and Fig. 2(b) the phase of the SPV signal for samples S2 and S2*. The band gap of the $Al_xGa_{1-x}As$ epilayer in these samples reveals itself in a jump both in SPV amplitude and phase at $\lambda \approx 730$ nm which corresponds to $x = 0.21$ [11]. The main characteristics of the SPV spectra of sample S2 remain unchanged upon hydrogenation and it shows features similar to the as-grown sample S1. However, on calculating the minority carrier diffusion length in the epilayer we find that after hydrogenation the hole diffusion length increases significantly, see Table 1. We observe that the SPV signal originating from the heterojunction of samples S2 and S2* are identical. Thus hydrogen passivation did not reach the heterojunction. This is

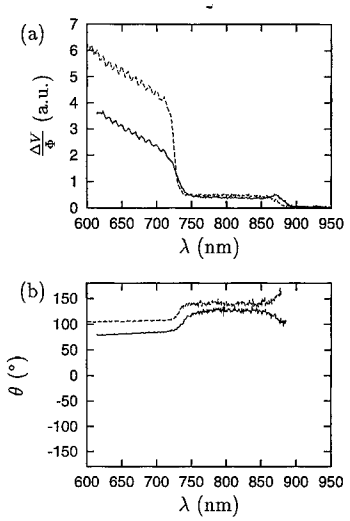

Fig. 2. (a) Normalized SPV amplitude $\Delta V/\Phi$ and (b) SPV phase as a function of wavelength λ for samples S2 (solid line) and S2* (dashed line). Measurements were made at room temperature using the constant flux method. The modulation frequency was $f = 890$ Hz.

to be expected, since the depth to which the carrier concentration is modified is inversely dependent on doping level [3].

SPV measurements on $Al_xGa_{1-x}As$/GaAs heterostructures have been used to distinguish the orientation of dipole moments at the heterojunction in p- and n-type $Al_xGa_{1-x}As$ epilayers grown on n^{++} GaAs [13]. Similarly, we apply the SPV data to predict the band structure in samples S1 and S1* at the heterojunction and near the surface. Fig. 3 shows a schematic of the band diagrams for the $Al_xGa_{1-x}As$/GaAs heterostructures in samples S1 and S1*. The right-hand side of the band diagrams represents the band structure of the GaAs substrate while the left-hand side shows the band structure of the $Al_xGa_{1-x}As$. The solid lines marked E_c and E_v represent the top of the valence band and the bottom of the conduction band, respectively, as a function of position. The dashed line represents the Fermi-level E_F. Hall measurements on the plain GaAs substrate show that the electron carrier concentration is $n \approx 3 \times 10^7\,\text{cm}^{-3}$. Thus, the substrate is semi-insulating and the Fermi-level will be close to the middle of the band gap. As stated above the $Al_xGa_{1-x}As$ epilayer is n-type with $n \approx 2 \times 10^{16}\,\text{cm}^{-3}$ for sample S1 and $n \approx 3 \times 10^{15}\,\text{cm}^{-3}$ for sample S1*. The location of the Fermi-level for these epilayers will thus be close to the conduction band. This is depicted in Fig. 3. We expect both the heterojunction and the surface to have a high concentration of defects that introduce energy levels within the band gap. These energy levels are represented in Fig. 3 by short horizontal

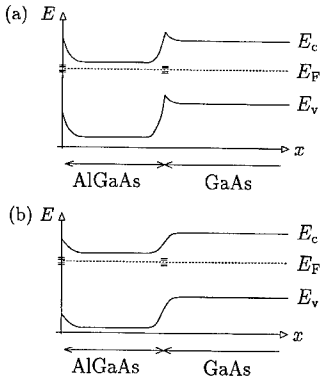

Fig. 3. Schematic band diagrams for the $Al_xGa_{1-x}As/GaAs$ heterostructures of samples S1 (a) and S1* (b). The dashed line represents the Fermi-level E_F. The short horizontal lines at the surface and the heterojunction represent localized energy levels introduced by impurities and defects.

lines within the band gap. Thus, at the heterojunction and at the surface the Fermi-level is displaced from the bulk or epilayer value, contributing to band bending.

Sample S1* shows a larger SPV signal originating from the heterojunction ($\lambda \in [720, 860\,\text{nm}]$) compared to the SPV signal from sample S1. We also see that there is a significant difference in the phase of the SPV signal originating from the heterojunctions of the two samples. We hypothesize that this is due to a difference in band bending at the heterojunction, as seen in Fig. 3. We conclude that this change in band bending is brought on by hydrogen passivation of impurities or defects at the heterojunction, which is at least 25 μm from the surface.

In summary we demonstrate the use of SPV measurements to investigate the effect of hydrogenation on $Al_xGa_{1-x}As/GaAs$ heterostructures. We demonstrate that the hydrogenation passivates interface states at the heterojunction. We measure the minority carrier diffusion length in the as-grown $Al_xGa_{1-x}As$ epilayer to be in the range 0.1–0.8 μm, increasing significantly upon hydrogenation. Furthermore, we apply the measured SPV spectrum to predict the band bending at the heterojunction.

Acknowledgements

This work was partially supported by the University of Iceland Research fund and the Icelandic Research Council. J.T.G. is grateful for the hospitality of Prof. M.A. Lieberman and the experimental assistance of A.M. Marakhtanov at University of California at Berkeley where the hydrogenation was performed.

References

[1] S.J. Pearton, J.W. Corbett, M. Stavola, in: H.-J. Queisser, (Ed.), Hydrogen in Crystalline Semiconductors, Springer, Berlin, 1992.
[2] H.P. Gislason, Phys. Scripta T 69 (1997) 40.
[3] J. Chevallier, W.C. Dautremont-Smith, C.W. Tu, S.J. Pearton, Appl. Phys. Lett. 47 (1985) 108.
[4] A.M. Goodman, J. Appl. Phys. 32 (1961) 2550.
[5] F391-96, Annual Book of ASTM Standards, American Society for Testing and Materials, Philadelphia, PA, 1996.
[6] J. Lagowski, P. Edelman, M.A. Dexter, W. Henley, Semicond. Sci. Technol. 7 (1992) A185.
[7] J.T. Gudmundsson, Plasma Sources Sci. Technol. 7 (1998) 330.
[8] J.T. Gudmundsson, Plasma Sources Sci. Technol. 8 (1999) 58.
[9] L.J. van der Pauw, Philips Res. Rep. 13 (1958) 1.
[10] H.Ö. Olafsson, Master's thesis, University of Iceland, 1999, http://www.raunvis.hi.is/reports/1999/RH-10-99.html.
[11] Swaminathan, A.T. Macrander, Material Aspects of GaAs and InP Based Structures, Prentice-Hall, Englewood Cliffs, NJ, 1992, p. 275.
[12] G.B. Lush, M.R. Melloch, M.S. Lundstrom, H.F. MacMillan, S. Asher, J. Appl. Phys. 74 (1993) 4694.
[13] S. Kumar, T. Ganguli, P. Bhattacharya, U.N. Roy, Appl. Phys. Lett. 23 (1998) 3020.

ELSEVIER

Physica B 273–274 (1999) 693–696

PHYSICA B

www.elsevier.com/locate/physb

Deep-level defects near the surface of Be-doped GaAs grown by molecular beam epitaxy

P. Krispin*, M. Asghar[1], H. Kostial, R. Hey

Paul-Drude-Institut für Festkörperelektronik, Hausvogteiplatz 5-7, D-10117 Berlin, Germany

Abstract

Metal–semiconductor contacts on highly Be-doped GaAs layers grown by molecular beam epitaxy are used to examine deep electronic states by deep-level transient Fourier spectroscopy. Two hole traps at 0.40 and 0.70 eV are found, which are associated with the Ga_{As} (Ga atom on As site) defect. The concentration versus depth profile demonstrates that the intrinsic defect is formed in a 100 nm thick layer near the as-grown surface. Our experimental results confirm thermodynamical calculations for nearly Ga-rich conditions during growth. The Ga_{As} formation energy strongly decreases, when the Fermi level is shifted from the valence band edge to midgap position. The concentration versus depth profile therefore reflects the change of the Ga_{As} formation energy near the GaAs surface during growth. The energy to form Ga_{As} defects at the surface of p-type GaAs is determined to be 1.1 eV, in full agreement with theoretical results.

Keywords: Be-doped GaAs; MBE growth; Ga_{As} hole traps; Ga_{As} defect formation energy

1. Introduction

For a variety of semiconductor devices based on GaAs, the examination of hole traps in p-type epitaxial layers is very important, since relatively low concentrations of defects can have a drastic effect, e.g., on scattering during electronic transport, the efficiency of light-emitting diodes or the series resistance of Bragg reflectors of surface-emitting laser diodes. Compared to n-type GaAs, little information is available about the actual electrical characteristics of p-type GaAs layers grown by molecular beam epitaxy (MBE). In early studies, impurities like Cu, Fe, and Cr, which were monitored as hole traps by deep-level transient spectroscopy [1], dominated the electrical characteristics of p-type GaAs layers [2–5]. However, Chand et al. [6] recently demonstrated that the concentration of impurity-related deep levels in p-type GaAs layers grown by MBE can be effectively reduced by proper selection of the source materials for the growth process. For low-doped GaAs layers with Be concentrations of 4×10^{14} cm^{-3}, it was later confirmed [7] that MBE layers contain several unidentified hole traps with maximal densities in the 10^{12} cm^{-3} range. Results on p-type GaAs layers with hole concentrations of 1×10^{17} cm^{-3} or higher, which are of particular interest for electronic device applications such as heterojunction bipolar transistors or vertical cavity surface-emitting lasers, were however not published up to now.

We have therefore investigated highly Be-doped GaAs layers grown by conventional MBE at 550°C. In particular, epitaxial Al layers have been used as metal-semiconductor (MS) contacts in order to examine deep electronic states in p-type GaAs by deep-level transient Fourier spectroscopy (DLTFS) [8]. The concentration of hole traps in the bulk of epitaxial GaAs layers with hole concentrations of about 1×10^{17} cm^{-3} is in the 10^{12} cm^{-3} range, i.e., highly Be-doped GaAs grown by MBE is practically defect-free as far as the levels in the lower half of the band gap are concerned. In a region near the as-grown surface, however, distinct deep-level defects with thermal activation energies of about 0.40 and

* Corresponding author. Tel.: + 49-30-20377-399; fax: + 49-30-20377-515.

E-mail address: krispin@pdi-berlin.de (P. Krispin)

[1] Permanent address. Department of Physics, Islamia University, Bahawalpur, Pakistan.

0921-4526/99/$ - see front matter
PII: S0921-4526(99)00612-2

0.70 eV are found having a remarkably high concentration of 3×10^{15} cm^{-3}. The electronic signatures of these hole traps are similar to the levels of the Ga_{As} (Ga atom on As site) antisite defect. Thermodynamical calculations for nearly Ga-rich growth conditions are fully confirmed by our experimental results. The energy for forming the Ga_{As} defect during growth at the surface is determined to be 1.1 eV.

2. Experimental details

The investigated Be-doped GaAs layers were grown under ultra-clean conditions by conventional MBE on p^+-type GaAs(0 0 1) substrates with a growth rate of 0.5 μm/h at a growth temperature of 550°C. The V/III beam equivalent pressure ratio was below 10. The hole concentration, which was determined by the capacitance–voltage (C–V) method [9], was about 1×10^{17} cm^{-3}. Ohmic contacts were realized with Au/Be alloys on the substrate. In order to inspect the as-grown surface of highly doped GaAs, Al with a thickness of 80 nm was epitaxially grown in the MBE system on p-type GaAs. Additionally, vacuum-deposited Ti/Au dots were applied as rectifying MS contacts. For examining larger depths, the GaAs layer was recess-etched.

Height of the Schottky barrier Φ_B and ideality factor n were determined by current–voltage and (C–V) measurements. For all studied contacts, Φ_B was about 0.58 eV and n between 1.02 and 1.10. Deep levels were investigated by the DLTFS technique [8], where the time transients of the capacitance C are digitized, and the discrete Fourier coefficients are calculated at each temperature T. The upper temperature was limited to about 300 K, since the low barrier height of the MS contact leads to high leakage currents at higher temperatures. The deep-level concentration N_T was determined from the DLTFS peak height $\Delta C_{max}/C$ according to the full correction given in Ref. [10]

$$\frac{\Delta C_{max}}{C} = \frac{N_T}{2N_A} \frac{(W_p - \lambda)^2 - (W_r - \lambda)^2}{W_p^2}, \quad (1)$$

where N_A is the shallow acceptor concentration, W_r and W_p the thicknesses of the depletion layer at the quiescent reverse bias and at the pulse voltage, respectively, and

$$\lambda = \sqrt{\frac{2\varepsilon\varepsilon_0(E_F - E_T)}{q^2 N_A}}, \quad (2)$$

where $\varepsilon\varepsilon_0$ is the dielectric permittivity, q the elementary charge, E_F the Fermi energy, and E_T the trap energy.

3. Results and discussion

For the epitaxial Al contact on the highly Be-doped GaAs layer, typical deep-level spectra of the DLTFS signal $\Delta C/C$ are displayed in Fig. 1 as curves 1–4. A dominant peak is found at about 300 K, which originates from a hole trap (label H_B). There is a small shift of the peak position to lower temperatures at lower biases opposite to an electric field-enhanced emission of holes. The thermal activation energy decreases from 0.70 to 0.65 eV at lower biases. The configuration around the corresponding point defect apparently changes approaching the as-grown GaAs surface. The broad responses at 180 and 260 K (curve 1 in Fig. 1) are due to interfacial states attributed to the MS contact. Spectra for Ti/Au contacts on GaAs after etching a recess of 80 nm are plotted as curves 5 and 6 in Fig. 1. Note the scaling factor for the spectra 5 and 6. These spectra show that at larger distances from the as-grown surface, the DLTFS signal $\Delta C/C$ of the level H_B is largely reduced and finally below the detection limit of 2×10^{-5}.

By recess etching and changing the reverse bias, the complete depth profile of the level density N_T is obtained for the trap H_B. It is shown in Fig. 2 for the same layer as studied in Fig. 1. It is obvious that the highly Be-doped GaAs layer contains near the as-grown surface a 100 nm thick layer with a remarkable defect concentration of 3×10^{15} cm^{-3}. Sufficiently far from the surface of the layer, the H_B density is found to be less than 10^{13} cm^{-3}. The apparent reduction of the level concentration towards the surface is not real. Because the H_B level with an activation energy of about 0.70 eV remains above the Fermi level for low reverse biases, it is no longer possible to recharge the trap by voltage pulses.

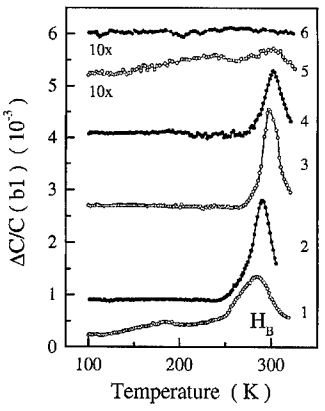

Fig. 1. Deep-level spectra (first sine coefficient $b1$) of GaAs grown by MBE with a hole density of 1×10^{17} cm^{-3}. Curves 1–4 (period 1 s, pulse width 0.1 s) were measured with the epitaxial Al contact on the as-grown surface. Curves 5 and 6 (period 0.1 s, pulse width 0.1 s) were measured with Ti/Au dots on the same layer, but after recess-etching of 80 nm. Note the smaller signals for the latter ones. The quiescent bias/pulse-height values are: (1) 0.6 V/0.1 V, (2) 1 V/0.5 V, (3) 1.5 V/1 V, (4) 2 V/1.5 V, (5) 1 V/0.5 V, and (6) 3 V/2 V. The DLTFS signal of the level H_B is indicated. The spectra are vertically shifted for clarity.

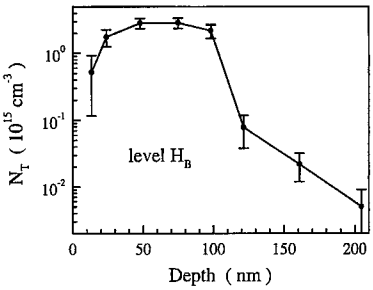

Fig. 2. Depth profile of the concentration N_T for the hole trap H_B in the Be-doped GaAs layer studied in Fig. 1.

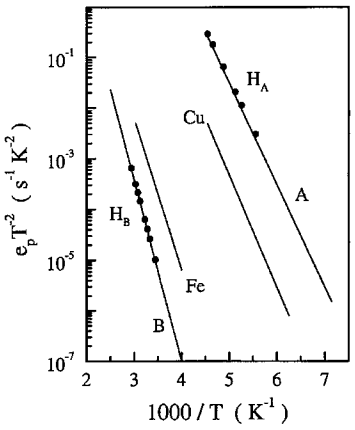

Fig. 3. Arrhenius plots of the hole traps H_A and H_B observed near the as-grown surface of a highly Be-doped GaAs MBE layer (points) compared with published data (lines) for the A and B levels typical of LPE-grown GaAs (Refs. [2,11,12]) and for Fe- and Cu-related hole traps in GaAs (Refs. [2,12]).

In order to identify the level H_B, the associated thermal emission rate e_p is compared in Fig. 3 to several hole traps, which are typical of p-type GaAs [2]. It is evident that the level H_B is identical to the well-known trap B, which is the dominant intrinsic level in GaAs grown by liquid-phase epitaxy (LPE) [11,12]. It originates from the Ga_{As} antisite defect [12,13] and is connected with the transition from the singly to the double negative charge state [14]. However, in contrast to LPE-grown GaAs, the defect is observed here only near the as-grown surface of highly Be-doped MBE layers and not in the bulk. The characteristics of Fe- and Cu-related traps in GaAs do not fit our experimental results (cf. Fig. 3). The concentrations of those impurities in the layers are below the detection limit of the DLTFS signal.

It is known that the Ga_{As} defect exhibits a second level A [11–14], which is connected with the transition from the neutral to the singly negative charge state [14]. Because the related activation energy of 0.40 eV is lower than the barrier height of the MS contacts, it is difficult to observe the associated transition at the as-grown surface.

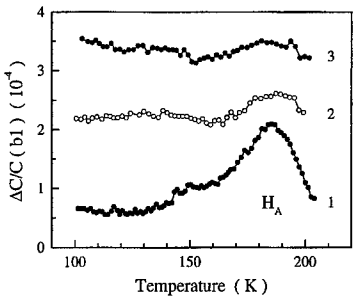

Fig. 4. Deep-level spectra (first sine coefficient $b1$, period 0.01 s, pulse width 0.01 s) of GaAs grown by MBE with a hole density of 1×10^{17} cm^{-3}. The spectra were measured with the epitaxial Al contact on the as-grown surface. The quiescent bias/pulse-height values are: (1) 0.5 V/0 V, (2) 1 V/0.5 V, and (3) 1.5 V/1 V. The DLTFS signal of the level H_A is indicated. The spectra are vertically shifted for clarity.

To detect the level A at low reverse biases, it is furthermore necessary to apply shorter pulses and higher rate windows in order to separate the level A response from MS-related signals. Fig. 4 shows for an epitaxial Al contact on the highly Be-doped GaAs layer a weak DLTFS response labeled H_A, which rapidly decreases with higher reverse biases. For this trap, the Arrhenius plot of the emission rate e_p entirely corresponds to the transition A of the Ga_{As} defect (cf. Fig. 3).

Our experimental results confirm calculations based on a thermodynamic model for the solid–vapor interface during growth [15]. Accordingly, Ga_{As} is the most dominant defect in GaAs grown by MBE under conditions close to those used for the current study. In Ref. [16] it was further shown that the energy for forming the Ga_{As} defect decreases by about 0.8 eV, when the Fermi level is shifted from the valence band edge to midgap position. It is therefore expected that Ga_{As} defects are predominantly formed at the surface of p-type GaAs, where the Fermi level is pinned to midgap position during growth. Thus, the depth profile in Fig. 2 reflects the variation of the defect formation energy near the GaAs surface during growth. The thickness of the layer, which contains the antisite defects, matches almost the depth of the space charge layer, since outside the depletion region the Fermi level is near to the valence band edge and the Ga_{As} defects are hardly formed. From the measured Ga_{As} concentration of 3×10^{15} cm^{-3}, the formation energy at the surface is estimated to be 1.1 eV, which is in perfect agreement with the calculations for nearly Ga-rich conditions during GaAs growth [16].

4. Conclusions

We have experimentally confirmed thermodynamical calculations for nearly Ga-rich conditions during growth.

The dominant defect at the surface of highly Be-doped GaAs is the Ga_{As} defect. Its formation energy depends strongly on the Fermi level and is found to be 1.1 eV at the GaAs surface. The intrinsic defect should be generated near the GaAs surface irrespective of the p-type dopant used. The bulk of the Be-doped GaAs layers is practically free of defects, which exhibit levels in the lower half of the band gap.

Acknowledgements

The authors are indebted to H.T. Grahn and L. Däweritz for comments and careful reading of the manuscript. We are grateful for the technical assistance of C. Dombrowski and E. Wiebicke.

References

[1] D.V. Lang, J. Appl. Phys. 45 (1974) 3023.
[2] A. Mitonneau, G.M. Martin, A. Mircea, Electron. Lett. 13 (1977) 666.
[3] P.K. Bhattacharya, H.-J. Bühlmann, M. Ilegems, J.L. Staehli, J. Appl. Phys. 53 (1982) 6391.
[4] P. Blood, J.J. Harris, J. Appl. Phys. 56 (1984) 993.
[5] A. Li, H.K. Kim, J.C. Jeong, D. Wong, J.H. Zhao, Z.-Q. Fang, T.E. Schlesinger, A.G. Milnes, J. Crystal Growth 95 (1989) 296.
[6] N. Chand, A.M. Sergent, J.P. van der Ziel, D.V. Lang, J. Vac. Sci. Technol. B 7 (1989) 399.
[7] F.D. Auret, S.A. Goodman, G. Myburg, J. Electron. Mater. 21 (1992) 1127.
[8] S. Weiss, R. Kassing, Solid State Electron. 31 (1988) 1733.
[9] P. Blood, J.W. Orton, The Electrical Characterization of Semiconductors: Majority Carriers and Electron States, Academic Press, London, 1992.
[10] J. Bourgoin, M. Lannoo, Point Defects in Semiconductors, Vol. II, Springer, Berlin, 1983, p. 167.
[11] Z.G. Wang, L.-A. Ledebo, H.G. Grimmeiss, J. Phys. C 17 (1984) 259.
[12] D.V. Lang, R.A. Logan, J. Electron. Mater. 4 (1975) 1053.
[13] P. Krispin, J. Appl. Phys. 65 (1989) 3470.
[14] G.A. Baraff, M. Schlüter, Phys. Rev. Lett. 55 (1985) 1327.
[15] M. Ichimura, T. Wada, J. Appl. Phys. 72 (1992) 1200.
[16] S.B. Zhang, J.E. Northrup, Phys. Rev. Lett. 67 (1991) 2339.

ELSEVIER

Physica B 273–274 (1999) 697–700

PHYSICA B

www.elsevier.com/locate/physb

Diffusivity of arsenic interstitials in GaAs studied by sulfur in-diffusion

H.S. Leipner[a,*], R.F. Scholz[b], N. Engler[a,b], F. Börner[a], P. Werner[b], U. Gösele[b]

[a]*Fachbereich Physik, Friedemann-Bach-Platz 6, Martin-Luther-Universität, D-06108 Halle, Germany*
[b]*Max-Planck-Institut für Mikrostrukturphysik, Weinberg 2, D-06120 Halle, Germany*

Abstract

Sulfur in-diffusion, which is governed by the kick-out mechanism, is a suitable tool to study the diffusion on the arsenic sublattice of GaAs. Sulfur diffuses for higher surface concentrations under non-equilibrium conditions of arsenic self-interstitials (I_{As}). The formation of extrinsic dislocation loops has been observed. The loop formation increases the concentration of Ga vacancies, which form complexes with S donors. The presence of such complexes has been investigated by cathodoluminescence, positron annihilation, and electrochemical capacity–voltage profiling. Taking into account the concentration of As interstitials agglomerated in faulted loops, the analysis of the sulfur profile can provide both the diffusion constant and the equilibrium concentration of I_{As}.

Keywords: Diffusion; Gallium arsenide; Interstitials; Vacancies

1. Introduction

Diffusion on the Ga sublattice of gallium arsenide is important for dopants such as Si, Be, or Zn. Many investigations have been done in this research field, and the diffusion process is quite well understood [1]. However, much less is known for the diffusion of impurities on the As sublattice. Furthermore, the fabrication of electrically homogeneous wafers requires the control of arsenic diffusion and precipitation during post-growth heat treatment. Recently, sulfur as n-type dopant has found increasing interest for device applications [2]. Uematsu et al. [3] concluded that different sets of experimental data of sulfur diffusion can be uniquely described by the kick-out mechanism,

$$i_S \rightleftarrows S_{As} + I_{As}. \quad (1)$$

i_S stands for sulfur atoms on interstitial lattice sites, S_{As} for sulfur on arsenic sites, and I_{As} for arsenic self-interstitials. Via reaction (1), sulfur diffusion should allow us in principle to determine the diffusion parameters of As self-interstitials. This requires the careful investigation of the defect reactions caused by in-diffusing sulfur.

2. Experimental details

Semi-insulating liquid-encapsulated Czochralski-grown GaAs was used for sulfur in-diffusion experiments. Annealing was carried out in sealed quartz ampoules after evacuating them to a pressure lower than 10^{-8} bar. To determine the small amounts of sulfur accurately, S was dissolved in benzene. For the results presented here, the sulfur density in the gas phase was 5 $\mu g/cm^3$. An arsenic pressure of 1 bar during the annealing experiment was established by adding the necessary amount of metallic arsenic to the ampoule. The in-diffusion was performed with various times and temperatures. The samples were either quenched in water or cooled down with a cooling rate of about 6 K/min. S in-diffusion profiles were measured by secondary ion mass spectroscopy (SIMS). The depth distribution of electrically active S, incorporated on As sites as donors, was monitored by electrochemical capacitance–voltage (ECV) profiling. Cathodoluminescence (CL) spectroscopy

* Corresponding author. Tel.: +49-345-55-25-453; fax: +49-345-55-27-563.
E-mail address: leipner@physik.uni-halle.de (H.S. Leipner)

0921-4526/99/$ - see front matter
PII: S0921-4526(99)00613-4

and microscopy were performed with an Oxford Mono-CL system attached to a Tesla BS 300 scanning electron microscope. A liquid-nitrogen-cooled germanium diode, which is sensitive from 800 to 1600 nm, was used as detector. The spectra shown are corrected with the sensitivity curve of the Ge diode. Transmission electron microscopy (TEM) was carried out with a JEOL JEM 1000 high-voltage transmission electron microscope. Additionally, we used a Vacuum Generators HB501-UX analytical electron microscope, equipped with a Kevex energy dispersive X-ray detector. Variable-energy positron annihilation measurements were carried out with a slow-positron beam system using a 0.5 GBq ^{22}Na β^+ emitter assembled with a 5 μm single-crystalline tungsten moderator in transmission geometry [4]. The Doppler broadening of the 511 keV annihilation line was measured as a function of the incident positron energy in the range 0.1–40 keV.

3. Results and discussion

The in-diffusion profiles strongly depend on the boundary conditions, i.e. on the equilibrium concentrations of i_S (c_{is}^{eq}) and S_{As} (c_S^{eq}) at the surface. The equilibrium surface concentration can be adjusted by the sulfur content in the gas phase over the GaAs sample. If the transport capacity of i_S is smaller than or equal to the transport capacity of I_{As}, i.e. $D_{is}\, c_{is}^{eq} \leqslant D_{I_{As}}\, c_{I_{As}}^{eq}$, then the diffusion proceeds under the equilibrium of intrinsic point defects (arsenic interstitials). In this case, I_{As} are quick enough that always $c_{I_{As}} = c_{I_{As}}^{eq}$. The effective diffusion coefficient is determined by

$$D_S^{eq} = \frac{D_{is}\, c_{is}^{eq}}{c_S^{eq}}.$$

Under this condition, error-function-like profiles and a constant sulfur diffusion coefficient is obtained.

On the other hand, if $D_{is}\, c_{is}^{eq} > D_{I_{As}}\, c_{I_{As}}^{eq}$, the effective diffusion coefficient is determined by the transport capacity of I_{As},

$$D_S^{noneq} = \frac{D_{I_{As}}\, c_{I_{As}}^{eq}}{c_S^{eq}} \left(\frac{c_S^{eq}}{c_S}\right)^2. \tag{2}$$

Eq. (2) is an approximation for the case when $c_{is} = c_{is}^{eq}$ in the diffused region. For S in-diffusion this is not valid even for long diffusion times, and the whole set of partial differential equations describing the diffusion [3] has to be used to evaluate experimental in-diffusion profiles. Under non-equilibrium conditions of Eq. (2), the diffusion profiles are non-error-function-like. The effective diffusion coefficient depends on the S concentration and provides information about I_{As} diffusion instead of S diffusion. The supersaturation of I_{As} may give rise to the formation of extended defects. TEM investigations of samples annealed at 1100°C show that small dislocation loops up to 2.5 nm in diameter were formed during in-diffusion. Their density is, however, very small, and they do not considerably influence the diffusion process. The behavior is different at 950°C annealing. Fig. 1a shows a TEM image of a sample annealed at 950°C with 5 μg/cm^3 S in the gas phase. Large loops were found near the surface. The defects were identified with the inside/outside contrast method as extrinsic dislocation loops. They lie on {1 1 1} lattice planes and are of the Frank type with the Burgers vector $\boldsymbol{b} = \frac{1}{3}\langle 1\,1\,1\rangle$. The fringe contrast of the corresponding extrinsic stacking faults is visible in Fig. 1a. The formation of the extrinsic dislocation loops may be described by one of the following reactions:

$$I_{As} + I_{Ga} \rightleftarrows \Phi \quad \text{or} \quad I_{As} \rightleftarrows \Phi + V_{Ga}. \tag{3}$$

Via loop formation – Φ stands for a pair of Ga and As atoms in the interstitial loop – the supersaturation of I_{As} is reduced. A remarkable fact is that the formation of extended defects occurs up to a depth of about 10 μm,

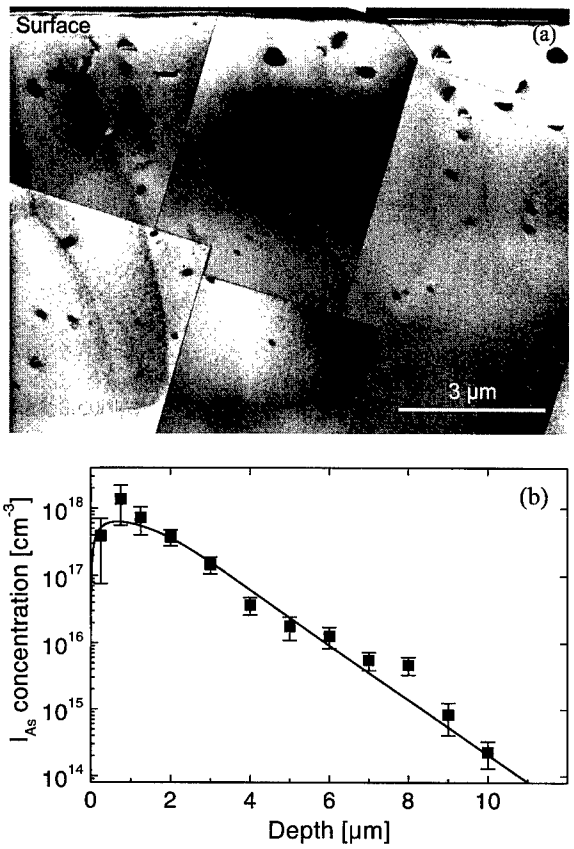

Fig. 1. GaAs sample annealed at 950°C for 20 min. (a) TEM cross-sectional image showing extrinsic stacking faults. (b) Depth profile of As interstitials agglomerated in faulted loops.

which is much deeper than the S in-diffusion profile (Fig. 2b). This indicates that the diffusion coefficient of I_{As} has to be much higher than the diffusion coefficient of i_S. The density of loops has been precisely determined from TEM images covering a large sample area. The size and their depth distribution have been measured. The depth profile of the concentration of I_{As} contained in faulted loops is plotted in Fig. 1b. The error bars mainly result from uncertainties in determining the thickness of the sample foil by counting the number of thickness extinction fringes.

The second type of reaction in Eq. (3) seems to be more likely than the first one, since sulfur in-diffusion leads only to a supersaturation of I_{As} and not of I_{Ga}. Thus, the formation and further growth of faulted loops make the supersaturation of As interstitials decrease at the expense of the formation of Ga vacancies. These vacancies, which are negatively charged acceptors, can form complexes with S donors according to the reaction

$$S_{As} + V_{Ga} \rightleftarrows (S_{As}V_{Ga}). \quad (4)$$

Similar defect complexes have been discussed for impurities such as Te, Sn, and Se. They exhibit a deep center luminescence band in the region 1.2–1.3 eV. It is thought to be a localized transition in the donor-V_{Ga} complex, the ground state of which is derived from the vacancy and the excited state in the configuration coordinate model from the donor [5].

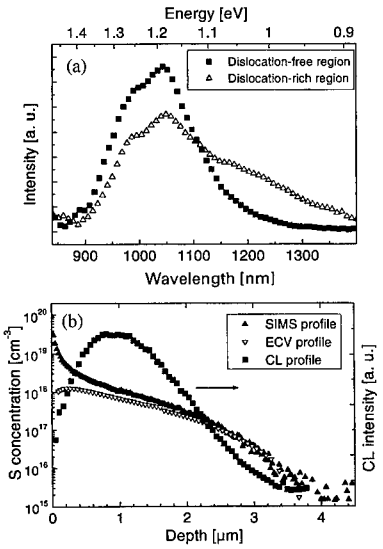

Fig. 2. Cathodoluminescence of GaAs samples after sulfur diffusion at 950°C. (a) CL spectra taken at 77 K in a dislocation-free and dislocation-rich region. (b) Depth profile of the peak intensity of the 1.2 eV CL band compared to the SIMS and the ECV profiles (diffusion time 1 h).

In dislocation-rich areas, an additional shoulder around 1 eV appears in the luminescence spectra (Fig. 2a). This may be related to the accumulation of sulfur and the depletion of arsenic at dislocations, which was found by analytical electron microscopy [6]. Various sulfur-rich phases or centers are under consideration for the 1 eV shoulder.

Fig. 2b compares the depth distribution of the in-diffused total amount of sulfur, as measured by SIMS, with the profile of the electrically active S_{As}, which has been determined by ECV profiling. The maximum S donor concentration amounts to 1.5×10^{18} cm^{-3}. The discrepancy between the total S concentration and the concentration of S_{As} may be explained by various compensation mechanisms. Two processes may be discussed here: the formation of sulfur clusters or precipitates and the formation of compensating $S_{As}V_{Ga}$ complexes. The former process has been observed preferably at dislocations introduced by plastic deformation [6]. It may play a minor role in as-grown GaAs wafers with a dislocation density of about 10^4 cm^{-2}. Thus, the main mechanism of electrical inactivation of in-diffusing sulfur is the formation of donor vacancy complexes via reaction (4). The depth profile of the intensity of the 1.2 eV CL line, which has been measured at a cross-sectional sample, is shown in Fig. 2b. At a depth of 2.5 μm the relative intensity decreases to 1/e, indicating that the concentration of $S_{As}V_{Ga}$ complexes becomes low. This corresponds to the course of the SIMS and ECV profiles, which indicate that for a depth > 2.5 μm the total S concentration equals roughly the concentration of electrically active sulfur. It should be noted that the drop in the CL intensity near the sample surface (depth below 500 nm) is related to a so-called dead layer of non-radiative recombination, which is caused by the pinning of the Fermi level by surface states and a space-charge region.

The question, whether gallium vacancies are released as a result of the in-diffusion of sulfur and the formation of faulted loops has been investigated by positron annihilation measurements. The *S* and *W* line shape parameters, which describe the Doppler broadening of the 511 keV annihilation line, have been measured as a function of the incident positron energy. The *W* parameter is distinctly lower in GaAs after sulfur in-diffusion. Accordingly, the *S* parameter increased. It is well known that this behavior can be described by the presence of vacancy-type defects [7]. Dependent on the annealing conditions (temperature and time), vacancies have been observed within a depth of 1–3 μm from the surface. As a result of the loop formation (3), vacancies may be also expected in a depth of up to 10 μm. However, it can be concluded from the positron results that in this region, V_{Ga} are not thermally stable. Such stable defects only appear in a region where the reaction (4) or the formation of other vacancy-sulfur complexes is possible.

In conclusion, the in-diffusion of sulfur results in the supersaturation of As interstitials, which may lead to the formation of interstitial dislocation loops. On the other hand, the supersaturation of I_{As} is reduced at the expense of the production of Ga interstitials. The latter gives rise to the compensation of S donors via the formation of $S_{As}V_{Ga}$ complexes. The influence of the formation of faulted loops on the shape of the diffusion profiles and hence on the diffusion parameters has been investigated [8]. It has been found that the tail of the profile depends on both factors contained in the transport capacity, i.e. on the diffusivity and the concentration of I_{As}. As a result of the simulation [8], the diffusivity of I_{As} has been determined. It amounts to 6.8×10^{-10} cm^2 s^{-1} for 950°C, while $c_{I_{As}}^{eq} = 3 \times 10^{14}$ cm^{-3}. The effective diffusion constant of i_S has been found to be 2.8×10^{-13} cm^2 s^{-1} for that temperature.

References

[1] U. Gösele et al., Defect Diff. Forum 143–147 (1997) 1079.
[2] J.-L. Lee, J. Appl. Phys. 85 (1999) 8.
[3] M. Uematsu et al., Appl. Phys. Lett. 48 (1995) 2863.
[4] F. Börner et al., J. Appl. Phys. 84 (1998) 2255.
[5] E.W. Williams, H.B. Bebb, Semicond. Semimet. 8 (1972) 321.
[6] N. Engler et al., Sol. State Phenomena 69–70 (1999) 443.
[7] R. Krause-Rehberg, H.S. Leipner, Positron Annihilation in Semiconductors, Springer, Berlin, 1999.
[8] R.F. Scholz et al., J. Appl. Phys. (1999), submitted for publication.

ELSEVIER

Physica B 273–274 (1999) 701–704

PHYSICA B

www.elsevier.com/locate/physb

Effect of lithium diffusion on the native defects in GaAs studied by positron annihilation spectroscopy

S. Arpiainen[a,*], K. Saarinen[a], J.T. Gudmundsson[b], H.P. Gislason[b]

[a]*Helsinki University of Technology, P.O. Box 1100, 02015 Hut, Finland*
[b]*Science Institute, University of Iceland, Iceland*

Abstract

The influence of Li diffusion on GaAs was studied by means of positron annihilation spectroscopy. Positron trapping at both gallium vacancy (V_{Ga}) and antisite (Ga_{As}) defects were found to increase after the in-diffusion, and increase further after the out-diffusion of Li. This indicates an increase in the concentrations of negative and neutral defects in both phases. Majority of the Ga vacancy and antisite defects is, however, supposed to be formed already during the in-diffusion phase at 800°C, but to remain passivated by Li prior to the out-diffusion phase at 400°C. The As antisite (EL2) and the As vacancy (V_{As}) defects were not detected after the incorporation of Li. All these results can be explained by a simple set of defect formation and reduction processes.

Keywords: GaAs; Li; Vacancies; Antisite defects

1. Introduction

Lithium (Li) diffusion into GaAs has been found to compensate both n- and p-type native defects and to produce semi-insulating GaAs when the incorporated Li concentration is high. The subsequent out-diffusion of Li produces p-type GaAs. This phenomenon was first detected by Fuller and Wolfstirn [1], but the defects and microscopic behavior responsible for the conductivity changes have not been fully identified. Earlier measurements of undoped and Zn-doped GaAs indicate increased resistivity of 3–4 orders of magnitude for Li diffusion temperatures up to 700°C, where a sharp increase in resistivity is observed, roughly 9 orders of magnitude [2]. It has been demonstrated that annealing of Li diffused GaAs at 400–500°C in pure Ga or Ar atmosphere reduces the Li concentration by about two orders of magnitude [3,4]. The final p-type conductivity indicates that additional acceptors are formed. These have been already earlier related to gallium vacancies [4,5].

In this study, the effect of lithium diffusion on the native defects in GaAs was studied by means of positron lifetime spectroscopy. Positrons get trapped at neutral and negative vacancy defects, which increases the positron lifetime above the bulk value τ_b. At low temperatures positrons get trapped also at negative ions, which are attributed to Ga antisites (Ga_{As}^{2-}). Some positive defects, like arsenic vacancy (V_{As}), can also be optically excited into negative charge state, that acts as an efficient positron trap [6].

2. Experimental

Thermal treatments for the in- and out-diffusion of Li, and for the reference samples, were made in open quartz ampoules under Ar ambient. The samples were immersed in an oversaturated Ga–As melt prepared from 6N Ga metal and GaAs, and from about 0.3 wt% of 99.9% Li metal in the in-diffusion phase. The in- and out-diffusion of Li were performed at 800°C for 8 h and at 400°C for 7 h, respectively. The doping of the samples prior to the incorporation of Li is presented in Table 1.

Positron lifetime in a defect free GaAs lattice (τ_b) is 231 ps. Positron lifetime increases when positrons

* Corresponding author. Tel.: + 358-9-451-3144; fax: + 358-9-451-3116.
E-mail address: san@fyslab.hut.fi (S. Arpiainen)

0921-4526/99/$ - see front matter
PII: S0921-4526(99)00614-6

Table 1
Sample identification and the vacancy and negative defect concentrations calculated from positron lifetime results measured in darkness. All Li diffusions were made at 800°C for 8 h, and subsequent out-diffusions at 400°C for 7 h

Sample	Vacancy concentration (cm^{-3})	Negative defect concentration (cm^{-3})
p-doped GaAs		
GaAs(Zn)	—	—
#17 Li in-diffused	2.2×10^{16}	3.1×10^{17}
#17a Li out-diffused	8.3×10^{16}	4.8×10^{17}
n-doped GaAs (10^{16} Si/cm^3)		
#15 GaAs(Si)	1.7×10^{16}	1.0×10^{17}
#18 Li in-diffused	2.2×10^{16}	1.6×10^{17}
#14 Li out-diffused	7.6×10^{16}	3.2×10^{17}

get trapped at negative and neutral vacancy defects. The increase of the average positron lifetime $\tau_{ave} = (1 - \eta_V)\tau_b + \eta_V\tau_V$ above τ_b is thus a direct sign of vacancy defects in the sample [6]. η_V is the fraction of annihilations at the vacancies. Negative ions, such as Ga_{As}^{2-}, trap positrons at their hydrogenic states ($\tau \sim 231$ ps) at low temperatures. This can be observed as decreasing τ_{ave} at low T, because less annihilations take place at vacancies [6].

The positron lifetime experiments were performed in a conventional way. The concentrations of $V_{Ga}^{0/-}$ and Ga_{As}^{2-} were measured in darkness. Negative charge state of the native donor defect V_{As} was maintained during the positron measurements by 1.42 eV illumination with a constant flux of $5 \times 10^{15}\ cm^{-2}\ s^{-1}$ [7]. EL2 (As antisite, As_{Ga}) was transformed into metastable state EL2* prior to the positron measurement in darkness. This was done at 10 K by illuminating with 1.15 eV photons with a total fluence of $3.6 \times 10^{19}\ cm^{-2}$ [8,9]. The carrier concentration and Hall mobility were measured on samples in the van der Pauw configuration.

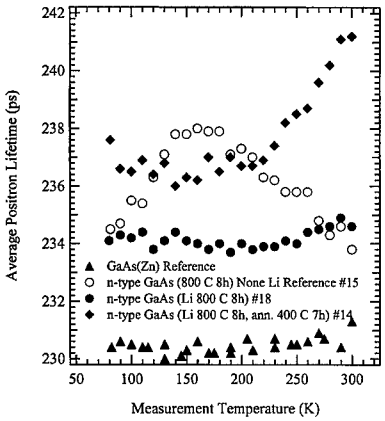

Fig. 1. Average positron lifetimes in darkness. Defect free GaAs(Zn) reference, GaAs(Si) reference #15, and Li in- and out-diffused samples with n-type conductivity prior to the incorporation of Li.

3. Gallium vacancies and antisites

The positron lifetime measurements in GaAs samples before and after Li diffusion revealed native Ga vacancies and antisites. The positron annihilation results are represented in Figs. 1 and 2. The first sample series (Fig. 1) was n-type conducting (10^{16} Si/cm^3) prior to the Li in-diffusion. The n-type starting material is converted to p-type by Li diffusion and baking. The as-grown material is n-type GaAs : Si with carrier concentration 2×10^{16} cm^{-3} and mobility 4000 Vs/cm^2 at room temperature. When diffused with lithium at 800°C for 10 h and annealed at 400°C for 7 h the hole concentration becomes $3.4 \times 10^{17}\ cm^{-3}$. For lithium-diffused samples annealed at temperatures below 400°C the mobility is very low, below 70 Vs/cm^2 at room temperature. As the annealing temperature is incresed the mobility increases.

The other sample series (Fig. 2) was p-type conducting prior to the incorporation of Li. The as-grown material GaAs : Zn with $p = 2 \times 10^{17}\ cm^{-3}$ remains $2 \times 10^{17}\ cm^{-3}$ after Li diffusion at 700°C for 10 h and annealing at 400°C for 4 h. The mobility of the as grown sample was 223 Vs/cm^2 and decreased to 141 Vs/cm^2 at room temperature upon Li diffusion and baking.

The shape of τ_{ave} in sample #15 is due to As vacancies that are highly efficient positron traps in n-GaAs at low T [10]. In both the sample series (Table 1), Li-diffusion increased τ_{ave} slightly, indicating an increased concentration of negative gallium vacancies (V_{Ga}^{-}). Out-diffusion of Li further increased τ_{ave}. Also, the gallium antisite (Ga_{As}^{-}) concentrations were increased in all the Li-diffused samples, but the major increase appeared only after the

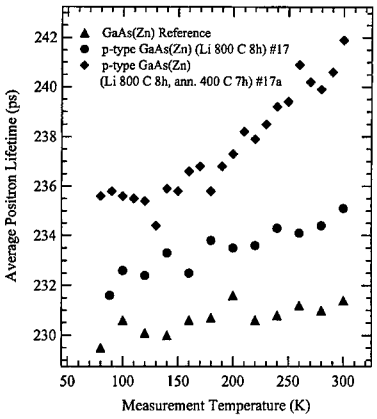

Fig. 2. Average positron lifetimes in darkness. Defect free GaAs(Zn) reference, and Li in- and out-diffused samples with p-type conductivity prior to the incorporation of Li.

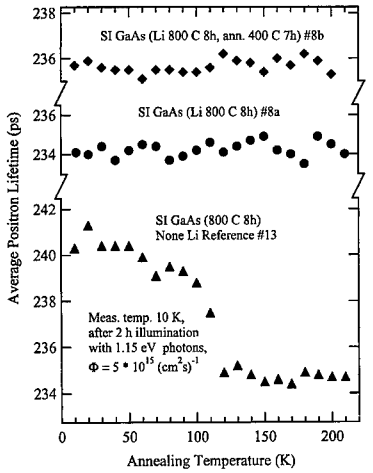

Fig. 3. Average positron lifetimes at 10 K after optical exitation of EL2 and subsequent annealings. Undoped SI-GaAs reference #13 and undoped Li in- and out-diffused samples.

out-diffusion of Li, as seen in Table 1. It is, however, not expected that the majority of the Ga-related defects would have been formed during the out-diffusion phase at 400°C, as the Li in-diffusion was performed at similar conditions but at a significantly higher temperature of 800°C. The results can only be explained by a formation of Li passivated (neutral) defect complexes like V_{Ga}^{-}–Li^{+} pairs, that are unable to trap positrons. This Li-passivation disappears in the out-diffusion phase at 400°C, converting V_{Ga} and Ga_{As} into efficient positron traps.

4. Optically excited arsenic vacancies and EL2

The effect of Li on the existence of EL2 and V_{As} in undoped GaAs was studied by optically turning the defects into efficient positron traps EL2* (V_{Ga}–As_i pair) and V_{As}^{-}, respectively. EL2* is a metastable state of EL2 that can be reached via optical excitation with 1.15 eV photons, and it anneals out at 120 K [8]. In the undoped GaAs reference sample #13 τ_{ave} increased persistently after illumination and decreased upon annealing at 120 K. This effect was not detected after Li in- and out-diffusions in samples #8a and #8b (Fig. 3). Similar results are obtained in IR absorption measurements, that revealed no transition from EL2 to EL2* upon illumination after the incorporation of Li.

The measurement of arsenic vacancy concentration in GaAs is based on the photoionization of V_{As}^{+} into V_{As}^{-}, the latter having $\tau = 257$ ps [7]. These photoinduced positron traps increase τ_{ave} from the value measured in darkness. This effect can be very clearly seen in the undoped GaAs reference #13 (Fig. 4). All the signs of the photoinduced defects disappeared with the in-diffusion of Li at 800°C (#8a), and no recovery occurred after the out-diffusion of Li (#8b).

Both defects were clearly visible in the undoped reference #13 with no Li, but disappeared totally in both in- and out-diffused samples. Since the Li passivation of donor type defects such as V_{As} and As_{Ga} is not expected, the data strongly suggest that V_{As} and As_{Ga} annihilate upon the Li diffusion into GaAs.

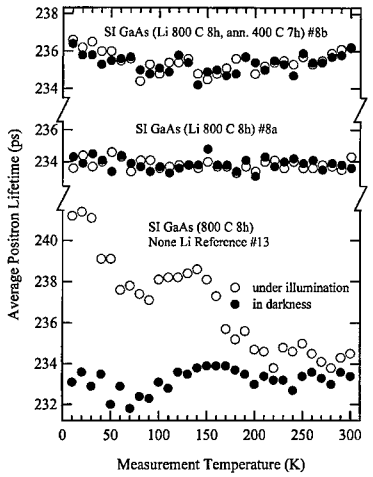

Fig. 4. Average positron lifetimes in darkness and under 1.42 eV illumination, reflecting the increase due to optically induced negative V_{As}. Same sample series as in Fig. 3.

5. Conclusions

Li diffusion at 700–800°C seems to induce the formation of neutral acceptor pairs like V_{Ga}^{-}–Li^{+} and Ga_{As}^{-}–Li^{+}. The passivation disappears with out-diffusion of Li, resulting in p-type conductivity. Both the As antisite (EL2) and the As vacancy are clearly visible in the

undoped reference sample, but disappear totally in both Li diffused and out-diffused samples. Since the Li passivation of donor-type defects such as V_{As} and As_{Ga} is not expected, the data suggest strongly that V_{As} and As_{Ga} annihilate upon the Li diffusion into GaAs.

All the detected phenomena, i.e. the disappearance of V_{As} and As_{Ga} as well as the generation of V_{Ga} and Ga_{As} can be understood as Li-induced defect formation and reduction processes. When the V_{Ga}^{-}–Li^{+} complexes are created, the associated Ga interstitials may get trapped by V_{As} thus producing Ga antisite defects. Similarly, the Li induced disappearance of As_{Ga} generates As interstitials, which are able to annihilate As vacancies. After the out-diffusion of Li increased concentrations of V_{Ga} and Ga_{As} acceptors remain in the samples, which explains the final p-type conductivity of the samples.

References

[1] C.S. Fuller et al., J. Appl. Phys. 33 (1962) 2507.
[2] H.P. Gislason et al., Materials Science Forum 83–87 (1992) 985.
[3] C.S. Fuller et al., J. Appl. Phys. 35 (1962) 1227.
[4] B.H. Yang et al., Phys. Rev. B 48 (1993) 12345.
[5] H.P. Gislason et al., Mater. Sci. Forum 258–263 (1997) 1813.
[6] K. Saarinen et al., in: M. Stavola (Ed.), Identification of Defects in Semiconductors Semiconductors and Semimetals, Vol. 51A, Academic Press, New York, 1998, p. 209.
[7] S. Kuisma et al., Phys. Rev. B 53 (1996) 9814.
[8] K. Saarinen et al., Phys. Rev. B 49 (1994) 8005.
[9] S. Kuisma et al., Phys. Rev. B 55 (1997) 9609.
[10] K. Saarinen et al., Phys. Rev. B 44 (1991) 10585.

ELSEVIER

Physica B 273–274 (1999) 705–709

PHYSICA B

www.elsevier.com/locate/physb

Influence of stoichiometry and doping on vacancies in n-type GaAs

J. Gebauer*, M. Lausmann, F. Redmann, R. Krause-Rehberg

Fachbereich Physik, Martin-Luther-Universität Halle-Wittenberg, Friedemann-Bach-platz 6, D-06099 Halle, Germany

Abstract

Native vacancies in n-type, Te-doped GaAs ($n = 5 \times 10^{16}$–5×10^{18} cm^{-3}) were studied by means of positron annihilation. We investigated the influence of doping, thermal treatment, and stoichiometry adjusted by changing the As pressure during annealing. Negatively charged monovacancies were found in all Te-doped samples under investigation. By using positron lifetime spectroscopy in conjunction with measurements of the annihilation momentum distribution and theoretical calculations, they can directly be identified to be V_{Ga}–Te_{As} complexes. After thermal treatment at 1100°C the density of the vacancies c_v increases with the As pressure (p_{As}) like $c_v = 0.1 c_d p_{As}^{1/4}$ where c_d is the donor concentration. For such a treatment, c_v depends only on p_{As} but not on the thermal history. The vacancy concentration was found to increase slightly with decreasing annealing temperature at a given p_{As}. This can be explained by the so-called Fermi level effect, i.e. the dependence of the equilibrium concentration of charged point defects on the position of the Fermi level.

Keywords: Gallium arsenide; Ga-vacancy–donor complex; Fermi level effect; Stoichiometry

1. Introduction

Point defects determine important properties of a semiconductor material like GaAs. Therefore, it is necessary to know microscopic nature and concentration of defects and the factors which influence them. Vacancies are among the most fundamental defects. However, the microscopic identification and therefore an estimation of the role native vacancies may have in GaAs was found to be difficult. Theoretical calculations indicate a dominating role of Ga vacancies in n-type, As-rich GaAs. The vacancy concentration depends on the doping level and has a negative temperature dependence in heavily n-doped GaAs (Fermi level effect) [1]. However, this has not yet been experimentally confirmed.

Positron annihilation is a powerful method for the detection of vacancies. It has been often used to study native vacancies in GaAs [2]. However, there is conflicting evidence for vacancies in the different sublattices of GaAs, emphasizing the difficulties of an unambiguous defect identification. Moreover, earlier studies were devoted to as-grown GaAs only and thus the factors leading to a certain defect type and concentration were often unknown. In the present work we investigate the influence of thermal treatment, stoichiometry, and (n-type) doping on vacancies in GaAs. An unambiguous defect identification in GaAs by positron annihilation has been achieved by using Doppler-broadening coincidence spectroscopy in conjunction with positron lifetime measurements and theoretical calculations of the annihilation parameters [3].

2. Experimental

The samples used in this work were GaAs : Te, grown by the LEC method. Crystals with carrier densities of 0.6, 4, 15 and 50×10^{17} cm^{-3} (determined by the Hall effect) were investigated. Te was chosen because it resides only on the As sublattice and acts as a donor. In the case of amphoteric dopants, e.g. Si, more complicated defect

* Corresponding author. Tel.: + 49-345-552-5570; fax: + 49-345-552-7160.

E-mail address: gebauer@physik.uni-halle.de (J. Gebauer)

0921-4526/99/$ - see front matter
PII: S0921-4526(99)00615-8

reactions are expected. Annealing was performed in sealed quartz-glass ampoules arranged in a two-zone furnace. The sample temperature (T_S) was independently varied from the temperature of the metallic As source ($T_{As} < T_S$). Then, T_{As} determines the As vapor pressure (p_{As}). p_{As} is obtained from Gokcen's review [4]. The ampoules were fast quenched in water after annealing.

Positrons can be trapped by vacancies during diffusion in a crystal. This results in an increasing positron lifetime and a narrowing of the annihilation momentum distribution. An increase of the average positron lifetime (τ_{av}) compared to the lifetime in defect-free material (τ_b) is a clear sign for positron trapping in vacancies. A decomposition of the lifetime spectra provides the vacancy-related lifetime (τ_v), specific for a given defect. The defect density (c_v) can be obtained from $c_v = 1/(\tau_{bulk}\mu)(\tau_{av} - \tau_b)/(\tau_v - \tau_{av})$ where μ is the trapping coefficient. μ is about $10^{15}\,s^{-1}$ for negatively charged monovacancies in semiconductors at 300 K [2]. We have to note that vacancy concentrations derived from positron annihilation have a systematic uncertainty in the order of 50% because the trapping coefficient is only known within this accuracy. Positron lifetime spectroscopy was performed with a conventional fast–fast system (resolution 250 ps) from 20–550 K. Doppler broadening coincidence spectroscopy was carried out with two Ge-γ-detectors (system resolution 1.1 keV). This technique allows the observation of annihilation with high-momentum electrons due to a reduction of the background which can be used to identify the chemical surrounding of a vacancy.

3. Results and discussion

Fig. 1 shows typical positron lifetime results in Te-doped GaAs annealed at 1100°C for different times and As vapor pressures. τ_{av} is above the value in the defect-free bulk, measured in a GaAs : Zn reference. This shows the presence of vacancies. The increase in τ_{av} with decreasing temperature is attributed to a negative charge state of the vacancies; positron trapping at neutral vacancies would be independent of temperature [5]. The decrease in τ_{av} at $T < 100$ K reveals the presence of negative, ions which trap positrons in their shallow potential only at low temperatures. The positron lifetime is close to τ_b [6]. However, the density is much lower than the vacancy concentration since the decrease of τ_{av} is weak. τ_v was ~ 254 ps in all samples, indicative for a monovacancy. It is somewhat shorter than the lifetime for V_{Ga}–Si_{Ga} complexes in GaAs : Si (262 ps). However, it is not clear which type of vacancy is detected because both, As and Ga vacancies, should have a similar positron lifetime of 250–260 ps [2].

An unambiguous identification of the vacancies has been possible using the Doppler-broadening coincidence technique, which measures the annihilation momentum

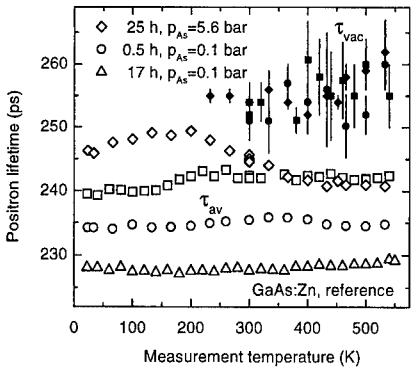

Fig. 1. Average (open symbols) and defect-related (solid symbols) positron lifetime versus the measurement temperature in GaAs : Te(2×10^{18} cm^{-3}) annealed at 1100°C, compared to a GaAs : Zn reference.

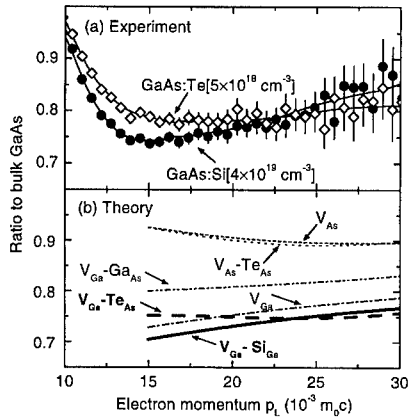

Fig. 2. (a) High momentum part of the annihilation momentum distribution for the vacancies in GaAs : Te and for V_{Ga}–Si_{Ga} in GaAs : Si. Lines result from smoothing. (b) Momentum distribution for different vacancies in GaAs from theoretical calculations. Theoretical curves are not accurate for $p_L < 15 \times 10^{-3}$ m_0c [7] and hence are omitted. (From Ref. [3])

distribution especially at high momenta [7]. In Fig. 2(a), the annihilation momentum distribution is shown for the vacancies in GaAs : Te and for V_{Ga}–Si_{Ga} complexes in highly Si-doped GaAs. The data are normalized by taking the ratio to a GaAs : Zn reference. The momentum distribution differs for differently doped GaAs. Together with the shorter positron lifetime in GaAs : Te, this indicates a different defect type. In Fig. 2(b), theoretical calculations (see, e.g. Ref. [7]) of the momentum distribution for different vacancies and vacancy complexes in GaAs are shown. The momentum distribution calculated for V_{Ga}–Si_{Ga} is in remarkable agreement with the experimental result. A similar good agreement is obtained for the V_{Ga}–Te_{As} complex and the vacancy in GaAs : Te.

The calculations revealed also a distinctly shorter positron lifetime for the V_{Ga}–Te_{As} complex in comparison to V_{Ga}–Si_{Ga} [3]. Calculations for any other defect have not shown any agreement to the experimental data. For example, the calculated momentum distribution for the As vacancy has a different shape and a much larger intensity compared to V_{Ga}–Si_{Ga}. Thus, the monovacancies in GaAs : Te are V_{Ga}–Te_{As} complexes. This holds for as-grown and annealed material as the same signals were found [3].

The positron lifetime results in Fig. 1 indicate a distinct relation between As pressure (p_{As}), vacancy concentration, and annealing time. τ_{As} (and hence c_v) is larger for short annealing times and higher p_{As}. Since we are interested in equilibrium defects, we checked the time dependence of c_v. The vacancy concentration remained at 3×10^{17} cm^{-3}, whereas the carrier concentration was 1.5×10^{18} cm^{-3} even after 180 h annealing at $p_{As} = 5.6$ bar and $T = 1100$°C. Contrary, annealing at $p_{As} = 0.1$ bar for times > 200 min significantly reduces c_v to a level of 6×10^{16} cm^{-3}, accompanied by an increase of the carrier concentration to 1.8–1.9×10^{18} cm^{-3}. The carrier concentration is in agreement with the total Te content determined by SIMS (2×10^{18} cm^{-3}). These values were also constant for longer annealing times (up to 180 h). In order to check for the reversibility of the process, samples first annealed at $p_{As} = 0.1$ bar were annealed for 24 h at $p_{As} = 5.6$ bar. This treatment increases the vacancy concentration to the same value as with annealing only at 5.6 bar. Thus, annealing for a sufficient long time allows a reversible adjustment of the vacancy concentration, which depends only on p_{As} but not on the thermal history of the sample. This is of course expected for a process in thermal equilibrium, however, it has not been confirmed before for a similar annealing process in GaAs.

In Fig. 3, the vacancy concentration is shown as a function of p_{As} for all Te concentrations investigated in this work. All samples were annealed at 1100°C for 24 h. We detected the same type of vacancies (i.e. V_{Ga}–Te_{As}) in all samples, indicated by the same τ_v and momentum distribution. The vacancy concentration was calculated from τ_{av} at high temperatures (550 K), where the influence of negative ions on positron trapping is negligible. We found an increasing vacancy concentration with increasing p_{As}, i.e. if the stoichiometry becomes more As-rich. Thus, equilibrium vacancies in n-GaAs must belong to the Ga-sublattice as it was independently shown with the identification of the V_{Ga}–Te_{As} complexes above. Note that the vacancy concentration is nearly constant for $p_{As} > 2.5$ bar. This is most probably related to the As-rich phase boundary of GaAs. For Ga vacancies, a kinetic equilibrium reaction like 1/4 As_4 (gas)$\leftrightarrow V_{Ga}$ + GaAs should apply (As_4 is the dominating As vapor [1]). Thus, the concentration of V_{Ga} is expected to be $\sim p_{As}^{1/4}$. A fit to the data (i.e. $c_v = K p_{As}^n$) yields consistently an exponent n close to 0.25 in agreement with this assumption. Moreover, all data could be described with the same constant $K = 0.1 c_d$ where c_d is the total donor (i.e. Te) concentration. The solid lines in Fig. 3 are obtained from $c_v = 0.1\, c_d p_{As}^{1/4}$ in good agreement to the data.

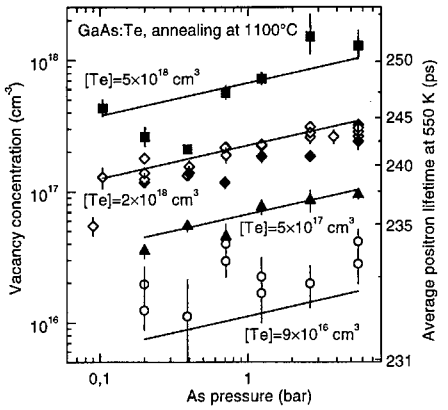

Fig. 3. Concentration of vacancies in Te-doped GaAs as a function of the p_{As} during annealing at 1100°C for 24 h. The respective Te densities (from SIMS) are indicated. Some of the samples with a Te concentration of 2×10^{18} cm^{-3} (indicated by solid diamonds, ◆) were first annealed at 0.1 bar and then annealed under the given As pressure, demonstrating the reversibility of the annealing process. Errors are due to statistical uncertainties of τ_{av} only, they are thus a measure for the relative accuracy.

It is expected that the negative vacancies compensate free carriers. Indeed, such compensation has often been observed [8]. According to our present and earlier results [9,10] we can expect that all n-GaAs is compensated by donor Ga-vacancy complexes. The highest degree of compensation reached under As-rich conditions in GaAs : Te is, however, only about 1/4 as was found earlier [8,9].

It has often been assumed that the concentration of V_{Ga} depends on the cube of c_d due to the 3 minus charge state of V_{Ga} in n-GaAs. According to the present results, c_v depends linearly on the donor concentration for constant p_{As}. Note that this is not necessarily in disagreement with a 3 minus charge state of V_{Ga}. Tan et al. [1] calculated the concentration of V_{Ga}^{3-} using equilibrium thermodynamics. The calculated vacancy concentrations exhibit a linear dependence on the donor concentration very similar to our experimental results. Moreover, the calculations for As-rich GaAs are in good quantitative agreement to our data as will be shown below for $c_d = 2 \times 10^{18}$ cm^{-3}. Thus, our results are indeed compatible with a 3 minus charge of V_{Ga}. This implies the assumption that the V_{Ga}–Te_{As} complex detected at room temperature is formed during cooling whereas V_{Ga}^{3-} is the equilibrium vacancy at high temperatures.

One of the most interesting features in the calculations of Tan et al. [1] is the negative temperature dependence of the V_{Ga} concentration in highly n-doped GaAs. Thus, we investigated GaAs : Te[2×10^{18} cm^{-3}] annealed at

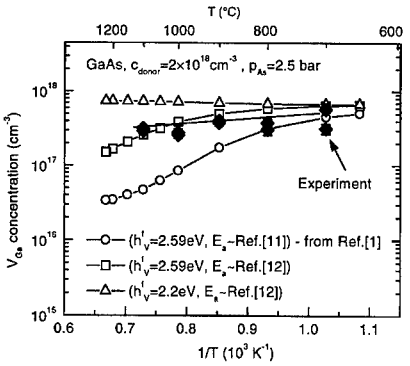

Fig. 4. Vacancy concentration in GaAs : Te as function of the temperature during annealing at $p_{As} = 2.5$ bar. The data are compared with theoretical calculations according to Tan et al. [1]. The parameters used for the calculations are indicated, see text.

different temperatures with a fixed As vapor pressure (2.5 bar). The samples were first annealed for 20 h at 1100°C in order to establish an equilibrium concentration of V_{Ga}. Then, the temperature was slowly (20 K/h) ramped down to the temperature intended (700–1000°C). This value was held for 24 h, finally, the samples were quenched in water. We found V_{Ga}–Te_{As} complexes in all samples regardless of the treatment. The resulting vacancy concentrations are shown in Fig. 4 (black dots). Indeed, c_v shows a slightly negative temperature dependence, i.e. it increases with decreasing temperature and thus confirms the results in Ref. [1].

Theoretical results according to the calculations of Tan et al. [1] are shown in Fig. 4 for comparison. At lower temperatures (700°C) the quantitative agreement is almost perfect. However, the theoretical results of Tan et al. [1] show a more pronounced negative temperature dependence than the experimental ones. There are at least two possible explanations: First, we cannot exclude that the cooling process is too slow to conserve the thermal equilibrium concentration of vacancies during quenching. At lower temperatures, the V_{Ga} concentration would be undersaturated and the crystal would seek to remove this undersaturation by the formation of additional V_{Ga}. Then, the measured c_v would not correspond the equilibrium concentration at the quenching temperature but rather to the equilibrium concentration at the temperature at which it is not further possible to create vacancies due to kinetic limitations. However, in that case we would not expect to see a temperature dependence of c_v at all. A second possibility to explain the differences between theory and experiment lies in the fact that the parameters used in the calculations are known with limited accuracy only. For example, the equilibrium concentration of the charged Ga vacancy depends sensitively on the position of their ionization levels because this determines the energy release by forming a charged vacancy. In Ref. [1], ionization levels for V_{Ga} according to Baraff and Schlüter [11] were used. By using the ionization levels calculated by Zhang and Northrup [12] which are closer to the valence band, the calculation yields a weaker negative temperature dependence of c_v (Fig. 4). If further the standard formation enthalpy h^f_V of V_{Ga} is slightly reduced (from 2.59 eV to 2.2 eV), the temperature dependence of c_v is in better agreement with the data. Thus, our data are indeed compatible with the theoretical model, however, it is necessary to include the formation of the V_{Ga}–Te_{As} complexes in the theory for further refinements. This requires further work beyond the scope of the present paper which is focussed on experimental results.

4. Summary

We have investigated native vacancies in Te-doped GaAs by means of positron annihilation. It is shown that native vacancies GaAs : Te can be unambiguously identified to be V_{Ga}–Te_{As} complexes by combining the results of positron lifetime and Doppler broadening coincidence measurement with theoretical calculations. The vacancy concentration depends on the doping level and increases linearly with the donor concentration c_d. A change of the stoichiometry by annealing under defined As vapor pressure allows a reversible adjustment of the vacancy concentration. The vacancy concentration c_v depends on p_{As} like $c_v = 0.1\, c_d p_{As}^{1/4}$ for the doping range under investigation ($n = 0.6$–50×10^{17} cm^{-3}). The vacancy concentration exhibits a weak negative temperature dependence in accordance with the Fermi level effect model of Tan et al. [1]. The data are the first direct experimental confirmation for this consequence of the model.

Acknowledgements

We like to thank Freiberger Compound Materials GmbH for the GaAs material. This work was supported by the Deutsche Forschungsgemeinschaft.

References

[1] T.Y. Tan, H.M. You, U.M. Gösele, Appl. Phys. A 56 (1993) 249.
[2] R. Krause-Rehberg, H.S. Leipner, Positron Annihilation in Semiconductors, Springer, Berlin, 1999.
[3] J. Gebauer, M. Lausmann, T.E.M. Staab, R. Krause-Rehberg, H. Hakala, M.J. Puska, Phys. Rev. B 60 (1999) 1464.
[4] N.A. Gokcen, Bull. of Alloy Phase Diagrams 10 (1989) 11.
[5] M.J. Puska, C. Corbel, R.M. Nieminen, Phys. Rev. B 41 (1990) 9980.

[6] K. Saarinen, P. Hautojärvi, A. Vehanen, R. Krause, G. Dlubek, Phys. Rev. B 39 (1989) 5287.
[7] M. Alatalo, B. Barbiellini, M. Hakala, H. Kaupinen, T. Korhonen, M.J. Puska, K. Saarinen, P. Hautojärvi, R.M. Nieminen, Phys. Rev. B 54 (1996) 2397.
[8] D.T.J. Hurle, J. Appl. Phys. 58 (1999) 6957.
[9] R. Krause-Rehberg, H.S. Leipner, A. Kupsch, A. Polity, T. Drost, Phys. Rev. B 49 (1994) 2385.
[10] J. Gebauer, R. Krause-Rehberg, C. Domke, P. Ebert, K. Urban, Phys. Rev. Lett. 78 (1997) 3334.
[11] G.A. Baraff, M. Schlüter, Phys. Rev. B 33 (1986) 7346.
[12] S.B. Zhang, J.E. Northrup, Phys. Rev. Lett. 67 (1991) 2339.

ELSEVIER

Physica B 273–274 (1999) 710–713

PHYSICA B

www.elsevier.com/locate/physb

Defect investigations in plastically deformed gallium arsenide

H.S. Leipner[a,*], C.G. Hübner[a,1], P. Grau[a], R. Krause-Rehberg[a]

[a]*Fachbereich Physik, Friedemann-Bach-Platz 6, Martin-Luther-Universität, D-06108 Halle, Germany*

Abstract

The defect formation during plastic deformation of GaAs has been investigated by means of the analysis of stress–strain curves including relaxation experiments and positron lifetime spectroscopy. The deformation creates a mixture of dislocations and point defects, which contribute to the positron lifetime spectra. Vacancy clusters can already be formed at rather low deformation temperatures via jog dragging. The concentration of generated defects depends on the number of activated slip systems for single-slip or multiple-slip orientation of the deformation axis.

Keywords: Deformation; Dislocations; Vacancies; Voids

1. Introduction

The strain rate and temperature dependence of the lower yield stress τ_{ly} of tetrahedrally coordinated semiconductors can be described within the Alexander–Haasen model in a wide range of temperature T by

$$\tau_{ly} = C\dot{\varepsilon}^{1/(2+m)}\exp\left[\frac{U}{(2+m)k_B T}\right]. \quad (1)$$

The underlying process is the movement of dislocations in the Peierls potential by nucleation and migration of double kinks. m is the stress exponent of the dislocation velocity (C is a model constant, k_B the Boltzmann factor, and $\dot{\varepsilon}$ the strain rate). Despite the fact that the activation energy U of the flow stress — which is identical to the activation energy of the glide velocity — has been found in a constant ratio to the self-diffusion energy [1], the generation of point defects during plastic deformation cannot be explained with Eq. (1). Another approach is the thermodynamic model of Schoeck [2]. The dislocation velocity v is determined in this description by the overcoming of glide obstacles with the spacing l. It is calculated by

$$v = lf\exp\left(-\frac{\Delta G}{k_B T}\right), \quad (2)$$

where f is the vibration frequency of the dislocation. The enthalpy term can be approximated by $\Delta G = Q - V\tau_{eff}$, with Q being the thermal contribution to the overcoming of the obstacles, $V = bdl$ the activation volume (b is the magnitude of the Burgers vector, d the diameter of an obstacle), and τ_{eff} the effective stress [3]. The Schoeck model allows the description of the formation of point defects by dislocation glide. The movement of a screw dislocation with jogs can formally be treated as the interaction of dislocations with obstacles, with the difference that the obstacles move along with the dislocation [4]. Zongo and Farvacque [3] analyzed the relation between the Alexander–Haasen and the Schoeck model. Despite the fact that point defect production can easily be included, the general weakness of the latter approach is the stress dependence of the activation energy of the dislocation velocity, which hardly corresponds to experimental findings. Also the stress dependence of the activation volume can scarcely be interpreted.

The main interest in our own investigations was the characterization of the point defect formation during plastic deformation of gallium arsenide single crystals. We used positron lifetime spectroscopy, which is mainly

* Corresponding author. Tel.: + 49-345-55-25-453; fax: + 49-345-55-27-563.

E-mail address: leipner@physik.uni-halle.de (H.S. Leipner)

[1] Present address: Eidgenössische Technische Hochschule, Department Chemie, CH-8092 Zürich, Switzerland.

0921-4526/99/$ - see front matter
PII: S0921-4526(99)00617-1

suited for the detection of vacancy-type defects. Stress–strain curves together with stress relaxations were measured and evaluated both with the Alexander–Haasen and the Schoeck model.

2. Experimental details

Bars of the dimension $4\times4\times12$ mm^3 with [0 0 1]-, [1 1 0]-, or [2 1 3]-oriented long axes were cut from undoped semi-insulating liquid-encapsulated Czochralski-grown gallium arsenide crystals (Freiberger compound materials). Uniaxial compression experiments were carried out in a hydraulic MTS testing machine at various constant strain rates and temperatures. The samples were kept during deformation in a protective Ar atmosphere. Positron lifetime measurements were performed using a fast–fast spectrometer. A ^{22}NaCl positron source was deposited on a thin Al foil and placed between a sandwich of identical samples cut from the middle of the plastically deformed bar. Positron measurements were carried out in a temperature range between 15 and 400 K. Events between 1.5×10^6 and 6×10^6 were collected for a complete positron lifetime spectrum.

3. Results and discussion

3.1. Deformation experiments

Fig. 1 shows stress–strain curves of undoped GaAs plastically deformed in different deformation directions in combination with strain rate changes. From the strain rate sensitivity,

$$I=\frac{\partial\tau}{\partial\ln\dot{\varepsilon}_{\text{plast}}}, \tag{3}$$

the activation volume can be determined via the equation $V=k_BT/I$. Since Eq. (3) requires a constant dislocation density, the differences of the yield stress maxima have been used for the calculation of I. For deformation in [1 1 0] and [2 1 3] directions, a strain rate sensitivity of $I=(1\pm0.05)$ MPa has been obtained. This corresponds to an activation volume of $V=(166\pm15)b^3$. Astié et al. [5] found for undoped GaAs deformed in [2 1 3] direction an activation volume of $240b^3$ for the applied stress used here. This higher activation volume may be due to the fact that pre-deformed samples having thus higher defect densities were used.

The activation volume of the sample deformed in [0 0 1] direction amounts to about twice the value of the other two deformation directions, $V=(308\pm35)b^3$. This increase cannot be explained with a higher yield stress, since V decreases with increasing yield stress. Rather, it may be a distinct indication for a variation in the deformation mechanism.

In addition to changes in the strain rate, also stress relaxation experiments have been carried out. At a certain value of the shear stress, the dynamical deformation has been stopped, and the total strain rate vanishes, $\dot{\varepsilon}=0$. In this case, the magnitude of the plastic strain rate is equal to the elastic strain rate, $\dot{\varepsilon}_{\text{plast}}=-\dot{\varepsilon}_{\text{elast}}$. The strain rate sensitivity can be determined in such an experiment as the slope of the straight line in the plot of the resolved shear stress versus the logarithm of the relaxation time. The activation volume determined in this way amounts to $(179\pm2)b^3$ for the [1 1 0] deformation axis. For [2 1 3] and [0 0 1], $(173\pm2)b^3$ and $(295\pm10)b^3$ have been obtained. These values correspond within the error bars those obtained in the strain rate change experiments.

From the jump in the stress $\Delta\tau$ occurring at a temperature change ΔT, the activation energy Q can be determined,

$$Q=\frac{k_BT}{I}\frac{\Delta\tau}{\Delta T}.$$

This activation energy has been determined to be (2.8 ± 0.3) eV for deformation in [2 1 3] direction with a strain rate of 8.3×10^{-5} s^{-1}. The value of Astié et al. is lower (2.2 eV). However, their method of the determination of Q is less correct than our approach, since in addition to the the Schoeck model (2), additional assumptions on a stress exponent m were used.

The stress–strain curves have been also evaluated within the framework of the Alexander–Haasen model (1). For the single-slip [2 1 3] deformation axis, the activation energy $U=2.1$ eV has been determined. The

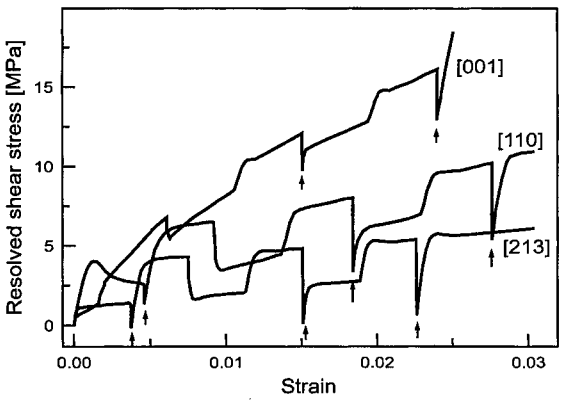

Fig. 1. Strain rate change experiments of undoped GaAs in combination with stress relaxations. The arrows indicate the strain where the relaxations started. The deformation temperature was 500°C. The starting strain rate was 7.5×10^{-6} s^{-1} for the [0 0 1] and 3.1×10^{-5} s^{-1} for the other two deformation directions. The ratio of the strain rates was 1 : 10.

stress exponent m amounts to 1.2. Whereas the latter value corresponds to data from the literature [1], the activation energy is lower than reported so far. This may be due to the production of point defects, which considerably influences dislocation motion in the range of temperatures and strain rates investigated here. Recently, Brion and Siethoff [6] have discussed the effect of a predeformation step on stress–strain curves of Zn-doped GaAs and the role of point defects. However, as far as intrinsic point defects are concerned, their contribution to the empirical parameters U and m has not been clarified yet.

3.2. Positron lifetime measurements

Fig. 2 shows the result of positron lifetime measurements of plastically deformed GaAs. The average positron lifetime $\bar{\tau}$ at room temperature is distinctly higher than in the undeformed sample, where a lifetime of 230 ps has been measured. This is a clear indication for the presence of vacancy-type defects. A distinct decrease in $\bar{\tau}$ appears at temperatures below 200 K. A three-component decomposition of the lifetime spectra can be carried out above 120 K. The course of the two defect-related positron lifetime components, $\tau_2 = \tau_{d1}$ and $\tau_3 = \tau_{d2}$ is shown in Fig. 2. The reduced positron bulk lifetime

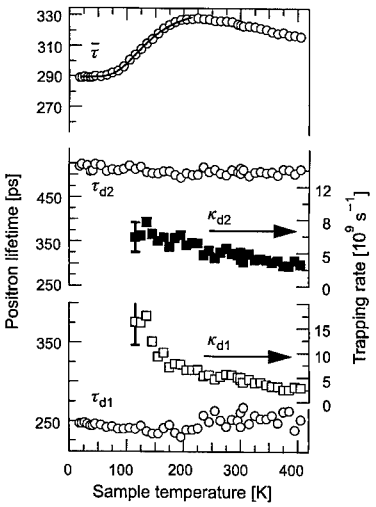

Fig. 2. Result of positron lifetime measurements of GaAs deformed in [1 1 0] direction at 800°C with a strain rate of 4.8×10^{-5} s^{-1} up to a strain of 10%. The upper panel shows the average positron lifetime $\bar{\tau}$ as a function of the sample temperature, the lower panels the result of the decomposition of the lifetime spectra with two defect-specific positron lifetimes, τ_{d1} and τ_{d2} and their trapping rates, κ_{d1} and κ_{d2}. The decomposition has been carried out with two lifetime components below 120 K and with three components above.

τ_1 has been omitted. A three-component decomposition is not possible in the low-temperature region. The component of the reduced bulk lifetime vanishes, and saturated positron trapping in defects occurs. The lifetime τ_2 amounts to (255 ± 7) ps above 200 K. The larger scatter in this lifetime component is due to higher uncertainties in the three-component decomposition in this range. The positron lifetime τ_{d1} lies close to values which are expected for monovacancies or complexes containing a monovacancy [7]. The question arises whether the deformation-induced monovacancy-type defect d1 is isolated or bound to dislocations. This problem has been tackled by annealing experiments of plastically deformed GaAs. Independent of the deformation conditions, the average positron lifetime decreased for annealing in the range 850–1000 K. This is related to the simultaneous annealing of defects d1 and d2, as reflected in the fall of the trapping rates κ_{d1} and κ_{d2}. As a consequence, the defect d1 cannot be related to isolated monovacancies, because it is known from electron-irradiation experiments that such defects anneal at much lower temperatures [8]. So it is concluded that d1 corresponds to vacancies stabilized on or close to dislocations.

Between 15 and 200 K, the shorter lifetime component is found between 240 and 247 ps. The decrease in this positron lifetime and in $\bar{\tau}$ at low temperatures in conjunction with saturated positron trapping can be uniquely explained with the activity of another defect, viz., a shallow positron trap. Such a defect is characterized by a weak potential, which is only able to capture positrons at low temperatures. With increasing temperature, there is an increasing probability of thermal escape of positrons, and such a shallow positron trap becomes "invisible". The positron lifetime specific for a shallow positron trap is close to the positron bulk lifetime, $\tau_{d3} \approx \tau_b$. Thus, the shorter lifetime component below 200 K can be understood as a mixture of τ_{d1} and τ_{d3}.

The nature of the shallow positron trap was studied by positron annihilation and electron paramagnetic resonance (EPR) [9]. The most probable candidate is the Ga_{As}^{-} antisite defect. With the independent determination of the concentration of antisites by EPR, the trapping coefficient as the proportionality constant between trapping rate and defect concentration, $\kappa = \mu C$, could be determined to be $\mu = (2.6 \pm 0.3) \times 10^{16}$ s^{-1} for temperatures below 200 K [9].

The lifetime component τ_{d2} amounts to (505 ± 10) ps. Such a high value can only be interpreted by the presence of large open-volume defects. Theoretical calculations with a local density-functional tight binding scheme provided as the most stable configuration clusters consisting of 12 vacancies [10]. The results of this simulation were used to calculate the positron lifetime. For the stable V_{12} configuration, 440 ps was obtained [10].

The mechanism of vacancy generation is directly related to dislocation motion. The jog dragging mechanism

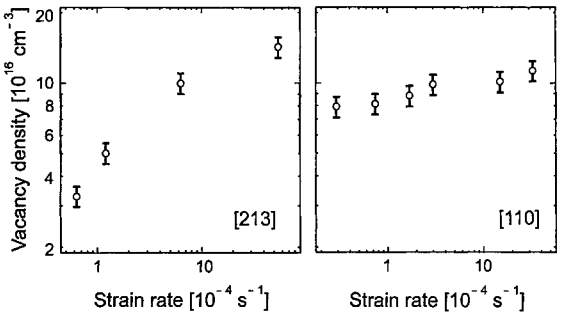

Fig. 3. Density of vacancies agglomerated in voids versus the strain rate. Undoped GaAs has been deformed at 500°C up to 3% in [2 1 3] (left panel) and [1 1 0] (right panel) directions.

is regarded as the primary source of point defects during plastic deformation. In contrast to earlier ideas, the formation of long rows of vacancies is energetically unfavorable [10], and three-dimensional vacancy clusters are generated.

The positron trapping rates obtained can be used to estimate the densities of defects formed during deformation. The density of vacancy clusters can be obtained from the trapping rate, $\kappa_{d2} = 2\pi Dr\rho$. D is the positron diffusion coefficient and ρ the density of voids. The stable cluster size of V_{12} has been assumed for the calculation of the void radius r. Defect densities have been determined for [0 0 1], [1 1 0], and [2 1 3] deformation axes. These orientations correspond to a different number of equivalent slip systems. Eight equivalent systems exist for [0 0 1] and four for [1 1 0]. [2 1 3] is a single-slip orientation. The influence of the orientation on the density of vacancies agglomerated in voids is shown in Fig. 3. The vacancy density is practically independent of the strain rate for a multiple-slip orientation such as [1 1 0]. In this case, there is always a high frequency of dislocation cutting, which leads to a high number of jogs being responsible for vacancy production. In contrast, for a [2 1 3] orientation, the vacancy density is low for low strain rates. The increase in the vacancy density with increasing strain rate may be related to a higher cross-slip activity or the activation of secondary slip systems. Consequently, the number of jogs increases and thus the number of vacancies produced by jog dragging.

Acknowledgements

The work was supported by the Deutsche Forschungsgemeinschaft.

References

[1] H. Siethoff, Phys. Stat. Sol. A 138 (1993) 591.
[2] G. Schoeck, Phys. Stat. Sol. 8 (1965) 499.
[3] I. Zongo, J.L. Farvacque, Phys. Stat. Sol. A 142 (1994) 383.
[4] G. Schöck, in: F.R.N. Nabarro (Ed.), Dislocations in Solids, Vol. 3, North-Holland, Amsterdam, 1980, pp. 63–163.
[5] P. Astié et al., Phys. Stat. Sol. A 96 (1986) 225.
[6] H.G. Brion, H. Siethoff, J. Appl. Phys. 84 (1998) 4885.
[7] R. Krause-Rehberg, H.S. Leipner, in: Positron Annihilation in Semiconductors, Springer, Berlin, 1999.
[8] C. Corbel et al., Phys. Rev. B 41 (1990) 10632.
[9] H.S. Leipner et al., Mater. Sci. Forum 258–263 (1997) 981.
[10] T.E.M. Staab et al., Phys. Rev. Lett. (1999), accepted for publication.

ELSEVIER

Physica B 273–274 (1999) 714–717

PHYSICA B

www.elsevier.com/locate/physb

Formation of vacancy clusters during copper diffusion in GaAs

R. Krause-Rehberg*, K. Petters, J. Gebauer

Martin-Luther-Universität Halle-Wittenberg, Fachbereich Physik, Fr.-Bach-Platz 6, D-06108 Halle, Germany

Abstract

Undoped and n-doped GaAs samples were studied after in-diffusion of copper by means of positron annihilation. During diffusion, small microvoids are formed which are decorated by copper atoms. The small clusters dissolve during annealing at $T > 850$ K.

Keywords: Gallium arsenide; Diffusion; Vacancy clusters; Copper–vacancy complex

1. Introduction

Copper is found as an unintentional impurity in most semiconductors. This is due to the fact that Cu is a rapidly diffusing contaminant already at low temperatures. In GaAs the diffusion coefficient was found to be as high as $D = 1.1 \times 10^{-5}$ cm^2 s^{-1} at 500°C [1]. Cu diffuses slowly by a substitutional process and very fast by interstitial diffusion (kick-out process) [2]. The solubility was reported to be in the range between 2×10^{16} cm^{-3} (500°C) and 7×10^{18} cm^{-3} (1100°C) [1]. The solubility was found to be a function of the initial doping concentration [1].

Cu is a double acceptor in GaAs, when being incorporated at a substitutional lattice site as Cu_{Ga}. It was found that Cu exhibits two ionization levels in the band gap [3]. Depending on the cooling speed after a diffusion process at elevated temperature, only a small fraction of the total Cu concentration is electrically active as acceptors. The inactive fraction forms Cu–Ga precipitates [3]. These precipitates have densities of about 10^{10} cm^{-3} when the sample is quenched from the temperature of highest Cu solubility. Their size was found to be 100–200 nm with a mean separation of 3 μm [3].

In this paper we show first the results of a comprehensive positron annihilation study of GaAs after Cu in-diffusion. Positron annihilation is a very sensitive tool for the detection of vacancy-type lattice defects in semiconductors [4]. We will show that vacancy clusters decorated with copper will be formed during annealing of GaAs when Cu is earlier introduced by diffusion.

2. Experimental details

Te-doped ($n = 4.5 \times 10^{17}$ cm^{-3}) and undoped semi-insulating GaAs samples of thickness of 0.4 mm were covered by 30 nm Cu by evaporating it under UHV conditions. This corresponds to a volume concentration of 6×10^{18} cm^{-3} which is approximately the upper solubility limit of Cu in GaAs [1]. The thickness of the deposited layer was controlled by a thickness measurement device (frequency shift of a crystal oscillator). After Cu deposition at one surface, the samples were annealed in a two-zone furnace at 1100°C (sample temperature) under an arsenic pressure of 2.6 bar for 3 h corresponding to a Cu diffusion length of about 1.5 cm. After annealing, the samples were quenched in the quartz ampoules into water at room temperature. The samples were measured in the as-quenched state by Hall effect and thermoprobe measurements. It was found that even the n-doped sample was converted to p-type conductivity. Thereafter, the samples were isochronally annealed in the temperature range up to 900 K. The samples were cooled down slowly after each annealing step. They were measured between the annealing steps with positron lifetime and Doppler-broadening spectroscopy. The resolution of

* Coresponding author. Tel.: + 49-345-552-5567; fax: + 49-345-552-7160.

E-mail address: krause@physik.uni-halle.de (R. Krause-Rehberg)

0921-4526/99/$ - see front matter
PII: S0921-4526(99)00618-3

the spectrometers was 240 ps and 1.4 keV, respectively. S and W Doppler parameters were calculated in the range of (511 ± 0.8) keV and (511 + 2.5 to 4) keV, respectively. The GaAs crystals were oriented with their (1 1 0) axis towards the Ge detector.

3. Results and discussion

3.1. Semi-insulating GaAs

A reference sample without any Cu deposition did not show any positron trapping. After Cu in-diffusion, a slight increase of the average positron lifetime indicates that a small number of vacancy-type defects is detected at higher temperatures. Fig. 1 shows the average positron lifetime after different annealing steps of the undoped sample after Cu in-diffusion. Almost no change was observed for the first annealing steps up to 550 K. The lifetime is about 226 ps at low sample temperatures, which is slightly lower than the value measured in GaAs:Zn (228 ps). The Doppler parameters more distinctly deviate from the bulk values: $S/S_b = 0.9915$ and $W/W_b = 1.047$. The positrons are obviously trapped at Cu acceptors which act as shallow positron traps [5]. The density of ionized Cu acceptors after quenching must be larger than 4.5×10^{17} cm^{-3} since the n-doped sample is converted to p-type conductivity. Assuming a trapping coefficient of 2×10^{16} s^{-1} for shallow traps at 20 K [6], almost complete positron trapping must be expected. However, the change in the lifetime and Doppler parameters is rather small because the positron is trapped and annihilates in the extended region of the Coloumbic potential, thus reflecting mainly the properties of the bulk.

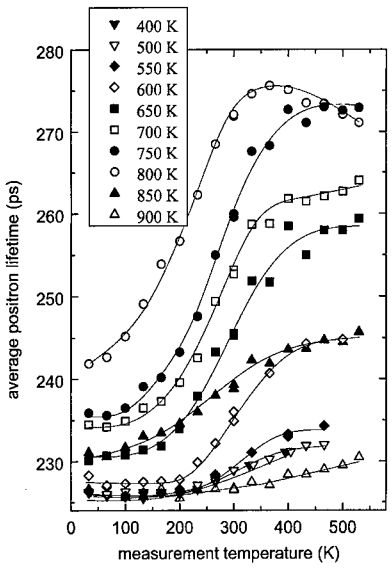

Fig. 1. Average positron lifetime as a function of sample temperature in undoped GaAs. Prior to the experiment, about 6×10^{18} cm^{-3} Cu atoms were introduced by evaporating 30 nm Cu to the sample surface and a subsequent annealing at 1100°C (3 h, quenched into water). The lifetime experiment was performed after each annealing step as indicated in the figure.

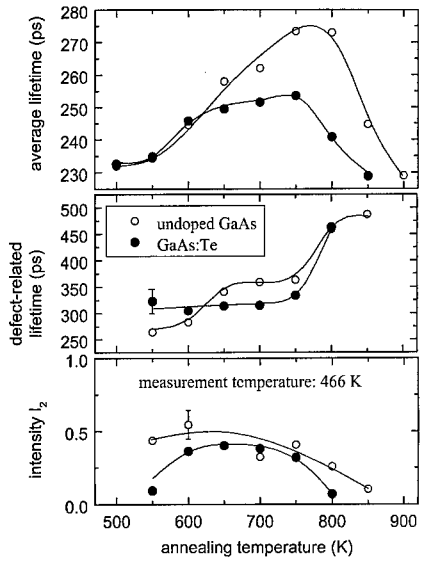

Fig. 2. Positron lifetime results of the annealing experiment of undoped (○) and n-doped (●) GaAs samples after in-diffusion of 6×10^{18} cm^{-3} Cu atoms. The lifetime and the intensity of the second component of a two-component spectra decomposition is plotted in the two lower panels. The spectra were measured at a sample temperature of 466 K to diminish the influence of the shallow traps (compare Fig. 1).

During annealing up to 800 K, the average positron lifetime increases strongly and reaches values as high as 275 ps. Thus, the detected vacancy must be distinctly larger than a gallium monovacancy (262 ps) [4]. The spectra could be decomposed into two lifetime components (for details of the spectra treatment see Ref. [4]). From the second lifetime component (defect-related lifetime), it must be concluded that the open volume increases during annealing (Fig. 2). A value of 480 ps can only be explained by positron trapping at larger microvoids (more than 10 vacancies) [7]. Large voids were also found after in-diffusion of Zn into GaAs [8]. During the last two annealing steps, this vacancy cluster signal almost disappears. The question arises whether these vacancy defects and clusters are isolated or decorated by Cu atoms. This cannot be decided from the positron lifetime results alone.

Fig. 3 shows the results of the Doppler-broadening measurements. The data were measured at 466 K where the influence of trapping to shallow positron traps can be

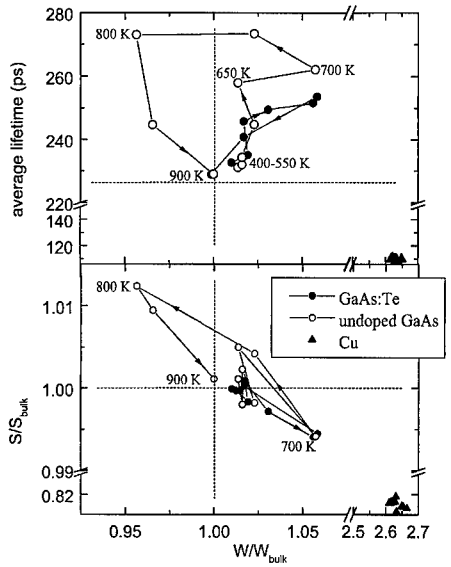

Fig. 3. Results of Doppler-broadening measurements obtained during annealing of undoped (○) and n-doped (●) GaAs after Cu in-diffusion. Average lifetime (upper panel) and S parameter (lower panel) are plotted versus W parameter. The spectra were measured at a sample temperature of 466 K. The course of the annealing treatment is indicated by arrows. Annealing temperatures given in the panels are valid for the undoped sample. The bulk values are marked by dashed lines.

neglected. When vacancies are detected by positron trapping, the S parameter usually increases and the W parameter decreases. Typical values for the isolated gallium vacancy in GaAs are $S/S_b = 1.02$ and $W/W_b = 0.80$ [4]. However, the experimental finding for the copper-diffused GaAs is in contradiction to this common experience. The normalized W parameter is larger than 1 for most data points, the S parameter is smaller than 1 for at least some points. Since the lifetime spectroscopy gives clear evidence for positron trapping in small vacancy clusters, the Doppler data can only be understood, when a change in the chemical surrounding of the open-volume defect is considered. It is impossible to explain the data when assuming vacancies or vacancy clusters in the otherwise undisturbed GaAs lattice. We have to conclude that the observed vacancy clusters are decorated with Cu atoms. Although no attempt has been made so far to simulate the data theoretically, it seems to be clear that the strong contradiction between defect-related lifetime (cluster size $n > 4$) and the W parameter ($W/W_b > 1$) cannot be explained by the assumption that only a single Cu atom is part of the defect complex. Furthermore, it is clear that for the observed reduction in the electron density in the open-volume defect (increase in lifetime) vacancies in both sublattices must be involved [7]. The distinct increase in the defect-related lifetime during the course of annealing indicates that the vacancy clusters under observation grow further and reach a size of $n > 10$ [7].

It should be noted that positron trapping by the above mentioned Cu–Ga precipitates could in principle also account for the observed strong effects in the annihilation parameters. However, the mean distance between the precipitates is much longer than the mean positron diffusion length, so that only a very weak effect is to be expected [9].

3.2. n-doped GaAs

A similar experiment was performed for Te-doped GaAs. Prior to Cu diffusion, i.e. in the as-grown state, a Te_{As}–V_{Ga} complex was identified as efficient positron trap [10,11]. We found an average lifetime of 236 ps. However, after Cu in-diffusion and quenching, the sample was converted to p-type conductivity. Thus, the charge state of the complex may be positive then (positrons will not be trapped). This fact, or the possibility that the Ga vacancies of the complex are filled by the diffusing Cu atoms may lead to the behavior that the average lifetime is distinctly smaller after Cu diffusion (Fig. 2, upper panel). After the first annealing steps, the average lifetime increases to a maximum of about 252 ps and the positron trapping is almost lost again after annealing at 850 K.

However, there are some differences to the undoped sample: The average lifetime remains smaller during annealing; the defect signal disappears 50 K earlier; the S and W parameters show smaller effects; and the defect-related lifetime seems to stay constant during annealing at least up to 750 K (due to the small intensity of this component after 800 K annealing, it is not entirely clear that the large τ_2 of about 450 ps is not an artifact of the spectra decomposition). However, it is obvious that the structure of the defect complex is different from the undoped sample, The defect-related lifetime of 300–330 ps is compatible with a V_{Ga}–V_{As} divacancy [7]. However, the large W/W_b parameter which is always > 1 strongly suggests that this complex is again decorated with Cu atoms. The difference to the undoped material may arise due to the different solubility of copper which is a function of initial doping [1].

4. Conclusions

Positron annihilation was applied to study undoped and n-type, Te-doped GaAs samples after in-diffusion of copper. The following conclusions can be derived from the experimental findings:

- Both samples were converted to p-type conductivity.

- After quenching from diffusion temperature, only weak positron trapping is found in both types of material and the positron trapping by V_{Ga}–Te_{As} complexes usually found in as-grown n-type GaAs : Te is lost.
- During annealing up to 750 K, vacancy clusters are formed which are decorated with at least one Cu atom (probably more).
- These clusters grow during annealing in undoped GaAs to a size of more than 10 vacancies (both sublattices). In n-type GaAs, the clusters seem to remain smaller, but this fact needs further experimental confirmation.
- The small Cu-vacancy clusters dissolve above 800 K.
- In the next step, electron microscopy and electrical measurements (Hall effect and DLTS) will be performed to characterize the precipitates and to obtain the number of ionized Cu acceptors (shallow positron traps). This will give us the opportunity to discuss the Cu distribution more quantitatively.

Acknowledgements

We would like to thank the Freiberger Compound Materials GmbH for supplying the GaAs material. This work was supported in part by the Deutsche Forschungsgemeinschaft.

References

[1] R.N. Hall, J.H. Racette, J. Appl. Phys. 35 (1964) 379.
[2] F.C. Frank, D. Turnball, Phys. Rev. 104 (1956) 617.
[3] R. Leon, P. Werner, K.M. Yu, M. Kaminska, E.R. Weber, Appl. Phys. A D61 (1995) 7.
[4] R. Krause-Rehberg, H.S. Leipner, Positron Annihilation in Semiconductors, Springer, Berlin, 1999.
[5] K. Saarinen, P. Hautojärvi, A. Vehanen, R. Krause, G. Dlubek, Phys. Rev. B 39 (1989) 5287.
[6] J. Mäkinen, P. Hautojärvi, C. Corbel, J. Phys.: Condens. Matter 4 (1992) 5137.
[7] T.E.M. Staab, M. Haugk, T. Frauenheim, H.S. Leipner, Physica B 273–274 (1999) 499, These Proceedings.
[8] T.Y. Tan, U. Gösele, S. Yu, Crit. Rev. Sol. State Mater. Sci. 17 (1991) 47.
[9] C. Hübner, T. Staab, R. Krause-Rehberg, Appl. Phys. A 61 (1995) 203.
[10] J. Gebauer, M. Lausmann, T.E.M. Staab, R. Krause-Rehberg, H. Hakala, M.J. Puska, Phys. Rev. B 60 (1999) 1464.
[11] R. Krause-Rehberg, H.S. Leipner, A. Kupsch, A. Polity, T. Drost, Phys. Rev. B 49 (1994) 2385.

ELSEVIER

Physica B 273–274 (1999) 718–721

PHYSICA B

www.elsevier.com/locate/physb

Deep levels in He^{++} irradiated Be-doped $Al_{0.5}Ga_{0.5}As$ MBE layers

J. Szatkowski[a,*], E. Płaczek-Popko[a], K. Sieranski[a], O.P. Hansen[b], A. Johansen[b], C. Soerensen[b]

[a]*Institute of Physics, Wrocław University of Technology, Wybrzeże Wyspiańskiego 27, 50-370 Wrocław, Poland*
[b]*Oersted Laboratory, University of Copenhagen, Universitetparken 5, DK-2100 Copenhagen, Denmark*

Abstract

He^{++} irradiation induced defects in Be-doped $Al_{0.5}Ga_{0.5}As$ MBE layers have been studied using the DLTS method. The samples were irradiated by He^{++} ions of an energy equal to 0.5 MeV and fluence of $10^{12}\,cm^{-2}$. In irradiated samples, persistent photocapacitance was observed after illumination of the samples at the liquid nitrogen ambient. Defect (or defects) introduced during irradiation can be responsible for the observed persistent photocapacitance effect.

Keywords: AlGaAs; Deep levels; DX centers

1. Introduction

P-type $Al_xGa_{1-x}As$ is used as an active material in many heterostructures. It has recently been shown that it can serve as window material in PIN heterostructures suitable for alpha particle detection [1]. Studies of the influence of radiation on the properties of this material are of crucial importance for radiation detection technology. Thus far, there is very little information about irradiation-induced defects in p-type GaAs and related $Al_{1-x}Ga_xAs$ mixed crystals.

The defects introduced in n-type GaAs during alpha irradiation have been studied earlier [2]. Alpha irradiation of Si-doped GaAs introduced several defects related to arsenic vacancies (V_{As}), to arsenic ions displaced to the interstitial locations (V_{As}–As_i) [3], as well as to metastable defects probably associated with vacancies and the Si impurity.

This work proves that low-dose He^{++} irradiation of epitaxial, Be-doped $Al_{0.5}Ga_{0.5}As$ layers results in the formation of additional deep levels.

2. Experimental details

The influence of He^{++} irradiation on Be-doped $Al_{0.5}Ga_{0.5}As$ layers grown by molecular beam epitaxy was studied in this work. The sample structure and the preparation method have been described elsewhere [4]. The irradiation was performed at Copenhagen University's accelerator laboratory using 0.5 MeV He^{++} ions with a fluence of $10^{12}\,cm^{-2}$. The penetration depth, estimated with TRIM software [5], was equal to 2 μm. The Schottky contacts were deposited after the irradiation. The depletion region of the Schottky contacts, estimated at 0.2 μm, is narrower than the region affected by the irradiation.

The net acceptor concentration (N_A–N_D) and the built voltage U_B were obtained from capacitance–voltage (C–V) measurements at 300 and 77 K. For non-irradiated (reference) samples $(N_A-N_D) = (2.0 \pm 0.1) \times 10^{17}\,cm^{-3}$ and built voltage $U_B = (1.1 \pm 0.1)$ V at both temperatures. For irradiated samples the net acceptor concentration was equal to $(2.0 \pm 0.1) \times 10^{17}\,cm^{-3}$ at 300 K and $(8.0 \pm 0.1) \times 10^{16}\,cm^{-3}$ at 77 K; the built voltage was equal to (1.0 ± 0.1) V at both temperatures.

Both the capacitance–voltage characteristics and the deep-level transient spectroscopy (DLTS) spectra were collected using a lock-in-type DLS-82E spectrometer,

* Corresponding author. Fax: + 48-71-328-3696.
E-mail address: jasza@rainbow.if.pwr.wroc.pl (J. Szatkowski)

0921-4526/99/$ - see front matter
PII: S0921-4526(99)00620-1

made by SEMITRAP, Hungary. The DLTS studies were carried out within the 77–380 K temperature range with 2 K/min rate. All measurements were made with increasing temperature. Finally, persistent photocapacitance measurements were performed. Until photocapacitance saturation was reached, the samples were illuminated at the temperature of liquid nitrogen using a halogen lamp. Placing a high-energy filter in front of the lamp allowed for illumination with photons of an energy lower than the energy gap of $Al_{0.5}Ga_{0.5}As$. After turning off the light, capacitance measurements were carried out while heating up the sample to room temperature. The capacitance measurements were performed on the samples reversely biased with -3 V.

3. Results and discussion

The properties of deep levels existing in the non-irradiated reference samples have already been presented in earlier publications [4,6–8]. Five hole traps, labeled as H1–H5, were found [4]. For traps H1, H3, H4 and H5 the activation energies for emission were $E_{T1} = 0.14$ eV, $E_{T3} = 0.40$ eV, $E_{T4} = 0.46$ eV and $E_{T5} = 0.77$ eV. The electric field enhancements of the emission rate from level H2 affirmed the acceptor-like nature of this defect. Two of the traps, H1 and H4, exhibited strong hole–lattice interaction with the capture energy barriers of 0.04 and 0.18 eV, respectively. Excluding the H3 and H5 traps, the concentration of deep levels was of the order of 10^{14} cm^{-3}. The remaining two traps had their concentration at approximately 10^{13} cm^{-3}.

In the He^{++} irradiated samples, five DLTS peaks have been observed within the accessible temperature range. Fig. 1 represents typical DLTS spectra for He^{++} ion-irradiated samples. In the figure, the DLTS signal versus temperature is shown for two different widths of the filling pulses, $t_{p1} = 0.5$ μs and $t_{p2} = 200$ μs. The temperature position of the first three DLTS peaks depends on the filling pulse width. For $t_{p2} = 200$ μs, the first two peaks are shifted towards a lower temperature as compared to $t_{p1} = 0.5$ μs. In contrast, the third peak is shifted towards a higher temperature. The temperature position of the last two peaks is independent of filling pulse width.

The shift of DLTS peaks with filling pulse width was not observed for the non-irradiated samples [4,6–8]. Therefore, we have assumed that each of the first three "peaks" originates from more than a single deep level. With the single-level assumptions, it was also impossible to fit a theoretical relation to the experimental data. The peaks are too broad for such an assumption, suggesting that in the irradiated samples, the number of deep traps increased.

In the first approximation, we assumed that each of the first three peaks results from two closely spaced peaks: one related to a deep level existing in the non-irradiated material and one related to a level introduced by irradiation. The additional peaks are labeled as H1R, H2R, and H3R. The remaining two peaks were assumed to result from the superposition of three peaks: H4, H4R and H5. The parameters for additional traps were found by fitting the theoretical curves to the experimental data. As an example, the result of the fitting to the experimental DLTS spectrum collected at 126 Hz is shown in Fig. 2. The open squares represent the experimental data for the irradiated sample. The open and solid circles result from the theoretically calculated DLTS spectrum. We assumed that theoretical curve is a sum of the DLTS spectrum calculated independently for each deep level. Solid circles represent data for traps observed in the non-radiated reference samples. Parameters for H1–H4 traps and H5 are taken from Szatkowski et al. [7]. During fitting

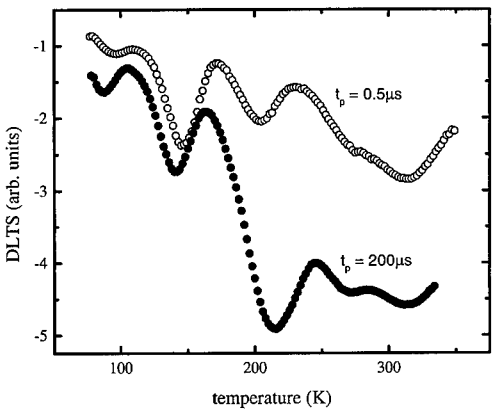

Fig. 1. DLTS spectra, with two different filling pulses, of an He^{++}-irradiated $Al_{0.5}Ga_{0.5}As$ layer MBE-grown on GaAs.

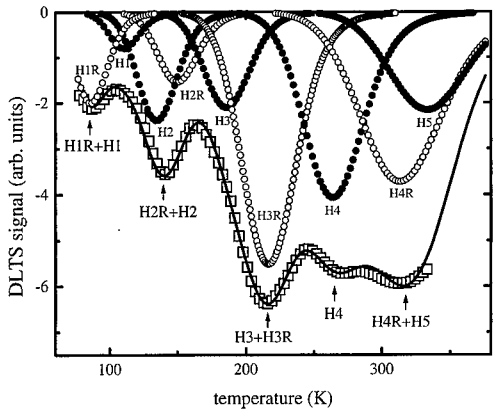

Fig. 2. The DLTS spectrum (squares) and the best fit (dashed curve) for MBE-grown $Al_{0.5}Ga_{0.5}As$. Theoretical DLTS peaks for the non-radiated (dotted line) and radiated (solid line) layers are included.

procedure only activation energy for H3 trap had to be changed from 0.40 eV as it was estimated for non-irradiated samples to 0.37 eV. Open circles represent data for new radiation-induced peaks. The solid line, being the best fit to the experimental data, is the sum of the functions represented by both open and solid circles. Parameters obtained with the fitting procedure for different lock-in frequencies are given in Table 1.

In the irradiated samples, persistent photocapacitance has been observed. Illumination of the samples at liquid nitrogen temperature caused an increase in capacitance by about 20%. After switching off the light, the photocapacitance remained on the new level for several hours. Only heating the samples to about 200 K restored its initial value. Since such an effect was not observed in the reference samples, this result indicates that irradiation either increased the concentration of some metastable defects or created new ones.

Fig. 3 shows the capacitance versus temperature plot after cooling the sample down to 77 K. One plot (i) represents its values while heating the samples in darkness, and the second plot (ii) was obtained while heating the samples after illuminating them at 77 K with the halogen lamp through the edge filter (with photons of an energy lower than 0.78 eV). The results prove the existence of persistent photocapacitance in the samples below the 225 K temperature.

Persistent photoeffects, observed in a variety of III–V and II–VI n-type semiconducting compounds, are due to metastable centers with a strong lattice coupling. Metastable defects are observed in both as-grown and processed semiconductors, mainly in n-type materials. In p-type, nitrogen-doped ZnSe the metastability of hole traps was observed [9].

In the studied samples, traps H3R, H4 and H4R, are the possible candidates for the metastable defects, responsible for the observed persistent photocapacitance. The H3R and H4R defects were found to be very sensitive to the filling pulse width and the DLTS peaks related to these traps do not saturate until several hundreds of microseconds. The H4 trap exhibited temperature-dependent capture cross section in the as-grown samples. Unfortunately, the H4 peak in the irradiated samples is accompanied by the H3R peak. The latter also probably has a very strong temperature-dependent capture cross section. It was also found that the peaks associated with both H3R and H4 traps increase significantly with filling pulse width. Therefore, based on this preliminary fitting, it is impossible to determine the energy barrier for capture for any of the traps.

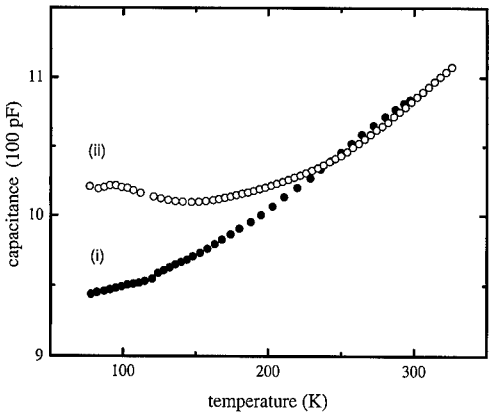

Fig. 3. Photocapacitance in MBE-grown $Al_{0.5}Ga_{0.5}As$. Plot (i) was collected while heating the samples without light. Plot (ii) represents results obtained while heating the samples after illumination at 77 K with a halogen lamp with an edge filter.

Table 1
Characteristics of the traps in the irradiated $Al_{0.5}Ga_{0.5}As$

Trap label	Activation energy (eV)	Capture cross section (cm^2)
H1R	0.11	8×10^{-17}
H1	0.15	8×10^{-17}
H2R	0.23	3×10^{-15}
H2	0.26	5×10^{-15}
H3	0.37	6.5×10^{-14}
H3R	0.38	3×10^{-15}
H4	0.46	2×10^{-15}
H4R	0.48	1×10^{-16}
H5	0.775	1×10^{-12}

4. Conclusions

The influence of irradiation on defects in Be-doped $Al_{0.5}Ga_{0.5}As$ MBE layers was studied. The samples were exposed to radiation with 0.5 MeV He^{++} ions at fluence of 10^{12} cm^{-2}. DLTS studies were performed within the 77–350 K temperature range on both reference and irradiated samples. He^{++} irradiation introduced four new levels in addition to those in the as-grown material. Persistent photocapacitance was observed for the irradiated samples. Thus, it has been assumed that irradiation increased the concentration of some metastable centers or introduced such centers, responsible for observed persistent photocapacitance effect.

Acknowledgements

This work has been partially supported by NATO Htech LG 974670 grant.

References

[1] L. Ryć, F. Riesz, in: Proceedings of the International Conference on Advanced Devices and Mikrosystems, ASDAM'96, Smolenice, October 20–24, 1996, Slovac Acad. of Sciences Bratislava, Slovakia, 1996, pp. 141–144.
[2] F.D. Auret, S.A. Goodman, G. Myburg, W.E. Myer, Appl. Phys. A 56 (1993) 547.
[3] F.D. Auret, S.A. Goodman, W.E. Meyer, Appl. Phys. Lett. 67 (1995) 3277.
[4] J. Szatkowski, E. Płaczek-Popko, K. Sierański, O.P. Hansen, Mater. Sci. Forum 258–263 (1997) 1653.
[5] J. Biersack, L. Häggmark, Nucl. Instr. and Meth. 174 (1980) 257.
[6] J. Szatkowski, E. Płaczek-Popko, K. Sierański, O.P. Hansen, Inst. Phys. Conf. Ser. 152 (1997) 789.
[7] J. Szatkowski, E. Płaczek-Popko, K. Sierański, O.P. Hansen, J. Appl. Phys. 86 (1999) 1433.
[8] J. Szatkowski, E. Płaczek-Popko, K. Sierański, O.P. Hansen, Acta Phys. Polon. 94 (1998) 565.
[9] K. Tanaka, Z. Zhu, T. Yao, Appl. Phys. Lett. 66 (1995) 3349.

ELSEVIER

Physica B 273–274 (1999) 722–724

PHYSICA B

www.elsevier.com/locate/physb

Native point defect analysis in non-stoichiometric GaAs: an annealing study

R.C. Lutz[a,*], P. Specht[a], R. Zhao[a], O.H. Lam[a], F. Börner[b], J. Gebauer[b], R. Krause-Rehberg[b], E.R. Weber[a]

[a]*Materials Science and Engineering Department, University of California at Berkeley, Berkeley, CA 94720, USA*
[b]*Fachbereich Physik, Martin-Luther-Universität Halle-Wittenberg, D-06099 Halle, Germany*

Abstract

The electronic properties of MBE-grown GaAs at temperatures well below 400°C are governed by its high concentration of native point defects. It is vital for device applications to understand and control the point defect concentrations in this non-stoichiometric III–V compound. In this paper, we present a detailed analysis of the changes of the point defect concentrations upon thermal annealing in both undoped and p-doped low-temperature-grown GaAs (LT-GaAs). The temperature-dependent concentration of residual arsenic antisites (As_{Ga}) after annealing is shown. Also the annealing behavior of the gallium vacancies (V_{Ga}) is investigated. Their role in the As diffusion will be discussed. The thermal stabilization of As_{Ga} will be demonstrated in LT-GaAs : Be for annealing temperatures as high as 700°C for 30 min.

Keywords: LT-GaAs; Molecular beam epitaxy; Native point defects; Annealing behavior; Thermal stabilization

1. Introduction

The primary identifying characteristic of low-temperature-grown GaAs (LT-GaAs) grown below 300°C by molecular beam epitaxy (MBE) is an excess of arsenic of up to 1.5%. Most of this excess takes the form of arsenic antisites (As_{Ga}), of which there may be as many as 10^{20}/cm^3 in epilayers grown at a substrate temperature of 200°C. Due to the presence of so many antisites, the *c*-axis lattice parameter of LT-GaAs is greater than that of bulk material [1]. Gallium vacancies, while present in much smaller concentrations than arsenic antisites, are important components of arsenic diffusion during high-temperature anneals.

Perhaps the biggest problem with LT-GaAs for device applications is its inability to withstand high-temperature anneals. On annealing at temperatures above 600°C for all but the shortest instants, the excess arsenic precipitates into small arsenic clusters [2–4]. The lattice parameter of the film relaxes back to that of the substrate [1]. Annealing is detrimental to the performance of neighboring layers, as defects outdiffuse from the LT layer and disrupt the current transport in adjacent layers [5].

The prevailing model of LT-GaAs annealing involves the vacancy-assisted diffusion of arsenic antisites to precipitate boundaries [6]. It was suggested that a possible solution to this arsenic precipitation might be a low-temperature pre-anneal [7]. The low-temperature anneal is believed to allow the diffusion of vacancies to vacancy sinks, thereby freezing the antisites in position and stabilizing them to subsequent high-temperature anneals. However, a successful thermal stabilization by such a pre-anneal has never been reported to date. Previous work found some evidence for improvements in thermal stability upon Be-doping [8].

2. Experimental

All films were grown in a Varian Gen II MBE chamber between 200°C and 295°C. Before LT-GaAs growth, a

* Corresponding author. Tel.: + 1-510-643-5304; fax: + 1-510-643-5304.
E-mail address: rlutz@uclink4.berkeley.edu (R.C. Lutz)

0921-4526/99/$ - see front matter
PII: S0921-4526(99)00621-3

0.5 μm GaAs buffer layer was grown at 580°C. The beam equivalent pressure ratio was 20, and the growth rate was 1 μm/h. The beryllium concentrations reported here are from SIMS measurements. Films were proximity annealed in a furnace with a sacrificial GaAs wafer on the face of the film to prevent outdiffusion of excess arsenic.

Infrared (IR) absorption and magnetic circular dichroism of absorption (MCDA) were used to determine the concentrations of neutral and ionized arsenic antisite defects, respectively. The concentrations were determined from the strength of the absorption or absorption difference using the established calibrations [9,10]. The raw substrate IR absorption spectrum and ionized antisites concentration measured were subtracted from the conjoined film/substrate spectrum or ionized antisite concentration. The measurement temperature was 1.8 K.

Vacancy characteristics were studied with slow positron annihilation spectroscopy. The positron annihilation data are reported in terms of the S and W parameters. These parameters are measures of the relative measure of the characteristic Doppler broadening of gamma radiation released by the annihilation reaction [11].

The lattice misfit between film and substrate was determined by X-ray diffraction using the (0 0 4) symmetric reflection.

3. Results and discussion

Fig. 1 shows the loss of arsenic antisites and change in c lattice misfit of a film grown at 200°C upon annealing at 400°C for varying periods of time. The lattice parameter and neutral antisite concentrations experience a decrease even at this low annealing temperature. However, even after the longest annealing time shown, some measurable lattice mismatch and quantity of neutral antisites remain in the film, while the concentration of ionized antisites is below the detection limit.

Fig. 2 shows the positron annihilation data for some of the same films. In this graph, moving right along the S-parameter axis indicates an increase in incident positron energy, and hence deeper penetration. From the slopes of the W versus S curve, the type of defect in which annihilation occurs can be acquired. The slope of the line for the two shortest annealing times, away from the surface, is no different from that of the as-grown material. This particular slope corresponds to annihilation at gallium vacancies. After annealing for 3 h 45 min, the slope of the line increases. This change indicates that vacancy clusters have formed. Vacancy clusters appear evident in the near-surface region of the sample annealed for 15 min as well.

These results are consistent with the optical spectroscopies. Annealing at this temperature for long times results in clustering of gallium vacancies. The vacancies are then no longer available to assist in antisite diffusion

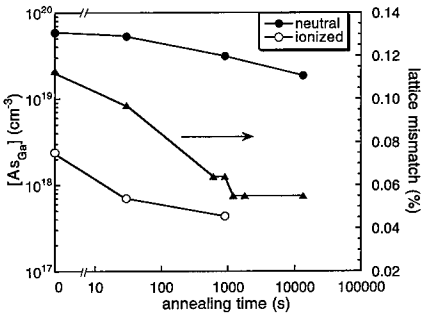

Fig. 1. Change in $[As_{GA}]$ and lattice parameter mismatch upon annealing films grown at 200°C at a temperature of 400°C.

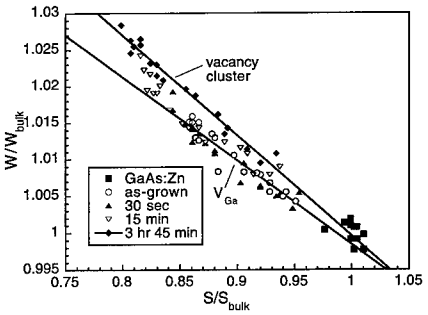

Fig. 2. Identification of gallium vacancies and vacancy clusters in films grown at 200°C and annealed at 400°C by slow positron annihilation spectroscopy. W and S parameters are normalized to those of bulk GaAs.

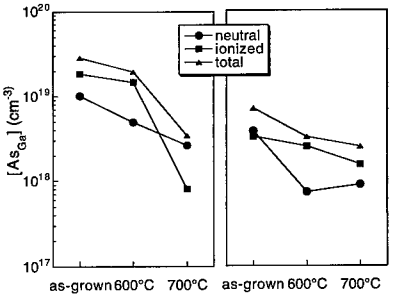

Fig. 3. Change in $[As_{Ga}]$ for films with growth parameters 250°C/6×10^{19} Be/cm^3 (left) and 295°C/3×10^{18} Be/cm^3 (right) upon annealing at 600°C and 700°C for 30 min.

to precipitate boundaries, and the concentration of antisites does not go to zero after annealing for extended periods of time. The disappearance of ionized antisites results from the clustering as well, as the isolated gallium vacancies were found to cause the ionization of antisite defects [8]. The presence of vacancy clusters is proof that vacancies have not diffused out of the epilayer, and as such the clusters may act as vacancy sources upon subsequent higher temperature anneals.

Fig. 3 shows the change in antisite concentration for two beryllium-doped films. The film grown at 250°C with 6×10^{19} Be/cm^3 shows improved thermal stability over undoped material grown at the same or lower temperatures, although significant antisite loss still results on annealing. The film grown at 295°C with 1×10^{18} Be/cm^3 has even better thermal stability, as the antisite concentration after the 700°C anneal is of the same magnitude as that of the as-grown film. Note that in undoped material annealed under similar conditions the concentration of arsenic antisites even after a 600°C anneal drops below the detection limit. The actual mechanism by which thermal stability is improved has not yet been determined, but it is likely that it is related to a reduction in the gallium vacancy concentration and/or strain compensation.

4. Conclusions

Annealing LT-GaAs at 400°C leads to vacancy clustering and a halt in antisite loss at that temperature. The vacancies remain in the epilayer, albeit in a slightly modified form, and these clusters may act as vacancy sources for future high-temperature anneals.

Beryllium doping improves the resistance to annealing. The mechanism may be related to a reduction in vacancy concentration and/or strain compensation due to the small size of the beryllium impurity.

Acknowledgements

This work has been supported by the Air Force Office of Scientific Research Grant #F49620-98-1-0135. Use of analytical equipment at the Lawrence Berkeley National Laboratory and the Integrated Materials Laboratory at UC Berkeley is gratefully acknowledged.

References

[1] M. Kaminska, Z. Liliental-Weber, E.R. Weber, T. George, J.B. Kortright, F.W. Smith, B.Y. Tsaur, A.R. Calawa, Appl. Phys. Lett. 54 (1989) 1881.
[2] A.C. Warren, J.M. Woodall, J.L. Freeouf, D. Grischkowsky, D.T. McInturff, M.R. Melloch, N. Otsuka, Appl. Phys. Lett. 57 (1990) 1331.
[3] Z. Liliental-Weber, Mater. Res. Soc. Symp. Proc. 198 (1990) 371.
[4] T.W. Fan, J.B. Liang, H.J. Deng, R.G. Li, Z.G. Wang, W. Gen, J. Crystal. Growth 143 (1994) 354.
[5] B.J.F. Lin, C.P. Kocot, D.E. Mars, R. Jaeger, IEEE Trans. Electron Dev. ED37 (1990) 46.
[6] D.E. Bliss, W. Walukiewicz, J.W. Ager, E.E. Haller, K.T. Chan, S. Tanigawa, J. Appl. Phys. 71 (1992) 1699.
[7] D.E. Bliss, W. Walukiewicz, E.E. Haller, J. Electron. Mater. 22 (1993) 1401.
[8] P. Specht, S. Jeong, H. Sohn, M. Luysberg, A. Prasad, J. Gebauer, R. Krause-Rehberg, E.R. Weber, in: G. Davies, M.H. Nazare (Eds.), Proceedings of the 20th International Conference on Defects in Semiconductors (ICDS-19), Mater. Sci. Forum 258–63 (1997) 951.
[9] G.M. Martin, Appl. Phys. Lett. 39 (1981) 747.
[10] D.M. Hoffmann, K. Krambrock, B.K. Meyer, J.M. Spaeth, Semicond. Sci. Technol. 6 (1991) 170.
[11] R. Krause-Rehberg, H.S. Leipuer, in: Positron Annihilation in Semiconductors, Springer, Heidlberg, 1999.

ELSEVIER

Physica B 273–274 (1999) 725–728

PHYSICA B

www.elsevier.com/locate/physb

As antisite incorporation in epitaxial growth of GaAs

J.C. Bourgoin[a,*], H. Hammadi[a], M. Stellmacher[b], J. Nagle[b], B. Grandidier[c], D. Stievenard[c], J.P. Nys[c], C. Delerue[c], M. Lannoo[c]

[a]*Laboratoire des Milieux Désordonnés et Hétérogènes, Université P. et M. Curie, C.N.R.S., UMR 7603, Tour 22, Casier 86, 4 place Jussieu, F-75252 Paris Cedex 05, France*

[b]*Thomson-CSF, Laboratoire Central de Recherches, Domaine de Corbeville, B.P. n° 10, F-91404 Orsay Cedex, France*

[c]*Institut d'Electronique et de Micro-Electronique du Nord, Département I.S.E.N., C.N.R.S. (UMR 8520), Avenue Poincaré, Cité Scientifique, B.P. n° 69, F-59652 Villeneuve d'Ascq Cedex, France*

Abstract

We have studied the incorporation of As antisite defects in GaAs during epitaxial growth. The growths have been performed by molecular beam epitaxy at low temperature, by metal organic chemical vapor deposition and by a special chemical vapor phase technique allowing to reach very high growth rates (up to 5 μm/min). The As antisite concentration is measured by electrical techniques or by infrared absorption at 1 μm, and through the change of the lattice mismatch and scanning tunneling microscopy in the case of large concentrations. The study is performed by monitoring the antisite concentration versus the growth temperature at constant growth rate and versus the growth rate at constant temperature. The results can be understood in terms of incorporation of As_2 molecules during the two different regimes by which epitaxial growth takes place.

Keywords: As antisite; GaAs; Epitaxial growth

1. Introduction

It is in principle possible to give special electronic properties to a given semiconductor material through the introduction of specific defects, by selecting the growth mode and the growth conditions. Indeed, the nature and concentration of the defects introduced during growth depend on the mode of growth. For instance, Czochralski (Cz) grown, nonintentionally doped GaAs contain, in addition to the contaminating impurities, As antisites (As_{Ga}) defects and dislocations (see for instance Ref. [1]). As a result such Cz material can be semi-insulating due to the presence of As_{Ga}-related defects (the so-called EL2 defects [2]) as deep donors which compensate the residual doping concentration. Such material engineering requires, first, a minimum understanding of the ways defects are incorporated during growth. Such understanding does not exist yet in the case of epitaxial growth. The aim of this communication is to present preliminary results concerning the introduction of As antisites related defects into GaAs by epitaxial techniques.

2. Principle of the study

We examine epitaxial grown GaAs layers obtained by molecular beam epitaxy (MBE) at low temperature, vapor-phase epitaxy (VPE) and metalorganic chemical vapor deposition (MOCVD). We study the introduction of As_{Ga}-related defects versus the growth rate V_g and versus the substrate (i.e. growth) temperature, T_g. These defects are labelled AARD in the following, and not EL2, because it is not established that in all cases, the same As antisite related defects are observed (see for instance in Ref. [3]).

The concentration C of these defects is measured by different techniques, depending on the experimental conditions. In layers grown at high temperature, by VPE or MOCVD, C is small compared to the free electron

* Corresponding author. Fax: + 33-1-4427-7998.
E-mail address: bourgoin@ccr.jussieu.fr (J.C. Bourgoin)

0921-4526/99/$ - see front matter
PII: S0921-4526(99)00622-5

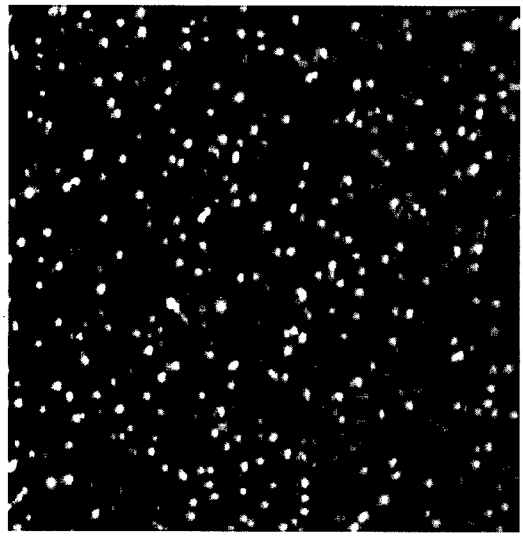

Fig. 1. Mapping of the electronic density obtained with scanning tunnelling microscopy for a -2 V bias (tunnelling current of 150 pA) of a sample grown by MBE at 225°C on a p^+-doped substrate. The thin lines, parallel to the diagonal of the image, correspond to rows of As atoms. The dots are related As antisites in the three top layers. For this sample, their concentration is estimated at $5 \pm 2 \times 10^{19}$ cm^{-3}. IR absorption at 1 μm gives a concentration of 7.5×10^{19} cm^{-3}.

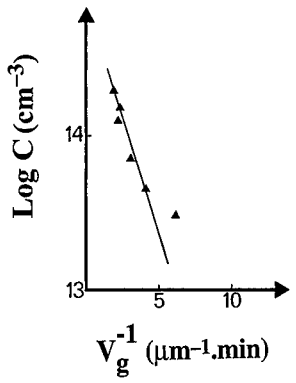

Fig. 2. Variation of the concentration of EL2 defects versus the inverse of the growth rate for a MOCVD growth at 770°C.

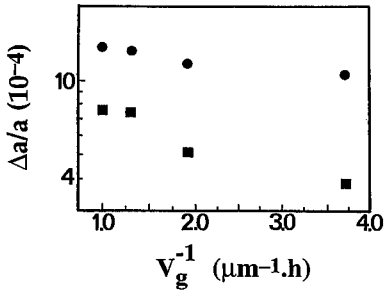

Fig. 3. Variation of the lattice change, proportional to the AARD concentration, versus the inverse of the MBE growth rate at two temperatures: 290°C (■) and 230°C (●).

concentration, and it is measured by deep level transient spectroscopy (DLTS). In this case, it is well established that the AARDs are the EL2 defects. In layers grown by MBE at low temperature, C being large (10^{18}–10^{19} cm^{-3}) is estimated by the lattice change (obtained by double X-ray diffraction), infrared absorption (IRA) at 1 μm [2,4] and scanning tunneling microscopy (STM) as illustrated in Fig. 1. In this case, we establish directly by STM that the defects we study are AARDs: evidence that the STM images are indeed related to AARDs is given by the energetical spectrum of the band of states inside the gap, which peaks between 0.25 and 0.5 eV above the valence band [5].

3. Results

Information concerning the growth processes are the following: (i) MOCVD growth is performed in a conventional H_2 reactor working in the 700–800°C range; the variation of the growth rate is achieved by varying the $AsCl_3$ mole fraction (from 10^{-4} to 10^{-2}); (ii) for VPE a specific technique, usually called close space vapor transport (CSVT), has been used; this technique (for a review see Ref. [6]) allows to reach very high growth rates [7] while producing layers exhibiting good electronic and optical properties [8]; (iii) MBE growth is performed in a Varian Gen II system. The growth temperature is monitored with the thermocouple of the molyblock. The temperature ranges in which activation energies are deduced, 50°C wide around 600 K, are such that the systematic error on the substrate temperature (10–20°C) induces a relative shift in these activation energies of the order of 5×10^{-2}. The growth rate is determined by RHEED oscillations and the ratio of the As_4 to Ga fluxes is calibrated by the determination of the transition point between the (2×4) As and the (4×2) Ga stabilized reconstruction.

Only typical results are presented here. First, the AARD concentration, C, is found to increase rapidly with the growth rate V_g. This is illustrated in Fig. 2 for MOCVD growth performed at 770°C. The results, similar to others given in Refs. [9,10], are presented under the form log C versus V_g^{-1} for a reason which will be made clear in the next section. MBE data obtained at different low temperatures present a similar behaviour (see Fig. 3) at constant As/Ga flux ratio (equal to 2.2). Other data obtained by CSVT are presented in Fig. 4.

The temperature dependence of C, illustrated in Fig. 5 in the case of MBE growth, shows that C is thermally activated. Below typically 300°C, the associated

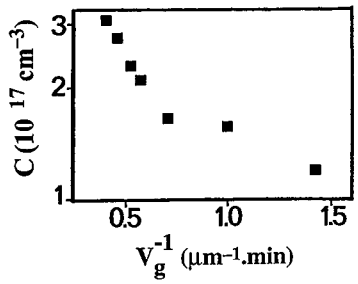

Fig. 4. Variation of the concentration of AARDs measured by IR absorption versus the inverse of the growth rate for close space vapor transport.

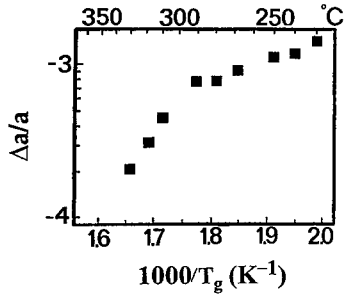

Fig. 5. Variation of the lattice change, proportional to the AARD concentration, versus the inverse of the MBE growth temperature.

activation energy is of the order of 0.3–0.4 eV. Above 300°C there is a strong change in the regime, the activation energy becoming of the order of 1.4 eV. This value of the activation energy, in the same temperature range, is also obtained in VPE growth [11].

4. Mechanism of antisite incorporation

The epitaxial growth of GaAs has been studied by Foxon and Joyce [12]. They showed that the growth is governed by two basically different mechanisms related to the interaction between As molecules and Ga atoms on the surface. One mechanism applies below 300°C, the other above 300°C, which is consistent with the change in the regime observed for AARDs incorporation in Fig. 5.

Below 300°C the growth is limited by the deposition of Ga atoms which are saturated by As_2 molecules, whose binding energy on the surface is 0.36 eV [12]. Because a systematic study correlating C with the stoechiometry shift suggests that AARDs are composed of two As atoms on a Ga site [13], we assume here that the induced AARDs result from the deposition of an As_2 molecule, which are located on a Ga site, giving an As antisite complexed with a neighbouring interstitial. The concentration C of such AARDs should therefore correspond to the fraction of As_2 molecules which are not desorbed. The time of As_2 desorption from the surface being characterized by an activation energy of 0.36 eV, we expect C to be characterized by the same activation energy. This is indeed observed, as shown in Fig. 5. The experimental value found for the activation energy being equal to that for As_2 desorption therefore demonstrates that the formation of As antisite related defects is directly correlated to the presence of As_2 molecules.

Above 300°C, the growth is limited by the dissociation of As_2 molecules [12]. Then C, like the rate of dissociation:

$$K = K_0 \exp(-E_d/kT), \tag{1}$$

should be thermally activated with the same activation energy E_d. We find experimentally $E_d = 1.4$ eV (see Fig. 5), a value coherent with the enthalpy for As dissociation [14].

The fraction dC of As_2 molecules which dissociate during the time dt is:

$$dC/dt = -KC. \tag{2}$$

This dissociation stops when a new layer (of thickness a) is added, i.e. after a time:

$$dt = a/V_g. \tag{3}$$

Then

$$C = C_0 \exp\left[\frac{K_0 a}{V_g} \exp(-E_d/kT)\right] \tag{4}$$

We obtain, as observed experimentally (see Figs. 2–4), a linear dependence of log C versus V_g^{-1}.

5. Conclusion

The temperature and growth rate dependences of the concentration of As antisite related defects (AARD), introduced during growth, obey the same laws for all vapor-phase epitaxy techniques. These dependences can be directly related to the density of As_2 molecules on the surface of the grown layer. We conclude that the AARDs are introduced as a result of As_2 molecules occupying Ga sites. This implies that an AARD is a defect associated with two As atoms on a Ga site.

References

[1] J.C. Bourgoin, H.J. von Bardeleben, D. Stievenard, J. Appl. Phys. 64 (1988) R65.
[2] G.M. Martin, Appl. Phys. Lett. 39 (1981) 747.
[3] G. Kowalski, A. Kurpiewski, M. Kaminska, E.R. Weber, Mater. Sci. Eng. B 22 (1993) 27.

[4] X. Liu, A. Prasad, J. Nishio, E.R. Weber, Z. Lilienthal-Weber, W. Walukiewicz, Appl. Phys. Lett. 67 (1995) 279.
[5] R.M. Feenstra, J.M. Woodall, G.P. Pettit, Phys. Rev. Lett. 71 (1993) 1176.
[6] J.C. Bourgoin, H. Samic-Sahinpasic, in: M.R. Brozel, G.E. Stillman (Eds.), Properties of GaAs, Inspec, Emis Data Reviews Series no. 16, 3rd Edition, London, UK, 1996, pp. 639–642.
[7] R. Castenado, J. Mimila-Arroyo, J.C. Bourgoin, J. Appl. Phys. 68 (1990) 6274.
[8] H. Samic, J.C. Bourgoin, Mater. Sci. Forum 258–263 (1997) 997.
[9] J.H. Neave, P. Blood, B.A. Joyce, Appl. Phys. Lett. 36 (1980) 311.
[10] A. Humbert, L. Hollau, D. Bois, J. Appl. Phys. 47 (1976) 4137.
[11] M. Ozeki, J. Komeno, A. Shikatomi, S. Ohkawa, J. Appl. Phys. 50 (1979) 4808.
[12] C.T. Foxon, B.A. Joyce, Surf. Sci. 50 (1975) 434.
[13] M. Stellmacher, J. Nagle, R. Bisaro, P. Galtier, J.C. Bourgoin, unpublished.
[14] D.R. Stull, G.C. Sinke, Thermodynamic Properties of the Elements, American Chemical Society, Washington, USA, 1956.

ELSEVIER

Physica B 273–274 (1999) 729–732

PHYSICA B

www.elsevier.com/locate/physb

Extrinsic and intrinsic defects at molecular-beam-epitaxy regrown GaAs interfaces

Nguyen Hong Ky*, D. Martin, F.K. Reinhart

Institute of Micro- and Optoelectronics, IMO-EPFL, Swiss Federal Institute of Technology, CH-1015 Lausanne, Switzerland

Abstract

To identify the defects responsible for anomalous electronic properties at the molecular-beam-epitaxy regrown interface, the interfaces of Si-doped GaAs epitaxial layers ($n = 7 \times 10^{16}\,cm^{-3}$) have been investigated. A significant reduction of the carrier concentration in a large region around the regrown interfaces has been observed by capacitance–voltage measurement. Photoluminescence spectra measured at different etching depths below the sample surface show that the intensity of the emissions associated with carbon acceptors and As vacancy–carbon acceptor complexes strongly increases in the interface region. The carbon-related emission line is absent in the photoluminescence spectra of the sample without regrown interface. The carrier concentration profiles obtained by capacitance–voltage measurements fit well that calculated numerically with the assumption that a high concentration of carbon is present at the interface. These results indicate that carbon and As vacancies are main defects responsible for the carrier depletion at the regrown interface. This carrier depletion is believed to be due to the direct compensation of Si donors by carbon acceptors. On the other hand, a high concentration of As vacancies at the interface is favorable for the formation of As vacancy-oxygen complexes that may act as deep-level electron traps.

Keywords: GaAs; MBE regrown interface; Carbon; Arsenic vacancies

1. Introduction

Molecular–beam epitaxy (MBE) is an extremely powerful technique for the fabrication of advanced electronic and optoelectronic devices. MBE is capable to produce multilayered III–V semiconductor structures with an excellent control of their thickness, composition, and doping profiles. A regrowth can be performed after a MBE growth interruption. This increases the degree of freedom for device design and device processing. Regrowth is an indispensable step in the fabrication of buried heterostructure lasers, distributed feedback lasers, and novel devices based on quantum wires and quantum dots. However, anomalous electronic properties including the formation of a highly resistive layer and the depletion or accumulation of carriers at MBE regrown GaAs interfaces have been observed [1–4]. In spite of intensive research efforts, the physical mechanisms of these anomalies at the regrown interfaces have not been fully understood. Arsenic vacancy (V_{As}) traps, site change of Si atoms, absorption of impurities such as C or O, and formation of a disordered region at the interface have been suggested to be the origin of the anomalies at the regrown interfaces. In this article, new results are reported on the observation of extrinsic and intrinsic defects at MBE regrown Si-doped GaAs interfaces. The carrier concentration profiles are obtained by capacitance–voltage (C–V) measurement. Extrinsic and intrinsic defects at the regrown interfaces are investigated using photoluminescence (PL) spectra measured at different etching depths, d_e, below the sample surface. C and V_{As} are the main defects detected in the region near the regrown interface. Their role in the formation of the carrier depletion at the interface will be discussed.

2. Experiment

Three samples are fabricated by MBE on Si-doped ($n \approx 10^{18}\,cm^{-3}$) (1 0 0)-oriented GaAs substrates in a

* Corresponding author. Fax: + 41-21-693-54-80.
E-mail address: ky.nguyen@epfl.ch (N.H. Ky)

0921-4526/99/$ - see front matter
PII: S0921-4526(99)00624-9

modified Varian 360 apparatus. Sample 1 is a 0.5 μm thick Si-doped ($n \approx 7 \times 10^{16}$ cm^{-3}) GaAs layer grown without interruption for use as reference. The As/Ga beam equivalent pressure ratio is 2.8, corresponding to an As-poor growth condition. The first fabrication step of samples 2 and 3 is to grow a 0.2 μm thick GaAs layer. After the first growth, both samples are removed from the growth chamber and exposed to the atmosphere during several minutes.

Before the regrowth, samples 2 and 3 are cleaned in a hydrogen-plasma processing chamber that is connected to the growth chamber by an ultrahigh vacuum transfer tube. A 13.56 MHz plasma radical source from Oxford Applied Research is used. Samples 2 and 3 are heated to 450°C and 536°C, respectively, in the hydrogen plasma for 15 min. The samples are then transferred to the growth chamber within 5 min and the regrowth is performed at 540°C. These samples consist of the following identical regrown layers: (i) a 0.15 μm thick GaAs layer, (ii) an $In_{0.17}Ga_{0.83}As$ quantum well (QW) with a thickness of 43 Å, and (iii) a 0.15 μm thick GaAs cap layer. Hence, the regrown interface is located at about 0.3 μm below the sample surface. The first-grown and regrown layers of samples 2 and 3 are uniformly doped with Si at a concentration of 7×10^{16} cm^{-3}. To perform the C–V measurements, Schottky diodes are produced by evaporating Cr and Au thin films onto the surface of samples 1–3. Ohmic contacts are formed by annealing the evaporated AuGe/Ni/Au sandwich on the substrate at 400°C for 1 min. The surface area of the Schottky diodes is about 0.25 mm^2. The C–V measurements are carried out at room temperature with a modified Boonton 72B capacitance meter. The measuring frequency is 1 MHz. The carrier concentration profile, $n(w)$, is deduced from the measured C–V curve using the formula [5]:

$$n(w) = \left[\frac{1}{2} q \varepsilon_s \frac{\mathrm{d}}{\mathrm{d}V}\left(\frac{1}{C^2}\right)\right]^{-1}, \tag{1}$$

where q is the electron charge, ε_s the dielectric permittivity, V the applied voltage, and C the measured capacitance. The depletion width, w, of the Schottky metal–semiconductor junction is given by

$$w = \frac{\varepsilon_s}{C}. \tag{2}$$

The PL spectra are measured at 77 K, using the 632.8 nm line of a He–Ne laser as excitation source and a Si photodiode as detector. The regrown samples are etched in a solution of $H_2SO_4 : H_2O_2 : H_2O = 1 : 8 : 10$ to form terraces with different d_e. The resolution of the measurement of d_e is 0.01 μm. The PL spectra taken at different d_e are characterized for a probe region within 0.5–0.7 μm below the etching surface.

3. Results and discussion

Fig. 1 shows typical carrier concentration profiles obtained by C–V measurements for samples 1 and 3. In sample 1, the carrier distribution is almost uniform with a concentration value, n, of about 7×10^{16} cm^{-3}. For sample 3, the carrier concentration profile is more complicated. At the depths, d, below 0.13 μm and between 0.2 and 0.23 μm, the carrier concentration is constant at 7×10^{16} cm^{-3}. The concentration profile exhibits a peak (QW) at $d = 0.15$ μm. This peak is due to the electron accumulation in the InGaAs well [6]. Because of the Debye spreading, the peak width is larger than the thickness of the QW. The difference between the full width of the peak and the well thickness is comparable to the double of the Debye length value $L_D \approx 0.015$ μm determined from the formula [5]:

$$L_D = \left(\frac{\varepsilon_s k_B T}{q^2 n}\right)^{1/2}, \tag{3}$$

where k_B and T are the Boltzmann constant and the temperature, respectively. Depletion layers of the InGaAs/GaAs heterojunctions are seen on both sides of the QW peak. A strong carrier depletion is observed in a 0.12 μm wide region around the regrown interface at $d = 0.3$ μm. At the regrown interface, n is significantly reduced to 2×10^{16} cm^{-3}.

The PL spectrum of the sample 1 (Fig. 2) shows a strong emission line at 822 nm or 1.509 eV (E_x). This emission line could be due to the recombination of free excitons in the epitaxial GaAs layer [7,8]. A broad emission band (V_{As}–C) is observed at 922 nm or 1.345 eV. The origin of the broad emission band at about 1.35 eV has been discussed previously [8,9]. This emission band could be associated with the recombination of the V_{As}–C acceptor complex [8]. C is a residual acceptor that is usually present in MBE grown GaAs [8]. V_{As} is abundant in the epitaxial layer that is grown under As-poor condition. The abundance of V_{As} in n-type GaAs is favorable for single hops of column-III atoms forming Ga antisite defects (Ga_{As}) and Ga

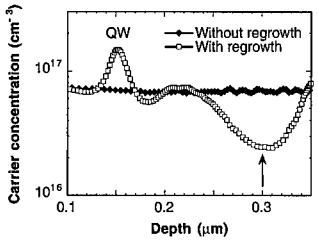

Fig. 1. Measured carrier concentration profiles in the reference sample 1 and in the regrown sample 3. The arrow indicates the location of the regrown interface.

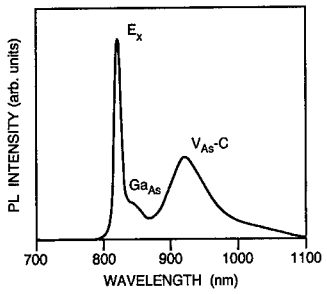

Fig. 2. 77 K PL spectrum taken on the surface of the reference sample 1.

vacancies (V_{Ga}) [9]:

$$Ga_{Ga} + V_{As} \Leftrightarrow V_{Ga} + Ga_{As}. \quad (4)$$

This is confirmed by the observation of the Ga_{As}-related emission band at 840 nm or 1.47 eV [9]. Moreover, the long-wavelength tail of the V_{As}–C emission band may be due to the presence of the Si donor-V_{Ga} complex emission band at about 1000 nm or 1.24 eV [9].

The PL spectrum taken on the surface of sample 3 (Fig. 3) is dominated by the emission line at 884 nm or 1.403 eV (QW). Since most of Si atoms occupy column-III sites and act as donors, electrons from the Si donors move into the InGaAs well and a pseudo-two-dimensional electron gas (2DEG) is formed due to high concentration of the free carriers confined in the well [6,10,11]. The broad QW emission line is related to the recombination involving electrons of the 2DEG which fill all of the confined states up to the Fermi level located above the lowest $n = 1$ electron quantized subband level in the well. The mixing of the heavy-hole and light-hole subbands could be induced by a "shake-up" of the Fermi sea [10–12]. The E_x line and the V_{As}–C band emitted from the adjacent GaAs layers are also observed in the spectrum. The QW emission line is no longer seen in the PL spectrum taken at $d_e = 0.26$ μm because the InGaAs well is removed. Beside the E_x line, the spectrum shows an intense emission line at 834 nm or 1.487 eV (eA_C). This emission line is due to the transition of free electrons to an acceptor level [9]. The acceptor ionization energy of 26 meV deduced from the peak position corresponds to that of C. The intensity of the V_{As}–C emission band is significant. At $d_e = 0.58$ μm, both eA_C and V_{As}–C emissions decrease in intensity. The intensity enhancement of eA_C and V_{As}-C emissions in the region around the regrown interface indicates high concentrations of V_{As} and C acceptors in this region. When the sample is exposed to the atmosphere after the first growth, C atoms could be absorbed at the sample surface. They can diffuse into the bulk during the regrowth. Fig. 4 shows a comparison between the carrier concentration profile measured for sample 3 and that calculated assuming a surface concentration $n_s = 4.5 \times 10^{11}$ cm^{-2} of C acceptor at the interface. In this calculation program, the electron and hole continuity equations and the Poisson's equation describing the relation between the electron potential and the charge density as a function of the position below the sample surface are solved self-consistently. The presence of the InGaAs well is not taken into account. The calculated carrier concentration profile fits well the measured curve, indicating that a direct compensation of Si donors by C acceptors results in the carrier depletion in the regrown interface region. In fact, high concentrations of C and O are detected at the regrown interface of this sample by secondary-ion mass spectrometry. The donor compensation in the region around the regrown interface may prevent the reaction of Eq. (4) from occurring. Hence, the V_{As} concentration is high in this region. Since V_{As} is positively charged and V_{As}–C complex is neutral, both V_{As} and V_{As}–C complex should not contribute directly to the carrier depletion. However, V_{As} at the interface can form complex with O interstitials. Two deep levels located between 0.57–0.75 eV and at 0.14 eV below the conduction band minimum, E_c, are found to be

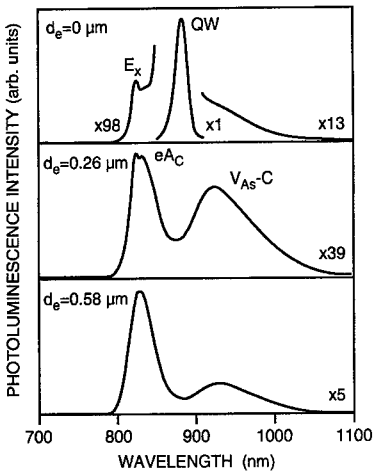

Fig. 3. 77 K PL spectra taken at different etching depths, d_e, below the surface of the regrown sample 3.

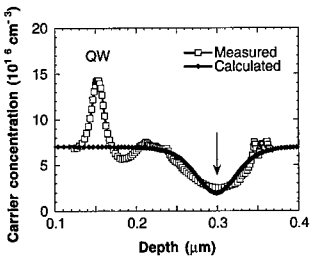

Fig. 4. Measured and calculated carrier concentration profiles in the regrown sample 3. The arrow indicates the location of the regrown interface.

Table 1
Summary of main experimental results obtained for samples 2 and 3

	Sample 2	Sample 3
Temperature during H-plasma cleaning, °C	450	536
Carrier loss at the regrown interface, 10^{16} cm^{-3}	6.4	5
Extent of the carrier depletion region, μm	0.22	0.12
Relative intensity the eA_C emission line	1.22	1
Relative intensity the V_{As}–C emission band	1.18	1

related to the O–V_{As} complex [13]. The $E_c - 0.14$ eV level is the donor state of the O–V_{As} complex, whereas the level near the midgap acts as an acceptor. Although the concentration of these deep-level traps is lower than that required to induce the observed carrier depletion by several order of magnitude [4], they may also be involved in the formation of the carrier depletion at the regrown interface.

A summary of the experimental results obtained for samples 2 and 3 is given in Table 1. The intensity of the eA_C and V_{As}–C emissions and the carrier depletion in the interface region are found to be dependent on the surface treatment procedure used to clean the sample surface before the regrowth. With increasing the heating temperature during hydrogen-plasma exposure from 450°C to 536°C, a reduction of carrier loss at the regrown interface from 1.4×10^{12} to 3×10^{11} cm^{-2} and a decrease in intensity of the eA_C and V_{As}–C emissions by a factor of about 1.2 are observed.

In conclusion, our results give evidences for the important role of C and V_{As} in the anomalous carrier depletion at MBE regrown interfaces. C acceptors are believed to be mainly responsible for the direct compensation of Si donors. In addition, a high V_{As} concentration may be favorable for the formation of O–V_{As} complexes that act as deep-level electron traps.

References

[1] A.Y. Cho, F.K. Reinhart, J. Appl. Phys. 45 (1974) 1812.
[2] D.L. Miller, R.T. Chen, K. Elliott, S.P. Kowalczyk, J. Appl. Phys. 57 (1985) 1922.
[3] E. Ikeda, H. Hasegawa, S. Ohtsuka, H. Ohno, Jpn. J. Appl. Phys. 27 (1988) 180.
[4] D. Biswas, P.R. Berger, U. Das, J.E. Oh, P.K. Bhattacharya, J. Electron. Mater. 18 (1989) 137.
[5] E.F. Schubert, J.M. Kuo, R.F. Kopf, J. Electron. Mater. 19 (1990) 521.
[6] R. Dingle, H.L. Störmer, A.C. Gossard, W. Wiegmann, Appl. Phys. Lett. 33 (1978) 665.
[7] N.H. Ky, J.D. Ganière, M. Gailhanou, F. Morier-Genoud, D. Martin, F.K. Reinhart, Phys. Rev. B 46 (1992) 6947.
[8] L. Pavesi, N.H. Ky, J.D. Ganière, F.K. Reinhart, N. Baba-Ali, I. Harrison, B. Tuck, M. Henini, J. Appl. Phys. 71 (1992) 2225.
[9] N.H. Ky, F.K. Reinhart, J. Appl. Phys. 83 (1998) 718.
[10] N.H. Ky, J.D. Ganière, F.K. Reinhart, B. Blanchard, J. Appl. Phys. 79 (1996) 4009.
[11] N.H. Ky, F.K. Reinhart, J.D. Ganière, B. Deveaud, B. Blanchard, J. Appl. Phys. 86 (1999) 259.
[12] G. Livescu, D.A.B. Miller, D.S. Chemla, M. Ramaswami, T.Y. Chang, N. Sauer, A.C. Gossard, J.H. English, IEEE J. Quantum Electron. 24 (1988) 1677.
[13] M. Skowronski, S.T. Neild, R.E. Kremer, Appl. Phys. Lett. 57 (1990) 902.

ELSEVIER

Physica B 273–274 (1999) 733–736

PHYSICA B

www.elsevier.com/locate/physb

Femtosecond nonlinear optics of low-temperature grown semiconductors

U. Siegner[a], M. Haiml[a,*], F. Morier-Genoud[a], R.C. Lutz[b], P. Specht[b], E.R. Weber[b], U. Keller[a]

[a]*Institute of Quantum Electronics, Swiss Federal Institute of Technology (ETH), ETH Honggerberg HPT, CH-8093 Zurich, Switzerland*
[b]*Materials Science and Mineral Engineering Department, University of California at Berkeley, Berkeley, CA 94720, USA*

Abstract

We investigate the nonlinear optical properties of low-temperature-grown (LT) GaAs. It is shown that the strength of the absorptive nonlinearity is weak in as-grown undoped LT-GaAs with a fast recovery time of the nonlinear absorption. The reason for this behavior is revealed by a quantitative study of the nonlinear optical properties of the most important defect transition from the neutral As antisite to the conduction band. Based on this analysis, we demonstrate two methods for the improvement of the ultrafast nonlinearity of LT-grown semiconductors: post-growth annealing or Be doping of LT-GaAs yields a material with a strong ultrafast nonlinear optical response.

Keywords: Low-temperature GaAs; Optical nonlinearity; Carrier dynamics

Low-temperature (LT) MBE-grown semiconductors will become increasingly important for future femtosecond all-optical switching applications due to the ultrafast recovery time of their optical nonlinearity after above-band-gap excitation. Already now, they are extensively used in optical communication [1] and laser physics [2]. Besides a fast recovery time, these applications require high nonlinear absorption modulation and small absorption losses at high pulse fluences (nonsaturable absorption losses). The ultrafast recovery time of the nonlinear absorption results from trapping of optically excited carriers into defect states introduced by the LT growth [3]. Carrier trapping into defects has been intensively investigated in recent years, in particular for LT-GaAs, which can serve as a model system [4,5]. However, the introduction of defect states may also give rise to new absorption channels, which can affect the strength of the nonlinear optical response [6–8].

In this paper, we present a comprehensive quantitative study of the nonsaturable absorption, the absorption modulation, and its recovery time in different modifications of LT-GaAs. It is shown that as-grown undoped LT-GaAs with a sub-picosecond recovery time suffers from small absorption modulation and large nonsaturable absorption. Therefore, this material is not well suited for ultrafast all-optical switching applications. This experimental result is traced back to the optical properties of the dominating defect transition from the neutral As antisites, As^0_{Ga}, to the conduction band (CB). Combining optical data with measurements of defect densities, we have quantitatively determined the optical absorption cross section and the saturation parameter of this transition for above-band-gap excitation. This data shows that, with reasonable pulse fluences, the As^0_{Ga}–CB transition is difficult to saturate and contributes a major fraction to the nonsaturable absorption losses. Therefore, as-grown undoped LT-GaAs with femtosecond recovery times and high As^0_{Ga} density suffers from high nonsaturable absorption losses. We demonstrate two methods to obtain an optimized material which combines fast recovery times with high modulation and small nonsaturable

* Corresponding author. Fax: + 41-1-633-1059.
E-mail address: haiml@iqe.phys.ethz.ch (M. Haiml)

0921-4526/99/$ - see front matter
PII: S0921-4526(99)00625-0

losses: (i) annealing of undoped LT-GaAs and (ii) beryllium doping of as-grown LT-GaAs. Both methods reduce the density of neutral As^0_{Ga} and the corresponding As^0_{Ga}–CB absorption, but maintain an ultrafast response. Our analysis shows that the Be concentration should be chosen to compensate the material in order to optimize the optical nonlinearity of LT-GaAs : Be.

We have studied 500 nm thick LT-GaAs layers, which were grown by MBE at an As_4/Ga-flux ratio of 4.5 and various growth temperatures (T_g = 220–580°C). The undoped layers are either as-grown or have been post-growth annealed at 600°C under arsenic overpressure for 75 min. Some of the as-grown layers are doped with Be at various concentrations. All layers have been grown on $Al_{0.15}Ga_{0.85}As$/AlAs Bragg mirrors and n+GaAs substrates. We have verified that the structural properties of LT-GaAs layers from our MBE system are independent of the substrate type [6]. The concentration of neutral arsenic antisites [As^0_{Ga}] was measured by near-infrared absorption (NIRA) [9] in the epilayers grown on n+substrates. The Bragg mirror samples have been antireflection (AR) coated on the front surface. These samples have been used for the optical studies in a reflection geometry.

Due to the good quality of the AR coating and the Bragg mirrors, the reflectivity R of the whole structure can be approximated by $R = \exp(-2\alpha d)$ [7] where α is the absorption coefficient, d the physical thickness of the LT-GaAs layer, and $2d$ the effective thickness in the reflection geometry. The linear absorption and the absorptive nonlinearity have been determined from measurements of the reflectivity R versus the pulse energy fluence F in a single-beam experiment [6]. The experimental data are extrapolated to the linear regime and to high fluences using the travelling wave rate equation model for a two-level absorber [10,11]. With respect to the concept of this model, we recall that the reflectivity of an ideal lossless absorber saturates at $R_{ns} = 1$ at high fluences. Here, $R_{ns} = 1$ corresponds to an absorption $\alpha_{ns} = 0$. The model assumes that the reflectivity of a real absorber saturates at $R_{ns} < 1$, corresponding to $\alpha_{ns} > 0$, and explicitly introduces $R_{ns} < 1$ as an additional parameter. R_{ns} (or α_{ns}) accounts for the differences between a two-level absorber and a real semiconductor. Different processes can contribute to α_{ns}: (i) absorption, which only decreases at fluences much higher than the fluences which fully saturate the two-level absorber, and (ii) induced absorption which only occurs in the nonlinear regime, e.g., absorption out of excited states. Very good fits to the experimental data are obtained with this model, see Ref. [6] for an example. From the fits, one determines the linear and nonsaturable reflectivities $R_{lin} = \exp(-2\alpha_{lin}d)$ and $R_{ns} = \exp(-2\alpha_{ns}d)$ (or the linear and nonsaturable absorption α_{lin} and α_{ns}), and the saturation fluence of the two-level absorber. The saturation fluence is a measure of the pulse fluence at which significant changes of the absorption occur. The absorption modulation is given by $\Delta\alpha = \alpha_{lin} - \alpha_{ns}$. With respect to applications, we note that an increase of α_{ns} increases the nonsaturable losses in reflectivity $\Delta R_{ns} = 1 - R_{ns}$ and decreases the reflectivity modulation $\Delta R = R_{ns} - R_{lin}$ of a saturable absorber device. Moreover, ΔR decreases with decreasing $\Delta\alpha$.

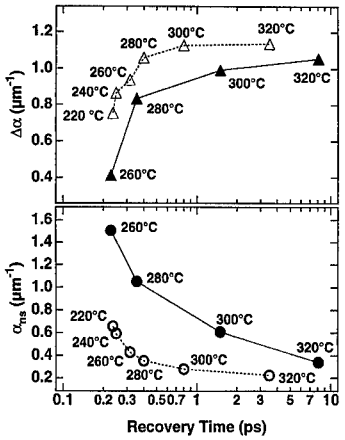

Fig. 1. Absorption modulation $\Delta\alpha$ (△, ▲) and nonsaturable absorption α_{ns} (○, ●) versus recovery times for undoped as-grown (filled symbols) and undoped annealed (open symbols) LT-GaAs. Labels: Growth temperatures. The recovery times have been determined at a carrier density of about 5×10^{18} cm^{-3}.

The time response of the absorption modulation has been determined by pump–probe experiments. We define the 1/e decay time of a pump–probe trace as the recovery time. All optical measurements have been performed at room temperature with 150 fs pulses for excitation above the band gap at 830 nm.

Fig. 1 shows the absorption modulation and the nonsaturable absorption versus the recovery time for undoped as-grown and annealed LT-GaAs. With decreasing growth temperature, the recovery time decreases in as-grown LT-GaAs [4] due to the increasing density of ionized As^+_{Ga} [9], which act as electron traps [5,12]. However, sub-picosecond recovery times in undoped as-grown LT-GaAs are only obtained at the expense of a small absorption modulation $\Delta\alpha$ and large nonsaturable absorption α_{ns}. For a given recovery time, annealed LT-GaAs has a much larger $\Delta\alpha$ and a much smaller α_{ns}. This is because annealing results only in a slight increase of the recovery time for $T_g \leqslant 280$°C and even yields a faster response at higher growth temperatures, but largely increases $\Delta\alpha$ and decreases α_{ns}. The latter point will be discussed in more detail below. Since annealing reduces the density of As^+_{Ga} electron traps [9], we conclude that a fast recovery time is maintained by the As precipitates [13] formed upon annealing.

Fig. 2 provides insight into the microscopic origin of the weak optical nonlinearity in undoped as-grown

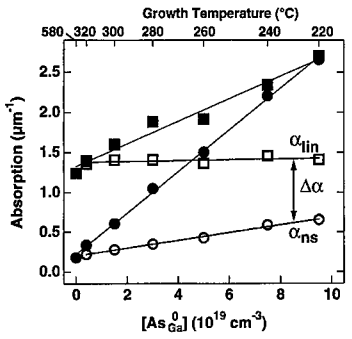

Fig. 2. Linear absorption α_{lin} (□, ■) and nonsaturable absorption α_{ns} (○, ●) for undoped as-grown LT-GaAs samples (filled symbols) and their annealed counterparts (open symbols) versus the neutral As antisite density in the as-grown LT-GaAs samples. The upper horizontal axis shows the growth temperature. The absorption modulation $\Delta\alpha = \alpha_{lin} - \alpha_{ns}$ is indicated by the arrow.

LT-GaAs with a fast recovery time. This figure shows α_{lin} and α_{ns} for the undoped as-grown LT-GaAs samples and their annealed counterparts versus the As^0_{Ga} density in the as-grown samples. It is found that the linear above-band-gap absorption strongly increases with increasing defect density in as-grown LT-GaAs, in agreement with Ref. [14]. We recall that, in undoped as-grown LT-GaAs, more than 90% of the As_{Ga} are neutral while the rest is ionized [9]. For below-band-gap energies, the As_{Ga}–CB transition has a much higher absorption cross section than the transition from the valence band (VB) to the ionized As^+_{Ga} [15] and the second optical ionization of As^+_{Ga} [16]. Consequently, we attribute the excess linear absorption in undoped as-grown GaAs to the As^0_{Ga}–CB transition. We refer to the As^0_{Ga}–CB absorption as to α_T, given by $\alpha_T = \alpha_{lin} - \alpha_{lin}(HT)$ ($\alpha_{lin}(HT)$ linear absorption in high-temperature grown undoped GaAs). Our quantitative data allows for the determination of the absorption cross section σ of this transition at 830 nm. One obtains $\sigma = 1.4 \times 10^{-16}$ cm^2 from $\alpha_T = \sigma[As^0_{Ga}]$ and the linear fit to the data in Fig. 2.

From σ, the saturation fluence $F_{sat} = \hbar\omega/\sigma$ ($\hbar\omega$ photon energy) [11] of the As^0_{Ga}–CB transition can be quantitatively determined: $F_{sat} = 1700$ μJ/cm^2. At this fluence, the absorption of the As^0_{Ga}–CB transition significantly decreases. In contrast, the saturation fluence of the interband transition in GaAs is typically below 50 μJ/cm^2. The comparison shows that α_T is hardly decreased by fluences which almost fully saturate the interband transition. Therefore, the As^0_{Ga}–CB absorption α_T fully contributes to the nonsaturable absorption α_{ns}.

Surprisingly, Fig. 2 shows that the absorption modulation $\Delta\alpha = \alpha_{lin} - \alpha_{ns}$ decreases with increasing As^0_{Ga} density. This decrease cannot be due to the nonsaturable trap absorption α_T since α_T equally contributes to both α_{lin} and α_{ns}. We conclude that there must be another mechanism which gives rise to additional nonsaturable absorption γ_{ns}. The mechanism responsible for the additional absorption γ_{ns} is not yet fully understood. A possible reason for γ_{ns} is free-carrier absorption due to carriers high in the CB. These carriers can be generated by the As^0_{Ga}–CB transition in as-grown undoped LT-GaAs.

The total nonsaturable absorption can be written as $\alpha_{ns} = \alpha_T + \gamma_{ns}$. A quantitative analysis of the data in Fig. 2 shows that γ_{ns} makes up about 40% of the total nonsaturable absorption α_{ns} in as-grown undoped LT GaAs. Thus the nonsaturable As^0_{Ga}–CB absorption α_T contributes the major fraction to α_{ns}. With respect to ultrafast all-optical switching applications, we note that the large nonsaturable As^0_{Ga}–CB absorption α_T in as-grown undoped LT-GaAs increases the nonsaturable losses in reflectivity ΔR_{ns} and limits the reflectivity modulation ΔR. Moreover, ΔR can be strongly reduced by γ_{ns} which contributes to the nonsaturable absorption and reduces the absorption modulation.

This analysis shows that LT-GaAs can be optimized for ultrafast all-optical switching applications if the density of neutral As^0_{Ga} is reduced while an ultrafast recovery time is maintained. This goal cannot be reached in as-grown undoped LT-GaAs since the incorporation of a large density of ionized As^+_{Ga} trap states results in the incorporation of even larger densities of neutral As^0_{Ga} [9] which deteriorate the optical nonlinearity.

Fig. 1 has shown that annealing of undoped LT-GaAs yields an optimized material with a strong optical nonlinearity and a fast recovery time due to the presence of As precipitates. In accordance with the guideline for optimization, annealing decreases the neutral As^0_{Ga} density [9] while the fast response is maintained by the precipitates. Due to the reduction of the neutral As^0_{Ga} density, the linear absorption of annealed undoped LT-GaAs in Fig. 2 increases only very slightly with the excess As content, in agreement with the surface plasmon model for precipitates [17]. The absorption α_T is almost totally removed by annealing which substantially decreases the nonsaturable absorption α_{ns}.

An alternative method for the optimization of LT-GaAs for ultrafast all-optical switching applications takes advantage of Be doping. Doping with Be acceptors reduces the neutral As^0_{Ga} density and increases the density of ionized As_{Ga} [18]. The latter insures ultrafast recovery times [6,18].

In order to examine the optical nonlinearity in LT-GaAs : Be, we have plotted the linear and the nonsaturable absorption versus Be doping concentration for as-grown LT-GaAs in Fig. 3. For a given growth temperature, the linear absorption α_{lin} decreases with the Be concentration. As long as α_{lin} is larger than the linear absorption of undoped high-temperature grown

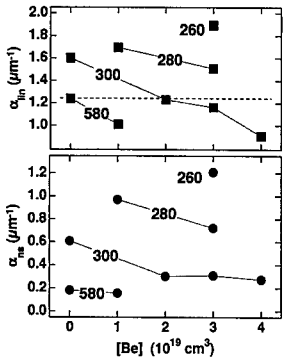

Fig. 3. Linear absorption α_{lin} and nonsaturable absorption α_{ns} versus Be concentration in as-grown LT-GaAs. The growth temperature in °C is indicated. The dashed line marks α_{lin} for undoped high-temperature grown GaAs.

GaAs α_{lin}(HT), this decrease is due to the ionization of the As_{Ga}. Consequently, also the nonsaturable absorption α_{ns} in LT-GaAs is seen to decrease for lower Be concentrations in Fig. 3. The reduced α_{ns} and the ultrafast recovery time [6,18] make LT-GaAs : Be a superior material for all-optical switching applications [6].

For higher Be concentrations, α_{lin} drops below α_{lin}(HT), seen for $T_g = 580$°C and 300°C in Fig. 3. The reduction of α_{lin} below $\alpha_{lin}(HT) = \alpha_{lin}([As^0_{Ga}] = 0)$ cannot be due to the decrease of the neutral As^0_{Ga} density. We conclude that this reduction results from holes in the valence band, which decrease the VB–CB absorption close to the band edge. The material is p-conductive for higher Be concentrations and all As_{Ga} are ionized. This interpretation is supported by the fact that the nonsaturable absorption stays constant in the Be concentration range in which $\alpha_{lin} < \alpha_{lin}$(HT) where the As^0_{Ga} density cannot be further reduced.

This analysis shows that compensated LT-GaAs : Be has the optimum nonlinearity. In compensated LT-GaAs : Be, all As_{Ga} are ionized, which minimizes the nonsaturable absorption α_{ns} due to the As^0_{Ga}–CB transition. Moreover, avoiding p-conductivity maximizes the linear absorption α_{lin} and, in turn, the absorption modulation $\Delta\alpha = \alpha_{lin} - \alpha_{ns}$.

In summary, we have investigated the key parameters for ultrafast all-optical switching in LT semiconductors and demonstrated strategies for their optimization.

This work has been supported by the Swiss National Science Foundation and the AFOSR grant no. F49620-98-1-0135. We would like to thank M. Moser, CSEM, Zurich, for the growth of the Bragg mirrors.

References

[1] R. Takahashi, Y. Kawamura, H. Iwamura, Appl. Phys. Lett. 68 (1996) 153.
[2] U. Keller, K.J. Weingarten, F.X. Kärtner, D. Kopf, B. Braun, I.D. Jung, R. Fluck, C. Hönninger, N. Matuschek, J. Aus der Au, IEEE J. Select Topics Quantum Electron. 2 (1996) 435.
[3] G.L. Witt, Mater. Sci. Eng. B 22 (1993) 9.
[4] S. Gupta, M.Y. Frankel, J.A. Valdmanis, J.F. Whitaker, G.A. Mourou, F.W. Smith, A.R. Calawa, Appl. Phys. Lett. 59 (1991) 3276.
[5] U. Siegner, R. Fluck, G. Zhang, U. Keller, Appl. Phys. Lett. 69 (1996) 2566.
[6] M. Haiml, U. Siegner, F. Morier-Genoud, U. Keller, M. Luysberg, P. Specht, E.R. Weber, Appl. Phys. Lett. 74 (1999) 1269.
[7] M. Haiml, U. Siegner, F. Morier-Genoud, U. Keller, M. Luysberg, R.C. Lutz, P. Specht, E.R. Weber, Appl. Phys. Lett. 74 (1999) 3134.
[8] H.S. Loka, S.D. Benjamin, P.W.E. Smith, IEEE J. Quantum Electron. 34 (1998) 1426.
[9] X. Liu, A. Prasad, W.M. Chen, A. Kurpiewski, A. Stoschek, Z. Liliental-Weber, E.R. Weber, Appl. Phys. Lett. 65 (1994) 3002.
[10] G.P. Agrawal, N.A. Olsson, IEEE J. Quantum Electron. 25 (1989) 2297.
[11] L.R. Brovelli, U. Keller, T.H. Chiu, J. Opt. Soc. Am. B 12 (1995) 311.
[12] Z. Liliental-Weber, J. Ager, D. Look, X.W. Lin, X. Liu, J. Nishio, K. Nichols, W. Schaff, W. Swider, K. Wang, J. Wasburn, E.R. Weber, J. Whitaker, in: M. Godlewski (Ed.), Proceedings of the Eight Conference on Semi-Insulating III–V Materials, World Scientific, 1994, p. 305.
[13] M.R. Melloch, N. Otsuka, J.M. Woodall, A.C. Warren, J.L. Freeouf, Appl. Phys. Lett. 57 (1990) 1531.
[14] S.U. Dankowski, D. Streb, M. Ruff, P. Kiesel, M. Kneissl, B. Knüpfer, G.H. Döhler, U.D. Keil, C.B. Sørenson, A.K. Verma, Appl. Phys. Lett. 68 (1996) 37.
[15] P. Silverberg, P. Omling, L. Samuelson, Appl. Phys. Lett. 52 (1988) 1689.
[16] P. Omling, P. Silverberg, L. Samuelson, Phys. Rev. B 38 (1988) 3606.
[17] D.D. Nolte, J. Appl. Phys. 76 (1994) 3740.
[18] P. Specht, S. Jeong, H. Sohn, M. Luysberg, A. Prasad, J. Gebauer, R. Krause-Rehberg, E.R. Weber, Mater. Sci. Forum 258–263 (1997) 951.

ELSEVIER

Physica B 273–274 (1999) 737–742

PHYSICA B

www.elsevier.com/locate/physb

Tunnel ionization of deep impurities in semiconductors induced by terahertz electric fields

S.D. Ganichev[a,b,*]

[a]*Institut für Exp. und Angew. Physik, Universität Regensburg, 93040 Regensburg, Germany*
[b]*A.F. Ioffe Physicotechnical Institute of the RAS, 194021 St. Petersburg, Russia*

Abstract

An analysis is made of the ionization of deep impurity centers induced by high-intensity terahertz radiation whose photon energies are tens of times lower than the impurity ionization energy. Under these conditions, ionization can be described as phonon-assisted tunneling in which carrier emission is accompanied by defect tunneling in configuration space and electron tunneling in the electric field of the radiation. At high intensities the ionization is caused by direct tunneling. Within a broad range of intensity, frequency and temperature, the terahertz electric field of the radiation acts like a static field. For very high frequencies and low temperatures an enhancement in tunneling as compared to static fields takes place.

Keywords: Tunnel ionization; Terahertz; Far-infrared; Deep centers

1. Introduction

The effect of high-frequency coherent radiation on tunneling in semiconductor superlattices and nanostructures has recently attracted considerable attention. The superposition of a static electric field and an alternating field causes a wealth of new phenomena as a result of photon assisted tunneling [1–3]. In all these cases tunneling is accomplished by a static electric field while the radiation influences the barrier penetration probability. An intense radiation field, however, can generate both the tunneling barrier and initiate tunneling. Such a tunneling process has been observed for deep impurities in semiconductors [4–6]. In contrast to tunneling ionization of atoms, where only electron tunneling takes place [7], phonon-assisted tunneling ionization of impurities in solids is accomplished by two simultaneous tunneling processes, electron tunneling and the redistribution of the vibrational system by defect tunneling [8,9]. With increasing electric field strength direct carrier tunneling from the ground state into continuum, without participation of phonons, becomes dominant.

2. Theoretical consideration

In most cases deep impurities have one bound state which phenomenologically can be approximated by a potential well. The emission and capture of electrons or holes by deep impurities in semiconductors can be considered in the adiabatic approximation. Due to strong electron–phonon interaction a system consisting of local impurity vibrations and an electron is characterized by two adiabatic potentials $U_1(x)$ and $U_2(x)$ as a function of a configuration coordinate x (see insets in Fig. 3) [8,10–13]. Following the Huang–Rhys model [10] these two adiabatic potentials correspond to the free electron bound to the impurity and to a free electron with zero kinetic energy, respectively. The energy separation between the minima of U_1 and U_2 is the thermal ionization energy ε_T of the electron. Thermal emission of carriers from the bound state into the continuum is accomplished

*Correspondence address: Institut für Exp. und Angew. Physik, Universität Regensburg, D-93040 Regensburg, Germany. Tel.: + 49-941-943-2050; fax: + 49-941-943-4223.

E-mail address: sergey.ganichev@physik.uni-regensburg.de (S.D. Ganichev)

0921-4526/99/$ - see front matter
PII: S0921-4526(99)00637-7

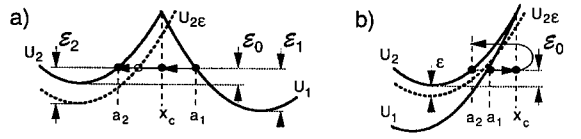

Fig. 1. Tunneling trajectories for the ionization of autolocalized (a) and substitutional (b) deep impurities.

by (i) thermal excitation of the system in the adiabatic bound state potential U_1 by a vibrational energy $\mathscr{E}_1$ and (ii) tunneling of the impurity configuration from this state into an excited state of the ionized configuration U_2 with energy $\mathscr{E}_2$ (Fig. 1) [8,9,14–16].

In the presence of an electric field the electron can be emitted at a negative kinetic energy $-\varepsilon$ due to tunneling through the triangular potential barrier formed by the potential well and the electric field (see inset in Fig. 4). Hence, the adiabatic potential of the ionized configuration U_2 is shifted to a lower energy $U_{2\varepsilon} \equiv U_2 - \varepsilon$ (Figs. 1 and 3). Thus electron emission in an electric field is achieved by two tunneling processes, electron tunneling with probability P_e and tunneling of the defect from the adiabatic potential $U_1(x)$ to potential $U_{2\varepsilon}$ with the probability P_d [8,9,14–16].

The ionization probability may be written as

$$e(E) = \iint P_e P_d \exp(-\mathscr{E}_1/k_B T)\,d\varepsilon\,d\mathscr{E}_1. \tag{1}$$

The Boltzmann factor takes into account the thermal excitation of the system in the adiabatic potential U_1.

In the semi-classical approximation, neglecting pre-exponential factors, the defect tunneling probability is given by [8,15,16]

$$P_d \propto \exp(-2(S_2 \mp S_1)),$$

$$S_i(\mathscr{E}_i) = \frac{\sqrt{2M}}{\hbar}\int_{a_i}^{x_c} dx\sqrt{U_i(x) - \mathscr{E}_i}, \quad i = 1,2, \tag{2}$$

where M is a mass corresponding to the mode of impurity vibration, a_i and x_c are shown in Fig. 1, and the minus and plus sign are related to the particular impurity configuration shown in Fig. 1a and b, respectively.

Electron tunneling in an alternating electric field $E = E_0\cos(\omega t)$ has been treated theoretically by Keldysh [7] (see also [17]). The tunneling probability is given by

$$P_e \propto \exp(-2S_e(\varepsilon)),$$

$$S_e(\varepsilon) = -\frac{\varepsilon}{\hbar}\int_0^{\tau_e}\frac{1}{\gamma^2}\sinh^2(\omega\tau)\,d\tau + \frac{\varepsilon\tau_e}{\hbar}. \tag{3}$$

Here $\gamma \equiv \sqrt{2m^*\varepsilon}\,\omega/eE$ and $\sinh(\omega\tau_e) = \gamma$; m^* and e are the electron effective mass and charge, respectively, and $\tau_e = \hbar\partial S_e/\partial\varepsilon$ has the meaning of an electron tunneling time [18,19].

The integral in Eq. (1) has been calculated using the saddle point method [6]. In the case of weak electric fields, i.e., as long as the saddle point energy $\varepsilon \ll \varepsilon_T$, the exponent can be expanded into a power series of ε. Taken into account that $\mathscr{E}_2 = \mathscr{E}_1 - (\varepsilon_T - \varepsilon)$ obtains

$$S_2 \mp S_1 \simeq (S_2 \mp S_1)|_{\varepsilon=0} - \frac{\varepsilon\tau_2}{\hbar}$$

$$\text{with} \quad \tau_2 = \frac{\hbar\partial|S_2|}{\partial\mathscr{E}_2}\bigg|_{\varepsilon=0}. \tag{4}$$

Then the saddle point condition gives

$$\tau_2 = \tau_e, \quad \tau_2 = \frac{\hbar}{2k_B T} \pm \tau_1, \tag{5}$$

where $\tau_1 = \hbar\partial|S_1|/\partial\mathscr{E}_1|_{\varepsilon=0}$. The first condition in Eq. (5) states that the electron tunneling time τ_e is equal to the defect tunneling time τ_2 for tunneling under the potential U_2.

Finally, the ionization probability of phonon-assisted tunneling is given by [6]

$$e(E) \propto \exp\left[\frac{E^2}{E_c^{*2}}\right] = \exp\left[\frac{E^2e^2(\tau_2^*)^3}{3m^*\hbar}\right], \tag{6}$$

$$(\tau_2^*)^3 = \frac{3}{4\omega^3}(\sinh(2\omega\tau_2) - 2\omega\tau_2). \tag{7}$$

This result shows that $(\tau_2^*)^3$ increases exponentially as a function of $\omega\tau_2$. As the ionization probability itself depends exponentially on the third power of τ_2^* the tunneling ionization is drastically enhanced with rising $\omega\tau_2$. This can be achieved not only by increasing the radiation frequency ω but also by lowering the temperature (Eq. (5)). In the limit $\omega\tau_2 \ll 1$ the time constant τ_2^* approaches the tunneling time τ_2 giving the same result as the static field regime obtained in Ref. [16].

3. Samples and experimental technique

The tunneling ionization of deep impurities by high-intensity FIR radiation with photon energies much smaller than the thermal impurity ionization energy ε_T has been studied for different types of deep impurities: substitutional impurities with weak electron–phonon coupling (Ge:Au, Ge:Hg, Ge:Cu, Ge:Zn, Si:Au, GaP:Te with acceptor concentrations in the range 10^{14}–10^{15} cm^{-3}) and autolocalized DX$^-$ centers with strong electron–phonon coupling ($Al_xGa_{1-x}As$:Te, $Al_xGa_{1-x}Sb$:Te with $x = 0.35$ and 0.5). In the investigated temperature range from 4.2 to 80 K or for autolocalized impurities up to 150 K, practically all impurities are occupied in thermal equilibrium.

The change of the ionization probability in the electric field which is proportional to the change in the free carrier concentration can be detected as photoconductive signal under FIR-laser illumination. The samples were placed in a temperature-controlled optical cryostat. Penetration of light in the medium IR range into the cryostat was prevented by the use of crystalline quartz filters, and in the visible, with a 1 mm-thick black-polyethylene filter. Measurements have been carried out using a standard 50 Ω load resistor circuit, taking care that the bias voltage across the sample was substantially below the threshold of electric breakdown, which for bulk samples is at about 5 V/cm.

The radiation sources used was a pulsed far-infrared molecular laser optically pumped by a TEA-CO_2 laser [20,21]. The CO_2 laser has been used for optical pumping because of its wavelength range from 9.2–10.6 μm, which includes strong vibrational–rotational absorption lines of many molecules. Commercial TEA-CO_2 lasers (URENKO-204) offer high stability and high power for this purpose. More than 10 strong single lines in the terahertz range from 3.78 to 68 THz (corresponding wavelengths are from 496 to 35 μm) have been obtained using NH_3, D_2O and CH_3F as the active gases for optically pumped laser [5]. The radiation pulse length varies for different lines from 10 to 100 ns. The radiation is focused to a spot of about 1 mm^2, with the maximum intensity reaching as high as 5 MW/cm^2 corresponding to electric fields up to about 50 kV/cm. The intensity, pulse shape and the spatial distribution of the laser radiation were measured with fast room temperature photodetectors based on the photon drag effect [22], intraband μ-photoconductivity [23] and the Spirikon pyroelectric camera, respectively.

Ionization of deep impurities by far infrared radiation has been observed for all samples in the whole frequency range investigated. A photoconductive signal increasing nonlinearly with incident power ($I \leqslant 5$ MW/cm^2, $E \leqslant 5 \times 10^4$ V/cm) has been observed in spite of the fact that the photon energies were much smaller than the binding energy of the impurities. Ionization can be attributed to phonon-assisted and direct tunneling over a wide range of temperature, frequency and electric field strength [5].

At not too low temperatures and not too high frequencies the tunneling probability is independent of frequency and exponentially increases with the square of the electric field strength[1] (see Eq. (6)). This is illustrated in Fig. 2a

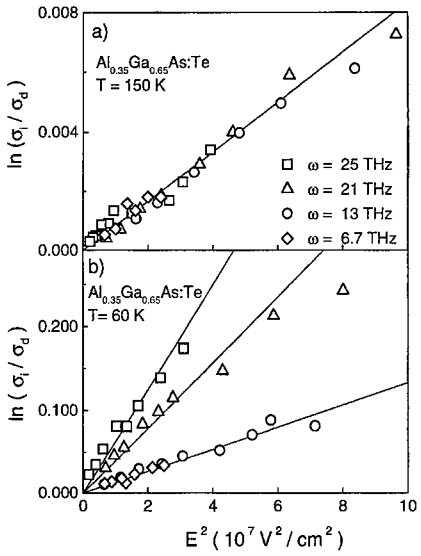

Fig. 2. The ionization probability (given by the ratio of the conductivity under illumination and in the dark σ_i/σ_d) of $Al_{0.35}Ga_{0.65}As$:Te as a function of the square of the electric field of the radiation. Lines shows $\propto \exp(E^2/E_c^{*2})$.

where experimental results obtained with AlGaAs:Te at $T = 150$ K are shown. In this quasi-static regime the electron tunnels at the instantaneous magnitude of the electric field in a time shorter than the period of oscillation and thus the electric field acts like a static field. Such a behaviour has been observed for all materials at sufficiently high temperatures. In this quasi-static regime [5] the characteristic field, which can be determined experimentally, is given by $E_c^{*2} = (3m^*\hbar)/(\tau_2^{*3}e^2)$ with $\tau_2^* = \tau_2$. Thus, the investigation of field dependence of ionization probability allows one to determine the defect tunneling time τ_2 [26]. Fig. 3 presents the temperature dependence of the tunneling time τ_2 obtained for various samples. For the purpose of comparison, $\hbar/2k_BT$ is also plotted in Fig. 3. Clearly, τ_2 is larger than $\hbar/2k_BT$ for substitutional impurities and smaller than $\hbar/2k_BT$ for the DX-centers. Thus, the tunneling time reflects the structure of the potential barriers which is distinct for the two potential configurations discussed here. The phonon-assisted ionization of deep impurities in semiconductors by contactless application of short pulses of terahertz radiation has been proposed as a method for the characterization of defects [5,26,30]. The field dependence of the signal allows one to determine the defect tunneling times, the Huang–Rhys parameter and the basic structure of the adiabatic defect potentials. The Poole–Frenkel effect, which can be observed for charged impurities only (see footnote 1), can be used to determine the defect charge state.

This frequency independent tunneling is limited to frequencies ω with $\omega\tau_2 < 1$ (Eq. (7)). The enhancement of

[1] In the case of charged impurities (all substitutional impurities investigated) a deviation from the field dependence $e(E) \propto \exp(E^2/E_c^{*2})$ can be seen in relatively low-field strength (up to 1 kV/cm) where the defects are thermally ionized through the Poole–Frenkel effect and the ionization probability is proportional to $e(E) \propto \exp(\sqrt{(Ze^3E/\kappa)}/k_BT)$ [5,24,25].

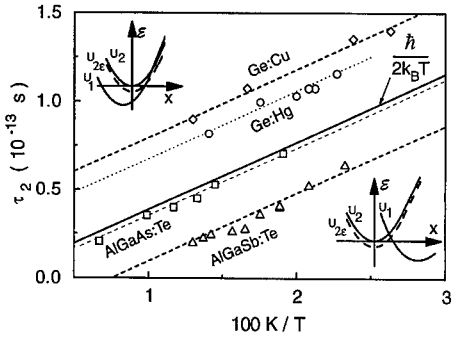

Fig. 3. Tunneling times τ_2 as a function of $1/T$ for different samples. The full line shows $\hbar/2k_BT$, the broken lines are plotted according to Eq. (5). Inset: Adiabatic potentials for substitutional impurities (top left) and autolocalized impurities (bottom right).

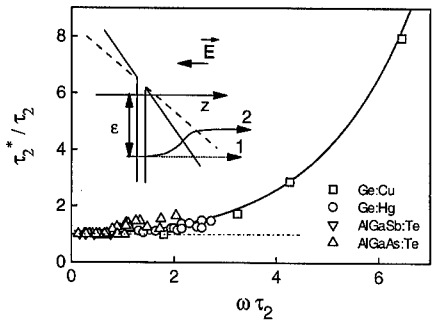

Fig. 4. Ratio τ_2^*/τ_2 as a function of $\omega\tau_2$. The line shows the dependence according to Eq. (7) Inset: Electron tunneling trajectory: (1) in a static electric field, and (2) in an alternating field.

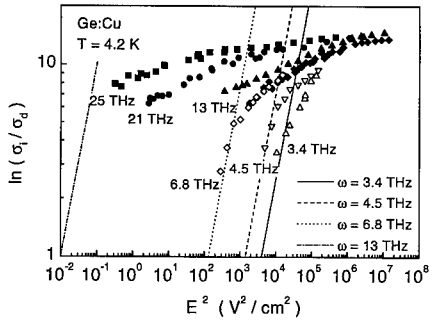

Fig. 5. The ionization probability (given by the ratio of the conductivity under illumination and in the dark σ_i/σ_d) of Ge : Cu at 4.2 K as a function of the square of the electric field of the radiation. Solid symbols are obtained with molecular optically pumped FIR laser and open symbols with Santa Barbara Free-Electron-Laser [6]. Lines show $\propto \exp(E^2/E_c^{*2})$ for four lowest frequencies used in experiment.

tunneling at frequencies higher than the reciprocal tunneling time has been anticipated in a number of theoretical papers [7,17,27–29], but has been demonstrated experimentally only recently [6]. In contrast to static electric fields where the electron tunnels at a fixed energy, the energy of the electron is not conserved during tunneling in alternating fields (see inset in Fig. 4). In this case the electron can absorb energy from the field, which leads to a sharp increase of the tunneling probability with increasing frequency. This effect has been observed for various impurities in different semiconductors and is demonstrated for AlGaAs:Te in Fig. 2b. For the case of $\omega\tau_2 \geqslant 1$ the ionization probability still depends exponentially on the square of the electric field strength but the characteristic field becomes frequency dependent and ionization is drastically enhanced with rising frequency.

In Fig. 4 the ratio τ_2^*/τ_2 calculated from Eq. (7) is plotted as a function of $\omega\tau_2$ and compared to experimental results obtained from the measured values of E_c^* for various the frequencies, temperatures and materials. The tunneling times τ_2 were determined from frequency independent values of E_c^*. The experimental results shown in Fig. 4 are grouped according to the materials. For each material the variation of the value of $\omega\tau_2$ has been obtained by applying different radiation frequencies in the range from 6.7 to 25 THz and different temperatures between 20 and 150 K. It should be pointed out that the theory leading to good agreement with experiment does not contain any fitting parameters.

Further decrease of the temperature leads to a much stronger frequency dependence of the ionization probability. Fig. 5 shows experimental results for Ge:Cu at $T = 4.2$ K in the frequency range between 3.4 and 25 Thz. In order to display in one figure the total set of data covering eight order of magnitude in the square of the electric field, $\log(E^2)$ has been plotted on the abscissa. To make a easy comparison to the $\exp(E^2/E_c^2)$ dependence of σ_i/σ_d possible, a log log presentation has been used for the ordinate.

At 4.2 K the condition $\omega\tau_2 \gg 1$ is valid for whole frequency range investigated here. The results in Fig. 5 show that at liquid helium temperature in the limit of $\omega\tau_2 \gg 1$ a drastic frequency dependence is observed. For a given constant signal a change of six orders of magnitude in electric fields squared needs only a factor of seven change in frequency. Note, that this effect is observed only for relatively low fields. In Fig. 5 the results of calculations for phonon-assisted tunneling with τ_2 determined at higher temperatures is plotted. It is seen that for the three lowest frequencies the experimental points at low field strength are reasonably well described by the emission probabilities of phonon-assisted tunneling calculated from Eqs. (6) and (7). However, for higher frequencies the calculated field dependence of

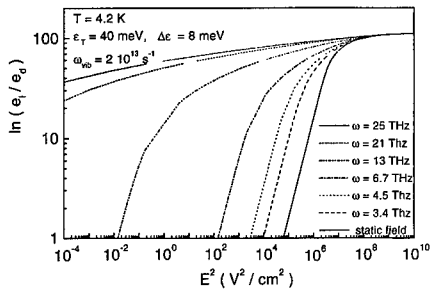

Fig. 6. Field dependence of ionization probability calculated after Eqs. (1)–(3) for all values of the energy of electron tunneling ε for Ge:Cu at 4.2 K and frequencies used in the experiments taking into account phonon-assisted and direct tunneling but ignoring Coulomb interaction.

phonon-assisted tunneling does not fit the experimental results in the whole range of electric fields where a signal could be detected. Furthemore, at higher field strengths the measured field dependence of the emission probability is much weaker than the theoretical result and the frequency dependence practically disappears. Similar results have been obtained for autolocalized DX-centers in AlGaAs:Te [31].

This complex dependence of ionization probability on field strength and radiation frequency is a result of the transition from phonon-assisted tunneling at low-field strength to direct tunneling without phonons at high fields. The emission probability for phonon-assisted tunneling as a function of the electric field strength given by Eq. (6) was obtained in the limit that corrections to thermal emission resulting from electron tunneling are small, i.e., the energy of electron tunneling ε is much smaller than the defect tunneling energy $\mathscr{E}_0$ and the energy of thermal ionization ε_T. In the opposite limit, $\varepsilon > \varepsilon_T, \mathscr{E}_0$, direct carrier tunneling from the ground state into the continuum, without participation of phonons, becomes dominant [5]. Direct electron tunneling occurs at the crossing of the $U_{2\varepsilon}$ and U_1 potential curves, where an electronic transition is possible without any change in the configuration coordinate. This effect, leading to weaker field dependence of the ionization probability in comparison to that of phonon-assisted tunneling dominates the ionization process at very high fields.

Fig. 6 shows the result of calculations based on Eqs. (1)–(3) for all values of the electron tunneling energy ε for Ge:Cu at 4.2 K and frequencies used in the experiments taking into account both processes but ignoring Coulomb interaction. It is seen that the theory describes well the experimentally observed features of the field and frequency dependence of tunneling ionization. The disappearence of frequency dependence of the ionization probability at high-field strengths is caused by a decrease in the tunneling time τ_2 with rising electric field strength resulting finally in $\omega\tau_2$ less than unity. This is due to the fact that at high-field strength defect tunneling occurs at energies much smaller than the energy of phonon-assisted tunneling which changes the tunneling trajectory. To achieve the quantitative agreement one needs to improve the theory by taking into account the charge of the impurities.

Finally, all our measurements have been carried out with deep impurities in semiconductors, however, because tunneling is crucial in numerous processes in physics, chemistry, and biology we expect that an enhancement of tunneling induced by application of high-intensity coherent radiation will have significant consequences.

Acknowledgements

The author would like to thank W. Prettl, I.N. Yassievich, V.I. Perel and E. Ziemann for active help and discussion. Financial support by the DFG and the RFFI is gratefully acknowledged.

References

[1] P.S.S. Guimaraes, B.J. Keay, J.P. Kaminski, S.J. Allen Jr., P.F. Hopkins, A.C. Gossard, L.T. Florez, J.P. Harbinson, Phys. Rev. Lett. 70 (1993) 3792.
[2] B.J. Keay, S.J. Allen Jr., J. Gallan, J.P. Kaminski, K.L. Campman, A.C. Gossard, U. Bhattacharya, J.W. Rodwell, Phys. Rev. Lett. 75 (1995) 4098.
[3] C.J.G.M. Langerak, B.N. Murdin, B.E. Cole, J.M. Chamberlain, M. Henini, M. Pate, G. Hill, Appl. Phys. Lett. 67 (1995) 3453.
[4] S.D. Ganichev, W. Prettl, P.G. Huggard, Phys. Rev. Lett. 71 (1993) 3882.
[5] S.D. Ganichev, W. Prettl, I.N. Yassievich, Rev. Phys. Solid State 39 (1997) 1703.
[6] S.D. Ganichev, E. Ziemann, Th. Gleim, W. Prettl, I.N. Yassievich, V.I. Perel, I. Wilke, E.E. Haller, Phys. Rev. Lett. 80 (1998) 2409.
[7] L.V. Keldysh, Sov. Phys. JETP 20 (1965) 1307.
[8] V.N. Abakumov, V.I. Perel, I.N. Yassievich, Nonradiative Recombination in Semiconductors, in: V.M. Agranovich, A.A. Maradudin (Eds.), Modern Problems in Condensed Matter Sciences, Vol. 33, North-Holland, Amsterdam, 1991.
[9] P.T. Landsberg, Recombination in Semiconductors, Cambridge University Press, New York, 1991.
[10] K. Huang, A. Rhys, Proc. Roy. Soc. London, Ser. A 204 (1950) 406.
[11] C.H. Henry, D.V. Lang, Phys. Rev. B 15 (1977) 989.
[12] P.M. Mooney, T.N. Theis, Comments Condens. Matter Phys. 16 (1992) 167.
[13] R.C. Newman, Semicond. Sci. Technol. 9 (1994) 1749.
[14] S. Makram-Ebeid, M. Lannoo, Phys. Rev. B 25 (1982) 6406.
[15] T. Markvart, J. Phys. C 17 (1984) 6303.
[16] V. Karpus, V.I. Perel, Sov. Phys. JETP 64 (1986) 1376.

[17] L.D. Landau, E.M. Livshitz, Quantum Mechanics, Pergamon, Oxford, 1977, p. 287.
[18] M. Büttiker, R. Landauer, Phys. Rev. Lett. 49 (1982) 1739.
[19] R. Landauer, Th. Martin, Rev. Mod. Phys. 66 (1994) 217.
[20] T.Y. Chang, T.J. Bridges, Opt. Commun. 1 (1970) 423.
[21] Th. de Temple, in: K.J. Button (Ed.), Infrared and Millimeter Waves, Vol. 1, 1979, p. 129.
[22] S.D. Ganichev, Ya.V. Terent'ev, I.D. Yaroshetskiĭ, Sov. Tech. Phys. Lett. 11 (1985) 20.
[23] S.D. Ganichev, S.A. Emel'yanov, A.G. Pakhomov, Ya.V. Terent'ev, I.D. Yaroshetskiĭ, Sov. Tech. Phys. Lett. 11 (1985) 377.
[24] S.D. Ganichev, J. Diener, I.N. Yassievich, W. Prettl, Europhys. Lett. 29 (1995) 315.
[25] S.D. Ganichev, E. Ziemann, W. Prettl, A. Istratov, E.R. Weber, MRS Symposium. Proceedings, San Francisco, 1999, to be published.
[26] S.D. Ganichev, J. Diener, I.N. Yassievich, W. Prettl, B.K. Meyer, K.W. Benz, Phys. Rev. Lett. 75 (1995) 1590.
[27] Yu.A. Bychkov, A.M. Dykhne, Sov. Phys. JETP 31 (1970) 928.
[28] B.I. Ivlev, V.I. Mel'nikov, Phys. Rev. Lett. 55 (1985) 1614.
[29] M.V. Ammosov, N.B. Delone, V.P. Krainov, Sov. Phys. JETP 64 (1986) 1191.
[30] E. Ziemann, S.D. Ganichev, I.N. Yassievich, K. Schmalz, W. Prettl, in: S. Ashok, J. Chevallier, K. Sumino, B.L. Sopori, W. Goetz (Eds.), Defect and Impurity Engineered Semiconductors and Devices II, Mater. Res. Soc. Symp. Proc. 510 (1998) 595.
[31] H. Ketterl, E. Ziemann, S.D. Ganichev, I.N. Yassievich, A. Belyaev, S. Schmult, W. Prettl, 1999, to be published.

ELSEVIER

Physica B 273–274 (1999) 743–745

PHYSICA B

www.elsevier.com/locate/physb

Hydrogen molecules in GaAs after hydrogen plasma treatment

A.W.R. Leitch[a,*], J. Weber[b]

[a]*Department of Physics, University of Port Elizabeth, P.O. Box 1600, Port Elizabeth 6000, South Africa*
[b]*Max-Planck-Institut für Festkörperforschung, Heisenbergstrasse 1, D-70569 Stuttgart, Germany*

Abstract

The exposure of GaAs to a hydrogen plasma at 250°C leads to the formation of isolated H_2 molecules positioned at interstitial tetrahedral T sites within the GaAs lattice. In this paper, we have measured the Raman vibrational mode for the H_2 molecule in GaAs within the 10–300 K temperature range. The H_2 vibrational mode at room temperature is measured at 3911 cm^{-1} and shifts to higher frequencies as the temperature is lowered, reaching a value of 3925 cm^{-1} at 10 K. A lack of splitting of the H_2 mode under applied uniaxial stress confirms that the H_2 molecule is free to rotate at the T site within the lattice.

Keywords: Gallium arsenide; Hydrogen; Spectroscopy

1. Introduction

Hydrogen is the most basic impurity that can occur in various configurations in a semiconductor. It was first proposed in 1983 [1,2] that energetic considerations would favour the formation of molecular hydrogen within the semiconductor lattice. Although these first calculations were made for Si, similar predictions were subsequently also made for the H_2 molecule in GaAs. As the molecule lacks a dipole moment and is electrically neutral, however, its presence in a semiconductor has until recently remained undetected.

In 1996 Vetterhöffer et al. [3] reported the first experimental evidence for isolated H_2 molecules in a crystalline semiconductor. A 77 K Raman spectrum of hydrogen plasma-treated GaAs revealed a line at 3925.9 cm^{-1}, which they attributed to the vibrational mode of the isolated H_2 molecule at an interstitial site within the zinc-blende lattice. This represents a substantial downward shift in frequency from the well-known value of 4161 cm^{-1} for gaseous H_2 [4]. They were also able to measure the vibrational lines due to the *para* and *ortho* states related to the lowest energy rotational quantum states $J = 0$ and 1 for the H_2 molecule, respectively. More recently, we have measured a room temperature Raman line at 3601 cm^{-1} in hydrogen-treated Si, and presented evidence that it is attributed to the vibrational mode of the isolated H_2 molecule in Si [5].

Two distinct and inequivalent tetrahedral interstitial (T) sites exist in the zinc-blende lattice; for GaAs these would be the T_{Ga} (surrounded by the Ga cations) and the T_{As} (surrounded by the As anions). Several theoretical studies [6–9] have predicted that the most stable position for the molecule in GaAs will be the T_{Ga} site, oriented along the $\langle 1\,0\,0\rangle$ axis. The calculations however also indicated that very little energy was required to rotate the molecule. In this paper, we extend the initial measurements of Vetterhöffer et al. [3] to room temperature and compare the results with what has been reported for Si.

2. Experimental details

Semi-insulating undoped GaAs as well as conducting n-type (Te-doped) and p-type (Zn-doped) GaAs, all grown by the horizontal Bridgman technique, were examined in this study. Hydrogen was introduced into the wafers by exposing them to a remote dc hydrogen

* Corresponding author: Tel.: + 27-41-504-2219; fax: + 27-41-504-2573.
E-mail address: phaawl@upe.ac.za (A.W.R. Leitch)

0921-4526/99/$ - see front matter
PII: S0921-4526(99)00638-9

plasma at typically 250°C for up to 8 h. The samples were mounted on a heater stage located downstream from the plasma. The hydrogen pressure was held constant at 1.5 mbar. For some of the samples the hydrogen atmosphere was replaced by either deuterium, or a mixture consisting of $H_2 : D_2$ (1 : 1).

Raman measurements were performed at various temperatures, with the sample mounted in a liquid helium exchange gas cryostat. For excitation, the 413 nm line of a Kr^+ laser was focussed onto the sample, making an angle of 40° with the sample normal. The laser intensity was typically 150 mW. The backscattered light, not analysed for its polarisation, was dispersed with a 0.3 m single grating spectrometer and detected with a cooled Si–CCD detector array. Appropriate holographic notch filters were used to reduce the scattered laser light.

3. Results and discussion

Fig. 1 demonstrates that the room temperature Raman peak, measured in GaAs after exposure to a hydrogen plasma, may be attributed to isolated H_2 molecules within the lattice. Spectrum (a) shows the H_2-related vibrational Raman line at 3911 cm^{-1}. When a similar GaAs sample is exposed to a deuterium plasma, the expected isotopic shift of the Raman line to 2827 cm^{-1} is measured (spectrum (b)). Exposure to a plasma containing a 1 : 1 $H_2 : D_2$ mixture produced three Raman lines at 3911, 2827 and 3429 cm^{-1} (spectrum (c)); these are attributed to H_2, D_2 and HD molecules, respectively. None of these Raman lines was present in the material before plasma treatment.

Due to the line width ($\sim 10\ cm^{-1}$) of the measured H_2 Raman line at room temperature, it was not possible to resolve the $Q_1(1)$ (*ortho*-H_2) and the $Q_1(0)$ (*para*-H_2) modes of the vibrational Raman lines. For temperatures below $\sim$ 100 K however, the $Q_1(0)$ mode becomes visible as a small peak on the high-frequency side of the dominant $Q_1(1)$ peak [3,10]. We have measured the frequency splitting of the two modes to be 8.0 cm^{-1}, while the ratio of the intensities is approximately 2.5 : 1, close to the expected ratio of 3 : 1. Due to the absence of strong nuclear spin-flip processes, the conversion of *ortho*-H_2 to *para*-H_2 is known to be a slow process at cryogenic temperatures (of the order of many days) [11]. The same intensity ratio of $\sim 3 : 1$ is therefore expected for all temperatures under investigation in this study.

Fig. 2 shows the measured H_2 peak position as function of temperature. At 8 K the H_2 Raman peak occurs at 3925.4 cm^{-1} and remains reasonably constant until $\sim$ 100 K, above which it progressively decreases by about 14 cm^{-1} to the room temperature value of 3911 cm^{-1}. This decrease in vibrational frequency with increasing temperature may be explained in terms of an increase in the bond length of the molecule. As the sample temperature is increased, the increased charge density surrounding the molecule leads to a weakening of the molecular bond and a corresponding decrease in the vibrational frequency. We have recently reported a similar trend for the Raman signal of the interstitial H_2 molecule in crystalline Si [12]. In the case of Si the Raman frequency decreases by about 17 cm^{-1} from the 10 K value of 3618 cm^{-1}. This again illustrates the influence of the matrix on the vibrating molecule.

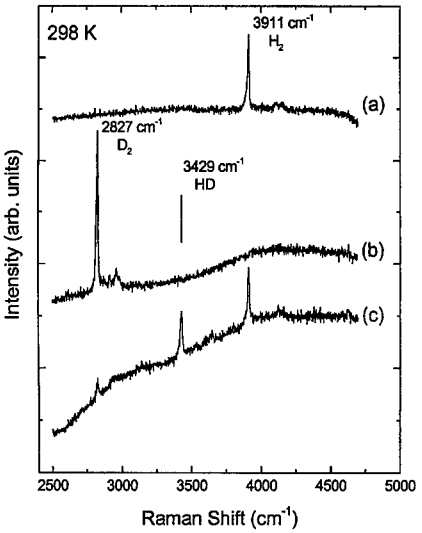

Fig. 1. Room temperature Raman spectra of GaAs, after exposure at 250°C for 8 h to: (a) H_2 plasma; (b) D_2 plasma; and (c) $H_2 : D_2$ (1 : 1) plasma.

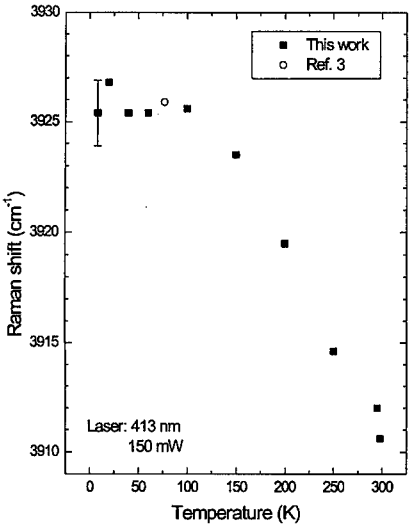

Fig. 2. Temperature dependence of the H_2 Raman peak position in GaAs.

Table 1
List of the reported Raman frequencies for interstitial H_2 in GaAs, together with data for H_2 in Si as well as H_2 in the gas phase for comparison

Matrix	H_2 (cm^{-1})	D_2 (cm^{-1})	HD (cm^{-1})	Reference
GaAs (295 K)	3911	2827	3429	This work
GaAs (77 K)	3925.9	2842.6	3446.5	3
GaAs (theory)	3704			8
GaAs (theory)	3824			9
Si (295 K)	3601	2622		5
Si (10 K)	3618.3	2642.5	3264.8	15
H_2 (gas)	4161.1	2993.6	3632.1	4

Uniaxial stress measurements performed at 60 K on specially cut [0 0 1], [1 1 0] or [1 1 1] aligned GaAs samples, failed to produce any splitting of the H_2 Raman line [10]. A defect having tetrahedral symmetry will not exhibit polarised splitting of the frequency for [0 0 1] stresses, but both [1 1 0] as well as [1 1 1] stresses will cause the frequency to split into two components of equal intensities [13]. The lack of splitting of the H_2 Raman line under uniaxial stress indicates that the H_2 molecule is isolated and free to rotate at the T_{Ga} site within the GaAs matrix. This confirms the theoretical calculations indicating that the rotational barrier is very small [14].

Finally, Table 1 compares the measured Raman frequencies with calculated values for GaAs, as well as the frequencies recently reported for interstitial H_2 molecules in Si [5,15]. For both semiconductors we find that the confinement of the isolated H_2 molecule at the interstitial site within the host matrix results in a dramatic decrease in the vibrational frequency from the value for H_2 in free space. This downward shift in frequency is greater for Si, due to the smaller lattice constant that leads to a stronger interaction between the H_2 molecule and the charge density of the neighbouring Si atoms. The decrease in frequency therefore confirms recent calculations for the vibrational frequency of the H_2 molecule trapped within the lattice of the semiconductor [8,9,14]. Both materials also show a similar variation in vibrational frequency of the H_2 line between 10 K and room temperature. One major difference however is that for GaAs it is possible to resolve the $Q_1(1)$ and $Q_1(0)$ modes, indicating that the molecule can freely rotate, while for Si the H_2 mode remains a single Raman line.

Acknowledgements

We gratefully acknowledge Prof. H.-J. Queisser for his interest and support throughout this work. We thank J. Wagner of the Fraunhofer-Institut für Angewandte Festkörperphysik, Freiburg, Germany, for fruitful discussions. We acknowledge the technical assistance of W. Heinz and W. Krause. One of us (AWRL) acknowledges the financial support of the South African National Research Foundation (NRF).

References

[1] A. Mainwood, A.M. Stoneham, Physica B 116 (1983) 101.
[2] J.W. Corbett, S.N. Sahu, T.S. Shi, L.C. Snyder, Phys. Lett. A 93 (1983) 303.
[3] J. Vetterhöffer, J. Wagner, J. Weber, Phys. Rev. Lett. 77 (1996) 5409.
[4] B.P. Stoicheff, Can. J. Phys. 35 (1957) 730.
[5] A.W.R. Leitch, V. Alex, J. Weber, Phys. Rev. Lett. 81 (1998) 421.
[6] L. Pavesi, P. Giannozzi, Phys. Rev. B 46 (1992) 4621.
[7] S.J. Breuer, R. Jones, P.R. Briddon, S. Öberg, Phys. Rev. B 53 (1996) 16 289.
[8] Y. Okamoto, M. Saito, A. Oshiyama, Phys. Rev. B. 56 (1997) R10016.
[9] C.G. Van de Walle, Phys. Rev. Lett. 80 (1998) 2177.
[10] A.W.R. Leitch, J. Weber, Phys. Rev. B Nov. 15 (1999) accepted for publication.
[11] G. Herzberg, in: Molecular Spectra and Molecular Structure: I. Spectra of Diatomic Molecules, Van Nostrand Reinhold, New York, 1950.
[12] A.W.R. Leitch, J. Weber, V. Alex, Mater. Sci. Eng. B 58 (1999) 6.
[13] A.A. Kaplyanskii, Opt. Spectrosc. (USSR) 16 (1964) 329.
[14] B. Hourahine, R. Jones, S. Öberg, R.C. Newman, P.R. Briddon, E. Roduner, Phys. Rev. B 57 (1998) 12 666.
[15] R.E. Pritchard, M.J. Ashwin, J.H. Tucker, R.C. Newman, E.C. Lightowlers, M.J. Binns, S.A. McQuaid, R. Falster, Phys. Rev. B 56 (1997) 13 118.

ELSEVIER

Physica B 273–274 (1999) 746–749

PHYSICA B

www.elsevier.com/locate/physb

Photo-ionization spectra for alloy-induced configurations of Si–DX center in AlGaAs

R. Piotrzkowski*

High Pressure Research Center, Polish Academy of Sciences, Sokolowska 29/37, 01-142 Warsaw, Poland

Abstract

We report, for the first time, the spectral dependencies of photo-ionization cross section for individual alloy-induced configurations in Si-doped $Al_xGa_{1-x}As$ ($x = 0.15$). We analyzed the build-up transients of the persistent photoconductivity at 77 K, in the spectral range $\lambda = 0.88$–1.1 μm. They were obtained by measuring Hall electron concentration as a function of time in the sample illuminated by the monochromatic light. The measured transients $\Delta n(t)$ were resolved into three exponential components. We demonstrate that they represent the photoionization of different local configurations of DX center (DX_1–DX_3). We found that the photo-ionization threshold for different DX configurations varies by the amount practically equal to the variation in their thermal energies. The spectral dependencies found here explain well the previously reported threshold dependence on the initial filling of the DX states.

Keywords: DX-centers; Photoionization; Alloy effects; AlGaAs

Since 1989 it has been known that the alloy effect on DX centers in AlGaAs consists in splitting of whole DX center population into four groups (configurations) DX_0–DX_3 [1,2]. This results from the fact that properties of the displaced DX^- ion depend on configuration of four (Al/Ga) ions in its immediate vicinity.

There were many papers concerning the configuration-dependent thermal emission energies and the energy level positions, but the first work related to the effect of alloying on the energy of the optical emission (photo-ionization energy) appeared only in 1992 [3]. In this paper Su and Farmer demonstrated for the first time the existence of non-exponential photo-ionization transients in Si-doped AlGaAs and their relation with the optical splitting of DX center (i.e. the fact that different configurations have different photo-ionization efficiency).

In 1996 we demonstrated the relevance of the method of 'pressure-assisted thermal emission from resonant levels' in determining the photo-ionization rates of individual DX configurations [4]. In this method, the Hall effect measurements enabled us a direct determination of the occupancies of individual DX configurations after photoionization with a given dose of light. After performing a series of experimental runs with various light exposures, the decay of individual DX configuration along the photo-ionization transient was determined (see Fig. 1). This experiment demonstrated that the decay of each DX configuration is exponential in time, but the time constants differ substantially (by the factor of 2–3 between the nearest configurations).

Experimental method of monitoring the occupancy of individual DX, used in Ref. [4] implies the use of hydrostatic pressure with the possibility of modifying it at low temperature in order to prepare the initial state of the sample. During such preparation procedure the sample is cooled to 77 K, at high pressure. At this temperature, the pressure is released. Due to metastable properties of DX center, the occupation reached at high pressure does not change any more (this method is sometimes referred to as 'high-pressure freeze-out' (HPFO)). Such pressure filling cycle must be performed (with maximum reproducibility) for each exposure point. This means that the discussed method is too time-consuming to be used for

* Tel.: + 48-22-632-3628; fax: + 48-3912-0331.
E-mail address: rp@unipress.waw.pl (R. Piotrzkowski)

0921-4526/99/$ - see front matter
PII: S0921-4526(99)00639-0

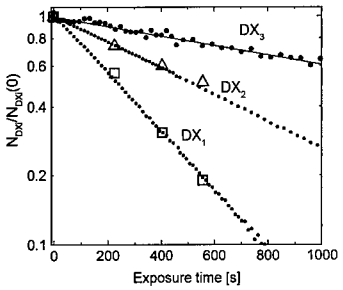

Fig. 1. Analysis of photo-ionization transient measured in $Al_{0.15}Ga_{0.85}As$: Si sample at $T = 77$ K ($\lambda = 1.033$ μm). The initial state of the sample was obtained by pressure freeze-out at 6 kbar. Large symbols denote the occupancies of individual DX configurations after photoionization during the given exposure time (taken from Ref. [4]). Small points correspond to the components found by fitting the measured full PPC transient. All occupancies are normalized to the initial value. To account for spread of measurements, $\frac{1}{3}$ of fitting error has been added to fitted exponential component.

determination of the photo-ionization spectra of individual DX configurations.

On the other hand, considering the differences in individual decay times as important as found, we can expect that the decay components can be determined from the full PPC transient $\Delta n(t)$. In this work, we have positively verified this possibility and determined the alloy splitting of optical-ionization spectra of Si–DX center in AlGaAs.

The sample studied was Si-doped $Al_xGa_{1-x}As$ MBE-grown 1.5 μm layer with the low Al contents x ($x = 0.15$). The characteristics of this sample, especially those related to the multiconfiguration character of DX centers are well known from our previous studies [5]. The important fact which permitted us to study the PPC transients at liquid nitrogen temperature is that in the sample with such low aluminum content, the capture barrier is so large that there is no recapture of electrons, even in the saturated PPC state. This means that the photoconductivity has really persistent character at $T = 77$ K, even at a pressure of 3 kbar. We have found out that this is not true for AlGaAs samples with higher Al contents (e.g. 26%).

The experimental setup was the same as in Ref. [4]. It was designed to study the transport phenomena (Hall effect and conductivity) under hydrostatic pressure at temperatures ranging from liquid nitrogen to ambient with the possibility of illuminating the samples with monochromatic light. We used Jobin–Yvon HR320 monochromator with 150 W tungsten halogen lamp. In this work, all measurements were made at a temperature of 77 K and at ambient pressure. In two cases, pressure was used to prepare the initial state of the sample. To find the PPC build-up transient, the Hall concentration n was measured as a function of time (max. repetition rate 1 aquisition/4 s) in illuminated sample. The time of measurement was long enough to reach maximum concentration n_{max} corresponding to total ionization of DX centers. The typical time was of the order of one hour. The analysis consisted in fitting the experimental dependence $\Delta n(t) = n_{max} - n(t)$ to exponential functions:

$$\Delta n(t) = \sum_i A_i \exp(-t/\tau_i). \quad (1)$$

The first step was to check if this decomposition procedure leads to the same results as in the method used in Ref. [4]. Accordingly, we analyzed the transient of PPC excited with $\lambda = 1.033$ μm for the initial state of the sample obtained by pressure filling at 6 kbar.

The three exponential components found for this transient are shown in Fig. 1 together with the results obtained previously in Ref. [4]. Two components track exactly the time dependences of occupation of the configuration DX_1 and DX_2, found in Ref. [4]. The amplitudes of these components ($A_1 = 9.65 \times 10^{17}$ cm^{-3}; $A_2 = 1.13 \times 10^{18}$ cm^{-3}) are equal to the concentrations of electrons frozen after pressure freeze-out at 6 kbar on respective configurations of DX i.e. N_{DX_1} and N_{DX_2} (see Ref. [4]). The third, slowest component corresponds to the DX_3 configuration, which cannot be accessed by the method used in Ref. [4].

In the next experiment, we measured the PPC build-up for the same photon energy, but without using the pressure to prepare the initial sample state. This is possible because the DX states of Si, although lying high above the conduction band minimum, are partly filled at ambient pressure (cf. Ref. [5]). In this case, the total amplitude of the transient was 3.6 times smaller than that obtained previously. Nevertheless, we resolved the three components which have the decay constants τ_i equal to those found in the first experiment (see the points at 1.2 eV in Fig. 3).

Next, we performed similar comparison of transients measured for different initial states for the wavelength 0.88 μm ($h\nu = 1.41$ eV). Also in this case, we found the same time constants for the corresponding components.

It should be noted here that when the initial state of sample is obtained at ambient pressure, the fast component is small (about 0.1–0.2 of the main DX_2 component). In the case of sample preparation at 6 kbar, the ratio N_{DX_1}/N_{DX_2} is close to one. On the other hand, the amplitude of the slowest component is practically the same in all cases.

The results of the experiments discussed above show that the photo-ionization rates of individual DX configurations can be obtained without the use of pressure. This motivated us to perform such measurements and analysis of the PPC transients for several photon energies. Fig. 2 shows an example of such analysis, which gives us the values of three time constants and of three amplitudes.

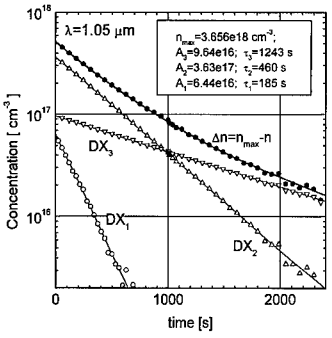

Fig. 2. An example of the PPC transient measured at 77 K and its components. Initial state obtained by simple cooling of the sample to 77 K. (Solid lines): fitted exponentials and their sum.

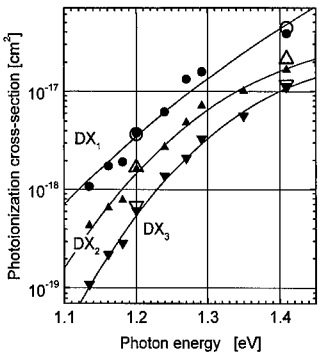

Fig. 3. Photo-ionization cross section found for different alloy-induced configurations of Si–DX center in AlGaAs as a function of light energy. Large open symbols indicate the result obtained after pressure filling at 6 kbar. The continuous lines are the interpolation functions, used to calculate the effective photo-ionization rate shown in Fig. 4.

Let us discuss first the amplitudes of the components A_i. They should correspond to occupancies of the individual configurations, N_{DX_i}, in the initial metastable state of sample at 77 K. These occupancies were determined in Ref. [5] and fitted to give the energy positions corresponding to the DX-center configurations DX_0–DX_2 and their pressure dependence. The calculations give for $P = 0$ the energy difference $E_{DX_2}-E_{DX_1}$ equal to 53 meV and the values of 5.7×10^{16} and 4.2×10^{17} cm^{-3} for the concentration of electrons frozen (at $P = 0$) on DX_1 and DX_2, respectively. The occupation of DX_3 configuration was also estimated assuming that the corresponding energy level was the lowest one and that the separations $E_{DX_3}-E_{DX_2}$ and $E_{DX_2}-E_{DX_1}$ were roughly the same. It was found out that in such a situation the configuration DX_3 was saturated even at $P = 0$. The saturated concentration of trapped electrons equals 10^{17} cm^{-3} — exactly as the amplitude of the slow decay component which, as we have remarked, was found not to be dependent on filling pressure. This justify the attribution of this component to DX_3.

On the other hand, from the analysis of transients we determined: for the main component DX_2 the amplitudes fall in the limits $4.15 \pm 0.5 \times 10^{17}$ cm^{-3}, and for the fast one (DX_1) the values are $6.4 \pm 3 \times 10^{16}$ cm^{-3}. The correspondence between the discussed amplitudes and occupations of the DX configurations at $P = 0$ is evident. This confirms that all the decay components represent photo-ionization of different local configurations of DX center (DX_1–DX_3).

We can calculate the photo-ionization cross sections σ_i for individual alloy-induced DX configurations from the decay times τ_i determined in our analysis. They are given by $\sigma_i(h\nu) = 1/(I(h\nu) \times \tau_i(h\nu))$ where $I(h\nu)$ is the intensity of photon flux, which is known from calibration of optical system.

The cross sections σ_i, thus obtained, are presented as a function of photon energy in Fig. 3, giving the alloy-splitted spectra. We see that photo-ionization threshold energies are different for different configurations of DX center. It should be interesting to compare the shift of this threshold to the splitting of other energetical parameters of DX center. The change of the threshold can be estimated from the horizontal shift of spectra in Fig. 3. The shift between DX_3 and DX_1 spectra, estimated from Fig. 3 for $\sigma_{opt} = 10^{-18}$ cm^2, is close to 0.1 eV which is practically equal to the difference between respective ground level energies found by us for $P = 0$.

The fact that different configurations have different photo-ionization threshold results in the dependence of actual photo-ionization threshold on the sample state. Such a dependence was reported in Ref. [4], where the spectral dependencies of effective photo-ionization cross section, defined as $\sigma_{eff} = 1/I \times d(\ln(N_{DX}))/dt$, were measured. It turned out that the effect produced by the different filling of DX configurations was comparable to the effect produced by application of pressure.

The effective photo-ionization cross section defined as above, is given by the expression

$$\sigma_{eff} = \sum_{i=0}^{3} \sigma_i(h\nu) N_{DX_i}(t) \Big/ \sum_{i=0}^{3} N_{DX_i}(t), \qquad (2)$$

where the variation of each configuration $N_{DX_i}(t)$ is determined from the equation

$$\frac{d(\ln(N_{DX_i}))}{dt} = -I(h\nu)\sigma_i(h\nu).$$

The right-hand side of this equation depends on time, because in the discussed measurement the wavelength was varied linearly with time. Using this equation we have simulated the variation of σ_{eff} for two different initial distributions $N_{DX_i}(t = 0)$: one corresponding to filling at $P = 11.8$ kbar and other one to $P = 0$. In these

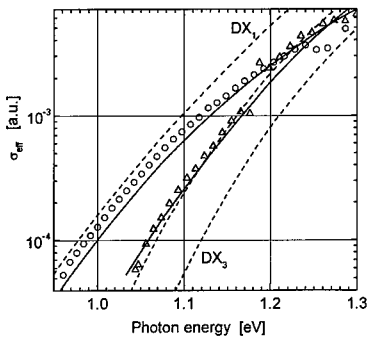

Fig. 4. Spectral dependencies of the effective photo-ionization rate for different filling of DX centers. Points denote two experimental dependencies (taken from Ref. [4]) measured at $P = 0$ and $T = 77$ K after initial pressure filling at 11.8 kbar (circles) and without such preparation (triangles). Solid lines are the results of corresponding numerical simulation (see Eq. (2)). Broken lines represent individual configuration-dependent spectra taken from Fig. 3.

calculations we used for the spectra σ_i the approximation curves shown in Fig. 3. As seen in Fig. 4, this well explains the observed evolution of σ_{eff}. The small shift between the curve corresponding to state prepared at 11.8 kbar and the experiment arises probably from the small accuracy of DX_1 spectrum, caused by small amplitude of the respective component.

The DX_0 configuration cannot be seen in the experiment described here. The energy level corresponding to this configuration is so high that even at the most elevated pressure its occupation is very low (see Ref. [5]) However, it can be filled by using the special filling procedure employed in Ref. [4]. Thus in principle the method of decomposition of PPC transient could be used to find the spectrum also for this configuration.

In summary, we have shown that the decomposition of non-exponential PPC transients provides a valuable method to find the individual photo-ionization spectra for alloy-induced configurations of Si–DX center in AlGaAs. We have found such spectra for the DX_1–DX_3 configurations, in the energy range 1.14–1.41 eV.

Our results suggest that the alloy effect leads to the same splitting of photo-ionization energy as that found for the ground state energy. The spectral dependencies found here explain well the previously reported dependence of the photo-ionization threshold on the initial filling of the DX states.

References

[1] P.M. Mooney, T.N. Theis, S.L. Wright, in: G. Ferenczi (Ed.), Defects in Semiconductors, Vol. 15, Trans. Tech. Publ, Switzerland, 1989, p. 1109.
[2] T.N. Morgan, in: G. Ferenczi (Ed.), Defects in Semiconductors, Vol. 15, Trans. Tech. Publ, Switzerland, 1989, p. 1079.
[3] Z. Su, J.W. Farmer, Phys. Rev. B 46 (1992) 9772.
[4] R. Piotrzkowski, E. Litwin-Staszewska, J. Przybytek, Phys. Stat. Sol. B 198 (1996) 205.
[5] R. Piotrzkowski, E. Litwin-Staszewska, P. Lorenzini, J.L. Robert, Semicond. Sci. Technol. 7 (1992) 103.

ELSEVIER

Physica B 273–274 (1999) 750–753

PHYSICA B

www.elsevier.com/locate/physb

Photoluminescence of highly compensated GaAs doped with high concentration of Ge

Masaru Watanabe[a], Akira Watanabe[b], Masashi Suezawa[a,*]

[a]*Institute for Materials Research, Tohoku University, Sendai 980-8577, Japan*
[b]*Institute for Chemical Reaction Science, Tohoku University, Sendai 980-8577, Japan*

Abstract

We have studied the photoluminescence (PL) properties of Ge-doped GaAs crystals to confirm the validity of a theory developed by Shklovskii and Efros to explain the donor–acceptor pair (DAP) recombination in potential fluctuation. GaAs crystals doped with Ge of various concentrations were grown by a liquid-encapsulated Czochralski method. They were homogenized by annealing at 1200°C for 20 h under the optimum As vapor pressure. Both quasi-continuous and time-resolved PL spectra were measured at 4.2 K. The quasi-continuous PL spectra showed that the peak position shifted to lower energy as the Ge concentration increased, which was consistent with the Shklovskii and Efros's theory. Under very strong excitation in time-resolved measurements, the exciton peak appeared within short periods after excitation and then the peak shifted to that of DAP recombination. This clearly showed that the potential fluctuation disappeared under strong excitation and then recovered as the recombination proceeded.

Keywords: GaAs; Ge; Photoluminescence; Compensation

1. Introduction

Photoluminescence (PL) spectra of semiconductors highly doped with donors and acceptors with similar concentrations, i.e., of highly compensated state, have been studied extensively by both experimental and theoretical approaches [1,2]. Characteristics of PL obtained from experimental study can be summarized as follows. The first characteristic is the absence of PL peaks due to ordinary donor–acceptor pair (abbreviated as DAP hereafter) recombination near the band-gap energy irrespective of co-doping of donors and acceptors. Instead, a broad PL line is observed at a much lower energy than that expected from ordinary DAP recombination. The second characteristic is the response of this broad peak to the excitation intensity and measurement temperature. The peak position shifts to a higher energy at higher excitation intensity with much greater rate than that expected from ordinary DAP recombination. In contrast to ordinary DAP recombination, the peak shifts to a lower energy at higher temperature. Such behaviors are well explained by Shklovskii and Efros [2]. They introduced the idea of potential fluctuation due to inhomogeneous distribution of ionized donors and acceptors in the highly compensated specimen. According to this theory, the above PL peak is due to the recombination of electrons and holes at donors and acceptors, respectively, which exist in potential fluctuation, namely, DAP recombination in the potential fluctuation. We describe this theory in the next section.

In a previous paper [3], we showed the results of PL study of Ge-doped GaAs grown by the LEC-method. Since Ga, Ge and As are neighboring elements on the same row of the periodic table of elements, Ge occupies Ga and As atom sites with almost equal probability in crystals grown from the melt. Hence Ge-doped GaAs is highly compensated. In this case, donors and acceptors are the same element, Ge, and there may be no complication arising from different atomic sizes and different

* Corresponding author. Tel.: + 81-22-215-2040; fax: + 81-22-215-2041.
E-mail address: suezawa@imr.tohoku.ac.jp (M. Suezawa)

0921-4526/99/$ - see front matter
PII: S0921-4526(99)00640-7

atomic numbers which occur when the species of donor and acceptor atoms are different. Our results were semi-quantitatively explained by Shklovskii and Efros's theory (we term their theory SET hereafter). In those studies, we used a quasi-continuous excitation method for PL measurement: Specimens were excited by a 514.5 nm line of Ar ion laser with weak excitation power at a chopping frequency of 75 Hz. According to a consideration shown in the next section, new features of DAP recombination in the potential fluctuation can be expected under much higher excitation intensity. On the other hand, the time-resolved PL spectra may give us invaluable information on the recombination process of DAP in various potential fluctuations. Moreover, the excitation intensity during the excitation period in the time-resolved experiment is very high, even though the average intensity is not high, making it possible to study recombination under very strong excitation. Hence, we studied PL of Ge-doped GaAs mainly concentrating on the time-resolved spectrum.

2. The model

As explained in Section 1, Shklovskii and Efros [2] proposed a theory for the recombination process of DAP in highly doped and highly compensated semiconductors. In such specimens, donors and acceptors are randomly distributed and hence donor- and acceptor-rich regions appear, which are positively and negatively charged, respectively, before excitation. We term the potential due to the above origin as built-in potential. Due to optical excitation, some donors and acceptors capture electron and holes, respectively. Then those electrons and holes recombine and emit light. According to SET, the PL peak ($h\nu$) is given by the following formula:

$$h\nu = E_g - (E_D + E_A) - 2\gamma(r_s), \quad (1)$$

where E_g, E_D and E_A are the band-gap energy, ionization energies of donor and acceptor, respectively, and

$$\gamma(r_s) = (e^2/4\pi\kappa r_s)(N_t r_s^3)^{1/2}, \quad (2)$$

Here, N_t and κ are the total concentration of charged impurities in the specimen and the dielectric constant, respectively, and r_s is the screening radius defined by Eq. (3) for an n-type sample,

$$r_s = N_t^{1/3}/n^{2/3}. \quad (3)$$

Here n is the free electron concentration. They derived the above equations by assuming Gaussian distributions of impurities. The difference in the emission energy between the model of recombination of ordinary DAP and that of DAP in a highly compensated specimen appears in the last term in Eq. (1), namely, $+ e^2/4\pi\kappa r_{D\text{-}A}$ and $- 2\gamma(r_s)$ where $r_{D\text{-}A}$ is the separation of D and A.

In SET, it is considered that highly doped and highly compensated semiconductors are composed of built-in potential due to the inhomogeneous distribution of donors and acceptors and that such potential itself is constant. On the other hand, we consider that such built-in potential itself changes due to excitation of carriers. According to this hypothesis, we roughly classify the excitation intensity into three cases. The first is a weak excitation case where excited carrier concentrations are much smaller than those of the dopants, i.e., donors and acceptors. This situation corresponds to SET since the perturbation of the built-in potential is very small. The second is a middle excitation case where excited carrier concentrations are slightly smaller than those of the dopants. The built-in potential partially disappears since a part of the ionized donors and acceptors becomes neutral by capturing carriers. The third is a strong excitation case where excited carrier concentrations are much larger than those of the dopants and, consequently, the built-in potential disappears. As the recombination proceeds, the built-in potential gradually reappears since donors and acceptors themselves do not change their states except their charge states during excitation and recombination. The PL spectrum in this case changes from that of exciton to that of DAP recombination with various potential fluctuations. As described in the introduction, time-resolved PL measurement is necessary to confirm the above model.

3. Experimental

Specimens were Ge-doped GaAs-grown by a liquid-encapsulated Czochralski method. After cutting and etching the specimens to a size of $6 \times 6 \times 6\ mm^3$, we annealed them at 1200°C for 20 h under the optimum As vapor pressure to homogenize them. Table 1 shows the concentrations of Ge, free carrier, and the conduction type. The free carrier concentrations are much smaller than those of Ge. This means that the concentrations of Ge_{Ga} (a donor. Ge at the Ga sublattice) and Ge_{As} (an acceptor. Ge at the As sublattice) are almost equal. Thus, we conclude that the above crystals are highly compensated. We measured both quasi-continuous and

Table 1
Concentrations of Ge and carriers, and the type of conduction of specimens used in this experiment

Specimen	Ge conc. (cm^{-3})	Carrier conc. (cm^{-3})	Type
#16	9×10^{16}	3×10^{12}	p
#17	3×10^{17}	2×10^{13}	p
#18	2×10^{18}	2×10^{15}	n
#19	2×10^{19}	8×10^{17}	n

time-resolved PL spectra. The quasi-continuous PL measurements were performed mainly at 4.2 K by exciting the specimens with an Ar ion laser (514.5 nm line) with a chopping frequency of 75 Hz, and by detecting PL with a Ge-photodetector. The time-resolved PL measurements were performed by excitation with a Ti-sapphire laser (720 nm line) pumped by an Ar ion laser, and by detecting emission with a picosecond fluorescence spectrometer based on a streak camera. The pulse width and the iteration frequency were about 1.5 ps and 4 MHz, respectively. This system enables photon counting measurements at multiple wavelengths.

4. Results and discussion

Fig. 1 displays quasi-continuous PL spectra of specimens doped with Ge of various concentrations. The excitation intensity was 1.6 mW. The peak position shifts to a lower energy and the line width increases as the Ge concentration increases. The peak position of specimen #16 agrees well with that expected from ordinary DAP recombination. The peak energies of #17, #18 and #19 are much lower than that of #16 and are qualitatively explained by SET. Hence, from the viewpoint of the PL spectrum, we concluded that specimens #17, #18 and #19 correspond to the highly compensated system.

To check the validity of our hypothesis described in Section 2, we measured the PL spectrum under pulse excitation. Fig. 2 displays the results of #17 under different excitation intensities. Signals were summed up within 1.4 ns after excitation. The thin and thick lines correspond to the average excitation intensities of 3.6 and 1.0 mW, respectively. In the case of 3.6 mW excitation, the excited electron concentration is estimated to be about $4.1 \times 10^{17}\,\mathrm{cm}^{-3}$. Hence, it corresponds to high excitation intensity, namely, the built-in potential fluctuation is expected to almost completely disappear because most of the donors and acceptors become neutral by capturing electrons and holes, respectively. In reality, the exciton line, even though the line width is very large, appeared as expected from this hypothesis. On the other hand, the 1 mW excitation corresponds to weak excitation and the built-in potential fluctuation is expected to become weaker but still exist. No exciton line was observed. Fig. 3 displays PL spectra of #17 and #16 with different excitation intensities. They agree well, even though their quasi-continuous PL spectra were much different as shown in Fig. 1. This also clearly supports the speculation that, under strong excitation, both specimens show similar behavior because of the disappearance of the built-in potential. Fig. 4 displays the dependence of the PL spectrum at various periods after excitation. As can be clearly seen, the exciton peak appears shortly after excitation, and then, as time proceeds, it disappears and a peak due to DAP recombination in the potential fluctuation appears at much lower energies. The peak shift to lower energy as the period becomes longer is due to the recovery of the built-in potential fluctuation. Fig. 5 displays the case of #18. In this case, our excitation intensity corresponds to the middle intensity and is not strong enough to make the bands flat. Hence, the PL peak position at 0.2 ns after excitation is rather near that of simple DAP recombination, not that of the exciton. The

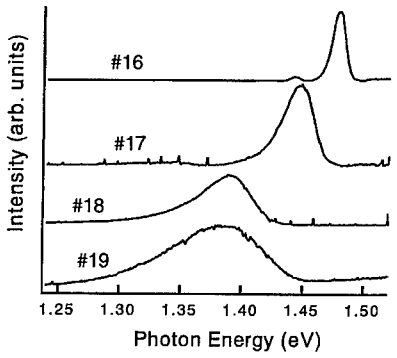

Fig. 1. Quasi-continuous PL spectra of specimens doped with Ge at various concentrations. Excitation intensity was 1.6 mW.

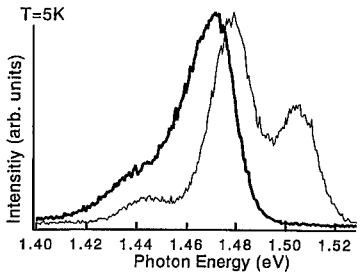

Fig. 2. Excitation intensity dependence of PL spectra of the specimen #17. Thick and thin spectra correspond to the average excitation intensities of 1.0 and 3.6 mW, respectively.

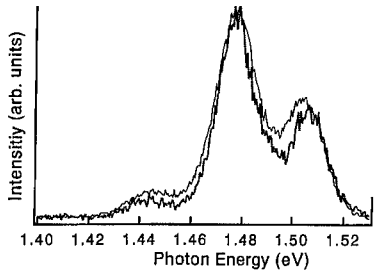

Fig. 3. Comparison of PL spectra of the #16 (dotted line) and #17 (solid line) under different excitation intensities which correspond to strong excitation for each case.

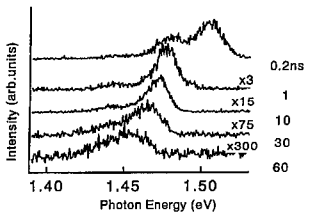

Fig. 4. Time-resolved PL spectra of #17, i.e., spectra at various periods after strong excitation. Numerals (n in xn) attached to spectra mean the multification factors for signal intensities.

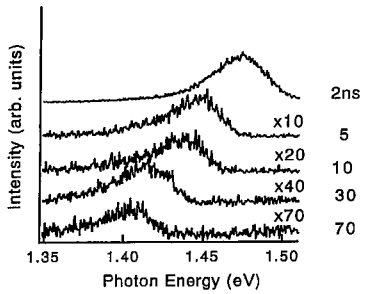

Fig. 5. Time-resolved PL spectra of #18 after middle excitation.

peak shifts to lower energy as the period after excitation becomes longer. This again corresponds to the recovery of built-in potential fluctuation.

5. Conclusion

We studied quasi-continuous and time-resolved PL spectra of GaAs doped with Ge with various concentrations to clarify the change of potential fluctuation in highly doped and highly compensated GaAs under various excitation intensities. Quasi-continuous PL spectra of Ge-doped GaAs were qualitatively explained by the Shklovskii and Efros's theory. Time-resolved PL spectra under strong excitation showed a change of potential fluctuations due to excitation and recombination.

References

[1] H.P. Gislason et al., Phys. Rev. B 47 (1993) 9418, and references therein.
[2] B.I. Shklovskii, A.L. Efros, Elecronic Properties of Doped Semiconductors, Springer, Berlin, 1984, pp. 52–73.
[3] T. Watanabe, M. Suezawa, Jpn. J. Appl. Phys. 36 (1997) 6787.

ELSEVIER

Physica B 273–274 (1999) 754–758

PHYSICA B

www.elsevier.com/locate/physb

Reactions of column-III vacancies and interstitials during Zn diffusion-induced disordering of GaAs/AlGaAs multiple-quantum-well structures

Nguyen Hong Ky*

Institute of Micro- and Optoelectronics, Swiss Federal Institute of Technology, IMO-EPFL, CH-1015 Lausanne, Switzerland

Abstract

Different effects related to the reactions of column-III vacancies and interstitials during Zn diffusion into undoped, Si-doped and Be-doped GaAs/$Al_xGa_{1-x}As$ multilayered structures are investigated by secondary-ion mass spectrometry and photoluminescence. The disordering is observed behind the Zn diffusion front in all multilayered structures. The disordering rate increases with increasing x. The Be out-diffusion is enhanced in the Zn-diffused region. The column-III interstitial supersaturation caused by Zn diffusion is believed to be responsible for the enhancements of Al–Ga interdiffusion and Be out-diffusion. The column-III interstitial supersaturation is affected by the presence of column-III vacancies. For undoped samples, the in-diffusion of column-III vacancies generated at the surface is a driving force for the out-diffusion of column-III interstitials. The effective Zn diffusivity and the disordering rate are enhanced by Be doping because of the increase in acceptor concentration and the abundance of column-III interstitials. For Si-doped samples that contain a high concentration of column-III vacancies, the increase in donor concentration and the mutual annihilation of column-III interstitials and vacancies leads to a retardation of the Zn diffusion.

Keywords: GaAs/AlGaAs; Column-III vacancies; Column-III interstitials; Zn diffusion

1. Introduction

The study of intrinsic defects in III–V semiconductors is an active field of research because the defects affect electrical and optical properties of semiconductor materials [1]. Six elementary intrinsic defect species exist in AlGaAs: vacancies in the column-III sublattice (V_{III}), vacancies in the As sublattice (V_{AS}), column-III interstitials (I_{III}), As interstitials (I_{As}), antisite defects formed by a column-III atom on an As site (III_{As}) or an As atom on a column-III site (AS_{III}). The reactions of intrinsic defects in bulk GaAs have been studied theoretically and experimentally [2–4]. In this article, the reactions of I_{III} and V_{III} during Zn diffusion-induced disordering in GaAs/AlGaAs multiple-quantum-well (MQW) structures are investigated systematically. Since the disordering of GaAs/AlGaAs MQW structures is due to an enhancement of Al–Ga interdiffusion at the layer interfaces [5], I_{III} and V_{III} should be involved in the disordering process.

2. Experiment

Six identical GaAs/AlGaAs MQW samples are grown by molecular-beam epitaxy (MBE) on Si-doped GaAs ($n \approx 2 \times 10^{18}$ cm^{-3}) substrates. These samples consist of the following layers (Fig. 1a): (i) a 0.1 μm thick GaAs cap layer, (ii) a MQW region with 29 GaAs wells (100 ± 4 Å) separated by $Al_xGa_{1-x}As$ barriers (195 ± 5 Å), (iii) a GaAs buffer layer, and (iv) an AlAs marker. The undoped samples A, B, C and D have the values $x \approx 0.1$, 0.2, 0.45, and 1, respectively. The multilayered structure ($x = 0.2$) of sample E is uniformly

* Fax: + 41-21-693-54-80.
E-mail address: ky.nguyen@epfl.ch (N.H. Ky)

0921-4526/99/$ - see front matter
PII: S0921-4526(99)00641-9

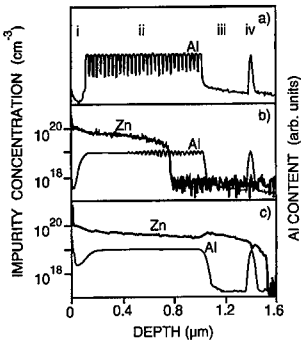

Fig. 1. SIMS concentration profiles of Al and Zn in sample B before (a), and after Zn diffusion at 575°C for 4 h (b) and 16 h (c).

doped with Be at a concentration of $1\times10^{19}\,cm^{-3}$, whereas that of samples F and G are uniformly doped with Si at 5×10^{18} and $1\times10^{19}\,cm^{-3}$, respectively. Zn diffusions are performed at 575°C for different times, t, using the sealed-ampoule technique [6–10] with $ZnAs_2$ source. The secondary-ion mass spectrometry (SIMS) profiles are obtained by a CAMECA IMS 300 system with a Xe^+ primary ion source. The photoluminescence (PL) spectra are measured at 77 K, using the 632.8 nm line of a He–Ne laser as excitation source. The Zn-diffused samples are etched in a solution of $H_2SO_4 : H_2O_2 : H_2O = 1 : 8 : 10$ to form terraces with different etching depths, d_e, below the sample surface. The PL spectra taken at different d_e are characterized for a probe region within 0.5–0.7 μm below the etching surface.

3. Results and discussion

After Zn diffusion into sample B for 4 h (Fig. 1b), a Zn profile with an abrupt diffusion front at 0.78 μm is observed. The Al profile exhibits an ordered region ahead of the Zn diffusion front where the MQW structure remains intact. Behind the diffusion front, the Al signal oscillation amplitude is gradually reduced, indicating the disordering of the MQW structure. A partially disordered region is followed by a totally disordered region where the MQW structure is converted into an AlGaAs alloy. After Zn diffusion for 16 h (Fig. 1c), the diffusion front passes beyond the MBE grown region, the whole MQW structure is totally disordered. An out-diffusion of Al from the disordered MQW region into adjacent GaAs layers is seen. Hence, Al atoms are immobile in the undiffused regions, whereas they become mobile in the Zn diffused regions. Fig. 2 shows that the effective Zn diffusivity, D_{Zn}, and the rate of total disordering, R_{tot} increase with increasing x. The values of D_{Zn} and R_{tot} are approximately estimated as $d^2/4t$, where d is the diffusion depth or the totally disordered depth.

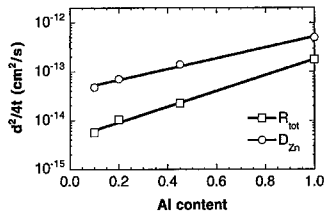

Fig. 2. The effective Zn diffusivity and the total disordering rate in undoped GaAs/$Al_xGa_{1-x}As$ MQW structures at 575°C as a function of x.

The PL spectrum of the as-grown sample B (Fig. 3a) shows PL lines at 1.535 eV (E_{el-hh1}) and 1.547 eV (E_{el-lh1}) due to the recombinations of $n = 1$ electron–heavy hole and $n = 1$ electron–light hole excitons confined in the quantum wells (QWs). The PL line at 1.511 eV (E_b) is related to excitonic recombinations in the GaAs buffer [11]. After Zn diffusion (Fig. 3b), a new PL line appears at 1.509 eV (eA_{Zn}). It is due to the recombination of electrons at the $n = 1$ subband with Zn acceptors in the Zn diffused QWs. At $d_e = 0.4$ μm, the eA_{Zn} line dominates the spectrum, but it disappears in the spectrum taken at $d_e = 0.9$ μm in the region ahead of the diffusion front. This indicates that the eA_{Zn} line comes from the QWs behind the diffusion front where Zn atoms incorporate onto column-III sites and act as acceptors (Zn_s). The Zn diffusion is performed by the fast diffusion of Zn interstitials (Zn_i) and their change-over to occupy column-III sites. The interchange between Zn_i and Zn_s can be described by the kick-out mechanism [12]:

$$Zn_i^+ \Leftrightarrow Zn_s^- + I_{III}^+ + h^+, \quad (1)$$

where h denotes a hole. Eq. (1) expects that I_{III} are formed at the Zn diffusion front. As the diffusivity of Zn_i, D_i, is larger than that of I_{III} [12], an I_{III} supersaturation develops behind the diffusion front. The excess I_{III} could nucleate to form dislocation loops that have been observed in the diffused region [13]. An expansion of the lattice constant due to the I_{III} supersaturation has been detected by X-ray diffraction technique [6]. The I_{III} supersaturation enhances the Ga–Al interdiffusion, resulting in the disordering of the MQW structure. Because of the interdiffusion at the barrier-well interface, a blue shift of excitonic peaks is seen in the PL spectra [6]. For MQW structures, the disordering levels of the wells are different. Therefore we observe a broad PL ban ($e–h_a$) on the high-energy side of the E_{el-hh1} line. The peak position of the $e–h_a$ band continues to shift to higher energy until the structure is completely disordered [6]. The PL band at 1.26 eV ($D–V_{III}$) due to the donor–V_{III} complex recombination [6–10] appears in the PL spectra (Fig. 3b). Since Zn diffusions are carried out under As-rich condition, the samples are surrounded by As_4 vapor. Gallium Frenkel defects could be formed at the surface of the GaAs cap

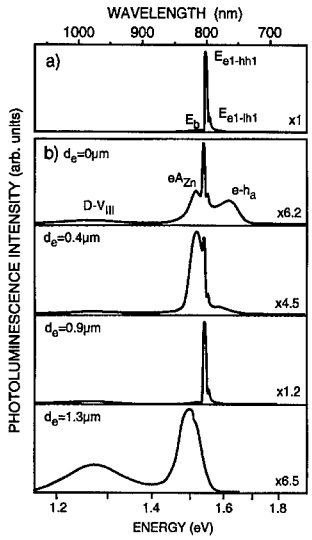

Fig. 3. 77 K PL spectra of sample B: (a) taken on the sample surface before Zn diffusion; (b) taken at different etching depths, d_e, after Zn diffusion at 575°C for 4 h.

layer:

$$Ga_{Ga} \Leftrightarrow V_{Ga} + I_{Ga}. \quad (2)$$

I_{Ga} can react with As atoms in the vapor to form additional unit cells:

$$\tfrac{1}{4}As_4 + I_{Ga} \Leftrightarrow GaAs. \quad (3)$$

Hence, V_{III} are generated at the sample surface. They diffuse into the bulk and form complexes with residual donors. At all values of the chemical potential, V_{III} and I_{III} have opposite charges and attract each other, increasing the probability of their mutual annihilation [2]. The I_{III} moving toward the surface can annihilate the V_{III} diffusing into the bulk. As a consequence, the intensity of the D–V_{III} band decreases with increasing d_e. The in-diffusion of V_{III} may be a driving force for the out-diffusion of I_{III}. At $d_e = 0.9$ μm, the spectrum is almost the same as that of the as-grown sample. The undiffused QWs are in the depletion region of the p–n junction formed at the Zn diffusion front. The electric field at the p–n junction induces a Stark shift of the E_{el-hh1} peak to lower energy (Fig. 3b). The disordering only occurs behind the diffusion front because the electric field prevents I_{III}^+ from diffusing into the n side of the junction. At $d_e = 1.3$ μm, we obtain the PL spectrum of the GaAs buffer and GaAs : Si substrate. Since the electric field keeps V_{III}^- on the n side of the junction, the observed increase in intensity of the D–V_{III} PL band in the region ahead of the Zn diffusion front is due to an accumulation of V_{III}.

SIMS profiles obtained for samples B, E, and G after Zn diffusion for 4 h (Fig. 4) clearly shows the effect of

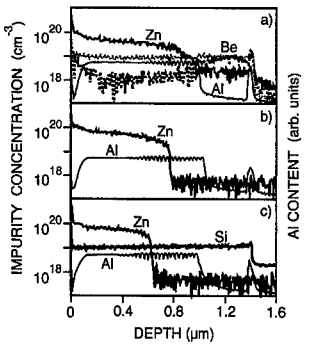

Fig. 4. SIMS concentration profiles of Al, Si, Be, and Zn in samples E (a), B (b) and G (c) after Zn diffusion at 575°C for 4 h. The Be profile before Zn diffusion (thin dot curve) is given in (a).

background doping on D_{Zn} and R_{tot}. The Zn diffused and totally disordered regions are largest in Be-doped sample E, while they are smallest in Si-dopped sample G. Moreover, an enhancement of Be out-diffusion is induced by Zn diffusion (Fig. 4a). The Be profile in the region ahead of the Zn diffusion front remains intact, whereas the Be concentration in the Zn-diffused region is significantly reduced. If Be diffuses via a substitutional-interstitial mechanism similar to that described by Eq. (1), the following equation can be written for Be out-diffusion:

$$Be_s^- + I_{III}^+ + h^+ \Leftrightarrow Be_i^+, \quad (4)$$

where Be_s^- and Be_i^+ are substitutional and interstitial Be atoms, respectively. Combining Eqs. (1) and (4), we obtain

$$Zn_i^+ + Be_s^- \Leftrightarrow Zn_s^- + Be_i^+. \quad (5)$$

Hence, the Be out-diffusion can be enhanced in the Zn-diffused region. We do not observe any change in the Si profiles after Zn diffusion (Fig. 4c). Using the electroneutrality conditions for Zn diffusion into n- and p-type semiconductors, and assuming that Zn_s^- are immobile, we can deduce D_{Zn} from the Fick's second law for Zn diffusion [3,7]:

$$D_{Zn} \cong D_i K[I_{III}](2[Zn_s] - N_D) \quad \text{for Si-doped samples,} \quad (6)$$

$$D_{Zn} \cong D_i K[I_{III}](2[Zn_s] - N_A) \quad \text{for Be-doped samples,} \quad (7)$$

where [ ] denotes concentration; K is the equilibrium constant of Eq. (1); N_A and N_D are the background concentrations of acceptor and donor, respectively. Eqs. (6) and (7) show that D_{Zn} is controlled by the I_{III} concentration behind the Zn diffusion front, $[I_{III}]$, and N_A or N_D. For undoped samples, N_A and N_D are negligible,

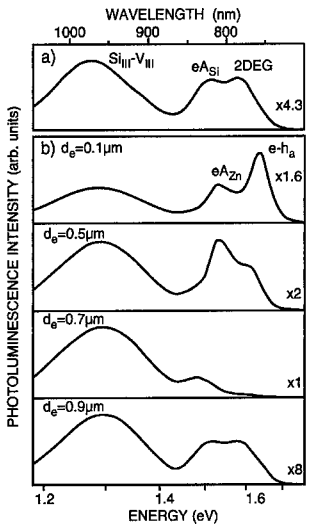

Fig. 5. 77 K PL spectra of sample F: (a) taken on the sample surface before Zn diffusion; (b) taken at different etching depths, d_e, after Zn diffusion at 575°C for 4 h.

D_{Zn} is determined by $[I_{III}]$ which is affected by V_{III} in-diffusion from the surface. For Si-doped samples, most of Si atoms occupy column-III sites and act as donors. A two-dimensional electron gas (2DEG) is formed due to a high concentration of the free carriers confined in the wells. A broad 2DEG-related PL line (2DEG) is observed in the PL spectrum of heavily Si-doped sample (Fig. 5a) [7]. Since Si atoms incorporate also into As sites and act as acceptors, the PL line at about 1.49 eV (eA_{Si}) is due to the transition of electrons in the 2DEG to the Si acceptors [7]. The PL band (Si_{III}–V_{III}) due to Si donor–V_{III} complex dominates the PL spectrum because heavily Si-doped samples contain a high concentration of V_{III} [3,7]. The intensity ratio between the Si_{III}–V_{III} band and the PL lines due to band-to-band transition is considered to be proportional to the concentration of the Si_{III}–V_{III} complex [3,7,8]. After Zn diffusion (Fig. 5b), the eA_{Zn} and e–h_a emission lines appear, indicating the incorporation of Zn atoms and the disordering in the Zn-diffused region at $d_e < 0.7$ μm. A V_{III} accumulation in the region ahead of the Zn diffusion front is clearly observed ($d_e = 0.7$ μm). At $d_e = 0.9$ μm the spectrum is similar to that of Fig. 5a. In particular, the concentration of the Si_{III}–V_{III} complex is significantly reduced in the Zn-diffused region. This indicates a strong mutual annihilation of V_{III} and I_{III}. According to Eq. (6), an increase in N_D and a reduction of $[I_{III}]$ result in a retardation of Zn diffusion in Si-doped samples. The PL spectrum of sample E before Zn diffusion (Fig. 6, $t = 0$ h) is dominated by the PL line at 1.513 eV due to the transition of electrons from the $n = 1$ subband to Be acceptor level in the QWs (eA_{Be}). The emission band due to the recombination of V_{As}–Be acceptor complex (V_{AS}–Be) is observed at 1.34 eV, indicating a high V_{As} concentration in sample E. The presence of high V_{As} concentration can result in single hops of column-III atoms forming III_{As} and V_{III}. This is confirmed by the observation of the III_{AS}-related PL line at 1.47 eV and the D–V_{III} PL band. On the other hand, sample E may contain I_{III} that can occupy V_{As} to form III_{As}. After Zn diffusion for 4 h, the eA_{Be} PL line is replaced by the eA_{Zn} and e–h_a PL lines. The decrease in intensity of the V_{As}–Be and D–V_{III} PL bands and the increase in intensity of the III_{As} PL line indicate that $[I_{III}]$ increases in the sample during Zn diffusion. The increase in N_A and $[I_{III}]$ in Be-doped samples leads to an enhancement of Zn diffusion, as expected in Eq. (7). Our results show that the combined effects of the Fermi-level and the reactions of V_{III} and I_{III} play an important role in the disordering process.

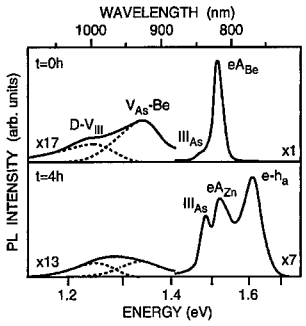

Fig. 6. 77 K PL spectra of sample E before Zn diffusion ($t = 0$ h) and after Zn diffusion at 575°C for 4 h.

Acknowledgements

The author thanks F. Morier-Genoud and D. Martin for the MBE growth of samples, B. Blanchard for SIMS measurements, J.D. Ganière and F.K. Reinhart for continuous support.

References

[1] J.C. Bourgoin, H.J. von Bardeleben, D. Stievenard, J. Appl. Phys. 64 (1988) R65.
[2] G.A. Baraff, M. Schlüter, Phys. Rev. Lett. 55 (1985) 1327.
[3] N.H. Ky, F.K. Reinhart, J. Appl. Phys. 83 (1998) 718.
[4] N.H. Ky, L. Pavesi, D. Araújo, J.D. Ganière, F.K. Reinhart, J. Appl. Phys. 70 (1991) 3887.
[5] D.G. Deppe, N. Holonyak Jr., J. Appl. Phys. 64 (1988) R93.
[6] N.H. Ky, J.D. Ganière, M. Gailhanou, B. Blanchard, L. Pavesi, G. Burri, D. Araújo, F.K. Reinhart, J. Appl. Phys. 73 (1993) 3769.
[7] N.H. Ky, J.D. Ganière, F.K. Reinhart, B. Blanchard, J. Appl. Phys. 79 (1996) 4009.
[8] N.H. Ky, J.D. Ganière, F.K. Reinhart, B. Blanchard, J.C. Pfister, J. Appl. Phys. 74 (1993) 5493.

[9] N.H. Ky, L. Pavesi, D. Araújo, J.D. Ganière, F.K. Reinhart, J. Appl. Phys. 69 (1991) 7585.
[10] N.H. Ky, F.K. Reinhart, J.D. Ganière, B. Deveaud, B. Blanchard, J. Appl. Phys. 86 (1999) 259.
[11] N.H. Ky, J.D. Ganière, M. Gailhanou, F. Morier-Genoud, D. Martin, F.K. Reinhart, Phys. Rev. B 46 (1992) 6947.
[12] T.Y. Tan, U. Gösele, S. Yu, Crit. Rev. Solid State Mater. Sci. 17 (1991) 47.
[13] I. Harrison, H.P. Ho, B. Tuck, M. Henini, O.H. Hughes, Semicond. Sci. Technol. 4 (1989) 841.

ELSEVIER

Physica B 273–274 (1999) 759–761

PHYSICA B

www.elsevier.com/locate/physb

Ab initio calculation of local vibrational modes. Application to GaAs:C and cubic GaN:As

C. Göbel, K. Petzke, C. Schrepel, U. Scherz*

Institut für Theoretische Physik, Technische Universität Berlin, Hardenbergstr. 36, D-10623 Berlin, Germany

Abstract

Ab initio density-functional theory is used to calculate interatomic forces and the dynamical matrix of cubic GaN and GaAs with and without point defects. The Green's function method and the Dyson equation is applied to obtain the change of the density of phonon states due to the defect, from which we find not only the local vibrational modes and their isotope shifts of GaAs:C outside the host-phonon bands, but also localized modes at the edges of the phonon bands and resonances inside the phonon bands. Our results indicate that recently observed low-energy Raman peaks at a layer of cubic GaN on a GaAs substrate can be interpreted as resonances inside the acoustical phonon bands of GaN or GaAs. The energetic positions of these resonances are not characteristic for the defect but occur at specific energies of the density of the host-phonon states.

Keywords: Local vibrations; Ab initio calculation; GaAs; GaN

1. Introduction

Density functional theory has successfully been used to calculate the phonon-dispersion curves of various crystals [1,2]. The Green's function technique together with a valence-force model to describe the defect properties has then been applied to calculate local vibrational modes (LVM) well above the optical phonon bands for point defects in GaAs [3]. The interatomic forces in the vicinity of the defect, however, can also be obtained from density-functional theory supercell methods [4,5]. This is shown by the comparison of the calculated local vibrational split-off mode of GaAs:C, its isotope shift and its ligand isotope shift with the experimental observation. Our method of the ab initio calculation of the dynamical matrix of the perfect crystal and of the crystal containing a defect is completed by the Green's function technique, which gives us the density of phonon states of the perfect crystal and the change of the density of phonon states due to the defect from first principles. This enables us to distinguish between the LVMs outside the host-phonon bands and localized modes inside but close to the edges of the host-phonon bands, which also show isotope shifts with respect to the masses of the defect atoms. We further find a number of resonances inside the host-phonon bands, the energy of which are nearly independent of the interatomic forces in the vicinity of the defect or the impurity mass. Especially in the acoustical phonon bands, these resonances occur at specific energies of the host-phonon bands and are not characteristic for the defect but are characteristic for the host crystal. We discuss our theoretical results of resonances inside the host-phonon bands of cubic GaN and GaAs with respect to observed Raman peaks at cubic GaN layers on a GaAs substrate [6].

2. Theoretical method

Our method is based on an ab initio calculation of the dynamical matrix for a perfect crystal and for

* Corresponding author. Tel.: + 49-30-314-23198; fax: + 49-30-314-21130.

E-mail address: scherz@physik.tu-berlin.de (U. Scherz)

0921-4526/99/$ - see front matter
PII: S0921-4526(99)00642-0

a crystal with a point defect. We used density-functional theory in the local density approximation applied to supercells and a plane wave expansion. We use fully separable pseudopotentials of the Troillier–Martins scheme for 3d valence electrons and of the Bachelet–Hamann–Schlüter–Chiang scheme for the 3d core electrons with a nonlinear core correction for the exchange and correlation potential. The inter-atomic forces were obtained from the displacements of one atom inside the supercell. Because of the periodicity with respect to the supercell, the displaced atom is repeated simultaneously giving a lattice of displaced atoms. We eliminate this effect by calculating an adequate number of supercells of different geometries [4]. The dynamical matrices were then set up by taking all forces up to the 11th nearest neighbour into account, leading to 72 different force constants according to symmetry requirements. The long-range electrostatic interaction was determined by an Ewald summation and the effective charge of the perfect crystal was fitted to reproduce the experimental splitting of the optical phonons at the Γ-point [2]. In the case of the perturbed crystal we took the lattice relaxation of the atoms up to the fourth nearest neighbour into account, which changed the force constants considerably.

We used a modified computer program from the Fritz–Haber Institute, Berlin [7], optimized for the massive parallel Cray computer. The supercells contained between 40 and 96 atoms, and the cut-off energy was between 33 and 60 Ry and 80 Ry when taking 3d-electrons into account.

The eigenvalues and eigenfunctions of the dynamical matrix of the perfect crystal were used to calculate the Green's function. The Green's function of the crystal containing a defect was then obtained from the change of the interatomic forces and atomic masses using the Dyson equation. The LVMs outside the host-phonon bands were obtained from the singularities of the Green's function of the perturbed crystal. The energies of the localized modes near the band edges and resonances inside the phonon bands were obtained from the difference of the density of phonon states (DPS) of the perturbed and of the perfect crystal.

3. Local vibrational modes at GaAs:C

The carbon impurity at arsenic site in GaAs has been extensively studied because of the remarkable isotopic fine structure of the LVM far above the optical phonon bands [8]. We calculated the energy of the LVM for the isotopes ^{12}C and ^{13}C and four nearest neighbours ^{69}Ga or ^{71}Ga, and compared our results in Table 1 with the corresponding Raman lines of Ref. [9]. It can be seen that the impurity isotope shift and the ligand isotope shift agree well with the experimental observation. The difference between the calculated and observed energies of the LVM is below 1% and is probably due to the approximations adopted here, e.g. the limited number of force constants and the neglect of anharmonic forces. The isotope shift of the energy $\hbar\omega$ of an LVM with respect to mass M of an atom is directly connected with the relative vibration amplitude $A/\sqrt{M}$ of that particular atom by the general formula

$$\frac{M\,\mathrm{d}\hbar\omega}{\hbar\omega\,\mathrm{d}M} = -\frac{1}{2}A^2$$

with $0 \leqslant A^2 \leqslant 1$. Therefore, correctly calculated isotope shifts due to impurity and ligand masses demonstrate that the interatomic forces had been calculated correctly.

Table 1
Comparison of the calculated energy of the LVM and impurity and ligand isotope shifts with experimental results after Ref. [7]. All energies are in meV

LVM	Exp.	Theory
^{13}C–^{69}Ga	69.67	69.22
^{12}C–^{69}Ga	72.27	71.93
^{12}C–^{71}Ga	72.21	71.85
Isotope shifts		
^{13}C–^{12}C	2.60	2.71
^{69}Ga–^{71}Ga	0.06	0.08

4. Low-energy Raman lines of cubic GaN/GaAs

Low-energy Raman peaks between 7.2 and 31.0 meV had been observed at a layer of cubic GaN on a GaAs substrate [6]. These energies are within the acoustical phonon bands of GaN and GaAs. In order to identify these defect-induced lines, we calculated arsenic defects at nitrogen site in GaN as a possible defect candidate. Because of the much heavier mass of As compared to N we calculated an As impurity at nitrogen site in cubic GaN and found localized modes near 43 meV, which had not been seen by Raman scattering [6]. However, the difference of the DPS between the perfect cubic GaN and the perturbed crystal showed a number of low-energy resonances inside the acoustical phonon bands. These resonances exhibited no isotope shifts and were nearly independent of the defect properties, but were characteristic for the DPS of the perfect crystal. It is therefore not a contradiction that some of these resonances coincide with the Raman peaks observed at a layer of cubic GaN on a GaAs substrate. As can be seen from Fig. 1, the calculated resonances were found at specific energies of typical changes of the DPS of the perfect crystal.

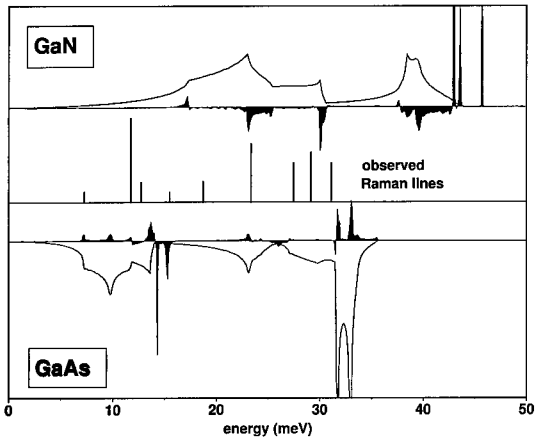

Fig. 1. Calculated density of acoustical phonon states of cubic GaN and resonances caused by an As impurity (upper part) and density of phonon states of GaAs and resonances due to a C impurity (lower part) together with Raman peaks of different intensity observed at a layer of cubic GaN on a GaAs substrate after Ref. [6].

Table 2
Calculated resonances inside the phonon bands of GaAs:C (first column) and inside the acoustical phonon bands of cubic GaN:As (second column) compared with Raman peaks observed by Siegle et al. [6] at a layer of cubic GaN on a GaAs substrate (third column). All energies are in meV

GaAs:C	GaN:As	GaN/GaAs
7.2		7.2
9.6		
11.7		11.8
13.6		12.7
		15.5
	17.2	18.7
23.1	23.1	23.3
	25.3	
26.9		27.4
	30.1	29.1
31.7		31.0
33.0		
	37.5	
	39.5	

We also calculated the carbon-induced localized modes and resonances inside the acoustical phonon bands of GaAs. A localized mode was found at 14.4 meV and is shown in Fig. 1 together with the resonances inside the GaAs phonon bands. There was no indication of the existence of the GaAs:C defect in the sample used for the Raman scattering of Ref. [6]. Nevertheless, the calculated resonances are not characteristic for this defect and may also be caused by other defects, which might be present at or close to the interface between the GaN layer and the GaAs substrate.

Our results of the resonances of GaAs and GaN are compiled in Table 2 together with the observed Raman peaks of Ref. [6]. Though our calculations of the localized modes of GaAs:C and GaN:As give no indication that these impurities were present in the samples used, several of the observed low-energy Raman peaks coincide with calculated resonances of GaAs or GaN. We therefore, tentatively assign these low-energy Raman peaks to resonances of GaAs or GaN, respectively. The observation of such low-energy Raman peaks is then an indication of defects in the sample, but contains little information about the chemical nature of these defects.

Acknowledgements

The authors are grateful to Matthias Scheffler for the provision of the computer program. We thank the Konrad-Zuse-Zentrum für Informationstechnik, Berlin and the Zentraleinrichtung Rechenzentrum of the Technische Universität, Berlin for their support and the provision of computing facilities.

References

[1] P. Giannozzi, S. de Gironcoli, P. Pavone, S. Baroni, Phys. Rev. B 43 (1993) 7231.
[2] K. Petzke, C. Schrepel, U. Scherz, Z. Phys. Chem. 201 (1997) 317.
[3] D.A. Robbie, M.J.L. Sangster, P. Pavone, Phys. Rev. B 51 (1995) 10489.
[4] K. Petzke, Phys. Rev. B, in press.
[5] C. Göbel, K. Petzke, C. Schrepel, U. Scherz, Eur. Phys. J. B 11 (1999) 559.
[6] H. Siegle, A. Kaschner, P. Thurian, A. Hoffmann, I. Broser, C. Thomsen, Mater. Sci. Forum 258–263 (1997) 1197.
[7] R. Stumpf, M. Scheffler, Comp. Phys. Commun. 79 (1994) 447.
[8] R.C. Newman, E.G. Grosche, M.J. Ashwin, B.R. Davidson, D.A. Robbie, R.S. Leigh, M.J.L. Sangster, Mater. Sci. Forum 258–263 (1997) 1.
[9] R.S. Leigh, R.C. Newman, M.J.L. Sangster, B.R. Davidson, M.J. Ashwin, D.A. Robbie, Semicond. Sci. Technol. 9 (1994) 1054.

ELSEVIER

Physica B 273–274 (1999) 762–765

PHYSICA B

www.elsevier.com/locate/physb

Dopant-related metastable defects in particle irradiated n-GaAs

M.J. Legodi*, F.D. Auret, S.A. Goodman

Department of Physics, University of Pretoria, Pretoria 0002, South Africa

Abstract

We show using deep-level transient spectroscopy (DLTS) that particle irradiation of GaAs : Si and GaAs : S introduces a defect Eα3 and a new defect EαIR10, respectively, and both these defects are metastable. We determine that Eα3 and EαIR10 are located 0.37 and 0.26 eV below the conduction band, respectively. Eα3 is removed by hole-injection and re-introduced during a first-order transformation under zero-bias annealing (at temperature $T > 160$ K, and activation energy $\Delta E = 0.40$ eV), or during reverse-bias annealing ($T > 190$ K and $\Delta E = 0.53$ eV). EαIR10 is removed by zero-bias annealing and re-introduced in the region 230–260 K, under predominantly first-order kinetics (activation energy $\Delta E = 0.58$ eV). Our results suggest that both defects Eα3 and EαIR10 are defect-impurity complexes that involve the Si and S dopants, respectively.

Keywords: GaAs; Defects; Radiation; Metastability

1. Introduction

Metastability refers to the reversible transformation of defects from one structural configuration to another, depending on the electric field in the semiconductor, the temperature and carrier injection conditions. Metastable defects are important from both a fundamental physics and a device application perspective. Buchwald et al. [1] and Wada et al. [2] have shown that metastability can affect semiconductor properties. Metastable defects lying deeper in the band gap could be important as irradiation-induced carrier removal centers. Recently, a memory devise employing the metastable property of the EL2 defect in GaAs has been demonstrated by Alex et al. [3]. It is thus necessary to study metastable defects in terms of their reversible transformations, in order to control and utilize them in devices. It has been suggested that some metastable defects are dopant related in GaAs [4]. DLTS is a convenient and powerful technique for studying metastable defects that are characterized by a deep level(s) in the band gap: cooling cycles and different biases can be used to induce controllably the different metastable states, and these could then be studied. In this paper, we study the DLTS-based reversible transformations of particle-irradiation-induced metastable defects, Eα3 and EαIR10, in epitaxial GaAs : Si and GaAS : S, respectively. We determine their activation energy for removal and re-introduction, their energy position in the band gap and their electron capture cross sections, and we conclude by suggesting that the two defects, Eα3 and EαIR10, are related to the silicon and sulfur dopants, respectively.

2. Experimental details

Metal-organic vapor-phase epitaxy (MOVPE) grown n-GaAs layers were used. Ni/AuGe/Au ohmic contacts were deposited on the n^+ backsides of the samples. Circular Pd Schottky barrier contacts, 1200 Å thick and 0.77 mm in diameter were resistively deposited on the epitaxial layers. Samples doped with silicon had free carrier densities: 1.1×10^{16} and 8×10^{16} cm^{-3}. Free carrier densities corresponding to the sulfur-doped samples were 1.7×10^{16} and 2.8×10^{16} cm^{-3}. Thereafter, the samples were irradiated with 5.4 MeV He-ions (α-particles) from an ^{241}Am radionuclide source to a dose of 1×10^{11} cm^{-2}. Furthermore, the sulfur-doped samples

* Corresponding author. Tel.: + 27-12-420-4413/2684; fax: + 27-12-362-5288.

E-mail address: mlegodi@scientia.up.ac.za (M.J. Legodi)

0921-4526/99/$ - see front matter
PII: S0921-4526(99)00643-2

were irradiated with 0.2–2.4 MeV electrons (β-particles) from Sr-90, 1 MeV protons and 10 and 12 MeV electrons from particle accelerators. Chemical cleaning was performed prior to the deposition of both ohmic and Schottky contacts.

DLTS using a lock-in amplifier-based system was used to study the defects. The bias and pulse sequence consisted of a reverse bias V_r on which pulses with amplitude V_p and frequency, f, were superimposed. The DLTS defect signatures (energy level in the band gap, E_T, and apparent capture cross section for electrons, σ_{na}) were calculated from Arrhenius plots of $\log(T^2/e)$ versus $1/T$, where e is the emission rate at the DLTS peak temperature T.

3. Results and discussions

After irradiation with 5.4 MeV α-particles, both the DLTS spectra of the Si- (Fig. 1(a)) and S-doped (Fig. 1(d)) samples show the presence of peaks: Eα1–Eα5 and Eα8 for the $1.1\times10^{16}\,cm^{-3}$ Si-doped samples; and EαIR1–EαIR4 and EαIR10, for the $1.7\times10^{16}\,cm^{-3}$ S-doped samples. The electronic properties of Eα1–Eα5 have been reported previously [5,6]; and, it was shown that Eαl, Eα2 and Eα4 have the same DLTS signatures as the well-known electron irradiation-induced defects E1, E2 and E3 [7], respectively, which in turn are related to vacancy-interstitial pairs in the As sublattice [7]. Also, the DLTS signatures of EαIR1, EαIR2 and EαIR4 are similar to those of Eα1, Eα2 and Eα4, respectively.

Auret et al. have reported on the metastable characteristics of Eα3 [4]. The defect Eα3 is present in Fig. 1(c),

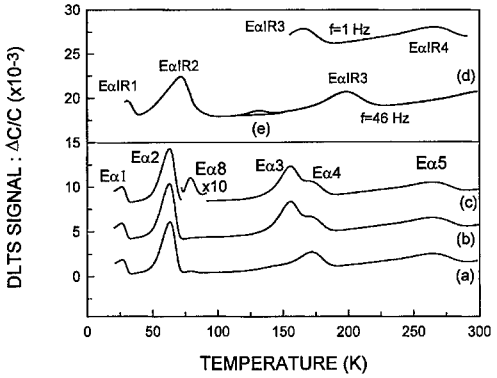

Fig. 1. DLTS spectra of α-particle-irradiated GaA : Si ($f=1$ Hz, $V_r=2$ V and $V_p=1.9$ V): (a) after applying a forward current density of 5.6 A cm^{-2} at 105 K; (b) after zero bias cooling; (c) after reverse bias (2 V) cooling; DLTS spectra of α-particle-irradiated GaAs : S ($V_r=3$ V and $V_p=2.8$ V): (d) after reverse bias (4 V) cooling; (e) after zero bias cooling.

recorded after cooling the $1.1\times10^{16}\,cm^{-3}$ Si-doped samples from room temperature under 2 V reverse bias (RB). Eα3 is also present in the DLTS spectra of Fig. 1(b), recorded after cooling down a similar Si-doped sample from 300–20 K, under zero bias (ZB). Fig. 1(a) was recorded after applying a forward current density of 5.6 A cm^{-2} for 10 s to the sample at 105 K and then cooling it down to 20 K, before recording the DLTS up-scan. We were able to reversibly introduce and remove Eα3 from the DLTS spectra through applying DLTS conditions used in recording Figs. 1(a)–(c). Fig. 1(d) and (e) are DLTS spectra of the $1.7\times10^{16}\,cm^{-3}$ S-doped GaAs, recorded after 5.4 MeV irradiation, showing the presence and absence, respectively, of the metastable EαIR10 defect. EαIR10 is present after 4 V reverse bias (RB) cooling of the samples and it disappears from the spectra (Fig. 1(e)) after zero bias cooling. The above appearance and disappearance of Eα3 and EαIR10 are completely reversible. Normally, when a stable defect, for example, Eα3, transforms into its metastable state the new (metastable) state appears as another deep level detectable by DLTS techniques. This is not always the case, and for both Eα3 and EαIR10, we have not been able to detect their metastable configurations through DLTS. This may be so because, the DLTS detection conditions, as used here, may modify or anneal these metastable states or they may not be suitable for their detection. For discussion, we will refer to these metastable states as Eα3* and EαIR10*.

The DLTS signatures of Eα3 and EαIR10 (E_T and σ_{na}) were determined as: ($E_C-0.37$ eV, $9\times10^{-14}\,cm^2$) and ($E_C-0.26$ eV, $4.4\times10^{-13}\,cm^2$), respectively. Also, the capture cross section of Eα3 was found to be thermally activated [4].

The temperature dependency of the removal and re-introduction reaction rates are found to obey the relation

$$\nu(T)=\nu_0\exp(-\Delta E/kT), \tag{1}$$

where ΔE is the energy barrier for removal or re-introduction. From the ν_0 and ΔE values so calculated, the Eα3 → Eα3* transformation can be summarized as [4]

$$E\alpha3\rightarrow E\alpha3^*:\quad \nu(T)=2.14\times10^4\exp(-0.041/kT).$$

This reaction involves the capture of holes [4].

Isochronal annealing indicated that Eα3 is re-introduced at temperatures above 160 K under ZB, or above 190 K under RB, and from isothermal annealing in these temperature ranges the transformation kinetics of Eα3* → Eα3 were obtained. Plots of $\ln[\{N_T-N(t)\}/N_T]$ versus time (t) at different temperatures were straight lines, indicating that the transformation obeys first-order kinetics. From the ν_0 and ΔE values calculated, the

Eα3* → Eα3 transformations can be summarized as [4]

Eα3* → Eα3:

$v = (6 \pm 2) \times 10^8 \exp[-(0.40 \pm 0.01)/kT]$ (zero bias),

$v = (6 \pm 2) \times 10^9 \exp[-(0.53 \pm 0.01)/kT]$

(2 V reverse bias).

The process Eα3* → Eα3 occurs via hole emission to the valence band [4].

For the introduction reaction EαIR10* → EαIR10, a plot of $\ln[\{N_T - N(t)\}/N_T]$ versus time (t) at different temperatures in the range 230–260 K also yielded a straight line, indicating a first-order reaction. The reaction rate for the first-order removal EαIR10 → EαIR10*, is given by a straight-line plot of $\ln[N(t)/N_T]$ versus time (t) at different temperatures in the range 230–260 K. The corresponding reaction rates were determined as

EαIR10 → EαIR10*:

$v = 1 \times 10^{12 \pm 1} \exp(-0.76 \pm 0.08/kT)$, ZB removal,

EαIR10* → EαIR10:

$v = 3 \times 10^{7 \pm 1} \exp(-0.58 \pm 0.08/kT)$

RB introduction.

The exponential pre-factor $\nu_0 = 1 \times 10^{12 \pm 1}\,s^{-1}$, relates to elementary atomic jumps [8], and the re-introduction could involve emission of electrons by multiphonon emission [8].

Fig. 2 is a possible configuration co-ordinate (C–C) diagram for the transformation of Eα3 to and from Eα3*, it shows also the thermal activation energy (0.05 eV) of the electron capture cross section of Eα3 [4]. Fig. 3 shows C–C diagram explaining the transformation of EαIR10 to and from EαIR10*.

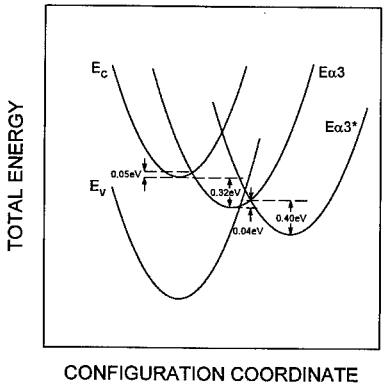

Fig. 2. Possible configuration co-ordinate (C–C) diagram for the transformation of Eα3 to and from Eα3*; it also shows the thermal activation energy (0.05 eV) of the electron capture cross section of Eα3 [4].

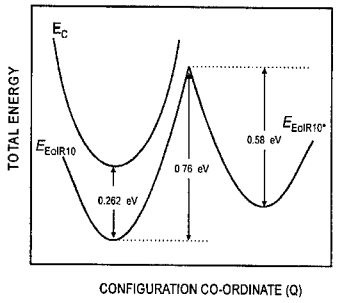

Fig. 3. Configuration coordinate diagram explaining the transformation of EαIR10 to and from EαIR10*.

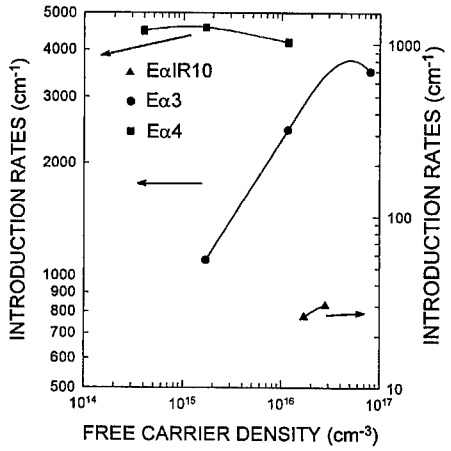

Fig. 4. Change in the introduction rates of Eα3 and EαIR10 as functions of the free carrier density of GaAs : Si and GaAs : S, respectively. The almost constant Eα4-introduction rate has also been included, the high doping density point is lowered by the higher electric field present.

It is of interest to note that, when GaAs : S is irradiated with electrons from the Sr-90 source with an energy of 0.2–2.4 MeV, EαIR10 is not detected by DLTS. However, irradiation by 1 MeV protons, 10 and 12 MeV electrons introduces EαIR10. This suggests that EαIR10 is a larger or complex defect. Auret et al. [4] have shown that Eα3 is a large defect and we found that the introduction rate of Eα3 increases with the free carrier density of GaAs : Si. We could not conclusively prove this for GaAs : S, as, increasing the free carrier density from 1.7×10^{16} to $2.8 \times 10^{16}\,cm^{-3}$, the introduction rate for EαIR10 only increased by about 15% from $26\,cm^{-1}$, as depicted in Fig. 4. The almost constant Eα4 introduction rate has also been included. Since Eα3 has only been detected in Si-doped GaAs and not in n-GaAs doped differently; and since the same applies to EαIR10, we suggest that Eα3 and EαIR10 are defect complexes linked to the Si and S dopants in n-GaAs.

4. Conclusions

We have shown using DLTS that particle irradiation introduces metastable defects Eα3 and EαIR10 in GaAs : Si and GaAs : S, respectively; and that Eα3 and EαIR10 have DLTS defect signatures, (0.37 eV, 9×10^{-14} cm^2) and (0.26 eV, 4.4×10^{-13} cm^2), respectively. Using DLTS, we detected Eα3 and EαIR10 only in GaAs doped with Si and S, respectively. This fact, the dependencies of Eα3 and EαIR10 introduction rates on the free carrier density, and the fact that Eα3 and EαIR10 are large defects, suggests Eα3 and EαIR10 as defect complexes linked to the dopant Si and S atoms.

Acknowledgements

We greatly acknowledge the financial assistance of the South African National Research Foundation (NRF) and Prof G. Myburg of the University of Pretoria for fabrication of the ohmic contacts.

References

[1] W.R. Buchwald et al., Phys. Rev. B 40 (1989) 2940.
[2] K. Wada et al., in: Defects in semiconductors, ICDS-19, Pt 2: Materials Science Forum, Trans Tech Publications, Switzerland, 1997, p. 1051.
[3] V. Alex et al., in: Defects in Semiconductors, ICDS-19, Pt 2: Materials Science Forum, Trans Tech Publications, Switzerland, 1997, p. 1009.
[4] F.D. Auret, S.A. Goodman, G. Myburg, W.E. Meyer, Appl. Phys. A 56 (1993) 547.
[5] S.A. Goodman, F.D. Auret, Jpn. J. Appl. Phys. Lett. 32 (1993) L1120.
[6] D. Pons, J.C. Bourgoin, J. Phys. C. Solid State Phys. 18 (1985) 3839.
[7] F.D. Auret, R.M. Erasmus, S.A. Goodman, W.E. Meyer, Phys. Rev. B 51 (1995) 17521.
[8] A. Chantre, Appl. Phys. A 48 (1989) 3.

ELSEVIER

Physica B 273–274 (1999) 766–769

PHYSICA B

www.elsevier.com/locate/physb

Terahertz tunnel ionization of DX-centers in AlGaAs : Te

H. Ketterl[a,*], E. Ziemann[a], S.D. Ganichev[a,b], I.N. Yassievich[b], A. Belyaev[c], S. Schmult[a], W. Prettl[a]

[a]*Institut für Exp. und Angew. Physik, Universität Regensburg, 93040 Regensburg, Germany*
[b]*A.F. Ioffe Physicotechnical Institute, RAS, St. Petersburg, 194021, Russia*
[c]*Institute of Semiconductor Physics, NASU, Kiev, 252028, Ukraine*

Abstract

Ionization of DX-centers in AlGaAs : Te has been investigated in strong terahertz electric fields of FIR-laser radiation with photon energies much smaller than the impurity binding energy. Detachment of electrons from DX-centers is caused by phonon-assisted tunneling being independent of the field frequency as long as the tunneling time is smaller than the field period. In the opposite case an enhancement of the emission probability with rising frequency has been observed. At very high-field strengths direct tunneling without involving phonons dominates and finally emission rates get frequency independent.

Keywords: DX-center; Persistent photoconductivity; Ionization; Tunneling

1. Introduction

The ionization of DX-centers in AlGaAs : Te in a strong terahertz electric field of a powerful far-infrared laser has been investigated. Although the quantum energy of radiation is much smaller than the binding energy of the impurities, a persistent photoconductive signal (PPC) due to the detachment of electrons from the DX-centers has been observed. In a wide range of temperatures, electric field strengths and frequencies, the emission process can be attributed to phonon-assisted tunneling, Refs. [1,2]. In contrast to tunneling ionization of atoms, where only electron tunneling takes place, ionization of impurities in solids is accomplished by two simultaneous tunneling processes, electron tunneling and the redistribution of the vibrational system by defect tunneling. Within a broad range of intensities and wavelengths, the terahertz electric field of the exciting radiation acts like a static field. In the case $\omega\tau < 1$, where ω is the radiation frequency and τ is the tunneling time, electrons tunnel at constant energy through the barrier formed by the impurity binding potential and that of the high-frequency electric field. The ionization probability is independent of frequency and increases with rising field strength E like $\exp(E^2/E_c^{*2})$ where E_c^* is a characteristic field. At higher frequencies and lower temperatures $\omega\tau > 1$ can be achieved, which leads to an increase of the ionization rate by an enhancement of the tunneling probability. In this high-frequency limit electrons can absorb energy from the radiation field during tunneling and thus leave the potential barrier at a higher energy level. By this the effective width of the tunneling barrier is reduced and thus, the tunneling probability enhanced. The ionization probability is characterized by the same field dependence, as in the quasi-static regime $\omega\tau < 1$, but substantially increases with increasing frequency. With increasing electric field strength direct carrier tunneling from the bound state into continuum, without participation of phonons, becomes dominant. Here, a less strong dependence of the ionization probability on the electric field strength is observed and the frequency dependence practically vanishes at very high fields.

* Corresponding author. Tel.: 0049-0-941-943-3301; fax: 0049-0-941-943-2177.

E-mail address: hermann.ketterl@physik.uni.regensburg.de (H. Ketterl)

0921-4526/99/$ - see front matter
PII: S0921-4526(99)00644-4

2. Experimental technique

The experimental investigations presented here have been carried out on DX-centers in $Al_{0.35}Ga_{65}As$: Te, Refs. [3,4]. Samples have been cooled that at thermal equilibrium practically all carriers were bound to deep impurities ($T = 4.2$–150 K). Terahertz electric fields have been applied using high-power FIR lasers pulses. The laser was a line-tunable NH_3-laser optically pumped by a high-power TEA-CO_2-laser, Ref. [5]. Electric field strengths in the semiconductor samples up to about 40 kV/cm ($\simeq 5$ MW/cm^2) could be achieved in the frequency range from 5 to 50 THz with 40 ns laser pulses. The ratio of irradiated conductivity σ_i and dark conductivity σ_d has been determined from peak values of photoconductive signals using a standard 50 Ω load resistor circuit, Ref. [5].

3. Results and discussion

Irradiation of the samples with FIR-radiation leads to positive persistent photoconductivity. Persistent photoconductivity can be attributed to the detachment of electrons from the DX-centers, Refs. [3,6,7], caused by simultaneous electron tunneling in the electric field of the radiation and tunneling redistribution of the defect vibrational system, shown in Fig. 1. In semiclassical approximation the probability of this process may be written as, Ref. [8],

$$e(E) = \iint P_e P_d \exp(-\mathscr{E}/k_B T)\, d\varepsilon\, d\mathscr{E}, \tag{1}$$

where P_e and P_d are the electron and the defect tunneling probability, respectively, T is the temperature, ε the electron energy at tunneling (see inset in Fig. 3) and $\mathscr{E}$ the corresponding defect tunneling energy (Fig. 1). The Boltzmann factor takes into account the thermal excitation of the system in the adiabatic potential U_1. For the electron energy smaller than the defect tunneling energy and the thermal binding energy, $\varepsilon \ll \varepsilon_T$, it has been shown that the dependence of the ionization probability on the alternating electric field strength E is given by, Ref. [8],

$$e(E) \propto \exp\left[\frac{E^2}{(E_c^*)^2}\right] \quad \text{with } (E_c^*)^2 = \frac{3m^*\hbar}{e^2(\tau_2^*)^3} \tag{2}$$

and

$$(\tau_2^*)^3 = \frac{3}{4\omega^3}(\sinh(2\omega\tau_2) - 2\omega\tau_2). \tag{3}$$

The tunneling process is controlled by $\omega\tau_2$ where the tunneling time τ_2 for $\varepsilon \ll \varepsilon_T$ depends on the temperature like, Ref. [9],

$$\tau_2 = \hbar/2kT - \tau_1. \tag{4}$$

Here τ_1 is of the order of the period of the impurity vibration. At $\omega\tau_2$ much smaller than unity $\tau_2^* \simeq \tau_2$ and the ionization probability is independent on frequency. Lowering the temperature leads to an increase of τ_2 according to Eq. (4) and in the same frequency range $\omega\tau_2$ becomes larger than unity. Now the ionization probability strongly depends on the laser frequency.

In AlGaAs:Te phonon-assisted tunneling has been observed over the entire range of available electric field strength. The ratio of the conductivity under irradiation to the dark conductivity σ_i/σ_d, which is proportional to the ionization probability $e(E)/e(0)$, is plotted in Fig. 2 as a function of the square of the peak electric field strength E. The ionization probability at $T = 100$ K (Fig. 2, top plate) is independent of the radiation frequency and increases with rising E like $\exp(E^2/E_c^{*2})$, according to Eqs. (2) and (3) with $\omega\tau_2 \ll 1$. Such a behavior has also been

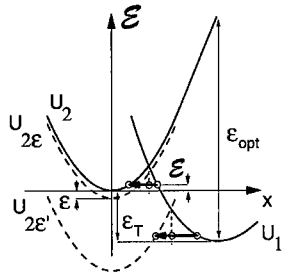

Fig. 1. Adiabatic potential configurations. The energy of vibration and electron is shown as a function of a configuration coordinate x. Potentials plotted in broken lines correspond to the electron with negative kinetic energy tunneling in electric fields of two different strengths.

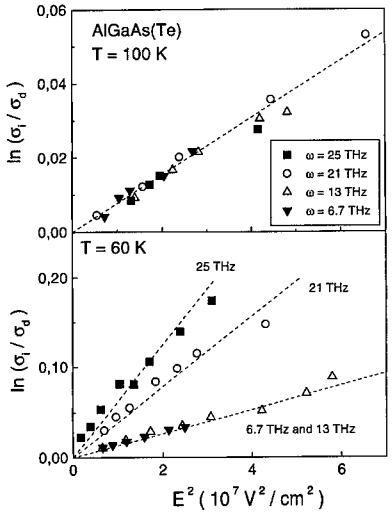

Fig. 2. Dependence of $\ln(\sigma_i/\sigma_d)$ on E^2 for $T = 100$ and $T = 60$ K.

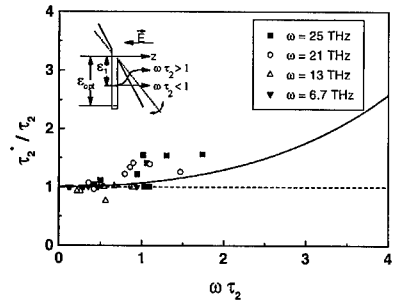

Fig. 3. Ratio τ_2^*/τ_2 as a function of $\omega\tau_2$. Experimentally obtained results are compared to calculations according to Eq. (2) (straight line). Inset: Electron tunneling in an electric field.

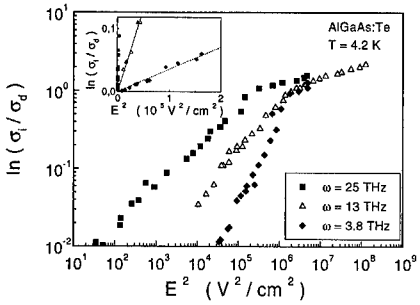

Fig. 4. Dependence of $\ln(\sigma_i/\sigma_d)$ on E^2 for $T = 4.2$ K, the inset shows the low field behavior.

observed for other materials like DX-centers in AlGaSb : Te and substitutional impurities in germanium at sufficiently high temperatures, Refs. [5,8,9]. Lowering the temperature leads to an increase of τ_2, given by Eq. (4), and thus in the same frequency range $\omega\tau_2$ becomes larger than unity. As shown in Fig. 2 (bottom plate) for $T = 60$ K, the ionization probability gets frequency dependent and is drastically enhanced with rising frequency ω. The ionization probability still depends exponentially on the square of the electric field strength, but the magnitude of E_c^* decreases strongly with increasing frequency.

Varying the temperature and the radiation frequency the dependence of the effective time τ_2^* has been obtained from the measured values of E_c^* for various frequencies and temperatures. In Fig. 3, the ratio τ_2^*/τ_2 determined experimentally is plotted as a function of $\omega\tau_2$ and compared to calculations after Eq. (2).

In order to get even larger values of $\omega\tau_2$ measurements at the temperature of liquid helium have been carried out. Because of the large binding energy of the DX-center, the sample resistance is too high to detect any signal at this temperature. Therefore, persistent photoconductivity has been used to reduce the sample resistance by several orders of magnitude by illumination with visible and near-infrared light. After this illumination has been switch off, positive persistent photoconductivity could be detected with FIR-radiation. Fig. 4 shows experimental results at $T = 4.2$ K in the frequency range between 3.8 and 25 THz. In order to display in one figure the total set of data covering seven orders of magnitude in the square of the electric field, E^2 has been plotted on the abscissa in a logarithmic scale. To make an easy comparison with the $\exp(E^2/E_c^{*2})$ dependence of σ_i/σ_d possible, a logarithmic presentation of $\ln(\sigma_i/\sigma_d)$ has been used for the ordinate.

At 4.2 K and at low field strengths the condition $\omega\tau_2 \gg 1$ is valid for the whole frequency range investigated here. The measurements of Fig. 4 show that at liquid helium temperature in the limit of $\omega\tau_2 \gg 1$ a drastic frequency dependence is observed. For a given constant signal a change of three orders of magnitude of electric fields squared needs only a six-times change in frequency. Note, that this large variation in the field strength yielding the same signal is valid only for the case of relatively low fields. As shown in the inset of Fig. 4, in this regime the ionization probability for the two lowest frequencies $\omega = 3.8$ and $\omega = 13$ THz can be described in terms of phonon-assisted tunneling $e(E) \propto \exp(E^2/E_c^{*2})$ as it was the case for higher temperatures. At higher field strength the field dependence of the emission probability is much weaker and the frequency dependence practically disappears.

These changes of the dependence of the ionization probability on the field strength and radiation frequency is a result of the transition from phonon-assisted tunneling at low field strengths to direct tunneling without involving phonons at high fields, Ref. [5]. The emission probability for phonon-assisted tunneling as a function of the electric field strength given by Eqs. (2) and (3) was obtained in the limit that corrections to thermal emission resulting from electron tunneling are small, i.e. the electron tunneling energy is much smaller than the thermal ionization energy, $\varepsilon \ll \varepsilon_T$. In the opposite limit, direct carrier tunneling from the ground state into continuum, without participation of phonons, becomes dominant. Direct electron tunneling occurs, if the potential $U_{2\varepsilon}$ crosses U_1 in its minimum, where an electronic transition is possible without any change in the configuration coordinate. This effect, leading to weaker growth of the ionization probability in comparison with the field dependence of phonon-assisted tunneling, extrapolated to higher field strengths, determines the ionization process at very high fields, Refs. [1,5].

In Fig. 5 solid lines show the result of calculations for AlGaAs : Te at 4.2 K and frequencies used in the experiments taking into account both processes, phonon-assisted tunneling and direct tunneling, but ignoring the change of carrier density due to pre-illumination.

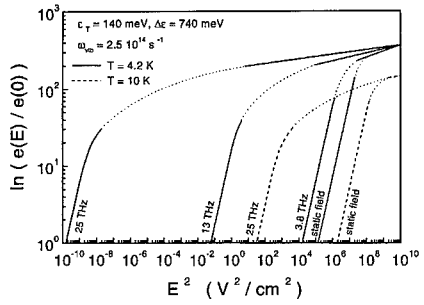

Fig. 5. Calculations of phonon-assisted and direct tunneling for $T = 4.2$ and $T = 10$ K.

Because of singularities, calculations at $\omega\tau_2 \gg 1$ have been carried out in limited and separated ranges of the electric field strength and the gaps have been interpolated. The theory qualitatively describes well the experimentally observed features of the field and frequency dependence of tunneling ionization. The disappearance of the frequency effects at very high fields can be explained by the electric field dependence of the tunneling time τ_2. In the high field regime the defect tunneling trajectory is shifted to lower energies, as shown in Fig. 1, leading to a decrease of τ_2. By this $\omega\tau_2$ becomes smaller than unity and the frequency dependence vanishes.

Theoretical expressions for tunneling ionization have been obtained under the condition that after excitation electrons and phonons remain in thermal equilibrium at liquid helium temperature. In experiment, pre-illumination and persistent photoconductivity has been used to increase the free carrier density by several orders of magnitude. Thus free electrons may be heated by FIR-radiation due to Drude absorption. To achieve quantitative agreement of theory and experiment, heating of the phonon system by energy transfer from the electrons should be taken into account. An increase of the sample temperature of just a few degrees leads to lower relative emission rates $e(E)/e(0)$ and a much weaker frequency dependence of the emission probability as demonstrated in Fig. 5 by broken lines.

Acknowledgements

Financial support by the DFG and the NATO Linkage Grant is gratefully acknowledged. S.D.G. and I.N.Y. wish to thank the RFFI grant 98-02-18268, H.K. the Hans-Böckler-Stiftung and E.Z. the Graduiertenkolleg *Komplexität in Festkörpern.*

References

[1] V.N. Abakumov, V.I. Perel, I.N. Yassievich, Nonradiative Recombination in Semiconductors, in: V.M. Agranovich, A.A. Maradudin (Eds.), Modern Problems in Condensed Matter Sciences, Vol. 33, North-Holland, Amsterdam, 1991.
[2] P.T. Landsberg, Recombination in Semiconductors, Cambridge University Press, Cambridge, 1991.
[3] H.J. von Bardeleben, I. Buyanova, A. Belyaev, M. Sheinkman, Phys. Rev. B 45 (1992) 11 667.
[4] A.E. Belyaev, Yu.S. Ryabchenko, M.K. Sheinkman, H.J. von Bardeleben, Semicond. Sci. Technol. 11 (1996) 68.
[5] S.D. Ganichev, W. Prettl, I.N. Yassievich, Phys. Solid State 39 (1997) 1703.
[6] P.M. Mooney, T.N. Theis, Comments Cond. Mat. Phys. 16 (1992) 167.
[7] R.C. Newman, Semicond. Sci. Technol. 9 (1994) 1749.
[8] S.D. Ganichev, E. Ziemann, Th. Gleim, W. Prettl, I.N. Yassievich, V.I. Perel, I. Wilke, E.E. Haller, Phys. Rev. Lett. 80 (1998) 2409.
[9] S.D. Ganichev, J. Diener, I.N. Yassievich, W. Prettl, B.K. Meyer, K.W. Benz, Phys. Rev. Lett. 75 (1995) 1590.

ELSEVIER

Physica B 273–274 (1999) 770–773

PHYSICA B

www.elsevier.com/locate/physb

Luminescence properties of Er,O-codoped III–V semiconductors grown by organometallic vapor phase epitaxy

Y. Fujiwara*, T. Kawamoto, T. Koide, Y. Takeda

Department of Materials Science and Engineering, Graduate School of Engineering, Nagoya University, Furo-cho, Chikusa-ku, Nagoya 464-8603, Japan

Abstract

We have grown Er,O-codoped GaAs and InP by organometallic vapor phase epitaxy (OMVPE) and investigated the growth condition dependences of the photoluminescence (PL) spectra due to intra-4f shell transitions of Er. The codoping of Er and oxygen (O) is performed using an O-containing Er source either with or without an additional O_2 flow. In GaAs, the addition of O_2 to the growth ambient is quite effective for the formation of an Er–2O center. The dependence of the PL spectra on growth temperature reveals the existence of a threshold growth temperature above which the formation of the Er–2O center is greatly suppressed. In Er-doped InP grown with a small amount of O_2, several extremely sharp emission lines are newly observed.

Keywords: Erbium; Oxygen; GaAs; InP

1. Introduction

Er^{3+} ions doped in III–V semiconductors and silicon exhibit sharp and temperature-stable photoluminescence (PL) at around 1.5 μm due to intra-4f shell transitions from the first excited state ($^4I_{13/2}$) to the ground state ($^4I_{15/2}$) of Er^{3+} (see, for example Ref. [1]). The wavelength of 1.5 μm lies in the minimum loss region of silica fibers. However, it has been found that Er^{3+} ions doped in semiconductors show various fine structures, depending on host materials and doping procedures. This indicates that various kinds of Er centers with different atom configurations are formed in a semiconductor, because the fine structures of PL spectra reflect atom configurations surrounding Er^{3+} ions. Selective formation of highly efficient Er centers for luminescence has strongly been desired for applications of Er-related luminescence to light-emitting devices.

We have intensively investigated Er-doped phosphorus-based III–V semiconductors such as InP and GaP grown by organometallic vapor phase epitaxy (OMVPE) [2–6]. In Er-doped InP, it has been found that there is a threshold growth temperature between 550°C and 580°C for Er incorporation into InP. The majority of Er atoms substitute the In sublattice in the lower-temperature grown InP, exhibiting high luminescence efficiency [3,4]. The threshold growth temperature depends on host materials. In Er-doped GaP, the temperature is higher, and the majority of Er atoms are incorporated into Ga sites in the GaP lattice even in samples grown at 650°C and 700°C [5].

Oxygen (O) has been recognized to influence strongly Er-related luminescence in semiconductors. Er doped in Czochralski-grown (CZ) Si containing 10^{18} cm^{-3} O atoms exhibits luminescence intensity 100 times more than that of Er in higher purity float-zone (FZ) material [7]. In Er-doped GaAs, the introduction of O_2 into the OMVPE growth ambient produces a sharp, simple PL spectrum of Er^{3+} [8]. The PL spectrum is dominated by seven emission lines under host-excited conditions at a low temperature. The Er center has been identified as an Er atom located at the Ga sublattice with two adjacent O atoms (hereafter referred as Er–2O) [9].

* Corresponding author. Fax: + 81-52-789-3239.
E-mail address: fujiwara@numse.nagoya-u.ac.jp (Y. Fujiwara)

0921-4526/99/$ - see front matter
PII: S0921-4526(99)00645-6

In this paper, we report luminescence properties of Er codoped with O in GaAs and InP by OMVPE using an O-containing Er source either with or without an additional O_2 flow.

2. Experimental

A low-pressure growth system with a vertical quartz reactor was employed in this work [2]. TEGa and TBAs were used as source materials for GaAs growth, and TMIn and TBP for InP growth. Er was doped using trisdipivaloylmethanatoerbium ($Er(C_{11}H_{19}O_2)_3$, $Er(DPM)_3$) as an Er source, which contains six O atoms bonded to one Er atom in one molecule. The Er source was maintained mainly at 40°C and introduced into the reactor by a H_2 flow through the Er source cylinder. Ar gas with 50 ppm of O_2 was used as an additional O source. The additional O_2 content in growth ambient was changed from 0 ppm up to 0.4 ppm for GaAs, and up to 0.3 ppm for InP. The growth temperature was in the range of 500–625°C for GaAs. It was fixed at 530°C for InP. The substrates for the growth were C-doped semi-insulating or Si-doped GaAs, and Fe-doped semi-insulating or Sn-doped InP. The surface orientation was (1 0 0) for both.

PL measurements were carried out with the samples directly immersed in liquid He at 4.2 K. The photoexcitation source was a cw mode Ar^+ laser with a beam diameter of 1 mm and an incident power of 200 mW. The luminescence of the sample was dispersed using a 0.91 m grating monochromator and detected with a liquid nitrogen-cooled Ge pin photodiode using a chopper and a lock-in amplifier. A spectral resolution of 0.3 nm in wavelength was used in this work.

3. Results and discussion

3.1. Er,O-codoped GaAs

Specular surface is successfully obtained in all Er-doped GaAs grown in this work.

The profiles and concentrations of Er and O in layers were characterized by secondary ion mass spectroscopy (SIMS) measurements using Cs^+ as a primary ion. Oxygen signal is clearly observed in the layers doped using $Er(DPM)_3$ without an additional O_2 flow as well as in those with the additional O_2 flow. The O-containing Er source is confirmed to supply oxygen to the layers. The in-depth profile of Er and O exhibits a uniform distribution along the growth direction in all the layers. The Er concentration in the layers, which is calibrated using an Er-implanted GaAs sample, is well controlled with the Er source temperature and the H_2 flow rate through the source cylinder. The Er concentration is 2×10^{20} cm^{-3} at maximum at present, which is limited by a mass flow controller attached to a supply line of the Er source. On the other hand, the O concentration is not calibrated, but it increases linearly with the Er concentration.

Fig. 1 shows Er-related PL spectrum in GaAs doped with Er and O using only $Er(DPM)_3$, which is compared with that in GaAs doped with Er using an O-free Er source (trismethylcyclopentadienylerbium, $Er(MeCp)_3$). In the O-free Er-doped GaAs, there are many emission lines, reflecting coexistence of various Er centers not identified. In the Er,O-codoped GaAs, weak emission lines from an Er–2O center [8] appear together with emission lines from other Er centers. It suggests difficulty in selective formation of Er centers using only $Er(DPM)_3$.

Fig. 2 shows a comparison of Er-related PL spectra in Er,O-codoped GaAs grown with and without an additional O_2 flow. The growth temperature and the H_2 flow rate through the Er source were 543°C and 125 sccm, respectively. In the sample grown with the additional O_2 flow (O_2 content of 0.2 ppm in the growth ambient), the Er-related PL spectrum reveals strong emission lines from only the Er–2O center as reported previously [8]. This indicates that O_2 added to the growth ambient is preferentially used for the formation of the Er–2O center.

We investigated the dependence of Er-related PL spectra on the growth conditions. The spectrum is almost independent of the Er concentration up to 2×10^{19} cm^{-3} and the O_2 content in the growth ambient up to 0.4 ppm. However, the formation of the Er–2O center is greatly influenced by the growth temperature. The growth temperature dependence of the PL spectra is shown in Fig. 3. In preparation of the samples, the H_2 flow rate through the Er source and O_2 content in the ambient were fixed at 125 sccm and 0.2 ppm, respectively. The PL spectrum

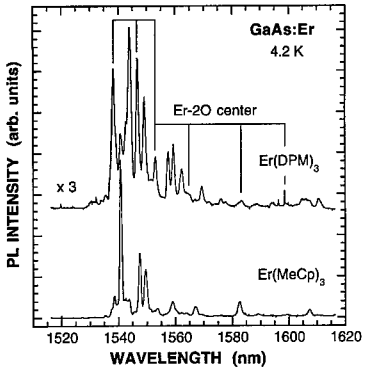

Fig. 1. Er-related PL spectrum in GaAs doped with Er and O using only $Er(DPM)_3$. The spectrum in GaAs doped with Er using O-free $Er(MeCp)_3$ is also shown for comparison. In Er,O-codoped GaAs, weak emission lines from the Er–2O center appear together with many emission lines from other Er centers formed simultaneously.

changes drastically between 543°C and 585°C, suggesting that there is a threshold growth temperature. In samples grown at temperatures higher than 585°C, the Er–2O emission lines become weak and the PL spectrum is dominated by emission lines from other Er centers. This result means that the formation of the Er–2O center is strongly suppressed above the threshold growth temperature.

SIMS measurements have been performed on the samples and it has been found that the concentrations of Er and O in the samples remain almost constant ([Er]: 8×10^{18} cm^{-3}, [O]: not calibrated) against the growth temperature. This suggests that the change in PL spectrum at higher growth temperature is not due to increase/decrease in concentrations of Er and O. Extended X-ray absorption fine structure (EXAFS) analysis on the samples is now in progress to clarify atom configurations around Er atoms.

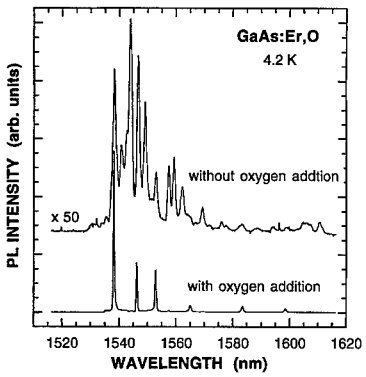

Fig. 2. Comparison of Er-related PL spectra in Er,O-codoped GaAs grown with and without an additional O_2 flow. In the sample with the O_2 flow, the PL spectrum is dominated by strong emission lines from only the Er–2O center.

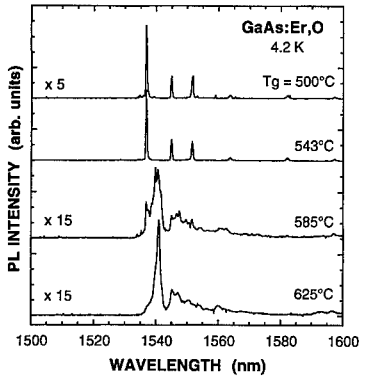

Fig. 3. Growth temperature dependence of Er-related PL spectra in Er,O-codoped GaAs grown with the additional O_2 flow. The spectral shape changes drastically between 543°C and 585°C, suggesting that there is a threshold growth temperature. Above the temperature, formation of the Er–2O center is greatly suppressed.

3.2. *Er,O-codoped InP*

Specular surface is obtained in Er-doped InP samples grown with the additional O_2 content in growth ambient up to 0.1 ppm as well as without the O_2 addition. The sample grown with the additional O_2 content of 0.3 ppm, however, exhibits extremely rough surface. It should be noted that Er-doped GaAs with specular surface can be grown with the 0.4 ppm O_2 content, suggesting that the situation in InP is quite different from that in GaAs.

SIMS analysis indicates obvious existence of oxygen even in layers doped using $Er(DPM)_3$ without an additional oxygen flow. As observed in Er,O-codoped GaAs, the in-depth profiles of Er and O exhibit a uniform distribution along the growth direction in all the layers. As for the dependence on the additional O_2 content in growth ambient, the concentration of O increases with the O_2 content, while the Er concentration remains almost constant. The increase of the O concentration might be due to preferential reaction between In and O.

Fig. 4 shows Er-related PL spectra in Er,O-codoped InP samples, which are compared with that in InP doped with Er using O-free $Er(MeCp)_3$ [2,3]. In Er-doped InP using only $Er(DPM)_3$, the PL spectrum has a main emission line at 1541.1 nm in wavelength. This is quite similar to the spectrum in InP doped with Er by the O-free Er source.

In the sample grown with a small amount of O_2 content (0.1 ppm) in the ambient, the intensity of the 1541.1 nm line is highly suppressed and several extremely sharp emission lines are newly observed. Peak positions

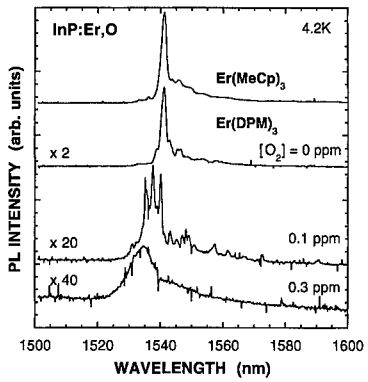

Fig. 4. Er-related PL spectra in InP doped with Er and O, which is compared with that in InP doped with Er using O-free $Er(MeCp)_3$. Under a small amount of O_2 content (0.1 ppm) in the ambient, three dominant emission lines are newly observed.

of dominant three new emission lines are 1535.1, 1537.5 and 1540.1 nm, respectively. Since the new emission lines are observed only in Er,O-codoped InP, they should originate from Er centers with O. Such PL spectrum with the sharp emission lines in Er-doped InP is the first observation to the best of our knowledge. In the sample grown with the additional O_2 content of 0.3 ppm, all the sharp emission lines disappear, and a weak broad band dominates the PL spectrum. The reduction in PL intensity and the appearance of the broad band reflect poor surface morphology, i.e., degraded crystal quality.

4. Conclusion

Er,O-codoped GaAs and InP have been grown by OMVPE using $Er(DPM)_3$ either with or without an additional O_2 flow, and the dependences of Er-related PL spectra on growth conditions have been investigated. In GaAs, the use of the O-containing source produces partial formation of an Er–2O center. As reported previously, the addition of O_2 to the growth ambient is quite effective for the formation of the Er–2O center. The dependence of PL spectra on growth temperature reveals the existence of a threshold growth temperature (543–585°C). Above the temperature, the formation of the Er–2O center is greatly suppressed. In InP, the situation is quite different from that in GaAs. The surface morphology is severely degraded under the additional O_2 content of 0.3 ppm. In the sample doped with a small amount of O_2 (0.1 ppm), the PL spectrum is dominated by three new sharp emission lines (1535.1, 1537.5 and 1540.1 nm in wavelength). Such PL spectrum with the sharp emission lines in Er-doped InP is the first observation to the best of our knowledge.

Acknowledgements

The authors would like to thank Tri Chemical Laboratory Inc. for the Er source, Hitachi Cable Ltd. for GaAs substrates, and Showa Denko K.K. for InP substrates. The work was supported in part by Grant-in-Aids for Scientific Research of Priority Areas, Spin Controlled Semiconductor Nanostructures No. 11125209, for Scientific Research (B)(2) No. 11450119, and for Exploration Research No. 10875070 from the Ministry of Education, Science, Sports and Culture.

References

[1] Mater. Res. Soc. Symp. Proc. 422 (1996).
[2] Y. Fujiwara, Y. Ito, Y. Nonogaki, N. Matsubara, K. Fujita, Y. Takeda, Mater. Sci. Forum 196–201 (1995) 621.
[3] Y. Fujiwara, N. Matsubara, J. Tsuchiya, T. Ito, Y. Takeda, Jpn. J. Appl. Phys. 36 (1997) 2587.
[4] H. Ofuchi, D. Kawamura, N. Matsubara, M. Tabuchi, Y. Fujiwara, Y. Takeda, Microelectron. Eng. 43/44 (1998) 745.
[5] Y. Fujiwara, T. Ito, H. Ofuchi, J. Tsuchiya, A. Tanigawa, M. Tabuchi, Y. Takeda, Institute of Physics Conference Series No. 156, Institute of Physics Publication, Bristol, 1998, p. 199.
[6] Y. Fujiwara, A.P. Curtis, G.E. Stillman, N. Matsubara, Y. Takeda, J. Appl. Phys. 83 (1998) 4902.
[7] P.N. Favennec, H. L'Haridon, D. Moutonnet, M. Salve, M. Gauneau, Jpn. J. Appl. Phys. 29 (1990) L524.
[8] K. Takahei, A. Taguchi, J. Appl. Phys. 74 (1993) 1979.
[9] K. Takahei, A. Taguchi, Y. Horikoshi, J. Nakata, J. Appl. Phys. 76 (1994) 4332.

ELSEVIER

Physica B 273–274 (1999) 774–777

PHYSICA B

www.elsevier.com/locate/physb

Direct observation of local structure of DX center by capacitance X-ray absorption fine structure

Masashi Ishii[a,*], Yoko Yoshino[b], Ken-ichi Takarabe[b], Osamu Shimomura[c]

[a]*Japan Synchrotron Radiation Research Institute (JASRI), SPring-8, Mikaduki, Sayo-gun, Hyogo 679-5198, Japan*
[b]*Okayama University of Science, Ridai, Okayama 700-0005, Japan*
[c]*Japan Atomic Energy Research Institute (JAERI), SPring-8, Mikaduki, Sayo-gun, Hyogo 679-5143, Japan*

Abstract

In order to discuss the crystal lattice relaxation in DX center, a new X-ray absorption fine structure (XAFS) analysis, 'capacitance XAFS', is applied to the $Al_{0.33}Ga_{0.67}As$: Se system. In capacitance XAFS, the X-ray absorption of a defect atom with a localized electron is selectively observed by measuring the photon-energy dependence of the capacitance. Capacitance XAFS at the Ga K-edge is different from conventional XAFS, although a similar absorption spectra are obtained at the As K-edge, suggesting that the DX center in this system originates from the trigonal broken bond (BB-DX) configuration rather than the cation–cation bonded (CCB-DX) state. © 1999 Elsevier Science B.V. All rights reserved.

Keywords: Capacitance XAFS; DX center; BB-DX; AlGaAs : Se

1. Introduction

Deep-level carrier traps in semiconductors have been investigated by many research groups [1–3] because they degenerate the device performance. Se-doped $Al_xGa_{1-x}As$ ($x \sim 0.3$) is a typical example that the deep-level electron trap, the DX center, is formed by the intrinsic property of the donor incorporated into the zinc-blende semiconductors [4,5]. The DX center exhibits metastability, which causes attractive properties such as persistent photoconductivity (PPC) [6]. Based on these practical and fundamental considerations, the DX center has been one of the main topics in the research field on semiconductor defects since the 1980s. Chadi and Chang explained the metastable DX center of AlGaAs : Se in terms of the large lattice relaxation (LLR) model in which Ga, the nearest neighbor of Se, is displaced from the lattice site instead of the donor itself, with the Ga–Se bond breaking [7]. Another possibility of LLR is that the cation adjacent to the donor pivots on As, resulting in cation–cation bonding without bond breaking [8]. These two LLR models are designated as the trigonal broken bond (BB-DX) configuration and the cation–cation bonded (CCB-DX) state, respectively. In contrast to the LLR model, the small lattice relaxation (SLR) model was also discussed based on the first-principal calculation [9]. Although various experiments have been performed to demonstrate these models [10,11], direct evidence has never been obtained. In this paper, a new X-ray absorption fine structure (XAFS) analysis method, 'capacitance XAFS', is applied to the AlGaAs : Se system for direct observation of the local structure of the DX center.

2. Experiment

The details of capacitance XAFS were discussed in a previous paper [12], therefore only a brief outline of the method is given. As is well known, a Schottky barrier diode can be fabricated by the evaporation of an appropriate metal electrode on an n-type semiconductor. The difference in work function between the metal and the

* Corresponding author. Tel.: + 81-791-58-0831; fax: + 81-791-58-2752.
E-mail address: ishiim@sp8sun.spring8.or.jp (M. Ishii)

PII: S0921-4526(99)00646-8

semiconductor forms a depletion layer in the semiconductor. The capacitance of this depletion layer depends on the density, N_d, of the ionized impurity acting as the donor in the depletion layer. When the DX center traps the electron in the semiconductor, N_d becomes less than the density of the donor impurity. In this situation, since the capacitance is sensitive to the localized electron in the DX center, the dropping of the electron into the core hole resulting from the X-ray absorption of the atom in the DX center, not the bulk atom, induces the ionization of the DX center, resulting in a change in the capacitance. Therefore, the X-ray photon-energy dependence of the capacitance is expected to correspond to the XAFS spectrum of the DX center atom only. Mizuta et al. performed conventional XAFS of AlGaAs : Se by detection of Se fluorescence, and reported no supporting evidence for the LLR model [13]. However, the atomic number of Se ($Z = 34$) is next to that of As ($Z = 33$), so the weak fluorescence signal from the dopant Se is difficult to isolate from the strong fluorescence of the bulk As, thereby inhibiting the estimation of the Ga relaxation. Since capacitance XAFS is unaffected by such absorption in the bulk, the local structure analysis of Ga and As in the DX center of AlGaAs : Se may be selectively analyzed.

Experiments using synchrotron radiation (SR) were carried out at the SPring-8 BL10XU high brilliance XAFS station in Hyogo Prefecture, Japan. SPring-8's standard monochromator equipped with an Si (1 1 1) double crystal was used to monochromatize the SR beam from an in-vacuum-type undulator. The $Al_{0.33}Ga_{0.67}As$ thin film was grown by molecular beam epitaxy (MBE). The substrate was (1 0 0)-oriented n-type GaAs. A concentration of the Se dopant was $5 \times 10^{17}/cm^3$. The electric properties of this sample were discussed in another paper [14]. As the metal electrode of the Schottky diode, an Al dot $\sim$500 μm in diameter and $\sim$100 nm thick was deposited by an evaporator. The hard X-rays can pass through this light metal electrode and ionize the DX center with the localized electron in the depletion layer. The capacitance of the Schottky diode was measured by a high-frequency capacitance meter, DA-1500 (Horiba Ltd.), with a 1 MHz oscillator.

3. Results and discussion

Fig. 1 shows the photon-energy dependence of the capacitance of AlGaAs : Se around the Ga K-edge (10.375 keV) with respect to various applied bias voltages ranging from -0.5 to -2.5 V. The sample temperature was fixed at 100 K. As shown in this figure, the absorption edge jump and the subsequent signal oscillation are clearly observed in all spectra, indicating that XAFS spectra can be obtained by this method. Nevertheless, an applied bias voltage dependence specific to capacitance XAFS is observed. In capacitance XAFS, the amplitude of the absorption signal increases with decreasing bias voltage until -1.5 V, after which the signal decreases with further decrease in the voltage. The edge jump is estimated to be $\sim$5 pF in the case of -1.5 V. A similar tendency is also observed at the As K-edge (11.875 keV). The bias voltage dependence of the peak height at the absorption edge is plotted in Fig. 2. In this figure, closed and open squares indicate the Ga and As K-edge peak heights, respectively. The maximum signal amplitude is obtained at ~ -1.5 V independent of the absorption atom.

In capacitance XAFS, a relaxation process by electron capture into the DX center also occurs; otherwise, the capacitance simply increases by photoionization, resulting

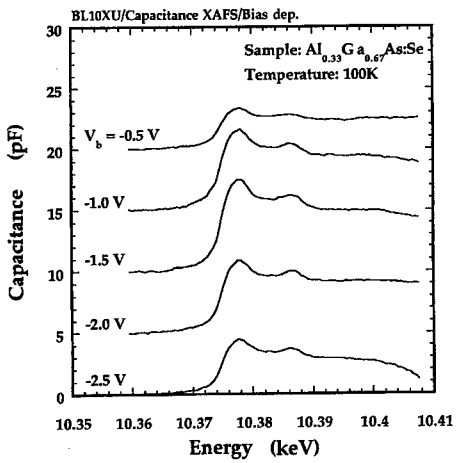

Fig. 1. The photon-energy dependence of the capacitance of $Al_{0.33}Ga_{0.67}As$: Se around the Ga K-edge.

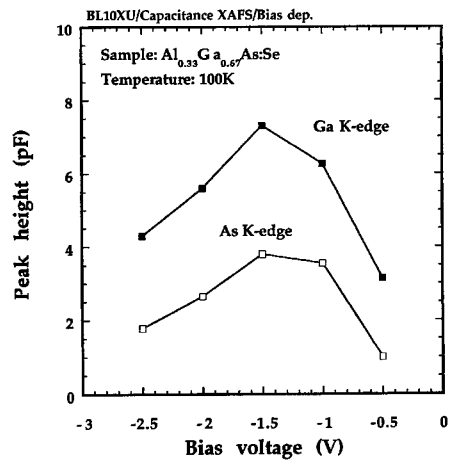

Fig. 2. The bias voltage dependence of the peak height at the absorption edge. The closed and the open squares indicate the Ga and As K-edge peak heights, respectively.

in the absence of XAFS oscillation. Since the signal amplitude of capacitance XAFS is determined by the ionization efficiency of the DX center with the localized electron, the experimental result of this bias voltage dependence is explained as follows. The thickness of the depletion layer, d, is expressed as

$$d = (2\varepsilon_r\varepsilon_0(V_d - V_b)/qN_d)^{1/2}, \quad (1)$$

where $\varepsilon_r\varepsilon_0$ is the dielectric constant of AlGaAs, V_d is the built-in potential, V_b is the bias voltage, q is the elementary electric charge, and N_d is the density of the ionized Se. The variation of N_d by capacitance XAFS is so small that d increases with V_b. In this situation, the total number of X-ray-induced photocarriers in the depletion layer increases with $d \propto (V_d - V_b)^{1/2}$. At a low bias voltage, the ionization of the DX center, rather than the electron capture, is dominant owing to the low number of the photocarriers in the depletion layer; the localized electron in the DX center is exhausted. Consequently, the XAFS signal amplitude becomes small. At a high bias voltage, on the other hand, the capture of the photocarriers becomes the dominant process with the result that the trapping level is always filled with the localized electron. The ionization efficiency decreases, so that the XAFS signal amplitude is again small. Hence, an optimal voltage for capacitance XAFS spectra should be in the intermediate range of the bias voltage; in this experiment, it is -1.5 V.

Because the optimal bias voltage has been determined above, V_b is fixed at -1.5 V in the following experiments. The solid line and the dashed line in Fig. 3(a) show the capacitance XAFS spectrum at the Ga K-edge and the conventional fluorescence XAFS spectrum obtained using an Si(Li) solid state detector (SEIKO EG & G Co., Ltd.), respectively. The substrate temperature was 60 K. Because all of the Ga, except for the minor Ga in the DX center, occupy a normal crystal lattice site in AlGaAs, the conventional XAFS spectrum is consistent with the Ga local structure in the zinc-blende structure. As shown in Fig. 3(a), the absorption edge peak in capacitance XAFS is sharp compared to that in conventional XAFS. Moreover, an energy shift of the absorption edge towards the low-energy side is observed in capacitance XAFS. This result could be attributable to the difference between the chemical environment of Ga in bulk and that in the DX center. The Ga in the DX center mixed in the bulk Ga is considered to be selectively observed by the capacitance XAFS. It can also be concluded that the difference of the chemical environment of Ga in the DX center from that in the bulk provides supporting evidence for the LLR. Fig. 3(b) shows another comparison between capacitance XAFS and the conventional XAFS at the As K-edge. In this figure, capacitance and the conventional XAFS spectra are also plotted by solid and dashed line, respectively. In contrast to the Ga K-edge, similar spectra are obtained, indicating that the local structure of As in the DX center is similar to that of the bulk zinc-blende structure. The DX center is generated by the LLR of only Ga in this system.

For a more detailed discussion, schematic diagrams of the two candidates of LLR, i.e., the CCB-DX and BB-DX models, are illustrated in Fig. 4. Fig. 4(a) is the atomic configuration of CCB-DX. The large lattice distortion of Ga and the simultaneous cation–cation bonding result in a significant coordination change of Ga in the DX center. In addition to the structural modification of Ga, it is important to note that As also suffers a change of the chemical environment according to the asymmetric cation distortion for As. As atoms marked with 'A' in this figure have a long chemical bond with the distorted Ga. If the CCB-DX configuration is the probable structure of the DX center, both the spectrum of Ga and that of As

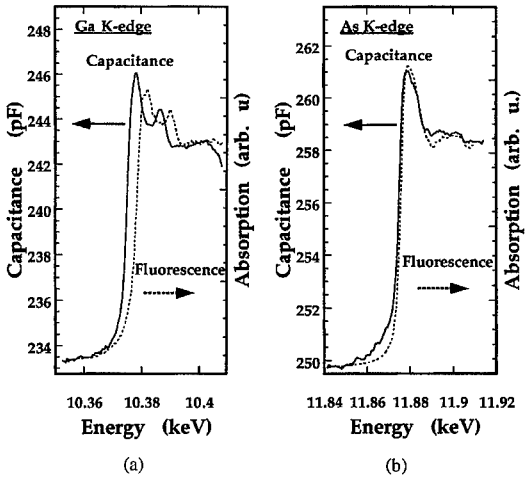

Fig. 3. Comparison between capacitance and conventional XAFS spectra at (a) the Ga and (b) the As K-edge. The solid line and the dashed line indicate capacitance and conventional XAFS spectra, respectively.

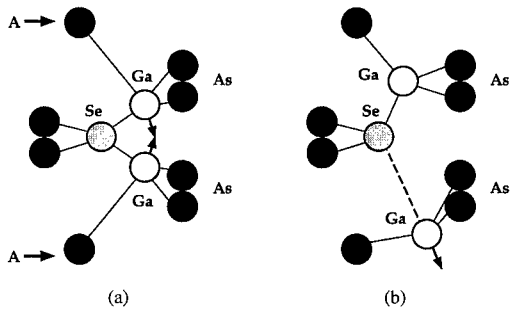

Fig. 4. Schematic diagrams of the (a) CCB-DX configuration and (b) BB-DX state predicted by theoretical calculations for the LLR model.

are expected to have an energy shift at the absorption edge. However, the results in Fig. 3 indicate only a local structural change in Ga. On the other hand, in the BB-DX state shown in Fig. 4(b), Ga in the DX center is expected to be surrounded by three As due to Se–Ga bond breaking. A fourfold structure of Ga in the zinc-blende structure should be observed by conventional XAFS of AlGaAs : Se. If the BB-DX model is acceptable for the local structure of the DX center in this system, the energy shift at the Ga K-edge in Fig. 3 is considered to indicate this change from a fourfold to a threefold structure. In this model, As neighboring Ga has little relaxation in the fourfold coordination. A similar X-ray absorption spectrum for As should be obtained. These qualitative considerations are consistent with the experimental results shown in Fig. 3. The experimental spectra at the near absorption edge provide no structural parameter for the DX center. However, the results of this study indicate that the BB-DX state is more probable as the DX center model.

4. Summary

The new X-ray absorption fine structure (XAFS) technique, 'capacitance XAFS', is performed to analyze the lattice relaxation of the DX center in the $Al_{0.33}Ga_{0.67}As$: Se system. The photon-energy dependence of the capacitance is expected to reveal the X-ray absorption spectrum of the DX center only. The capacitance XAFS spectrum at the Ga K-edge different from the conventional XAFS spectrum is obtained, whereas a similar absorption spectrum is observed at the As K-edge, indicating that only Ga suffers the change of local environment in the DX center caused by the large lattice relaxation. The large lattice relaxation of Ga and the small coordination change of As is considered with the probable structure of the DX center, the latter being the trigonal broken bond (BB-DX) configuration rather than the cation–cation bonded (CCB-DX) state.

Acknowledgements

The synchrotron radiation experiments were performed at the SPring-8 with the approval of the JASRI (Proposal No. 1999B0168-NX). The authors would like to thank Mr. H. Ohnishi of ATR Adaptive Communications Research and Mr. K. Matsuda of Horiba Ltd. for their technical assistance.

References

[1] D.V. Lang, R.A. Logan, J. Electron. Mater. 4 (1975) 1053.
[2] D. Pons, P.M. Mooney, J.C. Bourgoin, J. Appl. Phys. 51 (1980) 2038.
[3] J.Z. Yu et al., Jpn. J. Appl. Phys. 28 (1989) 2391.
[4] M. Mizuta, K. Mori, Phys. Rev. B 37 (1988) 1043.
[5] Y. Kajikawa, J. Appl. Phys. 69 (1991) 1429.
[6] J.Y. Lin, A. Dissanayake, G. Brown, H.X. Jiang, Phys. Rev. B 42 (1990) 5855.
[7] D.J. Chadi, K.J. Chang, Phys. Rev. B 39 (1989) 10063.
[8] C.H. Park, D.J. Chadi, Phys. Rev. B 15 (1996) R14246.
[9] E. Yamaguchi, K. Shiraishi, T. Ohno, J. Phys. Soc. Japan 60 (1991) 3093.
[10] H. Bemelmans, G. Borgh, G. Langouche, Phys. Rev. Lett. 72 (1994) 856.
[11] J. Mäkinen et al., Phys. Rev. B 53 (1996) 7851.
[12] M. Ishii, Y. Yoshino, K. Takarabe, O. Shimomura, Appl. Phys. Lett. 74 (1999) 2672.
[13] M. Mizuta, T. Kitano, Appl. Phys. Lett. 52 (1988) 126.
[14] K. Takarabe et al., Phys. Stat. Sol. 198 (1996) 187.

ELSEVIER

Physica B 273–274 (1999) 778–780

PHYSICA B

www.elsevier.com/locate/physb

Influence of oxygen co-doping on the thermal quenching property of Er-related emission in $Al_{0.70}Ga_{0.30}As$: Er

S. Uekusa[a], K. Uchiya[a,*], M. Kumagai[b]

[a]*Department of Electrical Engineering, Meiji University, 1-1-1 Higashimita, Tamaku, Kawasaki, Kanagawa 214-8571, Japan*
[b]*Kanagawa High-Technology Foundation, 3-2-1 Sakado, Takatsu-ku, Kawasaki, Kanagawa 213, Japan*

Abstract

Erbium (Er) was co-implanted with oxygen (O) into $Al_{0.70}Ga_{0.30}As$ substrates. Photoluminescence (PL) from Er^{3+}-related emission at 1.54 μm was enhanced by co-doping O. Furthermore, from the temperature dependence of the PL intensity and the lifetime of the sample implanted with Er and O, the value of E_2 (215 meV), the activation energy for rapid thermal quenching, was nearly equal to the value of E_A (206 meV), the activation energy for the decrease of the lifetime. Based on the results, the decrease of the lifetime confirms that the radiative efficiency is lower; therefore, we propose that rapid thermal quenching occurs above 200 K due to the decrease of the radiative efficiency.

Keywords: Aluminium gallium arsenide; Erbium; Photoluminescence; Thermal quenching

1. Introduction

Rare-earth (RE)-doped compound semiconductors are well known for their strong infrared intracenter emission [1,2]. Recently, the study of RE doped III–V semiconductors has attracted considerable attention due to their possible applications in optoelectronic devices. In particular, Er-doped semiconductors are a promising material for manufacturing optical devices emitting at 1.54 μm, which coincides with the wavelength of minimum loss in silica-based optical fibers, due to transitions between the crystal field split states $^4I_{13/2}$ and $^4I_{15/2}$ of Er^{3+}. Therefore, Er-doped semiconductors would be of great utility for light emitting diodes, lasers and amplifiers in optical fiber communication systems.

However, Er-doped semiconductors have problems such as a low-energy transition efficiency from the host semiconductor to the intra-4f-shell of Er^{3+} ions and a rapid thermal quenching property of the Er^{3+}-related emission. Therefore, it is important that we understand the mechanics of the energy transition and the thermal quenching property in Er-doped semiconductors. Numerous studies have been carried out in order to solve these problems. Recently, it was reported that the co-doping of O into Er-doped GaAs by metalorganic chemical vapor deposition (MOCVD) has a marked effect on its luminescence characteristics [3]. Thus, we are extremely interested in the influence of impurities on Er^{3+}-related emission in Er-doped semiconductors. We have previously reported the effect of N on Er^{3+}-related emission in AlGaAs : Er and GaP : Er [4,5].

In this work, in order to investigate the effect of O on Er^{3+}-related emissions in $Al_{0.70}Ga_{0.30}As$: Er, ion-implantation of Er and O co-doped into $Al_{0.70}Ga_{0.30}As$ were performed and their PL properties were systematically studied. Furthermore, the temperature dependence of the PL intensity and the lifetime was measured, and we also discussed the influence of oxygen co-doping on the thermal quenching property of Er^{3+}-related emission in $Al_{0.70}Ga_{0.30}As$: Er.

2. Experimental

Er^{3+} ions of 1 MeV were implanted into undoped molecular beam epitaxy (MBE) grown $Al_{0.70}Ga_{0.30}As$

* Corresponding author. Tel.: + 81-44-934-7171; fax + 81-44-934-7909.
E-mail address: ce88010@isc.meiji.ac.jp (K. Uchiya)

0921-4526/99/$ - see front matter
PII: S0921-4526(99)00647-X

with a dose of 1×10^{13} cm^{-2} at room temperature. For $Al_{0.70}Ga_{0.30}As$, the projected range (R_P) and straggling (ΔR_P) were calculated to be 205.7 and 58.4 nm, respectively, from the data for the transport ions in materials computer program (TRIM). O ions were implanted into $Al_{0.70}Ga_{0.30}As$: Er with a dose ranging from 3×10^{13} to 3×10^{15} at an energy of 130 keV. R_P of the implanted O ions was almost the same as that of Er ions. After implantation, these samples were isochronally annealed for 10 min at 800°C, using the proximity cap method in H_2 atmosphere. In order to characterize the specimens, PL measurements were carried out using a 1 m focal length double-grating monochromator and photomultiplier (Hamamatsu Photonics R5509-72). Samples were excited by the 488.0 nm line of an Ar ion laser with a power of 10 mW.

3. Results and discussion

Fig. 1 shows the PL spectra at 18 K obtained from (1) $Al_{0.70}Ga_{0.30}As$: Er,O and (2) $Al_{0.70}Ga_{0.30}As$: Er. The maximum PL intensity of Er^{3+} was obtained at an O dose of 1×10^{15} cm^{-2}. In both samples, various peaks (indicated by arrows) were observed from the PL spectra; however, the spectral shape of the Er^{3+}-related emission was changed by co-doping O. The main peak (*a*:1537.2 nm) in the spectrum of (1) $Al_{0.70}Ga_{0.30}As$: Er,O is more than threefold of that (*b*':1538.2 nm) in the spectrum of (2) $Al_{0.70}Ga_{0.30}As$: Er. In addition, the full-width of half-maximum (FWHM) of (1) $Al_{0.70}Ga_{0.30}As$: Er,O and (2) $Al_{0.70}Ga_{0.30}As$: Er was 1.6 and 3.0 nm, respectively. Furthermore, Fig. 2 shows the PL time decay of the domain peaks (a–e and a'–f' in Fig. 1) at 18 K, obtained from their samples. In (1)

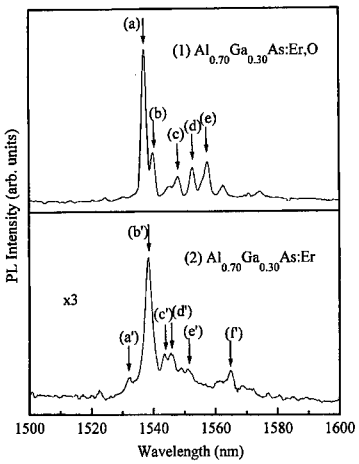

Fig. 1. PL spectra measured at 18 K for (1) $Al_{0.70}Ga_{0.30}As$: Er,O and (2) $Al_{0.70}Ga_{0.30}As$: Er.

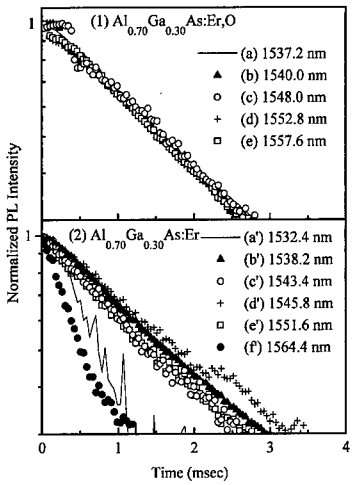

Fig. 2. PL time decay curves measured at various peaks for (1) $Al_{0.70}Ga_{0.30}As$: Er,O and (2) $Al_{0.70}Ga_{0.30}As$: Er at 18 K.

$Al_{0.70}Ga_{0.30}As$: Er,O, the PL time decay of all peaks (a–e) exhibit curves with nearly the same decay process. On the other hand, the curves for (2) $Al_{0.70}Ga_{0.30}As$: Er were different for each peak (a'–e'). We suggest that these results indicate that one kind of center is selectively formed by O co-doping. Furthermore, it has been reported previously that one kind of optically active Er–O complex luminescence center can be selectively formed into GaAs : Er,O grown by MOCVD [3], and the result in Ref. [3] agrees with our suggestion. This indicates that the mechanism of the Er^{3+}-related emission in (1) $Al_{0.70}Ga_{0.30}As$: Er,O is much simpler than that of (2) $Al_{0.70}Ga_{0.30}As$: Er. Therefore, we investigated the thermal quenching property for (1) $Al_{0.70}Ga_{0.30}As$: Er,O in detail.

Fig. 3 shows the temperature dependence of the PL intensity and the lifetime for $Al_{0.70}Ga_{0.30}As$: Er,O at an O dose of 1×10^{15} cm^{-2}. From Fig. 3, we can observe a peculiar two-step decrease of the PL intensity. The PL intensity slightly decreased below 200 K; however, it exhibited rapid thermal quenching above 200 K. The experimental data for $Al_{0.70}Ga_{0.30}As$: Er,O are plotted together with the theoretical lines of best fit (solid lines) obtained using Eqs. (1) and (2) [6–8] using the parameters (C_1, C_2, E_1, E_2, C_A, E_A) shown in Table 1.

$$I(T) = I_0/1 + C_1\exp(-E_1/kT) + C_2\exp(-E_2/kT)\}, \quad (1)$$

$$1/\tau(T) = 1/\tau_r + 1/\tau_n, \quad (2)$$

where τ_n (the non-radiative lifetime) was assumed as follows:

$$1/\tau_n = C_A\exp(-E_A/kT). \quad (3)$$

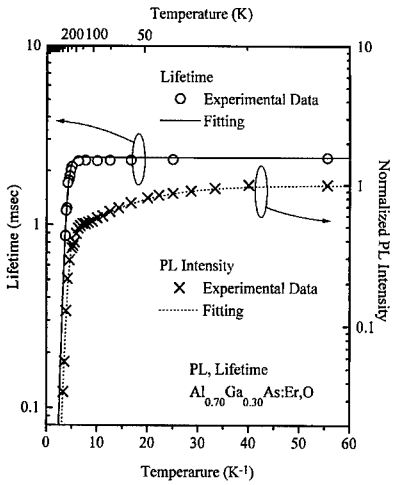

Fig. 3. Er^{3+}-related PL lifetime and intensity dependence on temperature for $Al_{0.70}Ga_{0.30}As$: Er,O.

Table 1
Activation energies obtained by fitting experimental results to Eqs. (1) and (2)

PL Intensity			
C_1	E_1 (meV)	C_2	E_2 (meV)
2.1	9.0	1×10^6	215
Lifetime			
C_A	E_A (meV)		
1×10^5	206		

Here, I_0 is the intensity when the electron emission from the Er-related trap is neglected. Therefore, it corresponds to the intensity at very low temperatures. T is the temperature, E_1, E_2 and E_A are the activation energies, and k is the Boltzmann constant. C_1, C_2 and C_A are the coupling coefficients at E_1, E_2 and E_A, respectively. τ and τ_r are the lifetime and the radiative lifetime, respectively. On the other hand, the value of E_2 (215 meV), the activation energy for rapid thermal quenching, was nearly equal to the value of E_A (206 meV), the activation energy for the decrease of the lifetime. Based on Eq. (2), the decrease of the lifetime confirms that the radiative efficiency is lower; therefore, we propose that rapid thermal quenching occurs above 200 K due to the decrease of the radiative efficiency. In addition, we infer that E_1 is the ionization energy of the e–h pair in the Er^{3+}-related trap level because it has been reported that the ionization energy is about 10 meV [7].

4. Conclusions

We studied Er^{3+}-related emission due to O co-doping in $Al_{0.70}Ga_{0.30}As$: Er using the co-implantation method. Er^{3+}-related emission at 1.54 μm was enhanced by O co-doping and we found that (i) the spectrum becomes sharper by O co-doping, and (ii) the various peaks exhibited similar decay curves as a result of O co-doping. We consider that these results indicate one kind of center selectively formed by O co-doping. Furthermore, from the temperature dependence of the PL intensity and the lifetime, E_2 (215 meV), the activation energy for rapid thermal quenching, was nearly equal to E_A (206 meV), the activation energy for the decrease of the lifetime. Based on the result, the decrease of the lifetime confirms that the radiative efficiency is lower; therefore, we propose that rapid thermal quenching occurs above 200 K due to the decrease of the radiative efficiency.

Acknowledgements

The authors thank Toshihiko Kanayama of the Electrotechnical Laboratory for technical support on low-energy ion implantation, and the personnel of Mitsubishi Kasei Corporation who provided the AlGaAs substrates. This work was supported in part by a Grant-in-Aid for Faculty Collaborative Research from the Institute of Science and Technology at Meiji University, Meiji High-Technology Research Center, and a General Scientific Research Grant (No. 10650020) from the Ministry of Education, Science, Sports and Culture, Japan.

References

[1] H. Katsumata, S. Uekusa, A. Majima, M. Kumagai, J. Appl. Phys. 77 (1995) 1881.
[2] H. Katsumata, S. Uekusa, H. Sai, J. Appl. Phys. 80 (1996) 2383.
[3] K. Takahei, A. Taguchi, J. Appl. Phys. 74 (1993) 1979.
[4] S. Uekusa, K. Utiya, M. Wakutani, M. Kumagai, Nucl. Instr. and Meth. B 148 (1999) 502.
[5] S. Uekusa, Y. Yano, K. Fukaya, M. Kumagai, Nucl. Instr. and Meth. B 127/128 (1997) 541.
[6] P. Wellmann, A. Winnacker, Mater. Res. Soc. Symp. Proc. 422 (1996) 255.
[7] A. Taguchi, K. Takahei, J. Appl. Phys. 79 (8) (1996) 4330.
[8] T. Kimura, H. Ishida, S. Yugo, R. Saito, H. Isshiki, T. Ikoma, Mater. Res. Soc. Symp. Proc. 301 (1993) 293.

ELSEVIER

Physica B 273–274 (1999) 781–783

PHYSICA B

www.elsevier.com/locate/physb

Optical ionization of DX center in AlGaAs : Se by inner-shell excitation

Y. Yoshino[a,*], K. Takarabe[a], M. Ishii[b], Y. Katayama[c], O. Shimomura[c]

[a]*Okayama University of Science, Ridai, Okayama 700-0005 Japan*
[b]*Japan Synchrotron Radiation Research Institute (JASRI), Sayo, Hyogo 679-5198 Japan*
[c]*Japan Atomic Energy Research Institute (JAERI), Sayo, Hyogo 679-5148 Japan*

Abstract

DX state is strongly localized. This nature could be investigated by observing relaxation process of localized electrons to emptied inner shells. We have found two different optical ionization processes of the DX center in $Al_xGa_{1-x}As$: Se ($x = 0.33$, $N_{Se} = 5 \times 10^{17}(cm^{-3})$) by using synchrotron radiation (SR). They are tentatively assigned to be a direct lift of an inner-shell electron to the conduction band (CB) followed by a capture of an electron at the DX center to the emptied inner shell ($DX^- + h\nu$(L, K-edge) $\rightarrow DX^0 + e_{CB}$) and the Auger ionization of one electron of the DX center to the CB followed by a capture of another electron to the emptied inner shell ($DX^- + h\nu$(L, K-edge) $\rightarrow DX^+ + e_{CB} + e_{vacuum}$).

Keywords: DX center; Inner-shell excitation; SR; ICTS

1. Introduction

Deep donor in n-AlGaAs has been studied for over two decades [1–3]. The deep donor called a DX center shows a persistent photoconductivity (PPC) [1] and a large Stokes shift between thermal and optical ionization energies [2]. This nature is understood by a large lattice-relaxation model [3]. The electronic ground state of the DX center is a strongly localized two-electron captured system. The localized nature could be investigated by exciting the inner shell of the DX center. We found new optical ionization processes of the DX center in AlGaAs : Se under synchrotron radiation (SR) which can excite the inner shell.

2. Experiment

$Al_xGa_{1-x}As$: Se ($x = 0.33$) sample is grown by molecular beam epitaxy (MBE) on n-type substrates, and the carrier concentration is $5 \times 10^{17}(cm^{-3})$. For the capacitance measurements, Al Schottky contacts, 500 μm in diameter, were evaporated onto AlGaAs : Se. Experiments using synchrotron radiation (SR) are performed at SPring-8 BL10XU high brilliance XAFS station in Hyogo Prefecture, Japan. An in-vacuum-type undulator is used for emitting source. SPring-8's standard monochromator equipped with a Si(1 1 1) double crystal is used to monochromatize the SR beam from the undulator. The sample temperatures are changed from 100 to 180 K.

The emission process of trapped electron at the DX center is monitored with isothermal capacitance transient spectroscopy (ICTS). The ICTS signal $S(t)$ for multiple electron emission rates is equal to :

$$S(t) = (q\varepsilon_r\varepsilon_0 A^2/2(V_d - V_b))\sum N_t^i(-e_n^i t)\exp(-e_n^i t) \quad (1)$$

where i denotes the ith component, q is electronic charge, ε_r and ε_0 are the dielectric constants of material and vacuum, respectively, A is diode area, V_d and V_b are the diffusion and bias voltage, and N_t and e_n the concentration of the filled trap (the electron occupancy of the center) and emission rate (relaxation time $\tau_n = e_n^{-1}$) for the center, respectively. The ICTS signal $S(t)$ has the

* Corresponding author. Tel.: 81-86-256-9440; fax: 81-86-256-8487.
E-mail address: yoko@das.ous.ac.jp (Y. Yoshino)

0921-4526/99/$ - see front matter
PII: S0921-4526(99)00648-1

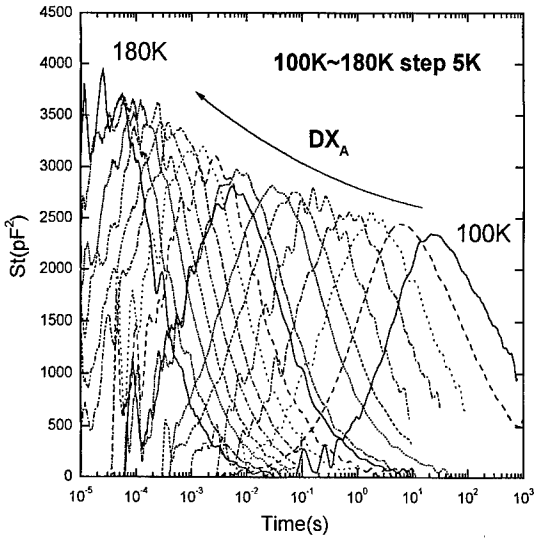

Fig. 1. ICTS spectra in AlGaAs : Se without SR irradiation in the range of temperature from 100 to 180 K.

maximum magnitude at $t = \tau_n = e_n^{-1}$ and the magnitude is proportional to the electron occupancy of the center.

3. Result and discussion

The ICTS spectra of the DX center in AlGaAs : Se without SR irradiation is shown in Fig. 1. The relaxation time becomes shorter as the temperature increases. The themal activation energy for this emission is evaluated to be 238 meV. This value is in good agreement with the reported result [4]. The ICTS spectra of the DX center with SR irradiation for photon energies of 10.2 and 12.8 keV are shown in Fig. 2(a) and (b), respectively. In the case of 10.2 keV photon, the L-shell is excited. The thermal emission is overlapped in the range of temperature, however it is seen that two optical emission of the DX center appear at the relaxation times of 1.2 and 9.0 s. These relaxation times are independent of temperature, which implies that the emission process is not by a thermal but optical excitation. In the case of 12.8 keV photon, the L- and K-shells are excited. Again, two optical emission with the same relaxation times for the L-shell excitation appear.

By comparing these two relaxation times, the optical cross section for the faster emission ($\tau = 1.2$ s) is larger by a factor of about 7.5 than that for the slower emission ($\tau = 9.0$ s). The optical cross section involves quantum mechanical information for the excitation of an electron at the DX center. The tentatively proposed model for the ionization of the DX center by the inner-shell excitation is shown in Fig. 3. Process (1) is a direct lift of the

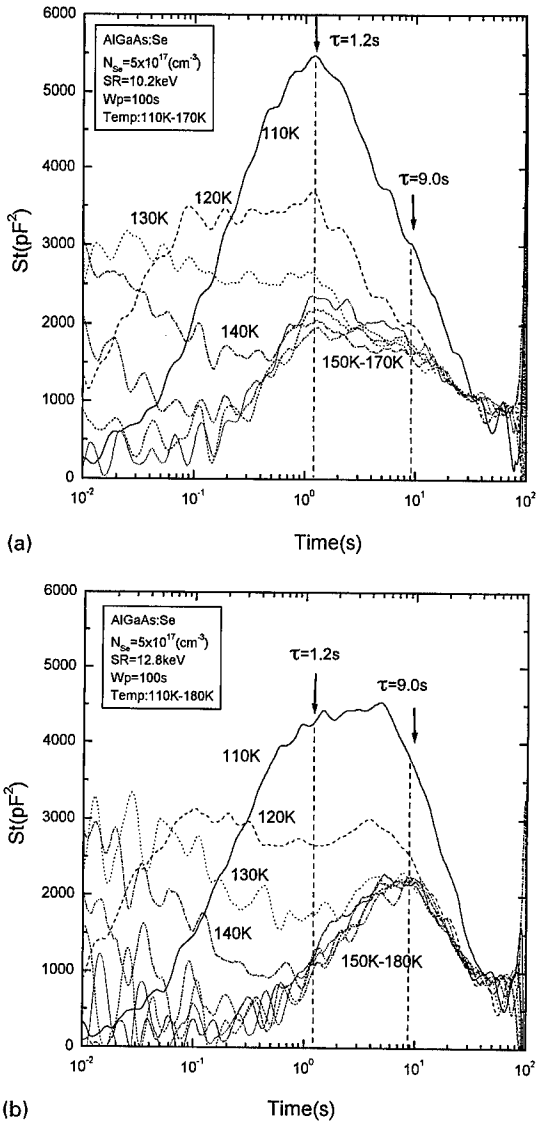

Fig. 2. (a) ICTS spectra in AlGaAs : Se under 10.2 keV SR irradiation in the range of temperature from 110 to 170 K; (b) ICTS spectra in AlGaAs : Se under 12.8 keV SR irradiation in the range of temperature from 110 to 180 K.

inner-shell electron to the conduction band (CB) followed by a capture of an electron at the DX center to the emptied inner shell. The other process (2) is the Auger excitation of one electron of the DX center to the CB followed by the capture of another electron to the emptied inner shell. The Auger process is a higher-order process, so the relaxation time is expected to be longer. The neutral DX^0 state is left for the process (1) and the positively changed DX^+ state is left for process (2). The SR photon energy is known to change the relative signal

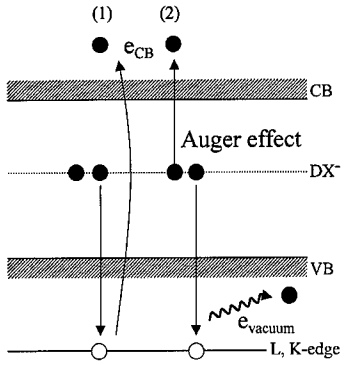

Fig. 3. A model for optical ionization of DX center by SR irradiation: (1) $DX^- + h\nu(\text{L, K-edge}) \rightarrow DX^0 + e_{CB}$; (2) $DX^- + h\nu(\text{L, K-edge}) \rightarrow DX^+ + e_{CB} + e_{vacuum}$.

intensity between the two processes. We need more study to have a clue for these phenomena. In particular, it is expected to investigate this by varying the SR photon energy.

4. Conclusion

When the sample is irradiated with SR, two different optical ionization processes appear in the ICTS spectra. They are tentatively explained by a direct lift of an inner-shell electron to the conduction band and the Auger ionization of an electron at the DX center.

Acknowledgements

We wish to thank Mr. Ohnishi of ATR for kindly providing us the samples. The synchrotron radiation experiments were performed at the SPring-8 with the approval of the JASRI (Proposal No. 1999A0117-NX).

References

[1] R.J. Nelson, Appl. Phys. Lett. 31 (1977) 351.
[2] D.V. Lang, R.A. Lorgan, M. Jaros, Phys. Rev. B 19 (1979) 1015.
[3] D.J. Chadi, K.J. Chang, Phys. Rev. B 39 (1989) 10063.
[4] E.G. Oh, M.C. Hanna, Z.H. Lu, D.M. Szmyd, A. Majerfeld, J. Appl. Phys. 74 (2) (1993) 1057.

ELSEVIER

Physica B 273–274 (1999) 784–787

PHYSICA B

www.elsevier.com/locate/physb

Mechanism for dicarbon defect formation in AlAs and GaAs

C.D. Latham[a,*], R. Jones[a], M. Haugk[b], Th. Frauenheim[c], P.R. Briddon[d]

[a]*School of Physics, University of Exeter, Exeter, EX4 4QL, UK*
[b]*Technische Universität, Institut für Physik, Theoretische Physik III, D-09107 Chemnitz, Germany*
[c]*Universität-GH Paderborn, Theoretische Physik, Fachbereich Physik, D-33098 Paderborn, Germany*
[d]*Department of Physics, University of Newcastle upon Tyne, Newcastle, NE1 7RU, UK*

Abstract

There is a need to understand the degradation mechanism which results in the loss of substitutional C_{As} shallow acceptors in AlAs and GaAs containing high concentrations ($\gtrsim 10^{20}\,cm^{-1}$) of carbon. The activation energy for the migration of interstitial carbon atoms, C_i, in AlAs and GaAs is calculated using a local-density functional-based method, *AIMPRO*, to be $\lesssim 1$ eV. This model is consistent with a 'kick-out' mechanism being responsible for the observed loss of C_{As}, and formation of dicarbon defects. Three local minima separated by only a few tenths of an eV are encountered by a diffusing carbon atom along its path through the crystal. These have $(C–As)_{As}$ split interstitial, bond-centred M–C–As, and $(C–M)_M$ split interstitial structures (M = Al, Ga). Interstitial dicarbon defects, $(C–C)_i$, or substitutional dicarbon defects, $(C–C)_{As}$, are produced depending on whether a C_i meets a $(C–M)_M$ split interstitial or a C_{As}. These possess Raman-active C–C vibrational modes near to that for a free dicarbon molecule, C_2.

PACS: 66.30.Jt; 61.72.Bb; 61.72.Ji; 71.15.Nc

Keywords: Aluminium-arsenide; Gallium-arsenide; Defects; Carbon; Diffusion

1. Introduction

In previous Raman scattering studies of heavily carbon-doped AlAs and GaAs it was found that the formation of dicarbon defects were the most likely explanation for the drastic fall in hole concentration, [p], observed upon annealing these materials at temperatures above ~ 600°C [1–3]. Two Raman-active C–C vibrational modes separated by $\approx 100\,cm^{-1}$ and near to that for a free C_2 molecule were detected, and the strength of the lines increased with the length and temperature of heat treatment. Supporting ab initio calculations considered three main alternative interpretations for the experimental findings. Firstly, it was suggested that the structure of the complexes had interstitial $(C–C)_i$ or substitutional $(C–C)_{As}$ forms which corresponded with the two Raman modes. This was rejected on the grounds that the ratio of the intensities of the two lines is nearly constant in both AlAs and GaAs, regardless of annealing time and temperature. If the lines were due to interstitial and substitutional types of defect, it would be expected that the formation rate of each would be different, and hence the intensity ratio of the lines would be variable. A second model was that the two lines were due to two different charge states of the same defect. The $(C–C)_{As}$ complex is a deep donor with a singly occupied level near mid-gap. In the neutral state, the carbon pair is aligned very nearly along a $\langle 1\,0\,0\rangle$ direction – exact D_{2d} symmetry is broken by the Jahn–Teller effect. When the defect is singly ionised, the alignment changes to $\langle 1\,1\,0\rangle$ with C_{2v} symmetry. This is accompanied by a slight shortening of the C–C distance and an increase in the frequency of the fundamental mode. However, as the Fermi level lies close to the top of the valence band in strongly p-type material, almost all the centres would be ionised, and the concentration of neutral complexes

* Corresponding author.
E-mail address: c.d.latham@ex.ac.uk (C.D. Latham)

0921-4526/99/$ - see front matter
PII: S0921-4526(99)00649-3

would be too small to give a detectable Raman signal. In the third model, it was found that the ionised $(C\text{–}C)^{+}_{As}$ complex aligned along a $\langle 1\,1\,1\rangle$ axis with C_{3v} symmetry is very nearly degenerate in energy with the $\langle 1\,1\,0\rangle$ form. Moreover, the calculated splitting in crystals doped with a mixture of ^{12}C and ^{13}C isotopes of the ^{12}C–^{13}C mode of $\langle 1\,1\,1\rangle$ oriented complexes ($\lesssim 4\,cm^{-1}$) is less than the resolution of the Raman scattering experiments. This would otherwise rule out this model as no splitting is observed. A number of other suggestions were also considered, but none of these turned out to be viable on closer scrutiny.

Having found these models for dicarbon defects in AlAs and GaAs it is now natural to consider mechanisms for their formation. A preliminary survey using self-consistent-charge density-functional tight-binding (*SCC-DFTB*) and fully selfconsistent density functional (*AIMPRO*) methods, examined the diffusion of interstitial carbon atoms in GaAs [4]. In p-type material these would be in the doubly ionised charge state, C_i^{2+}. It was first found with both theoretical methods that there are three metastable structures with low energy for a C_i^{2+} atom. In order of increasing stability these are (1) a $(C\text{–}As)^{2+}_{As}$ split interstitial, (2) a $(As\text{–}C\text{–}Ga)^{2+}$ bond-centred interstitial, and (3) a $(C\text{–}Ga)^{2+}_{Ga}$ split interstitial. Less than 0.4 eV separates the highest and lowest state, suggesting that a carbon atom may diffuse easily along a path connecting these structures – see Fig. 1. Subsequent simulations tested this idea. The largest energy barrier encountered is 0.7 eV which occurs when a carbon atom moves from a $(C\text{–}Ga)^{2+}_{Ga}$ split interstitial state to a $(As\text{–}C\text{–}Ga)^{2+}$ bond-centred interstitial position. This figure is in good agreement with the measured value of ~ 1 eV for the hole loss process [5].

If a similar mechanism is responsible for dicarbon defect formation in AlAs as in GaAs, the activation energy for the process is likely to be ~ 1 eV too. A critical difference between the two materials which has the potential to have a significant effect is the relative strength of C–Al and C–Ga bonds. In general carbon forms stronger bonds with aluminium than gallium. When a carbon atom moves from a $(C\text{–}As)^{2+}_{As}$ split interstitial state to a $(As\text{–}C\text{–}M)^{2+}$ bond-centred position (M = Al, Ga), it can be seen from Fig. 1 that a C–Al or C–Ga bond is broken and a C–As bond is formed. The differences in C–Al and C–Ga bond strengths are expected to result in different relative energies of the two states, and different activation energies for this step. The strength of Al–As and Ga–As bonds are very nearly equal. For the diatomic molecules the bond dissociation energy, D°_{298}, of an Al–As bond is $202.9\,kJ\,mol^{-1}$ (2.103 eV), and of a Ga–As bond is $209.6\,kJ\,mol^{-1}$ (2.172 eV) [6]. Hence no significant difference is expected for the second part of the reaction taking a carbon atom from the $(As\text{–}C\text{–}M)^{2+}$ bond-centred position to the $(C\text{–}M)^{2+}_{M}$ split interstitial configuration.

2. Methods

The calculations were performed in a similar manner to that described previously using the self-consistent local density functional based (*AIMPRO*) method [4]. This gives the total energy of H-terminated atomic clusters, using a Gaussian basis set with atom and bond-centred orbitals, a conjugate-gradient energy minimisation algorithm, and norm-conserving pseudopotentials [7]. Full details of the method are given in a recent review [8].

A system of constraints on the atomic coordinates is used to simulate reactions. Where pairs of bonds which are exchanged can be identified (i.e. one member of a pair breaks as the other forms), a convenient choice of reaction coordinates are the difference of the squares of the bond lengths of each bond pair. That is, $r_a^2 - r_b^2$, where r_a and r_b are the bond lengths of a given pair. Fig. 1

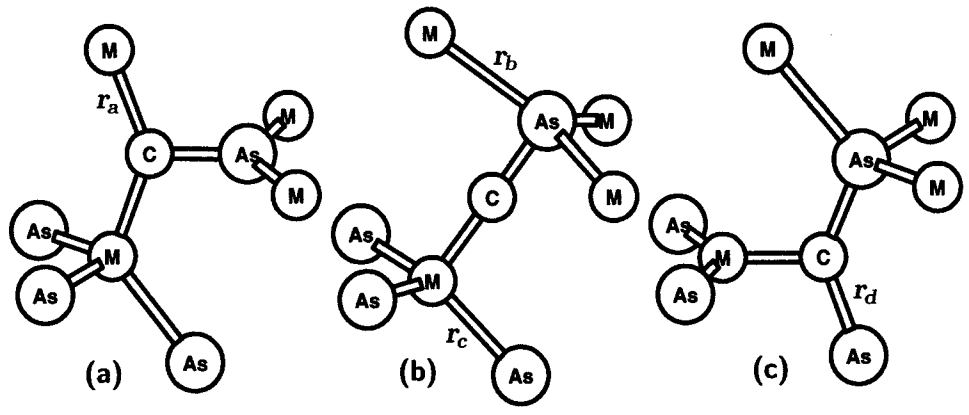

Fig. 1. Diffusion mechanism for C_i^{2+} in AlAs and GaAs: local minima are found at (a) $(C\text{–}As)^{2+}_{As}$ split interstitial, (b) bond-centred C interstitial, and (c) $(C\text{–}M)^{2+}_{M}$ split interstitial configurations along the migration path.

shows that when a carbon atom moves from either of the split interstitial states to a bond centred state, one pair of bonds is exchanged in each case.

These calculations used 135-atom clusters with the compositions $CAl_{34}As_{34}H_{66}$ and $CGa_{34}As_{34}H_{66}$. The unequal distribution of group III and group V atoms in these clusters imposes a significant dipole moment on them. This is compensated for by substituting the hydrogen atoms saturating the surface with 'pseudo-hydrogen' atoms. These have nuclear charges of $\frac{3}{4}$ or $\frac{5}{4}$ when an H-atom replaces, respectively, a group III or group V atom from the bulk.

3. Results

It is assumed throughout that in strongly p-type materials, the Fermi level lies near the top of the valence band, hence carbon interstitial defects always exist in a doubly ionised state, C_i^{2+}. The calculated relative energies of the split-interstitial and bond-centred structures for C_i^{2+} are given in Table 1.

Table 1
Calculated energies (eV) of the $(C\text{–}As)_{As}^{2+}$ and $(M\text{–}C\text{–}As)^{2+}$ defects in AlAs and GaAs relative to $(C\text{–}M)_M^{2+}$

	AlAs	GaAs[a]
$(C\text{–}As)_{As}^{2+}$	−0.16	0.38
$(M\text{–}C\text{–}As)^{2+}$	0.38	0.30

[a]Ref. [4].

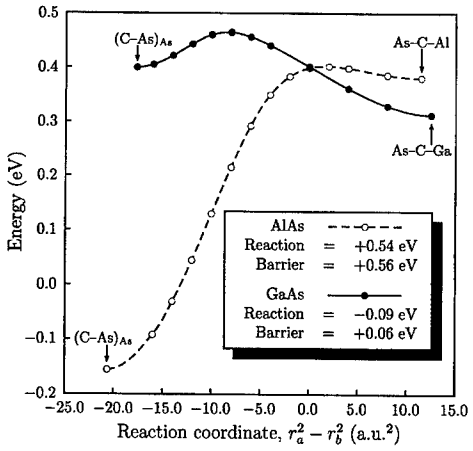

Fig. 2. Energy relative to the $(C\text{–}M)_M^{2+}$ complex plotted as a function of the reaction coordinate $r_a^2 - r_b^2$ described in the main text and Fig. 1. The reaction energy and barrier height are given relative to the initial $(C\text{–}As)_{As}^{2+}$ state.

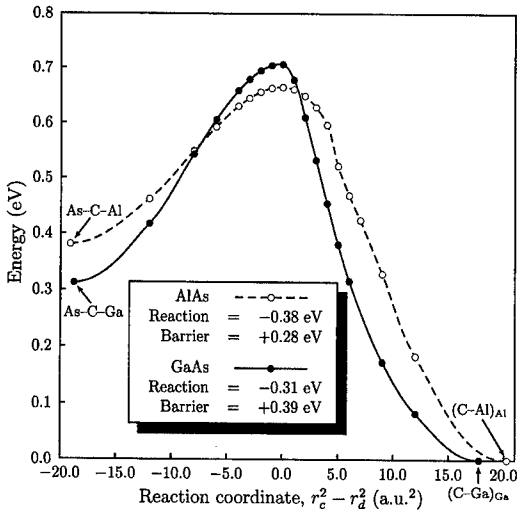

Fig. 3. Energy relative to the $(C\text{–}M)_M^{2+}$ complex plotted as a function of the reaction coordinate $r_c^2 - r_d^2$ described in the main text and Fig. 1. The reaction energy and barrier height are given relative to the intermediate $(M\text{–}C\text{–}As)^{2+}$ state.

Note that the $(C\text{–}As)_{As}^{2+}$ split interstitial state in AlAs has a relatively low energy, reflecting the strength of C–Al bonds as explained previously.

Figs. 2 and 3 plot the relative energy as a function of the reaction coordinates described previously in Section 2. This shows graphically the relative difficulty of breaking a C–Al compared with a C–Ga bond. Although the activation energy for this part of the migration path is much higher in AlAs than in GaAs, it is still somewhat smaller than the activation energy for a carbon atom to move from a $(C\text{–}Al)_{Al}^{2+}$ split interstitial state to a $(As\text{–}C\text{–}Al)^{2+}$ bond-centred state. The diffusion of C_i^{2+} from the group III split interstitial complex is, therefore, the rate-limiting step in both materials. Moreover, the activation energy for this step is approximately the same in both cases. In AlAs the calculated value is 0.67 eV, and in GaAs it is 0.71 eV. The difference – only 0.04 eV – is too small to be significant.

4. Conclusions

The main conclusion which can be drawn from the results of the local density functional theory-based calculations presented here is that the activation energy for the diffusion of C_i^{2+} atoms is approximately 0.7 eV in both AlAs and GaAs. The reaction path in both materials passes through three local minima in potential energy at split interstitial and bond-centred sites. This model reaction provides a mechanism for the formation of dicarbon defects in AlAs and GaAs once carbon atoms are present in the C_i^{2+} state. It strongly suggests that there is a source of highly mobile interstitial arsenic atoms, As_i, in the

material to displace C_{As} atoms creating, initially, $(C\text{–}As)^{2+}_{As}$ complexes. If this is the case, then the diffusion of C in AlAs and GaAs will cease if the supply of As_i is exhausted or suppressed. It is unknown what the source of As_i is, however, we suggest that extended defects similar to the {3 1 1} agglomerates in Si, or other As_i clusters are plausible candidates.

Acknowledgements

The Engineering and Physical Sciences Research Council (EPSRC), UK, is thanked for its financial support at Exeter University (contract GR/L34457).

References

[1] J. Wagner et al., Phys. Rev. Lett. 78 (1997) 74.
[2] C.D. Latham et al., Phys. Status Solidi B 210 (1998) 869.
[3] B.R. Davidson et al., Phys. Rev. B 60 (1999) 5447.
[4] C.D. Latham et al., Phys. Rev. B 60 (1999), in press.
[5] H. Fushimi, K. Wada, J. Appl. Phys. 82 (1997) 1208.
[6] L.D.R. (Ed.), CRC Handbook of Chemistry and Physics, 77 Edition, CRC Press, Boca Raton, FL, USA, 1996.
[7] G.B. Bachelet, D.R. Hamann, M. Schlüter, Phys. Rev. B 26 (1982) 4199.
[8] R. Jones, P.R. Briddon, in: M. Stavola (Ed.), Identification of Defects in Semiconductors, Vol. 51A of Semiconductors and Semimetals, Academic Press, Boston, 1998 (Chapter 6).

ELSEVIER

Physica B 273–274 (1999) 788–791

PHYSICA B

www.elsevier.com/locate/physb

Vibrational excited-state transitions of substitutional carbon in gallium arsenide

H.Ch. Alt*

Department of Engineering Physics, FHM - University of Applied Sciences, Lothstrasse 34, 80335 München, Germany

Abstract

New local modes due to substitutional carbon, C_{As}, have been detected at 566.2 cm^{-1} and at 1134.2 and 1149.3 cm^{-1}, respectively, by Fourier transform infrared absorption spectroscopy. The bands are attributed to excited-state transitions of the carbon local oscillator. Based on a comparison with recent theoretical predictions, the energy-level diagram including anharmonicity is discussed. © 1999 Elsevier Science B.V. All rights reserved.

Keywords: Gallium arsenide; Carbon acceptor; Local modes; Anharmonicity

1. Introduction

The fundamental of the local vibration of anion-site carbon in gallium arsenide, C_{As}, at 582 cm^{-1} is a prominent feature in the infrared (IR) absorption spectrum of gallium arsenide. The band has been studied thoroughly both experimentally and theoretically [1–4], because of the technological importance of carbon as the dominant acceptor in semi-insulating (SI) GaAs and because of the experimentally well-resolved impurity ($^{12}C/^{13}C$) and host ($^{69}Ga/^{71}Ga$) isotope shift which makes it to a model system for local modes in this III–V semiconductor.

Recently, a thermally activated sideband at 576.5 cm^{-1} (300 K) has been reported which can be attributed to a transition between the first- and the second-excited state ($T_2(v = 1) \rightarrow T_2(v = 2)$) of the carbon local oscillator [5,6]. The shift to lower energy is due to anharmonic contributions to the interatomic potential between carbon and its nearest gallium neighbors. However, two other $v = 1$ to 2 transitions with an A_1 singlet and E doublet, respectively, final state were not observed although IR active.

Using a four-parameter model for the interatomic potential Robbie et al. [7] carried out new calculations of the energy levels of the local oscillator. Including anharmonicity up to quartic terms, their results based on Schrödinger's perturbation theory also predict the energy positions of the missing $v = 1$ to 2 transitions. Furthermore, they extended the calculations to third harmonics and concluded that the observation of corresponding thermally activated absorption bands on the low-energy side of the second harmonic at 1156.2 cm^{-1} should be possible. In this paper we reinvestigate the absorption structure due to C_{As} in GaAs and compare the experimental findings with the theoretical predictions.

2. Experimental

Fourier transform infrared (FTIR) absorption measurements were carried out with a high-resolution vacuum instrument (Bruker IFS 113v) equipped with a globar source, a mercury cadmium telluride (MCT) detector, and a variable-temperature cryostat (10–300 K). The samples investigated were cut from SI single crystals grown by the liquid-encapsulated Czochralski (LEC) technique. The carbon concentration in the samples was selected between 5×10^{15} and 2×10^{16} cm^{-3} according to DIN 50449-1 [8] in order to obtain a sufficient absorption signal for the relatively weak excited-state transitions.

* Fax: + 49-89-1265-1480.
E-mail address: hchalt@rz.fh-muenchen.de (H.Ch. Alt)

0921-4526/99/$ - see front matter
PII: S0921-4526(99)00650-X

3. Results and discussion

A room-temperature FTIR absorption spectrum in the region of the fundamental is shown in Fig. 1. On the low-energy side of the fundamental at 579.8 cm^{-1} (300 K) three additional absorption bands are visible. The band at 576.5 cm^{-1} has been discussed in detail previously [5,6]. The correspondence to the excited-state transition $T_2(v=1) \rightarrow T_2(v=2)$ has been verified. The small peak at 558.8 cm^{-1} is due to the fundamental of the ^{13}C isotope (natural abundance 1.1%). The shift of 21.0 cm^{-1} is close to the value found previously [9]. Also, at low temperatures, the typical host-isotope ($^{69}Ga/^{71}Ga$) fine structure (not shown here) is observed.

The new band at 566.2 cm^{-1} is observed only in carbon-rich crystals and is attributed to the missing $T_2(v=1) \rightarrow A_1(v=2)$ transition. The experimentally observed shift of -10.3 cm^{-1} relative to the 576.5 cm^{-1} band has to be compared with the shift of -10.7 cm^{-1} predicted by Robbie et al. [7]. The Arrhenius plot (Fig. 2) of the temperature dependence of the strength of the band, measured as the integrated absorption, gives an activation energy of 68.1 meV. This is close to the activation energy expected from the occupation of the first excited state according to Boltzmann statistics, i.e. $\sim \exp(-E_A/k_B T)$, with $E_A = 71.9$ meV (579.8 cm^{-1}) being the energy difference between the ground state and the first excited state at 300 K. Using a similar argumentation as in Ref. [6], the expected strength of the band in harmonic approximation is proportional to

$$\omega|\langle\psi(1)_{T_2}||\psi(2)_{A_1}\rangle|^2 = \omega|\langle 1\,0\,0|x/\sqrt{3}|2\,0\,0\rangle|^2,$$

where $\psi(1)_{T_2}$ and $\psi(2)_{A_1}$ are the first- and second-excited state of T_2 and A_1 symmetry, respectively. At 300 K, the occupation of each of the triply degenerate first excited states is 6.2% relative to the ground state. As the strength of the fundamental is proportional to $\omega|\langle 0\,0\,0|x|1\,0\,0\rangle|^2$, it follows that the integrated absorption of the 566.2 cm^{-1} band should be $2/3 \times 6.2\% = 4.1\%$ relative to the fundamental. The experimental value derived from the spectrum shown in Fig. 1 is 3.9%. Therefore, the agreement is quite good and substantiates the assignment of the band.

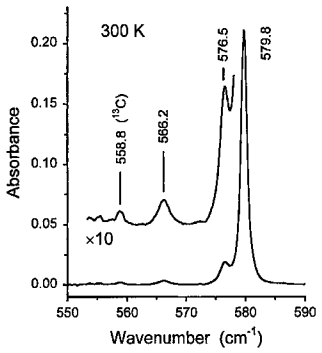

Fig. 1. Absorption spectrum of SI GaAs showing excited-state transitions of the $^{12}C_{As}$ local oscillator on the low-energy side of the fundamental. The band at 558.8 cm^{-1} is the fundamental of the $^{13}C_{As}$ isotope (natural abundance 1.1%).

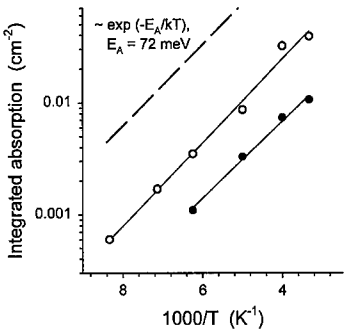

Fig. 2. Arrhenius plot of the intensity of the bands at 566.2 (full circles) and 576.5 cm^{-1} (open circles).

The question remains about the missing $T_2(v=1) \rightarrow E(v=2)$ transition. As theory predicts a frequency of 1165.2 cm^{-1} for the E doublet [7], the transition should be at 582.5 cm^{-1} (both at zero temperature). Assuming the same shift with temperature as it is found for the fundamental (2.9 cm^{-1}), at 300 K the transition is expected to occur at about 579.6 cm^{-1}. Therefore the transition would be hidden under the fundamental (579.8 cm^{-1}) and could not be observed directly. Nevertheless, we present some experimental evidence that this is actually the case. According to Boltzmann statistics, at 300 K 82.7% of the oscillators are in the ground state, 15.4% in the triply degenerate first-excited state, and 1.9% in the sixfold degenerate second-excited state (degeneracy in harmonic approximation). Summing up the expected intensity for the fundamental and the excited-state transitions $T_2(v=1) \rightarrow T_2(v=2)$ and $T_2(v=1) \rightarrow E(v=2)$ in a similar way as explained above, 99.8% of the intensity of the fundamental at low temperatures where excited states play no role ($T < 100$ K) is obtained. By contrary, the sum of the fundamental and the $T_2(v=1) \rightarrow T_2(v=2)$ transition alone gives only a value of 93.0%. This has to be compared with the experimentally observed value of $99.2 \pm 3.5\%$ (average over several samples) for the integrated absorption of the main band at 579.8 cm^{-1} and the sideband at 576.5 cm^{-1} relative to the integrated absorption of the fundamental at low temperatures. Keeping in mind that there is a tendency to underestimate systematically the integrated absorption at room temperature because of the broad tails of the absorption structure, the theoretical prediction that the $T_2(v=1) \rightarrow E(v=2)$ transition is hidden under the fundamental is clearly favored.

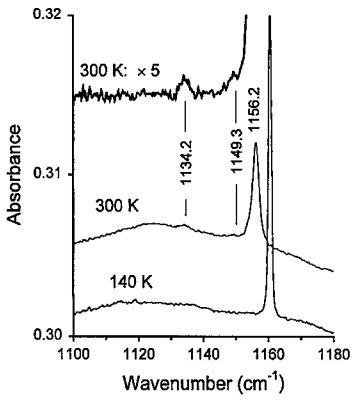

Fig. 3. Excited-state transitions ($v = 1 \rightarrow v = 3$) at 300 K in the neighborhood of the second-harmonic transition. The upper spectrum is obtained after subtraction of a smooth background. The spectrum at 140 K is shown for comparison.

Now, the spectral range in the neighborhood of the second-harmonic transition appearing at 1156.2 cm^{-1} (300 K) is considered (Fig. 3). Robbie et al. [7] calculate frequencies of the third excited states of 1744.1 cm^{-1} (T_2 symmetry), 1741.3 cm^{-1} (T_1 symmetry), 1738.2 cm^{-1} (A_1 symmetry), and 1721.6 cm^{-1} (T_2 symmetry). We looked at these frequencies, however, no carbon-related absorption could be detected. Even under vacuum conditions FTIR measurements are difficult in this spectral range because of interference with many absorption lines due to residual water vapor. Fortunately, these levels should be measurable as thermally activated ($v = 1$) $\rightarrow$ ($v = 3$) transitions on the low-energy side of the second-harmonic frequency. The calculated shifts are -0.6, -3.5, -6.6, and -23.1 cm^{-1} [7]. At 300 K the first two of these bands cannot be observed because the FWHM of the second harmonic is 2.4 cm^{-1} and the bands are hidden under the low-energy tail. However, the latter two are clearly separated from the second harmonic. Their intensity should again be proportional to $\exp(-E_A/k_B T)$.

Indeed, in the room-temperature absorption spectrum two weak absorption bands at 1149.3 ± 0.2 and at 1134.2 ± 0.1 cm^{-1} are detected. These bands are thermally activated as no corresponding bands are observed in the spectrum of the same sample taken at 140 K (Fig. 3). These new bands are attributed to the $T_2(v = 1) \rightarrow A_1(v = 3)$ and the lower-frequency $T_2(v = 1) \rightarrow T_2(v = 3)$ transition, respectively. The shifts are -6.9 and -22.0 cm^{-1}, in good agreement with the calculation. The activation energy cannot be determined because the bands are too weak. However, at 300 K the

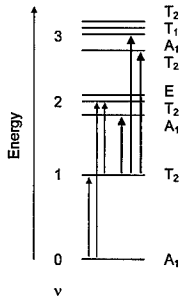

Fig. 4. Schematic energy-level diagram of the anharmonic C_{As} local oscillator. The new transitions are shown by bold arrows.

Table 1
Energy levels of the anharmonic $^{12}C_{As}$ oscillator. Experimental values are derived from the centroid of the transition. To obtain energies at low temperature from the excited-state transitions observed at 300 K the same relative shift with temperature is assumed as it is measured for the fundamental. All energies are given in cm^{-1}

Designation of the energy level		Theoretical prediction after Robbie et al. [7]	Experimental observation at 300 K	Experimental values at low temperature (extrapolated, if not observed)	Difference between experiment and theory
v	Type				
1	T_2	582.68[a]	579.8 ± 0.05	582.68	0.0
2	A_1	1151.4	1146.0 ± 0.1	1151.7	+0.3
2	T_2	1162.08[a]	1156.2 ± 0.1	1162.08	0.0
2	E	1165.2	?		
3	T_2	1721.6	1714.0 ± 0.2	1722.5	+0.9
3	A_1	1738.2	1729.1 ± 0.3	1737.7	−0.5
3	T_1	1741.3	?		
3	T_2	1744.1	?		

[a]Values fitted to the FTIR transition frequency observed at low temperatures.

integrated absorption of the 1149.3 cm^{-1} band is $5 \pm 3\%$ compared to the second harmonic, that of the 1134.2 cm^{-1} band is $4 \pm 1\%$, respectively. The expected values for the $T_2(v = 1) \rightarrow A_1(v = 3)$ transition are 6.2% and for both $T_2(v = 1) \rightarrow T_2(v = 3)$ transitions 12.4% [7]. The agreement is satisfactory in view of the relatively large experimental errors caused by the weakness of the bands.

All transitions observed are displayed schematically in the energy-level diagram shown in Fig. 4. Finally, a comparison between the frequencies determined experimentally and those predicted by calculation is given in Table 1.

4. Conclusion

The local vibration of substitutional carbon in GaAs, C_{As}, is the first example for a semiconductor crystal where anharmonic contributions to the interatomic oscillator potential have been both experimentally verified and theoretically calculated. The new $(v = 1) \rightarrow (v = 2)$ and $(v = 1) \rightarrow (v = 3)$ transitions reported here allow the comparison with energy levels predicted by quantum-mechanical perturbation theory. The good agreement found in this case may provide the basis to transfer the results to other light-impurity defect systems in semiconductors.

Acknowledgements

The author thanks M.J.L. Sangster of the University of Reading for helpful discussions and W. Ulrici for the possibility to carry out some FTIR measurements at the Paul-Drude-Institute in Berlin. The supply of samples with high carbon contents by FCM (Freiberger Compound Materials) is gratefully acknowledged.

References

[1] W.M. Theis, K.K. Bajaj, C.W. Litton, W.G. Spitzer, Appl. Phys. Lett. 41 (1982) 70.
[2] R.S. Leigh, R.C. Newman, J. Phys. C: Solid State Phys. 15 (1982) L1045.
[3] R.S. Leigh, R.C. Newman, M.J.L. Sangster, B.R. Davidson, M.J. Ashwin, D.A. Robbie, Semicond. Sci. Technol. 9 (1994) 1054.
[4] R.S. Leigh, M.J.L. Sangster, Phys. Rev. B 54 (1996) 5562.
[5] H.Ch. Alt, B. Dischler, Appl. Phys. Lett. 66 (1995) 61.
[6] H.Ch. Alt, in: M. Suezawa, H. Katayama-Yoshida (Eds.), Materials Science Forum, Vols. 196–201, Trans Tech, Zuerich, 1995, pp. 1577–1581.
[7] D.A. Robbie, R.S. Leigh, M.J.L. Sangster, Phys. Rev. B 56 (1997) 1381.
[8] DIN 50449-1, Deutsches Institut fuer Normung, 1995.
[9] M.J. Ashwin, R. Ware, R.C. Newman, Find an isotope shift of 21.06 cm^{-1} (at low temperatures), unpublished.

ELSEVIER

Physica B 273–274 (1999) 792–795

PHYSICA B

www.elsevier.com/locate/physb

New type of persistent photoconductivity related to DX-center: the study of interband PPC in Si-doped AlGaAs

R. Piotrzkowski[a,*], E. Litwin-Staszewska[a], F. Bosc[b], J. Sicart[b], J.L. Robert[b]

[a]*High Pressure Research Center, Polish Academy of Sciences, Sokolowska 29/37, 01-142 Warsaw, Poland*
[b]*GES, University Montpellier II, 34095 Montpellier, France*

Abstract

We studied the build-up of the persistent photoconductivity (PPC) in $Al_xGa_{1-x}As$ ($x = 0.15$) doped with Si. The Hall electron concentration and the conductivity were measured at 77 K as a function of time while the sample was illuminated by the monochromatic light. The case of excitation by photons with energy below the gap was compared to that by photons with energy just above the gap. The first mode leads to optical ionization of DX centers. The new mechanism of persistent emptying of DX centers, specific for inter-band PPC, is related to the capture of photo-created holes by negatively charged DX ions. Our results indicate the importance of effects of correlated space distribution of charges on impurity sites. The evolution of mobility during the build-up indicates that illumination with above-gap photons *increases* the degree of correlation, in contrast to the lower-energy ones. By analyzing the transients $n(t)$ we conclude that the effective cross section for hole capture decreases dramatically during the build-up process. This indicates that the hole capture by DX^- ions is strongly influenced by the Coulomb potential from the nearest impurity ions.

Keywords: DX-centers; Persistent photoconductivity; Hole capture; Charge correlation

The persistent photo-conductivity (PPC) is perhaps the most characteristic phenomenon related to DX-centers. As a result of their metastable character, if the sample is illuminated with the light which transfers electrons from DX-centers to the conduction band, the increased free electron concentration persists after the light is switched off. Using pulses of light, one can gradually increase the electron concentration in a given sample at a constant temperature. This possibility offered by the PPC was widely used in studying the effect of spatial correlation of impurity charges on free electron mobility (see review paper [1]). This effect is important in materials where a mean distance between DX donors is comparable with the screening length which determines the range of Coulomb interaction between the charged impurities. In systems where such correlations exist, the electron mobility limited by the ionized impurities cannot be represented as a function of the total density of charged scattering centers. Instead, a hysteresis of mobility is observed. Fig. 1 presents typical mobility loops observed in δ-doped 2-D $Al_{0.3}Ga_{0.7}As/In_{0.15}Ga_{0.85}As/GaAs$ structures (see Ref. [3]). A similar hysteresis was observed in 3-D $Al_{0.25}Ga_{0.75}As$ samples by Coz et al. [2]. In this case the mobility measured at $T = 7$ K, when the electron concentration was increased with PPC, corresponded to the lower branch of the hysteresis. To decrease this concentration in a stepwise fashion the sample was temporarily heated to temperatures high enough to overcome the barrier for capture of electrons by DX centers. Between these thermal transients, mobility measurements were taken at 7 K. These data traced the upper branch of hysteresis. Fig. 1 shows an alternative method of tuning the concentration, in this case filling by high-pressure freeze-out (HPFO) and emptying by thermally activated emission [1–3]. In each case, the upper branch of the mobility loop corresponds to gradual filling of empty donor states and the lower branch to gradual emptying of filled states. The increase of mobility along the upper branch (i.e. the branch related to capture of

* Corresponding author. Tel.: + 48-22-632-3628; fax: + 48-3912-0331.
E-mail address: rp@unipress.waw.pl (R. Piotrzkowski)

0921-4526/99/$ - see front matter
PII: S0921-4526(99)00651-1

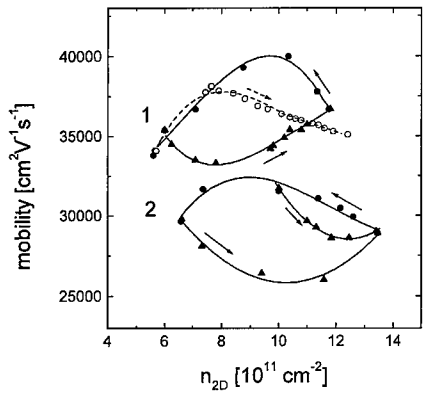

Fig. 1. Solid lines represent typical mobility versus electron concentration loops due to charge correlation effects. The data marked by dark points are taken from Ref. [3] and correspond to two AlGaAs/InGaAs/GaAs structures. (see text). Open points denotes the new results obtained by increasing the concentration with light pulses from IR LED.

electrons) was explained by the short-range ordering of impurity charges due to dependence of electron capture efficiency on local Coulomb fields. The electrons are captured preferentially by d^+ ions (i.e. the ionized states of DX center) which occur in closely spaced pairs. The result is conversion of close d^+–d^+ pairs into DX^-–d^+ dipoles which reduces considerably the scattering efficiency. Hence the upper branch corresponds to the strong correlation path. When the electron concentration is increased by thermal or optical ionization of the DX centers the mobility traces the lower branch (weak correlation path). This behavior was explained by the fact that emission is an intra-center process and its effectiveness does not depend on the center's environment. As a result the emission lowers the degree of charge correlation (it was demonstrated that both emissions are equivalent) [4].

The rule according to which an increase in carrier concentration causes the mobility to follow the weak correlation path seemed firmly established. Surprisingly, in two cases we have observed that the mobility followed the strong correlation path when the PPC was excited. The first case is shown by open points in Fig. 1 and corresponds to PPC excited by IR light emitting diode (LED). Other case was represented by experiments with AlAs/GaAs short period superlattices (characterized in Ref. [5]) which showed the anomaly when PPC was excited by a yellow LED, but showed the expected behavior when excited by IR emission. However, in both cases the enhancement of the mobility was observed when the light used was energetic enough to generate electron–hole (e–h) pairs. As was shown by Brunthaler et al. [6] the DX center is a very efficient hole trap with a cross section independent of temperature. This trapping can lead to an increase in the free electron concentration under illumination with the above band-gap light as the holes generated can be trapped by the DX-centers instead of recombining with photo-generated electrons. However, it should be noted that in both described cases the 'anomaly' was observed on modulated structures. In such cases, the influence of other PPC mechanisms associated with the physical separation of electrons and holes cannot be ruled out [7].

To make clear the role of trapping the holes by DX center in case of PPC associated with inter-band excitation, the experimental studies of this effect should be performed not on heterostructures, but on a 3-D sample. Therefore we decided to perform such studies on a $Al_{0.15}Ga_{0.85}As$: Si sample, the characteristics of which was known from our previous works (in particular: charge correlation effects [8] and PPC kinetics [9]). This was a MBE-grown sample with 1.5 μm thick layer doped with Si ($N_D - N_A = n_\infty = 3.65 \times 10^{18}$ cm^{-3}). The advantage of this low-Al content sample is the possibility of studying the PPC transients at liquid nitrogen temperature. The capture barrier (which decreases with Al content) is so large that there is no recapture of electrons at $T = 77$ K, even in the saturated PPC state. This means that the photoconductivity has very persistent character.

The experimental setup was described in detail in Ref. [9]. It was designed to study the transport phenomena (Hall effect and conductivity) under hydrostatic pressure at temperatures ranging from liquid nitrogen to ambient in samples illuminated by monochromatic light. All measurements in this work were made at ambient pressure and at temperature of 77 K. The pressure was used to initially fill the DX centers. To find the evolution of the free electron concentration n and mobility μ during the build-up of persistent photoconductivity, we have measured simultaneously Hall concentration and conductivity, using van der Pauw method.

We measured the efficiency of photo-excitation as a function of wavelength. A bound of efficiency about two order of magnitude was observed where photon energy increased above the energy gap in the studied material ($E_g = 1.7$ eV; $\lambda = 0.73$ μm). Such behavior was reported in Ref. [6]. Next, the transients of PPC in the regions below and above the gap were measured. In Fig. 2 two such transients, one measured with 0.65 μm light (above-gap excitation) and other with 0.88 μm light (below-gap excitation), are shown. In both cases the initial state of the sample was obtained by pressure freeze-out (at 4 ± 0.5 kbar). For the purpose of better comparison, the time scales were adjusted to give the same initial slope of both transients. Two kinks on the above-gap transient correspond to the points where we have increased the light intensity by a factor of ten. Without this, the time necessary to reach the saturated PPC would be about 300 times greater than the time to achieve saturation with below-gap excitation, supposing that the initial slopes dn/dt are the same.

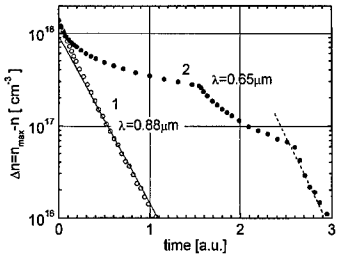

Fig. 2. Build-up transients of persistent photo-conductivity excited in $Al_{0.15}Ga_{0.85}As$:Si sample by the below-gap (1) and above-gap (2) photons at $T = 77$ K. Concentration of electrons localized on DX centers is presented in log scale (the straight lines correspond to exponential decay). The time scales were adjusted to obtain initial coincidence of curves.

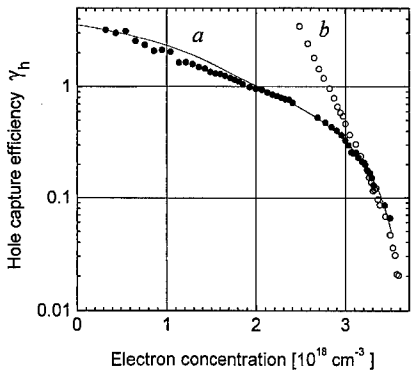

Fig. 3. Evolution of the coefficient of efficiency of hole capture during build-up of interband PPC: (a) for transient measured after pressure filling at 11.8 kbar, (b) for transient (2) in Fig. 2.

The final (saturated) state is the same for both types of excitations, which was verified by comparing both the final free electron concentration n_∞ and their mobility. This saturated PPC state corresponds to completely ionized DX donors. The difference $\Delta n = n_\infty - n$, which corresponds to concentration of the electron trapped on DX centers, is presented in Fig. 2 in log scale. The essential difference in kinetics of both processes is evident. The transient for below-gap excitation has a generally exponential character, as expected for the process of photo-ionization of donor centers. The transient of inter-band photoconductivity has extreme deviations from exponential character, but becomes exponential in the final stage. The decay rate of this final part permits us to attribute it to the process of optical emission of electrons from DX centers. However, the main part of the transient must be related to some other mechanism of persistent increase of the free electron concentration. This mechanism is likely related to capture of photo-created holes by the DX centers. Such capture is irreversible because the electrons from the conduction band (c.b.) cannot recombine with DX centers across the barrier. As a result, after switching off the light which excited the e–h pairs, a number of holes remains trapped on DX centers. The equal number of electrons remains in conduction band contributing to PPC.

The kinetics equation which takes into account both mechanisms has the form

$$\frac{dN_{DX}}{dt} = -I\sigma_{opt}N_{DX} - \frac{g\gamma_h}{(n/N_{DX}) + \gamma_h}, \quad (1)$$

where N_{DX} denotes the concentration of *occupied* (DX^-) centers, g is the e–h pairs generation rate, σ_{opt} is the photoionization cross section, and γ_h the ratio of hole capture coefficient to e–h recombination coefficient: $\gamma_h = \sigma_h \langle v_h \rangle / \gamma_r$

As we see from Eq. (1), when holes are generated, the kinetics of the photoconductivity are determined by the parameter γ_h. The magnitude of this parameter can be found with the aid of Eq. (1) from the measured rate dn/dt. In Fig. 3, the results of such calculation for two inter-band PPC transients are shown. It appears that the efficiency of capturing the holes (or effective capture cross section) is not constant, but diminishes considerably as the process proceeds.

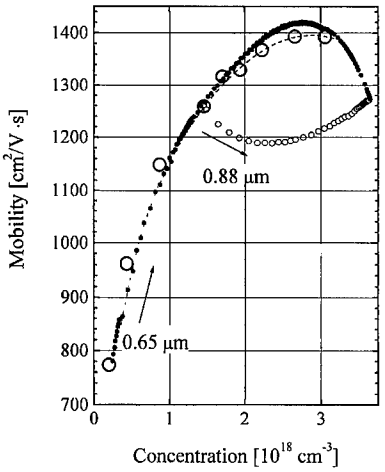

Fig. 4. Mobility of electrons as a function of Hall concentration, measured at 77 K in $Al_{0.15}Ga_{0.85}As$: Si sample. Different symbols correspond to different ways of changing the electron concentration: (Large circles) high-pressure freeze-out (HPFO) at pressures 0–12 kbar [10]. (Small close points) excitation of inter-band PPC (transient 'a' in Fig. 3); (Small open circles) mobility measured along the below-gap PPC transient (after 6 kbar filling).

The discussion of variations in the mobility during this process will contribute to understanding the possible reason of such behavior. Fig. 4 shows the variation of

mobility, measured during the transient 'a' in Fig. 3, i.e., for the initial filling obtained by HPFO at 11.8 kbar. We also present (large circles) the mobility obtained previously by pressure freeze-out at different pressures [10]. As we see, both $\mu(n)$ dependencies exhibit character which is typical for a strong-correlation path. For comparison the plot of $\mu(n)$ measured during the build-up of PPC excited by the below-gap light (0.88 μm) after filling at 6 kbar is shown. This latter follows a typical low-correlation path, as is expected for the process involving the direct ionization of DX centers.

The spectacular result of our experiment is that $\mu(n)$ measured in the process where *n increases* due to inter-band PPC follows exactly the same path as when *n decreases* due to the capture of electrons by DX centers. In the situation when spatial distribution of charge among impurities play an important role, such apparent reversibility of mobility strongly suggests that the observed coincidence of the mobility values is caused by coincidence of the spatial distribution of charges. As we have remarked, the evolution of this distribution in the *filling* process can be described as the creation of the short DX^--d^+ dipoles at the beginning and the non-correlated capture at the end of the process. The fact, that the process in which the holes are captured by the DX^- centers reproduces such evolution in the inverse order, indicates the importance of Coulomb interactions during the build-up of inter-band PPC. These interactions cause the holes to be attracted to the *isolated* DX^- centers. The dipoles, which do not attract the holes, can be destroyed only at very end of process. In other words, this means that cross section for capture of holes by DX^--d^+ dipoles is considerably smaller then that for the isolated DX^- ions. This explains why the observed effective cross section decreases as shown in Fig. 3.

The analysis presented above permits us to conclude that the spectacular difference between the two types of DX-related PPC results not only from the different mechanisms governing transfer of the localized electrons into the conduction band, but also from the effects of charge correlations in the studied sample. Our results permit us to conclude that the capture of holes by negative DX ions is sensitive to the local Coulomb field in a similar manner as is the capture of electrons by positive ions. Consequently, the inter-band PPC offers a new method of enhancing the degree of charge correlation, which works when the electron concentration increases.

References

[1] T. Suski, in: Semiconductors and Semimetals, Vol. 54, Academic Press, New York, 1998, p. 485.
[2] P.L. Coz, C. Ghezzi, A. Parisini, Semicond. Sci. Technol. 8 (1993) 13.
[3] E. Litwin-Staszewska, T. Suski, C. Skierbiszewski, F. Kobbi, J.L. Robert, V. Mosser, J. Appl. Phys. 77 (1994) 405.
[4] L. Dmowski et al., Jpn. J. Appl. Phys. 32 (Suppl. 32-1) (1993) 221.
[5] J.L. Robert, F. Bosc, J. Sicart, V. Mosser, Phys. Stat. Sol. B 211 (1999) 481.
[6] G. Brunthaler, K. Ploog, W. Jantsch, Phys. Rev. Lett. 63 (1989) 2276.
[7] R. Fletcher et al., Phys. Rev. B 41 (1990) 10649.
[8] R. Piotrzkowski, E. Litwin-Staszewska, J.L. Robert, in: H. Heinrich, W. Jantsch (Eds.), Proceedings of the 17th ICDS, Defect in Semiconductors 17, Mater. Sci. Forum, Vol. 143–147, Trans. Tech. Publications, Switzerland, 1993, p. 1135.
[9] R. Piotrzkowski, E. Litwin-Staszewska, J. Przybytek, Phys. Stat. Sol. B 198 (1996) 205.
[10] R. Piotrzkowski, E. Litwin-Staszewska, P. Lorenzini, J.L. Robert, Semicond. Sci. Technol. 7 (1992) 103.

ELSEVIER

Physica B 273–274 (1999) 796–802

PHYSICA B

www.elsevier.com/locate/physb

Comparison of electronic and mechanical contrast in scanning tunneling microscopy images of semiconductor heterojunctions

R.M. Feenstra*

Department of Physics, Carnegie Mellon University, Pittsburgh, PA 15213, USA

Abstract

The use of cross-sectional scanning tunneling microscopy (STM) to study strain in semiconductor heterostructures is discussed. In particular, intermixing between constituent heterostructure layers leads to internal strains in the heterostructure, and these strained regions are evident by displacement of the cleavage surface formed in the STM study. A theoretical analysis is made of the magnitude of electronic compared to mechanical contributions to the contrast of STM images, from which it is found that the former are relatively small, on the order of 0.1 Å, for typical $In_xGa_{1-x}As_yP_{1-y}$ heterostructures imaged with sufficiently large, positive sample bias.

Keywords: Semiconductor heterojunction; Scanning tunneling microscopy

1. Introduction

Within the area of semiconductor film growth, scanning tunneling microscopy (STM) has been used over the past 15 years to reveal many important aspects of atomic-scale structures and growth processes. A distinction can be made between *cross-sectional* imaging and *plan-view* imaging: the former is performed on (1 1 0) surfaces prepared by in situ cleavage and which are *not* reconstructed, whereas the latter is performed typically on (0 0 1) growth surfaces which are heavily reconstructed. Thus, in plan-view imaging, the information obtained pertains largely to the surface reconstruction itself, whereas for cross-sectional imaging one can study properties of the material which are not surface specific, e.g. concentration and types of defects in the semiconductor. For the case of heterostructures, cross-sectional imaging is useful for probing the structure of the interfaces between neighboring layers, as well as for studying the detailed properties of the individual layers themselves [1–4].

An example of point defect studies using cross-sectional STM (xSTM) is shown in Fig. 1 [5]. Those images were obtained from $In_{0.53}Ga_{0.47}As$ layers grown at a relatively low growth temperature of 240°C. Such material is known to contain excess arsenic, which predominantly forms antisite defects – arsenic on a gallium or indium site. The constant-current image of Fig. 1(a) shows one such defect, located near the center of the image. The same defect is also seen in the conductance image of Fig. 1(b), acquired simultaneously with Fig. 1(a). Detailed studies of As antisite defects in GaAs reveals that the antisite defects on different layers relative to the (1 1 0) cleavage plane can be distinguished, and spectroscopic studies reveal the gap states introduced by the antisites [6,7]. For the case of the $In_{0.53}Ga_{0.47}As$ investigation shown in Fig. 1, observation of the antisite defects in material of different doping concentrations and with different post-growth annealing conditions permitted an understanding of the electron–hole recombination dynamics on the ps time scale [5]. Many other point defect studies have been performed in recent years by Ebert and co-workers [8,9].

In addition to studies of point defects, xSTM has been very useful in probing properties of semiconductor heterostructures. An example is given in Fig. 2, which shows an

* Tel.: + 1-412-268-6961.
E-mail address: feenstra@andrew.cmu.edu (R.M. Feenstra)

0921-4526/99/$ - see front matter
PII: S0921-4526(99)00507-4

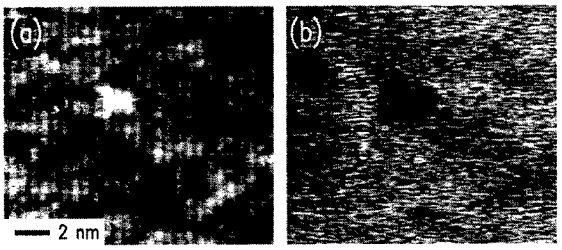

Fig. 1. (a) Constant-current image and (b) associated conductance image of the (1 1 0) cleaved surface of low-temperature-grown InGaAs, acquired with 0.1 nA tunnel current, at a sample bias of −1.45 V. A point defect with two satellite features is observed in both images. The gray-scale range in (a) is 0.08 nm. From Ref. [5].

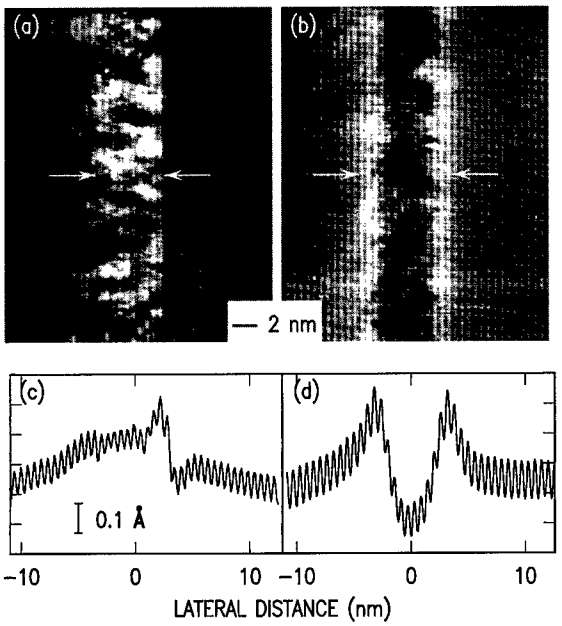

Fig. 2. Cross-sectional STM images of InGaAs/InP heterostructures, (a) as-grown sample; (b) implanted and annealed sample. Images were aquired at sample voltages of +2.5 and +2.0 V respectively, and gray-scale ranges are 0.05 and 0.06 nm, respectively. An average of the topographic line scans is shown in (c) and (d). Layer growth direction is from right to left. Arrows indicate approximate width of the quantum wells. From Ref. [8].

$In_{0.53}Ga_{0.47}As$ quantum well imbedded between InP barrier layers. Fig. 2(a) shows the as-grown heterostructure, and Fig. 2(b) shows the structure after ion implantation and subsequent annealing [10]. The ion implantation causes intermixing between the quantum well and the barrier layers. This intermixing, in turn, produces a *blue shift* in the optical transition energy of the quantum well, and thus the quantum well intermixing process can be used for tuning the emission wavelength of lasers and for other photonic integrated device applications [11]. The intermixing between quantum well and barrier layers is clearly evident in Fig. 2(b): we see some white (higher tip height) bands forming at the well/barrier interfaces, and the quantum well itself is darker (lower tip height) in Fig. 2(b) compared to Fig. 2(a). For the particular choice of implantation parameters used in this case [10] we have apparently produced a thin region near the well/barrier interface with new chemical composition which gives the white contrast in the STM images, along with modifying the overall quantum well composition thereby producing its darker contrast.

Given STM data of the type shown in Fig. 2, it is desirable to obtain a quantitative evaluation of chemical composition as a function of position in the heterostructure. Such an evaluation is, of course, quite difficult in general since the contrast in STM images contains significant contributions from electronic effects in the tunnel current and such effects are not easily quantified. However, in a series of studies of strained heterostructures, we have recently observed a second significant contribution to STM images, arising from displacement of the (1 1 0) cleavage face due to strain in the underlying material [12–14]. In cases where electronic effects can be shown to be small, this mechanical or elastic contribution to the STM contrast can be relatively simply evaluated using finite-element solutions of the elasticity equations, thus providing a means of determining strain and associated chemical composition in the heterostructure.

Fig. 3 illustrates these electronic and mechanical contributions to the STM contrast for the case of a semiconductor superlattice with compressively strained barriers and tensilely strained quantum well layers. In this particular case, the respective contributions have opposite sign, although for compressive wells with tensile barriers the electronic and mechanical effects would have the same sign. Let us consider the magnitude of the mechanical effect. As noted in the caption of Fig. 3, the peak-to-peak corrugation amplitude is approximately equal to $2\varepsilon L$ where L is the width of barrier and well, and their strains (in-plane, diagonal component) are $\pm\varepsilon$. For example, with 5 nm thick well and barrier, having strains of ± 0.01, the amplitude would be 1 Å. Offhand, this result is of the same order as typical electronic effects in the tunnel current between different materials, so it may seem difficult to distinguish between electronic and mechanical effects.

The main purpose of this paper is to provide a theoretical analysis of the tunnel current for $In_xGa_{1-x}As_yP_{1-y}$ heterostructures, with the goal of placing upper limits on the magnitude of electronic effects which may occur in the STM measurements. We demonstrate that for appropriate tunneling conditions (i.e. large, positive sample bias), the electronic effects are in fact remarkably small,

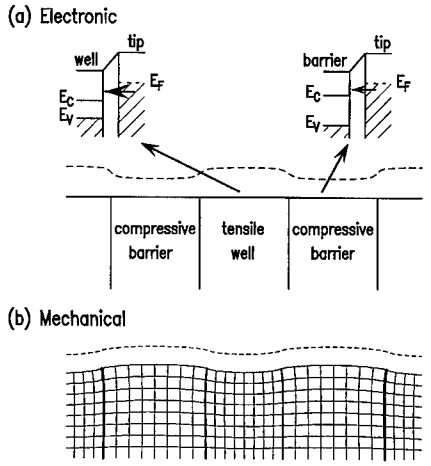

Fig. 3. Illustration of STM contrast mechanisms for a strained semiconductor superlattice containing quantum wells in tension and barrier layers in compression. The dashed line shows the constant-current contour followed by the STM probe tip considering (a) only electronic, and (b) only mechanical effects. For case (a), the barrier has a larger band gap than the quantum well, so for a given tip–sample voltage there are fewer states available for tunneling to the barrier. Thus, a lower current is produced for a fixed tip–sample separation, so that the tip moves towards the sample to maintain a constant tunnel current. For case (b), relaxation of the strain produces an undulating surface morphology across the superlattice. For a strain of $\pm\varepsilon$ in the layers and width of both barrier and well of L, the peak-to-peak amplitude $2h$ of the undulations is computed by finite elements to be $h/\varepsilon L \approx 1.0$ for Poisson ratio of 0.35. From Ref. [12].

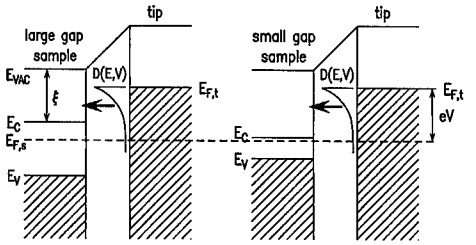

Fig. 4. Energy level diagram for the case of tunneling into two neighboring semiconductor materials, with aligned Fermi levels, $E_{F,s}$. The probe tip Fermi level is denoted by $E_{F,t}$, and is separated from the sample Fermi level by eV where V is the applied voltage. The vacuum level of the sample is denoted by E_{VAC} and electron affinity by ξ. The tunneling transmission term is indicated by $D(E, V)$.

on the order of 0.1 Å for typical heterostructures. Hence, it is possible to interpret many xSTM images of strained $In_xGa_{1-x}As_yP_{1-y}$ heterostructures directly in terms of the elastic displacement of the cleavage surface, thereby yielding a relatively direct measurement of the strain versus position in the heterostructure.

2. Results

The situation for which we compute the tunnel current is illustrated in Fig. 4. We consider two regions of neighboring semiconductor materials which are separated by an ideal interface. The Fermi levels in the two materials are aligned. An important starting point in our analysis is the use of the "electron affinity rule" which states that the conduction band offset between neighboring materials is determined by the difference in their electron affinities (distance from vacuum level to conduction band minimum). Dipoles forming at the interface may produce deviations in such offsets [15], but these effects appear to be small at least for the case of $In_{0.53}Ga_{0.47}As$ on InP [16]. For the materials GaAs, InP, InAs, and GaP, the electron affinities are given by 4.13, 4.50, 5.06, and 3.75 eV, respectively, with the latter value referring to the X-valley conduction band minimum of GaP [17]. Thus, offsets of the conduction band of GaAs, InP, and GaP relative to InAs are 0.93, 0.56, and 1.31 eV, respectively. In a heterostructure, the vacuum levels of the neighboring materials will be aligned as pictured in Fig. 4. The separation between vacuum level and Fermi level is the work function of the sample, ϕ, which is identical for all the materials we consider here due to our use of the electron affinity rule. We take the Fermi level to be located at the InAs CB minimum, so that the work function for all materials is 5.06 eV.

The goal of our study is to evaluate the material dependence of the tunnel current in $In_xGa_{1-x}As_yP_{1-y}$ alloys. In particular, if one moves across a heterointerface from one material to the next, by how much will the tunnel current change? We are interested in tunnel current variations in the immediate vicinity of the interface, so that band bending effects in the semiconductor (e.g. due to charge transfer across the interface in doped materials and the resulting formation of space charge regions) will not be included, although we return to this point at the end of Section 3.

Let us consider the tunnel currents in the materials pictured in Fig. 4. The separation between conduction band minimum and tip Fermi level is *larger* for the material with smaller band gap, which would imply a greater number of states available for tunneling and hence a larger tunnel current in that case compared to the larger band gap material. However, this conclusion is valid only for relatively small bias voltages between tip and semiconductor. For larger voltages, typically $\gtrsim 2$ V, one must explicitly include consideration of the voltage dependence of the transmission term for tunneling through the vacuum region, as pictured by the function $D(E, V)$ in Fig. 4. Assuming a simple trapezoidal barrier,

this function is given by

$$D(E,V) = \exp\left\{ -2s\left[\frac{2m}{\hbar^2}\left(\bar{\phi} - E + \frac{eV}{2}\right) + k_{||}^2\right]^{1/2}\right\}, \quad (1)$$

where $\bar{\phi}$ is the average work function between tip and sample, s is the tip–sample separation, V is the bias voltage applied to the sample relative to the tip, and E is the energy of a state in the sample relative to the sample Fermi-level, with E varying between 0 and eV. This formula also includes the dependence of the transmission term on the parallel wave vector of the tunneling electron, $k_{||}$. It is well known that the energy and voltage dependence of $D(E,V)$ is such that the highest lying states are favored in the tunneling process [18]. For $V > 0$ the maximum of $D(E,V)$ occurs at $E = eV$, and for $V < 0$ the maximum is at $E = 0$. The former case is illustrated in Fig. 4. The rate of decrease of $D(E,V)$ with decreasing E depends on the work function and tip–sample separation. For typical values of $\bar{\phi} = 4$ eV and $s = 6$ Å, $D(E,V)$ changes by a factor of 20 as E varies over a 2 eV interval. Thus, for tunneling voltages larger than about 2 V, increasing the voltage does *not* lead to a large difference in the number of states available for tunneling, and so an increase in the tunnel current is not expected. However, the $eV/2$ term in the exponent of Eq. (1), arising from the decrease in the average barrier height with increasing voltage, will still produce an overall increase in the current with increasing voltage.

Given an expression for the transmission term, the tunnel current between tip and sample can be computed according to [19]

$$J = \frac{2e}{(2\pi)^3\hbar}\int dk_\perp\, d^2k_{||}[f(E-eV) - f(E)]$$
$$D(E,k_{||})\left(\frac{\partial E}{\partial k_\perp}\right)\Theta\left(\frac{\partial E}{\partial k_\perp}\right), \quad (2)$$

where $f(E - eV)$ and $f(E)$ are Fermi–Dirac occupation factors in tip and sample, respectively, and $k_\perp$ is the component of the wavevector perpendicular to the surface. The step-function $\Theta(\partial E/\partial k_\perp)$ in this equation, which restricts the integral to positive values of $\partial E/\partial k_\perp$, arises from the assumption that waves traveling only in one direction can tunnel out of the material. (For the case of free electrons, this same factor is implicitly included in the integral by restricting it to run over only positive values of $k_\perp$ [19].) The bulk band structure is implicitly included in the formula by the dependence of E on $k_\perp$ and $k_{||}$, although, as is well known from early studies of tunneling, we expect the band structure effects to be small since the group velocity term $\partial E/\partial k_\perp$ in Eq. (2) is largely cancelled by a density of states term which appears when the integral over $k_\perp$ is performed [19]. In the computations below, we explicitly evaluate the dependence of the tunnel current on band structure, by computing it for GaAs, InP, InAs, and GaP materials.

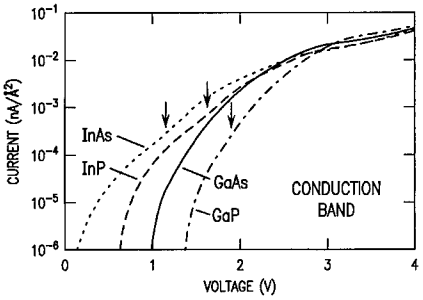

Fig. 5. Computed tunnel current for CB states of GaAs, InP, InAs, and GaP. Arrows indicate the location of inflection points seen for InAs and InP, and seen weakly for GaP.

To evaluate the tunnel current, band structure computations are performed using empirical nonlocal pseudopotentials. Spin–orbit coupling is not included. We focus on the materials GaAs, InP, InAs, and GaP which form the endpoints of the $In_xGa_{1-x}As_yP_{1-y}$ alloy system, since these alloys are most relevant to our prior xSTM measurements [5,10]. Results for the band structure and density of states of these materials are very similar to those given previously by Fischetti [20], and will not be repeated here. The tunnel current is computed by numerically evaluating the integral in Eq. (2). We use a wave vector spacing in reciprocal space of $0.01(2\pi/a_0)$, yielding 89076 points in the irreducible wedge of the first Brillouin zone. Computations are performed for a tip–sample separation of 6 Å, a temperature of 0 K, and a tip work function of 4 eV.

Results for tunneling into CB states are shown in Fig. 5. As seen there, at low voltages the tunnel current *does* vary considerably between the various materials. However, at higher voltage > 3 V, the current is practically the same amongst the different materials. We find less than a factor of 1.5 variation in the tunnel current, corresponding to a tip height variation of < 0.20 Å. The observed variation in tunnel current for voltages > 3 V arises in part from the differing lattice constant, a_0, of the materials. This dependence arises in Eq. (2) because the volume of the Brillouin zone is proportional to a_0^{-3}. Physically, a material with small lattice constant, like GaP, will have a greater state density than a material with large lattice constant, like InAs. However, this a_0 dependence is also partially compensated by the $k_{||}$ term in Eq. (1), which also depends on a_0. The resulting tunnel current varies approximately like a_0^{-n} where n is slightly greater than 1[1]. If we set all the lattice

[1] This dependence of the current on lattice constant will, of course, change slightly when one considers layers of $In_xGa_{1-x}As_yP_{1-y}$ biaxially strained on a particular substrate (such as InP).

constants to have the value for GaAs in the computation, then the resulting variation in tunnel current for voltages > 3 V is less than a factor of 1.35; this amount represents the effect of the differing band structures on the tunnel current.

We note that the zero of voltage in Fig. 5 is taken to be the CB minimum of InAs. In a typical experiment it would be at a different point, i.e. the lowest-lying conduction band minimum of the relevant alloy material, typically 0.5 V higher than that shown in Fig. 5. In that case, the voltage range for which the tunnel currents converge would be > 2.5 V. Furthermore, we consider experiments in which the $In_xGa_{1-x}As_yP_{1-y}$ alloy compositions used are in a rather restricted range, which is quite far from GaP [10,14]. In that case, the expected variation in tip height variation would be less, typically $\lesssim 0.07$ Å, and the minimum voltage needed to achieve this convergence of the tunnel currents is also less, typically $\gtrsim 2.0$ V. This voltage range is well within the parameters of usual xSTM experiments on $In_xGa_{1-x}As_yP_{1-y}$ alloys, which typically employ sample voltages with magnitude in the range 2.0–2.5 V. Values significantly less than this are generally avoided since they can lead to tip–sample contact, and values much larger than this are also dangerous since they may lead to material transfer between tip and sample.

A close inspection of the current versus voltage curves in Fig. 5 reveals some weak inflection points, seen most clearly for InAs and InP and indicated by arrows. These features correspond to the onset of tunneling into the L-valley conduction band, located at 0.98 and 0.85 eV above the Γ-valley minimum for InAs and InP, respectively. No such onset is seen for GaAs in Fig. 5; the L-valley is only 0.33 eV above the Γ-valley minimum in that case, which apparently prevents any clear discrimination of its onset. Experimentally, tunneling spectroscopy reveals clear L-valley onsets for InAs and InP, but no such feature is seen for GaAs [21], in good agreement with the results of Fig. 5. For the case of GaP, it is an indirect material with conduction band minimum at the X-point and with L-valley and Γ-valley minima located 0.33 and 0.42, respectively, above that. In Fig. 5, a very weak inflection point is seen for GaP approximately 0.5 V above the onset of the current, which corresponds to tunneling into these higher lying bands.

Fig. 6 shows results for tunneling into the valence band states. At voltage with low magnitude, the tunnel current again varies greatly between the various materials. At higher voltages, the tunnel currents tend to approach each, although their difference is significantly greater than that seen for the CB states. The states most responsible for the tunnel current originate from the top of the VB, and their barrier height for tunneling is the sum of the electron affinity and band gap. Those values vary considerably between the various materials, giving rise to the spread in current values seen in Fig. 6.

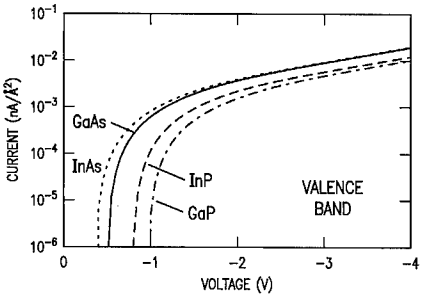

Fig. 6. Computed tunnel current for VB states of GaAs, InP, InAs, and GaP.

3. Discussion

The main result of the paper has been presented in the previous section, namely, that at large, positive sample voltages the tunnel current shows a relatively small variation between the various materials GaAs, InP, InAs, and GaP. In this section we examine some of the approximations and limitations of our theoretical treatment, in an effort to evaluate the reliability of our result.

One issue to be considered is our use of the electron affinity rule which led to equal work functions for all the materials. The band offsets derived above (0.93, 0.56, and 1.31 eV, respectively, for GaAs, InP, and GaP relative to InAs) differ slightly from those obtained from the model-solid theory of Van de Walle: 0.84, 0.55, and 1.11 eV, respectively [16]. These differences may be within the combined uncertainty of the experimental and theoretical determinations [16,17], but they may also reflect some real limitation of the electron affinity rule. In particular, the existence of a dipole layer on a surface will affect the electron affinity, and differing dipole layers for materials across a heterointerface will lead to differing work functions for those materials. In an effort to test the sensitivity of the computation on this effect, we vary the work functions of the materials. We use the band offsets from the model-theory solid, and add to them the experimental electron affinities to arrive at the work functions: 4.97, 5.05, 5.06 and 4.86 eV for GaAs, InP, InAs, and GaP, respectively (again, placing the Fermi-level at the CB minimum of InAs). Using these values, the main effect on the tunnel current at large, positive voltage is to increase the GaP result (due to its reduced work function) by a factor of 1.2, resulting in a total variation of a factor of 1.8 in the tunnel current between materials. Our previous upper limit of < 0.2 Å for the tip height variation would then increase to < 0.3 Å, although considering the restricted range of alloy compositions mentioned in Section 2 leads to an expected upper limit of $\lesssim 0.1$ Å.

Another important issue to consider is the role of strain in our results. Typically, $In_xGa_{1-x}As_yP_{1-y}$ alloys are grown coherently on InP, and the resulting biaxial

strain in the alloys will shift the energies of the electronic states. This effect will, of course, shift the onsets of the current versus voltage curves in Figs. 5 and 6. Nevertheless, it is important to realize that these shifts do *not* significantly change the results for the tunnel current at large, positive voltages. The reason for this insensitivity is that shifting the energy bands does *not* greatly change the number of states available for tunneling. For example, if we strain all the materials onto InP, then the strain-induced shifts for the conduction band minima are -0.29, $+0.27$, and $+0.14$ eV for GaAs, InAs, and GaP, respectively [16]. Applying these shifts to the *entire* band (i.e. neglecting the variation in deformation potential with energy), and recomputing the CB tunnel currents, we find for voltages > 3 V that the current varies by less than 15% from the results presented in Fig. 5.

The most significant approximation made in our computations is the neglect of surface state effects in the tunnel current. It is well known that the current is proportional to the local density of states at the surface, so that surface states will certainly play a role. However, for the (1 1 0) face of the III–V semiconductors, tunneling spectroscopy results demonstrate that, at energies $\gtrsim 2$ eV into the conduction band, the surface states make only a very small contribution to the tunnel current [21]. At these energies the surface states are all strongly mixed (resonant) with the bulk states, so that we expect Eq. (2) to provide a reasonably good estimate of the tunnel current. Certainly it would be desirable to include surface states in the computation, but we expect that the conclusions of this work will remain unchanged even in that case.

Finally, we return to one aspect of xSTM measurements which we mentioned briefly in Section 2, namely, the effect on the tunnel current of band bending (space charge regions) in the semiconductor, as encountered, e.g. in pn-junctions or around heterointerfaces in doped material. Such band bending produces significant effects in the tunnel current [22], although those effects are not important in the theory above since we focus only on the region *near* the heterointerface. However, our result that the tunnel current is insensitive to the material into which tunneling occurs can be used to develop a simple way for including band bending effects. Considering the case for large, positive voltages, we find above that the tunnel current can be expressed in the form $C\exp\{-2s\sqrt{(2m[\bar{\phi}-eV/2]/\hbar^2)}\}$ where the constant C is nearly independent of V and material parameters. In this case, a shift in the Fermi level of the semiconductor can be easily accounted for by taking the average work function $\bar{\phi}$ to be a function of position across the heterostructure (i.e. it would contain an additive term of $-e/2$ times the electrostatic potential). Computations of this sort could account for observed variations in current due to intrinsic electrostatic variations in the semiconductor material, although the effect of tip-induced band bending and/or band bending due to surface Fermi-level pinning are more complicated and would require additional considerations [22,23].

4. Conclusions

Based on the computations reported here, we find for large, positive voltages that the tunnel current expected from $In_xGa_{1-x}As_yP_{1-y}$ alloys of any composition will be nearly the same. Less than a factor of 2 variation is found between GaAs, InP, InAs, and GaP materials, corresponding to a tip height variation in the STM of < 0.3 Å. Typically in xSTM experiment one encounters alloy variations which span only a considerably restricted subset of the total range between GaAs, InP, InAs, and GaP. In that case, the expected variation in tip height due to electronic effects would be smaller, typically $\lesssim 0.1$ Å. As discussed above, the relatively small size of this electronic contribution to the tunnel current then enables the possibility of quantitatively determining strain variations in the heterostructures from the observed strain-induced displacement of the cleavage face.

Acknowledgements

We are most grateful to Max Fischetti for supplying the band structure code used in the computations reported here. We also thank Huajie Chen for many useful discussions during the course of this work, and Chris Van de Walle for a critical reading of the manuscript. We acknowledge Sung Ha Park and Li Zhang for assistance with the computer computations. This work was supported by the National Science Foundation under grant DMR-9615647.

References

[1] For review, R.M. Feenstra, Semicond. Sci. Technol. 9, (1994) 2157.
[2] For review, E.T. Yu, Mater. Sci. Eng. R: Rep. R17 (1996) 147.
[3] O. Albrektsen, D.J. Arent, H.P. Meier, H.W.M. Salemink, Appl. Phys. Lett. 57 (1990) 31.
[4] S. Gwo, K.-J. Chao, C.K. Shih, Appl. Phys. Lett. 64 (1994) 493.
[5] B. Grandidier, H. Chen, R.M. Feenstra, D.T. McInturff, P.W. Juodawlkis, S.E. Ralph, Appl. Phys. Lett. 74 (1999) 1439.
[6] R.M. Feenstra, J.M. Woodall, G.D. Pettit, Phys. Rev. Lett. 71 (1993) 1176.
[7] R.M. Feenstra, J.M. Woodall, G.D. Pettit, Mater. Sci. Forum 143–147 (1994) 1311.

[8] For example, J. Gebauer, R. Krause-Rehberg, C. Domke, Ph. Ebert, K. Urban, Phys. Rev. Lett. 78 (1997) 3334.
[9] Ph. Ebert, K. Urban, Phys. Rev. B 58 (1998) 1401.
[10] H. Chen, R.M. Feenstra, P.G. Piva, R.D. Goldberg, I.V. Mitchell, G.C. Aers, P.J. Poole, S. Charbonneau, Appl. Phys. Lett. 75 (1999) 79.
[11] S. Charbonneau, P.J. Poole, P.G. Piva, G.C. Aers, E.S. Koteles, M. Fallahi, J.-J. He, J.P. McCaffrey, M. Buchanan, M. Dion, R.D. Goldberg, I.V. Mitchell, J. Appl. Phys. 78 (1995) 3697.
[12] T. Pinnington, A. Sanderson, T. Tiedje, T.P. Pearsall, E. Kasper, H. Presting, Thin Solid Films 222 (1992) 259.
[13] H. Chen, R.M. Feenstra, R.S. Goldman, C. Silfvenius, G. Landgren, Appl. Phys. Lett. 72 (1998) 1727.
[14] B. Grandidier, R.M. Feenstra, C. Silfvenius, G. Landgren, J. Vac. Sci. Technol. A 17 (1999) 2251.
[15] W.A. Harrison, J. Tersoff, J. Vac. Sci. Technol. B 4 (1986) 1068.
[16] C.G. Van de Walle, Phys. Rev. B 39 (1989) 1871.
[17] J. van Laar, A. Huijser, T.L. van Rooy, J. Vac. Sci. Technol. 14 (1977) 894.
[18] R.M. Feenstra, J.A. Stroscio, A.P. Fein, Surf. Sci. 181 (1987) 295.
[19] C.B. Duke, Tunneling in Solids, Academic Press, New York, 1969, Eq. (7.8b) and discussion following.
[20] M.V. Fischetti, IEEE Trans. Electron Dev. 38 (1991) 634.
[21] R.M. Feenstra, Phys. Rev. B 50 (1994) 4561.
[22] R.M. Feenstra, E.T. Yu, J.M. Woodall, P.D. Kirchner, C.L. Lin, G.D. Pettit, Appl. Phys. Lett. 61 (1992) 795.
[23] R.M. Feenstra, J.A. Stroscio, J. Vac. Sci. Technol. B 5 (1987) 923.

ELSEVIER

Physica B 273–274 (1999) 803–806

PHYSICA B

www.elsevier.com/locate/physb

Complexes of group-VI donors with hydrogen in GaP

B. Clerjaud[a,*], D. Côte[a], W. Ulrici[b]

[a]*Laboratoire d'Optique des Solides - UMR 7601, Université Pierre et Marie Curie, case 80, 4 Place Jussieu, F-75252 Paris cedex 05, France*
[b]*Paul-Drude-Institut für Festkörperelektronik, D-10117 Berlin, Germany*

Abstract

Local vibrational modes due to complexes of hydrogen with sulfur, selenium and tellurium in gallium phosphide are reported together with the corresponding mode due to the deuterium–sulfur complex. The wave numbers of these modes indicate that hydrogen or deuterium binds to one of the host phosphorus atoms which are next-nearest neighbors of the group-VI donor. Experiments under uniaxial stress show that the complexes have C_s (C_{1h}) symmetry, the mirror planes being {1 1 0} planes. The orientation of the mode-induced electric dipole moment is determined for each of the complexes. The structure of the complexes of group-VI donors with hydrogen in GaP is different from the one determined previously in other III–V compounds such as GaAs or AlSb.

PACS: 61.72. – y; 63.20.Pw; 78.30.Fs

Keywords: Gallium phosphide; Hydrogen; Donor; Vibrational modes

1. Introduction

Hydrogen-acceptor complexes in semiconductors are presently well understood, but the situation concerning the donor hydrogen complexes is not yet very clear. In the case of III–V compounds, it has been shown [1–4] that in GaAs and AlSb, the complexes of group-VI donors with hydrogen have C_{3v} symmetry, with hydrogen sitting in an antibonding location close to one of the group-III host atoms nearest neighbor to the chalcogen. In the case of GaP, the situation is not clear [5]; photoluminescence experiments performed on hydrogenated sulfur doped samples were differently interpreted, Singh and Weber [6,7] suggesting that hydrogen was neutralizing the donors while Mizuta et al. [8] considered that this was not the case. In this paper, it will be shown that indeed hydrogen neutralizes the group-VI donors in GaP and the structure of the resulting complexes will be determined. This structure is different from the one determined previously in GaAs and AlSb.

2. Samples and experimental set-up

The samples investigated are bulk samples grown by the liquid encapsulation Czochralski (LEC) technique. As usual, they are contaminated with hydrogen, with this impurity coming from the wet boric oxide cap [9]. In order to introduce deuterium in one of the ingots, heavy water has been used for wetting the boric oxide. Another common impurity is sulfur; when not intentionally introduced, it comes from the phosphorus used, sulfur being the main residual impurity of phosphorus. For doping with group-VI donors, sulfur or tellurium were added into the melt; for doping with selenium, gallium selenide has been added into the melt.

Infrared experiments have been performed with either Bomem DA3 + or DA8 or Bruker IFS 120 HR interferometers equipped with CaF_2 beam splitters and cooled InSb detectors. The samples are cooled to liquid-helium temperature in Oxford Instruments CF 204 or CF 1204 cryostats. Uniaxial stresses were applied using a home made push rod apparatus inserted inside of the cryostats. All of the experiments under uniaxial stress reported in this paper have been performed at a temperature around 9 K.

* Corresponding author. Fax: + 33-1-44-27-44-47.
E-mail address: bec@ccr.jussieu.fr (B. Clerjaud)

0921-4526/99/$ - see front matter
PII: S0921-4526(99)00508-6

3. Local vibrational modes

In all of the n-type samples investigated, a sharp local vibrational mode (LVM) is observed at 2204.3 cm^{-1} at 5 K (2199.7 cm^{-1} at room temperature). This mode is known since the beginning of the investigation of hydrogen in III–V compounds by LVM spectroscopy [10]. This mode is stronger in samples in which sulfur is intentionally introduced. In sulfur-doped samples in which both hydrogen and deuterium are present, an extra LVM is observed at 1618.8 cm^{-1} at 5 K (1616.5 cm^{-1} at liquid-nitrogen temperature). This corresponds to a r factor slightly below $\sqrt{2}$ ($r = 1.362$) which proves that hydrogen is one of the partners of the complex and that only one hydrogen atom is involved.

In all of the tellurium doped samples, in addition to the 2204.3 cm^{-1} mode, a mode at 2217.1 cm^{-1} is observed. This mode has never been observed in a sample not intentionally doped with tellurium. In the selenium doped samples, a mode is observed at 2209.6 cm^{-1}. Even though these modes are quite sharp (≈ 0.1 cm^{-1} at 5 K) and intense, no isotopic structure could be detected.

These observations strongly suggest that the 2204.3, 2209.6 and 2217.1 cm^{-1} modes are due to complexes of hydrogen with S, Se and Te, respectively. The fact that the three modes show very similar shifts and broadening when temperature increases provides further support for their attribution to chalcogen–hydrogen complexes.

It has to be noted that no other mode which could be correlated with those described in this section have been observed.

4. Discussion

The mode at 2204.3 cm^{-1} which had been reported for already a dozen years [10] had been previously assigned to a mono-hydrogenated [11] or a tetra-hydrogenated [12] gallium vacancy. The origin of these misinterpretations arose from the assumption that the LVM observed at 2204.3 cm^{-1} (at 5 K) in as-grown LEC material and the one observed at 2204 cm^{-1} (at RT) in proton implanted material [13] have the same origin: Because the defect observed after proton implantation could be produced in very high concentrations, the participation of unintentional impurities in the complex was excluded. However, the observed frequencies at the same temperature for as grown materials on the one hand, and proton or deuteron implanted samples on the other hand are too different, especially for the deuterated complexes, for this assumption to be valid. Therefore, one should consider that the LVMs observed in as-grown and proton-implanted materials have different origins which allows for the assignment of the 2204.3 cm^{-1} to a complex involving a sulfur atom.

From the frequencies of the observed LVMs, one can deduce the atom to which hydrogen is bonded. Usually, in crystals, the frequency of a X–H bond is about 5% smaller than that of the same bond in a free molecule. The fact that the three LVMs observed lie within a very narrow range (< 15 cm^{-1}) excludes the direct bonding of hydrogen to the chalcogen. A Ga–H bond also has to be rejected because it should give rise to a stretching frequency around 1800 cm^{-1}. Phosphorus–hydrogen bonds in semiconductors such as InP or GaP are in the 2200 cm^{-1} range which matches perfectly the observed values. Therefore, it is concluded that the LVMs reported in the previous section correspond to the stretching modes of P–H (or P–D) bonds. This is confirmed by the absence of isotopic structure because phosphorus has only one natural isotope (^{31}P) whereas gallium and the chalcogens have several naturally abundant isotopes. Group-VI donors substitute for phosphorus atoms and therefore, hydrogen binds one of the next-nearest neighbors of the donor. This situation is not common and already at this stage, one notices that the complexes of group-VI donors with hydrogen in GaP behaves differently from the usual complexes of hydrogen with shallow dopants.

5. Experiments under uniaxial stress

Experiments under uniaxial stress have been performed with stresses applied along $\langle 0\,0\,1\rangle$, $\langle 1\,1\,1\rangle$ and $\langle 1\,1\,0\rangle$ crystallographic directions and polarized light parallel or perpendicular to the stress direction. When the stress is applied along the $[1\,\bar{1}\,0]$ axis, the selection rules depend upon the perpendicular direction investigated and experiments with the polarization of the light parallel to the [0 0 1], [1 1 0] and [1 1 1] axes have been performed.

The three LVMs associated with the three complexes split into two components under $\langle 0\,0\,1\rangle$ stress, both components being observed with both polarizations, however, the relative intensities of both components depend upon the polarization of the light.

Under $\langle 1\,1\,1\rangle$ stresses, one observes a splitting into three components of the three LVMs, some of the components being strongly polarized.

Under $\langle 1\,1\,0\rangle$ stresses, four components are observed in all cases, some of them being fully polarized.

Fig. 1 shows these splittings as a function of the applied stress in the case of the tellurium–hydrogen complex. The situation is very similar for the two other complexes.

6. The microscopic structure of the complexes

The modes for the three complexes have a very similar behavior under stress. This confirms both that they are

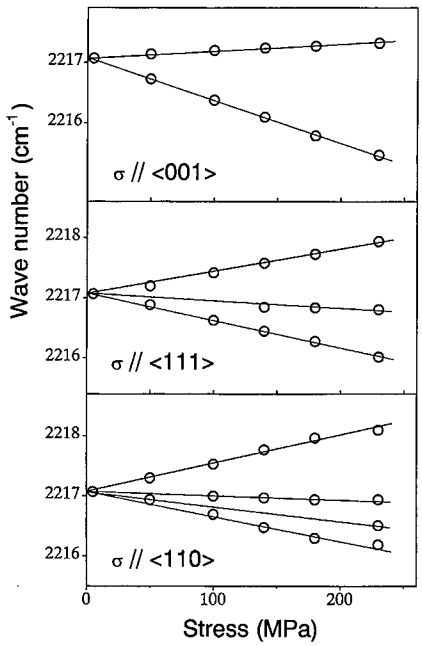

Fig. 1. Effects of ⟨0 0 1⟩, ⟨1 1 1⟩ and ⟨1 1 0⟩ uniaxial stresses on the mode due to the hydrogen–tellurium complex.

due to the same family of complexes and the assignment of the 2204.3 cm^{-1} mode to the sulfur–hydrogen complex.

The fact that the modes split into two components for stress along ⟨0 0 1⟩ clearly indicates that the complexes do not have trigonal symmetry and therefore that the complexes of group-VI donors with hydrogen in GaP behave differently from those in GaAs or AlSb.

Davies et al. [14] and Bech Nielsen and Grimmeiss [15] have analyzed the effects of stress on a complex having C_2 or C_s (C_{1h}) symmetry. The splittings correspond to those observed in the experiments reported in the previous section. It has been shown [14,15] that the intensities of the sub-components depend upon the angle θ in the {1 1 0} plane between the transition dipole moment of the vibrational mode and the ⟨0 0 1⟩ axis. For stresses applied along the [1 $\bar{1}$ 0] axis, the intensities of the sub-components were calculated only for parallel and for [0 0 1] and [1 1 0] perpendicular polarizations [14,15]; we have extended them to [1 1 1] polarization. These results match perfectly the experiments with $\theta = 35°$ for the sulfur–hydrogen complex and $\theta = 40°$ for the Se–H and Te–H complexes.

As hydrogen is very light, its motion is the most important one in the stretching modes. Therefore, the direction of transition dipole moment induced by the vibration should not be too far from the direction of the P–H bond involved in the vibration. The donor should be positively charged; because of the large electropositivity of hydrogen, in the P–H bond, the hydrogen atom should be positively charged; and the phosphorus atom should

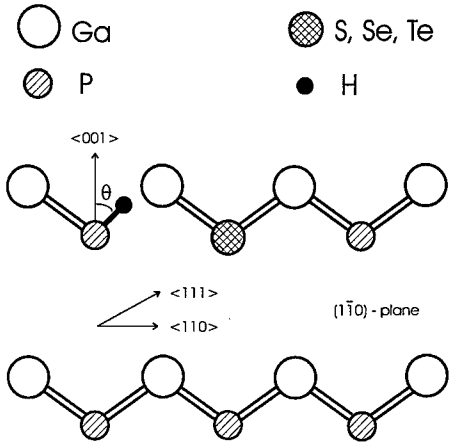

Fig. 2. Schematic representation in the {1 1 0} plane of the microscopic structure of the complexes of group-VI donors with hydrogen in GaP.

be negatively charged. Therefore, the donor exerts a torque on the P–H bond. The fact that $\theta < 54.7°$ indicates that hydrogen sits in a region of space between phosphorus and one of the gallium nearest neighbors to the group-VI donor. Consequently, one reaches the microscopic structure of the complex which is represented in Fig. 2. For symmetry reasons, there are twelve equivalent configurations of the complex. The complex has C_s (C_{1h}) symmetry with {1 1 0} mirror planes. In this model, there are two extra electrons not involved in covalent bonds (lone pair) that should be located in antibonding orbitals.

7. Conclusion

It has been shown that hydrogen forms complexes with group-VI donors in GaP and therefore that hydrogen neutralizes group-VI donors in this material. This confirms the photoluminescence results of Singh and Weber [6,7]. Hydrogen is bonded to phosphorus atoms which are next nearest neighbors to the group-VI donors. This clearly indicates that the microscopic structure of the complexes of group-VI donors with hydrogen in GaP is different than that of the same type of complexes in GaAs and AlSb. Experiments under uniaxial stress have led to the microscopic structure which is sketched in Fig. 2. To our knowledge, a structure of this type has never been suggested before. A theoretical investigation of these uncommon systems would be of interest.

Acknowledgements

The authors would like to thank M. Czupalla for growing the gallium phosphide ingots doped with

selenium and deuterium, C. Naud for his help with the stress experiments and H.v. Kiedrowski for the preparation of the oriented samples.

References

[1] J. Vetterhoffer, J.H. Svensson, J. Weber, A.W.R. Leitch, J.R. Botha, Phys. Rev. B 50 (1994) 2708.
[2] R. Rahbi, B. Theys, R. Jones, B. Pajot, S. Öberg, K. Somogyi, M.L. Fille, J. Chevallier, Solid State Commun. 91 (1994) 187.
[3] J. Vetterhoffer, J. Weber, Phys. Rev. B 53 (1996) 12 835.
[4] M.D. McCluskey, E.E. Haller, W. Walukiewicz, P. Becla, Phys. Rev. B 53 (1996) 16 297.
[5] B. Clerjaud, D. Côte, W.-S. Hahn, in: S.J. Pearton, (Ed.), Hydrogen in Compound Semiconductors, Trans Tech, Switzerland, 1994, Materials Science Forum, Vol. 148-149 pp. 281–294.
[6] J. Weber, M. Singh, Mater. Res. Soc. Symp. Proc. 104 (1988) 325.
[7] M. Singh, J. Weber, Appl. Phys. Lett. 54 (1989) 424.
[8] M. Mizuta, Y. Mochizuki, N. Takadoh, K. Asakawa, J. Appl. Phys. 66 (1989) 891.
[9] B. Clerjaud, D. Côte, W.-S. Hahn, W. Ulrici, Appl. Phys. Lett. 58 (1991) 1860.
[10] B. Clerjaud, D. Côte, C. Naud, Phys. Rev. Lett. 58 (1987) 1755.
[11] J. Chevallier, B. Clerjaud, B. Pajot, in: J.I. Pankove, N.M. Johnson (Eds.), Hydrogen in Semiconductors, Semiconductors and Semimetals, Vol. 34, Academic press, San Diego, 1991, pp. 447–510.
[12] B. Dischler, F. Fuchs, H. Seelewind, Physica B 170 (1991) 245.
[13] C. Ascheron, C. Bauer, H. Sobotta, V. Riede, Phys. Stat. Sol. A 89 (1985) 549.
[14] G. Davies, E.C. Lightowlers, M. Stavola, K. Bergman, B. Svensson, Phys. Rev. B 35 (1987) 2755.
[15] B. Bech Nielsen, H.G. Grimmeiss, Phys. Rev. B 40 (1989) 12 403.

ELSEVIER

Physica B 273–274 (1999) 807–810

PHYSICA B

www.elsevier.com/locate/physb

Local-vibrational-mode absorption of interstitial oxygen in GaP

W. Ulrici[a,*], B. Clerjaud[b], D. Côte[b]

[a]*Paul-Drude-Institut für Festkörperelektronik, Hausvogteiplatz 5–7, D-10117 Berlin, Germany*
[b]*Laboratoire d'Optique des Solides-UMR 7601, Université P. et M. Curie, Paris, France*

Abstract

A local-vibrational-mode absorption line is measured at 1006.8 cm^{-1} ($T = 7$ K) in GaP and identified as due to the antisymmetric stretching mode of interstitial oxygen (Ga–$^{16}O_i$–P). The line due to $^{18}O_i$ is found at 981.9 cm^{-1}. Uniaxial stress experiments indicate that the centre has a $C_s(C_{1h})$ symmetry. For stress applied parallel to $\langle 0\,0\,1\rangle$ direction, a low-temperature dichroism $I_{||}/I_{\perp} > 1$ is observed. This is due to a low-temperature reorientation of the centre among its three equivalent configurations around a trigonal axis.

Keywords: GaP; Interstitial oxygen; Vibrational modes; Stress-induced dichroism

1. Introduction

Oxygen is one of the most common and important impurities in technologically used semiconductors like Si, Ge, GaAs, and GaP. Most of the studies on oxygen have been performed for silicon, where it is present as an isolated oxygen atom bonded to two nearest-neighbour Si atoms, i.e. forming an interstitial oxygen (O_i). The main part of information about the microscopic structure of this centre has been derived from its vibrational properties measured by local-vibrational-mode (LVM) spectroscopy. Presently, there is a very detailed knowledge of the microscopic structure of O_i in Si as well as in Ge. An O_i centre of similar structure has been found in GaAs giving rise to the LVM absorption line at 845.7 cm^{-1}, where the Ga–O_i–As bonds are directed along $\langle 1\,1\,1\rangle$ directions [1,2]. This line is split by 0.4 cm^{-1} due to the ^{69}Ga, ^{71}Ga host isotope effect.

Oxygen in GaP has played an important role clarifying the light emitting properties of this material. Substitutional oxygen (O_P) forms a deep donor and is the partner in donor–acceptor (DA) pairs. Therefore, most of the information on substitutional oxygen and its vibrational properties comes from luminescence and excitation spectra [3]. The LVM of O_P was found in the phonon side bands of DA-photoluminescence spectra with an energy of 200 cm^{-1}, indicating a strong weakening of the O_P–Ga bonds compared with the bulk P–Ga bonds [4].

Interstitial oxygen in GaP was the subject of an early paper by Barker et al. [5]. They observed a prominent LVM absorption line at 1005 cm^{-1} ($T = 80$ K) and assigned this line to the antisymmetric stretching mode of the Ga–O_i–P interstitial oxygen. Their assignment was mainly supported by the comparison with Si and Ge and by calculations using a linear chain model. In the present paper, we investigate a vibrational absorption line at 1006.8 cm^{-1} ($T = 7$ K), which is found frequently in LEC–GaP, identify it as the O_i stretching mode, and analyse its response to uniaxial stress.

2. Experimental results

We have investigated a large number of different GaP samples (undoped as well as doped with donors, acceptors, and transition metals) grown by the liquid encapsulation Czochralski (LEC) technique under high-pressure N_2 inert gas. For all samples (except those

* Corresponding author. Fax: 49-30-20377-515.
E-mail address: ulrici@pdi-berlin.de (W. Ulrici)

0921-4526/99/$ - see front matter
PII: S0921-4526(99)00509-8

doped with titanium), a LVM absorption line was found at 1006.8 cm^{-1} with a half-width $\Gamma = 1.2\ cm^{-1}$ at $T = 7$ K as shown in Fig. 1. Related to this line, a weak line can be detected at 981.9 cm^{-1} with an intensity 0.2% of the 1006.8 cm^{-1} line (cf. inset in Fig. 1). This intensity ratio corresponds to the $^{18}O/^{16}O$ ratio of the natural isotopic abundances and indicates that these lines are due to vibrating oxygen. The high frequency of the vibration suggests that it is the antisymmetric stretching mode of an interstitially located oxygen in accordance with the observations and estimations of Barker et al. [5]. The absence of this line in GaP : Ti supports this interpretation, since Ti is known to be an effective gettering material for oxygen in III–V melts. The second-harmonic absorption line of this mode is detected at 1998.8 cm^{-1} with an intensity of 3×10^{-3} of the fundamental one, indicating an anharmonicity of the potential.

In Fig. 1 it can be seen that the line at 1006.8 cm^{-1} exhibits a complicated line shape, when the temperature is raised from 7 to 60 K. A detailed analysis (deconvolution into Lorentzians) of the temperature dependence of the line shape shows that low-energy vibrational levels become thermally populated and give rise to side bands on the low-energy side of the main line. This indicates that the stretching mode of O_i is coupled to a low-frequency mode. The position of the lowest excited level due to this coupling is estimated to be about 15 cm^{-1} above the ground level.

Uniaxial stress experiments on the 1006.8 cm^{-1} line were carried out up to stress values $|\sigma| = 270$ MPa along the three main crystallographic directions. Under stress $\sigma = \|\langle 0\,0\,1\rangle$, the line exhibits a complicated behaviour. At $T = 5$ K, the line apparently shifts to lower energies by about 2 cm^{-1}/GPa. At $T = 9$ K, a shoulder on the high-energy side of the mode is clearly seen for $|\sigma| = 200$ MPa. This shoulder is more clearly observed for the polarisation $\boldsymbol{E} \perp \sigma$ than for the polarisation $\boldsymbol{E} \parallel \sigma$.

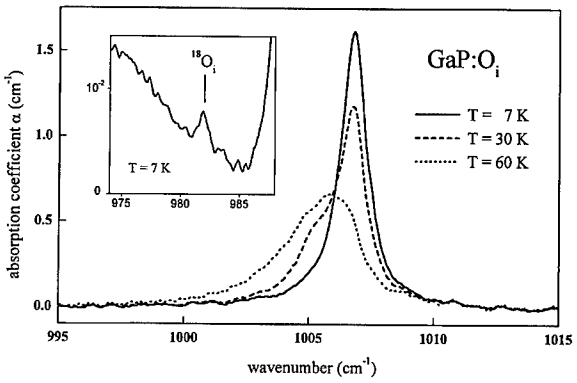

Fig. 1. Vibrational absorption line of interstitial oxygen $^{16}O_i$ in GaP at different temperatures. The inset shows the line due to the 0.2% natural abundant $^{18}O_i$ centre.

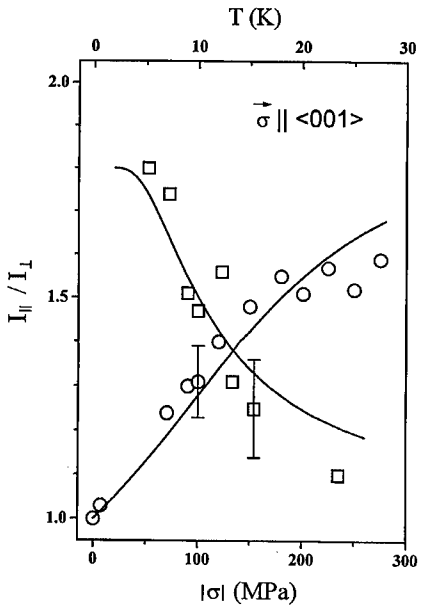

Fig. 2. Ratio $I_{\|}/I_{\perp}$ of the intensities I of the 1006.8 cm^{-1} line measured for stress $\sigma\|\langle 0\,0\,1\rangle$: (○) measured at $T = 9$ K for different stress values $|\sigma|$; (□) measured with $|\sigma| = 200$ MPa at different temperatures. The curves are fits to Eq. (1) using the values of Θ and B given in the text.

For $|\sigma| = 200$ MPa, the shoulder is observed up to $T = 15$ K; at higher temperature a general broadening hinders its detection. At $T = 9$ K and lower stresses, the shoulder is not clearly seen, but the maximum of the line seems to be polarisation dependent being at higher energies for $\boldsymbol{E} \perp \sigma$ than for $\boldsymbol{E} \parallel \sigma$. At low temperatures, one also clearly observes a linear dichroism of the overall mode under $\sigma\|\langle 0\,0\,1\rangle$ stress, the intensity for $\boldsymbol{E} \parallel \sigma$ being higher than for $\boldsymbol{E} \perp \sigma$. This dichroism increases with increasing stress and decreases with increasing temperature. This behaviour is shown in Fig. 2. These unusual results evidence that the centre does not have a trigonal symmetry [6].

Stress $\sigma \parallel [1\,1\,0]$ apparently splits the line into two components (shift of + 0.2 and − 2.0 cm^{-1}/GPa), which are polarised, the low-energy one with the light vector $\boldsymbol{E} \parallel \sigma$ and the other one with $\boldsymbol{E} \parallel [1\,\bar{1}\,0]$. Stress $\|\langle 1\,1\,1\rangle$ also splits the line into two components (shift of + 0.9 and − 1.8 cm^{-1}/GPa) polarised in the same way (the exact degree of polarisation is difficult to detect because of the large half width).

3. Discussion

The presented experimental results clearly suggest that the LVM line at 1006.8 cm^{-1} is due to the antisymmetric stretching mode of the Ga–O_i–P interstitial oxygen. The

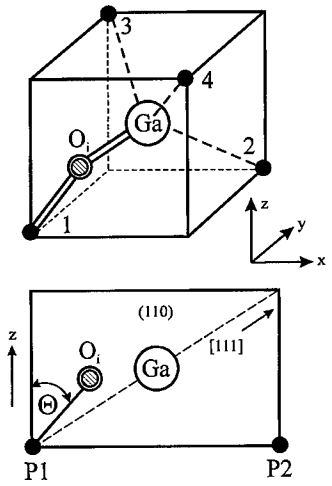

Fig. 3. Model of the Ga–O_i–P centre in GaP with the interstitial oxygen being off-axis around the trigonal axes. The lower part shows one of the 12 equivalent Ga–O_i–P configurations in a (1 1 0) plane.

smaller $^{16}O \rightarrow {}^{18}O$ isotope shift of the vibrational frequency, compared e.g. with GaAs : O_i [1], suggests that in GaP the O_i is more strongly bonded to P than to Ga. However, the behaviour under uniaxial stress leads to the conclusion that the oxygen atom is not in a bond-centred position between Ga and P, but off-axis. This was already suggested by theoretical considerations for O_i in GaAs and GaP [7]. The sidebands appearing at high temperature are probably due to the coupling of the mode with a very low-frequency mode such as observed in silicon [8].

To explain the results in more detail, we propose the model sketched in Fig. 3. The centre has $C_s(C_{1h})$ symmetry, the mirror planes being $\{1\,1\,0\}$ planes. There are 12 energetically equivalent configurations for the system. The centre is able to reorient even at low temperature. When a $\langle 0\,0\,1\rangle$ stress is applied, it favours four of the configurations with respect to the eight others, which means that the orientational degeneracy between the 12 configurations is lifted with a fourfold degenerate ground state (labelled z) and an eightfold degenerate excited one (labelled xy). If we assume the splitting to be proportional to the stress ($\Delta E = B\sigma$), the population ratio between the two configurations is: $n_{xy}/n_z = 2\exp(-\Delta E/kT)$. This decomposition into two classes involves also the splitting of the local mode into two components which is evidenced by the observation of the high-energy shoulder. If Θ is the angle between the $\langle 0\,0\,1\rangle$ axis and the electric dipole of the mode within the $\{1\,1\,0\}$ plane, the intensities at $T = 0$ under polarised light of each type of configuration are proportional to [9]:

$I_{\parallel}^{z} = 4\cos^2\Theta$, $I_{\perp}^{z} = 2\sin^2\Theta$, $I_{\parallel}^{xy} = 4\sin^2\Theta$, and

$I_{\perp}^{xy} = 4\cos^2\Theta + 2\sin^2\Theta$.

This leads to the intensity ratio for the overall line as a function of stress and temperature:

$$\frac{I_{\parallel}}{I_{\perp}}(\sigma, T) = \frac{2 + 2\cot^2\Theta\exp(B\sigma/kT)}{1 + 2\cot^2\Theta + \exp(B\sigma/kT)}. \quad (1)$$

The measured dependencies of $I_{\parallel}/I_{\perp}$ on σ and T can be reasonably fitted in the low-T and low-$|\sigma|$ region with Eq. (1) using the parameters $\Theta = 47°$ and $B = 70\,\mathrm{cm}^{-1}/\mathrm{GPa}$ as can be seen in Fig. 2. At higher temperature, the excited vibrational level responsible for the sideband seen in Fig. 1 becomes populated and at higher stress, these two levels are mixed by the stress. Our analysis does not take into account these phenomena and is therefore valid only at low temperature and low stress.

At this stage, we cannot state whether the reorientation is a general one or whether it only occurs among the three equivalent configurations around a trigonal axis. The fact that no dichroism is observed for $\langle 1\,1\,1\rangle$ stress seems to indicate that the reorientation occurs only among the three equivalent configurations around a trigonal axis, because these three configurations are affected in the same way by the $\langle 1\,1\,1\rangle$ stress. The fact that this reorientation occurs at very low temperature implies that the barriers E_b between the three equilibrium positions are very small. As on the time scale of the experiments no time-dependent effects could be observed, no estimation of E_b can be derived from the experiments.

Therefore, the model of Fig. 3 is able to explain the behaviour of the 1006.8 cm^{-1} line versus stress and temperature. As mentioned above, Θ is the angle between the dipole moment of the mode and the crystal axes. The angle Θ' between the [0 0 1] axis and the P–O bond should be smaller than Θ; if one assumes the bonding of oxygen to occur mainly with the phosphorus, Θ' might not be very different from Θ.

The calibration factor f, connecting the integrated intensity I of the LVM absorption line and the concentration of the defect, is not known for O_i in GaP. Using the value $f = 9.2 \times 10^{15}\,\mathrm{cm}^{-1}$ of O_i in Si and Ge, the highest concentration of O_i found in LEC–GaP amounts to about $8 \times 10^{16}\,\mathrm{cm}^{-3}$.

Acknowledgements

The authors would like to thank C. Naud for his help with the stress experiments and H.v. Kiedrowski for the preparation of the oriented samples.

References

[1] J. Schneider, B. Dischler, H. Seelewind, P.M. Mooney, J. Lagowski, M. Matsui, D.R. Beard, R.C. Newman, Appl. Phys. Lett. 54 (1989) 1442.

[2] C. Song, B. Pajot, C. Porte, Phys. Rev. B 41 (1990) 12330.

[3] P.J. Dean, in: S.T. Pantelides (Ed.), Deep Centers in Semiconductors, Gordon & Breach, New York, 1986, p. 185.
[4] R.J. Hauenstein, T.C. McGill, R.M. Feenstra, Phys. Rev. B 29 (1984) 1858.
[5] A.S. Barker, R. Berman, H.W. Verleur, J. Phys. Chem. Sol. 34 (1973) 123.
[6] A.A. Kaplyanskii, Opt. Spectrosc. 16 (1963) 329.
[7] M.A. Roberson, S.K. Estreicher, C.H. Chu, J. Phys.: Condens. Matter 5 (1993) 8943.
[8] D.R. Bosomworth, W. Hayes, A.R.L. Spray, G.D. Watkins, Proc. Roy. Soc. Lond. A 317 (1970) 133.
[9] B. Bech Nielsen, H.G. Grimmeis, Phys. Rev. B 40 (1989) 12403.

ELSEVIER

Physica B 273–274 (1999) 811–814

PHYSICA B

www.elsevier.com/locate/physb

Optical and magnetic resonance studies of As-impurities in AlSb: from isoelectronic point defects to planes

E.R. Glaser[a,*], T.A. Kennedy[a], B.R. Bennett[a], B.V. Shanabrook[a], L.A. Hemstreet[a], M.W. Bayerl[b], M.S. Brandt[b]

[a]*Naval Research Laboratory, Washington, DC, 20375-5347 USA*
[b]*Walter Schottky Institut, Technische Universität München, D-85748 Garching, Germany*

Abstract

Strong photoluminescence (PL) has been observed and assigned to excitons from superlattices (SL) composed of fractional or single planes of As atoms separated by 8–49 monolayers (ML) of AlSb, from a single As-impurity sheet embedded in AlSb, and from AlSb layers uniformly doped with As. The emission ($\sim$ 1.40–1.62 eV) from the SLs exhibits a weak dependence on period but a strong dependence on the amount of As in the plane. From optically detected magnetic resonance, the g-values and strength of the exchange interaction indicate that the SL recombination involves an exciton whose electron is strongly localized at the As-planes and whose hole is excluded to the AlSb layers. This assignment is supported by ab initio total energy calculations of the electronic band structure. Similar PL was found from the sample with a single As-impurity sheet. A PL band at 1.606 eV from the As-doped AlSb layer is ascribed to recombination of excitons bound to As-impurities that substitute isoelectronically on the Sb sites.

Keywords: Aluminum antimonide; Arsenic impurities; Photoluminescence; Magnetic resonance

1. Introduction

AlSb typically exhibits very weak bandedge recombination that reflects its indirect (X-point) band-gap property. Unexpectedly, strong photoluminescence (PL) was observed recently from superlattices (SLs) composed of fractional or single planes of As-atoms separated by 22–49 monolayers (MLs) of AlSb [1]. Optically detected magnetic resonance (ODMR) at 24 GHz revealed the excitonic character of this emission with the electron strongly localized at the As-planes and the hole bound to the electron but spatially excluded to the AlSb layers.

In this paper we extend these studies to a superlattice with a much shorter period, to a single As-impurity sheet embedded in AlSb, and to AlSb layers uniformly doped with As impurities. In addition, the ODMR was performed at a higher microwave frequency (35 GHz) in order to test the validity of the spin-Hamiltonian employed to model the earlier magnetic resonance results. Finally, ab initio total energy calculations have been made for the electronic band structure of the SLs, including the ground state wave functions and interband transition energies.

2. Experimental background

The PL and ODMR were performed on a set of $[(AlSb)_x(AlAs)_y]_{120}$ ($x = 8 - 49$, $y \sim 0.3, 1$) superlattices grown on semi-insulating GaAs (0 0 1) substrates by MBE at $\sim$ 500°C. Additional growth details, including those on the formation of the fractional or single planes of As-atoms, are given elsewhere [1]. Structures composed of a single As-impurity sheet buried 2000 Å below the surface of a 1 μm-thick AlSb layer and an AlSb film uniformly doped with As impurities ($\sim 5 \times 10^{19}$ cm^{-3}) were also investigated.

* Corresponding author. Tel.: + 1-202-404-4521; fax: + 1-202-767-1165.
E-mail address: glaser@bloch.nrl.navy.mil (E.R. Glaser)

0921-4526/99/$ - see front matter
PII: S0921-4526(99)00510-4

The PL at 1.6 K was excited by the 488 nm line of an Ar^+ laser at a power density of ~ 1 W/cm^2. The emission was analyzed with a $\frac{1}{4}$- m double-grating spectrometer and detected with a Si photodiode. The ODMR was carried out with 35 GHz spectrometers. The external magnetic field was supplied by a 7 T split-coil superconducting magnet or a 6-in pole-face electromagnet with a maximum field of 1.8 T. Photoexcitation power densities near 30 mW/cm^2 and microwave modulation frequencies between 3 and 10 kHz gave the best signal-to-noise ratios. Symmetry information was obtained from angular rotation studies with the field rotated in the $(1\,\bar{1}\,0)$ plane.

3. Results and discussion

3.1. As-planes and islands in AlSb

The photoluminescence from several $[(AlSb)_x(AlAs)_y]_{120}$ superlattices and from a single As-sheet embedded in AlSb is shown in Fig. 1. Several trends are evident. Most notably, the As-atoms introduce strong radiative recombination, in contrast to the weak emission typical of undoped epitaxial AlSb. The PL energies (~ 1.40–1.45 eV) for the SLs with x between 5 and 50 MLs and $y \sim 1$ ML and that for the single As-plane are very similar, ~ 250 meV below the AlSb band gap (1.7 eV). However, the PL exhibits a *strong* dependence on the amount of As in the ML. This is best demonstrated for the SL composed of fractional planes ("islands") of As-atoms with $y \sim 0.3$ separated by 31 MLs of AlSb where the PL is shifted to higher energy by ~ 170 meV. The small peaks found at 42 meV below the dominant PL bands are attributed to TO (AlSb) phonon replicas based on previous studies of bulk AlSb [2].

Previous ODMR at 24 GHz revealed the excitonic character of the emission from SLs with $x > 20$ MLs with the recombining electron strongly localized at the As-planes and the hole excluded to the AlSb layers [1]. The ODMR was analyzed with the following spin-Hamiltonian in the limit of weak elelctron–hole exchange interaction [3]:

$$H = \mu_B g_e \boldsymbol{S} \cdot \boldsymbol{B} + \mu_B g_h \boldsymbol{J} \cdot \boldsymbol{B} + a \boldsymbol{J} \cdot \boldsymbol{S}, \quad (1)$$

where the first two (field-dependent) terms are the Zeeman energies for an electron with spin $\frac{1}{2}$ and for a hole with spin $J = \frac{3}{2}$, μ_B is the Bohr magneton, g_e and g_h are the electron and hole g-values, and the last (field-independent) term describes the electron–hole exchange with strength a. This interaction is revealed through splittings of the electron and hole spin transitions as was found, for example, from ODMR of type-II short-period GaAs/AlAs superlattices [3–5].

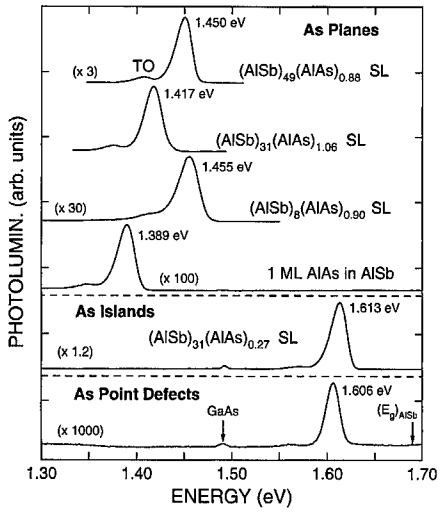

Fig. 1. PL spectra obtained at 1.6 K from several SLs composed of fractional or single planes of As-atoms separated by 8–49 MLs of AlSb, from a single As-impurity sheet embedded in AlSb, and from an AlSb layer uniformly doped with As at $\sim 5 \times 10^{19}$ cm^{-3}.

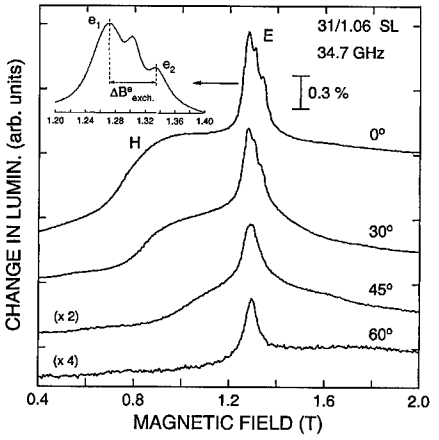

Fig. 2. ODMR spectra found at 35 GHz on the 1.417 eV PL from the $(AlSb)_{31}(AlAs)_{1.06}$ SL as a function of the angle between $\boldsymbol{B}$ and the [0 0 1] axis. Inset: Narrow-field scan about 1.30 T with $\boldsymbol{B} \parallel$ [0 0 1].

Wide-field ODMR scans at 35 GHz from the $[(AlSb)_{31}(AlAs)_{1.06}]_{120}$ SL for several orientations of $\boldsymbol{B}$ are shown in Fig. 2. Signals assigned to the recombining electrons and holes are discussed in turn.

Three luminescence-increasing features (labeled E) are resolved near 1.30 T for $\boldsymbol{B} \parallel$ [0 0 1]. A similar three-line spectrum was found at 24 GHz, including the $\cos(\theta)$ splitting dependence of the two outer lines (labeled e_1 and e_2 in the inset), where θ is the angle between $\boldsymbol{B}$ and the [0 0 1] SL axis [1]. From the first and third terms

in Eq. (1), lines e_1 and e_2 were ascribed to $S = \frac{1}{2}$ electron-spin transitions with $g^e_{\|} = 1.922$ and $g^e_{\perp} = 1.939$ split by an isotropic exchange interaction ($\Delta \equiv a/2 = (\mu_B/2)\Delta B^e_{exch} \cdot g^e_{\|}$, where ΔB^e_{exch}. is the field splitting with $\boldsymbol{B} \| [0\,0\,1]$) of 3.7 μeV with $J_z = \pm\frac{3}{2}$ heavy holes (characterized by $g_{\perp} \sim 0$). In support of that analysis, the *same* resonance parameters within error describe the 35 GHz ODMR results. These g-values lie between those reported for X-point electrons in AlAs [3–6] and AlSb [7]. This character indicates that the electron wave function is strongly localized (binding energy of ~ 250 meV) at the As-planes, with some penetration into the adjacent AlSb layers. A discussion of the unsplit line at ~ 1.30 T (described by the same g-tensor) is given elsewhere [1].

X-ray diffraction measurements revealed that the AlSb layers are under an average in-plane biaxial compression of $0.08 \pm 0.02\%$ [1]. This strain lifts the four-fold degeneracy of the $J = \frac{3}{2}$ valence band (VB) such that only states derived from the $J_z = \pm\frac{3}{2}$ heavy-hole VB are populated at 1.6 K. Most pertinent for the ODMR, the g-values for holes associated with this VB are highly anisotropic with $g(\theta) = g^h_{\|} \cos(\theta)$, where $g^h_{\|} \sim 2$–4 [8]. The broad resonance labeled H in Fig. 2 roughly exhibits such a g-tensor with $g^h_{\|} = 2.55 \pm 0.15$. A comparison of the line widths at 24 and 35 GHz indicates that this line is inhomogenously broadened due to a distribution of $g^h_{\|}$-values. We tentatively assign the feature to holes in the strained AlSb layers that participate in the excitonic recombination.

The exchange splittings obtained for the $[(AlSb)_x(AlAs)_1]_{120}$ SLs as a function of AlSb layer thickness are shown in Fig. 3. The exchange energy rapidly increases from 3.4 μeV for the SL with $x = 49$ MLs to 19.5 μeV for the SL with $x = 8$ MLs. This behavior reflects the strong increase in the degree of electron/hole wave function overlap with decreasing SL period. A similar dependence has been reported by several groups for type-II excitons in short-period GaAs/AlAs superlattices [3–5,9].

First-principles total energy calculations on 20- and 40-atom AlSb (0 0 1) SLs, both with and without an As-plane replacing a plane of Sb atoms, have been carried out to check the model employed to explain the salient features of the PL and ODMR results. The electronic properties were calculated within the local density approximation of density functional theory using the exchange-correlation potential of Ceperly–Alder [10,11], generalized norm-conserving pseudopotentials [12], and a plane-wave basis set with a kinetic energy cutoff of 12 Ry.

The key results can be summarized as follows. First, the presence of an As ML in the otherwise perfect AlSb SL leads to a lowering of the energy between the highest occupied and lowest unoccupied energy levels at the Γ-pt. by ~ 0.21–0.24 eV, in excellent agreement with the difference between the superlattice PL energies and the AlSb band gap. Second, the magnitude of this shift

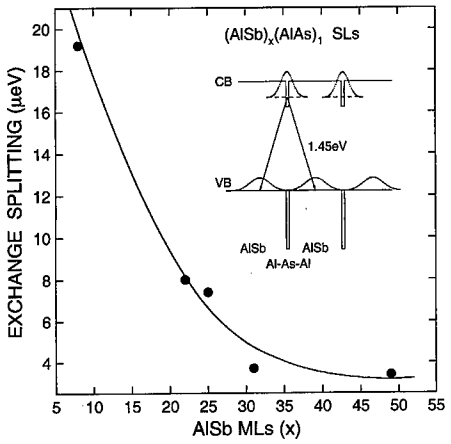

Fig. 3. Exchange splitting as a function of the AlSb layer thickness for $(AlSb)_x(AlAs)_1$ SLs. The curved line is a guide to the eye. Inset: Schematic diagram of proposed band structure for SLs based on the PL and ODMR studies.

shows little dependence on SL period but depends sensitively on the degree of strain in the Al–As layer. No reduction in transition energy was found when the atoms in the As ML were placed at the bulk Sb sites. However, the energy of the lowest unoccupied SL level decreased monotonically as the SL was allowed to relax around the As ML such that the Al–As interlayer spacing decreased by $\sim 14\%$ from that of bulk AlSb (1.53 Å) to the value predicted by elastic theory (1.31 Å). Third, the wave function associated with the lowest unoccupied level of the SL becomes localized about the As-plane as this level is pulled down into the bulk AlSb energy gap. This is illustrated in Fig. 4 where the dotted line represents the planar-averaged charge density of this state along [0 0 1] for the 20-atom $(AlSb)_9(AlAs)_1$ SL. Fourth, the highest occupied SL level derives from the AlSb $J_z = \pm\frac{3}{2}$ VB edge but the wave function of this state is pushed away from the As ML with an enhanced probability at the center of the AlSb layers as indicated by the full line in Fig. 4. Overall, these calculations offer strong support for the recombination model used to interpret the PL and ODMR data.

3.2. *As point defects in AlSb*

The PL at 1.6 K from an AlSb epitaxial layer uniformly doped with As impurites is given in Fig. 1. Strong emission is observed at 1.606 eV with similar phonon structure as found for the AlSb/AlAs superlattices and the single As-dopant sheet. Based on the strong degree of electron localization associated with the As-planar defects in those structures, this emission is ascribed to the recombination of excitons bound to the As-isovalent impurities.

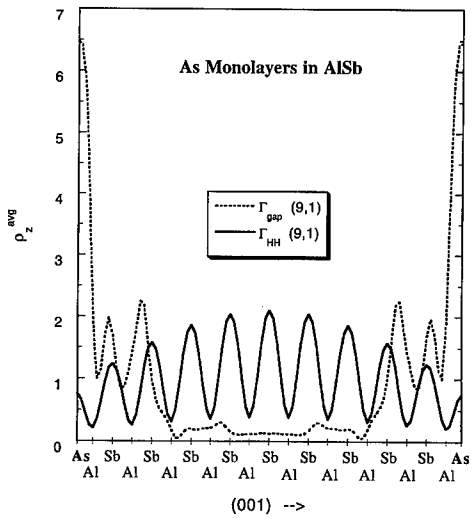

Fig. 4. The planar average charge densities associated with the electron (dashed line) and heavy-hole (solid line) ground states along the growth direction for a $(AlSb)_9(AlAs)_1$ SL as determined from ab initio total energy calculations.

The assignment of the PL to isovalent bound excitons also follows from the character of isoelectronic traps such as observed in N-doped GaP [13], Bi- and Sb-doped InP [14], and O-doped ZnTe [15]. In particular, it is known that isoelectronic impurities can form electron traps if their electronegativities are sufficiently larger than the atom of the host lattice for which they substitute. The electronegativity of As is indeed larger than that for Sb [16]. The short-range potential associated with the As-isovalent center traps an electron in a highly localized state. The exciton is formed when the Coulomb field of this charge binds a hole in a hydrogenic-like orbital. Thus, As can also be modeled as an "isoelectronic acceptor" in AlSb. Following previous analyses of isoelectronic bound excitons in Bi- and Sb-doped InP [14], the localization energy (E_{loc}) of the trapped electron at the As impurity is estimated by

$$E_{loc} = (E_g)_{AlSb} - E_{PL} - E_a \sim 55 \pm 3 \text{ meV}, \quad (2)$$

using an effective-mass acceptor binding energy (E_a) of ~ 37 meV [2]. It is interesting to note that E_{loc} is about $\frac{1}{3}$ of that reported for the effective-mass donor binding energy in AlSb [2].

4. Summary

Strong radiative recombination was observed from SLs composed of fractional or single planes of As-atoms separated by 8–49 MLs of AlSb, from a single As-impurity sheet in AlSb, and from an AlSb layer uniformly doped with As. ODMR studies revealed the excitonic character of the SL emission with the electron strongly localized at the As-planes and the hole excluded to the AlSb layers. This assignment is supported by total energy calculations of the electronic band structure that highlight the relaxation of the Al–As interlayer separation. A new PL band at 1.606 eV from the As-doped AlSb layer is ascribed to excitons bound to As-isovalent point defects. These studies provide a picture of the transition from recombination at an isoelectronic point defect to a planar defect.

Acknowledgements

This work was supported by the Office of Naval Research. We thank Prof. M. Stutzmann (TU-Munich) for stimulating discussions. ERG thanks the WSI for their hospitality and the financial support of the Deutsche Forschungsgemeinschaft during the time spent as a visiting scientist.

References

[1] E.R. Glaser, T.A. Kennedy, B.R. Bennett, B.V. Shanabrook, Phys. Rev. B 59 (1999) 2240.
[2] G. Hofmann, C.T. Lin, E. Schönherr, J. Weber, J. Appl. Phys. 67 (1990) 1478.
[3] H.W. van Kesteren, E.C. Cosman, W.A.J.A. van der Poel, Phys. Rev. B 41 (1990) 5283.
[4] J.M. Trombetta, T.A. Kennedy, D. Gammon, B.V. Shanabrook, S.M. Prokes, 20th International Conference on the Physics of Semiconductors, World Scientific, Singapore, 1990, p. 1361.
[5] P.G. Baranov, I.V. Mashkov, N.G. Romanov, P. Lavallard, R. Planel, Solid State Commun. 87 (1993) 649.
[6] E.R. Glaser, T.A. Kennedy, B. Molnar, R.S. Sillmon, M.G. Spencer, M. Mizuta, T.F. Kuech, Phys. Rev. B 43 (1991) 14540, and references therein.
[7] W. Wilkening, U. Kaufmann, J. Schneider, E. Schönherr, E.R. Glaser, B.V. Shanabrook, J.R. Waterman, R.J. Wagner, Mater. Sci. Forum 83–87 (1992) 793.
[8] See, e.g., E.R. Glaser, J.M. Trombetta, T.A. Kennedy, S.M. Prokes, O.J. Glembocki, K.L. Wang, C.H. Chern, Phys. Rev. Lett. 65 (1990) 1247, and references therein.
[9] B. Rejaei Salmassi, G.E.W. Bauer, Phys. Rev. B 39 (1989) 1970.
[10] D.M. Ceperly, B.J. Alder, Phys. Rev. Lett. 45 (1980) 5661.
[11] J.P. Perdew, A. Zunger, Phys. Rev. B 23 (1981) 5048.
[12] D. Hamann, Phys. Rev. B 40 (1989) 2980.
[13] D.G. Thomas, J.J. Hopfield, Phys. Rev. 150 (1966) 680.
[14] S.G. Bishop, B.V. Shanabrook, P.B. Klein, R.L. Henry, Phys. Rev. B 38 (1988) 8469, and references therein.
[15] M.J. Seong, I. Miotkowski, A.K. Ramdas, Phys. Rev. B 58 (1998) 7734, and references therein.
[16] J.C. Phillips, in: Bonds and Bands in Semiconductors, Academic Press, New York, 1973, p. 54.

ELSEVIER

Physica B 273–274 (1999) 815–818

PHYSICA B

www.elsevier.com/locate/physb

Deep electronic states near the surface of (In,Ga)P layers grown by MOVPE on GaAs

P. Krispin[a,*], M. Asghar[a,1], A. Knauer[b]

[a]*Paul-Drude-Institut für Festkörperelektronik, Hausvogteiplatz 5-7, D-10117 Berlin, Germany*
[b]*Ferdinand-Braun-Institut für Höchstfrequenztechnik, Albert-Einstein-Str. 11, D-12489 Berlin, Germany*

Abstract

Metal–semiconductor contacts are used to examine deep electronic states near the (In,Ga)P surface by deep-level transient Fourier spectroscopy. Towards the as-grown (In,Ga)P surface, the In mole fraction increases due to parasitic indium deposited from the horizontal reactor during cooling after growth. This process is accompanied by compressive strain, which leads to the formation of several deep-level defects near the surface of Si- as well as Zn-doped (In,Ga)P layers and their successive diffusion into the epitaxial layer. In contrast, Si-doped (In,Ga)P capped by a GaAs layer is practically free of deep-level defects. In the bulk of Zn-doped layers, a dominant hole trap is found at 0.91 eV with or without a GaAs cap layer.

Keywords: (In,Ga)P; Graded surface composition; Electron and hole traps; Depth profiles

1. Introduction

(In,Ga)P layers lattice-matched to GaAs are of vital importance for potential applications in semiconductor devices, i.e., heterojunction bipolar transistors, light-emitting and laser diodes, high electron mobility transistors, and solar cells. Despite a large number of investigations, the electrical characteristics of (In,Ga)P epitaxial layers are still controversial. Accurate lattice matching is a prerequisite for reproducible results. In addition, (In,Ga)P exhibits a tendency to decompose and order [1]. The electronic properties therefore strongly depend on the growth conditions. A large variety of deep electronic levels has been consistently found in layers realized by several epitaxial techniques. For n-type layers grown by metalorganic vapor-phase epitaxy (MOVPE), distinctly different traps have been detected with concentrations over a wide range from 10^{11} up to several 10^{17} cm^{-3} [1–5]. Mostly, ordered *n*-type layers grown at temperatures above 600°C have been studied up to now. A deep-level analysis of p-type (In,Ga)P layers grown by MOVPE has not been published yet. Our investigations focus on Si- as well as Zn-doped (In,Ga)P layers lattice-matched to GaAs and grown by MOVPE at about 580°C, where the disordered crystal structure prevails. Metal–semiconductor contacts have been used in order to examine deep electronic states near the (In,Ga)P surface by deep-level transient Fourier spectroscopy (DLTFS) [6].

The as-grown (In,Ga)P surface without a GaAs cap layer exhibits a compositional variation, which is due to parasitic indium deposited from the horizontal reactor during cooling after growth. By this process, deep-level defects are generated at the surface of Si- as well as Zn-doped (In,Ga)P layers. We find striking depth profiles of the trap concentrations near the as-grown surface of the epitaxial layers. The origin of these electronic states in the band gap of (In,Ga)P random alloys is discussed.

It is further shown that Si-doped (In,Ga)P with a GaAs cap layer is practically free of deep-level defects. Zn-doped layers with or without a GaAs cap contain a dominant level at 0.91 eV above the valence-band edge

* Corresponding author. Tel.: + 49-30-20377-399; fax: + 49-30-20377-515.

[1] Permanent address: Department of Physics, Islamia University, Bahawalpur, Pakistan.

E-mail address: krispin@pdi-berlin.de (P. Krispin)

0921-4526/99/$ - see front matter
PII: S0921-4526(99)00511-6

E_V, which is an effective candidate for non-radiative recombination.

2. Experimental details

The (In,Ga)P layers were grown with and without GaAs cap layers on highly doped GaAs(0 0 1) substrates at 580°C in a horizontal MOVPE reactor using TMGa, TMIn, DMZn, Si_2H8, PH_3, and AsH_3 as precursors. Typically, V/III input ratios of 70 and growth rates of 2.5 μm/h were used. The lattice mismatch of the layers was in all cases smaller than 5×10^{-4}. Si- and Zn-doped layers were grown with carrier concentrations of about 1×10^{17} cm^{-3} and thicknesses between 300 and 500 nm. Vacuum-deposited Ti/Au dots were applied as Schottky contacts. Deep levels were investigated by the DLTFS technique [6], where the time transients of the capacitance C are digitized, and the discrete Fourier coefficients are calculated at each temperature. The level concentration N_T was determined according to the corrections given in Ref. [7]. Secondary ion mass spectrometry (SIMS) was used to examine depth profiles of the composition.

3. Results and discussion

Fig. 1 displays typical deep-level spectra of a Si-doped (In,Ga)P layer grown without a GaAs cap layer for various values of the reverse bias. For pulse heights above the threshold voltage for bulk levels [8], a dominant, slightly broadened peak is found at about 365 K (cf. Fig. 1a), which originates from an electron trap E1 at 0.81 eV below the conduction-band edge E_C. The small shift of the peak position to lower temperatures is related to higher emission rates at higher electric fields. Spectra measured with small pulse heights, which are adequate to examine spatially confined traps, are shown in Fig. 1b for the same n-type (In,Ga)P layer as in Fig. 1a. In addition to the E1 response, sharp peaks labeled E2 appear, which strongly shift to lower temperatures at lower reverse biases. The thermal activation energy changes remarkably from 0.75 to 0.55 eV. Moreover, the peak height rises. It is important to note that the E1- and E2-related DLTFS peaks are totally missing in (In,Ga)P layers, when covered by a sufficiently thick GaAs layer. The concentration of other traps in these capped (In,Ga)P layers is found to be below 10^{14} cm^{-3}.

DLTFS curves typical of Zn-doped (In,Ga)P layers without a GaAs cap are given in Fig. 2 for different bias voltages. The peak at about 390 K in Fig. 2a with a position independent of the bias stems from a hole trap H1 at $E_V + 0.91$ eV in the bulk of the epitaxial layer. Its concentration approaches 10^{15} cm^{-3}. The capture cross section for holes is found to be about 10^{-14} cm^2. For lower

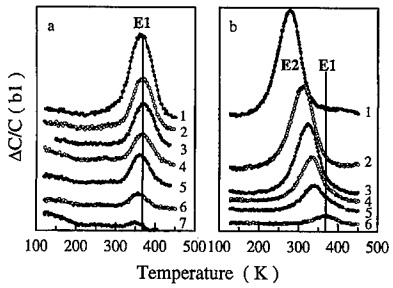

Fig. 1. Deep-level spectra (first sine coefficient $b1$, period 1 s, pulse width 0.1 s) of Si-doped (In,Ga)P without GaAs cap. The spectra are shifted vertically for clarity. The quiescent bias/pulse height values in (a) are: (1) −1.5/−1 V, (2) −2/−1.5 V, (3) −2.5/−2 V, (4) −3/−2.5 V, (5) −4/−3 V, (6) −5/−4 V, (7) −7/−5 V. The quiescent bias/pulse height values in (b) are: (1) 0/0.2 V, (2) −0.2/0 V, (3) −0.4/−0.2 V, (4) −0.6/−0.4 V, (5) −0.8/−0.6 V, (6) −1.5/−1.3 V. The temperature positions of the levels E1 and E2 are indicated.

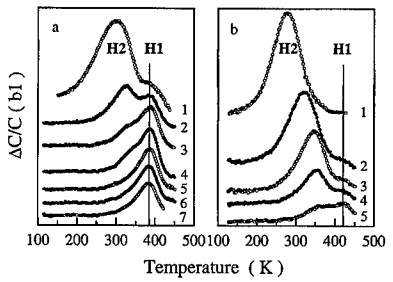

Fig. 2. Deep-level spectra (first sine coefficient $b1$) of Zn-doped (In,Ga)P without GaAs cap. The spectra in (a) were measured with 1 s period and 1s pulse width. The quiescent bias/pulse height values in (a) are: (1) 0.5/0 V, (2) 1/0.5 V, (3) 1.5/1 V, (4) 3/2 V, (5) 4/3 V, (6) 5/4 V, (7) 6/5 V. The spectra in (b) were measured with 0.1 s period and 0.01 s pulse width. The quiescent bias/pulse height values in (b) are: (1) 0/−0.2 V, (2) 0.2/0 V, (3) 0.4/0.2 V, (4) 0.6/0.4 V, (5) 1/0.8 V. The spectra are shifted vertically for clarity. The temperature positions of the levels H1 and H2 are indicated.

biases, a broad band appears at lower temperatures, which is analyzed in more detail in Fig. 2b with pulse heights of 0.2 V. The response H2 exhibits a large shift to lower temperatures, and the activation energy changes from about 0.78 to 0.58 eV. The H2 levels are not present in (In,Ga)P layers, when a GaAs layer is grown on top. The hole trap H1 is found in Zn-doped (In,Ga)P layers with and without the GaAs capping layer. Because of its high concentration and large capture cross section, it is a candidate for non-radiative recombination.

Since the peaks in Fig. 1b and 2b are well-defined, they are likely due to discrete levels. For each energy, there is a maximum response for a certain bias, if the Fermi level

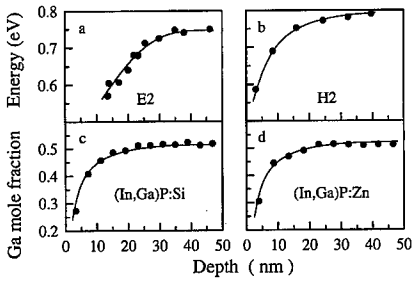

Fig. 3. Depth profiles of the level energies E2 in (a) and H2 in (b) as well as of the composition in (c) and (d) for Si- and Zn-doped (In,Ga)P, respectively.

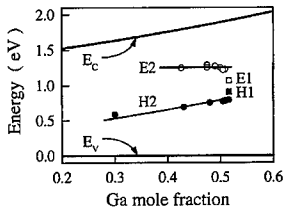

Fig. 4. Positions of the levels E1, E2, H1, and H2 within the band gap of disordered (In,Ga)P.

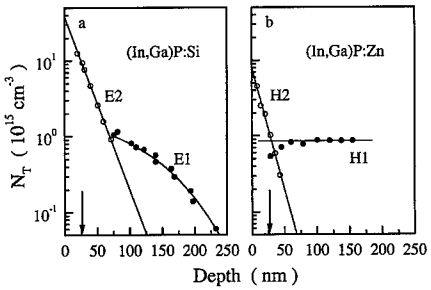

Fig. 5. Concentration versus depth profiles in (a) for the levels E1 and E2 in Si-doped (In,Ga)P and in (b) for the levels H1 and H2 in Zn-doped (In,Ga)P. The arrows at 25 nm indicate the thickness of the surface region exhibiting the gradual change of the composition.

crosses the particular level. The local origin of the individual deep-level contributions E2 and H2 can be determined from the thickness of the depletion layer taking the λ effect into account [7]. The change of the activation energies versus bias can thus be transformed into a depth dependence of the level energies. Fig. 3a and b demonstrate that the energies of the responses E2 and H2 substantially vary with the distance from the contact. It is suggested that it is always the same defect in Si-doped (In,Ga)P, which in Fig. 3a gives rise to the depth-dependent energy of the level E2 near the as-grown surface. For Zn-doped (In,Ga)P layers, the level H2 is in the same way related to a distinct defect with electronic properties, which change remarkably in a region of about 25 nm below the bare surface (see Fig. 3b).

The depth-dependent properties of the traps E2 and H2 are due to a gradual change of the composition near the (In,Ga)P surface. The bare (In,Ga)P surface exhibits, in contrast to (In,Ga)P layers with a GaAs cap layer, a compositional variation, which is due to parasitic indium deposited from the horizontal reactor during cooling after growth. Figs. 3c and d display the variation of the Ga mole fraction as deduced from SIMS depth profiles of the investigated layers. Identical compositional profiles appear for the Si- and Zn-doped (In,Ga)P layers grown under similar conditions. By comparing the depth profiles of the level energies with those of the Ga mole fraction, the compositional dependence of the levels E2 and H2 can be determined.

For the investigated Si- and Zn-doped random alloys of (In,Ga)P, the energy positions of the levels E1, E2, H1, and H2 in the band gap are compiled in Fig. 4 as determined from Fig. 3. Changing the Ga mole fraction, the activation energy of the electron trap E2 is fixed to the valence band at $E_V + 1.25$ eV, whereas the hole trap level H2 is attached to the conduction band at $E_C - 1.10$ eV. Both levels are obviously associated with different defects near the surface. The traps E2 and H2 are resolved in Fig. 1b and 2b with small pulse heights, i.e., under conditions for the examination of spatially confined levels. Nevertheless, both are associated with bulk defects, but in a region of gradual composition change. Thus, a certain level energy can be found only at a certain position.

Depth profiles of the trap concentrations are outlined in Fig. 5 including the full correction according to Ref. [7]. Whereas the E1-related defect is present near the surface with a density of about 10^{15} cm^{-3}, it disappears in the n-type layer for distances more than 250 nm from the surface (Fig. 5a). Since a similar electron trap has been found in (In,Ga)P with Ga mole fractions below 0.47 [3], its generation is apparently due to compressive strain. The trap E1 is missing in (In,Ga)P layers capped by GaAs. The internal strain near the as-grown surface obviously leads to the formation of an intrinsic defect with the band gap state E1. From the concentration versus depth plot for this defect in Fig. 5a, it further follows that the level E1 is not confined to the compositionally graded surface layer of 25 nm thickness. The E1-related defects also exist in the bulk of the (In,Ga)P layer, where the composition is found to be constant. Fig. 5a also shows that the density of the electron trap E2 decreases exponentially with depth. At the very surface, the concentration is found to be in the 10^{16} cm^{-3} range. The diffusion processes, which lead to the depth distributions of the E1- and E2-associated defects in Si-doped (In,Ga)P are apparently different. In Zn-doped (In,Ga)P

layers, the hole trap H2 exhibits also an exponential decay of the concentration versus depth (Fig. 5b). But, it can be ruled out that the levels E2 and H2 belong to the same defect, because the compositional variations of the level energies are different (see Fig. 4). As for the E1-related defect, the traps E2 and H2 are formed due to compressive strain at the bare surface. The depth distributions of both defects, however, extend into the region below the compositionally graded surface layer.

4. Conclusions

Disordered (In,Ga)P layers grown by MOVPE are very sensitive to local strain caused by deviations from the composition for lattice matching. We find that random alloys of (In,Ga)P, which are not capped by GaAs, exhibit an enhancement of the In mole fraction at the surface, which leads to compressive strain during cooling after growth and successive formation of deep-level defects and their diffusion into the epitaxial layer. It is suggested that the levels E1, E2, and H2 are associated with intrinsic lattice defects, which minimize the compressive strain near the surface, e.g., Frenkel defects.

Acknowledgements

The authors are indebted to H. T. Grahn and U. Jahn for comments and careful reading of the manuscript. We are grateful for the technical assistance of Ch. Dombrowski and E. Wiebicke.

References

[1] A. Ginoudi, E.C. Paloura, N. Frangis, J. Appl. Phys. 75 (1994) 2980.
[2] M.O. Watanabe, Y. Ohba, J. Appl. Phys. 60 (1986) 1032.
[3] Z.C. Huang, Bing Yang, H.K. Chen, J.C. Chen, in: S. Ashok, J. Chevallier, I. Akasaki, N.M. Johnson, B.L. Sopori (Eds.), Materials Research Society Symposium Proceedings, Vol. 378, 1995, p. 189.
[4] T. Kikkawa, K. Imanishi, K. Fukuzawa, T. Nishioka, M. Yokoyama, H. Tanaka, Inst. Phys. Conf. Ser. No. 155 (1997) 877.
[5] S. Anand, N. Carlsson, M.-E. Pistol, L. Samuelson, W. Seifert, J. Appl. Phys. 84 (1998) 3747.
[6] S. Weiss, R. Kassing, Solid State Electron. 31 (1988) 1733.
[7] J. Bourgoin, M. Lannoo, Point Defects in Semiconductors II, Springer, Berlin, 1983, p. 167.
[8] Jian H. Zhao, J.C. Lee, Z.Q. Fang, T.E. Schlesinger, A.G. Milnes, J. Appl. Phys. 61 (1987) 5303.

ELSEVIER

Physica B 273–274 (1999) 819–822

PHYSICA B

www.elsevier.com/locate/physb

Interplay between Jahn–Teller coupling and axial crystal fields: GaP:(Cr, S)

E. Baars[a], A. Dörnen[a,*], W. Ulrici[b]

[a] *4. Physikalisches Institut, Universität Stuttgart, D-70550 Stuttgart, Germany*
[b] *Paul-Drude-Institut, Hausvogteiplatz 5-7, D-10117 Berlin, Germany*

Abstract

We investigate the intracenter transitions $^5T_2(D) \rightarrow {}^5E(D)$ of negatively charged chromium $Cr^{2+}(3d^4)$ in GaP. The effect of uniaxial stress on the zero-phonon-absorption lines helps to identify the transitions and emphasizes the importance of the Jahn–Teller coupling of the ^5D states. In GaP codoped with chromium and sulfur a new spectrum is observed. The stress response of the corresponding optical center evidences trigonal symmetry C_{3v}. We identify the center with the $(Cr^{2+} - S)$ pair on substitutional next-neighbor sites. The trigonal crystal field strongly quenches the Jahn–Teller coupling inherent in isolated $GaP:Cr^{2+}$.

Keywords: , $GaP:(Cr^{2+}, S)$; Uniaxial stress; Jahn–Teller coupling

1. Introduction

From electron paramagnetic resonance (EPR) it is known that Cr^{2+} centers in GaAs, InP and GaP couple strongly to tetragonal phonon modes [1–3]. The ground state $^5T_2$ has been found to be split by a tetragonal term DS_z^2 with parameter D in the range of 1–2 cm^{-1}. In the optical spectra of the $^5T_2 \rightarrow {}^5E$ transition for $GaAs:Cr^{2+}$ [4] and $InP:Cr^{2+}$ [5] a strong and broad phonon sideband has been found in addition to the zero-phonon lines (ZPL), which also hints to a strong Jahn–Teller coupling. The ZPLs have been interpreted in terms of a dynamic Jahn–Teller model in which the orbital state T_2 is coupled to tetragonal phonon modes with the coupling close to the static limit [5–7]. This results in a tetragonally (D_{2d}) distorted center with the ground state $^5B_2$ manifold. Furthermore, to explain the structure of the ZPLs the excited state ^5E has been assumed to be much more weakly coupled to phonons so that tetrahedral symmetry is preserved in the excited state.

For GaP the situation remained unclear. In highly resolved absorption spectra eight ZPLs have been observed [3] whereas selection rules allow for seven lines only. The spectrum consisting of the series X, Y, and Z is shown in Fig. 1. The high-energetic line A, which does not fit into the level scheme as outlined above, has been tentatively assigned to a chromium associated defect [3]. To get more insight into the level scheme and into the importance of the Jahn–Teller coupling of the excited states ^5E we investigated the stress response of the ZPLs of $GaP:Cr^{2+}$ by uniaxial stress of up to 170 MPa. Additionally, in GaP codoped with chromium and sulfur a new spectrum shows up with a set of ZPLs centered at 7155 cm^{-1}. These ZPLs have been analyzed by uniaxial stress, too, and will be compared to the spectrum of the isolated substitutional Cr^{2+} ion.

For absorption experiments with external uniaxial stress rectangularly shaped rods were prepared with their axes along the directions [0 0 1], [1 1 1], and [1 1 0], respectively. The samples were placed between a pair of pistons to apply stress in a flow gas cryostat at temperatures of around 6 K. The measurements were carried out with a BOMEM Fourier spectrometer DA3 at a resolution of 0.1 cm^{-1}.

* Corresponding author. Tel.: 49-711-685-5150; fax: 49-711-685-5097.

E-mail address: a.doernen@physik.uni-stuttgart.de (A. Dörnen)

0921-4526/99/$ - see front matter
PII: S0921-4526(99)00512-8

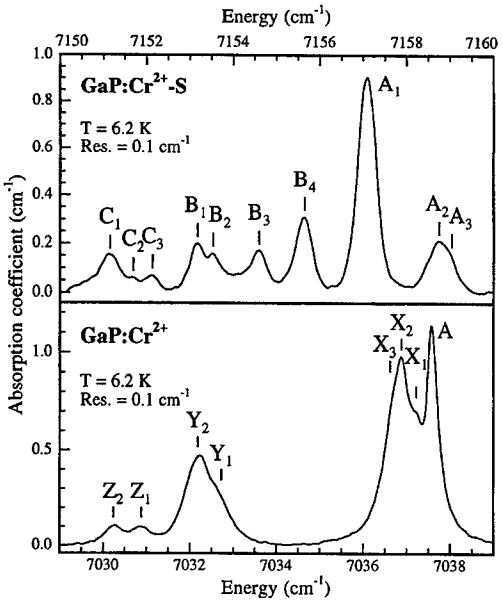

Fig. 1. Absorption spectrum of GaP:(Cr, S). The ZPLs at 7034 cm^{-1} are due to substitutional Cr^{2+} [3,12]. The ZPLs centered at 7155 cm^{-1} are related to Cr and S codoped GaP.

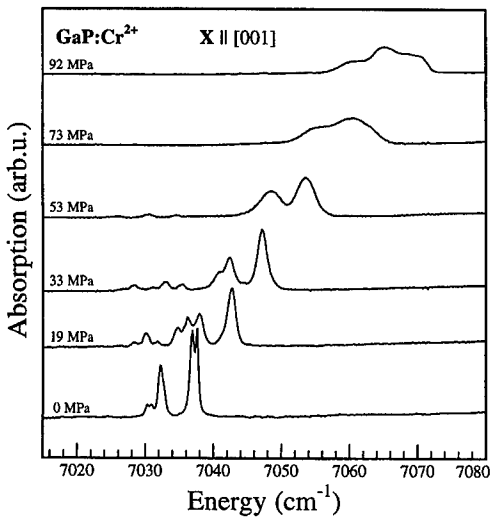

Fig. 2. Absorption spectra of GaP:Cr^{2+} with external stress X along the [0 0 1] direction.

2. GaP:Cr^{2+}

2.1. Stress response

Absorption spectra of the lines X, Y, Z, and A with stress applied along the [0 0 1] direction have been measured, see Fig. 2. Due to the line width, which gets rapidly larger with increasing stress, lines can be followed up to 150 MPa only. Lines which shift to lower energies become weaker as the population of the initial state reduces with increasing stress. As Fig. 3a shows, the lines split linearly with applied stress. We observe four different slopes for the eight lines resolved in total. For stress along the [111] crystal axis, the response of the center is much smaller (Fig. 3b). No splitting is being observed. All lines shift parallel to higher energies.

The experiments clearly show that the components of line A follow the same systematics as the components of the lines X, Y, and Z. As will be shown below, the splitting pattern also confirms the present understanding of a center, which is tetragonally distorted in the ground state $^5B_2$ but remains tetrahedral in the excited state ^5E [3]. To discuss the stress splitting of the spin–orbit (SO) coupled states we make use of the fact that the strain only affects the orbital part of the wave function.

According to the model introduced in Section 1, the orbital ground state T_2 is strongly coupled to tetragonal ε phonon modes. A spontaneous Jahn–Teller distortion reduces the symmetry of the center to tetragonal (D_{2d}) which splits the orbital state T_2 into a low lying level B_2 (nondegenerate) and a higher lying level E (two-fold degenerate). The latter level is not observed since it is not thermally populated. Therefore, the ground state levels observed consist of *one* B_2-type orbital wave function only. External stress removes the geometrical degeneracy of the three possible orientations of a tetragonal center in a tetrahedral crystal. The piezospectroscopic constants A_1 and A_2 of a tetragonal center as defined by Kaplyanskii [8] can be used to describe the stress response of the orbital ground state. As long as the strain splitting is smaller than the tetrahedral crystal-field splitting Δ into the $^5T_2$ and ^5E level or the Jahn–Teller coupling energy, orbital admixtures to the ground state are small. Then, in first order, all SO wave functions of a specific tetragonal center are affected by the same energetic shift when uniaxial stress is applied. This has been confirmed in the experiments as shown in Fig. 3. Thus only the piezospectroscopic constants A_1 and A_2 are required to describe the splitting of the $^5B_2$ manifold.

The levels of the excited state ^5E are split linearly for stress along the [0 0 1] direction by $\pm b$, where b denotes the piezospectroscopic constant of the E state. Stress along the [111] crystal axis does not split the orbital E state. Also, in this case no geometrical degeneracy is being lifted in the ground state. Therefore, no splitting is observed in the spectrum. The response to the hydrostatic component of the stress along [111] axis is about 20% smalle than along the [0 0 1] axis.

When the center is excited to the tetrahedral state ^5E the memory of the tetragonal distortion is lost. This mechanism explains the thermalization of the low energetic lines for stress applied along the [0 0 1] direction. In accordance with the values of A_1, A_2, and b, this shows

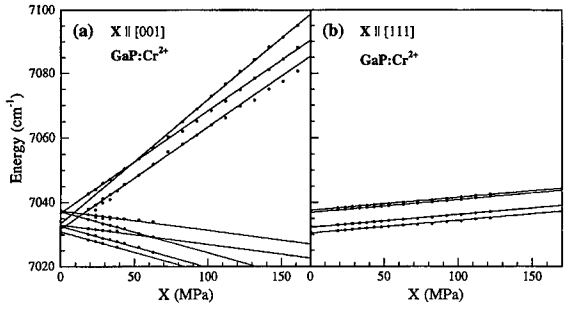

Fig. 3. The ZPLs of GaP : Cr^{2+}: Effect of uniaxial stress X along the [0 0 1] direction (a), and along the [111] direction (b), respectively.

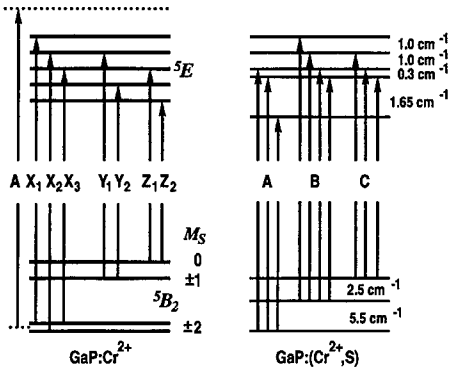

Fig. 4. (left): Level scheme of Cr^{2+}. The final state of line A, indicated as a dotted line, is discussed on the basis of a vibronically excited state. (right): Level scheme of the (Cr^{2+} – S) pair.

a much larger stress response of the ground state than of the excited state. The numerical analysis yields in units of cm^{-1}/MPa: $A_1 - a_h = -0.35$, $A_2 - a_h = 0.095$, and $b = 0.017$ (a_h: hydrostatic stress response of the excited state). The parameters show that the center with the tetragonal symmetry axis along the stress direction [0 0 1] is energetically lowered when the (compressional) stress increases. We therefore conclude that the Jahn–Teller distortion of the Cr^{2+} center in the ground state is a compressional one.

2.2. Level scheme and origin of the line A

For the excited state ^5E the situation of the Jahn–Teller coupling is less clear. In previous work on Cr^{2+} in GaAs and InP a series of equidistant SO levels has been assumed, according to SO coupling up to second order including a weak dynamic Jahn–Teller coupling [5,7]. From the corresponding ZPLs of Cr^{2+} in GaP severe deviation from equidistancy has been found [3]. According to selection rules three electric dipole transitions are allowed: X_1, X_2, and X_3 from the ground state levels $M_S = \pm 2$ to the ^5E states, as shown in Fig. 4. The highly resolved spectra indicate four absorption lines (X_1, X_2, X_3, and A) from the ground state.

An origin of line A could arise from a Jahn–Teller coupling in the excited state ^5E in the regime of intermediate coupling. In such a case the dynamics of the nuclei can be considered as a tunneling process between the three equivalent tetragonal distortions. In the excited state the center has full tetrahedral symmetry but the orbital E state is coupled to a vibronic level A_i (A_1 or A_2). The spacing between the two states E and A_i is denoted as tunneling splitting 3Γ. Ham [9] has given a theory which describes the coupled states ^5E and ^5A_i, including SO coupling. In the limit of small tunneling splitting the level $^5A_2$ yields two states which are lying energetically close. These two states, which would not be resolved in the absorption spectrum, could account for additional excited states (shown as a dashed line in Fig. 4) observed as final states of transition A.

Like the stress response reported in Section 2.1, the Zeeman effect of the ZPLs confirms that line A belongs to the transitions $^5T_2 \rightarrow {}^5E$ [10]. The Zeeman effect describes the experiments sufficiently well by a tunneling splitting of $\Gamma = 0.25\,cm^{-1}$.

Another possible explanation for line A emerges from a Jahn–Teller coupling in the excited state together with the action of random strains. At a specific relation between both effects a double-peaked feature for a single transition can appear [11]. This could also explain the observation of an additional line. On the other hand, no further splitting has been found in the other transitions Y_1 and Y_2 as well as in Z_1 and Z_2. More work is required to clarify the origin of line A.

3. Cr–S pair in GaP:(Cr^{2+},S)

Absorption measurements in the temperature range of 2 to 10 K reveal ten ZPLs in the spectrum at 7155 cm^{-1}, see Fig. 1. The lines originate from a manifold of three levels in the ground state with the upper two levels separated by 5.5 and 8 cm^{-1} from the lowest ground-state level, see Fig. 4. The five excited states are split in total by about 4.0 cm^{-1}.

As Fig. 5 shows, for stress along the [0 0 1] direction no splitting is observed. Only five lines can be resolved when stress is applied, due to the slightly enhanced line width. For stress of up to 50 MPa the lines shift nonlinearly with applied stress, which indicates electronic mixing rather than removal of geometrical degeneracy. A linear splitting of lines occurs for stress along the [111] direction. Up to 12 lines can be identified having three different slopes in the stress-dependent behavior. The splitting pattern is characteristic of a trigonal center. This strongly

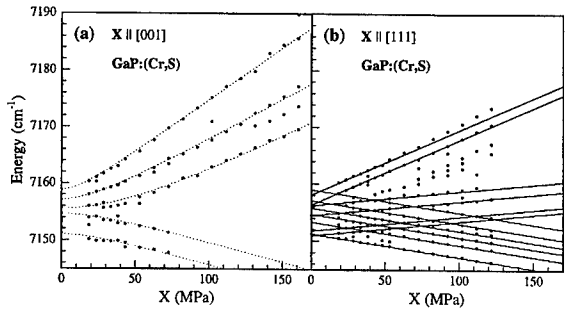

Fig. 5. The ZPLs assigned to the (Cr^{2+} – S) pair: Effect of uniaxial stress X along the [0 0 1] direction (a), and along the [111] direction (b), respectively (dotted lines are a guide to the eye).

supports the assignment of the corresponding optically active center to a Cr–S complex with the constituents on substitutional next-neighbor sites.

The lines for stress along the [111] direction do not thermalize, all lines can be observed for stress of up to 150 MPa. Thus reorientation of the center is not possible at cryogenic temperatures. Reorientation of the trigonal center requires site changes of an ion in this case. This again indicates that the origin of the symmetry lowering of the 7060 cm^{-1}-optical center is a Jahn–Teller effect, whereas in the 7155 cm^{-1}-optical center it is a bonding axis. Nevertheless the stress response along the [0 0 1] direction may be a remainder of the strong stress response of the Cr^{2+} ion due to the Jahn–Teller effect, which is strongly quenched by the action of the trigonal crystal field.

Acknowledgements

We are grateful to F.S. Ham for helpful discussions and to H.V. Kiedrowski for preparing the oriented samples.

References

[1] J.J. Krebs, G.H. Stauss, Phys. Rev. B 16 (1977) 971.
[2] G.H. Stauss, J.J. Krebs, R.L. Henry, Phys. Rev. B 16 (1977) 974.
[3] W. Ulrici, J. Kreissl, in: M. Scheffler, R. Zimmermann (Eds.), Proceedings of the 23rd International Conference Phys. Semicon. World Scientific, Singapore, 1996, p. 2833.
[4] A.M. Hennel et al., Phys. Rev. B 23 (1981) 3933.
[5] B. Clerjaud, C. Naud, G. Picoli, Y. Toudic, J. Phys. C 17 (1984) 6469.
[6] B. Clerjaud, J. Phys. C: Solid State Phys. 18 (1985) 3615.
[7] A.S. Abhvani, C.A. Bates, B. Clerjaud, D.R. Pooler, J. Phys. C 15 (1982) 1345.
[8] A.A. Kaplyanskii, Opt. Spectrosc. 16 (1964) 329.
[9] F.S. Ham, Phys. Rev. B 4 (1971) 3854.
[10] E. Baars, A. Dörnen, W. Ulrici, to be published.
[11] R.W. Reynolds, L.A. Boatner, Phys. Rev. B 12 (1975) 4735.
[12] U. Kaufmann, J. Schneider, in: J. Treusch (Ed.), Festkörperprobleme – Advances in Solid State Physics, Vol. XX, Vieweg, Braunschweig, 1980, p. 87.

ELSEVIER

Physica B 273–274 (1999) 823–826

PHYSICA B

www.elsevier.com/locate/physb

Modeling the diffusion of Be in InGaAs/InGaAsP epitaxial heterostructures under non-equilibrium point defect conditions

K. Ketata, M. Ketata, S. Koumetz*, J. Marcon, O. Valet

LEMI-UPRES.EA.2654-IUT, Université de Rouen, 76821 Mont Saint Aignan France

Abstract

Be diffusion from 0.2 μm Be doped (3×10^{19} cm^{-3}) $In_{0.53}Ga_{0.47}As$ layer sandwiched between 0.5 μm undoped $In_{0.73}Ga_{0.27}As_{0.58}P_{0.42}$ layers, grown by GSMBE has been studied. The samples were subjected to RTA in temperature range from 700°C to 900°C with time durations of 10–240 s. SIMS was employed for a quantitative determination of the Be depth profiles. Two kick-out models of substitutional–interstitial diffusion have been considered. To explain the obtained experimental results, the kick-out model, involving neutral Be interstitial species and singly positively charged Ga or In self-interstitials is proposed. The built-in electric field, bulk self-interstitial generation/annihilation, the Fermi-level and extended defect formation effects were taken into account in the simulations.

Keywords: Diffusion; Beryllium; InGaAs; InGaAsP

1. Introduction

Beryllium is one of the most commonly used acceptor dopants in the growth of III–V semiconductor compounds by molecular beam epitaxy (MBE) due to its high solubility and high sticking coefficient [1]. Indeed, the device performances of GaAs(Be)/GaAlAs heterojunction bipolar transistors (HBTs) could be strongly improved by the reduction of the GaAs base sheet resistance using high Be doping levels. However, an excessive diffusion of Be from the heavily doped base, which may occur during thermal post-growth technological processes, can cause severe degradations of the HBTs by reducing the emitter injection efficiency and increasing the generation-recombination current at the emitter/base junction [2].

The subject of this work is the modeling and simulation of the Be diffusion during post-growth rapid thermal annealing (RTA) in $In_{0.53}Ga_{0.47}As/In_{0.73}Ga_{0.27}As_{0.58}P_{0.42}$ heterojunction structures grown by gas source molecular beam epitaxy (GSMBE) technique. This diffusion could take place and consequently should be controlled during technological processes of highly Be-doped base InP/InGaAs double heterojunction bipolar transistors (DHBTs) with a step-graded collector.

In the literature, investigations on the diffusion of Be in III–V heterostructures are still limited [3,4]. The information related to the beryllium diffusion in InGaAs/InGaAsP systems is not available, to our knowledge.

2. Experimental procedure

Heterostructures of $In_{0.53}Ga_{0.47}As/In_{0.73}Ga_{0.27}As_{0.58}P_{0.42}$ were grown by GSMBE on an ⟨1 0 0⟩ oriented semi-insulating InP substrate in a V80 system from VG Semicon. The sources for group-V were cracked pure arsine AsH_3 and phosphine PH_3 as primary sources for As_2 and P_2. The group-III elements (Ga and In) and the dopant (Be) were coming from solid elemental sources using the standard Knudsen cells (K-cells). The growing sequence of the samples was as follows: at first, a 0.1 μm InP buffer layer was grown,

* Corresponding author. Tel.: + 33-235-14-63-55; fax: + 33-235-14-62-54.

E-mail address: serge.koumetz@univ-rouen.fr (S. Koumetz)

0921-4526/99/$ - see front matter
PII: S0921-4526(99)00513-X

followed by a 0.5 μm undoped $In_{0.73}Ga_{0.27}As_{0.58}P_{0.42}$ layer. Then a 0.2 μm Be-doped $In_{0.53}Ga_{0.47}As$ layer with a doping level of 3×10^{19} cm^{-3} was grown. Finally, an undoped $In_{0.73}Ga_{0.27}As_{0.58}P_{0.42}$ layer of 0.5 μm was grown on the Be doped layer. The layers were grown at a rate of 0.8–2 μm/h under "strongly" group-V stabilized conditions with a V/III flux ratio of 5 and a substrate temperature below 500°C. The values of the lattice mismatch ($\Delta a/a$) measured for these structures were better than 500 ppm. The error in layer thickness is expected to be not more than 5%. The post-growth RTA was performed in a halogen lamp furnace ADDAX XM using flowing Ar + 10%H_2 gas. The resulting samples were depth profiled in Cameca IMS-4F SIMS (secondary ion mass spectrometry) apparatus using an oxygen O_2^+ primary beam of 5.5 keV impact energy.

3. Results and discussion

Two kick-out models for substitutional–interstitial diffusion (SID), under point defect nonequilibrium conditions, have been studied to obtain quantitative data fits. The first model is based on the neutral Be interstitials Be_i^o and the singly positively ionized group III (In and Ga) self-interstitials I_{III}^+, the second model involves singly positively ionized Be interstitials Be_i^+ and doubly positively ionized group III self-interstitials I_{III}^{2+}:

$$Be_i^{n+} + \overset{K}{\Leftrightarrow} Be_s^- + I_{III}^{r+}, \tag{1}$$

where $n = 0, r = 1$ for the first model and $n = 1, r = 2$ for the second model; Be_s^- stands for the singly negatively charged Be substitutionals.

Suppose that the condition of local dynamic equilibrium between interstitial and substitutional Be species holds at any location and any moment, the law of mass action was applied to reaction (1):

$$\frac{C_i}{C_s C_I} = \frac{C_i^{eq}}{C_s^{eq} C_I^{eq}} = K, \tag{2}$$

where K is the reaction constant and C_i^{eq}, C_s^{eq}, C_I^{eq} denote the equilibrium concentrations of Be_i^{n+}, Be_s^- and I_{III}^{r+}, respectively, in the doped layer at the onset of annealing.

Assuming that the diffusivity of Be interstitials D_i is much greater than that of Be substitutionals D_s and taking into account the built-in electric field effect [5], the diffusion equation for Be species can be written as

$$\frac{\partial C_i}{\partial t} + \frac{\partial C_s}{\partial t} = \frac{\partial}{\partial x}\left(D_i \frac{\partial C_i}{\partial x} - D_i \frac{nC_i}{p}\frac{\partial p}{\partial x}\right) \tag{3}$$

with the local hole concentration $p = 0.5(C_s + \sqrt{C_s^2 + 4n_i^2})$.

Taking into consideration the built-in electric field effect and the phenomenon of the bulk annihilation or generation of self-interstitials by dislocation climb [6], the rate of the group III self-interstitial concentration change is given by

$$\frac{\partial C_I}{\partial t} = \frac{\partial}{\partial x}\left(D_I \frac{\partial C_I}{\partial x} - D_I \frac{rC_I}{p}\frac{\partial p}{\partial x}\right) + \frac{\partial C_s}{\partial t} - k_I(C_I - C_I^{eq}(p)), \tag{4}$$

where D_I is the I_{III}^{r+} diffusivity and $C_I^{eq}(p) = C_I^{eq}(n_i)\times(p/n_i)^r$ according to the Fermi-level effect [5]. The rate coefficient of the I_{III}^{r+} annihilation (in-diffusion) or generation (out-diffusion) k_I is directly proportional to the dislocation density ρ [6]: $k_I = \alpha_I \rho D_I$, where α_I is a geometrical constant of the order of unity. Eqs. (2)–(4) were numerically solved, for each model, using an explicit finite-difference method [7]. In order to model the Be diffusion after growth, the as-grown SIMS profile was used as the initial depth profile in our simulations. We added 4, 5 and 6 s to the annealing times for 700°C, 800°C and 900°C, respectively, to take into account the diffusion during the uphill and downhill temperature slope. On the other hand, as in the case of ternary and quaternary homojunctions, the extended defect formation effect was taken into account [8,9]. The intrinsic carrier concentrations for InGaAs and InGaAsP have been calculated as $n_i = 1.46\times10^{15}T^{3/2}\exp(-0.39\,\mathrm{eV}/k_B T)\mathrm{cm}^{-3}$ and $n_i = 3.31\times10^{15}T^{3/2}\exp(-0.52\,\mathrm{eV}/k_B T)\,\mathrm{cm}^{-3}$, respectively [8,9] (see Tables 1 and 2).

The SIMS depth profiles were fitted using the same parameters $C_I^{eq}(n_i)$, D_I, D_i and k_I, for InGaAs and In-

Table 1
The simulation parameters used by the first model in the ternary and quaternary layers

RTA T [°C]	700		800		900	
Compound	InGaAs	InGaAsP	InGaAs	InGaAsP	InGaAs	InGaAsP
n_i (cm^{-3})	4.0×10^{17}	1.9×10^{17}	7.7×10^{17}	4.2×10^{17}	1.3×10^{18}	8.0×10^{17}
$C_I^{eq}(n_i)$(cm^{-3})	1.7×10^{14}	2.0×10^{14}	1.8×10^{15}	1.5×10^{15}	1.3×10^{16}	8.0×10^{15}
C_i^{eq}(cm^{-3})	4.0×10^{16}	8.5×10^{16}	1.1×10^{17}	3.1×10^{17}	4.3×10^{17}	9.1×10^{17}
D_I(cm^2 s^{-1})	8.1×10^{-12}	3.5×10^{-12}	4.0×10^{-11}	2.2×10^{-11}	1.5×10^{-10}	1.0×10^{-10}
D_i(cm^2 s^{-1})	1.7×10^{-11}	2.7×10^{-11}	7.1×10^{-11}	1.0×10^{-10}	2.3×10^{-10}	3.0×10^{-10}
k_I(s^{-1})	0.1	0.04	1.4	0.7	14.0	8.0

Table 2
The simulation parameters used by the second model in the ternary and quaternary layers

RTA T [°C]	700		800		900	
Compound	InGaAs	InGaAsP	InGaAs	InGaAsP	InGaAs	InGaAsP
$n_i(cm^{-3})$	4.0×10^{17}	1.9×10^{17}	7.7×10^{17}	4.2×10^{17}	1.3×10^{18}	8.0×10^{17}
$C_I^{eq}(n_i)(cm^{-3})$	2.6×10^{12}	1.2×10^{12}	4.0×10^{13}	2.0×10^{13}	3.9×10^{14}	2.1×10^{14}
C_i^{eq} (cm^{-3})	1.1×10^{17}	2.8×10^{17}	2.5×10^{17}	6.0×10^{17}	7.8×10^{17}	1.6×10^{18}
D_I ($cm^2\ s^{-1}$)	1.4×10^{-11}	8.0×10^{-12}	7.0×10^{-11}	5.0×10^{-11}	2.7×10^{-10}	2.3×10^{-10}
$D_i(cm^2\ s^{-1})$	4.2×10^{-11}	6.7×10^{-11}	1.7×10^{-10}	2.4×10^{-10}	5.4×10^{-10}	6.9×10^{-10}
k_I (s^{-1})	0.1	0.04	1.4	0.7	14.0	8.0

GaAsP layers, which were found, using the first and the second models, for ternary and quaternary homostructures respectively [8,9]. Their values, for the first and the second models, respectively, are listed in Tables 1 and 2. The equations that fit those parameters are as follows:

InGaAs
$C_I^{eq}(n_i) = 1.90\times10^{25}\exp(-2.13\ eV/k_BT)\ cm^{-3}$,
$D_I = 2.20\times10^{-4}\exp(-1.44\ eV/k_BT)cm^2\ s^{-1}$,
$D_i = 7.34\times10^{-5}\exp(-1.28\ eV/k_BT)cm^2\ s^{-1}$,
$k_I = 6.50\times10^{11}\exp(-2.48\ eV/k_BT)\ s^{-1}$,

InGaAsS
$C_I^{eq}(n_i) = 4.98\times10^{23}\exp(-1.81\ eV/k_BT)cm^{-3}$
$D_I = 1.21\times10^{-3}\exp(-1.65\ eV/k_BT)cm^2\ s^{-1}$,
$D_i = 3.68\times10^{-5}\exp(-1.18\ eV/k_BT)cm^2\ s^{-1}$,
$k_I = 1.31\times10^{12}\exp(-2.62\ eV/k_BT)\ s^{-1}$

for the first model and

InGaAs
$C_I^{eq}(n_i) = 1.43\times10^{25}\exp(-2.46\ eV/k_BT)cm^{-3}$,
$D_I = 4.43\times10^{-4}\exp(-1.45\ eV/k_BT)\ cm^2\ s^{-1}$,
$D_i = 1.38\times10^{-4}\exp(-1.26\ eV/k_BT)\ cm^2\ s^{-1}$,
$k_I = 6.50\times10^{11}\exp(-2.48\ eV/k_BT)\ s^{-1}$,

InGaAsP
$C_I^{eq}(n_i) = 1.72\times10^{25}\exp(-2.54\ eV/k_BT)\ cm^{-3}$,
$D_I = 2.78\times10^{-3}\exp(-1.65\ eV/k_BT)\ cm^2\ s^{-1}$,
$D_i = 5.93\times10^{-5}\exp(-1.15\ eV/k_BT)\ cm^2\ s^{-1}$,
$k_I = 1.31\times10^{12}\exp(-2.62\ eV/k_BT)\ s^{-1}$

for the second model [8,9].

Figs. 1 and 2 show the Be SIMS concentration profiles of the samples annealed at temperatures 700°C, 800°C for 60, 120 s and at 900°C for 10, 20 s; as well as the simulated Be depth distributions according to the two kick-out models. It can be seen that the kick-out model involving the Be_i^o and I_{III}^+ species gives better simulation

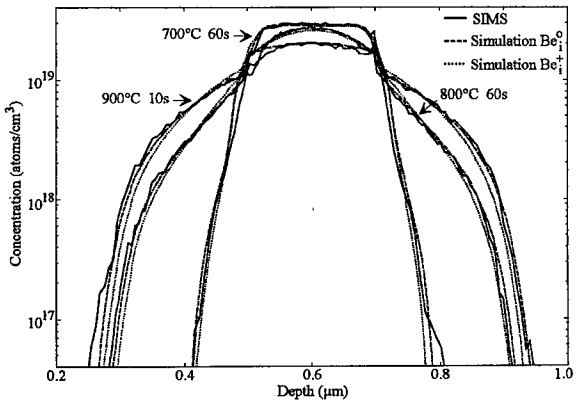

Fig. 1. The Be SIMS data and the simulated results for the samples annealed at 700°C and 800°C for 60 s, and at 900°C for 10 s.

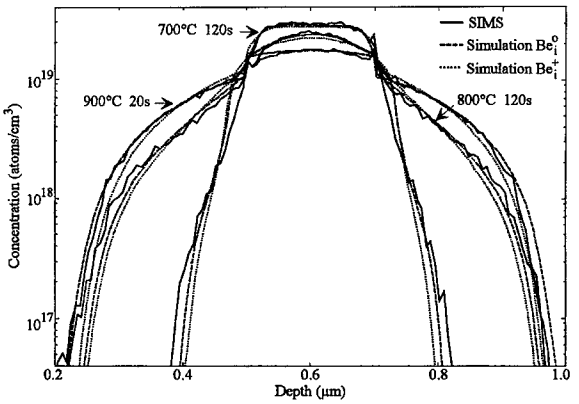

Fig. 2. The Be SIMS data and the simulated results for the samples annealed at 700°C and 800°C for 120 s, and at 900°C for 20 s.

results than that using the Be_i^+ and I_{III}^{2+} species, as in the case of the ternary and quaternary homostructures [8,9]. The data presented in these figures show relatively low Be gettering [10] at InGaAs/InGaAsP interfaces. This phenomenon, not taken into account in our simulations, could be responsible for lower C_i^{eq} values for InGaAs layers in heterostructures in comparison with these for InGaAs layers in homostructures [8].

4. Conclusion

We have shown that Be diffusion in $In_{0.53}Ga_{0.47}As/In_{0.73}Ga_{0.27}As_{0.58}P_{0.42}$ heterostructures can be described by kick-out models of SID. The Be interstitial diffusivity, the rate coefficient of self-interstitial generation or annihilation, the self-interstitial diffusivity, the self-interstitial equilibrium concentration, and intrinsic carrier concentration, all as a function of temperature are obtained for two models. The kick-out model, involving Be_i^o and I_{III}^+ species, gives better simulation results than that using Be_i^+ and I_{III}^{2+} species.

Acknowledgements

This research was supported by the CNET laboratories of Bagneux under contract 95 6B. The authors are indebted to C. Dubois for help in SIMS analysis and P. Blanconnier for performing RTA.

References

[1] M. Ilegems, J. Appl. Phys. 48 (1977) 1278.
[2] N. Jourdan, F. Alexandre, C. Dubon-Chevallier, J. Dangla, Y. Gao, IEEE Trans. Electron. Dev. 39 (1992) 767.
[3] M.B. Panish, R.A. Hamm, D. Ritter, H.S. Luftman, C.M. Cotell, J. Crystal Growth 112 (1991) 343.
[4] C.-H. Chen, U.M. Gösele, T.Y. Tan, Appl. Phys. A 68 (1999) 9.
[5] S. Yu, T.Y. Tan, U. Gösele, J. Appl. Phys. 69 (1991) 3547.
[6] A.H. van Ommen, J. Appl. Phys. 54 (1983) 5055.
[7] J. Crank, The Mathematics of Diffusion, Oxford University Press, Oxford, 1956, p. 186.
[8] K. Ketata, M. Ketata, S. Koumetz, J. Marcon, Europhys. Lett. 45 (1999) 348.
[9] S. Koumetz, K. Ketata, M. Ketata, J. Marcon, Comput. Mater. Science 15 (1999) 63.
[10] M. Geva, T.E. Seidel, J. Appl. Phys. 59 (1986) 2408.

ELSEVIER

Physica B 273-274 (1999) 827-830

PHYSICA B

www.elsevier.com/locate/physb

Local vibrational modes associated with semi-insulating InP : C, frequencies and line shapes

R.C Newman[a,*], B.R. Davidson[a], R.S. Leigh[b], M.J.L. Sangster[b], C.C. Button[c]

[a]*CEMD, The Blackett Laboratory, Imperial College of Science, Technology and Medicine, Prince Consort Road, London, SW7 2BZ, UK*
[b]*J.J. Thomson Physical Laboratory, Reading University, PO Box 220, Reading, RG6 6AF, UK*
[c]*Department of Electrical and Electronic Engineering, Sheffield University, Mappin Street, Sheffield, S1 3JD, UK*

Abstract

Infrared vibrational absorption spectra show that semi-insulating layers of InP grown by metal-organic vapour-phase epitaxy and doped with CCl_4 incorporate high concentrations of isolated carbon atoms and H–C pairs. Analyses of the spectra demonstrate that the carbon atoms occupy phosphorus lattice sites and are acceptors. The $^{12}C_P$ line is broad ($\sim 1.2\,cm^{-1}$) with a sharp central feature ($\sim 0.15\,cm^{-1}$). Homogeneous broadening by random electric fields from immobile charged impurities leads to an explanation of this observation.

PACS: 81.05.Ea; 63.20.Pw; 67.80.Mg

Keywords: InP : C; Internal electric fields; Infrared absorption; LVM line shapes

1. Introduction

Studies of the localized vibrational modes (LVM) of carbon atoms in GaAs, AlAs and GaP show that they are acceptors occupying group V lattice sites. Our understanding of InP : C is however unclear, as some epitaxial layers are n-type, implying that carbon atoms occupy In lattice sites (C_{In}) [1]. The only spectroscopic evidence is the observation by Raman scattering of a gap mode at $220\,cm^{-1}$ in n-type InP [2] but an expected high-frequency LVM from C_{In} donors was not detected. Other InP : C layers, doped from CCl_4, and grown by metal-organic vapour-phase epitaxy (MOVPE) at $T \sim 480°C$ were semi-insulating, although secondary ion mass spectrometry (SIMS) measurements showed high concentrations of carbon (10^{18}–$10^{20}\,cm^{-3}$) [3]. Our recent infrared (IR) LVM measurements of such samples demonstrated that C_P acceptors ($\sim 50\%$) were present, together with H–C_P pairs ($\sim 50\%$) [4]. The samples were fully compensated by unknown donors (possibly P_{In} anti-site defects [5] or VH_4 defects [6]). The C_P LVM has an unusual line shape and we now propose that this is due to perturbations arising from randomly distributed internal electric fields that are present because the layers are compensated and there are no mobile carriers to screen the charges.

2. Experimental details

Three semi-insulating InP epitaxial layers (MR923, MR950 and MR949) (Table 1) were grown by low-pressure MOVPE on (1 0 0) InP substrates at 500°C, using the precursors PH_3 and $In(CH_3)_3$, and were doped using CCl_4 diluted with H_2. SIMS measurements of ^1H, ^{12}C, ^{16}O, ^{35}Cl and ^{115}In led to determinations of the layer thicknesses (4.2, 10.3 and 8.0 μm) and the various impurity concentrations: further details are given in Ref. [4]. IR absorption measurements made at 10 K with a resolution of $0.01\,cm^{-1}$ allowed concentrations of isolated ^{12}C impurities of 1.8, 2.3 and $5.4 \times 10^{18}\,cm^{-3}$ (Table 1) to be determined by assuming that an integrated absorption coefficient $IA = 1\,cm^{-2}$ corresponds to $[C] = 0.7 \times 10^{16}\,cm^{-3}$ (as for GaAs). The LVM frequency is located in the gap of the 2-phonon density of

* Corresponding author. Tel.: + 44-207-594-6666; fax: + 44-0-207-581-3817.
E-mail address: r.newman@ic.ac.uk (R.C. Newman)

0921-4526/99/$ - see front matter
PII: S0921-4526(99)00514-1

Table 1
Carbon concentration [C] and fitted parameters for the three samples

Sample	MR949	MR923	MR950
[C] (10^{18} cm^{-3})	5.4	1.8	2.3
ω^* (cm^{-1})	0.25	0.12	0.175
γ (cm^{-1})	0.07	0.028	0.07
$\omega^*/[C]^{2/3}$ (10^{-14} cm)	8.1	8.1	10.0

perfect lattice modes, (from 517.5 to 612.4 cm^{-1}) [7]. Consequently, decay into two lattice phonons cannot occur, leading to very sharp lines.

3. LVMs of isolated carbon atoms and H–C pairs

Expanded plots (Fig. 1) of a line at 546.9 cm^{-1} show a broad profile with a width $\Delta \sim 1.2$ cm^{-1} and a sharp central feature with $\Delta \sim 0.15$ cm^{-1}. A second very weak line at 526.8 cm^{-1} is similarly broad: a corresponding sharp feature was not resolved but there was high background noise. The ratio of the IAs of $0.8 \pm 0.2\%$ (average for three samples) led to assignments of the lines to ^{12}C and ^{13}C, respectively, consistent with the natural abundance of ^{13}C of 1.1% and the mass difference. The two frequencies, ω_{imp}, should then satisfy the relationship,

$$(\omega_{\mathrm{imp}})^2 = k[1/m_{\mathrm{imp}} + 1/(\chi M_{\mathrm{NN}})], \quad (1)$$

where k is a force constant, m_{imp} is the mass of the impurity and M_{NN} is the mass of a nearest neighbour. χ is a numerical factor that has a value deduced from

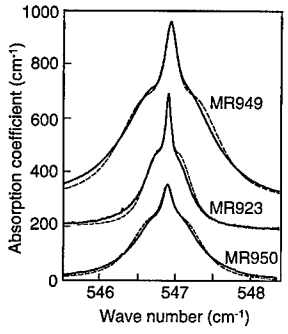

Fig. 1. Absorption coefficients for samples MR949 (top), MR923 and MR950 (bottom) with offsets of 350, 200 and 0 cm^{-1}, respectively. Continuous lines are experimental results: dashed lines are from theory with the parameters given in Table 1.

experiments of ~ 2 for all known isotopic tetrahedral substitutions. An acceptable value of $\chi = 1.5$ (see Ref. [8]), is obtained with an assignment of the lines to $C_{\mathrm{P}}(M_{\mathrm{NN}} = M_{\mathrm{In}} = 114.9$ amu: 95.7% abundance) but an assignment to $C_{\mathrm{In}}(M_{NN} = M_{\mathrm{P}} = 31$ amu) leads to an unacceptably high value of $\chi = 5.6$.

A previous suggestion [4] that there might be a very weak feature at 528.5 cm^{-1} due to $^{13}C_{\mathrm{In}}$ is discounted. Thus there is no evidence for the presence of these donors. However, we now report an LVM at 1091.0 cm^{-1} downshifted by 2.8 cm^{-1} from double the frequency of the $^{12}C_{\mathrm{P}}$ fundamental mode and with a relative strength of $\sim 1\%$. This line is assigned to the second harmonic of the $^{12}C_{\mathrm{P}}$ mode.

A line at 521.1 cm^{-1} is assigned to one of the two transverse E-modes of H–$^{12}C_{\mathrm{P}}$ pairs. More importantly, an LVM at 2703.3 cm^{-1} and a weaker ($\sim 1\%$) line at 2696.6 cm^{-1} are assigned to the stretch modes of H–$^{12}C_{\mathrm{P}}$ and H–$^{13}C_{\mathrm{P}}$, respectively [4]: another line at 413.5 cm^{-1} is assigned to the longitudinal symmetric A_1^+ mode. These data allow the longitudinal force constants for the H–C pair centre to be estimated (see Ref. [9]). In the model, the H and C atoms are each coupled to infinite masses by springs with force constants $k_{\mathrm{H}}^{\mathrm{L}}$ and $k_{\mathrm{C}}^{\mathrm{L}}$, respectively, and to each other by a spring with constant $k_{\mathrm{H-C}}^{\mathrm{L}}$. The calculated value of $k_{\mathrm{H}}^{\mathrm{L}} = 71$ N m^{-1} depends principally on the separation of the H–$^{12}C_{\mathrm{P}}$ and H–$^{13}C_{\mathrm{P}}$ modes but $k_{\mathrm{C}}^{\mathrm{L}} = 68$ N m^{-1} and $k_{\mathrm{H-C}}^{\mathrm{L}} = 394$ N m^{-1} are determined primarily from the A_1^+ and A_1^- frequencies. Values of $k_{\mathrm{H-C}}^{\mathrm{L}}$ for GaAs, AlAs, and GaP show only small changes, implying negligible changes in the H–C bond length: $k_{\mathrm{H}}^{\mathrm{L}}$ is always small, (a weak hydrogen-group III atom interaction): $k_{\mathrm{C}}^{\mathrm{L}}$ has values greater than 100 N m^{-1} for GaP, AlAs and GaAs, but a lower value of 68 N m^{-1} for InP, consistent with the known weak interaction of C–In bonds. These comparisons support the interpretation that the H-atom occupies a bond-centred site and is bonded directly to a C_{P} *acceptor*.

4. The line shape of the LVM of carbon acceptor

We now show that electric field broadening by randomly distributed immobile charged carbon impurities and compensating defects provides a satisfactory explanation of the line shape of the $^{12}C_{\mathrm{P}}$ LVM. Statistical theories of inhomogeneous line broadening go back to the work of Markoff [10]. For the effects of random electric fields on our triplet LVM absorption line, we require the statistical distribution of the total resultant electric field arising from all possible configurations of the positions of the impurities – the mean value is, of course, zero. This is the approach originally used by Holtsmark [11] in a study of broadening of spectral lines from molecules. His expression for $W(E)$, the three-dimensional probability distribution for the field from

a random distribution of charges, is

$$4\pi E^2 W(\boldsymbol{E}) = \frac{1}{E_0} H(E/E_0), \tag{2}$$

where $H(\beta) = (2\beta/\pi)\int_0^\infty ds \sin(\beta s) s \exp(-s^{3/2})$ is shown in the top part of Fig. 2. The reference electric field strength, E_0, is defined by

$$E_0 = \frac{2\pi e}{\varepsilon}\left[\frac{4}{15}\sum_k \rho_k |Z_k|^{3/2}\right]^{2/3}, \tag{3}$$

where the charge and number density of defects of type k are $Z_k e$ and ρ_k, respectively. Note that the probability distribution depends only on the magnitude of $\boldsymbol{E}$ and not on its direction.

The normalised absorption spectrum is

$$I(\omega) = \tfrac{1}{3}\sum_{j=1}^{3} \int d\boldsymbol{E}\, W(\boldsymbol{E}) \delta\{\omega - \omega_j(\boldsymbol{E})\}, \tag{4}$$

where $\omega_j(\boldsymbol{E})$ are the frequencies of the triplet after splitting by the perturbation $-\boldsymbol{E}.\boldsymbol{M}$ with $\boldsymbol{M}$ denoting the dipole moment associated with the atomic displacements. For any given direction of $\boldsymbol{E}$ the triplet is split by amounts that are proportional to the magnitude E. The frequency shifts may be denoted by $\hbar^{-1}\mathcal{M}E\lambda_j(\hat{\boldsymbol{E}})$ where $\mathcal{M}$ is the matrix element of $\boldsymbol{M}$ between any two of the triplet excited eigenstates. The middle part of Fig. 2 shows $D(\lambda)$, the density distribution of the $\lambda_j(\hat{\boldsymbol{E}})$ for $j = 1$, 2 and 3 and all directions of $\hat{\boldsymbol{E}}$. This may be considered as an accumulation of the appropriately scaled frequencies resulting from a *single* charged impurity moving over a sphere. $D(\lambda)$ is normalised to unity.

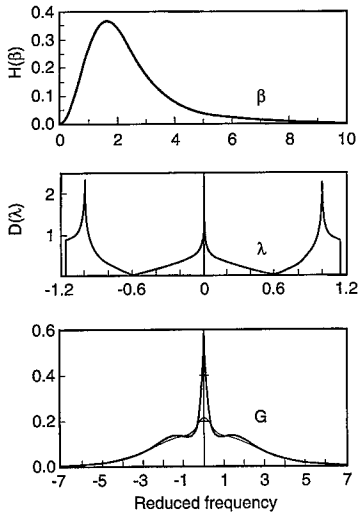

Fig. 2. Steps in the theory: top panel is the Holtsmark function; middle panel is the distribution of eigenfrequencies at fixed field strength; bottom panel combines these, as in Eq. (6), (heavy line with $\gamma = 0$ and light line with $\gamma = 0.3\omega^*$).

For given $\hat{\boldsymbol{E}}$ each of the three $\lambda_j(\hat{\boldsymbol{E}})$ falls into one of the three separated sections of the plot. The sharp peaks at 0 and ± 1 are in fact logarithmically divergent. Denoting the frequency of the unbroadened line by ω_0 and writing $\omega^* = \mathcal{M}E_0/\hbar$ Eq. (3) may be rewritten as

$$I(\omega) = \frac{1}{\omega^*} G\left(\frac{\omega - \omega_0}{\omega^*}\right), \tag{5}$$

where

$$G(\tilde{\omega}) = \int_0^\infty dE \frac{1}{E} H\left(\frac{E}{E_0}\right) D\left(\frac{\tilde{\omega}E_0}{E}\right). \tag{6}$$

The function G is shown as the bottom part of Fig. 2. The singularity at $G(0)$ survives since this occurs for every value of E, but the other two singularities are spread into shoulders at positions that relate directly to the maximum in the Holtsmark distribution.

To make comparison with the experimental line shapes other sources of broadening (e.g. from strains or instrumental broadening) have to be taken into consideration. We do this by replacing the delta function in Eq. (4) with a normalised Lorentzian of HWHM γ. The second trace in the bottom part of Fig. 2 shows the result of introducing extra broadening with $\gamma = 0.3\omega^*$. The theoretical traces shown in Fig. 1 are obtained by setting the parameters ω^* and γ as in Table 1. If the compensation mechanism is the same in all samples and no other charged defects are present in significant quantities we would expect from Eq. (3) that ω^* would be proportional to the concentration of carbon impurities to the power $\frac{2}{3}$ and, as demonstrated in Table 1, this is borne out in our three samples. The value of $\mathcal{M} \sim e \times (0.02\ \text{Å})$ required to achieve this agreement with the experimental line shapes turns out to be not unreasonable when a comparison is made with the strengths of the second harmonic.

In conclusion, the IR data indicate that carbon atoms are located on phosphorus lattice sites and that their unusual line shape is explained by broadening due to random electric fields.

Acknowledgements

RCN, BRD and CCB thank the EPSRC UK for their support on contract GR/K96977.

References

[1] W. Weyers, K. Shiraishi, Jpn. J. Appl. Phys. Part 1 31 (1992) 2483.
[2] M. Ramsteiner, P. Kleinert, K.H. Ploog, J. Oh, M. Konogai, Y. Takahashi, Appl. Phys. Lett. 67 (1995) 647.
[3] N.F. Gardner, Q.H. Hartmann, J.E. Baker, G.E. Stillman, Appl. Phys. Lett. 67 (1995) 3004.

[4] B.R. Davidson, R.C. Newman, C.C. Button, Phys. Rev. B 58 (1998) 15609.
[5] W.M. Chen, P. Dreszer, A. Prasad, A. Kurpiewski, W. Walukiewicz, E.R. Weber, E. Söman, B. Monemar, B.W. Liang, C.W. Tu, J. Appl. Phys. 76 (1994) 600.
[6] R. Darwich, B. Pajot, B. Rose, D. Robein, B. Theys, R. Rhabi, C. Porte, F. Gendron, Phys. Rev. B 48 (1993) 17776.
[7] B. Ulrici, E. Jahne, Phys. Stat. Sol. B 74 (1976) 601.
[8] R.S. Leigh, R.C. Newman, Semicond. Sci. Technol. 3 (1988) 84.
[9] B.R. Davidson, R.C. Newman, T.J. Bullough, T.B. Joyce, Phys Rev. B 48 (1993) 17106.
[10] A.A. Markoff, Wahrscheinlichkeitsrechnung, Teubner, Leipzig, 1912.
[11] J. Holtsmark, Ann. Physik 58 (1919) 577.

ELSEVIER

Physica B 273–274 (1999) 831–834

PHYSICA B

www.elsevier.com/locate/physb

Intrinsic doping in InP: ab initio calculations of P_{In} antisites

T.M. Schmidt[a], R.H. Miwa[a], A. Fazzio[b,*], R. Mota[c]

[a]*Depto de Física, Universidade Federal de Uberlândia, 38400-902, Uberlândia, MG, Brazil*
[b]*Instituto de Física, Universidade de São Paulo, C.P. 66318, 05315-970, São Paulo, SP, Brazil*
[c]*Depto de Física, Universidade Federal de Santa Maria, 97.105-900, Santa Maria, RS, Brazil*

Abstract

The electronic and structural properties of $[P_{In}]^{(n)}$ antisite clusters in InP are calculated using first principles total energy calculations. The results for the corresponding energy dispersions indicate that when n increases, from 1 to 4, an electronic confinement tendency is observed, mainly for clusters in two-dimensional topology. The calculations also indicate that the clustering of P_{In} antisites, forming low-dimensional systems, is an energetically favourable process, as the antisite relative formation energy is reduced when the number n increases. © 1999 Elsevier Science B.V. All rights reserved.

Keywords: Antisite; Defect; InP

1. Introduction

The confinement of high carrier concentrations has been an intensive area of study, particularly in doped III–V compounds [1] it has been recognized to be one of the most promising electronic material system, besides to provide an excellent area for the understanding of the quantum effects. Recent experimental results indicate the possibility of epitaxial growth of n-type modulation doping in InP-based heterostructures, where intrinsic defects can provide high concentration of carrier density [1]. The mechanism responsible for the n-type conductivity has been attributed to an abundant presence of P_{In} antisites, introduced during off-stoichiometric InP growth at low temperature [2]. The presence of carrier density has been explained by the autoionization of the P_{In}, via the excited (0/ +) level [3]. The antisite defects in III–V materials have been intensively studied, and particularly in GaAs, arsenic antisite (EL2 defect) is responsible for the semi-insulating behavior [4,5]. In InP the presence of these defects seems to have different character compared to other III–V compounds, and the origin of the conductivity is still not clear, and the chemical nature of the donors is unknown. High carrier concentrations are observed, implying high concentrations of defects, with the possibility of the presence of antisite complex defects and the formation of low-dimensional systems [1].

In this work, a systematic first principles calculations of the electronic and structural properties of P_{In} antisites is performed to discuss the confinement of the carrier density and the formation of antisite complex defects.

2. Method of calculation

The Kohn–Sham equations are solved in a basis of plane waves within local density approximation (LDA) [6]. The total energy and band-structure are self-consistently calculated, using norm-conserving fully separable pseudopotentials [7,8]. The k-summation in the reduced Brillouin zone has been checked to ensure a good description of the charge density and, consequently, the total energy. The k-sampling to describe correctly a system is dependent on the supercell size. A Chadi–Cohen [9] special points analysis is performed for different supercell sizes. Our results show that for 128 atoms supercell, the Γ-point describes appropriately the defect character and the ionization energies [10,11]. This is

* Corresponding author. Tel.: + 55-11-818-7039; fax: + 55-11-818-6983.
E-mail address: fazzio@if.usp.br (A. Fazzio)

PII: S0921-4526(99)00515-3

checked by the observation of similar results obtained using the first Chadi–Cohen special points for the same supercell in InP systems. The total energy convergency is reached to 20 Ry kinetic energy cutoff with the equilibrium lattice constant for bulk InP of 5.82 Å, which is close to the experimental value, 5.87 Å. The calculated band gap is 1.05 eV (difference between eigenvalues), which is smaller than the measured value 1.42 eV, as is expected in LDA-calculations. All studied systems have been relaxed until forces are lower than 0.025 eV/Å.

3. Results and discussions

Discussions on the origin of the n-type conductivity in InP growth at low temperature based on first principles calculations are presented elsewhere [12]. Isolated P_{In} neutral antisites (Fig. 1a) present a defect level *inside the band gap*, located around 0.70 eV from the valence band maximum (VBM) (at the Γ point), similarly to obtained by previous works [4,13]. This one-particle energy level presents a relative large energy dispersion (0.31 eV) along the Γ–X direction for unit cell with 128 atoms. This dispersion can be attributed to the interaction between the defects in the adjacent supercells, and is related to the origin of n-type conductivity, which comes from the auto-ionization of the antisite defect level, due to the interaction among them, in high concentration regime of P_{In} antisites. Small dispersion means more confinement. For the neutral charge state, a breathing mode relaxation of 0.16 Å of the impurity nearest neighbors is obtained.

Considering two nearest-neighbors P_{In} (see Fig. 1b), forming the complex defect $[P_{In}]^{(2)}$, two energy levels result in the gap, one at 0.77 eV and another at 0.20 eV above the VBM. The energy dispersions of the last occupied defect level in the ΓX direction is 0.17 eV. Both P impurities suffer a displacement towards each other by just 0.04 Å, while their nearest neighbors are displaced around 0.16 Å towards the impurities, maintaining almost the same relaxations observed for the nearest neighbors for the single P_{In} defect. The displacements between the two antisites are small due to the characters of the bonds.

For $n = 3$, we consider two possible configurations, one with the 3 antisites in the nearest-neighbor positions (3nn) (Fig. 1c), another with 2 antisites in the nearest-neighbor positions and the third one in the next nearest-neighbor position (2nn + 1nnn). In the second configuration, the distances between the P-impurities are kept almost the same of the In bulk atomic positions. In this configuration, the P-nearest neighbors to the impurities have two kinds of bonds: bonding and antibonding characters. Some bond lengths are reduced up to 0.34 Å, while others are increased up to 0.25 Å. We observe that each antisite always presents one bond with strong antibonding character. In the (2nn + 1nnn) configuration an energy dispersion of 0.15 eV for the upper level. This dispersion is smaller than the corresponding dispersion for the single defect P_{In} antisite.

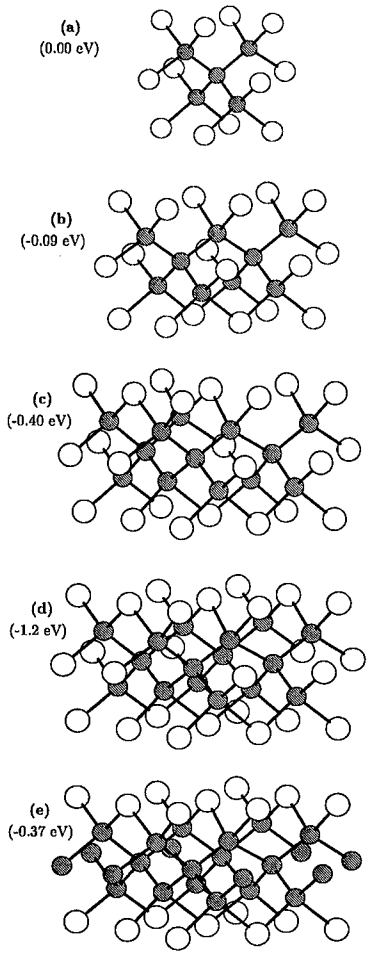

Fig. 1. Schematic representation of the 2D antisite clusters formation for: (a) one antisite; (b) two antisites; (c) three antisites (3nnn); (d) four antisites (4nnn), and (e) $\delta(P_{In})$-system. White balls represent In atoms and black balls P atoms. The energies in parenthesis are not normalized by the number of antisites.

For $n = 4$, two configurations are considered, one with the 4 antisites in the nearest-neighbor positions (4nn) forming a small three-dimensional (3D) cluster of P_{In}, and another with the 4 antisites in the closest positions in the same plane (0 0 1), forming a two-dimensional (2D) cluster (Fig. 1d). The last one is more stable by 0.12 eV/antisite related to the first one. For the 4 antisites in the same plane, the calculated dispersions of the last occupied defect level are 0.01 eV along the ΓZ direction, perpendicular to the (0 0 1) plane, and 0.23 eV along the ΓX direction, parallel to the (0 0 1) plane.

Fig. 2 shows the energy dispersions of the last occupied defect levels with n for 1–4. It is possible to observe the

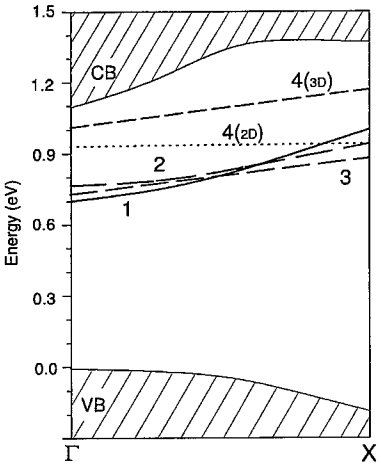

Fig. 2. Energy dispersions of the last occupied defect levels for the $[P_{In}]^{(n)}$ with n up to 4. 4(2D) is the dispersion perpendicular to the 2D plane. The dispersion lines for $n = 4$ are assumed straight to represent the calculated dispersions for the limits in the Γ and X points.

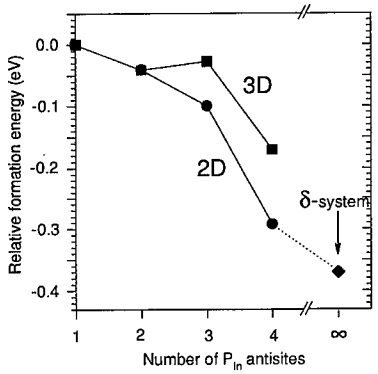

Fig. 3. Relative formation energy per antisite as a function of the number n of P_{In} antisites. Full squares are the energies corresponding to 3D defect clusters and full balls are the 2D defect clusters. The zero reference is the total energy difference between a cell of pure crystal and the same cell with one P_{In}.

tendency of the system to confine the electronic levels as the number n increases, in this case a carrier confinement with 2D character.

To consider the total energy calculation of $\delta(P_{In})$-system (Fig. 1e), we use a tetragonal unit cell [14,15], with 2×2 interface periodicity, and half a monolayer of P_{In} antisites in a plane perpendicular to the growth direction (0 0 1) are introduced. The distance between two δ layers, along the (0 0 1) direction, is equal to four lattice parameters of InP, ≈ 23 Å. The full relaxation of InP atomic layers results a P_{In}–P (first neighbours) bond length of 2.41 Å, which corresponds to the tetrahedric displacement of 0.11 Å towards the P_{In} antisite position, showing a very localized relaxation around the δ–P_{In} plane. The In–P bond length (near to the δ-plane) is 2.51 Å, which is very similar to the bond length of the bulk InP (2.52 Å), conserving the covalent character of these bonds.

In order to verify the possibility of the formation of $[P_{In}]^{(n)}$ antisite clusters, we have calculated the total energy differences between n antisites, close to each other, and n isolated P_{In} antisites. These total energy differences can be written as

$$\delta[\Delta E^{(n)}] = \frac{\Delta E[P_{In}]^{(n)}}{n} - \Delta E[P_{In}]^{(n=1)},$$

where $\Delta E[P_{In}]^{(n)}$ represents the total energy difference between a supercell of InP, with a cluster of n ($n = 1$, 2, 3 and 4) P_{In} antisites and a supercell of InP free of defects ($n = 0$). For an isolated P antisite, the lowest energy formation, in P-rich growth condiction materials, is around 2.0 eV[12]. We obtain a reduction of the total energy by 0.04 eV per antisite for two near-neighbour antisites ($\delta[\Delta E^{(n=2)}] = -0.04$ eV). For $n = 3$, forming a 3D cluster (3nn), the total energy decreases by 0.03 eV compared to one antisite ($n = 1$). For the (2nn + 1nnn) case, forming a 2D cluster, the total energy decreases 0.1 eV compared to the isolated antisite, $\delta[\Delta E^{(n=3(2nn+1nnn))}] = -0.1$ eV. For $n = 4$ (4nn) case, forming a 3D cluster, the total energy also decreases by 0.17 eV, $\delta[\Delta E^{n=4(4nn)}] = -0.17$ eV, and for $n = 4$ forming a 2D cluster, a planar topology, the total energy decreases by 0.29 eV. The relative formation energy per antisite as a function of the number of antisites can be seen in Fig. 3.

The reduction of the total energy ($\delta[\Delta E^{(n)}]$), as a function of the number n of antisites, up to $n = 4$, mainly in a planar topology for P_{In}, suggests the possibility of the formation of a planar $\delta(P_{In})$-system. Similar structures have been proposed, like InAs/AlSb interface [16], where the source of the donors was suggested to be antisite defects in a δ-configuration. The reduction of the total energy, for this configuration, is equal to 0.37 eV, $\delta[\Delta E] = -0.37$ eV per antisite, which indicates that the formation of P_{In} antisite, in a δ–P_{In} configuration, is energetically more favourable than the formation of P_{In} antisites isolated to each others.

4. Conclusions

The obtained results indicate that, when n increases from 1 to 4 P_{In} antisites, a confinement tendency is observed. The energy dispersions of the last occupied defect levels are 0.31 eV for $n = 1$, 0.17 eV for $n = 3$, and

0.01 eV for $n = 4$ in a two-dimensional system. Our total energy calculations also show that the clustering formation of P_{In} antisites is an energetically favourable process. The relative formation energy per antisite decreases as the number of antisites (close to each others) increases. The planar topology, 2D clusters, has been shown to be more stable than the 3D clusters. The reduction of the antisite relative formation energy in a 2D configuration suggests the formation of a low-dimensional system, δ–P_{In}.

Acknowledgements

This work was supported by the Brazilian agencies FAPEMIG, FAPERGS and CNPq.

References

[1] W.M. Chen, I.A. Buyanova, A.V. Buyanov, T. Lundstrom, Phys. Rev. Lett. 77 (1996) 2734.
[2] W.M. Chen, P. Dreszer, A. Prasad, A. Kurpiewski, W. Walukiewicz, E.R. Weber, E. Sorman, B. Monemar, B.W. Liang, C.W. Tu, J. Appl. Phys. 76 (1994) 1.
[3] P. Dreszer, W.M. Chen, K. Seendripu, J.A. Wolk, W. Walukiewicz, B.W. Liang, C.W. Tu, E.R. Weber, Phys. Rev. B 47 (1993) 4111.
[4] M.J. Caldas, J. Dabrowski, A. Fazzio, M. Scheffler, Phys. Rev. Lett. 65 (1990) 2046.
[5] M. Kamiska, E.R. Weber, Mater. Sci. Forum 83–87 (1991) 1033.
[6] M. Bockstedte, A. Kley, J. Neugebauer, M. Scheffler, Comp. Phys. Commun. 107 (1997) 187.
[7] G.B. Bachelet, D.R. Hamann, M. Schluter, Phys. Rev. B 26 (1982) 4199.
[8] L. Kleinman, D.M. Bylander, Phys. Rev. Lett. 48 (1982) 1425.
[9] D.J. Chadi, M.L. Cohen, Phys. Rev. B 8 (1973) 5747.
[10] A. Janotti, A. Fazzio, P. Piquini, R. Mota, Phys. Rev. B 56 (1997) 13073.
[11] A. Janotti, A. Fazzio, P. Piquini, R. Mota, Solid State Commun. 110 (1999) 457.
[12] T.M. Schmidt, R.H. Miwa, A. Fazzio, R. Mota, Phys. Rev. B, submitted for publication.
[13] A.P. Seitsonen, R. Virkkunen, M.J. Puska, R.M. Nieminen, Phys. Rev. B 49 (1994) 5253.
[14] T.M. Schmidt, A. Fazzio, Phys. Rev. B 51 (1995) 7898.
[15] R.H. Miwa, T.M. Schmidt, Appl. Phys. Lett. 74 (1999) 1999.
[16] G. Tuttle, H. Kroemer, J.H. English, J. Appl. Phys. 67 (1990) 3032.

ELSEVIER

Physica B 273–274 (1999) 835–838

PHYSICA B

www.elsevier.com/locate/physb

Structural and electronic properties of doped InP/InGaAs short period superlattices grown by LP-MOVPE

A.B. Henriques[a,*], L.K. Hanamoto[a], R.F. Oliveira[a], P.L. Souza[b], L.C.D. Gonçalves[b], B. Yavich[b]

[a]*Instituto de Física, Universidade de São Paulo, Caixa Postal 66318, 05389-970 São Paulo, Brazil*
[b]*Centro de Estudos em Telecomunicações, Pontifícia Universidade Católica, Rua Marques de São Vicente 225, Gávea, 22453-900 Rio de Janeiro, Brazil*

Abstract

We have studied the structural and electronic properties of lattice-matched InP/InGaAs superlattices with planar doping with Si in the center of the barrier layers, using X-ray spectroscopy, transport and photoluminescence (PL) measurements. The formation of superlattice minibands can be seen in the Shubnikov–de Haas (SdH) spectra. The PL spectra show an emission band at high energies, which is associated with carriers confined by the superlattice. As the thickness of the barriers was made smaller, the SdH oscillations decreased in frequency and the PL high-energy emission band narrowed, due to a reduction in the density of free carriers. A possible cause for this is the greater probability of the Si atoms being incorporated into acceptor sites, located within the interface layers, in samples with thinner barriers.

Keywords: InGaAs; InP; Interface; Superlattices

1. Introduction

Lattice-matched InGaAs/InP-based heterostructures have attracted wide interest due to their important applications in optoelectronic devices. In this work we studied InP/InGaAs superlattices doped with Si in the middle of the InP barriers. To investigate the influence of the tunneling probability of carriers through the barriers and of the density of carriers upon the properties of these systems we studied them as a function of the thickness of the barrier layers. The present work is distinguished from previous investigations [1–6] by the high density of free carriers present in our samples. The manifestation of free carriers in the transport and optical properties is correlated with the structural properties of the system, which are deduced from the X-ray spectra of the samples.

2. Experimental

Samples were grown by LP-MOVPE in an AIX200 reactor at 640°C and 20 mbar, using semi-insulating InP substrates, in the (1 0 0) direction. The sources used in the growth were TMIn, TMGa, arsine and phosphine. The growth rate was approximately 5 Å s. The InGaAs/InP superlattices consisted of nominally lattice-matched InGaAs wells separated by InP barriers (15 periods). The well thickness of the InGaAs layers was fixed at 50 Å; the samples differed in the thickness of the barrier material. The samples were delta-doped with Si in the middle of the InP layer. To achieve this, growth was interrupted halfway through the deposition of the barriers, by cutting the flux of TMIn. After 2 s, silane was introduced into the growth chamber, with a flux of either

* Corresponding author. Tel.: + 55-11-818-7049; fax: + 55-11-818-6984.
E-mail address: ahenriques@if.usp.br (A.B. Henriques)

0921-4526/99/$ - see front matter
PII: S0921-4526(99)00516-5

7.4 or 10 (in arbitrary units of flux). A new delay of 2 s was applied before resuming the growth, by restarting the TMIn flux. Growth interruption for 2 s was also employed at the interfaces. To start the growth of an InGaAs on top of InP, the TMIn and phosphine fluxes were suspended; after a 2-s delay, fluxes of TMIn, TMGa, and arsine were introduced into the growth chamber. To resume the growth of InP on top of the new InGaAs layer, the TMIn, TMGa and arsine fluxes were suspended, and after a delay of 2 s TMIn and phosphine were reintroduced into the reactor.

The X-ray measurements were performed with a commercially available double crystal X-ray diffractometer around the (4 0 0) diffraction peak of InP. The collection time per data point was 1 min and the density of points was one per 3-arcsec. The period of the superlattices and the alloy composition were determined assuming abrupt interfaces. The conventional measurements were carried out with the detector at a fixed position, while in the $\theta/2\theta$ experiments both the detector and the sample were moved simultaneously. Transport measurements were made on etched Hall bars. The sample was inserted inside a cryostat, which contained a superconducting coil, which supplied a magnetic field of 0–17 T. The temperature of the sample could be controlled within the 2–300 K interval. Photoluminescence measurements were made using a 0.75 m SPEX monochromator. Excitation of the sample was done using a 640 nm, 10 mW diode laser. Light was conveyed to the sample and collected from the sample using optical fibers. A Ge detector using standard phase-sensitive techniques gathered the PL signal.

3. Results and discussion

The alloy composition and the superlattice period were deduced from the X-ray spectra of the samples; the values obtained are shown in Table 1. This shows that the structures with 50 and 40 Å barriers are lattice matched, whereas in the structures with a barrier thickness of 30 Å the In content in the ternary layer is smaller than intended, leading to tensile strain in the ternary layer. A simulation of the X-ray spectrum was done for sample 327, using dynamical diffraction theory, which suggested that at each interface a thin strained layer exists, which is 2–3 monolayers wide, in agreement with previous investigations [2]. The strain built up at the interfaces enhances the X-ray satellite peaks [3].

Hall measurements as a function of temperature in the range 4.2–300 K were made for all samples. It is found that the carrier density is constant in the whole temperature range, indicating the absence of electron traps in the structure. The Hall mobility was constant in the range 4.2–100 K, above which temperature the mobility decreased due to the thermal activation of phonons. The Hall density and mobility at 4.2 K are shown in Table 1 for all samples.

The Shubnikov–de Haas (SdH) spectra of the samples were measured at 2 K in the range of fields 0–17 T. The Fourier transform of the SdH curves, plotted against $1/B$, are shown in Fig. 1. We can see that for the samples with the largest barrier thickness (50 Å) a single dominant peak characterizes the Fourier transform. As the thickness of the barrier is made smaller (40 Å), this Fourier develops a doublet structure and for the smallest barrier widths (30 Å) two peaks are completely resolved. This is an evidence of the formation of minibands. The Fermi surface evolves from a simple cylindrical shape (in the samples with thick barriers), which has a single extremal cross-sectional area, into a cylinder with a strongly modulated cross-section, which has two extremal cross-sectional areas ('belly' and 'neck') [7]. According to the semiclassical theory, the magnetoresistance oscillations are periodic in inverse field, displaying a set of periods that are associated with each one of the extremal cross-sectional areas of the Fermi surface. We denote the periodicities of the magnetoresistance oscillations in our superlattices by $\Delta(1/B)_{\mathrm{Neck}}$ and $\Delta(1/B)_{\mathrm{Belly}}$. The sheet density of carriers can be estimated by using the

Table 1
Parameters of the samples studied. d and x are the period of the superlattice and the indium content in the ternary layer, respectively, as deduced from the X-ray spectra. n_{Hall} and μ_{Hall} are the Hall density per superlattice period and mobility, respectively. n_{SdH} is the sheet density of carriers obtained from the Shubnikov–de Haas spectra by the use of Eq. (1)

Sample	Silane flux (arb. units)	d (Å)	X	n_{Hall} (cm^{-2})	μ_{Hall} ($\mathrm{cm}^2/\mathrm{Vs}$)	n_{SdH} (cm^{-2})
327	10	97	0.54	4.2×10^{12}	4320	4.7×10^{12}
326	7.4	95	0.54	3.3×10^{12}	6440	3.5×10^{12}
331	10	86	0.53	3.4×10^{12}	5460	3.4×10^{12}
332	7.4	86	0.52	2.6×10^{12}	5120	3.0×10^{12}
334	10	75	0.46	1.8×10^{12}	3360	1.9×10^{12}
333	7.4	77	0.44	1.6×10^{12}	3330	1.7×10^{12}

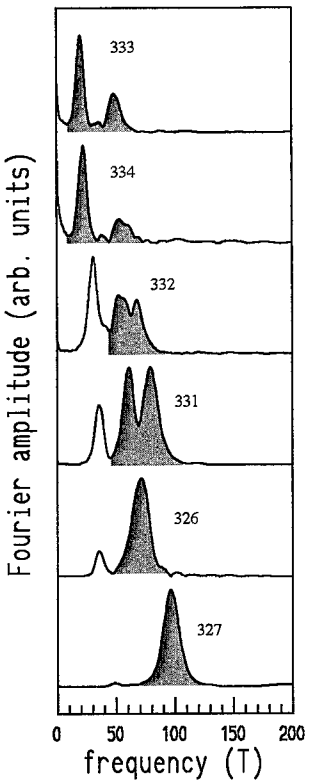

Fig. 1. Fourier transforms of the SdH spectra of the samples at $T = 2$ K. The number of the sample corresponding to each curve is indicated. The shaded area is the region of the spectrum associated with carriers occupying states in the fundamental electronic miniband.

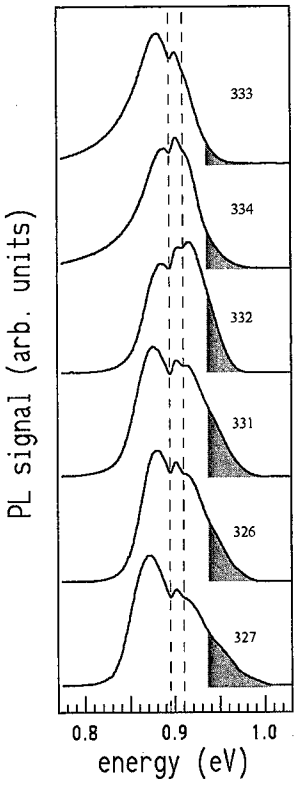

Fig. 2. Photoluminescence spectra of the samples at $T = 2$ K. The number of the sample corresponding to each curve is indicated. The shaded area is associated with the recombination of electrons confined by the superlattice potential and photoexcited holes. The dips in the spectra at the energies indicated by the dashed lines are due to absorption in the optical fiber used for light collection.

tight-binding approximation for the miniband dispersion, in which case the density of carriers will be given by

$$n_{\mathrm{SdH}} = \frac{e}{h}\left[\Delta\left(\frac{1}{B}\right)_{\mathrm{Belly}} + \Delta\left(\frac{1}{B}\right)_{\mathrm{Neck}}\right]^{-1}. \quad (1)$$

The carrier density estimated from the Shubnikov–de Haas spectra, obtained by the use of Eq. (1) is shown in Table 1. Fair agreement is obtained between the Shubnikov–de Haas and the Hall density of carriers, indicating that most of the free carriers in our samples occupy quantum states belonging to the fundamental electronic miniband. Samples 326, 331 and 332 also display a low-frequency oscillatory magnetoresistance, which might be due to a small population of electrons in the excited electronic miniband. The most striking feature, however, is the shift of the whole of the spectrum to lower frequencies as the thickness of the barriers is reduced, indicating a decrease in the density of free carriers.

Fig. 2 shows the photoluminescence of the samples at 2 K. A wide emission band centered on 0.9 eV characterized all spectra. At the high-energy side of this emission band, a tail is seen which we associate with the recombination of electrons confined by the superlattice potential and photoexcited holes. (This association is supported by the observation that when a magnetic field is applied parallel to the axis of the superlattice, the continuous high-energy emission tail splits into a fan of Landau levels.) The width of the high-energy tail in the PL spectrum narrows dramatically when the thickness of the barriers is reduced. This is in agreement with the results of the SdH measurements, since a decrease in the density of free carriers will lower the Fermi energy and hence narrow the PL spectrum.

In conclusion, we have studied the properties of InP/InGaAs superlattices doped with Si in the center of the InP barriers. X-ray measurements indicate that a strained layer of 2–3 monolayers exists at each interface of the structure. Transport and optical measurements show that for the same density of donor atoms the density of free carriers decreases when the thickness of the barrier layers is narrowed. While other explanations

cannot be ruled out, we propose that the smaller the density of free carriers in the samples with narrower barrier layers be due to the spread out of the Si atoms around the doping plane and to the presence of defects at the interfaces. As it is well known, the Si atoms will spread out around the delta-layer due to diffusion and segregation, and the density of doping atoms perpendicular to the doping plane can be described by a statistical distribution of Gaussian shape [8]. Assuming the statistical distribution of doping atoms to have the same width in all samples, in the samples with narrower barriers the Si doping atoms will have a greater probability of being incorporated into the interface layer. If the interface layer is of a lower crystalline quality than the rest of the structure, in these layers the Si atoms will have a greater chance of moving from donor to acceptor sites, hence the density of free carriers will be smaller.

Acknowledgements

A.B.H. thanks Dr. P.M. Koenraad, of the Eindhoven University of Technology, for help with the preparation of the samples and useful discussions, to Dr. M.T. Furtado and Dr. W. Carvalho Jr., of the Laboratório de Optoeletrônica/CPqD for the simulation of the X-ray spectrum, and to Dr. E. Abramoff of the Instituto Nacional de Pesquisas Espaciais for profitable discussions on the X-ray spectra. This work was supported in part by the government agencies FAPESP (grant 97/0635-7) and CNPq (grant 306335/88-3).

References

[1] A.R. Clawson, C.M. Hanson, J. Electron. Mater 24 (1994) 781.
[2] A.Y. Lew, C.H. Yan, R.B. Welstand, J.T. Zhu, C.W. Tu, P.K.L. Yu, E.T. Yu, J. Electron. Mater. 26 (1997) 64.
[3] Sang-Wan Ryu, Byung-Doo Choe, Weon Guk Jeong, Appl. Phys. Lett. 71 (1997) 1670.
[4] P.G. Piva et al., Appl. Phys. Lett. 72 (1998) 1599.
[5] T. Marschner, J. Brübach, C.A. Verschuren, M.R. Leys, J.H. Wolter, J. Appl. Phys. 83 (1998) 3630.
[6] P. Bönsch, D. Wüllner, H.H. Wehmann, A. Schalachetzki, F. Hitzel, D. Schneider, in: EW MOVPE VIII – Prague, 1999, unpublished.
[7] H.L. Störmer, J.P. Eisenstein, A.C. Gossard, W. Wiegmann, K. Balwin, Phys. Rev. Lett. 56 (1986) 85.
[8] E.F. Schubert, in: A.C. Gossard (Ed.), Semiconductors and Semimetals, Vol. 40, Academic Press, New York, 1994, p. 1.

ELSEVIER

Physica B 273–274 (1999) 839–842

PHYSICA B

www.elsevier.com/locate/physb

Deep levels associated with alpha irradiation of n-type MOCVD InP

M. Zafar Iqbal[a,*], U.S. Qurashi[a], A. Majid[a], Aurangzeb Khan[a], Nasim Zafar[a], A. Dadgar[b], D. Bimberg[b]

[a]*Semiconductor Physics Laboratory, Department of Physics, Quaid-i-Azam University, Islamabad, Pakistan*
[b]*Institut für Festkörperphysik, Technische Universität, Hardenbergstr. 36, 10623 Berlin, Germany*

Abstract

Deep level transient spectroscopy has been used to observe the effect of alpha particle irradiation on n-type InP grown by metal organic chemical vapour deposition (MOCVD). Eight majority carrier emitting levels Eα1, Eα2, ..., Eα8 are found to be produced as a result of this irradiation. At least two of the observed levels (Eα2 and Eα4) are found to show interesting metastable behaviour. One important result of this work is complete absence of the well-known metastable M-level (observed in electron irradiated LEC InP) in our alpha-irradiated MOCVD material. © 1999 Elsevier Science B.V. All rights reserved.

Keywords: InP; MOCVD; Deep-level defects; Irradiation

1. Introduction

Study of radiation-induced deep level defects in InP has attracted a great deal of attention over the last two decades or so [1]. This interest is stimulated largely by the potential of this material for devices meant for space use due to its much higher resistance to radiation as compared to other semiconductors, demonstrated in many studies [2,3]. Published investigations on n-type InP are mostly on liquid encapsulated Czochralski (LEC) [4–7] and liquid-phase epitaxy (LPE) [8–10] grown single-crystal material. We report here preliminary results of a study on n-type InP grown by metal-organic chemical vapour deposition (MOCVD) technique. Deep level transient spectroscopy (DLTS) has been used to investigate deep levels introduced by alpha radiation in p^+n junctions of InP. Apart from providing important information on the radiation-induced defects in this material, our study reveals some interesting but complex metastability effects.

2. Experimental details

Our samples consist of p^+n junctions grown by low-pressure metalorganic chemical vapour deposition (LP-MOCVD). The substrate used was a 350 μm thick n^+-InP layer doped with Si. On the top of this substrate a 3 μm thick n-InP : Si layer with a typical background donor doping 3×10^{15}–5×10^{16} cm^{-3} was grown. The top-most p^+ layer consists of ~0.7 μm thick InP : Zn. Nitrogen or hydrogen was used as the carrier gas for transporting the metalorganics and the epitaxy was carried out at a typical temperature and pressure of 640°C and 20 mbar, respectively. 600–800 μm diameter mesa diodes were prepared with suitable ohmic contacts. Irradiation was carried out by placing the samples in front of a 9 μCi ^{241}Am radioactive source, emitting alpha-particles of 5.48 MeV. DLTS measurements were carried out using a system based on the lock-in principle.

* Corresponding author.
E-mail address: mzi@splqau.sdnpk.undp.org (M.Z. Iqbal)

0921-4526/99/$ - see front matter
PII: S0921-4526(99)00517-7

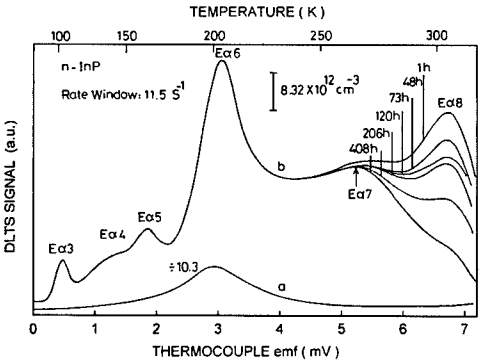

Fig. 1. DLTS majority carrier spectra of (a) unirradiated p^+n junction diodes; (b) after irradiation. The different scans for Eα8 show the room temperature (25°C) annealing and the numbers represent the storage time after irradiation.

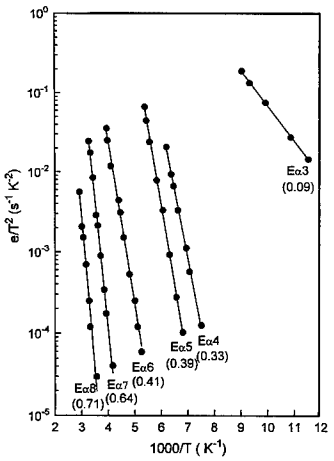

Fig. 2. Emission rate signatures of the α-irradiation-induced deep levels observed in Fig. 1. Filled circles are the experimental values, while the solid lines through these points are the least-squares fits to the data points. The numbers within brackets are the thermal activation energies (in eV) of the carriers to the conduction band.

3. Results

Fig. 1 shows the typical DLTS spectrum (trace a) obtained on our samples prior to irradiation. The spectrum exhibits one small peak around 200 K corresponding to a localized level at $E_C - 0.45$ eV with a concentration of 2.6×10^{12} cm^{-3}. The 5.48 MeV alpha particle irradiation produces six majority-carrier-emitting levels as shown in the DLTS spectrum (b) of Fig. 1, which we label as Eα3, Eα4, Eα5, Eα6, Eα7 and Eα8, respectively.

Table 1
Parameters of deep levels in α-irradiated MOCVD grown n-InP (Irradiation dose $= 1.8 \times 10^{11}$ cm^{-2})

Label	Energy position (eV)	Effective capture cross-section (cm^2)	Concentration ($\times 10^{13}$ cm^{-3})
Eα3	$E_C - 0.09$	7.82×10^{-20}	1.3
Eα4	$E_C - 0.33$	2.26×10^{-12}	—
Eα5	$E_C - 0.39$	8.50×10^{-12}	3.3
Eα6	$E_C - 0.41$	1.54×10^{-14}	8.2
Eα7	$E_C - 0.64$	3.3×10^{-12}	4.8
Eα8	$E_C - 0.71$	5.51×10^{-13}	5.5

The T^2-corrected Arrhenius plots of the measured electron emission rates for the observed levels are shown in Fig. 2. The respective thermal activation energy E_A and effective capture cross-section values obtained from the slopes and intercepts of these plots are given in Table 1 along with the concentrations of the observed deep levels.

The peak Eα8 was found to show a pronounced continuous decay during room temperature storage subsequent to irradiation at a significant rate until it completely disappears after about 408 h as shown by spectra (b) in Fig. 1. The remaining levels were found to be unaffected by room temperature isothermal annealing within the accuracy of our measurements.

As the LEC InP is well known to exhibit an interesting metastable deep level defect labelled as the M level [7], DLTS measurements were carried out by us to investigate any such effects in our spectrum for the MOCVD material. The experiments were carried out to investigate any charge-state-induced metastability leading to different defect configurations by the application or absence of reverse bias and/or excitation pulse during the cooling of the sample, prior to beginning of the DLTS scan. The DLTS spectra thus obtained are shown in Fig. 3 with the bias/pulse values given in the caption. These deep level spectra clearly demonstrate metastable character of the level Eα4 with its concentration in scan (a) decreasing to ~52% of its full concentration in scan (b). No increase in the concentration of the existing deep levels or appearance of a new defect state is observed with this reduction in concentration of Eα4. This type of metastability is in contrast with that observed for the M-level [7] where a complete transformation of one defect state into another is observed. The apparent decrease in the height of the peak Eα5 in spectra (a) and (c) relative to that in (b) may also suggest a similar metastability effect in the case of this peak, although at least part of this change must be due to the overlap of this peak with Eα4.

In addition to the above, preliminary DLTS measurements below 77 K were also carried out to look for any radiation-induced defects in the temperature range

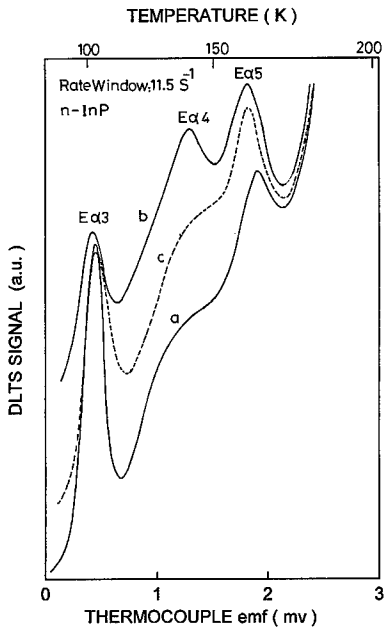

Fig. 3. DLTS spectra showing the metastable character of Eα4: (a) cooling without applied reverse bias; (b) cooling with applied reverse bias but no excitation pulse and (c) cooling with reverse bias and pulse. Reverse bias $V_R = -2.0$ V and pulse voltage $V_P = -0.5$ V.

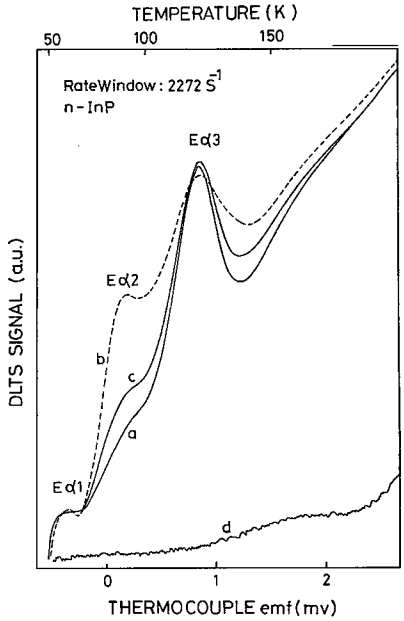

Fig. 4. DLTS spectra showing the metastable character of Eα2: (a) cooling without applied reverse bias; (b) cooling with applied reverse bias but no excitation pulse and (c) cooling with reverse bias and pulse. Trace d corresponds to the DLTS spectrum before irradiation. Reverse bias $V_R = -3.0$ V and pulse voltage $V_P = -0.5$ V.

10–77 K. Two more defect levels Eα1, Eα2 were observed in these spectra. The pronounced peak Eα2 is clearly found to display a strong charge-state-induced metastability effect as seen in spectra (a)–(c) of Fig. 4 for the three bias conditions. The emission rate signatures for this level could not be obtained accurately due to strong overlap with the level Eα3 at emission rates lower than 2260 s^{-1}. The peak Eα1 does not display any metastability effect. Its position and small magnitude also do not allow any detailed further characterization.

4. Discussion

We have presented the results of a DLTS study of the alpha radiation-induced defects in n-type InP crystals grown by LP-MOCVD. Irradiation by 5.48 MeV α-particles with a dose of $\sim 1.8 \times 10^{11}$ cm^{-2} results in eight electron emitting levels, Eα1–Eα8 with at least two (Eα2 and Eα4) metastable levels. The overall deep-level spectrum observed by us is found to be significantly different from the spectrum introduced by electron irradiation in n-type InP crystals grown by the LEC technique, reported by Levinson et al. [4].

No reported radiation-induced level in literature has similar emission rate signature as Eα3 (0.09 eV). Thus Eα3 is a new level observed by us. Our emission rate signature of the Eα5 (0.39 eV) level is in good agreement with the emission rate signature of the electron level E7 (0.37 eV) observed by Levinson et al. [4]. However, we do not observe as clear a charge-state-induced metastability effect for Eα5 due to its overlap with Eα4, as observed for the level E7 by Levinson et al. [7].

On comparison of emission rate signatures and temperature dependence of electron capture cross-section, we conclude that our level Eα6 (0.41 eV) is probably the same as observed by Tapster et al. [5] (0.44 eV) in n-InP crystals grown by LEC and VPE techniques and irradiated with electrons. The large capture barrier (~ 0.32 eV) observed by us for Eα6 suggests a strong lattice relaxation for the multiphonon emission model of capture. We also find that Eα6 is the dominant level observed in our case in contrast with the published reports on LEC InP where E10 (labelled as E11 by Suski et al. [10]) is observed to be the dominant level. The emission rate data of Eα6 are more or less coincident with that of the level observed in our sample before irradiation. This may indicate that Eα6 is the pre-existing level whose concentration has increased by α-irradiation. However, we also observed Eα6 in similar concentration in those samples in which this level was completely absent before the irradiation, indicating Eα6 to be a new defect state formed by α-irradiation. This suggests that this defect is either one of the primary radiation-induced

defects (In or P vacancy or self-interstitial) or a complex of these with some pre-existing impurity or intrinsic defect.

The activation energy and emission rates of Eα7 (0.64 eV) seem to be the same as those of a level E9 reported by Levinson et al. [4]. However, no electric field dependence of carrier emission was reported by them (although they do report [6] weak field dependence for the levels E1, E3 and EA) while we find the thermal emission from the level Eα7 to be strongly enhanced by the junction electric field. The detailed quantitative determination and analysis of this field dependence is in progress and will be reported elsewhere. This comparison suggests that Eα7 is not the same as the E9 defect state observed by Levinson et al.

The level Eα8 (0.71 eV) was found to be thermally unstable as it annealed out at room temperature (25°C). A similar thermally unstable level has been reported by Benton et al. [9] (E10) in LEC material and Suski et al. [10] (E11) in LPE material. However, the emission rate data for the level E10 (0.79 eV) and E11 are not in good agreement with the data for our level Eα8. Even if the level Eα8 is still identified with this deep level, it should be noted that in all cases of electron irradiation, the level E10(E11) has the highest concentration, dominating other radiation-induced levels. However, in our case of α-irradiation, Eα8 is not the dominant level. The E10(E11) defect, therefore, seems to be characteristic of LEC and LPE material only. Alternatively, there is, of course, the possibility that this may be interpreted as a major difference between the effects of electrons versus the α-radiation on n-InP.

4.1. Metastable defects

One important and interesting aspect of the present study is the complete absence of the well-known M-centre [7]. Electron-irradiation has been reported to result in this metastable level in LEC grown n-type samples. We did not observe a reversible, charge-state dependent, defect reaction in MOCVD-grown samples corresponding to the M centre as observed by Levinson et al. [7]. This would seem to indicate that the presence of M centre is specific to the method of crystal growth.

Another important feature of our spectra is the appearance of two new metastable levels Eα2 and Eα4. A detailed experimental investigation of the nature of these metastability effects, based on the variation of a number of DLTS parameters, such as temperature of application of bias and pulse, the magnitude and width of the bias and pulse, the history of the bias applied before the DLTS scan etc., is in progress and will be reported later. The kinetics governing the appearance/absence of these levels seem to be much more complex than for M-centre from our preliminary results.

5. Conclusions

The main conclusions of our study of α-irradiation on MOCVD n-type InP can be summarized as

(i) α-irradiation is seen to induce eight electron-emitting levels. The overall deep level spectra are observed to be quite different from those reported for electron irradiation of LEC and LPE n-InP.
(ii) Two of the new observed levels show interesting metastable behaviour.
(iii) The well-known M-centre in LEC material is not observed in α-irradiated MOCVD n-InP.
(iv) One of the levels, Eα8 is found to show strong room temperature isothermal annealing behaviour.

Acknowledgements

This work is supported in part by the Commission of European Communities project No. CI1-CT93-0076.

References

[1] A. Majerfeld, O. Wada, A.N.M.N. Choudhury, Appl. Phys. Lett. 33 (1978) 957.
[2] M. Yamaguchi, C. Uemura, A. Yamamoto, J. Appl. Phys. 55 (1984) 1429.
[3] K. Ando, M. Yamaguchi, Appl. Phys. Lett. 47 (1985) 846.
[4] M. Levinson, J.L. Benton, H. Temkin, L.C. Kimerling, Appl. Phys. Lett. 40 (1982) 990.
[5] P.R. Tapster, P.J. Dean, M.S. Skolnick, J. Phys. C: Solid State Phys. 15 (1982) L1007.
[6] M. Levinson, J.L. Benton, L.C. Kimerling, Phys. Rev. B 27 (1983) 6216.
[7] M. Levinson, M. Stavola, J.L. Benton, L.C. Kimerling, Phys. Rev. B 28 (1983) 5848.
[8] K. Ando, M. Yamaguchi, C. Uemura, J. Appl. Phys. 55 (1984) 4444.
[9] J.L. Benton, M. Levinson, A.T. Macrander, H. Temkin, L.C. Kimerling, Appl. Phys. Lett. 45 (1984) 566.
[10] J. Suski, A. Sibille, J.C. Bourgoin, Solid State Commun. 49 (1984) 875.

ELSEVIER

Physica B 273–274 (1999) 843–847

PHYSICA B

www.elsevier.com/locate/physb

Defect complexes induced by diffusion of group I acceptors into CdTe

H. Wolf, T. Filz, J. Hamann, S. Lany, V. Ostheimer, Th. Wichert*

Technische Physik, Universität des Saarlandes, Geb. 38, Postfach 15 11 50, D-66041 Saarbrücken, Germany

Abstract

The formation of defects following the diffusion of the group I acceptors Cu, Ag, or Au into CdTe was investigated by perturbed $\gamma\gamma$-angular correlation (PAC) using the radioactive donor $^{111}In_{Cd}$. The formation of A-centres (In_{Cd}–V_{Cd} pairs) with the donor $^{111}In_{Cd}$ was observed, indicating that the incorporation of the group I acceptors Cu, Ag, or Au is accompanied by the generation of cation vacancies. In addition, the formation of In_{Cd}–Ag_{Cd} or In_{Cd}–Au_{Cd} pairs was observed in CdTe. The concentration of cation vacancies formed after diffusion of Cu, Ag, or Au was found to depend only weakly on the respective group I element. In contrast, the migration energy of the cation vacancy was observed to be different in CdTe crystals doped with Ag or Au, yielding 0.76 (3) eV and 0.84 (3) eV, respectively. In Ag-doped CdTe the binding energies of the In_{Cd}–V_{Cd} pair and the In_{Cd}–Ag_{Cd} pair were determined to 0.18 (2) eV and 0.19 (2) eV, respectively.

Keywords: CdTe; Group I acceptors; Defect complexes; Diffusion

1. Introduction

Group I elements act as acceptors in CdTe if they are incorporated on Cd sites. The p-type conductivity of CdTe, however, that is achieved by doping with group I elements is strongly limited, yielding e.g. for Ag a maximum hole concentration of 2×10^{16} cm^{-3} [1], although the solubility of Ag is much higher. An effective p-type doping by group I elements may be prevented by the formation of compensating intrinsic defects or by the incorporation of group I elements also at interstitial lattice sites, acting there as donors. Thus, Chamonal et al. and Monemar et al. [2,3] proposed that close pairs of substitutional Ag_{Cd} acceptors and Ag_i donors are formed that passivate each other.

The formation of defect complexes upon doping of CdTe with group I acceptors was investigated by perturbed $\gamma\gamma$ angular correlation spectroscopy (PAC) using the radioactive donor $^{111}In_{Cd}$, which decays to the host atom ^{111}Cd. The PAC data yield information about acceptor-like defects, which form complexes with the donor probe $^{111}In_{Cd}$. Besides the group I acceptors, the acceptor-like cation vacancy is detected by PAC in CdTe. The migration energies of acceptor defects and the binding energies of defect complexes are determined by annealing the crystals after quenching and by variation of the sample temperature.

2. Experimental procedure

The ^{111}In probe atoms were diffused into the CdTe crystals at temperatures between 800 and 970 K for times between 1.5 and 8 h. The total number of ^{111}In atoms/crystal was about 10^{12}, the diffusion length L_{In} was between 3.5 and 14 μm depending on the individual diffusion conditions (see Table 1). The resulting maximum concentration of ^{111}In atoms was about 10^{15} cm^{-3} after diffusion and decreased well below

* Corresponding author: Tel.: + 49-681-302-4220; fax: + 49-681-302-4315.

E-mail address: thw@tech-phys.uni-sb.de (Th. Wichert)

0921-4526/99/$ - see front matter
PII: S0921-4526(99)00518-9

Table 1
Diffusion lengths $L = \sqrt{Dt}$ of the dopants [9] and site fractions f of the ^{111}In probe atoms at 295 K in thermal equilibrium

Dopant	L_{In} (μm)	L_A	f_c (%)	f_{In-V} (%)	f_{In-A} (%)
^{111}In	14	—	77	15	
^{111}In + Ag[a]	3.5	0.5 mm[c]	17	10	30
^{111}In + Ag[b]	3.5	0.5 mm[c]	31	26	17
^{111}In + Au	13	12 μm	55	38	—[d]
^{111}In + Cu	4	50 μm	25	46	—

[a]Variation of the measuring temperature (see Fig. 1).
[b]Annealing at 295 K (see Fig. 2a).
[c]Homogeneous distribution over the entire crystal assumed.
[d]Observable under altered diffusion conditions.

10^{15} cm^{-3} in the course of the experiments due to the radioactive decay.

For doping with Cu, Ag, or Au, a layer of 10 nm of the respective metal was evaporated onto the CdTe surface followed by a subsequent diffusion into the CdTe crystal. Since the metal layer on the surface represents an infinite diffusion source, the diffusion profile is described by the complementary error function, whereby the concentration at the surface is determined by the solubility. The diffusion lengths L_A of the group I dopants in the investigated crystals are listed in Table 1. As a reference, a CdTe crystal was diffused exclusively with ^{111}In at 860 K for 8 h and additionally treated at 1000 K for 10 min under Te pressure in order to generate cation vacancies.

In a PAC experiment, the site fractions of the probe atoms in specific local configurations are quantitatively detected. In the present experiments, the environment of ^{111}In probe atoms located on Cd lattice sites is of interest: whether they are incorporated isolated as electrically active donors or bound in pairs with either the cation vacancy V_{Cd} or the group I acceptors Ag_{Cd}, Au_{Cd}, or Cu_{Cd}. The different local configurations are distinguished by different electric field gradients (EFG), which are measured by PAC at the daughter isotope ^{111}Cd. The EFG tensor is usually expressed by the quadrupole coupling constant $\nu_Q = eQV_{zz}/h$ and the asymmetry parameter $\eta = (V_{xx} - V_{yy})/V_{zz}$. A detailed description of PAC spectroscopy in semiconductors can be found in the literature [4].

3. Results

In CdTe crystals exclusively doped with ^{111}In, the formation of $^{111}In_{Cd}$–V_{Cd} pairs is [5–7] observed after heating the crystal at 860 K under Te pressure. The presence of the cation vacancies is recognised by the EFG, characterised by $\nu_Q = 60.2$ (5) MHz and $\eta = 0.17$ (1). From the $^{111}In_{Cd}$ donors, the fraction $f_{In-V} = 15\%$ have formed In_{Cd}–V_{Cd} pairs and the fraction $f_c = 77\%$ are located on isolated Cd sites with cubic symmetry.

After diffusion of Cu, Ag, or Au into CdTe, the same EFG is observed; the fractions of In_{Cd}–V_{Cd} pairs, however, are often significantly larger than after thermal treatment under Te pressure. The diffusion of group I elements into CdTe obviously enhances the formation of cation vacancies. In case of Ag or Au diffusion, under suitable conditions a second EFG is observed, which is slightly smaller than the EFG corresponding to the cation vacancy and is assigned to the donor–acceptor pairs In_{Cd}–Ag_{Cd} ($\nu_Q = 56.6$ (5) MHz, $\eta = 0.11$ (2)) or In_{Cd}–Au_{Cd} ($\nu_Q = 54.2$ (5) MHz, $\eta = 0.07$ (2)), respectively. In contrast, after diffusion of Cu a second EFG is not observable, suggesting that no In_{Cd}–Cu_{Cd} pairs have been formed. The assignment of the detected EFG to these defect complexes will be discussed at an other place [8]. The present study focuses on the formation of In_{Cd}–V_{Cd} pairs (A-centres) accompanying the diffusion of Ag, Au, or Cu and, especially, on the mobility of the cation vacancy V_{Cd} and the stability of the A-centres formed with $^{111}In_{Cd}$ donors. In addition, the stability of the In_{Cd}–Ag_{Cd} pair is determined. The diffusion lengths of the dopants in the investigated samples are calculated on the basis of published data [9] and are listed in Table 1.

3.1. CdTe : Ag

Two ^{111}In-doped CdTe crystals were diffused with Ag at 550 K for 60 min. Based on the high mobility reported for Ag in CdTe [10], a homogeneous distribution of the Ag atoms over the entire crystal is assumed with a concentration of [Ag] = 10^{18} cm^{-3}. After diffusion, the first sample was cooled to 295 K and subsequently measured at different temperatures in the range 295–550 K. The PAC data at 295 K show the ^{111}In atoms to be located at lattice sites with cubic symmetry, bound in $^{111}In_{Cd}$–V_{Cd} pairs, and in $^{111}In_{Cd}$–Ag_{Cd} pairs with the fractions $f_c = 17\%$, $f_{In-V} = 10\%$, and $f_{In-Ag} = 30\%$, respectively. Increasing the sample temperature, f_{In-V} and f_{In-Ag} decrease, and f_c increases, whereas the sum $f_{tot} = f_c + f_{In-V} + f_{In-Ag} = 57\%$ remains constant. The ratios f_{In-V}/f_c and f_{In-Ag}/f_c (see. Eq. (3a) and (3b) below) are plotted as a function of the temperature in Fig. 1 in an Arrhenius plot. The second crystal was heated to 800 K, quenched to 260 K with a cooling rate of about 10^3 K/s, and immediately transferred into a LN_2 bath. The PAC data show that following the quench In_{Cd}–Ag_{Cd} pairs, but almost no In_{Cd}–V_{Cd} pairs are formed [11]. The In_{Cd}–V_{Cd} pairs are formed after annealing the crystal at 295 K. The fraction $f_{In-V}(t)$ measured within an isothermal annealing program is plotted in Fig. 2a. At the same time, the fraction of In_{Cd}–Ag_{Cd} pairs only slightly increases from

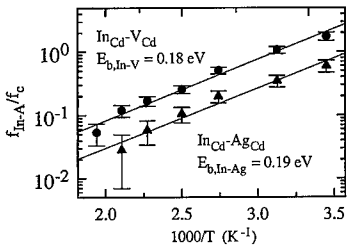

Fig. 1. Arrhenius plot of the ratio f_{In-V}/f_c and f_{In-Ag}/f_c in CdTe diffused with Ag.

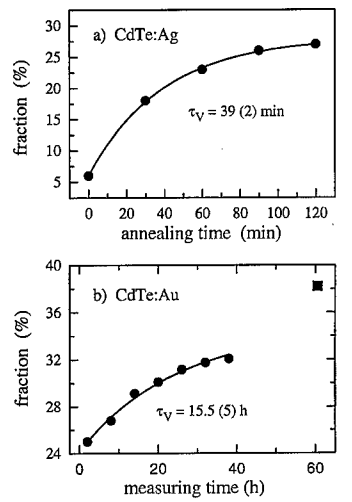

Fig. 2. Fraction of In_{Cd}-V_{Cd} pairs in (a) CdTe : Ag as a function of the annealing time at 295 K and (b) in CdTe : Au as a function of the accumulated measuring time. The last data point (square at 60 h) was taken after re-starting the measurement.

14% to 17%. The increase of the fraction of A-centres is well described by an exponential law with a time constant of $\tau_V = 39$ min (solid line in Fig. 2a). The time constant agrees fairly well with the time constant reported by Reislöhner et al. for the formation of $^{111}In_{Cd}$-V_{Cd} pairs after dipping a CdTe crystal in an aqueous solution of $AgNO_3$ [12].

3.2. CdTe : Au

An ^{111}In doped CdTe crystal was diffused with Au for 60 min at 900 K. The resulting diffusion lengths of the ^{111}In and the Au atoms were nearly identical (see Table 1). In this case, no In_{Cd}-Au_{Cd} pairs are formed, whereas the formation of In_{Cd}-V_{Cd} pairs is observed at ambient temperature like in the case of Ag. The time constant τ_V, however, is significantly larger than in the Ag-diffused sample. For practical reasons the experimental procedure was modified. After diffusion of Au, the crystal was measured at ambient temperature over a longer time, whereby the data were stored in time intervals of 6 h. The fraction of A-centres as a function of the accumulated measuring time is plotted in Fig. 2b. For the last data point (60 h after Au diffusion; square) the measurement was re-started, in this way yielding the equilibrium value of the fraction of In_{Cd}-V_{Cd} pairs, $f_{In-V} = 38\%$ directly.

3.3. CdTe : Cu

After diffusion of Cu into CdTe doped with ^{111}In, the formation of A-centres at ambient temperature happens faster than in case of Ag diffusion. The PAC data show that at thermal equilibrium $f_{In-V} = 46\%$ of the $^{111}In_{Cd}$ donors are bound in In_{Cd}-V_{Cd} pairs and $f_c = 25\%$ remained at lattice sites with cubic symmetry (see Table 1).

4. Discussion

A mechanism of the compensation of group I acceptors, involving the formation of cation vacancies V_{Cd}, is described by the defect reaction (e.g. for the Ag_{Cd} acceptor)

$$2Ag_{Cd}^{-} + 2h \rightarrow Ag_{Cd}^{-} + Ag_i^{+} + V_{Cd}^{0} \rightarrow (Ag_{Cd} - Ag_i)^0 + V_{Cd}^{0}. \quad (1)$$

It describes the conversion of the shallow level of the Ag_{Cd} acceptor into deep levels of the double acceptor defect V_{Cd}. Simultaneously, electrically inactive (Ag_{Cd}-Ag_i) pairs are formed as proposed by Chamonal et al. and by Monemar et al. [2,3]. The cation vacancies may be trapped at the surface of the crystal or at donor-like defects. The trapping at the radioactive donor $^{111}In_{Cd}$ enables the direct detection by PAC. Additionally, the $^{111}In_{Cd}$ donors form complexes with Ag_{Cd} acceptors that are not bound in Ag_{Cd}-Ag_i pairs.

The formation of close pairs of the $^{111}In_{Cd}$ donor with two different acceptor defects $A_{Cd,1}$ and $A_{Cd,2}$ during an annealing experiment is described by coupled rate equations. If the concentrations of the acceptor defects $[A_{Cd,k}]$ significantly exceed the total concentration of the involved ^{111}In atoms $[In_{Cd}]_{tot}$, as is the case in the present experiments, the rate equations are

$$\frac{d}{dt}[In_{Cd} - A_{Cd,k}] = -\lambda_k[In_{Cd} - A_{Cd,k}] + \mu_k[A_{Cd,k}][In_{Cd}] \quad (k = 1, 2) \quad (2)$$

with

$$\lambda_k = \nu_{0,k}\exp(-(E_{m,k} + E_{b,k})/kT),$$

$$\mu_k = \nu_{0,k}\Omega_k\exp(-E_{m,k}/kT),$$

and

$$[In_{Cd}]_{tot} = [In_{Cd}] + [In_{Cd} - A_{Cd,1}] + [In_{Cd} - A_{Cd,2}].$$

The decrease of $[In_{Cd}]_{tot}$ due to the radioactive decay can be separated from Eq. (2). Since in the following only the fractions of In atoms in specific configurations are of interest, $[In_{Cd}]_{tot}$ can be treated as constant. The rates of dissociation (λ_k) and formation (μ_k) depend on specific properties of the involved acceptor defects $A_{Cd,k}$, like the attempt frequency $\nu_{0,k}$ and the migration energy $E_{m,k}$. The trapping volume Ω_k and the binding energy $E_{b,k}$ are properties of the defect complexes In_{Cd}–$A_{Cd,k}$. In general, the fractions $f_{In-k}(t)$ of $^{111}In_{Cd}$ donors bound at the time t in the defect complexes In_{Cd}–$A_{Cd,k}$ are obtained by integrating the time -dependent solutions of Eq. (2) over the entire crystal and dividing the result by the total number of ^{111}In atoms. For the interpretation of the present data, however, only some special solutions are of interest.

4.1. CdTe : Ag

Since the concentrations of both defect complexes are in thermal equilibrium in the experiments shown in Fig. 1, the following solutions of the rate equations (Eq. (2)) are obtained

$$f_{In-V}/f_c = \Omega_V[V_{Cd}]\exp(E_{b,In-V}/kT) \quad (3a)$$

and

$$f_{In-Ag}/f_c = \Omega_{Ag}[Ag_{Cd}]\exp(E_{b,In-Ag}/kT), \quad (3b)$$

giving direct access to the binding energies of both defect complexes. The experimental data yield for the binding energies of the In_{Cd}–V_{Cd} pair and the In_{Cd}–Ag_{Cd} pair $E_{b,In-V} = 0.18$ (2) eV and $E_{b,In-Ag} = 0.19$ (2) eV, respectively, as well as $\Omega_V \cdot [V_{Cd}] = 4.6 \times 10^{-4}$ and $\Omega_{Ag} \cdot [Ag_{Cd}] = 1.0 \times 10^{-3}$. The binding energy of the In_{Cd}–V_{Cd} pair is somewhat larger than the value of 0.15 (1) eV reported by Griffith et al. [7], what, however, might be connected with the fact that a powder sample was used instead of a single crystal.

During the isothermal annealing experiment at 295 K, the fraction of In_{Cd}–Ag_{Cd} pairs remained almost constant, indicating that the concentration of the In_{Cd}–Ag_{Cd} pairs was in thermal equilibrium. The time constant τ_V, which describes the formation of the In_{Cd}–V_{Cd} pairs, is consequently mainly governed by the migration energy of the cation vacancy and is well approximated by

$$1/\tau_V = \nu_{0,V}\exp(-E_{m,V}/kT) \times (\Omega_V[V_{Cd}] + \exp(-E_{b,In-V}/kT)). \quad (4)$$

From this equation the migration energy $E_{m,V}$ of V_{Cd} is extracted. Using the values of $E_{b,In-V}$ and $\Omega_V \cdot [V_{Cd}]$ determined above, the attempt frequency $10^{12}\ s^{-1} < \nu_{0,V} < 10^{13}\ s^{-1}$, which is typical for phonon frequencies in solids, and the experimentally determined time constant of $\tau_V = 39$ min (Fig. 2a), the migration energy $E_{m,V} = 0.76(3)$ eV is deduced. This value is slightly smaller than the energy of 0.80 (5) eV reported in Ref. [11], using simplified assumptions for $\Omega_V \cdot [V_{Cd}]$ and a more simple model.

4.2. CdTe : Au

Since no In_{Cd}–Au_{Cd} pairs are observed during the isothermal annealing sequence (Fig. 2b), the formation of In_{Cd}–V_{Cd} pairs is described by a single rate equation. With regard to the evaluation of the time constant τ_V, two remarks have to be made. Firstly, the profile of V_{Cd} is assumed to be constant, which actually does not seem to be realistic because the diffusion length of the Au dopant is nearly identical with that of the ^{111}In dopant. Therefore, the time constant τ_V and consequently the expression $\Omega_V[V_{Cd}]$, have to be regarded as values averaged over the diffusion profiles. Secondly, it has to be considered that the fraction of In_{Cd}–V_{Cd} pairs $f_{In-V}(t)$ increases continuously during the PAC measurement and, at the same time, the counting rate decreases due to the radioactive decay of the ^{111}In atoms. The time dependent solution of the rate equation

$$f_{In-V}(t) = f_{In-V} + (f_{In-V,0} - f_{In-V})(1 - \exp(-t/\tau_V)), \quad (5)$$

therefore, has to be averaged over the measuring time, which, however, can be treated exactly. The symbols $f_{In-V,0}$ and f_{In-V} denote the fraction of In_{Cd}–V_{Cd} pairs at the beginning of the measurement and at thermal equilibrium, respectively. The fraction f_{In-V} was determined by starting a new measurement (square in Fig. 2b). From the experimental data, the time constant $\tau_V = 15.5(5)$ h and the fraction of $f_{In-V,0} = 24\%$ at the beginning of the experiment is determined (solid line in Fig. 2b). The ratio $f_{In-V}/f_c = 0.69$ is close to that observed at 295 K after Ag diffusion ($f_{In-V}/f_c = 0.59$), suggesting that the concentration of V_{Cd} is almost the same after Au and Ag diffusion. Since the attempt frequency $\nu_{0,V}$ is a property of the CdTe lattice, and Ω_V and $E_{b,In-V}$ are local properties of the In_{Cd}–V_{Cd} pair, the different time constants τ_V observed after Ag and Au diffusion can only be explained if the migration energy $E_{m,V}$ is different (see Eq. (4)). The extracted migration energy of the V_{Cd} defect in the Au-doped CdTe crystal is determined to be $E_{m,V} = 0.84(3)$ eV, as compared to 0.76 (3) eV in the Ag-doped crystal.

4.3. CdTe : Cu

From the present experimental data the migration energy of the cation vacancy cannot be determined. The ratio $f_{In-V}/f_c = 1.82$, however, is in the same order of magnitude as obtained after Ag or Au diffusion. Thus, the

concentration of V_{Cd} is obviously close to that observed after Ag or Au diffusion. It is suggested that at high concentration of the group I dopants the concentration of V_{Cd} is governed by intrinsic properties of CdTe.

5. Conclusion

In CdTe crystals, doped with the group I acceptors Ag, Au, or Cu, the formation of A-centres was investigated by PAC. The mobility of the cation vacancy V_{Cd} is different after diffusion of Ag or Au, whereas the concentration of the formed cation vacancies varies only slightly. Since the mobility of the cation vacancy can be affected by the presence of dopants, the observed differences might indicate different concentrations of the group I dopants. By Griffith et al. the mobility of the cation vacancy was observed in CdTe doped exclusively with ^{111}In. There, the mobility was significantly lower than in the present experiments. The lower mobility may be connected with the use of a powder sample, giving rise to a higher defect concentration. In contrast, the present experiments show that the concentration of the generated cation vacancies does not significantly depend on the nature of the introduced group I dopant Cu, Ag, or Au, nor on its concentration.

Acknowledgements

The financial support by the BMBF, grant No. WI04SAA, is gratefully acknowledged

References

[1] J.P. Chamonal, E. Molva, J.L. Pautrat, Solid State Commun. 43 (1982) 801.
[2] J.P. Chamonal, E. Molva, J.L. Pautrat, L. Revoil, J. Crystal Growth 59 (1982) 297.
[3] B. Monemar, E. Molva, Le Si Dang, Phys. Rev. B 33 (1986) 1134.
[4] Th. Wichert, M. Deicher, G. Grübel, G. Keller, N. Schulz, H. Skudlik, Appl. Phys. A 48 (1989) 59.
[5] R. Kalish, M. Deicher, G. Schatz, J. Appl. Phys. 53 (1982) 4793.
[6] Th. Wichert, Th. Krings, H. Wolf, Physica B 185 (1993) 297.
[7] J.W. Griffith, R. Lundquist, R. Platzer, J.A. Gardner, G. Karczewski, J.K. Furdyna, Mater. Sci. Forum 143-147 (1994) 405.
[8] V. Ostheimer, T. Filz, J. Hamann, S. Lany, H. Wolf, Th. Wichert, to be published.
[9] E.D. Jones, J.C. Clark, in: P. Capper (Ed.), Properties of Narrow Gap Cadmiumbased Compounds, (Ed), INSPEC, London UK, 1994, pp. 472–481.
[10] M.A. Kovalets, N.I. Kuchma, E.S. Nikonyuk, I.P. Chiokan, M.N. Skvydka, Fiz. Khim. Obrab. Mater. 3 (1987) 125.
[11] H. Wolf, T. Filz, J. Hamann, V. Ostheimer, S. Lany, Th. Wichert, M. Deicher, A. Burchard, ISOLDE Collaboration, Mater Res. Soc. Symp. Proc. 510 (1998) 337.
[12] U. Reislöhner, N. Achtziger, M. Rüb, W. Witthuhn, J. Crystal. Growth 159 (1996) 372.

ELSEVIER

Physica B 273–274 (1999) 848–851

PHYSICA B

www.elsevier.com/locate/physb

Intra-shell transitions of 3D metal ions (Fe, Co, Ni) in II–VI wide-gap semiconductor alloys

T.P. Surkova[a], M. Godlewski[b,*], K. Swiatek[b], P. Kaczor[b], A. Polimeni[c], L. Eaves[c], W. Giriat[d]

[a]*Institute of Metal Physics, Ural Division Russian Academy of Sciences, 620219 Ekaterinburg, GSP-170, Russia*
[b]*Institute of Physics, Polish Academy of Sciences, 02-668 Warsaw, Al. Lotnikow 32/46, Poland*
[c]*School of Physics and Astronomy, University of Nottingham, NG7 2RD Nottingham, UK*
[d]*IVIC, Centro de Fisica, Apto 1827, Caracas 1010A, Venezuela*

Abstract

We analyse ionisation and intra-shell transitions of iron, nickel and cobalt in bulk crystals of CdSe, ZnSe and ZnS and in their alloys. A multi-charge state of transition metal ions and observed nonlinear shifts of their intra-shell transitions clearly demonstrate deviations from the predictions of the Ludwig–Woodbury model. Studies of ionisation transitions allow us to verify the recent theoretical predictions on universal-reference-level due to transition metal ions. We report a relatively good agreement between predictions of the universal-level-model and band offsets in ZnCdSe/ZnSe and ZnSe/ZnSSe heterostructures.

Keywords: Transition metal ions; CdSe; ZnSe; ZnS; Ionisation and intra-shell transition

1. Introduction

There are several reasons for continuing interest in the properties of transition metal (TM) ions in wide-gap II–VI semiconductors. For example, TM ions are efficient activators of electroluminescence in a new generation of thin film EL devices, which are based on TM doped wide-gap II–VI semiconductors [1]. However, other TM ions act as efficient centres of nonradiative recombination in these compounds [2]. Recent theoretical works on universal-reference-level due to TM ions [3–6] also stem an interest in the studies of TM ions. In this work we first analyse ionisation and intra-shell transitions of three of TM ions (Fe, Co and Ni) in bulk crystals of CdSe, ZnSe and ZnS and in their solid alloys. We verify applicability of the Ludwig–Woodbury (LW) model to the description of these transitions. We then use the model of universal-reference-level for estimation of band offsets in the heterostructures of ZnCdSe/ZnSe and ZnSe/ZnSSe, which are presently intensively studied due to their possible application in green colour light emitting devices [7].

2. Experimental

Single crystals of CdSe, ZnSe and ZnS and their solid alloys were grown by a chemical transport method. Cd and S fraction in the alloys was controlled by EDXRF analysis. The crystals and the alloys were doped into melt with Ni, Co or Fe ions to the level about $1–5 \times 10^{19}$ cm^{-3}. Optical absorption, photoluminescence (PL), electron spin resonance (ESR) and photo-ESR [8] experiments were performed to analyse properties of TM ions in the crystals studied. These experiments were done at liquid helium temperature using conventional experimental set-ups described elsewhere.

* Corresponding author: Tel.: + 48-22-843-68-61; fax: + 48-22-843-09-26.
E-mail address: godlew@ifpan.edu.pl (M. Godlewski)

0921-4526/99/$ - see front matter
PII: S0921-4526(99)00519-0

3. Intra-shell and ionisation transitions of TM ions

Until recently, intra-shell transitions of TM ions in semiconductors were described by the Ludwig and Woodbury model [9]. This model, introduced to explain ESR data, assumes that a TM ion in a given II–VI compound gives two electrons to the bonds. The resulting 2+ ion has properties of 2+ ion in a vacuum, modified by dielectric constant of the material and by crystal field symmetry. The model assumes no hybridisation between t_2 orbitals of 3d electrons and p states of ligands. The LW model was first used to explain spin multiplicity of ground states of TM ions [9]. Then, the LW model was also used to describe intra-shell transitions of TM ions. It was pointed out that a multiplet structure of a given TM ion closely resembles that of a free ion. It was thus assumed that the only corrections to a multiplet structure of a TM ion in a crystal are due to dielectric constant of the medium and to a crystal field splitting.

The initial successes of the LW model relate to the fact that the model correctly describes spin properties of TM ions. However, our studies of ionisation transitions of TM ions clearly show the limitations of the LW model. The model fails to explain a multi-charge state of these ions, which we observed in wide-gap II–VI semiconductors. All TM ions studied by us introduce at least one energy level to a forbidden gap of CdSe, ZnSe and ZnS. Thus, these TM ions are observed in two or in three charge states. For example, we observed three charge states of Fe and Ni ions (3+, 2+ and 1+) in the lattice of ZnS. Such property of these two TM ions cannot be explained by slightly modified properties of a free ion. For a free TM ion different charge states differ in the energy by about 20 eV and not by 1–2 eV, as we observe in our experiments. Charge neutrality effects and hybridisation with ligand wave functions are necessary to explain the observed ionisation energies of TM ions [5,10].

We further test applicability of the LW model to the description of intra-shell transitions of Fe^{2+}, Ni^{2+} and Co^{2+} ions in CdSe, ZnSe and ZnS and in solid state alloys of ZnSSe and ZnCdSe. We studied the evolution of the shape and of spectral position of intra-shell absorption and PL transitions. The results of these experiments also deviate from the predictions of the LW model. For example, in Fig. 1 we show the evolution of the PL spectrum due to $^3T_1 \rightarrow {}^5E$ transition of Fe^{2+} in ZnSSe alloys. A fine structure of this PL emission (not shown) is only observed for ZnS : Fe. This structure is smeared out due to alloy broadening effects after adding 10% and more of Se and also is not observed for Fe^{2+} in ZnSe. We concentrate our attention on another property of the PL. The PL clearly shifts down in the energy when Cd (in ZnCdSe) and S (in ZnSSe, see Fig. 1) is introduced to the alloy. The observed energy dependence of intra-shell transition is nonlinear. For higher S fractions this shift

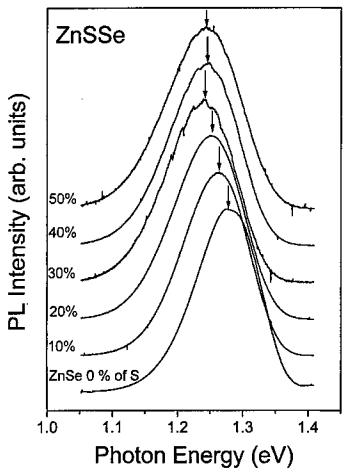

Fig. 1. Energy dependence of $^3T_1 \rightarrow {}^5E$ intra-shell transition of Fe^{2+} in the solid alloys of ZnSe and ZnS. Fine structure of the transition was resolved only for ZnS : Fe, not shown in the picture.

saturates and then the PL shifts up-in-the-energy. This cannot be explained within the framework of the LW model.

We also observed nonlinear shifts of the energy (and also alloy broadening) of intra-shell transitions of Ni^{2+} and Co^{2+} ions in the alloys of ZnSSe and ZnCdSe. Quite similar behaviour is observed for the alloys with the replacement of cation and anion. This we show in Figs. 2(a) and (b) on the example of $^3T_1(F) \rightarrow {}^3T_2(F)$ (a) and $^3T_1(F) \rightarrow {}^3A_2(F)$, $^1T_2(D)$, $^1E(D)$ (b) intra-shell transitions of Ni^{2+}. The relevant absorption peaks broaden due to the alloy broadening effects. They also shift in the energy and the shift is not linear. We propose that such nonlinear shift of the energy of intra-shell transitions is due to a hybridisation between t_2 3d electrons and p-states of ligands. The effect depends on a relative energy position of the relevant states (two t_2 (3d) states with different spin orientation and p orbital of ligands) and thus should be the alloy composition dependent. The nonlinear energy dependence can be more pronounced for intra-shell transitions between multiplets of a different spin multiplicity, which involve an excitation of a t_2 electron to an upper t_2 3d orbital, i.e., the transition between two hybridised t_2 states. A different situation will occur for those of TM intra-shell transitions, which involve the excitation of an electron between two e-symmetry orbitals (spin down and spin up) of a 3d ion. This is why different alloy composition dependencies are observed for us. Some transitions show only weak shifts of the transition energy, whereas for others this shift is more pronounced and often nonlinear.

A still different effect, which can also be related to a 3d-ligand hybridisation, is observed for intra-shell transitions of Co^{2+}. Whereas for ZnSe only the so-called

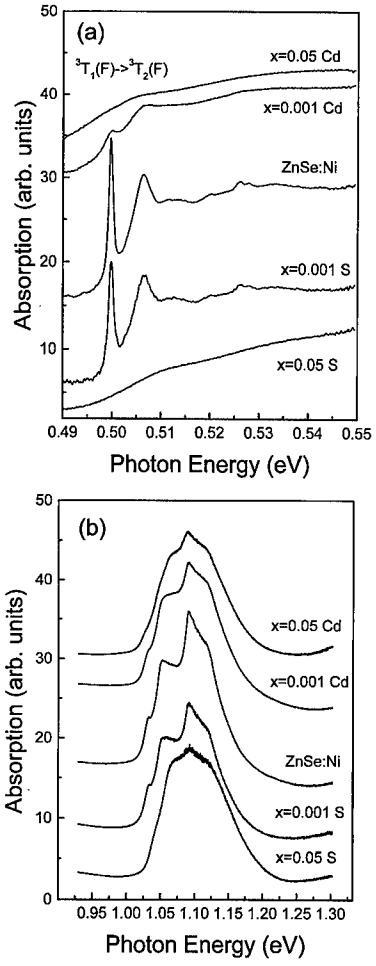

Fig. 2. Spectral evolution of $^3T_1(F) \rightarrow {}^3T_2(F)$ (a) and $^3T_1(F) \rightarrow {}^3A_2(F)$, $^1T_2(D)$, $^1E(D)$ (b) transitions of Ni^{2+} in ZnS, ZnSe and CdSe and in their alloys.

L-line PL is observed, two new PL emissions appear once 1% of S is introduced to the ZnSSe alloy. These are the so-called M- and N-lines, observed in ZnSe only in the absorption. This change of the PL spectrum is accompanied by a noticeable change of L-line PL decay time, as reported recently by us [11]. We relate both effects, the appearance of the new PL emissions and the nonlinear change of the PL decay time upon alloying, to hybridisation effects. As mentioned above hybridisation strongly depends on a relative energy position of two (spin up and spin down) t_2-like 3d levels and t_2-symmetry ligand level, and thus on the alloy composition.

4. Band offsets in CdSe/ZnSe/ZnS

Recent interest in the optical properties of TM ions in II–VI and III–V semiconductors was generated by the

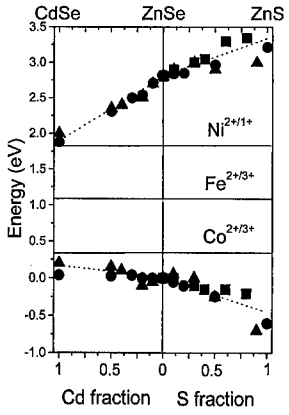

Fig. 3. Energy position of conduction and valence bands in CdSe, ZnSe and ZnS and in their alloys versus energy levels of iron, nickel and Co ions (solid lines). The experimentally determined ionisation energies are shown for Ni (●, 2 + -to-1 + transition), Co (▲, 2 + -to-3 + transition) and Fe (■, 2 + -to-3 + transition).

suggestion of the TM-related universal-reference-level [3]. It was proposed that energy levels of TM ions are pinned to a certain universal-reference-level [3–6]. If so, band offset in a given heterostructure can be predicted from a difference in conduction and valence band energies versus a fixed-energy-position of the TM-related level. We have recently tested validity of this model for $Ni^{2+} \rightarrow Ni^{1+}$ ionisation energies, estimated in the photo-ESR and optical absorption studies. We compared the predicted valence and conduction band offsets in ZnCdSe/ZnSe and ZnSe/ZnSSe quantum well structures with those known from other experiments [12]. The relevant experimental results are shown in Fig. 3, in which we summarise the experimental results obtained for Ni ion and we include new data on ionisation transitions of Co and Fe ions. The theory relatively well predicts band offsets in both ZnCdSe/ZnSe and ZnSe/ZnSSe heterostructures. For example, for ZnSe/CdSe heterostructure the extrapolated valence band offset is 0.15 ± 0.1 and is 0.35 ± 0.1 for ZnS/ZnSe heterostructure. These values agree relatively well with those measured experimentally [12,13]. We point out that a better agreement between the theory and the experiment is obtained if we include the data for $Co^{2+} \rightarrow Co^{3+}$ and $Fe^{2+} \rightarrow Fe^{3+}$ ionisation transitions.

We will now speculate why the use of Co and Fe energy levels as the universal-reference-level gives a better prediction of the band offsets. In our opinion this also relates to hybridisation effects discussed above. The crucial point in the universal-level-model is that the energy of TM ion is alloy composition independent. This is not the case for ionisation of t_2-symmetry 3d electron of a TM ion, which hybridises with t_2-symmetry p states of ligands. For Ni ion t_2-symmetry 3d electron participates

in the ionisation transition, whereas for Fe and Co ions we deal with the ionisation of e-symmetry 3d electrons. In the former case strong hybridisation with ligand t_2 orbitals is expected and thus some alloy composition dependence, which may result in a nonlinear energy dependence in the alloys. In the case of ionisation transitions of Fe and Co ions no hybridisation effects are expected, since e-symmetry 3d electrons participating in the ionisation transitions do not hybridise with ligand states.

Summarising, our experimental data indicate that both ionisation and intra-shell transitions of TM ions show clear deviations from the predictions of the LW model. The observed multi-charge state of TM ions and nonlinear shifts of their PL and absorption transitions we relate to effects of TM-ligand hybridisation and thus-induced modifications of the energy positions of the relevant states of TM ions and ligands. The strength of interaction should vary upon alloying, which can explain the observed nonlinearities in the energy level positions and in PL the transition energies.

Acknowledgements

This work was partly supported by grant no. 2P 03B 018 13 of KBN (M. Godlewski) and by grant no. 98-02-17560 of RFBR and a fellowship of the Royal Society (T.P. Surkova).

References

[1] M. Godlewski, M. Leskelä, CRC Crit. Rev. Solid State Mater. Sci. 19 (1994) 199.
[2] M. Godlewski, A. Zakrzewski, in: M. Jain (Ed.), II–VI Semiconductor Compounds, World Scientific, Singapore, 1993, p. 205.
[3] M.J. Caldas, A. Fazzio, A. Zunger, Appl. Phys. Lett. 45 (1984) 671.
[4] J.M. Langer, H. Heinrich, Phys. Rev. Lett. 55 (1985) 1414.
[5] A. Zunger, in: Solid State Physics, Vol. 89, Academic Press, New York, 1986, p. 275.
[6] J.M. Langer, C. Delarue, M. Lannoo, H. Heinrich, Phys. Rev. B 38 (1988) 7723.
[7] K. Ohkawa, M. Behringer, H. Wenisch, M. Fehrer, B. Jobst, D. Hommel, M. Kuttler, M. Strassburg, D. Bimberg, G. Bacher, D. Tönnies, A. Forchel, Phys. Stat. Sol. B 202 (1997) 683.
[8] M. Godlewski, Phys. Stat. Sol. A 90 (1985) 11.
[9] G.W. Ludwig, H.H. Woodbury, in: F. Seitz, D. Turnbull (Eds.), Solid State Physics, Vol. 13, Academic Press, New York, 1962, p. 223.
[10] M. Schefler, F. Beeler, O. Jepsen, O. Gunnarsson, O.K. Andersen, G.B. Bachelet, J. Electron. Mater. 14 (1985) 45.
[11] H. Born, P. Thurnian, T.P. Surkova, A. Hoffmann, W. Busse, H.-E. Gumlich, I. Broser, W. Giriat, J. Crystal Growth 184/185 (1998) 1132.
[12] T.P. Surkova, W. Giriat, M. Godlewski, P. Kaczor, M. Surma, S.A. Permogorov, L.N. Tenishev, Mater. Sci. Forum 196–201 (1995) 749.
[13] S. Lankes, T. Reisinger, B. Hahn, C. Meier, M. Meier, W. Gebhardt, J. Crystal Growth 159 (1996) 480.

ELSEVIER

Physica B 273–274 (1999) 852–855

PHYSICA B

www.elsevier.com/locate/physb

NMR study of bistable defects under in situ illumination

M. Shroyer[a], J.K. Furdyna[b], A.I. Ryskin[c], W.W. Warren, Jr[a,*]

[a]*Department of Physics, Oregon State University, Weniger Hall 301, Corvallis, OR 97331-6507, USA*
[b]*Department of Physics, University of Notre Dame, Notre Dame, IN 46556, USA*
[c]*S.I. Vavilov State Optical Institute, 199034, St. Petersburg, Russia*

Abstract

We report nuclear magnetic resonance (NMR) measurements with in situ optical excitation of metastable defects in CdTe : In, CdTe : Ga, and CdF_2 : In. ^{113}Cd nuclear spin–lattice relaxation rates ($1/T_1$) in CdTe : In are about two orders of magnitude greater than in undoped CdTe, while relaxation rates in CdTe : Ga are indistinguishable from those in the undoped material. These results are consistent with the known doping properties of these impurities. Under illumination at 31 K, a *non-persistent*, order-of-magnitude enhancement of the ^{113}Cd relaxation rate is observed. After illumination, the rate is *persistently* enhanced by about 50%. The ^{113}Cd relaxation rates in CdF_2 : In are strongly temperature-dependent as a result of interactions with thermally generated free carriers. This process is ineffective for ^{19}F. The temperature dependence of the ^{113}Cd rate yields an activation energy $\Delta E = 185 \pm 10$ meV. Below 77 K, the value of $1/T_1$ becomes independent of temperature. Under illumination, this rate is enhanced *persistently* by about a factor of two. These effects can be explained in terms of the "negative-U" DX model of bistability in these materials.

Keywords: Bistability; Nuclear magnetic resonance; Persistent photo-effects

1. Introduction

Group III impurities in II–VI compounds and CdF_2 provide fascinating examples of bistable and metastable defects. The carrier concentrations in gallium-doped CdTe-based materials, for example, are typically many orders of magnitude lower than the dopant concentration. It has been proposed that self-compensation is due to formation of DX-like deep centers [1]. Carriers can by excited optically into metastable states yielding persistent photoconductivity at low temperatures in these materials [2]. In contrast, indium is a more effective dopant and carrier concentrations on the order of 10^{18} cm^{-3} have been achieved [3,4].

Similarly, gallium or indium dopants in CdF_2 exhibit bistability that results in a strong photo-refractive effect. Bistability in this system has also been attributed to a "negative U" DX model [5–7], a particularly interesting result in this highly ionic material. The photo-refractive effect persists below approximately 80 K for indium and 200 K for gallium. These materials are of interest for potential holographic optical storage applications [8].

In this paper we describe a series of nuclear magnetic resonance (NMR) experiments that focus on the electronic excitations and bistability of group III dopants in CdTe and CdF_2. These studies exploit the highly local chemical specificity with which NMR characterizes atomic environments. We have emphasized investigation of the nuclear spin–lattice relaxation rates. These rates are strongly affected by interactions between the nuclear spins and the spins of localized paramagnetic centers or itinerant carriers in the conduction bands of the materials. Under in situ white-light illumination, we observe the effects on the nuclear environment of optically-induced changes of the electronic configuration of the impurities. Specifically, we report nuclear spin–lattice relaxation rates for ^{113}Cd and ^{19}F in various samples of group III-doped CdTe and CdF_2 over the temperature range 20 to 470 K. The effect of white-light illumination

* Corresponding author. Tel.: + 1-541-737-4631; fax: + 1-541-737-1683.
E-mail address: wwarren@physics.orst.edu (W.W. Warren Jr)

0921-4526/99/$ - see front matter
PII: S0921-4526(99)00520-7

on the relaxation rates was measured in the lower temperature ranges.

2. Experimental details

^{113}Cd and ^{19}F NMR spectra and spin–lattice relaxation rates were obtained in an 8 T magnetic field with a Chemagnetics/Varian CMX-360 spectrometer. Our homemade low temperature ($T < 150$ K) NMR probe incorporated a quartz light pipe to permit in situ illumination of the sample during NMR measurements. The light source was a tungsten filament lamp. The NMR probe was cooled by a He gas flow system operating an Oxford CF1200 Cryostat. Depending on the magnitude of the spin–lattice relaxation rates, these were measured by either the inversion-recovery or the saturation-recovery method. In most cases, the signal recovery could be fitted to a single exponential yielding a time constant, T_1.

For these experiments, samples were obtained from three sources. Nominally undoped CdTe powder of purity 99.999% was obtained from Johnson Matthey Electronics. Single crystals of CdTe : Ga ($\approx 10^{19}$ Ga/cm^3) and CdTe : In ($\approx 10^{19}$ In/cm^3) were prepared at Notre Dame University. Single crystals of semiconducting CdF_2 : In (3.5×10^{18} In/cm^3) were prepared in St. Petersburg as described previously [8].

3. Experimental results

3.1. ^{113}Cd relaxation in CdTe : In and CdTe : Ga

Nuclear spin-lattice relaxation rates ($1/T_1$) of ^{113}Cd are plotted against reciprocal temperature in Fig. 1 for CdTe : Ga, CdTe : In and nominally undoped CdTe powder [9]. The data cover a temperature range 200–500 K. The observed rates for CdTe : Ga are essentially identical with those of the undoped powder, a result that is consistent with the low carrier density of the Ga-doped material. In contrast, the rates in CdTe : In are one to two orders of magnitude greater, reflecting the much higher carrier density in this material.

The ^{113}Cd relaxation rates in CdTe : Ga are shown for a wider temperature range in Fig. 2. At 77 K and lower temperatures, the relaxation rates were measured in the dark, under in situ illumination with white light, and again in the dark after illumination. During illumination, the relaxation rate was enhanced significantly, with the enhancement increasing with decreasing temperature. At 31 K the rate increased by more than an order of magnitude during illumination. We have determined that this effect is not due to heating of the sample during illumination and have established an upper limit of about 2 K for any temperature increase from this source. At 31 K where the background (dark) relaxation is the weakest, a

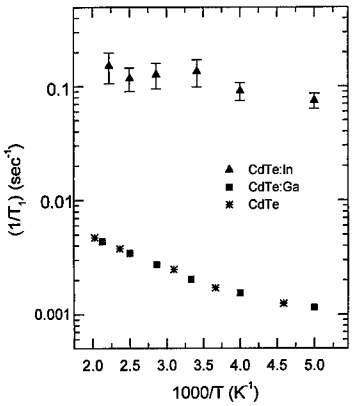

Fig. 1. ^{113}Cd spin–lattice relaxation rates versus reciprocal temperature for CdTe, CdTe : In, and CdTe : Ga.

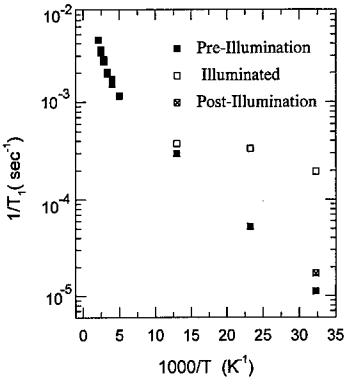

Fig. 2. ^{113}Cd spin–lattice relaxation rates versus reciprocal temperature for CdTe : Ga measured before illumination, under illumination, and after illumination.

persistent enhancement of the relaxation rate by about 50% remained after illumination was removed.

3.2. ^{113}Cd and ^{19}F relaxation in CdF_2 : In

^{113}Cd relaxation rates in CdF_2 : In are plotted against reciprocal temperature in Fig. 3 for a temperature range 25–470 K. In the high-temperature range (100–470 K), the relaxation is strongly temperature-dependent, increasing by nearly five orders of magnitude over this range. At lower temperatures (25–50 K), the rate is independent of temperature within the experimental resolution. After white-light illumination, the rates increased by a factor between two and three. This post-illumination effect persisted on the experimental time scale of several hours or until the sample was heated to temperatures in the range roughly 50–100 K. At these temperatures the post-illumination enhancement diminishes and just above 100 K the pre- and post-illumination relaxation rates become indistinguishable.

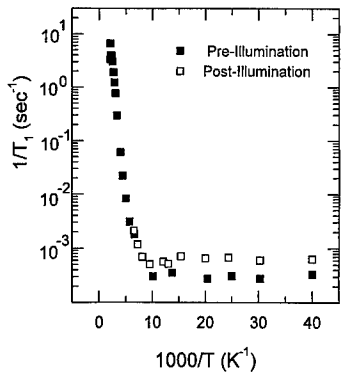

Fig. 3. ^{113}Cd spin–lattice relaxation rate versus reciprocal temperature before and after illumination in CdF_2 : In.

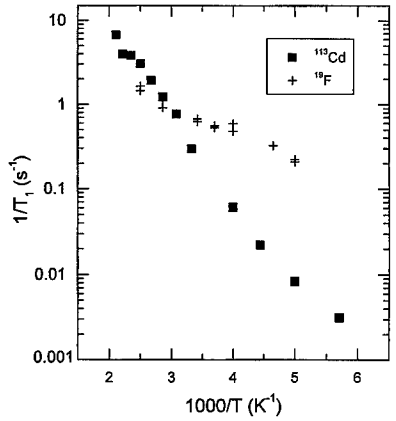

Fig. 4. ^{113}Cd and ^{19}F spin–lattice relaxation rates versus reciprocal temperature in CdF_2 : In.

We have also measured the ^{19}F relaxation rates in CdF_2 : In in the higher temperature range (200–500 K). These data are presented in Fig. 4 and compared with the ^{113}Cd rates in the same temperature range. Although the magnitudes of the rates are comparable, it is clear that ^{19}F does not share the same strong temperature dependence as ^{113}Cd in this temperature range. However, because of the much larger nuclear dipole moment of ^{19}F ($\mu_{19}/\mu_{113} = 4.2$) and the fact that the relaxation rates are proportional to the square of this quantity, the local field fluctuations experienced by ^{19}F are, in fact, much weaker than those at the cadmium sites. Relaxation of ^{19}F thus proceeds by a different mechanism than ^{113}Cd.

4. Discussion

4.1. CdTe

Indium impurities are shallow donors in CdTe. The doping effectiveness of indium compared with gallium is clearly indicated by the strongly enhanced nuclear spin–lattice relaxation rates of CdTe : In shown in Fig. 1. We attribute this relatively strong relaxation to dynamic interactions of ^{113}Cd nuclear dipole moments with the fluctuating local magnetic hyperfine fields produced by conduction electrons. The theory for this relaxation mechanism is well established; the relaxation rate is given by the following expression [10]:

$$\frac{1}{T_1} = \frac{64}{9}\pi N|\Psi(\mathrm{Cd})|^4\gamma_e^2\gamma_n^2\left(\frac{m^3kT}{2\pi}\right)^{1/2} \quad (1)$$

where N is the carrier (electron) density, $|\Psi(\mathrm{Cd})|^2$ is the conduction electron probability density at a cadmium nucleus, and γ_e and γ_{113} are, respectively, the electronic and nuclear gyromagnetic ratios. For the sample investigated, $N = 3.5\times10^{17}\,\mathrm{cm}^{-3}$ and is independent of temperature. The magnitude of the observed relaxation corresponds to a value $|\Psi(\mathrm{Cd})|^2 = 6.0\times10^{25}\,\mathrm{cm}^{-3}$ for the electronic probability density. This is a reasonable value for the hyperfine coupling of s-electrons to cadmium [11].

The electron concentration in our CdTe : Ga sample is only $2.5\times10^{15}\,\mathrm{cm}^{-3}$. At this level, there are too few conduction electrons to compete effectively with a background process which we believe to be associated with incidental paramagnetic impurities such as Mn^{2+}. Thus, essentially identical rates are observed in undoped CdTe and in CdTe : Ga (Fig. 1).

The ineffective doping behavior of gallium in CdTe-based materials has been attributed to formation of DX centers by the reaction $2d^0 \rightarrow DX^- + d^+$ in which the doubly occupied impurity DX^- is stabilized by a compensating lattice relaxation [1]. In alloys containing a few percent Zn or Mn, the impurity complex is transformed under illumination to a shallow donor leading to persistent photoconductivity at low temperatures [2]. Relaxation of electrons to the DX^- ground state is inhibited by a vibronic barrier. The strong *non-persistent* relaxation enhancement we observe in CdTe : Ga at low temperatures (Fig. 2) suggests relaxation by a steady-state density of conduction electrons maintained in the range $10^{15} - 10^{16}\,\mathrm{cm}^{-3}$ during illumination. The smaller effect we observe after illumination at 31 K reveals that a weak vibronic barrier is present even in material containing relatively low concentrations of Mn. Because they are localized, these "frozen out" shallow donor states are much less effective than conduction electrons in relaxing ^{113}Cd nuclei, most of which are located well away from the impurity.

4.2. CdF_2

The strength and temperature dependence of the ^{113}Cd relaxation rate above 100 K in CdF_2 : In suggest

that this relaxation is due to thermally generated conduction electrons. The magnitude, for example, is several orders of magnitude greater than we have observed in undoped CdF_2. The temperature dependence can be analyzed by fitting the data to the dependence $1/T_1 \propto e^{-\Delta/kT} T^{1/2}$ implied by Eq. (1). This procedure yields a value $\Delta = 185 \pm 10$ meV; we interpret this as the binding energy of the DX^- center. This value is slightly smaller than various previous estimates of the binding energy $E_b \approx 250$ meV [12–14]. A value of $|\Psi(Cd)|^2$ comparable with that inferred for CdTe : In would imply, according to Eq. (1), a carrier concentration $N \approx 1 \times 10^{17}\,cm^{-3}$ at room temperature. This is probably an overestimate since $|\Psi(Cd)|^2$ can be expected to be somewhat larger in the more ionic CdF_2. As discussed in Section 2, the ^{19}F relaxation rates, corrected for the difference in nuclear dipole moments, indicate that the ^{19}F relax by an independent and intrinsically weaker mechanism than ^{113}Cd. This is consistent with the expected predominantly Cd s-character of the conduction electron wave functions and correspondingly small values of $|\Psi(F)|^2$.

The weak, temperature-independent relaxation observed in the dark at low temperatures is characteristic of relaxation by incidental paramagnetic impurities, in this material mainly Mn^{2+} [15]. In this mode of nuclear relaxation, bulk nuclei far from the impurity couple to the electron spin of the impurity by nuclear spin diffusion [16].

Illumination at low temperatures leads to additional persistent nuclear relaxation with a magnitude and temperature dependence similar to the background impurity process. We attribute this additional relaxation to optically generated shallow donor states d^0, i.e. $In^{3+} + e^-$ where the electron is localized in a hydrogenic state. Similar effects have been detected previously in photo-EPR and photo-magnetism experiments [5,15,17]. The effectiveness of the shallow donors is roughly equal to that of the paramagnetic Mn^{2+} impurities whose concentration is known to be $4.1 \times 10^{17}\,Mn/cm^3$ in our sample.

Acknowledgements

This work was support by the U.S. National Science Foundation, grant DMR 96-23299.

References

[1] C.H. Park, D.J. Chadi, Phys. Rev. B 52 (1995) 11884.
[2] See, for example, N.G. Semaltianos et al., Phys. Rev. B 51 (1995) 17499.
[3] F. Bassani et al., J. Appl. Phys. 72 (1992) 2927.
[4] F. Bassani et al., Appl. Phys. Lett. 58 (1991) 2651.
[5] S.A. Kazanskii, A.I. Ryskin, V.V. Romanov, Appl. Phys. Lett. 70 (1997) 1272.
[6] A.I. Ryskin et al., Phys. Rev. Lett. 80 (1998) 2949.
[7] C.H. Park, D.J. Chadi, Phys. Rev. Lett. 82 (1999) 113.
[8] A.I. Ryskin, Appl. Phys. Lett. 67 (1995) 31.
[9] A. Göbel, Thesis Oregon State University, 1994.
[10] A. Abragam, Principles of Nuclear Magnetism, Oxford, London, 1961, p. 390.
[11] G.C. Carter, L.H. Bennett, D.J. Kahan, Metallic Shifts in NMR, Pergamon, London, 1977, pp. 8–10.
[12] J.M. Langer, Rev. Solid State Sci. 4 (1990) 297.
[13] J.E. Dmochowski et al., Phys. Rev. Lett. 56 (1986) 1735.
[14] U. Piekara, J.M. Langer, B. Krukowska-Fulde, Solid State Commun. 23 (1977) 583.
[15] Z. Wilamowski, J. Dmochowski, W. Jantsch, Mater. Sci. Forum 258–263 (1997).
[16] H.E. Rorschach Jr, Physica 30 (1964) 38.
[17] J.M. Langer, Mater. Sci. Forum 258–263 (1997) 1449.

ELSEVIER

Physica B 273–274 (1999) 856–860

PHYSICA B

www.elsevier.com/locate/physb

Shallow doping of wide band-gap II–VI compounds

B. Reinhold[a,*], M. Wienecke[b]

[a]*Hahn-Meitner-Institut Berlin GmbH, Bereich Festkörperphysik, Glienicker Str. 100, D-14109 Berlin, Germany*
[b]*Institut für Physik, Humboldt-Universität zu Berlin, Invalidenstr.110, D-10115 Berlin, Germany*

Abstract

Using radioactive isotopes of shallow dopants (Ag, As, Rb) as well as of native or isoelectronic elements (Se, Te, Cd) which were incorporated as host atoms and then transmute into relevant dopants (transmutation doping), we investigated the doping phenomena occurring in wide band-gap II–VI compounds CdTe, ZnTe and ZnSe by the classical methods of semiconductor physics Hall effect, *C–V* and photoluminescence measurements. Thus, we could assign unambiguously defect features in electrical and photoluminescence measurements to extrinsic dopants by means of the half lives of radioactive decay. In As-doped ZnSe samples we observed two states: a metastable effective mass-like state and a deep state. The occurrence of the latter state is always linked with the high resistivity of As-doped ZnSe crystals. The transmutation doping experiments reveal, that the so-called self-compensation being typical for wide band-gap II–VI compounds can be overcome if the thermal treatment for dopant incorporation is time separated from its electrical activation, here due to transmutation at room temperature.

Keywords: II–VI-compounds; Doping; Transmutation; Compensation

1. Motivation

Wide band-gap II–VI semiconductor compounds are important materials for optoelectronics in the visible spectral region. A crucial aspect for the creation of optoelectronic devices is the efficient incorporation of the dopants relevant for the respective application. All doping phenomena are affected, and in most cases controlled by the kinds and concentrations of the intrinsic defects occurring in the material as a consequence of doping and thermal treatments. Native defects determine the available sites on which the dopants can be incorporated, and, acting as donors or acceptors themselves, take part in the compensation processes. Additional residual impurities are involved in defect interactions in a similar way.

To investigate the properties of the relevant extrinsic and intrinsic defects, i.e. their electronic and structural features, it is necessary to combine several analyzing methods being sensitive to point defects. Thus we combined electrical measurements (Hall effect, *C–V*, DLTS), photoluminescence spectroscopy (PL) and structural (Perturbed Angular Correlation, PAC) investigations. The most reliable way of achieving assignments of measured features to specific kinds of dopant incorporation is to apply the method of nuclear transmutation process. Using the half lives as fingerprints, dopant atoms involved in the relevant centers can be unambiguous identified. Therefore we implanted besides stable elements radioactive isotopes of dopants decaying into inactive centers. On the other hand, we implanted radioactive isotopes of native or isoelectronic elements to incorporate them as host atoms at the desired lattice sites under defined annealing conditions and then we observed the electrical activation via radioactive decay at room temperature. The aim of these experiments is to understand the compensation phenomena typically occur due to doping of wide-gap II–VI compounds.

2. Experimental details

The experiments were performed with II–VI-bulk materials grown from the melt by the vertical Bridgman technique at the department of physics at the Humboldt

* Corresponding author. Fax: + 49-30-8062-2293.
E-mail address: reinhold@hmi.de (B. Reinhold)

0921-4526/99/$ - see front matter
PII: S0921-4526(99)00524-4

Table 1
Used isotopes for doping II–VI-materials

Isotope	Half-life $T_{1/2}$	Dose (cm^{-2})	Material
$^{73}Se \rightarrow As \rightarrow Ge$	80.3d	1 E 12	ZnSe
$^{75}Se \rightarrow As$	118.5d	2 E 11	ZnSe
$^{85}Sr \rightarrow Rb$	64.8d	1 E 10	ZnSe
$^{107}Cd \rightarrow Ag$	6.50h	1 E 12	CdTe, ZnSe
$^{115}Cd^{a} \rightarrow In$	44.8d (m) 53.4h (g)	1 E 12	CdTe, ZnTe

[a]Mixture of ground state g and metastable m isotopes.

University of Berlin (CdTe) or grown from the vapor phase by the Markov method and commercially purchased by CRYSTAL GmbH Berlin (ZnTe, ZnSe).

The deviation from stoichiometry was adjusted by a thermal treatment [1] to prepare a defined state of intrinsic point defect density. Prior to implantation the bulk samples ($5 \times 5 \times 1$ mm^3) were mechanically and chemically polished to remove any preparation damage.

The crystals were implanted at the isotope separator ISOLDE at CERN, Geneva [2]. The implantation energy was 60 or 260 keV. The isotopes used are listed in Table 1. The dose limits are given by the yield of the separator and the radioactivity limit for safe handling the samples. Depending on the mass of the implanted isotopes the expected implantation depths were between 22 and 28 nm for 60 keV and between 93 and 101 nm for 260 keV implantation, respectively (TRIM computer simulation [3]).

After implantation a thermal treatment was performed again, under metal- or chalcogen-rich conditions, to anneal the radiation damage and to reproduce the initial non-stoichiometry state of the samples. This annealing procedure had to be optimized to ensure a drive-in diffusion in order to adjust doping depths and concentration profiles as a basis for getting reliable information from the measurements carried out afterwards. Particular for the PL measurements we needed doping profiles of up to 10^{17}cm^{-3} in a depth up to 800 nm. Thus, the diffusion study was an important precondition for the following doping studies. Therefore, γ-spectroscopic investigation of the diffusion phenomena was performed by classical radio tracer sectioning. These experiments are described elsewhere [4]. Using ^{111m}Cd isotopes as probes, the occupation of unperturbed lattice sites was studied by perturbed angular correlation (PAC). This was published in Ref. [5]. A description of C–V measurements and Hall and resistivity investigations by the van der Pauw method is given in Refs. [4,6].

3. Results and discussion

Summarizing the results of the pre-investigation on incorporation and diffusion we have found that Te, Se, and As isotopes are incorporated on chalcogen lattice sites and Cd and Rb occupy sites in the metal sublattice [4]. This reflects as already known from literature that in II–VI compounds due to the high ionicity no amorphization occurs [7,8], i.e. most of the implants occupy lattice sites, and the recoil energy by transmutation is low compared to the displacement energy in this material group (see Table 2). Furthermore, the knowledge of the diffusion constants can be used to adjust the concentration and depth distribution by a proper choice of annealing parameters. These results are the basis of the following transmutation doping experiments.

By electrical measurements we could show that relevant dopants incorporated by transmutation from host isotopes act as highly effective shallow acceptors or donors, respectively. In CdTe we obtained a p-carrier concentration of 10^{17} cm^{-3} after transmutation from ^{107}Cd into Ag as expected according to the implanted dose, i.e. a 100% doping efficiency in contrast to any conventional doping techniques, whereby always autocompensation occurs [10,11]. Time-dependent measurements showed that the doping increased exactly with the half life of the radioactive decay, i.e. the transmutation occurs without any detectable compensation and distortion of the local structure by the recoil energy (Table 2) [6]. We could recently show by the assignment of the Ag bound exciton in time-dependent PL measurements too that Ag incorporated at Cd lattice site acts as shallow acceptor [12].

An 100% doping efficiency was found also in CdTe and ZnTe doped with In by transmutation of ^{115}Cd. Here the In donors compensate the p-type conductivity (about 10^{17} cm^{-3}) in bulk materials, and the samples became highly resistive [6].

Transmutation experiments were also performed on ZnSe, concentrating on acceptor dopants that do not form effective acceptors in conventional doping experiments. In time-dependent Hall effect measurements on samples implanted with $^{107}Cd \rightarrow Ag$ we obtained a decreasing n-type conductivity with exactly the half life of the radioactive decay (6.5 h). This is interpreted as caused by Ag acceptors compensating the n-type ZnSe. Finally, the sample became highly resistive.

The challenge was to observe the acceptor doping in ZnSe. This material is known for the impossibility of

Table 2
Comparison of displacement energies in II–VI compounds (after Watkins [9]) with the recoil energies calculated for the respective isotopes

	Metal sublattice			Chalcogen sublattice		
	Displacement energy (eV)	Isotope	Recoil energy (eV)	Displacement energy (eV)	Isotope	Recoil energy (eV)
CdTe	5.6–8.9	^{107}Cd(Ag)	8.8	5.0–7.8	—	—
		^{111}Ag(Cd)	5.11	—	—	—
ZnTe	4.2–13.1	^{115}Cd(In)	5.75	2.1–6.7	—	—
ZnSe	7.6–10.0	^{85}Sr(Rb)	1.91	6.2–8.2	^{73}As(Ge)	0.57
					^{75}Se(As)	1.54

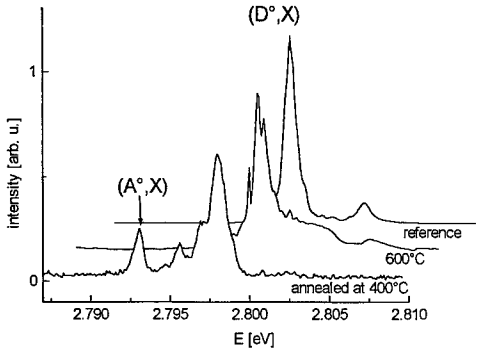

Fig. 1. Photoluminescence spectra of As-implanted ZnSe after two different annealing steps.

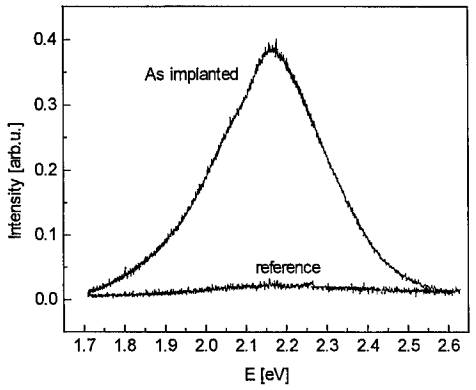

Fig. 2. Deep level in ZnSe after As-implantation, annealed at 600°C, for comparison an undoped reference is shown.

p-type doping by conventional methods. Particularly, the experiments done with ^{73}As in ZnSe turned out to be very instructive characterizing the compensation process: For these experiments we implanted ^{73}Se but annealed the samples only when most isotopes had been transmuted into As. Thus these experiments are comparable to our investigations performed with stable As. After implantation of As as stable element and an annealing procedure at 400°C, we observed an acceptor-bound exciton peak at 2.7931 eV in PL spectroscopy (Fig. 1). This peak disappears after annealing at temperatures above 600°C, and a weak deeper level at 2.16 eV was observed instead (Fig. 2). Here, a conflict arises between the need of using higher temperatures to anneal the radiation damage and the thermally induced disappearance of the shallow acceptor level. According to a theoretical work of Chadi [13,14], there are two possible states of As in ZnSe: a metastable shallow one, and a deep stable state. The second is characterized by a large lattice relaxation. The use of the radioactive ^{73}As isotope enables us to demonstrate the accordance of the observed two levels to the described states for As impurity via the characteristic radioactive decay time. The half life of the ^{73}As isotope is 80.3 days. Recording PL spectra right after implantation we found both, the shallow acceptor

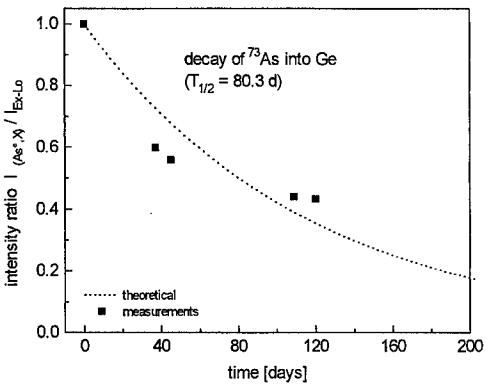

Fig. 3. Normalized intensity of the A^0,X line at 2.7931 eV (see text) versus time.

and the deep level. For the shallow level we observed a decreasing intensity in accordance to the decreasing As concentration in the crystal due to the radioactive decay of the implanted isotopes. This time-dependent decreasing is shown in Fig. 3. Obviously, the time dependence of the (A^0,X) line (normalized) can be well fitted with the

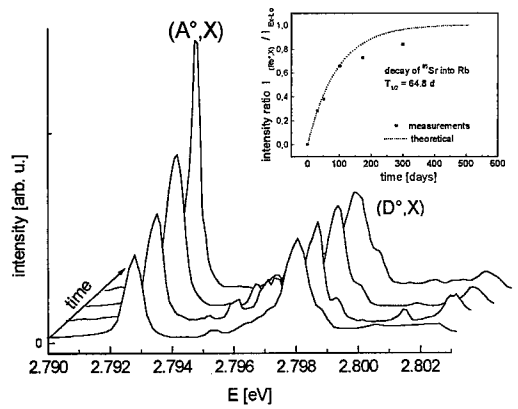

Fig. 4. Photoluminescence spectra of a ^{85}Sr implanted sample, ^{85}Sr decays into Rb ($t_{1/2}$ = 64.8 d), the inset shows the normalized intensities of the (A°,X) line at 2.7928 eV versus time.

half-life of ^{73}As decaying to Ge, which leads us to assign this line to the As acceptor. The weak deep level vanished too and was not detectable after one-and-a-half half lives of the isotope, indicating that the deep center contains the dopant As too, and is not, however, a thermal or implantation damage. Samples doped with As (stable or unstable) are always very high resistive.

Electrical measurements were carried out on crystals implanted with the ^{75}Se isotope as a host atom. The Se isotope was incorporated on lattice site, and after the decay of the Se into the As acceptor we detected a p-type conductivity. The p-carrier concentration of 10^{15} cm^{-3} agrees with the implanted dose of the Se isotope. Since these samples do not show the deep luminescence band we think that this deep center assigned by radioactive decay to a defect containing As is linked with the compensation process. Thus, we have an experimental evidence for the model theoretically proposed by Chadi [13].

Fig. 4 shows PL-spectra of ZnSe implanted with ^{85}Sr → Rb at several times after implantation. Unambiguously an acceptor bound exciton (A^0,X) at 2.7927 eV can be correlated to the Rb acceptors formed by radioactive decay from ^{85}Sr, which was incorporated as isoelectronic element on metal lattice sites. These samples show a p-type conductivity too in accordance to the implanted dose. The hole concentrations (p) achieved are relatively small due to the low yields available for those special radioactive ion beams. Nevertheless, these experiments reveal that As and Rb act as efficient acceptors in ZnSe. This has been concluded from photoluminescence investigations in the literature [15] but has not been demonstrated by electrical measurements until now.

4. Summary

From implantation and diffusion experiments on host or isoelectronic elements annealing conditions were derived in order to remove the implantation damage to a large extent and to achieve a well-defined incorporation. This is the proper starting point for the transmutation doping experiments. By transmutation experiments, relevant dopants, such as Ag, As, Rb and In are shown to act as highly efficient acceptors and donors, respectively, if they are incorporated undisturbed at the certain lattice sites in the metal or chalcogen sublattice. This implies that the main reason for inefficiency of conventional doping techniques like ionimplantation, diffusion or during crystal growth are defect reactions at high-temperature processes, which here are avoided if host elements are incorporated and then transmute into relevant dopants at room temperature. Thus, we reached for CdTe an uncompensated p-type carrier concentration up to 10^{17} cm^{-3} in contrast to any conventional Ag doping techniques. In As-doped ZnSe samples we observe two states: a metastable effective mass like state and a deep state. The occurrence of the latter state is always linked with the high resistivity of As-doped ZnSe crystals. The use of the radioactive ^{75}Se isotope, and their transmutation into the As acceptor at room temperature, enables us to avoid the formation of the deep state, and thus we achieve a doping efficiency of 100%. For As and Rb doping of ZnSe, we could show that they act as highly effective shallow acceptors. However, only low densities were investigated aiming at the comprehension of the compensation phenomenon model.

Our experiments revealed that the combination of classic techniques of semiconductor physics with the use of radioactive isotopes is a powerful tool to study the defects occurring due to doping and give considerable insight into the nature of defect interaction.

Acknowledgements

We thank Doris Forkel-Wirth and Angela Burchard for the helpful assistance and the ISOLDE-team for a good service during the beam times. Further it is a pleasure thanking all the collaborators in Berlin and Jena. This work was funded by the German Federal Ministry for Research and Technology (BMBF) under project number 03-HE5HUB-7.

References

[1] M. Wienecke, H. Berger, M. Schenk, Mater. Sci. Eng. B 16 (1993) 219.
[2] E. Kugler, D. Fiander, B. Jonson, H. Haas, A. Przwloka, H.L. Ravn, D.J. Simon, K. Zimmer, Nucl. Instr. and Meth. B 70 (1992) 41.
[3] J.F. Ziegler, J.P. Biersack, U. Littmark, The Stopping and Range of Ions in Solids, Pergamon, New York, 1985.

[4] M. Wienecke, B. Reinhold, J. Röhrich, J. Bollmann, N. Achtziger, U. Reislöhner, W. Witthuhn, S. Hermann, J. Phys. D: Appl. Phys. 32 (1999) 291.
[5] N. Achtziger, J. Bollmann, Th. Licht, B. Reinhold, U. Reislöhner, J. Röhrich, M. Rüb, M. Wienecke, W. Witthuhn, ISOLDE collaboration, Semicond. Sci. Technol. 11 (1996) 947.
[6] M. Wienecke, J. Bollmann, J. Röhrich, K. Maass, B. Reinhold, D. Forkel-Wirth, J. Crystal Growth 161 (1996) 82.
[7] H.M. Naguib, R. Kelly, Radiat. Effects 25 (1975) 1.
[8] K.M. Yu, E.D. Bourret-Courchesne, Appl. Phys. Lett. 69 (14) (1996) 2062.
[9] G.D. Watkins, Inst. Phys. Conference Series No. 31, 1977, p. 95.
[10] H. Zimmermann, R. Boyn, C. Albers, K.W. Benz, D. Sinerius, C. Eiche, B.K. Meyer, D.M. Hoffmann, J. Crystal Growth 128 (1993) 593.
[11] J. Bollmann, M. Wienecke, J. Röhrich, H. Kerkow, J. Crystal Growth 159 (1996) 384.
[12] B. Reinhold, M. Wienecke, F. Henneberger, A. Burchard, and the ISOLDE collaboration, Phys. Stat. Sol. B 210 (1998) 459.
[13] D.J. Chadi, J. Crystal Growth 138 (1994) 925.
[14] D.J. Chadi, Appl. Phys. Lett. 59 (27) (1991) 3589.
[15] Y. Zhang, B.J. Skromme, S.M. Shibli, C. Tamargo, Phys. Rev. B 48 (15) (1993) 10885.

ELSEVIER

Physica B 273–274 (1999) 861–865

PHYSICA B

www.elsevier.com/locate/physb

The electronic structure of interstitial zinc in its two T_d sites in ZnSe

K.H. Chow, G.D. Watkins*

Department of Physics, Lehigh University, Bethlehem, PA 18015-3182, USA

Abstract

We report ODEPR measurements in ZnSe which lead to the identification of $(Zn_i)^+_{Zn}$, i.e., the interstitial zinc located at the T_d site surrounded by four Zn atoms. Its central ^{67}Zn hyperfine interaction (1425 MHz) is isotropic and is significantly larger than that previously determined for $(Zn_i)^+_{Se}$ (1088 MHz), indicating that the unpaired electron is more highly localized on $(Zn_i)^+_{Zn}$. A "point-ion" envelope wave-function analysis which also takes into account the hyperfine interaction of the ^{77}Se atoms, in conjunction with other considerations, places the second donor level $(+/++)$ position for $(Zn_i)_{Se}$ and $(Zn_i)_{Zn}$ at ~ 1.0 and 1.6 eV below the conduction band respectively, with approximate error bars of ± 0.3 eV. Our experimental results are in good agreement with state-of-the-art ab initio calculations.

Keywords: ZnSe; Interstitial zinc; Frenkel pairs; ODEPR

Initially through the use of electron paramagnetic resonance (EPR) [1] and later by using optically detected EPR (ODEPR) [2–6] via the photoluminescence (PL), it has been well-established that in situ 4.2 K irradiation of ZnSe with 2.5 MeV electrons generates a large number (≈ 25) of distinct zinc-vacancy–zinc-interstitial, i.e., Zn_i–V_{Zn}, Frenkel pairs frozen into the lattice with a wide range of intramolecular separations. In addition to these Frenkel pairs, one can also detect zinc interstitials which are so far separated from their companion vacancies that they can be considered to be *isolated* [3]. In this early work, these interstitials were unambiguously identified as located at the T_d site with four nearest-neighbor Se atoms, henceforth denoted as $(Zn_i)^+_{Se}$, through detection of weakly resolved hyperfine interactions with the central ^{67}Zn ($I = \frac{5}{2}$, 4.1% abundant) and ^{77}Se ($I = \frac{1}{2}$, 7.6% abundant) atoms in the first and third neighbor shells. At that time, a significantly weaker co-existing signal with slightly larger g value, labelled X, was also observed which was *tentatively* identifed as $(Zn_i)^+_{Zn}$, where now the Zn_i^+ ion is located at the other T_d site surrounded by four Zn atoms. Recently, we have discovered that optical excitation, even at cryogenic temperatures, can efficiently convert between the $(Zn_i)^+_{Se}$ and X configurations in essentially a 1:1 fashion [7–9]. By capitalizing on our ability to selectively generate a strong X signal, we can now perform a detailed investigation of its electronic structure.

The results of these experiments are the subject of the current paper. These studies unambiguously confirm that X is indeed $(Zn_i)^+_{Zn}$ and also enable us to estimate the $(Zn_i)_{Zn}$ second donor $(+/++)$ level position in the band gap. These results, in addition to analogous ones made previously for $(Zn_i)^+_{Se}$, are then compared with state-of-the-art ab initio calculations.

The experiments were performed at 20 GHz in an EPR spectrometer capable of in situ 4.2 K electron irradiation with 2.5 MeV electrons from a Van de Graaf generator. The sample investigated was an as-grown high-resistivity ZnSe crystal supplied by Manuel Aven at G.E. Research and Development Center which we irradiated to a fluence of $\sim 1.5 \times 10^{17}/cm^2$ at 4.2 K. Subsequent ODEPR experiments at 1.5 K (pumped liquid helium temperatures) were accomplished by inserting a capillary tube, through which was threaded an optical fiber, into the

* Corresponding author. Tel.: +1-610-758-3961; fax: +1-610-758-4561.

E-mail address: gdw0@lehigh.edu (G.D. Watkins)

0921-4526/99/$ - see front matter
PII: S0921-4526(99)00525-6

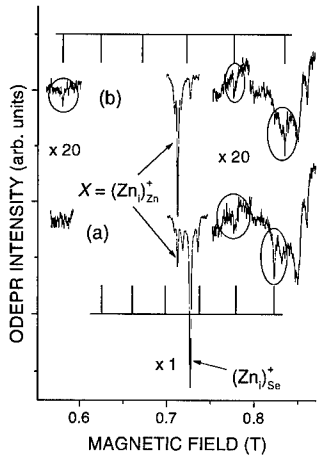

Fig. 1. The ODEPR spectra of the isolated zinc interstitials $(Zn_i)^+_{Se}$ and $X = (Zn_i)^+_{Zn}$ with $\boldsymbol{B}\|\langle 1\,0\,0\rangle$. (a) After anneal at 25 K in the dark, the $(Zn_i)^+_{Se}$ signal is dominant. (b) After 458 nm illumination at 25 K, the $X = (Zn_i)^+_{Zn}$ signal dominates. In both (a) and (b), observed satellites arising from hyperfine interaction with the central Zn_i ion are circled. Also shown for comparison are the theoretically predicted positions for all of the satellites, calculated using the relevant ^{67}Zn hyperfine parameters listed in Table 1.

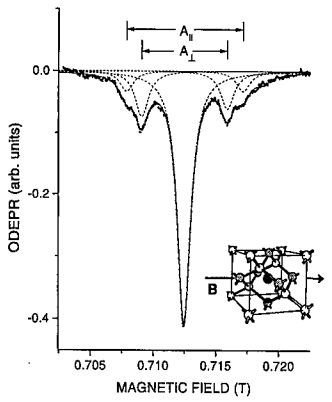

Fig. 2. The central $X = (Zn_i)^+_{Zn}$ ODEPR signal with $\boldsymbol{B}\|\langle 1\,0\,0\rangle$. The shoulders are due to the Se shell at second nearest-neighbor positions, as indicated by the darkened atoms in the inset. The solid line is a fit of the data assuming identical Lorentzian line shapes for the central and satellite lines. The dashed curves show the contributions of each individual line.

TE_{011} microwave cavity. The excitation of 458 nm was supplied by an argon ion laser through the fiber while the capillary served as a light guide for the PL, which was detected by a silicon EG&G 250 UV detector. The microwave power was on/off modulated at various audio frequencies, and synchronous changes in the PL were monitored with a lock-in detector (more details of the setup can be found in Ref. [5]).

In Fig. 1, we show the $(Zn_i)^+_{Se}$ and X PLODEPR signals. Let us first concentrate on the isolated interstitial $(Zn_i)^+_{Se}$ signal, as shown in Fig. 1a. It is negative and arises from a shallow donor ($\mathscr{D}$) to Zn_i^+ recombination, $Zn_i^+ + \mathscr{D}^0 \rightarrow Zn_i^0 + \mathscr{D}^+$, which competes with the 625 nm shallow donor to deep acceptor ($\mathscr{A}$) recombination luminescence being monitored, $\mathscr{A}^0 + \mathscr{D}^0 \rightarrow \mathscr{A}^- + \mathscr{D}^+ + h\nu$. Two of the six ^{67}Zn hyperfine satellites can be seen in Fig. 1a, corresponding exactly with the calculated positions using the previously measured isotropic hyperfine parameter of 1088 MHz for the central ^{67}Zn atom [3]. Note that the X signal can be seen in Fig. 1a also, but is significantly weaker than the main $(Zn_i)^+_{Se}$ line.

An anneal of the sample to 25 K in the dark has no effect on the $(Zn_i)^+_{Se}$ signal. However, as shown in Fig. 1b, if the sample is illuminated with visible light (458 nm) at 25 K, followed by rapid cooldown to 4.2 K, the X signal becomes dominant while the $(Zn_i)^+_{Se}$ signal decreases in proportion. Note that the two ^{67}Zn hyperfine satellites associated with $(Zn_i)^+_{Se}$ have decreased in size while three new satellites have appeared.[1] Furthermore, a closer examination of the X central line reveals that there is structure on its shoulders, as shown in the expanded magnetic field scale of Fig. 2. As in the case of $(Zn_i)^+_{Se}$, the positions of the central line, its shoulders, and its satellites can be fit by the $S = \frac{1}{2}$ spin Hamiltonian

$$\mathscr{H} = g\mu_B \mathrm{B}\cdot\boldsymbol{S} + \sum_j \boldsymbol{I}_j\cdot\boldsymbol{A}_j\cdot\boldsymbol{S}, \tag{1}$$

where the first term describes the isotropic electronic Zeeman interaction in a magnetic field $\boldsymbol{B}$ and the second term describes the hyperfine interactions with the central ^{67}Zn nucleus and neighboring ^{77}Se nuclei.

The hyperfine interaction with the central ^{67}Zn nucleus produces six $(2I + 1)$ satellites, whose positions, determined from the three detected, are indicated in Fig. 1b. The interaction (1425 MHz) is isotropic, consistent with the T_d symmetry of a $(Zn_i)_{Zn}$ site. The resolved structure on the shoulders of the central line, Fig. 2, matches well with the intensities predicted for a total of six ^{77}Se nuclei. These are identified to be due to the six Se second nearest-neighbor atoms which are equidistant in each of the six $\langle 1\,0\,0\rangle$ directions from the central $(Zn_i)^+_{Zn}$ ion. Consistent with this, angular dependence studies reveal that the interaction for each has axial symmetry about its corresponding $\langle 1\,0\,0\rangle$ axis. The data in Fig. 2, which was obtained with $\boldsymbol{B}$ parallel to a $\langle 1\,0\,0\rangle$ axis, should hence be made up of contributions due to two

[1] X was periodically regenerated with the 25 K optical excitation process since it was slowly converting back to $(Zn_i)^+_{Se}$ during the many signal averaged runs at 1.5 K required to detect the weak satellite structure.

Table 1
Experimental spin Hamiltonian parameters for isolated Zn_i^+ at the two interstitial T_d sites in ZnSe, compared with estimates from theory. The numbers in parentheses represent the error estimates in the last digit of each entry. The hyperfine parameters are given in MHz

$(Zn_i)^+_{Se}$			$X = (Zn_i)^+_{Zn}$		
	Expt[a]	Theory		Expt	Theory
g	1.9964(4)			2.0064(5)	
$a(^{67}Zn)$	1088(15)	1078[b], 1067[c]	$a(^{67}Zn)$	1425(8)	1252[b], 1739[c]
$a(^{77}Se)_{1NN}$	481(3)	736[b], 355[c]			
$b(^{77}Se)_{1NN}$	17(3)	11[b], 17[c]			
			$a(^{77}Se)_{2NN}$	215(3)	354[b], 227[c]
			$b(^{77}Se)_{2NN}$	23(2)	20.1[c]
$a(^{77}Se)_{3NN}$	37(3)	55[b]			

[a]Ref. [5].
[b]Ref. [13].
[c]Ref. [14].

equivalent nuclei with effective hyperfine interaction $A_\parallel$ and four equivalent nuclei with effective interaction $A_\perp$. This is indeed confirmed by the relative intensity of the shoulders compared to the central line where the indicated match in the figure corresponds to two and four equivalent nuclei being responsible for $A_\parallel$ and $A_\perp$, respectively. In contrast to $(Zn_i)^+_{Se}$, no additional structure is seen on the central line itself, which is narrower, indicating relatively weaker hyperfine interaction at the fourth, and more distant neighbor ^{77}Se shells.

These results demonstrate unambiguously therefore that, as tentatively suggested in previous work [3,5], the so-called X center is indeed $(Zn_i)^+_{Zn}$, the interstitial zinc atom located at the T_d site surrounded by four nearest-neighbor Zn atoms. The relevant parameters are summarized in Table 1, which also includes for comparison the previous experimental data on $(Zn_i)^+_{Se}$. We use the notation a and b to denote the isotropic and anisotropic parts respectively where $a = (A_\parallel + 2A_\perp)/3$ and $b = (A_\parallel - A_\perp)/3$. (Since the central ^{67}Zn hyperfine interaction is isotropic, only the parameter a is required for it.)

The central $^{67}(Zn_i)^+_{Zn}$ hyperfine interaction is 31% greater than that for $^{67}(Zn_i)^+_{Se}$ indicating that the unpaired electron is more highly localized on the former, and that its corresponding second donor level $(+/++)$ is therefore deeper in the gap. This can be quantified through a point-ion analysis, as was previously done [5] for $(Zn_i)^+_{Se}$, which utilizes both the central ^{67}Zn and neighboring ^{77}Se hyperfine parameters to estimate the electron's binding energy to the interstitial, and hence its level position below the conduction band edge.

In this approach, the electron is assumed to be bound in a spherically symmetric envelope function $\Phi(r)$ which, in turn, is orthogonalized to the ion cores of the lattice atoms to give the electron wave function $\psi(r)$. We are interested in obtaining $\Phi(r)$, from which we can ultimately estimate the electron's binding energy. Assuming that $\Phi(r)$ varies slowly over the extent of each of the core orbitals leads to the value for $\psi(r)$ at the position of the jth atom site, r_j, given by $\psi(r_j) \approx G_j N^2 |\Phi(r_j)|^2$. G_j can be calculated by using self-consistent Hartree–Fock functions for the free Zn^{2+} and Se^0 ions [10], and N is a normalization constant to be determined from the experimental data. The value of $|\psi(r_j)|^2$ can be estimated from the experimental isotropic part of the hyperfine constants a_j through the expression $a_j = (16\pi/3)(\mu_j/I_j)\mu_B|\psi(r_j)|^2$, where μ_j and I_j are the nuclear magnetic moment and spin of the jth nucleus while μ_B is the Bohr magneton. The results for the central zinc atom and the next neighbor Se shell for $(Zn_i)^+_{Zn}$ are plotted in Fig. 3, and are compared with the values previously determined for $(Zn_i)^+_{Se}$. For each, the straight line corresponds to a simple exponential dropoff, which, in turn, leads to a straight-forward determination of N [0.81 for $(Zn_i)^+_{Zn}$, 0.93 for $(Zn_i)^+_{Se}$], which is needed in the evaluation of $\Phi(r_j)$.

Finally, we assume that $\Phi(r_j)$ is similar to that of a $Z = 2$ hydrogenic atom in a uniform dielectric ε and furthermore, that for such a tightly bound state, the electron mass should be close to the free electron mass m. The solution is hence $\Phi_{He^+}(r) = [1/(\pi a_0^3)^{1/2}]\exp(-r/a_0)$ where the Bohr radius $a_0 = \hbar/\sqrt{2mE}$ gives the binding energy E.[2] In addition, the dielectric constant can be

[2] A more rigorous justification for this expression is to consider the Whittaker functions (see Ref. [11]) which are the correct solutions in spatial regions where a Coulomb potential is appropriate. The asymptotic form for large r is $\exp[-\sqrt{2mE}r/\hbar]$ independent of the form of the potential near the origin.

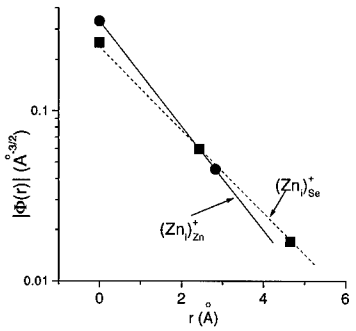

Fig. 3. The amplitude of the $\Phi(r)$ envelope wave function for $X = (Zn_i)^+_{Zn}$ (closed circles) deduced from hyperfine interactions and its corresponding fit (solid line) as described in the text. The $(Zn_i)^+_{Se}$ results from Ref. [5] are reproduced here for comparison (closed squares and dashed line).

calculated using $E = 2me^4/\varepsilon^2\hbar^2$. The slope of the straight line for $(Zn_i)^+_{Zn}$ gives $a_0 = 1.44$Å, corresponding to a binding energy of 1.8 eV and an effective dielectric constant $\varepsilon = 5.4$. (Note that as expected for a tightly bound state, ε is close to the high-frequency value $\varepsilon_\infty \sim 6$.) This result, when compared with that obtained for $(Zn_i)^+_{Se}$ by the same method of 1.2 eV, suggests that the second donor level ($+/+$) for $(Zn_i)_{Zn}$ could be as much as ~ 0.6 eV deeper than that for $(Zn_i)_{Se}$.

At this point, it is worthwhile noting that the earlier work [5] on $(Zn_i)_{Se}$ has suggested that $E_c - 0.9$ eV might be a more accurate value than $E_c - 1.2$ eV. This estimate was obtained by considering the PL energy of one of the Frenkel pairs, called X_8, whose intramolecular separation was believed to be established. If we assume that the $(Zn_i)_{Zn}$ level has been proportionally overestimated, a position of $E_c - 1.4$ eV is obtained instead of $E_c - 1.8$ eV above. Note however that recent measurements, as discussed in more detail in Ref. [9], bring up the possibility that the X_8 separation could be incorrectly assigned, which would in turn lead to different estimates of the $(Zn_i)_{Se}$ and $(Zn_i)_{Zn}$ level positions. Taking such uncertainties into account, we place the ($+/+$) levels at $E_c - 1.0$ eV and $E_c - 1.6$ eV for $(Zn_i)_{Se}$ and $(Zn_i)_{Zn}$ respectively, but with error bars of $\sim \pm 0.3$ eV.

It is of interest to compare the experimentally derived results with state-of-the-art ab initio local density calculations [12–14].[3] The theoretical hyperfine parameters have also been listed in Table 1. Note that for $(Zn_i)^+$ in both T_d sites, the agreement is excellent, leading to the conclusion that the theoretical calculations are remarkably accurate, at least for the $(Zn_i)^+$ charge states. Theoretical predictions of the level positions are also available [12], placing the ($+/+$) levels at $E_c - 1.35$ eV and $E_c - 1.79$ eV respectively for $(Zn_i)_{Se}$ and $(Zn_i)_{Zn}$. Once again, the agreement with the point-ion analysis is remarkable. However, this result is probably fortuitous. For example, theoretical uncertainties in estimating the band gap (~ 1 eV instead of 2.82 eV) could lead to substantial uncertainties in predicted level positions. Furthermore, the wave-function analysis described above may be faulty – the slope of the radial drop-off is only expected to reliably reflect the level positions for the part of the envelope wave function well-removed from the core (see foot note 2). Hence, it may be more meaningful to compare the estimates of the difference in the level positions of the two configurations instead. In this case, the agreement between theoretical calculations and the wave-function analysis, i.e., 0.44 eV versus 0.6 eV, still remains reasonable. Taken together, our results can be interpreted to provide a strong and unique confirmation of the reliability of such calculations for interstitial defects.

Finally, let us return to the optically induced conversion between X and $(Zn_i)^+_{Se}$, which we have recently demonstrated [7,8] to be occurring in both directions at low temperatures. With the current identification of X as $(Zn_i)^+_{Zn}$, it is now clearly established that we have observed the migration of interstitial zinc, and that the path taken in the one jump process is via the two T_d sites in ZnSe. This interesting observation has certain implications regarding the mechanism responsible, which are discussed in more detail in other works [8,9].

[3] The values indicated for the interstitial level positions can be derived from Ref. [12]. They were supplied to us privately by C.G. Van de Walle.

Acknowledgements

This research has been supported by the National Science Foundation Grant No. DMR-92-04114 and DMR-97-04386, and, initially, also by Office of Naval Research, Electronic Division, Grant No. N00014-94-0117.

References

[1] G.D. Watkins, Phys. Rev. Lett. 33 (1974) 223.
[2] F. Rong, G.D. Watkins, Phys. Rev. Lett. 56 (1986) 2310.
[3] F. Rong, G.D. Watkins, Phys. Rev. Lett. 58 (1987) 1486.
[4] F. Rong, W.A. Barry, J.F. Donegan, G.D. Watkins, Phys. Rev. B 37 (1988) 4329.
[5] F.C. Rong, W.A. Barry, J.F. Donegan, G.D. Watkins, Phys. Rev. B 54 (1996) 7789.
[6] W.A. Barry, G.D. Watkins, Phys. Rev. B 54 (1996) 7789.
[7] K.H. Chow, G.D. Watkins, Phys. Rev. Lett. 81 (1998) 2084.

[8] G.D. Watkins, K.H. Chow, Physica B 273–274 (1999) 7, These Proceedings.
[9] K.H. Chow, G.D. Watkins, Phys. Rev. B, 60 (1999) 8628.
[10] E. Clementi, C. Roetti, At. Data Nucl. Data Tables 14 (1974) 177.
[11] E.T. Whittaker, G.N. Watson, A Course in Modern Analysis, Cambridge University Press, Cambridge, 1952.
[12] D.B. Laks, C.G. Van de Walle, G.F. Neumark, P.E. Blöchl, S.T. Pantelides, Phys. Rev. B 45 (1992) 10965.
[13] C.G. Van de Walle, P.E. Blöchl, Phys. Rev. B 47 (1993) 4244.
[14] M. Illgner, H. Overhof, Phys. Rev. B 54 (1996) 2505.

ELSEVIER

Physica B 273–274 (1999) 866–869

PHYSICA B

www.elsevier.com/locate/physb

Ab initio study of local vibrational modes in II–VI semiconductors: ZnS : Se and ZnSe : N

K. Petzke*

Institut für Theoretische Physik, Technische Universität Berlin, Hardenbergstr. 36, D-10623 Berlin, Germany

Abstract

A parameter-free (with a single exception) method to calculate local vibrational modes from first principles is presented. It is applied to point defects in II–VI semiconductors: Se_S in ZnS shows a very pronounced fine structure, because there are six stable Se isotopes and five stable Zn isotopes. The calculated results agree very well with recent experiments. For N_{Se} in ZnSe, a recent assignment of FTIR absorption bands at 537 and 553 cm^{-1} is verified. The fine structure of the mode, which to our knowledge has not yet been observed, is calculated. © 1999 Elsevier Science B.V. All rights reserved.

Keywords: Ab initio; Local vibrational modes; Cubic ZnS; ZnS : Se; ZnSe; ZnSe : N

1. Method

The local vibrational modes are calculated in a two-step procedure: In step number one, an ab initio density-functional theory software package is used to calculate the inter-atomic force constants. In step number two, these force constants are used to calculate the vibrational modes.

For atoms closer than a cut-off radius r_{force}, individual force constants are calculated ab initio. For atoms, that are farther apart than the cut-off radius r_{force}, a long-range approximation is used, which replaces the atoms with effective point charges. These are calculated from the observed splitting of the LO and TO phonon bands at the Γ point of the undisturbed host crystal. This is the only parameter, which is not calculated ab initio.

For the atoms closer than r_{force}, the *force-constant separation approach* is used, which combines the *direct force-constant approach* introduced by Frank et al. [1] and the *planar force-constant separation approach* introduced by Wei and Chou [2].

The *direct force-constant approach* uses a large supercell. After displacing one atom slightly from its equilibrium position, density functional theory is used to calculate the resulting forces on the neighboring atoms. However, the supercell imposes a problem due to its periodicity: In reality, not only one atom is moved, but a super-lattice of atoms. Therefore, atom–atom forces cannot be calculated directly. Rather, the forces on any given atom in the supercell result from a superposition of the interaction of this atom with all the displaced atoms. However, in some systems like alkali metals, the forces decrease rapidly with increasing distance between the atoms. If the supercell is large enough, the interaction of a given atom with its closest displaced neighbor is much stronger than the interaction with the infinitely many other displaced atoms, so that they are neglected.

In addition, the harmonic approximation is applied. This allows to calculate a force constant as the quotient of the Hellmann–Feynman forces on a given atom and the amount of displacement used on the atoms, that had been moved.

The direct force-constant approach cannot be applied to semiconductors for two reasons: Due to the covalent bonds, there is no free electron gas, which efficiently screens the effects of the movement of a single ion. Therefore, the long-range interaction is much stronger than in

* Tel.: + 49-30-314-24-858; fax: + 49-30-314-23-198.
E-mail address: petzke@moldix.physik.tu-berlin.de (K. Petzke)

PII: S0921-4526(99)00526-8

alkali metals, so that larger supercells are required. In addition, semiconductors contain more valence electrons per unit cell than alkali metals. Both constraints make the direct force-constant approach impractical for semiconductors.

The *planar force-constant separation approach* uses planar force constants as an intermediate step. In this case, the supercell is large in one space direction but as small as possible in the other two. The long side is chosen long enough to reduce the effects due to the periodicity along this line below an acceptable threshold. The resulting planar force constants are superpositions of infinite atom–atom force constants. However, all force constants outside the cut-off radius r_{force} can be replaced with a long-range default or even with zero in case of homopolar semiconductors. This turns the infinite into a finite sum. To actually separate true atom–atom force constants, planar force constants are calculated for different space directions. In each configuration, the planar force constants are a superposition of different atom–atom force constants. When enough planar calculations have been made, the system of equations becomes over-defined and a least-squares fit is used to find individual constants.

The planar force-constant separation approach cannot be used to study point defects: If the supercell is small in two dimensions, defect–defect bonds will form along these lines, jeopardizing the goal of studying isolated defects.

However, the separation step used in the planar force-constant separation approach can be generalized to any shape of the supercell. This is the *generalized force-constant separation approach*: A set of differently shaped supercells is used. In each supercell, the forces acting on a given atom are a linear combination of the forces originating from an infinite number of atoms on the displaced superlattice. By using the long-range default for all far-away atoms, only a finite number of force constants inside r_{force} remains in that linear combination. For different shaped supercells, these linear combinations vary. The set of supercells is made large enough to make the system of linear equations over-defined. Then individual constants can be separated by using a least-squares fit. Further details of the method are described in Ref. [3].

Even though most of the vibrational energy of local vibrational modes is located at the defect site, a non-neglible fraction of the energy resides on atoms farther away. For those atoms, the force constants of the perfect, undisturbed crystal are used. In the vicinity of the defect, modified force constants are calculated separately. For the perfect crystal, the *force constant separation approach* is used. However, this method is not applicable to the disturbed system, as it requires a truely periodic crystal. Therefore, the *direct force-constant approach* is used for the crystal with the impurity.

In case of the perfect crystal, the dynamical matrix depends on the wave vector. At certain wave vectors, the matrix can contain different force constants. If these force constants are of the same order of magnitude, a small error in one constant can cause a large error in the dynamical matrix. The farther away two atoms are, the smaller the force constants are in general. But at the same time, the average number of atoms in a shell increases with distance. We found that it is necessary to include force constants for at least eleven shells in the calculation.

For local vibrational modes, the situation is different: The vibration is dominated by the central impurity atom. For example, it holds around 50% (ZnS : Se) respectively 91% ($ZnSe:N^-$) of the vibrational energy in the mode. Therefore, it is required to calculate the force constants for the impurity very precisely, but it is not necessary to go beyond the second shell around the impurity. In addition, modified force constants are calculated for the ligands, again up to the second shell.

So far, the harmonic approximation has been used all the time. In a truely harmonic case, force constants do not change, when atoms move. However, in earlier work for $GaAs:C^-$, we found non-neglible anharmonicity [4]. It is expected, that anharmonicity also plays a role with $ZnSe:N^-$. Therefore, the correct positions of all atoms in the vicinity of the defect are calculated. This relaxation is performed by gradually moving the atoms in the direction of the Hellmann–Feynman forces on them till the system comes to a rest. Only symmetry-conserving relaxations are included. All atoms up to the third covalent neighbour of the defect are considered, which are a total of 40 atoms located on four different shells.

In case of ZnS : Se, the situation is much better. The difference in size between Se and S is much smaller than that between Se and N. Furthermore, there is less anharmonicity in ZnS : Se. Therefore, we only relax two shells containing 16 atoms around the impurity.

All force constants are used to set up a cluster simulation. This is a purely classical procedure, where the atoms are simulated as point masses. The cluster contains the impurity and up to 488 atoms around it. The modes of this cluster are calculated by diagonalizing its dynamical matrix. Out of all vibrational modes, those with a large amplitude at the impurity atom and/or its four ligands are selected as local vibrational modes.

The stronger the localization of the mode, the better are the results of the cluster simulation. In case of $ZnSe:N^-$, the results for a cluster with 47 atoms differ by less than 0.2 cm^{-1} from the results for a 489 atom cluster.

In all calculations, the charged acceptor $ZnSe:N^-$ was preferred to the neutral ZnSe : N, because N^- is isoelectronic to the Se atom it replaces, so that no empty states have to be calculated. In case of neutral N, a single hole would exist, which requires a denser k-point sampling of the Brillouin zone and thus more CPU power [4]. The charge of the N^- is compensated by placing

a constant positive background charge inside the supercell. Because the defect is shallow, the extra electron bound to N^- is delocalized over a large area. Therefore, it does not contribute significantly to the strength of the bonds at the defect site, so that the frequency of the LVM is altered by less than 10 cm^{-1} for a similiar system [4].

All ab initio calculations are performed using density-functional theory with local density approximation (LDA) and a plane-wave basis set. Standard BHS pseudopotentials are used for S and Se, while Troullier–Martins potentials are used for Zn and N. In case of Zn, the 3d electrons are treated as valence electrons, but they are treated as core electrons for Se. Because of the large supercell size of 48–64 atoms, only one k-point is used to sample the Brillouin zone. The cut-off energy was up to 65 Ry.

2. Results for ZnSe:N

N impurities are used for p-type doping of ZnSe. However, if the impurity concentration is increased beyond 5×10^{19} cm^{-3}, self-compensation occurs, so that the carrier concentration drops. In Ref. [5], FTIR absorption bands in N-doped ZnSe at 537 and 553 cm^{-1} were assigned to substitutional $^{15}N_{Se}$ and $^{14}N_{Se}$, respectively.

To our knowledge, the fine structure of the line has not yet been measured. There are five stable Zn isotopes, so that 5^4 isotope combinations of the four Zn ligands of the N impurity are possible. Out of these 625 combinations, 70 are truely different, the others can be projected onto one another using symmetry operations. Depending on the ligand masses, the mode is a singlet (all masses equal), a doublet (three ligands with identical mass) or a triplet (at most two ligands with the same mass). The total number of modes is 180, resulting in a rich fine structure, see Fig. 1.

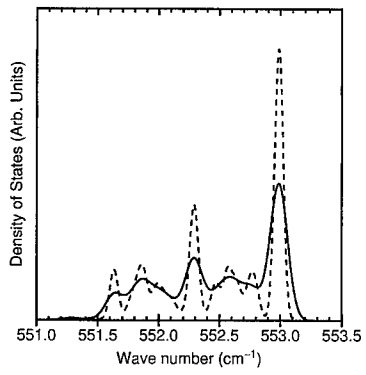

Fig. 1. Plot of the calculated fine structure of ^{14}C in ZnSe. The calculated sharp eigenfrequencies were broadened with gaussians with a half width of 0.1 cm^{-1} (solid line) and 0.05 cm^{-1} (dashed line), respectively.

The width of the fine structure is less than 2 cm^{-1}, so that the graphs for ^{14}N and ^{15}N center do not overlap. To calculate the average vibrational frequency, all fine structure modes are weighted with their probability according to the natural abundancy of the underlying isotopes. The result is 552.5 cm^{-1} for ^{14}N and 535.5 cm^{-1} for ^{15}N. Both values agree very well with the experimental results of 553 and 537 cm^{-1} [5].

3. Results for ZnS:Se

Substitutional Se in ZnS shows an even more detailed fine structure. This is because both the impurity and the four ligands each hold approximately 50% of the vibrational energy. The fine structure due to the five stable Zn isotopes is very similiar to the case ZnSe:N^-, but twice as wide because of the higher amplitude on the Zn ligands. The graphs belonging to the six different stable Se isotopes overlap, so that in experiments, only one mode with a very rich fine structure has been seen [6].

Our calculations (Fig. 2) reproduce the experiment of Ref. [6] with very good accuracy. It is found, that the second highest peak of the fine structure for a specific Se isotope has the same energy as the main peak for the Se isotope, whose atom mass is 2 u higher. This caused problems for semi-empirical models, which have been used so far [3]. Fig. 3

ZnS:^{80}Se and ZnSe:$^{14}N^-$ show similiar fine structures, despite the big difference of the impurity mass. This is, because in both cases, the Zn ligands are responsible for the splitting. However, the fine structure is wider for ZnS:^{80}Se than for ZnSe:$^{14}N^-$. The reason is the difference in vibrational energy at the ligands: Around 50% for ZnS:Se, but only around 9% for ZnSe:N^-.

To summarize, local vibrational modes have been calculated with ab initio density-functional theory. Our calculations for given impurity isotopes brought new insight into the systems ZnS:Se and ZnSe:N^-. Ab initio calculations allow to unambigiously interpret the fine structure of observed local vibrational modes.

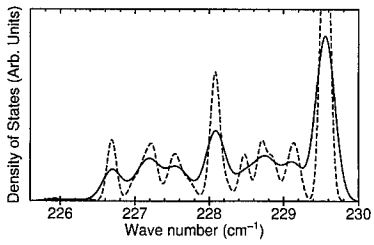

Fig. 2. Plot of the calculated fine structure of ^{80}Se in ZnS, the most abundant Se isotope. The half width used are 0.18 cm^{-1} (solid line) and 0.09 cm^{-1} (dashed line), respectively.

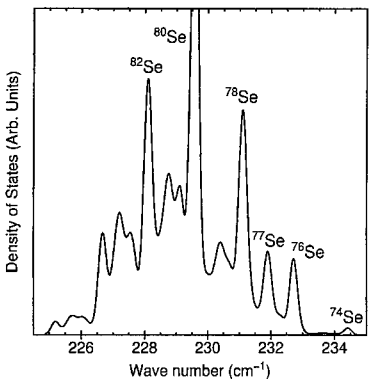

Fig. 3. Calculated fine structure for Se (all isotopes in their natural abundancy) in ZnS. All modes were broadened with Gaussians with a half width of 0.18 cm^{-1}.

Acknowledgements

The author thanks the Konrad-Zuse-Zentrum fr Informationstechnik, Berlin and the Zentraleinrichtung Rechenzentrum of the Technische Universität Berlin for their support and the provision of supercomputing facilities. The author also thanks the Fritz-Haber-Institut, Berlin, for the provision of the fhi94md [7] computer software, which was used for the ab initio calculations.

References

[1] W. Frank, C. Elsässer, M. Fähnle, Phys. Rev. Lett. 74 (1995) 1791.
[2] Siqing Wei, M.Y. Chou, Phys. Rev. Lett. 69 (1992) 2799.
[3] K. Petzke, Phys. Rev. B., in press.
[4] K. Petzke, C. Göbel, C. Schrepel, U. Scherz, Mater. Sci. Forum 258–263 (1997) 861.
[5] H.J. Stein, Appl. Phys. Lett. 64 (1994) 1520.
[6] M.D. Sciacca et al., Phys. Rev. B. 53 (1996) 12878.
[7] R. Stumpf, M. Scheffler, Comp. Phys. Commun. 79 (1994) 447.

ELSEVIER

Physica B 273–274 (1999) 870–874

PHYSICA B

www.elsevier.com/locate/physb

Luminescence and influence of defect concentration on excitons in ^{197}Hg/^{197}Au-doped CdTe

J. Hamann[a], A. Burchard[b,c], M. Deicher[b], T. Filz[a], V. Ostheimer[a], F. Strasser[a], H. Wolf[a], ISOLDE Collaboration[c], Th. Wichert[a,*]

[a]*Technische Physik, Universität des Saarlandes, Geb. 38, Postfach 15 1150, D-66041 Saarbrücken, Germany*
[b]*Fakultät für Physik, Universi... nstanz, D-78134 Konstanz, Germany*
[c]*CERN, Ge...eva, Switzerland*

Abstract

CdTe, implanted with ^{197}Hg ions, which decay to ^{197}Au with a half-life of 64.1 h, was investigated by photoluminescence (PL) spectroscopy. The results unambiguously verify the assignments of both, the donor–acceptor pair transition at 1.335 eV, which corresponds to an acceptor level with $E_A = 263$ meV, and the recombination of excitons bound to neutral acceptors at 1.57606 eV to single Au atoms on Cd sites. In addition, the dependence of the intensities of excitonic lines on the defect concentration was investigated quantitatively. The observed intensities are well explained, assuming that a defect can only bind an exciton if there is no additional defect within the volume of the bound exciton. The ratio between the exciton radii of the Cu- and Au-bound excitons $R_{exc}^{Cu}/R_{exc}^{Au} = 1.2 \pm 0.2$ obtained from this model is in good agreement with the ratio derived from the diamagnetic shift parameters of the two corresponding PL lines.

Keywords: Cadmium telluride; Gold; Photoluminescence; Radioactive isotope

1. Introduction

Photoluminescence spectroscopy (PL) provides a wealth of information on defects in semiconductors, but it is often difficult to identify the chemical identity of the defect causing a particular line in a PL spectrum. An unambiguous chemical identification becomes possible if radioactive isotopes are employed as dopants [1]. Depending on whether the parent or daughter isotope is the dopant element, the dopant concentration decreases or increases due to the radioactive decay, respectively. If the intensity of a PL line is correlated with the half-life of the radioactive decay, the parent or daughter isotope can be identified as a constituent of the defect causing the observed level.

After diffusion of stable Au into CdTe, E. Molva et al. observed a donor–acceptor pair transition (DAP) at 1.335 eV (maximum intensity at 1.27 eV), which corresponds to an acceptor level with $E_A = 263$ meV, and a recombination of excitons bound to neutral acceptors (A^0X) at 1.57606 eV. Both transitions were assigned to substitutional Au atoms on Cd sites (Au_{Cd}) [2]. Excitonic lines with nearly the same energy as the A^0X line, however, were observed after H^+ implantation [3,4] or electron irradiation [5] and were assigned to radiation damage. In order to verify the assignments of the DAP transition at 1.335 eV and of the A^0X line at 1.57606 eV to the Au_{Cd} acceptor, CdTe was implanted with ^{197}Hg ions, which decay to ^{197}Au with a half-life of 64.1 h by electron capture [6]. Hg, which is isoelectronic to Cd, is incorporated on a Cd site and does not form an electronic defect level. After the decay, the ^{197}Au atoms are still located on Cd sites because of the small recoil energy of 0.7 eV and are expected to form an acceptor level.

* Corresponding author. Tel.: + 49-681-3024219-4220; fax: + 49-681-3024315-4316.
E-mail address: thw@tech.phys.uni.sb.de (T. Wichert)

0921-4526/99/$ - see front matter
PII: S0921-4526(99)00533-5

It is known from the literature that the intensities of excitonic lines are reduced in semiconductors containing a high concentration of defects [7]. Intensive excitonic lines are, therefore, often used as an indicator of a good crystalline quality. Hence, additional information can be obtained from the present experiment, because the dopant concentration changes continuously due to the decay of ^{197}Hg to ^{197}Au. In this context, the fact that nothing but the elementary transmutation changes the sample, is even more important. To our knowledge, the dependence of the intensities of excitonic lines on the actual defect concentration has not yet been investigated quantitatively.

2. Experimental

The ^{197}Hg ions were implanted into Bridgman-grown, nominally undoped CdTe crystals at the ISOLDE mass-separator facility at CERN (Geneva) with a dose of 10^{13} cm^{-2} and an energy of 60 keV, resulting in an average implantation depth of 20 nm. After implantation, the crystals were annealed at 750 K for 1 h in vacuum in order to remove implantation-induced damage. The diffusion occurring during this annealing process distributes the ^{197}Hg atoms almost homogeneously within the layer of about 1 μm thickness probed by PL experiments [8,9]. The PL measurements were carried out at 1.8 K. The 351.1 nm line of an Ar laser was attenuated to 2 mW and focused to a diameter of about 200 μm. The luminescence was analysed by a 0.5 m grating monochromator and detected by a CCD camera.

3. Results and discussion

In order to observe the change of the PL spectrum due to the elementary transmutation, PL spectra were recorded at different times after annealing. Between these measurements, it was taken care that the sample temperature never exceeded 150 K in order to avoid modifications of the crystal besides those induced by the radioactive decay. A subset of the spectra is shown in Fig. 1. The intensity of each spectrum is normalised to the intensity of the DAP_{Cu} band at 1.455 eV [10]. Both Cu and effective-mass-like donors are usually present as unintentional impurities in CdTe. The data show that the intensity of the PL band around 1.27 eV increases with time. Both the energetic position and the phonon coupling constant of this band agree with the corresponding values of the DAP_{Au} band in the literature [2]. The intensity of this band was determined by integrating the intensities in the energy interval between 1.22 and 1.32 eV. The intensity $I(t)$ as a function of time t was fitted with

$$I(t) = I_0 + I_1(1 - e^{-(\ln 2)\cdot t/t_{1/2}}). \quad (1)$$

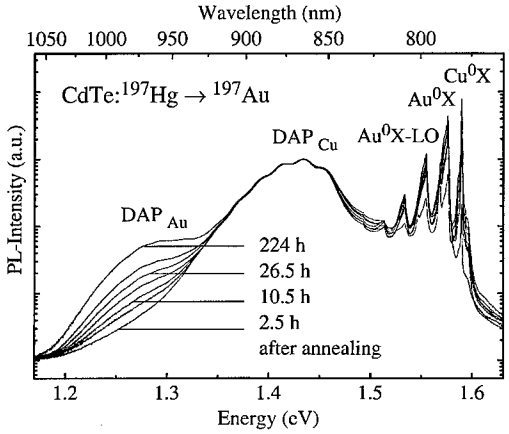

Fig. 1. PL spectra of a CdTe crystal implanted with ^{197}Hg, recorded at different times after annealing (1 h, 750 K, vacuum). The intensities of the spectra are normalised to the intensity of the DAP_{Cu} band.

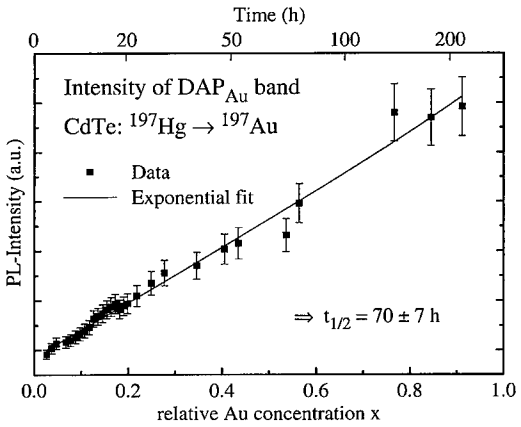

Fig. 2. Intensity of the DAP_{Au} band as a function of the relative Au concentration.

The best fit was obtained with $t_{1/2} = (70 \pm 7)$ h, which is in good agreement with the half-life of ^{197}Hg $t_{1/2} =$ 64.1 h. In Fig. 2 the data and the fit are plotted as a function of the relative Au concentration $0 \leqslant x \leqslant 1$, which is the ^{197}Au concentration normalised to the number of originally implanted ^{197}Hg atoms and is calculated from the radioactive decay ^{197}Hg → ^{197}Au using $t_{1/2} = 64.1$ h. From this linear dependence, it is obvious that the intensity of the band is proportional to the Au concentration. Therefore, it is concluded that the band is caused by a defect containing a single Au atom. Moreover, since the ^{197}Hg/^{197}Au atoms are incorporated on Cd sites, the acceptor level at 263 meV, which corresponds to this band, is caused by single Au atoms that reside on Cd sites.

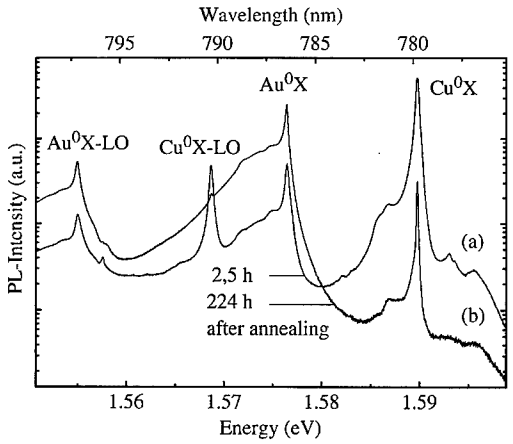

Fig. 3. Excitonic regions of the PL spectra of a CdTe crystal implanted with ^{197}Hg. The intensities of the two spectra are normalised to the intensity of the DAP_{Cu} band.

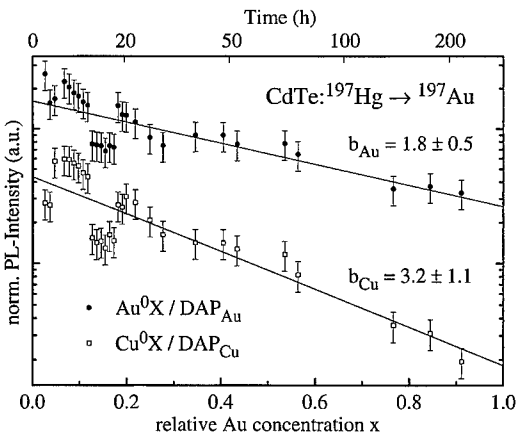

Fig. 4. Intensities of the Cu^0X line and the Au^0X line, normalised to the intensities of the DAP_{Cu} band and the DAP_{Au} band, respectively, plotted as a function of the relative Au concentration. The straight lines are fits to $p(x) = \exp(-bx)$, which yield $b_{Cu} = 3.2 \pm 1.1$ and $b_{Au} = 1.8 \pm 0.5$ (see Eq. (3)).

The excitonic regions of two PL spectra, which were recorded (a) 2.5 and (b) 224 h after annealing, are shown in Fig. 3. Their intensities are normalised to the intensity of the DAP_{Cu} band. At 1.5896 eV, the copper-bound exciton line (Cu^0X) [10] is observed, and at 1.5761 eV the line mentioned above is visible, which has been assigned to the Au_{Cd} defect (Au^0X) [2]. The dependence of the intensities of the excitonic lines on the Au concentration is obvious but more complex. Though the intensity of the Au^0X line increases by a factor of five, which suggests an assignment to ^{197}Au atoms, the radioactive decay ^{197}Hg $\rightarrow$ ^{197}Au should effect an increase by a factor of 34. Additionally, the intensity of the Cu^0X line changes as a function of time, too. It decreases by a factor of 20, although the Cu concentration in the crystal does not change. The reduced increase of the intensity of the Au^0X line and the decrease of the intensity of the Cu^0X line cannot be explained by a competition for the charge carriers created by the laser. Though additional decay channels for the charge carriers (DAP_{Au} band and Au^0X line) are created by the radioactive decay, the intensity of the DAP_{Cu} band does not significantly change in the non-normalised PL spectra. Therefore, the competition with the created decay channels for charge carriers should be neglectable.

Obviously, the probability of binding an exciton decreases for both Cu and Au acceptors, when the Au concentration increases. The intensities of the Cu^0X and the Au^0X lines as a function of the Au concentration are plotted in Fig. 4. They are normalised to the intensities of the DAP_{Cu} and DAP_{Au} bands, and thereby normalised to the actual Cu and Au concentrations, respectively. The decrease of intensity is more pronounced for the Cu-bound excitons than for the Au-bound excitons. This is expected because Cu-bound excitons with a binding energy of 7 meV are more extended and, therefore, more easily disturbed by an increasing defect concentration than Au-bound excitons with a binding energy of 20 meV. Since the binding energy is distributed among three particles (one hole and one electron from the exciton, one hole from the neutral acceptor), however, this argument provides an only qualitative estimate for the radius of the bound exciton.

In order to describe the intensities of the two A^0X lines quantitatively and to extract the exciton radii, we assume that a defect can only bind an exciton if there is no additional defect within the volume V_{exc} of the bound exciton. If V_{cell} denotes the volume of the unit cell and c is the defect concentration, for each unit cell the probability of containing a defect is cV_{cell}. Within the exciton volume, there are V_{exc}/V_{cell} unit cells. For each Cu or Au acceptor the probability for finding no additional defect within the volume of the bound exciton is

$$p(c) = (1 - cV_{cell})^{V_{exc}/V_{cell}} \approx \exp\left(-cV_{cell}\frac{V_{exc}}{V_{cell}}\right) = \exp(-\tfrac{4}{3}\pi R_{exc}^3 c), \quad (2)$$

where R_{exc} is the radius of the bound exciton. The defect concentration c is the sum of two contributions: the concentration of those ^{197}Hg atoms that have already decayed to ^{197}Au ($c_{impl} \cdot x$), where c_{impl} is the concentration of originally implanted ^{197}Hg ions and x is the time-dependent relative Au concentration, and the

concentration of all other defects c_0. This yields

$$p(x) = \exp(-\tfrac{4}{3}\pi R_{exc}^3[c_{impl}x + c_0]) = \text{const}\cdot\exp(-\tfrac{4}{3}\pi R_{exc}^3 c_{impl}x). \quad (3)$$

In our model, $p(x)$ is proportional to the intensity of a bound-exciton line normalised to the respective dopant concentration and, therefore, proportional to the intensity ratios Cu^0X/DAP_{Cu} and Au^0X/DAP_{Au} in Fig. 4. In fact, the data of both ratios, Cu^0X/DAP_{Cu} and Au^0X/DAP_{Au}, are well described by the function $p(x) = \exp(-b\cdot x)$ with $b_{Cu} = 3.2 \pm 1.1$ and $b_{Au} = 1.8 \pm 0.5$. The value of c_{impl} is estimated from the implantation dose of 10^{13} cm^{-2} and a diffusion length in the order of 1 μm for the ^{197}Hg atoms [8,9] to $c_{impl} = 10^{17}$ cm^{-3}. This yields excitonic radii of $R_{exc}^{Cu} = 20$ nm and $R_{exc}^{Au} = 16$ nm. These radii, however, are uncertain by a factor of about two because the uncertainty of c_{impl} is about one order of magnitude. Therefore, it is reasonable to consider the ratio of the excitonic radii $R_{exc}^{Cu}/R_{exc}^{Au} = 1.2 \pm 0.2$, which is independent of c_{impl}.

This ratio is compared with the ratio of the Bohr radii, which are obtained from the magneto-optical parameters of the corresponding PL lines [2,12,13]. In CdTe, the radius of an A^0X complex is determined by the more weakly bound electron. This follows from a pseudo-donor model, in which the two holes are tightly bound by the short-range potential of the acceptor, producing a long-range Coulomb potential, which binds the electron, similarly to a donor [11]. It has been shown that this model is valid for Cu^0X and Au^0X complexes in CdTe [2,12,13]. In an external magnetic field $\boldsymbol{B}$, an A^0X line exhibits a diamagnetic shift [14]. Because of the strong binding of the two holes and the quadratic dependence on the radii $|r_i|$, the contributions of the two holes to the diamagnetic shift ΔE is neglected:

$$\Delta E = \sum_{i=e,h,h} \left\langle \Psi_i \left| \frac{e^2}{8m_i^*}(\boldsymbol{r}_i \times \boldsymbol{B})^2 \right| \Psi_i \right\rangle \approx \frac{e^2}{8m_e^*}\langle \Psi_{1s}|(\boldsymbol{r}_e \times \boldsymbol{B})^2|\Psi_{1s}\rangle = c_{diam}\, B^2 \quad (4)$$

with

$$c_{diam} = \frac{e^2}{4m_e^*}a_0^2, \quad (5)$$

where e is the charge, m_e^* the effective mass, $\boldsymbol{r}_e$ the position of the electron, and Ψ_{1s} is the 1s wave function of a hydrogenic donor with Bohr radius a_0. With Eq. (5) the Bohr radius of the exciton can be estimated from the diamagnetic shift parameter c_{diam}. With $c_{diam}^{Cu} = (1.47 \pm 0.08)\times 10^{-2}$ meV/T^2 for the Cu^0X line [12] and $c_{diam}^{Au} = (1.1 \pm 0.1)\times 10^{-2}$ meV/T^2 for the Au^0X line [2,13], the Bohr radii $a_0^{Cu} = 5.7 \pm 0.2$ nm and $a_0^{Au} = 4.9 \pm 0.2$ nm are obtained. Their ratio is $a_0^{Cu}/a_0^{Au} = 1.16 \pm 0.09$, which is very close to the ratio $R_{exc}^{Cu}/R_{exc}^{Au} = 1.2 \pm 0.2$ obtained from the data in Fig. 4. The absolute values of the exciton radii determined from these data, $R_{exc}^{Cu} = 20$ nm and $R_{exc}^{Au} = 16$ nm (see above), are about 3.4 times the calculated Bohr radii, which is a reasonable factor since an electron described by a 1s wave function is found in a sphere with a diameter of $3.4a_0$ with a probability of 97%.

4. Summary

By doping CdTe with radioactive ^{197}Hg/^{197}Au, it is shown that the intensity of the DAP transition at 1.335 eV is proportional to the ^{197}Au concentration in the crystal. Therefore, the acceptor level at 263 meV, corresponding to this band, is caused by a defect containing a single Au atom. As the ^{197}Hg/^{197}Au atoms are incorporated on Cd sites, this acceptor consists of single Au atoms that reside on Cd sites. The dependence of the intensities of both the Cu^0X and the Au^0X lines are well explained quantitatively, assuming that a defect can only bind an exciton if there is no additional defect within the volume of the bound exciton. Since the intensity of the Au^0X line at 1.57606 eV is correctly described, the defect binding this exciton also contains a single Au atom. Therefore, the assignments of both the DAP transition at 1.335 eV and the A^0X line at 1.57606 eV to the Au_{Cd} acceptor are verified.

Acknowledgements

The financial support by the Bundesministerium für Bildung und Forschung under grant No. WI04SAA is gratefully acknowledged.

References

[1] R. Magerle, Mater. Res. Soc. Symp. Proc. 442 (1997) 3.
[2] E. Molva, J.M. Francou, J.L. Pautrat, K. Saminadayar, Le Si Dang, J. Appl. Phys. 56 (1984) 2241.
[3] L. Svob, Y. Marfaing, Mater. Sci. Forum 10–12 (1986) 857.
[4] A. Kozanecki, K. Paprocki, J. Tatarkiewicz, Solid State Commun. 76 (1990) 843.
[5] R. Legros, Y. Marfaing, G. Neu, R. Triboulet, Inst. Phys. Conf. Ser. 46 (1979) 392.
[6] see e.g. E. Browne, J.M. Dairiki, R.E. Doebler, Table of Isotopes, in: C.M. Lederer, V.S. Shirley (Eds.), Wiley, New York, 1978.
[7] P.J. Dean, D.C. Herbert, in: K. Cho (Ed.), Excitons, Springer, Berlin, 1979.
[8] E.D. Jones, V. Thambipillai, J.B. Mullin, J. Crystal Growth 118 (1992) 1.

[9] J.H.C. Hogg, A. Bairstow, G.W. Matthews, D. Shaw, J.D. Stedman, Mater. Sci. Eng. B 16 (1993) 195.
[10] J.P. Chamonal, E. Molva, J.L. Pautrat, Solid State Commun. 43 (1982) 801.
[11] W. Rühle, D. Bimberg, Phys. Rev. B 12 (1975) 2382.
[12] E. Molva, Le Si Dang, Phys. Rev. B 27 (1983) 6222.
[13] L. Worschech, W. Ossau, G. Landwehr, Proceedings of the 23rd International Conference on Physics of Semiconductors, Berlin, 1996, World Scientific, Singapore, 1996, p. 3001.
[14] see e.g. H. Ibach, H. Lüth, Festkörperphysik, Springer, Berlin, 1990.

ELSEVIER

Physica B 273–274 (1999) 875–878

PHYSICA B

www.elsevier.com/locate/physb

Lattice site and diffusion of ion-implanted Li in as-grown and Se-rich ZnSe

K. Bharuth-Ram[a,*], M. Restle[b], H. Hofsäss[c], C. Ronning[c], U. Wahl[d,e]

[a]*Physics Department, University of Durban-Westville, Private Bag X54001, Durban 4000, South Africa*
[b]*Fakultät für Physik, Universität Konstanz, D-78434 Konstanz, Germany*
[c]*II. Physik Institut, Universität Göttingen, D-37073 Göttingen, Germany*
[d]*Instituut voor Kern-en Stralingsfysica, KU-Leuven, B-3001 Leuven, Belgium*
[e]*ISOLDE Collaboration, CERN, Geneva, Switzerland*

Abstract

The implantation sites and diffusion of Li in as-grown and Se-rich ZnSe has been studied with emission channeling measurements on the α-particles emitted in the decay of radioactive ^{8}Li probes implanted in single-crystal samples. At implantation temperatures below 180 K the Li atoms are immobile at tetrahedral interstitial sites, but a site change sets in at 200 K, and above 250 K the Li atoms occupy mainly substitutional sites. In Se-rich ZnSe the interstitial Li fraction (f_T) shows partial recovery between 260 and 360 K, a phenomenon which may be attributed to Li trapping at interstitial Se. Implantation dose, however, has a strong influence on the observed channeling and blocking patterns. Maximum f_T is achieved at $T \geqslant 400$ K where the fraction at interstitial sites is an order of magnitude lower. At higher temperatures ($\approx$ 550 K) the Li atoms dissociate from their substitutional sites and diffuse to the surface in the Se-rich sample and to extended defects in the implantation region in the as-grown sample.

Keywords: ZnSe; Li; Implantation sites

1. Introduction

The properties of Li-doped ZnSe has been the subject of considerable study, both experimental and theoretical. While n-type doping (with Cl) poses little problem high levels of p-type doping has been difficult to achieve. Li as dopant produces low-resistivity p-type ZnSe [1,2], but the maximum net acceptor concentrations, $N_A - N_D$, are limited to $\leqslant 1 \times 10^{17}\,\mathrm{cm}^{-3}$ [3] and show no increase even with increasing Li concentrations [4]. Theoretical calculations [5,6] show that the acceptor doping levels are mainly constrained by two factors. Firstly, there is competition between substitutional and interstitial impurity configurations; secondly, the formation of a Li_2Se phase sets a limit on the achievable Li solubility level.

Ion implantation offers an obvious mechanism to overcome solubility limits. The quest then is to find the implantation conditions under which Li incorporation on substitutional Zn sites dominates. In this contribution we report on investigations on the lattice sites of ion-implanted Li in virgin and Se-enriched ZnSe as a function of implantation temperature, and compare the results with earlier measurements on Zn-enrichd ZnSe [7]. The investigations were carried out employing emission channeling measurements on the α-particles emitted in the decay of radioactive ^{8}Li probes implanted in single-crystal samples. These measurements allow studies of the site fractions and lattice site changes of the implanted dopant as a function of implantation temperature.

2. Experimental details

The emission channeling (EC) technique as applied to α-emitting probes implanted in single-crystal samples is

* Corresponding author. Tel.: + 27-31-204-4663; fax: + 27-31-204-4795 .
E-mail address: kbr@pixie.udw.ac.za (K. Bharuth-Ram)

0921-4526/99/$ - see front matter
PII: S0921-4526(99)00535-9

described in detail in Ref. [8]. For probes implanted at tetrahedral interstitial sites detection of the emitted α-particles as a function of tilt angle relative to the different crystallographic axes and planes, show that enhanced channeling yields along the ⟨1 1 0⟩ axial direction and blocking effects along the ⟨1 1 1⟩ and ⟨1 0 0⟩ directions; such measurements for α-emitters at substitutional sites, on the other hand, show blocking effects in all three major axial directions.

In our study of the implantation site and diffusion of Li we used as probe radioactive ^{8}Li which decays via β^- emission, with a half-life $t_{1/2} = 0.838$ s, to an excited state of ^{8}Be. This, in turn, breaks up, within 4×10^{-22} s, into two α-particles with energies continuously distributed around 1.6 MeV. The short half-life and the low recoil energy imparted to the product ^{8}Be ensures that the emitted α-particles reflect the lattice sites occupied by the implanted parent ions. This allows, within a time window of a few seconds between implantation and decay, studies of implantation site fractions and lattice site changes induced by Li-defect interactions.

The ZnSe crystals had a specific resistance of $> 10^8$ Ω cm, and were mechanically polished with a ⟨1 0 0⟩ orientation. Measurements were made on Se-enriched and virgin samples. Se enrichment was achieved by annealing a virgin ZnSe crystal in Se-rich atmosphere for 28 days at a temperature of 1200 K. The Se-rich crystal showed p-type characteristics, but was highly resistive with a nett acceptor density of 3×10^{11} cm^{-3}. For the channeling measurements each sample was pre-oriented with the aid of Laue X-ray photographs, and mounted in the vacuum chamber of a three-axis goniometer at the online isotope separator ISOLDE at Cern. The ^{8}Li probe ions were then implanted through a 0.5 mm diameter aperture into the crystal at a tilt angle of 10° with respect to the crystallographic axis. The emitted α-particles were detected in a two-dimensional position sensitive detector at 152° to the direction of the incident beam. Cooling and heating devices allowed the sample temperature to be set between 50 and 1000 K. The α-emission yield was measured over an angular range of ± 2.5° about different crystallographic directions, at several implantation temperatures between 150 and 560 K. The implantation dose needed to acquire a single spectrum with sufficient statistics, such as that shown in Fig. 1, was typically about 2×10^{12} cm^{-2}. The total implantation dose into the same beam spot on the sample surface did not exceed 2×10^{13} Li/cm^2.

3. Results and discussion

Figs. 1(a) and (b) show three-dimensional α-emission spectra about the ⟨1 1 0⟩ crystallographic direction observed for the as-grown ZnSe sample at 180 and 275 K, respectively. The plotted emission yield has been normalized to the mean yield for an off-axis random direction. The enhanced channeling effect with a maximum yield at 0° evident in Fig. 1(a), together with blocking effects along the (1 1 0)- and (1 0 0)-planes and channeling effect along the (1 1 1)-planes are clear signatures of Li atoms located at tetrahedral interstitial sites. The channeling pattern in Fig. 1(b), on the other hand, shows a pronounced blocking effect at 0°, as well as blocking effects of the {1 1 1}-planes, which provides evidence that most of the decaying Li are now on substitutional lattice sites.

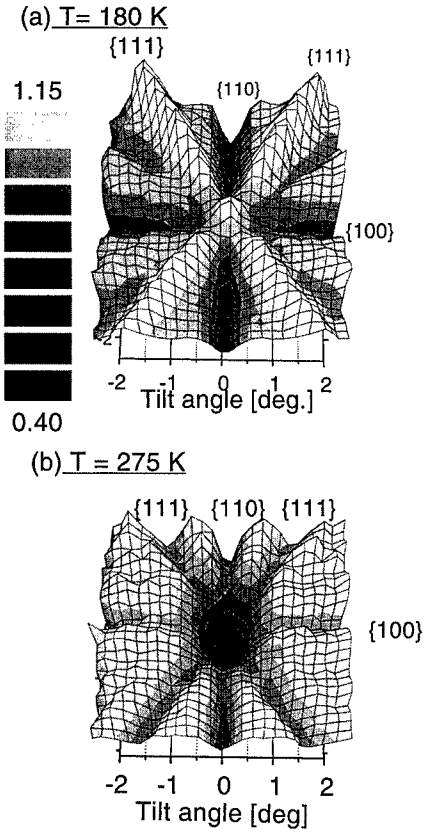

Fig. 1. Normalized α-emission yields from ^{8}Li implanted in ZnSe at (a) 180 K and (b) 270 K.

The Li site fractions were estimated from fits of the experimentally observed channeling spectra to α-emission channeling patterns simulated with the Monte Carlo simulation program FLUX [9], allowing for Li on substitutional (f_S), tetrahedral interstitial (f_T), and random sites (f_R). As input values for the theoretical calculations we used a TRIM [10] estimated mean range of the Li implantation profile (430 (200) nm), Debye temperatures of Θ_D(Zn) = 293 K, Θ_D(Se) = 266 K, and an experimental angular resolution of $\sigma = 0.12°$. The one-dimensional vibration amplitude u_1 of Li was treated as an additional fit parameter. Other regular lattice sites such

as bond-center, anti-bonding, hexagonal interstitial, split-⟨1 0 0⟩, were also modelled but no obvious evidence of Li at these sites was found. Li atoms decaying in highly disordered regions or within extended defects produce an isotropic α-emission yield, and have been included as contributing to the 'random' fraction. The best fit for the spectrum shown in Fig. 1(a) was obtained for $f_T = 68(4)\%$, $f_S = 8(3)\%$ $f_R = 24(4)\%$, and $u_1 = 0.12(1)$ Å, while that shown in Fig. 1(b) yielded $f_T = 9(3)\%, f_S = 54(4)\%, f_R = 37(4)\%$, and $u_1 = 0.19(1)$ Å.

Fig. 2 displays the Li site fractions f_T and f_S plotted as function of implantation temperature for the Se-rich and the virgin samples. At implantation temperatures below 180 K the majority (> 60%) of the Li atoms occupy tetrahedral interstitial sites but at temperatures between 180 and 275 K a $Li_T \rightarrow Li_S$ site change occurs. Between 400 and 500 K the maximum substitutional Li fraction ($f_S = 55(5)\%$) is achieved, while the interstitial fraction is an order of magnitude lower, a result in agreement with the theoretical calculations of Ref. [6]. At higher temperatures the blocking (and channeling) effects in all three principal axial directions rapidly decreases, and disappeared at 540 K, showing dissociation and diffusion of the Li_S.

Our results show that at low temperatures the most stable site for the implanted ^{8}Li is the interstitial lattice site with T_d symmetry (which has been shown to be the interstitial site surrrounded by four Se atoms [11]) and only a small fraction (8(3)%) recombines within the lifetime of ^{8}Li with a Zn vacancy. The Zn vacancy is stable within the temperature range of our measurements [11]. Hence the Li lattice site changes and the formation of substitutional Li (Li_S) observed at higher temperatures results from diffusion of the interstitial Li. Proceeding as described in Ref. [7], we estimate a migration energy of $E_m = 0.48(5)$ eV, a result which is in good agreement with theoretical estimates for the Li migration barrier in ZnSe of 0.5 eV [6].

In the Se-rich sample a similar general behaviour was observed. Our data suggests a partial recovery of the tetrahedral fraction at temperatures between 260 and 360 K. This effect may be attributed to the diffusing Li trapping at the enhanced Se interstitials (which are mobile at these temperatures [11]) in this sample, before they find a Zn vacancy. This interpretation, however, has to be treated with caution since the observed channeling effects are strongly influenced by implantation temperature and dose. This is illustrated in Fig. 3, in which the upper figure (a) shows a plot of the normalized channeling yield in the ⟨1 1 0⟩ axial direction observed in consecutive measurements as the sample temperature was changed. The arrows in the figure indicate the sequence in which the measurements were made. On average, a dose of 0.5×10^{12} Li/cm^2 was implanted at each stage, so that the dose at the end of the series amounted to about 6×10^{12} Li cm^{-2}. Fig. 3(b) shows the results of similar measurements on as-grown and Se-rich ZnSe samples, with the sample temperatures held at 300 K.

In both the virgin and the Se-rich samples the Li_S becomes unstable at higher temperatures, and at $T \geqslant 550$ K no channeling- and/or blocking effects are visible in the spectra. An approximate estimate of the Li_S dissociation energy E_D may be made by assuming that

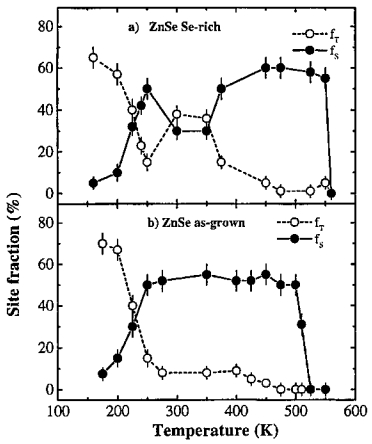

Fig. 2. Interstitial and substitutional lattice site fractions, f_T and f_S, of ^{8}Li implanted in (a) Se-rich ZnSe, and (b) as-grown ZnSe, as functions of implantation temperature.

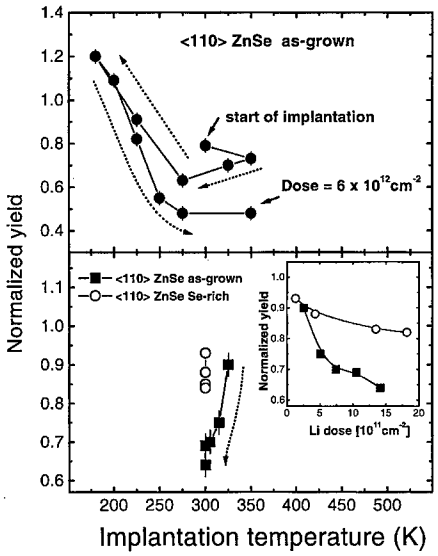

Fig. 3. Dose and temperature effects during Li implantation in ZnSe. The normalized yield in the ⟨1 1 0⟩ axial direction in consecutive measurements is plotted as a function of sample temperature. The arrow indicates the sequence of the measurements. The inset in (b) shows the dependence of the ⟨1 1 0⟩ yield on Li dose for Se-rich and as-grown ZnSe.

one jump is sufficient to cause dissociation (according to $Li_S \rightarrow Li_I + V_{Zn}$) within the lifetime of ^{8}Li, an attempt frequency of $\nu_0 = 10^{13}$ Hz, and a dissociation temperature of 510–550 K. The expression $\nu = \nu_0 \exp(-E_D/kT)$ then yields $E_D = 1.3 - 1.4$ eV. The question then arises as to where the Li atoms go after dissociating from their substitutional sites. An indication of this is provided by examining the energy spectra of the emitted α-particles, below and above the dissociation temperature. No change in α-particle energy is observed in the as-grown sample, which suggests that Li atoms diffuse to, and trap at, nearby extended defects presumably induced by the implantation process. In the Se-rich sample, on the other hand, the energy of the emitted α-particles is observed to increase by 110 keV. Using a TRIM estimated stopping power of 0.34 keV/nm for 1.6 MeV α-particles, this corresponds to a reduction of the mean path length of the α-particles of 325 nm. This is in reasonable agreement with the estimated mean implantation depth of 430 (200) nm, and indicates that in this case the Li atoms have diffused to the surface. This may suggest that lattice damage in the implantation region in Se-enriched ZnSe is very much reduced compared to the as-grown sample.

4. Conclusions

Our measurements show that at low temperatures the interstitial site with T_d symmetry is the preferred site for the Li atoms implanted in ZnSe. At temperatures between 180 and 275 K a site change of $Li_T \rightarrow Li_S$ is observed which may be attributed to interactions of diffusing Li^+ with Zn vacancies. This process occurs within a time scale of the ^{8}Li lifetime (≈ 1 s). Li shows similar behaviour in Se-rich ZnSe, except that the tetrahedral interstitial fraction remains appreciable up to 360 K, a phenomenon which can be attributed to Li^+ trapping at the enhanced concentration of interstitial Se.

The maximum substitutional fraction is achieved at 400–500 K, when the interstitial Li is an order of magnitude lower, a result in agreement with theoretical calculations [6]. At higher temperatures the substitutional Li dissociates and diffuse to extended defects or dislocations within the crystal in the as-grown sample, but to the surface in Se-rich ZnSe.

Acknowledgements

This work was financially supported by the National Research Foundation (S. Africa) and the Bundesministerium für Bildung und Forschung, Germany.

References

[1] J.G. Dieleman, J.W. De Jong, T. Meijer, J. Chem. Phys. 45 (1966) 3178.
[2] M. Behringer, P. Bäume, J. Gutwoski, D. Hommel, Phys. Rev. B 97 (1998) 12 869.
[3] J.M. De Puydt, M.A. Haase, H. Cheng, J.E. Potts, App. Phys. Lett. 55 (1989) 1103.
[4] H. Cheng, J.M. De Puydt, J.E. Potts, M.A. Haase, J. Crystal Growth 95 (1989) 512.
[5] D.B. Laks, C.G. Van de Walle, Physica B 185 (1993) 118.
[6] C.G. Van de Walle, D.B. Laks, G.F. Neumark, S. Pantelides, Phys. Rev. B 47 (1993) 9425.
[7] S.G. Jahn, U. Wahl, M. Restle, H. Quintel, H. Hofsäss, M. Wienecke, I. Trojahn, Mater. Sci. Forum 196–201 (1995) 315.
[8] U. Wahl, Phys. Rep. 280 (1997) 145.
[9] P.J. Smulders, D.O. Boerma, Nucl. Instr. and Meth. B 29 (1987) 471.
[10] J.F. Ziegler, J.P. Biersack, U. Littmark, The Stopping and Range of Ions in Solids, Pergamon, New York, 1985.
[11] G.D. Watkins, in: K. Sumino (Ed.), Defect Control in Semiconductors: Proceedings of the International Conference On Science and Technology of Defect Control in Semiconductors, North-Holland, Amsterdam, 1990.

ELSEVIER

Physica B 273–274 (1999) 879–882

PHYSICA B

www.elsevier.com/locate/physb

Persistent photoconductivity and DLTS in indium-doped $Cd_{0.9}Mn_{0.1}Te$

J. Szatkowski[a,*], E. Płaczek-Popko[a], K. Sierański[a], J. Fiałkowski[a], J.M. Wrobel[b], P. Becla[c]

[a]*Institute of Physics, Wrocław University of Technology, Wybrzeże Wyspiańskiego 27, 50-370 Wrocław, Poland*
[b]*Department of Physics, University of Missouri – Kansas City, Kansas City, MO 64110, USA*
[c]*Department of Materials Science and Engineering, Massachusetts Institute of Technology, Cambridge, MA 02139, USA*

Abstract

The properties of an indium-related DX center were determined in indium-doped $Cd_{0.9}Mn_{0.1}Te$ by deep-level transient spectroscopy (DLTS). These studies, carried out within a 77–360K temperature range, revealed the presence of five electron traps. It was possible to determine the activation energy for four of them. Their values were equal to 0.22–0.30, 0.43, 0.51 and 0.63 eV, respectively. For the first energy level, the concentration of the associated traps was higher than 10% of the concentration of the shallow levels and the capture cross section was thermally activated, with an energy barrier for capture equal to 0.1 eV. The concentration of the other three traps was lower than 10^{14} cm^{-3}. Persistent photoconductivity was also observed at low temperatures. At 77 K, the photoconductivity continued for a very long time after the light was extinguished, and was present until the temperature of the sample increased to 170 K. The very high concentration and thermally activated capture cross section for the first trap suggest its DX center nature.

Keywords: CdMnTe; Deep levels; DX centers

1. Introduction

It has been established that the presence of metastable DX centers is responsible for the persistent photoconductivity observed in many III–V and II–VI semiconducting compounds. For column III impurities in CdTe, i.e. Ga, In and Al, the large lattice relaxation model with the first-principles pseudopotential calculations has been used for analysis of DX centers [1]. From the model, the binding energies of the DX centers were determined to be equal to -0.42 eV for Al:DX, -0.04 eV for In:DX and $+0.08$ eV for Ga:DX. This implies that the conversion of the shallow hydrogenic donor into a deep relaxed one is only possible in Ga-doped CdTe. The shallow-to-deep transition in CdTe-based semiconductors, can be stimulated either by the formation of CdZnTe, CdMnTe or CdMgTe ternary compounds or by the application of hydrostatic pressure in n-type CdTe.

Metastable defects in CdTe and $Cd_{1-x}Mn_xTe$ have been observed before. In Ga-doped $Cd_{1-x}Mn_xTe$ metastable defects were investigated in Refs. [2–5] for $x = 0.01$, for $x = 0.03$ in Ref. [5] and $x = 0.05$ in Ref. [4]. Iseler et al. was the first to find that in CdTe:In there is a potential barrier to the transfer of electrons between the conduction band and the deep donor level [6]. Indium donors also form metastable DX centers in layers of CdTe:In [7,8] grown with molecular beam epitaxy. In indium-doped $Cd_{1-x}Mn_xTe$, both the metastability and the persistent photoconductivity were observed for $x > 7\%$ [9]. It has been suggested that the persistent photoconductivity is caused by the DX centers, which are introduced by indium donors. In our earlier paper [10]

* Corresponding author. Tel.: +48-71-320-2642; fax: +48-71-328-3696.
E-mail address: jasza@rainbow.if.pwr.wroc.pl (J. Szatkowski)

0921-4526/99/$ - see front matter
PII: S0921-4526(99)00539-6

we also observed metastable defects for In-doped $Cd_{1-x}Mn_xTe$ with $x = 0.2$.

In this work, we have used deep-level transient spectroscopy (DLTS) to investigate properties of deep levels, related to defects present in In-doped $Cd_{1-x}Mn_xTe$ for $x = 0.1$, and to identify the metastable defects responsible for persistent photoconductivity observed by us in this material.

2. Experimental details

The experiments were performed on $Cd_{0.9}Mn_{0.1}Te$ crystals grown by the Bridgman method. The studied wafers were annealed at 600°C in cadmium vapors for one week. Prior to the deposition of the contacts, the wafers were mechanically polished and etched in a 5% Br_2 solution in methanol. In order to perform DLTS measurements, Schottky barriers were prepared by the vacuum deposition of a 0.5 mm^2 gold layer on the front side of the samples. The ohmic contacts were obtained on the backside by indium soldering.

The capacitance–voltage and DLTS measurements were performed with the help of a DLS-82E spectrometer, based on a 1 MHz capacitance bridge and a lock-in integrator. The room temperature donor concentration, obtained from the capacitance–voltage measurements was approximately equal to $10^{16}\,cm^{-3}$.

3. Results and discussion

The DLTS studies, carried out within the 77–360 K temperature range, revealed the presence of five electron traps in In-doped $Cd_{0.9}Mn_{0.1}Te$ samples. A sample temperature scan of the DLTS signal, shown in Fig. 1, has five peaks labeled as E1–E5. At the temperature at which a DLTS peak is observed, the emission rate, e_n, and lock-in frequency f, are directly related by

$$e_n = 2.17f. \quad (1)$$

Taking temperature scans for several lock-in frequencies makes it possible to construct Arrhenius plots for each of the peaks. In Fig. 2, the plots for four traps are shown. The studies of the fifth peak were beyond the experimental capabilities of the system. The solid lines in the figure represent the best least-squares fit to the experimental data. Activation energies obtained from these plots for E2–E4 levels are equal to 0.43, 0.51 and 0.63 eV, respectively. The data for the trap E3 are ambiguous, as it was impossible to separate this peak from the neighboring peak related to trap E4. For E1 trap activation energy changed from 0.22 to 0.30 eV depending on measurements condition (amplitude of filling voltage and reverse bias).

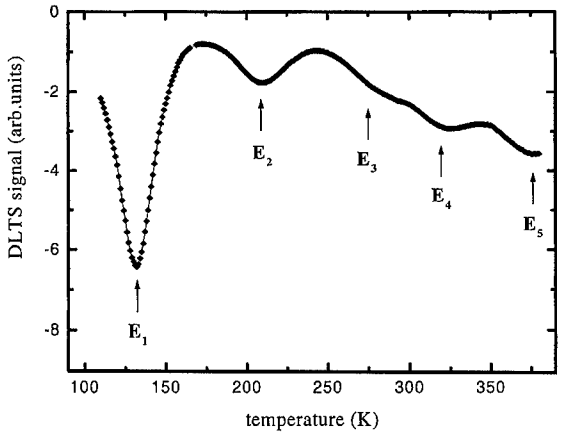

Fig. 1. DLTS temperature scans for $Cd_{0.9}Mn_{0.1}Te$:In at the 30 Hz lock-in frequency.

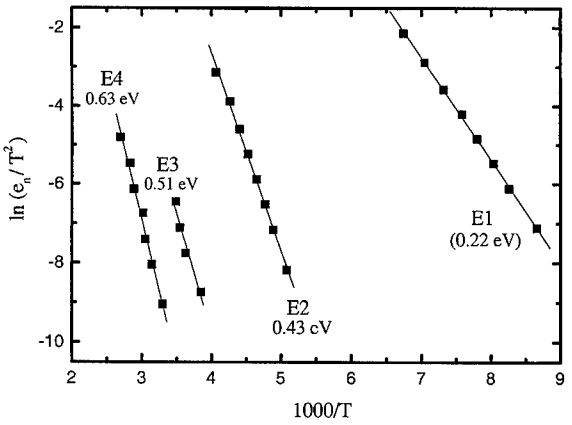

Fig. 2. The Arrhenius plots for the four deep levels observed by DLTS in $Cd_{0.9}Mn_{0.1}Te$:In. Solid lines are the best least-squares fit to the experimental data.

For levels E2–E4, the trap concentration obtained from the DLTS spectra constituted about 1% of the net donor concentration. These levels became completely filled by pulses lasting several microseconds. For level E1, the trap concentration was equal to more than 10% of the net donor concentration, and the DLTS signal related to this trap was not saturated until the filling pulse width reached 1 ms. An example of such a behavior is given in Fig. 3. In this figure, the DLTS spectra, collected at a 60 Hz lock-in frequency, are shown for different filling pulse widths. It is noticeable that for the first trap the DLTS signal increases significantly with increasing filling pulse width, whereas for the second trap it is saturated even for the shortest, 5 μs pulse. The DLTS peak saturating for very high pulse widths is a fingerprint for thermally activated capture cross section for a related

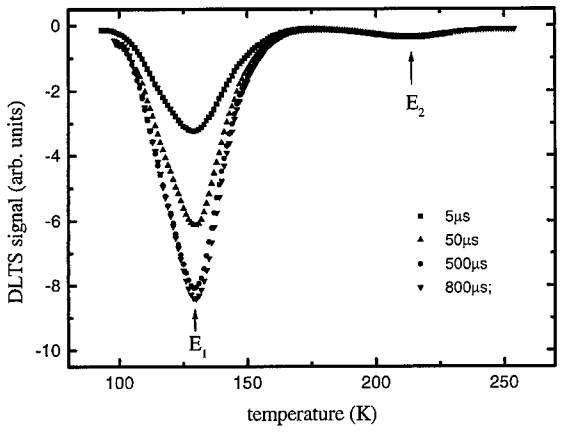

Fig. 3. DLTS temperature scans for $Cd_{0.9}Mn_{0.1}Te$:In collected at different times of the filling pulses: 5, 50, 500 and 800 μs.

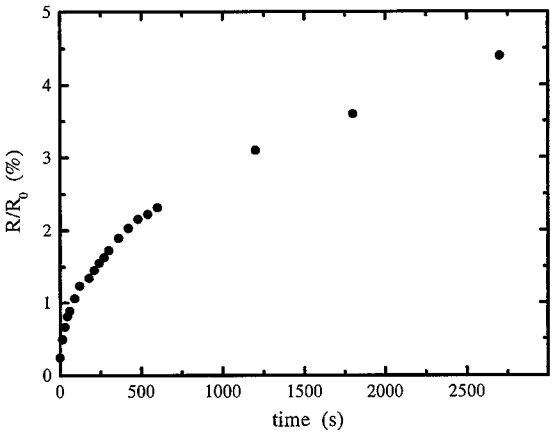

Fig. 4. Relative persistent photoconductivity in $Cd_{0.9}Mn_{0.1}Te$:In after halogen lamp illumination at 77 K. R_0 is the dark resistance at 77 K.

trap [11]. To find out if it was the case, the standard method of capture cross section measurement [11] was applied. In this method, the measurements of DLTS signal amplitude related to the peaks are carried out as a function of filling pulse width at different lock-in frequencies. The results of these measurements indicate that the capture cross section for trap E1 was indeed thermally activated and its activation barrier was equal to 0.1 eV.

The persistent photoconductivity was also studied in this experiment. The resistance of the samples was measured as a function of temperature in the 77–360 K range. When the temperature dropped below 120 K, the resistance rapidly increased by two orders of magnitude as compared to the room temperature resistance. This increase is caused by the carrier freezing associated with the high concentration of deep-level traps. Illumination of the samples at 77 K resulted in a drop in resistance by two orders of magnitude. After switching off the light, the relaxation of the resistance to its initial, dark value took a very long time. Even after 1 h, the resistance reached only about 5% of its dark value. The kinetics of the change in photoresistance after extinguishing the light is shown in Fig. 4.

Persistent photoconductivity in the indium-doped $Cd_{0.9}Mn_{0.1}Te$ proves the presence of some metastable defects in the material. For DX centers, it is required that their concentration is comparable with the net donor concentration. Also, the defects have to be strongly coupled to the surrounding lattice, which in DLTS manifests itself in very long filling pulses saturating the traps, and a thermally activated capture cross section. From the five electron traps observed in the indium-doped $Cd_{0.9}Mn_{0.1}Te$, only trap E1 satisfies these conditions. Its concentration is comparable to concentration of shallow donors and the capture cross section is thermally activated with a 0.1 eV energy barrier.

Comparing the results of this work with the results obtained by other authors supports the statement that level E1 is attributable to a DX center. Most likely, the donor-like indium impurity forms these centers.

4. Conclusions

Deep levels in $Cd_{0.9}Mn_{0.1}Te$:In were investigated using deep-level transient spectroscopy and persistent photoconductivity measurements. For full identification of the levels, the investigations were carried out within the 77–360 K temperature range. Five distinct peaks were observed in the DLTS spectra, one of which, E1, could be attributed to a DX center. The corresponding trap has a high concentration. There is strong lattice coupling for defect associated with this trap. Finally, the capture cross section, with a 0.1 eV barrier, can be thermally activated.

Exposing the $Cd_{0.9}Mn_{0.1}Te$:In sample, at 77 K, to illumination from a halogen lamp increased the conductivity of the material by about two orders of magnitude. This photoconductivity persisted for a very long time after extinguishing the light. It is reasonable to assume that trap E1 is related to indium impurity which forms DX centers in the studied $Cd_{0.9}Mn_{0.1}Te$:In. Therefore, trap E1 is responsible for the persistent photoconductivity observed in the material.

References

[1] C.H. Park, D.J. Chadi, Phys. Rev. B 52 (1995) 11 884.
[2] J. Szatkowski, E. Płaczek-Popko, K. Sierański, J. Fialkowski, B. Bieg, Mater. Sci. Forum 258–263 (1997) 1413.
[3] J. Szatkowski, E. Płaczek-Popko, K. Sierański, A. Hajdusianek, B. Bieg, Inst. Phys. Conf. Ser. 152 (1998) 793.

[4] J. Szatkowski, E. Płaczek-Popko, K. Sierański, B. Bieg, in: D. Gershoni (Ed.), Proceedings of the 24th International Conference on Phys. Semicond., August 2–7, 1998 Jerusalem, Israel, World Scientific, Singapore, 1999, CD-ROM 0804. pdf.
[5] N.G. Semaltianos, G. Karczewski, B. Hu, T. Wojtowicz, J.K. Furdyna, Phys. Rev. B 51 (1995) 17499.
[6] G.W. Iseler, J.A. Kafalas, A.J. Strauss, H.F. MacMillan, R.H. Bube, Solid State Commun. 10 (1972) 619.
[7] A.K. Zakrzewski, L. Dobaczewski, T. Wojtowicz, J. Kossut, G. Karczewski, in: M. Scheffler, R. Zimmerman (Eds.), Proceedings of the 23rd International Conference on the Physics of Semicond., Berlin Germany, July 21–26, 1996, World Scientific, Singapore, 1996, pp. 3005–3008
[8] G. Karczewski, A.K. Zakrzewski, L. Dobaczewski, W. Dobrowolski, E. Grodzicka, T. Wojtowicz, J. Kossut, Thin Solid Films 267 (1995) 79.
[9] I. Terry, I. Penny, S. Von Molnar, J.M. Rigotty, P. Becla, Solid State Commun. 84 (1992) 235.
[10] J. Szatkowski, E. Płaczek-Popko, K. Sierański, A. Hajdusianek, Proceedings of the SPIE International. Conference on Solid State Crystals'98, Single Crystal Growth, Characterisation, and Applications, Vol. 3724, 1999, p. 150.
[11] C.H. Henry, D.V. Lang, Phys. Rev. B 15 (1977) 989.

ELSEVIER

Physica B 273–274 (1999) 883–886

PHYSICA B

www.elsevier.com/locate/physb

Photoluminescence of deep levels in (CdZn) Te-correlation with diffusion length measurement

J. Franc[a,*], P. Hlídek[a], H. Sitter[b], E. Belas[a], A.L. Toth[c], L. Turjanska[a], P. Höschl[a]

[a]*Institute of Physics, Charles University, Ke Karlovu 5, CZ-121 16, Prague 2, Czech Republic*
[b]*Institute for Semiconductor Physics, Johannes Kepler University, Altenbergerstrasse 69, Linz, Austria*
[c]*MTA MFA, Structure Research, H-1535 Budapest-114 POB 49, Hungary*

Abstract

Photoluminescence of deep levels near mid-gap in P-($Cd_{1-x}Zn_x$)Te ($x \approx 0.03$–0.05) grown by the vertical gradient freezing method was investigated. Correlation with recombination properties manifested by temperature dependence of diffusion length of minority electrons and the corresponding mobility-lifetime product was studied. Low-temperature photoluminescence (PL) in the spectral range 0.68–1.3 eV and a temperature dependence of diffusion length of minority electrons (DL) measured by EBIC in the temperature range 60–300 K on both as-grown and annealed samples (800°C and 900°C) were investigated. We observed, that while as-grown samples exhibited a steep increase in DL with decreasing temperature in the temperature range 60–140 K, annealing and subsequent quenching resulted in a significant decrease of DL at these temperatures. Photoluminescence band with a peak at approx. 0.84 eV in annealed samples with increased recombination and therefore low DL was observed, while no such peak was detected in the as-grown samples with high DL. Luminescence in the ≈ 0.8 eV band is usually attributed to a V_{Cd} related defect which is supposed to act as a recombination centre. It can be concluded, that a correlation between effects of increased recombination manifested by decreased values of DL at temperatures 60–140 K and detection of the ≈ 0.8 eV PL band was observed. Reduction of the mobility-lifetime product by increased recombination in (CdZn)Te single crystals is therefore probably connected with a presence of a V_{Cd}-related defect.

Keywords: (CdZn)Te; Photoluminescence; Diffusion length

1. Introduction

(CdZn)Te has been in the centre of interest due to its applications in detection of X- and gamma rays, in electro-optic devices and also as a substrate for epitaxial growth of mercury cadmium telluride. While crystallographic quality and good optical properties are crucial for (CdZn)Te substrates, electrical properties like a high mobility-lifetime product, high resistivity connected with a low leakage current are important for its use as a gamma and X-ray detector. For a production of (CdZn)Te with pre-defined optical and electrical properties and low concentrations of point defects and precipitates, identification of basic defects and their influence on material properties is necessary. One of the most commonly used experimental techniques for material characterization is the low-temperature photoluminescence (PL). In this paper we concentrate on PL results from spectral range 0.68–1.3 eV, that includes also signal from deep levels near the mid-gap. Properties of deep levels in CdTe and (CdZn)Te were investigated by several authors by PL, DLTS and PICTS methods. Generally, three groups of PL bands located at 0.5, 0.8 and 1.1 eV are observed in CdTe [1–3]. The 1.1 eV band is usually attributed to tellurium vacancy V_{Te}^{+} [4–6]. The 0.8 eV band was reported to consist of two subbands [2] at 0.72 and 0.81 eV. It has been attributed to an acceptor complex involving the native V_{Cd} defect and an impurity [7,8]. This level was also reported to be a good candidate

* Corresponding author. Tel.: + 420-2-216-1320; fax: + 420-2-296764.
E-mail address: franc@karlov.mff.cuni.cz (J. Franc)

0921-4526/99/$ - see front matter
PII: S0921-4526(99)00545-1

to act as a recombination centre having comparable emission rates for electrons and holes [9].

The purpose of the present paper is to analyze deep PL bands in the spectral range (0.68–1.3 eV) in as-grown and annealed $Cd_{1-x}Zn_xTe$ ($x \approx 0.03$–0.05) and to investigate possible correlation with recombination effects in the samples analyzed from temperature dependence of diffusion length of minority carriers (DL) measured by electron beam-induced current (EBIC) method. This effect was already analyzed in Ref. [10], where correlation between DL and near band gap PL (≈ 1.5 eV) was looked for.

2. Experimental

(CdZn)Te samples used in this study were prepared in our laboratory by the Vertical gradient freezing method [11]. The as-grown samples were mostly P-type with a standard concentration of holes 10^{14}–10^{16} cm^{-3} and a mobility 30–70 cm^2/Vs at 300 K. Two sets of samples were fabricated. The first set was prepared from high-quality single crystalline (1 1 1) oriented P-(CdZn)Te slice (crystal A). Neighbor samples were annealed at 800°C and 900°C at different cadmium overpressures p_{Cd} (see Table 1) and after annealing quickly quenched to room temperature. The annealing procedure was performed in a one-zone furnace, when the p_{Cd} overpressure was created by additional Cd in the ampoule together with samples of (CdZn)Te powder being added in order to avoid surface damage during annealing. The annealing time was 10 days.

The second set of samples was prepared from the as-grown single crystal B by cutting samples along the [1 1 1] growth axis from the top to the bottom of the boule (height 2 cm) in order to characterize changing conditions during the growth (mainly due to changing p_{Cd} overpressure and Zn content) and their influence on basic electrical and PL properties.

PL measurements were performed in a FTIR spectrometer Bruker IFS66/S with a Ge and Si detectors in a spectral range (0.68–1.3 eV) at temperature 4.8 K in a continuous flow He cryostat. He–Ne laser with power ≈ 15 mW was used for excitation. Spectra were corrected with respect to sensitivity of the detectors. Diffusion length of minority carriers was measured by EBIC method in a JEOL-50 scanning electron microscope with a cooled holder for measurements in the temperature range 60–300 K [12]. Au-evaporated Schottky barrier was used for the separation of electron–hole pairs in the EBIC method.

3. Results and discussion

Results of measurements of DL of minority electrons on samples from the first set – annealed at 800°C and 900°C and different p_{Cd} overpressures together with an as-grown neighbor sample are presented in Fig. 1. Obviously, the as-grown sample shows a steep increase of DL and of the corresponding mobility-lifetime product (calculated from a standard relation $L^2 = (kT/e)\mu\tau$) at temperatures below 140 K. All three annealed neighbor samples show less steep increase of DL with decreasing temperature. The effect of increased recombination, which is manifested by shorter DL is stronger at higher annealing temperatures and lower p_{Cd} overpressure. These are experimental conditions that favor generation of cadmium vacancies V_{Cd} [13]. It is therefore a good reason to suppose, that the observed increased recombination is due to some V_{Cd} related defect or complex. Results of PL measurements are summarized in Table 1, where positions of the observed PL bands in the spectral range 0.68–1.3 eV are given for samples from both sets (the annealed set from single crystal A (samples No. 1–4), the as-grown set from single crystal B (samples No. 5–7). The PL band at 1.074–1.111 eV attributed to V_{Te} is present in all investigated samples and no correlation of its presence with recombination properties was found. The PL band at ≈ 1.23 eV is present only in one sample and also in this case we found no correlation with DL measurements. Other situation occurs in the case of the

Table 1

Crystal	Sample	T (anneal)	P_{Cd}	PL (eV) 1.2 eV band	PL (eV) 1.1 eV band	PL (eV) 0.8 eV band
A	1	as grown	×	×	1.08	×
A	2	800°C	8.7×10^{-4}	1.23	1.09	0.84
A	3	800°C	1.3×10^{-2}	×	1.07	0.75
A	4	900°C	0.3	×	1.07	0.85
B	5	as grown	×	×	1.08	×
B	6	as grown	×	×	1.09	0.84
B	7	as grown	×	×	1.11	0.84

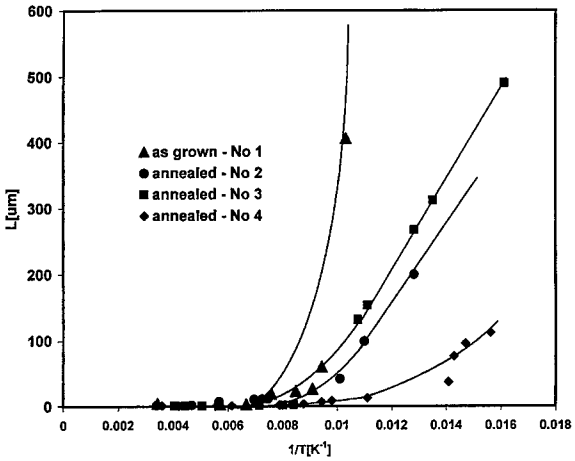

Fig. 1. Diffusion length of minority electrons in P-(CdZn)Te as-grown and annealed samples (crystal A).

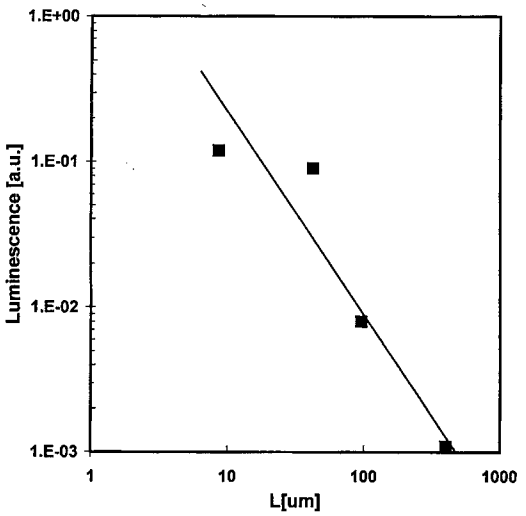

Fig. 3. Dependence of intensity of the ≈ 0.84 eV peak on diffusion length of minority electrons at 100 K (crystal A).

PL band at ≈ 0.84 eV. All annealed samples have a significant PL signal in this spectral range. In the case of sample No. 3 the peak was slightly shifted towards lower energies. PL spectra of as grown sample No. 1 and the neighbor No. 4 annealed at 900°C, $p_{Cd} \approx 0.3$ atm are given in Fig. 2. Dependence of the intensity of the ≈ 0.84 eV peak on DL of minority electrons at 100 K presented in Fig. 3 clearly shows the increase of PL intensity with decreasing DL.

Results of measurements of DL in samples from the second set (samples No. 5–7 cut along the growth axis of as-grown single crystal B) at room temperature and at 60 K are presented in Fig. 4. The top of the single crystal is N-type, the central part and the end are P-type. Diffusion length of both minority holes (N-type) and electrons (P-type) have a tendency to increase in the region, where

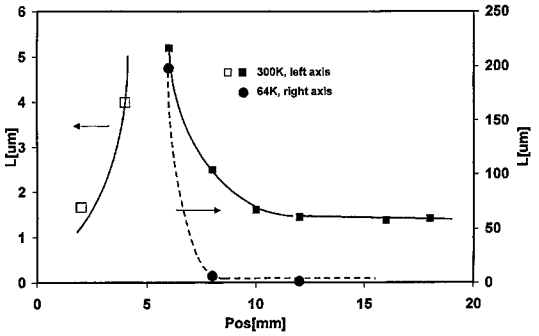

Fig. 4. Diffusion length of minority holes (open symbols) and electrons (full symbols) on a set of samples cut along the growth axis of crystal B at room temperature and at 64 K.

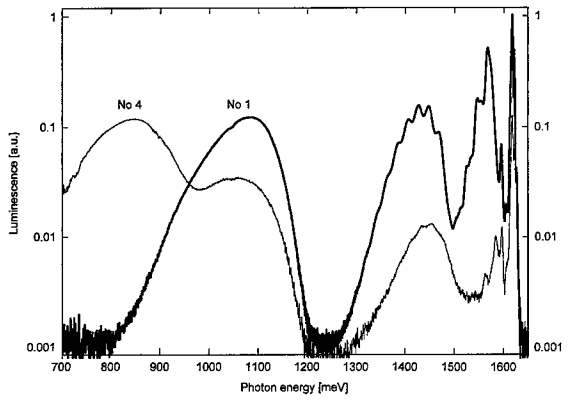

Fig. 2. Photoluminescence spectra of samples No. 1 and No. 4 (see Table 1).

P–N conversion occurs. Low-temperature (64 K) DL of minority electrons measured in the P-type part of the crystal are relatively long only in a very narrow region close to the P–N transition plain being very short in the rest part. PL analysis of these samples given in Table 1 shows, that the sample with relatively long DL at 64 K (No. 5) has only weak PL in the spectral range ≈ 0.84 eV, while the other two P-type samples representing the middle (No. 6) and the end of the single crystal (No. 7) have a clear PL band at ≈ 0.84 eV, whose intensity increases towards the crystal end.

The results can be explained as follows. The growth of crystal B occurred in a p_{Cd} overpressure ≈ 1 atm. While the top of the crystal had direct contact with the surrounding Cd atmosphere, the central part and the end solidified under Te rich conditions, which resulted in a higher concentration of V_{Cd}. The same effect was

reached by annealing and subsequent quenching of samples from the first set. The generated cadmium vacancies then could create complexes with some residual foreign impurities, which is manifested by increased PL at ≈ 0.84 eV. We conclude, that combined measurements of DL of minority electrons and PL in the spectral range (0.68–1.3 eV) indicate, that deep energy level ≈ 0.84 eV usually attributed to the V_{Cd} – foreign impurity complex, is responsible for increased recombination at temperatures below 140 K, which is manifested by shorter DL of minority electrons and of the corresponding mobility-lifetime product in P-(CdZn)Te samples.

Acknowledgements

This work was in part supported by the grant of the Czech ministry for schools, youth and education under No VS 97113, the grant agency of the Czech Republic under contract No. 202/97/8P072, the grant agency of the Charles University under No's 176/1996 and 42/1997, the Hungarian National Scientific Research Fund under contract No. T22545, the Austro-Hungarian Exchange Program TeT Project No. 19. and by the Austrian-Czech exchange program AKTION (ME 115).

References

[1] J.F. Bryant, E. Webster, Br. J. Appl. Phys. (J. Phys. D.) 1 (1968) 965.
[2] J. Krustok, A. Loo, T. Piibe, J. Phys. Chem. Sol. 52 (1991) 1037.
[3] He Xiang Han, B.J. Feldman, M.L. Wroge, D.J. Leopold, J.M. Ballingall, J. Appl. Phys. 61 (1987) 2670.
[4] W. Stadler, D.M. Hofmann, H.C. Alt, T. Muschik, B.K. Meyer, E. Weigel, G. Müller-Vogt, M. Salk, E. Rupp, K.W. Benz, Phys. Rev. B 51 (1995) 10 619.
[5] C. Barnett Davis, D.D. Allred, A. Reyes-Mena, J. Gonzales-Hernandez, D. Gonzales, B.C. Hess, W.P. Allred, Phys. Rev. B 47 (1993) 13 363.
[6] D.M. Hofmann, W. Stadler, K. Oettinger, B.K. Meyer, P. Omling, M. Salk, K.W. Benz, E. Weigel, G. Müller-Vogt, Mater. Sci. Eng. B 16 (1993) 128.
[7] A. Castaldini, A. Cavallini, B. Fraboni, P. Fernandez, J. Piqueras, J. Appl. Phys. 83 (1998) 2121.
[8] V. Pal, P. Fernandez, J. Piqueras, N.V. Sochinskii, E. Dieguez, J. Appl. Phys. 78 (1995) 1992.
[9] T. Takebe, J. Saraie, H. Matsunami, J. Appl. Phys. 53 (1982) 457.
[10] J. Franc, E. Belas, A.L. Toth, H. Sitter, P. Hlídek, P. Moravec, P. Höschl, J. Crystal Growth 197 (1999) 593.
[11] P. Höschl, Yu.M. Ivanov, E. Belas, J. Franc, R. Grill, P. Hlídek, P. Moravec, M. Zvára, H. Sitter, A.L. Toth, J. Crystal Growth 184/185 (1998) 1039.
[12] J. Franc, E. Belas, A.L. Toth, Yu.M. Ivanov, H. Sitter, P. Moravec, P. Höschl, Semicond. Sci. Technol. 13 (1998) 314.
[13] M.A. Berding, Appl. Phys. Lett. 74 (1999) 552.

ELSEVIER

Physica B 273–274 (1999) 887–890

PHYSICA B

www.elsevier.com/locate/physb

Study of microscopic mechanisms of electrical compensation of donors in CdS by fast diffusors (Cu, Ag, or Au)

I.D. Desnica-Frankovic[a,*], U.V. Desnica[a], A. Stötzler[b], M. Deicher[b]

[a]*R. Boskovic Institute, Mater. Physics Department, Bijenicka 54, 10000 Zagreb, Croatia*
[b]*Fakultät für Physik, Universität Konstanz, D-78457, Konstanz, Germany*

Abstract

The goal of this study was to identify microscopic causes of the extensive changes in electrical properties observed in CdS crystal when doped with some fast-diffusers (FD), Cu, Ag or Au. The compensation of donors and the dynamics of in-diffusion was quantitatively determined by C–V measurements, whereas the changes at the atomic level were followed by perturbed angular correlation (PAC) spectroscopy. The penetration of FDs, as deduced from C–V, correlated well with changes observed in PAC, which manifest as new defects and/or as the increase of the concentration of (V_{Cd}–In_{Cd}) pairs. Arguments are given that the new defects observed by PAC in CdS:Ag belong to $(In_{Cd}^{+}-V_{Cd}^{2-}-Ag_i^{+})^{o}$ and similar complexes in Cu. No indication of such complexes was observed in Au doped CdS. In CdS:Au practically all donors are passivated directly by pairing with V_{Cd} trapped at the nearest Cd site, whereas in Ag or Cu-doped CdS most of the donors are electrically compensated from the distance by FD_{Cd} acceptors. Our results suggest a complex microscopic mechanism by which the FD in-diffusion into CdS creates highly compensated semi-insulating material.

Keywords: II–VI; Electrical compensation; Fast diffusors; PAC

1. Introduction

Direct band gap II–VI semiconductors are very promising for realizing efficient diode lasers and light-emitting diodes over the visible portion of the spectrum, efficient solar cells, X-ray and gamma-detectors, and a number of other applications. However, the persistent technological problems — control of electrical properties being the most puzzling — still hinders a wider use of these materials.

Fast diffusors from the IB group, like Cu, Ag or Au, are important impurities or dopants in all semiconductors and in II–VI compounds in particular. It has been observed that they diffuse much faster in II–VI's at relatively low temperatures than they do in Si, Ge or III–V's [1], usually acting detrimentally on a number of desired properties, often in an uncontrollable way. The lowest temperatures at which diffusion coefficients in CdS monocrystals were hitherto determined are 160°C for Cu, $D_{Cu}(T) = 2.1 \times 10^{-3} \exp[-0.96(\text{eV})/kT]$ [2], 100°C for Ag, $D_{Ag}(T) = 2.6 \times 10^{-5} \exp[-0.75(\text{eV})/kT]$ [3]; and 500°C for gold, $D_{Au}(T) = 91 \exp(-2.1(\text{eV})/kT)$ [4]. To explain such extremely high diffusivities it is believed that FDs move through CdS as interstitials. However, since the in-diffusion of any of FD transforms n-type CdS into a highly compensated material [1–4], the effective electrical action of Cu, Ag or Au in CdS is clearly acceptor like. To clarify these controversies, we have monitored changes of electrical properties of CdS crystals due to in-diffusion of a particular fast diffusor (by C–V), in parallel with changes occurring at the microscopic level (by PAC). From the correlation between microscopic and macroscopic data it was possible to propose some compensation mechanisms (or exclude some others) by which FDs change the electrical properties of CdS.

* Corresponding author. Fax: + 385-1-4680-114.
E-mail address: ddesnica@rudjer.irb.hr (I.D. Desnica-Frankovic)

0921-4526/99/$ - see front matter
PII: S0921-4526(99)00546-3

2. Experimental details and methodology

2.1. Influence of FD in-diffusion on the electrical properties

The dynamics of the low-T in-diffusion was quantitatively determined by C–V measurements. The penetrating FD atoms compensate donors in n-CdS and therefore change the sample capacitance. A capacitor structure was created in which one 'plate' (and one contact) was the evaporated FD dot, while the other 'plate' was the rest of still conductive n-CdS, with alloyed In as a second contact. The typical area, A, of the dot was 10–20 mm^2. By measuring the capacitance $C = \varepsilon A/W$, the thickness of the SI-layer, W, reflecting the penetration of FD, was determined after each annealing step at temperature T_a. Furthermore, the C–V measurement enabled the profiling of effective, uncompensated, donor concentrations, $n = N_{D,eff.} \equiv N_D - N_A = 2/[(qA^2\varepsilon)d(1/C^2)/dV]$. By measuring $C(V)$ at various T_a as a function of time, the penetration rate, and then diffusion coefficients, of each FD could be determined with great precision and spatial resolution from

$$N_{FD}(x) = N_{FD}(0)\mathrm{erfc}[x/2(Dt)^{1/2}], \quad (1)$$

where $N_{FD}(0)$ is the concentration of dopants at the surface, $N_{FD}(x)$ the concentration of FD at depth x, diffused for time t at chosen T_a and diffusion coefficient $D(T_a)$. Measurements were done for Cu and Au, whereas for Ag the low-T diffusion data already exist [3].

Changes at the atomic level due to in-diffusion of FD

The perturbed $\gamma\gamma$ angular correlation (PAC) spectroscopy is a nuclear hyperfine technique which gives detailed and quantitative information about the immediate surrounding of the probe atom [5]. From the fit of a PAC spectrum $R(t)$, one can determine characteristic PAC parameters: the hyperfine interaction strength, ν_Q, and the asymmetry parameter η of the local electric field gradient (EFG). Each PAC 'signature' (ν_Q and η) unambiguously labels a particular probe-atom-defect configuration, allowing its easy qualitative and quantitative identification. The CdS samples were first pre-doped with very small amount ($\approx 10^{11}$ cm^{-3}) of radioactive ^{111}In probe atoms by diffusion at 800°C for 90 min under 2 atm vapor pressure of sulfur. Practically, all probe atoms were embedded within 1.5 μm from the surface (40% within first 0.2 μm), as determined by gradual etching. Two types of pre-doped samples were prepared: (a) Samples in which all ^{111}In atoms were incorporated at Cd donor-sites (In_{Cd}^{+}) [6], resulting in a single, 7.4 MHz frequency in PAC spectra (Fig. 4c, Site 1). (b) Samples in which about half of ^{111}In was incorporated as In_{Cd}, while the other half was paired with Cd vacancies, $(In_{Cd}^{+}-V_{Cd}^{2-})^{-}$, characterized by the 72.4 and 78.7 MHz frequencies [6] (Site 2 and 3, respectively). The $(In_{Cd}^{+}-V_{Cd}^{2-})^{-}$ pairs are acceptors, and hence pose a potential trap for any diffusing donors. On both types of samples a FD layer was evaporated. Annealing was performed either under S or Cd partial pressure, in the temperature interval from RT up to 700°C. After each annealing step a PAC spectrum was recorded.

3. Results and discussion

3.1. Influence of the FD in-diffusion on electrical properties

A gamut of C–V spectra measured on CdS:Cu annealed for up to 109 h at $T_a = 100$°C is shown in Fig. 1. At first, while the barrier is building up, the maximum of C only shifts away from the $V = 0$ position. Once the barrier has been formed, further annealing reduces C as the acceptors penetrate deeper into the CdS and the thickness of SI layer increases. The resulting decrease of the uncompensated donor concentration and the shifting of the penetration depth W is depicted in Fig. 2. Eq. (1) then enables the calculation of the penetration rate $N_{Cu}(x)/N_{Cu}(0)$ and the diffusion coefficient $D_{Cu}(100)$.

All results are summarized in Fig. 3. Full lines represent results from the present study while dotted lines are calculated from Refs. [2–4] including data for the lowest reported T_a. It can be seen that Cu was found to be the fastest diffusing for all also in the low T_a range, followed by Ag and Au. From the standpoint of the influence of FD on electrical properties, the most important fact is that all of the studied FD's in CdS act effectively as acceptors causing a complete compensation of donors (N_{Deff} in the 10^{15}–10^{16}/cm^3 range) in the surface region of n-CdS.

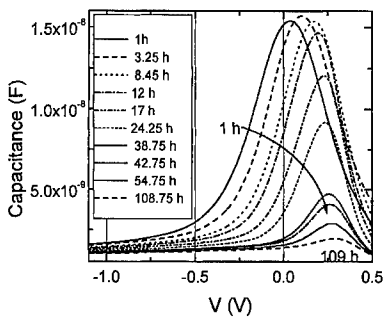

Fig. 1. A series of C–V spectra of CdS:Cu annealed at 100°C from 1 up to 108.75 h. For each curve the corresponding annealing time is given in the figure.

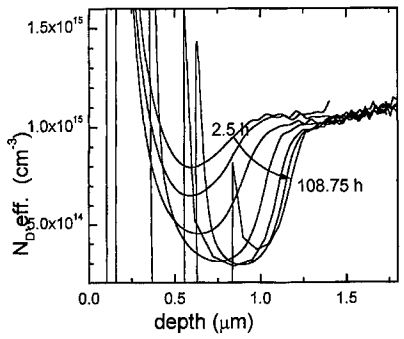

Fig. 2. Spatial distribution of the uncompensated donors concentration $N_{D,eff}$, for CdS:Cu sample annealed at 100°C for various annealing time, t_a, indicated in the figure. For larger t_a the penetration depth $W(t_a, T_a)$, and the whole profile of $N_{D,eff}(x)$, shifts deeper into the crystal.

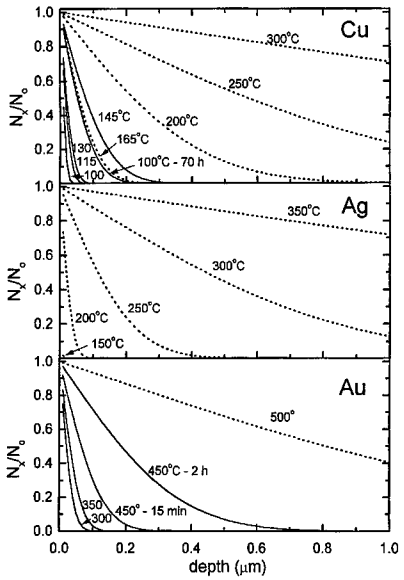

Fig. 3. Penetration rate $N_{FD}(x)/N_{FD}(0)$ for Cu, Ag, and Au diffusion in CdS, calculated from Eq. (1) with low-T values of diffusion coefficients obtained for Cu and Au from this work (full line), while D_{Ag} was taken from Ref. [2] (dashed line). For a comparison, lowest previously reported penetration rates for Cu are calculated from Ref. [2] and for Au from Ref. [4] (dashed). The diffusion time, t_a was 30 min, except for Cu at 100°C, 115°C and 130°C (2 h) or if indicated otherwise.

3.2. Changes at the atomic level due to in-diffusion of FD

Thermal treatment of CdS:FD brought about considerable changes in the microscopic surrounding of the ^{111}In probe atoms, observed at T_a as low as 145°C in CdS:Cu, at $T_a = 200$°C in CdS:Ag and at 450°C

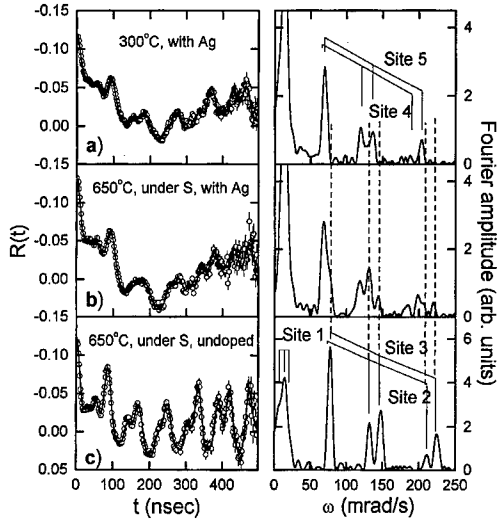

Fig. 4. PAC spectra (left) and their Fourier transforms (right) of a CdS sample pre-doped with ^{111}In probe atoms, after the evaporation of Ag at RT and annealing at indicated temperatures under S pressure (Figs. 4a and b). Spectrum of a sample without Ag is given for comparison (Fig. 4c).

in CdS:Au. In undoped samples (without intentionally added FD) first changes in PAC spectra were observed above 500°C [5,7].

Fig. 4 gives essential points regarding the changes in the surroundings of ^{111}In during in-diffusion of Ag. Prior to Ag evaporation the sample was annealed under Cd pressure to minimize V_{Cd} formation. Upon annealing at 200°C a new PAC signal appeared and already at $T_a = 300$°C a considerable fraction (35%) of probe atoms was involved in this configuration. Although the corresponding frequencies: $\nu_Q = 65.5$ MHz, $\eta = 0.30$ (Site 4) and $\nu_Q = 70.5$ and $\eta = 0.21$ (Site 5) are quite close to the values belonging to the ordinary pairs (Sites 2 and 3; Fig. 4c) they are clearly different and distinguishable (compare Fig. 4a and c). If, in addition, ordinary vacancies are created by heating the sample under S pressure above 500°C, a mixture of all 5 sites can be obtained (Fig. 4b).

In CdS:Cu samples the presence of Cu was revealed in several ways: as a new signal, also very similar to that belonging to $(In_{Cd}–V_{Cd})$ pairs, as an increase of the fraction of $(In_{Cd}–V_{Cd})$ pairs, and as an additional signal characterized by $\nu_Q = 20$ MHz, $\eta \leqslant 0.3$, the last one only in samples annealed under Cd pressure. This PAC signal was already observed in diffused CdS:In [6] but was not recognized as related to Cu.

In Au diffused samples no new frequencies were observed. However, vacancies appeared at $T_a = 450$°C, which is somewhat lower than the temperatures reported

for thermal creation of vacancies in undoped samples [5,7]. Furthermore, once created, V_{Cd} in Au-saturated samples cannot be easily annihilated by annealing under Cd pressure, as it is the case in undoped samples.

3.3. The correlation of microscopic and macroscopic results

By comparison of C–V and PAC results, the connection between microscopic and macroscopic properties in FD-doped CdS crystals could be established. We have found that:

(a) The appearance of new features in the PAC spectra, observed already at low T_a, correlates with the penetration of particular a FD into the 0.1–0.2 μm surface layer. Hence, these PAC features, in all cases, can be safely related to the in-diffusion of FDs.

(b) New configurations, observed in Ag and Cu doped samples, have PAC signatures so similar to those of the (In_{Cd}–V_{Cd}) pairs (Fig. 4) that they have to originate from complexes which contain (In_{Cd}–V_{Cd}). For these complexes we propose a microscopic structure $(In_{Cd}^{+}$–V_{Cd}^{2-}–$FD_i^{+})^{o}$, in which FD_i (Ag or Cu interstitial) should be 2.5 sites away from the probe atoms. Such assignment agrees with the expectation that the diffusing FD interstitals (Cu_i^{+} or Ag_i^{+}), which are donors, are attracted to the V_{Cd}^{2-} side of the pair whereas, at the same time, repulsed from the In_{Cd}^{+} side. This makes the interstitial lattice sites farthest from In_{Cd}^{+} energetically most favorable, and the observed small perturbation of the pair frequencies is then understandable. No indication of such complexes was observed in Au doped CdS. Since this complex should be neutral, it represents an efficient mechanism for the compensation of both In_{Cd} and FD_i donors.

(c) In CdS samples with evaporated Au, Cd vacancies were detected (through their pairing with $^{111}In_{Cd}$) already at 450°C. Taking into account the conclusions (a) and (b), it seems that due to the presence of FDs the V_{Cd} appear at T_a lower than in undoped CdS.

(d) The 20 MHz signal is now positively related to Cu, but its microscopic structure and possible electrical activity is yet to be identified.

(e) The formation of neutral donor–acceptor pairs of the (In_{Cd}–FD_{Cd}) type was not observed; hence, this is not the mechanism by which the substitutional donors (like $^{111}In_{Cd}$) in CdS are compensated. Even if one should prove that the 20 MHz PAC signal belongs to (In_{Cd}–Cu_{Cd}), its fraction never exceeded more than $\frac{1}{3}$ of In_{Cd} donors, indicating that most donors were compensated in some other way.

4. Conclusions

The presented results suggest a complex microscopic mechanism by which FD in-diffusion creates highly compensated semi-insulating Cds. Although all studied FD atoms act as acceptors, the microscopic mechanisms of compensation are multiple and differ for the different FDs, particularly in the relative importance of these mechanisms. The results are compatible with a notion that the diffusion of FD atoms into CdS provokes simultaneous in-diffusion of Cd vacancies. Some of these vacancies become trapped at donors resulting in a direct electrical passivation. The others create empty sites in the Cd sublattice (otherwise lacking in CdS), enabling the diffusing FD atoms to switch from interstitial donor sites (FD_i) onto substitutional acceptor sites (FD_{CD}). In Au doped CdS most of the donors are compensated directly by V_{Cd} trapped at the nearest Cd site, whereas in CdS:Ag or CdS:Cu the majority of donors are electrically compensated from the distance, most probably by FD_{Cd} acceptors.

Acknowledgements

This research was supported by the Ministry of Science and Technology of Croatia and by the Deutsche Forschugsgneischaft (SFB306). UVD gratefully acknowledges support of the Deutsche Akademishe Austauschdienst A/98/03073.

References

[1] D.L. Beke (Ed.), Landolt-Börnstein New Series Group III, Vol. 33, Subvol. A, Diffusion in Semiconductors, Springer, Berlin, 1998, and references therein.
[2] J.L. Sullivan, J. Phys. D 6 (1973) 552.
[3] J.-P. Sorbier, N. Sanguinetti, Rev. Phys. Appl. 9 (1974) 973.
[4] J.L. Sullivan, Phys. Rev. 184 (1969) 796.
[5] Th. Wichert, Th. Krings, H. Wolf, Physica B 185 (1993) 297.
[6] R. Magerle, M. Deicher, U. Desnica, R. Keller, W. Pfeiffer, F. Pleiter, H. Skudlik, Th. Wichert, Appl. Surf. Sci. 50 (1991) 169.
[7] U.V. Desnica, R. Magerle, I.D. Desnica-Frankovic, A. Burchard, M. Deicher, Phys. Rev. Lett., submitted for publication.

ELSEVIER

Physica B 273–274 (1999) 891–894

PHYSICA B

www.elsevier.com/locate/physb

Hydrogen passivation of nitrogen-related energy levels in ZnSe and ZnSSe grown by MBE

D. Seghier, J.T. Gudmundsson, H.P. Gislason*

Science Institute, University of Iceland, Dunhagi 3, IS-107 Reykjavik, Iceland

Abstract

In previous work we reported the observation of three hole traps in N-doped ZnSe and ZnS_xSe_{1-x} films grown by MBE. We attributed a trap T1 at $E_v + 0.11$ eV in ZnSe to a dominating nitrogen acceptor, but traps T2 at $E_v + 0.46$ and T3 at $E_v + 0.56$ eV to the N-doping process. In the present study we investigated the effect of hydrogenation on these hole traps. We found that samples with net acceptor concentrations less than few times 10^{16} cm^{-3} become highly resistive after the hydrogenation. In samples which remained conductive the hydrogenation caused a decrease in the DLTS peak heights of T2 and T3 within 0.4–0.5 μm from the surface. In samples with net acceptor concentration around $2–5 \times 10^{16}$ cm^{-3} we also observe a similar decrease in the DLTS peak height of level T1 and net charge density which shows its role in the hole conductivity of the samples. Hydrogenation of samples with net acceptor densities in the 10^{17} cm^{-3} range did not affect the net charge density or height of T1 much.

Keywords: ZnSe; Hydrogen; Passivation; Hole conductivity

The saturation of hole conductivity at high levels of p-type doping in ZnSe and ZnS_xSe_{1-x} alloys limits their potential for fabrication of devices operating in the blue portion of the visible spectrum. For some time the origin of this behaviour has been a topic of controversy. Nitrogen acts as an acceptor in ZnS_xSe_{1-x}. The highest active acceptor density obtained in nitrogen doped ZnSe is limited to about 10^{18} cm^{-3} in samples grown by molecular beam epitaxy (MBE) [1,2]. The origin of this charge compensation process is not well understood. One source of defect passivation in many semiconductors is hydrogen incorporated during the growth process.

There have been several investigations of the effect of hydrogen in N-doped ZnSe reported in the literature [3–6]. Most of them involved optical measurements. However, there is no direct evidence for the passivation of nitrogen acceptors by hydrogen from electrical measurements on samples measured before and after intentional hydrogenation. In an earlier work [7] we reported on deep-level transient spectroscopy (DLTS) and admittance spectroscopy on N-doped ZnSe and ZnSSe samples grown by MBE on GaAs substrates. In ZnSe we observed three hole traps T1–T3 located at 0.11, 0.46 and 0.56 eV, respectively, from the valence band. In ZnS_xSe_{1-x} with $x = 0.08$ slightly higher values were obtained. We attributed T1 to a dominating nitrogen acceptor, and T2 and T3 to other N-related defects [7] known to exist in the material [8]. In this work, we report on the effect of exposing the materials to hydrogen plasma. Our results from capacitance to voltage (C–V) profiling and DLTS show that the hydrogenation causes a direct passivation of the N acceptors.

The ZnSe epilayers were grown at Heriot-Watt University by MBE on GaAs substrates. The growth temperature was 300°C. Solid sources of zinc and selenium were used and the growth rate was 0.5 μm/h. The nitrogen was incorporated by using an Oxford Applied Instruments plasma source. The doped zinc selenide was grown directly onto the substrate without buffer layer. The thickness of the layer was approximately 1 μm. The N-doped ZnS_xSe_{1-x} layers with $x = 0.08$ were grown under

* Corresponding author. Fax: + 354-552-8911.
E-mail address: haflidi@raunvis.hi.is (H.P. Gislason)

0921-4526/99/$ - see front matter
PII: S0921-4526(99)00547-5

Table 1
List of samples used in the investigation. The net acceptor concentrations refer to as-grown samples

Sample	Material	$(N_a - N_d)$ (cm^{-3})
#1	ZnSe	8×10^{15}
#2	ZnSe	3×10^{16}
#2a	ZnSSe	5×10^{16}
#3	ZnSe	1.5×10^{17}
#3a	ZnSSe	4×10^{17}

similar conditions. The samples were exposed to H_2/Ar plasma, in a planar inductive discharge. The details of the inductive discharge used and plasma properties are given elsewhere [9,10]. The gas pressure was kept at 20 mTorr with fractional argon pressure of 0.3. The power applied to the plasma was 400 W for 45 min. No external heating was applied to the wafer. The plasma electron density was 6×10^{17} cm^{-3} [9] and the mean ion bombarding energy about 18 eV [10]. Schottky diodes with diameter 1 mm were made by evaporating Au and ohmic contacts were formed by evaporating Au–Zn alloy or using In–Ga alloy. The acceptor concentration determined from *C–V* measurements in the studied samples ranges between 8×10^{15} and 4×10^{17} cm^{-3}. Table 1 summarises some of the samples studied in this work. In the following results from the ZnSe samples labelled #2 and #3 will be presented since the ZnSSe samples #2a and #3a give similar results.

All Schottky diodes made from the samples were measured using *I–V* and *C–V* analysis. The net acceptor concentration $(N_a - N_d)$ was calculated from the *C–V* data before and after hydrogenation for comparison. After the hydrogenation samples with $(N_a - N_d) \approx 1 \times 10^{16}$ cm^{-3} were all highly resistive and the active layers completely depleted of free carriers. Thus, no capacitance measurements were possible on these samples. We infer that the acceptors were effectively charge compensated in these materials. We attribute this effect to N acceptors being passivated by hydrogen and deduce the concentration of hydrogen species involved in the passivation process as equal or higher than 1×10^{16} cm^{-3}. This assignment agrees with optical measurements using infrared absorption and Raman spectroscopy, which confirm that H forms complexes with N acceptors in ZnSe [3,4].

Fig. 1 shows $(N_a - N_d)$ measured in sample #2 before and after hydrogenation. The net charge profile is homogeneous in the as-grown sample, about 3×10^{16} cm^{-3} (curve *a*). The hydrogenation causes a decrease by a factor 2–3 in the net charge profile close to the surface (curve *b*). Farther into the sample $(N_a - N_d)$, increases continuously until it equals the original value around 0.4–0.5 μm from the surface. Curve *c* shows the effect of annealing

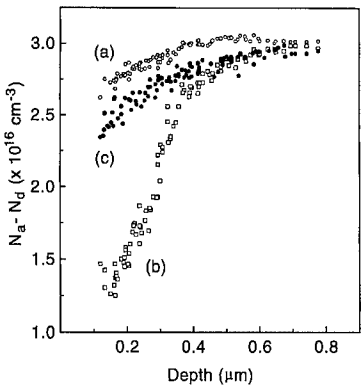

Fig. 1. Net acceptor concentration $(N_a - N_d)$ in sample #2. (a) as-grown (b) after hydrogenation (c) after annealing of the hydrogenated sample.

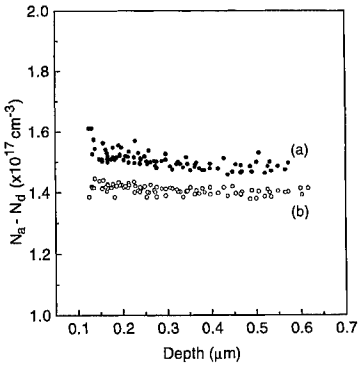

Fig. 2. Net acceptor concentration $(N_a - N_d)$ in sample #3. (a) as-grown (b) after hydrogenation.

the hydrogenated sample in curve *b* on the net acceptor concentration, to be discussed below. From the $(N_a - N_d)$ profile after hydrogenation we estimate that the passivation close to the surface corresponds to an effective density of hydrogen of about 2×10^{16} cm^{-3}, decreasing into the bulk. Fig. 2 presents $(N_a - N_d)$ in sample #3 before and after hydrogen exposure. It is clear that for $(N_a - N_d) = 1.5 \times 10^{17}$ cm^{-3} the hydrogenation has little effect on the active acceptor concentration.

In Fig. 3 we compare DLTS spectra of sample #2 as-grown (curve *a*) and after hydrogenation (curve *b*). For both curves a reverse bias of $V_r = 5$ V, a carrier filling pulse of 3 V and a DLTS rate window of $\tau = 2 \times 10^{-4}$ s were used. Similar DLTS spectra were obtained in all the samples before hydrogenation. The three dominant peaks in the DLTS spectrum, labelled T1, T2 and T3, have energy levels at 0.11, 0.46, and 0.56 eV from the valence band, respectively. Profiling of the DLTS signal shows homogeneous concentrations of the traps throughout the material. Details of the DLTS results were reported in a previous paper [7]. The T1 peak was

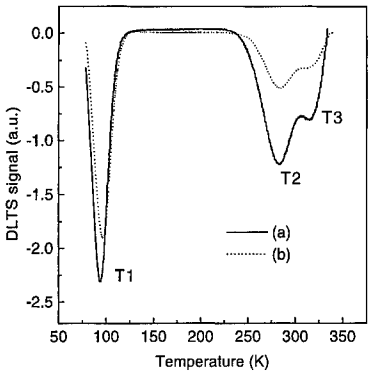

Fig. 3. DLTS spectra of sample #2 with reverse bias $V_r = 5$ V, carrier filling pulse 3 V and rate window $\tau = 2 \times 10^{-4}$ s. (a) as-grown (b) after hydrogenation.

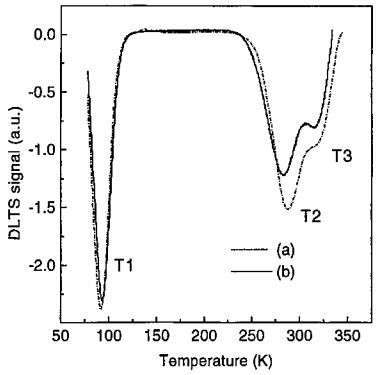

Fig. 4. DLTS spectra of sample #3 with reverse bias $V_r = 5$ V, carrier filling pulse 3 V and rate window $\tau = 2 \times 10^{-4}$ s. (a) as-grown (b) after hydrogenation.

attributed to a nitrogen acceptor level governing the free hole concentration in the samples. Traps T2 and T3 were attributed to the nitrogen doping process and found to have low concentration in all samples, the highest one $\approx 10^{14}$ cm^{-3} in the samples with highest net acceptor concentration. Curve *b* in Fig. 3 shows the DLTS spectrum of sample #2 after hydrogenation. By comparing the two curves, it is clear that the magnitude of all peaks T1–T3 has decreased in the hydrogenated sample. Profiling measurements show that the DLTS signal of traps T2 and T3 decreases in the same region as the net acceptor concentration $(N_a - N_d)$ as a result of the hydrogenation (see Fig. 1). The concentration of trap T1 also decreases with a similar profile after the hydrogenation. Since we attribute this energy level to a dominating acceptor, its peak height in DLTS is not a reliable measure of concentration, as explained in the previous work [7]. Nevertheless, the reduction of the peak height of T1 is consistent with the decrease in $(N_a - N_d)$ in the same sample. Fig. 4 compares the DLTS spectrum for the sample #3 before and after the hydrogenation. The measurement conditions were the same as in Fig. 3. We find that the hydrogenation decreases peaks T2 and T3. The height of peak T1 is virtually unchanged. This agrees with the *C–V* profiles in Fig. 2 which showed that the hydrogenation does not significantly affect this high net acceptor concentration.

From the collected evidence above we conclude that exposure to hydrogen simultaneously reduces the net acceptor concentration and the concentration of the 0.11 eV acceptor in N-doped ZnSe films grown by MBE. Moreover, the decrease of $(N_a - N_d)$ and the DLTS signal are correlated in magnitude. Identical results were obtained for the ZnSSe films in this study. This important observation is consistent with earlier work in which this acceptor was found to control the hole conductivity of the samples and attributed to a nitrogen acceptor. We also deduce that the concentration of hydrogen atoms which are active in passivating the N acceptor does not exceed few times 10^{16} cm^{-3} close to the surface where the hydrogen profile is strongest. We draw this conclusion since samples with $(N_a - N_d)$ lower than this value become highly resistive while samples with $(N_a - N_d)$ comparable with this value only exhibit a decrease in their net acceptor concentration by a factor of 2–3. Also, samples #3 and #3a with net acceptor concentration above 10^{17} cm^{-3} show negligible change in their net acceptor concentration after hydrogenation. In all conductive samples a decrease in the peak heights of the DLTS signal from traps T2 and T3 was observed. We observe less reduction in samples with higher net acceptor concentration, confirming that the concentration of these traps increases with $(N_a - N_d)$ since all the hydrogenated samples were subject to the same hydrogen exposure. The fact that incorporation of hydrogen which completely passivates about 10^{16} cm^{-3} of T1 traps only partially passivates less than 10^{14} cm^{-3} T2 and T3 traps requires further investigation.

Finally, we annealed the hydrogenated samples #2 and #2a at 200°C under reverse bias $V_r = 1$ V for about 10 min and repeated the above measurements. In order not to degrade the quality of the Schottky diodes we avoided higher annealing temperatures. We found that annealing partially restored both $(N_a - N_d)$ and the DLTS signal from all traps T1–T3. Curve *c* in Fig. 1 shows the effect of annealing on the net acceptor concentration in the hydrogenated sample #2. Similar annealing was performed on sample #1 which, however, remained highly resistive. In photoluminescence measurements on MBE-grown ZnSe:N samples which were as-grown and hydrogenated directly after growth Kim et al. [11] similarly found that annealing restored several properties of the samples. We attribute the increase of the net acceptor concentration to the dissociation of electri-

cally inactive complexes of nitrogen and hydrogen. By monitoring the DLTS signal from the nitrogen acceptor (as well as the T2 and T3) traps, which also increases upon annealing, we minimise the risk of misinterpreting the annealing results.

In conclusion we studied the net acceptor concentration ($N_a - N_d$) in nitrogen-doped p-type ZnSe and ZnS_xSe_{1-x} with $x = 0.08$ before and after exposure to H_2/Ar plasma. Our results from capacitance–voltage profiling and DLTS show that a direct passivation of the 0.11 eV acceptor level occurs after hydrogenation. At the same time there is a corresponding reduction of ($N_a - N_d$) in the samples. The results support the attribution of this dominating acceptor level to nitrogen.

This research was supported by the Icelandic Research Council and the University Research Fund. We are grateful to Prof. B.C. Cavenett and Prof. K.A. Prior for providing the samples used in this study. J.T.G. thanks the hospitality of Prof. M. A. Lieberman and the experimental assistance of A. M. Marakhtanov at University of California at Berkeley where the hydrogenation was performed.

References

[1] R.M. Park, M.B. Troffer, C.M. Rouleau, J.D. DePuydt, M.A. Haase, Appl. Phys. Lett. 57 (1990) 2127.
[2] J. Qiu, H. Cheng, J.M. DePuydt, M.A. Haase, J. Crystal Growth 127 (1993) 279.
[3] J.A. Wolk, J.W. Ager III, K.J. Duxstad, E.E. Haller, N.R. Taskar, D.R. Dorman, D.J. Olego, Mater. Res. Soc. Symp. Proc. 325 (1994) 347.
[4] J.A. Wolk, J.W. Ager III, K.J. Duxstad, E.E. Haller, N.R. Taskar, D.R. Dorman, D.J. Olego, Appl. Phys. Lett. 63 (1993) 2756.
[5] J. Yasuhisa Fujita, Toshiyuki Terada, Tetsuya Suzuki, Jpn. J. Appl. Phys. 34 (1995) L1034.
[6] S.J. Pearton, J.W. Corbett, T.S. Shi, Appl. Phys. A: Solids Surf. 43 (1987) 153.
[7] D. Seghier, H.P. Gislason, Appl. Phys. Lett. 71 (1998) 3026.
[8] I.S. Hauksson, J. Simpson, S.Y. Wang, K.A. Prior, B.C. Cavenett, Appl. Phys. Lett. 61 (1992) 2208.
[9] J.T. Gudmundsson, Plasma Sources Sci. Technol. 7 (1998) 330.
[10] J.T. Gudmundsson, Plasma Sources Sci. Technol. 8 (1999) 58.
[11] M.D. Kim, H.S. Park, T.W. Kim, J. Appl. Phys. 84 (1998) 3125.

ELSEVIER

Physica B 273–274 (1999) 895–897

PHYSICA B

www.elsevier.com/locate/physb

Anisotropic polarization of dislocation-related luminescence in thin ZnSe films

L. Worschech[a,*], W. Ossau[a], A. Waag[a], G. Landwehr[a], U. Hilpert[b], J. Schreiber[b], Y.T. Rebane[c], Y.G. Shreter[c]

[a]*Physikalisches Institut der Universität Würzburg, Am Hubland, 97074 Würzburg, Germany*
[b]*Fachbereich Physik, Martin-Luther-Universität Halle-Wittenberg, Friedemann-Bach-Platz 6, 06108 Halle (Saale), Germany*
[c]*A.F. Ioffe Physico-Technical Institute, Russian Academy of Science, 194021 St. Petersburg, Russia*

Abstract

We have investigated the strong anisotropic polarization of the prominent *Y* line luminescence at 2.62 eV in thin ZnSe layers grown by molecular beam epitaxy on (0 0 1)-oriented GaAs substrates. For thin ZnSe films a pronounced anisotropic polarization collinearly to the [$\bar{1}$ 1 0] crystallographic direction with intensity ratios up to 1 : 8 for polarizer orientations parallel and perpendicular to [1 1 0] is found. In this samples the matrix luminescence shows no preferential orientation of the electric field vector in the plane perpendicular to the axis of growth. For ZnSe films with a layer thickness just below the critical thickness we observed a fine structure of up to nine subcomponents in the *Y* line spectrum. We interpret the *Y* line as a radiative recombination of an exciton bound to a 60° α-dislocation, which is dissociated into a 90° and 30° Shockley partial dislocation bounding a stacking fault ribbon. We relate the fine structure to a discrete set of the stacking fault distances.

Keywords: Dislocations; ZnSe; Y-line; Polarization

1. Introduction

ZnSe films grown by molecular beam epitaxy on (0 0 1)-oriented GaAs substrates represent a mildly mismatched system. Up to a critical thickness of approximately 200 nm the ZnSe layer is fully elastically strained. With increasing layer thickness the residual strain is relieved by the formation of misfit dislocations. By scanning tunneling microscopy the majority of misfit dislocations could be identified as 60° dislocations [1].

Commonly high-resolution transmission electron microscopy techniques have been used to study dislocations down to an atomic scale. Only a few optical data could be directly correlated with dislocations [2]. Recently, anisotropically polarized luminescence from ZnSe-based laser structures and p-doped ZnSe films, respectively, has been observed. Different origins of the anisotropic polarization of the luminescence, e.g. asymmetric density of dislocations at the interface, the incorporation of oriented defects, and an asymmetric relaxation of the residual strain, have been identified [3]. Here we report on a fine structure of the prominent Y_0 line. Up to nine subcomponents of the Y_0 line in the photoluminescence spectrum can be observed when the ZnSe film has a thickness just below the critical layer thickness. A model is proposed, which explains the Y_0 line as an exciton bound to a 90° partial dislocation. The strain and electric fields of an adjacent 30° partial act as perturbation.

2. Experiment and results

The photoluminescence presented here was dispersed by a single grating spectrometer with 1 m focal length and detected by a cooled photomultiplier. The samples

* Corresponding author. Tel.: + 49-931-888-5895; fax: + 49-931-888-5142.
E-mail address: worschech@physik.uni-wuerzburg.de (L. Worschech)

0921-4526/99/$ - see front matter
PII: S0921-4526(99)00548-7

were immersed in liquid helium at 2 K and optically excited by the 351 nm line of an Ar-ion laser. A linear-polarizer was used to analyze the polarization of the luminescence. Special efforts were taken to ensure that polarization effects of the monochromator grating and excitation source were eliminated. The polarization of the lines was found to be almost independent of the laser polarization and excitation intensity.

The Y_0 line at an energy 2.62 eV is a dominating feature in the spectra of undoped or slightly doped ZnSe crystals with extended defects incorporated [4–8]. Photoluminescence (PL) bands with similar spectral properties have also been known for other II–VI semiconductors. In Fig. 1 the PL spectra of ZnSe films with a thickness of 200 nm is shown. A polarization of the Y_0 line collinear to the $[\bar{1}\,1\,0]$ crystallographic direction was found, whereas the electric field vector of the luminescence associated with the heavy hole (FX_{hh}) and the light hole (FX_{lh}) component of the free exciton and the exciton bound to an intrinsic point defect (BX) exhibits almost no preferential orientation in a plane perpendicular to the (0 0 1) axis of growth. In this sample the separation between the free exciton transitions associated with the split heavy-hole and light-hole valence bands is $\Delta E_{lh\text{-}hh} = 11$ meV. From this splitting a strain of 2×10^{-3} can be derived, which is found for fully elastically strained ZnSe/GaAs films [9]. Therefore, the strain induced by the lattice mismatch is not relaxed by the incorporation of misfit dislocations in a way that $\Delta E_{lh\text{-}hh}$ is reduced significantly. However, is has been shown by J. Saraie et al., that for thin ZnSe films the Y line is a good measure for the incorporation of misfit dislocations, when the number of dislocations incorporated is too small to reduce the residual strain in a way, that the the split of heavy-hole and light-hole valence bands is reduced.

In thin ZnSe films which show a drastic anisotropically polarized Y line we observe a new fine structure of the Y line. In Fig. 2 the photoluminescence spectrum of an 160 nm thick ZnSe sample is shown. It can be seen, that

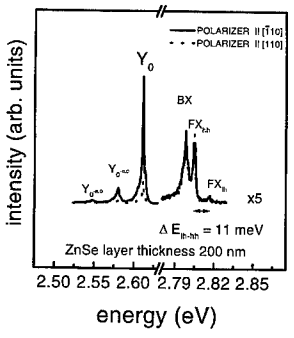

Fig. 1. Polarized photoluminescence spectra of a 200 nm thick ZnSe film grown on (0 0 1) GaAs.

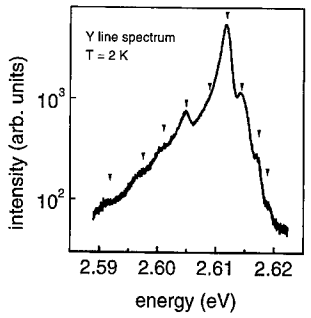

Fig. 2. Photoluminescence spectrum of 0.16 μm thick ZnSe layer. A fine structure of up to nine subcomponents of the no-phonon line appears.

the Y_0 line has a fine structure of up to nine subcomponents. In this sample a very strong anisotropic polarization of intensity ratios $Y_{0\bar{1}10}/Y_{0110}$ 8:1 were detected. The peak positions Y_0^n of the Y_0 line subcomponents are plotted versus integer numbers n in Fig. 3. The peak Y_0^0 with the highest photoluminescence intensity is used as a reference with $n = 0$. It is shown in Fig. 3 (solid line) that the energy E_n of each Y_0^n line can be described by the expression

$$E(n) = E_0 - A'/(r_0 - n \cdot b)^2 \qquad (1)$$

with $r_0 = (10.0 \pm 0.5)$ nm, $b = 5.7\ \mathring{A} \cdot \sqrt{3/8}$, $A' = (4.5 \pm 0.5) \times 10^2$ eV $\mathring{A}^2$ and $E_0 = 2.660 \pm 0.005$ eV, respectively. The constant b corresponds to the separation between two adjacent layers in [1 1 1] direction in a ZnSe crystal and is thus equal to the minimum step, which a dislocation that bounds a stacking fault may glide. The constant r_0 fits well to the observed equilibrium distance of dissociated 60° dislocations in ZnSe.

3. Discussion

Eq. (1) can be derived from a $k \cdot p$ Hamiltonian describing the influence of a deformation field and an electric

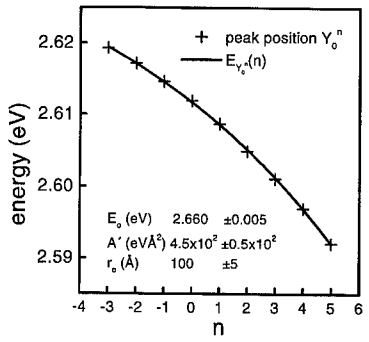

Fig. 3. Peak positions Y_0^n versus integer numbers n. The solid line was fitted with parameters listed in the figure.

field of 30° partial dislocations on the energy of an exciton localized at an adjacent 90° dislocation [10,11]. The theory describing excitons bound to dislocations lines in Si or Ge has to be modified regarding the interaction of electric fields, because in binary compound semiconductors dislocations are charged [12]. Therefore, we explain the fine structure of the Y_0 line observed in thin ZnSe films in the following way. The Y_0 line is interpreted in terms of an exciton bound to a $[\bar{1}\,1\,0]$ oriented 60° α-dislocation, which is dissociated into a 90° and a 30° Shockley partial dislocation. From high-resolution electron microscopy a distance of 11 nm was found for the equilibrium separation width of dissociated 60° dislocations [13], which fits well with the equilibrium distance $r_0 = 10$ nm extracted from the fit of Eq. (1) to the experimental data. The separation of partial dislocations can be changed only by integer multiples of $b = 5.7\ \mathring{A} \cdot \sqrt{3/8}$. Different widths change the strain and the electric fields acting on the electronic structure of the exciton. In thin compressively strained ZnSe films dislocations are incorporated mainly collinearly oriented to $[\bar{1}\,1\,0]$ with a concentration too small to affect the residual strain of the whole lattice. The different velocities of α- and β-dislocations result in a larger lattice relaxation along $[1\,1\,0]$ [14]. Therefore, a drastic polarization of the Y_0 line is observed for thin ZnSe films, whereas the luminescence associated with point defects and free excitons remains isotropically polarized, because the number of dislocations is too low.

Acknowledgements

This work was financially supported by the Deutsche Forschungsgemeinschaft Sonderforschungsbereich SFB 410. One of the authors (L.W.) is grateful for a fellowship granted by the Bayerisches Staatsministerium für Wissenschaft, Forschung und Kunst. Y.T.R. and Y.G.S. thank the Russian Fund for Fundamental Studies, grant no. 96-02-17825 and grant no. 98-01-01084, respectively.

References

[1] S. Guha, H. Munekata, L.L. Chang, J. Appl. Phys. Lett. 73 (1993) 2294.
[2] R. Sauer, Ch. Kisielowski-Kemmerich, H. Alexander, Phys. Rev. Lett. 57 (1986) 1472.
[3] L. Worschech, W. Ossau, Th. Behr, J. Nürnberger, G. Landwehr, Appl. Phys. Lett. 73 (1998) 835.
[4] J.W. Steeds, J.L. Batstone, Yu.T. Rebanne, Yu.G. Shreter, in: J.H. Werner, H.P. Strunk (Eds.), Springer Proceedings in Physics Polycrystalline Semiconductors II, Springer, Berlin, Heidelberg, 1991, p. 45.
[5] P.J. Dean, Phys. Stat. Sol 81 A (1984) 625.
[6] K. Shazad, J. Petruzello, D.J. Olego, D.A. Cammack, J.M. Gaines, Appl. Phys. Lett. 57 (1995) 2452.
[7] L.H. Kuo, L. Salamanca-Riba, J.M. DePuydt, H. Cheng, J. Qui, Appl. Phys. Lett. 63 (1993) 3197.
[8] P.J. Dean, G.M. Williams, G. Blackmore, J. Phys. D 17 (1984) 2291.
[9] K. Ohkawa, T. Mitsuyu, O. Yamazaki, Phys. Rev. B 38 (1988) 12465.
[10] Y.T. Rebanne, J.W. Steeds, Phys. Rev. Lett. 75 (1995) 3716.
[11] Y.T. Rebanne, Phys. Rev. B 52 (1995) 1590.
[12] Yu. Osip'yan, V.F. Petrenko, A.V. Zaretskii, R.W. Whitworth, Adv. Phys. 35 (1986) 115.
[13] Y. Chen, X. Liu, E. Weber, E.D. Bourret, Z. Liliental-Weber, E.E. Haller, D.J. Olego, D.R. Dorman, J.M. Gaines, N.R. Tasker, Appl. Phys. Lett. 65 (1994) 549.
[14] K. Nakano, H. Okuyama, T. Miyajima, K. Akimoto, J. Crystal Growth 117 (1992) 797.

ELSEVIER

Physica B 273–274 (1999) 898–901

PHYSICA B

www.elsevier.com/locate/physb

Induced defects in ZnS by electron and proton irradiation and defect-annealing behavior

S. Brunner[a,*], W. Puff[a], A.G. Balogh[b], P. Mascher[c]

[a]*Institut für Technische Physik, Technische Universität Graz, Petersgrasse 16, 8010 Graz, Austria*
[b]*Department of Materials Science, Technische Hochschule Darmstadt, Darmstadt, Germany*
[c]*Department of Engineering Physics, McMaster University, Hamilton, Ontario, Canada*

Abstract

In this contribution the positron annihilation technique is used, because of its specific sensitivity to vacancies, to investigate the effects of electron and proton irradiation on the lattice structure of ZnS and possible clustering mechanisms during isochronal annealing. Therefore, ZnS crystals were irradiated either with 3 MeV protons to a fluence of 1.2×10^{18} p/cm^2 or with 1 MeV electrons to a fluence of 1×10^{18} e/cm^2 or 5×10^{18} e/cm^2, respectively. It was found that electron and proton irradiation causes different changes in the positron annihilation characteristics. During isochronal annealing these defects agglomerate to larger vacancy complexes or even small voids. In both electron and proton irradiation several annealing stages can be observed, related to the annealing of variously sized vacancy complexes. Electron and proton irradiation leads to discoloration.

Keywords: ZnS; Irradiation; Point defects; Positron annihilation

1. Introduction

Because of the wide direct band gap (3.7 eV), zinc sulfide (ZnS), is well known as one of the promising II–VI compound semiconductors of a broad-band luminescence from the near UV to the near IR and, therefore, of prime interest for light emitting optoelectronic devices. In all the models for the light emitting mechanisms and for self-compensation which is responsible for doping limitation, point defects such as vacancies or interstitials play major roles. Much work on the basic understanding of intrinsic point defects in ZnS has been done by magnetic resonance studies [1–3].

The positron annihilation technique enables us to investigate the effects of electron and proton irradiation on the lattice structure of ZnS because positrons can get trapped in the introduced open-volume like defects in their neutral and negative charged state with subsequent changes in their annihilation characteristics. Due to the reduced electron density in open-volume-type defects, the lifetime of the trapped positrons increases and the electron momentum distribution narrows. Positive ion cores act as repelling centers for positrons and, therefore, are as isolated defect not evident for the positron annihilation technique. Nevertheless, only a few positron studies on ZnS crystals exist [4–9].

Isochronal annealing is a unique method to study the stability and migration behavior of defects induced by irradiation. However, the multitude of possible defects in compound semiconductors makes the interpretation of experimental results non-trivial.

2. Experimental details

The investigated ZnS samples were single crystals supplied from CrysTec, Berlin. The single crystals (SX-1) were irradiated with 1 MeV electrons at 4 K to a fluence of 1×10^{18} e/cm^2. Others (SX-2) were also irradiated with 1 MeV electrons but at 77 K and to a fluence of 5×10^{18} e/cm^2. Another set of single crystalline ZnS (SX-3) was

* Corresponding author. Tel.: + 43-316-873-8488; fax. + 43-316-873-8980 .
E-mail address: brunner@ifk.tu-graz.ac.at (S. Brunner)

0921-4526/99/$ - see front matter
PII: S0921-4526(99)00549-9

irradiated with 3 MeV protons at 223 K to a fluence of 1.2×10^{18} p/cm^2. The irradiated samples were isochronally annealed for 30 min at each temperature in an argon atmosphere to prevent oxidation [6].

The positron measurements were performed at room temperature and down to 10 K. From such low-temperature measurements one can obtain information about the charge state of the respective defects [10,11]. More experimental details are given in Ref. [8].

3. Results and discussion

Table 1 shows a summary of the positron lifetimes and the corresponding intensities together with the values of the Doppler S-parameters normalized to the value of the defect-free crystal for the respective samples. With the resolved positron annihilation parameters from the measured spectra one can calculate the mean lifetime according to $\tau_m = \sum_i \tau_i I_i$. From the simple two-state trapping model [12], the bulk lifetime, $\tau_b = (I_1/\tau_1 + I_d/\tau_d)^{-1}$, and the trapping rate $\kappa = I_d/I_1(1/\tau_b - 1/\tau_d)$ into the defects, can be obtained. The bulk lifetime is of particular importance since it refers to the annihilations from the perfect "crystalline" regions of the crystal and hence is a material constant.

In this contribution we present mainly the results of electron and proton-irradiated ZnS single crystals with a subsequent isochronal annealing of the electron irradiation-induced defects in SX-2 and proton irradiation-induced defects in SX-3. Some comparisons are made to an earlier investigation on SX-1 [6].

3.1. Electron irradiation

As one can see from Table 1, the positron lifetime measurements on as-grown ZnS single crystals (SX-1, SX-2, SX-3) reveal more or less only one lifetime component which can be attributed to annihilations from the bulk state. From the positrons' point of view the crystal appears defect free, with a positron bulk lifetime of $\tau_b = (218 \pm 2)$ ps.

This bulk lifetime agrees very well with the theoretically predicted bulk lifetime of $\tau_b = 217$–219 ps [13] and with other positron annihilation measurements, $\tau_b = (216 \pm 2)$ ps [5,9]. Irradiation of SX-1 with 1×10^{18} electrons [6] caused an increase in the mean lifetime, from 224 ps to 233 ps (see Fig. 1), indicating that open volume defects were introduced. For sample SX-2, electron irradiation with a 5 times higher fluence does not change the defect situation in a significant manner (see Table 1). For SX-2 the mean lifetime increases from 218 ps to 234 ps (see Fig. 1). The S-parameter normalized to the bulk value increases with the higher fluence from $S/S_b = 1.007$ for SX-1, to 1.009 for SX-2. For both, SX-1 and SX-2, a detailed analysis of the as-irradiated samples reveals a defect-related lifetime component with $\tau_d = (249 \pm 6)$ ps. Low-temperature measurements show that these defects are uncharged. A weak decrease of the defect lifetime, $\tau_d = (249 \pm 4)$ ps $\rightarrow \tau_d = (230 \pm 2)$ ps, of

Table 1
Observed positron lifetimes, τ_1,τ_d, intensities, I_1, I_d, and normalized S-parameter, S/S_b, together with calculated values of the mean lifetime, τ_m, the bulk lifetime, τ_b, for the respective ZnS samples before and after irradiation with 1 MeV electrons or 3 MeV protons and after annealing

ZnS	Status	Energy (MeV)	Fluenz $\times 10^{18}$/cm^2	τ_1 (ps) ± 5	I_1 (%) ± 2	τ_d (ps) ± 10	I_d (%) ± 2	τ_m (ps) ± 2	τ_b (ps) ± 2	S/S_b ± 0.001
	as–gr			219	94	304	6	224	223	1.001
SX-1	e–irr	1	1	154	18	250	82	233	225	1.007
	ann			221	100	—	—	221	221	1.001
	as–gr			218	100	—	—	218	218	1.000
SX-2	e–irr	1	5	136	13	249	87	234	225	1.009
	ann			216	216	—	—	216	216	1.000
	as–gr			219	100	—	—	219	219	1.001
SX-3	p–irr	3	1.2	167	22	311	78	279	261	1.031
	ann			219	100	—	—	219	219	0.999
ZnS[a]	Bulk*								218	
	V_{Zn}					233				
	$V_{Zn}V_S$					292				

[a]Ref. [13] (theoretical calculations).
*Theoretically predicted positron lifetimes for monovacancies, V_{Zn}, as well as for nearest-neighbour divacancies, ($V_{Zn}V_S$), and bulk lifetimes, τ_b [13].

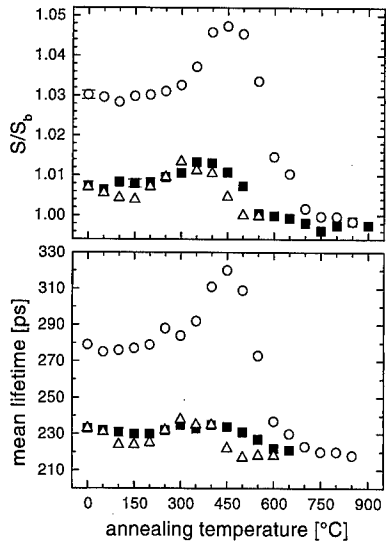

Fig. 1. Normalized S-parameter, S/S_b, and mean lifetime, τ_m, of SX-1 (■) and SX-2 (△) after electron irradiation and SX-3 (○) after proton irradiation as a function of the isochronal annealing temperature.

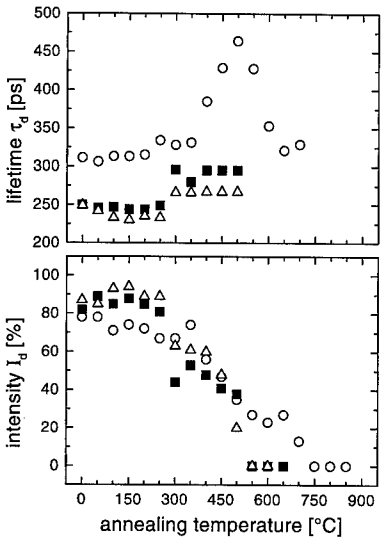

Fig. 2. Defect lifetimes, τ_d, of electron-irradiated SX-1 (■) and SX-2 (△) and proton-irradiated SX-3 (○) with the corresponding intensities, I_d, as a function of the isochronal annealing temperature.

SX-2 (see Fig. 2) during isochronal annealing up to 150°C is a manifestation that this defect is rather a composite lifetime of at least two lifetimes, one stemming from monovacancy-type defects and the other one from even bigger complexes which disappear up to 150°C. At 150°C the defect lifetime of SX-2 reaches a value of $\tau_d = (230 \pm 2)$ ps and (94 ± 4)%. Theoretical work on II–VI compound semiconductors using the local-density approximation (LDA) predicts for the zinc-vacancies, V_{Zn}, a positron lifetime of $\tau_V = 233$ ps, and for the nearest-neighbor divacancies, $V_{Zn}V_S$, a positron lifetime of $\tau_{DV} = 292$ ps [13]. Electron irradiation induces primarily Frenkel-pairs and isolated vacancies. Isolated Zn vacancies, V_{Zn}, induced by electron irradiation are stable up to ~ 100°C [3].

With a bulk lifetime of $\tau_b = (225 \pm 2)$ ps for SX-1 and SX-2 after irradiation we assume that the simple one-defect trapping model is applicable. Therefore, the trapping rate, which is proportional to the defect concentration can be determined. If we assume that a trapping rate of 1 ns^{-1} corresponds to a concentration of $\sim 10^{17}$ cm^{-3} neutral defects [10], we can estimate a concentration of about 2×10^{17} defects/cm^3 after electron irradiation to a fluence of 1×10^{18} e/cm^2 for SX-1 and 3×10^{17} defects/cm^3 after electron irradiation to a fluence of 5×10^{18} e/cm^2 for SX-2.

The irradiation with electrons causes a discoloration from glassy translucent to reddish. Such a discoloration is often ascribed to vacancies in the anion lattice, the well known F-centers [1,3].

In Fig. 2 both the defect lifetime and the corresponding intensity of SX-1 compared to SX-2 are shown as a function of isochronal annealing in an argon atmosphere. The behavior of the two electron-irradiated samples SX-1 reported earlier [6] and the SX-2 is very similar. Up to 250°C there was no change, neither in the defect lifetime, τ_d, nor in the intensity for SX-1. For SX-2 there is a small decrease in τ_d as mentioned before. At an annealing temperature of 200°C the lifetime τ_d of SX-2 starts to increse, reaching (267 ± 10) ps at 300°C, indicating that the defects agglomerate to bigger complexes. This behavior also can be seen in the mean lifetime and the normalized S-parameter (see Fig. 1). The increase of the defect lifetime can be attributed to monovacancies which become free and form more stable configurations such as divacancy-type defects like V_{Zn}-impurity (V_{Zn}-D^+), $(V_{Zn})_2$ or $V_{Zn}V_S$ in accordance with theoretical calculations [13]. Pareja et al. [4] reported a defect lifetime of 290 ps after electron irradiation of melt-grown ZnS single crystals. This comparison must be handled with care because his investigated as-grown single crystal showed a considerable higher bulk lifetime of 230 ps indicating that a very high concentration of grown in defects were present.

In our investigations these defect agglomerations disappear above 500°C. The mean lifetime as well as the S-parameter attain values lower than in the as-grown crystal, showing that all defects are now annealed out. At 550°C there is only one lifetime component observable, with a value of $\tau = 216$ ps. We therefore, attribute the lifetime of 216 ps to the bulk lifetime in ZnS, $\tau_b = 216$ ps. It's worth mentioning, that at a temperature of 250°C,

a third lifetime component with about (450 ± 50) ps appears, but with a marginal intensity. This defect component may originate from trapping at voids. Such defects also appear during annealing of proton-irradiated single crystals, which are discussed later. Adams et al. [5] also observed a positron lifetime of about 430 ps.

3.2. Proton irradiation

As mentioned, the analysis of the as-grown single crystals SX-3 reveals a positron bulk lifetime of $\tau_b = (219 \pm 2)$ ps, in excellent agreement with sample SX-2 and the theoretically predicted value.

The increased mean lifetime after proton irradiation to $\tau_m = (279 \pm 2)$ ps (see Table 1 and Fig. 1), gives clear evidence for positron trapping at vacancy-type defects. Since the value of the calculated bulk lifetime, $\tau_b = 261$ ps, is significantly higher than the assumed bulk lifetime, $\tau_b = 216$ ps, the simple one-defect trapping model is not applicable, likely because of saturation trapping, which means that all positrons annihilate from defect states. From the lifetime spectra after proton irradiation two lifetimes could be resolved. The short positron lifetime component, $\tau_1 = 167$ ps with an intensity of 22% might be a composition of a defect component near the bulk lifetime which cannot be separated and a small amount of annihilations from the bulk state. A detailed analysis reveals a defect-related lifetime of $\tau_d = (311 \pm 9)$ ps and an intensity of (78 ± 4)% (see Table 1). As discussed above (SX-2) and in a previous work (SX-1) [6], during isochronal annealing of electron-irradiated ZnS defect agglomerations to defect lifetimes of about (267–295) ps take place. These lifetimes were attributed to agglomerations of monovacancies, stabilized in small complexes, most likely divacancies. Since our observed lifetime is longer, this component might be a superposition of two lifetimes, one stemming from divacancies with about 290 ps and the other from even larger defect complexes which are observable during isochronal annealing (see Fig. 2). The defect lifetime, τ_d, reaches a value of about (460 ± 20) ps at 500°C. This is a very long lifetime, showing that the positrons annihilate from larger defect agglomerations or even small voids. These defects are not stable at temperatures higher than 550°C, and dissociate. Thereafter, the intensity of the defect lifetime decreases more and more. At a temperature of about 750°C only one lifetime component is observed indicating that all radiation-induced defects have annealed out.

4. Conclusions

A positron bulk lifetime for single crystal ZnS of $\tau_b = (216 \pm 2)$ ps has been obtained.

Electron irradiation of the ZnS single crystal reveals a defect component with a lifetime of (230 ± 2) ps, which can be attributed to the annihilation in monovacancies in their neutral state. Isochronal annealing causes agglomeration to larger defect complexes with a positron lifetime of about (267–295) ps, assigned to monovacancies stabilized at small complexes. The increase of the irradiation fluence from 1×10^{18} to 5×10^{18} e/cm^2 only causes a change in the defect concentration from 2×10^{17} to 3×10^{17} defects/cm^3. At an annealing temperature of 550°C all irradiation-induced defects are annealed out.

The proton irradiation of ZnS single crystals introduces defect complexes, most probably divacancies. During isochronal annealing these defects agglomerate to larger vacancy complexes or even small voids. After annealing at 750°C all defects are annealed out.

Electron and proton irradiation of ZnS leads to discoloration. The vanishing of the discoloration with annealing does not however, coincide with the disappearance of any specific lifetime component.

Acknowledgements

The proton irradiation was done at the Institut für Kernphysik, J.W. Goethe University, Frankfurt/Main. The electron irradiation was performed at the Institut für Festkörperforschung, Forschungszentrum Jülich and the Institut für Strahlenphysik, Universität Stuttgart. The authors wish to thank Dr. H. Baumann, Dr. F. Dworschak, and Dipl. Phys. K. Reichle for collaboration. This work has been supported by the Natural Sciences and Engineering Research Council of Canada.

References

[1] J. Schneider, A. Räuber, Solid State Commun. 5 (1967) 779.
[2] K. Leutwein, A. Räuber, J. Schneider, Solid State Commun. 5 (1967) 783.
[3] G.D. Watkins, J. Crystal Growth 159 (1996) 338, and references therein.
[4] R. Pareja, R.M. de la Cruz, P. Moser, J. Phys.: Condens. Matter 4 (1992) 7153.
[5] M. Adams, P. Mascher, A.H. Kitai, Appl. Phys. A 61 (1995) 217.
[6] S. Brunner, W. Puff, P. Mascher, A.G. Balogh, H. Baumann, Mater. Res. Soc. Symp. Proc. 438 (1997) 235.
[7] S. Brunner, W. Puff, P. Mascher, A.G. Balogh, H. Baumann, Mater. Sci. Forum 258–263 (1997) 1419.
[8] S. Brunner, W. Puff, P. Mascher, A.G. Balogh, Mater. Res. Soc. Symp. Proc. 510 (1998) 437.
[9] G. Tessaro, P. Mascher, Mater. Sci. Forum 258–263 (1997) 1335.
[10] P. Mascher, S. Dannefaer, D. Kerr, Phys. Rev. B 40 (1989) 11 764.
[11] M.J. Puska, C. Corbel, R.M. Nieminen, Phys. Rev. B 41 (1990) 9980.
[12] R.N. West, Adv. Phys. 22 (1973) 263.
[13] F. Plazaola, A.P. Seitsonen, M.J. Puska, J. Phys.: Condens. Matter 6 (1994) 8809.

ELSEVIER

Physica B 273–274 (1999) 902–906

PHYSICA B

www.elsevier.com/locate/physb

The deactivation of nitrogen acceptors in ZnS_xSe_{1-x} and $Mg_yZn_{1-y}S_xSe_{1-x}$ studied by combining positron annihilation, SIMS, and CV measurements

J. Oila[a,*], K. Saarinen[a], T. Laine[a], P. Hautojärvi[a], P. Uusimaa[b], M. Pessa[b], J. Likonen[c]

[a]*Laboratory of Physics, Helsinki University of Technology, P.O.Box 1100, FIN-02015 HUT, Finland*
[b]*Department of Physics, Tampere University of Technology, P.O.Box 692, 33101 Tampere, Finland*
[c]*Technical Research Centre of Finland, Chemical Technology, P.O.Box 1404, FIN-02044 VTT, Finland*

Abstract

We show that quantitative information on the electrical deactivation of doping can be obtained by combining the results of positron annihilation, secondary ion-mass spectrometry and capacitance–voltage measurements. We have applied this method to study the nitrogen doping in ZnS_xSe_{1-x} and $Mg_yZn_{1-y}S_xSe_{1-x}$ and we conclude that in addition to isolated acceptor impurities N_{Se}^-, nitrogen atoms are also situated at high concentrations in compensating donors, most probably in $(Zn_iN_{Se})^{1+}$ and $(V_{Se}N_{Se})^{1+}$ pairs, or in electrically neutral form, leading to electrical compensation of p-type material.

Keywords: ZnSSe; Compensation; Positron spectroscopy

ZnSe has been under intensive study for years as an attractive material for optoelectronic applications. The most crucial difficulty in ZnSe fabrication is in p-type doping: The charge carrier concentrations have been found to saturate at the moderate level of $\leqslant 10^{18}$ cm^{-3} regardless of much larger amount of incorporated nitrogen acceptors. On the basis of theoretical calculations it has been proposed that the deactivation could be caused e.g. by the formation of defect-impurity complexes [1], N_2 molecules [2] or instability of the lattice near the dopant atoms [3]. Recently, the calculations of Pöykkö et al. [4] show that the defects with the lowest formation energies, in addition to the isolated N_{Se}^- acceptor, are complexes consisting of the nitrogen dopant and a zinc interstitial Zn_i or a selenium vacancy V_{Se}. In previous positron experiments [5], Zn and Se vacancies were identified as compensating defects in n- and p-type ZnS_xSe_{1-x} material, respectively.

In this work we have combined the results of positron, secondary ion mass spectrometry (SIMS) and capacitance–voltage (C–V) measurements to study the deactivation of nitrogen impurities in ZnS_xSe_{1-x} [6] and $Mg_yZn_{1-y}S_xSe_{1-x}$. The concentrations of Se vacancies V_{Se} and ionic acceptors N_{Se}^- are estimated from the positron data. These values are related to the net acceptor concentration $N_A - N_D$ and to the total nitrogen concentration $[N]$ in order to determine the concentrations of various nitrogen-related defects. The applied method lets us to distinguish between electrical compensation and passivation processes and gives quantitative information on the compensating defects.

The studied samples were 1.5–2.2 μm thick N-doped ZnS_xSe_{1-x} (nine samples, $x \approx 0.06$) and $Mg_yZn_{1-y}S_xSe_{1-x}$ (five samples; $y = 0.05$–0.12, $x = 0.08$–0.14) overlayers grown by molecular beam epitaxy (MBE) on GaAs(1 0 0) substrate. The ZnS_xSe_{1-x} samples consisted of two sets (A and B) grown with different MBE systems. The p-type doping with N impurities was

* Corresponding author. Tel.: + 358-9-451-3142; fax: + 358-9-451-3116.
E-mail address: juha.oila@hut.fi (J. Oila)

0921-4526/99/$ - see front matter
PII: S0921-4526(99)00550-5

performed during the growth by a N_2 rf-plasma source. [N] was determined by SIMS, which was calibrated by implanting a known amount of N in undoped ZnSSe. The hole concentrations were determined by electrochemical C–V experiments at 300 K. In ZnSSe samples [N] varied between $1\text{–}30\times10^{18}$ cm^{-3} and the resulting p between $1\text{–}4\times10^{17}$ cm^{-3}, without correlation with [N]. In MgZnSSe samples the level of deactivation was even higher: With [N] = $6\text{–}66\times10^{18}$ cm^{-3} the achieved p was only $6\text{–}30\times10^{16}$ cm^{-3}.

Positron annihilation experiments were carried out using a beam of monoenergetic positrons. Neutral and negative vacancy-type defects, where the positive ion core is missing, act as efficient traps for positrons. Due to the reduced electron density in vacancies, the lifetime of the trapped positrons increases and the momentum distribution of the annihilating positron–electron pair narrows. The momentum of annihilating positron–electron pairs can be observed as the Doppler broadening of the 511 keV annihilation line. We use conventional lineshape parameters, the low-momentum parameter S and the high-momentum parameter W in describing the shape of the Doppler broadened line [7]. The narrowing momentum distribution due to positron trapping into vacancies is seen as an increase in the S parameter and decrease in the W parameter.

Fig. 1 shows the S parameter values at 25–500 K measured at a positron energy of 10 keV. With this energy all positrons annihilate inside the layer material. The S parameter increases with temperature in all samples, from a constant level at $T < 100$ K up to temperatures above 320 K, where it occupies an almost constant maximum level or starts to decrease. The behaviour of the W parameter is similar but just the opposite to that of the S parameter. The increasing S parameter indicates that positrons get trapped at vacancy-type defects. In ZnS_xSe_{1-x}:N these vacancies have been identified as Se vacancies by the shape of the core electron momentum distribution [5]. In a W–S plot the data in ZnS_xSe_{1-x}:N samples forms a straight line, giving the defect specific parameter $R = |\Delta S/\Delta W| \approx 5$, which can be used to characterize the Se vacancy [7]. The data in MgZnSSe:N samples form also a single line in W–S plot, with the same slope $R = |\Delta S/\Delta W| \approx 5$ as found in ZnSSe:N layers. This indicates that positron trapping at Se vacancies is observed also in N-doped $Mg_yZn_{1-y}S_xSe_{1-x}$. The charge state of an isolated Se vacancy is expected to be 2+ [1]. Because the positron does not get trapped into positive vacancies, an isolated V_{Se} cannot be observed. Therefore, the detected Se vacancy is most likely a part of a defect complex, probably with the N impurity, so that the total charge of the defect is negative or neutral. Supporting this identification, the recent theoretical calculations show that the $V_{Se}N_{Se}$ pair has the lowest formation energy of all defect complexes containing the Se vacancy [1,4].

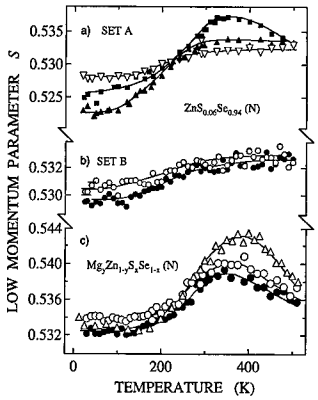

Fig. 1. The low momentum parameter S versus measurement temperature in some of the studied ZnS_xSe_{1-x}:N and $Mg_yZn_{1-y}S_xSe_{1-x}$:N layers.

The S parameter decreases when temperature is lowered, indicating smaller fraction of annihilations at vacancies (Fig. 1). The reduced trapping at vacancies at lower temperatures could be due to the change of the charge state of the vacancy by capturing a hole from the valence band. However, we do not consider this explanation likely. First, the vacancy concentrations, which are calculated below, are in some samples much larger than the hole concentration. Second, the levels of S at the high ($T > 300$ K) and low-temperature ($T < 100$ K) plateaus vary independently. Third, the increase of $S(T)$ takes place at $T = 130\text{–}300$ K in all samples and does not correlate with the Fermi level.

A more probable explanation for the reduced S parameter at low temperatures is the presence of negative ionic acceptors. Positrons can get trapped into the Rydberg states around negative ions such as N_{Se}^- acceptors. The negative ions do not contain open volume and the annihilation at this state yields the same S parameter as the annihilation in bulk lattice. When negative ions compete with vacancies in trapping positrons, the S parameter decreases towards the bulk value, because less annihilations take place at vacancies. The negative ions are efficient positron traps only at $T \leqslant 100$ K, above which positrons are able to escape from them [7]. In this temperature range the S parameter increases as seen in Fig. 1, because a larger fraction of positrons annihilate as trapped at vacancies.

At temperatures below 100 K, the S parameter is constant as a function of temperature. This indicates that the temperature dependencies of positron trapping at vacancies and negative ions cancel each other. In this temperature range the positron trapping coefficients at negative ions and negative vacancies both behave as $\sim T^{-1/2}$, whereas the trapping at neutral vacancies is

independent of temperature [7,8]. If neutral vacancies and negative ions were competing as positron traps, the S parameter would decrease when temperature is lowered at $T < 100$ K. The observed $V_{Se}N_{Se}$ complexes are thus negatively charged. Such a charge state is predicted for $V_{Se}N_{Se}$ also by recent theoretical calculations [4].

At high temperatures $T > 300$ K where no positrons annihilate at negative ions, the S parameter is a linear combination of the values S_b and S_V characteristic to the annihilations in the lattice and at vacancies, respectively. By using the standard positron trapping model [7] and the data recorded at 350 K, we can determine the concentrations of vacancies in ZnS_xSe_{1-x} layers as

$$c_V = \frac{N_{at}}{\mu_V \tau_b} \frac{(S/S_b - 1)}{(S_V/S_b - S/S_b)}, \quad (1)$$

where N_{at} is the atomic density and $\tau_b = 240$ ps is the positron lifetime in defect-free ZnSe lattice [9]. The value of S_b, the S parameter in the ZnS_xSe_{1-x} lattice, is taken from Ref. [5]. We use the value $\mu_V = 1.4 \times 10^{15}$ s^{-1} for the positron trapping coefficient at the Se monovacancy [7]. The exact value of the relative S parameter, S_V/S_b, for the Se monovacancies in ZnS_xSe_{1-x} is not known, but the present experimental data indicates that $S_V/S_b \geqslant 1.03$. We can further infer that $S_V/S_b \leqslant 1.04$, because larger S_V/S_b ratios correspond already to the open volume of divacancies [7]. For analogical vacancies in the anion sublattice, namely V_{As} in GaAs and V_P–Zn complex in InP, $S_V/S_b = 1.028$–1.035 can be determined depending slightly on the detector resolution [10,11]. The arguments lead us to choose $S_V/S_b = 1.034$. This estimation gives us vacancy concentrations between 2.4×10^{17} and 4.0×10^{18} cm^{-3} in ZnS_xSe_{1-x} layers.

At lower temperatures (< 50 K) the S parameter is a superposition of the values S_b, S_V and that obtained at negative ions $S_{ion} \approx S_b$. At 25 K we can estimate the concentration of negative ions as [7]

$$c_{ion} = \frac{N_{at}}{\mu_{ion}} \left(\frac{\mu_V c_V (S_V/S_b - S/S_b)}{N_{at}} \frac{}{(S/S_b - 1)} - \tau_b^{-1} \right). \quad (2)$$

For the trapping coefficients at 25 K we use the values determined earlier [7,12] for GaAs: For trapping at vacancies $\mu_V(25\text{ K}) = 1.4 \times 10^{16}$ s^{-1} and for trapping at negative ions $\mu_{ion}(25\text{ K}) = 1 \times 10^{16}$ s^{-1}. This gives us concentrations of negative ions in ZnS_xSe_{1-x} layers between 2.4×10^{17} and 1.1×10^{19} cm^{-3}.

In order to analyze quantitatively the electrical deactivation of nitrogen doping in ZnS_xSe_{1-x}, we combine the information obtained by positron, C–V and SIMS measurements. The positron data yields the total concentration of acceptor-type defects $[A^-] = c_V + c_{ion}$. The concentration of donor-type defects $[D^+]$ can thus be calculated from the hole concentration $p = [A^-] - [D^+]$ measured by C–V. The concentration of incorporated nitrogen $[N]$ obtained by SIMS is plotted in

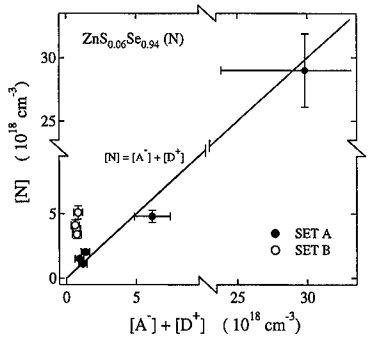

Fig. 2. The concentration of incorporated nitrogen atoms as a function of the sum of donor and acceptor concentrations in studied ZnS_xSe_{1-x}:N layers [6].

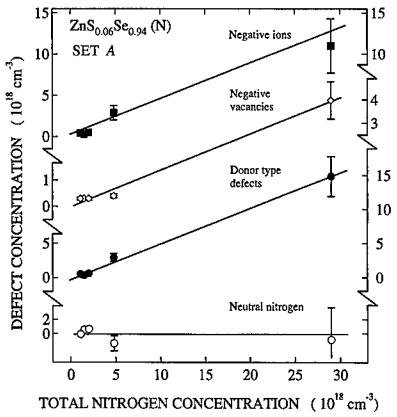

Fig. 3. The estimated defect concentrations as a function of the total concentration of incorporated nitrogen in the ZnS_xSe_{1-x} samples of set A. The solid lines indicate linear fits to various defect concentrations [6].

Fig. 2 [6] versus the sum of acceptor and donor concentrations, $[A^-] + [D^+]$. The samples from the set A are seen to fall quite well on the line $[N] = [A^-] + [D^+]$. As mentioned above, the theoretical calculations predict that the most probable defects in N-doped ZnSe are those related to nitrogen impurities. The correlation of Fig. 2 indicates that in the set A all nitrogen atoms are related to charged defects. The data obtained in the ZnS_xSe_{1-x} samples of the set B are seen to be clearly above the line $[N] = [A^-] + [D^+]$, indicating that these samples contain N atoms also in electrically neutral form.

In the samples of the set A the concentrations of negative vacancies, negative ions and donor defects are seen (Fig. 3 [6]) to increase linearly with the nitrogen incorporation. The negative vacancies were identified above as $V_{Se}N_{Se}$ complexes. According to calculations [4], the most likely assignment of the negative ions is

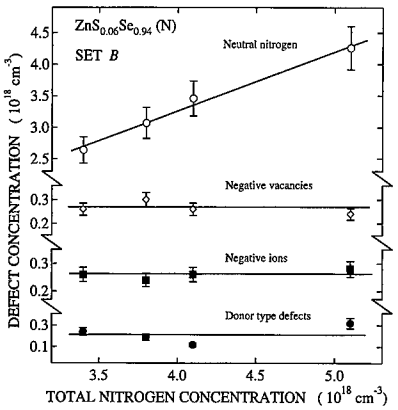

Fig. 4. The estimated defect concentrations as a function of the total concentration of incorporated nitrogen in the ZnS_xSe_{1-x} samples of set *B*. The concentration of electrically neutral nitrogen constitutes $\sim 80\%$ of total $[N]$.

isolated N_{Se}^- and that of the donor defect is either $(Zn_iN_{Se})^{1+}$ or $(V_{Se}N_{Se})^{1+}$. With these identifications we can say that in set *A* about 40% of all nitrogen impurities are situated as isolated acceptors N_{Se}^-. Another $\sim 40\%$ is in donor-type defect pairs $(Zn_iN_{Se})^{1+}$ or $(V_{Se}N_{Se})^{1+}$ and about $\sim 20\%$ is bound to the negative $(V_{Se}N_{Se})^{1-}$ pairs. The concentration of neutral nitrogen, defined as $[N]-[A^-]-[D^+]$, is negligible.

In the ZnS_xSe_{1-x} samples of the set *B* the mismatch of SIMS, *C–V* and positron data indicates that nitrogen exists in the lattice in electrically neutral form. This can be seen in Fig. 4: The concentration of electrically neutral N increases with the total nitrogen incorporation, being about 80% of $[N]$, while the concentrations of other defects occupy a much lower constant level. In principle, $\sim 80\%$ of nitrogen could be in neutral defect complexes, but the formation of such defects is unlikely according to theoretical calculations [4]. The electrical neutralization of N could result also from the passivation by hydrogen or the formation of nitrogen dimers or bigger clusters. Hydrogen passivation, however, is not a likely reason for the neutralization of N in set B, because SIMS experiments show no significant differences in $[H]$ between samples of set *A* and *B*. The existence of neutral N–N complexes is suggested by theory [2] and by an ion beam analysis on N-doped ZnSe [13].

Interestingly, the free hole concentrations are very similar in all ZnS_xSe_{1-x} samples of sets *A* and *B*, although the deactivation mechanisms are very different. This suggests that the details of the MBE growth system and the growth conditions may have a strong influence on the activation of nitrogen. The sample of the set *A*, where $[(V_{Se}N_{Se})^{1-}]$ is the largest (the rightmost point in Fig. 2), was grown at 335°C under Zn rich conditions. The other samples of the set *A* were grown at 270°C and under slightly more Se rich growth conditions than the set *B*, which was grown at 290°C. These results suggest that by adjusting the growth conditions for ZnS_xSe_{1-x}:N close to stoichiometric at 290°C the formation of electrically active nitrogen-related defects was suppressed. However, in this case the activation of impurities remained low due to the introduction of neutral nitrogen-related complexes.

In $Mg_yZn_{1-y}S_xSe_{1-x}$ samples a detailed quantitative estimation of defect concentrations, as presented above in case of ZnS_xSe_{1-x} samples, is not possible, because the annihilation parameter levels corresponding to defect-free MgZnSSe lattice cannot be determined on the basis of the studied set of samples. The large difference in annihilation parameters between the low-temperature ($T < 200$ K) and high-temperature ($T \sim 350$ K) values, however, suggest that the concentrations of acceptor-type defects (negative vacancies and negative ions) must be considerable. As the samples are still highly compensated, this leads to suggestion that the compensation must be caused by the formation of compensating donor defects rather than neutralization of N impurities.

In summary, the results of this work show that the combination of positron, SIMS and *C–V* measurements is very powerful in investigating the details of the deactivation mechanism. The method is able to yield quantitative estimates for the concentrations of compensating defects as well as information about their atomic structure. In the case of N doping of ZnS_xSe_{1-x}, the deactivation of N impurities is seen to take place by two different mechanisms. In some samples the deactivation by donors is the dominant effect: While 40% of the electrically active nitrogen occupy isolated acceptor configuration N_{Se}^-, another 40% is bound to compensating donor-type defect pairs, most probably to $(Zn_iN_{Se})^{1+}$ and $(V_{Se}N_{Se})^{1+}$ pairs, and about 20% is in the negative $(V_{Se}N_{Se})^{1-}$ complexes. The results give evidence on a similar deactivation mechanism also in N-doped $Mg_yZn_{1-y}S_xSe_{1-x}$ samples. In some ZnS_xSe_{1-x} samples the role of compensating donor defects is however minor, as the amount of electrically inactive nitrogen constitutes $\sim 80\%$ of the total N concentration.

References

[1] A. Garcia, J.E. Northrup, Phys. Rev. Lett. 74 (1995) 1131.
[2] B.-H. Cheong, C.H. Park, K.J. Chang, Phys. Rev. B 51 (1995) 10610.
[3] C.H. Park, D.J. Chadi, Phys. Rev. Lett. 75 (1995) 1134.
[4] S. Pöykkö, M.J. Puska, R.M. Nieminen, Phys. Rev. B 57 (1998) 12174.
[5] K. Saarinen, T. Laine, K. Skog, J. Mäkinen, P. Hautojärvi, K. Rakennus, P. Uusimaa, A. Salokatve, M. Pessa, Phys. Rev. Lett. 77 (1996) 3407.

[6] J. Oila, K. Saarinen, T. Laine, P. Hautojärvi, P. Uusimaa, M. Pessa, J. Likonen, Phys. Rev. B 59 (1999) 12736.
[7] K. Saarinen, P. Hautojärvi, C. Corbel, in: M. Stavola (Ed.), Identification of Defects in Semiconductors, Academic Press, New York, 1998, pp. 209.
[8] M.J. Puska, C. Corbel, R.M. Nieminen, Phys. Rev. B 41 (1990) 9980.
[9] F. Plazaola, A.P. Seitsonen, M.J. Puska, J. Phys.: Condens. Matter 6 (1994) 8809.
[10] R. Ambigapathy et al., Phys. Rev. B 50 (1994) 2188.
[11] M. Alatalo et al., Phys. Rev. B 51 (1995) 4176.
[12] K. Saarinen et al., Phys. Rev. B 51 (1995) 14152.
[13] H. Kobayashi et al., J. Crystal. Growth 184/185 (1998) 475.

ELSEVIER

Physica B 273–274 (1999) 907–910

PHYSICA B

www.elsevier.com/locate/physb

Compensating defects and electrical activation of donors in CdS

U.V. Desnica[a,*], I.D. Desnica-Frankovic[a], R. Magerle[b], M. Deicher[c]

[a]*Semiconductors Laboratory, R. Boskovic Institute, Physics Department, Material Physics Division, Bijenicka 54, 10000 Zagreb, Croatia*
[b]*Physikalische Chemie II, Universität Bayreuth, D-95440 Bayreuth, Germany*
[c]*Fakultät für Physik, Universität Konstanz, D-78457, Konstanz, Germany*

Abstract

Electrical deactivation of donors in CdS was studied by using Perturbed $\gamma\gamma$ Angular correlation (PAC) spectroscopy and temperature dependence of Hall mobility, resistivity, and free-carrier concentration. PAC spectra and electrical properties were monitored as a function of thermal treatment either under S or Cd pressure in a temperature range from RT to 1073 K. For samples annealed above 800 K under S pressure, Hall effect showed increased electrical compensation whereas PAC detected spontaneous creation of cadmium vacancies, V_{Cd}, via the formation of $(In_{Cd}–V_{Cd})$ pairs. The increase of the concentration of compensating acceptors, determined from electrical measurements, precisely correlates with the increase of the concentration of $(In_{Cd}–V_{Cd})$ pairs found by means of PAC. In contrast to that, thermal treatment under Cd pressure up to 1073 K does not provoke the formation of compensating native defects up to [In] $> 10^{19}/cm^3$.

Keywords: Compensation; Native defects; CdS; PAC; Hall effect

1. Introduction

Although doping problems and limits are among the main restraining factors for broader applications of the exceptional potentials of II–VI semiconductors, the microscopic causes of these difficulties still remain generally unknown. The main causes, reviewed recently [1], are claimed to be the spontaneous formation of native defects and/or pairs, the lattice relaxation around the doping atom resulting in the formation of compensating deep localized levels, mid-gap pinning of the Fermi level, the amphoteric behavior of some dopants, or the low solubility of others.

Indium is potentially an excellent donor to render CdS highly conductive (and hence promising for n-type side of the p–n junction or heterojunction) but its electrical activation depends strongly on thermal treatment conditions [2]. A microscopic explanation of these differences has only recently started to emerge [3]. The radioactive isotope ^{111}In enables the use of perturbed $\gamma\gamma$ angular correlation (PAC) spectroscopy, a powerful technique which gives information about the immediate surroundings of In probe atoms in the crystal. Each specific atomic configuration and surroundings of ^{111}In is unambiguously labeled by a characteristic electric field gradient (EFG) which is described by two parameters: the hyperfine interaction strength, ν_Q, and the asymmetry parameter η [4]. In this paper, we shall demonstrate that compensating acceptors, which cause electrical deactivation of donors (as revealed by electrical measurements), are being formed in the same concentrations as cadmium vacancies (as deduced from PAC), thus proving that this native defect plays a crucial role in electrical properties of the donor-doped CdS for a very wide range of In concentrations.

* Corresponding author. Tel.: 3851-4561-173; fax: +3851-4680-114.
E-mail address: desnica@rudjer.irb.hr (U.V. Desnica)

0921-4526/99/$ - see front matter
PII: S0921-4526(99)00551-7

2. Experimental details and measurements techniques

Commercial, undoped n-CdS single crystals were implanted at room temperature (RT) with 350 keV ^{111}In + ^{115}In ions in a non-channeling direction with doses ranging from 1.3×10^{11} to 1.3×10^{16}/cm^2 [3]. Both virgin and implanted samples were annealed for 10 min in 50 or 100 K steps up to 1073 K, either under Cd or S pressure. The free-electron concentration, n, and Hall mobility, μ_H, were measured from 20 to 300 K in a standard Van der Pauw configuration. After each annealing step experimental data for n were fitted using expression [5]:

$$n(n+[N_A])/([N_D]-n-[N_A]) = gN_C\exp(-E_D/kT) \quad (1)$$

with donor ionization energy E_D, concentration of donors, $[N_D]$, and acceptors, $[N_A]$, treated as fitting parameters. N_C is the effective conduction band-edge density of states and g is the degeneracy factor [5].

To explore the experimentally determined T-dependence of μ_H, all potentially relevant scattering mechanisms [6] were taken into account and the total Hall mobility, μ_H, was then calculated by applying Matthiesen's rule

$$1/\mu_H = 1/\mu_{po} + 1/\mu_{dp} + 1/\mu_{pe} + 1/\mu_N + 1/\mu_I, \quad (2)$$

where μ_{po}, μ_{dp}, μ_{pe}, μ_N and μ_I denote scattering-limited mobility by optical polar phonons, deformation potential acoustic phonons, piezoelectric scattering, neutral impurities, (N_N), and ionized impurities, (N_I), respectively. Each specific mobility was calculated by using corresponding formulae [6] and constants appropriate for CdS [2,5,7].

A PAC spectrum $R(t)$ was taken after each annealing step. From the fit of $R(t)$, the fractions of ^{111}In in different atomic configurations/surroundings were determined, each distinguished by its characteristic PAC 'signature' (ν_Q and η).

3. Results

Fig. 1 depicts the temperature dependence of the free-electron concentration, $n(T)$, of undoped CdS samples (with residual effective donor concentration in 10^{16}/cm^3 range) as a function of thermal treatment under either S or Cd vapor pressure. For Cd annealed sample practically no changes in $n(T)$ were observed from RT up to $T_a = 1073$ K (only the last curve is shown). On the other hand, for the S-annealed sample, changes were small up to $T_a = 773$ K, but above $T_a = 873$ K the slope increased significantly and n drastically decreased. For higher annealing steps n becomes immeasurably low and is estimated to be less than 10^4/cm^3.

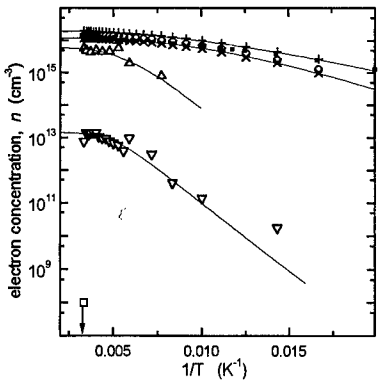

Fig. 1. Temperature dependence of the free-carrier concentration, n, after subsequent annealing under S pressure at T_a = RT (+), 573 K (○), 773 K (×), 823 K (△), 873 K (▽), and 923 K (□). $n(T)$ for the sample annealed under Cd pressure after $T_a = 1073$ K (■) is also shown. Full lines show the best fits according to Eq. (1).

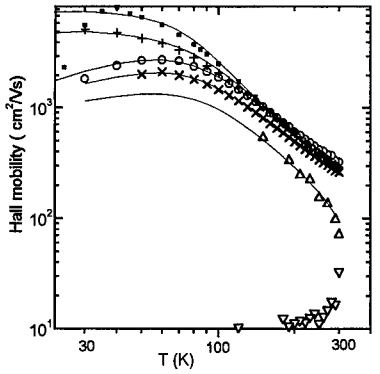

Fig. 2. Temperature dependence of the Hall mobility, μ_H, for the same samples and annealing conditions shown in Fig. 1. Symbols refer to the same T_a as in Fig. 1. Full lines show the calculated mobility, μ_H, following Eq. (2).

Hall mobility, $\mu_H(T)$, (Fig. 2) shows similar trends – small changes up to $T_a = 873$ K, and considerable, although much less dramatic, decrease of μ_H for higher T_a.

Several characteristic PAC spectra for a sample implanted with ^{111}In(1.3×10^{11}/cm^2) are shown in Fig. 3. All implantation-induced damage becomes completely annealed already after $T_a = 573$ K, and all of the In probe atoms are positioned in a single surrounding, distinguished by the characteristic PAC parameters $\nu_Q = 7.4$ MHz, and $\eta = 0$ (Site 1), which has been identified as substitutional In on Cd sites, In_{Cd} [8]. All probe atoms remain at In_{Cd} sites in unperturbed surroundings (Fig. 3a) up to $T_a \cong 800$ K independently of the annealing conditions.

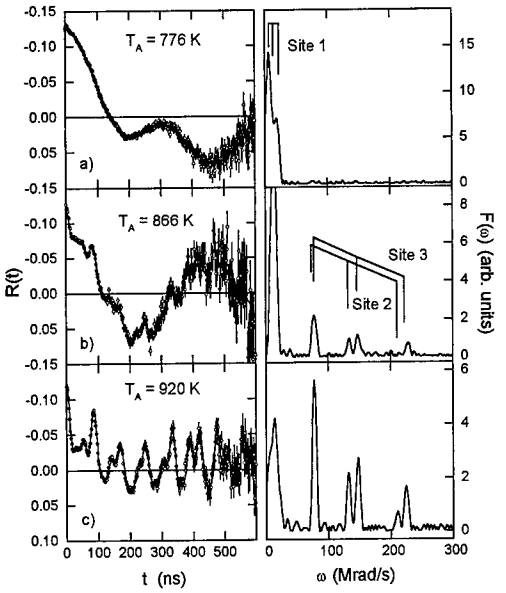

Fig. 3. PAC spectra (left) and their Fourier transforms (right) of In-implanted CdS after annealings up to 920 K under S pressure. The annealing temperature is indicated for each spectrum.

After annealing above 800 K under S pressure (Fig. 3b), two additional EFGs appear, assigned to (In_{Cd}–V_{Cd}) pairs [8] and characterized by a pair of frequencies, $\nu_Q = 72.4$ MHz with $\eta = 0.35$ (Site 2), and $\nu_Q = 78.7$ MHz with $\eta = 0.21$ (Site 3), respectively [4,8]. At higher T_a the fraction of (In_{Cd}–V_{Cd}) pairs becomes dominant although the signal belonging to In_{Cd} remains always present (Fig. 3c). We have observed a very similar behavior for higher In doses, up to In peak concentrations of $10^{20}/cm^3$ in the implanted layer. In those samples the fractions of pairs also similarly increased with the increase of T_a above 800 K. Above $T_a \cong 900$ K the fractions of pairs level up at around 50–70%, while the rest of the In atoms (30–50%) remains on Site 1 [3]. If the peak concentration of In exceeded $10^{20}/cm^3$, In started to precipitate into a second phase inside the CdS crystal [3].

The Cd annealed samples behaved differently: the PAC spectra with the single frequency 7.4 MHz (like in Fig. 3a) was obtained after each annealing step up to $T_a = 1073$ K. Furthermore, practically the same PAC spectrum was obtained for higher implantation doses as well, up to In peak concentrations of $10^{19}/cm^3$. For even higher doses, In started to precipitate into the second phase [3].

4. Discussion

The full lines in Fig. 1 are the results of fits of $n(T)$ using the Eq. (1). For $T_a = RT$, the E_D calculated from the fit is 27 meV, which is a very reasonable value for a shallow donor in the concentration range of $10^{16}/cm^3$ [2,5,7]. The increase of the annealing temperature up to 773 K does not induce virtually any change in E_D, indicating that the same shallow donors govern the electrical properties. The apparent small increase of the slope results from the small decrease of the effective donor concentration ($[N_D]_{eff} = [N_D] - [N_A]$) [2,5]. Above $T_a = 823$ K this shallow level becomes completely ionized i.e. all its electrons are trapped by compensating acceptors. The Fermi level is then lowered down to the next donor level deeper in the gap, which is, according to the fit, positioned at 70 meV below the conduction band. Above $T_a = 873$ K the same level still dominates the temperature dependence of n, but the concentrations $[N_D]$ and $[N_A]$ become very similar, primarily due to the stronger increase of $[N_A]$. Above $T_a = 923$ K, n becomes immeasurably low, indicating that the Fermi level is lowered much further down, close to or at the middle of the band-gap, due to the complete compensation of practically all donors by acceptors.

Fits of Eq. (2) to the experimental Hall mobility data are shown as full lines in Fig 2. The calculation showed that $\mu_{dp}(T)$ is unimportant throughout the whole T range. Similarly, μ_N is also insignificant, since unreasonably high concentrations of neutral scattering centers (above $10^{17}/cm^3$) would be needed to appropriately limit the maximal μ_H, and still the decrease of experimental μ_H observed at lower T_a could not be reproduced. Hence, this mechanism can be discarded as well. It was determined that at higher T optical phonons and piezoelectric scattering limit the mobility, while the maximum of $\mu_H(T)$ and its decrease at lower temperatures is limited by ionized impurities scattering, $\mu_I = A \cdot T^{3/2}/[N_I]$ (A is approximately a constant [5]). It was found that the $[N_I]$ values obtained from the fit to $\mu_H(T)$ were quite close to the sum of ($[N_D] + [N_A]$), determined independently from fitting of $n(T)$.

The agreement between measured μ_H and calculated μ_H breaks down for very high compensation (above $T_a = 873$ K, Fig. 2), since μ_H becomes rather low, and an unreasonable change of the material parameters in the expressions for μ_{po} and μ_{pe} would be needed to obtain a good fit. A considerable lowering of the mobility is often encountered in measurements of semi-insulating samples, ascribed to and convincingly explained by potential fluctuations [6]. Namely, when n is very low, any potential fluctuation becomes 'visible' since it affects/disrupts the continuity of the practically empty conduction band, thus lowering the measured mobility. In fact, the strong decrease of the mobility observed even at RT, provides independent proof that S annealing produces semi-insulating CdS samples.

The summary of the essential PAC, electrical experimental and calculated results for the $[N_D]_{eff.} \cong (10^{16}/cm^3$ donor level are given in Fig. 4 for S annealed samples.

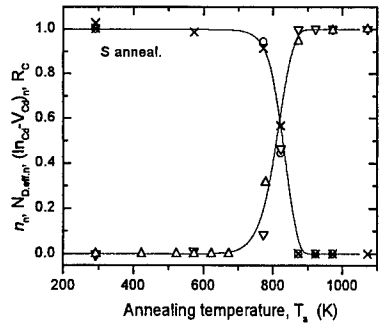

Fig. 4. Dependence of PAC and electrical properties (normalized values) of n-CdS annealed under S pressure (initial $[N_D]_{eff,RT} \cong 10^{16}/cm^3$) on the annealing temperature: n_n (○) – measured free-electron concentration normalized to its initial value at RT; $N_{D,eff,n}$ (×) – calculated effective donor concentration normalized to its initial value at RT; $(In_{Cd}-V_{Cd})_n$ (△) – fractions of pairs normalized to their saturating value at high T_a;(▽) – calculated compensation ratio, $R_C = 1 - ([N_D] - [N_A])/[N_D]$.

Above ≅800 K the $(In_{Cd}-V_{Cd})$ pairs appear and their fraction increases with higher T_a at the expense of the fraction of In_{Cd}. This change is closely matched with the increase of compensation, calculated from the fits of $n(T)$. The dynamics of the increase of $(In_{Cd}-V_{Cd})$ fraction, however, precisely correlates with the decrease of experimentally determined n, as well as with the decrease of the concentration of remaining donors, $[N_D]_{eff.}$. The fact that the sample becomes semi-insulating above $T_a \cong 800$ K means that not only the In_{Cd}^{+} donors but also all other donors are deactivated. Since PAC showed that In donors become compensated by pairing with spontaneously formed V_{Cd} acceptors, it seems plausible that the other donors are being compensated by the analogous mechanism.

The electrical measurements of the In-implanted layer ([In] up to $10^{20}/cm^3$) were also done after annealing at 923 K under S pressure, i.e. after the substrate was converted to semi-insulating (Fig. 1). Again, very low n (lower than $10^8/cm^3$) was obtained, pointing out to the full compensation of all In donors. Obviously, S annealing creates just a matching concentration of V_{Cd} to fully compensate foreign donors, indicating that the same compensation mechanisms deactivate donors over the range of 4 orders of In concentrations. This finding offers the experimental proof at a microscopic level of the self-compensation mechanism by spontaneously created native defects [3].

5. Conclusion

The electrical activation of donors in CdS was studied by using Perturbed γγ angular correlation (PAC) spectroscopy and temperature dependence of Hall mobility and electrical resistivity. It has been found that donors become electrically deactivated after thermal treatment under S pressure. The increase of the concentration of compensating acceptors, determined from the electrical measurements (temperature dependence $n(T)$ and $\mu_H(T)$) exactly correlates with the increase of the concentration of $(In_{Cd}-V_{Cd})$ pairs, as determined from PAC. This correlation identifies cadmium vacancies, which are created spontaneously under S pressure above 800 K, as native defects responsible for the electrical deactivation of donors in CdS. Only for $[In] > 10^{19}/cm^3$–$10^{20}/cm^3$, In starts to precipitate into other phases within CdS.

Acknowledgements

This research was supported by the Ministry of Science and Technology of Croatia and by the Deutsche Forschungsgemeinschaft (SFB 306).

References

[1] U.V. Desnica, Prog. Cryst. Growth Charact. Mater. 36 (1998) 291.
[2] H.W. Woodbury, Phys. Rev. B 9 (1974) 5188 and 5195.
[3] U.V. Desnica, R. Magerle, I.D. Desnica-Frankovic, M. Deicher, A. Burchard, Phys. Rev. Lett., submitted for publication.
[4] Th. Wichert, Th. Krings, H. Wolf, Physica B 185 (1993) 297.
[5] J.L. Boone, G. Cantwell, J. Appl. Phys. 57 (1985) 1171.
[6] D.C. Look, Electrical Characterization of GaAs Materials and Devices, Wiley, New York, 1989.
[7] K. Morimoto, M. Kitagawa, T. Toshida, J. Crystal Growth 59 (1982) 254.
[8] R. Magerle, M. Deicher, U. Desnica, R. Keller, W. Pfeiffer, F. Pleiter, H. Skudlik, Th. Wichert, Appl. Surf. Sci. 50 (1991) 169.

ELSEVIER

Physica B 273–274 (1999) 911–914

PHYSICA B

www.elsevier.com/locate/physb

Spin-flip Raman scattering in submonolayer CdSe/ZnSe structures

T. Ruf[a,*], O.Z. Karimov[b], D. Wolverson[b], J.J. Davies[b], A.N. Reznitsky[c], A.A. Klochikhin[d], S.Yu. Verbin[c], L.N. Tenishev[c], S.A. Permogorov[c], S.V. Ivanov[c]

[a]*Max-Planck-Institut für Festkörperforschung, Heisenbergstr. 1, D-70569 Stuttgart, Germany*
[b]*Department of Physics, University of Bath, Bath, BA2 7AY, UK*
[c]*A.F. Ioffe Physical-Technical Institute, 194021 St. Petersburg, Russia*
[d]*Petersburg Nuclear Physics Institute, 188350 St. Petersburg, Russia*

Abstract

We have used spin-flip Raman scattering in magnetic fields up to 14T to investigate g-factors and exchange constants of excitons related to a submonolayer insertion of CdSe in a ZnSe matrix. Sharp spectral signatures are obtained for excitation within the inhomogeneously broadened luminescence. The observed g factors are close to those of bulk ZnSe, a fact which is of particular relevance when considering the different models for the nature of excitons near submonolayer insertions and their microscopic structure (islands, homogeneous alloys, self-organized quantum dots). In measurements for different magnetic field directions we identify a "dark" (dipole-forbidden) exciton peak. Its exchange splitting from the dipole-allowed exciton increases linearly with the localization energy of the CdSe-related excitons.

Keywords: Spin-flip Raman scattering; CdSe/ZnSe heterostructures; Quantum dots; g factors; Exchange interaction

1. Introduction

Spin-flip Raman scattering (SFRS) has recently been applied intensively to investigate new materials, especially quantum wells and quantum dots made from wide-gap semiconductors. The SFRS efficiency resonates strongly at electronic interband transitions. According to the excitation wavelength, it is thus sensitive either to intrinsic or extrinsic (defect) material properties. As a result, the method possesses several unique features. For example, SFRS allows one to measure the g factors of excitons and their variation with the confinement conditions. In addition, by varying the angle between the quantum well planes and the magnetic field, the electron and hole g factors contributing to an exciton can be determined separately, unlike, e.g., in electron–spin resonance or photoluminescence (PL), where usually only one or a combination of these parameters is obtained. SFRS can also be applied to study excitons localized at defects, interface roughness or layer thickness fluctuations. Examples where these properties have been exploited include (i) studies of g factors, fundamental scattering mechanisms and selection rules for acceptor-bound excitons and excitons localized by interface disorder in GaAs/AlGaAs quantum wells [1,2], (ii) the determination of the electron g factor anisotropy and its variation with quantum well thickness in the GaAs/AlAs system [3], (iii) the identification of new defect states and the determination of the strain–spin Hamiltonian due to (nitrogen) doping in ZnSe [4,5], and (iv) a systematic study of exciton, electron, and hole g factors for quantum well excitons and different barrier materials in CdTe/CdMgTe quantum wells [6].

SFRS has recently been applied intensively also to study excitons in quantum dots formed by Stranski–Krastanov growth from thin (up to a few monolayers (ML) at most) layers of one material deposited between

* Corresponding author. Tel.: + 49-711-689-1735; fax: + 49-711-689-1712.
E-mail address: ruf@cardix.mpi-stuttgart.mpg.de (T. Ruf)

0921-4526/99/$ - see front matter
PII: S0921-4526(99)00552-9

much thicker sheets of another semiconductor (InAs/GaAs [7], InP/InGaP [8]) or by diffusion-controlled phase decomposition of solid solutions while annealing in a glass matrix (CdS [9]). In the CdS/glass system, the observed variation of the exciton g factor with the quantum dot size, measured by size selective excitation at different laser energies, could be explained well with CdS parameters when confinement effects were taken into account by using the excitation energy instead of the bulk CdS band gap [9]. This behavior reflects the fact that the excitons are strongly confined in the CdS dots. In contrast, g factors measured in the systems of Refs. [7,8] are rather close to those of the matrix surrounding the quantum dots. This indicates that the exciton wave function, e.g. in the submonolayer InAs/GaAs system, extends significantly into the barrier material and makes the correlation between SFRS data and the microscopic structure of these systems difficult. The wave function penetration could arise from weak exciton localization due either to a strong quantum confinement shift of the lowest quantum-dot state which is located near the barrier energy or to a dilute insertion. In such circumstances, SFRS cannot readily distinguish between several possible scenarios such as excitons localized at small InAs quantum dots, laterally extended islands with small thicknesses of only a few ML, or a homogeneous (alloy) InGaAs quantum well with low In content [7].

Here we report on an SFRS study of the CdSe/ZnSe system which has recently become interesting in the context of obtaining improved properties of green/blue II–VI semiconductor lasers [10–15]. Similar to the InAs/GaAs system, submonolayer deposition of CdSe in a ZnSe matrix leads to the formation of nanoscale objects. Their microscopic structure varies with the thickness of the insertion and has been discussed intensively in the literature. Deposition of more than 0.5 ML CdSe can lead to the formation of inhomogeneous (Zn, Cd)Se layers containing, e.g., two-dimensional (2D) islands acting as quantum dots or coexisting alloy and island phases [10,14,15]. For nominal CdSe compositions less than 0.5 ML the formation of a homogeneous $Zn_{1-x}Cd_xSe$ quantum well layer has been observed [10,12,13]. In this SFRS study, we investigate a sample at the border-line content of 0.5 ML.

2. Experiment

SFRS experiments have been performed on a structure with a period of 5.4 nm containing eleven sheets of nominally 0.5 ML CdSe in ZnSe (specimen B1485). Details of the sample growth have been described elsewhere [10]. Two experimental set-ups have been used [4]: (i) a split-coil 6 T system with the sample at 1.5 K, and detection by a multichannel spectrometer equipped with a CCD (Bath), and (ii) a 14 T magnet with sample temperatures around 4 K and signal detection by conventional single-photon counting and a double monochromator (Stuttgart). Tunable laser excitation was obtained from an Ar-ion laser pumped Stilbene 3 dye laser.

3. Results and discussion

Fig. 1 shows the PL and PL excitation (PLE) spectra of the 0.5 ML CdSe/ZnSe structure in the energy range of the CdSe-related emission. The peak position and the slight asymmetry of the PL spectrum towards lower energies are in good agreement with previous reports [10]. The location of the lowest-energy heavy-hole exciton E^{hh}, as determined from PLE measurements, is indicated. The light-hole exciton lies 40 meV higher in energy. Fig. 2 shows SFRS spectra in Voigt geometry for two different laser energies within the PL band. In this geometry, two types of lines appear on the Stokes (positive Raman shifts) and anti-Stokes sides: a sharp line (E) for which the Raman shift does not depend on the laser energy and a broad peak (DE) for which the shift changes when the laser energy is varied. The resonance behavior of these peaks is shown in Fig. 1. The maximum intensity of line E occurs between the maxima of the PL and PLE spectra; that of line DE is shifted towards lower energies by about 2 meV, and its profile closely follows the PL spectrum. The variation of these SFRS line positions with magnetic field B is shown in Fig. 3. For the E line the shift depends linearly on B and, within our

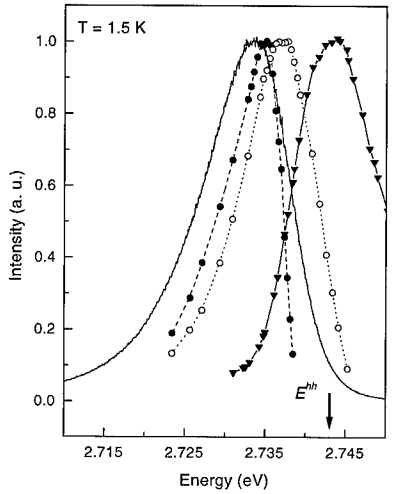

Fig. 1. CdSe-related PL (solid line) and PLE (filled triangles) spectra of a 0.5 ML CdSe/ZnSe multiple quantum well structure ($B = 6$ T, $E_{laser} = 2.88$ eV). The dotted (dashed) lines connect measurements of the scattering intensity resonance profiles (open (filled) circles) for the electron (E) and dark exciton (DE) SFRS lines, respectively.

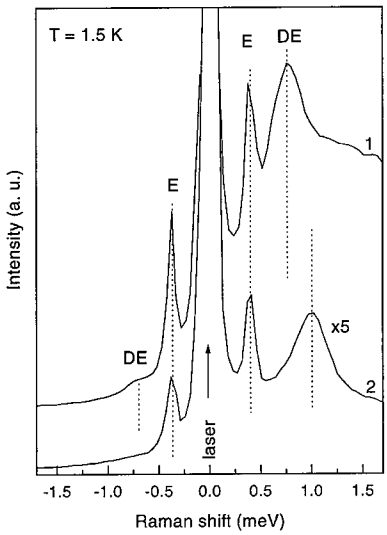

Fig. 2. SFRS spectra for laser energies within the broad PL band: (1) $E_{laser} = 2.7353$ eV, (2) $E_{laser} = 2.7248$ eV. Both spectra were measured in the $z(\pi,\sigma)\bar{z}$ polarization configuration with the magnetic field ($B = 6$ T) parallel to the CdSe layer (Voigt geometry). Spectrum 2 was magnified five times before plotting.

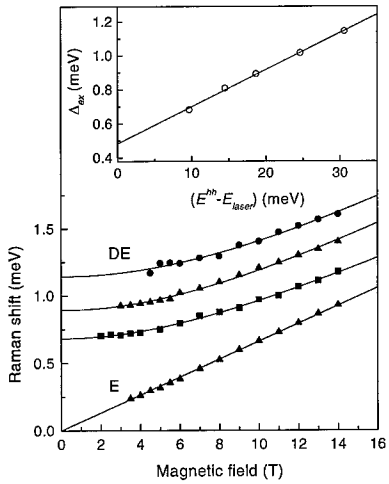

Fig. 3. Raman shifts of the SFRS lines E and DE vs. magnetic field. Line DE depends on the excitation energy as evidenced by measurements at $E_{laser} = 2.7338$ eV (squares), 2.7248 eV (triangles), and 2.7129 eV (circles) across the broad PL band. The inset shows the linear increase of the zero-field DE energy when E_{laser} becomes smaller than E^{hh}. The solid lines are fits to the data of a linear form (E) and $\sqrt{\Delta_{ex}^2 + (g\mu_B B)^2}$ (DE) (see Eq. (3) of Ref. [19]).

experimental accuracy, it vanishes at zero field. In contrast, the shift for line DE shows a nonlinear dependence on B and, even more interestingly, it increases (independently of B) when E_{laser} decreases. The inset of Fig. 3 shows a linear dependence of the zero-field limit Δ_{ex} of the DE line on the difference between the laser energy and E^{hh}. We have also performed SFRS measurements in which the direction of the field is varied and which will be discussed in detail elsewhere. Away from Voigt geometry, the DE line moves rapidly towards larger Raman shifts, and its intensity decreases strongly. In Faraday geometry (B perpendicular to the CdSe layer), this line is not observed. In addition to the E and DE lines, three other peaks appear for intermediate field directions.

Due to the large splitting between the heavy- and light-hole excitons (caused by a combination of confinement and strain effects) it suffices to consider only the $|J = \frac{3}{2}, J_z = \pm\frac{3}{2}\rangle$ hole and the $|S = \frac{1}{2}, S_z = \pm\frac{1}{2}|$ electron states in the data analysis. However, the exchange interaction between electrons and holes is known to play an important role in II–VI semiconductors. Its influence is even stronger in low-dimensional systems due to the larger wave function overlap compared to the bulk. This was already realized several years ago [17], and many theoretical and experimental investigations on quantum wells and quantum dots have been performed in the past few years [18]. In the above basis, the exchange interaction leads to the formation of two doublets with total angular momentum components of $|F_z = \pm 2\rangle$ and $|F_z = \pm 1\rangle$, which are dipole forbidden ("dark" excitons, DE) and allowed (bright excitons), respectively. Their separation is determined by the exchange coupling, which consists of two contributions, a short-range (analytical) and a long-range (roughly speaking: nonanalytical, see Ref. [18]) part, originating from contributions to the exchange integral within the same unit cell or from neighboring cells, respectively. For scattering geometries away from the Faraday configuration, the exciton wave functions in a magnetic field mix in a way similar to that caused by the application of a uniaxial stress. Dark exciton states may then become dipole-allowed and can be observed in optical experiments such as, e.g., the PL and SFRS study of Ref. [19] or the high-resolution SFRS data presented in Figs. 2 and 3.

We use a model Hamiltonian based on Fig. 10 of Ref. [20] to fit our angle-dependent data and obtain values of $\Delta_{ex} = 0.68$ meV for the exchange splitting, an electron g factor of $g_e = 1.2$, and a hole g factor of $g_{h\parallel} = 2.7$ (under excitation at the maximum of the resonance profile of the DE line, Fig. 1). g_e is isotropic, while g_h vanishes in Voigt geometry, thus exhibiting the well-known behavior for pure $|J_z = \pm\frac{3}{2}\rangle$ wave functions [1,2]. In the Voigt geometry only one SFRS line, involving dark exciton states, should occur according to our model. The observation of such transitions is possible in a magnetic field which mixes the $|F_z = \pm 2\rangle$ wave functions with the dipole-allowed $|F_z = \pm 1\rangle$ states. We therefore attribute the line marked DE (following the notation of Ref. [19]) in Figs. 2 and 3 to such a transition.

In addition, line E corresponds to an electron spin-flip, its g value ($g_e = 1.15(3)$) being very close to data for

donor-bound electrons [4] and calculations ($g_e = 1.19$) for intrinsic electrons in bulk ZnSe [21]. It is also worth to note that the measured hole g factor coincides to within experimental error with that observed in nitrogen-doped bulk ZnSe ($g_{h\|} = 2.5$–2.7 [4,22]). Since the exciton radius in both, bulk CdSe ($a_B = 44\,\AA$) and ZnSe ($a_B = 51\,\AA$) [16], is much larger than the maximum estimate for the thickness of the CdSe-related layer (about 1 nm [14]), such a similarity in the g factors may result from strong penetration of the exciton wave function into the ZnSe barriers.

Our results for the DE line are in many ways similar to those of Ref. [19]. However, in contrast to that work, we find a linear variation of the exchange splitting when E_{laser} is scanned across the CdSe-related PL band (g_e, on the other hand, remains constant) and an almost two-fold increase of Δ_{ex} at the lowest excitation energies. We attribute this enhancement to the larger wave function overlap for the more strongly localized excitons in the low-energy PL tail. Further work is required to decide whether this effect reflects a nonanalytical contribution to the (mostly analytical) exchange splitting, as one might conclude from the speculations in Ref. [19]. While it is qualitatively clear that the exchange splitting should vary strongly with the exciton radius (and thus the exciton localization energy) due to its strong sensitivity to changes in the wave function overlap, the exact functional form for this relation cannot be easily obtained. Note that this *increase* of Δ_{ex} for *lower* excitation energies is in contrast to the behavior of quantum dots with full three-dimensional confinement [14], where a *decrease* of the exchange splitting with increasing dot size, i.e., with lower exciton energy, is expected. Such an effect has been observed recently in pure CdSe dots [23]. The values of Δ_{ex} found here are 5–10 times larger than in bulk CdSe and ZnSe [16].

The present data are not consistent with a two-phase scenario, reported previously for insertion layers thicker than 0.7 ML, in which relatively large CdSe islands coexist with a homogeneous matrix (i.e., an alloy or, equivalently, a high density of 2D CdSe islands smaller than the exciton Bohr radius) [11–13]. For such a system, one would expect a discontinuous dependence of Δ_{ex} on the localization energy similar to Ref. [10] where two components in the PL decay curves have been observed for a 0.75 ML sample. Instead, the continuous, linear relation shown in the inset of Fig. 3 suggests that the microscopic structure of our 0.5 ML CdSe/ZnSe sample does not differ significantly from that of an alloy in which the Cd is randomly distributed. This is consistent with earlier reports for insertion thicknesses less than about 0.5 ML [11,13,14].

4. Conclusions

SFRS on a submonolayer CdSe/ZnSe multiple quantum well sample reveals g factors of electrons (presumably bound at donors) and of excitons localized at the CdSe-related insertion layer which are very close to the values for the surrounding ZnSe matrix. The exchange splitting between bright and dark excitons is enhanced and varies linearly with the exciton localization energy.

Acknowledgements

We would like to thank V.F. Sapega, A.A. Toropov, and E.L. Ivchenko for helpful discussions. We acknowledge technical assistance by P. Hiessl, H. Hirt, M. Siemers, and R.C.J. Draper. This work was supported in part by EPSRC grant GR/L62283, RFBR and Volkswagen-Stiftung grants.

References

[1] V.F. Sapega et al., Phys. Rev. B 45 (1992) 4320.
[2] V.F. Sapega et al., Phys. Rev. B 50 (1994) 2510.
[3] A.A. Sirenko et al., in: G. Landwehr, W. Ossau (Eds.), Proceedings of the 12th International Conference on High Magnetic Fields in Semiconductor Physics, World Scientific, Singapore, 1997, p. 561.
[4] C. Orange et al., Phys. Rev. B 55 (1997) 1607.
[5] D. Wolverson et al., J. Crystal Growth 159 (1996) 229.
[6] A.A. Sirenko et al., Phys. Rev. B 56 (1997) 2114.
[7] A.A. Sirenko et al., Solid State Commun. 97 (1996) 169.
[8] A.A. Sirenko et al., in: M. Scheffler, R. Zimmermann (Eds.), The Physics of Semiconductors, World Scientific, Singapore, 1996, p. 1385.
[9] A.A. Sirenko et al., Phys. Rev. B 58 (1998) 2077.
[10] S.V. Ivanov et al., J. Appl. Phys. 83 (1998) 3168.
[11] S.V. Ivanov et al., Appl. Phys. Lett. 74 (1999) 498.
[12] A.A. Toropov et al., Jpn. J. Appl. Phys. 38 (1999) 566.
[13] Z. Zhu et al., Appl. Phys. Lett. 63 (1993) 1678.
[14] M. Strassburg et al., Appl. Phys. Lett. 72 (1998) 942.
[15] T. Kümmell et al., Appl. Phys. Lett. 73 (1998) 3105.
[16] O. Madelung, M. Schulz, Landolt-Börnstein (Eds.), Intrinsic Properties of Group IV Elements and III–V, II–VI, and I–VII Compounds, New Series, Group III, Vol. 22a, Springer, Berlin, 1987.
[17] Y. Chen et al., Phys. Rev. B 37 (1988) 6429.
[18] H. Fu et al., Phys. Rev. B 59 (1999) 5568 and references therein.
[19] J. Puls, F. Henneberger, Phys. Stat. Solidi A 164 (1997) 499.
[20] D.G. Thomas, J.J. Hopfield, Phys. Rev. 128 (1962) 2135.
[21] M. Willatzen et al., Phys. Rev. B 51 (1995) 17992.
[22] C. Orange et al., J. Crystal Growth 184/185 (1998) 510.
[23] M. Nirmal et al., Phys. Rev. Lett. 75 (1995) 3728.

ELSEVIER

Physica B 273–274 (1999) 915–918

PHYSICA B

www.elsevier.com/locate/physb

Evidence on a bond-breaking relaxation in the bistable centers In and Ga in CdF_2

J. Nissilä[a,*], K. Saarinen[a], P. Hautojärvi[a], A. Suchocki[b], J.M. Langer[b]

[a]*Laboratory of Physics, Helsinki University of Technology, P.O. Box 1100, 02015 HUT, Finland*
[b]*Institute of Physics, Polish Academy of Sciences, 02-668 Warsaw, Poland*

Abstract

Positron annihilation experiments reveal an open-volume defect in the deep state atomic configurations of bistable donors In and Ga in CdF_2. The size of the open volume is at least half of a monovacancy. The results are similar to those obtained previously for the DX centers in the covalent system $Al_xGa_{1-x}As$. It is therefore likely that the bond-breaking mechanism (substitutional to interstitial atomic motion) responsible for metastability of point defects in covalent semiconductors is more universal and its validity extends to even some highly ionic compounds, like CdF_2.

Keywords: Bistable centers; DX-like centers; CdF_2

1. Introduction

Bistable centers are some of the most fascinating point defects in solids. The charge carriers are captured at these centers either on localized orbits or in effective mass bound states. The two types of states are separated by a vibronic barrier causing metastability of the shallower effective mass state at low temperature. Such defects are found from highly covalent (e.g., Si in $Al_xGa_{1-x}As$ [1]) to highly ionic crystals (e.g., Ga and In in CdF_2 [2–4]). In spite of the very different nature of the bonds in these crystals, bistable defects exhibit largely similar properties. The origin of the metastability is usually attributed to a large lattice relaxation taking place in the transition between the states [5]. In covalent hosts, the bond-breaking mechanism in which atoms change lattice position (e.g., from substitutional to interstitial) is responsible for the metastability [6]. In ionic hosts, such as CdF_2, a simple symmetric inward relaxation of the neighboring anions around the dopant atom was originally believed to be at the origin of the bistability [7–9]. Most surprisingly, recent experiments imply that the bistable centers in CdF_2 are negative-U type defects and an exotic asymmetric relaxation may be responsible for the phenomenon [10–14]. Interestingly, most recent theoretical computations of the defect structure of donors in these crystals also suggest a possibility of negative-U [15,16] and non-symmetric lattice relaxation with even a substitutional to interstitial dopant motion [16]. Such a relaxation would invariably produce a cation vacancy, which could possibly be observed by positron annihilation spectroscopy [17].

Positron annihilation is a well-established method to study vacancy-type defects in solids [18,19]. Positrons get trapped at negative and neutral vacancies due to the missing positive ion core. In a vacancy, the electron density is lower than in the lattice which leads to an increase in the positron lifetime and narrowing of the momentum distribution of the annihilating electron–positron pairs. Among the most exciting discoveries with this technique are the direct observations of vacancy-type defects related to the EL2 in GaAs and the DX center in $Al_xGa_{1-x}As$ [20,21].

* Corresponding author. Tel.: + 358-9-451-5802; fax: + 358-9-451-3116.
E-mail address: jaani.nissila@hut.fi (J. Nissilä)

0921-4526/99/$ - see front matter
PII: S0921-4526(99)00553-0

2. Experimental

The positron lifetime experiments were conducted in a conventional way [18,19]. Two identical sample pieces were sandwiched around a ^{22}NaCl positron source of 20–50 μCi. The lifetime spectra were measured with fast–fast spectrometers whose time resolutions were 210–250 ps (FWHM). To be able to vary the state of the bistable defects the samples were mounted into an optical cryostat (T = 8–350 K). The sample illumination was performed with monochromatic light ($h\nu$ = 1–4 eV, photon flux > 10^{12} cm^{-2} s^{-1}) (for technical details, see Ref. [22]).

The bulk CdF_2 crystals were grown by the modified Bridgman method. Two of the samples (#1 and #2) were doped with Ga, one (#3) with In, and one (#4) with Y (concentrations were in the range 10^{18}–10^{19} cm^{-3}). All of the samples were annealed in reducing Cd atmosphere to remove compensating F interstitials. Sample #2 was annealed more thoroughly than sample #1 to vary the concentration of bistable defects in the samples. The Y doped sample was suitable as a reference since Y is a simple effective mass shallow donor in CdF_2 crystals [2–4].

3. Results and discussion

The average positron lifetime results, measured in darkness from 10 to 300 K, are shown in Fig. 1. When positrons are trapped at open volume defects, the average lifetime τ_{av} increases compared with the value τ_{bulk} in the lattice. In all our samples, the lowest average lifetimes were measured at temperatures below 50 K. Raising the sample temperature towards room temperature leads to an increase of 5–15 ps in the lifetime values depending on the sample. The most natural explanation for this temperature dependence is positron trapping at two different types of point defects: some open-volume defects and some negative centers without any open volume [18]. At low temperatures, a considerable fraction of positrons gets trapped at negative ion-type defects, which prevents them from getting trapped at vacancies. Above 60 K, positrons are able to escape from the shallow state around the negative ions, which enhances trapping at vacancies, i.e., increases the average lifetime.

In a recent theoretical work, Mattila et al. performed ab initio calculations on the formation energies of point defects in CdF_2 [15]. They suggest that in n-type material the Cd vacancy is the most abundant vacancy defect. As shown, we observe native vacancies in Y, Ga and In doped material and it is thus natural to attribute them to V_{Cd}. In addition, the calculations [15] confirm the traditional assumption that F interstitials are abundantly formed as negatively charged compensating defects in n-type CdF_2. The positron data indicates the presence of negative ions in Y, Ga and In doped crystals. These defects are most probably the F interstitials.

The key experiment concerning defect bistability is to study whether illumination has an influence upon positron trapping. Illumination is known to induce deep–shallow transition of the bistable centers [2–4]. A most pronounced effect is observed in both In and Ga doped crystals at 15 K: the mean positron lifetime decreases with increasing photon fluence and saturates to a value of 1–4 ps lower than obtained before illumination. The data on samples #2 (Ga doped) and #3 (In doped) are presented in Fig. 2. The changes are persistent at 15 K based on the observation that after an illumination the average lifetime remains constant for days. In contrast to these effects, the illumination has no influence on the positron lifetime in the Y doped sample.

To study the thermal stability of the observed persistent change in the average lifetime, we performed an isochronal annealing experiment (Fig. 3). The samples

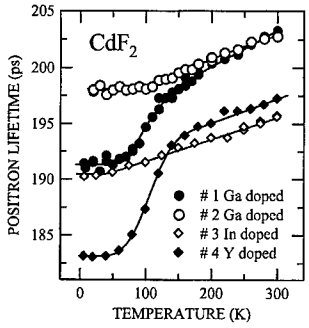

Fig. 1. The average positron lifetime in darkness as a function of the measurement temperature. The solid lines are guides to the eye.

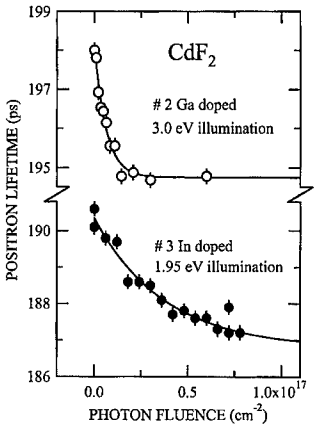

Fig. 2. The average positron lifetime in darkness versus the illumination fluence. The solid lines are exponential fits to the data.

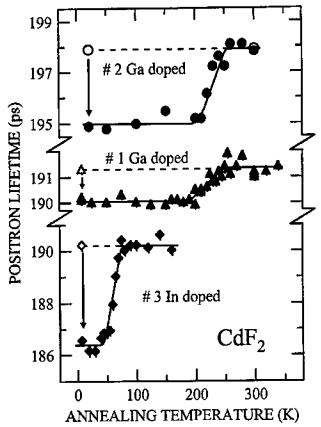

Fig. 3. The average positron lifetime measured at 15 K in darkness as a function of the annealing temperature. Before each 10 min annealing the samples were illuminated at 15 K with 1.95 eV (In doped) or 3.0 eV (Ga doped) light. The illumination was long enough to saturate the change in the average positron lifetime (photon fluence 2×10^{17} cm^{-2}). The open symbols and the dashed lines represent the lifetime levels before illumination. The solid lines are guides to the eye [17].

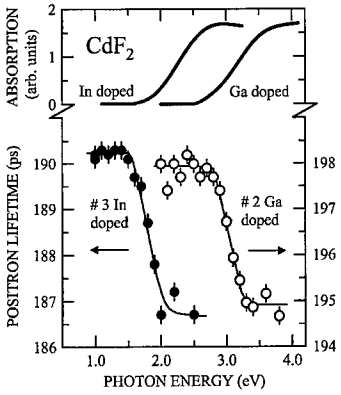

Fig. 4. The absorption spectra and the average positron lifetime versus the photon energy. The absorption data show a typical result for In and Ga in the deep state. The positron measurements were performed in darkness at 15 K after illuminating the sample to a constant fluence (3.6×10^{15} cm^{-2} for sample #2 and 8.0×10^{16} cm^{-2} for sample #3). After each measurement the samples were annealed at 300 K. The solid lines are guides to the eye [17].

were first illuminated with 1.95 eV (In doped) or 3.0 eV (Ga doped) photons whereafter the measurements and the heat treatments were performed in the dark. In In doped CdF_2, annealing in the range from 60 to 75 K restores the lifetime at the initial level before illumination. In the case of the Ga doped CdF_2, the recovery occurs between 200 and 250 K. These temperatures are the same at which the bistable centers make the transition from the shallow state to the deep state [2–4].

The positron lifetime can be directly correlated with the optical absorption of the bistable defects by performing the experiment as a function of the photon energy. The absorption related to the deep states of Ga and In begins to increase at 2.5 and 1.5 eV, respectively (Fig. 4). In the positron experiment the samples were illuminated at 15 K to a constant photon fluence. The positron lifetime spectra were measured in the dark at 15 K after each illumination (Fig. 4). In the Ga and In doped samples τ_{av} starts to decrease at about 2.7 and 1.5 eV, respectively. The average lifetime decreases with increasing absorption until the level corresponding to prolonged illumination (fully depleted deep state) is reached. The photon energy ranges at which τ_{av} decreases and the absorption increases match very well.[1]

[1] The minor differences in the absorption and positron data are due to different illumination conditions. The absorption data probes the deep state without effectively changing its electron population whereas the positron data is measured after partially converting the deep state into the shallow state.

The data in Figs. 2–4 show that the average positron lifetime is sensitive to the state of the bistable centers. Positron trapping at open-volume defects is enhanced, i.e. more vacancies are detected, when the deep state is occupied. Some vacancies (probably V_{Cd}) are, however, observed also when the bistable centers are in the shallow state. This is obvious since the average lifetime after illumination (Fig. 3) is higher than the lowest value 183 ps measured in the Y doped specimen (Fig. 1). A comparison of Doppler broadening and positron lifetime data implies that when the deep state is occupied there are at least two different open-volume defects [17]. Besides the evident V_{Cd} there is thus another vacancy which ceases trapping positrons when In and Ga are converted to the shallow state by illumination (Figs. 3 and 4). Hence, we infer that the vacancy defect is a constituent of the deep state atomic structure of the bistable centers in CdF_2. A likely configuration is a pair of V_{Cd} and Ga or In interstitial in its close vicinity. Such defect complex has an overall negative charge as In and Ga bistable donors form a negative-U system [10–13].

In sample #2, τ_{av} at 15 K decreases from 198 to 195 ps when the bistable centers are converted from the deep to the shallow state (Fig. 3). This implies that the characteristic positron lifetime in the deep state related vacancy $\tau_{DS} \geqslant 198$ ps. It is thus at least 15 ps longer than the lifetime in the lattice ($\tau_{bulk} \leqslant 183$ ps). On the other hand, the theoretical difference between τ_{bulk} and $\tau_{V_{Cd}}$ is about 35 ps ([23]; calculational scheme presented in Refs. [24,25]). Hence, we can deduce that the open volume in the deep state atomic configuration of the bistable centers is at least half of a Cd monovacancy.

The concentrations of different defects can be estimated based on the positron data [17]. As a result, we find that $[V_{Cd}]$ and $[F_i]$ are of the order of 10^{17}–$10^{18}\,cm^{-3}$ which are reasonable values in CdF_2. Furthermore, the concentration of the deep states [DS] is about $10^{18}\,cm^{-3}$ which is the same order of magnitude as estimated from electrical and optical measurements. This supports quantitatively our identification of the vacancy defect in the atomic structure of the deep state of In and Ga in CdF_2.

Most excitingly, the positron annihilation results on the DX center in $Al_xGa_{1-x}As$ [18,21] are qualitatively very similar to those in CdF_2. In $Al_xGa_{1-x}As$, the donor atom is believed to make a substitutional–interstitial jump leaving an open volume behind which positrons detect [18,21]. Recent calculations by Park and Chadi [16] suggest that also in CdF_2 In and Ga atoms can move from the substitutional site to an interstitial site in the neighboring lattice cell. This model is fully compatible with our positron data and indicates unexpected universality of the bond-breaking mechanism of bistability of defects in semiconductors.

4. Conclusions

We have studied n-type CdF_2 crystals doped with Y, Ga and In by positron annihilation spectroscopies. We found that an open-volume defect is included in the atomic configuration of the deep state of the bistable In and Ga related defects. Our data indicate that the size of the open volume is at least half a Cd monovacancy. The positron results imply that the bond-breaking mechanism resulting in asymmetric lattice relaxations is of more general validity than previously thought; it applies from covalent to predominantly ionic systems.

Acknowledgements

We are grateful to M.J. Puska, T. Mattila and S. Pöykko for invaluable discussions. We also acknowledge C.H. Park and D.J. Chadi for informing us of their results [16] before publication.

References

[1] P.M. Mooney, J. Appl. Phys. 67 (1990) R1.
[2] U. Piekara, J.M. Langer, B. Krukowska-Fulde, Solid State Commun. 23 (1977) 583.
[3] J.E. Dmochowski, J.M. Langer, Z. Kalinski, Phys. Rev. Lett. 56 (1986) 1735.
[4] J.E. Dmochowski, W. Jantsch, D. Dobosz, J.M. Langer, Acta Phys. Pol. A 73 (1988) 247.
[5] J.M. Langer, in: Reviews of Solid State Science, Vol. 4, World Scientific, Singapore, 1990, p. 297.
[6] D.J. Chadi, K.J. Chang, Phys. Rev. Lett. 61 (1988) 873.
[7] J.M. Langer, J. Phys. Soc. Jpn. 49A (Suppl.) (1980) 207.
[8] J.M. Langer, Radiat. Eff. 72 (1983) 55.
[9] J.M. Langer, Inst. Phys. Conf. Ser. 135 (1994) 197.
[10] A.S. Shcheulin, A.I. Ryskin, K. Swiatek, J.M. Langer, Phys. Lett. A 222 (1996) 107.
[11] A.I. Ryskin, A.S. Shcheulin, D.E. Onopko, Phys. Rev. Lett. 80 (1998) 2949.
[12] J.M. Langer, A. Suchocki, R. Szymczak, M. Baran, in: G. Davies, M.H. Nazare (Eds.), Defects in Semiconductors, Materials Science Forum Vols. 258–263, Trans Tech Publications, Switzerland, 1997, p. 1449.
[13] S.A. Kazanskii, A.I. Ryskin, V.V. Romanov, Appl. Phys. Lett. 70 (1997) 1272.
[14] A. Suchocki, J. Rauluszkiewicz, J.M. Langer, Appl. Phys. Lett. 71 (1997) 1552.
[15] T. Mattila, S. Pöykkö, R.M. Nieminen, Phys. Rev. B 56 (1997) 15665.
[16] C.H. Park, D.J. Chadi, Phys. Rev. Lett. 82 (1999) 113.
[17] J. Nissilä et al., Phys. Rev. Lett. 82 (1999) 3276.
[18] K. Saarinen, P. Hautojärvi, C. Corbel, in: M. Stavola (Ed.), Identification of Defects in Semiconductors, Academic Press, New York, 1998, p. 209.
[19] M.J. Puska, R.M. Nieminen, Rev. Mod. Phys. 66 (1994) 841.
[20] R. Krause et al., Phys. Rev. Lett. 65 (1990) 3329.
[21] J. Mäkinen et al., Phys. Rev. Lett. 71 (1993) 3154.
[22] S. Kuisma et al., Phys. Rev. B 53 (1996) 9814.
[23] M.J. Puska, unpublished.
[24] B. Barbiellini et al., Phys. Rev. B 51 (1995) 7341.
[25] B. Barbiellini et al., Phys. Rev. B 53 (1996) 16201.

ELSEVIER

Physica B 273–274 (1999) 919–922

PHYSICA B

www.elsevier.com/locate/physb

Analysis of secondary phases in InSbBi thin films

M.C. Wagener*, R.E. Kroon, J.R. Botha, A.W.R. Leitch

Department of Physics, University of Port Elizabeth, P.O. Box 1600, Port Elizabeth 6000, South Africa

Abstract

The secondary phases formed during the epitaxial growth of InSbBi by metal–organic vapor-phase epitaxy is reported. The material was grown on InSb and GaAs substrates at 455°C and was characterised using scanning electron microscopy (SEM), cross-sectional transmission electron microscopy (TEM) and X-ray diffraction. The formation of secondary phases was found to be critically dependent on the V/III ratio. A V/III ratio slightly below stoichiometry lead to InBi and In_2Bi phases forming on the surface, whereas a V/III ratio slightly above stoichiometry produced BiSb phases. Cross-sectional TEM revealed the formation of large Bi inclusions within layers grown on InSb substrates. The Bi inclusions ranged in size from 0.5 to 1 μm and were distributed throughout the epilayer. Bi–Ga inclusions were observed in the case of layers grown on GaAs substrates.

Keywords: Indium antimonide bismuth MOVPE

1. Introduction

The III–V compound $InSb_{1-x}Bi_x$ has received some attention in recent years [1–4] as a potential candidate for infrared applications in the 8–12 μm range. The band gap of the material can in principle be reduced from that of InSb (0.167 eV at 300°C) to that of the semi-metal InBi (−1.5 eV at 300°C [5]). Although a small concentration of Bi is required to decrease the band gap into the desired 8–12 μm range, the low solid solubility of 2.6 mol% InBi [6] in InSb has required the use of non-equilibrium growth techniques. Single-crystalline material has been grown by molecular beam epitaxy (MBE) [1] and metal–organic vapor phase epitaxy (MOVPE) [2,4]. Although the incorporation of Bi appeared to be enhanced, compared to equilibrium growth, the surface morphology was degraded by the formation of secondary condensed phases. Bi concentrations as high as 14 mol% InBi [2] have been measured by secondary ion mass spectrometry and energy dispersive X-ray spectroscopy (EDS), but no clear extension of the absorption edge to a longer wavelength was exhibited. The Bi was therefore most likely not incorporated substitutionally, but rather as interstitials or precipitates.

The range of group V to group III ratios giving featureless surfaces is expected to be extremely narrow due to the low-vapor pressures of In, Sb and Bi. Growth at near stoichiometric conditions is therefore required to ensure that the group V elements are sufficiently depleted at the growth interface [7], thereby preventing the formation of multiple phases. In order to deplete the group V elements at the growth front, these elements must incorporate efficiently into the lattice. However, in the case of Bi, this is complicated by the low activation energy of 0.2 eV [3] required for desorption from InSb. Hence, at sufficiently high growth temperatures (in MOVPE the minimum growth temperature is limited by the pyrolysis efficiency of the group V precursors), the formation of Bi related phases will be induced over the entire V/III range, thereby limiting the Bi content. In this paper, the secondary phases formed, and their dependence on the V/III ratio, are reported. The presence of precipitationally incorporated Bi is also shown.

2. Experimental details

A laboratory-scale horizontal MOVPE reactor was used at atmospheric pressure. Trimethylantimony

* Corresponding author. Tel.: +27-41504-2579; fax: +27-41504-2573.

E-mail address: phbmcw@upe.ac.za (M.C. Wagener)

0921-4526/99/$ - see front matter
PII: S0921-4526(99)00554-2

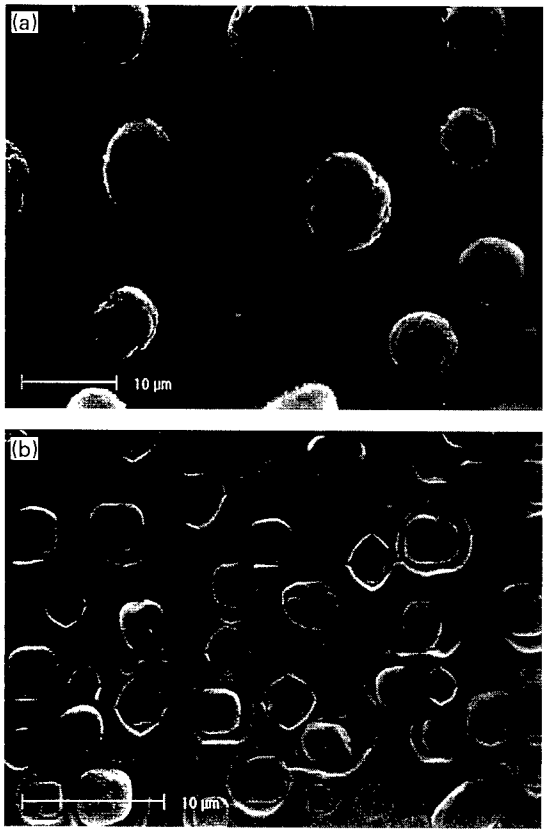

Fig. 1. Scanning electron micrographs of the surfaces of InSbBi layers grown under (a) In-rich and (b) Sb-rich growth conditions.

(TMSb), trimethylindium (TMIn) and trimethylbismuth (TMBi) were used as precursors. Epitaxial layers were grown on both InSb and GaAs substrates (orientated 2° off the (1 0 0) towards [1 1 0]) at a temperature of 455°C. Layers grown on InSb substrates were grown at a rate of 0.5 μm/h, whereas layers grown on GaAs substrates were grown at 2 μm/h. The epilayer thickness ranged from 1 to 4 μm. The epilayers were characterized using X-ray diffraction (XRD), scanning electron microscopy and transmission electron microscopy (TEM). The XRD spectra were obtained using a Phillips PW 1840 diffractometer and Fe K_α radiation.

3. Results and discussion

Preliminary attempts to incorporate Bi into InSb resulted in the formation of polycrystalline phases on the surface. The layers grown under In-rich conditions had a lustrous gray appearance, whereas layers grown under Sb-rich conditions had a mat gray appearance. Fig. 1a is a SEM micrograph of an epilayer grown under In-rich growth conditions. The surface is covered in InBi and

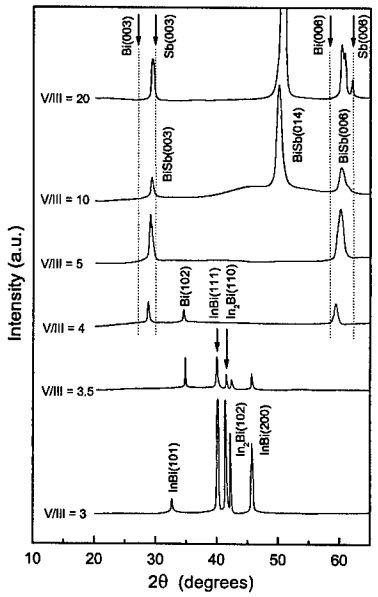

Fig. 2. X-ray diffraction spectra of InSbBi layers grown on InSb for different V/III ratios. The Bi/V ratio and TMIn flow rate were 0.01 and 1.4 μmol/min, respectively.

In_2Bi droplets. These alloys are liquids at the growth temperature and do not appear to impede epitaxial growth. The surface distribution density increased significantly with larger InBi mole fractions. The BiSb alloys formed under Sb-rich growth conditions are shown in Fig. 1b. The alloys are predominantly in the two-phase domain (45–85 at% Sb [9]) and consequently appear to impede epitaxial growth. This results in the crystallites becoming embedded in, and even covered by, the epitaxial layer. The structure of the BiSb crystallites ranged from droplet like (0–45 at% Sb) to more faceted as the Sb composition increased. Layers grown near stoichiometry were covered in Bi droplets and were nearly specular.

Fig. 2 shows the X-ray diffraction spectra of InSbBi layers grown at various V/III ratios. Diffraction peaks representing the phases InBi and In_2Bi were observed for layers grown at a V/III ratio of 3. As the V/III ratio was increased, these phases were replaced by pure Bi droplets (V/III = 3.5). A further increase in the V/III ratio produced BiSb alloys on the surface (V/III $\geqslant$ 4). The (0 0 3) and (0 0 6) reflections of BiSb were seen to shift towards higher angles as the V/III ratio was increased, indicating an increase in the Sb content (BiSb can form solutions of any composition, with the lattice spacing varying linearly with the Sb concentration [8]). The composition of the secondary phases was seen to vary significantly across each layer, with more Sb being available downstream in the reactor. The (0 0 6) reflection of the layer grown at a V/III ratio of 20 clearly consists of three peaks, indicating

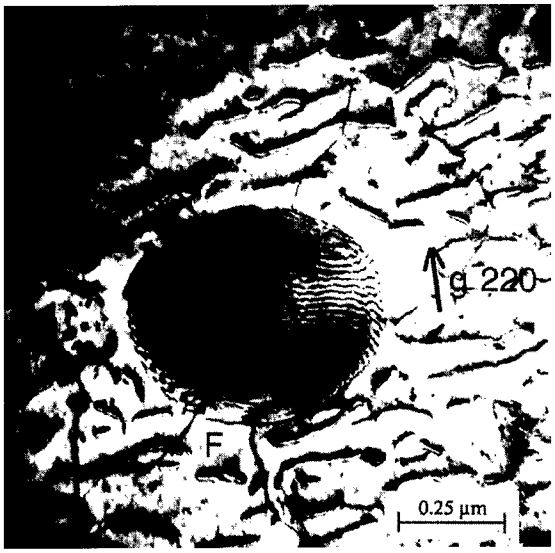

Fig. 3. Cross-sectional two-beam bright-field image of a bismuth inclusion in an InSbBi film grown on InSb. Beam direction along $[1\bar{1}0]$. $g = 220$, $s > 0$.

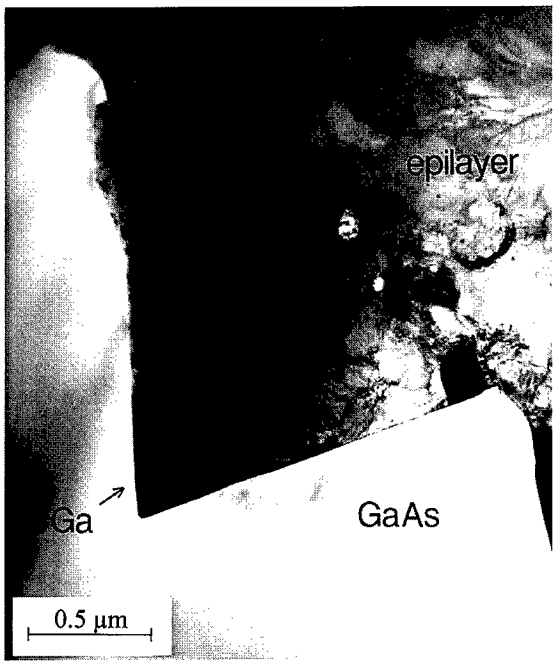

Fig. 4. Cross-sectional transmission electron micrograph of a Bi–Ga inclusion at the InSbBi/GaAs interface. Beam direction close to $[1\bar{1}0]$.

BiSb compositions of 47, 63 and 95 at% Sb. All of the detected phases were verified by EDS.

Fig. 3 shows a cross-sectional TEM image of an InSbBi layer grown with a V/III ratio of 5 and a Bi to group V ratio of 0.01. EDS measurements showed the elliptical feature to be an inclusion entirely composed of Bi. In Fig. 3, Moiré fringes, with spacing $D = 15.7$ nm occur on the border of the inclusion. These fringes occur almost perpendicular to the g vector and are characteristic of diffraction through two layers of material with slightly different interplanar spacings d_1 and d_2, where $D = (d_1 d_2)/|d_1 - d_2|$. Taking d_1 as the 220 interplanar spacing of InSb (0.2290 nm) gives $d_2 = 0.2257$ nm. This corresponds closely to the 110 interplanar spacings of hexagonal Bi (0.2273 nm). Bi is liquid at the growth temperature and contracts upon cooling. Stress fractures (F) can be seen pointing radially outwards from the Bi inclusion. EDS of the material around the inclusion detected no Bi and X-ray diffraction of the epilayer indicated no dilation of the lattice. The inclusions ranged in size from 0.5 to 1 μm. In all cases where EDS suggested a high Bi concentration in an epilayer, it was in fact due to Bi inclusions just below the surface.

In the case of layers grown on GaAs substrates, large Bi–Ga inclusions were observed along the interface. Fig. 4 shows an inclusion deep within the GaAs substrate. The inclusion is thought to be part of a segment projected along the $[1\bar{1}0]$ direction which crystallized with facets corresponding to the $\{1\,1\,1\}$ planes of the GaAs substrate. Although no crystalline Bi–Ga phase is known to exist, Bi appears to strongly interact with the GaAs substrate. It is though that the accompanying excess As is introduced into the epilayer, thereby causing lattice contraction and a reduction in the lattice mismatch. Selected area diffraction measurements of the lattice parameter in the epilayer indeed yielded a reduced value (6.3 Å) compared to that of InSb (6.48 Å).

4. Conclusions

A preliminary study of the MOVPE growth of InSbBi has revealed the various surface phases, ranging from InBi and In_2Bi formed under In-rich conditions, Bi droplets under stoichiometric growth conditions, to Bi–Sb alloys formed under Sb-rich conditions. X-ray diffraction indicated no measurable amount of substitutional Bi in the InSb matrix under any of the above growth conditions. Since the 0.2 eV desorption activation energy of Bi from InSb is significantly lower than the 1.8 eV activation energy for Bi evaporation, the formation of Bi-containing phases is thought to reduce the incorporation efficiency of Bi into InSb. The existence of large Bi inclusions was also shown. It is believed that this form of precipitational incorporation could explain reports of high Bi concentrations in InSbBi [2], coupled with no lattice dilation. Bi is also believed to adversely affect growth on GaAs substrates.

Acknowledgements

The authors wish to thank P. Gladkov from the Academy of Sciences in the Czech Republic (Institute of Radioengineering and Electronics) for valuable discussions. This work is financially supported by the National Research Foundation of South Africa.

References

[1] A.J. Noreika, W.J. Takei, M.H. Francombe, J. Appl. Phys. 53 (1982) 4932.
[2] T.P. Humphreys, P.K. Chiang, S.M. Bedair, Appl. Phys. Lett. 53 (1988) 142.
[3] J.L. Zilco, J.E. Greene, J. Appl. Phys. 51 (1980) 1549.
[4] L.L. Lee, J.D. Kim, M. Razeghi, Appl. Phys. Lett. 70 (1997) 3266.
[5] M.A. Berding, A. Sher, A.B. Chen, W.E. Miller, J. Appl. Phys. 63 (1988) 107.
[6] B. Joukoff, A.M. Jean-Louis, J. Crystal Growth 12 (1972) 169.
[7] G.B. Stringfellow, J. Crystal Growth 70 (1984) 133.
[8] W.B. Pearson, in: G.W. Raynor (Ed.), International Series of Monographs in Metal Physics and Physical Matallurgy, Vol. 8, Pergamon Press, Oxford, 1967, p. 719.
[9] ASM Handbook, Vol. 9, ASM International, 1992, p. 105.

ELSEVIER

Physica B 273–274 (1999) 923–926

PHYSICA B

www.elsevier.com/locate/physb

Determination of deep and shallow levels in conjugated polymers by electrical methods

Peter Stallinga[a,*], Henrique L. Gomes[a], H. Rost[b], A.B. Holmes[b], M.G. Harrison[c], R.H. Friend[c], F. Biscarini[d], C. Taliani[d], G.W. Jones[e], D.M. Taylor[e]

[a]*Universidade do Algarve, Optoelectronics UCEH, Campus de Gambelas, 8000 Faro, Portugal*
[b]*Melville Laboratory for Polymer Synthesis, Pembroke Street, Cambridge CB2 3RA, UK*
[c]*Cavendish Laboratory, Madingley Road, Cambridge CB3 OHE, UK*
[d]*CNR-Instituto di Spettroscopia Moleculare, Via Piero Gobetti 101, 40129 Bologna, Italy*
[e]*Institute of Molecular and Biomolecular Electronics, University of Wales, Dean Street, Bangor, Gwynnedd, LL57 1UT, UK*

Abstract

Conjugated organic semiconductors have been submitted to various electrical measurement techniques in order to reveal information about shallow levels and deep traps in the forbidden gap. The materials consisted of poly[2-methoxy, 5 ethyl (2′ hexyloxy) paraphenylenevinylene] (MEH-PPV), poly(3-methylthiophene) (PMeT), and α-sexithienyl (αT6) and the employed techniques were IV, CV, admittance spectroscopy, TSC, capacitance and current transients.

Keywords: Organic semiconductors; Electrical characterization

1. Introduction

Conjugated polymers have in common that you can locate a path with alternating single and double bonds somewhere in the molecule. The double bonds are made of overlapping p-orbitals which are relatively easily broken up. This makes the material (semi)conducting if it is possible to swap the position of the single and double bonds. The electrons are then delocalized along the backbone of the molecule. Furthermore, the π orbitals on neighboring molecules overlap with each other, especially when the molecular structures are flat, and therefore conduction can occur in three dimensions.

One of the most promising applications lies in the active element in displays and sensors. Because of the vast number of possible organic materials, they can be made to meet any requirements. For example, MEH-PPV has a band gap of approximately 2.5 eV and blue LEDS and detectors can be made from them. In fact, full-color displays, using three primary colors close to the CIE standards, and full-color scanners have already been made. They can also be used in for instance product tagging. In these low-end applications, silicon is overqualified for the job and their production cost prohibitively expensive. The great advantage that polymers offer is that they are easy to fabricate directly from solution and in contrast to inorganic semiconductors do not need surfaces with regularity at the atomic level; they do not have dangling bonds. Compare for instance the fabrication of our MEH-PPV devices, which were made by spin coating in ambient conditions (room temperature, room pressure and daylight) to the costly fabrication of GaN thin films or bulk crystals — a competitor for the blue LED. The thin GaN films require expensive MBE equipment running with ultra-high vacuum and well controlled environments, whereas the bulk materials require huge pressures. It is clear that the organic materials will be highly competitive in the consumer-electronics market of the future.

Semiconductor polymers still suffer from some problems. Most of these problems are caused by a lack of

* Corresponding author. Tel.: + 351-89-800-914; fax: + 351-89-818-560.
E-mail address: pjotr@ualg.pt (P. Stallinga)

0921-4526/99/$ - see front matter
PII: S0921-4526(99)00555-4

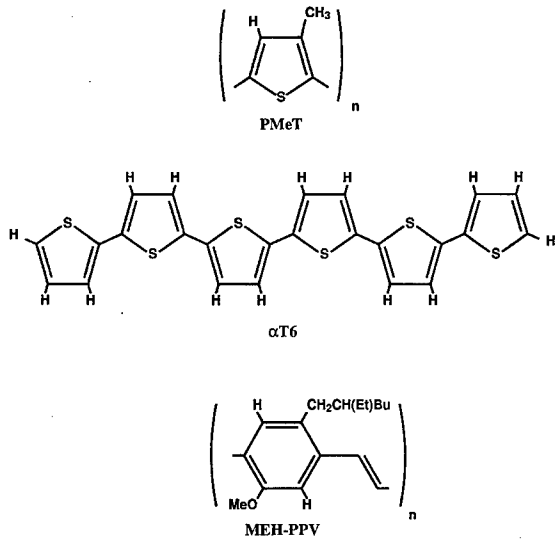

Fig. 1. The organic compounds studied in the current work. All contain a path along which the double and single bonds alternate. This causes delocalization of the charges and high conductivity.

understanding and control of the material properties. For instance, mid-gap states in wide-band-gap semiconductors have extremely long filling and emptying times. Hence, the understanding and possible elimination of these traps are mandatory for high-quality electronic devices. In the current work we review the possible experimental tools useful for the characterization of these novel semiconductors, especially applied to the deep and shallow levels. We will show how we can apply most of the standard techniques when we use them with care. Some critical remarks are placed where necessary.

The materials studied in the current work are PMeT (made by the Bangor group), MEH-PPV (made in Cambridge), and αT6 (made in Bologna). Fig. 1 summarizes these. Both PMeT and MEH-PPV are polymers with very long chains, while αT6 is an oligomer — a 'polymer' with constant, short chain length. These are just some examples of the vast number of possible structures.

2. Experimental details

The devices of the polymer PMeT were made by electro-polymerization, MEH-PPV by spin-coating the solution onto the substrates, and αT6 was deposited by vacuum sublimation. For the semiconductor/Al Schottky barriers the substrates were gold-coated glass plates where the gold-semiconductor interfaces produce good ohmic contacts. The aluminum electrodes where then vacuum sublimated on top of the polymers. For the hetero-junctions of silicon and the semiconductors, the substrates were heavily doped, n-type silicon single crystals. In that case, gold electrodes were made on top of the semiconductor. Circular electrodes with diameters of 1 and 2 mm were used.

After fabrication, the devices were exposed to air for long times before they were put in the measurement vacuum chamber. Gold wires were glued with silver paint to the substrate and the top electrode of a device. The chamber was then evacuated to 10^{-5} mbar so that it could be cooled or heated in the range 100–400 K. The temperature was measured with a thermocouple connected to a Keithley 2000 multimeter or a platinum, 100-Ω-standard resistor connected to an Oxford ITC 601 temperature controller. In either case, the sensor was placed close to the device to ensure accurate reading. The DC measurements were made with a Keithley 487 voltage source/picoammeter and the AC measurements (conductance G and capacitance C) were done on a Fluke PM6306 RCL bridge.

3. Results and discussion

3.1. Current–voltage measurements

The IV curves of all the three materials show good rectification ratios up to 10000 at $\pm$ 1 V. In most cases the ambient conditions have a huge effect on this. For one device of Si/MEH-PPV, for instance, we found how prolonged vacuum conditions can increase the rectification ratio from 16 (see Fig. 2) to 2600 [1]. For the heavily-doped PMeT devices hysteresis effects can be observed which are attributed to the normal (depletion) capacitance discharge currents, $J_C = C\,dV/dt$ (with the term containing dC/dV ignored). This current is visible when it is large compared to the normal DC conductance.

The devices made from the hetero-junctions with silicon all show a plateau in the IV curves — a range of reduced voltage dependence of the current. This we ascribe to the presence of a substantial minority-carrier

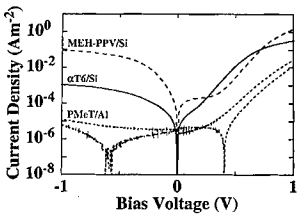

Fig. 2. Some IV curves of the studied materials. For the PMeT device a full-loop was made at a scanning speed of 1 mV/s and the observed hysteresis indicates a DC capacitance of 18 nF. The IV curves of the hetero-junctions both show a kink in the forward-bias range which we attribute to minority-carrier currents.

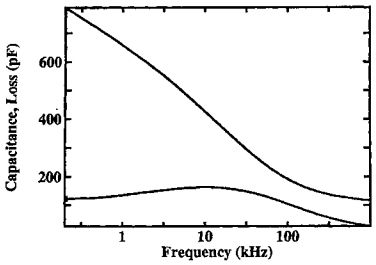

Fig. 3. Typical spectrum for a PMeT/Al Schottky barrier. The top trace shows the capacitance and the bottom trace shows the loss as a function of frequency. Up to the lowest frequencies the capacitance depends on the frequency indicating the presence of very deep level(s).

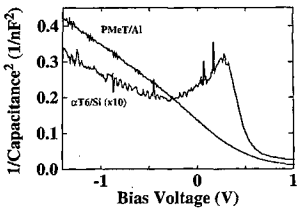

Fig. 4. Typical Mott–Schottky plots for a PMeT/Al Schottky barrier (at 200 Hz) and an αT6/Si hetero junction (at 60 Hz). The slope of the former indicates very high acceptor densities ($N_A = 10^{17}$ cm^{-3}). For reverse biases the slope changes slightly, indicating the presence of (a single) abundant deep level. For the hetero-junctions a peak is observed in forward bias, which can be assigned to minority-carrier currents.

(electron) current injected by the n-type silicon near zero bias [1]. Such currents are needed for good light-emitting devices where both types of carriers have to be brought together in the active region.

3.2. Admittance spectroscopy

Evidence for deep levels can be found in the measured capacitance (C) and loss (G/ω) as a function of the frequency. In the presence of only shallow levels, the measured capacitance should be flat up to a certain frequency, after which the measured capacitance switches to the much smaller value of the device-geometrical capacitance. In the presence of deep levels, the flat part of the C versus ω plot changes to a sloped part because the deep levels increasingly contribute to the capacitance when the frequency is lowered. Fig. 3 shows a typical plot of C and G/ω versus frequency for a PMeT/Al Schottky barrier. Up to the lowest frequencies the capacitance depends on the frequency, indicating deep levels present in the forbidden gap. For MEH-PPV and αT6 this effect is much smaller; the levels are more shallow here.

Note that at the frequency where the capacitance changes from the depletion value to the bulk value, the loss and the loss tangent $G/C\omega$ have a local maximum. The exact position of this peak depends reciprocally on the bulk resistance. Hence, from the temperature dependence of the value of this frequency we can determine the bulk activation energy [2]. For PMeT this energy was very high (0.47 eV) while for both MEH-PPV and αT6 this energy is 0.12 eV. The latter has to be placed in strong forward bias in order to be able to observe the peak.

3.3. Capacitance–voltage measurements

More evidence for deep levels can be found in the Mott–Schottky plots ($1/C^2$ versus V). The slope in a Mott–Schottky plot reveals the acceptor concentration, N_A. Note that in the presence of deep levels the slope can change with the bias, namely for voltages that put the Fermi level below the deep level somewhere in the depletion region. Fig. 4 shows such a plot with two different slopes for reverse and forward bias. This particular plot reveals a large acceptor concentration of $1\text{–}1.5 \times 10^{17}$ cm^{-3}. For both MEH-PPV and αT6 the plots are similar in shape, but the concentrations are typically an order of magnitude lower. For PMeT we also found that the apparent concentrations change when the device is placed under strong biases. After placing the device in strong forward bias for 20 min the slopes decrease and the apparent concentrations increase [2,3]. This is contradicting the common belief that the dopant ions in electro-deposited polymers can move under strong electrical fields. In that case the slopes would change in the other direction. What the cause is for the change in apparent acceptor concentration is not clear at this moment.

In the Mott–Schottky plots of the hetero-junctions (αT6/Si and MEH-PPV/Si) we observe on top of the linear behavior as described above some peaked structure in the small-bias range. This reduced capacitance is accompanied by an increased conductance and can be assigned to inductive effects of minority-carrier currents [4].

3.4. Transient spectroscopy

In the transients we also find evidence for deep levels. We recorded transients of the capacitance or DC current after switching the light or changing the voltage. By the illumination or bias the deep traps can be filled with holes which are, after switching off the light or switching the voltage back to its original value, re-emitted. The characteristic decay times of the transients are the trap-emptying times and these are exponentially depending on the trap depth divided by the temperature. For PMeT we recorded the slowest response times. Even at room temperature we recorded decay times in the order of 400 s in the optical-capacitance transients. See Fig. 5 for an example of such a transient.

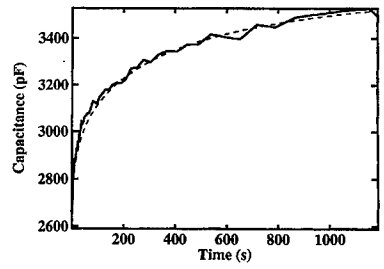

Fig. 5. Optical-capacitance transient for a PMeT/Al device. The extremely long decay time indicates a very large associated trap depth.

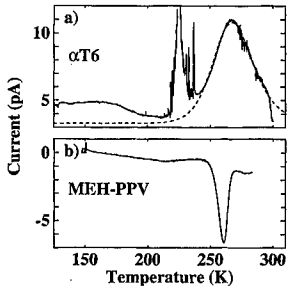

Fig. 6. TSC for αT6 (at 33 mK/s, cooled at +3 V bias) and MEH-PPV (at ca. 6 mK/s, cooled at +1 V). The peak in the former at 265 K can be related to a trap with depth 0.5 eV.

For MEH-PPV we made an extensive voltaic-transient-capacitance study and this revealed trap depths of 0.3, 0.45, 1.0 and 1.3 eV. Because here we used the n^+Si/MEH-PPV hetero junction we were able to observe both majority-carrier traps as well as minority-carrier traps [1,5]. By monitoring the transient amplitude as a function of the trap-filling time, we were able to determine that the trap that is visible at room temperature has point defect nature, rather than extended nature [1,5].

3.5. *Thermally stimulated current (TSC)*

For αT6 we did not find any transient response. This might be due to the fact that the cut-off frequency as described above for the loss tangents lies well below our measurement window (50 Hz–1 MHz) at 0 V and no response is expected from the interface. The best technique in such cases is to employ TSC, in which case the measurement is done at DC. The sample is cooled down at strong forward bias, thus filling all the traps. When it is warmed up without bias, the holes will be emitted when the emission time becomes appreciable. These holes drift towards the anode and a current is observed that mimics a reverse-bias current. When all the levels are emptied the current disappears again. For MEH-PPV we found a negative peak, in line with the above theory of a deep trap, see Fig. 6. The αT6 has a large positive peak at high temperatures and for this material we used the temperature controller to study it in more detail. The scanning rate dependence and overall fitting of the peak revealed that the associated trap is 0.5 eV deep.

In summary, the results presented here show that, in spite of the chemical differences between inorganic materials and conjugated polymers, the standard characterization techniques (CV, TSC and DLTS) can still be applied to these novel materials as long as care is taken. Polymers are low-mobility materials with large concentrations of deep impurities. Therefore one should use low-frequency-probing signals when doing AC measurements and long time scales when measuring transients.

Acknowledgements

This work was supported by a TMR grant, contract number FMRX-CT96-0083 (DG 12-BIUO).

References

[1] P. Stallinga et al., J. Appl. Phys. (1999) submitted for publication.
[2] P. Stallinga et al., Acta Phys. Polonica A 94 (1998) 545.
[3] P. Stallinga et al., Proceedings of the ICSM 1998 Conference in Montpellier.
[4] Toshio Misawa, J. Phys. Soc. Japan 12 (1957) 882.
[5] H.L. Gomes et al., Appl. Phys. Lett. 74 (1999) 1144.

ELSEVIER

Physica B 273–274 (1999) 927–929

PHYSICA B

www.elsevier.com/locate/physb

Differences in the electronic structure and compensation mechanism between n-type Zn- and Cd-doped $CuInS_2$ crystals

Tetsuya Yamamoto[a,*], Ilka V. Luck[b], Roland Scheer[b], Hiroshi Katayama-Yoshida[c]

[a]*Department of Electronic and Phonic Systems Engineering, Kochi University of Technology, 185 Miyanokuchi, Tosayamada-cho, Kami-gun, Kochi, 782-8502, Japan*

[b]*Department of Physical Chemistry/Interfaces, Hahn-Meitner Institute, Glienicker Straße 100, D-14109 Berlin, Germany*

[c]*Department of Condensed Matter Physics, The Institute of Scientific and Industrial Research, Osaka University, 8-1 Mihogaoka, Ibaraki, Osaka 567-0047, Japan*

Abstract

We investigate the electronic structures of n-type $CuInS_2$ crystals in the chalcopyrite structure using Zn or Cd species, Cu-substituting species, as donor dopants, based on the results of ab initio electronic band structure calculations. We find the strongly localized impurity states for n-type $CuInS_2$ doped with Zn, compared with that for n-type $CuInS_2$ crystals doped with Cd species. For n-type $CuInS_2$ doped with Zn species, total energy calculations show that the formation of a Cu vacancy in the vicinity of a Zn site, donor-impurity site, is energetically more favorable. From these findings for the electronic structure and the compensation mechanism, we predict that Cd species can be considered as suitable candidates for use as donor dopants.

Keywords: Copper indium disulfide; Compensation; Electronic structures; n-type

1. Introduction

Polycrystalline $CuInSe_2$ and $CuInS_2$ in the chalcopyrite structure in thin film photovoltaic technology is fast becoming a viable alternative to conventional silicon solar cell technology. One of the critical elements of this technology is the junction formation step. A cell structure consists of vacuum-evaporated p-type $CuInS(Se)_2$ in conjunction with chemical bath deposited (CBD) CdS layer and RF-sputtered ZnO. The quality of the $CdS/CuInSe_2$ or $CuInS_2$ junction is a key factor for high-performance solar cells. The above junction has been treated as an abrupt heterojunction. Recently, Ramanathan et al., pointed out that the CBD process caused the formation of both the Cd substituted $CuInSe_2$ thin films and single crystals, resulting in an n-type region [1,2]. On the other hand, $CuInSe_2$ homojunctions were obtained by converting the surface of p-type single crystals by extrinsic doping to n-type with Cd or Zn species [3]. Little is known about the electronic structures of Zn- or Cd-doped $CuInS(Se)_2$ crystals.

In our previous work, we studied the electronic structures of p-type $CuInS_2$ doped with the group V elements as acceptors using ab initio electronic structure calculations [4,5]. The aim of this work is to understand the difference in the effects of Cd and Zn dopings in $CuInS_2$ crystals. The $CuInS_2$ crystals have an energy band gap of almost 1.5 eV, close to the required value for achieving the optimum efficiency of solar photovoltaic conversion (approximately 1.5 eV). In addition, we propose a suitable candidate for donors in the fabrication of n-type $CuInS_2$ crystals.

* Corresponding author. Fax: + 81-88-757-2120.
E-mail address: yamateko@ele.kochi-tech.ac.jp (T. Yamamoto)

0921-4526/99/$ - see front matter
PII: S0921-4526(99)00556-6

2. Methodology

The results of our band structure calculations for $CuInS_2$ doped with Cd or Zn are based on the local-density-functional approximation to the electronic exchange and correlation potential [6–8] and on the augmented-spherical-wave (ASW) [9] formalism. The Brillouin-zone integration was carried out using 14-k points in an irreducible wedge. The Madelung energy, which reflects the long-range electrostatic interactions in the system, was assumed to be restricted to a sum over monopoles. For valence electrons, we employed 3d, 4s and 4p orbitals for the Cu and Zn atoms, 4d, 5s and 5p orbitals for the Cd atoms, and the outermost s and p orbitals for the other atoms.

We studied the crystal structure of doped $CuInS_2$ under periodic boundary conditions by generating supercells having 128 atoms, including 64 pseudoatoms with the atomic number $Z = 0$, that contain the object of interest: (1) for $CuInS_2$ with a Cu vacancy (V_{Cu}), we replace one of the 16 Cu sites by a vacancy in the supercell; (2) for Cd- or Zn-doped $CuInS_2$, we replace the above V_{Cu} site by the Cd or Zn atom; (3) for $CuInS_2 : (Cd(Zn)_{Cu}$ and $V_{Cu})$, we replace one of the 16 sites of the Cu atoms by a Cd(Zn) site and one of the remaining Cu sites by the vacancy site. In each case, we optimized crystal structure, by minimizing the total energy.

3. Results and discussion

We show the total density of states (DOS) of undoped $CuInS_2$ in Fig. 1(a) and the total and site-decomposed DOSs of $CuInS_2$ crystals doped with Zn_{Cu} in Figs. 1(b) and (c), and with Cd_{Cu} in Figs. 1(d) and (e). We present the DOS of s- and p-states at the Zn and Cd sites in Figs. 1(c) and (e), respectively. Energies are measured relative to the Fermi level (E_F). The arrows in Figs. 1(c) and (e) indicate the d states at the impurity sites in n-type doped $CuInS_2$.

In Fig. 1(a), A–D refer to the Cu 3d(dε)-S 3p antibonding states with a high Cu 3d(dε) contribution, Cu 3d nonbonding states (dγ), Cu 3d(dε)-S 3p bonding states with a high S 3p contribution, and In 5s-S 3p bonding states (the Cu 3d bands also have a small but finite intensity in this region), respectively. The S 3s states are not drawn in Fig. 1(a). More details are given elsewhere [10].

Figs. 1(b)–(e) show that the conduction type of the two $CuInS_2$ crystals doped with Zn or Cd species is n-type. For Zn-doped $CuInS_2$ crystals ($CuInS_2 : Zn$), we find that the strong attractive potential causes a shift in the weight of the impurity states, especially, the s states at the Zn sites, toward the lower-energy region, resulting in a sharp DOS peak near -8.1 eV.

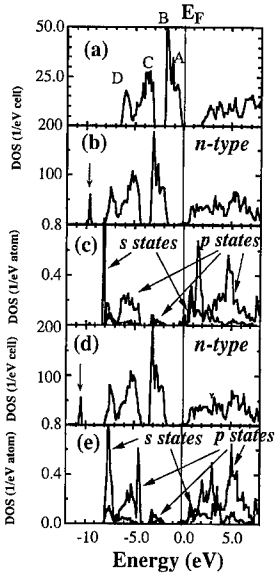

Fig. 1. (a) Total DOS of undoped $CuInS_2$, (b) total and (c) Zn-site decomposed DOS of $CuInS_2 : Zn_{Cu}$, (d) total and (e) Cd-site decomposed DOS of $CuInS_2 : Cd$. (c) and (e) show DOS of s and p states at the donor sites.

This finding indicates a deep impurity level in the band gap for $CuInS_2 : Zn$, which agrees well with experimental data [11]. This gives rise to localized impurity states at the Zn sites in Zn-doped $CuInS_2$, compared with those at the Cd sites in Cd-doped crystals. From the analysis of the total and site-decomposed DOSs, we find that the energy differences between the bonding and antibonding states of S p-donor(Zn or Cd) s orbitals in Zn- and Cd-doped $CuInS_2$ are 9.63 and 10.71 eV, respectively. In addition, we find that the Cd doping causes a 9.8 eV decrease in the Madelung energy, compared with the Zn doping. This result indicates that the Cd doping gives rise to a remarkable stabilization of the ionic charge distribution in $CuInS_2$ crystals. Thus, we suggest that Cd species are eminently suitable for donor dopants in the fabrication of low-resistivity n-type $CuInS_2$ crystals.

In our previous work [5,10], we studied the electronic structures of undoped $CuInS_2$ crystals and $CuInS_2$ with intrinsic defects such as cation vacancy and antisite defects: $CuInS_2$ crystals have two kinds of chemical bonds, the very weak Cu–S bonds and the strong In–S bonds. The reason why the Cu–S bonds are very weak is that the antibonding states of the Cu 3d(dε) and S 3p orbitals are not located in the conduction band but at the top of the valence band. Thus, we investigated the compensation mechanism by the Cu vacancy, acceptor, for Zn and Cd donors in $CuInS_2$ crystals.

First, we determined the crystal structure of p-type $CuInS_2$ with two Cu vacancies using the supercell

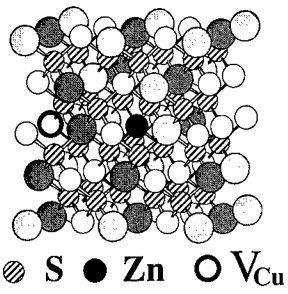

Fig. 2. Chalcopyrite structure of $CuInS_2$: with the Zn_{Cu} atoms at the body center, the Cu atoms (open circle), and the In (shaded circles). For Cu vacancy (V_{Cu}) and S atoms, see the figure.

method as a reference under the condition that the total energy is minimized. As a result, we find that the distance between the two Cu vacancies is 7.81 Å. In this case, we call the above Cu vacancies intrinsic defects (V_{Cu}^{in}) originated from the instability of the Cu–S chemical bonds. Next, we determined the crystal structure of intrinsic $CuInS_2$: (Zn_{Cu}, V_{Cu}^{ex}) crystals, where the letter V_{Cu}^{ex} means extrinsic Cu-vacancy defects induced by n-type doping using the Zn species. The total energy calculations show that the formation of the Cu vacancy whose site is 5.52 Å away from the Zn, Cu-substitution species, sites is energetically favorable (see Fig. 2). On the other hand, for intrinsic $CuInS_2$: (Cd_{Cu}, V_{Cu}^{ex}) crystals, we find that the formation of the Cu vacancy whose site is within a distance of 7.81 Å from the Cd, Cu-substitution species, site is not energetically favorable from the results of total energy calculations.

The total concentration of Cu vacancies, V_{Cu}, in $CuInS_2$ is given by

$$V_{Cu} = V_{Cu}^{in} + V_{Cu}^{ex}, \quad (1)$$

The above findings indicate that the concentration of V_{Cu}^{ex} in the vicinity of the Zn sites for Zn-doped $CuInS_2$ is larger than that for Cd-doped $CuInS_2$ crystals. In other words, n-type doping using the Zn species is easily compensated by the formation of the V_{Cu}^{ex} acceptors. We predict that for n-type $CuInS_2$: Zn, the additional energy such as that by light soaking to break the formation of the complex, Zn_{Cu}-V_{Cu}^{ex}, is necessary to generate free carriers.

4. Conclusions

We have investigated the differences in the electronic structures and compensation mechanism between n-type Zn- and Cd-doped $CuInS_2$ crystals. Our conclusions are as follows: (1) Cd species can be considered as suitable candidates for extrinsic n-type dopants because of the delocalization of its impurity states and the decrease of the Madelung energy; (2) Zn-doped $CuInS_2$ crystals exhibit n-type high-resistivity caused by the localization of the impurity states and the compensation due to Cu-vacancy defects, acceptors, in the vicinity of the Zn sites.

Acknowledgements

The authors thank Dr. Tokio Nakada of Aoyama Gakuin University for his fruitful discussion. In this study, we used ESOCS code by MSI. One of the authors, Yamamoto, thanks Dr. Jürgen Sticht for his technical support.

References

[1] K. Ramanathan, R.N. Bhattacharya, J. Granata, J. Webb, D. Nilles, M.A. Contreras, H. Wiesner, F.S. Hasoon, R. Noufi, Proceedings of the 26th IEEE PVSC, Anaheim, CA, 1997.
[2] K. Ramanathan, H. Wiesner, S. Asher, D. Nilles, R.N. Bhattacharya, J. Keane, M.A. Contreras, R. Noufi, Proceedings of the Second World Conference and Exhibition on Photovoltaic Solar Energy Conversion, Hofburg, Kongresszentrum, Wien, Austria, 6–10 July, 1998.
[3] B. Tell, P.M. Bridenbaugh, J. Appl. Phys. 48 (1977) 2477.
[4] T. Yamamoto, H. Katayama-Yoshida, Jpn. J. Appl. Phys. 36 (1996) L1562.
[5] T. Yamamoto, H. Katayama-Yoshida, in: R.D. Tomlinson, A.E. Hill, R.D. Pilkington (Eds.), Institute of Physics Conference Series, No. 152, Ternary and Multinary Compounds, IOP, London, 1998, pp. 37–40 (invited paper).
[6] W. Kohn, L.J. Sham, Phys. Rev. 140 (1965) A1133.
[7] L. Hedin, B.I. Lundquist, J. Phys. C 4 (1971) 3107.
[8] U. von Barth, L. Hedin, J. Phys. C 5 (1972) 1629.
[9] A.R. Williams, J. Kübler, C.D. Gelatt, Phys. Rev. B 19 (1979) 6094.
[10] T. Yamamoto, H. Katayama-Yoshida, Jpn. J. Appl. Phys. 34 (1995) L1584.
[11] H.Y. Ueng, H.L. Hwang, J. Phys. Chem. Solids 51 (1990) 11.

ELSEVIER

Physica B 273–274 (1999) 930–933

PHYSICA B

www.elsevier.com/locate/physb

Defects in CuIn(Ga)Se_2 solar cell material characterized by positron annihilation: post-growth annealing effects

F. Börner[a,*], J. Gebauer[a], S. Eichler[a], R. Krause-Rehberg[a], I. Dirnstorfer[b], B.K. Meyer[b], F. Karg[c]

[a]*Fachbereich Physik, Martin-Luther-Universität Halle-Wittenberg, D-06108 Halle (Saale), Germany*
[b]*I. Physikalisches Institut, Justus-Liebig-Universität, Heinrich-Buff-Ring 16, D-35392 Gießen, Germany*
[c]*Siemens Solar GmbH, PF 460705, D-80807 München, Germany*

Abstract

Thin (~1 μm) CuIn(Ga)Se_2 layers were grown by the rapid thermal processing technique under In-rich conditions. The as-grown samples were slightly p-type but highly compensated. They showed strong positron trapping in vacancies, indicated by a large valence annihilation parameter S. In order to identify the vacancies, we applied a novel PAS-method. In that, we compare the element-specific high-momentum part of the annihilation momentum distribution $f(p)$ in $CuInSe_2$ with $f(p)$ from the pure elements constituting the material (i.e. with Cu, In and Se). The results provide direct evidence that the vacancies in our as-grown $CuInSe_2$ layers are related to Cu vacancies. Annealing under Ar atmosphere did not alter the annihilation characteristics, i.e. it did not affect the vacancies. However, after annealing in air the samples become more heavily p-type and less compensated, whereas S is drastically reduced. PAS measurements as a function of temperature revealed that this effect is not due to a reduction of the vacancy concentration but due to the additional presence of negatively charged ions introduced by the annealing process. According to recent results, these ions are attributed to oxygen acceptors O_{Se}. These new acceptors account for the increase of p-type conductivity after air annealing.

Keywords: $CuInSe_2$; Cu vacancies; Post-growth annealing; Positron annihilation

1. Introduction

The chalcopyrite semiconductor $CuInSe_2$ (CIS) is a promising material for high-efficiency photovoltaic applications. The defect physics of that system is known to be complicated due to the large number of possible intrinsic defects and defect complexes. However, understanding of the material requires knowledge about native defects which are expected to dominate its properties. Although much effort has been devoted to the investigation of different electrical levels, little is known on the nature of the defects producing these levels. Recent theoretical calculations indicate that Cu vacancies (V_{Cu}) should be the most abundant defect in $CuInSe_2$ due to a low formation energy of V_{Cu} [1].

CIGS-layer grown under In-rich conditions are commonly used for solar cell applications. Such layers are highly defective and heavily compensated as indicated by, e.g., photoluminescence (PL). Post-growth annealing of CIGS-layers in oxygen or air atmosphere at temperatures of about 200–400°C is of great benefit to the solar cell efficiency [2,3]. However, the structural changes leading to this improvement are unknown. In this work we investigate CuIn(Ga)Se_2 (CIGS) thin solar cell layers using the method of positron annihilation spectroscopy (PAS) which provides structural sensitivity especially for vacancies and negative ions.

* Corresponding author. Tel.: + 49-345-5525570; fax: + 49-345-5527160.
E-mail address: boerner@physik.uni-halle.de (F. Börner)

0921-4526/99/$ - see front matter
PII: S0921-4526(99)00557-8

2. Experimental details

The CIGS samples studied in this work were grown by the rapid thermal processing (RTP) technique. The first step consists of a deposition of Cu, Ga, In and Se on a soda-lime glass substrate by sputtering and evaporation. The precursor was then annealed in a RTP-furnace at about 500°C. The Ga/Cu ratio was fixed at 10%. The final thickness of the CIGS-layer was about 1 μm. Details about the growth process can be found elsewhere [4]. Annealing was carried out in a conventional furnace at 400°C under air or Ar atmosphere.

The positron annihilation experiments were done with the slow positron beam system (POSSY) and the Doppler-coincidence setup in Halle. The POSSY consists of a ^{22}NaCl positron source (0.5 GBq), a linear accelerator (up to 40 keV) and a Ge-γ-detector. The resolution of the detector is 1.5 keV FHWM at 514 keV (^{85}Sr). The sample temperature could be varied from 20 to 600 K. The Doppler coincidence setup consists of two Ge-γ-detectors. The resolution of the system is 1.15 keV with a peak to background ratio of 10^5. Details about both setups can be found elsewhere [5].

During diffusion in a crystal a positron can be trapped by a vacancy. This results in a narrowing of the 511 keV annihilation line compared to defect free material. Experimentally, the annihilation line is characterized by the line shape parameters S and W. S is the relative fraction of counts in the center of the Doppler broadened annihilation spectrum (511 ± 0.8 keV), W is the relative fraction of counts in the wings of the spectrum (2.76 keV < $|E_\gamma$-511 keV| < 3.96 keV). Positron trapping at vacancy defects results in an increase (decrease) of S (W) since annihilation at defects occurs mainly with low momentum electrons. Every kind of annihilation site, e.g. bulk, surface, different defects, yields characteristic (W, S) values.

3. Results and discussion

The annealing of In-rich CIGS layer in air atmosphere reduces the high compensation of the charge carriers in the In-rich CIGS layers. This effect can be observed by PL. The dependence on the excitation power of the PL peak energy was reduced from 10 to 1 meV/dekade after annealing at 400°C in air [6]. This effect was not seen after annealing the layers in Ar atmosphere. The reduction of compensation is confirmed by Hall-measurements. The hole concentration of the as-grown In-rich layers is in the order of 10^{16} cm^{-3}. After annealing the layer in air this concentration increases to 5×10^{18} cm^{-3}. A more effective p-doping of the sample can be caused by an increasing number of acceptors or by a reduction of donors. The effect of the air annealing was interpreted as being likely due to a reduction of the donor density [6].

Positrons are sensitive for negative or neutral open-volume defects (vacancies, complexes containing vacancies, etc.). Vacancies were found in CIS bulk crystals by positron lifetime spectroscopy [7]. However, the identification was difficult due to the large number of possible vacancy defects and the insensitivity of positron lifetime spectroscopy to the chemical surrounding of a vacancy.

Fig. 1 shows the S parameter as a function of incident positron energy for the as-grown CIGS layer and the layers annealed in Ar atmosphere at 400°C or in air at 300°C and 400°C. S is normalized to the value we assign to bulk CIGS (see below). The S parameter profile reflects the structure of the layered CIGS/Mo/glass solar cell system. Up to positron energies of 18 keV (corresponding to about 1 μm mean implantation depth) the S parameter can be assigned to the CIGS layer. The variation of S at low energies ($E < 5$ keV) is due to positron trapping at the surface. For higher incident energies, S is due to annihilation in the Mo/glass substrate and is therefore not relevant for this study.

Annealing in air at 400°C distinctly reduces the S parameter of the CIGS layer. This decrease can only be explained as a lost of positron trapping at vacancies. This implies that the as-grown CIGS layer contains a high density of vacancy defects. The relative change of S is in the order 2%. However, annealing under Ar at 400°C or under air below $T = 400$°C did not change the annihilation signal in the CIGS layer at all. This indicates that a reaction with oxygen at higher temperatures is responsible for the change of the annihilation parameter. A S versus W analysis [8] showed that the defect distribution within all CIGS-layers is homogeneous for the high-temperature air-annealed sample this means especially that the oxygen reacts throughout the whole layer. This fact is also indicated by the constant S parameter (Fig. 1). This is in agreement with the results of Niki et al. [9], who detected Oxygen by SIMS throughout a CIS layer after similar air annealing. Moreover, the vacancy

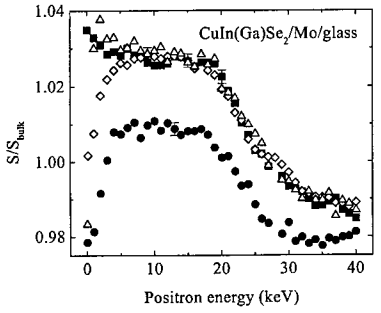

Fig. 1. The S parameter is shown as a function of the incident positron energy for the CuIn(Ga)Se_2/Mo/glass solar-cell layer structure in the as-grown state (■), annealed in air at 300°C (△) and at 400°C (●) and annealed in Ar at 400°C (◇).

type is the same in the as-grown, Ar-annealed and low-temperature air-annealed layers. Niki et al. [9] found a very similar effect, i.e. the average positron lifetime decreases in CIS-layers after annealing at 400°C under air. It was concluded that a structural change happens, i.e. the divacancies postulated to exist in as-grown CIS would change to monovacancy–oxygen complexes (e.g. V_{Cu}–$V_{Se} \rightarrow V_{Cu}$–$O_{Se}$) now dominating positron trapping.

In order to get further information about the charge state of the defects detected by positrons and the whole defect structure in the CIGS-layers we performed measurements as a function of temperature from 20–600 K (Fig. 2). In the as-grown layer, S decreases only very slightly as a function of temperature. This increase can be explained by thermal lattice expansion. There are two possibilities to explain this behavior. First, the vacancy defects obviously present are neutrally charged, thus positron trapping at vacancies would be independent of temperature. Secondly, the vacancies are negatively charged but their density is so large that all positrons are trapped. Than, the S parameter is independent of temperature too although positron trapping at negative vacancies is expected to increase strongly with decreasing temperature.

In contrast to as-grown material, the S parameter shows a distinct dependence on temperature in annealed CIGS. S is almost constant at $T < 300$ K and increases strongly when the temperature is further increased. This behavior can only be explained if a second defect is present which traps positrons only at low temperatures but with a S parameter much lower than that of the vacancies. Such defects are commonly attributed to ion-type acceptors which trap positrons in their attractive, shallow potential only at low temperatures. Since these defects do not have an open volume, the annihilation parameter are similar to the values found in defect-free material. Therefore, we attribute the S parameter at low temperatures ($T < 200$ K) to the bulk value, used also for the normalization of the data.

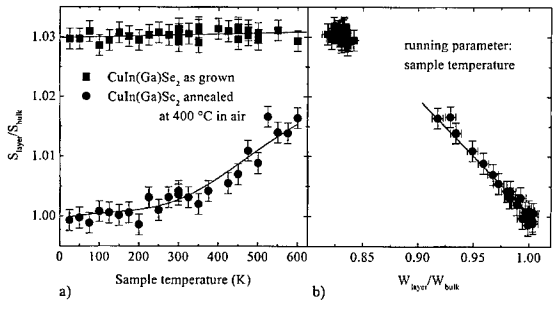

Fig. 2. (a) S parameter of the CIGS layers as a function of the measurement temperature for as-grown (■) and air-annealed (●) CIGS. (b) S parameter versus the W parameter for as grown and air annealed CIGS. The S parameters are the same ones as in part (a).

The strong increase of S at higher temperatures shows that vacancies are still present after annealing. The S versus W plot on the right-hand side of Fig. 2 shows that the vacancy type is similar to in as-grown and annealed CIGS since the data fall on a similar linear variation. The S parameter for the vacancies in as-grown CIGS must be at least 3% larger than the bulk value (Fig. 2). This is in the upper range expected for a monovacancy according to general knowledge. Indeed, Niki et al. [9] interpreted their lifetime results in as-grown CIS as being due to divacancies. However, the S parameter is not only dependent upon the open volume like the positron lifetime, i.e. it depends also on the chemical environment. Thus, we cannot definitely discriminate between mono- and divacancies in our samples.

The behavior of the S parameter in annealed CIGS is typical when positrons are trapped at neutral vacancies and negative ions. An according fit to the data (solid line in Fig. 2a) yields a binding energy to the negative ions of 93 ± 20 meV, in agreement to the value 88 ± 5 meV found in electron irradiated CIS bulk material [7].

A natural question is then the nature of the negative ions. Because the ions appear only after annealing in air they must be related to the oxygen known to penetrate the layer. In a recent work, Su-Huai Wei et al. [10] showed by theoretical calculations that oxygen on a Se site acts as deep acceptor although oxygen is formally isoelectronic. Thus, oxygen on a Se site is a perfect candidate for the negative ions detected by positrons. We conclude that the change in compensation ratio after air annealing is probably not alone due to a reduction of the donor concentration (e.g. V_{Se}) but rather due to an increase of the O_{Se} acceptor density.

The remaining problem is the nature of the vacancy defects which could not be addressed by the measurements above. For this reason we performed measurements with the Doppler broadening coincidence technique. With that technique, the annihilation momentum distribution can be measured up to rather high momenta due to a strong reduction of the background. It is known that the shape of the annihilation momentum distribution at high momenta ($p_L \geqslant 12 \times 10^{-3} m_0 c$) depends only on the chemical nature of the annihilation site because high-momentum core electrons retain their element specific properties even when atoms form a solid. In Fig. 3, the annihilation momentum distribution measured at room temperature is shown for as-grown and air-annealed CIGS and several reference samples. The spectra are normalized by taking the ratio to a GaAs : Zn reference sample free from positron trapping.

As references for the chemical environment we measured the single components of the chalcopyrite compound, i.e. Cu, In and Se. The references were annealed prior to the measurements, conventional positron

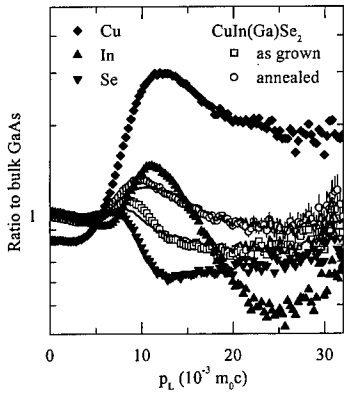

Fig. 3. Annihilation momentum distribution of the single elements Cu (◆), In (▲), Se (▼) and the chalcopyrite $CuInSe_2$ compound in the as-grown (□) and the annealed (○) state. The data are normalized by taking the ratio to a GaAs : Zn reference sample free from positron trapping.

lifetime spectroscopy confirmed that they are free from positron trapping at vacancies. Provided that the high momentum distribution depends only on the chemical nature of the annihilation site, it should be possible to find contributions from the single elements also in the spectra from CIGS. Thus, a fit of the momentum distribution according to $f_{CIGS}(p) = I_{Cu} \times f_{Cu}(p) + I_{In} \times f_{In}(p) + I_{Se} \times f_{Se}(p)$ was done. Here, $f_i(p)$ is the normalized annihilation momentum distribution for material i whereas the I_i characterizes its weight ($\Sigma I_i = 1$). Indeed, the spectra for as-grown and annealed CIGS could be well composed of the single-element contributions as indicated by the solid lines (Fig. 3). The resulting weights are $I_{Cu} = 0.079$, $I_{In} = 0.086$ and $I_{Se} = 0.835$ for as grown CIGS and $I_{Cu} = 0.205$, $I_{In} = 0.132$ and $I_{Se} = 0.663$ for annealed material. Note that absolute values of these weight factors are meaningless because they depend on the intensity of the spectra which is not only a function of the chemical environment but depends also on the lattice structure and interatomic distances. Only relative changes between different samples can be interpreted. In our data, obviously the fraction of Cu and, less distinctly, of In increases in annealed CIGS whereas the contribution from Se decreases. According to the results above, the annihilation momentum distribution in annealed CIGS should be close to that of the bulk. Thus, at the vacancy in as-grown CIGS annihilation takes place in a Cu-deficient environment, i.e. the vacancies should be related to V_{Cu}. This is in accordance with the theoretical calculations of Zhang et al. [1].

4. Conclusions

Native defects in $CuIn(Ga)Se_2$ were observed by means of positron annihilation. As grown samples are characterized by a high density of vacancy defects which are shown to be related to Cu vacancies. After annealing under air at 400°C negative ions acting as shallow positron traps were found. These ions are most probably O_{Se} acceptors. The decrease of compensation in $CuIn(Ga)Se_2$ annealed under air can thus be explained as being due to an increasing density of acceptors making the material more p-type.

Acknowledgements

This work was supported by the Bundesland Sachsen-Anhalt and in part by the Deutsche Forschungsgemeinschaft.

References

[1] S.B. Zhang, Su-Huai Wei, A. Zunger, H, Katayama-Yoshida, Phys. Rev. B 57 (1998) 9642.
[2] R.J. Matson, R. Noufi, K.J. Bachmann, D. Cahen, Appl. Phys. Let. 50 (1987) 158.
[3] E. Moons, D. Gal, J. Beier, G. Hodes, D. Cahen, L. Kronik, L. Burnstein, B. Mishori, Y. Shapira, D. Hariskos, H.W. Schock, Sol. Energy Mater. Sol. Cells 35 (1996) 73.
[4] V. Probst, F. Karg, J. Rimmasch, W. Riedl, W. Stetter, H. Harms, O. Eibl, in: D.C. Ginley, A. Schock, H.W. Eberspacher, C. Peterson, T.M. Wada, T. Pittsburgh (Eds.), Thin Films for Photovoltaic and Related Device Applications, Material Research Society 1996, p. 165.
[5] R. Krause-Rehberg, H.S. Leipner, Positron annihilation in semiconductors, Springer, Verlag, Berlin, 1999.
[6] I. Dirnstorfer, D.M. Hoffmann, D. Meister, B.K. Meyer, W. Riedl, F. Karg, J. Appl. Phys. 85 (1999) 1423.
[7] A. Polity, R. Krause-Rehberg, T.E.M. Staab, M.J. Puska, J. Klais, H.J. Möller, B.K. Meyer, J. Appl. Phys. 83 (1998) 71.
[8] L. Liszkay, C. Corbel, L. Baroux, P. Hautojärvi, M. Bayhan, A.W. Brinkmann, S. Tatarenko, Appl. Phys. Lett. 64 (1994) 1380.
[9] S. Niki, P. J. Fons, A. Yamada, R. Suzuki, T. Ohdaira, S. Ishibashi, H. Oyanagi, Proceedings of the 11th International Conference on Ternary and Multinary Compounds. Institute of Physics Publishing, 1998, p. 221.
[10] Wei. Su-Huai, S.B. Zhang, A. Zunger, J. Appl. Phys. 85 (1999) 7214.

ELSEVIER

Physica B 273–274 (1999) 934–937

PHYSICA B

www.elsevier.com/locate/physb

Do structural defects affect semiconducting properties of fullerene thin films?

E.A. Katz[a,*], A.I. Shames[b], D. Faiman,[a,b], S. Shtutina[b], Y. Cohen[a,b], S. Goren[b], W. Kempinski[c], L. Piekara-Sady[c]

[a]*The National Solar Energy Center, The Jacob Blaustein Institute for Desert Research, Ben-Gurion University of the Negev, Sede Boqer 84990, Israel*

[b]*Department of Physics, Ben-Gurion University of the Negev, Beersheba 84105, Israel*

[c]*Institute of Molecular Physics, Polish Academy of Science, 60-179 Poznan, Poland*

Abstract

We report on the time development of EPR signals ($g = 2.0026 \pm 0.0002$) from C_{60} films with various crystalline structure under air/light exposure. The time development consists of two clearly distinguished regions of fast and slow growth. Improvement of the film structure, and in particular the increase in grain size, leads to a deceleration of the "fast" growth. The results are explained assuming that EPR signal growth is controlled by oxygen diffusion, along grain boundaries and into grains, during the "fast" and "slow" periods, respectively. Fast decrease of the EPR signal as a result of in situ pumping strongly supports this model and indicates a correlation between crystalline structure and oxygen diffusion in C_{60} films. Such correlation is considered as one of the possible mechanisms which govern the semiconducting properties of the material.

Keywords: Fullerene; Paramagnetic centers; Grain boundaries; Recombination

1. Introduction

The discovery of C_{60} [1], the first of an entire class of fully conjugated, all-carbon molecules — the fullerenes (C_{60}, C_{70}, C_{82}, ...), has generated considerable interest in many areas of science and technology. There is a serious expectation that fullerenes will find practical use in electronics, electrooptics and photovoltaics [2]. However, even in the case of C_{60}, the simplest member of the fullerene family, many questions remain open at the most fundamental level.

Solid C_{60} is a molecular crystal with C_{60} molecules occupying, at room temperature, the sites of a face-centered cubic (FCC) lattice [3]. While the carbon atoms within each C_{60} molecule are held together by strong covalent bonding, weak van der Waals interactions are the dominant intermolecular forces [4]. Now crystals and thin films of pristine C_{60} are found to exhibit semiconductor-like behavior in their optical and electronic properties while, at the same time, retaining their molecular character [5]. One of the central issues that needs clarification concerns the effect of crystalline structure on the semiconducting properties of C_{60} thin films. Literature on this problem are fragmentary and often contradictory. One group of results indicates that the solid state packing has minimal effect on the optical [6], photoemission [7] and Raman [6] spectra of the material. Another research direction has recently demonstrated an influence of the crystalline structure of C_{60} films on electronic transport [8,9], optical absorption [10], photoluminescence [8], electron paramagnetic resonance (EPR) [11] and surface photovoltage (SPV) [12] spectra.

At the same time, a variety of experiments [9,12–17] has strongly suggested that oxygen affects properties of C_{60} films. Among them some studies [14,15] have revealed a drastic but reversible reduction of dark and

* Corresponding author. Tel.: + 972-7-6555057; fax: + 972-7-6596736.

E-mail address: keugene@bgumail.bgu.ac.il (E.A. Katz)

0921-4526/99/$ - see front matter
PII: S0921-4526(99)00558-X

photo-conductivity in C_{60} films upon their exposure to air. Given the large amount of interstitial volume in the C_{60} crystal molecular oxygen from the air readily diffuses into this solid [16]. It quenches the conductivity but does not react chemically with the C_{60} molecules. On the other hand, illumination of C_{60} films in air causes larger and irreversible changes in conductivity [9,14]. It has been suggested [14] that air/light exposure promotes C–O binding that damages the C_{60} molecules, producing dangling bonds or other defects with deep levels in the gap. Furthermore, a redistribution between fast and slow components of photoconductivity under the air/light exposure of C_{60} films [17] also points to a generation of recombination centers with deep levels. In a joint EPR/SPV experiment we demonstrated recently [12] that the air/light exposure of C_{60} films leads to the generation of the C_{60}^{+} paramagnetic centers and deep acceptor states at $E_v + 1.3$ eV. These acceptors act as recombination and/or scattering centers. The paramagnetic and recombination/scattering centers were suggested to have the same origin. Thus, we believe that monitoring the evolution of this EPR signal may be a relevant probe for studying the interaction of C_{60} films with oxygen and the corresponding effects on the material properties.

In this paper we vary the deposition conditions to produce C_{60} films with different crystalline structure and use X-ray diffraction and atomic force microscopy (AFM) for structural characterization as well as EPR spectroscopy to study its oxygen content. We present the first experimental evidence for the effect of crystalline structure on the rate of oxygen diffusion. The influence of this phenomenon on the semiconducting properties of the material is discussed.

2. Experimental

C_{60} thin films with a thickness of about 200 nm were grown on optical glass substrates of 3.5×20.0 mm^2 area predeposited with an Ag layer using vacuum evaporation of C_{60} powder (Hoechst AG 'Super Gold Grade', $> 99.9\%$). The vacuum chamber pressure was maintained at about 8×10^{-7} Torr. The temperature of the substrates was varied from 300 to 523 K.

Immediately after the end of vacuum deposition, the film samples were placed in EPR signalless Wilmad quartz tubes (5 mm o.d.). The tubes were then filled with Ar gas and sealed. It should be noted, however, that the samples were exposed to air and room light during this procedure (about 3 min). By room light we mean a combination of daylight and fluorescent room light. Finally, the tubes were kept in the dark till the beginning of the EPR measurements which were performed with a Bruker EMX-220 X-band digital spectrometer. An amplitude of 100 kHz modulation and a microwave power level were chosen as 1 G and 0.2 mW, respectively, to prevent saturation and to obtain good signal-to-noise ratio.

Crystalline structure of the C_{60} films was characterized by X-ray diffraction. Morphology of the front surface of the films, and in particular grain sizes, was studied by AFM.

3. Results and discussion

Sample 1 was grown on a substrate held at 473 K, using special conditions of C_{60} evaporation [18]. The X-ray diffraction pattern for this film is very similar to that shown in Fig. 2a in Ref. [19]. Only a narrow and intense Bragg peak (1 1 1) and its higher harmonics: (2 2 2) and (3 3 3) are observed, i.e. this film has a $\langle 1\,1\,1 \rangle$-texture. The sizes of crystalline domains are relatively high: AFM revealed grain size in the sample surface of about 200 nm. Sample 2 was grown by the same deposition process but on a substrate held at 300 K. The X-ray diffraction pattern for sample 2 is similar to that shown in Fig. 2b in Ref. [19]. The intensities of the broad peaks (1 1 1), (2 2 0) and (3 1 1) were almost the same but considerably lower than that of the (1 1 1)-peak for sample 1. This result corresponds to a lower grain size value, of about 20 nm, as recorded by AFM. These two samples are used as bench marks in the EPR study presented here. However, several other films with intermediate grain size values, grown by varying the deposition conditions, were also studied.

As we reported recently [11,12], well-structured C_{60} thin films in their as-grown state are practically EPR silent and only air/light exposure leads to the appearance of a sharp ($\Delta H_{pp} = 0.124 \pm 0.005$ mT) Lorentzian EPR signal with g-factor $g = 2.0026 \pm 0.0002$. Meanwhile no other EPR signals were observed. The signal is attributed to C_{60}^{+} centers which are located in the bulk of the film and generated due to oxygen diffusion into the C_{60} film and, presumably, formation of C–O chemical bonds [12]. In the present paper we study the time development of this signal air/room light exposure for C_{60} films with different crystalline structure. Since both line shape and line width of the EPR signal are found to remain the same during the exposure, the peak-to-peak intensity of the EPR signal is proportional to the total amount of paramagnetic centers. Fig. 1 displays peak-to-peak intensity of the EPR signal as a function of the light/air exposure time for samples 1 and 2. The first experimental point (at time, $t = 0$) was measured for the samples sealed in the Ar-filled tube. It is clearly seen that sample 2 (small-grain polycrystalline film) exhibits strong EPR signal with an intensity of about 150 a.u., while the initial signal for sample 1 ($\langle 1\,1\,1 \rangle$-textured film with the higher grain size) is very weak, with the intensity only slightly above the noise level (Fig. 1, inset). The Ar was then removed from the tubes and both samples were opened

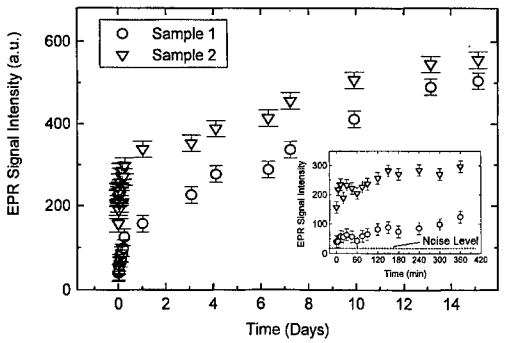

Fig. 1. Peak-to-peak intensity of the EPR signal as a function of the air/light exposure time for samples 1 and 2. Inset shows a zoom for the first 6 h of the exposure.

to the air. Starting from this point the signal in both samples begins to grow, but in essentially different ways. The time-dependent signal growth may be divided into at least two clearly distinguished regions of fast ($0 < t < 24$ h) and slow ($t > 24$ h) growth. For sample 2, one can observe a sharp increase in the signal intensity for about 140 a.u. during the first period followed by a slow growth for about 260 a.u. during the following two weeks of the exposure. On the contrary, for sample 1 the "sharp" component of the increase in the signal intensity was only 80 a.u. while the "slow" growth was much stronger (about 360 a.u.). It should be emphasized here that the difference in the behavior of the two samples during the first minutes of the exposure is found to be even more significant. For example, the signal intensity for sample 2 jumps in about 30% of its initial value immediately after the sample is exposed to air (first two experimental points in the inset in Fig. 1) while for sample 1 the initial signal remains relatively constant.

These results indicate that the improvement of the crystalline structure of C_{60} films, and in particular the increase in grain size, leads to a deceleration of the EPR signal growth in the "fast" period of the exposure and vice versa. Although, the time dependencies for the samples with intermediate grain size value are not shown in Fig. 1, all of them showed a similar tendency.

Studying conductivity of C_{60} films, Pevzner et al. [13] suggested that oxygen diffuses in fullerene films in two distinct ways. In the first few minutes of exposure oxygen diffuses along the grain boundaries (GB) rapidly decreasing conductivity by an order of magnitude. Then, in a slow process, that can run for days, oxygen diffuses into the grains, lowering conductivity by about two more orders of magnitude. Using this hypothesis and assuming that the observed evolution of the EPR signal is controlled by a change in oxygen content we can understand our results. Indeed, sample 2 has a higher area of GB surfaces than sample 1. This explains a higher rate of the EPR signal growth in sample 2 during the "GB diffusion" period. On the contrary, the signal growth in the "slow" period is higher in sample 1, which has a higher value of grain size. This model and the character of the signal change at the beginning of the exposure allow us to explain the difference in the initial signals (for $t = 0$) for the two samples by different amounts of oxygen diffused during the short period after the end of vacuum deposition until the filling of the sample tube by Ar.

In order to check the role of oxygen we performed the following experiment. Samples 1 and 2 exposed to air/light for 10 d were placed in quartz tubes connected to a rotary pump (10^{-2} Torr). The kinetics of the EPR signal intensity was recorded before, during and after the in situ pumping (Fig. 2). For this purpose the DC magnetic field was fixed at the maximum of the EPR signal and then the time scan was run. The figure clearly shows the moments, when the pump was turned on and off. The EPR signal intensity in both samples decreases when the pumping proceeds. After the samples were opened to air, the signals returned to their initial values, i.e. the process is fully reversible. It is worthwhile to note that all processes in sample 1 are characterized by longer times, than in sample 2. Since such a soft pumping may change only the amount of non-bound oxygen in the C_{60} host, these results strongly support our model. The removal of oxygen in sample 1 proceeds for 200 s, in comparison with 12 s in sample 2. The inverse process of oxygen embedding in sample 1 takes $\sim$ 50 s versus 8 s in sample 2.

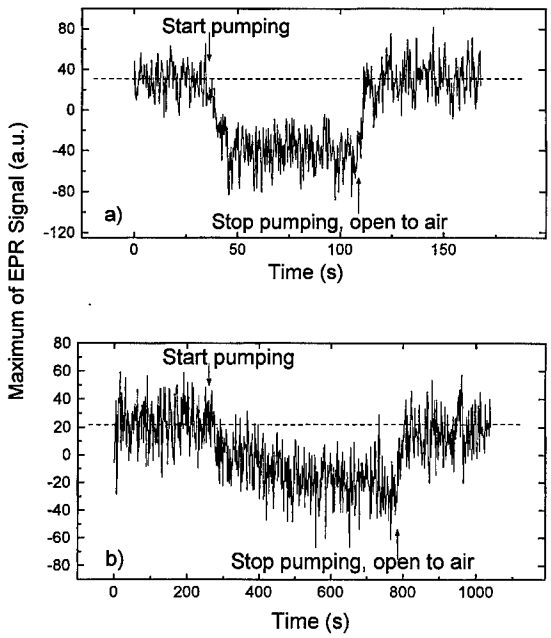

Fig. 2. Kinetics of changes in the EPR signal intensity in sample 2(a) and 1(b) before, during and after in situ pumping of the sample tube (see the text). The arrows point to the moments, when the pump was turned on and when the samples were opened to air.

In this manner, we present experimental evidence for the effect of crystalline structure on oxygen diffusion in C_{60} films. As already mentioned, oxygen affects the optical and electronic properties of this new semiconductor [12–17]. Hence, the reported influence of crystalline structure on C_{60} semiconducting properties which were measured in air [8–11] may originate, to a large extent, from the variation in oxygen content due to GB diffusion.

4. Conclusion

The time development of the EPR signal ($g = 2.0026 \pm 0.0002$) under air/light exposure of C_{60} films with various crystalline structure is presented. The time development consists of two clearly distinguished regions, of fast and slow growth. Improvement of the film structure leads to a deceleration of the "fast" growth. The results are explained assuming that the EPR signal growth is controlled by oxygen diffusion, along grain boundaries and into grains, during the "fast " and "slow" periods, respectively. An EPR experiment on in situ pumping strongly supports this model and also indicates a correlation between crystalline structure and oxygen diffusion in the C_{60} films. The influence of this phenomenon on the semiconducting properties of the material is discussed.

Acknowledgements

This work was funded partly by the Ministry of National Infrastructures and Sally Berg Foundation.

References

[1] H.W. Kroto, J.R. Heath, S.C. O'Brien, R.F. Curl, R.E. Smalley, Nature 318 (1985) 162.
[2] M.S. Dresselahaus, G. Dresselahaus, P.C. Eklund, in: Science of Fullerenes and Carbon Nanotubes, Academic Press, San Diego, 1996, p. 870.
[3] R. Tycko, G. Dabbagh, R.M. Fleming, R.C. Haddon, A.V. Makhia, S.M. Zahurak, Phys. Rev. Lett. 67 (1991) 1886.
[4] J.P. Lu, X.-P. Li, R.M. Martin, Phys. Rev. Lett. 68 (1992) 1551.
[5] E.A. Katz, Solid State Phenom. 67&68 (1999) 435.
[6] D.S. Bethune, G. Meijer, W.C. Tang, H.J. Rosen, W.G. Golden, H. Seki, C.A. Brown, M.S. de Vries, Chem. Phys. Lett. 179 (1991) 181.
[7] R.W. Lof, M.A. van Veenendaal, B. Koopmans, H.T. Jonkman, G.A. Sawatzky, Phys. Rev. Lett. 68 (1992) 3924.
[8] K. Kaneto, K. Rikitake, T. Aktyama, H. Hasegawa, Jpn. J. Appl. Phys. 36 (1997) 910.
[9] T. Asakawa, M. Sasaki, T. Shiraishi, H. Koinuma, Jpn. J. Appl. Phys. 34 (1995) 1958.
[10] D. Faiman, S. Goren, E.A. Katz, M. Koltun, N. Melnik, A. Shames, S. Shtutina, Thin Solid Films 295 (1997) 283.
[11] A. Shames, E.A. Katz, S. Goren, D. Faiman, Mater. Sci. Eng. B 45 (1997) 134.
[12] E.A. Katz, D. Faiman, B. Mishori, A.I. Yoram Shapira, Shames, S. Shtutina, S. Goren, J, Appl. Phys. 84 (1998) 3333.
[13] B. Pevzner, A.F. Hebard, M.S. Dresselhaus, Phys. Rev. B 55 (1997) 16439.
[14] A. Hamed, Y.Y. Sun, Y.K. Tao, R.L. Meng, P.H. Hor, Phys. Rev. B 47 (1993) 10873.
[15] S. Kazaoui, R. Ross, N. Minami, Solid State Commun. 90 (1994) 623.
[16] A. Assink, J. Schirber, D. Loy, B. Morosin, G.A. Carlson, J. Mater. Res. 7 (1992) 2136.
[17] E.A. Katz, V.M. Lyubin, D. Faiman, S. Shtutina, A. Shames, S. Goren, Solid State Commun. 100 (1996) 781.
[18] E.A. Katz, US Patent No. 5,876,790, Ormat Industries Ltd., Israel, 1999.
[19] E.A. Katz, D. Faiman, S. Shtutina, A. Shames, S. Goren, B. Mishori, Yoram Shapira, in: E.D. Jones, J. Kalejs, R. Noufi, B. Sopori (Eds.), Thin Films Structures for Photovoltaics, Materials Research Society Symposium Proceeedings, Vol. 485, 1997, p. 113.

ELSEVIER

Physica B 273–274 (1999) 938–943

PHYSICA B

www.elsevier.com/locate/physb

Confinement effects on phosphorus donors embedded in silicon nanocrystals

B.J. Pawlak*, T. Gregorkiewicz, C.A.J. Ammerlaan

Van der Waals–Zeeman Institute, University of Amsterdam, Valckenierstraat 65, NL-1018 XE Amsterdam, The Netherlands

Abstract

Magnetic resonance of shallow donor center phosphorus is used to track size-related changes of energy band structure in silicon powders. Small conduction band upshifts of several meV are determined for nanocrystals of approximately $d = 100$ nm diameter and smaller. These are interpreted as the onset of the quantum confinement-induced variations of silicon band structure. The conduction band upshift is experimentally found to follow the $1/d^{1.2}$ dependence in the investigated size range.

Keywords: Silicon nanocrystals; Electron paramagnetic resonance; Quantum confinement

1. Introduction

Silicon low-dimensional structures possess a variety of interesting electronic properties. It has been shown [1] that the decreasing size of crystallites leads to quantum confinement effect which enlarges the band-gap energy [2,3], and which can possibly also lead to change of its character from indirect to direct [4]. Both effects should be detectable by optical methods due to an increased efficiency of the emission and its gradual shift to higher energies upon size reduction. In line with that expectation visible luminescence in specially prepared silicon nanocrystal structures has been reported [5,6]. Unfortunately, low-dimensional structures are also characterized by a large surface-to-volume ratio. Surface-related effects obscure observation and conclusive identification of quantum-confinement-related effects. Consequently, to our knowledge, the onset of the size-induced changes of the energetic structure of silicon has been traced experimentally.

In this study we present experimental evidence of band structure changes in the relatively 'large' crystallites for which the theory-predicted conduction band upshift should be of the order of a few meV only. The experiment has been conducted on silicon nanocrystals prepared by mechanical milling. The size confinement is monitored by its effect on the electronic structure of phosphorus impurity as monitored by electron paramagnetic resonance (EPR). Substitutional phosphorus in silicon forms an effective-mass-theory (EMT) donor center; the extended character of its electronic wave function renders this center sensitive to variations of electronic structure of the conduction band minimum. Phosphorus donor in silicon is paramagnetic in its neutral charge state P^0 and is well-studied by EPR. It has cubic symmetry which is advantageous for randomly oriented grains. From the EPR spectrum the details of the wave function — spin localization on the phosphorus nucleus and mutual overlap of neighboring donors can be concluded. At the same time the observed spectrum is exclusive for a substitutional donor and therefore only the bulk of the nanocrystal is monitored. In this way, the volume and the surface effects can be separated. This in a clear advantage to other less discriminative techniques.

2. Silicon powders

For the current experiment two kinds of phosphorus-doped silicon have been used: Czochralski (CZ)

* Corresponding author. Tel.: + 31-20-525-5793; fax: + 31-20-525-5788.

E-mail address: bartek@wins.uva.nl (B.J. Pawlak)

0921-4526/99/$ - see front matter
PII: S0921-4526(99)00559-1

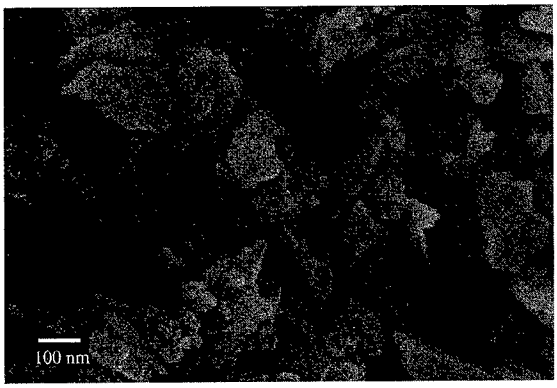

Fig. 1. Scanning electron microscopy picture of Si-powder before oxidation.

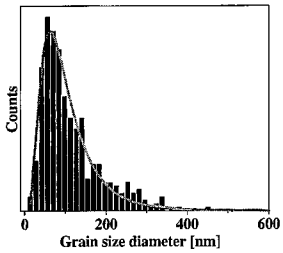

Fig. 2. Grain size distribution of one of the smallest powders obtained by ball milling, sedimentation, ultrasonic vibration and centrifuged sedimentation. The maximum of grain size distribution peaks at 60 nm. Almost no grains are bigger than 300 nm.

$[P] \approx 5 \times 10^{15}$ cm^{-3} and float-zoned (FZ) $[P] \approx 1.5 \times 10^{17}$ cm^{-3}. Nanocrystals have been prepared by mechanical ball milling for 1 h in ethanol (ZrO_2 balls and crucible). The milling step was followed by sedimentation of 15 h in order to remove the largest silicon grains. After that centrifuged sedimentation has been applied for size segregation. The actual size distribution was directly measured by scanning electron microscopy (SEM) (Figs. 1 and 2) and fitted with usual function $\exp(-\ln^2(d/x)/2w^2)$. For the particular set of powders investigated in this study the maxima of size distributions were determined at $x_B = 200$ nm for big, $x_{MB} = 110$ nm for medium big, $x_{MS} = 100$ nm for medium small and $x_S = 60$ nm for small nanocrystals. Further size reduction was achieved by oxidation; the powders were annealed at 1000°C in open air for time duration from 5 min to 3 h. By such a procedure the silicon core size was reduced by the formation of a SiO_2 layer. At the same time silicon surface was replaced by Si/SiO_2 interface.

The crystallinity of silicon powders was controlled by X-ray diffraction. Characteristic diffraction patterns of silicon crystal were clear and strong for as-milled and oxidized nanocrystals. Their intensity gradually decreased upon heat-treatment indicating the size reduction of the silicon core. After prolonged oxidation the X-ray pattern vanished completely as all the silicon has been transformed into SiO_2.

In addition to Röntgen diffraction, grain crystallinity was confirmed by other experiments. Raman spectroscopy revealed a strong first-order Stokes peak around 521 cm^{-1}. The line at 480 cm^{-1} which is characteristic of amorphous Si [7] was not observed. Also from transmission electron microscopy (TEM) related techniques of bright field/dark field (BF/DF) and selected area diffraction pattern (SADP) we obtained clear support that both as-milled and oxidized silicon grains retain their crystal structure. A TEM image of an oxidized silicon grain used in the present study is shown in Fig. 3; both the crystalline Si core and the external layer of SiO_2 developed by oxidation can be readily seen. By TEM we could also monitor how fast the SiO_2 layer develops at the surface of silicon grains. We conclude that the growth process proceeds according to the well-established formula $d_{SiO_2} = 10.78 \times \sqrt{t}$, where d_{SiO_2} is the oxide layer thickness (in nanometers) and t is the oxidation time (in min) [8]. From BF/DF and SADP we learn also that the SiO_2 layer is amorphous.

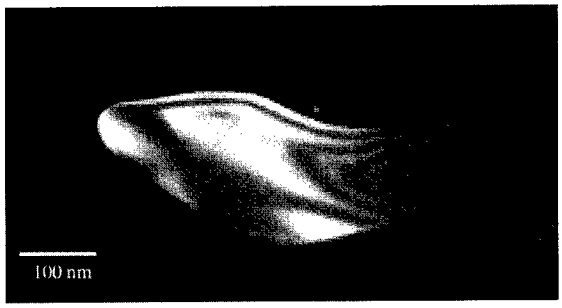

Fig. 3. Transmission electron microscopy picture of Si-grain after 1 h of oxidation at 1000°C. The SiO_2 thickness around the silicon core corresponds to approximately 80 nm. Evidence of crystallinity of the entire grain core is manifested by diffraction fringes in bright field/dark field method. The surrounding SiO_2 is amorphous.

3. Experimental results

The EPR measurements were performed at a temperature of $T = 4.2$ K in a superheterodyne EPR spectrometer operating at 23 GHz in the K-microwave band and tuned to detect the dispersive part of the signal. The EPR of P donor in bulk Si has been extensively investigated [9]. The spectrum consists of 2 lines separated due to the

hyperfine interaction. The hyperfine constant A, which is equal to the separation between the two resonance lines, is proportional to the localization of electron wave function on phosphorus nucleus and is given by the Fermi contact term: $A = (\mu_0/4\pi)g_e\mu_B g_N\mu_N|\Psi(0)|^2$. For P in bulk silicon it has $A = 4.2$ mT value. At higher doping levels an exchange interaction between individual P impurities appears. This shows in the EPR spectrum as components developing between the hyperfine lines at moderate concentrations ($[P] \leqslant 10^{16}\,\mathrm{cm}^{-3}$) and originating from donor pairs and larger clusters [10]. The spin Hamiltonian appropriate for a pair of donor atoms can be written as [11]

$$\mathcal{H} = g\mu_B B(S_1 + S_2) + A(I_1S_1 + I_2S_2) + J(S_1S_2), \quad (1)$$

where S_1, S_2 and I_1, I_2 are the electron and nuclear spins of the two donors, respectively, A is the hyperfine interaction constant, and J is the exchange coupling. At high concentrations ($[P] \geqslant 10^{17}\,\mathrm{cm}^{-3}$) the two-lines spectrum characteristic for an isolated donor decreases considerably and a strong Lorentzian-shaped line appears in the center of the spectrum. It exhibits exchange narrowing and evidences the donor-impurity band formation. The EPR spectrum of the bulk CZ-Si : P material used to prepare powders for this study is presented in Fig. 4. Also, EPR spectrum measured for powder sample prepared from this material is shown. As can be seen, in the EPR spectra of Si nanocrystals the lines originating from isolated donors are shifted towards the center and have a clearly asymmetric form, with the broadening also towards the center. This indicates a smaller hyperfine interaction for P donors embedded in the nanocrystals when compared to those in the bulk, and, also, size distribution within a given powder. Systematic EPR measurements of oxidized samples showed that a clear dependence exists between the value of the hyperfine splitting parameter A and an average volume of the silicon grain — see Fig. 5. A decrease of up to 6.5% for the smallest grains has been observed.

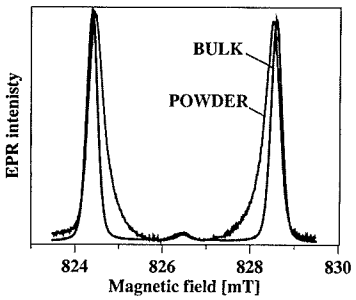

Fig. 4. EPR spectrum of the CZ-Si : P ($[P] = 5 \times 10^{15}\,\mathrm{cm}^{-3}$) bulk and nanocrystal sample. The hyperfine lines in powder sample are moved to the middle manifesting lowering of hyperfine splitting. The maximum of grain size distribution of powder before oxidation is $d \approx 200$ nm. Microwave frequency is $\nu = 23.11997$ GHz.

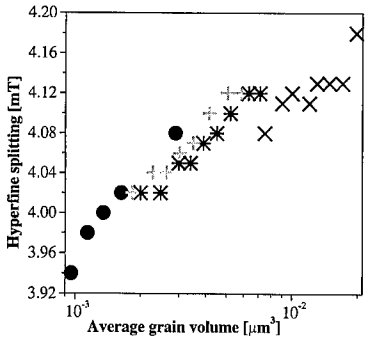

Fig. 5. Hyperfine splitting parameter for four different powders after oxidation versus average grain volume. For bulk silicon $A = 4.2$ mT. For powders the hyperfine parameter decreases with diminishing grain size. Oxidized powders has been marked with x-big; (*)-medium big; (+)-medium small and (o)-small ones.

By inspecting the EPR spectra of the nanocrystals we also note that the central lines originating from mutual interaction between donors have a slightly higher intensity than in the bulk material used for preparation of the powders. For the smallest nanocrystals the exchange interaction becomes very strong. An increased mutual interaction and a decreased hyperfine constant were observed consistently in all the nanocrystals investigated in the current study. For nanocrystals prepared from FZ-Si with a higher P-concentration ($[P] = 1.5 \times 10^{17}\,\mathrm{cm}^{-3}$), the signal from the isolated donors disappeared completely upon oxidation and a single central line, with a strong exchange narrowing dominated the spectrum.

4. Discussion

Before we assign the observed changes of the EPR spectrum of silicon powders (lowering of the hyperfine and increase of the exchange interactions) to the quantum confinement-induced perturbation of the ground state of P donor, we will first consider alternative mechanisms that could possibly account for the observed effects. The enhanced mutual interaction between phosphorus atoms could also be explained by an increase of P concentration caused by diffusion and the strain fields generated during mechanical milling, annealing and/or oxidation. In order to check this possibility non-oxidized silicon grains were heat-treated in argon atmosphere. In this way, grain reduction by oxidation is excluded, but thermal migration is allowed. No effect of heat treatment in an argon atmosphere on the EPR spectrum has been found. Also devoted measurements of oxidized silicon wafers by secondary ion mass spectroscopy (SIMS)

[12,13] showed that P indiffusion into silicon grain due to impurity pile-up at the Si–SiO_2 interface is negligible and cannot account for the effects observed here. Additional verification of importance of pile-up has been performed by oxidation of much bigger grains for times exceeding up to 100 h. In these powders the evaluated pile-up to grain core volume ratio is larger in comparison to samples used in our experiment. No traces of enhanced mutual interaction has been found by EPR.

Yet another possible explanation which has to be considered is the hydrogen passivation which could change the initial ratio between the isolated P impurities and their complexes. Hydrogen can easily be introduced into Si grains during oxidation, and passivation of donors renders them non-paramagnetic and non-detectable by EPR. We have made computer simulation of this process. The basic assumption of the program algorithm was to keep equal probability of passivation of all donors, the isolated ones and the ones forming pairs or larger aggregates. The simulation showed that the relative number of interacting donors would drop upon passivation, in contrary to experimental observation.

Based on the above, we conclude that the observed decrease of the hyperfine and increase of the exchange interactions of P donors in silicon nanocrystals reflects changes of the electronic structure of the donor centers, which appear upon grain size reduction.

Following the observation that the hyperfine splitting depends on the average volume of the grain, we attempt to analyze the effect in terms of the size confinement. Since P donor is well described by EMT we apply this formalism in our analysis of the effect. We describe the shallow donor electron wave function as a linear combination of envelope function, which is the solution of hydrogen-like Schrödinger equation, and propagating wave through the crystal modulated by Bloch function:

$$\Psi(r) = \sum_{j=1}^{6} \alpha^{(j)} F^{(j)}(r) u^{(j)}(r) e^{ik^{(j)}r} \tag{2}$$

$|\alpha^{(j)}|^2$ is the probability of finding an electron in the jth valley $j = 1, \ldots, 6$, as a consequence of the six-fold CB degeneracy in silicon. The 1s donor ground state is split by the cubic crystal field into the symmetric-singlet A_1 and asymmetric doublet E and triplet T_2. The separations of these energy levels have been directly measured by optical spectroscopy [14].

On basis of the EMT formalism we will derive an expression for the lowering of the hyperfine splitting and explain qualitatively the increased mutual interaction between donors. The ground state A_1 is symmetric with equal probability of finding the electron in all the 6 CB minima $\alpha = \frac{1}{\sqrt{6}}(1,1,1,1,1,1)$. It is the only state that has non-vanishing localization on the nucleus and, consequently, the only one contributing to the hyperfine interaction. The increased mutual interaction can be explained on the basis of admixing higher lying states which are anisotropic and are characterized by a more extended character. For simplicity we consider a tetragonal perturbation which can be characterized by a single parameter. Such a situation is similar to the symmetry perturbation induced in bulk Si : P by an application of a uniaxial stress along $\langle 1\,0\,0\rangle$ [15]. The interaction term of donor electron Hamiltonian with respect to the center of gravity has the form of the so-called valley-orbit matrix (6×6):

$$H_{vo} = -\Delta_2 \begin{vmatrix} -2x & 1+\delta & 1 & 1 & 1 & 1 \\ 1+\delta & -2x & 1 & 1 & 1 & 1 \\ 1 & 1 & x & 1+\delta & 1 & 1 \\ 1 & 1 & 1+\delta & x & 1 & 1 \\ 1 & 1 & 1 & 1 & x & 1+\delta \\ 1 & 1 & 1 & 1 & 1+\delta & x \end{vmatrix}. \tag{3}$$

The six-fold degeneracy of the CB is now lifted and we get 2 eigenvalues of the states, one corresponding to the ground state A_1:

$$E_{A_1} = \Delta_2[-(2+\delta) + \tfrac{1}{2}x - \tfrac{3}{2}\sqrt{x^2 + \tfrac{4}{3}x + 4}] \tag{4}$$

and the second to one of the admixed excited states E:

$$E_E = \Delta_2[-(2+\delta) + \tfrac{1}{2}x + \tfrac{3}{2}\sqrt{x^2 + \tfrac{4}{3}x + 4}]. \tag{5}$$

The hyperfine splitting is given by the expression: $A \sim |F^{(j)}(0)|^2 |u^{(j)}(0)|^2 |\sum_{j=1}^{6} \alpha^{(j)}|^2$. If we consider that CB degeneracy lifting affects only electron probability in the valleys then the reduction of hyperfine interaction can be expressed in terms of the $\alpha^{(j)}$ and the perturbation parameter $x_E = \Delta_2 x$ (meV) ($\Delta_2 = 2.17$ meV). We get then, for $j = 1, 2$:

$$(\alpha^{(j)})^2 = \frac{1}{4}\left[1 - \frac{x_E + 2/3}{\sqrt{x_E^2 + (4/3)x_E + 4}}\right] \tag{6}$$

and for $j = 3, 4, 5, 6$:

$$(\alpha^{(j)})^2 = \frac{1}{8}\left[1 + \frac{x_E + 2/3}{\sqrt{x_E^2 + (4/3)x_E + 4}}\right]. \tag{7}$$

For the hyperfine splitting reduction we obtain the following dependence on the perturbation parameter:

$$\frac{A'}{A} = \frac{1}{6}|\sum \alpha^{(j)}|^2 = \frac{1}{2}\left[1 + \frac{2 + \frac{1}{3}x_E}{\sqrt{x_E^2 + \frac{4}{3}x_E + 4}}\right]. \tag{8}$$

In our interpretation the perturbation of valley-orbit matrix is due to quantum confinement combined with

shape asymmetry of small grains. We assume further that the grains have shapes of cigars ($d_\perp \times d_\perp \times d_\parallel$). From SEM pictures of the powders we calculate the average asymmetry parameter defined as ratio of the shorter side to the longer side of grain $\gamma_0 = d_\perp/d_\parallel$ is $\gamma_0 \approx 0.6$.

Many experimental and theoretical publications derive expressions for enlarging the energy band gap [16–18,20] when diminishing grain size. The enlargement is made up of a downshift of the VB and an upshift of CB [2]. Since in our study we are dealing with EMT shallow donor, then only the upshift of CB will affect electronic structure of phosphorus. For the assumed cigar-shaped grains, the upshift in perpendicular directions will exceed that one along the axis. In our analysis we take the general expression for CB upshift to be $\Delta E_{CB} = \alpha/d^\beta$ [17]. In line with the tetragonal perturbation we assume further that the grains are oriented in such a way that their longitudinal axis coincides with one of the $\langle 1\,0\,0\rangle$ crystallographic directions. The correlation between the tetragonal perturbation in the valley-orbit matrix and the perturbation induced by quantum confinement takes the form: $3x_E = \Delta E(d_\perp) - \Delta E(d_\parallel) = (1-\gamma^\beta)\alpha/\gamma^\beta d_\parallel^\beta$. Knowing now the expression for the perturbation and for the hyperfine splitting, we can simulate our experimental results using α and β as fitting parameters, keeping the asymmetry parameter $\gamma = 0.6$. We find that the β parameter derived from fittings is not sensitive to the particular choice of γ. For all the powders; small, medium (big and small) and big, we get consistent results for β which are collected in the Table 1. Since homogeneity of grains was best for smallest powder, we consider the result $\beta = 1.2$ to be the most reliable. The α parameter changed from powder to powder and showed dependence on γ. For the fitting obtained for the smallest grains with γ taken from SEM pictures the explicit upshift of CB has the form $\Delta E_{CB}[\text{meV}] = 800/d^{1.2}[\text{nm}]$. This is far less rapid than expected from a simple EMT approximation. Expression for CB upshift is experimental result obtained for larger grains with broader size distributions than the theoretical calculations has been performed. Extrapolation of band-gap behaviour from small nanocrystals up to bulk material has been postulated by Delley et al. [19]. Our result is similar to that which has been calculated by pseudo-potential method by Öğüt et al. [1] for few nm Si grains. We note that our approximation holds for relatively small perturbations only, i.e., for relatively large grains. For large perturbations $-x \gg 1$ the 2 CB valleys distinguished by the perturbation become fully populated and the hyperfine splitting approaches in its limiting value $A' \to \frac{2}{3}A$. Any further upshift of CB, and thus an increased non-equivalence of the 6 CB minima, will not affect the hyperfine splitting A. Therefore for still smaller grains another experimental techniques should be more appropriate [20].

Finally we note that the second effect, an increased mutual interaction between donors, can be elucidated in terms of the admixing of the exited states E. The overlap between electron wave functions increases then due to the extended p-like character of the state E.

Table 1
Fitting parameters $\beta(\Delta E_{CB} \propto 1/d^\beta)$ for different silicon nanocrystals

Powder type	Parameter β
Big	1.17
Medium big	1.17
Medium small	1.27
Small	1.2

5. Summary

We show experimental evidence that the electronic structure of a shallow donor center phosphorus in silicon is changed when placed in a nanocrystal environment. The observed effects can be understood within the EMT by the ground state perturbation induced by the size confinement when combined with the asymmetry of the grains. The use of surface insensitive monitoring allows thus to observe the onset of the quantum confinement; it is shown to take place for relatively large grains of approximately 50–100 nm size. We conclude that in this range the confinement-induced CB upshift follows $\Delta E_{CB} \propto d^{-1.2}$ dependence.

Acknowledgements

For characterization of silicon powders the cooperation of W. Takkenberg (SEM), F. Tichelaar (TEM), R. Bacewicz (Raman), and P. Alkemade (SIMS) is gratefully acknowledged. Substantial improvement in sample preparation is due to P. Manshanden.

References

[1] S. Öğüt, J.R. Chelikowsky, S.G. Louie, Phys. Rev. Lett. 79 (1997) 1770.
[2] N.A. Hill, K.B. Whaley, J. Electron. Mater. 25 (1996) 269.
[3] L.E. Brus, J. Chem. Phys. 80 (1984) 4403.
[4] T. Takagahara, K. Takeda, Phys. Rev. B 46 (1992) 15 578.
[5] H. Takagi, H. Ogawa, Y. Yamazaki, A. Ishizaki, T. Nakagiri, Appl. Phys. Lett. 56 (1990) 2379.
[6] L.T. Canham, Appl. Phys. Lett. 57 (1990) 1046.
[7] S. Veprek, F.A. Sarott, Phys. Rev. B 36 (1987) 3344.
[8] Shaw-Kwen Ma, Juh Tzeng Lue, Thin Solid Films 304 (1997) 353.
[9] W. Kohn, J.M. Luttinger, Phys. Rev. 97 (1955) 883.
[10] C.P. Slichter, Phys. Rev. 99 (1955) 479.

[11] P.R. Cullis, J.R. Marko, Phys. Rev. B 1 (1970) 632.
[12] A.S. Grove, O. Leisteko, Jr., C.T. Sah, J. Appl. Phys. 35 (1964) 2695.
[13] P. Alkemade, private communication.
[14] R.L. Aggarwal, A.K. Ramdas, Phys. Rev. 140 (1965) A1246.
[15] D.K. Wilson, G. Feher, Phys. Rev. 124 (1961) 1068.
[16] C. Delerue, G. Allan, M. Lanoo, Phys. Rev. B 45 (1993) 11 024.
[17] V. Ranjan, V.A. Singh, G.C. John, Phys. Rev. B 58 (1998) 1158.
[18] G. Fisham, I. Mihalcescu, R. Romestain, Phys. Rev. B 48 (1993) 1464.
[19] B. Delley, E.F. Steigmeier, Phys. Rev. B 47 (1993) 1397.
[20] Y. Kanemitsu, H. Uto, Y. Masumoto, T. Matsumoto, T. Futagi, H. Mimura, Phys. Rev. B 48 (1993) 2827.

ELSEVIER

Physica B 273–274 (1999) 944–946

PHYSICA B

www.elsevier.com/locate/physb

Determination of potential fluctuations in modulation-doped SiGe-quantum wells from conduction electron spin resonance

W. Jantsch[a,*], Z. Wilamowski[b], N. Sandersfeld[a], F. Schäffler[a]

[a]*Institut für Halbleiterphysik, Johannes-Kepler Universität, Attenbergstrasse 69, A-4040 Linz, Austria*
[b]*Institute of Physics of the Polish Academy of Sciences, PL-0668 Warsaw, Poland*

Abstract

The spin resonance of conduction electrons in modulation-doped quantum wells is utilized to determine the density of states. The latter exhibits band tails resulting from potential fluctuations caused mainly by the distribution of charged impurities. Assuming a Gaussian distribution, we determine the fluctuation amplitude as a function of carrier density. For low-density screening becomes ineffective and we find a rapid increase of these fluctuations corresponding to the Anderson transition in two dimensions.

Keywords: Conduction electron spin resonance; Potential fluctuations; Two-dimensional conductance

The mobility of a two-dimensional (2D), modulation-doped quantum well is an essential parameter for many types of phenomena and investigations in basic science but also for the high-frequency behavior of high-mobility field effect transistors. The mobility depends on many extrinsic parameters, like fluctuations in the well width and height (alloy composition of the barriers), residual defects and impurities, fluctuations in the density and distance of the doping layer, etc. The mobility alone, being an integral quantity, does not permit to disentangle these different mechanisms for a given sample.

In this paper we invoke the recently observed conduction electron spin resonance (CESR) in SiGe or SiC quantum well structures [1–5] to derive information on the potential fluctuations and to evaluate them quantitatively as a function of carrier concentration. The latter can be conveniently derived from cyclotron resonance (CR) or the Shubnikov-de Haas effect seen frequently in the same type of experiment [6]. The fluctuations manifest themselves in the density of states, DOS, of the 2D electron gas, causing smooth bandtails extending below the ideal subband-edges instead of the sharp step-like DOS function expected for an ideal 2DEG. The CESR amplitude permits to investigate the DOS at the Fermi energy, ε_F, since the free carriers constitute a Pauli system rather than Curie behavior of independent paramagnetic spins of defects seen normally in ESR. The Pauli susceptibility is proportional to the DOS (ε_F) which can be thus determined from the integral CESR absorption.

CESR was recently identified as an outstandingly narrow line with a line width of 40 mG in a two-dimensional Si (or SiC) quantum well embedded between SiGe (Si) barriers [1–5]. Only this narrow line width allows its observation since the sensitivity of a conventional ESR instrument increases inversely proportional to the line width, thus allowing detection in this case starting from 10^9 electrons.

Typical spectra observed on an MBE grown modulation-doped Si quantum well are given in Fig. 1. The narrow CESR is superimposed on a broad background which was identified as CR of the 2DEG in the well. Since the CR signal is proportional to the total carrier density, n_s, rather than the DOS (ε_F), it allows independent determination of n_s. The Fermi level can be varied in our moderately modulation-doped samples since these

* Corresponding author: Tel.: +43-732-2468-9641; fax: +43-732-2468-9696.
E-mail address: wolfgang.jantsch@jk.uni-linz.ac.at (W. Jantsch)

0921-4526/99/$ - see front matter
PII: S0921-4526(99)00560-8

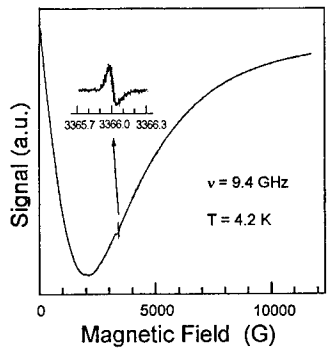

Fig. 1. First derivative of the microwave absorption signal with respect to magnetic field as a function of magnetic field obtained on the SiGe quantum well sample.

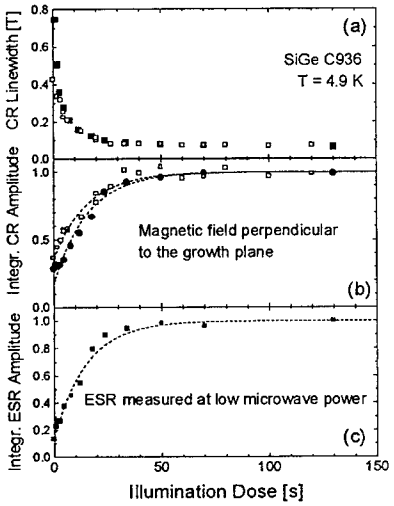

Fig. 2. (a) Cyclotron line width; (b) integrated cyclotron absorption and (c) integrated ESR absorption as a function of illumination dose after cooling the SiGe quantum well sample in darkness. The two sets of data were obtained after different surface cleaning.

exhibit persistent photoconductivity: after cooling in darkness, the samples are insulators and become gradually conducting with increasing illumination dose. The observed gradual increase of the CESR (see. Fig. 2b) and the integral CR amplitude (Fig. 2c) as a function of dose reflect the deviations from the sharp band edge and the constant DOS expected for a perfect two-dimensional electron gas. Finally, assuming a Gaussian distribution of the fluctuations we can evaluate their amplitude from the dependence of the DOS at the Fermi level as a function of the Fermi level.

In Fig. 3 we plot results for the fluctuation amplitude versus. n_s. After long illumination, the carrier concentration saturates, the mobility is high and the fluctuation

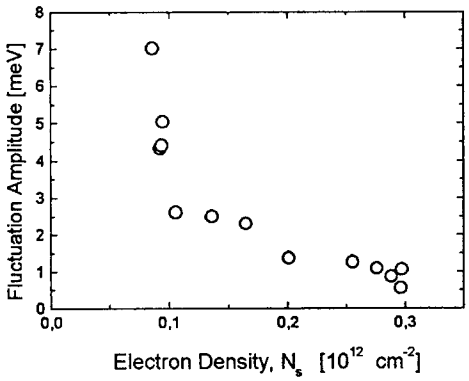

Fig. 3. Amplitude of potential fluctuations as obtained from CESR for two different samples as a function of the carrier density.

amplitude is the lowest. In the opposite limit (after short illumination), the concentration of mobile carriers and their mobility are low and the fluctuation amplitude (see Fig. 3) has a tendency to diverge. In order to understand this behavior we consider the effect of screening of potential fluctuations. The potential fluctuations are caused by fluctuations in the dimensions (well and spacer width), in the alloy composition x of the $Si_{1-x}Ge_x$ barriers, and, most important in our samples, by the distribution of ionized donors in the doping layer. For our weekly doped sample, the self-consistent calculation shows that the Fermi level is always below the donor states in the doping layer. Therefore this source (and all the others) of potential fluctuations are not affected by the population of the 2D channel and thus we can concentrate on the discussion of screening of the potential fluctuations by the 2DEG.

The simplest ansatz to discuss screening by the 2DEG is the Thomas–Fermi approach for the 2DEG in which the screening efficiency is given by: $q_s = 1/\lambda_s = 4/a_B$, where $a_B = 32$ Å is the Bohr radius. This expression is valid if the Fermi energy E_F^0 is above the band edge and bigger than δV. Since the screening length in this case is very short, $\lambda_s = 8$ Å, screening is very efficient and the resulting fluctuations are small in amplitude.

In the opposite limit, when the Fermi level is below the unperturbed band edge, the screening efficiency vanishes and the fluctuations caused by the quasi-2D doping layer diverge. In the transition regime the screening efficiency is proportional to the density of states at the Fermi level. The latter is a function of the potential fluctuations since the fluctuations are superimposed on the band structure of the idealized host. Now an increase in potential fluctuations causes additional states below the band edge and thus the Fermi level is lowered. This effect constitutes a positive feed-back mechanism: the lower Fermi level implies also a lower density of states and thus lower

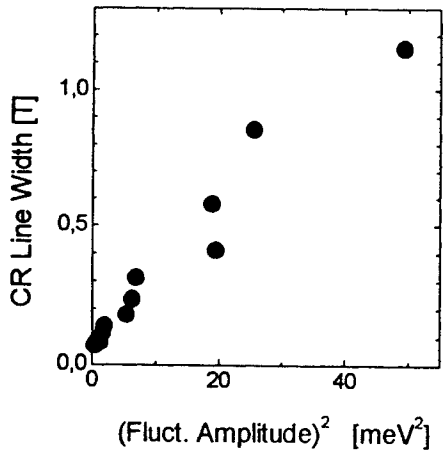

Fig. 4. Cyclotron resonance line width plotted as a function of the squared fluctuation amplitude.

screening efficiency. The latter, in turn, causes larger potential fluctuations, etc. Therefore we expect a highly non-linear dependence of the fluctuation amplitude on the 2D carrier concentration, or even a phase transition. Such behavior is seen in our experimental data (see Fig. 3) for low carrier concentration where the fluctuation amplitude δV increases drastically when the Fermi level becomes lower than δV.

Finally, we can also draw a conclusion on the effect of δV on the mobility. In Fig. 4, we plot the CR line width, which is proportional to the momentum scattering rate, as a function of $(\delta V)^2$. The linear dependence demonstrates that under all circumstances this type of sample scattering is dominated by the potential fluctuations, no matter whether we are in the metallic (high mobility) or nearly isolating case with low mobility.

In summary, we have demonstrated that the investigation of the 2DEG by ESR can yield information on the carrier density, the density of states, potential fluctuations, and the scattering rate in a single experiment. We obtained evidence for the divergence of the amplitude of potential fluctuations at low carrier density and an insulator-metal transition ruled by the density of the 2DEG via screening. At the same time, these potential fluctuations also constitute the main scattering mechanism for the 2DEG. This kind of transition is strongly reminiscent of the localization discussed by Anderson for the 3D case which should not exist in 2D [7] but whose existence has been demonstrated already by a number of other experiments [8].

Acknowledgements

Work supported in Austria by the Österreichischer Akademischer Austauschdienst, and the Fonds zur Förderung der Wissenschaftlichen Forschung, Vienna, Austria, and in Poland within the KBN grant 8 T11B 003 15.

References

[1] N. Nestle, G. Denninger, M. Vidal, C. Weinzierl, Phys. Rev. B 56 (1997) R4359.
[2] H.-J. Kümmerer, K. Hüftle, C. Weinzierl, G. Denninger, N. Nestle, K. Eberl, Phys. Rev. B 59 (1999) 12568.
[3] W. Jantsch, Z. Wilamowski, N. Sandersfeld, F. Schäffler, in: D. Gershoni (Ed.), Proceedings of the International Conference on Phys. Semiconductors, Jerusalem 1998, World Scientific, Singapore, 1999.
[4] W. Jantsch, Z. Wilamowski, N. Sandersfeld, F. Schäffler, Phys. Stat. Sol. B 210 (1998) 643.
[5] C.F.O. Graeff, M.S. Brandt, M. Stutzmann, M. Holzmann, G. Abstreiter, F. Schäffler, Phys. Rev. B 59 (1999) 13242.
[6] W. Timelthaler, W. Jantsch, G. Weimann, Semicond. Sci. Technol. 5 (1990) 686.
[7] E. Abrahams et al., Phys. Rev. Lett. 42 (1979) 673.
[8] S.V. Kravchenko et al., Phys. Rev. Lett. 77 (1996) 4938.

ELSEVIER

Physica B 273–274 (1999) 947–950

PHYSICA B

www.elsevier.com/locate/physb

Phonon resonances in optical spectra of donors in quantum wells

S. Bednarek[a], B. Szafran[a], J. Adamowski[a,*], I. Essaoudi[b], B. Stébé[c]

[a]*Faculty of Physics and Nuclear Techniques, University of Mining and Metallurgy (AGH), al. Mickiewicza 30, Kraków, Poland*
[b]*Department of Physics, University Moulay Ismail, Meknes, Morocco*
[c]*Institut de Physique et d'Electronique, Université de Metz, France*

Abstract

An influence of electron–phonon coupling and electron confinement on optical spectra is studied for donors in semiconductor quantum wells. A binding and 1s–2p transition energies have been calculated by the optimized canonical transformation method for GaAs/AlGaAs, CdTe/CdZnTe, and CdF_2/CaF_2 quantum wells. We have found that — in the quantum wells made from the ionic semiconductors — the 1s–2p transition energy exceeds the LO-phonon energy and the phonon resonances can appear in the optical spectra of donors. We have estimated the parameters of quantum wells, for which the phonon resonances can be detected in the absence of external magnetic field.

Keywords: Donor center; Electron–phonon coupling; Quantum well

Properties of donors substituting host-crystal atoms in a semiconductor quantum well (QW) are modified due to an electron confinement in the QW region. If the QW heterostructure is made from ionic materials, the electron–phonon coupling additionally modifies the donor spectra due to polaron effects. In semiconductor heterostructures, the polaron effects are more complicated than those in bulk semiconductors due to the occurrence of interface and confined phonon modes [1]. The polaron effects, which result by the presence of these phonon modes, were studied by Mori and Ando [1]. In the present paper, we study the QW-induced polaron effects of different nature, namely, the modification of donor spectra resulting from the electron–phonon interaction, that is changed due to the localization of the electron in the confinement potential of the QW.

A system under consideration consists of a single-electron donor impurity located at a center of the QW and interacting with LO phonons. It was shown [1] that electron–phonon interaction amplitudes for different phonon modes satisfy the sum rule. If dielectric properties of materials forming the heterostructure are similar, i.e., we can neglect the difference in coupling constants of phonon modes, then — according to the sum rule [1] — the Frőhlich interaction amplitude for bulk LO phonons can be used as an average amplitude of interaction between electrons and phonons in the QW. Therefore, we take on the electron–LO phonon coupling in the Frőhlich form. The Hamiltonian of the system after the Platzmann transformation [2] has the form

$$H = -\frac{\hbar^2}{2m_e}\nabla^2 - \frac{e^2}{4\pi\varepsilon_0\varepsilon r} + V_{\mathrm{conf}}(z) + \sum_k \hbar\omega_k a_k^\dagger a_k + \sum_k (v_k a_k e^{ikr} + \mathrm{h.c.}), \quad (1)$$

where m_e is the conduction band mass of the electron in the QW, ε is the static dielectric constant of the QW, $V_{\mathrm{conf}}(z)$ is the potential energy of electron confined in the QW, which is assumed to be a rectangular potential well

* Corresponding author. Tel.: + 4812-6172974; fax: + 4812-6340010.
E-mail address: adamowski@novell.ftj.agh.edu.pl (J. Adamowski)

0921-4526/99/$ - see front matter
PII: S0921-4526(99)00561-X

of finite depth (V_0) and thickness (L) measured in the growth (z) direction, $a_k^\dagger$ (a_k) is the LO-phonon creation (annihilation) operator, $\omega_k = \omega$ is the frequency of the LO phonon in the QW, and v_k is the Fröhlich interaction amplitude for the QW.

We solve the eigenvalue problem by a method of optimized canonical transformation [3,4], which has been adapted to the bound polarons in the QWs. According to this approach [3,4], the trial state of the electron–phonon system is taken on in the form

$$|\Psi\rangle = U\varphi(\boldsymbol{r})|0\rangle_{\mathrm{ph}}, \tag{2}$$

where U is the unitary operator of the canonical transformation, $\varphi(\boldsymbol{r})$ is the electronic trial wave function, and $|0\rangle_{\mathrm{ph}}$ is the phonon vacuum state. We take on the operator U in the form

$$U = \exp\left[\sum_k (F_k(\boldsymbol{r})a_k^\dagger - \mathrm{h.c.})\right], \tag{3}$$

where $F_k(\boldsymbol{r})$ is the displacement amplitude. In the first step of calculations, we transform Hamiltonian (1) with the help of U. Next, we solve the eigenequation obtained in the first step using the variational method with electronic trial wave function $\varphi(\boldsymbol{r})$, which has been expanded in the Gaussian basis $\exp[-\alpha_n(x^2+y^2)-\beta_n z^2]$, where α_n and β_n are nonlinear variational parameters. Test calculations of the lattice relaxation energy has been performed with one-element basis ($n = 1$) and calculations of energy spectra — with 15-element basis ($n = 1, \ldots, 15$). For the 2p states, the Gaussians were multiplied by (x, y, 0) and properly symmetrized.

We have performed a systematic search for the optimum displacement amplitude. In Fig. 1, we plot the results of test calculations obtained with the following displacement amplitudes:

$$F_k^{(1)}(\boldsymbol{r}) = f_k^{(1)}, \tag{4a}$$

$$F_k^{(2)}(\boldsymbol{r}) = f_k^{(2)}\exp(-\mathrm{i}\boldsymbol{k}\cdot\boldsymbol{r}), \tag{4b}$$

$$F_k^{(3)}(\boldsymbol{r}) = f_k^{(3)}\exp(-\mathrm{i}\boldsymbol{k}_\perp\cdot\boldsymbol{r}), \tag{4c}$$

$$F_k^{(4)}(\boldsymbol{r}) = f_k^{(4)}\exp(-\mathrm{i}\boldsymbol{k}_{||}\cdot\boldsymbol{r}), \tag{4d}$$

and their linear combinations of the forms, e.g., $F_k^{(12)} = F_k^{(1)} + F_k^{(2)}$ and $F_k^{(123)} = F_k^{(1)} + F_k^{(2)} + F_k^{(3)}$, where $\boldsymbol{k}_\perp$ and $\boldsymbol{k}_{||}$ denote the in-plane and z wave-vector components, respectively. Phonon amplitudes $f_k^{(i)}$ have been determined from minimum conditions for an expectation value of the Hamiltonian, i.e.,

$$\frac{\delta}{\delta f_k^{(i)}}\frac{\langle\Psi|H|\Psi\rangle}{\langle\Psi|\Psi\rangle} = 0. \tag{5}$$

Amplitudes $F_k^{(1)}$ and $F_k^{(2)}$ are appropriate for the strong and weak electron–phonon coupling, respectively, in bulk crystals, and $F_k^{(3)}$ and $F_k^{(4)}$ enable us to reproduce the lattice deformation, which results from the breaking of the crystal symmetry due to the presence of the QW.

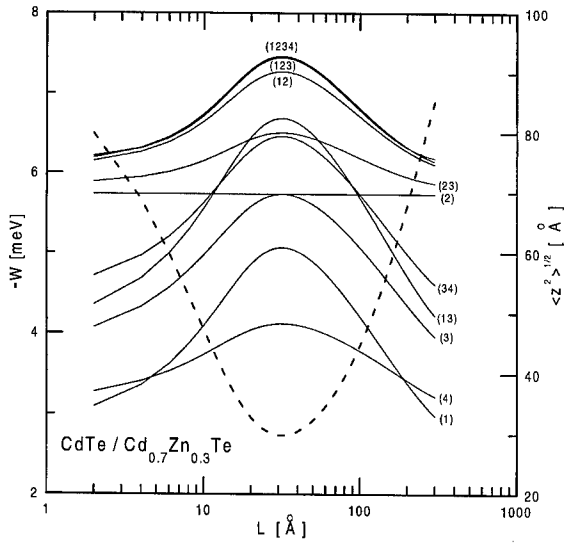

Fig. 1. Lattice relaxation energy W for the donor ground state as a function of QW thickness L for $CdTe/Cd_{0.7}Zn_{0.3}Te$. Solid curves display the results obtained with different displacement amplitudes and their linear combinations (see text), dashed curve shows the square-root mean value of z coordinate of electron.

Using the optimized phonon amplitudes, we have calculated the lattice relaxation energy, i.e., expectation value of the last two terms of Hamiltonian (1) representing the phonon field and electron–phonon interaction. The lattice relaxation energy W calculated with amplitude $F_k^{(123)}$ is given by

$$W = -\sum_k |v_k|^2\left[\frac{(1-|\rho_{||}|^2)^2}{T - T_\perp|\rho_{||}|^2 + \hbar\omega(1-|\rho|^2)(1-|\rho_{||}|^2)} + \frac{|\rho_{||}|^2(1-|\rho_\perp|^2)^2}{T_\perp + \hbar\omega(1-|\rho_\perp|^2)} + \frac{|\rho|^2}{\hbar\omega}\right], \tag{6}$$

where $\rho = \langle\varphi|\exp(\mathrm{i}\boldsymbol{k}\cdot\boldsymbol{r})|\varphi\rangle$, $\rho_{||} = \langle\varphi|\exp(\mathrm{i}\boldsymbol{k}_{||}\cdot\boldsymbol{r})|\varphi\rangle$, $\rho_\perp = \langle\varphi|\exp(\mathrm{i}\boldsymbol{k}_\perp\cdot\boldsymbol{r})|\varphi\rangle$, $T = \hbar^2k^2/2m_e$, $T_\perp = \hbar^2k_\perp^2/2m_e$. Analyzing Eq. (6), we can trace a mechanism of influence of the QW on the lattice relaxation energy. The QW confinement potential causes a stronger localization of electron in the z direction, which leads to an increase of absolute value of electron probability density $|\rho_{||}|$. This results in an enlarged absolute value of the lattice relaxation energy. Since the lattice relaxation energy is negative, this gives rise to a lowering of the total energy of the bound polaron. This effect is shown in Fig. 1, which displays the results of the test calculations for the ground state of the donor in the ionic QW heterostructure $CdTe/Cd_{0.7}Zn_{0.3}Te$. The larger estimated absolute values of the lattice relaxation energy correspond to

the improved variational upper bounds on the ground-state energy. The absolute value of the lattice relaxation energy takes its maximum for the QW thickness ~ 30Å, which corresponds to the largest electron localization in the z direction, i.e., minimum square-root mean value of the electron z coordinate (cf. Fig. 1). The best estimates have been obtained with the linear combination of all the four displacement amplitudes. Nevertheless, the results obtained with the use of the three amplitudes, i.e., $F_k^{(123)}$, almost indistinguishable from these best estimates. Therefore, we have used the amplitude $F_k^{(123)}$ in order to calculate the ground-state energies of the donor and polaron confined in the QW as well as the energy of the first excited state (2p) of the donor in the QW. The lattice-relaxation contributions to the energy of the donor and polaron in $CdTe/Cd_{0.7}Zn_{0.3}Te$ QW are displayed in Fig. 2. We note that the lattice relaxation energies for the delocalized states: the first excited 2p of the donor and ground state of the confined polaron, are approximately equal to each other and considerably different from this energy for the localized 1s donor ground state. In GaAs/AlGaAs QWs, the 1s and 2p donor states are weakly localized and the lattice relaxation energy is almost the same in both these states.

We have also determined the binding energy E_B and 1s–2p transition energy E_T for GaAs/AlGaAs, CdTe/CdZnTe, and CdF_2/CaF_2 QWs, that are representative for the weak, intermediate, and strong electron–phonon coupling, respectively. The lattice-relaxation energy contributions for the initial and final states, that are used to calculate the binding and transition energies, cancel each other for the donors in the weakly ionic GaAs/AlGaAs heterostructure. Therefore, the polaron effects for donors in GaAs/AlGaAs QWs are negligibly small and are not shown in figures. The results for the $CdTe/Cd_{0.7}Zn_{0.3}Te$ ($V_0 = 0.146$ eV) and CdF_2/CaF_2 ($V_0 = 3.0$ eV) heterostructures are plotted in Fig. 3.

In both the ionic heterostructures, the polaron effects are large and — together with the confinement of electrons — lead to a considerable enlargement of donor binding energy. The 1s binding energy and 1s–2p transition energy exhibit maxima for the QW thickness, that corresponds to the largest localization of electron in the z direction. According to Fig. 3, the 1s–2p transition energy exceeds the LO-phonon energy. This means that one can observe phonon resonances in optical spectra of the donors in these QWs. An appearance of the resonance corresponds to a crossing of the energy levels of states 2p and 1s + N phonons, where N is the number of phonons. Fig. 3 shows that in CdF_2/CaF_2 one can detect the phonon resonances involving $N = 2$, 3, and 4 phonons for the QWs with $L = \sim 60$, ~ 25 and ~ 15 Å, and for the energies 100, 150, and 200 meV, respectively. The four-phonon resonance at $L \leqslant \sim 2$ Å corresponds to the potential-well width smaller than the distance between the nearest-neighbor atoms in the fluorites. In

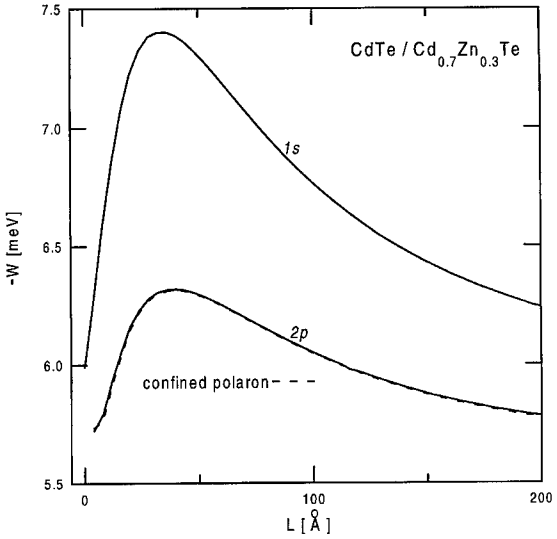

Fig. 2. Lattice relaxation energy W for 1s and 2p donor states (solid curves) and ground state of confined polaron (dashed curve) for $CdTe/Cd_{0.7}Zn_{0.3}Te$ QWs as a function of thickness L.

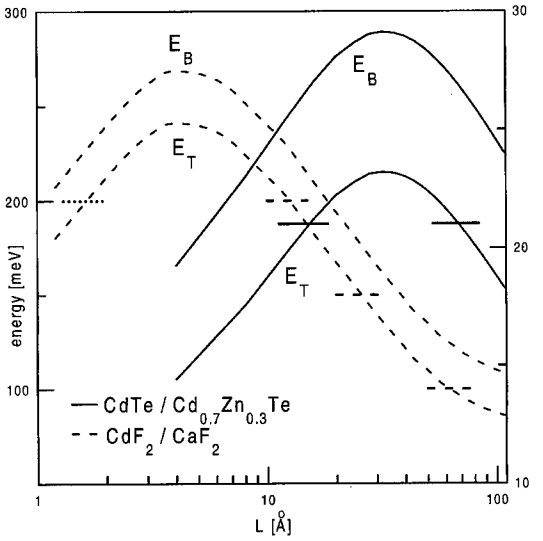

Fig. 3. Calculated 1s binding energy (E_B) and 1s–2p transition energy (E_T) as a function of QW thickness L for $CdTe/Cd_{0.7}Zn_{0.3}Te$ (solid curves, right energy scale) and CdF_2/CaF_2 (dashed curves, left energy scale) QWs. Short horizontal lines show the positions of phonon resonances.

$CdTe/Cd_{0.7}Zn_{0.3}Te$, the one-phonon resonances with the energy 21 meV are expected for $L = \sim 15$ and ~ 65 Å. A peak corresponding to the 1s–2p transition should be splitted in the close vicinity of the resonance. The present variational approach does not allow us to calculate a magnitude of this splitting. However, we

provide the values of the QW parameters, for which this splitting can occur. The similar phonon resonances were observed for polarons in GaAs/AlGaAs multiple QW structures in magnetic field [5]. The results of the present paper show that in the ionic QW heterostructures, the phonon resonances can be detected in the donor spectra even without the external magnetic field. For this purpose, one can either use several QWs of different thicknesses or a single wedge QW doped at the center. Recently, the impurity-related visible and ultraviolet luminescence was measured for Eu donors in CdF_2/CaF_2 superlattices [6]. The phonon resonances predicted in the present paper should be detected by the infrared spectroscopy.

In summary, we have shown that the joint effect of the electron–phonon coupling and electron confinement leads to the considerable increase of the binding energy and dipole transition energy for donors in QWs. In the ionic heterostructures, the appearance of phonon resonances in donor spectra is predicted.

Acknowledgements

This work is done in the frame of the French-Polish scientific cooperation programme POLONIUM and is partly supported by the Polish Government Scientific Committee (KBN Grant No. 2 P03B 5613).

References

[1] N. Mori, T. Ando, Phys. Rev. B 40 (1989) 6175.
[2] P.M. Platzmann, Phys. Rev. 125 (1962) 1961.
[3] S. Bednarek, J. Adamowski, M. Suffczyński, Solid State Commun. 21 (1997) 1.
[4] J. Adamowski, Phys. Rev. B 32 (1985) 2588.
[5] Y.J. Wang, H.A. Nickel, B.D. McCombe, F.M. Peeters, J.M. Shi, G.Q. Hai, X.-G. Wu, T.J. Eustis, W. Schaff, Phys. Rev. Lett. 79 (1997) 3226.
[6] N.S. Sokolov, S.V. Gastev, A.Yu. Khilko, S.M. Suturin, I.N. Yassievich, J.M. Langer, A. Kozanecki, Phys. Rev. B 59 (1999) R2525.

ELSEVIER

Physica B 273–274 (1999) 951–954

PHYSICA B

www.elsevier.com/locate/physb

Boron in mesoporous Si — Where have all the carriers gone?

G. Polisski[a,*], D. Kovalev[a], G. Dollinger[a], T. Sulima[b], F. Koch[a]

[a]*Physik-Department, Technische Universität München, D-85747 Garching, Germany*
[b]*Universität der Bundeswehr, D-85577 Neubiberg, Germany*

Abstract

Highly-doped p-type Si is electrochemically etched in an HF-based electrolyte to produce mesoporous surface layers. Using both elastic-recoil detection analysis and secondary ion mass spectroscopy it is concluded that B atoms are not removed from the porous layer. Crystallite size for the most porous samples is related to the average dopant spacing. It is argued that the electrolytic erosion of Si stops when B is in the surface layer and passivated.

Keywords: Porous silicon; Impurity concentration; Nanocrystals

1. Introduction and motivation

Porous Si is prepared from single-crystal wafers by electrochemical dissolution in an HF-based electrolyte. The surface layer formed in the process has a porosity ranging typically from a few tens of % to as much as 95%. Si atoms are removed from the crystalline lattice by an electrolytic process that involves a transfer of charge in the form of holes from the substrate to the electrolyte. It is for this reason that in the absence of illumination p-type material is etched, while the respective n-doped Si is not attacked by the electrolytic process.

The strong and visible luminescence (PL) of various forms of porous Si has attracted considerable attention and the phenomenon has been extensively, but not conclusively, researched by many groups. The PL has been found to depend greatly on the conditions of the etching process. The concentration and type of dopants, the exact composition of the electrolyte bath, the current density, the type and even polarization of the illumination during the processing all play a role. Under appropriate conditions the process is self-limiting with the remaining Si skeleton unable to support the flow of holes from the p-doped substrate. The original papers [1,2] on visibly luminescing porous Si formed from p^- material ($N_B \sim 10^{15}$–10^{16} cm^{-3}) argued that quantum-confinement effects along the current path blocked the movement of charge. This served at once to explain an enhanced bandgap with a PL in the yellow-red part of the spectrum (1.5–2.0 eV) and that the erosion of the Si would stop when the Si particles in the skeletal remains had reached sizes in the 2–3 nm range. The material thus formed is termed microporous Si.

By contrast, the mesoporous Si that is the subject of this report, is made from highly doped p^+-type Si with the B-acceptor density in the 1×10^{19} cm^{-3} range. Resistivities are typically in the mΩ cm range. The resulting pores and Si skeletal remains are between 6–20 nm. The material normally luminesces only weakly and with peak energies starting at the band gap of Si and increasing to about 1.4 eV depending on the preparation conditions. We have paid particular attention to the evolution of the PL starting at Si band gap and increasing in very small and controlled steps. In Ref. [3,4] has been demonstrated both a chemical layer-by-layer post-etching treatment and an electrochemical fine-tuning procedure which produced mesoporous Si whose PL covers the 1.1–1.4 eV range in arbitrarily small steps.

We show in Fig. 1, a set of luminescence spectra that are typical for the materials examined here. The PL-peak

* Corresponding author. Tel.: + + 49-89-289-12346; fax: + + 49-89-289-12317.
E-mail address: gpolissk@physik.tu-muenchen.de (G. Polisski)

0921-4526/99/$ - see front matter
PII: S0921-4526(99)00562-1

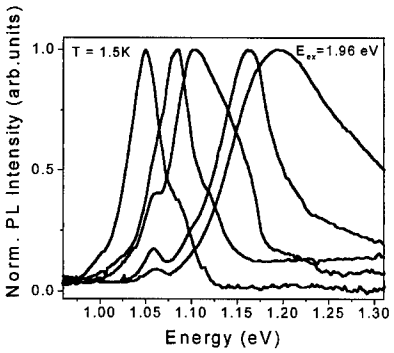

Fig. 1. Normalized PL spectra of mesoporous layers in the near band gap limit.

energies evolve from the Si band-edge value to about 1.2 eV. All the spectra were obtained at 1.5 K. The remaining small peak fixed at the 1.056 eV position is from the substrate and not from macrocrystalline inclusions in the porous layer. The spectra are normalized, but the porous film PL exceeds the substrate contribution by 1–2 orders of magnitude in the intensity. The PL lifetimes measured for the porous layer and substrate contributions differ greatly. It is ns for the substrate and up to ms for the porous layers. Details of these studies can be found elsewhere [5]. The exhibit in Fig. 1 is intended to make clear that the PL in mesoporous Si is related to the luminescence of crystalline Si. The energy shifts are so small that it is clear that quantum size effect blockade of the hole current cannot be the reason for self-limiting of the electrolytic process.

Porous Si layers, micro- or mesoporous, are always highly insulating. For the micro-type with an average dopant spacing of ~ 50 nm for p^- material ($N_B \sim 1 \times 10^{16}$ cm^{-3}) it is unlikely that B-acceptors are in a given 2–3 nm particle. In addition, the large surface area created by the electrolytic process provides a number of dangling bond sufficient to ionize the B-acceptor. We cannot expect free holes from these. The existence of an ESR signal [6] is an additional proof of the depletion.

The scenario for mesoporous Si is very different. The average dopant spacing for p^+-Si ($N_B \sim 1 \times 10^{19}$ cm^{-3}) is 5 nm. The particle size is on the average bigger than this. Moreover, there is growing experimental evidence that the electrochemical etching procedure actually enhances the B concentration. The electrochemical dissolution proceeds in a way that leaves the dopant impurities in the remaining Si skeleton. We will examine this aspects in the following Section 2.

In spite of the fact that each and every crystallite should have several impurity atoms, all the experiments point to a depletion of the holes in the mesoporous layer. After viewing the experimental evidence for this depletion of carriers in Section 3 we are left with the disturbing question: Where have all the carriers gone?

In the final Section 4 we will try to provide an answer to this challenging question by invoking the special role of the near-surface B-impurities.

2. ERDA and SIMS analytics. Where is the boron?

The mesoporous layers are prepared from (1 0 0) Si wafers with a resistivity specified as 5–15 mΩ cm. The electrochemical etching procedure is that described in Ref. [4]. Samples are typically 50 μm thick. The layers are freestanding to allow more precise porosity determination when this is of concern. For ease of handling in the SIMS/ERDA investigations the layers are kept on the wafer substrate.

In a brief report [7], the use of elastic-recoil detection analysis (ERDA), was introduced for the elemental composition analysis of the porous layer. It was shown that the H/Si and B/Si atomic ratios could be determined with good accuracy. The unexpected and remarkable result was that the B/Si ratio was increasing with the degree of porosity. While earlier secondary ion mass spectroscopy (SIMS) data had been inconclusive on this point [8,9], there was nuclear reaction data that pointed out such a possibility [10]. Because one is dealing with highly doped Si, it was unlikely that B-enhancement was the result of contamination and sample storage as reported in [11]. That ERDA data in Ref. [7] contained some error in plotting and also needed corrections for more precise porosity determination. This did not question the overall conclusion that there is B-enhancement in the remaining Si skeleton, but left open a precise quantitative statement. In a reanalysis of the original data in Fig. 2 we come to understand that the density increase is precisely such as to leave the original B-concentration intact. The electrochemical etching and post treatment that we use leaves all the B in the surface layer in spite of the very significant removal of Si (porosity up to 80%).

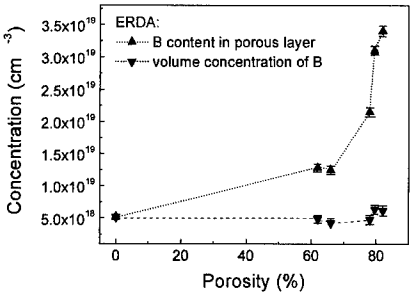

Fig. 2. B content in mesoporous Si from elastic-recoil detection analysis. I^- ions with energy more than 160 MeV have been used. Note that the volume concentration of B atoms remains constant if the porosity of the layer is taken into consideration.

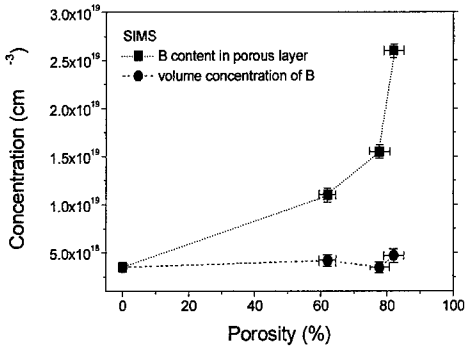

Fig. 3. B content in mesoporous Si from SIMS. The sputter source is O_2^- with the energy $E \sim 11$ eV.

From a new series of mesoporous Si layers we have obtained SIMS data. After extensive calibrations and scaling the atomic ratios to account for differences in the primary ion current from porous and solid materials, we reach with the data in Fig. 3 exactly the same conclusion. Also for the SIMS data the B/Si increases with porosity in such a way to keep all the B in the skeletal layer. B atoms are not removed with the electrolytic erosion in Si. This remarkable result applies for the processing details employed here. Different post-etching steps, such as the exact washing procedure, do not affect this conclusion.

3. Carrier depletion in mesoporous Si

The porous layer that is formed by the electrolytic processing is always highly insulating. The prima facie evidence for this is that it resists further erosion. Transport in mesoporous Si has been studied in many reports [12]. The charge transport is nonlinear and sensitive to adsorbed gases. The resistivity is roughly in the 1–10 MΩ cm range. Thus the electrochemical treatment has transformed mΩ cm wafer material into a MΩ cm skeleton. The resistivity is changed by a factor of 10^9 or more.

The lack of electrical conduction is not simply the result of the complicated topology of isolated nanocrystal segments, the lack of a continuos path for the current along the network of undulating columns. Microwave and far-infrared investigations show no significant free carrier contribution to the absorption. There is no evidence for infrared excitation of intraband resonant transitions that are expected for isolated particles which contain free charges.

Further evidence that the mesoporous layer is depleted comes from the existence of a spin resonance signal. Both Refs. [6,13] report for the porous layer on ESR signal of surface defects on Si even though it has been prepared from p^+-wafer. The dangling bond state apparently is occupied. For a granular, highly insulating material the existence of a spin resonance is not definitive proof of depletion, but together with the other observations it fits the pattern.

The same can be argued for the existence of PL. For particles containing a dopant impurity, the decay of the acceptor bound exciton is overwhelmingly nonradiative. Again this is only circumstantial evidence because of the discontinuous nature of the porous medium.

Taken together the observations leave no doubt that the high resistivity of porous Si is the result of carrier depletion. There are no free holes in the structure in spite of the high density of B atoms.

4. Conclusions — surface passivation of boron

The evidence of the previous two Sections is clear. There is an enhanced B concentration in the porous layers, reaching values of $(2\text{–}3) \times 10^{19}$ cm^{-3}. In spite of this the material is highly depleted. There are no free holes!

The peculiarity of electrochemical erosion has been to leave all the B atoms in the remnant skeleton. This means that the etching process has selectively evolved around the impurities, removing Si atoms between and around the dopants. An interesting and relevant observation can be made from a study of the topological features and the sizes of the nanoparticles in the porous layer. For the wafer doping with $N_B \sim 4 \times 10^{18}$ cm^{-3} the average impurity spacing is 6.2 nm. In Ref. [7] we had measured along with the B concentration, the hydrogen contained in the sample in terms of H/Si atomic ratio. For the 5 mesoporous layers in Fig. 2, the concentration values ranged from 13% to 21%. If one assumes a certain particle shape and a surface coverage with H atoms/cm^2, then this measurement provides a linear dimension for the particles that have formed. This approach was first applied in Ref. [14] and subsequently refined in Ref. [15].

From infrared spectroscopy of Si–H vibration modes on the surface of the Si particles it is of hydrided surface to the volume of an Si cube and taking into account the measured value of H/Si one arrives at the size given in Fig. 4. The porosity ranges from about 60% to 80% with the increasing ratio of H/Si. This determination of sizes has uncertainties related to shape, connectivity of the particles and the details of the H-bonding at the Si-surface but it does give a reliable estimate. We note that the limiting size in the most porous of the samples is 6.5 nm, nearly identical with the estimated average spacing of the B atoms. Further electroetching will not reduce this size or shift the PL to significantly higher values. We suggest that for this mode of electrolytic formation of porous Si, the ultimate particle size relates to the dopant density. The implication of not loosing B atoms from the Si matrix is that the removal of Si proceeds until B appears in a near-surface position. The dissolution of Si

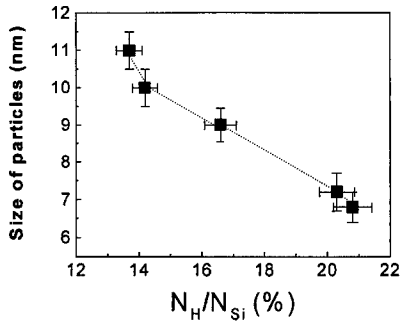

Fig. 4. Estimate of particle size from the atomic ratio of H to Si.

atoms requires the exchange of holes between the substrate and the electrolyte. Evidently these are not available with B at or near the surface.

In looking for reasons why the surface B atoms may be passivated, we could cite the well studied B–H complex [16]. After all the surface is covered with H both during the electrolytic treatment in HF and after drying. The problem with this explanation is that the B–H infrared local mode vibration is generally not seen in the porous layer, at least not with the appropriate signal strength.

Alternatively, one can think of passivation of the B acceptor by a nearby dangling bond defect. The transfer of charge, however, can take place over distances like a depletion layer width. Also there are not enough such defects to passivate more than 10^{19} cm^{-3} dopants. This process is not specific to B in a near surface layer position and could not explain the particle sizes.

We suggest that the passivation of B acceptors when these are at a distance of less than the impurity Bohr radius from a surface (in Si that is only 1–3 atomic layers!) is a very general result. At the surface itself, a B atom has the reduced coordination that is required. In a near surface position, the extra bonding charge is provided from Si orbitals in a way similar to how the dangling bond state ionizes the B acceptor in a depletion layer. In summary, the experiments show that B which is closer than a Bohr radius to a Si surface is not an acceptor.

References

[1] L.T. Canham, Appl. Phys. Lett. 57 (1990) 1046.
[2] V. Lehmann, U. Gösele, Appl. Phys. Lett. 58 (1991) 856.
[3] I.H. Libon, C. Voelkmann, V. Petrova-Koch, F. Koch, MRS Symp. Proc. 452 (1997) 511.
[4] G. Polisski, H. Heckler, D. Kovalev, M. Schwartzkopff, F. Koch, Appl. Phys. Lett. 73 (1998) 1107.
[5] D. Kovalev, H. Heckler, G. Polisski, F. Koch, Phys. Stat. Sol. (B) 214 (1999), in press.
[6] B.K. Meyer, D.M. Hofmann, P. Christmann, W. Stadler, A. Nikolov, A. Scharman, A. Hofstaeter, MRS Symp. Proc. 358 (1995) 453.
[7] G. Polisski, G. Dollinger, A. Bergmaier, H. Heckler, D. Kovalev, F. Koch, Phys. Stat. Sol. 168 (1998) R1.
[8] V. Lehmann, F. Hofmann, F. Möller, U. Grüning, Thin Solid. Films 255 (1995) 20.
[9] P. Allongue, C.H. Villeneuve, M.C. Bernard, J.E. Peou, A. Boutry-Forveille, C. Levy-Clement, Thin Solid Films 297 (1997) 1.
[10] A. Grosman, C. Ortega, in: L.T. Canham (ED.), Properties of Porous Silicon, EMIS Datareviews Series, INSPEC, Vol. 18, 1997, pp. 328–333.
[11] L.T. Canham, C.W. Blackmore, MRS Symp. Proc. 256 (1992) 63.
[12] M. Ben Chorin, F. Möller, F. Koch, Phys. Rev. B 49 (1994) 2891.
[13] H.J. von Bardeleben, J.L. Cantin, in: L.T. Canham (Ed.), Properties of Porous Silicon, EMIS Datareviews Series, INSPEC, Vol. 18 1997, pp. 319–327.
[14] Y. Diawara, J.F. Currie, A. Yelon, V.P.- Koch, A. Nikolov, MRS Symp.Proc. 358 (1995) 555.
[15] A. Nikolov, V.P.- Koch, G. Polisski, F. Koch, MRS Symp. Proc. 358 (1995) 423.
[16] N. Stavola, S. Pearson, J. Lopata, W.C. Deautremant-Smith, Appl. Phys. Lett. 50 (1987) 1086.

ELSEVIER

Physica B 273–274 (1999) 955–958

PHYSICA B

www.elsevier.com/locate/physb

OH-related emitting centers in interface layer of porous silicon

T.V. Torchynska[a,*], M.K. Sheinkman[b], N.E. Korsunskaya[b], L.Yu. Khomenkovan[b], B.M. Bulakh[b], B.R. Dzhumaev[b], A. Many[c], Y. Goldstein[c], E. Savir[c]

[a]*Material Science Department, ESFM-National Polytechnic Institute, U.P.A.L.M., Mexico D.F., 07738, Mexico*
[b]*Institute of Semiconductor Physics, National Academy of Sciences, Kiev, 252650, Ukraine*
[c]*Racah Institute of Physics, The Hebrew University, Jerusalem, Givat Ram, Israel*

Abstract

Photoluminescence and excitation spectra measurements as well as SIMS and FTIR techniques were used to investigate the photoluminescence excitation mechanism of porous silicon. It is shown that there are two types of photoluminescence excitation spectra which consist either of two, visible and ultraviolet, or one, only ultraviolet, bands. The dependence of photoluminescence excitation spectra upon the various treatment (aging in vacuum, in air and in liquids) indicates that the excitation in the visible range occurs via light absorption of some species on the porous Si surface.

Keywords: Porous silicon; Photoluminescence; Photoluminescence excitation

1. Introduction

In spite of numerous investigations of the photoluminescence, PL, of porous Si, PS, the origin of the visible emission and the mechanism of its excitation are still unknown. The current point of view on PL are as follows: quantum confinement effects in the silicon wires [1]; light emission of silicon clusters [2]; luminescence of polysilans [3]; siloxen [4] or silicon oxide [5]. In this paper these phenomena were studied by measurements of the PL and PL excitation, PLE, spectra, as well as SIMS and FTIR spectra and their variation during aging, in air, vacuum and liquids.

It should been noted that the PLE data are not numerous [2,6–8] and a systematic research of the dependence of the PLE spectra upon the preparation regimes and aging conditions have not been reported so far. All authors supposed that the luminescence and light absorption processes occurs in the same substance. Thus the light-emitting material was identified either as quantum confined silicon [2,7], silicon oxide [5] or siloxene [6]. But such assumption has no experimental confirmation or reasonable theoretical consideration.

2. Experimental results and discussion

The PS samples were prepared from p-type, B-doped, (1 0 0) oriented silicon wafers of 4.5 Ω cm resistivity. The porous layers were obtained by anodization in a solution of $HF : H_2O : C_2H_5OH$ (1 : 1 : 2). Several groups of 5–10 samples prepared at anodization current density 20–150 mA/cm^2 and anodization time 2–20 min were investigated. PL have been excited by a xenon-150 lamp with a grating monochromator MDR-23 and dispersed with a infrared spectrometer IKS-12 and photomultiplier FEU-79. PLE spectra were measured at 300 K for three wavelength values of the PL band: at the maximum, 645 nm, at the short wavelength side, 560 nm, and long wavelength side, 750 nm. PLE spectra were normalized to equal number of exited light quanta for different wavelengths.

Fig. 1 shows the PL spectra for PS samples obtained at the different anodization regimes. The PLE spectra, presented in Fig. 2, consist of two overlapping bands. One in the visible spectral range, 350–550 nm, V_{PLE}-band, has a

* Corresponding author.
E-mail address: ttorch@esfm.ipm.mx (T.V. Torchynska)

0921-4526/99/$ - see front matter
PII: S0921-4526(99)00563-3

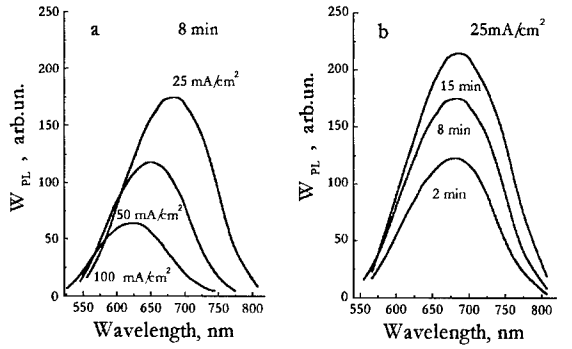

Fig. 1. PL spectra of as-prepared PS samples. The parameters of the different anodization regimes are shown in figures. The excitation wavelength was 330 nm.

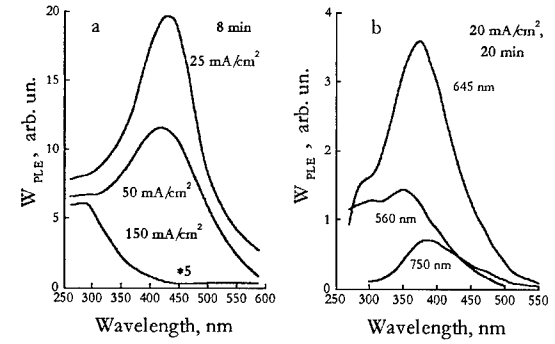

Fig. 2. PLE spectra for PS samples obtained at the shown anodization regimes, *a*, and detected at the different shown wavelength, *b*.

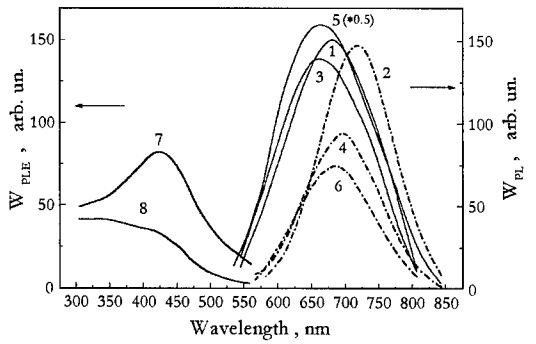

Fig. 3. The PL spectra, measured at the $\lambda_{exc} = 330$ nm (1, 3, 5) and 480 nm (2, 4, 6) for as-prepared (1, 2) and stored 7 days (3, 4) as well as 30 days (5, 6) at the air at 300 K PS samples, and the PLE spectra detected at 685 nm for as-prepared (7) and aged 7 days (8) PS samples.

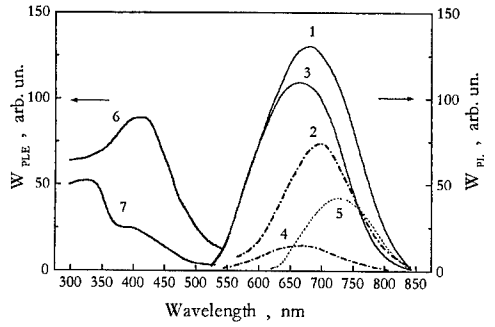

Fig. 4. The PL spectra, measured at the $\lambda_{exc} = 330$ nm (1, 3) and 480 nm (2, 4) for as-prepared (1, 2) and kept in vacuum during 2 h at 300 K (3, 4) PS samples, and the PLE spectra detected at 685 nm for as-prepared (6) and kept in vacuum (7) PS samples. Curve 5 represents the subtraction of curve 2 from curve 1.

broad maximum and the other in the ultraviolet, UV_{PLE}-band, exhibits a plateau towards shorter wavelengths.

An increase of the anodization current density, leads to a decrease of the visible band magnitude in the PLE spectrum and for 150 mA/cm^2 this band practically disappears (Fig. 2a). At the same time, there is a decrease of the PL intensity and its full-width on half-maximum (FWHM), as well as a blue shift of the PL peak position (Fig. 1a). Increasing the anodization time, on the other hand, results in an increase of the V_{PLE}-band intensity. In parallel, there is an enhancement of the PL intensity and its FWHM, as well as a small red shift of the PL peak position (Fig. 1b). Transformations of PL and PLE spectra during the PS aging process in air are shown in Fig. 3. The character of the PL variation is different for the various excitation light-wavelengths: the PL intensity excited by light in the V_{PLE}-band ($\lambda = 480$ nm), W_V, drops monotonously with time (Fig. 3).

The PL intensity excited by light in the UV_{PLE}-band ($\lambda = 330$ nm), W_{UV}, decreases insignificantly at first and then rises. It appears, that two processes during aging take place and they are characterized by the different excitation bands. The overlap of PLE bands is rather large (see Fig. 2). Thus, the non-monotony of PL variation at UV-excitation may be due to a competition between the two processes.

We have also studied the effect of keeping the samples in vacuum and in liquids. As liquids we used water and an aqueous solution of NaCl. The latter is often employed in electroluminescence studies. It turned out that in both cases keeping the samples in vacuum and liquids leads to a reduction in the PL intensity. The results for vacuum are plotted in Fig. 4. We see that W_V, W_{UV}, and the V_{PLE}-band intensity decrease. The shape of the PL spectra transforms similarly to the case of aging in air. It is noteworthy that the short-wavelength edges of the PL spectra before and after keeping in vacuum coincide. This fact means that the PL intensity reduction is mainly connected with the drop of the long-wavelength component. A similar PL behavior has been

observed when the PS samples were kept in a NaCl solution, Fig. 5.

Analysis of PL spectra (Fig. 4) shows that after keeping the samples in vacuum the peak positions of W_{UV} and W_V coincide with the peaks of as-prepared PS samples. It follows that after this process the contribution of the long-wavelength part becomes negligible. This can be seen clearly by subtracting curve 2 from curve 1. The result (Fig. 4 curve 5) shows that PL band is complete and the reduction in the PL intensity is due to the reduction in the long-wavelength band component.

The simultaneous decrease of long-wavelength PL band component and V_{PLE}-band in PLE spectra is the evidence that this PL band component excited by the V-band light mainly (Fig. 2b).

The PL variation after keeping the samples in the vacuum indicates that the decrease of PL intensity during aging is connected with the desorption of the some species from the Si wire surface. This may be the reason for the shift of the W_V and W_{UV} peak positions after aging. Because of the overlapping of the two excitation bands, the PL spectra excited by the light from both PLE bands may contain the long-wavelength component. Taking into account that PL long-wavelength band and V_{PLE}-band in PLE spectra decrease simultaneously it may be supposed that the excitation and recombination take place in the same object-adsorbed species on the Si wire surface, or that adsorbed species could transfer excitation to some other luminescent centers. If this center cannot be excited by another way the desorption of the species will lead to same experimental results.

In order to determine what species are present at the PS surface, we have measured the infrared absorption spectrum of a PS sample during aging (Fig. 6) as well as SIMS during desorption in vacuum. The FTIR-spectra of as-prepared samples exhibit a number of features that can be assigned to Si–H_2 and Si–O–Si bonds. It is seen that after 3 days storing in air the Si–H_2 band intensity decreases slightly probably due to H desorption and the Si–O–Si one rises due to oxidation. As SIMS measurements show the desorption takes place during 2 h. The majority of desorbing ions were H, OH and H_2O.

It thus appears that the surface channel of the PL excitation may be connected with H, OH or water molecules. The next facts allow to prefer OH groups or water molecules: (i) the small value (~0.5 eV) [9] of activation energy for decreasing of PL intensity during desorption is of the same order as the activation energy of H_2O molecules desorption from silicon oxide surface; (ii) consequent aqueous vapor treatment leads to the restoration of the PL [10]. Based on these results we can suggest that the long-wavelength part of PL band is not caused by emission from nanocrystallites, but rather by some surface emitting centers. As to water, it is known that water molecules do not have a light absorption band in the visible range (350–500 nm). However, water molecule

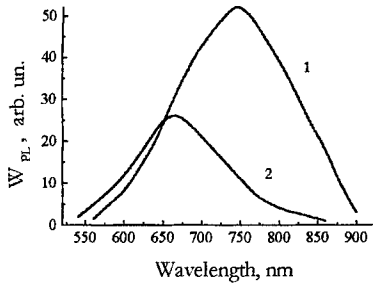

Fig. 5. PL spectra of as-prepared (curve 1) and after keeping in a NaCl solution (curve 2) of the PS samples.

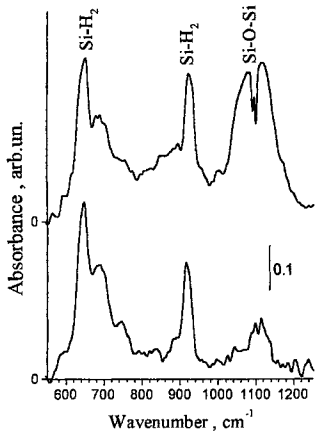

Fig. 6. FTIR spectra of as-prepared PS sample (curve 1) and after aging at 300 K for 3 days (curve 2).

complexes containing some impurities (Li, Na, K, H, CH_3 and, possibly, F and B) exhibit photoluminescence in this wavelength range [11]. This may suggest that the visible PL excitation involves water complexes with impurities.

Acknowledgements

This work was supported by the Ministry of Science and Technology of Ukraine and the Ministry of Science of Israel (grant 2M/1406) and CONACYT Mexico.

References

[1] A.G. Gullis, L.T. Canham, P.D.J. Calcott, Appl. Phys. Rev., J. Appl. Phys. 82 (3) (1997) 909.
[2] Y. Kanemitsu, T. Matsumoto, T. Futagi, H. Mimura, Jpn. J. Appl. Phys. 32 (1993) 411.

[3] J.M. Lavine, S.P. Sawan, Y.T. Shieh, A.J. Bellezza, Appl. Phys. Lett. 62 (1993) 1099.
[4] H.D. Fuchs, M. Stutzmann, M.S. Brandt, M. Rosenbauer, J. Weber, A. Breischwerdt, P. Deak, M. Cardona, Phys. Rev. B 48 (1993) 8172.
[5] S.M. Prokes, O.J. Glembocli, V.M. Berdudez, R. Kaplan, Phys. Rev. B 45 (1992) 13788.
[6] M.S. Brandt, H.D. Fuhs, M. Stutzmann, J. Weber, M. Cardona, Solid State Commun. 81 (1992) 307.
[7] H. Aoyagi, A. Motohashi, A. Kinoshita, T. Aono, A. Satou, Jpn. J. Appl. Phys. Part 2 32 (1A/B) (1993) L1.
[8] L. Wang, M.T. Wilson, N.M. Haegel, Appl. Phys. Lett. 62 (1993) 1113.
[9] T.V. Torchinskaya, N.E. Korsunskaya, L.Yu. Khomenkova, B.R. Dzhumaev, N.P. Baran, B.M. Bulakh, G. Polisskii, Ukr. J. Phys. 44 (N 3) (1999) 394.
[10] M.S. Brodin, V.N. Bykov, D.B. Dan'ko, A.A. Kipen, Ukr. Fiz. Zhurn. 40 (9) (1995) 933.
[11] G.I. Denisenko, Synthesis and properties of modifying zeolites, Author's Doctor Degree thesis, Institute of Physical Chemistry, Kyiv, Ukraine, 1995.

ELSEVIER

Physica B 273–274 (1999) 959–962

PHYSICA B

www.elsevier.com/locate/physb

Hole and electron traps in the InGaAs/GaAs heterostructures with quantum dots

M.M. Sobolev*, I.V. Kochnev, V.M. Lantratov, N.A. Cherkashin, V.V. Emtsev

A.F. Ioffe Physical Technical Institute, 26 Polytechnicheskaya ul., 194021 St. Petersburg, Russia

Abstract

Hole and electron traps at a p–n heterostructure with InGaAs/GaAs quantum dots (QD) grown by metal organic chemical vapor deposition (MOCVD) are investigated by capacitance–voltage (C–V) and deep level transient spectroscopy (DLTS). The C–V and DLTS measurements allowed to detect that the region of the accumulation of the electron concentration is characterized by the presence of hole and electron traps. We have observed by means of deep level defects, the population of the energy states of InGaAs quantum dots as a function of temperature of isochronous annealing as well as under bias-on–bias-off cooling conditions and white light illumination.

Keywords: Gallium arsenide; Quantum dot; Heterostructures

1. Introduction

Controlled tuning of height of electronic barriers [1] and population of quantum states [2,3] becomes an essential element in semiconductor technology. Capasso has proposed [1] the idea of change of height of band discontinuity at the heterointerface with the help of built-in potential of the doping interface dipole, created by placing equal numbers of donor and acceptor impurities on the two sides of the interface. It has recently been reported that the dipole formation occurs and in InAs/GaAs heterostructures with quantum dots (QD), produced by a method of a self-organized growth, when density of defects close with QD is comparable to density of dots [4,5]. There have also been some studies on controllable and reversible metastable population of the energy states of QD as a function of temperature of isochronous annealing as well as under bias-on–bias-off cooling conditions and light illumination [3,4]. It would be expected that effect of the controllable population of the energy states of QD occurs in structures containing the electron and hole traps with a concentration comparable to the carrier concentration in GaAs matrix, which embeds the QDs. In this case the optical and electrical recharge of deep levels will control the position of the Fermi level and the population of the energy states of QD. In this paper, effects of the population control of the energy states of InGaAs/GaAs quantum dots from defects with deep levels, and Coulomb interaction between carriers localized in QDs and ionized deep level defects are studied by C–V and DLTS methods.

2. Results and discussion

The structures under investigation were grown by MOCVD using an equipment with a horizontal, resistively, heated reactor at low pressure (76 Torr). The growth temperature was 480°C. After deposition on n^+-GaAs substrate of 0.5-μm-thick GaAs buffer undoped layer ($n = 3 \times 10^{15}\,cm^{-3}$) QD layer of InGaAs was deposited. Thereafter 1.0-μm-thick n-GaAs undoped layer and the top layer 0.3-μm-thick p-GaAs were grown. DLTS and C–V investigations were carried out by using a BIO-RAD DL4600 spectrometer. Prior to each C–V

* Corresponding author.
E-mail address: m.sobolev@pop.ioffe.rssi.ru (M.M. Sobolev)

0921-4526/99/$ - see front matter
PII: S0921-4526(99)00577-3

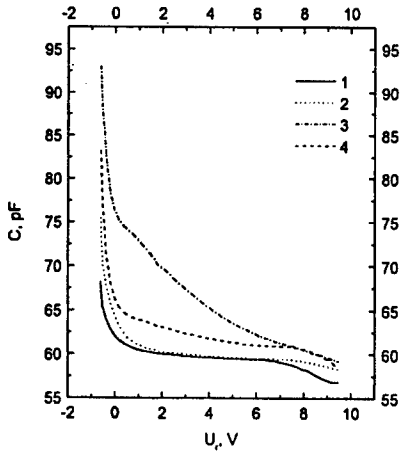

Fig. 1. C–V characteristic of the p–n heterostructure with InGaAs/GaAs quantum dots measured after previous isochronous annealing at $T_a = 450\,K$ and cooling down to $T = 80\,K$ wihtout illumination by white light and under: (1) applied reverse bias $U_{ra} < 0$, (2) zero bias $U_{ra} = 0$, and under illumination by white light: (3) $-U_{ra} < 0$, and cooling down to $T = 240\,K$ under (4) $U_{ra} < 0$.

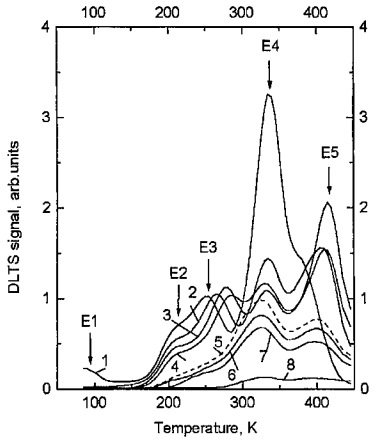

Fig. 2. DLTS spectra of the p–n heterostructure with InGaAs/GaAs quantum dots measured under various reverse bias U_r and filling pulse bias U_p, and a constant biad difference $\Delta U = (U_r - U_p) = 0.5\,V$ (U_r, V: (1) 0.5, (2) 1.0, (3) 1.5, (4) 2.0, (5) 3.5, (6) 4.0, (7) 4.5, (8) 8.0). All the spectra were taken for the rate window of 200 s^{-1} and the filling pulse duration was 5 ms.

and DLTS measurement the sample was subjected to isochronous annealing for 1 min at a fixed temperature under either of the three conditions: (i) reverse bias $U_{ra} < 0$, (ii) zero bias ($U_{ra} = 0$) and applied forward bias ($U_{fa} > 0$). The annealing temperature was varied in the 80–450 K range. After this was cooled down to $T = 80\,K$, the thermal activation energy E_a associated with the carrier emission from traps and their capture cross sections $\sigma_{p,n}$ were determined from Arrhenius plots. The results obtained by transmission electron microscopy (TEM) reveals that in the InGaAs/GaAs p–n heterostructure the formation of three-dimensional islands with misfit dislocation occurs. Fig. 1 shows the C–V characteristics of p–n InGaAs/GaAs structures measured at various temperatures and depending on conditions of isochronous annealing ($U_{ra} = 0$ and $U_{ra} < 0$) at light illumination.

The observed behavior of the C–V characteristics (extended plateau at low temperatures, as well as rise in capacitance in the region of the plateau at increasing of the temperatures and under white light illumination) reveals, that in this structure there are spatially localized states as well as electron and hole traps, on which accumulation of electrons occur. Moreover, concentrations of the traps in the GaAs layer are comparable to the concentration of shallow donors (N_d), and concentration of the hole traps (N_{ta}) exceeded that of the electron traps (N_{td}). When the measurement temperature is decreasing the rate of the electron emission from near-mid-gap traps is extremely small and the observed plateau of the C–V characteristics is defined by QD states. Width of this plateau depends on the population QD states at given temperatures. When the temperature rises the rate of the electron emission from deep levels is incresed and it becomes comparable to the emission rate from the QDs. This results in a substantial rise in the capacitance and in a deviation of the plateau from horizontal (Fig. 1). In the GaAs matrix the electron concentrations $n^*(x)$ was increased from 2×10^{15} at 77 K up to $3.4 \times 10^{16}\,cm^{-3}$ at 300 K. The subsequent measurements were performed varying the filling pulse bias U_p and detection reverse bias U_r and under the constant bias difference $\Delta U = (U_r - U_f) = 0.5\,V$ to determine the spatial localization of DLTS signals. The DLTS spectra (Fig. 2) were characterized with the presence of five peaks connected to emission of the electrons from traps.

Nothing unusual was observed in the behavior of the ED4 and ED5 peaks that obviously belong to well-known defects GaAs: E4 [7] and EL2 [6]. The maximal concentration of the ED4, ED5 and ED3 electron traps adjacent to QDs varies between 1.2 and $2.2 \times 10^{15}\,cm^{-3}$. In order to study hole traps we carried out the measurement of the DLTS spectrum at the various filling pulse bias U_p applied to a forward bias. We observed four hole traps (Fig. 3) three from which HD2, HD3 and HD4 are identified with well-known defects: HL3 [8], HS2 [8] and H5 [9].

The concentration hole traps were, approximately, ten times more, than electron traps. DLTS measurements demonstrate that the amplitudes of the ED1, ED2 ED3 peaks depend on temperature and conditions of the previous annealing ($U_{fa} > 0$, $U_{ra} < 0$, and $U_{ra} = 0$), cooling

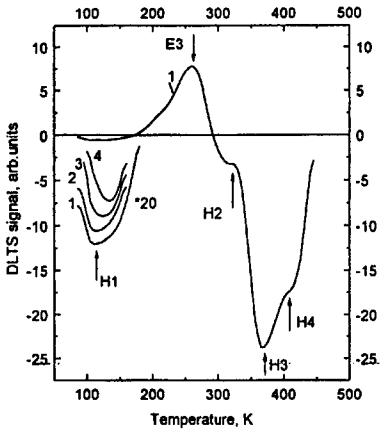

Fig. 3. DLTS spectra measured under U_r, V: (1) -2.5, (2 3 and 4) -2.0, and filling pulse bias applied to forward bias U_p, V: (1, 3) -1.84, (2) -1.4 and (4) -4.65.

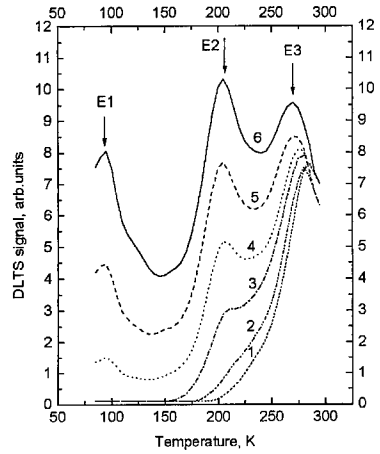

Fig. 4. DLTS spectra measured under $U_r = -1.5$ V and $U_p = -1.0$ V after previous isochronous annealing at $T_a = 450$ K and cooling down to 80 K without light illumination and under: (1) $U_{ra} = 0$, (2) $U_{ra} < 0$, (3) $U_{fa} = 1.9$ V, and at light illumination at different intensity of light I_n under $U_{ra} < 0$: (4) I_4, (5) I_5, (6) I_6 ($I_4 < I_5 < I_6$).

and optical illumination during measuring the DLTS spectra (Fig. 4). The parameters of the ED1 level are $E_a = 165$ meV, and $\sigma_n = 6.5 \times 10^{-14}$ cm^2, and that of the ED2 level are varied in the ranges of $E_a = 287$–252 meV, and $\sigma_n = 1.1$–0.24×10^{-16} m^2. The ED1 and ED2 peaks practically disappeared after annealing at $U_{ra} = 0$. The peak ED2 was designated after annealing at $U_{ra} < 0$. After annealing at $U_{fa} > 0$ amplitudes of the peak ED2 were increased and there appeared the ED1 peak. They became even more significant, when the measurements of DLTS spectra were carried out at illumination by white light. The amplitudes of both peaks rise with increasing a intensity of light. Simultaneously, we observed the change of the capacitance of the sample (Fig. 1). Earlier we established [3,4], that for the spatially localized states the amplitude of a DLTS signal ΔC depends on the change of the Fermi level position and populations of spatially localized states, and is defined by the relation $\Delta C/C \approx n_d L$, where n_d is the electron density trapped in the spatially localized quantum state, L is the distance between the dot plane and p–n junction. The dependence is the distinctive characteristic for the spatially localized state. The obsevable variation of the amplitudes of the ED1 and ED2 peaks depending on the conditions of the previous annealing and the optical illumination are connected with recharge of the electron and hole traps in the GaAs. From the above results, it follows that ED1 and ED2 peaks can be identified as spatially localized states. The region of the spatially localization ED1 and ED2 states coincides with the peak of the electron accumulation and position of the QDs determined from the TEM data. The HD1 and ED3 levels also revealed characteristic attributes of the spatially localized states, as well as they show a shift in the position of the DLTS peak maximum when V_r and U_p are varying (Figs. 2–4). Earlier [3,4] we have already observed similar dependencies for quantum and heterointerface state. The parameters of the ED3 level are changed in the ranges of $E_a = 347$–530 meV and $\sigma_n = 0.019$–3.4×10^{-14} cm^2. There is good reason to think that it represents the heterointerface state of the InGaAs/GaAs and coincide with the parameters of the EL3 [6]. The reasons for the observed change of activation energy can be attributed to the Coulomb interaction of carriers localized in the quantum well of the wetting layer with ionized interface defect. The built-in field of the dipole will be in opposition to a field of p–n junction, reducing an effective electrostatic field. The parameters of the HD1 level are varied in the ranges of $E_a = 126$–199 meV, and $\sigma_p = 0.16$–4.7×10^{-16} cm^2. The hole localized in the HD1 level, appear to be connected with the hole state of the InGaAs QD, is also formed from the electrostatic dipole with the deep acceptor-like levels of the GaAs. The electrostatic field of this dipole will be directed along the field of p–n junction. All changes of activation energy for the hole emission from HD1 state will be opposite to that observed for the ED3 level. Thus, we have established that the hole and electron traps are formed in a p–n heterostructure with InGaAs/GaAs quantum dots grown by MOCVD. The electron concentration in InGaAs/GaAs layer was comparable to the concentration of the electron traps, whereas that of the hole traps exceeded it. It is revealed that the filling of the ED1 and ED2 electron states of the QD and EL3 defect, localized in the InGaAs/GaAs heterointerface, is controlled by recharge electron and hole traps by isochronous annealing ($V_{ra} = 0$, $V_{ra} < 0$ and $V_{fa} > 0$) and white light. The behavior of the hole state of the QD in the structure at

isochronous annealing is defined by the formation of the electrostatic dipole and effect of the Coulomb interaction of carriers localized in the QD with ionized deep-level defects located close to QD.

Acknowledgements

The research was supported by Russian Ministry of Science under grants: Physics of Nanostructures No. 99-1115.

References

[1] F. Capasso et al., Appl. Phys. Lett. 46 (1985) 664.
[2] M.M. Sobolev et al., Semiconductors 33 (1999) 157.
[3] M.M. Sobolev et al., J. Electron. Mater. 28 (1999).
[4] M.M. Sobolev et al., Mater. Sci. Forum. 258–263 (1997) 1619.
[5] M.M. Sobolev et al., Semiconductors 31 (1997) 1074.
[6] G.M. Martin et al., Electron. Lett. 13 (1977) 191.
[7] D. Pons et al., J. Appl. Phys. 51 (1980) 2038.
[8] A. Mitonneau et al., Electron. Lett. 13 (1977) 666.
[9] D. Stievenard et al., J. Appl. Phys. 59 (1986) 743.

ELSEVIER

Physica B 273–274 (1999) 963–966

PHYSICA B

www.elsevier.com/locate/physb

Defect-limited carrier diffusion in $In_{0.53}Ga_{0.47}As$-InP single quantum well

A.F.G. Monte[a], S.W. da Silva[a], J.M.R. Cruz[a], P.C. Morais[a,*], H.M. Cox[b]

[a]*Universidade de Brasília, Instituto de Física, Núcleo de Física Aplicada, Campus Universitario, 70910-900, Brasília-DF, Brazil*
[b]*Lucent Technologies, Murray Hill, New Jersey 07974, USA*

Abstract

The diffusion of electron–hole plasma in an intrinsic $In_{0.53}Ga_{0.47}As$ single quantum well (SQW) was investigated by measurements of the PL intensity profile around the illuminated area. We found that the carrier diffusion length increases with the temperature, from 85 to 300 K, according to a defect-limited carrier diffusion. A change in the carrier expansion is observed at about 200 K, which appears to be correlated with the thermal activation of a defect center with activation energy of 120 meV. An Arrhenius function of the PL emission intensity confirms that a nonradiative recombination channel becomes visible with an energy of about 120 meV.

Keywords: Photoluminescence; Quantum wells; Defects

1. Introduction

Photocarrier transport properties in two-dimensional heterostructures have a great deal of interest, for they play a central role in the design and operation of photovoltaic devices. Lateral transport of electron–hole plasma in these structures is still a rather complex problem, since strong variations of the carrier density and strong temperature gradients must be placed together to render quantitative results [1]. This problem has been extensively studied in GaAs/AlGaAs systems [1–3], and experimental techniques, which incorporate spatial resolution capabilities, have been developed to investigate the physical processes of light emission and photocarrier dynamics in quantum wells (QW's). Cathodoluminescence (CL) [4,5] and optical beam-induced current (OBIC) [6] have been currently used to measure the carrier diffusion length. With a different configuration we have used the micro-luminescence surface scan technique (MSST) [7,8] to study the photocarrier transport mechanism in $In_{0.53}Ga_{0.47}As$ epilayers. In this technique, a tightly focused laser beam is used to excite the sample, and the lateral spread of electron–hole pairs is observed by scanning the microluminescence image at the system's image plane. The luminescent region was observed to broaden as a result of carrier diffusive processes, and to attenuate as a result of recombination processes. However, the temperature-dependent measurements indicate that charge traps may play a prominent role in the diffusion of the carriers. The investigation of the carrier trapping processes may be of use in the analysis of transport in QW heterostructures. A significant residual photoconductivity has been observed in low-temperature-grown InGaAs epilayers [9]. This residual conductivity may have significant consequences for device performance. Dislocations and interface defects may act as traps, and when this occurs the carrier diffusion length can be limited by nonradiative recombination at these traps [10,11]. In the present work, we have measured the temperature and excitation dependence of the photoluminescence (PL) signal and its spatial distribution. The results are consistent with a thermally activated diffusion process, where trapping and detrapping as well as radiative recombination play a significant role.

* Corresponding author. Tel.: + 55-61-2736655; fax: + 55-61-2723151.
E-mail address: pcmor@fis.unb.br (P.C. Morais)

0921-4526/99/$ - see front matter
PII: S0921-4526(99)00583-9

2. Experiment

The lattice-matched InGaAs-InP single QW used in this study was grown by vapor levitation epitaxy (VLE) [12]. The nominally undoped sample consists of a 0.6 μm InP buffer layer epitaxially grown on top of an InP substrate, followed by a 110 Å thick InGaAs layer and covered with a 600 Å InP cap-layer. The sample was mounted in a temperature-controlled optical cryostat and was optically excited using an Ar^+-ion laser tuned at 514 nm, which provided energy excitation above the InP band gap. The laser beam was focused down to a spot of 4 μm in diameter, thus allowing lateral PL measurements with very good resolution. Photoexcitation creates electron–hole pairs, which are quickly captured by the InGaAs single QW. The source of photoluminescence is the E_1–HH_1 transition of the QW. Lateral diffusion is observed by monitoring the luminescence region around the excitation spot. The luminescence is collected from the sample surface, through the cryostat window, and imaged at the plane of a scanning pinhole coupled to a liquid Nitrogen-cooled Germanium detector, as described elsewhere [7]. The laser line and the QW luminescence are separated through bandpass filters. The optical excitation intensity was set at a level strong enough to produce carrier density in the range of $1 - 5 \times 10^{11}\,cm^{-2}$.

3. Results and discussions

A spatial profile of the PL emission intensity (I_{PL}) is plotted in the inset of Fig. 1. The observed PL distribution gives the measurement of the local carrier density (n), considering that I_{PL} is proportional to the square of the density, $I_{PL} \propto n^2$. Beside this, important information can be obtained from the temperature dependence of the carrier expansion. Fig. 1 shows the variation of the carrier diffusion length at different temperatures, the data show a decrease in L with the inverse of temperature. In fact an increase of the carrier diffusion length at higher temperatures suggests that the in-plane carrier diffusion process is not a result of a purely free carrier motion, but it is some sort of thermally activated process. Since photocarriers are mainly confined in the InGaAs layer, carrier transport can be well described by the two-dimensional diffusion equation. In the steady-state regime, we have

$$D\frac{1}{r}\frac{\partial}{\partial r}\left[r\frac{\partial n}{\partial r}\right] = G(r) - \frac{n}{\tau} - Bn^2, \tag{1}$$

where D is the effective carrier diffusion coefficient, τ is the effective carrier lifetime, and B is the bimolecular recombination coefficient. $G(r)$ is the photocarrier generation term provided by a Gaussian-shaped laser spot, depending only upon the optical excitation intensity (I) and the laser spot size (Δ_0). The linear term $-n/\tau$ depends on recombination losses due to material quality factors, such as recombination at dislocations, and impurity sites and surface. As long as both the linear and quadratic terms are kept on the right-hand side of Eq. (1), numerical simulation shows that a Gaussian function represents a good solution for $n(r)$. Carriers are photogenerated in the laser spot with width Δ_0, and can be observed in a region of final width Δ. The carrier diffusion length, $L = \sqrt{D\tau}$, is then obtained from the spatial PL profile and is estimated from $L = (\Delta - \Delta_0)/2$.

Different mechanisms can account for the carrier scattering rate and, consequently, for the carrier diffusion length, including phonon scattering, interface roughness, and surface recombination [1,5,11,13,14]. The increase in the effective diffusion length with increasing temperature is not characteristic of the carrier acoustic-phonon scattering mechanism in two dimensions [15]. The mechanism of surface recombination can be disregarded either, since the sample is protected by a cap-layer. In $In_{0.53}Ga_{0.47}As$ the drift mobility at 77 K is lower than that of GaAs because of the increasing effect of alloy scattering at lower temperature [1]. As the temperature increases from 200 to 300 K, the diffusion length measured along the QW practically doubles (see Fig. 1). The change in the slope of the curve around 200 K suggests that a trap is involved in capturing the electrons, or holes, as the temperature is decreased, and then releasing them as the temperature is increased. The presence of such defects is expected to cause local potential fluctuations which could impede the diffusive transport and cause an increase in the recombination rate. For low carrier densities (far from the excitation spot) the quadratic recombination term is negligible, and we recover the linear equation whose asymptotic solution is exponential. We therefore assume that the decay is most likely due to falling into trap states, i.e., nonradiative recombination. In the laser spot, however, Coulomb interaction between carriers does not allow spatial charge separation, and carrier density reduction is dominated by ambipolar

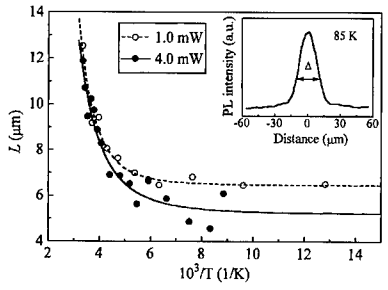

Fig. 1. Temperature dependence of the carrier diffusion length for a 110 Å $In_{0.53}Ga_{0.47}As$ SQW, revealing that carrier diffusion along the QW is thermally activated.

carrier recombination $B(T)np$. One physical mechanism for the trapping of the electrons was developed by Ongstad [16], who assumed that the mechanism of Schockley–Read (SR) is trapping of electrons from the conduction band by empty acceptor ions in the band gap. As the temperature is decreased, the SR recombination rate increases, and the reduction in electron momentum increases the effectiveness of the acceptor ions as traps, consequently reducing the nonradiative lifetime.

One possible explanation for our data is to assume that the diffusion coefficient D is temperature dependent, and has the form $D \sim e^{(-E_a/kT)}$, where k is the Boltzmann constant and E_a is the energy difference between the trap states and the free carrier band [13]. We also put the carrier lifetime in the form $\tau \sim T^m$, so that the diffusion length must be written as $L \sim T^{m/2} e^{(-E_a/2kT)}$. Best fits to the experimental data, present in Fig. 1, give $E_a = 120$ meV, and $m = 1.5$ for $I = 1$ mW and $m = 1.9$ for $I = 4$ mW.

Fig. 2 shows that the diffusion length decreases with increasing excitation laser intensity (I). To discuss the reasons for this intensity dependence, it is more convenient to use the carrier lifetime. The bimolecular recombination term renders a density-dependent carrier lifetime which is given by $\tau = 1/Bn$. Since the carrier density is proportional to the excitation intensity, $n \propto I$, the diffusion length reads

$$L = \sqrt{\frac{D}{B(T)I_0 I}}. \tag{2}$$

Hence, as we increase the intensity the diffusion length reduces. Saturation behavior occurs when the diffusion length becomes constant, and can be accounted for by the carrier lifetime saturation. The data also show that the diffusion length is higher at 300 K than 85 K, because of the high-temperature dependence of B(T).

In agreement with other reports [17,18], we find a strong thermal quenching of the PL efficiency, again denoting the relevance of the nonradiative losses at high temperature. In Fig. 3 the temperature dependence of the PL emission intensity (I_{PL}) is otherwise showing the strong influence of thermally activated nonradiative recombination. The origin of nonradiative recombination can be inferred from the activation energy of the nonradiative channel. Usually, the activation energy is evaluated from the slope of the Arrhenius plot, $\ln I_{PL} = f(1/T)$. In this model, the competing nonradiative process has an exponential dependence on temperature relative to some activation energy. The value of the activation energy is given by the slope, (E_a/kT), of the exponential quenching curve at the highest temperatures. Although we varied the power by four orders of magnitude, the activation energy did not show any power dependence, its value was about 120 meV. In summary, the PL quenching data are consistent with the value inferred previously from the temperature dependence of the diffusion length.

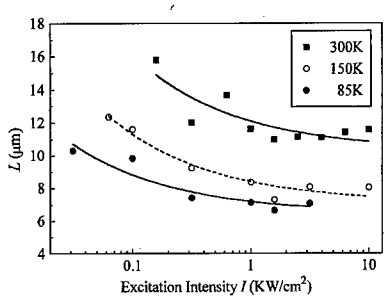

Fig. 2. Diffusion length as a function of the excitation intensity. Lines are only guide for the eyes.

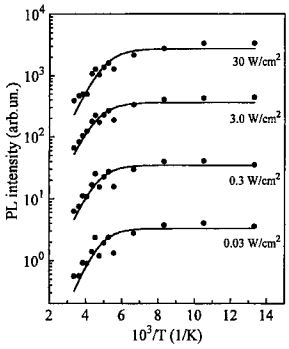

Fig. 3. Photoluminescence emission intensity as a function of the temperature. The fitting curves correspond to the Arrhenius plot and is a measure of the activation energy E_a.

The atomic structure of the trap detected in this work is not known at present. Because of heteroepitaxy, lattice mismatch and difference of thermal expansion coefficient between the substrate InP and $In_{0.53}Ga_{0.47}As$ would affect the mobility and its temperature dependence. The lattice thermal expansion characteristic for the ternary alloy $In_{0.53}Ga_{0.47}As$ is considerably larger than that for InP [19]. So, the nonradiative recombination process might be due to dislocations originating from the substrate and extending into the epitaxial layer. In fact, carrier trapping at the QW interfaces is reported to be the main mechanism reducing the efficiency of the radiative recombination [3,20]. More recently, a deep trap in $In_{0.53}Ga_{0.47}As$ grown by gas source molecular beam epitaxy was observed, although its origin is unknown, and it is not observed on material grown by conventional MBE method [21]. The effect of trapping of the two-dimensional electron gas is not only a property of the dislocations; trapping has also being observed at irradiation-induced defects [22]. It appears that the quality of the interface is a primordial factor for the carrier diffusion. It is also confirmed by Dosluoglu [14], who observed that electrons in InGaAs epilayers grown on semi-insulating InP substrates without any InP buffer layer had a lower mobility than those grown with an

undoped InP buffer layer. Hence, the inferior carrier transport properties are due to an enhanced scattering, most probably caused by a deep-level defect originating from the substrate epilayer interface.

4. Conclusions

In summary, the ambipolar diffusion length of carriers in the $In_{0.53}Ga_{0.47}As$ single QW was determined as a function of both temperature and optical excitation. We found that the carrier diffusion length increases with the temperature. A change in slope is observed at about 200 K, indicating a likely change of the dominant carrier scattering mechanism, and appears to be correlated with the thermal activation of a defect center with an activation energy of about 120 meV. The Arrhenius plot of the photoluminescence intensity confirms that the trap is indeed activated with the previous value of activation energy.

Acknowledgements

The authors would like to thank for financial support from FINATEC, CNPq, FAP-DF (Brazilian Agencies), and TWAS (Italy).

References

[1] H. Hillmer, A. Forchel, T. Kuhn, G. Mahler, H.P. Meier, Phys. Rev. B 43 (1991) 13 992.
[2] M. Gurioli, J. Martinez-Pastor, M. Colocci, C. Deparis, B. Chastaingt, J. Massies, Phys. Rev. B 46 (1992) 6922.
[3] Y.J. Ding, C.L. Guo, S. Li, J.B. Khurgin, K.-K. Law, J.L. Merz, Appl. Phys. Lett. 60 (1992) 154.
[4] H.A. Zarem, P.C. Sercel, J.A. Lebens, L.E. Eng, A. Yariv, K.J. Vahala, Appl. Phys. Lett. 55 (1989) 1647.
[5] Y. Tang, D.H. Rich, A.M. Moy, K.Y. Cheng, Appl. Phys. Lett. 72 (1998) 55.
[6] M. Gallant, A. Zemel, Appl. Phys. Lett. 52 (1988) 1686.
[7] A.F.G. Monte, J.M.R. Cruz, P.C. Morais, Rev. Sci. Instrum. 68 (1997) 3890.
[8] A.F.G. Monte, J.M.R. Cruz, P.C. Morais, H.M. Cox, Solid State Commun. 109 (1998) 163.
[9] Y. Chen, S.S. Prabhu, S.E. Ralph, D.T. McInturff, Appl. Phys. Lett. 72 (1998) 439.
[10] F. Buchali, R. Behrendt, G. Heymann, Electron. Lett. 27 (1991) 235.
[11] E. Ishimura, T. Kimura, T. Shiba, Y. Mihashi, H. Namizaki, Appl. Phys. Lett. 56 (1989) 644.
[12] H.M. Cox, S.G. Hummel, V.G. Keramidas, J. Cryst. Growth 79 (1986) 900.
[13] J. Qi, W. Angerer, M.S. Yeganeh, A.G. Yodh, W.M. Theis, Phys. Rev. B 51 (1995) 13 533.
[14] T. Dosluoglu, R. Solanki, J. Appl. Phys. 69 (1991) 7327.
[15] D.J. Westland, D. Mihailovic, J.F. Ryan, M.D. Scott, Appl. Phys. Lett. 51 (1987) 590.
[16] A.P. Ongstad, M.L. Tilton, E.J. Bochove, G.C. Dente, J. Appl. Phys. 80 (1996) 2866.
[17] J.D. Lambkin, D.J. Dunstan, K.P. Homewood, L.K. Howard, M.T. Emeny, Appl. Phys. Lett. 57 (1990) 1986.
[18] B. Bacher, H. Schweizer, J. Kovac, A. Forchel, H. Nickel, W. Schlapp, R. Lösch, Phys. Rev. B 43 (1991) 9312.
[19] R. Bisaro, P. Merenda, T.P. Pearsall, Appl. Phys. Lett. 34 (1979) 100.
[20] S. Marcinkevičius, U. Olin, G. Treideris, J. Appl. Phys. 74 (1993) 3587.
[21] Y. Takanashi, N. Kondo, J. Appl. Phys. 85 (1999) 633.
[22] M.O. Manasreh, H.J. von Bardeleben, A.M. Mousalitin, D.R. Khokhlov, J. Appl. Phys. 85 (1999) 630.

ELSEVIER

Physica B 273–274 (1999) 967–970

PHYSICA B

www.elsevier.com/locate/physb

Optical and magnetic properties for erbium-related centres in self-assembly silicon nanostructures

Nikolai T. Bagraev[a,*], Alexei D. Bouravleuv[a], Wolfgang Gehlhoff[b], Leonid E. Klyachkin[a], Anna M. Malyarenko[a], Margarita M. Mezdrogina[a], Alexander Naeser[b], Vladimir V. Romanov[a], Serguei A. Rykov[a]

[a]*Russian Academy of Sciences, A.F. Ioffe Physico-Technical Institute, Polytekhnicheskaya 26, 194021, St. Petersburg, Russia*
[b]*Institut fuer Festkoerperphysik, Technische Universitaet Berlin, D-10623 Berlin, Germany*

Abstract

We present the first findings of a highly efficient Er^{3+}-related electroluminescence $(^4I_{13/2}) \rightarrow (^4I_{15/2})$ from self-assembly silicon nanostructures with sizes varying from 1.0 to 10 nm that are naturally formed as a subsequence of quantum-size n^+–p junctions. The built-in electric field induced by these n^+–p junctions is found to result in the Stark effect that perturbs strong sp–f mixing due to the electron–hole localization on the Er^{3+} ions incorporated into nanostructures. This spatial confinement is shown to cause ultrafast energy transfer to the erbium-related centres which increases with decreasing size of nanostructures thereby enhancing the electroluminescent efficiency.

Keywords: Self-assembly quantum wells; Erbium-related centres; Electroluminescence

1. Introduction

The preparation of erbium-doped semiconductor materials in the nanometer scale is in progress to yield both high-efficiency and high-speed light emitters based on the electroluminescence induced by the Er^{3+} intra-4f-shell transition, $(^4I_{13/2}) \rightarrow (^4I_{15/2})$, near the wavelength equal to 1.54 μm that corresponds to minimal losses in optical fibers. Porous Si [1] and self-assembly quantum dots obtained within the framework of planar silicon technology [2] are of interest for the Er doping to provide a spatial confinement of non-equilibrium electrons and holes near the erbium-related centres in order to enhance the excitation of the Er^{3+} ions. Here we report on highly efficient and fast electroluminescence from quantum-size silicon n^+–p junctions doped with erbium which seems to be caused by strong interaction between the Er^{3+} ion f-electron states and the s–p electronic states of the host nanostructure.

2. Methods

The silicon (1 0 0) wafers of the p-type were doped with erbium in the process of long-time diffusion accompanied by surface injection of vacancies. The working and back sides of the wafers were previously oxidized. Erbium doping was done on the working side of the wafers after covering the oxide overlayer with a mask and subsequently performing the photolithography. Then, short-time phosphorus diffusion was performed at the diffusion temperature of 1100°C from gas phase into the same window on the working side under fine surface injection of self-interstitials which leads to the ultra-shallow n^+–p junctions ($\simeq$10 nm) controlled using the SIMS and STM techniques. The cyclotron resonance (CR) angular dependencies and current–voltage (CV) characteristics which brought about the deflection of the bias voltage

* Corresponding author. Tel.: 007-812-247-9311; fax: 007-812-247-1017.
E-mail address: impurity.dipole@pop.ioffe.rssi.ru (N.T. Bagraev)

0921-4526/99/$ - see front matter
PII: S0921-4526(99)00631-6

from the normal to the n^+–p junction plane show that the n^+-diffusion profiles doped preliminarily with erbium consist of both self-assembly longitudinal and lateral quantum wells (SQW) [2]. By varying the parameters of surface oxide overlayer, it was possible to change the dimensions of the nanostructures occurring near the SQW crossing points in the range from 1.0 to 10 nm. Here, the Er-doped nanostructures studied using the magnetic susceptibility and FIR electroluminescence techniques were shown to exhibit the quantum confinement phenomena in the Er^{3+}-related electroluminescence due to the intra-4f-shell transitions.

3. Results

The erbium-related centres introduced into the silicon wafers in the process of the crystal growth or impurity diffusion have been shown to predominantly represent the trigonal molecular defects, in which the antiferromagnetic erbium pairs are bound by the exchange interaction through the action of valence electrons from three oxygen atoms (Fig. 1) [3]. The temperature and magnetic-field dependencies of the magnetic susceptibility demonstrate that the antiferromagnetic erbium pairs being incorporated into SQW exhibit enhanced Van–Fleck paramagnetism as a result of the interplay between the spin correlations and the electron-vibration interaction (Fig. 2). The Er^{3+} ion f-states that belong to these molecular defects are found to act as efficient luminescent centres owing to strong interaction with s–p states of the host nanostructure (Fig. 3). The electron–hole localization due to such a spatial confinement increases with decreasing size of the nanostructures that leads to high-luminescent efficiency at room temperature without any quenching which is a direct consequence of the enlarged

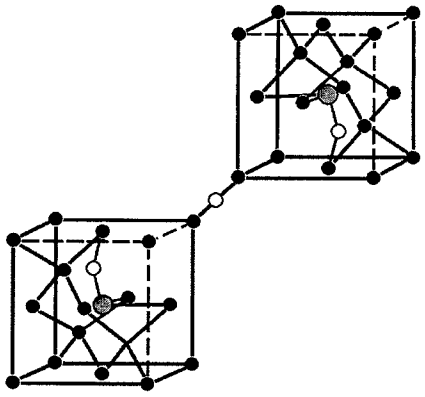

Fig. 1. A complex of two erbium atoms with bridge oxygen in silicon. The erbium atom is denoted by a hatched circle, silicon by black circles, and oxygen by a hollow circle.

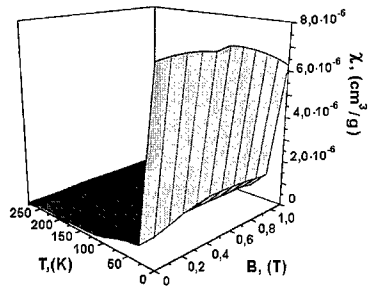

Fig. 2. The temperature–magnetic field diagram of the magnetic susceptibility revealed by studying the ultra-shallow silicon n^+–p junction that contains the self-assembly nanostructures doped with erbium.

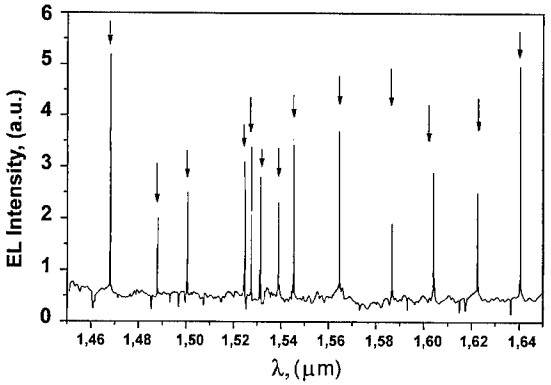

Fig. 3. The EL spectra from the ultra-shallow silicon p^+–n junction that consists of the self-assembly nanostructures containing trigonal erbium-related centres.

nanostructure's bandgap [4]. The maximum effective energy transfer is observed by studying the nanostructures with sizes lower than 2 nm, when the sp-electron bandgap value is found as being equal to 2.6 eV, that allows to determine the Er^{3+} multiplet structure (Fig. 4). The number of observed EL lines corresponds to the trigonal symmetry of the Er-related centre [5] as proposed preliminarly in Ref. [3] (Fig. 1) which is also revealed by the Stark effect induced by the built-in electric field of the quantum-size silicon n^+–p junctions (Figs. 5 and 6). Besides, owing to the quantum-confinement effect on the electron–hole energy spectra in the quantum-size n^+–p junctions, the Er^{3+}-related emission demonstrates an oscillating character as a function of the electric field value (Figs. 5 and 7) that is capable of accounting for, within the framework of the $(^4I_{15/2}) \rightarrow (^4I_{13/2})$, excitation induced by intraband transitions and/or the Auger recombination of non-equilibrium carriers tunnelling across the SQW planes (Fig. 8). The oscillations in the Er^{3+}-related electrolumines-

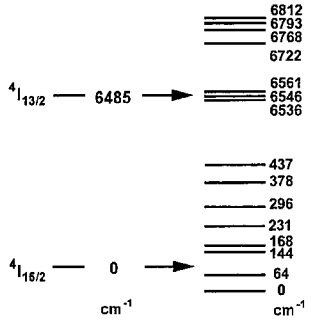

Fig. 4. Energy level diagram for the trigonal erbium-related centres incorporated into the self-assembly silicon nanostructures.

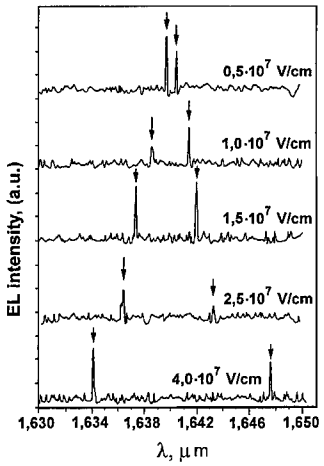

Fig. 5. The EL spectra obtained with increasing current densities through the ultra-shallow silicon n^+–p junction that consists of the self-assembly nanostructures containing trigonal erbium-related centres. The absence of the line's broadering is evidence of homogenius electric field in the dot system.

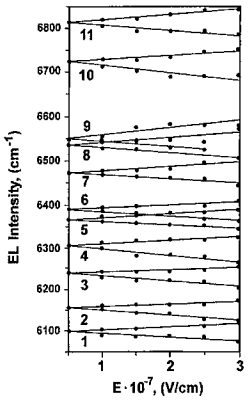

Fig. 6. The energy splitting revealed by EL spectral lines versus electric field applied to the self-assembly silicon nanostructures containing the erbium-related centres exhibiting a trigonal symmetry.

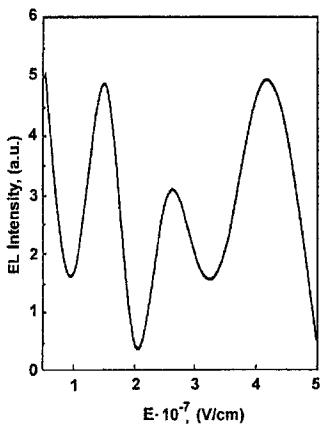

Fig. 7. The EL intensity of the 1639.5 nm spectral line versus electric field applied to the self-assembly nanostructures containing trigonal erbium-related centres.

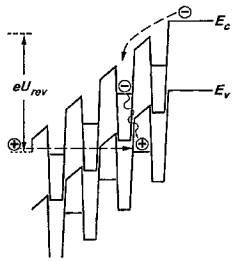

Fig. 8. The energy band diagram of quantum-size silicon n^+–p junctions.

cence are followed by the e–h quantum confinement determined by the dimensions of the silicon nanostructures (Fig. 8). The decay time of the enhanced $(^4I_{13/2}) \rightarrow (^4I_{15/2})$ transition and the energy-transfer time from recombined carriers to the Er-related centres should be decreased because of strong spatial overlap of the s–p states and the localized f-electron states in order to substantiate the high EL efficiency from the nanostructures forming near the SQW crossing points [4]. Ultra-shallow silicon n^+–p junctions that consist of the Er-doped nanostructures with sizes varying from 1 to 2 nm are observed to reveal an electroluminescent decay 6 orders of magnitude faster than the corresponding Er^{3+} transition in the bulk silicon crystals doped with erbium. Finally, the highly efficient electroluminescence found in the Er-doped silicon nanostructures seems to be due to a fast energy transfer into the Er^{3+} ions as well as fast radiative intra-4f-shell transitions induced by strong

sp–f mixing which are caused by the e–h localization at the nanostructures with size lower than 2 nm.

Acknowledgements

This work has been supported by the PhTNS, PTDNE and "Integratsiya" programma (Grants 97-1040; 02.04.301.89.5.2; 75:2.1.

References

[1] M. Stepikhova, W. Jantsch et al., Mater. Sci. Forum 258–263 (1997) 1533.
[2] N.T. Bagraev et al., Solid State Electron. 34 (1991) 1149.
[3] N.T. Bagraev et al., Semiconductors 30 (1996) 967.
[4] R.N. Bhargava et al., Phys. Rev. Lett. 72 (1994) 416.
[5] V.T. Gabrielyan et al., Phys. Stat. Sol. A 3 (1970) K37.

ELSEVIER

Physica B 273–274 (1999) 971–975

PHYSICA B

www.elsevier.com/locate/physb

Non-exponential capture of electrons in GaAs with embedded InAs quantum dots

C. Walther, J. Bollmann, H. Kissel, H. Kirmse, W. Neumann, W.T. Masselink*

Department of Physics, Humboldt-Universität zu Berlin, Invalidenstrasse 110, D-10115 Berlin, Germany

Abstract

InAs quantum dots grown in a GaAs matrix are investigated using capacitance transient spectroscopy and transmission electron microscopy (TEM). Trap states are measured which are associated with the presence of the quantum dots but are too deep to be interpreted as the intrinsic electronic levels of the quantum dots. TEM allows us to rule out traps caused by threading dislocations in the GaAs matrix. The trap occupation measured from capture data is a highly non-exponential function of the filling pulse duration and, together with double DLTS measurements, indicate that the traps are electrically coupled in two dimensions and located in the plane of the dots. We propose that the measured deep levels are due to point defects in or near the quantum dots.

Keywords: InAs quantum dots; DLTS

1. Introduction

Reduced dimensional semiconductor heterostructures such as quantum wells and quantum dots may be expected to be viewed as spatially extended electron traps and to be characterized using transient capacitive measurements such as deep level transient spectroscopy (DLTS). In the case of quantum wells, early DLTS investigations had difficulty measuring the quantum well depth [1], more recent studies have been able to accurately determine the conduction band offset, ΔE_c, using this technique [2–4]. Quantum dots are quasi-zero-dimensional structures and should behave more like conventional point defects than do quantum wells. Some results have been presented which appear to directly measure the energy difference between the matrix conduction band edge and the minimum electronic energy inside the dot [5–7]. Other studies have not presented such a straightforward picture [8,9].

This paper presents DLTS data analyzing trap levels in or near InAs quantum dots in a GaAs matrix. The thermal activation energy appears too deep to be explained as the quantum-confined electronic ground state within the dot. Additionally, the measured density is an order of magnitude lower than the dot density. Detailed line shape analysis of the non-exponential capture behavior indicate that the trap level is due to defects coupled in two dimensions, and in contrast to the one-dimensional coupling characteristic of dislocated material. We explain this behavior as being due to the Coulomb interaction of filled traps in the plane containing the quantum dots; to our knowledge, such a two-dimensional Coulomb coupling has not been previously reported. Furthermore, neither propagating dislocations nor in-plane dislocations could be detected by high-resolution transmission electron microscopy (TEM). It thus appears that the measured traps are point defects inside or very near the dots.

2. Growth and structural characterization

The structures investigated here consist of 1, 3, or 7 layers of InAs quantum dots embedded in a matrix of n-doped GaAs, vertically correlated in the cases of 3 and

* Corresponding author. Tel.: + 49-30-2093-7650; fax: + 49-30-2093-7659.

E-mail address: massel@physik.hu-berlin.de (W.T. Masselink)

0921-4526/99/$ - see front matter
PII: S0921-4526(99)00604-3

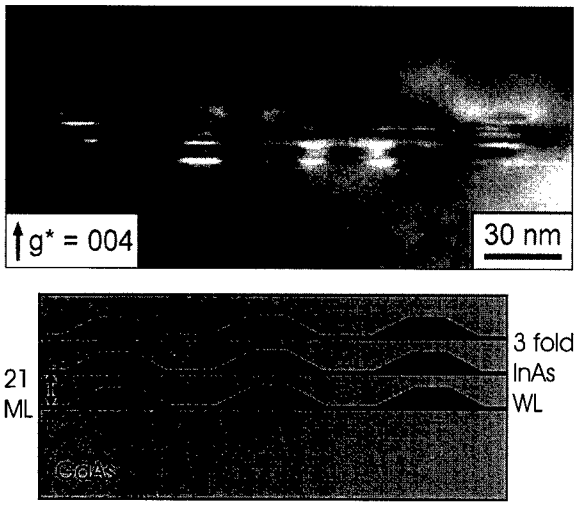

Fig. 1. Typical cross-section weak beam TEM image taken along [110] azimuth of a 3 layer stack of InAs quantum dots in GaAs grown by GSMBE. Below it is a cartoon showing the correlation of the dots in the multiple layers.

7 layers. They were grown by gas-source molecular beam epitaxy (GSMBE) on n-doped GaAs substrates. After a 500 nm n^+ GaAs buffer followed by 60 nm of n^- GaAs ($n = 3 \times 10^{16}$ cm^{-3}) is a 5-nm n^+ GaAs (2×10^{18} cm^{-3}) electron supply layer and 2.5 nm of undoped GaAs. Then the growth temperature was lowered to 500°C and another 10 monolayers (ML) of undoped GaAs were deposited followed by the InAs. The InAs coverage consists of 1, 3, or 7 repeated layers of 1.5–3.0 ML of InAs separated by 21 ML of GaAs. After that sequence the 10 ML and 2.5 nm of undoped GaAs and the 5 nm of n^+ GaAs were repeated, followed by 350 nm of n^- GaAs. We will concentrate on the 3-layer samples with 1.8 ML of InAs coverage per layer because the vertical correlation in the multi-layer samples results in more uniform dot size than in the single-layer samples. Further, the 7-layer samples contained dislocations due to excessive strain.

The samples were structurally characterized using in situ RHEED, double-crystal X-ray diffraction studies, and cross-section TEM. From the RHEED together with previous measurements using atomic force microscopy, we know that in all of the samples investigated, the InAs is contained in a thin wetting layer together with quantum dots. Fig. 1 depicts a 0 0 2 weak beam TEM image of a sample with three quantum dot layers taken using a Hitachi H-8110 200 keV microscope. The lateral extension of the dots is about 15–20 nm and the height is between 3 and 5 nm. The dots in the multiply repeated layers are vertically correlated, an effect which results in a more uniform size distribution [10–12]. The dot density is about 1×10^{10} cm^{-2} per layer. This density is also consistent with measurements of comparable samples using atomic force microscopy. Micro-twins and misfit dislocations were not found by TEM; 90° dislocations arising from Frank partial dislocations [13] were also not observed. Based on the area sampled, the density of threading dislocations is definitely $< 10^6$ cm^{-2} and the density of 90° dislocations definitely $< 10^3$ cm^{-1}. Similar samples with 7 layers of dots contained threading misfit dislocations which were clearly identified by TEM. X-ray analysis of the samples also shows that while the single layers and 3-layer samples appear to be fully strained, the InAs in the samples with 7 layers is relaxed by approximately 10%.

3. DLTS emission results

The samples have been further processed for electrical measurements by evaporating AuGe back contacts and TiAu Schottky front contacts in a set of circles with sub-millimeter diameter. The resulting Schottky diodes have excellent I–V characteristics with ideality factor of 1.019 and typical reverse saturation current densities of 15 μA/cm^{-2} at 77 K. C–V measurements have been performed using a HP 4285A LCR meter at 1 and 5 MHz and show three well-resolved free electron peaks at 77 K. These peaks correspond to the two n^+ GaAs electron supply layers, each with free electron concentration $n = 4.5 \times 10^{11}$ cm^{-2}, and a two-dimensional electron gas confined to the potential well associated with the In-containing region with $n = 5.5 \times 10^{11}$ cm^{-2}.

The DLTS measurements were carried out using a special DLTS system based on a fast capacitance meter with a signal frequency of 5 MHz and a modified lock-in filtering method. The emission rates detectable are within the range 10^{-1}–10^5 s^{-1}. Filling pulse durations as short as 10 ns are possible. The emission rate of electrons may be expressed as

$$e_n = \sigma_{na} \langle v_n(T) \rangle N_c(T) \exp(-E_{na}/k_B T), \quad (1)$$

where σ_{na} is the apparent trap cross section for electrons, $\langle v_n(T) \rangle$ and $N_c(T)$ are the electron thermal velocity and the effective density of states of the conduction band, and E_{na} is the activation energy of the thermal emission rate. Fig. 2 shows the reciprocal emission rates for the two detected peaks in a sample with 3 layers of InAs as a function of temperature and the raw DLTS signal in the insert. To extract E_{na}, the temperature dependence of the pre-factor $\sigma_{na} \langle v_n(T) \rangle N_c(T)$ is taken as T^2. The resulting activation energies E_{na} are found to be 400 and 322 meV and the values σ_{na} 3.2 and 10.7 $\times 10^{-15}$ cm^2 for the levels A and B, respectively. Similar results are found for the single layer sample with 2.4 ML InAs coverage. No DLTS signal was detected in samples with smaller InAs coverage (including no InAs at all) or heavy n-doping in the dots.

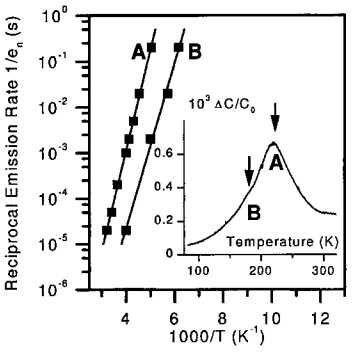

Fig. 2. Arrhenius plots of the two deep levels present in a sample with 3-layers of correlated InAs dots. In the inset the DLTS spectrum for a rate window of 20 ms is given.

We also used the double DLTS [15] technique to profile the position of the deep levels. The signal arises from the difference of two capacitance transients with different filling pulse heights. We find that the trap-related peak is localized at the InAs-containing layer as are the free electrons measured seen in the C–V profile. The measured concentration of the inhomogeneously distributed deep levels $N_T(x)$ never gets greater than $0.003n$, where n is the free electron concentration. Furthermore, the total trap density is determined to be approximately $4 \times 10^9\,\mathrm{cm}^{-2}$, an order of magnitude smaller than the total dot density. This result suggests that the dots are not acting as traps themselves and that the traps are something other than the electronic subband in the dots. Small peak B is not so well localized and appears to have another physical origin, although its appearance coincides with that of peak A. For the rest of this study, we restrict our comments to the large peak of samples with 3 layers of 1.7 ML InAs shown in Figs. 1 and 2 and a sample with a single layer of 2.4 ML of InAs.

Using Ref. [14] to estimate the band gap of the strained InAs and its conduction and valence band offsets with respect to GaAs, along with an estimate of the subband energies in the quantum dot due to size quantization effects, the energy difference between the conduction band of GaAs and the lowest quantized subband in the InAs quantum dot is estimated as approximately 200 meV. We have measured the low-temperature photoluminescence spectrum from these samples and find two peaks at 1.13 and 1.16 eV with full-width at half-maximum (FWHM) of 29 and 40 meV from the 3-layer sample. This recombination energy is consistent with the band picture described above. The value $E_c - E_T$ of 200 meV is significantly smaller than the activation energy of the thermal emission rate measured using DLTS and further suggests that the measured trap levels are not the electronic levels of the dots.

The activation energy for the thermal emission rate E_{na} is generally larger than $E_t = E_c - E_T$, the optical trapping energy, because of the temperature effects of the change in entropy when the occupation of the trap is changed and due to the temperature dependence of the band gap. This change in entropy ΔS can be obtained from the relationship between the true capture cross section σ_n measured from capture data and the apparent one obtained from the Arrhenius plot, $\Delta S = k_B \ln(\sigma_{na}/\sigma_n)$.

4. Non-exponential capture

We have measured the capture behavior of electrons into the trap states by varying the filling pulse t_p over a wide range. The experiment shows a strong deviation from the exponential capturing behavior characteristic of isolated traps. In Fig. 3, the relative trap occupation $\eta = n_T(t_p)/N_T$ is plotted as a function of the filling pulse duration t_p for a rate window of 2 ms at 245 K; n_T and N_T are the occupied and total areal trap densities, respectively. Isolated trap states result in an exponential behavior given by $\eta = 1 - \exp(t_p/\tau_1)$ [16]; this relationship is represented in Fig. 3 as the dashed line. Because of the large range of filling pulse durations needed to measure η in the entire range of 0–1, we were unable to vary the temperature significantly. The limited data which we do have, however, indicate that the capture cross section is relatively independent of temperature.

Non-exponential trapping behavior is indicative of extended defects [16–18]. When trap states are strongly coupled with their neighbors, a logarithmic behavior typically results in which $\eta \sim \ln(t_p)$ [16]. For Coulomb coupling in d dimensions, a potential caused by neighboring occupied traps hinders electron capture by the

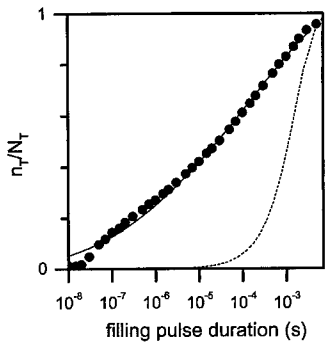

Fig. 3. Measurement of the relative trap occupation η at a rate window of 2 ms and a temperature of 245 K. The dashed line is for isolated traps ($E_1 = 0$) and the full line is a best fit assuming Coulomb coupling in two dimensions with $E_1 = 225$ meV and $\tau_1 = 2.4 \times 10^{-8}$ s in Eq. (3).

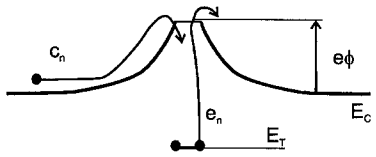

Fig. 4. Cartoon diagram of the potential near the plane of the traps due to the Coulomb field when they are charged.

next unoccupied trap through a potential change given by

$$\phi_1 = \frac{E_1}{e}\left(\frac{n_T}{N_T}\right)^{1/d}, \tag{2}$$

where e is the electronic charge and E_1/e is the potential when all traps are occupied (see Fig. 4). The rate equation for electron capture in the presence of a d-dimensional aggregate of traps is given by [17]

$$\frac{d\eta}{dt_p} = \frac{1-\eta}{\tau_1}\exp\left(\frac{-\eta^{1/d}E_1}{k_B T}\right). \tag{3}$$

We have numerically fit our data to Eq. (3) for $d = 1$, 2, and 3. The best fit for the 3-layer sample has been obtained for $d = 2$, $E_1 = 225$ meV and $\tau_1 = 2.4 \times 10^{-8}$ s. In particular, the $d = 2$ fit and the measured data differ from the previously reported $d = 1$ solution [18] in its second derivative, $d^2\eta/d\ln(t_p)^2$, which over four decades is positive for $d = 2$ (and for our data) but negative for $d = 1$. We interpret the apparent two-dimensionality of the coupling as an indication that the traps are *not* coupled along dislocations (consistent with the TEM results), but are relatively symmetrically coupled in a plane. The measured value of τ_1 for the 3-layer sample gives a true capture cross-section of $\sigma_n = 3 \times 10^{-17}$ cm^2, which in turn implies a change in entropy $\Delta S = 4.6k_B$.

The relationship between the distance separating neighboring traps a_t and the coupling energy E_1 depends critically on the screening, which again depends on the electronic configuration of the traps. Coupling in 1-d has typically resulted from inter-trap spacing a_t of several nm [16,18], while a homogeneous distribution of our 4×10^9 traps/cm^2 implies a much larger spacing. While a different screening could allow a large a_t to result in the measured E_1, it is also possible that the traps are inhomogeneously clustered.

The TEM result that the threading dislocation density is $< 10^6$ cm^{-2} allows us to rule out traps coupled along such dislocations because 4×10^9 traps/cm^2 would require a distance between the traps of only 0.1 Å since the traps are confined to a region < 400 Å thick. On the other hand, if we indeed have the maximum density of 90° or loop dislocations consistent with their not being seen with TEM, we could still have 4×10^9 traps/cm^2 with an inter-trap distance of 2.5 nm. Thus, the trap density together with the TEM data allows us to rule out threading dislocations as the source of the traps, but not in-plane dislocations [13]. To fit the capture data to 1-d coupling, however, requires that $\sigma_n = 1.5 \times 10^{-18}$ cm^2, a value 20 times smaller than fit for 2-d coupling and, we believe, unrealistically small compared to σ_{na}.

5. Conclusions

To conclude, we have characterized deep levels associated with InAs quantum dots in a GaAs matrix. Through C–V and double DLTS, we are able to ascertain that the DLTS signal is located at precisely the depth of the quantum dots. The measured activation energy is 400 meV, significantly deeper than the 200 meV expected energy difference between the ground state of the quantum dot and the GaAs conduction band edge. No other states are measurable in the energy range of 100–700 meV below the GaAs conduction band edge and no signal is measured in samples with a thin 2-d InAs layer, but without dots. Detailed TEM investigations allow us to rule out propagating dislocations or stacking faults in the samples and also give no evidence for in-plane dislocations. The non-exponential capture behavior of the traps is consistent with a coupling in two dimensions, again inconsistent with traps along dislocations, but consistent with traps distributed in the plane of the quantum dots. We propose that these measurements indicate point defects inside (or within a couple of nm of) the quantum dots producing deep levels.

Acknowledgements

The authors like to express their thanks to A. Laws and E. Wiebecke for their technical assistance.

References

[1] P.A. Martin et al., J. Appl. Phys. 54 (1983) 4689.
[2] N. Debbar, P. Bhattacharya, J. Appl. Phys. 62 (1987) 3845.
[3] K.L. Juao, W.A. Anderson, J. Appl. Phys. 73 (1993) 271.
[4] L. Lu et al., J. Appl. Phys. 83 (1998) 2093.
[5] S. Anand et al., Appl. Phys. Lett. 69 (1995) 3016.
[6] S. Anand et al., J. Appl. Phys. 84 (1998) 3747.
[7] C.M.A. Kapteyn et al., in: Proceedings of the 24th International Conference on The Physics of Semiconductors, Jerusalem, 1998.
[8] P. Krispin et al., J. Appl. Phys. 84 (1998) 6135.
[9] F. Chen et al., Phys. Low-Dim. Struct. 11/12 (1997) 179.

[10] Q. Xie et al., Proc. Mat. Res. Soc. 379 (1995) 177.
[11] Q. Xie et al., Phys. Rev. Lett. 75 (1995) 2542.
[12] J. Tersoff et al., Phys. Rev. Lett. 76 (1996) 1675.
[13] Y. Chen et al., Appl. Phys. Lett. 68 (1996) 111.
[14] C.G. Van de Walle, Phys. Rev. B 39 (1989) 1871.
[15] H. Lefévre, M. Schulz, Appl. Phys. 12 (1977) 45.
[16] P. Omling et al., Phys. Rev. B. 32 (1985) 6571.
[17] G. Ferenczi, L. Dosza, Cryst. Res. Technol. 16 (1981) 203.
[18] K. Zdansky, N.T. Thuc Hien, Phys. Stat. Sol. A 85 (1984) 219.

ELSEVIER

Physica B 273–274 (1999) 976–980

PHYSICA B

www.elsevier.com/locate/physb

Overcoming doping bottlenecks in semiconductors and wide-gap materials

S.B. Zhang*, S.-H. Wei, A. Zunger

National Renewable Energy Laboratory, 1617 Cole Building, Golden, CO 80401, USA

Abstract

There often exist strong doping bottlenecks that may severely restrict potential applications of semiconductors, especially in wide-band-gap materials where bipolar doping is impossible. Recent rapid progress in semiconductor research has reached a point where these doping limitations must be overcome in order to tune semiconductors for precisely required properties. Here, we discuss how to find out what causes the doping bottlenecks. We based our discussion on a set of recent, novel developments regarding the doping limitations: the "doping limit rule" distilled from both phenomenological studies and from first-principles calculations. The thermodynamic doping bottlenecks are identified as due mainly to the formation of intrinsic defects whose formation enthalpies depend on the Fermi energy, and always act to negate the effect of doping. © 1999 Elsevier Science B.V. All rights reserved.

Keywords: Doping; Defect compensation; Wide-gap materials; Semiconductors

1. Introduction

Semiconductor-based high-tech owes its existence, in large part, to the fact that semiconductors can be doped. Materials that cannot be doped are useless for most electronic and optoelectronic applications. Indeed, failure-to-dope a class of materials is often the single most important bottleneck for advancing a semiconductor technology based on these materials. Overcoming this bottleneck can enable a whole new technology. Examples of past and present doping roadblocks include (i) p-type doping of wide-gap II–VI compounds for blue lasers, (ii) p-type doping of nitrides, (iii) the elusive n-type doping of diamond, (iv) p-type doping of (transparent conducting) oxides for displays, and (v) doping of alkali halides, wide-gap carbides and fluorides. Case (i) has been recently solved for ZnSe alone [1,2] and case (ii) for GaN alone [3,4]. All other cases remain unsolved.

The vast experimental literature on doping shows that there are three main modes of failure-to-dope:

(i) *Insoluble dopants*: The desired impurity atom cannot be introduced into the appropriate host crystal site because of limited solubility. This includes cases of formation of competing compound phases (e.g., Zn_3N_2 in ZnSe : N [5]), impurity segregation or precipitation (e.g., large impurity atoms such as Ba, Hg in III–V compounds), and substitution on the "wrong site" (e.g., the amphoteric center where the dopant may occupy different sites, thus being either a donor or an acceptor [6]).

(ii) *Deep-level dopants*: The desired dopant *is* soluble in the host, but it produces a deep, rather than shallow level, so the impurity remains un-ionized at normal temperatures. Examples of such "localized centers" include *Cd*S : Cu, *Zn*Se : Cu [7], or Diamond : P [8], in which the impurity substitutes the underlining atoms.

(iii) *Compensated dopants*: The impurity atom is both soluble and ionizable, but as it produces free carriers, a spontaneous-generated, opposite-charged native defect forms, which compensates and negates the effect of the intentional dopant. Examples include the DX center in

* Corresponding author. Tel.: 303-384-6622; fax: 303-384-6531.

E-mail address: szhang@nrel.gov (S.B. Zhang)

PII: S0921-4526(99)00605-5

Si-doped GaAlAs [9,10], and the AX center in N-doped ZnSe [11].

Categories (i) and (ii) of failure-to-dope can sometimes be circumvented by changing the dopant or by co-doping. For example, (i) If Ba is insoluble in III–V compounds, one can attain p-doping by using instead a smaller divalent cation such as Zn. (ii) If Cu creates a deep level in ZnSe, one can use N that forms a shallower level [11]. If P in diamond is too deep, 2P + H can create a shallower center [12]. However, category (iii) of failure-to-dope is terminal, since it is not the chemical impurity that causes the failure-to-dope, but the free carriers. Thus, category (iii) represents the true "doping limit" of a material. For example, no impurity or chemical treatment has so far resulted in any p-doping of main group oxides (e.g., ZnO, CaO, MgO), or n-doping of alkali halides or stable n-doping of diamond. Also, GaAs cannot be doped p-type in excess of 10^{19} cm^{-3} [13] (while it can be doped n-type in excess of 10^{21} cm^{-3} [14]) independent of the impurity and chemical treatment. Thus, there must be a yet unknown intrinsic and fundamental doping-limiting process. We will thus focus our attention on this intrinsic limit.

In olden days, it was believed that such "doping limits" are caused by the very existence of a large band gap [15]. As evidence, it was customary to cite the fact that large gap materials cannot be doped, e.g., GaN, diamond, and oxides. Today, it is clear that this is not the case. We know that some large gap materials can be doped, e.g., n-ZnO [16], n-CdS [17], p-diamond [18] and n-GaN [19]. Surprisingly, however, doping can be strongly asymmetric with respect to holes and electrons. These "doping anomalies" include [20] the facts that (i) ZnO, ZnS, and CdS can be doped only n-type, while ZnTe can be doped only p-type. (ii) $CuAlSe_2$ cannot be doped either p- or n-type, while $CuGaSe_2$ can be doped p-type only, and $CuInSe_2$ can be doped both p- and n-type, and (iii) Si, Ge can be doped both p- and n-type while diamond can be doped only p-type. The existence of such a pronounced asymmetry between n-type and p-type dopability cannot be explained simply by the existence of a large gap. We need another explanation.

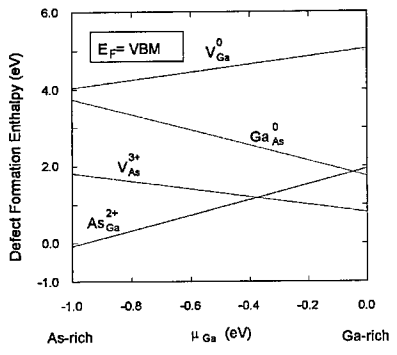

Fig. 1. Calculated point defect formation enthalpy in GaAs as a function of μ_{Ga}.

In the past, each case of failure-to-dope in semiconductors and insulators was treated surprisingly as an isolated issue. Thus, the literature on the failure to p-dope ZnSe is divorced from the literature on the failure to n-dope diamond or from the literature on doping difficulties in nitrides and carbides. It appears that there is a need to study the "science of failure-to-dope" as a generic discipline to frog-leap in this important field because as we will show, there is a common phenomenon that underlies to all of these failures.

2. Thermodynamics of doping

A key realization regarding doping is that the formation enthalpy of a charged defect A in a solid often depends on the atomic chemical potential, μ_A, and always depends on the electron Fermi level, ε_F, as described below. This holds the key to understand, and overcome, doping compensation.

2.1. Dependence of formation enthalpy on chemical potentials

The formation enthalpy of a charge-neutral intrinsic defect A^0 often depends on the atomic chemical potentials of the host atoms. For example, to form a cation vacancy in a binary compound, one cation atom is removed from the host and is placed in the atomic "reservoir" of energy, μ_A. The formation enthalpy is thus

$$\Delta H(A^0) = E_{tot}(A^0) - E_{tot}(0) + \mu_A, \quad (1)$$

where $E_{tot}(A^0)$ is the total energy of the host crystal having a neutral defect A, $E_{tot}(0)$ is the total energy of the host without any defect. Fig. 1 shows [21] a few calculated formation enthalpies of native defects in p-type GaAs as a function of the Ga chemical potential. We see that the Ga-on-As antisite (Ga_{As}) and the As vacancy (V_{As}) are easier to form in Ga-rich conditions, while in As-rich conditions, As-on-Ga antisite (As_{Ga}) and Ga vacancy (V_{Ga}) are instead easier to form. To suppress compensation by intrinsic defect formation, it is always advantageous to prepare materials at the chemical potentials that maximize the formation enthalpy of the specific defect.

2.2. Dependence of defect formation enthalpy on the Fermi level

The formation enthalpy of a neutral defect A^0 does not depend on the Fermi energy, ε_F. However, the formation enthalpy of a charged defect does. For example, the

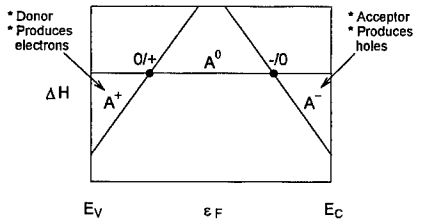

Fig. 2. Schematic change of the defect formation enthalpies (ΔH), as a function of the Fermi energy (ε_F).

formation enthalpy of a positively charged defect A^+ is equal to the energy of a neutral defect A^0, minus the energy $\varepsilon(0/+)$ needed to ionize A^0 to form A^+, plus the energy of the ionized electron. Since this electron resides in the Fermi reservoir, its energy is ε_F:

$$\Delta H(A^+) = \Delta H(A^0) - \varepsilon(0/+) + \varepsilon_F. \quad (2)$$

For a double donor we will have $+2\varepsilon_F$, etc. Thus, as shown in Fig. 2, the higher the Fermi energy, the larger the energy needed to form A^+. So donors (that produce electrons in the reaction $A^0 \rightarrow A^+ + e^-$) are more difficult to form in electron-rich (n-type) materials. Similarly, for acceptors, the formation energy decreases as ε_F increases:

$$\Delta H(A^-) = \Delta H(A^0) + \varepsilon(-/0) - \varepsilon_F. \quad (3)$$

So acceptors (that produce holes in the reaction $A^- + h^+ \rightarrow A^0$) are more difficult to form in hole-rich (p-type) materials.

These simple considerations show that

(a) If we dope a material intentionally n-type via some donor impurity, as ε_F moves up in the gap, the formation energy of native-acceptors $\Delta H(A^-)$ decreases. At some points, the formation energy is so low that such native acceptors (e.g., cation vacancy or DX centers) could form spontaneously, thus negating the effect of the intentionally introduced donors.

(b) If we dope a material intentionally p-type via some acceptor impurity, as ε_F moves down in the gap, the formation energy of native donors $\Delta H(A^+)$ decreases. At some point the formation energy is so low that such native donors (e.g., the AX center) could form spontaneously, thus negating the effects of the intentionally introduced acceptors.

Thus, the spontaneous formation of native defects determines the maximum and minimum pinning energy positions over which the Fermi energy can vary.

3. The phenomenological "doping limit rule"

Based on an earlier "vacuum pinning rule" [22] (that established the universality of the energetic positions of deep, transition-metal-impurity levels in semiconductors), Walukiewicz [23–25] studied the trends in doping limits in many semiconductors. This study and the follow-on studies by Tokumitsu [26], Ferreira et al. [27], and more recently by Zhang et al. [20] established a remarkable "phenomenological doping limit rule". It showed that there are common and surprisingly simple principles that cut across failure to dope in different material classes. Failure-to-dope is not related to the size of the band gap per-se, but rather to the position of the valence band maximum (VBM) with respect to the p-like pinning energy $\varepsilon_{pin}^{(p)}$, and the position of the conduction band minimum (CBM) with respect to the n-like pinning energy $\varepsilon_{pin}^{(n)}$.

From the discussion in Section 2, doping stops when there are too many spontaneously generated defects that compensate the intentional dopants. The net concentration $N^{(n/p)}(T, \varepsilon_F)$ of free carriers (electrons or holes) in a semiconductor is determined, in the single, parabolic band approximation, by the position of the pinning Fermi energy,

$$N^{(n/p)}[T, \varepsilon_F^{(n/p)}] = \frac{1}{2\pi^2}[2m^{*,(n/p)}]^{3/2} \times \int_0^4 \frac{\varepsilon^{1/2} d\varepsilon}{\exp[\beta(\varepsilon - \varepsilon_F^{(n/p)})] + 1}, \quad (4)$$

where $\beta = 1/kT$ is the temperature factor, and m^* is the appropriate effective mass. If we know the measured maximum electron or hole concentration, $N_{max}^{(n/p)}$, we may obtain $\varepsilon_{pin}^{(n)}$ and $\varepsilon_{pin}^{(p)}$ simply by inverting Eq. (4).

Fig. 3 shows the values of $\varepsilon_{pin}^{(n)}$ and $\varepsilon_{pin}^{(p)}$ obtained from measured maximum doping in all the III–V compounds. In this figure, the VBMs were aligned. While the data for $\varepsilon_{pin}^{(p)}$ are scattered within a relatively small range of 0.5 eV, the data for $\varepsilon_{pin}^{(n)}$ are scattered over a wide range of 1.2 eV, showing no emerging trend.

A similar problem of absence of apparent trends in energy levels existed in another field, namely that of

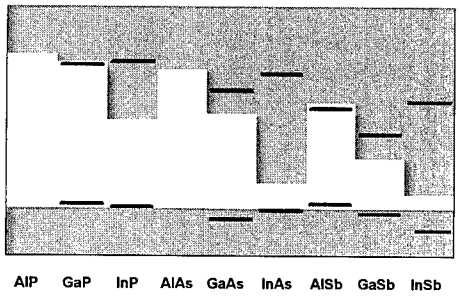

Fig. 3. Calculated pinning energies, by inverting Eq. (4), for conventional III–V compounds. The valence band maxima are lined up in the plot, without any absolute energy scale. Not large scatter near the conduction band.

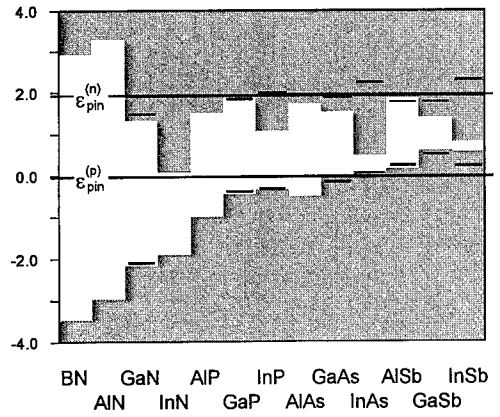

Fig. 4. Phenomenological pinning energies in III–V compounds (solid bars) obtained by inverting Eq. (4). The bands were aligned with calculated valence band offsets on an absolute energy scale. The heavy lines denote the average pinning energies. The energy zero is the VBM of GaAs.

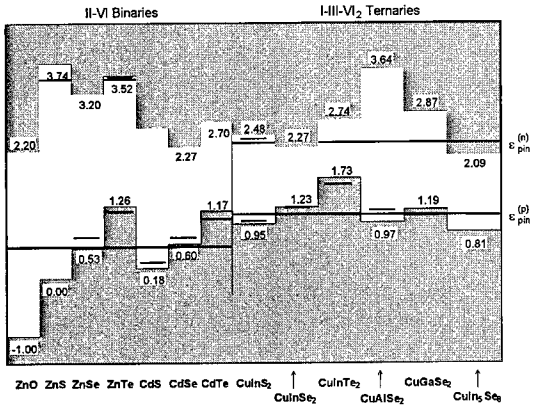

Fig. 5. Phenomenological pinning energies in II–VI and I–III–VI_2 compounds. The legend is the same as in Fig. 4. The energy zero is the VBM of ZnS.

transition metal impurities in semiconductors. However, Caldas et al. [22] showed that if one refers the impurity levels to the vacuum level, the states of a given impurity in different hosts all line up.

Thus, following Walukiewicz [23–25] we will do the same for our calculated p- and n-type Fermi energy pinning levels. However, now we will use modern, calculated values of unstrained band offsets [28] that are believed to have correct chemical trends. This is shown in Fig. 4 for III–V compounds. The scatter in $\varepsilon_{pin}^{(n)}$ is approximately 0.5 eV while the scatter in $\varepsilon_{pin}^{(p)}$ is somewhat larger, most noticeably for p-type GaN. Results for II–VI and I–III–VI_2 ternary compounds are shown in Fig. 5. This newly discovered doping limit rule tells us that when

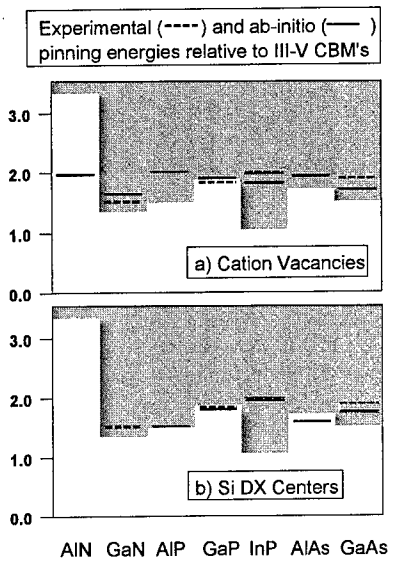

Fig. 6. LDA (solid lines) vs. the experimental (dashed lines) n-type pinning energies in seven III–V compounds. The energy zero is the VBM of GaAs.

referred to an absolute energy scale, all $\varepsilon_{pin}^{(n)}$ and separately all $\varepsilon_{pin}^{(p)}$ tend to align for each class of materials. The emerging "doping limit rule" is:

(a) A material for which $\varepsilon_{pin}^{(n)} \ll \varepsilon_{CBM}$ cannot be doped n-type.

(b) A material for which $\varepsilon_{pin}^{(p)} \gg \varepsilon_{VBM}$ cannot be doped p-type.

This remarkable rule permits one to guess rather accurately if a material can be doped or not merely by positioning its band-edge energies on a diagram such as Figs. 4 and 5. This phenomenological rule explains all the "doping anomalies" noted in Section 1. However, the microscopic origin of this generally successful rule, i.e., the identity of the compensating defects, remains unclear.

4. First-principles study of the n-doping limit in III–V compounds

Our recent first-principles pseudopotential total energy calculations reveal that for n-doping of III–V compounds, the spontaneously-formed acceptor "killer defects" are indeed the microscopic origin of failure-to-dope. These defects are the cation vacancies and the DX centers depending on host materials. For the cation vacancies, the pinning energy $\varepsilon_{pin}^{(n)}$ is defined as the Fermi energy at which the vacancy formation enthalpy is zero,

$$\Delta H(\varepsilon_F = \varepsilon_{pin}^{(n)}) = 0. \quad (5)$$

For the DX centers, $\varepsilon_{pin}^{(n)}$ is defined as the defect transition energy $\varepsilon(+/-)$ at which the donor to acceptor transition takes place,

$$\varepsilon_F = \varepsilon_{pin}^{(n)} = \varepsilon(+/-). \quad (6)$$

Fig. 6 compares the ab initio $\varepsilon_{pin}^{(n)}$ values in seven III–V materials whose band diagram is aligned with ab initio band offsets [28]. The dashed lines give the experimental pinning energies. Fig. 6 shows a clear tendency of line-up of $\varepsilon_{pin}^{(n)}$ with respect to the vacuum level. In the case of the cation vacancy, the scatter among 7 calculated $\varepsilon_{pin}^{(n)}$ is less than 0.4 eV. This scatter would, however, be an order of magnitude larger (3.3 eV), should one line up, as in Fig. 3 the valence band edges without the band offsets.

5. Strategies to suppress the "killer defects"

The understanding in (a) the identity of the "killer defects" and in (b) the microscopic meaning of the phenomenological doping limit rule in a series of key materials enables new ways of overcoming the doping limit. For example, a long-standing problem in the field of oxides is that while they can be made n-type, they cannot be made p-type. It will be a great success to be able to make a "p-type transparent conductor". Doping of carbides and fluorides poses another outstanding milestone challenge — so far, most experimental attempts at doping had failed (except, in part, SiC [29] and CdF_2 [30]) for reasons that remain a rather mysterious puzzle. Success here will open a hitherto unexplored future class of electronic materials and possibly pave the way for new technologies. How could this study lead to new design principles to overcome such doping roadblocks?

(i) Work within the bulk defect thermodynamics. One may design new dopable materials by adjusting the band edges with respect to the pinning energies. Suppose that the pinning energy $\varepsilon_{pin}^{(p)}$ is too high relative to the VBM so the material cannot be made p-type. Since $\varepsilon_{pin}^{(p)}$ is fixed, one may consider increasing ε_{VBM}, as an alternative. Thus, one strategy to suppress the killer defect would be to modify the host material so that its VBM will be higher with respect to the vacuum level (i.e., reduce the work function).

(ii) "Defeat" bulk defect thermodynamics. An example is [31–33] the co-doping of GaN by Mg and H. Mg is a substitutional acceptor while H is an interstitial donor. The two forms a charge neutral defect pair [33], thus the Fermi energy is not moved away from near the midgap during the growth and the formation enthalpy of the killer defect (according to Eq. (1)) remains to be high. After growth, the H atoms can be removed at low-enough temperatures at which no killer defect can form, thus freeing the Mg as acceptors. This may explain the apparent discrepancy of the p-type GaN from the "doping limit rule" in Fig. 4.

Acknowledgements

Supported by the US Department of Energy under contract No. DE-AC36-98-GO10337.

References

[1] R.M. Park, M.B. Troffer, C.M. Rouleau, J.M. DePuydt, M.A. Haase, Appl. Phys. Lett. 57 (1990) 2127.
[2] K. Ohkawa, T. karasawa, T. Mitsuyu, Jpn. J. Appl. Phys. 30 (1991) L152.
[3] S. Nakamura, J. Vac. Sci. Technol. A 13 (1995) 705.
[4] I. Akasaki, S. Sota, H. Sakai, T. Tanaka, M. Koike, H. Amano, Electron Lett. 32 (1996) 1105.
[5] D.B. Laks, C.G. Van de Walle, G.F. Neumark, P.E. Blochl, S.T. Pantelides, Phys. Rev. B 45 (1992) 10965.
[6] J.E. Northrup, S.B. Zhang, Phys. Rev. B 47 (1993) 6791.
[7] A. Zunger, in: H. Ehrenreich, D. Turnbull (Eds.), Solid State Physics, 39, Academic Press, New York, 1986, p. 275.
[8] T. Nishimori, K. Nakano, H. Sakamoto, Y. Takakuwa, S. Kono, Appl. Phys. Lett. 71 (1997) 945.
[9] D.J. Chadi, K.J. Chang, Phys. Rev. Lett. 61 (1988) 873.
[10] S.B. Zhang, D.J. Chadi, Phys. Rev. B 42 (1990) 7174.
[11] C.H. Park, D.J. Chadi, Pyhs. Rev. Lett. 75 (1995) 1134.
[12] H. Katayama-Yoshida et al., Centennial Meeting, Bulletin Am. Phys. Society (1999) 1194.
[13] M.C. Wu, Y.K. Su, K.Y. Cheng, C.Y. Chang, Solid State Electron. 31 (1988) 251.
[14] T. Yamada, E. Tokumitsu, K. Saito, T. Akatsuka, M. Miyauchi, M. Konagai, K. Takahashi, J. Crystal Growth 95 (1989) 145.
[15] J. Van Vechten, in: T.S. Moss (Ed.), Handbook of Semiconductors, Vol. 3, Amsterdam, North-Holland, 1980, p. 3.
[16] H.L. Hartnagel et al., Semiconducting Transparent Thin Films, Inst. Of Physics, Bristol, 1995.
[17] J.L. Boone, G. Cantwell, J. Appl. Phys. 57 (1985) 1171.
[18] T.H. Borst, O. Weis, Phys. Stat. Sol. A 154 (1996) 423.
[19] J. Neugbauer, C.G. Van de Walle, Phys. Rev. B 50 (1994) 8067 and references therein.
[20] S.B. Zhang, S.-H. Wei, A. Zunger, J. Appl. Phys. 83 (1998) 3192.
[21] S.B. Zhang, J.E. Northrup, Phys. Rev. Lett. 67 (1991) 2339.
[22] M. Caldas, A. Fazzio, A. Zunger, Appl. Phys. Lett. 45 (1984) 671.
[23] W. Walukiewicz, J. Vac. Sci. Technol. B 5 (1987) 1062.
[24] W. Walukiewicz, J. Vac. Sci. Tech. B 6 (1988) 1257.
[25] W. Walukiewicz, in: K. Wada, S. Pang (Eds.), Defects in Optoelectronic Materials. C&B Science Publishers, Newark, 1999, and references therein.
[26] E. Tokumitsu, Jpn. J. Appl. Phys. 29 (1990) L698.
[27] S.O. Ferreira, H. Sitter, W. Faschinger, R. Krump, G. Brunthaler, J. Crystal Growth 146 (1995) 418.
[28] S.-H. Wei, A. Zunger, Appl. Phys. Lett. 72 (1998) 2011.
[29] H. Wirth et al., Appl. Phys. Lett. 74 (1999) 979.
[30] R.P. Khosla, Phys. Rev. 183 (1969) 695.
[31] S. Nakamura, N. Iwasa, M. Senoh, T. Mukai, Jpn. J. Appl. Phys. 31 (1992) 1258.
[32] J.A. Van Vechten, J.D. Zook, R.D. Hornig, B. Goldenberg, Jpn. J. Appl. Phys. 31 (1992) 3662.
[33] J. Neugebauer, C.G. Van de Walle, Appl. Phys. Lett. 68 (1996) 1829.

ELSEVIER

Physica B 273–274 (1999) 981–986

PHYSICA B

www.elsevier.com/locate/physb

Diffusion in isotopically controlled semiconductor systems

H. Bracht*

Institut für Metallforschung, University of Münster, Wilhelm-Klemm-Str. 10, D-48149 Münster, Germany

Abstract

Isotopically controlled heterostructures of $^{28}Si/^{nat}Si$ and $Al^{71}GaAs/Al^{69}GaAs/^{71}GaAs$ have been used to study the self-diffusion process in this elemental and compound semiconductor material. The directly measured Si self-diffusion coefficient is compared with the self-interstitial and vacancy contribution to self-diffusion which were deduced from metal diffusion experiments. The remarkable agreement between the Si self-diffusion coefficients and the individual contributions to self-diffusion shows that both self-interstitials and vacancies mediate Si self-diffusion. The Ga self-diffusion in undoped AlGaAs was found to decrease with increasing Al concentration. The activation enthalpy of Ga and Al diffusion in GaAs and of Ga diffusion in AlGaAs all lie in the range of (3.6 ± 0.1) eV, but with different pre-exponential factors. The doping dependence of Ga self-diffusion reveals a retardation (enhancement) of Ga diffusion under p-type (n-type) doping compared to intrinsic conditions. All experimental results on the group-III atom diffusion are accurately described if vacancies on the group-III sublattice are assumed to mediate the Ga self- and Al–Ga interdiffusion in undoped AlGaAs and the Ga self-diffusion in Be- and Si-doped GaAs with an active dopant concentration of 3×10^{18} cm^{-3}. The doping dependence of Ga self-diffusion in GaAs provides strong evidence that neutral, singly and doubly charged Ga vacancies govern the self-diffusion process.

Keywords: Silicon; Aluminum-gallium arsenic; Self-diffusion; Isotope heterostructures

1. Introduction

Self-diffusion studies in solids are of fundamental significance for obtaining information about the properties of native defects in the material under investigation. Self-diffusion with radioactive isotopes has proven to be a powerful technique but it also bears some disadvantages. Radiotracer self-diffusion experiments are often limited with respect to the activity and half-life of the radiotracer and special safety requirements are necessary. Self-diffusion studies in compound materials can be affected by the deposition of the radiotracer through altering the composition near the surface. These disadvantages can be overcome by self-diffusion studies with isotopically controlled materials if at least two stable isotopes of the element of interest exist.

This paper summarizes results of recently performed self-diffusion experiments with $^{28}Si/^{nat}Si$ [1] and $Al^{71}GaAs/Al^{69}GaAs/^{71}GaAs/^{nat}GaAs$ isotope heterostructures [2] and includes new data on the effect of doping on Ga self-diffusion in GaAs. In Section 2.1 directly measured Si self-diffusion coefficients are compared with the self-interstitial and vacancy contribution to Si self-diffusion which were extracted from Zn diffusion profiles in Si. The thermodynamic properties of native defects in Si which are considered to be most reliable are given in Section 2.2.

Results on Ga self- and Al–Ga interdiffusion in undoped AlGaAs/GaAs isotope heterostructures are summarized in Section 3.1. In Section 3.2 new experimental data of the effect of doping on Ga self-diffusion in Si- and Be-doped $^{71}GaAs/^{nat}GaAs$ isotope heterostructures are presented. Neutral, singly and doubly negatively charged Ga vacancies are concluded to mainly determine the self-diffusion under the particular doping levels with relative contributions which change with temperature and doping.

* Tel.: + 49-251-833-9004; fax: + 49-251-833-8346.
E-mail address: bracht@nwz.uni-muenster.de (H. Bracht)

0921-4526/99/$ - see front matter
PII: S0921-4526(99)00606-7

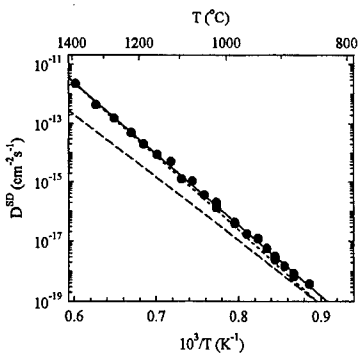

Fig. 1. Temperature dependence of Si self-diffusion coefficients D^{SD} (symbols) [1,5] compared to $0.73C_I^{eq}D_I + 0.5C_V^{eq}D_V$ (solid line). $0.73C_I^{eq}D_I$ (finely dashed line) and $0.5C_V^{eq}D_V$ (dashed line) were deduced from Zn in-diffusion [8] and out-diffusion experiments [10], respectively.

2. Silicon self-diffusion in isotope heterostructures

Earlier self-diffusion experiments which utilize either the short-lived radiotracer ^{31}Si or the stable isotope ^{30}Si in the presence of a high ^{30}Si background were limited to a narrow temperature range [3,4]. Using isotopically enriched ^{28}Si layers grown on natural Si, self-diffusion experiments could be performed over a wide temperature range [1]. After annealing the distribution of ^{30}Si which is diffused from the natural Si into the ^{28}Si layer was followed with the help of secondary ion mass spectrometry (SIMS). Details about the Si isotope heterostructure and the diffusion experiments have already been published [1,5]. The Si self-diffusion coefficients D^{SD} obtained from the analysis of all experimental profiles measured after annealing at temperatures between 855°C and 1388°C are shown in Fig. 1. The temperature dependence of Si self-diffusion is accurately described by an Arrhenius equation with one single activation enthalpy Q = 4.76 eV and a pre-exponential factor $D_o = 560$ cm^2 s^{-1} [1,5].

2.1. Self-interstitial and vacancy contribution

Taking into account all possible contributions to Si self-diffusion, the self-diffusion coefficient is given by

$$D^{SD} = f_I C_I^{eq} D_I + f_V C_V^{eq} D_V + D_{ex}. \quad (1)$$

The first two terms represent the self-interstitial and the vacancy contribution to Si self-diffusion where $C_{I,V}^{eq}$ and $D_{I,V}$ are the equilibrium concentrations in atomic fractions (unitless) and diffusion coefficients of I and V, respectively. $f_{I,V}$ denote the correlation factors for the corresponding diffusion mechanism, which were calculated to be $f_I = 0.73$ [6] and $f_V = 0.5$ [7] for the interstitialcy and vacancy mechanism in the diamond lattice. The last term accounts for a direct exchange between two adjacent lattice atoms or an exchange between lattice sites via a ring mechanism. Eq. (1) shows that self-diffusion experiments cannot determine the relative contribution of each individual self-diffusion mechanism. However, information about the transport coefficients $C_I^{eq}D_I$ and $C_V^{eq}D_V$ can be deduced from Au, Pt, and Zn diffusion profiles in Si whose diffusion behavior is governed by the kick-out and dissociative diffusion mechanisms [3]. Analysis of Zn in-diffusion in Si yielded the following temperature dependence of the transport coefficient of Si self-interstitials [8]

$$C_I^{eq}D_I = 3000 \exp\left(-\frac{4.95\ \text{eV}}{k_B T}\right) \text{cm}^2\ \text{s}^{-1}. \quad (2)$$

In comparison to the in-diffusion of Zn, out-diffusion of Zn from homogenously Zn-doped Si samples provides data for $C_V^{eq}D_V$ which are best reproduced by [9,10]

$$C_V^{eq}D_V = 2.1 \exp\left(-\frac{4.24\ \text{eV}}{k_B T}\right) \text{cm}^2\ \text{s}^{-1}. \quad (3)$$

Fig. 1 illustrates the temperature dependence of $C_I^{eq}D_I$ and $C_V^{eq}D_V$ according to Eqs. (2) and (3) in comparison to the Si self-diffusion data. The sum of the self-interstitial and vacancy contribution to Si self-diffusion determined independently from the metal diffusion experiments is in remarkable agreement with the direct Si self-diffusion data taking into account $f_I = 0.73$, $f_V = 0.5$ and $D_{ex} = 0$. This implies that Si self-diffusion is mediated by vacancies and self-interstitials with their individual contributions given by Eqs. (2) and (3).

Recently Ural et al. [11] have analysed the effect of both vacancy- and self-interstitial injection on Si self-diffusion at 1000°C and 1100°C. The relative contributions of vacancies and self-interstitials to Si self-diffusion reported by these authors are in good agreement with the results deduced from the Zn diffusion experiments.

2.2. Formation and migration enthalpies of vacancies and self-interstitials

The activation enthalpy of self-diffusion via self-interstitials and vacancies given by Eqs. (2) and (3) equals the sum of the enthalpy of formation and migration of the particular native defect. The pre-exponential factor is correlated with the corresponding entropy. The activation enthalpy $H_{I,V}^{SD}$ and entropy $S_{I,V}^{SD}$ of I- and V-mediated self-diffusion which were deduced from Eqs. (2) and (3) are listed in Table 1. These values are considered to be fairly reliable since the Si self-diffusion coefficients calculated with Eq. (1) are in excellent agreement with the directly measured self-diffusion data. The individual values for the formation enthalpy $H_{I,V}^{f}$ and migration enthalpy $H_{I,V}^{m}$ of the native defects are not as accurately known as the sum of the individual quantities. Recently,

Table 1
Thermodynamic properties of Si self-interstitials I and vacancies V obtained from experimental and theoretical studies (see Ref. [4] and references therein)

X	H_X^{SD} (eV)	S_X^{SD} (k_B)	H_X^f (eV)	S_X^f (k_B)	H_X^m (eV)	S_X^m (k_B)
I	4.95	13.2	3.2–3.5	4–6	1.4–1.8	7–9
V	4.24	6.3	2.0–4.0	1–6	0.2–2.2	0–6

the present author has reviewed data for $H_{I,V}^f$ and $H_{I,V}^m$ reported in the literature [4]. It has been concluded that the properties of self-interstitials in Si extracted experimentally and calculated theoretically are in good agreement. Values for H_I^f, H_I^m, S_I^f and S_I^m which are considered to be fairly reliable are given in Table 1. The corresponding data reported for the vacancies are also given in this table. The migration enthalpy of vacancies in different charge states was found to be between 0.18 –0.45 eV [12] at cryogenic temperature. However, some experimental results point to a higher migration enthalpy at higher temperatures [4]. More reliable information about the thermodynamic properties of vacancies at high temperatures are required in order to clarify whether the properties of this defect depend on temperature or not. In the case the vacancy in Si is spread out over several atomic volumes, a temperature dependence can be expected. This concept of extended native point defects was first proposed by Seeger and Chik [13] and explains the high pre-exponential factor which is observed in the temperature dependence of Si self-diffusion.

3. Diffusion of group-III atoms in III–V compound semiconductors

3.1. Ga self- and Al–Ga interdiffusion in AlGaAs/GaAs isotope heterostructures

The Ga self-diffusion in $Al_xGa_{1-x}As$ with x between 0 and 1 and the Al–Ga interdiffusion at AlGaAs/GaAs interfaces has been investigated with the help of $Al^{71}GaAs/Al^{69}GaAs/^{71}GaAs/^{nat}GaAs$ isotope heterostructures. Details about the structure of the isotope samples and the diffusion experiments have been published recently [2]. The experimental results of the diffusion study are explained if vacancies on the Ga sublattice are assumed to mediate the Ga self- and Al–Ga interdiffusion under intrinsic conditions and are summarized in the following: (i) Ga diffusion in AlGaAs decreases with increasing Al concentration. This is explained with a lower thermal equilibrium concentration of vacancies in AlAs as compared to GaAs which is caused by the different locations of the intrinsic Fermi energy level E_f^{in} with respect to the vacancy charge transition state [2]. Different positions of E_f^{in} in GaAs and AlAs are expected since the effective density of state masses for holes and electrons are different in these materials. (ii) The experimentally observed higher Al diffusivity in GaAs as compared to Ga self-diffusion is attributed to the higher jump frequency of ^{27}Al as compared to ^{71}Ga which is caused by the differences in their masses. (iii) The activation enthalpy of Al diffusion in GaAs and of Ga diffusion in $Al_xGa_{1-x}As$ with x between 0 and 1 is in the range of (3.6 ± 0.1) eV. This value represents the sum of the vacancy formation and migration enthalpy and is consistent with recent theoretical calculations which yield about 4 eV for the activation enthalpy of Ga self-diffusion [14]. (iv) The Al–Ga interdiffusion is described by a concentration-dependent interdiffusion coefficient taking into account the individual diffusion coefficients of Ga and Al in AlAs and GaAs, respectively.

3.2. Ga self-diffusion in Si- and Be-doped GaAs

In addition to our group-III atom diffusion experiments in undoped AlGaAs/GaAs isotope heterostructures the doping dependence of Ga self-diffusion in GaAs was investigated with Si- and Be-doped samples. Details about the isotope structures used for the diffusion experiments and about the analysis of the doping dependence of Ga self-diffusion are published elsewhere [15]. The doping levels of the n- and p-type structures were determined by electrochemical capacitance voltage (C–V) profiling to be 3×10^{18} cm^{-3} for each structure. The self-diffusion coefficients D_{Ga} which were extracted from Ga diffusion profiles measured with SIMS on undoped, Si- and Be-doped isotope samples are shown in Fig. 2. Solid lines in Fig. 2 represent the best fit to the experimental data assuming that vacancies govern the Ga diffusion under the present doping conditions. This assumption is consistent with data for the self-interstitial contribution to Ga self-diffusion [16] showing that the I_{Ga}^{2+} contribution to Ga diffusion for a p-doping level of 3×10^{18} cm^{-3} is still smaller than the measured Ga self-diffusion coefficient at this doping level (see Fig. 2). Fitting of the doping

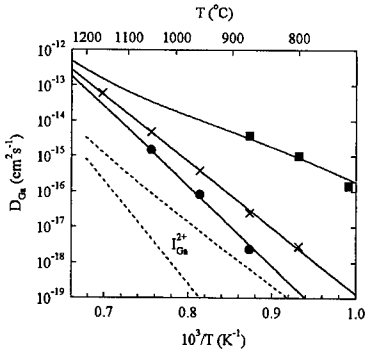

Fig. 2. Temperature dependence of the Ga self-diffusion coefficient D_{Ga} in undoped (×), Si-doped (■), and Be-doped (●) GaAs for $P_{As_4} = 1$ atm. Solid lines represent the best fit to the experimental data which yields that neutral, singly and doubly charged Ga vacancies govern the Ga self-diffusion under the particular doping conditions. Finely dashed lines represent the contribution of the doubly positively charged Ga self-interstitial I^{2+}_{Ga} to Ga self-diffusion. Lower dashed line: I^{2+}_{Ga} contribution for intrinsic conditions and $P_{As_4} = 1$ atm [16]; upper dashed line: I^{2+}_{Ga} contribution calculated for a hole concentration of 3×10^{18} cm^{-3}.

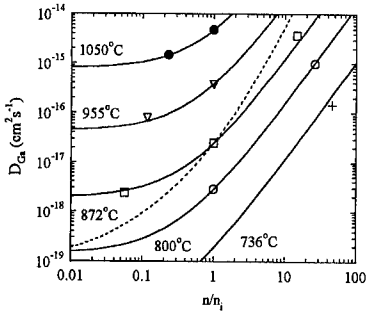

Fig. 3. Ga self-diffusion coefficients D_{Ga} versus the ratio n/n_i between the free carrier concentration under extrinsic and intrinsic doping conditions for $P_{As_4} = 1$ atm and different temperatures as indicated. Solid lines were calculated via Eq. (4) taking into account the vacancy related energy levels $E_{V^-} - E_v = 0.42$ eV and $E_{V^{2-}} - E_v = 0.60$ eV which were deduced from fitting the doping dependence of Ga self-diffusion. The dashed line shows the doping dependence of D_{Ga} for 872°C which was calculated for $E_{V^-_{Ga}} - E_v \approx 0.20$ eV, $E_{V^{2-}_{Ga}} - E_v \approx 0.52$ eV and $E_{V^{3-}_{Ga}} - E_v \approx 0.72$ eV given by Baraff and Schlüter [20].

dependence of Ga self-diffusion is based on [15]

$$\frac{D_{Ga}(n)}{D_{Ga}(n_i)} = \frac{1+\sum_{m=1}^{3}\left(\frac{n}{n_i}\right)^m \exp(mE_f^i - \sum_{m=1}^{3} E_{V^{m-}_{Ga}})/k_B T}{1+\sum_{m=1}^{3}\exp(mE_f^i - \sum_{m=1}^{3} E_{V^{m-}_{Ga}})/k_B T} \quad (4)$$

and the neutrality equation which is used to calculate the free electron concentration n. A compensation of Si donors by negatively charged vacancies was included in the neutrality equation. Both equations were solved simultaneously in order to extract the vacancy-related energy levels $E_{V^{m-}_{Ga}}$ with $m \in \{1,2,3\}$ from the ratio $D_{Ga}(n)/D_{Ga}(n_i)$ between the experimental Ga self-diffusion coefficients in doped and undoped GaAs. In Eq. (4) n_i and E_f^i denote the free electron concentration and Fermi level position, respectively, in intrinsic GaAs. Values reported by Blakemore [17] were used for these quantities. In the case that only one charge state dominates Ga self-diffusion, Eq. (4) is reduced to

$$\frac{D_{Ga}(n)}{D_{Ga}(n_i)} = \left(\frac{n}{n_i}\right)^r. \quad (5)$$

This simplified relationship has been generally used to analyze the doping dependence of Ga self- and Al–Ga interdiffusion [18]. Here the more general Eq. (4) is preferred, since this equation takes into account that the charge state of the vacancy mediating Ga self-diffusion may change with doping and temperature.

A representation of the Ga self-diffusion data versus the ratio n/n_i is given by Fig. 3. Again the solid lines represent the best fit of the doping dependence of Ga self-diffusion. This fit yields that neutral, singly and doubly negatively charged Ga vacancies govern the self-diffusion. The energy levels $E_{V^-} - E_v = 0.42$ eV and $E_{V^{2-}} - E_v = 0.60$ eV for the singly and doubly charged vacancy have been extracted from the doping dependence of Ga self-diffusion [15]. No significant contribution from the triply charged vacancy was found. In contrast to this finding, Tan and Gösele [18] have proposed that triply negatively charged vacancies govern Ga self-diffusion under intrinsic and n-type background doping [18]. These authors have analyzed data given by Mei et al. [19] for Al–Ga interdiffusion in Si-doped AlAs/GaAs superlattices. According to Tan and Gösele, the doping dependence of interdiffusion is representative for Ga self-diffusion $D_{Ga}(n)$ in n-type GaAs and accurately reproduced by Eq. (5) with $r = 3$. At first sight their analysis appears to be correct, but a closer inspection reveals that their interpretation is not conclusive. More specifically, Tan and Gösele have determined via Eq. (5) and Mei's interdiffusion data both the exponent r and $D_{Ga}(n_i)$. Since different choices for $D_{Ga}(n_i)$ also change r, their analysis is not unambigous. In this context, the activation enthalpy of 6 eV reported by Tan and Gösele [18] for the Ga self-diffusion in GaAs under intrinsic conditions also appears to be questionable. Our investigation of Ga self-diffusion in undoped isotope heterostructures yielded a much lower activation enthalpy of 3.71 eV [2]. With these results for $D_{Ga}(n_i)$ [2], the former interdiffusion

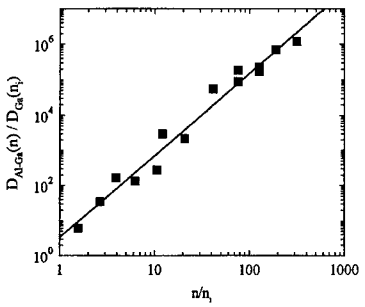

Fig. 4. Al–Ga interdiffusion coefficients $D_{Al-Ga}(n)$ of Mei et al. [19] normalized by $D_{Ga}(n_i)$ [2] as a function of n/n_i. The solid line represents the best fit which is reproduced by $D_{Al-Ga}(n)/D_{Ga}(n_i) = 3.4(n/n_i)^{2.3}$.

data of Mei et al. [19] were reanalysed. Since the Al–Ga interdiffusion experiments of Mei et al. were performed under As poor conditions, the diffusion data were reduced to an arsenic pressure of $P_{As_4} = 1$ atm using the As_4 vapor pressure data reported by Arthur [21]. Fig. 4 illustrates the ratio between the Al–Ga interdiffusion coefficient of Mei et al. and our data for $D_{Ga}(n_i)$ as a function of n/n_i. In this double logarithmic representation the slope of the experimental data equals the exponent r. The best fit yields $r = 2.3$ showing that V_{Ga}^{2-} rather than V_{Ga}^{3-} mediate the Al–Ga interdiffusion in agreement with the results of the present work. The earlier conclusions of Tan and Gösele [18] that V_{Ga}^{3-} mediates the self- and interdiffusion in n-type GaAs and that the Ga self-diffusion under intrinsic conditions is described by an activation enthalpy of 6 eV, mainly suffers from the fact that no reliable Ga self-diffusion data were available at that time. It should be noted that for $n/n_i = 1$ the fit illustrated in Fig. 4 yields $D_{Ga}(n)/D_{Ga}(n_i) = 3.4$ instead of 1.0. This indicates that the As_4 pressure during the Al–Ga interdiffusion experiments was most probably higher than the values given by Arthur for As poor conditions. Indeed this is expected since Mei's diffusion experiments were performed with the superlattice structure in close contact to a GaAs wafer.

Further seemingly inconsistent literature data on the doping dependence of group-III atom diffusion in GaAs can be described consistently on the basis of the vacancy energy levels reported in this paper. This is shown in a more comprehensive paper [15].

4. Conclusion

Isotopically controlled semiconductor heterostructures offer the unique possibility to study the self-diffusion across buried interfaces and to overcome the experimental problems which are associated with the limited half-life of radiotracers generally used for self-diffusion studies. Self-diffusion experiments with $^{28}Si/^{nat}Si$ and $Al^{71}GaAs/Al^{69}GaAs/^{71}GaAs$ isotope structures yield reliable information about the native point defects mediating the self-diffusion process in these materials.

Comparison of the direct Si self-diffusion data with the self-interstitial and vacancy contribution to Si self-diffusion, which were deduced from Zn diffusion experiments, shows that Si self-diffusion is mediated by both native defects with relative contributions given by Eqs. (2) and (3). The thermodynamic properties of self-interstitials and vacancies are summarized in Table 1 which are considered to be fairly reliable.

The activation enthalpies of Ga diffusion in undoped AlGaAs with different Al concentrations and of Al diffusion in undoped GaAs all lie in the range of (3.6 ± 0.14) eV, but with different pre-exponential factors [2]. An enhanced (retarded) Ga diffusion in Si-doped (Be-doped) GaAs with an active dopant concentration of 3×10^{18} cm^{-3} was observed and attributed to the effect of the Fermi level on the concentration of charged native point defects. All experimental results on the group-III atom diffusion are accurately described if Ga vacancies are assumed to govern the self-diffusion under the present doping conditions. The doping dependence of Ga self-diffusion provides strong evidence that neutral, singly and doubly negatively charged Ga vacancies mediate the self-diffusion process in intrinsic, Si- and Be-doped GaAs with relative contributions of the various charged vacancies which change with temperature and doping. The energy levels $E_{V^-} - E_v = 0.42$ eV and $E_{V^{2-}} - E_v = 0.60$ eV for the singly and doubly charged vacancy were deduced from the doping dependence of Ga self-diffusion.

Acknowledgements

The present author gratefully acknowledges a Feodor Lynen fellowship of the Alexander von Humboldt-Stiftung and is indebted to E.E. Haller at the Lawrence Berkeley National Laboratory (USA) for his support and very fruitful collaboration in the diffusion experiments with isotope heterostructures. He is thankful to S. Burden from Isonics corporation and M. Cardona and K. Eberl from the Max-Planck-Institute (Stuttgart, Germany) for providing the Si isotope heterostructures and the AlGaAs/GaAs isotope samples, respectively.

References

[1] H. Bracht, E.E. Haller, R. Clark-Phelps, Phys. Rev. Lett. 81 (1998) 393.
[2] H. Bracht, E.E. Haller, K. Eberl, M. Cardona, Appl. Phys. Lett. 74 (1999) 49.

[3] N.A. Stolwijk, H. Bracht, in: D.L. Beke, Landolt-Börnstein (Eds.), Diffusion in Semiconductors and Non-metallic Solids, New Series, Group III, vol. 33a, Springer, Berlin, 1998.
[4] H. Bracht, Proc. Electrochem. Soc. 99-1 (1999) 357.
[5] H. Bracht, E.E. Haller, K. Eberl, M. Cardona, R. Clark-Phelps, Mat. Res. Soc. Symp. Proc. 527 (1998) 335.
[6] K. Compaan, Y. Haven, Trans. Faraday Soc. 54 (1958) 1498.
[7] K. Compaan, Y. Haven, Trans. Faraday Soc. 52 (1956) 786.
[8] H. Bracht, N.A. Stolwijk, H. Mehrer, Phys. Rev. B 52 (1995) 16542.
[9] A. Giese, H. Bracht, N.A. Stolwijk, J.T. Walton, J. Appl. Phys. 83 (1998) 8062.
[10] A. Giese, H. Bracht, N.A. Stolwijk, D. Baither, Mater. Sci. Eng. B, to be published.
[11] A. Ural, P.B. Griffin, J.D. Plummer, Appl. Phys. Lett. 73 (1998) 1706.
[12] G.D. Watkins, J.R. Troxell, A.P. Chatterjee, Inst. Phys. Conf. Ser. 46 (1979) 16.
[13] A. Seeger, K.P. Chik, Phys. Stat. Sol. 29 (1968) 455.
[14] M. Bockstedte, M. Scheffler, Z. Phys. Chem. 200 (1997) 195.
[15] H. Bracht, M. Norseng, E.E. Haller, K. Eberl, M. Cardona, Solid State Communications 112 (1999) 30.
[16] G. Bösker, N.A. Stolwijk, H. Mehrer, U. Södervall, W. Jäger, J. Appl. Phys. 86 (1999) 791.
[17] J.S. Blakemore, J. Appl. Phys. 53 (1982) R123.
[18] T.Y. Tan, U. Gösele, Appl. Phys. Lett. 52 (1988) 1240.
[19] P. Mei, H.W. Yoon, T. Venkatesan, S.A. Schwarz, J.P. Harbison, Appl. Phys. Lett. 50 (1987) 1823.
[20] G.A. Baraff, M. Schlüter, Phys. Rev. Lett. 55 (1985) 1327.
[21] J.R. Arthur, J. Phys. Chem. Solids 28 (1967) 2257.

ELSEVIER

Physica B 273–274 (1999) 987–990

PHYSICA B

www.elsevier.com/locate/physb

Calculation of the line shapes of electronic transitions at defects using the frozen Gaussian technique

Barbara McKinnon[a], Alison Mainwood[b,*], A.M. Stoneham[a]

[a]*Physics Department, University College London, Gower St, London WC1E 6BT, UK*
[b]*Physics Department, King's College London, Strand, London WC2R 2LS, UK*

Abstract

Calculations of the optical properties of defects in semiconductors or multiphonon transition rates presently make far more severe approximations than standard electronic structure calculations. One major challenge is how one can handle realistically the lattice vibrations, including quantum nuclear dynamics when those are necessary. The semi-classical frozen Gaussian technique allows us to calculate the line shapes of electronic transitions at defects using molecular dynamic simulation data from the initial and final states. Approximate nuclear wave functions are constructed from classical trajectories on nuclear potential energy surfaces for the two states. The method expands the system initial and final states (functions of position and momentum), as a sum of Gaussians, whose centres evolve classically on the relevant potential surface. An expression for the transition probability is then derived from the time-dependent overlap of the two wave functions. The frozen Gaussian method has been tested on the core exciton in diamond. The potential energy surfaces are calculated using an approximate but self-consistent molecular orbital technique, while simultaneously performing molecular dynamics. The results of our calculations show a Stokes shift of 3.64 eV, similar to the value of "up to 5 eV" obtained experimentally. We predict a fine structure with much narrower lines than those observable in the (low-resolution) experimental spectra.

Keywords: Transitions; Line shapes; Defects; Diamond; Core exciton

1. Introduction

The advances made in computational modelling of condensed matter systems in the last decade make it possible to predict many quantities, such as electronic energy levels, wave functions, charge densities and vibrational modes of defects in crystals, reliably and accurately. Yet, while there is much experimental data available for optical line shapes and non-radiative transitions, it can only currently be compared with the most approximate theoretical models (typically single-frequency models or weak coupling models). For these line shapes and rates, a key quantity is the line-shape function.

Here, a new method is proposed to calculate the line-shape function, namely the frozen Gaussian approximation [1,2]. The approach does not make the usual analysis of the motion into normal modes, and can exploit the more flexible tool of molecular dynamics. The frozen Gaussian approximation (FGA) is a mathematical device whereby an approximate nuclear wave function is constructed from ensembles of classical nuclear trajectories on excited and ground state electronic potential energy surfaces (PES). The line-shape function is given by the Fourier transform of the time-dependent overlap of the excited and ground state phonon wave functions. The method is described in detail in Section 2. The principal advantage of the method over previous techniques is that it is not limited to a harmonic description of the nuclear motion, nor to one or just a few phonon modes. The problems encountered when applying this technique are discussed in Section 3, and a simple illustration of the method shown in Section 4.

* Corresponding author. Tel.: + 44-(0)-171-848-2044; fax: + 44-(0)-171-848-2420.
E-mail address: alison.mainwood@kcl.ac.uk (A. Mainwood)

0921-4526/99/$ - see front matter
PII: S0921-4526(99)00607-9

2. The calculation of transition rates

A transition between two states can be described to first order in time-dependent perturbation theory, using Fermi's Golden Rule. The initial and final states of the system, Ψ_i and Ψ_f (with energies E_i and E_f, respectively), are assumed to be eigenstates of the system Hamiltonian H_0. The transition is driven by the perturbation H_1 which can impart energy E to the system. The resultant expression for the transition rate is

$$W_{if} = \frac{2\pi}{\hbar}|\langle\Psi_i|H_1|\Psi_f\rangle|^2\delta(E_f - E_i - E). \quad (1)$$

In the Born Oppenheimer approximation, the eigenstates of H_0, $\Psi_{i\mu}$ are separated into products of electronic states ψ_i and phonon states $\chi_{i\mu}$, where the electronic states are eigenstates of the Hamiltonian for a given instantaneous nuclear configuration and the phonon states are eigenstates of the nuclear kinetic energy operator and the potential field provided by the electrons. To evaluate the transition between electronic levels i and f it is therefore necessary to average over the initial distribution of phonon states and sum over all final phonon states, arriving at the following expression for the rate:

$$W_{if} = \frac{2\pi}{\hbar}\sum_{\mu\nu}\frac{e^{-\beta E_{i\mu}}}{Z} \times |\langle\psi_i\chi_{i\mu}|H_1|\psi_f\chi_{f\nu}\rangle|^2\delta(E_{f\nu} - E_{i\mu} - E), \quad (2)$$

where

$$Z = \sum_{\mu} e^{-\beta E_{i\mu}}.$$

For allowed optical transitions, we make the standard Condon approximation that the transition operator H_1 is independent of the nuclear configuration [3]. Eq. (2) is then simplified by replacing the delta function by its Fourier transform, expressing the phonon state χ_μ at time t propagated on potential energy surface i as $e^{-iH_i t/\hbar}|\chi_\mu(0)\rangle = |\chi_\mu(t)\rangle_i$, and replacing the complete sum over final phonon states by unity. Hence the transition rate reduces to thermal average of the Fourier transform of the overlap of the phonon state χ_μ propagated on the initial, i, and final, f, potential energy surfaces:

$$W_{if}(E) = \frac{|\langle\psi_f|H_1|\psi_i\rangle|^2}{\hbar^2} \times \sum_{\mu}\frac{e^{-\beta E_{i\mu}}}{Z}\int_{-\infty}^{\infty} dt\, e_f^{iEt/\hbar}\langle\chi_\mu(t)|\chi_\mu(t)\rangle_i. \quad (3)$$

Eq. (3) is still difficult to evaluate because it depends upon the phonon state as a function of time. The frozen Gaussian approach can be used to construct an approximate nuclear wave function rendering the above expression tractable. The mathematical derivation of the method is given elsewhere [4–8], but the essentials for its use on condensed matter systems follow.

The initial state of the system is approximated by a product of Gaussians, each one describing one of the $3N$ coordinates of the system, whether normal modes or components of individual atomic displacements.

$$\chi(0, R) = \prod_j^{3N}\left(\frac{2\gamma}{\pi}\right)^{1/4}\exp(-\gamma(R - R_j)^2 + iP_j(R - R_j)), \quad (4)$$

where R_j and P_j are the initial positions and momenta of the atoms (or normal mode coordinates). The product is over the $3N$ atom coordinates (or normal modes) of a system containing N atoms, and γ is the Gaussian width, which will be discussed later. Then it can be shown that at later times, t, the nuclear wave function becomes:

$$\chi(t, R) = \exp(iS(t)/\hbar)\prod_j^{3N}\left(\frac{2\gamma}{\pi}\right)^{1/4} \times \exp(-\gamma(R - R_j(t))^2 + iP_j(t)(R - R_j(t))), \quad (5)$$

where $S(t) = \int_0^t L\, dt$, where L closely related to the Lagrangian of the system: $L = KE - PE +$ zero point energy for the oscillators. The expressions for the absorption and emission spectra for the transition are proportional to the line-shape function $G_{if}(E)$ [3]:

$$G_{if}(E) = \sum_{\mu}\frac{\exp(-\beta E_{i\mu})}{Z}\int_{-\infty}^{\infty} dt\, e_f^{iEt/\hbar}\langle\chi_\mu(t)|\chi_\mu(t)\rangle_i. \quad (6)$$

The sum is over all possible starting configurations, μ. The sum is approximated by selecting a number of starting configurations with random displacements of the atoms about their initial state equilibrium positions.

This treatment has made a number of assumptions, which have been explored in more detail elsewhere [4–10]:

1. The expansion of each degree of freedom in the exact wave function into an overcomplete set of Gaussians is replaced by a single Gaussian per degree of freedom [7,8,10].
2. The nuclear overlap is independent of the Gaussian's width, γ [9]. There proves to be a weak dependence, because of the finite number of starting configurations, but the results are largely independent of γ.
3. A complex function of the momenta and positions of the atoms (or normal modes) ($C(R_i, P_i, t)$ of Ref. [9]) arising in the exact propagation of the Gaussians has been approximated by a constant. This is examined and partially justified in Refs. [2,7,10].

To summarise, one must calculate the positions and momenta of the atoms near the excitation position, both in the excited state of the transition and in its ground state, as functions of time. For each pair of dynamic runs, which start with the same initial positions, the overlap between the Gaussians is calculated as a function of time. For finite temperatures, either the normal mode phonons of the atoms concerned are excited, or sufficient different random displacements of the atoms around their equilibrium positions are included. The number of dynamic runs required before the line-shape function converges depends upon the system. In this case less than ten runs were required.

3. Using the frozen Gaussian method

In the past, the frozen Gaussian method has only been used for a very limited set of systems, but it has huge potential in the field of condensed matter physics. Much information on the structure and properties of defects is contained in the vibronic line shapes of their transitions, and they have only been interpreted by simple weak-coupling or single-frequency models.

Blake and Metiu [8] have studied the absorption lineshape for electrons solvated in halo-sodalites. A mixture of the more sophisticated Herman and Kluk approach [2] and the original frozen Gaussian method [1] has been implemented by Ovchinnikov and Apkarian [10] to study Cl_2 in solid Ar clusters.

The implementation of the method has the following requirements:

- A number of long dynamic runs (of the order of picoseconds) is required to obtain sufficient resolution in the spectra,
- short time steps must be used in the dynamics, to obtain sufficient accuracy in the numerical integration of the action, S,
- reasonably accurate electronic and vibrational states must be modelled,
- the ground state and the excited state must be modelled simultaneously,
- neither calculation must diverge (many methods that force convergence also damp the nuclear motion, and this would not be acceptable).

Many of the familiar state-of-the-art methods are unsuitable for these calculations. Any of the calculation methods based on density functional theory (DFT) can calculate the properties of the ground state, but they are not designed for excited state calculations. Many of the calculation methods based on Hartree–Fock (HF) approximations, although capable in principle of calculating excited states, have severe convergence problems when these are attempted. At present, these considerations severely limit the classes of problems and the methods of calculation that can be treated by this theory. Fortunately, it is possible to use simpler self-consistent methods based on HF and LDA approaches.

4. An illustration of the use of the frozen Gaussian method

A core exciton is created in diamond when an X-ray of approximately 285 eV is absorbed by a 1 s electron, promoting it to the conduction band [11]. The excited state is therefore very similar to a nitrogen substitutional atom in diamond [12] — a very deep donor which has a very large trigonal distortion. Hence, one would expect the core exciton to have a substantial Stokes shift; it is estimated to be as large as 5 eV [13].

The core exciton in diamond has been modelled using the molecular dynamics code CHEMOS [14] in which the nuclei follow classical trajectories on adiabatic potential energy surfaces calculated self-consistently within the CNDO approximation. The diamond cluster we use consists of 65 carbon atoms of which the central 29 are free to move and the outer 36 are fixed. The creation of the core exciton is modelled by introducing an extra electron into the conduction band and replacing the C core by N. The runs were started from different initial nuclear configurations in order to perform the classical average over nuclear phase space.

An approximate nuclear wave function $\chi(t, R)$ was constructed consisting of the product of Gaussians of the form of Eq. (5). We used one Gaussian per atomic degree of freedom. The sum over starting configurations was made by selecting a number of sets of atomic positions. For the absorption spectra, these configurations were produced by displacing each atom a random, but small distance from its equilibrium in the ground state and introducing a small random momentum to each atom. For the emission spectra the atoms were displaced from their excited state equilibrium positions.

The time dependence of the overlap of the Gaussian wave functions on the initial and final state potential energy surfaces depends upon the widths of the Gaussians and the relaxation of the system upon excitation. We have chosen a width consistent with the frequency of the dominant mode in the cluster namely 60 meV for both the ground and excited states. We selected several values for the Gaussian width to verify that this choice has little effect upon the lineshape function.

To obtain an accurate Fourier transform of the correlation function care must be taken to have a sufficiently long simulation. In this work the period of the oscillatory component was about 60 fs, whereas data was collected every 0.25 fs so that the numerical integration of the action integral was sufficiently accurate. The simulations ran for 0.5 ps, to give a resolution in the Fourier transform, and hence in the spectra, of 8.3 meV.

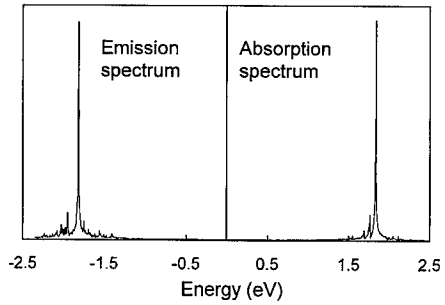

Fig. 1. The spectra calculated by the FGA technique, associated with the creation and destruction of a core exciton in diamond.

5. Results

Fig. 1 illustrates the spectrum corresponding to (a) the creation and (b) subsequent destruction of a core exciton. The absorption peak is obtained from the average over five runs and the emission peak from the average over four runs, where each run has a different set of initial positions and momenta.

The important features of the spectrum are the separation of the absorption and emission spectrum, the existence and position of the side bands on each peak and the origin of the finite width of the peaks. The separation of the peaks should correspond to the Stokes' shift, which is defined as the difference between the absorption and emission energies from the relaxed ground and excited states, respectively. The Stokes' shift as measured from the simulation data is 3.64 eV. This is in fully satisfactory accord with experimental estimates of "up to 5 eV" [13]. The spacing of the side bands seen in Fig. 1 correspond to about 70 meV and are the harmonic overtones associated with the breathing mode-like vibration. Experimentally, these would need special methods to detect.

6. Discussion and conclusion

The frozen Gaussian technique has been applied to obtain the line shapes corresponding to the creation and destruction of the core exciton in diamond. To judge the quality of the result it is necessary to compare it with experimental spectra. However, the experimental spectra have insufficient resolution for any but the most crude comparisons to be possible. The Stokes shift agrees well, but the finer structure that are predicted by this simulation are not resolved in the experimental spectra.

There are no numerical difficulties in implementing the FGA for a system of this size; it should prove to be extremely suitable for application to condensed matter problems. The problem is that most of the methods of calculating PES are not, at present, suitable for dynamic runs on excited states. The method used here, based on a particular form of self-consistent molecular dynamics, is fully adequate for demonstration purposes, or for scoping a problem, but does not achieve the accuracy of which the frozen Gaussian method is capable.

References

[1] E.J. Heller, J. Chem. Phys. 75 (1981) 2923.
[2] M.F. Herman, E. Kluk, Chem. Phys. 91 (1984) 27.
[3] A. M. Stoneham, Theory of Defects in Solids, Oxford University Press, reprinted 1996 (Chapter 10).
[4] J.H. Van Vleck, Proc. Nat. Acad. Sci. USA 14 (1928) 178.
[5] W. Dittrich, M. Reuter, Classical and Quantum Dynamics, 2nd Edition, Springer, Berlin, 1994.
[6] E. Kluk, M. Herman, H. Davis, J. Chem. Phys. 84 (1986) 326.
[7] E. Neria, A. Nitzen, J. Chem. Phys. 99 (1993) 1109.
[8] N.P. Blake, H. Metiu, J. Chem. Phys. 103 (1995) 4455.
[9] B.A. McKinnon, A. Mainwood, A.M. Stoneham, Phys. Rev. B, 1999, submitted for publication.
[10] M. Ovchinnikov, V.A. Apkarian, J. Chem. Phys. 108 (1998) 1.
[11] Y. Ma, P. Skytt, N. Wassdahl, P. Glans, D.C. Mancini, J. Guo, J. Nordgren, Phys. Rev. Lett. 71 (1993) 3725.
[12] A. Mainwood, A.M. Stoneham, J. Phys.: Condens. Matter 6 (1994) 4917.
[13] Ref. 11 interpreted by F. Mauri, R. Car, Phys. Rev. Lett. 75 (1995) 3166.
[14] D.S. Wallace, A.M. Stoneham, W. Hayes, A.J. Fisher, A.H. Harker, J. Phys: Condens. Matter 3 (1991) 3879.

ELSEVIER

Physica B 273–274 (1999) 991–994

PHYSICA B

www.elsevier.com/locate/physb

First-principles dynamics of defect reactions triggered by electronic excitation

Yoshiyuki Miyamoto*, Osamu Sugino, Yasunori Mochizuki

Fundamental Research Laboratories, NEC Corporation, 34 Miyukigaoka, Tsukuba, 305-8501, Japan

Abstract

We investigated the influence of electronic excitation on reactivation of H-passivated impurities in GaAs. By applying the recently developed scheme for the first-principles molecular dynamics coupled with the real-time electron dynamics, the electronic excitation that significantly reduces the dissociation barrier heights of a Si_{Ga}–H complex in GaAs was found. This fact indicates strong enhancement of H-dissociation upon the excitation and subsequent reactivation of the Si donors. Moreover, the reactivation mechanisms of the C acceptor are partially reviewed.

Keywords: Impurity reactivation; First-principles MD; Electron dynamics

1. Introduction

Since hydrogen is inevitably or intentionally contained in semiconductors during the device-fabrication processes, formation of hydrogen-impurity complexes often occurs and neutralizes the impurities [1]. Reactivation of the H-passivated impurities is an important technique for achieving high device performance, so microscopic understanding of the reactivation is of great importance. In the case of Si donors in GaAs, the Si_{Ga}–H complex was identified by measuring the corresponding vibrational mode by infrared (IR) spectroscopy [2,3]. Reactivation of these Si donors can be achieved by thermal annealing [4] or by applying an electric field [5]. Very recently, disappearance of the Si_{Ga}–H vibrational mode coupled with recovery of *n*-carrier density upon laser illumination has been reported [6]. This experiment suggests that an electronic excitation assists the H-dissociation. The threshold of the optical excitation energy was 3.5 eV, exceeding the band gap of GaAs (about 1.5 eV). This fact indicates that the excitation corresponds to the resonance of the GaAs band structures, so the nonradiative decay of the excited state can occur. If this decay occurs, the direct H-dissociation should be disturbed.

Besides the Si donors, considerable attention has been paid to C acceptors because of their potential for heavy doping (δ-doping) when metalorganic molecular (MO) beam epitaxy is applied [7,8]. H-incorporation may occur during the MO epitaxy, and postannealing is necessary for the reactivation [9]. The existence of the C_{As}–H complexes was confirmed by IR spectroscopy [10], and this bond was found to be broken during minority carrier injection [11] in which electronic excitations may play a key role.

In this paper, we demonstrate that an electronic excitation in the Si_{Ga}–H complexes indeed assists H-dissociation. We performed the first-principles molecular dynamics (MD) simulation, within the framework of the density functional theory, using the local density approximation (LDA) and the pseudopotentials. In order to examine the nonradiative decay of the excited state, the electron dynamics must be explicitly treated by solving the time-dependent Schrödinger equation during the

* Corresponding author. Tel.: + 81-298-50-1586; fax: + 81-298-50-2647.

E-mail address: miyamoto@frl.cl.nec.co.jp (Y. Miyamoto)

0921-4526/99/$ - see front matter
PII: S0921-4526(99)00608-0

classical MD simulation for ions. This time-dependent calculation was very difficult when the self-consistent field (SCF) remained between the Hartree-exchange-correlation potentials and the charge densities. We have recently developed an efficient and numerically stable scheme for solving the time-dependent Schrödinger equation within the framework of the SCF-LDA and the nonlocal pseudopotentials [12]. By applying this scheme, we found that the dissociation barrier height of the Si_{Ga}–H can be reduced upon electronic excitation. On the other hand, the mechanisms of the C_{As}–H bond breaking were only partially revealed from conventional LDA-pseudopotential calculations.

2. Computational methods

The present MD simulations under electronic excitation were performed by the following procedures with LDA, the pseudopotentials, and the plane-wave basis sets. First, we compute the relaxed atomic geometry with the electronic ground state by using the total-energy band structure and force calculations. Then, electronic occupation is promoted to mimic the electron–hole excitation pair, and the static SCF calculation is performed. Finally, the classical MD simulation (coupled with the real-time electron dynamics) for ions is run until the system significantly deviates from the adiabatic surface. All these procedures are done by using the 64-atom supercell of GaAs and the Γ sampling point. The exchange-correlation potential of the LDA is expressed by an analytic form [13] fitted with the numerical results [14]. The soft pseudopotentials [15] in the separable forms [16] are used to express the effect of ions on valence electrons. And the Kohn–Sham Hamiltonian of the LDA (H_{KS}) is used to express the time-evolution operator

$$e^{-iH_{KS}\Delta t} \quad (1)$$

for electronic wavefunctions, which is treated by the Suzuki–Trotter split-operator method [17]. Other details of the computational methods are presented in Ref. [12]. Whether the simulation runs on the adiabatic potential energy surface (PES) can be judged by monitoring the matrix of H_{KS} with respect to wavefunctions. (The present simulation for the excited Si_{Ga}–H complex showed no appearance of off-diagonal elements of the matrix. This means that the excited state survives during the present simulations.) The planewave basis set with kinetic energy cutoff of 8 Ry was used in the Si_{Ga}–H case, whereas, in the C_{As}–H case, only the static calculations were done since a higher cutoff energy of 40 Ry was necessary, making the present scheme of the dynamics very time consuming.

3. Results — H-passivated Si donors in GaAs

3.1. Electronic structure and vibrations

Under the electronic ground states, the most stable geometry of the Si_{Ga}–H complex is shown in Fig. 1. This geometry has the H atom at the anti-bonding (AB) site which was established by former works [2,3,18–20]. We found an electron–hole pair localized around the Si_{Ga}–H complex by investigating the wavefunction characteristics of the states with their levels near the band edge. Then this pair was chosen to be a single excitation. Fig. 2 illustrates the pair obtained by the SCF static calculation when the electronic occupations are promoted to mimic this single excitation. Assuming no change in the atomic structure, we compared the total energies of this excited state with that of the ground state. The calculated difference in energy was 4.0 eV, which reasonably agrees with but slightly overestimates the experimental threshold of 3.5 eV [6]. The neglect of contributions from the Franck–Condon lattice relaxation and from the zero-point vibrational energy in the present calculation may be the origin of the overestimation which overcomes the LDA underestimation. At this atomic geometry, the Hellmann–Feynman forces were found in the directions of the Si_{Ga}–H elongation and the Si_{Ga}–As shortening upon this electronic excitation. These forces triggered coupled vibrations of Si_{Ga}–H and Si_{Ga}–As bonds. During these vibrations, no off-diagonal element was observed in the matrix element, meaning the survival of the excited state. Since the Si_{Ga}–H vibrations can be a considerable perturbation on the excited state, the survival of the excited state for several periods of

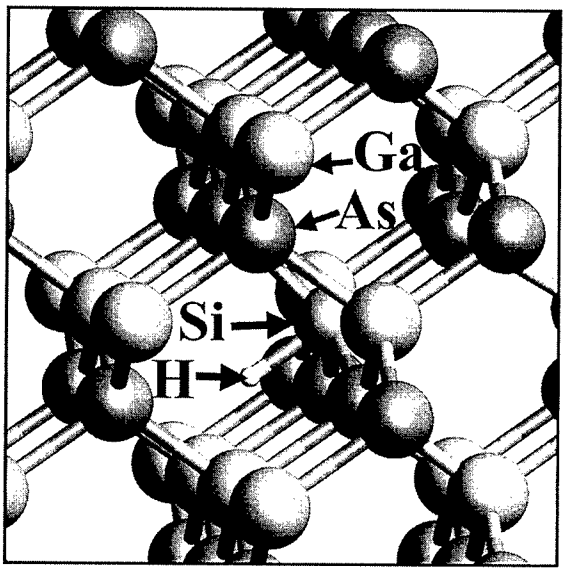

Fig. 1. Stable atomic geometry of the Si_{Ga}–H complex in GaAs. H, Si, Ga, and As atoms are indicated by arrows.

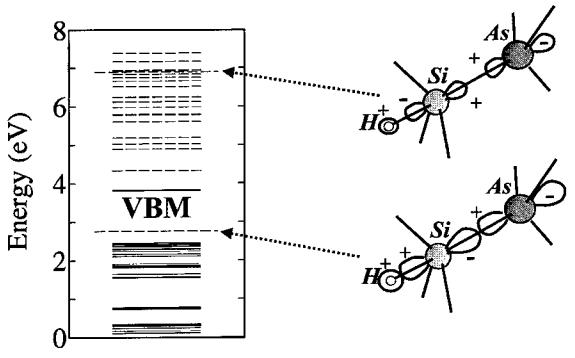

Fig. 2. One-electron energy levels (with the atomic geometry of Fig. 1) obtained with a promotion of electronic occupations. Solid and dotted bars denote occupied and empty states. Longer dotted bars are (upper) electron and (lower) hole states for the considered excitation. Schematic pictures of the wavefunction characteristics of the electron–hole pair are shown in the right panel. ("VBM" denotes the valence band maximum.)

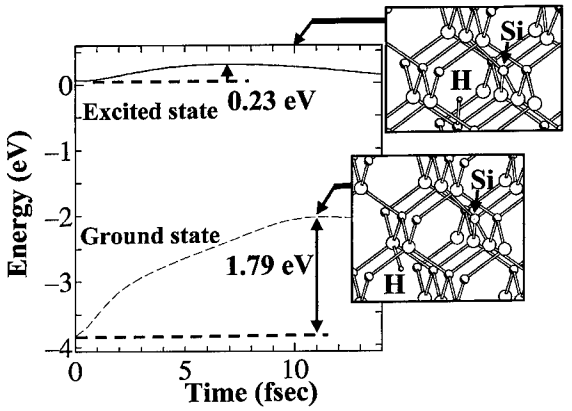

Fig. 3. Time evolution of the potential energies for the ground state (dotted) and the excited state (solid). The 0 eV of the potential was chosen arbitrarily. Two vertical arrows denote the existence of the potential barrier for breaking the Si_{Ga}–H bond. Two insets are atomic structures near the dissociation barriers for the excited state (upper) and for the ground state (lower).

these vibrations suggests that the excited state can hold till the time of the onset of the H-dissociation in the thermal equilibrium condition.

3.2. Electron-ion dynamics of H-dissociation

We compared the Si_{Ga}–H dissociation barrier heights between the ground state and the excited state. That is, MD simulations giving initial velocity to the H atom were performed in order to initiate breaking of the Si_{Ga}–H bond. In the case of the ground state, we gave the initial velocity corresponding to a kinetic energy of 4.50 eV in the direction of the dissociation. Fig. 3 shows the plotted potentials during the MD simulation and indicates the barrier height of 1.79 eV. In the case of the excited state, on the other hand, the given initial kinetic energy of 0.45 eV was enough to ensure the dissociation and the computed barrier height was 0.23 eV (see Fig. 3 again). The barrier height of 1.79 eV in the ground state shows reasonable agreement with the experimental value of 2.1 eV obtained by thermal annealing [4], indicating that the atomic trajectory of the present MD simulation passed near the point of a true transition state. Meanwhile, the significantly reduced dissociation barrier height upon electronic excitation suggests that the Si_{Ga}–H bond breaking is strongly enhanced and, thus, well explains a recent experiment [6]. A more accurate barrier height can be computed when we use a scheme beyond LDA and obtain the true transition state, but this is an issue for later works. We should mention here that the true time constant for H-dissociation should be the time needed for initiating H-dissociation with the aid of the thermal motion rather than the time scale illustrated in Fig. 3. During the dissociation, no-growth of the off-diagonal elements in the matrix of H_{KS} was seen, denoting the survival of the excited state. Since the survival of the excited state was seen in simulations of both Si_{Ga}–H vibration and bond breaking, we suppose the lifetime of the present excitation is long enough for H-dissociation. The lifetime can be more accurately estimated by performing a longer MD simulation accounting for the temperature effect instead of giving artificial velocities, but this simulation is beyond the scope of our present work.

4. Results — H-passivated C-acceptors in GaAs

The location of the H atom in the C_{As}–H complex was determined to be the bond-center (BC) site [10] (Fig. 4(a)). This geometry was optimized in the electronic ground state. We did not consider heavy-doping, i.e., the aligned defect complex C_{As}–H–Ga–C_{As} [21]. Contrary to that in the Si_{Ga}–H complex, the ⟨1 1 1⟩ direction in the C_{As}–H complex is unlikely to be a trajectory of the dissociation even when an electronic excitation to the C_{As}–H antibonding orbital occurs. This is because the C_{As}–H stretching is blocked by the adjacent Ga atom. On the other hand, when the H atom diffuses from the BC site to the AB site with the aid of thermal activation, it can be easily imagined that possible dissociation occurs along another ⟨1 1 1⟩ direction. Fig. 4(b) shows the AB site, which was also determined in the electronic ground state.[1] With this geometry, a single electron–hole excita-

[1] The present calculated total energy of the AB site is lower than that of the BC site, but only by 51 meV. The higher cutoff energy or an approach beyond LDA might be necessary to determine the most stable site theoretically.

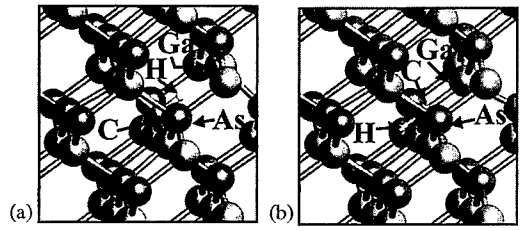

Fig. 4. Atomic structures of the C_{As}–H complex in GaAs with (a) H atom located at the bond-center site and (b) at the anti-bonding site.

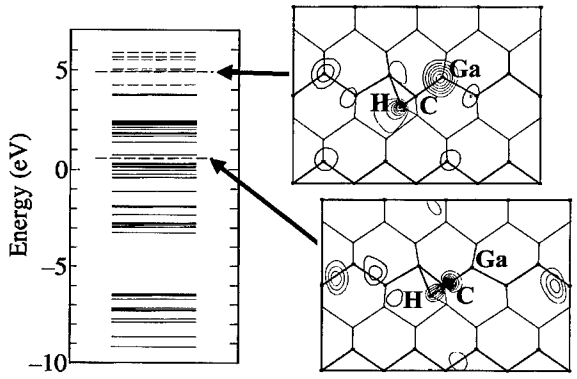

Fig. 5. One-electron energy levels for the C_{As}–H complex with the H atom at the anti-bonding site. The two right panels are the charge densities of the electron–hole pairs (two longer dotted bars in the left panel) for the considered excitations of the excited electron (upper) and the hole (lower). The contour maps are drawn along the $\langle 1\,1\,0\rangle$ plane including the H–C_{As}–Ga line (common minimum value used for the charge densities).

tion pair was found to push the H atom away from the C atom with a force of 0.10 Hartree/(Bohr radius). Fig. 5 shows the one-electron energy levels and the corresponding charge densities of the excitation pair obtained by the present static SCF calculation. The computed vertical excitation energy was 4.30 eV in the LDA level. We suppose that carrier injection can cause this excitation. Indeed, H-emission from the C_{As}–H complexes in GaAs induced by minority carrier injection has been reported [9]. Since this complex system requires a higher cutoff energy when using the planewave basis sets and a very long CPU time, the MD simulation coupled with the time-dependent Schrödinger equation has not been done. The length of the lifetime of this excited state therefore remains an open question.

5. Summary

We have investigated the mechanisms of the reactivation of H-passivated impurities in GaAs. In the case of Si_{Ga}–H complexes, we found an electron–hole excitation pair whose excitation energy reasonably agrees with the experimental one [5]. The MD simulation coupled with the time-dependent Schrödinger equation showed that this electronic excitation assists H-dissociation by lowering the activation barrier height. In the case of C_{As}–H, we proposed possible mechanisms of the reactivation; that is, a combination of thermal diffusion of the H atom and electronic excitation.

Acknowledgements

All calculations were performed by using the SX4 supercomputer system at the NEC Tsukuba Laboratories.

References

[1] S.J. Pearton, J.W. Corbett, M. Stavola (Eds.), Hydrogen in Crystalline Semiconductors, Springer, Berlin, 1991.
[2] B. Pajot et al., Phys. Rev. B 37 (1988) 4188.
[3] B. Pajot et al., Physica B 170 (1991) 371.
[4] P.R. Pearton et al., J. Appl. Phys. 59 (1986) 2821.
[5] H.Y. Cho et al., J. Appl. Phys. 68 (1990) 5077.
[6] D. Loridant-Bernard et al., Appl. Phys. Lett. 73 (1998) 644.
[7] C.R. Abernathy et al., Appl. Phys. Lett. 55 (1989) 1750.
[8] G. Li, M. Petravić, C. Jagadish, J. Appl. Phys. 79 (1996) 3554.
[9] see for example, G. Li, C. Jagadish, Appl. Phys. Lett. 69 (1996) 2551.
[10] B. Clerjaud et al., Phys. Rev. Lett. 65 (1990) 1800.
[11] H. Fushimi, K. Wada, Mater. Sci. Forum 196–201 (1995) 957.
[12] O. Sugino, Y. Miyamoto, Phys. Rev. B 59 (1999) 2579.
[13] J.P. Perdew, A. Zunger, Phys. Rev. B 23 (1981) 5048.
[14] D.M. Ceperley, B.J. Alder, Phys. Rev. Lett. 45 (1980) 566.
[15] N. Troullier, J.L. Martins, Phys. Rev. B 43 (1991) 1993.
[16] L. Kleinman, D.M. Bylander, Phys. Rev. Lett. 48 (1982) 1425.
[17] M. Suzuki, J. Phys. Soc. Japan 61 (1992) 3015.
[18] P.R. Briddon, R. Jones, Phys. Rev. Lett. 64 (1990) 2535.
[19] K.J. Chang, Solid State Commun. 78 (1991) 273.
[20] L. Pavesi, P. Giannozzi, Phys. Rev. B 43 (1991) 2446.
[21] Y. Cheng et al., Phys. Rev. B 49 (1994) 2469.

ELSEVIER

Physica B 273–274 (1999) 995–998

PHYSICA B

www.elsevier.com/locate/physb

Numerical determination of one-dimensional energy bands bound to dislocations

J.L. Farvacque*, Ph. François

Université de Lille 1, CNRS UPRESA 8008, 59650 Villeneuve d'Ascq Cedex, France

Abstract

It is assumed that the dislocation binding potential issues from their strain field through the deformation potential and the piezoelectric coupling. Dislocation states are then determined by solving the envelop function Schrödinger equation by means of a standard numerical method which consists in making a plane wave decomposition of the components of the spinor wave function. Numerical results give relatively strong binding energies and large 1D effective masses, in the case of the valence band, leading probably to large effects on the doping possibilities for large dislocation densities.

Keywords: Electronic levels; Dislocations

1. Introduction

Untill now, the theoretical determination of dislocation states has been mainly undertaken by means of cluster ab initio calculations in the local density approximation [1–4]. Such approaches have systematically shown that the dislocation core structure is strongly reconstructed and indicate that only shallow bound states may be associated with dislocations (we exclude from this conclusion possible "extrinsic" states bound by reconstruction defects or impurities of the Cottrell atmosphere). Thus, dislocation "intrinsic" states originate only from the long-range potentials generated by the dislocation strain fields, we have undertaken their determination in the effective mass approximation which is particularly well designed for the description of shallow states.

2. Background of the numerical method

It is straightforward to show that shallow states bound by a weak potential $V(r)$ are described, in the effective mass approximation, by the solution of the envelop function Schrödinger equation whose general form is $(\boldsymbol{T} + \boldsymbol{V})\varphi = E\varphi$. The operator $\boldsymbol{T}$ represents the kinetic energy term. It is obtained by making the subsitution $\boldsymbol{k} = -i\hbar\boldsymbol{\nabla}$ in the dispersion relation $E(k)$ found in the effective mass approximation. $\boldsymbol{V}$ is the operator associated with the binding potential. In the case of band degeneracy (generally the valence bands), φ is a spinor wave function whose dimension corresponds to the band degeneracy p. The kinetic energy operator takes a matricial form as for instance the 4×4 Luttinger hamiltonian [5] when the large spin orbit coupling allows to forget about the third valence band. The binding potential $\boldsymbol{V}$ has also to be expressed under a matricial form. For a nondegenerated band (generally the conduction band), the Schrödinger equation simplifies into a scalar equation where the kinetic energy operator is expressed in terms of the conduction band effective mass.

We now consider a straight dislocation whose line is along the Oz-axis. Obviously its binding potential will be of the form $V(x, y)$ and the wave function may then be written in the form $\varphi(x, y, z) = \boldsymbol{F}(x, y)\exp(ik_z z)$. The component k_z remains a good quantum number, so that all happens as if it was sufficient to make in the kinetic operators the following substitution $-i\hbar\partial/\partial z \rightarrow k_z$ for obtaining the Schrödinger equation verified by the spinor $\boldsymbol{F}(x, y)$. Then, the various solutions of the

* Corresponding author.

0921-4526/99/$ - see front matter
PII: S0921-4526(99)00609-2

energy E become k_z dependent and describe the one-dimensional energy bands associated with the dislocation.

The binding potentials associated with the dislocation strain field turn out to be complicated spatial functions. This rules out the possibility to find any reliable analytical solution of the corresponding envelop Schrödinger equation. However, the present dislocation problem is exactly identical to the case of quantum wires for which various and now standard numerical methods have been developed as for instance the plane wave (PW) decomposition of the various spinor components which we now briefly recall. Since the binding potential results into localized states (at least in the Oxy plane for dislocations), it is expected that the various components of the spinor vanish at a given distance of the defect. We then localize the defect at the center of a square whose width L is chosen in such a way that the wave function vanishes at the square boundaries. This allows to define a infinite set of G reciprocal vectors of the form $2\pi\{n_x/L, n_y/L\}$ and to express each spinor component as a Fourier series. Inserted into the Schrödinger equation, the problem is then transformed into the search of the eigen-elements of an infinite matrix in which the kinetic energy contribution is now obtained by making the substitution $-\mathrm{i}\partial/\partial x \to G_x$ and $-\mathrm{i}\partial/\partial y \to G_y$. Its general element is

$$H_{mn}(\boldsymbol{G}, \boldsymbol{G}') = H^{Lutt}_{mn}(G_x, G_y, k_z)\delta_{GG'} + \tilde{V}_{mn}(\boldsymbol{G}' - \boldsymbol{G})/L^2, \tag{2.1}$$

where $\tilde{V}_{mn}(\boldsymbol{G}' - \boldsymbol{G})$ is the Fourier transform of the binding potential. It is not numerically possible to determine the eigen-elements of an infinite matrix and therefore to consider an infinite set of G vectors to express the wave functions. In practice, a maximum number of G vectors are selected so that $G^2/2m^*$ is lower than a given energy cutoff E_{cut}. This limitation leads to an approximated representation of the real function which may be considered as a trial function depending on the choice of the square width L. The eigen-energies also depend on L and this "variational" parameter is finally adjusted in order to minimize the ground state energy $E(L, k_z)$.

3. Dislocation binding potentials

In the case of the diamond or the sphalerite structures, the Burgers vectors are of $\langle 1\,1\,0 > a/2$ type. Peierls forces tend to maintain the dislocation lines in the $\langle 1\,1\,0\rangle$ lattice directions. Thus, for these materials, two kinds of straight dislocations are generally considered: the 60° dislocation whose line and Burgers vector make a 60° angle and the screw dislocation whose line and Burgers vectors are parallel. Obviously, the orientation of dislocation lines does not coincide with the choice of the $x-, y-, z$-axis (the $\langle 0\,0\,1\rangle$ directions) used to express the Luttinger hamiltonian. Thus, prior to any calculation, it is necessary to rewrite the Luttinger operator in the natural dislocation reference system.

The binding potentials associated with dislocations are connected with their strain field through the deformation potential and the piezoelectric coupling (in polar materials).

For the nondegenerated conduction band and in the case of direct band-gap semiconductors, the scalar deformation potential $V_{DP}(r) = \Xi : \varepsilon(r)$ is characterized by a Ξ tensor which reduces to a constant E_1 times a 3×3 identity matrix. For the degenerated valence bands, the deformation potential coupling is expressed by Bir and Pikus hamiltonians [6] which have the same symmetries than Luttinger ones, since they are written in the same spinor basis. Their shape are identical but each of the components are now function of the deformation tensor components $H^{BP}_{mn} = C^{ij}_{mn}k_i k_j$ Here again, the Bir and Pikus hamiltonian must be rewritten in the natural reference system of the dislocation.

In the case of noncentrosymmetric crystals, the piezoelectric potential may be deduced from the second Voigt equation which gives: $D = \chi E + \mathrm{e} : \varepsilon$ where ε is the strain tensor, e the piezoelectric tensor, E the electric field, D the displacement vector and χ the dielectric constant. Since no net charge may be introduced by the dislocation strain field, $\mathrm{div}(D) = 0$ so that the Fourier transform of the piezoelectric potential is given by $V_{pz}(q) = \mathrm{i}q \cdot \{\mathrm{e} : \varepsilon(q)\}/\varepsilon_0\varepsilon_r q^2$. For the conduction band the piezoelectric potential is directly used as a scalar potential. For the valence band it is necessary to give it a matricial form by multiplying it by the 4×4 identity matrix.

4. Numerical results, discussion and conclusion

The shallow states bound to the conduction band have been computed for various III–V and II–VI semiconductors of the sphalerite structure. For GaN, the study is restricted to conduction band bound states, using the cubic approximation. The various coefficients used in the calculation correspond to standard values found in the literature.

Table 1 shows the values of the 2 "deeper" bound states. Generally, larger binding energies are found for larger gap semiconductor like GaN, ZnSe or ZnS: a consequence of larger effective masses and lower dielectric constants. It is worth noting that the dislocation binding energies are found to be systematically much larger than impurity binding energies calculated in the hydrogen model and whose values are also recalled in Table 1.

Numerical results show that generally the piezoelectric potential contribute slightly to the binding energy and a discrete set of bound states are found as it is illustrated by the difference between the first and the secondary bound state. The square modulus of the wave functions associated with the two first fundamental dislocation ground states are shown in Figs. 1 and 2 in the case of

Table 1
The 2 first bound states below the conduction band calculated using 841 waves. The second line indicates the shallow impurity ground state calculated in the hydrogenoid model

MeV	GaN	GaAs	InP	InSb	ZnSe	ZnS(β)	CdTe
Imp. level	37	5.43	7.08	0.60	31.10	54.6	13.91
Ground state	103.3	47.90	22.04	23.49	131.55	104.75	61.77
Dislo level 2	11.72	28.17	5.87	10.35	19.60	49.46	9.08

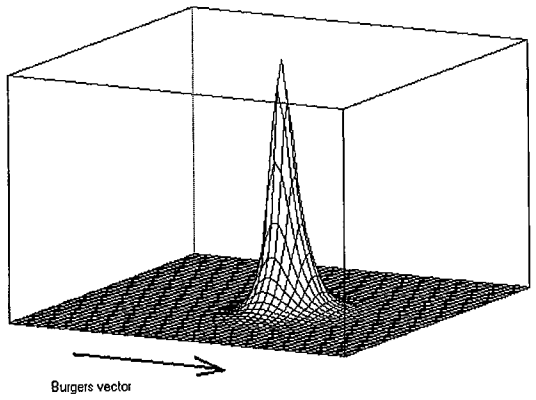

Fig. 1. Squared modulus of the wave function of the ground energy state bound to the conduction band.

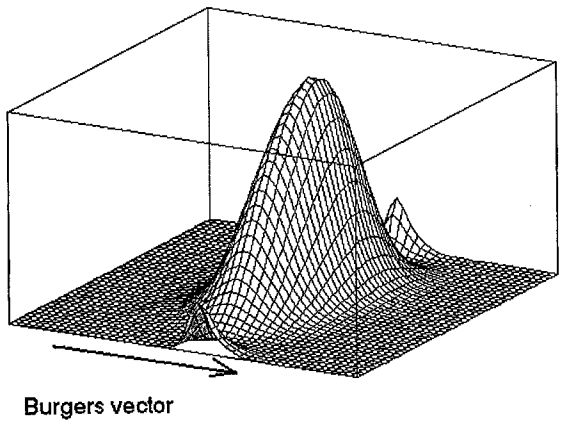

Fig. 2. Squared modulus of the wave function of the second energy state bound to the conduction band.

GaAs. It is worth noting that the actual shape of the second wave function is strongly determined by the piezoelectric contribution even if it does not drastically modify the binding energy. This fact is illustrated in Fig. 3 which represents the wave function obtained, instead of Fig. 2, when the piezoelectric coupling has been neglected.

Table 2 gives the values of the two first bound states at $k_z = 0$ bound above the valence band. Similarly to the case of quantum lines along $\langle 1\,1\,0\rangle$ directions, these

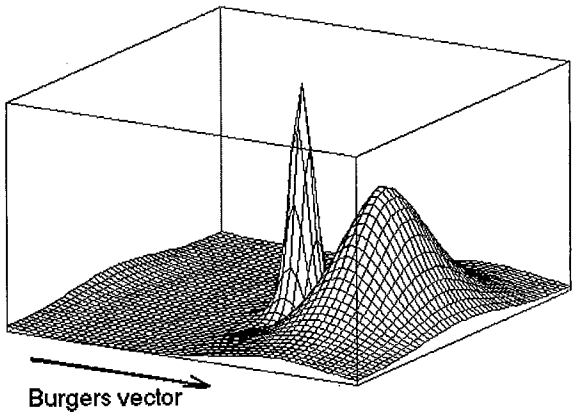

Fig. 3. Squared modulus of the wave function of the second energy state bound to the conduction band calculated without the piezoelectric coupling.

Table 2
The two first shallow energy states bound to the valence bands and their associated 1D effective masses

MeV m^*/m_0	GaAs	InP	InSb	ZnSe	ZnS	CdTe
m_{lh}	0.074	0.046	0.015	0.149	0.23	0.103
m_{hh}	0.62	0.49	9.47	1.44	1.76	1.38
m_1	0.514	0.624	0.203	1.214	1.531	1.30
E_1	93.45	62.27	33.64	72.42	87.18	100.84
m_2	0.526	0.630	0.226	1.247	1.560	1.25
m_3	0.73	0.69	0.25	1.45	1.70	0.69
E_2	36.39	35.75	18.12	30.95	39.38	67.36
m_4	0.80	0.68	0.23	1.53	1.73	0.67

levels split into 4 distinct bands shown in Fig. 4 and lead to heavy 1D effective masses.

In conclusion, using numerical techniques previously developed for the determination of quantum wires energy states, we have found exact numerical solutions of the one-dimensional energy bands associated with the dislocation strain fields. Ground states are found systematically deeper than those associated with impurities. They are expected to play a signifiant role on the doping possibilities for large dislocation densities (case of the actual bulk GaN).

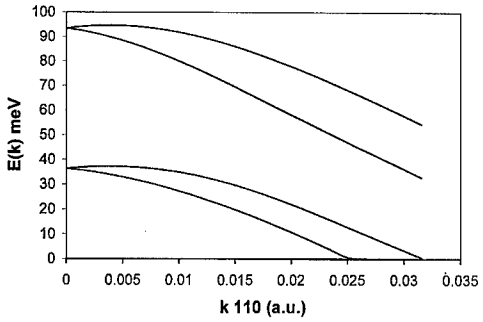

Fig. 4. 1D valence bands associated with dislocation in the case of GaAs.

Acknowledgements

This work has been financially supported by the PICS no. 630 CNRS.

References

[1] A. Umerski, R. Jones, Philos. Mag. A 67 (1992) 905.
[2] R. Jones, A. Umerski, P. Sitch, M.I. Heggie, S. Öberg, Phys. Stat. Sol. A 137 (1993) 389.
[3] P.K. Sitch, R. Jones, S. Öberg, M.I. Heggie, Phys. Rev. B 50 (1995) 17717.
[4] P.K. Sitch, R. Jones, S. Öberg, M.I. Heggie, J. Phys. III France 7 (1997) 1381.
[5] J.M. Luttinger, Phys. Rev. 102 (1956) 1030.
[6] See for instance, G.L. Bir, G.E. Pikus (Eds.), Symmetry and Strain-induced Effects in Semiconductors, Keter Publishing House, Jerusalem, 1974.

ELSEVIER

Physica B 273–274 (1999) 999–1002

PHYSICA B

www.elsevier.com/locate/physb

Transient lattice vibration induced by coherent carrier captures at a deep-level defect and the effect on defect reactions

Yuzo Shinozuka[a,b,*], Tetsuya Karatsu[a]

[a]*Faculty of Engineering, Yamaguchi University, Tokiwadai 2557, Ube 755-8611, Japan*
[b]*Faculty of Systems Engineering, Wakayama University, Sakaedani 930, Wakayama 640-8510, Japan*

Abstract

We study theoretically the dynamics of the transient lattice vibrations induced by successive carrier captures by a deep-level defect. After each carrier capture, the interaction mode $Q_1(t)$ coupled to the defect level shows a damping oscillation in a period $\sim 2\pi/\Delta\omega$, where $\Delta\omega$ is the width of the phonon frequency distribution. The induced vibration in turn enhances the next carrier capture. The induced lattice vibration energy induced by a nonradiative recombination of an electron–hole pair is larger for shorter time interval between two captures. The possibility of defect reaction is discussed in connection with the coherence in successive captures and the induced vibration, which depend on the carrier densities, $n_{e(h)}$, the capture cross sections, $\sigma_{e(h)}$, the activation energies, $E^{act}_{e(h)}$ and $\Delta\omega$.

Keywords: Deep level; Multiphonon recombination; Coherent capture; Defect reaction

1. Introduction

The nonradiative multiphonon recombination in semiconductors takes place as successive captures of an electron and a hole by a deep-level defect. After an electron (hole) capture, the lattice relaxation takes place around the defect and an electronic energy equal to the thermal depth $E^{th}_e(E^{th}_h)$ of an electron (hole) is converted into phonon energies. The whole process of nonradiative multiphonon recombination can be described consistently only by using a proper configuration coordinate diagram with many electron representation [1,2]. It has been suggested that the transient vibration induced by a carrier capture enhances a following capture of the opposite carrier [1–4]. These coherent captures are considered as a key mechanism for recombination-enhanced defect reactions, which are observed in many optical semiconductor devices [5]. The purpose of the present paper is to study theoretically the dynamics of the transient lattice vibration induced by successive carrier captures by a deep-level defect [6–8]. The induced lattice vibration energy induced by a nonradiative recombination of an electron-hole pair is larger for shorter time interval between the two captures. Possibility of defect reaction is discussed in connection with the coherence in successive captures and the induced vibration, which depend on the carrier densities, $n_{e(h)}$, the capture cross sections, $\sigma_{e(h)}$, the activation energies, $E^{act}_{e(h)}$, and the width of the phonon frequency distribution $\Delta\omega$.

2. Model Hamiltonian

A classical treatment of the transient lattice vibrations induced by successive carrier captures at a deep-level defect in a semiconductor has been developed in the preceding paper [6]. Here we briefly summarize the results. Let q_k denote the normal mode of the lattice vibration and p_k its conjugate momentum with an angular frequency ω_k. The suffix k stands for the wave numbers and the modes. Without loss of generality, we assume that the equilibrium positions of lattice modes are $q_k = 0$ when the defect is neutral (D^0) and $q_k = \bar{q}_k$ when the

* Corresponding author. Tel.: + 81-734-57-8236; fax: + 81-734-57-8237.
E-mail address: yuzo@sys.wakayama-u.ac.jp (Y. Shinozuka)

0921-4526/99/$ - see front matter
PII: S0921-4526(99)00616-X

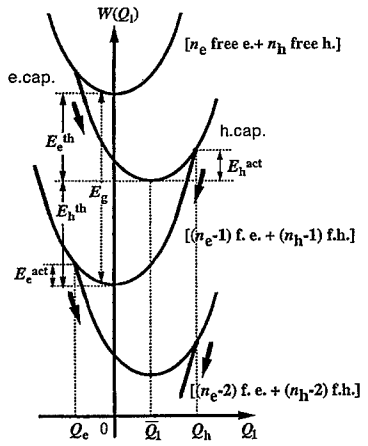

Fig. 1. The configuration coordinate model for a deep-level defect with many carriers.

defect is occupied by an electron (D^-). The Hamiltonian of the system for D^0 with n_e free electrons in the conduction band and n_h free holes in the valence band is written as

$$H_{n_e,n_h} = \frac{1}{2}\sum_k (p_k^2 + \omega_k^2 q_k^2) + n_e E_g + \sum_{i=1}^{n_e} \varepsilon_i^e + \sum_{j=1}^{n_h} \varepsilon_j^h. \quad (1)$$

The origin of the total energy is measured from that for D^0 with $(n_h - n_e)$ free holes and no electron. Here, E_g is the band gap energy, ε_i^e and ε_j^h are the kinetic energy of ith electron and jth hole, respectively. The Hamiltonian for D^- where one of the electrons is captured is written as

$$H_{n_e-1,n_h} = \frac{1}{2}\sum_k [p_k^2 + \omega_k^2(q_k - \bar{q}_k)^2] + n_e E_g - E_e^{th} + \sum_{i=1}^{n_e-1} \varepsilon_i^e + \sum_{j=1}^{n_h} \varepsilon_j^h. \quad (2)$$

Here, E_e^{th} presents the thermal depth of a bound electron. The quantity $E_h^{th} = E_g - E_e^{th}$ presents the thermal depth of a bound hole assuming that a hole is bound in D^0. The interaction between free carriers and the lattice is neglected, for simplicity and the phonon modes ω_k are assumed to be unchanged for D^0 and D^-.

Let us introduce an orthogonal transformation from $\{\omega_k q_k\}$ to $\{Q_l\}$, in which the interaction mode Q_1 is taken as

$$Q_1 = \frac{1}{\bar{Q}_1}\sum_k \omega_k^2 \bar{q}_k q_k. \quad (3)$$

Here $\bar{Q}_1$ denotes its equilibrium position. The effect of the lattice distortions to the electron–hole system appears only through Q_1 (Fig. 1). The lattice relaxation energy is given by $E_{LR} = \frac{1}{2}\sum_k \omega_k^2 \bar{q}_k^2 \equiv \frac{1}{2}\bar{Q}_1^2$.

3. Transient lattice vibration

If an electron is captured by D^0 at time τ_e, the time evolution of the interaction mode is given by

$$Q_1(t) = \frac{1}{\bar{Q}_1}\sum_k \omega_k^2 \bar{q}_k \{q_k^{before}(t) + \bar{q}_k[1 - \cos\omega_k(t - \tau_{ej})]\}$$

for $\tau_e < t$. (4a)

Here $q_k^{before}(t)$ is the time dependence of the kth lattice mode before the electron capture. Next, a hole is captured at time $\tau_h (> \tau_e)$, it is given by

$$Q_1(t) = \frac{1}{\bar{Q}_1}\sum_k \omega_k^2 \bar{q}_k \{q_k^{before}(t) + \bar{q}_k[- \cos\omega_k(t - \tau_{ej}) + \cos\omega_k(t - \tau_{hj})]\} \text{ for } \tau_h < t. \quad (4b)$$

If N pairs of electrons and holes have been captured, each occurred at $\tau_{e1} < \tau_{h1} < \tau_{e2} < \tau_{h2} < \cdots < \tau_{eN} < \tau_{hN}$, the time evolution of $Q_1(t)$ is given by

$$Q_1(t) = Q_1^{before}(t) + \bar{Q}_1\left\{1 - \sum_j^N \exp[-\Delta\omega^2(t - \tau_{ej})^2/4]\cos\omega_0(t - \tau_{ej}) + \sum_j^{N-1} \exp[-\Delta\omega^2(t - \tau_{hj})^2/4]\cos\omega_0(t - \tau_{hj})\right\},$$

for $\tau_{eN} < t < \tau_{hN}$, (5a)

$$Q_1(t) = Q_1^{before}(t) + \bar{Q}_1\left\{-\sum_j^N \exp[-\Delta\omega^2(t - \tau_{ej})^2/4]\cos\omega_0(t - \tau_{ej}) + \sum_j^N \exp[-\Delta\omega^2(t - \tau_{hj})^2/4]\cos\omega_0(t - \tau_{hj})\right\},$$

for $\tau_{hN} < t$ (5b)

for a system whose phonon frequency ω_k distribution is given by a Gaussian with the central frequency ω_0 and the width $\Delta\omega$. Here $Q_1^{before}(t)$ is the time dependence before the captures of N pairs. Thus, $Q_1(t)$ is shown to be a linear combination of damping oscillations, each starts at time τ_{ej} or τ_{hj} and lasts in the common period $\sim 2\pi/\Delta\omega$. It should be reminded here that the nonradiative capture time τ_{ej} and τ_{hj} cannot take an arbitrary value but should obey a probability process which takes place only when $Q_1(t)$ crosses a critical point Q_e or Q_h, the intersection of two adiabatic potentials (Fig. 1).

4. Correlation between two captures

Next, let us discuss the possibility of coherent captures of an electron and a hole, starting from the first electron capture which takes place by a thermal activation

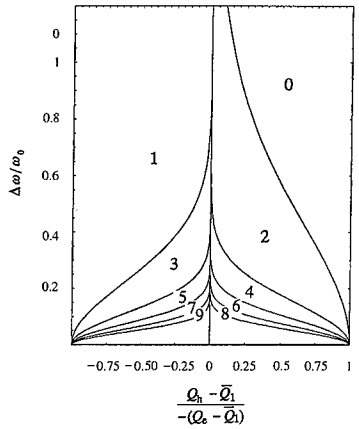

Fig. 2. How many times $Q_1(t)$ can cross at Q_h after an electron capture, as a function of $\Delta\omega/\omega_0$ and the relative positions of Q_e, Q_h and $\bar{Q}_1$. Each number denotes the number of crossing times.

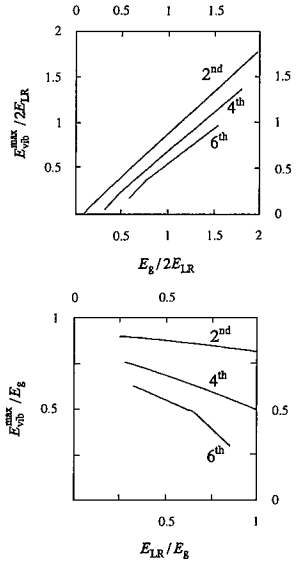

Fig. 3. The maximum lattice vibration energy generated after a pair of coherent captures of an electron and a hole for $\Delta\omega/\omega_0 = 0.1$.

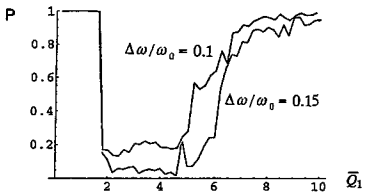

Fig. 4. The probability $P_{reaction}$ of a defect reaction as a function of $\bar{Q}_1$, i.e., the strength of the electron-lattice interaction, for a case where $p_e = 0.05$ and $p_h = 0.1$, $E_e^{th} = E_g/2$, and $Q_c^2/2 = E_g$.

$Q_1 \Rightarrow Q_e$. After the electron capture, $Q_1(t)$ shows a damping oscillation around $\bar{Q}_1$ and may cross a point Q_h, at which a nonradiative capture of a hole can take place [3,4]. It should be noted that only when $Q_1(t)$ is decreasing the level crossings correspond the real capture process: transition from one of the free continuum states to a bound state. Fig. 2 shows how many times $Q_1(t)$ can cross at Q_h after an electron capture, as a function of $\Delta\omega/\omega_0$ and the relative positions of Q_e, Q_h and $\bar{Q}_1$. When the parameters allow $Q_1(t)$ to cross Q_h N_h-times, a nonradiative coherent capture of a hole, which does not need the activation energy E_h^{act}, is probable for a case $p_h N_h/2 \sim 1$. Here the capture rate p_i (i = e, h) is related with the capture cross section $\sigma^i = \sigma_\infty^i \exp(-E_i^{act}/k_B T)$ as $p_i = n_i v_T^i \sigma_\infty^h$, where n_i is the carrier density, v_T^i the thermal carrier velocity.

Fig. 3 shows the maximum lattice vibration energy $E_{vib}^{max} = \mathrm{Max}[Q_1(t)^2/2]$ induced after a set of coherent captures of an electron and a hole. It is readily seen that an enhancement of the lattice vibration is more remarkable for quicker hole capture, i.e., at earlier crossing of $Q_1(t)$ at Q_h. If E_{vib}^{max} exceeds the activation energy E_e^{act} for an electron capture, the second electron capture will also be enhanced and a coherent capture may take place for a case $p_e N_e/2 \sim 1$ where N_e is the number of crossing times at Q_e.

5. Coherent captures and the effect on defect reaction

Finally, we will simulate the dynamics of the transient vibration and a series of coherent captures. We will use the following assumptions:

(1) The first electron capture takes place by a thermal activation $Q_1 \Rightarrow Q_e$ with an activation energy E_e^{act}.
(2) If $Q_1(t)$ crosses the point $Q_e(Q_h)$ of the adiabatic potentials, there is a probability $p_e(p_h)$ per time to capture an electron (hole) nonradiatively.
(3) If the vibration $Q_1(t)$ is damped out so that it is not enough to reach $Q_e(Q_h)$ before the next carrier capture, the coherence in successive captures will be lost. The next capture is again a thermally activated process.
(4) If the induced lattice vibration enables $Q_1(t)$ to overcome the critical point $Q_1(t) \Rightarrow Q_c$, the defect reaction takes place.

Fig. 4 shows a typical example of the simulation for the probability $P_{reaction}$ of a defect reaction per set of coherent captures as a function of $\bar{Q}_1$, i.e., the strength of the electron–lattice interaction. The values of parameters are: $p_e = 0.05$, $p_h = 0.1$, the energy of defect reaction is $Q_c^2/2 = E_g$ and the localized electron level is fixed at the middle of

the gap ($E_e^{th} = E_g/2$). The regions of $\bar{Q}_1 < 2$ and $\bar{Q}_1 > 6$ are not probable because a large activation energy E_e^{act} is necessary for the first capture (see the above assumption 1). In the region $2 < \bar{Q}_1 < 6$ the probability of the defect reaction is very sensitive to $\Delta\omega/\omega_0$. Details of the result of the simulation will be shown elsewhere.

6. Summary

We have studied theoretically the dynamics of the transient lattice vibrations induced by successive carrier captures by a deep-level defect. After each carrier capture, the interaction mode $Q_1(t)$ coupled to the defect-level shows a damping oscillation in a period $\sim 2\pi/\Delta\omega$, where $\Delta\omega$ is the width of the phonon frequency distribution. The induced vibration in turn enhances the next carrier capture. The induced lattice vibration energy induced by a nonradiative recombination of an electron–hole pair is larger for shorter time interval between two captures. The possibility of defect reaction is discussed in connection with the values of the capture rates, p_e and p_h, the activation energies, E_e^{act} and E_h^{act}, and $\Delta\omega$. In the diabatic limit it is theoretically shown that $p_{e(h)} \sim \omega_0/2\pi$ [3,4]. Then the condition for the coherent captures turns out to be $p_e\tau \sim p_h\tau \sim \omega_0/\Delta\omega > 1$. The details also depend on the parameters: Q_e, Q_h, $\bar{Q}_1, \ldots$.

If several pairs of electrons and holes are captured within a short period $\sim 2\pi/\Delta\omega$, the amplitude of the interaction mode $Q_1(t)$ increases remarkably, and it may overcome the potential barrier for a defect reaction [5]. More than the band gap energy, $E_g = E_e^{th} + E_h^{th}$ can be transformed into the lattice vibration energy by a series of coherent carrier captures, and will be used for the phonon kick mechanism.

Acknowledgements

The present work was supported by the Grand-in-Aid of the Japanese Ministry of Education, Science, Sports and Culture.

References

[1] Y. Shinozuka, J. Phys. Soc. Japan 51 (1982) 2852.
[2] Y. Shinozuka, Jpn. J. Appl. Phys. 32 (1993) 4560.
[3] H. Sumi, Phys. Rev. B 29 (1985) 4616.
[4] H. Sumi, J. Phys. C 17 (1984) 6071.
[5] O. Ueda, Reliability and Degradation of III–V Optical Devices, Artech House Publishers, Boston-London, 1996.
[6] Y. Shinozuka, T. Karatsu, Mater. Sci. Forum 258–263 (1997) 659.
[7] Y. Shinozuka, in: J. Michel, T. Kennedy, K. Wada, K. Thonke (Eds.), Defects in Electronic Materials II, Proceedings of the MRS 1996 Fall Meeting, Vol. 442, p. 225.
[8] Y. Shinozuka, in: K. Wada, S.W. Pang (Eds.), Defect in Optoelectronic Materials, Gordon and Bleach Publisher, London, 1999, Chapter 2.1.

ELSEVIER

Physica B 273–274 (1999) 1003–1006

PHYSICA B

www.elsevier.com/locate/physb

Real-space electronic structure calculations of charged clusters and defects in semiconductors using a multigrid method

Young-Gu Jin, J.-W. Jeong, K.J. Chang*

Department of Physics, Korea Advanced Institute of Science and Technology, 373-1 Kusung-dong Yusung-ku, Taejon 305-701, South Korea

Abstract

We present an efficient real-space multigrid method for first-principles electronic structure calculations, based on the pseudopotential method within the local-density-functional approximation. The Poisson and Kohn-Sham equations are accurately discretized by a higher-order finite difference method, and solved efficiently by a multigrid technique, which uses different relaxations for different sets of real-space grids. Testing various systems, we find the convergence to be nearly independent of the number of real-space grids. We demonstrate that our method is very useful for charged clusters and defects in localized bulk systems. © 1999 Elsevier Science B.V. All rights reserved.

Keywords: Multigrid; Real space; Cluster; Defect

1. Introduction

Real-space electronic structure calculations [1–7] have several advantages over the conventional method using a plane wave basis. Periodic boundary conditions which are commonly used in the plane wave method are not necessary in real-space techniques, and thereby total energies especially for charged clusters can be accurately calculated. Other advantage is that the local potential has only diagonal elements and the kinetic operator is sparse if a finite difference method is used. In addition, the real-space method can maintain the sparsity of the Hamiltonian, in conjunction with the multigrid technique [8] as a preconditioner, which accelerate the convergence by varying the resolution of grids. The convergence is nearly independent of the length scale of systems and the number of grids. Successful applications of the multigrid method for condense matter systems have been demonstrated by Briggs and coworkers [6,7].

In this work, we present an efficient real-space multigrid method for first-principles electronic structure calculations. Our techniques used for the discretization of the kinetic operator and the diagonalization of the Hamiltonian are different from those of Briggs et al. [6,7]. A higher-order finite difference method [9] is used to discretize the Laplacian and gradient operators. The Poisson and Kohn-Sham equations are solved by a multigrid method using different relaxations for different sets of real-space grids. We use the V-cycle of multigrids. Introducing an energy shift parameter in the Kohn-Sham equation, we are able to accelerate greatly the convergence without using complicated algorithms such as a full multigrid (FMG) method. For charged Si clusters, we calculate the total energies with and without periodic boundary conditions and examine the effect of the periodic boundary conditions on the energies. We also test several charged defects such as N-vacancy, hydrogen-N-vacancy pair, and Mg-interstitial-N-vacancy complex in GaN, including the localized Ga 3d electrons in the valence states.

2. Calculational method

Using a higher-order finite difference method, the Laplacian and gradient operators are expanded up to the 12th order on fine grids. Norm-conserving

* Corresponding author. Tel.: + 82-42-869-2531; fax: + 82-42-869-2510.

E-mail address: kchang@hanbit.kaist.ac.kr (K.J. Chang)

0921-4526/99/$ - see front matter
PII: S0921-4526(99)00619-5

pseudopotentials are generated by the scheme of Troullier and Martins [10] and transformed into the Kleinman–Bylander separable form [11]. We employ the Ceperley and Alder form of the exchange-correlation potential within the local-density-functional approximation (LDA) [12–15]. The Kohn-Sham and Poisson equations are solved very efficiently in real space, using the V-cycle of multigrids, which spans from coarse grids to fine grids back and forth. We also test other complicated cycles of multigrids that give better convergence, but find their computational costs much higher.

For a given electron charge density $\tilde{\rho}$, the Hamiltonian made of $\tilde{\rho}$ satisfies the following equation:

$$H_{\mathrm{KS}}[\tilde{\rho}]\psi_i = \varepsilon_i \psi_i. \tag{1}$$

Instead of solving directly Eq. (1), we use an inverse iteration method to obtain ε_i and ψ_i. For trial wave functions $\tilde{\psi}_i$, a relaxation step of the wave functions is made as follows. We first calculate the estimated eigenvalue $\tilde{\varepsilon}_i$ and residual vector r,

$$\tilde{\varepsilon}_i = \langle \tilde{\psi}_i | H_{\mathrm{KS}}[\tilde{\rho}] | \tilde{\psi}_i \rangle, \tag{2}$$

$$r = (\tilde{\varepsilon}_i - H_{\mathrm{KS}}[\tilde{\rho}])\tilde{\psi}_i. \tag{3}$$

Then, we obtain a correction $\Delta\psi_i$ to ψ_i from the equation,

$$(H_{\mathrm{KS}}[\tilde{\rho}] - \tilde{\varepsilon}_i + \delta)\Delta\psi_i = r. \tag{4}$$

In this case, $\Delta\psi_i$ is calculated using the multigrid method with one V-cycle. Here δ denotes a deviation of $\tilde{\varepsilon}_i$ from ε_i and decreases as $\tilde{\psi}_i$ becomes close to ψ_i. When $\tilde{\psi}_i$ is sufficiently close to ψ_i, δ is approximately proportional to the magnitude of the residual vector,

$$\delta \approx \tilde{\varepsilon}_i - \varepsilon_i \propto \sqrt{\langle r|r\rangle}. \tag{5}$$

With a proper choice of δ, the residual vector can be reduced very rapidly and thereby the fast convergence can be achieved. Adding $\Delta\psi_i$ to $\tilde{\psi}_i$, we obtain new wave functions, which are orthonormalized to each other. To maintain the numerical stability, on the coarse grids, the ionic potential is taken as purely local, i.e., the s-component in angular momentum, and a larger value of δ is used, as compared to the fine grids.

After each V-cycle, i.e., one self-consistent loop, the charge density and the Hamiltonian are updated for self-consistency using new wave functions. A subspace diagonalization with the wave functions $\tilde{\psi}_i$ as a basis set is performed every five self-consistent steps, so that the eigenstates close in energy are unmixed, improving the numerical convergence. We point out that this procedure should be performed more frequently for large metallic systems, which have many electrons thereby the eigenstates close in energy.

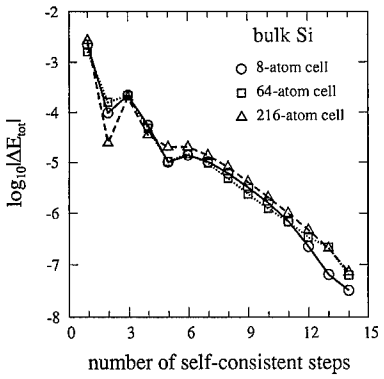

Fig. 1. Total energy convergence for the 8-, 64-, and 216-atom supercells of bulk Si. Here ΔE_{tot} represents the energy difference from the converged value.

3. Results and discussion

The test of the total energy convergence for bulk Si is drawn in Fig. 1. The energy converges almost linearly with increasing the number of self-consistent interations. Since the number of iterations required for self-consistency is independent of the supercell size, the total computational cost is nearly proportional to $O(N^2)$, where N is the number of atoms in the supercell. Although the orthogonalization procedure requires the computational cost of $O(N^3)$, it is negligible for supercells containing up to 216 atoms in bulk Si.

In the calculations with nonperiodic boundary conditions, the calculated total energies of charged clusters or defects are considered to be exact. Since supercells are commonly used in the plane-wave method, periodic boundary conditions are intrinsic and a neutralizing background charge is inevitably required for charged clusters or defects in materials. In supercell calculations, if the supercell size is sufficiently large, the total energies can be accurately calculated for neutral clusters or defects. However, for charged systems, considerable and spurious interactions between the neutralizing background and the lattice of excess or deficit charges from the neutral system are induced. Fig. 2(a) shows the total energies calculated for neutral and charged Si atoms with nonperiodic and periodic boundary conditions, as a function of the cell size. The energies are well converged with nonperiodic boundary conditions, while the calculations with periodic boundary conditions need large supercells to obtain the convergenece, as expected. It is interesting to note that the errors of the energies caused by the use of supercells become significant as the deficit charge Q from the neutral state increases. For a cubic supercell with a length L, we find that these errors are due to the Coulomb energy between the charged cells, wich is simply expressed as $\Delta E \approx \alpha Q^2/2L$, where α is the Madelung constant. In Fig. 2(b), we also compare the total energies

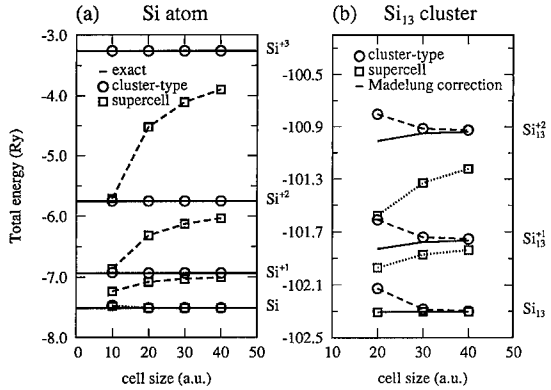

Fig. 2. Total energy convergence for (a) Si atom and (b) Si_{13} cluster in different charge states. The energies calculated with nonperiodic periodic boundary conditions (cluster-type calculation) are compared with those from periodic supercell calculations.

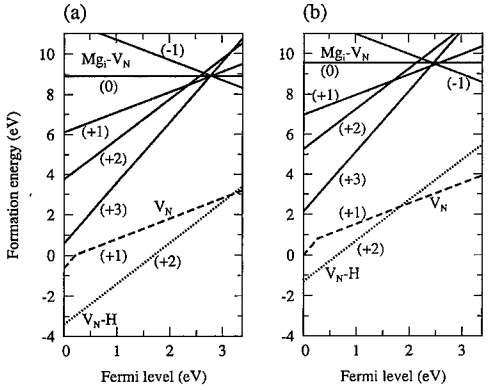

Fig. 3. The formation energies calculated in real space (a) with only the partial core corrections and (b) with the Ga 3d electrons in the valence shell are compared for various defects in GaN under Ga-rich conditions.

calculated with periodic and nonperiodic boundary conditions for charged Si_{13} clusters in the surface-like icosahedron structure [16]. In the cluster-type calculations which use nonperiodic boundary conditions, the total energies are well converged for the cell size of 40 a.u. Compared with the exact energies calculated with nonperiodic boundary conditions, the supercell calculations underestimate the total energies of charged clusters; the error increases as Q increases. With the Madelung correction, the total energies can be improved, lying close to the exact values. For clusters, however, since excess or deficit charges cannot be simply expressed by a monopole interaction, higher-order (Makov–Payne) correction terms [17] are needed for better comparison.

Similarly, the total energies of charged defects in bulk materials can be improved by including the Madelung and Makov–Payne corrections with the dielectric constant, which represents the screening effect between the charged defects in supercells. However, if defect charges are not well localized and supercells are not sufficiently large, these corrections cannot be accurately estimated. Moreover, the accurate evaluation of the dielectric constant is computationally very difficult. As an alternative way, the Slater–Janak transition-state theorem [18,19] can be used efficiently in practical calculations.

We test various charged defects such as N-vacancy, Mg-interstitial-N-vacancy complex, and H–N-vacancy pair in wurtzite GaN. Including the Ga 3d electrons in the valence states, the total energy for each defect is calculated in real space, while in previous plane-wave-basis calculations [21–24] the Ga 3d electrons were treated as the core shell, with partial core corrections [20] in the exchange-correlation potential. We use a supercell containing 64 atoms for charged defects. For the summation of the charge density in the Brillouin zone, only the Γ-point is used over the irreducible sector of the supercell Brillouin zone. The Slater–Janak transition-state theory is used to calculate the total energies for different charged states, and the resulting formation energies are plotted as a function of the Fermi level in Fig. 3. Our real-space calculations with the Ga 3d electrons in the core shell but with the partial core corrections are in good agreement with the previous plane-wave-basis calculations [21–24]. Including the 3d electrons in the valence shell, the formation energy of the N-vacancy increases by about 0.6 eV mainly due to the extra cost to remove interactions between the Ga 3d and N orbitals [22,23]. Similar behavior is also found in the Mg-interstitial-N-vacancy complex, which was suggested to be the origin of the red shift of luminescence in heavily Mg-doped GaN [25]. For all the defects considered, the atomic relaxations are generally reduced by including the Ga 3d electrons in the valence shell. For the H–N-vacancy complex, because of the repulsive interactions between the H atom and the neighboring Ga 3d electrons, the increase in the formation energy is much higher, about 2 eV. Our results demonstrate that the real-space technique is very powerful for future calculations of defects in localized or large systems.

4. Summary

In summary, we have demonstrated that the real-space multigrid method is a very powerful technique for the electronic structure calculations of defects in localized or large systems. The total energies of charged clusters calculated within this scheme are exact, as compared to the plane-wave-basis supercell calculations. For charged defects in bulk materials, the error caused by the use of the periodic boundary conditions may be enlarged as the defect charge increases.

Acknowledgements

This work was supported by the MOST-FOTD project and the CMS at KAIST.

References

[1] J.R. Chelikowsky, N. Troullier, Y. Saad, Phys. Rev. Lett. 72 (1994) 1240.
[2] J.R. Chelikowsky, N. Troullier, K. Wu, Y. Saad, Phys. Rev. B 50 (1994) 11 355.
[3] F. Gygi, G. Galli, Phys. Rev. B 52 (1995) R2229.
[4] G. Zumbach, N.A. Modine, E. Kaxiras, Solid State Commun. 99 (1996) 57.
[5] N.A. Modine, G. Zumbach, E. Kaxiras, Phys. Rev. B 55 (1997) 10 289.
[6] E.L. Briggs, D.J. Sullivan, J. Bernholc, Phys. Rev. B 52 (1995) R5471.
[7] E.L. Briggs, D.J. Sullivan, J. Bernholc, Phys. Rev. B 54 (1996) 14 362.
[8] W. Hackbusch, Multigrid Methods and Applications, Springer, Berlin, 1985.
[9] B. Fornberg, D.M. Sloan, in: A. Iserles (Ed.), Acta Numerica 94, Cambridge University Press, Cambridge, 1994.
[10] N. Troullier, J.L. Martins, Phys. Rev. B 43 (1991) 1993.
[11] L. Kleinman, D.M. Bylander, Phys. Rev. Lett. 48 (1982) 1425.
[12] P. Hohenberg, W. Kohn, Phys. Rev. 136 (1964) B864.
[13] W. Kohn, L.J. Sham, Phys. Rev. 140 (1965) A1133.
[14] D.M. Ceperley, B.J. Alder, Phys. Rev. Lett. 45 (1980) 566.
[15] J.P. Perdew, A. Junger, Phys. Rev. B 23 (1981) 5048.
[16] J.-W. Jeong, I.-H. Lee, J.H. Oh, K.J. Chang, J. Phys.: Condens. Matter 10 (1998) 5851.
[17] G. Makov, M.C. Payne, Phys. Rev. B 51 (1995) 4014.
[18] J.C. Slater, The Self-Consistent Field for Molecules and Solids, McGraw-Hill, New York, 1974.
[19] J.F. Janak, Phys. Rev. B 18 (1978) 7165.
[20] S.G. Louie, S. Froyen, M.L. Cohen, Phys. Rev. B 26 (1982) 1738.
[21] C.H. Park, D.J. Chadi, Phys. Rev. B 55 (1997) 12 995.
[22] J. Neugebauer, C.G. Van der Walle, Phys. Rev. B 50 (1994) 8067.
[23] J. Neugebauer, C.G. Van der Walle, Mat. Res. Soc. Symp. Proc. 339 (1994) 687.
[24] C.G. Van der Walle, Phys. Rev. B 56 (1997) R10 020.
[25] S.-G. Lee, K.J. Chang, Semicond. Sci. Technol. 14 (1999) 138.

ELSEVIER

Physica B 273–274 (1999) 1007–1010

PHYSICA B

www.elsevier.com/locate/physb

Magnetic field effect on tunnel ionization of deep impurities by far-infrared radiation

A.S. Moskalenko[a], S.D. Ganichev[a,b], V.I. Perel[a,*], I.N. Yassievich[a,c]

[a]*A.F. Ioffe Physico-Technical Institute RAS, 194021, Polytechnicheskaya 26, St. Petersburg, Russia*
[b]*Institut für Exp. und Angew. Physik, Universität Regensburg, 93040 Regensburg, Germany*
[c]*Department of Theoretical Physics, Lund University, S-223 62, Lund, Sweden*

Abstract

The probability of electron tunneling from a bound to a free state in an alternating electric and a constant magnetic field is calculated in the quasiclassical approximation. It is shown that the magnetic field reduces the probability of electron tunneling. The application of the external magnetic field perpendicular to the electric field reduces the ionization probability at high magnetic fields, when cyclotron resonance frequency becomes larger than reciprocal tunneling time. The increase of electric field frequency to values larger than the same reciprocal tunneling time enhances the influence of magnetic field.

Keywords: Magnetic field; Far infrared; Ionization rate; Deep centers

1. Introduction

Recently, it has been demonstrated theoretically and experimentally that the ionization of deep impurities in semiconductors in the presence of static as well as high-frequency electric fields occurs via the multiphonon-assisted tunneling Refs. [1–4]. In contrast to tunneling ionization of atoms, where only electron tunneling takes place, ionization of impurities in solids is accomplished by two simultaneous processes: electron tunneling and the redistribution of the vibrational system by defect tunneling [1,4]. Recently, using results [5] for the probability of electron tunneling, it has been shown that an external magnetic field applied perpendicular to the electric field, suppresses the multiphonon-assisted tunneling in a static electric field at $\omega_c\tau_2 > 1$, where ω_c is the cyclotron frequency and τ_2 the defect tunneling time [6].

In this work we study theoretically the influence of an external magnetic field on the thermally activated ionization of impurities in the presence of an alternating electric field. The interest to this problem is caused by the observation of an enhancement of multiphonon-assisted tunnel ionization of deep impurities in various semiconductors in terahertz electric fields as compared to static fields [3]. As shown in Ref. [3], this process is also controlled by the defect tunneling time τ_2. At $\Omega\tau_2 > 1$, where Ω is the frequency of electric field the probability of tunnel ionization increases drastically with rising frequency.

The work consists of two parts. In the first part an expression for the probability of tunneling of an electron through an alternating barrier is obtained. In this part we use the method similar to used in Ref. [8]. In the second part we study the thermally activated tunneling in the presence of an alternating electric field and an external magnetic field in semiclassical approximation and neglecting preexponential factors. We show that in this approximation the logarithm of the ionization rate linearly depends on the square of the electric field amplitude, as it has already been obtained for phonon-assisted tunneling without magnetic field [7,3]. The application of the external magnetic field perpendicular to the electric field reduces the ionization probability at $\omega_c\tau_2 > 1$. At

* Corresponding author. Tel.: + 7-812-247-93-80; fax: + 7-812-247-10-17.
E-mail address: perel@vip1.ioffe.rssi.ru (V.I. Perel)

0921-4526/99/$ - see front matter
PII: S0921-4526(99)00623-7

frequencies of the electric field high enough to achieve the regime $\Omega\tau_2 > 1$, the influence of the magnetic field drastically increases.

2. Quasiclassical wave function of tunneling electron

The quasiclassical wave function in quasiclassical approximation and neglecting preexponential factors is given by the expression

$$\Psi(\boldsymbol{r},t) \sim \mathrm{e}^{(i/\hbar)\cdot\tilde{S}(\boldsymbol{r},t)}, \tag{1}$$

where the action $\tilde{S}(\boldsymbol{r},t)$ must confirm to the Hamilton–Jacobi equations

$$\frac{\partial\tilde{S}}{\partial t} = -\mathscr{H}(\boldsymbol{P},\boldsymbol{r},t), \quad \nabla\tilde{S} = \boldsymbol{P} \tag{2}$$

with the boundary condition $\tilde{S}(\boldsymbol{r},t) = -\varepsilon t$ at $\boldsymbol{r} = 0$, where ε is the energy of an electron bound to the center ($\varepsilon < 0$). In Eq. (2) $\mathscr{H}$ is the Hamilton function, $\boldsymbol{P}$ is the generalized momentum. In our case

$$\mathscr{H}(\boldsymbol{P},\boldsymbol{r},t) = \frac{(\boldsymbol{P} - e/c\boldsymbol{A})^2}{2m} - ZF(t), \quad P = m\dot{r} + \frac{e}{c}A, \tag{3}$$

where $F(t) = F\cos\Omega t$ is the force applied to an electron from an electric field of a wave, $F = eE$. We consider that the electric field $\boldsymbol{E}$ is directed along the axis Z, and a constant magnetic field H along the axis Z. Below we use the calibration $A_x = A_z = 0$; $A_y = -Hz$.

The action $\tilde{S}$, which confirms to required conditions can be written

$$\tilde{S} = S_0 - \varepsilon t_0, \quad S_0 = \int_{t_0}^{t} \mathscr{L}(\boldsymbol{r}',\dot{\boldsymbol{r}}',t')\,\mathrm{d}t', \tag{4}$$

where $\mathscr{L}$ is the Lagrange function

$$\mathscr{L}(\boldsymbol{r}',\dot{\boldsymbol{r}}',t') = \frac{m\dot{r}'^2}{2} - z'\left[\frac{eH}{c}\dot{y}' - F(t')\right]. \tag{5}$$

The radius-vector $\boldsymbol{r}'(t')$ confirms to the motion laws

$$\ddot{x}' = 0, \qquad \ddot{y}' = \omega_c\dot{z}', \qquad \ddot{z}' = \frac{F}{m}\cos\Omega t' - \omega_c\dot{y}' \tag{6}$$

with conditions

$$\boldsymbol{r}'(t_0) = 0, \quad \boldsymbol{r}'(t) = r. \tag{7}$$

In Eq. (4) t_0 is a function $\boldsymbol{r}$ and t determined by the condition

$$\left(\frac{\mathrm{d}\tilde{S}}{\mathrm{d}t_0}\right)_{r,t} = 0. \tag{8}$$

We want to emphasize that due to the sense of wave functions values of $\boldsymbol{r}$ and t are real, while $\boldsymbol{r}'$, t' and t_0 can be complex. Using equation of Ref. [9]

$$\left(\frac{\mathrm{d}S_0}{\mathrm{d}t_0}\right)_{r,t} = \mathscr{H}|_{t=t_0}$$

and the first boundary condition of Eqs. (7) and (8) can be written as

$$\frac{m}{2}(v_{0x}^2 + v_{0y}^2 + v_{0z}^2) = \varepsilon, \tag{9}$$

where $\boldsymbol{v}_0 = \dot{\boldsymbol{r}}(t_0)$ is the velocity at the beginning of motion t_0. The value of this velocity is purely imaginary due to the condition $\varepsilon < 0$ in Eq. (9). This is natural because an electron is under the barrier.

3. Probability of direct electron tunneling

After solving of the motion equation (6) with conditions (7), it is possible to get $\boldsymbol{v}_0$ as a function of $\boldsymbol{r}$, t, t_0. Then Eq. (9) determines t_0 as a function of $\boldsymbol{r}$, t. Finally, we find the action $\tilde{S}$ as a function $\boldsymbol{r}$, t, and therefore wave function $\Psi(\boldsymbol{r},t)$.

To find the density current from the center, which is proportional to $|\Psi|^2$, it is enough to find $\mathrm{Im}\tilde{S}$ in the area of space, where it reaches its maximum, e.g. with the values of $\boldsymbol{r}$, where $\nabla\mathrm{Im}\tilde{S} = 0$. The probability of ionization P_e can be written as

$$P_e \sim \exp[-2S_e(\varepsilon)], \tag{10}$$

where $S_e(\varepsilon) = \mathrm{Im}\,\tilde{S}/\hbar$ in the area of space, which determines the result of tunneling. Then $S_e(\varepsilon)$ can be found as

$$S_e(\varepsilon) = \frac{m}{2\hbar}\int_0^{\tau_e}(\dot{z}'^2 - \dot{y}'^2)\,\mathrm{d}\tau - \frac{\varepsilon\tau_e}{\hbar}, \tag{11}$$

where τ_e is defined by the equation

$$\mathrm{sh}^2\Omega\tau_e\left[1 - \left(\frac{\Omega\omega_c}{\Omega^2 - \omega_c^2}\right)^2\left(\mathrm{cth}\Omega\tau_e - \frac{\omega_c}{\Omega}\mathrm{cth}\omega_c\tau_e\right)^2\right] = \frac{\Omega^2}{F^2}2m|\varepsilon|, \tag{12}$$

and

$$\dot{y}' = \frac{F\omega_c}{m(\Omega^2 - \omega_c^2)}\left[-\mathrm{ch}\Omega\tau + \frac{\omega_c}{\Omega}\frac{\mathrm{sh}\Omega\tau_e}{\mathrm{sh}\omega_c\tau_e}\mathrm{ch}\omega_c\tau\right], \tag{13a}$$

$$\dot{z}' = \frac{F\omega_c}{m(\Omega^2 - \omega_c^2)}\left[\frac{\Omega}{\omega_c}\mathrm{sh}\Omega\tau - \frac{\omega_c}{\Omega}\frac{\mathrm{sh}\Omega\tau_e}{\mathrm{sh}\omega_c\tau_e}\mathrm{sh}\omega_c\tau\right]i. \tag{13b}$$

Thus, the probability of ionization, neglecting pre-exponential factors, is given by Eq. (10), where $S_e(\varepsilon)$ and $\tau_e(\varepsilon)$ are defined by Eqs. (11) and(12). Note that the

parameter:

$$\tau_e = -\hbar\frac{\partial S_e}{\partial \varepsilon}, \tag{14}$$

and thus can be named as time of electron tunneling. Without magnetic field (with $\omega_c = 0$) Eqs. (10)–(13) coincide with the result of Ref. [8] for the tunnel ionization in an alternating electric field and when $\Omega = 0$ with the result of Ref. [5] for the tunnel ionization in a constant electric field in the presence of the magnetic field.

The probability of the ionization decreases and tunneling time increases when the magnetic field increases.

4. Thermally activated tunnel ionization of deep center

The probability of tunnel ionization with participation of phonons can be considered as a result of three processes: (i) thermal excitation of the system to a vibrational level $\mathscr{E}_1$ in the adiabatic potential $U_1(x)$, corresponding to an electron bound to the center (x is the vibrational coordinate), (ii) tunnel transition of the vibrational system to the adiabatic potential $U_{2\varepsilon}(x)$, corresponding to free electron with potential energy ε and (iii) tunnel transition of an electron under influence of an electric field out of the well to the free state with negative energy ε.

In quasiclassical approximation the probability of ionization with fixed ε and $\mathscr{E}_1$ is proportional to the expression:

$$\exp\left(-\frac{\mathscr{E}_1}{kT}\right)\exp[-2(S_{2\varepsilon} - S_{1\varepsilon})]\exp[-2S_e(\varepsilon)], \tag{15}$$

where the three factors are probabilities of the three processes enumerated above,

$$S_{1\varepsilon} = \frac{\sqrt{2M}}{\hbar}\int_{a_1}^{x_{c\varepsilon}}\sqrt{U_1(x) - \mathscr{E}}\,dx, \quad \mathscr{E} = \mathscr{E}_1 - \varepsilon_T, \tag{16a}$$

$$S_{2\varepsilon} = \frac{\sqrt{2M}}{\hbar}\int_{a_2\varepsilon}^{x_{c\varepsilon}}\sqrt{U_{2\varepsilon}(x) - \mathscr{E}}\,dx, \quad U_{2\varepsilon}(x) = U_2(x) + \varepsilon, \tag{16b}$$

where M is a mass, corresponding to the vibrational mode, which plays the main role in the process. $\mathscr{E}$ and $\mathscr{E}_1$ are local vibration energies, counted from the bottom of potentials U_2 and U_1, respectively. The scheme of adiabatic potentials and the tunneling trajectories are shown in Fig. 1.

The total probability of ionization is obtained by integrating product (15) over $\mathscr{E}_1$ and ε. Calculation of this integral by the saddle-point method yields two equations for the optimal values $\mathscr{E}_{1m}$ and ε_m:

$$\tau_{2\varepsilon} = \tau_{1\varepsilon} + \hbar/2kT, \quad \tau_{2\varepsilon} = \tau_e, \tag{17}$$

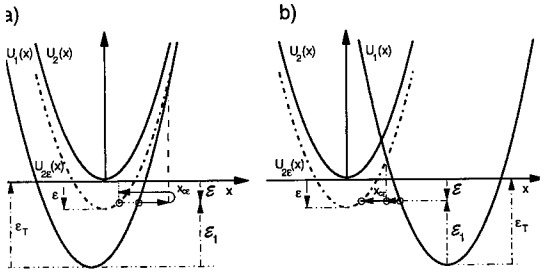

Fig. 1. Adiabatic potential configurations for: (a) weak electron–phonon coupling and (b) strong electron–phonon coupling (autolocalization). Potentials plotted in broken lines correspond to the electron with negative kinetic energy tunneling in electric fields of two different strengths. Solid arrows show the tunneling trajectories of vibrational system.

where the "tunneling times" of the vibrational system $\tau_{n\varepsilon}$ are determined by the expression

$$\tau_{n\varepsilon} = -\hbar\frac{\partial S_{n\varepsilon}}{\partial \mathscr{E}}.$$

For sufficiently weak fields the value of ε_m is small and in the first Eq. (17) we can consider $\varepsilon = 0$. Then it determines the energy $\mathscr{E}_{1m}$, which does not depend on the electric field. In Eq. (15) the difference $S_{2\varepsilon} - S_{1\varepsilon}$ can be expanded in a power series of ε and only the first term in the expansion need be retained

$$S_{2\varepsilon} - S_{1\varepsilon} = S_2 - S_1 + \frac{\varepsilon\tau_2}{\hbar}, \tag{18}$$

where S_2, S_1, τ_2 are the values of $S_{2\varepsilon}$, $S_{1\varepsilon}$ and $\tau_{2\varepsilon}$ at $\varepsilon = 0$. Then using Eq. (11) at $\tau_e = \tau_2$ we can get for the ionization probability $e(F)$:

$$e(F) = e(0)\exp\frac{F^2}{F_c^{*2}}, \tag{19}$$

where it is convenient to write

$$F_c^{*2} = \frac{3m\hbar}{\tau_2^{*3}}, \tag{20a}$$

$$\tau_2^{*3} = \frac{3\omega_c^2}{(\Omega^2 - \omega_c^2)^2}\int_0^{\tau_2}\left\{\left[-\mathrm{ch}\Omega\tau + \frac{\omega_c\,\mathrm{sh}\Omega\tau_2}{\Omega\,\mathrm{sh}\omega_c\tau_2}\mathrm{ch}\omega_c\tau\right]^2 + \left[\frac{\Omega}{\omega_c}\mathrm{sh}\Omega\tau - \frac{\omega_c\,\mathrm{sh}\Omega\tau_2}{\Omega\,\mathrm{sh}\omega_c\tau_2}\mathrm{sh}\omega_c\tau\right]^2\right\}d\tau. \tag{20b}$$

The dependence of τ_2^* on the magnetic field is illustrated in Fig. 2.

Without magnetic field ($\omega_c \to 0$) Eqs. (19) and (20) coincide with expression for the probability of multiphonon thermally activated tunneling under the influence of an alternating electric field obtained in Ref. [3], and at $\Omega \to 0$ with results of Ref. [6].

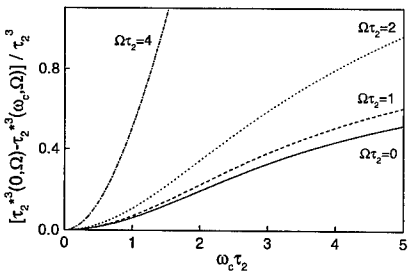

Fig. 2. The ratio $(\tau_2^{*3}(0,\Omega) - \tau_2^{*3}(\omega_c,\Omega))/\tau_2^3$ versus $\omega_c\tau_2$ calculated after Eq. (20b) for various values of the $\Omega\tau_2$. Note, that the only parameter in Eq. (20b) which determines a scale for the frequency is the tunneling time τ_2.

Note, that we can use Eqs. (19) and (20) when $F \gg F_c^*$ and $|\varepsilon_m| \ll \varepsilon_T$, where $|\varepsilon_m|$ is determined by Eq. (12) at $\tau_e = \tau_2$. Corresponding to the first formula (17) at $\varepsilon = 0$

$$\tau_2 = \tau_1 + \hbar/2kT, \tag{21}$$

where τ_1 practically does not depend on temperature. At adiabatic potentials (autolocalization) $\tau_1 < 0$ (Fig. 1b).

5. Summary

In this work an expression for the probability of electron tunneling from a bound to a free state under an alternating electric field in the presence of constant magnetic field is obtained. The result is used for the calculation of the rate of thermally activated ionization of impurities by alternating electric fields. It is shown that the application of the external magnetic field perpendicular to the electric field declines carriers which increases the tunneling trajectory. Thus, magnetic field reduces the ionization probability at $\omega_c\tau_2 > 1$. This effect is enhanced at frequencies, when $\Omega\tau_2$ becomes larger than unity.

Acknowledgements

This work was supported by RFFI grants 98-02-18268 and 96-15-96392, I.N.Y. thanks also Swedish NSRC grant O-AH/KG 03996-322, S.D.G thanks DFG and NATO-Linkage grant for support.

References

[1] V.N. Abakumov, V.I. Perel, I.N. Yassievich, Nonradiative recombination in semiconductors, in: V.M. Agranovich, A.A. Maradudin (Eds.), Modern Problems in Condensed Matter Sciences, Vol. 33, North-Holland, Amsterdam, 1991.
[2] P.T. Landsberg, in: Recombination in Semiconductors, Cambridge University Press, UK, 1991.
[3] S.D. Ganichev, E. Ziemann, Th. Gleim, W. Prettl, I.N. Yassievich, V.I. Perel, I. Wilke, E.E. Haller, Phys. Rev. Lett. 80 (1998) 2409.
[4] S.D. Ganichev, I.N. Yassievich, W. Prettl, Sov. Phys. Solid State 39 (1997) 1703.
[5] V.S. Popov, A.V. Sergeev, Sov. Phys. JETP 86 (1998) 1122.
[6] V.I. Perel, I.N. Yassievich, JETP Lett. 68 (1998) 804.
[7] V. Karpus, V.I. Perel, JETP Lett. 42 (1985) 403.
[8] L.D. Landau, E.M. Livshitz, Quantum Mechanics, Pergamon Press, Oxford, 1977, p. 287.
[9] L.D. Landau, E.M. Livshitz, in: Mechanics, Pergamon Press, Oxford, 1976.

ELSEVIER

Physica B 273–274 (1999) 1011–1014

PHYSICA B

www.elsevier.com/locate/physb

Study of bound exciton excited state structure using photothermal ionisation spectroscopy

M. Gibson*, E. McGlynn, M.O. Henry

School of Physical Sciences, Dublin City University, Glasnevin, Dublin 9, Ireland

Abstract

Photothermal ionisation spectroscopy (PTIS) has been used for many years to study the electronic structure of dopants in semiconductors, but to our knowledge it has been applied only once to the study of isoelectronic bound exciton (BE) states. The absence of any substantial literature on the subject raises the question as to whether some fundamental factors preclude the observation of the sharp line transitions from the exciton excited states. We have attempted to measure PTIS effects in a range of BE systems in silicon, but only certain systems prove amenable to the technique. In addition to data on the C-line (which has been reported in another study), PTIS spectra of BE complexes at two other well-studied centres in silicon are reported, which are generally comparable to published photoluminescence excitation (PLE) and absorption spectra. The intensities of the lines do not show, in all cases, the expected systematic temperature dependence, demonstrating extreme temperature sensitivity, with thermal activation energies different to those obtained from photoluminescence (PL) temperature dependence data. Finally, we comment on the potential of the technique for the study of excited states of BE in silicon.

Keywords: Photothermal; Spectroscopy; Defect; Exciton

1. Introduction

The study of bound exciton (BE) excited state structure provides a valuable source of information on the detailed nature of the particle binding mechanisms at a defect site, and about the nature of the underlying defect. The majority of optical measurements on defect BE systems utilise the technique of photoluminescence (PL), which, in combination with perturbative mechanisms such as uniaxial stress and magnetic fields, can provide much information on the physical and chemical nature of the defect [1]. However, by the virtue of thermalisation effects at low temperatures, PL mainly probes the first few excited states of the exciton system, and information obtained on higher states is very limited.

The main technique used to study the full BE excited state spectrum is that of photoluminescence excitation (PLE), and this has been applied to a number of the common BE systems in silicon, for example [2,3]. For the particular case of defects in silicon, the poor optical efficiency of the material means that a tunable laser is generally required to obtain good signal levels. However, a number of workers have also successfully applied simple Fourier transform (FT)-based techniques (with the associated advantage of high system throughput), including photo-thermal ionisation spectroscopy (PTIS), to the study of the excited state structure of the well-known C-line centre (PL photon energy $\sim$790 meV) in silicon [4,5]. PTIS is a hybrid electro-optical technique, utilising a photon to excite a particle from a low-lying energy state up to a state close to the ionisation edge. The particle is then ionised into the continuum by a phonon, contributing to an increase in sample conductivity, as shown in Fig. 1. This technique is well established for the study of donor and acceptor levels in the far-infra red (IR) as described in the review articles [6,7], and in principle should allow the study of BE states in the near-IR. The PTIS technique in the far-IR allows measurement of extremely low-defect concentrations ($<10^{10}$cm^{-3}) [6,7],

* Corresponding author. Tel.: 353-1-704-5730; fax: 353-1-704-5384.

E-mail address: mdg@alice.physics.dcu.ie (M. Gibson)

0921-4526/99/$ - see front matter
PII: S0921-4526(99)00626-2

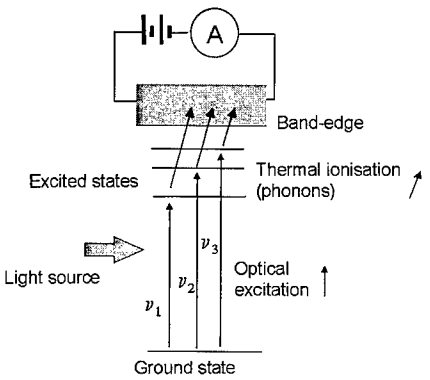

Fig. 1. Schematic diagram of photothermal ionisation process for a defect. (See text.)

which has prompted us to examine the possible advantages it may offer in the near-IR. To the best of our knowledge however, there have been no published reports on the observation of the excited state spectrum of BE in silicon other than the C-centre [4] using PTIS.

It is the purpose of this report to outline the results of our first investigations of the use of FT-based PTIS to the study of a number of BE systems in silicon, and to comment on the potential of the technique for such measurements in general.

2. Experimental

A variety of samples of silicon were used in an attempt to study various BE systems. For the three centres which proved amenable to the PTIS technique the following sample types and preparation were used.

The samples used for the C- and P-line centres were nominally intrinsic high-purity CZ bulk silicon. To produce the C-line centre these samples were irradiated with 2 MeV electrons to a dose of 5×10^{17} cm^{-2} [1,4]. C-line spectra were obtained from these samples with no further treatment. P-line spectra were obtained from the same samples after further annealing at 450°C for 2 h [2]. The samples used in the Beryllium measurements were p-type high-resistivity FZ silicon doped with Be by diffusion. In all cases the sample were RCA cleaned before preparation.

We have examined two simple methods of making ohmic contacts to the samples. Either by pressing a mixture of indium and gallium on to the samples [8] or by scratching the silicon surface with an aluminium bar coated with gallium [4,9]. For most of the results presented in this paper the latter was used.

The PTIS measurements were carried out using the internal quartz halogen source of a BOMEM DA8 Fourier transform spectrometer with a Stanford Model DR570 low-noise current preamplifier and home made amplifier combination. The internal light source was suitably filtered to match the photon energy range of interest, which optimised the PTIS signals. It was also ensured that no above band-gap radiation was incident on the sample, eliminating band-to-band excitations which would completely obscure the PTIS signals.

The prepared samples were placed in a Janis model CCS-500 closed cycle refrigeration cryostat and an Oxford instruments automatic temperature controller ITC4 was used to control the temperature. For most of our measurements sample voltages in the range 0–5 V were applied using a high stability power supply.

3. Results and discussion

As mentioned above, two different methods of making ohmic contacts to the samples were examined; In–Ga and Al–Ga. Fig. 2 shows a comparison of the PTIS spectra of the C-line centre after initial contact. In the inset a plot of the signal-to-noise ratio (SNR) taken over a number of days (with the samples being cycled to room temperature a number of times during the period) is shown. As can be seen from the plot the Al–Ga contacts, while having a poorer SNR initially, show improved behaviour over a longer period of time, while the In–Ga contacts appear to degrade quite considerably over the same period. For this reason we have used the Al–Ga contacts for all further spectra shown in this report.

A range of excitonic systems seen in PL were investigated including the 983 meV Cd-related defect [10], the 1138 meV Be-related defect [11], the 1078 meV Be–Be defect [12] and the 790 meV C-line [1,2] and 767 meV P-line [1,3] centres. A PTIS signal corresponding to the BE was seen only for three of these systems, specifically the C-line and the P-line (Both of which have also been seen by Klevermann) [4,9] and the Be–Be centre. These spectra are shown in Fig. 3 with the C-line centre showing the best SNR and the Be–Be system the worst. In all cases, the features observed in PTIS are in good agreement with those obtained in either PLE [2,3] or absorption [13] measurements.

Because of the thermal ionisation stage of the PTIS process, the line intensities are expected to show a characteristic variation with temperature related by a Boltzmann factor to their particle ionisation energies. This effect was examined in depth by other workers for the C-line [4] and good agreement with experiment was found for this system. We have performed similar temperature dependence measurements on our C-line, P-line, and Be–Be samples. For the C-line sample we find results in general agreement with Klevermann et al. [4], giving reasonable estimates of the particle ionisation energy, albeit over a narrower temperature range ($\sim$15 K) for our study (Fig. 4) compared to agreement over a range $>$ 30 K in Ref. [4]. We feel that the one cause of this

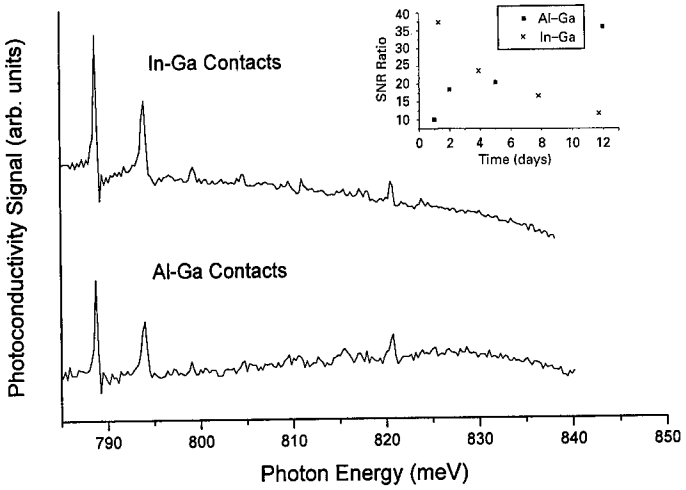

Fig. 2. PTIS spectra of the same sample using the two contact methods discussed above. The inset shows signal-to-noise ratio measured over a period of days using both contacting methods.

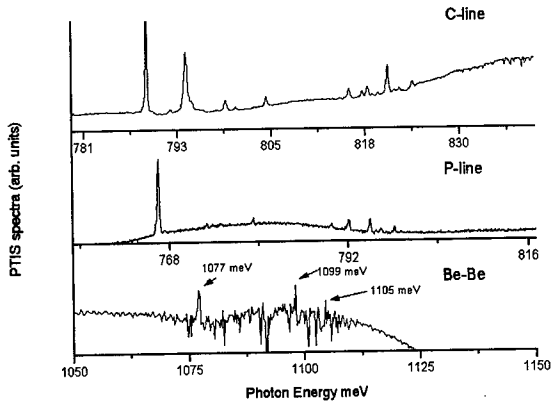

Fig. 3. Measured PTIS spectra of the three defect centres which proved amenable to the technique.

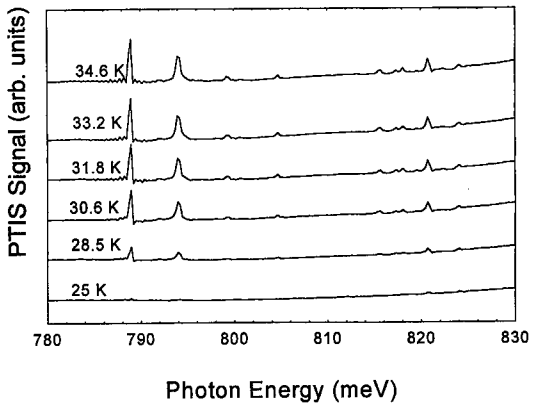

Fig. 4. Measured PTIS spectra of C-line centre in temperature range 25–35 K.

difference may be in our use of nominally undoped high purity starting material compared to the use of starting material of higher conductivity. A theoretical analysis [4,9] predicts a simple thermal behaviour in the cases where the thermally ionised particles are either a small fraction of the total number of carriers in the band or are the sole source of carriers in the band, but the intermediate case yields more complicated behaviour. The use of nominally undoped high purity starting material, which may have small residual doping of either type, may have placed our samples in this intermediate regime. Our attempts to measure the C-line PTIS signal in the starting material of higher conductivities (both n- and p-type) which received identical sample treatments have been unsuccessful, in spite of the fact that strong C-line PL was observed in these samples. Thus, the choice of starting material appears to be crucial for observing the PTIS signal.

In the case of both the P-line and the Be–Be pair systems, attempts to study temperature dependence were unsuccessful, with the spectra being observable over an extremely limited range of $\sim$5 K. This precludes any study of the relation of thermal to spectral ionisation energies, and shows that the theories applied to temperature-dependent PTIS in the far-IR [14,15] do not fully account for the behaviour when applied to the study of BE systems.

Finally, we note that the thermal activation energy obtained from temperature dependence studies of PL data from the same C-line sample (shown in Fig. 5) is 24 meV which does not agree with the ionisation energy from the $1s(A_1)$ to continuum value obtained from PTIS

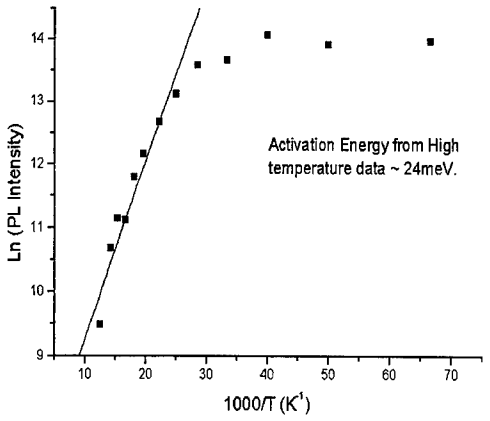

Fig. 5. Plot of PL intensity as a function of temperature, and calculated thermal activation energy.

and PLE of ~32 meV. This is most probably due to the dissociation of the free exciton as a limiting process in PL, and indicates the difficulty in drawing any firm conclusions about the exciton binding energy from PL temperature dependence measurements.

Our results demonstrate the difficulty of using the PTIS technique for the study of BE systems in general in the near-IR in silicon. Of the range of samples we have attempted to measure using the technique, only the aforementioned three systems have been observed. It is interesting to examine these three systems more closely in an attempt to discern some common features which may explain this behaviour.

One significant point may be the fact that all three are either so-called pseudo-donor BE (in the case of the C- and P-line centres [1]) or pseudo-acceptor BE (in the case of the Be–Be centre [12]). Such centres consist of one tightly bound particle, with the other in an effective mass orbit around it. The crucial step in the PTIS process is the optical absorption transition from the ground state into the higher excited states. For most BE systems in silicon, the indirect gap means that such an absorption is weak, making it difficult to measure excitonic absorption spectra. In the case of some pseudo-donor/acceptor systems, however, the tightly bound particle state localised in space spreads in k-space and relaxes this selection rule, allowing reasonably strong absorption. The fact that the three defects mentioned above are some of the relatively few excitonic systems in silicon studied by absorption [1,13] supports this point. We intend to further examine this aspect by making measurements on excitonic systems in a direct gap material such as GaAs.

4. Conclusions

We have examined the potential of the PTIS technique for the study of BE systems in silicon generally and have found that only a limited number of systems yield sharp line BE spectra. These systems have a similar electronic structure of the pseudo-donor/acceptor type. It appears from our measurements that PTIS offers no advantage for the measurement of BE excited state structure over conventional optical absorption, with the weakness of the oscillator strength between the ground and excited states fundamentally limiting both processes. Additional complications are introduced by both the contact-making process and the observed sensitivity to starting material type. Temperature-dependence measurements on these systems indicate that in two of the cases the expected Boltzmann dependence is not observed and a more complicated behaviour is seen.

Further work, including study of direct gap materials such as GaAs is required and study of temperature-dependent behaviour in starting material of different conductivity types, is needed to clarify some of the issues raised by our measurements.

Acknowledgements

The authors acknowledge financial support from an Enterprise Ireland Basic Research Grant (grant number SC97/700) during the course of this work.

EM gratefully acknowledges the hospitality of Prof. M. Klevermann, Drs. P. Tidlund and J. Olajos during a visit to the University of Lund, and the helpful discussions during and after that period.

References

[1] G. Davies, Phys. Rep. 176 (1989) 34.
[2] J. Wagner et al., Phys. Rev. B 29 (1984) 7051.
[3] J. Wagner et al., Phys. Rev. B 31 (1985) 5561.
[4] M. Klevermann et al., Phys. Rev. B 37 (1988) 10199.
[5] M.L.W. Thewalt et al., Matter. Res. Soc. Symp. Proc. 163 (1990) 221.
[6] M. Kogan et al., Phys. Stat. Sol. A 39 (1977) 11.
[7] T.M. Lifshits, Inst. Expt. Techol. 36 (1993) 1.
[8] J.M. Caywoood et al., Appl. Phys. Lett. 20 (1972) 326.
[9] M. Klevermann, private communication, 1996.
[10] E. McGlynn et al., Phys. Rev. B 54 (1996) 14494.
[11] S.E. Daly et al., Semicond. Sci. Technol. 11 (1996) 996.
[12] N. Killoran et al., J. Phys. C 15 (1982) 6067.
[13] M.L.W. Thewalt et al., Solid State Commun. 44 (1982) 573.
[14] H.W.H.M. Jongbloets et al., J. Phys. C 13 (1980) 2139.
[15] G. Bambakidis et al., Phys. Rev. B 33 (1986) 8180.

ELSEVIER

Physica B 273–274 (1999) 1015–1021

PHYSICA B

www.elsevier.com/locate/physb

Electron spin resonance study of the interaction of hydrogen with the (1 1 1)Si/SiO_2 interface: P_b-hydrogen interaction kinetics

A. Stesmans*

Department of Physics, University of Leuven, Celestijnenlaan 200D, 3001 Leuven, Belgium

Abstract

The thermal interaction kinetics of interfacial Si dangling bond P_b defects ($Si_3 \equiv Si\cdot$) in (1 1 1)Si/SiO_2, including passivation in molecular hydrogen (pictured as P_bH formation) and dissociation in vacuum, is readdressed. An initial simple thermal model had concluded simple exponential decay for both processes characterised by single-valued activation energies E_f and E_d, respectively. The picture, however, is found inadequate. In the first part, the results are reviewed of a previous expanded electron spin resonance (ESR) study of the passivation step, leading to a consistent model for passivation, in which the existence of a significant spread σ_{E_f} in E_f was exposed. In the present work, the results are presented of a similar study on the dissociation kinetics, providing distinct extension of the data set based on proper ESR defect density probing. Unlike previous conclusion, manifest non-simple exponential decay is exposed, which within the simple thermal model reveals the existence of a distinct spread σ_{E_d} in E_d. Incorporation of this results in a consistent generalised thermal model, the solid set of data enabling unbiased extraction of the pertinent physical parameters, such as the attempt frequency $k_{d0} = (1.6 \pm 0.5) \times 10^{13}\ s^{-1}$, close to the Si–H bending mode. The spreads in E_d and E_f are the natural manifestation of the stress-induced non-uniformity in atomic P_b morphology. The combination of both studies leads to a consistent unified picture of the P_b-(molecular) hydrogen interaction kinetics that matches underlying physical insight, based on the rate limiting reactions $P_b + H_2 \rightarrow P_b + H$ and $P_bH \rightarrow P_b + H$. It is evidenced that the model also applies to the interfacial Si dangling bond defects in (1 0 0)Si/SiO_2.

Keywords: Defects; Si/SiO_2 interface; Silicon; Magnetic resonance

1. Introduction

The presence of electrically active centers at the Si/SiO_2 interface has early on been recognized as a major obstacle in metal-oxide-semiconductor device technology. Later, it was realised that hydrogen plays an important role in this matter as it turned out, at least for some types of defects, chemical reaction with hydrogen is a prime means of inactivation [1]. Hydrogen is always found to be present in Si/SiO_2 entities because of its universal presence during fabrication.

The subject is encountered in numerous studies [1–11]. Yet, only few works have aimed at inferring the specific trap–hydrogen interaction kinetics [12,13]. Techniques used are electrical current–voltage (*CV*) measurements and positron annihilation spectroscopy [14,15], albeit restricted to passivation and dissociation, respectively. However, these techniques, inherently lacking atomic discriminative power, have appeared little decisive in model assessment. As known, there exist various types of interface traps [16,17].

* Tel.: + 32-16-327179; fax: + 32-16-327987.

E-mail address: andre.stesmans@fys.kuleuven.ac.be (A. Stesmans)

0921-4526/99/$ - see front matter
PII: S0921-4526(99)00627-4

When it concerns paramagnetic traps, a most adequate technique that may be applied is the defect-type-specific electron spin resonance (ESR). Yet, only few ESR-based works have been carried out [18–24], exclusively dealing with P_b-type defects. The latter is the generic ESR name for the particular class of paramagnetic coordination point defects [2], inherently generated at the interface as a result of mismatch [25,26]. Their appearance depends on the crystallographic interface orientation. At the (1 1 1)Si/SiO_2 interface, only one type is generally observed — specifically termed P_b —, identified as trivalent interfacial Si, denoted $Si_3 \equiv Si\cdot$. The (1 0 0)Si/SiO_2 exhibits two prominent types, termed P_{b0} and P_{b1}. For standard oxidation temperatures (800–950°C), intrinsic (N_i) areal densities of physical defect sites (including both ESR active and inactivated ones) of $[P_b] \sim 5 \times 10^{12}$ cm^{-2} [25] and $[P_{b0}]$, $[P_{b1}] \sim 1 \times 10^{12}$ cm^{-2} [27] are naturally incorporated. All three P_b variants were shown to be trivalent Si centers, where the consensus is that P_{b0} is the equivalent of P_b, but now residing at (imperfections of) a macroscopic (1 0 0) oriented Si/SiO_2 interface. P_{b1} is hinted [28] to be a distorted defected interfacial Si dimer. For this important class of Si dangling bond centers, electrical inactivation is generally pictured as chemical saturation of the failing bond by hydrogen, symbolized as SiH formation [2–4,18].

2. P_b–molecular hydrogen interaction

2.1. Initial canonical picture

Some preliminary atomic insight on P_b–hydrogen bonding, albeit somewhat scattered, was provided by initial ESR work [29–32], some in combination with an electrical technique. In pioneering ESR work [18,19], Brower was the first to fully quantify the hydrogen interaction kinetics of P_bs with molecular H_2. His model, henceforth called the simple thermal (ST) scheme, concerns a least-complications scheme, the red wire being that the key interactions are simply rate limited by the availability of 'reactive' P_b sites, i.e., $[P_b]$ and $[P_b\,H]$ for passivation and dissociation, respectively. The P_b passivation in *molecular* H_2 and dissociation in vacuum [studied in the temperature (T_{an}) ranges 230–260 and 500–590°C, respectively] is modelled by the simple chemical reactions

$$P_b + H_2 \rightarrow P_b + H, \tag{1}$$

$$P_bH \rightarrow P_b + H, \tag{2}$$

leading to the respective first-order differential rate equations $d[P_b]/dt = -k_f[H_2][P_b]$ and $d[P_b]/dt = k_d(N_0 - [P_b])$, with solutions

$$[P_b]/N_0 = \exp(-k_f\,[H_2]t), \tag{3}$$

$$[P_b]/N_0 = 1 - \exp(-k_d t), \tag{4}$$

where the rate constants are given by the Arrhenius equations $k_f = k_{f0}\exp(-E_f/kT)$ and $k_d = k_{d0}\exp(-E_d/kT)$. Here, N_0 is the initial density of P_b and HP_b (maximum number of recoverable ESR-active P_b centers) entities, respectively, $[H_2]$ the volume concentration of H_2 at the interface, and k Boltzmann's constant. The inferred parameters were $E_f = 1.66 \pm 0.06$ eV, $E_d = 2.56 \pm 0.06$, and preexponential factors $k_{f0} = 1.94\,(+2/-1) \times 10^{-6}$ cm^3/s, $k_{d0} \sim 1.2 \times 10^{12}$ s^{-1}.

The sequence of the Eqs. (1) and (2) is equivalent to the dissociation of the H_2 molecule (at the Si/SiO_2 interface), with a net energy ~ 4.2 eV, close to the value of 4.52 eV for dissociation in vacuo. It exposes P_b as a catalyst for cracking H_2.

Regarding passivation, basic ingredients of the ST model include: (i) H_2 is physically absorbed into the SiO_2 layer and diffuses molecularly among the accessible interstices of the SiO_2 network, including the reaction site at the P_b center; (ii) Rather than diffusion, the passivation is limited by direct P_b–H_2 reaction at the P_b reaction site; (iii) there is no preliminary cracking at internal sites in the SiO_2 on their way towards the interface; (iv) The interfacial concentration of H_2 is assumed equal to the physical solubility of H_2 in bulk vitreous silica, and the supply of H_2 considered unlimited. (v) For both the passivation and dissociation steps, single-valued activation energies (E_f and E_d) are presumed. (v) It was argued that the deduced activation energies for Eqs. (1) and (2) are equal or only slightly larger than the energy difference between the respective initial and final constituents. Hence, the reverse passivation and dissociation reactions would proceed essentially spontaneously (little or no barrier) in the presence of atomic hydrogen.

The ST model enjoyed theoretical support [33] from semiempirical spin-unrestricted molecular orbital cluster calculations on P_b. The values $E_f = 1.32$ eV and $E_d = 2.7$ eV were reported, in fair agreement with Brower's data [18,19] (1.66 and 2.56 eV, respectively). Also of interest may be the theoretical results [34] for the case of the Si–H bond placed in bulk Si. The work reports an $E_d = 2.5$ eV for removing H to a position 'far' away from the dangling bond, while a value $E_d = 1.5$ eV is found for moving the H atom to a neighboring Si–Si bond-center site. A more recent ESR study [23] of P_b H dissociation utilizing isochronal (2h) annealing, when interpreted within the ST model, largely affirmed Brower's results [19]. However, the interpretation was carried out assuming first-order kinetics, whereby an appropriate value for k_{d0} was postulated — it could not be inferred independently. The intertwined effect of E_d and k_{d0} in Eq. (4), in

conjunction with the limitation in data, resulted in equally 'good' fits for a broad range of k_{d0}–E_d values, i.e., $E_d = 2.4$–2.9 eV for k_{d0} varying from 1×10^{11} to 1×10^{14} s^{-1}, a broad range indeed, of little decisive use.

2.2. Revised passivation scheme

Although the ST model was soon accepted as definitive upon disclosure, it later on appeared to be based on indequate data [21,22], of insufficient extent. In a recent extensive ESR work [21], the passivation model, as embraced by Eq. (3), dramatically fell short in accounting for expanded sets of data. In that ESR work, revisiting the interaction kinetics, a consistent passivation scheme for P_bs was attained — termed the generalised simple thermal (GST) model —, also based on the chemical pathway represented by Eq. (1). Within the GST model, a major finding was the demonstration of the existence of a significant spread σ_{E_f} in the activation energy E_f for passivation. Without this recognition, no consistent description could be attained. As outlined there, the inferred values of physical parameters, in particular the average activation energy and preexponential factor, now match the underlying physical insight.

The kinetics of passivation as a function of time t was found reliably described by the convolution

$$\frac{[P_b]}{N_0} = \frac{1}{\sqrt{2\pi}\sigma_{E_f}} \times \int_0^\infty e^{-[(E_{fi}-E_f)^2/(2\sigma_{E_f}^2)+tk_{f0}[H_2]\exp(-E_{fi}/kT)]}\, dE_{fi}. \quad (5)$$

It accounts for all experimental data, the inferred values of the pertinent physical parameters being surveyed in Table 1. As explained, the spread just traces back to the stress-induced variations in the P_b atomic morphology over the various sites.

The passivation of P_{b0} and P_{b1} has also been extensively studied [22] (isothermally) by ESR, giving as mean values, respectively, $E_f = 1.51 \pm 0.04$ and 1.57 ± 0.04 eV, and revealing for both defects (similar as for P_b) a spread $\sigma_{E_f} = 0.15 \pm 0.03$ eV. Thus, identical E_f values are found for P_b and P_{b0} passivation (cf. Table 1).

Table 1
Results within the generalized simple thermal (GST) model for the kinetics of thermal passivation in H_2 and dissociation in vacuum of P_b (P_bH) defects at the interface of standard (1 1 1)Si/SiO_2 (oxidation temperature $\gtrsim$800°C)

Dissociation		
E_d (eV)	σ_{E_d} (eV)	k_{d0} (10^{13} s^{-1})
2.83 ± 0.02	0.08 ± 0.03	1.6 ± 0.5
Passivation[a]		
E_f (eV)	σ_{E_f} (eV)	k_{f0} (10^{-8} cm^3 s^{-1})
1.51 ± 0.04	0.06 ± 0.004	$9.8\ (+8/-5)$

[a]Ref. [21].

3. Revisiting P_b–hydrogen dissociation kinetics

Clearly, there are various reasons to readdress the ST model for P_b passivation in H_2. These include the necessary alleviation of a previous [18,19] inadvertent flaw in ESR experimenting regarding the monitoring of the P_b defect density and the above-mentioned inadequacy of the ST model to account for experimental data. With the unveiled intrinsic spread σ_{E_f} in E_f, it is then conceivable to expect a correlated analogous spread in the activation energy E_d for P_bH dissociation. Three, the previously inferred k_{d0} value appears unrealistically low (vide infra). The present work intends to thoroughly verify the ST model, and if applicable, to determine E_d and k_{d0} independently. This is realized through providing broad data ranges, combination of both isothermal and isochronal annealing, enhanced ESR sensitivity, and extension to enhanced P_b density. In combination with the previous consolidated passivation picture, it will be outlined that an overall consistent model for the P_b–H_2 interaction is attained, matching underlying physical insight.

3.1. Experimental details

Slices of 2×9 mm^2 main face, appropriate fore ESR, were cut from 2-in-diameter float zone (1 1 1) Si wafers ($> 100\ \Omega$ cm, p-type, two side polished) of thickness ~ 70 μm. Their 9-mm edge was a ⟨1 1 0⟩ direction. After wet cleaning, multiple samples (each comprising ~ 10 slices) were submitted to various thermal steps in a high-vacuum laboratory set up, as described elsewhere [21,25].

Briefly, samples were first oxidised at ~ 970°C (1.1 atm dry O_2; 99.9995%; oxide thickness $d_{ox} \sim 42$ nm), terminated by rapid cooling to room temperature in O_2. It was standardly followed by a ~ 40-min treatment in H_2 (1.1 atm; 99.9999%) at 405°C in order to passivate [18,21,35] all P_bs, as affirmed by ESR. This then establishes the starting condition for the dissociation study. Samples were heated for appropriate times and at desired temperatures in the range 480–970°C, either isochronically or isothermally. The isochronal mode implied two types of investigations: In a first one, a freshly oxidized and subsequently fully passivated sample was used for each isochronal (62 min) vacuum annealing step — henceforth referred to as the fresh-oxide samples set. In a second type, physically only two specimens were used. Upon oxidation, each was first submitted to a post oxidation anneal (POA) in high vacuum at 968 or

~ 1000°C for 1 h, in order to increase the P_b density (different for the two temperatures) through the creation mechanism [35]. These are referred to as POA samples. They were then repeatedly submitted to alternately isochronal annealing and exhaustive repassivation. The dissociation results of both procedures are found to coincide.

Conventional absorption mode ESR (~ 20.6 GHz) measurements were carried out at 4.3 K, with the applied microwave power levels P_μ ($\lesssim 0.3$ nW) and modulation amplitude (~ 0.25 G) restricted to linear signal response levels [21]. Spin densities were determined by regular double numerical integration of the dP_μ/dB spectra relative to that of a comounted isotropic spin standard recorded in one trace. This contrasts with the previous work [18,19], which rather used the peak-to-peak height $2V_D$ of the derivative–absorption signal to monitor [P_b.]. But as noticed [21] that procedure is spectroscopically justified only if both the line width and shape remain unchanged — neither of which holds as later on manifestly exposed by analysing dipolar interactions [36].

3.2. Experimental results and interpretation

Three sets of isochronal (~ 62 min) data on depassivation of P_b defects by vacuum annealing were measured. Fig. 1 represents the fresh oxide set, characterised by $N_0 = (4.7 \pm 0.2) \times 10^{12}$ cm^{-2}, the intrinsic P_b density. The two sets of data shown in Fig. 2, by contrast, were each obtained on one state-of-the-art oxidized sample, first submitted after the oxidation to a high-temperature vacuum anneal for ~ 1 h at ~ 967 [Fig. 2(a)] or ~ 1000°C [Fig. 2(b)], resulting in $N_0 = (12.2 \pm 0.2)$ and $(14.0 \pm 0.2) \times 10^{12}$ cm^{-2}, respectively. Within a set, each data point is thus obtained by repeated desorption and exhaustive repassivation.

According to the ST model, the data should check with the first-order kinetics Eq. (4). However, fitting this equation faces two major obstacles. First, with k_{d0} and E_d as fitting parameters, no satisfactory fit can be attained. The failure is blatently exposed in Fig. 1 by the dotted curve, representing a 'best' fit obtained with $E_d = 2.83$ eV for a *postulated* value $k_{d0} = 1.6 \times 10^{13}$ s^{-1}. The major shortcoming is clear: the dissociation behavior as a function of T_{an} prescribed by Eq. (4) appears far too abrupt for the more stretched out data. The same conclusion applies for the high-N_0 samples. For comparison, also shown in Fig. 2(a) (dashed line) is the prescribed dissociation behavior [Eq. (4)] using the previous values [19] ($k_{d0} = 1.2 \times 10^{12}$ s^{-1}; $E_d = 2.56$ eV), exposing the inadequacy of the initial model. Second, with respect to the aimed inference of k_{d0} and E_d, the fitting to the isochronal data is far from unique — not even with a much improved set of data as shown — due to the strong correlation of these parameters in Eq. (4).

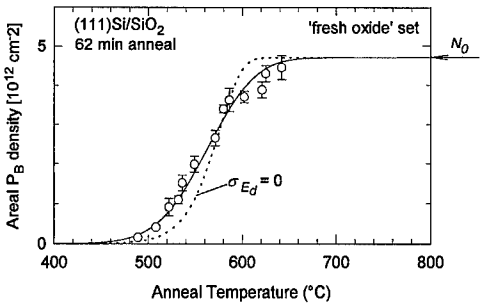

Fig. 1. Recovery of paramagnetic P_b defects (P_bH dissociation) by isochronal annealing in vacuum of as-oxidized (1 1 1)Si/SiO_2 ('fresh oxide' sample set): for each data point, a freshly oxidized specimen is used, subsequently exhaustively passivated in H_2 (405°C). The solid curve represents an optimised fit of the generalized simple thermal model [Eq. (6)], with the inferred parameters collected in Table 1. The dotted curve corresponds to an 'optimized' fit for the ST model [Eq. (4)] using the same parameter values as listed in Table 1, but with spread $\sigma_{E_d} = 0$.

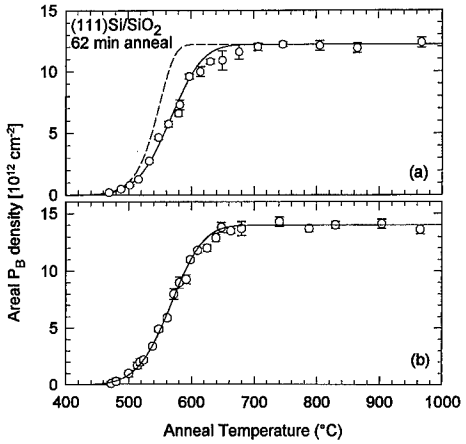

Fig. 2. Recovery of P_b defects by isochronal annealing in vacuum of (1 1 1)Si/SiO_2 structures initially 'degraded' by POA at 968 (a) and ~ 1000°C (b), resulting in $N_0 = (12.2 \pm 0.2)$ and $(14 \pm 0.2) \times 10^{12}$ cm^{-2}, respectively. Solid curves are fits of the GST model [Eq. (6)] using the data in Table 1. The dashed curve is calculated from Eq. (4) (the ST model) using Brower's parameters (Ref. [19]): $E_d = 2.56$ eV; $k_{d0} = 1.2 \times 10^{12}$ cm^{-2}.

Improvement of fitting significance is achieved by resorting to isothermal study. The results, obtained for $T = 538$, 561, and 592°C on one sample of $N_0 = (14.0 \pm 0.2) \times 10^{12}$ cm^{-2} are assembled in Fig. 3(a). According to Eq. (4) (the ST model), the data, when plotted as log of the fraction of P_b H centers ($= 1 - [P_b]/$

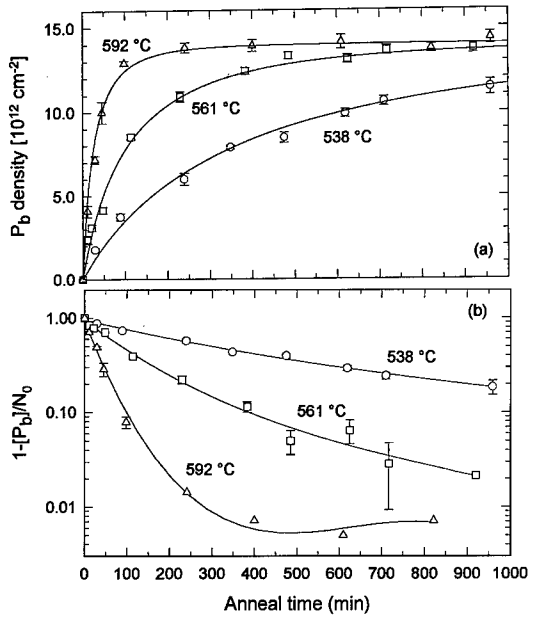

Fig. 3. (a) Isothermal recovery of P_b centers in the degraded (1 1 1)Si/SiO_2 sample of $N_0 \sim 14 \times 10^{12}$ cm^{-2}. The curves represent a global fit of the GST model [Eq. (6)], giving the parameters collected in Table 1; (b) same data plotted semilogarithmically in terms of [P_bH]. Curves guide the eye.

N_0) versus time, should exhibit a linear behavior. Such a plot is shown in Fig. 3(b), from where, quite in contrast, there is little evidence for straight lines, exposing an alarming discrepancy. Here, it should be recalled that in a similar semilogarithmic plot using the relative P_b signal heights ($1 - V_D/V_D$) versus t, Brower [19] could fit his data with straight lines, which suggested true exponential decay of [P_b] versus t. It was this apparent simple exponential decay that was taken as proof for the first-order kinetics [Eq. (4)]. Apparently then, the prime motive for the simple model embraced by Eqs. (2) and (4) is invalidated. Rather, main observations are: (i) as most prominent from the highest T_{an} data, an initial steep drop in P_bH density over about the first hour of dissociation; (ii) a gradual curving down with increasing t, without, however, much linear trend.

One could then conclude the deduced P_bH dissociation model to be plainly incorrect. Yet, with the GST passivation model as backdrop, where the existence of σ_{E_f} was demonstrated, one might expect a similar, correlated spread σ_{E_d} in E_d. Including this might improve the model. The existance of such spread is also hinted by the current data. For one, there is the remarkable observation of the steep drop in [P_bH] over the first period of dissociation [cf. Fig. 3(a)]. In one opinion, this may indeed be reminiscent of a nonuniformity of E_d within the P_b system, i.e., the existence of a spread. Also, regarding the isochronal data shown in Figs. 1 and 2, as already mentioned, the experimental dissociation is pertinently more stretched out than predicted by the ST model [Eq. (4)], which may be accounted for by a spread in E_d; It would provide a direct experimental evidence for the existence of such spread.

Accordingly, the ST model is amended for the existence of a spread in E_d, henceforth also referred to as part of the GST model. This is simply accomplished starting from Eq. (4), by assuming, as a first approach, a Gaussian distribution in E_d of standard deviation σ_{E_d}, leading to the generalized dissociation formula

$$\frac{[P_b]}{N_0} = 1 - \frac{1}{\sqrt{2\pi}\sigma_{E_d}} \times \int_0^\infty e^{-[(E_{di}-E_d)^2/(2\sigma_{E_d}^2)+tk_{d0}\exp(-E_{di}/kT)]}\, dE_{di}, \quad (6)$$

where E_d now represents the *mean* activation energy and where the integration extends over all possible E_d values. Clearly, a pay off is that the much enhanced complexity of this model [Eq. (6)] hampers data interpretation; one can no longer resort to the simple fitting of straight lines, enabling straightforward extraction of E_d and k_{d0}. Instead, all data must be self-consistantly fitted together. Yet, though interpretatively more cumbersome than Eq. (4), a successful fit is readily obtained, as illustrated by the solid lines in Fig. 3(a). The deduced parameters are listed in Table 1, revealing a spread $\sigma_{E_d} = 0.08 \pm 0.03$ eV. An equally satisfactory fit (solid lines) is obtained for the isochronal data displayed in Figs. 1 and 2, with the *same* values of the parameters as given in Table 1.

4. Discussion

We first comment on the inferred existence of the previously unrecognized spread σ_{E_d} in E_d. As to its physical origin, one may refer to a pertinent aspect of P_b defects, i.e., their interfacial location. The P_bs, as archetype interface defects, reside in the non-ideal transition region between c-Si and a-SiO_2, dispersed by interface strain as a result of crystal-network mismatch. Hence, unlike the case of a defect system embedded in a bulk single crystal, the physical environment over the individual P_b sites will not be non-uniform. This must reflect back as a variation in defect bonding configuration, hence also in P_bH bond strength, and a fortiori E_d and E_f. In this view, the existence of the spread in E_d appears just natural.

There exist other evidences for the existence of σ_{E_d} from at least three sides. First, as mentioned, there is the previous ESR work [25] on the relationship between P_b and strain, providing direct evidence for the existence of a spread in the P_b defect configuration over the various sites. Second, perhaps most convincing, there is the long

known electrical fact that the P_b energy levels in the band gap exhibit a significant distribution [2,30,31] (several tenths of eV).

Next, the derived value for k_{d0} is addressed. As outlined, fitting of the GST model to all data sets globally very convincingly gives $k_{d0} = (1.6 \pm 0.5) \times 10^{13}\,s^{-1}$, thus differing significantly from the previously suggested low value [19] of $\sim 1.2 \times 10^{12}\,s^{-1}$. The latter may appear inconsistently low. Within the simple reaction rate theory, the preexponential factor k_{d0} represents an attempt frequency, which for the current Si–hydrogen interaction case should be accounted for by an appropriate Si–H vibrational mode. The k_{d0} value inferred here within the GST model is now found to be reassuringly close to the known low-frequency ($Si_3 \equiv$)Si–H bending mode [37] at 1.86×10^{13} Hz, in agreement with theoretical expectations [34]. It thus appears that with the GST scheme, fitting all available experimental data, a truly consistent *interpretative* model has been attained. The fact, now, that the inferred k_{d0} value is in accordance with a consolidated vibration frequency (bending mode) of the Si–H bond strongly suggests its underlaying basis also constituting the correct physical picture.

The results may be put in the perspective of the technologically dominant (1 0 0)Si/SiO_2 interface. A major result of the present study in conjunction with previous work [21] carried out along the same lines (extended sets of data, proper ESR signal intensity probing) is the demonstration of the existence of distinct spreads in both E_f and E_d for P_b. Interestingly, similar work [22] on passivation in H_2 for (1 0 0)Si/SiO_2 has also revealed significant spreads in E_f for both P_{b0} and P_{b1}: $\sigma_{E_f}(P_{b0})$, $\sigma_{E_f}(P_{b1}) \sim 0.15$ eV. Hence, when transposing from the P_b case, the activation energy for *dissociation* of inactivated P_{b0} and P_{b1} centers is also expected to exhibit noticeable spreads. This is more so for P_{b0}, pictured as the equivalent of P_b at the (1 0 0)Si/SiO_2 interface. Among others, the existence of spreads in activation energies has repercussions for technological interface defect control. For one, the existence of $\sigma_{E_f}(P_{b0}, P_{b1})$ reduces the passivation efficiency of these defects in a typical H_2 ($\sim$ 400°C; 30′) treatment.

5. Concluding remarks

The dissociation kinetics of the P_b interface defects in standard thermal (1 1 1)Si/SiO_2 has been extensively studied with particular attention to correct ESR spectroscopy, providing a sufficiently broad set of data, both isothermally and isochronically, so as to enable conclusive model verification and decisive objective parameter determination. The isothermal dissociation data $[P_bH]$ versus time is found to exhibit a manifest non-simple exponential decay. Within the ST model, this reveals the existence of a spread σ_{E_d} ($\sim$0.08 eV) around the mean activation energy E_d (2.83 $\pm$ 0.03 eV). Such spread is the natural result of the interfacial position of the P_bs, that is, a nonuniform strained environment. The attractive ST model for P_b recovery has been upgraded to a consistent model by incorporation of the spread σ_{E_d}. The inferred Arrhenius preexponential factor (attempt frequency) k_{d0} is found close to Si–H wagging mode frequency. While reflecting the self-consistency of the underlying dissociation model, it suggests that the wagging vibration provides the relevant attempt frequency.

Recent extensive ESR work on *passivation* kinetics of P_b in H_2 has also demonstrated the presence of a spread σ_{E_f} in E_f, which when taken into account, led to a consistent picture in compliance with underlying physics. Hence, when combined with the present results, it appears a truly unified consistent picture of the P_b–H_2 interaction kinetics has been attained, that matches physical insight. The attained model also applies to the trivalent Si P_{b0} and P_{b1} defects in (1 0 0)Si/SiO_2.

References

[1] Y.C. Cheng, Prog. Surf. Sci. 8 (1977) 181, and references therein.
[2] R. Helms, E. Poindexter, Rep. Prog. Phys. 57 (1994) 791, and references therein.
[3] E. Kooi, Philips Res. Rep. 20 (1965) 528.
[4] F. Montillo, P. Balk, J. Electrochem. Soc. 118 (1971) 1463.
[5] D.L. Griscom, J. Appl. Phys. 58 (1985) 2524.
[6] P.L. Castro, B.E. Deal, J. Electrochem. Soc. 118 (1971) 280.
[7] S. Kar, S. Ashok, J. Appl. Phys. 73 (1993) 2187.
[8] H. Li, E.A. Ogryzlo, Can. J. Phys. (Supp.) 74 (1996) S233.
[9] L. Do Thanh, P. Balk, J. Electrochem. Soc. 135 (1988) 1797.
[10] S.M. Meyers, P.M. Richards, J. Appl. Phys. 67 (1990) 4064.
[11] S.R. Hofstein, Solid-State Electron. 10 (1967) 657.
[12] M.L Reed, J.D. Plummer, J. Appl. Phys. 63 (1988) 5776.
[13] E.P. Burte, J. Appl. Phys. 64 (1988) 5013.
[14] K.G. Lynn, B. Nielsen, D.O. Welch, Can. J. Phys. 67 (1989) 818.
[15] R. Khatri, P. Asoka-Kumar, B. Nielsen, L.O. Roellig, K.G. Lynn, Appl. Phys. Lett. 65 (1994) 330.
[16] C.-T. Sah, J.Y.- C Sun, J.J.-T. Tsou, J. Appl. Phys. 55 (1984) 1525.
[17] L. Trombetta, G. Gerardi, D.J. DiMaria, E. Tierney, J. Appl. Phys. 64 (1988) 2434.
[18] K.L. Brower, Phys. Rev. 38 (1988) 9657.
[19] K.L. Brower, Phys. Rev. B 42 (1990) 3444.
[20] K.L. Brower, S.M. Myers, Appl. Phys. Lett. 57 (1990) 162.
[21] A. Stesmans, Appl. Phys. Lett. 68 (1996) 2723.
[22] A. Stesmans, Appl. Phys. Lett. 68 (1996) 2076.
[23] J.H. Stathis, J. Appl. Phys. 77 (1995) 6205.
[24] J.H. Stathis, J. Appl. Phys. 78 (1995) 5215.
[25] A. Stesmans, Phys. Rev. B 48 (1993) 2418.
[26] A. Stesmans, Solid State Commun. 96 (1995) 397.
[27] A. Stesmans, V.V. Afanas'ev, J. Phys.: Condens. Matter 10 (1998) L19.

[28] A. Stesmans, B. Nouwen, V.V. Afanas'ev, Phys. Rev. 58 (1998) 15801.
[29] Y. Nishi, Jpn. J. Appl. Phys. 10 (1971) 52.
[30] E.H. Poindexter, P. Caplan, B. Deal, R. Razouk, J. Appl. Phys. 52 (1981) 879.
[31] N.M. Johnson, D.K. Biegelsen, M.D. Moyer, J. Vac, Sci. Technol. 19 (1981) 390.
[32] E.H. Poindexter, P.J. Caplan, Prog. Surf. Sci. 14 (1983) 201.
[33] A.H. Edwards, Phys. Rev. B 44 (1991) 1832.
[34] C.G. Van de Walle, R.B. Street, Phys. Rev. B 49 (1994) 14766.
[35] A. Stesmans, V.V. Afanas'ev, Phys. Rev. B 54 (1996) R11129.
[36] A. Stesmans, G. Van Gorp, Phys. Rev. B 42 (1990) 3765.
[37] A. Stesmans, G. Van Gorp, Phys. Rev. 45 (1992) 4344.

ELSEVIER

Physica B 273–274 (1999) 1022–1026

PHYSICA B

www.elsevier.com/locate/physb

Aspects of defects in silica related to dielectric breakdown of gate oxides in MOSFETs

Peter E. Blöchl[a,*], James H. Stathis[b]

[a]*IBM Research, Zurich Research Laboratory, CH-8803 Rüschlikon, Switzerland*
[b]*IBM Research, Thomas J. Watson Research Center, Yorktown Heights, NY 10596, USA*

Abstract

Defects in silica related to hydrogen and oxygen vacancies have been analyzed using first principles density functional calculations. The hydrogen bridge has been identified as the defect responsible for the stress-induced leakage current, a forerunner of dielectric breakdown. The question of Joule heating of the oxide as a result of dielectric breakdown is discussed. A classification scheme for defects in the short-range structure of silica is presented. © 1999 Elsevier Science B.V. All rights reserved.

Keywords: Silicon dioxide; Tunneling; Dielectric breakdown

1. Introduction

Recent extrapolations of the lifetime of metal-oxide-semiconductor field-effect transitors (MOSFETs) predict an early breakdown of gate oxides [1]. This obviously shortens the lifetime of semiconductor components. The stress-induced leakage current (SILC), a tunneling current through the oxide that increases during device operation, is considered a forerunner and possible cause of dielectric breakdown. The present understanding is that hot electrons crossing the oxide release hydrogen bound into the lattice near or in the gate electrode, or that hydrogen is released by hot electrons in or near the channel [2–4]. We analyzed the defects related to hydrogen and oxygen vacancies. The latter must be considered because the thermal oxides used as gate oxides are oxygen-deficient. These studies allowed us to identify the hydrogen bridge, i.e. a complex of a hydrogen atom with an oxygen vacancy, as the defect responsible for SILC [5]. In this paper, we summarize the main results and discuss selected topics of interest related to dielectric breakdown.

We begin by presenting a classification scheme and a notation for the short-range order in silica. Then we discuss in some detail the definition of charge-state levels, which have been evaluated to determine the defect responsible for SILC [5]. After a summary of the results that identify the hydrogen bridge as the defect responsible for SILC, we discuss the problem that the heat dissipation of the SILC is apparently insufficient to induce the catastrophic material failure observed during the dielectric breakdown of the oxide.

2. Short-range order defects

The short-range order of silica is determined by each silicon atom being bonded to four oxygen neighbors and each oxygen being bonded to two silicon neighbors. Any network of this type will be called an ideal, i.e. a defect-free, silica framework. This framework can be classified further for example by its ring size distribution. Defects of the short-range structure can be over- or under-coordinated atoms,"wrong bonds" such as Si–Si or O–O bonds, and impurities. Hydrogen is an impurity that is so common in silica that it is often considered an intrinsic rather than an extrinsic defect.

In the following, a defect notation is proposed that we found convenient and transparent. We found it useful to

* Corresponding author. Tel.: + 41-1-7248-656; fax: + 41-1-7248-953.

E-mail address: blo@zurich.ibm.com (P.E. Blöchl)

0921-4526/99/$ - see front matter
PII: S0921-4526(99)00628-6

denote an ill-coordinated atom by its element symbol followed by its coordination number, i.e. the number of bonds, in parentheses, such as $[O(3)^+]$ for an over-coordinated oxygen atom in the positive charge state. The preferred coordination of hydrogen is one. "Wrong bonds" are indicated by writing out the entire cluster participating in wrong bonds, such as [SiSi] for an oxygen vacancy. If a defect consists of parts that are connected only by an ideal silica network, we connect the parts by a plus sign such as $[Si(3) + O(3)^+]$ for the so-called E'_γ center, an oxygen vacancy where one of the silicon atoms is inverted and forms a bond with an oxygen bridge.

For atoms that are connected as in the ideal silica network, the coordination number is omitted.

With this classification of defect structures, it is straightforward to set up a hierarchy of intrinsic defects in silica:

- Singly over-coordinated and under-coordinated defects

  - The classical silicon dangling bond center [Si(3)] gives rise to a suite of E′ centers. The primitive defect is called E'_s or surface E′ center [6].
  - The over-coordinated oxygen atom $[O(3)^+]$ is the classical positive charge defect in silica and an important precursor of [Si(3)]. The dangling bond center [Si(3)] is obtained from $[O(3)^+]$ by adding an electron and breaking one SiO bond.
  - The classical negative charge defect in silica is $[Si(5)^-]$, which is closely related to $[O(1)^-]$. The latter is obtained from $[Si(5)^-]$ by breaking a Si–O bond.
  - The non-bridging oxygen hole center, i.e. the oxygen radical [O(1)], is obtained from the precursor $[O(1)^-]$ after hole capture [7]. It occurs predominantly in synthetic silica with excess oxygen.

- "Wrong" bonds:

  - The oxygen vacancy [SiSi].
  - The peroxy bridge [OO] [8] is closely related to [O(3)O(1)]. The latter is obtained by rotating the peroxy bond perpendicular to the line connecting the two silicon atoms it bridges.
  - The hydroxyl group [OH] attached to a silicon site is an important ingredient of the oxide framework. This defect is of particular importance in optical fibers because the first overtone of the OH stretch vibration lies close to the signal transmission window. Thus the hydroxyl group is an important source of the absorption losses in the signal transmission. Special care must be taken to remove hydroxyl groups, which are annealed out as water and oxygen bridges are formed.
  - The fragment [SiH]. This defect can also be detected by infrared (IR) absorption because the stretch vibration gives rise to a characteristic band above the framework vibrations.

- Interstitial hydrogen.

  - In the positive charge state, hydrogen binds to an oxygen bridge and forms a threefold coordinated oxygen atom $[O(3)^+H]$ [9].
  - In the neutral charge state hydrogen is a clearly distinguishable ESR (electron spin resonance) active defect [H(0)] that does not form bonds to the lattice but rather occupies the centers of the cages in silica [10].
  - In the negative charge state, hydrogen forms bonds with a silicon atom, resulting in a defect $[Si(5)H^-]$ [9].

Increasingly more complex defects can be built up from the basic building blocks described here. It should be noted that this structural notation is not completely unambiguous because weak bonds may be considered in some cases or neglected in other cases, resulting in different (Table 1) notations for the same defect.

The composite defects considered by us so far are the following: The metastable oxygen vacancy is called the E'_γ center in amorphous silica and E'_1 center in quartz [11,12]. This defect, the structure of which has the form $[O(3)^+ + Si(3)]$, has been widely studied. The E'_γ or E'_1 center has a clear ESR spectrum resulting from the electron in the dangling bond of the under-coordinated silicon atom. We find this defect to be several electron volts less stable than the neutral oxygen vacancy assuming that the Fermi level is located near the mid-gap energy of silicon at the interface. It can, however, be created by avalanche hole injection, which substantially lowers the effective Fermi level, and thus stabilizes the positive charge states of the oxygen vacancy, namely $[SiSi^+]$ and $[O(3)^+ + Si(3)]$.

The oxygen vacancy can capture an interstitial hydrogen atom and form a hydrogen bridge [SiH(2)Si], which exists in three charge states. The structures of the three

Table 1
Notation of the most common paramagnetic defects in amorphous silica (first column), quartz (second column), and the notation proposed in this paper

E'_γ	E'_1	$[O(3)^+ + Si(3)]$
E'_β	E'_2	[SiH + Si(3)]
	E'_4	[SiH(2)Si]
E'_δ		$[SiSi^+]$
E'_s		[Si(3)]
NBOHC		[O(1)]
Peroxy		$[OO^+]$ or [O(3)O(1)]

charge states — positive, neutral, and negative — have similar structures, the main difference being that the hydrogen atom localizes increasingly on one or the other silicon atom with increasing number of electrons. This defect has been observed sofar only in α-quartz [13], and our calculations [5] provide the first evidence of its existence in the amorphous matrix.

The hydrogen bridge is not the most stable configuration, but transforms into [SiH + Si(3)], which is known as the E'_β center in amorphous silica or as the E'_2 center in quartz [12,14]. When an electron is removed from the paramagnetic [SiH + Si(3)] defect, the now-empty dangling bond on the silicon atom binds to an oxygen bridge, forming [SiH + $O(3)^+$]. If an electron is added to [SiH + Si(3)] the filled dangling attaches to a nearby silicon atom, forming [SiH + $SiSi(5)^-$].

An important aspect of any defect is its stoichiometry. Local transformations of defects or defect reactions must conserve the stoichiometry. This results in selection rules for chemical transformations.

The stoichiometry of a defect can be derived from the notation by the following steps: "Wrong" bonds are broken and the coordination number of the bond partners is reduced accordingly. The hydrogen content is thus readily obtained. The oxygen deficiency is obtained by adding any missing bond of a silicon atom and any additional bond of an oxygen atom as one one-half oxygen vacancy each.

3. Charge-state levels

Owing to the flexible bond network, it is important to distinguish carefully among various definitions of charge-state levels. We will discuss here the thermodynamic and switching charge-state levels.

The stability of the charge state of a defect as a function of the Fermi level is what we call the thermodynamic charge-state level. In a typical experiment the Fermi level is determined by the Fermi levels of the contacts, which typically lie about 3 eV below the oxide conduction band edge. Using electron or avalanche hole injection it is possible to shift the Fermi level far from the position determined by the band offsets, and thus make charge states accessible that do not normally occur in the unperturbed devices.

The thermodynamic charge-state level can be regarded as a reaction energy where, for example, an electron moves from a reservoir, e.g. the contacts, onto an uncharged defect X^0 to charge it negatively, i.e.

$$X^0 + e \rightarrow X^-.$$

The energy cost to add the electron to the defect is

$$\Delta E = E[X^-] - E[X^0] - \varepsilon_F,$$

where the Fermi energy ε_F of the contacts defines the energy of the electron. The energies for both X^0 and X^- are determined with the structure individually relaxed.

The charge-state level is then defined as

$$\varepsilon_{0/-} = E[X^-] - E[X^0].$$

The physical significance of the charge-state level is that the corresponding orbital is occupied if the Fermi level lies above the charge-state level, and is unoccupied if the Fermi level lies below the charge-state level.

A tunneling process proceeds far from thermal equilibrium. It should be noted that the Fermi level itself is an ill-defined concept in the presence of a high applied voltage.

We discuss here the switching charge-state level that is relevant for the two-step tunneling process. The tunneling event of an electron from the cathode moving to an empty defect level in the oxide is a instantaneous process compared to the time scales of the atomic motion. Hence the electron encounters an essentially frozen atomic structure. The relevant charge-state level is that of adding an electron to the defect but now, in contrast to the calculation of the thermodynamic charge-state level, the atomic structure is held fixed in the structure obtained with the empty orbital. The lifetime of the electron on the defect is of the order of nanoseconds, which is long compared to the time scales of the atomic motion.

The tunneling frequency on the other hand, being of the order of one electron per nanosecond, is low compared to the atomic motion. The defect will therefore relax in order to lower the energy of the additional electron. Silica is special in this regard, as it combines a large band gap of 8–9 eV with a soft lattice. The energy gain from lowering the defect level can therefore be large and the price paid to distort the lattice is relatively minor. During this process, which occurs on a sub-picosecond time scale, the energy level drops, in some cases by as much as 7 eV.

If the energy relaxation is too large, larger than the applied voltage, it is impossible for the electron to proceed to the anode. Hence the electron is trapped. Only electrons with relaxation energies lower than the applied voltage can proceed to the anode and contribute to the tunneling current. (We do not discuss here the resonant tunneling, which is the dominant defect mediated tunneling mechanism, if the more efficient two-step tunnel processes are blocked.)

This criterion provides us with a guideline for selecting the defects responsible for SILC. Candidates should have relaxation energies below about 3 eV, which is the voltage above which electrons are injected into the oxide conduction band.

4. Origin of stress-induced leakage current

Gate oxides exposed to strong electric fields exhibit a tunneling current that increases with the amount of

charge transported through the oxide. This SILC is a forerunner of dielectric breakdown of gate oxides and is even considered a possible cause of it. The current understanding is based on the hydrogen model of Griscom and DiMaria [2–4], who proposed that hydrogen bound into the lattice is released near or in the gate electrode by hot electrons. The released hydrogen diffuses into the oxide and induces defects. Electrons tunnel across the oxide preferentially using these defects as stepping stones. The nature of these defects has only been resolved recently [5].

Our identification of the defect responsible for SILC is based on the fact that most defects in silica trap electrons strongly, and thus do not contribute appreciably to the tunneling current. Only few defects bind the electron sufficiently loosely, for it to proceed towards the anode. The tendency towards strong electron trapping originates from the significant structural relaxation that defects can undergo while capturing electrons or holes.

The only defect for which electrons can pass at a voltage lower than 3 eV is the hydrogen bridge, [SiH(2)Si], a complex between an oxygen vacancy and a hydrogen atom, where the hydrogen atom occupies the bond center of a SiSi bond similar to interstitial hydrogen in silica [15,16]. The relaxation energies of this defect are particularly small because the electron enters a nonbonding orbital of the three-center bond formed by the dangling bonds on silicon with the hydrogen atom in the center.

The prediction that the hydrogen bridge is responsible for SILC explains for the first time the electrically detected magnetic resonance (EDMR) experiments of Stathis [17]. In this experiment, the result of which is displayed in Fig. 1, the shoulder at $g = 2.0076$ in the current induced by magnetic resonance could not be attributed to any of the known defects in amorphous silica. However, this shoulder is naturally explained by the hydrogen hyperfine splitting of the hydrogen bridge. The g-values and hyperfine parameters of the hydrogen bridge have been measured in quartz, where the hydrogen bridge is known as the E_4' center [13]. Our own calculations for the hyperfine parameters of the E_4' center reproduce the small hydrogen hyperfine parameter, whereas the asymmetry of the two participating silicon atoms is underestimated.

The central band of the EDMR spectra can be attributed to the stable partner of the hydrogen bridge, namely the E_β' center, which according to our prediction contributes at voltages beyond 3 eV. The experiments have been done at this high voltage to optimize the signal-to-noise ratio.

The energy loss during stress-induced tunneling has been measured by Takagi et al. [18] to be 1.5 eV, which agrees very well with our prediction of 1.7 eV for the relaxation energy of the hydrogen bridge.

All other properties of the hydrogen bridge derived from electrical measurements [4], namely that the defect

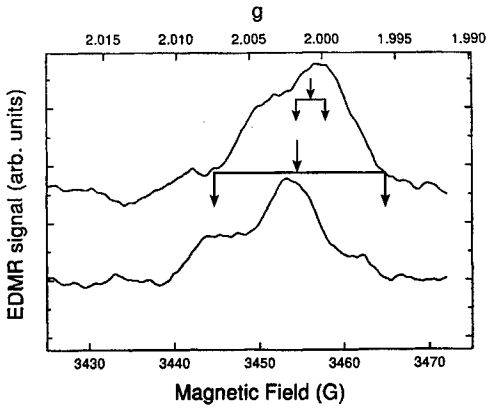

Fig. 1. Electrically detected magnetic resonance of stress-induced leakage current. The lower line refers to collinear magnetic field and current, whereas the upper line refers to perpendicular magnetic field and current. Thus the upper line describes in this case the equatorial components and the lower line describes the axial components of Zeemann and hyperfine splittings. The arrows indicate the Zeeman and hyperfine splittings of the hydorgen bridge [SiH(2)Si] (outer arrows) and of the E_2' center (inner arrow).

is related to hydrogen and is a neutral electron trap, are fulfilled by the hydrogen bridge.

Our work is the first identification of the hydrogen bridge in amorphous silica. The defect is well characterized in quartz, but has never been observed in amorphous silica. A possible reason may be that the hydrogen bridge is not thermodynamically stable, and therefore exists in small quantities. The EDMR experiment of the SILC, however, is only sensitive to the defects that contribute to the tunnel current irrespective of their relative concentrations, and therefore is selective to the hydrogen bridge. Another reason may be that the hydrogen bridge is created by the tunnel current from its stable partner. Our simulations indicate that the neutral [SiH + Si(3)] defect does not transform into [SiH + $O(3)^+$] under hole capture, but into the positive hydrogen bridge. Thus the precursor of the neutral hydrogen bridge is generated via the non-equilibrium tunneling process. It might be of interest to exploit this mechanism in ESR measurements to enhance the ESR signal of the hydrogen bridge.

5. Joule heating due to SILC

Estimates of the power dissipated by two step tunneling processes appear to be too low for it to induce damage in the oxide. This indicates that SILC is not the cause of breakdown, but rather some other aspect of the material changes in the oxide that ultimately lead to breakdown. In this section we discuss the local Joule heating via the two-step tunneling processes.

We use a model where the power P is dissipated uniformly in a volume Ω of radius r_0. Let us consider the change of the thermal energy U under the influence of the power $p(r)$ dissipated locally in Ω and the thermal current j_Q that transports heat away from this region

$$\partial_t U(r) = -\nabla j_Q + p(r), \tag{1}$$

where $p(r)$ is equal to $p_0 = 3P/(4\pi r_0^3)$ inside Ω and zero otherwise.

The heat current is related to the temperature gradient via

$$j_Q = -\kappa \nabla T, \tag{2}$$

where κ is the thermal conductivity.

By combining Eqs. (1) and (2) and assuming steady-state conditions, we obtain the differential equation for the temperature profile

$$\nabla^2 T = \frac{1}{\kappa} p(r), \tag{3}$$

which has the solution

$$T(r) = \frac{p_0}{4\pi\kappa r} \quad \text{for } r > r_0, \tag{4}$$

$$T(r) = \left[\frac{3}{2} - \frac{1}{2}\left(\frac{r}{r_0}\right)^2\right]\frac{p_0}{4\pi\kappa r_0} \quad \text{for } r < r_0. \tag{5}$$

Thus the maximum temperature reached is

$$T_x = \frac{3P}{8\pi\kappa r_0}. \tag{6}$$

Let us take representative data from Stathis and DiMaria [1]. The SILC I_S at breakdown for a 3-nm-thick oxide and a gate area of 5×10^{-4} cm^2 is $I_S = 5$ nA at 2 V, resulting in a power dissipation of 10^{-8} W. If the power is generated at a single defect site, and if we assume a conservative estimate of $r_0 = 1$ Å radius as the region Ω, we obtain

$$T_x = \frac{33\times10^{-8}\ \text{W}}{8\pi\times1.5\ \text{W/Km}\ 10^{-10}\ \text{m}} = 10\ \text{K} \tag{7}$$

for the maximum temperature. Here we used a value of $\kappa = 1.5$ W/(Km) for the thermal conductivity of silica.

Thus our estimate indicates that the Joule heating of SILC is insufficient to destroy the material thermally.

The estimates are taken conservative and assume the validity of steady-state conditions, and that the SILC measured at sensing voltage of 2 eV is identical to that at breakdown voltage. It should be noted that the electrons crossing the oxide by direct tunneling dissipate their energy in the gate, the thermal conductivity of which is two orders of magnitude higher than that of silica. Thus most of the power dissipated due to tunneling electrons will not affect the oxide directly.

This simple analysis indicates that the breakdown of the oxide is not yet fully understood, as the connection between leakage current and material damage remains unexplained.

Acknowledgements

One of us (PEB) thanks Emily Carter for critically reading the manuscript and Chris Van de Walle for interesting discussions.

References

[1] J.H. Stathis, D.J. DiMaria, in: IEDM '98 Technical Digest, IEEE, Piscataway, 1998, p. 167.
[2] D.L. Griscom, J. Electron. Mater. 21 (1992) 762.
[3] D.J. DiMaria, E. Cartier, D. Arnold, J. Appl. Phys. 73 (1993) 3367.
[4] D.J. DiMaria, E. Cartier, J. Appl. Phys. 78 (1995) 3883.
[5] P.E. Blöchl, J.H. Stathis, Phys. Rev. Lett. 83 (1999) 372.
[6] G. Hochstrasser, J.F. Antonini, Surf. Sci. 32 (1972) 644.
[7] M. Stapelbroek, D.L. Griscom, E.J. Friebele, G.H. Sigel Jr., J. Non-Cryst. Solids 32 (1979) 313.
[8] E.J. Friebele, D.L. Griscom, M. Stapelbroek, R.A. Weeks, Phys. Rev. Lett. 42 (1979) 1346.
[9] A. Yokozawa, Y. Miyamoto, Phys. Rev. B 55 (1998) 13 783.
[10] R.A. Weeks, M. Abraham, J. Chem. Phys. 42 (1965) 68.
[11] C.M. Nelson, R.A. Weeks, J. Am. Ceram. Soc. 43 (1960) 396.
[12] R.A. Weeks, C.M. Nelson, J. Am. Ceram. Soc. 43 (1960) 399.
[13] J. Isoya, J.A. Weil, L.E. Halliburton, J. Chem. Phys. 74 (1981) 5436.
[14] R.A. Weeks, Phys. Rev. 130 (1963) 570.
[15] C.G. Van de Walle, Y. Bar-Yam, S.T. Pantelides, Phys. Rev. Lett. 60 (1988) 2761.
[16] C.G. Van de Walle, P.J.H. Denteneer, Y. Bar-Yam, S.T. Pantelides, Phys. Rev. B 39 (1989) 10 791.
[17] J.H. Stathis, Appl. Phys. Lett. 68 (1996) 1669.
[18] S. Takagi, N. Yasuda, A. Toriumi, in: IEDM '96 Technical Digest, IEEE, Piscataway, 1996, p. 323.

ELSEVIER

Physica B 273–274 (1999) 1027–1030

PHYSICA B

www.elsevier.com/locate/physb

Capacitively detected magnetic resonance of defects in MOSFETs

M.S. Brandt*, R. Neuberger, M. Stutzmann

Walter Schottky Institut, Technische Universität München, Am Coulombwall, D 85748 Garching, Germany

Abstract

In p-channel enhancement MOSFETs, a spin-dependent change of the drain-gate capacitance is observed at bias voltages near accumulation. Two resonances, with $g_\perp = 1.9979$ and $g_\parallel = 2.008$ as well as $g \approx 4.9$ are attributed to defects induced by processing as well as to transition metal impurities. The signal intensity of the capacitively detected magnetic resonance (CDMR) is approx. 30 aF, corresponding to about 400 electrons additionally trapped at the edge of the space-charge region under spin resonance conditions. © 1999 Elsevier Science B.V. All rights reserved.

Keywords: MOSFET; CV-characteristic; Electron–spin resonance; Electron paramagnetic resonance

1. Introduction

Defects in metal-oxide-semiconductor field-effect transistors (MOSFETs) continue to be of interest both from a fundamental and applied point of view. A notable example is the observation of an increased stability in deuterated MOSFETs compared to hydrogenated devices [1]. The microscopic identification of such defects with conventional electron spin resonance (ESR) is difficult due to the low defect concentration and the small size of the actual devices. However, the detection of the spin resonance of defects via the measurement of resonantly induced changes of the conductivity (electrically detected magnetic resonance, EDMR) leads to a significant increase in the sensitivity. Spin-dependent recombination both at E′-centers in the gate oxide as well as at P_b-centers at the Si/SiO_2-interface have been observed in EDMR, as reviewed in Refs. [2,3]. In polycrystalline thin-film transistors, spin-dependent recombination at grain boundaries as well as spin-dependent hopping through the gate dielectric have been reported [4]. Similarly, Stathis has observed spin-dependent processes in the tunneling current through a gate oxide which has been current stressed [5].

Electrically detected magnetic resonance is sensitive to changes of the resistance of the device investigated. The effects of spin-dependent transport processes on the capacitance of semiconductor structures have not been studied with a similar intensity as spin-dependent changes of the resistance. In fact, a combination of capacitive methods like deep-level transient spectroscopy (DLTS) with ESR would lead to a spectroscopy which would have a high sensitivity as well as the ability to determine both the energy level of interface defects and their microscopic chemical identity. As first steps towards such an experimental method, Chen and Lang have shown that the current transient caused by thermal re-emission of charge carriers trapped at the Si/SiO_2-interface is spin-dependent [6]. Later, Cavenett et al. [7] have reported that the capacitance of a crystalline Si pin-diode can be spin-dependent under large forward biases. Finally, Stathis and Nishikawa have successfully demonstrated spin-dependent charge pumping in MOSFETs [8]. Here, we present measurements of capacitively detected magnetic resonance (CDMR) on p-channel MOSFETs. We show that under bias voltages near accumulation, spin-dependent trapping of charge carriers by shallow defects at the edge of a space-charge region is observed as a resonant change of the capacitance. Two different defects, tentatively assigned to a defect caused by processing and a transition

* Corresponding author. Tel.: + 49-89-289-12758; fax: + 49-89-289-12737.

E-mail address: mbrandt@physik.tu-muenchen.de (M.S. Brandt)

0921-4526/99/$ - see front matter
PII: S0921-4526(99)00629-8

metal impurity, are resolved. In contrast to conventional EDMR, the method presented here has the potential to allow a quantitative estimation of the defect density.

2. Experimental details

Commercial p-channel enhancement MOSFETs have been used in this study. The device is a short-channel DMOS or DIMOS (double-diffused or double-implanted MOS) field-effect transistor, with the drain contact at the back-side of the p^--doped substrate. Our original intention was to use the device as a simple MOS test structure on p-type Si for CDMR due to its comparatively large gate area and the resulting large capacitance. The room temperature CV-characteristic of the drain-gate and the source-gate capacitance of the device is shown in Fig. 1. The capacitance is measured with a capacitance bridge (Boonton 7200) operating at a test frequency of 1 MHz. In deviation from the simple CV-characteristic of a MOS diode, an additional step is observed in the drain-gate capacitance at a bias of ≈ -1.5 V near accumulation, caused by the presence of a p^-n-junction at the source contact.

For the CDMR measurements, the MOSFET is inserted in the standard TE_{102} cavity of an X-band ESR spectrometer. For certain bias voltages U_{bias}, the resonant change of the drain-gate capacitance is detected with a lock-in amplifier using magnetic field modulation. As usual, a compensating capacitor allows to use the most sensitive measurement range of the capacitance bridge. Since the analog output of the bridge used as the input of the lock-in has a low-pass filter with a cut-off frequency of 20 kHz, the modulation frequency of the magnetic field was kept below 2 kHz. To increase the signal-to-noise ratio of the CDMR spectra, a more stable external power supply was used to apply the bias voltage. All experiments were performed at room temperature using a microwave power of 2 W.

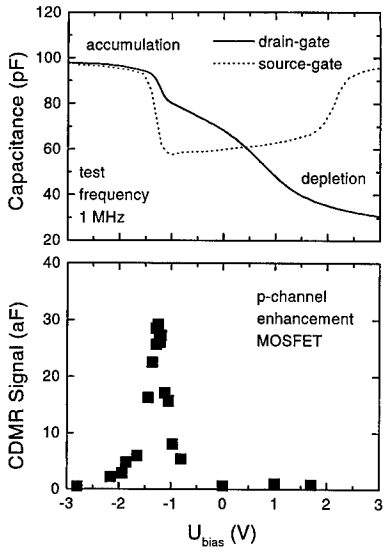

Fig. 1. Capacitance–voltage characteristic of the drain-gate and the source-gate capacitance of the commercial MOSFET investigated. The lower part shows the change of the drain-gate capacitance under spin resonance conditions of the defect at $g \approx 2$.

3. Results and discussion

Fig. 2 shows the CDMR spectrum obtained on the drain-gate capacitance at a bias voltage of -1.3 V for a sample orientation with respect to the magnetic field of H_0 perpendicular to the surface normal [1 0 0]. Two resonances are observed, a narrow resonance with a peak-to-peak linewidth $\Delta H_{pp} = 15$ G at $g = 1.9979$ and a broad, asymmetric resonance at $g = 4.9$. The anisotropy of the narrow resonance is shown in Fig. 3. For all sample orientations with respect to the magnetic field, only a single resonance line is observed. For $H_0 \| [1\,0\,0]$, the g-factor shifts to 2.008. The resonant change of the capacitance ΔC is 30 aF at $U_{bias} = -1.3$ V, corresponding to a relative change of $\Delta C/C \approx 4 \times 10^{-7}$. Towards higher and lower bias voltages, ΔC decreases rapidly, and outside a range of $-2.5\text{ V} < U_{bias} < -0.5$ V, no CDMR is detectable with our experimental set-up (lower part of Fig. 1).

To investigate the influence of current-induced stress on the CDMR, the MOSFET was degraded by applying a bias of 100 V (leading to a current of 0.2 nA) across the gate for 1 h. As a result, the CV-characteristic shifted to lower voltages by about 2.5 V but otherwise remained unchanged, indicating the trapping of charge in the gate oxide (Fig. 4). The only consequence of the degradation on the CDMR is that the bias dependence of the signal

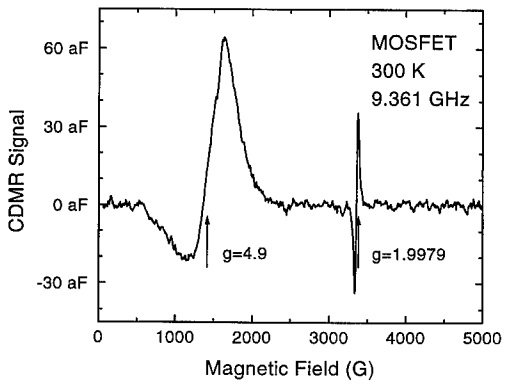

Fig. 2. Capacitively detected magnetic resonance spectrum of the p-channel enhancement MOSFET at a drain-gate bias of -1.3 V using a microwave power of 2 W. Two resonances are clearly resolved.

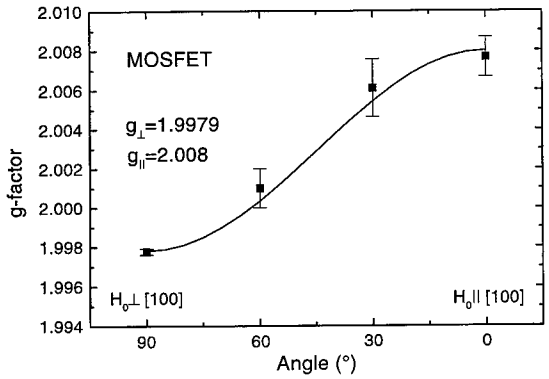

Fig. 3. Anisotropy of the g-factor of the narrow CDMR resonance at $g \approx 2$.

intensity is shifted accordingly. As an example, the CDMR lines obtained from both the as-shipped and the degraded device at a capacitance of 90 pF are also given in Fig. 4. It is evident that g-factor and ΔC are unchanged under degradation and that the CDMR signal does not originate from the trapped charge.

The g-factor observed is markedly different from that of the E'- and P_b-centers usually observed in EDMR experiments on MOSFETs. In fact, the thermal emission rate at room temperature from these deep defect states is much smaller (10^3–10^4 Hz) than the test frequency of 10^6 Hz used in the CDMR experiments. These defects will therefore only be accessible by CDMR experiments at much smaller test frequencies or by spin-dependent DLTS measurements. Instead, the defects observed here are most likely near the Fermi level. Accordingly, the defects could be located at either of the two different space-charge regions present in the device, at the p^--oxide interface or at the p^-n-junction. The fact that the CDMR signal is only observed at the characteristic step of the capacitance caused by the p^-n-junction indicates that the defects are located there. Since the formation of this p^-n-junction involves in-diffusion or implantation, it is indeed to be expected that even after a suitable anneal a small defect concentration remains in this region.

Very few defects in crystalline Si have been found with g-factors similar to those observed here [9]. The most similar g-values have been reported for the G1 defect, assigned to a positively charged vacancy V^+ [10]. The charge state of the G1 defect would indeed agree with the defect being located in the p^--substrate. The vacancy should exists in different crystallographic orientations giving rise to more resonance lines than the single one observed in CDMR. However, preferential alignment of defects after implantation has been observed previously [11]. A stronger argument against the assignment of the narrow CDMR signal to the G1 center is the reported anneal temperature of the G1 center of 150–180 K [12],

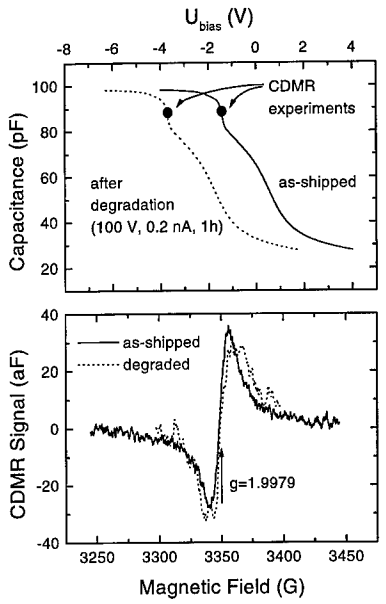

Fig. 4. CV-characteristic of the drain-gate capacitance of the MOSFET in the as-shipped state and after degradation. The CDMR signature and signal intensity measured at a capacitance of 90 pF are the same for both states.

well below room temperature at which the CDMR was performed. Concerning the asymmetric resonance at low magnetic fields, several iron-related complexes have been reported with similar g-factors [13,14]. Although both resonances observed with CDMR cannot be definitely assigned to particular defects at present, it is very likely that the defects are induced by processes involved in the fabrication of the device.

While being very sensitive, electrically detected magnetic resonance cannot provide a quantitative determination of the concentration of defects giving rise to the observed changes in the conductivity. In contrast, CDMR has the potential of providing an estimate of the defect concentration. Under spin resonance conditions, the spin-dependent trapping of charge carriers at paramagnetic defects is enhanced. The reverse process of thermal emission from diamagnetic defects is not spin-dependent. Therefore, an additional charge ΔQ is resonantly stored at the edge of the space-charge region. This charge leads to a change of the voltage across the space-charge region of $\Delta U = \Delta Q/C$. However, since the capacitance C depends on the voltage U as evidenced by the CV-characteristic, a change in voltage leads to a change in the capacitance, which is to first order given by $\Delta C = (dC/dU)\Delta Q/C$. Using the data shown in Fig. 1, we deduce that only about 400 electrons are trapped additionally under spin resonance conditions. For a determination of the total number of defects present, we would however have to correct for the probability of a single

trapping event to be spin-dependent. A measure for this probability are the EDMR signal intensities $\Delta R/R$, which for silicon are typically 10^{-4}–10^{-6}. Together with an estimation of the volume of the space-charge region, we can finally determine the local defect density to between 10^{15} and 10^{17} cm^{-3} in the space-charge region.

4. Conclusion

We have shown that electron spin resonance can lead to resonant changes in the capacitance of MOSFET structures. Two different defects haven been observed in DMOS transistors and have been attributed to process-induced defects at the p^-n-junction. From the above discussion we would expect that the technique could similarly be useful to detect shallow defect states in basic MOS diode structures whose thermal emission can follow the test frequency. The energy level of the defect could then, e.g., be determined from CDMR experiments at different frequencies. Together with the possibility to quantitatively estimate the defect density, this shows that capacitively detected magnetic resonance could develop into a useful defect spectroscopy.

Acknowledgements

The authors acknowledge helpful discussions with and experimental support by R. Zeisel, M.W. Bayerl, S.T.B. Goennenwein and C.E. Nebel. This work was supported by the Deutsche Forschungsgemeinschaft (SFB 348).

References

[1] J.W. Lyding, K. Hess, I.C. Kizilyalli, Appl. Phys. Lett. 68 (1996) 2526.
[2] B. Henderson, M. Pepper, R.L. Vranch, Semicond. Sci. Technol. 4 (1989) 1045.
[3] P.M. Lenahan, M.A. Jupina, Colloids and Surfaces 45 (1990) 191.
[4] G. Kawachi, C.F.O. Graeff, M.S. Brandt, M. Stutzmann, Extended Abstracts of the 1996 International Conference on Solid State Devices and Materials, Yokohama, Japan, 1996, p. 248.
[5] J. Stathis, Appl. Phys. Lett. 68 (1996) 1669.
[6] M.C. Chen, D.V. Lang, Phys. Rev. Lett. 51 (1983) 427.
[7] B.C. Cavenett, M.X. Yan, Semicond. Sci. Technol. 1 (1986) 180.
[8] J. Stathis, H. Nishikawa, unpublished.
[9] E.G. Sieverts, Phys. Stat. Sol. B 120 (1983) 11.
[10] G.D. Watkins, J. Phys. Soc. Jpn. 18 (Suppl. II) (1963) 22.
[11] A. Stesmans, A.G. Revesz, H.L. Hughes, J. Appl. Phys. 69 (1991) 175.
[12] M. Sprenger, S.H. Muller, E.G. Sieverts, C.A.J. Ammerlaan, Phys. Rev. B 35 (1987) 1566.
[13] S.H. Muller, G.M. Tuynman, E.G. Sieverts, C.A.J. Ammerlaan, Phys. Rev. B 25 (1982) 25.
[14] A.A. Ezhevskii, C.A.J. Ammerlaan, Sov. Phys. Semicond. 24 (1990) 851.

ELSEVIER

Physica B 273–274 (1999) 1031–1033

PHYSICA B

www.elsevier.com/locate/physb

Radiation-induced lattice defects in InGaAsP laser diodes and their effects on device performance

H. Ohyama[a,*], E. Simoen[b], C. Claeys[b,c], T. Hakata[a], T. Kudou[a], M. Yoneoka[a], K. Kobayashi[a], M. Nakabayashi[a], Y. Takami[d], H. Sunaga[e]

[a]*Department of Electronic Engineering, Kumamoto National College of Technology, 2659-2 Suya Nishigoshi Kumamoto, 861-1102 Japan*
[b]*IMEC, Kapeldreef 75, B-3001 Leuven, Belgium*
[c]*KU Leuven, ESAT-INSYS, Kard. Mercierlaan 95, B-3001 Leuven, Belgium*
[d]*Rikkyo University, 2-5-1, Nagasaka Yokosuka Kanagawa, 240-0101 Japan*
[e]*Takasaki JAERI, 1233 Watanuki Takasaki Gunma, 370-1292 Japan*

Abstract

Results are presented of an extended study on the degradation and recovery behavior of optical and electrical performance and on induced lattice defects of 1.3 μm InGaAsP double channel planar buried heterostructure laser diodes with an $In_{0.76}Ga_{0.24}As_{0.55}P_{0.45}$ multi-quantum well active region, subjected to 1-MeV fast neutron and 1-MeV electron irradiation. The degradation of the device performance increases with increasing fluence. Two hole capture traps with near midgap energy level in the $In_{0.76}Ga_{0.24}As_{0.55}P_{0.45}$ multi-quantum well active region are observed after 1×10^{16} n/cm^2 irradiation. These deep levels are thought to be associated with a Ga-vacancy. The decrease of optical power is related to the induced lattice defects, leading to reduction of the non-radiative recombination lifetime and of the carrier mobility due to scattering.

Keywords: InGaAsP laser diodes; Radiation damage; Induced deep levels

Extensive studies aiming at the development of semiconductor devices which can operate normally in a radiation environment have been undertaken, as there is an expansion in the utilization of hardened electronic circuits. The $In_{1-x}Ga_xAs_yP_{1-y}$/InP semiconductor system has attained much interest for optoelectronic devices in the 0.95–1.65 μm wavelength region. Especially InGaAsP/InP buried heterostructure (BH) laser diodes have considerable potential for use in long distance and high capacity optical fiber communication systems from the viewpoint of their low threshold current, high differential quantum efficiency, stable fundamental lateral-mode operation and carrier wave operability at high temperature. It is worthwhile to investigate the operation of such photodevices in a radiation environment, representative for space or a nuclear plant. Some papers on degradation of laser diode performance by irradiation have been published so far (e.g. Refs. [1,2]). However, detailed considerations on the induced lattice defects in the InGaAsP multi-quantum well active region, its radiation source dependence and recovery behavior are not available.

In the present paper, the degradation of InGaAsP laser diodes by 1-MeV fast neutrons is studied with special emphasis on the optical characteristics. The radiation-induced lattice defects of InGaAsP laser diodes by irradiation and their effect on device performance are investigated. The radiation source dependence of the damage is also discussed by a comparison with 1-MeV electron irradiation data taking into account the nonionizing energy loss (NIEL).

1.3 μm InGaAsP double channel planar BH laser diodes with an $In_{0.76}Ga_{0.24}As_{0.55}P_{0.45}$ multi-quantum well active region were used in this study. The thickness

* Corresponding author. Tel.: + 81-96-242-6079; fax: + 81-96-242-6079.
E-mail address: ohyama@cc.knct.ac.jp (H. Ohyama)

0921-4526/99/$ - see front matter
PII: S0921-4526(99)00630-4

of the multi-quantum well active region fabricated by MOVPE is 0.22 μm. Diodes were fabricated by a two-step LPE process. Pairs of 7 μm-wide and 3 μm-deep channels were formed by chemical etching to make a stripe mesa on a double heterostructure wafer which consisted of an n-InP buffer layer, an undoped InGaAsP active layer and a p-InP cladding layer on a (0 0 1) n-InP substrate. The stripe mesa direction was chosen to be ⟨1 1 0⟩. In the embedding LPE process, a p-InP blocking and an n-InP confining layer were grown first on the whole prepared double heterostructure wafer surface, except on the mesa top surface. A p-InP embedding layer and a p-InGaAsP cap layer were successively grown to embed these layers completely. CrAu/TiPtAu and AuGeAuNi/TiAu were evaporated for anode and cathode contacts, respectively.

The diodes were irradiated by fast 1-MeV neutrons at room temperature in the irradiation tube of the Rikkyo University reactor (Triga Mark II). The neutron fluence was varied between 10^{12} and 10^{16} n/cm^2. The diodes were also irradiated with 1-MeV electrons using the linear electron accelerator at the Takasaki JAERI (Dynamitron) at room temperature to investigate the radiation source dependence of the degradation. The electron fluence was varied from 10^{13} to 10^{16} e/cm^2. Both irradiations were performed through the borosilicate glass and package and without applied bias.

Before and after irradiation, the current/voltage (I/V) and capacitance/voltage (C/V) characteristics of the diodes were measured at room temperature. The optical power (P_L) as a function of forward current (I_F) was also characterised at 300 K. Threshold current (I_{th}) before irradiation is around 9.4 mA. The induced deep levels in the $In_{0.76}Ga_{0.24}As_{0.55}P_{0.45}$ multi-quantum well active region were studied using the deep level transient spectroscopy (DLTS) method in the temperature range between 77 and 300 K. The emission rate window used in this measurement ranged from 1.18 to 26.51 ms. The applied filling pulse ranged from -1 to 0 V, allowing to observe electron capture levels, and from -1 to 0.8 V to observe hole capture levels as well.

Fig. 1 shows the DLTS spectra corresponding to minority carrier traps, before and after neutron irradiation. In the figure, two hole capture traps with near midgap energy levels, H_1 ($E_v + 0.25$ eV) and H_2 ($E_v + 0.49$ eV), are observed after a 1×10^{16} n/cm^2 irradiation. Cross section of those deep levels are 2×10^{-15} and 8×10^{-16} cm^2, respectively. Defect origin of these levels is not known now. The capacitance decreases after irradiation. Fig. 2 shows the typical P_L/I_F characteristics, following irradiation by 1-MeV neutrons, for different fluences. It is found from the figure that P_L decreases after irradiation, while I_{th} increases. The reason for the positive shift of I_{th} is mainly related to a decrease of the electron density due to the formation of radiation-induced lattice defects in the $In_{0.76}Ga_{0.24}As_{0.55}P_{0.45}$ multi-quantum well active region. The decrease of optical power is also related to thee induced lattice defects in the $In_{0.76}Ga_{0.24}As_{0.55}P_{0.45}$ multi-quantum well active region, causing a reduction of the non-radiative recombination lifetime and of the mobility due to carrier scattering.

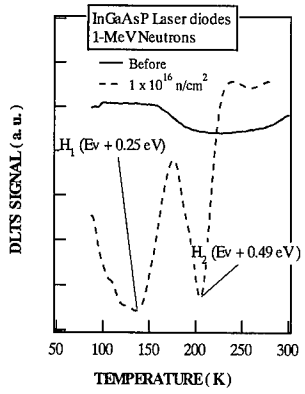

Fig. 1. DLTS spectra in the $In_{0.76}Ga_{0.24}As_{0.55}P_{0.45}$ epitaxial layer before and after 1-MeV neutron irradiation.

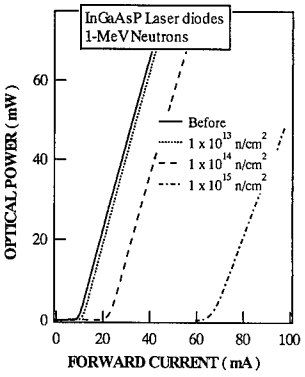

Fig. 2. Influence of 1-MeV neutron irradiation on P_L/I_F characteristics.

Fig. 3 shows the typical P_L/I_F characteristics after 1-MeV neutron and 1-MeV electron irradiation. From this figure it is noted that the degradation of the diode performance for neutron irradiation is about two orders of magnitude larger than for electron irradiation.

Assuming a linear relationship between the radiation damage and fluence, the damage coefficient of the P_L at $I_F = 30$ mA (K_{PL}), defined by the following equation [3]:

$$P_L(\Phi) = P_L(0) + K_{PL}\Phi, \quad (1)$$

where Φ is the radiation fluence. $P_L(\Phi)$ and $P_L(0)$ are the optical power after and before irradiation, respectively.

To investigate the radiation source dependence of the performance degradation, one can calculate the

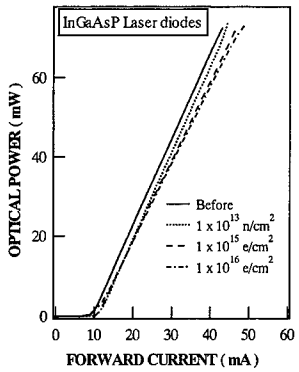

Fig. 3. Comparison of optical power damage for 1-MeV neutrons and 1-MeV electrons.

nonionizing energy loss (NIEL) in the $In_{0.76}Ga_{0.24}As_{0.55}P_{0.45}$ multi-quantum well active region. The NIEL is quantitatively similar to the amount of energy transfer to the lattice during irradiation. The damage coefficient for neutron and electron irradiation is calculated to be $-3.4\times10^{-13}\,n^{-1}mWcm^2$ and $-6.4\times10^{-16}\,e^{-1}mW\,cm^2$, respectively. The same tendency is observed for the I/V and C/V characteristics. The calculated NIEL values for 1-MeV neutron and 1-MeV electron irradiation are calculated to be 0.8×10^{-3} and 1.8×10^{-6} MeV cm^2g^{-1}, respectively. Based on this consideration, the radiation source dependence of the performance degradation is attributed to the difference of mass of the incident particle and the possibility of nuclear collision for the formation of lattice defects [4].

In conclusion, both reverse and forward current increase after irradiation. The optical power decreases after irradiation, while the threshold current increases. The reason for the positive shift of the threshold current is mainly related to a decrease of the electron density due to the formation of radiation-induced lattice defects in the $In_{0.76}Ga_{0.24}As_{0.55}P_{0.45}$ multi-quantum well active region. The capacitance decreases after irradiation. Two hole capture traps with near midgap energy level are observed after a 1×10^{16} n/cm^2 irradiation. The decrease of optical power is related to the induced lattice defects in the $In_{0.76}Ga_{0.24}As_{0.55}P_{0.45}$ multi-quantum well active region, causing a reduction of the non-radiative recombination lifetime and of the mobility due to carrier scattering. The degradation of the diode performance for neutron irradiation is about two orders of magnitude larger than for electron irradiation. The radiation source dependence of the performance degradation is attributed to the difference of mass of the incident particle and the possibility of nuclear collision for the formation of lattice defects.

Part of this work was supported by Grant-in-Aid for Scientific Research (No. 11695065 and 116507727) from the Japanese Ministry of Education for Science, by Sagawa foundation for promotion of frontier science and by Inter-University Laboratory for the Joint Use of JAERI Facilities. Mr. H. Takizawa of Takasaki JAERI is thanked for his cooperation on the irradiation experiments.

References

[1] B.D. Evans et al., IEEE Trans. Nucl. Sci. 40 (1993) 1645.
[2] Y.F. Zhao et al., IEEE Trans. Nucl. Sci. 45 (1998) 2826.
[3] H. Ohyama et al., Appl. Phys. Lett. 69 (1996) 2429.
[4] H. Ohyama et al., IEEE Trans. Nucl. Sci. 45 (1998) 2861.

ELSEVIER

Physica B 273–274 (1999) 1034–1036

PHYSICA B

www.elsevier.com/locate/physb

Impact of induced lattice defects on performance degradation of AlGaAs/GaAs p-HEMTs

T. Hakata[a], H. Ohyama[a,*], S. Kuroda[b], E. Simoen[c], C. Claeys[c,d], T. Kudou[a], K. Kobayashi[a], M. Nakabayashi[a], M. Yoncoka[a], Y. Takami[e], H. Sunaga[f], K. Miyahara[g]

[a]*Department of Electronic Engineering, Kumamoto National College of Technology, 2659-2 Suya Nishigoshi Kumamoto, 861-1102, Japan*
[b]*Fujitsu quantum device Ltd., Syouwa-machi Yamanashi, 409-3883, Japan*
[c]*IMEC, Kapeldreef 75, B-3001 Leuven, Belgium*
[d]*KU Leuven, ESAT-INSYS, Kard. Mercierlaan 95, B-3001 Leuven, Belgium*
[e]*Rikkyo University, 2-5-1, Nagasaka Yokosuka Kanagawa, 240-0101 Japan*
[f]*Takasaki JAERI, 1233 Watanuki Takasaki Gunma, 370-1292 Japan*
[g]*Kumamoto University, 39-1 Kurokami Kumamoto 860-8555, Japan*

Abstract

Irradiation damage and its recovery behavior resulting from thermal annealing in AlGaAs/GaAs pseudomorphic HEMTs, subjected to 1-MeV electrons, 1-MeV fast neutrons and 220-MeV carbon, are studied. The drain current and effective mobility decrease after irradiation, while the threshold voltage increases in positive direction. The decrease of the mobility is thought to be due to the scattering of channel electrons with the induced lattice defects and also to the decrease of the electron density in the two-dimensional electron gas (2DEG) region.

Keywords: AlGaAs/GaAs p-HEMTs; Radiation damage; Induced deep levels

It is well known that low-noise high electron mobility transistors (HEMTs) are commercially available in the microwave and millimeter-wave range, for example for satellite direct broadcasting receiver systems. In space-born applications, their radiation hardness becomes a key factor to be considered. Although there are some reports on radiation damage of InGaAs photodiodes and InGaP p-HEMT devices [1,2], little is known on the detailed degradation and recovery behavior of AlGaAs/GaAs pseudomorphic HEMTs. In this paper, the radiation damage of AlGaAs/GaAs pseudomorphic HEMTs by 1-MeV electrons, 1-MeV fast neutrons and 220-MeV carbon particle irradiation and their recovery behavior resulting from thermal annealing are studied. A comparison is made with results obtained on irradiated InGaP/InGaAs p-HEMTs in order to investigate the effect of the constituent atom on the radiation damage for HEMTs.

N-AlGaAs/GaAs HEMTs fabricated on undoped GaAs channel layers with 600 nm thickness grown on a (1 0 0) semi-insulating GaAs substrate by MOCVD are used in this study. The concentration and thickness of the Si-doped $Al_{0.26}Ga_{0.74}As$ donor layer are 3.0×10^{18} cm^{-3} and 46 nm, respectively. AuGe/Ni/Au is evaporated for source, drain and gate contacts. The latter contact is Al. Both gate length and width are 10 μm. AlGaAs HEMTs were irradiated by 220-MeV carbon particles at room temperature by the AVF cyclotron in TIARA at Takasaki JAERI. The fluence of the carbon particles was varied between 10^9 and 5×10^{13} cm^{-2}. In addition, 1-MeV electron and 1-MeV fast neutron irradiations were done at Takasaki JAERI and at Rikkyo university, respectively. The irradiation was performed

* Corresponding author. Tel.: + 81-96-242-6079; fax: + 81-96-242-6079.
E-mail address: ohyama@cc.knct.ac.jp (H. Ohyama)

0921-4526/99/$ - see front matter
PII: S0921-4526(99)00632-8

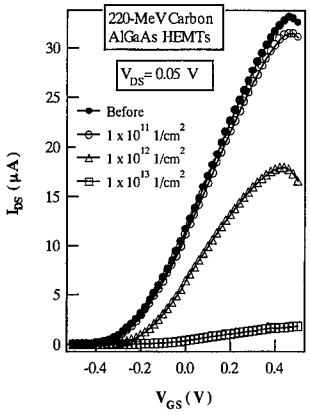

Fig. 1. Degradation of input characteristics by 220-MeV carbon irradiation.

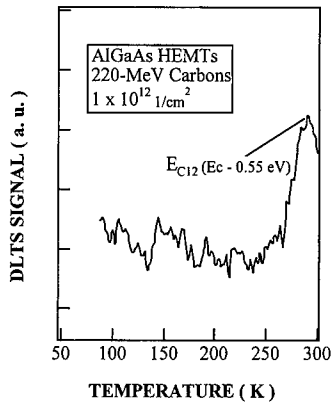

Fig. 2. DLTS spectra in the Si-doped $Al_{0.26}Ga_{0.74}As$ donor layer.

without applied bias to the transistors. The drain source current (I_{DS}) as a function of V_{GS} (input characteristics) and V_{DS} (output characteristics) were measured at room temperature before and after irradiation. The effective mobility (μ_{eff}) prior to the irradiation is typically 6800 cm^2/Vs. Current/voltage (I/V) and capacitance/voltage (C/V) characteristics of the Schottky diode structures between gate and source contact were also measured. The deep levels induced in the Si-doped $Al_{0.26}Ga_{0.74}As$ donor layer were studied using deep level transient spectroscopy (DLTS) in the temperature range from 77 to 300 K. The applied filling pulse ranged from -1 to 0 V for observing electron capture levels. To investigate the recovery behavior of the irradiated devices, isochronal thermal anneals were carried out at temperatures between 50°C and 300°C under nitrogen flow. An annealing time of 15 min was chosen, while the temperature was varied in steps of 25°C with an accuracy of 1°C.

Fig. 1 shows the typical input characteristics, following irradiation by 220-MeV carbon particles, for different fluences. From these figures it is first of all noted that I_{DS} decreases after irradiation and that the threshold voltage, which corresponds to the intercept of the extrapolated drain current with the x-axis, increases in the positive direction. The reason for the positive shift of the threshold voltage is mainly related to a decrease of the electron density due to the formation of radiation-induced lattice defects in the $Al_{0.26}Ga_{0.76}As$ donor layer as mentioned below.

For a carbon irradiation with a fluence of $1 \times 10^{13}\,cm^{-2}$, μ_{eff} is calculated to be 900 cm^2/Vs, which is 13% of the pre-rad value. Fig. 2 shows the typical DLTS spectra in the Si-doped $Al_{0.26}Ga_{0.74}As$ donor layer for $1 \times 10^{12}\,cm^{-2}$ carbon irradiation. One electron ($E_c - 0.55$ eV) trap level, which is associated with As vacancy-related defects, is observed. Based on this result, the decrease of the mobility is thought to be due to the scattering of channel electrons with the induced lattice defects and also due to the decrease of the electron density in the two-dimensional electron gas (2DEG) region for the GaAs channel layers.

Similar performance degradation was observed for electron and fast-neutron irradiation. Assuming a linear relationship between the radiation damage and fluence, the damage coefficient of the linear I_{DS} at $V_{GS} = 0.2$ V can be calculated (K_{DI}), defined by the following equation, and used to compare the radiation damage between AlGaAs and InGaP HEMTs.

$$I_{DS}(\Phi) = I_{DS}(0) + K_{DI}\Phi, \tag{1}$$

where Φ is the radiation fluence. $I_{DS}(\Phi)$ and $I_{DS}(0)$ are the drain current after and before irradiation, respectively.

Table 1 lists K_{DI} values of AlGaAs and InGaP HEMTs for different radiation sources. As shown in Table 1, the radiation damage for carbon irradiation is the largest, and it exceeds about three orders of magnitude the value for electron irradiation. The damage coefficient of AlGaAs HEMTs is about one order larger than that of InGaP HEMTs for the same radiation source. The same tendency is observed for the output characteristics.

To investigate the material and radiation source dependence of the performance degradation, one can calculate the number of knock-on atoms (N_d) and nonionizing energy loss (NIEL) in the active region composed of the undoped channel layer and the donor layers. The NIEL is quantitatively similar to the amount of energy transfer to the lattice during irradiation. The corresponding values for 1-MeV electron irradiation of InGaP material are calculated to be $3.0 \times 10^{-2}\,cm^{-3}$ and 1.8×10^{-6} MeV $cm^2\,g^{-1}$, respectively. For 220-MeV carbon irradiation, they are $124\,cm^{-3}$ and 1.9×10^{-3} MeV $cm^2\,g^{-1}$, respectively. From this follows that the K_{DI} value is in the first instance proportional to the calculated energy transfer. For AlGaAs material of

Table 1
Damage coefficient of I_{DS} of input characteristics of AlGaAs and InGaP HEMTs for different radiation sources

	1-MeV electrons (e^{-1} Acm^2)	1-MeV neutrons (n^{-1} Acm^2)	220-MeV carbons (Acm^2)
AlGaAs HEMTs	1.8×10^{-19}	4.3×10^{-18}	2.3×10^{-17}
InGaP HEMTs	3.6×10^{-21}	1.3×10^{-19}	3.0×10^{-18}

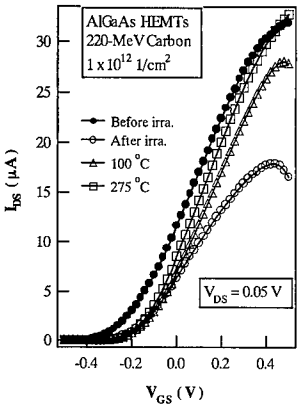

Fig. 3. Recovery behavior of the input characteristics by a 220-MeV carbon ray with a fluence of 1×10^{12} cm^{-2}.

220-MeV carbon irradiation, N_d and NIEL are 978 cm^{-3} and 1.0×10^{-2} MeV cm^2 g^{-1}, respectively. Those values are about one order larger than those for InGaP material. Based on this consideration, the material and radiation source dependence of the performance degradation is thought to be attributed to the difference of mass of the incident particle and the possibility of nuclear collision for the formation of lattice defects [2].

Fig. 3 shows the result of isochronal anneals of the input characteristics, after a 220-MeV carbon irradiation with a fluence of 1×10^{12} cm^{-2}. As shown in this figure, the decreased I_{DS} recovers by thermal annealing, and the recovery increases with increasing annealing temperature. After a 275°C annealing, a complete recovery of I_{DS} at $V_{GS} = 0.4$ V is observed.

In conclusion, the degradation of AlGaAs/GaAs pseudomorphic HEMTs by 220-MeV carbon, 1-MeV neutrons and 1-MeV electrons increases with increasing fluence. The drain current and effective mobility decrease after irradiation, while the threshold voltage increases in the positive direction. The decrease in the mobility is thought to be due to the scattering of channel electrons with induced lattice defects and also due to the decrease of the electron density in the two-dimensional electron gas (2DEG) region. The damage coefficient for carbon and alpha ray are nearly the same, and are about two orders of magnitude larger than that for electron irradiation. This difference is due to the different number of knock-on atoms, which is correlated with the difference in mass and the possibility of nuclear collisions in the formation of lattice defects. The degraded device performance completely recovers by a 275°C thermal annealing for a carbon irradiation with a fluence of 10^{12} 1/cm^2.

Part of this work was supported by Giant-in-Aid for Scientific Research (No. 11695065 and 116507727) from the Japanese Ministry of Education for Science, by Sagawa foundation for promotion of frontier science and by Inter-University Laboratory for the Joint Use of JAERI Facilities. Mr. H. Takizawa of Takasaki JAERI is thanked for his cooperation on the irradiation experiments.

References

[1] H. Ohyama et al., IEEE Trans. Nucl. Sci. NS-43 (1996) 3019.
[2] H. Ohyama et al., IEEE Trans. Nucl. Sci. NS-45 (1998) 2861.

ELSEVIER

Physica B 273–274 (1999) 1037–1040

PHYSICA B

www.elsevier.com/locate/physb

Mechanism of injection-enhanced defect transformation in LPE GaAs structures

Tetyana V. Torchynska[a,*], Georgiy P. Polupan[a], Vladimir I. Kooshnirenko[b], Evgeniy Scherbina[c]

[a]*National Polytechnic Institute, Ed. 9, U.P.A.L.M., 07738, Mexico D.F., Mexico*
[b]*Institute of Semiconductor Physics, National Academy of Sciences, Kiev, Ukraine*
[c]*National Technical University-"KPI", Kiev 252056, Ukraine*

Abstract

It has been shown that the electroluminescence variation in LEDs based on LPE GaAs : Si structures is a complex phenomenon, which is due to recombination-enhanced decomposition of the original complex defects with intrinsic defect appearance, subsequent diffusion of intrinsic defects and microprecipitate creation on final stage. A theoretical model of these processes has been created. The numerical calculation results of the kinetics of GaAs : Si LED EL variation and intrinsic defect transformation have been presented, which enabled us to estimate the recombination-enhanced efficiency of complex defect decomposition and the diffusion coefficient for intrinsic lattice defects, apparently interstitial Ga atoms, as well as to prove that the processes of this intrinsic defect diffusion in GaAs layer is not recombination-enhanced one.

Keywords: Kinetics; Electroluminescence; Recombination-enhanced process; Microprecipitate

1. Introduction

Defect transformation processes in semiconductor materials and devices under conditions of photoexcitation, injection or exposure by different kind radiation have been attracted great attention [1]. These processes are known to limit the efficiency as well as the lifetime and radiation reliability of micro- and optoelectronic devices.

The present work related to GaAs : Si light-emitting diodes (LEDs) which are characterised by high external quantum efficiency but exhibit electroluminescence (EL) power degradation at a forward current flowing [2–4]. The essential degradation of GaAs : Si LED efficiency gives the possibility to investigate the degradation kinetics in great detail, to create the theoretical model of injection-enhanced defect transformation process at degradation as well as to compare the experimental dates and the numerical calculated results.

2. Experimental results and discussion

GaAs : Si LEDs prepared by the liquid-phase epitaxy (LPE) were studied using EL, current–voltage (I–V), capacitance–voltage (C–V), emitting power–current (P–I) and emitting-power–voltage (P–U) characteristics, photocurrent, thermostimulated current (TSC) and deep level transient spectroscopy (DLTS), as well as by the metallographic and transmission electron microscopy (TEM) methods. It is well known that Si is the amphoteric impurity in GaAs crystal [2–4]. The investigated GaAs LEDs had the structure p-GaAs : Si (LPE active layer)–n-GaAs : Si (LPE layer)–n-GaAs (wafer). The degradation of LED groups consisting of 15–25 devices was carried out at forward current J_d = 2–40 A/cm^2 and temperatures T_d of 340, 355 and 380 K during 10^4 h.

* Corresponding author. Tel.: + 52-572-96-000; fax: + 52-572-96-000.
E-mail address: ttorch@esfm.ipn.mx (T.V. Torchynska)

0921-4526/99/$ - see front matter
PII: S0921-4526(99)00633-X

The main experimental results which characterise the LED degradation process are as follows.

1. The time dependence of the intensity of the main ($h\nu_m = 1.30$ eV) EL band $W_{1,3}$ during LEDs operation was nonmonotonic (Fig. 1b). The increase of $W_{1,3}$ (first I stage) can be described is $W_{1,3} \sim [1 - \exp(-t/\tau)]$, where τ is a function of the current flowing through the diode [4]. The fall of $W_{1,3}$ (second II stage) was characterised by $W_{1,3} \sim (\alpha t) - 2/3$, where α depends on the current and temperature (Fig. 2).

2. The $W_{1,3}$ intensity changes is accompanied by a considerable shift at 300 K of the EL band maximum $h\nu_m$ (Fig. 1c) [3].

3. Five peaks corresponding to hole traps in p-layer were observed by TSC and DLTS methods (Table 1). When the intensity $W_{1,3}$ increases the concentration of H5 traps decreases and shallow acceptors H1 appear. During the period of $W_{1,3}$ decreasing no new peaks appear.

4. Metallographic studies demonstrate no changes in the pattern of structural defects at $W_{1,3}$ increase, while during $W_{1,3}$ decrease microdefects give rise to irregular flat bottom etch pits (Fig. 3). TEM studies have shown a diffraction contrast with a size of 50–150 A corresponding to microprecipitate (MP), which are coherent formations in crystal [4].

Radiative recombination in investigated GaAs : Si structures occur primarily in the p-layer as a result of a recombination (Fig. 1a) of electrons from the conduction band (c-band) with holes localised in tails of the valence band (v-band), with the internal quantum efficiency η_{in}. The latter at 300 K for GaAs : Si LEDs can be represented as follows [5]:

$$\eta_{in} = \frac{p_{eq} S_a^e v_e [1 - \exp(-\varphi/kT)]}{p_{eq} S_a^e v_e [1 - \exp(-\varphi/kT)] + p_{eq} S_r^e v_e \exp(-\varphi/kT) + N_n S_n^e v_e}, \quad (1)$$

where S_a^e is the radiative capture cross-section of electrons by holes in v-band tails, S_r^e, S_n^e are the cross-sections of a radiative and nonradiative capture of electrons for an over-barrier radiative recombination and a nonradiative recombination through defects with level N_n, respectively.

The equilibrium hole concentration p_{eq} can be estimated from the maximum position ($h\nu_m$) of main EL

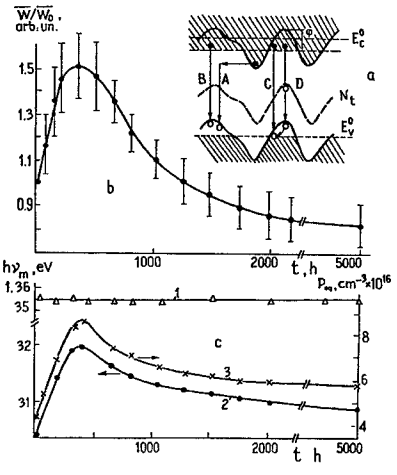

Fig. 1. (a) Energy band diagram of highly compensated active p-layer in GaAs : Si LEDs. (b) Kinetics of injection-enhanced variation of GaAs : Si LED electroluminescence intensity at $I_d = 10$ A/cm^2. (c) Time variation of the maximum position of main luminescence band at 77 (1) and 300 K (2) as well as of equilibrium hole concentration p_{eq} at 300 K (3).

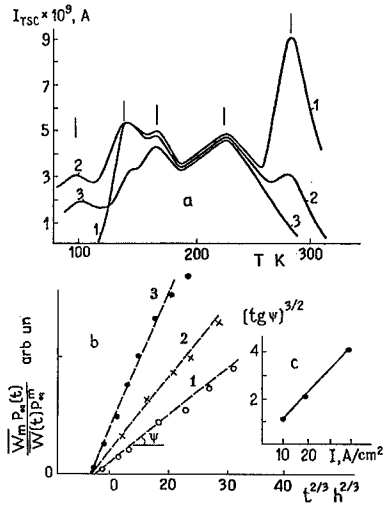

Fig. 2. (a) Spectra of the thermostimulated current before (1) and after (2,3) GaAs : Si LEDs degradation: $t = 0$ (1), 300 (2) and 2000 (3) h. (b) The curves of GaAs : Si LED EL degradation kinetics at different current $I_d = 10$ (1), 20 (2) and 40 (3) A/cm^2 replotted on the form $W_{max} p_{eq}(t)/W(t) p_{eq}^{max} \sim t^{2/3}$. (c) Dependence of the slope of the curves of Fig. 2b on the total current density I_d.

Table 1
The parameters of the hole traps measured by DLTS method

Peak no.	E_t, (eV)	σ (cm^2)	N_t (cm^{-3})
H1	0.11 ± 0.03	$(1–2) \times 10^{-20}$	
H2	0.20 ± 0.02	$(2–5) \times 10^{-19}$	
H3	0.25 ± 0.02	$(4–6) \times 10^{-19}$	
H4	0.41 ± 0.02	$(3–5) \times 10^{-17}$	
H5	0.53 ± 0.02	$(1–3) \times 10^{-16}$	2×10^{16}

Fig. 3. Photomicrograph of a (1 1 0) cleavage plane of GaAs LED excepted by double etching method before (a) and after (b) degradation during 10^3 h at $I_d = 4$ A/cm^2 and $T_{p-n} = 300$ K.

band in GaAs : Si LEDs [5]. Thus the EL band intensity increase and shift during I stage of LED operation is associated with the change of the η_{in} due to p_{eq} rise (Fig. 1c). At the II stage of degradation the intensity of the main EL band decreases much more rapidly than does the $p_{eq}(t)$ one (Fig. 1 b and c), which is indicated by the appearance of new nonradiative recombination channels in the active p-layer [3,4].

We have postulated, that additional acceptors, apparently Si_{As} atoms, and new types of nonradiative recombination centres appeared at the degradation as a consequence of the same process (1) the recombination-enhanced decomposition of initial clusters ($Si_{As} + k\,I$), where Si_{As} are the impure atoms, I represents mobile intrinsic defects, apparently interstitial Ga_i, k is the number of mobile atoms in complex, and (2) coagulation of mobile defects on some nuclei with the formation of MP [4]:

$$I + \cdots + I = (I)_m.$$

These MP are nonradiative recombination centres due to fast recombination of curries on the surface of MP with the some surface recombination velocity σ. Their appearance cause a reduction of η_{in} coefficients and $W_{1,3}$ intensity in the p-layer.

The theoretical model of this complete processes has been proposed by us in Ref. [4], where we attempted to describe the dynamics of the processes of formation and growth of MP in GaAs : Si LEDs using the theory of condensation of excitons into electron–hole drops, suggested in Ref. [6].

The dependence of the mobile intrinsic defect concentration, N, on the time and coordinate was determined by the diffusion equation

$$\frac{\partial N}{\partial t} + \operatorname{div}(-D \operatorname{grad} N) + \frac{N}{\tau} = G - MS, \tag{2}$$

where D is the diffusion coefficient of intrinsic defects, τ is their lifetime in a free state, limited by the process of the reverse association into complexes, M is the concentration of MP, $S = 4\pi R^2 v_t[N(R) - N_t(R)]$ is the flow of defects to MP which is proportional to MP surface, $v_t = (kT/m)^{1/2}$ is the thermal velocity of a defect, m is its mass, $N_t = N_t^o \exp(2\alpha/RkTN_o)$ is the thermodynamically equilibrium concentration of intrinsic defects over a spherical MP whose size is R [4], α is the surface tension coefficient and G is the rate of recombination-enhanced generation of mobile defects. We have shown in Ref. [4] that the average size of the MP increases with time asymptotically in accordance with the law

$$\bar{R} = \left(\frac{8\alpha N_t^0}{9N_0^2 kT} Dt\right)^{1/3}. \tag{3}$$

The recombination flow of electrons in the p-layer to M microprecipitates with size R, proceeding from the solution of the diffusion equation for electrons, was derived in Ref. [7]:

$$J = 4\pi \bar{R}^2 M D_e g \tau_e \frac{(1 + \bar{R}/L_0)\sigma\bar{R}/D_e}{(1 + \sigma\bar{R}/D_e + \bar{R}/L_0)}, \tag{4}$$

where g is the rate of free curries generation, $n_{in} = g\tau_e$, $L_o = D_e\tau_e^o$ is the diffusion length of electrons in the p-layer up to formation of microprecipitates. Taking into account that $R/L_o < 1$ and $\sigma R/D_e < 1$, we obtained

$$J = 4\pi \bar{R}^2 M \sigma n_{in} \frac{\tau_e}{\tau_{eff}}. \tag{5}$$

3. Comparison of numerical calculations and experimental results

To compare the experimental GaAs : Si LEDs emitting power variation with calculated one, it is necessary to solve system of equations, evaluated in Ref. [4], for describing the variation with the time the concentration of intrinsic mobile defect $N(t)$, the radius of MP $R(t)$ and relative EL intensity $W(t)/W_{max}$. The relative variation of EL intensity was determined in Ref. [4] using expressions (1), (3) and (5), as

$$\frac{\bar{W}_{max} p_{eq}(t)}{W(t) p_{eq}^{max}} = 1 + \frac{4\pi M\sigma(\tau_0/\tau_{eff})(8\alpha N_t^0/9N_0^2 kT)^{2/3} D^{2/3} t^{2/3}}{p_{eq} S_a^e v_e[1 - \exp(-\varphi/kT)] + p_{eq} S_r^e v_e \exp(-\varphi/kT) + N_n S_n^e v_e}, \tag{6}$$

where $\tau_{o,eff}$ is the lifetime for curries at W_{max} and $W(t)$, respectively.

Figs. 4 and 5 give the data of calculation done for $N(t)$, $R(t)$, $W(t)/W_{max}$ dependences for various J_d and T_d of p–n junction during degradation and experiment. The calculated curves are obtained for the following parameter values: $k = 10$, $M = 10^{15}$cm^{-3}, $N_t^o = 10^{11}$cm^{-3}, $\alpha = 3 \times 10^{13}$eV cm^{-2}, concentration

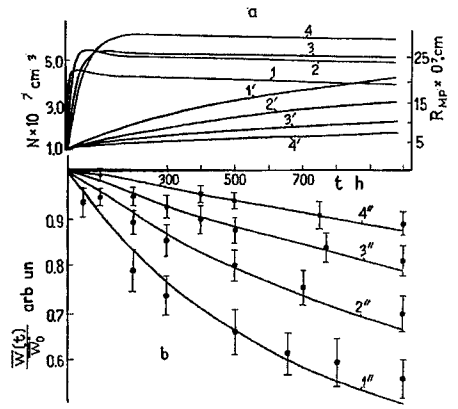

Fig. 4. Variation with (a) operation time of the defect concentration $N(t)$ and MP radius $R(t)$, as well as (b) the relative values of LED electroluminescence intensity for various currents I_d: (1) 40 A/cm^2 ($\beta = 6 \times 10^3$ s^{-1}, $T_{p\text{-}n} = 360$ K); (2) 20 A/cm^2 ($\beta = 3 \times 10^3$ s^{-1}, $T_{p\text{-}n} = 330$ K); (3) 10 A/cm^2 ($\beta = 1{,}5 \times 10^3$ s^{-1}, $T_{p\text{-}n} = 315$ K); (4) 4 A/cm^2 ($\beta = 6 \times 10^2$ s^{-1}, $T_{p\text{-}n} = 300$ K).

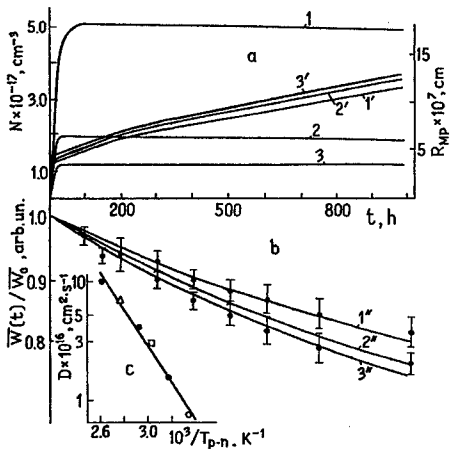

Fig. 5. (a) Variation with operation time of the defect concentration N, radius MP and the average values of LED electroluminescence intensity at $I_d = 10$ A/cm^2, $\beta = 1.5 \times 10^3$ s^{-1} for various values of $T_{p\text{-}n}$; (1) 315, (2) 340, (3) 380 K. (b) Dependence of the diffusion coefficient D on $T_{p\text{-}n}$ at various I_d values: (○) 4 A/cm^2, (●) 10 A/cm^2, (□) 20 A/cm^2, (△) 40 A/cm^2.

intrinsic defects in MP $N_o = 5 \times 10^{20}$ cm^{-3}, fluctuation of the potential in the tail of the zone $\varphi = 0.11$ eV, $\sigma = 750$ cm s^{-1}, efficiency of complex decomposition $\gamma = 5 \times 10^{-10}$, concentration of the original complexes $n_o = 10^{18}$ cm^{-3}, compensation rate $K = 0.95$ and initial values of intrinsic defect concentration $N_t = 10^{12}$ cm^{-3}.

The more effective acceleration of LED degradation is achieved by increasing I_d, not T_d what is observed experimentally. The latter is due to the increase in the rate of recombination-stimulated decay of complexes with I_d growth, a higher concentration in the p-layer of mobile defects N and a growth as a result of the variation rate of MP radius (Figs. 4 and 5). The process of mobile defects, apparently interstitial Ga_i atoms, as it follows from the temperature dependence of D coefficient at various I_d (Fig. 5b) turns out to be thermally activated only with activation energy $\varepsilon_a = 0.35$ eV and not a recombination-stimulated one.

It is essential to note that the formation of clusters of intrinsic defects under unequilibrium conditions had been observed in CdS, Si and AgBr crystals. The proposed model can in a principle be useful for explanation of the blue II–VI and III–V LED and laser degradation kinetics [8].

Acknowledgements

This work was partially supported by Ministry of Sciences of Ukraine and CONACYT Mexico.

References

[1] J. Bourgoin, M. Lanno, Point defects in Semiconductors, Part II, Springer, Berlin, 1993, p. 304.
[2] R.G. Waters, Degradation of LEDs, Prog. in Quant. Electron. 15 (1991) 153.
[3] T.V. Torchinskaya, G.N. Semenova, Quantum Electronics, Naukova Dumka, Kiev, Ukraine N 37 (1989) 53.
[4] B.I. Lev, T.V. Torchinskaya, P.M. Tomchuk, M.K. Sheinkman, Sov. Phys. Semiconductors (USA) 23 (1989) 949.
[5] A.P. Levanjuk, V.V. Osipov, Sov. Phys. Semiconductors (USA) 12 (1973) 1069.
[6] V.S. Bagaev, L.V. Keldysh, Sov. J. Exp. Theor. Phys. 70 (4) (1976) 1501.
[7] N.N. Grigorev, T.A. Kudykina, Ukrain Phys. Zh. 32 (10) (1987) 1460.
[8] S.L. Chuang, M. Ukita, S. Kijima, S. Taniguchi, Appl. Phys. Lett. 69 (1996) 1588.

ELSEVIER

Physica B 273–274 (1999) 1041–1044

PHYSICA B

www.elsevier.com/locate/physb

The bulk damaged effects of clustered defects in irradiated silicon detectors

Shahyar Saramad*, Ali Moussavi Zarandi

Physics Department, Amir Kabir University, Tehran, Iran

Abstract

In this paper a new semiconductor device model based on deep acceptor states and clustered defects are used to explain the significant fraction of discrepancies in effective doping data from neutron-irradiated devices. It is postulated that the main difference between neutron and gamma damage is in the formation of dense cluster during neutron irradiation. So V2, E70, E170 and P6 defects that are estimated to be present inside the dense cluster will be responsible for leakage current annealing by exchange charge reaction. This mechanism can lead to an increase in electron–hole pair generation rate around two-orders of magnitude. Therefore by using the annealing behavior of leakage current, the concentration and spatial distribution of these defects are calculated and can be used to explain the effective doping concentration versus fluence truly.

Keywords: Cluster; Leakage current; Effective doping

1. Introduction

High-resistivity silicon detectors are planned to be used for many applications at CERN Large Hadron Collider where high radiation levels will cause significant bulk damages. In addition to increased leakage current which worsens the signal-to-noise ratio, changes in effective doping concentration have been observed after irradiation which is a limiting factor for long-term operation of detectors [1]. In other words at high fluences the depletion voltage required to operate the silicon detector exceeds the breakdown voltage of the device and the detector cannot operate efficiently.

Although many radiation damage models of silicon detectors have been extensively represented for describing the large amount of experimental data, until recently these changes in doping concentration were poorly understood. The deep level acceptor model can predict gamma irradiation results with reasonable agreement, but there is a large discrepancy between the model and data for fast neutron damage effects [2]. However charge exchange reaction between divacancy defects in high density cluster which is formed with neutron damage can resolve this discrepancy [3], recent experimental results have shown that two unidentified defects termed E70, E170 [4] and P6 di-interstitial defect are correlated with leakage current after neutron irradiation, which must be considered in this model [5].

In this paper a semiconductor simulation which includes Poisson and continuity equations and exchange charge reaction between clustered defects, has been successfully used to describe the observed evolution of effective doping concentration with fluence after neutron irradiation which may lead to ideas for defect engineering of more radiation-tolerant silicon detectors.

2. Bulk damage models in silicon

One of the earliest plausible models of doping changes under irradiation was based on donor removal through electrical deactivation of phosphorus dopant by combining with a lattice vacancy [6]. The introduction of shallow acceptor was then assumed to give rise to the type

* Correspondence address. Faculty of Physics and Nuclear Science, Amir Kabir University, P.O. Box 14155-1734, Tehran, Iran. Tel.: 0098-021-64954320; fax: 0098-021-6419506.

E-mail address: s7312909@cic.aku.ac.ir (S. Saramad)

0921-4526/99/$ - see front matter
PII: S0921-4526(99)00634-1

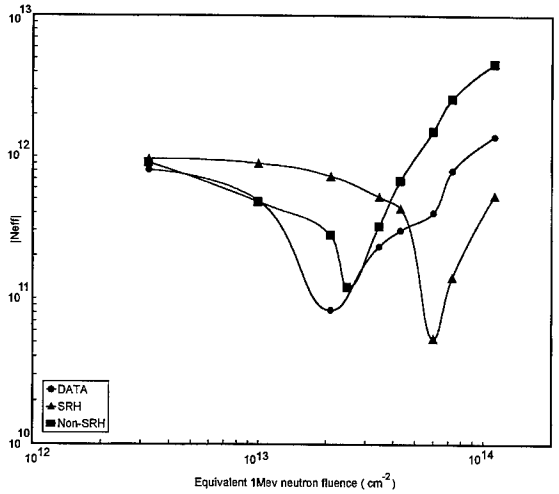

Fig. 1. Data and SRH and non-SRH models for the evolution of effective doping concentration with 1 MeV neutron fluence.

inversion once the phosphorus was exhausted, therefore the combination of phosphorus removal and acceptor creation provides a successful description of the data on doping changes without explaining anti-annealing effect. But recent DLTS studies [7] on detector diodes after low fluence irradiations have shown a phosphorus removal rate about 30 times smaller than this model suggests. An alternative hypothesis is that the introduction of deep level acceptors, close to the center of the band gap, which are known to exist in the material in the presence of trap defects, will cause type inversion. It is clear that if this new explanation is correct it must be able to predict the N_{eff} behavior against neutron fluence.

For model calculations of N_{eff}, the measured leakage current density was used as an input parameter to determine free carrier concentration, n and p from the current continuity and Poisson's equations. The measured and calculated change in N_{eff} for neutron irradiation using Shockley–Read–Hall (SRH) statistic is shown in Fig. 1. In contrast to the gamma damage results the deep level model cannot predict the observed change in N_{eff} accurately. If the deep level acceptor model is complete it should also be able to explain the different defect contributions to leakage current with SRH statistic, the ideas of which were first presented by Shockley et al. [8,9].

Although the calculations of leakage current after gamma irradiation show that the results are in reasonable agreement with measured data, there is a large discrepancy in leakage current of neutron-irradiated detectors due to different defects by around two-orders of magnitude which is shown in Table 1. This correlation between leakage current and effective doping suggests that a single mechanism must be responsible for the two effects, which will be described in the next section [10].

Table 1
The enhancement factors necessary to supply the observed currents using SRH statistic

	Observed current (nA)	SRH calculated current (nA)	Enhancement factor
V2(− /0)	1	0.00806	116
E170	3	0.003	1000
E70	4	0.05	80

3. Charge exchange reaction model

Since the deep level idea appears to be reasonable, different explanations can be given for solving these discrepancies. One possible explanation for resolving this problem is the existence of an unidentified trap very close to the center of the band gap which could be responsible for extra leakage current. However, the introduction rate of such a defect would be $\sim 8\,cm^{-1}$, which no obvious candidate has been observed [3].

The discrepancy may correspond to clusters in neutron-irradiated silicon which are absent in gamma irradiation materials. These clusters that contain V2, E170, E70 and P6 defects in a region of volume (~ 100 Å)^3, can modify the normal SRH picture of generation recombination. In other words it is possible that part of these defects which are sufficiently close together, can participate to exchange charge reaction. This mechanism [11] has been recently observed [12,13] which enhanced diode currents and might be the answer for our present and future unsolved questions.

Charge exchange reaction which influences the generation rate will also affect the occupancy of charge states, since a new steady-state situation will arise in comparison to a system of isolated defects. This can also influence the effective doping concentration in a significant way. Although this phenomenon is almost unique to divacancy due to its multivalent nature but the presence of other defects in the cluster can modify this model. For example our simulation has shown that without considering P6 defect, the observed variations in leakage current cannot be well described by the hypothesis of inter center charge transfer between cluster divacancy or even unidentified E70, E170 defects detected by DLTS method.

If the effective local density of V2 in the cluster is left as a free parameter, by using the annealing behavior of leakage current, the concentration and spatial distribution of E70, E170, P6 and V2 defects are calculated with the following assumptions. (1) Since interstitial atoms diffuse out more rapidly than vacancies, it is natural that P6 defects are considered in the outer part of the dense cluster, with a uniform distribution, and V2 as an uniform distributed defect in the whole of cluster. (2) Because

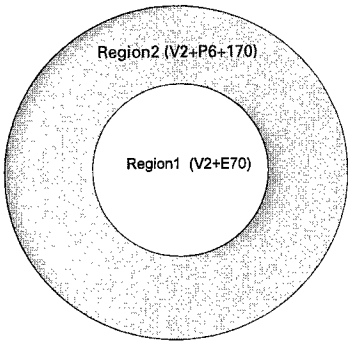

Fig. 2. Distribution of V2, E170, E70 and P6 defects in the cluster.

of the unknown nature of E70 defect, with an initial assumption its position is considered in the inner core of cluster, where its trueness is also verified in our modeling. (3) Because of the statistical nature of damage process, only part of V2 defects can participate in exchange charge reaction which can be taken as an unknown parameter in this model. (4) The temperature dependence of leakage current contribution from clustered defects after neutron irradiation must be $E_a = 0.62 \pm 0.02$ eV, consistent with the measured data.

With these assumptions we found that the average density of V2 defect in the cluster is approximately $2.6 \times 10^{17}\,\mathrm{cm}^{-3}$ and 95% of these defects can participate in exchange charge reaction and this can be used to explain the significant fraction of discrepancy in the effective doping observed in neutron-irradiated detectors. This cluster model also predicts that E170 is a multi-interstitial and E70 is a multi-vacancy related defect in the outer edge and inner core of cluster (Fig. 2) and E170 can participate in the reverse annealing effect by releasing interstitials which is also consistent with the increasing Ci-related defects (Cc, Co) in the E170 annealing temperature range [14].

4. Device modeling of effective doping

By considering all possible exchange charge reactions we found that clustered defects can also have significant effect on effective doping concentration. For example, at experimental inversion fluence $2 \times 10^{13}\,\mathrm{cm}^{-2}$, the net density of acceptor states will be $4 \times 10^{11}\,\mathrm{cm}^{-3}$ (Table 2), which has a similar value to $[V2O]^-$ and $[p]^+$ at this fluence. For modeling the effective doping concentration, first of all by using Davies kinetics and exchange-charge model, the production rate of various defects are calculated and secondly a device model takes this information and predicts the macroscopic parameters of detector.

For this purpose the coupled differential current transport and continuity equations and Poisson's equation are transformed to different equations and then by applying the Newton's iteration principle and boundary conditions the final matrix equation is extracted and solved using a recursive method. So by using the electron (n) and hole (p) concentrations the density of filled acceptors ($\Sigma f_a N_a$) and empty donors ($\Sigma(1-f_d)N_d$) can be determined and can be used to calculate the effective doping concentration (N_{eff}).

$$N_{eff} = \Sigma(1-f_d)N_d - \Sigma f_a N_a + p - n - N_{cl}, \quad (1)$$

where N_{cl} is the net acceptor concentration calculated by exchange charge model. As shown in Fig. 1 with this cluster model, it is possible to explain the type inversion fluence ($\phi_{inv} = 2.6 \times 10^{13}$) and effective doping concentration quite well. Since at high fluences, experimental results show the broadening of DLTS peak near $V2^-$ energy level in neutron and proton-irradiated detectors [15], the discrepancies between our model and data in higher fluences may correspond to the formation of larger clusters. Since the larger clusters are more stable than smaller ones, different clusters have different activation energies which may lead to logarithmic annealing behavior [16].

5. Conclusions

A numerical model has been used to investigate the effect of clustered defects on macroscopic behavior in fast neutron-irradiated silicon detectors. Our conclusions reveal that defects coupling in terminal cluster can make a significant contribution to both N_{eff} and leakage current in case of heavy particle irradiation, which has serious consequences in defect engineering a radiation tolerant silicon device.

Table 2
Concentration of clustered V2, E170, E70 and P6 (cm^{-3}) defects at fluence $2 \times 10^{13}\,\mathrm{cm}^{-2}$

	[V2(+)]	[V2(−)]	[V2(-)]	[E70(−)]	[E170(−)]	[P6(+)]
Region 1	6.66E + 8	2.41E + 10	8820	4.46E + 11	0	0
Region 2	3.12E + 8	7.36E + 9	5290	0	1.11E + 10	9.1E + 10

Acknowledgements

The authors would like to thank M. Moll, K. Gill and S.J. Watts for many useful discussions and suggestions.

References

[1] G. Hall, Rep. Prog. Phys. 57 (1994) 481.
[2] B.C. MacEvoy, Nucl. Instr. and Meth. A 388 (1997) 365.
[3] K. Gill et al., J. Appl. Phys. 82 (1997) 126.
[4] S.J. Watts et al., IEEE Trans. Nucl. Sci. NS-43 (1996) 2587.
[5] S. Saramad et al., The exchange charge model of clustered defects in bulk damaged slicon detectors, presented at International Conference on Atomic Collisions in Solids, Odense University, 3–8 August, 1999.
[6] RD2 Collaboration, Nucl. Phys. B 32 (1993) 415.
[7] J. Matheson et al., RD20/TN/36, 1994.
[8] W. Schockley et al., Phys. Rev. 87 (1952) 835.
[9] R. Hall, Phys. Rev. 87 (1952) 387.
[10] J. Matheson et al., Nucl. Instr. and Meth. A 371 (1996) 575.
[11] A. Shenk et al., J. Appl. Phys. 78 (1995) 3185.
[12] W.M. Chen et al., Phys. Rev. Lett. 67 (1991) 1914.
[13] A. Frens et al., Phys. Rev. Lett. 72 (1994) 2939.
[14] M. Moll, private communication.
[15] V. Eremin et al., Nucl. Instr. and Meth. A 426 (1999) 120.
[16] M. Moll et al., Nucl. Instr. and Meth. A 426 (1999) 87.

ELSEVIER

Physica B 273–274 (1999) 1045–1049

PHYSICA B

www.elsevier.com/locate/physb

Defect-engineering rad-hard particle detectors: the role of impurities and inter-defect charge exchange

B.C. MacEvoy*, A. Santocchia, G. Hall

Imperial College of Science Technology and Medicine, London SW7 2BZ, UK

Abstract

Silicon detectors in particle physics experiments at the CERN Large Hadron Collider will be exposed to unprecedented levels of radiation. The principal obstacle to long-term operation in this environment is changes in detector effective doping concentration (N_{eff}). We present a model of defect evolution during gamma and hadron irradiation which has been combined with Shockley–Read–Hall (SRH) statistics to predict N_{eff} and dark current in irradiated devices. These predictions are compared with experimental results from detectors with various oxygen and carbon concentrations. In the case of gamma irradiation, the electrical characteristics are described satisfactorily by the production of divacancy–oxygen (V_2O) defects. In the case of hadron irradiation, however, the experimental data cannot be explained in the conventional SRH picture. We propose a model whereby states in the terminal defect clusters exchange charge directly. This mechanism leads to a marked increase in carrier generation rate and an enhancement in the acceptor-like contribution to N_{eff}. We conclude that only limited improvements in radiation hardness to hadrons can be achieved by altering detector impurity levels, since the changes in N_{eff} are dominated by intrinsic defects within the terminal clusters.

Keywords: Silicon; Particle detector; Radiation; Defect engineering

1. Introduction

Silicon detectors will be used extensively in experiments at the CERN Large Hadron Collider (LHC), where they will be exposed to fast hadron fluences equivalent to $\sim 10^{14}\,cm^{-2}$ 1 MeV neutrons and an ionising dose of ~ 10 Mrad over their operational lifetime [1]. Particle detectors typically consist of a series of p-type strips implanted on an n-type high resistivity ($\sim 5\,k\Omega$ cm) Fz substrate. The principal obstacle to long-term operation arises from atomic displacement damage, which ultimately increases the effective doping concentration of the substrate (N_{eff}) and thus operational voltage. Recently, significant effort has been devoted by the particle physics community to understanding the microscopic origins of these doping changes, with the goal of defect-engineering rad-hard detectors [2]. Studies have focussed on the effect of carbon and oxygen concentrations. The 'standard' Fz material used in conventional detectors contains both impurities at levels of $\sim 10^{15}\,cm^{-3}$, but novel samples with concentrations in the range 10^{14}–$10^{17}\,cm^{-3}$ have now been produced.

In this paper, we present the most complete model of defect evolution and detector behaviour to date. In Section 2, a brief review of bulk damage effects is given. This is followed by the modelling of data from gamma-irradiated devices in Section 3. The purpose of this modelling is to evaluate the contribution of point defects to device characteristics. In Section 4, we turn to the modelling of data from hadron-irradiated devices, with particular emphasis on the phenomenon of inter-defect charge exchange. Lastly, we evaluate the consequences of this work for the prospects of producing truly rad-hard devices in Section 5.

* Corresponding author. Tel.: + 44-171-594-7797; fax: + 44 171 823 8830.

E-mail address: b.macevoy@ic.ac.uk (B.C. Mac Evoy)

0921-4526/99/$ - see front matter
PII: S0921-4526(99)00635-3

2. Radiation effects

Detector leakage currents increase significantly during irradiation. The bulk current is described in terms of J_v, which is the leakage current per unit volume. The increase in J_v is directly proportional to particle fluence:

$$\Delta J_v = \alpha \Phi, \tag{1}$$

where α is known as the 'damage constant' and has the value $5\text{–}10 \times 10^{-17}$ A cm^{-1} at 20°C for fast hadrons immediately after irradiation [3]. The damage constant for ^{60}Co photons is very much less, with a value of $\sim 7 \times 10^{-23}$ A cm^{-1} [4].

With regard to effective doping concentration, the space-charge in an unirradiated device arises from the shallow dopants present, usually phosphorus with some small degree of compensation ($< 20\%$) by boron. Irradiation results in an accumulation of negative space-charge in the depletion region. n-type detectors therefore become progressively less n-type with increasing hadron fluence until they invert to effectively p-type at around 2×10^{13} n cm^{-2} and then continue to become more p-type beyond this point [5]. In the case of ^{60}Co γ-irradiation, standard Fz detectors undergo type inversion at a dose of ~ 100 Mrad [6].

The effective doping concentration can be inferred from the voltage required to obtain full depletion, V_{depl}:

$$N_{eff} = \frac{2\varepsilon_0 \varepsilon_{Si}}{ed^2} V_{depl}, \tag{2}$$

where d is the diode thickness. At high fluences, N_{eff} can be such that V_{depl} exceeds the breakdown voltage of the device and efficient operation is no longer possible.

3. Modelling data from gamma-irradiated devices

The modelling is based on a numerical calculation of defect evolution first suggested by Davies and co-workers to explain the effects of electron irradiation [7]. This defect kinetics model has been developed and adapted for detector material to predict defect concentrations after irradiation with ^{60}Co photons and fast hadrons. The reactions used in the model are listed in Table 1. In the case of hadron irradiation, the struck atom has sufficient recoil energy to cause further displacements, giving rise to several terminal clusters containing a high initial density of interstitial (I) and vacancy (V) defects [8]. The processes in list A only have a significant chance of occurring within these clusters. The processes in list B occur as the primary defects diffuse away from the cluster region; these are also the processes that occur during gamma irradiation, where the recoil energy of the struck atom is sufficient to displace only one or two atoms from their lattice sites [9].

Table 1
Defect kinetics model reaction scheme

I reactions	V reactions	C_i reactions
(A) *Cluster reactions*		
$I + V \rightarrow Si$	$V + V \rightarrow V_2$	...
(B) *Diffusion reactions*		
$I + C_s \rightarrow C_i$	$V + V \rightarrow V_2$	$C_i + C_s \rightarrow CC$
$I + CC \rightarrow CCI$	$V + V_2 \rightarrow V_3$	$C_i + O \rightarrow CO$
$I + CCI \rightarrow CCII$	$V + O \rightarrow VO$	
$I + CO \rightarrow COI$	$V + VO \rightarrow V_2O$	
$I + COI \rightarrow COII$	$V + P \rightarrow VP$	
$I + VO \rightarrow O$		
$I + V_2O \rightarrow VO$		
$I + V_2 \rightarrow V$		
$I + VP \rightarrow P$		

Table 2
Defect states considered in the SRH calculation

Identity	Energy (eV)	Type	Charge
VO	$E_c - 0.17$	Acceptor	(0/−)
V_2O	$E_c - 0.50 \pm .05$	Acceptor	(0/−)
V_2	$E_v + 0.20$	Donor	(+/0)
	$E_c - 0.41$	Acceptor	(0/−)
	$E_c - 0.23$	Acceptor	(−/=)
VP	$E_c - 0.45$	Acceptor	(0/−)
CO	$E_v + 0.36$	Donor	(+/0)
CC	$E_c - 0.17$	Acceptor	(0/−)

Reaction rates are controlled by the concentrations of impurities and their relative capture radii. Full details may be found in Ref. [10]. The input parameters required by the model are the oxygen and carbon impurity concentrations (determined by SIMS, IR absorption etc.) and the introduction rates of the primary defects. These are $\eta_V = 2.7 \times 10^{-4}$ cm^{-1}, $\eta_{V2} = 7.1 \times 10^{-6}$ cm^{-1} for ^{60}Co gammas, $\eta_V = 0.58$ cm^{-1}, $\eta_{V2} = 0.96$ cm^{-1} for 1 MeV neutrons and $\eta_V = 0.61$ cm^{-1}, $\eta_{V2} = 0.46$ cm^{-1} for 24 GeV protons [11,12]. In order to calculate device characteristics, the theory of Shockley et al. [13,14] is combined with the predicted defect concentrations. The states included in the calculation of N_{eff} and ΔJ_v are listed in Table 2. It should be noted that there is some uncertainty in the energy level assignment of the divacancy–oxygen (V_2O) defect [15].

The predictions of the model for the evolution of N_{eff} during gamma irradiation are compared with experimental data from detectors with various oxygen concentrations in Fig. 1. The agreement between the model and data is impressive. The dominant contribution to

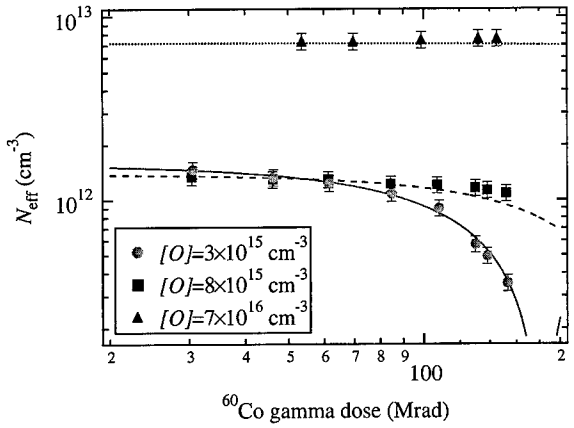

Fig. 1. Model predictions (lines) and experimental data (markers) for ^{60}Co gamma irradiation of samples with various oxygen concentrations and a carbon concentration of $\sim 10^{16}$ cm^{-3}.

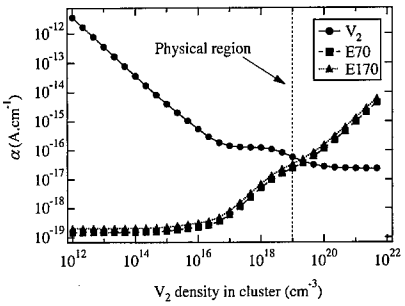

Fig. 2. Contribution of V_2, E70 and E170 to α as a function of V_2 density within the cluster assuming inter-defect charge exchange. The densities of E70 and E170 are held at 10^{19} cm^{-3}.

N_{eff} arises from the V_2O state; an energy level of $E_{V_2O} = E_c - 0.54$ eV is required to obtain agreement with the data, a value which lies within 1σ of the experimental energy measurement. Oxygenated material is more radiation hard to gammas because V_2O production is suppressed by the competing reaction $V + O \rightarrow VO$. The leakage current in these detectors has also been modelled. The V_2O defect dominates on account of its proximity to mid-gap. The model therefore suggests that α is reduced as the oxygen content rises, a prediction which has recently been borne out by experiment [16].

4. Modelling data from hadron-irradiated devices

Using the value of E_{V_2O} fixed by the gamma data, the same modelling procedure was applied to the case of hadron irradiation. For 1 MeV neutrons, it was found that the predicted type inversion fluence was an order of magnitude higher than that observed experimentally. The dominant contribution to the doping changes predicted by the model again arose from the V_2O defect. The leakage current was underestimated by some 2 orders of magnitude. The potential errors in the model were examined carefully but could not possibly explain these discrepancies.

The presence of defect clusters in hadron-irradiated material, and their absence in gamma-irradiated material, suggests a possible cause. Several defects are strongly produced within the terminal clusters, including the divacancy (V_2) and two defects known as E70 and E170. The E70 state is multivalent, giving rise to acceptor levels at $E_c - 0.45$ eV (0/−) and $E_c - 0.35$ eV (−/=), whereas E170 gives rise to a single acceptor at $E_c - 0.37$ eV (0/−) [17]. E70 and E170 are strongly correlated with annealing of the leakage current after irradiation, but neither state is sufficiently close to mid-gap to explain the magnitude of the observed current decrease in the conventional SRH picture [18].

Simple calculations indicate that the local density of V_2, E70 and E170 within the terminal clusters is of the order of 10^{19} cm^{-3}. It is evident, therefore, that some of these defects are close enough to exchange charge directly. There is compelling experimental evidence in the literature for such inter-defect charge exchange (see, for example, Ref. [19]). By writing general expressions for the rates of emission and capture between all levels of the V_2, E70 and E170 defects, and assuming equal carrier capture cross sections throughout, it is possible to calculate the steady-state occupancy of each defect and the carrier generation rate numerically. The model predictions for the damage constant, α, are shown in Fig. 2. The predicted value, which is the sum of the three components, is $\sim 10 \times 10^{-17}$ A cm^{-1} in the physical region, in close agreement with what is actually observed.

Fig. 3 shows the predicted occupancy fractions as a function of V_2 density within the cluster, with the densities of E70 and E170 held at 10^{19} cm^{-3}. It can be seen that, as the density of V_2 increases, the occupancies of all defects are enhanced over the SRH value. The introduction rate of negative space charge is now $\sim 5 \times 10^{-3}$ cm^{-1}. To explain the experimental data, however, an introduction rate of $\sim 25 \times 10^{-3}$ cm^{-1} is required. Given that our preliminary calculation has assumed equal carrier capture cross sections, which is known not to be the case, it is not surprising that there is not a perfect agreement with the data. A more complete calculation is now in progress; from work to date it is evident that even small deviations from unity in the capture cross-section ratios can cause further enhancements in the introduction rate of negative space-charge. While it would be foolish to pre-empt the final results of these calculations, in order to make a step forward we assume that the total contribution of the clustered defects

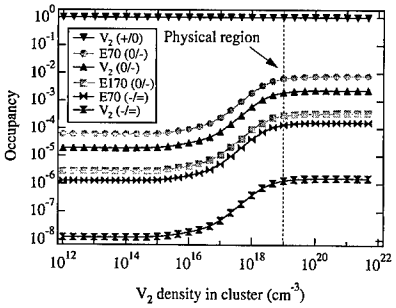

Fig. 3. Occupancies of V_2, E70 and E170 charge states as a function of V_2 density within the cluster assuming inter-defect charge exchange. The densities of E70 and E170 are held at $10^{19}\,cm^{-3}$.

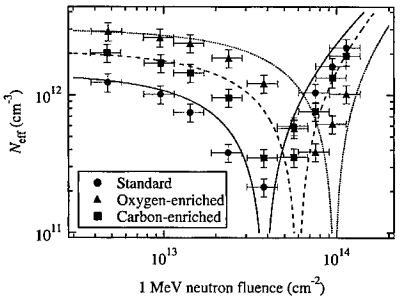

Fig. 4. Model predictions (lines) and experimental data (markers) for 1 MeV neutron irradiation. (Circles) $[O] = 3\times 10^{15}\,cm^{-3}$, $[C] = 5\times 10^{15}\,cm^{-3}$; (triangles) $[O] = 1.7\times 10^{16}\,cm^{-3}$, $[C] < 2\times 10^{16}\,cm^{-3}$; (squares) $[O] < 5\times 10^{16}\,cm^{-3}$, $[C] = 1.8\times 10^{16}\,cm^{-3}$.

to the space charge is indeed of the order of $\sim 25\times 10^{-3}\,cm^{-1}$ for 1 MeV neutrons and scales with the cluster defect introduction rates.

The results of combining the standard SRH calculation for point defects and the non-SRH calculation for clustered defects with this assumption are shown in Figs. 4 and 5. The plots show the predicted evolution of N_{eff} for various detector impurity concentrations for 1 MeV neutrons and 24 GeV protons, respectively. The experimental data are described well. There are several points to note. In the case of neutron irradiation, the various detectors display similar radiation tolerance; the only differences observed are due to differences in the initial resistivity of the devices. In the case of proton irradiation, however, the oxygen-enriched detector is more rad-hard and the carbon-enriched detector less rad-hard than the standard device. The reason for this is that, in the case of proton irradiation, the primary introduction rate of the vacancy, η_V, is proportionally larger than in the case of neutron irradiation. Hence, the role

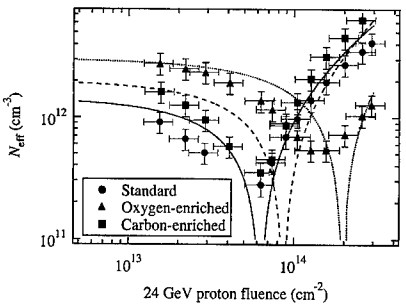

Fig. 5. Model predictions (lines) and experimental data (markers) for 24 GeV proton irradiation: Circles $[O] = 3\times 10^{15}\,cm^{-3}$, $[C] = 5\times 10^{15}\,cm^{-3}$; (triangles) $[O] = 1.7\times 10^{16}\,cm^{-3}$, $[C] < 2\times 10^{16}\,cm^{-3}$; (squares) $[O] < 5\times 10^{16}\,cm^{-3}$, $[C] = 1.8\times 10^{16}\,cm^{-3}$.

played by V_2O in determining N_{eff} is greater for protons. As in the case of gamma irradiation, a high oxygen concentration suppresses V_2O production and thus the changes in N_{eff}. Conversely, a high carbon concentration encourages V_2O production because substitutional carbon acts as a sink for interstitials and suppresses capture of interstitials at V_2O itself and its pre-cursor states (Table 1).

5. Conclusions

The changes in N_{eff} and dark current during gamma irradiation have been modelled satisfactorily in terms of production of the V_2O defect. In the case of hadron irradiation, electrical characteristics are controlled by cluster defects, with a contribution to N_{eff} from the V_2O state. The V_2O defect is more copiously produced during proton irradiation on account of the proportionally higher vacancy introduction rate, hence the radiation hardness of materials to protons is more sensitive to impurity concentrations than in the case of neutrons.

In terms of the prospects of improving radiation hardness for the LHC experiments, it is clear from both the experimental data and the modelling presented here that only limited improvements can be made by altering initial impurity concentrations. Production of cluster defects can only be influenced by relatively high ($\sim 10^{20}\,cm^{-3}$) impurity concentrations, which may be impractical. Notwithstanding, work is now underway to understand the charge exchange processes more thoroughly, since it is the clusters that hold the key to improving radiation tolerance.

References

[1] CMS Collaboration, CERN/LHCC 98-6, 1998, p. 541.
[2] ROSE Collaboration, CERN/LHCC 96-23, 1996.

[3] S. Sotthibandhu, Rutherford Appleton Laboratory Thesis RALT-025, 1994, p. 55.
[4] B. MacEvoy, Rutherford Appleton Laboratory Thesis RAL-TH-97-003, 1997, p. 128.
[5] K. Gill et al., Nucl. Instr. and Meth. A 322 (1992) 177.
[6] B. MacEvoy, Rutherford Appleton Laboratory Thesis RAL-TH-97-003, 1997, p. 138.
[7] G. Davies et al., Semicond. Sci. Technol. 2 (1987) 524.
[8] V.A.J. van Lint et al., IEEE Trans. Nucl. Sci. NS-19 (1972) 181.
[9] J.H. Cahn, J. Appl. Phys. 30 (1959) 1310.
[10] K. Gill et al., J. Appl. Phys. 82 (1997) 126.
[11] S. J. Watts et al., CERN/LEB 98-11, 1998, p. 432.
[12] M. Moll et al., Nucl. Instr. and Meth. A 388 (1997) 335.
[13] W. Shockley, W.T. Read, Phys. Rev. 87 (1952) 835.
[14] R.N. Hall, Phys. Rev. 87 (1952) 387.
[15] Y.H. Lee et al., Radiat. Eff. 29 (1976) 7.
[16] E. Fretwurst et al., CERN/LEB 98-11, 1998, p. 221.
[17] M. Ahmed, Ph.D. Thesis Brunel University, 1998.
[18] S.J. Watts et al., IEEE Trans. Nucl. Sci. NS-43 (1996) 2587.
[19] A. Frens et al., Phys. Rev. Lett. 72 (1994) 2939.

ELSEVIER

Physica B 273–274 (1999) 1050–1053

PHYSICA B

www.elsevier.com/locate/physb

Point defect reaction in (Al)GaInP STQW lasers enhanced by laser operation

A. Ihara[a], Y. Ohno[a,*], S. Takeda[a], S. Nagao[b], D. Diffily[b], Y. Satoh[b], K. Shimoyama[b], N. Hosoi[b]

[a]*Department of Physics, Graduate School of Science, Osaka University, 1-16, Machikane-yama, Toyonaka, Osaka 560-0043, Japan*
[b]*Mitsubishi Chemical Corporation, Tsukuba Plant, 1000, Higashi-Mamiana, Ushiku, Ibaraki 300-1201, Japan*

Abstract

We have found that a large number of dislocation loops of interstitial type are introduced in the active region of (Al)GaInP strained triple quantum wells (STQW) lasers by the effect of laser operation. These loops were always generated in the lasers, the driving current of which increased gradually as operating time increased. We have shown that the dislocation cores act as nonradiative recombination centers and therefore the loops cause the *gradual* degradation. The migration of interstitial atoms enhanced by laser operation are essential for the degradation of the lasers. © 1999 Elsevier Science B.V. All rights reserved.

Keywords: (Al)GaInP STQW laser; Interstitial atoms; Laser operation-induced migration; Interstitial clustering

1. Introduction

Ridge stripe laser and buried heterostructure laser have been of great interest for optoelectronic applications during the last decade. Since the active region of these lasers is surrounded by materials with wider band gap and smaller refractive index, both carriers and laser light are effectively confined in the region, and these lasers therefore produce high output powers with a low driving current compared with that of planar lasers such as double heterostructure (DH) lasers.

It is known that the driving current under a constant output power increases with increasing laser-operation time: lasers degrade by their operation. The degradation is due to the nonradiative recombination of a part of electrons and holes at laser operation-induced defects; the recombination creates not photons but multiple-phonons [1]. For DH planar lasers, the degradation is explained by recombination-enhanced dislocation climb, recombination-enhanced dislocation glide, and the formation of point defect clusters [1]. Ridge stripe lasers have also been studied, but their degradation process is still unclear. In this paper, we will show that point defect reactions under laser operation are essential for the degradation.

2. Experiments

Samples were AlGaInP/GaInP-strained triple quantum wells (STQW) ridge stripe lasers emitting at 680 nm wavelength region (with the stripe width of 3500 nm). The laser consists of: (1) p-GaAs contact layer (1300 nm), (2) p-AlGaAs cladding layer (1200 nm), (3) p-AlGaInP cladding layer (100 nm), (4) STQW active layer, (5) n-AlGaInP cladding layer (100 nm), (6) n-AlGaAs cladding layer (1500 nm), and (7) n-GaAs substrate.

The driving current under a constant output power (60 mW) was measured during laser operation (at the temperature of 60°C). The operated sample was then characterized by means of cross-sectional transmission electron microscopy (TEM) with microscopes, JEM-2010 and JEM-2000EX operated at 160 kV. TEM specimens were prepared by a conventional etching method with Ar^+ ions.

* Corresponding author. Tel.: + 81-6-6850-5753; fax: + 81-6-6850-5764.
E-mail address: ohno@tem.phys.wani.osaka-u.ac.jp (Y. Ohno)

0921-4526/99/$ - see front matter
PII: S0921-4526(99)00636-5

3. Results

3.1. Generation of dislocation loops in operated lasers

The thick lines in Figs. 1a and b show the change of the driving current $\Delta I(t)$, where $\Delta I(t) = 1 - I(t)/I(0)$ and $I(t)$ is the driving current at an operation time t. ΔI increases gradually up to ΔI_g with increasing t in both Figs. 1a and b (the so-called *gradual* degradation). In Fig. 1b, ΔI increases rapidly subsequent to the gradual increase (*sudden* degradation). We found that a large number of dislocation loops are introduced in these degraded lasers (Fig. 1c and d). High-resolution (HR) TEM revealed that the loops are of interstitial type (Fig. 2). The loops were generated only in the active and the AlGaInP cladding regions in which carriers are confined (just under the ridge). We could not find extended defects such as dislocation loops and misfit dislocations in lasers without operation or those annealed at 800 K without operation. The migration energy of interstitial atoms is smaller than that of point defects of the other kinds, and the energy may be reduced on the condition of an electronic excitation such as laser operating condition. We have therefore considered that the enhancement of the migration of interstitial atoms by the effect of laser operation results in the generation of the loops.

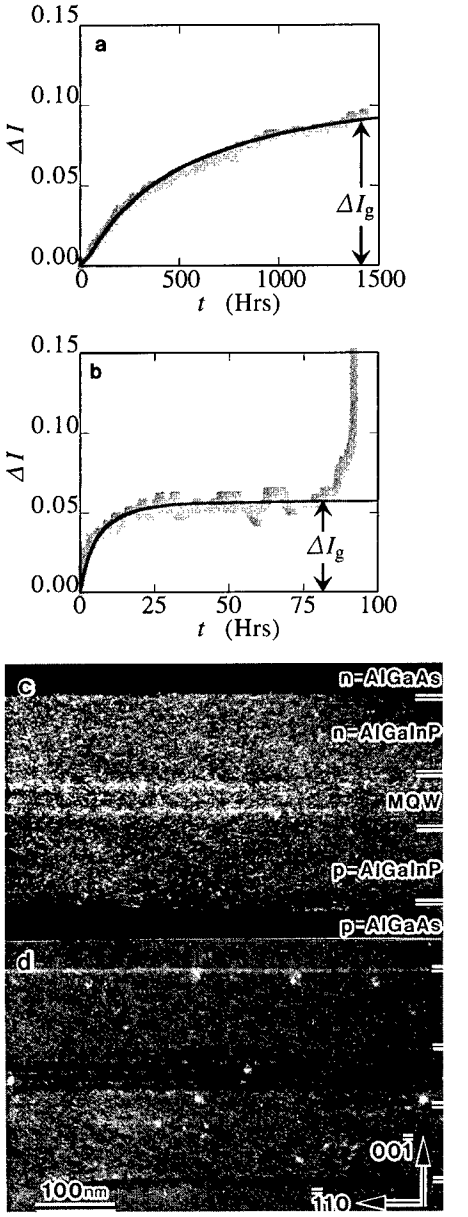

Fig. 1. The change of the driving current ΔI vs. the operation time t (a) for a *gradual* and (b) for a *gradual/sudden* degraded lasers. TEM images (c) of the *gradual* and (d) of the *gradual/sudden* degraded lasers of (a) and (b), respectively.

3.2. Size and spatial distribution of the dislocation loops

Fig. 3 shows the size distribution of the loops (a) in a *gradual* and (b) in a *gradual/sudden* degraded lasers. The number of the loops in (a) peaks at the loop radius

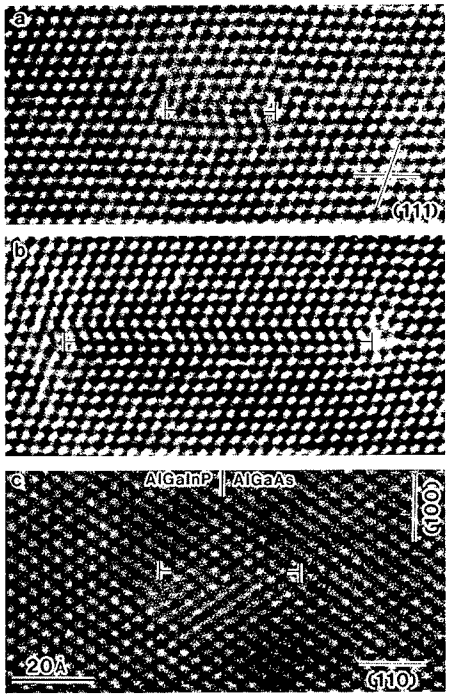

Fig. 2. HRTEM images of the dislocation loops (a) in the active region (STQW), in the cladding regions (b) near and (c) close to the n-AlGaAs/n-AlGaInP interface, respectively.

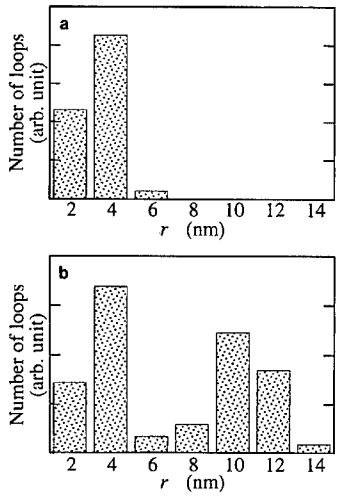

Fig. 3. The number of the loops (a) in a *gradual* and (b) in a *gradual/sudden* degraded lasers vs. the radii of the loops r.

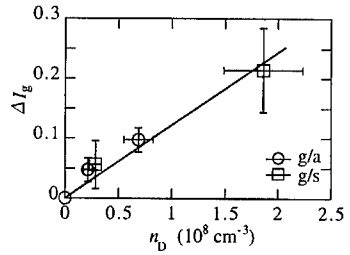

Fig. 4. The change of the driving current after the *gradual* degradation ΔI_g vs. the total number density of interstitial atoms in the dislocation cores in the active region n_D. ΔI_g is in proportion to n_D.

r of 4 nm, while that in (b) has two peaks at $r = 4$ and 10 nm. Most of the loops with $r = 2$–6 nm are homogeneously generated in the active regions in both (a) and (b). Similar loops are also observed in gradually degraded lasers of the other kind [1]. We have proposed a model that the loops in the active region are related to the *gradual* degradation. In Section 4, we discuss quantitatively the generation process of the loops with the model.

The loops with $r = 8$–14 nm, observed only in *gradual/sudden* degraded lasers, are generated in the cladding region near the n-AlGaInP/n-AlGaAs interface. These loops are presumably related to the *sudden* degradation, even though the degradation may be due to other kinds of point defects that cannot be observed by TEM. The generation and growth processes of the loops will be discussed elsewhere.

4. Discussion

We found the formation of dislocation loops in the active layer in the *gradual* degraded lasers. It is generally considered that dislocation cores act as nonradiative recombination centers and they may capture the carriers. Due to the capture, the flow of the carriers is disturbed and the driving current under a constant output power will increase. Suppose the cores of the dislocation loops in the active region act as nonradiative recombination centers, the number density of the centers is αn_D where n_D and α represent the total number density of interstitial atoms in the cores and the number of the centers per interstitial atom in the core, respectively. ΔI may be given as [2]

$$\Delta I = (\alpha v \sigma_D \tau) n_D$$

in which v and σ_D represent the carrier velocity and the nonradiative capture cross section, and τ the radiative recombination time for a dislocation-free sample. Since ΔI_g is in proportion to n_D (Fig. 4), the *gradual* degradation is obviously due to the loops in the active region. $\alpha v \sigma_D \tau$ was estimated to be 1.2×10^{-9} cm^3.

The volume number density of interstitial atoms aggregated in all the loops in the active region was estimated to be about $(1\text{–}10) \times 10^{17}$ cm^{-3}, and the value is much higher than the equilibrium density of interstitial atoms in the crystal. Frenkel-pairs may be created during laser operation due to the effect of nonradiative recombination of injected carriers, as is proposed in AlGaAs DH diodes [3]. The density of the pairs is presumably negligible, since the driving current density used in the present study is smaller than that in Ref. [3]. Since the interstitial density is in the same order of the dopant density (1×10^{18} cm^{-3}), these interstitials may be introduced by the kick out mechanism of dopant interstitials. These results imply that interstitial atoms of high density exist in the lasers without operation. We should point out the importance of the estimation of the interstitial density to the fabrication of laser diodes of high reliability, since the interstitials may form deep levels by their migration under laser operation and vary drastically the optical properties as discussed above. So far, the interstitials of high density have not been observed in lasers without operation by optical and electrical measurements. We consider that they may be inactive optically and electrically. More experiments to provide the evidence for the existence of the interstitials is needful.

Isolated interstitials in III–V compound semiconductors can migrate thermally even at a temperature below room temperature. Since no loop was observed in lasers annealed at 800 K, the loops in the active region are not generated by the thermal migration of isolated interstitials. The migration of the interstitials may be enhanced by the absorption of laser light. Moreover, it is proposed that, in GaP and InP, the migration of isolated interstitials under the irradiation of an electron beam

(i.e., under the flow of an electric current) results in the formation of interstitial pairs, and dislocation loops of interstitial type are formed by the migration of the pairs [4]. Such reactions may occur in the active region, since both intense laser light and carriers of high density exist in the region. We simulated $\Delta I(t)$ on trial with the model in Ref. [4]. In the simulation, we assumed the initial density of interstitial pairs to be zero. The experimental data shown in Figs. 1a and b (thick lines) are well explained by the model under the assumption that the mobilities of isolated interstitials and interstitial pairs are about 10^{-3} and $10^{-4}\,s^{-1}$, respectively; thin lines in the figures show the best fit of the experiments. This result suggests that the reduction of the initial density of isolated interstitials in the active region is necessitous to eliminate the *gradual* degradation. The reduction may be achieved by an annealing before laser operation to generate the dislocation loops outside the active region, since the loops do not interact with the carriers during laser operation.

5. Conclusion

We have proposed a model for the *gradual* degradation: (1) the migration of interstitial atoms by the effect of laser operation results in the generation of dislocation loops of interstitial type, (2) the dislocation core act as nonradiative recombination centers, and (3) the driving current under a constant output power will increase due to the capture of the carriers by the centers. We have pointed out that the reduction of the interstitial density is of importance to fabricate laser diodes of high reliability.

References

[1] O. Ueda, in: Reliability and Degradation of III–V Optical Devices, Artech House, Boston, 1996.
[2] Y. Ohno, Y. Kawai, S. Takeda, Phys. Rev. B 59 (1999) 2694.
[3] S. Yamakoshi, O. Hasegawa, H. Hamaguchi, M. Abe, T. Yamaoka, Appl. Phys. Lett. 31 (1977) 627.
[4] Y. Ohno, S. Takeda, M. Hirata, Phys. Rev. B 54 (1996) 4642.

ELSEVIER

Physica B 273–274 (1999) 1054–1059

PHYSICA B

www.elsevier.com/locate/physb

List of Contributors

ELSEVIER

Physica B 273–274 (1999) 1060–1063

PHYSICA B

www.elsevier.com/locate/physb

Subject Index

REPORT DOCUMENTATION PAGE

Form Approved
OMB No. 0704-0188

1. REPORT DATE (DD-MM-YYYY)	2. REPORT DATE	3. DATES COVERED (From - To)
12-11-1999		6/1/99 - 5/31/99

4. TITLE AND SUBTITLE

20th International Conference on Defects in Semiconductors

5a. CONTRACT NUMBER

5b. GRANT NUMBER
N00014-99-1-0656

5c. PROGRAM ELEMENT NUMBER

6. AUTHOR(S)

Eugene E. Haller

5d. PROJECT NUMBER
99PR05022-00

5e. TASK NUMBER

5f. WORK UNIT NUMBER

7. PERFORMING ORGANIZATION NAME(S) AND ADDRESS(ES)

The Regents of the University of California
Berkeley, CA 94720-5940

8. PERFORMING ORGANIZATION REPORT NUMBER
442427-23138

9. SPONSORING/MONITORING AGENCY NAME(S) AND ADDRESS(ES)

Larry R. Cooper
Office of Naval Research, ONR 312
Ballston Centre Tower One, 800 North Quincy Street
Arlington, VA 22217-5660

10. SPONSOR/MONITOR'S ACRONYM(S)
ONR

11. SPONSORING/MONITORING AGENCY REPORT NUMBER

12. DISTRIBUTION AVAILABILITY STATEMENT

APPROVED FOR PUBLIC RELEASE

13. SUPPLEMENTARY NOTES

none

14. ABSTRACT

These are the proceedings of the 20th International Conference on Defects in Semiconductors, ICDS-20, which was held in Berkeley, California, between July 26-30, 1999. The 278 registered attendees from 25 countries presented and discussed a wide range of new experimental and theoretical results. Three plenary talks, all focusing on wide bandgap semiconductors, 19 invited presentations, 82 contributed talks and 218 posters, for a total of 322 presentations, gave a comprehensive panorama of the continuously evolving field. The group III-nitrides and related materials, diamond and the effects of hydrogen represented a major portion of the conference content.

15. SUBJECT TERMS

16. SECURITY CLASSIFICATION OF:			17. LIMITATION OF ABSTRACT	18. NUMBER OF PAGES	19a. NAME OF RESPONSIBLE PERSON
a. REPORT	b. ABSTRACT	c. THIS PAGE			Eugene E. Haller
UNCLASS	UNCLASS	UNCLASS	UL		19b. TELEPONE NUMBER (*Include area code*) 510-486-5294

PHYSICA B

INSTRUCTIONS TO AUTHORS

Submission of papers
Manuscripts (one original + two copies) should be sent to one of the following regular editors:

Original material: Submission of a manuscript implies that it is not being simultaneously considered for publication elsewhere and that the authors have obtained the necessary authority for publication.

Types of contributions
Original research papers and letters to the editor are welcomed. Both should contain an Abstract (of up to 200 words) and a Conclusions section, which, particularly in the case of theoretical papers, translates the results into terms readily accessible to most readers.

Manuscript preparation
All manuscripts should be written in proper English. The paper copies of the text should be prepared with double line spacing and wide margins, on numbered sheets.
Structure: Please adhere to the following order of presentation: Article title, Author(s), Affiliation(s), Abstract, PACS codes and keywords, Main text, Acknowledgements, Appendices, References, Figure captions, Tables.
Corresponding author: The name, complete postal address, telephone and fax numbers and the E-mail address of the corresponding author should be given on the first page of the manuscript.
PACS codes/Keywords: Please supply one to four classification codes (PACS and/or MSC) and up to six keywords of your own choice that describe the content of your article in more detail.
References: References to other work should be consecutively numbered in the text using square brackets and listed by number in the Reference list.

Illustrations
Illustrations should also be submitted in triplicate: one master set and two sets of copies. The *line drawings* in the master set should be original laser printer or plotter output or drawn black india ink, with careful lettering, large enough (3–5 mm) to remain legible after reduction for printing. The *photographs* should be originals, with somewhat more contrast than is required in the printed version. They should be unmounted unless part of a composite figure. Any scale markers should be inserted on the photograph itself, not drawn below it.
Colour plates: Figures may be published in colour, if this is judged essential by the editor. The publisher and the author will each bear part of the extra costs involved. Further information is available from the publisher.

After acceptance
Notification: You will be notified by the Editor of the journal of the acceptance of your article.
Copyright transfer: In the course of the production process you will be asked to transfer the copyright of the article to the publisher. This transfer will ensure the widest possible dissemination of information.

Electronic manuscripts
The publisher welcomes the receipt of an electronic version of your accepted manuscript. If there is not already a copy of this (on diskette) with the journal editor at the time the manuscript is being refereed, you are invited to send a file with the text of the accepted manuscript directly to the Publisher on diskette (allowed formats 3.5″ or 5.25″ MS-DOS, or 3.5″ Macintosh) to the address given below. Please note that no deviations from the version accepted by the Editor of the journal are permissible without the prior and explicit approval of the Editor. Such changes should be clearly indicated on an accompanying printout of the file.

Author benefits
No page charges: Publishing in Physica B is free of charge.
Free offprints: The corresponding author will receive 25 offprints free of charge. An offprint order form will be supplied by the publisher for ordering any additional paid offprints.
Discount: Contributors to Elsevier Science journals are entitled to a 30% discount on all Elsevier Science books.

Further information (after acceptance):

Issue Manager Physica B
Elsevier Science B.V.
P.O. Box 2759
1000 CT Amsterdam
The Netherlands
Telefax: +31-20-485 2319
E-mail: j.leest@elsevier.nl

North-Holland, an imprint of Elsevier Science